PET and SPECT of Neurobiological Systems

Rudi A. J. O. Dierckx
Andreas Otte
Erik F. J. de Vries
Aren van Waarde

Editors

Adriaan A. Lammertsma
Guest Editor

Second Edition

🐎 Springer

PET and SPECT of Neurobiological Systems

Rudi A. J. O. Dierckx • Andreas Otte
Erik F. J. de Vries • Aren van Waarde
Editors

Adriaan A. Lammertsma
Guest Editor

PET and SPECT of Neurobiological Systems

Second Edition

Springer

Editors
Rudi A. J. O. Dierckx
Nuclear Medicine and Molecular Imaging
University Medical Center Groningen
Groningen
The Netherlands

Erik F. J. de Vries
Nuclear Medicine and Molecular Imaging
University Medical Center Groningen
Groningen
The Netherlands

Guest Editor
Adriaan A. Lammertsma
Department of Radiology
and Nuclear Medicine
Amsterdam University Medical Centers
location VUmc
Amsterdam
The Netherlands

Andreas Otte
Faculty of Electrical Engineering, Medical
Engineering and Computer Science
Offenburg University
Offenburg
Germany

Aren van Waarde
Nuclear Medicine and Molecular Imaging
University Medical Center
Groningen
The Netherlands

Foreword

When in 2014 the editors published the first edition of this three-volume series, dedicated to the use of PET and SPECT in the CNS, a major undertaking saw the light in print. These were significant multi-authored books, providing the most comprehensive review of this challenging field at the time.

Now in 2020, a second edition is launched, demonstrating the success of this initial endeavor. With a further major effort, over 50 % of the numerous chapters are either entirely novel or rewritten anew, by an impressive list of international contributors. The team from Groningen deserve warm congratulations for this achievement.

In 2004, PETMR had just emerged as a novel imaging modality, and the medical applications of machine learning, or artificial intelligence, had hardly surfaced. PET imaging of Tau had just made it.

Now in 2020, amazing progress in the understanding of the brain is being made, and even dedicated brain PET and PETMR imaging instruments are in development (Catana 2019). Yet, with its hundred billion neurons, the brain keeps its mystery and continues to engage and stimulate our enquiry.

Little by little progress is being made, from decoding consciousness (Sohn 2019) to growing neurons from reprogrammed skin fibroblasts (Kofler 2019). We now understand that protein deposits in the brain may precede clinical manifestations by years, great advances have been made in extracting quantitative data from such studies (as shown with PETCT and amyloid and tau numerical data) and that we can intervene effectively, inter alia, in receptor deficiencies and in deep brain stimulation. The brain connectome is unravelling, with it, greater understanding of, among others, pain and drug-induced addictions, the dementias, and the movement disorders. All of this and much more is being critically reviewed by 119 chapters spread into these three major volumes.

It is hence perfect timing that the second edition shines a new light at the significant progress made in PET and SPECT, describing and analyzing latest information from novel biological radionuclide probes, neuroreceptors, and the clinical progress achieved.

<div align="right">

Peter Josef Ell
University College London
London, UK

</div>

References

1. Catana C (2019) Development of Dedicated Brain PET Imaging Devices: Recent Advances and Future Perspectives. J Nucl Med 60:1044–52
2. Kofler N (2019) Brain in a Dish, Babies by Design: What It Means to Be Human. Nature 569:333–34
3. Sohn E (2019) Decoding the Neuroscience of Consciousness. Nature 571:S2–S5

Preface

Neuroscientists of today dispose of a powerful armament for functional, physiological, and molecular imaging that has never made more impressive advances than before, helping to better understand the mechanisms of diseases and to develop and design drug treatment options with a superior efficacy and safety profile. Among these instruments, positron emission tomography (PET) and single-photon emission computed tomography (SPECT) have become forerunners in the in vivo imaging arena, and for this reason, the present trilogy, now in its second, completely revised and supplemented edition, is dedicated to PET and SPECT. The volumes of this trilogy are *PET and SPECT in Psychiatry*, *PET and SPECT in Neurology*, and *PET and SPECT in Neurobiological Systems*. In all volumes, we have again assembled the combined expertise of the renowned authors of the first edition and expanded this by some new authors for the second edition, whose dedication to the investigation of psychiatric and neurological disorders or of neurobiological systems through nuclear medicine technology has achieved international recognition.

The editors, who are nuclear medicine specialists, radiochemists, and biologists with a strong exposure to neurosciences, have again invited experts from the psychiatry, neurology, and medical physics fields to enhance the editorial board as guest editors for each volume of the trilogy. For *PET and SPECT in Psychiatry*, this was Iris Sommer, professor of cognitive aspects of neurological and psychiatric disorders; for *PET and SPECT in Neurology*, it remained Klaus (Nico) L. Leenders, emeritus professor of neurology; and for *SPECT in Neurobiological Systems*, it was Adriaan A. Lammertsma, professor of medical physics and positron emission tomography.

We are very happy that our trilogy has become a state-of-the-art compendium with top downloads already for the first edition. This is certainly also due to the production and distribution by one of the premier publishers in the field, guaranteeing a high quality of reproduction and allowing for the inclusion of many color figures, which is essential in the field of neuroimaging. We are intrigued by the enthusiastic response from contributors from all over the world who made this endeavor successful and are confident that the second edition continues to live up to this onus. Finally, we would like to thank Mrs. Gesa Frese from *Springer-Verlag* for her continuous help and support during the development of the second edition of this book series.

We sincerely hope that the new trilogy will still serve as a key tool not only for all physicians in nuclear medicine, psychiatry, neurology, or geriatrics, but also for all professionals working to understand or treat brain disorders. With today's ageing population, PET and SPECT imaging can provide new insights into the processes that may lead to unhealthy ageing of the brain. May this book series serve as a guide towards the present use of PET and SPECT in brain disorders and as a catalyst for future research. The progress achieved by PET and SPECT in the diagnosis of the many facets of diseases disposed in the neurosciences has been astounding. Nevertheless, in line with the Socratic paradox "*I know that I know nothing,*" it seems that we are still at the beginning of understanding the brain. This book hopes to provide a renewed platform to further contribute to this quest at the benefit of patients suffering from neurologic and psychiatric disorders.

Groningen, The Netherlands   Rudi A. J. O. Dierckx
Offenburg, Germany   Andreas Otte
Groningen, The Netherlands   Erik F. J. de Vries
Groningen, The Netherlands   Aren van Waarde

Contents

Part I
Basics

Animal Models for Brain Research

1

Debby Van Dam and Peter Paul De Deyn

Contents

D. Van Dam (✉)
Laboratory of Neurochemistry and Behaviour, Institute Born-Bunge, University of Antwerp, Wilrijk, Belgium

Department of Neurology and Alzheimer Center Groningen, University of Groningen and University Medical Center Groningen (UMCG), Groningen, GZ, The Netherlands
e-mail: debby.vandam@antwerpen.be

P. P. De Deyn
Laboratory of Neurochemistry and Behaviour, Institute Born-Bunge, University of Antwerp, Wilrijk, Belgium

Department of Neurology and Alzheimer Center Groningen, University of Groningen and University Medical Center Groningen (UMCG), Groningen, GZ, The Netherlands

Department of Neurology and Memory Clinic, Hospital Network Antwerp (ZNA), Middelheim and Hoge Beuken, Antwerp, Belgium

Abstract

Animal models are important experimental tools in neuroscience research since they allow appraisal of selected and specific brain pathogenesis-related questions—often not easily accessible in human patients—in a temporal and spatial pattern. Translational research based on valid animal models may aid in alleviating some of the unmet needs in the current pharmaceutical market. Of primary concern to a neuroscience researcher is the selection of the most relevant animal model to achieve pursued research goals. Researchers are challenged to develop models that recapitulate the disorder in question, but are quite often confronted with the choice between models that reproduce cardinal pathological features of the disorders caused by mechanisms that may not necessarily occur in the patients versus models that are based on known aetiological mechanisms that may not reproduce all clinical features. Besides offering some general concepts concerning the relevance, validity and generalisation of animal models for brain disorders, this chapter focuses in detail on animal models of brain disease, in particular schizophrenia models as examples of animal models of psychiatric disorders and Alzheimer's disease models as examples of animal models of neurological/neurodegenerative disorders.

Abbreviations

AChE	Acetylcholinesterase
AD	Alzheimer's disease
APP	Amyloid precursor protein
Aβ	Amyloid β
BPSD	Behavioural and psychological signs and symptoms of dementia
ChAT	Choline O-acetyltransferase
DISC1	Disrupted in schizophrenia-1 gene
DSM	Diagnostic and Statistical Manual of Mental Disorders
DTNBP1	Dysbindin gene
ERBB4	Neuregulin 1 receptor gene
FRL	Flinders resistant line
FSL	Flinders sensitive line
HAB	High-anxiety-related behaviour Wistar rat line
LAB	Low-anxiety-related behaviour Wistar rat line
LI	Latent inhibition
NFT	Neurofibrillary tangle
NGF	Nerve growth factor
NMDA	N-methyl-D-aspartate
NPS	Neuropsychiatric symptoms
NRG1	Neuregulin 1 gene
PCP	Phencyclidine
PDAPP	Platelet-derived growth factor promoter-driven APP

PPI   Prepulse inhibition
PSEN   Presenilin
RDoC   Research Domain Criteria
RELN   Reelin gene
SAM   Senescence-accelerated mouse
SAMP   SAM-prone substrain
SNP   Single nucleotide polymorphism
TDP-43 TAR DNA-binding protein 43

1.1 Introduction to Animal Modelling for Human Brain Disease

Animal models aiming at studying human disorders emerged in the 1800s and experienced a major boost over the last decades. The value of animal experimentation in the advances of human health is exemplified by the list of Nobel Prizes awarded for Physiology or Medicine. Since the beginning of the twentieth century, these prizes have chronicled the world's greatest medical advances. Of the 109 Nobel Prizes awarded for Physiology or Medicine up to 2018, at least 87 were directly dependent on animal-based research or the discovery relied on crucial data obtained from animal studies by other research groups.

Basic neuroscience research on animal models is essential to understand the nature of brain disorders that afflict humans and develop purposeful therapies. In the mid-1960s, the neural circuits containing and utilising the neurotransmitters dopamine and norepinephrine were visualised for the first time in rodent brain (Glowinski et al. 1966; Glowinski and Iversen 1966a, b; Iversen and Glowinski 1966). Further development of other (antibody-based) methods allowed neuroscientists to link synaptic molecules to neural circuits in rodent and nonhuman primate brains, thereby coordinating neuroanatomy, neuropharmacology and neurophysiology into a cohesive view of biochemically coded brain circuitry. Application of these techniques in human brain aided in elucidating the neurotransmitter-based nature of specific brain circuits affected in disease, e.g. the degeneration of cholinergic neurons in the basal forebrain of Alzheimer's disease (AD) patients (Whitehouse et al. 1982). The concept of synaptic communication between nerve cells as the key level of interaction in the brain further culminated with the work of E. Kandel and colleagues, who were awarded the Nobel Prize in 2000. More recently, the 2013 Nobel Prize in Physiology or Medicine was awarded jointly to J.E. Rothman, R.W. Schekman and T.C. Südhof for their discoveries of machinery regulating vesicle traffic, a major transport system in our cells. The synapse has become a key target for pharmaceutical intervention in many brain disorders that are now understood at the level of synaptic circuitry and functional brain organisation, including multiple psychiatric disorders (e.g. schizophrenia, depression), as well as neurodegenerative disorders (e.g. AD, amyotrophic lateral sclerosis, Parkinson's disease).

The starting point for the development of a new animal model for a specific brain disease is mostly the current dominant theory about the disorder. Although a logical first approach, it is essential to broaden the focus of animal models under development based on the increasing knowledge of underlying disease mechanisms.

Animal models of human disease can be classified into spontaneous, induced, negative and orphan models, of which the two latter types are in general not relevant for psychiatric and neurological disorders. Negative models after all are models in which a specific human disorder does not develop, while orphan models display a condition which has never been described in man or other target species. Spontaneous models are presumed to develop their condition without experimental manipulation, but selective breeding is often compulsory to establish and maintain the desired line. Especially for psychiatric and neurological conditions, few spontaneous models exist, and experimentally induced pathology is often required. Such artificial manipulations include surgical procedures, administration or withdrawal of biologically active substances, application of physical or physicochemical stimuli and genetic manipulations.

1.1.1   Relevance of Animal Models

Relevance reflects the meaningfulness and usefulness of results obtained with an animal model for a particular scientific and/or clinical purpose (van der Staay 2006). The two most important clinically inspired applications of animal models in neuroscience research are (1) the development and evaluation of mechanistic hypotheses about neurological and psychiatric disorders in general and their neural substrates in particular (i.e. brain–behaviour relation) and (2) the identification and screening of novel therapeutic approaches, most frequently drugs.

Opponents of animal research often question the relevance of animal models to understanding diseases and disease processes in humans. The disputed similarities between human and other species at the structural and functional level of the CNS are often considered a major hurdle for the use of animal models in studies of human neurological and psychiatric conditions.

Neuroscientists are far from reaching consensus about the level of similarity between the brains and 'minds' of humans and other species. Comparative neuroscience can provide essential information for the adequate comparison of both structural and functional aspects of human and nonhuman brain and thereby identify research areas in which animal models are likely to be useful, as well as the appropriate species for such studies. Specifically when considering models of psychiatric disease, the issue of similarities between the mental lives of animals and humans is fundamental. Animal consciousness or unconsciousness is difficult, if not impossible, to corroborate. On the other hand, one could argue whether it is necessary for the animal mind to be as complex as the human mind. Behavioural responses and brain mechanisms associated with anxiety, fear, aggression and coping serve such a crucial adaptive function that they must have evolved very early in the development of mammalian species and are probably highly conserved (Steimer 2011).

Other classes of vertebrates and even lower invertebrates may display some form of anxiety and have the capacity to detect danger and react to threat, i.e. display a fight-or-flight response. Components of emotional processes, as well as the biological and neuronal logistic systems essential for their realisation, gain in complexity higher up in the phylum. Species located higher in the phylogenetic tree gain additional capabilities (e.g. autonoetic consciousness in humans, orang-utans, chimpanzees and bonobos), but never lose the more primitive abilities shared with lower invertebrates (Belzung and Philippot 2007), thereby opening perspectives for the use of lower species like zebrafish (Gerlai 2010), or even fruit flies (Iliadi 2009), in the studies of emotional responses and specific psychiatric disorders. The further focus of this chapter will be, however, on rodent models given their widespread use and applicability of microimaging techniques in these species.

Although some attributes still appear to be rather unique to the human brain, other aspects seem to be shared with more species than originally believed. Also at the neuroanatomical level, major species differences should be taken into consideration. The complex pattern of human cortical sulci and gyri, as well the extent of the prefrontal cortex, the neural substrate of many higher functions, is beyond compare in the rest of the animal kingdom (Fuster 1980). The prefrontal cortex may be present, however, in more species than initially thought, and the prefrontal to nonprefrontal cortical surface ratio in itself may not be an optimal index of evolution. Improved knowledge of rat prefrontal cortex anatomy has modified strategies to manipulate specific cortical areas to model prefrontal involvement, although reports delineating boundaries between prefrontal cortical subareas of the rat in comparison with the primate homologues show some dissimilarities. Nevertheless, current anatomical and functional data indicate that rats do have a prefrontal cortex, although not as differentiated as the primate prefrontal cortex. Rats have a functionally divided prefrontal cortex that includes not only features of the medial and orbital areas in primates, but also some features of the primate dorsolateral prefrontal cortex (Uylings et al. 2003).

1.1.2 Validity of Animal Models

The conclusions drawn from animal models largely depend on the validity of the model in representing the human condition. The more levels of validity a model satisfies, the greater its value, utility and relevance to the human condition. The validity of a model can only be determined in a multidisciplinary approach. A 'perfect' model would account for aetiology, symptomatology, treatment response and physiological basis, as originally proposed by McKinney and Bunney in 1969 (McKinney Jr and Bunney Jr 1969). Animal models in general do not meet all of these criteria. Moreover, in developing and assessing an animal model, it is critical to consider the explicit purpose intended for the model, because the intended purpose determines the criteria that the model must satisfy to establish its validity. The following perspectives are commonly used in the characterisation of a model's validity (Van Dam and De Deyn 2006, 2011a).

1.1.2.1 Face Validity

Face validity refers to the resemblance between the animal model and the situation or process being modelled. It refers to the phenomenological similarity between the model and the human condition. Similarity of symptoms is most commonly used to assess face validity in animal models of behavioural dysfunction. Throughout this chapter, several behavioural paradigms will be mentioned. Writing a complete 'how-to manual' for the behavioural phenotyping of a new brain disease model would go beyond the scope of this chapter. For further reading, we would like to refer the readers to excellent manuals on behavioural neuroscience as, e.g. 'What's wrong with my mouse?' (Crawley 2000) and 'Methods of Behavior Analysis in Neuroscience' (Buccafusco 2008).

1.1.2.2 Construct Validity

Construct validity refers to the theoretical clarification of what a test measures or a model is supposed to mimic. Because a given condition may manifest itself in different ways in different species, the behaviour used in the animal model may not match that of humans, yet the test or model may still be valid. Construct validation is useful in the incessant process of further developing and refining an animal model.

1.1.2.3 Aetiological Validity

Aetiological validity is closely related to construct validity and refers to identical aetiologies or phenomena in the model and the human condition. Models with high aetiological validity are most valuable in drug development and discovery.

1.1.2.4 Predictive Validity

Predictive validity represents the extent to which the performance of the animal model in a test predicts the performance in the condition being modelled. This level of validation necessitates parallel development of clinical measures for meaningful comparisons between model and man. In a more narrow sense, this term is sometimes used to indicate pharmacological isomorphism, i.e. the model's ability to identify compounds with potential therapeutic effects in the human condition.

1.1.3   Homology, Analogy and Isomorphism

As a consequence of the different validation levels, validity is highest in the so-called homologous models, where the symptoms displayed and the cause of the condition in the animal are identical to those of the human condition. Especially in neurosciences, homologous models are very rare and mostly limited to well-defined lesion syndromes. Analogous or isomorphic models are more common, but, although they display similar symptoms, the condition is not provoked by the same events as the human condition. In reality, most animal models are partial models, focusing only on restricted aspects of a disease, and modelling the complete condition is often not pursued. Of primary concern to neuroscientists is the selection of

the most relevant animal model to achieve his/her research goals. Researchers are challenged to develop models that recapitulate the disorder in question, which is often not as straightforward as it may seem. Quite often they are confronted with the choice between models that reproduce cardinal pathological features of the disorders caused by mechanisms that may not necessarily occur in the patients versus models that are based on known etiological mechanisms that may not reproduce all clinical features. Although animal models cannot replicate human pathophysiology or psychopathology in every detail, we should envisage them as experimental systems in which selected and specific CNS pathogenesis-related questions—often not easily accessible in human patients—can be studied in a temporal and spatial pattern. Partial models may be of substantial value in the gradual process of building a more complete image of the disease and underlying pathophysiological mechanisms, whereas more complete and complex models are only possible in case of better understood diseases (De Deyn and Van Dam 2011).

1.1.4   Generalisation and Extrapolation

The ultimate goal of animal modelling is the generalisation of results and insights to the target species, which in most occasions of course is man. The term extrapolation is also often used to describe how data obtained from animal studies can be reliably used to apply to the human condition. Extrapolation is therefore not performed in its mathematical sense, in which data fit a certain function that may be described graphically and the graph extends beyond the highest or lowest sets of data to describe a situation outside the window of observation. Generalisation across species is intrinsically based on the Darwinian evolutionary concept. Phylogenetic similarity in morphology and physiology between different species allows observations made in animals to be translated to the human condition based on homology. Related to animal models for psychiatric and neurological disorders, this cross-species comparison may focus or be based on the biological, genetic or environmental basis of personality traits (Gosling 2001), or neuroanatomical structures and their function (Striedter 1998). Uncritical generalisation or extrapolation of animal findings to the human condition may lead to unreliable or even dangerous conclusions. As a general rule, extrapolation tends to be most reliable when a plurispecies approach is taken and the condition is studied in a variety of relatively unrelated laboratory animals. Differences in metabolic patterns and speed, as well as several other confounding variables (e.g. age, sex, distress, diet, housing condition, route of administration, rhythmic variations), need to be taken into account, particularly when quantitative extrapolation is intended (De Deyn and Van Dam 2011).

Generalisation may be advanced by the development of translatable preclinical biomarkers, including small animal imaging (Kaimal and McConville 2009; Sakoğlu et al. 2011), and biochemical assays on biological fluids such as plasma and cerebrospinal fluid (Liu and Duff 2008). These biomarkers could be used to characterise the translatability of animal models, determine the translatability of a

novel therapeutic intervention if the same biomarker can be used in a clinical trial, assess target engagement of investigational treatments and monitor biological responses to treatment in real time.

1.2   Animal Models of Psychiatric Disorders

Psychiatric disorders represent a diverse set of conditions, variously affecting all domains of mental function and affecting the most fundamental human attributes, namely, language, thought, perception, mood and sense of self. Many psychiatric symptoms, e.g. hallucinations, delusions, sadness, guilt and suicidal thoughts, are probably uniquely human and cannot be convincingly ascertained in animals. Researchers should also refrain from uncritical anthropomorphising of emotional behaviour in general. Feeling anxious or depressed are subjective emotional experiences that may require a certain minimal level of consciousness that may well be uniquely human.

The evaluation of animal models of neuropsychiatric disorders is further challenged by the use of the Diagnostic and Statistical Manual of Mental Disorders (DSM), criteria in the clinical diagnosis, combined with the lack of knowledge of pathophysiological mechanisms and objective diagnostic tests. Both in the fourth (American Psychiatric Association 2000) and fifth edition (American Psychiatric Association 2013) of the DSM, the diagnosis is based on phenomenology (i.e. signs, symptoms, course of illness), and mostly, a minimal number of symptoms should be present for at least a specified period of time. In the case of schizophrenia, two (or more) of the following symptoms should be present for a significant portion of time during a 1-month period (or less if successfully treated): delusions, hallucinations, disorganised speech, grossly disorganised or catatonic behaviour and negative symptoms, i.e. affective flattening, alogia, or avolition, in addition to social/occupational dysfunction (American Psychiatric Association 2000, 2013). Two individuals with the same DSM diagnosis of schizophrenia may therefore present with extremely heterogeneous symptom combinations. Similar problems exist for most DSM-based diagnoses, thereby further complicating the evaluation and validation process of newly developed mouse models for psychiatric illnesses (Nestler and Hyman 2010).

1.2.1   The Endophenotype Concept in Psychiatry

The concept of endophenotypes appears to be unique to the broad field of psychiatry. An endophenotype is a biomarker associated with genetic components, as well as the clinical symptoms of neuropsychiatric disorders. In that way they differ from biomarkers in general that often lack the genetic link. Endophenotypes play an important role to bridge the gap between the microscopic and macroscopic level of neuropsychiatric disorders. It is per definition any hereditary characteristic that is normally associated with some condition but is not a direct symptom of that condition. Criteria useful for the identification of endophenotypes of diseases that display

complex inheritance patterns have been suggested (Gottesman and Gould 2003; Gould and Gottesman 2006):

1. The endophenotype is associated with illness in the population.
2. The endophenotype is heritable.
3. The endophenotype is primarily state-independent (manifests in an individual whether or not illness is active), but age-normed and may need to be elicited by a challenge.
4. Within families, endophenotypes and illness co-segregate.
5. The endophenotype found in affected family members is found in nonaffected family members at a higher rate than in the general population.

Endophenotype analysis can be based on neuroanatomical, neurophysiological, biochemical, endocrinological, cognitive and neuropsychological/behavioural measures (Leboyer et al. 1998). Advanced neuroimaging techniques, including PET and SPECT, have left little doubt that specific structural CNS anomalies can be linked to particular neurological and psychiatric diseases. Neuroimaging endophenotypes are vitally important to the identification of genetic determinants of complex brain-related disorders (Glahn et al. 2007).

Especially with regard to behavioural measures, the endophenotype approach is considered particularly relevant in the context of the Research Domain Criteria (RDoC) framework from the National Institute of Mental Health for new approaches to investigate psychopathologies by bridging basic neuroscience and mental health and supporting the concept of a normality and pathology continuum. According to the RDoC system, behavioural endophenotypes attribute five main domains, including arousal and regulation, negative valence, positive valence, social processes and cognitive systems. Changes at all neurobiological levels, ranging from molecules to brain networks, are related to the specified behavioural domains (Anderzhanova et al. 2017; Maximino and van der Staay 2019) (Fig. 1.1).

The study of endophenotypes is particularly useful to understanding underlying disease mechanisms in neuropsychiatric disorders, essential for the accurate diagnosis, classification, early detection purposes, the development and evaluation of valid animal models and accelerating the drug discovery pipeline concerned.

1.2.2   Approaches to Modelling Psychiatric Disease

1.2.2.1 Behavioural Approach
In the absence of knowledge of underlying genetic causes, the first attempts to model psychiatric disturbances in animals consisted of the behavioural approach that defined behavioural assays thought to mimic particular psychiatric symptoms. Animals with specific behavioural deficits were generated through pharmacological, surgical or genetic (e.g. comparison of inbred strains) procedures. Well-known examples are the learned helplessness model of depression, spontaneous alternation indexing working memory in schizophrenia, decreased social interaction linked to
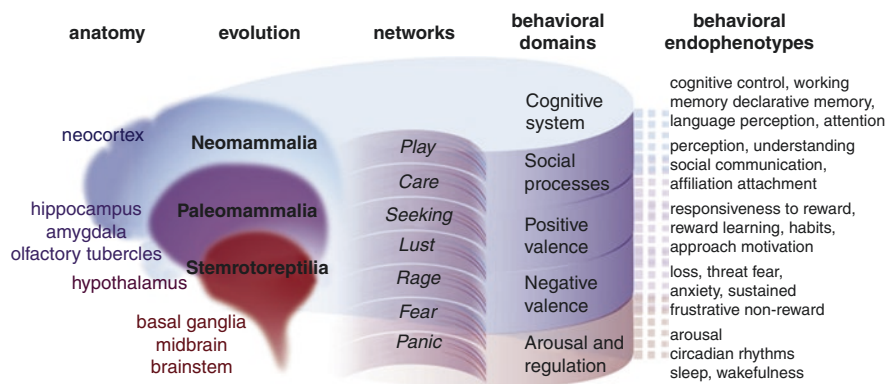
Fig. 1.1 According to the RDoC system, behavioural endophenotypes attribute five main behavioural domains. These five domains and their respective constructs can be used to comprehensively profile behaviour (i.e. behavioural endophenotypes). They are not only distinct but describe personality as an interacting and dynamic individual trait. The domains are objectively different, determined by particular neuronal networks. Separation of the networks is due to a distinction in the functions they serve (The Affective Neuroscience Scale, Panksepp, 1998). This distinction corresponds well with the concept of a gradual evolution of the brain (the triune brain model of MacLean 1970). Legend: RDoC, Research Domain Criteria. Adapted from Anderzhanova et al. (2017) Neurobiol Stress 7:47–56 (Anderzhanova et al. 2017) under the CC-BY license 4.0 (http://creativecommons.org/licenses/by/4.0). Copyright © 2017 Anderzhanova, Kirmeier and Wotjak

autism spectrum disorder and approach–avoidance conflict behaviours associated with anxiety disorders (Crawley 2000; Mitchell et al. 2011). The development of valid behavioural models and paradigms is currently still ongoing, but with more attention for the neurobiological and clinical relevance (Baker 2011). A rodent behavioural paradigm has neurobiological construct validity if it isolates and measures a behavioural process with similar environmental regulators and neural mediators as the human process of interest. However, many behavioural assays lack sufficient construct validity, and their use in the development of rodent models for psychiatric disorder is mainly based on face validity (Moore 2010). These translational challenges are—at least partially—tackled by the development of reverse translational tools that take the rodent paradigm as a starting point to develop a human variant that allows appraisal of construct validity. Relevant examples include human real-life or virtual reality analogues of visual spatial learning and memory as tested in a water maze (Laczó et al. 2010; Woolley et al. 2013; Fajnerová et al. 2014), or a tool to assess unconditioned locomotor behaviour similarly as in rodents (Young et al. 2007).

Although brain–behaviour relationships are assumed to be conserved across evolution for many aspects of normal motor and sensory functions, this may not be translated as easily to abnormal behaviour, let alone psychiatric disease. Animal brain circuitry and neurochemical systems involved may differ from the complex human (disease) system. A mental disorder is not characterised by an aberration in one single feature, but is a syndrome with a myriad of deviations in behaviour,

cognition and/or emotion. Behavioural models of psychiatric disease, like the learned helplessness model of depression, are of course partial models that mimic only one single isolated feature of the human condition (Insel 2007).

1.2.2.2 Pharmacological Models

The administration of certain chemicals may induce behavioural changes reminiscent of specific psychiatric symptoms based on interference with central neurotransmission pathways. Understanding the mechanisms of these actions might contribute to our fundamental understanding of the illness. Drug-based models include the reserpine model of depression (Hendley and Welch 1975) and N-methyl-D-aspartate (NMDA) receptor antagonist-based models of psychosis (Andiné et al. 1999).

1.2.2.3 Genetic Models

Genetic models of psychiatric disorders were initially dominated by inbred strains, often after selection for a relevant psychiatric-like phenotype. Examples include the selectively bred Flinders Sensitive Line and the Flinders Resistant Line of rats (FSL versus FRL), a genetic animal model of depression (Overstreet et al. 1989); selectively bred Wistar rat lines with high- versus low-anxiety-related behaviour (HAB versus LAB) (Liebsch et al. 1998); and the continuous distribution of PPI (see paragraph on "Sensory Discrimination" in Sect. 1.2.3.2) response amongst mouse inbred strains, which indicates PPI to be a polygenetic trait (Willott et al. 1994; Bullock et al. 1997; Paylor and Crawley 1997). The success of inbred and selectively bred strains was closely followed by single-gene models developed through homologous recombination in embryonic stem cells, as illustrated by neurokinin-1 receptor knockout mice that display significantly reduced anxiety and stress-related responses (Santarelli et al. 2001), and the glutathione S-transferase M1-knockout mouse model for autism (Yochum et al. 2010). Based on information obtained from genome-wide association studies, single-gene knockout or mutation models will undoubtedly maintain a stable position in the field of psychiatry models. They aid in assessing the putative link between gene and disorder using increasingly powerful and sophisticated tools to elucidate underlying neurobiology and disease mechanisms from the level of synapses over brain circuitry to behavioural outcome (Mitchell et al. 2011). With the advancement of genetic engineering techniques, the number of genetic mouse—and even rat—models is strongly increasing. The development of genetic rat models is of specific value for the study of psychiatric disorders, since they display more complex and sociable behaviour compared to mice. Genetic possibilities in rodents include full knockouts, spatial and/or temporal knockouts, knock-in of human alleles, and precisely engineered chromosomal rearrangements (e.g. inversions, deletions, translocations or duplications) into syntenic animal genes (van der Weyden and Bradley 2006). Although novel molecular tools, like the bacterial CRISPS/Cas9 system, mainly promote in vitro genome editing, the ability of CRISPR/Cas9 to directly target any gene of interest in the embryonic genome holds great promise to faster, less expensively and more reliably generate in vivo psychopathology models (Tscharganeh et al. 2016).

The theory that genes and environment combine to confer susceptibility to the development of diseases surfaced in the early half of the last century, but the use of such a framework for exploring the aetiology of psychiatric disorders is more recent. Given the fact that many—if not all—psychiatric disorders are multifactorial, sophisticated genetically engineered animal models can of course also be used to disentangle complex aetiological mechanisms with the appraisal of gene–environment interactions. For example, the effect of repeated maternal separation or exposure to pesticides early in ontogeny on the reelin-deficient mouse, i.e. the reeler model that has been linked to autism and schizophrenia, has been studied (Laviola et al. 2009).

1.2.3 Animal Models of Schizophrenia

1.2.3.1 Aetiology and Symptomatology of Schizophrenia

Schizophrenia is a devastating and common psychiatric disorder that is associated with a high degree of medical morbidity and reduced life span. Both incidence and prevalence estimates vary across the world, and even within countries, and at the local and neighbourhood level. The median lifetime prevalence was estimated at 4/1000 and the lifetime morbid risk at 7.2/1000, while the median incidence was estimated at 15.2/100,000 individuals. Incidence rates differ between sexes with a male to female ratio of 1.4:1 (McGrath et al. 2008). These variations are supportive of the assumption that schizophrenia is a clinical syndrome, perhaps comprising several disease entities.

Symptoms cluster into three categories: positive symptoms (including hallucinations, delusions, thought disorder and conceptual disorganisation), negative symptoms (including emotional blunting, social withdrawal, anhedonia, avolition, poverty of thought and content of speech) and cognitive dysfunction (including impaired executive functioning, working memory and attention) (Andreasen 1995). The onset of some aspects of the disease may be observed from birth onward, but psychotic symptoms generally become manifest in late adolescence and early adulthood in males, with an extended onset period in females (McGrath et al. 2008; Carpenter and Koenig 2008).

The dopamine hypothesis of schizophrenia proposes that dysfunction in dopaminergic neurotransmission, specifically hyperactivity of dopaminergic neurons in the limbic system and striatum, produces the positive symptoms, while underactive mesocortical dopaminergic neurons cause the negative, cognitive and affective symptoms of schizophrenia (Seeman 1987). Dopamine dysfunction and its treatment are not sufficient to explain the psychopathology of schizophrenia and its treatment outcomes (Yang and Tsai 2017; Stępnicki et al. 2018). Besides the dopaminergic hypothesis, dysfunction of the glutamatergic system has been implicated in schizophrenia (Olney and Farber 1995; Tsai and Coyle 2002). Glutamate is the major excitatory neurotransmitter in the CNS. The glutamate hypothesis posits that the function of the NMDA receptor is compromised in this disease. NMDA

receptors mediate slow excitatory postsynaptic potentials, which are considered critical for the proper expression of complex behaviours, such as associative learning, working memory, behavioural flexibility and attention, many of which are impaired in schizophrenia. These neurochemical hypotheses have been further extended to include contributions of other neurotransmitter systems in the pathophysiology of schizophrenia (Yang and Tsai 2017; Stępnicki et al. 2018). The serotonin (5-hydroxytryptamine; 5-HT) hypothesis of schizophrenia is derived from early studies of interactions between two major classes of psychedelic hallucinogens, the indoleamines (e.g., lysergic acid diethylamide, LSD) and phenethylamines (e.g., mescaline) and the serotonergic system, i.e. via 5-HT2A receptor agonisms (Aghajanian and Marek 2000). Although no direct evidence of serotonergic dysfunction in the pathogenesis of schizophrenia is yet available, specific 5-HT receptors continue to be a focus of interest in schizophrenia (Yang and Tsai 2017; Stępnicki et al. 2018). Of relevance in this matter is of course the serotonergic inhibitory modulation of dopaminergic neurotransmission in midbrain and forebrain (Kapur and Remington 1996), and the 5-HT-related enhancement of glutamatergic transmission in for example frontal cortex (Aghajanian and Marek 2000). Gamma-aminobutyric acid (GABA) is the main inhibitory neurotransmitter in the CNS. GABAergic dysfunction leads to an imbalance between inhibitory and excitatory activity in cortical areas which has been implemented in the pathophysiology of schizophrenia (Yang and Tsai 2017; Stępnicki et al. 2018; Guidotti et al. 2005). The high prevalence of smoking in schizophrenia, motivated the evaluation of nicotinic acetylcholine receptors, but also muscarinergic receptors are, respectively, potential targets for cognitive symptoms and positive symptoms (Yang and Tsai 2017; Stępnicki et al. 2018; Raedler et al. 2007; Brunzell and McIntosh 2012). In addition, several other systems including the histaminergic, adrenergic and endocannabinoid systems, as well as various neuropeptides have been implicated in the pathomechanisms of schizophrenia (Yang and Tsai 2017; Stępnicki et al. 2018).

1.2.3.2 Validating Animal Models of Schizophrenia

When validating animal models of schizophrenia, behavioural and electrophysiological endophenotypes are commonly employed, in addition to alternative endophenotypes focussing on neurochemical alterations, e.g. brain dopamine levels (Winter et al. 2009; Ayhan et al. 2011), or other neurochemical readouts (Corcoba et al. 2015; Puhl 2015), in addition to neuroanatomical changes, like reduction of brain (region) volume (Ayhan et al. 2011; Drew et al. 2011), ventricular enlargement (Ayhan et al. 2011; Corcoba et al. 2015; Puhl 2015; Li et al. 2009), and dendritic spine density (Ayhan et al. 2011; Berlanga et al. 2011; Jaehne et al. 2015; Nakao 2017).

Electrophysiological Endophenotypes

Electroencephalography recordings have been widely used to assess sensory processing deficits in schizophrenia. Analogous human and rodent auditory-evoked event-related potentials that are similarly affected by pharmacological interventions

and stimulus manipulations were described. The human auditory-evoked potential waveform shows characteristic positive deflections 50, 200 and 300 ms poststimulus (respectively, P50, P200 and P300) and a negative deflection 100 ms poststimulus (N100). The rodent analogues are P20, N40, P80 and P120 in order of occurrence. When exposed to a paired-click paradigm (S1–500 ms interval—S2), the waveform amplitudes are lower after S2 than after S1. Schizophrenia patients display a gating deficit based on a decreased response to S1 and/or a failure to inhibit S2 that results in similar amplitudes after S1 and S2. Useful endophenotypes with acknowledged heritability include decreased P50 (P20), N100 (N40) and P200 (P80) amplitude and gating, as well as decreased P300 (P120) amplitude. Schizophrenia patients also show a reduced ability to detect changes in the auditory environment, which is measured with a mismatch negativity paradigm, an exaggerated negative voltage deflection following N100 (N40), elicited when the qualitative features of a novel tone fail to match the pattern of a previous series of repetitive tones. Electrophysiological endophenotypes may aid in understanding schizophrenia mechanistically as gene and neurobiological associations have been described (Amann et al. 2010; Rosen et al. 2015; Owens et al. 2016).

Cognitive Endophenotypes

The cognitive phenotype can be evaluated using various protocols and paradigms (Crawley 2000), including a wide range of dry land (e.g. radial arm maze) and water mazes (e.g. Morris water maze) to specifically assess working memory. Contextual and fear conditioning are based on learning the association of a nonaversive context or cue with an aversive stimulus and the evaluation of freezing responses. The novel object recognition task is based on the rodents' tendency to focus attention on novel objects in their surroundings and the evaluation of exploration of a familiar versus a new object. Impairments in different forms of behavioural flexibility are commonly associated with schizophrenia. A number of behavioural paradigms using different sensory modalities and classes of stimuli have been developed to assess behavioural flexibility, in particular reversal learning, in rodents (Floresco et al. 2009).

Locomotor Activity

The majority of early tests for schizophrenia-related behaviours in rodents were based on the antipsychotic activity of dopamine D2 receptor antagonists (Ellenbroek and Cools 1990), with behavioural outcome parameters including locomotor hyperactivity and stereotyped sniffing and/or grooming. Locomotor activity can be scored in an open-field arena equipped with a video tracking system or infrared sensors to detect spontaneous exploration and ambulatory horizontal locomotion over a specific time frame (Crawley 2000). Motor stereotypy is mostly scored in rodents employing the Creese–Iversen stereotypy scale ranging from 0 (mouse either sleeping or inactive) to 6 (mouse engaged in continuous and nonstop route-tracing stereotypic behaviours) (Creese and Iversen 1973). Repeated administration of psychostimulants, including amphetamine, causes sensitisation to the motor-activating properties, as exemplified by enhanced hyperlocomotion and increased neuronal release of dopamine after the second or third administration. Behavioural

sensitisation is quantified by repeatedly testing spontaneous ambulatory locomotion in an open-field arena (Crawley 2000).

Sensory Discrimination

Abnormalities in the automatic processes of sensory discrimination, orienting and reorienting of attention are evident in the early phases of schizophrenia. Two attentional tasks were developed to be used both in humans and rodents: latent inhibition (LI) and PPI of the startle reflex. LI is the retarded conditioning to a stimulus that is repeatedly presented without reinforcement. In other words, the prior experience that a stimulus does not have a consequence makes it less likely that the brain will form an association with that stimulus later. LI is widely considered to relate to the cognitive abnormalities that characterise schizophrenia because it reflects an organism's ability to ignore irrelevant stimuli. One major strength of the LI task is that it can be applied across (mammalian) species (Amann et al. 2010; Lubow and Gewirtz 1995).

PPI of the startle reflex is a neurophysiological and behavioural measure of sensorimotor gating. One of its primary advantages is its ability to translate between mice and humans, as it is one of the few tests that is largely conserved across all vertebrate species. In rodents, the startle response is typically evoked using either acoustic or tactile stimuli and is characterised by contractions of the major muscles of the body, generally leading to extension of the forepaws and hind paws followed by muscle flexion into a hunched position. PPI is evoked when a weak stimulus (e.g. a 70- to 80-dB tone or a puff of air) inhibits the subsequent startle response to a strong stimulus (e.g. a 120-dB tone or a second puff of air) if presented within 100 ms. The whole-body startle from the rodent, restrained in a cylindrical holder, is quantified with piezoelectric motion sensors. Abnormal sensory inhibition may reflect a deficit in processing and prioritising incoming sensory information (Crawley 2000; Amann et al. 2010). A genetic component underlying PPI was suggested based on inbred mouse strain differences (Paylor and Crawley 1997).

Negative Symptoms

Certain negative symptoms, like poverty of speech, may be uniquely human, but other negative symptoms can be assessed in rodents using relatively simple behavioural paradigms. Anhedonia is studied with the sucrose preference test, which measures reduction in reward function in rodents (Crawley 2000). Deficits in social functioning is best scrutinised in rodents using a range of behavioural protocols, which may include a social choice paradigm for spontaneous affiliative behaviour, assessments of social recognition–discrimination, play-soliciting behaviour, social grooming, dominance, aggression and social defeat. Other negative symptoms, including avolition and blunted affect, have been studied in rodents using respectively behavioural despair tests (forced swim test and tail suspension test) and general anxiety tests, but interpretation is rather controversial (O'Tuathaigh et al. 2010). The controverse surrounding behavioural despair tests (Reardon 2019; Trunnell 2019), quite recently lead to the ban of the FST by several large pharma companies.

1.2.3.3 Neurodevelopmental Schizophrenia Models

Epidemiological evidence indicates gestational or perinatal exposure to adverse environmental events, like maternal stress, malnutrition and infection, and obstetric complication (e.g. hypoxia) increases the risk of developing schizophrenia (Lewis and Levitt 2002). Exposure to early-life adverse events combined with genetic predisposition is hypothesised to trigger deviating neuronal development and connectivity leading to the development of schizophrenia. When developing animal models based on this neurodevelopmental hypothesis, the timing of the exposure to a certain adverse event during the sensitive perinatal period is critical. Various adverse events have been applied, including postweaning social isolation (Fone and Porkess 2008), sometimes combined with physical stressors like e.g. alternating warm and cold temperature exposures (Hohmann et al. 2012), gestational exposure to the DNA-alkylating agent methylazoxymethanol acetate (Lodge and Grace 2008; Gulchina et al. 2017), exposure to bacterial or viral infection of pregnant rats (Gayle et al. 2004; Buka et al. 2008), or maternal exposure to stress (Martínez-Téllez et al. 2009; Markham et al. 2010). Depending on the chosen procedure and timing, these models may display, amongst others, disrupted sensory gating, decreased social interaction, cognitive deficits, enhanced drug-induced locomotion, neuroanatomical, neurostructural and neurochemical alterations.

1.2.3.4 Drug-Induced Schizophrenia Models

The development of an animal model is often based on the observation that certain drugs produce abnormal behaviour in healthy people. Usually the following steps are included in the process of developing an animal model based on pharmacological compounds: (1) the drug in question induces behavioural effects in healthy people that resemble human psychiatric pathology; (2) the drug induces specific biochemical alterations in animals; (3) the drug produces similar behavioural effects in animals, allowing for any species differences in behaviour; (4) the biochemical observations in animals provide insight into the behavioural effects of the drug in humans; and (5) if the behavioural effect of the drug in humans has the same characteristics as pathological behaviour, then the biochemical changes produced by the drug in animals may also provide data relevant for the understanding of the abnormal human behaviour. The vast majority of schizophrenia-related models have been based on the induction of abnormal behaviour by psychotomimetics, including both psychostimulants and hallucinogens. These drug-induced states, however, resemble the early stages of a range of psychotic disorders, and not necessarily the diagnostic syndrome of schizophrenia.

Psychostimulant Models

The most widely studied class of drug-induced animal models of schizophrenia is based on behavioural effects of psychostimulant drugs, such as amphetamine. Amphetamine-induced psychosis has been used as a model to support the dopaminergic hypothesis of schizophrenia (Seeman 1987). A hypodopaminergic state in the frontal-cortical terminal fields of mesocortical dopaminergic neurons has also been proposed to be the basis of negative symptoms (Dworkin and Opler 1992), but

these are relatively rare in amphetamine-induced psychosis, due to the hyperdopa-minergic nature of this model. One of the primary consequences of amphetamine treatment is the release of catecholamines from nerve terminals. In addition to its effects on release, amphetamine also blocks the reuptake of catecholamines from the synaptic cleft, and in high dosages, it is a potent monoamine oxidase inhibitor (Kokkinidis and Anisman 1981).

In rodents, chronic amphetamine administration induces a persistent sensitisa-tion that, both behaviourally and neurochemically, mirrors several features linked to the positive symptoms of schizophrenia. Behavioural alterations include locomotor hyperactive and/or stereotypy or perseverative behaviours, reduced PPI and dis-rupted LI (Featherstone et al. 2007). While amphetamine sensitisation does not pro-duce memory impairments similar to those seen in schizophrenia, it does produce strong impairments in set-shifting, suggesting schizophrenia-like changes in pre-frontal functioning (Featherstone et al. 2007, 2008). Interestingly, rhesus monkeys displayed behavioural alterations reminiscent of schizophrenia-like hallucination, including tracking, grasping 'at thin air', manipulating nonapparent stimuli (e.g. picking at imaginary parasites) and hypervigilance after amphetamine administra-tion (Castner and Goldman-Rakic 1999, 2003).

Hallucinogen Models

NMDA receptor antagonists, such as phencyclidine (PCP, 'angel dust') and ket-amine, produce psychotic symptoms and cognitive disturbances reminiscent of schizophrenia (Cohen et al. 1962; Krystal et al. 1994), findings that have contrib-uted to the hypoglutamatergic hypothesis of schizophrenia. As opposed to amphetamine-induced psychosis, hallucinogen-induced psychosis encompasses negative symptoms (e.g. emotional withdrawal) as well. Positive schizophrenia-like symptoms induced in laboratory animals include hyperlocomotion, stereotyped movements, circling and ataxia, while deficits in social behaviour are reminiscent of negative symptoms typical for schizophrenia. PCP and PCP-like drugs impair sen-sorimotor discrimination (LI and PPI) and affect performance in several cognitive paradigms, both in rats and monkeys (Javitt and Zukin 1991; Jentsch and Roth 1999). Also the serotonin 5-HT2A receptor agonist LSD has been applied to develop a rodent model with a schizophrenia-related behavioural state entailing e.g. psycho-sis, hyperactivity and hyperirritability, increased locomotor activity, anhedonia, cognitive and/or impairment in social interaction (Marona-Lewicka et al. 2011; Moreno et al. 2013).

1.2.3.5 Lesion-Induced Schizophrenia Models

To address some of the issues surrounding progressive neurodevelopmental or neu-rodegenerative changes in schizophrenia, a number of targeted lesion animal mod-els have been developed. Besides electrolytic and aspiration lesions, the majority of models is based on the application of excitotoxic agents (Marcotte et al. 2001). Three major sites of actions were chosen based on their presumed involvement in schizophrenia, i.e. the prefrontal cortex, hippocampus and thalamus. The prefrontal cortex is involved in higher cognitive functions, including attention, working

memory, emotional expression and social interaction. Executive function allows us to interact with the world in a purposive, goal-directed manner. It relies on several cognitive control operations that are mediated by different regions of the prefrontal cortex. The hippocampus modulates activity of the prefrontal cortex and thus exerts direct control over the schizophrenia-linked mesolimbic dopaminergic system. The thalamus is the brain's relay station that filters and gates sensory information and is therefore involved in PPI. Despite reasonable claims of predictive and face validity for many adult lesion models, the required size and temporal nature of these lesions limits their construct validity as animal models of schizophrenia. The neonatal ventral hippocampus lesion model is the best characterised model to test neurodevelopmental hypotheses of schizophrenia. This excitotoxicity model leads to dopamine-related behavioural alterations in adolescence or early adulthood, which include hyperlocomotion in response to stress, sensory gating deficits (PPI and LI), disturbed working memory and reduced social contacts, as well as psychotomimetic-induced hyperactivity, apomorphine-induced stereotypies and reduced catalepsy in response to haloperidol. Aberrant development of the prefrontal cortex, illustrated by molecular changes in this region, in response to neonatal hippocampal damage may be a critical factor in the onset of symptoms (Lipska and Weinberger 2000; Lipska 2004). Based on the neonatal disconnection of the ventral hippocampus presumably altering the development and plasticity of prefrontal cortical circuitry, the neonatal rat excitotoxic brain lesion model was also adapted to the ventral thalamus (Wolf et al. 2010, 2018), and the prefrontal cortex (Klein et al. 2008; Lazar et al. 2008).

1.2.3.6 Genetic Schizophrenia Models

As exemplified by twin studies, schizophrenia has a substantial genetic compound (Cardno et al. 1999). An important shift can be observed in the way animal models are being used for the genetic dissection of psychiatric disease. Initially, inbred strains, often selectively bred for a disease-specific trait, dominated the literature, followed by single-gene knockout or mutation models developed with homologous recombination in embryonic stem cells. Whole-genome association studies are presently expected to provide strong evidence for the involvement of susceptibility genes that will lead to attempts to model multiple susceptibility genes. In addition, the development of microarray and proteomic technology has enabled global description of gene expression in schizophrenia, although it may be difficult to distinguish between primary aetiology and secondary pathology, confounding influences or compensatory mechanisms. Changes in gene expression with a primary etiopathological role may arise from sequence variants in regulatory regions of genomic DNA, epigenetic/stochastic variation or environmental influences, while secondary changes may reflect points of convergence in the action of individual susceptibility genes (Bray 2008). Given the complex aetiological nature of schizophrenia, genetic models expressing risk genes may form the basis to study the effect of environmental manipulation on such mutant phenotypes at specific developmental stages and may help in defining the trajectory, relative contribution of and

interaction between genes and environmental factors in the emergence of the schizophrenia phenotype (Desbonnet et al. 2009).

Inbred and Selectively Bred Rodent Strains

Remarkable variability in outcome of specific cognitive and behavioural tasks is evident in different rodent strains (Crawley 2000; van der Staay and Blokland 1996; Crawley et al. 1997). Genetic factors determine sensory and sensorimotor gating in rodents, and consequently, strain differences in baseline startle response and PPI have been described (Paylor and Crawley 1997; Palmer et al. 2000; Willott et al. 2003; Pietropaolo and Crusio 2009). Moreover, strain and substrain differences for pharmacological (e.g. amphetamine-based) disruption of sensorimotor gating were observed (Kinney et al. 1999; Swerdlow et al. 2000, 2012; Varty et al. 2001). Interestingly, strain-dependent changes across adolescence have been observed, indicating that genetic factors and the early adolescent phase are critically important considerations in the design of animal models of neuropsychiatric disturbances (Pietropaolo and Crusio 2009). Variations between strains and substrains, whether or not accomplished through selective breeding, form a good basis to study the underlying biological mechanisms and hence, therapeutic strategies in schizophrenia (Swerdlow et al. 2005, 2012; Dieckmann et al. 2007; Gogos et al. 2008; Flood et al. 2011). Selective breeding also forms an excellent basis for the development of highly relevant multiple-hit models (Kekesi et al. 2015; Horvath et al. 2016; Büki et al. 2019).

Genetically Modified Models

Candidate genes for schizophrenia are dysbindin (*DTNBP1*) (Williams et al. 2005); neuregulin 1 (*NRG1*) and its receptor *ERBB4* (Banerjee et al. 2010); *DISC1* (i.e. disrupted in schizophrenia-1) (Muir et al. 2008); reelin (*RELN*) (Grayson et al. 2006); components of the Akt-GSK3β signalling pathway, including AKT1 (Freyberg et al. 2010); and genes located in chromosomal region Δ22q11.2, which has been implicated in schizophrenia based on the 22q11.2 deletion syndrome (Paylor and Lindsay 2006). For an updated list of published genetic associations studies for schizophrenia readers are referred to the comprehensive, multi-omics online SZGR 2.0 database (https://bioinfo.uth.edu/SZGR/). Besides genetics studies that reported variants and genes potentially associated with schizophrenia, SZGR 2.0 also compiles transcriptome and epigenetic information (Peilin et al. 2017).

Several spontaneous mutant rodent models have been studied as presumed phenocopies of schizophrenia. The *sandy* mouse has a deletion of two of the exons of the dysbindin gene and is therefore a naturally occurring dysbindin-knockout model. *Sandy* mice display some behavioural phenotypes with relevance to schizophrenia, including increased anxiety and deficits in social interaction (Hattori et al. 2008). After the discovery of *DISC1* as a potential schizophrenia candidate gene, some of the earliest animal studies on its potential role included the detection of

natural mutations in different mouse strains. All 129 mouse substrains carry a 25-bp deletion in the *mDISC1*, which modulates working memory (Clapcote and Roder 2006; Koike et al. 2006). Reeler is an autosomal recessive mutant mouse with reduced cerebellar size, disruption of the laminar organisation in several brain regions and inversion of neocortical cellular layers (Falconer 1951; Caviness Jr 1976). The reelin-haploinsufficient heterozygous reeler mouse has been used as an animal model for schizophrenia based on several neuropathological and behavioural abnormalities homologous to schizophrenia. Heterozygous reeler mice exhibit alterations in sensorimotor gating (Barr et al. 2008), deficits in working memory (Brigman et al. 2006), impaired social interaction (Podhorna and Didriksen 2004), but also neurochemical, neuroanatomical and protein expression alterations relevant to schizophrenia have been reported (Schmitt et al. 2013; Nullmeier et al. 2014; Varela et al. 2015).

DNA variation that affects expression of candidate disease genes can take various forms, including single nucleotide polymorphisms (SNPs), deletions, insertions, variable repeat sequences, rearrangements or duplications (copy number variations). Downregulation of individual susceptibility genes can be mimicked via gene knockout or via RNA interference, while upregulation can be achieved with gene knock-in techniques or RNA activation.

Multiple genes (perhaps thousands) of small effect are thought to exist for the illness, given its status as a complex genetic illness (Peilin et al. 2017; Gejman et al. 2011). Nonetheless, tissue effects in animals with risk mutations are presumed to be associated in some way with schizophrenia pathophysiology. The biological characterisation of animals with risk genes is highly relevant to ultimately discovering disease pathophysiology, even though every aspect of the biology may not be critical. For the currently most promising risk genes, few transgenic mouse models will be briefly discussed.

Many mouse models with manipulated expression levels of the different NRG1 isoforms have been created. Mutants with heterozygous deletion of the transmembrane domain exhibit hyperactivity, a deficit in PPI, selective impairment in social novelty preference and altered patterns of social interaction. Studies focusing on deletion of specific NRG1 isoforms have shown that type III NRG1 mutant mice display even more pronounced PPI deficits in addition to working memory dysfunction (Desbonnet et al. 2009). Homozygous knockout of *NRG1* is developmentally lethal in mice, but viable heterozygous, hypomorphic/conditional knockouts that can modulate neuregulin–ErbB4 signalling have been developed, all with distinct 'schizophrenia-like' alterations, including—depending on the genetic models studied—hyperactivity, PPI, LI and social interaction deficits, impairment in contextual fear conditioning and mismatch negativity (Harrison and Law 2006; Mei and Xiong 2008; Jones et al. 2011). At least seven different strains of transgenic mice containing inducible and/or partial *DISC1* gene mutations resulting in a (partial) loss of DISC-1 function have been created (Jaaro-Peled 2009). These mice exhibit enlarged lateral ventricles and reduced cortical thickness and brain volume, mimicking some characteristics of schizophrenia. Some mutants display reductions in hippocampal dendritic complexity, structure and density. Some *DISC1* mice display PPI deficits

that are attenuated with antipsychotics, while hyperactivity, reduced sociability, working memory and executive function impairments have been described as well.

Over the past decades a multitude of genetically modified schizophrenica models has been developed. Discussing all currently developed genetic models of schizophrenia would go beyond the scope of this chapter. Readers are referred to several excellent review papers (Jones et al. 2011; Leung and Jia 2016; Moran et al. 2016; St Clair and Johnstone 2018).

1.3   Animal Models of Neurological Disorders

The discovery of new therapies for neurological disorders is predicated on the use of animal models both to identify new therapeutic targets and to perform preclinical trials of drugs prior to clinical application. In both cases, the challenge is to develop models that recapitulate the disorder. The starting point for the development of a new animal model for a specific neurological condition is often the current dominant theory about the disease. Although a logical first approach, it is essential to broaden the focus of animal models under development based on the increasing knowledge of underlying disease mechanisms. The development of animal models for Alzheimer's disease (AD) serves an excellent example of such a strategy.

Advances in biochemical pathology and human genetics have yielded striking progress in our understanding of molecular mechanisms underlying nervous system diseases such as AD, Parkinson's and Huntington's disease. Of great importance is the pivotal concept that certain normally soluble neuronal proteins can misfold and aggregate into oligomers and fibrils, which can confer profound cytotoxicity. Perhaps the foremost example, both in terms of its societal impact and how far knowledge has moved toward the clinic, is that of AD, hence the focus of the following paragraphs.

1.3.1   Approaches to Modelling Neurological Disorders

In contrast to psychiatric disorders, approaches to model neurological conditions are not easily categorised. The approach largely depends on the aetiology of the human neurological condition, which may be acquired or degenerative. Specific approaches when developing new animal models should be applied depending on the aetiology, which may be amongst others infectious (e.g. Creutzfeldt–Jakob disease, HIV dementia), immune-related (e.g. multiple sclerosis), genetic (e.g. Charcot–Marie–Tooth disease; leukodystrophies), lesion-based (e.g. head trauma), and environmental/toxicity-related (e.g. alcohol-related dementia, toxic-metabolic encephalopathy).

1.3.2   Animal Models of Alzheimer's Disease

1.3.2.1 Aetiology and Symptomatology of Alzheimer's Disease

As the prototype of cortical dementias, AD is characterised by prominent cognitive deficits. Patients initially exhibit limited forgetfulness with disturbance of memory imprinting, which further evolves to short-term memory disruption and, ultimately, to long-term memory deficits. At more advanced stages, patients display executive dysfunctioning leading to advanced helplessness (Selkoe 2000). Besides cognitive deterioration, patients demonstrate behavioural and psychological signs and symptoms of dementia (BPSD), including paranoid and delusional ideation, hallucinations, activity disturbances, aggressiveness, diurnal rhythm disturbances, affective disturbances, anxieties and phobias (Reisberg et al. 1987). BPSD are nowadays also often referred to as neuropsychiatric symptoms or NPS (Lyketsos et al. 2011; Van Dam et al. 2016). The histopathological hallmarks of AD brain are extracellular amyloid-β (Aβ) plaques and intracellular neurofibrillary tangles (NFT), accompanied by decreased synaptic density, which eventually leads to widespread neurodegeneration and failure of neurotransmitter pathways, particularly those of the basal forebrain cholinergic system (Van Dam et al. 2016; Selkoe 2001). The number of affected individuals is likely to grow in the decades to come as a result of demographic changes and rising life expectancy. It is forecast that the worldwide number of elderly people suffering from dementia will rise to 63 million in 2030 and to 114 million in 2050 (Wimo et al. 2003).

1.3.2.2 Validating Animal Models of Alzheimer's Disease

Cognitive Symptoms

A variety of paradigms and protocols has been developed to assess cognitive functions in rodents (Crawley 2000; Buccafusco 2008). Ideally, several paradigms requiring distinct sensory and motor abilities are chosen when phenotyping a new dementia model. Protocols distinguishing explicit versus implicit memory can be chosen, as well as designs assessing short-term versus long-term memory (Tulving 1987). The Morris water maze is presently the most widely used paradigm for the evaluation of hippocampus-dependent visual-spatial learning and memory skills in rodents, which represents the highest cognitive level appreciable in rodents (D'Hooge and De Deyn 2001). Besides the Morris water maze, several other mazes could be employed, which are all based on the same principle; successfully passing through the maze is rewarded by escaping from the water in wet mazes or by food as a positive reinforcer in dry-land mazes. Examples include the plus-shaped water maze, radial arm mazes, multiple Y mazes and the Barnes maze. Complex nonspatial hippocampus-dependent tasks like the odour paired-associates task (Bunsey and Eichenbaum 1996), are analogous to the verbal paired-association task for humans, but the long duration of the protocol, which requires several months, makes it unsuitable for the assessment of memory in progressing phenotypes (Van Dijck et al. 2008). The same disadvantage may arise when using schedule-induced

operant tasks employing operant conditioning or Skinner boxes. Both active and passive avoidance learning protocols are widely used to assess cognitive function in a short time frame. However, procedural components of the task are not easily distinguishable from declarative memory components as is the case in the Morris water maze or in cued and contextual learning (Crawley 2000). Associative learning (cued and contextual conditioning) requires a different set of sensory and motor functions, so that the procedural components of associative tasks do not overlap. Other potentially useful learning and memory tasks include novel object recognition, conditioned taste aversion, social recognition and discrimination learning (Crawley 2000).

BPSD-Related Symptoms

In accordance with the increased clinical focus on BPSD, major efforts have been made to mimic specific behavioural alterations in animal models and to develop useful tools (Crawley 2000; Buccafusco 2008), to evaluate new psychopharmacological strategies to replace atypical antipsychotics or classic neuroleptics, which display only modest effect size and are frequently associated with significant side effects (De Deyn et al. 2005).

Activity and circadian rhythm disturbances can be easily screened using infrared sensors surrounding the animal's home cage. The number of beam interruptions over a specific time interval is recorded as a measure of activity comparable to actigraphic measurements in the clinical setting (Vloeberghs et al. 2004). Aggressive behaviour in male rodents can be provoked using a variety of behavioural protocols based on dominance hierarchy, as is the case in the commonly used isolation-induced resident–intruder protocol (Valzelli 1973). Anxiety and fear-related behaviours can be assessed using both conditioned (i.e. conflict tests like the Vogel's lick-suppression test) and unconditioned response tests, which are based on the quantification of fear-related responses like freezing, defecation and thigmotaxis, and the conflict between the innate trait of nocturnal animal like mice and rats to prefer narrow, dark enclosures and the tendency to explore new environments (Crawley 2000). Appraisal of depression-related symptoms in rodents is based on learned helplessness and behavioural despair phenomena, in which animals are exposed to uncontrollable and inescapable stress, e.g. the Porsolt forced swim test, the tail suspension test and inescapable shock paradigms. Failure to try to escape from this type of aversive stimulus in rodents is considered to model a depression-like state (Chourbaji et al. 2005). Anhedonia, a core symptom of clinical depression, which is defined as the loss of sensitivity to reward, can be assessed in rodents with a sucrose preference test during which the consumption of a 0.8% sucrose solution is compared to the simultaneous consumption of tap water (Sanchis-Segura et al. 2005). Phenotyping can also focus on ingestive behaviour. The intake of food and water can be screened using metabolic cages. More detailed analysis of food intake is possible in operant conditioning boxes equipped with pellet dispensers and optical lick-o-meters that allow appraisal of the circadian rhythm of ingestive behaviour (Vloeberghs et al. 2008).

Pathological Alterations

The neuropathological hallmarks of AD include "positive" lesions such as amyloid plaques, cerebral amyloid angiopathy, neurofibrillary tangles, and neuroinflammatory responses, and "negative" lesions, such as neuronal and synaptic dysfunction and loss (Van Dam et al. 2016). Amyloid structure is most commonly stained using congo red, thioflavin S or Aβ-specific antibodies (Castellani et al. 2007; Vidal and Ghetti 2011). Amyloid plaque burden can be evaluated by employing stereological methods, which allow a three-dimensional geometrical interpretation of structures based on observations made on two-dimensional sections. Levels of Aβ peptides and other APP-derived molecules can be quantified using ELISA or Western blotting techniques. While ELISA is a very sensitive method to detect and quantify total Aβ levels, commercially available kits provide no or very little information on the possible aggregation state and structure of Aβ. Western blotting, on the other hand, is less suited for quantification but makes it possible to detect aggregates and roughly estimate their size. However, it still only provides very limited information about the structure and composition of the aggregates. Researchers more interested in the molecular structure, composition and formation of the oligomers turned to mass spectrometry techniques, which allow very accurate determination of protein identity, amino acid sequence and presence of modifications, or even—when using nondenaturing approaches—the macromolecular structure (Ashcroft 2010; Bleiholder et al. 2011). Tau pathology can be assessed at various levels, including a quantitative assessment using Western blot, biochemical and immunohistochemical determination of different phosphorylation states and sites, as well as the immunohistochemical assessment (e.g. with the ALZ-50 monoclonal antibody) of the spatiotemporal progression of tau pathology (Rankin and Gamblin 2008). Monitoring inflammatory processes can be based on the use of histopathological and immunohistochemical markers of astrocyte and microglia activation, as well as on various biochemical assays of inflammatory markers in body fluids (McGeer and McGeer 2003). Potential biomarkers of oxidative stress, including an imbalance between free radicals (reactive oxygen and nitrogen species) and the antioxidant response (free radical scavengers and antioxidant enzymes), as well as the subsequent damage to macromolecules (lipids, proteins, nucleic acids and sugars), can be determined in body fluids or brain using a wide range of biochemical techniques, including spectrophotometric, fluorometric, chromatographic and immunohistochemical assays (Migliore et al. 2005). Degenerative processes (e.g. neuritic spheroids) can be visualised by silver impregnation, neurofilament or ubiquitin immunostaining (Castellani et al. 2007).

Neurochemical Alterations

The cholinergic hypothesis of AD is based on the fact that degeneration of cholinergic neurons in the nucleus basalis of Meynert, situated in the basal forebrain and primarily projecting to the neocortex, occurs early in the course of the disease and leads to a marked decline in the activities of choline O-acetyltransferase (ChAT) and acetylcholinesterase (AChE) (Contestabile 2011). In rodent models, the presence of cholinergic deficits can be scrutinised with the determination of ChAT or AChE enzyme activities based on, respectively, a radiochemical (Fonnum 1975), and a spectrophotometric protocol (Ellman et al. 1961). Microdialysis extraneuronal

sampling coupled with a high-sensitivity HPLC detection and quantification method has been often used for assessing the cholinergic impairment and its recovery in many AD models (Pepeu and Giovannini 2007). Moreover, immunohistochemical visualisation and quantification of ChAT- or AChE-positive neurons and fibres has been employed, as well as determination of high-affinity choline uptake, considered a biochemical marker of the localisation and integrity of the cholinergic nerve endings and a measure of the activity of the cholinergic neurons (Pepeu and Rosi 2011).

Neurochemical alterations observed in AD brain, however, are not confined to the cholinergic system. Moreover, many data indicate that the neurochemical alterations underlying cognitive deterioration and related disturbances in cortical processing implicate more widespread neurodegeneration that cannot be attributed solely to the cholinergic system (Dringenberg 2000). Neuronal loss and, inherently, alterations in the concentration of neurotransmitters and metabolites of the noradrenergic, adrenergic, dopaminergic and serotonergic system, as well as neurotransmitter amino acids, have been described in AD (Van Dam et al. 2016; Vermeiren et al. 2014a, b; Gsell et al. 2004). In rodent models, chromatography-based determination of neurotransmitter (and metabolite) levels in microdialysis samples or brain (region) homogenates can be employed to assess neurotransmitter alterations. Deficits in peptidergic neurotransmission (or co-transmission) have been implicated in AD. Classically, neuropeptides are mainly studied by radioimmunoassay and immunohistochemistry, but recently researchers have shifted to mass spectrometry-based methodologies (Van Dam et al. 2013).

1.3.2.3 Spontaneous and Selectively Bred Alzheimer's Disease Models

Various species across the phylogenetic tree, ranging from invertebrates like *Drosophila melanogaster* and *Caenorhabditis elegans* (Mhatre et al. 2013), up to non-human primates have been applied in AD-related research (Van Dam and De Deyn 2017). Some species, including dogs (Cummings et al. 1993, 1996; Rofina et al. 2006), cats (Head et al. 2005; Gunn-Moore et al. 2006), bears (Cork et al. 1988; Tekirian et al. 1996; Uchida et al. 1995), goats and sheep (Braak et al. 1994), wolverine (Roertgen et al. 1996), as well as several non-human primate species (Van Dam and De Deyn 2017; Bons et al. 1994; Gearing et al. 1994, 1997; Lane 2000; Geula et al. 2002; Kimura et al. 2003; Sani et al. 2003; Lemere et al. 2004, 2008), spontaneously develop plaque pathology and some species even display tauopathies. These histopathological changes can be accompanied by cognitive decline (Cummings et al. 1996; Rofina et al. 2006; Gunn-Moore et al. 2006; Voytko and Tinkler 2004). The use of these species for experimental research is however limited by availability, economical (based on long lifespan) and/or ethical reasons (Van Dam and De Deyn 2017).

Rodents are unequivocally the front runners as model organisms in this field. Rodents are easier and cheaper to house and maintain than larger mammals, and they display a fast generation time with large numbers of offspring. Moreover, rodents and humans do share approximately 95% of their genome, and standardized breeding gives researchers access to various inbred strains contributing to a less variable phenotype (Van Dam and De Deyn 2006, 2011a). Ageing rodents do not spontaneously develop histopathological AD-like hallmarks, but do display

senescence-related cognitive decline and behavioural alterations associated with neurochemical and morphological alterations (Erickson and Barnes 2003), including age-associated cholinergic hypofunction (Sherman and Friedman 1990). In addition, they aid in uncovering the boundary between normal and pathological ageing, allowing in-depth investigation of basic neural mechanisms underlying brain ageing.

Selective breeding from a genetic pool of AKR/J mice has led to the development of the senescence-accelerated mouse (SAM) model, which includes nine major SAM-prone (SAMP) substrains and three major SAM-resistant substrains. The SAMP8 substrain is of particular interest given the development of age-associated learning and memory deficits in association with Aβ deposition (Butterfield and Poon 2005; Renã and Butterfield 2011).

Pharmacological, Chemical and Lesion-Induced Rodent Models of Alzheimer's Disease

Disruption of multiple neurotransmitter systems underlies the cognitive and behavioural disturbances associated with AD. The majority of animal models that fall within this category are based on the cholinergic hypothesis of AD, which states that degeneration of cholinergic neurons in the nucleus basalis of Meynert, located in the basal forebrain and projecting to the neocortex, occurs early in the course of the disease (Whitehouse et al. 1982; Davies and Maloney 1976). The most widely used pharmacological model is scopolamine-induced amnesia (Sunderland et al. 1986; Ebert and Kirch 1998). The application of this muscarinic antagonist has increased our knowledge of the role of the cholinergic system in cognition and allows pre-clinical evaluation of symptomatic efficacy of cholinomimetics. The applicability of this model is however limited by the fact that cholinergic hypofunction is not associated with the development of AD-typical pathology, and the lack of disease progression both at the cholinergic and cognitive level. Blockade of nicotinic receptors by mecamylamine also induces learning impairment (Moran 1993; Estapé and Steckler 2002). Since AD brain shows both reduced muscarinic and nicotinic acetylcholine receptor densities (Whitehouse and Au 1986; Nordberg et al. 1989), blockade of both receptors may offer a better animal model for AD-related amnesia (Levin et al. 1990; Riekkinen Jr et al. 1990).

In addition to scopolamine-induced amnesia, cortical cholinergic involution has been replicated in lesion models that focus on specific cholinergic centres of the basal forebrain, as well as more general lesions of all basal forebrain cholinergic neurons. Focal lesions are most often directed at the nucleus basalis magnocellularis (Lescaudron and Stein 1999; Vale-Martínez et al. 2002), the rodent analogue of the nucleus basalis of Meynert, the septal area (Mulder et al. 2005), or include fimbria/fornix transection leading to septo-hippocampal cholinergic denervation (He et al. 1992; Alonso 1996). Lesions can be induced by mechanical, i.e. knife cut, or electrolytic procedures and intraparenchymal or intracerebroventricular microinjections of neurotoxic substances, such as quinolic, kainic, ibotenic and quisqualic acids, NMDA, the cholinotoxin AF64, and the immunotoxin 192 IgG-saporin (Toledana and Alvarez 2011). Such lesion models increase our understanding of the role of cholinergic innervations in the aetiology and treatment of cognitive disorders.

AD-related memory deficits can also be (partially) reproduced by lesioning brain structures or pathways essential for different aspects of learning and memory, such as the hippocampus, striatal or cortical regions (Gray and McNaughton 1983; Glenn et al. 2003; Sloan et al. 2006; Castañé et al. 2010). These models increase our knowledge of the neural mechanisms underlying memory dysfunction, but of course lack disease progression and do not develop AD-like pathological hallmarks. Moreover, selected lesions are compared with the more global disease process of AD.

Certain chemically induced models focus on one specific pathophysiological pathway thought to underlie AD, such as neuroinflammation or glucose/energy metabolism impairment, and their effects on neurodegeneration. Neuroinflammation develops upon the infusion of endotoxins, like lipopolysaccharide (Hauss-Wegrzyniak et al. 1998), or proinflammatory cytokines (Wenk et al. 2003). Brain metabolism can be disrupted through interference with mitochondrial metabolic pathways (Szabados et al. 2004), or neuronal insulin signal transduction (Ishrat et al. 2009).
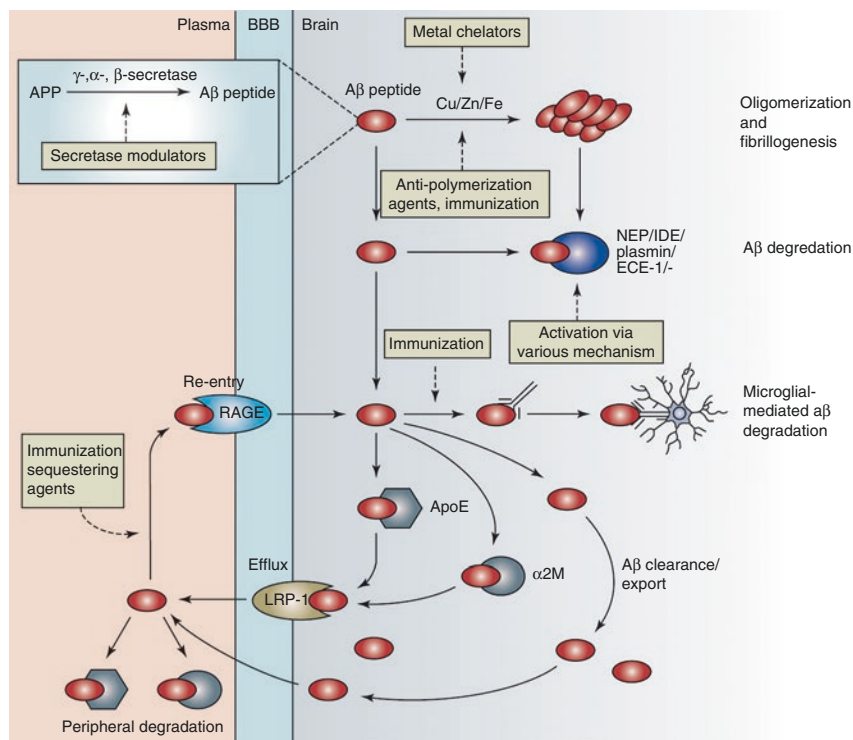
Fig. 1.2 This figure represents the major processing pathways of amyloid precursor protein (APP) and amyloid β (Aβ) peptides, including the potential therapeutic targets and therapeutic interventions. *APP* amyloid precursor protein, *CTF* C-terminal fragment, *NTF* N-terminal fragment, *Aβ* amyloid β peptide, *ApoE* apolipoprotein E, *BBB* blood–brain barrier, *CSF* cerebrospinal fluid, *ECE-1* endothelin-converting enzyme-1, *IDE* insulin-degrading enzyme, *LRP-1* low-density lipoprotein receptor-related protein-1, *NEP* neprilysin, *RAGE* receptor for advanced glycation end products, *α2M* α-2-macroglobulin. Repinted with permission from Van Dam and De Deyn (2006)

1.3.2.4 Amyloid-β Infusion Rodent Models of Alzheimer's Disease

The amyloid cascade hypothesis states that cerebral accumulation and aggregation of Aβ peptides into amyloid plaques is the primary culprit in AD (Selkoe 2000; Hardy and Selkoe 2002). More recently, a key role was assigned to soluble Aβ oligomers (Gong et al. 2003; Lacor et al. 2004; Walsh and Selkoe 2007; Selkoe 2008) (Fig. 1.2).

Aspects of AD can be modelled by acute or repetitive intracerebral or intracerebroventricular infusion of Aβ peptides in rodent brain (Lawlor and Young 2011). To better mimic the progressive nature of AD, chronic and continuous administration is accomplished by connecting an implanted cannula to an osmotic mini-pump (Nakamura et al. 2001; Olariu et al. 2002), or a micro-infusion pump (Nag et al. 1999), or with microdialysis (Harkany et al. 2000). In addition to measurable adverse effects on memory and behaviour (Harkany et al. 1998; Yamada et al. 2005; Sipos et al. 2007), exogenous administration of Aβ peptides can lead to AD-like neuropathological alterations (Sipos et al. 2007; Frautschy et al. 1996), although the full complexity of the human pathology is not reproduced and pathology is not widespread as in patients. Accumulation of Aβ deposits can be associated with, e.g. inflammation and microglial activation, oxidative stress and local cell loss (Weldon et al. 1998). More specifically, disruption of cholinergic function was reported (Harkany et al. 1998; Yamada et al. 2005).

CNS Aβ infusion animal models provide insight into the mechanisms and secondary effects of Aβ toxicity and allow preclinical evaluation of drugs targeting Aβ, as well as evaluation of protective efficacy of pharmacological modulation of microglial signalling. Rodent infusion models have some advantages over transgenic amyloid-related models. Infusion models can deliver the desired (pathological) outcome within a time frame of a few weeks (Frautschy et al. 1996), versus several months or years in transgenic models. Moreover, they allow researchers to administer defined amounts of a specific Aβ species of known sequence and length or to introduce controlled cofactors related to plaque development, while transgenic overexpression of APP results not only in increased production of Aβ1–40 and/or Aβ1–42, but in elevated levels of other APP fragments, which can have neuroprotective, neurotoxic or signalling functions and influence learning and memory. On the other hand, major caveats of infusion models are the fact that administered Aβ concentrations are much higher than Aβ levels found in the brain or cerebrospinal fluid of AD patients (Vickers et al. 2000), and that effects of ageing on AD progression are lacking. Moreover, the invasive nature of Aβ infusion inevitably brings about brain injury, which—in addition to the potential neurotoxic effects of vehicles used—may contribute to the induction of inflammation observed in these models. These potentially confounding effects should be controlled for by including proper sham and/or scrambled peptide groups.

1.3.2.5 Genetically Modified Alzheimer's Disease Mouse Models

Modelling of AD in transgenic mouse models became reality in the mid-1990s with the development of the platelet-derived growth factor promoter-driven APP (PDAPP) model (Games et al. 1995; Basak and Holtzman 2011), followed in

subsequent years by the Tg2576 (Hsiao et al. 1996; Deacon 2011), and the APP23 mouse model (Sturchler-Pierrat et al. 1997; Van Dam and De Deyn 2011b), currently the most widely used amyloidosis models in AD-related research. The choice of *APP* as the incorporated transgene was based on two lines of evidence: APP is the precursor of Aβ and it is the target of the first described early-onset AD mutations. The PDAPP model expresses human *APP* carrying the Indiana familial AD mutation driven by the platelet-derived growth factor-β promoter, whereas both the Tg2576 and APP23 model express human APP with the Swedish mutation driven by the hamster prion protein and murine Thy-1 promoter, respectively. The discovery of familial AD mutations in the presenilin (PSEN) genes, which influence APP processing, opened the path for PSEN1 and PSEN2 transgenic mouse models and double-cross APP/PSEN models. Although early-onset AD accounts for only a small proportion of AD cases, models expressing pathogenic mutations of human genes have become crucial tools in unravelling disease processes and have boosted drug discovery and development.

Several major genetic risk factors for developing late-onset AD have been identified, among which apolipoprotein E (ApoE) and triggering receptor expressed on myeloid cells 2 (TREM2). Mice expressing a human ApoE isoform, such as Apoε4 (Huber et al. 2000), and TREM2 (Kleinberger et al. 2017) have been developed to study the pathophysiological link between, respectively, ApoE and TREM2, and AD.

Genetically modified mouse models based on other aetiological hypotheses that are considered relevant to the preclinical AD field include, e.g. mutated human α-synuclein models (Freichel et al. 2007), TAR DNA-binding protein 43 (TDP-43)-related models (Wu et al. 2010; Wils et al. 2012), mutated human cyclooxygenase-2 overexpression models (Andreasson et al. 2001), anti-nerve growth factor (NGF) mice (in which NGF activity is neutralised using antibodies) (Capsoni et al. 2000), neprilysin (Iwata et al. 2001), insulin-degrading enzyme knockout mice (Farris et al. 2003), and crosses between mutated human APP overexpression strains and nitric oxide synthase 2 knockouts (Colton et al. 2008). For more in-depth information and latest updates, readers are referred to the Alzheimer Research Forum website (http://www.alzforum.org), which includes an online compendium of relevant mouse models for AD and related disorders. Most of these models robustly mimic a subset of AD features, including Aβ deposition, plaque formation and cerebral amyloid angiopathy, as well as neurodegeneration, synaptic dysfunction and inflammation, in addition to cognitive decline.

The major limitation of the above-mentioned models, i.e. the lack of NFT formation, was partially counterbalanced with the development of several (mutated) tau models, and the crossing of tau and amyloidosis models, which featured enhanced amyloid deposition accompanied by tau phosphorylation, NFT-like formation and overt neuronal loss (Götz et al. 2004; Ribé et al. 2005). It has proven challenging to develop mice in which both histopathological hallmarks occur in AD-relevant brain regions, such as the hippocampus and cortex. However, the development of triple transgenic (3 × Tg) mice seems to have overcome this hurdle (Oddo et al. 2003; Sy et al. 2011). Rather than crossing independent mutant mouse lines, two transgenes

(mutant APP and tau) were microinjected into single-cell embryos from homozygous mutant PSEN1 mice. The major advantages of this approach are the integration of APP and tau at the same genetic locus (which prevents segregation in subsequent generations), more cost-effective breeding requirements and the fact that there is no mixing or altering of the genetic background. In accordance with the amyloid cascade theory, these 3 × Tg mice develop Aβ plaques prior to NFT pathology with a temporal and spatial profile equivalent to AD. Studies using the 3 × Tg-AD mice have revealed a strong interaction between Aβ and tau, which synergistically drive the pathogenesis in the brain. The first signs of cognitive decline manifest at age 4 months as a deficit in long-term retention and correlate with accumulation of intraneuronal Aβ in the hippocampus and amygdala (Billings et al. 2005). Similarly, the 5 × FAD model was developed that expresses human APP and PSEN1 transgenes with a total of five AD-linked mutations: the Swedish (K670N/M671L), Florida (I716V), and London (V717I) mutations in APP, and the M146L and L286V mutations in PSEN1. The Swedish mutation results in higher levels of total Aβ, whereas the other mutations specifically increase the production of Aβx-42. Already at age 2 months, extracellular amyloid plaques are detected by immunohistochemistry in hippocampus, cortex, and thalamus (Oakley et al. 2006). At the age of 1 year, 5 × FAD mice display a 40% loss of layer V pyramidal neurons (Oakley et al. 2006; Neuman et al. 2015). The model develops age-dependent cognitive (spatial, associative and working) decline from the age of 3 months onwards (Girard et al. 2013), as well as non-cognitive behavioural abnormalities (Jawhar et al. 2012).

Of interest is the development of genetically modified rat models for AD, which may serve better tools then mouse models for microPET/SPECT applications. TgF344-AD rats for example express human APP with the Swedish mutation and human PSEN1 with the Δ exon 9 mutation. The rat model shows an age-dependent accumulation of amyloid plaques between 6 and 26 months of age, with plaque-associated neuritic dystrophies, cerebral amyloidosis, tauopathy, gliosis, apoptotic loss of neurons in the cerebral cortex and hippocampus, and cognitive disturbances (Cohen et al. 2013), as well as enhanced anxiety-like behaviour (Pentkowski et al. 2018).

More recently, the use of viral vector gene transfer technology has allowed the development of 'somatic transgenic' models, whereby genes putatively involved in AD pathogenesis can be selectively overexpressed in specific brain regions involved in AD (Lawlor and Young 2011; Jaworski et al. 2010). Viral transgenesis also allows investigators to explore the role of newly discovered genetic linkages in a more efficient and cost effective manner, indeed, viral technologies can be used to introduce many genetic changes at once for the screening of many individual factors (and their interactions) simultaneously (Platt et al. 2013). The CRISPR/Cas9 system further improves the biological toolkit to develop genetically modified animals (Tschaharganeh et al. 2016). For an updated list of genetically modified AD-related models, readers are referred to the website of the Alzheimer Research Forum (http://www.alzforum.org).

1.4 Imaging in Rodent Models of Brain Disease

This chapter does not aim at giving an overview of neuroimaging involving PET and SPECT in models of brain disease, but rather serves as an introduction to models of brain disorders with a selected overview of modelling approaches and methodological aspects with regard to phenotyping. We will briefly describe some relevant imaging techniques and show a couple of examples related to schizophrenia and AD.

With the development of more sophisticated techniques, neuroimaging has become an essential component of studying brain structure and function in the diseased state. In drug development research, utilising methodology and results that can easily be translated from preclinical to clinical platforms will facilitate the identification and the assessment of efficacy of neuroprotective therapeutic compounds to treat CNS diseases. Translational neuroimaging can provide information on brain morphology and function in preclinical models of CNS diseases, healthy human subjects and patients. Amongst the variety of imaging methods used for understanding and treating brain diseases are PET, SPECT, X-ray/computed tomography, near-infrared optical imaging and magnetic resonance imaging.

Normal laboratory rodents may be used for *in vivo* biodistribution experiments focussing on CNS penetration and washout of radiotracers, while (transgenic) disease models may form the basis for *ex vivo* autoradiography to assess binding of probes to the targeted molecule on brain slices, or of course the *in vivo* evaluation of tracer retention in brain.

1.4.1 Imaging in Schizophrenia

Advances in the development and applications of neurochemical brain imaging have improved the ability to study the neurochemistry of the living brain in psychiatric disorders. In particular, PET and SPECT have been used to determine neurochemical substrates of schizophrenia and to uncover the mechanism of action of antipsychotic medications. The growing availability of radiotracers for monoaminergic neurotransmitter synthesis, transporters and receptors has enabled the evaluation of hypotheses regarding neurotransmitter function in schizophrenia derived from preclinical and clinical observations. Clinical schizophrenia PET-/SPECT-based trials study (1) abnormalities in indices of neurotransmitter systems with an established role in schizophrenia in patients versus controls, (2) new tools to study other neurotransmitter systems or potential biomarkers (e.g. inflammation markers) (Doorduin et al. 2009, 2010) (Figs. 1.3 and 1.4) and (3) characterisation of target occupancy by antipsychotic drugs, as well as its relationship to efficacy and side effects (Urban and Abi-Dargham 2010; Kirino et al. 2017); see also http://www.clinicaltrials.gov.

A variety of PET tracers has been used to identify brain abnormalities in schizophrenia based on kinetic modelling. The most consistent early findings showed a difference in the dopamine content in the prefrontal cortex, anterior cingulate gyrus
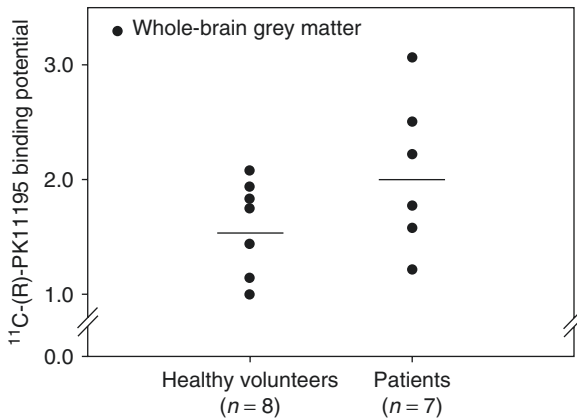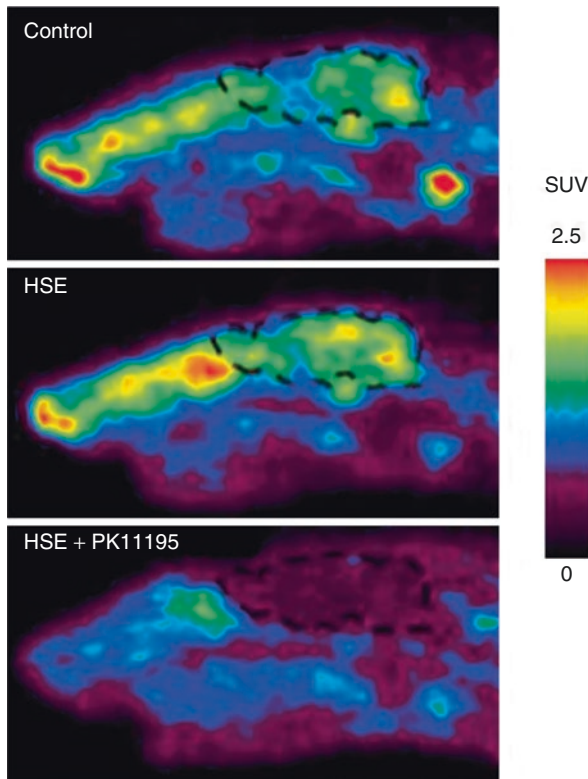
Fig. 1.3 Binding potential of the PET marker *(R)*-[^{11}C]-PK11195 that binds to translocator protein (TSPO), a biomarker to study activated microglia cells, in healthy volunteers and schizophrenia patients. All schizophrenia patients met the DSM-IV criteria of schizophrenia spectrum disorders. Each dot represents an individual subject, and horizontal lines represent mean values. Whole-brain grey matter binding potential was 30% higher in patients versus healthy controls, although this difference did not reach statistical significance (Reprinted from (Doorduin et al. 2009); Doorduin et al. (2009) with permission. Copyright@2009 Society of Nuclear Medicine and Molecular Imaging)

and hippocampus between healthy controls and schizophrenia patients. In addition, a higher density of D2 receptors in the striatum and neural brain dysconnectivity was observed (Patel et al. 2010), while [^{11}C]SCH23390 and [^{11}C]N-methyl-spiperone to map D1/D2 receptors identified reduced D1R densities in the prefrontal cortex (Okubo et al. 1997). Dopaminergic abnormalities have been further substantiated in a large number of PET/SPECT-based studies in recent years (Kambeitz et al. 2014; Weinstein et al. 2017; Kim 2018; Avram et al. 2019).

In addition, other neurotransmitter systems, including the serotonergic (Milak et al. 2008; Huang et al. 2010; Herth et al. 2016; Petersen et al. 2016), and the cholinergic system (Horti et al. 2010; Wong 2018), are being targeted in more recent years by PET/SPECT imaging in line with the elaboration of the neurochemical hypothesis in schizophrenia as discussed in Sect. 1.2.3.1. Aetiology and Symptomatology of Schizophrenia.

There have been some PET studies of the behavioural sensitisation to psychostimulant drugs in dogs (Nakamura et al. 1997), rhesus monkeys (Castner 2000), and rats (Kilbourn and Domino 2011). Given the presumed contribution of excitatory NMDA-linked neurotransmission to schizophrenia, PET/SPECT has scarcely been used for investigations of NMDA perturbations in experimental animals, including rats (Reith et al. 1998), cats (Vollenweider et al. 2000), and monkeys (Tsukada et al. 2000; van Berckel et al. 2006). Albeit the application of microPET/SPECT in schizophrenia remains currently still limited, insight in disease processes underlying schizophrenia, with of course an important focus on the dopaminergic aspects, lay at the basis of the development of novel genetically modified rodent

Fig. 1.4 Many neurological and psychiatric disorders are associated with neuroinflammation, which can be studied using PET markers like *(R)*-[^{11}C]-PK11195 that binds to translocator protein (TSPO), a biomarker to study activated microglia cells. The sensitivity of *(R)*-[^{11}C]-PK11195 may however be insufficient to visualise mild neuroinflammation. [^{11}C]-N-(2,5-dimethoxybenzyl)-N-(4-fluoro-2-phenoxyphenyl)-acetamide, [^{11}C]-DAA1106, proposed as a potentially more sensitive neuroinflammation tracer, was evaluated in a rat model of herpes encephalitis (*HSE*). Sagittal view of the head of a control rat (*control*), a rat with HSE and a HSE rat pretreated with 5 mg/kg of unlabeled PK11195 (*HSE + PK11195*), in which the brain is delineated by a dashed line. The images represent tracer uptake between 30 and 60 min after injection of [^{11}C]-DAA1106 (44 ± 14 MBq). Images show a high uptake of [^{11}C]-DAA1106 in the brainstem. Pretreatment with unlabeled PK11195 resulted in effective blocking of [^{11}C]-DAA1106 uptake. *In vivo* uptake, however, did not significantly differ between control and HSE rats. [^{11}C]-DAA1106 may not be an ideal tracer to perform longitudinal PET studies in small animals to study the role of neuroinflammation in neurological and psychiatric disorders (Reprinted from (Doorduin et al. 2010); Doorduin et al. (2010) with permission. Copyright@2010 Elsevier)

models. In an interesting bedside-to-bench approach, the enhanced D2 stimulation in the dorsal striatum formed the basis for the development of the D2R-OE mouse model designed to overexpress dopaminergic D2 receptors in dorsal striatum during development, thereby modelling the temporal and regional-specific state of D2 hyperstimulation in schizophrenia (Abi-Dargham 2020). Interestingly, in a non-human primate model of maternal immune activation showing schizophrenia-like

aberrant behavior, PET imaging indicated increased striatal dopamine in late ado-lescence—a hallmark molecular biomarker of schizophrenia (Bauman et al. 2019).

This recent moving into gear with the development of various relevant schizo-phrenia animal models will undoubtedly boost valuable insights into disease-causative molecular and cellular pathology of schizophrenia and other psychiatric disorders, as well as the application of these models for the evaluation of novel PET/SPECT tracers.

1.4.2 Imaging in AD

Aβ plaque-bearing mice are obviously a potentially interesting tool for the develop-ment of PET/SPECT tracers aiming at the visualisation of amyloid plaques and/or other AD-typical pathological alterations. With the development of a specific tracer that reliably visualises AD pathology in an amyloidosis mouse model, small animal imaging techniques may be used to assess treatment efficacy of anti-Aβ leads in the AD drug discovery pipeline. More in general, the impact of PET/SPECT imaging on drug discovery can also be situated at various levels, including validation of mechanisms of drug localisation, establishing transport efficiency of a drug to the target, establishing drug occupancy of saturable receptor sites and determining half-time of occupancy of the drug (Eckelman 2003).

2-Deoxy-2(^{18}F)fluoro-D-glucose-based PET, [^{18}F]FDG-PET, is a sensitive surro-gate marker for AD diagnosis. A typical activity pattern shows decreased metabo-lism in the posterior cingulate and temporoparietal and prefrontal association cortex, while metabolism is maintained in the primary sensorimotor cortex and basal gan-glia. Changes in [^{18}F]FDG-PET are evident prior to the onset of cognitive symptoms in AD-related mutation carriers. Moreover, [^{18}F]FDG-PET has predictive power for conversion of MCI to AD (Zhang et al. 2012). However, given the lack of specificity of [^{18}F]FDG-PET for AD, much efforts are directed at the development of Aβ-specific radioligands. [N-methyl-11C]2-(4′-methylaminophenyl)-6-hydroxybenzothiazole, a fluorescent analogue of thioflavin T better known as Pittsburgh compound B, [^{11}C]PiB-PET, emerged as the lead Aβ-specific PET ligand to proceed to clinical development. [^{11}C]PiB-PET studies have demonstrated significant regional reten-tion of radioactive signal in CNS areas with extensive plaque burden in AD brain, including the frontal, parietal and lateral temporal cortex and the striatum (Klunk et al. 2004; Price et al. 2005). [^{18}F]FDDNP (2-(1-{6-[(2-[fluorine-18]fluoroethyl) (methyl)amino]-2-naphthyl}-ethylidene)malononitrile) is the only currently avail-able PET radiotracer to image neurofibrillary tangles, besides Aβ aggregates, and it is also the only radiotracer to visualise AD pathology in the hippocampal region of living humans (Shin et al. 2011).

Mid-2012, [^{18}F]AV-45 (Amyvid™) became the first FDA-approved PET ligand. The search for other Aβ-binding radiopharmaceuticals is still ongoing, and several [^{18}F]- and [^{11}C]-labelled tracers have been developed that underwent or are still undergoing extensive clinical evaluation. Besides amyloid-targeting tracers, also tau PET as a biomarker of tau pathology in AD is being scrutinized (Okamura et al. 2014; Maass et al. 2017). More information concerning current clinical trials in AD

with PET and/or SPECT imaging can be obtained at http://www.clinicaltrials.gov, while some excellent reviews summarize the state-of-the-art in radioligand-based imaging in AD (Koric et al. 2016; Cistaro et al. 2018; Femminella et al. 2018), as well as in several interesting chapters included in this book series.

Based on often disappointing PET imaging results in AD mouse models (Klunk et al. 2005; Toyama et al. 2005; Kuntner et al. 2009; Luo et al. 2012), the usefulness of currently available transgenic mouse models for the identification and optimisation of imaging tracers is somewhat controversial. The spatial resolution of PET is often insufficient to allow reliable estimation of Aβ-specific tracer binding. Repeated PET imaging in the same mouse, however, may be applied to study the evolution of plaque burden and may be useful to complement *ex vivo* autoradiographic radionuclide imaging of brain slices, which provides sufficient spatial resolution for assessment of specific tracer binding but of course lacks the possibility of time-linked observations (Wirths et al. 2009; Teipel et al. 2011). Substantial differences in pharmacokinetics and pharmacodynamics are often observed between animals and humans for CNS targeted molecules (Carpenter Jr et al. 2009). Moreover, the detection of amyloid plaques often depends on the presence of one specific Aβ subtype that may not be present in the same proportion in mouse versus man, or in different transgenic amyloidosis mouse models, as is the case for AβN3-pyroglutamate recognised by [^{11}C]PiB (Maeda et al. 2007). In addition, the presence of high-affinity binding sites may differ between species, as well as between the sources of Aβ even within the same species (Klunk et al. 2005; Rabinovici and Jagust 2009; Rosen et al. 2011). Latter hurdle may be overcome, however, by increasing the specific activity of [^{11}C]PiB to afford an Aβ-specific binding signal in transgenic mouse brain that could be quantified with small animal PET (Maeda et al. 2007) (Fig. 1.5).

Despite differences between humans and animals, the development of new radioligands for AD brain lesions still strongly relies on preclinical tests in transgenic amyloidosis mice. For example, the [^{18}F]AV-45 ligand, which allows significant discrimination between AD patients and healthy control individuals (Wong et al. 2010), has first been successfully tested in transgenic amyloidosis mice (Choi et al. 2009). Noteworthy is the fact that given the (relative) similarity in brain structure, as well as important protein homology (Van Dam and De Deyn 2017; Podlisny et al. 1991), non-human primates still also play an important role in the preclinical evolution of radiopharmaceuticals with regard to safety, kinetics, selectivity and specificity.

The most important advantage of (micro)PET imaging over (micro)SPECT is that of exhibiting a much higher sensitivity, while (micro)SPECT offers the possibility to widen the observational time window (based on the longer half-life of single-photon emitters) thus allowing the observation of biological processes *in vivo* several hours or days after administration of the labelled compound. By using different energy radioisotopes conjugated to different molecular targets, (micro)SPECT has the advantage over (micro)PET in being able to image several molecular events simultaneously. *In vivo* evaluation of novel SPECT tracers in AD rodent models is however limited. Most studies evaluate the *in vivo* biodistribution and brain penetration of newly developed SPECT tracers in normal mice and Aβ-specific
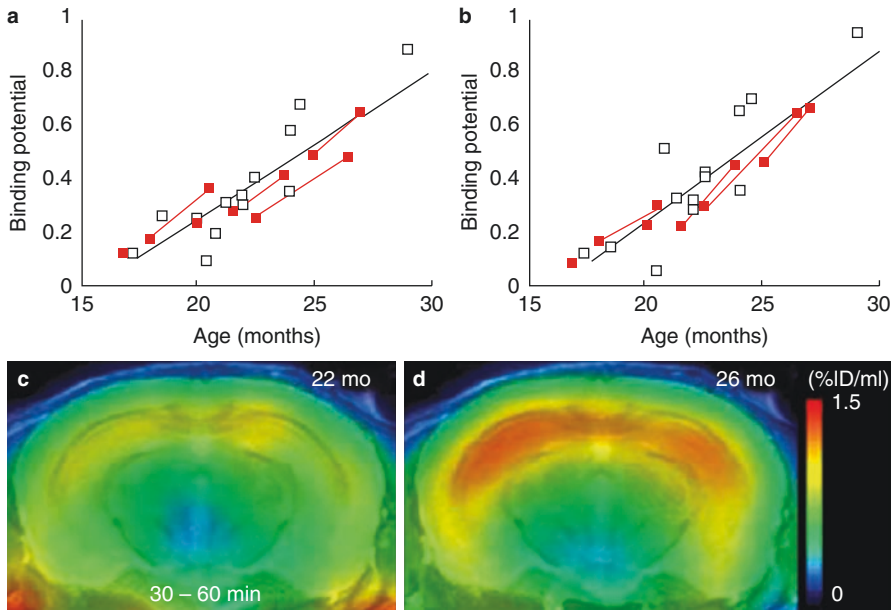
Fig. 1.5 Ability of mouse PET to capture age-dependent evolution of brain amyloidosis. (**a**, **b**) Represent scatter plots of binding potential of N-[^{11}C]methyl-2-(4-methylaminophenyl)-6-hydroxybenzothiazole (or [^{11}C]PIB for 'Pittsburgh compound B') versus age in the hippocampus (**a**) and neocortex (**b**) of Tg2576 mice, with the correlation of the two parameters being statistically significant in both regions. Black lines represent regression, and red elements indicate longitudinal analysis of the same individuals ($n = 5$). (**c**, **d**) Represent PET images to illustrate [^{11}C]PIB's substantial increase in tracer binding in the hippocampal formations of the same animal at the age of 22 (**c**) and 26 months (**d**), indicating progression of amyloid accumulation. Images were generated by averaging dynamic scan data at 30–60 min after tracer injection and were merged onto an MRI template. *mo* month (Reprinted from (Maeda et al. 2007); Maeda et al. (2007) with permission. Copyright@2007 Society for Neuroscience)

binding via *ex vivo* autoradiography on brain slices or brain homogenates of plaque-bearing rodents, often in addition to post-mortem brain tissue (extracts) of AD patients (Cui et al. 2011; Cheng et al. 2012; Martins et al. 2013; Fuchigami 2014; Molavipordanjani et al. 2019). Few published studies, however, also compared tracer retention in plaque-bearing versus control animals (Opazo et al. 2006; Ono et al. 2013; Chen et al. 2015; Kiritsis et al. 2017; Sagnou et al. 2019), and few examples of tau pathology-targeting SPECT tracer development based on tau rodent models (ex vivo or in vivo) have been published up to date (Ono 2016; Watanabe 2017).

MicroSPECT imaging is not only useful for tracer development and evaluation, but may also be used to characterize novel biological targets, with the aim to elevate the accuracy of AD diagnosis. Since amyloid or tau-related neuropathological changes may also occur in cognitively normal individuals (Johnson et al. 2013), there is a need for additional and more accurate biomarkers, or biomarker combinations. As butyrylcholinesterase (BuChE) becomes associated with amyloid and
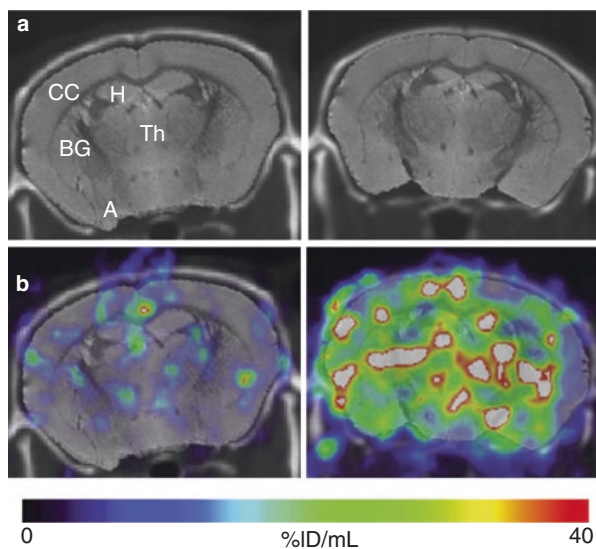
Fig. 1.6 Comparison of BuChE activity at mid coronal level in specific brain regions of WT (left) and 5× FAD (right) mice detected with radiotracer SPECT analysis. (**a**) CT with coregistered MR. (**b**) SPECT images acquired at 4-minute post-injection with coregistered CT/MR and ROIs. Marked retention in the $5 \times$ FAD cerebral cortex is evident in the $5 \times$ FAD brain compared to WT with less difference in retention evident in amygdala, hippocampus, basal ganglia, and thalamus. Image intensities expressed as %ID/mL and set to a common scale of 0%ID/mL–40%ID/mL. Abbreviations: A, amygdala; BuChE, butyrylcholinesterase; BG, basal ganglia; CC, cerebral cortex; CT, computed tomography; H, hippocampal formation; MR, magnetic resonance; ROIs, regions of interest; SPECT, single photon emission computed tomography; Th, thalamus;WT, wild-type; 5 × FAD, B6SJL-Tg(APPSwFlLon, PSEN1*M146 L*L286 V) 6799Vas/Mmjax mouse strain. (Adapted from (DeBay et al. 2017); DeBay et al. (2017) Alzheimers Dement (N Y) 3:166–176 under the CC-BY license 4.0 (http://creativecommons.org/licenses/by/4.0). Copyright © 2017 DeBay, Reid, Pottie, Martin, Bowen and Darvesh)

tau deposits in AD, BuChE pathology in the cerebral cortex, a region of scant BuChE activity in healthy brain, was targeted by N-methylpiperidin-4-yl 4-[123I]iodobenzoate, a BuChE radiotracer, in the 5 × FAD mouse model. Tracer retention was consistently higher in the 5 × FAD mouse versus healthy control animals, and differences were particularly evident in the cerebral cortex, paving the way for further investigation of BuChE-specific radiotracers as AD diagnostic agents (DeBay et al. 2017) (Fig. 1.6).

1.5 Conclusion

Patho(physio)logical alterations in rodent models of human disease are usually studied using invasive techniques, requiring sacrificing of the animals. This approach implies, amongst other, the use of a large number of animals to reach statistical significance, high associated (labour) costs and follow-up or longitudinal studies are impossible in the same animal. Recent improvements in molecular imaging

technologies employed to image small animal models, at least partially, overcome these limitations. Small animal imaging is increasingly recognised as an important facet of preclinical and translational (neuroscience) research. Perhaps most significant amongst the clear advantages of imaging experimental animals is that physiology, pathology and novel phenotypes can be understood in the most relevant milieu—in an intact, living system. Moreover, longitudinal imaging studies will allow researchers to gain more insight into the (developmental) time course of the modelled endophenotypes. The nuclear imaging modalities PET and SPECT can provide the sensitivities required to obtain the same physiological imaging acuity in small animals as can be obtained in humans, which will greatly facilitate the translation of preclinical studies to applications in the clinic. Valid animal models provide essential tools for the preclinical development of novel PET/SPECT tracers, be it via *ex vivo* autoradiography or *in vivo* tracer biodistribution and brain penetration. Besides in the framework of tracer development and evaluation, microPET/SPECT imaging support the identification of novel biological targets to elevate the accuracy of AD diagnosis.

References

Abi-Dargham A (2020) From "bedside" to "bench" and back: A translational approach to studying dopamine dysfunction in schizophrenia. Neurosci Biobehav Rev 110:174–179

Aghajanian GK, Marek GJ (2000) Serotonin model of schizophrenia: emerging role of glutamate mechanisms. Brain Res Brain Res Rev 31:302–312

Alonso JR, HS U, Amaral DG (1996) Cholinergic innervation of the primate hippocampal formation: II. Effects of fimbria/fornix transection J Comp Neurol 375:527–551

Amann LC, Gandal MJ, Halene TB et al (2010) Mouse behavioral endophenotypes for schizophrenia. Brain Res Bull 83:147–161

American Psychiatric Association (2000) Diagnostic and statistical manual of mental health disorders, 4th edn. American Psychiatric Publishing, Washington, DC. https://doi.org/10.1176/appi.books.9780890423349

American Psychiatric Association (2013) Diagnostic and statistical manual of mental disorders, American Psychiatric Publishing, 5th edn, Washington, DC. https://doi.org/10.1176/appi.books.9780890425596

Anderzhanova E, Kirmeier T, Wotjak CT (2017) Animal models in psychiatric research: The RDoC system as a new framework for endophenotype-oriented translational neuroscience. Neurobiol Stress 25:47–56

Andiné P, Widermark N, Axelsson R et al (1999) Characterization of MK-801-induced behavior as a putative rat model of psychosis. J Pharmacol Exp Ther 290:1393–1408

Andreasen NC (1995) Symptoms, signs, and diagnosis of schizophrenia. Lancet 346:477–481

Andreasson KI, Savonenko A, Vidensky S et al (2001) Age-dependent cognitive deficits and neuronal apoptosis in cyclooxygenase-2 transgenic mice. J Neurosci 21:8198–8209

Ashcroft AE (2010) Mass spectrometry and the amyloid problem–how far can we go in the gas phase? J Am Soc Mass Spectrom 21:1087–1096

Avram M, Brandl F, Cabello J et al (2019) Reduced striatal dopamine synthesis capacity in patients with schizophrenia during remission of positive symptoms. Brain 142:1813–1826

Ayhan Y, Abazyan B, Nomura J, Kim R et al (2011) Differential effects of prenatal and postnatal expressions of mutant human DISC1 on neurobehavioral phenotypes in transgenic mice: evidence for neurodevelopmental origin of major psychiatric disorders. Mol Psychiatry 16:293–306

Baker M (2011) Animal models: inside the minds of mice and men. Nature 475:123–128

Banerjee A, Macdonald ML, Borgmann-Winter KE et al (2010) Neuregulin 1-erbB4 pathway in schizophrenia: from genes to an interactome. Brain Res Bull 83:132–139

Barr AM, Fish KN, Markou A et al (2008) Heterozygous reeler mice exhibit alterations in sensorimotor gating but not presynaptic proteins. Eur J Neurosci 27:2568–2574

Basak JM, Holtzman DM (2011) APP-based transgenic models: the PDAPP model. In: De Deyn PP, Van Dam D (eds) Animal models of dementia, 1st edn. Springer Science + Business Media, New York

Bauman MD, Lesh TA, Rowland DJ et al (2019) Preliminary evidence of increased striatal dopamine in a nonhuman primate model of maternal immune activation. Transl Psychiatry 9:135

Belzung C, Philippot P (2007) Anxiety from a phylogenetic perspective: is there a qualitative difference between human and animal anxiety? Neural Plast 2007:59676

Berlanga ML, Price DL, Phung BS et al (2011) Multiscale imaging characterization of dopamine transporter knockout mice reveals regional alterations in spine density of medium spiny neurons. Brain Res 1390:41–49

Billings LM, Oddo S, Green KN et al (2005) Intraneuronal abeta causes the onset of early Alzheimer's disease-related cognitive deficits in transgenic mice. Neuron 45:675–688

Bleiholder C, Dupuis NF, Wyttenbach T et al (2011) Ion mobility-mass spectrometry reveals a conformational conversion from random assembly to β-sheet in amyloid fibril formation. Nat Chem 3:172–177

Bons N, Mestre N, Ritchie K et al (1994) Identification of amyloid beta protein in the brain of the small, short-lived lemurian primate microcebus murinus. Neurobiol Aging 15:215–220

Braak H, Braak E, Strothjohann M (1994) Abnormally phosphorylated tau protein related to the formation of neurofibrillary tangles and neuropil threads in the cerebral cortex of sheep and goat. Neurosci Lett 171:1–4

Bray NJ (2008) Gene expression in the etiology of schizophrenia. Schizophr Bull 34:412–418

Brigman JL, Padukiewicz KE, Sutherland ML et al (2006) Executive functions in the heterozygous reeler mouse model of schizophrenia. Behav Neurosci 120:984–998

Brunzell DH, McIntosh JM (2012) Alpha7 nicotinic acetylcholine receptors modulate motivation to self-administer nicotine: implications for smoking and schizophrenia. Neuropsychopharmacology 37:1134–1143

Buccafusco JJ (2008) Methods of behavior analysis in neuroscience. CRC Press/Taylor & Francis Group, Boca Raton

Buka SL, Cannon TD, Torrey EF, Collaborative Study Group on the Perinatal Origins of Severe Psychiatric Disorders et al (2008) Maternal exposure to herpes simplex virus and risk of psychosis among adult offspring. Biol Psychiatry 63:809–815

Büki A, Horvath G, Benedek G et al (2019) Impaired GAD1 expression in schizophrenia-related WISKET rat model with sex-dependent aggressive behavior and motivational deficit. Genes Brain Behav 18:e12507

Bullock AE, Slobe BS, Vazquez V et al (1997) Inbred mouse strains differ in the regulation of startle and prepulse inhibition of the startle response. Behav Neurosci 111:1353–1360

Bunsey M, Eichenbaum H (1996) Conservation of hippocampal memory function in rats and humans. Nature 379:255–257

Butterfield DA, Poon HF (2005) The senescence-accelerated prone mouse (SAMP8): a model of age-related cognitive decline with relevance to alterations of the gene expression and protein abnormalities in Alzheimer's disease. Exp Gerontol 40:774–783

Capsoni S, Ugolini G, Comparini A et al (2000) Alzheimer-like neurodegeneration in aged anti-nerve growth factor transgenic mice. Proc Natl Acad Sci U S A 97:6826–6831

Cardno AG, Marshall EJ, Coid B et al (1999) Heritability estimates for psychotic disorders: the Maudsley twin psychosis series. Arch Gen Psychiatry 56:162–168

Carpenter AP Jr, Pontecorvo MJ, Hefti FF et al (2009) The use of the exploratory IND in the evaluation and development of 18F-PET radiopharmaceuticals for amyloid imaging in the brain: a review of one company's experience. Q J Nucl Med Mol Imaging 53:387–393

Carpenter WT, Koenig JI (2008) The evolution of drug development in schizophrenia: past issues and future opportunities. Neuropsychopharmacology 33:2061–2079

Castañé A, Theobald DE, Robbins TW (2010) Selective lesions of the dorsomedial striatum impair serial spatial reversal learning in rats. Behav Brain Res 210:74–83

Castellani RJ, Alexiev BA, Phillips D et al (2007) Microscopic investigations in neurodegenerative diseases. In: Méndez-Vilas A, Díaz J (eds) Modern research and educational topics in microscopy. Formatex, Badajoz

Castner SA, al-Tikriti MS, Baldwin RM et al (2000) Behavioral changes and [123I]IBZM equilibrium SPECT measurement of amphetamine-induced dopamine release in rhesus monkeys exposed to subchronic amphetamine. Neuropsychopharmacology 22:4–13

Castner SA, Goldman-Rakic PS (1999) Long-lasting psychotomimetic consequences of repeated low-dose amphetamine exposure in rhesus monkeys. Neuropsychopharmacology 20:10–28

Castner SA, Goldman-Rakic PS (2003) Amphetamine sensitization of hallucinatory-like behaviors is dependent on prefrontal cortex in nonhuman primates. Biol Psychiatry 54:105–110

Caviness VS Jr (1976) Patterns of cell and fiber distribution in the neocortex of the reeler mutant mouse. J Comp Neurol 170:435–447

Chen CJ, Bando K, Ashino H et al (2015) In vivo SPECT imaging of amyloid-β deposition with radioiodinated imidazo[1,2-a]pyridine derivative DRM106 in a mouse model of Alzheimer's disease. J Nucl Med 56:120–126

Cheng Y, Ono M, Kimura H et al (2012) Technetium-99m labeled pyridyl benzofuran derivatives as single photon emission computed tomography imaging probes for β-amyloid plaques in Alzheimer's brains. J Med Chem 55:2279–2286

Choi SR, Golding G, Zhuang Z et al (2009) Preclinical properties of 18F-AV-45: a PET agent for Abeta plaques in the brain. J Nucl Med 50:1887–1894

Chourbaji S, Zacher C, Sanchis-Segura C et al (2005) Learned helplessness: validity and reliability of depressive-like states in mice. Brain Res Brain Res Protoc 16:70–78

Cistaro A, Alongi P, Caobelli F, Cassalia L (2018) Radiotracers for Amyloid Imaging in Neurodegenerative Disease: State-of-the-Art and Novel Concepts. Curr Med Chem 25:3131–3140

Clapcote SJ, Roder JC (2006) Deletion polymorphism of Disc1 is common to all 129 mouse substrains: implications for gene-targeting studies of brain function. Genetics 173:2407–2410

Cohen BD, Rosenbaum G, Luby ED et al (1962) Comparison of phencyclidine hydrochloride (Sernyl) with other drugs. Simulation of schizophrenic performance with phencyclidine hydrochloride (Sernyl), lysergic acid diethylamide (LSD-25), and amobarbital (Amytal) sodium; II. Symbolic and sequential thinking. Arch Gen Psychiatry 6:395–401

Cohen RM, Rezai-Zadeh K, Weitz TM et al (2013 Apr 10) (2013) A transgenic Alzheimer rat with plaques, tau pathology, behavioral impairment, oligomeric aβ, and frank neuronal loss. J Neurosci 33(15):6245–6256

Colton CA, Wilcock DM, Wink DA et al (2008) The effects of NOS2 gene deletion on mice expressing mutated human AbetaPP. J Alzheimers Dis 15:571–587

Contestabile A (2011) The history of the cholinergic hypothesis. Behav Brain Res 221:334–340

Corcoba A, Steullet P, Duarte JM et al (2015) Glutathione deficit affects the integrity and function of the Fimbria/Fornix and anterior commissure in mice: relevance for Schizophrenia. Int J Neuropsychopharmacol 19:pyv110

Cork LC, Powers RE, Selkoe DJ et al (1988) Neurofibrillary tangles and senile plaques in aged bears. J Neuropathol Exp Neurol 47:629–641

Crawley J (2000) What's wrong with my mouse? Behavioral phenotyping of transgenic and knockout mice. Wiley-Liss, Wilmington

Crawley JN, Belknap JK, Collins A et al (1997) Behavioral phenotypes of inbred mouse strains: implications and recommendations for molecular studies. Psychopharmacology 132:107–124

Creese I, Iversen SD (1973) Blockage of amphetamine induced motor stimulation and stereotypy in the adult rat following neonatal treatment with 6-hydroxydopamine. Brain Res 55:369–382

Cui M, Ono M, Kimura H et al (2011) Radioiodinated benzimidazole derivatives as single photon emission computed tomography probes for imaging of β-amyloid plaques in Alzheimer's disease. Nucl Med Biol 38:313–320

Cummings BJ, Head E, Ruehl W et al (1996) The canine as an animal model of human aging and dementia. Neurobiol Aging 17:259–268

Cummings BJ, Su JH, Cotman CW et al (1993) Beta-amyloid accumulation in aged canine brain: a model of early plaque formation in Alzheimer's disease. Neurobiol Aging 14:547–560

D'Hooge R, De Deyn PP (2001) Applications of the Morris water maze in the study of learning and memory. Brain Res Brain Res Rev 36:60–90

Davies P, Maloney AJ (1976) Selective loss of central cholinergic neurons in Alzheimer's disease. Lancet 2:1403

De Deyn PP, Katz IR, Brodathy H et al (2005) Management of agitation, aggression, and psychosis associated with dementia: a pooled analysis including three randomized, placebo-controlled double-blind trials in nursing home residents treated with risperidone. Clin Neurol Neurosurg 107:497–508

De Deyn PP, Van Dam D (2011) General introduction to animal models of human conditions. In: De Deyn PP, Van Dam D (eds) Animal models of dementia, 1st edn. Springer Science + Business Media, New York

Deacon R (2011) APP-based transgenic models: the Tg2576 model. In: De Deyn PP, Van Dam D (eds) Animal models of dementia, 1st edn. Springer Science + Business Media, New York

DeBay DR, Reid GA, Pottie IR et al (2017) Targeting butyrylcholinesterase for preclinical single photon emission computed tomography (SPECT) imaging of Alzheimer's disease. Alzheimers Dement (N Y) 3:166–176

Desbonnet L, Waddington JL, O'Tuathaigh CM (2009) Mutant models for genes associated with schizophrenia. Biochem Soc Trans 37:308–312

Dieckmann M, Freudenberg F, Klein S et al (2007) Disturbed social behavior and motivation in rats selectively bred for deficient sensorimotor gating. Schizophr Res 97:250–253

Doorduin J, de Vries EF, Willemsen AT et al (2009) Neuroinflammation in schizophrenia-related psychosis: a PET study. J Nucl Med 50:1801–1807

Doorduin J, Klein HC, de Jong JR et al (2010) Evaluation of [11C]-DAA1106 for imaging and quantification of neuroinflammation in a rat model of herpes encephalitis. Nucl Med Biol 37:9–15

Drew LJ, Stark KL, Fénelon K et al (2011) Evidence for altered hippocampal function in a mouse model of the human 22q11.2 microdeletion. Mol Cell Neurosci 47:293–305

Dringenberg HC (2000) Alzheimer's disease: more than a 'cholinergic disorder'—evidence that cholinergic–monoaminergic interactions contribute to EEG slowing and dementia. Behav Brain Res 115:235–249

Dworkin RH, Opler LA (1992) Simple schizophrenia, negative symptoms, and prefrontal hypodopaminergia. Am J Psychiatry 149:1284–1285

Ebert U, Kirch W (1998) Scopolamine model of dementia: electroencephalogram findings and cognitive performance. Eur J Clin Investig 28:944–949

Eckelman WC (2003) The use of PET and knockout mice in the drug discovery process. Drug Discov Today 8:404–410

Ellenbroek BA, Cools AR (1990) Animal models with construct validity for schizophrenia. Behav Pharmacol 1:469–490

Ellman GL, Courtney KD, Andres J Jr et al (1961) A new and rapid colorimetric determination of acetylcholinesterase activity. Biochem Pharmacol 7:88–95

Erickson CA, Barnes CA (2003) The neurobiology of memory changes in normal aging. Exp Gerontol 38:61–69

Estapé N, Steckler T (2002) Cholinergic blockade impairs performance in operant DNMTP in two inbred strains of mice. Pharmacol Biochem Behav 72:319–334

Fajnerová I, Rodriguez M, Levčík D et al (2014) A virtual reality task based on animal research - spatial learning and memory in patients after the first episode of schizophrenia. Front Behav Neurosci 8:157

Falconer DS (1951) Two new mutants, Trembler and 'Reeler', with neurological actions in the house mouse. J Genetics 50:182–201

Farris W, Mansourian S, Chang Y et al (2003) Insulin-degrading enzyme regulates the levels of insulin, amyloid beta-protein, and the beta-amyloid precursor protein intracellular domain in vivo. Proc Natl Acad Sci U S A 100:4162–4167

Featherstone RE, Kapur S, Fletcher PJ (2007) The amphetamine-induced sensitized state as a model of schizophrenia. Prog Neuro-Psychopharmacol Biol Psychiatry 31:1556–1571

Featherstone RE, Rizos Z, Kapur S et al (2008) A sensitizing regimen of amphetamine that disrupts attentional set-shifting does not disrupt working or long-term memory. Behav Brain Res 189:170–179

Femminella GD, Thayanandan T, Calsolaro V et al (2018) Imaging and Molecular Mechanisms of Alzheimer's Disease: A Review. Int J Mol Sci 19. pii: E3702

Flood DG, Zuvich E, Marino MJ et al (2011) Prepulse inhibition of the startle reflex and response to antipsychotic treatments in two outbred mouse strains in comparison to the inbred DBA/2 mouse. Psychopharmacology 215:441–454

Floresco SB, Zhang Y, Enomoto T (2009) Neural circuits subserving behavioral flexibility and their relevance to schizophrenia. Behav Brain Res 204:396–409

Fone KC, Porkess MV (2008) Behavioural and neurochemical effects of post-weaning social isolation in rodents-relevance to developmental neuropsychiatric disorders. Neurosci Biobehav Rev 32:1087–1102

Fonnum F (1975) A rapid radiochemical method for the determination of choline acetyltransferase. J Neurochem 24:407–409

Frautschy SA, Yang F, Calderón L et al (1996) Rodent models of Alzheimer's disease: rat A beta infusion approaches to amyloid deposits. Neurobiol Aging 17:311–321

Freichel C, Neumann M, Ballard T et al (2007) Age-dependent cognitive decline and amygdala pathology in alpha-synuclein transgenic mice. Neurobiol Aging 28:1421–1435

Freyberg Z, Ferrando SJ, Javitch JA (2010) Roles of the Akt/GSK-3 and Wnt signaling pathways in schizophrenia and antipsychotic drug action. Am J Psychiatry 167:388–396

Fuchigami T, Yamashita Y2, Haratake M et al (2014) Synthesis and evaluation of ethyleneoxylated and allyloxylated chalcone derivatives for imaging of amyloid β plaques by SPECT. Bioorg Med Chem 22:2622–2628

Fuster JM (1980) The prefrontal cortex. Anatomy, physiology, and neuropsychology of the frontal lobe. Raven Press, New York

Games D, Adams D, Alessandrini R et al (1995) Alzheimer-type neuropathology in transgenic mice overexpressing V717F beta-amyloid precursor protein. Nature 373:523–527

Gayle DA, Beloosesky R, Desai M et al (2004) Maternal LPS induces cytokines in the amniotic fluid and corticotropin releasing hormone in the fetal rat brain. Am J Physiol Regul Integr Comp Physiol 286:R1024–R1029

Gearing M, Rebeck GW, Hyman BT et al (1994) Neuropathology and apolipoprotein E profile of aged chimpanzees: implications for Alzheimer's disease. Proc Natl Acad Sci U S A 91:9382–9386

Gearing M, Tigges J, Mori H et al (1997) β-amyloid (Aβ) deposition in the brains of aged orangutans. Neurobiol Aging 18:139–146

Gejman PV, Sanders AR, Kendler KS (2011) Genetics of schizophrenia: new findings and challenges. Annu Rev Genomics Hum Genet 12:121–144

Gerlai R (2010) Zebrafish antipredatory responses: a future for translational research? Behav Brain Res 207:223–231

Geula C, Nagykery N, Wu CK (2002) Amyloid-beta deposits in the cerebral cortex of the aged common marmoset (Callithrix jacchus): incidence and chemical composition. Acta Neuropathol 103:48–58

Girard SD, Baranger K, Gauthier C et al (2013) Evidence for early cognitive impairment related to frontal cortex in the 5XFAD mouse model of Alzheimer's disease. J Alzheimers Dis 33:781–796

Glahn DC, Thompson PM, Blangero J (2007) Neuroimaging endophenotypes: strategies for finding genes influencing brain structure and function. Hum Brain Mapp 28:488–501

Glenn MJ, Nesbitt C, Mumby DG (2003) Perirhinal cortex lesions produce variable patterns of retrograde amnesia in rats. Behav Brain Res 141:183–193

Glowinski J, Axelrod J, Iversen LL (1966) Regional studies of catecholamines in the rat brain. IV. Effects of drugs on the disposition and metabolism of H3-norepinephrine and H3-dopamine. J Pharmacol Exp Ther 153:30–41

Glowinski J, Iversen L (1966a) Regional studies of catecholamines in the rat brain. 3. Subcellular distribution of endogenous and exogenous catecholamines in various brain regions. Biochem Pharmacol 15:977–987

Glowinski J, Iversen LL (1966b) Regional studies of catecholamines in the rat brain. I. The disposition of [3H]norepinephrine, [3H]dopamine and [3H]dopa in various regions of the brain. J Neurochem 13:655–669

Gogos A, Bogeski M, van den Buuse M (2008) Role of serotonin-1A receptors in the action of antipsychotic drugs: comparison of prepulse inhibition studies in mice and rats and relevance for human pharmacology. Behav Pharmacol 19:548–561

Gong Y, Chang L, Viola KL et al (2003) Alzheimer's disease-affected brain: presence of oligomeric A beta ligands (ADDLs) suggests a molecular basis for reversible memory loss. Proc Natl Acad Sci U S A 100:10417–10422

Gosling SD (2001) From mice to men: what can we learn about personality from animal research? Psychol Bull 127:45–86

Gottesman II, Gould TD (2003) The endophenotype concept in psychiatry: etymology and strategic intentions. Am J Psychiatry 160:636–645

Götz J, Schild A, Hoerndli F et al (2004) Amyloid-induced neurofibrillary tangle formation in Alzheimer's disease: insight from transgenic mouse and tissue-culture models. Int J Dev Neurosci 22:453–465

Gould TD, Gottesman II (2006) Psychiatric endophenotypes and the development of valid animal models. Genes Brain Behav 5:113–119

Gray JA, McNaughton N (1983) Comparison between the behavioural effects of septal and hippocampal lesions: a review. Neurosci Biobehav Rev 7:119–188

Grayson DR, Chen Y, Costa E et al (2006) The human reelin gene: transcription factors (+), repressors (−) and the methylation switch (+/−) in schizophrenia. Pharmacol Ther 111:272–286

Gsell W, Jungkunz G, Riederer P (2004) Functional neurochemistry of Alzheimer's disease. Curr Pharm Des 10:265–293

Guidotti A, Auta J, Davis JM et al (2005) GABAergic dysfunction in schizophrenia: new treatment strategies on the horizon. Psychopharmacology 180:191–205

Gulchina Y, Xu SJ, Snyder MA et al (2017) Epigenetic mechanisms underlying NMDA receptor hypofunction in the prefrontal cortex of juvenile animals in the MAM model for schizophrenia. J Neurochem 143:320–333

Gunn-Moore DA, McVee J, Bradshaw JM et al (2006) Ageing changes in cat brains demonstrated by beta-amyloid and AT8-immunoreactive phosphorylated tau deposits. J Feline Med Surg 8:234–242

Hardy J, Selkoe DJ (2002) The amyloid hypothesis of Alzheimer's disease: progress and problems on the road to therapeutics. Science 297:353–356

Harkany T, O'Mahony S, Kelly JP et al (1998) Beta-amyloid(Phe(SO3H)24)25-35 in rat nucleus basalis induces behavioral dysfunctions, impairs learning and memory and disrupts cortical cholinergic innervation. Behav Brain Res 90:133–145

Harkany T, Penke B, Luiten PG (2000) beta-Amyloid excitotoxicity in rat magnocellular nucleus basalis. Effect of cortical deafferentation on cerebral blood flow regulation and implications for Alzheimer's disease. Ann N Y Acad Sci 903:374–386

Harrison P, Law A (2006) Neuregulin 1 and schizophrenia: genetics, gene expression, and neurobiology. Biol Psychiatry 60:132–140

Hattori S, Murotani T, Matsuzaki S et al (2008) Behavioral abnormalities and dopamine reductions in sdy mutant mice with a deletion in Dtnbp1, a susceptibility gene for schizophrenia. Biochem Biophys Res Commun 373:298–302

Hauss-Wegrzyniak B, Dobrzanski P, Stoehr JD et al (1998) Chronic neuroinflammation in rats reproduces components of the neurobiology of Alzheimer's disease. Brain Res 780:294–303

He Y, Yao Z, Gu Y et al (1992) Nerve growth factor promotes collateral sprouting of cholinergic fibers in the septohippocampal cholinergic system of aged rats with fimbria transection. Brain Res 586:27–35

Head E, Moffat K, Das P et al (2005) β-amyloid deposition and tau phosphorylation in clinically characterized aged cats. Neurobiol Aging 26:749–763

Hendley ED, Welch BL (1975) Electroconvulsive shock: sustained decrease in norepinephrine uptake affinity in a reserpine model of depression. Life Sci 16:45–54

Herth MM, Petersen IN, Hansen HD et al (2016) Synthesis and evaluation of (18)F-labeled 5-HT2A receptor agonists as PET ligands. Nucl Med Biol 43:455–462

Hohmann CF, Beard NA, Kari-Kari P et al (2012) Effects of brief stress exposure during early postnatal development in Balb/CByJ mice: II. Altered cortical morphology. Dev Psychobiol 54:723–735

Horti AG, Gao Y, Kuwabara H, Dannals RF (2010) Development of radioligands with optimized imaging properties for quantification of nicotinic acetylcholine receptors by positron emission tomography. Life Sci 86:575–584

Horvath G, Petrovszki Z, Kekesi G et al (2016) Electrophysiological alterations in a complex rat model of schizophrenia. Behav Brain Res 307:65–72

Hsiao K, Chapman P, Nilsen S et al (1996) Correlative memory deficits, Abeta elevation, and amyloid plaques in transgenic mice. Science 274:99–102

Huang Y, Zheng MQ, Gerdes JM et al (2010) Development of effective PET and SPECT imaging agents for the serotonin transporter: has a twenty-year journey reached its destination? Curr Top Med Chem 10:1499–1526

Huber G, März W, Martin JR et al (2000) Characterization of transgenic mice expressing apolipoprotein E4(C112R) and apolipoprotein E4(L28P; C112R). Neuroscience 101:211–218

Iliadi KG (2009) The genetic basis of emotional behavior: has the time come for a Drosophila model? J Neurogenet 23:136–146

Insel TR (2007) From animal model to model animals. Biol Psychiatry 62:1337–1339

Ishrat T, Parveen K, Khan MM et al (2009) Selenium prevents cognitive decline and oxidative damage in rat model of streptozotocin-induced experimental dementia of Alzheimer's type. Brain Res 1281:117–127

Iversen LL, Glowinski J (1966) Regional studies of catecholamines in the rat brain. II Rate of turnover of catecholamines in various brain regions J Neurochem 13:671–682

Iwata N, Tsubuki S, Takaki Y et al (2001) Metabolic regulation of brain Abeta by neprilysin. Science 292:1550–1552

Jaaro-Peled H (2009) Gene models of schizophrenia: DISC1 mouse models. Prog Brain Res 179:75–86

Jaehne EJ, Ramshaw H, Xu X et al (2015) In-vivo administration of clozapine affects behaviour but does not reverse dendritic spine deficits in the 14-3-3ζ KO mouse model of schizophrenia-like disorders. Pharmacol Biochem Behav 138:1–8

Javitt DC, Zukin SR (1991) Recent advances in the phencyclidine model of schizophrenia. Am J Psychiatry 148:1301–1308

Jawhar S, Trawicka A, Jenneckens C et al (2012) Motor deficits, neuron loss, and reduced anxiety coinciding with axonal degeneration and intraneuronal Aβ aggregation in the 5XFAD mouse model of Alzheimer's disease. Neurobiol Aging 33:196.e29-40

Jaworski T, Dewachter I, Seymour CM et al (2010) Alzheimer's disease: old problem, new views from transgenic and viral models. Biochim Biophys Acta 1802:808–818

Jentsch JD, Roth RH (1999) The neuropsychopharmacology of phencyclidine: from NMDA receptor hypofunction to the dopamine hypothesis of schizophrenia. Neuropsychopharmacology 20:201–225

Johnson KA, Minoshima S, Bohnen NI et al (2013) Appropriate use criteria for amyloid PET: a report of the Amyloid Imaging Task Force, the Society of Nuclear Medicine and Molecular Imaging, and the Alzheimer's Association. J Nucl Med 54:476–490

Jones CA, Watson DJ, Fone KC (2011) Animal models of schizophrenia. Br J Pharmacol 164:1162–1194

Kaimal V, McConville P (2009) Importance of preclinical imaging in drug discovery. Charles River. https://pdfs.semanticscholar.org/f049/5930b61a7c117704f1467a98aa1e75dd1d3e.pdf. Accessed 23 July 2019

Kambeitz J, Abi-Dargham A, Kapur S, Howes OD (2014) Alterations in cortical and extrastriatal subcortical dopamine function in schizophrenia: systematic review and meta-analysis of imaging studies. Br J Psychiatry 204:420–429

Kapur S, Remington G (1996) Serotonin-dopamine interaction and its relevance to schizophrenia. Am J Psychiatry 153:466–476

Kekesi G, Petrovszki Z, Benedek G, Horvath G (2015) Sex-specific alterations in behavioral and cognitive functions in a "three hit" animal model of schizophrenia. Behav Brain Res 284:85–93

Kilbourn MR, Domino EF (2011) Increased in vivo [11C]raclopride binding to brain dopamine receptors in amphetamine-treated rats. Eur J Pharmacol 654:254–257

Kim S, Jung WH2, Howes OD et al (2018) Frontostriatal functional connectivity and striatal dopamine synthesis capacity in schizophrenia in terms of antipsychotic responsiveness: an [18F]DOPA PET and fMRI study. Psychol Med 21:1–10

Kimura N, Tanemura K, Nakamura S et al (2003) Age-related changes of Alzheimer's disease-associated proteins in cynomolgus monkey brains. Biochem Biophys Res Commun 310:303–311

Kinney GG, Wilkinson LO, Saywell KL et al (1999) Rat strain differences in the ability to disrupt sensorimotor gating are limited to the dopaminergic system, specific to prepulse inhibition, and unrelated to changes in startle amplitude or nucleus accumbens dopamine receptor sensitivity. J Neurosci 19:5644–5653

Kirino S, Suzuki T, Takeuchi H (2017) Representativeness of clinical PET study participants with schizophrenia: A systematic review. J Psychiatr Res 88:72–79

Kiritsis C, Mavroidi B, Shegani A et al (2017) 2-(4'-Aminophenyl)benzothiazole Labeled with 99mTc-Cyclopentadienyl for Imaging β-Amyloid Plaques. ACS Med Chem Lett 8:1089–1092

Klein S, Koch M, Schwabe K (2008) Neuroanatomical changes in the adult rat brain after neonatal lesion of the medial prefrontal cortex. Exp Neurol 209:199–212

Kleinberger G, Brendel M, Mracsko E et al (2017) The FTD-like syndrome causing TREM2 T66M mutation impairs microglia function, brain perfusion, and glucose metabolism. EMBO J 36:1837–1853

Klunk WE, Engler H, Nordberg A et al (2004) Imaging brain amyloid in Alzheimer's disease with Pittsburgh Compound-B. Ann Neurol 55:306–319

Klunk WE, Lopresti BJ, Ikonomovic MD et al (2005) Binding of the positron emission tomography tracer Pittsburgh compound-B reflects the amount of amyloid-beta in Alzheimer's disease brain but not in transgenic mouse brain. J Neurosci 25:10598–10606

Koike H, Arguello PA, Kvajo M et al (2006) Disc1 is mutated in the 129S6/SvEv strain and modulates working memory in mice. Proc Natl Acad Sci U S A 103:3693–3697

Kokkinidis L, Anisman H (1981) Amphetamine psychosis and schizophrenia: a dual model. Neurosci Biobehav Rev 5:449–461

Koric L, Guedj E, Habert MO et al (2016) Molecular imaging in the diagnosis of Alzheimer's disease and related disorders. Rev Neurol (Paris) 172:725–734

Krystal JH, Karper LP, Seibyl JP et al (1994) Subanesthetic effects of the noncompetitive NMDA antagonist, ketamine, in humans. Psychotomimetic, perceptual, cognitive, and neuroendocrine responses. Arch Gen Psychiatry 51:199–214

Kuntner C, Kesner AL, Bauer M et al (2009) Limitations of small animal PET imaging with [18F]FDDNP and FDG for quantitative studies in a transgenic mouse model of Alzheimer's disease. Mol Imaging Biol 11:236–240

Lacor PN, Buniel MC, Chang L et al (2004) Synaptic targeting by Alzheimer's-related amyloid beta oligomers. J Neurosci 24:10191–10200

Laczó J, Andel R, Vyhnalek M et al (2010) Human analogue of the morris water maze for testing subjects at risk of Alzheimer's disease. Neurodegener Dis 7:148–152

Lane MA (2000) Nonhuman primate models in biogerontology. Exp Gerontol 35:533–541

Laviola G, Ognibene E, Romano E et al (2009) Gene-environment interaction during early development in the heterozygous reeler mouse: clues for modelling of major neurobehavioral syndromes. Neurosci Biobehav Rev 33:560–572

Lawlor PA, Young D (2011) Aβ infusion and related models of Alzheimer dementia. In: De Deyn PP, Van Dam D (eds) Animal models of dementia, 1st edn. Springer Science + Business Media, New York

Lazar NL, Rajakumar N, Cain DP (2008) Injections of NGF into neonatal frontal cortex decrease social interaction as adults: a rat model of schizophrenia. Schizophr Bull 34:127–136

Leboyer M, Bellivier F, Nosten-Bertrand M et al (1998) Psychiatric genetics: search for phenotypes. Trends Neurosci 21:102–105

Lemere CA, Beierschmitt A, Iglesias M et al (2004) Alzheimer's disease abeta vaccine reduces central nervous system abeta levels in a non-human primate, the Caribbean vervet. Am J Pathol 165:283–297

Lemere CA, Oh J, Stanish HA et al (2008) Cerebral amyloid-beta protein accumulation with aging in cotton-top tamarins: a model of early Alzheimer's disease? Rejuvenation Res 11:321–332

Lescaudron L, Stein DG (1999) Differences in memory impairment and response to GM1 ganglioside treatment following electrolytic or ibotenic acid lesions of the nucleus basalis magnocellularis. Restor Neurol Neurosci 15:25–37

Leung C, Jia Z (2016) Mouse Genetic Models of Human Brain Disorders. Front Genet 7:40

Levin ED, Rose JE, McGurk SR et al (1990) Characterization of the cognitive effects of combined muscarinic and nicotinic blockade. Behav Neural Biol 53:103–112

Lewis DA, Levitt P (2002) Schizophrenia as a disorder of neurodevelopment. Annu Rev Neurosci 25:409–432

Li Q, Cheung C, Wei R et al (2009) Prenatal immune challenge is an environmental risk factor for brain and behavior change relevant to schizophrenia: evidence from MRI in a mouse model. PLoS One 4:e6354

Liebsch G, Linthorst AC, Neumann ID et al (1998) Behavioral, physiological, and neuroendocrine stress responses and differential sensitivity to diazepam in two Wistar rat lines selectively bred for high- and low-anxiety-related behavior. Neuropsychopharmacology 19:381–396

Lipska BK (2004) Using animal models to test a neurodevelopmental hypothesis of schizophrenia. J Psychiatry Neurosci 29:282–286

Lipska BK, Weinberger DR (2000) To model a psychiatric disorder in animals: schizophrenia as a reality test. Neuropsychopharmacology 23:223–239

Liu L, Duff K (2008) A technique for serial collection of cerebrospinal fluid from the cisterna magna in mouse. J Vis Exp 21:e960

Lodge DJ, Grace AA (2008) Hippocampal dysfunction and disruption of dopamine system regulation in an animal model of schizophrenia. Neurotox Res 14:97–104

Lubow RE, Gewirtz JC (1995) Latent inhibition in humans: data, theory, and implications for schizophrenia. Psychol Bull 117:87–103

Luo F, Rustay NR, Ebert U et al (2012) Characterization of 7- and 19-month-old Tg2576 mice using multimodal in vivo imaging: limitations as a translatable model of Alzheimer's disease. Neurobiol Aging 33:933–944

Lyketsos CG, Carrillo MC, Ryan JM et al (2011) Neuropsychiatric symptoms in Alzheimer's disease. Alzheimers Dement 7:532–539

Maass A, Landau S, Baker SL et al (2017) Comparison of multiple tau-PET measures as biomarkers in aging and Alzheimer's disease. NeuroImage 157:448–463

MacLean PD (1970) The Triune Brain, Emotion and Scientific Bias. In: Schmitt FO (Ed.) The Neurosciences: Second Study Program. New York: Rockefeller University Press, 336–349

Maeda J, Ji B, Irie T et al (2007) Longitudinal, quantitative assessment of amyloid, neuroinflammation, and anti-amyloid treatment in a living mouse model of Alzheimer's disease enabled by positron emission tomography. J Neurosci 27:10957–10968

Marcotte ER, Pearson DM, Srivastava LK (2001) Animal models of schizophrenia: a critical review. J Psychiatry Neurosci 26:395–410

Markham JA, Taylor AR, Taylor SB et al (2010) Characterization of the cognitive impairments induced by prenatal exposure to stress in the rat. Front Behav Neurosci 4:173

Marona-Lewicka D, Nichols CD, Nichols DE (2011) An animal model of schizophrenia based on chronic LSD administration: old idea, new results. Neuropharmacology 61:503–512

Martínez-Téllez RI, Hernández-Torres E, Gamboa C et al (2009) Prenatal stress alters spine density and dendritic length of nucleus accumbens and hippocampus neurons in rat offspring. Synapse 63:794–804

Martins AF, Morfin JF, Kubíčková A et al (2013) PiB-Conjugated, Metal-Based Imaging Probes: Multimodal Approaches for the Visualization of β-Amyloid Plaques. ACS Med Chem Lett 4:436–440

Maximino C, van der Staay FJ (2019) Behavioral models in psychopathology: epsitemic and semantic considerations. Behav Brain Funct 15:1

McGeer EG, McGeer PL (2003) Inflammatory processes in Alzheimer's disease. Prog Neuro-Psychopharmacol Biol Psychiatry 27:741–749

McGrath J, Saha S, Chant D et al (2008) Schizophrenia: a concise overview of incidence, prevalence, and mortality. Epidemiol Rev 30:67–76

McKinney WT Jr, Bunney WE Jr (1969) Animal model of depression. I. Review of evidence: implications for research. Arch Gen Psychiatry 21:240–248

Mei L, Xiong W (2008) Neuregulin 1 in neural development, synaptic plasticity and schizophrenia. Nat Rev Neurosci 9:437–452

Mhatre SD, Paddock BE, Saunders AJ, Marenda DR (2013) Invertebrate models of Alzheimer's disease. J Alzheimers Dis 33:3–16

Migliore L, Fontana I, Colognato R et al (2005) Searching for the role and the most suitable biomarkers of oxidative stress in Alzheimer's disease and in other neurodegenerative diseases. Neurobiol Aging 26:587–595

Milak MS, Severance AJ, Ogden RT et al (2008) Modeling considerations for 11C-CUMI-101, an agonist radiotracer for imaging serotonin 1A receptor in vivo with PET. J Nucl Med 49:587–596

Mitchell KJ, Huang ZJ, Moghaddam B et al (2011) Following the genes: a framework for animal modelling of psychiatric disorders. BMC Biol 9:76

Molavipordanjani S, Emami S, Mardanshahi A et al (2019) Novel 99mTc-2-arylimidazo[2,1-b]benzothiazole derivatives as SPECT imaging agents for amyloid-β plaques. Eur J Med Chem 175:149–161

Moore H (2010) The role of rodent models in the discovery of new treatments for schizophrenia: updating our strategy. Schizophr Bull 36:1066–1072

Moran P, Stokes J, Marr J et al (2016) Gene × Environment Interactions in Schizophrenia: Evidence from Genetic Mouse Models. Neural Plast 2173748

Moran PM (1993) Differential effects of scopolamine and mecamylamine on working and reference memory in the rat. Pharmacol Biochem Behav 45:533–538

Moreno JL, Holloway T, Umali A et al (2013) Persistent effects of chronic clozapine on the cellular and behavioral responses to LSD in mice. Psychopharmacology 225:217–226

Muir WJ, Pickard BS, Blackwood DH (2008) Disrupted-in-schizophrenia-1. Curr Psychiatry Rep 10:140–147

Mulder J, Harkany T, Czollner K et al (2005) Galantamine-induced behavioral recovery after sublethal excitotoxic lesions to the rat medial septum. Behav Brain Res 163:33–41

Nag S, Yee BK, Tang F (1999) Chronic intracerebroventricular infusion of beta-amyloid (1-40) results in a selective loss of neuropeptides in addition to a reduction in choline acetyltransferase activity in the cortical mantle and hippocampus in the rat. Ann N Y Acad Sci 897:420–422

Nakamura H, Hishinuma T, Tomioka Y et al (1997) Effects of haloperidol and cocaine pretreatments on brain distribution and kinetics of [11C]methamphetamine in methamphetamine sensitized dog: application of PET to drug pharmacokinetic study. Nucl Med Biol 24:165–169

Nakamura S, Murayama N, Noshita T et al (2001) Progressive brain dysfunction following intracerebroventricular infusion of beta(1-42)-amyloid peptide. Brain Res 912:128–136

Nakao A, Miyazaki N2, Ohira K et al (2017) Immature morphological properties in subcellular-scale structures in the dentate gyrus of Schnurri-2 knockout mice: a model for schizophrenia and intellectual disability. Mol Brain 10:60

Nestler EJ, Hyman SE (2010) Animal models of neuropsychiatric disorders. Nat Neurosci 13:1161–1169

Neuman KM, Molina-Campos E, Musial TF et al (2015) Evidence for Alzheimer's disease-linked synapse loss and compensation in mouse and human hippocampal CA1 pyramidal neurons. Brain Struct Funct 220:3143–3165

Nordberg A, Nilsson-Håkansson L, Adem A et al (1989) Multiple actions of THA on cholinergic neurotransmission in Alzheimer brains. Prog Clin Biol Res 317:1169–1178

Nullmeier S, Panther P, Frotscher M et al (2014) Alterations in the hippocampal and striatal catecholaminergic fiber densities of heterozygous reeler mice. Neuroscience 275:404–419

O'Tuathaigh CM, Kirby BP, Moran PM et al (2010) Mutant mouse models: genotype-phenotype relationships to negative symptoms in schizophrenia. Schizophr Bull 36:271–288

Oakley H, Cole SL, Logan S et al (2006) Intraneuronal beta-amyloid aggregates, neurodegeneration, and neuron loss in transgenic mice with five familial Alzheimer's disease mutations: potential factors in amyloid plaque formation. J Neurosci 26:10129–10140

Oddo S, Caccamo A, Kitazawa M et al (2003) Amyloid deposition precedes tangle formation in a triple transgenic model of Alzheimer's disease. Neurobiol Aging 24:1063–1070

Okamura N, Harada R, Furumoto S et al (2014) Tau PET imaging in Alzheimer's disease. Curr Neurol Neurosci Rep 14:500

Okubo Y, Suhara T, Suzuki K et al (1997) Decreased prefrontal dopamine D1 receptors in schizophrenia revealed by PET. Nature 385:634–636

Olariu A, Yamada K, Mamiya T et al (2002) Memory impairment induced by chronic intracerebroventricular infusion of beta-amyloid (1-40) involves downregulation of protein kinase C. Brain Res 957:278–286

Olney JW, Farber NB (1995) Glutamate receptor dysfunction and schizophrenia. Arch Gen Psychiatry 52:998–1007

Ono M, Watanabe H, Kitada A et al (2016) Highly Selective Tau-SPECT Imaging Probes for Detection of Neurofibrillary Tangles in Alzheimer's Disease. Sci Rep 6:34197

Ono M, Cheng Y, Kimura H et al (2013) Development of novel 123I-labeled pyridyl benzofuran derivatives for SPECT imaging of β-amyloid plaques in Alzheimer's disease. PLoS One 8:e74104

Opazo C, Luza S, Villemagne VL et al (2006) Radioiodinated clioquinol as a biomarker for beta-amyloid: Zn complexes in Alzheimer's disease. Aging Cell 5:69–79

Overstreet DH, Double K, Schiller GD (1989) Antidepressant effects of rolipram in a genetic animal model of depression: cholinergic supersensitivity and weight gain. Pharmacol Biochem Behav 34:691–696

Owens EM, Bachman P, Glahn DC, Bearden CE (2016) Electrophysiological Endophenotypes for Schizophrenia. Harv Rev Psychiatry 24:129–147

Palmer AA, Dulawa SC, Mottiwala AA et al (2000) Prepulse startle deficit in the Brown Norway rat: a potential genetic model. Behav Neurosci 114:374–388

Patel NH, Vyas NS, Puri BK et al (2010) Positron emission tomography in schizophrenia: a new perspective. J Nucl Med 51:511–520

Paylor R, Crawley JN (1997) Inbred strain differences in prepulse inhibition of the mouse startle response. Psychopharmacology 132:169–180

Paylor R, Lindsay E (2006) Mouse models of 22q11 deletion syndrome. Biol Psychiatry 59:1172–1179

Peilin J, Guangchun H, Junfei Z et al (2017) SZGR 2.0: a one-stop shop of schizophrenia candidate genes. Nucleic Acids Res 45(Database issue):D915–D924

Pentkowski NS, Berkowitz LE, Thompson SM et al (2018) Anxiety-like behavior as an early endophenotype in the TgF344-AD rat model of Alzheimer's disease. Neurobiol Aging 61:169–176

Pepeu G, Giovannini MG (2007) Changes in acetylcholine extracellular levels during cognitive processes. In: Westerink BH, Cremers TI (eds) Handbook of microdialysis. Methods, applications and perspectives. Elsevier, Amsterdam

Pepeu G, Rosi MC (2011) Validation of animal models of dementia: neurochemical aspects. In: De Deyn PP, Van Dam D (eds) Animal models of dementia, 1st edn. Springer Science + Business Media, New York

Petersen IN, Villadsen J, Hansen HD et al (2016) Convergent 18F-labeling and evaluation of N-benzyl-phenethylamines as 5-HT2A receptor PET ligands. Bioorg Med Chem 24:5353–5356

Pietropaolo S, Crusio WE (2009) Strain-dependent changes in acoustic startle response and its plasticity across adolescence in mice. Behav Genet 39:623–631

Platt TL, Reeves VL, Murphy MP (2013) Transgenic models of Alzheimer's disease: better utilization of existing models through viral transgenesis. Biochim Biophys Acta 1832:1437–1448

Podhorna J, Didriksen M (2004) The heterozygous reeler mouse: behavioural phenotype. Behav Brain Res 153:43–54

Podlisny MB, Tolan DR, Selkoe DJ (1991) Homology of the amyloid beta protein precursor in monkey and human supports a primate model for beta amyloidosis in Alzheimer's disease. Am J Pathol 138:1423–1435

Price JC, Klunk WE, Lopresti BJ et al (2005) Kinetic modeling of amyloid binding in humans using PET imaging and Pittsburgh Compound-B. J Cereb Blood Flow Metab 25:1528–1547

Puhl MD, Mintzopoulos D2, Jensen JE et al (2015) In vivo magnetic resonance studies reveal neuroanatomical and neurochemical abnormalities in the serine racemase knockout mouse model of schizophrenia. Neurobiol Dis 73:269–274

Rabinovici GD, Jagust WJ (2009) Amyloid imaging in aging and dementia: testing the amyloid hypothesis in vivo. Behav Neurol 21:117–128

Raedler TJ, Bymaster FP, Tandon R et al (2007) Towards a muscarinic hypothesis of schizophrenia. Mol Psychiatry 12:232–246

Rankin CA, Gamblin TC (2008) Assessing the toxicity of tau aggregation. J Alzheimers Dis 14:411–416

Reardon S (2019) Depression researchers rethink popular mouse swim tests Nature 571: 456–457. https://www.nature.com/articles/d41586-019-02133-?utm_source=fbk_nnc&utm_medium=social&utm_campaign=naturenews&sf216017303=1&fbclid=IwAR0gq-hnRrXCld-fHPZdoN-gCnfUY2IfbzqzvHJi5v8WGdBdNAqGp7WSA__E. Accessed 23 July 2019

Reisberg B, Borenstein J, Salob SP et al (1987) Behavioral symptoms in Alzheimer's disease: phenomenology and treatment. J Clin Psychiatry 48:9–15

Reith J, Cumming P, Gjedde A (1998) Enhanced [3H]DOPA and [3H]dopamine turnover in striatum and frontal cortex in vivo linked to glutamate receptor antagonism. J Neurochem 70:1979–1985

Renã AS, Butterfield DA (2011) Spontaneous vertebrate models of Alzheimer dementia: selectively bred strains (SAM strains). In: De Deyn PP, Van Dam D (eds) Animal models of dementia, 1st edn. Springer Science + Business Media, New York

Ribé EM, Pérez M, Puig B et al (2005) Accelerated amyloid deposition, neurofibrillary degeneration and neuronal loss in double mutant APP/tau transgenic mice. Neurobiol Dis 20:814–822

Riekkinen P Jr, Sirviö J, Aaltonen M et al (1990) Effects of concurrent manipulations of nicotinic and muscarinic receptors on spatial and passive avoidance learning. Pharmacol Biochem Behav 37:405–410

Roertgen KE, Parisi JE, Clark HB et al (1996) A beta-associated cerebral angiopathy and senile plaques with neurofibrillary tangles and cerebral hemorrhage in an aged wolverine (Gulo gulo). Neurobiol Aging 17:243–247

Rofina JE, van Ederen AM, Toussaint MJ et al (2006) Cognitive disturbances in old dogs suffering from the canine counterpart of Alzheimer's disease. Brain Res 1069:216–226

Rosen AM, Spellman T, Gordon JA (2015) Electrophysiological endophenotypes in rodent models of schizophrenia and psychosis. Biol Psychiatry 77:1041–1049

Rosen RF, Walker LC, Levine H 3rd (2011) PIB binding in aged primate brain: enrichment of high-affinity sites in humans with Alzheimer's disease. Neurobiol Aging 32:223–234

Sagnou M, Mavroidi B, Shegani A et al (2019) Remarkable Brain Penetration of Cyclopentadienyl $M(CO)_3^+$ (M = ^{99m}Tc, Re) Derivatives of Benzothiazole and Benzimidazole Paves the Way for Their Application as Diagnostic, with Single-Photon-Emission Computed Tomography (SPECT), and Therapeutic Agents for Alzheimer's Disease. J Med Chem 62:2638–2650

Sakoğlu U, Upadhyay J, Chin CL et al (2011) Paradigm shift in translational neuroimaging of CNS disorders. Biochem Pharmacol 81:1374–1387

Sanchis-Segura C, Spanagel R, Henn FA et al (2005) Reduced sensitivity to sucrose in rats bred for helplessness: a study using the matching law. Behav Pharmacol 16:267–270

Sani S, Traul D, Klink A et al (2003) Distribution, progression and chemical composition of cortical amyloid-β deposits in aged rhesus monkeys: similarities to the human. Acta Neuropathol 105:145–156

Santarelli L, Gobbi G, Debs PC et al (2001) Genetic and pharmacological disruption of neurokinin 1 receptor function decreases anxiety-related behaviors and increases serotonergic function. Proc Natl Acad Sci U S A 98:1912–1917

Schmitt A, Turck CW, Pilz PK et al (2013) Proteomic similarities between heterozygous reeler mice and schizophrenia. Biol Psychiatry 74:e5–e10

Seeman P (1987) Dopamine receptors and the dopamine hypothesis of schizophrenia. Synapse 1:133–152

Selkoe DJ (2000) Toward a comprehensive theory for Alzheimer's disease. Hypothesis: Alzheimer's disease is caused by the cerebral accumulation and cytotoxicity of amyloid beta-protein. Ann N Y Acad Sci 924:17–25

Selkoe DJ (2001) Alzheimer's disease: genes, proteins, and therapy. Physiol Rev 81:741–766

Selkoe DJ (2008) Soluble oligomers of the amyloid beta-protein impair synaptic plasticity and behavior. Behav Brain Res 192:106–113

Sherman KA, Friedman E (1990) Pre- and post-synaptic cholinergic dysfunction in aged rodent brain regions: new findings and an interpretive review. Int J Dev Neurosci 8:689–708

Shin J, Kepe V, Barrio JR et al (2011) The merits of FDDNP-PET imaging in Alzheimer's disease. J Alzheimers Dis 26:135–145

Sipos E, Kurunczi A, Kasza A et al (2007) Beta-amyloid pathology in the entorhinal cortex of rats induces memory deficits: implications for Alzheimer's disease. Neuroscience 147:28–36

Sloan HL, Good M, Dunnett SB (2006) Double dissociation between hippocampal and prefrontal lesions on an operant delayed matching task and a water maze reference memory task. Behav Brain Res 171:116–126

St Clair D, Johnstone M (2018) Using mouse transgenic and human stem cell technologies to model genetic mutations associated with schizophrenia and autism. Philos Trans R Soc Lond B Biol Sci 373:pii:20170037

Steimer T (2011) Animal models of anxiety disorders in rats and mice: some conceptual issues. Dialogues Clin Neurosci 13:495–506

Stępnicki P, Kondej M, Kaczor AA (2018) Current concepts and treatments of Schizophrenia. Molecules 23. pii: E2087

Striedter GF (1998) Progress in the study of brain evolution: from speculative theories to testable hypotheses. Anat Rec 253:105–112

Sturchler-Pierrat C, Abramowski D, Duke M et al (1997) Two amyloid precursor protein trans-genic mouse models with Alzheimer disease-like pathology. Proc Natl Acad Sci U S A 94:13287–13292

Sunderland T, Tariot PN, Weingartner H et al (1986) Pharmacologic modelling of Alzheimer's disease. Prog Neuro-Psychopharmacol Biol Psychiatry 10:599–610

Swerdlow NR, Kuczenski R, Goins JC et al (2005) Neurochemical analysis of rat strain differ-ences in the startle gating-disruptive effects of dopamine agonists. Pharmacol Biochem Behav 80:203–211

Swerdlow NR, Martinez ZA, Hanlon FM et al (2000) Toward understanding the biology of a complex phenotype: rat strain and substrain differences in the sensorimotor gating-disruptive effects of dopamine agonists. J Neurosci 20:4325–4336

Swerdlow NR, Shilling PD, Breier M et al (2012) Fronto-temporal-mesolimbic gene expres-sion and heritable differences in amphetamine-disrupted sensorimotor gating in rats. Psychopharmacology 224:349–362

Sy M, Kitazawa M, LaFerla F (2011) The 3xTg-AD mouse model: reproducing and modulating plaque and tangle pathology. In: De Deyn PP, Van Dam D (eds) Animal models of dementia, 1st edn. Springer Science + Business Media, New York

Szabados T, Dul C, Majtényi K et al (2004) A chronic Alzheimer's model evoked by mitochondrial poison sodium azide for pharmacological investigations. Behav Brain Res 154:31–40

Teipel SJ, Buchert R, Thome J et al (2011) Development of Alzheimer-disease neuroimaging-biomarkers using mouse models with amyloid-precursor protein-transgene expression. Prog Neurobiol 95:547–556

Tekirian TL, Cole GM, Russell MJ et al (1996) Carboxy terminal of beta-amyloid deposits in aged human, canine, and polar bear brains. Neurobiol Aging 17:249–257

Toledana A, Alvarez MI (2011) Lesion-induced vertebrate models of Alzheimer dementia. In: De Deyn PP, Van Dam D (eds) Animal models of dementia, 1st edn. Springer Science + Business Media, New York

Toyama H, Ye D, Ichise M et al (2005) PET imaging of brain with the beta-amyloid probe, [11C]6-OH-BTA-1, in a transgenic mouse model of Alzheimer's disease. Eur J Nucl Med Mol Imaging 32:593–600

Trunnell ER (2019) Use of the forced swim test to assess "despair". Brain Stimul pii: S1935-861X(19)30277-3

Tsai G, Coyle JT (2002) Glutamatergic mechanisms in schizophrenia. Annu Rev Pharmacol Toxicol 42:165–179

Tschaharganeh DF, Lowe SW, Garippa RJ, Livshits G (2016) Using CRISPR/Cas to study gene function and model disease in vivo. FEBS J 283:3194–3203

Tsukada H, Harada N, Nishiyama S et al (2000) Ketamine decreased striatal [(11)C]raclopride binding with no alterations in static dopamine concentrations in the striatal extracellular fluid in the monkey brain: multiparametric PET studies combined with microdialysis analysis. Synapse 37:95–103

Tulving E (1987) Multiple memory systems and consciousness. Hum Neurobiol 6:67–80

Uchida K, Yoshino T, Yamaguchi R et al (1995) Senile plaques and other senile changes in the brain of an American black bear. Vet Pathol 32:412–414

Urban N, Abi-Dargham A (2010) Neurochemical imaging in schizophrenia. Curr Top Behav Neurosci 4:215–242

Uylings HB, Groenewegen HJ, Kolb B (2003) Do rats have a prefrontal cortex? Behav Brain Res 146:3–17

Vale-Martínez A, Guillazo-Blanch G, Martí-Nicolovius M et al (2002) Electrolytic and ibotenic acid lesions of the nucleus basalis magnocellularis interrupt long-term retention, but not acqui-sition of two-way active avoidance, in rats. Exp Brain Res 142:52–66

Valzelli L (1973) The "isolation syndrome" in mice. Psychopharmacologia 31:305–320

van Berckel BN, Kegeles LS, Waterhouse R et al (2006) Modulation of amphetamine-induced dopamine release by group II metabotropic glutamate receptor agonist LY354740 in non-human primates studied with positron emission tomography. Neuropsychopharmacology 31:967–977

Van Dam D, De Deyn PP (2006) Drug discovery in dementia: the role of rodent models. Nat Rev Drug Discov 5:956–970

Van Dam D, De Deyn PP (2011a) The role of rodent models in the drug discovery pipeline for dementia. In: De Deyn PP, Van Dam D (eds) Animal models of dementia, 1st edn, Neuromethods series. Springer Science + Business Media, New York

Van Dam D, De Deyn PP (2011b) APP-based transgenic models: the APP23 model. In: De Deyn PP, Van Dam D (eds) Animal models of dementia, 1st edn. Springer Science + Business Media, New York

Van Dam D, De Deyn PP (2017) Non human primate models for Alzheimer's disease-related research and drug discovery. Expert Opin Drug Discov 12:187–200

Van Dam D, Van Dijck A, Janssen L et al (2013) Neuropeptides in Alzheimer's disease: from pathophysiological mechanisms to therapeutic opportunities. Curr Alzheimer Res 10(5):449–468

Van Dam D, Vermeiren Y, Dekker AD et al (2016) Neuropsychiatric Disturbances in Alzheimer's Disease: What Have We Learned from Neuropathological Studies? Curr Alzheimer Res 13:1145–1164

van der Staay FJ (2006) Animal models of behavioral dysfunctions: basic concepts and classifications, and an evaluation strategy. Brain Res Rev 52:131–159

van der Staay FJ, Blokland A (1996) Behavioral differences between outbred Wistar, inbred Fischer 344, brown Norway, and hybrid Fischer 344 x brown Norway rats. Physiol Behav 60:97–109

van der Weyden L, Bradley A (2006) Mouse chromosome engineering for modeling human disease. Annu Rev Genomics Hum Genet 7:247–276

Van Dijck A, Vloeberghs E, Van Dam D et al (2008) Evaluation of the APP23-model for Alzheimer's disease in the odour paired-associate test for hippocampus-dependent memory. Behav Brain Res 190:147–151

Varela MJ, Lage S, Caruncho HJ et al (2015) Reelin influences the expression and function of dopamine D2 and serotonin 5-HT2A receptors: a comparative study. Neuroscience 290:165–174

Varty GB, Walters N, Cohen-Williams M et al (2001) Comparison of apomorphine, amphetamine and dizocilpine disruptions of prepulse inhibition in inbred and outbred mice strains. Eur J Pharmacol 424:27–36

Vermeiren Y, Van Dam D, Aerts T et al (2014a) (2014) Brain region-specific monoaminergic correlates of neuropsychiatric symptoms in Alzheimer's disease. J Alzheimers Dis 41(3):819–833

Vermeiren Y, Van Dam D, Aerts T et al (2014b Dec) (2014) Monoaminergic neurotransmitter alterations in postmortem brain regions of depressed and aggressive patients with Alzheimer's disease. Neurobiol Aging 35(12):2691–2700

Vickers JC, Dickson TC, Adlard PA et al (2000) The cause of neuronal degeneration in Alzheimer's disease. Prog Neurobiol 60:139–165

Vidal R, Ghetti B (2011) Characterization of amyloid deposits in neurodegenerative diseases. In: Manfredi G, Kawamata H (eds) Neurodegeneration: methods and protocols, 1st edn. Springer Science + Business Media, New York

Vloeberghs E, Van Dam D, Engelborghs S et al (2004) Altered circadian locomotor activity in APP23 mice: a model for BPSD disturbances. Eur J Neurosci 20:2757–2766

Vloeberghs E, Van Dam D, Franck F et al (2008) Altered ingestive behavior, weight changes, and intact olfactory sense in an APP overexpression model. Behav Neurosci 122:491–497

Vollenweider FX, Vontobel P, Oye I et al (2000) Effects of (S)-ketamine on striatal dopamine: a [11C]raclopride PET study of a model psychosis in humans. J Psychiatr Res 34:35–43

Voytko ML, Tinkler GP (2004) Cognitive function and its neural mechanisms in nonhuman primate models of aging, Alzheimer disease, and menopause. Front Biosci 9:1899–1914

Walsh DM, Selkoe DJ (2007) A beta oligomers—a decade of discovery. J Neurochem 101:1172–1184

Watanabe H (2017) [Development of SPECT Probes for In Vivo Imaging of β-Amyloid and Tau Aggregates in the Alzheimer's Disease Brain]. [Article in Japanese]. Yakugaku Zasshi 137:1361–1365

Weinstein JJ, Chohan MO, Slifstein M et al (2017) Pathway-Specific Dopamine Abnormalities in Schizophrenia. Biol Psychiatry 81:31–42

Weldon DT, Rogers SD, Ghilardi JR et al (1998) Fibrillar beta-amyloid induces microglial phagocytosis, expression of inducible nitric oxide synthase, and loss of a select population of neurons in the rat CNS in vivo. J Neurosci 18:2161–2173

Wenk GL, McGann K, Hauss-Wegrzyniak B et al (2003) The toxicity of tumor necrosis factor-alpha upon cholinergic neurons within the nucleus basalis and the role of norepinephrine in the regulation of inflammation: implications for Alzheimer's disease. Neuroscience 121:719–729

Whitehouse PJ, Au KS (1986) Cholinergic receptors in aging and Alzheimer's disease. Prog Neuro-Psychopharmacol Biol Psychiatry 10:665–676

Whitehouse PJ, Price DL, Struble RG et al (1982) Alzheimer's disease and senile dementia: loss of neurons in the basal forebrain. Science 215:1237–1239

Williams NM, O'Donovan MC, Owen MJ (2005) Is the dysbindin gene (DTNBP1) a susceptibility gene for schizophrenia? Schizophr Bull 31:800–805

Willott JF, Carlson S, Chen H (1994) Prepulse inhibition of the startle response in mice: relationship to hearing loss and auditory system plasticity. Behav Neurosci 108:703–713

Willott JF, Tanner L, O'Steen J et al (2003) Acoustic startle and prepulse inhibition in 40 inbred strains of mice. Behav Neurosci 117:716–727

Wils H, Kleinberger G, Pereson S et al (2012) Cellular ageing, increased mortality and FTLD-TDP-associated neuropathology in progranulin knockout mice. J Pathol 228:67–76

Wimo A, Winblad B, Aguero-Torres H et al (2003) The magnitude of dementia occurrence in the world. Alzheimer Dis Assoc Disord 17:63–67

Winter C, Djodari-Irani A, Sohr R et al (2009) Prenatal immune activation leads to multiple changes in basal neurotransmitter levels in the adult brain: implications for brain disorders of neurodevelopmental origin such as schizophrenia. Int J Neuropsychopharmacol 12:513–524

Wirths O, Breyhan H, Cynis H et al (2009) Intraneuronal pyroglutamate-Abeta 3-42 triggers neurodegeneration and lethal neurological deficits in a transgenic mouse model. Acta Neuropathol 118(4):487–496

Wolf R, Dobrowolny H, Nullmeier S et al (2018) Effects of neonatal excitotoxic lesions in ventral thalamus on social interaction in the rat. Eur Arch Psychiatry Clin Neurosci 268:461–470

Wolf R, Matzke K, Paelchen K et al (2010) Reduction of Prepulse Inhibition (PPI) after neonatal excitotoxic lesion of the ventral thalamus in pubertal and adult rats. Pharmacopsychiatry 43:99–109

Wong DF, Kuwabara H1, Horti AG et al (2018) Brain PET Imaging of α7-nAChR with [18F]ASEM: Reproducibility, Occupancy, Receptor Density, and Changes in Schizophrenia. Int J Neuropsychopharmacol 21:656–667

Wong DF, Rosenberg PB, Zhou Y et al (2010) In vivo imaging of amyloid deposition in Alzheimer disease using the radioligand 18F-AV-45 (florbetapir [corrected] F 18). J Nucl Med 51:913–920

Woolley DG, Laeremans A, Gantois I et al (2013) Homologous involvement of striatum and prefrontal cortex in rodent and human water maze learning. Proc Natl Acad Sci U S A 110:3131–3136

Wu LS, Cheng WC, Hou SC et al (2010) TDP-43, a neuro-pathosignature factor, is essential for early mouse embryogenesis. Genesis 48:56–62

Yamada M, Chiba T, Sasabe J et al (2005) Implanted cannula-mediated repetitive administration of Abeta25-35 into the mouse cerebral ventricle effectively impairs spatial working memory. Behav Brain Res 164:139–146

Yang AC, Tsai SJ (2017) New targets for Schizophrenia treatment beyond the dopamine hypothesis. Int J Mol Sci 18. pii: E1689

Yochum CL, Bhattacharya P, Patti L et al (2010) Animal model of autism using GSTM1 knockout mice and early post-natal sodium valproate treatment. Behav Brain Res 210:202–210

Young JW, Minassian A, Paulus MP et al (2007) A reverse-translational approach to bipolar disorder: rodent and human studies in the Behavioral Pattern Monitor. Neurosci Biobehav Rev 31:882–896

Zhang S, Han D, Tan X et al (2012) Diagnostic accuracy of 18F-FDG and 11 C-PIB-PET for prediction of short-term conversion to Alzheimer's disease in subjects with mild cognitive impairment. Int J Clin Pract 66:185–198

The Use of Small Animal Molecular Imaging (µPET) Exemplified in a Neurobiological Pathology

2

Dorien Glorie, Stijn Servaes, Alan Miranda, Daniele Bertoglio, Jeroen Verhaeghe, and Steven Staelens

Contents

Abstract

Positron emission tomography (PET) imaging is a molecular imaging modality with an extreme high versatility. Theoretically, all biological processes can be visualized longitudinally and quantified in vivo with high sensitivity, once a radioli-

D. Glorie · S. Servaes · A. Miranda · D. Bertoglio · J. Verhaeghe · S. Staelens (✉)
Molecular Imaging Center Antwerp (MICA), University of Antwerp,
Antwerp (Wilrijk), Belgium
e-mail: steven.staelens@uantwerpen.be

gand for a certain target of interest is developed. This chapter introduces the principle of PET and how relevant biological parameters can be extracted from PET images using pharmacokinetic modelling. In addition, we discuss awake PET imaging in small animal (μPET) studies. The novelty of point source tracking enables to follow tracer distribution in the brain of rodents during the conduct of certain (pathological) behavior. As a consequence, anesthesia-related factors are eliminated which continue to be an obstacle for bench-to-bedside translation. Lastly, this chapter emphasizes the value of μPET in the exploration and evaluation of disease mechanisms, as illustrated by a pharmacological and genetic rodent model for obsessive compulsive disorder (OCD). Longitudinal brain PET studies can be set up to investigate whether behavioral alterations parallel changes in the binding of radioligands for multiple targets. Altogether, μPET imaging provides unique whole brain information on underlying disease mechanisms and potential treatment targets, especially when the PET data are collected in awake animals.

2.1   Introduction on μPET

Positron emission tomography (PET) is a noninvasive imaging technique which detects the distribution of radionuclide-labelled molecules to visualize and quantify biochemical and physiological processes on a molecular level. While the first human PET cameras date back to the 1970s (Phelps et al. 1975), the application of PET imaging in rodents started about 15 years later (Ingvar et al. 1991; Hume et al. 1992). This preceded the introduction of miniaturized systems with higher spatial resolution given the smaller brain size compared to humans (Watanabe et al. 1992; Shuping et al. 1994; Bloomfield et al. 1995; Lecomte et al. 1996; Cherry et al. 1997). MPET imaging has a moderate spatial resolution (typically 1.0–1.5 mm); however, its ability to detect picomolar changes makes PET imaging the most sensitive noninvasive functional imaging technique available. PET imaging can be theoretically applied to image all biological processes once a radioligand for the target of interest has been developed, indicating the extremely high versatility of the technique. In addition, PET imaging has the potential to assess target engagement through quantitative measurements of receptor occupancy when a radioligand shares the same binding site as a drug of interest, allowing to estimate the optimal treatment dosage in vivo. Most importantly, given its noninvasive character and high sensitivity, it is well suited for longitudinal study designs and allows relatively small sample sizes to perform adequately powered experiments.

2.1.1   Physics and Principle of PET

PET imaging relies on the use of radioisotopes, which are unstable isotopes undergoing radioactive decay in order to form a more stable element. The radioactivity decays exponentially with a half-life, $t_{1/2}$, which is constant for a certain

Fig. 2.1 Principle of
PET. The radioisotope of
the radioligand emits a
positron (β⁺), which
annihilates with an electron
(e⁻) present in the
surrounding medium and
generates two antiparallel
gamma (γ)-ray photons
with an energy of 511 keV
each. In the process of
positron emission, also a
neutrino (ν) is released.
The photons are detected
in coincidence by the PET
ring detector as one event.
Image reconstruction
algorithms use the detected
events to generate a
PET image
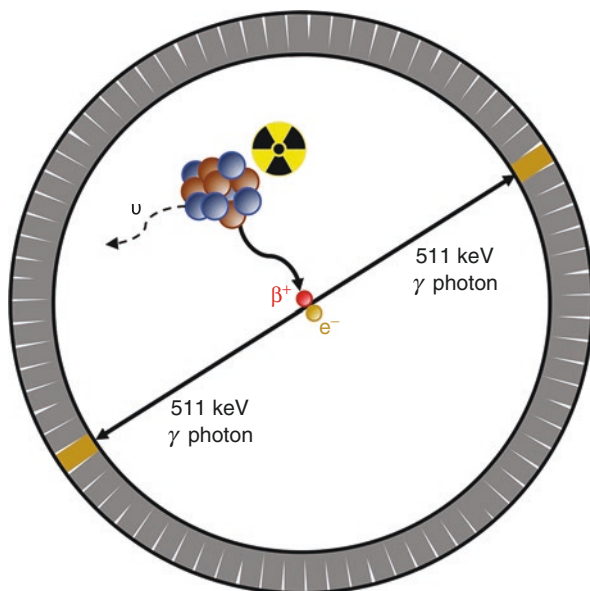
radioisotope. Radioisotopes suited for PET imaging decay through positron (β⁺) emission, a positron being the antiparticle to the electron (e⁻). Once emitted, the positron loses energy and collides with an electron from the surrounding medium, a process known as the annihilation reaction (Fig. 2.1). This results in the generation of two antiparallel γ-ray photons with an energy of 511 keV each. The coincident detection of two photons at opposite sides of the PET ring detector (composed of scintillation crystals) generates an event. The collection of these events, followed by the application of image reconstruction algorithms, informs about the position of the radioligand in the tissue.

The selection of a specific radioisotope mainly depends on the atomic structure of the ligand, the possible radiolabelling reaction, and the half-life. The two most commonly employed radioisotopes are [^{18}F] and [^{11}C]. The former features a relatively long half-life ($t_{1/2}$ = 109.8 minutes); thus, it is generally preferred as it allows to perform acquisitions of multiple subjects with the same radiosynthesis and it can be transported to imaging centers without an on-site cyclotron. However, a fluor atom in the structure of the ligand is required, but radiofluorination is not always a viable option. On the other hand, Carbon-11 has the main advantage that C atoms are present in all molecular structures; therefore, [^{11}C] labelling can virtually always be applied. However, this latter radioisotope is characterized by a shorter half-life ($t_{1/2}$ = 20.39 minutes), which requires a higher number of radiosyntheses, and it cannot be used by imaging centers lacking an on-site cyclotron. Nevertheless, a benefit of its short half-life is the possibility of performing repeated PET imaging studies in the same subject in a short time frame as well as the low radiation burden for the subjects.

2.1.2 Pharmacokinetic Modelling

Following systemic injection of a radioligand, dynamic PET imaging measures the concentration of radioactivity as a function of time. As a result, serial PET images depicting sequential time windows (frames) are created. Thus, dynamic acquisition allows the generation of a time-activity curve (TAC) of the radioligand in the region of interest over time. By combining the tissue TAC with the quantitative measurement of the plasma radioactivity (input function), it is possible to derive quantitative information about, for instance, the blood flow, enzymatic activity, and protein densities (Fig. 2.2).

A large number of factors and variables come into play when characterizing the dynamic biodistribution of a radioligand. Mathematical models simplifying the biological system can be helpful in summarizing the main relevant variables in a limited number of parameters.

Radioligand dynamics can be modelled in order to allow a quantitative prediction of the parameter of interest. The selection of an appropriate pharmacokinetic model, describing the underlying biology of the tissue, is crucial to obtain accurate parameter estimates. Since irreversible binding kinetics are not commonly used in PET imaging, only reversible binding kinetics are described. Overall, kinetic models can be divided into two main categories: compartment models, when no reference tissue is available, and reference tissue models, when a reference tissue is available.
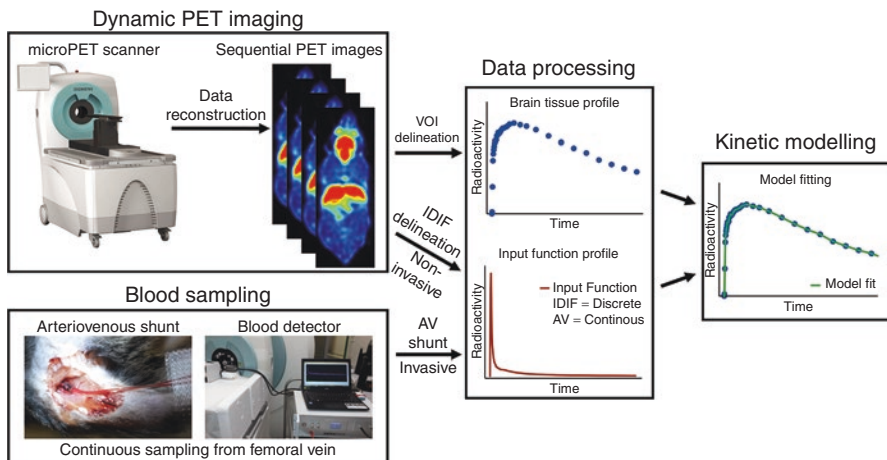
Fig. 2.2 Principle of dynamic PET. The radioligand is injected in the vascular system (via tail vein for rodents) and distributes with specific in vivo kinetics. The profile of the radioligand in the volumes of interest (VOI) and the amount of radioactivity in the blood (input function) can both be measured as a function of time. The input function can be obtained with either invasive (arteriovenous, AV shunt) or noninvasive (image-derived input function (IDIF)) approaches. Pharmacokinetic modelling can be performed in order to fit a specific model to the data and to derive the parameter estimations

2.1.3   Compartment Models

Compartment models are applied when no reference tissue is available. These models require knowledge of an input function, which can be measured with invasive or noninvasive approaches as later described. The physiological system is decomposed into a number of compartments, each contributing to the overall PET signal. Each compartment represents a part of the physiological system and is characterized by a pool of homogenous radioligand that changes over time as a consequence of the exchange of radioligand between compartments. According to compartment models, the radioactivity measured in a region of interest is composed of the radioligand distributed in different compartments at any given time. The fitting of a model to the measured radioligand profile allows to generate a model estimate of the radioligand's steady-state parameters such as the volume of distribution (described in the next section), which is related to receptor density and affinity (Gunn et al. 2001). Thus, if affinity of the radioligand toward the target is not altered, the model estimate informs about changes in receptor density.

2.1.3.1 Volume of Distribution

For receptor radioligands with no reference tissue, the gold standard outcome parameter to estimate is the volume of distribution (V_T). V_T is defined as the ratio of radioligand concentration in the tissue of interest (C_T) (measured in kBq/cm^3) to the concentration of intact radioligand in plasma (C_P) (measured as kBq/mL) *at equilibrium* (Innis et al. 2007). It is measured in mL/cm^3 and can be expressed as follows:

$$V_T = \frac{C_T}{C_P} \tag{2.1}$$

This can be visually depicted when infusion of radioligand is performed. After a certain period of time, the TAC of the radioligand will reach *equilibrium*, and its measurement could provide the V_T (Fig. 2.3). For instance, a V_T equal to five means that the radioligand is concentrated in tissue by five times compared to the blood.

The C_T component of the V_T measurement is composed of three parameters in total:

$$C_T = C_{FT} + C_{NS} + C_S \tag{2.2}$$

where C_{FT} represents the concentration of free radioligand in the tissue, C_{NS} the nonspecifically bound radioligand, and C_S the radioligand bound to the receptor of interest (Fig. 2.4). C_{FT} and C_{NS} can be combined as a single measurement, as they represent the total non-displaceable (C_{ND}) radioligand uptake. This component is independent of the presence of the receptor in the tissue of interest. Thus, Eq. (2.1) can be substituted as follows:

$$V_T = V_S = V_{ND} \tag{2.3}$$

where the total volume of distribution (V_T) is a combination of the specific (V_S) and non-displaceable (V_{ND}) volume of distribution.
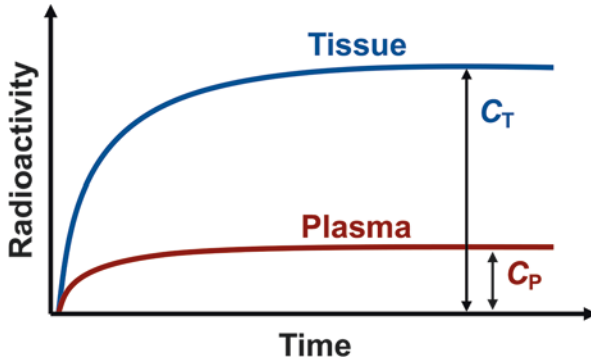
Fig. 2.3 Schematic representation of the radioactivity in tissue and plasma *at equilibrium*. Following radioligand infusion, it is possible to reach *equilibrium* after a certain amount of time, as shown here. At *equilibrium*, the V_T can be measured as the ratio of the concentration in the tissue (C_T) to the concentration in plasma (C_P) as described in Eq. (2.1)

$$C_P = C_{FT} + C_{NS} \qquad C_T = C_{FT} + C_{NS} + C_S$$
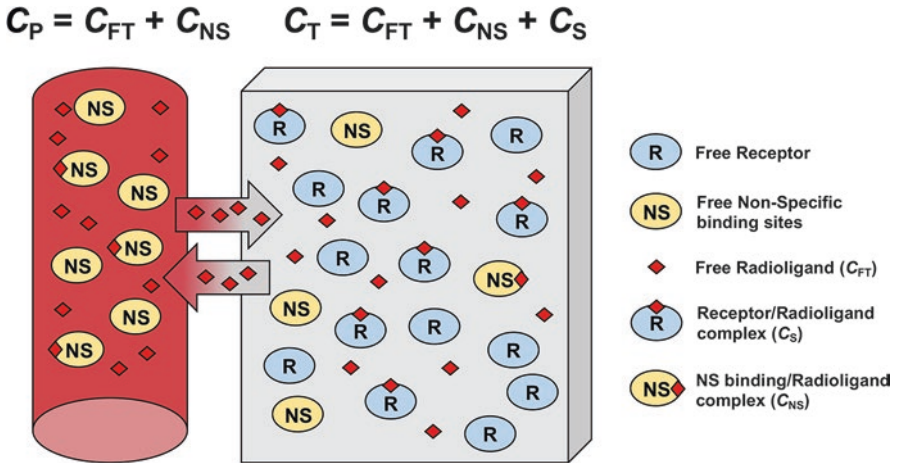
Fig. 2.4 Schematic representation of the components contributing to the radioligand signal in the tissue and the plasma. The concentration of radioligand in the plasma (C_P) is the summation of the concentration of free radioligand (C_{FT}) and the concentration of nonspecifically bound radioligand (C_{NS}). The concentration of radioligand in the target tissue (C_T) is constituted by C_{FT} and C_{NS}, which represent the non-displaceable component (C_{ND}), with the addition of the concentration of specifically bound radioligand to the receptor (C_S)

V_s and thus V_T are linked to the receptor density in the region of interest and the binding affinity and thus to the binding potential, which will be described later.

2.1.3.2 Input Function

In order to perform accurate quantification of the PET data, an input or reference tissue is required to provide information of the amount of available radioligand. A plasma input function is used for compartment models, while a brain region TAC is

employed in reference tissue models. The selection of one over the other depends on the distribution of the radioligand's target in the brain. If a region devoid of a target is present in the brain, that region can be used as reference tissue; otherwise, a plasma input function is required. The use of a brain region as reference tissue will be discussed in Sect. 2.1.4.

The input function describes the concentration of intact radioligand in arterial plasma as a function of time and represents the delivery of the radioligand to the brain. Subject cannulation for continuous arterial blood sampling with correction for radiometabolites in plasma represents the gold standard in quantitative PET data analysis. However, this procedure is laborious and invasive for patients (or small animals) (Jons et al. 1997), including many challenges and possible biases related to blood sampling, peripheral metabolism, and plasma protein binding. In particular, arterial blood sampling is specifically required for accurate measurement of the plasma radioactivity; however, arterial cannulation is invasive and, while it may be well tolerated in healthy subjects, is often a concern in ill or aged subjects with arteriosclerosis, especially for longitudinal studies. Venous blood sampling is less invasive and laborious, improving the comfort of the patient. However, radioligand venous concentration is never consistent with the arterial concentration since the venous concentration is dependent on the clearance of the compound from the tissue, thus the sampling site (Chiou 1989; Gumbleton et al. 1994; Zanotti-Fregonara et al. 2011).

Alternatively, blood sampling at a few precise moments during the scan is a valid alternative but still requires the arterial cannulation of the subject. Although blood sampling is also possible in rodents (Weber et al. 2002), it often represents a terminal procedure. Therefore, it cannot be applied for longitudinal studies. In addition, in mice, blood sampling has further limitations because the amount of available blood is extremely limited (usually 1.5–2 mL, around 58.5 mL/kg of body weight).

A possible alternative is the noninvasive extraction of the blood radioactivity data using the dynamic µPET data, an approach referred to as image-derived input function (IDIF). IDIF application is relevant in small animal imaging due to the difficulty of regular blood sampling without altering the physiological state (Laforest et al. 2005), especially in longitudinal study paradigms that require serial PET acquisitions. The majority of IDIF approaches use the signal from a large blood vessel or the left cardiac ventricle from the dynamic PET acquisition. However, IDIF approaches have many challenges (Zanotti-Fregonara et al. 2011) since the quality of the IDIF is affected by several factors: the measurement of whole blood, the accumulation of radiometabolites, the cardiac or large vessel region in the µPET scanner field of view (FOV), the sampling rate (PET frames), the cardiac rhythm, the sensitivity of the µPET scanner, and the quality of the reconstruction software. As many of these limitations are related to the individual µPET scanner and/or reconstruction software, it is usually recommended to validate an IDIF protocol in each laboratory independently. An important drawback of IDIFs is the presence of blood radiometabolites, which cannot be distinguished from the signal provided by the intact radioligand. A possible approach to overcome this restriction is the application of a population-based input function. For this approach, in vivo radioligand

metabolism is calculated at different times postinjection in an animal cohort representative of the overall population, and the average profile is calculated. However, this method has the limitation of requiring extremely highly comparable metabolic profiles of the radioligand across subjects, which, if not the case, may introduce under-corrections or overcorrections in the estimation of the parent radioligand contribution, thus in the V_T.
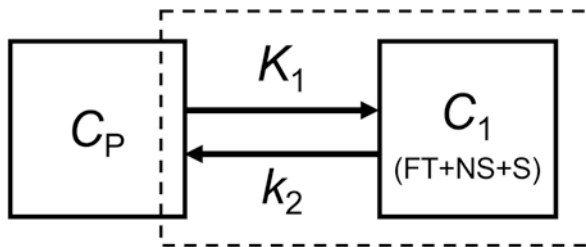
2.1.3.3 One-Tissue Compartment Model

The one-tissue compartment model (1TCM) is composed of two compartments (Fig. 2.5). As for all compartment models, the first compartment is described by the input function C_P. The concentration of radioligand in the region of interest is defined by a single compartment, and thus, C_{FT}, C_{NS}, and C_S are lumped together. Exchange of radioligand between the two compartments is represented by the rate constants K_1 and k_2 (Koeppe et al. 1991; Lassen 1992), and the change of activity in the tissue compartment is given by the following differential equation:

$$\frac{dC_1(t)}{dt} = K_1 C_P(t) - k_2 C_1(t) \tag{2.4}$$

When applying the 1TCM, the volume of distribution can be determined as follows *at equilibrium*, hence the first order derivative being zero:

$$V_T = \frac{K_1}{k_2} \tag{2.5}$$

The two rate constants K_1 and k_2 represent the transport of radioligand from and to the plasma compartment, respectively. K_1 denotes the unidirectional transport of the radioligand from plasma to the tissue. Its value depends on perfusion and plasma extraction, which is a combination of capillary permeability and capillary surface area. Thus, K_1 is representative of the delivery rate in the region of interest. For radioligands featuring high brain permeability, it nearly equals perfusion. K_1 is measured as mL/cm^3 per minute, while k_2 describes the fractional rate constant for the washout of free radioligand transferred to plasma per unit time, measured as 1/minute.

Fig. 2.5 Schematic overview of the one-tissue compartment model. Following the injection into the vascular system (C_P), the radioligand is transported from the plasma to the tissue (C_1) at a certain delivery rate (K_1), with the free radioligand component (C_{FT}) transferred back to plasma at a fractional rate constant (k_2). The dashed box indicates the total component present in the tissue of interest, as a vascular component is within the brain region and cannot be separated

2.1.3.4 Two-Tissue Compartment Model

The two-tissue compartment model (2TCM) is composed of three compartments, as depicted in Fig. 2.6. Analogous to 1TCM, the first compartment is described by the input function C_P. In the 2TCM, the concentration of the radioligand in the region of interest is defined by two compartments: the first compartment (C_1) is the non-displaceable contribution ($C_{FT} + C_{NS}$), while the second component (C_2) represents the specific binding to the receptor (C_S).

Exchange of radioligand between the three compartments is described by the rate constants K_1, k_2, k_3, and k_4 (Koeppe et al. 1991; Lassen 1992) with the following differential equations:

$$\frac{dC_1(t)}{dt} = K_1 C_P(t) - (k_2 + k_3)C_1(t) + k_4 C_2(t) \tag{2.6}$$

$$\frac{dC_2(t)}{dt} = k_3 C_1(t) - k_4 C_2(t) \tag{2.7}$$

When applying the 2TCM, the volume of distribution can be determined as follows:

$$V_T = \frac{K_1}{k_2}\left(1 + \frac{k_3}{k_4}\right) \tag{2.8}$$

Compared to 1TCM, 2TCM includes two additional rate constants. k_3 represents the association rate constant to the specific binding site, while k_4 describes the dissociation rate constant of the receptor-radioligand complex. Analogous to k_2, both k_3 and k_4 are reported per unit time (1/minute).

Although 2TCM has a larger number of parameters to fit, thus it is more sensitive to noise, and it has the advantage of allowing estimation of more complex kinetics, including approximation of V_{ND} and V_S. V_{ND} can be seen as the V_T of the first compartment C_1, and thus, it is described by a 1TCM equation as follows:

$$V_{ND} = \frac{K_1}{k_2} \tag{2.9}$$
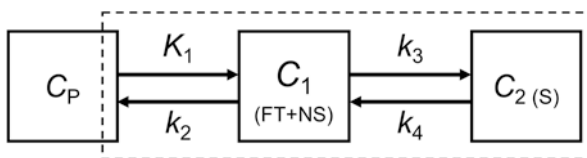
Fig. 2.6 Schematic overview of the two-tissue compartment model. Following the radioligand injection into the vascular system (C_P), the tracer is transported from the plasma to the tissue (C_1) at a certain delivery rate (K_1), with the free radioligand component (C_{FT}) transferred back to plasma at a fractional rate constant (k_2). The radioligand binds specifically to the receptor (C_2) at an association rate (k_3) and dissociates from the receptor at a precise rate (k_4). The dashed box indicates the total component present in the tissue of interest, as a vascular component is within the brain region and cannot be separated

In addition, as the main interest relies on specific binding of the radioligand to the receptor, 2TCM allows to estimate the V_S as the difference between V_T and V_{ND} based on Eq. (2.3).

2.1.3.5 Logan Plot

One- and two-tissue compartment models, as full kinetic models, are very informative and provide estimations for the microparameters K_1, k_2, k_3, and k_4. However, due to the number of variables that needs to be fitted, they are sensitive to noise, and in certain situations, the accuracy of the estimation might be compromised. Therefore, the Logan plot (Logan et al. 1990) represents a robust alternative for radioligands with reversible kinetics. It is a "graphical" method that normalizes the measurements using a mathematical transformation, which simplifies the differential equations of the more complex compartment models to a linearized model:

$$\frac{\int_0^t C_T(\tau)\,d\tau}{C_T(t)} = K\frac{\int_0^t C_P(\tau)\,d\tau}{C_T(t)} + b \tag{2.10}$$

As a result, the estimation of the V_T (slope K) using a Logan plot is easier compared to using compartment models (Fig. 2.7). However, also the Logan plot is susceptible to noise in the data for low activities, which can result in an underestimation of the V_T (Logan et al. 2001; Varga and Szabo 2002). For this reason, before application of this linearization approach, it is always recommended to verify its stability over the compartment models.
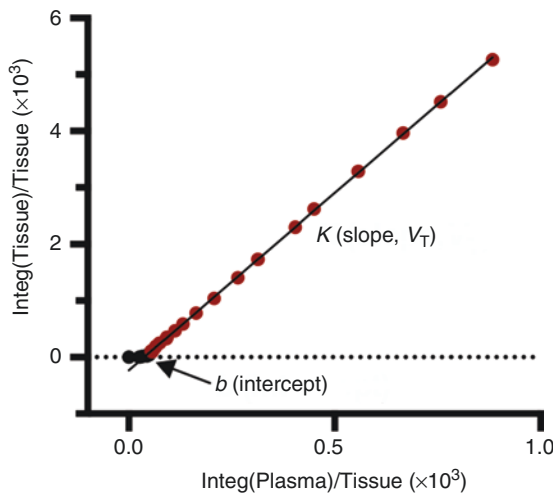
Fig. 2.7 Representative Logan plot fitting. As described in Eq. (2.10), when applying the Logan plot graphical analysis, the integral of the tissue activity over the tissue activity is plotted versus the integral of the input function over the tissue activity. The result of the fitting is a straight line (black line) starting after an equilibration period defined as t^*. The slope of the fitting, K, depicts the V_T value. The tissue activity values considered for the linearization are depicted in red, while values before t^* are depicted in black

2.1.4   Reference Tissue Models

Unlike compartment models, reference tissue models have the advantage of not requiring a vascular input function. Thus, all challenges and possible biases related to blood sampling, peripheral metabolism, and plasma protein binding are absent. These models provide an estimate of the binding potential (BP) of a radioligand-receptor complex. The concept of BP is described in the next section.

To apply reference tissue models, there are two conditions that need to be met: (i) A reference tissue completely devoid of target, i.e., with no (or negligible) specific binding of the radioligand, is required (Lammertsma and Hume 1996). (ii) The V_{ND} of the radioligand should be similar in all investigated regions, i.e., the ratio K_1 over k_2 is comparable. Thus:

$$\frac{K_1}{k_2} = \frac{K_1^{'}}{k_2^{'}}$$

(2.11)

where K_1' and k_2' are the microparameters of the reference tissue.

Based on the equation above, it is possible to estimate the delivery ratio R_1:

$$R_1 = \frac{K_1}{K_1^{'}} = \frac{k_2}{k_2^{'}}$$

(2.12)

which describes the ratio of relative influx in the region of interest and in the reference tissue. As a ratio, R_1 is unitless.

2.1.4.1   Binding Potential

When applying reference tissue models, the gold standard is represented by the binding potential (BP). BP is the ratio of the total density of receptors in the tissue (receptor concentration) (B_{max}) to the equilibrium dissociation constant of the radioligand (K_D) (Mintun et al. 1984). Thus, *BP* is given by a combination of receptor density and affinity of the radioligand toward the receptor as follows:

$$BP = \frac{B_{max}}{K_D} = \text{receptor density} \times \text{affinity}$$

(2.13)

When performing PET imaging, *BP* can be determined in vivo if a region with only non-displaceable uptake exists, in order to estimate the so-called non-displaceable *BP* (BP_{ND}) (Innis et al. 2007). BP_{ND} quantifies the equilibrium concentration of specific binding as compared to a region with only non-displaceable binding (reference tissue) and can be calculated as follows:

$$BP_{ND} = \frac{(V_T - V_{ND})}{V_{ND}} = \frac{V_T}{V_{ND}} - 1 = \frac{k_3}{k_4}$$

(2.14)

The ratio V_T to V_{ND} is referred to as distribution volume ratio (DVR) (Logan et al. 1996), and it can be determined using the compartment models if a reference tissue region is available for calculation of V_{ND}. BP_{ND} is a ratio of two volumes of distribution and is therefore unitless.

2.1.4.2 Simplified Reference Tissue Model

The simplified reference tissue model (SRTM) is a simplification of the full reference tissue model in which no distinction is made between the non-displaceable and specific components of the target region, as depicted in Fig. 2.8. For this reason, it performs the best when the kinetic of the radioligand could be described using 1TCM (Lammertsma and Hume 1996). In the SRTM, a total of three components can be identified: the input function (C_P), the region of interest (C_{ROI}), and the reference tissue (C_{REF}). As the input function C_P is the same for both C_{ROI} and C_{REF}, its measurement is not required if the delivery rates (K_1 and K_1') are similar. In addition, the C_{REF} needs to be devoid of specific binding (Lammertsma and Hume 1996).

Exchange of radioligand for SRTM can then be described by the following differential equation:

$$\frac{dC_{ROI}(t)}{dt} = R_1 \frac{dC_{REF}(t)}{dt} + k_2 C_{REF}(t) - \frac{k_2}{1 + BP_{ND}} C_{ROI}(t) \qquad (2.15)$$

2.1.5 Receptor Occupancy and Displacement

In addition to quantification of receptor density, PET imaging has the potential to assess target engagement through quantitative measurements of receptor occupancy (RO) (Lassen et al. 1995; Cunningham et al. 2010). RO of the radioligand binding site by a treatment drug can be described as follows:

$$RO = \left(1 - \frac{B_{avialble}(\text{treatment})}{B_{available}(\text{baseline})} \right) \times 100\% \qquad (2.16)$$

where $B_{available}$ (treatment) and $B_{available}$ (baseline) represent the density of available receptors for the radioligand under the drug condition and during baseline,
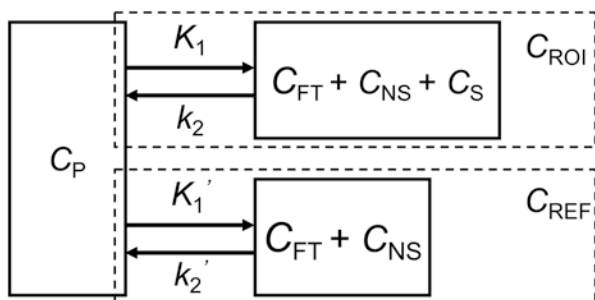
Fig. 2.8 Schematic overview of the simplified reference tissue model. Following the injection into the vascular system (C_P), the radioligand is transported from the plasma to the tissue of interest (C_{ROI}) and the reference (C_{REF}) at a similar delivery rate (K_1 and K_1' prime), with the free radioligand component (C_{FT}) transferred back to the plasma at a fractional rate constant (k_2 and k_2'). The non-displaceable binding ($C_{FT} + C_{NS}$) is comparable between the tissue of interest (C_{ROI}) and the reference (C_{REF}). The dashed box indicates the total component present in the tissue regions
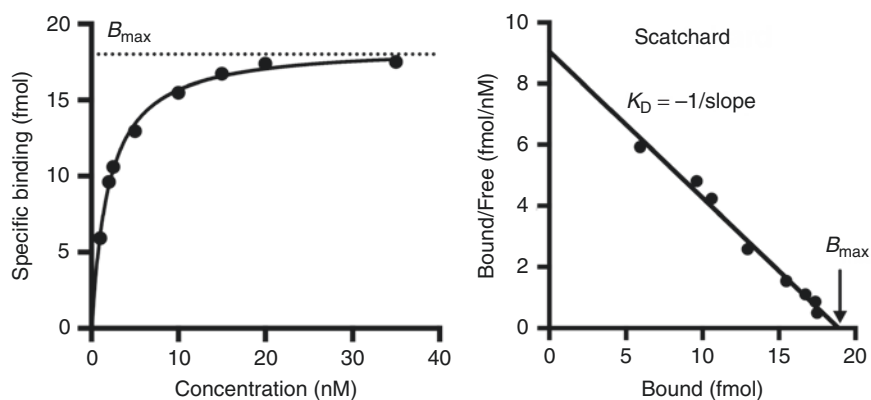
Fig. 2.9 Representative saturation study to estimate B_{max} and K_D. The receptor density (B_{max}) and equilibrium dissociation constant (K_D) can be estimated by generating a saturation curve where the specific binding of a compound is measured at different doses (concentrations of compound) (left). The estimation can be linearized by transforming the data of the saturation curve in a Scatchard plot (right), where the intercept with the *x*-axis represented the B_{max} and the K_D is -1/slope

respectively (Innis et al. 2007). For instance, this paradigm is extremely useful in the determination of drug dosage to determine the desired in vivo target occupancy (Cunningham et al. 2005). Additionally, B_{max} and K_D can be estimated by performing a saturation binding study to generate a curve where the specific binding of the compound of interest is measured at different doses (concentrations of compound) (Fig. 2.9). This estimation can also be represented linearly by transforming the data of the saturation curve in a Scatchard plot, where the intercept with the *X*-axis represented the B_{max} and the K_D is -1/slope (Fig. 2.9). Notably, by performing serial PET scans with increasing amounts of cold ligand, thus with cumulative target saturation studies, an estimation of the in vivo B_{max} and K_D can be determined. Alternatively, PET scans can be performed using a competitive ligand to block or displace the receptor. This approach has the potential to confirm the specificity of the binding of novel radioligands, to provide an estimate of the amount of non-displaceable binding contributing to the PET signal in the tissue of interest, and to investigate whether a reference tissue region devoid of specific binding exists.

2.1.6   Semiquantitative Approach

When a radioligand presents slow and stable (reversible or irreversible) kinetics, the quantitative pharmacokinetic modeling based on dynamic imaging may be replaced by a simpler semiquantitative static approach. The most common static measurement is the standardized uptake value (SUV). Unlike dynamic imaging, SUV is based on a static acquisition starting when, following radioligand system injection,

the kinetics of the radiotracer have stabilized. SUV typically lasts for a time window of 15–20 minutes, and it is measured as follows:

$$\text{SUV} = \frac{C_t}{\text{ID} / \text{BW}} \tag{2.17}$$

where C_t represents the concentration of activity in the tissue of interest, ID is the dose injected into the animal, and BW is the body weight of the subject.

The most common radioligand measured with semiquantitative approaches is [18F]2-fluoro-2-deoxy-D-glucose ([18F]FDG), thanks to its semi-irreversible kinetics. [18F]FDG is a glucose analogue; therefore, it can be used to measure glucose metabolism.

Following system injection, [18F]FDG enters the brain via glucose transporters. Due to its similarity to glucose, [18F]FDG directly competes with glucose for the binding to the glucose transporters in the brain. Because of this competition, animals are generally fasted several hours before [18F]FDG administration in order to guarantee low blood glucose levels and, consequently, high cerebral [18F]FDG uptake (Deleye et al. 2014). Once in the brain, free [18F]FDG can either be transported back to the vascular system (C_P) or be phosphorylated by hexokinase to [18F]FDG-6-phosphate ([18F]FDG-6-P). The latter cannot be further metabolized through metabolic pathways and remains trapped into the tissue. Thus, as depicted in Fig. 2.10, [18F]FDG kinetics for glucose transport and phosphorylation in the brain resemble the 2TCM, as described above. Although the [18F]FDG-6-P uptake is not fully irreversible, its efflux constant (k_4) is much slower than the metabolic rate (k_3); therefore, k_4 can be assumed to be equal to zero.

2.1.7 Radioligands

Given the versatility of PET imaging, this technique can be theoretically applied to image all biological processes if a radioligand for the target of interest is available.
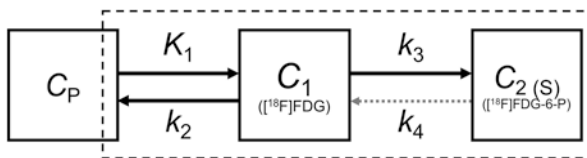
Fig. 2.10 Schematic overview of the 2TCM applied to [18F]FDG. Following [18F]FDG injection into the vascular system (C_P), the radiotracer is transported from the plasma to the tissue (C_1) at a certain delivery rate (K_1), with the free radioligand component (C_{FT}) transferred back to the plasma at a fractional rate constant (k_2). [18F]FDG is phosphorylated into [18F]FDG-6-P (C_2) at a certain metabolic rate (k_3), and its efflux from the tissue (k_4) occurs at a much slower rate; thus, it is assumed to be negligible. The dashed box indicates the total component present in the tissue of interest, as a vascular component is within the brain region and cannot be separated

Nonetheless, reversibly binding radioligands feature a series of requirements that need to be met in order to be suitable for receptor imaging:

– *Availability of the target*: The amount of target available for the radioligand depends on the specific target. For receptor imaging, this amount is generally in the nanomolar range; thus, the amount of radioligand injected into the animal has to be consistent (and low) to avoid any target saturation or pharmacological effect.

– *Specificity toward the target*: In order to investigate the pharmacokinetics, the process of reversible binding of the radioligand from the target should be the main, if not the only, process to occur in the region of interest. This means that the presence of labelled metabolites should be minimal or absent and a low specific binding toward any other molecule is desired. For instance, the radioligands for the dopaminergic D_1 receptor, namely, [^{11}C]SCH23390 and [^{11}C]NNC-112, feature affinity toward serotonin 2A receptors (Ekelund et al. 2007).

– *Radiometabolites*: Following injection into the vascular system, radioligands undergo metabolism, which results in the generation of radiometabolites as a consequence of xenobiotic-degrading enzymes in the blood, liver, and kidneys. For brain imaging, this does not represent a major drawback as long as the radiometabolites generated in plasma are polar and cannot penetrate the blood-brain barrier (BBB) and no metabolism occurs in the brain.

– *Low nonspecific binding*: Another variable that might hamper the sensitivity of a radioligand is the amount of nonspecific binding in the tissue of interest. Ideally, a good radioligand washes out from a region quickly if no target is present. However, radioligands might have nonspecific binding toward other undefined molecules causing longer retention. This represents the major contributor to the non-displaceable binding component and cannot be avoided.

– *Trace amount*: The radioligand introduced to the system needs to be in trace amount in order to avoid perturbation of the process meant to be measured. Accordingly, less than 5% of receptors should be occupied by the radioligand (Hume et al. 1998). However, this is challenging in small animals because of the low amount of total target available, which demands extremely high molar activities. Molar activity is a measure of the amount of radioactivity in a given number of moles of ligand. Thus, the higher the molar activity, the less non-labelled molecules of the radioligand are injected into the system and compete for the receptor (Elsinga 2002). This is particularly relevant for small animal imaging where the amount of injected radioligand is often above the 5% occupancy (trace amount) and a high-affinity radioligand is used. Thus, the calculated injected mass of each animal should always be corrected for the molar activity of the specific radiosynthesis in order to avoid changes in receptor occupancy across subjects. This erroneous methodology can generate artificial changes in radioligand binding.

– *Low plasma protein binding*: Following injection into the vascular system, a portion of the total radioligand binds to plasma proteins. The binding to plasma proteins means less free fraction of radioligand available to reach the region of interest, and high protein binding leads to prolonged blood circulation. Plasma protein binding is generally related to the lipophilicity of the molecule.
– *Target accessibility*: The major factor avoiding target accessibility in brain imaging is the BBB. While radiometabolites should not cross the BBB, high penetrance by the radioligand is critical to allow in vivo pharmacokinetic analysis. It is poorly understood which factors contribute to membrane permeability, with the exception of lipophilicity.
– *Appropriate in vivo pharmacokinetics*: In order to perform dynamic PET imaging and obtain accurate parameter estimations for a radioligand, it is critical that the in vivo pharmacokinetic profile is in the time window of PET scan acquisition time and isotope decay. For instance, PET imaging is sensitive to noise; thus, the temporal sampling rate of the kinetic data has some restrictions. However, if radioligand efflux from the region of interest is extremely fast, the PET scanner cannot detect it accurately. Conversely, if the influx and efflux of the radioligand labelled with C-11 ($t_{1/2}$ = 20.39 minutes) into the region of interest is too slow, thus requiring a longer acquisition time, the kinetic data may become too noisy for accurate quantification.

2.2   PET Motion Correction: State of the Art

One technological innovation in small animal PET imaging that is of particular interest to imaging of neurobiological systems is PET imaging of awake unconstrained animal. As such, an approach has the potential to circumvent the, often unknown, impact of anesthesia on the PET reading of the brain function. Since the first demonstration of awake animal imaging, now already 10 years ago, a few research groups have worked on further improving the technology (Kyme et al. 2008). Our group has mainly focused on making the method practically feasible in a routine small animal PET imaging setting. As this technology is now becoming available, we can not only avoid the impact of anesthesia on the PET outcome, but we can also implement previously unfeasible experimental paradigms where we can monitor and/or alter behavior during PET imaging. Indeed, this approach has great potential to dynamically monitor brain uptake of a radioligand during the occurrence of, for example, compulsive-like behaviors in animal models for obsessive compulsive disorder, as discussed in Sect. 2.3. In addition, the method also allows to image interacting animals in larger imaging systems (Miranda et al. 2019b). The next paragraphs introduce the problem of anesthesia, give a brief overview of several approaches to awake animal imaging, and finally demonstrate the technique in a typical small animal brain PET study with excessive animal motion due to pharmacological stimulation.

2.2.1   The Need for Awake PET: Anesthesia, Stress, and Its Impact on Small Animal PET

A major difference between preclinical brain PET research in small animals and human brain PET is the use of anesthesia to immobilize the animal during the study to avoid image blurring caused by animal motion. In contrast, human subjects are usually scanned in a conscious state. Several studies have investigated to which degree anesthesia affects the animal's brain response for specific PET radiotracers as reviewed by Alstrup and colleagues (Alstrup et al. 2013). For example, in line with previous ex vivo studies using 2-[^{14}C]-deoxyglucose (Sokoloff et al. 1977; Lenz et al. 1998), an overall lower [^{18}F]FDG brain uptake was observed in anesthetized animals (Toyama et al. 2004; Mizuma et al. 2010). However, for certain radiotracers, the effect of anesthesia on the PET uptake is still unknown.

Injectable and inhalant anesthetic agents are used to immobilize small animals to perform imaging scans. Due to its practicality, inhalant anesthetic agents are more commonly used.

Since scanning of awake animals under physical restraint has been proposed to avoid the effects of anesthesia, studies have also been performed to assess the impact of restraining stress on the radiotracer brain uptake. Sung et al. (2009) performed [^{18}F]FDG scans of rats that underwent restraining stress 1 and 2 h prior to a PET scan. It was shown that restraining stress, induced by fixing the rat limbs, modifies the [^{18}F]FDG brain uptake in comparison with unrestrained rats. Even after a 1 h recovery from restraining, the change in [^{18}F]FDG brain uptake in comparison with control rats endured.

The effect of anesthesia and stress on the animal's brain response have motivated research in performing brain PET scans of awake and unrestrained small animals. A method proposed by Schulz et al. (2011) makes use of a specially designed miniaturized PET scanner attached to a rat's head. A mechanical system is needed to counterbalance the weight of the PET scanner and allow motion of the rat. Another approach proposed by Balasse et al. (2015) measures the activity in small regions of the awake rat brain using a beta-probe. A portable wireless measurement system for the beta-probe was built inside a backpack that is placed on the rat. These methods require specially designed devices and surgical implantation of the device in the skull of the rat.

A different approach that makes use of typical preclinical PET scanners to perform awake rat PET scans was proposed by Kyme et al. (2008). In this method, the motion of the rat head is measured while it is scanned, and the PET data is corrected for motion using the tracking data. Awake mouse brain scanning has also been investigated (Baba et al. 2013), although the problem is more challenging than rat awake scanning due to the smaller size of the animal.

Finally, awake brain scanning not only avoids undesired effects on the animal's brain response from anesthesia and stress; it would also allow to expand the experimental design to setups where the conscious response of the subject to external sensorial stimuli could be investigated, similar to what has been done for several years in human brain PET and MRI studies (Frith et al. 1991; Reiman et al. 1997; Crespo-Facorro et al. 2001).

2.2.2   Motion Correction in PET Reconstruction

In order to perform brain PET scans in awake animals, methods for human brain rigid motion correction can be adapted to be used in preclinical PET scanners. One of these methods consists of measuring the six degrees of freedom (DOF) motion of the human head and relocating each line-of-response (LOR) back to a reference pose (translation and rotation) according to the measured motion with (Menke et al. 1996) or without (Rahmim et al. 2004) additional rebinning to a sinogram. This approach is convenient to use when continuous motion is present and is therefore the usual method for small animal PET brain motion correction. The method requires data acquisition in list-mode format, a condition fulfilled in most modern PET scanners. In the next section, methods to perform the motion tracking of the animal head are detailed.

2.2.3   Head Motion Tracking for Awake Small Animal PET

The challenges in awake small animal brain PET scanning are considerably greater than in human brain PET motion correction. The motion of freely running small animals is considerably larger than the motion of a human head inside a scanner. In addition, the tracking devices need to be able to track inside smaller bore size scanners than in human motion tracking. Also, the tracking accuracy needs to be higher to avoid image degradation in preclinical scanners with finer spatial resolution. Moreover, different correction approaches in the motion correction algorithm need to be implemented or developed to obtain reconstructions with quantitative information.

2.2.3.1   State of the Art

Several approaches have been proposed to track the animal head motion. One of the earliest methods is the one proposed by Kyme et al. (2008). In this method the marker-based optical tracking camera MicronTracker (Claron Technology Inc., Toronto, Canada) is used to measure the motion of the rat's head during the PET scan. A small rectangular marker is pasted on the head to measure its motion. This method performs well if the motion of the rat is restricted to face toward the tracking camera, normally placed in front of the scanner. If the rat turns around or the marker is occluded by the scanner bore, the tracking information is lost. With this method, motion-corrected images are obtained by repositioning of the LORs and performing LOR rebinning or list-mode motion correction.

Kyme et al. (2014) also developed a markerless rat head tracking method. By acquiring different views from the rat head and matching face features in the different views, the pose of the head is determined. Although in theory natural features of the rat head can be used (e.g., eyes), in this work, it was found that painting a pattern on the rat fur is necessary to increase the accuracy of the motion tracking data.

2.2.3.2 Optical Tracking Methods

Optical tracking methods work with the principle of stereovision. For these methods, features in different views of the space that needs to be mapped are used to determine the 3D location of points in this space. In addition, since the tracking data is measured with respect to the camera coordinate system and time, a spatial and temporal calibration needs to be performed to transform the camera tracking information to the coordinate system and time of the PET scanner.

Stereovision

Two 2D images acquired from two different views of the same scene can be used to calculate the 3D position of points in the scene. A 2D image can be seen as a planar projection of a 3D scene on which each point in the 2D image plane is the image of a 3D point on the scene which intersects a 3D ray (line) coming from the camera that forms the image. By triangulation of two of these rays that intersect the same point (from different views), the 3D coordinate of the point can be calculated (Fig. 2.11). If all points (up to the image resolution) on the two different images can be related to a point in the other image, a disparity map can be calculated by triangulating all points. The disparity map is then a 3D surface mapped space.

There also exist other devices that could be used for motion tracking using 3D vision. These devices have different working principles. For example, time-of-flight (TOF) cameras measure the distance from several points on the surface of objects to the camera by measuring the distance travelled from light projected and detected back to the camera. This information renders a 3D map of the object. Most of these cameras are used for broad-field applications, such as geological surface mapping
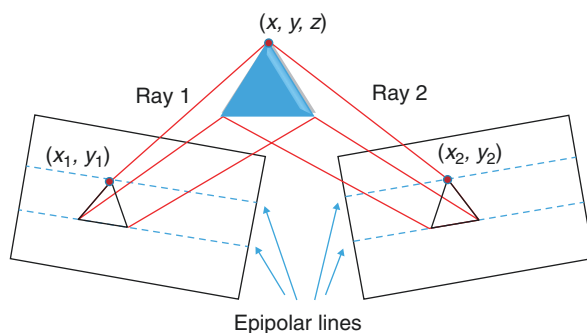
Fig. 2.11 By determining that the point (x_1, y_1) on image 1 corresponds to the image of the point (x_2, y_2) on the second image, e.g., using image correlation, and with knowledge of the camera intrinsic parameters, the 3D point (x, y, z) can be calculated. The intrinsic parameters of the camera serve to determine the equations of ray 1 and 2. The 3D point (x, y, z) can be found by triangulation of these two rays. The search for the corresponding 2D point in the other image can be simplified by calculating the epipolar lines. The epipolar line in one image will contain all points of the corresponding epipolar line of the other image (if the points are within the corresponding field of view of the camera)

and atmospheric mapping. To our knowledge, no high precision TOF camera for small-scale applications with high frame rate, such as that required for PET motion tracking, is commercially available.

### 2.2.3.3 PET-Based Motion Tracking

As the PET image provides the 3D location in space of the radiotracer, in theory, this information could be used to determine the pose of the object containing the radiotracer. However, short time-frame PET images, required to determine fast motion, present high noise, thereby hindering the possibility of accurate image registration. In addition, the radiotracer distribution changes over time, making it difficult to define a unique image to perform the registration.

The problem of high image noise in the short time frames and changing tracer distribution can be solved by using radioactive point sources as fiducial markers. The point sources can be accurately reconstructed in short time frames, and their activity distribution does not change over time.

Point Source Tracking

For this method, radioactive point sources are used as markers attached to the object to be tracked. By detecting the position of at least three noncollinear points in 3D space arranged in an asymmetric cluster, the six DOF of the point configuration (and of the object they are attached to) can be uniquely defined. This method performs the motion tracking without additional hardware, and therefore, a spatial and temporal synchronizations are not necessary, which avoid any associated calibration errors.

The point sources used as markers are prepared using sodium polyacrylate grains with sizes of less than 1 mm. The grains are repeatedly soaked in [^{18}F]FDG for a few seconds until an activity between 148 and 222 kBq is reached. The radioactive point sources are attached to the object prior to the PET scan. At least three point sources must be attached to the head of the rat or mouse (Fig. 2.12).
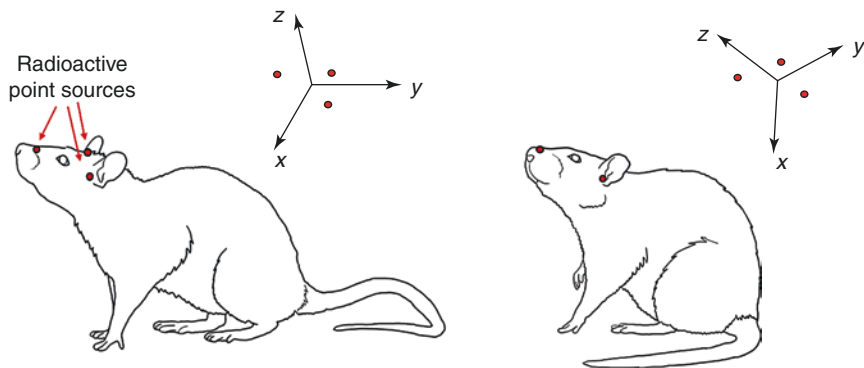
Fig. 2.12 By attaching radioactive point sources to the head of the rat (or mouse), its rigid motion can be determined by defining a rigid coordinate system fixed with respect to the point source geometry

The tracking algorithm works by identifying the position of point sources in the image space. In order to track high-speed motion, the PET data is divided in short time frames, and these frames are reconstructed. The duration of every frame is 32 ms, i.e., a tracking frame rate of 31.2 Hz.

2.2.4   Awake [18F]FDG PET Imaging of Memantine-Induced Brain Activation and Test-Retest in Freely Running Mice

The point source tracking method has been used to perform a [18F]FDG brain uptake experiment in freely running mice (Miranda et al. 2019a). A test-retest and challenge study using the stimulant drug memantine was performed. For these experiments, point sources were attached to the head of the mouse to track their motion during the PET scan. Awake mice were placed on a cylindrical holder inside the PET scanner and scanned during 20 minutes. A test, a retest, and a memantine challenge scan were performed in 8 mice (24 scans in total). Additionally, eight mice were scanned in the same three conditions under anesthesia to obtain a motion-free image for comparison. Since an awake [18F]FDG uptake period of 20/30 minutes was allowed before the beginning of the PET scan for both the awake and the anesthesia scans, [18F]FDG brain uptake in the anesthesia and the awake state should be similar (Matsumura et al. 2003).

2.2.4.1 Mouse Behavior in Awake Scans
The average speed of the mice during the test-retest scans was 2.09 cm/s and more than doubled during the memantine scans to 4.25 cm/s. The travelled distance during the memantine scans (18.2 m) was significantly higher compared to the test-retest conditions (6.49 m). During test-retest scans, mice moved sporadically and remained in the same location for long periods of time. On the other hand, during memantine scans, mice moved constantly during the entire scan duration with short resting periods.

2.2.4.2 Brain Regional Quantification
Figure 2.13 shows the regional brain [18F]FDG uptake in the test, retest, and memantine conditions, in both awake and anesthetized mice. The uptake in the cortex, the caudate putamen, the thalamus, the hippocampus, and the cerebellum was investigated. In both the anesthesia and the awake state, there is a significant difference ($p < 0.05$) in regional brain uptake between test-retest and memantine conditions, except in the thalamus and cerebellum in the anesthesia state. Differences between test–retest and memantine conditions were more pronounced in the awake state in comparison with the anesthesia state. This might be caused by the use of anesthesia before (awake) [18F]FDG injection to attach the point sources in awake mice. In both the awake and the anesthesia state, there was no significant difference between the test and the retest conditions.

When comparing the uptake in the anesthesia and awake groups, the test and retest uptake tends to be lower in the awake state. On the other hand, there was no significant difference in uptake when comparing anesthetized with awake animals in the
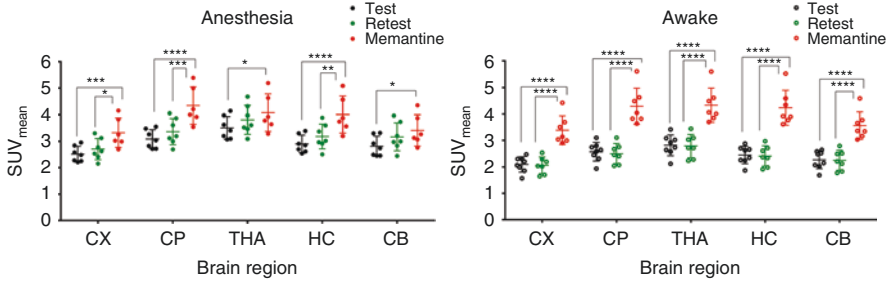
Fig. 2.13 Scatter plot of [^{18}F]FDG standard uptake values (SUV) for different brain regions in the test, the retest, and the memantine challenge conditions for both the anesthesia and the awake group. (Significance level $^*p < 0.05$, $^{**}p < 0.01$, $^{***}p < 0.001$, $^{****}p < 0.0001$. *CX* cortex, *CP* caudate putamen, *TH* thalamus, *HC* hippocampus, *CB* cerebellum. This research was originally published in JNM. Miranda A, et al. Awake ^{18}F-FDG PET Imaging of Memantine-Induced Brain Activation and Test–Retest in Freely Running Mice. *J Nucl Med*. 2019;60:844–850. © SNMMI)
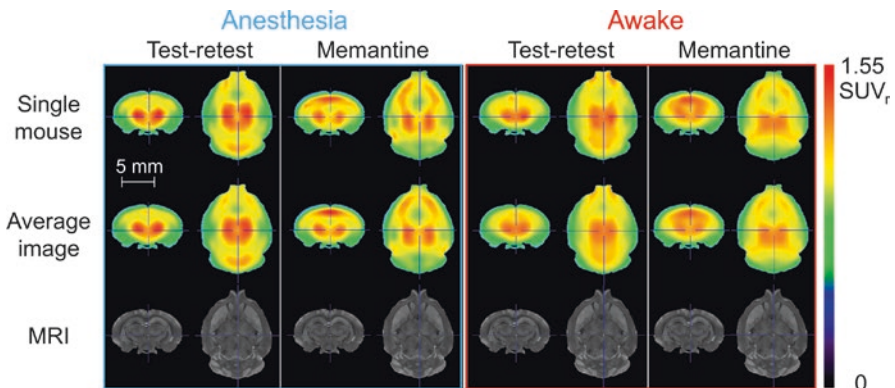
Fig. 2.14 The anesthesia and awake [^{18}F]FDG images for a single mouse and averaged over all mice from each group. MRI template images are included as an anatomical reference. The test-retest and the memantine challenge conditions are displayed for each group. Image values are normalized to whole brain uptake for visualization purposes. (SUV ratio (SUV$_r$); This research was originally published in *JNM*. Miranda A, et al. Awake ^{18}F-FDG PET Imaging of Memantine-Induced Brain Activation and Test–Retest in Freely Running Mice. J Nucl Med. 2019;60:844–850. © SNMMI)

memantine condition. This might be caused by the longer waiting period between the administration of the anesthesia to paste the point sources and the [^{18}F]FDG injection in the memantine scans (40 minutes), compared to the test-retest scans (10 minutes).

Figure 2.14 shows the brain reconstructions for all conditions in the anesthetized and the awake mice. The brain uptake pattern is similar between the anesthesia and the awake states, but awake reconstructions show a lower spatial resolution. There is a change in the memantine condition brain uptake pattern compared to the test-retest condition. This change is observable in both the anesthesia and the awake states. Compared to the test-retest uptake, the memantine brain uptake is reduced in the cerebellum and increased in the hippocampus, relative to other brain regions.

2.3   Illustration of PET Applications Exemplified for a Neuropsychiatric Disorder

Previously, ex vivo techniques are predominated in basic research to obtain information on pathological processes in animal models of disease. The development of dedicated small animal imaging equipment enabled the opportunity to collect such information in vivo. With µPET, interactions between a radioligand and its target can be quantified on a molecular level within a picomolar range and with high sensitivity. In this way, µPET has acquired an important role in preclinical research. This modality creates the opportunity to perform longitudinal study designs, wherein each animal can function as its own control. This allows noninvasive monitoring of biological processes and disease progression but also therapy response, thereby improving the scientific value of the obtained data using paired observations. Also, fewer animals can be used. In addition, exploring (patho)physiology in small animals using µPET is associated with a high potential for translation to a clinical setting. The same radioligands can be used for both animal and human research.

In disease model studies, for example, the animal's behavior can function as a readout for the presence of a certain pathology. Longitudinal brain PET studies can be designed to explore whether characteristic behavioral changes parallel alterations in a relevant target. Using PET, a wide range of molecular targets and entities such as brain receptors can be visualized in the same animal. Hence, information about, for example, different neuroreceptors belonging to separate neurotransmitter systems can be integrated. This provides us with unique information on underlying disease mechanisms. In this section, we provide an illustration of the application of µPET in obsessive compulsive disorder (OCD) animal models and how this imaging modality can provide new insights in the complex pathophysiology of OCD.

2.3.1   Obsessive Compulsive Disorder

OCD is a chronic disabling psychiatric disease with a lifetime prevalence of 1–3% (Ruscio et al. 2010). The two hallmark symptoms include unwanted obsessions and compulsions (Abramowitz et al. 2009). Obsessions are recurrent and persistent thoughts (e.g., of contamination), urges (e.g., to stab someone), or images (e.g., of violent or horrific scenes) causing anxiety or distress. Also, individuals attempt to suppress or ignore these thoughts, urges, or images or to neutralize these with another thought or action (compulsion). These compulsions include repetitive behaviors (e.g., washing, checking) and mental acts (e.g., counting, repeating words silently), which are driven by an uncontrollable need to be performed in response to the obsession. Clearly, this condition causes serious impairment in daily functioning, which drastically reduces the patient's quality of life. OCD often remains underdiagnosed, resulting in a treatment gap of 57.3% (Kohn et al. 2004). The first-line treatment consists of selective serotonin reuptake inhibitors (SSRIs) and cognitive behavioral therapy (CBT) and was shown to reduce symptoms with circa 50% in half of the patients (Denys et al. 2010). A substantial part of patients remains

treatment refractory (Denys 2006). This emphasizes the need for an improved treatment approach to tackle this disease.

Despite the extensive research focusing on OCD in recent years, the exact mechanism of action is not known. One of the more consistent findings has been the identification of alterations in cortico-striato-thalamocortical (CSTC) circuitry (Pauls et al. 2014), which was mainly established via a range of imaging studies (Bandelow et al. 2016), although additional brain regions are likely to be involved in the pathogenesis as well (Milad and Rauch 2012; Lapidus et al. 2014). Furthermore, it is hypothesized that an altered local neurotransmission lies at the basis of a behavioral disinhibition (Fineberg et al. 2011), which is not fully characterized yet. More specifically, as illustrated in Fig. 2.15, when dopamine (DA) from nigral projections is released in the striatum, a direct pathway is activated. This results in a disinhibition of the thalamus with activation of excitatory projections returning to the cortex. Alternatively, when striatal DA is absent, an indirect
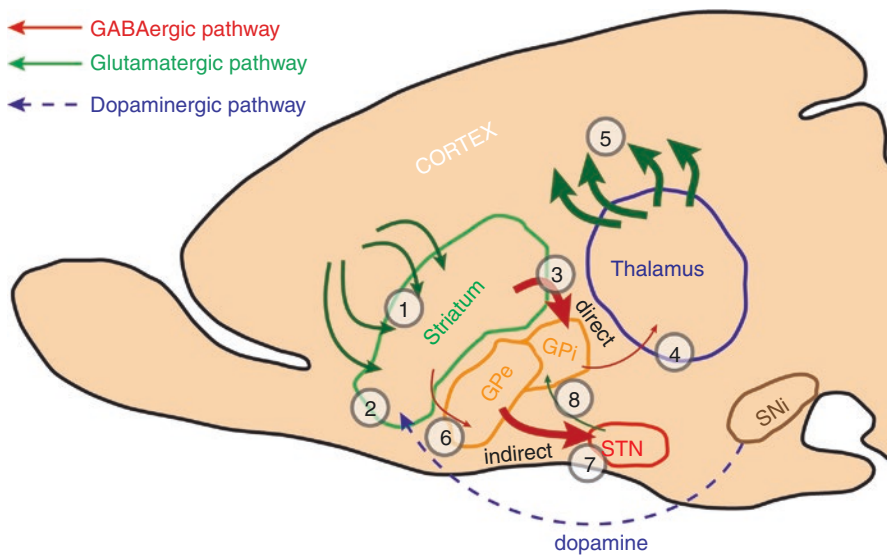
Fig. 2.15 Simplified scheme of the basal ganglia circuitry in the presence of dopamine. The striatum receives (*1*) glutamatergic projections from the entire neocortex, which is involved in higher functioning, and (*2*) dopaminergic projections originating from the substantia nigra (SNi). Dependent on the dopamine (DA) levels in the striatum, a direct or indirect pathway is chosen: (i) When dopamine (DA) is present, GABAergic projections (*3*) from the striatum will inhibit the globus pallidus interna (GPi) through the direct pathway, leading to less inhibition of the thalamus (*4*). The thalamus then projects back to the cortex completing the loop (*5*). Furthermore, the inhibitory projections (*6*) from the indirect pathway to the globus pallidus externa (GPe) are inhibited themselves due to binding of DA on the dopamine D2 receptor (D2R). This will lead to inhibition (*7*) of the subthalamic nucleus (STN), followed by less activation of the GPi (*8*), again resulting in less inhibition of the thalamus (*4*). (ii) However, the opposite occurs when less DA is present. The inhibitory projections from the striatum to the GPe will become active, leading to less inhibition of the subthalamic nucleus (STN), excitation of the GPi, and inhibition of the thalamus

pathway is activated, thereby inhibiting the thalamus resulting in less signalling to the cortex (Milad and Rauch 2012). OCD is hypothesized to have an excessive relative activation of this aforementioned direct pathway. Other neurotransmitters, such as serotonin and glutamate, likely play a role in the manifestation of this complex pathology as well (Kariuki-Nyuthe et al. 2014; Pauls et al. 2014). Also, new evidence points out synaptic pathology "synaptopathies" as a potential cornerstone in the development of OCD (Bienvenu et al. 2009; Züchner et al. 2009; Ting et al. 2012; Stewart et al. 2013; Mattheisen et al. 2015).

Taken together, OCD is a complex disease involving alterations in multiple brain regions and neurotransmitter systems. Therefore, PET is a promising tool to use in the context of OCD research. PET enables whole brain visualization of multiple targets, e.g., dopamine and glutamate receptors can be visualized in the same animal (model). Also, the use of PET enables regional quantification of radioligand binding. Hence, it can be demonstrated whether or not a certain brain region is involved in the origin and/or progression of OCD or OCD-like behavior(s) in an animal model.

2.3.2   Animal Models for Obsessive Compulsive Disorder

The heterogeneous OCD patient population and the presence of comorbidities hamper clinical research. Also, the majority of patients are already receiving treatment, thereby potentially modifying existing disease processes. This further complicates the investigation of underlying pathological mechanisms. Therefore, animal models serve as a valuable tool to dissect mechanisms underlying pathological behavior such as excessive self-grooming and compulsive-like checking behavior. They allow to investigate circuit dysfunction on an experimental level, which is not possible in clinical OCD research. Besides the classic methods such as electrophysiology, the use of in vivo methods like optogenetics and molecular imaging is indispensable to obtain a more in-depth comprehension of underlying neuropathology at a molecular, cellular, and circuit level.

Here, we focus on two common OCD disease models to illustrate the value and applicability of μPET imaging within this field.

2.3.2.1 A Pharmacological Rat Model

The pharmacological-induced quinpirole (QP) model belongs to the most used models for OCD and was already extensively validated (Stuchlik et al. 2016) and proven to be effective in a wide variety of studies. In this model, rats receive a biweekly dose of QP for a total duration of 10 weeks. QP is a dopamine D2 receptor (D2R) agonist, causing a sensitization effect on the receptor (Janikova et al. 2019). Activation of D2R, being an inhibitory receptor, results in an inhibition of the inhibitory indirect pathway, thus activating the downstream striatal circuit (Fig. 2.15). This results in ritual-like repetitive checking behavior combined with hyperlocomotion (Szechtman et al. 1998). Fifteen minutes after the QP injection, the animal is placed on a large open field table with four different cubes for a duration of 30 minutes to evaluate such behavior (Fig. 2.16a). This results in a characteristic pattern of locomotion that differs from the pattern of saline-treated control animals, as illustrated in Fig. 2.16b,
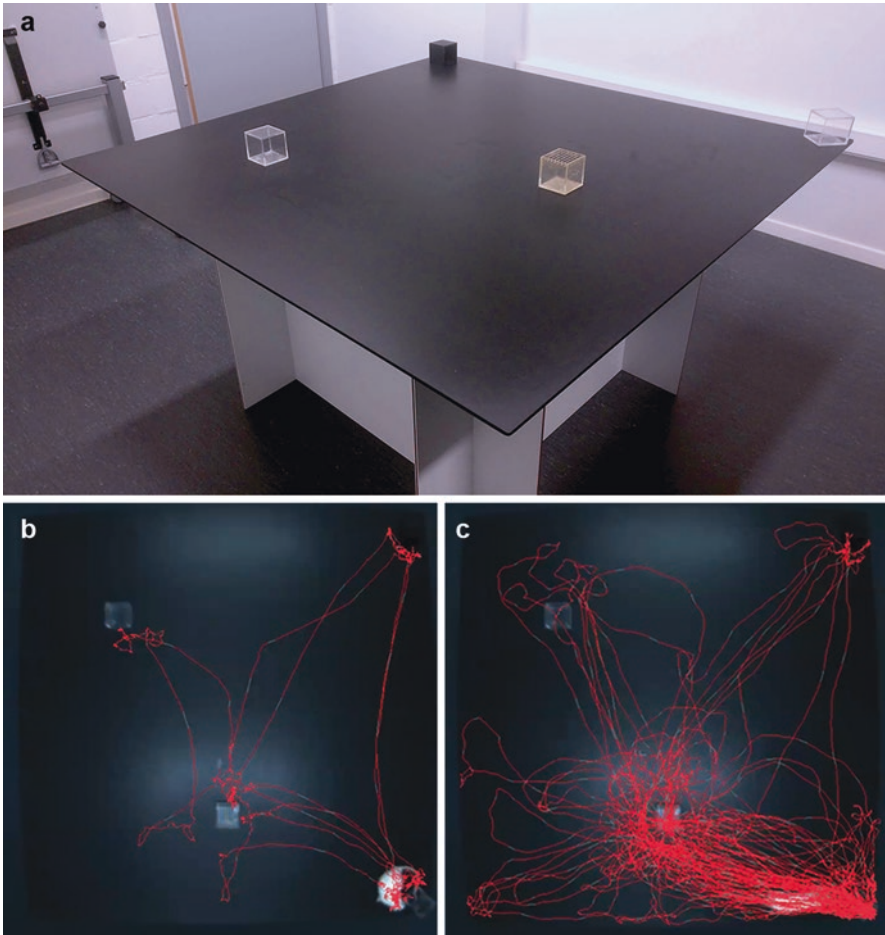
Fig. 2.16 Behavioral testing. The open field table (OFT) that was used to setup the model is shown here (**a**). In total, 4 objects are placed on the surface of the table at the specified locations. Panel (**b**) and (**c**) show a 30-minute exemplary trajectory of (**b**) a control animal and (**c**) a quin-pirole animal with a visible contrast between the two trajectories with regard to compulsive-like checking and hyperlocomotion

c. Despite the extensive amount of behavioral studies done with the QP model (Zadicario et al. 2007; Winter et al. 2008; De Carolis et al. 2011; De Haas et al. 2011; Eagle et al. 2014; Hatalova et al. 2014), no in vivo longitudinal data was collected in this model, and the currently available in vivo imaging data is sparse. This is where μPET enters the picture, because it could provide new insights on regional brain metabolism and the interplay between neurotransmitter systems in this model. For example, a μPET study permits to visualize what happens to the D2R within the interval at which the pathological behavior occurs. In the future, awake PET imaging could be applied in this context (cf. Sect. 2.2).

Imaging of Cerebral Glucose Consumption

We reported on a first imaging study in the QP model, using the glucose analogue [^{18}F]FDG as a marker for cerebral glucose consumption expressed via the rodent standardized uptake value (rSUV) parameter (cf. Sect. 2.1.6 semiquantitative approach). A baseline [^{18}F]FDG μPET scan was acquired of both the acute and chronic groups prior to (i) an acute QP or saline injection or (ii) twice weekly injections of either QP or saline, each time paired with an open field test. Further, follow-up scans to stage the pathology, after the first injection for the acute group and after the tenth injection (in week 5) for the chronic group, were acquired. This study established significant decreases in [^{18}F]FDG uptake in cortical and striatal regions of chronic QP-treated rats (Fig. 2.17) (Servaes et al. 2016), consistent with the hypothesis stating involvement of the CSTC circuit in the pathophysiology of this OCD model and the process of inefficient thalamic gating (Del Casale et al. 2011). Furthermore, they showed alterations in other key structures such as the amygdala, the hippocampus, and the entorhinal cortex, which are directly involved in memory and fear processing, pointing toward a more extensive disease mechanism. These findings further hint toward a dysregulation of a neural feedback circuit that includes not only the cortical and striatal structures but also the (para)limbic regions in this model.
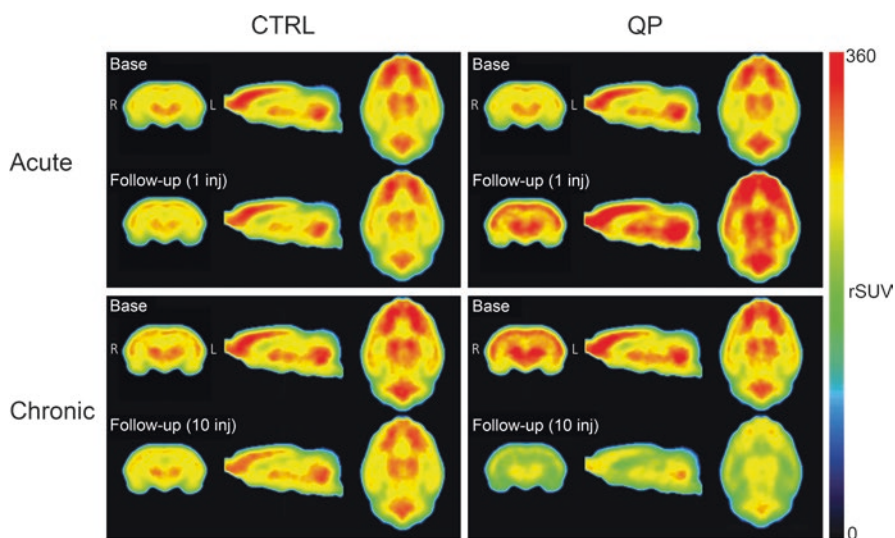
Fig. 2.17 Rodent standardized uptake value (SUV$_r$) averaged [^{18}F]FDG images at baseline and follow-up for both the acute and chronic quinpirole (QP) group in both conditions (saline control and QP). Acute exposure increased while chronic exposure to quinpirole decreased the total glucose consumption in the brain. Strong reductions were seen within the cortico-striato-thalamocortical (CSTC) circuit after chronic QP exposure. Additional alterations in the (para)limbic regions suggest a more extensive disease mechanism. (*CTRL* control, *inj* injection, *QP* quinpirole, *SUV$_r$* rodent standardized uptake value; acute group, $n = 8$/group; chronic group, $n = 7$/group)

Dopamine D2 Receptor Imaging

A second μPET study used [^{11}C]raclopride to visualize the striatal dopamine D2 receptor availability in QP rats with compulsive-like checking behavior (Servaes et al. 2017). This study clearly showed that animals receiving acute and chronic QP had a reduction in D2R availability in the striatum (expressed as the BP$_{ND}$ cf. Sect. 2.1.4.2 SRTM), which was more pronounced after chronic injections (Fig. 2.18). Since QP is a D2R agonist, it most likely competes with [^{11}C]raclopride for the same binding site. Hence, a reduced uptake was to be expected. However, rats receiving chronic QP had significantly lower striatal BP$_{ND}$ levels compared to rats
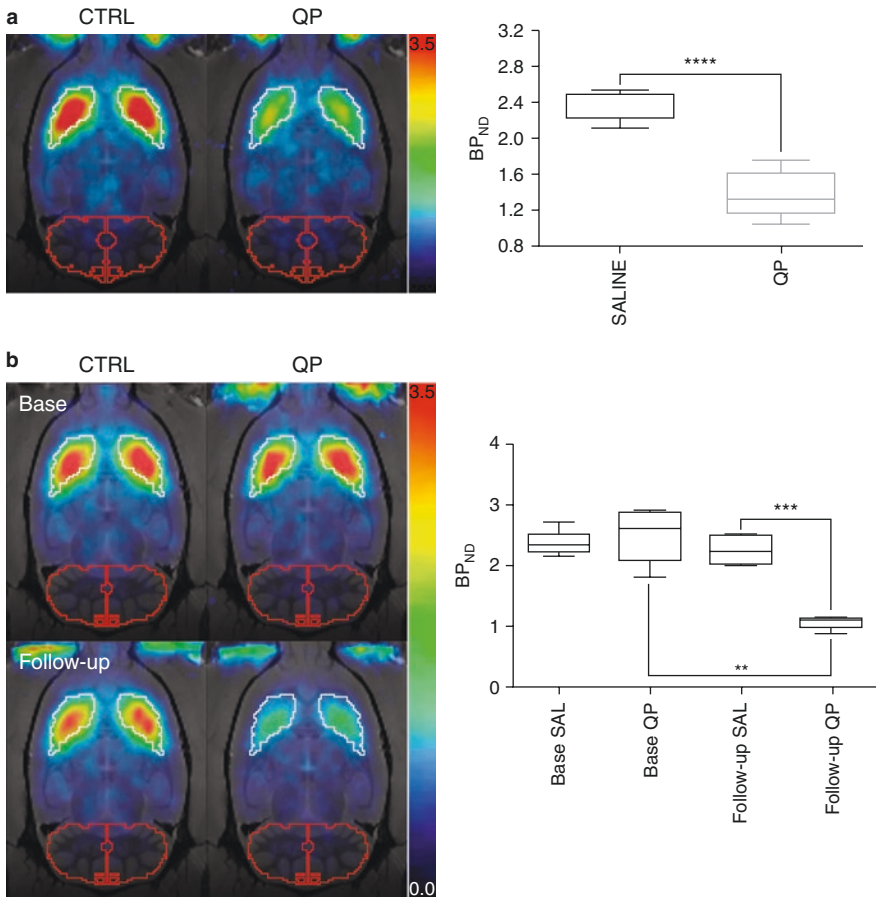
Fig. 2.18 Panel (**a**) displays the [^{11}C]raclopride BP$_{ND}$ maps (left) and the corresponding striatal BP$_{ND}$ values (right) after acute administration of quinpirole and saline. Panel (**b**) shows the [^{11}C]raclopride BP$_{ND}$ maps (left) and the corresponding striatal BP$_{ND}$ values (right) for the chronic groups at baseline and after chronic administration of quinpirole and saline. (*BP$_{ND}$* non-displaceable binding potential, *CTRL* control, *QP* quinpirole; $n = 8$/group; p-values t tests (unpaired and paired): **<0.01, ***<0.001, ****<0.0001)

receiving only one QP injection (Fig. 2.18). Therefore, we hypothesized that repeated administration of QP causes a decreased number of available binding sites due to receptor internalization (Goggi et al. 2007), or tolerance development (Lomanowska et al. 2004), while also influencing extracellular DA levels (De Haas et al. 2011).

2.3.2.2 A Genetic Mouse Model

As mentioned before, repeated μPET acquisitions can be combined with the setup of a pharmacological model to provide information on alterations linked to the provoked behavior. Furthermore, similar study designs allow us to follow pathological changes in genetic models during the entire lifespan of the animal. For example, μPET acquisitions can be performed in the same animal prior and during the expression and/or progression of certain pathological behavior. This approach enables imaging of secondary effects to a primum movens. In the next example, the primum movens is the loss of a synaptic protein.

Mice with a genetic deletion of the SAP-90/PSD95-associated protein 3 (Sapap3) exhibit an OCD-like phenotype with pathological self-grooming and increased anxiety (Welch et al. 2007). Sapap3 is a scaffolding protein localized in the postsynaptic density (PSD) of excitatory synapses with a high expression in the striatum (Welch et al. 2004). The PSD is a dense multiprotein complex consisting of neurotransmitter receptors, scaffolding proteins, adhesion molecules, signalling enzymes, and cytoskeletal components (Kim and Sheng 2004; Bourgeron 2015). Spatial and temporal organization of these components plays a central role in neurotransmission and synaptic plasticity (Zhu et al. 2016). This widely used model was previously characterized with an abnormal striatal output based on an imbalance between direct and indirect pathway medium spiny neurons located within the CSTC "OCD" circuit (Fig. 2.15) (Ade et al. 2016).

In this model, the grooming phenotype was shown to worsen with age with the development of skin lesions (Fig. 2.19, Glorie et al. 2020). Furthermore, young adult Sapap3 ko mice already have significantly higher grooming frequencies in the
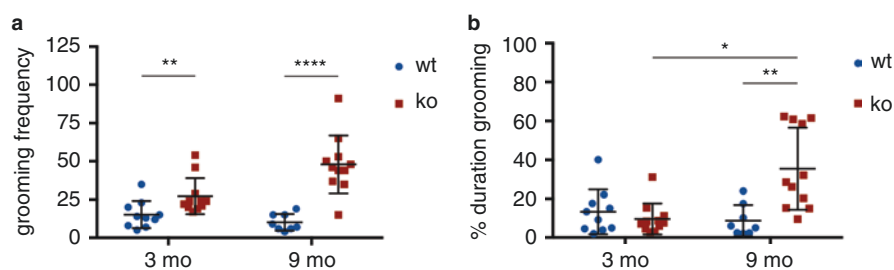
Fig. 2.19 Progression of compulsive-like grooming in Sapap3 ko mice reflected by behavioral parameters (**a**) grooming frequency and (**b**) % duration grooming, compared to wt controls. Both parameters were collected from a 30-minute video recording. (mo, months; wt, wild types; ko, knockouts; animal numbers, wt 3 mo $n = 10$, ko 3 mo $n = 11$, wt 9 mo $n = 8$, ko 9 mo $n = 11$; p-values Mann-Whitney and Wilcoxon matched pairs signed rank test: *<0.05, **<0.01, ****<0.0001)

absence of visible skin lesions. Longitudinal in vivo µPET imaging provides the opportunity to further investigate changes in relevant molecular targets such as glutamate receptors and other synaptic targets related to Sapap3, parallel to the aggravation of this phenotype.

Metabotropic Glutamate Receptor 5 PET Imaging

Sapap3 belongs to a group of scaffolding proteins that links metabotropic glutamate receptors (mGluRs i.a. mGluR5) to ionotropic glutamate receptors (iGluRs i.a. NMDAR and AMPAR) anatomically and functionally (Zhu et al. 2016). Sapap3 ko mice are characterized by glutamatergic abnormalities: (i) an altered N-methyl-D-aspartate receptor (NMDAR) composition (Welch et al. 2007), (ii) a reduction in corticostriatal synaptic strength driven by metabotropic glutamate receptor 5 (mGluR5)-dependent α-amino-3-hydroxy-5-methyl-4-isoxazolepropionic acid receptor (AMPAR) endocytosis (Wan et al. 2011), and (iii) an elevated mGluR5 signalling driving OCD-relevant behavior (Ade et al. 2016). These findings substantiate the application of in vivo [^{11}C]ABP688 µPET imaging to longitudinally visualize mGluR5 availability (Ametamey et al. 2006) in the brain of Sapap3 ko mice, expressed as the non-displaceable binding potential BP_{ND} (cf. Sect. 2.1.4.2 SRTM) (Lammertsma and Hume 1996).

The results of this study emphasize the potential of µPET to follow disease progression in vivo. We established a significant progressive decline in the availability of the mGluR5 allosteric site (expressed via [^{11}C]ABP688 BP_{ND}) in both striatal and extra-striatal brain regions of Sapap3 ko mice (Fig. 2.20). This parallels an increase in compulsive-like grooming behavior (Fig. 2.19) (Glorie et al. 2020). In line with previous findings (Ade et al. 2016), our data, showing dynamic changes in mGluR5 availability during the lifespan of Sapap3 ko mice, support the hypothesis of excessive mGluR5 activation as a driver of the OCD-like phenotype in this model. Previously, the mGluR5 was shown to be constitutively activated, not via the conventional binding of its orthosteric ligand glutamate. Lower mGluR5 availability for [^{11}C]ABP688 in ko mice could be related to this aberrant activation pattern. Altogether, these findings suggest a promising role for [^{11}C]ABP688 as a biomarker for constitutive mGluR5 activation and to study disease progression in this model. Also, this study points out the potential of [^{11}C]ABP688 µPET to evaluate drugs targeting mGluR5 together with the drug's effect on the behavioral readout.

2.4   Summary/Conclusion

This chapter highlights the added value of PET imaging in the preclinical research setting, with its high versatility and its ability to collect in vivo molecular information during the lifespan of a laboratory animal. Indeed, an illustration of the use of µPET with multiple radiotracers in OCD animal models confirms these characteristics. Beside the pharmacokinetic modelling methods to extract biologically relevant
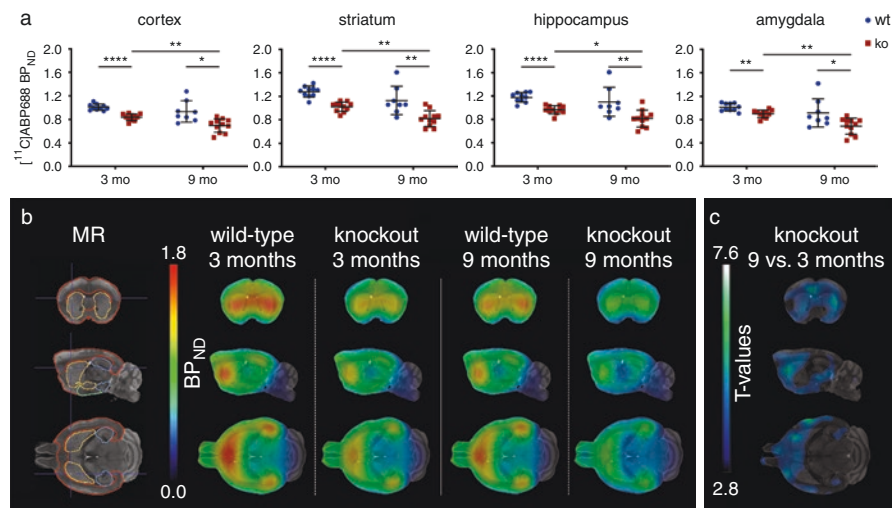
Fig. 2.20 Sapap3 ko mice show cross-sectional differences and a longitudinal decline in mGluR5 availability for [^{11}C]ABP688. (**a**) Averaged BP$_{ND}$ values showing a progressive decline in BP$_{ND}$ in the brain of Sapap3 ko mice in the cortex, striatum, hippocampus, and amygdala. Cross-sectionally, the averaged BP$_{ND}$ value of Sapap3 ko mice is significantly lower in all four analyzed regions compared to their wt counterparts both at the age of 3 and 9 months. (**b**) Corresponding averaged [^{11}C]ABP688 BP$_{ND}$ images superimposed on a mouse MR template at both time points (3 and 9 months) and for both groups separately (wt versus ko). (**c**) Hypo T-map (voxel-based statistical parametric mapping (SPM) analysis) showing clusters of voxels (voxel threshold = 100) with a significantly ($p < 0.01$) decreased BP$_{ND}$ at 9 mo, when compared to the 3 mo time point in Sapap3 ko mice. (MR, magnetic resonance; MR delineation, *red* cortex, *yellow* striatum, *blue* hippocampus, *green* amygdala; wt, wild type; ko, knockout; animal numbers, wt 3 mo $n = 10$, ko 3 mo $n = 11$, wt 9 mo $n = 8$, ko 9 mo $n = 11$; statistical analysis, cross-sectional data with a two-way ANOVA with post hoc Bonferroni correction for multiple comparisons and longitudinal data with a mixed effects model; p-values, *<0.05, **<0.01, ***<0.001, ****<0.0001)

information from PET images, we describe the new and promising method of point source tracking with the possibility to perform high-throughput awake µPET in a routine small animal setting. Further work should focus on combining awake µPET imaging paradigms with animal models of brain disease, thereby collecting unique information on underlying pathological mechanisms and eliminating anesthesia-related disturbances. In this context, the use of multiple tracers within one animal enables the study of the interplay between different targets of interest during the conduct of behavior. With this progress, an important problem associated with translation to a clinical setting will be tackled.

References

Abramowitz JS, Taylor S, McKay D (2009) Obsessive-compulsive disorder. Lancet 374:491–499. https://doi.org/10.1016/S0140-6736(09)60240-3

Ade KK, Wan Y, Hamann HC et al (2016) Increased metabotropic glutamate receptor 5 signaling underlies obsessive-compulsive disorder-like behavioral and striatal circuit abnormalities in mice. Biol Psychiatry 80:522–533

Alstrup AKO, Landau AM, Holden JE et al (2013) Effects of anesthesia and species on the uptake or binding of radioligands in vivo in the Göttingen minipig. Biomed Res Int. https://doi.org/10.1155/2013/808713

Ametamey SM, Kessler LJ, Honer M et al (2006) Radiosynthesis and preclinical evaluation of 11C-ABP688 as a probe for imaging the metabotropic glutamate receptor subtype 5. J Nucl Med 47:698–705

Baba JS, Endres CJ, Foss CA et al (2013) Molecular imaging of conscious, unrestrained mice with AwakeSPECT. J Nucl Med. https://doi.org/10.2967/jnumed.112.109090

Balasse L, Maerk J, Pain F et al (2015) PIXSIC: a wireless intracerebral radiosensitive probe in freely moving rats. Mol Imaging. https://doi.org/10.2310/7290.2015.00020

Bandelow B, Baldwin D, Abelli M et al (2016) Biological markers for anxiety disorders, OCD and PTSD—a consensus statement. Part I: Neuroimaging and genetics. World J Biol Psychiatry 17(5):321–365

Bienvenu OJ, Wang Y, Shugart YY et al (2009) Sapap3 and pathological grooming in humans: results from the OCD collaborative genetics study. Am J Med Genet Part B Neuropsychiatr Genet. https://doi.org/10.1002/ajmg.b.30897

Bloomfield PM, Rajeswaran S, Spinks TJ et al (1995) The design and physical characteristics of a small animal positron emission tomography. Phys Med Biol. https://doi.org/10.1088/0031-9155/40/6/010

Bourgeron T (2015) From the genetic architecture to synaptic plasticity in autism spectrum disorder. Nat Rev Neurosci 16(9):551–563

Cherry SR, Shao Y, Silverman RW et al (1997) MicroPET: a high resolution PET scanner for imaging small animals. IEEE Trans Nucl Sci. https://doi.org/10.1109/23.596981

Chiou WL (1989) The phenomenon and rationale of marked dependence of drug concentration on blood sampling site: implications in pharmacokinetics, pharmacodynamics, toxicology and therapeutics (Part II). Clin Pharmacokinet 17(3):175–199

Crespo-Facorro B, Paradiso S, Andreasen NC et al (2001) Neural mechanisms of anhedonia in schizophrenia: a PET study of response to unpleasant and pleasant odors. J Am Med Assoc. https://doi.org/10.1001/jama.286.4.427

Cunningham VJ, Parker CA, Rabiner EA et al (2005) PET studies in drug development: methodological considerations. Drug Discov Today Technol 2(4):–311, 315

Cunningham VJ, Rabiner EA, Slifstein M et al (2010) Measuring drug occupancy in the absence of a reference region: the Lassen plot re-visited. J Cereb Blood Flow Metab. https://doi.org/10.1038/jcbfm.2009.190

De Carolis L, Schepisi C, Milella MS, Nencini P (2011) Clomipramine, but not haloperidol or aripiprazole, inhibits quinpirole-induced water contrafreeloading, a putative animal model of compulsive behavior. Psychopharmacology. https://doi.org/10.1007/s00213-011-2372-7

De Haas R, Nijdam A, Westra TA et al (2011) Behavioral pattern analysis and dopamine release in quinpirole-induced repetitive behavior in rats. J Psychopharmacol. https://doi.org/10.1177/0269881110389093

Del Casale A, Kotzalidis GD, Rapinesi C et al (2011) Functional neuroimaging in obsessive-compulsive disorder. Neuropsychobiology 64(2):61–85

Deleye S, Verhaeghe J, Wyffels L et al (2014) Towards a reproducible protocol for repetitive and semi-quantitative rat brain imaging with 18 F-FDG: Exemplified in a memantine pharmacological challenge. NeuroImage. https://doi.org/10.1016/j.neuroimage.2014.04.004

Denys D (2006) Pharmacotherapy of obsessive-compulsive disorder and obsessive-compulsive spectrum disorders. Psychiatr Clin North Am 29(2):553

Denys D, Mantione M, Figee M et al (2010) Deep brain stimulation of the nucleus accumbens for treatment-refractory obsessive-compulsive disorder. Arch Gen Psychiatry. https://doi.org/10.1001/archgenpsychiatry.2010.122

Eagle DM, Noschang C, d'Angelo LSC et al (2014) The dopamine D2/D3 receptor agonist quinpirole increases checking-like behaviour in an operant observing response task with uncertain reinforcement: a novel possible model of OCD. Behav Brain Res. https://doi.org/10.1016/j.bbr.2013.12.040

Ekelund J, Slifstein M, Narendran R et al (2007) In vivo DA D 1 receptor selectivity of NNC 112 and SCH 23390. Mol Imaging Biol. https://doi.org/10.1007/s11307-007-0077-4

Elsinga PH (2002) Radiopharmaceutical chemistry for positron emission tomography. Methods 27:208–217. https://doi.org/10.1016/S1046-2023(02)00076-2

Fineberg N, Chamberlain S, Hollander E et al (2011) Translational approaches to obsessive-compulsive disorder: from animal models to clinical treatment. Br J Pharmacol 164(4):1044–1061

Frith CD, Friston K, Liddle PF, Frackowiak RSJ (1991) Willed action and the prefrontal cortex in man: a study with PET. Proc R Soc B Biol Sci. https://doi.org/10.1098/rspb.1991.0077

Glorie D, Verhaeghe J, Miranda A, et al (2020) Progression of obsessive compulsive disorder-like grooming in Sapap3 knockout mice: a longitudinal [11C]ABP688 PET study. Neuropharm. https://doi.org/10.1016/j.neuropharm.2020.108160

Goggi JL, Sardini A, Egerton A et al (2007) Agonist-dependent internalization of D2 receptors: Imaging quantification by confocal microscopy. Synapse. https://doi.org/10.1002/syn.20360

Gumbleton M, Oie S, Verotta D (1994) Pharmacokinetic-pharmacodynamic (PK-PD) modelling in non-steady-state studies and arterio-venous drug concentration differences. Br J Clin Pharmacol. https://doi.org/10.1111/j.1365-2125.1994.tb04372.x

Gunn RN, Gunn SR, Cunningham VJ (2001) Positron emission tomography compartmental models. J Cereb Blood Flow Metab. https://doi.org/10.1097/00004647-200106000-00002

Hatalova H, Radostova D, Pistikova A et al (2014) Spatial reversal learning in chronically sensitized rats and in undrugged sensitized rats with dopamine d2-like receptor agonist quinpirole. Front Behav Neurosci. https://doi.org/10.3389/fnbeh.2014.00122

Hume SP, Gunn RN, Jones T (1998) Pharmacological constraints associated with positron emission tomographic scanning of small laboratory animals. Eur J Nucl Med. https://doi.org/10.1007/s002590050211

Hume SP, Myers R, Bloomfield PM et al (1992) Quantitation of Carbon-11-labeled raclopride in rat striatum using positron emission tomography. Synapse. https://doi.org/10.1002/syn.890120106

Ingvar M, Eriksson L, Rogers GA et al (1991) Rapid feasibility studies of tracers for positron emission tomography: High-resolution PET in small animals with kinetic analysis. J Cereb Blood Flow Metab. https://doi.org/10.1038/jcbfm.1991.157

Innis RB, Cunningham VJ, Delforge J et al (2007) Consensus nomenclature for in vivo imaging of reversibly binding radioligands. J Cereb Blood Flow Metab Metab 27:1533–1539

Janikova M, Brozka H, Radostova D et al (2019) No effect of riluzole and memantine on learning deficit following quinpirole sensitization—an animal model of obsessive-compulsive disorder. Physiol Behav. https://doi.org/10.1016/j.physbeh.2019.01.013

Jons PH, Ernst M, Hankerson J et al (1997) Follow-up of radial arterial catheterization for positron emission tomography studies. Hum Brain Mapp. https://doi.org/10.1002/(SICI)1097-0193(1997)5:2<119::AID-HBM5>3.0.CO;2-6

Kariuki-Nyuthe C, Gomez-Mancilla B, Stein DJ (2014) Obsessive compulsive disorder and the glutamatergic system. Curr Opin Psychiatry 27(1):32–37

Kim E, Sheng M (2004) PDZ domain proteins of synapses. Nat Rev Neurosci 5(10):–771, 781

Koeppe RA, Holthoff VA, Frey KA et al (1991) Compartmental analysis of [11C]flumazenil kinetics for the estimation of ligand transport rate and receptor distribution using positron emission tomography. J Cereb Blood Flow Metab. https://doi.org/10.1038/jcbfm.1991.130

Kohn R, Saxena S, Levav I, Saraceno B (2004) The treatment gap in mental health care. Bull World Health Organ 82:858–866

Kyme A, Se S, Meikle S et al (2014) Markerless motion tracking of awake animals in positron emission tomography. IEEE Trans Med Imaging. https://doi.org/10.1109/TMI.2014.2332821

Kyme AZ, Zhou VW, Meikle SR, Fulton RR (2008) Real-time 3D motion tracking for small animal brain PET. Phys Med Biol. https://doi.org/10.1088/0031-9155/53/10/014

Laforest R, Sharp TL, Engelbach JA et al (2005) Measurement of input functions in rodents: challenges and solutions. Nucl Med Biol 32(7):679–685

Lammertsma AA, Hume SP (1996) Simplified reference tissue model for PET receptor studies. Hum Brain Mapp J 4:153–158

Lapidus KAB, Stern ER, Berlin HA, Goodman WK (2014) Neuromodulation for obsessive–compulsive disorder. Neurotherapeutics 11:485–495. https://doi.org/10.1007/s13311-014-0287-9

Lassen NA (1992) Neuroreceptor quantitation in vivo by the steady-state principle using constant infusion or bolus injection of radioactive tracers. J Cereb Blood Flow Metab. https://doi.org/10.1038/jcbfm.1992.101

Lassen NA, Bartenstein PA, Lammertsma AA et al (1995) Benzodiazepine receptor quantification in vivo in humans using [11C]flumazenil and PET: application of the steady-state principle. J Cereb Blood Flow Metab. https://doi.org/10.1038/jcbfm.1995.17

Lecomte R, Cadorette J, Rodrigue S et al (1996) Initial results from the Sherbrooke avalanche photodiode positron tomograph. IEEE Trans Nucl Sci. https://doi.org/10.1109/23.507252

Lenz C, Rebel A, Van Ackern K et al (1998) Local cerebral blood flow, local cerebral glucose utilization, and flow- metabolism coupling during sevoflurane versus isoflurane anesthesia in rats. Anesthesiology. https://doi.org/10.1097/00000542-199812000-00026

Logan J, Fowler JS, Volkow ND et al (1990) Graphical analysis of reversible radioligand binding from time-activity measurements applied to [N-11C-methyl]-(−)-cocaine PET studies in human subjects. J Cereb Blood Flow Metab. https://doi.org/10.1038/jcbfm.1990.127

Logan J, Fowler JS, Volkow ND et al (1996) Distribution volume ratios without blood sampling from graphical analysis of PET data. J Cereb Blood Flow Metab. https://doi.org/10.1097/00004647-199609000-00008

Logan J, Fowler JS, Volkow ND et al (2001) A strategy for removing the bias in the graphical analysis method. J Cereb Blood Flow Metab. https://doi.org/10.1097/00004647-200103000-00014

Lomanowska A, Gormley S, Szechtman H (2004) Presynaptic stimulation and development of locomotor sensitization to the dopamine agonist quinpirole. Pharmacol Biochem Behav. https://doi.org/10.1016/j.pbb.2003.12.018

Matsumura A, Mizokawa S, Tanaka M et al (2003) Assessment of microPET performance in analyzing the rat brain under different types of anesthesia: Comparison between quantitative data obtained with microPET and ex vivo autoradiography. NeuroImage. https://doi.org/10.1016/j.neuroimage.2003.08.020

Mattheisen M, Samuels JF, Wang Y et al (2015) Genome-wide association study in obsessive-compulsive disorder: results from the OCGAS. Mol Psychiatry. https://doi.org/10.1038/mp.2014.43

Menke M, Atkins MS, Buckley KR (1996) Compensation methods for head motion detected during pet imaging. IEEE Trans Nucl Sci. https://doi.org/10.1109/23.485971

Milad MR, Rauch SL (2012) Obsessive-compulsive disorder: beyond segregated cortico-striatal pathways. Trends Cogn Sci 16:43–51

Mintun MA, Raichle ME, Kilbourn MR et al (1984) A quantitative model for the in vivo assessment of drug binding sites with positron emission tomography. Ann Neurol. https://doi.org/10.1002/ana.410150302

Miranda A, Glorie D, Bertoglio D et al (2019a) Awake 18F-FDG PET imaging of memantine-induced brain activation and test–retest in freely running mice. J Nucl Med. https://doi.org/10.2967/jnumed.118.218669

Miranda A, Kang MS, Blinder S et al (2019b) PET imaging of freely moving interacting rats. NeuroImage. https://doi.org/10.1016/j.neuroimage.2019.02.064

Mizuma H, Shukuri M, Hayashi T et al (2010) Establishment of in vivo brain imaging method in conscious mice. J Nucl Med. https://doi.org/10.2967/jnumed.110.075184

Pauls DL, Abramovitch A, Rauch SL, Geller DA (2014) Obsessive-compulsive disorder: an integrative genetic and neurobiological perspective. Nat Rev Neurosci 15:410–424

Phelps ME, Hoffman EJ, Mullani NA, Ter Pogossian MM (1975) Application of annihilation coincidence detection to transaxial reconstruction tomography. J Nucl Med 16(3):210–224

Rahmim A, Bloomfield P, Houle S et al (2004) Motion compensation in histogram-mode and list-mode EM reconstructions: beyond the event-driven approach. IEEE Trans Nucl Sci. https://doi.org/10.1109/TNS.2004.835763

Reiman EM, Lane RD, Ahern GL et al (1997) Neuroanatomical correlates of externally and internally generated human emotion. Am J Psychiatry. https://doi.org/10.1176/ajp.154.7.918

Ruscio AM, Stein DJ, Chiu WT, Kessler RC (2010) The epidemiology of obsessive-compulsive disorder in the National Comorbidity Survey Replication. Mol Psychiatry. https://doi.org/10.1038/mp.2008.94

Schulz D, Southekal S, Junnarkar SS et al (2011) Simultaneous assessment of rodent behavior and neurochemistry using a miniature positron emission tomography. Nat Methods. https://doi.org/10.1038/nmeth.1582

Servaes S, Glorie D, Verhaeghe J et al (2016) [18F]-FDG PET neuroimaging in rats with quinpirole-induced checking behavior as a model for obsessive compulsive disorder. Psychiatry Res Neuroimaging. https://doi.org/10.1016/j.pscychresns.2016.10.003

Servaes S, Glorie D, Verhaeghe J et al (2017) Preclinical molecular imaging of glutamatergic and dopaminergic neuroreceptor kinetics in obsessive compulsive disorder. Prog Neuro-Psychopharmacol Biol Psychiatry. https://doi.org/10.1016/j.pnpbp.2017.02.027

Shuping Z, Bruyndonckx P, Goldberg MB, Tavernier S (1994) Study of a high resolution 3D PET scanner. Nucl Inst Methods Phys Res A. https://doi.org/10.1016/0168-9002(94)90808-7

Sokoloff L, Reivich M, Kennedy C et al (1977) The [14C]deoxyglucose method for the measurement of local cerebral glucose utilization: theory, procedure, and normal values in the conscious and anesthetized albino rat. J Neurochem. https://doi.org/10.1111/j.1471-4159.1977.tb10649.x

Stewart SE, Yu D, Scharf JM et al (2013) Genome-wide association study of obsessive-compulsive disorder. Mol Psychiatry. https://doi.org/10.1038/mp.2012.85

Stuchlik A, Radostová D, Hatalova H et al (2016) Validity of quinpirole sensitization rat model of OCD: Linking evidence from animal and clinical studies. Front Behav Neurosci 10:209

Sung KK, Jang DP, Lee S et al (2009) Neural responses in rat brain during acute immobilization stress: a [F-18]FDG micro PET imaging study. NeuroImage. https://doi.org/10.1016/j.neuroimage.2008.09.032

Szechtman H, Sulis W, Eilam D (1998) Quinpirole induces compulsive checking behavior in rats: A potential animal model of obsessive-compulsive disorder (OCD). Behav Neurosci. https://doi.org/10.1037/0735-7044.112.6.1475

Ting JT, Peça J, Feng G (2012) Functional consequences of mutations in postsynaptic scaffolding proteins and relevance to psychiatric disorders. Annu Rev Neurosci. https://doi.org/10.1146/annurev-neuro-062111-150442

Toyama H, Ichise M, Liow JS et al (2004) Absolute quantification of regional cerebral glucose utilization in mice by 18F-FDG small animal PET scanning and 2-14C-DG autoradiography. J Nucl Med 45(8):1398–1405

Varga J, Szabo Z (2002) Modified regression model for the Logan plot. J Cereb Blood Flow Metab. https://doi.org/10.1097/00004647-200202000-00012

Wan Y, Feng G, Calakos N (2011) Sapap3 Deletion causes mGluR5-dependent silencing of AMPAR synapses. J Neurosci. https://doi.org/10.1523/JNEUROSCI.2533-11.2011

Watanabe M, Uchida H, Okada H et al (1992) A high resolution PET for animal studies. IEEE Trans Med Imaging. https://doi.org/10.1109/42.192694

Weber B, Burger C, Biro P, Buck A (2002) A femoral arteriovenous shunt facilitates arterial whole blood sampling in animals. Eur J Nucl Med. https://doi.org/10.1007/s00259-001-0712-2

Welch JM, Lu J, Rodriguiz RM et al (2007) Cortico-striatal synaptic defects and OCD-like behaviours in Sapap3-mutant mice. Nature. https://doi.org/10.1038/nature06104

Welch JM, Wang D, Feng G (2004) Differential mRNA expression and protein localization of the SAP90/PSD-95-associated proteins (SAPAPs) in the nervous system of the mouse. J Comp Neurol 472:24–39

Winter C, Mundt A, Jalali R et al (2008) High frequency stimulation and temporary inactivation of the subthalamic nucleus reduce quinpirole-induced compulsive checking behavior in rats. Exp Neurol. https://doi.org/10.1016/j.expneurol.2007.10.020

Zadicario P, Ronen S, Eilam D (2007) Modulation of quinpirole-induced compulsive-like behavior in rats by environmental changes: Implications for OCD rituals and for exploration and naviga-tion. BMC Neurosci. https://doi.org/10.1186/1471-2202-8-23

Zanotti-Fregonara P, Chen K, Liow JS et al (2011) Image-derived input function for brain PET studies: many challenges and few opportunities. J Cereb Blood Flow Metab 31(10):1986–1998

Zhu J, Shang Y, Zhang M (2016) Mechanistic basis of MAGUK-organized complexes in synaptic development and signalling. Nat Rev Neurosci 17(4):209

Züchner S, Wendland JR, Ashley-Koch AE et al (2009) Multiple rare SAPAP3 missense variants in trichotillomania and OCD. Mol Psychiatry 14(1):6–9

Total-Body PET

3

Charlotte Thyssen and Stefaan Vandenberghe

Contents

Abstract

Since the introduction of positron emission tomography (PET) in the mid-1970s, multiple attempts were made to build a scanner able to cover a large portion of the body, but none led to a clinical research system. However, many research centers remained interested in the idea, and with the help of simulation studies, the potential of total-body PET was shown. The building of a system was started only 2 years ago, and the first clinical studies were performed at UC Davis in 2019. The reason for the success of total-body PET is the increased angle coverage of the subject. The larger this angle, the more coincidences are potentially detected by the system. Studies showed that a gain in sensitivity up to a factor 40

C. Thyssen · S. Vandenberghe (✉)

Faculty of Engineering and Architecture, Department of Electronics and Information Systems, MEDISIP, Ghent University, Ghent, Belgium

e-mail: cathysse.Thyssen@UGent.be; Stefaan.Vandenberghe@UGent.be

can be obtained with this new scanner design. This allows a reduction in administered dose as well as acquisition time, paving the way for dynamic PET imaging and long-term follow-up of patients. Although the main application of PET is in oncology, other disciplines like neurology, pediatrics, and pharmaceutical (drug) development can take advantage of the increased sensitivity.

3.1   Introduction

It is safe to say that since the introduction of positron emission tomography (PET) in the mid-1970s (Phelps et al. 1975), nothing fundamentally changed to the original idea. We inject the patient with a short living radiotracer, and we attempt to trace its biodistribution by detecting the annihilation photons that are produced inside the body. However, the sensitive detectors that surround the patient have changed in several ways. Already in the early 1990s, Terry Jones came up with the idea of a PET system that covers the whole body of a human subject (Vandenberghe et al. 2020). The following years, only prototypes of such systems were produced, and the idea never led to a scanner for clinical research. In 2015, a consortium called EXPLORER was founded, committed to build a long field-of-view (FOV) PET scanner, and this resulted in the first publication of a human study with a total-body PET system in 2019 (Badawi et al. 2019). In order to understand the added value of total-body imaging, the present chapter starts with a discussion of the importance of coincidence detection in PET imaging and how this is influenced by scanner length.

3.2   The Importance of Detection

In medical imaging, very good spatial resolution is important in order to detect small lesions and abnormalities. Spatial resolution is the ability to distinguish two objects (like lesions) from their surrounding tissue. However, the spatial resolution cannot be improved infinitely without simultaneously increasing the signal-to-noise ratio (SNR) (Nesterets and Gureyev 2015; Gureyev et al. 2014). In order to explain this, one could draw the analogy with photography where enough light exposure on the sensor is necessary in order to see the image appear against the black background. The longer we expose the camera to the object we want to capture, the better it appears on the resulting image. Reverting back to medical imaging, multiple sources of noise exist that each individually adds to this background signal. In the specific case of PET, these sources include, among others, the scintillation process, the movement of charge carriers in the p-n junction of the silicon photomultiplier (SiPM), the electronic noise from the readout circuit, and the random process of radioactive decay of the radioisotopes.

Detection of this radioactive decay is a perfect example of a Poisson distribution. The Poisson distribution is a statistical distribution that exists for situations in which an experiment is repeated a large number of times with a low probability of success, as is photon detection in PET imaging. The Poisson distribution predicts a noise
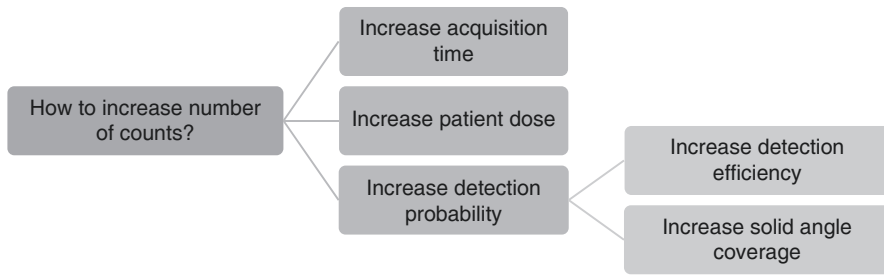
Fig. 3.1 Schematic overview of three main strategies for increasing the number of counts

level that equals the square root of the number of detected photons. This implies that the SNR of measured data is equal to (Tsui et al. 1981):

$$\text{SNR} = \frac{n}{\sqrt{n}} = \sqrt{n} \qquad (3.1)$$

In words, the square of the SNR scales linearly with the detected number of photons. In its turn, better SNR implies a better ability to distinguish the signal from the background. The schematic overview in Fig. 3.1 shows how the number of detected photons can be increased in PET. We distinguish three main strategies. The number of detections could be increased by increasing (i) the acquisition time, (ii) the amount of radioactivity administered to the patient, and (iii) the sensitivity—the ability to detect photons – of the set of detectors surrounding the patient. However, increasing the acquisition time (of each static image, strategy 1) will decrease the image quality due to movement artifacts. This is not favorable, and the acquisition time should therefore be as short as possible. Also, increasing the radioactive dose (strategy 2) increases the risk of radiation-induced problems. Therefore, the only sustainable solution is to improve the probability of detection of photons by the PET ring (strategy 3). This can be done either on the detector level, by increasing detection probability when a photon hits the sensitive ring, or on the system level, by increasing the probability of a gamma photon hitting the ring.

3.3 The Effect of the Scanner Configuration on the Sensitivity

The sensitivity of a PET scanner is a measure for the counting efficiency of the system. It is defined as the count rate of incoming coincidences, in counts per second (cps), divided by the activity, often expressed in Becquerel (Bq). Since both count rate and activity are essentially expressed in the unit 1/s, the sensitivity can be thought of as a unitless number expressing the fraction of radioactive decays, captured by the system. As stated by Habte et al. (2007), the sensitivity (S) can be estimated as:

$$S = E_g \times E_i \qquad (3.2)$$

Fig. 3.2 Definition of the opening angle of the detectable solid angle of a PET scanner
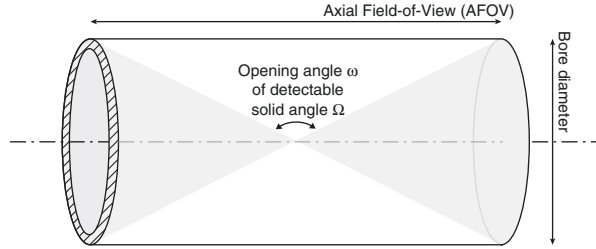
The sensitivity can thus be written as the product of the geometric efficiency, E_g, depending on the geometry of the system, and the intrinsic detection efficiency, E_i, depending among other things on the atomic number of the detecting material. The geometric detection efficiency, E_g, equals the (fractional) solid angle Ω that is covered by the PET system. This solid angle expresses what portion of an imaginary sphere in the center of the scanner is covered by detectors. The magnitude of Ω will vary with the opening angle ω of the triangle, as defined in Fig. 3.2, and is also referred to as the detectable solid angle or solid angle coverage. The magnitude of this angle is defined as:

$$\tan(\omega/2) = \frac{\text{AFOV}}{\text{Diameter}} \tag{3.3}$$

Since all emission directions falling inside ω will possibly lead to a coincidence on the scanner, the number of coincidences will increase according to the magnitude of ω. When the axial length (also called axial field of view (AFOV)) is increased, Eq. (3.3) proves that the solid angle coverage will increase accordingly. The detected count rate per unit of activity will thus be higher, which implies a higher geometric sensitivity of the system.

Since only ~1.6% of all decays inside the body are captured in state-of-the-art PET systems (Van Sluis et al. 2019), there is clearly a lot of space for further improvement in terms of sensitivity. As sensitivity is dependent on geometrical and intrinsic sensitivity, it can be improved in two ways (Fig. 3.1).

1. Increasing detection efficiency
2. Increasing solid angle coverage

Increased solid angle coverage can be achieved by increasing the AFOV of the scanner or reducing the diameter. Figure 3.3 sketches the concept of total-body PET and highlights the differences between conventional and total-body PET systems. On the one hand, the geometric efficiency is increased, and on the other, a larger portion of the body is imaged at once which makes translation (i.e., stepwise horizontal movement of the human subject) in the system redundant (Vandenberghe et al. 2020).
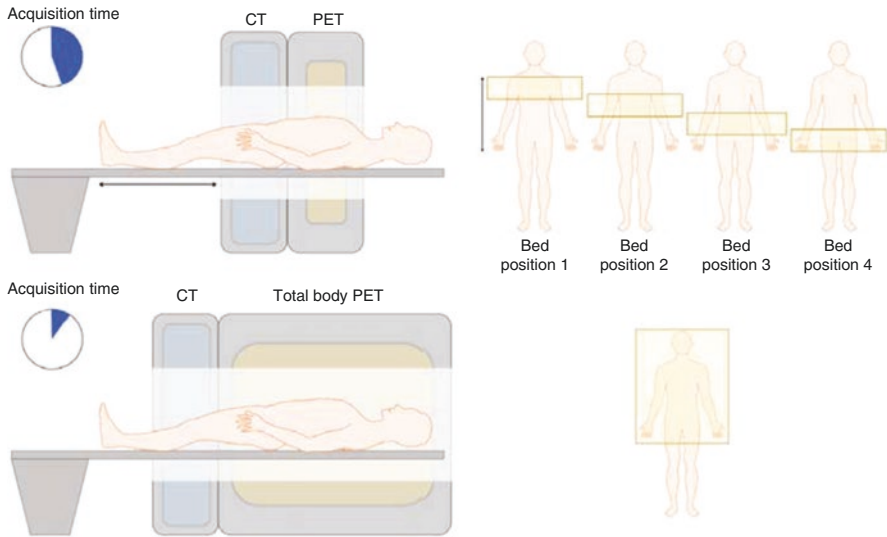
Fig. 3.3 Comparison between normal PET as we find it today in clinic and total-body PET. In the first situation, the patient has to move through the scanner while this is not the case in total-body PET. Here, the patient is scanned at once

The idea of drastically increasing the scanner length as a solution to the limited sensitivity has recently (re)gained a lot of attention from the PET community. The idea was already considered in the early 1990s but never became reality. This was mainly due to limitations in the performance of the scintillators and detectors to do fully 3D acquisitions.

Also, today there are obstacles on the road toward a system able to cover the complete human body. The major obstacle here is the cost of the system, since cost increases linearly with length of the system. Also, component choices affect the price significantly. Among others, the choice of scintillator material is a decisive factor for total-body PET designs since it forms the largest component cost of the system; the choice of photosensor and electronics has a large impact on the total price as well.

Apart from the financial obstacles that will arise, there are some other, more practical, problems that will have to be overcome. One of these is the claustrophobic feeling that might be evoked from the long and narrow tunnel in which the patient will have to lie during image acquisition. It might be necessary to incorporate screens inside the scanner bore or to go for an adaptive design, for example, in which there exist gaps between the detectors. Via such gaps, the patient is able to see outside the scanner which will counteract the feeling of claustrophobia.

3.4 State of the Art in Total-Body PET

3.4.1 The Road Toward Total-Body PET

Although total-body PET scanners are a new member of the nuclear imaging family, the idea to extend the axial FOV had already been suggested in the early 1900s by Terry Jones (Vandenberghe et al. 2020). Ever since, it has fascinated scientists around the world, and it led to several research projects (Watanabe et al. 2003; Wong et al. 2007; Poon et al. 2012; Freedenberg et al. 2014; Mikhaylova et al. 2017; Schmall et al. 2016; Crosetto 2003; Conti et al. 2006). In 2003, a 68.5-cm-long prototype was built by Hamamatsu with 96 rings and pixelated BGO crystals read out by flat panel PS-PMTs (Watanabe et al. 2003). However, the detector's energy resolution—36% on average—was not sufficient to obtain qualitative images.

3.4.2 The EXPLORER Project

In 2015, a research consortium, called EXPLORER, was founded by the University of California (UC) at Davis, University of Pennsylvania (Upenn), and Lawrence Berkeley National Laboratory based on the idea of scanning the entire body of a patient at once. This consortium led to the construction of a total-body PET system by United Imaging under the control of UC Davis. This system is called uEXPLORER and has an AFOV of 194 cm. First images were taken mid-2018 (Reardon 2019) followed by a study on healthy volunteers (Badawi et al. 2019). Since the acquisition time per image can be reduced to a few seconds or even less, it becomes possible to image the distribution of a radiotracer in the patient as a function of time. A second system, the PennPET Explorer, is under construction at the University of Pennsylvania. This system is scalable since it comprises multiple ring segments. Recently, a 64-cm-long prototype of the PennPET Explorer consisting of three ring segments has been completed and tested on human subjects. This system also allows dynamic imaging. Table 3.1 gives an overview of the performance parameters of both systems in the EXPLORER project.

Table 3.1 Overview of the performance parameters of both scanners in the EXPLORER project

| System	uEXPLORER (Badawi et al. 2019)	PennPET Explorer (Karp et al. 2019)
Length AFOV	194 cm	64 cm[a]
Bore diameter	78.6 cm	76.4 cm
Spatial resolution center (FBP)	~ 2.9 mm	~ 4.0 mm
Energy resolution	~ 11.7%	~ 12%
Time resolution	~ 430 ps	~ 256 ps
Sensitivity NEMA	~ 191.5 kcps/MBq	~ 55 kcps/MBq

[a]This is the active AFOV of the current prototype comprising three ring segments. The scanner is scalable in length and in the future more rings will be added (Karp et al. 2019)

3.4.3   Gain Versus System Length

As mentioned before, moving to a scanner with a long bore affects the sensitivity of the scanner. The actual gain in image quality depends not only on the geometry of the system but also on the object under study. Figure 3.4 gives a graphical overview of how the predicted sensitivity of the scanner improves with increasing length for different line sources. In case of single organ examinations, the sensitivity gain is limited to a factor between 3 and 4 depending on the final size of the system, and the primary gain in sensitivity is already in the first 50 cm of the system. This is also visible in Fig. 3.4, where the sensitivity is going up in the beginning of the curve in case of a point source and a 10-cm-long source but stabilizes after the 50-cm point. Both sources can act as surrogate for a single organ examination. However, the real added value of a total-body system is not in single organ examinations but in the ability to image a large portion of a tall object at once. This comes forward in both blue and black curves in Fig. 3.4. Gain for a 2-m source is predicted to range between 15, for a 1-m-long scanner, and 40, for a 2-m-long scanner (Vandenberghe et al. 2020).

A side note to these results can be drawn when one looks at a nationwide study in the Netherlands, the country known to have the tallest average inhabitant (Risk and Collaboration F 2016). This study shows that 99% of male adults have a sitting height (torso and head) below 104 cm (Fredriks et al. 2005). Since most relevant information is confined in head and torso, a 100-cm source is an accurate estimate for a patient under study. From Fig. 3.4, we see that for a 1-m source, only limited extra sensitivity gain is expected between 100-cm and 200-cm AFOV. This supports the idea of limiting the AFOV of a total-body PET system to around 1 m in order to reduce cost and make this new technology more accessible for research centers and clinics.

Fig. 3.4 Evolution of the sensitivity gain as a function of system length for different line sources. This figure was originally published in EJNMMI Physics. Vandenberghe S, Moskal P, Karp J. State of the art in Total Body PET. EJNMMI Phys (Vandenberghe et al. 2020)
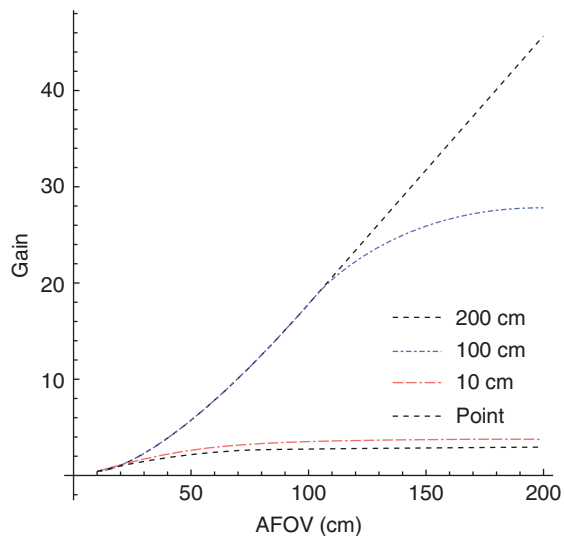
3.5   Total-Body PET Applications

It is a well-known fact that early detection of diseases is very important in order to improve the quality of life of the patient and to prolong his/her lifespan. In many diseases, like cancer and dementia, changes happen to the physiology (e.g., metabolism and signaling pathways) long before anatomical changes (e.g., tumor formation and neuron degradation) occur. Therefore, in order to diagnose a patient in the early disease stage, focus on physiology over anatomy is important. For this purpose, PET is the modality of choice. In anno 2020, it is the most powerful molecular imaging modality with main applications in oncology. Early detection is not only important for the patient, but it also makes expensive and specific treatments redundant. The follow-up of patient treatments is one step further in the direction of personalized medicine, where therapy can be adapted to the patient and revised through the treatment cycle.

The gain in sensitivity in total-body PET systems has a big impact not only on the image quality but also on the possibilities and applications of molecular imaging. Basically, the advantages can be split up into four categories: signal-to-noise ratio (SNR), dynamic imaging, injected dose, and acquisition time.

(a) **Better SNR:** When the dose and the acquisition time are kept constant, the increased sensitivity can be used to visualize tracers in tissues or lesions with only small uptake or with tracers that could not be visualized before because they only send out a very small number of positrons. One particular example of this is visualization of therapeutic isotopes like ^{90}Y that do not have positrons as primary emission source. Moreover, the increased sensitivity allows to visualize the radiotracer distribution at later time points—e.g., the next day—when they have already decayed for several half-lives.

(b) **Dynamic image:** The increased sensitivity of a large system can also be applied to reduce the length of the acquisition frames (to an order of magnitude of 1 s). Thus, the tracer can be followed from the moment of administration while it spreads in the patient's body.

(c) **Lower dose:** Since a larger portion of the emitted photons are captured in total-body PET, another possibility is the reduction of the administered dose to the patient. Especially for children who are much more likely to develop radiation-induced tumors, this is very important. The uEXPLORER claims to have a sensitivity gain of ~20 for children (Berg et al. 2018). An extra advantage is the ability to scan a larger number of patients with the same amount of tracer. This makes rare tracers accessible for more patients, and it reduces the need for an expensive on-site cyclotron.

(d) **Faster:** Instead of using the decreased acquisition time for dynamic imaging, one could also use this to reduce the overall acquisition time per patient without decreasing image quality. This allows to image patients faster and to increase scanner throughput. Especially in regions with limited availability of PET systems – e.g., in regions with a high population density – this is very desirable.

3.5.1 Applications in Oncology

Since the invention of positron emission tomography in 1975, it lasted until the early 2000s before PET established itself in clinical routine. Ever since, PET has been used mostly for diagnosis, staging, and follow-up of cancer patients. In order to diagnose and stage a patient, it is typically necessary to scan a large portion of the patient's body in order not to miss metastases that have spread to other body parts far from the primary tumor. However, conventional systems only allow to scan a small portion of the body at once. By the time an image of a certain body portion is acquired, the uptake of a rapidly changing radioactive tracer might already have altered, leading to the possible loss of detection of metastatic lesions. By scanning the whole body at once and in a dynamic way, no lesions will be missed in this way.

Already at the turn of the century, it was shown that malignant carcinomas have more tracer uptake at later time points (Kubota et al. 2001; Cherry et al. 2017) and normal tissue uptake decreases at later time points (Cheng et al. 2013). However, at late time points, the radioactivity of the tracer will have decayed already significantly, and visibility is poor with conventional scanners. The higher sensitivity of a total-body PET system makes it possible to acquire a delayed image of the patient with sufficient image quality for lesion detection.

3.5.2 Applications in Neurology

Many diseases that were thought to be confined to one single organ in the past now appear to be much more complex and involve interactions between organs. Total-body PET imaging, i.e., simultaneous imaging of the brain and torso, allows the medical doctor to look at these interactions during a single examination. This interaction of peripheral organ pathologies and the brain or the interaction between the body and the brain is an interesting topic of novel neurological studies that could lead to new information and a more thorough understanding on the origin of CNS diseases. One example of this is the gut-brain axis or the relationship between the brain and the microbiota in the gastrointestinal tract. It has been shown that changes in the gut microbiota induce activation of certain pathways in the central nervous system and may even lead to conditions like anxiety and depression (Foster and McVey Neufeld 2013; Cryan and O'Mahony 2011). The introduction of total-body PET and the ability to visualize the whole body and the dynamics of the tracer at once can lead to breakthroughs in neurological research.

3.5.3 Research on New Radiopharmaceuticals

One of the main driving factors for the realization of total-body PET is its potential use for research. The first research advantage is the ability to visualize the complete body of the patient at once and in a dynamic way. Thus, the effect and the

time-dependent distribution of a drug can be studied in the entire body. A second reason is the ability to scan patients with a radioactive dose lower than the monthly background radiation. This makes it safe for healthy subjects to participate in clinical trials, which will make new radiotracers more rapidly available. One example of a new tracer under investigation is the use of radioactively labeled nanobodies for the detection of breast carcinoma (Keyaerts et al. 2016).

3.6   Conclusion

Since PET physics is based on electronic collimation by means of coincidence detection, its sensitivity is highly restricted by the geometry of the system. Because of the limited length of clinically available system (~20 cm), they are only able to detect less than 2% of all emitted activity from inside the patient. For this reason, the patient has to be injected with a high dose of radioactivity and lie still in the scanner for a long time. The first requirement is associated with an increased risk for radiation-induced cancers, while the latter may introduce artefacts due to small movements of the patient. The only way to drastically increase the fraction of detected photons is by increasing the length of the scanner and making it cover a larger portion of the patient's body. This is exactly what was done in the EXPLORER project. This project resulted in the construction of two total-body PET systems with lengths of 1 and 2 m and up to 15 and 40× higher sensitivity, respectively. The highest gain is in applications where the full length of the scanner is used, meaning where the whole body is under examination. A typical application of PET where this is the case is in oncology where PET is used for diagnosis, staging, and follow-up of patients. Although the main application of PET is in oncology, other disciplines like neurology, pediatrics and pharmacology can take advantage of the increased sensitivity.

References

Badawi RD, Shi H, Hu P, Chen S, Xu T, Price PM et al (2019) First human imaging studies with the explorer total-body PET scanner. J Nucl Med 60(3):299–303

Berg E, Liu W, Zhao Y, Dong Y, Lv X, Ding Y, et al. (2018) Physical performance of the first total-body EXPLORER PET scanner and preclinical applications with mini-EXPLORER systems [Internet]. Available from https://explorer.ucdavis.edu/sites/g/files/dgvnsk6796/files/inline-files/Berg_EXPLORER_TotalBodyPETWorkshop_wm.pdf

Cheng G, Alavi A, Lim E, Werner TJ, Del Bello CV, Akers SR (2013) Dynamic changes of FDG uptake and clearance in normal tissues. Mol Imaging Biol 15(3):345–352

Cherry SR, Jones T, Karp JS, Qi J, Moses WW, Badawi RD. Total-Body PET: Maximizing sensitivity to create new opportunities for clinical research and patient care. J Nucl Med 2017;59(1):3–12

Conti M, Bendriem B, Casey M, Eriksson L, Jakoby B, Jones WF et al (2006 Jun) Performance of a high sensitivity PET scanner based on LSO panel detectors. IEEE Trans Nucl Sci 53(3):1136–1142

Crosetto D. (2003) The 3-D Complete Body Screening (3D-CBS) features and implementation. In: IEEE Nuclear Science Symposium Conference Record, vol. 4. pp. 2415–2419

Cryan JF, O'Mahony SM (2011 Mar) The microbiome-gut-brain axis: from bowel to behavior. Neurogastroenterol Motil 23(3):187–192

Foster JA, McVey Neufeld K-A (2013 May) Gut–brain axis: how the microbiome influences anxiety and depression. Trends Neurosci 36(5):305–312

Fredriks AM, Van Buuren S, Van Heel WJM, Dijkman-Neerincx RHM, Verloove-Vanhorick SP, Wit JM (2005) Nationwide age references for sitting height, leg length, and sitting height/height ratio, and their diagnostic value for disproportionate growth disorders. Arch Dis Child 90(8):807–812

Freedenberg MI, Badawi RD, Tarantal AF, Cherry SR (2014 Feb) Performance and limitations of positron emission tomography (PET) scanners for imaging very low activity sources. Phys Med 30(1):104–110

Gureyev TE, Nesterets YI, de Hoog F, Schmalz G, Mayo SC, Mohammadi S et al (2014) Duality between noise and spatial resolution in linear systems. Opt Express 22(8):9087–9094

Habte F, Foudray AMK, Olcott PD, Levin CS (2007) Effects of system geometry and other physical factors on photon sensitivity of high-resolution positron emission tomography. Phys Med Biol 52(13):3753–3772

Karp JS, Viswanath V, Geagan MJ, Muehllehner G, Pantel AR, Parma MJ et al (2019) PennPET explorer: design and preliminary performance of a whole-body imager. J Nucl Med 61:136–143

Keyaerts M, Xavier C, Heemskerk J, Devoogdt N, Everaert H, Ackaert C et al (2016) Phase I Study of 68Ga-HER2-nanobody for PET/CT assessment of HER2 expression in breast carcinoma. J Nucl Med 57(1):27–33

Kubota K, Itoh M, Ozaki K, Ono S, Tashiro M, Yamaguchi K et al (2001) Advantage of delayed whole-body FDG-PET imaging for tumour detection. Eur J Nucl Med 28(6):696–703

Mikhaylova E, Tabacchini V, Borghi G, Mollet P, D'Hoe E, Schaart DR et al (2017 Oct) Optimization of an ultralow-dose high-resolution pediatric PET scanner design based on monolithic scintillators with dual-sided digital SiPM readout: a simulation study. Phys Med Biol 62(21):8402–8418

Nesterets YI, Gureyev TE (2015) Young's double-slit experiment: noise-resolution duality. Opt Express 23(3):3373–3380

Phelps ME, Hoffman EJ, Mullani NA, Ter-pogossian MM (1975) Application of annihilation coincidence detection to transaxial reconstruction tomography. J Nucl Med 16(3):210–224

Poon JK, Dahlbom ML, Moses WW, Balakrishnan K, Wang W, Cherry SR et al (2012 Jul) Optimal whole-body PET scanner configurations for different volumes of LSO scintillator: a simulation study. Phys Med Biol 57(13):4077–4094

Reardon S (2019) Whole-body PET scanner produces 3D images in seconds. Nature 570(7761):285–286

Risk NCD, Collaboration F (2016) A century of trends in adult human height. elife 5:1–29

Schmall JP, Karp JS, Werner M, Surti S (2016 Jul) Parallax error in long-axial field-of-view PET scanners - a simulation study. Phys Med Biol 61(14):5443–5455

Tsui BMW, Beck RN, Doi K, Metz CE (1981) Analysis of recorded image noise in nuclear medicine. Phys Med Biol 26(5):883–902

Van Sluis J, De Jong J, Schaar J, Noordzij W, Van Snick P, Dierckx R et al (2019) Performance characteristics of the digital biograph vision PET/CT system. J Nucl Med 60(7):1031–1036

Vandenberghe S, Moskal P, Karp J (2020) State of the art in total body PET. EJNMMI Phys. (Accepted for publication)

Watanabe M, Shimizu K, Omura T, Sato N, Takahashi M, Kosugi T, et al. (2003) A high-throughput whole-body PET scanner using flat panel PS-PMTs. In: 2003 IEEE Nuclear Science Symposium Conference Record, vol. 4. pp. 2442–2446

Wai-Hoi Wong, Yuxuan Zhang, Shitao Liu, Hongdi Li, Hossain Baghaei, Ramirez R, et al. (2007) The initial design and feasibility study of an affordable high-resolution 100-cm long PET. In: 2007 IEEE Nuclear Science Symposium Conference Record. pp. 4117–4122

Cerebral Glucose Metabolism

4

Wolf-Dieter Heiss and Olivier Zaro-Weber

Contents

Abstract

Glucose is the main substrate for energy metabolism of the brain, and the regional cerebral metabolic rate is directly related to regional brain activity. Therefore, the measurement of regional glucose metabolism is of great importance for the assessment of regional normal function and of pathological changes. Quantitation of glucose metabolism by PET is based on the 2-deoxyglucose method developed by Sokoloff and colleagues: F18-labelled deoxyglucose (FDG) is transported into the brain and phosphorylated, but cannot be further metabolised and therefore is accumulated intracellularly. The concentration of the tracer can be

W.-D. Heiss (✉)
Max Planck Institute for Neurological Research, Cologne, Germany
e-mail: wdh@nf.mpg.de

O. Zaro-Weber
Max Planck Institute for Neurological Research, Cologne, Germany

Department of Neurology and Center for Stroke Research Berlin (CSB),
Charité – Universitätsmedizin, Berlin, Germany
e-mail: zaroweber@nf.mpg.de

measured three dimensionally by PET, and together with the arterial tracer concentration, the kinetics of glucose uptake can be assessed, and the regional cerebral metabolic rates for glucose (rCMRGlc) can be calculated.

rCMRGlc is high in cortex and grey matter structures and low in white matter, but there are significant differences among various regions. Metabolic rate is slightly reduced with ageing and changed by sleep, dream, and functional activation. CMRGlc is significantly affected in pathological states, and the regional and global changes are important for assessing the severity of disorders and for differential diagnosis of diseases of the brain. Therefore, FDG-PET has still great importance in brain research and many applications in clinical neurology.

4.1   Energy Requirements of Brain Tissue

The energy demand of the nervous tissue is very high, and therefore sufficient blood supply to the brain must be maintained consistently. A normal adult male's brain containing approximately 130 billion neurons (21.5 billion in the neocortex) (Pakkenberg and Gundersen 1997) comprises only 2% of the total body mass yet consumes at rest approximately 20% of the body's total basal oxygen consumption supplied by 16% of the cardiac blood output. The brain's oxygen consumption is almost entirely for the oxidative metabolism of glucose, which in normal physiological conditions is the almost exclusive substrate for the brain's energy metabolism (Clarke and Sokoloff 1999). It must be kept in mind that the glucose metabolised in neuronal cell bodies is mainly to support cellular vegetative and housekeeping functions, e.g. axonal transport, biosynthesis of nucleic acids, proteins, lipids, as well as other energy-consuming processes not related directly to action potentials. Therefore, the rate of glucose consumption of neuronal cell bodies is essentially unaffected by neuronal functional activation. Increases in glucose consumption (and regional blood flow) evoked by functional activation are confined to synapse-rich regions, i.e. neuropil which contains axonal terminals, dendritic processes, and also astrocytic processes that envelope the synapses. The magnitudes of these increases are linearly related to the frequency of action potentials in the afferent pathways, and increases in the projection zones occur regardless of whether the pathway is excitatory or inhibitory. Only at the next downstream projection zones glucose utilisation (and, as a consequence, blood supply) is depressed in inhibited neurons and increased in excited neurons. Energy metabolism by functional activation is due mostly to the stimulation of the $Na + K + -ATPase$ activity to restore the ionic gradients across the cell membrane and the membrane potentials that were degraded by the spike activity and is rather high compared to the demand of neuronal cell bodies (Sokoloff 1999). Overall, 87% of the total energy consumed is required by signalling, mainly action potential propagation and postsynaptic ion fluxes, and only 13% is expended in maintaining membrane resting potential (Attwell and Laughlin 2001).

4.2   Brain Energy Metabolism

Glucose is the obligatory energy substrate for the brain, and it is almost entirely oxidised to CO_2 and H_2O. Although the brain represents only 2% of the body weight, it receives 15% of the cardiac output, 20% of the total body oxygen consumption, and 25% of the total body glucose utilisation (Villien et al. 2014). With a global blood flow of 57 mL/100 g min, the brain extracts approximately 50% of oxygen and 10% of glucose from the arterial blood. Hence, the glucose utilisation of the brain, as assessed by measuring the arterial-venous difference (Kety and Schmidt 1948), is 31 mmol/100 g min. Oxygen consumption is 160 mmol/100 g min; because CO_2 production is almost identical, the respiratory quotient (RQ) of the brain is nearly 1, indicating that carbohydrates are the substrates for oxidative metabolism (Sokoloff 1989). Given a theoretical stoichiometry of 6 mmol of oxygen consumed for each mmole of glucose, glucose utilisation by the brain should in theory be 26.6 mmol/100 g min. As indicated earlier, the measured glucose utilisation is 31 mmol/100 g min, indicating that an excess of 4.4 mmol/100 g min of glucose follows other metabolic fates. Glucose can produce metabolic intermediates, such as lactate and pyruvate, which do not enter necessarily in the tricarboxylic acid cycle, but rather can be released and removed by circulation. Glucose can be incorporated into lipids, proteins, and glycogen, and it is also the precursor of certain neurotransmitters such as gamma-aminobutyric acid (GABA), glutamate, and acetylcholine (Sokoloff 1989).

Of molecules that could substitute for glucose as an alternative substrate for brain energy metabolism, mannose is the only one that can sustain normal brain function in the absence of glucose. Lactate and pyruvate can sustain synaptic activity in vitro. Because of their limited permeability across the blood–brain barrier, they cannot substitute for plasma glucose to maintain brain function (Pardridge and Oldendorf 1977). However, if formed inside the brain parenchyma, they are useful metabolic substrates for neural cells (review in Magistretti and Allaman 2015).

Whole-organ studies, which allowed the determination of the substrate requirements for the brain, failed to provide the appropriate level of resolution to appreciate two major features of brain energy metabolism: (a) its regional heterogeneity and (b) its tight relationship with the functional activation of specific pathways. The autoradiographic 2-deoxyglucose (2-DG) method developed by Sokoloff and colleagues afforded a sensitive means to measure local cerebral metabolic rates of glucose (LCMRGlc) with a spatial resolution of approximately 50–100 μm (Sokoloff et al. 1977). The method is based on the fact that tracer amounts of radioactive 2-DG are taken up by glucose transporters and phosphorylated by hexokinase with kinetics that are similar to those for glucose; however, unlike glucose-6-phosphate, 2-deoxyglucose-6-phosphate cannot be metabolised further and therefore accumulates intracellularly, thus providing, after appropriate corrections (Sokoloff et al. 1977), an accurate measurement of the amount of glucose utilised. Using this method, LCMRGlc have been determined in virtually all morphologically and

functionally defined brain structures in various physiological and pathological states including sleep, seizures, and dehydration and following a variety of pharmacological treatments. Furthermore, the increase in glucose utilisation following activation of pathways subserving specific modalities, such as visual, auditory, olfactory, or somatosensory stimulations, as well as during motor activity, has been revealed in the pertinent brain structures.

Basal glucose utilisation of the grey matter as determined by the 2-DG technique varies, depending on the brain structure, between 50 and 150 μmol/100 g wet weight/min in the rat (Sokoloff et al. 1977). Physiological activation of specific pathways results in a 1.5–3-fold increase in LCMRGlc as determined by the 2-DG technique.

With the advent of PET and the use of positron-emitting isotopes such as ^{18}F, local glucose utilisation has been studied in humans with 2-(^{18}F)fluoro-2-deoxyglucose (Reivich et al. 1979). Changes in local brain energy metabolism can now be studied in humans with PET by monitoring alterations in glucose utilisation, oxygen consumption, and blood flow during activation of specific areas. Studies in which these three parameters have been analysed during activation of a given modality have yielded an uncoupling between glucose uptake and oxygen consumption during activation, since the increase in blood flow and in glucose utilisation in the activated cortical area was not matched by an equivalent increase in oxygen consumption (Fox et al. 1988; Madsen et al. 1995; Blomqvist et al. 1994). This observation raises the puzzling possibility that, at least during the early stages of activation, the increased energy demand is met by glycolysis rather than by oxidative phosphorylation (Vaishnavi et al. 2010; Raichle and Mintun 2006).

4.2.1 Glycolysis and Oxidative Phosphorylation

Glycolysis (Embden–Meyerhof pathway) is the metabolism of glucose to pyruvate and lactate. It results in the net production of only 2 mol of adenosine triphosphate (ATP)/mol of glucose as well as in the regeneration of reducing equivalents (the oxidised form of nicotinamide adenine dinucleotide (NAD+)) through the conversion of pyruvate into lactate. Alternatively, pyruvate can enter the tricarboxylic acid (TCA) cycle (or the Krebs cycle) and produce 30 mol of ATP/mol of glucose via the mitochondrial oxidative phosphorylation cascade. The energetic value of oxidative phosphorylation over glycolysis is thus obvious. The respiratory quotient of the brain is virtually 1; PET studies indicate an uncoupling between glucose uptake and oxygen consumption during activation (Fox et al. 1988; Madsen et al. 1995), and rises in lactate have been monitored. During activation, lactate may normally be taken up by neurons as an energy fuel. It should be remembered that after conversion to pyruvate, lactate can enter the TCA cycle with the potential to generate a total of 36 mol of ATP/mol of glucose. Activation-induced glycolysis may provide ATP to fuel energy-dependent ion transport, in particular the Na+/K + −ATPase, which represents the main energy-consuming process in neural cells (Siesjo 1978).

4.2.2   Determination of the Regional Cerebral Metabolic Rate for Glucose (rCMRGlc)

The study of glucose metabolism with 18FDG is a direct application of the autoradiographic technique of Sokoloff et al. (1977) with [^{14}C]deoxyglucose. The model developed by Sokoloff et al. can be applied directly because the fluorodeoxyglucose labelled at point 2 behaves in the same way as deoxyglucose. It is transported into the cell in the same way as glucose and, with the aid of hexokinase, is phosphorylated to [^{18}F]deoxyglucose-6-phosphate. Deoxyglucose-6-phosphate, however, cannot be further converted to fructose-6-phosphate and degraded to CO_2 and H_2O, but accumulates in the cell. The kinetics of the back reaction (phosphatase) to deoxyglucose is much slower, and the deoxyglucose-6-phosphate can penetrate through the cell membrane only in small amounts. The kinetics of the accumulation of deoxyglucose-6-phosphate can be described with the transport and enzyme constants of a three-compartment model (Fig. 4.1). The corresponding complex formula (Reivich et al. 1979) for calculating the regional cerebral metabolic rate of glucose (rCMRGlc) (Fig. 4.2) can be simplified to the following form (Phelps et al. 1979):

$$rCMRGl = \frac{(GI)}{LC} \bullet \frac{C\left(^{18}F\right) - C\left(FDG\right)}{A_b}$$

where $C(^{18}F)$ is the total fluorine activity measured in the tissue, which is determined directly in the PET, and $C(FDG)$ is the concentration of free FDG in the tissue, calculated from the plasma concentration up to time point T with the aid of the

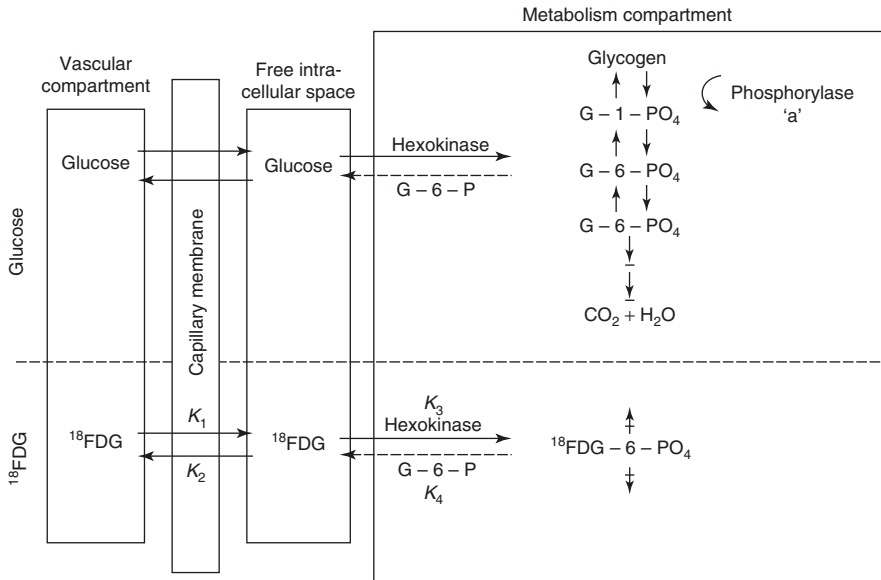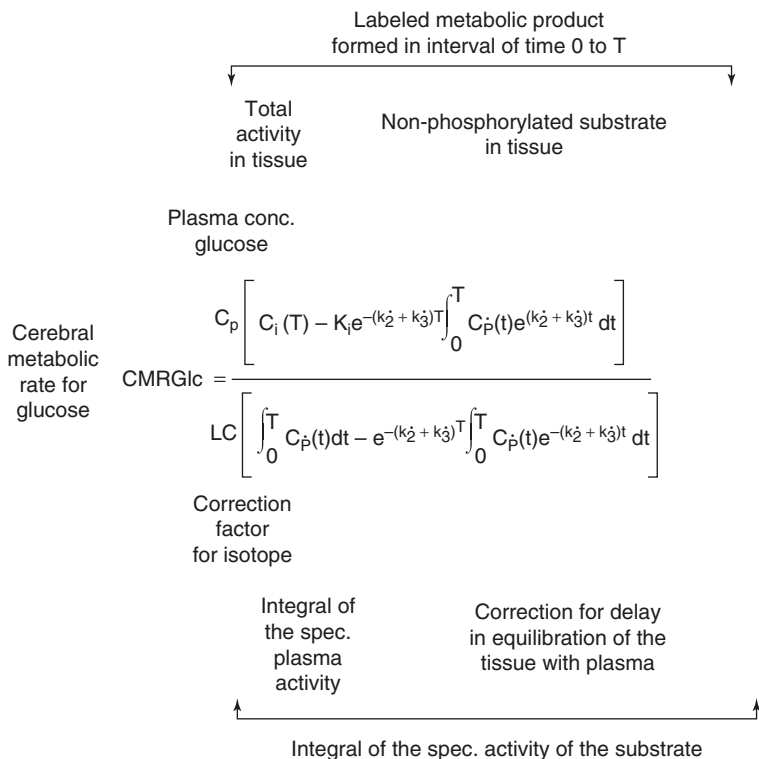**Fig. 4.1** Transport and metabolism of glucose and ^{18}F-FDG in brain tissue (see text for details)

$$\text{CMRGlc} = \frac{C_p\left[C_i(T) - K_i e^{-(k_2^* + k_3^*)T} \int_0^T C_{\dot{p}}(t) e^{(k_2^* + k_3^*)t}\, dt\right]}{LC\left[\int_0^T C_{\dot{p}}(t)\, dt - e^{-(k_2^* + k_3^*)T} \int_0^T C_{\dot{p}}(t) e^{-(k_2^* + k_3^*)t}\, dt\right]}$$

Labeled metabolic product
formed in interval of time 0 to T

Total activity in tissue

Non-phosphorylated substrate in tissue

Plasma conc. glucose

Cerebral metabolic rate for glucose

Correction factor for isotope

Integral of the spec. plasma activity

Correction for delay in equilibration of the tissue with plasma

Integral of the spec. activity of the substrate

Operational equation for calculation of rCMRGl

Fig. 4.2 Equation for calculation of regional cerebral metabolic rate of glucose (rCMRGlc) in the brain

constants of the model. The difference between these two values gives the local tissue concentration of FDG-6-phosphate; A_b is the total quantity of FDG released into the tissue and is calculated from the plasma FDG concentration curve up to time point T, decreased by the delay in the tissue equilibration using the corresponding model constants. The quotient therefore gives the proportional phosphorylation rate of FDG. Multiplication by the plasma concentration of glucose (Glc) would yield the rate of glucose phosphorylation if it behaved in the same way as FDG. Since the arterial-venous extraction of glucose is not identical with that of FDG, the value must be corrected with an experimentally determined constant (LC = lumped constant). For the measurement of the regional glucose consumption in the brain, therefore, after i.v. administration of 3–6 mCi 18FDG, the plasma curve of 18FDG from the injection to the measurement time point (usually determined in arterialised venous blood), the glucose value in plasma, and the regional ^{18}F activity in the brain must be determined.

Errors resulting with this model from widely diverging kinetic constants in pathological tissue (Hawkins et al. 1981) can be reduced by dynamic PET. For this purpose, the tissue activity is determined at short time intervals from the time point of injection. By variation of the values for the kinetic constants, the curve deriving from the model equation is adapted to the measured regional activity time curve. The kinetic constants thus determined correspond best to the activity uptake in the corresponding tissue segment. They allow the regional metabolic rate for glucose to be directly calculated (Wienhard et al. 1985). It is now only necessary to assume a known value for the LC.

There remains some uncertainty as to the exact value of the normal "lumped constant" (LC) for FDG. The initial value empirically derived by Phelps et al. (1979) was 0.42. It has been directly measured by Reivich et al. (1985), who found a value of 0.52, assuming $k_4 = 0$. But LC could be even as high as 0.65 (Wu et al. 2003). However, regional changes in LC are small. For the sake of uniformity, the actual value used should be quoted in all publications. This will allow direct comparison of numerical values because the LC is a linear scaling factor in the operational equations. With rate constants measured by dynamic curve fitting or by integration techniques, the equation for calculation of CMRGlc is:

$$\text{CMRglc} = C_a \ / \ \text{LC} \times \left(k_1 k_3 \ / \left(k_2 + k_3 \right) \right)$$

The term $k_1 k_3/(k_2 + k_3)$, representing the metabolic rate of FDG, can be substituted by the influx rate constant ki determined with the linear approximation of Patlak et al. (1983). There have also been modifications that avoid the assumption of a fixed LC and refer instead to the Michaelis–Menten equation to account for the relations between enzyme affinities for FDG and glucose (Kuwabara et al. 1990).

Determination of individual rate constants is not very practical in many clinical applications, and methods are preferred that can be done with a single scan, a situation similar to the original development of the method for autoradiography. Then the deviation from population average CMRGlc (given by the average rate constants) is estimated from a single scan. Actual measured FDG activity is compared with the activity that would have been expected at the time of the scan with the individual's blood activity time course and average rate constants (Wienhard et al. 1985).

To avoid the conversion factor needed with the analogue tracer FDG, native glucose labelled with 11C in the 1-position (1-11C-d-glucose) has also been used for quantitation of CMRGlc (Raichle et al. 1975). Modelling is based on the same two-tissue compartment model as with FDG, but an additional term is necessary to account for labelled metabolites (mainly lactate and other monocarboxylic acids and CO_2). Metabolites occur in the plasma and in the brain, and loss of labelled CO_2 from the brain is dependent on CBF. Data indicate that there is a rapid loss of labelled lactate from the brain, suggesting that it represents a significant nonoxidative part of glucose metabolism in the brain (approximately 10% of the total CMRGlc) (Blomqvist et al. 1990).
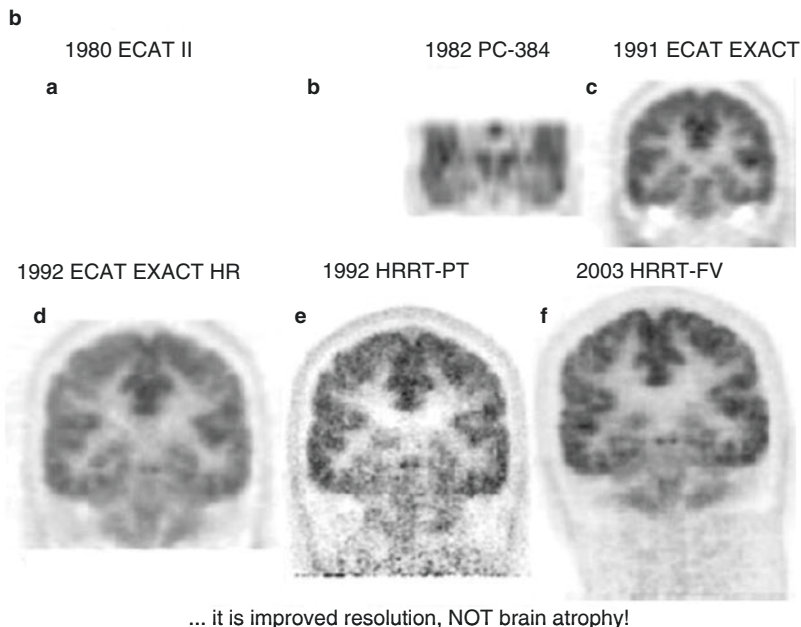
4.2.3 Normal Glucose Consumption of the Brain

In healthy volunteers, a mean glucose consumption of 29–32 µmol/100 g/min was found by means of FDG and PET (Reivich et al. 1979; Heiss et al. 1984), which correspond well to whole-brain metabolic rates provided by the Kety–Schmidt method. Under controlled conditions (darkened laboratory and steady noise from fans of equipment cooling systems), the functional anatomy of the brain is reflected in the metabolic activity of the individual regions. However, reliable regional values for cerebral metabolic rate of glucose (rCMRGlc) can only be obtained by equipment permitting high 3D resolution of tracer concentration in the brain tissue (Heiss et al. 2004). This progressively improved spatial resolution of PET is documented in Fig. 4.3 showing FDG images of the brain in the same volunteer assessed with different tomographs over the years (Heiss 2009a, b). Typical resting state grey matter CMRGlc values are in the range of 40–60 µmol/100 g/min, and the corresponding level in the white matter is about 15 µmol/100 g/min. There are significant differences among regions with highest values in the basal ganglia, primary visual cortex, and cingulate and frontal cortex (42–50 µmol/100 g/min) and lower values in other cortical and subcortical areas (35–42 µmol/100 g/min) and in the structures of the brain stem (25–30 µmol/100 g/min) and the cerebellum (33 µmol/100 g/min). There exist also significant asymmetries with largely right hemispheric predominance (Pawlik and Heiss 1989), review in Silverman and Melega (2004). The resting regional metabolism and its asymmetry are highly dependent on the state of resting wakefulness (e.g. apprehensive or relaxed) and background conditions (e.g. laboratory noise).

Local CMRGlc measured with PET is influenced by age: glucose metabolism of various grey matter structures was low at birth (13–25 µmol/100 g/min), reached a level of 19–33 µmol/100 g/min by 2 years and continued to rise until age 3–4 years, and was maintained at a high level (49–55 µmol/100 g/min) until age of 10 years (Chugani et al. 1987). At about 10 years, CMRGlc began to decline with a rather uniform decrease by 26% in all investigated brain regions of 40 healthy resting subjects between the ages of 18 and 78 years (Kuhl et al. 1982). However, these age-dependent changes were not observed in all studies (Duara et al. 1984). In our own study on 42 normal subjects aged 15–85 years, a small (0.65 µmol/100 g/min per decade/$p < 0.05$) age-dependent decrease in global CMRGlc was found (Fig. 4.4). However, as demonstrated in Fig. 4.4, the various regions contributed differently to this overall effect: decreases of 16.6–11.3% in cingulate, frontal, parietal, insular, temporal, and sensorimotor cortex, virtually no change in the primary visual cortex and cerebellum (Pawlik and Heiss 1989). Similar age-dependent changes of rCMRGlc were described in further studies (Kalpouzos et al. 2009; Hsieh et al. 2012; Chetelat et al. 2013; Berti et al. 2014; Shen et al. 2012; Bonte et al. 2017; Jiang et al. 2018).
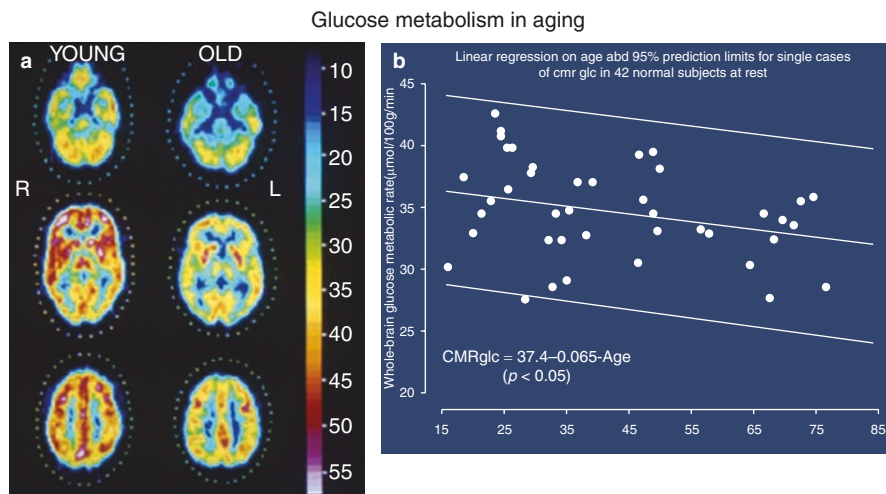
Hardly any normal functional state is as regularly associated with as dramatic changes of general behaviour and shifting of attention as is sleep. The conclusion of no effect of sleep on human cerebral haemodynamics and metabolism, derived from early Kety–Schmidt studies (Mangold et al. 1955), could be disproved with PET (Heiss et al. 1985). As shown in Fig. 4.5, during stages II–IV sleep, a significant ($P < 0.001$) global decrease of brain functional activity was observed, with the
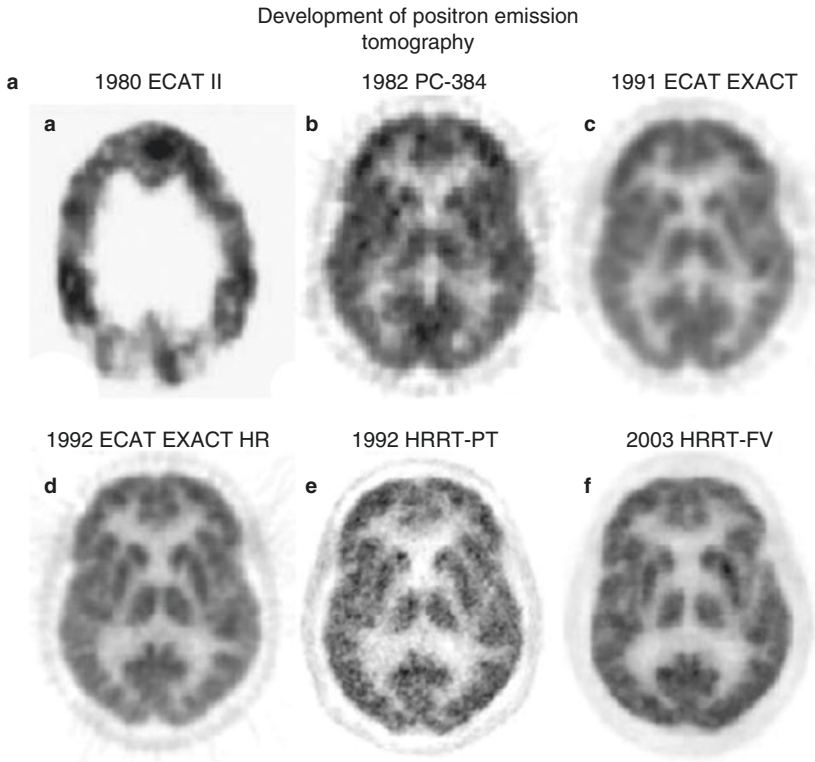

Fig. 4.3 (**a**) Development of PET: a horizontal slice. Various PET systems over the years demonstrate improvement in image quality and spatial resolution. (*a*) ECAT II, spatial resolution 15 mm. (*b*) PC-384, FWHM 8.4 mm. (*c*) ECAT EXACT, FWHM 6.5–7 mm. (*d*) ECAT EXACT HR, FWHM 3.6–4.5 mm. (*e*) *f* HRRT PET: *e* prototype. (*f*) final version (HRRT-FV), FWHM 2.3–3.2 mm. Images of glucose metabolism were acquired for 20 min of steady-state starting 30 min after tracer administration. (**b**) Coronal views of glucose consumption of the brain in a volunteer acquired with various PET systems over the years demonstrate improvement in axial resolution due to decreased slice thickness and advances in image reconstruction. (*a*) ECAT II (1980) was a single-ring camera; axial reconstruction was therefore not feasible. (*b*) PC-384, slice thickness 12 mm. (*c*) ECAT EXACT, axial FWHM 5–8 mm. (*d*) ECAT EXACT HR, axial FWHM 4.0–6.7 mm. (*e*) *f* HRRT PET: *e* prototype. (*f*) final version (HRRT-FV), axial FWHM 2.5–3.4 mm

b

1980 ECAT II   1982 PC-384   1991 ECAT EXACT

1992 ECAT EXACT HR   1992 HRRT-PT   2003 HRRT-FV

... it is improved resolution, NOT brain atrophy!

Fig. 4.3 (continued)

Glucose metabolism in aging

$CMRglc = 37.4 - 0.065 \cdot Age$
($p < 0.05$)

Fig. 4.4 (**a**) PET scans of glucose metabolism (μmol/100 g/min according to scale) in cerebral sections at the level of the cerebellum, basal ganglia, thalamus, and semioval centre in young (23 years) and old (67 years) healthy subjects. The individual brain structures can be differentiated according to different metabolic rates; metabolism decreases slightly in all regions in older patients. (**b**) Decrease of mean global glucose metabolic rate in 42 healthy subjects with increasing age. The regression line shows a significant relationship despite the large range of variation
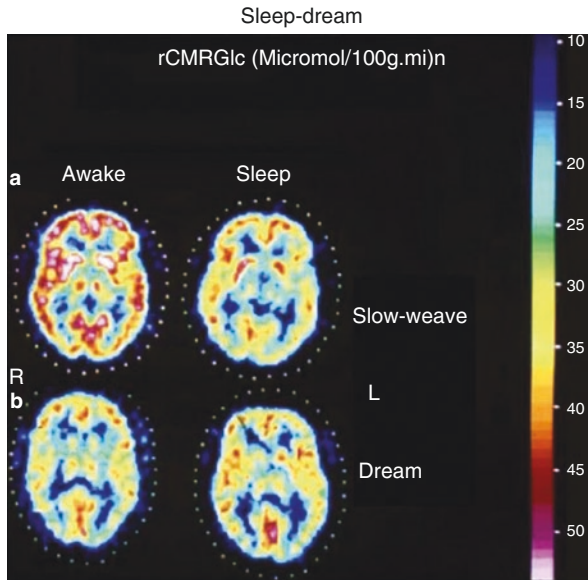
Fig. 4.5 (**a**) Corresponding images of the local cerebral metabolic rate for glucose determined by FDG-PET in a characteristic horizontal brain slice across the basal ganglia of a healthy 37-year-old male subject representative of the non-dreamers group, showing nonselective decrease in glucose utilisation from wakefulness (W) to sleep (S). Frontal poles are on top, occipital poles at bottom, sides as marked (R, L). Values on reference scale are in μmol/100 g min. (**b**) Corresponding metabolic maps of a 28-year-old normal volunteer's brain slice recorded by FDG-PET while the subject was awake (W) and asleep dreaming (S). A generalised activation, most marked in the insular regions, visual cortex, and hippocampal formations, is clearly demonstrated during sleep with dreaming

largest declines in the orbitofrontal cortex and in the thalamus. In dream sleep, by contrast, both a general metabolic increase and conspicuous regional activations of superior frontal, insular, inferior parietal, hippocampal, and visual association cortex (Heiss et al. 1985) were found. Increased CMRGlc during REM sleep has also been observed in limbic and paralimbic regions including hypothalamus, amygdala, orbitofrontal cingulate, entorhinal, and insular cortices (Nofzinger et al. 1997).

4.2.4   Coupling of Neuronal Activity to Metabolism and Flow

The activation of Na+, K +-ATPase represents the coupling mechanism between the increase in glucose utilisation and functional activity of the nervous tissue. The activation- induced increase in glucose uptake is visualised in the neuropil, that is, where synapses ensheathed by astrocytes are present, not at the level of the neuronal perikarya. Glucose, taken up by astrocytic processes, is metabolised glycolytically to lactate and pyruvate, which are then released as substrates for oxidative

phosphorylation in neurons (Wyss et al. 2011; Juaristi et al. 2019). Mapping of neuronal activity in the brain can be primarily achieved by quantitation of the regional cerebral metabolic rate for glucose (rCMRGlc), as introduced for autora-diographic experimental studies by Sokoloff (1977) and adapted for positron emission tomography (PET) in humans (Reivich et al. 1979). Functional mapping, as it is widely used now, relies primarily on the hemodynamic response assuming a close association between energy metabolism and blood flow. While it is well documented that increases in blood flow and glucose consumption are closely coupled during neuronal activation, the increase in oxygen consumption is considerably delayed leading to a decreased oxygen extraction fraction (OEF) during activation (Villien et al. 2014; Mintun et al. 2001). PET detects and, if required, can quantify changes in CBF and CMRGlc accompanying different activation states of the brain tissue. The regional values of CBF or CMRGlc represent the brain activity due to a specific state, task, or stimulus, in comparison to the resting condition, and colour-coded maps can be analysed or coregistered to morphologic images.

Due to the radioactivity of the necessary tracers, activation studies with PET are limited to a maximum of 12 doses of 15O-labelled tracers, e.g. 12 flow scans, or 2 doses of ^{18}F-labelled tracers, e.g. 2 metabolic scans. Especially for studies of glucose consumption, the time to metabolic equilibrium (20–40 min) as well as the time interval between measurements required for isotope decay (HT for ^{18}F 108 min, for 15O 2 min) must be taken into consideration. FDG-PET was the leading method to investigate functional activation in humans in the 1980s (Pawlik and Heiss 1989; Phelps et al. 1981). PET-FDG activation studies assess task-induced CMRGlc changes either by performing the bolus method, with one or two separate PET scans, or as described recently by constant infusion of FDG during the entire scan for rest and activation condition (Villien et al. 2014; Hahn et al. 2016). FDG activation studies can also be applied in patients with functional disorders due to localised brain damage, e.g. by stroke and tumour (review in Chiaravalloti et al. (2019)), and has found broad application to patients with aphasia (Heiss 2009a, b). An example is given in Fig. 4.6 showing different activation patterns in poststroke aphasia which are related to prognosis and recovery of language function.

4.2.5   Clinical Applications of FDG-PET

Since its introduction, FDG-PET has been applied for studying the pathophysiology and for differential diagnosis of several neurological and psychiatric disorders (Chiaravalloti et al. 2019; Herholz et al. 2013; Jones et al. 2012). These applications will be described in the special clinical chapters of this book series. Some examples where FDG-PET has gained special importance are shown here.

In dementias, FDG-PET has attained a special role to detect progression of regional functional disturbance related to severity of cognitive and memory impairment (Fig. 4.7) and for differential diagnosis to other degenerative disorders

Reserve capacity of the brain
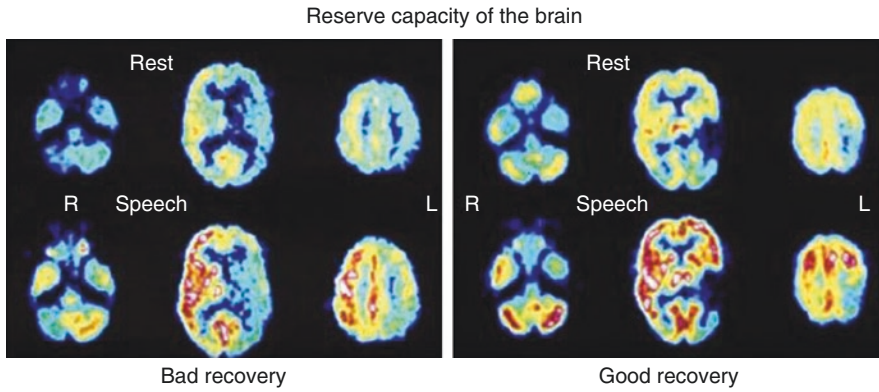
Fig. 4.6 Resting and speech-activated regional glucose metabolism in two patients with aphasia after ischemic stroke: if only contralateral regions are activated by speech, the prognosis is poor. If activation takes also place in homolateral periinfarct regions, prognosis is better, and speech performance shows satisfactory recovery
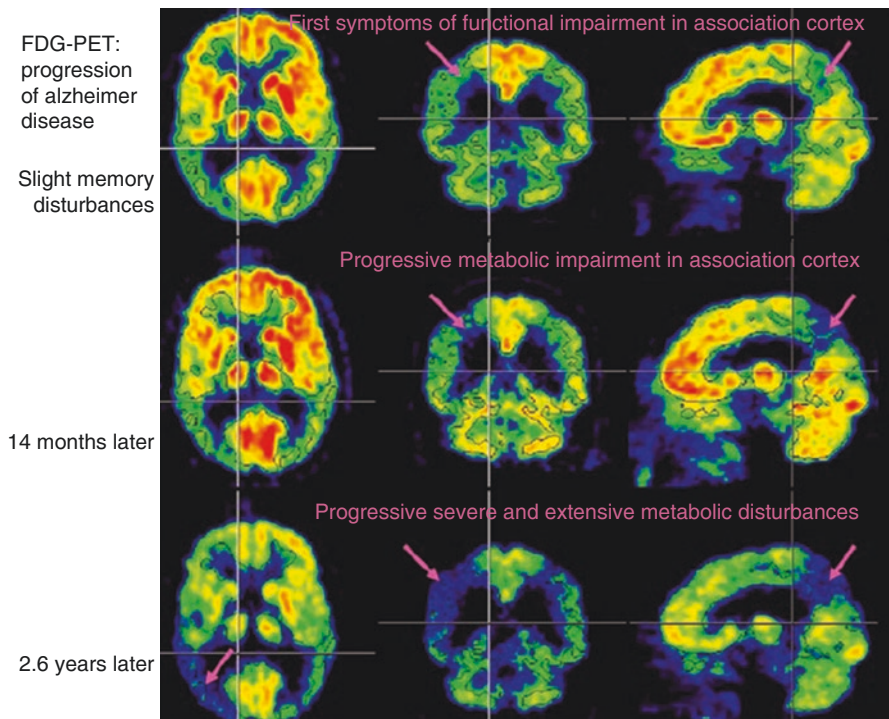
Fig. 4.7 Decline of cerebral metabolic rate (glucose) (CMRGlc) in association areas with progression of AD from the clinical stage of mild cognitive impairment (MCI) to mild dementia (three follow-up FDG-PET scans, each showing the same orthogonal slices at position marked by crosshairs)

Differential diagnosis of dementias by FDG-PET
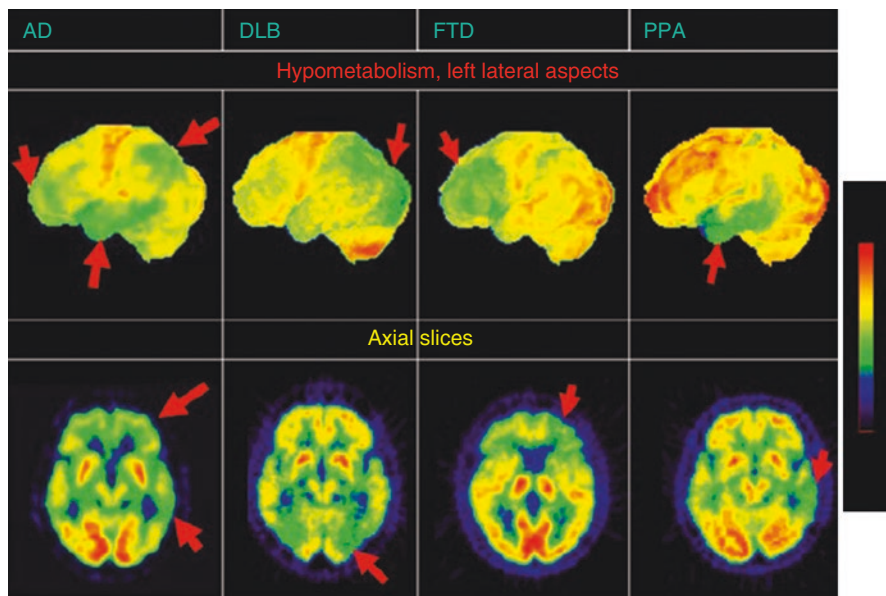
Fig. 4.8 FDG-PET in the differential diagnosis of various degenerative dementias. *Upper row*: typical transaxial slices. *Lower row*: reconstructed surface view. *AD* Alzheimer dementia, characterised by the decreases in temporoparietal and temporal association and in cingulate cortex; *FTD* frontotemporal dementia, the metabolic decrease is most severe in the anterior frontal and temporal regions; *DLB* dementia with Lewy body (Parkinson's disease), the metabolic disturbance also affects the visual cortex; *PPA* primary progressive aphasia, the disturbance is most accentuated in the temporal (Wernicke) area. *Arrows* indicate most prominent changes

(Fig. 4.8) and to vascular dementia (Fig. 4.9) (Drzezga 2009; Drzezga et al. 2018; Heiss and Zimmermann-Meinzingen 2012; Heiss 2018; Bohnen et al. 2012; Choo et al. 2013; Garibotto et al. 2017).

In brain tumours, FDG-PET has been successful in differentiating between necrosis and recurrent tumour (Fig. 4.10) and has value for grading of gliomas and for assessing the effect of chemotherapy (Heiss et al. 2011; Chierichetti and Pizzolato 2012; Herholz 2017; Herholz et al. 2012).

FDG-PET is the most common tracer used in epilepsy since epileptogenic foci are hypometabolic on interictal imaging, and FDG imaging is a commonly used tool in presurgical assessment of epilepsies (von Oertzen 2018; Broski et al. 2018; Lotan et al. 2020).

FDG-PET imaging has also been extensively performed in Parkinson's disease and is able to distinguish between several other movement disorders (Meyer et al. 2017; Meles et al. 2020).
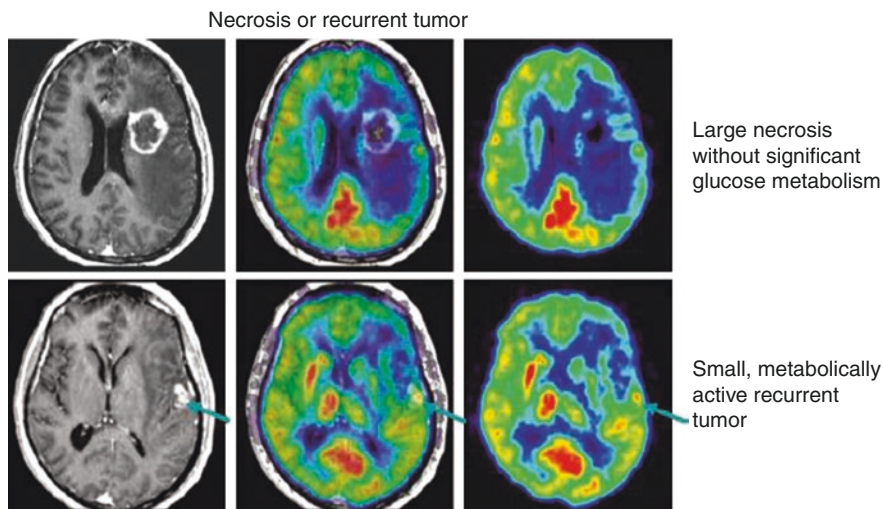
Metabolic pattern in dementia:
VaD ns AD
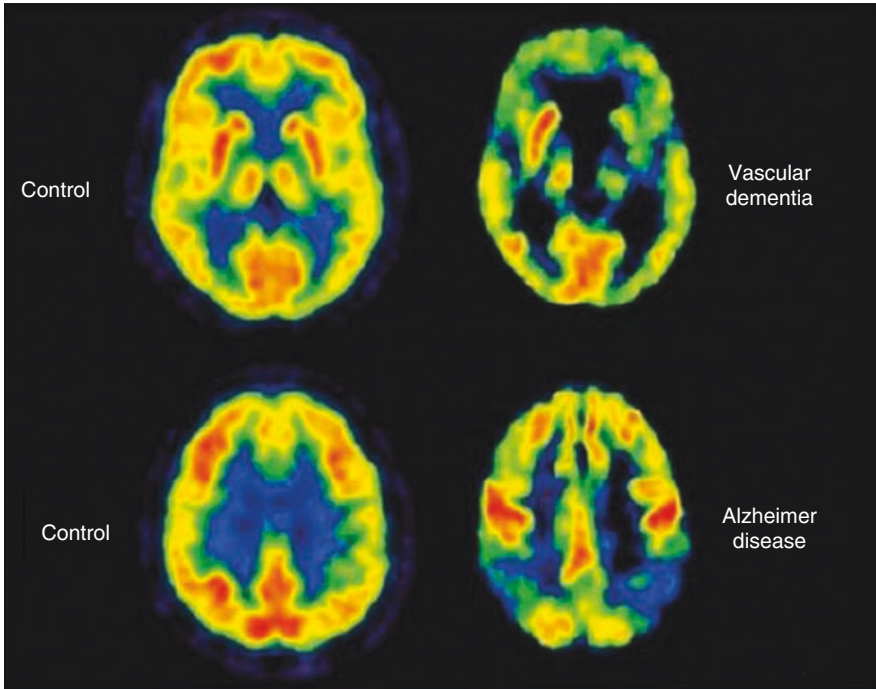
Fig. 4.9 Glucose metabolism in a normal control, in a patient with vascular dementia and a patient with Alzheimer's disease. The severity of dementia was comparable; the pattern of pathological changes differentiated these two cases: patchy metabolic defects in VaD in the frontal lobe, basal ganglia, and thalamus and hypometabolism in AD bilateral in parieto-temporal cortex and to a lesser degree in the frontal association areas, whereas primary cortical regions are spared

Neuroimaging of sleep disorders such as narcolepsy and primary hypersomnias with FDG-PET combined with other MR-based measures has given insight into the neural basis and pathogenesis of narcolepsy and primary or idiopathic hypersomnias (for review, see Cavaliere et al. 2020).

In ischemic stroke, 18FDG-PET has a role in discriminating recoverable ischemic brain tissue (penumbra) from infarcted tissue (infarct core) to predict along with 15O-PET tissue fate in acute and subacute ischemic stroke (Fig. 4.11) (Heiss et al. 1992; Nasu et al. 2002; Bunevicius et al. 2013).

Since plaque inflammation contributes to stroke and FDG identifies carotid plaque inflammation-related metabolism, FDG-PET is suitable to independently predict future recurrent stroke which may improve patient selection for revascularisation therapies as well as anti-inflammatory therapy (Marnane et al. 2012; Kelly et al. 2019).

Necrosis or recurrent tumor

Large necrosis
without significant
glucose metabolism

Small, metabolically
active recurrent
tumor

Fig. 4.10 FDG-PET and coregistered MRI in a patient with a large contrast-enhancing radiation necrosis (*top row*) and a small recurrent active carcinoma metastasis (*bottom row*)
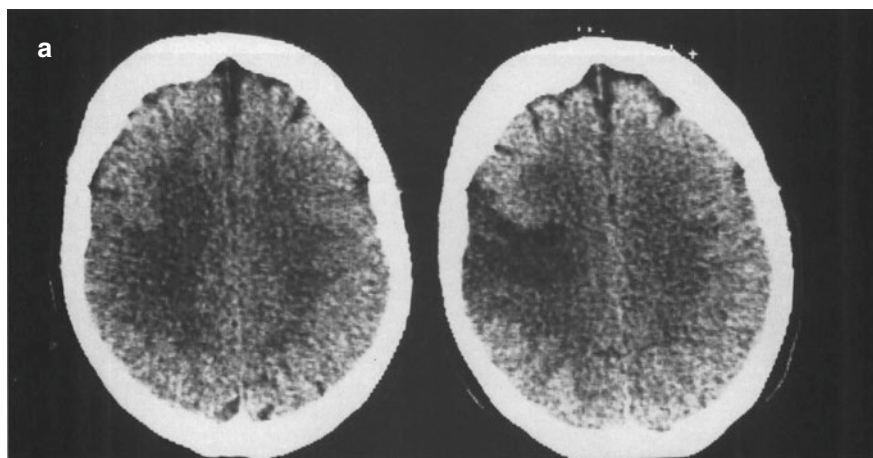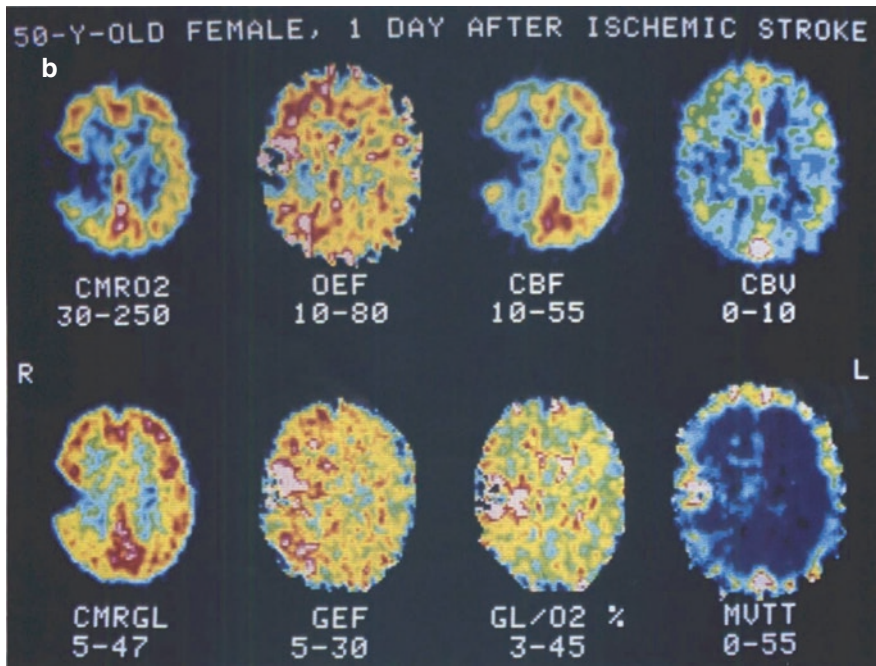

Fig. 4.11 CT and multitracer PET study of a patient 24 h after ischemic stroke in the territory of the right middle cerebral artery. CT and PET images of a brain slice 55 mm above the canthomeatal plane are presented. (**a**) While the initial CT is inconclusive, the ischemic infarct is clearly demarcated on the CT 4 days later. (**b**) PET images of the measured variables clearly demonstrate the flow defect (on CBF image) and the metabolic disturbance (CMRO2 and CMRGlc): the flow defect, however, is larger than the CMRO2 and CMRGlc defect, leaving border zone regions with preserved oxygen and glucose consumption and therefore increased oxygen extraction fraction (OEF) and glucose extraction fraction (GEF). This anterior portion is preserved at the later CT. In the posterior rim, however, CMRO2 is more severely impaired than CMRGlc leading to an increase in the ratio of glucose to oxygen consumption indicative of anaerobic glycolysis. On later CT, this area is infarcted. In the infarct, CBV is increased in relation to CBF leading to an increased transit time (TT). Due to the occlusion of the right internal carotid artery, CBF in the ipsilateral hemisphere outside the infarct is reduced without effect on CMRO2 and CMRGlc since OEF and GEF are increased

50-Y-OLD FEMALE, 1 DAY AFTER ISCHEMIC STROKE

CMRO2 30–250	OEF 10–80	CBF 10–55	CBV 0–10
CMRGL 5–47	GEF 5–30	GL/O2 % 3–45	MVTT 0–55

Fig. 4.11 (continued)

The impact of PET has further increased by the advent of integrated MRI-PET facilities (Broski et al. 2018; Catana et al. 2012; Portnow et al. 2013; Tondo et al. 2019; Shepherd and Nayak 2019; Shiyam Sundar et al. 2020).

References

Attwell D, Laughlin SB (2001) An energy budget for signaling in the grey matter of the brain. J Cereb Blood Flow Metab 21(10):1133–1145

Berti V, Mosconi L, Pupi A (2014) Brain: normal variations and benign findings in fluorodeoxyglucose-PET/computed tomography imaging. PET Clin 9(2):129–140

Blomqvist G, Seitz RJ, Sjogren I, Halldin C, Stone-Elander S, Widen L et al (1994) Regional cerebral oxidative and total glucose consumption during rest and activation studied with positron emission tomography. Acta Physiol Scand 151(1):29–43

Blomqvist G, Stone-Elander S, Halldin C, Roland PE, Widen L, Lindqvist M et al (1990) Positron emission tomographic measurements of cerebral glucose utilization using [1-11C]D-glucose. J Cereb Blood Flow Metab 10(4):467–483

Bohnen NI, Djang DS, Herholz K, Anzai Y, Minoshima S (2012) Effectiveness and safety of ^{18}F-FDG PET in the evaluation of dementia: a review of the recent literature. J Nucl Med 53(1):59–71

Bonte S, Vandemaele P, Verleden S, Audenaert K, Deblaere K, Goethals I et al (2017) Healthy brain ageing assessed with ^{18}F-FDG PET and age-dependent recovery factors after partial volume effect correction. Eur J Nucl Med Mol Imaging 44(5):838–849

Broski SM, Goenka AH, Kemp BJ, Johnson GB (2018) Clinical PET/MRI: 2018 update. Am J Roentgenol 211(2):295–313

Bunevicius A, Yuan H, Lin W (2013) The potential roles of ^{18}F-FDG-PET in management of acute stroke patients. Biomed Res Int 2013:634598

Catana C, Drzezga A, Heiss WD, Rosen BR (2012) PET/MRI for neurologic applications. J Nucl Med 53(12):1916–1925

Cavaliere C, Longarzo M, Fogel S, Engstrom M, Soddu A (2020) Neuroimaging of narcolepsy and primary hypersomnias. Neuroscientist:1073858420905829

Chetelat G, Landeau B, Salmon E, Yakushev I, Bahri MA, Mezenge F et al (2013) Relationships between brain metabolism decrease in normal aging and changes in structural and functional connectivity. NeuroImage 76:167–177

Chiaravalloti A, Micarelli A, Ricci M, Pagani M, Ciccariello G, Bruno E et al (2019) Evaluation of task-related brain activity: is there a role for (18)F FDG-PET imaging? Biomed Res Int 2019:4762404

Chierichetti F, Pizzolato G (2012) ^{18}F-FDG-PET/CT. Q J Nucl Med Mol Imaging 56(2):138–150

Choo IH, Ni R, Scholl M, Wall A, Almkvist O, Nordberg A (2013) Combination of ^{18}F-FDG PET and cerebrospinal fluid biomarkers as a better predictor of the progression to Alzheimer's disease in mild cognitive impairment patients. J Alzheimers Dis 33(4):929–939

Chugani HT, Phelps ME, Mazziotta JC (1987) Positron emission tomography study of human brain functional development. Ann Neurol 22(4):487–497

Clarke D, Sokoloff L (1999) Circulation and energy metabolism of the brain. In: Siegel GJ (ed) Basic neurochemistry: molecular, cellular, and medical aspects, 6th edn. Lippincott Williams & Wilkins, Philadelphia, p xxi, 1183 p

Drzezga A (2009) Diagnosis of Alzheimer's disease with [^{18}F]PET in mild and asymptomatic stages. Behav Neurol 21(1):101–115

Drzezga A, Altomare D, Festari C, Arbizu J, Orini S, Herholz K et al (2018) Diagnostic utility of ^{18}F-Fluorodeoxyglucose positron emission tomography (FDG-PET) in asymptomatic subjects at increased risk for Alzheimer's disease. Eur J Nucl Med Mol Imaging 45(9):1487–1496

Duara R, Grady C, Haxby J, Ingvar D, Sokoloff L, Margolin RA et al (1984) Human brain glucose utilization and cognitive function in relation to age. Ann Neurol 16(6):703–713

Fox PT, Raichle ME, Mintun MA, Dence C (1988) Nonoxidative glucose consumption during focal physiologic neural activity. Science 241(4864):462–464

Garibotto V, Herholz K, Boccardi M, Picco A, Varrone A, Nordberg A et al (2017) Clinical validity of brain fluorodeoxyglucose positron emission tomography as a biomarker for Alzheimer's disease in the context of a structured 5-phase development framework. Neurobiol Aging 52:183–195

Hahn A, Gryglewski G, Nics L, Hienert M, Rischka L, Vraka C et al (2016) Quantification of task-specific glucose metabolism with constant infusion of ^{18}F-FDG. J Nucl Med 57(12):1933–1940

Hawkins RA, Phelps ME, Huang SC, Kuhl DE (1981) Effect of ischemia on quantification of local cerebral glucose metabolic rate in man. J Cereb Blood Flow Metab 1(1):37–51

Heiss WD (2009a) WSO Leadership in Stroke Medicine Award Lecture Vienna, September 26, 2008: functional imaging correlates to disturbance and recovery of language function. Int J Stroke 4(2):129–136

Heiss WD (2009b) The potential of PET/MR for brain imaging. Eur J Nucl Med Mol Imaging 36(Suppl 1):S105–S112

Heiss WD (2018) The additional value of PET in the assessment of cerebral small vessel disease. J Nucl Med 59(11):1660–1664

Heiss WD, Habedank B, Klein JC, Herholz K, Wienhard K, Lenox M et al (2004) Metabolic rates in small brain nuclei determined by high-resolution PET. J Nucl Med 45(11):1811–1815

Heiss WD, Huber M, Fink GR, Herholz K, Pietrzyk U, Wagner R et al (1992) Progressive derangement of periinfarct viable tissue in ischemic stroke. J Cereb Blood Flow Metab 12(2):193–203

Heiss WD, Pawlik G, Herholz K, Wagner R, Goldner H, Wienhard K (1984) Regional kinetic constants and cerebral metabolic rate for glucose in normal human volunteers determined by dynamic positron emission tomography of [^{18}F]-2-fluoro-2-deoxy-D-glucose. J Cereb Blood Flow Metab 4(2):212–223

Heiss WD, Pawlik G, Herholz K, Wagner R, Wienhard K (1985) Regional cerebral glucose metabolism in man during wakefulness, sleep, and dreaming. Brain Res 327(1–2):362–366

Heiss WD, Raab P, Lanfermann H (2011) Multimodality assessment of brain tumors and tumor recurrence. J Nucl Med 52(10):1585–1600

Heiss WD, Zimmermann-Meinzingen S (2012) PET imaging in the differential diagnosis of vascular dementia. J Neurol Sci 322(1–2):268–273

Herholz K (2017) Brain tumors: an update on clinical PET research in gliomas. Semin Nucl Med 47(1):5–17

Herholz K, Herscovitch P, Heiss WD (2013) NeuroPET positron emission tomography in neuroscience and clinical neurology. Springer, Berlin

Herholz K, Langen KJ, Schiepers C, Mountz JM (2012) Brain tumors. Semin Nucl Med 42(6):356–370

Hsieh TC, Lin WY, Ding HJ, Sun SS, Wu YC, Yen KY et al (2012) Sex- and age-related differences in brain FDG metabolism of healthy adults: an SPM analysis. J Neuroimaging 22(1):21–27

Jiang J, Sun Y, Zhou H, Li S, Huang Z, Wu P et al (2018) Study of the influence of age in (18) F-FDG PET images using a data-driven approach and its evaluation in Alzheimer's disease. Contrast Media Mol Imaging 2018:3786083

Jones T, Rabiner EA, Company PETRA (2012) The development, past achievements, and future directions of brain PET. J Cereb Blood Flow Metab 32(7):1426–1454

Juaristi I, Contreras L, Gonzalez-Sanchez P, Perez-Liebana I, Gonzalez-Moreno L, Pardo B et al (2019) The response to stimulation in neurons and astrocytes. Neurochem Res 44(10):2385–2391

Kalpouzos G, Chetelat G, Baron JC, Landeau B, Mevel K, Godeau C et al (2009) Voxel-based mapping of brain gray matter volume and glucose metabolism profiles in normal aging. Neurobiol Aging 30(1):112–124

Kelly PJ, Camps-Renom P, Giannotti N, Marti-Fabregas J, Murphy S, McNulty J et al (2019) Carotid plaque inflammation imaged by (18)F-Fluorodeoxyglucose positron emission tomography and risk of early recurrent stroke. Stroke 50(7):1766–1773

Kety SS, Schmidt CF (1948) The nitrous oxide method for the quantitative determination of cerebral blood flow in man: theory, procedure and normal values. J Clin Invest 27(4):476–483

Kuhl DE, Metter EJ, Riege WH, Phelps ME (1982) Effects of human aging on patterns of local cerebral glucose utilization determined by the [^{18}F]fluorodeoxyglucose method. J Cereb Blood Flow Metab 2(2):163–171

Kuwabara H, Evans AC, Gjedde A (1990) Michaelis-Menten constraints improved cerebral glucose metabolism and regional lumped constant measurements with [^{18}F]fluorodeoxyglucose. J Cereb Blood Flow Metab 10(2):180–189

Lotan E, Friedman KP, Davidson T, Shepherd TM (2020) Brain ^{18}F-FDG-PET: utility in the diagnosis of dementia and epilepsy. Isr Med Assoc J 22(3):178–184

Madsen PL, Hasselbalch SG, Hagemann LP, Olsen KS, Bulow J, Holm S et al (1995) Persistent resetting of the cerebral oxygen/glucose uptake ratio by brain activation: evidence obtained with the Kety-Schmidt technique. J Cereb Blood Flow Metab 15(3):485–491

Magistretti PJ, Allaman I (2015) A cellular perspective on brain energy metabolism and functional imaging. Neuron 86(4):883–901

Mangold R, Sokoloff L, Conner E, Kleinerman J, Therman PO, Kety SS (1955) The effects of sleep and lack of sleep on the cerebral circulation and metabolism of normal young men. J Clin Invest 34(7, Part 1):1092–1100

Marnane M, Merwick A, Sheehan OC, Hannon N, Foran P, Grant T et al (2012) Carotid plaque inflammation on ^{18}F-fluorodeoxyglucose positron emission tomography predicts early stroke recurrence. Ann Neurol 71(5):709–718

Meles SK, Renken RJ, Pagani M, Teune LK, Arnaldi D, Morbelli S et al (2020) Abnormal pattern of brain glucose metabolism in Parkinson's disease: replication in three European cohorts. Eur J Nucl Med Mol Imaging 47(2):437–450

Meyer PT, Frings L, Rucker G, Hellwig S (2017) (18)F-FDG PET in Parkinsonism: differential diagnosis and evaluation of cognitive impairment. J Nucl Med 58(12):1888–1898

Mintun MA, Lundstrom BN, Snyder AZ, Vlassenko AG, Shulman GL, Raichle ME (2001) Blood flow and oxygen delivery to human brain during functional activity: theoretical modeling and experimental data. Proc Natl Acad Sci U S A 98(12):6859–6864

Nasu S, Hata T, Nakajima T, Suzuki Y (2002) Evaluation of ^{18}F-FDG PET in acute ischemic stroke: assessment of hyper accumulation around the lesion. Kaku Igaku 39(2):103–110

Nofzinger EA, Mintun MA, Wiseman M, Kupfer DJ, Moore RY (1997) Forebrain activation in REM sleep: an FDG PET study. Brain Res 770(1-2):192–201

Pakkenberg B, Gundersen HJ (1997) Neocortical neuron number in humans: effect of sex and age. J Comp Neurol 384(2):312–320

Pardridge WM, Oldendorf WH (1977) Transport of metabolic substrates through the blood-brain barrier. J Neurochem 28(1):5–12

Patlak CS, Blasberg RG, Fenstermacher JD (1983) Graphical evaluation of blood-to-brain transfer constants from multiple-time uptake data. J Cereb Blood Flow Metab 3(1):1–7

Pawlik G, Heiss WD (1989) Positron emission tomography and neuropsychological function. In: Bigler ED, Yeo RA, Turkheimer E (eds) Neuropsychological function and brain imaging. Springer, New York, NY, pp 65–138

Phelps ME, Huang SC, Hoffman EJ, Selin C, Sokoloff L, Kuhl DE (1979) Tomographic measurement of local cerebral glucose metabolic rate in humans with (F-18)2-fluoro-2-deoxy-D-glucose: validation of method. Ann Neurol 6(5):371–388

Phelps ME, Mazziotta JC, Kuhl DE, Nuwer M, Packwood J, Metter J et al (1981) Tomographic mapping of human cerebral metabolism visual stimulation and deprivation. Neurology 31(5):517–529

Portnow LH, Vaillancourt DE, Okun MS (2013) The history of cerebral PET scanning: from physiology to cutting-edge technology. Neurology 80(10):952–956

Raichle ME, Larson KB, Phelps ME, Grubb RL Jr, Welch MJ, Ter-Pogossian MM (1975) In vivo measurement of brain glucose transport and metabolism employing glucose--^{11}C. Am J Phys 228(6):1936–1948

Raichle ME, Mintun MA (2006) Brain work and brain imaging. Annu Rev Neurosci 29:449–476

Reivich M, Alavi A, Wolf A, Fowler J, Russell J, Arnett C et al (1985) Glucose metabolic rate kinetic model parameter determination in humans: the lumped constants and rate constants for [^{18}F]fluorodeoxyglucose and [^{11}C]deoxyglucose. J Cereb Blood Flow Metab 5(2):179–192

Reivich M, Kuhl D, Wolf A, Greenberg J, Phelps M, Ido T et al (1979) The [^{18}F]fluorodeoxyglucose method for the measurement of local cerebral glucose utilization in man. Circ Res 44(1):127–137

Shen X, Liu H, Hu Z, Hu H, Shi P (2012) The relationship between cerebral glucose metabolism and age: report of a large brain PET data set. PLoS One 7(12):e51517

Shepherd TM, Nayak GK (2019) Clinical use of integrated positron emission tomography-magnetic resonance imaging for dementia patients. Top Magn Reson Imaging 28(6):299–310

Shiyam Sundar LK, Muzik O, Rischka L, Hahn A, Lanzenberger R, Hienert M et al (2020) Promise of fully integrated PET/MRI: noninvasive clinical quantification of cerebral glucose metabolism. J Nucl Med 61(2):276–284

Siesjo BK (1978) Brain energy metabolism and catecholaminergic activity in hypoxia, hypercapnia and ischemia. J Neural Transm Suppl 14:17–22

Silverman DHS, Melega WP (2004) Molecular imaging of biologic processes with PET: evaluation biologic bases of cerebral function. In: MEPD P (ed) Pet: molecular imaging and its biological applications. Springer, pp 509–583

Sokoloff L (1989) Circulation and energy metabolism of the brain. In: Siegel GJ (ed) Basic neurochemistry: molecular, cellular, and medical aspects, 4th edn. Raven Press, New York, p xviii. 984 p

Sokoloff L (1999) Energetics of functional activation in neural tissues. Neurochem Res 24(2):321–329

Sokoloff L, Reivich M, Kennedy C, Des Rosiers MH, Patlak CS, Pettigrew KD et al (1977) The [^{14}C]deoxyglucose method for the measurement of local cerebral glucose utilization: theory, procedure, and normal values in the conscious and anesthetized albino rat. J Neurochem 28(5):897–916

Tondo G, Esposito M, Dervenoulas G, Wilson H, Politis M, Pagano G (2019) Hybrid PET-MRI applications in movement disorders. Int Rev Neurobiol 144:211–257

Vaishnavi SN, Vlassenko AG, Rundle MM, Snyder AZ, Mintun MA, Raichle ME (2010) Regional aerobic glycolysis in the human brain. Proc Natl Acad Sci U S A 107(41):17757–17762

Villien M, Wey HY, Mandeville JB, Catana C, Polimeni JR, Sander CY et al (2014) Dynamic functional imaging of brain glucose utilization using fPET-FDG. NeuroImage 100:192–199

von Oertzen TJ (2018) PET and ictal SPECT can be helpful for localizing epileptic foci. Curr Opin Neurol 31(2):184–191

Wienhard K, Pawlik G, Herholz K, Wagner R, Heiss WD (1985) Estimation of local cerebral glucose utilization by positron emission tomography of [^{18}F]2-fluoro-2-deoxy-D-glucose: a critical appraisal of optimization procedures. J Cereb Blood Flow Metab 5(1):115–125

Wu HM, Bergsneider M, Glenn TC, Yeh E, Hovda DA, Phelps ME et al (2003) Measurement of the global lumped constant for 2-deoxy-2-[^{18}F]fluoro-D-glucose in normal human brain using [15O]water and 2-deoxy-2-[^{18}F]fluoro-D-glucose positron emission tomography imaging. A method with validation based on multiple methodologies. Mol Imaging Biol 5(1):32–41

Wyss MT, Jolivet R, Buck A, Magistretti PJ, Weber B (2011) In vivo evidence for lactate as a neuronal energy source. J Neurosci 31(20):7477–7485

Cerebral Blood Flow Measurement with Oxygen-15 Water Positron Emission Tomography

5

Henryk Barthel, Vilia Zeisig, Björn Nitzsche, Marianne Patt, Jörg Patt, Georg Becker, Antje Dreyer, Johannes Boltze, and Osama Sabri

Contents

H. Barthel (✉) · V. Zeisig · B. Nitzsche · M. Patt · J. Patt · G. Becker · O. Sabri
Department of Nuclear Medicine, University Hospital Leipzig, University of Leipzig, Leipzig, Germany
e-mail: henryk.barthel@medizin.uni-leipzig.de; vilia.zeisig@medizin.uni-leipzig.de; marianne.patt@medizin.uni-leipzig.de; joerg.patt@medizin.uni-kleipzig.de; georg.becker@medizin.uni-leipzig.de; osama.sabri@medizin.uni-leipzig.de

A. Dreyer
Department of Cell Therapy, Ischemia Research Unit, Fraunhofer Institute for Cell Therapy and Immunology, Leipzig, Germany
e-mail: antje.dreyer@izi.fraunhofer.de

J. Boltze
School of Life Sciences, The University of Warwick, Gibbet Hill Campus, Coventry, UK
e-mail: johannes.boltze@warwick.ac.uk

Abstract

The human brain receives approximately 15% of the cardiac output and therefore is the most demanding organ in respect to blood flow supply. This fact emphasizes the importance of perfusion as a key factor in a variety of cerebrovascular and other diseases including stroke, migraine, and brain tumors. Today, numerous imaging techniques are able to visualize brain perfusion, but only few of them provide quantitative information. In the field of modern in vivo imaging techniques, positron emission tomography (PET) is considered to be the gold standard to give reliable results about major aspects of cerebral physiology. [^{15}O]H$_2$O allows for quantitative cerebral blood flow (CBF) measurement within a few minutes, and subsequent ^{15}O[O$_2$] imaging can provide precise information on oxygen metabolism like cerebral oxygen metabolism and oxygen extraction fraction. As a result, PET has become an extremely useful research tool for defining cerebral blood flow and physiology. However, complex methodological logistics and a limited availability of the imaging system hamper the widespread use of CBF PET in clinical routine. The chapter aims at summarizing the radiosynthesis, data acquisition, and analysis, as well as major preclinical and clinical applications of [^{15}O]H$_2$O PET.

Abbreviations

$c_a(t)$	Arterial input function (arterial activity concentration over time)
CBF	Cerebral blood flow
CBV	Cerebral blood volume
CMRO$_2$	Cerebral metabolic rate of oxygen
CT	Computed tomography
$c_v(t)$	Activity concentration in venous blood over time
f_a	Arterial blood flow
GBq	Gigabecquerel
GM	Gray matter
IAP	Iodoantipyrine
iNO	Inhaled nitric oxide
k	Washout constant
kBq	Kilobecquerel
MBq	Megabecquerel
MRI	Magnetic resonance imaging
NIRS	Near-infrared spectroscopy
NO	Nitric oxide
OEF	Oxygen extraction fraction
PET	Positron emission tomography
rCBF	Regional cerebral blood flow
ROI	Region of interest
S/N	Signal-to-noise
SPECT	Single-photon emission computed tomography

TSE   Turbo spin echo
V_d Partition coefficient
V_{tissue} Tissue volume
WM   White matter
Xe   Xenon

5.1   Introduction

Although the adult human brain assumes only about 2% of the total body weight, it receives nearly 15% of the resting cardiac output and 20% of the total body oxygen consumption. This high metabolic rate reveals the need to ensure a constant delivery of oxygen and energy-providing substrates at the capillary level and to remove the waste products of metabolism. Owing to a complex autoregulatory mechanism, the cerebral perfusion is maintained relatively constant over a wider range of mean arterial pressures. A complete interruption of brain–blood supply, however, leads immediately to neuronal impairments because of the limited availability of nutrition and energy reserves in the brain. Hence, perfusion parameters are important key factors involved in major cerebrovascular and other brain diseases. Important information about cerebral characteristics is given by measurement of the cerebral blood flow (CBF) which describes the rate of blood delivery to the brain parenchyma. Traditionally, the respective literature reports CBF units in mL blood/100 g of tissue per minute. Other authors use mL instead of gram tissue to describe the volumetric character especially with imaging techniques. Due to the fact that 1 g of brain tissue nearly corresponds to 1 mL, both values can be more or less used interchangeably.

Global average CBF values in middle-aged healthy human subjects are around 55 mL/100 g/min (Kety and Schmidt 1945). However, CBF values vary regionally: In cortical gray matter, the CBF is 60–100 mL/100 g/min (Slosman et al. 2001; Sokoloff et al. 1957) and around 20 mL/100 g/min for white matter (Law et al. 2000). It has been demonstrated that neuronal activity as well as CBF is closely coupled to brain metabolism (Pantano et al. 1984; Roy and Sherrington 1890). This may explain the generally higher blood flow in younger subjects which is typically exceeding values that are 50–85% higher than those of adults (age: 6–7 years, Chiron et al. 1992). This age dependency of CBF is probably caused, at least in parts, by an age effect on the gray-to-white matter ratio. Additionally, a decline of CBF with age is described (Brody 1955).

Kety and Schmidt (1945) were the first who introduced a method for quantitative CBF measurement in the unanesthetized human. This method is based on the Fick principle. During the inhalation of the freely diffusible nitrous oxide, the brain perfusion was calculated by measuring the amount of gas removed from the blood by the brain per minute and dividing this by the arteriovenous difference of N_2O. This method was an important step to study brain function in humans and has contributed fundamentally to our understanding of physiological and pathological cerebral processes. However, this first technique lacked the possibility to measure CBF in different brain subregions. This limitation has led to further developments in perfusion

imaging techniques. As important examples, radioactive agents such as ^{133}Xe and ^{85}Kr were later used to measure their washout with external radiation detectors (Lassen and Ingvar 1961; Veall and Mallett 1967; Bruce et al. 1973; Obrist et al. 1975). Today, a wide variety of brain perfusion imaging techniques is available for preclinical and clinical research settings as well as clinical routine applications. CBF measurement using positron emission tomography (PET) became available in the 1970s, followed by other in vivo imaging techniques, like single-photon emission computed tomography (SPECT), magnetic resonance imaging (MRI), and transmission computed tomography (CT), to obtain CBF readouts (Hoeffner 2005). This chapter will focus on CBF PET with [^{15}O]H$_2$O as this represents the gold standard technique for in vivo CBF measurements (Carroll et al. 2002; Hoeffner 2005). One possible application for its usage is studying CBF in brain activation studies to localize brain segments involved in processing certain tasks. More important today, however, is the diagnostic potential of CBF PET imaging mainly in cerebrovascular disorders and oncology. Hence alterations of cerebral perfusion can theoretically be detected by quantitative CBF measurement leading to optimal therapy and providing estimates of the potentially salvable part of the affected brain.

5.2   Radiochemistry of [^{15}O]H$_2$O

Oxygen-15 can be produced by different nuclear reactions using both high- and low-energy protons as well as deuterons as projectiles. The ^{14}N(d, n)^{15}O nuclear reaction is the most efficient and economic production pathway and is therefore applied most frequently. For cyclotrons that do not have the possibility of accelerating deuterons, either the ^{15}N(p, n)^{15}O (Powell and O'Neil 2006) for low-energy protons (>3.7 MeV) or the ^{16}O(p, pn)^{15}O (Beaver et al. 1976; Krohn et al. 1986) for high-energy protons (>16.6 MeV) nuclear reactions can be used as an alternative.

Two methods are available for conversion of the ^{15}O to [^{15}O]H$_2$O, the in-target production method and the out-of-target external conversion method. In case of the in-target production method, [^{15}O]H$_2$O is produced by either addition of small amounts of hydrogen to the target gas or direct irradiation of H$_2$^{16}O. For the first approach, the ^{15}N(p, n)^{15}O nuclear reaction is used (Powell and O'Neil 2006), and the trace amounts of H$_2$ in the target lead to the formation of [^{15}O]H$_2$O by radiolytic reactions which can be trapped in a cooled stainless steel loop. The possible radioactive impurities such as ^{11}CH$_4$ and ^{13}NH$_3$ (resulting from trace amounts of N-14 and O-16 in the target gas) are directed to the exhaust. By heating the loop, [^{15}O]H$_2$O vapor is released and can be trapped again in a sterile water or saline solution. The major drawbacks are the high costs for enriched ^{15}N$_2$ which is used as target material. An alternative approach for [^{15}O]H$_2$O in-target production is the direct irradiation of H$_2$^{16}O in a liquid target (Mulholland et al. 1990; van Naemen et al. 1996). As mentioned above this method is feasible only with high-energy protons, a restriction that excludes this approach for commonly used cyclotrons in a clinical setting.

As an alternative to the in-target production of [^{15}O]H$_2$O, external out-of-target tracer production by catalytic conversion of a mixture of H$_2$ and [^{15}O]O$_2$ has been

demonstrated for all abovementioned nuclear reactions, i.e., $^{16}O(p, pn)^{15}O$ (Krohn et al. 1986), $^{15}N(p, n)^{15}O$ (Explora®H$_2$O module, Siemens Healthcare, Erlangen, Germany), and $^{14}N(d, n)^{15}O$ (Clark et al. 1987; Clark and Tochon-Danguy 1991; Sajjad et al. 2000). For the $^{14}N(d, n)^{15}O$ nuclear reaction, N$_2$ with up to 4% O$_2$ is irradiated with deuterons ($\approx$7 MeV). In most cases, Pd is used as the catalyst; however, if the same target is used as well for production of C^{15}O, it might be necessary to reduce the amount of O$_2$ in order to minimize the production of toxic carrier CO. Under these conditions it has been shown that Pt as catalyst is superior (Berridge et al. 1990). The most simple production and application approach consists of an H$_2$ supply that is connected to the target line via a T connector. The target gas/H$_2$ mixture (2–10%, Berridge et al. 1990; Sajjad et al. 2000) is then directed over the heated catalyst ($\approx$170 °C, temperatures up to 450 °C have been reported as well (Berridge et al. 1990)), and the resulting [^{15}O]H$_2$O vapor is bubbled into a sterile reservoir containing water, saline, or preferably buffer since the catalyst might as well generate trace amounts of ammonia which un-buffered may lead to elevated pH values. The [^{15}O]H$_2$O-containing solution is then drawn up into a syringe and manually applied to the investigated subject. However, due to the relatively high radiation exposure of the medical personnel, it might be worth to automate the injection procedure. In a relatively simple setup, the injection is performed by means of two infusion pumps and a 4-port valve (Sajjad et al. 2000). A more sophisticated method uses a dialysis membrane to enable exchange of [^{15}O]H$_2$O with sterile water (Clark and Tochon-Danguy 1991) together with an infusion pump and several valves to enable automatic injection. This system is commercially available (Veenstra Instruments, Joure, Netherlands).

5.3 [^{15}O]H$_2$O Brain PET Data Generation

Over the years, different methods to perform [^{15}O]H$_2$O CBF measurements have been developed and applied. Early users employed a technique originally developed by Kety and coworkers to determine rCBF with tissue autoradiography in laboratory animals (Kety 1951). Later on, groups used the steady-state technique developed by Jones and colleagues in which [^{15}O]CO$_2$ needs to be continuously inhaled over the examination time (Jones et al. 1976).

For the dynamic PET scanning method which is the current standard approach, the emission scan is, after a transmission scan for attenuation correction, acquired preferentially in 3D mode and initiated immediately before tracer administration. The tracer is injected as a fast bolus followed by a flush of inert saline solution. The amount of injected tracer in humans typically ranges between 550 and 1000 MBq for an adult subject, but studies using up to 2.2 GBq were also found in the literature (Heiss et al. 2000). For this bolus injection method, Kanno et al. (1991) investigated an optimal scan time for [^{15}O]H$_2$O to improve image quality and signal-to-noise ratios. A minimum scan duration of 90 s was recommended. For most applications, however, scan durations of 2–5 min are chosen. A typical protocol for a 5-min dynamic data acquisition is shown in Table 5.1.

Table 5.1 Acquisition protocol for a 5-min PET scan with [^{15}O]H$_2$O

Frame duration [s]	5	10	30
Number of frames	24	12	2

The advantageous short half-life of the tracer (122 s) enables the performance of multiple image acquisition scans in rapid sequence. Inter-scan intervals should, however, not be shorter than 15 min to allow isotope decay. Due to the fast radioactive decay, an on-site cyclotron or linear accelerator for isotope production becomes necessary. Further data analyses generally include the absolute quantification of CBF. For this purpose, the experimental setting implies arterial blood sampling in parallel to the PET acquisition. This is preferably performed using an automated sampling system (e.g., ALLOGG AB blood sampler; Allogg Mariefred, Sweden) with a peripheral artery, e.g., the radial artery. Using such a device, arterial blood samples are continuously drawn at a constant speed with activity measurements for every 0.5 or 1 s. The blood sampler needs to be cross-calibrated to the PET scanner, allowing the decay-corrected blood data to be used as input function for kinetic modeling.

Obtaining arterial blood samples via the placement of an arterial catheter is accepted as the gold standard method for CBF quantification. However, there are some limitations, like invasiveness, complications for the patient, and sensitivity to errors (Hall 1971; Machleder et al. 1972). Aiming to replace the arterial canalization and corresponding input function, alternatives were suggested, like image-derived input functions (Zanotti-Fregonara et al. 2011) and methods without the need of any input function (Lammertsma 1994; Watabe et al. 1996). Another possibility to avoid arterial canalization is the use of arterialized venous blood, which is an often used method also with other PET tracers. With this technique, the hand of the patient or volunteer is heated well above 37 °C to achieve a shunting of arterial blood to the venous system (Wakita et al. 2000). Nevertheless, all alternative techniques have their drawbacks, and the CBF values obtained by them need to be handled with caution.

As for all brain PET tracers, the resulting PET data require a correlation with structural information from MRI (preferably 3D-T1 data). In this regard, the use of combined PET/MRI scanners might improve this situation in the future. Combined PET/MR imaging gives the opportunity for accurate registration and exact correlation of PET functional aspects with anatomical information from MRI. This will result in better image quality because of the comparably lower spatial resolution of PET in contrast to MRI and also shortens imaging times for the patients/anesthetized research animals.

5.4   Kinetic Modeling of CBF

The first method to measure CBF in humans was proposed by Kety and Schmidt in 1945 who utilized nitrous oxide for CBF detection. Later, other tracers like ^{133}Xenon (Veall and Mallett 1967) were applied within this concept which was based on the
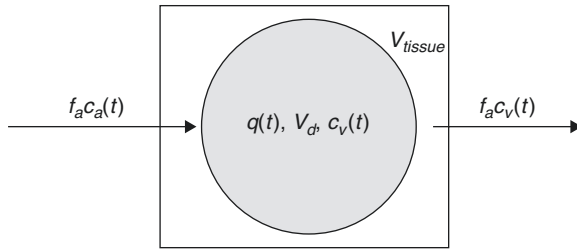
Fig. 5.1 Schematic description of a single-tissue compartment. V_{tissue} is the anatomical tissue volume (1 cm³), and V_d is the volume of the tissue compartment accessible to the tracer. The products of flow and concentration describe the amount of tracer which enters or leaves the tissue compartment per time unit. Please refer to the main text for further explanation of the other symbols

Fick principle and a single-tissue compartment model. It states that the amount of a metabolically inert and freely diffusible gas that is taken up by a tissue per unit of time is equal to the product of the blood flow through that tissue and the difference between the amount of gas entering it via the arterial blood and the gas leaving in the venous blood.

The single-tissue compartment model describes the behavior of a freely diffusible tracer like [¹⁵O]H₂O in tissue as shown in Fig. 5.1 and can be used to determine the local arterial blood flow in the brain (on a region of interest (ROI) or voxel basis). The model consists of two parameters that have to be estimated from the data of a dynamic PET scan ($q(t)$) and from the measured arterial input function $c_a(t)$.

Assuming that the transport of tracer from the vessel into the tissue compartment is fast (high permeability surface area product) compared to the delivery by the arterial blood flow, the tracer dynamics can be described by a one-tissue compartment model with one input function. The mass balance for the tracer (Fick principle) yields the differential equation

$$\frac{dq(t)}{dt} = f_a c_a(t) - f_a c_v(t) \tag{5.1}$$

where $q(t)$ is the quantity of tracer per unit volume of tissue (kBq cm⁻³), f_a is the local arterial blood flow per unit volume (mL min⁻¹ cm⁻³), and $c_a(t)$ and $c_v(t)$ are the tracer concentrations in arterial and venous blood (kBq cm⁻³).

The tracer concentration in the venous blood ($c_v(t)$) is related to the tracer concentration in the tissue space ($q(t)$) through the relative volume of distribution (V_d (mL cm⁻³)) by the Kety–Schmidt assumption:

$$q(t) = V_d c_v(t) \tag{5.2}$$

reflecting the assumption that the concentrations in the water spaces of venous blood and tissue are always equilibrated (this assumption is not generally valid, because a diffusion limitation exists for [¹⁵O]H₂O at low CBF rates).

From Eqs. (5.1) and (5.2), the differential equation

$$\frac{dq(t)}{dt} = f_a c_a(t) - kq(t) \tag{5.3}$$

is obtained with the washout constant k (min^{-1}) defined to be

$$k = \frac{f_a}{V_d}. \tag{5.4}$$

By estimating values of f_a and k, the partition coefficient of the tracer can be calculated for every tissue voxel. An example of parameter estimation for a cortical region of interest based on the arterial input function is shown in Fig. 5.2.
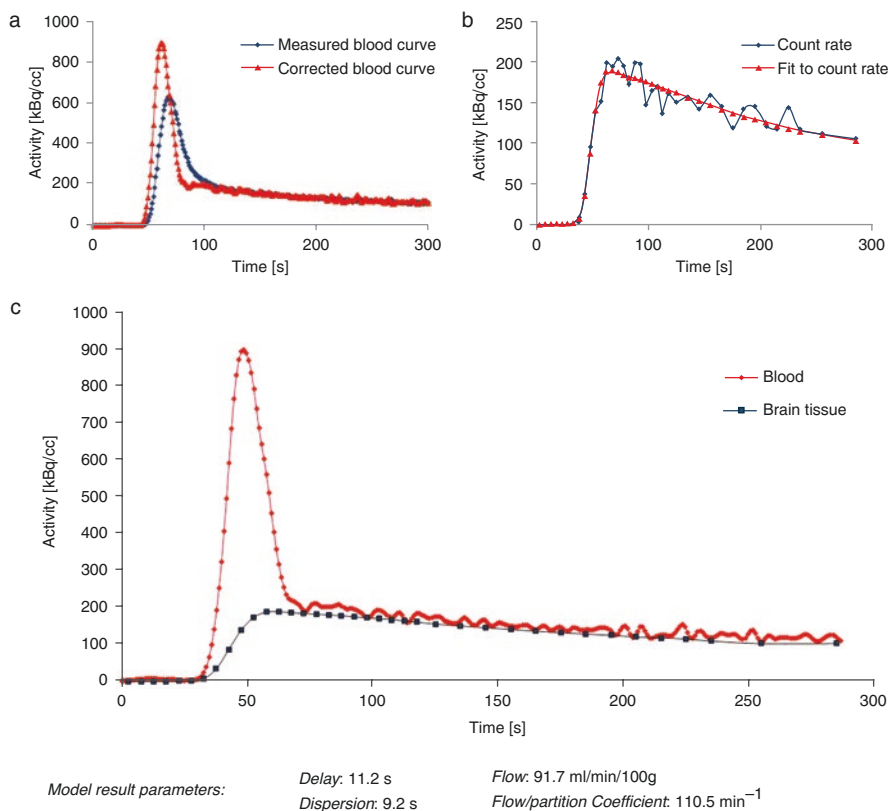
Fig. 5.2 Model parameter estimation. The arterial input function (**a**) and corresponding tissue response in a cortical ROI (**b**) after bolus injection of [^{15}O]H$_2$O are shown. Blood activity data were determined by taking arterial blood samples with a dedicated sampling device. The input function and tissue response are corrected for tracer arrival times and bolus dispersion. Further kinetic modeling is based on the resulting corrected curves (**c**)

Equation (5.3) has the solution

$$q(t) = f_a e^{-kt} \otimes c_a(t) \tag{5.5}$$

where $\otimes$ describes the convolution of an exponential function with the arterial input function $c_a(t)$:

$$e^{-kt} \otimes c_a(t) = \int_0^t e^{-k\tau} c_a(t-\tau) \, \mathrm{d}\tau \tag{5.6}$$

The experimental design is further specified in a way that the tissue response, $q(t)$, as well as the arterial, $c_a(t)$, input is measured and thus known for the duration of the experiment. Additionally, $q(0) = 0$.

$[^{15}O]H_2O$ is the most commonly used tracer for brain perfusion imaging and CBF quantification with PET. However, there are some notable restrictions concerning the diffusion limitation of $[^{15}O]H_2O$. A study of Eichling et al. investigated the cerebral behavior of $[^{15}O]H_2O$ after administration to rhesus monkeys. They found that only about 90% of the injected tracer freely exchanges with the brain tissue, with even lower rates at higher flow rates. This incomplete first-pass extraction (80–90% in gray matter structures) resulted in a slightly underestimation of CBF especially in high-flow regions (Eichling et al. 1974; Bolwig and Lassen 1975; Raichle et al. 1983).

In this respect, lipophilic gaseous tracers (like nitrous oxide and xenon) behave superior for CBF measurements as compared with $[^{15}O]H_2O$.

Further consideration should be done concerning partial volume effect that among others derive from relatively low spatial resolution of typically 6–10 mm in PET. The resulting spread out of signal is a phenomenon that introduces distortion effects in the targeted region and adjacent tissue (Links et al. 1996). The partial volume effect primarily leads to an increased bias for small anatomical structures (like vessels) in the brain (Rousset et al. 1998).

Since the early 1980s, several methods have been described to calculate CBF from PET measurements with $[^{15}O]H_2O$, including simplified techniques that include parameter fixation, e.g., fixation of the partition coefficient (Watabe et al. 1996). The partition coefficient of $[^{15}O]H_2O$ is a parameter that has been investigated in many studies and varies from 0.77 to 1.05 mL/mL (Herscovitch and Raichle 1985; Iida et al. 1993; Kanno et al. 1991). A good approximation for the whole brain was considered by Herscovitch and Raichle to be 0.9 mL/mL (Herscovitch and Raichle 1985). However, CBF calculation methods with fixed values for V_d are only applicable to identify global blood flow changes. In presence of regional blood flow deficits, CBF calculation results in incorrect values.

5.5 Role of PET for CBF Measurements

5.5.1 General Principles for CBF Measurements

A general distinction must be made between the behaviors of different CBF tracers. One class of techniques utilizes agents which are restricted to the intravascular space and do not interact with the nonvascular space. These can be, in cases of an

intact blood–brain barrier, referred to as nondiffusible CBF tracers. Many brain imaging techniques, such as contrast-enhanced MR and CT, use these intravascular tracers to calculate CBF on the basis of the indicator dilution theory (Meier and Zierler 1954; Zierler 1962). In contrast, a direct tracer exchange from the arterial vascularity to the parenchyma occurs in case of freely diffusible CBF tracers and enables to give a direct measurement of parenchymal blood flow, as originally described by Kety (1951). This concept is utilized, for example, with [^{15}O]H$_2$O PET, Xenon CT, and Xenon SPECT. Some basic characteristics appear to be necessary for a useful CBF measurement method: Ideally, the incorporated indicator should be early and completely mixed with blood and must stay identifiable for position and concentration in time of image acquisition. Further, the indicator should be metabolically inert and rapidly eliminated.

5.5.2 Advantages and Disadvantages of Perfusion Imaging Methods

Various modalities have been developed to obtain hemodynamic parameters in research and clinical settings. These include the older ^{133}Xe inhalation method, PET, SPECT, X-ray computed tomography methods, and several MRI techniques. However, each technique has its own advantages and drawbacks. It depends on the study subject and the targeted question which method to choose appropriately. A review from Wintermark et al. (2005) gives a comparative overview of current brain perfusion measurement techniques and their clinical relevance. At this point, a brief overview is given on the role of [^{15}O]H$_2$O PET in this context.

5.5.2.1 Nuclear Medicine Methods

CBF can be measured after incorporation of radioactive agents which are detected outside the investigated subject with dedicated scintillation detectors. Based on this principle, tracers like [^{99m}Tc]HMPAO or [^{99m}Tc]ECD and ^{133}Xe were commonly used for CBF measurements with SPECT (Barthel et al. 2001; Lass et al. 1998; Sakai et al. 1987). In comparison with the coincidence method in PET imaging, the detection of single photons is less sensitive. SPECT imaging with [^{99m}Tc]HMPAO or [^{99m}Tc]ECD only allows for semiquantitative CBF estimation (Markus 2004). In contrast, the ^{133}Xe SPECT method relies on the Kety–Schmidt model (Kety and Schmidt 1945) and is considered to give quantitative measures of CBF (Wintermark et al. 2005). In several studies, however, a systematic CBF overestimation was reported in low-flow areas, as well as an underestimation of cortical CBF (Matsuda et al. 1996; Skyhøj Olsen et al. 1981).

However, the coincidence PET technique is commonly accepted to be the reference standard for CBF imaging. With PET, the tissue perfusion can be directly measured by using the diffusible radiotracer [^{15}O]H$_2$O. This method is well validated and combines several favorable properties. The tracer is easy to produce, and the fast acquisition time permits repetitive measurements with whole brain coverage. Additionally, the major advantage of CBF measurement with PET is the high

accuracy for assessing quantitative parameter maps as well as a high reproducibility (Carroll et al. 2002; Matthew et al. 1993).

Additionally, PET imaging with ^{15}O-labeled compounds is of special interest for studying cerebrovascular diseases and if a comprehensive view on brain hemodynamic is demanded. In addition to the determination of CBF with [^{15}O]H$_2$O, a successive ^{15}O[O$_2$] inhalation allows for quantitative determination of essential parameters of hemodynamics and energy metabolism like oxygen consumption (cerebral metabolic rate of oxygen; CMRO$_2$) and oxygen extraction fraction (OEF) (Frackowiak et al. 1980; Ibaraki et al. 2004). Further, because of its binding to hemoglobin in red blood cells (Martin et al. 1987), [^{11}C]CO is used as an intravascular tracer to measure the cerebral blood volume (CBV). Compared to other modalities, PET is the only technique which is able to gain all of these different functional parameters noninvasively and in 3D for the entire brain, a fact which allowed PET imaging to become the gold standard method in the field of brain circulation physiology and pathophysiology imaging (Hoeffner 2005).

In comparison with SPECT, which is widely accessible and a routine perfusion imaging tool, PET imaging is technically more demanding, and its availability is limited by complex logistics. Not only a PET scanner but also the constant access to a cyclotron producing the radiopharmaceutical online is required, a fact limiting the application of the method especially in emergency settings. A further restriction occurs in patients who will receive a thrombolytic therapy. Because quantitative PET preferentially requires invasive arterial blood sampling in order to obtain an input function for kinetic CBF modeling, this procedure is not applicable in these patients. As a consequence, [^{15}O]H$_2$O PET did not manage to become a clinical routine imaging tool in the acute stroke situation. Clinical applications instead mainly refer to chronic cerebrovascular disorders, brain tumors, and brain activation studies. Moreover, due to the wide acceptance of PET as standard for CBF visualization and quantification, the method is used as the reference to validate other brain perfusion imaging techniques, like perfusion-weighted or arterial spin labeling MRI (Zaro-Weber et al. 2010a, b; Chen et al. 2008).

Apart from [^{15}O]H$_2$O PET, [^{11}C]butanol has been suggested to be an alternative tracer for CBF measurements with PET. In comparison with radiolabeled water, butanol has the advantage of being permeable through the blood–brain barrier to 100%. However, this tracer is not used in routine practice because of its complex and radiochemical synthesis (Herscovitch et al. 1987).

[^{14}C]iodoantipyrine (IAP) autoradiography is another nuclear medicine perfusion imaging method used in preclinical research (Hatakeyama et al. 1992; Jay et al. 1988). As with butanol and H$_2$O, IAP is also able to freely cross the blood–brain barrier. It is not metabolized and as such accumulates in the brain tissue depending on the regional CBF. After tracer application, the animals need to be sacrificed to prevent tracer diffusion and to autoradiographically determine the CBF at the time point of tracer injection. Sequential arterial blood samples can be used for absolute CBF quantification. This autoradiographic ex vivo method provides accurate and high-resolution quantitative CBF values at a specific time point and is therefore mainly used in small animal studies.

5.5.2.2 Computed Tomography Methods

The physical principle that underlies the CT technique is based on tissue-specific attenuation of X-rays that are directed to the body. The image contrast then resulted from variations in attenuation depending on tissue density. Due to similar densities in white and gray matter structures, this technique is not the ideal tool to image anatomical brain structures (Griffiths et al. 2001). However, with a bolus injection of a contrast agent, such as iodine, most prerequisites of the abovementioned indicator dilution theory are satisfied to measure blood flow in the brain. However, due to different acquisition hardware, acquisition protocols, varying post-processing protocols, and differences in the interpretation of perfusion CT data, a reliable CBF quantification remains challenging and varies widely between centers (Kudo et al. 2010). A further approach for CBF measurement uses inhaled Xenon to detect concentration changes of the substance (Pindzola and Yonas 1998). The lipophilic gas is soluble in water, and its X-ray attenuation is similar to that of iodine. As in ^{133}Xe SPECT, the Xe–CT technique also utilizes the Kety–Schmidt method to calculate quantitative CBF maps with sufficient accuracy (Wintermark et al. 2005). Although newer CT scanners are able to achieve whole brain coverage, a main limitation of commonly used CT scanners derives from the limited anatomical coverage, which is restricted to few brain slices.

5.5.2.3 Magnetic Resonance Methods

Several methods for CBF estimation by means of MR have been developed. The most commonly used method for neuroimaging studies is the dynamic susceptibility contrast (DSC) MRI method. It relies on changes in relaxation time on T2*-weighted images. With the bolus of a paramagnetic contrast agent (e.g., gadolinium-DTPA) passing through the vascular system, a detectable signal loss occurs in T2*-weighted sequences. Mathematical conclusions were then drawn from the signal reductions to further calculate several perfusion or perfusion-related parameters including mean transit time (MTT), time to peak (TTP), relative cerebral blood volume (rCBV), and relative CBF (Ostergaard et al. 1996a, b). Contrast agents for MR imaging are not radioactive and relatively inexpensive as compared with PET and SPECT tracers. A further advantage of this method is the short acquisition time that enables to visualize perfusion-weighted measurements within a few minutes. However, the absolute quantification of CBF remains unsolved (Wintermark et al. 2005). The use of a local internal input function (Calamante et al. 2004) is necessary to receive parametric maps. As such, the detection of a plausible AIF which is influenced by numerous factors, such as partial volume effects, is important for reproducible and reliable perfusion values (van Osch et al. 2001). Another respective challenge is the localization of the intracranial region of interest for the AIF calculation (Zaro-Weber et al. 2012). Thus, most of the calculated parameter maps in perfusion MR are named as "relative" (Griffiths et al. 2001; Jezzard 1998). Nevertheless, perfusion MRI is employed for diagnostic purposes, for instance, in acute stroke and in clinical settings regarding the combination of the various readout parameters. In comparison with gadolinium-based MRI, the arterial spin labeling approach is another promising MR perfusion

technique. Here, magnetically labeled water protons are used as endogenous tracer. However, problems with image interpretation may occur due to a limited signal-to-noise ratio and in the presence of prolonged blood transit times, like in patients with stroke or atherosclerosis (Petersen et al. 2006). In latter cases (e.g., stroke patients), the labeled water spins did not reach the target brain tissue within a given time, with the consequence of underestimating the real blood flow values (Jezzard 1998; Kimura et al. 2005).

5.6   Applications for CBF PET

5.6.1   Acute Cerebral Ischemia

The increasing incidence of vascular diseases, like atherosclerosis, is associated with a worldwide increasing number of ischemic attacks (Feigin et al. 2009). Interruptions in brain–blood supply rapidly leads to ischemic cell damage that results in necrotic tissue if no sufficient therapy or spontaneous reperfusion becomes available. Current therapies aim to restore perfusion in the ischemic, salvageable brain tissue. In order to determine this hypoperfused yet viable tissue—the so-called ischemic penumbra (Astrup et al. 1981)—in acute stroke patients, perfusion imaging techniques were developed to identify this "tissue at risk" and to separate it from the already necrotic infarction core. The transition from reversible to irreversible damage is a function of ischemia duration as well as of CBF. A hemodynamic determination of the ischemic penumbra is used for many research studies in laboratory animals and humans, and CBF thresholds to characterize different tissue states were proposed: While normal human CBF is in the range of 50–80 mL/100 g/min, reversible ischemia ("ischemic penumbra") is evident when CBF drops below values around 22 mL/100 g/min, and neuronal cell death occurs below a CBF of 8 mL/100 g/min (Baron 2001). However, penumbra detection, based on CBF thresholds, is highly dependent on a reliable and accurate quantitative imaging method in an acute stroke diagnostic setting.

The opportunity to investigate different parameters of brain function, like CBF, CBV, OEF, and $CMRO_2$, within one PET imaging session is a further advantage in the investigation of cerebrovascular diseases such as ischemic stroke. A first example for the use of the steady-state $[^{15}O]CO_2$ inhalation technique to determine CBF (together with most of the abovementioned parameters) in acute stroke patients was provided by Wise et al. (1983).

In general, it is essential to reliably separate primary perfusion deficits from events of decreased metabolic demand. This is as CBF decreases may not only appear in the surrounding tissue of the stenotic vessel but sometimes also distant from the obviously damaged part of the brain. This well-recognized phenomenon is called "diaschisis." One example is the so-called crossed cerebellar diaschisis in which a CBF reduction in the cerebellum contralateral to the stroke-affected brain hemisphere occurs as a result of crossed functional deafferentiation (Baron et al. 1981; Feeney and Baron 1986).

### 5.6.1.1 PET Perfusion Imaging in Preclinical Stroke Research

This paragraph will handle the employment of $[^{15}O]H_2O$ PET in translational research studies of experimental stroke.

In 2008, our group proposed a new large animal model that is applicable for acute and chronic stroke induction (Boltze et al. 2008) and is highly suitable to reflect the human brain pathophysiology. Due to a similar cerebral anatomy and the favorable ovine brain size, brain imaging protocols, scanners, and data analysis techniques as used in clinical routine become feasible. This enables us to perform studies while meeting main conditions for translational research. Like in humans, in sheep, the middle cerebral artery (MCA) usually gives rise to three arterial branches. Different stroke sizes can be induced by permanent transcranial occlusion of one, two, or all three MCA branches, with the latter being referred to as permanent MCA occlusion (pMCAO). Figure 5.3 shows examples of different occlusion types for experimental pMCAO in sheep. One, two, and three branch (total) occlusions of the MCA could clearly be visualized by magnetic resonance angiography (MRA), together with the resulting CBF defects in $[^{15}O]H_2O$ PET. In addition, slight CBF decreases, probably due to the transcranial surgery, were also detected in the sham-operated animals. Further, it was possible to demonstrate that the ischemic strokes induced by the transcranial pMCAO lead to reproducible CBF deficits, which remain stable over time and eventually leading to necrotic brain tissue.

The major advantage of $[^{15}O]H_2O$ PET is the option to perform serial scans in a short time period due to the short half-life of the ^{15}O (122 s). As an example, CBF PET measurements were applied for a controlled preclinical study that aimed to test inhaled nitrous oxide (iNO) for its potential to protect the ischemic tissue in the penumbra in acute ischemic stroke. All animals were subjected to repeated PET scans at 110, 150, 175, and 210 min following pMCAO (a total of four PET scans within 100 min). In the treatment group, 50 ppm iNO were applied from 120 to 180 min after pMCAO. By using kinetic modeling, parametric CBF maps were
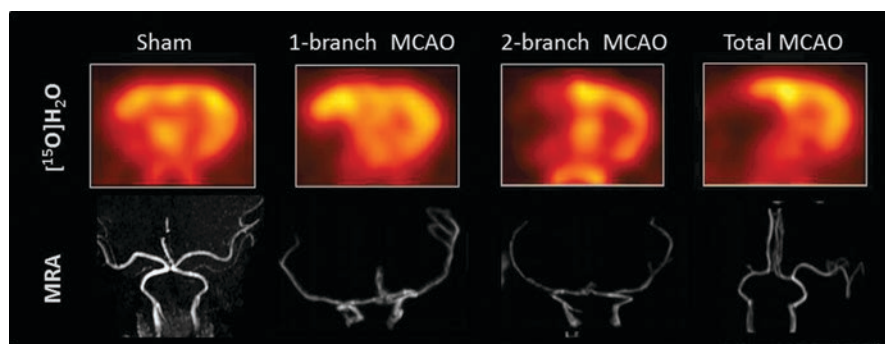
Fig. 5.3 Differential CBF deficits dependent on extent of experimental permanent middle cerebral artery occlusion in sheep. The extent of the post-pMCAO CBF deficit is clearly visualized with $[^{15}O]H_2O$ PET. Corresponding to angiographic MRI findings, the CBF deficit increases in the order sham >1-branch pMCAO >2-branch pMCAO > total pMCAO. *MCAO* middle cerebral artery occlusion, *MRA* magnetic resonance angiography (Modified from Boltze et al. (2008))
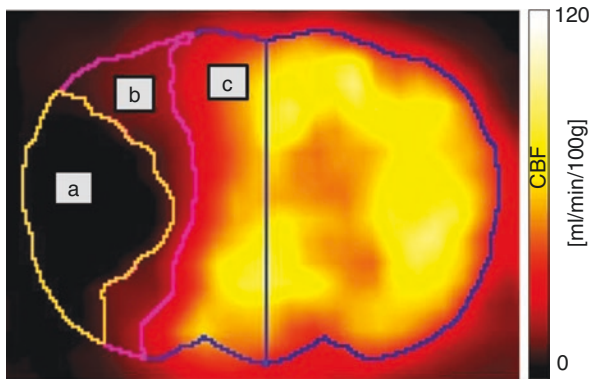
Fig. 5.4 Parametric CBF map as obtained by [^{15}O]H$_2$O PET in the Leipzig permanent middle cerebral artery occlusion sheep stroke model. For volume of interest analysis, the stroke-related regions were defined as follows: infarction core (**a**), <8 mL/100 g/min; ischemic penumbra, (**b**) 8–22 mL/100 g/min; normal brain tissue (**c**), >22 mL/100 g/min

created. Based on the abovementioned commonly accepted CBF thresholds (Baron 2001), operator-independent brain volumes of interest were defined for penumbra, infarction core, and remaining normal brain tissue (Fig. 5.4). Our experiments showed that iNO selectively restores CBF in the ischemic penumbra. While the volume of the necrotic core was not affected, the volume of the penumbra decreased by up to 50% turning into normally perfused tissue (>22 mL/100 g/min) under iNO application but remained unchanged in the untreated control animals ($p < 0.05$ vs. baseline and vs. control; Figs. 5.5 and 5.6; Terpolilli et al. 2012).

To give an outlook for further projects on CBF PET imaging in the Leipzig sheep pMCAO stroke model, Fig. 5.7 shows first images acquired by a simultaneous PET/3T-MRI system (Biograph mMR, Siemens). Comparative PET and MR imaging studies in acute stroke setting will greatly benefit from the new possibility to acquire data of both modalities simultaneously. This will significantly improve the investigation of the very fast pathophysiological processes in early ischemia. The first experience with this new simultaneous imaging approach, however, triggers great enthusiasm to employ this new technique for further preclinical and clinical research in the acute stroke situation.

With regard to the abovementioned possibility of PET imaging to provide multi-parameter readouts (CBF, OEF, CMRO$_2$, CBV), in experimental ischemic stroke, so far mainly the brains of monkeys (Kuge et al. 2001; Pappata et al. 1993), pigs (Sakoh et al. 2000a), and felines (Heiss et al. 1994) were investigated by using [^{15}O]H$_2$O for CBF measurements. With examinations of different time points after stroke, the studies by Heiss et al. aimed at monitoring important parameters of the temporal transversion of penumbral tissue to the final infarct core. The ischemic penumbra is characterized by an initial increase of OEF and CBV and preserved values of CMRO$_2$. In progress of the infarct and decreasing blood flow supply, CMRO$_2$ declines to values of 25% of baseline within the first hour after stroke,
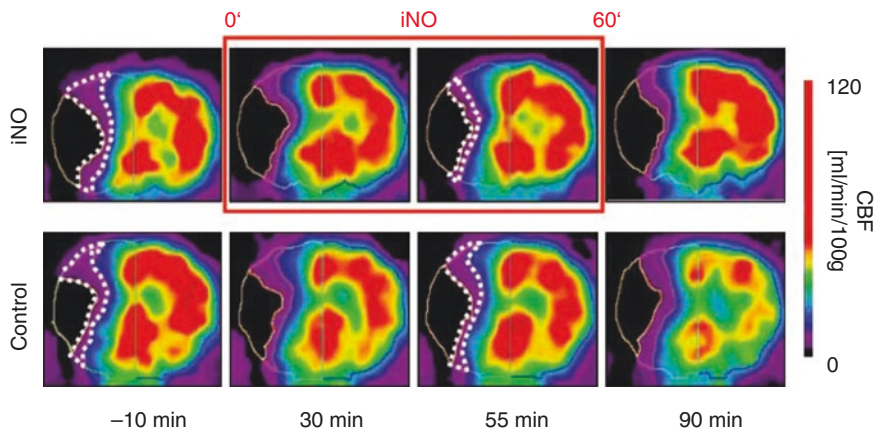
Fig. 5.5 Serial [^{15}O]H$_2$O PET scans show therapeutic effect of iNO in the Leipzig permanent middle cerebral artery occlusion sheep stroke model. Stroke-related tissue regions were defined on the basis of quantitative CBF maps. Volumetric analysis showed a significant decrease of the penumbra volume under iNO therapy in favor of the normal brain tissue compartment. This beneficial effect was not detected in control animals (Terpolilli et al. 2012)
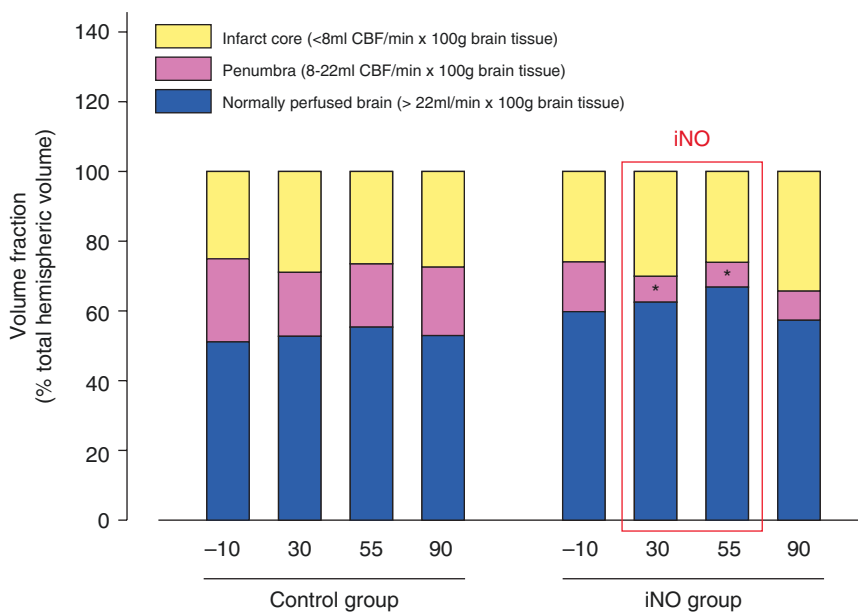
Fig. 5.6 iNO improves penumbral blood flow after permanent middle cerebral artery occlusion in sheep. Quantification of normally perfused, ischemic, and penumbral tissue volumes revealed that penumbral volume decreased significantly during NO inhalation ($n = 3$ per group; *$p < 0.05$ vs. control and vs. baseline PET at $t − 10$ min) in favor of the normally perfused brain tissue (Terpolilli et al. 2012)
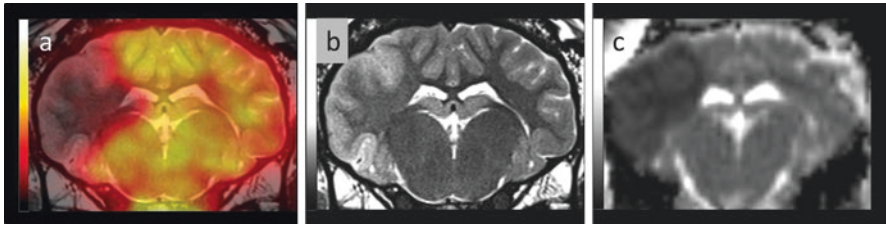
Fig. 5.7 Multimodal PET–MRI imaging in the Leipzig sheep stroke model. Four hours after permanent middle cerebral artery occlusion, (**a**) CBF was determined by [^{15}O]H$_2$O PET (shown here in overlay with anatomical T2-MRI) demonstrating the typical post-stroke deficit. (**b**) T2-MRI acquired to exclude hemorrhage. (**c**) Diffusion-weighted MRI with deficit similar to the CBF abnormality. The image data were acquired simultaneously using a PET/3 T-MR (Siemens mMR) system

while the initial increase of OEF becomes less prominent. In the final stage, the lack of CBF is associated with a decrease in OEF and the occurrence of brain tissue necrosis. This progress from still viable to necrotic tissue was defined as a function of duration and severity of stroke (Heiss et al. 1994, 1997; Heiss and Rosner 1983). In further experiments from the Cologne group, postischemic hemodynamic and metabolic processes were investigated after temporary MCAO (from 30 to 120 min of duration) in anesthetized cats (Heiss et al. 1997). CBF PET was performed immediately after MCAO and was repeated at 30-min intervals. After reopening the vessel, a distinct hyperperfusion was found in all animals, depending on the duration of the MCAO. After 30 min of ischemia, the reactive CBF increase was found to be transient with a fast normalization to pre-occlusion CBF values and without major tissue necrosis. By comparison, the reperfusion period after 60 or 120 min of ischemia was associated with severe hyperperfusion (CBF increase up to 300% compared to basal levels) and irreversible tissue damage, depending on the severity of prior ischemia. Approximately 50% of animals died after the prolonged ischemic period and suffered from higher CBF than the surviving animals from the same group. One explanation might be the hyperperfusion processes with massive cerebral edema that resulted in malignant brain swelling. These observations let to assume a relatively high tolerance against moderate hyperemia, whereas extensive hyperperfusion leads to an increased mortality (Heiss et al. 1997).

Other large animal experiments utilized [^{15}O]H$_2$O (Sakoh et al. 2000a, b) in combination with [^{15}O]CO PET to study regional correlations of CBF and CBV after acute stroke and in cases of reperfusion (Sakoh et al. 2000a). For that purpose, 13 pigs underwent PET, and the results were compared to MRI measurements of the same parameters. A good agreement was found between the values of both modalities in the ischemic tissue. After MCAO, a significant correlation between CBF reduction and CBV increase was observed. However, the decrease of CBF below 60% of the contralateral side was found to induce a reduction in CBV. In contrast, both parameters were less correlated in cases of reperfusion (Sakoh et al. 2000a).

5.6.2   Chronic Cerebral Ischemia

Earliest human work on CBF visualization and quantification by PET in chronic cerebrovascular disease was carried out by Gibbs and coworkers (1984). They successfully imaged, by using the steady-state $[^{15}O]CO_2$ inhalation technique, the consequences of carotid artery occlusion on brain hemodynamics in their patients (Gibbs et al. 1984). Currently, $[^{15}O]H_2O$ PET imaging is used as a diagnostic standard tool in specialized centers handling patients with Moyamoya disease (Taki et al. 1988). In this chronic occlusive cerebrovascular disorder of unknown etiology which is most prevalent in East Asia, cerebral angiography and cerebral MRI are often accompanied by testing the hemodynamic consequences of the eminent arterial occlusion on the brain parenchyma by PET (Zhang et al. 2019).

5.6.3   Brain Activation Studies

Perfusion parameters are closely coupled with changes in neuronal activity (Roy and Sherrington 1890; Fox et al. 1988; Villringer and Dirnagl 1995). In the last decades, numerous neuronal activation studies have reported this effect, which, nevertheless, is not completely understood (Peterson et al. 2011). The possibility to perform sequential measurements within a certain time window made CBF PET an attractive tool to study perfusion during cognitive, motor, or sensomotor tasks in humans. During local brain activation, cerebral areas that are involved in task performance were identified by CBF changes (Feng et al. 2004; Worsley et al. 1992). It is also worth noting that many tools to analyze brain activation studies, like the Statistical Parametric Mapping (SPM) toolbox (Friston et al. 1991), which are nowadays intensively employed to analyze functional MRI data, were originally developed to process $[^{15}O]H_2O$ brain PET studies.

5.6.4   Other Applications for CBF PET

In general, PET is a useful tool to study perfusion and oxygen metabolism in any cerebral disease, such as dementia (Yao et al. 1990; Cohen et al. 1997), schizophrenia (Ragland et al. 2001), and migraine. Latter approaches addressed hemodynamic changes and oxygen metabolism during and between acute attacks. An increase in CBF was found in cortical areas and in the brainstem which appeared to be pain related (Andersson et al. 1997; Cutrer et al. 2000). Similar to these migraine studies, other preclinical and clinical investigations focus on epilepsy to determine perfusion changes during and between epileptic seizures (Szabo et al. 2007; Kahane 1999; Gaillard et al. 1995). A few studies also used CBF PET (mostly in combination with other PET readouts, like oxygen metabolism from ^{15}O inhalation) for detailed characterization of brain tumors (Lammertsma et al. 1985; Leenders 1994; Hino et al. 1990; Tomura et al. 1993). Due to the newly formed vessels which often

appear in the tumor parenchyma or its surrounding tissue, a regional CBF increase could be detected and may provide additionally useful information about the progression of the brain tumors.

5.7 Simplification/Improvement of CBF Quantification by [^{15}O]H$_2$O PET

There are ongoing efforts to simplify and/or improve CBF quantification by [^{15}O]H$_2$O PET. For instance, ways to replace invasive blood sampling to derive the required arterial input function have been suggested. Here, Jochimsen et al. (2016) and Khalighi et al. (2018) proposed to generate image-derived input functions on hybrid PET/MRI systems. This was realized by the help of arterial vessel segmentation on time of flight MR angiography images perfectly aligned to the PET data, with convincing results as compared to the arterial sampling gold standard. Nevertheless, Koopman et al. (2019) recently compared different non-invasive [^{15}O]H$_2$O PET CBF quantification methods and pointed out that absolute CBF quantification is limited using these approaches regarding accuracy, while relative—in relation to a reference region—CBF determination (CBF pattern determination as used in most clinical routine applications) is possible with sufficient reliability. Contributing to an improvement of the quality of kinetic modeling of [^{15}O]H$_2$O PET data, Kudomi et al. (2013) proposed to directly determine the appearance time of the tracer to the brain which is also called the delay time. This parameter which is important for accurate modeling would be determined separately for different brain pixels in an image-based manner.

5.8 Future Alternatives to [^{15}O]H$_2$O PET Imaging in Determining CBF

Different strategies were tested over the last years to potentially substitute the challenging [^{15}O]H$_2$O PET approach by more convenient imaging techniques. This search was significantly stimulated by the appearance of the hybrid PET/MRI technology by which it is now possible to cross-evaluate certain MR techniques which were developed to deliver CBF surrogates simultaneously against the gold standard [^{15}O]H$_2$O PET. Also, the future possibility to obtain CBF information via MRI in parallel to other (for instance, neuropathology or neurotransmitter) PET readouts is seen by many as promising, not only to improve brain research but also different neuropsychiatric diagnoses. Following this line, several versions of the arterial spin labeling MRI technique (van Golen et al. 2014; Schmid et al. 2015; Heijtel et al. 2016), phase contrast mapping MRI (Puig et al. 2018), the classical contrast medium-based perfusion-weighted MRI (Werner et al. 2015), and blood oxygenation level-dependent functional MRI (Fierstra et al. 2018) were cross-evaluated against [^{15}O]H$_2$O PET over the last years with success for most techniques, at least

for the clinically relevant relative CBF determination. Another technique with potential for delivering CBF surrogate readouts is near-infrared spectroscopy (NIRS). Recently, Polinder-Bos et al. (2018) cross-evaluated NIRS against [^{15}O]H$_2$O PET. As a drawback, a CBF underestimation was reported by the authors. Thus, more work is required to establish this non-radioactive technology for reliable CBF determination. Finally, there is the concept of substituting CBF imaging with [^{15}O]H$_2$O PET by blood flow surrogate information as obtained by dynamic data acquisition, early after administration of certain brain PET tracers, with amyloid PET tracers currently being in the main focus. The clinical concept here is that it would be possible to obtain both histopathology (amyloid load) and neurodegeneration (blood flow surrogate) biomarker information in dementia disorders after a single tracer administration. To test this approach, three recent studies head-to-head compared [^{15}O]H$_2$O PET against different blood flow or blood flow surrogate readouts obtained from amyloid PET imaging (Sojkova et al. 2015; Ottoy et al. 2019; Bilgel et al. 2019). All these studies concluded that the data obtained after amyloid tracer administration is of sufficient quality to obtain clinically relevant blood flow pattern information.

5.9   Summary and Conclusions

PET imaging with [^{15}O]H$_2$O represents the gold standard to visualize and quantify CBF in vivo. As such, this method plays a relevant role mainly for the investigation of cerebrovascular diseases. Despite advantageous characteristics of the tracer, like the possibility to monitor CBF changes over time in sequential scans, [^{15}O]H$_2$O PET imaging remains a technological and infrastructural challenge, preventing it from gaining a wider acceptance in a clinical routine setting. In contrast to clinical routine, [^{15}O]H$_2$O PET plays an important role in preclinical and clinical research, for instance, in (1) clarifying the pathophysiology of ischemic stroke and other cerebrovascular disorders, (2) cross-evaluation of alternative imaging methods to estimate CBF, and (3) the testing of new stroke treatment concepts.

References

Andersson JL, Muhr C, Lilja A et al (1997) Regional cerebral blood flow and oxygen metabolism during migraine with and without aura. Cephalalgia 17(5):570–579
Astrup J, Siesjö BK, Symon L (1981) Thresholds in cerebral ischemia—the ischemic penumbra. Stroke 12(6):723–725

Baron JC (2001) Perfusion thresholds in human cerebral ischemia: historical perspective and therapeutic implications. Cerebrovasc Dis 11(Suppl 1):2–8

Baron JC, Bousser MG, Comar D et al (1981) "Crossed cerebellar diaschisis" in human supratentorial brain infarction. Trans Am Neurol Assoc 105:459–461

Barthel H, Hesse S, Dannenberg C et al (2001) Prospective value of perfusion and X-ray attenuation imaging with single-photon emission and transmission computed tomography in acute cerebral ischemia. Stroke 32(7):1588–1597

Beaver J, Finn RD, Hupf HB et al (1976) A new method for the production of high concentration oxygen-15 labeled carbon dioxide with protons. Appl Radiat Isot 27:195–197

Berridge MS, Terries AH, Cassidy EH et al (1990) Low-carrier production of [15O]oxygen, water and carbon monoxide. Appl Radiat Isot 41:1173–1175

Bilgel M, Beason-Held L, An Y et al (2019) Longitudinal evaluation of surrogates of regional cerebral blood flow computed from dynamic amyloid PET imaging. J Cereb Blood Flow Metab:271678X19830537

Boltze J, Forschler A, Nitzsche B et al (2008) Permanent middle cerebral artery occlusion in sheep: a novel large animal model of focal cerebral ischemia. J Cereb Blood Flow Metab 28(12):1951–1964

Bolwig TG, Lassen NA (1975) The diffusion permeability to water of the rat blood–brain barrier. Acta Physiol Scand 93(3):415–422

Brody H (1955) Organization of the cerebral cortex. III. A study of aging in the human cerebral cortex. J Comp Neurol 102(2):511–516

Bruce DA, Langfitt TW, Miller JD et al (1973) Regional cerebral blood flow, intracranial pressure, and brain metabolism in comatose patients. J Neurosurg 38(2):131–144

Calamante F, Morup M, Hansen LK (2004) Defining a local arterial input function for perfusion MRI using independent component analysis. Magn Reson Med 52(4):789–797

Carroll TJ, Teneggi V, Jobin M et al (2002) Absolute quantification of cerebral blood flow with magnetic resonance, reproducibility of the method, and comparison with H215O positron emission tomography. J Cereb Blood Flow Metab 22:1149–1156

Chen JJ, Wieckowska M, Meyer E et al (2008) Cerebral blood flow measurement using fMRI and PET: a cross-validation study. Int J Biomed Imaging 2008:516359

Chiron C, Raynaud C, Maziere B et al (1992) Changes in regional cerebral blood flow during brain maturation in children and adolescents. J Nucl Med 33(5):696–703

Clark JC, Crouzel C, Meyer GJ et al (1987) Current methodology for oxygen-15 production for clinical use. Int J Rad Appl Instrum A 38(8):597–600

Clark JC, Tochon-Danguy H (1991) R2D2—a bedside [oxygen-15]water infuser. PSI Proceedings 92-01, pp 234–235. ISSN 1019-6447. Proc. IV. Int. Workshop on Targetry and Target Chemistry; Sept 9–12th; Villigen, Switzerland, 1991. (Abstract)

Cohen RM, Andreason PJ, Doudet DJ et al (1997) Opiate receptor avidity and cerebral blood flow in Alzheimer's disease. J Neurol Sci 148(2):171–180

Cutrer FM, O'Donnell A, Sanchez del Rio M (2000) Functional neuroimaging: enhanced understanding of migraine pathophysiology. Neurology 55(9 Suppl 2):S36–S45

Eichling JO, Raichle ME, Grubb RL et al (1974) Evidence of the limitations of water as a freely diffusible tracer in brain of the rhesus monkey. Circ Res 35(3):358–364

Feeney DM, Baron JC (1986) Diaschisis. Stroke 17(5):817–830

Feigin VL, Lawes CMM, Bennett DA et al (2009) Worldwide stroke incidence and early case fatality reported in 56 population-based studies: a systematic review. Lancet Neurol 8(4):355–369

Feng C, Narayana S, Lancaster JL et al (2004) CBF changes during brain activation: fMRI vs PET. NeuroImage 22(1):443–446

Fierstra J, van Niftrik C, Warnock G et al (2018) Staging hemodynamic failure with blood oxygen-level-dependent functional magnetic resonance imaging cerebrovascular reactivity: a comparison versus gold standard (15O-)H2O-positron emission tomography. Stroke 49(3):621–629

Fox PT, Mintun MA, Reiman EM et al (1988) Enhanced detection of focal brain responses using intersubject averaging and change-distribution analysis of subtracted PET images. J Cereb Blood Flow Metab 8(5):642–653

Frackowiak RS, Lenzi GL, Jones T et al (1980) Quantitative measurement of regional cerebral blood flow and oxygen metabolism in man using 15O and positron emission tomography: theory, procedure, and normal values. J Comput Assist Tomogr 4(6):727–736

Friston K et al (1991). https://www.fil.ion.ucl.ac.uk/spm/software/

Gaillard WD, Fazilat S, White S et al (1995) Interictal metabolism and blood flow are uncoupled in temporal lobe cortex of patients with complex partial epilepsy. Neurology 45(10):1841–1847

Gibbs JM, Wise RJ, Leenders KL et al (1984) Cerebral haemodynamics in occlusive carotid-artery disease. Lancet 1(8434):933–934

Griffiths PD, Hoggard N, Dannels WR et al (2001) In vivo measurement of cerebral blood flow: a review of methods and applications. Vasc Med 6(1):51–60

Hall R (1971) Vascular injuries resulting from arterial puncture of catheterization. Br J Surg 58(7):513–516

Hatakeyama T, Sakaki S, Nakamura K et al (1992) Improvement in local cerebral blood flow measurement in gerbil brains by prevention of postmortem diffusion of ^{14}C iodoantipyrine. J Cereb Blood Flow Metab 12(2):296–300

Heijtel DF, Petersen ET, Mutsaerts HJ et al (2016) Quantitative agreement between [(15)O]H$_2$O PET and model free QUASAR MRI-derived cerebral blood flow and arterial blood volume. NMR Biomed 29(4):519–526

Heiss W, Kracht L, Grond M et al (2000) Early [^{11}C]flumazenil/H$_2$O positron emission tomography predicts irreversible ischemic cortical damage in stroke patients receiving acute thrombolytic therapy. Stroke 31(2):366–369

Heiss WD, Graf R, Lottgen J et al (1997) Repeat positron emission tomographic studies in transient middle cerebral artery occlusion in cats: residual perfusion and efficacy of postischemic reperfusion. J Cereb Blood Flow Metab 17(4):388–400

Heiss WD, Graf R, Wienhard K et al (1994) Dynamic penumbra demonstrated by sequential multitracer PET after middle cerebral artery occlusion in cats. J Cereb Blood Flow Metab 14(6):892–902

Heiss WD, Rosner G (1983) Functional recovery of cortical neurons as related to degree and duration of ischemia. Ann Neurol 14(3):294–301

Herscovitch P, Raichle ME (1985) What is the correct value for the brain–blood partition coefficient for water? J Cereb Blood Flow Metab 5(1):65–69

Herscovitch P, Raichle ME, Kilbourn MR et al (1987) Positron emission tomographic measurement of cerebral blood flow and permeability-surface area product of water using 15Owater and 11Cbutanol. J Cereb Blood Flow Metab 7(5):527–542

Hino A, Imahori Y, Tenjin H et al (1990) Metabolic and hemodynamic aspects of peritumoral low-density areas in human brain tumor. Neurosurgery 26(4):615–621

Hoeffner EG (2005) Cerebral perfusion imaging. J Neuroophthalmol 25(4):313–320

Ibaraki M, Shimosegawa E, Miura S et al (2004) PET measurements of CBF, OEF, and CMRO2 without arterial sampling in hyperacute ischemic stroke: method and error analysis. Ann Nucl Med 18(1):35–44

Iida H, Jones T, Miura S (1993) Modeling approach to eliminate the need to separate arterial plasma in oxygen-15 inhalation positron emission tomography. J Nucl Med 34(8):1333–1340

Jay TM, Lucignani G, Crane AM et al (1988) Measurement of local cerebral blood flow with [^{14}C]iodoantipyrine in the mouse. J Cereb Blood Flow Metab 8(1):121–129

Jezzard P (1998) Advances in perfusion MR imaging. Radiology 208(2):296–299

Jochimsen TH, Zeisig V, Schulz J et al (2016) Fully automated calculation of image-derived input function in simultaneous PET/MRI in a sheep model. EJNMMI Phys 3(1):2

Jones T, Chester DA, Ter-Pogossian MM (1976) The continuous inhalation of oxygen-15 for assessing regional cerebral oxygen extraction in the brain of man. Br J Radiol 49:339

Kahane P (1999) An H215O-PET study of cerebral blood flow changes during focal epileptic discharges induced by intracerebral electrical stimulation. Brain 122(10):1851–1865

Kanno I, Iida H, Miura S et al (1991) Optimal scan time of oxygen-15-labeled water injection method for measurement of cerebral blood flow. J Nucl Med 32(10):1931–1934

Kety SS (1951) The theory and applications of the exchange of inert gas at the lungs and tissues. Pharmacol Rev 3:1–41

Kety SS, Schmidt CF (1945) The determination of cerebral blood flow in man by use of nitrous oxide in low concentrations. Am J Phys 143:53–66

Khalighi MM, Deller TW, Fan AP et al (2018) Image-derived input function estimation on a TOF-enabled PET/MR for cerebral blood flow mapping. J Cereb Blood Flow Metab 38(1):126–135

Kimura H, Kado H, Koshimoto Y et al (2005) Multislice continuous arterial spin-labeled perfusion MRI in patients with chronic occlusive cerebrovascular disease: a correlative study with CO_2 PET validation. J Magn Reson Imaging 22(2):189–198

Koopman T, Yaqub M, Heijtel DF et al (2019) Semi-quantitative cerebral blood flow parameters derived from non-invasive [15O]H_2O PET studies. J Cereb Blood Flow Metab 39(1):163–172

Krohn K, Link JM, Lewellen TK et al (1986) The use of 50 MeV protons to produce C-11 and O-15. J Label Compd Radiopharm 23:1190–1192

Kudo K, Sasaki M, Yamada K et al (2010) Differences in CT perfusion maps generated by different commercial software: quantitative analysis by using identical source data of acute stroke patients. Radiology 254(1):200–209

Kudomi N, Maeda Y, Sasakawa Y et al (2013) Imaging of the appearance time of cerebral blood using [15O]H_2O PET for the computation of correct CBF. EJNMMI Res 3(1):41

Kuge Y, Yokota C, Tagaya M et al (2001) Serial changes in cerebral blood flow and flow-metabolism uncoupling in primates with acute thromboembolic stroke. J Cereb Blood Flow Metab 21(3):202–210

Lammertsma AA (1994) Noninvasive estimation of cerebral blood flow. J Nucl Med 35(11):1878–1879

Lammertsma AA, Wise RJS, Cox TCS et al (1985) Measurement of blood flow, oxygen utilisation, oxygen extraction ratio, and fractional blood volume in human brain tumours and surrounding oedematous tissue. Br J Radiol 58:725–734

Lass P, Koseda M, Romanowicz G et al (1998) Cerebral blood flow assessed by brain SPECT with 99mTc-HMPAO utilising the acetazolamide test in systemic lupus erythematosus. Nucl Med Rev Cent East Eur 1(1):20–24

Lassen NA, Ingvar DH (1961) The blood flow of the cerebral cortex determined by radioactive krypton. Experientia 17:42–43

Law I, Iida H, Holm S et al (2000) Quantitation of regional cerebral blood flow corrected for partial volume effect using O-15 water and PET: II. Normal values and gray matter blood flow response to visual activation. J Cereb Blood Flow Metab 20(8):1252–1263

Leenders KL (1994) PET: blood flow and oxygen consumption in brain tumors. J Neuro-Oncol 22(3):269–273

Links JM, Zubieta JK, Meltzer CC et al (1996) Influence of spatially heterogeneous background activity on "hot object" quantitation in brain emission computed tomography. J Comput Assist Tomogr 20(4):680–687

Machleder HI, Sweeney JP, Barker WF (1972) Pulseless arm after brachial-artery catheterisation. Lancet 1(7747):407–409

Markus HS (2004) Cerebral perfusion and stroke. J Neurol Neurosurg Psychiatry 75(3):353–361

Martin WR, Powers WJ, Raichle ME (1987) Cerebral blood volume measured with inhaled C15O and positron emission tomography. J Cereb Blood Flow Metab 7(4):421–426

Matsuda M, Lee H, Kuribayashi K et al (1996) Comparative study of regional cerebral blood flow values measured by Xe CT and Xe SPECT. Acta Neurol Scand Suppl 166:13–16

Matthew E, Andreason P, Carson RE et al (1993) Reproducibility of resting cerebral blood flow measurements with H2(15)O positron emission tomography in humans. J Cereb Blood Flow Metab 13(5):748–754

Meier P, Zierler KL (1954) On the theory of the indicator-dilution method for measurement of blood flow and volume. J Appl Physiol 6(12):731–744

Mulholland GK, Kilbourn MR, Moskwa JJ (1990) Direct simultaneous production of 15Owater and 13Nammonia or 18Ffluoride ion by 26 MeV proton irradiation of a double chamber water target. Int J Rad Appl Instrum A 41(12):1193–1199

Obrist WD, Thompson HKJR, Wang HS et al (1975) Regional cerebral blood flow estimated by 133-xenon inhalation. Stroke 6(3):245–256

Ostergaard L, Sorensen AG, Kwong KK et al (1996b) High resolution measurement of cerebral blood flow using intravascular tracer bolus passages. Part II: Experimental comparison and preliminary results. Magn Reson Med 36(5):726–736

Ostergaard L, Weisskoff RM, Chesler DA et al (1996a) High resolution measurement of cerebral blood flow using intravascular tracer bolus passages. Part I: Mathematical approach and statistical analysis. Magn Reson Med 36(5):715–725

Ottoy J, Verhaeghe J, Niemantsverdriet E et al (2019) ^{18}F-FDG PET, the early phases and the delivery rate of ^{18}F-AV45 PET as proxies of cerebral blood flow in Alzheimer's disease: validation against 15O-H_2O PET. Alzheimers Dement S1552–5260(19):30151–30157

Pantano P, Baron JC, Lebrun-Grandie P et al (1984) Regional cerebral blood flow and oxygen consumption in human aging. Stroke 15(4):635–641

Pappata S, Fiorelli M, Rommel T et al (1993) PET study of changes in local brain hemodynamics and oxygen metabolism after unilateral middle cerebral artery occlusion in baboons. J Cereb Blood Flow Metab 13(3):416–424

Petersen ET, Zimine I, Ho YL et al (2006) Non-invasive measurement of perfusion: a critical review of arterial spin labelling techniques. Br J Radiol 79(944):688–701

Peterson EC, Wang Z, Britz G (2011) Regulation of cerebral blood flow. Int J Vasc Med 2011:1–8

Pindzola RR, Yonas H (1998) The xenon-enhanced computed tomography cerebral blood flow method. Neurosurgery 43(6):1488–1492

Polinder-Bos HA, Elting JWJ, Aries MJ et al (2018) Changes in cerebral oxygenation and cerebral blood flow during hemodialysis—a simultaneous near-infrared spectroscopy and positron emission tomography study. J Cereb Blood Flow Metab 12:271678X18818652

Powell J, O'Neil JP (2006) Production of 15Owater at low-energy proton cyclotrons. Appl Radiat Isot 64(7):755–759

Puig O, Vestergaard MB, Lindberg U et al (2018) Phase contrast mapping MRI measurements of global cerebral blood flow across different perfusion states: a direct comparison with 15O-H_2O positron emission tomography using a hybrid PET/MR system. J Cereb Blood Flow Metab 11:271678X18798762

Ragland JD, Gur RC, Raz J et al (2001) Effect of Schizophrenia on frontotemporal activity during word encoding and recognition: a PET cerebral blood flow study. Am J Psychiatry 158(7):1114–1125

Raichle ME, Martin WR, Herscovitch P et al (1983) Brain blood flow measured with intravenous H2(15)O. II. Implementation and validation. J Nucl Med 24(9):790–798

Rousset OG, Ma Y, Evans AC (1998) Correction for partial volume effects in PET: principle and validation. J Nucl Med 39(5):904–911

Roy CS, Sherrington CS (1890) On the regulation of the blood-supply of the brain. J Physiol 11(1–2):85–158

Sajjad M, Liow JS, Moreno-Cantu J (2000) A system for continuous production and infusion of 15OH_2O for PET activation studies. Appl Radiat Isot 52(2):205–210

Sakai Y, Kasuga T, Nakanishi F et al (1987) Cerebral blood flow study by ^{133}Xe inhalation and single photon emission CT in occlusive cerebrovascular diseases. Kaku Igaku 24(1):47–54

Sakoh M, Ostergaard L, Røhl L et al (2000b) Relationship between residual cerebral blood flow and oxygen metabolism as predictive of ischemic tissue viability: sequential multitracer positron emission tomography scanning of middle cerebral artery occlusion during the critical first 6 hours after stroke in pigs. J Neurosurg 93(4):647–657

Sakoh M, Rohl L, Gyldensted C et al (2000a) Cerebral blood flow and blood volume measured by magnetic resonance imaging bolus tracking after acute stroke in pigs: comparison with [15O]H_2O positron emission tomography. Stroke 31(8):1958–1964

Schmid S, Heijtel DF, Mutsaerts HJ et al (2015) Comparison of velocity- and acceleration-selective arterial spin labeling with [15O]H$_2$O positron emission tomography. J Cereb Blood Flow Metab 35(8):1296–1303

Skyhøj Olsen T, Larsen B, Bech Skriver E et al (1981) Focal cerebral ischemia measured by the intra-arterial 133xenon method. Limitations of 2-dimensional blood flow measurements. Stroke 12(6):736–744

Slosman DO, Chicherio C, Ludwig C et al (2001) (133)Xe SPECT cerebral blood flow study in a healthy population: determination of T-scores. J Nucl Med 42(6):864–870

Sojkova J, Goh J, Bilgel M et al (2015) Voxelwise relationships between distribution volume ratio and cerebral blood flow: implications for analysis of β-amyloid images. J Nucl Med 56(7):1042–1047

Sokoloff L, Perlin S, Kornetsky C et al (1957) The effects of D-lysergic acid diethylamide on cerebral circulation and overall metabolism. Ann N Y Acad Sci 66(3):468–477

Szabo CA, Narayana S, Kochunov PV et al (2007) PET imaging in the photosensitive baboon: case-controlled study. Epilepsia 48(2):245–253

Taki W, Yonekawa Y, Kobayashi A et al (1988) Cerebral circulation and oxygen metabolism in moyamoya disease of ischemic type in children. Childs Nerv Syst 4(5):259–262

Terpolilli NA, Kim S, Thal SC et al (2012) Inhalation of nitric oxide prevents ischemic brain damage in experimental stroke by selective dilatation of collateral arterioles. Circ Res 110(5):727–738

Tomura N, Kato T, Kanno I et al (1993) Increased blood flow in human brain tumor after administration of angiotensin II: demonstration by PET. Comput Med Imaging Graph 17(6):443–449

van Golen LW, Kuijer JP, Huisman MC et al (2014) Quantification of cerebral blood flow in healthy volunteers and type 1 diabetic patients: comparison of MRI arterial spin labeling and [(15)O]H$_2$O positron emission tomography (PET). J Magn Reson Imaging 40(6):1300–1309

van Naemen J, Monclus M, Damhaut P et al (1996) Production, automatic delivery and bolus injection of 15Owater for positron emission tomography studies. Nucl Med Biol 23(4):413–416

van Osch MJ, Vonken EJ, Bakker CJ et al (2001) Correcting partial volume artifacts of the arterial input function in quantitative cerebral perfusion MRI. Magn Reson Med 45(3):477–485

Veall N, Mallett BL (1967) The Xe133 inhalation technique for regional cerebral blood flow studies. Strahlentherapie Sonderb 65:166–173

Villringer A, Dirnagl U (1995) Coupling of brain activity and cerebral blood flow: basis of functional neuroimaging. Cerebrovasc Brain Metab Rev 7(3):240–276

Wakita K, Imahori Y, Ido T et al (2000) Simplification for measuring input function of FDG PET: investigation of 1-point blood sampling method. J Nucl Med 41(9):1484–1490

Watabe H, Itoh M, Cunningham V et al (1996) Noninvasive quantification of rCBF using positron emission tomography. J Cereb Blood Flow Metab 16:311–319

Werner P, Saur D, Zeisig V et al (2015) Simultaneous PET/MRI in stroke: a case series. J Cereb Blood Flow Metab 35(9):1421–1425

Wintermark M, Sesay M, Barbier E et al (2005) Comparative overview of brain perfusion imaging techniques. J Neuroradiol 32(5):294–314

Wise RJ, Bernardi S, Frackowiak RS et al (1983) Serial observations on the pathophysiology of acute stroke the transition from ischaemia to infarction as reflected in regional oxygen extraction. Brain 106:197–222

Worsley KJ, Evans AC, Marrett S et al (1992) A three-dimensional statistical analysis for CBF activation studies in human brain. J Cereb Blood Flow Metab 12(6):900–918

Yao H, Sadoshima S, Kuwabara Y et al (1990) Cerebral blood flow and oxygen metabolism in patients with vascular dementia of the Binswanger type. Stroke 21(12):1694–1699

Zanotti-Fregonara P, Chen K, Liow J et al (2011) Image-derived input function for brain PET studies: many challenges and few opportunities. J Cereb Blood Flow Metab 31(10):1986–1998

Zaro-Weber O, Moeller-Hartmann W, Heiss W et al (2010a) Maps of time to maximum and time to peak for mismatch definition in clinical stroke studies validated with positron emission tomography. Stroke 41(12):2817–2821

Zaro-Weber O, Moeller-Hartmann W, Heiss W et al (2010b) MRI perfusion maps in acute stroke validated with 15O-water positron emission tomography. Stroke 41(3):443–449

Zaro-Weber O, Moeller-Hartmann W, Heiss W et al (2012) Influence of the arterial input function on absolute and relative perfusion-weighted imaging penumbral flow detection: a validation with ^{15}O-water positron emission tomography. Stroke 43(2):378–385

Zhang H, Zheng L, Feng L (2019) Epidemiology, diagnosis and treatment of Moyamoya disease. Exp Ther Med 17(3):1977–1984

Zierler K (1962) Theoretical basis of indicator-dilution methods for measuring flow and volume. Circ Res 10:393–407

The Impact of Genetic Polymorphisms on Neuroreceptor Binding: Results from PET and SPECT Neuroreceptor Imaging Studies

6

Irene Graf, Matthäus Willeit, Siegfried Kasper, and Nicole Praschak-Rieder

Contents

I. Graf · M. Willeit (✉) · S. Kasper · N. Praschak-Rieder
Division of General Psychiatry, Department of Psychiatry and Psychotherapy, Medical University Vienna, Vienna, Austria
e-mail: irene.graf@meduniwien.ac.at; matthaeus.willeit@meduniwien.ac.at; siegfried.kasper@meduniwien.ac.at; nicole.praschak-rieder@meduniwien.ac.at

Abstract

Major psychiatric disorders are highly heritable. Nevertheless, more than three decades of candidate gene studies and genome-wide association studies have yielded few, if any, unambiguous and replicable results that would be strong enough as to direct research toward new pharmacological targets. This is in part due to the complex non-Mendelian inheritance patterns and difficult-to-define phenotypes of psychiatric disorders. In addition, the relationship between genetic risk and phenotypic expression is blurred by the strong contribution of environmental factors and epigenetic modification. A research strategy that has successfully been pursued over the last years with magnetic resonance-based methods is imaging of endophenotypes. However, these techniques have the drawback that their results are not easily transferable to a molecular level potentially accessible to therapeutic drugs. Neuroreceptor imaging methods such as positron emission tomography (PET) and single photon emission computer tomography (SPECT) make it possible to explore the impact of genetic variation on neuroreceptor binding and function of transporters and other molecules that play a central role in neuropsychiatric disorders, besides certain aspects of molecules that play a central role in our understanding and treatment of psychiatric disorders. This chapter tries to cover the current state of knowledge about the impact of genetic variation on the behavior of PET and SPECT radioligands in the living human brain.

6.1 Introduction

Since more than a century, diagnoses in psychiatry are syndrome based, that is, the diagnostic process relies on the presence (or absence) of a bundle of more or less specific symptoms that are either reported by the patient or observed by the physician. The diagnostic classification is the ground for prognosis and treatment decision. However, diagnosis cannot be related to putative neurochemical alterations thought to be the pathogenic substrate of major psychiatric disorders. The high heritability of disorders such as schizophrenia or affective illness, together with enormous advances in molecular genetics made in the last decades, has incited the hope that molecular genetics might be able to contribute substantially to our knowledge on molecular alterations associated with specific disorders. Moreover, it is anticipated that these methods would help identify biomarkers that would make the diagnostic process more reliable and objective.

Until recently, case-control studies comparing frequencies of putative risk alleles in patient groups and healthy subjects were the predominant research strategy in psychiatric genetics. Candidate genes were selected a priori on grounds of hypotheses on the pathogenesis and available knowledge on genetic variation in these

targets (so-called biological candidate genes). In keeping with the predominant pathogenetic hypotheses, many of the investigated polymorphisms (polymorphisms are frequent genetic variants) were in one or the other way related to brain monoamine neurotransmission. However, it is now increasingly evident that the genetic mechanisms associated with heritability of psychiatric disorders are far more complex than initially thought and that the variance introduced by single genetic variants is rarely strong enough for having relevant influence on a specific disease risk. Results of recent genome-wide association studies (GWAS) rather suggest that the genetic risk for disorders such as schizophrenia is due to a combination of common low-risk and rare high-risk variants (Purcell et al. 2009; Shi et al. 2009; Stefansson et al. 2009). One of the major advantages of the methodology employed in GWAS is that it does not rely on *a priori* hypotheses. Thus, results surviving the extremely rigid statistical thresholds merit further scientific attention. Functional gene variants derived from GWAS have been termed "positional candidate genes." In contrast to biological candidate genes, the function and biological role of positional candidate genes is frequently unknown and needs to be determined in sometimes complicated follow-up studies. A possible way to relate the function of biological and positional candidate genes to the actual body of knowledge on pathogenesis and neuropharmacology of psychiatric disorders is certainly imaging genetics.

Imaging genetics uses magnetic resonance imaging (MRI)-based methods such as functional MRI (fMRI) or voxel-based morphometry (VBM) and radiation-based methods such as single photon emission computer tomography (SPECT) and positron emission tomography (PET) to study the effects of genetic variants in the living brain. While MRI-based methods can provide information on brain structure, regional brain metabolism, and functional or anatomical connectivity between brain regions, radiation-based methods allow investigating distribution and, in part, function of selected molecules in the brain.

In this chapter, we will review the scientific evidence on the influence of genetic variation upon neuroreceptor PET and SPECT radioligand binding in the brain.

6.2   Serotonin

Serotonin is a phylogenetically ancient modulatory neurotransmitter that is synthesized in the brain and periphery from the essential amino acid tryptophan. The rate-limiting step of serotonin synthesis is hydroxylation of tryptophan by the enzyme tryptophan hydroxylase (TPH). Two isoenzymes are known in humans: TPH-1 catalyzes the reaction in the periphery, whereas TPH-2 (Walther et al. 2003; Zill et al. 2004) is found in the central nervous system (CNS). The serotonin system is involved in the regulation of circadian and seasonal rhythms, mood, sleep, feeding behavior, and energy homeostasis and consequently in a number of psychiatric problems and disorders, notably depression, anxiety, obsessive-compulsive disorder, impulsivity, self-harm, and suicide.

6.2.1   The Serotonin Transporter

The presynaptic serotonin transporter (5-HTT) is a key regulator of serotonin signaling and a major target for antidepressant medications and psychostimulants. The 5-HTT takes up serotonin after its release into the extracellular space, thereby controlling the magnitude and duration of serotonergic responses (Bel and Artigas 1992; Shen et al. 2004; Jennings et al. 2006). High presynaptic 5-HTT density is associated with low extracellular serotonin (Jennings et al. 2006), and raising extracellular serotonin by pharmacological blocking 5-HTT is the main mechanism of action of many antidepressant drugs.

6.2.2   Serotonin Transporter Gene-Linked Polymorphic Region (5-HTTLPR)

An insertion-deletion polymorphism in the promoter region of the 5-HTT transporter gene, the serotonin transporter-linked polymorphic region (5-HTTLPR; Heils et al. 1996), has been extensively studied in psychiatry. In human cell lines, the 5-HTTLPR long (or *l*-allele) is associated with 30–40% higher 5-HTT expression than the short (or *s*-allele) (Heils et al. 1996; Lesch et al. 1996). Initially, 5-HTTLPR was found to be associated with anxiety-related traits: individuals carrying the short allele had higher neuroticism scores than individuals homozygous for the long allele (Lesch et al. 1996). Several studies were able to find associations between 5-HTTLPR and neuropsychiatric illness (Collier et al. 1996; Kunugi et al. 1997; Malhotra et al. 1998; Rosenthal et al. 1998; Anguelova et al. 2003; Bondy et al. 2006; Grunblatt et al. 2006; Premi et al. 2015) However, there are many studies who failed to replicate earlier results (Seretti et al. 1999; Johansson et al. 2003; Willeit et al. 2003). An intensively discussed finding was the association with the 5-HTTLPR s-allele and risk for depression in interaction with traumatic life events (Caspi et al. 2003, 2010). Although this finding has been replicated several times (see, e.g., Zalsman et al. 2006), meta-analyses of this finding are conflicting (Risch et al. 2009; Karg et al. 2011).

In light of inconsistent and contradicting results, it is a rational research strategy to investigate biological endophenotypes associated with the 5-HTTLPR genotype, such as amygdala reactivity (Hariri et al. 2002; Hariri and Holmes 2006) or the influence of 5-HTTLPR on the interaction between brain areas relevant for psychiatric disorders (Pezawas et al. 2005). Today, the s-allele is not seen any more as a variant leading to deficient function of brain proteins or brain circuits. Interestingly, s-allele carriers were found to outperform subjects carrying the long allele in a number of cognitive and social tasks (for review, see Homberg and Lesch 2010). Hyperactivity in corticolimbic structures associated with the s-allele resulting in hypervigilance in the sense of increased sensitivity to both aversive and rewarding stimuli and possibly greater mood reagibility (Willeit et al. 2003) may have beneficial or negative consequences, depending on the environmental circumstances (Homberg and Lesch 2010).

6.2.3   Effects of 5-HTTLPR on Serotonin Transporter Binding

First studies in human platelets investigated the effects of 5-HTTLPR on serotonin transporter expression and function. The amount of transporter protein was not found to be altered, but an influence of 5-HTTLPR on maximal serotonin uptake velocity was described in some (Greenberg et al. 1999; Nobile et al. 1999; Patkar et al. 2004) but not all (Willeit et al. 2008) studies. Two of these studies also showed a significant effect of season on functional 5-HTT parameters (Greenberg et al. 1999; Nobile et al. 1999), and one study also found a significant interaction between 5-HTTLPR genotype and seasonal change in serotonin uptake velocity (Greenberg et al. 1999).

Studies on the effects of 5-HTTLPR on 5-HTT availability in the human brain using the radiolabeled cocaine-analog on [^{123}I]-2-β-carbomethoxy-3-b-(4-iodophenyl)tropane ([^{123}I]β-CIT; Neumeyer et al. 1991) and SPECT (Table 6.1) found higher (Heinz et al. 2000b) or unchanged (Jacobsen et al. 2000; Willeit et al. 2001) binding in carriers of the high-expressing *l*-allele, while other studies found higher binding in subjects homozygous for the low-expressing *s*-allele (Van Dyck et al. 2004). However, rather than being selective for the 5-HTT, [^{123}I]β-CIT is a nonspecific monoamine transporter ligand. Moreover, [^{123}I]β-CIT binding shows a clear age-dependent decrease (Pirker et al. 2000), and a major limitation of the van Dyck et al. study is that *s/s* homozygous subjects were significantly younger than *l/l* and *l/s*-carriers. A more recent study using the β-CIT derivative [^{123}I]nor-β-CIT described slightly higher [^{123}I]nor-β-CIT binding in the thalamus of *s*-allele carriers (Kauppila et al. 2013).

The effects of 5-HTTLPR or the so-called triallelic 5-HTTLPR – a functional single-nucleotide variant within the 5-HTTLPR *l*-allele termed *LA* and *LG*, with only *LA* being associated with high levels of 5-HTT mRNA, whereas *LG* is more similar to the *s*-allele (Nakamura et al. 2000; Kraft et al. 2005)—have also been studied with two PET ligands that are selective for the 5-HTT, [^{11}C]-(+)-6beta-(4-methylthiophenyl)-1,2,3,5,6alpha,10beta-hexahydropyrrolo[2,1-a]isoquinoline ([^{11}C]McN 5652; Suehiro et al. 1993) and [^{11}C]-3-amino-4-(2-dimethylaminomethylphenylthio)benzonitrile ([^{11}C]DASB; Wilson and Houle 1999; Houle et al. 2000; Wilson et al. 2000). [^{11}C]DASB is currently the method of choice for PET imaging of the 5-HTT, and it has been shown to be superior to [^{11}C]McN 5652 in several aspects (Huang et al. 2002; Szabo et al. 2002; Frankle et al. 2004).

In contrast to studies using [^{11}C]McN 5652 (Shioe et al. 2003; Parsey et al. 2006a), three studies using [^{11}C]DASB were able to detect higher serotonin transporter binding in *LA/LA* homozygous subjects (Praschak-Rieder et al. 2007; Reimold et al. 2007; Kalbitzer et al. 2009). The three studies disagree on the location of higher [^{11}C]DASB binding in *LA/LA* homozygous subjects in the brain: Praschak-Rieder et al. found significant 5-HTTLPR effects in the putamen, Reimold et al. in the midbrain, and Kalbitzer et al. in the caudate nucleus. What these regions have in common is that they contain large amounts of serotonin transporter protein, and it is inherent to PET methodology that accuracy of measurements is greater in

Table 6.1 Effects of serotonin transporter-linked polymorphic region (5-HTTLPR), brain-derived neurotrophic factor (BDNF) Val66Met, and 5-HT2A receptor polymorphisms on serotonin transporter binding

	Polymorphism	Number of subjects[a]	Radioligand	Results	Region	Comment
Heinz et al. (2000b)	5-HTTLPR	22 (14 AD)[b]	[123I]β-CIT	ll > s-carriers (healthy subjects)	Brainstem	Opposite genotype effects in AD[b]
Willeit et al. (2001)	5-HTTLPR	11	[123I]β-CIT	No effect	Midbrain	
Van Dyck et al. (2004)	5-HTTLPR	96	[123I]β-CIT	ss > ll > ls	Midbrain	s/s Homozygotes younger than other genotypes
Shioe et al. (2003)	5-HTTLPR	27	[11C]McN 5652	No effect	Midbrain	
Parsey et al. (2006a)	Triallelic 5-HTTLPR	67 (25 MDD)[c]	[11C]McN 5652	No effect	Serotonin-rich regions	
Praschak-Rieder et al. (2007)	Triallelic 5-HTTLPR	43	[11C]DASB	La/La > s-carriers	Putamen	Results clearer when covarying for ethnicity and effects of season
Reimold et al. (2007)	Triallelic 5-HTTLPR	19	[11C]DASB	La/La > s-carriers	Midbrain	
Kalbitzer et al. (2009)	Triallelic 5-HTTLPR	50	[11C]DASB	La/La > s-carriers	Caudate	
Murthy et al. (2010)	Triallelic 5-HTTLPR	63	[11C]DASB	No effect	Serotonin-rich regions	Only male Caucasians, no effects of daylight
Kauppila et al. (2013)	5-HTTLPR	30	[123I]nor-β-CIT	s-carriers > ll	Thalamus	No effect in other regions
Premi et al. (2015)	5-HTTLPR	76[d]	99mTc-ECD	Blood flow ll < s/l < ss	Frontal lobes	Additive effect of CR and ll
Laje et al. (2010)	5-HT1A	43	[11C]DASB	rs7333412 AA < AG < GG	Thalamus	rs7333412, rs7997012, rs977003
Henningsson et al. (2009)	BDNF Val66Met	25	[11C]MADAM	Val/Val > Met+	Serotonin-rich regions	Finding significant in males only

Klein et al. (2010)	BDNF Val66Met	49	[¹¹C]DASB	No effect	Caudate, putamen, thalamus	Also no effect of plasma BDNF levels
Peciña et al. (2014)	BDNF Val66Met	49	[¹¹C]raclopride	Met > Val/Val	VTA, NaC	Met: no reaction to monetary gains, attenuated dopamine response to analgesic placebo in NAc
Kraus et al. (2014)	BDNF Val66Met	41 (16 MDD)[c]; 51	[¹¹C]DASB; [¹¹C]WAY 100635	No effect	Serotonin-rich regions	
Fisher et al. (2015)	BDNF Val66Met; 5-HTTLPR	68	[¹¹C]SB207145	Val/Val < Met+; s-carriers < ll	Neocortex, subcortical structures	Effects of 5-HTTLPR in neocortex
Fisher et al. (2017)	BDNF Val66Met; 5-HTTLPR	144	[¹¹C]DASB	Val/Val < Met+; No effect	Subcortical structures	No BDNF Val66Met effect in neocortex; no significant effect of 5-HTTLPR

Adapted from Willeit and Praschak-Rieder (2010)

[a]Healthy subjects if not otherwise indicated

[b]AD Patients with alcohol dependence

[c]MDD Major depressive disorder

[d]FTD Frontotemporal dementia

regions with high density of the target molecule than in those who express the target scarcely (Willeit and Praschak-Rieder 2010). Kalbitzer et al. also showed that light-dependent changes in serotonin transporter binding (Praschak-Rieder et al. 2008; Ruhe et al. 2009) were influenced by 5-HTTLPR genotype, with *LA/LA* carriers showing greater seasonal fluctuation in serotonin transporter binding. However, another recent study did not find any relevant effects of 5-HTTLPR on [^{11}C]DASB binding in the human brain (Murthy et al. 2010).

In summary, the literature reports contradictory results on the influence of 5-HTTLPR genotype on serotonin transporter binding in the living human brain. Apart from the natural variation in individual 5-HTT density, one major factor may be the quality of the imaging methods applied. [^{11}C]DASB is clearly superior to [^{11}C]McN 5652 or [^{123}I]β-CIT for imaging the 5-HTT in vivo (Huang et al. 2002; Szabo et al. 2002; Frankle et al. 2004). Moreover, nongenetic aspects have been shown to influence or associate with 5-HTT binding. These include ethnicity (Praschak-Rieder et al. 2007), personality (Kalbitzer et al. 2009), biography (Miller et al. 2009), and psychiatric diagnoses (Malison et al. 1998; Willeit et al. 2000; Meyer et al. 2004; Selvaraj et al. 2009; for review, see Stockmeier 2003; Meyer 2007) and the intensity of environmental light at the time of the year when scanning takes place (Buchert et al. 2006; Praschak-Rieder et al. 2008; Ruhe et al. 2009; Kalbitzer et al. 2010). Studies on the effects of season show that 5-HTT binding is higher in fall and winter as compared to spring and summer, and covarying for season in the Praschak-Rieder et al. sample (Praschak-Rieder et al. 2007) increased the significance of the effects of 5-HTTLPR on [^{11}C]DASB binding (Praschak-Rieder et al. 2008). Thus, three of four PET imaging studies using [^{11}C]DASB support the notion that 5-HTTLPR is indeed associated with 5-HTT binding in the living human brain. However, in contrast to restricted systems like human cell lines, where a 30–40% difference in 5-HTT binding between high- and low-expressing genotypes has been observed, genotype effects of 5-HTTLPR, if any, were found to be quite small.

6.2.4 Serotonin 2A Receptor Polymorphisms

A relatively large study has investigated the effects of several single-nucleotide polymorphisms (SNPs) in the serotonin 2A (5-HT$_{2A}$) receptor gene on [^{11}C]DASB binding in the brain (Laje et al. 2010). Genetic variation in this region had previously been associated with antidepressant treatment response to citalopram (McMahon et al. 2006). An association between 5-HTT binding in thalamus and three SNPs (rs7333412, rs7997012, rs977003) was found, and results were suggestive for a gene-dose effect (rs7333412 AA < AG < GG). This study may thus help to explain differences in treatment response to SSRIs due to genetic variation in the 5-HT$_{2A}$ receptor gene. This result is among the few ones in the literature strong enough as to survive correction for multiple testing.

6.2.5 Brain-Derived Neurotrophic Factor (BDNF) Polymorphisms (Val66Met)

Brain-derived neurotrophic factor (BDNF) is a relatively well-characterized neuro-trophic protein that supports survival, sprouting, and synaptogenesis of neurons. It is encoded on chromosome 11p13–14 (Jones and Reichardt 1990; Maisonpierre et al. 1991). Polymorphisms within the BDNF gene have been shown to influence brain structure and function (Egan et al. 2003; Hariri et al. 2003; Pezawas et al. 2004, 2008) and have been associated with affective disorders, antidepressant treatment response, substance abuse, eating disorders, and schizophrenia (Neves-Pereira et al. 2002; Sklar et al. 2002; Castren 2004; Gratacos et al. 2007; Brunoni et al. 2008). Experimental and clinical evidence suggests that there is a close interaction between BDNF and brain serotonin transmission (Neumeister et al. 2005; Brunoni et al. 2008; Maynard et al. 2016).

Two PET studies have investigated a possible association of the BDNF Val66Met polymorphism and binding to brain 5-HT_{2A} receptors (Klein et al. 2010) and to 5-HT_{1A} receptors and the serotonin transporter (Henningsson et al. 2009). While there was no effect of the BDNF Val66Met polymorphism on 5-HT_{1A} or 5-HT_{2A} receptor binding, one study (Henningsson et al. 2009) found significantly higher binding of the serotonin transporter radioligand [^{11}C]MADAM in male subjects. This finding was replicated in the same study at a trend level in second cohort using the radioligand [^{123}I]β-CIT and SPECT. However, the studies by Klein et al. (2010) and Kraus et al. (2014) using the radioligand [^{11}C]DASB did not find any effect of the BDNF Val66Met polymorphism or BDNF plasma levels (Klein et al.(2010)) on brain serotonin transporter binding in larger samples. As part of the same study, Kraus et al. (2014) also performed [^{11}C]WAY 100635 PET scans but did not demonstrate effects of BDNF Val66Met on 5-HT_{1a} binding either.

Effects on 5-HT_4 receptor binding were reported in a PET study using [^{11}C]SB207145 that demonstrated increased BP_{ND} for Val66met met carriers compared with Val/Val carriers across regions (Fisher et al. 2015). The group also predicted latent variable model (LVM) for the serotonin transporter-linked polymorphic region (5-HTTLPR) and showed lower neocortical binding for s-carriers relative to LL homozygotes.

The same group further researched effects of 5-HTTLPR and BDNF Val66met on 5-HTT binding ([^{11}C]DASB PET) in 144 healthy humans and demonstrated 2–7% higher subcortical 5-HTT binding for met carriers compared with Val/Val individuals of BDNF Val66met on 5-HTT (Fisher et al. 2017). No significant effect was shown for 5-HTTLPR or BDNF Val66met in neocortex (Table 6.1).

6.2.6 The Serotonin 1A Receptor

The serotonin 1A (5-HT_{1A}) receptor is a G-protein-coupled transmembrane protein whose main signaling effect is a reduction in the formation of cyclic adenosine monophosphate (cAMP). 5-HT_{1A} receptors are abundantly expressed in the frontal and

temporal cortex, hippocampus, septum, amygdala, and the raphe nuclei, and lower levels are found in basal ganglia and the thalamus (Ito et al. 1999; de Almeida and Mengod 2008; Storvik et al. 2009). 5-HT$_{1A}$ receptors are considered inhibitory as, upon activation, they reduce the probability of neuronal discharge. Cortical and subcortical 5-HT$_{1A}$ receptors are mostly postsynaptic receptors located on glutamatergic and GABAergic neurons (Freund et al. 1990; Palchaudhuri and Flugge 2005; de Almeida and Mengod 2008), while 5-HT$_{1A}$ receptors in the raphe nuclei, the origin of brain serotonin innervation, are somatodendritic autoreceptors that reduce serotonergic output from the raphe into the respective target areas (Sprouse and Aghajanian 1988).

Reductions in brain 5-HT$_{1A}$ receptor binding have been described in anxiety disorders (Neumeister et al. 2004; Lanzenberger et al. 2007; for review, see Akimova et al. 2009), depression (Drevets et al. 1999, 2000; Meltzer et al. 2004; Hirvonen et al. 2008, but see Parsey et al. 2006b) (for review, see Drevets et al. 2007; Savitz et al. 2009), and schizophrenia (Tauscher et al. 2002; but see Frankle et al. 2006). Results on the effects of antidepressant treatment with selective serotonin reuptake inhibitors or electroconvulsive therapy on 5-HT$_{1A}$ binding are mixed (Moses-Kolko et al. 2007; Spindelegger et al. 2009; Saijo et al. 2010; Lanzenberger et al. 2012a). Increased 5-HT1A receptor binding has been observed in anorexia nervosa (Bailer et al. 2005, 2007) and post-traumatic stress disorder (Sullivan et al. 2013).

Several polymorphisms in 5-HT$_{1A}$ receptor gene (located on chromosome 5q11.2-q13; Fargin et al. 1989; Albert et al. 1990) have been studied for association with psychiatric disorders (for review, see Drago et al. 2008; Le Francois et al. 2008). The best studied polymorphism is a functional SNP in a palindromic region within the 5-HT$_{1A}$ promoter region (C($-$1019)G; rs6295; Wu and Comings 1999) that influences gene expression by modulating the interaction of the promoter with transcription factors. The C($-$1019)G *C*-allele has been associated with reduced 5-HT$_{1A}$ expression (Pernhorst et al. 2013) and was found to be associated with affective disorders in a recent meta-analysis (Kishi et al. 2012).

There is only limited evidence on the in vivo influence of the C($-$1019)G polymorphism on brain 5-HT$_{1A}$ receptor binding. One study did not show any effect of the C($-$1019)G polymorphism on brain 5-HT$_{1A}$ receptor binding but instead reduced 5-HT$_{1A}$ binding in carriers of the 5-HTTLPR short allele (David et al. 2005). Another study (Parsey et al. 2006b, c) showed increased binding of the selective 5-HT$_{1A}$ receptor radioligand [^{11}C]WAY100635 in carriers of the C($-$1019)G *G*-allele. This study also showed higher 5-HT$_{1A}$ receptor binding in antidepressant-naïve subjects. *GG*-homozygous subjects were overrepresented in the group of depressed patients in this study; however, the majority of studies find the low-expressing *C*-allele of C($-$1019)G to be overrepresented in major depression (Kishi et al. 2012). A recent study in a relatively large collective of healthy subjects (Lanzenberger et al. 2012b) did not show any effect of C($-$1019)G on brain [^{11}C]WAY100635 binding. Kautzky et al. (2017) also researched the C($-$1019)G polymorphism with [^{11}C]WAY100635 PET in 19 patients with MDD and 62 healthy volunteers. Receptor binding was calculated for ROIs, and a mixed model was applied that showed an interaction effect of seven ROIs (hippocampus, parahippocampus, medial and lateral

occipitomporal, inferior frontal occipital and rectal gyrus, and supplementary motor area) and genotype in patients but not healthy volunteers. Further, machine learning was used to classify genotypes but didn't result with significant predictions.

The literature also reports some studies that investigated the influence of the 5-HTTLPR polymorphism on 5-HT$_{1A}$ receptor binding in the brain (Table 6.2). Two studies (one of them was performed in a relatively large sample of nonhuman primates) describe lower 5-HT$_{1A}$ receptor binding in carriers of the low-expressing 5-HTTLPR *s*-allele (David et al. 2005; Christian et al. 2013). Two further studies describe higher 5-HT$_{1A}$ receptor binding in female carriers of the 5-HTTLPR *l*-allele (Lee et al. 2005; Borg et al. 2009), and a third study does not detect any effect of 5-HTTLPR on 5-HT$_{1A}$ receptor binding in a relatively large sample of healthy subjects (Borg et al. 2009). Finally, a fourth study (Kautzky et al. 2019) researched epistasis of risk alleles in both C($-$1019)G (5-HT$_{1A}$ gene) and Val66Met (BDNF gene) via [*carbonyl*-^{11}C]WAY-100635 PET imaging and observed an average of 17% increase in 5-HT$_{1A}$ receptor binding within risk genotypes. In sum, the evidence concerning the impact of genetic polymorphisms on 5-HT$_{1A}$ receptor binding in the brain is, as of yet, inconclusive.

6.2.7 The Serotonin 4 Receptor

The 5-HT$_4$ receptor is abundant in serotonin-rich areas of the brain like the basal ganglia and hippocampus (Waeber et al. 1996; Varnas et al. 2003) and plays a role in anxiety- and depression-like behavior. Studies in mice using autoradiography have shown that modification of 5-HTT gene expression was associated with alterations in 5-HT$_4$ density: 5-HTT knockout mice showed reduced 5-HT$_4$ density, and mice overexpressing 5-HTT showed increased 5-HT$_4$ density (Jennings et al. 2011). 5-HT$_4$ receptor expression and function seem to be influenced by extracellular serotonin levels, as increases in extracellular serotonin induced by paroxetine given for several weeks are associated with low 5-HT$_4$ levels (Licht et al. 2009; Vidal et al. 2009).

The PET radioligand [^{11}C]SB207145 is a newly developed selective tracer for imaging 5-HT$_4$ receptors in the human brain (Marner et al. 2009, 2010; Paterson et al. 2010). Since a study in healthy volunteers suggested that acute administration of citalopram does not alter binding of [^{11}C]SB207145 (Marner et al. 2010), it was speculated that [^{11}C]SB207145 PET could be a useful tool for indirectly measuring chronic, but not acute, changes in extracellular serotonin levels. Fisher et al. thus conducted a study on the effects of 5-HTTLPR on binding of the selective 5-HT$_4$ radioligand [11C]SB207145 in healthy subjects (Fisher et al. 2012). 5-HT$_4$ receptor binding in the neocortex was 9% lower in *s*-allele carriers compared to *l/l* homozygous subjects, providing further evidence that 5-HTTLPR genotype may influence serotonin transmission in humans. No effect of season or season-by-5-HTTLPR interaction on [11C]SB207145 binding was found in this sample. Limitations of this study are that l/l subjects were older than *s*-allele carriers and that datasets were collected on two different PET scanners with a significant effect of scanner type.

Table 6.2 Effects of polymorphisms on serotonin 1A (5-HT1A), serotonin 2A (5-HT2A), and serotonin 4 (5-HT4) receptor binding

	Polymorphism	Number of subjects[a]	Radioligand	Results	Region	Comment
David et al. (2005)	5HT1A C(−1019)G	35	[11C]WAY 100635 (5-HT1A)	No effect	5HT1A receptor-rich regions	Subjects also genotyped for 5-HTTLPR (see below)
Parsey et al. (2006b)	5HT1A C(−1019)G	71 (28 MDD)[b]	[11C]WAY 100635 (5-HT1A)	GG > CG > CC	Raphe nuclei	
Lanzenberger et al. (2012b)	5HT1A C(−1019)G	50	[11C]WAY 100635 (5-HT1A)	No effect	5HT1A receptor-rich regions	
Kautzky et al. (2017)	5HT1A C(−1019)G	81 (19 MDD)[b]	[11C]WAY 100635 (5-HT1A)	BP_{ND} GG < C	Dorsal raphe projections	No effect in healthy subjects
Kautzky et al. (2019)	5HT1A C(−1019)G/BDNF Val66Met	46	[11C]WAY 100635 (5-HT1A)	Increased BP_{ND} in GG/AA	Cortical surface	
David et al. (2005)	5-HTTLPR	35	[11C]WAY 100635 (5-HT1A)	ll > ls/ss	Widespread	Subjects also genotyped for 5-HT1A C(−1019)G (see above)
Lee et al. (2005)	5-HTTLPR	16	[11C]WAY 100635 (5-HT1A)	ll < ls/ss	Anterior cingulum	All female study sample
Borg et al. (2009)	5-HTTLPR	54	[11C]WAY 100635 (5-HT1A)	No effect	–	5-HTTLPR effects cognitive performance
Lothe et al. (2009)	Triallelic 5-HTTLPR	38	[18F]MPPF (5-HT1A)	La carriers <ss, females only	Widespread except raphe nuclei	No genotype effect in males (n = 13)
Fisher et al. (2012)	Triallelic 5-HTTLPR	47	[11C]SB207145 (5-HT4)	ll > ls/ss	Neocortex	ll Subjects older than ls/ss
Henningsson et al. (2009)	BDNF Val66Met	53	[11C]WAY 100635 (5-HT1A)	No effect	Cortex and pons	
Klein et al. (2010)	BDNF Val66Met	133	[18F]altanserin (5-HT2A)	No effect	Cortex	

Adapted from Willet and Praschak-Rieder (2010)

[a]Healthy subjects if not otherwise indicated

[b]*MDD* major depressive disorder

6.2.8   The Serotonin 2C Receptor

Serotonin binding to the 5-HT2C receptor causes inhibition of dopamine release in specific areas of the brain, such as the striatum, prefrontal cortex, nucleus accumbens, and the hippocampus (Alex et al. 2005). The receptor has therefore been implemented in the regulation of mood, anxiety, stress, and pain. An abundant missense SNP in the 5-HT2C receptor gene (HTR2C) (rs6318, Cys23Ser) has previously been linked to an in vitro activity change and also with mood disorders in humans. A group (Mickey et al. 2012) studied 54 healthy adults using PET and [^{11}C]raclopride and detected increased dopamine release in the nucleus accumbens, caudate nucleus, and putamen in Ser23 carriers, after controlling for sex, age, and ethnicity, but there was no connection of Cys23Ser with baseline BPND.

6.3   Dopamine

Due to their preeminent role in addiction and psychotic disorders, brain dopamine systems have been extensively studied with PET and SPECT imaging techniques in psychiatric populations (see Cumming 2009 for in-depth review of dopamine imaging). Dopamine neurons in the brain originate almost exclusively in the brainstem substantia nigra and the more medially located ventral tegmental area. Important projection areas for dopamine neurons are the frontal cortex and subcortical structures, especially the striatum. The best studied dopaminergic region in the brain is the striatum, since it has a high density of dopamine nerve terminals and is thus a region that is particularly well suited for PET and SPECT imaging. Frequently targeted molecules are G-protein-coupled postsynaptic dopamine receptors and the dopamine transporter (DAT).

6.3.1   Dopamine D$_{2/3}$ Receptors

According to their effects on postsynaptic levels of cyclic adenosine monophosphate (cAMP), dopamine receptors are grouped into two families, the D$_1$ receptor family (dopamine D$_1$ and D$_5$ receptors) and the D$_2$ receptor family (dopamine D$_2$, D$_3$, and D$_4$ receptors). As the main target of antipsychotic medication, dopamine D$_{2/3}$ receptors have been of particular interest for imaging studies in schizophrenia. Moreover, D$_{2/3}$ receptor imaging techniques have successfully been used to demonstrate alterations in brain dopamine transmission in addictive disorders (Volkow et al. 2009; Urban and Martinez 2012). While current evidence speaks against a relevant alteration in the quantity of D$_{2/3}$ receptors that are accessible to PET imaging in schizophrenia (Howes et al. 2012), several studies have shown a reduction of D$_{2/3}$ binding in addictive disorders (Volkow et al. 2009; Urban and Martinez 2012).

There are several studies on the influence of genetic variation on D$_{2/3}$ receptor binding in the literature (Table 6.4; for review, see Willeit and Praschak-Rieder 2010). To our knowledge, the only replicated finding as of yet is a reduction in

binding of the $D_{2/3}$ radioligand [^{11}C]raclopride in carriers of the Taq1 A1 allele as compared to A2 homozygotes (Pohjalainen et al. 1998; Jonsson et al. 1999; Joutsa et al. 2014). However, a study of this polymorphism with SPECT and the radioligand [^{123}I]IBZM did not show differences between the genotypic groups (Laruelle et al. 1998). Other polymorphisms in the D2 receptor gene showed in part significant effects but still warrant replication (Table 6.3). A recent study investigated a possible association between polymorphisms in the Period2 (PER2) gene and dopamine $D_{2/3}$ receptor binding as measured using [^{11}C]raclopride and PET (Shumay et al. 2012a). PER2 is part of the clock-gene family and involved in the reaction of organisms to circadian and circannual changes in lighting conditions and day length. Dopamine transmission shows circadian and seasonal changes in rodents and humans (Castaneda et al. 2004; Tsai et al. 2011; Eisenberg et al. 2010). The authors report on a newly identified VNTR polymorphism in the human PER2 gene that was associated with cocaine craving and striatal dopamine $D_{2/3}$ receptor binding. This finding is so far very exciting as it brings together several research strings on the physiology of dopamine function and its implication in addiction (see also Praschak-Rieder and Willeit 2012 for further discussion).

The effect of the BDNF Val(66)Met polymorphism, priorly implicated in MDD (see above), on dopamine-mediated responses to stress, cognitive regulation, and anticipatory responses in ventral tegmental area (VTA) and nucleus accumbens (NAc) circuitry were researched in a different study (Peciña et al. 2014) via [^{11}C]raclopride PET scans with or without placebo administration of a potentially analgesic substance. A significant effect of BDNF Val(66)Met was demonstrated on baseline D2/3 receptor availability and pain-stress-induced dopamine release in the NAc and responses to anticipation of monetary losses (Met > Val/Val). On the other hand, met carriers didn't react to monetary gains and presented with attenuated dopamine response to analgesic placebo in NAc. This study provides first human evidence on the effect of BDNF Val(66)Met on dopaminergic responses.

6.3.2 The Dopamine Transporter

Another frequently studied target is the dopamine transporter (DAT), a member of the monoamine transporter family that transports dopamine back into the presynaptic neuron immediately after its release into the extracellular space. DAT is the main target of therapeutic drugs, for example, methylphenidate, used to treat attention-deficit hyperactivity disorder (ADHD) or the antidepressant bupropion. DAT is also the main site of action of drugs of abuse such as cocaine or amphetamines. Radiolabeled DAT blockers such as [^{11}C]methylphenidate or [^{11}C]cocaine have successfully been used to quantify DAT availability in the human brain.

Several polymorphisms within the DAT gene or in its promoter region have been identified and studied for association with psychiatric disorders, and there is extensive literature on imaging the effects of some of these polymorphisms on DAT binding in the human brain (Willeit and Praschak-Rieder 2010). The most frequently imaged polymorphism is a 40-bp (base pair) VNTR (variable number of tandem

Table 6.3 Effects of dopamine D2 receptor polymorphisms on D2 receptor binding, dopamine transporter (DAT) binding, and dopamine synthesis

	Polymorphism	Number of subjects[a]	Radioligand	Results	Region	Comment
Pohjalainen et al. (1998)	Taq1 A	54	[^{11}C]raclopride (2 scans)	A1 carriers < A2/A2	Striatum	No effect on D2 affinity
Laruelle et al. (1998)	Taq1 A, Taq1 B	70 (23 SCZ)[b]	[^{123}I]IBZM	No effect	Striatum	
Jönsson et al. (1999)	Taq1 A	56	[^{11}C]raclopride	A1 carriers < A2/A2	Striatum	
	Taq1 B			B1 carriers < B2/B2		
	$-^{141}$C Ins/Del			Del carriers > Ins/Ins		
Pohjalainen et al. (1999)	$-^{141}$C Ins/Del	52	[^{11}C]raclopride	No effect	Striatum	Same sample as in Pohjalainen et al. (1998)
Hirvonen et al. (2004)	C957T	45	[^{11}C]raclopride	T/T > C/T > CC	Striatum	Same sample as in Pohjalainen et al. (1998)
Hirvonen et al. (2009)	C957T	45	[^{11}C]raclopride (2 scans)	Effect on affinity: K_D C/C > C/T > TT	Striatum	Same sample as in Pohjalainen et al. (1998)
				No effect on B_{max}		
Bertolino et al. (2010)	D2 rs1076560 (G > T)	37	[^{123}I]IBZM	D2 binding T < G	Striatum	Effect on correlation between D_2 binding and prefrontal activity
			[^{123}I]FP-CIT	DAT binding T < G		
Laakso et al. (2005)	Taq1 A	33	[^{18}F]FDOPA	Higher uptake in A1 carriers; no effect of $-^{141}$C Ins/Del, C957T	Striatum	
	$-^{141}$C Ins/Del					
	C957T					
Laine et al. (2001)	Taq1 A	29 AD[c]	[^{123}I] ß-CIT	Higher DAT binding in A1 carriers	Striatum	

(continued)

Table 6.3 (continued)

	Polymorphism	Number of subjects[a]	Radioligand	Results	Region	Comment
Sambataro et al. (2011)	D2 rs1076560 (G > T)	28	[^{123}I]FP-CIT	No effect	Striatum	
Shumay et al. (2012a)	PER2 (Period2)	52	[^{11}C]raclopride	Higher binding in 4R and 3R homozygotes	Striatum	Clock-gene family
Joutsa et al. (2014)	Taq1 A	24 (12[d])	[^{11}C]raclopride	A1 carriers < A2/A2	Striatum	Especially for high-reward gambling

Adapted from Willeit and Praschak-Rieder (2010)
[a]Healthy subjects if not otherwise indicated
[b]Schizophrenia
[c]Alcohol dependence
[d]Pathologic gamblers

repeats) polymorphism in the 3′ untranslated region of exon 15 of the DAT gene SLC6A3 (Vandenbergh et al. 1992, 2000). These studies included healthy subjects as well as patients with alcohol dependence, schizophrenia, ADHD, and Parkinson's disease (Heinz et al. 2000a; Jacobsen et al. 2000; Martinez et al. 2001; Lynch et al. 2003; Cheon et al. 2005; van Dyck et al. 2005; Krause et al. 2006; Lafuente et al. 2007; van de Giessen et al. 2009; Kasparbauer et al. 2015; Table 6.4). A recent methodologically sound meta-analysis (Costa et al. 2011) provides no evidence to support the hypothesis that the DAT 40-bp VNTR is significantly associated with interindividual differences in DAT availability in the striatum. A SPECT study investigating a cluster of polymorphisms flanking a recently described splice variant in the DAT gene (Talkowski et al. 2010) did not show significant differences in [^{123}I]-β-CIT binding (van de Giessen et al. 2012). Another group (Pak et al. 2018) investigated impacts of 19 different SNPs previously implicated in Parkinson's disease on DAT and SERT availability with ^{123}I-FP-CIT SPECT. None of the tested SNPs impacted DAT availability but SERT availability in midbrain and pons ($p = 0.0007$) of healthy males was significantly influenced by rs591323 in Fibroblast Growth Factor 20 on chromosome 8. In summary, the results of these studies give no clear picture on the effects of the DAT 40-bp VNTR polymorphism. However, the number of studies is relatively small, and there is significant heterogeneity between the studies.

6.3.3 Measuring Dopamine Transporter Function

Radiolabeled dopamine precursors able to cross the blood-brain barrier (e.g., [^{18}F]dihydroxyphenylalanine, [^{18}F]DOPA) are converted into the DAT substrate [^{18}F]dopamine in dopaminergic neurons. The striatal [^{18}F]DOPA influx constant Ki reflects presynaptic dopamine uptake, synthesis, and storage capacity and is regarded as a good proxy for presynaptic dopamine metabolism in the brain (Cumming 2009). Together with so-called "competition" paradigms, a research technique that allows for measuring the inhibition of radioligand binding at D$_{2/3}$ receptors by endogenous dopamine, [^{18}F]DOPA studies have now clearly shown that presynaptic dopamine synthesis capacity (Reith et al. 1994; Hietala et al. 1995, 1999; Lindstrom et al. 1999; Meyer-Lindenberg et al. 2002; McGowan et al. 2004; Kumakura et al. 2007; Bose et al. 2008; Nozaki et al. 2009), baseline synaptic dopamine levels (Abi-Dargham et al. 2000, 2009; Kegeles et al. 2010; Weidenauer et al. 2020), and pharmacologically induced dopamine release (Laruelle et al. 1996; Breier et al. 1997; Abi-Dargham et al. 1998, 2009) are increased in schizophrenia (for review, see Howes et al. 2012).

Imaging measures of the hyper-dopaminergic state in schizophrenia can as well be conceptualized as an endophenotype of the disorder. Indeed, there are a number of studies on the genetic background of in vivo imaging measures of presynaptic

Table 6.4 Effects of polymorphisms within the dopamine transporter gene SLC6A3 on in vivo dopamine transporter binding in humans

	Polymorphism	Number of subjects[a]	Radioligand	Results	Region	Comment
Heinz et al. (2000a)	DAT 3′ VNTR	25 (14 AD)[b]	[^{123}I]-β-CIT	9-repeat carriers <10/10	Putamen	Alcohol not associated with DAT binding genotype
Jacobsen et al. (2000)	DAT 3′ VNTR	44 (14 CA)[c]	[^{123}I]-β-CIT	9-repeat carriers >10/10	Striatum	5-HTTLPR not associated with [^{123}I]-β-CIT binding in midbrain
Martinez et al. (2001)	DAT 3′ VNTR	43 (22 SCZ)[d]	[^{123}I]-β-CIT	No effect	Striatum	No genotype effect on amphetamine-induced dopamine release
Lynch et al. (2003)	DAT 3′ VNTR	166 (100 PD)[e]	[^{99m}Tc]TRODAT-1	No effect	Striatum	Also no effect of COMT and MAO-B polymorphisms
Van Dyck et al. (2005)	DAT 3′ VNTR	96	[^{123}I]-β-CIT	9-repeat carriers >10/10	Striatum	
Cheon et al. (2005)	DAT 3′ VNTR	11 children with ADHD[f]	[^{123}I] IPT	9-repeat carriers <10/10	Basal ganglia	Response to methylphenidate better in 9-repeat-allele carriers
Krause et al. (2006)	DAT 3′ VNTR	22 ADHD[f]	[^{99m}Tc]TRODAT	No effect	Striatum	
Lafuente et al. (2007)	DAT 3′ VNTR	15 SCZ[d]	[^{123}I] FP-CIT	No effect	Striatum	
van de Giessen et al. (2009)	DAT 3′ VNTR	79	[^{123}I]-β-CIT	9-repeat carriers >10/10	Striatum	Haplotype 5′ T-A 3′ 9R highest DAT binding
	DAT 5′ VNTR					

Drgon et al. (2006)	DAT 5′ VNTR (rs2652511, rs2937639)	15 (6 ADHD)[f]	[11C]-cocaine PET	C-G > T-A	Ventral striatum	5′ C-G combination confirmed postmortem
Szobot et al. (2010)	DAT 3′ VNTR DRD4 48-bp VNTR	17 ADHD[f]	[99mTc]TRODAT	Reduced occupancy in DAT10R homozygotes/ DRD4-7R carriers	Striatum	Subjects scanned before and after 3 weeks of methylphenidate treatment
Kasparbauer et al. (2015)	DAT 3′ VNTR	35	[123I] FP-CIT	9-repeat carriers >10/10	Striatum	Methylphenidate induced increase of blood oxygen for 9R carriers

Adapted from Willeit and Praschak-Rieder (2010)

[a]Healthy subjects if not otherwise indicated

[b]AD Alcohol dependence

[c]CA Cocaine abuse

[d]Schizophrenia

[e]Parkinson's disease

[f]Attention-deficit hyperactivity disorder

dopamine function (Table 6.5). These studies investigated the influence of polymorphisms in the DAT gene (Martinez et al. 2001; Brody et al. 2006), in D_2 and D_3 receptor-related genes (Brody et al. 2006; Peciña et al. 2012; Savitz et al. 2013), in the gene coding for oxytocin (Love et al. 2012), in the μ-opioid receptor gene (Domino et al. 2010), leptin gene (Burghardt et al. 2012), and AKT1 gene (Shumay et al. 2017) on DAT function. In these studies, dopamine release was induced either by administration of d-amphetamine, by nicotine from cigarettes or by behavioral stimuli such as stress and pain. All of the abovementioned studies describe an association with reductions in $D_{2/3}$ radioligand binding (as an indirect measure for dopamine release) and the respective candidate genes. Although there emerges no consistent picture due to the variety of polymorphisms and the different methods used, all of these studies were able to show that results of "competition studies" are in part driven by genetic variation. Some of the information collected in these studies might thus be used for refining future studies in patients with schizophrenia. Perhaps even more important, these studies were able to show that several neurochemical pathways are involved in regulating dopamine release in the living human brain. Regulatory mechanisms include feedback regulation in dopamine terminal fields (see, e.g., Savitz et al. 2013, brain opioid systems (Domino et al. 2010), and the neuropeptide oxytocin (Love et al. 2012)).

6.4   Other Polymorphisms

6.4.1   The Catechol-O-methyltransferase Val158Met Polymorphism

Catechol-O-methyltransferase (COMT) is an enzyme that catalyzes degradation of catecholamines (including epinephrine, norepinephrine, and dopamine) in the periphery and the brain. While regulation of extracellular dopamine levels is heavily dependent on DAT function in subcortical brain areas, COMT is believed to be a key mechanism regulating dopamine activity in cortical, especially frontal cortical brain areas (Ciliax et al. 1999; Lewis et al. 2001; Matsumoto et al. 2003).

Several SNPs have been described in the COMT gene, but without doubt, the SNP causing a valine-to-methionine substitution at position 158 (COMT Val158Met) is one of the most studied polymorphisms in psychiatry and a series of other disorders. The COMT 158Val variant degrades dopamine more efficiently than the COMT 158Met variant (Lachman et al. 1996), and the polymorphism has been associated with several psychiatric and other disorders. A finding that seems to hold true is a difference in executive function mediated mainly by prefrontal cortex dopamine between carriers of the gene variants. Thus, several studies have investigated behavioral, cognitive, functional, and anatomical variance associated with this gene as an endophenotype in various disorders (see, e.g., Schosser et al. 2011; Witte and Floel 2011; Ira et al. 2013).

Two studies investigated the effects of COMT Val158Met using [^{18}F]DOPA and PET. A study (Meyer-Lindenberg et al. 2005) in healthy volunteers found increased

Table 6.5 Effects of genetic polymorphisms on dopamine-induced reductions in $D_{2/3}$ receptor binding

	Polymorphism	Number of subjects[a]	Outcome measure	Results	Region	Comment
Martinez et al. (2001)	DAT 3′ VNTR	59 (28 SCZ)[b]	d-Amphetamine-induced decrease in [^{123}I]IBZM binding	No effect	Striatum	Greater reductions in patients; trend for greater reductions in 9-repeat carriers
Brody et al. (2006)	DAT 3′ VNTR, D2 Taq A1/A, D4 VNTR, COMT Val158Met	45	Nicotine-induced decrease in [^{11}C]raclopride binding	DAT: 9R > 10/10R D2: no effect D4: greater in <7R Val/Val > Met	Striatum	
Peciña et al. (2012)	D2 rs4274224 (A > G)	52	Stress-induced decrease in [^{11}C] raclopride binding	AG > AA/GG	Caudate, putamen, ventral striatum	
Savitz et al. (2013)	D3 Ser9Gly	36 (10 MDD)[c]	Reward-induced decrease in [^{11}C] raclopride binding	Gly > Ser	Caudate, ventral striatum	No genotype effect on baseline $D_{2/3}$ binding
Love et al. (2012)	Oxytocin Rs4813625	55	Pain-stress-induced decrease in [^{11}C] raclopride binding	GC/CC > GG	Ventromedial caudate	Significant effects in females (n = 32) but not males
Domino et al. (2012)	μ-Opioid 1 receptor A118G	19 males	Nicotine-induced decrease in [^{11}C]carfentanyl binding	AG/GG > AA	Caudate, ventral putamen	Significant effect of the polymorphism also on plasma cortisol levels
Burghardt et al. (2012)	Leptin rs12706832	50	Stress/pain -induced [^{11}C] raclopride binding	GG > AG/AA	Caudate, putamen, ventral striatum, Nucl. accumbens	Plasma leptin levels also correlated to challenged dopamine release.
Shumay et al. (2017)	AKT1 VNTR	91; 54	Baseline DRD2 availability; methylphenidate-induced dopamine release	LL > HL > HH	Caudate, Putamen	Only in ventral striatum, highest in HH > HI > LL

[a]Healthy subjects if not otherwise indicated
[b]SCZ schizophrenia
[c]MDD major depressive disorder

striatal [^{18}F]DOPA uptake in 158Val carriers when compared to 158Met homozygotes. Another study in patients with early Parkinson's disease (Wu et al. 2012) describes higher [^{18}F]DOPA uptake measured between 150 and 210 min after radioligand injection in 158Met homozygous patients. Besides differences between study samples (young healthy volunteers versus patients with Parkinson's disease), the difference might be due to the fact that higher [^{18}F]DOPA in 158VMet homozygous patients with Parkinson's disease was measured from 150 min after tracer injection onward. At this time, the [^{18}F]DOPA signal is believed to reflect rates of dopamine metabolism to 3,4-dihydroxyphenylacetic acid and homovanillic acid (Ruottinen et al. 2001; Ceravolo et al. 2002).

A study in healthy volunteers investigated the effects of COMT Val158Met on dopamine $D_{2/3}$ receptor binding using PET and the radioligands [^{11}C]raclopride and [^{11}C]FLB457 for assessing striatal and cortical $D_{2/3}$ binding, respectively. Since genotype had no effect on binding of either radioligand, the authors concluded that baseline in vivo $D_{2/3}$ receptor availability does not differ between COMT Val158Met genotypic groups. In contrast, another study using the dopamine D_1 receptor radioligand [^{11}C]NNC112 (Slifstein et al. 2008) found significantly higher cortical D_1 receptor binding in Val158 homozygotes, while no difference was found in striatum. This finding is in good agreement with the functional role of COMT Val158Met, as low dopamine levels have been found to cause upregulation of dopamine D_1 receptors in the rodent brain, while dopamine transmission in the basal ganglia is less affected due to the prominent role of DAT in these brain areas (Gogos et al. 1998; Guo et al. 2003). Hernaus et al. investigated the effect of COMT Val158Met on prefrontal [^{18}F]fallypride displacement in PET and subjective stress response to a psychosocial stress challenge in a mixed sample of healthy volunteers and healthy first-degree relatives of patients with psychotic disorders (Hernaus et al. 2013). They showed less [^{18}F]fallypride displacement in Val/Met and Met/Met than Val/Val and Met-allele carriers also experienced larger subjective stress responses than Val-homozygotes. Separated analysis for controls/ first-degree relatives didn't change the direction of these effects. A different group performed [^{11}C]FLB 457 PET in healthy controls to investigate dopamine release in the PFC and were neither able to show a relationship between COMT genotype and dopamine release nor COMT genotype and baseline D2/3 receptor BPND (Narendran et al. 2016). A study investigating the effects of the COMT Val158Met polymorphism on brain 5-HT$_{1A}$ receptor binding found significantly higher [^{11}C]WAY100635 binding in Val158 homozygotes in orbitofrontal and cingulate cortex, insula, and amygdala (Baldinger et al. 2014). Peak differences were found in the posterior cingulate cortex.

6.4.2 Monoamine Oxidase A

Monoamine oxidase is an enzyme that catalyzes the oxidative degradation of biogenic amines. There are two isoforms, MAO-A and MAO-B. MAO-A has high affinity for serotonin, norepinephrine, and epinephrine. MAO-B mainly degrades phenethylamine, a so-called trace amine. Dopamine is a substrate of both

isoenzymes (Kalgutkar et al. 2001). The gene for MAO-A is located on the X chromosome (Xp11.23–11.4). A rare loss-of-function mutation of the gene is associated with behavioral features such as impulsive aggression, hypersexuality, and reduced intelligence (Brunner et al. 1993). A polymorphism in the promoter region of the MAO-A gene affecting transcriptional activity (Sabol et al. 1998) has been linked to aggressive or antisocial behavior in subjects exposed to childhood maltreatment (Caspi et al. 2002; Fergusson et al. 2011) or brain injury (Pardini et al. 2011). The polymorphism consists of a 30-bp repeat sequence present in three to five copies and is termed MAO-A *high* and *low* according to the amount of MAO-A produced in cell lines. As the polymorphism is located on the X chromosome, males are hemizygous for either the MAO-A *high* or *low* allele.

Radioligands for quantifying MAO-A activity in the brain are modified MAO-A inhibitors such as [^{11}C]clorgyline (MacGregor et al. 1985) or [^{11}C]harmine (Bergstrom et al. 1997; Ginovart et al. 2006). Both radioligands have successfully been used to study the role of MAO-A in aggression (Alia-Klein et al. 2008) or affective disorders (Meyer et al. 2006; Sacher et al. 2010).

To our knowledge, there are no studies published on the effects of genetic heterogeneity on [^{11}C]harmine binding in the human brain. A study investigating the MAO-A *high/low* polymorphism in 38 healthy subjects using [^{11}C]clorgyline (Fowler et al. 2007) did not find any relationship between genotype and the brain [^{11}C]clorgyline binding. Males are hemizygous for this polymorphism (the MAO-A gene is located on the X chromosome); the effects of this polymorphism, if functional in vivo, should therefore be clearest in a male-only sample. A possible explanation for the negative finding is epigenetic regulation: methylation of the MAO-A promoter has indeed been shown to have a clear influence on brain [^{11}C]clorgyline distribution volumes (Shumay et al. 2012b). Another study investigating the effects of this polymorphism on binding of the 5-HT$_{1A}$ receptor radioligand [^{11}C]WAY 100635 (Mickey et al. 2008) found higher binding in females carrying the MAO-A *high* allele. No genotype effect was found in males.

6.4.3 18-kD Translocator Protein

Immune cells express an 18-kD translocator protein (TSPO) formerly known as the peripheral benzodiazepine receptor (Anholt et al. 1986). Expression of TSPO has been studied as a marker of microglia activation and inflammation in various disorders, including Alzheimer's disease, multiple sclerosis, frontotemporal dementia, and schizophrenia (Debruyne et al. 2002; Cagnin et al. 2004; Edison et al. 2008; Kreisl et al. 2012) using a variety of TSPO radioligands. The TSPO radioligand [^{11}C]PBR28 was observed to bind to TPSO with high affinity in some subjects, with low affinity in others and with intermediate affinity in a third group (Fujita et al. 2008; Kreisl et al. 2009; Owen et al. 2010, 2011), an observation that has been related to a polymorphism (rs6971) affecting binding of the radioligand PBR28 to TSPO in human platelets (Owen et al. 2011).

A study using the TSPO radioligand [^{18}F]FEPPA (Wilson et al. 2008) has shown clear effects of the rs6971 polymorphism in the human brain (Mizrahi et al. 2012). Another study using the radioligand [^{11}C]PBR28 confirmed these effects and showed increased [^{11}C]PBR28 binding in patients with schizophrenia when accounting for genotype effects (Kreisl et al. 2012). This study showed that data on TSPO binding need to be stratified by genotype in order to get information on TSPO expression in various disorders.

6.4.4 Translocase of Outer Mitochondrial Membrane 40 (TOMM40)

The encoded protein of the translocase of outer mitochondrial membrane 40 gene (TOMM40) is a channel-forming subunit of the translocase that is essential for import of protein precursors to mitochondria. Different splice variants of the gene have been identified and linked to Alzheimer's disease because of its linkage disequilibrium with the apolipoprotein E gene and its neurotoxic potential (Roses 2010). Morphology changes of the medial temporal lobe manifest early within the disease progression of Alzheimer's disease. A group (Siddarth et al. 2018) therefore researched the effects of the two genes via regional brain PET with 2-(1-{6-[(2 [F18]fluoroethyl) (methyl) amino]-2-naphthyl}ethylidene)malononitrile (FDDNP) in the medial temporal lobe. FDDNP binding differed significantly between groups and TOMM40 S/S exhibited significantly lower binding compared to TOMM40 S/VL and APOE-4 carriers.

6.4.5 AKT1

AKT1 is a protein kinase, also referred to as protein kinase B (PKB), that can be found in different cell types of the human body and is involved in various signaling pathways, such as cell apoptosis, proliferation, differentiation, and metabolism. The AKT1 gene is located on chromosome 14 (14q32.33), and somatic mutations have been implemented for different types of cancer. Further, several polymorphisms in the AKT1 gene have been linked to schizophrenia and dopamine neurotransmission, which might be due to the function of AKT1 in G-protein-independent DA receptor signaling, particularly internalization and desensitization of the receptor (Li et al. 2016). The AKT1 activity is further inversely regulated by extracellular DA content, and binding to the DRD2 induces phosphorylation of AKT1 (Zheng et al. 2013; Jönsson et al. 1999).

A fairly recently discovered variant number of tandem repeat (VNTR) polymorphism in AKT1, intron3 [major alleles: L- (eight repeats), H- (nine repeats)], has lately been tied to striatal dopamine D2/3 receptor availability and dopamine release in a healthy cohort. The high CG content of the gene (amenability to DNA methylation) and the location of the considered polymorphism within the nucleosome exclusion region highlight its susceptibility to epigenetic modification.

Shumay et al. used [^{11}C]raclopride and PET to determine baseline D2R availability and methylphenidate-induced dopamine release. LL phenotypes showed higher D2R availability than HH in caudate and putamen but not ventral striatum. Dopamine increases further were stronger in the ventral striatum in HH phenotypes, but no increases were observed in caudate or putamen after methylphenidate administration (Shumay et al. 2017). These results suggest a modulating role of AKT1 in striatal dopamine signaling but lack conclusions for schizophrenia or acute (drug-induced) psychoses.

The finding that AK1−/− mice present with an amplified reaction to amphetamine and ketamine (Emamian et al. 2004; Featherstone 2013) leads to the belief that a reduced AKT function might cause a supersensitive DA state. Therefore, the HH allele of the gene, for which increased DA release in VS was demonstrated, might serve as a marker for schizophrenia and other psychotic disorders.

6.5   Summary and Outlook

This review shows that combining genetic research with neuroreceptor imaging using PET and SPECT has produced a large array of findings suggesting effects of genetic variants on protein expression in the living brain. Some genetic effects, for example, those of polymorphisms in the TSPO gene, seem strong enough as to produce plausible results with large effect sizes in PET imaging studies. Other results, such as those on the effects of 5-HTTLPR on 5-HTT binding or Taq1 A on dopamine $D_{2/3}$ receptor binding in the brain, show less clear-cut effects, and despite having been replicated independently, they are contrasted by studies with differing or negative results. Many studies in the field either are not replicated at all or are replicated with slightly different imaging methods or in differing study collectives, thus creating a "penumbra" of a 0.05 significance level (Kapur et al. 2012) around the original findings without being able to answer the question whether a certain genetic variant does really have an effect on protein binding in the brain.

The way genetic research in psychiatry is conducted has changed dramatically in the last years. Typical studies at the beginning of this research had sample sizes in the low three-digit number range. The picture that emerged from these studies was quite similar to what we see in PET and SPECT imaging genetics today: many significant findings, few replications, and no definite answers on candidate gene loci. Researchers have thus started to combine their efforts and to implement logistics for large international consortia that are able to collect data from tens or hundreds of thousands of subjects (Sullivan 2010). Similar efforts have been made in the field of MRI-based imaging genetics (the IMAGEN consortium started in 2007 is a good example; http://www.imagen-europe.com).

The single most important limitation of all studies reviewed here is a lack of power. Sample sizes in PET and SPECT imaging genetic studies are maybe even a bit larger than those in other PET and SPECT studies, most probably because genotyping is sometimes used to extract some additional scientific output from already existing projects sharing a radioligand (the mean sample size in the here reported

studies is 44 subjects, the range 11–166). Still, due to the relatively small effect of most genetic variants and the large number of other factors influencing availability of target receptors, much larger samples would be needed to have adequately powered studies in this field. Neuroreceptor PET is an expensive and logistically difficult research technology available in a limited number of research centers around the world. It is time for the field to follow the example of other research areas and to start combining efforts and cooperate. This would benefit not only imaging genetics but also all other research topics addressed with PET and SPECT imaging techniques.

References

Abi-Dargham A, Gil R, Krystal J et al (1998) Increased striatal dopamine transmission in schizophrenia: confirmation in a second cohort. Am J Psychiatry 155(6):761–767

Abi-Dargham A, Rodenhiser J, Printz D et al (2000) Increased baseline occupancy of D2 receptors by dopamine in schizophrenia. Proc Natl Acad Sci U S A 97(14):8104–8109

Abi-Dargham A, van de Giessen E, Slifstein M, Kegeles LS, Laruelle M (2009) Baseline and amphetamine-stimulated dopamine activity are related in drug-naive schizophrenic subjects. Biol Psychiatry 65(12):1091–1093

Akimova E, Lanzenberger R, Kasper S (2009) The serotonin-1A receptor in anxiety disorders. Biol Psychiatry 66(7):627–635

Albert PR, Zhou QY, Van Tol HH, Bunzow JR, Civelli O (1990) Cloning, functional expression, and mRNA tissue distribution of the rat 5-hydroxytryptamine1A receptor gene. J Biol Chem 265(10):5825–5832

Alex KD, Yavanian GJ, McFarlane HG et al (2005) Modulation of dopamine release by striatal 5-HT2C receptors. Synapse 55(4):242–251

Alia-Klein N, Goldstein RZ, Kriplani A et al (2008) Brain monoamine oxidase A activity predicts trait aggression. J Neurosci 28(19):5099–5104

Anguelova M, Benkelfat C, Turecki G (2003) A systematic review of association studies investigating genes coding for serotonin receptors and the serotonin transporter: II. Suicidal behavior. Mol Psychiatry 8(7):646–653

Anholt RR, Pedersen PL, De Souza EB, Snyder SH (1986) The peripheral-type benzodiazepine receptor. Localization to the mitochondrial outer membrane. J Biol Chem 261(2):576–583

Bailer UF, Frank GK, Henry SE et al (2005) Altered brain serotonin 5-HT1A receptor binding after recovery from anorexia nervosa measured by positron emission tomography and [carbonyl11C]WAY-100635. Arch Gen Psychiatry 62(9):1032–1041

Bailer UF, Frank GK, Henry SE et al (2007) Exaggerated 5-HT1A but normal 5-HT2A receptor activity in individuals ill with anorexia nervosa. Biol Psychiatry 61(9):1090–1099

Baldinger P, Hahn A, Mitterhauser M et al (2014) Impact of COMT genotype on serotonin-1A receptor binding investigated with PET. Brain Struct Funct 219(6):2017–2028

Bel N, Artigas F (1992) Fluvoxamine preferentially increases extracellular 5-hydroxytryptamine in the raphe nuclei: an in vivo microdialysis study. Eur J Pharmacol 229(1):101–103

Bergstrom M, Westerberg G, Langstrom B (1997) 11C-harmine as a tracer for monoamine oxidase A (MAO-A): in vitro and in vivo studies. Nucl Med Biol 24(4):287–293

Bertolino A, Taurisano P, Pisciotta NM et al (2010) Genetically determined measures of striatal D2 signaling predict prefrontal activity during working memory performance. PLoS One 5(2):e9348

Bondy B, Buettner A, Zill P (2006) Genetics of suicide. Mol Psychiatry 11(4):336–351

Borg J, Henningsson S, Saijo T et al (2009) Serotonin transporter genotype is associated with cognitive performance but not regional 5-HT1A receptor binding in humans. Int J Neuropsychopharmacol 12(6):783–792

Bose SK, Turkheimer FE, Howes OD et al (2008) Classification of schizophrenic patients and healthy controls using [18F] fluorodopa PET imaging. Schizophr Res 106(2–3):148–155

Breier A, Su TP, Saunders R et al (1997) Schizophrenia is associated with elevated amphetamine-induced synaptic dopamine concentrations: evidence from a novel positron emission tomography method. Proc Natl Acad Sci U S A 94(6):2569–2574

Brody AL, Mandelkern MA, Olmstead RE et al (2006) Gene variants of brain dopamine pathways and smoking-induced dopamine release in the ventral caudate/nucleus accumbens. Arch Gen Psychiatry 63(7):808–816

Brunner HG, Nelen MR, van Zandvoort P et al (1993) X-linked borderline mental retardation with prominent behavioral disturbance: phenotype, genetic localization, and evidence for disturbed monoamine metabolism. Am J Hum Genet 52(6):1032–1039

Brunoni AR, Lopes M, Fregni F (2008) A systematic review and meta-analysis of clinical studies on major depression and BDNF levels: implications for the role of neuroplasticity in depression. Int J Neuropsychopharmacol 11(8):1169–1180

Buchert R, Schulze O, Wilke F et al (2006) Is correction for age necessary in SPECT or PET of the central serotonin transporter in young, healthy adults? J Nucl Med 47(1):38–42

Burghardt PR, Love TM, Stohler CS et al (2012) Leptin regulates dopamine responses to sustained stress in humans. J Neurosci 32(44):15369–15376

Cagnin A, Rossor M, Sampson EL, Mackinnon T, Banati RB (2004) In vivo detection of microglial activation in frontotemporal dementia. Ann Neurol 56(6):894–897

Caspi A, Hariri AR, Holmes A, Uher R, Moffitt TE (2010) Genetic sensitivity to the environment: the case of the serotonin transporter gene and its implications for studying complex diseases and traits. Am J Psychiatry 167(5):509–527

Caspi A, McClay J, Moffitt TE et al (2002) Role of genotype in the cycle of violence in maltreated children. Science 297(5582):851–854

Caspi A, Sugden K, Moffitt TE et al (2003) Influence of life stress on depression: moderation by a polymorphism in the 5-HTT gene. Science 301(5631):386–389

Castaneda TR, de Prado BM, Prieto D, Mora F (2004) Circadian rhythms of dopamine, glutamate and GABA in the striatum and nucleus accumbens of the awake rat: modulation by light. J Pineal Res 36(3):177–185

Castren E (2004) Neurotrophic effects of antidepressant drugs. Curr Opin Pharmacol 4(1):58–64

Ceravolo R, Piccini P, Bailey DL et al (2002) 18F-dopa PET evidence that tolcapone acts as a central COMT inhibitor in Parkinson's disease. Synapse 43(3):201–207

Cheon KA, Ryu YH, Kim JW, Cho DY (2005) The homozygosity for 10-repeat allele at dopamine transporter gene and dopamine transporter density in Korean children with attention deficit hyperactivity disorder: relating to treatment response to methylphenidate. Eur Neuropsychopharmacol 15(1):95–101

Christian BT, Wooten DW, Hillmer AT et al (2013) Serotonin transporter genotype affects serotonin 5-HT1A binding in primates. J Neurosci 33(6):2512–2516

Ciliax BJ, Drash GW, Staley JK et al (1999) Immunocytochemical localization of the dopamine transporter in human brain. J Comp Neurol 409(1):38–56

Collier DA, Stober G, Li T et al (1996) A novel functional polymorphism within the promoter of the serotonin transporter gene: possible role in susceptibility to affective disorders. Mol Psychiatry 1(6):453–460

Costa A, Riedel M, Muller U, Moller HJ, Ettinger U (2011) Relationship between SLC6A3 genotype and striatal dopamine transporter availability: a meta-analysis of human single photon emission computed tomography studies. Synapse 65(10):998–1005

Cumming P (2009) Imaging dopamine. Cambridge University Press, New York

David SP, Murthy NV, Rabiner EA et al (2005) A functional genetic variation of the serotonin (5-HT) transporter affects 5-HT1A receptor binding in humans. J Neurosci 25(10):2586–2590

de Almeida J, Mengod G (2008) Serotonin 1A receptors in human and monkey prefrontal cortex are mainly expressed in pyramidal neurons and in a GABAergic interneuron subpopulation: implications for schizophrenia and its treatment. J Neurochem 107(2):488–496

Debruyne JC, Van Laere KJ, Versijpt J et al (2002) Semiquantification of the peripheral-type benzodiazepine ligand [11C]PK11195 in normal human brain and application in multiple sclerosis patients. Acta Neurol Belg 102(3):127–135

Domino EF, Evans CL, Ni L et al (2010) Tobacco smoking produces greater striatal dopamine release in G-allele carriers with mu opioid receptor A118G polymorphism. Prog Neuro-Psychopharmacol Biol Psychiatry 38(2):236–240

Domino EF, Evans CL, Ni L et al (2012) Tobacco smoking produces greater striatal dopamine release in G-allele carriers with mu opioid receptor A118G polymorphism. Prog Neuro-Psychopharmacol Biol Psychiatry 38(2):236–240

Drago A, Ronchi DD, Serretti A (2008) 5-HT1A gene variants and psychiatric disorders: a review of current literature and selection of SNPs for future studies. Int J Neuropsychopharmacol 11(5):701–721

Drevets WC, Frank E, Price JC et al (1999) PET imaging of serotonin 1A receptor binding in depression. Biol Psychiatry 46(10):1375–1387

Drevets WC, Frank E, Price JC et al (2000) Serotonin type-1A receptor imaging in depression. Nucl Med Biol 27(5):499–507

Drevets WC, Thase ME, Moses-Kolko EL et al (2007) Serotonin-1A receptor imaging in recurrent depression: replication and literature review. Nucl Med Biol 34(7):865–877

Drgon T, Lin Z, Wang GJ et al (2006) Common human 5′ dopamine transporter (SLC6A3) haplotypes yield varying expression levels in vivo. Cell Mol Neurobiol 26(4–6):875–889

Edison P, Archer HA, Gerhard A et al (2008) Microglia, amyloid, and cognition in Alzheimer's disease: an [11C](R)PK11195-PET and [11C]PIB-PET study. Neurobiol Dis 32(3):412–419

Egan MF, Kojima M, Callicott JH et al (2003) The BDNF val66met polymorphism affects activity-dependent secretion of BDNF and human memory and hippocampal function. Cell 112(2):257–269

Eisenberg DP, Kohn PD, Baller EB et al (2010) Seasonal effects on human striatal presynaptic dopamine synthesis. J Neurosci 30(44):14691–14694

Emamian ES, Hall D, Birnbaum MJ et al (2004) Convergent evidence for impaired AKT1-GSK3beta signaling in schizophrenia. Nat Genet 36:131–137

Fargin A, Raymond JR, Regan JW et al (1989) Effector coupling mechanisms of the cloned 5-HT1A receptor. J Biol Chem 264(25):14848–14852

Featherstone RE, Tatard-Leitman VM, Suh JD et al (2013) Electrophysiological and behavioral responses to ketamine in mice with reduced Akt1 expression. Psychopharmacology 227:639–649

Fergusson DM, Boden JM, Horwood LJ, Miller AL, Kennedy MA (2011) MAOA, abuse exposure and antisocial behaviour: 30-year longitudinal study. Br J Psychiatry 198(6):457–463

Fisher PM, Holst KK, Adamsen D et al (2015) BDNF Val66met and 5-HTTLPR polymorphisms predict a human in vivo marker for brain serotonin levels. Hum Brain Mapp 36:313–323

Fisher PM, Holst KK, Mc Mahon B et al (2012) 5-HTTLPR status predictive of neocortical 5-HT4 binding assessed with [(11)C]SB207145 PET in humans. NeuroImage 62(1):130–136

Fisher PM, Ozenne B, Svarer C et al (2017) BDNF val66met association with serotonin transporter binding in healthy humans. Transl Psychiatry 7(2):e1029

Fowler JS, Alia-Klein N, Kriplani A et al (2007) Evidence that brain MAO A activity does not correspond to MAO A genotype in healthy male subjects. Biol Psychiatry 62(4):355–358

Frankle WG, Huang Y, Hwang DR et al (2004) Comparative evaluation of serotonin transporter radioligands 11C-DASB and 11C-McN 5652 in healthy humans. J Nucl Med 45(4):682–694

Frankle WG, Lombardo I, Kegeles LS et al (2006) Serotonin 1A receptor availability in patients with schizophrenia and schizo-affective disorder: a positron emission tomography imaging study with [11C]WAY 100635. Psychopharmacology 189(2):155–164

Freund TF, Gulyas AI, Acsady L, Gorcs T, Toth K (1990) Serotonergic control of the hippocampus via local inhibitory interneurons. Proc Natl Acad Sci U S A 87(21):8501–8505

Fujita M, Imaizumi M, Zoghbi SS et al (2008) Kinetic analysis in healthy humans of a novel positron emission tomography radioligand to image the peripheral benzodiazepine receptor, a potential biomarker for inflammation. NeuroImage 40(1):43–52

Ginovart N, Meyer JH, Boovariwala A et al (2006) Positron emission tomography quantification of [11C]-harmine binding to monoamine oxidase-A in the human brain. J Cereb Blood Flow Metab 26(3):330–344

Gogos JA, Morgan M, Luine V et al (1998) Catechol-O-methyltransferase-deficient mice exhibit sexually dimorphic changes in catecholamine levels and behavior. Proc Natl Acad Sci U S A 95(17):9991–9996

Gratacos M, Gonzalez JR, Mercader JM et al (2007) Brain-derived neurotrophic factor Val66Met and psychiatric disorders: meta-analysis of case-control studies confirm association to substance-related disorders, eating disorders, and schizophrenia. Biol Psychiatry 61(7):911–922

Greenberg BD, Tolliver TJ, Huang SJ et al (1999) Genetic variation in the serotonin transporter promoter region affects serotonin uptake in human blood platelets. Am J Med Genet 88(1):83–87

Grunblatt E, Loffler C, Zehetmayer S et al (2006) Association study of the 5-HTTLPR polymorphism and depression in 75-year-old nondemented subjects from the Vienna transdanube aging (VITA) study. J Clin Psychiatry 67(9):1373–1378

Guo N, Hwang DR, Lo ES et al (2003) Dopamine depletion and in vivo binding of PET D1 receptor radioligands: implications for imaging studies in schizophrenia. Neuropsychopharmacology 28(9):1703–1711

Hariri AR, Goldberg TE, Mattay VS et al (2003) Brain-derived neurotrophic factor val66met polymorphism affects human memory-related hippocampal activity and predicts memory performance. J Neurosci 23(17):6690–6694

Hariri AR, Holmes A (2006) Genetics of emotional regulation: the role of the serotonin transporter in neural function. Trends Cogn Sci 10(4):182–191

Hariri AR, Mattay VS, Tessitore A et al (2002) Serotonin transporter genetic variation and the response of the human amygdala. Science 297(5580):400–403

Heils A, Teufel A, Petri S et al (1996) Allelic variation of human serotonin transporter gene expression. J Neurochem 66(6):2621–2624

Heinz A, Goldman D, Jones DW et al (2000a) Genotype influences in vivo dopamine transporter availability in human striatum. Neuropsychopharmacology 22(2):133–139

Heinz A, Jones DW, Mazzanti C et al (2000b) A relationship between serotonin transporter genotype and in vivo protein expression and alcohol neurotoxicity. Biol Psychiatry 47(7):643–649

Henningsson S, Borg J, Lundberg J et al (2009) Genetic variation in brain-derived neurotrophic factor is associated with serotonin transporter but not serotonin-1A receptor availability in men. Biol Psychiatry 66(5):477–485

Hernaus D, Collip D, Lataster J et al (2013) COMT Val158Met genotype selectively alters prefrontal [18F]fallypride displacement and subjective feelings of stress in response to a psychosocial stress challenge. PLoS One 8(6):e65662

Hietala J, Syvalahti E, Vilkman H et al (1999) Depressive symptoms and presynaptic dopamine function in neuroleptic-naive schizophrenia. Schizophr Res 35(1):41–50

Hietala J, Syvalahti E, Vuorio K et al (1995) Presynaptic dopamine function in striatum of neuroleptic-naive schizophrenic patients. Lancet 346(8983):1130–1131

Hirvonen J, Karlsson H, Kajander J et al (2008) Decreased brain serotonin 5-HT1A receptor availability in medication-naive patients with major depressive disorder: an in-vivo imaging study using PET and [carbonyl-11C]WAY-100635. Int J Neuropsychopharmacol 11(4):465–476

Hirvonen M, Laakso A, Nagren K et al (2004) C957T polymorphism of the dopamine D2 receptor (DRD2) gene affects striatal DRD2 availability in vivo. Mol Psychiatry 9(12):1060–1061

Hirvonen MM, Laakso A, Nagren K et al (2009) C957T polymorphism of dopamine D2 receptor gene affects striatal DRD2 in vivo availability by changing the receptor affinity. Synapse 63(10):907–912

Homberg JR, Lesch KP (2010) Looking on the bright side of serotonin transporter gene variation. Biol Psychiatry 69(6):513–519

Houle S, Ginovart N, Hussey D, Meyer JH, Wilson AA (2000) Imaging the serotonin transporter with positron emission tomography: initial human studies with [C-11]DAPP and [C-11]DASB. Eur J Nucl Med 27(11):1719–1722

Howes OD, Kambeitz J, Kim E et al (2012) The nature of dopamine dysfunction in schizophrenia and what this means for treatment. Arch Gen Psychiatry 69(8):776–786

Huang TY, Hwang DR, Narendran R et al (2002) Comparative evaluation in nonhuman primates of five PET radiotracers for imaging the serotonin transporters: [C-11]McN 5652, [C-11]ADAM, [C-11]DASB, [C-11]DAPA, and [C-11]AFM. J Cereb Blood Flow Metab 22(11):1377–1398

Ira E, Zanoni M, Ruggeri M, Dazzan P, Tosato S (2013) COMT, neuropsychological function and brain structure in schizophrenia: a systematic review and neurobiological interpretation. J Psychiatry Neurosci 38(3):120178

Ito H, Halldin C, Farde L (1999) Localization of 5-HT1A receptors in the living human brain using [carbonyl-11C]WAY-100635: PET with anatomic standardization technique. J Nucl Med 40(1):102–109

Jacobsen LK, Staley JK, Zoghbi S et al (2000) Prediction of dopamine transporter binding availability by genotype: a preliminary report. Am J Psychiatry 157(10):1700–1703

Jennings KA, Licht CL, Bruce A et al (2011) Genetic variation in 5-hydroxytryptamine transporter expression causes adaptive changes in 5-HT(4) receptor levels. Int J Neuropsychopharmacol 15(8):1099–1107

Jennings KA, Loder MK, Sheward WJ et al (2006) Increased expression of the 5-HT transporter confers a low-anxiety phenotype linked to decreased 5-HT transmission. J Neurosci 26(35):8955–8964

Johansson C, Willeit M, Levitan R et al (2003) The serotonin transporter promoter repeat length polymorphism, seasonal affective disorder and seasonality. Psychol Med 33(5):785–792

Jones KR, Reichardt LF (1990) Molecular cloning of a human gene that is a member of the nerve growth factor family. Proc Natl Acad Sci U S A 87(20):8060–8064

Jonsson EG, Nothen MM, Grunhage F et al (1999) Polymorphisms in the dopamine D2 receptor gene and their relationships to striatal dopamine receptor density of healthy volunteers. Mol Psychiatry 4(3):290–296

Jönsson EG, Nöthen MM, Grünhage F et al (1999) Polymorphisms in the dopamine D2 receptor gene and their relationships to striatal dopamine receptor density of healthy volunteers. Mol Psychiatry 4:290–296

Joutsa J, Hirvonen MM, Arponen E et al (2014) DRD2-related TaqIA genotype is associated with dopamine release during a gambling task. J Addict Med 8(4):294–295

Kalbitzer J, Erritzoe D, Holst KK et al (2010) Seasonal changes in brain serotonin transporter binding in short serotonin transporter linked polymorphic region-allele carriers but not in long-allele homozygotes. Biol Psychiatry 67(11):1033–1039

Kalbitzer J, Frokjaer VG, Erritzoe D et al (2009) The personality trait openness is related to cerebral 5-HTT levels. NeuroImage 45(2):280–285

Kalgutkar AS, Dalvie DK, Castagnoli N Jr, Taylor TJ (2001) Interactions of nitrogen-containing xenobiotics with monoamine oxidase (MAO) isozymes A and B: SAR studies on MAO substrates and inhibitors. Chem Res Toxicol 14(9):1139–1162

Kapur S, Phillips AG, Insel TR (2012) Why has it taken so long for biological psychiatry to develop clinical tests and what to do about it? Mol Psychiatry 17(12):1174–1179

Karg K, Burmeister M, Shedden K, Sen S (2011) The serotonin transporter promoter variant (5-HTTLPR), stress, and depression meta-analysis revisited: evidence of genetic moderation. Arch Gen Psychiatry 68(5):444–454

Kasparbauer AM, Rujescu D, Riedel M et al (2015) Methylphenidate effects on brain activity as a function of SLC6A3 genotype and striatal dopamine transporter availability. Neuropsychopharmacology 40(3):736–745

Kauppila E, Vanninen E, Kaurijoki S et al (2013) Influence of serotonin transporter gene polymorphism (5-HTTLPR polymorphism) on the relation between brain 5-HT transporter binding and heart rate corrected cardiac repolarization interval. PLoS One 8(1):e50303

Kautzky A, James GM, Phillipe C et al (2017) The influence of the rs6295 gene polymorphism on serotonin-1A receptor distribution investigated with PET in patients with major depression applying machine learning. Transl Psychiatry 7:e1150

Kautzky A, James GM, Phillipe C et al (2019) Epistasis of HTR1A and BDNF risk genes alters cortical 5-HT1A receptor binding: PET results link genotype to molecular phenotype in depression. Transl Psychiatry 9(1):5

Kegeles LS, Abi-Dargham A, Frankle WG et al (2010) Increased synaptic dopamine function in associative regions of the striatum in schizophrenia. Arch Gen Psychiatry 67(3):231–239

Kishi T, Yoshimura R, Fukuo Y et al (2012) The serotonin 1A receptor gene confer susceptibility to mood disorders: results from an extended meta-analysis of patients with major depression and bipolar disorder. Eur Arch Psychiatry Clin Neurosci 263(2):105–118

Klein AB, Trajkovska V, Erritzoe D et al (2010) Cerebral 5-HT2A receptor and serotonin transporter binding in humans are not affected by the val66met BDNF polymorphism status or blood BDNF levels. J Cereb Blood Flow Metab 30(11):e1–e7

Kraft JB, Slager SL, McGrath PJ, Hamilton SP (2005) Sequence analysis of the serotonin transporter and associations with antidepressant response. Biol Psychiatry 58(5):374–381

Kraus C, Baldinger P, Rami-Mark C et al (2014) Exploring the Impact of BDNF Val66Met Genotype on Serotonin Transporter and Serotonin-1A Receptor Binding. PLoS One 9(9):e106810

Krause J, Dresel SH, Krause KH et al (2006) Striatal dopamine transporter availability and DAT-1 gene in adults with ADHD: No higher DAT availability in patients with homozygosity for the 10-repeat allele. World J Biol Psychiatry 7(3):152–157

Kreisl WC, Fujita M, Fujimura Y et al (2009) Comparison of [(11)C]-(R)-PK 11195 and [(11)C]PBR28, two radioligands for translocator protein (18 kDa) in human and monkey: implications for positron emission tomographic imaging of this inflammation biomarker. NeuroImage 49(4):2924–2932

Kreisl WC, Jenko KJ, Hines CS et al (2012) A genetic polymorphism for translocator protein 18 kDa affects both in vitro and in vivo radioligand binding in human brain to this putative biomarker of neuroinflammation. J Cereb Blood Flow Metab 33(1):53–58

Kumakura Y, Cumming P, Vernaleken I et al (2007) Elevated [18F]fluorodopamine turnover in brain of patients with schizophrenia: an [18F]fluorodopa/positron emission tomography study. J Neurosci 27(30):8080–8087

Kunugi H, Hattori M, Kato T et al (1997) Serotonin transporter gene polymorphisms: ethnic difference and possible association with bipolar affective disorder. Mol Psychiatry 2(6):457–462

Laakso A, Pohjalainen T, Bergman J et al (2005) The A1 allele of the human D2 dopamine receptor gene is associated with increased activity of striatal L-amino acid decarboxylase in healthy subjects. Pharmacogenet Genomics 15(6):387–391

Lachman HM, Morrow B, Shprintzen R et al (1996) Association of codon 108/158 catechol-O-methyltransferase gene polymorphism with the psychiatric manifestations of velo-cardio-facial syndrome. Am J Med Genet 67(5):468–472

Lafuente A, Bernardo M, Mas S et al (2007) Dopamine transporter (DAT) genotype (VNTR) and phenotype in extrapyramidal symptoms induced by antipsychotics. Schizophr Res 90(1–3):115–122

Laine TP, Ahonen A, Rasanen P et al (2001) The A1 allele of the D2 dopamine receptor gene is associated with high dopamine transporter density in detoxified alcoholics. Alcohol Alcohol 36(3):262–265

Laje G, Cannon DM, Allen AS et al (2010) Genetic variation in HTR2A influences serotonin transporter binding potential as measured using PET and [11C]DASB. Int J Neuropsychopharmacol 13(6):715–724

Lanzenberger R, Baldinger P, Hahn A et al (2012a) Global decrease of serotonin-1A receptor binding after electroconvulsive therapy in major depression measured by PET. Mol Psychiatry 18(1):93–100

Lanzenberger R, Mitterhauser M, Hahn A et al (2012b) Molecular imaging genetics of the serotonin-1A receptor investigating the common rs6295 single nucleotide polymorphism. J Cereb Blood Flow Metab 32(Suppl 1):S85

Lanzenberger RR, Mitterhauser M, Spindelegger C et al (2007) Reduced serotonin-1A receptor binding in social anxiety disorder. Biol Psychiatry 61(9):1081–1089

Laruelle M, Abi-Dargham A, van Dyck CH et al (1996) Single photon emission computerized tomography imaging of amphetamine-induced dopamine release in drug-free schizophrenic subjects. Proc Natl Acad Sci U S A 93(17):9235–9240

Laruelle M, Gelernter J, Innis RB (1998) D2 receptors binding potential is not affected by Taq1 polymorphism at the D2 receptor gene. Mol Psychiatry 3(3):261–265

Le Francois B, Czesak M, Steubl D, Albert PR (2008) Transcriptional regulation at a HTR1A polymorphism associated with mental illness. Neuropharmacology 55(6):977–985

Lee M, Bailer UF, Frank GK et al (2005) Relationship of a 5-HT transporter functional polymorphism to 5-HT1A receptor binding in healthy women. Mol Psychiatry 10(8):715–716

Lesch KP, Bengel D, Heils A et al (1996) Association of anxiety-related traits with a polymorphism in the serotonin transporter gene regulatory region. Science 274(5292):1527–1531

Lewis DA, Melchitzky DS, Sesack SR et al (2001) Dopamine transporter immunoreactivity in monkey cerebral cortex: regional, laminar, and ultrastructural localization. J Comp Neurol 432(1):119–136

Li YC, Yang SS, Gao WJ (2016) Disruption of Akt signaling decreases dopamine sensitivity in modulation of inhibitory synaptic transmission in rat prefrontal cortex. Neuropharmacology 108:403–414

Licht CL, Marcussen AB, Wegener G et al (2009) The brain 5-HT4 receptor binding is down-regulated in the Flinders Sensitive Line depression model and in response to paroxetine administration. J Neurochem 109(5):1363–1374

Lindstrom LH, Gefvert O, Hagberg G et al (1999) Increased dopamine synthesis rate in medial prefrontal cortex and striatum in schizophrenia indicated by L-(beta-11C) DOPA and PET. Biol Psychiatry 46(5):681–688

Lothe A, Boni C, Costes N et al (2009) Association between triallelic polymorphism of the serotonin transporter and [F-18] MPPF binding potential at 5-HT1A receptors in healthy subjects. NeuroImage 47(2):482–492

Love TM, Enoch MA, Hodgkinson CA et al (2012) Oxytocin gene polymorphisms influence human dopaminergic function in a sex-dependent manner. Biol Psychiatry 72(3):198–206

Lynch DR, Mozley PD, Sokol S et al (2003) Lack of effect of polymorphisms in dopamine metabolism related genes on imaging of TRODAT-1 in striatum of asymptomatic volunteers and patients with Parkinson's disease. Mov Disord 18(7):804–812

MacGregor RR, Halldin C, Fowler JS et al (1985) Selective, irreversible in vivo binding of [11C]clorgyline and [11C]-L-deprenyl in mice: potential for measurement of functional monoamine oxidase activity in brain using positron emission tomography. Biochem Pharmacol 34(17):3207–3210

Maisonpierre PC, Le Beau MM, Espinosa R 3rd et al (1991) Human and rat brain-derived neurotrophic factor and neurotrophin-3: gene structures, distributions, and chromosomal localizations. Genomics 10(3):558–568

Malhotra AK, Goldman D, Mazzanti C et al (1998) A functional serotonin transporter (5-HTT) polymorphism is associated with psychosis in neuroleptic-free schizophrenics. Mol Psychiatry 3(4):328–332

Malison RT, Price LH, Berman R et al (1998) Reduced brain serotonin transporter availability in major depression as measured by [123I]-2 beta-carbomethoxy-3 beta-(4-iodophenyl)tropane and single photon emission computed tomography. Biol Psychiatry 44(11):1090–1098

Marner L, Gillings N, Comley RA et al (2009) Kinetic modeling of 11C-SB207145 binding to 5-HT4 receptors in the human brain in vivo. J Nucl Med 50(6):900–908

Marner L, Gillings N, Madsen K et al (2010) Brain imaging of serotonin 4 receptors in humans with [11C]SB207145-PET. NeuroImage 50(3):855–861

Martinez D, Gelernter J, Abi-Dargham A et al (2001) The variable number of tandem repeats polymorphism of the dopamine transporter gene is not associated with significant change in dopamine transporter phenotype in humans. Neuropsychopharmacology 24(5):553–560

Matsumoto M, Weickert CS, Akil M et al (2003) Catechol O-methyltransferase mRNA expression in human and rat brain: evidence for a role in cortical neuronal function. Neuroscience 116(1):127–137

Maynard KR, Hill JL, Calcaterra NE et al (2016) Functional Role of BDNF Production from Unique Promoters in Aggression and Serotonin Signaling. Neuropsychopharmacology 41(8):1943–1955

McGowan S, Lawrence AD, Sales T, Quested D, Grasby P (2004) Presynaptic dopaminergic dysfunction in schizophrenia: a positron emission tomographic [18F]fluorodopa study. Arch Gen Psychiatry 61(2):134–142

McMahon FJ, Buervenich S, Charney D et al (2006) Variation in the gene encoding the serotonin 2A receptor is associated with outcome of antidepressant treatment. Am J Hum Genet 78(5):804–814

Meltzer CC, Price JC, Mathis CA et al (2004) Serotonin 1A receptor binding and treatment response in late-life depression. Neuropsychopharmacology 29(12):2258–2265

Meyer JH (2007) Imaging the serotonin transporter during major depressive disorder and antidepressant treatment. J Psychiatry Neurosci 32(2):86–102

Meyer JH, Ginovart N, Boovariwala A et al (2006) Elevated monoamine oxidase A levels in the brain: an explanation for the monoamine imbalance of major depression. Arch Gen Psychiatry 63(11):1209–1216

Meyer JH, Houle S, Sagrati S et al (2004) Brain serotonin transporter binding potential measured with carbon 11-labeled DASB positron emission tomography – effects of major depression episodes and severity of dysfunctional attitudes. Arch Gen Psychiatry 61(12):1271–1279

Meyer-Lindenberg A, Kohn PD, Kolachana B et al (2005) Midbrain dopamine and prefrontal function in humans: interaction and modulation by COMT genotype. Nat Neurosci 8(5):594–596

Meyer-Lindenberg A, Miletich RS, Kohn PD et al (2002) Reduced prefrontal activity predicts exaggerated striatal dopaminergic function in schizophrenia. Nat Neurosci 5(3):267–271

Mickey BJ, Ducci F, Hodgkinson CA et al (2008) Monoamine oxidase A genotype predicts human serotonin 1A receptor availability in vivo. J Neurosci 28(44):11354–11359

Mickey BJ, Sanford BJ, Love TM et al (2012) Striatal dopamine release and genetic variation of the serotonin 2C receptor in humans. J Neurosci 32(27):9344–9350

Miller JM, Kinnally EL, Ogden RT et al (2009) Reported childhood abuse is associated with low serotonin transporter binding in vivo in major depressive disorder. Synapse 63(7):565–573

Mizrahi R, Rusjan PM, Kennedy J et al (2012) Translocator protein (18 kDa) polymorphism (rs6971) explains in-vivo brain binding affinity of the PET radioligand [(18)F]-FEPPA. J Cereb Blood Flow Metab 32(6):968–972

Moses-Kolko EL, Price JC, Thase ME et al (2007) Measurement of 5-HT1A receptor binding in depressed adults before and after antidepressant drug treatment using positron emission tomography and [11C]WAY-100635. Synapse 61(7):523–530

Murthy NV, Selvaraj S, Cowen PJ et al (2010) Serotonin transporter polymorphisms (SLC6A4 insertion/deletion and rs25531) do not affect the availability of 5-HTT to [11C] DASB binding in the living human brain. NeuroImage 52(1):50–54

Nakamura M, Ueno S, Sano A, Tanabe H (2000) The human serotonin transporter gene linked polymorphism (5-HTTLPR) shows ten novel allelic variants. Mol Psychiatry 5(1):32–38

Narendran R, Tumuluru D, May MA et al (2016) cortical dopamine transmission as measured with the [11C]FLB 457—Amphetamine PET imaging paradigm is not influenced by COMT genotype. PLoS One 11(6):e0157867

Neumeister A, Bain E, Nugent AC et al (2004) Reduced serotonin type 1A receptor binding in panic disorder. J Neurosci 24(3):589–591

Neumeister A, Yuan P, Young TA et al (2005) Effects of tryptophan depletion on serum levels of brain-derived neurotrophic factor in unmedicated patients with remitted depression and healthy subjects. Am J Psychiatry 162(4):805–807

Neumeyer JL, Wang SY, Milius RA et al (1991) [123I]-2 beta-carbomethoxy-3 beta-(4-iodophenyl) tropane: high-affinity SPECT radiotracer of monoamine reuptake sites in brain. J Med Chem 34(10):3144–3146

Neves-Pereira M, Mundo E, Muglia P et al (2002) The brain-derived neurotrophic factor gene confers susceptibility to bipolar disorder: evidence from a family-based association study. Am J Hum Genet 71(3):651–655

Nobile M, Begni B, Giorda R et al (1999) Effects of serotonin transporter promoter genotype on platelet serotonin transporter functionality in depressed children and adolescents. J Am Acad Child Adolesc Psychiatry 38(11):1396–1402

Nozaki S, Kato M, Takano H et al (2009) Regional dopamine synthesis in patients with schizophrenia using L-[beta-11C]DOPA PET. Schizophr Res 108(1–3):78–84

Owen DR, Howell OW, Tang SP et al (2010) Two binding sites for [3H]PBR28 in human brain: implications for TSPO PET imaging of neuroinflammation. J Cereb Blood Flow Metab 30(9):1608–1618

Owen DR, Yeo AJ, Gunn RN et al (2011) An 18-kDa translocator protein (TSPO) polymorphism explains differences in binding affinity of the PET radioligand PBR28. J Cereb Blood Flow Metab 32(1):1–5

Pak K, Nam HY, Shin S et al (2018) Effects of rs591323 on serotonin transporter availability in healthy male subjects. Ann Nucl Med 32:431

Palchaudhuri M, Flugge G (2005) 5-HT1A receptor expression in pyramidal neurons of cortical and limbic brain regions. Cell Tissue Res 321(2):159–172

Pardini M, Krueger F, Hodgkinson C et al (2011) Prefrontal cortex lesions and MAO-A modulate aggression in penetrating traumatic brain injury. Neurology 76(12):1038–1045

Parsey RV, Hastings RS, Oquendo MA et al (2006a) Effect of a triallelic functional polymorphism of the serotonin-transporter-linked promoter region on expression of serotonin transporter in the human brain. Am J Psychiatry 163(1):48–51

Parsey RV, Olvet DM, Oquendo MA et al (2006b) Higher 5-HT1A receptor binding potential during a major depressive episode predicts poor treatment response: preliminary data from a naturalistic study. Neuropsychopharmacology 31(8):1745–1749

Parsey RV, Oquendo MA, Ogden RT et al (2006c) Altered serotonin 1A binding in major depression: a [carbonyl-C-11]WAY100635 positron emission tomography study. Biol Psychiatry 59(2):106–113

Paterson LM, Tyacke RJ, Nutt DJ, Knudsen GM (2010) Measuring endogenous 5-HT release by emission tomography: promises and pitfalls. J Cereb Blood Flow Metab 30(10):1682–1706

Patkar AA, Berrettini WH, Mannelli P et al (2004) Relationship between serotonin transporter gene polymorphisms and platelet serotonin transporter sites among African-American cocaine-dependent individuals and healthy volunteers. Psychiatr Genet 14(1):25–32

Peciña M, Martínez-Jauand M, Love T et al (2014) Valence-specific effects of BDNF Val66Met polymorphism on dopaminergic stress and reward processing in humans. J Neurosci 34(17):5874–5881

Peciña M, Mickey BJ, Love T et al (2012) DRD2 polymorphisms modulate reward and emotion processing, dopamine neurotransmission and openness to experience. Cortex 49(3):877–890

Pernhorst K, van Loo KM, von Lehe M et al (2013) Rs6295 promoter variants of the serotonin type 1A receptor are differentially activated by c-Jun in vitro and correlate to transcript levels in human epileptic brain tissue. Brain Res 1499:136–144

Pezawas L, Meyer-Lindenberg A, Drabant EM et al (2005) 5-HTTLPR polymorphism impacts human cingulate-amygdala interactions: a genetic susceptibility mechanism for depression. Nat Neurosci 8(6):828–834

Pezawas L, Meyer-Lindenberg A, Goldman LA et al (2008) Evidence of biologic epistasis between BDNF and SLC6A4 and implications for depression. Mol Psychiatry 13(7):709–716

Pezawas L, Verchinski BA, Mattay VS et al (2004) The brain-derived neurotrophic factor val66met polymorphism and variation in human cortical morphology. J Neurosci 24(45):10099–10102

Pirker W, Asenbaum S, Hauk M et al (2000) Imaging serotonin and dopamine transporters with 123I-beta-CIT SPECT: binding kinetics and effects of normal aging. J Nucl Med 41(1):36–44

Pohjalainen T, Nagren K, Syvalahti EK, Hietala J (1999) The dopamine D2 receptor 5′-flanking variant, -141C Ins/Del, is not associated with reduced dopamine D2 receptor density in vivo. Pharmacogenetics 9(4):505–509

Pohjalainen T, Rinne JO, Nagren K et al (1998) The A1 allele of the human D2 dopamine receptor gene predicts low D2 receptor availability in healthy volunteers. Mol Psychiatry 3(3):256–260

Praschak-Rieder N, Kennedy J, Wilson AA et al (2007) Novel 5-HTTLPR allele associates with higher serotonin transporter binding in putamen: a [C-11] DASB positron emission tomography study. Biol Psychiatry 62(4):327–331

Praschak-Rieder N, Willeit M (2012) Imaging of seasonal affective disorder and seasonality effects on serotonin and dopamine function in the human brain. Curr Top Behav Neurosci 11:149–167

Praschak-Rieder N, Willeit M, Wilson AA, Houle S, Meyer JH (2008) Seasonal variation in human brain serotonin transporter binding. Arch Gen Psychiatry 65(9):1072–1078

Premi E, Archetti S, Pilotto A, Seripa D, Paghera B, Padovani A, Borroni B (2015) Functional genetic variation in the serotonin 5-HTTLPR modulates brain damage in frontotemporal dementia. Neurobiol Aging 36(1):446–451

Purcell SM, Wray NR, Stone JL et al (2009) Common polygenic variation contributes to risk of schizophrenia and bipolar disorder. Nature 460(7256):748–752

Reimold M, Smolka MN, Schumann G et al (2007) Midbrain serotonin transporter binding potential measured with [C-11]DASB is affected by serotonin transporter genotype. J Neural Transm 114(5):635–639

Reith J, Benkelfat C, Sherwin A et al (1994) Elevated dopa decarboxylase activity in living brain of patients with psychosis. Proc Natl Acad Sci U S A 91(24):11651–11654

Risch N, Herrell R, Lehner T et al (2009) Interaction between the serotonin transporter gene (5-HTTLPR), stressful life events, and risk of depression: a meta-analysis. JAMA 301(23):2462–2471

Rosenthal NE, Mazzanti CM, Barnett RL et al (1998) Role of serotonin transporter promoter repeat length polymorphism (5-HTTLPR) in seasonality and seasonal affective disorder. Mol Psychiatry 3(2):175–177

Roses AD (2010) An inherited variable poly-T repeat genotype in TOMM40 in Alzheimer disease. Arch Neurol 67(5):536–541

Ruhe HG, Booij J, Reitsma JB, Schene AH (2009) Serotonin transporter binding with [I-123]beta-CIT SPECT in major depressive disorder versus controls: effect of season and gender. Eur J Nucl Med Mol Imaging 36(5):841–849

Ruottinen HM, Niinivirta M, Bergman J et al (2001) Detection of response to COMT inhibition in FDOPA PET in advanced Parkinson's disease requires prolonged imaging. Synapse 40(1):19–26

Sabol SZ, Hu S, Hamer D (1998) A functional polymorphism in the monoamine oxidase A gene promoter. Hum Genet 103(3):273–279

Sacher J, Wilson AA, Houle S et al (2010) Elevated brain monoamine oxidase A binding in the early postpartum period. Arch Gen Psychiatry 67(5):468–474

Saijo T, Takano A, Suhara T et al (2010) Effect of electroconvulsive therapy on 5-HT1A receptor binding in patients with depression: a PET study with [11C]WAY 100635. Int J Neuropsychopharmacol 13(6):785–791

Sambataro F, Fazio L, Taurisano P et al (2011) DRD2 Genotype-based variation of default mode network activity and of its relationship with striatal DAT binding. Schizophr Bull 39(1):206–216

Savitz J, Hodgkinson CA, Martin-Soelch C et al (2013) The functional DRD3 Ser9Gly polymorphism (rs6280) is pleiotropic, affecting reward as well as movement. PLoS One 8(1):e54108

Savitz J, Lucki I, Drevets WC (2009) 5-HT(1A) receptor function in major depressive disorder. Prog Neurobiol 88(1):17–31

Schosser A, Calati R, Serretti A et al (2011) The impact of COMT gene polymorphisms on suicidality in treatment resistant major depressive disorder–a European multicenter study. Eur Neuropsychopharmacol 22(4):259–266

Selvaraj S, Murthy NV, Bhagwagar Z et al (2009) Diminished brain 5-HT transporter binding in major depression: a positron emission tomography study with [11C]DASB. Psychopharmacology 213(2–3):555–562

Seretti A, Cusin C, Lattuada E et al (1999) Serotonin transporter gene (5-HTTLPR) is not associated with depressive symptomatology in mood disorders. Mol Psychiatry 4(3):280–283

Shen HW, Hagino Y, Kobayashi H et al (2004) Regional differences in extracellular dopamine and serotonin assessed by in vivo microdialysis in mice lacking dopamine and/or serotonin transporters. Neuropsychopharmacology 29(10):1790–1799

Shi J, Levinson DF, Duan J et al (2009) Common variants on chromosome 6p22.1 are associated with schizophrenia. Nature 460(7256):753–757

Shioe K, Ichimya T, Suhara T et al (2003) No association between genotype of the promoter region of serotonin transporter gene and serotonin transporter binding in human brain measured by PET. Synapse 48(4):184–188

Shumay E, Fowler JS, Wang GJ et al (2012a) Repeat variation in the human PER2 gene as a new genetic marker associated with cocaine addiction and brain dopamine D2 receptor availability. Transl Psychiatry 2:e86

Shumay E, Logan J, Volkow ND, Fowler JS (2012b) Evidence that the methylation state of the monoamine oxidase A (MAOA) gene predicts brain activity of MAO A enzyme in healthy men. Epigenetics 7(10):1151–1160

Shumay E, Wiers CE, Shokri-Kojori E et al (2017) New repeat polymorphism in the AKT1 gene predicts striatal dopamine D2/D3 receptor availability and stimulant-induced dopamine release in the healthy human brain. J Neurosci 37(19):4982–4991

Siddarth P, Burggren AC, Merrill DA et al (2018) Longer TOMM40 poly-T variants associated with higher FDDNP-PET medial temporal tau and amyloid binding. PLoS One 13(12):e0208358

Sklar P, Gabriel SB, McInnis MG et al (2002) Family-based association study of 76 candidate genes in bipolar disorder: BDNF is a potential risk locus. Brain-derived neurotrophic factor. Mol Psychiatry 7(6):579–593

Slifstein M, Kolachana B, Simpson EH et al (2008) COMT genotype predicts cortical-limbic D1 receptor availability measured with [11C]NNC112 and PET. Mol Psychiatry 13(8):821–827

Spindelegger C, Lanzenberger R, Wadsak W et al (2009) Influence of escitalopram treatment on 5-HT(1A) receptor binding in limbic regions in patients with anxiety disorders. Mol Psychiatry 14(11):1040–1050

Sprouse JS, Aghajanian GK (1988) Responses of hippocampal pyramidal cells to putative serotonin 5-HT1A and 5-HT1B agonists: a comparative study with dorsal raphe neurons. Neuropharmacology 27(7):707–715

Stefansson H, Ophoff RA, Steinberg S et al (2009) Common variants conferring risk of schizophrenia. Nature 460(7256):744–747

Stockmeier CA (2003) Involvement of serotonin in depression: evidence from postmortem and imaging studies of serotonin receptors and the serotonin transporter. J Psychiatr Res 37(5):357–373

Storvik M, Hakkinen M, Tupala E, Tiihonen J (2009) 5-HT(1A) receptors in the frontal cortical brain areas in Cloninger type 1 and 2 alcoholics measured by whole-hemisphere autoradiography. Alcohol Alcohol 44(1):2–7

Suehiro M, Scheffel U, Ravert HT, Dannals RF, Wagner HN (1993) [C-11] (+)MCN5652 as a radiotracer for imaging serotonin uptake sites with PET. Life Sci 53(11):883–892

Sullivan GM, Ogden RT, Huang YY et al (2013) Higher in vivo serotonin-1a binding in post-traumatic stress disorder: a pet study with [11C]way-100635. Depress Anxiety 30(3):197–206

Sullivan PF (2010) The psychiatric GWAS consortium: big science comes to psychiatry. Neuron 68(2):182–186

Szabo Z, McCann UD, Wilson AA et al (2002) Comparison of (+)-C-11-McN5652 and C-11-DASB as serotonin transporter radioligands under various experimental conditions. J Nucl Med 43(5):678–692

Szobot CM, Roman T, Hutz MH et al (2010) Molecular imaging genetics of methylphenidate response in ADHD and substance use comorbidity. Synapse 65(2):154–159

Talkowski ME, McCann KL, Chen M et al (2010) Fine-mapping reveals novel alternative splicing of the dopamine transporter. Am J Med Genet B Neuropsychiatr Genet 153B(8):1434–1447

Tauscher J, Kapur S, Verhoeff NP et al (2002) Brain serotonin 5-HT(1A) receptor binding in schizophrenia measured by positron emission tomography and [11C]WAY-100635. Arch Gen Psychiatry 59(6):514–520

Tsai HY, Chen KC, Yang YK et al (2011) Sunshine-exposure variation of human striatal dopamine D(2)/D(3) receptor availability in healthy volunteers. Prog Neuro-Psychopharmacol Biol Psychiatry 35(1):107–110

Urban NB, Martinez D (2012) Neurobiology of addiction: insight from neurochemical imaging. Psychiatr Clin North Am 35(2):521–541

van de Giessen E, Nimgaonkar VL, Watson AM et al (2012) Association tests of striatal DAT availability and SNPs that impact a novel splice variant in the DAT gene. J Nucl Med 53(5):839

van de Giessen EM, de Win MM, Tanck MW et al (2009) Striatal dopamine transporter availability associated with polymorphisms in the dopamine transporter gene SLC6A3. J Nucl Med 50(1):45–52

van Dyck CH, Malison RT, Jacobsen LK et al (2005) Increased dopamine transporter availability associated with the 9-repeat allele of the SLC6A3 gene. J Nucl Med 46(5):745–751

Van Dyck CH, Malison RT, Staley JK et al (2004) Central serotonin transporter availability measured with [I-123]beta-CIT SPECT in relation to serotonin transporter genotype. Am J Psychiatry 161(3):525–531

Vandenbergh DJ, Persico AM, Hawkins AL et al (1992) Human dopamine transporter gene (DAT1) maps to chromosome 5p15.3 and displays a VNTR. Genomics 14(4):1104–1106

Vandenbergh DJ, Thompson MD, Cook EH et al (2000) Human dopamine transporter gene: coding region conservation among normal, Tourette's disorder, alcohol dependence and attention-deficit hyperactivity disorder populations. Mol Psychiatry 5(3):283–292

Varnas K, Halldin C, Pike VW, Hall H (2003) Distribution of 5–HT4 receptors in the postmortem human brain–an autoradiographic study using [125I]SB 207710. Eur Neuropsychopharmacol 13(4):228–234

Vidal R, Valdizan EM, Mostany R, Pazos A, Castro E (2009) Long-term treatment with fluoxetine induces desensitization of 5-HT4 receptor-dependent signalling and functionality in rat brain. J Neurochem 110(3):1120–1127

Volkow ND, Fowler JS, Wang GJ, Baler R, Telang F (2009) Imaging dopamine's role in drug abuse and addiction. Neuropharmacology 56(Suppl 1):3–8

Waeber C, Sebben M, Bockaert J, Dumuis A (1996) Regional distribution and ontogeny of 5-HT4 binding sites in rat brain. Behav Brain Res 73(1–2):259–262

Walther DJ, Peter JU, Bashammakh S et al (2003) Synthesis of serotonin by a second tryptophan hydroxylase isoform. Science 299(5603):76

Weidenauer A, Bauer M, Sauerzopf U, Bartova L, Nics L, Pfaff S, Philippe C, Berroterán-Infante N, Pichler V, Meyer BM, Rabl U, Sezen P, Cumming P, Stimpfl T, Sitte HH, Lanzenberger R, Mossaheb N, Zimprich A, Rusjan P, Dorffner G, Mitterhauser M, Hacker M, Pezawas L, Kasper S, Wadsak W, Praschak-Rieder N, Willeit M. (2020) On the relationship of first-episode psychosis to the amphetamine-sensitized state: a dopamine D2/3 receptor agonist radioligand study. Transl Psychiatry. 8;10(1):2. https://doi.org/10.1038/s41398-019-0681-5. PMID: 32066718; PMCID: PMC7026156

Willeit M, Praschak-Rieder N (2010) Imaging the effects of genetic polymorphisms on radioligand binding in the living human brain: a review on genetic neuroreceptor imaging of monoaminergic systems in psychiatry. NeuroImage 53(3):878–892

Willeit M, Praschak-Rieder N, Neumeister A et al (2000) [I-123]-beta-CIT SPECT imaging shows reduced brain serotonin transporter availability in drug-free depressed patients with seasonal affective disorder. Biol Psychiatry 47(6):482–489

Willeit M, Praschak-Rieder N, Neumeister A et al (2003) A polymorphism (5-HTTLPR) in the serotonin transporter promoter gene is associated with DSM-IV depression subtypes in seasonal affective disorder. Mol Psychiatry 8(11):942–946

Willeit M, Sitte HH, Thierry N et al (2008) Enhanced serotonin transporter function during depression in seasonal affective disorder. Neuropsychopharmacology 33(7):1503–1513

Willeit M, Stastny J, Pirker W et al (2001) No evidence for in vivo regulation of midbrain serotonin transporter availability by serotonin transporter promoter gene polymorphism. Biol Psychiatry 50(1):8–12

Wilson AA, Garcia A, Parkes J et al (2008) Radiosynthesis and initial evaluation of [18F]-FEPPA for PET imaging of peripheral benzodiazepine receptors. Nucl Med Biol 35(3):305–314

Wilson AA, Ginovart N, Schmidt M et al (2000) Novel radiotracers for imaging the serotonin transporter by positron emission tomography: synthesis, radiosynthesis, and in vitro and ex vivo evaluation of C-11-labeled 2-(phenylthio)araalkylamines. J Med Chem 43(16):3103–3110

Wilson AA, Houle S (1999) Radiosynthesis of carbon-11 labelled N-methyl-2-(arylthio)benzylamines: potential radiotracers for the serotonin reuptake receptor. J Label Compd Radiopharm 42(13):1277–1288

Witte AV, Floel A (2011) Effects of COMT polymorphisms on brain function and behavior in health and disease. Brain Res Bull 88(5):418–428

Wu K, O'Keeffe D, Politis M et al (2012) The catechol-O-methyltransferase Val(158)Met polymorphism modulates fronto-cortical dopamine turnover in early Parkinson's disease: a PET study. Brain 135(Pt 8):2449–2457

Wu S, Comings DE (1999) A common C-1018G polymorphism in the human 5-HT1A receptor gene. Psychiatr Genet 9(2):105–106

Zalsman G, Huang YY, Oquendo MA et al (2006) Association of a triallelic serotonin transporter gene promoter region (5-HTTLPR) polymorphism with stressful life events and severity of depression. Am J Psychiatry 163(9):1588–1593

Zheng H, Wang X, Tang Z et al (2013) The PI3K/Akt and ERK1/2 signaling pathways mediate the erythropoietin-modulated calcium influx in kainic acid-induced epilepsy. Neuroreport 24:335–341

Zill P, Buttner A, Eisenmenger W, Bondy B, Ackenheil M (2004) Regional mRNA expression of a second tryptophan hydroxylase isoform in postmortem tissue samples of two human brains. Eur Neuropsychopharmacol 14(4):282–284

Part II

Systems

PET Imaging of Acetylcholinesterase

7

Hitoshi Shinotoh, Shigeki Hirano, and Hitoshi Shimada

Contents

H. Shinotoh (✉)
Department of Functional Brain Imaging Research, National Institutes for Quantum and Radiological Science and Technology, Chiba, Japan

Neurology Clinic Chiba, Chiba, Japan
e-mail: hitoshi.shinoto@nifty.com

S. Hirano
Department of Functional Brain Imaging Research, National Institutes for Quantum and Radiological Science and Technology, Chiba, Japan

Department of Neurology, Graduate School of Medicine, Chiba University, Chiba, Japan

H. Shimada
Department of Functional Brain Imaging Research, National Institutes for Quantum and Radiological Science and Technology, Chiba, Japan

Abstract

Acetylcholinesterase (AChE) is an enzyme that hydrolyzes acetylcholine and thereby regulates the concentration of the transmitter at the cholinergic synapse. AChE is frequently described as a marker of cholinergic neurons in the brain. Several cholinesterase inhibitors have been labeled with carbon-11 as radiotracers for visualizing AChE-binding sites. Among these, carbon-11-labeled methyl-4-piperidyl acetate (MP4A) and methyl-4-piperidyl propionate (MP4P or PMP) are successfully in clinical use for in vivo measurement of AChE activity. Both [^{11}C]MP4A and [^{11}C]PMP opened a window on cerebral cholinergic function in the human brain and have elucidated the role of cholinergic system in Alzheimer's disease, Parkinson's disease, and related disorders.

7.1 Introduction

Acetylcholine-mediated neurotransmission has been implicated in complex functions such as attention, memory, cognition, and consciousness (Bartus et al. 1982; Benarroch 2010). Its gradual loss, as in Alzheimer's disease (AD) and Parkinson's disease (PD), is associated with progressive deterioration of cognitive function (Bartus et al. 1982; Benarroch 2010; Hampel et al. 2018). Choline acetyltransferase (ChAT) is an enzyme that synthesizes acetylcholine, and acetylcholinesterase (AChE) is an enzyme that hydrolyzes acetylcholine and thereby regulates the concentration of the transmitter at the cholinergic synapse. ChAT is cytoplasmic within cholinergic neurons, mainly presynaptic, but also axonal (Mesulam and Geula 1992). In contrast, AChE is localized within the intersynaptic space, membrane bound predominantly on presynaptic cholinergic neurons, and on postsynaptic cholinoceptive neurons (Mesulam and Geula 1992). AChE and ChAT are frequently described as equivalent markers of cholinergic neurons in the brain.

AChE activity varies grossly across cerebral structures. The relative ratio of cerebral cortex/thalamus/cerebellar hemispheres/striatum is 1/3.5/10/33–45 for AChE activity in postmortem normal human brains (Atack et al. 1986; Arai et al. 1984). It may be challenging to obtain accurate measurement of AChE binding or activity in all regions with a single radiotracer. There are also species differences in brain AChE activity. AChE activity in the cerebellar hemispheres is similar to or smaller than that in the cerebral cortex of mice, rats, and rabbits (Shinotoh et al. 2004; Tavitian et al. 1993a; De Vos et al. 2000), while human cerebellar AChE activity is ten times higher than that in the cerebral cortex.

Acetylcholine is also cleaved by a less specific enzyme, butyrylcholinesterase (BuChE). BuChE can act as a molecular décor for natural anti-AChEs by reacting with these toxins before they reach AChE, but may also play a role in the regulation of cholinergic neurotransmission in specific brain regions (Darvesh et al. 2003). In postmortem AD brains, BuChE activity was found to be increased as the number of

senile plaques increased, while ChAT and AChE activities decreased (Perry et al. 1978). Therefore, radiotracers for AChE are required to have high selectivity for AChE over BuChE.

7.2   PET Radiotracers for Acetylcholinesterase

Several positron-emission tomography (PET) radiotracers for AChE binding sites or activity have been developed since the 1990s, while no PET radiotracer has been developed to measure ChAT-binding sites or activity until now. There are two major approaches to measuring AChE-binding sites or activity by radiotracers. One is the use of cholinesterase (ChE) inhibitors that bind to AChE. Another approach is the use of acetylcholine analogues that serve as substrates for AChE.

7.2.1   Cholinesterase Inhibitors

Several ChE inhibitors have been labeled with carbon-11 as radiotracers for visualizing AChE-binding sites (Shinotoh et al. 2004). Tacrine (THA) is a potent ChE inhibitor. An analogue of tacrine, 1,2,3,4-tetrahydro-9-methyl-amino-acridine (N-methylTHA, MTHA), was labeled with carbon-11, and the kinetics of [^{11}C]MTHA in baboon brains were investigated by PET (Tavitian et al. 1993a, b). The regional distribution of [^{11}C]MTHA, however, did not parallel that of AChE concentrations in baboon or human brains. This could be attributed to the fact that THA does not have selectivity for AChE over BuChE.

Physostigmine is a competitive ChE inhibitor that reversibly binds to AChE. Radioactivity distribution in the brain following intravenous injection of [^{11}C]physostigmine was found to correspond to the known distribution of AChE in baboons and humans (Tavitian et al. 1993b; Blomqvist et al. 2001). However, the kinetics of [^{11}C]physostigmine are so complex in vivo that this may hamper the quantitative assessment of AChE-binding sites (Blomqvist et al. 2001).

Some N-benzylpiperidines are potent and selective AChE inhibitors. Of these compounds, carbon-11-labeled CP126,998 was developed as a PET radiotracer for AChE (Bencherif et al. 2002). The regional brain uptake of [^{11}C]CP126,998 corresponded to the rank order of regional AChE distribution in mouse and human brains. The demethylated form of CP126,998 (CP118,954) is a more potent and selective AChE inhibitor than CP126,998. CP118,954 was labeled with fluorine-18 and evaluated for in vivo mapping of AChE in the mouse (Lee et al. 2004). Autoradiography showed high radioactivity accumulation in the striatum, an AChE-rich region.

Donepezil is a noncompetitive, high-affinity, reversible AChE inhibitor, and is widely used for the treatment of AD. Donepezil has over thousandfold more selectivity of AChE over BuChE. Donepezil was initially labeled with carbon-11 at the 6′ position (De Vos et al. 2000). Regional distribution studies in rabbit, however, did not show any correlation between the uptake of radioactivity and the amount of AChE. Subsequently, donepezil was labeled with carbon-11 at the 5′ position

([5-^{11}C-methoxy]donepezil), and the regional distribution study demonstrated heterogenous radioactivity uptake (striatum, brainstem > cerebral cortex > cerebellum) in the rat brain (Funaki et al. 2003). A PET study in humans demonstrated that intravenously injected [5-^{11}C methoxy]donepezil rapidly enters the brain and is mainly distributed in the striatum, thalamus, and cerebellum, which contain high densities of AChE compared with the cerebral cortex (Okamura et al. 2008). However, donepezil has moderate binding affinity for σ1-receptors that are widely distributed throughout the brain including the cerebral cortex, hippocampus, and cerebellum (De Vos et al. 2000; Ishikawa et al. 2009). Therefore, [5-^{11}C-methoxy]donepezil may not be a suitable PET ligand for measuring AChE-binding sites in the brain. Recently, [5-^{11}C-methoxy]donepezil has been used for the measurement of AChE density in human peripheral organs (Gjerløff et al. 2014).

7.2.2 Acetylcholine Analogue Substrates

7.2.2.1 Carbon-11-Labeled Compounds

Irie et al. (1994, 1996; Namba et al. 1994) examined several piperidyl esters as acetylcholine analogue substrates as radiotracers for the measurement of AChE activity in vivo in the brain (Fig. 7.1). N-methyl-3-piperidyl esters and N-methyl-4-piperidyl esters have a tertiary-amine structure, thereby making them lipophilic, and readily cross the blood-brain barrier. Both compounds are hydrolyzed by AChE in the brain, and yield a hydrophobic and polar metabolite, N-methylpiperidinol, which does not readily cross the blood-brain barrier and is thus trapped locally in the brain. Esters with a different acyl group or its position on the piperidine ring showed a wide range of enzymatic reactivity, about 40-fold, and specificity of the esters to AChE depends

Fig. 7.1 Two-tissue compartment model with three parameters describing the kinetic behavior of acetylcholine analogue substrates in the brain. AChE: acetylcholinesterase, BBB: blood-brain barrier
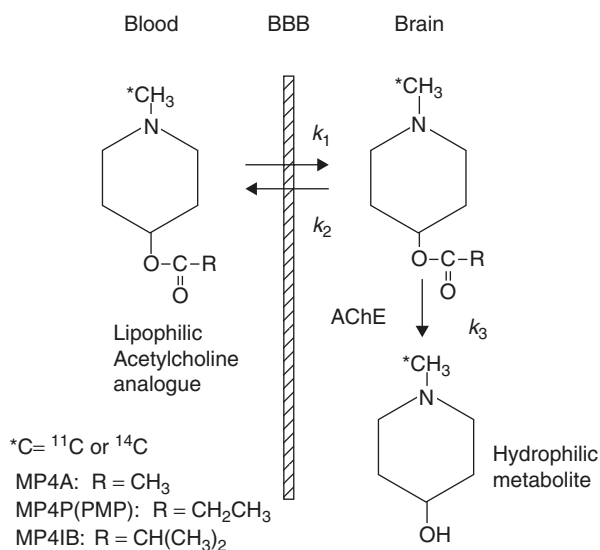
on the acyl group. The acetates (methyl-3-piperidyl acetate: MP3A; methyl-4-piperidyl acetate: MP4A) and propionates (methyl-3-piperidyl propionate: MP3P; methyl-4-piperidyl propionate: MP4P) have high specificity of more than 96% for AChE, followed by isobutyrates (methyl-3-piperidyl isobutyrate: MP3IB, 89%; methyl-4-piperidyl isobutyrate: MP4IB, 82%) and butyrate (MP3B, 45%). All of the esters (after labeling with carbon-14) showed rapid and high uptakes in the mouse brain followed by a slow decrease of radioactivity. Rank orders of brain uptake of these esters at 30 min postinjection were in accord with that of AChE activity in the mouse brain: striatum > cerebral cortex > cerebellar cortex. Chemical forms of ^{14}C radioactivity in the mouse brain after intravenous injections of MP3A and MP4A were analyzed by a thin-layer chromatography method. More than 95% of radioactivity was found to exist as hydrolytic metabolites ([^{14}C]MP3OH or [^{14}C]MP4OH). When [^{14}C]MP3OH or [^{14}C]MP4OH was intravenously injected in the mouse, only low brain uptakes were observed, indicating that these N-methylpiperidinols are so hydrophilic that they do not readily cross the blood-brain barrier. The 4-piperidyl series do not have asymmetrical carbon, while the 3-piperidyl series are asymmetrical and thus have optical isomers, and their kinetics have to be taken as averaged values of two optical isomers, a confounding factor in the interpretation of the kinetics of these radiotracers. Taken together, MP4A and MP4P are thought to be the most promising radiotracers for the measurement of AChE activity in the brain.

Furthermore, the brain kinetics of [^{14}C]MP4A and [^{14}C]MP4P were investigated in rats with a unilateral lesion in the nucleus basalis magnocellularis (nBM) (Irie et al. 1996). The nBM lesion reduced cortical AChE activity by 30–50% compared with that in the contralateral side of the cerebral cortex. Radioactivity uptakes 30 min postinjection of [^{14}C]MP4A and [^{14}C]MP4P were reduced by 21% and 27%, respectively, in the lesioned side of the cortex, suggesting that both radiotracers have sufficient sensitivity to capture less than 50% of AChE activity changes in the cerebral cortex (Irie et al. 1996).

Kilbourn et al. (1996) examined the kinetics of [^{11}C]MP4A and [^{11}C]MP4P (or [^{11}C]PMP; they preferred to call [^{11}C]PMP) in mice and monkeys. They found that regional brain distributions after intravenous injection of [^{11}C]PMP showed better discrimination between regions of high, intermediate, and low AChE activities than [^{11}C]MP4A because the hydrolysis rate of acetylcholine by MP4P is about one-fourth that by MP4A (Table 7.1) (Shinotoh et al. 2004; Irie et al. 1996; Kilbourn et al. 1996).

Currently, both [^{11}C]MP4A and [^{11}C]PMP are in clinical use for studies of various neurodegenerative diseases by PET (Tables 7.2 and 7.3). [^{11}C]MP4A has higher specificity for AChE over BuChE than [^{11}C]PMP in the human cerebral cortex (Table 7.1) (Shinotoh et al. 2004; Irie et al. 1996). [^{11}C]MP4A-PET gives precise estimates of k_3, an index of AChE activity, in the cerebral cortex, while [^{11}C]PMP provides precise measurement of k_3 in the cerebral cortex and thalamus. In the striatum, both radiotracers give poor estimates of k_3 values because of the delivery limitation effect.

Table 7.1 Characteristics of two radiotracers for measurement of acetylcholinesterase activity

| Radiotracer | Selectivity for AChE | | Relative hydrolysis rate (Irie et al. 1994) | PET scan time | Optimum brain regions for measurement in humans |
	Mouse brain (Irie et al. 1994)	Human cerebral cortex (Irie et al. 1996)			
[11C]MP4A	99%	94%	4.43	40–60 min	Cerebral cortex (thalamus)
[11C]PMP	97%	86%	0.97	60–80 min	Cerebral cortex, thalamus, (cerebellar cortex) (striatum)

AChE: acetylcholinesterase, [11C]MP4A: [11C]N-methylpiperidine-4-yl acetate, [11C]PMP: [11C]N-methylpiperidine-4-yl propionate

Table 7.2 PET studies in Alzheimer's disease and related disorders

Radiotracer	Author	Year	Subjects	Main findings on AChE activity
[11C] MP4A	Iyo et al. (1997)	1997	5 AD, 8 HC	Reduction in neocortex (19–38%) in AD patients
[11C]PMP	Kuhl et al. (1999)	1999	14 AD, 26 HC	Reduction in neocortex and hippocampus (25–33%) in AD patients
				Inhibition (50%) in brain AChE activity after 1.5 mg dose of physostigmine infusion
[11C] MP4A	Shinotoh et al. (2000)	2000	30 AD, 14 HC	Reduction in neocortex (23%), hippocampus (21%), and amygdala (27%) in EOAD Reduction in temporoparietal cortex (14%, 18%) and amygdala (26%) in LOAD Progressive loss of cortical AChE activity in 7 repeat PET scans in AD Correlation between cortical AChE activity and MMSE scores in 37 AD patients
[11C]PMP	Kuhl et al. (2000)	2000	9 AD	Inhibition (27%) of cortical AChE activity after 5–10 mg/day donepezil treatment
[11C] MP4A	Shinotoh et al. (2001)	2001	3 AD	Inhibition (39 ± 5%) of cortical AChE activity after 3–5 mg/day donepezil treatment
[11C] MP4A	Kaasinen et al. (2002)	2002	11 AD	Inhibition (28–39%) of cortical AChE activity after 10 mg/day donepezil treatment Inhibition (28–37%) of cortical AChE activity after 9 mg/day rivastigmine treatment
[11C] MP4A	Rinne et al. (2003)	2003	13 AD, 12 MCI, 12 HC	Reduction of AChE activity in hippocampus in MCI patients (17%) and in AD patients (27%)
[11C] MP4A	Herholz et al. (2004)	2004	9 AD, 13 HC	Reduction of cortical AChE activity (18–34%) in AD, [11C]MP4A uptake preserved in nbM
[11C]PMP	Bohnen et al. (2005a)	2005	15 AD, 12 HC	Cortical AChE activity associated with performance on a test of attention and working memory

Table 7.2 (continued)

Radiotracer	Author	Year	Subjects	Main findings on AChE activity
[^{11}C]PMP	Bohnen et al. (2005b)	2005	14 AD	Inhibition (19.1%) of cortical AChE after 10 mg/day donepezil treatment. Degree of cortical AChE inhibition correlates with executive and attentional functional changes
[^{11}C] MP4A	Eggers et al. (2006)	2006	19 AD	Preserved cortical AChE activity in ApoE4-positive patients compared with negative patients
[^{11}C] donepezil	Okamura et al. (2008)	2007	10 AD, 6 HC	Reduction (18–30%) of cortical [^{11}C] donepezil binding in AD. Inhibition (62–63%) of cortical [^{11}C] donepezil binding after 5 mg/day donepezil treatment
[^{11}C]PMP	Kadir et al. (2008)	2008	18 AD	Inhibition (30–40%) of cortical AChE activity after galantamine (16–24 mg/day) treatment
[^{11}C]PMP	Bohnen et al. (2009a)	2009	28 elderly subjects	Severity of periventricular WMH was related to cortical AChE activity
[^{11}C] MP4A	Marcone et al. (2012)	2012	10 MCI, 7 AD, 4 DLB, 9 HC	Reduction of cortical and hippocampal AChE activity in MCI patients and in AD patients
[^{11}C] MP4A	Haense et al. (2012)	2012	17 MCI, 21 HC	Decline of cortical AChE activity, most pronounced in temporal regions in MCI
[^{11}C] MP4A	Garibotto et al. (2013)	2013	9 MCI, 7 AD, 9 HC	Correlation between education and hippocampal AChE activity. Correlation between occupation and AChE activity in right posterior cingulate cortex
[^{11}C] MP4A	Richter et al. (2014)	2014	14 elderly subjects	AChE activity in right medial temporal lobe correlated with episodic memory function
[^{11}C] MP4A	Shimada et al. (2015)	2015	14 DLB, 25 AD, 18 HC	Reduction of cortical AChE activity was consistently prominent in DLB than AD patients
[^{11}C] MP4A	Richter et al. (2017)	2017	17 MCI, 18 HC	Periventricular WML negatively correlated with brain AChE activity in MCI and HC
[^{11}C] MP4A	Richter et al. (2018)	2018	14 MCI, 16HC	Reduction of cortical AChE, especially in lateral temporal lobe. Association of change in neural activation in response to rivastigmine with local AChE activity
[^{11}C] MP4A	Hirano et al. (2018)	2018	22 EOAD, 26 LOAD, 16 HC	Reduction of wider cortical AChE activity in EOAD than LOAD

AD: Alzheimer's disease, HC: healthy controls, EOAD: early-onset AD, LOAD: late-onset AD, MCI: mild cognitive impairment, nbM: nucleus basalis of Meynert, WMH(L): white matter hyper-intensities (load), DLB: dementia with Lewy bodies

Table 7.3 PET studies in Parkinson's disease and related disorders

Radiotracer	Author	Year	Subjects	Main findings on AChE activity
[¹¹C]MP4A	Shinotoh et al. (1999)	1999	16 PD, 12 PSP, 13 HC	Reduction of cortical (17%) and thalamic (13%) AChE activity in PD Prominent reduction (38%) of thalamic but not cortical AChE activity in PSP
[¹¹C]PMP	Bohnen et al. (2003)	2003	11 PD, 14 PDD, 12 AD, 10 HC	More severe reduction of cortical AChE activity in PD with dementia than AD
[¹¹C]MP4A	Hilker et al. (2005)	2005	17 PD, 1 PDD, 31 HC	Reduction (10.7%, 29.7%) of cortical AChE activity in PD and PDD
[¹¹C]MP4A	Hirano et al. (2006)	2006	2 FTDP-17	Prominent reduction of cortical (13% to 44%) and thalamic (57%) AChE activity
[¹¹C]PMP	Bohnen et al. (2007)	2006	12 PD, 6 PDD, 10 HC	Inverse correlation between cortical AChE activity and depression scale
[¹¹C]PMP	Hirano et al. (2008)	2008	8 MSA-C, 7 SCA-3, 3 SCA-6, 13 HC	Reduction of AChE activity in thalamus (27%) and cerebellar cortex (36%) in MSA-C Reduction of AChE activity in thalamus (23%) in SCA-3
[¹¹C]MP4A	Shimada et al. (2009)	2009	18 PD, 21 PDD/DLB, 26HC	Reduction (12%) of cortical activity, especially in medial occipital cortex in PD Severe reduction (27%) of cortical AChE activity in PDD/DLB
[¹¹C]PMP	Bohnen et al. (2009b)	2009	44 PD, 15 HC	Reduction of cortical (12.3%) and thalamic (11.8%) AChE activity in PD fallers PD non-fallers showed reduction (6.6%) of AChE activity only in cortex
[¹¹C]MP4A	Hirano et al. (2010)	2010	7 CBS, 12 PSP, 8 FTD, 16 HC	Reduction of cortical (17.5%) but not thalamic AChE activity in CBS Reduction of cortical (9.4%) and thalamic (24%) AChE activity in PSP No reduction of brain AChE activity in FTD
[¹¹C]PMP	Gilman et al. (2010)	2010	12 PD, 13 MSA-P, 4 PSP, 22 HC	Cortical AChE reductions were 15.3%, 14.6%, 13.2% in PD, MSA-P, PSP Subcortical AChE activities were more decreased in MSA-P and PSP than in PD

Table 7.3   (continued)

Radiotracer	Author	Year	Subjects	Main findings on AChE activity
[^{11}C] MP4A	Miyoshi et al. (2010)	2010	3 Presymptomatic FTDP-17	One presymptomatic subject showed reduction of cortical AChE activity
[^{11}C]PMP	Bohnen et al. (2012)	2012	101 PD, 29 HC	Low neocortical AChE activity PD subgroup had lower cognitive performance More than half of low thalamic AChE activity PD subgroup had history of falls
[^{11}C]PMP	Kotagal et al. (2012)	2012	80 PD	Reduction of cortical and thalamic AChE activity in PD with RBD ($n = 27$) in comparison to those without RBD ($n = 53$)
[^{11}C]PMP	Bohnen et al. (2013)	2013	125 PD, 32 HC	PD group with low cortical AChE activity had slower gait speed
[^{11}C]PMP	Bohnen et al. (2014)	2014	143 PD	90% of PD with freezing of gait had cortical AChE activity reduction or amyloid deposition
[^{11}C]PMP	Weather et al. (2014)	2014	30 PD	Less thalamic ACh activity in risky drivers compared to safe drivers
[^{11}C]PMP	Bohnen et al. (2015)	2015	143 PD	Cortical cholinergic denervation frequency increased with increasing cognitive impairment
[^{11}C]PMP	Müller et al. (2015)	2015	137 PD	Combination of RBD and fall history is a predictor for thalamic and cortical deficits
[^{11}C]PMP	Chou et al. (2016)	2016	133 PD	Cholinergic uptake was not a predictor of fatigue in PD
[^{11}C] donepezil	Gjerløff et al. (2015)	2015	12 PD, 12 HC	Reduction of [^{11}C]donepezil binding in small intestine (35%), and pancreas (22%)
[^{11}C] donepezil	Fedorova et al. (2017)	2017	19 early PD, 16 HC	Reduction of [^{11}C]donepezil binding in small intestine (14%), colon (22%), and kidney (14%)
[^{11}C]PMP	Liu et al. (2018)	2018	14 LRRK2 PD, 16 LRRKs mutation carriers, 8 PD, 11 HC	Increased cortical AChE activity in LRRK2 mutation carriers compared with HC Increased cortical and thalamic AChE activity in LRRK2 PD compared with PD

PD: Parkinson's disease, PSP: progressive supranuclear palsy, HC: healthy controls, PDD: PD with dementia, FTDP-17: frontotemporal dementia with parkinsonism linked to chromosome 17, MSA-C: cerebellar syndrome of multiple system atrophy, SCA-3: spinocerebellar atrophy type 3, DLB: dementia with Lewy bodies, CBS: corticobasal syndrome, FTD: frontotemporal dementia, MSA-P: parkinsonian syndromes of multiple system atrophy, RBD: REM sleep behavior disorder

7.2.2.2 Kinetics Analysis of [^{11}C]MP4A and [^{11}C]PMP

[^{11}C]MP4A and [^{11}C]PMP are irreversible PET radiotracers. Irreversible tracers are generally analyzed using a two-tissue compartment model—one representing an authentic radiotracer, and a second representing a metabolically trapped radiotracer (Fig. 7.1). The two-tissue compartment configuration has three rate parameters, K_1 to k_3. K_1 is defined as the transfer rate of an authentic tracer from plasma to tissue, k_2 is the efflux rate of authentic tracer from tissue to plasma, and k_3 is the hydrolysis rate of authentic tracer by AChE. The model does not require the parameter k_4 because hydrolysis by AChE is completely irreversible. The three parameters are estimated by fitting regional brain time-radioactivity curves with plasma input function to the following theoretical function in a nonlinear least-squares method:

$$C_t = C_b + C_m, \tag{7.1}$$

$$C_b = \int_0^T K_1 C e^{-(k_2+k_3)(T-t)} dt, \tag{7.2}$$

$$C_m = \int_0^T k_3 C_b dt, \tag{7.3}$$

where C_b and C_m represent authentic and metabolized tracers, respectively.

An irreversible radiotracer is required to be matched well between the rate of trapping (k_3) and the rate of blood-brain barrier transport (K_1 and k_2) (Koeppe et al. 1999). The ratio of the metabolic rate (k_3) and the efflux rate (k_2), i.e., $\alpha \equiv k_3/k_2$, can affect the reliability of data from compartment model analysis (Koeppe et al. 1999). A simulation study showed that the optimal α-value with the maximal precision of k_3 parameter is around 0.2 in the two-tissue compartment model with the three parameters (Ohya et al. 2011). The good precision of k_3 estimates was maintained when the tracer α-value was within a range of approximately 0.05–1.0 (optimal α range). With k_2 values of about 0.13 min^{-1} (Namba et al. 1999), the α-value was calculated to be 0.48–0.73 in the cerebral cortex in healthy volunteers in a [^{11}C]MP4A PET study, although α-values in the thalamus, cerebellum, and striatum fell outside of the optimal range. In a [^{11}C]PMP PET study, the α-value was about 0.15–3.3 in the brain, and α-values in the striatum fell outside of the optimal range (Koeppe et al. 1999).

Radioactivity in the cerebral cortex gradually decreased, reaching a plateau after an initial high uptake following intravenous injection of [^{11}C]MP4A in 20 healthy volunteers, while that in the cerebellum and striatum gradually increased to reach a plateau at about 20 min following an initial rapid uptake (Fig. 7.2) (Namba et al. 1999). The radioactivity curve of the thalamus is between those of the cerebellum and the cerebral cortex. The plateau level of radioactivity in those regions suggests that washout of the radioactive metabolite from the brain is negligible during PET measurement. Each of the plateau levels was in accord with the regional distribution of AChE activity in the brain (Figs. 7.2 and 7.3). The fraction of [^{11}C]MP4A in the total plasma radioactivity rapidly decreases along bi-exponential curves to reach a

Fig. 7.2 Time-activity curves in the brain and plasma in a 66-year-old healthy man following intravenous injection of [^{11}C]MP4A (**a**), and time-activity curves in the brain in a 63-year-old healthy man following intravenous injection of [^{11}C]PMP (**b**)
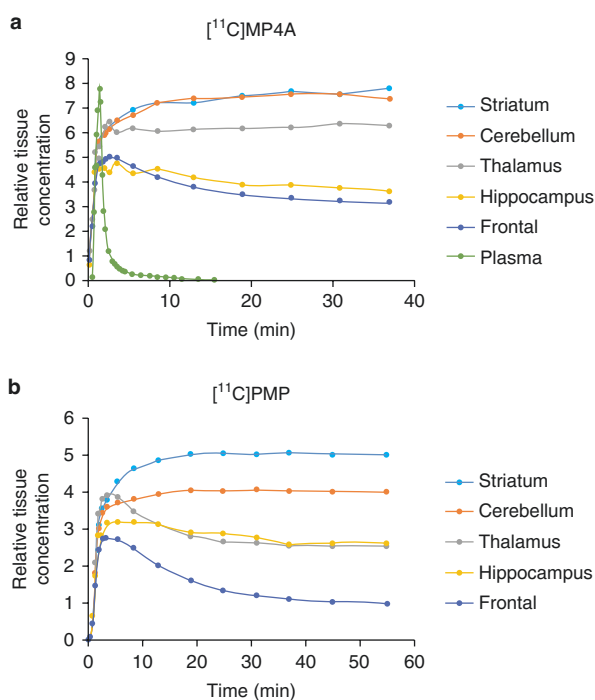
low level of less than 5% within 15 min (Fig. 7.2a) (Namba et al. 1999). [^{11}C]MP4A PET scans are usually performed for 40–60 min. In the two-tissue compartment model with the three parameters, the k_3 values in the cerebral cortices were estimated with coefficients of variation of less than 15% in 20 healthy subjects by a nonlinear least-squares method (Namba et al. 1999). In the regions with higher AChE activity (thalamus, cerebellum, and striatum), an obvious washout phase of time-activity curves is not observed, and thus k_2 is estimated to be almost zero, leading to underestimation of k_3 values. Reasonable k_3 values in the regions with high AChE activity would be obtained by constraining K_1/k_2 values. We constrained the K_1/k_2 values in the thalamus, cerebellum, and striatum to be the mean ± 2SD of fitted K_1/k_2 values in the cerebral cortices for each subject (Namba et al. 1999). This constraint of the K_1/k_2 values was based on the assumption that the tissue distribution volume of authentic tracers is approximately uniform across the brain. In this analysis, the k_3 values in the thalamus were estimated with coefficients of variation of 20% (Namba et al. 1999). The coefficients of variation of k_3 values in the cerebellum and striatum were 46% and 161% in this analysis, suggesting that k_3 estimates in those regions are not reliable.

Based on the characteristic kinetics of [^{11}C]MP4A, a unique kinetic analysis was developed (Nagatsuka et al. 2001; Herholz et al. 2001). Since metabolism of [^{11}C]MP4A by AChE in the striatum and cerebellum is very high, it is assumed that all [^{11}C]MP4A molecules entering these regions would be trapped there (metabolic
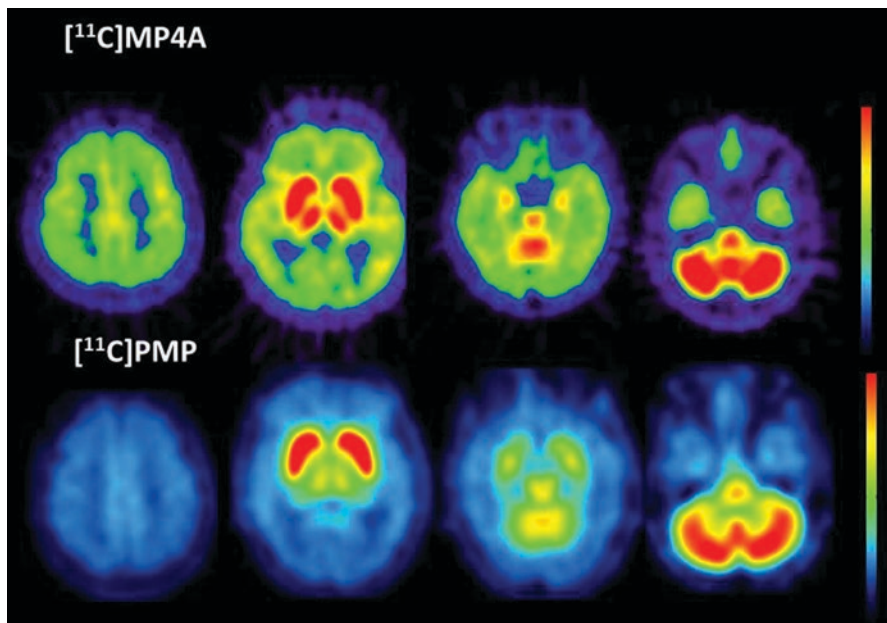
Fig. 7.3 PET images of a 66-year-old healthy man 20–40 min following intravenous injection of [^{11}C]MP4A (upper row), and PET images of a 63-year-old healthy man 40–60 min following i.v. injection of [^{11}C]PMP. These images were scanned at the National Institutes for Quantum and Radiological Science and Technology, Japan

trapping). This assumption allows the use of the striatum or cerebellum as reference regions to obtain input function data in the form of a single integral with respect to PET scan time:

$$C_R(t) = K_1^{REF} \int_0^t Ca(\theta) d\theta$$

where $C_R(t)$ is radioactivity in the reference region, and K_1^{REF} is the value of K_1 in this region.

When such input function data is applied to Blomqvist's linear approach (Blomqvist 1984), the kinetics parameter k_3 can be estimated from PET data alone without arterial blood sampling: (Nagatsuka et al. 2001; Herholz et al. 2001)

$$C_T(t) = p_1 CR(t) + p_2 \int_0^t CR(\theta) d\theta + p_3 \int_0^t CT(\theta) d\theta \tag{7.4}$$

$$p_1 = \frac{K_{1Target}}{K_{1REF}} \equiv K_R \tag{7.5}$$

$$p_2 = K_R \cdot k_3 \tag{7.6}$$

$$p_3 = -(k_2 + k_3) \tag{7.7}$$
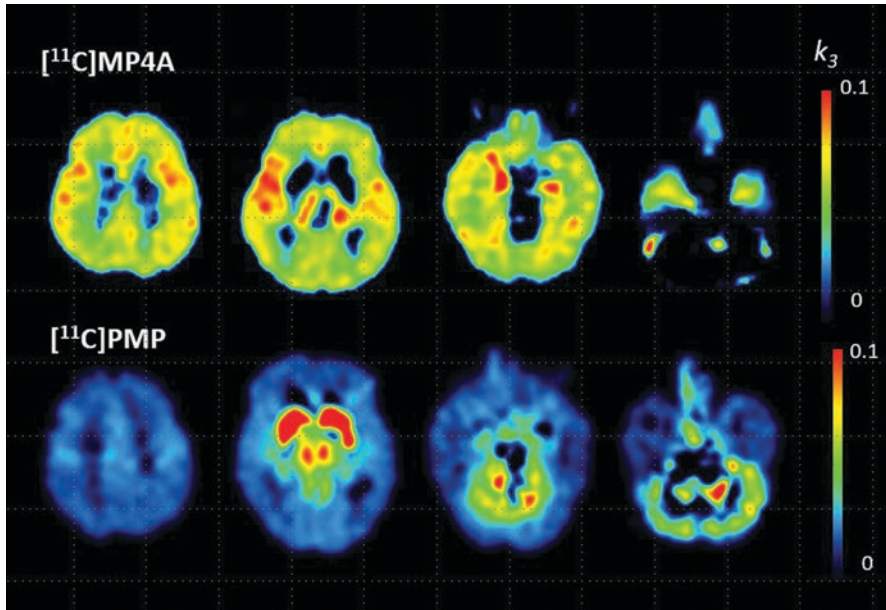
Fig. 7.4 Parametric (k_3) images of a 66-year-old healthy man in a [11C]MP4A PET study (upper row), and parametric (k_3) images of a 63-year-old healthy man in a [11C]PMP PET study. Both parametric images of [11C]MP4A were obtained by Nagatsuka's reference tissue-based linear least-squares (RLS) analysis implemented in PMOD 4.0 (PMOD Technologies LLC, Zürich, Switzerland). Note that k_3 could not be estimated in the striatum and cerebellum by [11C]MP4A PET and a part of the cerebellum and brainstem by [11C]PMP PET

In this approach, the rate of tracer influx into the target region is obtained as a relative value K_R.

This method is applicable to [11C]PMP PET. In the case of [11C]PMP, the striatum is preferable to the cerebellum because of its slower kinetics. This kinetic analysis without blood sampling is known as reference tissue-based linear-least squares (RLS) analysis, and is often employed in clinical [11C]MP4A or [11C]PMP PET studies (Fig. 7.4).

The time-activity curves of [11C]PMP in the brain and blood are similar but slower than those of [11C]MP4A. Koeppe et al. (1999) examined the kinetics of [11C]PMP in 12 healthy volunteers. Sequential [11C]PMP PET scans were performed for 80 min. They found that [11C]PMP can be used with dynamic PET to provide an in vivo index of local AChE activity (k_3) with excellent precision in the cerebral cortex (coefficient of variation less than 10% in healthy volunteers) and other regions of low enzyme activity by unconstrained nonlinear least-squares fit to the theoretical model. The excellent precision was thought to be due to its bolus-like input function shape, complete irreversibility, and near-optimal kinetic properties. Estimates of k_3 were poorer in regions of high enzyme activity such as the striatum and cerebellum because of excessive bias and variability caused by

delivery-limitation effects. The constraint on K_1/k_2 was required to yield meaningful estimates. Koeppe et al. constrained K_1/k_2 values by two methods. In one method, the K_1/k_2 ratio was fixed at 4.0. This estimate of the AChE activity index was referred to as the constrained least-squares estimate of k_3c. In the other method, $* k_3$ (modified k_3) was defined as unconstrained k_3 multiplied by unconstrained K_1/k_2. This was based on the following facts. In regions with high AChE activity, the estimates of k_2 and k_3 become extremely variable, but they remain highly correlated. If k_3 is underestimated, k_2 is underestimated, while K_1 continues to be estimated precisely. Modified k_3 value was defined as follows:

$$*k_3 = k_3 \left[\left(K_1 / k_2 \right) / 4.0 \right] \left(\text{min}^{-1} \right) \tag{7.8}$$

This estimate of the AChE activity index was referred to as the constrained least-squares estimate of $* k_3$. These constrained least-square estimates of k_3c and $* k_3$ yielded meaningful estimates of AChE activity in the thalamus, cerebellum, and striatum in the [11C]PMP PET study.

Koeppe et al. (1999) proposed another method to estimate k_3 entirely from the shape of the tissue time-activity curve without arterial blood sampling or plasma metabolite analysis (shape analysis) (Koeppe et al. 1999). The following conditions are required for this approach to be valid: the concentration of authentic tracer in arterial plasma must reach zero during the study period, and hydrolysis of the substrate PMP is completely irreversible. Under these assumptions, two further conditions hold: (Bartus et al. 1982) all radiotracer in brain is in the free compartment at the start of the study, and all radiotracer in the brain is in the metabolite compartment by the end of the study. Shape analysis is applicable only to brain areas of low activity such as the cerebral cortex because estimates of k_3 values in brain regions with high enzyme activity become progressively more inaccurate. This shape analysis is also applicable to [11C]MP4A, although the sensitivity of shape analysis for detecting neocortical regions with abnormally low k_3 in AD patients is less than the conventional compartment analysis with arterial sampling (Tanaka et al. 2001).

7.2.2.3 Fluorine-18-Labeled Compounds

There have been several attempts to develop acetylcholine analogues labeled with fluorine-18 (Kikuchi et al. 2005, 2010, 2013; Shao et al. 2005; Zhang et al. 2003). Fluorine-18-labeled derivatives of MP4A or PMP may allow for the delivery of radiotracers to other PET centers since fluorine-18 has a longer half-life (109.8 min) than carbon-11 (20.4 min). N-[18F]fluoroethylpiperidin-4-yl acetate ([18F]FEtP4A) was synthesized as an [18F]fluoroethylated MP4A derivative.[33] Disappointingly, an in vitro study of [18F]FEtP4A showed that this compound has a much lower specificity for AChE compared with [11C]MP4A and a much slower (approximately one-twentieth) AChE-mediated hydrolysis rate compared with MP4A in rat cerebral cortical homogenate or test tube with pure enzyme.

A series of N-[14C]ethylpiperidin-3-yl or -4-ylmethanol esters (acetyl and propionyl esters) were newly designed and evaluated in an in vitro screening study (Kikuchi et al. 2005, 2010, 2013). N-[18F]fluoroethylpiperidin-4-ylmethyl acetate ([18F]FEP-4MA) was identified as a potential 18F-labeled compound for measuring

cerebral AChE activity. In rat experiments, [^{18}F]FEP-4MA showed high brain uptake of the authentic ester, high AChE specificity, a moderate hydrolysis rate, and low membrane permeability of the metabolite, although the metabolite was slowly eliminated from the brain, probably by efflux transporters (Kikuchi et al. 2010, 2013). A simulation study and a monkey study of [^{18}F]FEP-4MA were performed. In the simulation study, it was investigated how the tracer α-value affected k_3 precision under a different efflux rate constant (k_{el}) (Ohya et al. 2011). A nonlinear least-squares analysis of the [^{18}F]FEP-4MA PET data showed that the precision of the k_3 estimate was as high as that for [^{11}C]MP4A, as the ratio of k_{el} to the efflux rate (k_2) was relatively small (<0.1), suggesting that [^{18}F]FEP-4MA may be useful as a radiotracer for the measurement of AChE activity in humans (Ohya et al. 2011).

7.3 Clinical Applications of Acetylcholinesterase Imaging

7.3.1 Healthy Older Adults

Aging is a major risk factor for AD, and it is therefore of interest to study the effect of age on brain AChE activity. There was no alteration of cortical AChE activity in 23 healthy volunteers ranging in age from 24 to 89 years old in a [^{11}C]MP4A PET study (Namba et al. 1998, 1999). Likewise, Kuhl et al. (1999) did not find any effect of age on cortical AChE activity measured by [^{11}C]PMP PET in 26 healthy volunteers ranging in age from 23 to 80 years. There was also no gender effect on cortical AChE activity (Kuhl et al. 1999).

Richter et al. (2014) investigated the relationship between brain AChE activity measured by [^{11}C]MP4A PET and memory performance in 14 healthy older adults ranging in age from 53 to 77 years. They found a significant correlation between AChE activity in the right medial temporal lobe and number of words recalled after a delay, suggesting that the integrity of the cholinergic system underlies interindividual variability in memory function.

7.3.2 Alzheimer's Disease and Related Disorders

Impairment of memory and learning by cholinergic antagonists was demonstrated by pharmacological studies of healthy volunteers in the 1970s (Bartus et al. 1982). In the mid-1970s, depletions of presynaptic cholinergic markers, ChAT and AChE activity, were found in postmortem brains with AD (Perry et al. 1978; Davies and Maloney 1976). In 1982, pronounced loss of cholinergic neurons in the nucleus basalis of Meynert in postmortem brains with AD was demonstrated (Whitehouse et al. 1982). These discoveries led to the cholinergic hypothesis of AD (Bartus et al. 1982).

In 1997, we showed an average reduction of 31% of cortical AChE activity in 5 mild AD patients compared with 12 healthy controls in a [^{11}C]MP4A PET study with arterial input function (Iyo et al. 1997). Subsequently, we showed different reduced distributions of brain AChE activity between 14 patients with early-onset

AD (EOAD) and 14 patients with late-onset AD (LOAD) by [^{11}C]MP4A PET (Shinotoh et al. 2000). AChE activity was reduced in the entire neocortex (23% on average), hippocampus (21%), and amygdala (27%) in EOAD patients, while AChE activity was reduced only in the temporoparietal cortex (14, 18%) and amygdala (26%) in LOAD patients. Seven AD patients had repeat PET scans with a mean interval of 2 years, and cortical AChE activity had reduced further in the second PET scans, suggesting a progressive loss of the ascending cholinergic system from the nucleus basalis of Meynert in AD. There was a highly significant correlation between cortical AChE activity and Mini-Mental State Examination (MMSE) scores, supporting the cholinergic hypothesis in AD. Recently, we conducted voxel-based AChE activity estimation of [^{11}C]MP4A PET data in an unconstrained nonlinear least-squares method with arterial input in 22 EOAD patients, 26 LOAD patients, and 16 healthy controls (Hirano et al. 2018). Both the EOAD and LOAD groups showed cortical AChE activity decrement in parietal, temporal, and occipital cortices, with wider and stringent cortical involvement in the EOAD group, most prominently in the temporal region, compared with healthy controls (Fig. 7.5). Herholz
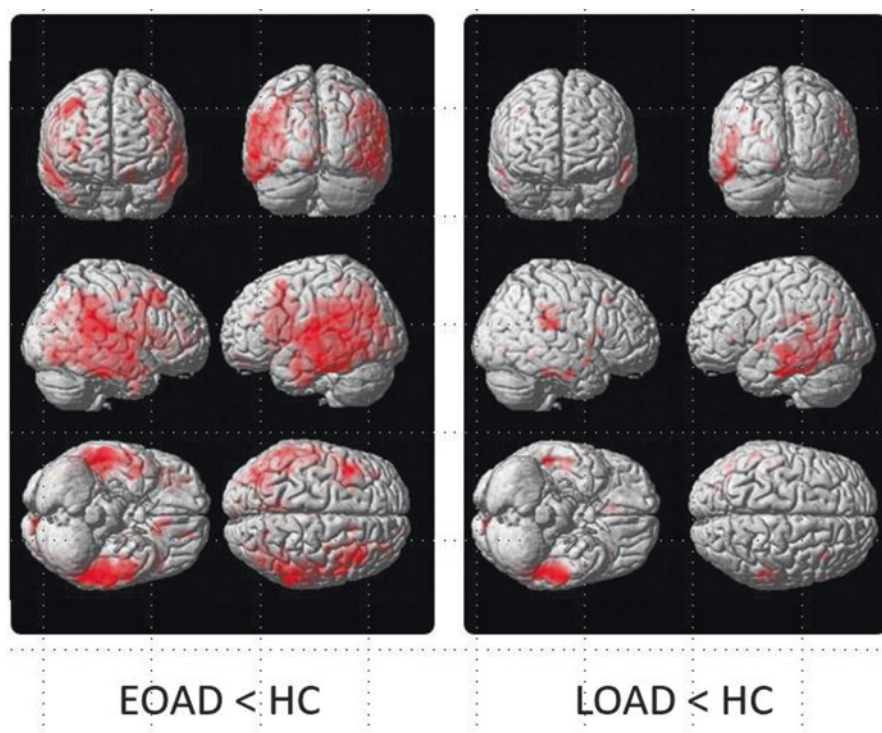
Fig. 7.5 Acetylcholinesterase (AChE) activity reduction in early-onset AD (EOAD) ($n = 22$) and late-onset AD (LOAD) ($n = 26$) in comparison with 16 healthy controls (HC). Statistical parametric T-score maps, with red-yellow color representing AChE activity reduction, are superimposed on a single subject T1, thresholded at voxel-level $p < 0.05$; family-wise error (FEW) corrected with cluster above 30 voxels

et al. (2004) found reduction of AChE activity in the cerebral cortex and amygdala but not in the nucleus basalis of Meynert in mild-to-moderate AD in a [^{11}C]MP4A PET study, suggesting that neocortical and amygdaloid function changes of the cholinergic system are an early and leading event in AD, rather than the consequence of neurodegeneration of basal nuclei.

Kuhl et al. (1999) found a reduction of neocortical (25–33%) and hippocampal AChE activity in 14 moderate-severe AD patients with a mean MMSE score of 14 by [^{11}C]PMP PET. There was no reduction of AChE activity in the caudate, putamen, thalamus, pons, and cerebellum.

Bohnen et al. (2005a) found that cortical AChE activity is more robustly associated with functions of attention and working memory (WAIS-III Digit Span, $R = 0.46$, $P = 0.01$) compared to performance on primary memory tests (California Verbal Learning Test).

The E4 allele of apolipoprotein ε (ApoE4) is the major genetic risk factor for AD, and increases the formation of amyloid plaques and neurofibrillary tangles. Eggers et al. (2006) examined the relation between ApoE genotype and cortical AChE activity in 19 patients with mild-to-moderate AD by [^{11}C]MP4A PET. The ApoE4-positive patients ($n = 11$) had significantly higher AChE levels than the ApoE4-negative ($n = 8$) patients, while the two groups were comparable with regard to age and dementia severity. Higher AChE levels in ApoE4-positive patients could be attributed to AChE activity in amyloid plaque in the brain.

Rinne et al. (2003) measured brain AChE activity in 12 patients with mild cognitive impairment (MCI), 13 AD patients, and 12 healthy elderly volunteers by [^{11}C]MP4A PET. There was a significant difference in AChE activity only in the hippocampus between the groups, and hippocampal AChE activity was only slightly reduced in MCI (17%) and early AD (27%). They concluded that the value of in vivo AChE activity measurements in detecting early AD is limited.

Marcone et al. (2012) assessed AChE activity with [^{11}C]MP4A PET in 10 patients with multi-domain amnestic MCI (aMCI), 7 AD patients, and 9 healthy controls. They found widespread AChE reductions in several cortical regions and in hippocampus in all AD and aMCI patients who progressed to AD with a follow-up of 2 years. There was also a significant correlation between hippocampal AChE activity and long-term verbal and nonverbal memory. In addition, Haense et al. (2012) found a significant decline of cortical AChE activity in 17 MCI patients.

Richter et al. (2018) measured brain AChE activity by [^{11}C]MP4A PET in 14 patients with MCI due to AD who had positive cerebrospinal fluid biomarkers indicative of AD pathology, and 16 age-matched healthy controls. AChE activity was significantly decreased in the cerebral cortex (11%), and this decrease was most pronounced in the lateral temporal lobes of MCI patients relative to healthy controls. The MCI patients showed less memory-related neural activation in the fusiform gyrus and impaired deactivation in the posterior cingulate cortex, relative to heathy controls, by functional magnetic resonance imaging (fMRI). These differences were attenuated under cholinergic stimulation with rivastigmine. The change in neural activation in response to rivastigmine was negatively associated with local AChE activity.

Garibotto et al. (2013) investigated reserve capacity by [^{11}C]MP4A PET in nine patients with MCI, seven patients with early AD, and nine healthy controls. They found a positive correlation between education and AChE activity in the hippocampus bilaterally, and between occupation and AChE activity in the right posterior cingulate gyrus.

White matter lesions (WML) are observed in cognitively normal older persons and may be associated with cognitive dysfunction. One possible mechanism of cognitive decline in individuals with WML is disruption of cholinergic fibers by strategically located WMLs. Bohnen et al. (2009a) investigated the relationship between WML and cortical cholinergic AChE activity in 18 subjects without dementia ranging in age from 55 to 84 years. The severity of periventricular WML but not nonperiventricular WMH was inversely related to global cortical AChE activity. There was an inverse correlation between cortical AChE activity and reaction time in Conners Continuous Performance Test. On the way from the nucleus basalis of Meynert, cholinergic fibers are initially tightly packed in bundles, fanning out toward the cortex after passing the basal ganglia and ventricles (Selden et al. 1998). In proximity to the ventricles, their density is much higher than in deep white matter, which could explain why only periventricular white matter is related to cortical AChE activity.

Richter et al. (2017) investigated the relationship between periventricular WML, cortical AChE activity, and memory function in 18 patients with MCI due to AD and 18 cognitively normal older participants. Only periventricular, not non-periventricular, WML load negatively correlated with cortical AChE activity in both groups. AChE activity predicted memory function better than WML load, suggesting that the effects of WML load on memory were fully mediated by AChE activity.

AChE PET allows a direct measurement of the degree of AChE inhibition by therapeutic AChE inhibitors. Kuhl et al. (2000) found that mean AChE inhibition in the cerebral cortex of AD patients was $26 \pm 12\%$ and $27 \pm 11\%$ after donepezil doses of 5 or 10 mg/day for at least 5 weeks. Since 80–90% red blood cell AChE inhibition in humans by these doses of donepezil had been reported, they concluded that AChE inhibition in vivo in living Alzheimer cerebral cortex by these doses of donepezil was limited. We found that 3–5 mg/day donepezil treatment reduced cortical AChE activity by 29–39% in three AD patients (Shinotoh et al. 2001). Bohnen et al. (2005b) observed a correlation between the degree of cortical AChE inhibition and changes in executive and attentional function by donepezil treatment in AD patients in a [^{11}C]PMP study. Kaasinen et al. (2002) reported a similar inhibition of cortical AChE activity between 10 mg/day donepezil and 9 mg/day rivastigmine (28–39% vs. 28–37%). They also found that the pooled effects of donepezil and rivastigmine are greater in the frontal cortex compared to the temporal cortex in AD, which could be attributed to the prominent temporoparietal reduction of AChE in AD. Kadir et al. (2008) observed 30–40% inhibition of cortical AChE activity after 16–24 mg/day of galantamine treatment.

Dementia with Lewy bodies (DLB) is the second most frequent neurodegenerative dementia after AD. We measured brain AChE activity in 14 DLB patients, 25 late-onset AD patients, and 18 age-matched healthy controls (Shimada et al. 2015).

Cortical AChE activity was more prominently reduced in DLB patients (27.8%) than late-onset AD patients (8.2%). Regional brain AChE activity was well able to discriminate DLB from late-onset AD.

Perry et al. (1978) found that BuChE activity is increased by 40% in the cerebral cortex of postmortem AD brains. It has not been settled, however, whether cholinesterase inhibitor therapy should target BuChE in AD, not AChE alone, because both enzymes hydrolyze acetylcholine. Snyder et al. (2001) investigated a series of 1-methyl-4-piperidinyl esters, and identified 1-[^{11}C]methyl-4-piperidinyl n-butyrate ([^{11}C]BMP) as a most promising ligand for the in vivo measurement of cerebral BuChE activity. Kuhl et al. (2006) performed [^{11}C]BMP PET scan in 15 AD patients and 12 healthy controls. Contrary to prediction, cerebral BuChE activity was decreased by 18%. BuChE in the neuritic plaques is considered to account for the incremental BuChE observed in postmortem AD cerebral cortex tissue homogenates. The PET method would underestimate BuChE activity in plaques, because delivery of [^{11}C]BMP tracer to the plaque enzyme would be limited.

7.3.3 Parkinson's Disease and Related Disorders

Neurochemical analysis of postmortem brains with PD in the 1980s revealed a decrement of AChE activity in association with ChAT activity (Ruberg et al. 1986). Since then, however, cholinergic deficits in PD had not drawn much attention. PET imaging of AChE has elucidated the role of cholinergic dysfunction in PD and related disorders in the last 20 years.

We measured brain AChE activity in 16 patients with PD, 12 patients with progressive supranuclear palsy (PSP), and 13 age-matched healthy controls by [^{11}C]MP4A PET (Shinotoh et al. 1999). We found a significant reduction (17%) of cortical AChE activity associated with a nonsignificant reduction (13%) of thalamic AChE activity in PD patients compared with healthy controls. PD patients with dementia and hallucination showed more prominent reduction of cortical AChE activity than PD without dementia. PSP patients showed a nonsignificant reduction (10%) of cortical AChE activity but a prominent reduction (38%) of thalamic AChE activity. There is a second major set of cholinergic nuclei in the brainstem, the pedunculopontine nucleus, and the laterodorsal tegmental nucleus, which gives rise to a major ascending projection to the thalamus (Mesulam et al. 1984; Tubert et al. 2019). The pedunculopontine nucleus plays a major role in the control of gait (Tubert et al. 2019). The prominent reduction of thalamic AChE activity suggests that the ascending cholinergic system from the brainstem to the thalamus is severely impaired in PSP, probably leading to gait instability.

By voxel-by-voxel analysis of AChE activity, we found a significant reduction (12%) in the cerebral cortex, and especially in the medial occipital cortex in PD patients (*n* = 18) in comparison with healthy controls (*n* = 26) (Fig. 7.6) (Shimada et al. 2009). AChE activity reduction was seen in the medial occipital cortex even in de novo PD patients (*n* = 5), suggesting that cholinergic denervation occurs early in
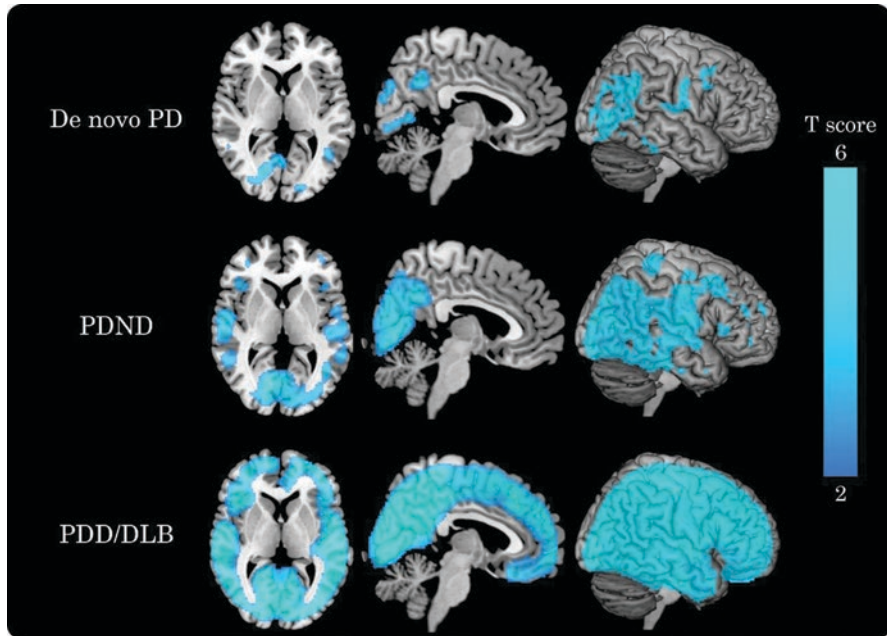
Fig. 7.6 Cortical AChE activity reduction in de novo Parkinson's disease (PD) ($n = 5$), PD without dementia (PDND) ($n = 18$), and PD with dementia (PDD), and dementia with Lewy bodies (DLB) ($n = 21$), compared with 26 healthy controls. Statistical parametric T-score maps with blue color representing AChE activity reduction are superimposed on SPM T1 MRI template, thresholded at voxel-level $p < 0.01$; false discovery rate (FDR) corrected with cluster above 26 voxels, age as covariate

PD. There was more profound (27%) and widespread reduction of cortical AChE activity in both PDD and DLB patients.

Bohnen et al. (2003) found that cortical AChE activity is more severely affected in PD patients with dementia (20%, $n = 14$) than in patients with mild AD (9.1%, $n = 12$) relative to healthy controls ($n = 10$) in a [^{11}C]PMP PET study with shape analysis. PD patients without dementia showed intermediate cortical AChE activity reduction (12.9%, $n = 11$).

Hilker et al. (2005) found severe reduction (29.7%) of cortical AChE activity in PDD ($n = 10$) and moderate reduction of cortical AChE activity in PD ($n = 17$) in comparison with healthy controls ($n = 31$) in their [^{11}C]MP4A-PET study. They also found a significant covariance of striatal reduction of [^{18}F]fluorodopa uptake and decreased cortical AChE activity in PDD, suggesting a common disease process leading to a transmitter deficiency syndrome in PDD.

Bohnen et al. (2009b) compared brain ACh activity between 17 PD patients with a history of falls and 27 PD patients without such a history. Cortical AChE activity was reduced in the PD fallers group (12.3%), followed by PD non-fallers (6.6%), compared with healthy controls ($n = 15$). Thalamic AChE activity was lower only in the PD fallers (11.8%), suggesting that impairment of the pedunculopontine nucleus

contributes to postural control and gait dysfunction in PD, like in PSP. In another study, Bohnen et al. (2013) also found that low cortical AChE activity was associated with slow gait speed. Subsequently, Chung et al. (2010) did clinical trials of donepezil, a central cholinesterase inhibitor, in 23 PD patients who reported falling or nearly falling more than twice per week and found that subjects with PD fell approximately half as often during the 6 weeks on donepezil than on placebo. A randomized, double-blind, placebo-controlled, phase 2 trial of rivastigmine in 130 PD patients showed that PD patients who were assigned to rivastigmine had improved gait stability and possible reduction in the frequency of falls (Henderson et al. 2016).

Bohnen et al. (2010) investigated olfactory dysfunction, brain AChE activity, and cognitive impairment in 58 PD patients, and found that odor identification scores correlated positively with AChE activity in hippocampal, amygdala, and cortical AChE activity, and scores on cognitive measures of episodic verbal learning. The results suggest that greater deficits in odor identification may identify patients with PD at risk for cognitive impairment. Bohnen et al. found heterogeneity of cholinergic denervation in PD. (Bohnen et al. 2012) They found that cortical cholinergic denervation frequency increased monotonically with increasing cognitive impairment in 143 non-demented PD patients (Bohnen et al. 2015). They investigated the relationship of brain AChE activity with depressive symptoms, rapid eye movement sleep behavior disorder, freezing of gait, risky driving, and fatigue (Bohnen et al. 2007, 2014, 2015; Kotagal et al. 2012; Müller et al. 2015; Weathers et al. 2014; Chou et al. 2016).

We investigated brain AChE activity in corticobasal syndrome and found a significant reduction of cortical (17.5%) but not thalamic AChE activity by [¹¹C]MP4A PET (Hirano et al. 2010). AChE activity was reduced in the thalamus and the posterior lobe of the cerebellar cortex but not in the cerebral cortex in seven patients with cerebellar syndrome of multiple system atrophy (MSA-C) (Hirano et al. 2008). Gilman et al. (2010) found prominent reduction of AChE activity in the thalamus, mesencephalon, pons, cerebellum, and caudate putamen and mild reduction in the cerebral cortex in patients with parkinsonian syndrome of multiple system atrophy (MSA-P) in a [¹¹C]PMP PET study.

Two symptomatic patients with frontotemporal dementia with parkinsonism linked to chromosome 17 (FTDP-17) carrying N279K mutation showed prominent reduction of cortical and thalamic AChE activity (Hirano et al. 2006). One of the three asymptomatic gene carriers with N279K mutation showed a decrease in temporal and parietal AChE activity (Miyoshi et al. 2010).

[¹¹C]donepezil is used for assessment of the autonomic nervous system in the abdomen in PD. Gjerløff et al. (2015) found reduction of [¹¹C]donepezil binding in the small intestine (35%) and pancreas (22%) in 12 PD patients. Reduction of [¹¹C]donepezil binding is also seen in early PD patients (Fedorova et al. 2017).

Autosomal dominant inherited PD caused by LRRK2 mutations is one of the commonest forms of genetic parkinsonism. Liu et al. (2018) found that LRRK2 mutation carriers without PD ($n = 16$) had increased cortical AChE activity compared with healthy controls ($n = 11$). PD patients with LRRK2 mutations had

significantly higher AChE activity in some cortical regions and thalamus compared with idiopathic PD patients. Changes in cholinergic activity might represent early and sustained attempts to compensate for LRRRK2-related dysfunction. Another possible cause for increased AChE activity might represent alteration of AChE activity in non-neuronal cells.

7.3.4　Other Disorders

Östberg et al. (2018) investigated cholinergic function in 17 subjects with traumatic brain injury (TBI). They found significant reduction of neocortical AChE activity in TBI subjects compared to healthy controls ($n = 12$).

Patients with multiple sclerosis (MS) often present with cognitive impairment. Virta et al. (2011) investigated the brain cholinergic system in ten MS patients with marked cognitive impairment by [11C]MP4A PET. There were no differences in cortical AChE activity between the MS patients and ten healthy controls.

AChE is expressed in the inflamed vessel wall of patients with giant-cell arteritis. Two patients with large-vessel giant-cell arteritis were scanned with [11C]donepezil and [18F]fluorodeoxy glucose. PET scan revealed extensive vascular FDG uptake but no [11C]donepezil (Therkildsen et al. 2019).

7.4　Conclusions

1. *N*-methylpiperidyl esters have been extensively characterized as synthetic substrates for AChE.
2. Carbon-11-labeled analogues of two of these esters, [11C]MP4A and [11C]PMP, are in successful clinical use for in vivo measurement of AChE activity. These radiotracers give precise estimates of AChE activity in brain regions with low enzyme activity because of its bolus-like input function shape, complete irreversibility, and near-optimal kinetic properties. It is challenging to estimate AChE activity in regions with high enzyme activity such as the striatum.
3. [11C]MP4A and [11C]PMP opened a window on cerebral cholinergic function (Reed and Jagust 1999) and have elucidated the role of the cholinergic system in AD, PD, and related disorders.

References

Arai H, Kosaka K, Muramoto O, Iizuka R (1984) A biochemical study of cholinergic neurons of the post-mortem brains from the patients with Alzheimer-type dementia. Rinsho Shinkeigaku 24:1128–1135

Atack JR, Perry EK, Bonham JR, Candy JM, Perry RH (1986) Molecular forms of acetylcholinesterase and butyrylcholinesterase in the aged human central nervous system. J Neurochem 47:263–277

Bartus RT, Dean RL 3rd, Beer B, Lippa AS (1982) The cholinergic hypothesis of geriatric memory dysfunction. Science 217(4558):408–414

Benarroch E (2010) Acetylcholine in the cerebral cortex. Effects and clinical implications. Neurology 75:659–665

Bencherif B, Endres CJ, Musachio JL, Villalobos A, Hilton J, Scheffel U, Dannals RF, Williams S, Frost JJ (2002) PET imaging of brain acetylcholinesterase using [^{11}C]CP-126,998, a brain selective enzyme inhibitor. Synapse 45:1–9

Blomqvist G, Tavitian B, Pappata S, Crouzel C, Jobert A, Doignon I, Di Giamberardino L (2001) Quantitative measurement of cerebral acetylcholinesterase using [^{11}C]physostigmine and positron emission tomography. J Cereb Blood Flow Metab 21:114–131

Blomqvist GJ (1984) On the construction of functional maps in positron emission tomography. J Cereb Blood Flow Metab 4:629–632

Bohnen NI, Albin RL, Müller ML, Petrou M, Kotagal V, Koeppe RA, Scott PJ, Frey KA (2015) Frequency of cholinergic and caudate nucleus dopaminergic deficits across the predemented cognitive spectrum of Parkinson disease and evidence of interaction effects. JAMA Neurol 72:194–200

Bohnen NI, Frey KA, Studenski S, Kotagal V, Koeppe RA, Constantine GM, Scott PJ, Albin RL, Müller M (2014) Extra-nigral pathological conditions are common in Parkinson's disease with freezing of gait: an in vivo positron emission tomography study. Mov Disord 29:1118–1124

Bohnen NI, Frey KA, Studenski S, Kotagal V, Koeppe RA, Scott PJ, Albin RL, Müller ML (2013) Gait speed in Parkinson disease correlates with cholinergic degeneration. Neurology 81:1611–1616

Bohnen NI, Kaufer DI, Hendrickson R, Constantine GM, Mathis CA, Moore RY (2007) Cortical cholinergic denervation is associated with depressive symptoms in Parkinson's disease and parkinsonian dementia. J Neurol Neurosurg Psychiatry 78:641–643

Bohnen NI, Kaufer DI, Hendrickson R, Ivanco LS, Lopresti B, Davis JG, Constantine G, Mathis CA, Moore RY, DeKosky ST (2005a) Cognitive correlates of alterations in acetylcholinesterase in Alzheimer's disease. Neurosci Lett 380:127–132

Bohnen NI, Kaufer DI, Hendrickson R, Ivanco LS, Lopresti BJ, Koeppe RA, Meltzer CC, Constantine G, Davis JG, Mathis CA, Dekosky ST, Moore RY (2005b) Degree of inhibition of cortical acetylcholinesterase activity and cognitive effects by donepezil treatment in Alzheimer's disease. J Neurol Neurosurg Psychiatry 76:315–319

Bohnen NI, Kaufer DI, Ivanco LS, Lopresti B, Koeppe RA, Davis JG, Mathis CA, Moore RY, DeKosky ST (2003) Cortical cholinergic function is more severely affected in parkinsonian dementia than in Alzheimer disease: an in vivo positron emission tomographic study. Arch Neurol 60:1745–1748

Bohnen NI, Müller ML, Koeppe RA, Studenski SA, Kilbourn MA, Frey KA, Albin RL (2009b) History of falls in Parkinson disease is associated with reduced cholinergic activity. Neurology 73(20):1670–1676

Bohnen NI, Müller ML, Kotagal V, Koeppe RA, Kilbourn MA, Albin RL, Frey KA (2010) Olfactory dysfunction, central cholinergic integrity and cognitive impairment in Parkinson's disease. Brain 133:1747–1754

Bohnen NI, Müller ML, Kotagal V, Koeppe RA, Kilbourn MR, Gilman S, Albin RL, Frey KA (2012) Heterogeneity of cholinergic denervation in Parkinson's disease without dementia. J Cereb Blood Flow Metab 32:1609–1617

Bohnen NI, Müller ML, Kuwabara H, Constantine GM, Studenski SA (2009a) Age-associated leukoaraiosis and cortical cholinergic deafferentation. Neurology 72:1411–1416

Chou KL, Kotagal V, Bohnen NI (2016) Neuroimaging and clinical predictors of fatigue in Parkinson disease. Parkinsonism Relat Disord 23:45–49

Chung KA, Lobb BM, Nutt JG, Horak FB (2010) Effects of a central cholinesterase inhibitor on reducing falls in Parkinson disease. Neurology 75:1263–1269

Darvesh S, Hopkins DA, Geula C (2003) Neurobiology of butyrylcholinesterase. Nat Rev Neurosci 4:131–138

Davies P, Maloney AJF (1976) Selective loss of central cholinergic neurons in Alzheimer's disease. Lancet 2:1403

De Vos F, Santens P, Vermeirsch H, Dewolf I, Dumont F, Slegers G, Dierckx RA, De Reuck J (2000) Pharmacological evaluation of [^{11}C]donepezil as a tracer for visualization of acetylcholinesterase by PET. Nucl Med Biol 27:745–747

Eggers C, Herholz K, Kalbe E, Heiss WD (2006) Cortical acetylcholine esterase activity and ApoE4-genotype in Alzheimer disease. Neurosci Lett 408:46–50

Fedorova TD, Seidelin LB, Knudsen K, Schacht AC, Geday J, Pavese N, Brooks DJ, Borghammer P (2017) Decreased intestinal acetylcholinesterase in early Parkinson disease: an ^{11}C-donepezil PET study. Neurology 88:775–781

Funaki Y, Kato M, Iwata R, Sakurai E, Sakurai E, Tashiro M, Ido T, Yanai K (2003) Evaluation of the binding characteristics of [5-(11)C-methoxy]-donepezil in the rat brain for in vivo visualization of acetylcholinesterase. J Pharmacol Sci 91:105–112

Garibotto V, Tettamanti M, Marcone A, Florea I, Panzacchi A, Moresco R, Virta JR, Rinne J, Cappa SF, Perani D (2013) Cholinergic activity correlates with reserve proxies in Alzheimer's disease. Neurobiol Aging 34:2694.e13–2694.e18

Gilman S, Koeppe RA, Nan B, Wang CN, Wang X, Junck L, Chervin RD, Consens F, Bhaumik A (2010) Cerebral cortical and subcortical cholinergic deficits in Parkinsonian syndromes. Neurology 74:1416–1423

Gjerløff T, Fedorova T, Knudsen K, Munk OL, Nahimi A, Jacobsen S, Danielsen EH, Terkelsen AJ, Hansen J, Pavese N, Brooks DJ, Borghammer P (2015) Imaging acetylcholinesterase density in peripheral organs in Parkinson's disease with ^{11}C-donepezil PET. Brain 138:653–663

Gjerløff T, Jakobsen S, Nahimi A, Munk OL, Bender D, Alstrup AK, Vase KH, Hansen SB, Brooks DJ, Borghammer P (2014) In vivo imaging of human acetylcholinesterase density in peripheral organs using ^{11}C-donepezil: dosimetry, biodistribution, and kinetic analyses. J Nucl Med 55:1818–1824

Haense C, Kalbe E, Herholz K, Hohmann C, Neumaier B, Krais R, Heiss WD (2012) Cholinergic system function and cognition in mild cognitive impairment. Neurobiol Aging 33:867–877

Hampel H, Mesulam MM, Cuello AC, Farlow MR, Giacobini E, Grossberg GT, Khachaturian AS, Vergallo A, Cavedo E, Snyder PJ, Khachaturian ZS (2018) The cholinergic system in the pathophysiology and treatment of Alzheimer's disease. Brain 141:1917–1933

Henderson EJ, Lord SR, Brodie MA, Gaunt DM, Lawrence AD, Close JC, Whone AL, Ben-Shlomo Y (2016) Rivastigmine for gait stability in patients with Parkinson's disease (ReSPonD): a randomised, double-blind, placebo-controlled, phase 2 trial. Lancet Neurol 15:249–258

Herholz K, Lercher M, Wienhard K, Bauer B, Lenz O, Heiss WD (2001) PET measurement of cerebral acetylcholine esterase activity without blood sampling. Eur J Nucl Med 28:472–477

Herholz K, Weisenbach S, Zündorf G, Lenz O, Schröder H, Bauer B, Kalbe E, Heiss WD (2004) In vivo study of acetylcholine esterase in basal forebrain, amygdala, and cortex in mild to moderate Alzheimer disease. NeuroImage 21:136–143

Hilker R, Thomas AV, Klein JC, Weisenbach S, Kalbe E, Burghaus L, Jacobs AH, Herholz K, Heiss WD (2005) Dementia in Parkinson disease: functional imaging of cholinergic and dopaminergic pathways. Neurology 65:1716–1722

Hirano S, Shinotoh H, Arai K, Aotsuka A, Yasuno F, Tanaka N, Ota T, Sato K, Fukushi K, Tanada S, Hattori T, Irie T (2008) PET study of brain acetylcholinesterase in cerebellar degenerative disorders. Mov Disord 23:1154–1160

Hirano S, Shinotoh H, Kobayashi T, Tsuboi Y, Wszolek ZK, Aotsuka A, Tanaka N, Ota T, Fukushi K, Tanada S, Irie T (2006) Brain acetylcholinesterase activity in FTDP-17 studied by PET. Neurology 66:1276–1277

Hirano S, Shinotoh H, Shimada H, Aotsuka A, Tanaka N, Ota T, Sato K, Ito H, Kuwabara S, Fukushi K, Irie T, Suhara T (2010) Cholinergic imaging in corticobasal syndrome, progressive supranuclear palsy and frontotemporal dementia. Brain 133:2058–2068

Hirano S, Shinotoh H, Shimada H, Ota T, Sato K, Tanaka N, Zhang MR, Higuchi M, Fukushi K, Irie T, Kuwabara S, Suhara T (2018) Voxel-based acetylcholinesterase PET study in early and late onset Alzheimer's disease. J Alzheimers Dis 62:1539–1548

Irie T, Fukushi K, Akimoto Y, Tamagami H, Nozaki T (1994) Design and evaluation of radioactive acetylcholine analogs for mapping brain acetylcholinesterase (AchE) in vivo. Nucl Med Biol 21:801–808

Irie T, Fukushi K, Namba H, Iyo M, Tamagami H, Nagatsuka S, Ikota N (1996) Brain acetylcholinesterase activity: validation of a PET tracer in a rat model of Alzheimer's disease. J Nucl Med 37:649–655

Ishikawa M, Sakata M, Ishii K, Kimura Y, Oda K, Toyohara J, Wu J, Ishiwata K, Iyo M, Hashimoto K (2009) High occupancy of sigma1 receptors in the human brain after single oral administration of donepezil: a positron emission tomography study using [^{11}C]SA4503. Int J Neuropsychopharmacol 12:1127–1131

Iyo M, Namba H, Fukushi K, Shinotoh H, Nagatsuka S, Suhara T, Sudo Y, Suzuki K, Irie T (1997) Measurement of acetylcholinesterase by positron emission tomography in the brains of healthy controls and patients with Alzheimer's disease. Lancet 349:1805–1809

Kaasinen V, Någren K, Järvenpää T, Roivainen A, Yu M, Oikonen V, Kurki T, Rinne JO (2002) Regional effects of donepezil and rivastigmine on cortical acetylcholinesterase activity in Alzheimer's disease. J Clin Psychopharmacol 22:615–620

Kadir A, Darreh-Shori T, Almkvist O, Wall A, Grut M, Strandberg B, Ringheim A, Eriksson B, Blomquist G, Långström B, Nordberg A (2008) PET imaging of the in vivo brain acetylcholinesterase activity and nicotine binding in galantamine-treated patients with AD. Neurobiol Aging 29:1204–1217

Kikuchi T, Okamura T, Zhang MR, Fukushi K, Irie T (2010) In vivo evaluation of N-[^{18}F]fluoroethylpiperidin-4ylmethyl acetate in rats compared with MP4A as a probe for measuring cerebral acetylcholinesterase activity. Synapse 64:209–215

Kikuchi T, Okamura T, Zhang MR, Irie T (2013) PET probes for imaging brain acetylcholinesterase. J Labelled Comp Radiopharm 56:172–179

Kikuchi T, Zhang MR, Ikota N, Fukushi K, Okamura T, Suzuki K, Arano Y, Irie T (2005) N-[^{18}F]fluoroethylpiperidin-4ylmethyl acetate, a novel lipophilic acetylcholine analogue for PET measurement of brain acetylcholinesterase activity. J Med Chem 48:2577–2583

Kilbourn MR, Snyder SE, Sherman PS, Kuhl DE (1996) In vivo studies of acetylcholinesterase activity using a labeled substrate, N-[^{11}C]methylpiperidin-4-yl propionate ([^{11}C]PMP). Synapse 22:123–131

Koeppe RA, Frey KA, Snyder SE, Meyer P, Kilbourn MR, Kuhl DE (1999) Kinetic modeling of N-[^{11}C]methylpiperidin-4-yl propionate: alternatives for analysis of an irreversible positron emission tomography trace for measurement of acetylcholinesterase activity in human brain. J Cereb Blood Flow Metab 19:1150–1163

Kotagal V, Albin RL, Müller ML, Koeppe RA, Chervin RD, Frey KA, Bohnen NI (2012) Symptoms of rapid eye movement sleep behavior disorder are associated with cholinergic denervation in Parkinson disease. Ann Neurol 71:560–568

Kuhl DE, Koeppe RA, Minoshima S, Snyder SE, Ficaro EP, Foster NL, Frey KA, Kilbourn MR (1999) In vivo mapping of cerebral acetylcholinesterase activity in aging and Alzheimer's disease. Neurology 52:691–699

Kuhl DE, Koeppe RA, Snyder SE, Minoshima S, Frey KA, Kilbourn MR (2006) In vivo butyrylcholinesterase activity is not increased in Alzheimer's disease synapses. Ann Neurol 59:13–20

Kuhl DE, Minoshima S, Frey KA, Foster NL, Kilbourn MR, Koeppe RA (2000) Limited donepezil inhibition of acetylcholinesterase measured with positron emission tomography in living Alzheimer cerebral cortex. Ann Neurol 48:391–395

Lee SY, Choe YS, Kim YR, Paik JY, Choi BW, Kim SE, Lee KH, Choi Y, Kim BT (2004) Synthesis and evaluation of 5,7-dihydro-3-[2-[1-(4-[^{18}F]-fluorobenzyl)-4-piperidinyl]ethyl]-6H-pyrrolo[3,2-f]-1,2-benzisoxazol-6-one for in vivo mapping of acetylcholinesterase. Nucl Med Commun 25:591–596

Liu SY, Wile DJ, Fu JF, Valerio J, Shahinfard E, McCormick S, Mabrouk R, Vafai N, McKenzie J, Neilson N, Perez-Soriano A, Arena JE, Cherkasova M, Chan P, Zhang J, Zabetian CP, Aasly JO, Wszolek ZK, McKeown MJ, Adam MJ, Ruth TJ, Schulzer M, Sossi V, Stoessl AJ (2018)

The effect of LRRK2 mutations on the cholinergic system in manifest and premanifest stages of Parkinson's disease: a cross-sectional PET study. Lancet Neurol 17:309–316

Marcone A, Garibotto V, Moresco RM, Florea I, Panzacchi A, Carpinelli A, Virta JR, Tettamanti M, Borroni B, Padovani A, Bertoldo A, Herholz K, Rinne JO, Cappa SF, Perani D (2012) [^{11}C]-MP4A PET cholinergic measurements in amnestic mild cognitive impairment, probable Alzheimer's disease, and dementia with Lewy bodies: a Bayesian method and voxel-based analysis. J Alzheimers Dis 31:387–399

Mesulam MM, Geula C (1992) Overlap between acetylcholinesterase-rich and choline acetyltransferase-positive (cholinergic) axons in human cerebral cortex. Brain Res 577:112–120

Mesulam MM, Mufson EJ, Levey AI, Wainer BH (1984) Atlas of cholinergic neurons in the forebrain and upper brainstem of the macaque based on monoclonal choline acetyltransferase immunohistochemistry and acetylcholinesterase histochemistry. Neuroscience 12:669–686

Miyoshi M, Shinotoh H, Wszolek ZK, Strongosky AJ, Shimada H, Arakawa R, Higuchi M, Ikoma Y, Yasuno F, Fukushi K, Irie T, Ito H, Suhara T (2010) In vivo detection of neuropathologic changes in presymptomatic MAPT mutation carriers: a PET and MRI study. Parkinsonism Relat Disord 16:404–408

Müller ML, Bohnen NI, Kotagal V, Scott PJ, Koeppe RA, Frey KA, Albin RL (2015) Clinical markers for identifying cholinergic deficits in Parkinson's disease. Mov Disord 30:269–273

Nagatsuka S, Fukushi K, Shinotoh H, Namba H, Iyo M, Tanaka N, Aotsuka A, Ota T, Tanada S, Irie T (2001) Kinetic analysis of [(11)C]MP4A using a high-radioactivity brain region that represents an integrated input function for measurement of cerebral acetylcholinesterase activity without arterial blood sampling. J Cereb Blood Flow Metab 21:1354–1366

Namba H, Irie T, Fukushi K, Iyo M (1994) In vivo measurement of acetylcholinesterase activity in the brain with a radioactive acetylcholine analog. Brain Res 667:278–282

Namba H, Iyo M, Fukushi K, Shinotoh H, Nagatsuka S, Suhara T, Sudo Y, Suzuki K, Irie T (1999) Human cerebral acetylcholinesterase activity measured with positron emission tomography: procedure, normal values and effect of age. Eur J Nucl Med 26:135–143

Namba H, Iyo M, Shinotoh H, Nagatsuka S, Fukushi K, Irie T (1998) Preserved acetylcholinesterase activity in aged cerebral cortex. Lancet 351:881–882

Ohya T, Okamura T, Nagai Y, Fukushi K, Irie T, Suhara T, Zhang MR, Fukumura T, Kikuchi T (2011) Effect of radiolabeled metabolite elimination from the brain on the accuracy of cerebral enzyme activity estimation using positron emission tomography with substrate tracers. NeuroImage 56:1105–1110

Okamura N, Funaki Y, Tashiro M, Kato M, Ishikawa Y, Maruyama M, Ishikawa H, Meguro K, Iwata R, Yanai K (2008) In vivo visualization of donepezil binding in the brain of patients with Alzheimer's disease. Br J Clin Pharmacol 65:472–479

Östberg A, Virta J, Rinne JO, Oikonen V, Luoto P, Någren K, Arponen E, Tenovuo O (2018) Brain cholinergic function and response to rivastigmine in patients with chronic sequels of traumatic brain injury: a PET study. J Head Trauma Rehabil 33:25–32

Perry EK, Tomlinson BE, Blessed G, Bergmann K, Gibson PH, Perry RH (1978) Correlation of cholinergic abnormalities with senile plaques and mental test scores in senile dementia. Br Med J 2:1457–1459

Reed BR, Jagust WJ (1999) Opening a window on cerebral cholinergic function: PET imaging of acetylcholinesterase. Neurology 52:680–682

Richter N, Allendorf I, Onur OA, Kracht L, Dietlein M, Tittgemeyer M, Neumaier B, Fink GR, Kukolja J (2014) The integrity of the cholinergic system determines memory performance in healthy elderly. NeuroImage 100:481–488

Richter N, Beckers N, Onur OA, Dietlein M, Tittgemeyer M, Kracht L, Neumaier B, Fink GR, Kukolja J (2018) Effect of cholinergic treatment depends on cholinergic integrity in early Alzheimer's disease. Brain 141:903–915

Richter N, Michel A, Onur OA, Kracht L, Dietlein M, Tittgemeyer M, Neumaier B, Fink GR, Kukolja J (2017) White matter lesions and the cholinergic deficit in aging and mild cognitive impairment. Neurobiol Aging 53:27–35

Rinne JO, Kaasinen V, Järvenpää T, Någren K, Roivainen A, Yu M, Oikonen V, Kurki T (2003) Brain acetylcholinesterase activity in mild cognitive impairment and early Alzheimer's disease. J Neurol Neurosurg Psychiatry 74:113–115

Ruberg M, Rieger F, Villageois A, Bonnet AM, Agid Y (1986) Acetylcholinesterase and butyryl-cholinesterase in frontal cortex and cerebrospinal fluid of demented and non-demented patients with Parkinson's disease. Brain Res 362:83–91

Selden NR, Gitelman DR, Salamon-Murayama N, Parrish TB, Mesulam MM (1998) Trajectories of cholinergic pathways within the cerebral hemispheres of the human brain. Brain 121:2249–2257

Shao X, Koeppe RA, Butch ER, Kilbourn MR, Snyder SE (2005) Evaluation of ^{18}F-labeled acetyl-cholinesterase substrates as PET radiotracers. Bioorg Med Chem 13:869–875

Shimada H, Hirano S, Shinotoh H, Aotsuka A, Sato K, Tanaka N, Ota T, Asahina M, Fukushi K, Kuwabara S, Hattori T, Suhara T, Irie T (2009) Mapping of brain acetylcholinesterase altera-tions in Lewy body disease by PET. Neurology 73:273–278

Shimada H, Hirano S, Sinotoh H, Ota T, Tanaka N, Sato K, Yamada M, Fukushi K, Irie T, Zhang MR, Higuchi M, Kuwabara S, Suhara T (2015) Dementia with Lewy bodies can be well-differentiated from Alzheimer's disease by measurement of brain acetylcholinesterase activity-a [^{11}C]MP4A PET study. Int J Geriatr Psychiatry 30:1105–1113

Shinotoh H, Aotsuka A, Fukushi K, Nagatsuka S, Tanaka N, Ota T, Tanada S, Irie T (2001) Effect of donepezil on brain acetylcholinesterase activity in patients with AD measured by PET. Neurology 56:408–410

Shinotoh H, Fukushi K, Nagatsuka S, Irie T (2004) Acetylcholinesterase imaging: its use in ther-apy evaluation and drug design. Curr Pharm Des 10:1505–1517

Shinotoh H, Namba H, Fukushi K, Nagatsuka S, Tanaka N, Aotsuka A, Ota T, Tanada S, Irie T (2000) Progressive loss of cortical acetylcholinesterase activity in association with cogni-tive decline in Alzheimer's disease: a positron emission tomography study. Ann Neurol 48: 194–200

Shinotoh H, Namba H, Yamaguchi M, Fukushi K, Nagatsuka S, Iyo M, Asahina M, Hattori T, Tanada S, Irie T (1999) Positron emission tomographic measurement of acetylcholinesterase activity reveals differential loss of ascending cholinergic systems in Parkinson's disease and progressive supranuclear palsy. Ann Neurol 46:62–69

Snyder SE, Gunupudi N, Sherman PS, Butch ER, Skaddan MB, Kilbourn MR, Koeppe RA, Kuhl DE (2001) Radiolabeled cholinesterase substrates: in vitro methods for determining structure-activity relationships and identification of a positron emission tomography radiopharmaceu-tical for in vivo measurement of butyrylcholinesterase activity. J Cereb Blood Flow Metab 21:132–143

Tanaka N, Fukushi K, Shinotoh H, Nagatsuka S, Namba H, Iyo M, Aotsuka A, Ota T, Tanada S, Irie T (2001) Positron emission tomographic measurement of brain acetylcholinesterase activ-ity using N-[(11)C]methylpiperidin-4-yl acetate without arterial blood sampling: methodology of shape analysis and its diagnostic power for Alzheimer's disease. J Cereb Blood Flow Metab 21:295–306

Tavitian B, Pappata S, Bonnot-Lours S, Prenant C, Jobert A, Crouzel C, Di Giamberardino L (1993a) Positron emission tomography study of [^{11}C]methyl-tetrahydroaminoacridine (methyl-tacrine) in baboon brain. Eur J Pharmacol 236:229–238

Tavitian B, Pappata S, Planas AM, Jobert A, Bonnot-Lours S, Crouzel C, DiGiamberardino L (1993b) In vivo visualization of acetylcholinesterase with positron emission tomography. Neuroreport 4:535–538

Therkildsen P, Nielsen BD, Hansen IT, Keller KK, Steiniche T, Gormsen LC, Borghammer P, Hauge EM (2019) Acetylcholinesterase-associated inflammation in patients with giant cell arteritis. Evaluation by histology and ^{11}C-donepezil PET/CT. Clin Exp Rheumatol 37(Suppl 117):20–25

Tubert C, Galtieri D, Surmeier DJ (2019) The pedunculopontine nucleus and Parkinson's disease. Neurobiol Dis 128:3–8

Virta JR, Laatu S, Parkkola R, Oikonene V, Rinne JO, Ruutiainen J (2011) Cerebral acetylcholinesterase is not decreased in MS patients with cognitive impairment. Mult Scler 17:931–938

Weathers SP, Kotagal V, Bohnen NI, Chou KL (2014) Risky driving and pedunculopontine nucleus-thalamic cholinergic denervation in Parkinson disease. Parkinsonism Relat Disord 20:13–16

Whitehouse PJ, Price DL, Struble RG, Clark AW, Coyle JT, Delon MR (1982) Alzheimer's disease and senile dementia: loss of neurons in the basal forebrain. Science 215:1237–1239

Zhang MR, Furutsuka K, Maeda J, Kikuchi T, Kida T, Okauchi T, Irie T, Suzuki K (2003) N-[18F]fluoroethyl-4-piperidyl acetate ([18F]FEtP4A): a PET tracer for imaging brain acetylcholinesterase in vivo. Bioorg Med Chem 11:2519–2527

Imaging of Adenosine Receptors

David Elmenhorst, Dirk Bier, Marcus Holschbach,
and Andreas Bauer

Contents

8.1 Introduction

Adenosine is a fundamental molecule of life. It is a part of the DNA and the main degradation product of the central currency of energy metabolism in humans and animals—adenosine triphosphate (ATP). The nucleoside adenosine is composed of the nucleobase adenine and the sugar ribose. It has a short biological half-life of about 1–2 s and the endogenous extracellular level of adenosine is in the range of several hundred nano mol in heart and brain of humans (Zeitzer et al. 2006). Adenosine is formed by breakdown of ATP to ADP to AMP and finally to adenosine by the enzyme 5′-nucleotidase. Adenosine is metabolized by adenosine deaminase to inosine and mainly by

D. Elmenhorst (✉)
Institute of Neuroscience and Medicine, INM-2, Forschungszentrum Jülich, Jülich, Germany
e-mail: d.elmenhorst@fz-juelich.de

D. Bier · M. Holschbach
Institute of Neuroscience and Medicine, INM-5, Forschungszentrum Jülich, Jülich, Germany

A. Bauer
Institute of Neuroscience and Medicine, INM-2, Forschungszentrum Jülich, Jülich, Germany

Department of Neurology, Heinrich-Heine-University Düsseldorf, Düsseldorf, Germany

phosphorylation by adenosine kinase to AMP. Extra- and intracellular concentrations of adenosine can equilibrate quickly by equilibrative nucleoside transporters. Under pathological conditions like hypoxia the adenosine concentration can rise severalfold—up to micromolar concentrations. Adenosine is a part of the heterogeneous group of neuromodulators. In contrast to classical neurotransmitters it is not stored and released from vesicles. The net effect of adenosine on excitable tissue is inhibitory affecting the release of classical neurotransmitters like glutamate, GABA (gamma-aminobutyric acid), and dopamine. Adenosine, for example, reduces the contraction frequency of a tachycardic heart or reduces epileptic activity in the brain. The most prominent and most widespread used substance that interacts with adenosine in daily life is caffeine. The widely used neurostimulant caffeine exerts its effects as an antagonist at adenosine receptors. Four different types of adenosine receptors have been described in mammals: A_1, A_{2A}, A_{2B}, and A_3 which are all G-protein-coupled receptors (Fredholm et al. 2001; Hess 2001; Palmer and Stiles 1995). The coupling of A_1 and A_3 to a G_i-protein leads to inhibition of adenylate cyclase whereas the coupling of A_{2A} and A_{2B} to G_s- or G_o-proteins leads to stimulation of adenylate cyclase. In humans the A_1 adenosine receptor (A_1AR) shows the most abundant distribution and highest concentrations (in descending order) in brain, heart, adipose tissue, stomach, testis, spleen, kidney, aorta, liver, eye, and bladder. The A_{2A} adenosine receptor ($A_{2A}AR$) can be found in striatum, nucleus accumbens, olfactory tubercle, heart, lung, and blood vessels. A_{2B} adenosine receptors ($A_{2B}AR$) are expressed in low levels in all tissues and A_3 adenosine receptors (A_3ARs) show low levels in brain and high levels in lung and liver (Jacobson and Gao 2006). The affinities of endogenous adenosine for the A_1AR and the $A_{2A}AR$ are in the nanomolar range whereas the affinities for the $A_{2B}AR$ and the A_3AR are in the micromolar range (Dunwiddie and Masino 2001). This discrepancy in affinity in combination with normal adenosine levels in the nanomolar range suggests that $A_{2B}AR$ and A_3AR are primarily activated under pathological conditions and massively increased levels of intracellular adenosine. An important aspect is that $A_{2A}ARs$ form heterodimers with A_1ARs or dopamine D_2 receptors and A_1AR with dopamine D_1 receptors which in turn influence the affinity of the adenosine receptors (Ciruela et al. 2006; Franco et al. 2007; Cristovao-Ferreira et al. 2011).

Over the last 30 years adenosine receptor ligands, agonists, as well as antagonists have emerged as a class of useful therapeutics (for a comprehensive review see van Waarde et al. 2018; Jacobson 2009; Jacobson and Gao 2006). The requirements for compounds suitable for noninvasive in vivo imaging of adenosine receptors (radiopharmaceuticals, radiotracers) with positron-emission tomography (PET) are in some aspects different from those for therapeutic drugs. This difference is even more pronounced in the case of radiotracers involved in neurotransmission research. One possible process for adenosine receptor ligand development in combination with adequate evaluation methods is depicted in Table 8.1.

In contrast to therapeutically dosed drugs the amounts of intravenously (i.v.) administered radiopharmaceuticals are extremely small. Thus, biochemical equilibriums are not or only marginally disturbed allowing quantitative receptor scintigraphy (determination of concentration of binding sites, B_{max}).

Depending on the amount of applied radioactivity and on the molar activity of the respective radiotracer the applied mass of a PET-radiopharmaceutical typically lies in the range of nano- to micrograms. Thus, even toxic drugs, which are not suitable as therapeutics, can be used as radiotracers for PET.

Table 8.1 Requirements for a suitable radiotracer

Criterion	Requirements	Evaluation system
Affinity and reversibility	K_D or K_I in nM range	Assays with brain tissue or cell homogenates, autoradiography
Specificity	Selectivity compared to receptors of the same subfamily and to receptors mainly present in the region of interest	
Nonspecific binding potential	Low	
Agonism	Antagonists (usually for receptor quantification; for determination of endogenous ligand concentrations agonistic or partially agonistic properties are useful)	Functional assays, for instance cAMP
Penetration of BBB	>1% ID/g @ t_{max}	Organ distribution in animals, animal PET or SPECT
Metabolism	Preferably no metabolism in the target organ (brain) or biologically inactive metabolites	
Bioavailability	Half-life of radionuclide compatible with physiological kinetics	
	Fraction of "free" ligand should be as high as possible (>1%)	
Mutagenicity	Very low	Specific assays for instance chromosome aberration, Ames test
Toxicity	Low << effects thousandfold of applied mass	Theoretically: **Q**uantitative **S**tructure-**A**ctivity **R**elationship Animal experiments LD$_{50}$
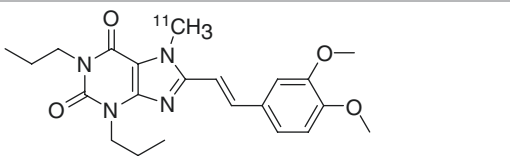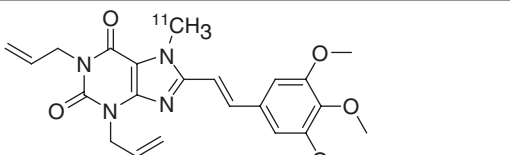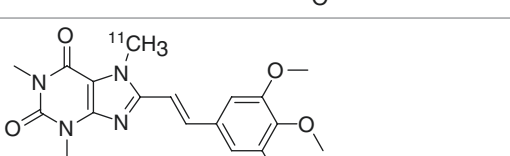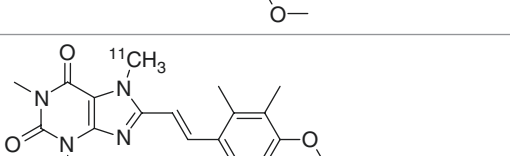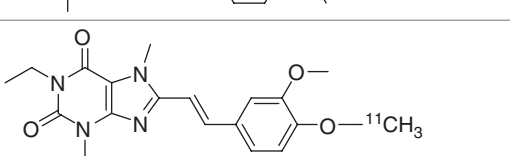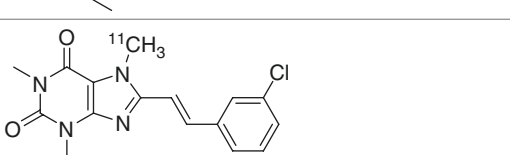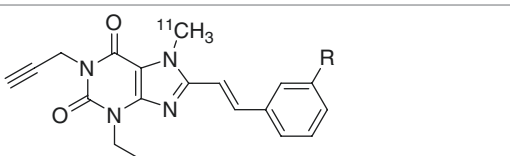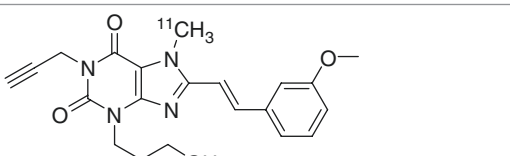
A brain radiotracer, in order to be suitable for imaging, has to fulfill a number of criteria with regard to its physical and physiological properties (Ding and Fowler 2005; Halldin et al. 2001; Mason and Mathis 2003). The ligand should have nanomolar to subnanomolar affinity (K_D) and sufficient selectivity for the target receptor. Ideally, binding to the receptor should be reversible over the experimental time range because this allows the use of biomathematical equilibrium approaches for the quantification of ligand-receptor interaction. Lipophilicity (log P) of the tracer should be appropriate for crossing the blood-brain barrier (BBB). For neuroradioligands there is an optimal, rather narrow "window" of lipophilicity in the log P range between 1 and 4 (Dishino et al. 1983; Moerlein et al. 1985). As a rule of thumb molecules with a log P value <1 will not cross the BBB, while those with a log P > 4 generally tend to exhibit high nonspecific binding. Other criteria for a successful radiotracer are sufficient in vivo stability in plasma and, in respect to tracer availability, low affinity for plasma proteins. With regard to image analysis, there should be no radiolabeled metabolites which are capable of crossing the BBB. Further, a suitable radiotracer should show a kinetic profile that allows adequate quantification of the obtained data.

Radiolabeled subtype-specific adenosine receptor ligands currently under development are depicted in Table 8.2.

Table 8.2 Selection of PET ligands for adenosine receptors

A$_1$	R=CH$_3$CH$_2$^{11}CH$_2$, [^{11}C] KF15372 R=CH$_3$^{11}CH$_2$, [^{11}C]EDPX R=^{11}CH$_3$, [^{11}C]MDPX (Ishiwata et al. 1995; Noguchi et al. 1997)	
	[^{18}F]CPFPX (Holschbach et al. 2002)	
	R=H, [^{18}F]CBX R=CH$_3$, [^{18}F]1-MCBX (Kreft et al. 2017)	
	R=H, [^{18}F]CBX R=CH$_3$, [^{18}F]1-MCBX (Schneider et al. 2019a, b)	
	[^{11}C]FR194921 (Matsuya et al. 2005)	
	[^{131}I]CPIPX (Sihver et al. 2003)	
A$_1$	[^{11}C]22b A$_1$AR partial agonist radioligand (Guo et al. 2018)	
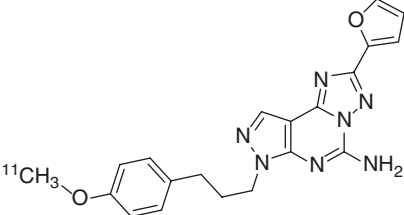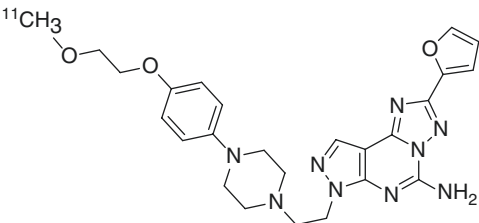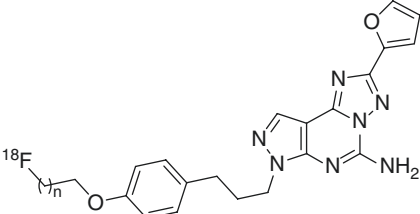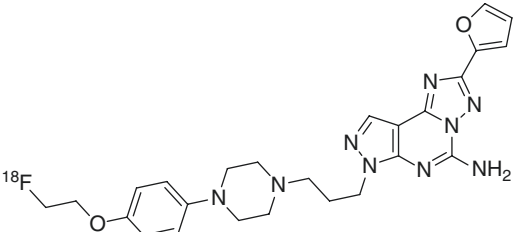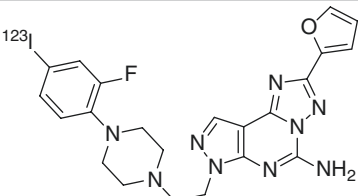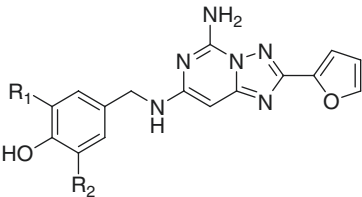
Table 8.2   (continued)

A₂ₐ	[¹¹C]KF117837 (Ishiwata et al. 1996)	
	[¹¹C]KF19631 (Ishiwata et al. 2000a, b)	
	[¹¹C]KF18446, [¹¹C]TMSX (Ishiwata et al. 2000a, b, c, d)	
	[¹¹C]KF21213 (Wang et al. 2000)	
	[¹¹C]KW6002 (Hirani et al. 2001)	
	[¹¹C]CSC (Ishiwata et al. 2000a, b, c, d; Marian et al. 1999)	
	R=Br, [¹¹C]BS-DMPX R=I, [¹¹C]IS-DMPX (Ishiwata et al. 2000a, b, c, d)	
	[¹¹C]MSX-2 (Holschbach et al., 2000)	
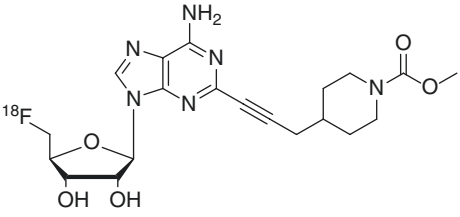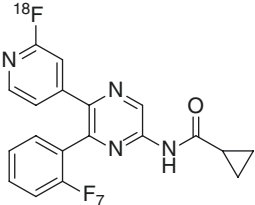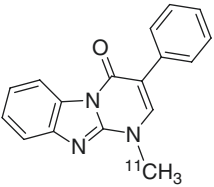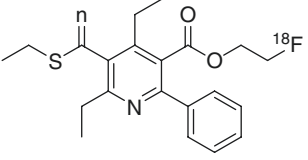
Table 8.2 (continued)

[^{11}C]SCH442416 (Moresco et al. 2005; Todde et al. 2000)	
[^{11}C]SCH420814, [^{11}C] Preladenant (Zhou et al. 2014)	
$n = 1$, [^{18}F]fluoroethyl SCH420814 $n = 2$, [^{18}F]fluoropropyl SCH420814 (Khanapur et al. 2014a, b)	
[^{18}F]MNI-444 (Barret et al. 2015; Vala et al. 2016)	
[^{123}I]MI-420 (Vala et al. 2016; Tavares et al. 2013)	
$R_1 = H$, $R_2 = {}^{131}$I: [^{131}I]iodo-ZM241385 $R_1 = I$, $R_2 = {}^{131}$I: [^{131}I]diiodo-ZM241385 (Poucher et al. 1995; Sihver et al. 2004)	

Table 8.2   (continued)

	[^{18}F]FDA-PP1-labeled A$_{2A}$AR agonist (enzymatic fluorination) (Lowe et al. 2017)	
A$_{2B}$	[^{18}F]7a-pyrazine based radioligand (Lindemann et al. 2018)	
	[^{11}C]-labeled triazinobenzimidazole radioligand (Petroni et al. 2016)	
A$_3$	[^{18}F]FE@SUPPY (Wadsak et al. 2008)	

A$_1$AR and A$_{2A}$AR antagonists are either xanthines or non-xanthine monocyclic or fused bi- or tricyclic substituted heteroaromatic compounds, some of them containing hetero ring atoms such as nitrogen, oxygen, and sulfur.

Three characteristics identify xanthines that are potent and selective antagonists at the A$_1$AR. They possess long alkyl chains in positions 1 and 3 as well as a bulky (bi)cycloalkyl substituent at C-8, with the optimum substituents at N-1- and N-3 being propyl groups. Additionally, N-7 must be unsubstituted in order to act as a hydrogen bond donor, a feature which is essential for binding to the A$_1$AR. Whereas some modifications of the 1- and 3-substituents (fluorination, iodination, substitution of an aralkyl group at N-3) preserve or at least do not seriously affect activity, the criteria based on N-7 and C-8 are required for antagonist activity at the A$_1$AR.

Xanthine-type A$_{2A}$AR antagonists with high A$_{2A}$AR affinity contain a (substituted) (*E*)-styryl substituent at C-8 in combination with alkyl/alkynyl moieties at N-1 and N-3; a methyl group at N-7 reduces affinity to the A$_1$AR by suppressing the formation of hydrogen bonds and can sterically interact with the styryl group by

forcing the vinylic double bond into a favored conformation for binding to the $A_{2A}AR$.

Non-xanthine A_1AR antagonists are often structurally based on adenine, having a 6-amino group substituted with bulky cycloaliphatic moieties and variable nitrogen atoms in the heterocyclic core.

Nitrogen polyheterocyclic $A_{2A}AR$ ligands, especially those based on a triazolo-pyrimidine structure, display good affinity and selectivity when they bear a furan moiety of the core aromatic scaffold, a prerequisite which is crucial for binding. Moreover, bi- and tricyclic fused nitrogen heterocyclic antagonists, in order to be active, often contain a long-chain aralkyl moiety. PET ligands for adenosine receptors at different states of development have been reviewed recently (Vuorimaa et al. 2017; Li et al. 2019; Mishina and Ishiwata 2014; Khanapur et al. 2014a, b; Bauer and Ishiwata 2009; Ishiwata et al. 2007a, b).

8.2 A$_1$ Adenosine Receptor Ligands

So far two PET tracers have been applied and evaluated to image A_1ARs in humans: [^{11}C]MPDX (Noguchi et al. 1997) and [^{18}F]CPFPX (Holschbach et al. 2002). Both are xanthine derivates. Potential scientific applications and findings for A_1AR imaging have been reviewed (Paul et al. 2011a, b; Mishina and Ishiwata 2014; Li et al. 2019).

The antagonist [^{18}F]CPFPX (Log P = 2.1) shows a high affinity (K_D 1.26 nM in cells constitutively expressing the human A_1AR) and high selectivity ($A_{2A}AR$ affinity 940 nM) for the A_1AR (Bauer et al. 2003; Holschbach et al. 2002). After i.v. injection it rapidly (within 5 min) reaches a maximum brain uptake of approximately 3% of injected dose (Bauer et al. 2003; Meyer et al. 2004) (Fig. 8.1). Free
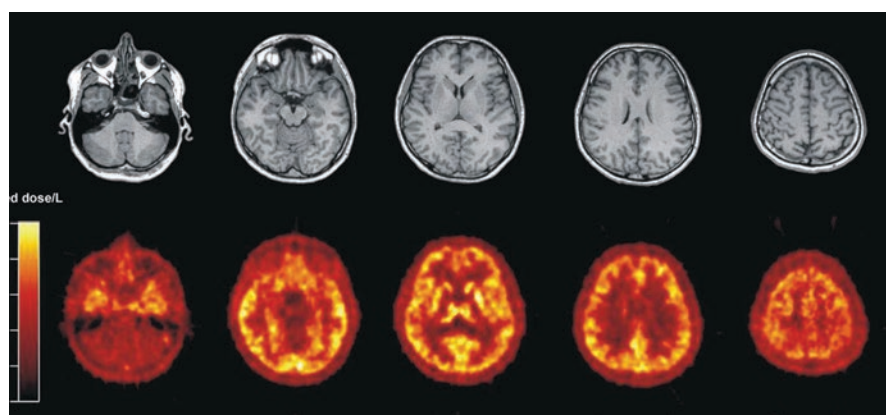
Fig. 8.1 In vivo distribution of [^{18}F]CPFPX: individual MRI (top) and summed (5–60 min postinjection) PET (bottom) of a representative healthy volunteer. Note the high accumulation of [^{18}F]CPFPX in cerebral cortex, basal ganglia, and thalamus
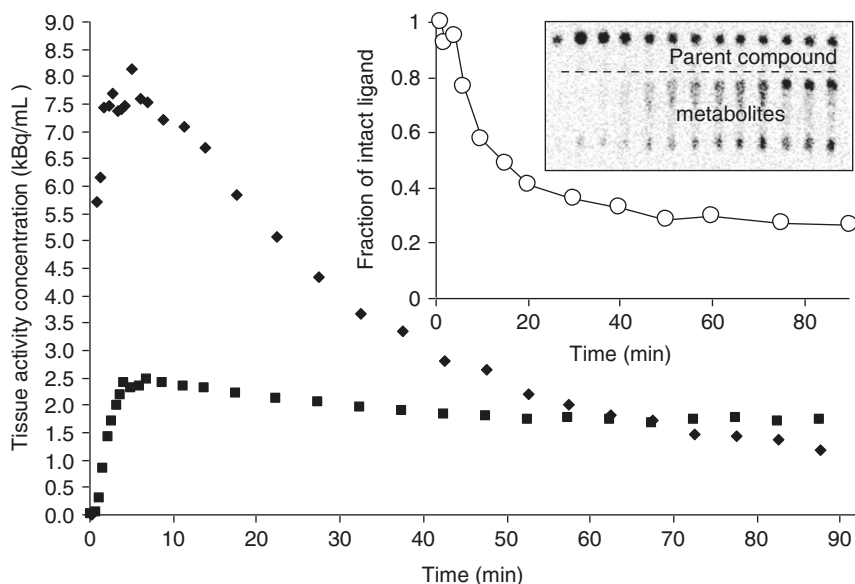
Fig. 8.2 Examples of representative bolus (diamonds) and bolus plus constant infusion (boxes) experiments in humans with [^{18}F]CPFPX. Depicted is the tissue time-activity curve of the frontal lobe. Steady state is reached after approximately 50 min. Inserted figure shows [^{18}F]CPFPX metabolism, fraction of parent compound of the bolus/infusion experiment, and thin-layer chromatography radioactivity distribution

fraction of parent compound in plasma is about 1–2%. [^{18}F]CPFPX is metabolized fast in the liver by the cytochrome isoenzyme CYP1A2 so that the fraction of parent compound is reduced to approximately 50% after 10 min and to less than 10% after 60 min (Matusch et al. 2006; Meyer et al. 2004). Formed metabolites are hydrophilic and do not cross the blood-brain barrier (>98% unchanged ligand in mouse brain tissue after 60 min) (Holschbach et al. 2002). The chemical structure of seven main metabolites (Fig. 8.2) and their pathways have been described (Holschbach et al. 2009, 2017; Bier et al. 2006). The regional cortical and subcortical distribution of in vivo binding is in agreement with the human *postmortem* distribution in autoradiographic measurements.

The suitability of [^{18}F]CPFPX for clinical applications has been shown in a dosimetry study (Herzog et al. 2008) which revealed that an injected dose of 300 MBq posed a radiation burden of 5.3 mSv on a patient. This dose is comparable to other ^{18}F-labeled PET tracers in clinical use.

[^{18}F]CPFPX has been administered i.v. as bolus and as bolus plus subsequent infusion (Meyer et al. 2004, 2005a, b). Pharmacokinetic modeling of an injection of a bolus can be described significantly better with a two-compartment model than with a one-compartment model. Nevertheless the individual rate constants were highly correlated leading to high standard errors of the estimates and the derived outcome parameter BP_P denoting the specific binding (Meyer et al. 2004). The

parameter total distribution volume (V_T) is a more valid measure as it combines the specific and nonspecific binding. V_T can also be determined with Logan's graphical analysis which allows voxel-wise determination and statistical parametric mapping. The noise-dependent bias in V_T parametric images can be reduced by spatial smoothing before applying the graphical analysis. A relatively short scan duration of 60 min is sufficient (Meyer et al. 2006a). Including the free fraction into the model increases variation and is therefore often omitted. Because of the high fraction of metabolites at late time points a blood volume correction should be applied. It had been shown that not only arterial but also venous input function for the graphical analysis allows reliable quantification of V_T (Meyer et al. 2005a, b).

Displacement studies with unlabeled CPFPX revealed that about one-third of cerebellar binding and at least two-thirds of cortical binding (depending on the cortical region) are specific (V_S) (Meyer et al. 2006b). [^{18}F]CPFPX is displaceable by caffeine in rats (Meyer et al. 2003) and humans (Elmenhorst et al. 2012). Therefore it is compulsory that subjects refrain from caffeine intake at least 36 h before participating in a PET study. Due to the selective liver metabolism special caution has to be taken in patients with liver dysfunction where the elimination half-life of caffeine is extremely prolonged (Matusch et al. 2006).

The in vitro inhibitory concentration of caffeine that displaces 50% of the binding (IC_{50}) of [^{3}H]CPFPX at human brain *postmortem* A_1ARs is in the range of 113–170 µM (Elmenhorst et al. 2011). Therefore the dose of caffeine after common consumption of coffee or tea has probably a direct impact on the in vivo quantification of A_1ARs with the PET ligand [^{18}F]CPFPX. Despite the acute effects of caffeine and various contradicting in vitro findings of the long-term effects of caffeine, an effect on A_1AR availability was not observed in a rat model of chronic caffeine exposure (30 mg/kg body weight/day, corresponding to 4–5 cups of coffee per day in humans for 12 weeks) (Nabbi-Schroeter et al. 2018).

The bolus plus subsequent infusion method allows quantifying modulations of binding (e.g., displacement) within a single scan. After establishing a steady state of ligand concentration in plasma and brain tissue, the total distribution volume V_T can be determined as a ratio of the concentrations in brain tissue and plasma. Due to the fast kinetics of [^{18}F]CPFPX equilibrium can be achieved within approximately 60 min (Meyer et al. 2005a, b).

In the case of [^{18}F]CPFPX the relatively low fraction of specific binding (about 2/3 of V_T) reduces the sensitivity for possible changes in V_T. Another shortcoming is the dependence on error-prone individual plasma input functions, which increases variability. These drawbacks can be avoided by using a reference region input for BP_{ND} (specific vs. non-displaceable input) which is independent on blood sampling (Meyer et al. 2006b; Elmenhorst et al. 2007a, b). The cerebellar cortex is used as a reference region. Although the cerebellar cortex is the region with the lowest A_1AR density in the human brain, one-third of the V_T is displaceable with unlabeled CPFPX (Meyer et al. 2006b). Therefore changes in BP_{ND} deserve careful consideration with regard to their dependency on V_S changes in the reference region. BP_{ND} can be determined by Logan's noninvasive graphical analysis. Test-retest evaluation of the variability and reproducibility revealed that reference-based measures were

superior to those based on plasma input function (Elmenhorst et al. 2007a, b). Exemplary values for V_T and BP_{ND} in the frontal cortex are 0.80 mL/mL and 0.92, respectively.

In an approach to determine the in vivo IC_{50} value of caffeine at the A_1AR in humans 18 subjects underwent bolus plus constant-infusion PET experiments after caffeine abstinence. Caffeine in varying concentrations (0.5–4.3 mg/kg body weight) was administered during the steady-state phase of ligand delivery (Fig. 8.3). [^{18}F]CPFPX binding was displaced in a concentration-dependent manner ranging from 5 to 44% (Fig. 8.4). No displacement (0.3%) was found after placebo administration. IC_{50} was estimated to be 65 µM in plasma which corresponds to 460 mg in a 70 kg subject (approximately 4.5 cups of coffee). Given both the biological
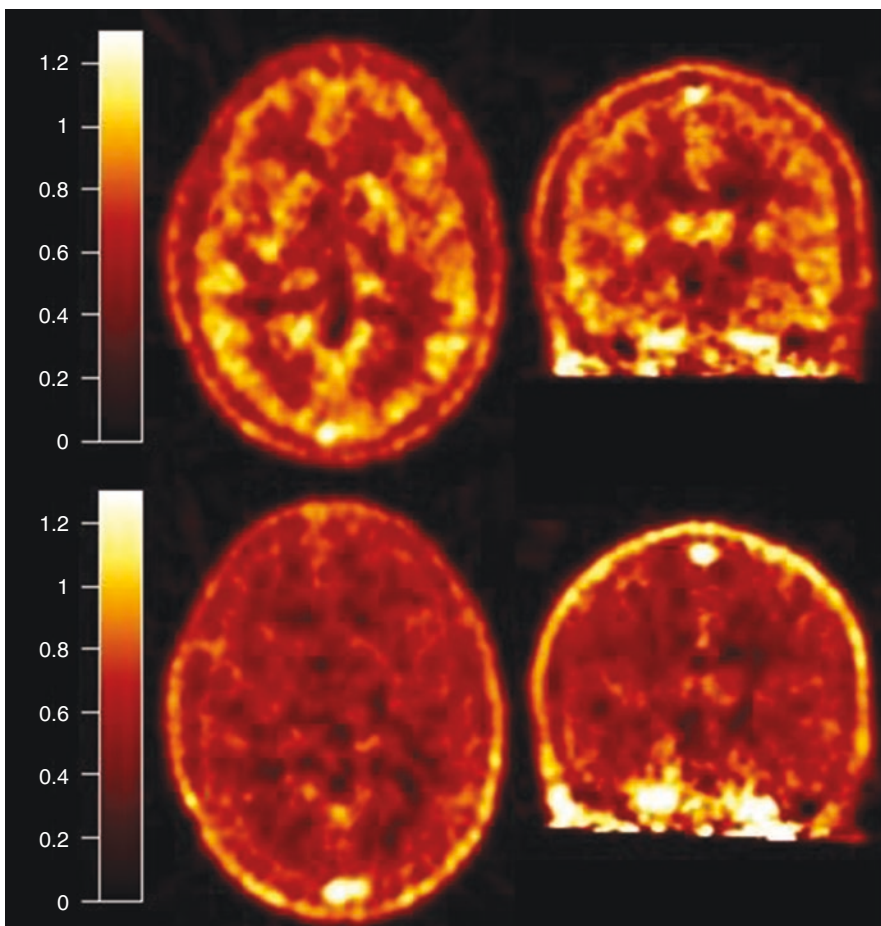
Fig. 8.3 Equilibrium imaging of caffeine action: parametric total distribution volume PET images before (50–90 min, top) and after caffeine infusion (100–140 min, bottom) of a subject receiving 4.3 mg caffeine per kg body weight
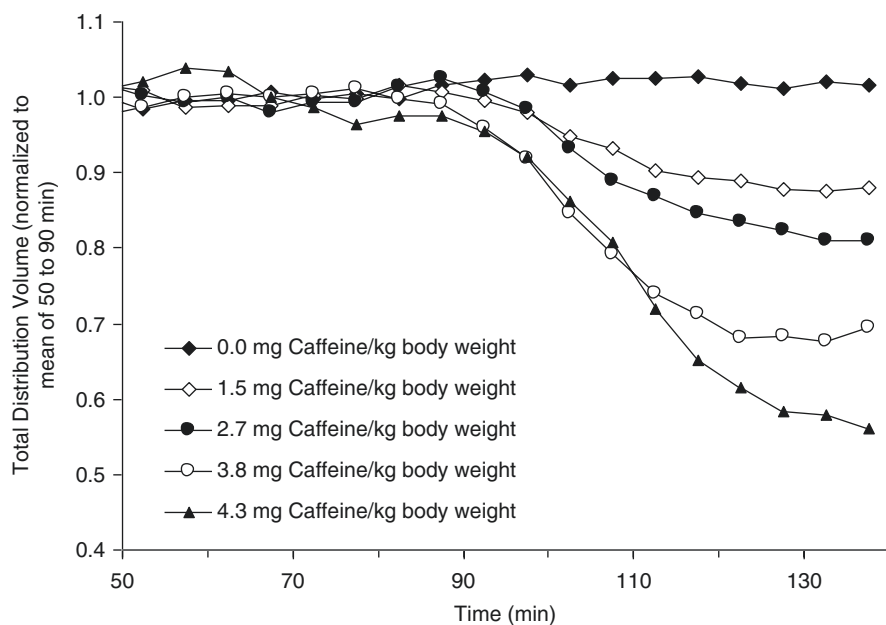
Fig. 8.4 Displacement of [^{18}F]CPFPX A$_1$AR binding by caffeine under equilibrium conditions (bolus/infusion PET scanning): Representative [^{18}F]CPFPX displacement studies employing increasing doses of caffeine. Intravenous infusion of 0.0–4.3 mg caffeine per kg body weight (equivalent to approximately 0–4 cups of coffee) between 90 and 100 min. Note the rapid and dose-dependent displacement of [^{18}F]CPFPX (x-axis: time after start of bolus/infusion study, y-axis: total volume of distribution normalized to the mean of 50–90 min)

half-life of caffeine of about 5 h and the repeated consumption of caffeinated beverages during a day, occupancies of 50% of the cerebral A$_1$AR are probably common conditions in caffeine consumers (Elmenhorst et al. 2012).

The A$_1$AR is known to be involved in numerous physiological and pathophysiological processes. Age-related changes were investigated over a time span of approximately 50 years showing a range of decline of BP_{ND} between −17% (putamen) and −34% (postcentral gyrus) (Meyer et al. 2006c). Further, it is hypothesized that adenosine is involved in the induction of sleep after prolonged wakefulness. 24 and 52 h of sleep deprivation lead to increased V_T values in a region-specific pattern in the brain with a maximum increase in the orbitofrontal cortex (15.3%). The upregulation in cortical and subcortical brain regions after prolonged wakefulness is likely to indicate that A$_1$AR expression is contributing to the homeostatic sleep regulation. Furthermore, correlations with psychomotor vigilance underscore the importance of A$_1$AR for cognitive performance (Elmenhorst et al. 2007a, b, 2017, 2018).

Interestingly ethanol exposure leads to an increase in A$_1$AR availability in humans measured with [^{18}F]CPFPX (Elmenhorst et al. 2018) which confirms previous reports of in vitro and in vivo experiments in rodents. In rats a 35–55% increase in [^{11}C]MPDX distribution volume was measured shortly after ethanol exposure along with an adenosine kinase inhibitor (Paul et al. 2011a, b). Recent results from
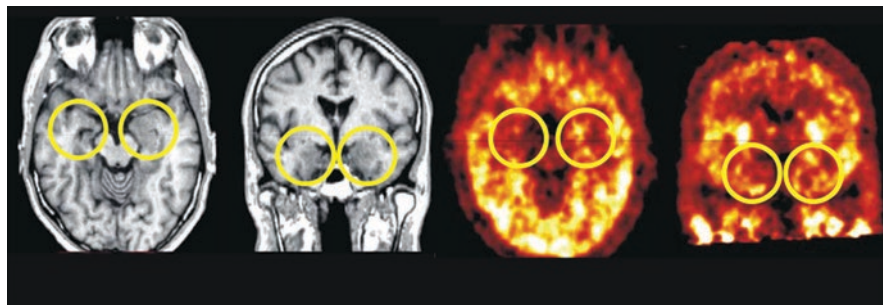
Fig. 8.5 Corresponding MRI (left) and [^{18}F]CPFPX PET (right) planes of a patient suffering from mesial temporal lobe epilepsy (focus in the right hemisphere). Note the considerably reduced A$_1$AR binding in the left mesial temporal lobe

mice suggest that sleep deprivation attenuates the sensitivity to ethanol via reduction of extracellular adenosine accumulation. The magnitude of the 35% increase in cerebral [^{18}F]CPFPX V_T after ethanol is comparable to a respective decrease observed after four cups of espresso.

In a pilot study on a patient with recurrent glioblastoma multiforme increases in A$_1$AR density in the direct vicinity of the tumor confirmed corresponding results in a F98 glioma-bearing rat model (Bauer et al. 2005). In a case of temporal lobe epilepsy there was evidence that A$_1$AR binding is reduced in the epileptic focus (Fig. 8.5).

The inverse antagonist [^{11}C]MPDX (log $P < 2.2$) (Ishiwata et al. 1995) shows a slightly lower affinity (K_i 4.2 nM) (Noguchi et al. 1997) for the A$_1$AR compared to [^{18}F]CPFPX. After i.v. injection it rapidly (within 2.5 min) reaches a maximum brain uptake of approximately 6% of injected dose (Kimura et al. 2004). [^{11}C]MPDX is metabolized slowly, so that the fraction of parent compound is reduced to approximately 75% after 60 min. The relative density distribution pattern of [^{11}C]MPDX is comparable to [^{18}F]CPFPX. Pharmacokinetic modeling of V_T was evaluated and performed with both a two-tissue-compartment model (with K_1/k_2 parameter estimates based on cerebellum as a reference region) and a graphical approach in the time span between 10 and 60 min (Logan plot) (Fukumitsu et al. 2003). Using an arterial input function with and without metabolite correction produced only a small negative bias of 4%. Parametric BP_{ND} images based on V_T determined by graphical analysis and cerebellum as reference region have been published (Fukumitsu et al. 2003). A blocking experiment in cats with DPCPX revealed that about 53% of V_T was specific binding. Exemplary values for V_T and BP_{ND} in the frontal cortex are 0.82 mL/mL and 0.23, respectively (Kimura et al. 2004). Interestingly, the radioactivity concentration of [^{11}C]MPDX in whole blood was slightly higher than in plasma suggesting an uptake in or binding to red blood cells (Fukumitsu et al. 2005). A noninvasive method to determine the outcome parameters based on independent component analysis has been proposed. Plasma time-activity curves could be estimated from dynamic PET images because the slow metabolization of [^{11}C]MPDX allowed to disregard metabolite correction. P-gp regulates the ability of endogenous and exogenous compounds to cross the BBB. Pretreatment of mice with the P-gp

blocker cyclosporine A before [11C]TMSX and [11C]MPDX PET increased both the blood-to-brain ratio and the cerebral uptake (Ishiwata et al. 2007a, b). [11C]TMSX and [11C]MPDX binding are therefore dependent on P-gp function (at least in mice).

The suitability of [18F]CPFPX and [11C]MPDX for investigating cerebral A_1ARs in longitudinal study protocols has been reported repeatedly for A_1AR availability and occupancy in a reliable (test-retest) and quantitative (pharmacokinetic modelling) manner in rats (Elmenhorst et al. 2013; Kroll et al. 2014; Paul et al. 2014a, b; Sijbesma et al. 2016).

PET imaging of A_1ARs has been evaluated as a tool to predict the severity of ischemic cerebral insults. In 13 cats the right middle cerebral artery was occluded transiently. [11C]MPDX uptake was significantly lower in those animals with a severe ischemic damage and the authors concluded that the binding after reperfusion was a sensitive predictor of severity (Nariai et al. 2003). Stimulation of cerebral A_1AR dampens microglial activaton after tissue trauma and has neuroprotective effects in animal models. Neuroinflammatory processes (HSV-1 infection) increased [11C]MPDX uptake in infected regions in concordance with immunohistochemical analyses (Paul et al. 2014).

The previously mentioned decline of adenosine receptor densities in human brains with increasing age measured with [18F]CPFPX was replicated for the A_1 subtype with [11C]MPDX (Mishina et al. 2012, 2017a, b). Interestingly, in the same study no effect of aging on the $A_{2A}AR$ was found. In an explorative study though, a putative interaction of $A_{2A}ARs$ and A1ARs in an inverse manner was observed between carriers of specific single-nucleotide polymorphisms in the $A_{2A}AR$ gene who showed a regionally higher A_1AR density (Hohoff et al. 2014).

A_1ARs have been investigated so far in various neurodegenerative diseases: In patients suffering from Alzheimer's disease a decreased binding of [11C]MPDX was detected in temporal cortex and thalamus (Fukumitsu et al. 2008). As the pattern of binding differs from the widely used [18F]FDG, adenosine receptor imaging might provide an additional diagnostic value. A cross sectional investigation of Huntington's disease patients indicated a switch of A_1AR availability from supra- to subnormal levels during phenoconversion of the disease (Matusch et al. 2014). [11C]MPDX PET in 10 drug-naïve patients with early Parkinson's disease did not show altered A_1AR in comparison to controls (Mishina et al. 2017). In patients in chronic stages of traumatic brain injury (diffuse axonal injury, n = 10) an increased [11C]MPDX BP_{ND} was measured in lower frontal and posterior cingulate cortex and the Rolandic area (Hayashi et al. 2018). The recent preclinical evaluation of [11C]22b, a A_1AR partial agonist PET radiotracer, showed besides suitable uptake, region-specific distribution, selective blocking, and test-retest stability the promise of detecting endogenous adenosine fluctuations (Guo et al. 2018). This feature might open up a new field of in vivo adenosine imaging.

8.3 A_{2A} Adenosine Receptor Ligands

The $A_{2A}AR$ antagonist [11C]TMSX (calculated log P = 1.1) (Ishiwata et al. 2000a, b, c, d) was the first radioligand to visualize $A_{2A}ARs$ in humans (Ishiwata et al. 2005). The compound presents a high affinity to $A_{2A}ARs$ (K_i = 5.9 nM) and a high

selectivity compared to the A_1AR (K_i = 1600 nM) (Ishiwata et al. 2003). It was confirmed in vitro that TMSX has a very low affinity for 13 different neuroreceptors (Ishiwata et al. 2000a, b, c, d). After i.v. injection it rapidly (within 1.5–2.5 min) reaches a maximum brain uptake of approximately 1–2% of injected dose (estimated from the data provided by Naganawa et al. 2007). In humans [^{11}C]TMSX is very slowly metabolized (over 90% parent compound after 60 min) (Naganawa et al. 2007). Exemplary values for V_T and BP_{ND} in the putamen are 1.75 mL/mL and 1.26, respectively. In a single subject Ishiwata et al. (2005) showed that [^{11}C]TMSX binding is blocked by a simultaneous and constant infusion of theophylline. V_T was reduced 8% in caudate nucleus and 4.5% in putamen but not in other brain areas. Theophylline infusion had an inhibiting effect on the metabolism of [^{11}C]TMSX. Quantification of $A_{2A}ARs$ based on arterial blood samples and metabolite analyses in five healthy volunteers were described by a two-compartment model and showed highest distribution volumes in putamen and thalamus (Mishina et al. 2007). Simplified methods for the determination of BP_{ND} by Logan's graphical analysis and distribution volume ratio to the reference region (centrum semiovale) have been reported for [^{11}C]TMSX. One method is based on the generation of an estimated plasma time-activity curve by independent component analysis (EPICA), which is applicable to [^{11}C]TMSX modeling because of the negligible metabolism of the compound (Naganawa et al. 2007). The second method using an intersectional searching algorithm and clustering (called EPISA) is independent of the metabolism of a ligand. In contrast to Logan, noninvasive EPISA-based V_T calculations to obtain BP_{ND} with a reference region circumvent k_2 parameter determinations which necessitate arterial blood sampling and metabolite correction (Naganawa et al. 2008). This is achieved by obtaining an unscaled integral of the metabolite-corrected plasma input function which is determined by clusters of distinct tissue time-activity curves. An alternative approach extracted reference region data from the PET images (cortical gray matter by using supervised clustering) and linked those to a population-based arterial input function which correlated well with standard plasma input analyses (Rissanen et al. 2015). Test-retest stability of [^{11}C]TMSX V_T and BP_{ND} was confirmed in five subjects (Naganawa et al. 2014).

Analogs of SCH442416 called [^{18}F]-FESCH and [^{18}F]-FPSCH were preclinically evaluated in rats (Khanapur et al. 2017). Blocking studies and pharmacokinetic modeling revealed that a 60-min dynamic scan of [^{18}F]-FESCH is suitable for blood- or reference region (cerebellum)-based $A_{2A}R$ quantification. The same group developed a radiolabeled version of the drug preladenant. The in vivo assessment of [^{11}C]preladenant in rats showed a larger striatum-to-cerebellum ratio compared to previously presented $A_{2A}R$ radioligands in rats. Pharmacokinetic quantification of $A_{2A}R$ (striatal $BP_{ND} \sim 6$, $V_T \sim 10$) in a rat model was possible and reliable, and formation of metabolites in plasma was low (17% after 60 min) (Zhou et al. 2017a, b, c). Transferring organ residence times of the rat model to a human radiation dosimetry model estimated common ^{11}C radiotracer doses of 6 μSv/MBq for [^{11}C]preladenant (Zhou et al. 2017a, b, c). Finally, first human data ($n = 8$) confirmed the low effective dose range, slow metabolization (23% after 60 min), and high target-to-background ratio (putamen $BP_{ND} \sim 5$, $V_T \sim 8$) (Sakata et al. 2017).

Another promising, although from a PET imaging perspective less favorable, derivate of preladenant called [^{18}F]-MNI-444 was recently tested in monkeys (Barret et al. 2014) and human subjects (Barret et al. 2015). Kinetics in humans were relatively slower (90-min scanning overestimated 210-min striatal BP_{ND} by ~10%). Binding in putamen was high ($BP_{ND} \sim 5$, $V_T \sim 3$) and the effective dose comparable to other [^{18}F] radioligands.

Due to the heterodimerization between dopamine D_2 and $A_{2A}ARs$, adenosine antagonists were explored as therapeutics for Parkinson's disease. Using PET it was investigated whether the disease affects basal cerebral $A_{2A}AR$ density and whether therapeutic interventions with standard antiparkinsonian medication had an impact on $A_{2A}AR$ binding. It was found that the binding potential in the putamen was higher in patients with additional dyskinetic symptoms compared to controls (Mishina et al. 2011). In another study with the $A_{2A}AR$ ligand [^{11}C]SCH442416 this finding could be reproduced as patients with dyskinesia had higher binding potentials in contrast to patients without dyskinesia who showed binding potentials comparable to the control subjects (Ramlackhansingh et al. 2011). In a preliminary analysis the EPICA method has been used to determine the BP_{ND} of patients with Parkinson's disease. BP_{ND} was significantly lower on the more affected side of the posterior putamen in Parkinson's disease while [^{11}C]raclopride binding to dopamine receptors was increased. A recent study with the new $A_{2A}AR$ ligand [^{11}C]preladenant showed no significant differences in the basal ganglia between Parkinson's disease and control groups in BP_{ND} values (Ishibashi et al. 2018). In the 6-hydroxydopamine rat model [^{11}C]preladenant binding was reduced after induction and increased after L-DOPA treatment (Zhou et al. 2017a, b, c).

[^{11}C]TMSX was used to investigate the changes of $A_{2A}AR$ availability in patients ($n = 8$) with normal-appearing white matter of secondary progressive multiple sclerosis. Patients showed an ~20% higher V_T compared to healthy controls (Rissanen et al. 2015).

Besides the aforementioned application of [^{11}C]TMSX in brain imaging studies it has additionally been used to study the human $A_{2A}AR$ in skeletal muscle, heart, and brown adipose tissue. An infusion of theophylline resulted in a reduction of binding suggesting specific binding of [^{11}C]TMSX in human muscles (Ishiwata et al. 2004). Increased adenosine $A_{2A}AR$ densities were found in the muscles of endurance-trained vs. untrained men (Mizuno et al. 2005). This finding could not be confirmed in a subsequent study (Heinonen et al. 2008). Exposure to cold ambient temperature (16 °C) leads to a reduction of [^{11}C]TMSX binding in brown adipose tissue (neck region) which was interpreted as an occupancy by endogenous adenosine (Lahesmaa et al. 2019).

Regarding human occupancy studies of drug candidates, [^{11}C]SCH442416 has been used to assess adenosine $A_{2A}AR$ occupancy of vipadenant (BIIB014) in healthy subjects (Brooks et al. 2010) and [^{11}C]KW-6002 (istradefylline) to find optimal oral doses of the same unlabeled compound (Brooks et al. 2008). The human in vivo $A_{2A}AR$ occupancy of this Parkinson medication was measured with the new radioligand [^{11}C]preladenant confirming the approved dose range (Ishibashi et al. 2018).

8.4   A$_{2B}$ Adenosine Receptor

Although several A$_{2B}$AR agonists and antagonists have been evaluated for preclinical applications (Kalla et al. 2009), none of these compounds has so far been introduced as a preclinical or clinical PET ligand.

[^{11}C]4a triazinobenzimidazole-based radioligand has been introduced and tested in vivo showing very high chemical and blood stability but low brain uptake in rats (Petroni et al. 2016). The [^{18}F]7a pyrazine-based radioligand (K_D for A$_{2B}$AR = 4.2 nM) (Lindemann et al. 2018) showed brain uptake in mice (SUV = 1) but formation of a blood-brain barrier-penetrating metabolite. Another drawback of this compound is its low A$_1$AR selectivity (K_D 19 nM).

8.5   A$_3$ Adenosine Receptor

There are no reports on A$_3$AR in vivo imaging studies so far although some radioligands were evaluated in biodistribution studies in rodents. Distribution and metabolism experiments have been performed in rodents with the fluoroethyl ester [^{18}F]FE@SUPPY and its fluoroethyl thioester analog [^{18}F]FE@SUPPY:2 (Haeusler et al. 2015, 2010; Wadsak et al. 2008). Unfortunately, both tracers are metabolized to BBB-permeating metabolites which complicate pharmacokinetic evaluation of the binding. Fifteen minutes after injection of [^{18}F]FE@SUPPY:2 the metabolites accounted for ~40% of brain tissue radioactivity and this fraction increased to ~80% after 60 min. [^{18}F]FE@SUPPY was more favorable in this respect as no metabolites were detected in the brain tissue up to 15 min after injection. However, the concentration increased to ~80% after 60 min (Haeusler et al. 2010). In another biodistribution study the [^{76}Br]-labeled antagonist MRS5147 was evaluated in rats showing an increased uptake in A$_3$AR-rich testes (Kiesewetter et al. 2009). However, in a dipping study with whole brain and testes no specific binding of [^{76}Br]MRS5147 was detected. In colorectal cancer A$_3$ARs are described to be highly expressed. In a xenograft mouse model in vivo detection of A$_3$AR with [^{18}F]FE@SUPPY was tested but showed insufficient tumor uptake (Balber et al. 2018).

8.6   Conclusion

Adenosine and its receptors play an important role in the physiology and pathophysiology of the brain as well as in other organs, particularly kidney, bowel, and vascular system, and in tumors. At present, only the A$_1$AR and the A$_{2A}$AR are accessible with molecular in vivo imaging. So far, these tools revealed important insights into neurologic and psychiatric disorders, sleep physiology, and cancer. The constantly increasing amount of data on adenosine and its important role in multiple organ systems as well as in the pathophysiology of frequent diseases underscore the need for further research in the field of ligand development for adenosine receptors.

References

Balber T, Singer J, Berroteran-Infante N, Dumanic M, Fetty L, Fazekas-Singer J, Vraka C, Nics L, Bergmann M, Pallitsch K, Spreitzer H, Wadsak W, Hacker M, Jensen-Jarolim E, Viernstein H, Mitterhauser M (2018) Preclinical in vitro and in vivo evaluation of [(18)F]FE@SUPPY for cancer PET imaging: limitations of a xenograft model for colorectal cancer. Contrast Media Mol Imaging 2018:1269830

Barret O, Hannestad J, Alagille D, Vala C, Tavares A, Papin C, Morley T, Fowles K, Lee H, Seibyl J, Tytgat D, Laruelle M, Tamagnan G (2014) Adenosine 2A receptor occupancy by tozadenant and preladenant in rhesus monkeys. J Nucl Med 55:1712–1718

Barret O, Hannestad J, Vala C, Alagille D, Tavares A, Laruelle M, Jennings D, Marek K, Russell D, Seibyl J, Tamagnan G (2015) Characterization in humans of ^{18}F-MNI-444, a PET radiotracer for brain adenosine 2A receptors. J Nucl Med 56:586–591

Bauer A, Holschbach MH, Meyer PT, Boy C, Herzog H, Olsson RA, Coenen HH, Zilles K (2003) In vivo imaging of adenosine A1 receptors in the human brain with [^{18}F]CPFPX and positron emission tomography. NeuroImage 19:1760–1769

Bauer A, Ishiwata K (2009) Adenosine receptor ligands and PET imaging of the CNS. Handb Exp Pharmacol:617–642

Bauer A, Langen KJ, Bidmon H, Holschbach MH, Weber S, Olsson RA, Coenen HH, Zilles K (2005) ^{18}F-CPFPX PET identifies changes in cerebral A1 adenosine receptor density caused by glioma invasion. J Nucl Med 46:450–454

Bier D, Holschbach MH, Wutz W, Olsson RA, Coenen HH (2006) Metabolism of the A1 adenosine receptor positron emission tomography ligand [^{18}F]8-cyclopentyl-3-(3-fluoropropyl)-1-propylxanthine ([^{18}F]CPFPX) in rodents and humans. Drug Metab Dispos 34:570–576

Brooks DJ, Doder M, Osman S, Luthra SK, Hirani E, Hume S, Kase H, Kilborn J, Martindill S, Mori A (2008) Positron emission tomography analysis of [11C]KW-6002 binding to human and rat adenosine A2A receptors in the brain. Synapse 62:671–681

Brooks DJ, Papapetropoulos S, Vandenhende F, Tomic D, He P, Coppell A, O'Neill G (2010) An open-label, positron emission tomography study to assess adenosine A2A brain receptor occupancy of vipadenant (BIIB014) at steady-state levels in healthy male volunteers. Clin Neuropharmacol 33:55–60

Ciruela F, Casado V, Rodrigues RJ, Lujan R, Burgueno J, Canals M, Borycz J, Rebola N, Goldberg SR, Mallol J, Cortes A, Canela EI, Lopez-Gimenez JF, Milligan G, Lluis C, Cunha RA, Ferre S, Franco R (2006) Presynaptic control of striatal glutamatergic neurotransmission by adenosine A1-A2A receptor heteromers. J Neurosci 26:2080–2087

Cristovao-Ferreira S, Navarro G, Brugarolas M, Perez-Capote K, Vaz SH, Fattorini G, Conti F, Lluis C, Ribeiro JA, McCormick PJ, Casado V, Franco R, Sebastiao AM (2011) Modulation of GABA transport by adenosine A1R-A2AR heteromers, which are coupled to both Gs- and G(i/o)-proteins. J Neurosci 31:15629–15639

Ding Y-S, Fowler J (2005) New-generation radiotracers for nAChR and NET. Nucl Med Biol 32:707–718

Dishino DD, Welch MJ, Kilbourn MR, Raichle ME (1983) Relationship between lipophilicity and brain extraction of C-11-labeled radiopharmaceuticals. J Nucl Med 24:1030–1038

Dunwiddie TV, Masino SA (2001) The role and regulation of adenosine in the central nervous system. Annu Rev Neurosci 24:31–55

Elmenhorst D, Elmenhorst EM, Hennecke E, Kroll T, Matusch A, Aeschbach D, Bauer A (2017) Recovery sleep after extended wakefulness restores elevated A1 adenosine receptor availability in the human brain. Proc Natl Acad Sci U S A 114:4243–4248

Elmenhorst D, Garibotto V, Prescher A, Bauer A (2011) Adenosine A(1) receptors in human brain and transfected CHO cells: inhibition of [(3)H]CPFPX binding by adenosine and caffeine. Neurosci Lett 487:415–420

Elmenhorst D, Kroll T, Wedekind F, Weisshaupt A, Beer S, Bauer A (2013) In vivo kinetic and steady-state quantification of ^{18}F-CPFPX binding to rat cerebral A1 adenosine receptors: validation by displacement and autoradiographic experiments. J Nucl Med 54:1411–1419

Elmenhorst D, Meyer PT, Matusch A, Winz OH, Bauer A (2012) Caffeine occupancy of human cerebral A1 adenosine receptors: in vivo quantification with ^{18}F-CPFPX and PET. J Nucl Med 53:1723–1729

Elmenhorst D, Meyer PT, Matusch A, Winz OH, Zilles K, Bauer A (2007a) Test-retest stability of cerebral A(1) adenosine receptor quantification using [(18)F]CPFPX and PET. Eur J Nucl Med Mol Imaging 34:1061–1070

Elmenhorst D, Meyer PT, Winz OH, Matusch A, Ermert J, Coenen HH, Basheer R, Haas HL, Zilles K, Bauer A (2007b) Sleep deprivation increases A1 adenosine receptor binding in the human brain: a positron emission tomography study. J Neurosci 27:2410–2415

Elmenhorst EM, Elmenhorst D, Benderoth S, Kroll T, Bauer A, Aeschbach D (2018) Cognitive impairments by alcohol and sleep deprivation indicate trait characteristics and a potential role for adenosine A1 receptors. Proc Natl Acad Sci U S A 115:8009–8014

Franco R, Lluis C, Canela EI, Mallol J, Agnati L, Casado V, Ciruela F, Ferre S, Fuxe K (2007) Receptor-receptor interactions involving adenosine A1 or dopamine D1 receptors and accessory proteins. J Neural Transm 114:93–104

Fredholm BB, IJzerman AP, Jacobson KA, Klotz KN, Linden J (2001) International union of pharmacology. XXV. Nomenclature and classification of adenosine receptors. Pharmacol Rev 53:527–552

Fukumitsu N, Ishii K, Kimura Y, Oda K, Hashimoto M, Suzuki M, Ishiwata K (2008) Adenosine A(1) receptors using 8-dicyclopropylmethyl-1-[(11)C]methyl-3-propylxanthine PET in Alzheimer's disease. Ann Nucl Med 22:841–847

Fukumitsu N, Ishii K, Kimura Y, Oda K, Sasaki T, Mori Y, Ishiwata K (2003) Imaging of adenosine A1 receptors in the human brain by positron emission tomography with [11C]MPDX. Ann Nucl Med 17:511–515

Fukumitsu N, Ishii K, Kimura Y, Oda K, Sasaki T, Mori Y, Ishiwata K (2005) Adenosine A1 receptor mapping of the human brain by PET with 8-dicyclopropylmethyl-1-11C-methyl-3-propylxanthine. J Nucl Med 46:32–37

Guo M, Gao ZG, Tyler R, Stodden T, Li Y, Ramsey J, Zhao WJ, Wang GJ, Wiers CE, Fowler JS, Rice KC, Jacobson KA, Kim SW, Volkow ND (2018) Preclinical evaluation of the first adenosine A1 receptor partial agonist radioligand for positron emission tomography imaging. J Med Chem 61:9966–9975

Haeusler D, Kuntner C, Nics L, Savli M, Zeilinger M, Wanek T, Karagiannis P, Lanzenberger RR, Langer O, Shanab K, Spreitzer H, Wadsak W, Hacker M, Mitterhauser M (2015) [18F]FE@SUPPY: a suitable PET tracer for the adenosine A3 receptor? An in vivo study in rodents. Eur J Nucl Med Mol Imaging 42:741–749

Haeusler D, Nics L, Mien LK, Ungersboeck J, Lanzenberger RR, Shanab K, Spreitzerf H, Sindelar KM, Viernstein H, Wagner KH, Dudczak R, Kletter K, Wadsak W, Mitterhauser M (2010) [18F]FE@SUPPY and [18F]FE@SUPPY:2--metabolic considerations. Nucl Med Biol 37:421–426

Halldin C, Gulyas B, Langer O, Farde L (2001) Brain radioligands--state of the art and new trends. Q J Nucl Med 45:139–152

Hayashi S, Inaji M, Nariai T, Oda K, Sakata M, Toyohara J, Ishii K, Ishiwata K, Maehara T (2018) Increased binding potential of brain adenosine A1 receptor in chronic stages of patients with diffuse axonal injury measured with [1-methyl-(11C)] 8-dicyclopropylmethyl-1-methyl-3-propylxanthine positron emission tomography imaging. J Neurotrauma 35:25–31

Heinonen I, Nesterov SV, Liukko K, Kemppainen J, Nagren K, Luotolahti M, Virsu P, Oikonen V, Nuutila P, Kujala UM, Kainulainen H, Boushel R, Knuuti J, Kalliokoski KK (2008) Myocardial blood flow and adenosine A2A receptor density in endurance athletes and untrained men. J Physiol 586:5193–5202

Herzog H, Elmenhorst D, Winz O, Bauer A (2008) Biodistribution and radiation dosimetry of the A1 adenosine receptor ligand ^{18}F-CPFPX determined from human whole-body PET. Eur J Nucl Med Mol Imaging 35:1499–1506

Hess S (2001) Recent advances in adenosine receptor antagonist research. Expert Opin Ther Pat 11:1533–1561

Hirani E, Gillies J, Karasawa A, Shimada J, Kase H, Opacka-Juffry J, Osman S, Luthra SK, Hume SP, Brooks DJ (2001) Evaluation of [4-O-methyl-(11)C]KW-6002 as a potential PET ligand for mapping central adenosine A(2A) receptors in rats. Synapse 42:164–176

Hohoff C, Garibotto V, Elmenhorst D, Baffa A, Kroll T, Hoffmann A, Schwarte K, Zhang W, Arolt V, Deckert J, Bauer A (2014) Association of adenosine receptor gene polymorphisms and in vivo adenosine A1 receptor binding in the human brain. Neuropsychopharmacology 39:2989–2999

Holschbach M, Müller CE, Wutz W, Schüller M, Coenen HH (2000) C-11 Markierung und erste ex vivo Evaluierung des Adenosin A2A Rezeptorliganden MSX-2 an NMRI Mäusen. Nuklearmedizin 39:P154

Holschbach MH, Bier D, Sihver W, Schulze A, Neumaier B (2017) Synthesis and pharmacological evaluation of identified and putative metabolites of the A1 adenosine receptor antagonist 8-cyclopentyl-3-(3-fluoropropyl)-1-propylxanthine (CPFPX). ChemMedChem 12:770–784

Holschbach MH, Olsson RA, Bier D, Wutz W, Sihver W, Schuller M, Palm B, Coenen HH (2002) Synthesis and evaluation of no-carrier-added 8-cyclopentyl-3-(3-[(18)F]fluoropropyl)-1-propylxanthine ([(18)F]CPFPX): a potent and selective A(1)-adenosine receptor antagonist for in vivo imaging. J Med Chem 45:5150–5156

Holschbach MH, Bier D, Wutz W, Willbold S, Olsson RA (2009) Synthesis of the main metabolite in human blood of the A1 adenosine receptor ligand [^{18}F]CPFPX. Org Lett 11:4266–4269

Ishibashi K, Miura Y, Wagatsuma K, Toyohara J, Ishiwata K, Ishii K (2018) Occupancy of adenosine A2A receptors by istradefylline in patients with Parkinson's disease using (11)C-preladenant PET. Neuropharmacology 143:106–112

Ishiwata K, Furuta R, Shimada J, Ishii S, Endo K, Suzuki F, Senda M (1995) Synthesis and preliminary evaluation of [11C]KF15372, a selective adenosine A1 antagonist. Appl Radiat Isot 46:1009–1013

Ishiwata K, Kawamura K, Yanai K, Hendrikse NH (2007a) In vivo evaluation of P-glycoprotein modulation of 8 PET radioligands used clinically. J Nucl Med 48:81–87

Ishiwata K, Kimura Y, de Vries J, Erik F, Elsinga PH (2007b) PET tracers for mapping adenosine receptors as probes for diagnosis of CNS disorders. CNS Agents Med Chem (Formerly Current Medicinal Chemistry-Central Nervous System Agents) 7(1):57–77

Ishiwata K, Mishina M, Kimura Y, Oda K, Sasaki T, Ishii K (2005) First visualization of adenosine A(2A) receptors in the human brain by positron emission tomography with [11C]TMSX. Synapse 55:133–136

Ishiwata K, Mizuno M, Kimura Y, Kawamura K, Oda K, Sasaki T, Nakamura Y, Muraoka I, Ishii K (2004) Potential of [11C]TMSX for the evaluation of adenosine A2A receptors in the skeletal muscle by positron emission tomography. Nucl Med Biol 31:949–956

Ishiwata K, Noguchi J, Toyama H, Sakiyama Y, Koike N, Ishii S, Oda K, Endo K, Suzuki F, Senda M (1996) Synthesis and preliminary evaluation of [11C]KF17837, a selective adenosine A2A antagonist. Appl Radiat Isot 47:507–511

Ishiwata K, Noguchi J, Wakabayashi S, Shimada J, Ogi N, Nariai T, Tanaka A, Endo K, Suzuki F, Senda M (2000a) 11C-labeled KF18446: a potential central nervous system adenosine A2a receptor ligand. J Nucl Med 41:345–354

Ishiwata K, Ogi N, Shimada J, Nonaka H, Tanaka A, Suzuki F, Senda M (2000b) Further characterization of a CNS adenosine A2a receptor ligand [11C]KF18446 with in vitro autoradiography and in vivo tissue uptake. Ann Nucl Med 14:81–89

Ishiwata K, Ogi N, Shimada J, Wang W, Ishii K, Tanaka A, Suzuki F, Senda M (2000c) Search for PET probes for imaging the globus pallidus studied with rat brain ex vivo autoradiography. Ann Nucl Med 14:461–466

Ishiwata K, Shimada J, Wang WF, Harakawa H, Ishii S, Kiyosawa M, Suzuki F, Senda M (2000d) Evaluation of iodinated and brominated [11C]styrylxanthine derivatives as in vivo radioligands mapping adenosine A2A receptor in the central nervous system. Ann Nucl Med 14:247–253

Ishiwata K, Kawamura K, Kimura Y, Oda K, Ishii K (2003) Potential of an adenosine A2A receptor antagonist [11C]TMSX for myocardial imaging by positron emission tomography: a first human study. Ann Nucl Med 17:457–462

Jacobson KA (2009) Introduction to adenosine receptors as therapeutic targets. Handb Exp Pharmacol 193:1–24. https://doi.org/10.1007/978-3-540-89615-9_1

Jacobson KA, Gao ZG (2006) Adenosine receptors as therapeutic targets. Nat Rev Drug Discov 5:247–264

Kalla RV, Zablocki J, Tabrizi MA, Baraldi PG (2009) Recent developments in A2B adenosine receptor ligands. Handb Exp Pharmacol 193:99–122

Khanapur S, Av W, Ishiwata K, Leenders KL, Dierckx RA, Elsinga PH (2014b) Adenosine A(2A) receptor antagonists as Positron Emission Tomography (PET) tracers. Curr Med Chem 21:312–328

Khanapur S, Paul S, Shah A, Vatakuti S, Koole MJ, Zijlma R, Dierckx RA, Luurtsema G, Garg P, van Waarde A, Elsinga PH (2014a) Development of [18F]-labeled pyrazolo[4,3-e]-1,2,4-triazolo[1,5-c]pyrimidine (SCH442416) analogs for the imaging of cerebral adenosine A2A receptors with positron emission tomography. J Med Chem 57:6765–6780

Khanapur S, van Waarde A, Dierckx RA, Elsinga PH, Koole MJ (2017) Preclinical evaluation and quantification of (18)F-fluoroethyl and (18)F-fluoropropyl analogs of SCH442416 as radioligands for PET imaging of the adenosine A2A receptor in rat brain. J Nucl Med 58:466–472

Kiesewetter DO, Lang L, Ma Y, Bhattacharjee AK, Gao ZG, Joshi BV, Melman A, de Castro S, Jacobson KA (2009) Synthesis and characterization of [76Br]-labeled high-affinity A3 adenosine receptor ligands for positron emission tomography. Nucl Med Biol 36:3–10

Kimura Y, Ishii K, Fukumitsu N, Oda K, Sasaki T, Kawamura K, Ishiwata K (2004) Quantitative analysis of adenosine A1 receptors in human brain using positron emission tomography and [1-methyl-11C]8-dicyclopropylmethyl-1-methyl-3-propylxanthine. Nucl Med Biol 31:975–981

Kreft S, Bier D, Holschbach MH, Schulze A, Coenen HH (2017) New potent A1 adenosine receptor radioligands for positron emission tomography. Nucl Med Biol 44:69–77

Kroll T, Elmenhorst D, Weisshaupt A, Beer S, Bauer A (2014) Reproducibility of non-invasive A adenosine receptor quantification in the rat brain using [18F]CPFPX and Positron Emission Tomography. Mol Imaging Biol 16(5):699–709

Lahesmaa M, Oikonen V, Helin S, Luoto P, Din MU, Pfeifer A, Nuutila P, Virtanen KA (2019) Regulation of human brown adipose tissue by adenosine and A2A receptors—studies with [(15)O]H$_2$O and [(11)C]TMSX PET/CT. Eur J Nucl Med Mol Imaging 46:743–750

Li J, Hong X, Li G, Conti PS, Zhang X, Chen K (2019) PET imaging of adenosine receptors in diseases. Curr Top Med Chem 19(16):1445–1463

Lindemann M, Hinz S, Deuther-Conrad W, Namasivayam V, Dukic-Stefanovic S, Teodoro R, Toussaint M, Kranz M, Juhl C, Steinbach J, Brust P, Muller CE, Wenzel B (2018) Radiosynthesis and in vivo evaluation of a fluorine-18 labeled pyrazine based radioligand for PET imaging of the adenosine A2B receptor. Bioorg Med Chem 26:4650–4663

Lowe PT, Dall'Angelo S, Mulder-Krieger T, IJzerman AP, Zanda M, O'Hagan D (2017) a new class of fluorinated A2A adenosine receptor agonist with application to last-step enzymatic [(18)F]fluorination for PET imaging. Chembiochem 18:2156–2164

Marian T, Boros I, Lengyel Z, Balkay L, Horvath G, Emri M, Sarkadi E, Szentmiklosi AJ, Fekete I, Tron L (1999) Preparation and primary evaluation of [11C]CSC as a possible tracer for mapping adenosine A2A receptors by PET. Appl Radiat Isot 50:887–893

Mason NS, Mathis CA (2003) Positron emission tomography radiochemistry. Neuroimaging Clin N Am 13:671–687

Matsuya T, Takamatsu H, Murakami Y, Noda A, Ichise R, Awaga Y, Nishimura S (2005) Synthesis and evaluation of [(11)C]FR194921 as a nonxanthine-type PET tracer for adenosine A(1) receptors in the brain. Nucl Med Biol 32:837–844

Matusch A, Meyer PT, Bier D, Holschbach MH, Woitalla D, Elmenhorst D, Winz OH, Zilles K, Bauer A (2006) Metabolism of the A(1) adenosine receptor PET ligand [(18)F]CPFPX by CYP1A2: implications for bolus/infusion PET studies. Nucl Med Biol 33:891–898

Matusch A, Saft C, Elmenhorst D, Kraus PH, Gold R, Hartung HP, Bauer A (2014) Cross sectional PET study of cerebral adenosine A(1) receptors in premanifest and manifest Huntington's disease. Eur J Nucl Med Mol Imaging 41:1210–1220

Meyer PT, Bier D, Holschbach MH, Boy C, Olsson RA, Coenen HH, Zilles K, Bauer A (2004) Quantification of cerebral A1 adenosine receptors in humans using [18F]CPFPX and PET. J Cereb Blood Flow Metab 24:323–333

Meyer PT, Bier D, Holschbach MH, Cremer M, Tellmann L, Bauer A (2003) Image of the month. In vivo imaging of rat brain A1 adenosine receptor occupancy by caffeine. Eur J Nucl Med Mol Imaging 30:1440

Meyer PT, Elmenhorst D, Bier D, Holschbach MH, Matusch A, Coenen HH, Zilles K, Bauer A (2005a) Quantification of cerebral A1 adenosine receptors in humans using [18F]CPFPX and PET: an equilibrium approach. NeuroImage 24:1192–1204

Meyer PT, Elmenhorst D, Boy C, Winz O, Matusch A, Zilles K, Bauer A (2006c) Effect of aging on cerebral A(1) adenosine receptors: a [(18)F]CPFPX PET study in humans. Neurobiol Aging 28:1914–1924

Meyer PT, Elmenhorst D, Matusch A, Winz O, Zilles K, Bauer A (2006a) 18F-CPFPX PET: on the generation of parametric images and the effect of scan duration. J Nucl Med 47: 200–207

Meyer PT, Elmenhorst D, Zilles K, Bauer A (2005b) Simplified quantification of cerebral A1 adenosine receptors using [18F]CPFPX and PET: analyses based on venous blood sampling. Synapse 55:212–223

Meyer PT, Elmenhorst D, Matusch A, Winz O, Zilles K, Bauer A (2006b) A1 adenosine receptor PET using [18F]CPFPX: displacement studies in humans. NeuroImage 32: 1100–1105

Mishina M, Ishii K, Kimura Y, Suzuki M, Kitamura S, Ishibashi K, Sakata M, Oda K, Kobayashi S, Kimura K, Ishiwata K (2017a) Adenosine A1 receptors measured with (11) C-MPDX PET in early Parkinson's disease. Synapse 71(8):e21979

Mishina M, Ishiwata K (2014) Adenosine receptor PET imaging in human brain. Int Rev Neurobiol 119:51–69

Mishina M, Ishiwata K, Kimura Y, Naganawa M, Oda K, Kobayashi S, Katayama Y, Ishii K (2007) Evaluation of distribution of adenosine A(2A) receptors in normal human brain measured with [C-11]TMSX PET. Synapse 61:778–784

Mishina M, Ishiwata K, Naganawa M, Kimura Y, Kitamura S, Suzuki M, Hashimoto M, Ishibashi K, Oda K, Sakata M, Hamamoto M, Kobayashi S, Katayama Y, Ishii K (2011) Adenosine A(2A) receptors measured with [C]TMSX PET in the striata of Parkinson's disease patients. PLoS One 6:e17338

Mishina M, Kimura Y, Naganawa M, Ishii K, Oda K, Sakata M, Toyohara J, Kobayashi S, Katayama Y, Ishiwata K (2012) Differential effects of age on human striatal adenosine A(1) and A(2A) receptors. Synapse 66:832–839

Mishina M, Kimura Y, Sakata M, Ishii K, Oda K, Toyohara J, Kimura K, Ishiwata K (2017b) Age-Related Decrease in Male Extra-Striatal Adenosine A1 Receptors Measured Using (11) C-MPDX PET. Front Pharmacol 8:903

Mizuno M, Kimura Y, Tokizawa K, Ishii K, Oda K, Sasaki T, Nakamura Y, Muraoka I, Ishiwata K (2005) Greater adenosine A(2A) receptor densities in cardiac and skeletal muscle in endurance-trained men: a [11C]TMSX PET study. Nucl Med Biol 32:831–836

Moerlein SM, Laufer P, Stocklin G (1985) Effect of lipophilicity on the in vivo localization of radiolabelled spiperone analogues. Int J Nucl Med Biol 12:353–356

Moresco RM, Todde S, Belloli S, Simonelli P, Panzacchi A, Rigamonti M, Galli-Kienle M, Fazio F (2005) In vivo imaging of adenosine A2A receptors in rat and primate brain using [11C]SCH442416. Eur J Nucl Med Mol Imaging 32:405–413

Nabbi-Schroeter D, Elmenhorst D, Oskamp A, Laskowski S, Bauer A, Kroll T (2018) Effects of long-term caffeine consumption on the adenosine A1 receptor in the rat brain: an in vivo PET Study with [(18)F]CPFPX. Mol Imaging Biol 20:284–291

Naganawa M, Kimura Y, Mishina M, Manabe Y, Chihara K, Oda K, Ishii K, Ishiwata K (2007) Quantification of adenosine A2A receptors in the human brain using [11C]TMSX and positron emission tomography. Eur J Nucl Med Mol Imaging 34:679–687

Naganawa M, Kimura Y, Yano J, Mishina M, Yanagisawa M, Ishii K, Oda K, Ishiwata K (2008) Robust estimation of the arterial input function for Logan plots using an intersectional searching algorithm and clustering in positron emission tomography for neuroreceptor imaging. NeuroImage 40:26–34

Naganawa M, Mishina M, Sakata M, Oda K, Hiura M, Ishii K, Ishiwata K (2014) Test-retest variability of adenosine A2A binding in the human brain with (11)C-TMSX and PET. EJNMMI Res 4:76

Nariai T, Shimada Y, Ishiwata K, Nagaoka T, Shimada J, Kuroiwa T, Ono K, Ohno K, Hirakawa K, Senda M (2003) PET imaging of adenosine A(1) receptors with (11)C-MPDX as an indicator of severe cerebral ischemic insult. J Nucl Med 44:1839–1844

Noguchi J, Ishiwata K, Furuta R, Simada J, Kiyosawa M, Ishii S, Endo K, Suzuki F, Senda M (1997) Evaluation of carbon-11 labeled KF15372 and its ethyl and methyl derivatives as a potential CNS adenosine A1 receptor ligand. Nucl Med Biol 24:53–59

Palmer TM, Stiles GL (1995) Adenosine receptors. Neuropharmacology 34:683–694

Paul S, Elsinga PH, Ishiwata K, Dierckx RA, van Waarde A (2011a) Adenosine A(1) receptors in the central nervous system: their functions in health and disease, and possible elucidation by PET imaging. Curr Med Chem 18:4820–4835

Paul S, Khanapur S, Boersma W, Sijbesma JW, Ishiwata K, Elsinga PH, Meerlo P, Doorduin J, Dierckx RA, van Waarde A (2014) Cerebral adenosine A(1) receptors are upregulated in rodent encephalitis. NeuroImage 92:83–89

Paul S, Khanapur S, Rybczynska AA, Kwizera C, Sijbesma JW, Ishiwata K, Willemsen AT, Elsinga PH, Dierckx RA, van Waarde A (2011b) Small-animal PET study of adenosine A(1) receptors in rat brain: blocking receptors and raising extracellular adenosine. J Nucl Med 52:1293–1300

Paul S, Khanapur S, Sijbesma JW, Ishiwata K, Elsinga PH, Meerlo P, Dierckx RA, van Waarde A (2014b) Use of 11C-MPDX and PET to study adenosine A1 receptor occupancy by nonradioactive agonists and antagonists. J Nucl Med 55:315–320

Petroni D, Giacomelli C, Taliani S, Barresi E, Robello M, Daniele S, Bartoli A, Burchielli S, Pardini S, Salvadori PA, Da Settimo F, Martini C, Trincavelli ML, Menichetti L (2016) Toward PET imaging of A2B adenosine receptors: a carbon-11 labeled triazinobenzimidazole tracer: Synthesis and imaging of a new A2B PET tracer. Nucl Med Biol 43:309–317

Poucher SM, Keddie JR, Singh P, Stoggall SM, Caulkett PW, Jones G, Coll MG (1995) The in vitro pharmacology of ZM 241385, a potent, non-xanthine A2a selective adenosine receptor antagonist. Br J Pharmacol 115:1096–1102

Ramlackhansingh AF, Bose SK, Ahmed I, Turkheimer FE, Pavese N, Brooks DJ (2011) Adenosine 2A receptor availability in dyskinetic and nondyskinetic patients with Parkinson disease. Neurology 76:1811–1816

Rissanen E, Tuisku J, Luoto P, Arponen E, Johansson J, Oikonen V, Parkkola R, Airas L, Rinne JO (2015) Automated reference region extraction and population-based input function for brain [(11)C]TMSX PET image analyses. J Cereb Blood Flow Metab 35:157–165

Sakata M, Ishibashi K, Imai M, Wagatsuma K, Ishii K, Zhou X, de Vries EFJ, Elsinga PH, Ishiwata K, Toyohara J (2017) Initial evaluation of an adenosine A2A receptor ligand, (11)C-preladenant, in healthy human subjects. J Nucl Med 58:1464–1470

Schneider D, Bier D, Bauer A, Neumaier B, Holschbach M (2019a) Influence of incubation conditions on microsomal metabolism of xanthine-derived A1 adenosine receptor ligands. J Pharmacol Toxicol Methods 95:16–26

Schneider D, Oskamp A, Holschbach M, Neumaier B, Bauer A, Bier D (2019b) Relevance of in vitro metabolism models to PET radiotracer development: prediction of in vivo clearance in rats from microsomal stability data. Pharmaceuticals (Basel) 12

Sihver W, Bier D, Holschbach MH, Schulze A, Wutz W, Olsson RA, Coenen HH (2004) Binding of tritiated and radioiodinated ZM241,385 to brain A2A adenosine receptors. Nucl Med Biol 31:173–177

Sihver W, Holschbach MH, Bier D, Wutz W, Schulze A, Olsson RA, Coenen HH (2003) Evaluation of radioiodinated 8-Cyclopentyl-3-[(E)-3-iodoprop-2-en-1-yl]-1-propylxanthine ([*I]CPIPX) as a new potential A1 adenosine receptor antagonist for SPECT. Nucl Med Biol 30:661–668

Sijbesma JW, Zhou X, Vallez Garcia D, Houwertjes MC, Doorduin J, Kwizera C, Maas B, Meerlo P, Dierckx RA, Slart RH, Elsinga PH, van Waarde A (2016) Novel approach to repeated arterial blood sampling in small animal PET: application in a test-retest study with the adenosine A1 receptor ligand [(11)C]MPDX. Mol Imaging Biol 18:715–723

Tavares AADS, Batis J, Barret O, Alagille D, Vala C, Kudej G, Koren A, Cosgrove KP, Nice K, Kordower JH, Seibyl J, Tamagnan GD (2013) In vivo evaluation of [(123)I]MNI-420: a novel single photon emission computed tomography radiotracer for imaging of adenosine 2A receptors in brain. Nucl Med Biol 40:403–409

Todde S, Moresco RM, Simonelli P, Baraldi PG, Cacciari B, Spalluto G, Varani K, Monopoli A, Matarrese M, Carpinelli A, Magni F, Kienle MG, Fazio F (2000) Design, radiosynthesis, and biodistribution of a new potent and selective ligand for in vivo imaging of the adenosine A(2A) receptor system using positron emission tomography. J Med Chem 43:4359–4362

Vala C, Morley TJ, Zhang X, Papin C, Tavares AA, Lee HS, Constantinescu C, Barret O, Carroll VM, Baldwin RM, Tamagnan GD, Alagille D (2016) Synthesis and in vivo evaluation of Fluorine-18 and Iodine-123 Pyrazolo[4,3-e]-1,2,4-triazolo[1,5-c]pyrimidine derivatives as PET and SPECT radiotracers for mapping A2A receptors. ChemMedChem 11:1936–1943

van Waarde A, Rajo D, Zhou X, Khanapur S, Tsukada H, Ishiwata K, Luurtsema G, de Vries EFJ, Elsinga PH (2018) Potential Therapeutic applications of adenosine A2A receptor ligands and opportunities for A2A receptor imaging. Med Res Rev 38:5–56

Vuorimaa, A., E. Rissanen, and L. Airas. 2017. In vivo PET imaging of adenosine 2A receptors in neuroinflammatory and neurodegenerative disease, Contrast Media Mol Imaging, 2017:6975841

Wadsak W, Mien LK, Shanab K, Ettlinger DE, Haeusler D, Sindelar K, Lanzenberger RR, Spreitzer H, Viernstein H, Keppler BK, Dudczak R, Kletter K, Mitterhauser M (2008) Preparation and first evaluation of [(18)F]FE@SUPPY: a new PET tracer for the adenosine A(3) receptor. Nucl Med Biol 35:61–66

Wang WF, Ishiwata K, Nonaka H, Ishii S, Kiyosawa M, Shimada J, Suzuki F, Senda M (2000) Carbon-11-labeled KF21213: a highly selective ligand for mapping CNS adenosine A(2A) receptors with positron emission tomography. Nucl Med Biol 27:541–546

Zeitzer JM, Morales-Villagran A, Maidment NT, Behnke EJ, Ackerson LC, Lopez-Rodriguez F, Fried I, Engel J, Wilson CL (2006) Extracellular adenosine in the human brain during sleep and sleep deprivation: an in vivo microdialysis study. Sleep 29:455–461

Zhou X, Doorduin J, Elsinga PH, Dierckx R, de Vries EFJ, Casteels C (2017a) Altered adenosine 2A and dopamine D2 receptor availability in the 6-hydroxydopamine-treated rats with and without levodopa-induced dyskinesia. NeuroImage 157:209–218

Zhou X, Elsinga PH, Khanapur S, Dierckx RA, de Vries EF, de Jong JR (2017b) Radiation dosimetry of a novel adenosine A2A receptor radioligand [(11)C]preladenant based on PET/CT imaging and ex vivo biodistribution in rats. Mol Imaging Biol 19:289–297

Zhou X, Khanapur S, de Jong JR, Willemsen AT, Dierckx RA, Elsinga PH, de Vries EF (2017c) In vivo evaluation of [(11)C]preladenant positron emission tomography for quantification of adenosine A2A receptors in the rat brain. J Cereb Blood Flow Metab 37:577–589

Zhou X, Khanapur S, Huizing AP, Zijlma R, Schepers M, Dierckx RA, van Waarde A, de Vries EF, Elsinga PH (2014) Synthesis and preclinical evaluation of 2-(2-furanyl)-7-[2-[4-[4-(2-[11C]methoxyethoxy)phenyl]-1-piperazinyl]ethyl]7H-pyr azolo[4,3-e][1,2,4]triazolo[1,5-c]pyrimidine-5-amine ([11C]Preladenant) as a PET tracer for the imaging of cerebral adenosine A2A receptors. J Med Chem 57:9204–9210

Imaging of Central Benzodiazepine Receptors in Chronic Cerebral Ischemia

9

Hiroshi Yamauchi

Contents

Abstract

In patients with atherosclerotic internal carotid artery (ICA) or middle cerebral artery (MCA) occlusive disease, fluctuation of cerebral perfusion under conditions of chronic hemodynamic compromise may cause not only cerebral infarction but also selective neuronal damage in the cerebral cortex that is not detectable as infarction on CT or MRI. Imaging of the central-type benzodiazepine receptors (cBZR), which are expressed by most cortical neurons, has enabled visualization of neuronal alterations induced by ischemia in vivo, in humans. Using PET and ^{11}C-flumazenil, we showed that selective neuronal damage demon-

H. Yamauchi (✉)

Division of PET Imaging, Shiga Medical Center Research Institute, Moriyama, Shiga, Japan
e-mail: yamauchi@kuhp.kyoto-u.ac.jp

strated as a decrease in cBZR in the normal-appearing cerebral cortex was associated with increased oxygen extraction fraction (OEF), the so-called misery perfusion, in patients with atherosclerotic ICA or MCA occlusive disease in the chronic stage. Follow-up examinations of the patients without ischemic episode showed that a decrease in cBZR was associated with an increase in OEF (hemodynamic deterioration). A decrease in cBZR was also associated with executive dysfunction. Chronic hemodynamic ischemia causes selective neuronal damage observed as a decrease in cBZR that has an impact on the functional outcomes. Therapies for preventing neuronal damage are needed, and imaging of cBZR may be useful to monitor the effects of such therapies.

9.1 Introduction

9.1.1 Chronic Hemodynamic Compromise and Risk for Stroke

In patients with atherosclerotic internal carotid artery (ICA) or middle cerebral artery (MCA) occlusive disease, chronic reduction in cerebral perfusion pressure (chronic hemodynamic compromise) increases the risk of cerebral ischemic damage (Baron et al. 1981; Klijn and Kappelle 2010; Powers 1991; Yamauchi et al. 1992). Previous studies have shown that chronic hemodynamic compromise, as indicated by increased oxygen extraction fraction (OEF; misery perfusion) (Baron et al. 1981) on positron-emission tomography (PET) or severely decreased vasodilatory capacity, is a risk factor for subsequent ischemic stroke in atherosclerotic ICA or MCA occlusive disease (Derdeyn et al. 1999; Grubb et al. 1998; Kuroda et al. 2001; Markus and Cullinane 2001; Ogasawara et al. 2002; Vernieri et al. 1999; Yamauchi et al. 1996b, 1999, 2012). Furthermore, follow-up examinations of patients without ischemic episodes showed that an increase in OEF (hemodynamic deterioration) was associated with an increase in the risk for subsequent stroke (Yamauchi et al. 2000b). Thus, understanding the pathophysiology of chronic hemodynamic cerebral ischemia is essential for the management of patients with atherosclerotic ICA or MCA occlusive disease.

Vascular reconstruction surgery can improve chronic hemodynamic compromise (Yamauchi et al. 1994), which may prevent subsequent ischemic stroke of hemodynamic origin (Fig. 9.1). Extracranial-to-intracranial (EC-IC) bypass surgery—which has no benefit in patients with ICA or MCA occlusive disease in general (The EC/IC Bypass Study Group 1985)—may prevent recurrent strokes in select patients with hemodynamic compromise. Two randomized clinical trials used hemodynamic criteria for patient selection (Ogawa 2012; Powers et al. 2011), to test this hypothesis. One trial in Japan (Japanese EC-IC bypass trial; JET study) demonstrated a benefit from bypass surgery for preventing disabling stroke (modified Rankin scale >2) (2-year ipsilateral ischemic stroke rate including perioperative stroke: 2.9% in
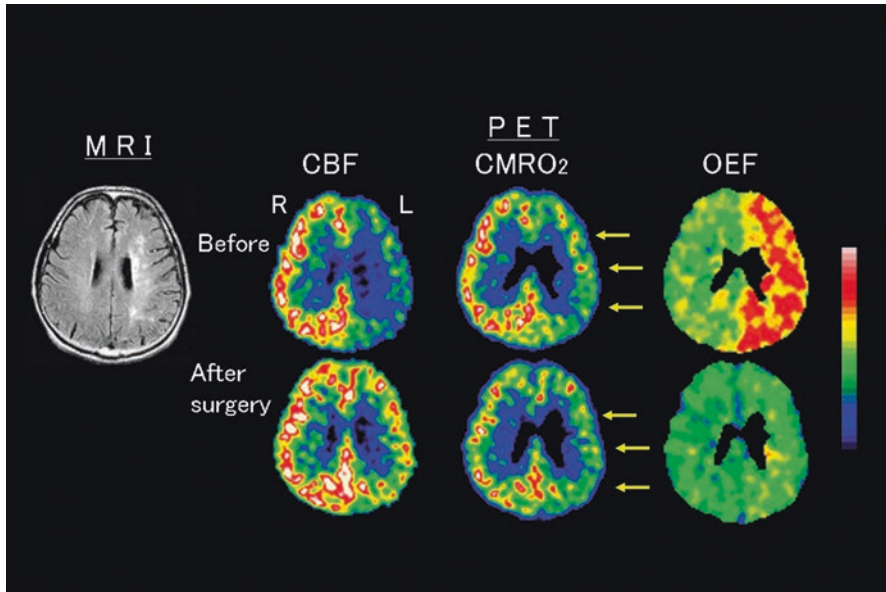
Fig. 9.1 Reduced cerebral cortical oxygen metabolism without morphological changes. A patient with occlusion of the left internal carotid artery showed decreased cerebral blood flow (CBF) and increased oxygen extraction fraction (OEF, misery perfusion) in the hemisphere with occlusion. Surgical reperfusion with bypass improved misery perfusion. However, we should note that cerebral metabolic rate of oxygen, which was decreased in the normal-appearing cerebral cortex before surgery, was unchanged after surgical reperfusion. Some irreversible damage may occur in the cerebral cortex

the surgical group vs. 10.7% in the medical group) (Ogawa 2012); in contrast, another study (Carotid Occlusion Surgery Study; COSS) did not demonstrate a benefit (any stroke, 21% vs. 23%) (Powers et al. 2011). The perioperative stroke rate in the two studies differed (disabling stroke, 0% vs. any stroke, 15%), which may have led to their different conclusions. Because of the high prevalence of Moyamoya disease, EC-IC bypass with postoperative management has been an essential skill for neurosurgeons in Japan (Kuroda and Houkin 2008), which may have resulted in the 0% perioperative disabling stroke rate of the Japanese EC/IC Bypass Trial (Ogawa 2012). Achieving low operative risk could lead to the benefit of bypass surgery.

Although correct evaluation of hemodynamic status is essential to determine prognosis, therapeutic strategies to prevent recurrent strokes, which should differ between patients with and those without hemodynamic compromise, are not clearly established. Continuing efforts are warranted to determine the strategies for selecting treatments based on hemodynamic measurements.

9.1.2 Selective Neuronal Damage/Loss or Incomplete Infarction

In atherosclerotic ICA or MCA occlusive disease, chronic hemodynamic compromise increases the risk for cerebral ischemic damage regardless of the development of symptoms. Hemodynamic cerebral ischemia due to ICA or MCA occlusive disease may cause not only cerebral infarction but also minor tissue damage in the cerebral cortex that is not detectable as infarction on CT or magnetic resonance imaging (MRI). Neuropathological studies have demonstrated cortical granular atrophy or watershed territory microemboli in the cerebral cortex distal to a large cerebral arterial occlusion (Graham 1992). Observations in both humans and animals also suggest that cortical selective neuronal loss results from acute occlusion of the large cerebral arteries accompanied by ischemia of moderate severity (Garcia et al. 1996; Lassen et al. 1983). Fifteen-minute distal MCA occlusion in spontaneously hypertensive rats, mimicking true cortical TIA, resulted in normal MRI findings, but consistent cortical selective neuronal loss was observed (Ejaz et al. 2015a, b). However, selective neuronal loss in patients with atherosclerotic ICA or MCA disease has not been confirmed pathologically in the human brain. It is unclear whether selective neuronal ischemic change develops in patients with atherosclerotic occlusion of the large cerebral arteries because a direct demonstration of the cortical neuronal loss in the living brain is not possible.

Indirect markers for neuronal damage, including decreased metabolism and brain atrophy, have been investigated to address the issue of neuronal loss without infarction in ICA or MCA occlusive diseases. Decrease in glucose or oxygen metabolism in the normal-appearing cerebral cortex is one of the sequalae of ischemic damage to the tissue; however, it can also be caused by a decrease in neural input from distant regions with fiber connections (Feeney and Baron 1986). CT studies in ICA occlusive disease have revealed only hemiatrophy in some patients (Radu and Moseley 1978). In patients with ICA or MCA occlusive disease, including Moyamoya disease, MRI studies have shown decreases in cortical thickness in the hemispheres with arterial disease (Fierstra et al. 2010). Atrophy of the corpus callosum may be an indirect but sensitive indicator of ischemic cortical neuronal loss. The largest fraction of neurons projecting into the corpus callosum comprises the large pyramidal cells in layer 3, which constitute one of the groups of cortical neurons most vulnerable to ischemia (Graham 1992). Therefore, cortical ischemic loss may lead to callosal atrophy. Reduced cerebral cortical oxygen metabolism in the normal-appearing cerebral cortex, which surgical reperfusion cannot improve, has been demonstrated by using PET in ICA or MCA occlusive disease, suggesting that selective neuronal damage may occur (Powers et al. 1984; Yamauchi et al. 1990). Our studies showed that a decrease in bilateral cerebral cortical oxygen metabolism occurs in association with callosal atrophy in patients with ICA occlusive disease, suggesting that ischemic neuronal loss may contribute to the reduced cortical oxygen metabolism (Yamauchi et al. 1993, 1995, 1996a, 2000b). However, to explore this aspect further, a more direct marker for neuronal damage is needed.

9.2   Imaging of Central-Type Benzodiazepine Receptors

Development of imaging techniques makes it possible to visualize the distribution of central-type benzodiazepine receptors (cBZRs) in humans by using ^{11}C-labeled flumazenil (FMZ) for PET or ^{123}I-labeled iomazenil (IMZ) for single-photon emission computed tomography (SPECT) (Beer et al. 1990; Persson et al. 1985; Samson et al. 1985). cBZR is coupled with γ-aminobutyric acid receptors (GABAA/BZ receptor complex), and cBZR exists in the membrane of neurons (Olsen 1981). Most cortical neurons express cBZR. Binding of FMZ is high in the cerebral cortex and low in the cerebellum, thalamus, and basal ganglia, while it is lacking in the white matter (Fig. 9.2). As shown in the case of crossed cerebellar diaschisis, a decrease in neural input may not decrease cBZR (Dong et al. 1997; Hatazawa et al. 1995a). Thus, imaging of the cBZR may detect cortical neuronal damage, which could not be evaluated directly by other neuroimaging modalities (Baron et al. 2014; Garcia et al. 1996; Hatazawa and Shimosegawa 1998; Sette et al. 1993). Cortical neuronal damage should lead to a decrease in cBZR.

Histopathological correlations between decreased cBZR and selective neuronal loss have recently been confirmed (Ejaz et al. 2013). A rat ischemia-reperfusion model with 45-min occlusion of the distal MCA was examined with FMZ PET and immunohistochemistry 28 days after ischemia. The study showed that a decrease in
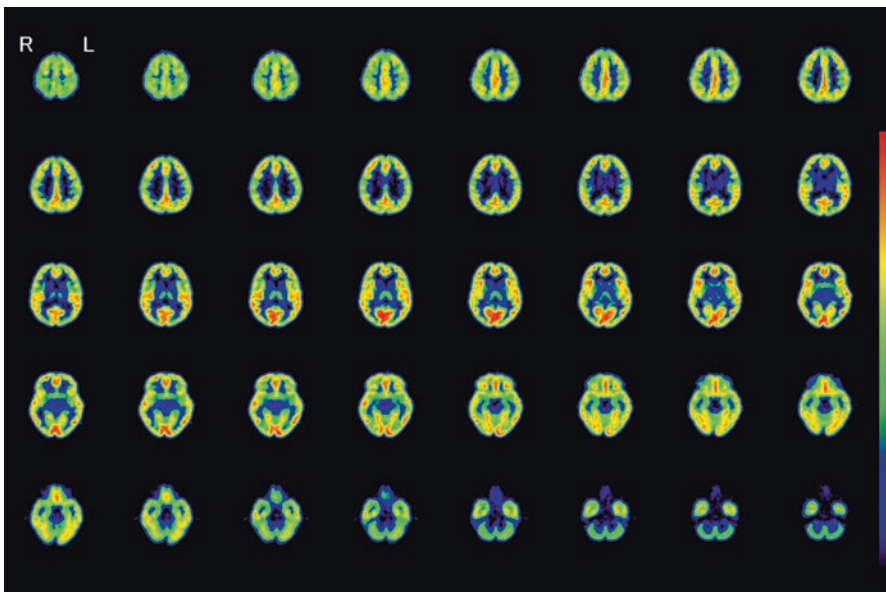
Fig. 9.2 BZR imaging with ^{11}C-flumazenil PET. Images of a male normal volunteer of 49 years old show high binding in the cerebral cortex

FMZ binding in the normal-appearing cerebral cortex on T2-weighted MRI was associated with selective neuronal loss on stains with an antibody for neurons. Imaging of cBZR by using ^{11}C-FMZ and PET can detect selective neuronal damage or loss.

9.3 Pathophysiology of Selective Neuronal Damage Demonstrated as Decreased BZR

9.3.1 Selective Neuronal Damage and Chronic Hemodynamic Cerebral Ischemia

Several small studies in patients with atherosclerotic ICA or MCA disease in the chronic stage demonstrated a reduction in cBZR in the normal-appearing cortical areas on CT or MRI, suggesting selective neuronal damage (Dong et al. 1997; Kuroda et al. 2004, 2006; Moriwaki et al. 1998; Sasaki et al. 1997; Yamauchi et al. 2000a). The IMZ uptake on SPECT was significantly but weakly correlated with the cerebral metabolic rate of oxygen, while no significant correlation was found of the IMZ uptake with the blood flow, the cerebrovascular reactivity, or the cerebral metabolic rate of glucose, which suggested that the reduction in IMZ uptake may be due to selective neuronal loss that may not be revealed by other imaging tracers (Dong et al. 1997; Moriwaki et al. 1998; Sasaki et al. 1997). These findings were also shown by using FMZ and PET (Kuroda et al. 2004, 2006). A decrease in cortical BZR binding was correlated with corpus callosum atrophy, which supported that decreased cortical BZR binding may reflect cortical neuronal damage (Yamauchi et al. 2000a).

However, the incidence, extent, and severity of selective neuronal damage demonstrated as decreased cBZR are unclear. Furthermore, the factors responsible for decreased cBZR are not well understood. Specifically, although a chronic hemodynamic mechanism may be responsible for the decreased cBZR, the relationship between decreased BZR and chronic hemodynamic compromise is unknown. The clarification of this relationship is essential because vascular reconstruction surgery can improve chronic hemodynamic compromise, which may prevent the development of selective neuronal damage as well as infarction.

9.3.2 Selective Neuronal Damage and Low-Flow Infarction

Border zone infarction has been demonstrated to be associated with ICA occlusive disease and hemodynamic compromise (Momjian-Mayoy and Baron 2005; Yamauchi et al. 1990, 1991). Hemodynamic ischemia due to ICA occlusive disease may cause not only border-zone infarction but also selective neuronal damage beyond the regions of infarcts that may be detected by a decrease in cBZR in the normal-appearing cerebral cortex. To determine whether selective neuronal damage is associated with border-zone infarction in ICA occlusive disease, we measured

cBZR using PET and ^{11}C-FMZ in 62 nondisabled patients with ICA steno-occlusive lesions in the chronic stage (Yamauchi et al. 2005). FMZ-binding potential (BP) was calculated using the dynamic data and Logan graphical analysis with the reference tissue, with the pons as a reference region (Logan et al. 1996; Okazawa et al. 2004). The infarcts on MRI, which were categorized as territorial, border zone (external or internal), striatocapsular, lacunar, and other white matter infarcts, were correlated with mean cerebral/cerebellar cortical BP ratio in the hemisphere with ICA occlusive disease. Patients with border-zone infarction ($n = 18$) had significantly decreased FMZ-BP ratio in the hemisphere with ICA disease, compared with patients without border-zone infarction ($n = 44$) and normal control subjects ($n = 10$). Both external and internal border-zone infarctions were associated with a decreased FMZ-BP ratio. Multivariate analysis showed that external border-zone infarction was an independent predictor of the decreased FMZ-BP ratio. In ICA occlusive disease, selective neuronal damage demonstrated as decreased cBZR is associated with border-zone infarction. Microemboli can cause border-zone infarction, particularly in cases of ICA stenosis (Moustafa et al. 2010). However, it is less likely that border-zone infarction due to microemboli causes a significant decrease in BZR beyond the regions of the infarct because ischemia due to microemboli is restricted to the border zone region. Therefore, hemodynamic ischemia leading to border-zone infarction may cause selective neuronal damage beyond the regions of infarcts in the chronic stage.

Decreased cBZR was strongly associated with decreased oxygen metabolism. However, the correlation of decreased cBZR with increased OEF (hemodynamic compromise) was weak. Selective neuronal damage caused by hemodynamic ischemia, consequently, decreases the degree of hemodynamic compromise due to ICA occlusive disease by causing reduced metabolic demand of the tissue (Kuroda et al. 2004; Yamauchi et al. 2004), which may lead to normalization of OEF after the development of selective neuronal damage. The association of decrease in cBZR with border-zone infarction suggests that severe hemodynamic compromise, which was present in the acute stage of infarction, disappeared according to the decrease in the metabolic needs of the tissue within the surviving penumbra between the time of infarction and PET examination (Morris et al. 2018). Careful medical management in the acute stage for patients with border-zone infarction should prevent selective neuronal damage, even when infarct size is small, and symptom is mild. Subsequently, the preserved metabolic needs of the cortical tissue in the chronic stage may permit the persistence of the hemodynamic compromise that can be improved by vascular reconstruction surgery. This strategy results in preservation of cortical metabolism that may lead to good functional outcomes. Recognition and prevention of selective neuronal damage are important for the management of patients with ICA occlusive disease.

The association between border-zone infarction (internal border-zone infarction) and a decrease in cBZR in the overlying cerebral cortex was also found in 62 nondisabled patients with atherosclerotic occlusive disease of the MCA and no cortical infarction (Yamauchi et al. 2009).

9.3.3 Selective Neuronal Damage and Misery Perfusion

9.3.3.1 A Cross-Sectional Study

The notion that normalization of OEF may occur after the development of selective neuronal damage suggests that it may not be easy to demonstrate an association of decreased cBZR with chronic hemodynamic compromise (increased OEF) in the chronic stage. To overcome this issue, we studied 105 nondisabled patients with atherosclerotic ICA or MCA occlusive disease and *no cortical infarction* on routine MRI images (T1-, T2-weighted, or fluid-attenuated inversion recovery images) and measured cBZR and OEF using PET. We investigated the association of selective neuronal damage demonstrated as a decrease in cBZR in the normal-appearing cerebral cortex with increased OEF (misery perfusion) (Yamauchi et al. 2007).

A three-dimensional stereotactic surface projection (3D-SSP) technique was used to analyze FMZ BP (Minoshima et al. 1995). After anatomical standardization, a method of data extraction is performed in which the cortical activity is projected onto the brain surface. The algorithm searches the highest pixel value in an inward direction along the vector to a six-pixel depth into the cortex on an individual's anatomically standardized PET image set and assigns the maximum value to the surface pixel. The surface projection technique minimizes the effect of cortical atrophy. Then, a comparison of the resultant cortical projections between a patient and controls is performed. Pixel-by-pixel *Z* scores were used. *Z* scores (([mean normalized pixel value of controls] − [normalized pixel value of each patient])/[SD of controls]) were calculated for each surface pixel (*Z* score map) (Fig. 9.3) to quantify a decrease in FMZ BP. A positive *Z* score represents a reduced FMZ BP in patients relative to controls. To assess the degree of abnormal FMZ BP reduction in each patient quantitatively, the BZR index [(the extent of the pixels with *Z* score more than 2 compared with controls) • (average *Z* score in those pixels)] of the MCA distribution with arterial disease in the cerebral cortex was calculated by the stereotactic extraction estimation (SEE) method (Mizumura et al. 2003).

All patients had pixels with abnormally decreased cBZR in the cerebral cortex of the MCA distribution, with the extent varying from 0.04% to 60.91% (Fig. 9.4). The BZR index was significantly correlated with the mean hemispheric value of OEF or CBF in the ipsilateral hemisphere. Multivariate analysis showed that the BZR index was positively correlated with the value of OEF and the history of stroke, which suggested that misery perfusion might cause selective neuronal damage. On the other hand, the BZR index was negatively correlated with the presence of statin treatment. Several studies have shown that statins have beneficial effects on the cerebral circulation and brain parenchyma during ischemic stroke and reperfusion (Vaughan and Delanty 1999). The antioxidative properties of statins might be involved in their beneficial effects against neuronal damage in cerebral ischemia (Nagotani et al. 2005). Statins might also reduce microemboli by plaque stabilization in patients with ICA or MCA stenosis. Therefore, statins may reduce the occurrence of selective neuronal damage due to ischemia in atherosclerotic ICA or MCA occlusive disease.
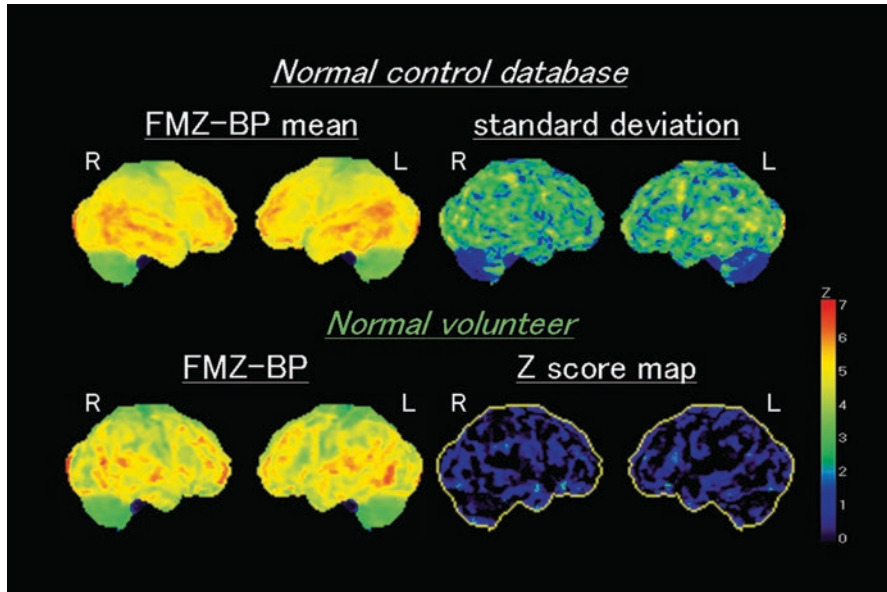
Fig. 9.3 Three-dimensional stereotactic surface projection (3D-SSP) analysis. Upper row: 3D-SSP images showing the value of mean and standard deviation for normal control database ($N = 10$, mean age 57 years). Lower row: 3D-SSP images and Z score maps of a male normal volunteer of 49 years old shown in Fig. 9.2

9.3.3.2 Follow-Up Study

It is essential to show a correlation between an increase in OEF and progression of selective neuronal damage using a longitudinal study to demonstrate a causal relationship between misery perfusion and selective neuronal damage more directly. Therefore, we evaluated the distribution of cBZRs twice using PET and ^{11}C-flumazenil over time in 80 medically treated patients, aged 63 ± 8 years, with atherosclerotic ICA or MCA occlusive disease who had no ischemic episodes during follow-up (Yamauchi et al. 2016). The total change of the BZR index or the OEF value in the cerebral cortex of the MCA distribution with arterial disease was calculated by subtracting the value obtained at the second scanning from that obtained at the first scanning.

Follow-up examinations in seven normal subjects, aged 56 ± 8 years, demonstrated no significant change in Z index during follow-up (mean 41 ± 3 months). The mean $\pm$ SD value of changes in the index in the controls was 0.94 ± 1.38. In patients, an increase of the index beyond the upper 95% limit (the mean plus $_6 t_{0.05}$SD) defined in normal subjects (above 4.32) was considered to be an increased BZR index (progression of neuronal damage) during follow-up.
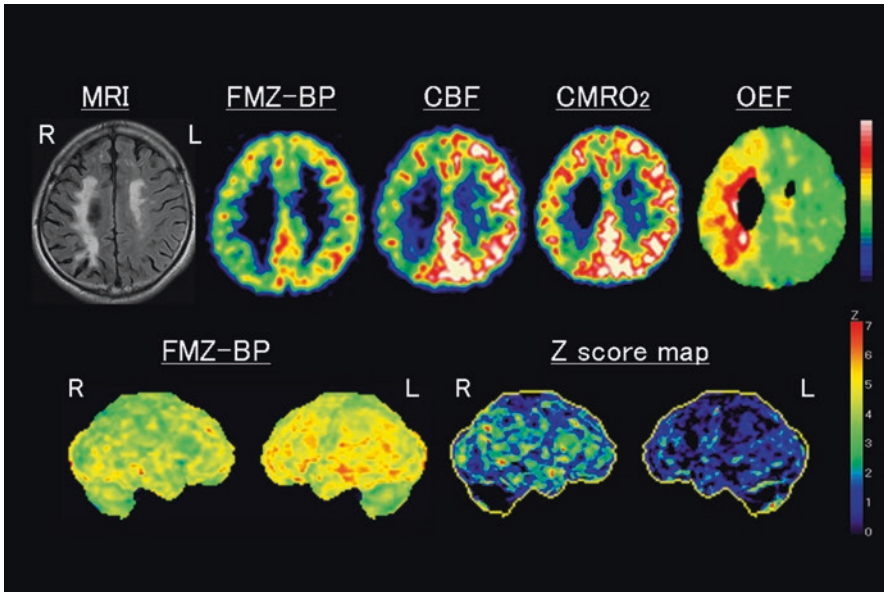
Fig. 9.4 Selective cortical neuronal damage and misery perfusion. Upper row: Examples of PET images showing a decrease of flumazenil-binding potential (FMZ-BP), cerebral blood flow (CBF), and cerebral metabolic rate of oxygen (CMRO$_2$) with increased oxygen extraction fraction (OEF) in a patient with right (R) internal carotid artery occlusion who showed internal border-zone infarction on the corresponding MRI images. This patient presented with left hemiparesis and spatial neglect. Lower row: 3D-SSP images and Z score maps showing a decrease of FMZ-BP in the right hemisphere. The extent of abnormally decreased benzodiazepine receptors (BZR) was 47.6% in the right middle cerebral artery distribution; the mean z score in those pixels was 2.92, and the BZR index was 139.2

In the hemisphere affected by arterial disease, the BZR index in 40 patients (50%) was increased during follow-up (mean 26 ± 20 months). In multivariable logistic regression analyses, increases in the BZR index were associated with the decreased CBF at baseline and an increased OEF during follow-up. Increases in the OEF during follow-up were associated with a lack of statin use. In patients with atherosclerotic ICA or MCA disease, the progression of cortical neuronal damage was associated with hemodynamic impairment at baseline and hemodynamic deterioration during follow-up. Statin use may be beneficial against hemodynamic deterioration and therefore be neuroprotective.

Follow-up data show that hemodynamic deterioration causes selective neuronal damage demonstrated as decreased BZR without an overt episode of stroke. This study confirmed the relationship between selective neuronal damage and chronic hemodynamic compromise for the first time. In patients with chronic hemodynamic compromise, the perfusion may fall below the penumbra threshold for a matter of minutes, causing selective neuronal damage.

9.4   Silent Cortical Neuronal Damage in Asymptomatic Patients

The finding that selective neuronal damage manifested as loss of cBZR occurs in association with hemodynamic deterioration without an overt episode of stroke suggests that selective neuronal damage may occur in association with hemodynamic compromise in patients whose atherosclerotic ICA or MCA disease is asymptomatic. To test this hypothesis, we measured cBZR using PET and ^{11}C-FMZ in 79 patients with asymptomatic atherosclerotic ICA or MCA disease and no cortical infarction (Yamauchi et al. 2011b). 3D-SSP was used to calculate the BZR index, a measure of abnormally decreased cBZR in the cerebral cortex within the MCA distribution. The BZR index was abnormal (>5.84) in 71% of the asymptomatic patients compared to that in healthy control subjects. This abnormality was mild compared with that previously reported for symptomatic patients (the BZR index, 16.0 ± 14.5 vs. 48.2 ± 54.1). Multiple regression analysis showed the BZR index to be positively correlated with the value of OEF, presence of silent subcortical infarcts, and presence of ischemic heart disease, which suggested that hemodynamic compromise is associated with selective neuronal damage in asymptomatic patients. Hemodynamic compromise may cause silent cortical neuronal damage in asymptomatic patients as well. Patients at elevated risk of stroke may have already suffered ischemic cerebral damage by the time their asymptomatic ICA or MCA disease is discovered. Therapeutic strategies to prevent neuronal damage, including vascular reconstruction surgery, may be called for in asymptomatic patients with chronic hemodynamic compromise.

On the other hand, the BZR index was negatively correlated with the treatment of hypertension with angiotensin receptor blockers (ARBs). ARBs were associated with preservation of cortical cBZR. Several experimental studies have shown that ARBs can attenuate ischemic neuronal injury through various mechanisms, including decreased oxidative stress and improved arterial compliance (Mogi and Horiuchi 2009). ARBs might have beneficial effects against neuronal damage in atherosclerotic ICA or MCA disease.

9.5   Clinical Impact of Selective Neuronal Damage: Cognitive Impairment

In atherosclerotic ICA or MCA disease, chronic hemodynamic compromise causes selective neuronal damage, which can be detected as a decrease in cBZR in the normal-appearing cerebral cortex. However, the impact of selective neuronal damage on clinical outcomes is unclear.

One to three months after acute stroke, selective neuronal loss—as documented by a decrease in cBZR—within the rescued penumbra was shown to impede neural activation on functional MRI, suggesting the presence of functional impairments

(Carrera et al. 2013). In cases of subcortical hemorrhage, patients with aphasia or anopsia showed an ipsilateral/contralateral IMZ uptake ratio of ≤0.78 in the cortical area (Hatazawa et al. 1995b). Another SPECT study also showed that cerebral hyperperfusion after carotid endarterectomy resulted in a postoperative decrease in IMZ uptake that correlated with postoperative cognitive impairment (Chida et al. 2009). Therefore, selective neuronal damage may contribute to the development of subtle poststroke cognitive impairment, depending on the degree of neuronal damage.

In patients with atherosclerotic ICA or MCA disease, a few subjects with reduced cBZR in the cerebral cortex overlying subcortical infarcts were reported to show aphasia (Hatazawa et al. 1995a; Moriwaki et al. 1998), and a decrease in cortical cBZR was shown to be correlated with the atrophy of corpus callosum that is associated with global cognitive impairment (Yamauchi et al. 1996a, 2000a). However, the relationship between a decrease in cBZR and neurological symptoms has not been systematically investigated. Clinical correlates are essential to establish the clinical significance of cBZR imaging.

Executive dysfunction may be an early sign of vascular cognitive impairment and may have a considerable impact on the functional outcomes of patients with stroke (Roman and Royall 1999). The Wisconsin Card Sorting Test (WCST) is a widely used clinical test for assessing executive functions (Nagahama et al. 1996; Nelson 1976). To determine whether a decrease in the cBZRs in the non-infarcted cerebral cortex is associated with poor performance on the WCST, we measured cBZR using PET and ^{11}C-FMZ in 60 nondisabled patients with unilateral atherosclerotic ICA or MCA disease and no cortical infarction (Yamauchi et al. 2011a). Using 3D-SSP, the BZR indices in the cerebral cortex of the anterior cerebral artery (ACA) and the MCA territories were calculated and found to be correlated with the patient's score on the WCST. We used the Keio-Fukuoka-Shimane version of the WCST that can be performed on a personal computer (Kobayashi 2002). Because the WCST method used in this study needs verbal mediation during the performance, the language-related left hemisphere may contribute more than the right hemisphere to the performance of the WCST. The BZR index was associated with an increase in OEF in the ACA and MCA territories of the hemisphere with ICA or MCA disease. Based on the WCST results, 39 patients were considered abnormal (low categories achieved) for their age. The BZR index of the ACA territory in the hemisphere affected by arterial disease was significantly higher in abnormal patients than in normal patients. The BZR index of the MCA territory differed significantly between the two groups when patients with left arterial disease ($n = 28$) were analyzed separately. Among the BZR indices for the subregions of the ACA territory, those of the anterior cingulate gyrus and the medial frontal gyrus were positively correlated with the total number of errors after controlling for the effect of age through multiple regression analysis. In patients with left arterial diseases, among the BZR indices for the subregions of the MCA territory, the BZR index of the middle frontal gyrus was also positively correlated with the total number of errors. These subregions have been reported to be essential for the performance on WCST (Buckley et al. 2009; Nagahama et al. 1996).

In atherosclerotic ICA or MCA disease, selective neuronal damage that manifests as a decrease in cBZR in the non-infarcted cerebral cortex may contribute to the development of executive dysfunction. PET imaging of cBZR may be useful as an objective measure of cognitive impairments in atherosclerotic occlusive disease of the major cerebral artery. In this study, a decrease in cBZR was also associated with hemodynamic compromise. Interestingly, a recent IMZ SPECT study showed that improvement of hemodynamic compromise after carotid endarterectomy resulted in a postoperative increase in IMZ uptake that correlated with postoperative improvement of cognitive impairment (Chida et al. 2010). In patients with severe hemodynamic compromise, a part of the cBZR decrease may be reversible, and improvement of hemodynamic compromise may lead to the improvement of cognitive impairment with cBZR reduction.

9.6   Selective Neuronal Damage as Outcome Measures

In patients with atherosclerotic ICA or MCA disease, the progression of selective cortical neuronal damage occurs in the absence of an overt stroke episode and is associated with both decreased CBF at baseline and an increased OEF during follow-up. Decreased CBF at baseline may reflect misery perfusion with cortical neuronal damage, while an increased OEF during follow-up may reflect hemodynamic deterioration. Thus, to prevent the progression of selective cortical neuronal damage, vascular reconstruction surgery to improve hemodynamic impairment and appropriate control of vascular risk factors (e.g., the use of statin or antihypertensive agents) may be useful. ^{11}C-flumazenil PET would be useful to monitor the effects of the therapies.

9.6.1   Vascular Reconstruction Surgery

Bypass surgery can improve misery perfusion and may prevent neuronal damage. A recent IMZ SPECT study showed that improvement of hemodynamic compromise after bypass surgery resulted in a postoperative improvement of BZR that was associated with cognitive improvement (Chida et al. 2011). An MRI study also showed an improvement in cortical thinness after bypass surgery in patients with ICA or MCA occlusive diseases, including Moyamoya disease (Fierstra et al. 2011). However, surgery often involves a potential risk for neuronal damage.

To determine whether the progression of cortical neuronal damage in surgically treated patients with misery perfusion is more significant than in those without, or in medically treated patients with misery perfusion, we evaluated the distribution of cBZRs using ^{11}C-flumazenil PET in patients with atherosclerotic ICA or MCA disease, including 18 surgically treated patients with no history of perioperative stroke, among which 9 presented with misery perfusion, and 8 medically treated patients with misery perfusion but no intervening ischemic event (Yamauchi et al. 2017).

We quantified abnormal decreases in the cBZRs distributed within the MCA of the cerebral cortex, and compared the changes in the BZR index among the three groups. The change in the BZR index in surgically treated patients with misery perfusion (27.5 ± 15.6) during 7 ± 5 months was significantly greater than that in surgically treated patients without misery perfusion (−5.2 ± 9.4) during 6 ± 4 months ($p < 0.001$), and in medically treated patients with misery perfusion (3.2 ± 15.4) during 16 ± 6 months ($p < 0.01$).

Therefore, the results suggest that the progression of cortical neuronal damage in surgically treated patients with misery perfusion and no perioperative stroke may be more extensive than in medically treated patients with misery perfusion and no intervening ischemic event. The progression of cortical neuronal damage should be considered while using bypass surgery for treating patients with misery perfusion.

9.6.2 Blood Pressure Control

The treatment of hypertension is generally beneficial to patients with atherosclerotic major cerebral artery diseases (Rashid et al. 2003); however, the optimal blood pressure (BP) level to achieve maximal benefits among patients with this condition remains unknown. In patients with atherosclerotic major cerebral artery disease, low BP may impair cerebral perfusion, thereby worsening the risk of ischemic cerebral damage. It is thus debatable whether BP regulated to lower levels may be associated with the reduced risks of a recurrent stroke and hemodynamic impairment in these patients (Amin-Hanjani et al. 2017; Powers et al. 2014; Yamauchi et al. 2013, 2015).

Our previous studies in patients with ICA or MCA disease showed that the incidence of ischemic stroke in the territory of the diseased artery was significantly higher in patients with low systolic BP (SBP) (<130 mmHg) (Yamauchi et al. 2013, 2015). This was particularly true in patients with impaired perfusion, characterized by a decreased CBF/cerebral blood volume ratio. Furthermore, low SBP during follow-up may be associated with hemodynamic deterioration (Yamauchi et al. 2019a) and consequently with a risk of selective neuronal damage.

To determine whether low BP at follow-up is associated with increased selective neuronal damage, we retrospectively analyzed data from 76 medically treated patients with atherosclerotic ICA or MCA disease with no ischemic episodes reported on a follow-up of 6 months or more (Yamauchi et al. 2019b). In all patients the distribution of cBZR was measured using ¹¹C-flumazenil PET. The changes in the BZR index during follow-up were negatively correlated with SBP at follow-up. More significant increases in the BZR index indicating neuronal damage were observed in patients with lower SBP levels and decreased CBF than in patients without such decreases (Fig. 9.5). Therefore, low SBP may contribute to the risk of cortical neuronal damage in hemispheres with decreased CBF.

Further studies are needed to determine the optimal BP in patients with atherosclerotic major cerebral artery disease for favorable management of the condition.
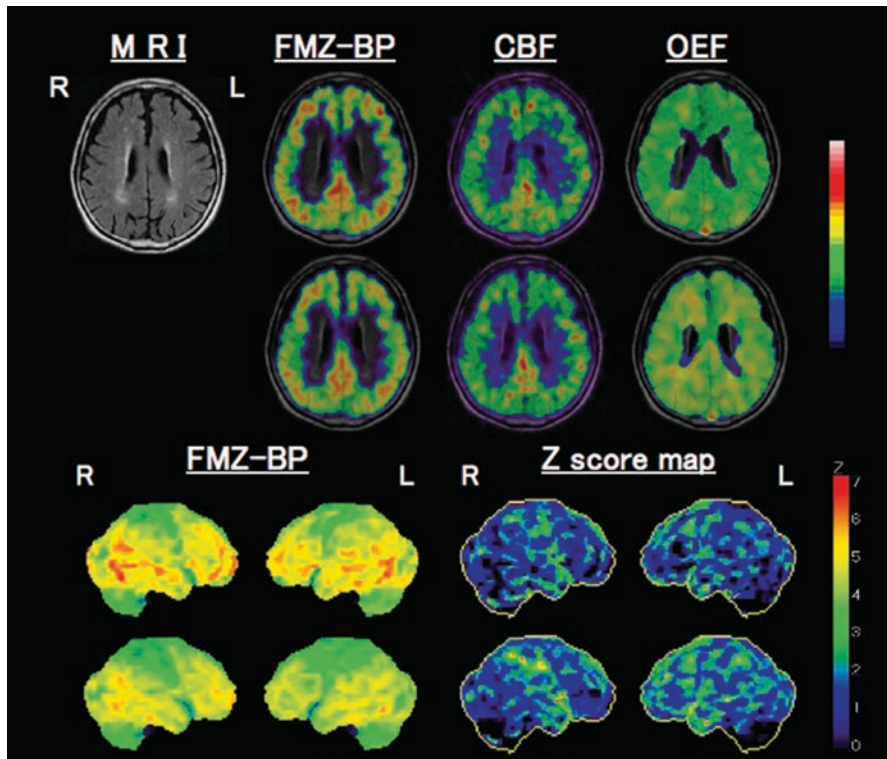
Fig. 9.5 Progressive cortical neuronal damage and low blood pressure in a patient with a right internal carotid artery occlusion and a left internal carotid artery stenosis (mild). Collateral pathways included the anterior communicating artery and leptomeningeal collaterals from the posterior cerebral artery. The first PET study (first row) revealed a mild decrease in flumazenil-binding potential (FMZ-BP) in the right (R) hemisphere with internal carotid artery occlusion and subcortical ischemic lesions (MRI), while cerebral blood flow (CBF) was decreased and oxygen extraction fraction (OEF) was increased slightly. A follow-up 48 months later (second row) revealed decreased FMZ-BP and CBF with increased OEF in the right hemisphere. Mean hemispheric CBF decreased from 28.4 to 27.5 (mL/100 g/min) while OEF increased from 51.5 to 57.0 (%). 3D-SSP images and Z score maps from the first (third row) and second (fourth row) examinations demonstrated a decrease in FMZ-BP in the right hemisphere, especially in the frontoparietal region. The BZR index increased from 35.9 to 103.1 between baseline and follow-up. The patient's systolic blood pressure was 119 (mmHg) at baseline and 107 at follow-up. Antihypertensive therapy was discontinued proximally to the follow-up examinations. The patient showed a mild attention deficit (a Mini Mental State Examination score, 26) (Yamauchi et al. 2019b)

9.7 Conclusions

1. In patients with atherosclerotic ICA or MCA occlusive disease, misery perfusion contributes to selective neuronal damage characterized by a decreased cBZR distribution in the apparently unremarkable cerebral cortex.
2. Hemodynamic deterioration may contribute to selective neuronal damage in the absence of an overt episode of stroke.
3. Selective neuronal damage may affect the functional outcomes.
4. Careful medical management and successful vascular reconstruction surgery in patients with misery perfusion may prevent selective neuronal damage.
5. Statins and angiotensin receptor blockers may reduce the occurrence of selective neuronal damage.
6. Imaging of cBZR is a potential technique to quantitatively evaluate the success of future therapeutic interventions to protect neurons from ischemic damage.

References

Amin-Hanjani S, Turan TN, Du X, Pandey DK, Rose-Finnell L, Richardson D, Elkind MS, Zipfel GJ, Liebeskind DS, Silver FL, Kasner SE, Gorelick PB, Charbel FT, Derdeyn CP (2017) Higher stroke risk with lower blood pressure in hemodynamic vertebrobasilar disease: analysis from the VERiTAS study. J Stroke Cerebrovasc Dis 26:403–410

Baron JC, Bousser MG, Rey A, Guillard A, Comar D, Castaigne P (1981) Reversal of focal "misery-perfusion syndrome" by extra-intracranial arterial bypass in hemodynamic cerebral ischemia. A case study with ^{15}O positron emission tomography. Stroke 12:454–459

Baron JC, Yamauchi H, Fujioka M, Endres M (2014) Selective neuronal loss in ischemic stroke and cerebrovascular disease. J Cereb Blood Flow Metab 34:2–18

Beer HF, Blauenstein PA, Hasler PH, Delaloye B, Riccabona G, Bangerl I, Hunkeler W, Bonetti EP, Pieri L, Richards JG et al (1990) In vitro and in vivo evaluation of iodine-123-Ro 16-0154: a new imaging agent for SPECT investigations of benzodiazepine receptors. J Nucl Med 31:1007–1014

Buckley MJ, Mansouri FA, Hoda H, Mahboubi M, Browning PG, Kwok SC, Phillips A, Tanaka K (2009) Dissociable components of rule-guided behavior depend on distinct medial and prefrontal regions. Science 325:52–58

Carrera E, Jones PS, Morris RS, Alawneh J, Hong YT, Aigbirhio FI, Fryer TD, Carpenter TA, Warburton EA, Baron JC (2013) Is neural activation within the rescued penumbra impeded by selective neuronal loss? Brain 136:1816–1829

Chida K, Ogasawara K, Aso K, Kuroda H, Saito H, Kobayashi M, Yoshida K, Ogawa A (2011) Postoperative resolution of ^{123}I-iomazenil uptake and metabolic rate of oxygen in the cerebral cortex accompanied by postoperative improvement of cognition in a patient undergoing extracranial-intracranial arterial bypass surgery for internal carotid artery occlusion: a case report. Clin Nucl Med 36:361–362

Chida K, Ogasawara K, Aso K, Suga Y, Kobayashi M, Yoshida K, Terasaki K, Tsushina E, Ogawa A (2010) Postcarotid endarterectomy improvement in cognition is associated with resolution of crossed cerebellar hypoperfusion and increase in ^{123}I-iomazenil uptake in the cerebral cortex: a SPECT study. Cerebrovasc Dis 29:343–351

Chida K, Ogasawara K, Suga Y, Saito H, Kobayashi M, Yoshida K, Otawara Y, Ogawa A (2009) Postoperative cortical neural loss associated with cerebral hyperperfusion and cognitive impairment after carotid endarterectomy: ^{123}I-iomazenil SPECT study. Stroke 40:448–453

Derdeyn CP, Grubb RL Jr, Powers WJ (1999) Cerebral hemodynamic impairment: methods of measurement and association with stroke risk. Neurology 53:251–259

Dong Y, Fukuyama H, Nabatame H, Yamauchi H, Shibasaki H, Yonekura Y (1997) Assessment of benzodiazepine receptors using iodine-123-labeled iomazenil single-photon emission computed tomography in patients with ischemic cerebrovascular disease. A comparison with PET study. Stroke 28:1776–1782

Ejaz S, Emmrich JV, Sawiak SJ, Williamson DJ, Baron JC (2015a) Cortical selective neuronal loss, impaired behavior, and normal magnetic resonance imaging in a new rat model of true transient ischemic attacks. Stroke 46:1084–1092

Ejaz S, Williamson DJ, Ahmed T, Sitnikov S, Hong YT, Sawiak SJ, Fryer TD, Aigbirhio FI, Baron JC (2013) Characterizing infarction and selective neuronal loss following temporary focal cerebral ischemia in the rat: a multi-modality imaging study. Neurobiol Dis 51:120–132

Ejaz S, Williamson DJ, Jensen-Kondering U, Ahmed T, Sawiak SJ, Baron JC (2015b) What is the optimal duration of middle-cerebral artery occlusion consistently resulting in isolated cortical selective neuronal loss in the spontaneously hypertensive rat? Front Neurol 6:64

Feeney DM, Baron JC (1986) Diaschisis. Stroke 17:817–830

Fierstra J, Maclean DB, Fisher JA, Han JS, Mandell DM, Conklin J, Poublanc J, Crawley AP, Regli L, Mikulis DJ, Tymianski M (2011) Surgical revascularization reverses cerebral cortical thinning in patients with severe cerebrovascular steno-occlusive disease. Stroke 42:1631–1637

Fierstra J, Poublanc J, Han JS, Silver F, Tymianski M, Crawley AP, Fisher JA, Mikulis DJ (2010) Steal physiology is spatially associated with cortical thinning. J Neurol Neurosurg Psychiatry 81:290–293

Garcia JH, Lassen NA, Weiller C, Sperling B, Nakagawara J (1996) Ischemic stroke and incomplete infarction. Stroke 27:761–765

Graham DI (1992) Hypoxia and vascular disorders. Edward Arnord, London

Grubb RL Jr, Derdeyn CP, Fritsch SM, Carpenter DA, Yundt KD, Videen TO, Spitznagel EL, Powers WJ (1998) Importance of hemodynamic factors in the prognosis of symptomatic carotid occlusion. JAMA 280:1055–1060

Hatazawa J, Satoh T, Shimosegawa E, Okudera T, Inugami A, Ogawa T, Fujita H, Noguchi K, Kanno I, Miura S, Murakami M, Iida H, Miura Y, Uemura K (1995a) Evaluation of cerebral infarction with iodine 123-iomazenil SPECT. J Nucl Med 36:2154–2161

Hatazawa J, Shimosegawa E (1998) Imaging neurochemistry of cerebrovascular disease with PET and SPECT. QJ Nucl Med 42:193–198

Hatazawa J, Shimosegawa E, Satoh T, Kanno I, Uemura K (1995b) Central benzodiazepine receptor distribution after subcortical hemorrhage evaluated by means of [^{123}I]iomazenil and SPECT. Stroke 26:2267–2271

Klijn CJ, Kappelle LJ (2010) Haemodynamic stroke: clinical features, prognosis, and management. Lancet Neurol 9:1008–1017

Kobayashi S (2002) Neuropsychological test using personal computer. Japan J Neuropsychol 18:188–193

Kuroda S, Houkin K (2008) Moyamoya disease: current concepts and future perspectives. Lancet Neurol 7:1056–1066

Kuroda S, Houkin K, Kamiyama H, Mitsumori K, Iwasaki Y, Abe H (2001) Long-term prognosis of medically treated patients with internal carotid or middle cerebral artery occlusion: can acetazolamide test predict it? Stroke 32:2110–2116

Kuroda S, Shiga T, Houkin K, Ishikawa T, Katoh C, Tamaki N, Iwasaki Y (2006) Cerebral oxygen hypometabolism and neuronal integrity in patients with impaired vasoreactivity attributable to occlusive carotid artery diseases. Stroke 37:393–398

Kuroda S, Shiga T, Ishikawa T, Houkin K, Narita T, Katoh C, Tamaki N, Iwasaki Y (2004) Reduced blood flow and preserved vasoreactivity characterize oxygen hypometabolism due to incomplete infarction in occlusive carotid artery diseases. J Nucl Med 45:943–949

Lassen NA, Losen TS, Højgaard K, Skriver E (1983) Incomplete infarction: a CT-negative irreversible ischemic brain lesion. J Cereb Blood Flow Metab 3(Suppl 1):S602–S603

Logan J, Fowler JS, Volkow ND, Wang GJ, Ding YS, Alexoff DL (1996) Distribution volume ratios without blood sampling from graphical analysis of PET data. J Cereb Blood Flow Metab 16:834–840

Markus H, Cullinane M (2001) Severely impaired cerebrovascular reactivity predicts stroke and TIA risk in patients with carotid artery stenosis and occlusion. Brain 124:457–467

Minoshima S, Frey KA, Koeppe RA, Foster NL, Kuhl DE (1995) A diagnostic approach in Alzheimer's disease using three-dimensional stereotactic surface projections of fluorine-18-FDG PET. J Nucl Med 36:1238–1248

Mizumura S, Kumita S, Cho K, Ishihara M, Nakajo H, Toba M, Kumazaki T (2003) Development of quantitative analysis method for stereotactic brain image: assessment of reduced accumulation in extent and severity using anatomical segmentation. Ann Nucl Med 17:289–295

Mogi M, Horiuchi M (2009) Effects of angiotensin II receptor blockers on dementia. Hypertens Res 32:738–740

Momjian-Mayoy I, Baron JC (2005) The pathophysiology of watershed infarction in internal carotid artery disease. Review of cerebral perfusion studies. Stroke 36:567–577

Moriwaki H, Matsumoto M, Hashikawa K, Oku N, Ishida M, Seike Y, Fukuchi K, Hori M, Nishimura T (1998) Iodine-123-iomazenil and iodine-123-iodoamphetamine SPECT in major cerebral artery occlusive disease. J Nucl Med 39:1348–1353

Morris RS, Simon Jones P, Alawneh JA, Hong YT, Fryer TD, Aigbirhio FI, Warburton EA, Baron JC (2018) Relationships between selective neuronal loss and microglial activation after ischaemic stroke in man. Brain 141:2098–2111

Moustafa RR, Izquierdo-Garcia D, Jones PS, Graves MJ, Fryer TD, Gillard JH, Warburton EA, Baron JC (2010) Watershed infarcts in transient ischemic attack/minor stroke with > or = 50% carotid stenosis: hemodynamic or embolic? Stroke 41:1410–1416

Nagahama Y, Fukuyama H, Yamauchi H, Matsuzaki S, Konishi J, Shibasaki H, Kimura J (1996) Cerebral activation during performance of a card sorting test. Brain 119(Pt 5):1667–1675

Nagotani S, Hayashi T, Satoh K, Zhang W, Deguchi K, Nagano I, Shoji M, Abe K (2005) Reduction of cerebral infarction in stroke-prone spontaneously hypertensive rats by statins associated with amelioration of oxidative stress. Stroke 36:670–672

Nelson HE (1976) A modified card sorting test sensitive to frontal lobe defects. Cortex 12:313–324

Ogasawara K, Ogawa A, Yoshimoto T (2002) Cerebrovascular reactivity to acetazolamide and outcome in patients with symptomatic internal carotid or middle cerebral artery occlusion: a xenon-133 single-photon emission computed tomography study. Stroke 33:1857–1862

Ogawa A (2012) Beneficial effect of extracranial-intracranial arterial bypass for symptomatic hemodynamic cerebral ischemia due to cerebrovascular steno-occlusive disease: Japanese extracranial-intracranial bypass trial. Cerebrovasc Dis 34(Suppl 1):7

Okazawa H, Yamauch IH, Sugimoto K, Magata Y, Kudo TYY (2004) Effects of metabolite correction for arterial input function on quantitative receptor images with 11C-Flumazenil in clinical positron emission tomography studies. J Comput Assist Tomogr 28:428–435

Olsen RW (1981) The GABA postsynaptic membrane receptor-ionophore complex. Site of action of convulsant and anticonvulsant drugs. Mol Cell Biochem 39:261–279

Persson A, Ehrin E, Eriksson L, Farde L, Hedstrom CG, Litton JE, Mindus P, Sedvall G (1985) Imaging of [11C]-labelled Ro 15-1788 binding to benzodiazepine receptors in the human brain by positron emission tomography. J Psychiatr Res 19:609–622

Powers WJ (1991) Cerebral hemodynamics in ischemic cerebrovascular disease. Ann Neurol 29:231–240

Powers WJ, Clarke WR, Grubb RL Jr, Videen TO, Adams HP Jr, Derdeyn CP (2014) Lower stroke risk with lower blood pressure in hemodynamic cerebral ischemia. Neurology 82:1027–1032

Powers WJ, Clarke WR, Grubb RL Jr, Videen TO, Adams HP Jr, Derdeyn CP, Investigators C (2011) Extracranial-intracranial bypass surgery for stroke prevention in hemodynamic cerebral ischemia: the Carotid Occlusion Surgery Study randomized trial. JAMA 306:1983–1992

Powers WJ, Martin WRW, Herscovitch P, Raichle ME, Grubb RL (1984) Extracranial-intracranial bypass surgery: hemodynamic and metabolic effects. Neurology 34:1168–1174

Radu EW, Moseley IF (1978) Carotid artery occlusion and computed tomography. A Clinicoradiological study. Neuroradiology 17:7–12

Rashid P, Leonardi-Bee J, Bath P (2003) Blood pressure reduction and secondary prevention of stroke and other vascular events: a systematic review. Stroke 34:2741–2748

Roman GC, Royall DR (1999) Executive control function: a rational basis for the diagnosis of vascular dementia. Alzheimer Dis Assoc Disord 13(Suppl 3):S69–S80

Samson Y, Hantraye P, Baron JC, Soussaline F, Comar D, Maziere M (1985) Kinetics and displacement of [11C]RO 15-1788, a benzodiazepine antagonist, studied in human brain in vivo by positron tomography. Eur J Pharmacol 110:247–251

Sasaki M, Ichiya Y, Kuwabara Y, Yoshida T, Fukumura T, Masuda K (1997) Benzodiazepine receptors in chronic cerebrovascular disease: comparison with blood flow and metabolism. J Nucl Med 38:1693–1698

Sette G, Baron JC, Young AR, Miyazawa H, Tillet I, Barre L, Travere JM, Derlon JM, MacKenzie ET (1993) In vivo mapping of brain benzodiazepine receptor changes by positron emission tomography after focal ischemia in the anesthetized baboon. Stroke 24:2046–2057

The EC/IC Bypass Study Group (1985) Failure of extracranial-intracranial arterial bypass to reduce the risk of ischemic stroke. Results of an international randomized trial. The EC/IC Bypass Study Group. N Engl J Med 313:1191–1200

Vaughan CJ, Delanty N (1999) Neuroprotective properties of statins in cerebral ischemia and stroke. Stroke 30:1969–1973

Vernieri F, Pasqualetti P, Passarelli F, Rossini PM, Caltagirone C, Silvestrini M (1999) Outcome of carotid artery occlusion is predicted by cerebrovascular reactivity. Stroke 30:593–598

Yamauchi H, Fukuyama H, Dong Y, Nabatame H, Nagahama Y, Nishizawa S, Konishi J, Shio H (2000a) Atrophy of the corpus callosum associated with a decrease in cortical benzodiazepine receptor in large cerebral arterial occlusive diseases. J Neurol Neurosurg Psychiatry 68:317–322

Yamauchi H, Fukuyama H, Fujimoto N, Nabatame H, Kimura J (1992) Significance of low perfusion with increased oxygen extraction fraction in a case of internal carotid artery stenosis. Stroke 23:431–432

Yamauchi H, Fukuyama H, Kimura J, Ishikawa M, Kikuchi H (1994) Crossed cerebellar hypoperfusion indicates the degree of uncoupling between blood flow and metabolism in major cerebral arterial occlusion. Stroke 25:1945–1951

Yamauchi H, Fukuyama H, Kimura J, Konishi J, Kameyama M (1990) Hemodynamics in internal carotid artery occlusion examined by positron emission tomography. Stroke 21:1400–1406

Yamauchi H, Fukuyama H, Nabatame H, Harada K, Kimura J (1993) Callosal atrophy with reduced cortical oxygen metabolism in carotid artery disease. Stroke 24:88–93

Yamauchi H, Fukuyama H, Nagahama Y, Katsumi Y, Dong Y, Konishi J, Kimura J (1996a) Atrophy of the corpus callosum associated with cognitive impairment and widespread cortical hypometabolism in carotid artery occlusive disease. Arch Neurol 53:1103–1109

Yamauchi H, Fukuyama H, Nagahama Y, Nabatame H, Nakamura K, Yamamoto Y, Yonekura Y, Konishi J, Kimura J (1996b) Evidence of misery perfusion and risk for recurrent stroke in major cerebral arterial occlusive diseases from PET. J Neurol Neurosurg Psychiatry 61:18–25

Yamauchi H, Fukuyama H, Nagahama Y, Nabatame H, Ueno M, Nishizawa S, Konishi J, Shio H (1999) Significance of increased oxygen extraction fraction in 5-year prognosis of major cerebral arterial occlusive diseases. J Nucl Med 40:1992–1998

Yamauchi H, Fukuyama H, Nagahama Y, Oyanagi C, Okazawa H, Ueno M, Konishi J, Shio H (2000b) Long-term changes of hemodynamics and metabolism after carotid artery occlusion. Neurology 54:2095–2102

Yamauchi H, Fukuyama H, Yamaguchi S, Miyoshi T, Kimura J, Konishi J (1991) High-intensity area in the deep white matter indicating hemodynamic compromise in internal carotid artery occlusive disorders. Arch Neurol 48:1067–1071

Yamauchi H, Higashi T, Kagawa S, Kishibe Y, Takahashi M (2013) Impaired perfusion modifies the relationship between blood pressure and stroke risk in major cerebral artery disease. J Neurol Neurosurg Psychiatry 84:1226–1232

Yamauchi H, Higashi T, Kagawa S, Nishii R, Kudo T, Sugimoto K, Okazawa H, Fukuyama H (2012) Is misery perfusion still a predictor of stroke in symptomatic major cerebral artery disease? Brain 135:2515–2526

Yamauchi H, Kagawa S, Kishibe Y, Takahashi M, Higashi T (2015) Misery perfusion, blood pressure control, and 5-year stroke risk in symptomatic major cerebral artery disease. Stroke 46:265–268

Yamauchi H, Kagawa S, Kishibe Y, Takahashi M, Higashi T (2016) Progressive cortical neuronal damage and chronic hemodynamic impairment in atherosclerotic major cerebral artery disease. Stroke 47:1534–1541

Yamauchi H, Kagawa S, Kishibe Y, Takahashi M, Higashi T (2017) Progressive cortical neuronal damage and extracranial-intracranial bypass surgery in patients with misery perfusion. AJNR Am J Neuroradiol 38:935–941

Yamauchi H, Kagawa S, Takahashi M, Higashi T (2019a) Long-term hemodynamic changes and blood pressure in atherosclerotic major cerebral artery disease. J Cereb Blood Flow Metab 39:324–331

Yamauchi H, Kagawa S, Takahashi M, Kusano K, Okuyama C (2019b) Selective neuronal damage and blood pressure in atherosclerotic major cerebral artery disease. J Neurol Neurosurg Psychiatry 90(9):975–980. https://doi.org/10.1136/jnnp-2019-320326. [Epub ahead of print]

Yamauchi H, Kudoh T, Kishibe Y, Iwasaki J, Kagawa S (2005) Selective neuronal damage and border-zone infarction in carotid artery occlusive disease: a ^{11}C-flumazenil PET study. J Nucl Med 46:1973–1979

Yamauchi H, Kudoh T, Kishibe Y, Iwasaki J, Kagawa S (2007) Selective neuronal damage and chronic hemodynamic cerebral ischemia. Ann Neurol 61:454–465

Yamauchi H, Kudoh T, Sugimoto K, Takahashi M, Kishibe Y, Okazawa H (2004) Pattern of collaterals, type of infarcts, and hemodynamic impairment in carotid artery occlusion. J Neurol Neurosurg Psychiatry 76:1697–1701

Yamauchi H, Nishii R, Higashi T, Kagawa S, Fukuyama H (2009) Hemodynamic compromise as a cause of internal border-zone infarction and cortical neuronal damage in atherosclerotic middle cerebral artery disease. Stroke 40:3730–3735

Yamauchi H, Nishii R, Higashi T, Kagawa S, Fukuyama H (2011a) Selective neuronal damage and Wisconsin Card Sorting Test performance in atherosclerotic occlusive disease of the major cerebral artery. J Neurol Neurosurg Psychiatry 82:150–156

Yamauchi H, Nishii R, Higashi T, Kagawa S, Fukuyama H (2011b) Silent cortical neuronal damage in atherosclerotic disease of the major cerebral arteries. J Cereb Blood Flow Metab 31:953–961

Yamauchi H, Pagani M, Fukuyama H, Ouchi Y, Nagahama Y, Matsuzaki S, Kimura J, Yonekura Y, Konishi J (1995) Progression of atrophy of the corpus callosum with deterioration of cerebral cortical oxygen metabolism after carotid artery occlusion: a follow up study with MRI and PET. J Neurol Neurosurg Psychiatry 59:420–426

PET Imaging of Cyclooxygenases in Neuroinflammation

10

Atul Bhardwaj and Frank Wuest

Contents

A. Bhardwaj
Cross Cancer Institute, Department of Oncology, University of Alberta, Edmonton, AB, Canada

Faculty of Pharmacy and Pharmaceutical Sciences, University of Alberta, Edmonton, AB, Canada
e-mail: abhardwa@ualberta.ca

F. Wuest (✉)
Cross Cancer Institute, Department of Oncology, University of Alberta, Edmonton, AB, Canada

Faculty of Pharmacy and Pharmaceutical Sciences, University of Alberta, Edmonton, AB, Canada

Department of Chemistry, University of Alberta, Edmonton, AB, Canada
e-mail: wuest@ualberta.ca

Abstract

Neuroinflammation has detrimental effects on brain functions and plays critical roles in the pathogenesis and progression of several neurodegenerative diseases, including Alzheimer's and Parkinson's disease, and dementia. Cyclooxygenase isoenzymes COX-1 and COX-2 are responsible for the conversion of arachidonic acid to prostanoids such as prostaglandins, thromboxanes, and prostacyclins. Aberrant expression and function of COX-1 and COX-2 isoforms in the brain are linked to various inflammatory conditions leading to neural death and manifestation of neurodegenerative disorders. Consequently, COX-1 and COX-2 have emerged as important biomarkers for functional imaging of neuroinflammation and associated neurodegenerative diseases with positron-emission tomography (PET). This chapter reviews recent advances of PET imaging agents for the noninvasive visualization and characterization of COX-1 and COX-2 enzymes in neuroinflammation.

10.1 Introduction

10.1.1 Neuroinflammation

Inflammation is an essential and vital part of the body's defense mechanism to respond to injuries and infections. The inflammatory response is a crucial signal to the body's immune system to trigger the healing and repair of injured tissue, as well as to mobilize the defense system against invasive microbes such as viruses and bacteria (Medzhitov 2008; DiSabato et al. 2016; Schmid et al. 2009; Schain and Kreisl 2017a; Glass et al. 2010). If the inflammatory response is not successful and fails to counteract the effects of tissue injury and infection, conditions can lead to chronic inflammation and start of vicious processes resulting in further damage of injured tissue and surrounding healthy tissue. Aberrant inflammatory responses have detrimental effects on organ and tissue function and contribute to the development and manifestation of many chronic diseases. Molecular imaging of inflammatory processes and crucial biomarkers of inflammation represents an important tool for early and accurate diagnosis and staging of inflammatory disease as well as for monitoring the response to therapeutic interventions (Narayanaswami et al. 2018; Winkeler et al. 2010).

This becomes particularly important when the inflammatory response is linked to the central nervous system (CNS) as damaged neural tissues can remain unnoticed for several years before the development of symptoms. Inflammation of the CNS (neuroinflammation) is a primary driver and contributor to the development and progression of several neurodegenerative diseases such as Alzheimer's disease (Graeber 2010; Wyss-Coray and Rogers 2012; Glass et al. 2010; Ransohoff 2016; Schain and Kreisl 2017b; Wyss-Coray and Mucke 2012; Craft et al. 2005), Parkinson's disease (Chen et al. 2005; Hirsch and Hunot 2009; Phani et al. 2012),

amyotrophic lateral sclerosis, multiple sclerosis, and traumatic brain injury (Bartels and Leenders 2010; Calsolaro and Edison 2016; Stephenson et al. 2018; Amor et al. 2014; Lymana et al. 2014; Tansey et al. 2007; Ransohoff 2016).

10.1.2 Cyclooxygenases, Neuroinflammation, and Neurodegenerative Diseases

Cyclooxygenases (COXs) play a central role in the arachidonic acid metabolism cascade. COXs are involved in the activation of various inflammatory pathways that generate prostaglandins (PGs), chemokines, and cytokines as well as various reactive oxygen species (Smith et al. 2011; van der Donk et al. 2002; Blobaum and Marnett 2007; Marnett 2009). The excessive and sustained release of these substances can lead to chronic inflammation and oxidative stress which is harmful to any organ, including the brain. The COX-mediated release of prostaglandins as inflammatory mediators is a significant contributor to neuroinflammation and neurodegenerative diseases (Choi et al. 2009a; Ricciotti and FitzGerald 2011; Aïd and Bosetti 2011; Dargahi et al. 2011; Phillis et al. 2006). Therefore, COXs continue as a primary drug target for the treatment and as a biomarker for the diagnosis of chronic inflammatory conditions, including pain, fever, rheumatoid arthritis, cancer, and neurodegenerative diseases. Several classes of COX inhibitors have been developed, also referred to as nonsteroidal anti-inflammatory drugs (NSAIDs). Many COX inhibitors were tested as therapeutic candidates for various CNS disorders (Imbimbo et al. 2010; Vlad et al. 2008; Rogers et al. 1993; McGeer and McGeer 2007; Cudaback et al. 2014).

COXs are rate-limiting enzymes in the arachidonic acid pathway (Fig. 10.1).

COXs first oxidize arachidonic acid to prostaglandin G2 (PGG2) which is further reduced into prostaglandin H2 (PGH2) (Smith et al. 1996; Kurumbail et al. 1996a; Smith et al. 2000; Simmons et al. 2004; Chandrasekharan et al. 2002a; Mitchell and Warner 1999). Various tissue-specific enzymes (isomerases) metabolize PGH_2 into prostanoids, including prostaglandins (PGs: PGE2, PGD2, PGF2α), prostacyclin (PGI2), and thromboxanes (TXs). Prostanoids bind to G-protein-coupled receptors (e.g., EP_{1-4}) and mediate a variety of physiological and pathological processes, including inflammation.

COXs exist in three isoforms: a constitutive isoform, COX-1; a mitogen-inducible isoform, COX-2; and a splice variant of COX-1, COX-3 (Smith et al. 1996; Marnett et al. 1999; Kurumbail et al. 1996b; Chandrasekharan et al. 2002b; Choi et al. 2009b). The human COX-1 enzyme (599 amino acids, 68.686 kDa) is constitutively expressed in most tissues and responsible for the physiological production of PGs involved in the regulation of processes such as thrombogenesis and homeostasis of the gastrointestinal tract and kidneys.

In addition to its homeostatic functions in various organs, the COX-1 isoform is also considered as a major player in neuroinflammation. Several studies indicated that COX-1 is expressed in the midbrain, pons, and medulla. Moreover, COX-1 plays a critical role in brain injuries induced by pro-inflammatory stimuli including
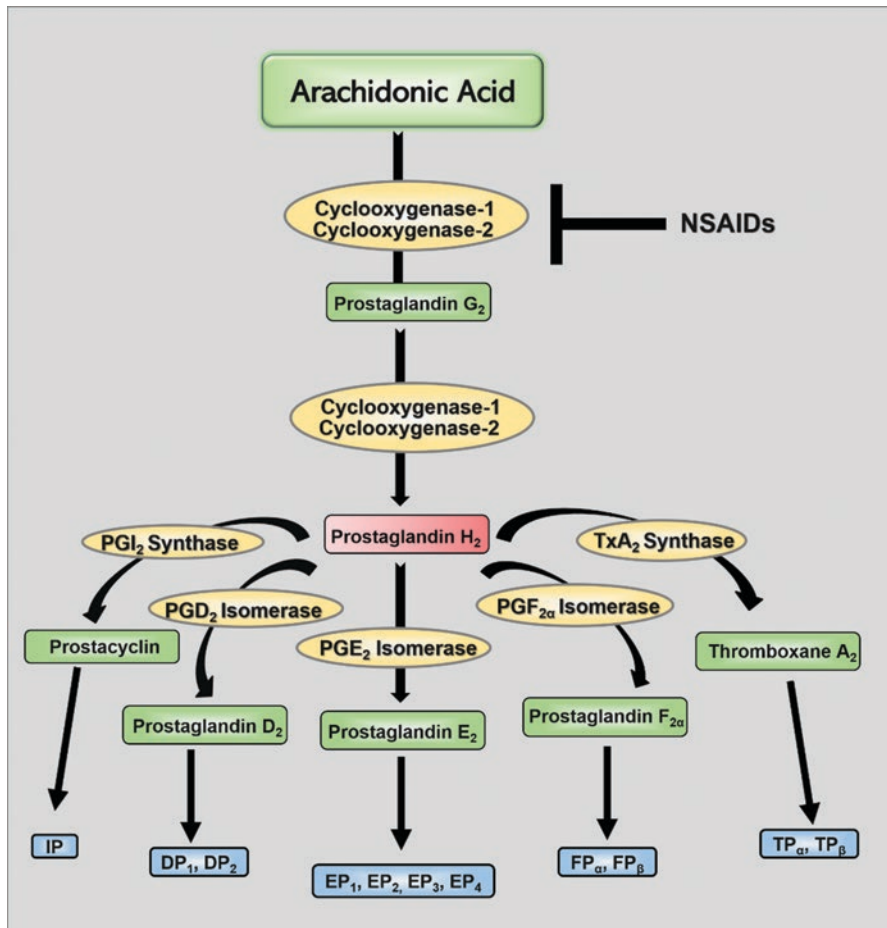
Fig. 10.1 Cyclooxygenase-mediated metabolic pathway of arachidonic acid

prostaglandin E2 (PGE2) or cytokines such as interleukin (IL)-1β, lipopolysaccharide, IL-1β, and TNFα (Hoozemans et al. 2001; García-Bueno et al. 2009; Yermakova et al. 1999; Bosetti 2007). COX-1 is also involved in microglial activation during neuroinflammation (Aid et al. 2010; Toscano et al. 2007). The pharmacological inhibition or genetic deletion of COX-1 isoform resulted in the reduction of oxidative stress and neuronal damage (Choi et al. 2008; Choi and Bosetti 2009; Matousek et al. 2010).

The human COX-2 isoform (604 amino acids, 68.996 kDa) is only scarcely expressed in most tissues and organs under normal conditions and is mainly induced by several inflammatory stimuli, hormones, and growth factors. COX-2 is an established therapeutic target for various chronic inflammatory diseases, including cancer (Wang and DuBois 2010, 2013; Meric et al. 2006). Although COX-2 is mostly referred to as the "inducible" COX isoform, COX-2 is constitutively expressed throughout the forebrain, including hippocampal and cortical glutamatergic

neurons. The COX-2 isoform plays a central role in synaptic activity and long-term synaptic plasticity (Wang et al. 2005; Stefanovic et al. 2006; Hewett et al. 2006; Slanina and Schweitzer 2005). Possible involvement of COX-2 isoform in neurotoxicity is still subject to controversial debates but several studies demonstrated that overexpression of COX-2 drives neurological disorders such as Alzheimer's disease, Parkinson's disease, multiple sclerosis, long-term potentiation (LTP), stroke, epilepsy, schizophrenia, and bipolar disorder (Yamagata et al. 1993; Yang and Chen 2008; Teismann et al. 2003; Blais et al. 2005).

The discovery of novel COX-1 and COX-2 selective inhibitors also referred to as Coxibs has stimulated the development of COX-imaging agents for imaging biomarker research (Bhardwaj et al. 2013, 2017; Marnett 2012; Uddin et al. 2010; Kaur et al. 2015; Laube et al. 2013; Morgenroth et al. 2017; Tietz et al. 2016). During the last two decades, several COX-1 and COX-2 selective fluorescent and radiolabeled imaging agents have been developed and tested. A selection of [11]C- and ^{18}F-labeled PET imaging agents is depicted in Fig. 10.2 (Tietz et al. 2013; Pacelli et al. 2014; de Vries 2006).
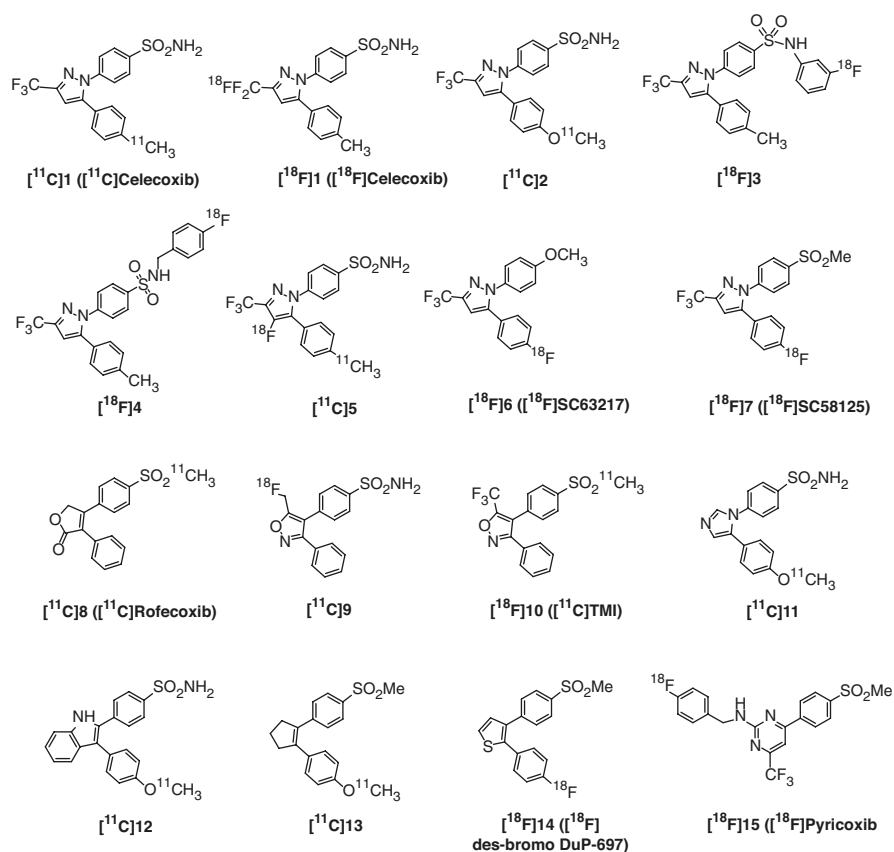
Fig. 10.2 COX-1- and COX-2-targeted PET imaging probes labeled with ^{11}C and [18]F

However, to date, no COX PET imaging agent has received approval for clinical use. Significant challenges and limitations of PET imaging agents for COXs include low in vivo affinity, high blood pool retention, poor metabolic stability, low uptake in target organs and tissues, and nonspecific binding. The following sections discuss the current status of radiotracer development for PET imaging of COX-1 and COX-2 in the brain.

10.2 PET Imaging Agents for COX-1

10.2.1 [¹¹C]Ketoprofen Methyl Ester

PET imaging of COX-1 was advanced to clinical testing using ¹¹C-labeled ketoprofen methyl ester (¹¹C-KTP-Me, [¹¹C]**24**) as a radiotracer. The first PET imaging of COX-1 in activated microglia was successfully achieved with racemic (*R,S*)-¹¹C-KTP-Me) (Takashima-Hirano et al. 2010). The radiosynthesis of racemic (*R,S*)-¹¹C-KTP-Me was reported along with the preparation of a series of ¹¹C-labeled arylpropionic acids of six NSAIDs (ibuprofen, naproxen, flurbiprofen, fenoprofen, ketoprofen, and loxoprofen) and their respective methyl esters (Fig. 10.3).

COX-1 selective inhibitor ketoprofen is widely used as an analgesic and antipyretic drug. The use of the respective methyl ester (*R,S*)-11C-KTP-Me was motivated to overcome the poor blood-brain barrier (BBB) permeability of ketoprofen. Racemic (*R,S*)-¹¹C-KTP-Me was synthesized by a [¹¹C]methylation reaction of (3-benzophenyl)acetic acid methyl ester with [¹¹C]CH₃I in the presence of NaH at 30 °C, and the obtained chemical and radiochemical purity was >99% (Takashima-Hirano et al. 2010). Corresponding (*R,S*)-[¹¹C]ketoprofen was prepared by treating methyl ester (*R,S*)-¹¹C-KTP-Me with 2 M NaOH. Extension of the [¹¹C]methylation reaction time beyond 2 min and use of reaction temperatures of 50 °C resulted in lower yield and decomposition of (*R,S*)-¹¹C-KTP-Me into unknown side products.
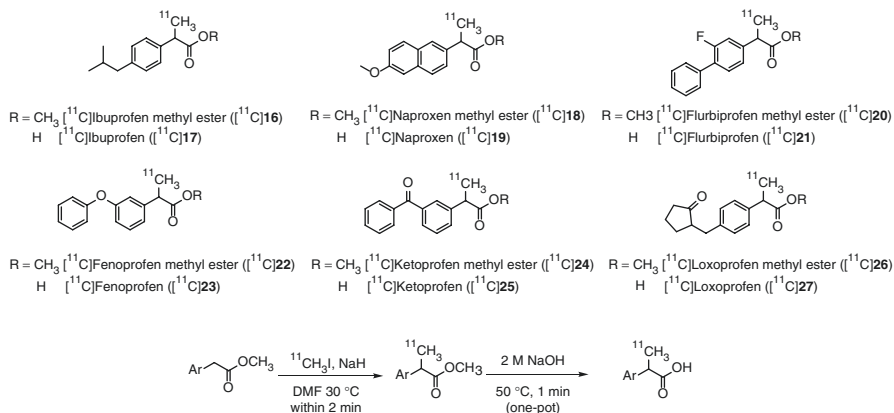
Fig. 10.3 ¹¹C-labeled arylpropionic acid derivatives (Takashima-Hirano et al. 2010)
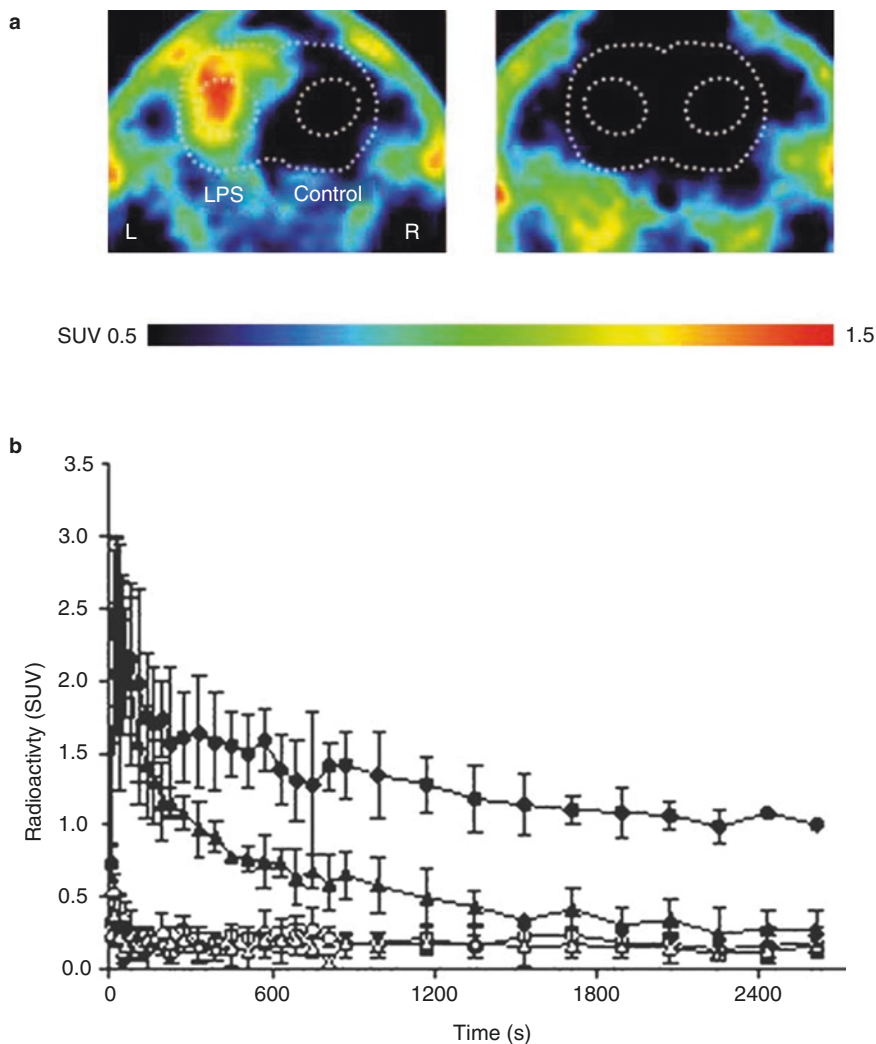
Fig. 10.4 (**a**) Summarized PET images (from 5 to 45 min after radiotracer injection) of [^{11}C]**24** (left panel) and [^{11}C]**25** (right panel) in rat brain inflammation induced by LPS (50 mg) injection into the left striatum. (**b**) Time-activity curves of [^{11}C]**24** (*n* = 2) and [^{11}C]**25** (*n* = 3) in LPS-injected inflammatory area (LPS) and contralateral region (control). Data are expressed as mean ± SD (●: LPS [^{11}C]**24**, ▲: control [^{11}C]**25**; ○: LPS [^{11}C]**24**, Δ: control [^{11}C]**25**) (Takashima-Hirano et al. 2010)

PET imaging with (*R*,*S*)-^{11}C-KTP-Me in rat brain demonstrated specific accumulation of radioactivity in the inflamed region (Fig. 10.4) (Takashima-Hirano et al. 2010). The obtained SUV of (*R*,*S*)-^{11}C-KTP-Me was comparable to that of [^{11}C]PK11195, a commonly used PET radiotracer for imaging peripheral benzodiazepine receptors in activated microglia during neuroinflammation. Radiotracer

(R,S)-^{11}C-ketoprofen ([11]C**24**) was not accumulated in the brain due to its poor blood-brain barrier (BBB) permeability (Fig. 10.4) (Takashima-Hirano et al. 2010).

Metabolite analysis of (R,S)-^{11}C-KTP-Me in the rat brain and blood showed that >90% of the radiotracer hydrolyzed to its pharmacologically active form (R,S)-^{11}C-ketoprofen within 5 min postinjection. In the rat model of neuroinflammation model, all 2-aryl [^{11}C]propionic acid methyl esters showed high accumulation in the area of lipopolysaccharide (LPS)-induced inflammation, except for [^{11}C]ibuprofen methyl ester [11]C**24** (Fig. 10.5) (Takashima-Hirano et al. 2010).

(R,S)-^{11}C-KTP-Me displayed the highest radioactivity accumulation in inflammatory regions compared to all other tested radiotracers. The observed significant blocking effect with pharmacological doses of ketoprofen methyl ester on the radioactivity accumulation of (R,S)-11C-KTP-Me in brain regions of inflammation was indicative of high binding specificity of the radiotracer to COX.

Additional research involved ex vivo and in vivo imaging studies with ^{11}C-KTP-Me to study the COX-1 and COX-2 selectivity and specificity profile of the radiotracer (Shukuri et al. 2011). High accumulation of radiotracer of ^{11}C-KTP-Me was observed in the hippocampus, cerebral cortex, and cerebellum of wild-type (COX-1^{+/+}, COX-2^{+/+}) mice, whereas uptake of ^{11}C-KTP-Me was significantly lower in COX-1^{−/−} mice (Fig. 10.6a). No differences were detected between COX-2^{−/−} and wild-type COX-2^{+/+} mice (Fig. 10.6b).

This experiment provided important evidence that radiotracer ^{11}C-KTP-Me selectively binds to the COX-1 isoform in the brain (Fig. 10.6) (Shukuri et al. 2011).
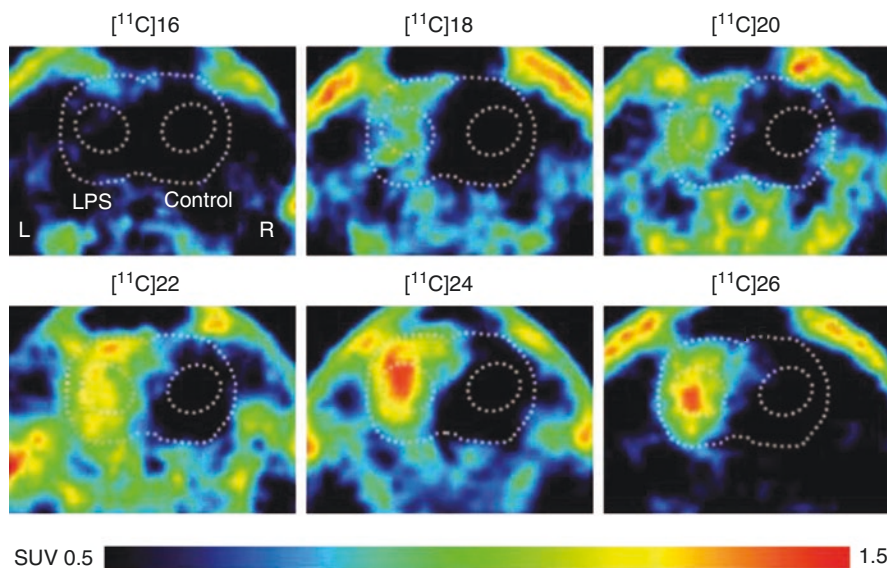
Fig. 10.5 PET images of 2-aryl[11]C]propionic acid methyl esters in rat brain inflammation induced by LPS (50 mg) injection into the left striatum (Takashima-Hirano et al. 2010)
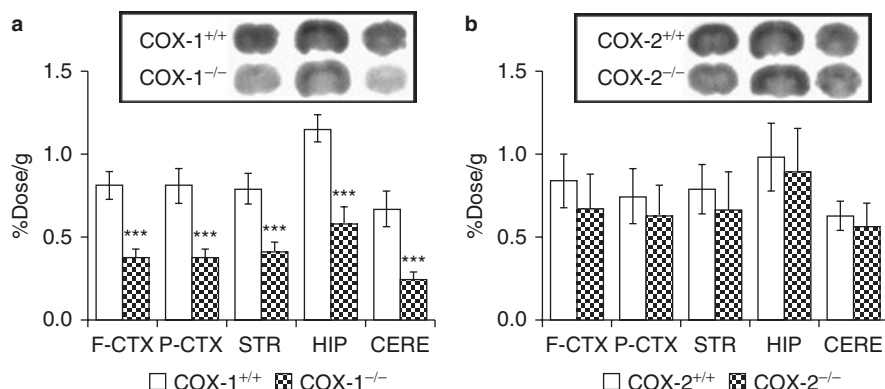
Fig. 10.6 Accumulation of ^{11}C-ketoprofen methyl ester ^{11}C-KTP-Me in the brain of COX-1$^{-/-}$ and COX-2$^{-/-}$ mice. Ex vivo autoradiography and regional brain tissue uptake of ^{11}C-KTP-Me in COX-1$^{+/+}$ and COX-1$^{-/-}$ mice (**a**) and COX-2$^{+/+}$ and COX-2$^{-/-}$ mice (**b**) were obtained 15 min after injection of the radiotracer. F-CTX 5 frontal cortex; P-CTX 5 parietal cortex; STR 5 striatum; HIP 5 hippocampus; CERE 5 cerebellum. Data are mean ± SD ($n = 6$). $^{***}P$, 0.001 *versus* wild-type mice (Shukuri et al. 2011)
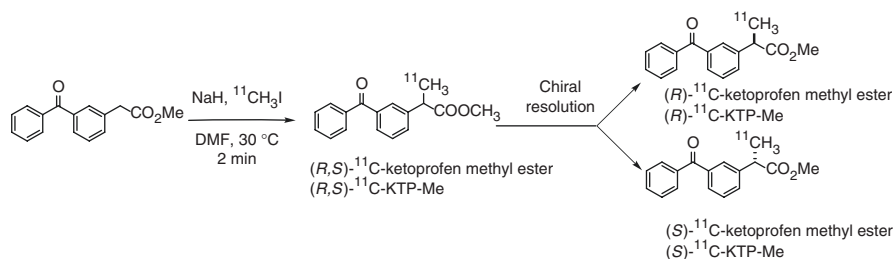
Fig. 10.7 Synthesis of (*R*)- and (*S*)-^{11}C-KTP-Me via rapid *C*-^{11}C-methylation and chiral resolution (Shukuri et al. 2016)

To this point, racemic (*R*,*S*)-^{11}C-KTP-Me was used for all COX-targeted PET imaging studies in the brain, although the (S)-enantiomer of ketoprofen is known to be pharmacologically more active than the (*R*)-enantiomer. Thus, Onoe et al. separated both isomers using a solid chiral resolution method with semi-preparative high-performance liquid chromatography (HPLC) (Fig. 10.7) (Shukuri et al. 2016).

The (*S*)-^{11}C-KTP-Me enantiomer was identified as an improved PET imaging agent with high COX-1 specificity. Radiotracer (*S*)-^{11}C-KTP-Me was further investigated for COX-1 imaging during the progression of Alzheimer's disease in a transgenic mouse model. In contrast to COX-1 inhibitory activity of (*R*)-^{11}C-KTP-Me (IC$_{50}$ = 126.7 μM), both racemic (*R*,*S*)-^{11}C-KTP-Me (IC$_{50}$ = 0.031 μM) and (*S*)-^{11}C-KTP-Me (IC$_{50}$ = 0.011 μM) showed higher inhibitory potency for COX-1 (Shukuri et al. 2016). Moreover, PET imaging of neuroinflammation in rat brain also showed 1.5-fold higher radioactivity accumulation in LPS-induced inflamed region after

injection of (S)-^{11}C-KTP-Me compared to racemic (R,S)-^{11}C-KTP-Me. Enantiomer (R)-^{11}C-KTP-Me displayed only low and nonspecific radioactivity accumulation in the brain (Shukuri et al. 2016). Time-activity curve analyses of all three radiotracers revealed rapid washout from the brain within 15 min under normal conditions, whereas radioactivity remained in the striatum for 45 min in the case of (R,S)-^{11}C-KTP-Me and (S)-^{11}C-KTP-Me after the LPS-induced neuroinflammation. Moreover, retention of radioactivity was improved significantly for (S)-^{11}C-KTP-Me compared to racemic (R,S)-^{11}C-KTP-Me (Fig. 10.8) (Shukuri et al. 2016).

Ex vivo autoradiography analyses showed an age-dependent increase in (S)-^{11}C-KTP-Me accumulation in all brain regions of amyloid precursor protein transgenic (APP-Tg) mice in direct comparison with radiotracer accumulation in wild-type mice (Fig. 10.9) (Shukuri et al. 2016).
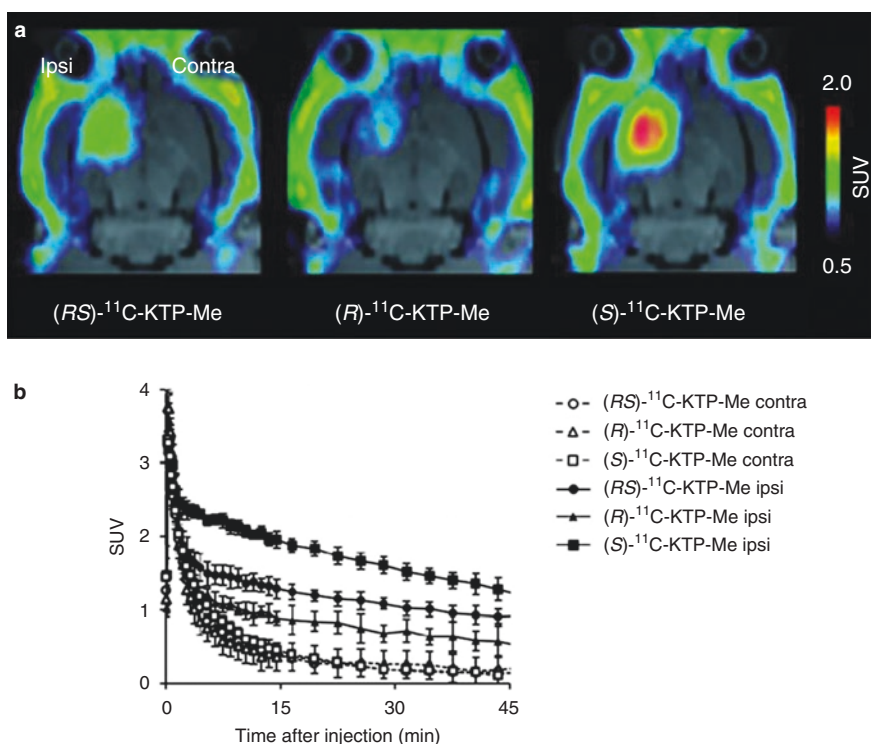
Fig. 10.8 Representative PET images and time-radioactivity curves of each ^{11}C-KTP-Me enantiomer in rat brain after LPS injection. (**a**) Transaxial rat brain views of SUV-summed PET images from 5 to 45 min after tracer injection were coregistered with individual MR images at baseline. (S)-^{11}C-KTP-Me showed higher accumulation and superior specificity in rat brain hemisphere than (R,S)- and (R)-11CKTP-Me. (**b**) Quantitative time-radioactivity curves of each 11C-KTP-Me enantiomer in contralateral (Contra) and ipsilateral (Ipsi) striatum. Data are expressed as SUV and are mean ± SD ((R)-[11C]KTP-Me, $n = 3$; others, $n = 4$) (Shukuri et al. 2016)
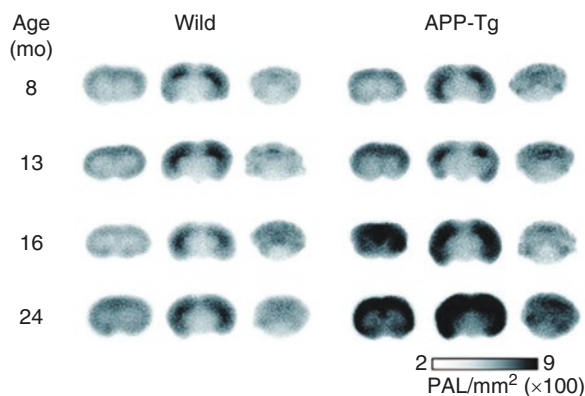
Fig. 10.9 Age-dependent changes in (*S*)-^{11}C-KTP-Me accumulation in the brain of APP-Tg 2576 and wild-type mice. Representative ex vivo autoradiographs of coronal sections of mice at 15 min after PET tracer injection. Progressive and remarkable increases in (*S*)-^{11}C-KTP-Me in the frontal cortex, parietal occipital cortex, and hippocampus of APP-Tg mice of 16 months old. The range bar represents the intensity of photostimulated luminescence (PSL/mm^2)
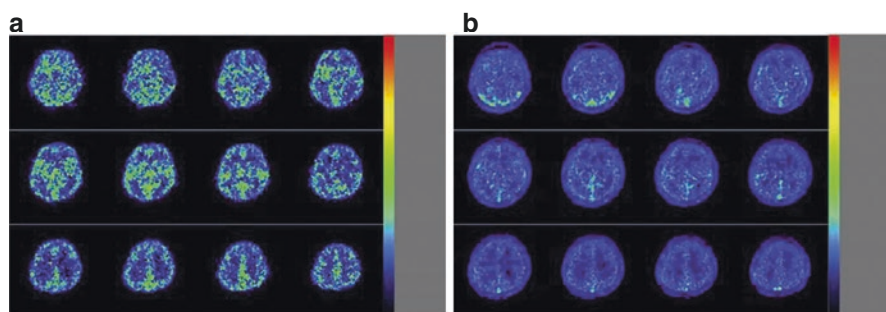
Fig. 10.10 Brain summation image during 2 min after injection of (*R,S*)-[^{11}C]KTP-Me in a young normal volunteer (**a**). Late-phase brain summation image created from three whole-body scans (8, 20, and 40 min postinjection) (**b**) (Ohnishi et al. 2014)

The encouraging PET imaging results in animals stimulated efforts to explore the clinical utility of racemic (*R,S*)-[^{11}C]KTP-Me for PET imaging of COX-1 in neuroinflammation, and a first-in-human study was performed in healthy volunteers (Ohnishi et al. 2014). In this study, the safety, radiation dosimetry, pharmacokinetics, biodistribution, and brain uptake of (*R,S*)-^{11}C-KTP-Me were investigated. Optimization of the radiosynthesis in an automated synthesis unit based on previously reported methods provided the radiotracer in high radiochemical purity >99%. No adverse effects were observed after radiotracer administration. The radiotracer was rapidly metabolized to more hydrophilic ^{11}C-KTP ([^{11}C]**17**) and cleared from the blood. The whole-brain and cerebral cortex time-activity curves indicated that radioactivity readily entered the brain, with an average peak cortical SUV of 1.5 in the cortex at 2 min postinjection. Then, radioactivity was gradually washed out presumably due to the lack of neuroinflammation (Fig. 10.10) (Ohnishi et al. 2014).
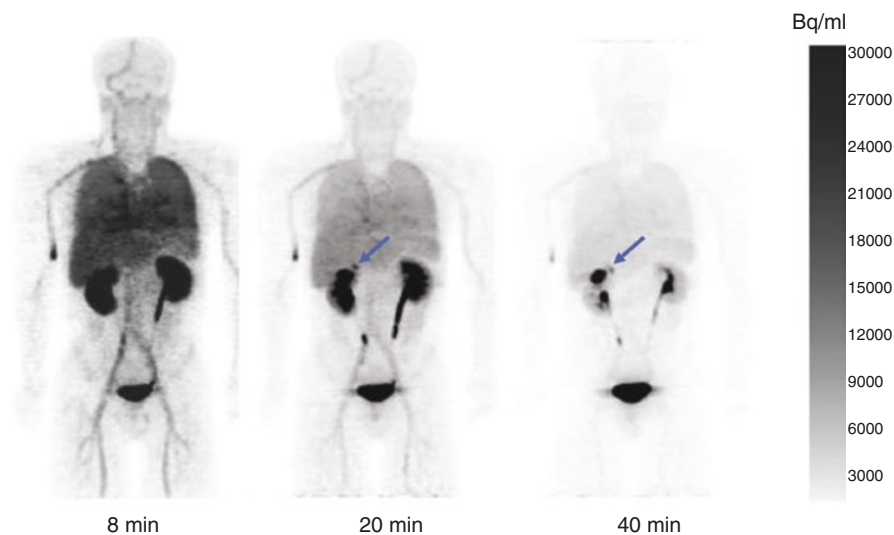
Fig. 10.11 Biodistribution of radioactivity in a healthy volunteer obtained with whole-body scans starting 8, 20, and 40 min after injection of (R,S)-[^{11}C]KTP-Me. Images are decay corrected. Arrows (←) indicate biliary excretion (Ohnishi et al. 2014)

The biodistribution analyses revealed that urinary bladder was the major excretory pathway, and the organs with the highest absorbed radioactivity dose were the urinary bladder (41 μGy/MBq), the kidneys (23 μGy/MBq), and the lungs (13 μGy/MBq) (Fig. 10.11). Similar to other ^{11}C-labeled PET radiotracers the calculated effective dose of (R,S)-^{11}C-KTP-Me was 4.7 μSv/MBq.

Radiotracer (R,S)-^{11}C-KTP-Me was further investigated as a diagnostic biomarker for neuroinflammatory processes in Alzheimer's disease (AD) (Ohnishi et al. 2016). (R,S)-^{11}C-KTP-Me was intravenously administered to healthy subjects, Pittsburgh compound-B (PiB)-positive patients with mild cognitive impairment (MCI), and PiB-positive AD patients. PET scans were recorded for 70 min (Fig. 10.12) (Ohnishi et al. 2016).

In all subjects, no abnormal symptoms, physical examination, vital signs, electrocardiogram, urine tests, or blood tests after injection of (R,S)-[11C]KTP-Me were observed. Unfortunately, the analyses of average peak cortical SUV revealed no statistically significant difference between healthy and MCI/AD patients (Fig. 10.13) (Ohnishi et al. 2016).

The evaluation of regional uptake in healthy subjects and patients showed no connection between the distribution profile of (R,S)-[^{11}C]KTP-Me and [^{11}C]PiB in the patient population. Overall, the results of this study indicated that [^{11}C]KTP-Me enters the human brain but it was found not useful as a diagnostic biomarker for neuroinflammation in MCI/AD. Because of better COX-1 affinity of (S)-^{11}C-KTP-Me over racemic [^{11}C]KTP-Me, the authors suggested the evaluations with S-enantiomer in AD, MCI, and other neuroinflammatory conditions.
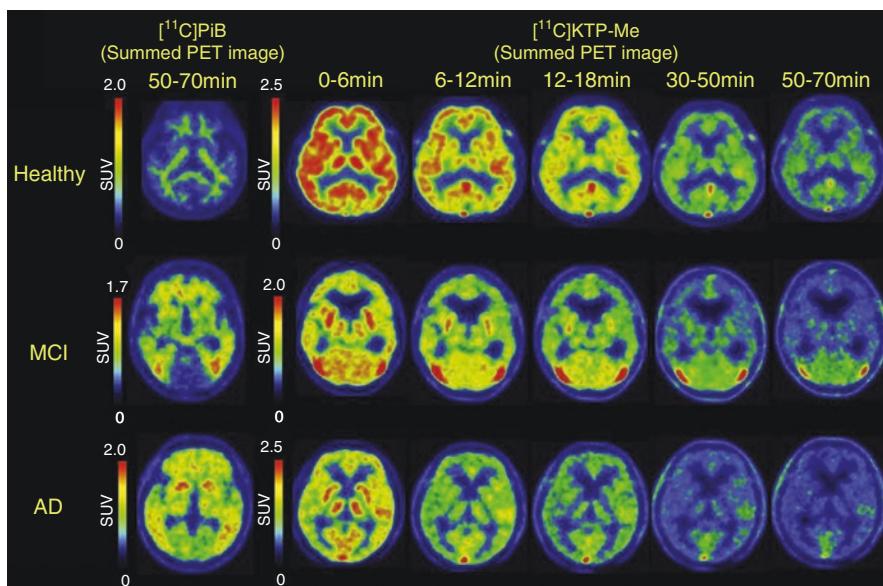
Fig. 10.12 Brain summation images 50–70 min after injection of [^{11}C]PiB and during 0–6 min, 6–12 min, 12–18 min, 30–50 min, and 50–70 min after injection of (*R,S*)-[^{11}C]KTP-Me in a representative healthy subject, MCI patient, and AD patient. No obvious differences were observed in cortical or regional retention among the subjects (Ohnishi et al. 2016)
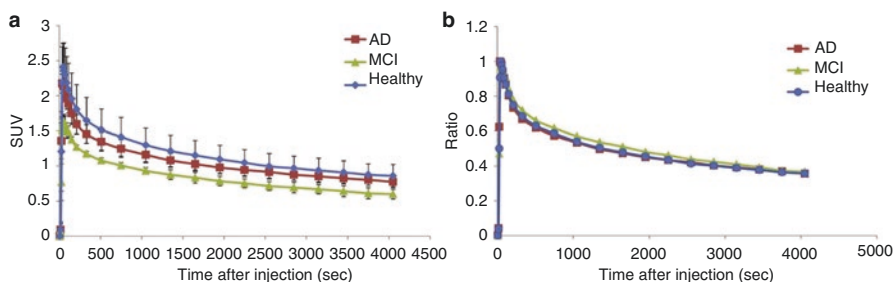
Fig. 10.13 (**a**) Mean time-activity curves and SD of the cerebral cortex after injection of (*R,S*)-[^{11}C]KTP-Me in healthy subjects, MCI patients, and AD patients. (**b**) Time course of the ratio to the peak of each curve. No apparent differences were observed in the washout curve among the three groups (Ohnishi et al. 2016)

10.2.1.1   [^{11}C](1,5-bis(4-methoxyphenyl)-3-(2,2,2-trifluoroethoxy)-1*H*-1,2,4 triazoles ([^{11}C]PS13, [^{11}C]PS1, [^{2}H$_{2}$,^{18}F]PS2, and [^{11}C]PS13)

The limitations of using radiotracer [^{11}C]KTP-Me for PET imaging of COX-1 prompted the development of other ^{11}C-labeled imaging agents such as [^{11}C]PS13 (1,5-bis(4-methoxyphenyl)-3-(2,2,2-trifluoroethoxy)-1H-1,2,4   triazole)   for

studying neuroinflammation in monkeys and humans. Seventeen analogs of potent and selective COX-1 inhibitor FK881 (PS1) (IC_{50} = 4.9 nM (COX-1); IC_{50} = 3.2 μM (COX-2); clog D = 3.72) were prepared and tested (Imanishi et al. 2011; Singh et al. 2018).

The high inhibitory potency and COX-1 selectivity profile and calculated moderate lipophilicities drove the development of [11]C- and ^{18}F-labeled radiotracer candidates for PET imaging in monkeys: 1,5-(4-methoxyphenyl)-1H-1,2,4-triazole [^{11}C]PS1; 3-[^{18}F]fluoromethoxy-substituted and deuterated compound [^{18}F]PS2; and 3-(1,1,1-trifluoroethoxy) compound [^{11}C]PS13 (Fig. 10.14).

Radiotracer [^{11}C]PS1 was synthesized by O-methylation of the 1,5-bis-(4-methoxy-phenyl)-1H-[1,2,4]triazol-3-ol with [^{11}C]MeI in 20 ± 3% radiochemical (from [^{11}C]CO$_2$) in >99% radiochemical purity and with a molar activity of 125 ± 62 GBq/μmol, radiotracer [^{18}F]PS2 was obtained in 14 ± 4% radiochemical yield in >99% radiochemical purity and with a molar activity of 53 ± 17 GBq/μmol by treating 1,5-bis-(4-methoxy-phenyl)-1H-[1,2,4]triazol-3-ol with deuterated d2-[^{18}F]fluorobromomethane, and compound [^{11}C]PS13 was prepared in 9.8 ± 3.5% radiochemical yield (from [^{11}C]CO$_2$) with >99% radiochemical purity and with a molar activity of 176 ± 73 GBq/μmol by the reaction of desmethoxy precursor 4-[2-(4-methoxy-phenyl)-5-(2,2,2-trifluoro-ethoxy)-2H-[1,2,4]triazol-3-yl]-phenol with [^{11}C]MeI (Singh et al. 2018; Shrestha et al. 2018).

The PS1 displayed a high COX1 affinity (IC_{50} = 5 nM) and selectivity over COX-2. In the monkey brain, radioactivity concentration for radioligand [^{11}C]PS1 peaked at an SUV of 4.26 at 1.75 min, followed by a washout reaching an SUV of
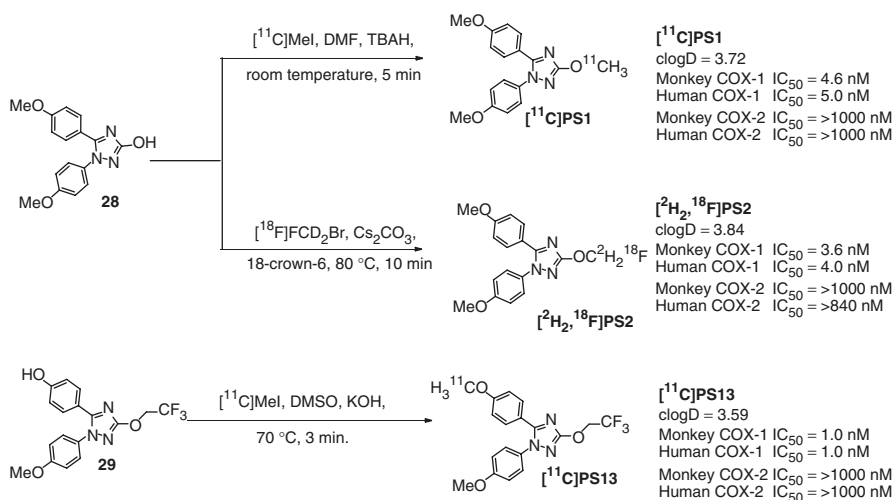
Fig. 10.14 Radiosynthesis of [^{11}C]PS1, [^{18}F]PS2, and [^{11}C]PS13 (Singh et al. 2018; Shrestha et al. 2018)

Fig. 10.15 PET time-activity curves from rhesus monkey whole brain (gray matter) following intravenous injection of [^{11}C]PS1 ($n = 1$), [^{2}H$_2$,^{18}F]PS2 ($n = 1$), and [^{11}C]PS13 (mean ± SD, $n = 3$). The inset expands the data presentation over the early stage of scanning (Shrestha et al. 2018)
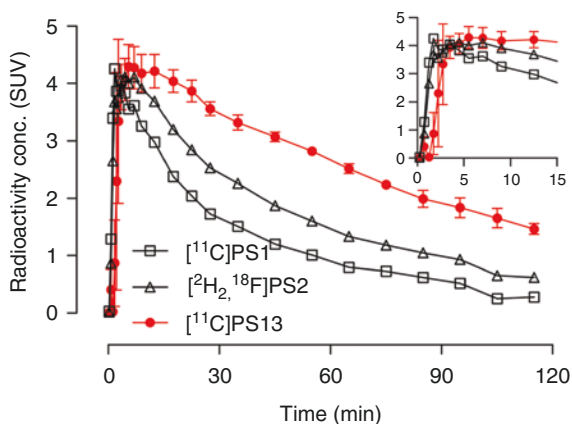
0.62 at 85 min. Compound PS2 also showed a high affinity for human COX1 (4 nM) with >200 selectivity over COX-2. In the monkey brain, radiotracer [^{2}H$_2$,^{18}F]PS2 showed an SUV of 4.11 at 7 min postinjection which declined by 74% reaching an SUV = 1.05 at 85 min (Fig. 10.15) (Singh et al. 2018; Shrestha et al. 2018).

Despite the use of two deuterium atoms in the [^{2}H$_2$,^{18}F]fluoromethoxy group to reduce in vivo radiodefluorination, brain images with radiotracer [H$_2$,^{18}F]PS2 confirmed high radioactivity uptake in the skull which is indicative of radiodefluorination. Radiodefluorination and accumulation of radioactivity in the skull challenged the quantification of radiotracer [^{2}H$_2$,^{18}F]PS2 in the monkey brain, and radiotracer [^{2}H$_2$,^{18}F]PS2 was not used for further studies. COX-1 inhibitor PS13 had a high affinity for both monkey and human COX-1 (IC$_{50}$ ~1 nM) and a thousandfold selectivity over COX-2.

Radiotracer [^{11}C]PS13 showed high radioactivity concentration in the monkey brain (SUV = 4.3, at 9 min) which was washed out by 54% reaching an SUV of 1.99 at 85 min (Fig. 10.15) (Shrestha et al. 2018). Among all tested 1,2,4-triazole radioligands (PS1, PS2, PS3), radiotracer [^{11}C]PS13 displayed the most favorable characteristics for COX-1 imaging and quantification in the brain.

The COX-1 specificity of [^{11}C]PS13 was further confirmed with blocking experiments, using pharmacological doses of PS13 and KTP-Me. From brain volume distribution (V_T) estimations, high uptake of [^{11}C]PS13 in the monkey brain was noticed in the neocortex, temporal cortex, striatum, thalamus, midbrain, and hippocampus, in descending order (Fig. 10.16, top row). Blocking with PS13 or KTP-Me resulted in a reduction in V_T (Figs. 10.16 and 10.17) (Shrestha et al. 2018).

The excellent in vivo selectivity and PET imaging profile of radiotracer [^{11}C]PS13 encouraged biodistribution studies in healthy human subjects (Anaya et al. 2019).
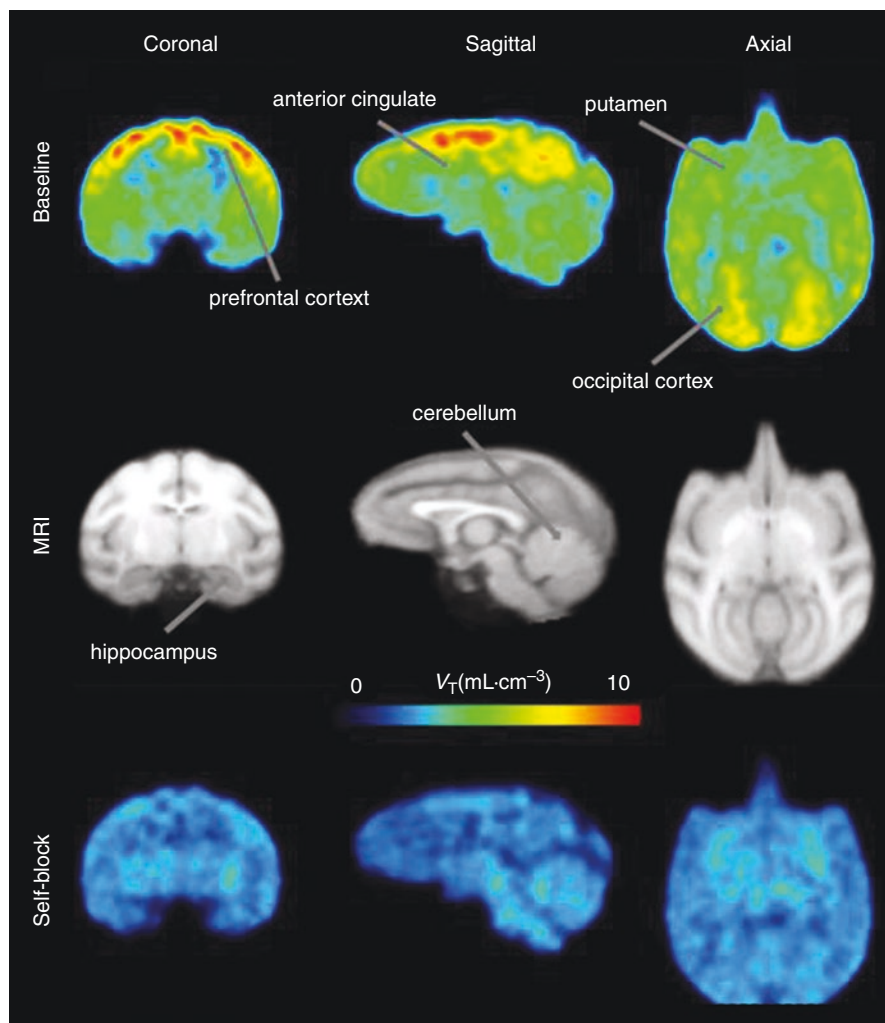
Fig. 10.16 Parametric images of V_T for [^{11}C]PS13 in the brain of a normal rhesus monkey at baseline (top row) and after blocking with PS13 (1 mg/kg, i.v., bottom row). Kinetic analysis was performed at the voxel level using a Logan plot so that the resulting V_T values are shown as PET images. The middle row shows template MRI scans (Shrestha et al. 2018)

10.3 PET Imaging Agents for COX-2

Despite the remarkable success in the development of potent and selective COX-2 inhibitors, no COX-2 targeted radioligands are currently available for clinical use. Research progress for the development of radiotracers for molecular imaging of

Fig. 10.17 [^{11}C]PS13 binds selectively to COX-1. Parametric images of V_T in the brain of a normal rhesus monkey at baseline (top row) and after administration of either KTP-Me (3 mg/kg, i.v.; as prodrug of COX-1-specific KTP; middle row) or MC1 (0.3 mg/kg, i.v.; COX-2-specific; bottom row). Only KTP-Me reduced whole-brain uptake of [^{11}C]PS13 (Shrestha et al. 2018)
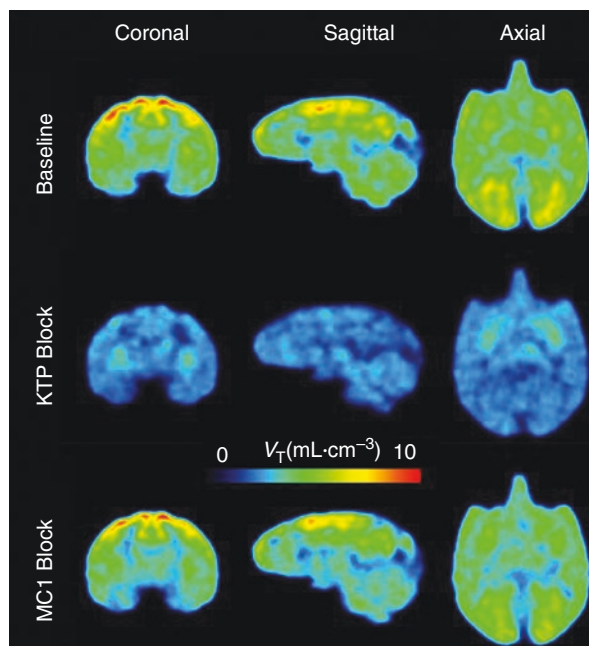
COX-2 has been summarized in several comprehensive review articles (Tietz et al. 2013; Pacelli et al. 2014; de Vries 2006). Selected examples of COX-2-targeted radiotracers are presented in Fig. 10.1. Among available COX-2 radiotracers, two compounds ([^{11}C]MC1 and [^{11}C]VA426) have recently been reported for PET imaging of COX-2 in the brain.

10.3.1 (6-[^{11}C]Methoxy-2-(4-(methylsulfonyl)phenyl)-N-(thiophen-2-ylmethyl)-pyrimidin-4-amine ([^{11}C]MC1)

In parallel to studies with COX-1-specific radiotracer [^{11}C]PS13, compound 6-methoxy-2-(4-(methylsulfonyl)phenyl)-N-(thiophen-2-ylmethyl)pyrimidin-4-amine) (MC1) was tested and also evaluated as a COX-2 selective inhibitor (Singh et al. 2018). The radiosynthesis [^{11}C]MC1 and related ^{18}F-labeled imaging agents **32** and **33** are displayed in Fig. 10.18.

Compound MC1 displayed high affinity and selectivity for monkey (IC_{50} = 2.58 nM) and human (IC_{50} = 2.89 nM) COX-2 and a favorable logD (3.74) (Cortes-Salva et al. 2018).

Radiotracer [^{11}C]MC1 was used for whole-body biodistribution and specific binding studies (Kim et al. 2018). The highest uptake of [^{11}C]MC1 in rhesus monkeys was noticed in excretory organs liver, gallbladder, and urinary bladder
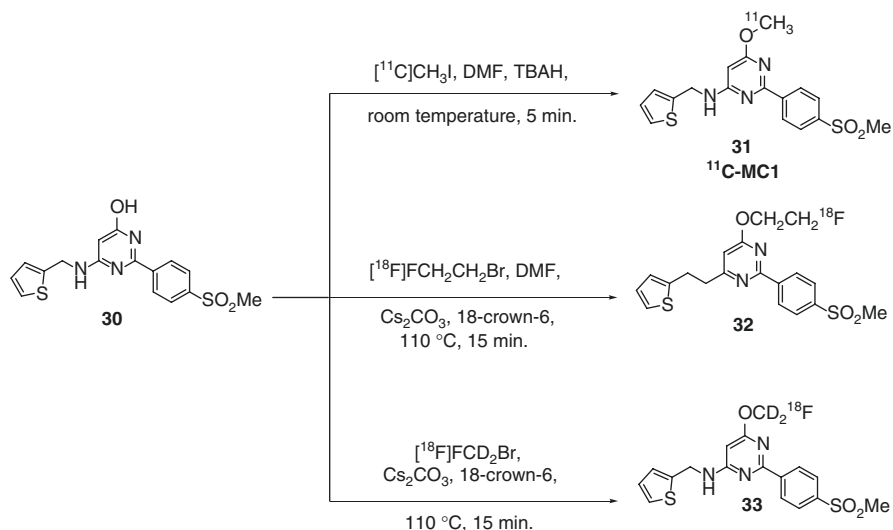
Fig. 10.18 Radiosynthesis of [^{11}C]MC1 and radiotracers **32** and **33** (Cortes-Salva et al. 2018)

Fig. 10.19 Maximum-intensity projections after injection of [^{11}C]MC1 under baseline conditions (**a**) and after injection of MC1 (0.3 mg/kg) (**b**). High uptake was observed only in excretory organs at baseline and was not blocked by pharmacologic doses of MC1 (Kim et al. 2018)
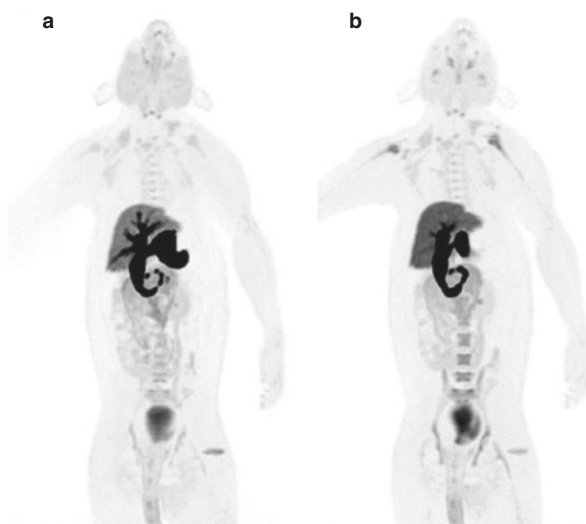
(Fig. 10.19). No blocking effect was noticed with MC1 in excretory organs, although a significant blocking by MC1 and celecoxib was observed in the ovaries (Table 10.1 and Fig. 10.20).

In a follow-up study, the brain uptake of [^{11}C]MC1 in LPS-neuroinflammation monkey model was investigated, and percentage of specific uptake was 41% and 35% on postinjection days 3 and 8, respectively (Cortes et al. 2017).

Table 10.1 Uptake of [^{11}C]MC1 in monkeys and percentage blockade with pharmacologic doses of COX-1 and COX-2 inhibitors (Kim et al. 2018)

| Organ | SUV1$_{0-90}$ (n = 8) | Blocking effect (%)[a] | | | |
| | | COX-1 | | COX-2 | |
		PS13 (n = 1)	Aspirin (n = 1)	MC1 (n = 1)	Celecoxib (n = 1)
Brain	1.22 ± 0.25	17	0	21	0
Lungs	0.22 ± 0.05	7	0	0	0
Heart	0.70 ± 0.11	7	0	0	0
Liver	9.10 ± 2.42	21	0	0	14
Spleen	0.63 ± 0.10	12	0	0	5
Gastrointestinal tract	1.10 ± 0.26	19	0	14	0
Kidney cortex	1.73 ± 0.36	16	5	16	22
Kidney medulla	1.91 ± 0.27	22	12	35	30
Ovaries	0.82 ± 0.23	12	12	38	46

[a]Corrected by plasma parent radioactivity at four time points

10.3.1.1 [1-(4-Fluorophenyl)-3-(2-[^{11}C]methoxyethyl)-2-methyl-5-(4-(methylsulfonil)phenyl)-1*H*-pyrrole] (^{11}C-VA426)

The favorable COX-2 inhibitory activity and selectivity profile of 1-(4-fluorophenyl)-3-(2-methoxyethyl)-2-methyl-5-(4-(methylsulfonyl)phenyl)-1H-pyrrole (VA426) (Anzini et al. 2008) prompted Carpinelli et al. to optimize and validate an automated radiosynthesis of [^{11}C]VA426 (Fig. 10.21) (Carpinelli et al. 2019).

The radiotracer was synthesized in 15 ± 2% radiochemical yield (based on [11C]MeOTf) and high radiochemical purity >95%. The molar activity ranged between 37 and 148 GBq/μmol. Radiotracer [^{11}C]VA426 was studied in models of LPS-induced brain neuroinflammation (Carpinelli et al. 2019). Ex vivo biodistribution experiments with radiotracer [^{11}C]VA426 confirmed fast radioactivity uptake in the peripheral organs (kidney, lung, and heart). Highest uptake values were observed in the liver and kidneys at 10 min postinjection, and the kidney radioactivity was washed out thereafter whereas liver radioactivity slightly increased over time (Fig. 10.22).

Radioactivity peaked at 10 min in the analyzed brain regions followed by slow washout. Ex vivo study in the LPS-induced neuroinflammation model revealed no significant difference between radioactivity levels in the LPS-treated and healthy striatal regions (Carpinelli et al. 2019).

PET imaging studies with radiotracer [^{11}C]VA426 in healthy mice showed rapid radioactivity accumulation mainly in the liver and kidneys which slightly decreased at 30 min (Fig. 10.23).

Pre-dosing with pharmacological doses of celecoxib resulted in some reduction of radioactivity uptake in the intestine regions (Carpinelli et al. 2019). Moreover, PET imaging of [^{11}C]VA426 under blocking conditions with celecoxib in a model of peripheral inflammation revealed a reduced radioactivity uptake in all organs,
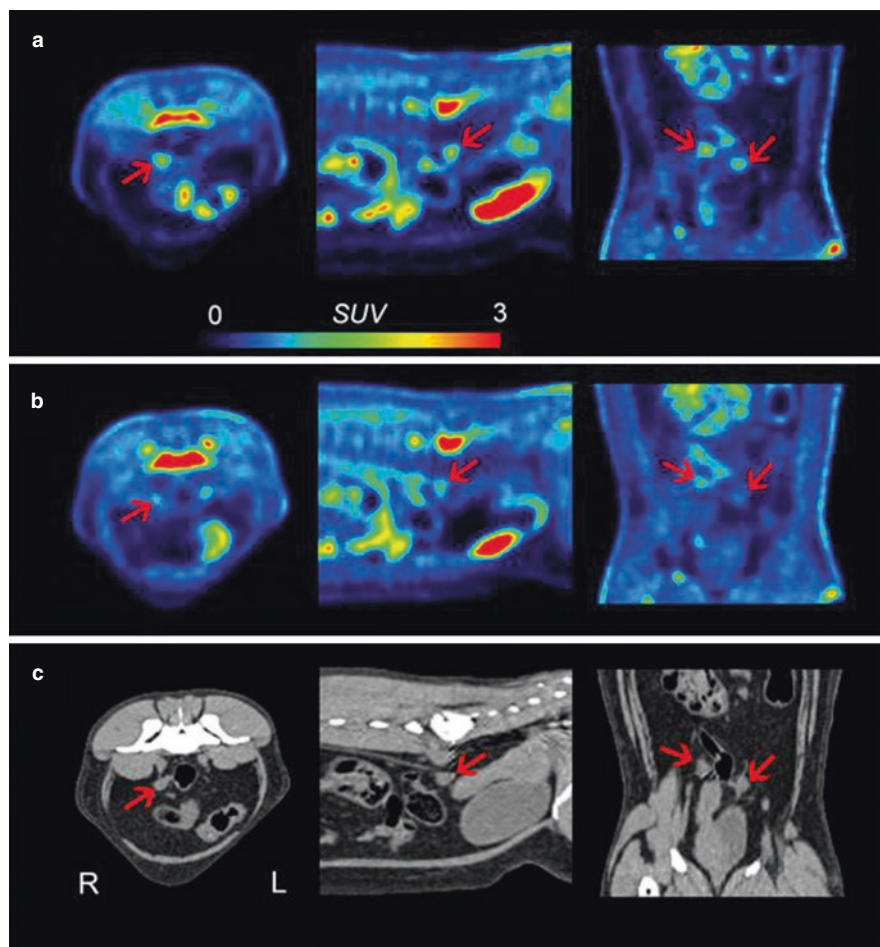
Fig. 10.20 Whole-body PET images after the injection of [^{11}C]MC1 under baseline conditions (**a**) and after injection of MC1 (0.3 mg/kg) (**b**), as well as corresponding CT images (**c**). High uptake was observed in both ovaries (arrows) and was blocked by a pharmacologic dose of MC1, consistent with specific binding to COX-2. PET images are shown as SUV[91]


Fig. 10.21 Radiosynthesis of [^{11}C]VA426
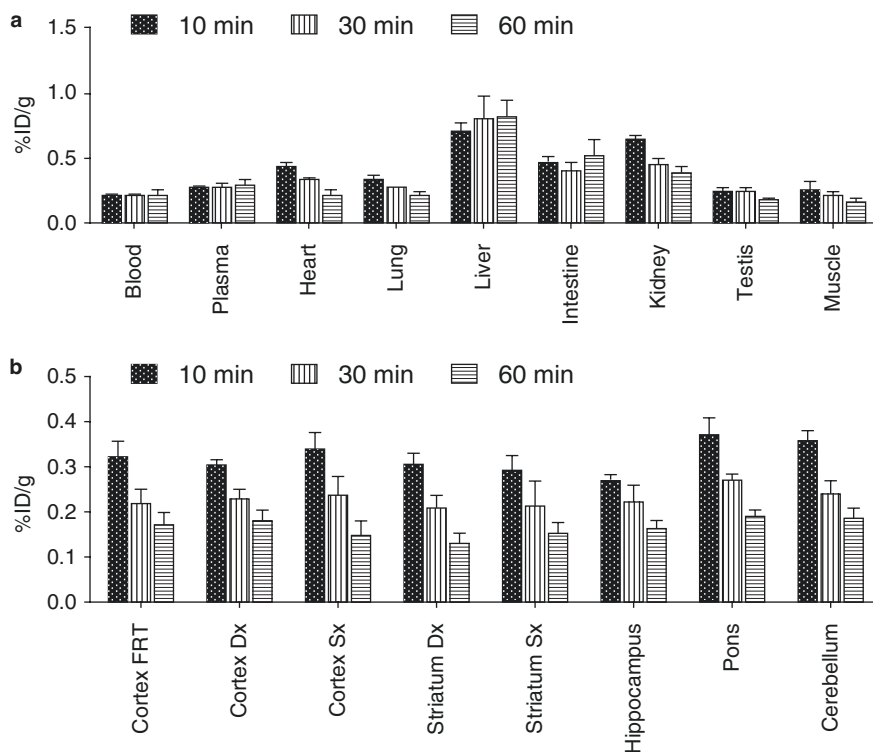
Fig. 10.22 Ex vivo biodistribution of [^{11}C]VA426 (**a**) in the periphery and (**b**) in the brain of healthy rats ($n = 9$, three per time point). Uptake value areas are expressed as %ID/g[94]

including blood and plasma indicating that the blocking effect was not linked to the inhibition of COX-2-binding sites (Fig. 10.24).

In vivo stability analyses showed that [^{11}C]VA426 was not metabolically stable, and more than 50% of the detected radioactivity was related to radiometabolites of [^{11}C]VA426. Taken together, despite the favorable COX-2 inhibitory and selectivity profile of VA426, radiotracer [^{11}C]VA426 was not suitable for further development as a clinical COX-2 PET imaging agent.

10.3.1.2 4-(5-([^{11}C]Methoxymethyl)-3-phenylisoxazol-4-yl) benzenesulfonamide ([^{11}C]MOV)

Prabhakaran et al. used hydroxymethyl valdecoxib **35**, an in vivo metabolite of valdecoxib, for the development and evaluation of novel COX-2 imaging agent [^{11}C]MOV (Prabhakaran et al. 2018). The first step of synthesis involved the protection of the sulfonamide group of hydroxymethyl valdecoxib **35** to form dimethoxytrityl (DMT) intermediate **36**. Compound **36** was reacted with [^{11}C]CH$_3$I in DMF with KO^{t}Bu as a base. Upon the removal of DMT-protecting group, radiotracer [^{11}C]MOV was obtained in 40 ± 10% radiochemical yield (based on [^{11}C]CH$_3$I) (Fig. 10.25) (Prabhakaran et al. 2018).
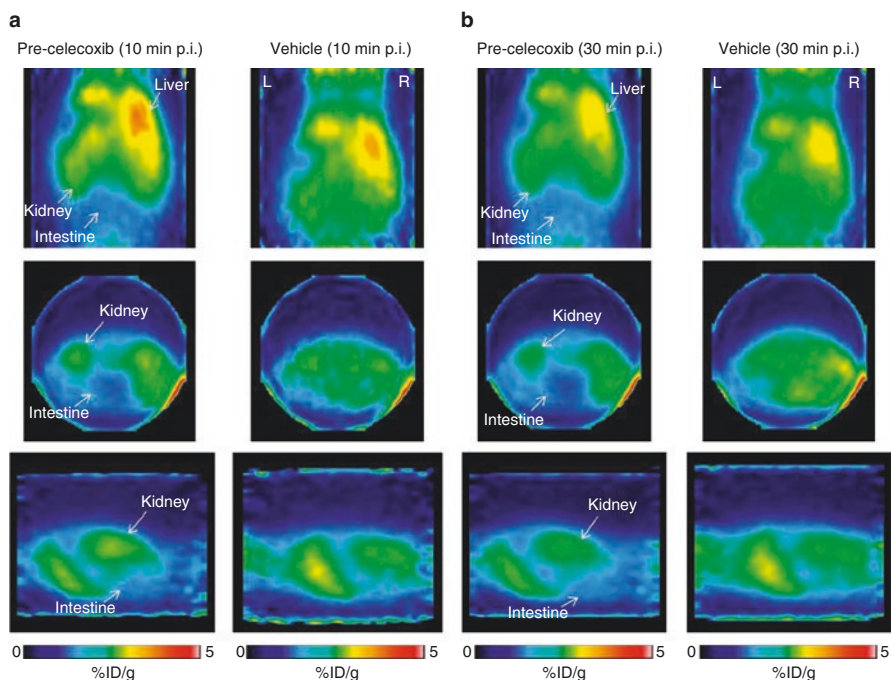
Fig. 10.23 PET images of [^{11}C]VA426 distribution in mouse (**a**) at 10 and (**b**) 30 min after injection. Each acquisition was shown in coronal, transaxial, and sagittal sections, respectively. Mice were anesthetized with a mixture of 2% isoflurane in air, injected intravenously with 1.85 MBq (mouse 1) and 3.7 MBq (mouse 2) of [^{11}C]VA426 and, respectively, pretreated (5 min before) with celecoxib or vehicle (DMSO). Dynamic PET data were acquired for 30 min (four scans of 2.5 min followed by four of 5 min). White arrow indicates the main anatomical regions of [^{11}C]VA426 distribution. In coronal views, R (right) and L (left) indicate the spatial orientation of mouse (Carpinelli et al. 2019)
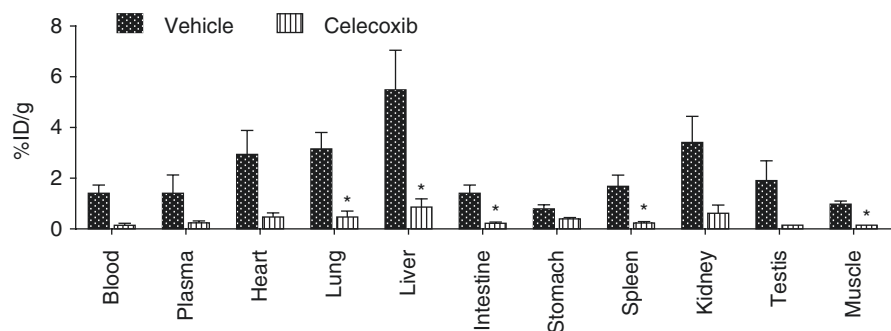
Fig. 10.24 Inhibition study in the peripheral inflammation model; inflammation was induced by intraperitoneal injection of LPS 6 h before the study. Mice were treated with celecoxib ($n = 3$) or vehicle ($n = 3$) prior to ^{11}C-VA426 injection and sacrificed after 10 min. Uptake values in peripheral areas are expressed as a percentage of injected dose per gram of tissue (%ID/g) (*$p < 0.05$ vs. vehicle) (Carpinelli et al. 2019)
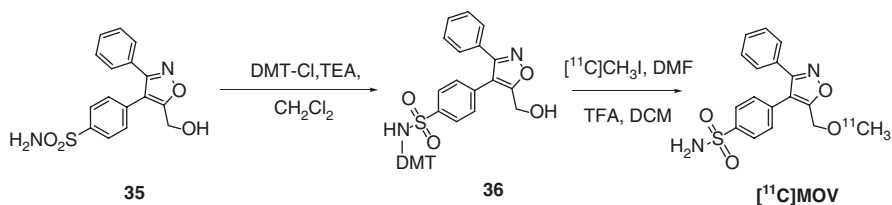
Fig. 10.25 Radiosynthesis of [^{11}C]MOV
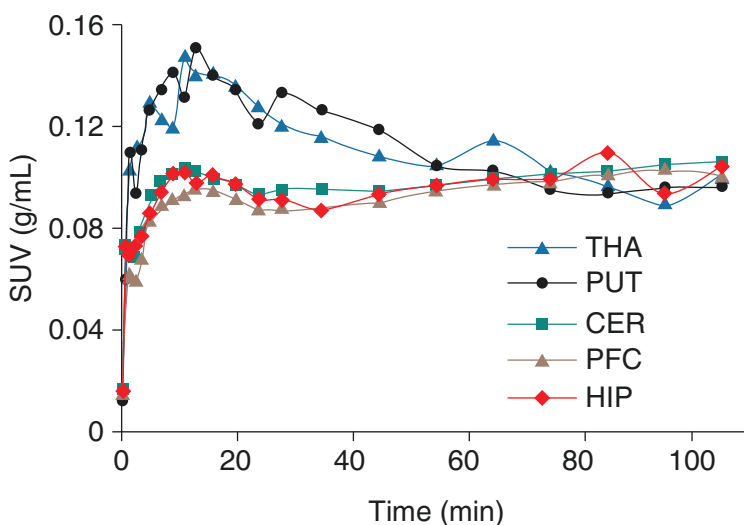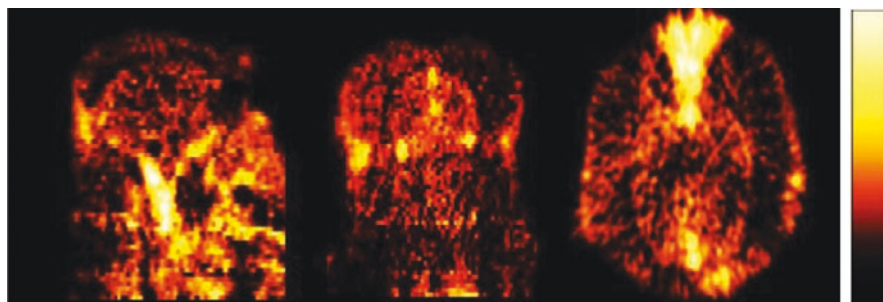
Fig. 10.26 Top: Sum of 0–120 min PET images of [^{11}C]MOV in a representative anesthetized baboon (left: sagittal, middle: coronal, right: transaxial). Bottom: Time-activity curves of [^{11}C]MOV in baboon brain (*CER* cerebellum, *HIP* hippocampus, *PFC* prefrontal cortex, *PUT* putamen, *THA* thalamus) (Prabhakaran et al. 2018)

PET imaging with [^{11}C]MOV in anesthetized baboons confirmed blood-brain barrier penetration of the radiotracer. However, the retention of radioactivity in the brain was very low (Fig. 10.26) (Prabhakaran et al. 2018).

Radioactivity accumulation was observed in the heart and duodenum. Metabolite analysis of [^{11}C]MOV confirmed a rapid metabolism of the radiotracer. Both the very low retention of radioactivity in the brain and the rapid metabolic degradation make radiotracer [^{11}C]MOV not suitable for COX-2 imaging in neuroinflammation.

10.4   Summary and Conclusion

Despite their structural similarities, both cyclooxygenase isozymes (COX-1 and COX-2) display quite different distribution and regulation patterns in various tissues and organs. In the central nervous system (CNS), the COX-1 isoform is particularly upregulated in the midbrain, pons, and medulla. Moreover, COX-1 upregulation and activation in the CNS are part of the defense mechanism in response to acute and chronic neuroinflammatory conditions. Overall, recent data demonstrated that COX-1 plays a crucial role in the process of neuroinflammation and neurodegeneration. The role of inducible COX-2 isoform in neuroinflammation is more controversial. COX-2 may mediate a neurotoxic or anti-inflammatory role depending on the stimulus and cell type. As COX-1 and COX-2 have become important drug targets in neuroinflammatory and neurodegenerative diseases, imaging techniques like positron-emission tomography (PET) have emerged as valuable tools to detect and visualize the functional expression of COXs in vivo.

The development of PET imaging agents is most advanced for COX-1-targeted radiotracers with a clear dominance for compounds labeled with the short-lived positron emitter carbon-11 (^{11}C, $t_{1/2}$ = 20.4 min). The COX-1 radiotracer (S)-[^{11}C]KTP-Me has progressed to first-in-human studies in healthy volunteers and patients with mild cognitive impairment and Alzheimer's disease. However, the radiotracer (S)-[^{11}C]KTP-Me was not successful as a COX-1-imaging agent in neuroinflammation, and radiotracer [^{11}C]PS3 was developed as a more potent and COX-1 selective PET imaging agent. The obtained excellent PET images with radiotracer [^{11}C]PS3 in monkeys encouraged first human biodistribution and dosimetry studies in healthy volunteers, but detailed clinical studies in patients with neurodegenerative diseases are still pending.

To date, no COX-2 radiotracers were tested in humans for PET imaging of neuroinflammatory conditions. Despite favorable COX-2 inhibitory potencies and selectivities, most radiotracers lack sufficient COX-2 binding capacity in the brain in vivo.

As a result, all tested COX-2 radiotracers displayed rapid washout from the brain without retention of radioactivity related to COX-2-binding sites as demonstrated in rat brains with neuroinflammation after intracerebral LPS injection.

Overall, the most promising radiotracers [^{11}C]PS3 and [^{11}C]MC1 represent interesting lead compounds for further optimization towards the development of suitable PET imaging agents for detecting and visualizing COX-1 and COX-2 in neuroinflammation. Optimization should involve the use of the positron emitter fluorine-18 (^{18}F, $t_{1/2}$ = 109.8 min) which would allow the preparation of COX1/2 PET imaging

agents at higher molar activities. High molar activity is an essential requirement to achieve favorable PET imaging contrast in vivo for saturable binding sites and intracellular targets with low abundance like COX-1 and COX-2.

References

Aïd S, Bosetti F (2011) Targeting cyclooxygenases-1 and -2 in neuroinflammation: therapeutic implications. Biochimie 93:46–51

Aid S, Silva AC, Candelario-Jalil E, Choi SH, Rosenberg GA, Bosetti F (2010) Cyclooxygenase-1 and -2 differentially modulate lipopolysaccharide-induced blood-brain barrier disruption through matrix metalloproteinase activity. J Cereb Blood Flow Metab 30:370–380

Amor S, Peferoen LA, Vogel DY, Breur M, van der Valk P, Baker D, van Noort JM (2014) Inflammation in neurodegenerative diseases--an update. Immunology 142(2):151–166

Anaya FJ et al (2019) Human biodistribution and dosimetry of C-PS13, a novel radioligand for cyclooxygenase-1. J Nucl Med 60:1629

Anzini M et al (2008) Synthesis, biological evaluation, and enzyme docking simulations of 1,5-diarylpyrrole- 3-alkoxyethyl ethers as selective cyclooxygenase-2 inhibitors endowed with anti-inflammatory and antinociceptive activity. J Med Chem 51:4476–4481

Bartels AL, Leenders KL (2010) Cyclooxygenase and neuroinflammation in Parkinson's disease neurodegeneration. Curr Neuropharmacol 8(1):62–68

Bhardwaj A, Kaur J, Sharma SK, Huang Z, Wuest F, Knaus EE (2013) Hybrid fluorescent conjugates of COX-2 inhibitors: search for a COX-2 isozyme imaging cancer biomarker. Bioorg Med Chem Lett 23(1):163–168

Bhardwaj A, Kaur J, Wuest M, Wuest F (2017) In situ click chemistry generation of cyclooxygenase-2 inhibitors. Nat Commun 8(1):1–13

Blais V, Turrin NP, Rivest S (2005) Cyclooxygenase 2 (COX-2) inhibition increases the inflammatory response in the brain during systemic immune stimuli. J Neurochem 95:1563–1574

Blobaum AL, Marnett LJ (2007) Structural and functional basis of cyclooxygenase inhibition. J Med Chem 50:1425–1441

Bosetti F (2007) Arachidonic acid metabolism in brain physiology and pathology: lessons from genetically altered mouse models. J Neurochem 102:577–586

Calsolaro V, Edison P (2016) Neuroinflammation in Alzheimer's disease: current evidence and future directions. Alzheimers Dement 12(6):719–732

Carpinelli A et al (2019) Radiosynthesis and preclinical evaluation of 11C-VA426, a cyclooxygenase-2 selective ligand. Contrast Media Mol Imaging 2019:5823261

Chandrasekharan NV, Dai H, Roos KL, Evanson NK, Tomsik J, Elton TS, Simmons DL (2002b) COX-3, a cyclooxygenase-1 variant inhibited by acetaminophen and other analgesic/antipyretic drugs: cloning, structure, and expression. Proc Natl Acad Sci U S A 99:13926–13931

Chandrasekharan NV et al (2002a) COX-3, a cyclooxygenase-1 variant inhibited by acetaminophen and other analgesic/antipyretic drugs: cloning, structure, and expression. Proc Natl Acad Sci U S A 99:13926–13931

Chen H, Jacobs E, Schwarzschild MA, McCullough ML, Calle EE, Thun MJ, Ascherio A (2005) Nonsteroidal anti-inflammatory drug use and the risk for Parkinson's disease. Ann Neurol 58:963–967

Choi SH, Aid S, Bosetti F (2009a) The distinct roles of cyclooxygenase- 1 and -2 in neuroinflammation: implications for translational research. Trends Pharmacol Sci 30(4):174–181

Choi SH, Aid S, Bosetti F (2009b) The distinct roles of cyclooxygenase-1 and -2 in neuroinflammation for translational research. Trends Pharmacol Sci 30:174–181

Choi SH, Bosetti F (2009) Cyclooxygenase-1 null mice show reduced neuroinflammation in response to beta-amyloid. Aging 1:234–244

Choi SH, Langenbach R, Bosetti F (2008) Genetic deletion or pharmacological inhibition of cyclo-oxygenase-1 attenuate lipopolysaccharide-induced inflammatory response and brain injury. FASEB J 22(5):1491–1501

Cortes M et al (2017) Novel PET radioligands show that, in rhesus monkeys, COX-1 is constitutively expressed and COX-2 is induced by inflammation. J Nucl Med 58:203

Cortes-Salva MY, Shrestha S, Singh P, Morse CL, Jenko KJ, Montero Santamaria JA, Zoghbi SS, Innis RB, Pike VW (2018) 2-(4-Methylsulfonylphenyl)pyrimidines as prospective radioligands for imaging cyclooxygenase-2 with PET-synthesis, triage, and radiolabeling. Molecules 23:E2850

Craft JM, Watterson DM, Van Eldik LJ (2005) Neuroinflammation: a potential therapeutic target. Expert Opin Ther Targets 9(5):887–900

Cudaback E, Jorstad NL, Yang Y, Montine TJ, Keene CD (2014) Therapeutic implications of the prostaglandin pathway in Alzheimer's disease. Biochem Pharmacol 88(4):565–572

Dargahi L, Nasiraei-Moghadam S, Abdi A, Khalaj L, Moradi F, Ahmadiani A (2011) Cyclooxygenase (COX)-1 activity precedes the COX-2 induction in Aβ-induced neuroinflammation. J Mol Neurosci 45:10–21

de Vries EF (2006) Imaging of cyclooxygenase-2 (COX-2) expression: potential use in diagnosis and drug evaluation. Curr Pharm Des 12(30):3847–3856

DiSabato DJ, Quan N, Godbout JP (2016) Neuroinflammation: the devil is in the details. J Neurochem 139(Suppl. 2):136–153

García-Bueno B, Serrats J, Sawchenko PE (2009) Cerebrovascular cyclooxygenase-1, expression, regulation, and role in hypothalamic-pituitary-adrenal axis activation by inflammatory stimuli. J Neurosci 29:12970–12981

Glass CK, Saijo K, Winner B, Marchetto MC, Gage FH (2010) Mechanisms underlying inflammation in neurodegeneration. Cell 140(6):918–934

Graeber MB (2010) Changing face of microglia. Science 330(6005):783–788

Hewett SJ, Bell SC, Hewett JA (2006) Contributions of cyclooxygenase-2 to neuroplasticity and neuropathology of the central nervous system. Pharmacol Ther 112:335–357

Hirsch EC, Hunot S (2009) Neuroinflammation in Parkinson's disease: a target for neuroprotection? Lancet Neurol 8(4):382–397

Hoozemans JJ, Rozemuller AJ, Janssen I, De Groot CJ, Veerhuis R, Eikelenboom P (2001) Cyclooxygenase expression in microglia and neurons in Alzheimer's disease and control brain. Acta Neuropathol 101:2–8

Imanishi J et al (2011) Pharmacological profile of FK881 (ASP6537), a novel potent and selective cyclooxygenase-1 inhibitor. Biochem Pharmacol 82:746–754

Imbimbo BP, Solfrizzi V, Panza F (2010) Are NSAIDs useful to treat Alzheimer's disease or mild cognitive impairment? Front Aging Neurosci 2:19

Kaur J, Tietz O, Bhardwaj A, Marshall A, Way J, Wuest M, Wuest F (2015) Design, synthesis, and evaluation of an (18)F-labeled radiotracer based on celecoxib-NBD for positron emission tomography (PET) imaging of cyclooxygenase-2 (COX-2). ChemMedChem 10:1635–1640

Kim MJ et al (2018) Evaluation of two potent and selective PET radioligands to image COX-1 and COX-2 in rhesus monkeys. J Nucl Med 59(12):1907–1912

Kurumbail RG, Stevens AM, Gierse JK, McDonald JJ, Stegeman RA, Pak JY, Gildehaus D, Miyashiro JM, Penning TD, Seibert K, Isakson PC, Stallings WC (1996b) Structural basis for selective inhibition of cyclooxygenase-2 by anti-inflammatory agents. Nature 384:644–648

Kurumbail RG et al (1996a) Structural basis for selective inhibition of cyclooxygenase-2 by anti-inflammatory agents. Nature 384:644–648

Laube M, Kniess T, Pietzsch J (2013) Radiolabeled COX-2 inhibitors for non-invasive visualization of COX-2 expression and activity—a critical update. Molecules 18(6):6311–6355

Lymana M, Lloyda DG, Ji X, Vizcaychipia MP, Maa D (2014) Neuroinflammation: the role and consequences. Neurosci Res 79:1–12

Marnett LJ (2009) The COXIB experience: a look in the rearview mirror. Annu Rev Pharmacol Toxicol 49:265–290

Marnett LJ (2012) Inflammation and cancer: chemical approaches to mechanisms, imaging, and treatment. J Org Chem 77:5224–5238

Marnett LJ, Rowlinson SW, Goodwin DC, Kalgutkar AS, Lanzo CA (1999) Arachidonic acid oxygenation by COX-1 and COX-2. J Biol Chem 274:22903–22906

Matousek SB, Hein AM, Shaftel SS, Olschowka JA, Kyrkanides S, O'Banion MK (2010) Cyclooxygenase-1 mediates prostaglandin E(2) elevation and contextual memory impairment in a model of sustained hippocampal interleukin-1 beta expression. J Neurochem 114:247–258

McGeer PL, McGeer EG (2007) NSAIDs and Alzheimer disease: epidemiological, animal model and clinical studies. Neurobiol Aging 28:639–647

Medzhitov R (2008) Origin and physiological roles of inflammation. Nature 454:428–435

Meric JB et al (2006) Cyclooxygenase-2 as target of anticancer drug development. Crit Rev Oncol Hematol 59:51–64

Mitchell JA, Warner TD (1999) Cyclo-oxygenase-2: pharmacology, physiology, biochemistry and relevance to NSAID therapy. Br J Pharmacol 128:1121–1132

Morgenroth A, Vogg AT, Neumaier B, Mottaghy FM, Zlatopolskiy BD (2017) Radioiodinated indomethacin amide for molecular imaging of cyclooxygenase-2 expressing tumors. Oncotarget 8:18059–18069

Narayanaswami V, Dahl K, Bernard-Gauthier V, Josephson L, Cumming P, Vasdev N (2018) Emerging PET radiotracers and targets for imaging of neuroinflammation in neurodegenerative diseases: outlook beyond TSPO. Mol Imaging 17:1536012118792317

Ohnishi A et al (2014) Human whole-body biodistribution and dosimetry of a new PET tracer, [11C]ketoprofen methyl ester, for imagings of neuroinflammation. Nucl Med Biol 41:594–599

Ohnishi A et al (2016) Exploratory human PET study of the effectiveness of 11C-ketoprofen methyl ester, a potential biomarker of neuroinflammatory processes in Alzheimer's disease. Nucl Med Biol 43:438–444

Pacelli A, Greenman J, Cawthorne C, Smith G (2014) Imaging COX-2 expression in cancer using PET/SPECT radioligands: current status and future directions. J Labelled Comp Radiopharm 57(4):317–322

Phani S, Loike JD, Przedborski S (2012) Neurodegeneration and inflammation in Parkinson's disease. Parkinsonism Relat Disord Suppl 1:S207–S209

Phillis JW, Horrocks LA, Farooqui AA (2006) Cyclooxygenases, lipoxygenases, and epoxygenases in CNS: their role and involvement in neurological disorders. Brain Res Rev 52(2):201–243

Prabhakaran J et al (2018) Radiosynthesis and in vivo evaluation of [11C]MOV as a PET imaging agent for COX-2. Bioorg Med Chem Lett 28(14):2432–2435

Ransohoff RM (2016) How neuroinflammation contributes to neurodegeneration. Science 353(6301):777–783

Ricciotti E, FitzGerald GA (2011) Prostaglandins and inflammation. Arterioscler Thromb Vasc Biol 31:986–1000

Rogers J, Kirby LC, Hempelman SR, Berry DL, McGeer PL, Kaszniak AW et al (1993) Clinical trial of indomethacin in Alzheimer's disease. Neurology 43(8):1609–1611

Schain M, Kreisl WC (2017a) Neuroinflammation in neurodegenerative disorder—a review. Curr Neurol Neurosci Rep 17(3):25

Schain M, Kreisl WC (2017b) Neuroinflammation in neurodegenerative disorders—a review. Curr Neurol Neurosci Rep 201717(3):25

Schmid CD, Melchior B, Masek K et al (2009) Differential gene expression in LPS/IFNgamma activated microglia and macrophages: in vitro versus in vivo. J Neurochem 109(suppl 1):117–125

Shrestha S et al (2018) 3-Substituted 1,5-diaryl-1H-1,2,4-triazoles as prospective PET radioligands for imaging brain COX-1 in monkey. Part 2: Selection and evaluation of [11C]PS13 for quantitative imaging. ACS Chem Neurosci 9:2620–2627

Shukuri M, Mawatari A, Ohno M, Suzuki M, Doi H, Watanabe Y, Onoe H (2016) Detection of cyclooxygenase-1 in activated microglia during amyloid plaque progression: PET studies in Alzheimer's disease model mice. J Nucl Med 57(2):291–296

Shukuri M, Takashima-Hirano M, Tokuda K, Takashima T, Matsumura K, Inoue O, Doi H, Suzuki M, Watanabe Y, Onoe H (2011) In vivo expression of cyclooxygenase-1 in activated microglia

and macrophages during neuroinflammation visualized by PET with 11C-ketoprofen methyl ester. J Nucl Med 52(7):1094–1101

Simmons DL, Botting RM, Hla T (2004) Cyclooxygenase isozymes: the biology of prostaglandin synthesis and inhibition. Pharmacol Rev 56:387–437

Singh P, Shrestha S, Cortes-Salva MY, Jenko KJ, Zoghbi SS, Morse CL, Innis RB, Pike VW (2018) 3-Substituted 1,5-diaryl-1H-1,2,4-triazoles as prospective PET radioligands for imaging brain COX-1 in monkey. Part 1: Synthesis and pharmacology. ACS Chem Neurosci 9:2610–2619

Slanina KA, Schweitzer P (2005) Inhibition of cyclooxygenase-2 elicits a CB1-mediated decrease of excitatory transmission in rat CA1 hippocampus. Neuropharmacology 49:653–659

Smith W, Garavito RM, DeWitt DL (1996a) Prostaglandin endoperoxide H synthases (cyclooxygenases)-1 and -2. J Biol Chem 271:33157–33160

Smith WL, DeWitt DL, Garavito RM (2000) Cyclooxygenases: structural, cellular, and molecular biology. Annu Rev Biochem 69:145–182

Smith WL, Urade Y, Jakobsson PJ (2011) Enzymes of the cyclooxygenase pathways of prostanoid biosynthesis. Chem Rev 111:5821–5865

Stefanovic B, Bosetti F, Silva AC (2006) Modulatory role of cyclooxygenase-2 in cerebrovascular coupling. NeuroImage 32:23–32

Stephenson J, Nutma E, van der Valk P, Amor S (2018) Inflammation in CNS neurodegenerative diseases. Immunology 154(2):204–219

Takashima-Hirano M, Shukuri M, Takashima T, Goto M, Wada Y, Watanabe Y, Onoe H, Doi H, Suzuki M (2010) General method for the (11)C-labeling of 2-arylpropionic acids and their esters: construction of a PET tracer library for a study of biological events involved in COXs expression. Chemistry 16(14):4250–4258

Tansey MG, McCoy MK, Frank-Cannon TC (2007) Neuroinflammatory mechanisms in Parkinson's disease: potential environmental triggers, pathways, and targets for early therapeutic intervention. Exp Neurol 208(1):1–25

Teismann P et al (2003) Cyclooxygenase-2 is instrumental in Parkinson's disease neurodegeneration. Proc Natl Acad Sci U S A 100:5473–5478

Tietz O, Marshall A, Wuest M, Wang M, Wuest F (2013) Radiotracers for molecular imaging of cyclooxygenase-2 (COX-2) enzyme. Curr Med Chem 20(35):4350–4369

Tietz O et al (2016) PET imaging of cyclooxygenase-2 (COX-2) in a colon cancer model. EJNMMI Res 6:37

Toscano CD, Prabhu VV, Langenbach R, Becker KG, Bosetti F (2007) Differential gene expression patterns in cyclooxygenase-1 and cyclooxygenase-2 deficient mouse brain. Genome Biol 8:R14

Uddin MJ et al (2010) Selective visualization of cyclooxygenase-2 in inflammation and cancer by targeted fluorescent imaging agents. Cancer Res 70(9):3618–3627

van der Donk WA, Tsai AL, Kulmacz RJ (2002) The cyclooxygenase reaction mechanism. Biochemistry 41:15451–15458

Vlad SC, Miller DR, Kowall NW, Felson DT (2008) Protective effects of NSAIDs on the development of Alzheimer disease. Neurology 70(19):1672–1677

Wang D, DuBois RN (2010) Eicosanoids and cancer. Nat Rev Cancer 10:181–193

Wang D, DuBois RN (2013) The role of anti-inflammatory drugs in colorectal. Cancer Rev Med 64:131–144

Wang H, Hitron IM, Iadecola C, Pickel VM (2005) Synaptic and vascular associations of neurons containing cyclooxygenase-2 and nitric oxide synthase in rat somatosensory cortex. Cereb Cortex 15:1250–1260

Winkeler A, Boisgard R, Martín A, Tavitian B (2010) Radioisotopic imaging of neuroinflammation. J Nucl Med 51:1–4

Wyss-Coray T, Mucke L (2012) Inflammation in neurodegenerative disease—a double-edged sword. Neuron 35(3):419–432

Wyss-Coray T, Rogers J (2012) Inflammation in Alzheimer disease-a brief review of the basic science and clinical literature. Cold Spring Harb Perspect Med 2(1):a006346

Yamagata K, Andreasson KI, Kaufmann WE, Barnes CA, Worley PF (1993) Expression of a mitogen-inducible cyclooxygenase in brain neurons: regulation by synaptic activity and gluco-corticoids. Neuron 11(2):371–386

Yang H, Chen C (2008) Cyclooxygenase-2 in synaptic signaling. Curr Pharm Des 14(14):1443–1451

Yermakova AV, Rollins J, Callahan LM, Rogers J, O'Banion MK (1999) Cyclooxygenase-1 in human Alzheimer and control brain: quantitative analysis of expression by microglia and CA3 hippocampal neurons. J Neuropathol Exp Neurol 58:1135–1146

PET and SPECT Imaging of the Central Dopamine System in Humans

Jan Booij, Jan-Peter van Wieringen,
Elsmarieke van de Giessen, Remco J. J. Knol,
and Sjoerd J. Finnema

Contents

J. Booij (✉) · J.-P. van Wieringen · E. van de Giessen
Department of Radiology and Nuclear Medicine, Amsterdam University Medical Centers,
University of Amsterdam, Amsterdam, AZ, The Netherlands
e-mail: j.booij@amsterdamumc.nl; e.m.vandegiessen@amsterdamumc.nl

R. J. J. Knol
Department of Nuclear Medicine, Noordwest Ziekenhuisgroep, Alkmaar, The Netherlands
e-mail: r.j.j.knol@nwz.nl

S. J. Finnema
Department of Radiology and Biomedical Imaging, Yale Positron Emission Tomography
Center, Yale University, New Haven, CT, USA

Integrated Science and Technology, Translational Imaging, AbbVie, North Chicago, IL, USA
e-mail: sjoerd.finnema@yale.edu

Abstract

The neurotransmitter dopamine plays a role in many different functions of the human brain, ranging from psychomotor planning to cognition. This short review addresses which parts of the dopamine system can be imaged quantitatively in the living human brain using positron-emission tomography (PET) or single-photon emission computed tomography (SPECT).

Nowadays, imaging of the nigrostriatal dopaminergic pathway in humans can be performed quantitatively using radiotracers like the aromatic amino acid decarboxylase (AADC) substrate [^{18}F]FDOPA, vesicular monoamine transporter 2 (VMAT-2) radioligands derived from tetrabenazine or PET/SPECT radioligands that bind to the dopamine transporter (DAT). Using PET, also several other dopaminergic projection pathways (e.g. mesocortical projections) can be assessed in humans. Several antagonist PET radioligands for the dopamine D_1 receptor have been developed successfully. In addition, well-validated antagonist PET and SPECT radioligands are available for imaging of dopamine D_2 and dopamine D_3 ($D_{2/3}$) receptors in the living human brain. Also agonist PET radioligands for the dopamine $D_{2/3}$ receptors have become available, which afford the opportunity to evaluate the existence of the high-affinity state of these receptors in vivo. These agonist radiopharmaceuticals may also prove more sensitive to changes in dopamine concentrations (e.g. induced by the dopamine releaser amphetamine). Finally, selective antagonist PET radioligands for the dopamine D_4 receptor have recently been synthesized and evaluated successfully in small laboratory animals, although these radioligands have not yet been reported as applied in human subjects.

In conclusion, after almost four decades of research, several relevant parts of the central dopamine system can be assessed quantitatively in the living human brain using PET or SPECT. Future studies may include application of agonist radioligands and more dopamine receptor subtype selective radioligands.

11.1   Introduction

Numerous cognitive, psychomotor and emotional functions are regulated, at least in part, by dopaminergic circuits in the brain. The neurotransmitter dopamine plays, for example, an important role in movement and the experience of pleasure (hedonia). Dopaminergic neurons in the midbrain area are relevant in coding the value of neuronal signals, and indeed, these neurons are activated by rewarding stimuli (such as amphetamines, which induce dopamine release), but may also play a role in reward learning, prediction of error signalling and interpretation of the salience of events (Fiorillo et al. 2003; Nakahara et al. 2004; Morris et al. 2006; Zijlstra et al. 2008; Enomoto et al. 2011; Schultz, 2016; Takahashi et al. 2017; Wang et al. 2019). In addition, neurodegeneration of the dopaminergic neurons in the midbrain can lead to severe locomotor dysfunction such as in Parkinson's disease. Given the broad spectrum of functions of dopamine in the brain, it is reasonable that imaging

of the central dopamine system has been used frequently as a tool to assess different aspects of dopaminergic functioning in health and disease, particularly in a variety of neuropsychiatric disorders.

Here we review shortly which parts of the central dopamine system can be imaged quantitatively in the living human brain using positron-emission tomography (PET) or single-photon emission computed tomography (SPECT). The findings of SPECT and PET studies of the dopamine system in different neuropsychiatric disorders will be discussed only shortly, since they will be discussed in depth in other chapters of this book.
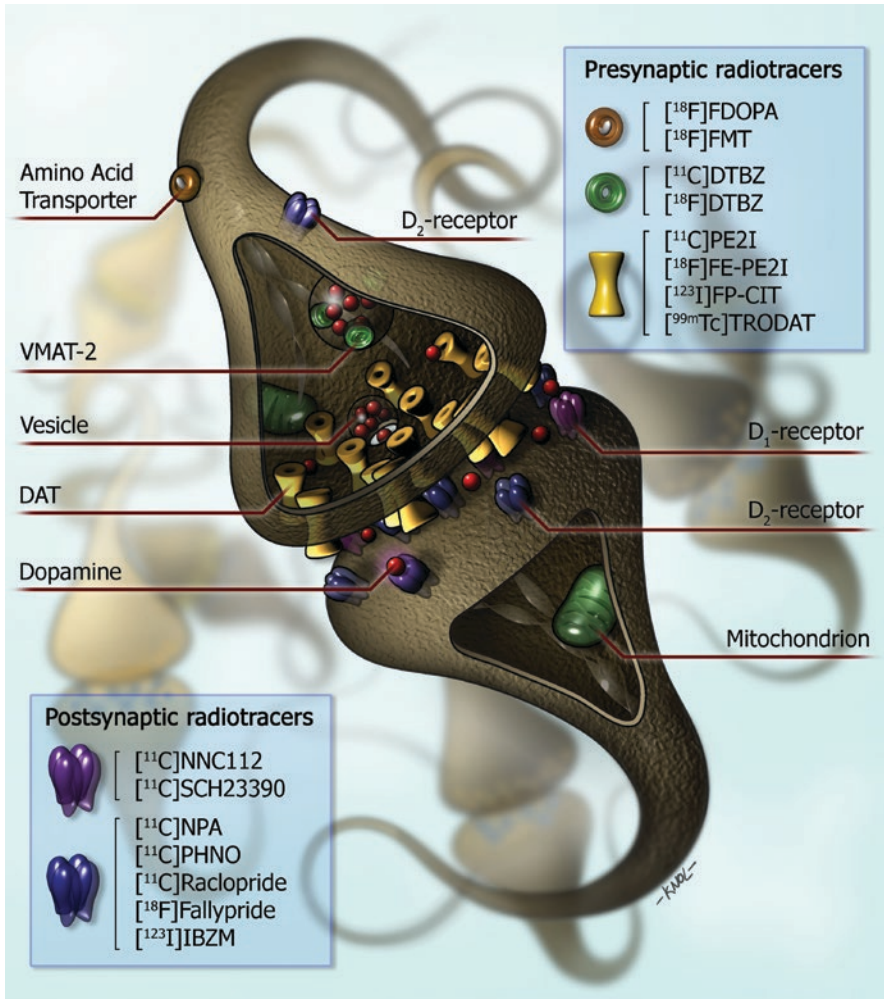
11.2 Imaging of the Presynaptic Dopamine System

11.2.1 [^{18}F]FDOPA and [^{18}F]FMT

The majority of the cell bodies of dopaminergic neurons are located in the midbrain area, with axons predominantly projecting to the striatum (the nigrostriatal dopaminergic pathway). The scintigraphic techniques PET and SPECT offer unique means to assess the in vivo integrity of the nigrostriatal pathway. The biochemical integrity of presynaptic dopamine neurons can be assessed with the PET radioligands 6-^{18}F-fluoro-*L*-DOPA ([^{18}F]FDOPA) or 6-^{18}F-fluoro-meta-tyrosine ([^{18}F]FMT) (for reviews, see Booij et al. 1999; Kumakura and Cumming 2009; Sarikaya 2015).

[^{18}F]FDOPA is a widely applied PET tracer commonly radiolabelled with fluorine-18, although in some clinical studies DOPA has been applied as radiolabelled with carbon-11. After injection, the radiotracer will be taken up into dopaminergic neurons by the amino acid transporter (Fig. 11.1), decarboxylated (by aromatic amino acid decarboxylase; AADC) to [^{18}F]fluorodopamine (or [^{11}C]dopamine when [^{11}C]DOPA is administered) and then temporarily stored in vesicles within the nerve terminals. Therefore, [^{18}F]FDOPA accumulation in dopamine neurons reflects a regulated aspect of the synthesis of dopamine in presynaptic neurons. The trapping of [^{18}F]fluorodopamine in nigrostriatal dopamine terminals has, however, been demonstrated not to be completely irreversible (Holden et al. 1997; Cumming et al. 2001). Indeed, steady-state kinetic analyses of [^{18}F]FDOPA PET studies have shown that besides the synthesis, also the turnover of [^{18}F]FDOPA to *O*-methyl-[^{18}F]FDOPA can be assessed (Kumakura et al. 2005). Importantly, in most clinical studies, static striatal [^{18}F]FDOPA uptake was assessed relative to uptake in a reference tissue (reflecting the nonspecific radioactivity concentration) and using linear graphical analysis. This approach is convenient for clinical studies in which radioactivity in arterial blood is commonly not measured (Kumakura and Cumming 2009; Jauhar et al. 2018; Majuri et al. 2018). However, the kinetic properties of [^{18}F]FDOPA are complex and include not only the washout of radiotracer but also the entry of a radiolabelled metabolite of [^{18}F]FDOPA into the brain. Consequently, relatively long acquisitions of dynamic PET images, as well as the analysis of the metabolite-corrected arterial [^{18}F]FDOPA input function, are required to yield a more physiological index of [^{18}F]FDOPA utilization, including [^{18}F]FDOPA turnover (for a review, see Kumakura and Cumming 2009).

Fig. 11.1 Simplified diagram of a striatal dopaminergic synapse. On the presynaptic side, potential markers for imaging of the integrity of dopaminergic neurons in humans are shown. [18F]FDOPA and [18F]FMT PET provide measures of the structural and biochemical integrity of the dopaminergic neurons. [11C]DTBZ and [18F]DTBZ are commonly used radiopharmaceuticals for the vesicular monoaminergic transporter. Substituted (nor)phenyltropanes ([11C]PE2I, [18F]FE-PE2I, [123I]FP-CIT and [99mTc]TRODAT) are frequently used PET and SPECT radioligands for imaging of the DAT in humans. On the postsynaptic side, [11C]NNC112 and [11C]SCH23390 are commonly used antagonist radiopharmaceuticals for the dopamine D_1 receptor. Dopamine D_2 receptors are predominantly expressed on the postsynaptic side as compared to the presynaptic side of the dopaminergic synapse. [11C]NPA and [11C]PHNO are agonist radioligands for dopamine $D_{2/3}$ receptors. Commonly used antagonist radioligands for $D_{2/3}$ receptors are substituted benzamides ([11C]raclopride, [11C]FLB 457, [18F]fallypride and [123I]IBZM). *DAT* dopamine transporter, *VMAT-2* vesicular monoaminergic transporter 2

As an alternative to [18F]FDOPA, the tyrosine derivative [18F]FMT has been developed. This radiotracer is similar to [18F]FDOPA in that both radiotracers are substrates of AADC. However, unlike [18F]FDOPA, [18F]FMT is not a substrate for catechol-O-methyl-transferase (COMT), an enzyme essential in the breakdown of dopamine. Therefore, there are no radioactive *O*-methyl-metabolites which contribute to the nonspecific radioactivity in the brain, which enables the use of simplified kinetic modelling approaches (Dejesus et al. 2001).

The enzyme AADC plays an important role in the synthesis of dopamine, in that it converts *L*-DOPA to dopamine. It is important to consider that AADC also plays a role in the synthesis of other monoamine transmitters, e.g. in the conversion of 5-hydroxytryptophan to serotonin (5-HT). Since both [18F]FDOPA and [18F]FMT are substrates of AADC, these tracers are converted not only in dopaminergic neurons but also in serotonergic and noradrenergic neurons (Brown et al. 1999; Moore et al. 2003). The striatal accumulation of these tracers does however predominantly reflect conversion in nigrostriatal dopaminergic neurons (Pavese et al. 2012).

Initial PET studies applying [18F]FDOPA or [18F]FMT focused on the evaluation of the nigrostriatal pathway, by studying the distribution of these tracers in the striatum (Antonini et al. 1995). Due to the better performance characteristics of the PET systems, as well as improved PET data analysis methods, also extrastriatal radioactivity concentrations can nowadays be quantified (e.g. cortical areas). However, and as mentioned before, due to the expression of AADC in all monoaminergic neurons, accumulation in the raphe nuclei and locus coeruleus likely reflects predominantly serotonergic and noradrenergic activity, respectively, instead of accumulation in dopaminergic neurons (Ito et al. 2008; Lewis et al. 2012; Pavese et al. 2012), while accumulation in the thalamus may represent a combination of serotonergic and noradrenergic activity (Stokholm et al. 2018). An important consideration when studying extrastriatal brain regions is that the reliability of measurements in extrastriatal regions is lower than in striatum (Egerton et al. 2010).

Neuropsychiatric diseases like Parkinson's disease and dementia with Lewy bodies are characterized by severe loss of dopaminergic nigrostriatal neurons (Fig. 11.2; for more details on imaging of the dopaminergic system in Parkinsonian syndromes, see Chap. 27 in "PET and SPECT in Neurology"). Consequently, many PET studies have utilized [18F]FDOPA and [18F]FMT to demonstrate the ability to detect loss of dopaminergic neurons in cohorts of these patients (Brooks et al. 1990; Antonini et al. 1995; Hu et al. 2000; Pavese et al. 2012). Also, [18F]DOPA may already detect the loss of dopaminergic neurons in idiopathic rapid eye movement (REM) sleep behaviour disorder, a prodromal phenotype of Parkinson's disease (Stokholm et al. 2017; Knudsen et al. 2018). In addition, several [18F]FDOPA PET studies have been performed in patients suffering from psychosis, with the majority of them demonstrating an elevated striatal [18F]FDOPA accumulation, which suggests an increased synthesis rate as well as dopamine turnover in these patients (Kumakura et al. 2007; Howes and Kapur 2009; for systematic reviews see Fusar-Poli and Meyer-Lindenberg 2013; McCutcheon et al. 2018). Interestingly, the results of recent studies suggested that the increased [18F]FDOPA uptake may be
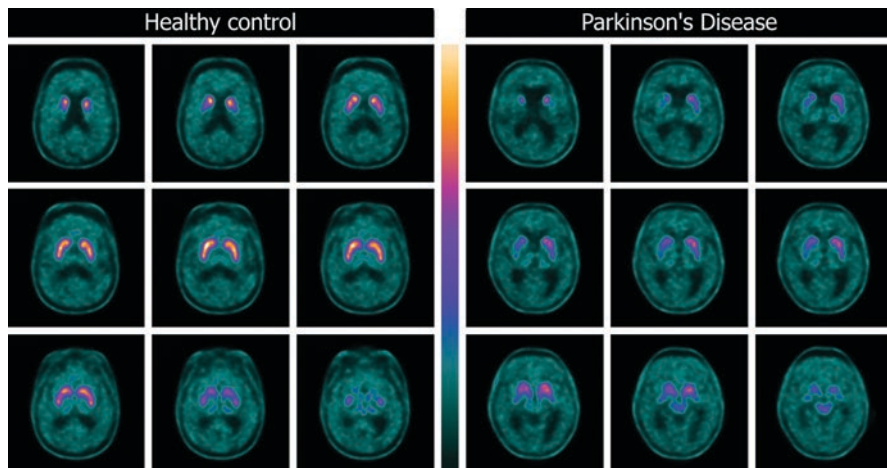
Fig. 11.2 Transversal planes of a [^{18}F]DOPA PET image obtained in a subject without nigrostriatal cell loss (left panel), and in a patient suffering from Parkinson's disease (PD; right panel). Please note the asymmetric striatal uptake as well as the severe loss of [^{18}F]DOPA uptake particularly in the putamen of the PD case

only observed in patients that respond to classic antipsychotics, but not in patients with treatment-resistant schizophrenia (Demjaha et al. 2012; Kim et al. 2017).

[^{18}F]FDOPA and [^{18}F]FMT PET have also been applied to evaluate the role of dopamine in the human reward system (Dreher et al. 2008; Schlagenhauf et al. 2013; Deserno et al. 2015; Smith et al. 2016). Finally, in healthy controls [^{18}F]FDOPA and [^{18}F]FMT PET have been used to assess ageing effects and cognitive functions (Braskie et al. 2008; Dreher et al. 2008; Kumakura et al. 2010).

11.2.2 Imaging of the VMAT-2

The vesicular monoamine transporter type 2 (VMAT-2; Fig. 11.1) is located in presynaptic dopaminergic neurons. Initially, carbon-11-labelled tetrabenazine derivatives were developed for PET imaging to visualize and quantify the VMAT-2 in humans (for a review, see Kilbourn 1997). More recently, also fluorine-18-labelled radioligands for the VMAT-2 have been developed successfully (Lin et al. 2010; for a recent review see Kilbourn and Koeppe, 2019), which provides the opportunity to use these radioligands also in hospitals not equipped with a cyclotron.

VMAT-2 is not exclusively present in dopaminergic neurons, but also in other monoaminergic neurons, including serotonergic (Guillot and Miller 2009), although the vast majority of the striatal radioactivity concentration represents binding in dopaminergic nerve terminals (Wang et al. 2010). In this regard, it is of interest that it has been suggested that VMAT-2 radioligands can also be used to visualize loss of pancreatic beta-cell mass in type 1 and type 2 diabetes (Goland et al. 2009; Cline et al. 2018), since beta-cells express VMAT-2. However, the specific binding of VMAT-2 PET radioligands binding to beta-cell mass has been disputed (Virostko

et al. 2011). Like [¹⁸F]FDOPA and [¹⁸F]FMT use in PET studies, VMAT-2 studies in humans have demonstrated that VMAT-2 imaging is a sensitive technique to detect reductions of nigrostriatal dopaminergic terminals in patients suffering from Parkinson's disease or dementia with Lewy bodies (Frey et al. 1996; Okamura et al. 2010; Burke et al. 2011a; Villemagne et al. 2011; Shah et al. 2016). In addition, VMAT-2 binding has been evaluated in relation to natural ageing effects (Bohnen et al. 2006), although findings are not consistent (Lin et al. 2013). Until now, SPECT radioligands have not been developed successfully for imaging of the VMAT-2.

11.2.3 Imaging of the Dopamine Transporter

The dopamine transporter (DAT) is mainly located in the membrane of terminals of presynaptic dopaminergic neurons (Fig. 11.1), but is also expressed at much lower levels in cell bodies in the substantia nigra (Ma et al. 1999; Fazio et al. 2018). Radioligands for the DAT have been developed successfully for both PET and SPECT. Regarding SPECT radioligands, radiopharmaceuticals derived from cocaine, e.g. [⁹⁹ᵐTc]TRODAT-1, [¹²³I]β-CIT and [¹²³I]FP-CIT, are nonselective DAT radioligands, although binding in the striatum predominantly reflects binding to DAT (Laruelle et al. 1993; Booij et al. 1997a, 2007; Dresel et al. 1998; Ziebell et al. 2010; Koopman et al. 2012; Fig. 11.3). Indeed, [¹²³I]FP-CIT SPECT studies have
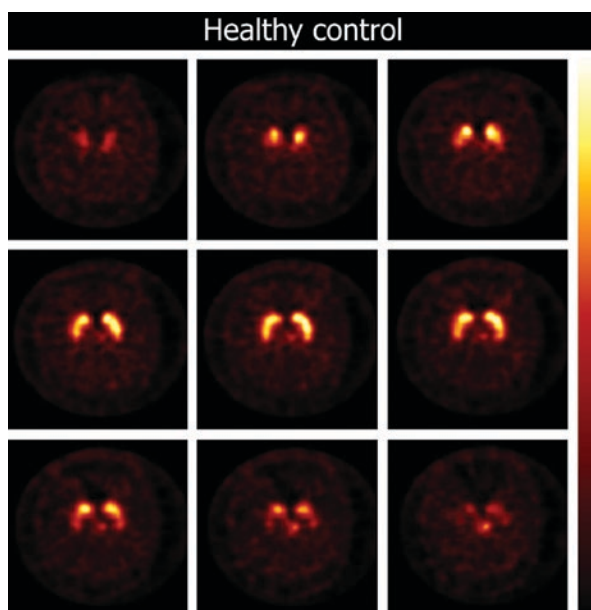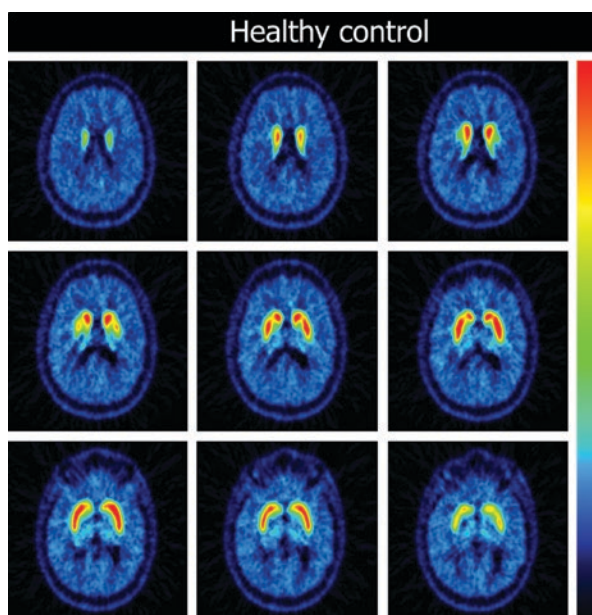

Fig. 11.3 Transversal SPECT images obtained 3 h after i.v. injection of [¹²³I]FP-CIT (radiotracer for the dopamine transporter) into a healthy female control subject. Intense symmetric and specific binding is visible in the caudate nucleus and putamen. The used colour scale represents a maximum intensity scale. This study has been acquired on a brain-dedicated SPECT system (InSPira)

shown that extrastriatal binding (in the diencephalon and midbrain) can be blocked by a selective serotonin reuptake inhibitor, indicating predominant binding to serotonin transporters in these brain areas (Booij et al. 2007; Ziebell et al. 2010). In addition, also promising and DAT-selective SPECT ligands, like [^{123}I]PE2I, have been developed and used in human subjects (Kuikka et al. 1998; Ziebell et al. 2010; Thomsen et al. 2013).

PET radioligands for imaging of the DAT have been developed numerously over the last two decades (see for reviews Varrone and Halldin 2012a, b). Initially, non-selective DAT radioligands (e.g. [^{11}C/^{18}F]CFT, Rinne et al. 2002; Nurmi et al. 2003; [^{18}F]FP-CIT; Oh et al. 2012) were applied in human studies, but more recently reported radioligands have an improved DAT selectivity (e.g. [^{11}C]PE2I (Hirvonen et al. 2008) (Fig. 11.4) or [^{18}F]FE-PE2I (Varrone et al. 2009; Sasaki et al. 2012; Sonni et al. 2016)). The developed PET radioligands also afford the opportunity to assess extrastriatal DAT binding, i.e. binding in the midbrain area and the orbitofrontal area (Jucaite et al. 2005; Hirvonen et al. 2008; Yagi et al. 2010; Fazio et al. 2018), while with SPECT only DAT binding in the striatum can be assessed accurately.

The DAT plays an important role in regulating dopaminergic neurotransmission. In this regard, appropriate regulation of the DAT expression is critical. Indeed, the

Fig. 11.4 Transversal planes of a mean PET summation image (6–93 min) obtained after i.v. injection of [^{11}C]PE2I (selective radiotracer for the dopamine transporter) into a healthy male control subject. Intense specific binding is visible in the caudate nucleus and putamen and lower specific binding in extrastriatal brain areas (thalamus/midbrain). This study has been acquired on a brain-dedicated PET system (HRRT) (images courtesy of Dr. Andrea Varrone and Professor Christer Halldin, Karolinska Institutet)

DAT expression undergoes dynamic control by cellular protein kinases and phosphatases (Ramamoorthy et al. 2011; Won et al. 2018). So, the DAT is not only expressed on the plasma membrane of dopaminergic neurons, as internalization of the DAT has been reported (Eriksen et al. 2009; Chen et al. 2010). Until now, it is not clear whether the abovementioned DAT radioligands label only plasma membrane-bound transporters or also internalized transporters when applied in PET/SPECT studies evaluating in vivo conditions (Earley et al. 2011), although a recent PET study provided indirect evidence that DAT PET tracers may bind preferentially to DAT located on cell membrane (Kim et al. 2016). More specifically, in mice it was shown that environmental enrichment induced internalization of the DAT (confirmed by surface biotinylation studies) and reduced striatal [^{18}F]FP-CIT binding. It might thus be that such tracers do not pass the cell membrane or, more likely, the radioligand binding characteristics to internalized transporters may differ from those transporters that are not internalized. For example, Afonso-Orama and co-workers showed that downregulation of the DAT consisted of a decrease of glycosylated (mature) DAT on the plasma membrane and accumulation of non-glycosylated (immature) DAT intracellularly (Afonso-Oramas et al. 2010). So, it might be that tracers like [^{18}F]FP-CIT bind with higher affinity to the mature than immature DAT. Interestingly, Guo and co-workers have demonstrated that radioligands that bind to the dopamine $D_{2/3}$ receptors have a lower affinity to internalized than to non-internalized receptors (Guo et al. 2010). Future studies are necessary to evaluate whether DAT internalization is a relevant consideration for in vivo imaging of DAT.

Numerous PET and SPECT studies evaluating DAT binding have shown the possibility to detect in vivo degeneration of nigrostriatal cells in disorders like Parkinson's disease and dementia with Lewy bodies (Booij et al. 1997b; Varrone et al. 2001; McKeith et al. 2007; Yagi et al. 2010; Oh et al. 2012; Fazio et al. 2018). Also, DAT binding has been examined in relation to ageing and gender effects in healthy controls, as well as the effects of polymorphism of the DAT gene (Lavalaye et al. 2000; van Dyck et al. 2005; van de Giessen et al. 2009; Troiano et al. 2010; Burke et al. 2011b; Varrone et al. 2013). Generally speaking, brain SPECT imaging of neuroreceptors/transporters is more accessible and cheaper than PET imaging, and consequently DAT imaging with SPECT is more commonly used in routine clinical studies to exclude or detect loss of nigrostriatal neurons in individual patients (Booij et al. 2001; Løkkegaard et al. 2002; Catafau et al. 2004; Ziebell et al. 2012; for reviews see Ba and Martin 2015; Suwijn et al. 2015).

11.3 Imaging of the Postsynaptic Dopaminergic System

11.3.1 Imaging of Dopamine D_1 Receptors

Dopamine exerts its pharmacological action through G-protein-coupled receptors. These transmembrane receptors can be divided into two subfamilies based on their pharmacological properties: the D_1- (D_1, D_5) and D_2-like receptor subfamily (D_2, D_3, D_4; Stoof and Kebabian 1981; Strange 1993; Beaulieu and Gainetdinov 2011).
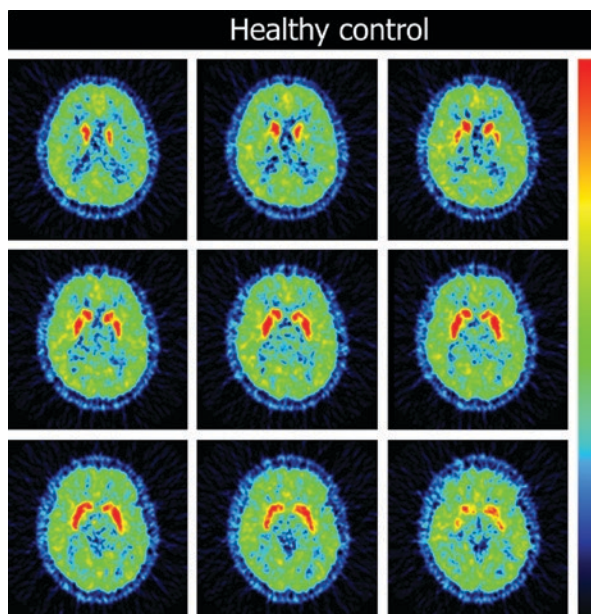
Fig. 11.5 Transversal plane of a mean PET summation image (12–63 min) obtained after i.v. injection of [^{11}C]SCH23390 (radiotracer for the dopamine D_1 receptor) into a healthy male control subject. Intense specific binding is visible in the caudate and putamen, and lower specific binding in the extrastriatal brain areas (cortex). This study has been acquired on a brain-dedicated PET system (ECAT EXACT HR) (images are courtesy of Per Stenkrona and Professor Christer Halldin, Karolinska Institutet)

The dopamine D_1 receptor is a highly prevalent dopamine receptor in the striatum and neocortex and is located postsynaptically (Cortés et al. 1989; Volkow et al. 1996). The radiopharmaceuticals [^{11}C]NNC 112 and [^{11}C]SCH23390 have successfully been developed to image dopamine D_1 receptors in the living human brain using PET (Fig. 11.5; for a recent review see Cervenka, 2019). Both radioligands are high-affinity dopamine D_1 receptor antagonists, although they also have been reported to bind to serotonin 2A (5-HT_{2A}) receptors, estimated as approximately 25% of cortical binding being due to binding to 5-HT_{2A} receptors (Ekelund et al. 2007). To circumvent this limitation, a study proposed the use of the 5-HT_{2A} receptor antagonist ketanserin. After ketanserin administration, the 5-HT_{2A} receptor binding is inhibited, and cortical D_1 receptor binding can be accurately assessed using [^{11}C]NNC 112 in humans (Catafau et al. 2010).

Although [^{11}C]NNC 112 and [^{11}C]SCH23390 bind to both dopamine D_1 and 5-HT_{2A} receptors, their affinity to dopamine D_2-like receptors is substantially lower (Andersen et al. 1992) although binding to dopamine D_5 receptors cannot be excluded (Sunahara et al. 1991; Chou et al. 2006). While dopamine D_1 receptors are expressed at high levels in the striatum and cortical areas, the expression of dopamine D_5 receptors in the brain is low (Beaulieu and Gainetdinov 2011). Consequently,

in vivo binding to dopamine D_5 receptors, as compared to D_1 receptors, with PET radioligands like [^{11}C]NNC 112 is likely negligible.

Dopamine receptors have been demonstrated to exist in two affinity states in vitro. The two receptor states are convertible and consist of a state of high and low affinity for the endogenous agonist dopamine (or exogenous agonists) (Sibley et al. 1982; Chio et al. 1994). The high-affinity state represents the active form of the receptors that are coupled to G-proteins (Zahniser and Molinoff 1978). Regarding dopamine D_1 receptors, results of in vitro experiments suggest that 20–40% of these receptors are in the high-affinity state (Richfield et al. 1989; Mamelak et al. 1993; McCauley et al. 1995). Importantly, while antagonist radioligands label both the high- and low-affinity state of the receptors, agonist radioligands may label receptors only in its high-affinity state (for a recent review see Shalgunov et al. 2019). So far, the available radioligands [^{11}C]NNC 112 and [^{11}C]SCH23390 are both antagonists for the dopamine D_1 receptor. Developments of agonist radioligands for the dopamine D_1 receptor are ongoing and will enable to examine in future studies whether the high-affinity state of the dopamine D_1 receptor exists in living humans (Palner et al. 2010; Finnema et al. 2013), although human studies with such novel tracers have not been performed yet. Also, dopamine agonist radioligands may be more sensitive to detect changes in dopamine concentrations in the synapse, e.g. changes induced by dopamine releasers like amphetamines (see the following section).

Since dopamine D_1 receptors have been implicated in cognitive performance, dopamine D_1 PET studies in healthy volunteers have been used to examine changes in working memory (McNab et al. 2009; Roffman et al. 2016), reward learning (de Boer et al. 2019), amygdala response to affective stimuli (Takahashi et al. 2010) and natural ageing (Jucaite et al. 2010) and to study the effects of genes involved in the dopaminergic tone (Slifstein et al. 2008). Dopamine D_1 receptor imaging in neuropsychiatric disorders has so far focused on schizophrenia (and the mechanism of action of antipsychotics), cocaine addiction and movement disorders (Nordström et al. 1995; Karlsson et al. 2002; Hirvonen et al. 2006; Martinez et al. 2009; Karimi et al. 2013; Thompson et al. 2014). Until now, the development of SPECT radioligands for the dopamine D_1 receptor has not been successful.

11.3.2 Imaging of Dopamine D_2-Like Receptors

11.3.2.1 Dopamine $D_{2/3}$ Receptor Imaging

In the past three decades, PET as well as SPECT radioligands have been developed successfully to image and quantify dopamine $D_{2/3}$ receptors in the human brain.

Regarding SPECT imaging, the commonly used benzamide [^{123}I]IBZM is an antagonist radioligand which binds with high affinity to dopamine $D_{2/3}$ receptors (i.e. in the low nanomolar range) (Verhoeff et al. 1993; Videbaek et al. 2000; de Haan et al. 2003; Boot et al. 2008; Visser et al. 2008; Figee et al. 2014). With this radioligand striatal dopamine $D_{2/3}$ receptors can be assessed accurately, and extrastriatal distribution may be visualized, particularly when using brain-dedicated SPECT systems (Fig. 11.6). The radioligand [^{123}I]epidepride is a dopamine $D_{2/3}$
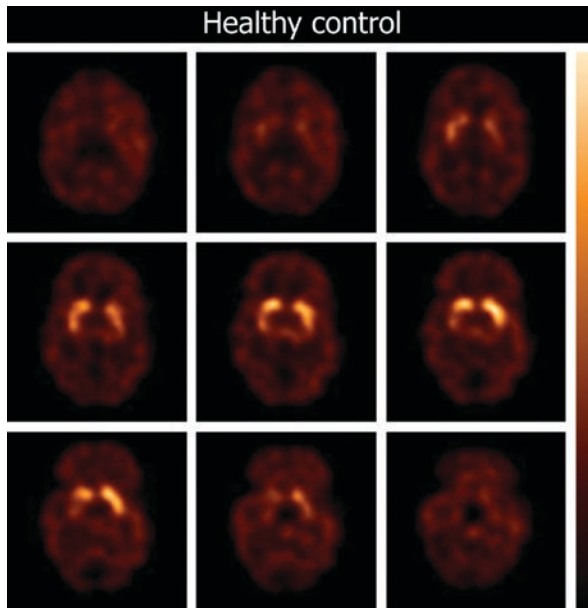
Fig. 11.6 Transversal [123I]IBZM slices obtained in a healthy control, 2 h after start of bolus/constant infusion. Intense specific binding is visible in the striatum, and much lower specific binding in the extrastriatal brain areas (thalamus/midbrain). The used colour scale represents a maximum intensity scale. This study has been acquired on a brain-dedicated SPECT system (NeuroFocus)

receptor antagonist with an enhanced affinity (picomolar range) for the dopamine $D_{2/3}$ receptors (Kessler et al. 1991). This ultrahigh-affinity SPECT radioligand allows assessing dopamine $D_{2/3}$ receptor availability in extrastriatal brain areas, such as the midbrain, diencephalon and cortical areas (Kornhuber et al. 1995; Varrone et al. 2000; Glenthoj et al. 2006; Tuppurainen et al. 2010; Nørbak-Emig et al. 2016).

Regarding PET imaging, the benzamide [11C]raclopride is an antagonist radioligand that binds with high affinity to dopamine $D_{2/3}$ receptors (in the low nanomolar range; Farde et al. 1986) and is commonly used in human studies (Ito et al. 2011; Martinez et al. 2011; Wang et al. 2019). The radioligand [11C]N-methylspiperone binds also with high affinity to dopamine $D_{2/3}$ receptors, although binding has been shown to be partly related to 5-HT_{2A} receptors (Nyberg et al. 1999). Also antagonist PET radioligands with ultrahigh affinity for the dopamine $D_{2/3}$ receptors have been developed successfully. For example, [11C]FLB 457 (Halldin et al. 1995) and [18F]fallypride (Mukherjee et al. 1995; Kasanova et al. 2018) are radioligands with a very high dopamine $D_{2/3}$ receptor affinity allowing for evaluation of extrastriatal dopamine $D_{2/3}$ receptors (picomolar range; Mukherjee et al. 1995; for a review see Högberg 1993). Finally, the antagonist [18F]N-methylbenperidol binds selectively to dopamine D_2 receptors (Karimi et al. 2011).

More recently, many agonist PET radioligands for dopamine $D_{2/3}$ receptors have been synthesized and evaluated (for a recent review see Shalgunov et al. 2019), and at least three were tested successfully in humans, that is, [^{11}C]PHNO, [^{11}C]NPA and [^{11}C]MNPA (Willeit et al. 2006; Laymon et al. 2009; Otsuka et al. 2009). The apomorphine derivatives NPA and MNPA bind with high affinity to both dopamine D_2 and dopamine D_3 receptors (Seeman et al. 1985; Neumeyer et al. 1990). In contrast, in vitro studies have shown that the affinity of PHNO is 30- to 50-fold lower for the dopamine D_2 than for the dopamine D_3 receptor (Freedman et al. 1994; van Vliet et al. 2000). Indeed, a recent study in humans demonstrated that binding of [^{11}C]PHNO in several brain regions, e.g. hypothalamus, substantia nigra, ventral pallidum and globus pallidus, is predominantly to dopamine D_3 receptors. On the other hand, in striatal subregions, in vivo binding is predominant to dopamine D_2 receptors (Tziortzi et al. 2011). Although the agonist [^{11}C]PHNO binds predominantly to dopamine D_3 receptors in certain brain areas, selective agonist radioligands for dopamine D_2 or dopamine D_3 receptors are not available yet.

Regarding dopamine D_2 receptors, in vitro experiments on homogenized striata from rats and mice show that roughly 15–30% of the receptors are in the high-affinity state with a range up to 80% depending on the detection method used. In more intact tissue (brain slices), 90% of these receptors may even be in the high-affinity state (for review see van Wieringen et al. 2013). Initial results of in vivo PET measurements using amphetamine in nonhuman primates suggested that 60–80% of these receptors are in the high-affinity state (Narendran et al. 2004). However, although several attempts have been made, formally the existence of the high- and low-affinity state has until now not been confirmed or disputed in vivo (Finnema et al. 2009; see for reviews Finnema et al. 2010; Skinbjerg et al. 2012; Shalgunov et al. 2019). The results of the recent application of agonist radioligands in human PET studies suggest that 60–65% of dopamine D_2 receptors are in the high-affinity state in vivo (Narendran et al. 2010; Shotbolt et al. 2012).

As discussed earlier, dopamine agonist radioligands may be more sensitive to detect changes in dopamine concentrations in the synapse, e.g. changes induced by dopamine releasers like amphetamines (Laruelle et al. 1995) or depletion induced by AMPT (Laruelle et al. 1997; Boot et al. 2008). Indeed, recent studies have indicated that the agonist radioligands ([^{11}C]NPA and [^{11}C]PHNO) are more vulnerable to endogenous striatal dopamine competition than the antagonist radioligand [^{11}C]raclopride in humans (Narendran et al. 2010; Shotbolt et al. 2012; Gallezot et al. 2014). Also, it may be possible to use [^{11}C]PHNO PET as a tool to assess not only striatal dopamine release but also release in the substantia nigra (Tseng et al. 2018). It can be concluded that agonist dopamine $D_{2/3}$ receptor radioligands hold promise for studying changes in dopamine concentrations although further confirmation in human subjects is required.

The dopamine $D_{2/3}$ receptors are expressed not only on the plasma membrane of postsynaptic neurons, but also presynaptically (Fig. 11.1). There are two splice variants of dopamine D_2 receptors, the dopamine D_2 long (D_2L) and the short variant (D_2S) (Chio et al. 1990). These isoforms have different localizations, with D_2S

primarily located presynaptically (as an autoreceptor) (Khan et al. 1998). From a pharmacological point of view, these splice variants cannot be discriminated, and consequently, radioligands for the dopamine $D_{2/3}$ receptors may bind to both D_2L and D_2S. However, since the striatal density of D_2L is much higher than that of D_2S (Rani and Kanungo 2006), imaging of dopamine $D_{2/3}$ receptors is frequently referred to as imaging of postsynaptic dopamine $D_{2/3}$ receptors. Also, imaging of the midbrain dopamine $D_{2/3}$ receptors may predominantly visualize dopamine $D_{2/3}$ autoreceptors (Buckholtz et al. 2010).

Dopamine D_2 receptors can internalize into the intracellular compartment after agonist stimulation, similar as for other G-protein-coupled receptors. Interestingly, Guo and co-workers have reported that dopamine D_2 receptor radioligands have a lower affinity to internalized than to non-internalized receptors (Guo et al. 2010). A frequently used approach to assess dopamine release in vivo is the use of dexamphetamine (see for review Laruelle 2000). Administration of dexamphetamine intravenously or orally in doses of 0.2–0.3 mg/kg body weight induces a substantial release of endogenous dopamine, which will result in a displacement of radioligand binding to dopamine $D_{2/3}$ receptors (i.e. decrease of, e.g., striatal [^{123}I]IBZM or [^{11}C]raclopride binding; Laruelle et al. 1995; Breier et al. 1997). Typically, administration of dexamphetamine leads to a rapid release of extracellular dopamine which is not long lasting (Breier et al. 1997). However, in imaging studies a prolonged displacement of radioligand binding has been observed, which may be caused (partly) by receptor internalization (Laruelle 2000; Cárdenas et al. 2004; Scott et al. 2007). Indeed, studies in knockout mice, which are incapable of internalizing dopamine D_2 receptors, suggest that the prolonged displacement is mainly due to internalization of D_2 receptors (Skinbjerg et al. 2010). Interestingly, a recent human [^{11}C]raclopride PET study examined whether the prolonged displacement (or return of the [^{11}C]raclopride binding to baseline), as a measure of dopamine $D_{2/3}$ receptor internalization, was impaired in schizophrenia (Weinstein et al. 2018). Their findings suggested that this was not the case. Additional studies are needed to demonstrate whether molecular imaging studies are indeed able to assess internalization of dopamine D_2 receptors in humans, preferentially using simpler paradigms than that presented by Weinstein and co-workers (Weinstein et al. 2018), which may be relevant to study the role of a possible abnormal internalization of these receptors in neuropsychiatric disorders.

11.3.2.2 Dopamine D_4 Receptor Imaging

The dopamine D_4 receptor was cloned for the first time in 1991 (Van Tol et al. 1991) and is thought to play a role in a variety of neuropsychiatric disorders. This receptor is predominantly expressed postsynaptically (Rivera et al. 2002). In contrast to dopamine $D_{2/3}$ receptors, dopamine D_4 receptors do not internalize after agonist stimulation (Spooren et al. 2010). Interestingly, the antipsychotic clozapine, for instance, demonstrates a substantially higher affinity for the dopamine D_4 than for the dopamine D_2 receptor subtype (Van Tol et al. 1991; Eisenegger et al. 2010; Smith 2010). Recently, progress has been reported on the development of dopamine D_4 receptor radioligands. This has been a challenging task as the density of

dopamine D_4 receptors in the human brain is much lower than that of other dopamine D_2-like receptors (Marazziti et al. 2009; Lacivita et al. 2010; Kügler et al. 2011). Although Lacivita and co-workers reported that their radioligand mainly demonstrated high binding in the retina of non-primates (Lacivita et al. 2010), it is promising that a relatively recent study demonstrated clear brain uptake of a dopamine D_4 receptor antagonist radioligand in mice (Kügler et al. 2011), although it remains challenging to identify an optimized radiotracer (Leopoldo et al. 2014).

11.4   Conclusion

Imaging of the nigrostriatal pathway in humans can be performed quantitatively with PET and SPECT techniques, using the PET radiotracer [^{18}F]FDOPA or [^{18}F]FMT, PET radioligands for the VMAT-2 and PET or SPECT radioligands for the DAT. With PET, also several other dopaminergic projections (e.g. mesocortical projections) can be assessed adequately in the human brain. Several antagonist PET radioligands for the dopamine D_1 receptor have been developed successfully. In addition, well-validated antagonist PET and SPECT radioligands are available to image dopamine $D_{2/3}$ receptors in the living human brain. Relatively recently, also agonist PET radioligands for the dopamine $D_{2/3}$ receptors have been developed, which affords the opportunity to evaluate the existence of the high-affinity state of these receptors in vivo, and these radiopharmaceuticals may be more sensitive to detect changes in dopamine concentrations. Finally, although selective antagonist PET radioligands for the dopamine D_4 receptor have been synthesized and evaluated successfully in small laboratory animals, these radioligands have not yet been applied in human research.

References

Afonso-Oramas D, Cruz-Muros I, Barroso-Chinea P, Álvarez de la Rosa D, Castro-Hernández J, Salas-Hernández J, Giráldez T, González-Hernández T et al (2010) The dopamine transporter is differentially regulated after dopaminergic lesion. Neurobiol Dis 40:518–530

Andersen PH, Grønvald FC, Hohlweg R et al (1992) NNC-112, NNC-687 and NNC-756, new selective and highly potent dopamine D1 receptor antagonists. Eur J Pharmacol 219:45–52

Antonini A, Vontobel P, Psylla M et al (1995) Complementary positron emission tomographic studies of the striatal dopaminergic system in Parkinson's disease. Arch Neurol 52:1183–1190

Ba F, Martin WR (2015) Dopamine transporter imaging as a diagnostic tool for parkinsonism and related disorders in clinical practice. Parkinsonism Relat Disord 21:87–94

Beaulieu JM, Gainetdinov RR (2011) The physiology, signaling, and pharmacology of dopamine receptors. Pharmacol Rev 63:182–217

Bohnen NI, Albin RL, Koeppe RA (2006) Positron emission tomography of monoaminergic vesicular binding in aging and Parkinson disease. J Cereb Blood Flow Metab 26:1198–1212

Booij J, Andringa G, Rijks LJ et al (1997a) [123I]FP-CIT binds to the dopamine transporter as assessed by biodistribution studies in rats and SPECT studies in MPTP-lesioned monkeys. Synapse 27:183–190

Booij J, de Jong J, de Bruin K, Knol R, de Win MM, van Eck-Smit BL (2007) Quantification of striatal dopamine transporters with 123I-FP-CIT SPECT is influenced by the selective sero-

tonin reuptake inhibitor paroxetine: a double-blind, placebo-controlled, crossover study in healthy control subjects. J Nucl Med 48:359–366

Booij J, Speelman JD, Horstink MW, Wolters EC (2001) The clinical benefit of imaging striatal dopamine transporters with [123I]FP-CIT SPET in differentiating patients with presynaptic Parkinsonism from those with other forms of Parkinsonism. Eur J Nucl Med 28:266–272

Booij J, Tissingh G, Boer GJ (1997b) [123I]FP-CIT SPECT shows a pronounced decline of striatal dopamine transporter labelling in early and advanced Parkinson's disease. J Neurol Neurosurg Psychiatry 62:133–140

Booij J, Tissingh G, Winogrodzka A, van Royen EA (1999) Imaging of the dopaminergic neuro-transmission system using single-photon emission tomography and positron emission tomography in patients with parkinsonism. Eur J Nucl Med 26:171–182

Boot E, Booij J, Hasler G et al (2008) AMPT-induced monoamine depletion in humans: evaluation of two alternative [123I]IBZM SPECT procedures. Eur J Nucl Med Mol Imaging 35:1350–1356

Braskie MN, Wilcox CE, Landau SM et al (2008) Relationship of striatal dopamine synthesis capacity to age and cognition. J Neurosci 28:14320–14328

Breier A, Su T-P, Saunders R, Carson R et al (1997) Schizophrenia is associated with elevated amphetamine-induced synaptic dopamine concentrations: evidence from a novel positron emission tomography method. Proc Natl Acad Sci U S A 94:2569–2574

Brooks DJ, Ibanez V, Sawle GV et al (1990) Differing patterns of striatal 18F-dopa uptake in Parkinson's disease, multiple system atrophy, and progressive supranuclear palsy. Ann Neurol 28:547–555

Brown WD, DeJesus OT, Pyzalski RW (1999) Localization of trapping of 6-[^{18}F]fluoro-L-m-tyrosine, an aromatic L-amino acid decarboxylase tracer for PET. Synapse 34:111–123

Buckholtz JW, Treadway MT, Cowan RL et al (2010) Dopaminergic network differences in human impulsivity. Science 329:532

Burke JF, Albin RL, Koeppe RA et al (2011a) Assessment of mild dementia with amyloid and dopamine terminal positron emission tomography. Brain 134:1647–1657

Burke SM, van de Giessen E, de Win M et al (2011b) Serotonin and dopamine transporters in relation to neuropsychological functioning, personality traits and mood in young adult healthy subjects. Psychol Med 41:419–429

Cárdenas L, Houle S, Kapur S, Busto UE (2004) Oral D-amphetamine causes prolonged displacement of [11C]raclopride as measured by PET. Synapse 51:27–31

Catafau AM, Searle GE, Bullich S (2010) Imaging cortical dopamine D1 receptors using [11C]NNC112 and ketanserin blockade of the 5-HT 2A receptors. J Cereb Blood Flow Metab 30:985–993

Catafau AM, Tolosa E, DaTSCAN Clinically Uncertain Parkinsonian Syndromes Study Group (2004) Impact of dopamine transporter SPECT using 123I-Ioflupane on diagnosis and management of patients with clinically uncertain Parkinsonian syndromes. Mov Disord 19:1175–1182

Cervenka S (2019) PET radioligands for the dopamine D1-receptor: application in psychiatric disorders. Neurosci Lett 691:26–34

Chen R, Furman CA, Gnegy ME (2010) Dopamine transporter trafficking: rapid response on demand. Future Neurol 5:123

Chio CL, Hess GF, Graham RS, Huff RM (1990) A second molecular form of D2 dopamine receptor in rat and bovine caudate nucleus. Nature 343:266–269

Chio CL, Lajiness ME, Huff RM (1994) Activation of heterologously expressed D3 dopamine receptors: comparison with D2 dopamine receptors. Mol Pharmacol 45:51–60

Chou YH, Halldin C, Farde L (2006) Clozapine binds preferentially to cortical D1-like dopamine receptors in the primate brain: a PET study. Psychopharmacology 185:29–35

Cline GW, Naganawa M, Chen L et al (2018) Decreased VMAT2 in the pancreas of humans with type 2 diabetes mellitus measured in vivo by PET imaging. Diabetologia 61:2598–2607

Cortés R, Gueye B, Pazos A, Probst A, Palacios JM (1989) Dopamine receptors in human brain: autoradiographic distribution of D1 sites. Neuroscience 28:263–273

Cumming P, Munk OL, Doudet D (2001) Loss of metabolites from monkey striatum during PET with FDOPA. Synapse 41:212–218

de Boer L, Axelsson J, Chowdhury R et al (2019) Dorsal striatal dopamine D1 receptor availability predicts an instrumental bias in action learning. Proc Natl Acad Sci U S A 116:261–270

de Haan L, van Bruggen M, Lavalaye J, Booij J, Dingemans PM, Linszen D (2003) Subjective experience and D2 receptor occupancy in patients with recent-onset schizophrenia treated with low-dose olanzapine or haloperidol: a randomized, double-blind study. Am J Psychiatry 160:303–309

Dejesus OT, Endres CJ, Shelton SE, Nickles RJ, Holden JE (2001) Noninvasive assessment of aromatic L-amino acid decarboxylase activity in aging rhesus monkey brain in vivo. Synapse 39:58–63

Demjaha A, Murray RM, McGuire PK, Kapur S, Howes OD (2012) Dopamine synthesis capacity in patients with treatment-resistant schizophrenia. Am J Psychiatry 169:1203–1210

Deserno L, Beck A, Huys QJ et al (2015) Chronic alcohol intake abolishes the relationship between dopamine synthesis capacity and learning signals in the ventral striatum. Eur J Neurosci 41:477–486

Dreher JC, Meyer-Lindenberg A, Kohn P, Berman KF (2008) Age-related changes in midbrain dopaminergic regulation of the human reward system. Proc Natl Acad Sci U S A 105:15106–15111

Dresel SH, Kung MP, Plössl K, Meegalla SK, Kung HF (1998) Pharmacological effects of dopaminergic drugs on in vivo binding of [99mTc]TRODAT-1 to the central dopamine transporters in rats. Eur J Nucl Med 25:31–39

Earley CJ, Kuwabara H, Wong DF et al (2011) The dopamine transporter is decreased in the striatum of subjects with restless legs syndrome. Sleep 34:341–347

Egerton A, Demjaha A, McGuire P, Mehta MA, Howes OD (2010) The test-retest reliability of 18 F-DOPA PET in assessing striatal and extrastriatal presynaptic dopaminergic function. NeuroImage 50:524–531

Eisenegger C, Knoch D, Ebstein RP, Gianotti LR, Sándor PS, Fehr E (2010) Dopamine receptor D4 polymorphism predicts the effect of L-DOPA on gambling behavior. Biol Psychiatry 67:702–706

Ekelund J, Slifstein M, Narendran R et al (2007) In vivo DA D1 receptor selectivity of NNC 112 and SCH 23390. Mol Imaging Biol 9:117–125

Enomoto K, Matsumoto N, Nakai S et al (2011) Dopamine neurons learn to encode the long-term value of multiple future rewards. Proc Natl Acad Sci U S A 108:15462–15467

Eriksen J, Rasmussen SG, Rasmussen TN et al (2009) Visualization of dopamine transporter trafficking in live neurons by use of fluorescent cocaine analogs. J Neurosci 29:6794–6808

Farde L, Hall H, Ehrin E, Sedvall G (1986) Quantitative analysis of D2 dopamine receptor binding in the living human brain by PET. Science 231:258–261

Fazio P, Svenningsson P, Cselényi Z, Halldin C, Farde L, Varrone A (2018) Nigrostriatal dopamine transporter availability in early Parkinson's disease. Mov Disord 33:592–599

Figee M, de Koning P, Klaassen S et al (2014) Deep brain stimulation induces striatal dopamine release in obsessive-compulsive disorder. Biol Psychiatry 75:647–652

Finnema SJ, Bang-Andersen B, Jørgensen M et al (2013) The dopamine D_1 receptor agonist (S)-[^{11}C]N-methyl-NNC 01-0259 is not sensitive to changes in dopamine concentration--a positron emission tomography examination in the monkey brain. Synapse 67:586–595

Finnema SJ, Bang-Andersen B, Wikström HV, Halldin C (2010) Current state of agonist radioligands for imaging of brain dopamine D2/D3 receptors in vivo with positron emission tomography. Curr Top Med Chem 10:1477–1498

Finnema SJ, Halldin C, Bang-Andersen B, Gulyás B, Bundgaard C, Wikström HV, Farde L (2009) Dopamine $D_{2/3}$ receptor occupancy of apomorphine in the nonhuman primate brain-a comparative PET study with [11C]raclopride and [11C]MNPA. Synapse 63:378–389

Fiorillo CD, Tobler PN, Schultz W (2003) Discrete coding of reward probability and uncertainty by dopamine neurons. Science 299:1898–1902

Freedman SB, Patel S, Marwood R et al (1994) Expression and pharmacological characterization of the human D3 dopamine receptor. J Pharmacol Exp Ther 268:417–426

Frey KA, Koeppe RA, Kilbourn MR et al (1996) Presynaptic monoaminergic vesicles in Parkinson's disease and normal aging. Ann Neurol 40:873–884

Fusar-Poli P, Meyer-Lindenberg A (2013) Striatal presynaptic dopamine in schizophrenia, part II: meta-analysis of [(18)F/(11)C]-DOPA PET studies. Schizophr Bull 39:33–42

Gallezot JD, Kloczynski T, Weinzimmer D et al (2014) Imaging nicotine- and amphetamine-induced dopamine release in rhesus monkeys with [(11)C]PHNO vs [(11)C]raclopride PET. Neuropsychopharmacology 39:866–874

Glenthoj BY, Mackeprang T, Svarer C et al (2006) Frontal dopamine D(2/3) receptor binding in drug-naive first-episode schizophrenic patients correlates with positive psychotic symptoms and gender. Biol Psychiatry 60:621–629

Goland R, Freeby M, Parsey R et al (2009) 11C-dihydrotetrabenazine PET of the pancreas in subjects with long-standing type 1 diabetes and in healthy controls. J Nucl Med 50:382–389

Guillot TS, Miller GW (2009) Protective actions of the vesicular monoamine transporter 2 (VMAT2) in monoaminergic neurons. Mol Neurobiol 39:149–170

Guo N, Guo W, Kralikova M et al (2010) Impact of D2 receptor internalization on binding affinity of neuroimaging radiotracers. Neuropsychopharmacology 35:806–817

Halldin C, Farde L, Högberg T et al (1995) Carbon-11-FLB 457: a radioligand for extrastriatal D2 dopamine receptors. J Nucl Med 36:1275–1281

Hirvonen J, Johansson J, Teräs M (2008) Measurement of striatal and extrastriatal dopamine transporter binding with high-resolution PET and [11C]PE2I: quantitative modeling and test-retest reproducibility. J Cereb Blood Flow Metab 28:1059–1069

Hirvonen J, van Erp TG, Huttunen J et al (2006) Brain dopamine d1 receptors in twins discordant for schizophrenia. Am J Psychiatry 163:1747–1753

Högberg T (1993) The development of dopamine D2-receptor selective antagonists. Drug Des Discov 9:333–350

Holden JE, Doudet D, Endres CJ et al (1997) Graphical analysis of 6-fluoro-L-dopa trapping: effect of inhibition of catechol-O-methyltransferase. J Nucl Med 38:1568–1574

Howes OD, Kapur S (2009) The dopamine hypothesis of schizophrenia: version III—the final common pathway. Schizophr Bull 35:549–562

Hu XS, Okamura N, Arai H (2000) 18F-fluorodopa PET study of striatal dopamine uptake in the diagnosis of dementia with Lewy bodies. Neurology 55:1575–1577

Ito H, Kodaka F, Takahashi H et al (2011) Relation between presynaptic and postsynaptic dopaminergic functions measured by positron emission tomography: implication of dopaminergic tone. J Neurosci 31:7886–7890

Ito H, Takahashi H, Arakawa R, Takano H, Suhara T (2008) Normal database of dopaminergic neurotransmission system in human brain measured by positron emission tomography. NeuroImage 39:555–565

Jauhar S, McCutcheon R, Borgan F et al (2018) The relationship between cortical glutamate and striatal dopamine in first-episode psychosis: a cross-sectional multimodal PET and magnetic resonance spectroscopy imaging study. Lancet Psychiatry 5:816–823

Jucaite A, Fernell E, Halldin C, Forssberg H, Farde L (2005) Reduced midbrain dopamine transporter binding in male adolescents with attention-deficit/hyperactivity disorder: association between striatal dopamine markers and motor hyperactivity. Biol Psychiatry 57:229–238

Jucaite A, Forssberg H, Karlsson P, Halldin C, Farde L (2010) Age-related reduction in dopamine D1 receptors in the human brain: from late childhood to adulthood, a positron emission tomography study. Neuroscience 167:104–110

Karimi M, Moerlein SM, Videen TO, Su Y, Flores HP, Perlmutter JS (2013) Striatal dopamine D1-like receptor binding is unchanged in primary focal dystonia. Mov Disord 28:2002–2006

Karimi M, Moerlein SM, Videen TO, Luedtke RR, Taylor M, Mach RH, Perlmutter JS (2011) Decreased striatal dopamine receptor binding in primary focal dystonia: a D2 or D3 defect? Mov Disord 26:100–106

Karlsson P, Farde L, Halldin C, Sedvall G (2002) PET study of D(1) dopamine receptor binding in neuroleptic-naive patients with schizophrenia. Am J Psychiatry 159:761–767

Kasanova Z, Ceccarini J, Frank MJ et al (2018) Daily-life stress differentially impacts ventral striatal dopaminergic modulation of reward processing in first-degree relatives of individuals with psychosis. Eur Neuropsychopharmacol 28:1314–1324

Kessler RM, Ansari MS, de Paulis T et al (1991) High affinity dopamine D2 receptor radioligands. 1. Regional rat brain distribution of iodinated benzamides. J Nucl Med 32:1593–1600

Khan ZU, Mrzljak L, Gutierrez A, de la Calle A, Goldman-Rakic PS (1998) Prominence of the dopamine D2 short isoform in dopaminergic pathways. Proc Natl Acad Sci U S A 95: 7731–7736

Kilbourn MR (1997) In vivo radiotracers for vesicular neurotransmitter transporters. Nucl Med Biol 24:615–619

Kilbourn MR, Koeppe RA (2019) Classics in neuroimaging: radioligands for the vesicular monoamine transporter 2. ACS Chem Neurosci [Epub ahead of print]

Kim E, Howes OD, Veronese M et al (2017) Presynaptic dopamine capacity in patients with treatment-resistant schizophrenia taking clozapine: an [^{18}F]DOPA PET Study. Neuropsychopharmacology 42:941–950

Kim MS, Yu JH, Kim CH et al (2016) Environmental enrichment enhances synaptic plasticity by internalization of striatal dopamine transporters. J Cereb Blood Flow Metab 36:2122–2133

Knudsen K, Fedorova TD, Hansen AK et al (2018) In-vivo staging of pathology in REM sleep behaviour disorder: a multimodality imaging case-control study. Lancet Neurol 17:618–628

Koopman KE, la Fleur SE, Fliers E, Serlie MJ, Booij J (2012) Assessing the optimal time-point for the measurement of extrastriatal serotonin transporter binding with ^{123}I-FP-CIT SPECT in healthy, male subjects. J Nucl Med 53:1087–1090

Kornhuber J, Brücke T, Angelberger P, Asenbaum S, Podreka I (1995) SPECT imaging of dopamine receptors with [123I]epidepride: characterization of uptake in the human brain. J Neural Transm Gen Sect 101:95–103

Kügler F, Sihver W, Ermert J et al (2011) Evaluation of 18 F-labeled benzodioxine piperazine-based dopamine D4 receptor ligands: lipophilicity as a determinate of nonspecific binding. J Med Chem 54:8343–8352

Kuikka JT, Baulieu JL, Hiltunen J et al (1998) Pharmacokinetics and dosimetry of iodine-123 labelled PE2I in humans, a radioligand for dopamine transporter imaging. Eur J Nucl Med 25:531–534

Kumakura Y, Cumming P (2009) PET studies of cerebral levodopa metabolism: a review of clinical findings and modeling approaches. Neuroscientist 15:635–650

Kumakura Y, Cumming P, Vernaleken I et al (2007) Elevated [18 F]fluorodopamine turnover in brain of patients with schizophrenia: an [18 F]fluorodopa/positron emission tomography study. J Neurosci 27:8080–8087

Kumakura Y, Vernaleken I, Buchholz HG et al (2010) Age-dependent decline of steady state dopamine storage capacity of human brain: an FDOPA PET study. Neurobiol Aging 31:447–463

Kumakura Y, Vernaleken I, Gründer G, Bartenstein P, Gjedde A, Cumming P (2005) PET studies of net blood–brain clearance of FDOPA to human brain: age-dependent decline of [^{18}F]fluorodopamine storage capacity. J Cereb Blood Flow Metab 25:807–819

Lacivita E, De Giorgio P, Lee IT et al (2010) Design, synthesis, radiolabeling, and in vivo evaluation of carbon-11 labeled N-[2-[4-(3-cyanopyridin-2-yl)piperazin-1-yl]ethyl]-3-methoxybenzamide, a potential positron emission tomography tracer for the dopamine D4 receptors. J Med Chem 53:7344–7355

Laruelle M (2000) Imaging synaptic neurotransmission with in vivo binding competition techniques: a critical review. J Cereb Blood Flow Metab 20:423–451

Laruelle M, Abi-Dargham A, van Dyck CH et al (1995) SPECT imaging of striatal dopamine release after amphetamine challenge. J Nucl Med 36:1182–1190

Laruelle M, Baldwin RM, Malison RT (1993) SPECT imaging of dopamine and serotonin. transporters with [123I]beta-CIT: pharmacological characterization of brain uptake in nonhuman primates. Synapse 13:295–309

Laruelle M, D'Souza CD, Baldwin RM et al (1997) Imaging D2 receptor occupancy by endogenous dopamine in humans. Neuropsychopharmacology 17:162–174

Lavalaye J, Booij J, Reneman L, Habraken JB, van Royen EA (2000) Effect of age and gender on dopamine transporter imaging with [123I]FP-CIT SPET in healthy volunteers. Eur J Nucl Med 27:867–869

Laymon CM, Mason NS, Frankle WG et al (2009) Human biodistribution and dosimetry of the D2/3 agonist 11C-N-propylnorapomorphine (11C-NPA) determined from PET. J Nucl Med 50:814–817

Leopoldo M, Selivanova SV, Müller A, Lacivita E, Schetz JA, Ametamey SM (2014) In vitro and in vivo evaluation of N-{2-[4-(3-Cyanopyridin-2-yl)piperazin-1-yl]ethyl}-3-[(11) C]methoxybenz-amide, a positron emission tomography (PET) radioligand for dopamine D4 receptors, in rodents. Chem Biodivers 11:1298–1308

Lewis SJ, Pavese N, Rivero-Bosch M et al (2012) Brain monoamine systems in multiple system atrophy: a positron emission tomography study. Neurobiol Dis 46:130–136

Lin KJ, Weng YH, Hsieh CJ et al (2013) Brain imaging of vesicular monoamine transporter type 2 in healthy aging subjects by 18F-FP-(+)-DTBZ PET. PLoS One 8:e75952

Lin KJ, Weng YH, Wey SP et al (2010) Whole-body biodistribution and radiation dosimetry of 18 F-FP-(+)-DTBZ (18 F-AV-133): a novel vesicular monoamine transporter 2 imaging agent. J Nucl Med 51:1480–1485

Løkkegaard A, Werdelin LM, Friberg L (2002) Clinical impact of diagnostic SPET investigations with a dopamine re-uptake ligand. Eur J Nucl Med Mol Imaging 29:1623–1629

Ma SY, Ciliax BJ, Stebbins G et al (1999) Dopamine transporter-immunoreactive neurons decrease with age in the human substantia nigra. J Comp Neurol 409:25–37

Majuri J, Joutsa J, Arponen E, Forsback S, Kaasinen V (2018) Dopamine synthesis capacity correlates with μ-opioid receptor availability in the human basal ganglia: a triple-tracer PET study. NeuroImage 183:1–6

Mamelak M, Chiu S, Mishra RK (1993) High- and low-affinity states of dopamine D1 receptors in schizophrenia. Eur J Pharmacol 233:175–176

Marazziti D, Baroni S, Masala I et al (2009) [(3)H]-YM-09151-2 binding sites in human brain postmortem. Neurochem Int 55:643–647

Martinez D, Carpenter KM, Liu F (2011) Imaging dopamine transmission in cocaine dependence: link between neurochemistry and response to treatment. Am J Psychiatry 168:634–641

Martinez D, Slifstein M, Narendran R et al (2009) Dopamine D1 receptors in cocaine dependence measured with PET and the choice to self-administer cocaine. Neuropsychopharmacology 34:1774–1782

McCauley PG, O'Boyle KM, Waddington JL (1995) Dopamine-induced reduction in the density of guanine nucleotide-sensitive D1 receptors in human postmortem brain in the absence of apparent D1:D2 interactions. Neuropharmacology 34:777–783

McCutcheon R, Beck K, Jauhar S, Howes OD (2018) Defining the locus of dopaminergic dysfunction in schizophrenia: a meta-analysis and test of the mesolimbic hypothesis. Schizophr Bull 44:1301–1311

McKeith I, O'Brien J, Walker Z et al (2007) Sensitivity and specificity of dopamine transporter imaging with 123I-FP-CIT SPECT in dementia with Lewy bodies: a phase III, multicentre study. Lancet Neurol 6:305–313

McNab F, Varrone A, Farde L et al (2009) Changes in cortical dopamine D1 receptor binding associated with cognitive training. Science 323:800–802

Moore RY, Whone AL, McGowan S, Brooks DJ (2003) Monoamine neuron innervation of the normal human brain: an 18 F-DOPA PET study. Brain Res 982:137–145

Morris G, Nevet A, Arkadir D, Vaadia E, Bergman H (2006) Midbrain dopamine neurons encode decisions for future action. Nat Neurosci 9:1057–1063

Mukherjee J, Yang ZY, Das MK, Brown T (1995) Fluorinated benzamide neuroleptics–III. Development of (S)-N-[(1-allyl-2-pyrrolidinyl)methyl]-5-(3-[18 F]fluoropropyl)-2, 3-dimethoxybenzamide as an improved dopamine D-2 receptor tracer. Nucl Med Biol 22:283–296

Nakahara H, Itoh H, Kawagoe R, Takikawa Y, Hikosaka O (2004) Dopamine neurons can represent context-dependent prediction error. Neuron 41:269–280

Narendran R, Hwang DR, Slifstein M et al (2004) In vivo vulnerability to competition by endogenous dopamine: comparison of the D2 receptor agonist radiotracer (−)-N-[11C]propyl-norapomorphine ([11C]NPA) with the D2 receptor antagonist radiotracer [11C]-raclopride. Synapse 52:188–208

Narendran R, Mason NS, Laymon CM et al (2010) A comparative evaluation of the dopamine D$_{2/3}$ agonist radiotracer [^{11}C](−)-N-propyl-norapomorphine and antagonist [^{11}C]raclopride to measure amphetamine-induced dopamine release in the human striatum. J Pharmacol Exp Ther 333:533–539

Neumeyer JL, Gao YG, Kula NS, Baldessarini RJ (1990) Synthesis and dopamine receptor affinity of (R)-(−)-2-fluoro-N-n-propylnorapomorphine: a highly potent and selective dopamine D$_2$ agonist. J Med Chem 33:3122–3124

Nørbak-Emig H, Ebdrup BH, Fagerlund B et al (2016) Frontal D2/3 receptor availability in schizophrenia patients before and after their first antipsychotic treatment: relation to cognitive functions and psychopathology. Int J Neuropsychopharmacol 19:5

Nordström AL, Farde L, Nyberg S, Karlsson P, Halldin C, Sedvall G (1995) D1, D2, and 5-HT2 receptor occupancy in relation to clozapine serum concentration: a PET study of schizophrenic patients. Am J Psychiatry 152:1444–1449

Nurmi E, Bergman J, Eskola O, Solin O, Vahlberg T, Sonninen P, Rinne JO (2003) Progression of dopaminergic hypofunction in striatal subregions in Parkinson's disease using [18F]CFT PET. Synapse 48:109–115

Nyberg S, Eriksson B, Oxenstierna G, Halldin C, Farde L (1999) Suggested minimal effective dose of risperidone based on PET-measured D2 and 5-HT2A receptor occupancy in schizophrenic patients. Am J Psychiatry 156:869–875

Oh M, Kim JS, Kim JY et al (2012) Subregional patterns of preferential striatal dopamine transporter loss differ in Parkinson disease, progressive supranuclear palsy, and multiple-system atrophy. J Nucl Med 53:399–406

Okamura N, Villemagne VL, Drago J et al (2010) In vivo measurement of vesicular monoamine transporter type 2 density in Parkinson disease with ^{18}F-AV-133. 2010. J Nucl Med 51:223–228

Otsuka T, Ito H, Halldin C et al (2009) Quantitative PET analysis of the dopamine D2 receptor agonist radioligand 11C-(R)-2-CH3O-N-n-propylnorapomorphine in the human brain. J Nucl Med 50:703–710

Palner M, McCormick P, Parkes J, Knudsen GM, Wilson AA (2010) Systemic catechol-O-methyl transferase inhibition enables the D1 agonist radiotracer R-[11C]SKF 82957. Nucl Med Biol 37:837–843

Pavese N, Simpson BS, Metta V, Ramlackhansingh A, Chaudhuri KR, Brooks DJ (2012) [^{18}F]FDOPA uptake in the raphe nuclei complex reflects serotonin transporter availability. A combined [^{18}F]FDOPA and [^{11}C]DASB PET study in Parkinson's disease. NeuroImage 59:1080–1084

Ramamoorthy S, Shippenberg TS, Jayanthi LD (2011) Regulation of monoamine transporters: role of transporter phosphorylation. Pharmacol Ther 129:220–238

Rani M, Kanungo MS (2006) Expression of D2 dopamine receptor in the mouse brain. Biochem Biophys Res Commun 344:981–986

Richfield EK, Penney JB, Young AB (1989) Anatomical and affinity state comparisons between dopamine D1 and D2 receptors in the rat central nervous system. Neuroscience 30:767–777

Rinne JO, Laine M, Kaasinen V, Norvasuo-Heilä MK, Någren K, Helenius H (2002) Striatal dopamine transporter and extrapyramidal symptoms in frontotemporal dementia. Neurology 58:1489–1493

Rivera A, Cuéllar B, Girón FJ, Grandy DK, de la Calle A, Moratalla R (2002) Dopamine D4 receptors are heterogeneously distributed in the striosomes/matrix compartments of the striatum. J Neurochem 80:219–229

Roffman JL, Tanner AS, Eryilmaz H et al (2016) Dopamine D1 signaling organizes network dynamics underlying working memory. Sci Adv 2:e1501672

Sarikaya I (2015) PET imaging in neurology: Alzheimer's and Parkinson's diseases. Nucl Med Commun 36:775–781

Sasaki T, Ito H, Kimura Y et al (2012) Quantification of dopamine transporter in human brain using PET with 18 F-FE-PE2I. J Nucl Med 53:1065–1073

Schlagenhauf F, Rapp MA, Huys QJ et al (2013) Ventral striatal prediction error signaling is associated with dopamine synthesis capacity and fluid intelligence. Hum Brain Mapp 34: 1490–1499

Schultz W (2016) Dopamine reward prediction-error signalling: a two-component response. Nat Rev Neurosci 17:183–195

Scott DJ, Stohler CS, Koeppe RA, Zubieta JK (2007) Time-course of change in [11C]carfentanil and [11C]raclopride binding potential after a nonpharmacological challenge. Synapse 61:707–714

Seeman P, Waanabe M, Grigoriadis D et al (1985) Dopamine D2 receptor binding sites for agonists. A tetrahedral model. Mol Pharmacol 28:391–399

Shah N, Frey KA, Müller ML et al (2016) Striatal and cortical β-amyloidopathy and cognition in Parkinson's disease. Mov Disord 31:111–117

Shalgunov V, van Waarde A, Booij J, Michel MC, Dierckx RAJO, Elsinga PH (2019) Hunting for the high-affinity state of G-protein-coupled receptors with agonist tracers: Theoretical and practical considerations for positron emission tomography imaging. Med Res Rev 39: 1014–1052

Shotbolt P, Tziortzi AC, Searle GE et al (2012) Within-subject comparison of [11C]-(+)-PHNO and [11C]raclopride sensitivity to acute amphetamine challenge in healthy humans. J Cereb Blood Flow Metab 32:127–136

Sibley DR, De Lean A, Creese I (1982) Anterior pituitary dopamine receptors. Demonstration of interconvertible high and low affinity states of the D-2 dopamine receptor. J Biol Chem 257:6351–6361

Skinbjerg M, Liow JS, Seneca N et al (2010) D2 dopamine receptor internalization prolongs the decrease of radioligand binding after amphetamine: a PET study in a receptor internalization-deficient mouse model. NeuroImage 50:1402–1407

Skinbjerg M, Sibley DR, Javitch JA, Abi-Dargham A (2012) Imaging the high-affinity state of the dopamine D2 receptor in vivo: fact or fiction? Biochem Pharmacol 83:193–198

Slifstein M, Kolachana B, Simpson EH et al (2008) COMT genotype predicts cortical-limbic D1 receptor availability measured with [11C]NNC112 and PET. Mol Psychiatry 13:821–827

Smith CT, Wallace DL, Dang LC, Aarts E, Jagust WJ, D'Esposito M, Boettiger CA (2016) Modulation of impulsivity and reward sensitivity in intertemporal choice by striatal and midbrain dopamine synthesis in healthy adults. J Neurophysiol 115:1146–1156

Smith TF (2010) Meta-analysis of the heterogeneity in association of DRD4 7-repeat allele and AD/HD: stronger association with AD/HD combined type. Am J Med Genet B Neuropsychiatr Genet 153B:1189–1199

Sonni I, Fazio P, Schain M, Halldin C, Svenningsson P, Farde L, Varrone A (2016) Optimal acquisition time window and simplified quantification of dopamine transporter availability using 18F-FE-PE2I in healthy controls and parkinson disease patients. J Nucl Med 57:1529–1534

Spooren A, Rondou P, Debowska K et al (2010) Resistance of the dopamine D4 receptor to agonist-induced internalization and degradation. Cell Signal 22:600–609

Stokholm MG, Iranzo A, Østergaard K et al (2017) Assessment of neuroinflammation in patients with idiopathic rapid-eye-movement sleep behaviour disorder: a case-control study. Lancet Neurol 16:789–796

Stokholm MG, Iranzo A, Østergaard K et al (2018) Extrastriatal monoaminergic dysfunction and enhanced microglial activation in idiopathic rapid eye movement sleep behaviour disorder. Neurobiol Dis 115:9–16

Stoof JC, Kebabian JW (1981) Opposing roles for D-1 and D-2 dopamine receptors in efflux of cyclic AMP from rat neostriatum. Nature 294:366–368

Strange PG (1993) New insights into dopamine receptors in the central nervous system. Neurochem Int 22:223–236

Sunahara RK, Guan HC, O'Dowd BF et al (1991) Cloning of the gene for a human dopamine D5 receptor with higher affinity for dopamine than D1. Nature 350:614–619

Suwijn SR, van Boheemen CJ, de Haan RJ, Tissingh G, Booij J, de Bie RM (2015) The diagnostic accuracy of dopamine transporter SPECT imaging to detect nigrostriatal cell loss in patients with Parkinson's disease or clinically uncertain parkinsonism: a systematic review. EJNMMI Res 5:12

Takahashi H, Takano H, Kodaka F et al (2010) Contribution of dopamine D1 and D2 receptors to amygdala activity in human. J Neurosci 30:3043–3047

Takahashi YK, Batchelor HM, Liu B, Khanna A, Morales M, Schoenbaum G (2017) Dopamine neurons respond to errors in the prediction of sensory features of expected rewards. Neuron 95:1395–1405

Thompson JL, Rosell DR, Slifstein M et al (2014) Prefrontal dopamine D1 receptors and working memory in schizotypal personality disorder: a PETstudy with [11C]NNC112. Psychopharmacology 231:4231–4240

Thomsen G, Ziebell M, Jensen PS, da Cuhna-Bang S, Knudsen GM, Pinborg LH (2013) No correlation between body mass index and striatal dopamine transporter availability in healthy volunteers using SPECT and [123I]PE2I. Obesity (Silver Spring) 21:1803–1806

Troiano AR, Schulzer M, de la Fuente-Fernandez R et al (2010) Dopamine transporter PET in normal aging: dopamine transporter decline and its possible role in preservation of motor function. Synapse 64:146–151

Tseng HH, Watts JJ, Kiang M et al (2018) Nigral stress-induced dopamine release in clinical high risk and antipsychotic-naïve schizophrenia. Schizophr Bull 44:542–551

Tuppurainen H, Kuikka JT, Viinamäki H, Husso M, Tiihonen J (2010) Extrapyramidal side-effects and dopamine $D_{2/3}$ receptor binding in substantia nigra. Nord J Psychiatry 64:233–238

Tziortzi AC, Searle GE, Tzimopoulou S et al (2011) Imaging dopamine receptors in humans with [11C]-(+)-PHNO: dissection of D3 signal and anatomy. NeuroImage 54:264–277

van de Giessen E, de Win MM, Tanck MW, van den Brink W, Baas F, Booij J (2009) Striatal dopamine transporter availability associated with polymorphisms in the dopamine transporter gene SLC6A3. J Nucl Med 50:45–52

van Dyck CH, Malison RT, Jacobsen LK et al (2005) Increased dopamine transporter availability associated with the 9-repeat allele of the SLC6A3 gene. J Nucl Med 46:745–751

Van Tol HHM, Bunzow JR, Guan HC et al (1991) Cloning of the gene for a human D4 receptor with high affinity for the antipsychotic clozapine. Nature 350:610–614

van Vliet L, Rodenhuis N, Dijkstra D et al (2000) Synthesis and pharmacological evaluation of thiopyran analogues of the dopamine D3 receptor-selective agonist (4aR,10bR)-(þ)-trans-3,4,4a,10b-tetrahydro-4-n-propyl-2H,5H-[1]benzopropyno[4,3-b]-1,4-oxazin-9-ol (PD128907). J Med Chem 43:2871–2882

van Wieringen J-P, Booij J, Shalgunov V et al (2013) Agonist high- and low-affinity states of dopamine D_2 receptors: methods of detection and clinical implications. Naunyn Schmiedeberg's Arch Pharmacol 386:135–154

Varrone A, Dickson JC, Tossici-Bolt L et al (2013) European multicentre database of healthy controls for [123I]FP-CIT SPECT (ENC-DAT): age-related effects, gender differences and evaluation of different methods of analysis. Eur J Nucl Med Mol Imaging 40:213–227

Varrone A, Fujita M, Verhoeff NP et al (2000) Test-retest reproducibility of extrastriatal dopamine D2 receptor imaging with [123I]epidepride SPECT in humans. J Nucl Med 41:1343–1451

Varrone A, Halldin C (2012a) New developments of dopaminergic imaging in Parkinson's disease. Q J Nucl Med Mol Imaging 56:68–82

Varrone A, Halldin C (2012b) Molecular imaging of the dopamine transporter. J Nucl Med 51:1331–1334

Varrone A, Marek KL, Jennings D, Innis RB, Seibyl JP (2001) [123I]beta-CIT SPECT imaging demonstrates reduced density of striatal dopamine transporters in Parkinson's disease and multiple system atrophy. Mov Disord 16:1023–1032

Varrone A, Steiger C, Schou M et al (2009) In vitro autoradiography and in vivo evaluation in cynomolgus monkey of [18 F]FE-PE2I, a new dopamine transporter PET radioligand. Synapse 63:871–880

Verhoeff NP, Kapucu O, Sokole-Busemann E, van Royen EA, Janssen AG (1993) Estimation of dopamine D2 receptor binding potential in the striatum with iodine-123-IBZM SPECT: technical and interobserver variability. J Nucl Med 34:2076–2084

Videbaek C, Toska K, Scheideler MA, Paulson OB, Moos Knudsen G (2000) SPECT tracer [123I]IBZM has similar affinity to dopamine D2 and D3 receptors. Synapse 38:338–342

Villemagne VL, Okamura N, Pejoska S et al (2011) In vivo assessment of vesicular mono-amine transporter type 2 in dementia with Lewy bodies and Alzheimer disease. Arch Neurol 68:905–912

Virostko J, Henske J, Vinet L et al (2011) Multimodal image coregistration and inducible selective cell ablation to evaluate imaging ligands. Proc Natl Acad Sci U S A 108:20719–20724

Visser I, Lavini C, Booij J et al (2008) Cerebral impairment in chronic solvent-induced encepha-lopathy. Ann Neurol 63:572–580

Volkow ND, Fowler JS, Gatley SJ, Logan J, Wang GJ, Ding YS, Dewey S (1996) PET evaluation of the dopamine system of the human brain. J Nucl Med 37:1242–1256

Wang GJ, Wiers CE, Shumay E (2019) Expectation effects on brain dopamine responses to meth-ylphenidate in cocaine use disorder. Transl Psychiatry 9:93

Wang JL, Oya S, Parhi AK et al (2010) In vivo studies of the SERT-selective [18 F]FPBM and VMAT2-selective [18 F]AV-133 radiotracers in a rat model of Parkinson's disease. Nucl Med Biol 37:479–486

Weinstein JJ, van de Giessen E, Rosengard RJ et al (2018) PET imaging of dopamine-D2 receptor internalization in schizophrenia. Mol Psychiatry 23:1506–1511

Willeit M, Ginovart N, Kapur S et al (2006) High-affinity states of human brain dopamine D2/3 receptors imaged by the agonist [11C]-(+)-PHNO. Biol Psychiatry 59:389–394

Won JH, Kim SK, Shin IC et al (2018) Dopamine transporter trafficking is regulated by neutral sphingomyelinase 2/ceramide kinase. Cell Signal 44:171–187

Yagi S, Yoshikawa E, Futatsubashi M et al (2010) Progression from unilateral to bilateral par-kinsonism in early Parkinson disease: implication of mesocortical dopamine dysfunction by PET. J Nucl Med 51:1250–1257

Zahniser NR, Molinoff PB (1978) Effect of guanine nucleotides on striatal dopamine receptors. Nature 275:453–455

Ziebell M, Andersen BB, Thomsen G et al (2012) Predictive value of dopamine transporter SPECT imaging with [123I]PE2I in patients with subtle parkinsonian symptoms. Eur J Nucl Med Mol Imaging 39:242–250

Ziebell M, Holm-Hansen S, Thomsen G et al (2010) Serotonin transporters in dopamine trans-porter imaging: a head-to-head comparison of dopamine transporter SPECT radioligands 123I-FP-CIT and 123I-PE2I. J Nucl Med 51:1885–1891

Zijlstra F, Booij J, van den Brink W, Franken IH (2008) Striatal dopamine D2 receptor binding and dopamine release during cue-elicited craving in recently abstinent opiate-dependent males. Eur Neuropsychopharmacol 18:262–270

PET Imaging of the Endocannabinoid System

12

Garth E. Terry, Vanessa Raymont, and Andrew G. Horti

Contents

G. E. Terry (✉)
Mental Illness Research, Education, and Clinical Center, Department of Veterans Affairs, VA Puget Sound, Seattle, WA, USA

Department of Psychiatry and Behavioral Sciences, University of Washington School of Medicine, Seattle, WA, USA
e-mail: geterry@uw.edu

V. Raymont
Department of Psychiatry, University of Oxford, Oxford, UK

A. G. Horti
Division of Nuclear Medicine and Molecular Imaging, Department of Radiology, Johns Hopkins School of Medicine, Baltimore, MD, USA

Abstract

The endocannabinoid system consists of cannabinoid receptors (which mediate the actions of cannabis), their endogenous ligands (endocannabinoids), and the enzymes and proteins associated with their regulation. In brain, the endocannabinoid system, in part, functions to modulate the release of other neurotransmitters via the subtype 1 (CB₁) receptor. Abnormalities of CB₁ receptor expression or endocannabinoid transmission have been associated with several neuropsychiatric diseases. Subtype 2 (CB₂) receptors are found primarily on immune and neuroimmune cells, and are overexpressed in activated microglia and neuroinflammation. Both receptors are of particular interest for biomarker development and therapeutic targets. Fatty acid amide hydrolase (FAAH) and monoacylglycerol lipase (MAGL) are responsible for the breakdown of endocannabinoids. Growing evidence supports the regulation of endocannabinoids as involved in neuropsychiatric and neuroinflammatory diseases. However, the function of endocannabinoid system components *in vivo* remains difficult to assess. Therefore, the use of functional imaging techniques, such as positron-emission tomography (PET), may be particularly useful in the assessment and quantification of the endocannabinoid system. This review covers the current understanding of PET imaging that directly targets the endocannabinoid system.

Abbreviations

2-AG	2-Arachidonoyl glycerol
AAI	Aminoalkylindoles
AChE	Acetylcholinesterase
AD	Alzheimer's disease
AEA	N-arachidonoylethanolamine, aka anandamide
AIDS	Acquired immunodeficiency syndrome
ALS	Amyotrophic lateral sclerosis

AM404	An endocannabinoid transporter inhibitor
BAT	Brown adipose tissue
BBB	Blood-brain barrier
B_{max}	Binding maximum (i.e., total receptor density)
BMI	Body mass index
BP	Binding potential
cAMP	$3'$–$5'$-Cyclic adenosine monophosphate
CB_1	Cannabinoid subtype 1
CB_2	Cannabinoid subtype 2
CNR1	Gene encoding cannabinoid subtype 1 receptor
CNR2	Gene encoding cannabinoid subtype 2 receptor
CNS	Central nervous system
COX-2	Cyclooxygenase type 2
CP-55,940	A nonclassical cannabinoid agonist
D_2	Dopamine subtype 2
DAGL	Diacylglycerol lipase
EAE	Experimental autoimmune encephalomyelitis
ECS	Endocannabinoid system
FAAH	Fatty acid amide hydrolase
FUR	Fractional uptake ratio
GABA	Gamma-aminobutyric acid
GPCR	G-protein-coupled receptor
GPR55	G-protein-coupled receptor 55
GTP	Guanosine-$5'$-triphosphate
HD	Huntington's disease
HRRT	High-resolution research tomograph
ICC	Intraclass correlation coefficient
K_D	Dissociation constant
K_i	Inhibition constant
LTD	Long-term depression
LTP	Long-term potentiation
MAGL	Monoacylglycerol lipase
MDR1	Multidrug resistance gene 1 (encodes P-gp)
mRNA	Messenger ribonucleic acid
MS	Multiple sclerosis
MS	Multiple sclerosis
mSUV	Modified standardized uptake value
MW	Molecular weight
NAPE-PLD	N-acyl-phosphatidylethanolamine-selective phospholipase D
PANSS	Positive and negative syndrome scale
PD	Parkinson's disease
PET	Positron-emission tomography
P-gp	P-glycoprotein (an efflux transporter)
PSA	Polar surface area
SNP	Single-nucleotide polymorphism

SPECT	Single-photon emission computed tomography
SUV	Standardized uptake value
TCM	Tissue compartment model
TGN	Trigeminal nerve
THC, Δ^9-THC	Δ^9-Tetrahydrocannabinol
TRPV1	Transient receptor potential vanilloid 1 (a cation channel)
TSPO	Translocator protein (18 kDa)
URB597	A FAAH inhibitor
V_T	Total distribution volume
WIN 55,212-2	An aminoalkylindole cannabinoid agonist

12.1 Introduction

12.1.1 Endocannabinoid System

Cannabis has been known to have medicinal and narcotic effects for thousands of years and is the most commonly used illegal drug in the world today (Anthony et al. 2017; Copeland and Swift 2009). However, it was not until 1964 that Δ^9-tetrahydrocannabinol (Δ^9-THC) was described by Gaoni and Mechoulam as the principal psychoactive component of cannabis (Gaoni and Mechoulam 1964) (Fig. 12.1). While over 100 plant-derived cannabinoids (phytocannabinoids) have been discovered, to date most remain insufficiently characterized (Turner et al. 2017). For approximately the last 20 years, Δ^9-THC and cannabidiol (CBD) have received increasingly focused attention for their potential therapeutic effects and their greater concentration in cultivated cannabis. In particular, Δ^9-THC

Δ^9-THC

anandamide (AEA)

arachidonoylglycerol (2-AG)
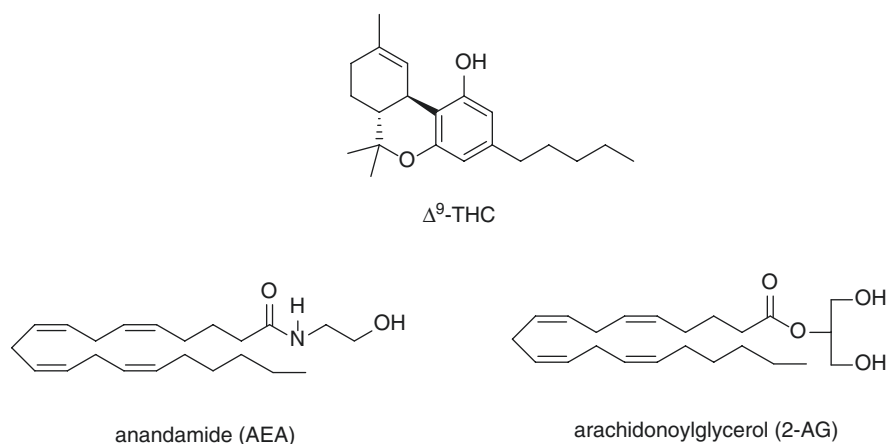
Fig. 12.1 Structure of Δ^9-THC and the endocannabinoids, anandamide (AEA), and 2-arachidonoylglycerol (2-AG)

concentration in cannabis has increased from less than 1.5% in 1980 to over 17% in 2017, and nearly 30% in regions with legalized cannabis[1] (ElSohly et al. 2000; Chandra et al. 2019; Smart et al. 2017). This has prompted the need for additional research of cannabis and cannabinoids, their impact on health, and the biology and pharmacology they have uncovered.

The effects of Δ^9-THC are primarily mediated by G-protein-coupled receptors (GPCR) discovered in the 1990s and termed cannabinoid receptors. The first cannabinoid receptor subtype, CB_1, is highly concentrated in brain and was found to be responsible for the psychotropic effects of cannabinoids (Matsuda et al. 1990; Devane et al. 1988). CB_1 receptors are abundantly expressed in hippocampus, striatum, cerebral cortex, and molecular layer of the cerebellum, and with the lowest density in the brainstem, thalamus, and white matter (Howlett et al. 2002; Lynn and Herkenham 1994; Herkenham et al. 1990, 1991; Glass et al. 1997; Iversen 2003). CB_1 is also widely expressed in the gut, liver, brown adipose tissue, and bone marrow (Massa et al. 2005).

The second cannabinoid receptor subtype, CB_2, was discovered shortly thereafter and found primarily on cells associated with the immune system (Howlett et al. 2002; Munro et al. 1993). Broadly CB_2 receptors participate in the regulation of cytokine release and function (Klein 2005). They are typically in low density in the brain (Van Sickle et al. 2005; Onaivi et al. 2006), but are overexpressed during states of neuroinflammation on activated microglia (Howlett et al. 2002). In the periphery, they have high density in spleen and leukocytes, particularly B-lymphocytes (Munro et al. 1993).

The discovery of cannabinoid receptors prompted the search for their endogenous ligands, termed endocannabinoids (*endo*genous *cannabinoids*), which could activate them. The first identified endocannabinoid, anandamide (N-arachidonoylethanolamine; AEA), was named for the Sanskrit word ananda, meaning "bliss," and has been characterized as a partial agonist for cannabinoid receptors (Fig. 12.1) (Devane et al. 1992). Subsequently, 2-arachidonoylglycerol (2-AG) was identified as a full agonist and at substantially higher concentrations in brain than anandamide, though with a lower binding affinity (Stella et al. 1997). Both anandamide and 2-AG are able to mimic several pharmacological effects of Δ^9-THC (Paradisi et al. 2006).

In contrast to monoamine neurotransmitters which are synthesized, stored in vesicles, and released upon signaling by presynaptic neurons, endocannabinoids are synthesized on demand following Ca^{2+} elevation in the postsynaptic neuron. Anandamide is cleaved from N-acyl-phosphatidylethanolamine by phospholipase D (NAPE-PLD), and 2-AG is generated from diacylglycerol hydrolyzed by

---

[1] As of this writing (mid-2019) cannabis remains largely illegal throughout the world. Uruguay and Canada have legalized cannabis for recreational use, while South Africa and Georgia have legalized the possession and consumption, but not the sale, of cannabis for recreational use. Many other countries have legalized cannabis for medicinal uses only. Cannabis remains illegal in the United States on a federal level, while laws are mixed across states and territories ranging from legal for recreational and medical use, legal for medical use only, and illegal but decriminalized to fully illegal.

diacylglycerol lipase (DAG-L) (Di Marzo et al. 2011; Marsicano et al. 2003). They subsequently diffuse across the synapse in a retrograde manner where they act on presynaptic CB_1 receptors, which in turn propagate second messenger signaling through G-stimulatory and G-inhibitory proteins, among other mechanisms. The resulting cascade of events leads to decreased cAMP production, closing of Ca^{2+} channels, and reduced mobilization of neurotransmitter-containing vesicles, and therefore an inhibition of neurotransmitter release (e.g., GABA, glutamate, dopamine).

Endocannabinoids undergo a reuptake and degradation process. Fatty acid amide hydrolase (FAAH) is primarily responsible for the breakdown of anandamide, whereas the monoacylglycerol lipase (MAGL) plays a key role in the enzymatic hydrolysis of about 85% of 2-AG (Dinh et al. 2002), with α/β hydrolase domain-6 and -12 (ABHD6 and ABHD12) additionally contributing to 2-AG catabolism. Cyclooxygenase 2 (COX-2), in addition to its production of prostaglandins from arachidonic acid, metabolizes endocannabinoids to prostacannabinoids, which in turn can participate in cell signaling (Kozak et al. 2002). Indirect evidence supports the presence of an endocannabinoid transporter on postsynaptic membranes; however no protein structure has been elucidated to confirm its existence (Felder et al. 2006; Fowler 2012). Acetaminophen (paracetamol), a widely used pain reliever which has long lacked an understood mechanism, is metabolized *in vivo* to N-(4-hydroxyphenyl)arachidonoylethanolamide (AM404), an inhibitor of the putative endocannabinoid transporter and a compound known to reduce pain (Hogestatt et al. 2005; La Rana et al. 2006; Bertolini et al. 2006).

Cannabinoid receptors, endocannabinoids, and enzymes for endocannabinoid synthesis, uptake, and degradation constitute the endocannabinoid system (ECS) (Fig. 12.2) (Joshi and Onaivi 2019). Other receptors identified as targets of
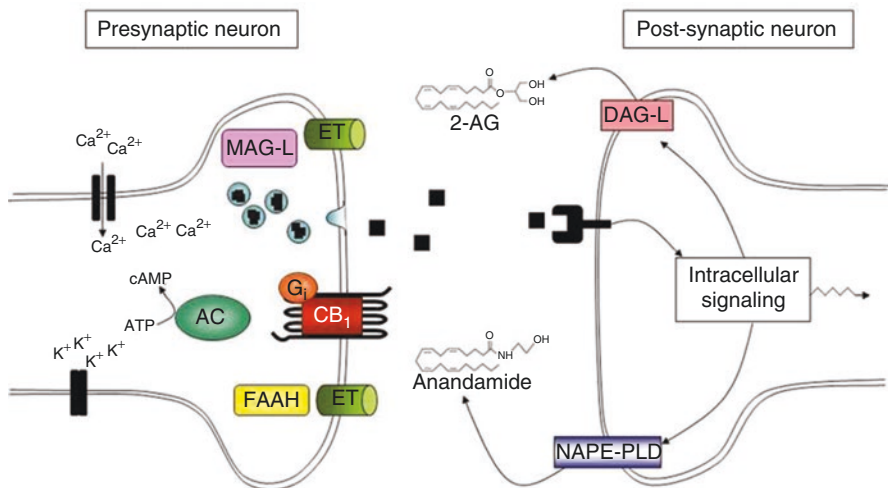
Fig. 12.2 Endocannabinoid system signaling (reprinted from Terry (2009))

phyto- and endocannabinoids (e.g., transient receptor potential cation channel sub-family V member 1 [TRPV1], orphan receptors such as GPR18 and GPR55) (Di Marzo and De Petrocellis 2010; Irving et al. 2017), putative endocannabinoids (e.g., 2-arachidonyl glyceryl ether [noladin ether]), endocannabinoid-like compounds (e.g., N-palmitoylethanolamide [PEA]), and cannabinoid receptor-binding endoge-nous compounds (e.g., hemopressin-like peptides) are considered to be closely involved with the ECS, but not definitively classified as part of it (Pertwee 2015; Pertwee et al. 2010). In particular, TRPV1 is a receptor at which anandamide has been identified as a full agonist, and may be partly responsible for the analgesic properties of the phytocannabinoid cannabidiol (CBD), which has low binding affinity to CB_1 and CB_2 (Muller et al. 2018). The ECS is fundamental to physiology, and has widespread influences on the human brain, immune system, and other organs. It is found in fish, reptiles, and all mammals, suggesting that the ECS is evolutionarily an ancient system (Elphick and Egertova 2005). Abnormalities of this system have been implicated in many cognitive, neuropsychiatric, and meta-bolic disorders (Pacher et al. 2006).

12.1.2 Physiology of the Endocannabinoid System

The ECS plays an important modulating role in homeostasis, metabolism, and immunological reactions as well as motor functions, learning, and reward process-ing. In the brain, endocannabinoids mostly act on presynaptic CB_1 receptors as ret-rograde messengers and modulate the neurotransmitters GABA-A, dopamine, glutamate, and opioids, as described above (Schlicker and Kathmann 2001; Wilson and Nicoll 2002). While this represents a rather straightforward model, cannabinoid receptors possess a richness of pharmacology and present challenges for research. For example, CB_1 and CB_2 receptors are associated with a variety of GPCR-associated second messenger systems other than G-inhibitory and G-stimulatory proteins, such as mitogen-activated protein kinase (MAPK), phosphatidylinositol-3-kinases (PI3K), and G-protein inward-rectifying potassium (GIRK) channels. In addition, as GPCRs they have the ability to be in high-affinity states (G-protein coupled and agonist preferring), in low-affinity states (G-protein uncoupled), and constitutively active (*i.e.*, engaging in signal transduction without the binding of a ligand). However, due to the lipophilicity of endocannabinoids and their ability to travel within the plasma membrane, they may laterally translocate to the binding site; thus, the description of true inverse agonist activity of these receptors has been called into question in lieu of antagonist and/or partial agonist inhibition of baseline endocannabinoid activity. A substantial portion of CB_1 receptors can be internalized in endosomes, or located on intracellular lysosomes and mitochondria, increasing its receptor reserve (Zou and Kumar 2018). Finally, cannabinoid receptors are able to undergo homo- and heteromerization with other GPCRs with cross-cell transduc-tion signaling.

Generally, increased or decreased endocannabinoid neurotransmission results in decreases or increases in neurotransmitter release, respectively (Iversen 2003),

and additionally, changes in neurotransmitter function can modulate endocannabinoid signaling (Degroot and Nomikos 2007). By inhibiting excitatory or inhibitory signals, endocannabinoids facilitate long-term potentiation (LTP) or depression (LTD) between neurons both directly and indirectly, which enables the process of learning and memory formation (Di Marzo et al. 2004; Riedel and Davies 2005). The process of learning and memory formation likely depends on the timing and location of endocannabinoid release, which permits the extinction of previous memories (Chhatwal et al. 2005). Understandably then, the ECS plays an important role in neural development and synaptic formations given that repeated stimulation between excitatory and inhibitory connections is part of synaptic pruning and neuronal maturation (Dow-Edwards and Silva 2017). Therefore, global stimulation of CB_1 receptors, as from cannabis, interrupts the local formation of LTP and LTD and delays learning and memory, and can impact neuronal development. As well, aberrant expression or function of the ECS may represent change of the system itself, or compensatory changes of other neurotransmission systems, and thus has the potential as a biomarker or therapeutic target in numerous neuropsychiatric disorders.

CB_1 receptors are associated with a wide range of behaviors, including cognition, pain perception, movement, drug addiction, and memory consolidation. Stimulation of these receptors also has anti-inflammatory, antioxidant, and neuroprotective effects (Drysdale and Platt 2003), as well as a role in neuronal gene expression (Piomelli 2003) and endocrinological modulation (Cota et al. 2007). CB_1 receptor expression is affected by the estrous cycle in females (Rodriguez de Fonseca et al. 1994), suggesting its sensitivity to estrogen and potential for sex-related differences in expression or function. As such, when examining the ECS, differences between males, females, and phases of the estrous cycle may need to be taken into consideration.

Less is known about the physiological role of CB_2 receptors. In the absence of inflammatory CNS disease, CB_2 receptors are not expressed in any significant amount in the human brain with the exception of the brainstem, where low concentrations can be found (Van Sickle et al. 2005). However, in inflammatory conditions such as cancer, atherosclerosis, peripheral inflammation, and several brain disorders there is a marked upregulation of CB_2 receptors, primarily in activated microglia, which can be ten times that of basal levels (Maresz et al. 2005; Cabral and Marciano-Cabral 2005). In neurodegenerative brain disorders, CB_2 receptor upregulation was noted postmortem in microglia surrounding and coincident with the beta-amyloid plaques of patients with Alzheimer's disease (Benito et al. 2003), and related to the extent and progression of neuronal loss in Huntington's disease (Sapp et al. 2001). CB_2 agonists have been found to stimulate human macrophages to remove beta-amyloid in in vitro studies, thereby representing a potential therapeutic approach in the treatment of neurodegenerative disorders (Tolon et al. 2009). CB_2 receptors have been implicated in mediating pain transmission (*i.e.*, nociception) and in the function and communication of immune cells (*e.g.*, mediating cytokine release). CB_2 receptor agonists have been shown to have analgesic effects and decrease lymphocyte function (Hsieh et al. 2011; Cencioni et al. 2010). In brain cancers, CB_2

receptor expression has been found to correlate with the stage of tumor malignancy (Ellert-Miklaszewska et al. 2007; Calatozzolo et al. 2007).

As FAAH is highly involved in controlling the concentration of endocannabinoids, it has a key role in determining endocannabinoid tone. In brain, FAAH expression differs from that of CB_1 receptors with regard to distribution and density. The gene encoding FAAH, *FAAH*, contains an estrogen-binding site on the promoter region (Waleh et al. 2002), again suggesting sex differences in the ECS. Genetic knockout or pharmacologic blockade of FAAH has been shown to reduce anxiety and depression in animal models (Moreira et al. 2008), and an identified single-nucleotide polymorphism on *FAAH* and microdeletion on a pseudogene leading to FAAH loss of function have been associated with reduced anxiety and pain sensitivity (Habib et al. 2019).

12.1.3 Pharmacology of the Endocannabinoid System

Cannabis has been consumed in its natural form since 3000 years, and has been utilized as an analgesic, appetite stimulant, anti-inflammatory, and decongestant, among other uses (Booth 2005). The ECS is vital to learning, memory, motor behavior, pain and weight control, as well as inflammation, gut motility, and intracellular apoptosis. Thus, cannabinoid drugs are being used or have the potential for use in treating multiple pathologies, including anorexia (in AIDS and cachexia secondary to cancer), emesis, obesity, pain, inflammation, schizophrenia, multiple sclerosis, neurodegenerative disorders, epilepsy, stroke, glaucoma, osteoporosis, cardiovascular disorders, and cancer (Di Marzo et al. 2004; Kogan and Mechoulam 2007; Howlett 1995; Pertwee 1999; Timpone et al. 1997).

Despite the potential therapeutic value of the cannabinoid partial agonist Δ^9-THC and its analogues, side effects have been a problem and the potential for abuse has been a concern (Howlett et al. 2002; Howlett 1995, 2002; Murray et al. 2007), although it has become apparent that adverse effects may be reduced by developing subtype-selective drugs (Hertzog 2004). Two cannabinoid agonists on the market in the United States, dronabinol (Marinol, Δ^9-THC) and nabilone (Cesamet, a THC synthetic analogue), are approved for treatment of nausea, vomiting, and appetite stimulation in cancer and AIDS. Nabiximols (Sativex®), a Δ^9-THC and cannabidiol mixture, is available in some EU countries and Canada, as the treatment for symptoms of multiple sclerosis. Cannabidiol (Epidiolex) has been approved in the United States for seizures associated with the severe pediatric disorders Lennox-Gastaut and Dravet syndromes.

The first clinically useful selective CB_1 inverse agonist, rimonabant, has been used as an anti-obesity medication, and was investigated for use in alcohol and tobacco addiction (Van Gaal et al. 2005; Pi-Sunyer et al. 2006; Rosenstock et al. 2008; Despres et al. 2009; Nissen et al. 2008; Soyka et al. 2008; Cahill and Ussher 2007). In addition to its central mechanism by decreasing appetite, rimonabant mediated improvements in peripheral comorbidities of obesity, including increased HDL, decreased triglyceride levels, and decreased hemoglobin A_{1c} (Van Gaal et al.

2005). Later, rimonabant was withdrawn from the market due to its central side effects of depression and anxiety. CB_1 inverse agonists that act predominantly peripherally (thus avoiding psychiatric side effects (Cluny et al. 2010)) are under preclinical investigation (Chorvat 2013). A number of FAAH inhibitors (notably PF-04457845 and URB597) are also under preclinical investigation to target anxiety disorders (Piomelli et al. 2006) and cannabis withdrawal (D'Souza et al. 2019).

12.1.4 Special Considerations for Radioligand Development and PET Imaging of the Endocannabinoid System

Until recently, only *in vitro*, animal model, electrophysiological, behavioral, and postmortem data existed on the ECS. However, there is a need for direct functional measurement in human subjects given the differences between species (Howlett et al. 2002; Pertwee et al. 2010). There are several important applications of functional imaging of the central CB_1 receptor using PET and SPECT (Horti and Van Laere 2008; Van Laere 2007). They have a role in planning drug therapy using inverse agonists or antagonists. Quantitative information about the receptor occupancy can be obtained after a titration of individual doses and existing radioligands. They also allow for the investigation of CNS side effects, which are frequent problems, particularly with CB_1 receptor blockade. PET or SPECT imaging allows information from preclinical models to be tested in humans, and may also lead to the development of novel diagnostic biomarkers where marked regional up- or downregulation is present. These imaging techniques can be used to examine the interactions of the ECS with other neurotransmitter systems (*e.g.*, GABA-A, dopamine, and opioid systems). Functional imaging could provide quantitative measurements of endocannabinoid release and allow study of its effects in pathological and cognitive states. However, more data is needed on the sensitivity of existing cannabinoid ligands to displacement by endocannabinoids.

Multiple efforts have been undertaken to probe the ECS through imaging. Methods such as $[^{15}O]H_2O$ or $[^{18}F]FDG$ PET, or fMRI, do not directly probe the ECS, though they have provided information regarding the effects of cannabinoids on the brain and behavior. Several studies have evaluated the effect of cannabis and Δ^9-THC on the dopaminergic system with mixed results; while animal studies have demonstrated dopamine release in the nucleus accumbens after exposure to Δ^9-THC, *in vivo* human studies using PET have demonstrated little to no dopamine release, suggesting alternative neuromolecular mechanisms for reinforcement and addiction (Zehra et al. 2018; Bloomfield et al. 2016; Urban and Martinez 2012). While these results are intriguing, they are outside the scope of this review, and have been described elsewhere (Martin-Santos et al. 2010; Bloomfield et al. 2019).

12.1.4.1 Radioligand Requirements

Generally, PET radioligands for quantification of cerebral receptors must possess a variety of imaging properties which have been previously described (Eckelman et al. 1979; Waterhouse 2003; Pike 2009; Zhang and Villalobos 2017). Briefly, the

most important characteristics of successful radioligands include high binding affinity with high selectivity for the intended target and low nonspecific binding, and characteristics generally predictive of blood-brain barrier penetration including moderate lipophilicity, low-to-moderate molecular weight, and appropriate polar surface area (PSA). Rapid clearance from the blood, appropriate brain kinetics, and absence of active radiometabolites are also among the crucial imaging properties of cerebral PET radioligands. As well, radioligands must be safe for human use, and possess a low radiation burden and low toxicity. There is certain serendipity in the development of novel PET radioligands because relationships of some physical-chemical properties with imaging properties are still not fully understood.

The typical range of essential parameters for successfully developed PET radioligands is summarized in Table 12.1. It is conventionally agreed that most good CNS PET radioligands with reasonable BBB permeability and minimal nonspecific binding should exhibit lipophilicity of $\log D_{7.4} = 0–4$. Radioligands with a low value of $\log D_{7.4}$ are likely to exhibit a low BBB permeability, whereas very lipophilic compounds bind to plasma proteins and produce a low concentration of free radioligand in the blood and, correspondingly, show poor permeability through the BBB, and can produce high nonspecific binding. The high lipophilicity of most cannabinoids and cannabinomimetic ligands ($\log D_{7.4} \gg 4$) remains a main concern of medicinal radiochemists who are involved in the development of CB_1 and CB_2 PET radioligands. A number of high-affinity-labeled cannabinoids demonstrated poor imaging properties due to their high lipophilicity. Development of high-affinity cannabinoids with reduced lipophilicities represents a difficult undertaking (Katoch-Rouse et al. 2003). Most successful CB_1 and CB_2 radiotracers reviewed and shown below that were developed in the last few years exhibit relatively high lipophilicity values ($\mathrm{clog}D_{7.4} = 3.3–6.0$).

The classic Lipinski "rule of 5" that proposes an upper limit of molecular weight (MW) of 500 as acceptable for orally absorbed drugs seems to be valid for the majority of successful PET radiotracers for brain imaging that are administered intravenously in humans. PSA is used for characterization of the transport and partitioning properties of cerebral drugs and radiotracers. PSA embodies an optimal combination of H-bonding, molecular polarity, and solubility. A common measure of brain/blood distribution (logBB) can be calculated as a simple function of lipophilicity and PSA. The great majority of CNS drugs exhibit a PSA value of <70 Å^2 (Ertl 2008). Calculation of PSA for all currently available PET radioligands for CNS receptor imaging in humans suggests a window of opportunity PSA <84 Å^2 (Table 12.1) (Horti 2011). It is likely that successful CB_1 and CB_2 radioligands for

Table 12.1 Molecular descriptors of successful PET radioligands ($n = 23$) for imaging of brain-binding sites in humans (Horti 2011)

Molecular property	Range	Mean ± SD
Molecular weight (Dalton)	157–490	319 ± 87
Lipophilicity, clogD$_{7.4}$	−1.65 to 6.00	2.1 ± 1.8
Polar surface area, PSA (Å^2)	23–84	47 ± 19

PET imaging should display the molecular property range that is shown in Table 12.1.

An additional component to the BBB is the presence of efflux transporters, which prevent entry and/or eject substrates from the brain (Pike 2009). In particular, permeability glycoprotein (P-gp)-mediated efflux has proven to be a burden to CNS drug and radiotracer development. Δ^9-THC and several other cannabinoid ligands are partial substrates for this particular transporter (Bonhomme-Faivre et al. 2008a). P-gp is normally expressed at the BBB and blood-testes barrier to protect these sensitive tissues from potentially harmful compounds, and is sometimes overexpressed on cancer cells, causing multidrug resistance (hence the gene name, *MDR1*) (Ambudkar et al. 2003). As a result, compounds that act as substrates for P-gp are prevented from entering and accumulating in the brain; many CNS drug and radiotracer candidates have been abandoned due to this limitation.

12.1.4.2 Binding Site Density and the Radioligand Binding Affinity

An advantage of PET is its quantitative ability, and the main quantitative measures are typically standardized uptake value (SUV), distribution volume (V_T), and binding potential (*BP*). Organ uptake of radioactivity is generally measured as SUV (or %SUV), which corrects only for injected radioactivity and total body weight, but does not adjust for nonspecific binding, free and unbound radioligand, and peripheral metabolism of the radioligand. Therefore, SUV and its derivative measures can reflect relative biodistribution of the imaging target, but might not accurately reflect target density. At equilibrium, both *BP* and V_T are proportional to the density of available receptor-binding sites (B_{max}) and the binding affinity of the radioligand; a ligand's binding affinity is inversely proportional to its K_D (binding affinity = $1/K_D$; $BP = B_{max}/K_D$). A full description, derivation, and definition of related parameters can be reviewed elsewhere (Innis et al. 2007). The cerebral receptors with a greater value of B_{max} exhibit greater *BP* values than those of the receptors with low B_{max}. Obviously, the binding affinity of a cerebral radioligand has to be optimally high in order to gather sufficiently quantitative data. However, it is also essential to keep in mind that CNS radioligands with binding affinities that are too high can demonstrate slow or even seemingly irreversible brain kinetics that may complicate quantification of the receptor. Additionally, radioligands must demonstrate sufficient specific signal, and thus have low affinity for other nontarget receptors or proteins, and low nonspecific binding to proteins, lipids, or extracellular matrix.

CB_1 receptor radioligands have been successfully developed in spite of their moderately high lipophilicity due in part to the high B_{max} of CB_1 receptors in the CNS (Howlett et al. 2002). The low density of CB_2 receptors then likely creates an additional need for CNS radioligands to have a lower or more moderate lipophilicity.

Estimation of required binding affinities using a conventional approach (Eckelman et al. 1979) suggests that a successful CB_1 receptor PET radioligand should exhibit a moderately high binding affinity with a low nanomolar value of K_i or even lower. B_{max} data for the CB_2 subtype in normal mammalian brain tissue and during neuroinflammation are not available yet, but expression of *CNR1* gene

transcripts in the normal mouse brain stem is 100 times the *CNR2* gene expression (Onaivi et al. 2006). These results make us to believe that a good CB_2 receptor radioligand for PET should exhibit very high binding affinities with K_i values in the picomolar range.

12.2   Imaging of CB_1 Receptors

Radioligands that have been developed for imaging CB_1 receptors may be broadly categorized as first- and second-generation compounds. As discussed below, first-generation compounds were limited by their low specific binding and poor brain uptake. Second-generation compounds achieved success largely by retaining a high binding affinity with more moderate lipophilicity. Pharmacokinetic modeling of these radioligands is challenging; however these compounds have been used in numerous clinical investigations.

### 12.2.1   Initial CB_1 Radioligands and Imaging Studies

12.2.1.1   (−)-5′-[^{18}F]-Δ^8-THC

The starting point in the development of CB_1 receptor PET radioligands was established when a ^{18}F-derivative of Δ^8-THC (Fig. 12.3), one of the active constituents of marijuana, was synthesized in 1991 (Charalambous et al. 1991). The radioligand was studied in mice and baboons. The mouse study demonstrated some initial brain uptake of (−)-5′-[^{18}F]-Δ^8-THC (1% ID/g tissue, 5 min) with rapid clearance. The clearance of radioactivity from the baboon brain was also rapid and no specific binding was observed. The relatively low binding affinity of the radioligand (K_i = 57 nM) (Compton et al. 1993), its potentially P-gp-mediated efflux (Bonhomme-Faivre et al. 2008b), and, most importantly, its high lipophilicity (clogD$_{7.4}$ = 6.9) are the likely factors behind the discouraging imaging results.

12.2.1.2   Radiolabeled CB_1 Antagonists, Derivatives of SR141716 (Rimonabant)

In 1994 the discovery of rimonabant, a highly selective and potent CB_1 receptor antagonist, by Sanofi-Aventis (Rinaldi-Carmona et al. 1994) stimulated progress in the development of PET and SPECT radioligands for imaging CB_1 receptors. Several research groups synthesized many analogues of rimonabant and

Fig. 12.3 Structure of (−)-5′-[^{18}F]-Δ^8-THC, the first cannabinoid PET radioligand

(-)-5′-[^{18}F]fluoro-Δ^8-THC
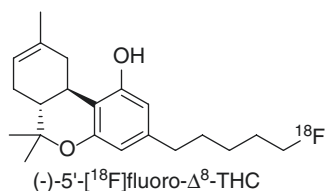
radiolabeled some of them for emission tomography studies (Katoch-Rouse et al. 2003; Lan et al. 1996, 1999; Gatley et al. 1996, 1998; Mathews et al. 1999, 2000, 2002; Katoch-Rouse et al. 2002; Nojiri and Ishiwata 2008) (Fig. 12.4). While more
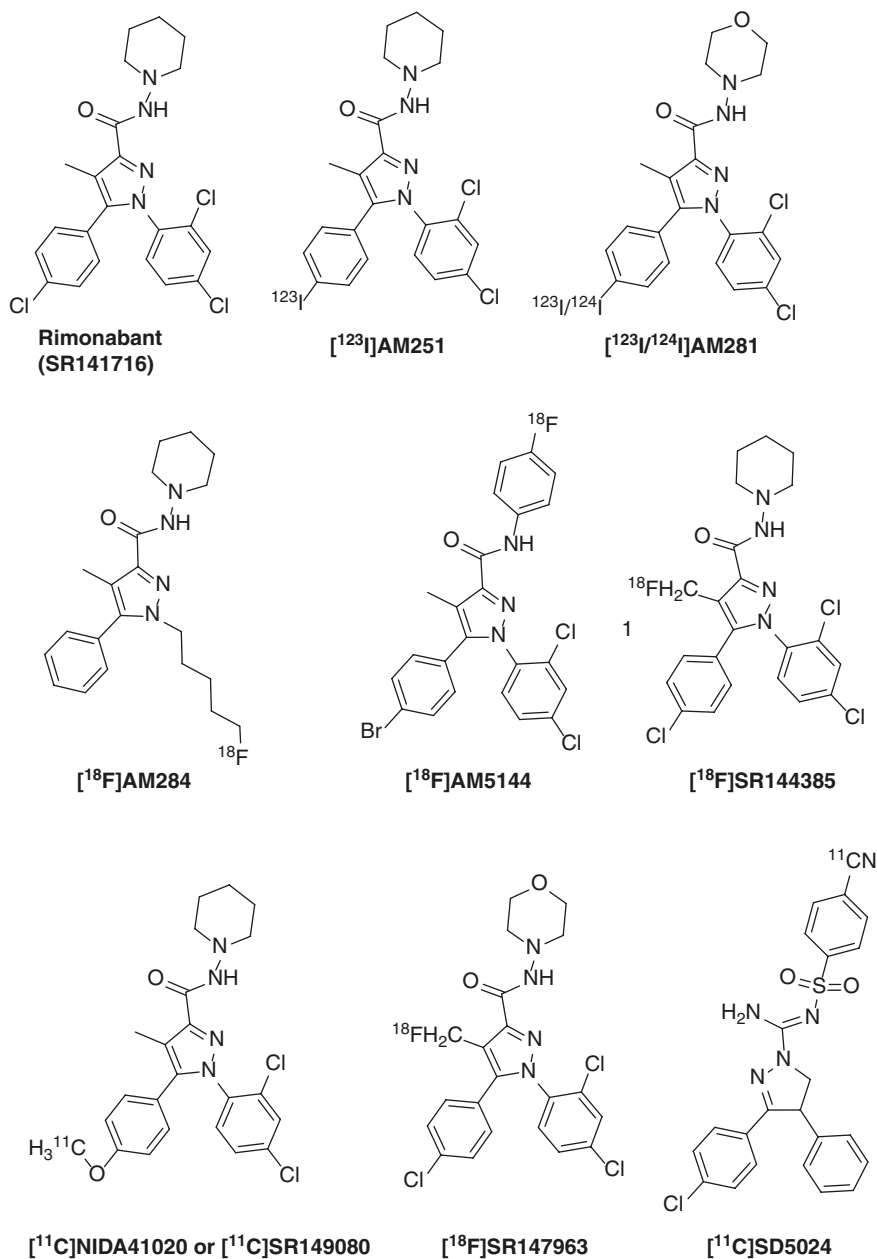
Fig. 12.4 Initial radiolabeled analogues of rimonabant and structurally related compounds

details on the initial stage of CB_1 radioligand development can be obtained from the original literature and previous reviews (Horti and Van Laere 2008; Gatley et al. 2004) a brief summary of the most representative initial radioprobes is given below.

Iodinated analogues of SR141716, AM251 and AM281, exhibited high and moderate CB_1 receptor-binding affinity, respectively, and good CB_1/CB_2 selectivity (Lan et al. 1999) and were radiolabeled with ^{123}I for SPECT studies (Lan et al. 1996; Gatley et al. 1998) (Fig. 12.4). The molecular weights of AM251 and AM281 are rather high (>500) for passive BBB transport (Table 12.2). In mouse experiments, $[^{123}I]$AM251 and $[^{123}I]$AM281 demonstrated reasonable specific brain uptake (Table 12.2) and both radioligands were found to be suitable for further baboon SPECT studies. In baboon experiments, $[^{123}I]$AM251 exhibited little brain uptake, whereas $[^{123}I]$AM281 showed good permeation of the blood-brain barrier (Gatley et al. 1998). A likely explanation for these results is the high lipophilicity of $[^{123}I]$AM251 and lower lipophilicity of $[^{123}I]$AM281 (Table 12.2) that is within the conventional range for *in vivo* radioligands. Notably, both radioligands manifest PSAs that are within the range for passive blood-brain transport (Table 12.2). The highest regional accumulation of $[^{123}I]$AM281 in the baboon brain was in the cerebellum, cortex, and striatum, and lower in the other regions. A blocking study with rimonabant demonstrated that $[^{123}I]$AM281 specifically bound to CB_1 receptors in baboon cerebellum but the value of the signal-to-noise ratio was moderate (Table 12.2). Substantial nonspecific binding was observed in other brain regions. In spite of the modest imaging results in animals $[^{123}I]$AM281 remained the best available CB_1 receptor radioligand for almost a decade and the only hope for *in vivo* CB_1 receptor imaging in humans.

The first CB_1 receptor SPECT imaging study in humans was performed with $[^{123}I]$AM281 in six patients suffering from Tourette's syndrome before and after Δ^9-THC treatment (Berding et al. 2004). The radioligand displayed some brain uptake that did not change significantly after Δ^9-THC treatment. However, V_3" declined in the only patient that showed a treatment response suggesting that specific binding of $[^{123}I]$AM281 in human subjects is mediated by CB_1 receptors. Because of the low specific signal and high nonspecific binding in human subjects, it was concluded that $[^{124}I]$AM281/PET could give better results than $[^{123}I]$AM281/SPECT because PET provides better image statistics than SPECT.

Human PET imaging with $[^{124}I]$AM281 in a single patient with schizophrenia was performed by a research group from MHH (Berding et al. 2006). The radioligand manifested limited accumulation in regions enriched with CB_1 receptors: the striatum and pallidum (DVR − 1 = 0.3–0.4), and cerebral cortex and cerebellum (DVR − 1 = 0.2). It was also stated that the high radiation burden of ^{124}I, a radionuclide with 4-day half-life, represents a radiation safety issue in human subjects. The low specific signal, high nonspecific binding, and safety concerns were the main reasons why $[^{124}I]$AM281-PET was never used again in clinical experiments.

In summary, initial studies with radiolabeled analogues of rimonabant (Table 12.2) demonstrated that CB_1 receptor imaging is a tough nut to crack. Structure-imaging properties of these radioligands suggest that most of them exhibit lipophilicity that is too high ($logD_{7.4} > 4$) and/or binding affinity that is too low

Table 12.2 Physical-chemical and *in vivo* imaging characteristics of the first generation of radioligands for PET/SPECT imaging of CB_1

Code name	M.W.[a] (Dalton)	K_i^{CB1} (nM)	K_i^{CB2} (nM)	$clogD_{7.4}$[b]	PSA[b]	Target-to-nontarget region ratio − 1			References
						Mouse	Monkey	Human	
Analogues of rimonabant									
[123I]AM251	555	0.6–1	2290	5.3	50	0.7[d]	Low uptake	–	Lan et al. (1999), Gatley et al. (1996, 1998)
[123I]AM281 or [124I] AM281	557	4.5	4200	3.9	59	~0.9[d]	~0.4[e]	0.21[i] 0.37[i]	Gatley et al. (1998), Berding et al. (2004, 2006); Gifford et al. (1997)
[18F]AM284	372	30	–	5.0	50	0.4[f]	–	–	Gatley et al. (2004), Li et al. (2005)
[18F]AM5144	519	31	–	5.7	47	–	0.5[g]	–	Li et al. (2005)
[18F]SR144385	482	14[c]	1000[e]	4.8	50	1.5[h]	–	–	Mathews et al. (1999, 2000)
[18F]SR147963	484	120[c]	–	3.4	59	0.7[h]	–	–	Mathews et al. (2000)
[11C]NIDA41020 or [11C] SR149080	459	4.1–16	800	4.0	59	1.2[g]	0.5[g]	–	Katoch-Rouse et al. (2002, 2003); Mathews et al. (2002)
[11C]SD5024	464	0.5	>5000	2.8	120	–	0.8[l]	–	Donohue et al. (2008a)
Indole derivatives									
[18F]NIDA54	400	0.7	–	3.8[j]	25	–	0.7	–	Willis et al. (2005)
[18F]PipISB	492	1.5[k]	–	5.0	80	–	0.9	–	Finnema et al. (2009), Donohue et al. (2008b)

[a]Molecular weight
[b]Lipophilicity ($clogD_{7.4}$) and polar surface area (PSA) are calculated with ACD/Structure Designer software
[c]IC_{50} (Mathews et al. 2000)
[d]Cerebellum/brain stem ratio −1
[e]Cerebellum baseline/cerebellum block with rimonabant ratio −1
[f]Whole-brain baseline/whole brain blocked with rimonabant ratio −1
[g]Cerebellum/thalamus ratio −1
[h]Hippocampus/thalamus ratio −1
[i]Binding potential
[j]Experimental data
[k]In vitro functional binding activity (K_b)
[l]Striatum/pons−1 (time-uptake curves)

(Table 12.2). As a result, animal studies with these radioligands showed either little brain uptake or some brain uptake with high nonspecific binding and relatively low target-to-nontarget ratio − 1 value (<1). It is noteworthy that within the initial series of radioligands the most reasonable imaging properties were exhibited by the least lipophilic radioligand [123/124I]AM281, which also manifested a moderate CB_1 receptor-binding affinity (Table 12.2). [123I]AM251, an analogue of AM281 with excellent binding affinity but high lipophilicity, showed little brain uptake in monkey and was clearly not suitable for PET studies.

12.2.1.3   Radiolabeled Aminoalkylindole Derivatives and Structurally Related Compounds

Aminoalkylindoles (AAI) that are exemplified by WIN-55,212–2 (Fig. 12.5) represent a large group of compounds that exhibit typical cannabinoid pharmacology. Because the structure-activity relationship for AAIs is well developed (Huffman et al. 2005) and many AAI display excellent CB_1 affinity, it is not a surprise that several compounds of this class have been radiolabeled for PET or SPECT application (Willis et al. 2005; Finnema et al. 2009; Donohue et al. 2008b; Deng et al. 2005; Makriyannis and Deng 2001; Willis et al. 2003; Tamagnan et al. 1999).

The most notable PET radioligands among AAI are [18F]NIDA54 (Willis et al. 2005) and [18F]PipISB (Finnema et al. 2009; Donohue et al. 2008b). [18F]NIDA54 manifests greater binding affinity and more appropriate molecular weight, PSA, and lipophilicity for a CNS radioligand, but both radioligands exhibit comparable specific binding in monkey brain. This finding can be explained by the functional properties of the inverse agonist [18F]PipISB that should bind with a greater population of CB_1 receptors than agonist [18F]NIDA54. Neither [18F]NIDA54 nor [18F]PipISB were sufficiently good CB_1 radiotracers in animal experiments to initiate further clinical investigation.

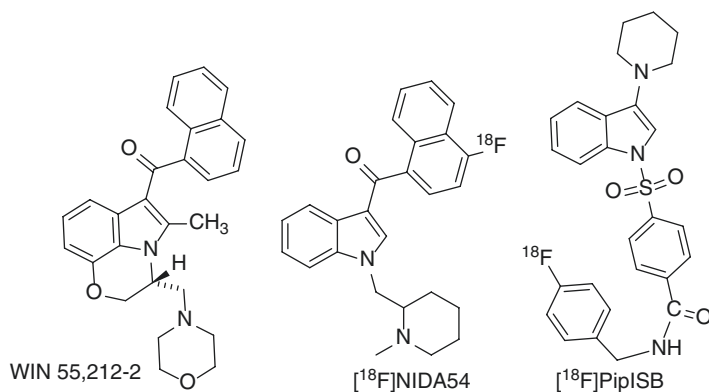**Fig. 12.5** Aminoalkylindole derivatives

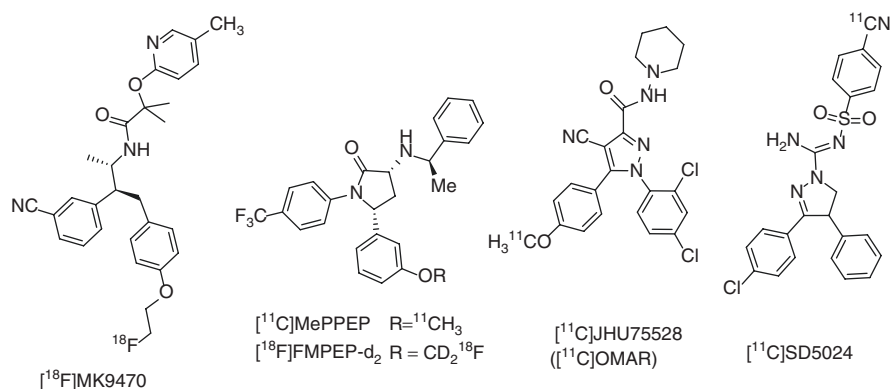## 12.2.2 Current CB$_1$ Receptor Radioligands for Human PET Imaging

12.2.2.1 [^{11}C]OMAR ([^{11}C]JHU75528)

[^{11}C]OMAR ([^{11}C]JHU75528) was the first CB$_1$ selective radioligand with adequate properties for PET imaging (Horti et al. 2006; Fan et al. 2006). Structurally [^{11}C]OMAR (Fig. 12.6) is an analog of rimonabant (Fig. 12.4) with comparable CB$_1$ receptor-binding affinity and good CB$_1$/CB$_2$ selectivity. The lipophilicity of OMAR is considerably lower because the hydrophobic methyl and chlorine substituents of the rimonabant molecule are replaced with cyano- and methoxy-groups that exhibit negative constants of lipophilicity ($\pi = 0.56$, 0.71, -0.57, and -0.02, correspondingly (Kubinyi 1995)), but the PSA value of OMAR is relatively high (Table 12.3). An *in vitro* functional assay demonstrated that OMAR is a cannabinoid antagonist (Fan et al. 2009).

Radiosynthesis of [^{11}C]OMAR is straightforward (Fan et al. 2006) and is achieved by ^{11}C-methylation of the corresponding phenol precursor that is currently commercially available, or can be prepared as described (Gao et al. 2012).

In mice and baboon studies, [^{11}C]OMAR manifested promising imaging results (Table 12.3). In comparison with the previously reported CB$_1$ receptor radiotracers of the first generation (Table 12.2), [^{11}C]OMAR showed substantially greater signal-to-noise ratios. Pharmacological evaluation of [^{11}C]OMAR in mice demonstrated that the radioligand labels CB$_1$ receptors specifically and selectively and does not bind to various other cerebral receptors including D$_1$, D$_2$, D$_5$, 5-HT$_{2A}$, 5-HT$_{1C/2C}$, opioid, and α4β2-nAChR. The specific *in vivo* binding of [^{11}C]OMAR in CD1 mice was blocked by selective CB$_1$ antagonists in a dose-dependent manner (Horti et al. 2006). MicroPET studies with [^{11}C]OMAR showed a 50% higher brain uptake in wild-type mice versus CB$_1$ knockout animals (Herance et al. 2011).

Baboon PET studies demonstrated that [^{11}C]OMAR exhibits good values of BP in CB$_1$ receptor-rich brain regions (Table 12.3) and reasonable total brain uptake

Fig. 12.6 Currently available CB$_1$ receptor PET radioligands for human studies

Table 12.3 Physical–chemical and *in vivo* imaging characteristics of the clinical radioligands for PET imaging of CB_1

Code name	M.W.[a] (Dalton)	clog$D_{7.4}$[b]	PSA	K_i^{CB1} (nM)	K_i^{CB2} (nM)	Target-to-nontarget region ratio −1			References
						Mouse	Nonhuman primate	Human	
[¹¹C]OMAR	470	3.3–3.6[c]	83	11; 2.05[f]	2700 5250	2.4	1.4	1.0	Horti et al. (2006), Fan et al. (2006), Wong et al. (2010a), Tsujikawa et al. (2014)
[¹⁸F] MK-9470	489	4.9	84	0.7; 0.10	44	–	~3–4	3	Burns et al. (2007), Van Laere et al. (2008a), Tsujikawa et al. (2014)
[¹¹C] MePPEP	454	4.77 ± 0.27[c]	42	0.5[d] 0.11[f]	363	2.3	~2	1.4	Terry et al. (2008), Yasuno et al. (2008), Tsujikawa et al. (2014)
[¹⁸F] FMPEP-d_2	474	4.24 ± 0.08[c]	42	0.2[d] 0.11[f]	669	–	~2.2	1.8[e]	Donohue et al. (2008c), Terry et al. (2009), Tsujikawa et al. (2014)
[¹¹C] SD5024	464	3.79 ± 0.09[c]	120	0.47[f]	n/a		~2.2	~1.1	Tsujikawa et al. (2014)

[a]Molecular weight
[b]Lipophilicity (clog$D_{7.4}$) and PSA are calculated with ACD/Structure Designer software
[c]Experimental data
[d]In vitro functional binding activity (K_b)
[e]2-h scanning
[f]Measured in human parietal cortex

(%SUV = 150%). A blockade PET study with rimonabant showed that *in vivo* binding of [^{11}C]OMAR in baboon brain is mediated by CB_1 receptors (Horti et al. 2006). Kinetic analysis suggests that [^{11}C]OMAR rapidly reaches the steady state in the baboon brain before the end of the 90-min PET scanning session, which is a logistical advantage of [^{11}C]OMAR versus other available PET radioligands (see below).

[^{11}C]OMAR was used by the Johns Hopkins group under an Investigational New Drug Application, approved by the FDA, for quantification of cerebral CB_1 receptors in healthy subjects (Fig. 12.7) and schizophrenia patients (see Sect. 3.3) (Wong et al. 2010a). Within ten control male subjects, [^{11}C]OMAR peaked at approximately 20 min postinjection (% SUV = 136–207% in the putamen, Table 12.4) and decreased gradually thereafter to reach a SUV between 80 and 117% at 90 min. The globus pallidus showed the highest V_T (1.47 ± 0.25), with a range of 0.95–1.82 in individual subjects. The cingulate cortex (mean 1.23 ± 0.16) and the putamen (mean 1.32 ± 0.20) also showed high binding. White matter, pons, and thalamus were the regions with the lowest accumulation of [^{11}C]OMAR radioactivity. [^{11}C]OMAR binding in healthy controls appeared to decline with increasing age in the globus pallidus and putamen, the regions with the highest values of V_T.

Given the relatively fast kinetics of [^{11}C]OMAR, measurements of brain uptake can be quantified as V_T using two-tissue compartment model (2-TCM) with vascular component and multilinear analysis (MA1) modeling, which are the preferred analytical methods. Interestingly, human V_T was about 20% of that in rhesus monkey, which may have been due to low estimations of brain entry (human K_1 parameter was approximately 25% of that in monkey) (Normandin et al. 2010a), and as other studies have shown human CB_1 receptor density to be a similar fraction compared
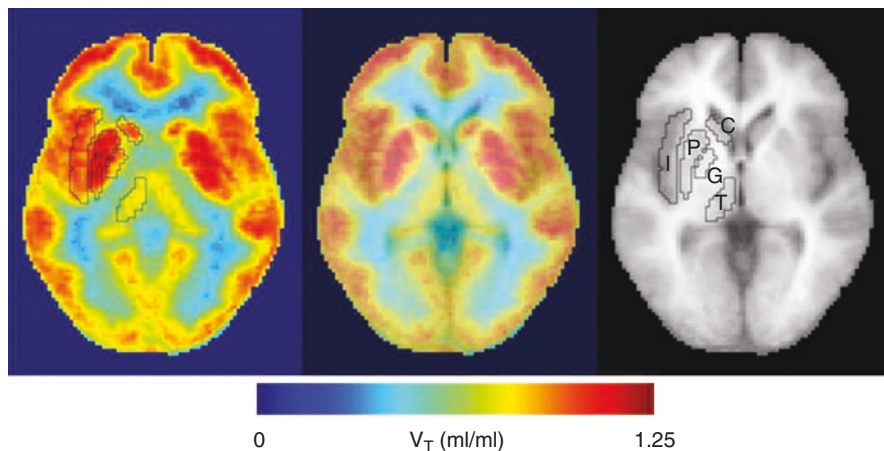
Fig. 12.7 Trans-axial images of distribution volume (V_T) of [^{11}C]OMAR, mean of ten healthy subjects in a standard space (left panel), a standard MRI (right), and merged image (middle). Volumes of interest of selected structures in the standard space are shown on the V_T image and MRI. Regions are insula (I), putamen (P), globus pallidus (G), thalamus (T), and caudate nucleus (C) (reprinted from Wong et al. (2010a, b) with permission of Copyright Clearance Center)

to nonhuman primate. An initial modeling study in baboons tested if the simpler reference tissue model could be used for [^{11}C]OMAR data analysis (Horti et al. 2006). When pons was used as a reference tissue the resulting values of BP fluctuated by 10–20%, further suggesting that it leads to low precision and is an unstable method to use for quantifying CB$_1$ receptors. An alternative candidate for use as a reference tissue, white matter, did not appear to reach equilibrium in the course of the scan, and indeed had a small increase of radioactivity over the course of 90 min, eliminating it as a choice for analytic method.

Test-retest analysis of V_T in healthy human subjects demonstrated that [^{11}C]OMAR has reasonably good precision with ~3% within-subject variability, ~9% intersubject variability, and ICC ~0.7 (Table 12.4). (Normandin et al. 2015) Analysis of potential modeling errors suggested that measurement error in the input function is the likely source for variability in V_T. Both peak brain uptake and fraction of parent tracer in plasma were found to be higher in men than women. V_T was significantly higher in women than men, presumably due to the faster plasma clearance in women than in men, and could be measured using 90 min of data (and as little as 60 min for some regions using the MA1 model) (Normandin et al. 2010b; Neumeister et al. 2013). Since brain uptake is higher and V_T is lower in men compared to women, it is recommended that V_T derived via metabolite-corrected arterial input function be used in patient population assessments with sex-matched controls, as brain uptake alone and sex differences could result in misleading or confounding results. The free fraction of [^{11}C]OMAR is ~0.1–0.2% (Normandin et al. 2015; Ranganathan et al. 2016; D'Souza et al. 2016a).

[^{11}C]OMAR demonstrated an age-related decline trending in nearly all regions and attaining statistical significance in the region with the highest V_T (globus pallidus) (Wong et al. 2010a; Neumeister et al. 2013).

Table 12.4 *In vivo* properties of CB$_1$ receptor radioligands in humans

Radioligand	[^{11}C]OMAR	[^{18}F]MK-9470	[^{18}F]FMPEP-d_2	[^{11}C]SD5024
Peak brain uptake (SUV)	~2	1.2	~4	~3
Retest variability	–	~7%	16%	–
Intersubject variability	–	16%	14%	–
V_T (mL/cm^3)	~1.5	~22	~23	~2.5–3.0
Retest variability	~3%	10–30%	14%	–
Intersubject variability	~9–15%	~55–66% (35% with FUR)	26%	22%
Effective dose (μSv/MBq)	–	22.8	19.7	–
References	Wong et al. (2010a), Normandin et al. (2015, 2010b)	Burns et al. (2007), Van Laere et al. (2008a, b), Addy et al. (2008)	Terry et al. (2010a, b)	Tsujikawa et al. (2014)

Human PET studies with the CB_1 antagonist blocker AVE1625 demonstrated the utility of [^{11}C]OMAR for successful occupancy evaluation of cannabinoid receptors by drugs in human brain (Wong et al. 2010b). Because of the short half-life of ^{11}C ($t_{1/2}$ = ~20 min), the baseline and drug challenge scans with [^{11}C]OMAR can be done in the same subject in a single day, an advantage of [^{11}C]OMAR over ^{18}F-labeled CB_1 receptor radioligands for drug development research.

The biodistribution and radiation dosimetry estimates for [^{11}C]OMAR have not yet been reported.

12.2.2.2 [^{18}F]MK-9470

Discovery of the selective CB_1 inverse agonist rimonabant by Sanofi-Aventis (Rinaldi-Carmona et al. 1994), available in the UK and the EU as anti-obesity drug in 2006–2009, stimulated the development of cannabinoid drugs by many pharmaceutical companies. As a result, a large number of rimonabant analogs and structurally different CB_1 inverse agonists have been developed. Merck disclosed a series of non-rimonabant-based CB_1 receptor inverse agonists (Lin et al. 2006). The best compound of the Merck series, taranabant, demonstrated a substantially higher affinity (0.4 nM) than that of rimonabant (Lin et al. 2008). Using taranabant as a lead compound Merck has developed MK-9470, a CB_1 receptor-selective fluoroalkyl analogue of taranabant with high CB_1 receptor-binding affinity, but also relatively high values of $\log D_{7.4}$ and PSA (Burns et al. 2007) (Fig. 12.6, Table 12.3). Radiolabeling of [^{18}F]MK-9470 was performed in two steps by preparation of [^{18}F]fluoroethylbromide and [^{18}F]fluoroethylation of the corresponding phenol with moderate radiochemical yield. [^{18}F]MK-9470 can also be produced in a simplified, one-step synthesis using a GE TRACERlab FX$_{FN}$ with the tosylate precursor and [^{18}F]fluoride in high yield for routine GMP production (Thomae et al. 2014).

In vitro autoradiography of [^{18}F]MK-9470 in rhesus monkey brain slices (Burns et al. 2007) produced images with a high signal in cerebral cortex, cerebellum, caudate/putamen, globus pallidus, substantia nigra, and hippocampus, which is consistent with the reported localization of CB_1 receptors in the brain of various mammalian species. Additional *in vitro* studies showed that [^{18}F]MK-9470 is not a P-gp substrate.

Preclinical studies using [^{18}F]MK-9470 in rodents have provided additional information on the radioligand's characterization. [^{18}F]MK-9470 is about 80% specific in wild-type compared to CB_1 receptor knockout mice. In rats, [^{18}F]MK-9470 shows a distribution consistent with known CB_1 receptor distribution, a test-retest variability of <5%, and a 58% decrease of radioactivity following blockade by rimonabant (Miederer et al. 2013). Serial arterial blood sampling can permit kinetic modeling of both [^{18}F]MK-9470 and radioactive metabolites in brain, which accounts for approximately 10–30% of radioactivity, and demonstrates that radiometabolites cause an overestimation of V_T. Measurements of V_T were better approximated after 10 h of scanning, which was independent of radiometabolites. Although it was concluded that compartmental modeling and measurements of V_T are superior to those of brain uptake alone, simplified measurements using SUV or mSUV correlated with V_T and may be preferred over the onerous arterial sampling and

extensive scan time required to measure V_T (Casteels et al. 2012). In a separate analysis, kinetic modeling with arterial blood sampling demonstrated a better fit with 2-TCM compared to 1-tissue compartment model (1-TCM), but due to micro-parameter poor identification, a coupled fitting approach improved parameter stability. However, radioactivity in brain from [^{18}F]MK-9470 was observed to plateau from ~60 to 90 min and therefore an irreversible model was assessed and found to fit the data well (Miederer et al. 2018). [^{18}F]MK-9470 uptake was found to increase with age when comparing adolescent and adult male rats, although this study was limited by its lack of kinetic modeling. Nevertheless, the main effect was replicated with [^{3}H]CP-55,940 (a CB_1, CB_2 high-affinity agonist) *in vitro* binding, though with one-quarter the magnitude (Verdurand et al. 2011).

Additional rodent studies demonstrated that anesthetics affected brain uptake of [^{18}F]MK-9470, and suggest an indirect action of $GABA_A$ receptors on CB_1 receptor binding (Casteels et al. 2010a). Following 2 weeks of treatment with anti-epileptic agents, valproic acid produced a significant increase in [^{18}F]MK-9470 uptake while levetiracetam did not (Goffin et al. 2008). These results from rodents were not corrected for plasma concentrations of parent radioligand across conditions (*i.e.*, drug treatments) which might be expected to change with altered hepatic metabolism, and potentially confound independent measurements of brain uptake. In rats, *ex vivo* biodistribution studies were in good agreement with *in vivo* PET imaging data, with which organs known to have CB_1 receptor expression and involvement in metabolism were grossly well delineated (Buchholz et al. 2017).

Baseline PET scans in the rhesus monkey showed gradual brain penetration and accumulation of [^{18}F]MK-9470 in gray matter regions of the brain as expected for binding to CB_1 receptors and consistent with autoradiography studies. The specificity of the *in vivo* binding was confirmed in a blockade study with MK-0364, a CB_1-selective inverse agonist.

After bolus injection of [^{18}F]MK-9470 in human controls the radioactivity reached a plateau at ~120 min (Burns et al. 2007) (Fig. 12.8). The distribution of radioactivity corresponded to the known CB_1 receptor distribution and regional concentrations remained nearly unchanged for 2–6 h postinjection. Despite the seemingly irreversible brain kinetics the excellent signal-to-noise characteristics of [^{18}F]MK-9470 (Table 12.3) made it suitable for several human PET imaging studies (Burns et al. 2007; Gerard et al. 2010, 2011; Sanabria-Bohorquez et al. 2010; Van Laere et al. 2008a, b, c, 2009) that were performed by the imaging group from K.U. Leuven in collaboration with Merck.

A methoxy analogue of MK-9470, CB-119, was designed as a carbon-11 alternative for PET imaging (Hamill et al. 2009). While it showed nearly identical binding characteristics to [^{18}F]MK-9470, it was not able to achieve equilibrium within the scanning time. [^{11}C]CB-119 was therefore abandoned for further clinical development in lieu of [^{18}F]MK-9470.

[^{18}F]MK-9470 demonstrates many favorable properties for characterizing CB_1 receptors with *in vivo* imaging including good brain uptake and low nonspecific uptake (Tables 12.3 and 12.4). However, its slow pharmacokinetics has proven to be a challenge for modeling accepted outcome measures such as V_T. In both monkeys
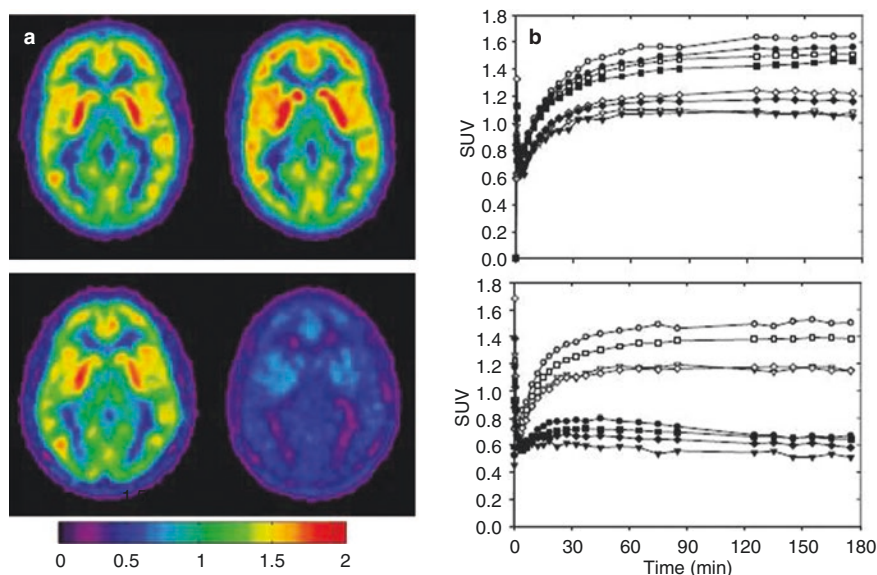
Fig. 12.8 ^{18}F-MK-9470 PET images of CB_1 receptors were acquired in normal healthy male subjects before and after treatment with MK-3640 or placebo. (**a**) Representative transverse parametric SUV images at the level of the basal ganglia for two human subjects, acquired before (*left*) and 24 h after (*right*) treatment with either placebo (*upper*) or a 7.5 mg dose of MK-0364 (*lower*). (**b**) Graphs show the corresponding TACs. The open symbols denote baseline values, and the closed symbols denote the scan after treatment (reprinted from Burns et al. (2007) with permission of Copyright National Academy of Sciences, U.S.A., PNAS)

and humans, radioactivity increased in brain up to about 120 min after bolus injection with [^{18}F]MK-9470, and concentrations of radioactivity did not appear to decline, even though concentrations of the radioligand in arterial plasma decreased throughout the length of the scan (Burns et al. 2007). For these reasons, brain studies using [^{18}F]MK-9470 were analyzed using a pharmacokinetic method designed for irreversible PET radioligands (Koeppe et al. 1999) which simply uses the area under the curve (AUC) of radioactivity in brain after a period when measurements have stabilized (e.g., 120–180 min after injection), termed fractional uptake ratio (FUR). However, when challenged with another CB_1 inverse agonist the radioactivity quickly washed out of brain, indicating that [^{18}F]MK-9470 undergoes reversible binding at the CB_1 receptor, which runs counter to the rationale of using an irreversible model.

Indeed, when scanning is continued for 12 h a slow washout of the radioligand can be detected, and sufficient data is then available for analysis by 2-TCM (Sanabria-Bohorquez et al. 2010). However, even with this additional data only macroparameters from modeling could be distinguished, and the individual parameter that is proportional to receptor density (k_3) could not be identified in any individual brain region. Using 2-TCM the test-retest variability of V_T was 10–30%, indicating that it had poor precision. After making the assumption that dissociation from the receptor

(k_4) is constant throughout the brain *in vivo*, multiple serial correlations were made linking V_T to irreversible measurements and to FUR. It was further assumed that in cases when plasma measurements are not statistically different, brain uptake measured as SUV or modified SUV (mSUV) is a sufficient outcome measurement, as they would correlate with FUR and be interpreted as CB_1 receptor availability. These models do not fully account for the full clearance of radioligand (*i.e.*, AUC extrapolated to infinity), and therefore do not correct the amount of radioligand in brain to that in plasma, and dissociation from receptors is not always constant *in vivo*. Thus, while the precision of these model outcomes can be assessed by test-retest studies, their accuracy remains uncertain, particularly in conditions where metabolic processes or changes in receptor density may affect radioligand concentration in plasma or local dissociation rate. Nevertheless, using this analytical method, [^{18}F]MK-9470 has shown good precision (retest variability <7% within 24 h) and intersubject variability (16–35%) (Burns et al. 2007; Addy et al. 2008).

Gender-dependent increases of [^{18}F]MK-9470 uptake with age were measured in women but not in men, particularly in the basal ganglia and hippocampus (Van Laere et al. 2008a). These results were obtained with and without partial volume correction of the brain images with presumably no loss of effect; partial volume effects have been minimal and likely insignificant for other studies using [^{18}F]MK-9470. Metabolism of the radioligand was not dependent on age, although there were measured differences in metabolism between sexes. Similarly, sex-dependent differences were measured for the slow parameter of arterial input function (*i.e.*, elimination phase of clearance). However, when applied to pharmacokinetic modeling no significant difference was measured in arterial plasma input function using a three-parameter bi-exponential model. Larger intersubject variability (COV 15–20%) and region-dependent differences (up to 230%) were found than in the smaller sample size of the initial human study (Burns et al. 2007).

In part to assess this large variation within groups, additional information was obtained from subjects to find correlations between receptor availability and temperament traits, as have been shown for other receptor systems (Farde et al. 1997). Novelty-seeking traits were found to be inversely correlated to [^{18}F]MK-9470 uptake throughout the brain, with the strongest correlation in the left amygdala (Van Laere et al. 2009). The trait subtypes of extravagance and disorderliness maintained significance even after strict limitations, while trait subtypes of exploratory excitability and impulsiveness, and trait types harm avoidance, reward dependence, and persistence, failed to attain significant correlations with CB_1 receptor availability. As novelty-seeking traits are associated with thrill seeking, addiction behavior (including overeating, and substance dependence), and impulsive aggression (Hiroi and Agatsuma 2005), their association with CB_1 receptor imaging, and particular location in the amygdala, is intriguing.

In humans, [^{18}F]MK-9470 has shown to be useful in estimating receptor occupancy of other inverse agonists (Burns et al. 2007; Addy et al. 2008). Clinical trials of taranabant for weight loss showed that 10–40% receptor occupancy was sufficient to produce significant amounts of weight loss in a dose-dependent fashion, which is in agreement with estimates from preclinical rodent studies.

Whole-body imaging studies using [^{18}F]MK-9470 demonstrated the radiation burden to be acceptable for completion of multiple brain studies per year (22.8 ± 4.3 μSv/MBq), and similar to that of other commonly used PET tracers (Van Laere et al. 2008b). Brain uptake of the radioligand was about 3.2–4.9% of the total dose, and receptor occupancy was estimated to be well below 1%. [^{18}F]MK-9470 undergoes predominantly hepatobiliary excretion, with significant radiation burden to the gallbladder which was the radiation dose-limiting organ. Although measured radioactivity in the periphery likely originates from a mixture of parent compound and its metabolites, an appreciable amount of radioactivity was measured in liver, small intestine, and red bone marrow, sites known to have CB_1 receptors.
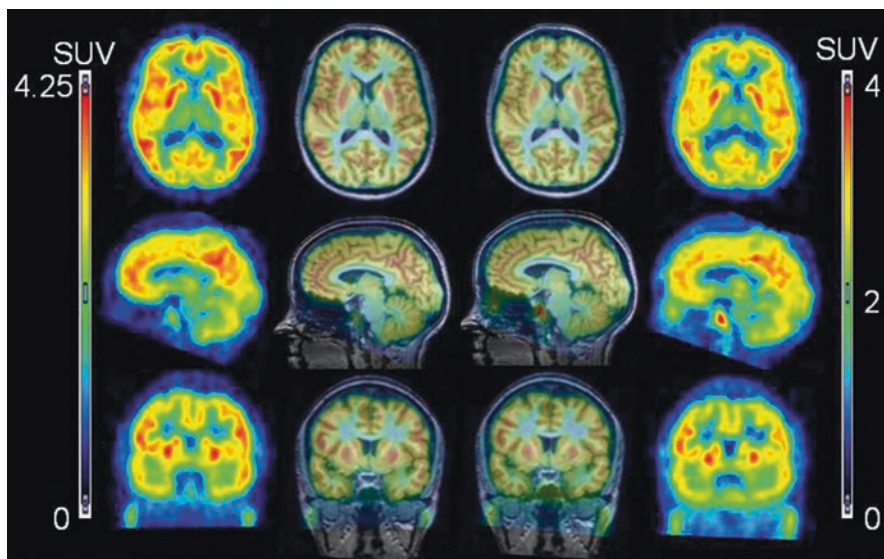
12.2.2.3 [^{11}C]MePPEP and [^{18}F]FMPEP-d_2

A collaborative group from Eli Lilly, NIH, and Karolinska University developed two structurally similar CB_1 radioligands, [^{11}C]MePPEP and [^{18}F]FMPEP-d_2 (Fig. 12.6), for human PET studies (Terry et al. 2008; Yasuno et al. 2008; Donohue et al. 2008c; Suter et al. 2010). Both compounds are CB_1 receptor inverse agonists with high CB_1 receptor-binding affinity and selectivity (Table 12.3). MePPEP has about 10 times higher binding affinity compared to rimonabant, and has >700 times greater selectivity for CB_1 than CB_2. The lipophilicity values of MePPEP and FMPEP-d_2 are high, but the PSAs are in the acceptable range for passive BBB transport and lower than those of OMAR and MK-9470 (Table 12.3).

Radiosynthesis of [^{11}C]MePPEP is simple and can be performed by reaction of the corresponding desmethyl precursor with [^{11}C]methyliodide (Terry et al. 2009). In the monkey brain, [^{11}C]MePPEP showed very high uptake with a good specific signal, reaching >89% in high-binding regions (prefrontal cortex) and ~75% in low-binding regions (pons, thalamus) (Table 12.3) (Yasuno et al. 2008). Preclinical studies in rodents further defined the *in vivo* characteristics of [^{11}C]MePPEP (Terry et al. 2008). According to data from both genetic and pharmacologic rodent models, [^{11}C]MePPEP is not a substrate for P-gp and has high specificity for the CB_1 receptor. Approximately two-thirds of radioactivity after injection of [^{11}C]MePPEP is specific for CB_1 receptors in mouse and rat brain, and *ex vivo* mass spectrometry demonstrated >90% specific binding. Serial arterial blood sampling permitted kinetic modeling of [^{11}C]MePPEP and measurements of CB_1 receptors as V_T in rats within 70 min of scan time. A constant percentage (13%) of the radioactivity present in rat brain was in the form of metabolites, which may cause a stable, overestimated value of V_T. High doses of CB_1 receptor agonists, including the endocannabinoid anandamide and the high-affinity synthetic cannabinoid CP 55,940, were unable to cause any displacement or blockade of [^{11}C]MePPEP binding in brain; these findings were independently confirmed by *ex vivo* mass spectrometry. Despite the much higher affinity of MePPEP over lower affinity agonists (*e.g.*, endocannabinoids) for CB_1 receptors, the severalfold higher concentration of agonists would be expected to compete and potentially displace or block the tracer dose of radioligand. The inability of [^{11}C]MePPEP to be displaced by agonist *in vivo* suggests either non-overlapping binding sites of MePPEP and agonists or a large receptor reserve; that is, a small percentage of CB_1 receptors are in the high-affinity, agonist-preferring,

state *in vivo*, and displacement of that small proportion might not be detected by PET. It was previously shown that *in vitro* agonism was achieved by CB_1 receptor occupancy of 7.5%, suggesting a >92% receptor reserve (Gifford et al. 1999).

An IND approval for the radioligand was obtained and [11C]MePPEP was initially studied in 17 human control subjects (Terry et al. 2009). The radioligand exhibited high human brain uptake in a regional distribution consistent with that of CB_1 receptors (Fig. 12.9), and slow washout from brain. [11C]MePPEP provided acceptable quantification of receptor density using V_T 2-TCM as the outcome measure. However, the precision and accuracy of quantification of CB_1 receptor with [11C]MePPEP in human brain may have been diminished by slow brain kinetics and a very low fraction of free radioligand in plasma (f_P) (Terry et al. 2009) that can be explained by the high lipophilicity of this compound (Table 12.3). Further studies determined that quantification was not limited by measurements from brain, but rather by measurements of radioligand in plasma (see Sect. 12.2.3). Despite the relatively low test-retest variability (8%) and low intersubject variability (16%) of brain uptake, when combined with concentrations of parent radioligand in arterial plasma to calculate V_T, the intersubject variability was much higher (>50%). Assuming that the slow washout of [11C]MePPEP from brain limited a sufficient amount of pharmacokinetic data from being collected, an increased scan time of 210 min demonstrated that measurements of V_T were affected not by the washout

Fig. 12.9 [11C]MePPEP and [18F]FMPEP-d_2 in human brain. PET images from 40 to 80 min after injection of [11C]MePPEP were averaged (left column) and co-registered to the subject's MR images (middle left column). In the same individual, PET images from 30 to 60 min after injection of [18F]FMPEP-d_2 were averaged (right column) and co-registered to the subject's MR images (middle right column). Color bars on left and right correspond to SUV for [11C]MePPEP and [18F]FMPEP-d_2, respectively

rate of [^{11}C]MePPEP, but rather by the low concentration of [^{11}C]MePPEP in plasma and the radioactive half-life of ^{11}C. Thus, the relatively poor precision of the plasma measurements contributed to the higher within- and between-subject variabilities of V_T compared to those of brain uptake. Nevertheless, measurements of V_T within subjects were highly stable over time, and consistent values were observed 60 min after injection. The test-retest variability was acceptable (~15%) and the intraclass correlation coefficient (ICC) of V_T (*i.e.*, the sensitivity of distinguishing variability between subjects from within subjects) was considered good to excellent (0.87), and better than that of brain uptake measured alone (0.77). Taken together, the stable measures of V_T, the high ICC of V_T, and the theoretically superior outcome measure of V_T compared to brain uptake suggest that V_T remains the more accurate index of CB$_1$ receptor density, in spite of the poor precision of plasma measurements. In computer simulations in which CB$_1$ receptor density was varied, V_T was much more sensitive than brain uptake alone in measuring increases, but not sensitive for decreases, of receptor density, and therefore might be expected to require fewer sample points (*i.e.*, study subjects) to detect significant differences between groups. Therefore, it was recommended using V_T as the primary outcome measure for [^{11}C]MePPEP; however brain uptake could be used for within-subject studies (e.g., receptor occupancy).

A replication test-retest study of [^{11}C]MePPEP in 15 subjects examined multiple kinetic modeling methods (Riano Barros et al. 2014). The 1-TCM demonstrated comparable test-rest reliability (19.7 ± 8.7%) and ICC (0.82 ± 0.09) with high pallidum-to-pons ratio (suggesting low bias), but the 2-TCM did not. This may be due in part to the difficulty with measuring radioactivity in later blood samples, with an inability to measure the parent fraction at 90 min, and therefore affecting the modeling of the input function. This in turn is likely due to injection of about ½ the amount of radioactivity compared to the prior studies (~360 MBq vs. ~650 MBq in Terry 2009). All three spectral analyses (a "model free" approaching using an input function) demonstrated good test-retest reliability (13.5–15.5%) and ICC (0.76–0.83), though the ROI-based and voxel-based models demonstrated bias to overestimating V_T in high-binding regions, while the rank-shaping model restricted the range of V_T and underestimated those regions. While the input function free modified SUV (mSUV) method demonstrated satisfactory test-retest variability and ICC for most regions, it performed poorly for the low-binding region pons, and yielded the most regional heterogeneity of models tested. The simplified reference tissue model (with pons as reference) produced highly variable results across regions, with very poor test-retest and ICC outcomes, likely due to the presence of specific binding in pons.

Several modeling methods have been assessed in an effort to improve the parent fraction arterial plasma input function of [^{11}C]MePPEP. Comparison of standard and convoluted (by incorporating injection time duration as a variable) exponential, Hill, and power models demonstrated improved modeling of the input function data using the convoluted Hill model compared to the standard exponential model, but this had negligible effect on V_T and its related micro- and macroparameters (Tonietto

et al. 2015). A follow-up analysis implemented an automated, user-independent pipeline on a combination of continuous (first 15 min) and discrete (up to 90 min) arterial plasma samples in comparison to the standard exponential approach. A small (3%), but statistically significant, reduction of weighted residual sum of squares for V_T suggested improvement of the input function model, though the effect on V_T itself was small (2 ± 1%) (Tonietto et al. 2019). In an effort to more accurately quantify the later time points of parent compound in arterial plasma, LC-MS/MS was tested as a way to measure the nonradioactive MePPEP from the carrier of [^{11}C]MePPEP in a single test-retest study. While the method was highly correlated with the standard radio-HPLC method and could calculate V_T with equal test-retest variability, LC-MS/MS determinations were consistently lower by 25–30%, demonstrating a promising option for input function measures when radioactivity might be difficult or impossible to detect (Victor et al. 2010).

In an effort to develop a radioligand with improved measurements of radioactivity for an extended time, several fluorinated analogues of [^{11}C]MePPEP were developed and tested in monkeys, yielding [^{18}F]FMPEP-d_2 as suitable for human studies (Terry et al. 2010a). Other fluorinated radioligands tested had either less specific binding, or showed higher amounts of radioactivity bound to bone, presumably due to free [^{18}F]fluoride which was formed as a metabolite from the parent radioligand. Indeed, deuterium substitution on the fluoromethoxy radiolabel to inhibit defluorination resulted in about 1/3 less radioactivity uptake in bone than was observed after injection of the native hydrogen version.

The same precursor was used for the preparation of [^{18}F]FMPEP-d_2 and [^{11}C]MePPEP. The radiosynthesis of [^{18}F]FMPEP-d_2 involves [^{18}F]fluorination of dibromomethane-d_2, purification of [^{18}F]fluorobromomethane-d_2, and [^{18}F]fluoromethylation of the phenol precursor (Donohue et al. 2008c). In a rhesus monkey study, [^{18}F]FMPEP-d_2 peaked in the brain at 20 min post-bolus injection (SUV 4.5–6.5) with gradual washout thereafter. The blocking experiment revealed that specific binding in the monkey brain was 80–90% of total tissue uptake. Radioactivity concentration in the mandible reached an SUV of approximately 2.0 by the end of the 3-h scan (Terry et al. 2009). Following injection with [^{18}F]FMPEP-d_2 in mice, radioactivity is comprised of about 56% parent compound in plasma at 15 min, decreasing to about 19% by 240 min, and radioactivity is about 86% parent compound in cortex, with the remainder accounted by a single metabolite, and remains essentially unchanged from 60 to 240 min after injection. Similar to [^{11}C]MePPEP, about 2/3 radioactivity was displaced by rimonabant following [^{18}F]FMPEP-d_2 injection in mice (Takkinen et al. 2018).

After injection of [^{18}F]FMPEP-d_2 in human, radioactivity peaked in putamen (SUV = 5) by 30 min post-bolus administration followed by slow washout (Terry et al. 2010a). The regional distribution of radioactivity matched the density of CB_1 receptors in human brain (Fig. 12.9). The skull had substantial uptake of radioactivity that reached a peak SUV value of 4.5 by the end of 5 h of scanning. Pharmacokinetic modeling demonstrated that 60–120 min of human imaging gives the most accurate measurements of V_T, whereas a longer acquisition is likely vulnerable to

contamination of the brain with radiometabolites and/or spillover of radioactivity from the skull, which presumably outweighs any added accuracy from a more extended scan time.

In test-retest studies similar to those done for [^{11}C]MePPEP, [^{18}F]FMPEP-d_2 yielded similar between-subject variability for brain uptake; however [^{18}F]FMPEP-d_2 demonstrated a much better test-retest variability of plasma measurements (16% vs. 58% for [^{11}C]MePPEP), and acceptable test-retest variability of V_T (14%) (Table 12.4). This increased precision of plasma measurements led to a much reduced intersubject variability of V_T (26%), and, in conjunction with an extremely good ICC (0.89), suggests an improved accuracy of V_T. When changes of receptor density were simulated, V_T was shown to be more sensitive for detecting both increases and decreases of receptor density. The test-retest studies of both [^{11}C]MePPEP and [^{18}F]FMPEP-d_2 were conducted with at least 2-week intervals, strengthening the robustness of radioligands' precision. In conclusion, using [^{18}F]FMPEP-d_2 to measure CB$_1$ receptor density as V_T was determined to be more precise, accurate, and sensitive than [^{11}C]MePPEP or using brain uptake alone as outcome measurement.

Two significant limitations of [^{18}F]FMPEP-d_2 were identified in early human studies. First, values of V_T increased after 120 min. While the exact cause was not identified, such a trend is consistent with an accumulation of radioactive metabolites in brain. Simulations demonstrated that radioactivity originating from neighboring bone would account for <2% of the total amount. Fortunately, V_T was measured with consistent and stable values from 60 to 120 min after injection, and therefore limiting scan duration to 120 min should avoid confounding changes to the accuracy of V_T. Second, the plasma free fraction of both [^{11}C]MePPEP and [^{18}F]FMPEP-d_2 in humans is very low (approximately 0.05% and 0.63%, respectively). The test-retest variability of plasma free fraction is excellent; however, the intersubject variability was quite large. This is likely due in part to the nature of such low values, since small measured differences would be disproportionately large in percentage. Since correction of V_T with free fraction (which would be a more correct quantitation of radioligand binding in brain) added too much noise to the final outcome measurements, it was excluded from the calculation of V_T. Thus, it is recommended that potential changes of free fraction be accounted for in future studies, particularly those with pharmacological challenges, as a proportionately large amount of radioligand could be displaced from plasma proteins and made available to enter brain.

In an effort to reduce the burden related to arterial sampling, a population-based input function (PBIF) was compared to full arterial sampled input function (Zanotti-Fregonara et al. 2013). Using the Logan plot to determine V_T (which was equivalent to that determined by the 2-TCM with similar ICC of 0.88, but slightly higher test-retest variability of 16%), a PBIF function derived from 42 healthy individuals yielded nearly identical estimates of V_T compared to the individually measured input function (13.2 mL/cm^3 vs. 13.3 mL/cm^3; $R^2 = 0.8765$, $p < 0.001$). This method was able to replicate the main finding in a study of individuals with alcohol-use disorder, but underestimated global V_T from those with cannabis-use disorder at

baseline (see Sect. 12.3.1.1), suggesting that the method may be used within healthy populations, but should be avoided in the analysis of clinical groups.

The PBIF with Logan plot was utilized to explore sex differences of CB_1 receptor expression (Laurikainen et al. 2019). V_T of [^{18}F]FMPEP-d_2 was consistently high in all regions (grouped bilaterally) in males compared to females, with occipital, parietal, and posterior cingulate cortex demonstrating the largest effect. The intersubject variability was similar within males and females; however females taking oral contraceptives were noted to have lower V_T than those not taking contraceptives or recent menopause. Neuropsychological testing revealed a negative correlation between V_T and visual-spatial working memory, with sex as a covariate, though there were no differences in test performance.

Whole-body imaging studies using [^{11}C]MePPEP and [^{18}F]FMPEP-d_2 demonstrated the radiation burden to be acceptable for both radioligands (4.6 ± 0.3 μSv/MBq and 19.7 ± 2.1 μSv/MBq, respectively) for completion of multiple brain studies per year (Terry et al. 2010b). Brain uptake of both radioligands was about 7–8% of the total dose, and receptor occupancy is estimated to be well below 1% (0.3% for [^{11}C]MePPEP, and 0.06% for [^{18}F]FMPEP-d_2). Both radioligands undergo hepatobiliary excretion, [^{11}C]MePPEP exclusively, while [^{18}F]FMPEP-d_2 undergoes also some urinary excretion. Similar to [^{18}F]MK-9470, and as first reported for [^{11}C]OMAR, an appreciable amount of radioactivity was measured in red bone marrow. To determine if radioactivity was concentrated in bone tissue rather than bone marrow, additional analysis showed that the pattern of accumulation in bone was consistent with areas rich in bone marrow, such as vertebrae, pelvis, and ribs. A comparison of bones rich in marrow to those devoid of marrow demonstrated that radioactivity was not largely due to accumulation in bone. In addition, studies using monkeys demonstrated that about 20% of the radioactivity in bone marrow was due to specific binding to CB_1 receptors.

12.2.2.4   [^{11}C]SD5024

A collaborative group from NIH and Karolinska University developed CB_1 radiotracer [^{11}C]SD5024 (Fig. 12.6) (Donohue et al. 2008a; Tsujikawa et al. 2014). The tracer was evaluated *in vitro* and *in vivo* and compared with other CB_1 receptor ligands previously used in humans, *i.e.*, [^{11}C]MePPEP, [^{11}C]OMAR, [^{18}F]MK-9470, and [^{18}F]FMPEP-d_2. The negative enantiomer of SD5024 exhibited intermediate binding affinity (K_i = 0.47 nM) between MePPEP, MK-9470, FMPEP-d_2 (0.1 nM), and OMAR (2 nM) (Table 12.3). The lipophilicity of SD5024 is lower than MePPEP and FMPEP-d_2 (Tsujikawa et al. 2014), but slightly greater than that of OMAR.

The radiosynthesis of SD5024 was performed via a palladium catalyst-assisted reaction of [^{11}C]cyanide and corresponding Br precursor with radiochemical yield of 36% (n = 2) (Donohue et al. 2008a), high radiochemical purity (>98%), and moderate specific activity of 41 ± 31 GBq/μmol (n = 4) (Tsujikawa et al. 2014). [^{11}C]SD5024 demonstrates high uptake in nonhuman primate brain in a distribution consistent with CB_1 receptor density, peaking at ~30–60 min and decreasing thereafter, and can be displaced and blocked with the antagonists PipISB and rimonabant. The lower affinity positive enantiomer (K_i = 16.9 nM) demonstrated an immediate

peak at 1.5 min after injection followed by rapid decline in all regions, consistent with a high proportion of nonspecific binding. Pharmacokinetic modeling with an arterial input function demonstrated best fit with the 1-TCM, and was well identified with standard error of 3.8% across brain regions, suggesting that the majority of binding is specific. Indeed, specific binding is ~80% in high-binding regions, and ~66% in low-binding regions, as determined by rimonabant preblockade.

[11C]SD5024 was applied for the comparison of rimonabant, taranabant, and three novel rimonabant-related CB_1 receptor antagonists, developed by AstraZeneca, in nonhuman primate (Hjorth et al. 2016). Using pons as a pseudoreference region (arterial sampling for kinetic analysis was not possible as those samples were needed for measuring test drug plasma concentration), [11C]SD5024 demonstrated a test-retest variability of 12%, and escalating displacement after 4–6 escalating doses of test drugs. Taranabant demonstrated greater potency, achieving similar receptor occupancy at lower doses and plasma concentrations than the other drugs tested. When these nonhuman receptor occupancy doses of taranabant and rimonabant were compared to clinically effective doses for weight loss, it was estimated that only 20–30% of occupancy might be needed to result in weight loss (slightly less or similar to that estimated using [18F]MK-9470, see Sect. 12.2.2.2).

In humans, [11C]SD5024 peaked at 1.5–3.0 SUV at about 40 min and decreased by 20% at the end of 120 min (Fig. 12.10). Notably, the fraction of parent [11C]SD5024 in plasma decreased slowly during the study, reaching ~50% by 75 min. Brain uptake was best fit by the 1-TCM with well-identified V_T, similar to nonhuman primate, and could be reliably measured with as little as 80 min of data. Subtracting activity from the vascular compartment in the modeling improved fitting of the data. The intersubject variability ($n = 7$) was substantially lower than [11C]MePPEP at 22% (Table 12.4), likely due to its moderate binding affinity and slower metabolism, suggesting that [11C]SD5024 provides less noise (*i.e.*, greater precision) in its measurements. While a head-to-head comparison with test-retest and receptor blockade studies would better identify the preferred radioligand for human studies, the current data suggests that [11C]SD5024 might be one of the best available 11C-labeled radioligand for CB_1 receptor neuroimaging, being superior to [11C]MePPEP (due to better plasma measures and intersubject variability) and equivalent or slightly better than [11C]OMAR (due to greater brain uptake and V_T) (Tsujikawa et al. 2014).

12.2.3 Considerations in Imaging CB₁ Receptors and Its Interpretation

An advantage of PET over other imaging modalities is its quantitative ability, and quantitative analysis is achieved in large part through pharmacokinetic modeling. Pharmacokinetic modeling of CB_1 receptor PET radioligands in brain poses some particular challenges compared to more established compounds. These challenges include the high concentration of receptors throughout the brain, lack of a
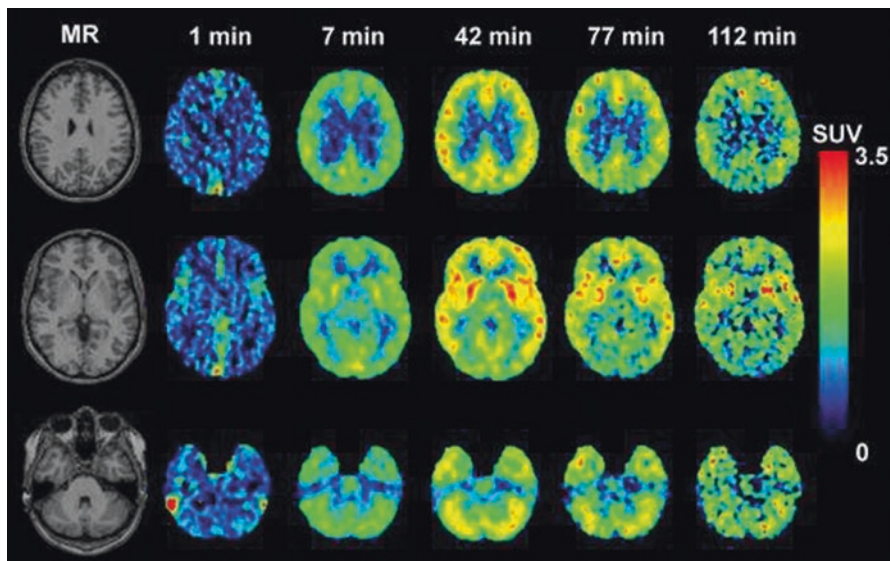
Fig. 12.10 [^{11}C]SD5024 in human brain. Magnetic resonance anatomic images at the levels of centrum semiovale (top row), nucleus basalis (middle row), and pedunculus cerebellaris medius (bottom row) correspond to dynamic PET images obtained at 1, 7, 42, 77, and 112 min after [^{11}C]SD5024 injection (from right to left). Each PET image represents standard uptake value (SUV) and is indicated in the SUV color scale on the right. Reprinted from Tsujikawa et al. (2014), Copyright 2014, with permission from Elsevier

receptor-devoid region, slow pharmacokinetics of the radioligands, low plasma concentrations of parent radioligand, and very high plasma protein binding. Careful consideration should be made when interpreting data from clinical PET studies, as radioligand properties and modeling methods may potentially confound results or their interpretation. To better appreciate such potential confounding variables, a brief review of modeling considerations is discussed here.

The noninvasive nature of *in vivo* PET imaging limits the ability to establish a "gold standard" method to validate endpoint measurements such as receptor density, as absolute measurements might require surgical excision followed by *in vitro* quantitation of receptors. Using a 2-TCM the radioligand can be conceptualized as being in a "non-displaceable compartment," which represents radioligand nonspecifically bound to proteins or lipids or is free in tissue, and a "specifically bound" compartment, which represents radioligand bound to a receptor and is potentially displaceable. Both compartments are detected as radioactivity by the PET camera, and so pharmacokinetic analysis with mathematical modeling serves to separate out these two compartments as discernible and quantitative measures. In doing so, estimates of receptor density and/or receptor occupancy can be calculated. Estimates of receptor density are approximated by V_T (Innis et al. 2007), which in turn can be

conceptualized as the ratio of areas under the curve of radioligand in tissue (*e.g.*, brain) divided by radioligand in arterial plasma. Over the course of the entire study the brain was exposed to the amount of radioligand available in plasma (*i.e.*, the input function), and the brain responded by taking up the radioligand. Unfortunately, we cannot always measure the complete area under the curve because of the short radioactive half-life or slow pharmacokinetics of the radioligand. Using mathematical modeling the curves can be extrapolated to infinity (or, in practice, described using rate constants) with only part of the entire curve of brain or plasma data; however enough of the curve shape must be observed for it to be successful, in particular the tissue uptake, peak, and initial decline.

The additional steps required to perform compartment modeling and calculate V_T yield theoretically more accurate outcome measures than simple methods, as it avoids potentially confounding variables. At equilibrium radioligand in brain changes proportionally by the amount of radioligand in arterial plasma, and is therefore susceptible to pharmacokinetic variables from the periphery that may affect the delivery of the radioligand to brain (*e.g.*, metabolism, distribution, excretion which could change radioligand concentration) (Liow et al. 2007). Additionally, compartment models account for radioligand in brain that is both receptor bound and unbound or free. Even for radioligands that have nearly 90% receptor specificity, not accounting for unbound radioligand may reduce the significance or obscure results.

The high density and widespread location of CB_1 receptors are likely the cause for several hurdles when performing pharmacokinetic modeling of its radioligands (Hirvonen et al. 2010). First, extremely slow washout of CB_1 inverse agonists may be due to a rapid process of reversible binding and rebinding to receptors, a phenomenon known as "synaptic barrier" (Frost and Wagner Jr. 1984). Similar kinetics suggestive of synaptic barrier has been seen with other radioligands targeting receptors found in high density (*e.g.*, iomazenil and benzodiazepine receptors) (Laruelle et al. 1994). Second, the widespread location of CB_1 receptors in brain eliminates the use of reference tissue modeling methods, an alternative to compartment modeling using arterial plasma samples. Even areas of relatively low receptor density show up to 90% specific binding by some radioligands, and small changes in receptor binding in these regions would lead to potentially large systemic errors in outcome measurements. A potential advantage of high receptor density is that radioligands with lower specific activity could be used while maintaining the principle of tracer dosing. Tracer doses are needed to avoid inducing pharmacological effects, such as receptor internalization, and are generally accepted at 5–10% receptor occupancy or less; CB_1 receptor imaging studies are well below this threshold, even in rodents, and typically maintain <1% receptor occupancy in humans.

The CB_1 receptor radioligands discussed here demonstrate slow pharmacokinetics. Slow pharmacokinetics implies that ligands take a longer time to reach steady state when equilibrium has been achieved, and for reversible radioligands, after the identifiable peak in brain concentration has been achieved. This is a particular problem in PET imaging, as data acquisition time is typically limited by the radioactive half-life of the radioligand, as measured in brain and/or plasma. Thus, there is a

chance that insufficient data may be collected within the time allowed, and consequently an increased likelihood that measurement errors can be introduced. Test-retest studies are particularly useful to identify potential sources of error in kinetic modeling in measurements (brain uptake, plasma) and outcome measures (brain uptake, V_T).

Additional potential causes of error are likely due to the high lipophilicity of CB_1 receptor radioligands. First, most of the ligands have a relatively rapid distribution phase, followed by a very slow excretion phase (taken together as clearance). As a result, the excretion phase of plasma clearance typically has very low concentrations of parent radioligand, which are difficult to measure accurately. Second, CB_1 receptor ligands tend to exhibit very high plasma protein binding, sometimes >99%, meaning that free ligand available to cross the BBB may be very small (*e.g.*, <1%). Thus, when comparing between groups or conditions, brain uptake or V_T should be corrected for differences in free fraction (not the fraction bound to proteins), as low absolute changes in free fraction can produce large proportional changes. For example, a change of bound fraction from 99.9% to 99.8%, which could be caused by competitive binding by a drug, would correspond to a change of free fraction from 0.1% to 0.2%, or a 100% increase; such a phenomenon may have been the cause of about 17% increased brain uptake of one radioligand when a co-administered drug caused about 10% increased free fraction (Yasuno et al. 2008). It is generally assumed that metabolites more polar than the parent tracer are unable to cross the BBB. However, ligands for cannabinoid receptors have a higher lipophilicity than more typical PET tracers, and their metabolites, though relatively more polar, may retain a lipophilicity sufficient to cross the BBB. Thus, additional consideration should be made to the radiometabolite profile of cannabinoid PET tracers to avoid confounding results from pharmacokinetic modeling. Finally, the high lipophilicity of CB_1 receptor radioligands may permit passage not only through the BBB, but also through cell membranes and into intracellularly localized receptors where a substantial population may be present (*e.g.*, 85% in hippocampus) (Coutts et al. 2001). While it is assumed that the only receptors binding radioligand are membrane surface bound, the degree that differences in lipophilicity may confer for intracellular passage of these radioligands remains unknown, and could theoretically account for differences in brain uptake, washout, and estimation of receptor density of these PET tracers.

What does the data from CB_1 receptor radioligand studies imply physiologically? It is generally assumed that differences or changes to receptor binding are due to changes of receptor density; however outcome measurements using PET alone cannot distinguish receptor density from receptor-binding affinity; indeed, until recently few examples of decreased binding affinity had been reported (Itoh et al. 2009). Changes observed in studies using these radioligands are likely to demonstrate changes in receptor density, whether due to direct downregulation or by indirect downregulation due to increased endocannabinoid tone (Romero et al. 1995; Sim-Selley and Martin 2002). As GPCRs, cannabinoid receptors are found in both a protein-coupled or high-affinity and agonist-preferring state and an uncoupled or low-affinity inverse agonist-preferring state. As demonstrated by *in vitro*

studies (Rinaldi-Carmona et al. 1996), high-affinity inverse agonists bind to all available receptors, and thus it is assumed that at tracer doses inverse agonist radioligand binding represents the entire population of available receptors. Regional changes relative to global V_T or brain uptake likely reflect local variations in CB_1 receptor availability or density, as tracer uptake is unlikely affected by regional flow effects. However, when relative values of brain uptake are taken alone it could mask the absolute effect of receptor availability: For example, does a local increase of tracer uptake in brain with globally decreased uptake represent a true, and potentially abnormal, increase in receptor availability, or does it represent a local sparing or preservation of receptor expression with global reductions? Such relative changes may be open to wider interpretation when presented without more absolute measurements, as can be obtained with V_T. Nevertheless, relative changes can be sensitive measures, and may provide additional insight into regional alterations of CB_1 receptor availability or expression (Van Laere et al. 2002).

Finally, as noted above, variabilities in CNS outcome measures of these radioligands have been described across populations of healthy individuals. In particular, sex differences (with males having lower outcomes with [^{11}C]OMAR and greater outcomes with [^{18}F]FMPEP-d_2 and [^{18}F]MK-9470), BMI correlation (see Sect. 3.2), and CB_1 receptor SNPs (see Sect. 3.1.1) suggest that care should be made when selecting comparison groups, with appropriate controls and adjustments in study design and analysis. The extent that medications may confound CNS imaging results remains incompletely known, with the exception of CB_1 receptor antagonists/inverse agonists which can displace all radioligands described, and therefore may also require control in sample selection, or be appropriately adjusted for via pharmacokinetic modeling.

12.3 CB$_1$ Receptor Imaging in Neuropsychiatric Disorders

12.3.1 Substance-Use Disorders

Multiple preclinical and clinical studies have suggested that CB_1 antagonists could be used as treatments for multiple types of drug dependence (Le Foll and Goldberg 2005). Cannabis itself has the highest level of substance abuse, after alcohol and nicotine (Compton et al. 2005). Postmortem studies have shown that the density of CB_1 mRNA-positive neurons is significantly lower in long-term cannabis users in the striatum, nucleus accumbens, and hippocampal regions (Villares 2007). Rimonabant blocks effects induced by Δ^9-THC in humans and has been found to increase smoking cessation (Soyka et al. 2008; Cahill and Ussher 2007; Huestis et al. 2001).

While the synergism between alcohol and cannabinoid agonists (in various forms) creates undesirable side effects when the two are consumed together, the administration of CB_1 antagonists leads to a significant reduction in alcohol consumption and cannabinoid antagonists also mitigate alcohol-withdrawal symptoms (Kleczkowska et al. 2016). Several preclinical studies have provided evidence that

CB_1 receptors significantly contribute to the behavioral properties of alcohol and that the chronic consumption alters CB_1 receptor expression in the brain nuclei associated with addiction pathways. Additionally, recent studies have further established the role of the ECS in the development of fetal alcohol spectrum disorders (FASD) (Basavarajappa et al. 2019), yet few trials have investigated cannabinergic medications for alcohol-use disorder. Although animal studies suggested that rimonabant would be a useful agent for treating alcohol dependence, the results in clinical trials were negative (Soyka et al. 2008; George et al. 2010). In animal models using both pharmacologic and genetic knockout methods, blocking or eliminating CB_1 receptor activity decreases the rewarding effects of opiates and alcohol, and reduces cocaine-seeking behavior (Le Foll and Goldberg 2005).

The ECS is central in the brain's reward circuitry, and interacts with the opioid and dopamine system circuitry and thus plays a role in other addictions (Nowak et al. 2006; Hungund and Basavarajappa 2004; Moranta et al. 2006; Economidou et al. 2006; Gonzalez et al. 2004; Caille et al. 2007). In both *CNR1* and *FAAH*, human genetic polymorphisms have been associated with increased risk of alcohol or drug use (Zhang et al. 2004; Hutchison et al. 2008; Sipe et al. 2002). Addiction remains a major public health concern and current evidence suggests that pharmacotherapies containing Δ^9-THC, such as dronabinol and nabiximols, could still be effective treatments for a variety of disorders. Development of novel medications such as fatty acid amide hydrolase (FAAH) inhibitors and neutral CB_1 receptor antagonists promises to extend the range of available interventions (Sloan et al. 2017).

12.3.1.1   Cannabis-Use Disorder

In cannabis users, [^{18}F]MK-9470 binding is ~12% lower in cortical, but not most subcortical, brain regions compared to non-cannabis user controls, about 5 days after last use of cannabis reaching significance in temporal lobe, anterior and posterior cortex, and nucleus accumbens (Ceccarini et al. 2015). Binding was not correlated with any clinical characteristics including amount of cannabis consumption, cannabinoid metabolite concentration, duration or initial age of cannabis use, or status of tobacco use.

[^{18}F]FMPEP-d_2 also demonstrated a regionally selective downregulation of CB_1 receptors in chronic cannabis smokers, and also showed that it was reversible (Hirvonen et al. 2012a). Compared to healthy controls, V_T of [^{18}F]FMPEP-d_2 in chronic daily cannabis smokers was ~20% lower in all regions of neocortex, but not subcortex, including basal ganglia a day after last use of cannabis (Fig. 12.11). Years of smoking correlated negatively with V_T (*i.e.*, more years of smoking correlated with smaller V_T), as V_T of [^{18}F]FMPEP-d_2 was independent of age in healthy males. As there was no significant difference between groups for V_T in cerebellum, this tissue was used as a reference tissue for additional analysis; it should be noted that this was performed only after the lack of difference for V_T was established between groups using the standard method correcting for radioligand in plasma, and may not be directly applicable to other between-group analyses. Following approximately 1 month of cannabis abstinence V_T increased in all affected regions except

hippocampus, demonstrating that the downregulation of CB_1 receptors was reversible. In addition, V_T correlated negatively with BMI; therefore BMI was used as an adjustment variable in all findings. BMI or cannabis use did not correlate with free fraction of the radioligand, a potential confounding variable of the study. Neither the initial V_T nor the amount of recovery of V_T after 4-week abstinence correlated with the age of first use, amount of current daily use, or any clinical rating scales measuring withdrawal or craving. Tobacco smoking did not affect the results when included as a confounding variable in cannabis abusers (see below Sect. 12.3.1.3 for additional review). Interestingly, three control subjects of Indian descent had significantly lower V_T, but there was no difference for subjects of African or European descent, compared to the rest of the control group.

[^{11}C]OMAR was used to examine cannabis users in a similar study; however in this instance participants used less cannabis daily and were scanned three times: at baseline while not intoxicated or in withdrawal from cannabis, after 2 days, and after 28 days of monitored abstinence (D'Souza et al. 2016a). This paradigm permitted detection of the rapid time course by which CB_1 receptors reverse, as the 15% lower V_T in cannabis users compared to controls at baseline were essentially reversed within 2 days and remained nonsignificantly through 28 days. In contrast to that seen using [^{18}F]FMPEP-d_2, [^{11}C]OMAR binding was globally lower in cannabis users compared to controls, with the exception of thalamus and cerebellum, and there were no correlations with CB_1 receptor availability and cannabis use patterns. [^{11}C]OMAR binding was negatively correlated to cannabis withdrawal symptoms on day 2 (*e.g.*, more severe withdrawal symptoms with lower [^{11}C]OMAR V_T).

12.3.1.2 Alcohol-Use Disorder

In alcohol-dependent patients, [^{18}F]FMPEP-d_2 demonstrated reduced CB_1 receptor binding that did not recover after 2–4 weeks of abstinence (Fig. 12.11) (Hirvonen et al. 2013). Compared to healthy controls ($n = 19$), alcohol-dependent patients ($n = 18$) had approximately 20–30% lower V_T adjusted for BMI across all brain regions when scanned during the first week of alcohol cessation. Years of alcohol use correlated negatively with V_T, which was not confounded by age. Differences between controls and alcohol-dependent patients could not be accounted for by clinical rating scales for alcohol use or withdrawal, or by tobacco use, and remained significant after partial volume correction. Repeat scans 2–4 weeks after abstinence did not result in any significant change in V_T. In both groups, those individuals carrying the *rs2023239 C* allele of *CNR1* had higher V_T (31% higher in patients, 19% in controls), although no statistical differences were detected between carriers and noncarriers based on demographic or clinical variables.

In contrast, V_T of [^{11}C]OMAR was approximately 20% higher in alcohol-dependent patients ($n = 8$) compared to healthy controls ($n = 8$) when measured 4 weeks after abstinence. Anterior and posterior cingulate and orbitofrontal cortices, hippocampus, insula, and putamen were chosen *a priori* for their involvement in alcohol dependence, and analysis of other brain regions did not demonstrate any significant between-group differences. These findings were neither affected by age,
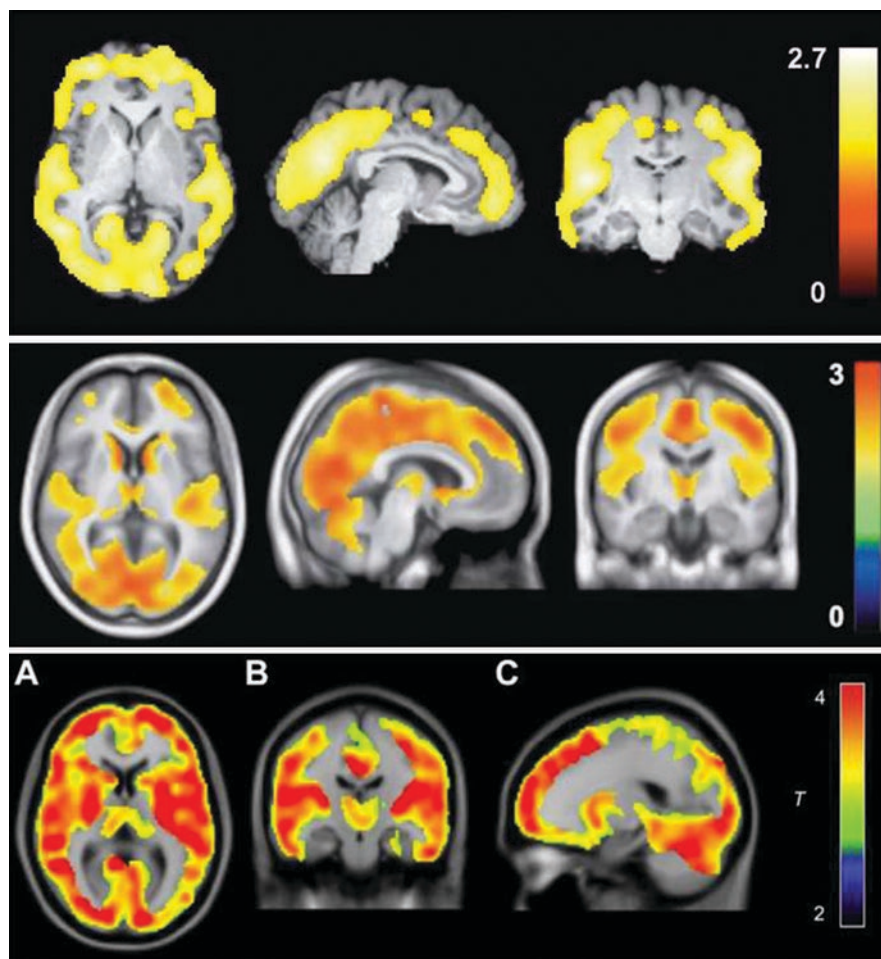
Fig. 12.11 Statistical parametric mapping (SPM) of [^{18}F]FMPEP-d_2 in three different substance-use disorders. Top: Chronic daily cannabis smokers ($n = 30$) have lower V_T than control subjects ($n = 28$) at baseline as a large single cluster that includes only cortical regions, and cluster-level corrected p-value of 0.043 (reprinted from Hirvonen et al. (2012b) with permission of Nature Publishing Group). Middle: Patients with alcohol dependence ($n = 18$) have lower V_T than control subjects ($n = 19$) at baseline as a large single cluster, with cluster-level family-wise error-corrected P-value of 0.038 (reprinted from Hirvonen et al. (2013) with permission of Nature Publishing Group). Bottom: Male tobacco smokers ($n = 18$) have lower V_T than nonsmokers ($n = 28$) as a large single cluster, with cluster-level family-wise error-corrected p-value of 0.001 (reprinted from Biological Psychiatry, Hirvonen et al. (2018) Copyright (2018) with permission from Elsevier). For each, corresponding color bar represents t value in each voxel within the significant cluster

body mass index (BMI), or use of tobacco, nor did they correlate with any alcohol-related or other clinical measures (Neumeister et al. 2012).

The effects of both acute and chronic alcohol exposure on CB$_1$ receptor availability were examined with [^{18}F]MK-9470 in rats. Acute alcohol exposure resulted

in ~7% increase of CB_1 receptor binding in nucleus accumbens and it highly correlated with an approximate doubling of anandamide concentration (measured by microdialysis), while chronic alcohol exposure resulted in ~5% decrease of CB_1 receptor binding in right hippocampus and striatum, and insular and primary sensory cortices, which correlated with the amount of ethanol consumed, and it was reversible in hippocampus and striatum after 7–14-day abstinence. Anandamide was no difference in nucleus accumbens after chronic alcohol exposure or abstinence (Ceccarini et al. 2013a). [18F]MK-9470 was used to study both acute and chronic effects of alcohol on CB_1 receptor availability in humans, yielding bidirectional results. In social drinkers ($n = 20$), intravenous ethanol caused ~16% increase of [18F]MK-9470 binding, while alcohol-use disorder patients had 16% lower ($n = 26$) [18F]MK-9470 binding immediately after chronic heavy drinking compared to nondrinking healthy controls ($n = 17$), which remained lower (17%, $n = 19$) after 1-month abstinence from alcohol (Ceccarini et al. 2014). In social drinkers, the change in [18F]MK-9470 binding was less in those with more previous drinking, and correlated with some subjective effects of alcohol intoxication. There were no correlations with [18F]MK-9470 binding to clinical characteristics or patterns of alcohol, tobacco, or caffeine use.

12.3.1.3 Tobacco Use and Nicotine Exposure

In a study examining the impact of nicotine on receptor binding, 2 weeks of nicotine exposure did not produce significant change in [18F]MK-9470 uptake in rat brain (Gerard et al. 2010).

Similar to that seen in cannabis- and alcohol-using subjects, [18F]FMPEP-d_2 demonstrated ~20% lower V_T in male tobacco smokers ($n = 18$) compared to nonsmoker controls ($n = 28$) (Fig. 12.11) (Hirvonen et al. 2018). Decreased CB_1 receptor availability was observed throughout the entire brain, persisted before and after accounting for corrections of BMI and *rs2023239* genotype, and could not be accounted for by change in plasma free fraction of the radioligand. Characteristics of smoking (cigarettes per day, age of onset, years smoked, Fagerström Test for Nicotine Dependence [FTND]) were not correlated with whole-brain V_T. In an exploratory re-examination of studies using [18F]FMPEP-d_2 in cannabis- and alcohol-using subjects (see above), the prior results were not affected by tobacco use; that is, CB_1 receptor downregulation resulting from cannabis or alcohol use was not furthered by tobacco use.

In a study using [11C]OMAR examining patients with schizophrenia (see below, Sect. 12.3.3), tobacco smokers with schizophrenia had greater V_T than nonsmoking patients (D'Souza and Ranganathan 2015). While both groups were lower than nonsmoking controls (no tobacco smoking controls were included in the study, and therefore conclusions about tobacco smoking alone cannot be drawn with regard to [11C]OMAR binding), smokers with schizophrenia were not significantly different from controls. CB_1 receptor availability did not correlate with FTND or other smoking-related characteristics; however more smokers were on antipsychotic medications, which increased [11C]OMAR binding in that group, and may have confounded this result.

12.3.2 Eating and Metabolic Disorders

There is overwhelming evidence that the ECS plays a central role in the control of food intake and in eating disorders (Gerard et al. 2011; Di Marzo et al. 2001; Cooper 2004; Maresz et al. 2007; Morton et al. 2006). The administration of cannabinoid CB_1 receptor agonists can promote body weight gain (Cota et al. 2003; Vickers and Kennett 2005), anandamide causes overeating in rats because of its ability to activate cannabinoid receptors (Gaetani et al. 2008), and CB_1 receptor agonists have been used as appetite stimulants in AIDS and cancer patients (Croxford 2003). Conversely, antagonists or inverse agonists are associated with long-term weight loss (Vickers and Kennett 2005; Smith and Fathi 2005; Hsiao et al. 2015). Mechanism-of-action studies have shown that the effect of inverse agonists is likely caused by a combination of central effects (e.g., reduction in food intake) (Nogueiras et al. 2008) and peripheral effects (increased resting energy expenditure and fat oxidation) (Addy et al. 2008; Jbilo et al. 2005). In addition, different alleles of the gene encoding the CB_1 receptor (*CNR1*) and FAAH (*FAAH*) have been associated with anorexia nervosa (Siegfried et al. 2004; Monteleone et al. 2009) and obesity (Benzinou et al. 2008; Sipe et al. 2005). An analysis pooling data from two studies found a negative association between [^{18}F]MK-9470 CB_1 binding in regions associated with homeostasis (*e.g.*, hypothalamus, pons, medulla) and reward (*e.g.*, nucleus accumbens, amygdala, insula, orbitofrontal cortex, striatum) and body mass index (BMI) (Ceccarini et al. 2016), replicating an association observed in some but not all CB_1 PET studies (Sloan et al. 2019). This association raises the possibility that the fluctuations in BMI associated with disordered eating may explain the observed alterations in radiotracer binding, suggesting that altered CB_1 availability may be a result of disordered eating rather than a causal factor.

The highly selective CB_1 inverse agonist SR141716 (rimonabant) was developed by Sanofi-Aventis in the European Union to treat obesity (Rinaldi-Carmona et al. 1994), and has been found to improve lipid and glucose metabolism in obese humans. However, shortly after its introduction to the market, the safety of rimonabant was called into question due to the side effects that included severe depression and suicidal thoughts (Kelly et al. 2011; Lee et al. 2009; Le Foll et al. 2009). After the collection of additional clinical data, and preclinical results with taranabant showing similar side effects, rimonabant was withdrawn from the market and further development of centrally acting CB_1 inverse agonists was largely abandoned (Le Foll et al. 2009). Due to the structural dissimilarity of taranabant from rimonabant, and preclinical data from animal studies, the adverse effects are thought to be mechanism-dependent, and not merely compound-specific, effects. As previously discussed, the brain receptor occupancy necessary for clinical weight loss with rimonabant and taranabant is estimated at 20–30% (see Sect. 12.2.2.4).

Following the failures of rimonabant and taranabant due to anxiety, depression, and suicidal thoughts, a second generation of CB_1 receptor antagonists that are peripherally restricted have been developed that might confer benefit on metabolic profile but without CNS penetration and psychiatric side effects. One such compound, TM38837, was assessed for CNS penetration in nonhuman primates using

[^{11}C]MePPEP with brain uptake as the within-subject outcome measure, as previously recommended, for calculating receptor occupancy by the Lassen plot (Takano et al. 2014). Compared to rimonabant, TM38837 required about 10 times higher dose and 100 times higher plasma concentration to achieve a similar CNS CB_1 receptor occupancy, and it was concluded that the clinically relevant doses of TM38837 would have low CB_1 receptor occupancy. This study demonstrated the potential of using CNS-penetrant CB_1 receptor radioligands in the assessment of peripherally restricted drugs, by screening for a lack of meaningful receptor occupancy.

There is evidence that people with anorexia nervosa do not exhibit normal endocannabinoid responses to food consumption (Monteleone et al. 2015). In a rat model of anorexia, [^{18}F]MK-9470 cortical and subcortical binding was substantially higher in male (67%) and female (>51%) rats following weight loss by food restriction and exercise, which normalized after weight gain (Casteels et al. 2014). In an assessment of anorexia nervosa patients, [^{18}F]MK-9470 demonstrated ~25% globally increased uptake in brain compared to healthy controls (Gerard et al. 2011). The amount of uptake was also significantly more than bulimia nervosa patients, though bulimia nervosa patients were not statistically different from controls. Uptake was relatively increased in insula for anorexia (right side) and bulimia (left side) patients, and in areas of frontotemporal cortex in anorexia patients. In addition, scores rating drive for thinness in anorexia patients correlated with [^{18}F]MK-9470 uptake in the superior temporal region. Increased uptake was interpreted as increased CB_1 receptor availability, and therefore hypoactive endocannabinoid transmission. Similarly, [^{18}F]MK-9470 was about 24% greater in multiple regions throughout brain in those with functional dyspepsia compared to BMI-matched controls (Ly et al. 2015). While no correlations could be associated with symptom severity or clinical characteristics, the regions identified are implicated in visceral nociception, homeostasis, and reward, and remained stable over the course of about 3 years.

CB_1 receptor expression has been identified in metabolically active brown adipose tissue (BAT), and both [^{11}C]MePPEP/[^{18}F]FMPEP-d_2 and [^{18}F]MK-9470 binding can be observed in regions of human BAT distribution (Van Laere et al. 2008b; Terry et al. 2010b). In rats, CB_1 receptors were found to colocalize with the BAT marker uncoupling protein-1; were selectively expressed in BAT but not white adipose tissue; could be imaged with [^{18}F]FMPEP-d_2 in BAT, with kinetic analysis conducted using an image-derived input function; and increased following β_3 agonist treatment to stimulate BAT activity (Eriksson et al. 2015; Lahesmaa et al. 2018). In follow-up, cold exposure increased [^{18}F]FMPEP-d_2 binding in human BAT, and overweight subjects were found to have lower CB_1 receptor availability in BAT compared to lean subjects both by imaging and biopsy histochemical analysis (Lahesmaa et al. 2018). In brain, overweight subjects had about 23% lower CB_1 receptor availability compared to their lean counterparts, with a correlation during cold condition between midbrain and BAT, suggesting sympathetic nervous and endocannabinoid system-mediated connection during thermoregulation.

Furthering the investigation of peripheral CB_1 receptor-rich targets in obesity, [^{11}C]OMAR was assessed in heart muscle in obese mice and humans (Valenta et al.

2018). Uptake of [¹¹C]OMAR was greater in heart of genetically modified obese mice compared to wild type, which was reflected in high CB_1 expression detected by PCR and RNA *in situ* hybridization. [¹¹C]OMAR had significantly greater retention in hearts of obese vs. health weight controls.

12.3.3 Schizophrenia

Cannabis has long been associated with schizophrenia (Ortiz-Medina et al. 2018), and the evidence between cannabis use and development of a psychotic disorder has been mounting (D'Souza et al. 2016b). Large epidemiological studies have suggested an overall increased and potentially dose-dependent risk for developing schizophrenia after cannabis use (Fernandez-Espejo et al. 2009; Malone et al. 2010; Marconi et al. 2016), and a genetic susceptibility has been found in subjects who develop psychotic symptoms after cannabis use (Caspi et al. 2005; Ho et al. 2011). Additional genetic studies have reported an association between the CB_1 receptor-encoding gene, *CNR1*, and schizophrenia, especially the disorganized subtype (Ujike et al. 2002); individuals with a 9-repeat allele of an AAT-repeat polymorphism of the gene have a 2.3-fold higher susceptibility to schizophrenia (Leroy et al. 2001). A meta-analysis has demonstrated greater CSF and blood anandamide, and blood CB_1 receptor expression in those with schizophrenia compared to controls was greater during earlier stage of the illness and before antipsychotic treatment, was inversely associated with symptom severity, and normalized following successful treatment (Minichino et al. 2019).

In schizophrenia, hyperactivity of dopamine neurotransmission in the mesencephalic projections to the nucleus accumbens appears to contribute to the psychotic (positive) symptoms, and hypodopaminergic and hypoglutamatergic transmission in the prefrontal cortex to the negative symptoms (van der Stelt and Di Marzo 2003). These transmitters are under CB_1 receptor signaling control, and hyperactivity of the central ECS has been shown to be involved in the pathogenesis of schizophrenia and its symptoms (Vinod and Hungund 2006a; Laviolette and Grace 2006; Ujike and Morita 2004; Zavitsanou et al. 2004; Dean et al. 2001). Since increasing evidence from the anatomical, pharmacological, and behavioral studies points to functional interactions between the cannabinoid and dopamine receptor systems (Laviolette and Grace 2006), this could be a key to the development of innovative therapy for psychotic illnesses (Ujike and Morita 2004).

Interestingly, there is growing evidence that cannabidiol acts as a negative allosteric modulator of the CB_1 receptor, and reduces psychotic symptoms in patients with schizophrenia, both as a monotherapy (Leweke et al. 2012) and as an adjunctive treatment (McGuire et al. 2018). Conversely, blockade of CB_1 receptors has been found to be ineffective at reducing psychotic symptoms in schizophrenia and schizoaffective disorder (Meltzer et al. 2004), suggesting the possibility that cannabidiol may exert its antipsychotic effects through other molecular targets.

Studies measuring CB_1 receptor density in postmortem tissue have been inconsistent. Significantly greater CB_1 receptor binding in the frontal and cingulate cortex

was found in subjects with schizophrenia (Dean et al. 2001), and has also been reported to be increased by up to 25% in the posterior cingulum (Newell et al. 2006). In contrast, other studies have shown a decrease in CB_1 receptor mRNA and protein by nearly 15% and 12%, respectively (Eggan et al. 2008). While discrepancies could be attributed to methodology (e.g., autoradiography generally reflecting higher CB_1 receptor expression in schizophrenia vs. vice versa for immunodetection), receptor trafficking and localization, and/or allosteric modulation changing affinity of ligands at the allosteric site (Price et al. 2005), confounding factors such as lifetime antipsychotic exposure which has been shown to affect CB_1 receptor expression (Secher et al. 2010) might also contribute. Therefore, *in vivo* imaging studies would be of great assistance in distinguishing the changes in receptor expression due to disease, and control for effects of medication.

Prior to imaging, [³H]MePPEP was assessed in postmortem human brain tissue to estimate the difference in CB_1 receptor binding in those with schizophrenia ($n = 47$) versus controls ($n = 43$), and the number of participants to enroll in subsequent PET studies (Jenko et al. 2012). Specific binding was about 20% higher in dorsolateral prefrontal cortex from those with schizophrenia compared to controls; this result was significant ($p = 0.050$) when controlling numerous categorical and continuous variables (*e.g.*, gender, age of onset, duration of illness, age of death, antipsychotic exposure, alcohol and substance abuse), and more so when the variables, all of which were not statistically significant, were omitted ($p = 0.021$). Binding affinity of MePPEP was the same between groups, and the *rs2023239C* allele was not found to affect results between groups; allele carriers had higher binding than noncarriers within groups, though not reaching statistical significance. A power analysis using this in vitro data suggested that 53 subjects per group would be needed for an *in vivo* PET study using [¹⁸F]FMPEP-d_2 with 80% power and $p < 0.05$.

In a subsequent study, [¹¹C]MePPEP and [¹⁸F]FMPEP-d_2 were used to image CB_1 receptors in separate cohorts of males with first-episode psychosis (*i.e.*, diagnosis or high risk for development of schizophrenia) (Borgan et al. 2019). [¹¹C]MePPEP was imaged in patients and controls ($n = 20$ each) for 90 min with arterial sampling, and demonstrated lower V_T in anterior cingulate cortex, hippocampus, thalamus, and striatum in those with psychosis compared to controls; results were significant by group, but not group × region. Significant associations were found between lower V_T in hippocampus with greater symptom severity (as measured by the Positive and Negative Syndrome Scale [PANSS]), and lower V_T in striatum and anterior cingulate cortex with worse cognitive performance. [¹⁸F]FMPEP-d_2 was imaged in patients ($n = 7$) and controls ($n = 11$) from 0 to 60 and 90 to 120 min with arterial sampling, and demonstrated significantly lower V_T in anterior cingulate cortex, hippocampus, thalamus, and striatum of those with psychosis compared to controls. As predicted by the previous ex vivo study, antipsychotic treatment did not affect the outcome in either cohort, as treatment status did not affect the results.

Autoradiography with [³H]OMAR was performed in the same schizophrenia and matched control subjects previously analyzed by *in situ* hybridization (for mRNA) and radioimmunohistochemistry (for protein) (Eggan et al. 2008; Volk et al. 2014).

[^{3}H]OMAR was grossly 8% higher in all layers of prefrontal cortex from schizophrenia subjects compared to matched controls, and did not differ by multiple clinical characteristics (*e.g.*, psychiatric medications, cannabis use, history of suicide). [^{3}H]OMAR correlated negatively with CB_1 receptor mRNA, which may reflect altered trafficking of CB_1 receptors with a nonlinear 1:1 relationship between transcription and translation, higher CB_1 receptor affinity leading to reduced expression, or reduced expression (*e.g.*, from loss of receptor reserve pools) leading to higher affinity of the remaining receptors. [^{3}H]OMAR positively correlated with ABHD6 (which metabolizes 2-AG) mRNA expression, suggesting that lower 2-AG levels could be associated with CB_1 receptor upregulation.

In an initial study, patients with schizophrenia ($n = 10$) trended towards higher measurements of V_T with [^{11}C]OMAR compared to healthy controls ($n = 10$). There was no significant difference in V_T between healthy controls and schizophrenia patients, with the exception of that in pons (Wong et al. 2010a); however this finding did not survive correction for multiple comparisons. Patients in the study were on either olanzapine or risperidone monotherapy, and antipsychotics have been shown to have a mixed effect on CB_1 receptor binding or availability; in subgroup analysis, no difference was found between patients on the two medications. Within the schizophrenia patient group, there was no association of V_T with Brief Psychotic Rating Score (BPRS); however when scores were taken as a ratio of positive over negative symptoms, there was a positive correlation with V_T in several areas of neocortex (Wong et al. 2008).

In a follow-up study, patients with schizophrenia ($n = 25$) demonstrated ~12% significantly lower global V_T with [^{11}C]OMAR compared to healthy controls ($n = 18$) (Ranganathan et al. 2016). Patients with schizophrenia treated with antipsychotic medications ($n = 18$) had higher V_T with [^{11}C]OMAR compared to untreated patients ($n = 7$), and while the two patient groups had no significant differences in PANSS, CB_1 receptor availability and PANSS were positively correlated in hippocampus, hypothalamus, and thalamus. As mentioned above, schizophrenia patients who used tobacco had CB_1 receptor availability that was greater than that of nonsmoking patients, and it was nonsignificantly lower than that of nonsmoking controls.

In contrast to results obtained using [^{11}C]MePPEP, [^{18}F]FMPEP-d_2, and [^{11}C]OMAR, [^{18}F]MK-9470 demonstrated 5–10% higher binding in brains of individuals with schizophrenia ($n = 51$ with antipsychotic treatment, $n = 6$ after antipsychotic washout, $n = 10$ first-episode psychosis and antipsychotic naive) compared to healthy controls ($n = 12$) (Ceccarini et al. 2013b). Specifically, binding was higher in regions of the mesocortical limbic circuit (nucleus accumbens, insula, cingulate cortex, inferior frontal cortex, and areas of the parietal and mediotemporal lobes), and was negatively correlated with PANSS negative symptom and depression scores in the antipsychotic free subgroup. In a rodent model of schizophrenia mimicking the *in utero* exposure to infectious agents hypothesized to contribute to risk of disease in humans, [^{18}F]MK-9470 reflected reduced CB_1 receptor availability in globus pallidus of adolescent rats, and increased receptor availability in sensory cortex and hypothalamus in adult rats after prenatal exposure to a viral mimic agent, compared to controls (Verdurand et al. 2014).

12.3.4 Mood and Anxiety Disorders

Cannabinoid agonists demonstrate mood-altering effects (Degenhardt et al. 2003). The location of CB_1 receptors in limbic and cerebral cortex suggests that they are involved in mood dysfunction, and endocannabinoid stimulation does indeed have anxiolytic and antidepressant effects on animals (Gobbi et al. 2005). Inhibitors of FAAH are a hopeful and novel target for anxiety and depression, suggesting that enhancement of local endocannabinoid tone is preferred to exogenous cannabinoid agonists, which are potentially anxiogenic (more commonly at high doses) as well as anxiolytic (Moreira and Wotjak 2010). While the effect of cannabinoid agonists on depression is unclear, they generally have a negative effect on symptoms when used chronically (Lowe et al. 2019), and inverse agonists have been shown to increase depression and suicidal thoughts (as previously discussed). Several genetic polymorphisms have been identified in association with mood and anxiety disorders, and likely cause alterations to endocannabinoid signaling (Hillard et al. 2011). Genetic and postmortem studies have implicated the ECS in depression and suicide, and CB_1 receptors have been found to be upregulated in suicide victims (Vinod and Hungund 2006b). A recent review concluded that cannabinoid receptors, particularly CB_1 receptors, may become promising targets for the development of novel therapeutic tools for the treatment of suicidal behavior (Colino et al. 2018). Several studies have found reductions in circulating endocannabinoid levels in individuals with PTSD (Neumeister et al. 2013; Hill et al. 2013). Since endocannabinoids appear to influence stress, anxiety, and reversal learning related to aversive memories, cannabinoid receptor agonists have been proposed as a potential treatment for PTSD. One small randomized placebo-controlled crossover trial indicated that nabilone, a synthetic analogue of Δ^9-THC, reduced PTSD symptoms in male military personnel compared to placebo (Jetly et al. 2015). While a follow-up study also demonstrated reduced PTSD-related nightmares (Jetly et al. 2015), several others have found that cannabis can worsen PTSD symptoms and increase the risk of violence and suicidal behaviors (Wilkinson et al. 2015; Barrett et al. 2011; Kimbrel et al. 2018; Borges et al. 2016; Moller et al. 2013). A recent review suggested that cannabidiol (CBD), while representing a less specific pharmacological approach, may be another way to treat trauma-related and anxiety disorders (Patel et al. 2017).

[^{11}C]OMAR demonstrated ~20% higher V_T in the brain of individuals with PTSD ($n = 25$) compared to trauma-exposed controls ($n = 12$) and healthy controls without trauma history ($n = 23$) (Fig. 12.12) (Neumeister et al. 2013). While cortisol was lower in the trauma-control and PTSD groups, peripheral anandamide, but not other endocannabinoids, was >50% lower in the PTSD group compared to either control group. As well, [^{11}C]OMAR V_T was negatively correlated to peripheral anandamide in the PTSD group, and other demographic and clinical comorbidities and variables were not correlated with [^{11}C]OMAR V_T. Combination of [^{11}C]OMAR V_T, anandamide, and cortisol levels could identify ~85% PTSD individuals. The low anandamide concentration suggests compensatory CB_1 receptor upregulation, and together could be reflective of an ineffective modulation of stress response which results in PTSD symptoms, compared to those exposed to trauma without developing symptoms.
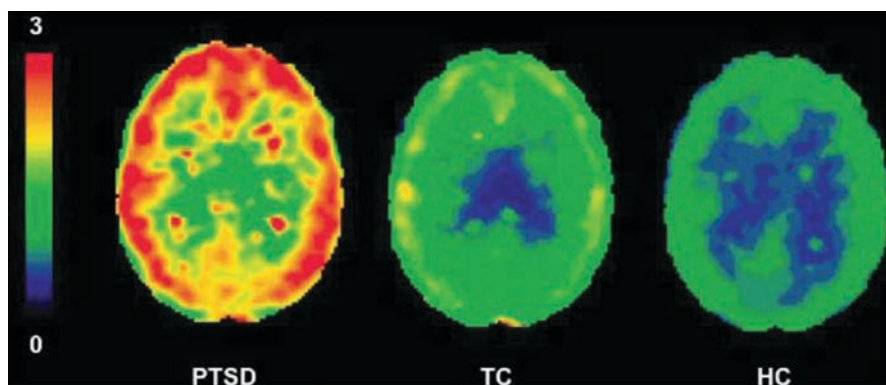
Fig. 12.12 [^{11}C]OMAR volume of distribution (V_T) values in post-traumatic stress disorder (PTSD, $n = 25$) and trauma-exposed control (TC, $n = 12$) groups relative to healthy control (HC, $n = 23$) group (reprinted from Neumeister et al. (2013) with permission of Nature Publishing Group)

While the role of the amygdala on the anxiogenic effects of cannabis had been examined in preclinical studies, use of PET provided an opportunity to assess this association in humans *in vivo*. Using [^{11}C]OMAR, CB_1 receptor availability in amygdala was found to be positively correlated to attentional bias to threat and severity of threat symptomatology (using the dot-probe task measuring reaction and bias to threatening versus neutral words) across a group of individuals with PTSD ($n = 12$), trauma exposed without PTSD ($n = 4$), and nontrauma-exposed controls ($n = 4$) (Pietrzak et al. 2014). Moreover, a mediation analysis demonstrated that the endophenotype of attentional bias to threat better explains and connects the association between higher amygdala CB_1 receptor availability and trauma-related psychopathology than a direct relationship alone. Similar to that seen in the PTSD study, peripheral anandamide concentrations were negatively correlated with CB_1 receptor availability, as well as attentional bias to threat. In a separate study, male participants ($n = 14$) with experiential use of cannabis were given THC 10 mg orally and assessed for anxiety (state-trait anxiety inventory), psychosis (PANSS), and response to fearful vs. neutral faces during fMRI imaging, and were found to have significantly greater anxiety and psychosis ratings during peak levels of THC, and activation of right amygdala and adjacent limbic and associated areas (Bhattacharyya et al. 2017). CB_1 receptor V_T was measured with [^{11}C]MePPEP (by spectral analysis), and right amygdala V_T was positively correlated with the anxiogenic (but not psychotogenic) effect of THC, and positively correlated with the activation seen during fMRI fear processing task.

12.3.5   Neurodegenerative Diseases

Cannabinoids exert a neuroprotective influence on some neurological diseases, including Alzheimer's disease (AD), Parkinson's disease (PD), Huntington's disease (HD), multiple sclerosis, and epilepsy. Synthetic cannabinoid receptor

agonists/antagonists or compounds can provide symptom relief or control the progression of neurological diseases. However, the molecular mechanism and the effectiveness of these agents in controlling the progression of most of these diseases remain unclear (Agar 2015).

12.3.5.1 Alzheimer's Disease

Alzheimer's disease (AD) is one of many neurodegenerative disorders that are associated with excitotoxicity, oxidative stress, and neuroinflammation, and certain cannabinoids have been demonstrated to inhibit these events to halt the progression of neurodegeneration. CB_1 and CB_2 receptors and FAAH have found to be co-localized with amyloid plaques in Alzheimer's disease (AD). CB_2-selective agonists were shown to block amyloid-induced activation of cultured microglial cells (Ramirez et al. 2005), and would presumably decrease neuroinflammation in AD. In postmortem studies, [^{125}I]SD7015, a CB_1 selective ligand, has demonstrated an inverse correlation of CB_1 receptor density and Braak tau pathology staging (Farkas et al. 2012), suggesting a novel *in vivo* method of staging AD progression. Independent of cannabinoid receptor activation, Δ^9-THC competitively inhibits acetylcholinesterase (AChE) and prevents AChE-induced amyloid beta-peptide aggregation (Eubanks et al. 2006). Study of CB_1 and CB_2 receptors in correlation with amyloid load could lead to new treatment options for AD.

Activating CB_1 receptors has been demonstrated to produce certain therapeutic effects on animal models of AD (Aso et al. 2018). [^{18}F]FMPEP-d_2 was longitudinally assessed in a mouse model of AD (Takkinen et al. 2018). Compared to wild-type littermates, APP/PS1–21 transgenic mice, which produce amyloid β_{42} around 6 weeks and peaking at 9 months of age, were found to have lower [^{18}F]FMPEP-d_2 uptake in parietotemporal cortex (at 9, 12, and 15 months), hippocampus (at 9 and 12 months), and cerebellum (at 9 months) relative to thalamus (used as a pseudoreference region and with no significant difference between groups). *Ex vivo* autoradiography also demonstrated reduced [^{18}F]FMPEP-d_2 binding in amyloid-overproducing mice, but with difference by sex and time (males with lower binding in striatum at 15 months, females with lower binding in parietotemporal cortex, striatum, and posterior hippocampus). Immunohistochemical staining of CB_1 receptors demonstrated visible loss in amyloid-overproducing mice compared to wild type at 15 months. However, measured by Western blot, CB_1 receptor expression was not different by genotype at 9 months, though males were significantly lower than females.

The activity of CB_1 receptors was studied in postmortem brain samples of AD patients during clinical deterioration. CB_1 receptor activity was higher at earlier AD stages in hippocampal areas and internal layers of frontal cortex, but a decrease was observed at the advanced stages. The pattern of modification appears to indicate initial hyperactivity of the endocannabinoid system in brain areas that lack classical histopathological markers at earlier stages of AD, indicating an attempt to compensate for the initial synaptic impairment, which is then surpassed by disease progression. These results suggest that initial CB_1 receptor stimulation might have therapeutic relevance (Manuel et al. 2014). However, another study found no

evidence for a difference in CB_1 receptor availability in AD compared to age-matched controls (Ahmad et al. 2014) using combined [^{18}F]MK-9470 and [^{11}C]PIB PET scans. When compared with reported CB_1 receptor changes in Parkinson's and Huntington's disease (see below), this suggests that CB_1 receptors maybe differentially involved in neurodegenerative disorders.

12.3.5.2   Huntington's Disease

Huntington's disease (HD) is caused by a trinucleotide repeat expansion on the *HTT* gene, leading to a polyglutamine tail of the huntingtin protein. Although the normal physiologic function of the protein remains unclear, this pathological variant has been shown to cause disruptions in nuclear transcription factors, presumably leading to a decrease in normal expression of certain proteins. The pathological characteristic is progressive neuronal loss, preferentially affecting the caudate nucleus, resulting in motor (choreiform movements), cognitive (early-onset dementia), and psychiatric symptoms (behavioral changes, e.g., disinhibition, aggression). One of the earliest neurochemical alterations in HD is the loss of CB_1 receptors in the basal ganglia (Glass et al. 2000), which occurs before the D_1/D_2 receptor dopaminergic dysfunction and characteristic choreic motor dysfunction and is strongly correlated with chorea and cognitive deficit (Laprairie et al. 2016). In animal models, the ECS is hypofunctional (Lastres-Becker et al. 2003). A huntingtin/CB_1 double-knockout mouse model demonstrated that endocannabinoid signaling was essential to the neuropathologic symptoms, and that CB_1 receptor loss may sensitize cells to additional excitotoxic damage (Blazquez et al. 2011). Oom et al. found early decreased CB_1 receptor binding in the bilateral caudate, putamen, globus pallidus, and thalamic nucleus of presymptomatic HD (R6/2) mice, with further progressive decline using [^{18}F]MK-9470, suggesting that PET quantification of *in vivo* CB_1 binding may be a useful early biomarker for HD (Ooms et al. 2014).

In HD, there is also selective loss of spinal neurons and the appearance of activated microglia in striatum, cortex, and white matter. The number of activated microglia in the striatum and cortex has been shown to correlate with the extent and progression of neuronal loss (Sapp et al. 2001), and CB_2 agonists show neuroprotective effects in an HD animal model (Sagredo et al. 2009; Paldy et al. 2008). In this way, CB_2 receptor imaging may be useful in monitoring the progression of neuronal loss in HD. In addition, early regional dysfunctions in CB_1 receptor signaling, involving the lateral globus pallidus and caudate-putamen, have been found, suggesting another useful early biomarker for HD. Decreased [^{18}F]MK-9470 brain uptake was observed in a rat genetic model of Huntington's disease when compared to wild-type littermates (Casteels et al. 2011); however, this was observed in a regionally selective fashion limited to the basal ganglia, rather than the global reduction described below in humans. A rat model of HD using unilateral quinolinic acid lesion demonstrated a disproportionately modest decrease of [^{18}F]MK-9470 uptake compared to the severity of the lesion, and an increase in contralateral basal ganglia and cerebellum, the latter of which corresponded to improved functional outcome (Casteels et al. 2010c).
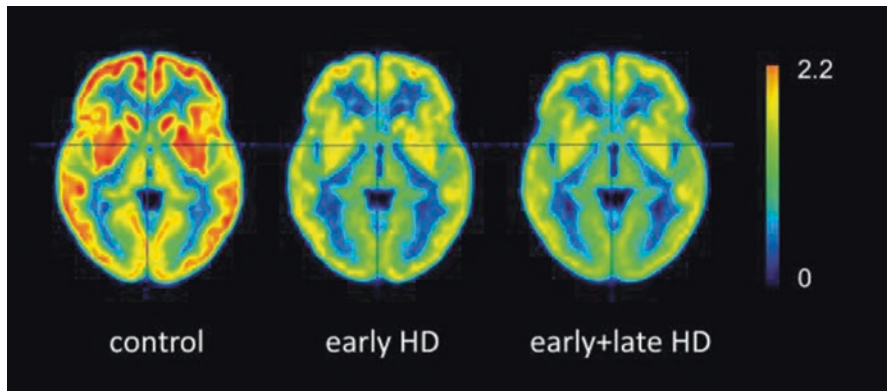
Fig. 12.13 Cross-sectional, partial-volume-corrected, modified standardized uptake value (mSUV) parametric images of [^{18}F]MK-9470, averaged for all controls ($n = 14$), early-HD patients ($n = 7$), and total group of HD patients ($n = 19$) (courtesy of Dr. Koen Van Laere, KU Leuven)

Given the high concentration of CB$_1$ receptors in the basal ganglia, neuropsychiatric and movement disorders known to affect those regions present themselves as potentially sensitive and particularly interesting targets for CB$_1$ receptor PET imaging. In humans with HD, [^{18}F]MK-9470 uptake was decreased in all areas of brain except white matter compared to healthy controls (Fig. 12.13) (Van Laere et al. 2010). Intriguingly, this was also observed in early symptomatic patients, even in areas with minimal volume loss. Decreased uptake was presumably due to reduced CB$_1$ receptor availability, as huntingtin is known to interfere with protein and receptor expression. Therefore, CB$_1$ PET imaging may be a useful tool to assess early symptomatic, and potentially presymptomatic, Huntington's disease onset. As well, decreased [^{18}F]MK-9470 uptake was found in pre-HD subjects in the prefrontal cortex and cingulate cortex, with depression, apathy, and irritability inversely correlating with the binding (Ceccarini et al. 2019a). This suggests that a potential molecular basis of neuropsychiatric symptoms in pre-HD could lead to new therapeutic avenues. It has previously been suggested that CB$_1$ agonists may delay the development of this disease (Lastres-Becker et al. 2003; Glass et al. 2004), and at least one clinical study has shown that they improve neuropsychiatric symptoms (Curtis et al. 2009). However, in a double-blind, randomized, placebo-controlled, crossover pilot clinical trial, no significant differences on motor, cognitive, behavioral, and functional scores were detected among HD patients treated with Sativex (a botanical extract with an equimolecular combination of Δ^9-THC and cannabidiol) and placebo (Lopez-Sendon Moreno et al. 2016).

12.3.5.3 Parkinson's Disease

Several studies have reported neuroprotective effects of cannabinoids in glutamatergic excitotoxicity, oxidative damage, traumatic injury, ischemia, and neurodegeneration models (Paradisi et al. 2006; Sarne and Mechoulam 2005). CB$_1$ receptors are densely located in the basal ganglia, and the ECS has a modulatory effect on

excitation and inhibition, as evident in movement disorders. Parkinson's disease (PD) leads to a decrease in voluntary movements, secondary to insufficient striatal dopamine, causing a subsequent increase in GABAergic activity (Pacher et al. 2006). Early on CB_1 receptor density is reduced, but later the density is increased to compensate for the subsequent overexcitation of GABA (Orgado et al. 2009). mRNA expression of CB_1 is changed and an increased binding capacity has been observed in postmortem tissue of subjects with PD (Lastres-Becker et al. 2001). It is hypothesized that alterations of endocannabinoid synthesis stimulate increased dopamine release (Giuffrida et al. 1999), and cannabinoids inhibit the excitotoxic glutamate release and counteract oxidative stress to dopaminergic neurons which is responsible for nigrostriatal damage (Levenes et al. 1998). Deficiency in endocannabinoid transmission is thought to contribute to late-stage dyskinesias. Thus, modulation of CB_1 receptor-mediated basal ganglia transmission can be used to suppress or prevent the development of these complications (Segovia et al. 2003; Sevcik and Masek 2000; Di Marzo et al. 2000; Sieradzan et al. 2001; Fox et al. 2002); however, the results to date have been mixed (Carroll et al. 2004).

One recent study designed to detect potential alterations in the CB_1 and CB_2 (A isoform, CB2Ar) receptors and monoacylglycerol lipase (MAGL) gene expression in the substantia nigra and putamen found them to be closely related to the neuropathological processes of PD. Therefore, the pharmacological modulation of these targets could represent a new potential therapeutic tool for the management of PD (Navarrete et al. 2018). Most interestingly, a recent study (Ceccarini et al. 2019b) found decreased CB_1 receptor availability in the prefrontal and midcingulate cortex in PD patients using [18F]MK-9470 PET imaging which strongly correlated with the level of disturbed executive functioning, episodic memory, and visuospatial functioning. Thus, further investigation of regional CB_1 receptor expression in varying levels of PD-related cognitive impairment may be useful. In recent study, upregulation of CB_2 receptors was shown in a PD rat model (Concannon et al. 2016). Although more studies are necessary, these findings suggest that CB_2 receptor-selective agonists may provide neuroprotection against the neurodegenerative processes of PD.

Rodent models of PD using 6-hydroxydopamine showed decreased [18F]MK-9470 uptake in bilateral striatum and contralateral cerebellum relative to the lesioned side. Additional correlations were observed with an inverse relationship of tyrosine hydroxylase-containing neurons (*i.e.*, dopaminergic neurons) to [18F]MK-9470 uptake in ipsilateral cerebellum, and a positive relationship of [18F]MK-9470 uptake and contralateral limb impairment (*i.e.*, disease severity) (Casteels et al. 2010b).

[18F]MK-9470 uptake was altered in a region-specific pattern in individuals with PD (Van Laere et al. 2012). In ventral midbrain (site of the substantia nigra) tracer uptake was decreased for early and late stages of PD patients compared to healthy controls, likely representing reduced CB_1 receptor expression in the pars reticulata, irrespective of disease progression, rather than simply a marker of neuronal loss. However in putamen, prefrontal cortex, midcingulate, anterior insula, and hippocampus (regions correlating to dopaminergic projections) tracer uptake was increased relative to total brain uptake in comparison to healthy controls. Regionally

increased CB_1 receptor availability could be explained by compensatory processes of reducing glutamatergic drive in the absence of normally inhibitory dopamine (in striatum) in glutamatergic neurons, and disinhibition of dopaminergic neurons in the ventral tegmental area via a feedback mechanism from mesocortical and meso-limbic regions. Comparison of PD patients with or without levodopa-induced dys-kinesias did not reveal any differences in [^{18}F]MK-9470 uptake, as was also shown in healthy rats receiving L-DOPA or bromocriptine (Casteels et al. 2010d).

12.3.5.4 Multiple Sclerosis

Meta-analyses have supported the beneficial effect of cannabinoid agonists as treat-ment for neuropathic pain (Iskedjian et al. 2007; Rog et al. 2005) and muscle spas-ticity (Pryce and Baker 2007; Mori et al. 2014) in multiple sclerosis (MS). Selective CB_1 receptor overexpression on various glial cells and CB_2 receptor-positive microglia is located within active plaques and in the periphery of chronic active plaques, supporting a role for the ECS as a biomarker or therapeutic target for MS (Bifulco et al. 2007; Benito et al. 2007). Treatment of MS with cannabinoids appears to be based on two mechanisms: (i) reducing excitotoxicity by CB_1 receptors on glia and neurons and (ii) reducing inflammation by CB_2 receptors on microglia (Rossi et al. 2010; Pryce and Baker 2015). Nabiximols is a sublingual spray developed by GW Pharmaceuticals for the treatment of MS using a proprietary blend of a Δ^9-THC and cannabidiol, which show differing affinities for CB_1 and CB_2 receptors, as well as other targets. Although MS has been considered mainly an inflammatory disorder, recent evidence, has revealed the importance of neurodegenerative events, opening the possibility that cannabinoid agonists, given their cytoprotective proper-ties, may also serve to reduce oligodendrocyte death and axonal damage in MS. Thus, the treatment with WIN55,512–2, a potent CB_1 and CB_2 agonist, was reported to be effective to ameliorate tremor and spasticity in mice with chronic relapsing experimental autoimmune encephalomyelitis (EAE), a commonly used murine model of MS (de Lago et al. 2012). Growing evidence suggests that target-ing the hydrolysis of 2-AG may offer a more favorable benefit-to-risk balance in MS than existing cannabinoid medicines (Manterola et al. 2018). While CB_1 receptor imaging might potentially be useful for probing neuroadaptations related to gluta-matergic excess or other interactions between the ECS and MS pathology, no stud-ies have yet been reported.

CB_2 receptor imaging may be useful to identify MS plaques of the active type. Ten days after EAE induction in mice, CB_2 receptor gene (*CNR2*) mRNA was ten-fold higher in activated microglia compared to microglia in a resting state. In total brain, *CNR2* mRNA was upregulated 100-fold (Maresz et al. 2005). In humans, CB_2-expressing microglial cell staining was observed in spinal cord and brain sec-tions of patients with MS and amyotrophic lateral sclerosis (Yiangou et al. 2006; Palazuelos et al. 2008). CB_2 receptor-positive microglial cells were homogenously distributed within active MS plaques, but were found only in the periphery of chronic active plaques (Benito et al. 2007). However, to date, no CB_2 receptor imag-ing studies of MS patients have yet been reported.

12.3.5.5 Amyotrophic Lateral Sclerosis

Amyotrophic lateral sclerosis (ALS) is a rapidly progressing neurodegenerative disease accelerated by neuroinflammation. CB_2 receptors are dramatically upregulated in the spinal cords of mice with ALS, and CB_2 agonists have been shown to slow motor neuron degeneration (Shoemaker et al. 2007). Animal models have demonstrated that increased endocannabinoid tone delays disease progression (Kim et al. 2006), though the limited clinical data available to date has not shown cannabinoid agonists to be helpful in ongoing disease. Nevertheless, the potential for ECS to affect neuroinflammatory and glutamate-mediated processes in ALS, along with the sparse number of therapeutics available, should prompt additional investigation.

12.3.6 Pain and Migraine

Cannabinoids are antinociceptive in several types of animal models, acute tissue injury and nerve injury-induced nociception, and play a role in transmission, processing, perception, and modulation of pain (Hohmann and Suplita 2nd. 2006; Anand et al. 2009). Cannabinoid agonists and endocannabinoids act on CB_1 receptors in the brain, dorsal root ganglia, and peripheral nerves (Pacher et al. 2006). Activation of CB_2 receptors has been shown to reduce inflammatory pain (see above, Multiple Sclerosis). In addition, anti-inflammatory and analgesic medications affect proteins involved in lowering endocannabinoid levels (*e.g.*, COX-2, endocannabinoid transporter), and act synergistically with cannabinoid agonists in animal studies (Guindon et al. 2006). Interestingly, cannabidiol, which behaves as a cannabinoid receptor-negative allosteric modulator and TRPV1 agonist among other roles, has shown anti-inflammatory properties as well (Booz 2011). In humans, the mechanism of cannabinoid receptor-mediated analgesia is less clear. The exact mechanism of pain suppression is unknown, but synergistic actions and interactions with the endogenous opioid system have been reported (Corchero et al. 2004), and the ECS modulates the actions of cytokines and glucocorticoids (Hill and McEwen 2009), which play important roles in inflammation. In female migraine patients, platelets have been observed to have an increased rate of endocannabinoid metabolism, suggesting a decreased endocannabinoid tone in patients suffering from migraine headaches (Cupini et al. 2006). In addition, TRPV1 receptors are directly linked to pain transmission, and are affected by the ECS. Thus, the modulation of pain by the endocannabinoid system is likely a mixed interplay between central and peripheral mechanisms, CB_1, CB_2, TRPV1, and 5-HT_{1a} receptors, and signal propagation to other neurotransmitter systems to affect the sensation and affective (and anxiety-related component) of pain. Cannabinoids are effective in suppressing pain symptoms of chemotherapy-induced and other peripheral neuropathies, but their widespread use is limited by CNS-mediated and anticholinergic side effects (Mulpuri et al. 2018). However, cannabinoid-based drugs appear to heterogeneously influence the perception of pain, causing a reduction in the affective, but not the sensory, perception of pain (Lotsch et al. 2018; Lee et al. 2013; De Vita et al. 2018).

Several synthetic cannabinomimetic drugs are being developed to treat pain and depression. However, the precise mode of action of endocannabinoids on different targets in the body and whether their effects on pain and depression follow the same or different pathways remain to be determined (Huang et al. 2016).

In women with episodic migraine, [^{18}F]MK-9470 uptake was globally increased by about 16%, with focal increases found in anterior cingulate, mesial temporal, prefrontal, and superior frontal cortices (Van der Schueren et al. 2011). No significant clinical correlations could be made between CB_1 receptor availability and migraine characteristics (*e.g.*, with or without aura, age of onset, migraine frequency).

12.3.7 Epilepsy

In epilepsy, an uncontrolled excitatory signal causes an epileptic seizure. Endocannabinoid-mediated self-inhibition reduces excitability of neocortical interneurons (Bacci et al. 2004). The CB_1 receptor acts as an important endogenous locus of epileptic seizure modulation (Wallace et al. 2002) and endocannabinoids block status epilepticus in hippocampal neurons (Deshpande et al. 2007). There is evidence of a compensatory upregulation of CB_1 receptors in epilepsy (Wallace et al. 2003; Chen et al. 2003). Both animal and human clinical studies have shown mixed results on the use of cannabinoid agents for seizure depending on model, pathology, and dose of the agent. This is likely due to the complex interplay of multiple actions of cannabinoid receptors, and their dual association with excitatory and inhibitory neurotransmitters.

An examination of patients with mesial temporal lobe epilepsy due to hippocampal sclerosis provided an in vivo perspective on the role of CB_1 receptors in a locally hyperexcitable and excitotoxic environment. Compared to healthy controls, [^{18}F]MK-9470 uptake was increased in the ipsilateral temporal lobe, and decreased in ipsilateral and, to a lesser extent, contralateral insula relative to the affected lobe (Goffin et al. 2011). Insufficient data is available to distinguish whether these changes are acute or chronic; however there were significant correlations to relative uptake in the seizure focus: a positive correlation with the number of seizures in the month prior to scanning, and a negative correlation to the number of days since the last seizure before scanning.

A recent study using [^{18}F]MK-9470 PET imaging in an amygdala kindling model of epileptogenesis in rhesus monkeys (Cleeren et al. 2018) found evidence that the CB_1 receptors may be dynamically and progressively involved in the early development of mesial temporal lobe epileptogenesis.

12.3.8 Stroke

CB_2 receptor-positive cells occur in the brain within minutes following stroke (Ashton et al. 2007), and CB_1 receptor expression is increased in the ischemic zone

(Jin et al. 2000). In a CB_1 receptor knockout mouse model of stroke, mortality was increased and infarct size and ischemia were more severe compared to wild-type mice (Parmentier-Batteur et al. 2002). This suggests that endogenous cannabinoid signaling pathways may protect against additional anoxic and inflammatory injury following ischemic stroke. CB_2 receptor activation has been proven to produce protective effects against acute poststroke inflammation (Capettini et al. 2012) and a CB_1 receptor antagonist has been found to be protective in an ischemic mouse model (Reichenbach et al. 2016). Studies have also indicated that CB_2 receptor agonists reduce neurodegeneration after stroke through anti-inflammatory activity (Yu et al. 2015). Vandeputte et al. (Vandeputte et al. 2012) found that [^{18}F]MK-9470 PET demonstrated a strong increase in CB_1 receptor availability 24 and 72 h after stroke surrounding the lesion, in a photothrombotic stroke model, suggesting that time-dependent and regionally increased CB_1, but not CB_2, binding is an early consequence of photothrombotic stroke. This implies that pharmaceutical interventions should primarily aim at CB_1 receptors.

12.3.9 Non-CNS Applications

Cannabinoid drugs have recently also become candidates for peripheral inflammatory and degenerative disorders such as atherosclerosis (Steffens et al. 2005) and in the field of oncology (Herrera et al. 2005). For example, CB_2 receptors have been shown to be involved in the apoptotic pathway in certain tumor cell lines, and have correlated with certain brain tumor grades (Ellert-Miklaszewska et al. 2007). In tissues with normally low receptor expression, there may be a >1000-fold increase in receptor density in the presence of certain tumor types (Oesch et al. 2009). [^{18}F]MK-9470 has been assessed in prostate cancer and found to bind in both benign and malignant prostate tissue, but could not reliably distinguish between the two (with notably weak CB_1 receptor detection by immunohistochemistry), and could visualize metastases in the appendicular skeleton but not reliably in the axial skeleton (Emonds et al. 2013). Peripheral CB_1 receptors have been considered a target of therapy in metabolic and cardiac diseases (see above Sect. 12.3.2 for imaging applications in brown adipose tissue and myocardium). Finally, CB_1 and CB_2 receptors are upregulated in liver fibrosis as a consequence of cirrhosis (Wasmuth and Trautwein 2007; Teixeira-Clerc et al. 2008).

12.3.10 Considerations and Conclusions on the Use of Current CB_1 Receptor PET Radioligands

The development and evaluation of CB_1 receptor PET radioligands have presented both insight into CB_1 receptor pathophysiology and challenges to PET radiochemistry and pharmacokinetic modeling. The primary breakthrough in CB_1 receptor imaging was the development of ligands with lower lipophilicity and higher binding affinity. However, high lipophilicity continues to present anticipated challenges, and

high binding affinity and slow clearance of the radioligands have presented new ones. The results from [¹¹C]OMAR and [¹¹C]MePPEP exemplify the need for accurate plasma measurements when determining V_T, and show that peak uptake alone is not an appropriate outcome measure when comparisons are made between subjects. The development of additional radioligands with improved properties would be of value. To improve the measurements of parent ligand in plasma, alternative approaches with higher sensitivity could be used. Assays or spectroscopic methods with high accuracy for detecting very low concentrations of drug in plasma should be considered (*e.g.*, LC-MS).

Insights gained regarding the ECS include an understanding that CB_1 receptor density decreases after direct agonist stimulation. For example, cannabis abusers had lower V_T and/or radioligand binding compared to controls in all studies to date, and in diseases regarded to have increased endocannabinoid tone (*e.g.*, Huntington's disease) leading to receptor downregulation. However, these results have assumed that decreased radioligand outcome measures are the result of receptor downregulation and not occupancy; the inability of cannabinoid agonists to displace these radioligands has only been definitively demonstrated in rodents, and has been assumed via data interpretation but not yet demonstrated and reported in humans. Conversely, at least one study has suggested that decreased endocannabinoid tone is associated with upregulation of CB_1 receptors (Neumeister et al. 2013). Also, changes observed in CB_1 receptor density or availability were often region dependent, and in one case, a region-specific lesion resulted in contralateral changes (Casteels et al. 2010b); while unilateral lesions or comparisons across hemispheres are commonly performed for other tracers, findings from these CB_1 receptor imaging studies suggest that this may not always be an appropriate method.

Inverse discrepancy has been reported for CB_1 receptor imaging across several studies. For example, in alcohol-dependent patients [¹¹C]OMAR demonstrated a 20% increase of V_T while [¹⁸F]FMPEP-d_2 demonstrated a 20–30% decrease, and [¹⁸F]MK-9470 demonstrated increased binding in chronic alcohol dependence but lower binding acute alcohol exposure in social drinkers. As well, [¹¹C]MePPEP, [¹⁸F]FMPEP-d_2, and [¹¹C]OMAR all demonstrated lower V_T in schizophrenia patients compared to controls, while [¹⁸F]MK-9470 demonstrated high binding in the schizophrenia group. Whether these differences are due to study design or methods remains unclear, and therefore additional investigations are warranted.

The radioligands presented here have their particular pros and cons (Table 12.4). [¹¹C]OMAR and [¹¹C]SD5024, with their relatively fast kinetics and C-11 radiolabel, have the advantage that subjects could quickly complete multiple PET studies in one day, and receptor density could be quantified by V_T. Faster kinetics are attributed in part by their more modest binding affinity, which in turn likely contributes to less brain uptake and lower measures of V_T. [¹¹C]OMAR binding was shown to decrease with age, and thus age should be analyzed as a clinical variable. [¹⁸F]MK-9470 has been studied extensively in healthy controls and in patients with several neuropsychiatric disorders, providing a wealth of data and observations. Its simplified outcome measure does not require arterial blood sampling, greatly easing subject burden and data analysis. However, this comes at the expense of potentially

less accurate measurements, as differences in metabolism and excretion are not accounted for in the final outcome measurement. These initial studies also uncovered several clinical variables that should be accounted for when analyzing [^{18}F]MK-9470 data, including age, sex, and weight. [^{18}F]FMPEP-d_2 has high brain uptake which can be quantified by V_T, and therefore is more likely to detect small changes in CB$_1$ receptor availability, and more accurately measure an index of receptor density. It is available in C-11 form ([^{11}C]MePPEP) in addition to F-18 form, should same-day repeat studies be preferred, and studies with either radioligand can be completed with about 90–120 min of scanning. Longer scan times with [^{18}F]FMPEP-d_2 may be vulnerable to radioactivity accumulation in the brain, possibly due to radioactive metabolites. Analysis of [^{18}F]FMPEP-d_2 should account for BMI as a clinical variable. Due to their lipophilicity, the free fraction of all radioligands should be measured when comparing group differences or studying the effect of drugs. To date, partial volume correction has not affected data for any of the radioligands.

Several uncertainties remain when interpreting data from CB$_1$ receptor imaging studies. It has been assumed that changes in [^{18}F]MK-9470 uptake or [^{11}C]OMAR and [^{18}F]FMPEP-$d_2 V_T$ likely represent changes in receptor availability. However, it is unknown whether changes in uptake or V_T are due to altered receptor density, internalization and/or changes in receptor trafficking (Coutts et al. 2001), or changes in receptor-binding affinity (including that occurring from allosteric modulation of other drugs), as these cannot be distinguished with PET (Martin et al. 2004). Additionally, the degree to which genetic polymorphisms of *CNR1* affect receptor density, binding affinity of the radioligands, or both has been inconsistent and remains to be more fully assessed (Zhang et al. 2004; Hutchison et al. 2008; Hirvonen et al. 2012b). Finally, most of the results presented here were all obtained either in a single study or within a relatively short time span. Therefore, little information is available regarding longitudinal changes of CB$_1$ receptor expression over extended periods of time, and the results may suggest either a causal relationship or merely significant correlations.

Development of a CB$_1$ receptor agonist radioligand remains an unmet need. As demonstrated by [^{11}C]MePPEP, this class of radioligand (inverse agonist) is not displaced in vivo by endogenous or synthetic agonists. Therefore, these PET tracers can only be used for measuring changes or differences in receptor density, or for measuring receptor occupancy by inverse agonists. They cannot be used for measuring receptor occupancy by agonists, and estimates of endocannabinoid tone are only assessed indirectly. Therefore, an agonist radioligand that demonstrates preference for the high-affinity state and is therefore more susceptible to competition by endogenous agonists would be of great value. For example, a radioligand for high-affinity dopamine D$_2$ receptors, [^{11}C]MNPA, is displaced nearly twice as much by dopamine than an antagonist, such as [^{11}C]raclopride (Seneca et al. 2006). Given that only a small proportion of receptors may be in the high-affinity state, the distribution and normal physiology of CB$_1$ receptors may appear quite different when an agonist radioligand is used for *in vivo* PET. Therefore, development of an agonist

radiotracer may provide tremendous insight into the regulation of the endocannabinoid system.

If an agonist radiotracer for the CB_1 receptor were developed, several experiments probing the endocannabinoid system could be conceived. First, increasing endocannabinoid concentrations by inhibiting their degradation or reuptake (via FAAH, MAG lipase, or other proteins) would provide better understanding of this dynamic and possibly regionally selective process. Second, studies involving stimulation or inhibition of the release of primary neurotransmitters could be performed to assess the relative response of endocannabinoids to neuromodulation of GABA, glutamate, and dopamine. Third, a radioligand sensitive to dynamic changes in endocannabinoid concentration would allow for *in vivo* studies with behavioral components, such as acute stress response (Gorzalka et al. 2008).

Development of an agonist radiotracer is likely to be difficult, primarily due to their high lipophilicity. Very few CB_1 agonists have the moderate lipophilicity required for a PET tracer; a notable exception is the aminoalkylindole class of agonists, typified by WIN-55,212–2. In addition, most existing agonists do not have high selectivity for the CB_1 receptor. Indeed, one of the first attempts to develop a radioligand to image CB_1 receptors was $[^{18}F]\Delta^8$-THC, which exhibited a prohibitively high lipophilicity and has nearly equal affinity for CB_1 and CB_2 receptors, as well as likely having P-gp substrate affinity. Given the relatively low expression of CB_2 compared to CB_1 receptors and the availability of selective antagonists, it is unknown if high selectivity would be an absolute requirement for an agonist radioligand. Finally, the development of an agonist radioligand may face the complexities posed by partial agonism and functional selectivity, which may present the CB_1 receptor with altered binding conformations and possibly differing binding affinities for agonists depending on the intracellular coupling of the receptor (Georgieva et al. 2008).

Lastly, there are many potential non-CNS applications for CB_1 receptor imaging, including liver fibrosis, metabolic diseases such as diabetes, and cancer. At present, insufficient data is available to determine if the existing CB_1 receptor radioligands would be optimal for use in the imaging of diseases outside the CNS, and, if so, what the optimal method of analysis would be (radioactivity concentration vs. V_T). More research concerning the appropriate use of these tracers for imaging CB_1 receptors outside the brain needs to be performed.

12.4 Imaging of CB_2

The CB_2 receptor is expressed primarily by the immune system (Munro et al. 1993; Schatz et al. 1997; Galiegue et al. 1995), but has been found in intact CNS tissue in tiny concentrations (Van Sickle et al. 2005; Gong et al. 2006; Ashton et al. 2006). Importantly, CB_2 receptors are highly expressed in disorders that are associated with inflammation including cancer, pain, osteoporosis, and liver diseases (see for review (Pertwee 2009; Pisanti and Bifulco 2009; Ashton 2007)). The entire functional role of CB_2 receptor expression in the inflammatory processes has yet to be clarified,

though its upregulation makes CB_2 a unique biomarker of microglial/macrophage cell-specific activity in these neuroinflammatory processes.

Recent studies have demonstrated high expression of CB_2 receptors in CNS microglia in patients with various neuroinflammatory disorders (Benito et al. 2008). Postmortem tissue studies from patients with AD demonstrate dramatically increased expression of CB_2 receptors in areas of beta-amyloid (Aβ) plaque deposition (Benito et al. 2003). CB_2 receptor expression increases both in striatal microglia of transgenic mouse models of HD and in patients with HD (Palazuelos et al. 2009). Better understanding of the immune-modifying role and principal mechanisms of CB_2 receptor agonists in the human CNS could facilitate the development of disease-modifying treatments and preventive agents, as proposed for AD (Tolon et al. 2009). Induced expression of CB_2 receptors in neuroinflammatory disease is also observed in tissue samples from human and animal models of HIV-induced encephalitis and multiple sclerosis (Benito et al. 2005) (see for review (Tolon et al. 2009)). Traumatic brain injury (TBI) leads to the release of pro-inflammatory cytokines in the brain, which then cause neuronal cell death and secondary damage. Simultaneously, there is "on-demand" synthesis of cannabinoid receptors including CB_2, which in turn inhibit inflammatory responses (Stella 2010; Shohami et al. 2011).

There are also unique therapeutic implications afforded by a better understanding of the endocannabinoid system and supported by recent studies of CB_2-specific agonists (Tolon et al. 2009; Ehrhart et al. 2005). Recent studies demonstrated that brain CB_2 receptors modulate the rewarding and locomotor-stimulating effects of cocaine (Xi et al. 2011). CB_2 receptors are involved in some of the effects mediated by alcohol (Ishiguro et al. 2007) in rodent brains and expression of CB_2 in microglia increases in response to MDMA ("ecstasy") treatment (Torres et al. 2010).

In summary, the CB_2 receptor that is nearly absent in the normal brain and highly expressed in activated microglia in neuroinflammation is an attractive target for PET imaging of a large variety of disorders that are associated with neuroinflammation. Although substantial progress has been made in the development of radioligands to image CB_1 with PET, the absence of suitable PET radioligands has hampered the noninvasive imaging of CB_2. Several CB_2 radioligands have recently been synthesized and evaluated in animals as potential PET radioligands (Evens et al. 2008, 2009a; Fujinaga et al. 2010; Gao et al. 2010).

12.4.1 Development of First-Generation CB₂ Radioligands

Pioneer work of researchers from Canada and France revealed the first selective CB_2 agonists (Gallant et al. 1996) and inverse agonists (Rinaldi-Carmona et al. 1998) with nanomolar affinity, and additional review of early CB_2 PET imaging and radioligand development has been described in an excellent review (Evens and Bormans 2010). Several CB_2 receptor radioligands have been developed, including the oxoquinoline derivatives [^{11}C]KD2, [^{11}C]KP23, [^{11}C]RS016, [^{11}C]RSR-056, [^{11}C]RS-028, and [^{18}F]RS-126 and [^{11}C]NE40, and the thiazole derivatives [^{11}C]A-836339, [^{18}F]JHU94620, and [^{18}F]2f (Ni et al. 2019). In the last few years a large

number of selective high-affinity CB_2 ligands have been developed and they were a basis for the recent development of CB_2 PET radioligands (Tables 12.5, 12.6, and 12.7; Fig. 12.14).

The group from KU Leuven reported that [^{11}C]**1** had high CB_2-binding affinity (Evens et al. 2008), but it exhibited low brain uptake (Tables 12.5 and 12.7). This is in accord with the high PSA value and high molecular weight (MW = 540) of this radioligand that are above the conventional limits for passive BBB transport. However, brain uptake increased following the administration of cyclosporine A, which inhibits several BBB efflux transporters including P-gp, indicating that the radioligand is an efflux transporter substrate. No further studies on [^{11}C]**1** have been published. Researchers from the same group presented radioligands based on the compound GW405833, [^{11}C]**2** and [^{18}F]**3**, which have more moderate CB_2-binding affinities (Table 12.5) (Evens et al. 2011a). Both [^{11}C]**2** and [^{18}F]**3** showed good BBB permeability (Table 12.7), in agreement with their molecular properties. Unfortunately, [^{18}F]**3** had much slower washout of radioactivity from mouse brain than [^{11}C]**2**, which was due to a large fraction of radiometabolites in brain (50% at 30 min after injection), limiting its further development.

The same group (Evens et al. 2009b; Vandeputte et al. 2011) took advantage of the low expression of CB_2 receptors in normal brain by using the CB_2/[^{11}C]**2** reporter gene/reporter probe combination as a possible way to follow suitably transfected cells. [^{11}C]**2** is capable of selective CB_2 imaging in rats with an induced overexpression of the CB_2 receptor, but due to their relatively low binding affinity both [^{11}C]**2** and [^{18}F]**3** are unlikely candidates for imaging in neuroinflammatory disorders. Also, [^{11}C]**2** exhibited low washout and high nonspecific binding in healthy monkey brain (Vandeputte et al. 2011).

A research group from Indiana synthesized a CB_2 ligand [^{11}C]**4** (Gao et al. 2010) with moderate CB_2-binding affinity and low CB_2/CB_1 selectivity (Table 12.5). No animal studies have been published.

The Chiba University PET center presented a series of triaryl CB_2 radioligands (Fujinaga et al. 2010). One of these compounds [^{11}C]**5** exhibited high binding affinity (Table 12.5). In a mouse study [^{11}C]**5** manifested good BBB penetration, but its slow brain washout suggests substantial nonspecific binding, which can be explained by the high lipophilicity of this radioligand (Tables 12.5 and 12.7).

The JHU group synthesized [^{11}C]A836339 ([^{11}C]**6**) (Horti et al. 2010), a selective CB_2 agonist with high binding affinity, moderate lipophilicity, and an adequate PSA value for CNS activity (Table 12.5). In healthy control CD1 mice [^{11}C]**6** shows specific binding (Horti et al. 2010) (50%, Table 12.7) in the spleen, an organ with high CB_2 receptor density. In control mice [^{11}C]**6** exhibited good BBB permeability, and little specific in vivo binding in the mouse brain, which is in agreement with low expression of CB_2 receptors in the intact brain (Munro et al. 1993; Schatz et al. 1997). The specific cerebral binding of [^{11}C]**6** was studied in two animal models of neuroinflammation, a lipopolysaccharide (LPS)-induced mouse model (Qin et al. 2007) and a transgenic amyloid mouse model of AD (APPswe/PS1dE9 mice). The dissection study (baseline and blockade (Horti et al. 2010)) showed that [^{11}C]**6** exhibits high specific binding to CB_2 receptors (78–84%) in LPS-treated mice.

Table 12.5 Physical-chemical properties of first-generation CB$_2$ radioligands

Compound	M.W.	clogD$_{7.4}$[a]	PSA	Experimental CB$_2$K$_i$, nM (CB$_2$/CB$_1$ selectivity)	Reference
[^{11}C]**1**	540	2.8	158	0.4 (2263)	Evens et al. (2008)
[^{11}C]**2**	447	4.5 2.5[b]	44	35 (171)	Evens and Bormans (2010), Evens et al. (2007), Baekelandt et al. (2010)
[^{18}F]**3**	356	4.7 2.8[b]	44	27 (370)	Evens and Bormans (2010), Evens et al. (2011a)
[^{11}C]**4**	393	3.6	60	6.9 (28)	Gao et al. (2010)
[^{11}C]**5**	395	4.6	39	0.3 (3333)	Fujinaga et al. (2010)
[^{11}C]**6,** [^{11}C] A836339	310	3.37 ± 0.08[b]	42	0.7 (450)	Yao et al. (2009), Horti et al. (2010)
[^{11}C]NE40	372	3.9 ± 0.01[b]	77	9.6 (>100)	Evens et al. (2009a)
[^{18}F]**7**	398	4.4[b]	77	3.4	Turkman et al. (2012)

[a]Lipophilicity log$D_{7.4}$ and PSA values were calculated with ACD/Structure Designer Suite (Toronto, Canada)
[b]Experimental data

Table 12.6 Physical–chemical properties of most recent CB$_2$ radioligands

Compound	M.W.	clogD$_{7.4}$[a]	PSA	Experimental CB$_2$K$_i$, nM (CB$_2$/CB$_1$ selectivity)	Reference
[^{11}C]RSR-056	418	1.94	89	2.5 (>1000)	Slavik et al. (2015a)
[^{11}C]RS-016	424	2.8	68	0.7 (>10,000)	Slavik et al. (2015b)
[^{11}C]AAT-778	376	6.0	55	4.3 (256)	Haider et al. (2016)
[^{11}C]AAT-015	389	4.11	76	3.3 (303)	Haider et al. (2016)
[^{18}F]RS-126	442	2.74	68	1.2 (>10,000)	Haider et al. (2018)
[^{11}C]RS-028	440	0.94	88	0.8 (>10,000)	Haider et al. (2018)
[^{18}F] (Z)-N-(3-(4-fluorobutyl)-4,5-dimethylthiazol-2(3H)-ylidene)-2,2,3,3-tetramethyl-cyclopropanecarboxamide	325	3.22 ± 0.03	33	0.39 (>1000)	Moldovan et al. (2016)

Table 12.7 Imaging properties of PET CB$_2$ radioligands

Radioligand	Spleen uptake (%ID/g)	Brain uptake (%ID/g)	Brain BP (animal model)	Reference
[^{11}C]**1**	–	Low	–	Evens et al. (2008)
[^{11}C]**2**	1 (2 min), 1 (1 h)	1.4 (2 min), 0.1(1 h)	>1[a]	Evens and Bormans (2010)
[^{11}C]**3**	0.9 (2 min), 0.7 (1 h)	1.7 (1 h)	–	Evens and Bormans (2010)
[^{11}C]**4**	–	–	–	Gao et al. (2010)
[^{11}C]**5**	n/a	1.9 (1 min), 0.7 (1 h)	–	Fujinaga et al. (2010)
[^{11}C]**6**, [^{11}C] A836339	1.3 (1 h)—control 0.6 (1 h)—CB$_2$ block Control/block = 2.2	0.4 (1 h)	1.4[b], 2.5[c]	Horti et al. (2010)
[^{11}C]NE40	Control/block = 1.9	0.8 (2 min) 0.1 (60 min)	~3[a]	Evens et al. (2011b)
[^{18}F]**7**	Insignificant	–	~1[d]	Turkman et al. (2012)

[a]Rat model of CB$_2$ overexpression
[b]Mouse model of Alzheimer's disease
[c]LPS mouse model of neuroinflammation
[d]U87/CB$_2$-expressing tumor in mice
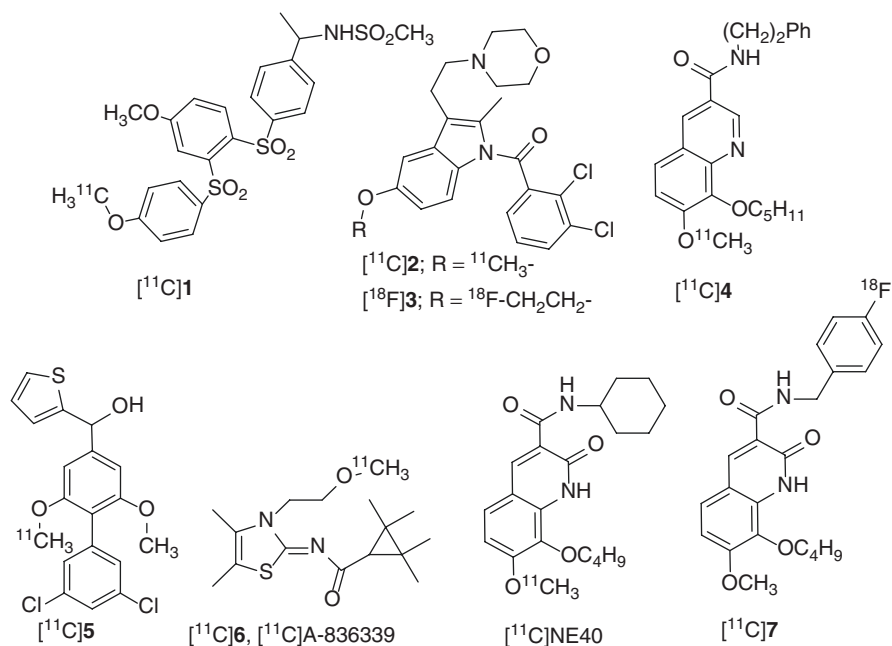
Fig. 12.14 First generation of CB$_2$ receptor radioligands

These results were also confirmed in a small-animal PET/[^{11}C]**6** study with control- and LPS-treated mice (standardized uptake value (SUV) = 0.7 and 2.3, respectively). The cerebral specific binding of [^{11}C]**6** in the LPS-treated mice is in accordance with a previously found upregulation of CB_2 in this neuroinflammation model (Mukhopadhyay et al. 2006). The very high total cerebral uptake of [^{11}C]**6** in LPS-treated mice may be associated in part with dysfunction of the BBB (Sumi et al. 2010). Recent study in rat models of neuroinflammation induced by LPS or AMPA showed no specific binding of [^{11}C]**6** (Pottier et al. 2017). The inconsistency between the [^{11}C]**6** imaging results in mouse and rat models of neuroinflammation may be due to the species difference and other experimental differences. The species difference in the LPS-induced neuroinflammation models was observed previously in baboon and human PET studies. Thus, the conventional TSPO radiotracer [^{11}C]PBR28 showed that human subjects required only a low dose of LPS (1 ng/kg, IV) for quantifiable PET imaging of neuroinflammation (Hannestad et al. 2012). Baboons, which are less sensitive to LPS than humans, required a dose of LPS that was five orders of magnitude greater (0.1 mg/kg, IV) for quantifiable PET with [^{11}C]PBR28 (Sandiego et al. 2015).

Brain distribution of [^{11}C]**6** in the AD mouse model demonstrated that [^{11}C]**6** displays significant specific CB_2 binding (29–33%) in various brain regions, which is consistent with the distribution of the Aβ amyloid plaques in this mouse model of AD. Previous in vitro studies showed that CB_2 receptors are abundantly and selectively expressed in microglia in human brain tissue from patients with AD, whereas the expression of the CB_1 subtype remains unchanged (Benito et al. 2003). These results suggest the potential of the CB_2 radioligand [^{11}C]**6** for PET imaging of neuroinflammation in neurodegenerative disorders. The radiotracer [^{11}C]**6** is currently approved by the FDA for human PET scans under eIND, but the human PET results have not been published yet.

The compound of the KU Leuven group [^{11}C]NE40 (Evens et al. 2009a) displays favorable molecular properties for BBB transport, but its binding affinity is moderate (Table 12.5). [^{11}C]NE40 was successfully evaluated in a substantial number of preclinical safety studies (Evens et al. 2011b). [^{11}C]NE40 showed specific CB_2 receptor binding in the spleen and blood of normal rats and high initial brain uptake in rhesus monkeys. In a rat model with local h-CB_2 receptor overexpression [^{11}C]NE40 demonstrated specific and reversible binding to h-CB_2 receptors. [^{11}C]NE40 is the first CB_2 receptor PET radioligand that was selected for human PET studies (see below for additional discussion).

A group from MD Anderson Cancer Center has published a series of 2-oxoquinoline derivatives (Turkman et al. 2011), and reported one as a candidate for PET studies (Turkman et al. 2012). Designed to be a more metabolically stable fluorine-18 compound, [^{18}F]**7** (Log*P* 4.4) had poor uptake in spleen and only about 50% specific binding on CB_2 receptor-positive tumor cells transfected into mouse. Both the preclinical applications and the clinical potential of this compound are limited by its poor solubility.

12.4.2 Update of CB$_2$ PET Tracer Development

The main goal of the many CB$_2$ receptor studies published after 2013 was to synthesize new PET tracers with very high CB$_2$ receptor-binding affinities and selectivity and optimal structural properties (see Fig. 12.15 and Table 12.6).

Group from Zurich synthesized [^{11}C]RSR-056 with CB$_2$ receptor K_i = 2.5 nM, log$D_{7.4}$ = 1.94, and SI over hCB$_1$ > 1000 (Slavik et al. 2015a). High specific binding of [^{11}C]RSR-056 to CB$_2$-positive tissue was demonstrated in vitro using rodent spleen sections. In the mouse LPS model of neuroinflammation [^{11}C]RSR-056 demonstrated a strikingly increased brain uptake versus control animals, but the blocking with GW405833 showed only a slight reduction of the uptake. The authors concluded that to which extent binding to CB$_2$ and disruption of blood-brain barrier are involved in [^{11}C]RSR-056 accumulation in experimental neuroinflammation remains to be elucidated. The same group also synthesized a 4-oxo-quinoline-based radiotracer [^{11}C]RS-016 with binding affinity K_i of 0.7 nM and log$D_{7.4}$ = 2.8 (Slavik et al. 2015b). [^{11}C]RS-016 exhibited excellent specific binding *in vitro* in rat spleen and human ALS spinal cord. In the LPS neuroinflammation model in rodents [^{11}C]RS-016 exhibited specific binding in the range of 10–30% suggesting that [^{11}C]RS-016 may be suitable for PET imaging of CB$_2$ receptors in neuroinflammation. In a separate report (Haider et al. 2018) two more radiotracers of the
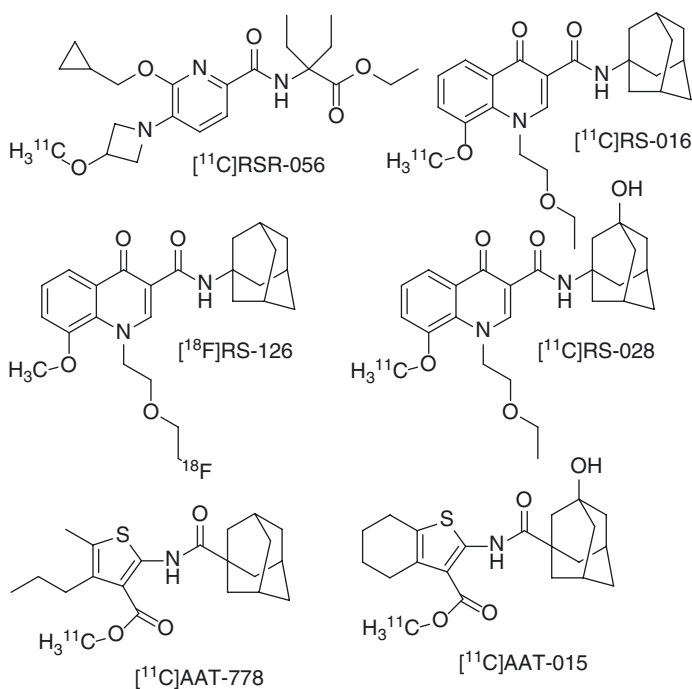
Fig. 12.15 Novel radioligands for CB$_2$ receptor since 2013

4-oxo-quinoline series ([^{18}F]RS-126 and [^{11}C]RS-028) showed some specific binding by *in vitro* autoradiography in postmortem human ALS spinal cord tissue, but showed no *in vivo* specific binding in Huntington's disease model in rodents. The same group also synthesized a series of thiophene-based CB_2 receptor ligands with good binding affinities (K_i = 3–4 nM), but ^{11}C-labeled compounds of that series failed to demonstrate *in vivo* specific binding in animals (Haider et al. 2016).

Moldovan et al. synthesized a series of fluoro analogues of A836339 with a wide range of CB_2 receptor-binding affinities (K_i = 0.3–1100 nM) (Moldovan et al. 2016). Compound (Z)-N-(3-(4-fluorobutyl)-4,5-dimethylthiazol-2(3H)-ylidene)-2,2,3,3-tetramethyl-cyclopropanecarboxamide was selected as the ligand with the highest CB_2 receptor affinity (K_i = 0.39 nM) and selectivity over those of CB_1 receptor (factor of 1000). Radiolabeled [^{18}F](Z)-N-(3-(4-fluorobutyl)-4,5-dimethylthiazol-2(3H)-ylidene)-2,2,3,3-tetramethyl-cyclopropanecarboxamide was tested in rodents and demonstrated high brain uptake and 20–30% specific binding in the LPS model of neuroinflammation, but rapid metabolism was a drawback of this radiotracer.

Chemists from Australia developed a series of ^{18}F-labeled benzimidazole sulfones as CB_2 receptor PET radioligands with binding affinities in low nanomolar range (Kallinen et al. 2019). The best compounds of the series have been radiolabeled with ^{18}F and showed 32–44% specific binding in rat spleen, but neuroinflammation animal studies have not been reported.

Lately, several other research groups worked on CB_2 receptor PET tracer development, but no promising *in vivo* data have been presented yet (Saccomanni et al. 2015; Yrjola et al. 2015; Heimann et al. 2018a, b).

12.4.3 CB$_2$ Imaging Studies

Apart from initial demonstration of *in vivo* potential and proof of target, few CB_2 imaging studies have been reported. In animals, [^{11}C]**6** has been shown to have sufficient brain uptake and receptor binding in models of substantial receptor expression; however, the preliminary findings were less favorable in rodent models of Alzheimer's related neuroinflammation (Horti et al. 2010).

In animal studies [^{11}C]NE40 was shown to have rapid brain uptake and washout, and relatively rapid plasma metabolism; however, at 10 min after injection approximately 10% of radioactivity in brain was due to radiometabolites (Horti et al. 2010). [^{11}C]NE40 has been used to demonstrate a PET reporter gene system in rats using an adeno-associated viral vector, a potentially useful application in gene or stem cell therapy (Vandeputte et al. 2011).

The only PET radioligand for CB_2 receptors reported in human use is [^{11}C]NE40. In healthy human brain [^{11}C]NE40 exhibited rapid uptake and washout (Ahmad et al. 2011). Latest human PET studies with [^{11}C]NE40 demonstrated a lack of upregulation of CB_2 receptors in the brain of AD patients *in vivo* compared with age-matched controls without correlation with regional amyloid deposition. In contrast, CB_2 receptor availability was significantly lower in AD patients (Ahmad et al. 2016). The authors explained the results as an indication of a relative loss of

neuronal expression rather than absence of microglial expression, therefore making the CB_2 receptor target less promising as a biomarker for neuroinflammation in AD. In addition, the relatively low binding affinity of NE40 ($K_i = 9.6$ nM, Table 12.5) may be the reason of this result.

[^{11}C]NE40 has an effective dose of 4.4 μSv/MBq, as determined in three healthy males. In addition to intestine, liver, and lungs, radioactivity was observed in lymph nodes and spleen, suggestive of CB_2 receptor localization.

To date, no pharmacokinetic modeling from *in vivo* imaging of CB_2 receptors has been reported; however several predictions can be made based on preliminary studies and previous experience with CB_1 receptor imaging. Although CB_2 receptors are found at much lower density in brain than CB_1 receptors, image analysis and pharmacokinetic modeling of CB_2 receptor radioligands may have some potential sources of error. First, similar to CB_1 receptor ligands, CB_2 receptor radioligands are higher in lipophilicity than more commonly used PET tracers, and similar complications as described for CB_1 receptor radioligands should be anticipated. Second, many systemic or local inflammatory conditions can cause disruption of the BBB, causing brain uptake of the radioligand to be affected by flow in addition to specific binding. Third, given the low density of CB_2 receptors normally found in brain, simpler methods for quantifying receptor density might be employed (*e.g.*, reference tissue modeling with pseudoreference region). However, such methods should be validated using compartmental modeling with plasma measurements prior to routine use of alternative methods, with particular attention to states of systemic inflammation, as increased expression of CB_2 receptors may not be a region-specific phenomenon. Fourth, specific binding may occur to circulating leukocytes in addition to nonspecific binding to plasma proteins, potentially complicating measurements of plasma free fraction. As an additional consequence, competition studies with cannabinoid ligands (agonists or inverse agonists) might be expected to have a more significant effect on plasma free fraction due to preferential displacement of radioligand from specific binding sites. Finally, it is unknown if the expression of CB_2 receptors during neuroinflammation or pathological conditions is consistently correlated to any clinical measures, making efforts towards quantitation both a challenge and an exciting prospect.

12.4.4 Potential Clinical Application of CB_2 Imaging

The paucity of reported results for CB_2 receptor imaging with PET is striking, as is its potential as a clinical biomarker. As noted, multiple inflammatory conditions could be probed by a reliable CB_2 receptor radioligand. Multiple sclerosis, ALS, Huntington's disease, and Alzheimer's disease have already been discussed as neuroinflammatory conditions associated with CB_2 receptor upregulation. In particular, *in vivo* and dynamic monitoring of MS in response to treatment with cannabinoid

agonists or other investigatory drugs may be of particular interest. Yet few clinical evaluations of CB_2 receptor PET imaging have been reported (Ahmad et al. 2016; Ahmad et al. 2013). The hurdles in CB_2 receptor radioligand development and translation include (1) differences between humans and rodents in their immune systems, microglia subtypes, and levels of CB_2 receptor expression (Smith and Dragunow 2014), as well as distinct age-related changes (Galatro et al. 2017); (2) low expression level of CB_2 receptors in the brain (Chen et al. 2017); (3) lack of specific CB_2 receptor antibody for postmortem validation of *in vivo* imaging results (England et al. 2015); (4) lack of full CB_2 receptor knockout mice (Constantinescu et al. 2011); and (5) developing a reference region for modeling (Li and Kim 2015). In addition, as age-related inflammation is also a confounding factor in mouse models, these models might not be ideal for evaluating CB_2 receptor tracers (Ni et al. 2019). A greater density of CB_2 receptor-positive microglia and macrophages has been observed in the postmortem spinal cord tissues from patients with ALS compared to healthy controls (Taylor et al. 2016). And similar increases were reported in other studies on ASL spinal cord tissues using [^{11}C]RS-028 and [^{11}C]KD2 (Mu et al. 2013). Emerging evidence indicates the involvement of CB_2 receptor and increased levels of complements, cytokines, and chemokines in the brain of patients with AD. Reactive astrocytes, activated microglia, and upregulated CB_2 receptor have been observed in the vicinity of Aβ plaques in postmortem AD mouse model brains and patients with AD (Ni et al. 2019).

Vasculitis and cerebritis are often difficult to diagnose, in part due to their frequent normal appearance on conventional imaging, and can be difficult to treat. Thus, CB_2 receptor imaging could potentially provide assistance in both diagnosis and therapy monitoring. A study on rats with a poststroke model demonstrated CB_2 receptor activation related to the neuroprotective responses that likely occur at an early stage of brain disorders (Hosoya et al. 2017). The advent of CB_2 receptor PET radiotracers has enabled the visualization of CB_2 receptor distribution in vivo in animal models of central nervous system inflammation; however translation to humans has been less successful. Certain types of cancer have demonstrated CB_2 receptor expression, and *in vivo* imaging could assist in identifying tumor type and grade prior to surgery, and identify tumors susceptible to treatment with cannabinoids to induce apoptosis. Peripherally, CB_2 receptor imaging may assist in deepening an understanding of inflammation in atherosclerotic (Steffens 2008) and cardiovascular diseases (Patel et al. 2010). As described elsewhere (Vandeputte et al. 2011), *in vivo* imaging of CB_2 receptors with a reporter gene/reporter probe system provides an excellent opportunity to monitor gene therapy with PET, and may have other potential applications. Finally, inflammatory states have been associated with mood disorders, such as seen in patients treated with PEGylated interferon, and a genetic polymorphism of the CB_2 receptor has been associated with bipolar disorder (Minocci et al. 2011). Whether CB_2 receptors are a suitable *in vivo* biomarker for mood disorders remains unknown.
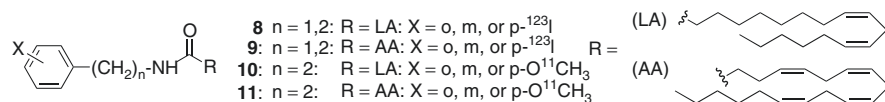
12.5 Imaging of FAAH

FAAH is a serine hydrolase enzyme that is responsible for the breakdown of AEA, and is found in the CNS and periphery (Egertova et al. 1998; Thomas et al. 1997). FAAH inhibitors are considered to be an important therapeutic target, allowing a means to increase endocannabinoid tone in a more regionally selective and physiologically relevant manner than administration of exogenous agonists (Otrubova et al. 2011). Clinical applications of FAAH inhibition include treatment of anxiety, PTSD, substance-use disorders (particularly cannabis-use disorder and cannabis withdrawal), depression, Alzheimer's disease, Parkinson's disease, and neuropathic pain (D'Souza et al. 2019; Pertwee 2014; Fowler 2015). As FAAH is found throughout human brain in variable concentration, it is not amenable to a reference region approach for imaging (Romero et al. 2002).

Radioligand design for enzymes is approachable from three different paradigms: reversible binding, tissue or metabolic trapping, and irreversible binding or suicide inactivation (Fowler et al. 2002; Rempel et al. 2017). Reversible binding is most similar to receptor binding and is potentially amenable to compartment kinetic modeling and could measure enzyme availability. Tissue trapping and irreversible binding via suicide inactivation could both potentially inform enzymatic activity as well as tissue distribution. In both cases, molecular design and radiolabel position should be carefully selected to ensure that the enzymatically processed trapped compound retains the radiolabel. The majority of FAAH inhibitors, including the prototypical URB597, are irreversible suicide inhibitors based on either carbamate or urea cleavage by Ser_{241} leading to a covalent bond. It should be noted that the FAAH inhibitory potency of unlabeled compounds that was used to predict specific binding of the corresponding radiotracers does not directly correlate with specific binding of these radiotracers. The lack of binding affinity data for the most promising FAAH inhibitors is an obstacle for development of FAAH radioligands for PET. Nevertheless, the latest studies revealed radioligands for imaging FAAH with adequate properties for PET quantification (Wilson et al. 2011a; Li et al. 2011).

12.5.1 Tissue-Trapped FAAH Substrates

Initial attempts of a group from Belgium to develop PET- and SPECT-labeled FAAH radioligands have dealt with aryl analogues of anandamide using a tissue trapping approach (Fig. 12.16). Analogue compounds [123I]8 and [123I]9 (Fig. 12.14) exhibited poor binding to FAAH in mice, likely due to steric hinderance from the


Fig. 12.16 Radiolabeled analogues of AEA for PET and SPECT imaging of FAAH

iodine, and were abandoned (Wyffels et al. 2009). Compounds [^{11}C]**10** and [^{11}C]**11** displayed moderate inhibitory potency of AEA metabolism (pIC$_{50}$ ranges = 4.34–5.64, 4.46–5.56, respectively) and demonstrated some brain uptake in mice (Wyffels et al. 2009), but no further *in vivo* evaluation has been presented. Another tissue-trapping radioligand reported, [^{18}F]FHEA, was designed and intended for the lysosomal enzyme (and therefore acidic environment functioning) *N*-acylethanolamine-hydrolyzing amidase (NAAA), an enzyme functionally similar to membrane-bound FAAH (preferring basic conditions) in that it can inactivate anandamide, though it is more associated with inactivating palmitoylethanolamide (PEA). [^{18}F]FHEA, a PEA analogue, demonstrated stable brain uptake in mice from 1 to 60 min after injection, though levels in brain were no different after administration of either an NAAA inhibitor or an FAAH inhibitor. However, [^{18}F]FHEA metabolism was reduced following FAAH, but not NAAA, inhibition, suggesting that [^{18}F]FHEA is at least a partial substrate for FAAH (Pandey et al. 2014).

12.5.2   Irreversible FAAH Inhibitors

In a follow-up attempt from the same Belgian group, [^{11}C]-4-methoxyphenylcarbamate (**12**, Fig. 12.17), a radiolabeled analoge of URB597, inhibited the hydrolysis of AEA with an IC$_{50}$ value of 436 nM (compared to 40 nM for that of URB597) and
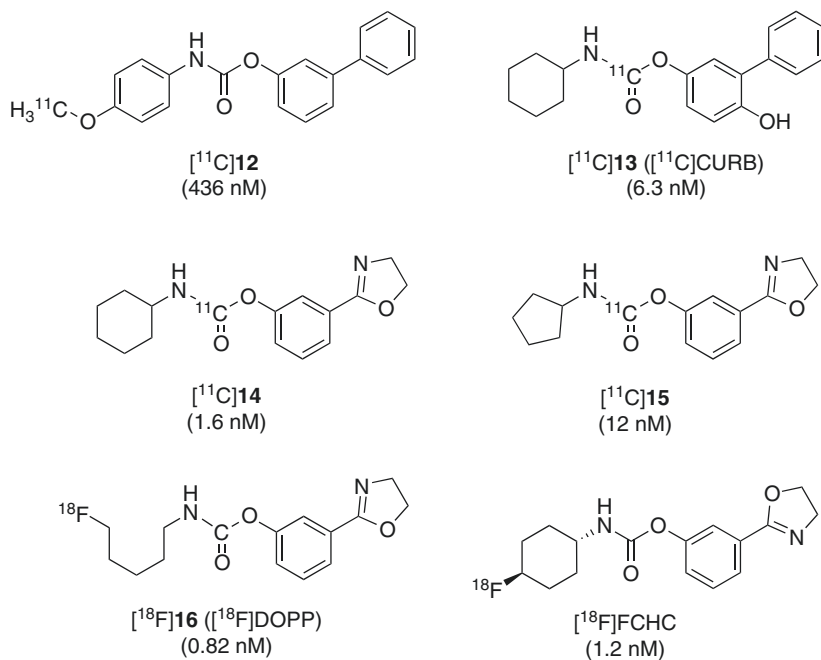

Fig. 12.17 Radiolabeled carbamate-based FAAH irreversible inhibitors and analogues of URB597, with their IC$_{50}$

manifested good initial brain uptake (anticipated with good lipophilicity of $\log D = 2.27$), but no specific binding was observed in mouse biodistribution studies (Wyffels et al. 2010). It was concluded that this negative result is due to insufficient affinity of [^{11}C]**12**.

Researchers from Toronto have reported a series of ^{11}C-radiolabeled analogues of URB597 with low-nanomolar inhibitory potency values (Wilson et al. 2011a, b; Wilson et al. 2013). [^{11}C]CURB (Fig. 12.17) (aka, URB694) showed high brain uptake in rats (SUV of 1.5–2.5 at 5 min) with no washout, which is characteristic of irreversible binding. Regional distribution of radioactivity was found to be high in the cortex, intermediate in the cerebellum, and low in the hypothalamus, which corresponds to the known distribution of FAAH in the rat brain (Egertova et al. 1998; Thomas et al. 1997). Pretreatment with unlabeled URB694 reduced binding in all brain regions by 62–86%, and URB597 reduced binding in brain by 72–88%. It was concluded that [^{11}C]CURB represents a highly promising radiotracer for imaging FAAH using PET (Wilson et al. 2011b).

Human PET studies using [^{11}C]CURB have demonstrated its ability to quantify FAAH activity in CNS. Following injection of [^{11}C]CURB, radioactivity in brain peaked at ~4.3 SUV within 2–3 min, and after a washout period of ~30 min remained relatively stable at levels ~25–33% below that of peak for the remaining 90-min scan, consistent with irreversible binding. Radioactivity quickly declined in plasma, and the parent fraction quickly declined over the first several minutes and then slowly from 20 min (48%) to 90 min (37%). The free fraction of [^{11}C]CURB is low, at ~0.9%. Data were well described with good identifiability using the 2-TCM with irreversible binding (2-TCMi; $k_4 \equiv 0$), with as little as 60 min of data. Though some high-uptake regions had better model fitting in a 2-TCM with reversible binding and most others in a three-tissue compartment model with irreversible binding, they were not statistically superior to the 2-TCMi and had poor identifiability in some microparameters. Binding was not limited by cerebral blood flow, and simulation studies predicted that λk_3 is the optimal parameter to quantify FAAH binding (with $\lambda = K_1/k_2$, or V_T of ligand in the free and nonspecific compartment at equilibrium, available for binding). The Patlak analysis for irreversible kinetics (*e.g.*, [^{18}F]FDG as a prototypical application) was unsuccessful, likely due to the late time it could be implemented (40 min) with the remaining data containing too much noise (Rusjan et al. 2013). Subsequent analysis demonstrated that voxel-wise modeling was achievable for high-resolution data (HRRT camera; Fig. 12.18) using a basis function model (BAFPIC for 2-TCMi with arterial input function), though with higher bias and variability than ROI data outcomes, but ~60% reduced variability compared to Patlak plot derivations (Rusjan et al. 2018). [^{11}C]CURB has an effective dose of 5.2 μSv/MBq in women, and 4.6 μSv/MBq when estimated in both men and women, with highest radioactivity uptake in liver, gallbladder, and small intestine, within the range of other carbon-11 radioligands (Boileau et al. 2014).

[^{11}C]CURB has been further examined in clinical studies. It has excellent reproducibility with test-retest variability of 9%, and good reliability with ICC of 0.79. The C385A single-nucleotide polymorphism (SNP) of the *FAAH* gene (rs324420), known to result in reduced FAAH expression (*i.e.*, loss of function) with
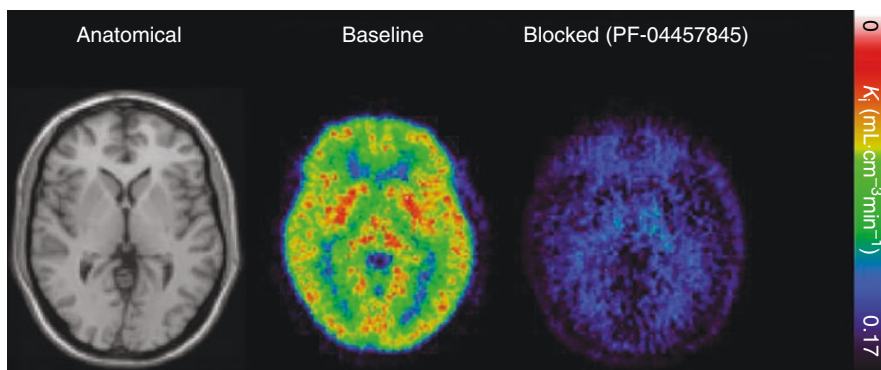
Fig. 12.18 [^{11}C]CURB in human brain. Axial slice of reference MRI (right, MNI $z = +2$ mm), and of [^{11}C]CURB parametric maps of K_i at baseline condition (middle, averaged of $n = 6$) and 2 h after an oral dose $\geq$1 mg of PF-04457845 (right). Figure courtesy of Dr. Pablo Rusjan, University of Toronto

corresponding increase of anandamide, has been associated with increased risk for trait impulsiveness, cannabis sampling, and higher reward reactivity, but lower anxiety, and cannabis liking, craving, and withdrawal. [^{11}C]CURB demonstrated lower binding in brains of A allele holders (~20% in A/C heterozygotes, ~50% in the lone A/A homozygote imaged) compared to C/C homozygotes, as would be predicted with the loss of function and decreased FAAH expression (Boileau et al. 2015a). [^{11}C]CURB was able to estimate brain FAAH occupancy of the high-potency FAAH inhibitor PF-04457845 across 1 mg, 4 mg, and 20 mg, quantified using λk_3 and 60 min of scan data, yielding a ~91% reduction (Fig. 12.18). Following blockade, the time-activity curves had a reversible appearance, and the 1-TCM fit equally well as the 2-TCMi, confirming that the first compartment of the latter model represents non-displaceable binding. Since the non-displaceable represents <10% of λk_3, FAAH occupancy was therefore estimated as >95%, confirming high potency and occupancy of FAAH by PF-04457845 at 1 mg (Boileau et al. 2015b). In cannabis users ($n = 10$), compared to healthy controls ($n = 22$), [^{11}C]CURB reflected 14–20% reduced FAAH binding, which was not correlated with clinical characteristics of cannabis use (years of use, days and amount used per week, craving, withdrawal symptoms), or influenced by cigarette or alcohol use, or global cerebral blood flow. High cannabinoid and associated metabolite concentrations in blood and urine and greater impulsivity traits correlated with lower FAAH binding (Boileau et al. 2016). Among the explanations for lower FAAH binding in cannabis users 1 day after abstinence include presence of metabolites binding or modulating FAAH, related downregulation of CB_1 receptors, compensation for downregulated AEA, or suppression of immune cells given identification of FAAH in microglia. However, increased translocator protein (TSPO) binding imaged in cannabis users suggests an increase of neuroinflammation, casting this last possibility in doubt (Da Silva et al. 2019).

Additional clinical studies with [¹¹C]CURB have been briefly reported. Despite an association between C385A with obesity and metabolic syndrome, neither [¹¹C]CURB binding nor peripheral endocannabinoid levels were different between overweight healthy subjects ($n = 10$) and age-matched controls ($n = 20$) (Best et al. 2017). Similarly, those with PTSD ($n = 7$) had no difference in [¹¹C]CURB binding compared to healthy controls ($n = 30$); however, [¹¹C]CURB binding in amygdala did correlate across both groups with fMRI BOLD response to fearful faces, suggesting the role of endocannabinoid tone in fear processing more generally. In contrast to the finding of reduced peripheral anandamide levels in PTSD patients (see above Sect. 12.3.4 (Neumeister et al. 2013)), there was a significant elevation in peripheral 2-AG, but no difference in anandamide levels in those with PTSD compared to controls (Isabelle Boileau et al. 2018). Across healthy subjects ($n = 51$), [¹¹C]CURB binding in prefrontal cortex was negatively correlated with impulsivity (total Barratt Impulsiveness Scale), and in whole brain, prefrontal cortex, and ventral striatum with the self-control factor (Esmaeil Mansouri et al. 2018). Young heavy drinkers (age 19–25) with ($n = 14$) or without ($n = 17$) a family history of alcohol-use disorder had no difference in FAAH brain levels; however across groups lower FAAH levels (and therefore increased anandamide levels) were correlated with greater Alcohol Use Disorder Identification Test (AUDIT) scores and lower subjective sedative effects of alcohol (Best et al. 2018).

Several analogues of CURB ([¹¹C]**14**, [¹¹C]**15**, [¹⁸F]**16**, or [¹⁸F]DOPP; Fig. 12.17) also demonstrated high specific FAAH uptake in the brain of rats and nonhuman primates (Wilson et al. 2011a; Wilson et al. 2013; Sadovski et al. 2013; Rotstein et al. 2014; Shoup et al. 2015). [¹⁸F]DOPP, synthesized with a multistep procedure with alkyl radiolabeling followed by coupling reaction, demonstrated good uptake in rat brain and greater than that of [¹¹C]CURB, in a distribution consistent with FAAH, to which the ¹⁸F-radiolabel was bound irreversibly; notably, the compound was stable in human, but not rat, plasma, possibly due to the presence of species-specific carboxylesterases (Sadovski et al. 2013). Follow-up studies in nonhuman primate demonstrated good brain uptake (2.2–2.8 SUV), kinetic modeling best fit with 2-TCMi using λk_3 as an outcome measure consistent to that described with [¹¹C]CURB, rapid metabolism, and significantly reduced binding after blocking with URB597 suggesting specificity to FAAH (Rotstein et al. 2014). No data in human subjects has yet been reported.

[¹⁸F]DOPP was utilized in a rat study to investigate the *in vivo* potency of BIA 10–2474, a putative FAAH inhibitor that caused one death and five serious neurological injuries during a Phase I dose escalation study. *Ex vivo* measures of [¹⁸F]DOPP demonstrated BIA 10–2474 to have high potency at FAAH in rats with IC_{50} ~ 65 µg/kg, comparable to other FAAH inhibitors (e.g., URB597 at 0.15 µg/kg, URB694 aka CURB at 40 µg/kg, PF-04457935 at 30–100 µg/kg); in contrast the pre-trial reported that IC_{50} for BIA 10–2474 was 1.1–1.7 nM, reflecting a much lower potency (Tong et al. 2017). It has since been understood that several off-target mechanisms at high doses likely led to its toxicity, possibly inhibition of other serine hydrolases or disruption of neuronal lipid metabolism (Chaikin 2017); preclinical occupancy studies might have identified FAAH saturation at lower doses and potentially prevented the tragic trial outcomes.

A second [^{18}F]fluorine-labeled carbamate radioligand, [^{18}F]FCHC (IC$_{50}$ = 1.2 nM; Fig. 12.17), has been evaluated in preclinical studies. [^{18}F]FCHC is radiosynthesized in a one-pot, three-step process with 10–20% radiochemical yield. Both *ex vivo* and *in vivo* studies demonstrated that [^{18}F]FCHC uptake in rat brain was initially rapidly followed by a slow increase to >5 SUV in high-FAAH-rich regions, which was about twice as high as low regions, and was >95% blocked by URB597. Metabolism was initially rapid (75% parent at 2 min) with no lipophilic metabolites and 16% parent remaining by 40 min. [^{18}F]FCHC has higher brain uptake (about two times greater than [^{18}F]DOPP and about four times greater than [^{11}C]CURB), greater specific binding, and faster blood clearance than other carbamate FAAH inhibitor radioligands (Shoup et al. 2015). Despite the promising characteristics of [^{18}F]FCHC and [^{18}F]DOPP, no fluorine-18 radioligand for FAAH has yet advanced into human studies.

Scientists from Chiba (Japan) recently developed two high-binding-affinity FAAH PET tracers [^{11}C]MFTC (IC$_{50}$ = 0.34 nM, clogD = 3.6) (Kumata et al. 2015) and [^{11}C]DFMC (IC$_{50}$ = 6.1 nM, clogD = 3.43) (Shimoda et al. 2016). [^{11}C]MFTC, a [^{11}C-carbonyl]carbamate, was synthesized via [^{11}C]phosgene and [^{11}C]carbonate intermediate in a two-step reaction with 20% radiochemical yield, had good and rapid uptake that plateaued in mouse and rat brain in a distribution consistent with FAAH, and was >80% blocked by cold MFTC or URB597 in rat brain. In nonhuman primates, [^{11}C]MFTC had rapid uptake in a FAAH regional distribution, and slow washout over 90 min that suggests nonspecific binding. However, while cold MFTC reduced radioactivity by 70–80% with homogenous regional time-activity curves, URB597 reduced radioactivity by 50–60% with heterogenous regional time-activity curves, suggesting the presence of off-target binding (Kumata et al. 2015). [^{11}C]DFMC, a urea-based FAAH inhibitor, was synthesized via [^{11}C]methylation with 20% radiochemical yield, and had rapid and high uptake in mouse (*ex vivo*) and rat (*in vivo* PET) brain in a FAAH distribution. However, uptake was disproportionly high in the cerebellar nucleus (2.4 SUV) compared to other FAAH-containing regions (1.6–2.0 SUV), though after blockade by URB597 60–70% of radioactivity was reduced in brain with nearly homogenous regional time-activity curves suggesting specificity for FAAH. Brain extracts largely confirmed this with ~95% of radioactivity in brain at 30 min being irreversibly bound to brain tissue, which dropped to <2% after pretreatment with URB597 (Shimoda et al. 2016).

A group from Pfizer has released a series of publications on a novel FAAH inhibitor (Ahn et al. 2011; Johnson et al. 2010) and its closely related radiotracer, [^{18}F]PF-9811 (Fig. 12.19). Using a three-step one-pot reaction sequence [^{18}F]PF-9811 can be attained in high yield (~11%). Using an activity-based protein profiling probe for FAAH, [^{18}F]PF-9811 achieved an IC$_{50}$ = 16 nM (compared to IC$_{50}$ = 7.2 nM for PF-04457845). Following injection of [^{18}F]PF-9811, distribution of radioactivity was as previously described for FAAH and [^{11}C]CURB in rat brain. Both *in vitro* and *in vivo* measurements of [^{18}F]PF-9811 were reduced after pretreatment with PF-04457845 in rats, with ~40% reduction of SUV as measured by PET after 90 min (Skaddan et al. 2012).

Structurally similar [^{11}C-carbonyl]PF-04457845 (Fig. 12.19) was reported by the Toronto group. Radiolabeling was accomplished by [^{11}C]CO$_2$ fixation to the urea carbonyl position in a one-pot reaction with radiochemical yield ~4.5%. It demonstrated good imaging properties with appropriate lipophilicity (Log$P_{7.4}$ = 3.48), good brain uptake consistent with FAAH distribution in rats and approximately double that achieved by [^{11}C]CURB, and an estimated >95% specific binding in brain (Hicks et al. 2013). As a therapeutic compound, PF-04457845 has demonstrated an ability to reduce cannabis withdrawal symptoms (D'Souza et al. 2019), but not pain related to osteoarthritis of the knee (Huggins et al. 2012).

12.5.3 Reversible FAAH Inhibitors

The Merck PET group has presented data on [^{11}C]MK-3168 (Fig. 12.20), a radiolabeled inhibitor of FAAH with reversible binding (Li et al. 2011; Liu et al. 2013). The compound demonstrated a favorable *in vitro* profile with IC$_{50}$ = 1.0 nM and K_D 0.8 nM (both human cortex), lipophilicity by HPLC log D of 3.3, >1000-fold selectivity over other targets, and lack of rat and human P-gp sensitivity. Autoradiographic studies in rhesus monkey and human brain slices showed highest binding in striatum, frontal cortex, and hippocampus, consistent with FAAH distribution. PET studies of [^{11}C]MK-3168 in rhesus monkeys confirmed this uptake pattern with total to nonspecific signal ~2:1 and pre-administration of a FAAH inhibitor provided evidence that in vivo binding of [^{11}C]MK-3168 is mediated by FAAH (Liu et al. 2013). Kinetic modeling in monkeys showed 2-TCM V_T of 3–4 mL/cm^3, and small

[^{18}F]**PF-9811**
(16 nM)

[^{11}C-carbonyl]**PF-04457845**
(7.2 nM)
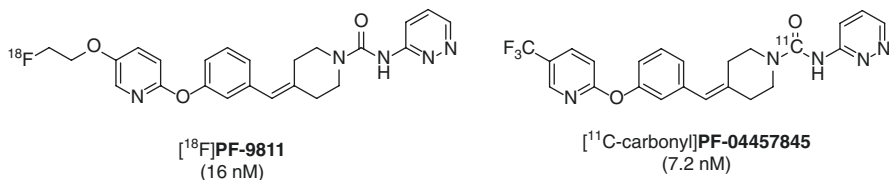
Fig. 12.19 Radiolabeled urea-based FAAH irreversible inhibitors and analogues of PF-0445784, with their IC$_{50}$

Fig. 12.20 [^{11}C]MK-3168, first FAAH PET tracer for imaging in human subjects
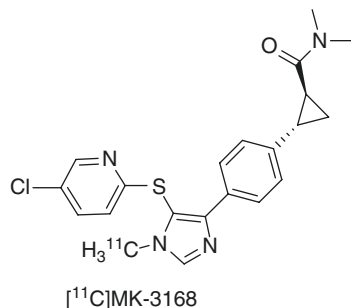
[^{11}C]MK-3168

changes (<15%) in white matter between baseline and blocked scans provided BP_{ND} 0.4–1 with a modest test-retest variability at <20% (Joshi et al. 2012). Human [^{11}C]MK-3168 PET demonstrated high brain uptake (peak SUV ~3–3.5), rapid metabolism with parent radioligand comprising 30–40% of radioactivity at 10 min and essentially eliminated at 60 min after injection, 2-TCM V_T of 14–20 mL/cm^3, good test-retest variability (<12%), and acceptable radiation burden for PET studies (effective dose of 4.65 μSv/MBq) (Li et al. 2011; Joshi et al. 2012; Postnov et al. 2018). [^{11}C]MK-3168 was used to assess FAAH occupancy by another inhibitor, JNJ-42165279, first in rhesus macaque, and then in humans using a 2-TCM, demonstrating that 10 mg achieved >95% occupancy (Fig. 12.21) (Postnov et al. 2015, 2018).

A second reported reversible FAAH inhibitor, [^{11}C]MPPO, is based on an α-ketoheterocyclic scaffold that promotes binding at the serine hydrolase site without cleavage. [^{11}C]MPPO has high binding at FAAH (*in vitro* IC_{50} = 10 nM), greater than 500-fold selectivity over triglycerol hydrolase, and acceptable lipophilicity (log $D_{7.4}$ = 3.43). [^{11}C]MPPO was radiolabeled with ^{11}C with 13% radiochemical yield and demonstrated moderate brain uptake (0.6–0.8 SUV) with FAAH distribution and rapid washout in *ex vivo* mouse studies and *in vivo* PET rat studies, generating time-activity curve profiles consistent with reversible binding. In rats,

Fig. 12.21 Distribution of [^{11}C]MK-3168 in human brain under baseline and blocked conditions. Top image: [^{11}C]MK-3168 PET scan at baseline. Bottom image: [^{11}C]MK-3168 PET scan in the same volunteer after receiving 10 mg JNJ-42165279. Figure reproduced from Postnov et al. (2018)
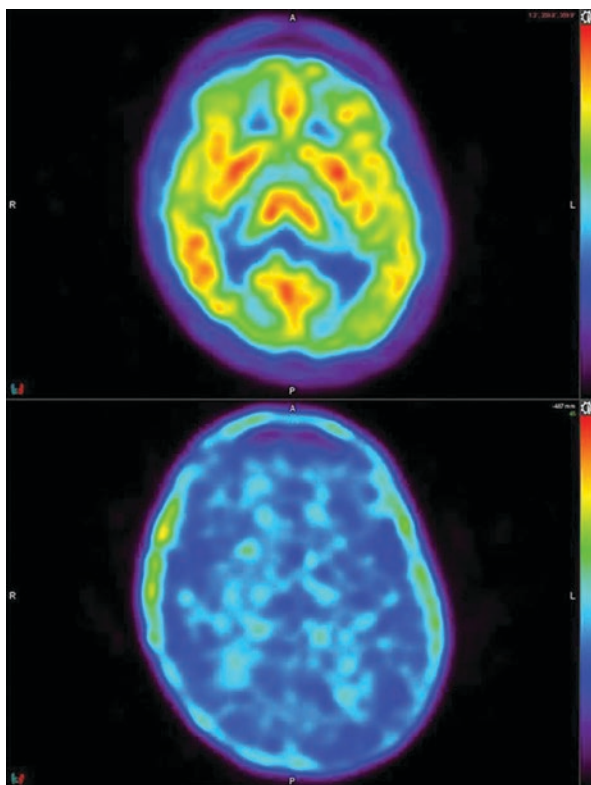
pretreatment with URB597 had little effect on [^{11}C]MPPO brain uptake, but abolished regional uptake heterogeneity and increased washout, suggesting that uptake and/or binding is modest but specific for FAAH. The relatively low PET signal may have been due to the very rapid metabolism of the radioligand, with hydrophilic radiometabolites comprising 75% and 90% of radioactivity in brain and plasma at 15 min, respectively. [^{11}C]MPPO was assessed for sensitivity to P-gp and Bcrp efflux transporters, and while wild-type controls had higher brain uptake compared to P-gp/Bcrp knockout mice, the amount was considered insufficient to account for the limited brain uptake (Wang et al. 2016a).

12.6   Imaging of MAGL

Similar to inhibition of FAAH, monoacylglycerol lipase (MAGL), an enzyme responsible for the breakdown of ~85% of 2-AG, has been the target for pharmacologic inhibitor and radioligand development. MAGL is also a serine hydrolase enzyme and is co-localized with CB_1 receptors in axon terminals. MAGL inhibitors may have application in anxiety disorders, traumatic brain injury, substance-use disorders, Alzheimer's disease, and Parkinson's disease (Pertwee 2014; Fowler 2015).

Several PET tracers for imaging MAGL have been published in recent years. An initial evaluation of several candidate radiotracers by the Toronto group based on known MAGL inhibitors (KML29, JJKK-048, ML30, JW642) and five novel analogues led to [^{11}C]carbonyl radiolabeling, similar to that performed for FAAH radiotracers, of the most promising candidates based on favorable affinity (IC_{50} range 0.36–5.9 nM) and selectivity. The two hexafluoroisopropanol carbamates and three triazole urea evaluated *ex vivo* in rodents had modest nonspecific brain uptake, but only [^{11}C]JJKK-048 had reduced uptake (by 42%) after preblockade with unlabeled compound. Several compounds also demonstrated reduced retention in blood after preblockade, possibly due to plasma and leukocyte MAGL which could confound attempts at designing brain-penetrant MAGL radiotracers (Hicks et al. 2014), and potentially affect kinetic modeling estimates that do not account for a vascular compartment.

The Leuven group modified JW642 to create [^{11}C]MA-PB-1 (IC_{50} = 26 nM, clog$D$ = 3.4; Fig. 12.22), which has similar MAGL affinity but lower and more acceptable lipophilicity. [^{11}C]MA-PB-1 has high brain uptake in mice (ex vivo SUV 2.6, decreasing to 1.6), which was ~70% blocked by itself and MJN110, an unrelated MAGL inhibitor, with fast metabolism and no significant MAGL binding in blood. *In vivo* PET imaging in rats demonstrated similar kinetics, albeit with lower peak uptake (~1.6 SUV) and washout to a lower plateau from 30 to 90 min (~0.6), which was blocked ~60% by pre-administration of MJN110, but not by challenge administration, consistent with [^{11}C]MA-PB-1 having irreversible binding at MAGL. The tracer was advanced to nonhuman primate imaging studies, in which it demonstrated high uptake (~4.2 SUV) with washout to plateau by 20 min (~2.5 SUV), and could be blocked by ~ ≥88% by MJN110 (Ahamed et al. 2017).
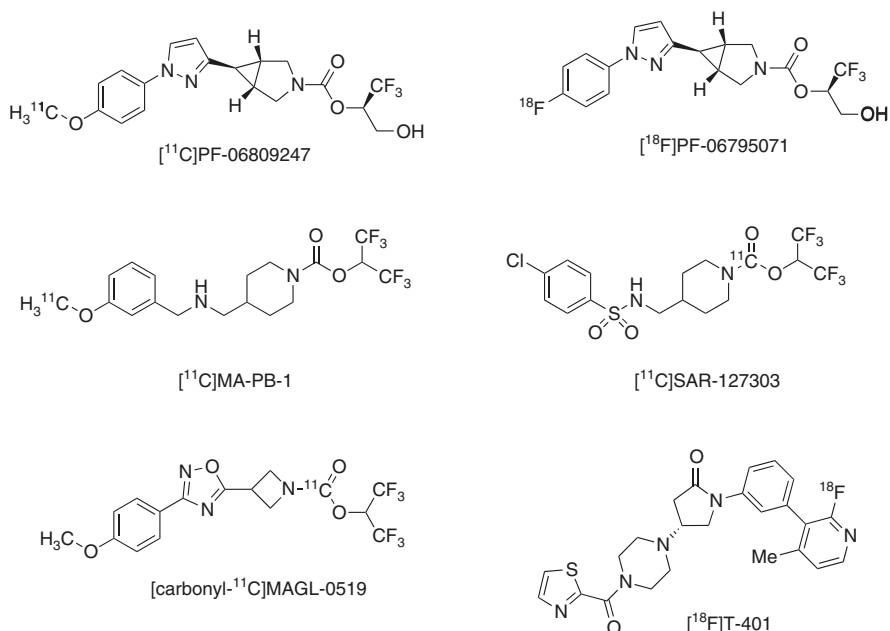
Fig. 12.22 Radioligands for MAGL

A high-potency carbamate with structurally distinct sulfonamido-piperidine platform was selected as a candidate radiotracer. SAR127303 (IC_{50} = 36 nM, $\log D$ = 3.69; Fig. 12.22) and the novel urea-based TZPU (IC_{50} = 39 nM, $\log D$ = 1.85) were selected from a series of analogues, with SAR127303 having better selectivity for MAGL over FAAH. *Ex vivo* studies in mice demonstrated [^{11}C]TZPU to have poor brain uptake, while [^{11}C]SAR127303 had rapid and persisting brain uptake from 1 to 60 min after injection. *In vivo* PET imaging reflected these results, with [^{11}C]TZPU achieving ~0.4 SUV in rat brain which was reduced by ~48% with unlabeled TZPU, and not substantially accounted for by P-gp/Bcrp. In contrast, [^{11}C]SAR127303 achieved ~1.5 SUV in rat brain throughout the 60-min scan, in a distribution pattern consistent with MAGL expression (cortex, striatum > cerebellum > hippocampus > > pons), and could be ~50–67% reduced by self-block with loss of regional heterogeneity, suggesting that ~1/3 of radioactivity is from nonspecific binding. [^{11}C]SAR127303 was partially reduced after pretreatment with MAGL inhibitor KML29, but not after JZL184 (consistent with prior literature) or FAAH inhibitor URB597 (as anticipated for MAGL selectivity). [^{11}C]SAR127303 uptake was not altered by P-gp inhibitor cyclosporin A suggesting lack of P-gp substrate affinity, and could not be competed off by unlabeled SAR127303, confirming irreversible binding in rat brain (Wang et al. 2016b, c). Follow-up assessment and kinetic modeling with arterial input function in rats demonstrated that [^{11}C]SAR127303 binding could be quantified with the 2-TCMi (similar to FAAH, described above) with good identifiability of microparameters, and provided

supporting evidence that radiometabolites do not enter brain. Results with 2-TCMi were highly correlated with those obtained by Patlak values, and K_i from both 2-TCMi and Patlak as well as λk_3 from 2-TCMi, but not k_3, all correlated with *in vitro* binding data; however, λk_3 had higher variability making K_i the preferred outcome parameter. Thus, Patlak K_i parametric images of [^{11}C]SAR127303 in rat brain could be used to reflect MAGL availability (Yamasaki et al. 2018). Advancement of [^{11}C]SAR127303 to nonhuman primate imaging provided encouraging results, with sufficient (peak ~1 SUV) and persistent brain uptake from 20 to 90 min (consistent with a profile of irreversible binding) in a MAGL distribution (Wang et al. 2016c).

A series of azetidine scaffold compounds were developed as a novel class of MAGL radiotracers in an effort to lower lipophilicity. MAGL-0519 (IC_{50} = 12.7 nM, $LogP$ = 1.23) was selected as the most favorable candidate, as it had the highest affinity for MAGL and selectivity over FAAH (30- to 50-fold), with no P-gp substrate affinity by *in vitro* assay. [Methyl-^{11}C] and [carbonyl-^{11}C]MAGL-0519 (Fig. 12.22) were assessed by PET in rat brain and demonstrated nearly identical kinetic profiles, with rapid heterogenous uptake (peak ~1.5 SUV), followed by gradual washout for 90 min, and could be blocked, but not displaced, by unlabeled MAGL-0519 or KML29 (~40–50% reduction), and had no significant reduction with pretreatment of FAAH inhibitor URB597. Although blocking and challenge studies were consistent with irreversible binding at MAGL, the slow washout of both [^{11}C]methyl- and [^{11}C]carbonyl-radiolabeled could not otherwise be explained by nonspecific binding or radiometabolites (<10%), and therefore likely reflected ongoing dissociation between the azetidine carbonyl and the MAGL serine residue. Initial PET studies in nonhuman primates showed [carbonyl-^{11}C]MAGL-0519 to have similar kinetics with high heterogenous uptake ($\geq$1.5 SUV), with gradual washout over 90 min (~0.5 SUV) (Cheng et al. 2018). In a separate attempt, another azetidine-based [^{11}C]carbonyl-radiolabeled tracer (1,1,1,3,3,3-hexafluoropropan-2-yl-3-(1-benzyl-1H-pyrazol-3-yl)azetidine-1-[^{11}C]carboxylate) was evaluated with improved affinity and reasonable lipophilicity (IC_{50} = 0.41 nM, $LogD$ = 3.69). The radioligand was shown to be irreversibly bound in rat brain tissue, have high brain uptake in mice (*ex vivo*) and rats (*in vivo* PET) in a distribution consistent with MAGL, and be ~40% reduced by pretreatment with unlabeled compound or MAGL inhibitor JW642, but not during challenge in rats. However, it also demonstrated washout from brain over time, similar to MAGL-0519 (Mori et al. 2019).

In a follow-up effort, another series of azetidines were designed for more favorable properties, including candidates as reversible binding radioligands for MAGL. An irreversible binding carbamate with high affinity (MAGL-2-11, IC_{50} = 0.88 nM, $LogD$ = 1.9) and two reversibly binding compounds, designed by altering and stabilizing the leaving group (PAD, IC_{50} = 2.7 nM, $LogD$ = 3.35; MAGL-4-11, IC_{50} = 11.7 nM, $LogD$ = 2.7), were evaluated. These three new compounds are selective for MAGL, and in silico studies predicted MAGL-2-11 and PAD to have full inhibition of MAGL, while MAGL-4-11 had only partial docking in the binding site but would block 2-AG from entering the catalytic site. PET imaging of [carbonyl-^{11}C]PAD in rats showed high and heterogenous brain uptake (2.2

SUV) with very little washout over 90 min, and was ~50% blocked with KML29, suggesting improved irreversible kinetics compared to [11C]MAGL-0519. PET imaging of [11C]PAD and [18F]MAGL-4-11 in rats showed poor brain uptake (~0.4 and ~0.3 SUV, respectively), though substantial uptake was seen in brown adipose tissue that could be substantially blocked by KML29, suggesting peripheral specificity for MAGL. P-gp/Bcrp knockout mice had high brain uptake of both [11C]PAD and [18F]MAGL-4-11 compared to wild-type mice with plateaued kinetics, demonstrating that the inadequate blood-brain barrier permeability for CNS imaging is due to ABC efflux transporters (Chen et al. 2019a).

A Pfizer and Karolinska Institute collaborative effort identified [11C]PF-06809247 (Fig. 12.22) as an irreversible binding PET radioligand for MAGL. Initial *in silico* assessment identified PF-06809247 from reported and Pfizer library MAGL inhibitors as having optimal properties including blood-brain barrier penetration and lipophilicity (Clog$D$ = 2.7), and measured assays confirmed high affinity (IC$_{50}$ = 13 nM), low cross-species affinity differences, >1000-fold selectivity for MAGL over FAAH, and very good selectivity overall (Zhang et al. 2019). *Ex vivo* assessments in rats demonstrated ligand uptake consistent with brain and peripheral organ MAGL distribution that was reduced by another MAGL inhibitor. PET imaging in nonhuman primates showed [11C]PF-06809247 to have high, heterogenous uptake (~3.0–3.5 SUV) peaking at 40 min and with minimal washout to 120 min, and could be ~90% blocked by MAGL inhibitor pretreatment (Fig. 12.23). [11C]PF-06809247 has entered into human testing for test-retest reliability; however results have not yet been reported (ClinicalTrials.gov Identifier: NCT03100136). Very shortly after the report of [11C]PF-06809247, another collaborative group assessed its analogue [18F]PF-06795071 (Fig. 12.22) as a [18F]fluorine-labeled PET radioligand for MAGL. Compared to its analogues also assessed, PF-06795071 possesses good affinity and lipophilicity (IC$_{50}$ = 2.3 nM, Log$D$ = 3.3), with high selectivity, and demonstrated irreversible binding by *in vitro* assay. Autoradiography of [18F]PF-06795071 in rat brain resulted in 26–49% specific binding when blocked by itself or KML29 in a MAGL distribution. In vivo PET in rat brain showed good uptake (~1.75 SUV) and moderate washout over 90 min, which was 56% and 61% blocked by pretreatment with KML29 and unlabeled PF-06795071, respectively (Chen et al. 2019b).

[18F]T-401 (Fig. 12.22) is the first reversibly binding MAGL PET radioligand reported to successfully enter brain. [18F]T-401 (IC$_{50}$ = 4.0 nM, Log$D$ = 1.86) was designed following the discovery of piperazinyl pyrrolidine-2-one scaffold of reversible MAGL compounds, and selected from a series of analogues due to its favorable binding affinity, lipophilicity, good mouse brain uptake by *ex vivo* assessment, and low P-gp affinity. [18F]T-401 immediately peaks (~0.6 SUV) followed by rapid washout with heterogenous brain uptake in mouse brain, with very little retention in MAGL knockout mice. T-401 was demonstrated to be selective and reversibly bound to MAGL by *in vitro* assays. In monkey brain, [18F]T-401 had similar kinetics as seen in mice, and could be blocked by unlabeled compound; an analogue developed alongside [18F]T-401 demonstrated poor washout and increasing brain radioactivity over time, leading to the selection of [18F]T-401 as the preferred
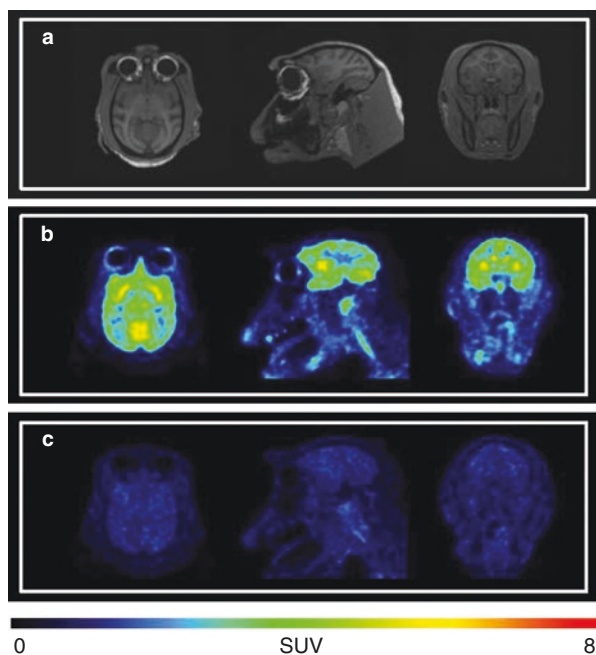
Fig. 12.23 [^{11}C]PF-06809247 in nonhuman primate brain. MRI (**a**) and PET images summed from 0 to 123 min under baseline (**b**) and blocking condition with (**c**) pretreatment of MAGL inhibitor. Reprinted with permission from Zhang et al. Copyright (2019) American Chemical Society (Zhang et al. 2019)

radiotracer. The estimated effective dose of [^{18}F]T-401 as derived from monkey data is 25 μSv/MBq, in range for human use; [^{18}F]T-401 has reportedly entered into human testing; however no additional details are yet available (Hattori et al. 2019).

12.7 Imaging of TRPV1

Although TRPV1 receptors are not currently considered part of the ECS, they function in close relation to each other as evidenced by cannabinoids and anandamide (which is sometimes even referred to as an endovanilloid) acting meaningfully as agonists. To date, four radioligands for TRPV1 have been reported. The first, [^{11}C]SB366791, a cinnamide-derived antagonist developed at GlaxoSmithKline with good selectivity (Gunthorpe et al. 2004), had relatively poor binding affinity (K_D = 280 ± 56 nM in human TRPV1 expressing CHO), acceptable lipophilicity (LogD = 3.5), and an increase of proportional radioactivity due to metabolites from 2 to 10 min in mouse brain (15–33% of total radioactivity), but appropriate biodistribution and good retention in target-rich trigeminal nerve (TGN) (van Veghel et al. 2013a). In follow-up, [^{11}C]DVV24 (a trifluoromethyl- for chloro- substitution of

[^{11}C]SB366791) had improved binding affinity (K_D = 163 ± 28 nM) and about ~2.5 times mouse TGN-to-blood binding ratio compared to blocked conditions, but rapid washout from mouse brain and a similar increase of radiometabolites from 2 to 10 min (~10–45% of total radioactivity) (van Veghel et al. 2013b). [^{18}F]DVV54, an aminoquinazoline, demonstrated similar binding affinity (K_D = 171 ± 48 nM) and slower clearance from blood, but poorer brain and TGN uptake attributed to its high lipophilicity (cLogD 6.51) and PSA (50.70) (van Veghel et al. 2013b). Carbon-11-labeled capsaicin accumulated in rat tissues known to express TRPV1, including low, but measurable, uptake in brain, suggesting capsaicin as a potential platform for generating analogue radioligands (Goto et al. 2015). Most recently, the TRPV1 antagonist BCTC, known to have high selectivity and high CNS penetration, was labeled with carbon-11 and found to have higher ex vivo TGN-to-blood ratio and specific binding than the other radioligands (Kumata et al. 2017), though no report of brain uptake was made.

12.8 Conclusion and Future Directions

Herein we have described the utility of ECS imaging with PET, its historical development, the current understanding and experience with it, and its potential applications and developments in the future. Akin to its description as a nonclassical neurotransmitter system, it has pushed the boundaries of classical PET radioligand and pharmacokinetic techniques. Given the established roles of the ECS in physiological function, it is not surprising that direct *in vivo* imaging has provided a window into basic workings of the normal brain and a wide variety of neuropsychiatric diseases. It is therefore expected to continue yielding additional new insights for those, as well as for inflammatory, immunological, and non-CNS diseases.

Progress in the medicinal chemistry of cannabinoid drugs stimulated discovery of radiotracers for imaging the ECS. Most PET imaging studies on the ECS have been done with CB_1 receptor radioligands. There are at least five radiolabeled CB_1 receptor inverse agonists ([^{11}C]OMAR, [^{18}F]MK-9470, [^{11}C]MePPEP, [^{18}F]FMPEP-d_2, and [^{11}C]SD5024) that are suitable for PET imaging in human subjects. All of these radioligands are not free of drawbacks and better compounds are under development. Combination of excellent specific signal, high brain uptake, appropriate brain kinetics, absence of active radiometabolites, and radiochemical availability are a must for a successful radioligand for PET imaging in humans, but this is a tough nut to crack. The high density of CB_1 receptors in brain, which has proved a challenge, masks the true physiology of the receptor system; a series of radioligands that can distinguish agonist-preferring coupled receptors or their associated second messenger systems would provide additional information on the pathophysiology that has already been probed. A useful radiolabeled CB_1 receptor agonist for PET imaging in humans remains to be discovered and is an unmet need.

Successful development and human study of CB_2 receptor radioligands remain a challenge. Several research groups are actively working on the development of CB_2

PET radioligands as potential probes for imaging inflammation in various disorders. Very low expression of CB_2 in the intact CNS dictates a necessity for a CB_2 PET radioligand with very high binding affinity likely requiring subnanomolar to picomolar range. So far only one radioligand, [^{11}C]NE40, has been studied and reported in humans, but its binding affinity is rather moderate considering the expected requirement of very high affinity. The major obstacle in the development of CB_1 and CB_2 receptor radioligands is a very high lipophilicity of compounds with sufficiently high binding affinities. While CB_2 receptor imaging remains with substantial promise for numerous CNS diseases, the lackluster and mixed results to date may call into question this target as a useful biomarker of neuroinflammation when contrasted with other well-established imaging targets such as TSPO. However, its potential as a druggable target, similar to the neuroinflammatory targets cyclooxygenases and $P2X_7$ receptor, may reveal yet unrealized dividends in developing novel treatments for debilitating neuropsychiatric disorders.

The recent report of several FAAH and MAGL radioligands advanced into human study has opened new avenues for understanding the ECS. Imaging of FAAH, a pharmacological target with exceptional promise, has the potential to broaden our understanding of the regulation of anandamide. As well, using PET to quantify the dose to percent enzyme saturation of investigational drugs demonstrates the power of this *in vivo* imaging technique, as sadly illustrated in preclinical studies following the tragedy of the BIA 10–2474 trial. Imaging MAGL, an equally promising target for drug development, may improve the understanding of 2-AG regulation, which given its ~1000-fold higher concentration than anandamide in brain (Buczynski and Parsons 2010) may provide more salient understanding to the *in vivo* regulation of ECS neurotransmission.

Non-cannabinoid targets involved in the ECS, such as TRPV1, are underexplored targets for radioligand development, and likewise represent exciting possibilities for creating tools for probing this nearly ubiquitous and far-reaching system. Radioligands for GPR18, GPR55, and the putative endocannabinoid transporter remain essentially unexplored and would add to our knowledge of endocannabinoid physiology and cannabinoid pharmacology.

The complexity of the ECS and its seemingly unending connectivity to organ and biochemical systems afford it a vast potential for future development and investigations for *in vivo* imaging. As the depths of the ECS continue to be sounded, the drive for novel radioligands remains an exciting pursuit.

References

Addy C, Wright H, Van Laere K, Gantz I, Erondu N, Musser BJ et al (2008) The acyclic CB1R inverse agonist taranabant mediates weight loss by increasing energy expenditure and decreasing caloric intake. Cell Metab 7(1):68–78

Agar E (2015) The role of cannabinoids and leptin in neurological diseases. Acta Neurol Scand 132(6):371–380

Ahamed M, Attili B, van Veghel D, Ooms M, Berben P, Celen S et al (2017) Synthesis and pre-clinical evaluation of [(11)C]MA-PB-1 for in vivo imaging of brain monoacylglycerol lipase (MAGL). Eur J Med Chem 136:104–113

Ahmad R, Evens N, Koole M, Serdons K, Verbruggen A, Bormans G et al (2011) Whole-body bio-distribution and radiation dosimetry of the human cannabinoid type-2 receptor ligand [11C]-NE40 in healthy subjects. J Nucl Med 52(Suppl 1):1470

Ahmad R, Koole M, Evens N, Serdons K, Verbruggen A, Bormans G et al (2013) Whole-body bio-distribution and radiation dosimetry of the cannabinoid type 2 receptor ligand [^{11}C]-NE40 in healthy subjects. Mol Imaging Biol 15(4):384–390

Ahmad R, Goffin K, Van den Stock J, De Winter FL, Cleeren E, Bormans G et al (2014) In vivo type 1 cannabinoid receptor availability in Alzheimer's disease. Eur Neuropsychopharmacol 24(2):242–250

Ahmad R, Postnov A, Bormans G, Versijpt J, Vandenbulcke M, Van Laere K (2016) Decreased in vivo availability of the cannabinoid type 2 receptor in Alzheimer's disease. Eur J Nucl Med Mol Imaging 43(12):2219–2227

Ahn K, Smith SE, Liimatta MB, Beidler D, Sadagopan N, Dudley DT et al (2011) Mechanistic and pharmacological characterization of PF-04457845: a highly potent and selective fatty acid amide hydrolase inhibitor that reduces inflammatory and noninflammatory pain. J Pharmacol Exp Ther 338(1):114–124

Ambudkar SV, Kimchi-Sarfaty C, Sauna ZE, Gottesman MM (2003) P-glycoprotein: from genomics to mechanism. Oncogene 22(47):7468–7485

Anand P, Whiteside G, Fowler CJ, Hohmann AG (2009) Targeting CB2 receptors and the endocannabinoid system for the treatment of pain. Brain Res Rev 60(1):255–266

Anthony JC, Lopez-Quintero C, Alshaarawy O (2017) Cannabis epidemiology: a selective review. Curr Pharm Des 22(42):6340–6352

Ashton JC (2007) Cannabinoids for the treatment of inflammation. Curr Opin Investig Drugs 8(5):373–384

Ashton JC, Friberg D, Darlington CL, Smith PF (2006) Expression of the cannabinoid CB2 receptor in the rat cerebellum: an immunohistochemical study. Neurosci Lett 396(2):113–116

Ashton JC, Rahman RM, Nair SM, Sutherland BA, Glass M, Appleton I (2007) Cerebral hypoxia-ischemia and middle cerebral artery occlusion induce expression of the cannabinoid CB2 receptor in the brain. Neurosci Lett 412(2):114–117

Aso E, Andres-Benito P, Ferrer I (2018) Genetic deletion of CB1 cannabinoid receptors exacerbates the Alzheimer-like symptoms in a transgenic animal model. Biochem Pharmacol 157:210–216

Bacci A, Huguenard JR, Prince DA (2004) Long-lasting self-inhibition of neocortical interneurons mediated by endocannabinoids. Nature 431(7006):312–316

Baekelandt V, Bormans G, Debyser Z, Deroose C, Evens N, Toelen J, et al. (2010) Reporter gene constructs and radioligand probes for positron emission tomography in nervous system patent WO 2010105315

Barrett EL, Mills KL, Teesson M (2011) Hurt people who hurt people: violence amongst individuals with comorbid substance use disorder and post-traumatic stress disorder. Addict Behav 36(7):721–728

Basavarajappa BS, Joshi V, Shivakumar M, Subbanna S (2019) Distinct functions of endogenous cannabinoid system in alcohol abuse disorders. Br J Pharmacol 176(17):3085–3109

Benito C, Nunez E, Tolon RM, Carrier EJ, Rabano A, Hillard CJ et al (2003) Cannabinoid CB2 receptors and fatty acid amide hydrolase are selectively overexpressed in neuritic plaque-associated glia in Alzheimer's disease brains. J Neurosci 23(35):11136–11141

Benito C, Kim WK, Chavarria I, Hillard CJ, Mackie K, Tolon RM et al (2005) A glial endogenous cannabinoid system is upregulated in the brains of macaques with simian immunodeficiency virus-induced encephalitis. J Neurosci 25(10):2530–2536

Benito C, Romero JP, Tolon RM, Clemente D, Docagne F, Hillard CJ et al (2007) Cannabinoid CB1 and CB2 receptors and fatty acid amide hydrolase are specific markers of plaque cell subtypes in human multiple sclerosis. J Neurosci 27(9):2396–2402

Benito C, Tolon RM, Pazos MR, Nunez E, Castillo AI, Romero J (2008) Cannabinoid CB2 receptors in human brain inflammation. Br J Pharmacol 153(2):277–285

Benzinou M, Chevre JC, Ward KJ, Lecoeur C, Dina C, Lobbens S et al (2008) Endocannabinoid receptor 1 gene variations increase risk for obesity and modulate body mass index in European populations. Hum Mol Genet 17(13):1916–1921

Berding G, Muller-Vahl K, Schneider U, Gielow P, Fitschen J, Stuhrmann M et al (2004) [123I]AM281 single-photon emission computed tomography imaging of central cannabinoid CB1 receptors before and after Delta9-tetrahydrocannabinol therapy and whole-body scanning for assessment of radiation dose in tourette patients. Biol Psychiatry 55(9):904–915

Berding G, Schneider U, Gielow P, Buchert R, Donnerstag F, Brandau W et al (2006) Feasibility of central cannabinoid CB1 receptor imaging with [124I]AM281 PET demonstrated in a schizophrenic patient. Psychiatry Res 147(2–3):249–256

Bertolini A, Ferrari A, Ottani A, Guerzoni S, Tacchi R, Leone S (2006) Paracetamol: new vistas of an old drug. CNS Drug Rev 12(3–4):250–275

Best L, Tong J, Le Foll B, Bazinet R, Tyndale RF, Mizrahi R et al (2017) Brain levels of fatty acid amide hydrolase are not altered in overweight healthy individuals: a pilot PET Study with [11C]CURB. Biol Psychiatry 81(10):S250–S2S1

Best LM, Hendershot CS, Samantha J, Tong J, Le Foll B, Houle S et al (2018) Endocannabinoid metabolism and alcohol consumption in youth: A PET study with the fatty acid amide hydrolase radioligand [11C]CURB. Biol Psychiatry 83(9):S451

Bhattacharyya S, Egerton A, Kim E, Rosso L, Riano Barros D, Hammers A et al (2017) Acute induction of anxiety in humans by delta-9-tetrahydrocannabinol related to amygdalar cannabinoid-1 (CB1) receptors. Sci Rep 7(1):15025

Bifulco M, Laezza C, Malfitano AM (2007) From anecdotal evidence of cannabinoids in multiple sclerosis to emerging new therapeutic approaches. Mult Scler 13(1):133–134

Blazquez C, Chiarlone A, Sagredo O, Aguado T, Pazos MR, Resel E et al (2011) Loss of striatal type 1 cannabinoid receptors is a key pathogenic factor in Huntington's disease. Brain 134(Pt 1):119–136

Bloomfield MA, Ashok AH, Volkow ND, Howes OD (2016) The effects of Delta(9)-tetrahydrocannabinol on the dopamine system. Nature 539(7629):369–377

Bloomfield MAP, Hindocha C, Green SF, Wall MB, Lees R, Petrilli K et al (2019) The neuropsychopharmacology of cannabis: a review of human imaging studies. Pharmacol Ther 195:132–161

Boileau I, Bloomfield PM, Rusjan P, Mizrahi R, Mufti A, Vitcu I et al (2014) Whole-body radiation dosimetry of 11C-carbonyl-URB694: a PET tracer for fatty acid amide hydrolase. J Nucl Med 55(12):1993–1997

Boileau I, Tyndale RF, Williams B, Mansouri E, Westwood DJ, Le Foll B et al (2015a) The fatty acid amide hydrolase C385A variant affects brain binding of the positron emission tomography tracer [11C]CURB. J Cereb Blood Flow Metab 35(8):1237–1240

Boileau I, Rusjan PM, Williams B, Mansouri E, Mizrahi R, De Luca V et al (2015b) Blocking of fatty acid amide hydrolase activity with PF-04457845 in human brain: a positron emission tomography study with the novel radioligand [(11)C]CURB. J Cereb Blood Flow Metab 35(11):1827–1835

Boileau I, Mansouri E, Williams B, Le Foll B, Rusjan P, Mizrahi R et al (2016) Fatty acid amide hydrolase binding in brain of cannabis users: imaging with the novel radiotracer [^{11}C]CURB. Biol Psychiatry 80(9):691–701

Bonhomme-Faivre L, Benyamina A, Reynaud M, Farinotti R, Abbara C (2008a) Disposition of Delta tetrahydrocannabinol in CF1 mice deficient in mdr1a P-glycoprotein. Addict Biol 13(3–4):295–300

Bonhomme-Faivre L, Benyamina A, Reynaud M, Farinotti R, Abbara C (2008b) Disposition of Delta(9) tetrahydrocannabinol in CF1 mice deficient in mdr1a P-glycoprotein. Addict Biol

Booth M (2005) Cannabis: a history. Picador, A Thomas Dunne Book, St. Martin's Press, New York

Booz GW (2011) Cannabidiol as an emergent therapeutic strategy for lessening the impact of inflammation on oxidative stress. Free Radic Biol Med 51(5):1054–1061

Borgan F, Laurikainen H, Veronese M, Marques TR, Haaparanta-Solin M, Solin O et al (2019) In vivo availability of Cannabinoid 1 receptor levels in patients with first-episode psychosis. JAMA Psychiat 76(10):1074–1084

Borges G, Bagge CL, Orozco R (2016) A literature review and meta-analyses of cannabis use and suicidality. J Affect Disord 195:63–74

Buchholz HG, Uebbing K, Maus S, Pektor S, Afahaene N, Weyer-Elberich V et al (2017) Whole-body biodistribution of the cannabinoid type 1 receptor ligand [18F]MK-9470 in the rat. Nucl Med Biol 52:63–69

Buczynski MW, Parsons LH (2010) Quantification of brain endocannabinoid levels: methods, interpretations and pitfalls. Br J Pharmacol 160(3):423–442

Burns HD, Van Laere K, Sanabria-Bohorquez S, Hamill TG, Bormans G, Eng WS et al (2007) [18F]MK-9470, a positron emission tomography (PET) tracer for in vivo human PET brain imaging of the cannabinoid-1 receptor. Proc Natl Acad Sci U S A 104(23):9800–9805

Cabral GA, Marciano-Cabral F (2005) Cannabinoid receptors in microglia of the central nervous system: immune functional relevance. J Leukoc Biol 78(6):1192–1197

Cahill K, Ussher MH (2007) Cannabinoid type 1 receptor antagonists for smoking cessation. Cochrane Database Syst Rev 4:CD005353

Caille S, Alvarez-Jaimes L, Polis I, Stouffer DG, Parsons LH (2007) Specific alterations of extra-cellular endocannabinoid levels in the nucleus accumbens by ethanol, heroin, and cocaine self-administration. J Neurosci 27(14):3695–3702

Calatozzolo C, Salmaggi A, Pollo B, Sciacca FL, Lorenzetti M, Franzini A et al (2007) Expression of cannabinoid receptors and neurotrophins in human gliomas. Neurol Sci 28(6):304–310

Capettini LS, Savergnini SQ, da Silva RF, Stergiopulos N, Santos RA, Mach F et al (2012) Update on the role of cannabinoid receptors after ischemic stroke. Mediat Inflamm 2012:824093

Carroll CB, Bain PG, Teare L, Liu X, Joint C, Wroath C et al (2004) Cannabis for dyskinesia in Parkinson disease: a randomized double-blind crossover study. Neurology 63(7):1245–1250

Caspi A, Moffitt TE, Cannon M, McClay J, Murray R, Harrington H et al (2005) Moderation of the effect of adolescent-onset cannabis use on adult psychosis by a functional polymorphism in the catechol-O-methyltransferase gene: longitudinal evidence of a gene X environment interaction. Biol Psychiatry 57(10):1117–1127

Casteels C, Bormans G, Van Laere K (2010a) The effect of anaesthesia on [(18)F]MK-9470 binding to the type 1 cannabinoid receptor in the rat brain. Eur J Nucl Med Mol Imaging 37(6):1164–1173

Casteels C, Lauwers E, Baitar A, Bormans G, Baekelandt V, Van Laere K (2010b) In vivo type 1 cannabinoid receptor mapping in the 6-hydroxydopamine lesion rat model of Parkinson's disease. Brain Res 1316:153–162

Casteels C, Koole M, Celen S, Bormans G, Van Laere K (2012) Preclinical evaluation and quantification of [(1)(8)F]MK-9470 as a radioligand for PET imaging of the type 1 cannabinoid receptor in rat brain. Eur J Nucl Med Mol Imaging 39(9):1467–1477

Casteels C, Gerard N, van Kuyck K, Pottel L, Nuttin B, Bormans G et al (2014) Small animal PET imaging of the type 1 cannabinoid receptor in a rodent model for anorexia nervosa. Eur J Nucl Med Mol Imaging 41(2):308–321

Casteels C, Vandeputte C, Rangarajan JR, Dresselaers T, Riess O, Bormans G et al (2011) Metabolic and type 1 cannabinoid receptor imaging of a transgenic rat model in the early phase of Huntington disease. Exp Neurol 229(2):440–449

Casteels C, Martinez E, Bormans G, Camon L, de Vera N, Baekelandt V et al (2010c) Type 1 cannabinoid receptor mapping with [¹⁸F]MK-9470 PET in the rat brain after quinolinic acid lesion: a comparison to dopamine receptors and glucose metabolism. Eur J Nucl Med Mol Imaging 37(12):2354–2363

Casteels C, Vanbilloen B, Vercammen D, Bosier B, Lambert DM, Bormans G et al (2010d) Influence of chronic bromocriptine and levodopa administration on cerebral type 1 cannabinoid receptor binding. Synapse 64(8):617–623

Ceccarini J, Casteels C, Koole M, Bormans G, Van Laere K (2013a) Transient changes in the endocannabinoid system after acute and chronic ethanol exposure and abstinence in the rat: a combined PET and microdialysis study. Eur J Nucl Med Mol Imaging 40(10):1582–1594

Ceccarini J, De Hert M, Van Winkel R, Peuskens J, Bormans G, Kranaster L et al (2013b) Increased ventral striatal CB1 receptor binding is related to negative symptoms in drug-free patients with schizophrenia. NeuroImage 79:304–312

Ceccarini J, Hompes T, Verhaeghen A, Casteels C, Peuskens H, Bormans G et al (2014) Changes in cerebral CB1 receptor availability after acute and chronic alcohol abuse and monitored abstinence. J Neurosci 34(8):2822–2831

Ceccarini J, Kuepper R, Kemels D, van Os J, Henquet C, Van Laere K (2015) [¹⁸F]MK-9470 PET measurement of cannabinoid CB1 receptor availability in chronic cannabis users. Addict Biol 20(2):357–367

Ceccarini J, Weltens N, Ly HG, Tack J, Van Oudenhove L, Van Laere K (2016) Association between cerebral cannabinoid 1 receptor availability and body mass index in patients with food intake disorders and healthy subjects: a [(18)F]MK-9470 PET study. Transl Psychiatry 6(7):e853

Ceccarini J, Ahmad R, Van de Vliet L, Casteels C, Vandenbulcke M, Vandenberghe W et al (2019a) Behavioral symptoms in premanifest Huntington disease correlate with reduced frontal CB1R levels. J Nucl Med 60(1):115–121

Ceccarini J, Casteels C, Ahmad R, Crabbe M, Van de Vliet L, Vanhaute H et al (2019b) Regional changes in the type 1 cannabinoid receptor are associated with cognitive dysfunction in Parkinson's disease. Eur J Nucl Med Mol Imaging 46(11):2348–2357

Cencioni MT, Chiurchiu V, Catanzaro G, Borsellino G, Bernardi G, Battistini L et al (2010) Anandamide suppresses proliferation and cytokine release from primary human T-lymphocytes mainly via CB2 receptors. PLoS One 5(1):e8688

Chaikin P (2017) The bial 10-2474 Phase 1 Study-A drug development perspective and recommendations for future first-in-human trials. J Clin Pharmacol 57(6):690–703

Chandra S, Radwan MM, Majumdar CG, Church JC, Freeman TP, ElSohly MA (2019) New trends in cannabis potency in USA and Europe during the last decade (2008–2017). Eur Arch Psychiatry Clin Neurosci 269(1):5–15

Charalambous A, Marciniak G, Shiue CY, Dewey SL, Schlyer DJ, Wolf AP et al (1991) PET studies in the primate brain and biodistribution in mice using (−)-5'-18F-delta 8-THC. Pharmacol Biochem Behav 40(3):503–507

Chen K, Ratzliff A, Hilgenberg L, Gulyas A, Freund TF, Smith M et al (2003) Long-term plasticity of endocannabinoid signaling induced by developmental febrile seizures. Neuron 39(4):599–611

Chen DJ, Gao M, Gao FF, Su QX, Wu J (2017) Brain cannabinoid receptor 2: expression, function and modulation. Acta Pharmacol Sin 38(3):312–316

Chen Z, Mori W, Deng X, Cheng R, Ogasawara D, Zhang G et al (2019a) Design, synthesis, and evaluation of reversible and irreversible monoacylglycerol lipase Positron Emission Tomography (PET) tracers using a "Tail Switching" strategy on a piperazinyl azetidine skeleton. J Med Chem 62(7):3336–3353

Chen Z, Mori W, Fu H, Schafroth MA, Hatori A, Shao T et al (2019b) Design, synthesis, and evaluation of (18)F-labeled monoacylglycerol lipase inhibitors as novel positron emission tomography probes. J Med Chem 62(19):8866–8872

Cheng R, Mori W, Ma L, Alhouayek M, Hatori A, Zhang Y et al (2018) In vitro and in vivo evaluation of (11)C-labeled azetidinecarboxylates for imaging monoacylglycerol lipase by PET imaging studies. J Med Chem 61(6):2278–2291

Chhatwal JP, Davis M, Maguschak KA, Ressler KJ (2005) Enhancing cannabinoid neurotransmission augments the extinction of conditioned fear. Neuropsychopharmacology 30(3):516–524

Chorvat RJ (2013) Peripherally restricted CB1 receptor blockers. Bioorg Med Chem Lett 23(17):4751–4760

Cleeren E, Casteels C, Goffin K, Koole M, Van Laere K, Janssen P et al (2018) Positron emission tomography imaging of cerebral glucose metabolism and type 1 cannabinoid receptor availability during temporal lobe epileptogenesis in the amygdala kindling model in rhesus monkeys. Epilepsia 59(5):959–970

Cluny NL, Vemuri VK, Chambers AP, Limebeer CL, Bedard H, Wood JT et al (2010) A novel peripherally restricted cannabinoid receptor antagonist, AM6545, reduces food intake and body weight, but does not cause malaise, in rodents. Br J Pharmacol 161(3):629–642

Colino L, Herranz-Herrer J, Gil-Benito E, Ponte-Lopez T, Del Sol-Calderon P, Rodrigo-Yanguas M et al (2018) Cannabinoid receptors, mental pain and suicidal behavior: a systematic review. Curr Psychiatry Rep 20(3):19

Compton DR, Rice KC, De Costa BR, Razdan RK, Melvin LS, Johnson MR et al (1993) Cannabinoid structure-activity relationships: correlation of receptor binding and in vivo activities. J Pharmacol Exp Ther 265(1):218–226

Compton WM, Thomas YF, Conway KP, Colliver JD (2005) Developments in the epidemiology of drug use and drug use disorders. Am J Psychiatry 162(8):1494–1502

Concannon RM, Okine BN, Finn DP, Dowd E (2016) Upregulation of the cannabinoid CB2 receptor in environmental and viral inflammation-driven rat models of Parkinson's disease. Exp Neurol 283(Pt A):204–212

Constantinescu CS, Farooqi N, O'Brien K, Gran B (2011) Experimental autoimmune encephalomyelitis (EAE) as a model for multiple sclerosis (MS). Br J Pharmacol 164(4):1079–1106

Cooper SJ (2004) Endocannabinoids and food consumption: comparisons with benzodiazepine and opioid palatability-dependent appetite. Eur J Pharmacol 500(1–3):37–49

Copeland J, Swift W (2009) Cannabis use disorder: epidemiology and management. Int Rev Psychiatry 21(2):96–103

Corchero J, Manzanares J, Fuentes JA (2004) Cannabinoid/opioid crosstalk in the central nervous system. Crit Rev Neurobiol 16(1–2):159–172

Cota D, Marsicano G, Lutz B, Vicennati V, Stalla GK, Pasquali R et al (2003) Endogenous cannabinoid system as a modulator of food intake. Int J Obes Relat Metab Disord 27(3):289–301

Cota D, Steiner MA, Marsicano G, Cervino C, Herman JP, Grubler Y et al (2007) Requirement of cannabinoid receptor type 1 for the basal modulation of hypothalamic-pituitary-adrenal axis function. Endocrinology 148(4):1574–1581

Coutts AA, Anavi-Goffer S, Ross RA, MacEwan DJ, Mackie K, Pertwee RG et al (2001) Agonist-induced internalization and trafficking of cannabinoid CB1 receptors in hippocampal neurons. J Neurosci 21(7):2425–2433

Croxford JL (2003) Therapeutic potential of cannabinoids in CNS disease. CNS Drugs 17(3):179–202

Cupini LM, Bari M, Battista N, Argiro G, Finazzi-Agro A, Calabresi P et al (2006) Biochemical changes in endocannabinoid system are expressed in platelets of female but not male migraineurs. Cephalalgia 26(3):277–281

Curtis A, Mitchell I, Patel S, Ives N, Rickards H (2009) A pilot study using nabilone for symptomatic treatment in Huntington's disease. Mov Disord 24(15):2254–2259

D'Souza DC, Ranganathan M (2015) Medical marijuana: is the cart before the horse? JAMA 313(24):2431–2432

Da Silva T, Hafizi S, Watts JJ, Weickert CS, Meyer JH, Houle S et al (2019) In vivo imaging of translocator protein in long-term Cannabis users. JAMA Psychiat 76(12):1305–1313

de Lago E, Moreno-Martet M, Cabranes A, Ramos JA, Fernandez-Ruiz J (2012) Cannabinoids ameliorate disease progression in a model of multiple sclerosis in mice, acting prefer-

entially through CB1 receptor-mediated anti-inflammatory effects. Neuropharmacology 62(7):2299–2308

De Vita MJ, Moskal D, Maisto SA, Ansell EB (2018) Association of cannabinoid administration with experimental pain in healthy adults: a systematic review and meta-analysis. JAMA Psychiat 75(11):1118–1127

Dean B, Sundram S, Bradbury R, Scarr E, Copolov D (2001) Studies on [³H]CP-55940 binding in the human central nervous system: regional specific changes in density of cannabinoid-1 receptors associated with schizophrenia and cannabis use. Neuroscience 103(1):9–15

Degenhardt L, Hall W, Lynskey M (2003) Exploring the association between cannabis use and depression. Addiction 98(11):1493–1504

Degroot A, Nomikos GG (2007) In vivo neurochemical effects induced by changes in endocannabinoid neurotransmission. Curr Opin Pharmacol 7(1):62–68

Deng H, Gifford AN, Zvonok AM, Cui G, Li X, Fan P et al (2005) Potent cannabinergic indole analogues as radioiodinatable brain imaging agents for the CB1 cannabinoid receptor. J Med Chem 48(20):6386–6392

Deshpande LS, Blair RE, Ziobro JM, Sombati S, Martin BR, DeLorenzo RJ (2007) Endocannabinoids block status epilepticus in cultured hippocampal neurons. Eur J Pharmacol 558(1–3):52–59

Despres JP, Ross R, Boka G, Almeras N, Lemieux I (2009) Effect of rimonabant on the high-triglyceride/low-HDL-cholesterol dyslipidemia, intraabdominal adiposity, and liver fat: the ADAGIO-lipids trial. Arterioscler Thromb Vasc Biol 29(3):416–423

Devane WA, Dysarz FA 3rd, Johnson MR, Melvin LS, Howlett AC (1988) Determination and characterization of a cannabinoid receptor in rat brain. Mol Pharmacol 34(5):605–613

Devane WA, Hanus L, Breuer A, Pertwee RG, Stevenson LA, Griffin G et al (1992) Isolation and structure of a brain constituent that binds to the cannabinoid receptor. Science 258(5090):1946–1949

Di Marzo V, De Petrocellis L (2010) Endocannabinoids as regulators of transient receptor potential (TRP) channels: a further opportunity to develop new endocannabinoid-based therapeutic drugs. Curr Med Chem 17(14):1430–1449

Di Marzo V, Hill MP, Bisogno T, Crossman AR, Brotchie JM (2000) Enhanced levels of endogenous cannabinoids in the globus pallidus are associated with a reduction in movement in an animal model of Parkinson's disease. FASEB J 14(10):1432–1438

Di Marzo V, Goparaju SK, Wang L, Liu J, Batkai S, Jarai Z et al (2001) Leptin-regulated endocannabinoids are involved in maintaining food intake. Nature 410(6830):822–825

Di Marzo V, Bifulco M, De Petrocellis L (2004) The endocannabinoid system and its therapeutic exploitation. Nat Rev Drug Discov 3(9):771–784

Di Marzo V, Piscitelli F, Mechoulam R (2011) Cannabinoids and endocannabinoids in metabolic disorders with focus on diabetes. Handb Exp Pharmacol 203:75–104

Dinh TP, Carpenter D, Leslie FM, Freund TF, Katona I, Sensi SL et al (2002) Brain monoglyceride lipase participating in endocannabinoid inactivation. Proc Natl Acad Sci U S A 99(16):10819–10824

Donohue SR, Pike VW, Finnema SJ, Truong P, Andersson J, Gulyas B et al (2008a) Discovery and labeling of high-affinity 3,4-diarylpyrazolines as candidate radioligands for in vivo imaging of cannabinoid subtype-1 (CB1) receptors. J Med Chem 51(18):5608–5616

Donohue S, Halldin C, Schou M, Hong J, Phebus L, Chernet E et al (2008b) Radiolabeling of a high potency cannabinoid subtype-1 receptor ligand, N-(4-fluoro-benzyl)-4-(3-(piperidin-1-yl)-indole-1-sulfonyl)benzamide(PipISB), with carbon-11 or fluorine-18. J Label Compd Radiopharm 51:146–152

Donohue SR, Krushinski JH, Pike VW, Chernet E, Phebus L, Chesterfield AK et al (2008c) Synthesis, ex vivo evaluation, and radiolabeling of potent 1,5-diphenylpyrrolidin-2-one cannabinoid subtype-1 receptor ligands as candidates for in vivo imaging. J Med Chem 51(18):5833–5842

Dow-Edwards D, Silva L (2017) Endocannabinoids in brain plasticity: cortical maturation, HPA axis function and behavior. Brain Res 1654(Pt B):157–164

Drysdale AJ, Platt B (2003) Cannabinoids: mechanisms and therapeutic applications in the CNS. Curr Med Chem 10(24):2719–2732

D'Souza DC, Cortes-Briones JA, Ranganathan M, Thurnauer H, Creatura G, Surti T et al (2016a) Rapid changes in cannabinoid 1 receptor availability in cannabis-dependent male subjects after abstinence from cannabis. Biol Psychiatry Cogn Neurosci Neuroimaging 1(1):60–67

D'Souza DC, Radhakrishnan R, Sherif M, Cortes-Briones J, Cahill J, Gupta S et al (2016b) Cannabinoids and psychosis. Curr Pharm Des 22(42):6380–6391

D'Souza DC, Cortes-Briones J, Creatura G, Bluez G, Thurnauer H, Deaso E et al (2019) Efficacy and safety of a fatty acid amide hydrolase inhibitor (PF-04457845) in the treatment of cannabis withdrawal and dependence in men: a double-blind, placebo-controlled, parallel group, phase 2a single-site randomised controlled trial. Lancet Psychiatry 6(1):35–45

Eckelman WC, Reba RC, Gibson RE (1979) Receptor-binding radiotracers: a class of potential radiopharmaceuticals. J Nucl Med 20(4):350–357

Economidou D, Mattioli L, Cifani C, Perfumi M, Massi M, Cuomo V et al (2006) Effect of the cannabinoid CB(1) receptor antagonist SR-141716A on ethanol self-administration and ethanol-seeking behaviour in rats. Psychopharmacology 183(4):394–403

Egertova M, Giang DK, Cravatt BF, Elphick MR (1998) A new perspective on cannabinoid signalling: complementary localization of fatty acid amide hydrolase and the CB1 receptor in rat brain. Proc Biol Sci 265(1410):2081–2085

Eggan SM, Hashimoto T, Lewis DA (2008) Reduced cortical cannabinoid 1 receptor messenger RNA and protein expression in Schizophrenia. Arch Gen Psychiatry 65(7):772–784

Ehrhart J, Obregon D, Mori T, Hou H, Sun N, Bai Y et al (2005) Stimulation of cannabinoid receptor 2 (CB2) suppresses microglial activation. J Neuroinflammation 2:29

Ellert-Miklaszewska A, Grajkowska W, Gabrusiewicz K, Kaminska B, Konarska L (2007) Distinctive pattern of cannabinoid receptor type II (CB2) expression in adult and pediatric brain tumors. Brain Res 1137(1):161–169

Elphick MR, Egertova M (2005) The phylogenetic distribution and evolutionary origins of endocannabinoid signalling. Handb Exp Pharmacol 168:283–297

ElSohly MA, Ross SA, Mehmedic Z, Arafat R, Yi B, Banahan BF 3rd. (2000) Potency trends of delta9-THC and other cannabinoids in confiscated marijuana from 1980–1997. J Forensic Sci 45(1):24–30

Emonds KM, Koole M, Casteels C, Van den Bergh L, Bormans GM, Claus F et al (2013) 18F-MK-9470 PET imaging of the type 1 cannabinoid receptor in prostate carcinoma: a Pilot Study. EJNMMI Res 3(1):59

England TJ, Hind WH, Rasid NA, O'Sullivan SE (2015) Cannabinoids in experimental stroke: a systematic review and meta-analysis. J Cereb Blood Flow Metab 35(3):348–358

Eriksson O, Mikkola K, Espes D, Tuominen L, Virtanen K, Forsback S et al (2015) The Cannabinoid Receptor-1 Is an imaging biomarker of brown adipose tissue. J Nucl Med 56(12):1937–1941

Ertl P (2008) Polar surface area. In: Mannhold R (ed) Molecular drug properties measurements and predictions. Wiley-VCH Verlag GmbH & Co., Weinheim, pp 111–126

Esmaeil Mansouri LMB, Le Foll B, Hendershot CS, Tyndale RF, Ksh S, Tong J, Boileau I (2018) Involvement of the endocannabinoid enzyme fatty acid amide hydrolase in the neurobiology of impulsivity: positron emission tomography studies with [11C]CURB. Biol Psychiatry 83(9):S158

Eubanks LM, Rogers CJ, Beuscher AE, Koob GF, Olson AJ, Dickerson TJ et al (2006) A molecular link between the active component of marijuana and Alzheimer's disease pathology. Mol Pharm 3(6):773–777

Evens N, Bormans GM (2010) Non-invasive imaging of the Type 2 cannabinoid receptor, focus on positron emission tomography. Curr Top Med Chem 10(15):1527–1543

Evens N, Bosier B, Van Laere K, Verbruggen A, Bormans G (2007) Synthesis and evaluation of (2,3-dichloro-phenyl)-[5-[11C]methoxy-2-methyl-3-(2-morpholin-4-yl-ethyl)-indol-1-yl]-methanone as a PET radioligand with affinity for the CB2 receptor. J Nucl Med 48:133P

Evens N, Bosier B, Lavey BJ, Kozlowski JA, Vermaelen P, Baudemprez L et al (2008) Labelling and biological evaluation of [(11)C]methoxy-Sch225336: a radioligand for the cannabinoid-type 2 receptor. Nucl Med Biol 35(7):793–800

Evens N, Muccioli GG, Houbrechts N, Lambert DM, Verbruggen AM, Van Laere K et al (2009a) Synthesis and biological evaluation of carbon-11- and fluorine-18-labeled 2-oxoquinoline derivatives for type 2 cannabinoid receptor positron emission tomography imaging. Nucl Med Biol 36(4):455–465

Evens N, Vandeputte C, Toelen J, Baekelandt V, Debyser Z, Verbruggen A, et al., (eds.) (2009b) Validation of PET radioligands for visualisation of the type 2 cannabinoid receptor in a rat model with local cerebral CB2R overexpression. In: Annual Congress of the European Association of Nuclear Medicine; 2009; Barcelona, Spain: Eur. J. Nucl. Med. Mol. Imaging; 2009

Evens N, Vandeputte C, Muccioli GG, Lambert DM, Baekelandt V, Verbruggen AM et al (2011a) Synthesis, in vitro and in vivo evaluation of fluorine-18 labelled FE-GW405833 as a PET tracer for type 2 cannabinoid receptor imaging. Bioorg Med Chem 19(15):4499–4505

Evens N, Vandeputte C, Coolen C, Janssen P, Sciot R, Baekelandt V et al (2011b) Preclinical evaluation of [(11)C]NE40, a type 2 cannabinoid receptor PET tracer. Nucl Med Biol

Fan H, Ravert HT, Holt D, Dannals RF, Horti AG (2006) Synthesis of 1-(2,4-dichlorophenyl)-4-cyano-5-(4-[11C]methoxyphenyl)-N-(piperidin-1-yl)-1H-pyrazole-3-carboxamide ([11C]JHU75528) and 1-(2-bromophenyl)-4-cyano-5-(4-[11C]methoxyphenyl)-N-(piperidin-1-yl)-1H-pyrazole-3-carboxamide ([11C]JHU75575) as potential radioligands for PET imaging of cerebral cannabinoid receptor. J Label Compd Radiopharm 49:1021–1036

Fan H, Kotsikorou E, Hoffman AF, Ravert HT, Holt D, Hurst DP et al (2009) Analogs of JHU75528, a PET ligand for imaging of cerebral cannabinoid receptors (CB1): development of ligands with optimized lipophilicity and binding affinity. Eur J Med Chem 44(2):593–608

Farde L, Gustavsson JP, Jonsson E (1997) D2 dopamine receptors and personality traits. Nature 385(6617):590

Farkas S, Nagy K, Palkovits M, Kovacs GG, Jia Z, Donohue S et al (2012) [(1)(2)I]SD-7015 reveals fine modalities of CB cannabinoid receptor density in the prefrontal cortex during progression of Alzheimer's disease. Neurochem Int 60(3):286–291

Felder CC, Dickason-Chesterfield AK, Moore SA (2006) Cannabinoids biology: the search for new therapeutic targets. Mol Interv 6(3):149–161

Fernandez-Espejo E, Viveros MP, Nunez L, Ellenbroek BA, Rodriguez de Fonseca F (2009) Role of cannabis and endocannabinoids in the genesis of schizophrenia. Psychopharmacology 206(4):531–549

Finnema SJ, Donohue SR, Zoghbi SS, Brown AK, Gulyas B, Innis RB et al (2009) Evaluation of [11C]PipISB and [18F]PipISB in monkey as candidate radioligands for imaging brain cannabinoid type-1 receptors in vivo. Synapse 63(1):22–30

Fowler CJ (2012) Anandamide uptake explained? Trends Pharmacol Sci 33(4):181–185

Fowler CJ (2015) The potential of inhibitors of endocannabinoid metabolism for drug development: a critical review. Handb Exp Pharmacol 231:95–128

Fowler JS, Logan J, Volkow ND, Wang GJ, MacGregor RR, Ding YS (2002) Monoamine oxidase: radiotracer development and human studies. Methods 27(3):263–277

Fox SH, Henry B, Hill M, Crossman A, Brotchie J (2002) Stimulation of cannabinoid receptors reduces levodopa-induced dyskinesia in the MPTP-lesioned nonhuman primate model of Parkinson's disease. Mov Disord 17(6):1180–1187

Frost JJ, Wagner HN Jr (1984) Kinetics of binding to opiate receptors in vivo predicted from in vitro parameters. Brain Res 305(1):1–11

Fujinaga M, Kumata K, Yanamoto K, Kawamura K, Yamasaki T, Yui J et al (2010) Radiosynthesis of novel carbon-11-labeled triaryl ligands for cannabinoid-type 2 receptor. Bioorg Med Chem Lett 20(5):1565–1568

Gaetani S, Kaye WH, Cuomo V, Piomelli D (2008) Role of endocannabinoids and their analogues in obesity and eating disorders. Eat Weight Disord 13(3):e42–e48

Galatro TF, Holtman IR, Lerario AM, Vainchtein ID, Brouwer N, Sola PR et al (2017) Transcriptomic analysis of purified human cortical microglia reveals age-associated changes. Nat Neurosci 20(8):1162–1171

Galiegue S, Mary S, Marchand J, Dussossoy D, Carriere D, Carayon P et al (1995) Expression of central and peripheral cannabinoid receptors in human immune tissues and leukocyte subpopulations. Eur J Biochem 232(1):54–61

Gallant M, Dufresne C, Gareau Y, Guay D, Leblanc R, Petpiboon P et al (1996) New class of potent ligands for the human peripheral cannabinoid receptor. J Med Chem 6(19):2263–2268

Gao M, Wang M, Miller KD, Hutchins GD, Zheng QH (2010) Synthesis and in vitro biological evaluation of carbon-11-labeled quinoline derivatives as new candidate PET radioligands for cannabinoid CB2 receptor imaging. Bioorg Med Chem 18(6):2099–2106

Gao M, Wang M, Zheng QH (2012) A new high-yield synthetic route to PET CB1 radioligands [^{11}C]OMAR and its analogs. Bioorg Med Chem Lett 22(11):3704–3709

Gaoni Y, Mechoulam R (1964) Isolation structure + partial synthesis of active constituent of Hashish. J Am Chem Soc 86(8):1646

Gatley SJ, Gifford AN, Volkow ND, Lan R, Makriyannis A (1996) 123I-labeled AM251: a radioiodinated ligand which binds in vivo to mouse brain cannabinoid CB1 receptors. Eur J Pharmacol 307(3):331–338

Gatley SJ, Lan R, Volkow ND, Pappas N, King P, Wong CT et al (1998) Imaging the brain marijuana receptor: development of a radioligand that binds to cannabinoid CB1 receptors in vivo. J Neurochem 70(1):417–423

Gatley SJ, Gifford AN, Ding Y-S, Volkow ND, Lan R, Liu Q et al (2004) Development of PET and SPECT radioligands for cannabinoid receptors. Drug Discov Strategies Methods:129–146

George DT, Herion DW, Jones CL, Phillips MJ, Hersh J, Hill D et al (2010) Rimonabant (SR141716) has no effect on alcohol self-administration or endocrine measures in nontreatment-seeking heavy alcohol drinkers. Psychopharmacology 208(1):37–44

Georgieva T, Devanathan S, Stropova D, Park CK, Salamon Z, Tollin G et al (2008) Unique agonist-bound cannabinoid CB1 receptor conformations indicate agonist specificity in signaling. Eur J Pharmacol 581(1–2):19–29

Gerard N, Ceccarini J, Bormans G, Vanbilloen B, Casteels C, Goffin K et al (2010) Influence of chronic nicotine administration on cerebral type 1 cannabinoid receptor binding: an in vivo micro-PET study in the rat using [^{18}F]MK-9470. J Mol Neurosci 42(2):162–167

Gerard N, Pieters G, Goffin K, Bormans G, Van Laere K (2011) Brain Type 1 cannabinoid receptor availability in patients with anorexia and bulimia nervosa. Biol Psychiatry 70(8):777–784

Gifford AN, Tang Y, Gatley SJ, Volkow ND, Lan R, Makriyannis A (1997) Effect of the cannabinoid receptor SPECT agent, AM 281, on hippocampal acetylcholine release from rat brain slices. Neurosci Lett 238(1–2):84–86

Gifford AN, Bruneus M, Gatley SJ, Lan R, Makriyannis A, Volkow ND (1999) Large receptor reserve for cannabinoid actions in the central nervous system. J Pharmacol Exp Ther 288(2):478–483

Giuffrida A, Parsons LH, Kerr TM, Rodriguez de Fonseca F, Navarro M, Piomelli D (1999) Dopamine activation of endogenous cannabinoid signaling in dorsal striatum. Nat Neurosci 2(4):358–363

Glass M, Dragunow M, Faull RL (1997) Cannabinoid receptors in the human brain: a detailed anatomical and quantitative autoradiographic study in the fetal, neonatal and adult human brain. Neuroscience 77(2):299–318

Glass M, Dragunow M, Faull RL (2000) The pattern of neurodegeneration in Huntington's disease: a comparative study of cannabinoid, dopamine, adenosine and GABA(A) receptor alterations in the human basal ganglia in Huntington's disease. Neuroscience 97(3):505–519

Glass M, van Dellen A, Blakemore C, Hannan AJ, Faull RL (2004) Delayed onset of Huntington's disease in mice in an enriched environment correlates with delayed loss of cannabinoid CB1 receptors. Neuroscience 123(1):207–212

Gobbi G, Bambico FR, Mangieri R, Bortolato M, Campolongo P, Solinas M et al (2005) Antidepressant-like activity and modulation of brain monoaminergic transmission by blockade of anandamide hydrolysis. Proc Natl Acad Sci U S A 102(51):18620–18625

Goffin K, Bormans G, Casteels C, Bosier B, Lambert DM, Grachev ID et al (2008) An in vivo [(18)F]MK-9470 microPET study of type 1 cannabinoid receptor binding in Wistar rats after chronic administration of valproate and levetiracetam. Neuropharmacology

Goffin K, Van Paesschen W, Van Laere K (2011) In vivo activation of endocannabinoid system in temporal lobe epilepsy with hippocampal sclerosis. Brain 134(Pt 4):1033–1040

Gong JP, Onaivi ES, Ishiguro H, Liu QR, Tagliaferro PA, Brusco A et al (2006) Cannabinoid CB2 receptors: immunohistochemical localization in rat brain. Brain Res 1071(1):10–23

Gonzalez S, Valenti M, de Miguel R, Fezza F, Fernandez-Ruiz J, Di Marzo V et al (2004) Changes in endocannabinoid contents in reward-related brain regions of alcohol-exposed rats, and their possible relevance to alcohol relapse. Br J Pharmacol 143(4):455–464

Gorzalka BB, Hill MN, Hillard CJ (2008) Regulation of endocannabinoid signaling by stress: implications for stress-related affective disorders. Neurosci Biobehav Rev 32(6):1152–1160

Goto M, Mizuma H, Wada Y, Suzuki M, Watanabe Y, Onoe H et al (2015) 11C-Labeled capsaicin and its in vivo molecular imaging in rats by positron emission tomography. Food Nutr Sci 6:216–220

Guindon J, De Lean A, Beaulieu P (2006) Local interactions between anandamide, an endocannabinoid, and ibuprofen, a nonsteroidal anti-inflammatory drug, in acute and inflammatory pain. Pain 121(1–2):85–93

Gunthorpe MJ, Rami HK, Jerman JC, Smart D, Gill CH, Soffin EM et al (2004) Identification and characterisation of SB-366791, a potent and selective vanilloid receptor (VR1/TRPV1) antagonist. Neuropharmacology 46(1):133–149

Habib AM, Okorokov AL, Hill MN, Bras JT, Lee MC, Li S et al (2019) Microdeletion in a FAAH pseudogene identified in a patient with high anandamide concentrations and pain insensitivity. Br J Anaesth 123(2):e249–ee53

Haider A, Muller Herde A, Slavik R, Weber M, Mugnaini C, Ligresti A et al (2016) Synthesis and biological evaluation of thiophene-based cannabinoid receptor Type 2 radiotracers for PET imaging. Front Neurosci 10:350

Haider A, Spinelli F, Herde AM, Mu B, Keller C, Margelisch M et al (2018) Evaluation of 4-oxo-quinoline-based CB2 PET radioligands in R6/2 chorea Huntington mouse model and human ALS spinal cord tissue. Eur J Med Chem 145:746–759

Hamill TG, Lin LS, Hagmann W, Liu P, Jewell J, Sanabria S et al (2009) PET imaging studies in rhesus monkey with the Cannabinoid-1 (CB1) receptor ligand [(11)C]CB-119. Mol Imaging Biol 11(4):246–252

Hannestad J, Gallezot JD, Schafbauer T, Lim K, Kloczynski T, Morris ED et al (2012) Endotoxin-induced systemic inflammation activates microglia: [(1)(1)C]PBR28 positron emission tomography in nonhuman primates. NeuroImage 63(1):232–239

Hattori Y, Aoyama K, Maeda J, Arimura N, Takahashi Y, Sasaki M et al (2019) Design, synthesis, and evaluation of (4 R)-1-{3-[2-((18)F)Fluoro-4-methylpyridin-3-yl]phenyl}-4-[4-(1,3-thiazol-2-ylcarbo nyl)piperazin-1-yl]pyrrolidin-2-one ([(18)F]T-401) as a Novel positron-emission tomography imaging agent for monoacylglycerol lipase. J Med Chem 62(5):2362–2375

Heimann D, Borgel F, de Vries H, Bachmann K, Rose VE, Frehland B et al (2018a) Optimization of pharmacokinetic properties by modification of a carbazole-based cannabinoid receptor subtype 2 (CB2) ligand. Eur J Med Chem 143:1436–1447

Heimann D, Borgel F, de Vries H, Patberg M, Jan-Smith E, Frehland B et al (2018b) Optimization of the metabolic stability of a fluorinated cannabinoid receptor subtype 2 (CB2) ligand designed for PET studies. Eur J Med Chem 146:409–422

Herance R, Rojas S, Abad S, Jimenez X, Gispert JD, Millan O et al (2011) Positron emission tomographic imaging of the cannabinoid Type 1 receptor system with [(11)C]OMAR ([(11) C]JHU75528): improvements in image quantification using wild-type and knockout mice. Mol Imaging 10(6):481–487

Herkenham M, Lynn AB, Little MD, Johnson MR, Melvin LS, de Costa BR et al (1990) Cannabinoid receptor localization in brain. Proc Natl Acad Sci U S A 87(5):1932–1936

Herkenham M, Lynn AB, Johnson MR, Melvin LS, de Costa BR, Rice KC (1991) Characterization and localization of cannabinoid receptors in rat brain: a quantitative in vitro autoradiographic study. J Neurosci 11(2):563–583

Herrera B, Carracedo A, Diez-Zaera M, Guzman M, Velasco G (2005) p38 MAPK is involved in CB2 receptor-induced apoptosis of human leukaemia cells. FEBS Lett 579(22):5084–5088

Hertzog DL (2004) Recent advances in the cannabinoids. Expert Opin Ther Pat 14(10):1435–1452

Hicks JW, Parkes J, Sadovski O, Tong J, Houle S, Vasdev N et al (2013) Synthesis and preclinical evaluation of [^{11}C-carbonyl]PF-04457845 for neuroimaging of fatty acid amide hydrolase. Nucl Med Biol 40(6):740–746

Hicks JW, Parkes J, Tong J, Houle S, Vasdev N, Wilson AA (2014) Radiosynthesis and ex vivo evaluation of [(11)C-carbonyl]carbamate- and urea-based monoacylglycerol lipase inhibitors. Nucl Med Biol 41(8):688–694

Hill MN, McEwen BS (2009) Endocannabinoids: The silent partner of glucocorticoids in the synapse. Proc Natl Acad Sci U S A 106(12):4579–4580

Hill MN, Bierer LM, Makotkine I, Golier JA, Galea S, McEwen BS et al (2013) Reductions in circulating endocannabinoid levels in individuals with post-traumatic stress disorder following exposure to the World Trade Center attacks. Psychoneuroendocrinology 38(12):2952–2961

Hillard CJ, Weinlander KM, Stuhr KL (2011) Contributions of endocannabinoid signaling to psychiatric disorders in humans: genetic and biochemical evidence. Neuroscience 204:207–229

Hiroi N, Agatsuma S (2005) Genetic susceptibility to substance dependence. Mol Psychiatry 10(4):336–344

Hirvonen J, Terry GE, Halldin C, Pike VW, Innis RB (2010) Approaches to quantify radioligands that wash out slowly from target organs. Eur J Nucl Med Mol Imaging 37(5):917–919

Hirvonen J, Goodwin RS, Li CT, Terry GE, Zoghbi SS, Morse C et al (2012a) Reversible and regionally selective downregulation of brain cannabinoid CB(1) receptors in chronic daily cannabis smokers. Mol Psychiatry 17(6):642–649

Hirvonen J, Goodwin RS, Li CT, Terry GE, Zoghbi SS, Morse C et al (2012b) Reversible and regionally selective downregulation of brain cannabinoid CB1 receptors in chronic daily cannabis smokers. Mol Psychiatry 17(6):642–649

Hirvonen J, Zanotti-Fregonara P, Umhau JC, George DT, Rallis-Frutos D, Lyoo CH et al (2013) Reduced cannabinoid CB1 receptor binding in alcohol dependence measured with positron emission tomography. Mol Psychiatry 18(8):916–921

Hirvonen J, Zanotti-Fregonara P, Gorelick DA, Lyoo CH, Rallis-Frutos D, Morse C et al (2018) Decreased cannabinoid CB1 receptors in male tobacco smokers examined with positron emission tomography. Biol Psychiatry 84(10):715–721

Hjorth S, Karlsson C, Jucaite A, Varnas K, Wahlby Hamren U, Johnstrom P et al (2016) A PET study comparing receptor occupancy by five selective cannabinoid 1 receptor antagonists in non-human primates. Neuropharmacology 101:519–530

Ho BC, Wassink TH, Ziebell S, Andreasen NC (2011) Cannabinoid receptor 1 gene polymorphisms and marijuana misuse interactions on white matter and cognitive deficits in schizophrenia. Schizophr Res 128(1–3):66–75

Hogestatt ED, Jonsson BA, Ermund A, Andersson DA, Bjork H, Alexander JP et al (2005) Conversion of acetaminophen to the bioactive N-acylphenolamine AM404 via fatty acid amide hydrolase-dependent arachidonic acid conjugation in the nervous system. J Biol Chem 280(36):31405–31412

Hohmann AG, Suplita RL 2nd. (2006) Endocannabinoid mechanisms of pain modulation. AAPS J 8(4):E693–E708

Horti AG (2011) Unpublished results

Horti AG, Van Laere K (2008) Development of radioligands for in vivo imaging of type 1 cannabinoid receptors (CB1) in human brain. Curr Pharm Des 14(31):3363–3383

Horti AG, Fan H, Kuwabara H, Hilton J, Ravert HT, Holt DP et al (2006) 11C-JHU75528: a radiotracer for PET imaging of CB1 cannabinoid receptors. J Nucl Med 47(10):1689–1696

Horti AG, Gao Y, Ravert HT, Finley P, Valentine H, Wong DF et al (2010) Synthesis and biodistribution of [^{11}C]A-836339, a new potential radioligand for PET imaging of cannabinoid type 2 receptors (CB2). Bioorg Med Chem 18(14):5202–5207

Hosoya T, Fukumoto D, Kakiuchi T, Nishiyama S, Yamamoto S, Ohba H et al (2017) In vivo TSPO and cannabinoid receptor type 2 availability early in post-stroke neuroinflammation in rats: a positron emission tomography study. J Neuroinflammation 14(1):69

Howlett AC (1995) Pharmacology of cannabinoid receptors. Annu Rev Pharmacol Toxicol 35:607–634

Howlett AC (2002) The cannabinoid receptors. Prostaglandins Other Lipid Mediat 68-69:619–631

Howlett AC, Barth F, Bonner TI, Cabral G, Casellas P, Devane WA et al (2002) International Union of Pharmacology. XXVII. Classification of cannabinoid receptors. Pharmacol Rev 54(2):161–202

Hsiao WC, Shia KS, Wang YT, Yeh YN, Chang CP, Lin Y et al (2015) A novel peripheral cannabinoid receptor 1 antagonist, BPR0912, reduces weight independently of food intake and modulates thermogenesis. Diabetes Obes Metab 17(5):495–504

Hsieh GC, Pai M, Chandran P, Hooker BA, Zhu CZ, Salyers AK et al (2011) Central and peripheral sites of action for CB receptor mediated analgesic activity in chronic inflammatory and neuropathic pain models in rats. Br J Pharmacol 162(2):428–440

Huang WJ, Chen WW, Zhang X (2016) Endocannabinoid system: role in depression, reward and pain control (Review). Mol Med Rep 14(4):2899–2903

Huestis MA, Gorelick DA, Heishman SJ, Preston KL, Nelson RA, Moolchan ET et al (2001) Blockade of effects of smoked marijuana by the CB1-selective cannabinoid receptor antagonist SR141716. Arch Gen Psychiatry 58(4):322–328

Huffman JW, Zengin G, Wu MJ, Lu J, Hynd G, Bushell K et al (2005) Structure-activity relationships for 1-alkyl-3-(1-naphthoyl)indoles at the cannabinoid CB(1) and CB(2) receptors: steric and electronic effects of naphthoyl substituents. New highly selective CB(2) receptor agonists. Bioorg Med Chem 13(1):89–112

Huggins JP, Smart TS, Langman S, Taylor L, Young T (2012) An efficient randomised, placebo-controlled clinical trial with the irreversible fatty acid amide hydrolase-1 inhibitor PF-04457845, which modulates endocannabinoids but fails to induce effective analgesia in patients with pain due to osteoarthritis of the knee. Pain 153(9):1837–1846

Hungund BL, Basavarajappa BS (2004) Role of endocannabinoids and cannabinoid CB1 receptors in alcohol-related behaviors. Ann N Y Acad Sci 1025:515–527

Hutchison KE, Haughey H, Niculescu M, Schacht J, Kaiser A, Stitzel J et al (2008) The incentive salience of alcohol: translating the effects of genetic variant in CNR1. Arch Gen Psychiatry 65(7):841–850

Innis RB, Cunningham VJ, Delforge J, Fujita M, Gjedde A, Gunn RN et al (2007) Consensus nomenclature for in vivo imaging of reversibly binding radioligands. J Cereb Blood Flow Metab 27(9):1533–1539

Irving A, Abdulrazzaq G, Chan SLF, Penman J, Harvey J, Alexander SPH (2017) Cannabinoid receptor-related Orphan G protein-coupled receptors. Adv Pharmacol 80:223–247

Isabelle Boileau DW, Richardson D, Rhind S, Tyndale RF, Lanius R, Bazinet R, Lobaugh NJ, Houle S (2018) Investigating endocannabinoid mechanisms in posttraumatic stress disorder: neuroimaging studies with the novel fatty acid amide hydrolase probe [^{11}C]CURB. Biol Psychiatry 83(9):S21

Ishiguro H, Iwasaki S, Teasenfitz L, Higuchi S, Horiuchi Y, Saito T et al (2007) Involvement of cannabinoid CB2 receptor in alcohol preference in mice and alcoholism in humans. Pharmacogenomics J 7(6):380–385

Iskedjian M, Bereza B, Gordon A, Piwko C, Einarson TR (2007) Meta-analysis of cannabis based treatments for neuropathic and multiple sclerosis-related pain. Curr Med Res Opin 23(1):17–24

Itoh T, Abe K, Zoghbi SS, Inoue O, Hong J, Imaizumi M et al (2009) PET measurement of the in vivo affinity of 11C-(R)-rolipram and the density of its target, phosphodiesterase-4, in the brains of conscious and anesthetized rats. J Nucl Med 50(5):749–756

Iversen L (2003) Cannabis and the brain. Brain 126(Pt 6):1252–1270

Jbilo O, Ravinet-Trillou C, Arnone M, Buisson I, Bribes E, Peleraux A et al (2005) The CB1 receptor antagonist rimonabant reverses the diet-induced obesity phenotype through the regulation of lipolysis and energy balance. FASEB J 19(11):1567–1569

Jenko KJ, Hirvonen J, Henter ID, Anderson KB, Zoghbi SS, Hyde TM et al (2012) Binding of a tritiated inverse agonist to cannabinoid CB1 receptors is increased in patients with Schizophrenia. Schizophr Res 141(2–3):185–188

Jetly R, Heber A, Fraser G, Boisvert D (2015) The efficacy of nabilone, a synthetic cannabinoid, in the treatment of PTSD-associated nightmares: a preliminary randomized, double-blind, placebo-controlled cross-over design study. Psychoneuroendocrinology 51:585–588

Jin KL, Mao XO, Goldsmith PC, Greenberg DA (2000) CB1 cannabinoid receptor induction in experimental stroke. Ann Neurol 48(2):257–261

Johnson DS, Stiff C, Lazerwith SE, Kesten SR, Fay LK, Morris M et al (2010) Discovery of PF-04457845: a highly potent, orally bioavailable, and selective urea FAAH inhibitor. ACS Med Chem Lett 2(2):91–96

Joshi N, Onaivi ES (2019) Endocannabinoid system components: overview and tissue distribution. Adv Exp Med Biol 1162:1–12

Joshi A, Li W, Sanabria S, Holahan M, Purcell M, Declercq R et al (2012) Translational studies with [^{11}C]MK-3168, a PET tracer for fatty acid amide hydrolase (FAAH). J Nucl Med 53(Suppl. 1):397

Kallinen A, Boyd R, Lane S, Bhalla R, Mardon K, Stimson DHR et al (2019) Synthesis and in vitro evaluation of fluorine-18 benzimidazole sulfones as CB2 PET-radioligands. Org Biomol Chem 17(20):5086–5098

Katoch-Rouse R, Chefer SI, Pavlova OA, Vaupel DB, Matochik JA, Caulder T, et al., (Eds.) (2002) Development of C-11-NIDA-41020, a potential radiotracer for studying cerebral cannabinoid receptors (CB1) by PET. In: IX Symposium on the Medical Applications of Cyclotrons. Turku, Finland

Katoch-Rouse R, Pavlova OA, Caulder T, Hoffman AF, Mukhin AG, Horti AG (2003) Synthesis, structure-activity relationship, and evaluation of SR141716 analogues: development of central cannabinoid receptor ligands with lower lipophilicity. J Med Chem 46(4):642–645

Kelly DL, Gorelick DA, Conley RR, Boggs DL, Linthicum J, Liu F et al (2011) Effects of the cannabinoid-1 receptor antagonist rimonabant on psychiatric symptoms in overweight people with Schizophrenia: a randomized, double-blind, pilot study. J Clin Psychopharmacol 31(1):86–91

Kim K, Moore DH, Makriyannis A, Abood ME (2006) AM1241, a cannabinoid CB(2) receptor selective compound, delays disease progression in a mouse model of amyotrophic lateral sclerosis. Eur J Pharmacol 542(1–3):100–105

Kimbrel NA, Meyer EC, BB DB, Gulliver SB, Morissette SB (2018) The impact of Cannabis use disorder on suicidal and nonsuicidal self-injury in Iraq/Afghanistan-Era veterans with and without mental health disorders. Suicide Life Threat Behav 48(2):140–148

Kleczkowska P, Smaga I, Filip M, Bujalska-Zadrozny M (2016) Cannabinoid ligands and alcohol addiction: a promising therapeutic tool or a Humbug? Neurotox Res 29(1):173–196

Klein TW (2005) Cannabinoid-based drugs as anti-inflammatory therapeutics. Nat Rev Immunol 5(5):400–411

Koeppe RA, Frey KA, Snyder SE, Meyer P, Kilbourn MR, Kuhl DE (1999) Kinetic modeling of N-[^{11}C]methylpiperidin-4-yl propionate: alternatives for analysis of an irreversible positron emission tomography trace for measurement of acetylcholinesterase activity in human brain. J Cereb Blood Flow Metab 19(10):1150–1163

Kogan NM, Mechoulam R (2007) Cannabinoids in health and disease. Dialogues Clin Neurosci 9(4):413–430

Kozak KR, Crews BC, Morrow JD, Wang LH, Ma YH, Weinander R et al (2002) Metabolism of the endocannabinoids, 2-arachidonoylglycerol and anandamide, into prostaglandin, thromboxane, and prostacyclin glycerol esters and ethanolamides. J Biol Chem 277(47):44877–44885

Kubinyi H (1995) The quantitative analysis of structure-activity relationships. In: Wolff ME (ed) Burger's medicinal chemistry and drug discovery, pp 497–571

Kumata K, Yui J, Hatori A, Maeda J, Xie L, Ogawa M et al (2015) Development of [(11)C]MFTC for PET imaging of fatty acid amide hydrolase in rat and monkey brains. ACS Chem Neurosci 6(2):339–346

Kumata K, Yui J, Zhang Y, Kurihara Y, Ogawa M, Mori W et al (2017) [(11)C]BCTC: Radiosynthesis and in vivo binding to transient receptor potential vanilloid subfamily member 1 (TRPV1) receptor in the mouse trigeminal nerve. Bioorg Med Chem Lett 27(19):4521–4524

La Rana G, Russo R, Campolongo P, Bortolato M, Mangieri RA, Cuomo V et al (2006) Modulation of neuropathic and inflammatory pain by the endocannabinoid transport inhibitor AM404 [N-(4-hydroxyphenyl)-eicosa-5,8,11,14-tetraenamide]. J Pharmacol Exp Ther 317(3):1365–1371

Lahesmaa M, Eriksson O, Gnad T, Oikonen V, Bucci M, Hirvonen J et al (2018) Cannabinoid Type 1 receptors are upregulated during acute activation of brown adipose tissue. Diabetes 67(7):1226–1236

Lan R, Gatley SJ, Makriyannis A (1996) Preparation of iodine-123 labeled AM251: a potential SPECT radioligand for the brain cannabinoid CB1 receptor. J Label Compd Radiopharm 38(10):875–881

Lan R, Liu Q, Fan P, Lin S, Fernando SR, McCallion D et al (1999) Structure-activity relationships of pyrazole derivatives as cannabinoid receptor antagonists. J Med Chem 42(4):769–776

Laprairie RB, Bagher AM, Kelly ME, Denovan-Wright EM (2016) Biased Type 1 cannabinoid receptor signaling influences neuronal viability in a cell culture model of Huntington disease. Mol Pharmacol 89(3):364–375

Laruelle M, Abi-Dargham A, al-Tikriti MS, Baldwin RM, Zea-Ponce Y, Zoghbi SS et al (1994) SPECT quantification of [123I]iomazenil binding to benzodiazepine receptors in nonhuman primates: II. Equilibrium analysis of constant infusion experiments and correlation with in vitro parameters. J Cereb Blood Flow Metab 14(3):453–465

Lastres-Becker I, Cebeira M, de Ceballos ML, Zeng BY, Jenner P, Ramos JA et al (2001) Increased cannabinoid CB1 receptor binding and activation of GTP-binding proteins in the basal ganglia of patients with Parkinson's syndrome and of MPTP-treated marmosets. Eur J Neurosci 14(11):1827–1832

Lastres-Becker I, De Miguel R, Fernandez-Ruiz JJ (2003) The endocannabinoid system and Huntington's disease. Curr Drug Targets CNS Neurol Disord 2(5):335–347

Laurikainen H, Tuominen L, Tikka M, Merisaari H, Armio RL, Sormunen E et al (2019) Sex difference in brain CB1 receptor availability in man. NeuroImage 184:834–842

Laviolette SR, Grace AA (2006) The roles of cannabinoid and dopamine receptor systems in neural emotional learning circuits: implications for schizophrenia and addiction. Cell Mol Life Sci 63(14):1597–1613

Le Foll B, Goldberg SR (2005) Cannabinoid CB1 receptor antagonists as promising new medications for drug dependence. J Pharmacol Exp Ther 312(3):875–883

Le Foll B, Gorelick DA, Goldberg SR (2009) The future of endocannabinoid-oriented clinical research after CB1 antagonists. Psychopharmacology 205(1):171–174

Lee HK, Choi EB, Pak CS (2009) The current status and future perspectives of studies of cannabinoid receptor 1 antagonists as anti-obesity agents. Curr Top Med Chem 9(6):482–503

Lee MC, Ploner M, Wiech K, Bingel U, Wanigasekera V, Brooks J et al (2013) Amygdala activity contributes to the dissociative effect of cannabis on pain perception. Pain 154(1):124–134

Leroy S, Griffon N, Bourdel MC, Olie JP, Poirier MF, Krebs MO (2001) Schizophrenia and the cannabinoid receptor type 1 (CB1): association study using a single-base polymorphism in coding exon 1. Am J Med Genet 105(8):749–752

Levenes C, Daniel H, Soubrie P, Crepel F (1998) Cannabinoids decrease excitatory synaptic transmission and impair long-term depression in rat cerebellar Purkinje cells. J Physiol 510(Pt 3):867–879

Leweke FM, Piomelli D, Pahlisch F, Muhl D, Gerth CW, Hoyer C et al (2012) Cannabidiol enhances anandamide signaling and alleviates psychotic symptoms of schizophrenia. Transl Psychiatry 2:e94

Li Y, Kim J (2015) Neuronal expression of CB2 cannabinoid receptor mRNAs in the mouse hippocampus. Neuroscience 311:253–267

Li Z, Gifford A, Liu Q, Thotapally R, Ding YS, Makriyannis A et al (2005) Candidate PET radio-ligands for cannabinoid CB1 receptors: [¹⁸F]AM5144 and related pyrazole compounds. Nucl Med Biol 32(4):361–366

Li W, Sanabria-Bohorquez S, Joshi A, Cook J, Halahan M, Posaves D et al (2011) The discovery and characterization of [¹¹C]MK-3168, a novel PET tracer for imaging Fatty Acid Amide Hydrolase (FAAH). J Label Compd Radiopharm 54(Suppl 1):S38

Lin LS, Lanza TJ Jr, Jewell JP, Liu P, Shah SK, Qi H et al (2006) Discovery of N-[(1S,2S)-3-(4-Chlorophenyl)-2-   (3-cyanophenyl)-1-methylpropyl]-2-methyl-2-{5-(trifluoromethyl)pyridin-2-yl]oxy}propanamide (MK-0364), a novel, acyclic cannabinoid-1 receptor inverse agonist for the treatment of obesity. J Med Chem 49(26):7584–7587

Lin LS, Ha S, Ball RG, Tsou NN, Castonguay LA, Doss GA et al (2008) Conformational analysis and receptor docking of N-[(1S,2S)-3-(4-chlorophenyl)-2-(3-cyanophenyl)-1-methylpropyl]-2-methyl-2 -{5-(trifluoromethyl)pyridin-2-yl]oxy}propanamide (taranabant, MK-0364), a novel, acyclic cannabinoid-1 receptor inverse agonist. J Med Chem 51(7):2108–2114

Liow JS, Lu S, McCarron JA, Hong J, Musachio JL, Pike VW et al (2007) Effect of a P-glycoprotein inhibitor, Cyclosporin A, on the disposition in rodent brain and blood of the 5-HT1A receptor radioligand, [11C](R)-(−)-RWAY. Synapse 61(2):96–105

Liu P, Hamill TG, Chioda M, Chobanian H, Fung S, Guo Y et al (2013) Discovery of MK-3168: A PET tracer for imaging brain fatty acid amide hydrolase. ACS Med Chem Lett 4(6):509–513

Lopez-Sendon Moreno JL, Garcia Caldentey J, Trigo Cubillo P, Ruiz Romero C, Garcia Ribas G, Alonso Arias MA et al (2016) A double-blind, randomized, cross-over, placebo-controlled, pilot trial with Sativex in Huntington's disease. J Neurol 263(7):1390–1400

Lotsch J, Weyer-Menkhoff I, Tegeder I (2018) Current evidence of cannabinoid-based analgesia obtained in preclinical and human experimental settings. Eur J Pain 22(3):471–484

Lowe DJE, Sasiadek JD, Coles AS, George TP (2019) Cannabis and mental illness: a review. Eur Arch Psychiatry Clin Neurosci 269(1):107–120

Ly HG, Ceccarini J, Weltens N, Bormans G, Van Laere K, Tack J et al (2015) Increased cerebral cannabinoid-1 receptor availability is a stable feature of functional dyspepsia: a [F]MK-9470 PET study. Psychother Psychosom 84(3):149–158

Lynn AB, Herkenham M (1994) Localization of cannabinoid receptors and nonsaturable high-density cannabinoid binding sites in peripheral tissues of the rat: implications for receptor-mediated immune modulation by cannabinoids. J Pharmacol Exp Ther 268(3):1612–1623

Mach F, Steffens S (2008) The role of the endocannabinoid system in atherosclerosis. J Neuroendocrinol 20(Suppl 1):53–57

Makriyannis A, Deng H (2001) Preparation of cannabimimetic indole derivatives with cannabi-noid CB1 or CB2 receptor binding affinity patent WO 01/28557

Malone DT, Hill MN, Rubino T (2010) Adolescent cannabis use and psychosis: epidemiology and neurodevelopmental models. Br J Pharmacol 160(3):511–522

Manterola A, Bernal-Chico A, Cipriani R, Canedo-Antelo M, Moreno-Garcia A, Martin-Fontecha M et al (2018) Deregulation of the endocannabinoid system and therapeutic potential of ABHD6 blockade in the cuprizone model of demyelination. Biochem Pharmacol 157:189–201

Manuel I, Gonzalez de San Roman E, Giralt MT, Ferrer I, Rodriguez-Puertas R (2014) Type-1 cannabinoid receptor activity during Alzheimer's disease progression. J Alzheimers Dis 42(3):761–766

Marconi A, Di Forti M, Lewis CM, Murray RM, Vassos E (2016) Meta-analysis of the association between the level of cannabis use and risk of psychosis. Schizophr Bull 42(5):1262–1269

Maresz K, Carrier EJ, Ponomarev ED, Hillard CJ, Dittel BN (2005) Modulation of the canna-binoid CB2 receptor in microglial cells in response to inflammatory stimuli. J Neurochem 95(2):437–445

Maresz K, Pryce G, Ponomarev ED, Marsicano G, Croxford JL, Shriver LP et al (2007) Direct suppression of CNS autoimmune inflammation via the cannabinoid receptor CB1 on neurons and CB2 on autoreactive T cells. Nat Med 13(4):492–497

Marsicano G, Goodenough S, Monory K, Hermann H, Eder M, Cannich A et al (2003) CB1 can-nabinoid receptors and on-demand defense against excitotoxicity. Science 302(5642):84–88

Martin BR, Sim-Selley LJ, Selley DE (2004) Signaling pathways involved in the development of cannabinoid tolerance. Trends Pharmacol Sci 25(6):325–330

Martin-Santos R, Fagundo AB, Crippa JA, Atakan Z, Bhattacharyya S, Allen P et al (2010) Neuroimaging in cannabis use: a systematic review of the literature. Psychol Med 40(3):383–398

Massa F, Storr M, Lutz B (2005) The endocannabinoid system in the physiology and pathophysiology of the gastrointestinal tract. J Mol Med 83(12):944–954

Mathews WB, Ravert HT, Musachio JL, Frank RA, Rinaldi-Carmona M, Barth F et al (1999) Synthesis of [18F] SR144385: A selective radioligand for positron emission tomographic studies of brain cannabinoid receptors. J Label Compd Radiopharm 42:589–596

Mathews WB, Scheffel U, Finley P, Ravert HT, Frank RA, Rinaldi-Carmona M et al (2000) Biodistribution of [18F] SR144385 and [18F] SR147963: selective radioligands for positron emission tomographic studies of brain cannabinoid receptors. Nucl Med Biol 27(8):757–762

Mathews WB, Scheffel U, Rauseo PA, Ravert HT, Frank RA, Ellames GJ et al (2002) Carbon-11 labeled radioligands for imaging brain cannabinoid receptors. Nucl Med Biol 29(6):671–677

Matsuda LA, Lolait SJ, Brownstein MJ, Young AC, Bonner TI (1990) Structure of a cannabinoid receptor and functional expression of the cloned cDNA. Nature 346(6284):561–564

McGuire P, Robson P, Cubala WJ, Vasile D, Morrison PD, Barron R et al (2018) Cannabidiol (CBD) as an adjunctive therapy in Schizophrenia: a multicenter randomized controlled trial. Am J Psychiatry 175(3):225–231

Meltzer HY, Arvanitis L, Bauer D, Rein W, Meta-Trial SG (2004) Placebo-controlled evaluation of four novel compounds for the treatment of schizophrenia and schizoaffective disorder. Am J Psychiatry 161(6):975–984

Miederer I, Maus S, Zwiener I, Podoprygorina G, Meshcheryakov D, Lutz B et al (2013) Evaluation of cannabinoid type 1 receptor expression in the rat brain using [(1)(8)F]MK-9470 microPET. Eur J Nucl Med Mol Imaging 40(11):1739–1747

Miederer I, Buchholz HG, Kronfeld A, Maus S, Weyer-Elberich V, Mildenberger P et al (2018) Pharmacokinetics of the cannabinoid receptor ligand [(18) F]MK-9470 in the rat brain - Evaluation of models using microPET. Med Phys 45(2):725–734

Minichino A, Senior M, Brondino N, Zhang SH, Godwlewska BR, Burnet PWJ et al (2019) Measuring disturbance of the endocannabinoid system in psychosis: a systematic review and meta-analysis. JAMA Psychiat

Minocci D, Massei J, Martino A, Milianti M, Piz L, Di Bello D et al (2011) Genetic association between bipolar disorder and 524A>C (Leu133Ile) polymorphism of CNR2 gene, encoding for CB2 cannabinoid receptor. J Affect Disord 134(1–3):427–430

Moldovan RP, Teodoro R, Gao Y, Deuther-Conrad W, Kranz M, Wang Y et al (2016) Development of a high-affinity PET radioligand for imaging cannabinoid subtype 2 receptor. J Med Chem 59(17):7840–7855

Moller CI, Tait RJ, Byrne DG (2013) Self-harm, substance use and psychological distress in the Australian general population. Addiction 108(1):211–220

Monteleone P, Bifulco M, Di Filippo C, Gazzerro P, Canestrelli B, Monteleone F et al (2009) Association of CNR1 and FAAH endocannabinoid gene polymorphisms with anorexia nervosa and bulimia nervosa: evidence for synergistic effects. Genes Brain Behav 8(7):728–732

Monteleone AM, Di Marzo V, Aveta T, Piscitelli F, Dalle Grave R, Scognamiglio P et al (2015) Deranged endocannabinoid responses to hedonic eating in underweight and recently weight-restored patients with anorexia nervosa. Am J Clin Nutr 101(2):262–269

Moranta D, Esteban S, Garcia-Sevilla JA (2006) Ethanol desensitizes cannabinoid CB(1) receptors modulating monoamine synthesis in the rat brain in vivo. Neurosci Lett 392(1–2):58–61

Moreira FA, Wotjak CT (2010) Cannabinoids and anxiety. Curr Top Behav Neurosci 2:429–450

Moreira FA, Kaiser N, Monory K, Lutz B (2008) Reduced anxiety-like behaviour induced by genetic and pharmacological inhibition of the endocannabinoid-degrading enzyme fatty acid amide hydrolase (FAAH) is mediated by CB1 receptors. Neuropharmacology 54(1):141–150

Mori F, Ljoka C, Nicoletti CG, Kusayanagi H, Buttari F, Giordani L et al (2014) CB1 receptor affects cortical plasticity and response to physiotherapy in multiple sclerosis. Neurol Neuroimmunol Neuroinflamm 1(4):e48

Mori W, Hatori A, Zhang Y, Kurihara Y, Yamasaki T, Xie L et al (2019) Radiosynthesis and evaluation of a novel monoacylglycerol lipase radiotracer: 1,1,1,3,3,3-hexafluoropropan-2-yl-3-(1-benzyl-1H-pyrazol-3-yl)azetidine-1-[(11)C]carboxylate. Bioorg Med Chem 27(16):3568–3573

Morton GJ, Cummings DE, Baskin DG, Barsh GS, Schwartz MW (2006) Central nervous system control of food intake and body weight. Nature 443(7109):289–295

Mu L, Bieri D, Slavik R, Drandarov K, Muller A, Cermak S et al (2013) Radiolabeling and in vitro/in vivo evaluation of N-(1-adamantyl)-8-methoxy-4-oxo-1-phenyl-1,4-dihydroquinoline-3-carboxamide as a PET probe for imaging cannabinoid type 2 receptor. J Neurochem 126(5):616–624

Mukhopadhyay S, Das S, Williams EA, Moore D, Jones JD, Zahm DS et al (2006) Lipopolysaccharide and cyclic AMP regulation of CB(2) cannabinoid receptor levels in rat brain and mouse RAW 264.7 macrophages. J Neuroimmunol 181(1–2):82–92

Muller C, Morales P, Reggio PH (2018) Cannabinoid ligands targeting TRP channels. Front Mol Neurosci 11:487

Mulpuri Y, Marty VN, Munier JJ, Mackie K, Schmidt BL, Seltzman HH et al (2018) Synthetic peripherally-restricted cannabinoid suppresses chemotherapy-induced peripheral neuropathy pain symptoms by CB1 receptor activation. Neuropharmacology 139:85–97

Munro S, Thomas KL, Abu-Shaar M (1993) Molecular characterization of a peripheral receptor for cannabinoids. Nature 365(6441):61–65

Murray RM, Morrison PD, Henquet C, Di Forti M (2007) Cannabis, the mind and society: the harsh realities. Nat Rev Neurosci 8(11):885–895

Navarrete F, Garcia-Gutierrez MS, Aracil-Fernandez A, Lanciego JL, Manzanares J (2018) Cannabinoid CB1 and CB2 receptors, and monoacylglycerol lipase gene expression alterations in the Basal Ganglia of patients with Parkinson's disease. Neurotherapeutics 15(2):459–469

Neumeister A, Normandin MD, Murrough JW, Henry S, Bailey CR, Luckenbaugh DA et al (2012) Positron emission tomography shows elevated cannabinoid CB1 receptor binding in men with alcohol dependence. Alcohol Clin Exp Res 36(12):2104–2109

Neumeister A, Normandin MD, Pietrzak RH, Piomelli D, Zheng MQ, Gujarro-Anton A et al (2013) Elevated brain cannabinoid CB1 receptor availability in post-traumatic stress disorder: a positron emission tomography study. Mol Psychiatry 18(9):1034–1040

Newell KA, Deng C, Huang XF (2006) Increased cannabinoid receptor density in the posterior cingulate cortex in Schizophrenia. Exp Brain Res 172(4):556–560

Ni R, Mu L, Ametamey S (2019) Positron emission tomography of type 2 cannabinoid receptors for detecting inflammation in the central nervous system. Acta Pharmacol Sin 40(3):351–357

Nissen SE, Nicholls SJ, Wolski K, Rodes-Cabau J, Cannon CP, Deanfield JE et al (2008) Effect of rimonabant on progression of atherosclerosis in patients with abdominal obesity and coronary artery disease: the STRADIVARIUS randomized controlled trial. JAMA 299(13):1547–1560

Nogueiras R, Veyrat-Durebex C, Suchanek PM, Klein M, Tschop J, Caldwell C et al (2008) Peripheral, but not central, CB1 antagonism provides food intake-independent metabolic benefits in diet-induced obese rats. Diabetes 57(11):2977–2991

Nojiri Y, Ishiwata K (2008) Qinggeletu, Tobiishi S, Sasada T, Yamamoto F, et al. Radiosynthesis and biodistribution in mice of a 18F-labeled analog of O-1302 for use in cerebral CB1 cannabinoid receptor imaging. Biol Pharm Bull 31(6):1274–1278

Normandin MD, Weinzimmer DP, Ropchan J, Labaree D, Lin KS, Mason NS et al (2010a) Kinetic modeling of CB1 PET tracer [11C]OMAR in rhesus monkeys and humans. J Nucl Med 51(Suppl 2):216

Normandin MD, Zheng M-Q, Ropchan J, Najafzadeh S, Hull R, Quin W et al (2010b) Test-retest reproducibility and gender differences in binding of CB1 PET tracer [^{11}C]OMAR in humans. J Nucl Med 51(Suppl 2):51

Normandin MD, Zheng MQ, Lin KS, Mason NS, Lin SF, Ropchan J et al (2015) Imaging the cannabinoid CB1 receptor in humans with [^{11}C]OMAR: assessment of kinetic analysis methods, test-retest reproducibility, and gender differences. J Cereb Blood Flow Metab 35(8):1313–1322

Nowak KL, Vinod KY, Hungund BL (2006) Pharmacological manipulation of cb1 receptor function alters development of tolerance to alcohol. Alcohol Alcohol 41(1):24–32

Oesch S, Walter D, Wachtel M, Pretre K, Salazar M, Guzman M et al (2009) Cannabinoid receptor 1 is a potential drug target for treatment of translocation-positive rhabdomyosarcoma. Mol Cancer Ther 8(7):1838–1845

Onaivi ES, Ishiguro H, Gong JP, Patel S, Perchuk A, Meozzi PA et al (2006) Discovery of the presence and functional expression of cannabinoid CB2 receptors in brain. Ann N Y Acad Sci 1074:514–536

Ooms M, Rietjens R, Rangarajan JR, Vunckx K, Valdeolivas S, Maes F et al (2014) Early decrease of type 1 cannabinoid receptor binding and phosphodiesterase 10A activity in vivo in R6/2 Huntington mice. Neurobiol Aging 35(12):2858–2869

Orgado JM, Fernandez-Ruiz J, Romero J (2009) The endocannabinoid system in neuropathological states. Int Rev Psychiatry 21(2):172–180

Ortiz-Medina MB, Perea M, Torales J, Ventriglio A, Vitrani G, Aguilar L et al (2018) Cannabis consumption and psychosis or Schizophrenia development. Int J Soc Psychiatry 64(7):690–704

Otrubova K, Ezzili C, Boger DL (2011) The discovery and development of inhibitors of fatty acid amide hydrolase (FAAH). Bioorg Med Chem Lett 21(16):4674–4685

Pacher P, Batkai S, Kunos G (2006) The endocannabinoid system as an emerging target of pharmacotherapy. Pharmacol Rev 58(3):389–462

Palazuelos J, Davoust N, Julien B, Hatterer E, Aguado T, Mechoulam R et al (2008) The CB(2) cannabinoid receptor controls myeloid progenitor trafficking: involvement in the pathogenesis of an animal model of multiple sclerosis. J Biol Chem 283(19):13320–13329

Palazuelos J, Aguado T, Pazos MR, Julien B, Carrasco C, Resel E et al (2009) Microglial CB2 cannabinoid receptors are neuroprotective in Huntington's disease excitotoxicity. Brain 132(Pt 11):3152–3164

Paldy E, Bereczki E, Santha M, Wenger T, Borsodi A, Zimmer A et al (2008) CB(2) cannabinoid receptor antagonist SR144528 decreases mu-opioid receptor expression and activation in mouse brainstem: role of CB(2) receptor in pain. Neurochem Int 53(6–8):309–316

Pandey MK, DeGrado TR, Qian K, Jacobson MS, Hagen CE, Duclos RI Jr et al (2014) Synthesis and preliminary evaluation of N-(16-18F-fluorohexadecanoyl)ethanolamine (18F-FHEA) as a PET probe of N-acylethanolamine metabolism in mouse brain. ACS Chem Neurosci 5(9):793–802

Paradisi A, Oddi S, Maccarrone M (2006) The endocannabinoid system in ageing: a new target for drug development. Curr Drug Targets 7(11):1539–1552

Parmentier-Batteur S, Jin K, Mao XO, Xie L, Greenberg DA (2002) Increased severity of stroke in CB1 cannabinoid receptor knock-out mice. J Neurosci 22(22):9771–9775

Patel KD, Davison JS, Pittman QJ, Sharkey KA (2010) Cannabinoid CB(2) receptors in health and disease. Curr Med Chem 17:1393–1410

Patel S, Hill MN, Cheer JF, Wotjak CT, Holmes A (2017) The endocannabinoid system as a target for novel anxiolytic drugs. Neurosci Biobehav Rev 76(Pt A):56–66

Pertwee RG (1999) Pharmacology of cannabinoid receptor ligands. Curr Med Chem 6(8):635–664

Pertwee RG (2009) Emerging strategies for exploiting cannabinoid receptor agonists as medicines. Br J Pharmacol 156(3):397–411

Pertwee RG (2014) Elevating endocannabinoid levels: pharmacological strategies and potential therapeutic applications. Proc Nutr Soc 73(1):96–105

Pertwee RG (2015) Endocannabinoids and their pharmacological actions. Handb Exp Pharmacol 231:1–37

Pertwee RG, Howlett AC, Abood ME, Alexander SP, Di Marzo V, Elphick MR et al (2010) International Union of Basic and Clinical Pharmacology. LXXIX. Cannabinoid receptors and their ligands: beyond CB and CB. Pharmacol Rev 62(4):588–631

Pietrzak RH, Huang Y, Corsi-Travali S, Zheng MQ, Lin SF, Henry S et al (2014) Cannabinoid type 1 receptor availability in the amygdala mediates threat processing in trauma survivors. Neuropsychopharmacology 39(11):2519–2528

Pike VW (2009) PET radiotracers: crossing the blood-brain barrier and surviving metabolism. Trends Pharmacol Sci 30(8):431–440

Piomelli D (2003) The molecular logic of endocannabinoid signalling. Nat Rev Neurosci 4(11):873–884

Piomelli D, Tarzia G, Duranti A, Tontini A, Mor M, Compton TR et al (2006) Pharmacological profile of the selective FAAH inhibitor KDS-4103 (URB597). CNS Drug Rev 12(1):21–38

Pisanti S, Bifulco M (2009) Endocannabinoid system modulation in cancer biology and therapy. Pharmacol Res 60(2):107–116

Pi-Sunyer FX, Aronne LJ, Heshmati HM, Devin J, Rosenstock J (2006) Effect of rimonabant, a cannabinoid-1 receptor blocker, on weight and cardiometabolic risk factors in overweight or obese patients: RIO-North America: a randomized controlled trial. JAMA 295(7):761–775

Postnov A, Schmidt M, Penson J, Van Hecken A, Zannikos P, Pemberton D et al (2015) Kinetic modeling of Fatty Acid Amide Hydrolase (FAAH) enzyme occupancy after JNJ-42165279 inhibition based on ^{11}C-MK-3168 PET imaging of human brain. J Nucl Med 56(Suppl. 3):362

Postnov A, Schmidt ME, Pemberton DJ, de Hoon J, van Hecken A, van den Boer M et al (2018) Fatty acid amide hydrolase inhibition by JNJ-42165279: a multiple-ascending dose and a positron emission tomography study in healthy volunteers. Clin Transl Sci 11(4):397–404

Pottier G, Gomez-Vallejo V, Padro D, Boisgard R, Dolle F, Llop J et al (2017) PET imaging of cannabinoid type 2 receptors with [(11)C]A-836339 did not evidence changes following neuroinflammation in rats. J Cereb Blood Flow Metab 37(3):1163–1178

Price MR, Baillie GL, Thomas A, Stevenson LA, Easson M, Goodwin R et al (2005) Allosteric modulation of the cannabinoid CB1 receptor. Mol Pharmacol 68(5):1484–1495

Pryce G, Baker D (2007) Control of spasticity in a multiple sclerosis model is mediated by CB1, not CB2, cannabinoid receptors. Br J Pharmacol 150(4):519–525

Pryce G, Baker D (2015) Endocannabinoids in multiple sclerosis and amyotrophic lateral sclerosis. Handb Exp Pharmacol 231:213–231

Qin L, Wu X, Block ML, Liu Y, Breese GR, Hong JS et al (2007) Systemic LPS causes chronic neuroinflammation and progressive neurodegeneration. Glia 55(5):453–462

Ramirez BG, Blazquez C, Gomez del Pulgar T, Guzman M, de Ceballos ML (2005) Prevention of Alzheimer's disease pathology by cannabinoids: neuroprotection mediated by blockade of microglial activation. J Neurosci 25(8):1904–1913

Ranganathan M, Cortes-Briones J, Radhakrishnan R, Thurnauer H, Planeta B, Skosnik P et al (2016) Reduced brain cannabinoid receptor availability in Schizophrenia. Biol Psychiatry 79(12):997–1005

Reichenbach ZW, Li H, Ward SJ, Tuma RF (2016) The CB1 antagonist, SR141716A, is protective in permanent photothrombotic cerebral ischemia. Neurosci Lett 630:9–15

Rempel BP, Price EW, Phenix CP (2017) Molecular imaging of hydrolytic enzymes using PET and SPECT. Mol Imaging 16:1536012117717852

Riano Barros DA, McGinnity CJ, Rosso L, Heckemann RA, Howes OD, Brooks DJ et al (2014) Test-retest reproducibility of cannabinoid-receptor type 1 availability quantified with the PET ligand [(1)(1)C]MePPEP. NeuroImage 97:151–162

Riedel G, Davies SN (2005) Cannabinoid function in learning, memory and plasticity. Handb Exp Pharmacol 168:445–477

Rinaldi-Carmona M, Barth F, Heaulme M, Shire D, Calandra B, Congy C et al (1994) SR141716A, a potent and selective antagonist of the brain cannabinoid receptor. FEBS Lett 350(2–3):240–244

Rinaldi-Carmona M, Pialot F, Congy C, Redon E, Barth F, Bachy A et al (1996) Characterization and distribution of binding sites for [3H]-SR 141716A, a selective brain (CB1) cannabinoid receptor antagonist, in rodent brain. Life Sci 58(15):1239–1247

Rinaldi-Carmona M, Barth F, Millan J, Derocq JM, Casellas P, Congy C et al (1998) SR 144528, the first potent and selective antagonist of the CB2 cannabinoid receptor. J Pharmacol Exp Ther 284(2):644–650

Rodriguez de Fonseca F, Cebeira M, Ramos JA, Martin M, Fernandez-Ruiz JJ (1994) Cannabinoid receptors in rat brain areas: sexual differences, fluctuations during estrous cycle and changes after gonadectomy and sex steroid replacement. Life Sci 54(3):159–170

Rog DJ, Nurmikko TJ, Friede T, Young CA (2005) Randomized, controlled trial of cannabis-based medicine in central pain in multiple sclerosis. Neurology 65(6):812–819

Romero J, Garcia L, Fernandez-Ruiz JJ, Cebeira M, Ramos JA (1995) Changes in rat brain cannabinoid binding sites after acute or chronic exposure to their endogenous agonist, anandamide, or to delta 9-tetrahydrocannabinol. Pharmacol Biochem Behav 51(4):731–737

Romero J, Hillard CJ, Calero M, Rabano A (2002) Fatty acid amide hydrolase localization in the human central nervous system: an immunohistochemical study. Brain Res Mol Brain Res 100(1–2):85–93

Rosenstock J, Hollander P, Chevalier S, Iranmanesh A (2008) The SERENADE Trial: effects of monotherapy with rimonabant, the first selective CB1 receptor antagonist, on glycemic control, body weight and lipid profile in drug-naive Type 2 diabetes. Diabetes Care

Rossi S, Bernardi G, Centonze D (2010) The endocannabinoid system in the inflammatory and neurodegenerative processes of multiple sclerosis and of amyotrophic lateral sclerosis. Exp Neurol 224(1):92–102

Rotstein BH, Wey HY, Shoup TM, Wilson AA, Liang SH, Hooker JM et al (2014) PET imaging of fatty acid amide hydrolase with [(18)F]DOPP in nonhuman primates. Mol Pharm 11(11):3832–3838

Rusjan PM, Wilson AA, Mizrahi R, Boileau I, Chavez SE, Lobaugh NJ et al (2013) Mapping human brain fatty acid amide hydrolase activity with PET. J Cereb Blood Flow Metab 33(3):407–414

Rusjan PM, Knezevic D, Boileau I, Tong J, Mizrahi R, Wilson AA et al (2018) Voxel level quantification of [^{11}C]CURB, a radioligand for fatty acid amide hydrolase, using high resolution positron emission tomography. PLoS One 13(2):e0192410

Saccomanni G, Pascali G, Carlo SD, Panetta D, De Simone M, Bertini S et al (2015) Design, synthesis and preliminary evaluation of (18)F-labelled 1,8-naphthyridin- and quinolin-2-one-3-carboxamide derivatives for PET imaging of CB2 cannabinoid receptor. Bioorg Med Chem Lett 25(12):2532–2535

Sadovski O, Hicks JW, Parkes J, Raymond R, Nobrega J, Houle S et al (2013) Development and characterization of a promising fluorine-18 labelled radiopharmaceutical for in vivo imaging of fatty acid amide hydrolase. Bioorg Med Chem 21(14):4351–4357

Sagredo O, Gonzalez S, Aroyo I, Pazos MR, Benito C, Lastres-Becker I et al (2009) Cannabinoid CB2 receptor agonists protect the striatum against malonate toxicity: relevance for Huntington's disease. Glia 57(11):1154–1167

Sanabria-Bohorquez SM, Hamill TG, Goffin K, De Lepeleire I, Bormans G, Burns HD et al (2010) Kinetic analysis of the cannabinoid-1 receptor PET tracer [(18)F]MK-9470 in human brain. Eur J Nucl Med Mol Imaging 37(5):920–933

Sandiego CM, Gallezot JD, Pittman B, Nabulsi N, Lim K, Lin SF et al (2015) Imaging robust microglial activation after lipopolysaccharide administration in humans with PET. Proc Natl Acad Sci U S A 112(40):12468–12473

Sapp E, Kegel KB, Aronin N, Hashikawa T, Uchiyama Y, Tohyama K et al (2001) Early and progressive accumulation of reactive microglia in the Huntington disease brain. J Neuropathol Exp Neurol 60(2):161–172

Sarne Y, Mechoulam R (2005) Cannabinoids: between neuroprotection and neurotoxicity. Curr Drug Targets CNS Neurol Disord 4(6):677–684

Schatz AR, Lee M, Condie RB, Pulaski JT, Kaminski NE (1997) Cannabinoid receptors CB1 and CB2: a characterization of expression and adenylate cyclase modulation within the immune system. Toxicol Appl Pharmacol 142(2):278–287

Schlicker E, Kathmann M (2001) Modulation of transmitter release via presynaptic cannabinoid receptors. Trends Pharmacol Sci 22(11):565–572

Secher A, Husum H, Holst B, Egerod KL, Mellerup E (2010) Risperidone treatment increases CB1 receptor binding in rat brain. Neuroendocrinology 91(2):155–168

Segovia G, Mora F, Crossman AR, Brotchie JM (2003) Effects of CB1 cannabinoid receptor modulating compounds on the hyperkinesia induced by high-dose levodopa in the reserpine-treated rat model of Parkinson's disease. Mov Disord 18(2):138–149

Seneca N, Finnema SJ, Farde L, Gulyas B, Wikstrom HV, Halldin C et al (2006) Effect of amphetamine on dopamine D2 receptor binding in nonhuman primate brain: a comparison of the agonist radioligand [^{11}C]MNPA and antagonist [^{11}C]raclopride. Synapse 59(5):260–269

Sevcik J, Masek K (2000) Potential role of cannabinoids in Parkinson's disease. Drugs Aging 16(6):391–395

Shimoda Y, Fujinaga M, Hatori A, Yui J, Zhang Y, Nengaki N et al (2016) N-(3,4-Dimethylisoxazol-5-yl)piperazine-4-[4-(2-fluoro-4-[(11)C]methylphenyl)thia zol-2-yl]-1-carboxamide: A promising positron emission tomography ligand for fatty acid amide hydrolase. Bioorg Med Chem 24(4):627–634

Shoemaker JL, Seely KA, Reed RL, Crow JP, Prather PL (2007) The CB2 cannabinoid agonist AM-1241 prolongs survival in a transgenic mouse model of amyotrophic lateral sclerosis when initiated at symptom onset. J Neurochem 101(1):87–98

Shohami E, Cohen-Yeshurun A, Magid L, Algali M, Mechoulam R (2011) Endocannabinoids and traumatic brain injury. Br J Pharmacol 163(7):1402–1410

Shoup TM, Bonab AA, Wilson AA, Vasdev N (2015) Synthesis and preclinical evaluation of [(1)(8)F]FCHC for neuroimaging of fatty acid amide hydrolase. Mol Imaging Biol 17(2):257–263

Siegfried Z, Kanyas K, Latzer Y, Karni O, Bloch M, Lerer B et al (2004) Association study of cannabinoid receptor gene (CNR1) alleles and anorexia nervosa: differences between restricting and binging/purging subtypes. Am J Med Genet B Neuropsychiatr Genet 125B(1):126–130

Sieradzan KA, Fox SH, Hill M, Dick JP, Crossman AR, Brotchie JM (2001) Cannabinoids reduce levodopa-induced dyskinesia in Parkinson's disease: a pilot study. Neurology 57(11):2108–2111

Sim-Selley LJ, Martin BR (2002) Effect of chronic administration of R-(+)-[2,3-Dihydro-5-methyl-3-[(morpholinyl)methyl]pyrrolo[1,2,3-de]-1,4-benzoxaz inyl]-(1-naphthalenyl)methanone mesylate (WIN55,212-2) or delta(9)-tetrahydrocannabinol on cannabinoid receptor adaptation in mice. J Pharmacol Exp Ther 303(1):36–44

Sipe JC, Chiang K, Gerber AL, Beutler E, Cravatt BF (2002) A missense mutation in human fatty acid amide hydrolase associated with problem drug use. Proc Natl Acad Sci U S A 99(12):8394–8399

Sipe JC, Waalen J, Gerber A, Beutler E (2005) Overweight and obesity associated with a missense polymorphism in fatty acid amide hydrolase (FAAH). Int J Obes Relat Metab Disord 29(7):755–759

Skaddan MB, Zhang L, Johnson DS, Zhu A, Zasadny KR, Coelho RV et al (2012) The synthesis and in vivo evaluation of [(18)F]PF-9811: a novel PET ligand for imaging brain fatty acid amide hydrolase (FAAH). Nucl Med Biol

Slavik R, Grether U, Muller Herde A, Gobbi L, Fingerle J, Ullmer C et al (2015a) Discovery of a high affinity and selective pyridine analog as a potential positron emission tomography imaging agent for cannabinoid type 2 receptor. J Med Chem 58(10):4266–4277

Slavik R, Herde AM, Bieri D, Weber M, Schibli R, Kramer SD et al (2015b) Synthesis, radiolabeling and evaluation of novel 4-oxo-quinoline derivatives as PET tracers for imaging cannabinoid type 2 receptor. Eur J Med Chem 92:554–564

Sloan ME, Gowin JL, Ramchandani VA, Hurd YL, Le Foll B (2017) The endocannabinoid system as a target for addiction treatment: trials and tribulations. Neuropharmacology 124:73–83

Sloan ME, Grant CW, Gowin JL, Ramchandani VA, Le Foll B (2019) Endocannabinoid signaling in psychiatric disorders: a review of positron emission tomography studies. Acta Pharmacol Sin 40(3):342–350

Smart R, Caulkins JP, Kilmer B, Davenport S, Midgette G (2017) Variation in cannabis potency and prices in a newly legal market: evidence from 30 million cannabis sales in Washington state. Addiction 112(12):2167–2177

Smith AM, Dragunow M (2014) The human side of microglia. Trends Neurosci 37(3):125–135

Smith RA, Fathi Z (2005) Recent advances in the research and development of CB(1) antagonists. IDrugs 8(1):53–66

Soyka M, Koller G, Schmidt P, Lesch OM, Leweke M, Fehr C et al (2008) Cannabinoid Receptor 1 blocker rimonabant (SR 141716) for treatment of alcohol dependence: results from a placebo-controlled. Double-Blind Trial. J Clin Psychopharmacol 28(3):317–324

Steffens S, Veillard NR, Arnaud C, Pelli G, Burger F, Staub C et al (2005) Low dose oral cannabinoid therapy reduces progression of atherosclerosis in mice. Nature 434(7034):782–786

Stella N (2010) Cannabinoid and cannabinoid-like receptors in microglia, astrocytes, and astrocy-tomas. Glia 58(9):1017–1030

Stella N, Schweitzer P, Piomelli D (1997) A second endogenous cannabinoid that modulates long-term potentiation. Nature 388(6644):773–778

Sumi N, Nishioku T, Takata F, Matsumoto J, Watanabe T, Shuto H et al (2010) Lipopolysaccharide-activated microglia induce dysfunction of the blood-brain barrier in rat microvascular endothe-lial cells co-cultured with microglia. Cell Mol Neurobiol 30(2):247–253

Suter TM, Chesterfield AK, Bao C, Schaus JM, Krushinski JH, Statnick MA et al (2010) Pharmacological characterization of the cannabinoid CB receptor PET ligand ortholog, [(3) H]MePPEP. Eur J Pharmacol 649(1–3):44–50

Takano A, Gulyas B, Varnas K, Little PB, Noerregaard PK, Jensen NO et al (2014) Low brain CB1 receptor occupancy by a second generation CB1 receptor antagonist TM38837 in comparison with rimonabant in nonhuman primates: a PET study. Synapse 68(3):89–97

Takkinen JS, Lopez-Picon FR, Kirjavainen AK, Pihlaja R, Snellman A, Ishizu T et al (2018) [(18) F]FMPEP-d2 PET imaging shows age- and genotype-dependent impairments in the avail-ability of cannabinoid receptor 1 in a mouse model of Alzheimer's disease. Neurobiol Aging 69:199–208

Tamagnan G, Lu XJ, Gao Y, Amici LA, Baldwin RM, Innis RB (1999) Potential SPECT radioli-gand for cannabinoid receptor. J Label Compd Radiopharm 43:S191–S1S3

Taylor JP, Brown RH Jr, Cleveland DW (2016) Decoding ALS: from genes to mechanism. Nature 539(7628):197–206

Teixeira-Clerc F, Julien B, Grenard P, Tran Van Nhieu J, Deveaux V, Hezode C et al (2008) The endocannabinoid system as a novel target for the treatment of liver fibrosis. Pathol Biol (Paris) 56(1):36–38

Terry G (2009) In vivo imaging of the cannabinoid CB1 receptor using positron emission tomog-raphy. Stockholm, Sweden, Karolinska Institutet

Terry G, Liow JS, Chernet E, Zoghbi SS, Phebus L, Felder CC et al (2008) Positron emission tomography imaging using an inverse agonist radioligand to assess cannabinoid CB1 receptors in rodents. NeuroImage 41(3):690–698

Terry GE, Liow JS, Zoghbi SS, Hirvonen J, Farris AG, Lerner A et al (2009) Quantitation of can-nabinoid CB1 receptors in healthy human brain using positron emission tomography and an inverse agonist radioligand. NeuroImage 48(2):362–370

Terry GE, Hirvonen J, Liow JS, Zoghbi SS, Gladding R, Tauscher JT et al (2010a) Imaging and quantitation of cannabinoid CB1 receptors in human and monkey brains using (18)F-labeled inverse agonist radioligands. J Nucl Med 51(1):112–120

Terry GE, Hirvonen J, Liow JS, Seneca N, Tauscher JT, Schaus JM et al (2010b) Biodistribution and dosimetry in humans of two inverse agonists to image cannabinoid CB1 receptors using positron emission tomography. Eur J Nucl Med Mol Imaging 37(8):1499–1506

Thomae D, Morley TJ, Hamill T, Carroll VM, Papin C, Twardy NM et al (2014) Automated one-step radiosynthesis of the CB1 receptor imaging agent [(18) F]MK-9470. J Labelled Comp Radiopharm 57(10):611–614

Thomas EA, Cravatt BF, Danielson PE, Gilula NB, Sutcliffe JG (1997) Fatty acid amide hydrolase, the degradative enzyme for anandamide and oleamide, has selective distribution in neurons within the rat central nervous system. J Neurosci Res 50(6):1047–1052

Timpone JG, Wright DJ, Li N, Egorin MJ, Enama ME, Mayers J et al (1997) The safety and phar-macokinetics of single-agent and combination therapy with megestrol acetate and dronabinol for the treatment of HIV wasting syndrome. The DATRI 004 Study Group. Division of AIDS Treatment Research Initiative. AIDS Res Hum Retrovir 13(4):305–315

Tolon RM, Nunez E, Pazos MR, Benito C, Castillo AI, Martinez-Orgado JA et al (2009) The acti-vation of cannabinoid CB2 receptors stimulates in situ and in vitro beta-amyloid removal by human macrophages. Brain Res 1283:148–154

Tong J, Mizrahi R, Houle S, Kish SJ, Boileau I, Nobrega J et al (2017) Inhibition of fatty acid amide hydrolase by BIA 10-2474 in rat brain. J Cereb Blood Flow Metab 37(11):3635–3639

Tonietto M, Veronese M, Rizzo G, Zanotti-Fregonara P, Lohith TG, Fujita M et al (2015) Improved models for plasma radiometabolite correction and their impact on kinetic quantification in PET studies. J Cereb Blood Flow Metab 35(9):1462–1469

Tonietto M, Rizzo G, Veronese M, Borgan F, Bloomfield PS, Howes O et al (2019) A unified framework for plasma data modeling in dynamic positron emission tomography studies. IEEE Trans Biomed Eng 66(5):1447–1455

Torres E, Gutierrez-Lopez MD, Borcel E, Peraile I, Mayado A, O'Shea E et al (2010) Evidence that MDMA ('ecstasy') increases cannabinoid CB2 receptor expression in microglial cells: role in the neuroinflammatory response in rat brain. J Neurochem 113(1):67–78

Tsujikawa T, Zoghbi SS, Hong J, Donohue SR, Jenko KJ, Gladding RL et al (2014) In vitro and in vivo evaluation of (11)C-SD5024, a novel PET radioligand for human brain imaging of cannabinoid CB1 receptors. NeuroImage 84:733–741

Turkman N, Shavrin A, Ivanov RA, Rabinovich B, Volgin A, Gelovani JG et al (2011) Fluorinated cannabinoid CB2 receptor ligands: synthesis and in vitro binding characteristics of 2-oxoquinoline derivatives. Bioorg Med Chem 19:5698–5707

Turkman N, Shavrin A, Paolillo V, Yeh HH, Flores L, Soghomonian S et al (2012) Synthesis and preliminary evaluation of [(18)F]-labeled 2-oxoquinoline derivatives for PET imaging of cannabinoid CB(2) receptor. Nucl Med Biol 39(4):593–600

Turner SE, Williams CM, Iversen L, Whalley BJ (2017) Molecular pharmacology of phytocannabinoids. Prog Chem Org Nat Prod 103:61–101

Ujike H, Morita Y (2004) New perspectives in the studies on endocannabinoid and cannabis: cannabinoid receptors and Schizophrenia. J Pharmacol Sci 96(4):376–381

Ujike H, Takaki M, Nakata K, Tanaka Y, Takeda T, Kodama M et al (2002) CNR1, central cannabinoid receptor gene, associated with susceptibility to hebephrenic schizophrenia. Mol Psychiatry 7(5):515–518

Urban NB, Martinez D (2012) Neurobiology of addiction: insight from neurochemical imaging. Psychiatr Clin North Am 35(2):521–541

Valenta I, Varga ZV, Valentine H, Cinar R, Horti A, Mathews WB et al (2018) Feasibility evaluation of myocardial cannabinoid Type 1 receptor imaging in obesity: a translational approach. JACC Cardiovasc Imaging 11(2 Pt 2):320–332

Van der Schueren BJ, Van Laere K, Gerard N, Bormans G, De Hoon JN (2011) Interictal Type 1 cannabinoid receptor binding is increased in female migraine patients. Headache 52(3):433–440

van der Stelt M, Di Marzo V (2003) The endocannabinoid system in the basal ganglia and in the mesolimbic reward system: implications for neurological and psychiatric disorders. Eur J Pharmacol 480(1–3):133–150

Van Gaal LF, Rissanen AM, Scheen AJ, Ziegler O, Rossner S (2005) Effects of the cannabinoid-1 receptor blocker rimonabant on weight reduction and cardiovascular risk factors in overweight patients: 1-year experience from the RIO-Europe study. Lancet 365(9468):1389–1397

Van Laere K (2007) In vivo imaging of the endocannabinoid system: a novel window to a central modulatory mechanism in humans. Eur J Nucl Med Mol Imaging 34(11):1719–1726

Van Laere KJ, Versijpt J, Koole M, Vandenberghe S, Lahorte P, Lemahieu I et al (2002) Experimental performance assessment of SPM for SPECT neuroactivation studies using a sub-resolution sandwich phantom design. NeuroImage 16(1):200–216

Van Laere K, Goffin K, Casteels C, Dupont P, Mortelmans L, de Hoon J et al (2008a) Gender-dependent increases with healthy aging of the human cerebral cannabinoid-type 1 receptor binding using [(18)F]MK-9470 PET. NeuroImage 39(4):1533–1541

Van Laere K, Koole M, Sanabria Bohorquez SM, Goffin K, Guenther I, Belanger MJ et al (2008b) Whole-body biodistribution and radiation dosimetry of the human cannabinoid type-1 receptor ligand 18F-MK-9470 in healthy subjects. J Nucl Med 49(3):439–445

Van Laere K, Casteels C, Lunskens S, Goffin K, Gerard N, Bormans G, et al., (eds.) (2008c) In vivo PET brain imaging of the Type 1 cannabinoid receptor in early and advanced Parkinson's disease. In: Annual Meeting of European Association of Nuclear Medicine; October 10–13; Munich

Van Laere K, Goffin K, Bormans G, Casteels C, Mortelmans L, de Hoon J et al (2009) Relationship of type 1 cannabinoid receptor availability in the human brain to novelty-seeking temperament. Arch Gen Psychiatry 66(2):196–204

Van Laere K, Casteels C, Dhollander I, Goffin K, Grachev I, Bormans G et al (2010) Widespread decrease of type 1 cannabinoid receptor availability in Huntington disease in vivo. J Nucl Med 51(9):1413–1417

Van Laere K, Casteels C, Lunskens S, Goffin K, Grachev ID, Bormans G et al (2012) Regional changes in type 1 cannabinoid receptor availability in Parkinson's disease in vivo. Neurobiol Aging 33(3):620-e1–620-e8

Van Sickle MD, Duncan M, Kingsley PJ, Mouihate A, Urbani P, Mackie K et al (2005) Identification and functional characterization of brainstem cannabinoid CB2 receptors. Science 310(5746):329–332

van Veghel D, Cleynhens J, Pearce LV, Blumberg PM, Van Laere K, Verbruggen A et al (2013a) Synthesis and biological evaluation of [(1)(1)C]SB366791: a new PET-radioligand for in vivo imaging of the TRPV1 receptor. Nucl Med Biol 40(1):141–147

van Veghel D, Cleynhens J, Pearce LV, DeAndrea-Lazarus IA, Blumberg PM, Van Laere K et al (2013b) New transient receptor potential vanilloid subfamily member 1 positron emission tomography radioligands: synthesis, radiolabeling, and preclinical evaluation. ACS Chem Neurosci 4(4):624–634

Vandeputte C, Evens N, Toelen J, Deroose CM, Bosier B, Ibrahimi A et al (2011) A PET brain reporter gene system based on Type 2 cannabinoid receptors. J Nucl Med. Epub ahead of print

Vandeputte C, Casteels C, Struys T, Koole M, van Veghel D, Evens N et al (2012) Small-animal PET imaging of the type 1 and type 2 cannabinoid receptors in a photothrombotic stroke model. Eur J Nucl Med Mol Imaging 39(11):1796–1806

Verdurand M, Nguyen V, Stark D, Zahra D, Gregoire MC, Greguric I et al (2011) Comparison of cannabinoid CB(1) receptor binding in adolescent and adult rats: a positron Emission Tomography Study using [F]MK-9470. Int J Mol Imaging 2011:548123

Verdurand M, Dalton VS, Nguyen V, Gregoire MC, Zahra D, Wyatt N et al (2014) Prenatal poly I:C age-dependently alters cannabinoid type 1 receptors in offspring: a longitudinal small animal PET study using [(18)F]MK-9470. Exp Neurol 257:162–169

Vickers SP, Kennett GA (2005) Cannabinoids and the regulation of ingestive behaviour. Curr Drug Targets 6(2):215–223

Victor W, Pike SSZ, Shetty HU, Hirvonen J, Anderson KB, Jenko KJ, Morse C, Innis RB (2010) Comparison of human plasma arterial input function for [11C]MePPEP determined with LC-MS/MS and radiometric methods. NeuroImage 52:S162

Villares J (2007) Chronic use of marijuana decreases cannabinoid receptor binding and mRNA expression in the human brain. Neuroscience 145(1):323–334

Vinod KY, Hungund BL (2006a) Cannabinoid-1 receptor: a novel target for the treatment of neuropsychiatric disorders. Expert Opin Ther Targets 10(2):203–210

Vinod KY, Hungund BL (2006b) Role of the endocannabinoid system in depression and suicide. Trends Pharmacol Sci 27(10):539–545

Volk DW, Eggan SM, Horti AG, Wong DF, Lewis DA (2014) Reciprocal alterations in cortical cannabinoid receptor 1 binding relative to protein immunoreactivity and transcript levels in schizophrenia. Schizophr Res 159(1):124–129

Waleh NS, Cravatt BF, Apte-Deshpande A, Terao A, Kilduff TS (2002) Transcriptional regulation of the mouse fatty acid amide hydrolase gene. Gene 291(1–2):203–210

Wallace MJ, Martin BR, DeLorenzo RJ (2002) Evidence for a physiological role of endocannabinoids in the modulation of seizure threshold and severity. Eur J Pharmacol 452(3):295–301

Wallace MJ, Blair RE, Falenski KW, Martin BR, DeLorenzo RJ (2003) The endogenous cannabinoid system regulates seizure frequency and duration in a model of temporal lobe epilepsy. J Pharmacol Exp Ther 307(1):129–137

Wang L, Yui J, Wang Q, Zhang Y, Mori W, Shimoda Y et al (2016a) Synthesis and preliminary PET imaging studies of a FAAH Radiotracer ([(1)(1)C]MPPO) based on alpha-ketoheterocyclic scaffold. ACS Chem Neurosci 7(1):109–118

Wang C, Placzek MS, Van de Bittner GC, Schroeder FA, Hooker JM (2016b) A novel radiotracer for imaging monoacylglycerol lipase in the brain using positron emission tomography. ACS Chem Neurosci 7(4):484–489

Wang L, Mori W, Cheng R, Yui J, Hatori A, Ma L et al (2016c) Synthesis and preclinical evaluation of sulfonamido-based [(11)C-Carbonyl]-carbamates and ureas for imaging monoacylglycerol lipase. Theranostics 6(8):1145–1159

Wasmuth HE, Trautwein C (2007) CB1 cannabinoid receptor antagonism: a new strategy for the treatment of liver fibrosis. Hepatology 45(2):543–544

Waterhouse RN (2003) Determination of lipophilicity and its use as a predictor of blood-brain barrier penetration of molecular imaging agents. Mol Imaging Biol 5(6):376–389

Wilkinson ST, Stefanovics E, Rosenheck RA (2015) Marijuana use is associated with worse outcomes in symptom severity and violent behavior in patients with posttraumatic stress disorder. J Clin Psychiatry 76(9):1174–1180

Willis PG, Katoch-Rouse R, Horti AG (2003) Regioselective F-18 radiolabeling of AM694, a CB1 cannabinoid receptor ligand. J Label Compd Radiopharm 46(9):799

Willis PG, Pavlova OA, Chefer SI, Vaupel DB, Mukhin AG, Horti AG (2005) Synthesis and structure-activity relationship of a novel series of aminoalkylindoles with potential for imaging the neuronal cannabinoid receptor by positron emission tomography. J Med Chem 48(18):5813–5822

Wilson RI, Nicoll RA (2002) Endocannabinoid signaling in the brain. Science 296(5568):678–682

Wilson A, Garcia A, Parkes J, Sadovski O, Houle S, Vasdev N (2011a) 3-Oxazolinylphenyl N-Alkylcarbamates as promising radiotracers for imaging Fatty Acid Amide Hydrolase (FAAH). J Label Compd Radiopharm 54(Suppl 1):S-37

Wilson AA, Garcia A, Parkes J, Houle S, Tong J, Vasdev N (2011b) [11C]CURB: Evaluation of a novel radiotracer for imaging fatty acid amide hydrolase by positron emission tomography. Nucl Med Biol 38(2):247–253

Wilson AA, Hicks JW, Sadovski O, Parkes J, Tong J, Houle S et al (2013) Radiosynthesis and evaluation of [(1)(1)C-carbonyl]-labeled carbamates as fatty acid amide hydrolase radiotracers for positron emission tomography. J Med Chem 56(1):201–209

Wong DF, Kuwabara H, Horti AG, Kumar A, Brasic J, Ye W et al (2008) Imaging of human cannabinoid CB1 receptors with [11C]OMAR. J Nucl Med 49(Suppl 1):131P

Wong DF, Kuwabara H, Horti AG, Raymont V, Brasic J, Guevara M et al (2010a) Quantification of cerebral cannabinoid receptors subtype 1 (CB1) in healthy subjects and schizophrenia by the novel PET radioligand [11C]OMAR. NeuroImage 52(4):1505–1513

Wong DF, Kuwabara H, Hussain B, Horti AG, Brasic J, Raymont V et al (2010b) Evaluation of occupancy of cannabinoid CB1 receptors by a novel antagonist drug with [11C]OMAR and PET. NeuroImage 52(Suppl. 1):S64

Wyffels L, Muccioli GG, De Bruyne S, Moerman L, Sambre J, Lambert DM et al (2009) Synthesis, in vitro and in vivo evaluation, and radiolabeling of aryl anandamide analogues as candidate radioligands for in vivo imaging of fatty acid amide hydrolase in the brain. J Med Chem 52(15):4613–4622

Wyffels L, Muccioli GG, Kapanda CN, Labar G, De Bruyne S, De Vos F et al (2010) PET imaging of fatty acid amide hydrolase in the brain: synthesis and biological evaluation of an 11C-labelled URB597 analogue. Nucl Med Biol 37(5):665–675

Xi ZX, Peng XQ, Li X, Song R, Zhang HY, Liu QR et al (2011) Brain cannabinoid CB receptors modulate cocaine's actions in mice. Nat Neurosci 14(9):1160–1166

Yamasaki T, Mori W, Zhang Y, Hatori A, Fujinaga M, Wakizaka H et al (2018) First demonstration of in vivo mapping for regional brain monoacylglycerol lipase using PET with [(11)C]SAR127303. NeuroImage 176:313–320

Yao BB, Hsieh G, Daza AV, Fan Y, Grayson GK, Garrison TR et al (2009) Characterization of a cannabinoid CB2 receptor-selective agonist, A-836339 [2,2,3,3-tetramethyl-cyclopropanecarboxylic acid [3-(2-methoxy-ethyl)-4,5-dimethyl-3H-thiazol-(2Z)-ylidene]-amide], using in vitro pharmacological assays, in vivo pain models, and pharmacological magnetic resonance imaging. J Pharmacol Exp Ther 328(1):141–151

Yasuno F, Brown AK, Zoghbi SS, Krushinski JH, Chernet E, Tauscher J et al (2008) The PET radioligand [^{11}C]MePPEP binds reversibly and with high specific signal to cannabinoid CB1 receptors in nonhuman primate brain. Neuropsychopharmacology 33(2):259–269

Yiangou Y, Facer P, Durrenberger P, Chessell IP, Naylor A, Bountra C et al (2006) COX-2, CB2 and P2X7-immunoreactivities are increased in activated microglial cells/macrophages of multiple sclerosis and amyotrophic lateral sclerosis spinal cord. BMC Neurol 6:12

Yrjola S, Sarparanta M, Airaksinen AJ, Hytti M, Kauppinen A, Pasonen-Seppanen S et al (2015) Synthesis, in vitro and in vivo evaluation of 1,3,5-triazines as cannabinoid CB2 receptor agonists. Eur J Pharm Sci 67:85–96

Yu SJ, Reiner D, Shen H, Wu KJ, Liu QR, Wang Y (2015) Time-dependent protection of CB2 receptor agonist in stroke. PLoS One 10(7):e0132487

Zanotti-Fregonara P, Hirvonen J, Lyoo CH, Zoghbi SS, Rallis-Frutos D, Huestis MA et al (2013) Population-based input function modeling for [(18)F]FMPEP-d 2, an inverse agonist radioligand for cannabinoid CB1 receptors: validation in clinical studies. PLoS One 8(4):e60231

Zavitsanou K, Garrick T, Huang XF (2004) Selective antagonist [^{3}H]SR141716A binding to cannabinoid CB1 receptors is increased in the anterior cingulate cortex in schizophrenia. Prog Neuro-Psychopharmacol Biol Psychiatry 28(2):355–360

Zehra A, Burns J, Liu CK, Manza P, Wiers CE, Volkow ND et al (2018) Cannabis addiction and the brain: a review. J Neuroimmune Pharmacol 13(4):438–452

Zhang L, Villalobos A (2017) Strategies to facilitate the discovery of novel CNS PET ligands. EJNMMI Radiopharm Chem 1(1):13

Zhang PW, Ishiguro H, Ohtsuki T, Hess J, Carillo F, Walther D et al (2004) Human cannabinoid receptor 1: 5′ exons, candidate regulatory regions, polymorphisms, haplotypes and association with polysubstance abuse. Mol Psychiatry 9(10):916–931

Zhang L, Butler CR, Maresca KP, Takano A, Nag S, Jia Z et al (2019) Identification and development of an irreversible Monoacylglycerol Lipase (MAGL) Positron Emission Tomography (PET) radioligand with high specificity. J Med Chem 62(18):8532–8543

Zou S, Kumar U (2018) Cannabinoid receptors and the endocannabinoid system: signaling and function in the Central Nervous System. Int J Mol Sci 19(3):833

Current Radioligands for the PET Imaging of Metabotropic Glutamate Receptors

13

Linjing Mu and Simon M. Ametamey

Contents

L. Mu
Department of Nuclear Medicine, Center for Radiopharmaceutical Sciences of ETH,
PSI and USZ, University Hospital Zurich, Zurich, Switzerland
e-mail: linjing.mu@pharma.ethz.ch

S. M. Ametamey (✉)
Department of Chemistry and Applied Biosciences, Center for Radiopharmaceutical Sciences
of ETH, PSI and USZ, ETH Zurich, Zurich, Switzerland
e-mail: simon.ametamey@pharma.ethz.ch

Abstract

Glutamate receptors are divided into two main groups: ionotropic glutamate receptors (iGluRs) and metabotropic glutamate receptors (mGluRs). Modulation of iGluRs and mGluRs has potential for the treatment of psychiatric and neurological diseases such as depression, anxiety, schizophrenia, and Parkinson's disease. Positron emission tomography (PET) might offer the possibility to visualize glutamate receptors and presents an interesting tool for studying these receptors under physiologic and pathologic conditions. MGluR PET radioligands reported till August 2019 are summarized, and also a summary of some of the most important prerequisites for CNS PET radioligands is provided. Emphasis is given to mGluR1 and mGluR5, the two receptor subtypes for which most advances in radioligand development and human studies have been made. In addition, recent research efforts toward the development of PET radioligands for other receptor subtypes more specifically, mGluR2/mGluR3 and mGluR4 are also outlined alongside their in vitro/in vivo properties and clinical applications where available.

Abbreviations

ABP688	3-(6-methyl-pyridin-2-ylethynyl)-cyclohex-2-enonemethyl-oxime
AMPA	2-amino-3-(3-hydroxy-5-methyl-isoxazol-4-yl)-propionic acid
BBB	Blood-brain barrier
B_{max}	Maximal binding capacity
BP_{ND}	Binding potential relative to the no displaceable compartment
Bq	Becquerel
BSA	Bovine serum albumin
CAMP	Cyclic adenosine monophosphate
CNS	Central nervous system
DMF	Dimethylformamide
DMSO	Dimethyl sulfoxide
DV	Distribution volume
EOB	End of bombardment
EOS	End of synthesis
Et_3N	Triethylamine
GPCR	G-protein-coupled receptor
HBD	Hydrogen bond donors
HPLC	High-pressure liquid chromatography
i.v	Intravenous
IC_{50}	Inhibition constant required for displacement of 50% of radioligand binding
ID	Injected dose
IDnorm./g	Injected dose normalized to body weight per tissue weight

iGluR	Ionotropic glutamate receptor
K_d	Dissociation constant
K_i	Inhibition constant
ko	Knockout
LPS	Lipopolysaccharide
LTP	Long-term potentiation
MeI	Methyl iodide
M-FPEP	2-methyl-6-(3-fluoro-phenylethynyl)-pyridine
mGluR	Metabotropic glutamate receptor
mGluR5	Metabotropic glutamate receptor subtype 5
min	Minute(s)
M-MPEP	2-methyl-6-((methoxyphenyl)ethynyl)-pyridine
MPO	Multi-parameter optimization
MW	Microwave
NAC	*N*-acetylcysteine
NMDA	*N*-methyl-D-aspartate
NMDAR	*N*-methyl-D-aspartate receptor
p.i.	Postinjection
PBS	Phosphate-buffered saline
PET	Positron emission tomography
P-gp	P-glycoprotein
PI	Phosphoinositol
PLC	Phospholipase C
ROI	Region of interest
RT	Room temperature
SAR	Structure-activity relationship
SUV	Standard uptake value
TAC	Time activity curve
TEMPO	2,2,6,6-Tetramethylpiperidine-1-oxyl
THF	Tetrahydrofuran
TM	Transmembrane domain
TPSA	Topological polar surface area
wt	Wild-type

13.1 Introduction

13.1.1 Gutamate Receptors

Glutamate (L-glutamic acid) serves as the neurotransmitter at the majority of excitatory synapses in the mammalian central nervous system (CNS). Glutamate receptors are divided into two main groups, namely, ionotropic glutamate receptors (iGluRs) and metabotropic glutamate receptors (mGluRs) (Fig. 13.1).
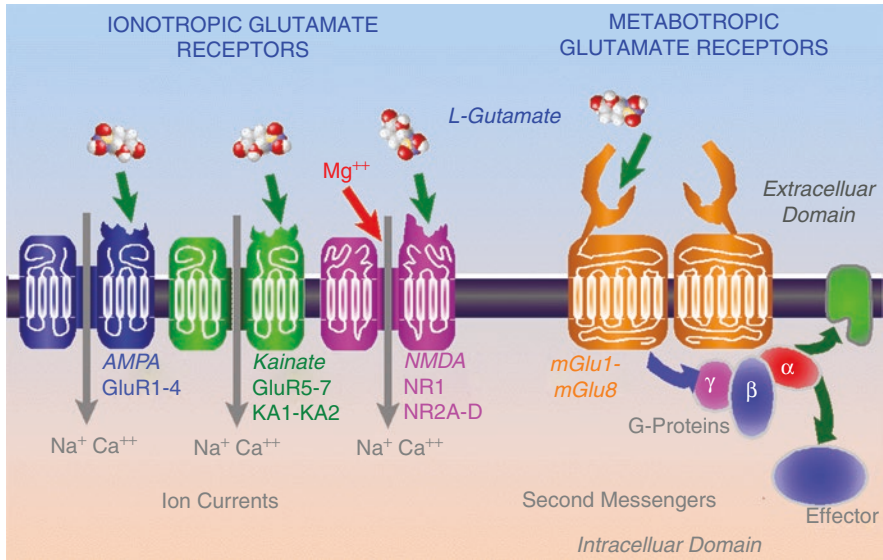
Fig. 13.1 Ionotropic and metabotropic glutamate receptors (*Source*: http://www.ucl.ac.uk/ioo/research/salt/glutamat.htm (Prof. Tom Salt))

The iGluRs are the principal mediators of excitatory neurotransmission. These are ligand-gated cationic-selective channels which are permeable to Na$^+$, K$^+$, and Ca^{2+} ions. They are subdivided into three major classes based on structural similarities and named according to the type of synthetic agonist that activates them. These three selective agonists are NMDA (*N*-methyl-D-aspartate), AMPA (α-amino-3-hydroxy-5-methyl-isoxazole-4-propionate), and kainate (Bettler and Mulle 1995; Mori and Mishina 1995). Native receptors of all of these families are likely heteromeric assemblies comprising more than one type of subunit. *N*-methyl-D-aspartate (NMDA) tetrameric receptors consist of subunits NR1 and NR2. There are four NR2 subunit types, NR2A, B, C, and D. AMPA receptors are composed of a four-subunit family (GluR1–4) with members that are products of separate genes and are believed to assemble as functional tetramers. Kainate receptors are composed of two related subunit families, GluR5–7 and KA-1 and 2.

Metabotropic glutamate receptors (mGluRs) are G-protein-coupled receptors (GPCR), which activate intracellular secondary messenger systems when bound by the physiological ligand glutamate. From a structural viewpoint, mGluRs belong to the seven-transmembrane protein family and have been classified into three subgroups. Group I mGluRs (mGluR1 and mGluR5) are coupled to phospholipase C and upregulate or downregulate neuronal excitability (Gereau and Conn 1995). Group II (mGluR2 and mGluR3) and group III (mGluR4 and mGluR6–8) inhibit adenylate cyclase and hence reduce synaptic transmission (Bradley et al. 2000; Ritzen et al. 2005). The mGluRs are expressed on neuronal and glial cells, with each receptor subtype exhibiting distinct spatial and temporal expression profiles in the

brain (Shigemoto et al. 1997; Thomas et al. 2001), with the exception of mGluR6 existing in the retina. In neurons, group I mGluRs are mainly localized in somato-dendritic domains and postsynaptically regulate neuronal excitability and synaptic transmission via several intracellular second messenger systems, whereas group II and III mGluRs are predominantly localized in axonal domains and axon terminals to presynaptically regulate neurotransmitter release (Cartmell and Schoepp 2000). MGluRs function as dimers, with two glutamate molecules being required for full receptor activation (Shin et al. 2008; Tsuchiya et al. 2002).

13.1.2 PET

Positron emission tomography (PET) is a noninvasive imaging technology, allowing for the quantitative imaging of physiologic and pathophysiologic processes in vivo (Ametamey et al. 2008; Piel et al. 2014). High resolution of about 1–2 mm can be achieved with small animal imaging systems and 4–6 mm for clinical PET scanners. The visualization of biological targets and systems is of special interest in this research field. Specific PET tracers for labeling such targets are potential future diagnostics of various diseases and provide elegant tools for drug development (Fowler 1999), especially for the development of drugs with less side effects. Besides oncologic and cardiac applications, there is a growing demand for specific and selective radiopharmaceuticals in the field of neuroscience. PET can be used to image receptor distribution, concentration, and functions in normal and pathological states and has proven to be a powerful technique in neurological research (Passchier et al. 2002). Due to the convenient half-lives of carbon-11 and fluorine-18 and their chemical properties, most effort has been put into the development of tracers labeled with one of these isotopes. In general, carbon-11 and fluorine-18 are produced by nuclear reactions which require the bombardment of convenient stable isotopes with high energetic protons provided by a cyclotron. Carbon-11 can easily be introduced into biologically interesting compounds without changing their biochemical and pharmacological properties. The relatively short physical half-life of ^{11}C (20 min) allows for multiple imaging studies in a short period of time, which makes it advantageous for sequential investigations with short time intervals in the same individual (animal or human), thereby allowing the subject to serve as its own control. Therefore ^{11}C-labeled compounds can be used for instance in a receptor occupancy paradigm or in cognitive intervention studies where several PET investigations are usually needed within a few hours apart from each other. The short half-life of ^{11}C, however, is disadvantageous for commercial production. Fluorine-18 has long physical half-life of 110 min allowing more complex synthesis, extended in vivo investigation, and, most importantly, satellite distribution of the radiotracer to clinical PET centers that do not have radiochemistry facilities. In addition, it shows better imaging characteristics than carbon-11 due to its lower positron energy (0.64 MeV vs. 0.96 MeV for ^{11}C). The larger the positron energy, the larger the average distance the positron travels

before annihilating and as such more loss in spatial resolution will be expected. Thus, efforts have been put into developing ^{18}F-labeled radiotracers. Radiolabeling methods with either carbon-11 or fluorine-18 will not be discussed in this chapter. Several review papers on this topic can be found in the literature (Dahl et al. 2017; Deng et al. 2018; van der Born et al. 2017).

13.1.3 General Requirements for CNS Radiotracers

The general requirements for successful PET radiotracers for the imaging of specific brain targets such as transporters, receptors, and enzymes also hold true for glutamate receptors. Several excellent review papers have been published on this topic (Eckelman et al. 2006; Van de Bittner et al. 2014; Waterhouse 2003). A summary of some of the most major points is provided below.

13.1.3.1 High Affinity and Selectivity

The affinity of the radiotracer relative to the concentration of binding site present in the target tissue is an important characteristic of site-specific radiotracers (Eckelman et al. 2006). The ability to image a receptor is determined by delivery, by retention at the specific binding site, and by washout of nonspecifically associated radiotracer. Two terms are related to the affinity of a ligand toward its target, and depending on how the value is obtained, the K_d (equilibrium dissociation constant) and the K_i (inhibition constant) express the affinity of a ligand to the target. Usually, binding affinities should be in the low nanomolar to subnanomolar range. With regard to selectivity, the radioligand in question should have the highest affinity for the actual target and only low affinity for any other binding site.

13.1.3.2 Concentration of Target Sites (B_{max})

A high ratio of binding site concentration toward radiotracer concentration is a requirement for a valid response to changes in binding site concentration caused by diseases or drug occupancy during a PET experiment. Therefore, it is important that the B_{max} value exceeds the affinity (K_d) of the radioligand, and this positively affects the target-to-nontarget ratio and the imaging quality. It is considered that PET tracers with an in vitro B_{max}/K_d ratio (also called binding potential) of at least ten have a high chance of providing a specific signal in vivo. A high level of nondisplaceable binding in vivo may require an in vitro B_{max}/K_d much greater than ten to provide a useful specific signal in vivo (Eckelman and Mathis 2006).

13.1.3.3 BBB Permeability

Lipophilicity is a measure of how much of a compound partitions into a lipid environment compared to an aqueous environment. CNS compounds have to pass the blood-brain barrier (BBB) and ideally should therefore have log$P$ values well above 1 to allow free diffusion across the BBB. Nonspecific binding is known to be higher with increasing lipophilicity, and high nonspecific binding in target tissues reduces the signal-to-noise ratio and, thus, the ability to detect the specific signal (Pike 2009). It has been recommended that the log$P$ values of potential CNS compounds

should be between 1 and 3.5 (Waterhouse 2003; Clark 2003). It should also be pointed out that lipophilicity values (normally log$P$ or log$D$) are highly variable, depending on the methodology used for their determination. Values obtained using the traditional "shake-flask" method tend to be lower than those obtained by HPLC, C18, and calculation methods. Log$P$ values determined using in silico methodology are also highly variable, depending on the algorithm used. Therefore, it has been suggested that log$P$ should not be relied upon as a sole predictor of BBB penetration during brain radiotracer discovery. HPLC measurement of permeability, percentage of plasma protein binding, and membrane interactions may be potentially useful in predicting a radioligand's in vivo performance (Tavares et al. 2012). Additionally, the BBB possesses efflux pumps which can prevent compounds from effectively accumulating in the brain, of which P-glycoprotein (P-gp) is a key efflux pump (Ohe et al. 2003). Therefore, a PET tracer should not be a substrate for P-gp. There are in vitro assays to determine whether a compound is a P-gp substrate or not (Wanger-Baumann et al. 2011).

13.1.3.4   In Vivo Stability

The formation of radioactive metabolites which might enter into the brain and confound the brain signals is undesired. Unfavorable is also the metabolic elimination of the radioactive nuclide from the radiotracer. Thus, the radioligand should be resistant to unfavorable metabolism during the acquisition time, and radioactive metabolites should not be taken up in the target area.

13.1.3.5   Efficient Radiosynthesis

Due to the short half-lives of common PET nuclides, a rapid and efficient radiolabeling process is crucial. The best radiosynthetic scheme should incorporate the radionuclide at the last synthetic step. Typically, the reaction time for synthetic schemes with multiple steps should be accomplished within two half-lives of the radioisotope. The establishment of a one-step radiosynthesis is desired for obtaining high radiochemical yields with high molar activities. The ratio between labeled and unlabeled tracer is defined by the molar activity. Low molar activities result in low-quality PET images especially for saturable systems such as enzymes, transporter proteins, and receptors. For receptors with low binding sites (low B_{max}), very high molar activity is required in order to exclude substantial occupation of target sites by unlabeled ligand and the saturation of the biological system of interest.

It should be stressed that these criteria do not necessarily guarantee a successful glutamate radiotracer. They are merely guidelines to assist in the selection of potentially useful CNS imaging ligands. Recently, multiparameter optimization methods have been used to assess ligands which have central nervous drug-like properties. The parameters are (1) lipophilicity, calculated distribution coefficient (Clog$P$); (2) calculated distribution coefficient at pH = 7.4 (Clog$D$); (3) molecular weight (MW); (4) topological polar surface area (TPSA); (5) number of hydrogen bond donors (HBD); and (6) pK_a (Wager et al. 2010a; Wager et al. 2010b; Zhang et al. 2013). This multiparameter optimization method has successfully been used to develop CNS PET tracers (Zhang et al. 2013; Chen et al. 2016; Zhang et al. 2017a).

When a potential radiotracer has been selected and a radiolabeling method has been developed, some preclinical evaluations and acute toxicity studies have to be performed prior to PET studies in humans. The characterization of a new radioligand includes autoradiography, biodistribution, and metabolite studies as well as pretreatment and displacement studies, using in vitro, in vivo, and ex vivo techniques. With the increasing ability to carry out PET studies in rodents, using dedicated small animal PET cameras, the evaluation of PET tracers is simplified and serves as an important bridge between laboratory and clinical science (Myers 2001; Xi et al. 2011; Xu and Li 2019).

13.2   MGluR1 PET Tracers

MGluR1 has been implicated in neuroprotection, chronic and neuropathic pain, multiple sclerosis, motor dysfunction, epilepsy, cerebral ischemia, and cerebellar long-term depression (Ito et al. 2009; Kohara et al. 2008; Yamasaki et al. 2017). Hence, monitoring mGluR1 in vivo and noninvasively would lead to a better understanding of the role of this receptor in the pathophysiology of biological processes mediated through glutamatergic pathways. It has been reported that the highest expression of mGluR1 in rat brain is in the cerebellum; moderate or low level in the thalamus, striatum, hippocampus, and cerebral cortex; and very low level in the brain stem (Fotuhi et al. 1993; Lavreysen et al. 2004a). Since noncompetitive ligands do not bind to the evolutionarily conserved glutamate binding site, they offer the potential for improved selectivity for mGluR subtypes (Parmentier et al. 2000). Therefore, potent and selective allosteric mGluR1 antagonists such as CPCCOEt (Annoura et al. 1996), JNJ-16259685 (Lavreysen et al. 2004b), YM-298198 (Kohara et al. 2005), FTIDC (Suzuki et al. 2007), and MK-5435 (Ito et al. 2009) have been developed (Fig. 13.2). Subsequently, several radiolabeled
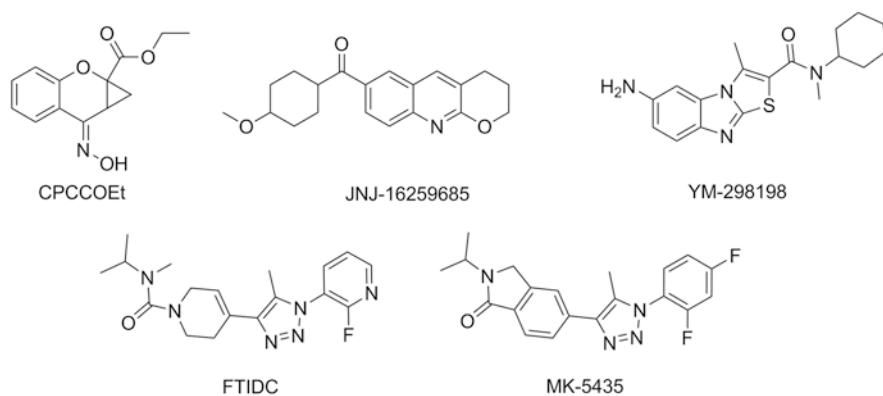
Fig. 13.2 Structures of some mGluR1 allosteric antagonists

[^{11}C]JNJ-16567083 (K_i 0.87nM)

[^{18}F]cEFQ (K_i 1.07 nM)

[^{11}C]MMTP (K_i 7.9 nM)

[^{18}F]MK-1312 (K_d 0.84); R = propyl
[^{18}F]FPIT (IC$_{50}$ 5.4 nM); R = isopropyl

[^{11}C]YM-202074 (K_i 4.8 nM)

[^{18}F]FPTQ (IC$_{50}$ 3.6 nM)

[^{11}C]ITMM (K_i 12.6 nM); R = O^{11}CH3
[^{11}C]ITDM (K_i 13.6 nM); R = ^{11}CH3

[^{18}F]FITM (IC$_{50}$ 5.1 nM); R = isopropyl
[^{18}F]FIMX (IC$_{50}$ 1.8 nM); R = CH$_3$

[^{11}C]LY2428703 (K_i 8.9 nM)

[^{11}C]FIMX (IC$_{50}$ 1.8 nM)
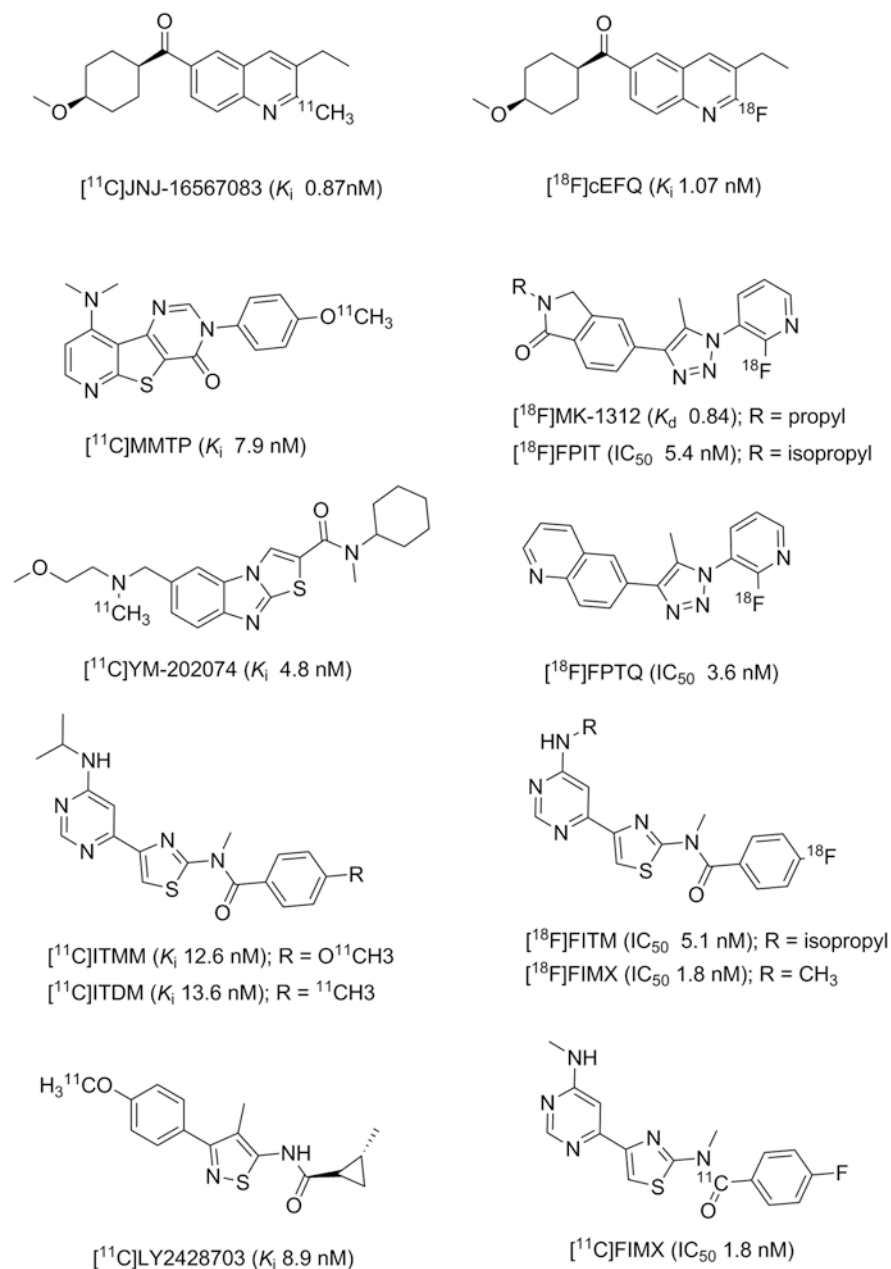
Fig. 13.3 Structures of some important mGluR1 PET tracers

Table 13.1 Summary of affinity, lipophilicity values, and in vivo specificity of mGluR1 radioligands

Radioligand	Binding affinity (nM)	Lipophilicity (LogD)	Specificity in the brain
[11C]JNJ-16567083	K_i 0.87 (4 °C); 3.49 (37 °C)[a] K_i 0.57 (4 °C); 4.41 (37 °C)[b] K_i 4.75 (4 °C); 13.3 (37 °C)[c]	3.38	No (rat, baboon)
[11C]MMTP	K_i 7.9[b]; IC50 9.5[c]	3.15	Not clear
[11C]YM-202074	IC_{50} 4.8[c]	2.7	Yes (rat), no (monkey and human)
[11C]LY2428703	IC_{50} 8.9[c]	4.02	Yes (rat), no (monkey and human)
[11C]ITMM	K_i 12.6[b]	2.57	Yes (rat and human)
[11C]ITDM	K_i 13.6		Yes (monkey)
[18F]FPTQ	IC_{50} 3.6 [c]	2.53	Confound by radiometabolites (rat)
[18F]FPIT	IC_{50} 5.4[c]	2.53	Confound by radiometabolites (rat, monkey)
[18F]cEFQ	K_i 0.87(4 °C); 3.38 (37 °C)[a] K_i 1.07 (4 °C); 1.77 (37 °C)[b] K_i 3.74 (4 °C); 24.7 (37 °C)[c]	3.54	Yes (rat), no (baboon)
[18F]MK-1312	IC_{50} 0.84[c]	2.3	Yes (monkey)
[18F]FITM	IC_{50} 5.1[c]	1.5	Yes (rat, monkey)
[18F]FIMX	IC_{50} 1.8[c]	2.52	Yes (monkey, human)

[a]Determined in ligand competition binding assays using cloned rat mGluR1 membrane
[b]Using rat cerebellum homogenate
[c]Using cloned human mGluR1

ligands for PET studies were synthesized and evaluated for their utility as potential imaging agents for mGluR1 (Xu and Li 2019; Li and Huang 2014) (Fig. 13.3). Their binding affinities, lipophilicities, and in vivo specificity to mGluR1 are summarized in Table 13.1.

13.2.1 11C-Labeled mGluR1 Tracers

The most important carbon-11 radioligands for mGluR1 are described below.

(3-Ethyl-2-[11C]-methyl-6-quinolinyl)(cis-4-methoxycyclohexyl)-methanone, also denoted as [11C]JNJ-16567083, was the first reported allosteric antagonist PET tracer for imaging mGluR1 in the rodent brain (Huang et al. 2005). High binding affinity of JNJ-16567083 toward rat mGluR1 receptor was discovered with a K_i value of 0.87 nM. [11C]JNJ-16567083 was synthesized via palladium-mediated
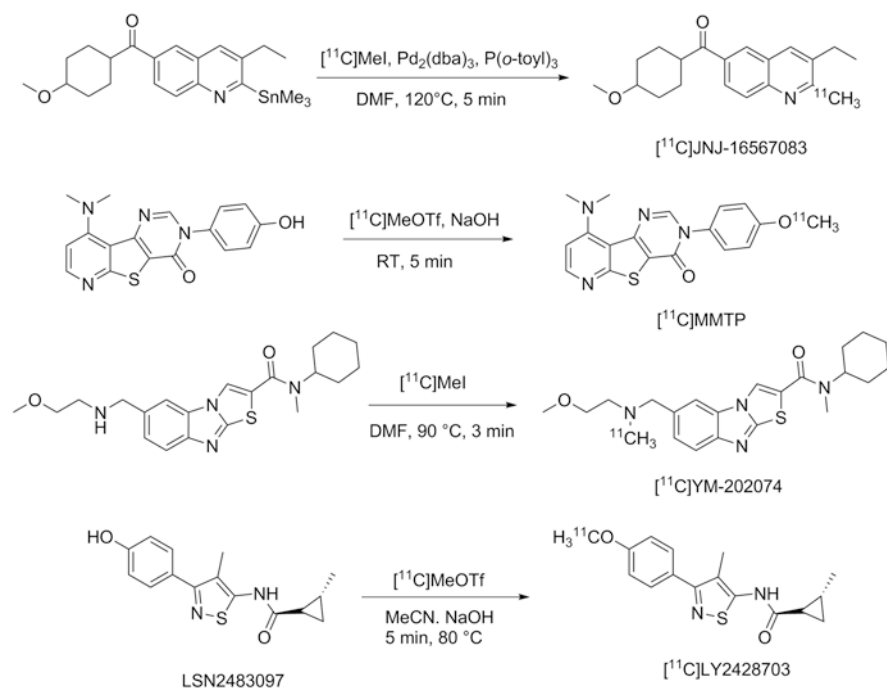
Scheme 13.1 Radiosyntheses of [¹¹C]JNJ-16567083, [¹¹C]MMTP, [¹¹C]YM-202074, and [¹¹C]LY2428703

Stille coupling of the trialkyltin precursor with [¹¹C] methyl iodide (Scheme 13.1). Biodistribution studies in rats under baseline and blockade conditions showed that [¹¹C]JNJ-16567083 is selective and binds specifically to the mGluR1. Among the brain regions examined, the cerebellum, a region with the highest expression of the mGluR1, exhibited the highest uptake of radioactivity and highest specific binding of 81%. Further studies with [¹¹C]JNJ-16567083 in rodents and nonhuman primates revealed species differences in the binding affinities toward mGluR1 (Table 13.1). A higher specificity of binding was obtained in rat brain, compared to baboon brain (Huang et al. 2012).

[¹¹C]MMTP, [O-methyl-¹¹C]dimethylamino-3(4-methoxyphenyl)-3H-pyrido[3′,2′:4,5] thieno[3,2-d]pyrimidin-4-one is another promising carbon-11-labeled mGluR1 PET radioligand, which was synthesized by methylation of the corresponding desmethyl precursor using [¹¹C]MeOTf in the presence of NaOH at room temperature (Scheme 13.1) (Prabhakaran et al. 2010). [¹¹C]MMTP selectively labeled mGluR1 binding sites in postmortem human brain slices containing the cerebellum, hippocampus, frontal cortex, and striatum using phosphor imaging autoradiography. The densities of binding sites (B_{max}) for the various brain regions estimated from these autoradiography studies were 140, 110, 85, and 20 fmol/cm^2 for cerebellum, hippocampus, frontal cortex, and striatum, respectively. The authors

performed PET studies in a baboon and showed that [¹¹C]MMTP penetrates the BBB and accumulated in mGluR1-rich regions. The highest uptake was observed in the cerebellum, a region known to have the highest level of mGluR1 expression. However, it was not clear whether the binding in the cerebellum was specific, given that no blocking experiment was performed.

N-cyclohexyl-6-{[*N*-(2-methoxyethyl)-*N*-methylamino]methyl-*N*-methylthiazolo[3,2-a]benzimidazole-2-carboxamide (YM-202074) is a derivative of YM-298198 (Fig. 13.2) and exhibits an inhibition constant (K_i) of 4.8 nM toward mGluR1 and no inhibition up to 1 μM for mGluR5 (Kohara et al. 2008). [¹¹C]YM-202074 was synthesized by N-[¹¹C] methylation of its desmethyl precursor with [¹¹C] methyl iodide in DMF at 90 °C for 3 min (Scheme 13.1). [¹¹C]YM-202074 exhibited optimal lipophilicity with a log*D* value of 2.7. High specific binding of [¹¹C]YM-202074 for mGluR1 in rat brain was confirmed by in vitro autoradiography under blockade conditions with nonradioactive mGluR1 antagonists YM-202074, JNJ-16259685, and CPCCOEt. However, ex vivo autoradiography and PET study showed that the in vivo radioactivity distribution of [¹¹C]YM-202074 in rat brain region did not reflect the distribution pattern obtained from in vitro autoradiographic results. It was suggested that the discrepancy between in vitro and in vivo distributions might be caused by radiometabolite(s) of [¹¹C]YM-202074 in the brain, and less than 10% intact compound was found in mouse plasma at 30 min p.i. Therefore, it was concluded that [¹¹C]YM-202074 may not be a useful PET ligand for the in vivo imaging of mGluR1 (Yanamoto et al. 2010).

(1S,2R)-N-(3-(4-(methoxy)phenyl)-4-methylisothiazol-5-yl)-2-methylcyclo propane-1-carboxamide (LY2428703) exhibits an IC$_{50}$ value of 8.9 nM to human mGluR1. [¹¹C]LY2428703 was prepared by reacting the phenolic precursor, LSN2483097, with [¹¹C]methyl triflate (Scheme 13.1) (Zanotti-Fregonara et al. 2013a). PET studies showed that [¹¹C]LY2428703 readily penetrated the rat brain and distributed preferentially in the target-rich cerebellum. Its in vivo specificity and selectivity were confirmed by using mGluR1 and mGluR5 blocking agents, respectively. To verify species differences, a saturation binding assay was used to estimate its in vitro binding potential. The values for the binding potential expressed as B_{max}/K_d were 25.3, 18.2, and 16.9 for rat, monkey, and human, respectively (Zanotti-Fregonara et al. 2013b). PET imaging studies in rhesus monkeys under baseline and blocking conditions with and without nonradioactive LY2428703 (2.0 mg/kg) showed that although the brain uptake in the cerebellum was slightly higher than other brain regions, the uptake was not specific. In humans, a low and a homogeneous brain uptake was observed with [¹¹C]LY2428703. The unspecific and low brain uptake was suspected to be due to high plasma protein binding given that the plasma free fraction of [¹¹C]LY2428703 was 0.094% as measured by ultrafiltration. In summary, despite the promising in vitro and in vivo results in rodents, [¹¹C]LY2428703 is unsuitable for imaging mGluR1 expression in monkey and human brain.

N-(4-(6-(isopropylamino)pyrimidin-4-yl)-1,3-(thiazol-2-yl)-4-[¹¹C]methoxy-N-methylbenzamide ([¹¹C]ITMM, Fig. 13.3) was prepared by reacting the corresponding phenolic precursor with [¹¹C]MeI (Scheme 13.2) (Fujinaga et al. 2012c). A K_i
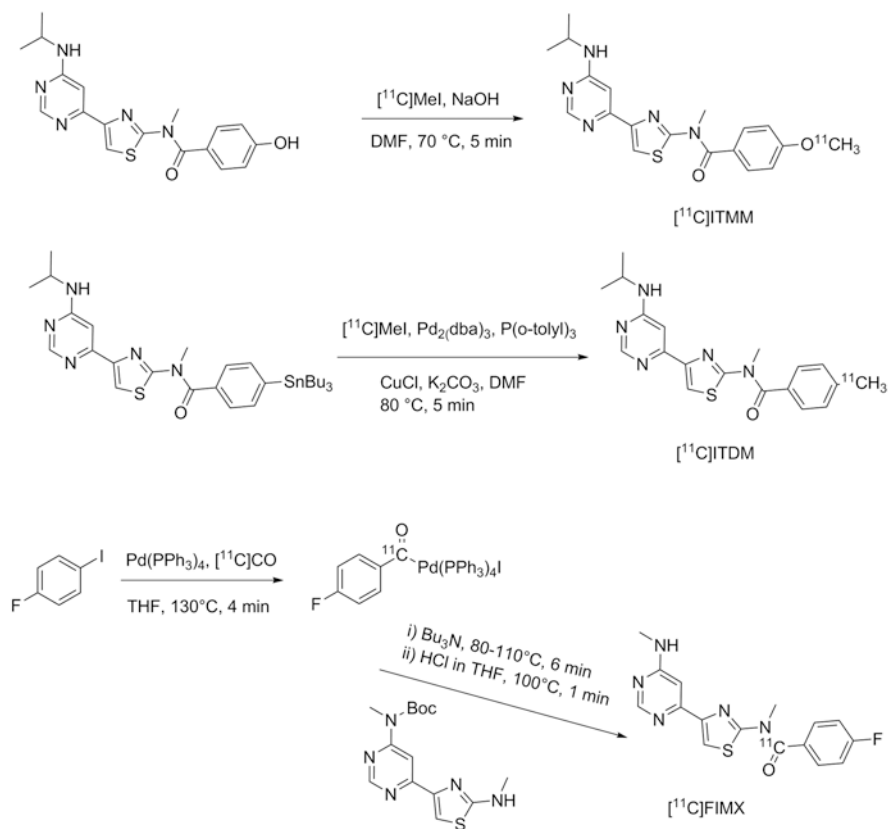
Scheme 13.2 Radiosyntheses of [^{11}C]ITMM, [^{11}C]ITDM and [^{11}C]FIMX

value of 12.6 nM was determined toward mGluR1 using rat brain homogenates in competition binding experiments. [^{11}C]ITMM was demonstrated to have high selectivity over mGluR5 (K_i mGluR5/mGluR1, >306) and low binding affinity to 28 major neurotransmitter receptors, uptake systems, and ion channels (Toyohara et al. 2013a). The log$D$ value of [^{11}C]ITMM was 2.57 using shake-flask method in octanol/phosphate buffer at pH 7.4. In vitro autoradiography on sagittal section of rat brain slices showed heterogeneous distribution of [^{11}C]ITMM, with highest uptake in the cerebellum, moderate radioactivity in the thalamus, and low in the striatum. The lowest radioactivity was detected in the brain stem. The in vivo PET results confirmed the expected distribution pattern of [^{11}C]ITMM in rat brain with the highest uptake in the cerebellum, followed by thalamus and striatum. Pretreatment with unlabeled ITMM (1 mg/kg) significantly reduced the uptake compared to the control group, and the distribution of radioactivity became fairly uniform throughout the brain. The maximum reduction of radioactivity uptake exceeded 85% in the thalamus and striatum, demonstrating that [^{11}C]ITMM binds specifically to mGluR1 in the rat brain. The specificity of binding of [^{11}C]ITMM was also

confirmed in mGluR1-knockout mouse brain. Although rapid metabolism was observed in the plasma, > 80% total radioactivity in the rat brain homogenate was intact [^{11}C]ITMM (Fujinaga et al. 2012b). PET imaging studies were performed in eight healthy male volunteers (aged 21–27y) with [^{11}C]ITMM (Toyohara et al. 2013b). Five of the eight subjects underwent dynamic brain PET study, and the other three subjects a whole-body distribution study. The uptake of [^{11}C]ITMM was consistent with the known distribution of mGluR1 in the human brain. Brain uptake kinetics was slow, with a continuing increase of activity in the cerebellar cortex, and little washout in other brain regions during the 90 min dynamic PET scan. Small individual differences of [^{11}C]ITMM distribution and brain TACs were detected in the five healthy young male subjects. A two-tissue-compartment model was used to analyze the regional TACs with the input function based on the metabolite-corrected arterial plasma concentration curve. Brain mGluR1 densities were estimated as distribution volume (V_T), and the values for the cerebellar cortex and thalamus were 2.7 and 1.1 mL/cm^3, respectively. The whole-body distribution studies revealed that the urinary bladder wall absorbed the highest dose, followed by the small intestine, liver, and heart wall. No adverse or clinically detectable pharmacologic effects were detected in any of the eight subjects. The authors concluded that [^{11}C]ITMM is suitable for imaging cerebellar mGluR1 with acceptable dosimetry and pharmacologic safety at the dose required for adequate PET imaging (Toyohara et al. 2013b).

N-(4-(6-(isopropylamino)pyrimidin-4-yl)thiazol-2-yl)-N-methyl-4-^{11}C]methyl benzamide ([^{11}C]ITDM), a structurally similar compound to ITMM, was developed by the same research group by replacing the O-[^{11}C]methyl group in [^{11}C]ITMM with C-[^{11}C]methyl group. ITDM displayed a binding affinity (K_i) value of 13.6 nM toward mGluR1, which is similar to ITMM (K_i value of 12.6 nM). The [^{11}C]methyl group was introduced to the benzene ring via cross-coupling reaction of arylstannane precursor with [^{11}C]MeI in the presence of palladium(0) complex (Scheme 13.2) (Fujinaga et al. 2012b). [^{11}C]ITDM showed high specific binding in the cerebellum and thalamus in in vitro autoradiographic studies using rat brain sections. PET studies with [^{11}C]ITDM in monkeys confirmed the high brain uptake and mGluR1 specificity in vivo. Metabolite analysis showed more than 95% intact [^{11}C]ITDM at 60 min postinjection in rat brain extracts.

Yamasaki et al. used R6/2 mice, the most widely used animal model of Huntington's disease, for the measurement of nondisplaceable binding potential (BP_{ND}) of [^{11}C]ITMM (Yamasaki et al. 2014). It was established that the pons, a part of the brainstem with negligible mGluR1 expression, could be used as the reference tissue for the in vivo measurement of mGluR1 levels without the need for arterial blood sampling. Reduced radioactivity uptake was observed in cerebellum, thalamus, striatum, and cingulate cortex brain regions in R6/2 mice compared with control mice. The BP_{ND} measurements based on the Logan reference (Logan Ref) method indicated decreased BP_{ND} values in several R6/2 mice brain regions with highest in the striatum of roughly 35% followed by thalamus, cingulate cortex, and cerebellum at 20% to 30%. These percentage decreases in various of R6/2 mice brain regions were similar to the decreased mRNA levels reported previously in these brain regions (Cha et al. 1998). A close correlation between changes in

radioactive signal intensity and the degree of mGluR1 expression was found by comparison of the autoradiograms of R6/2 mouse brain sections with immunohistochemical images. Similar to the PET results, autoradiographic and immunohistochemical images of R6/2 mouse brain sections showed a heterogeneous decrease of signal in striatum, thalamus, and cerebellum, suggesting that the radioactive signal intensity corresponded with mGluR1 expression. The roles of mGluR1 were further investigated in chronic PD pathology by performing longitudinal [^{11}C]ITDM PET imaging in A53T transgenic (A53T-Tg) rats expressing an abnormal human α-synuclein (ASN) gene (Yamasaki et al. 2016). A53T-Tg rats showed a dramatic decline in general motor activities with age, along with abnormal ASN aggregation and striatal neuron degeneration. In longitudinal PET imaging, dynamic changes associated with PD progression were observed. Using the same reference tissue as mentioned above (Yamasaki et al. 2014), striatal BP_{ND} values of [^{11}C]ITDM were higher in A53T-Tg rats than control rats prior to PD pathology onset but dramatically decreased afterward with age. [^{11}C]ITDM was further assessed in pilocarpine-induced status epilepticus (PISE), a rat model of neuroinflammation (Yamasaki et al. 2017). PET with [^{11}C]ITDM showed significant decreases of mGluR1 availability (BP_{ND}) in the thalamus and hippocampus after PISE over the chronic period. PET with [^{11}C]ITDM could successfully visualize hippocampal and thalamic declines of mGluR1 related to neuroinflammation. These results demonstrated that monitoring mGluR1 in vivo may provide beneficial information to further understand central nervous system disorders.

[Carbonyl-^{11}C]4-fluoro-N-methyl-N-(4-(6-(methylamino)pyrimidin-4-yl)thiazol-2-yl) benzamide ([^{11}C]FIMX) is the C-11 version of [^{18}F]FIMX, which has been demonstrated as an effective radioligand for imaging brain mGluR1 with PET (Hong et al. 2015; Xu et al. 2013). [^{11}C]FIMX with a short physical half-life was developed to allow PET imaging of mGluR1 in the same animal subject on the same day, for example, in receptor occupancy studies. [^{11}C]FIMX was prepared via a two-step synthetic approach (Scheme 13.2). The intermediate [^{11}C]acyl-palladium complex was prepared by Pd-promoted carbonylation of 1-fluoro-4-iodobenzene with [^{11}C]carbon monoxide, which was prepared online from cyclotron-produced [^{11}C]carbon dioxide. THF was the preferred solvent because of its low boiling point, allowing it to be easily removed during the next step. To achieve optimal [^{11}C]carbon monoxide insertion and avoid the formation of [^{11}C]4-fluorobenzoic acid, the authors recommend the use of fresh and anhydrous THF. Boc-protected [^{11}C]FIMX was formed by reacting [^{11}C]acyl-palladium complex with the Boc-protected pyrimidine-thiazol amine; the aminolysis reaction went smoothly upon the complete evaporation of THF. Removal of the Boc-protecting group with 1.1 M HCl at 100 °C for 1 min led to the formation of the final product [^{11}C]FIMX, which was separated from the reaction mixture by reversed-phase HPLC and formulated as a sterile solution for intravenous injection. The radiochemical yield was about 5% (d.c.) with a molar activity of about 100 GBq/μmol. The total synthesis time was ca. 40 min. [^{11}C]FIMX was evaluated in anesthetized rhesus monkey. High radioactivity uptake (SUV 8.5) was observed in mGluR1-rich cerebellum after intravenous injection. The signal was abolished after pretreatment with the selective antagonist

JNJ16259685 (3 mg/kg, i.v.), confirming the specificity of uptake in rhesus monkey brain.

13.2.2 ^{18}F-Labeled mGluR1 Tracers

A number of fluorine-18-labeled compounds have been evaluated as potential PET ligands for imaging mGluR1. Some of the most important ^{18}F-labeled mGluR1 radioligands reported so far are described below.

13.2.2.1 ^{18}F-Labeled Triazole Analogues

Based on the structure of MK-5435, a potent and selective mGluR1 allosteric antagonist (Ito et al. 2009), several pyridyl triazole derivatives have been developed for imaging mGluR1. Depicted in Fig. 13.3 are the structures of three triazole analogues [^{18}F]MK-1312, [^{18}F]FTIDC, and [^{18}F]FPIT.

[^{18}F]MK-1312 was synthesized via reaction of [^{18}F]KF with the corresponding chloropyridine in DMSO with microwave heating (Scheme 13.3) (Hostetler et al. 2011). Saturation binding studies in cerebellum homogenates with [^{18}F]MK-1312 revealed a K_d value of 0.40 and 0.84 nM for rhesus monkey and human cerebellum, respectively. Autoradiography was performed with both human and monkey brain slices. The cerebellum exhibited the highest accumulation of activity for both species. Baseline PET studies in a monkey showed that this radiotracer rapidly penetrates the BBB, which is in line with its optimal lipophilicity value of 2.3. The distribution of [^{18}F]MK-1312 was heterogeneous, with highest uptake observed in the cerebellum and moderate uptake in the thalamus and striatum. Displacement studies with an mGluR1 allosteric antagonist, MK-5435, indicated specific binding of [^{18}F]MK-1312 to mGluR1 in the cerebellum of rhesus monkey, and blockade was concentration dependent (Hostetler et al. 2011). Measurement of in vivo tracer metabolism in plasma revealed that 17% of plasma radioactivity was due to [^{18}F]MK-1312 at the end of a 90-min baseline PET scan. [^{18}F]MK-1312 shows the desired characteristics as a potential mGluR1 PET tracer with respect to its lipophilicity, affinity, and specificity toward mGluR1. However, a direct comparative study with [^{18}F]FITM indicated a lower brain uptake and specificity for [^{18}F]MK-1312 (Yamasaki et al. 2012b).

R = propyl
R = isopropyl

R = propyl ([^{18}F]MK-1312)
R = isopropyl ([^{18}F]FPIT)
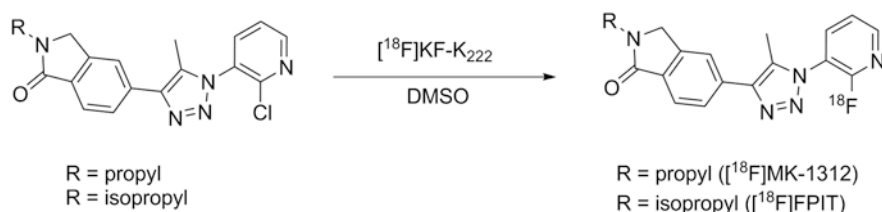
Scheme 13.3 Radiosynthetic scheme for [^{18}F]MK-1312 and [^{18}F]FPIT

[^{18}F]FPTQ, 6-[1-(2-[^{18}F]fluoro-3-pyridyl)-5-methyl-1H-1,2,3-triazol-4-yl]quino-lone, was synthesized by heating the bromo precursor with [^{18}F]KF in anhydrous DMSO at 150 °C for 10 min. High binding affinities (IC$_{50}$ values) of FPTQ toward mouse and human mGluR1 of 1.4 and 3.6 nM, respectively, have been reported (Suzuki et al. 2009). In vitro autoradiographic results showed that the distribution pattern of [^{18}F]FPTQ in the brain of rats was consistent with the distribution of mGluR1 reported previously (Lavreysen et al. 2004a). The specific binding of [^{18}F]FPTQ accounted for higher than 97% of total binding, as determined by incubating with unlabeled FPTQ or mGluR1-selective JNJ-16259685 in rat brain slices. PET imaging showed that the distribution and uptake of [^{18}F]FPTQ in the rat brain was consistent with the results obtained by dissection as well as by in vitro autoradiography. The maximum standard uptake values (SUV) were 2.3 in the cerebellum, 2.1 in the thalamus, and ranged from 1.1 to 1.5 in the hippocampus, striatum, cerebral cortex, and medulla. However, the presence of a radiolabeled metabolite in the brain may confound the specific binding of this radioligand in vivo. Thus, [^{18}F]FPTQ may be of limited utility for the in vivo investigation of mGluR1 (Fujinaga et al. 2011).

[^{18}F]FPIT, 1-(2-[^{18}F]fluoro-3-pyridyl)-4-(2-isopropyl-1-oxoisoindoline-5-yl)-5-methyl-1H-1,2,3-triazole, an analogue of [^{18}F]MK-1312, was synthesized by reacting the bromo precursor with [^{18}F]KF in anhydrous DMSO at 150 °C for 10 min (Scheme 13.3). FPIT was shown to have an IC$_{50}$ value of 5.4 nM for mGluR1 and 2500 nM for mGluR5 (Hostetler et al. 2011). The experimentally determined log$D$ value of [^{18}F]FPIT was 2.53, suggesting good BBB penetration. Autoradiography showed that the binding of [^{18}F]FPIT is consistent with the reported distribution of mGluR1 with high specific binding in the cerebellum and thalamus of rat and monkey brains. [^{18}F]FPIT displayed a similar distribution of radioactivity in both monkey and rat brains. The sequence of radioactivity level in the brain regions was cerebellum >thalamus >hippocampus >cerebral cortex >striatum >pons-medulla. Pretreatment with FPIT or JNJ-16259865 showed substantial inhibition of [^{18}F]FPIT binding in these brain regions to a level close to or lower than that in the pons-medulla and almost diminished the difference in radioactivity among all brain regions. As indicated by the authors, a disadvantage of [^{18}F]FPIT is its slow kinetics in the monkey brain and also the generation of a radiolabeled metabolite in the brain that could hamper accurate modeling and quantification with PET (Fujinaga et al. 2012a).

13.2.2.2 ^{18}F-Labeled Thiazole Analogues

[^{18}F]FITM (4-[^{18}F]fluoro-*N*-[4-[6-(isopropylamino)pyrimidin-4-yl]-1,3-thiazol-2-yl]-*N*-methylbenzamide) has a novel chemical structure that does not contain a triazole ring. Moreover, instead of the 2-[^{18}F]fluoropyridine ring, [^{18}F]FITM contains a [^{18}F]fluorobenzene ring, which is expected to be stable against defluorination. [^{18}F]FITM was synthesized by [^{18}F]fluorination of its corresponding nitro precursor with [^{18}F]KF in the presence of Kryptofix 222 (Scheme 13.4). FITM was shown to have potent antagonistic activity against human mGluR1 with an IC$_{50}$ value of 5.1 nM. Excellent selectivity over other subtypes has been reported whereby the IC$_{50}$ values were 7000 nM for human mGluR5, >10,000 nM for mGluR2, and
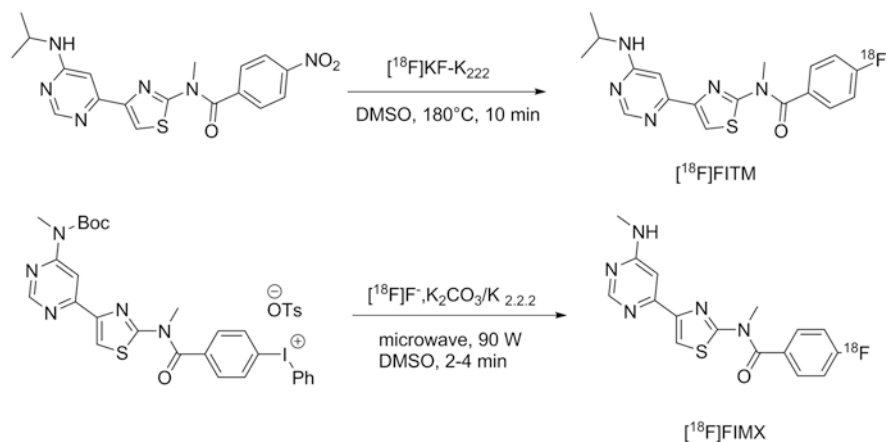
Scheme 13.4 Radiosynthetic scheme for [¹⁸F]FITM and [¹⁸F]FIMX

>10,000 nM for mGluR8 (Satoh et al. 2009). The distribution coefficient (log$D$) of [¹⁸F]FITM was 1.46 using the shake-flask method at pH 7.4. Strong signals of radio-activity were found in known mGluR1-rich regions such as the cerebellum and thalamus in in vitro autoradiographic studies using rat brain sections. By co-incubation with the nonradioactive reference FITM or mGluR1 antagonist JNJ-16259685, radioactivity throughout the brain section decreased significantly compared with those in the control section. Upon co-incubation with MPEP, an antagonist for mGluR5, no change in radioactivity accumulation was observed. The signals of radioactivity in ex vivo autoradiography in the brain sections of rat co-injected with JNJ-16259685 decreased by 86–91% in mGluR1-rich regions compared with those of the control, indicating the tracer was specifically bound to mGluR1 (Yamasaki et al. 2011). Very recently, the same research group reported on the further evaluation of [¹⁸F]FITM in a monkey brain. High in vivo stability was also observed. The uptake of [¹⁸F]FITM in the monkey brain was not only high in mGluR1-rich cerebellum but also in brain regions such as the thalamus and hippocampus which have moderate expression levels of mGluR1. Specific binding of [¹⁸F]FITM could be demonstrated in all the aforementioned brain regions by pretreatment with JNJ-16259685 (Yamasaki et al. 2012a).

In order to circumvent the harsh radiolabeling conditions and also to improve the brain washout of [¹⁸F]FITM, a new thiazole derivative code named [¹⁸F]FIMX (4-[¹⁸F]Fluoro-N-methyl-N-(4-(6-(methylamino)pyrimidin-4-yl)thiazol-2-yl)benzamide) was developed (Yamasaki et al. 2012a). Structurally, the N-isopropyl group in FITM was replaced by the less lipophilic N-methyl group in FIMX. FIMX displayed a threefold higher human mGluR1 affinity (IC$_{50}$ = 1.8 nM) than FITM and high selectivity over mGluR5 and a wide range of other receptors, transporters, and binding sites (Xu et al. 2013; Satoh et al. 2009). For the F-18 radiolabeling, a diaryliodonium salt served as the precursor (Scheme 13.4). Various radiolabeling conditions were investigated including heating sources (conventional heating and

microwave), reaction time and temperature, solvent, and the influence of free-radical scavenger TEMPO. High radiolabeling yield (40%) was obtained using both conventional and microwave heating; however, microwave heating could remove the Boc-protecting group without the addition of acid which simplified the radiolabeling process. The most suitable solvent was DMF or DMSO. The addition of TEMPO improved the incorporation of [18F]fluoride ion from 26 to 42% under thermal conditions (100 °C bath temperature, 5 min) in DMF (Scheme 13.4). [18F]FIMX was produced in high radiochemical purity (96–100%) with molar activities of ca. 105 GBq/μmol. The decay-corrected radiochemical yield was 20%. The specificity and selectivity of [18F]FIMX were confirmed by imaging the mGluR1 expression in a rhesus monkey brain. Radioactivity signal distribution in monkey brain was consistent with the known mGluR1 expression. The highest uptake was in the receptor-rich cerebellum (5.3 SUV at 12 min). Moderate uptake values were observed in the thalamus (2.9 SUV), frontal cortex (2.7 SUV), hippocampus (2.5 SUV), putamen (2.5 SUV), and anterior cingulate (2.4 SUV). The regional time-activity curves were almost indistinguishable after i.v. injection of the mGluR1 selective antagonist, JNJ-16259685 (3 mg/kg) 30 min postinjection of the radiotracer. In sharp contrast, no changes of radioactivity distribution were observed using the mGluR5-selective ligand MTEP (5 mg/kg). Encouraged by the promising results, the same research group translated [18F]FIMX into humans. Twelve healthy volunteers were included for dynamic PET scan over 120 min, and four other subjects underwent whole-body scan to estimate radiation exposure (Zanotti-Fregonara et al. 2016). PET imaging revealed high [18F]FIMX uptake (SUV = 4–6) in mGluR1-rich cerebellum, and washout was faster than that of [11C]ITMM. The high density of mGluR1 in the cerebellum was quantified based on an unconstrained two-tissue-compartment model, and values of distribution volume (V_T) ranged from 1.5 in the caudate to 11 mL·cm^{-3} in the cerebellum. Stable V_T values could be obtained in 120 min scan in all regions except the cerebellum, for which an acquisition time of at least 170 min was necessary. Regional V_T values of [18F]FIMX correlated well with mGluR1 transcript density, indicating that [18F]FIMX could be used for mapping mGluR1 in the human brain. The estimated effective dose of [18F]FIMX was 23 μSv/MBq and compares favorably with other 18F-labeled ligands (Zanotti-Fregonara et al. 2013c).

13.2.2.3   [18F]cEFQ

(3-Ethyl-2-[18F]fluoroquinolin-6-yl) cis-(4-methoxycyclohexyl)methanone ([18F]cEFQ), the 18F-labeled analogue of JNJ-16567083, was prepared by nucleophilic substitution of chloroquinoline precursor with [18F]KF in DMSO in the presence of Kryptofix 222 at 100 °C for 5 min (Huang et al. 2012; Lee et al. 2017). It was found that even when a pure cis-form precursor was used, both cis and trans isomers [18F]cEFQ and [18F]tEFQ were obtained under the abovementioned radiolabeling conditions. Separation of the isomers was possible using a reversed-phase HPLC column. Higher amount of the trans isomer, [18F]tEFQ, was obtained compared to the cis-isomer [18F]cEFQ (60% vs. 40%) due to the more stable thermodynamic nature of the trans product. It was reported that the trans isomers bearing methoxy-,

methyl, and chloro-quinoline functionalities were 20–100-fold less potent toward GluR1 compared to their cis counterparts (Mabire et al. 2005). For biological evaluations, it is therefore essential to separate [^{18}F]cEFQ from [^{18}F]tEFQ by HPLC. In vitro stability studies indicated no cis-trans isomerization in human serum at body temperature. [^{18}F]cEFQ was shown to be stable at 4 °C but slowly degraded into free [^{18}F]fluoride and other radioactive metabolites over time at 37 °C. The binding affinity of [^{18}F]cEFQ to mGluR1 was also shown to be temperature-dependent (Table 13.1). Species differences were found for [^{18}F]cEFQ in vitro and in vivo studies. [^{18}F]cEFQ was more potent for cloned rat mGluR1 than human mGluR1 (3.38 nM vs. 24.7 nM at 37 °C). PET images and TACs with [^{18}F]cEFQ in rat brain indicated highest radioactivity uptake in the cerebellum. Moderate radioactivity uptake was found in the thalamus, hippocampus, and striatum. The pattern of radioactivity distribution was in line with the expected mGluR1 expression in the rat brain. The amount of the intact [^{18}F]cEFQ in the brain was 88.9% and 59.5% at 5 and 30 min, respectively. Polar radiometabolites did not confound with the radiosignals in the brain tissue. Specificity and selectivity of binding were confirmed by blocking studies using the known mGluR1 antagonist JNJ16259685 and mGluR5 selective antagonist ABP688, respectively. [^{18}F]cEFQ, however, did not show any detectable specific binding in the baboon brain, which impeded its further evaluation in human subjects.

So far, three mGluR1 PET ligands, [^{11}C]YM-202074, [^{11}C]ITMM, and [^{18}F]FIMX, were evaluated in human subjects. [^{11}C]YM-202074 failed to visualize mGluR1 in humans, whereas both [^{11}C]ITMM and [^{18}F]FIMX demonstrated potential for mapping mGuR1 in the human brain.

13.3   mGluR2/3 PET Tracers

Group II mGluRs consists of mGluR2 and mGluR3. They couple negatively to adenylyl cyclase through Gi/Go proteins. Emerging preclinical and clinical data suggested that group II mGluRs are implicated in various neurological and psychiatric disorders including anxiety disorders (Swanson et al. 2005), schizophrenia (Ghose et al. 2008; Muguruza et al. 2016; Patil et al. 2007), drug addiction (Moussawi and Kalivas 2010), Parkinson's disease (Dickerson and Conn 2012), and pain states (Chiechio 2016; Mazzitelli et al. 2018; Neugebauer et al. 2009). Specifically, high potent mGluR2 allosteric modulators have advanced to phase 2 clinical trials in patients with schizophrenia and MDD (Trabanco et al. 2019). In the brain, mGluR2 is highly expressed in the cerebral cortex, striatum, hippocampus, and amygdala (Richards et al. 2005). So far, several PET ligands targeting mGluR2 have been developed, and one of them has been evaluated in human subjects.

(S,S,S)-2-(2-carboxycyclopropyl)-2-(3-[^{11}C]methoxyphenethyl) glycine dimethyl ester ([^{11}C]CMGDE) was the first PET tracer developed as a prodrug for imaging group II metabotropic glutamate receptors in vivo. Its hydrolyzed product cyclopropane amino-diacid CMG was designed based on an mGluR2/3 antagonist LY341495 (IC$_{50}$ = 21 nM for mGluR2; 14 nM for mGluR3) (Ornstein et al. 1998). CMG
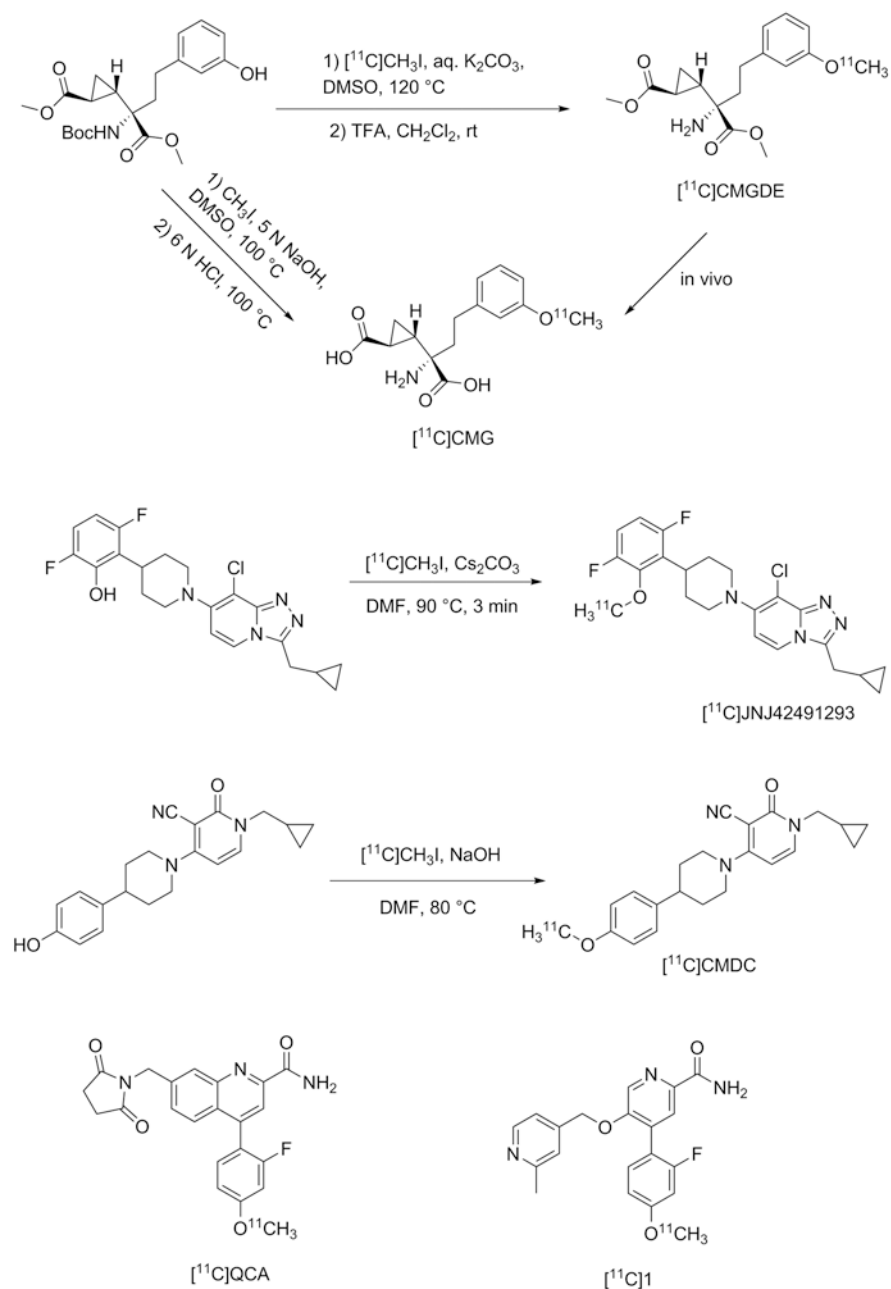
Scheme 13.5 Radiosynthetic scheme for mGluR2 radioligands and structures of [¹¹C]QCA and [¹¹C]1

displayed a IC_{50} value of 94 nM toward mGluR2/3 with the mixture of its four constituent isomers (R,S,S-, S,S,S-, S,R,R- and R,R,R-isomer). As the binding affinities of the S,S,S-isomer of several CMG derivatives surpassed that of the corresponding isomer mixture by factors of 3.4–6.9 (Ornstein et al. 1998), the S,S,S-isomers of CMG and CMGDE were radiolabeled with carbon-11 as illustrated in Scheme 13.5 (Wang et al. 2012). As expected, the high hydrophilic tracer [11C]CMG showed no brain penetration after injection into male Sprague-Dawley rats. However, its prodrug [11C]CMGDE readily accumulated into mGluR2/3-rich rat brain regions such as striatum, hippocampus, and cortical areas. The maximum accumulation (2.5–3.5% of the injected dose per cm^3) was observed at 2 min after the tracer application. Pretreatment with LY341495, a highly potent mGluR2/3 ligand, induced 29.5% decrease of [11C]CMGDE accumulation in the whole brain, indicating relatively low in vivo specificity.

1-(Cyclopropylmethyl)-4-(4-[11C]methoxyphenyl)piperidin-1-yl-2-oxo-1,2-dihydro pyridine-3-carbonitrile ([11C]CMDC) was synthesized by O-[11C]methylation of its corresponding phenolic precursor with [11C]methyl iodide under basic conditions (Ma et al. 2017). CMDC showed potent functional activity (EC_{50}: 98 nM) for human mGluR2 in vitro (Cid et al. 2014). The logD value of [11C]CMDC as measured by the shake flask method was 3.1 ± 0.2. This value lies in the range normally considered favorable for CNS PET radiotracers. In vitro autoradiography indicated that the distribution pattern of radioactivity was heterogeneous with high expression in mGluR2-rich brain regions of cerebral cortex, striatum, hippocampus, and granular layer of the cerebellum. Co-incubation with unlabeled CMDC demonstrated its specificity in rat brain sections. However, limited brain penetration (peak brain uptake ca. 0.6 SUV) and low in vivo specific binding of [11C]CMDC in rat brain suggest that [11C]CMDC has limited potential as a PET tracer for mapping brain mGluR2 in vivo. Replacing the C-11 labeled methoxy group with F-18 labeled fluoroethoxyl and shifting the methoxy group from para- to meta- or ortho-position of the benzene ring resulted in similar or slightly increased binding affinities compared to CMDC (Kumata et al. 2017). In vitro specificities were demonstrated by autoradiographic studies using rat brain sections. No in vivo studies have been disclosed so far.

7-((2,5-dioxopyrrolidin-1-yl)methyl)-4-(2-fluoro-4-[11C]-methoxyphenyl) quinoline-2-carboxamide ([11C]QCA) was prepared in a similar way as [11C]CMDC (Zhang et al. 2017b). The EC_{50} value reported for QCA was 8 nM. Heterogeneous brain distribution and moderate-to-high level specific binding were obtained in vitro autoradiographic studies using rat brain sections applying [11C]QCA. Dynamic PET imaging using [11C]QCA showed limited radioactivity uptake (ca. 0.3 SUV) in the rat brain. Pretreatment with unlabeled QCA (1 mg/kg) failed to show significant reduction of brain uptake. PET imaging studies in PgP/Bcrp knockout mice indicated that [11C]QCA had intensive interactions with brain efflux pumps at the murine blood-brain barrier. These results suggest that [11C]QCA is not a suitable tracer for imaging mGluR2 in rodent brain.

4-(2-Fluoro-4-[11C]methoxyphenyl)-5-((2-methylpyridin-4-yl)methoxy)picolinamide ([11C]1) was synthesized by O-[11C]-methylation of the phenolic precursor with [11C]methyl iodide (Kumata et al. 2019). This compound displayed nanomolar

binding affinity for mGluR2 (IC_{50} = 26 nM). Although this radioligand showed high in vitro specific binding to mGluR2 in autoradiographic studies, its in vivo properties (low binding and substrate of ATP binding cassette efflux transporters) were very similar to the lead compound [^{11}C]QCA; therefore it could not be taken into consideration as a potential PET radiotracer candidate.

8-Chloro-3-(cyclopropylmethyl)-7-(4-(3,6-difluoro-2-[^{11}C](methoxyphenyl) piperidin-1-yl)-[1,2,4]triazolo[4,3-a]pyridine ([^{11}C]JNJ42491293) was selected as a potential PET tracer from a series of C-11 labeled 7-(phenyl-piperidinyl)-1,2,4-triazolo[4,3-a]pyridine derivatives (Andres et al. 2012). JNJ42491293 binds to an allosteric modulator site of the human mGluR2 with 9.6 nM binding affinity and has a calculated logP value of 4.84. PET studies in rats indicated that [^{11}C]JNJ42491293 binds specifically and reversibly to mGluR2. The intensity of the PET signals were in the order of cerebellum > striatum > thalamus > whole brain > hippocampus > cortex. The maximum radioactivity concentration (SUV 1.7) in the brain was reached at 12 min p.i. and remained constant until 27 min followed by a slow washout. A clear displacement of radioactivity in all the brain regions was observed after injection of JNJ42153605, a high affinity, and selective ligand for mGluR2. Ex vivo radiometabolite studies revealed that the radioactivity signal in the rat brain was attributed to the intact parent compound (> 95%). Given these promising results in rat, [^{11}C]JNJ42491293 was further studied in mGluR2 knockout rats and humans (Leurquin-Sterk et al. 2017). The brain uptake of [^{11}C]JNJ42491293 in human subjects peaked at around 30 min after bolus injection and showed a gradual brain washout over the next hour. However, unexpected high cardiac retention was observed in a human subject, which prompted the authors to re-examine the tracer's specificity by extending preclinical research including the mGluR2 knockout rat and rhesus monkey. Similar [^{11}C]JNJ42491293 uptake was obtained in both mGluR2 knockout and wild-type rat brain, suggesting non-specific binding. Using JNJ-46356479, another mGluR2 selective positive allosteric modulator, also failed to show specific binding of [^{11}C]JNJ42491293 in rat and monkey brains. The unknown in vivo off-target binding in the knockout rat and the lack of in vivo specificity precluded [^{11}C]JNJ42491293 as a useful mGluR2 PET tracer.

Apart from [^{11}C]JNJ42491293, two structurally unknown PET tracers, one was labeled with F-18 ([^{18}F]ER-000604699), and the other with with C-11 have been reported as mGluR2 PET tracers (Li et al. 2017; Lohith et al. 2016). However, limited information is available on these two radioligands as only conference abstracts are available.

13.4   mGluR4 PET Tracers

mGluR4 belongs to the group III metabotropic glutamate receptors along with mGluR6, mGluR7, and mGluR8. Based on mRNA studies, mGluR4 has high expression in cerebellar cortex, moderate in thalamus and hippocampus (Corti et al. 2002). Compared to other groups of the mGlu receptor family, less attention has been received for group III mGluRs in the field of drug discovery. The identification

mGluR4
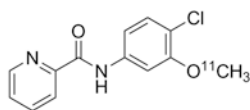
[11C]ML128
rEC50 = 110 nM; hEC50=240 nM
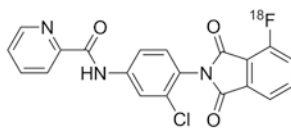
[18F]KALB001
hEC50 = 50.4 nM; IC50 = 5.1 nM
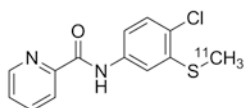
[11C]PXT012253
IC50= 3.4 nM
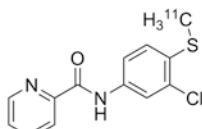
[11C]iso-PXT012253
IC50= 3.1 nM
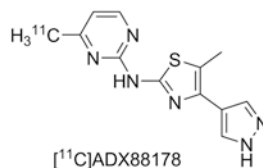
[11C]ADX88178
EC50 = 4 nM

Fig. 13.4 Structures of mGluR4 radioligands

of a partially selective mGluR4 positive allosteric modulator (PAM), N-phenyl-7-(hydroxyimino)cyclopropa[b]-chromen-1a-carboxamide (PHCCC), and its antiparkinsonian activity in animal models of PD has prompted intense interest for this target (Marino et al. 2003). Compound PXT002331 was the first mGluR4 PAM to enter into a clinical trial study (Charvin et al. 2018). Several PET tracers for imaging mGluR4 were developed since 2013 (Fig. 13.4); however, as of today none of them has advanced through to human studies.

N-(4-chloro-3-[11C]methoxyphenyl)picolinamide ([11C]ML128) was synthesized by reacting its corresponding phenolic precursor with [11C]CH$_3$I (Kil et al. 2013). ML128, a positive allosteric modulator for mGluR4 (rEC_{50} = 110 nM and hEC_{50} = 240 nM), showed efficacy in a preclinical rodent model of motor impairments associated with PD (Engers et al. 2009; Lindsley et al. 2009). Fast accumulation of [11C]ML128 (peak activity between 1–3 min) was observed in several rat brain regions including striatum, thalamus, hippocampus, and cerebellum, which reflected the distribution pattern of mGluR4 in rodent brain. Partial blocking effect (22–28%) was demonstrated by using N-(3-(difluoromethoxy)phenyl)picolinamide, a potent mGluR4 modulator, suggesting low in vivo specificity. [11C]ML128 is the first reported mGluR4 PET tracer and may serve as a lead compound for future mGluR4 PET imaging agents.

N-(4-chloro-3-([11C]methyl)thiophenyl)picolinamide ([11C]PXT012253) was developed as an analog of [11C]ML128. (Kil et al. 2016). It emerged from a series of ML128 derivatives which were synthesized and evaluated for their binding affinities toward mGluR4. PXT012253 and its regioisomer exhibited high in vitro binding affinity for mGluR4 with IC_{50} values of 3.4 nM and 3.1 nM, respectively. Both compounds were radiolabeled with C-11 and characterized in vivo using PET. [11C]PXT012253 outperformed its regioisomer and the lead compound

[^{11}C]ML128 as it showed the highest uptake in rat brain and 25% increased signal-to-noise ratio compared to [^{11}C]ML128. [^{11}C]PXT012253 was therefore selected for further evaluation in cynomolgus monkeys (Takano et al. 2019). The uptake of [^{11}C]PXT012253 peaked at 4 min and decreased to half in around 40 min on average. The mean %ID (injected dose) of the whole brain was 3.6% with the highest binding in the thalamus and putamen, and the lowest in the cortexes, which was similar to that previously reported in the rat brain with the same PET ligand (Kil et al. 2013). A two-tissue compartment model (2TC) fitted well to the brain regional TACs of [^{11}C]PXT012253. Competition with PXT002331 showed that the SUV values at the peak under the blocking conditions were higher than those at baseline conditions. The authors suggested that blocking compounds other than PXT002331 should be evaluated.

N-(3-chloro-4-(4-[^{18}F]fluoro-1,3-dioxoisoindolin-2-yl)phenyl)picolinamide ([^{18}F]KALB001) was prepared by nucleophilic substitution of the nitro group with [^{18}F]fluoride in the presence of Kryptofix 222 and potassium carbonate at 120 °C for 5 min (Kil et al. 2014). KALB001 was developed from picolinamide ML128 by introducing the phthalimide group at the 4-position on the phenyl ring. It exhibited enhanced activity (hEC$_{50}$ = 50.4 nM) compared to ML128 (hEC$_{50}$ = 240 nM) and excellent binding affinity (IC$_{50}$ = 5.1 nM) to mGluR4. The characterization of [^{18}F]KALB001was conducted in both rats and monkeys. It was found that [^{18}F]KALB001 occupied brain areas known to express mGluR4 and showed better permeability in the monkey brain than in the rat brain. Blocking studies revealed 10–20% reduced uptake in the rat brain pretreated with mGluR4-specific blocking agent N-(3-(difluoromethoxy)phenyl)-2-picolinamide (10 mg/kg). Negligible blocking effect was observed when mGluR5 antagonist MTEP was used, indicating good selectivity to mGluR4. [^{18}F]KALB001 is the first ^{18}F-labeled mGluR4 radioligand, and further structural modification to improve its specificity may lead to the discovery of a suitable radioligand for imaging mGluR4 in human subjects.

5-Methyl-N-(4-[^{11}C]methylpyrimidin-2-yl)-4-(1H-pyrazol-4-yl)thiazol-2-amine ([^{11}C]ADX88178) was reported in 2016 (Fujinaga et al. 2016). ADX88178 potentiated glutamate-mediated activation of human mGluR4 with an EC$_{50}$ value of 4 nM without significant effects on other mGluRs (EC$_{50}$ > 30 μM). The [^{11}C]methyl group at position 4 in pyrimidine was introduced by Stille coupling. Protecting the pyrazole ring with p-methoxybenzyl (PMB) was required for the C-C cross-coupling reaction. The accumulation pattern of [^{11}C]ADX88178 was consistent with the reported biological distribution of mGluR4 in the rat brain. Although low in vitro and in vivo specificity to mGluR4 was observed, compound ADX88178 may serve as a new chemical scaffold for structural optimization.

13.5   mGluR5 PET Tracers

MGluR5 is an important target for PET imaging with potential for application in drug development, diagnosis, and therapy monitoring. Metabotropic glutamate subtype 5 receptor (mGluR5) was cloned in 1992 and exists as a covalently bound

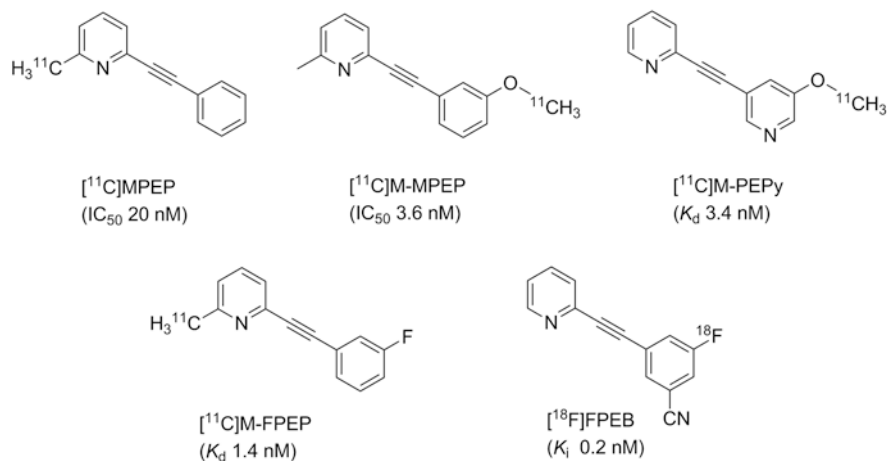**Fig. 13.5** Chemical structures of MPEP and MTEP
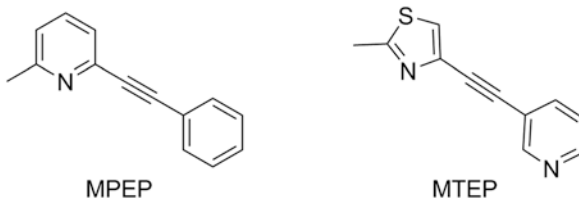
homodimer in heterologous expression system as well as in native tissue (Abe et al. 1992; Romano et al. 1996). It is expressed in brain regions such as the hippocampus, basal ganglia (striatum and nucleus accumbens), amygdala, and cortex (Romano et al. 1996; Gupta et al. 2005). mGluR5 has been implicated in a number of central nervous system disorders including depression, anxiety, addiction, schizophrenia, Parkinson's disease, and fragile X syndrome (Bear 2005; Carroll 2008; Ohnuma et al. 1998; Palucha et al. 2005; Pietraszek et al. 2007; Rouse et al. 2000; Spooren et al. 2003; Spooren and Gasparini 2004; Spooren et al. 2000; Tatarczynska et al. 2001; Tsai et al. 2005). As such, this receptor provides a novel target for the development of therapeutic drugs for the aforementioned neurological disorders. A number of noncompetitive mGluR5 ligands have been developed during the past years, and their potential as therapeutic drugs for some of the abovementioned CNS disorders has been investigated (Augelli-Szafran and Schwarz 2003; Chen and Conn 2008; Chua et al. 2005; Emmitte 2011; Gasparini et al. 2008; Jaeschke et al. 2008; Kulkarni et al. 2009; Lindemann et al. 2011; Lindsley and Emmitte 2009; Porter et al. 2005; Ritzen et al. 2009; Varney et al. 2002). In addition to CNS disorders, mGluR5 was found to be upregulated in CNS tumors and some non-CNS tumors (Brocke et al. 2010; Choi et al. 2011), participating in tumor growth and aggression.

The first potent and selective noncompetitive mGluR5 antagonists reported were the diaryl alkynes, 2-methyl-6-(phenylethynyl)pyridine (MPEP) (Gasparini et al. 1999; Lea and Faden 2006), and 3-[(2-methyl-1,3-thiazol-4-yl)ethynyl]pyridine (MTEP) (Fig. 13.5) (Cosford et al. 2003a; Cosford et al. 2002; Cosford et al. 2003b). Since their publication, MPEP and MTEP have been used as templates for the design of noncompetitive mGluR5 antagonists. Also a series of PET radioligands based on their core structures have been labeled with either carbon-11 or fluorine-18 and evaluated in in vitro and in vivo studies. Three reviews providing an overview on available mGluR5 PET ligands have been published (Mu et al. 2010; Pillai and Tipre 2016; Yu 2007).

13.5.1   MPEP-Derived mGluR5 Tracers

MPEP and its methyl analogue M-MPEP have been identified as potent, highly selective, noncompetitive antagonists for mGluR5. Derivatives of MPEP that have been labeled with either carbon-11 or fluorine-18 are depicted in Fig. 13.6.

Fig. 13.6 Chemical structures of [11]C- and ^{18}F-labeled MPEP derivatives

The high binding affinity of MPEP (IC$_{50}$ 20 nM) (Gasparini et al. 1999; Gasparini et al. 2002) to the heptahelical domain mGluR5 initiated the first radiolabeling of this compound with tritium. The identification of high-affinity analogues of M-MPEP (2-(2-(3-methoxyphenyl)ethynyl)pyridine, IC$_{50}$ 3.6 nM) (Gasparini et al. 2002), and M-PEPy (3-methoxy-5-pyridin-2ylethynyl)pyridine, K_d 3.4 nM) (Cosford et al. 2003a; Anderson et al. 2003; Patel et al. 2003) prompted the radiolabeling of these derivatives with carbon-11 for evaluation as potential candidates for imaging mGluR5.

[^{11}C]MPEP was prepared via Stille coupling reaction of 2-(phenylethynyl)-6-(trimethylstannyl)pyridine with [^{11}C]MeI (Scheme 13.6) in high radiochemical purity and good molar activity (33–44 GBq/μmol) (Yu et al. 2005). In vivo PET imaging studies of [^{11}C]MPEP in Sprague-Dawley rats showed high accumulation of [^{11}C]MPEP in brain areas such as the olfactory bulb, striatum, hippocampus, frontal cortex, and cerebellum. Pre-administration of unlabeled MPEP (10 mg/kg) 5 min prior to administration of [^{11}C]MPEP led to a decreased [^{11}C]MPEP binding in the olfactory bulb. In contrast, an increased uptake was noted for the hippocampus and striatum, suggesting that [^{11}C]MPEP binds nonspecifically to these brain regions. No reasons have been provided by the authors to explain this phenomenon. For the olfactory bulb, the extent of specific binding was 45 and 61% at 5 and 40 min postinjection, respectively.

The radiosynthesis of [^{11}C]M-MPEP was accomplished by reacting [^{11}C]MeI with phenolic precursor in the presence of solid KOH powder in 85% radiochemical yield and 98% radiochemical purity (Scheme 13.6) (Yu et al. 2005). Moderate uptake was observed after tail vein injection of [^{11}C]M-MPEP into rats. Pre-administration of MPEP (10 mg/kg) induced a 60% decrease in [^{11}C]M-MPEP binding in the olfactory bulb 5 min postinjection. In other brain regions, the mGluR5 antagonist, MPEP, decreased [^{11}C]M-MPEP binding only during the early time
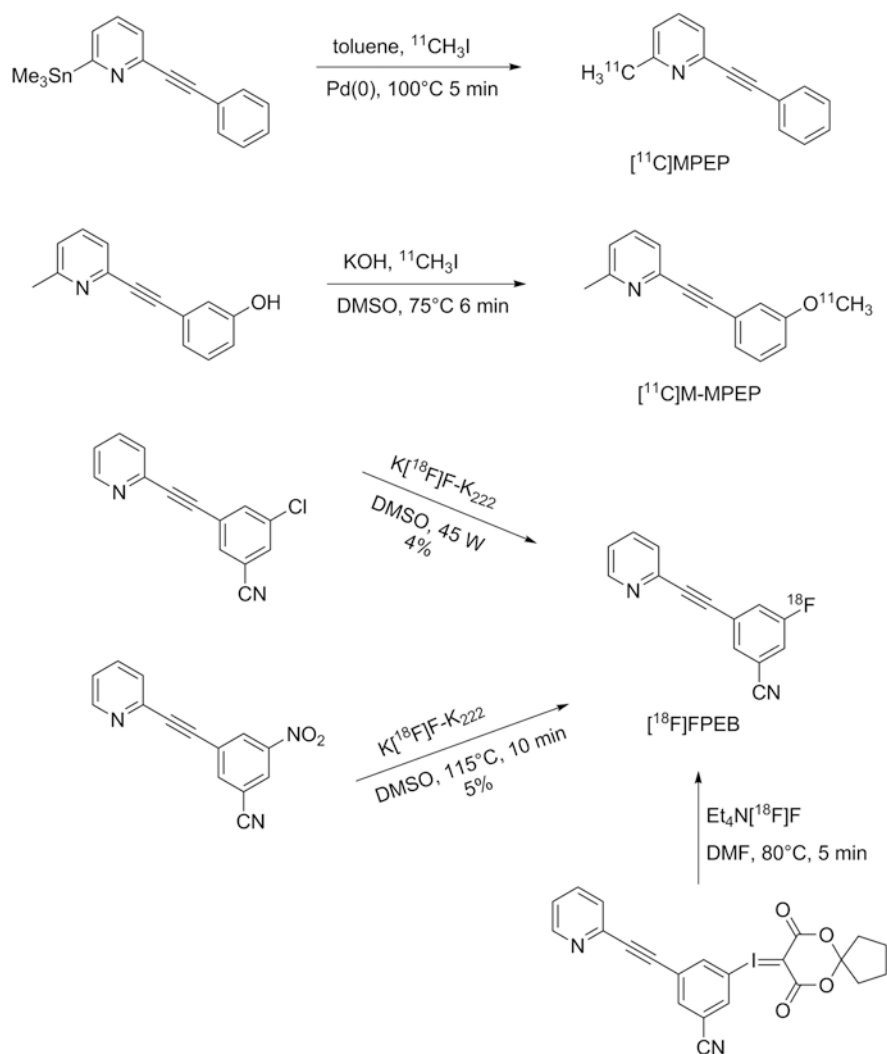
Scheme 13.6 Radiosyntheses of [¹¹C]MPEP, [¹¹C]M-MPEP, and [¹⁸F]FPEB

points: 45% in the cortex, 14% in the hippocampus, and 29% in the striatum at 5 min postinjection. At 40 min postinjection, a binding ratio of olfactory bulb to cerebellum was 4.2. Kokic et al. also reported on the radiosynthesis and the in vivo evaluation of [¹¹C]M-MPEP albeit in an abstract (Kokic et al. 2002). In their study, Kokic and colleagues found an increased uptake of [¹¹C]M-MPEP radioactivity 30 min postinjection in the rat brain after co-injection with unlabeled M-MPEP (1 mg/kg). However, no information was provided on radioactivity uptake in the olfactory bulb.

[^{11}C]M-PEPy was obtained by reacting the desmethyl precursor with either [^{11}C]MeI (Yu et al. 2005) or [^{11}C]CH$_3$OTf (Severance et al. 2006) in the presence of KOH or NaOH in moderate radiochemical yield. In vitro phosphor imaging with [^{11}C]M-PEPy using human and rat brain tissues demonstrated high specific binding in the hippocampus, striatum, and cortex with minimal specific binding in the cerebellum. The hippocampus-to-cerebellum ratio found in this study was 37 in rats and 8 in humans. However, further in vivo micro-PET studies in rats using urethane anesthesia, PET studies in baboons using isoflurane anesthesia, and ex vivo studies in rats showed little specific binding in the brain and very fast tracer washout (Severance et al. 2006). One possible explanation is that [^{11}C]M-PEPy is actively extruded from the brain by P-gp or some other multidrug-resistant like transport protein in the blood-brain barrier. Despite the promising in vitro results, the low signal-to-noise ratio found in vivo did not justify the use of [^{11}C]M-PEPy as a PET radiotracer in humans (Severance et al. 2006).

Kessler labeled 2-methyl-6-(3-fluoro-phenylethynyl)-pyridine (M-FPEP), another analogue of MPEP, with ^{11}C (Kessler 2014). [^{11}C]M-FPEP was prepared in good radiochemical yields and high molar activity starting from its bromo-pyridine precursor. Saturation assays of [^{11}C]M-FPEP binding resulted in a single high-affinity binding site with a K_d of 1.4 ± 0.1 nM and a B_{max} value of 563 ± 190 fmol/mg protein. Dynamic PET studies in a rat indicated rapid uptake of [^{11}C]M-FPEP in rat brain, followed by a fast clearance. Classical biodistribution studies in rats showed a homogeneous distribution of [^{11}C]M-FPEP in all brain regions examined, suggesting nonspecific uptake in the brain, which was also confirmed in blocking studies.

Based on the data summarized in Table 13.2, although moderate to high binding affinities toward mGluR5 for all the ^{11}C-labeled MPEP derivatives have been observed, their utility as mGluR5 imaging agents has been limited due to their unfavorable in vivo properties. The radiosynthesis of [^{18}F]FPEB ([^{18}F]3-fluoro-5-[(pyridin-3-yl)ethynyl] benzonitrile), a structural analogue of M-FPEP, was accomplished via a nucleophilic aromatic substitution reaction using either nitro or Cl$^-$ as a leaving group under conventional or microwave heating conditions (Belanger et al. 2008; Hamill et al. 2005; Patel et al. 2007; Wang et al. 2007). Low radiochemical yields were obtained under both conditions (Scheme 13.6). The low radiochemical yields may be due to the position of the leaving group which is not activated enough for aromatic nucleophilic substitution. Increased radiochemical yield (20% ± 5%, $n = 3$) was achieved when using a hypervalent spirocyclic iodonium(III) ylide precursor (Stephenson et al. 2015). High binding affinities of

Table 13.2 Lipophilicity, in vitro binding affinity, and specificity of ^{11}C-labeled MPEP derivatives

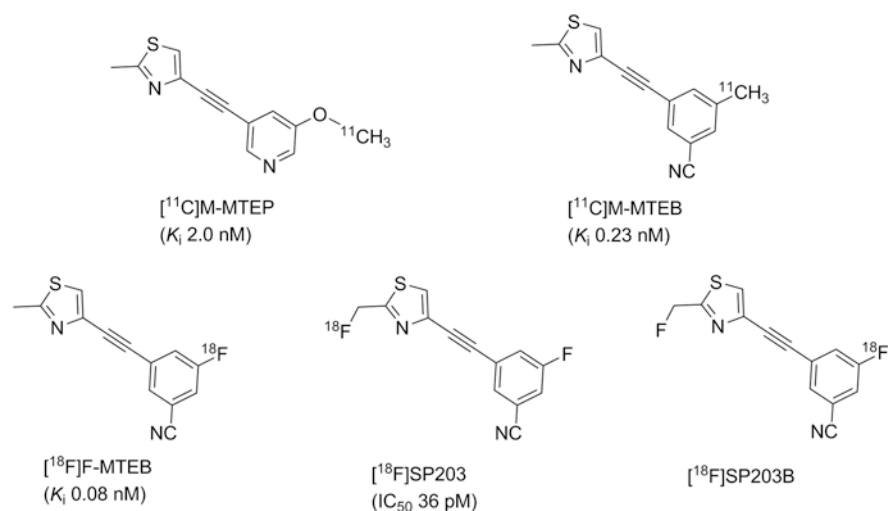| Compd	CLog$P$ [a]	IC$_{50}$	Specificity (brain)
[^{11}C]MPEP	3.6	20 nM	No
[^{11}C]M-MPEP	3.7	3.6 nM	Low
[^{11}C]M-PEPy	1.5	3.4 nM (K_d)[b]	Middle
[^{11}C]M-FPEP	2.5	1.4 nM (K_d)[b]	No

[a]CLog$P$ values were calculated based on ChemBioDraw software
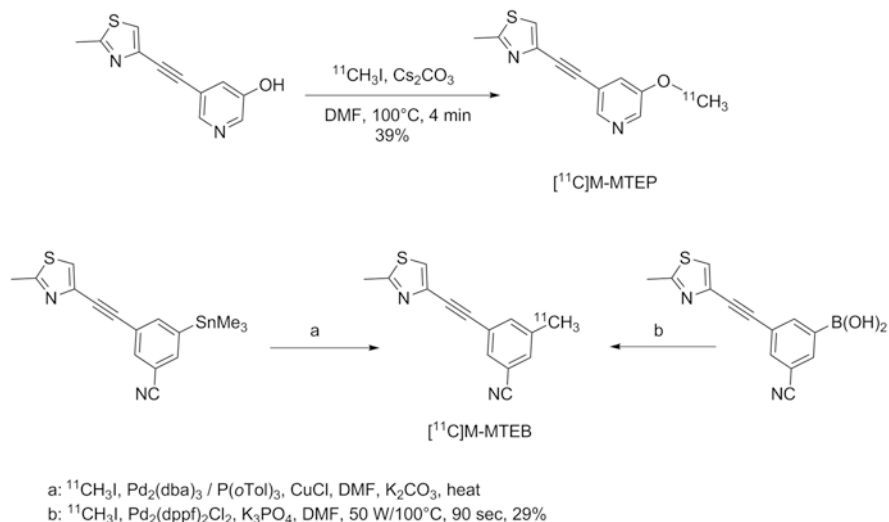[b]Obtained from saturation assays using [^{3}H]M-FPEP or [^{11}C]M-FPEP

[^{18}F]FPEB toward mGluR5 in rat, rhesus, and human brain sections have been reported (K_d = 0.1–0.15 nM, $n \geq 3$) (Patil et al. 2007). [^{18}F]FPEB showed an approximately 70% specific signal in the cortex and caudate-putamen of rat, rhesus, and human brain (Patil et al. 2007). Small animal PET imaging studies using Sprague-Dawley rats demonstrated that [^{18}F]FPEB accumulated in mGluR5-rich regions of the brain such as striatum and hippocampus with 77% specific binding after 20 min postinjection (Patel et al. 2005). In blocking studies of [^{18}F]FPEB, pretreatment with 3 mg/kg, MTEP did not result in identical residual uptake in all regions. When [^{18}F]FPEB was blocked with 10 mg/kg MTEP, nearly homogeneous uptake of tracer in all regions was observed, indicating full blockade had been achieved. It was also found that blocking mGluR5 is more efficient with MTEP than MPEP under the same conditions (Wang et al. 2007). PET imaging studies in a monkey also showed that [^{18}F]FPEB readily enters the brain and provides mGluR5-specific signal in all gray matter regions, including the cerebellum (Hamill et al. 2005). Initial human studies have been reported by Tamagnan (Tamagnan et al. 2009). Dynamic PET images of six human subjects examined so far revealed excellent penetration of [^{18}F]FPEB into human brain with initial visualization of anterior cingulate, thalamus, caudate, and midbrain, while cerebellum showed low uptake.

13.5.2 MTEP-Derived mGluR5 Tracers

Structural modification of MTEP (Fig. 13.5) led to M-MTEP (4-(5-methoxypyridin-3-yl)ethynyl-2-methyl-4,5-dihydrothiazole, K_i 2.0 nM) (Cosford et al. 2003a; Patel et al. 2005) and M-MTEB (3-methyl-5-[(2-methyl-1,3-thiazol-4-yl)

Fig. 13.7 Chemical structures of ^{11}C- and ^{18}F-labeled MTEP derivatives

a: [11C]CH$_3$I, Pd$_2$(dba)$_3$ / P(oTol)$_3$, CuCl, DMF, K$_2$CO$_3$, heat
b: [11C]CH$_3$I, Pd$_2$(dppf)$_2$Cl$_2$, K$_3$PO$_4$, DMF, 50 W/100°C, 90 sec, 29%

Scheme 13.7 Radiosynthetic routes to [11C]M-MTEP and [11C]M-MTEB

ethynyl]benzonitrile, K_i 0.23 nM) with improved binding affinity to mGluR5. The corresponding carbon-11- and fluorine-18-labeled PET radioligands derived from MTEP are shown in Fig. 13.7.

[11C]M-MTEP was synthesized by reacting the cesium salt of 5-((2-methyl-4,5-di-hydrothiazol-4-yl)ethynyl)pyridin-3-ol with [11C]MeI in 39% radiochemical yield (Patel et al. 2005). The [11C]methyl group in [11C]M-MTEB can be introduced by using either Stille (Suzuki et al. 1997) or Suzuki (Hostetler and Burns 2003) coupling reaction with [11C]MeI as shown in Scheme 13.7. However, due to the ease of precursor synthesis and radiolabeling, the Suzuki route (Scheme 13.7, pathway b) with aryl boronic acid as the precursor was chosen (Hamill et al. 2005). A radiochemical yield of 29% was obtained for [11C]M-MTEB using DMF as solvent. The total synthesis time was ~20–23 min, and the molar activity achieved was 70 GBq/μmol.

PET imaging studies with [11C]M-MTEP in a rat and a rhesus monkey showed a uniform distribution across most cerebral regions, and its clearance from the brain was also rapid, suggesting little retention by mGluR5 (Hamill et al. 2003; Krause et al. 2003). More promising results were obtained with [11C]M-MTEB. [11C]M-MTEB showed rapid uptake into the brain of rhesus monkey and provided large, long-lasting specific signals in mGluR5-rich regions such as the striatum, lower uptake in the frontal cortex, but surprisingly also specific uptake in the cerebellum, a region known to contain low densities of mGluR5. Species differences in the distribution of mGluR5 may account for this uptake in the cerebellum (Hamill et al. 2005).

[18F]F-MTEB ([18F]3-Fluoro-5-[(2-methyl-1,3-thiazol-4-yl)ethynyl]benzonitrile) was synthesized (Scheme 13.8) by the same synthetic route as shown for [18F]FPEB (Scheme 13.6) in low radiochemical yields (Hamill et al. 2005; Patel et al. 2005). The binding affinity (K_i) of F-MTEB toward mGluR5 was in the
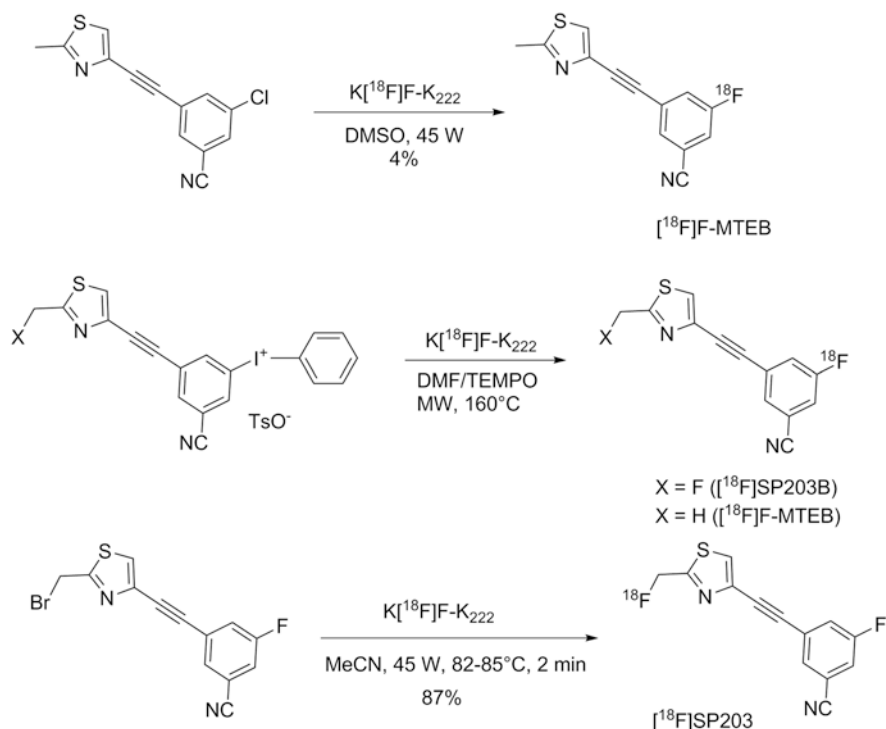
Scheme 13.8 Radiosynthetic routes to [18F]F-MTEB, [18F]SP203, and [18F]SP203B

subnanomolar range (80 pM). High-quality mGluR5-specific images in rat and rhesus monkey PET studies were obtained with [18F]F-MTEB. The low radiochemical yield of 4% would limit its application in human subjects; however, the recently reported high yielding method that uses iodonium salt as a precursor in the presence of TEMPO could increase the RCY of [18F]F-MTEB threefold to 20% (Telu et al. 2011). This is a step forward which would make possible the application of [18F]F-MTEB in humans.

3-Fluoro-5-(2-(2-(fluoromethyl)thiazol-4-yl)ethynyl) benzonitrile (designated SP203) an analogue of F-MTEB was found to have unusually high affinity (IC$_{50}$ = 36 pM) and potency in a phosphoinositol hydrolysis assay (IC$_{50}$ = 0.71 pM) for mGluR5 (Simeon et al. 2007). SP203 was labeled with fluorine-18 by treatment of its bromomethyl analogue with [18F]-fluoride in high radiochemical yield (87%, Scheme 13.8).

The PET evaluation of [18F]SP203 in a monkey demonstrated that a high proportion of radioactivity in brain was bound to mGluR5. However, radioactivity also accumulated in the bone, suggesting in vivo defluorination (Simeon et al. 2007). Ex vivo analysis of metabolites in rat brain extracts indicated that defluorination of [18F]SP203 occurs by glutathionylation at the 2-fluoromethyl group in [18F]SP203 (Shetty et al. 2008). [18F]SP203 was further evaluated in human subjects by the same group (Brown et al. 2008; Kimura et al. 2010). The results showed that

defluorination of [18F]SP203 was relatively small and that brain uptake could be robustly quantified. A recent study in nine healthy subjects using a bolus plus constant infusion protocol (equilibrium method) showed that this method is a viable alternative method and is slightly more precise than the standard bolus injection and kinetic modeling method (Kimura et al. 2012). To circumvent the problem of in vivo radiodefluorination, the aryl fluorine part of SP203 was recently labeled with 18F at the meta-position on the aromatic ring (Telu et al. 2011). Because this position is not activated enough toward aromatic nucleophilic substitution, iodonium salt was used as a precursor. A radiochemical yield of 33% was obtained (Scheme 13.8). Compared to [18F]SP203, it is expected that [18F]SP203B will show a higher in vivo stability with respect to in vivo 18F-defluorination.

13.5.3 ABP688-Related mGluR5 Tracers

Chemical modification of the original MPEP series allowed the identification of ABP688, a derivative in which the aromatic ring of the MPEP series is replaced by a functionalized cyclohexanone moiety (Fig. 13.8).

[11C]ABP688(3-(6-methyl-pyridin-2-ylethynyl)-cyclohex-2-enone-*O*-11C-methyl-oxime) was described in 2006 by Ametamey et al. (Ametamey et al. 2006). The radiosynthesis of ABP688 was accomplished by reacting desmethyl-ABP688 in anhydrous DMF with [11C]MeI at 90 °C for 5 min using sodium hydride as a base (Scheme 13.9). [11C]ABP688 showed an optimal log*D* value of 2.4 and high binding
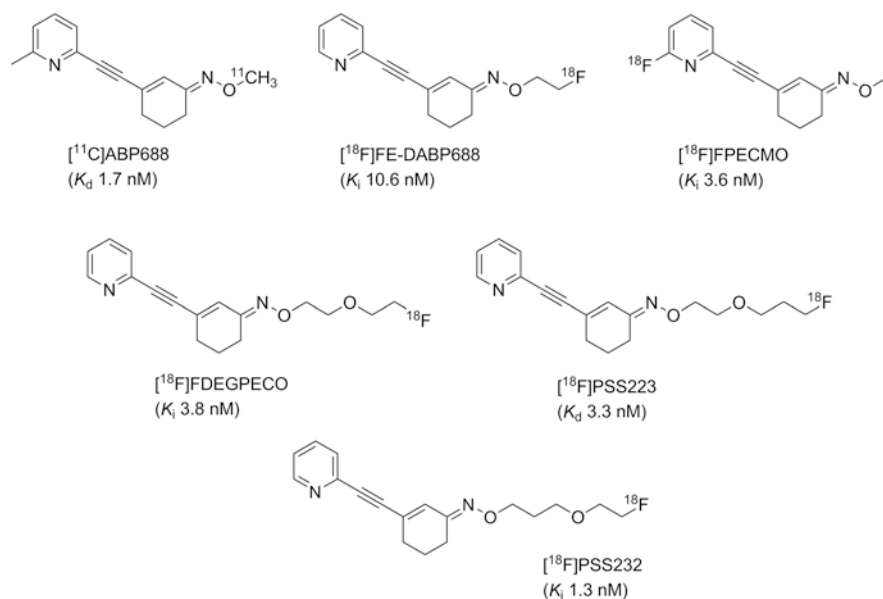
**Fig. 13.8** Chemical structures of 11C- and 18F-labeled ABP derivatives
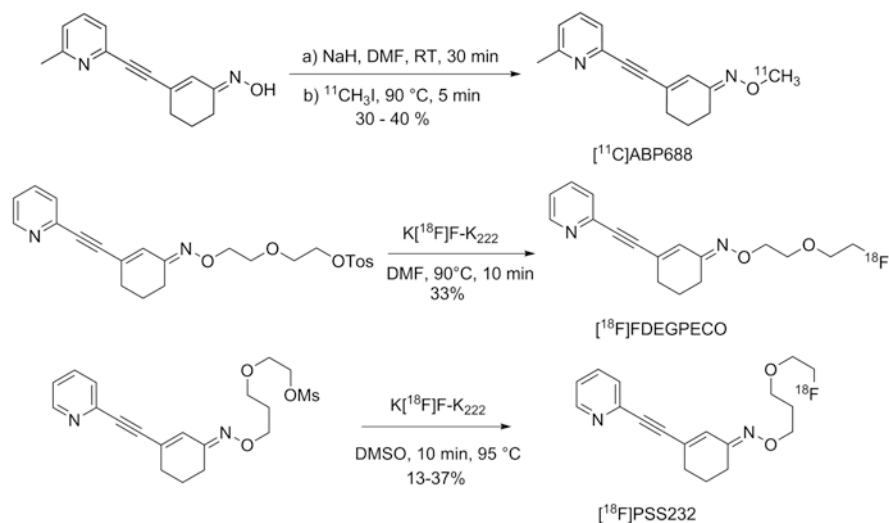
Scheme 13.9 Radiosyntheses of [^{11}C]ABP688, [^{18}F]FDEGPECO, and [^{18}F]PSS232

affinity to mGluR5 (K_d 1.7 nM in rat) with a B_{max} value of 231 ± 18 pmol/mg protein. Ex vivo autoradiography in wild-type mice and rats showed that the brain uptake of [^{11}C]ABP688 was highly selective and specific, with high heterogeneous accumulation in known mGluR5-rich regions such as the hippocampus, caudate putamen, and cortex. The specificity of [^{11}C]ABP688 binding was confirmed by blockade studies with M-MPEP (1 mg/kg), an antagonist for mGluR5. Up to 80% reduction in radioactivity uptake in mGluR5-rich regions (hippocampus, striatum) was observed; however, no blocking effect was observed in the cerebellum. The observed heterogeneity of tracer uptake is consistent with the known distribution of mGluR5 in the brain. The specificity of binding of [^{11}C]ABP688 was also confirmed in mGluR5-knockout mouse brain. Using the cerebellum as a reference region, radioactivity uptake ratios of 6.6 ± 0.1, 5.4 ± 0.1, and 4.6 ± 0.1 were obtained for the striatum, hippocampus, and cortex, respectively.

PET studies in rats and mice using a small animal PET scanner also demonstrated receptor-specific uptake in the brain regions known to be rich in mGluR5.

The first human PET studies on six healthy male volunteers using [^{11}C]ABP688 as the PET tracer were reported by the same group (Ametamey et al. 2007; Treyer et al. 2008). Relatively high radioactivity concentrations were observed in mGluR5-rich brain regions such as the anterior cingulate, medial temporal lobe, amygdala, caudate, and putamen, whereas radioactivity uptake in the cerebellum and white matter, regions known to contain low densities of mGluR5, was low (Fig. 13.9). Specific distribution volume as an outcome measure of mGluR5 density in the various brain regions ranged from 5.45 ± 1.47 (anterior cingulate) to 1.91 ± 0.32 (cerebellum), and the rank order of the corresponding specific distribution volumes of [^{11}C]ABP688 in cortical regions was temporal >frontal >occipital >parietal. The rank order of specific distribution volume obtained was in
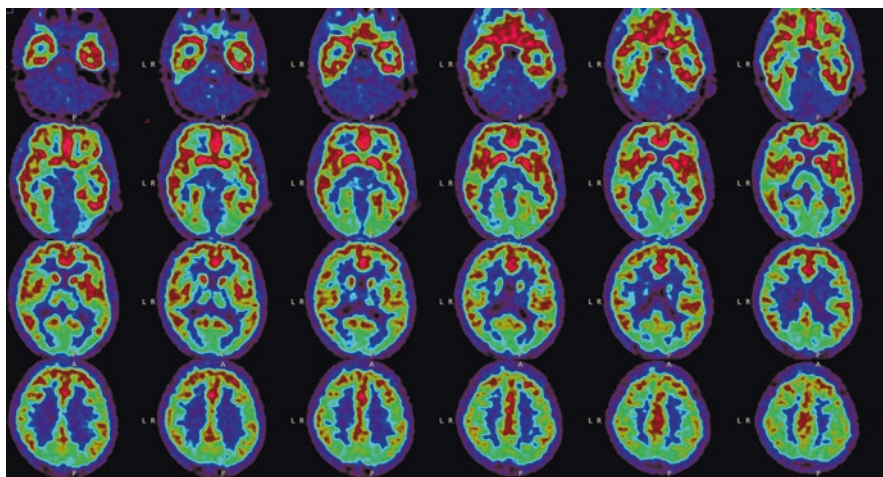
Fig. 13.9 Uptake of [^{11}C]ABP688 in a healthy volunteer

accordance with the reported distribution pattern of mGluR5 in rodents and humans. These results indicated that [^{11}C]ABP688 has suitable characteristics in humans and is a promising PET ligand for imaging mGluR5 distribution in humans.

Encouraged by the animal and human PET imaging results of [^{11}C]ABP688, several novel ^{18}F-labeled ABP688 derivatives have been evaluated as potential mGluR5 imaging agents by the group that first reported on [^{11}C]ABP688 (Wanger-Baumann et al. 2011; Baumann et al. 2010; Honer et al. 2007; Lucatelli et al. 2009; Sephton et al. 2012; Sephton et al. 2015).

[^{18}F]FE-DABP688 was produced by reacting 2-[^{18}F]-fluoroethyl tosylate with the sodium salt of 3-(pyridin-2-ylethynyl)-cyclohex-2-enone-oxime in dry DMF. The isolated radiochemical yield was $25 \pm 8\%$ (Honer et al. 2007). Saturation assays of [^{18}F]FE-DABP688 revealed a single high-affinity binding site with a K_d of 1.6 nM and a B_{max} value of 119 ± 24 fmol/mg protein. Biodistribution and PET studies of [^{18}F]FE-DABP688 in rats indicated radioactivity uptake in mGluR5-rich regions such as the hippocampus, striatum, and cortex, while radioactivity accumulation in the cerebellum was significantly low. Although the obtained PET image quality of [^{18}F]FE-DABP688 was comparable to that of [^{11}C]ABP688, [^{18}F]FE-DABP688 displayed unfavorable pharmacokinetics in the anesthetized rat with a fast washout from the forebrain resulting in a relatively short-lived signal. Consequently, [^{18}F]FE-DABP688 was abandoned and was not further exploited in primates.

[^{18}F]-(E)-3-((6-Fluoropyridin-2-yl)ethynyl)cyclohex-2-enone O-methyl oxime ([^{18}F]FPECMO) is another derivative of [^{11}C]ABP688 (Lucatelli et al. 2009). It was synthesized in a one-step reaction sequence by reacting K[^{18}F]F–K$_{222}$ complex with (E)-3-((6-bromopyridin-2-yl)ethynyl)cyclohex-2-enone O-methyl oxime in dry DMSO. The radiochemical yield after semi-preparative HPLC was 35%, and molar
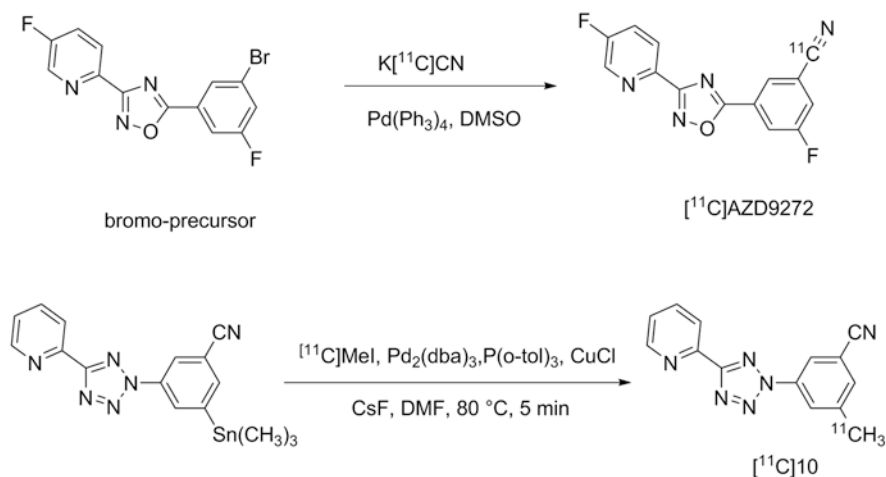
Scheme 13.10 Radiosynthesis of [^{11}C]AZD9272 and [^{11}C]10

activity was greater than 240 GBq/µmol. [^{18}F]FPECMO exhibited optimal lipophilicity (log$D$ = 2.1) and high metabolic stability in vitro. Displacement studies revealed a K_i value of 3.6 nM for FPECMO. Biodistribution studies and ex vivo autoradiographies confirmed this specificity revealing highest radioactivity accumulation in mGluR5-rich brain regions. Despite high metabolic stability in various in vitro test systems, a rapid defluorination of the radiolabeled substance was observed in rats in vivo.

[^{18}F]FDEGPECO   (*E*)-3-(pyridin-2-ylethynyl)cyclohex-2-enone   *O*-2-(2-fluoroethoxy)ethyl oxime is one of the most recently developed ABP688 derivatives (Wanger-Baumann et al. 2011; Baumann et al. 2010). A K_i value of 3.8 ± 0.4 (*n* = 3) nM was obtained for FDEGPECO, and the radioligand was synthesized in one-step reaction sequence by reacting K[^{18}F]F–K$_{222}$ complex with the corresponding tosyl precursor in anhydrous DMF (Scheme 13.10) in good radiochemical yield and high molar activity. Scatchard plot analysis indicated two affinity binding sites with dissociation constants of 0.6 ± 0.2 nM and 13.7 ± 4.7 nM (*n* = 3) and B_{max1} and B_{max2} values ranging from 470 to 1870 fmol/mg and from 4.0 to 15.6 pmol/mg protein, respectively. The in vitro autoradiography on rat brain slices showed a heterogeneous uptake consistent with the distribution of mGluR5 in the rat brain. PET imaging on rats revealed specific uptake of radioactivity in the mGluR5-rich brain regions. Postmortem biodistribution studies in rats that received intravenous injections of 8–16 MBq [^{18}F]FDEGPECO at 15 min p.i. confirmed the distribution pattern observed in PET. The highest radioactivity concentrations were observed in mGluR5-rich brain regions. The hippocampus/cerebellum and striatum/cerebellum ratios were 2.8 and 3.3, respectively. [^{18}F]FDEGPECO is one of the most promising fluorine-18-labeled ABP688 analogues so far although its background activity is relatively high and the radioactivity ratios when compared to [^{11}C]ABP688 (Ametamey et al. 2006) are lower.

[^{18}F]PSS223   ((*E*)-3-(pyridin-2-ylethynyl)cyclohex-2-enone   *O*-(2-(3-18F-fluoropropoxy)ethyl) oxime), an [^{18}F]FDEGPECO analogue, was designed with the aim to increase the lipophilicity of the ligand, in which the side chain was extended by one methylene group (Sephton et al. 2012). [^{18}F]PSS223 was obtained in 20% decay-corrected radiochemical yield. Experimentally determined log*D* value of [^{18}F]PSS223 was 1.89, which is 0.2 log units higher than that of [^{18}F]FDEGPECO (Baumann et al. 2010) as expected. The in vitro binding affinity of [^{18}F]PSS223 was measured directly in a Scatchard assay to give a K_d value of 3.34 ± 2.05 nM. In vitro autoradiography on horizontal rat brain slices showed heterogeneous distribution of [^{18}F]PSS223 with the highest accumulation in brain regions where mGluR5 is highly expressed (hippocampus, striatum, and cortex). Autoradiography in vitro under blockade conditions with ABP688 also confirmed the high specificity of [^{18}F]PSS223 for mGluR5. Under the same blocking conditions but using the mGluR1 antagonist, JNJ-16259685, no blockade was observed demonstrating the selectivity of [^{18}F]PSS223 for mGluR5 over mGluR1. [^{18}F]PSS223 was stable in PBS and rat plasma but was significantly metabolized by rat liver microsomal enzymes and to a lesser extent by human liver microsomes. Within 60 min, 90 and 20% of [^{18}F]PSS223 were metabolized by rat and human microsome enzymes, respectively. PET studies showed that [^{18}F]PSS223 has a fast clearance and only a weak accumulation in mGluR5-rich brain regions. A significant accumulation of radioactivity in the skull and jaws was also observed suggesting in vivo defluorination of [^{18}F]PSS223. Consequently a clear-cut visualization of mGluR5-rich brain regions in vivo in rats was not possible.

The difference in the in vivo behavior of [^{18}F]PSS223 and [^{18}F]FDEGPECO could be attributed to the β-heteroatom effect (French et al. 1993), by which primary aliphatic ^{18}F-atoms in a β-position to heteroatom (e.g., [^{18}F]FCH$_2$CH$_2$OR) are found to be metabolized at a slower rate. This is in line with the absence of in vivo radiodefluorination of [^{18}F]FDEGPECO and also (E)-3-(pyridin-2-ylethynyl) cyclohex-2-enone O-(3-(2-[^{18}F]-fluoroethoxy)propyl) oxime ([^{18}F]PSS232). [^{18}F]PSS232 was designed by our group to improve the metabolic stability of [^{18}F]PSS223 by switching the oxygen atom located between the ethylene and the fluoropropyl moieties by one CH$_2$ unit to the right in the side chain (Fig. 13.8). From the two geometrical E and Z isomers of PSS232, the E-geometrical isomer was shown to exhibit a higher binding affinity when compared to the Z-isomer (1 nM for E-isomer vs. 15 nM for Z-isomer). The E-isomer was radiolabeled in one step via nucleophilic substitution of a mesylate leaving group and evaluated in vitro and in vivo (Sephton et al. 2015; Sephton et al. 2013). As expected, increased in vitro stabilities were observed with rat and human microsomal enzymes in 60 min (20% hydrophilic radiometabolites for rat, 4% for human, respectively). No hydrophilic decomposition products or radiometabolites were found in PBS or plasma. The specificity of [^{18}F]PSS232 was confirmed in in vitro autoradiography on rat brain slices and in vivo PET images. Radioactivity distribution pattern was consistent with the known distribution of mGluR5 in rat brain with high binding to hippocampal and cortical regions and negligible radioactivity in the cerebellum. Under displacement conditions with MMPEP, reduced [^{18}F]PSS232 binding was found in all brain regions except the

cerebellum. Test-retest studies were reproducible with a variability ranging from 6.8% to 8.2%. An extended single-dose toxicity study in Wistar rats showed no compound-related adverse effects (Sephton et al. 2015). Encouraged by the promising preclinical data obtained with [18F]PSS232 in rodents, its potential for imaging mGluR5 density in humans was investigated by the same research group (Warnock et al. 2018). [18F]PSS232 was evaluated in ten healthy male volunteers aged 20–40 years old, and seven of the volunteers were additionally scanned with [15O]water for cerebral blood flow determination. Arterial blood activity was measured using an online blood counter. Brain uptake of [18F]PSS232 was very similar to its analog [11C]ABP688 and matched the distribution pattern of mGluR5. The uptake kinetics of [18F]PSS232 followed a two-tissue compartment model (Warnock et al. 2018). [18F]PSS232 is thus the only fluorinated derivative of [11C]ABP688 which has so far shown utility for imaging mGluR5 in humans, and it is hoped that this new fluorinated version of ABP688 will find a wider application in clinical studies in the near future. Recently, [18F]PSS232 was evaluated in our group for its usefulness to measure mGluR5 expression levels in LPS-induced murine neuroinflammation model and postmortem tissue samples from AD and amyotrophic lateral sclerosis (ALS) patients (Muller Herde et al. 2019). The results indicated that LPS-induced neuroinflammation lead to increased mGluR5 expression in mouse brain. Levels of mGluR5 in human AD and ALS postmortem brain tissues were also found to be several-fold increased compared to control brains. These results suggest that mGluR5 is a useful target to consider in neuroinflammation diseases and that diagnosis and the therapy monitoring of AD and ALS patients could be accomplished via mGluR5 imaging.

13.5.4 Other Type of mGluR5 Radioligands Without Alkyne Moiety in MPEP

[11C]AZD9272 (3-fluoro-5-(3-(5-fluoropyridin-2-yl)-1,2,4-oxadiazol-5-yl)benzo-[11C]nitrile) was labeled using palladium mediated 11C-cyanation (Andersson et al. 2013). Reacting the bromo-precursor 5-(3-bromo-5-fluorophenyl)-3-(5-fluoropyridin-2-yl)-1,2,4-oxadiazol with K[11C]CN in the presence of Pd(PPh₃) (5.5 mg, 4.8 μmol) afforded [11C]AZD9272 over 50% incorporation yield from hydrogen [11C]cyanide in a total synthesis time of 45–50 min (Scheme 13.10). AZD9272 showed high affinity ($K_D = 3.8 \pm 0.7$ nM) toward human mGluR5 and shared the same allosteric binding site as MPEP (Raboisson et al. 2012). In PET studies using Cynomolgus monkeys, high and heterogeneous brain uptake were demonstrated. The highest radioactivity was seen in the caudate, cingulate gyrus, and thalamus, whereas uptake was moderate in temporal cortex and lower in the cerebellum. Co-injection of unlabeled AZD9272 led to significantly decreased radioactivity in many brain regions (Andersson et al. 2013). Further studies revealed unique binding sites of [11C]AZD9272 in primate brain (Varnas et al. 2018). The binding of [11C]AZD9272 in NHP was almost completely inhibited by the structurally unique mGluR5 compound fenobam (2.0 mg/kg; 98% occupancy). In contrast, unlabeled

MTEP and ABP688 (2.0 mg/kg) inhibited [^{11}C]AZD9272 binding only partially by 20% and 46%, respectively. The authors concluded that additional PET studies employing multiple doses of fenobam should be done to further assess the binding of fenobam at AZD9272 binding sites (Varnas et al. 2018).

3-(−[^{11}C]methyl)-5-(5-(pyridin-2-yl)-2H-tetrazol-2-yl)benzonitrile   designated as [^{11}C]10 in the publication of Shimodu and co-workers (Shimoda et al. 2016) has similar structural attributes as AZD9272, i.e., a tetrazole ring instead of the alkyne group (in MPEP) between two the aromatic rings. A binding affinity (K_i) of 9.4 nM and moderate lipophilicity (cLogD, 2.4) have been reported for this compound. The radiolabeling was performed by reacting the arylstannyl precursor with [^{11}C]methyl iodide (Scheme 13.10). PET imaging with [^{11}C]10 in rats visualized the regional distribution of mGluR5 and demonstrated high reliability for quantification of mGluR5 density in test-retest PET studies. This radioligand might serve as a useful lead compound for development new PET ligands with higher affinity and more specific binding to mGluR5 (Shimoda et al. 2016).

Among all the abovementioned mGluR5 PET ligands, [^{11}C]ABP688 and [^{18}F]FPEB are the most successful and widely used PET tracers for imaging mGluR5 in humans. The first-in-man PET studies with [^{18}F]PSS232 confirmed its utility for mapping mGluR5 in humans. The longer physical half-life of F-18 (110 min) and its easy/high yield radiolabeling process will make [^{18}F]PSS232 a very attractive mGluR5 tracer for PET centers without cyclotron facilities.

13.6   Application of mGluR Tracers

With the availability of suitable mGluR5 radioligands, the utility of mGluR5 PET radioligands for drug development and the study of psychiatric and neurological diseases have been demonstrated by various studies in humans and rodents as illustrated in Table 13.3. As mentioned earlier, [^{11}C]ABP688 and [^{18}F]FPEP are the most widely used tracers for imaging mGluR5 densities in the brain. Compared to healthy individuals, altered mGluR5 availability was observed in the brain of stressed subjects, epilepsy, Parkinson's disease, and adults with autism and behavioral variant frontotemporal dementia patients (DuBois et al. 2016a; Fatemi et al. 2018; Holmes et al. 2017; Kang et al. 2019; Lam et al. 2019; Leuzy et al. 2016). Downregulation of mGluR5 was demonstrated in smokers and patients with depression, while sleep-deprived subjects and alcohol use disorders showed an increased mGluR5 availability compared to the healthy controls (Akkus et al. 2013; Akkus et al. 2018; Hefti et al. 2013; Holst et al. 2017). Species difference was realized in the studies of drug induced changes in extracellular glutamate levels on mGluR5 tracer binding in the brains of humans and rodents. In humans, lower [^{11}C]ABP688 binding was observed after administration of ketamine, known to increase glutamate levels (DeLorenzo et al. 2015; Esterlis et al. 2018a), while contradictory results were obtained in rat studies. Increased mGluR5 availability was visualized in rats after administration of ceftriaxone, which decreases glutamate (Zimmer et al. 2015); however, no change in mGluR5 availability was indicated when [^{11}C]ABP688 or [^{18}F]PSS232 was used

Table 13.3 Application of mGluR5 PET tracers and main findings

PET tracer	Application	Subject	Main findings	Reference
[¹¹C] ABP688	Major depressive disorder	Human	Severity of depression correlated negatively with mGluR5 binding in the hippocampus	Deschwanden et al. (2011)
[¹¹C] ABP688	Nicotine addiction	Human	Marked global reductions in mGluR5 binding in smokers and ex-smokers	Akkus et al. (2013)
[¹¹C] ABP688	Pilocarpine-induced chronic epilepsy	Rat	mGluR5 availability changes during epileptogenesis in the rat models	Choi et al. (2014)
[¹¹C] ABP688	Ketamine administration	Human	Decreased mGluR5 binding after ketamine administration	DeLorenzo et al. (2015)
[¹⁸F] FPEB	Receptor occupancy	Rat	Useful as a biomarker for drug development, but in vitro/in vivo difference exists	Rook et al. (2015)
[¹⁸F] FPEB	ALS model expressing SOD1- G93A gene	Mouse	Enhanced expression of mGluR5	Brownell et al. (2015)
[¹¹C] ABP688	Epilepsy (ocal cortical dysplasia, FCD)	Human	Reduced mGluR5 availability in FCD	DuBois et al. (2016a)
[¹¹C] ABP688	Age/sex difference	Human	No sex/age effect in healthy subjects	DuBois et al. (2016b)
[¹¹C] ABP688	Behavioral variant frontotemporal dementia (bvFTD)	Human	Decreased availability of mGluR5 in bvFTD	Leuzy et al. (2016)
[¹⁸F] FPEB	Novelty-seeking temperament	Human	High novelty-seeking temperament was robustly associated with increased mGluR5 availability	Leurquin-Sterk et al. (2016)
[¹⁸F] FPEB	Posttraumatic stress disorder (PTSD)	Human	Higher mGluR5 availability in PTSD	Holmes et al. (2017)
[¹⁸F] FPEB	Major depressive disorder	Human	No significant difference of mGluR5 availability	Abdallah et al. (2017)
[¹¹C] ABP688	Schizophrenia	Human	mGluR5 binding has no difference in schizophrenia from healthy control	Akkus et al. (2017)
[¹¹C] ABP688	Huntington disease (Q175 mouse model)	Mouse	Reduced mGluR5 availability in Q175 mouse	Bertoglio et al. (2018)
[¹⁸F] FPEB	Parkinson's disease (6-OHDA); levodopa-induced dyskinesia (LID)	Rat	Alterated mGluR5 availability in PD and LID rats	Crabbe et al. (2018)
[¹⁸F] PSS232	Ketamine or ceftriaxone	Rat	No change of mGluR5 availability	Muller Herde et al. (2018)

Table 13.3 (continued)

PET tracer	Application	Subject	Main findings	Reference
[^{18}F] FPEB	Adults with autism	Human	mGluR5 binding is altered in critical brain areas of subjects with autism	Fatemi et al. (2018)
[^{18}F] FPEB	Cocaine self-administration	Rat	Reduced mGluR5 availability in rats	de Laat et al. (2018)
[^{11}C] ABP688	Ketamine infusion	Rat	No change of mGluR5 availability	Kosten et al. (2018)
[^{11}C] ABP688	Alcohol use disorder	Human	Altered mGluR5 signaling in the amygdala in alcohol use disorder	Akkus et al. (2018)
[^{11}C] ABP688	Major depressive disorder	Human	Ketamine-induced reduction in mGluR5 availability is associated with an antidepressant response	Esterlis et al. (2018b)
[^{18}F] PSS232	LPS-induced Neuroinflammation	Mouse	Increased mGluR5 levels in LPS-treated mouse brain	Muller Herde et al. (2019)
[^{18}F] FPEB	Alcohol exposure	Rat	Decreased mGluR5 availability in the hippocampus	de Laat et al. (2019)
[^{18}F] FPEB	Parkinson's disease (PD)	Human	Slightly increased mGluR5 availability	Kang et al. (2019)
[^{11}C] ABP688	Sex differences	Human	PET [^{11}C]ABP688 is higher in healthy men than women	Smart et al. (2019b)
[^{11}C] ABP688	Mesial temporal lobe epilepsy (MTLE)	Human	Reduced mGluR5 availability	Lam et al. (2019)

to assess endogenous glutamate fluctuations induced by either ketamine or ceftriaxone (Kosten et al. 2018; Muller Herde et al. 2018). [^{11}C]ABP688 binding to brain tissue was reported to be higher in healthy men than in women (Akkus et al. 2013; Smart et al. 2019b); however, some other studies found no effect of gender on radioligand binding (Abdallah et al. 2017; DuBois et al. 2016b). Given that the (Z)-isomer of [^{11}C]ABP688 has a low affinity and affects binding potential values (Smart et al. 2019a), efforts should be undertaken to minimize the amount of the (Z)-isomer in the formulated solution of [^{11}C]ABP688. [^{11}C]ABP688 has shown good reproducibility of mGluR5 quantification in rodents and non-human primates (DeLorenzo et al. 2011b; Elmenhorst et al. 2012). In humans, high within-subject variability of V_T and BP_{ND} in the same-day scans was observed in test-retest studies with [^{11}C]ABP688 (DeLorenzo et al. 2017; DeLorenzo et al. 2011a); however, variability was low when the time interval between the scans was greater than 7 days (Burger et al. 2010). Test-retest variability for [^{18}F]FPEB was also high when scans were performed on the same day. Because similar high same-day within-subject variability was observed for both [^{11}C]ABP688 and [^{18}F]FPEB, it is suggested that this phenomenon may be related to alterations in glutamatergic activity which cause

up- and downregulation of mGluR5 (DeLorenzo et al. 2017; DeLorenzo et al. 2011a). It is further suggested that studies using these radiotracers should be carefully controlled and that further work should be done to determine sources and mechanisms of mGluR5 PET tracer variability in humans (Smart et al. 2018).

The mGluR1 PET tracer [^{11}C]ITMM has been used for several clinical studies since its first-in-man study in 2013 (Toyohara et al. 2013b). Decreased mGluR1 availability was observed in a patient with spinocerebellar ataxia type 6 compared to age-matched healthy controls (Ishibashi et al. 2015). In comparison with the most often used [^{18}F]FDG, [^{11}C]ITMM demonstrated higher specificity for evaluating cerebellar ataxia in human subjects (Ishibashi et al. 2017). Recently, [^{11}C]ITMM was also used in a PET study to measure mGluR1 in relatively early stage of Alzheimer's disease patients; however, no significant changes in mGluR1 availability were found in these patients (Ishibashi et al. 2019). Future studies in patients with the fluorinated derivative, [^{18}F]FIMX, for imaging mGluR1 are highly expected given its demonstrated utility in first-in-man studies (Zanotti-Fregonara et al. 2016).

In summary, a number of group I mGluRs ligands have been successfully used to label mGluR1 and mGluR5 in vitro. The development of these ligands into useful PET tracers in vivo, however, in most cases failed due to high nonspecific binding, unfavorable brain uptake kinetics, and/or limited metabolic stability. So far, only three mGluR5 and two mGluR1 PET radioligands have demonstrated their usefulness in human studies. Several chemical scaffolds as lead structures for targeting mGluR2 and mGluR4 subtypes are currently under evaluation as potential PET radioligands. We are optimistic that the translation of the pre-clinical results to the clinic will be feasible in the near future for radioligands targeting mGluR2 and mGluR4. There are currently no PET radioligands for mGluR subtypes 6, 7, and 8. Different mGluR subtype PET radioligands would have high utility in drug development programs by supporting the selection of appropriate doses of clinically relevant drugs and the determination of receptor occupancy of drugs, guiding proof of concept studies, and characterizing various disease states related to the type of receptor involved. Furthermore, they will have great implications for the identification of potential molecular therapeutic targets, in the development of new treatment strategies, and in helping to understand psychiatric and neurological diseases.

References

Abdallah CG, Hannestad J, Mason GF, Holmes SE, DellaGioia N, Sanacora G, Jiang L, Matuskey D, Satodiya R, Gasparini F et al (2017) Metabotropic glutamate receptor 5 and glutamate involvement in major depressive disorder: a multimodal imaging study. Biol Psychiatry Cogn Neurosci Neuroimaging 2:449–456

Abe T, Sugihara H, Nawa H, Shigemoto R, Mizuno N, Nakanishi S (1992) Molecular characterization of a novel metabotropic glutamate receptor Mglur5 coupled to inositol phosphate/Ca2+ signal transduction. J Biol Chem 267:13361–13368

Akkus F, Ametamey SM, Treyer V, Burger C, Johayem A, Umbricht D, Gomez Mancilla B, Sovago J, Buck A, Hasler G (2013) Marked global reduction in mGluR5 receptor binding in smokers

and ex-smokers determined by [11C]ABP688 positron emission tomography. Proc Natl Acad Sci U S A 110:737–742

Akkus F, Treyer V, Ametamey SM, Johayem A, Buck A, Hasler G (2017) Metabotropic glutamate receptor 5 neuroimaging in schizophrenia. Schizophr Res 183:95–101

Akkus F, Mihov Y, Treyer V, Ametamey SM, Johayem A, Senn S, Rosner S, Buck A, Hasler G (2018) Metabotropic glutamate receptor 5 binding in male patients with alcohol use disorder. Transl Psychiatry 8:17

Ametamey SM, Kessler LJ, Honer M, Wyss MT, Buck A, Hintermann S, Auberson YP, Gasparini F, Schubiger PA (2006) Radiosynthesis and preclinical evaluation of C-11-ABP688 as a probe for imaging the metabotropic glutamate receptor subtype 5. J Nucl Med 47:698–705

Ametamey SM, Treyer V, Streffer J, Wyss MT, Schmidt M, Blagoev M, Hintermann S, Auberson Y, Gasparini F, Fischer UC, Buck A (2007) Human PET studies of metabotropic glutamate receptor subtype 5 with C-11-ABP688. J Nucl Med 48:247–252

Ametamey SM, Honer M, Schubiger PA (2008) Molecular imaging with PET. Chem Rev 108:1501–1516

Anderson JJ, Bradbury MJ, Giracello DR, Chapman DF, Holtz G, Roppe J, King C, Cosford NDP, Varney MA (2003) In vivo receptor occupancy of mGlu5 receptor antagonists using the novel radioligand [H-3]3-methoxy-5-(pyridin-2-ylethynyl)pyridine. Euro J Pharmacol 473:35–40

Andersson JD, Seneca N, Truong P, Wensbo D, Raboisson P, Farde L, Halldin C (2013) Palladium mediated (1)(1)C-cyanation and characterization in the non-human primate brain of the novel mGluR5 radioligand [(1)(1)C]AZD9272. Nucl Med Biol 40:547–553

Andres JI, Alcazar J, Cid JM, De Angelis M, Iturrino L, Langlois X, Lavreysen H, Trabanco AA, Celen S, Bormans G (2012) Synthesis, evaluation, and radiolabeling of new potent positive allosteric modulators of the metabotropic glutamate receptor 2 as potential tracers for positron emission tomography imaging. J Med Chem 55:8685–8699

Annoura H, Fukunaga A, Uesugi M, Tatsuoka T, Horikawa Y (1996) A novel class of antagonists for metabotropic glutamate receptors, 7-(hydroxyimino)cyclopropa[b]chromen-1a-carboxylates. Bioorg Med Chem Lett 6:763–766

Augelli-Szafran CE, Schwarz RD (2003) Metabotropic glutamate receptors: agonists, antagonists and allosteric modulators. Ann Rep Med Chem 38:21–30

Baumann CA, Mu L, Johannsen S, Honer M, Schubiger PA, Ametamey SM (2010) Structure-activity relationships of fluorinated (E)-3-((6-methylpyridin-2-yl)ethynyl)cyclohex-2-enone-O-methyloxime (ABP688) derivatives and the discovery of a high affinity analogue as a potential candidate for imaging metabotropic glutamate recepors subtype 5 (mGluR5) with positron emission tomography (PET). J Med Chem 53:4009–4017

Bear MF (2005) Therapeutic implications of the mGluR theory of fragile X mental retardation. Genes Brain Behav 4:393–398

Belanger MJ, Krause SM, Ryan C, Sanabria-Bohorquez S, Li WP, Hamill TG, Burns HD (2008) Biodistribution and radiation dosimetry of [F-18]F-PEB in nonhuman primates. Nucl Med Commun 29:915–919

Bertoglio D, Kosten L, Verhaeghe J, Thomae D, Wyffels L, Stroobants S, Wityak J, Dominguez C, Mrzljak L, Staelens S (2018) Longitudinal characterization of mGluR5 using (11)C-ABP688 PET imaging in the Q175 mouse model of Huntington disease. J Nucl Med 59:1722–1727

Bettler B, Mulle C (1995) Review: neurotransmitter receptors. II AMPA and kainate receptors. Neuropharmacology 34:123–139

van der Born D, Pees A, Poot AJ, Orru RVA, Windhorst AD, Vugts DJ (2017) Fluorine-18 labelled building blocks for PET tracer synthesis. Chem Soc Rev 46:4709–4773

Bradley SR, Marino MJ, Wittmann M, Rouse ST, Awad H, Levey AI, Conn PJ (2000) Activation of group II metabotropic glutamate receptors inhibits synaptic excitation of the substantia nigra pars reticulata. J Neurosci 20:3085–3094

Brocke KS, Staufner C, Luksch H, Geiger KD, Stepulak A, Marzahn J, Schackert G, Temme A, Ikonomidou C (2010) Glutamate receptors in pediatric tumors of the central nervous system. Cancer Biol Ther 9:455–468

Brown AK, Kimura Y, Zoghbi SS, Simeon FG, Liow J-S, Kreisl WC, Tau A, Fujita M, Pike VW, Innis RB (2008) Metabotropic glutamate subtype 5 receptors are quantified in the human brain with a novel radioligand for PET. J Nucl Med 49:2042–2048

Brownell AL, Kuruppu D, Kil KE, Jokivarsi K, Poutiainen P, Zhu A, Maxwell M (2015) PET imaging studies show enhanced expression of mGluR5 and inflammatory response during progressive degeneration in ALS mouse model expressing SOD1-G93A gene. J Neuroinflammation 12:217

Burger C, Deschwanden A, Ametamey S, Johayem A, Mancosu B, Wyss M, Hasler G, Buck A (2010) Evaluation of a bolus/infusion protocol for 11C-ABP688, a PET tracer for mGluR5. Nucl Med Biol 37:845–851

Carroll FI (2008) Antagonists at metabotropic glutamate receptor subtype 5 structure activity relationships and therapeutic potential for addiction. Addict Rev 1141:221–232

Cartmell J, Schoepp DD (2000) Regulation of neurotransmitter release by metabotropic glutamate receptors. J Neurochem 75:889–907

Cha JH, Kosinski CM, Kerner JA, Alsdorf SA, Mangiarini L, Davies SW, Penney JB, Bates GP, Young AB (1998) Altered brain neurotransmitter receptors in transgenic mice expressing a portion of an abnormal human Huntington disease gene. Proc Natl Acad Sci U S A 95:6480–6485

Charvin D, Di Paolo T, Bezard E, Gregoire L, Takano A, Duvey G, Pioli E, Halldin C, Medori R, Conquet F (2018) An mGlu4-positive allosteric modulator alleviates parkinsonism in Primates. Mov Disord 33:1619–1631

Chen YL, Conn PJ (2008) mGluR(5) positive allosteric modulators. Drugs Future 33:355–360

Chen L, Nabulsi N, Naganawa M, Zasadny K, Skaddan MB, Zhang L, Najafzadeh S, Lin SF, Helal CJ, Boyden TL et al (2016) Preclinical evaluation of 18F-PF-05270430, a novel PET radioligand for the phosphodiesterase 2A enzyme. J Nucl Med 57:1448–1453

Chiechio S (2016) Modulation of chronic pain by metabotropic glutamate receptors. Adv Pharmacol 75:63–89

Choi KY, Chang K, Pickel JM, Badger JD 2nd, Roche KW (2011) Expression of the metabotropic glutamate receptor 5 (mGluR5) induces melanoma in transgenic mice. Proc Natl Acad Sci U S A 108:15219–15224

Choi H, Kim YK, Oh SW, Im HJ, Hwang DW, Kang H, Lee B, Lee YS, Jeong JM, Kim EE et al (2014) In vivo imaging of mGluR5 changes during epileptogenesis using [11C]ABP688 PET in pilocarpine-induced epilepsy rat model. PLoS One 9:e92765

Chua PC, Nagasawa JY, Bleicher LS, Munoz B, Schweiger EJ, Tehrani L, Anderson JJ, Cramer M, Chung J, Green MD et al (2005) Cyclohexenyl- and dehydropiperidinyl-alkynyl pyridines as potent metabotropic glutamate subtype 5 (mGlu5) receptor antagonists. Bioorg Med Chem Lett 15:4589–4593

Cid JM, Tresadern G, Duvey G, Lutjens R, Finn T, Rocher JP, Poli S, Vega JA, de Lucas AI, Matesanz E et al (2014) Discovery of 1-butyl-3-chloro-4-(4-phenyl-1-piperidinyl)-(1H)-pyridone (JNJ-40411813): a novel positive allosteric modulator of the metabotropic glutamate 2 receptor. J Med Chem 57:6495–6512

Clark DE (2003) In silico prediction of blood-brain barrier permeation. Drug Discov Today 8:927–933

Corti C, Aldegheri L, Somogyi P, Ferraguti F (2002) Distribution and synaptic localisation of the metabotropic glutamate receptor 4 (mGluR4) in the rodent CNS. Neuroscience 110:403–420

Cosford NDP, Tehrani L, Arruda J, King C, McDonald IA, Munoz B, Roppe J, Anderson E, Bristow L, Brodkin J et al (2002) 3-[(2-methyl-1,3-thiazol4-yl)etrynyl]pyredine (MTEP): design and synthesis of a potent and highly selective metabotropic glutamate subtype 5 (mGlu5) receptor antagonist with anxiolytic activity. Neuropharmacology 43:282–283

Cosford NDP, Roppe J, Tehrani L, Schweiger EJ, Seiders TJ, Chaudary A, Rao S, Varney MA (2003a) [H-3]-methoxymethyl-MTEP and [H-3]-methoxy-PEPy: potent and selective radioligands for the metabotropic glutamate subtype 5 (mGlu5) receptor. Bioorg Med Chem Lett 13:351–354

Cosford NDP, Tehrani L, Roppe J, Schweiger E, Smith ND, Anderson J, Bristow L, Brodkin J, Jiang XH, McDonald I et al (2003b) 3-[(2-methyl-1,3-thiazol-4-yl)ethynyl]-pyridine: a potent and highly selective metabotropic glutamate subtype 5 receptor antagonist with anxiolytic activity. J Med Chem 46:204–206

Crabbe M, Van der Perren A, Weerasekera A, Himmelreich U, Baekelandt V, Van Laere K, Casteels C (2018) Altered mGluR5 binding potential and glutamine concentration in the 6-OHDA rat model of acute Parkinson's disease and levodopa-induced dyskinesia. Neurobiol Aging 61:82–92

Dahl K, Halldin C, Schou M (2017) New methodologies for the preparation of carbon-11 labeled radiopharmaceuticals. Clin Transl Imaging 5:275–289

DeLorenzo C, Kumar JSD, Mann JJ, Parsey RV (2011a) In vivo variation in metabotropic glutamate receptor subtype 5 binding using positron emission tomography and [(11)C]ABP688. J Cereb Blood Flow Metab 31:2169–2180

DeLorenzo C, Milak MS, Brennan KG, Kumar JSD, Mann JJ, Parsey RV (2011b) In vivo positron emission tomography imaging with [(11)C]ABP688: binding variability and specificity for the metabotropic glutamate receptor subtype 5 in baboons. Euro J Nucl Med Mol Imaging 38:1083–1094

DeLorenzo C, DellaGioia N, Bloch M, Sanacora G, Nabulsi N, Abdallah C, Yang J, Wen R, Mann JJ, Krystal JH et al (2015) In vivo ketamine-induced changes in [(1)(1)C]ABP688 binding to metabotropic glutamate receptor subtype 5. Biol Psychiatry 77:266–275

DeLorenzo C, Gallezot JD, Gardus J, Yang J, Planeta B, Nabulsi N, Ogden RT, Labaree DC, Huang YH, Mann JJ et al (2017) In vivo variation in same-day estimates of metabotropic glutamate receptor subtype 5 binding using [(11)C]ABP688 and [(18)F]FPEB. J Cereb Blood Flow Metab 37:2716–2727

Deng X, Rong J, Wang L, Vasdev N, Zhang L, Josephson L, Liang SH (2018) Chemistry for positron emission tomography: recent advances in (11) C-, (18) F-, (13) N-, and (15) O-labeling reactions. Angew Chem Int Ed Engl 58:2580–2605

Deschwanden A, Karolewicz B, Feyissa AM, Treyer V, Ametamey SM, Johayem A, Burger C, Auberson YP, Sovago J, Stockmeier CA et al (2011) Reduced metabotropic glutamate receptor 5 density in major depression determined by [(11)C]ABP688 positron emission tomography and postmortem study. Curr Neuropharmacol 9:15–15

Dickerson JW, Conn PJ (2012) Therapeutic potential of targeting metabotropic glutamate receptors for Parkinson's disease. Neurodegener Dis Manag 2:221–232

DuBois JM, Rousset OG, Guiot MC, Hall JA, Reader AJ, Soucy JP, Rosa-Neto P, Kobayashi E (2016a) Metabotropic glutamate receptor type 5 (mGluR5) cortical abnormalities in focal cortical dysplasia identified in vivo with [11C]ABP688 positron-emission tomography (PET) imaging. Cereb Cortex 26:4170–4179

DuBois JM, Rousset OG, Rowley J, Porras-Betancourt M, Reader AJ, Labbe A, Massarweh G, Soucy JP, Rosa-Neto P, Kobayashi E (2016b) Characterization of age/sex and the regional distribution of mGluR5 availability in the healthy human brain measured by high-resolution [(11) C]ABP688 PET. Eur J Nucl Med Mol Imaging 43:152–162

Eckelman WC, Mathis CA (2006) Targeting proteins in vivo: in vitro guidelines. Nucl Med Biol 33:161–164

Eckelman WC, Kilbourn MR, Mathis CA (2006) Discussion of targeting proteins in vivo: in vitro guidelines. Nucl Med Biol 33:449–451

Elmenhorst D, Aliaga A, Bauer A, Rosa-Neto P (2012) Test-retest stability of cerebral mGluR(5) quantification using [(1)(1)C]ABP688 and positron emission tomography in rats. Synapse 66:552–560

Emmitte KA (2011) Recent advances in the design and development of novel negative allosteric modulators of mGlu(5). ACS Chem Neurosci 2:411–432

Engers DW, Niswender CM, Weaver CD, Jadhav S, Menon UN, Zamorano R, Conn PJ, Lindsley CW, Hopkins CR (2009) Synthesis and evaluation of a series of heterobiarylamides that are centrally penetrant metabotropic glutamate receptor 4 (mGluR4) positive allosteric modulators (PAMs). J Med Chem 52:4115–4118

Esterlis I, DellaGioia N, Pietrzak RH, Matuskey D, Nabulsi N, Abdallah CG, Yang J, Pittenger C, Sanacora G, Krystal JH et al (2018a) Ketamine-induced reduction in mGluR5 availability is associated with an antidepressant response: an [(11)C]ABP688 and PET imaging study in depression. Mol Psychiatry 23:824–832

Esterlis I, Holmes SE, Sharma P, Krystal JH, DeLorenzo C (2018b) Metabotropic glutamatergic receptor 5 and stress disorders: knowledge gained from receptor imaging studies. Biol Psychiatry 84:95–105

Fatemi SH, Wong DF, Brasic JR, Kuwabara H, Mathur A, Folsom TD, Jacob S, Realmuto GM, Pardo JV, Lee S (2018) Metabotropic glutamate receptor 5 tracer [(18)F]-FPEB displays increased binding potential in postcentral gyrus and cerebellum of male individuals with autism: a pilot PET study. Cerebellum Ataxias 5:3

Fotuhi M, Sharp AH, Glatt CE, Hwang PM, von Krosigk M, Snyder SH, Dawson TM (1993) Differential localization of phosphoinositide-linked metabotropic glutamate receptor (mGluR1) and the inositol 1,4,5-trisphosphate receptor in rat brain. J Neurosci 13:2001–2012

Fowler CJ. PET and drug research and Development_Fowler_1999.Pdf. 1999.

French AN, Napolitano E, VanBrocklin HF, Hanson RN, Welch MJ, Katzenellenbogen JA (1993) Synthesis, radiolabeling and tissue distribution of 11 beta-fluoroalkyl- and 11 beta-fluoroalkoxy-substituted estrogens: target tissue uptake selectivity and defluorination of a homologous series of fluorine-18-labeled estrogens. Nucl Med Biol 20:31–47

Fujinaga M, Yamasaki T, Kawamura K, Kumata K, Hatori A, Yui J, Yanamoto K, Yoshida Y, Ogawa M, Nengaki N et al (2011) Synthesis and evaluation of 6-[1-(2-[(18)F]fluoro-3-pyridyl)-5-methyl-1H-1,2,3-triazol-4-yl]quinoline for positron emission tomography imaging of the metabotropic glutamate receptor type 1 in brain. Bioorg Med Chem 19:102–110

Fujinaga M, Maeda J, Yui J, Hatori A, Yamasaki T, Kawamura K, Kumata K, Yoshida Y, Nagai Y, Higuchi M et al (2012a) Characterization of 1-(2-[(18) F]fluoro-3-pyridyl)-4-(2-isopropyl-1-oxo- isoindoline-5-yl)-5-methyl-1H-1,2,3-triazole, a PET ligand for imaging the metabotropic glutamate receptor type 1 in rat and monkey brains. J Neurochem 121:115–124

Fujinaga M, Yamasaki T, Maeda J, Yui J, Xie L, Nagai Y, Nengaki N, Hatori A, Kumata K, Kawamura K, Zhang MR (2012b) Development of N-[4-[6-(isopropylamino)pyrimidin-4-yl]-1,3-thiazol-2-yl]-N-methyl-4-[11C]methylb enzamide for positron emission tomography imaging of metabotropic glutamate 1 receptor in monkey brain. J Med Chem 55:11042–11051

Fujinaga M, Yamasaki T, Yui J, Hatori A, Xie L, Kawamura K, Asagawa C, Kumata K, Yoshida Y, Ogawa M et al (2012c) Synthesis and evaluation of novel radioligands for positron emission tomography imaging of metabotropic glutamate receptor subtype 1 (mGluR1) in rodent brain. J Med Chem 55:2342–2352

Fujinaga M, Yamasaki T, Nengaki N, Ogawa M, Kumata K, Shimoda Y, Yui J, Xie L, Zhang Y, Kawamura K, Zhang MR (2016) Radiosynthesis and evaluation of 5-methyl-N-(4-[(11) C]methylpyrimidin-2-yl)-4-(1H-pyrazol-4-yl)thiazol-2-amine ([(11)C]ADX88178) as a novel radioligand for imaging of metabotropic glutamate receptor subtype 4 (mGluR4). Bioorg Med Chem Lett 26:370–374

Gasparini F, Lingenhoehl K, Flor PJ, Stoehr N, Stierlin C, Heinrich M, Vranesic I, Allgeier H, Biollaz M, Heckendorn R et al (1999) Discovery of 2-methyl-6-(phenylethynyl)-pyridine (MPEP): a highly potent and selective mGluR5 antagonist. Neuropharmacology 38:52

Gasparini F, Andres H, Flor PJ, Heinrich M, Inderbitzin W, Lingenhohl K, Muller H, Munk VC, Omilusik K, Stierlin C et al (2002) [H-3]-M-MPEP, a potent, subtype-selective radioligand for the metabotropic glutamate receptor subtype 5. Bioorg Med Chem Lett 12:407–409

Gasparini F, Bilbe G, Gomez-Mancilla B, Spooren W (2008) mGluR5 antagonists: discovery, characterization and drug development. Curr Opin Drug Discovery Develop 11:655–665

Gereau RW, Conn PJ (1995) Roles of specific metabotropic glutamate-receptor subtypes in regulation of hippocampal Ca1 pyramidal cell excitability. J Neurophysiol 74:122–129

Ghose S, Crook JM, Bartus CL, Sherman TG, Herman MM, Hyde TM, Kleinman JE, Akil M (2008) Metabotropic glutamate receptor 2 and 3 gene expression in the human prefrontal cortex and mesencephalon in schizophrenia. Int J Neurosci 118:1609–1627

Gupta DS, McCullumsmith GE, Beneyto M, Haroutunian V, Davis KL, Meador-Woodruff JH (2005) Metabotropic glutamate receptor protein expression in the prefrontal cortex and striatum in schizophrenia. Synapse 57:123–131

Hamill TG, Seiders TJ, Krause S, Ryan C, Sanabria S, Gibson RE, Patel S, Cosford NDP, Roppe J, Yang J et al (2003) The synthesis and characterization of mGluR5 receptor PET ligands. J Label Compd Radiopharm 46:S184

Hamill TG, Krause S, Ryan C, Bonnefous C, Govek S, Seiders TJ, Cosford NDP, Roppe J, Kamenecka T, Patel S et al (2005) Synthesis, characterization, and first successful monkey imaging studies of metabotropic glutamate receptor subtype 5 (mGluR5) PET radiotracers. Synapse 56:205–216

Hefti K, Holst SC, Sovago J, Bachmann V, Buck A, Ametamey SM, Scheidegger M, Berthold T, Gomez-Mancilla B, Seifritz E, Landolt HP (2013) Increased metabotropic glutamate receptor subtype 5 availability in human brain after one night without sleep. Biol Psychiatry 73:161–168

Holmes SE, Girgenti MJ, Davis MT, Pietrzak RH, DellaGioia N, Nabulsi N, Matuskey D, Southwick S, Duman RS, Carson RE et al (2017) Altered metabotropic glutamate receptor 5 markers in PTSD: in vivo and postmortem evidence. Proc Natl Acad Sci U S A 114:8390–8395

Holst SC, Sousek A, Hefti K, Saberi-Moghadam S, Buck A, Ametamey SM, Scheidegger M, Franken P, Henning A, Seifritz E et al (2017) Cerebral mGluR5 availability contributes to elevated sleep need and behavioral adjustment after sleep deprivation. Elife 6:e28751

Honer M, Stoffel A, Kessler LJ, Schubiger PA, Ametamey SM (2007) Radiolabeling and in vitro and in vivo evaluation of [F-18]-FE-DABP688 as a PET radioligand for the metabotropic glutamate receptor subtype 5. Nucl Med Biol 34:973–980

Hong J, Lu S, Xu R, Liow JS, Woock AE, Jenko KJ, Gladding RL, Zoghbi SS, Innis RB, Pike VW (2015) [carbonyl-11C]4-Fluoro-N-methyl-N-(4-(6-(methylamino)pyrimidin-4-yl)thiazol-2-yl)benzamide ([11C]FIMX) is an effective radioligand for PET imaging of metabotropic glutamate receptor 1 (mGluR1) in monkey brain. Nucl Med Biol 42:967–974

Hostetler ED, Burns HD (2003) An improved synthesis of substituted [C-11]toluenes via Suzuki coupling with [C-11]methyl iodide. J Label Compd Radiopharm 46:S75

Hostetler ED, Eng W, Joshi AD, Sanabria-Bohorquez S, Kawamoto H, Ito S, O'Malley S, Krause S, Ryan C, Patel S et al (2011) Synthesis, characterization, and monkey PET studies of [(18)F]MK-1312, a PET tracer for quantification of mGluR1 receptor occupancy by MK-5435. Synapse 65:125–135

Huang YY, Narendran R, Bischoff F, Guo NN, Zhu ZH, Bae SA, Lesage AS, Laruelle M (2005) A positron emission tomography radioligand for the in vivo labeling of metabotropic glutamate 1 receptor: (3-ethyl-2-[C-11]methyl-6-quinolinyl) (cis-4-methoxycyclohexyl)methanone. J Med Chem 48:5096–5099

Huang Y, Narendran R, Bischoff F, Guo N, Bae SA, Hwang DR, Lesage AS, Laruelle M (2012) Synthesis and characterization of two PET radioligands for the metabotropic glutamate 1 (mGlu1) receptor. Synapse 66:1002–1014

Ishibashi K, Miura Y, Ishikawa K, Ishii K, Ishiwata K (2015) Decreased metabotropic glutamate receptor type 1 availability in a patient with spinocerebellar ataxia type 6: a (11)C-ITMM PET study. J Neurol Sci 355:202–205

Ishibashi K, Miura Y, Toyohara J, Ishii K, Ishiwata K (2017) Comparison of imaging using (11)C-ITMM and (18)F-FDG for the detection of cerebellar ataxia. J Neurol Sci 375:97–102

Ishibashi K, Miura Y, Toyohara J, Ishiwata K, Ishii K (2019) Unchanged type 1 metabotropic glutamate receptor availability in patients with Alzheimer's disease: a study using (11)C-ITMM positron emission tomography. Neuroimage Clin 22:101783

Ito S, Hirata Y, Nagatomi Y, Satoh A, Suzuki G, Kimura T, Satow A, Maehara S, Hikichi H, Hata M et al (2009) Discovery and biological profile of isoindolinone derivatives as novel metabotropic glutamate receptor 1 antagonists: a potential treatment for psychotic disorders. Bioorg Med Chem Lett 19:5310–5313

Jaeschke G, Wettstein JG, Nordquist RE, Spooren W (2008) mGlu5 receptor antagonists and their therapeutic potential. Expert Opin Ther Patents 18:123–142

Kang Y, Henchcliffe C, Verma A, Vallabhajosula S, He B, Kothari PJ, Pryor KO, Mozley PD (2019) 18F-FPEB PET/CT shows mGluR5 upregulation in Parkinson's disease. J Neuroimaging 29:97–103

Kessler LJ. Development of novel ligands for PET imaging of metabotropic glutamate receptor subtype 5 (mGLuR5). Dissertation No 15633, ETH-Zürich. 2014

Kil KE, Zhang Z, Jokivarsi K, Gong C, Choi JK, Kura S, Brownell AL (2013) Radiosynthesis of N-(4-chloro-3-[(11)C]methoxyphenyl)-2-picolinamide ([(11)C]ML128) as a PET radiotracer for metabotropic glutamate receptor subtype 4 (mGlu4). Bioorg Med Chem 21:5955–5962

Kil KE, Poutiainen P, Zhang Z, Zhu A, Choi JK, Jokivarsi K, Brownell AL (2014) Radiosynthesis and evaluation of an 18F-labeled positron emission tomography (PET) radioligand for metabotropic glutamate receptor subtype 4 (mGlu4). J Med Chem 57:9130–9138

Kil KE, Poutiainen P, Zhang Z, Zhu A, Kuruppu D, Prabhakar S, Choi JK, Tannous BA, Brownell AL (2016) Synthesis and evaluation of N-(methylthiophenyl)picolinamide derivatives as PET radioligands for metabotropic glutamate receptor subtype 4. Bioorg Med Chem Lett 26:133–139

Kimura Y, Simeon FG, Hatazawa J, Mozley PD, Pike VW, Innis RB, Fujita M (2010) Biodistribution and radiation dosimetry of a positron emission tomographic ligand, (18) F-SP203, to image metabotropic glutamate subtype 5 receptors in humans. Euro J Nucl Med Mol Imaging 37:1943–1949

Kimura Y, Simeon FG, Zoghbi SS, Zhang Y, Hatazawa J, Pike VW, Innis RB, Fujita M (2012) Quantification of metabotropic glutamate subtype 5 receptors in the brain by an equilibrium method using 18F-SP203. NeuroImage 59:2124–2130

Kohara A, Toya T, Tamura S, Watabiki T, Nagakura Y, Shitaka Y, Hayashibe S, Kawabata S, Okada M (2005) Radioligand binding properties and pharmacological characterization of 6-amino-N-cyclohexyl-N,3-dimethylthiazolo[3,2-a]benzimidazole-2-carboxamide (YM-298198), a high-affinity, selective, and noncompetitive antagonist of metabotropic glutamate receptor type 1. J Pharmacol Exp Ther 315:163–169

Kohara A, Takahashi M, Yatsugi S, Tamura S, Shitaka Y, Hayashibe S, Kawabata S, Okada M (2008) Neuroprotective effects of the selective type 1 metabotropic glutamate receptor antagonist YM-202074 in rat stroke models. Brain Res 1191:168–179

Kokic M, Honer M, Kessler LJ, Grauert M, Schubiger PA, Ametamey SM (2002) Synthesis and in vitro and in vivo evaluation of [C-11]methyl-BIII277CL for imaging the PCP-binding site of the NMDA receptor by PET. J Recept Signal Transduct Res 22:123–139

Kosten L, Verhaeghe J, Wyffels L, Stroobants S, Staelens S (2018) Acute ketamine infusion in rat does not affect in vivo [(11)C]ABP688 binding to metabotropic glutamate receptor subtype 5. Mol Imaging 17:1536012118788636

Krause SM, Hamill TG, Seiders TJ, Ryan C, Sanabria S, Gibson RE, Patel S, Cosford NDP, Roppe JR, Hargreaves RJ, Burns HD (2003) In vivo characterization of PET ligands for the mGluR5 receptor in rhesus monkey. Mol Imaging Biol 5:166

Kulkarni SS, Zou MF, Cao JJ, Deschamps JR, Rodriguez AL, Conn PJ, Newman AH (2009) Structure-activity relationships comparing N-(6-methylpyridin-yl)-substituted aryl amides to 2-Methyl-6-(substituted-arylethynyl)pyridines or 2-Methyl-4-(substituted-arylethynyl) thiazoles as novel metabotropic glutamate receptor subtype 5 antagonists. J Med Chem 52:3563–3575

Kumata K, Yamasaki T, Hatori A, Zhang Y, Mori W, Fujinaga M, Xie L, Okubo T, Nengaki N, Zhang MR (2017) Synthesis and in vitro evaluation of three novel radiotracers for imaging of metabotropic glutamate receptor subtype 2 in rat brain. Bioorg Med Chem Lett 27:3139–3143

Kumata K, Hatori A, Yamasaki T, Zhang Y, Mori W, Fujinaga M, Xie L, Nengaki N, Zhang MR (2019) Synthesis and evaluation of 4-(2-fluoro-4-[(11)C]methoxyphenyl)-5-((2-methylpyridin-4-yl)methoxy)picolinamide for PET imaging of the metabotropic glutamate receptor 2 in the rat brain. Bioorg Med Chem 27:483–491

de Laat B, Weerasekera A, Leurquin-Sterk G, Bormans G, Himmelreich U, Casteels C, Van Laere K (2018) Glutamatergic biomarkers for cocaine addiction: a longitudinal study using MR spectroscopy and mGluR5 PET in self-administering rats. J Nucl Med 59:952–959

de Laat B, Weerasekera A, Leurquin-Sterk G, Gsell W, Bormans G, Himmelreich U, Casteels C, Van Laere K (2019) Effects of alcohol exposure on the glutamatergic system: a combined longitudinal (18) F-FPEB and (1) H-MRS study in rats. Addict Biol 24:696–706

Lam J, DuBois JM, Rowley J, Gonzalez-Otarula KA, Soucy JP, Massarweh G, Hall JA, Guiot MC, Rosa-Neto P, Kobayashi E (2019) In vivo metabotropic glutamate receptor type 5 abnormalities localize the epileptogenic zone in mesial temporal lobe epilepsy. Ann Neurol 85:218–228

Lavreysen H, Pereira SN, Leysen JE, Langlois X, Lesage AS (2004a) Metabotropic glutamate 1 receptor distribution and occupancy in the rat brain: a quantitative autoradiographic study using [3H]R214127. Neuropharmacology 46:609–619

Lavreysen H, Wouters R, Bischoff F, Nobrega Pereira S, Langlois X, Blokland S, Somers M, Dillen L, Lesage AS (2004b) JNJ16259685, a highly potent, selective and systemically active mGlu1 receptor antagonist. Neuropharmacology 47:961–972

Lea PM, Faden AI (2006) Metabotropic glutamate receptor subtype 5 antagonists MPEP and MTEP. CNS Drug Rev 12:149–166

Lee B, Kim YK, Lee JY, Kim YJ, Lee YS, Lee DS, Chung JK, Jeong JM (2017) Preclinical anaylses of [(18)F]cEFQ as a PET tracer for imaging metabotropic glutamate receptor type 1 (mGluR1). J Cereb Blood Flow Metab 37:2283–2293

Leurquin-Sterk G, Van den Stock J, Crunelle CL, de Laat B, Weerasekera A, Himmelreich U, Bormans G, Van Laere K (2016) Positive association between limbic metabotropic glutamate receptor 5 availability and novelty-seeking temperament in humans: an 18F-FPEB PET study. J Nucl Med 57:1746–1752

Leurquin-Sterk G, Celen S, Van Laere K, Koole M, Bormans G, Langlois X, Van Hecken A, Te Riele P, Alcazar J, Verbruggen A et al (2017) What we observe in vivo is not always what we see in vitro: development and validation of 11C-JNJ-42491293, a novel radioligand for mGluR2. J Nucl Med 58:110–116

Leuzy A, Zimmer ER, Dubois J, Pruessner J, Cooperman C, Soucy JP, Kostikov A, Schirmaccher E, Desautels R, Gauthier S, Rosa-Neto P (2016) In vivo characterization of metabotropic glutamate receptor type 5 abnormalities in behavioral variant FTD. Brain Struct Funct 221:1387–1402

Li SY, Huang YY (2014) In vivo imaging of the metabotropic glutamate receptor 1 (mGluR1) with positron emission tomography: recent advance and perspective. Curr Med Chem 21:113–123

Li Z, Hagiwara H, Takaishi M, Teceno T, Krause S, Sasaki T, McCracken P, Koyama T, Terauchi T (2017) Discovery of a new class of mGluR2 selective group II mGluR NAM PET tracer. J Nucl Med 58:548

Lindemann L, Jaeschke G, Michalon A, Vieira E, Honer M, Spooren W, Porter R, Hartung T, Kolczewski S, Buttelmann B et al (2011) CTEP: a novel, potent, long-acting, and orally bio-available metabotropic glutamate receptor 5 inhibitor. J Pharmacol Exp Ther 339:474–486

Lindsley CW, Emmitte KA (2009) Recent progress in the discovery and development of negative allosteric modulators of mGluR5. Curr Opin Drug Discovery Develop 12:446–457

Lindsley CW, Niswender CM, Engers DW, Hopkins CR (2009) Recent progress in the development of mGluR4 positive allosteric modulators for the treatment of Parkinson's disease. Curr Top Med Chem 9:949–963

Lohith T, McQuade P, Salinas C, Anderson M, Reynders T, Bautmans A, Bormans G, Serdons K, Van Laere K, Hostetler E (2016) First-in-human PET imaging of mGluR2 receptors. J Nucl Med 57:213

Lucatelli C, Honer M, Salazar JF, Ross TL, Schubiger PA, Ametamey SM (2009) Synthesis, radio-labeling, in vitro and in vivo evaluation of [F-18]-FPECMO as a positron emission tomography radioligand for imaging the metabotropic glutamate receptor subtype 5. Nucl Med Biol 36:613–622

Ma Y, Kumata K, Yui J, Zhang Y, Yamasaki T, Hatori A, Fujinaga M, Nengaki N, Xie L, Wang H, Zhang MR (2017) Synthesis and evaluation of 1-(cyclopropylmethyl)-4-(4-[(11) C]methoxyphenyl)-piperidin-1-yl-2-oxo-1,2-dihydro pyridine-3-carbonitrile ([(11)C]CMDC) for PET imaging of metabotropic glutamate receptor 2 in the rat brain. Bioorg Med Chem 25:1014–1021

Mabire D, Coupa S, Adelinet C, Poncelet A, Simonnet Y, Venet M, Wouters R, Lesage AS, Van Beijsterveldt L, Bischoff F (2005) Synthesis, structure-activity relationship, and receptor phar-

macology of a new series of quinoline derivatives acting as selective, noncompetitive mGlu1 antagonists. J Med Chem 48:2134–2153

Marino MJ, Williams DL Jr, O'Brien JA, Valenti O, McDonald TP, Clements MK, Wang R, DiLella AG, Hess JF, Kinney GG, Conn PJ (2003) Allosteric modulation of group III metabotropic glutamate receptor 4: a potential approach to Parkinson's disease treatment. Proc Natl Acad Sci U S A 100:13668–13673

Mazzitelli M, Palazzo E, Maione S, Neugebauer V (2018) Group II metabotropic glutamate receptors: role in pain mechanisms and pain modulation. Front Mol Neurosci 11:383

Mori H, Mishina M (1995) Structure and function of the NMDA receptor channel. Neuropharmacology 34:1219–1237

Moussawi K, Kalivas PW (2010) Group II metabotropic glutamate receptors (mGlu2/3) in drug addiction. Eur J Pharmacol 639:115–122

Mu L, Schubiger PA, Ametamey SM (2010) Radioligands for the PET imaging of metabotropic glutamate receptor subtype 5 (mGluR5). Curr Top Med Chem 10:1558–1568

Muguruza C, Meana JJ, Callado LF (2016) Group II metabotropic glutamate receptors as targets for novel antipsychotic drugs. Front Pharmacol 7:130

Muller Herde A, Boss SD, He Y, Schibli R, Mu L, Ametamey SM (2018) Ketamine and ceftriaxone-induced alterations in glutamate levels do not impact the specific binding of metabotropic glutamate receptor subtype 5 radioligand [(18)F]PSS232 in the rat brain. Pharmaceuticals (Basel) 11(3):83

Muller Herde A, Schibli R, Weber M, Ametamey SM (2019) Metabotropic glutamate receptor subtype 5 is altered in LPS-induced murine neuroinflammation model and in the brains of AD and ALS patients. Eur J Nucl Med Mol Imaging 46:407–420

Myers R (2001) The biological application of small animal PET imaging. Nucl Med Biol 28:585–593

Neugebauer V, Galhardo V, Maione S, Mackey SC (2009) Forebrain pain mechanisms. Brain Res Rev 60:226–242

Ohe T, Sato M, Tanaka S, Fujino N, Hata M, Shibata Y, Kanatani A, Fukami T, Yamazaki M, Chiba M, Ishii Y (2003) Effect of P-glycoprotein-mediated efflux on cerebrospinal fluid/plasma concentration ratio. Drug Metab Dispos 31:1251–1254

Ohnuma T, Augood SJ, Arai H, McKenna PJ, Emson PC (1998) Expression of the human excitatory amino acid transporter 2 and metabotropic glutamate receptors 3 and 5 in the prefrontal cortex from normal individuals and patients with schizophrenia. Mol Brain Res 56:207–217

Ornstein PL, Bleisch TJ, Arnold MB, Kennedy JH, Wright RA, Johnson BG, Tizzano JP, Helton DR, Kallman MJ, Schoepp DD, Herin M (1998) 2-substituted (2SR)-2-amino-2-((1SR,2SR)-2-carboxycycloprop-1-yl)glycines as potent and selective antagonists of group II metabotropic glutamate receptors. 2. Effects of aromatic substitution, pharmacological characterization, and bioavailability. J Med Chem 41:358–378

Palucha A, Branski P, Szewczyk B, Wieronska JM, Klak K, Pilc A (2005) Potential antidepressant-like effect of MTEP, a potent and highly selective mGluR5 antagonist. Pharmacol Biochem Behav 81:901–906

Parmentier ML, Galvez T, Acher F, Peyre B, Pellicciari R, Grau Y, Bockaert J, Pin JP (2000) Conservation of the ligand recognition site of metabotropic glutamate receptors during evolution. Neuropharmacology 39:1119–1131

Passchier J, Gee A, Willemsen A, Vaalburg W, van Waarde A (2002) Measuring drug-related receptor occupancy with positron emission tomography. Methods 27:278–286

Patel S, Krause SM, Hamill T, Chaudhary A, Burns DH, Gibson RA (2003) In vitro characterization of [H-3]MethoxyPyEP, an mGluR5 selective radioligand. Life Sci 73:371–379

Patel S, Ndubizu O, Hamill T, Chaudhary A, Burns HD, Hargreaves R, Gibson RE (2005) Screening cascade and development of potential positron emission tomography radiotracers for mGluR5: in vitro and in vivo characterization. Mol Imaging Biol 7:314–323

Patel S, Hamill TG, Connolly B, Jagoda E, Li W, Gibson RE (2007) Species differences in mGluR5 binding sites in mammalian central nervous system determined using in vitro binding with [F-18]F-PEB. Nucl Med Biol 34:1009–1017

Patil ST, Zhang L, Martenyi F, Lowe SL, Jackson KA, Andreev BV, Avedisova AS, Bardenstein LM, Gurovich IY, Morozova MA et al (2007) Activation of mGlu2/3 receptors as a new approach to treat schizophrenia: a randomized phase 2 clinical trial. Nat Med 13:1102–1107

Piel M, Vernaleken I, Rosch F (2014) Positron emission tomography in CNS drug discovery and drug monitoring. J Med Chem 57:9232–9258

Pietraszek M, Nagel J, Gravius A, Schafer D, Danysz W (2007) The role of group I metabotropic glutamate receptors in schizophrenia. Amino Acids 32:173–178

Pike VW (2009) PET radiotracers: crossing the blood-brain barrier and surviving metabolism. Trends Pharmacol Sci 30:431–440

Pillai RL, Tipre DN (2016) Metabotropic glutamate receptor 5-a promising target in drug development and neuroimaging. Eur J Nucl Med Mol Imaging 43(6):1151–1170

Porter RHP, Jaeschke G, Spooren W, Ballard TM, Buttelmann B, Kolczewski S, Peters JU, Prinssen E, Wichmann J, Vieira E et al (2005) Fenobam: a clinically validated nonbenzodiazepine anxiolytic is a potent, selective, and noncompetitive mGlu5 receptor antagonist with inverse agonist activity. J Pharmacol Exp Ther 315:711–721

Prabhakaran J, Majo VJ, Milak MS, Kassir SA, Palner M, Savenkova L, Mali P, Arango V, Mann JJ, Parsey RV, Kumar JSD (2010) Synthesis, in vitro and in vivo evaluation of [(11)C]MMTP: a potential PET ligand for mGluR1 receptors. Bioorg Med Chem Lett 20:3499–3501

Raboisson P, Breitholtz-Emanuelsson A, Dahllof H, Edwards L, Heaton WL, Isaac M, Jarvie K, Kers A, Minidis AB, Nordmark A et al (2012) Discovery and characterization of AZD9272 and AZD6538-two novel mGluR5 negative allosteric modulators selected for clinical development. Bioorg Med Chem Lett 22:6974–6979

Richards G, Messer J, Malherbe P, Pink R, Brockhaus M, Stadler H, Wichmann J, Schaffhauser H, Mutel V (2005) Distribution and abundance of metabotropic glutamate receptor subtype 2 in rat brain revealed by [3H]LY354740 binding in vitro and quantitative radioautography: correlation with the sites of synthesis, expression, and agonist stimulation of [35S]GTPgammas binding. J Comp Neurol 487:15–27

Ritzen A, Mathiesen JM, Thomsen C (2005) Molecular pharmacology and therapeutic prospects of metabotropic glutamate receptor allosteric modulators. Basic Clin Pharmacol Toxicol 97:202–213

Ritzen A, Sindet R, Hentzer M, Svendsen N, Brodbeck RM, Bundgaard C (2009) Discovery of a potent and brain penetrant mGluR5 positive allosteric modulator. Bioorg Med Chem Lett 19:3275–3278

Romano C, Yang WL, OMalley KL (1996) Metabotropic glutamate receptor 5 is a disulfide-linked dimer. J Biol Chem 271:28612–28616

Rook JM, Tantawy MN, Ansari MS, Felts AS, Stauffer SR, Emmitte KA, Kessler RM, Niswender CM, Daniels JS, Jones CK et al (2015) Relationship between in vivo receptor occupancy and efficacy of metabotropic glutamate receptor subtype 5 allosteric modulators with different in vitro binding profiles. Neuropsychopharmacology 40:755–765

Rouse ST, Marino MJ, Bradley SR, Awad H, Wittmann M, Conn PJ (2000) Distribution and roles of metabotropic glutamate receptors in the basal ganglia motor circuit: implications for treatment of Parkinson's disease and related disorders. Pharmacol Ther 88:427–435

Satoh A, Nagatomi Y, Hirata Y, Ito S, Suzuki G, Kimura T, Maehara S, Hikichi H, Satow A, Hata M et al (2009) Discovery and in vitro and in vivo profiles of 4-fluoro-N-[4-[6-(isopropylamino) pyrimidin-4-yl]-1,3-thiazol-2-yl]-N-methylbenzamide as novel class of an orally active metabotropic glutamate receptor 1 (mGluR1) antagonist. Bioorg Med Chem Lett 19:5464–5468

Sephton SM, Dennler P, Leutwiler DS, Mu L, Schibli R, Kramer SD, Ametamey SM (2012) Development of [(18)F]-PSS223 as a PET tracer for imaging of metabotropic glutamate receptor subtype 5 (mGluR5). Chimia (Aarau) 66:201–204

Sephton SM, Mu LJ, Dragic M, Kramer SD, Schibli R, Ametamey SM (2013) Synthesis and in vitro evaluation of E- and Z-geometrical isomers of PSS232 as potential metabotropic glutamate receptors subtype 5 (mGlu(5)) binders. Synthesis-Stuttgart 45:1877–1885

Sephton SM, Herde AM, Mu L, Keller C, Rudisuhli S, Auberson Y, Schibli R, Kramer SD, Ametamey SM (2015) Preclinical evaluation and test-retest studies of [(18)F]PSS232, a novel radioligand for targeting metabotropic glutamate receptor 5 (mGlu5). Eur J Nucl Med Mol Imaging 42:128–137

Severance AJ, Parsey RV, Kumar JSD, Underwood MD, Arango V, Majoa VJ, Prabhakaran J, Simpson NR, Van Heertum RL, Mann JJ (2006) In vitro and in vivo evaluation of [C-11]MPEPy as a potential PET ligand for mGlu(5) receptors. Nucl Med Biol 33:1021–1027

Shetty HU, Zoghbi SS, Simeon FG, Liow JS, Brown AK, Kannan P, Innis RB, Pike VW (2008) Radiodefluorination of 3-Fluoro-5-(2-(2-[F-18](fluoromethyl)-thiazol-4-yl) ethynyl)benzonitrile ([F-18]SP203), a radioligand for imaging brain metabotropic glutamate Subtype-5 receptors with positron emission tomography, occurs by Glutathionylation in rat brain. J Pharmacol Exp Ther 327:727–735

Shigemoto R, Kinoshita A, Wada E, Nomura S, Ohishi H, Takada M, Flor PJ, Neki A, Abe T, Nakanishi S, Mizuno N (1997) Differential presynaptic localization of metabotropic glutamate receptor subtypes in the rat hippocampus. J Neurosci 17:7503–7522

Shimoda Y, Yamasaki T, Fujinaga M, Ogawa M, Kurihara Y, Nengaki N, Kumata K, Yui J, Hatori A, Xie L et al (2016) Synthesis and evaluation of novel radioligands based on 3-[5-(Pyridin-2-yl)-2H-tetrazol-2-yl]benzonitrile for positron emission tomography imaging of metabotropic glutamate receptor subtype 5. J Med Chem 59:3980–3990

Shin SS, Martino JJ, Chen S (2008) Metabotropic glutamate receptors (mGlus) and cellular transformation. Neuropharmacology 55:396–402

Simeon FG, Brown AK, Zoghbi SS, Patterson VM, Innis RB, Pike VW (2007) Synthesis and simple F-18-labeling of 3-fluoro-5-(2-(2-(fluoromethyl)thiazol-4-yl)ethynyl)benzonitrile as a high affinity radioligand for imaging monkey brain metabotropic glutamate subtype-5 receptors with positron emission tomography. J Med Chem 50:3256–3266

Smart K, Cox SML, Nagano-Saito A, Rosa-Neto P, Leyton M, Benkelfat C (2018) Test-retest variability of [(11)C]ABP688 estimates of metabotropic glutamate receptor subtype 5 availability in humans. Synapse 72:e22041

Smart K, Cox SML, Kostikov A, Shalai A, Scala SG, Tippler M, Jaworska N, Boivin M, Seguin JR, Benkelfat C, Leyton M (2019a) Effect of (Z)-isomer content on [(11)C]ABP688 binding potential in humans. Eur J Nucl Med Mol Imaging 46:1175–1178

Smart K, Cox SML, Scala SG, Tippler M, Jaworska N, Boivin M, Seguin JR, Benkelfat C, Leyton M (2019b) Sex differences in [(11)C]ABP688 binding: a positron emission tomography study of mGlu5 receptors. Eur J Nucl Med Mol Imaging 46:1179–1183

Spooren W, Gasparini F (2004) mGluS receptor antagonists: a novel class of anxiolytics? Drug News Perspect 17:251–257

Spooren WPJM, Vassout A, Neijt HC, Kuhn R, Gasparini F, Roux S, Porsolt RD, Gentsch C (2000) Anxiolytic-like effects of the prototypical metabotropic glutamate receptor 5 antagonist 2-methyl-6-(phenylethynyl)pyridine in rodents. J Pharmacol Exp Ther 295:1267–1275

Spooren W, Ballard T, Gasparini F, Amalric M, Mutel V, Schreiber R (2003) Insight into the function of group I and group II metabotropic glutamate (mGlu) receptors: behavioural characterization and implications for the treatment of CNS disorders. Behav Pharmacol 14:257–277

Stephenson NA, Holland JP, Kassenbrock A, Yokell DL, Livni E, Liang SH, Vasdev N (2015) Iodonium ylide-mediated radiofluorination of 18F-FPEB and validation for human use. J Nucl Med 56:489–492

Suzuki M, Doi H, Bjorkman M, Andersson Y, Langstrom B, Watanabe Y, Noyori R (1997) Rapid coupling of methyl iodide with aryltributylstannanes mediated by palladium(0) complexes: a general protocol for the synthesis of (CH3)-C-11-labeled PET tracers. Chem Eur J 3:2039–2042

Suzuki G, Kimura T, Satow A, Kaneko N, Fukuda J, Hikichi H, Sakai N, Maehara S, Kawagoe-Takaki H, Hata M et al (2007) Pharmacological characterization of a new, orally active and potent allosteric metabotropic glutamate receptor 1 antagonist, 4-[1-(2-fluoropyridin-3-yl)-

5-methyl-1H-1,2,3-triazol-4-yl]-N-isopropyl-N-methyl- 3,6-dihydropyridine-1(2H)-carbox-amide (FTIDC). J Pharmacol Exp Ther 321:1144–1153

Suzuki G, Kawagoe-Takaki H, Inoue T, Kimura T, Hikichi H, Murai T, Satow A, Hata M, Maehara S, Ito S et al (2009) Correlation of receptor occupancy of metabotropic glutamate receptor subtype 1 (mGluR1) in mouse brain with in vivo activity of allosteric mGluR1 antagonists. J Pharmacol Sci 110:315–325

Swanson CJ, Bures M, Johnson MP, Linden AM, Monn JA, Schoepp DD (2005) Metabotropic glutamate receptors as novel targets for anxiety and stress disorders. Nat Rev Drug Discov 4:131–144

Takano A, Nag S, Jia Z, Jahan M, Forsberg A, Arakawa R, Gryback P, Duvey G, Halldin C, Charvin D (2019) Characterization of [(11)C]PXT012253 as a PET radioligand for mGlu4 allosteric modulators in nonhuman Primates. Mol Imaging Biol 21:500–508

Tamagnan GD, Batis J, Koren AO, Lee H, Alagille D, Jennings D, Russell D, Carson R, Marek K, Seibyl JP (2009) Initial human studies of [18]-FPEB, a selective metabotropic glutamate receptor 5. Eur J Nucl Med Mol Imaging 36(Suppl 2):S223

Tatarczynska E, Klodzinska A, Chojnacka-Wojcik E, Palucha A, Gasparini F, Kuhn R, Pilc A (2001) Potential anxiolytic- and antidepressant-like effects of MPEP, a potent, selective and systemically active mGlu5 receptor antagonist. Br J Pharmacol 132:1423–1430

Tavares AA, Lewsey J, Dewar D, Pimlott SL (2012) Radiotracer properties determined by high performance liquid chromatography: a potential tool for brain radiotracer discovery. Nucl Med Biol 39:127–135

Telu S, Chun J, Simeon FG, Lu S, Pike VW (2011) Syntheses of an mGlurR5 PET radio-ligands through the radiofluorination of a diaryliodonium tosylates. Org Biomol Chem 9:6629–6638

Thomas NK, Wright RA, Howson PA, Kingston AE, Schoepp DD, Jane DE (2001) (S)-3,4-DCPG, a potent and selective mGlu8a receptor agonist, activates metabotropic glutamate receptors on primary afferent terminals in the neonatal rat spinal cord. Neuropharmacology 40:311–318

Toyohara J, Sakata M, Fujinaga M, Yamasaki T, Oda K, Ishii K, Zhang MR, Moriguchi Jeckel CM, Ishiwata K (2013a) Preclinical and the first clinical studies on [11C]ITMM for mapping metabotropic glutamate receptor subtype 1 by positron emission tomography. Nucl Med Biol 40:214–220

Toyohara J, Sakata M, Oda K, Ishii K, Ito K, Hiura M, Fujinaga M, Yamasaki T, Zhang MR, Ishiwata K (2013b) Initial human PET studies of metabotropic glutamate receptor type 1 ligand 11C-ITMM. J Nucl Med 54:1302–1307

Trabanco AA, Bartolome JM, Cid JM (2019) mGluR2 positive allosteric modulators: an updated patent review (2013-2018). Expert Opin Ther Pat 29:497–507

Treyer V, Streffer J, Ametamey SM, Bettio A, Blauenstein P, Schmidt M, Gasparini F, Fischer U, Hock C, Buck A (2008) Radiation dosimetry and biodistribution of 11C-ABP688 measured in healthy volunteers. Euro J Nucl Med Mol Imaging 35:766–770

Tsai VWW, Scott HL, Lewis RJ, Dodd PR (2005) The role of group I metabotropic glutamate receptor's in neuronal excitotoxicity in Alzheimer's disease. Neurotox Res 7:125–141

Tsuchiya D, Kunishima N, Kamiya N, Jingami H, Morikawa K (2002) Structural views of the ligand-binding cores of a metabotropic glutamate receptor complexed with an antagonist and both glutamate and Gd3+. Proc Natl Acad Sci U S A 99:2660–2665

Van de Bittner GC, Ricq EL, Hooker JM (2014) A philosophy for CNS radiotracer design. Acc Chem Res 47:3127–3134

Varnas K, Jureus A, Finnema SJ, Johnstrom P, Raboisson P, Amini N, Takano A, Stepanov V, Halldin C, Farde L (2018) The metabotropic glutamate receptor 5 radioligand [(11)C]AZD9272 identifies unique binding sites in primate brain. Neuropharmacology 135:455–463

Varney M, Anderson J, Bradbury M, Bristow L, Brodkin J, Giracello D, Jachec C, Holtz G, Prasit P, Rao S et al (2002) 3-[(2-methyl-1,3-thiazol-4-yl)ethynyl]pyridine (MTEP): a potent and highly selective metabotropic glutamate subtype 5 (mGlu5) receptor antagonist with anxiolytic activity. Neuropharmacology 43:311–311

Wager TT, Chandrasekaran RY, Hou X, Troutman MD, Verhoest PR, Villalobos A, Will Y (2010a) Defining desirable central nervous system drug space through the alignment of molecular properties, in vitro ADME, and safety attributes. ACS Chem Neurosci 1:420–434

Wager TT, Hou X, Verhoest PR, Villalobos A (2010b) Moving beyond rules: the development of a central nervous system multiparameter optimization (CNS MPO) approach to enable alignment of druglike properties. ACS Chem Neurosci 1:435–449

Wang JQ, Tueckmantel W, Zhu AJ, Pellegrino D, Brownell AL (2007) Synthesis and preliminary biological evaluation of 3-[F-18]Fluoro-5-(2-pyridinylethynyl)benzonitrile as a PET radiotracer for imaging metabotropic glutamate receptor subtype 5. Synapse 61:951–961

Wang JQ, Zhang Z, Kuruppu D, Brownell AL (2012) Radiosynthesis of PET radiotracer as a prodrug for imaging group II metabotropic glutamate receptors in vivo. Bioorg Med Chem Lett 22:1958–1962

Wanger-Baumann CA, Mu L, Honer M, Belli S, Alf MF, Schubiger PA, Kramer SD, Ametamey SM (2011) In vitro and in vivo evaluation of [F-18]-FDEGPECO as a PET tracer for imaging the metabotropic glutamate receptor subtype 5 (mGluR5). NeuroImage 56:984–991

Warnock G, Sommerauer M, Mu L, Pla Gonzalez G, Geistlich S, Treyer V, Schibli R, Buck A, Kramer SD, Ametamey SM (2018) A first-in-man PET study of [(18)F]PSS232, a fluorinated ABP688 derivative for imaging metabotropic glutamate receptor subtype 5. Eur J Nucl Med Mol Imaging 45:1041–1051

Waterhouse RN (2003) Determination of lipophilicity and its use as a predictor of blood-brain barrier penetration of molecular imaging agents. Mol Imaging Biol 5:376–389

Xi W, Tian M, Zhang H (2011) Molecular imaging in neuroscience research with small-animal PET in rodents. Neurosci Res 70:133–143

Xu YW, Li ZZ (2019) Imaging metabotropic glutamate receptor system: application of positron emission tomography technology in drug development. Med Res Rev 39:1892–1922

Xu R, Zanotti-Fregonara P, Zoghbi SS, Gladding RL, Woock AE, Innis RB, Pike VW (2013) Synthesis and evaluation in monkey of [(18)F]4-fluoro-N-methyl-N-(4-(6-(methylamino) pyrimidin-4-yl)thiazol-2-yl)benzami de ([(18)F]FIMX): a promising radioligand for PET imaging of brain metabotropic glutamate receptor 1 (mGluR1). J Med Chem 56:9146–9155

Yamasaki T, Fujinaga M, Yoshida Y, Kumata K, Yui JJ, Kawamura K, Hatori A, Fukumura T, Zhang MR (2011) Radiosynthesis and preliminary evaluation of 4-[(18)F]fluoro-N-[4-[6-(isopropylamino)pyrimidin-4-yl]-1,3-thiazol-2-yl]-N-methylbenzamide as a new positron emission tomography ligand for metabotropic glutamate receptor subtype 1. Bioorg Med Chem Lett 21:2998–3001

Yamasaki T, Fujinaga M, Kawamura K, Yui J, Hatori A, Ohya T, Xie L, Wakizaka H, Yoshida Y, Fukumura T, Zhang MR (2012a) In vivo measurement of the affinity and density of metabotropic glutamate receptor subtype 1 in rat brain using 18F-FITM in small-animal PET. J Nucl Med 53:1601–1607

Yamasaki T, Fujinaga M, Maeda J, Kawamura K, Yui J, Hatori A, Yoshida Y, Nagai Y, Tokunaga M, Higuchi M et al (2012b) Imaging for metabotropic glutamate receptor subtype 1 in rat and monkey brains using PET with [18F]FITM. Eur J Nucl Med Mol Imaging 39:632–641

Yamasaki T, Fujinaga M, Yui J, Ikoma Y, Hatori A, Xie L, Wakizaka H, Kumata K, Nengaki N, Kawamura K, Zhang MR (2014) Noninvasive quantification of metabotropic glutamate receptor type 1 with [(1)(1)C]ITDM: a small-animal PET study. J Cereb Blood Flow Metab 34:606–612

Yamasaki T, Fujinaga M, Kawamura K, Furutsuka K, Nengaki N, Shimoda Y, Shiomi S, Takei M, Hashimoto H, Yui J et al (2016) Dynamic changes in striatal mGluR1 but not mGluR5 during pathological progression of Parkinson's disease in human alpha-synuclein A53T transgenic rats: a multi-PET imaging study. J Neurosci 36:375–384

Yamasaki T, Fujinaga M, Mori W, Zhang Y, Wakizaka H, Nengaki N, Xie L, Hatori A, Zhang MR (2017) In vivo monitoring for regional changes of metabotropic glutamate receptor subtype 1 (mGluR1) in pilocarpine-induced epileptic rat brain by small-animal PET. Sci Rep 7:14945

Yanamoto K, Konno F, Odawara C, Yamasaki T, Kawamura K, Hatori A, Yui J, Wakizaka H, Nengaki N, Takei M, Zhang MR (2010) Radiosynthesis and evaluation of [(11)C]YM-202074

as a PET ligand for imaging the metabotropic glutamate receptor type 1. Nucl Med Biol 37:615–624

Yu M (2007) Recent developments of the PET imaging agents for metabotropic glutamate receptor subtype 5. Curr Top Med Chem 7:1800–1805

Yu MX, Tueckmantel W, Wang XK, Zhu AJ, Kozikowski AP, Brownell AL (2005) Methoxyphenylethynyl, methoxypyridylethynyl and phenylethynyl derivatives of pyridine: synthesis, radiolabeling and evaluation of new PET ligands for metabotropic glutamate subtype 5 receptors. Nucl Med Biol 32:631–640

Zanotti-Fregonara P, Barth VN, Liow JS, Zoghbi SS, Clark DT, Rhoads E, Siuda E, Heinz BA, Nisenbaum E, Dressman B et al (2013a) Evaluation in vitro and in animals of a new 11C-labeled PET radioligand for metabotropic glutamate receptors 1 in brain. Eur J Nucl Med Mol Imaging 40:245–253

Zanotti-Fregonara P, Barth VN, Zoghbi SS, Liow JS, Nisenbaum E, Siuda E, Gladding RL, Rallis-Frutos D, Morse C, Tauscher J et al (2013b) 11C-LY2428703, a positron emission tomographic radioligand for the metabotropic glutamate receptor 1, is unsuitable for imaging in monkey and human brains. EJNMMI Res 3:47

Zanotti-Fregonara P, Lammertsma AA, Innis RB (2013c) Suggested pathway to assess radiation safety of (1)(8)F-labeled PET tracers for first-in-human studies. Eur J Nucl Med Mol Imaging 40:1781–1783

Zanotti-Fregonara P, Xu R, Zoghbi SS, Liow JS, Fujita M, Veronese M, Gladding RL, Rallis-Frutos D, Hong J, Pike VW, Innis RB (2016) The PET radioligand 18F-FIMX images and quantifies metabotropic glutamate receptor 1 in proportion to the regional density of its gene transcript in human brain. J Nucl Med 57:242–247

Zhang L, Villalobos A, Beck EM, Bocan T, Chappie TA, Chen L, Grimwood S, Heck SD, Helal CJ, Hou X et al (2013) Design and selection parameters to accelerate the discovery of novel central nervous system positron emission tomography (PET) ligands and their application in the development of a novel phosphodiesterase 2A PET ligand. J Med Chem 56:4568–4579

Zhang L, Chen L, Beck EM, Chappie TA, Coelho RV, Doran SD, Fan KH, Helal CJ, Humphrey JM, Hughes Z et al (2017a) The discovery of a novel phosphodiesterase (PDE) 4B-preferring Radioligand for positron emission tomography (PET) imaging. J Med Chem 60:8538–8551

Zhang X, Kumata K, Yamasaki T, Cheng R, Hatori A, Ma L, Zhang Y, Xie L, Wang L, Kang HJ et al (2017b) Synthesis and preliminary studies of a novel negative allosteric modulator, 7-((2,5-dioxopyrrolidin-1-yl)methyl)-4-(2-fluoro-4-[(11)C]methoxyphenyl) quinoline-2-carboxamide, for imaging of metabotropic glutamate receptor 2. ACS Chem Neurosci 8:1937–1948

Zimmer ER, Parent MJ, Leuzy A, Aliaga A, Aliaga A, Moquin L, Schirrmacher ES, Soucy JP, Skelin I, Gratton A et al (2015) Imaging in vivo glutamate fluctuations with [(11)C]ABP688: a GLT-1 challenge with ceftriaxone. J Cereb Blood Flow Metab 35:1169–1174

PET and SPECT Imaging of Steroid Hormone Receptors in the Brain

14

Rodrigo Moraga-Amaro, Janine Doorduin,
Rudi A. J. O. Dierckx, and Erik F. J. de Vries

Contents

Abstract

Steroid hormones, like sex hormones and corticosteroids, are involved in normal brain function. They can influence behavior and higher functions via binding to the corresponding hormone receptors. Steroid hormones also play a crucial role in psychiatric disorders by interacting with different neurotransmitter systems in the brain. Most of the studies in this field have been performed on postmortem

R. Moraga-Amaro · J. Doorduin · R. A. J. O. Dierckx · E. F. J. de Vries (✉)
Department of Nuclear Medicine and Molecular Imaging, University Medical Center Groningen, University of Groningen, Groningen, The Netherlands
e-mail: e.f.j.de.vries@umcg.nl

tissue of animals and humans. However, noninvasive techniques could provide new insight into the role that steroid hormones play in normal and pathological brain function. PET and SPECT are techniques that allow noninvasive quantitative analysis of the expression of steroid hormone receptors. This chapter will briefly explain the role of steroid hormones in physiological and pathological conditions and provide an overview of the available PET and SPECT imaging methods that could be used to study the role steroid hormones and their receptors in the brain.

Abbreviations

(Z)-[125I]MIVE	(20Z)-11beta-methoxy-17alpha-[123I]iodovinylestradiol
[123I]IES	16alpha-[123I]iodo-17beta-estradiol
[123I]IVMMNT	17alpha-[123I]iodovinyl-18-methyl-11-methylene-19-nortestosterone
[123I]TAM	[123I]iodotamoxifen
[125I]IVNT	(20Z)-17alpha-[125I]iodovinyl-19-nortestosterone
[125I]MIE	16alpha-[125I]iodo-11beta-methoxy-17beta-estradiol
[18F]betaFMOX	17alpha-ethynyl-16beta-[18F]fluoro-11beta-methoxy-estradiol
[18F]FDHT	16beta-[18F]fluorodihydrotestosterone
[18F]FENP	21-[18F]fluoro-16alpha-ethyl-19-norprogesterone
[18F]FES	16alpha-[18F]fluoro-17beta-estradiol
[18F]FFNP	21-[18F]fluoro-16alpha,17alpha-[(R)-(1′alpha-furylmethylidene)dioxy]-19-norpregn-4-ene-3,20-dione
[18F]-FHNP	2-[18F]fluoro-6-[6-hydroxynaphthalen-2-yl]pyridin-3-ol
[18F]FMDHT	7alpha-[18F]fluoro-17-methyl-5-dihydrotestosterone
[18F]FMNP	21-[18F]fluoro-16alpha-methyl-19-norprogesterone
[18F]FPTP	4-[18F]fluoropropyl-tanaproget
[18F]FTX	[18F]Fluoromethyl-*N*,*N*-dimethyltamoxifen
16alpha-[18F]FMNT	16alpha-[18F]fluoro-7alpha-methyl-19-nortestosterone
16beta-[18F]FMNT	16beta-[18F]fluoro-7alpha-methyl-19-nortestosterone
16beta-[18F]FT	16beta-[18F]fluorotestosterone
20-[18F]Fmib	20-[18F]fluoromibolerone
20-[18F]R1881	20-[18F]fluorometribolone
4F-M[18F]FES	11beta-methoxy-4,16alpha-[18F]difluoroestradiol
7alpha-[125I]IDHT	7alpha-[125I]iodo-5alpha-dihydrotestosterone
8beta-[18F]FEE	8beta-(2-[18F]fluoroethyl)estradiol
AR	Androgen receptors
CNS	Central nervous system
DES	Diethylstilbestrol
ER	Estrogen receptors
GR	Glucocorticoid receptors
HPA axis	Hypothalamic-pituitary-adrenal axis

HRE   Hormone response elements
MR   Mineralocorticoid receptors
PR   Progesterone receptors
SHBG   Sex hormone-binding globulin
SHR   Steroid hormone receptors

14.1   Introduction

Steroid hormones are messenger molecules that are produced and secreted by endocrine glands, such as ovaries, testes, and adrenal cortex. Structurally all steroid hormones consist of a steroidal scaffold, which is composed of three six-membered rings and one five-membered ring; nonsteroidal hormones lack this steroid scaffold. Secreted steroid hormones can travel through the blood vessels toward their receptors and can easily cross cell membranes, including the blood-brain barrier, because of their high lipophilicity. Steroidal hormones can be classified into two main families: sex hormones and corticosteroids. In general, they are responsible for biological responses in a wide range of endocrine processes, including sexual differentiation, reproductive physiology, glucose metabolism, and maintenance of cell homeostasis. The sex hormones can be further classified into three subfamilies: progestins, estrogens, and androgens.

The brain is an important target organ for circulating steroid hormones. It is known that these molecules can affect several brain functions (McEwen and Milner 2017; Zalachoras et al. 2013). Steroid hormones can either bind directly to their respective membrane receptors or cross the cell membrane and bind to intracellular receptors (Gray et al. 2017; Kawata et al. 2008; Mani et al. 2012). Although circulating steroid hormones can diffuse across the blood-brain barrier, the brain itself is also capable of synthesizing steroid hormones de novo from cholesterol (Fig. 14.1), as was first discovered in studies, in which peripheral organs that produce steroid hormones were surgically removed (Porcu et al. 2016). Neuroactive steroids (neurosteroids) produce their effects by autocrine or endocrine pathways (Baulieu 1998) and act mostly as allosteric modulators of different neurotransmitter receptors (for a review on the functions of neurosteroids, see Rupprecht (2003)).

Neuroactive steroids can act as allosteric modulators of ligand-gated ion channels ($GABA_A$), NMDA, and sigma receptors. Because of these interactions, neuroactive steroids have sleep-inducing, anticonvulsant, anesthetic, nootropic, and antipsychotic properties, among others (Rupprecht 2003). They also play a crucial role in neuronal development and plasticity, including processes like learning, memory, emotion, behavior, synaptic transmission, and neuroprotection (Giatti et al. 2012). Because of these neuroprotective properties, neurosteroids have been proposed as adjuvant treatment for neurodegenerative diseases and neuropsychiatric disorders like Alzheimer's disease, multiple sclerosis, Parkinson's disease, depression and anxiety-related disorders, among others (Borowicz et al. 2011; Eser et al. 2006).
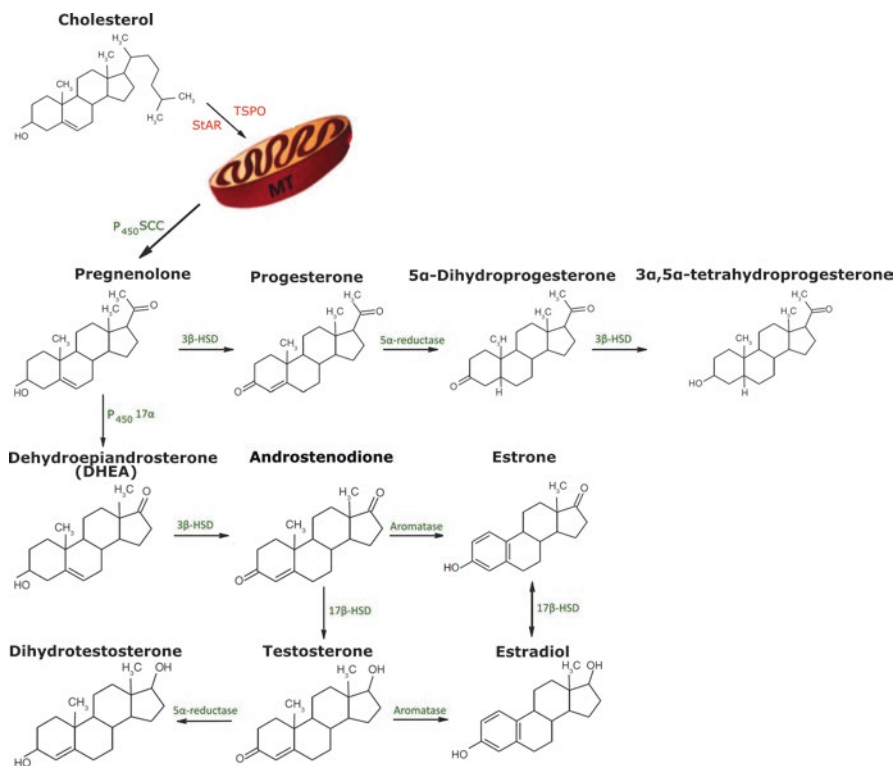
Fig. 14.1 Scheme of neurosteroidogenesis. Steroidogenesis follows a sequential, highly compartmentalized procedure, starting with the translocation of cholesterol from cytoplasm to mitochondria in the cells of the CNS, which is mediated by steroidogenic acute regulatory protein (StAR) and an 18 kDa translocator protein (TSPO). In the mitochondria, P450 side-chain cleavage (P450SCC) cleaves the side chain from cholesterol, resulting in the formation of pregnenolone. Pregnenolone is subsequently converted to progesterone and dehydroepiandrosterone in endoplasmic reticulum. The lipophilic nature of these compounds allows them to diffuse from one cell to another. Progesterone and dehydroepiandrosterone are further metabolized to form other neuroactive metabolites like testosterone, estrone, and estradiol

In this chapter, we will provide an overview of the available literature about PET and SPECT imaging techniques that can be applied to study the role of steroid hormones and their receptors in the brain. We will start discussing the role of steroidal hormones in the brain and subsequently provide an overview of the available PET and SPECT tracers for imaging of steroid hormone receptors and their applicability in brain research.

14.2 Steroid Hormones and Their Receptors in Brain Disorders

Steroid hormones exert their biological effects through specific steroid hormone receptors (SHR) that are expressed by the target cells. To date, two estrogen receptor (ER) subtypes (ERα and ERβ) with several isoforms (Ogino et al. 2018; Tonn

Fig. 14.2 Functional domains of steroid hormone receptors (SHR). All the SHRs share common structural domains; the N-terminal transcription activation-1 domain (*A/B*), which regulates the ligand-independent transcription; a DNA-binding domain (*C*) which recognizes and binds with the steroid hormone-responsive elements on DNA; a flexible hinge domain (*D*) which carries information for the posttranscriptional modification; and a multifunctional ligand-binding domain (*E*) which recognizes and binds the ligand and acts as a ligand-dependent transcription activation function. ERα contains an extra region (*F*). Numbers represent the number of amino acids in each receptor. *ER*, estrogen receptor; *PR*, progesterone receptor; *AR*, androgen receptor; *MR*, mineralocorticoid receptor; *GR*, glucocorticoid receptor; *AF*, activation function; *DBD*, DNA-binding domain; *LBD*, ligand-binding domain. Figure modified from (Griekspoor et al. 2007)

Eisinger et al. 2018), two progesterone receptors (PR) subtypes (PR$_A$ and PR$_B$) with several splice variants (Brinton et al. 2008; Knutson and Lange 2014), and two types of androgen receptor (AR) subtypes have been identified (AR$_A$ and AR$_B$) (Ogino et al. 2018; Pelletier et al. 2000). All SHR share similar functional domains but differ in the length of the amino acid chain (Fig. 14.2).

In steroid-responsive cells, SHR are mainly present in the cytoplasm and the nucleus, although SHR are also found on the cell membrane (Schwartz et al. 2016). When SHR are activated by the corresponding steroid hormone, they dimerize and move into the nucleus of the cell, where they bind to the hormone-responsive element in the promoter region of specific target genes. SHR may act as transcriptional activators or transcriptional suppressors, resulting in the induction or suppression of the expression of hormone-responsive genes. These responsive genes may evoke a wide variety of physiological responses. Some rapid actions of estrogens and progestins are directly mediated by cell surface receptors in a non-genomic manner (Fig. 14.3). Although the involvement of steroid hormones in various brain disorders has been demonstrated, the mechanisms by which they exert their effects are still largely unknown.

Animal experiments and postmortem brain analyses using molecular biology techniques, such as western blot and immunohistochemistry, have shown that sex hormone receptors are expressed in various regions of the brain. ER, PR, and AR are expressed in those brain areas that are associated with emotion, cognition, and behavior, such as the hypothalamus, amygdala, cerebral cortex, hippocampus, and brainstem (Marrocco and McEwen 2016). This expression pattern is in agreement with the association of sex hormones with psychiatric disorders. Literature suggests that the neuroprotective effects of estrogens are mainly due to ERα-mediated signaling (Ooishi et al. 2012), whereas the effect on mood and cognitive functions is
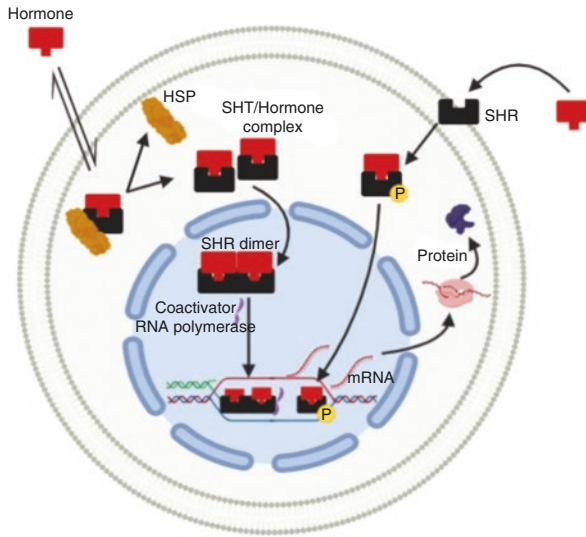
Fig. 14.3 Generalized mechanisms of action of steroid hormones in the cell. All the steroid hormone receptors mediate their action by a common genomic pathway, upon entering the cell by passive diffusion. Hormones can bind to either cytoplasmic, nuclear, or membrane receptors. In the cytoplasm, they exist as complexes with heat shock proteins (HSP) in an inactive form. When a steroid hormone binds, the receptor complex releases the HSP and becomes activated. The activated receptor forms a homodimer or heterodimer, which subsequently enters into the nucleus. The dimer binds to the specific hormone-responsive element in DNA and initiates or inhibits the process of gene transcription. Hormones with receptors in the nucleus get activated by their ligands and follow the same signaling pathway as the cytoplasmic receptors. In the case of membrane receptors, binding of the target molecule will induce a signaling cascade or the translocation of the receptor to the nucleus. In the nucleus, the receptor complex will activate the transcription to mRNA of certain genes and their following translation into functional proteins

mainly mediated by ERβ (Foster 2012). A study on patients with depression or schizophrenia, who committed suicide, showed downregulation of ERβ expression in the limbic system (Östlund et al. 2003). To our knowledge, no data exist on altered expression of PR and AR in the human brain in mood and behavioral disorders. Alternatively, steroid hormones may be acting indirectly through regulation of neurotransmission of serotonin and dopamine among others (Bristot et al. 2014; Fink et al. 1999; MacKenzie and Maguire 2014).

Not only sex hormone receptor expression but also polymorphisms in their genes were found to be implicated in psychiatric diseases. Sex hormone receptor polymorphisms have been associated with an increased risk for schizophrenia, depression, anxiety traits, and cognitive impairment. The association of polymorphisms in estrogen and androgen receptors with psychiatric disorders has been reviewed recently (Zhang et al. 2017).

The corticosteroid receptors may be divided into two classes: mineralocorticoid receptors (MR) and glucocorticoid receptors (GR) (Barabás et al. 2018). MR are mainly expressed in the limbic system, hypothalamus, and circumventricular

regions and to a lesser extent in other parts of the brain. GR expression is mainly observed in subregions of the cerebral cortex, olfactory cortex, hippocampus, amygdala, dorsal thalamus, hypothalamus, cerebellar cortex, trapezoid body, locus coeruleus, and dorsal raphe nucleus in rats (Morimoto et al. 1996; Owen 2002). Both the corticosteroid receptors are co-expressed in the hippocampus, amygdala, inferior frontal gyrus, cingulate gyrus, and nucleus accumbens in the human brain, whereas predominantly MR were found in the hippocampus (Klok et al. 2011).

Corticosteroids have the ability to bind to the corresponding MR or GR, via which they can exert behavioral changes. In clinical studies, a reduction in MR and GR expression and an increase in corticosteroid levels are suggested to be associated with suicide in different brain disorders (López et al. 1998; Xing et al. 2004; Young et al. 2003). Prolonged (chronic) stress has been reported to downregulate the expression of GR in the prefrontal cortex in rats (Chiba et al. 2012) and to reduce GR mRNA in the basolateral/lateral nuclei in patients with schizophrenia or bipolar disorder (Perlman et al. 2007, 2004). Increased production of cortisol causes a downregulation of GR receptors and desensitization of the GR signaling pathway, which in turn leads to an increase in the levels of cortisol (Sapolsky 2000).

14.2.1 Estrogens in Brain Disorders

Estrogens are a family of steroidal hormones that regulate reproductive and nonreproductive functions in both males and females. These hormones exert their pleiotropic effects through a combination of nuclear and membrane-associated receptors, which are often associated with different latencies of action (Cornil 2018; Micevych et al. 2015). Binding of estrogens to intracellular nuclear ER (mostly ERα but also ERβ) leads to a transcriptional regulation of estrogen-related genes, through the activation of the hormone response element (HRE). On the other hand, estrogens can also bind to membrane receptors to induce fast responses through non-genomic signaling, affecting various aspects of brain function and behavior. For a review on the molecular mechanisms, see (Kawata et al. 2008).

Although both male and female subjects produce estrogens, the major source of estrogens are the ovaries, which is responsible for the difference in estrogen quantities and functions between both sexes. Changes of circulating estrogens in women, e.g., due to pregnancy or menopause, have been associated with an increased prevalence of brain disorders like reduced cognitive function, depression, and anxiety-related and eating disorders (Holsen et al. 2011). This hypothesis is supported by the observation that several mental changes occur during the transition of women from pre- to postmenopause, including reduced sexual drive and premenstrual or perimenopausal dysphoria induced by oral contraceptives or hormone replacement therapy (Eriksson et al. 2002; Rubinow and Schmidt 2006; Steiner et al. 2006). Other studies showed that during menopause, when circulating levels of estrogens are strongly reduced, there is a higher prevalence of social and psychological changes in women, like anxiety, irritability, stress, memory loss, lack of concentration, and loss of libido, which eventually may culminate into depression (Bryant

et al. 2012). Moreover, prolonged deficiency of estrogens also increases the risk to develop dementia (Sherman et al. 2005), including Alzheimer's disease (Pike et al. 2009). One possible explanation for these phenomena is that changes in circulating estrogens can induce changes in neurotransmitters like acetylcholine, dopamine, noradrenaline, and serotonin (McEwen and Milner 2017).

Maintenance of estrogen levels seems essential for normal physiological and mental status. In fact, estrogen replacement therapies have shown to have neuroprotective effects. Studies in humans and animal models have shown positive effects on perimenopausal and postmenopausal depression (Grigoriadis and Kennedy 2002), a reduction of ischemia-induced brain injury (Carswell et al. 2000), improvement of cognition (McCarrey and Resnick 2015), and neuroprotection against other neurodegenerative diseases like multiple sclerosis, Parkinson's disease and Alzheimer's disease (Chakrabarti et al. 2014). This protective effect was partly ascribed to the anti-inflammatory activity of estrogens (Resnick and Henderson 2002; Vegeto et al. 2008). Neurosteroids produced by activated microglia are able to shift a pro-inflammatory immune response into an anti-inflammatory phenotype. This effect seems to be dependent on both the expression level and the extent of stimulation of ER in the CNS (Giatti et al. 2012).

14.2.2 Progestins in Brain Disorders

Progestins have been demonstrated to play an important role in neuroprotection in experimental models and clinical trials in patients with stroke and traumatic brain injury. Progestins are able to decrease the lesion volume progression in the brain of stroke patients. A few studies were performed to assess the role of PR in experimental animal models of stroke, traumatic brain injury, and spinal cord injury (for a review see (Gibson et al. 2008)). For example, Liu et al. found that ischemia to the brain for 6 h resulted in a rapid increase in the progesterone and 5α-dihydroprogesterone levels both in wild-type and PR knockout mice, suggesting a possible role of progestins in the salvage of neurons at risk (Liu et al. 2012). Progestins are also involved in cellular processes related to maintenance of myelin integrity, regulation of spinogenesis, synaptogenesis, neuronal survival, and dendritic growth (McEwen and Woolley 1994; Mellon 2007; Schumacher et al. 2012; Zhang et al. 2009). These observations suggest that neuroprotective effects of progestins may be mainly due to cellular maintenance processes.

Changes in steroid hormone levels affected the expression of membrane PR, especially PRα, in rats and mice. Upon treatment with estradiol or progesterone, significant expression of PRα was observed in neurons of the olfactory bulb, striatum, cortex, thalamus, hypothalamus, septum, hippocampus, and cerebellum, but not on oligodendrocytes or astrocytes. Moreover, traumatic brain injury induced the expression of PRα not only on neurons but also on oligodendrocytes, astrocytes, and reactive microglia, suggesting a role of progestins and PR in inflammation in the injured brain (Meffre et al. 2013). The neuroprotective mechanisms and

anti-inflammatory effects of progestins have been reviewed by several authors (De Nicola et al. 2009; Giatti et al. 2012; Grandi et al. 2017; Luoma et al. 2012; Singh and Su 2013). Progestins can inhibit the activation of microglia, which prevents NO and TNF-alpha production and the release of other inflammatory cytokines, such as IL-1beta, IL-6, complement factor C3 and C5, and macrophage-inducing factor-1.

Other mechanisms of action for the neuroprotective effects of progestins have been suggested. Progestins may prevent brain damage by controlling edema formation (vasogenic or cytogenic) via modulation of the expression of the aquaporin-4 water transporter, moderating Ca^{2+} flux caused by excitotoxicity, and reconstitution of the blood-brain barrier (O'Connor et al. 2005). Additionally, it has been reported that the antioxidant properties of progestins can prevent cellular insults by oxidative stress induced by free radicals (Ishihara et al. 2015). Besides the aforementioned roles in neuroprotection, progestins also play a role in neuronal remodeling by upregulating several neurotrophic factors, such as brain-derived neurotrophic factor (BDNF), Na/K ATPase, microtubule-associated protein 2 (MAP-2), choline acetyltransferase (ChAT), and glial-derived neurotrophic factor (GDNF) (Singh and Su 2013).

To investigate progestins as neuroprotective agents in patients, a clinical trial (phase IIa) was conducted in 100 male and female patients with blunt head trauma with moderate-to-severe damage. Treatment with progesterone was associated with a significant reduction in mortality compared to the vehicle group (Wright et al. 2007). However, the follow-up phase III clinical study could not demonstrate any neuroprotective effect of progestins in moderate-to-severe traumatic brain injury (Goldstein et al. 2017; Skolnick et al. 2014). Discussions about this lack of efficacy are suggesting a dose calibration problem (Howard et al. 2017). On the other hand, administration of progestins in combination with estrogens showed efficacy as treatment for multiple sclerosis in both animal models and in patients. The beneficial effect was mediated by modulation of peripheral and brain-intrinsic immune responses and regulation of local growth factor supply, oligodendrocytes, and astrocytes (Kipp et al. 2012). The combination of progestins and estrogens was also found to be an effective treatment for postmenopausal symptoms.

14.2.3 Androgens in Brain Disorders

Androgens are known to affect various brain functions and behavior. The most common central effect of androgens is the induction of aggression. Several studies have shown that excessive levels of testosterone induce aggression in both males and females of various species (Carré et al. 2011). Additionally, studies have shown that androgens play a role in depression-like and anxiety-like disorders, especially after menopause in women and during hypogonadism (andropause) in men. Changes in circulating androgens have been suggested to increase the risk of mood disorders,

depression, and psychosis (McHenry et al. 2014; Talih et al. 2007). Other studies reported that changes in circulating androgen levels have effects on cognition and cell survival (Lašaitė et al. 2017; Spritzer and Galea 2007).

Testosterone is converted to estradiol in the CNS, which plays a pivotal role in the feedback regulation in the hypothalamus. The hypothalamus can induce hormone release by the endocrine system through the pituitary. When men show hypogonadism, there are very low circulating androgen concentrations, which causes impairment of the higher functions in the brain, as described above (Ciocca et al. 2016). Testosterone replacement therapy (THT) showed either positive effects or no improvements in higher brain function (Ciocca et al. 2016; Corona et al. 2017; Davis et al. 2013). For this reason, the use of THT as a therapy for brain-related dysfunctions due to androgen hypogonadism is still under debate (Corona et al. 2015; Scovell and Khera 2018).

14.2.4 Corticosteroids in Brain Disorders

Corticosteroids, such as glucocorticoids and mineralocorticoids, are produced by the adrenal glands and liver and by the placenta and maternal glands during pregnancy. In stressful conditions, the glucocorticoid cortisol is rapidly synthesized and secreted in response to adrenocorticotropic hormone, released from the pituitary, and corticotrophin-releasing hormone, secreted by the hypothalamus. Cortisol stimulates the production of energy-rich compounds such as glucose, free fatty acids, and amino acids in different tissues. On the other hand, the mineralocorticoid aldosterone is produced in response to angiotensin II and promotes sodium reabsorption and fluid retention. Both cortisol and aldosterone release are controlled by the hypothalamic-pituitary-adrenal (HPA) axis. The HPA axis is a neuroendocrine system that has complex interactions with the serotonergic, noradrenergic, and dopaminergic systems in the brain. This axis regulates our body's responses to stress, and its dysregulation may lead to brain disorders (Stratakis and Chrousos 1995).

Excessive activity of the HPA axis or enlargement of the pituitary or adrenal gland cause an increase in cortisol levels, which in turn leads to hypercortisolemia. The overactivity of the HPA axis in stressful conditions may lead to dysregulation of the serotonergic system and is one of the most important predictors of suicide attempts in depressed patients (Pompili et al. 2010). Depression, on the other hand, is one of the major causes of hypercortisolemia, which may lead to neurotoxicity and reduced neurogenesis in the hippocampus in depressed patients (Axelson et al. 1993). Besides their role in glucose and mineral metabolism, corticosteroids are also implicated in the regulation of brain functions like sleep, ingestive behavior, behavioral adaptation, learning, and memory. In addition, corticosteroids play a significant role in brain damage, aging, mood, mental performance, and the pathogenesis of neuropsychiatric disorders, such as depression and Alzheimer's disease (de Kloet et al. 1986; McEwen and Sapolsky 1995; Sapolsky 2004).

14.3   Radiopharmaceuticals for Imaging of Steroid Hormone Receptors

Up to now, almost all information about the role of steroid hormones and their receptors in the healthy and diseased brain is obtained from experimental animals and postmortem human studies, because brain biopsy in patients is generally not feasible or highly undesirable. In order to facilitate research on the role of steroid hormones in neurodegenerative and psychiatric diseases, it is therefore of importance to have noninvasive techniques available to measure the expression of SHR in the brain. PET and SPECT are noninvasive nuclear imaging techniques that allow measurement of receptor expression and receptor occupancy in the living brain. Until now, several PET and SPECT tracers have been developed to image the SHR. Most of these radiopharmaceuticals, however, were developed for applications in oncology, in particular for imaging of receptor expression and occupancy in steroid hormone-sensitive tumors like breast and prostate cancer (de Vries et al. 2007; Hospers et al. 2008).

So far, only a few studies on imaging of SHR in the brain have been reported. However, it is expected that most radiopharmaceuticals that have been developed for tumor imaging can also be applied in brain imaging. Although many tracers have been described for each SHR, most of these tracers did not provide satisfactory results and consequently did not enter clinical studies. In the following paragraphs, we will not provide a complete overview of all tracers for SHR that have been reported but only discuss the most promising candidate tracers for PET and SPECT imaging of SHR in the brain.

14.3.1 Estrogen Receptor Imaging

The ER is the most widely studied SHR. Although literature exists on western blotting and in situ hybridization studies to determine the expression of the ER in the rodent brain, hardly any data exists on ER expression in the human brain. For this purpose, imaging methods to measure ER expression could certainly be of added value. Several tracers have been developed for PET and SPECT imaging of ER, in particular for imaging breast cancer.

14.3.1.1   PET Tracers for Estrogen Receptors

[^{18}F]FES (16alpha-[^{18}F]fluoro-17beta-estradiol) was one of the first PET tracers introduced for imaging of ER in the 1980s (Kiesewetter et al. 1984), and it is still used in the clinic today. In rats and mice, [^{18}F]FES presented highest uptake in tissues with high ER expression, such as the uterus and ovaries (Aliaga et al. 2004; Kiesewetter et al. 1984; Sasaki et al. 2000; Seimbille et al. 2004; Yoo et al. 2005). [^{18}F]FES uptake in ER-rich organs could be blocked with unlabeled estradiol in a dose-dependent manner, indicating that the tracer uptake is ER-mediated (Katzenellenbogen et al. 1993). Treatment of mice bearing ER-positive breast tumors with fulvestrant, an irreversible ER antagonist, also reduced the uptake of

[^{18}F]FES (Fowler et al. 2012). [^{18}F]FES binds to both ERα and ERβ, but the affinity of [^{18}F]FES is 6.3-fold higher for ERα than for ERβ (Yoo et al. 2005). Both ER subtypes are expressed in breast tumors, but ERα is usually the major type expressed (Fox et al. 2008). ERα is associated with tumor growth and development (Dotzlaw et al. 1997; Järvinen et al. 2000), while the function of ERβ is not well understood yet but is suggested to be involved in the inhibition of ERα signaling (Fox et al. 2008). In breast cancer patients, [^{18}F]FES PET has been applied successfully for the diagnosis and monitoring of anticancer treatment efficacy in ER-positive breast cancer. Previous studies showed ER expression in primary breast tumors and in metastases, in which the accumulation of [^{18}F]FES in these tumors correlated well with ER density, as determined by immunohistochemistry (Dehdashti et al. 1995; Mintun et al. 1988). In ER-positive breast cancer patients, [^{18}F]FES PET displays an excellent specificity (98%) and fairly good sensitivity (85%) for tumor detection (van Kruchten et al. 2013). In human plasma, [^{18}F]FES binds to sex hormone-binding globulin (SHBG) (Tewson et al. 1999), which improves the plasma stability of the tracer, although substantial metabolism is still observed. The radiation burden associated with [^{18}F]FES PET is within the normal range of other nuclear medicine procedures: a typical dose of 200 MBq (6 mCi) causes a radiation burden to the patient of 4.4 mSv (Mankoff et al. 2001; Mortimer et al. 1996; Peterson et al. 2008). [^{18}F]FES PET has now been used in many clinical studies in ER-positive cancer patients and is nowadays even used in routine clinical practice in our institution.

In order to increase the binding affinity and in vivo stability of the tracer, several analogues of [^{18}F]FES have been developed. One of these candidates, 11beta-methoxy-4,16alpha-[^{18}F]difluoroestradiol (4F-M[^{18}F]FES), showed high uptake and high target-to-background ratios in ER-rich organs like the uterus (VanBrocklin et al. 1994). 4F-M[^{18}F]FES has a low affinity toward the SHBG, but studies in humans showed a significant, potentially ER-mediated uterus uptake in both pre- and postmenopausal women (Beauregard et al. 2008). A preclinical study performed by Paquette and colleagues compared both 4F-M[^{18}F]FES and [^{18}F]FES, showing a higher specific tumor uptake and better contrast for 4F-M[^{18}F]FES (Paquette et al. 2013). Some years later, the same research group performed a comparative phase II clinical study in ER+ breast cancer patients and showed that 4F-M[^{18}F]FES yielded a lower nonspecific signal and better tumor contrast than [^{18}F]FES (Paquette et al. 2018). More studies should be performed to determine if 4F-M[^{18}F]FES is indeed more suitable than [^{18}F]FES for diagnosis and treatment evaluation of ER+ breast cancer patients.

Besides [^{18}F]FES and 4F-M[^{18}F]FES, several other radiolabeled estradiol derivatives and ER-targeting anticancer drugs have been evaluated as candidate PET tracers for imaging ER density and occupancy (Fig. 14.4). The potent estrogen 17alpha-ethynyl-16beta-[^{18}F]fluoro-11beta-methoxy-estradiol ([^{18}F]betaFMOX) showed promising results in rodents with a fourfold higher uptake in immature rat uterus than [^{18}F]FES. [^{18}F]betaFMOX was considered to be a highly sensitive tracer for imaging of the ER, as [^{18}F]betaFMOX also exhibited specific binding in organs with low ER density, such as the kidney, muscle, and thymus (VanBrocklin et al. 1993a, b). Despite the promising results in rodents, [^{18}F]betaFMOX PET failed to
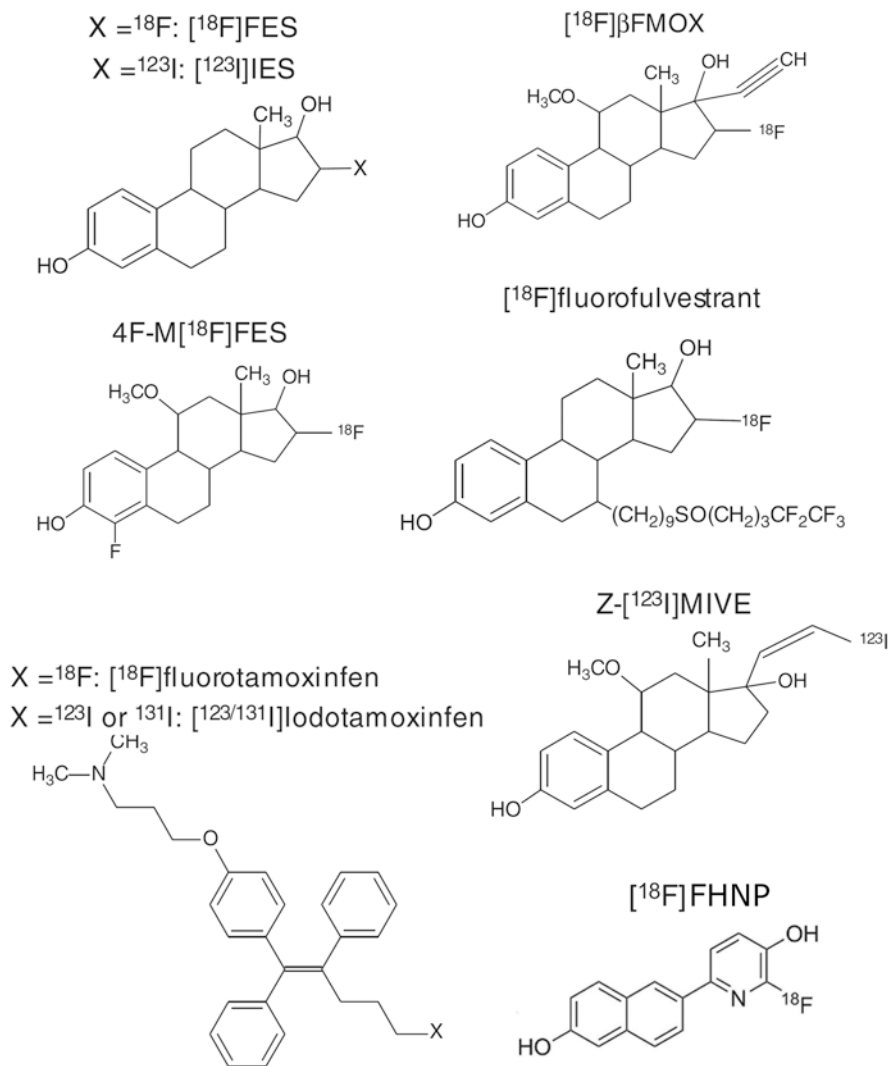
Fig. 14.4 Chemical structures of tracers that have been evaluated for PET or SPECT imaging of estrogen receptors

detect ER-positive lesions in breast cancer patients. This lack of sensitivity in humans may be due to the fast metabolism of the tracer, because it exhibited low binding to SHBG, which protects steroids from metabolic degradation (Jonson et al. 1999). Other ethynyl analogues of FES were tested for breast cancer imaging. These tracers also showed faster degradation in vivo, due to low SHGB binding, although they showed better target-to-background ratios (VanBrocklin et al. 1992).

In addition to estradiol derivatives, radiolabeled derivatives of anticancer drugs, such as tamoxifen and fulvestrant, were evaluated for imaging of ER. ^{18}F-labeled

tamoxifen, [^{18}F]fluoromethyl-*N*,*N*-dimethyltamoxifen ([^{18}F]FTX), exhibited specific uptake in the uterus and mammary tumors, which could be blocked with an excess of estradiol (Yang et al. 1994) and appeared to correlate with tamoxifen treatment outcome (Inoue et al. 1996). So far, no additional studies have been performed to prove the clinical utility of [^{18}F]FTX. Labeling of fulvestrant, a full antagonist of the ER, resulted in a reduced binding affinity due to the addition of ^{18}F. Consequently, ^{18}F-labeled fulvestrant is not suitable for PET imaging of ER (Seimbille et al. 2004).

The discovery of ERβ in breast cancer initiated the search for ERβ-selective PET tracers. Lee and colleagues developed two beta-selective tracers: 8beta-(2-[^{18}F]fluoroethyl)estradiol (8beta-[^{18}F]FEE), a derivative of the potent ERβ-selective steroid 8beta-vinylestradiol, and [^{76}Br]BrERB-041 derived from the nonsteroidal ERβ ligand ERB-041 (Lee et al. 2012). Although both 8beta-[^{18}F]FEE and [^{76}Br]BrERB-041 showed high binding affinities in a radiometric assay, ex vivo biodistribution studies in rats and mice could not demonstrate ERβ-mediated uptake (Lee et al. 2012). On the other hand, Antunes and colleagues recently synthesized a fluorinated pyridinic tracer [^{18}F]FHNP for selective binding to ERβ. [^{18}F]FHNP showed a higher affinity toward ERβ than ERα, showing selective binding of the tracer to ERβ in tumor-bearing mice, which makes this tracer a possible candidate for the measurement of ERβ in vivo (Antunes et al. 2017a, b). However, more studies are needed for the validation of this tracer.

In summary, at this moment [^{18}F]FES remains the best validated tracer for molecular imaging of ER expression and is currently used in clinical studies. Even though its characteristics are not ideal, [^{18}F]FES is an adequate tracer for PET imaging of ER in humans (van Kruchten et al. 2013). Efforts to develop better alternatives for [^{18}F]FES are still made (e.g., 4F-M[^{18}F]FES), but no phase III clinical studies have been performed yet. So far, [^{18}F]FHNP is the only PET tracer showing ERβ-selectivity in vivo, but this ligand needs further evaluation.

14.3.1.2 SPECT Tracers for Estrogen Receptors

In addition to PET tracers, some SPECT tracers have been developed for imaging of ER (Fig. 14.4) (for a review see (Liu et al. 2016)). Among the first successful SPECT tracers for ER was 16alpha-[^{125}I]iodo-11beta-methoxy-17beta-estradiol ([^{125}I]MIE) (Zielinski et al. 1986). In rodents, [^{125}I]MIE was found to accumulate in ER-rich areas, such as the uterus. [^{125}I]MIE showed higher uterus-to-blood ratios than 16alpha-[^{125}I]iodoestradiol. 16alpha-[^{123}I]iodo-17beta-estradiol ([^{123}I]IES) and (20Z)-11beta-methoxy-17alpha-[^{123}I]iodovinylestradiol (Z-[^{123}I]MIVE) have not only been applied in animals but also in clinical studies. [^{123}I]IES showed ER-mediated uptake in the rabbit reproductive system and in ER-positive tumors in breast cancer patients, but no specificity or sensitivity data were reported (Kenady et al. 1993; Pavlik et al. 1990; Scheidhauer et al. 1991; Schober et al. 1990). Both stereoisomers of [^{123}I]MIVE were evaluated for ER imaging. The (Z)-isomer of [^{123}I]MIVE showed highest ER-mediated specific uptake in rodents and in clinical studies in breast cancer patients. The tracer uptake could be blocked by saturation of the ER with tamoxifen (Bennink et al. 2004, b; Rijks et al. 1997a, b). Although both [^{123}I]IES and (Z)-[^{123}I]MIVE showed ER-mediated specific uptake, these

tracers also displayed fast metabolism and low SHBG binding (Nachar et al. 1999; Rijks et al. 1998a; Rijks et al. 1998b).

Attempts have been made to generate a SPECT tracer for ER by labeling derivatives of the anticancer drug tamoxifen. In rodents, the uptake of [123I]iodotamoxifen ([123I]TAM) was found to be high in ER-rich organs (Biber Muftuler et al. 2008). In clinical studies, [123I]TAM showed ER-specific uptake in breast tumors (Hanson and Seitz 1982; Van de Wiele et al. 2001). Recently tamoxifen was also labeled with 131I ([131I]TAM). Biodistribution studies in rodents proved that the uptake of this tracer was ER-mediated in the uterus and breast tissue (Biber Muftuler et al. 2008). No further studies on iodine-labeled tamoxifen have been published lately.

Estradiol and anticancer drug derivatives have also been labeled with 99mTc. A few of them have even been successfully evaluated in rodents (Arterburn et al. 2003; Nayak et al. 2008, 2014; Ramesh et al. 2006; Takahashi et al. 2007a, b; Xia et al. 2016; Yurt et al. 2009; Zhu et al. 2010). However, the usefulness of these tracers for brain imaging is questionable, because of the high hydrophilicity of the 99mTc conjugates, which likely precludes efficient brain penetration.

14.3.2 Progesterone Receptor Imaging

14.3.2.1 PET Tracers for Progesterone Receptors

A few substrates of PR have been labeled with 18F, 76Br, 123I, and 125I for imaging of PR with PET and SPECT (Fig. 14.5) (for a review, see Linden et al. 2018). The 18F-labeled candidate PET tracers for PR include 21-[18F]fluoro-16alpha-ethyl-19-norprogesterone ([18F]FENP) (Dehdashti et al. 1991; Jonson and Welch 1998; Pomper et al. 1988; Verhagen et al. 1991a), 21-[18F]fluoro-16alpha-methyl-19-norprogesterone([18F]FMNP)(Verhagenetal.1991a),and21-[18F]fluoro-16alpha,7alpha-[(R)-(1′alpha-furylethylidene)dioxy]-19-norpregn-4-ene-3,20-dione (Buckman et al. 1995). [18F]FMNP exhibited PR-mediated uptake in the uterus and tumors in rats (Verhagen et al. 1991b), but no further studies in humans were reported. [18F]FENP showed highly selective PR-mediated uptake in the uterus of estrogen-primed rats (Pomper et al. 1988)) and in PR-positive carcinoma in mice (Verhagen et al. 1991b). In eight breast cancer patients, however, [18F]FENP could only detect 50% of PR-positive lesions, and tracer uptake did not correlate with PR expression (Dehdashti et al. 1991). The major reason for failure of [18F]FENP in clinical studies was its extensive metabolism in humans (Verhagen et al. 1994).

To overcome this problem, several ketals of 16alpha,17alpha-dihydroxyprogesterone were labeled with positron-emitting isotopes (Buckman et al. 1995; Vijaykumar et al. 2002; Zhou et al. 2006), with 21-[18F]fluoro-16alpha,17alpha-[(R)-(1′-alpha-furylmethylidene)dioxy]-19-norpregn-4-ene-3,20-dione ([18F]FFNP) being the most studied one. In a study performed in mice with mammary tumors, treatment with estradiol, letrozole, or fulvestrant showed treatment-induced changes in the uptake of [18F]FFNP, suggesting that early evaluation of response to the anticancer treatment could be feasible (Fowler et al. 2012; Salem et al. 2018, 2019). A study in breast cancer patients showed that [18F]FFNP PET is
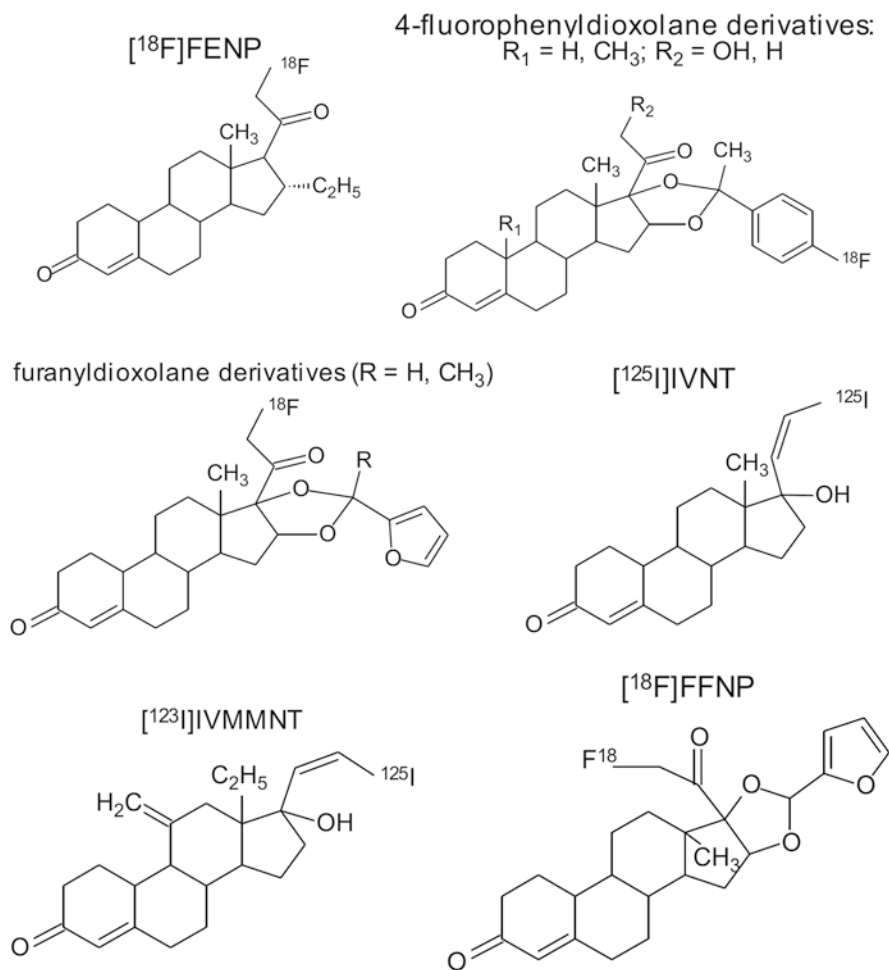
Fig. 14.5 Chemical structures of tracers that have been evaluated for PET or SPECT imaging of progesterone receptors

a safe, noninvasive method to evaluate the tumor's PR status in vivo (Dehdashti et al. 2012). Brain uptake of [18F]FFNP seems to be acceptable, but further studies are needed to prove its suitability for brain imaging.

Another series of candidate PET tracers for PR imaging comprised the derivatives of the nonsteroidal PR agonist tanaproget. Several derivatives of tanaproget were evaluated (Zhou et al. 2010), and 4-[18F]fluoropropyl-tanaproget ([18F]FPTP) demonstrated highest uptake in the target tissues like uterus and ovaries. The biodistribution pattern of [18F]FPTP in rats was comparable with other PR tracers, such as FENP and FFNP (Lee et al. 2010). Furthermore, synthesis of tanaproget-based compounds labeled with 11C is currently ongoing. Haywood and colleagues successfully tested the synthesis of different 11C-based molecules, but further

preclinical studies are needed to characterize the pharmacokinetics of these compounds (Haywood et al. 2015).

At the moment, [¹⁸F]FFNP seems to be the most promising candidate tracer for imaging PR, but more studies are required to validate the utility of this tracer in humans.

14.3.2.2   SPECT Tracers for Progesterone Receptors

A few iodinated tracers for PR imaging have been developed, but none of these candidate tracers showed promising results. (20Z)-17alpha-[¹²⁵I]iodovinyl-19-nortestosterone ([¹²⁵I]IVNT) had interesting binding properties, but lacked selectivity in vivo (Ali et al. 1994). Later, both isomers of 17alpha-[¹²³I]iodovinyl-18-methyl-11-methylene-19-nortestosterone ([¹²³I]IVMMNT) were investigated in rats and rabbits. (Z)-[¹²³I]IVMMNT displayed highest in vivo binding in target organs, such as in uterus and ovaries. The uptake of (Z)-[¹²³I]IVMMNT was found to be PR-mediated (Rijks et al. 1998b). So far, no human data exist to prove the feasibility of PR imaging with these tracers.

14.3.3   Androgen Receptor Imaging

14.3.3.1   PET Tracers for Androgen Receptors

Several promising PET tracers for imaging of androgen receptors have been successfully developed (Fig. 14.6). 20-[¹⁸F]fluoromibolerone (20-[¹⁸F]Fmib) was the first radiolabeled PET tracer for AR that showed promising uptake in the prostate of rats and in baboons (Bonasera et al. 1996; Liu et al. 1991). Several other fluorinated compounds have been developed, and some of them showed promising results, such as 16beta-[¹⁸F]fluorodihydrotestosterone ([¹⁸F]FDHT), 16beta-[¹⁸F]fluorotestosterone (16beta-[¹⁸F]FT), 16beta-[¹⁸F]fluoro-7alpha-methyl-19-nortestosterone (16beta-[¹⁸F]FMNT), 16alpha-[¹⁸F]fluoro-7alpha-methyl-19-nortestosterone (16alpha-[¹⁸F]FMNT), and 20-[¹⁸F]fluorometribolone (20-[¹⁸F]R1881) (Liu et al. 1992). Most of these tracers showed quick clearance from the body and rapid metabolism.

[¹⁸F]FDHT is so far the most promising tracer, showing the best results in rats and baboons. Uptake of [¹⁸F]FDHT in the prostate was specific and AR-mediated. Metabolism of [¹⁸F]FDHT was slower than metabolism of the other candidate tracers (Bonasera et al. 1996; Choe et al. 1995). [¹⁸F]FDHT showed specific binding to AR and was able to detect changes in AR availability in preclinical studies (Larimer et al. 2018). Currently, [¹⁸F]FDHT is the only PET tracer that has proceeded into the clinical evaluation phase (Beattie et al. 2010; Dehdashti et al. 2005; Kramer et al. 2019; Larson et al. 2019; Zanzonico et al. 2004). The radiation burden associated with [¹⁸F]FDHT PET is within the normal range of other clinical nuclear medicine procedures: 0.018 mSv/MBq; for the maximum administered dose of 331 MBq, the total radiation burden is 6.0 mSv. Furthermore, recent studies aimed to position this tracer as a biomarker for metastatic castration-resistant prostate cancer patients have shown positive results (Cysouw et al. 2019; Fox et al. 2018; Jansen et al. 2019). In addition, [¹⁸F]FDHT has also been

20-[18F]FMib: R₁= CH₂¹⁸F, R₂ =H
16-[18F]FMib: R₁= CH₃,R₂ = ¹⁸F
16-[18F]FMNT: R₁= H,R₂ = ¹⁸F

[¹⁸F]FDHT

16β–[¹⁸F]FT

[¹⁸F]FMDHT

[¹⁸F]R1881
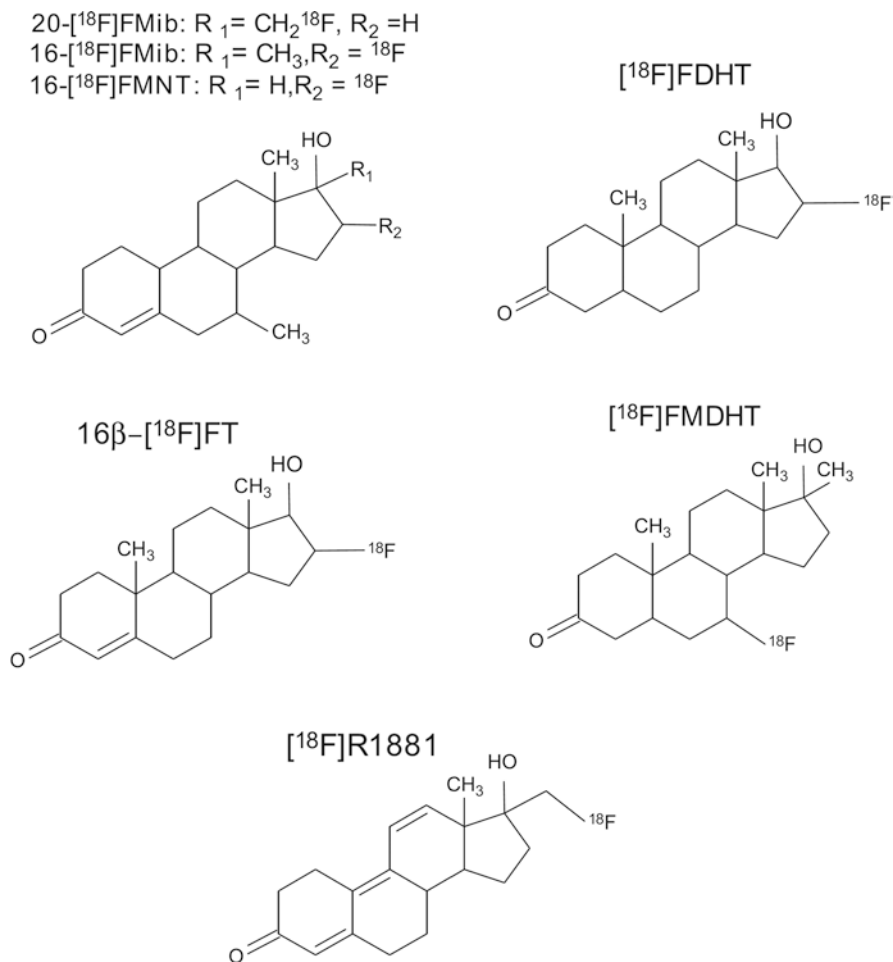
Fig. 14.6 Chemical structures of tracers that have been evaluated for PET or SPECT imaging of androgen receptors

investigated as a PET tracer for detection of AR expression in breast cancer (Venema et al. 2017) and for detection of intra-abdominal testicles (Glaudemans et al. 2015).

The major drawback of [¹⁸F]FDHT is its rapid metabolism. This led to the investigation of nonsteroidal derivatives with better in vivo stability, like ¹¹C-labeled derivatives of propanamide, a selective androgen receptor modulator (Gao et al. 2011). Some nonsteroidal antagonists of AR have been radiolabeled, such as a ¹¹C-labeled diethylamine flutamide derivative (Jacobson et al. 2006), a ¹⁸F-labeled hydroxyflutamide derivative (Jacobson et al. 2005), 3-[⁷⁶Br]bromohydroxyflu-tamide (Parent et al. 2006), [¹⁸F]bicalutamide, 4-[⁷⁶Br]bromobicalutamide, and [⁷⁶Br]bromo-thiobicalutamide (Parent et al. 2007). However, none of these compounds showed promising results that warranted further evaluation.

Another interesting candidate PET tracer is 7alpha-[^{18}F]fluoro-17-methyl-5-di-hydrotestosterone ([^{18}F]FMDHT), although the first results reported for this tracer were not very promising. The uptake of [^{18}F]FMDHT in the prostate was low; results were not reproducible and not comparable with other labeled steroids like [^{18}F]FDHT. In these first experiments, [^{18}F]FMDHT was investigated in rats treated with DES to suppress endogenous testosterone production (Garg et al. 2001). The same authors reevaluated the suitability of [^{18}F]FMDHT for AR imaging in chemically castrated rats. In this animal model, uptake in the prostate was proven to be AR-mediated. Prostate uptake was comparable to other ^{18}F-labeled steroids and twofold higher than [^{18}F]FMDHT uptake in DES-treated rats (Garg et al. 2008).

The most recent attempt for the synthesis of fluorinated androgen analogues was made by Okamoto and colleagues (2017). They could successfully synthesize two ^{18}F-labeled derivatives of 7α-(3-[^{18}F]fluoropropyl)-testosterone that showed proper affinity for AR. However, further studies are needed to determine if these tracers could be useful in determining AR changes in the brain.

So far, [^{18}F]FDHT is the only AR tracer that has proceeded into the clinical evaluation phase. Clinical studies confirmed that this tracer is suitable for AR imaging in cancer patients. However, it still remains to be evaluated whether [^{18}F]FDHT PET is also able to monitor AR expression in the human brain. In addition, preclinical data of [^{18}F]FMDHT suggest that it may have favorable characteristics for AR imaging as well, but further evaluation is required to establish the merit of this tracer.

14.3.3.2 SPECT Tracers for Androgen Receptors

The radioiodinated steroid 2alpha-[^{125}I]dihydrotestosterone was the first SPECT tracer showing high uptake in AR-rich organs like the prostate, epididymis, and testis in rats. Pretreatment with dihydrotestosterone reduced the uptake in these organs, suggesting that tracer uptake is specific and AR-mediated (Tarle et al. 1981). 7alpha-[^{125}I]iodo-5alpha-dihydrotestosterone (7alpha-[^{125}I]IDHT) is another analogue of testosterone that was labeled with [125]I. 7alpha-[^{125}I]IDHT showed AR-mediated uptake in the prostate of rats. In vitro autoradiography of 7alpha-[^{125}I]IDHT produced excellent autoradiograms with low nonspecific binding in the prostate of rats (Labaree et al. 1997), but no further studies were published to demonstrate the usefulness of this tracer in vivo.
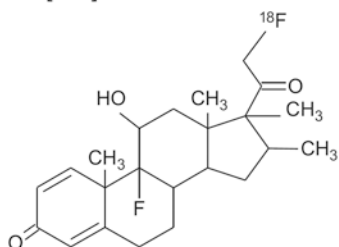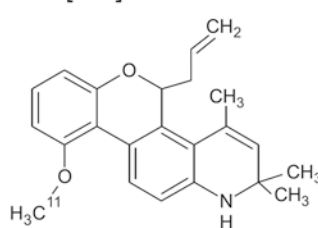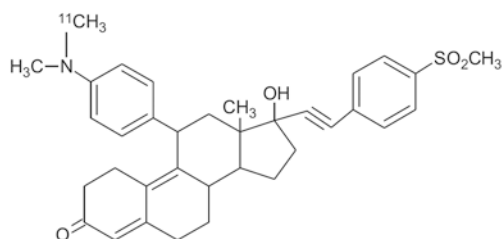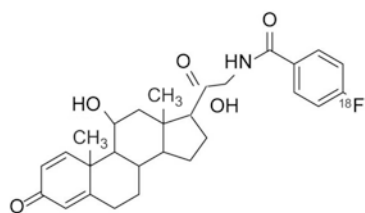
Some steroid and flutamide derivatives have been labeled with ^{99m}Tc and tested as SPECT tracers for AR. However, in vivo evaluation in rats did not show any AR-mediated specific binding for any of these compounds (Dallagi et al. 2010; Dhyani et al. 2011).

14.4 Corticoid Receptor Imaging

14.4.1 PET Tracers for Glucocorticoid Receptors

So far, only a few radiolabeled GR ligands have been synthesized and evaluated for the potential use as PET tracer (Fig. 14.7). Most of these candidate tracers showed disappointing results in rodents and baboons. The first labeled compound that was
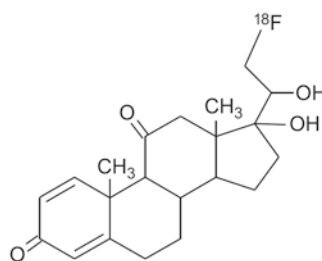
Fig. 14.7 Chemical structures of tracers that have been evaluated for PET imaging of glucocorticoid receptors

introduced as ligand for the imaging of GR was 21-[^{18}F]fluoroprednisone. 21-[^{18}F]fluoroprednisone was rapidly metabolized, leading to low uptake in rat brain (Feliu and Rottenberg 1987). Additionally, an analogue of the selective GR agonist RU28362 was tested. The biodistribution of [^{18}F]RU52461 showed high GR-mediated uptake in the adrenals and pituitary in rats. PET imaging studies in baboons, however, showed low uptake of [^{18}F]RU 52461 in the brain (Dasilva et al. 1992). In another study in rats, [^{18}F]RU52461 uptake in the hippocampus could only be partially blocked with an excess of the unlabeled ligand, whereas complete blocking of tracer uptake in peripheral organs was observed (Pomper et al. 1992). The potent GR ligand [^{18}F]ORG6141 was evaluated in adrenalectomized and sham-operated rats. Ex vivo biodistribution 3 h postinjection revealed higher uptake of tracer in the hippocampus and brain stem of adrenalectomized animals as compared to sham-operated controls. However, GR-mediated specific retention of activity in these brain areas could not be demonstrated (Visser et al. 1995).

Wuest et al. synthesized a series of novel 4-fluorophenylpyrazolo steroids and tested their binding affinities to GR. Some of these compounds showed binding affinities up to 56% relative to dexamethasone (100%) (Wüst et al. 2003). One of these compounds, 2′-(4-fluorophenyl)-21-[^{18}F]fluoro-20-oxo-11beta,17alpha-dihydroxy-pregn-4-eno[3,2-c]pyrazole, was evaluated in rats using autoradiography and small animal PET imaging. Brain uptake of this tracer was found to be constant between 5 and 60 min after tracer injection. However, brain uptake was not specifically GR-mediated (Wüst et al. 2005) but only due to nonspecific binding. Another high-affinity GR antagonist Org34850 was labeled with ^{11}C. [N-methyl-^{11}C]Org34850 was found to rapidly metabolize in rats. Ex vivo biodistribution and small animal PET studies demonstrated that [N-methyl-^{11}C]Org34850 was not able to penetrate the blood-brain barrier (Wuest et al. 2009).

Additional attempts were made with nonsteroidal molecules. The selective GR modulator AL-438 was labeled with ^{11}C. The biodistribution of [^{11}C]AL-438 showed high uptake in the pituitary and the brain, but treatment with a high dose of the GR antagonist corticosterone did not result in any blocking of tracer uptake, suggesting that the uptake was not GR-mediated (Wuest et al. 2007).

Thus, none of the aforementioned studies were successful, and consequently suitable tracers for imaging GR expression are currently not available. Nonetheless, in a recent work performed by Truillet and colleagues, a set of GR ligands was synthesized and labeled with ^{18}F (Truillet et al. 2018). One of these tracers, [^{18}F]GR02, showed promising results. In vitro and in vivo testing in rats showed sufficient binding affinity to GR in GR-rich tissue. Additionally, they found uptake in the brain, which was increased substantially in adrenalectomized animals. Further studies are needed to validate this compound as a tracer for GR.

14.4.2 PET Tracers for Mineralocorticoid Receptors

There is only one report that describes a series of MR-specific compounds that have been labeled with fluorine-18 for PET imaging. These compounds include
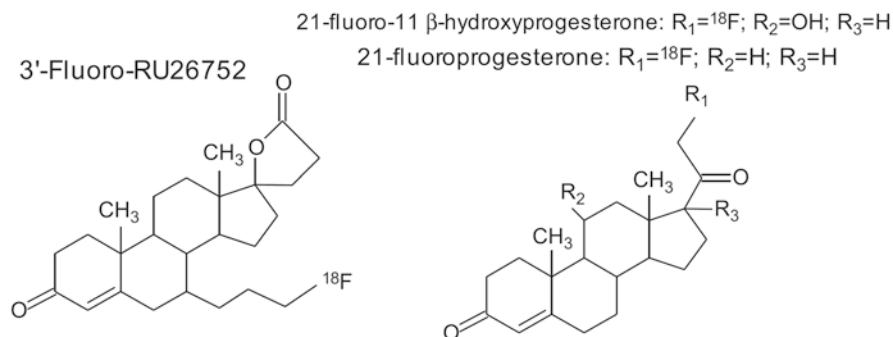
Fig. 14.8 Chemical structures of tracers that have been evaluated for PET imaging of mineralo-corticoid receptors

21-[^{18}F]fluoroprogesterone,   21-[^{18}F]fluoro-11beta-hydroxyprogesterone,   and 3′-[^{18}F]fluoro-RU26752 (Fig. 14.8). Unfortunately, none of these compounds displayed the characteristics that are required for PET imaging of MR (Pomper et al. 1992).

14.5   Imaging of Steroid Hormone Receptors in the Brain

Although several tracers for imaging of SHR have now been applied in humans, hardly any studies on imaging of these receptors in the brain have been published. So far, mostly tracers for ER have been successfully used in rodents for imaging SHR in the brain.

14.5.1 Imaging of Estrogen Receptors in the Brain

So far, there is one study testing the usefulness of 16alpha-[^{125}I]iodoestradiol for the detection of ER in the brain. Stumpf and colleagues (1987) used ex vivo autoradi-ography of the brain of prepubertal Sprague Dawley rats injected with 16alpha-[^{125}I]iodoestradiol and showed high concentrations of radioactivity in the marginal zone of the mid-region anterior lobe of the pituitary and in preoptic neurons 1 h after tracer injection. The intermediate lobe and most cells in the anterior lobe, together with the dorsocaudal paraventricular nucleus and the medial amygdaloid region showed only a weak signal. Long-term exposure of the photographic plate allowed topographical recognition of tracer binding to cells in the medial amygdala, medio-dorsal and cortical nuclei, and piriform cortex. However, 16alpha-[^{125}I]iodoestradiol uptake in the brain could not be significantly blocked with an excess of unlabeled estradiol, which was ascribed to deiodination of the tracer, leading to nonspecific binding of ^{125}I within the myelin sheaths.

In addition to 16alpha-[^{125}I]iodoestradiol, the SPECT tracer 11beta-methoxy-16alpha-[^{125}I]iodoestradiol ([^{125}I]MIE$_2$) has also been evaluated as tracer for ER in binding and displacement studies in rat, rabbit, and human brain slices. A

dose-dependent uptake of [^{125}I]MIE$_2$ in pituitary and brain cell nuclei was observed in 25-day-old female rats (Brown et al. 1989), suggesting specific binding to the ER with no cross-reactivity with the other SHR. Additional experiments by Toran-Allerand and colleagues (1992) combined autoradiography with in situ hybridization and revealed a correlation between SPECT tracer uptake and binding of the mRNA probe in the cerebral cortex of female rats. In another study, ER expression during brain development was studied with [^{125}I]MIE$_2$ in mice of both sexes. This study demonstrated the presence of ER-positive cells in the early postnatal cortex and showed a profound change in the topography and number of ER-positive cells during development (Shughrue et al. 1990). The most recent study used ex vivo autoradiography with [^{125}I]MIE$_2$ to evaluate the effect of long-term treatment (21–60 days) with estradiol and tamoxifen on ER occupancy in the brain. The distribution of [^{125}I]MIE$_2$ uptake was in agreement with the expected ER distribution in ovariectomized rats: highest uptake in the preoptic and hypothalamic nuclei, followed by the amygdala, hippocampus, midbrain, and frontal cortex. In the tamoxifen-treated rats, a reduction in [^{125}I]MIE$_2$ binding was mainly seen in ERα-dominated regions like the cortical amygdala, central gray, and anterior paraventricular thalamus. A moderate inhibition of tracer uptake was found in the regions where both ER subtypes are expressed, like the ventrolateral-ventromedial hypothalamus, medial preoptic area, medial amygdala, and arcuate nucleus. After estradiol treatment, [^{125}I]MIE$_2$ showed a low and homogenous uptake in the brain, with an overall reduction in ER binding of 87% as compared to untreated controls (Pareto et al. 2004).

Fluoroestradiol ([^{18}F]FES) is the only PET tracer that has been used to assess ER expression in rat brain. In a very detailed study, the suitability of [^{18}F]FES for in vivo quantification of ER was tested by both equilibrium and dynamic kinetic analysis (Moresco et al. 1995). Uptake of [^{18}F]FES was mainly seen in ER-rich regions in the brain, such as in the pituitary and hypothalamus, with a maximum uptake observed between 25 and 30 min postinjection, reaching a pseudoequilibrium at 30 min. Blocking with increasing doses of unlabeled estradiol reduced the accumulation in the pituitary and hypothalamus in a dose-dependent manner, whereas no effect was observed in the hippocampus, cortex, and striatum. The specific binding of [^{18}F]FES was calculated by equilibrium analysis considering the striatum as a reference tissue where the expression of the ER was expected to be very low. The equilibrium analysis showed saturable binding in the pituitary and hypothalamus with highest binding potential (B_{max}/K_d) in the pituitary (16.11) and hypothalamus (1.97). The B_{max} and the K_d were found to be much higher in the pituitary (124.01 ± 12.36 pmol/g and 7.70 ± 1.07) and then in the hypothalamus (11.85 ± 0.16 pmol/g and 6.01 ± 0.41). The in vivo quantification of ER gave similar results in the pituitary and hypothalamus when either equilibrium or graphical analysis was used (Moresco et al. 1995). In another study, the effect of long-term treatment of estradiol and tamoxifen on ER occupancy in rat brain was studied by ex vivo autoradiography with [^{18}F]FES. Although this study showed marked reduction in the uptake of [^{18}F]FES in ER-rich areas, such as the hypothalamus, preoptic area, amygdala, and frontal cortex in the treatment groups, no differences in cerebellar uptake was observed (Pareto et al. 2004).

All the aforementioned studies were performed by ex vivo measurement of tracer uptake, without the use of in vivo imaging. We studied the feasibility of [^{18}F]FES to monitor ER in the rat brain by small animal PET, and the results were in agreement with the ones found by Moresco et al. (1995). The brain time-activity curves of [^{18}F]FES showed a quick peak uptake immediately after intravenous tracer injection, which was followed by a washout leading to a state of pseudoequilibrium after 25 min. Highest uptake was seen in the pituitary gland, followed by the hypothalamus. The rest of the brain areas showed low uptake. Blocking of the receptor with an excess of estradiol resulted in a statistically significant reduction in tracer uptake only in the pituitary gland and hypothalamus. A statistically significant higher volume of distribution and binding potential was found in the pituitary, when compared to other brain regions. [^{18}F]FES uptake was not significantly affected by differences in plasma estrogen levels (Khayum et al. 2014).

So far, [^{18}F]FES is the only tracer that was tested for in vivo visualization of ER in the brain of rats. [^{18}F]FES showed promising results, as it displayed highest uptake in the regions of the brain with high expression of ER. It has also been shown that using this tracer, ER-positive tumors can be identified in the brain (Moresco et al. 1997). Nonetheless, further research is necessary to validate this tracer for ER imaging in the human brain. We recently used [^{18}F]FES PET to determine the receptor occupancy of a novel ER-binding drug in postmenopausal women (Conlan et al. 2020). Highest [^{18}F]FES uptake was observed in pituitary, with low tracer uptake in all other brain regions. After treatment with the ER-binding drug, [^{18}F]FES uptake was significantly reduced in pituitary only, suggesting that [^{18}F]FES PET can only show ER-specific binding in this brain region.

Moreover, the availability of a new ERβ-selective tracer would be highly desirable, since the different isoforms of ER have different expression patterns and different functions in neuroprotection, mood, and memory (Foster 2012; Ooishi et al. 2012). [^{18}F]FHNP seems to be a good candidate for selective binding to ERβ in the brain (Antunes et al. 2017a; Antunes et al. 2017b). However, further studies are needed to validate this tracer.

14.5.2 Imaging of Other Hormone Receptors in the Brain

The only tracer that has been tested for AR imaging in the brain is [^{18}F]FDHT. Although this tracer is already used in the clinical studies in cancer patients, it proved not suitable for the detection of AR in the brain of rats. Fast metabolism, low and nonspecific binding are the main issues that were encountered (Khayum et al. 2015). [^{18}F]FPTP is the only tracer that could visualize PR both in humans and in experimental animals so far, but further evaluation of the tracer for brain imaging is required. Additionally, [^{18}F]FFNP PET was found to be a safe, noninvasive method to evaluate tumor PR in vivo in patients with breast cancer, positioning this tracer as a candidate to be used for brain research (Fowler

et al. 2012; Salem et al. 2018, 2019). Unfortunately, no selective tracers for the different isoforms of the PR and AR are available yet. No suitable tracers for GR and MR imaging are available either. Although some studies explored the used of some PET tracers for GR and MR receptors in the brain, none of them proved to be suitable.

14.6 Conclusion and Perspectives

Despite the large amount of research focusing on SHRs and their functions in the brain, many questions still remain unanswered. PET and SPECT imaging could be attractive tools for studying SHR function in the brain in living subjects. Several PET and SPECT tracers have been already evaluated for detection of SHR in oncology, and some of them have already entered into the clinical setting. Tracers that are used for diagnosis and monitoring of therapy response in hormone-sensitive cancers can easily be tested for applications in neurological and psychiatric disorders as well. So far, [18F]FES, [18F]FFNP, and [18F]FDHT have been used successfully in cancer patients for imaging of ER, PR, and AR, respectively. Only [18F]FES and [18F]FDHT have been tested to detect ER and AR in the brain of rodents. More studies using these tracers are needed to validate their use in brain research. The development of new tracers with higher affinity and specificity can help to increase the use of molecular imaging of sex hormone receptors in the brain.

Development of tracers for corticoid receptors has long been attempted, but these efforts have not yet produced any promising results. When tracers for corticoid receptors finally become available, however, they will be valuable assets for research in stress, mood, and neuropsychiatric disorders that are known to be associated with dysregulation of the HPA axis.

Aging and lifestyle-associated stress are known to change SHR expression. Because SHR receptors are associated with many brain functions, imaging of SHR in the brain could be a valuable tool to study disease mechanisms associated with, e.g., changes in expressional levels of SHR, which can ultimately culminate into neurological and psychiatric disorders. Understanding disease mechanisms could provide a rationale for treatment regimens based on pharmacological compounds associated with SHR. PET and SPECT imaging of SHR could also be helpful in drug discovery for individual SHR-associated disorders. PET and SPECT may provide information about the amount of a test drug that binds to the target and about the residence time of the drug in the brain. Such information about a new drug is highly valuable for decision-making in drug development and optimizing the dose and route of administration.

Thus, PET and SPECT imaging of SHR may not only be helpful in the diagnosis of neurological and psychiatric disorders associated with altered SHR expression but could also be instrumental in providing a better understanding of disease mechanisms and the development of new intervention strategies.

References

Ali H, Rousseau AJ, van Lier JE (1994) Synthesis of (17 alpha,20E/Z)iodovinyl testosterone and 19-nortestosterone derivatives as potential radioligands for androgen and progesterone receptors. J Steroid Biochem Mol Biol 49(1):15–29

Aliaga A, Rousseau JA, Ouellette R, Cadorette J, van Lier JE, Lecomte R, Bénard F (2004) Breast cancer models to study the expression of estrogen receptors with small animal PET imaging. Nucl Med Biol 31(6):761–770. https://doi.org/10.1016/j.nucmedbio.2004.02.011

Antunes IF, van Waarde A, Dierckx RAJ, de Vries EGE, Hospers GAP, de Vries EFJ (2017a) Synthesis and evaluation of the estrogen receptor β–selective radioligand 2–18 F-fluoro-6-(6-hydroxynaphthalen-2-yl)pyridin-3-ol: comparison with 16α- 18 F-fluoro-17β-estradiol. J Nucl Med 58(4):554–559. https://doi.org/10.2967/jnumed.116.180158

Antunes IF, Willemsen ATM, Sijbesma JWA, Boerema AS, van Waarde A, Glaudemans AWJM, Dierckx RA, de Vries EFJ (2017b) In vivo quantification of ERβ expression by pharmaco-kinetic modeling: studies with 18 F-FHNP PET. J Nucl Med 58(11):1743–1748. https://doi.org/10.2967/jnumed.117.192666

Arterburn JB, Corona C, Rao KV, Carlson KE, Katzenellenbogen JA (2003) Synthesis of 17-α-substituted estradiol-pyridin-2-yl hydrazine conjugates as effective ligands for labeling with Alberto's complex f ac -[Re(OH 2) 3 (CO) 3] + in water. J Org Chem 68(18):7063–7070. https://doi.org/10.1021/jo034780g

Axelson DA, Doraiswamy PM, McDonald WM, Boyko OB, Tupler LA, Patterson LJ, Nemeroff CB, Ellinwood EH Jr, Krishnan KR (1993) Hypercortisolemia and hippocampal changes in depression. Psychiatry Res 47(2):163–173

Barabás K, Godó S, Lengyel F, Ernszt D, Pál J, Ábrahám IM (2018) Rapid non-classical effects of steroids on the membrane receptor dynamics and downstream signaling in neurons. Horm Behav 104:183–191. https://doi.org/10.1016/j.yhbeh.2018.05.008

Baulieu E (1998) Neurosteroids: a novel function of the brain. Psychoneuroendocrinology 23(8):963–987. https://doi.org/10.1016/S0306-4530(98)00071-7

Beattie BJ, Smith-Jones PM, Jhanwar YS, Schoder H, Schmidtlein CR, Morris MJ, Zanzonico P, Squire O, GSP M, Finn R, Namavari M, Cai SD, Scher HI, Larson SM, Humm JL (2010) Pharmacokinetic assessment of the uptake of 16 -18f-fluoro-5 -dihydrotestosterone (FDHT) in prostate tumors as measured by PET. J Nucl Med 51(2):183–192. https://doi.org/10.2967/jnumed.109.066159

Beauregard J-M, Croteau E, Ahmed N, van Lier JE, Benard F (2008) Assessment of human bio-distribution and dosimetry of 4-fluoro-11 -methoxy-16 -18F-fluoroestradiol using serial whole-body PET/CT. J Nucl Med 50(1):100–107. https://doi.org/10.2967/jnumed.108.057000

Bennink RJ, Van Tienhoven G, Rijks LJ, Noorduyn AL, Janssen AG, Sloof GW (2004) In vivo prediction of response to antiestrogen treatment in estrogen receptor – positive breast cancer. J Nucl Med 45(1):1–7

Biber Muftuler FZ, Unak P, Teksoz S, Acar C, Yolcular S, Yürekli Y (2008) 131I labeling of tamoxifen and biodistribution studies in rats. Appl Radiat Isot 66(2):178–187. https://doi.org/10.1016/j.apradiso.2007.08.005

Bonasera TA, O'Neil JP, Xu M, Dobkin JA, Cutler PD, Lich LL, Katzenellenbogen JA, Welch MJ (1996) Preclinical evaluation of fluorine-18-labeled androgen receptor ligands in baboons. J Nucl Med 37(6):1009–1015

Borowicz KK, Piskorska B, Banach M, Czuczwar SJ (2011) Neuroprotective actions of neuros-teroids. Front Endocrinol 2:1–10. https://doi.org/10.3389/fendo.2011.00050

Brinton RD, Thompson RF, Foy MR, Baudry M, Wang J, Finch CE, Morgan TE, Pike CJ, Mack WJ, Stanczyk FZ, Nilsen J (2008) Progesterone receptors: form and function in brain. Front Neuroendocrinol 29(2):313–339. https://doi.org/10.1016/j.yfrne.2008.02.001

Bristot G, Ascoli B, Gubert C, Panizzutti B, Kapczinski F, Rosa AR (2014) Progesterone and its metabolites as therapeutic targets in psychiatric disorders. Expert Opin Ther Targets 18(6):679–690. https://doi.org/10.1517/14728222.2014.897329

Brown TJ, MacLusky NJ, Toran-Allerand CD, Zielinski JE, Hochberg RB (1989) Characterization of 11 beta-methoxy-16 alpha-[125I]iodoestradiol binding: neuronal localization of estrogen-binding sites in the developing rat brain. Endocrinology 124(5):2074–2088. https://doi.org/10.1210/endo-124-5-2074

Bryant C, Judd FK, Hickey M (2012) Anxiety during the menopausal transition: a systematic review. J Affect Disord 139(2):141–148. https://doi.org/10.1016/j.jad.2011.06.055

Buckman BO, Bonasera TA, Kirschbaum KS, Welch MJ, Katzenellenbogen JA (1995) Fluorine-18-labeled progestin 16.alpha.,17.alpha.-dioxolanes: development of high-affinity ligands for the progesterone receptor with high in vivo target site selectivity. J Med Chem 38(2):328–337. https://doi.org/10.1021/jm00002a014

Carré JM, McCormick CM, Hariri AR (2011) The social neuroendocrinology of human aggression. Psychoneuroendocrinology 36(7):935–944. https://doi.org/10.1016/j.psyneuen.2011.02.001

Carswell HV, Dominiczak AF, Macrae IM (2000) Estrogen status affects sensitivity to focal cerebral ischemia in stroke-prone spontaneously hypertensive rats. Am J Physiol Heart Circ Physiol 278(1):H290–H294

Chakrabarti M, Haque A, Banik NL, Nagarkatti P, Nagarkatti M, Ray SK (2014) Estrogen receptor agonists for attenuation of neuroinflammation and neurodegeneration. Brain Res Bull 109:22–31. https://doi.org/10.1016/j.brainresbull.2014.09.004

Chiba S, Numakawa T, Ninomiya M, Richards MC, Wakabayashi C, Kunugi H (2012) Chronic restraint stress causes anxiety- and depression-like behaviors, downregulates glucocorticoid receptor expression, and attenuates glutamate release induced by brain-derived neurotrophic factor in the prefrontal cortex. Prog Neuropsychopharmacol Biol Psychiatry 39(1):112–119. https://doi.org/10.1016/j.pnpbp.2012.05.018

Choe YS, Lidstroem PJ, Chi DY, Bonasera TA, Welch MJ, Katzenellenbogen JA (1995) Synthesis of 11.beta.-[18f]fluoro-5.alpha.-dihydrotestosterone and 11.beta.-[18f]fluoro-19-nor-5.alpha.-dihydrotestosterone: preparation via halofluorination-reduction, receptor binding, and tissue distribution. J Med Chem 38(5):816–825. https://doi.org/10.1021/jm00005a009

Ciocca G, Limoncin E, Carosa E, Di Sante S, Gravina GL, Mollaioli D, Gianfrilli D, Lenzi A, Jannini EA (2016) Is testosterone a food for the brain? Sex Med Rev 4(1):15–25. https://doi.org/10.1016/j.sxmr.2015.10.007

Conlan MG, de Vries EFJ, Glaudemans AWJM, Wang Y, Troy S (2020) Pharmacokinetic and pharmacodynamic studies of elacestrant, a novel oral selective estrogen receptor degrader, in healthy post-menopausal women. Eur J Drug Metab Pharmacokinet [published online ahead of print, 2020 Jul 13]. https://doi.org/10.1007/s13318-020-00635-3

Cornil CA (2018) On the role of brain aromatase in females: why are estrogens produced locally when they are available systemically? J Comp Physiol A 204(1):31–49. https://doi.org/10.1007/s00359-017-1224-2

Corona G, Ratrelli G, Maggi M (2015) The pharmacotherapy of male hypogonadism besides androgens. Expert Opin Pharmacother 16(3):369–387. https://doi.org/10.1517/14656566.2015.993607

Corona G, Sforza A, Maggi M (2017) Testosterone replacement therapy: long-term safety and efficacy. World J Men's Health 35(2):65. https://doi.org/10.5534/wjmh.2017.35.2.65

Cysouw MCF, Kramer GM, Heijtel D, Schuit RC, Morris MJ, van den Eertwegh AJM, Voortman J, Hoekstra OS, Oprea-Lager DE, Boellaard R (2019) Sensitivity of 18F-fluorodihydrotestosterone PET-CT to count statistics and reconstruction protocol in metastatic castration-resistant prostate cancer. EJNMMI Res 9(1):70. https://doi.org/10.1186/s13550-019-0531-8

Dallagi T, Top S, Masi S, Jaouen G, Saidi M (2010) Synthesis and biodistribution of [99mTc]-N-[4-nitro-3-trifluoromethyl-phenyl] cyclopentadienyltricarbonyltechnetium carboxamide, a nonsteroidal antiandrogen flutamide derivative. Metallomics 2(4):289. https://doi.org/10.1039/b925224j

Dasilva JN, Crouzel C, Stulzaft O, Khalili-Varasteh M, Hantraye P (1992) Synthesis, tissue distribution in rats and PET studies in baboon brain of no-carrier-added [18F]RU 52461: in vivo evaluation as a brain glucocorticoid receptor radioligand. International Journal of Radiation Applications and Instrumentation. Part B, Nuclear Medicine and Biology 19(2):167–173

Davis SR, Davison SL, Gavrilescu M, Searle K, Gogos A, Rossell SL, Egan GF, Bell RJ (2013) Effects of testosterone on visuospatial function and verbal fluency in postmenopausal women. Menopause 21(4):1. https://doi.org/10.1097/GME.0b013e3182a065ed

De Nicola AF, Labombarda F, Deniselle MCG, Gonzalez SL, Garay L, Meyer M, Gargiulo G, Guennoun R, Schumacher M (2009) Progesterone neuroprotection in traumatic CNS injury and motoneuron degeneration. Front Neuroendocrinol 30(2):173–187. https://doi.org/10.1016/j.yfrne.2009.03.001

Dehdashti F, McGuire AH, Van Brocklin HF, Siegel BA, Andriole DP, Griffeth LK, Pomper MG, Katzenellenbogen JA, Welch MJ (1991) Assessment of 21-[18F]fluoro-16 alpha-ethyl-19-nor-progesterone as a positron-emitting radiopharmaceutical for the detection of progestin receptors in human breast carcinomas. J Nucl Med 32(8):1532–1537

Dehdashti F, Mortimer JE, Siegel BA, Griffeth LK, Bonasera TJ, Fusselman MJ, Detert DD, Cutler PD, Katzenellenbogen JA, Welch MJ (1995) Positron tomographic assessment of estrogen receptors in breast cancer: comparison with FDG-PET and in vitro receptor assays. J Nucl Med 36(10):1766–1774

Dehdashti F, Picus J, Michalski JM, Dence CS, Siegel BA, Katzenellenbogen JA, Welch MJ (2005) Positron tomographic assessment of androgen receptors in prostatic carcinoma. Eur J Nucl Med Mol Imaging 32(3):344–350. https://doi.org/10.1007/s00259-005-1764-5

Dehdashti F, Laforest R, Gao F, Aft RL, Dence CS, Zhou D, Shoghi KI, Siegel BA, Katzenellenbogen JA, Welch MJ (2012) Assessment of progesterone receptors in breast carcinoma by PET with 21-18F-fluoro-16 ,17 -[(R)-(1′- -furylmethylidene)dioxy]-19-norpregn-4-ene-3,20-dione. J Nucl Med 53(3):363–370. https://doi.org/10.2967/jnumed.111.098319

Dhyani MV, Satpati D, Korde A, Banerjee S (2011) Synthesis and preliminary bioevaluation of 99m Tc(CO) 3 -17α-triazolylandrost-4-ene-3-one derivative prepared via click chemistry route. Cancer Biother Radiopharm 26(5):539–545. https://doi.org/10.1089/cbr.2011.0966

Dotzlaw H, Leygue E, Watson PH, Murphy LC (1997) Expression of estrogen receptor-beta in human breast tumors. J Clin Endocrinol Metab 82(7):2371–2374. https://doi.org/10.1210/jcem.82.7.4212

Eriksson E, Andersch B, Ho HP, Landén M, Sundblad C (2002) Diagnosis and treatment of premenstrual dysphoria. J Clin Psychiatry 63(Suppl 7):16–23

Eser D, Schüle C, Romeo E, Baghai TC, di Michele F, Pasini A, Zwanzger P, Padberg F, Rupprecht R (2006) Neuropsychopharmacological properties of neuroactive steroids in depression and anxiety disorders. Psychopharmacology (Berl) 186(3):373–387. https://doi.org/10.1007/s00213-005-0188-z

Feliu AL, Rottenberg DA (1987) Synthesis and evaluation of fluorine-18 21-fluoroprednisone as a potential ligand for neuro-PET studies. J Nucl Med 28(6):998–1005

Fink, G., Sumner, B., Rosie, R., Wilson, H., & McQueen, J. (1999). Androgen actions on central serotonin neurotransmission: relevance for mood, mental state and memory. Behavioural Brain Research, 105(1), 53–68

Foster TC (2012) Role of estrogen receptor alpha and beta expression and signaling on cognitive function during aging. Hippocampus 22(4):656–669. https://doi.org/10.1002/hipo.20935

Fowler AM, Chan SR, Sharp TL, Fettig NM, Zhou D, Dence CS, Carlson KE, Jeyakumar M, Katzenellenbogen JA, Schreiber RD, Welch MJ (2012) Small-animal PET of steroid hormone receptors predicts tumor response to endocrine therapy using a preclinical model of breast cancer. J Nucl Med 53(7):1119–1126. https://doi.org/10.2967/jnumed.112.103465

Fox EM, Davis RJ, Shupnik MA (2008) ERβ in breast cancer – onlooker, passive player, or active protector? Steroids 73(11):1039–1051. https://doi.org/10.1016/j.steroids.2008.04.006.ER

Fox JJ, Gavane SC, Blanc-Autran E, Nehmeh S, Gönen M, Beattie B, Vargas HA, Schöder H, Humm JL, Fine SW, Lewis JS, Larson SM (2018) Positron emission tomography/computed tomography–based assessments of androgen receptor expression and glycolytic activity as a prognostic biomarker for metastatic castration-resistant prostate cancer. JAMA Oncol 4(2):217. https://doi.org/10.1001/jamaoncol.2017.3588

Gao M, Wang M, Miller KD, Zheng Q (2011) Facile radiosynthesis of new carbon-11-labeled propanamide derivatives as selective androgen receptor modulator (SARM) radioli-

gands for prostate cancer imaging. Steroids 76(13):1505–1512. https://doi.org/10.1016/j.
steroids.2011.08.005

Garg PK, Labaree DC, Hoyte RM, Hochberg RB (2001) [7alpha-18F]fluoro-17alpha-methyl-
5alpha-dihydrotestosterone: a ligand for androgen receptor-mediated imaging of prostate can-
cer. Nucl Med Biol 28(1):85–90

Garg S, Lynch AJH, Doke AK, Minton RC, Garg PK (2008) A remote controlled system
for the preparation of 7 alpha-[18F]fluoro-17 alpha-methyl 5 alpha-dihydrotestosterone
([18F]FMDHT) using microwave. Appl Radiat Isot 66(5):612–618. https://doi.org/10.1016/j.
apradiso.2008.01.017

Giatti S, Boraso M, Melcangi RC, Viviani B (2012) Neuroactive steroids, their metabolites, and neu-
roinflammation. J Mol Endocrinol 49(3):R125–R134. https://doi.org/10.1530/JME-12-0127

Gibson CL, Gray LJ, Bath PMW, Murphy SP (2008) Progesterone for the treatment of experi-
mental brain injury; a systematic review. Brain 131(2):318–328. https://doi.org/10.1093/
brain/awm183

Glaudemans AWJM, de Vries EFJ, Luurtsema G, Cornelissen EAM, Feitz WF, Antunes IF, Slart
RH, Bongaerts AH, Kömhoff M (2015) Detection of intra-abdominal testicles with 16β-[18F]-
Fluoro-5α-dihydrotestosterone positron emission tomography/computed tomography in a
pubertal boy. J Pediatr 166(3):774–774.e1. https://doi.org/10.1016/j.jpeds.2014.11.017

Goldstein FC, Caveney AF, Hertzberg VS, Silbergleit R, Yeatts SD, Palesch YY, Levin HS,
Wright DW (2017) Very early administration of progesterone does not improve neuropsycho-
logical outcomes in subjects with moderate to severe traumatic brain injury. J Neurotrauma
34(1):115–120. https://doi.org/10.1089/neu.2015.4313

Grandi G, Mueller MD, Bersinger NA, Facchinetti F, McKinnon BD (2017) The association
between progestins, nuclear receptors expression and inflammation in endometrial stromal
cells from women with endometriosis. Gynecol Endocrinol 33(9):712–715. https://doi.org/1
0.1080/09513590.2017.1314458

Gray JD, Kogan JF, Marrocco J, McEwen BS (2017) Genomic and epigenomic mechanisms of
glucocorticoids in the brain. Nat Rev Endocrinol 13(11):661–673. https://doi.org/10.1038/
nrendo.2017.97

Griekspoor A, Zwart W, Neefjes J, Michalides R (2007) Visualizing the action of steroid hormone
receptors in living cells. Nucl Recept Signal 5(1):nrs.05003. https://doi.org/10.1621/nrs.05003

Grigoriadis S, Kennedy SH (2002) Role of estrogen in the treatment of depression. Am J Ther
9(6):503–509. https://doi.org/10.1097/00045391-200211000-00008

Hanson RN, Seitz DE (1982) Tissue distribution of the radiolabeled antiestrogen [125I]iodota-
moxifen. Int J Nucl Med Biol 9(2):105–107

Haywood T, Kealey S, Sánchez-Cabezas S, Hall JJ, Allott L, Smith G, Plisson C, Miller PW
(2015) Carbon-11 radiolabelling of organosulfur compounds: 11 C synthesis of the progester-
one receptor agonist Tanaproget. Chem A Eur J 21(25):9034–9038. https://doi.org/10.1002/
chem.201501089

Holsen LM, Spaeth SB, Lee J, Ogden LA, Klibanski A, Whitfield-Gabrieli S, Goldstein JM (2011)
Stress response circuitry hypoactivation related to hormonal dysfunction in women with major
depression. J Affect Disord 131(1–3):379–387. https://doi.org/10.1016/j.jad.2010.11.024

Hospers G, Helmond F, de Vries E, Dierckx R, de Vries E (2008) PET imaging of steroid recep-
tor expression in breast and prostate Cancer. Curr Pharm Des 14(28):3020–3032. https://doi.
org/10.2174/138161208786404362

Howard RB, Sayeed I, Stein DG (2017) Suboptimal dosing parameters as possible factors in the
negative phase III clinical trials of progesterone for traumatic brain injury. J Neurotrauma
34(11):1915–1918. https://doi.org/10.1089/neu.2015.4179

Inoue T, Kim EE, Wallace S, Yang DJ, Wong FCL, Bassa P, Cherif A, Delpassand E, Buzdar A,
Podoloff DA (1996) Positron emission tomography using [18 F]fluorotamoxifen to evalu-
ate therapeutic responses in patients with breast cancer: preliminary study. Cancer Biother
Radiopharm 11(4):235–245. https://doi.org/10.1089/cbr.1996.11.235

Ishihara Y, Takemoto T, Ishida A, Yamazaki T (2015) Protective actions of 17 β -estradiol and progesterone on oxidative neuronal injury induced by organometallic compounds. Oxid Med Cell Longev 2015:1–16. https://doi.org/10.1155/2015/343706

Jacobson O, Bechor Y, Icar A, Novak N, Birman A, Marom H, Fadeeva L, Golan E, Leibovitch I, Gutman M, Even-Sapir E, Chisin R, Gozin M, Mishani E (2005) Prostate cancer PET bioprobes: synthesis of [18F]-radiolabeled hydroxyflutamide derivatives. Bioorg Med Chem 13(22):6195–6205. https://doi.org/10.1016/j.bmc.2005.06.033

Jacobson O, Laky D, Carlson KE, Elgavish S, Gozin M, Even-Sapir E, Leibovitcf I, Gutmang M, Chisina R, Katzenellenbogen JA, Mishani E (2006) Chiral dimethylamine flutamide derivatives—modeling, synthesis, androgen receptor affinities and carbon-11 labeling. Nucl Med Biol 33(6):695–704. https://doi.org/10.1016/j.nucmedbio.2006.05.010

Jansen BHE, Kramer GM, Cysouw MCF, Yaqub MM, de Keizer B, Lavalaye J, Booij J, Vargas HA, Morris MJ, Vis AN, van Moorselaar RJA, Hoekstra OS, Boellaard R, Oprea-Lager DE (2019) Healthy tissue uptake of 68 Ga-prostate-specific membrane antigen, 18 F-DCFPyL, 18 F-fluoromethylcholine, and 18 F-dihydrotestosterone. J Nucl Med 60(8):1111–1117. https://doi.org/10.2967/jnumed.118.222505

Järvinen TA, Pelto-Huikko M, Holli K, Isola J (2000) Estrogen receptor beta is coexpressed with ERalpha and PR and associated with nodal status, grade, and proliferation rate in breast cancer. Am J Pathol 156(1):29–35. https://doi.org/10.1016/s0002-9440(10)64702-5

Jonson SD, Welch MJ (1998) PET imaging of breast cancer with fluorine-18 radiolabeled estrogens and progestins. Q J Nucl Med 42(1):8–17

Jonson SD, Bonasera TA, Dehdashti F, Cristel ME, Katzenellenbogen JA, Welch MJ (1999) Comparative breast tumor imaging and comparative in vitro metabolism of 16alpha-[18F]fluoroestradiol-17beta and 16beta-[18F]fluoromoxestrol in isolated hepatocytes. Nucl Med Biol 26(1):123–130

Katzenellenbogen JA, Mathias CJ, VanBrocklin HF, Brodack JW, Welch MJ (1993) Titration of the in vivo uptake of 16 alpha-[18F]fluoroestradiol by target tissues in the rat: competition by tamoxifen, and implications for quantitating estrogen receptors in vivo and the use of animal models in receptor-binding radiopharmaceutical deve. Nucl Med Biol 20(6):735–745

Kawata M, Nishi M, Matsuda K, Sakamoto H, Kaku N, Masugi-Tokita M, Fujikawa K, Hirahara-Wada Y, Mori H (2008) Steroid receptor signalling in the brain - lessons learned from molecular imaging. J Neuroendocrinol 20(6):673–676. https://doi.org/10.1111/j.1365-2826.2008.01727.x

Kenady DE, Pavlik EJ, Nelson K, van Nagell JR, Gallion H, DePriest PD, Ryo UY, Baranczuk RJ (1993) Images of estrogen-receptor-positive breast tumors produced by estradiol labeled with iodine I 123 at 16 alpha. Archiv Surg (Chicago, Ill : 1960) 128(12):1373–1381. https://doi.org/10.1001/archsurg.1993.01420240081016

Khayum MA, de Vries EFJ, Glaudemans AWJM, Dierckx RAJO, Doorduin J (2014) In vivo imaging of brain estrogen receptors in rats: a 16α-18F-fluoro-17β-estradiol PET study. J Nucl Med 55(3):481–487. https://doi.org/10.2967/jnumed.113.128751

Khayum MA, Doorduin J, Antunes IF, Kwizera C, Zijlma R, den Boer JA, Dierckx RA, de Vries EFJ (2015) In vivo imaging of brain androgen receptors in rats: a [18F]FDHT PET study. Nucl Med Biol 42(6):561–569. https://doi.org/10.1016/j.nucmedbio.2015.02.003

Kiesewetter, D. O., Kilbourn, M. R., Landvatter, S. W., Heiman, D. F., Katzenellenbogen, J. A., & Welch, M. J. (1984). Preparation of four fluorine- 18-labeled estrogens and their selective uptakes in target tissues of immature rats. J Nucl Med, 25(11), 1212–1221.

Kipp M, Amor S, Krauth R, Beyer C (2012) Multiple sclerosis: Neuroprotective alliance of estrogen–progesterone and gender. Front Neuroendocrinol 33(1):1–16. https://doi.org/10.1016/j.yfrne.2012.01.001

de Kloet ER, Reul JM, de Ronde FS, Bloemers M, Ratka A (1986) Function and plasticity of brain corticosteroid receptor systems: action of neuropeptides. J Steroid Biochem 25(5B):723–731. https://doi.org/10.1016/0022-4731(86)90301-8

Klok MD, Alt SR, Irurzun Lafitte AJM, Turner JD, Lakke EAJF, Huitinga I, Muller CP, Zitman FG, De Kloet ER, DeRijk RH (2011) Decreased expression of mineralocorticoid receptor mRNA

and its splice variants in postmortem brain regions of patients with major depressive disorder. J Psychiatr Res 45(7):871–878. https://doi.org/10.1016/j.jpsychires.2010.12.002

Knutson TP, Lange CA (2014) Tracking progesterone receptor-mediated actions in breast cancer. Pharmacol Ther 142(1):114–125. https://doi.org/10.1016/j.pharmthera.2013.11.010

Kramer GM, Yaqub M, Vargas HA, Schuit R, Windhorst AD, van den Eertwegh A, van der Veldt AAM, Bergman AM, Burnazi EM, Lewis JS, Chua S, Staton KD, Beattie BJ, Humm JL, Davis ID, Weickhardt AJ, Scott AM, Morris MJ, Hoekstra OS, Lammertsma AA, Lammertsma AA (2019) Assessment of simplified methods for quantification of 18 F-FDHT uptake in patients with metastatic castration-resistant prostate cancer. J Nucl Med 60(9):1221–1227. https://doi.org/10.2967/jnumed.118.220111

van Kruchten M, de Vries EGE, Brown M, de Vries EFJ, Glaudemans AWJM, Dierckx RAJO, Schröder CP, Hospers GAP (2013) PET imaging of oestrogen receptors in patients with breast cancer. Lancet Oncol 14(11):e465–e475. https://doi.org/10.1016/S1470-2045(13)70292-4

Labaree DC, Brown TJ, Hoyte RM, Hochberg RB (1997) 7α-Iodine-125-Iodo-5α-dihydrotestosterone: a radiolabeled ligand for the androgen receptor. J Nucl Med 38(3):402–409

Larimer BM, Dubois F, Bloch E, Nesti S, Placzek M, Zadra G, Hooker JM, Loda M, Mahmood U (2018) Specific 18 F-FDHT accumulation in human prostate cancer xenograft murine models is facilitated by prebinding to sex hormone–binding globulin. J Nucl Med 59(10):1538–1543. https://doi.org/10.2967/jnumed.118.208785

Larson SM, Morris M, Gunther I, Beattie B, Humm JL, Akhurst TA, Finn RD, Erdi Y, Pentlow K, Dyke J, Squire O, Bornmann W, McCarthy T, Welch M, Scher H (2019) Tumor localization of 16β-18F-5α-dihydrotestosterone versus 18F-FDG in patients with progressive, metastatic prostate cancer. J Nucl Med 45:366–374

Lašaitė L, Čeponis J, Preikša RT, Žilaitienė B (2017) Effects of two-year testosterone replacement therapy on cognition, emotions and quality of life in young and middle-aged hypogonadal men. Andrologia 49(3):e12633. https://doi.org/10.1111/and.12633

Lee JH, Zhou H, Dence CS, Carlson KE, Welch MJ, Katzenellenbogen JA (2010) Development of [F-18]fluorine-substituted tanaproget as a progesterone receptor imaging agent for positron emission tomography. Bioconjug Chem 21(6):1096–1104. https://doi.org/10.1021/bc1001054

Lee JH, Peters O, Lehmann L, Dence CS, Sharp TL, Carlson KE, Zhou D, Jeyakumar M, Welch MJ, Katzenellenbogen JA (2012) Synthesis and biological evaluation of two agents for imaging estrogen receptor β by positron emission tomography: challenges in PET imaging of a low abundance target. Nucl Med Biol 39(8):1105–1116. https://doi.org/10.1016/j.nucmedbio.2012.05.011

Liu AJ, Katzenellenbogen JA, VanBrocklin HF, Mathias CJ, Welch MJ (1991) 20-[18F]fluoromibolerone, a positron-emitting radiotracer for androgen receptors: synthesis and tissue distribution studies. J Nucl Med 32(1):81–88

Liu A, Dence CS, Welch MJ, Katzenellenbogen JA (1992) Fluorine-18-labeled androgens: radiochemical synthesis and tissue distribution studies on six fluorine-substituted androgens, potential imaging agents for prostatic cancer. J Nucl Med 33(5):724–734

Liu A, Margaill I, Zhang S, Labombarda F, Coqueran B, Delespierre B, Liere P, Marchand-Leroux C, O'Malley BW, Lydon JP, De Nicola AF, Sitruk-Ware R, Mattern C, Plotkine M, Schumacher M, Guennoun R (2012) Progesterone receptors: a key for neuroprotection in experimental stroke. Endocrinology 153(8):3747–3757. https://doi.org/10.1210/en.2012-1138

Liu H, Chen Y, Wu S, Song F, Zhang H, Tian M (2016) Molecular imaging using PET and SPECT for identification of breast cancer subtypes. Nucl Med Commun 37(11):1116–1124. https://doi.org/10.1097/MNM.0000000000000576

López JF, Chalmers DT, Little KY, Watson SJ (1998) A.E. Bennett research award. Regulation of serotonin1A, glucocorticoid, and mineralocorticoid receptor in rat and human hippocampus: implications for the neurobiology of depression. Biol Psychiatry 43(8):547–573. https://doi.org/10.1016/s0006-3223(97)00484-8

Luoma JI, Stern CM, Mermelstein PG (2012) Progesterone inhibition of neuronal calcium signaling underlies aspects of progesterone-mediated neuroprotection. J Steroid Biochem Mol Biol 131(1–2):30–36. https://doi.org/10.1016/j.jsbmb.2011.11.002

MacKenzie G, Maguire J (2014) The role of ovarian hormone-derived neurosteroids on the regulation of GABAA receptors in affective disorders. Psychopharmacology (Berl) 231(17):3333–3342. https://doi.org/10.1007/s00213-013-3423-z

Mani S, Mermelstein P, Tetel M, Anesetti G (2012) Convergence of multiple mechanisms of steroid hormone action. Horm Metab Res 44(08):569–576. https://doi.org/10.1055/s-0032-1306343

Mankoff DA, Peterson LM, Tewson TJ, Link JM, Gralow JR, Graham MM, Krohn KA (2001) [18F]fluoroestradiol radiation dosimetry in human PET studies. J Nucl Med 42(4):679–684

Marrocco J, McEwen BS (2016) Sex in the brain: hormones and sex differences. Dialogues Clin Neurosci 18(4):373–383

McCarrey AC, Resnick SM (2015) Postmenopausal hormone therapy and cognition. Horm Behav 74:167–172. https://doi.org/10.1016/j.yhbeh.2015.04.018

McEwen BS, Milner TA (2017) Understanding the broad influence of sex hormones and sex differences in the brain. J Neurosci Res 95(1–2):24–39. https://doi.org/10.1002/jnr.23809

McEwen BS, Sapolsky RM (1995) Stress and cognitive function. Curr Opin Neurobiol 5(2):205–216

McEwen BS, Woolley CS (1994) Estradiol and progesterone regulate neuronal structure and synaptic connectivity in adult as well as developing brain. Exp Gerontol 29(3–4):431–436. https://doi.org/10.1016/0531-5565(94)90022-1

McHenry J, Carrier N, Hull E, Kabbaj M (2014) Sex differences in anxiety and depression: role of testosterone. Front Neuroendocrinol 35(1):42–57. https://doi.org/10.1016/j.yfrne.2013.09.001

Meffre D, Labombarda F, Delespierre B, Chastre A, De Nicola AF, Stein DG, Schumacher M, Guennoun R (2013) Distribution of membrane progesterone receptor alpha in the male mouse and rat brain and its regulation after traumatic brain injury. Neuroscience 231:111–124. https://doi.org/10.1016/j.neuroscience.2012.11.039

Mellon SH (2007) Neurosteroid regulation of central nervous system development. Pharmacol Ther 116(1):107–124. https://doi.org/10.1016/j.pharmthera.2007.04.011

Micevych PE, May Wong A, Mittelman-Smith MA (2015) Estradiol membrane-initiated signaling and female reproduction. Compr Physiol 5:1211–1222. https://doi.org/10.1002/cphy.c140056

Mintun MA, Welch MJ, Siegel BA, Mathias CJ, Brodack JW, McGuire AH, Katzenellenbogen JA (1988) Breast cancer: PET imaging of estrogen receptors. Radiology 169(1):45–48. https://doi.org/10.1148/radiology.169.1.3262228

Moresco RM, Casati R, Lucignani G, Carpinelli A, Schmidt K, Todde S, Colombo F, Fazio F (1995) Systemic and cerebral kinetics of 16α[18 F]Fluoro-17β-estradiol: a ligand for the in vivo assessment of estrogen receptor binding parameters. J Cereb Blood Flow Metab 15(2):301–311. https://doi.org/10.1038/jcbfm.1995.35

Moresco RM, Scheithauer BW, Lucignani G, Lombardi D, Rocca A, Losa M, Casati R, Giovanelli M, Fazio F (1997) Oestrogen receptors in meningiomas: a correlative PET and immunohistochemical study. Nucl Med Commun 18(7):606–615

Morimoto M, Morita N, Ozawa H, Yokoyama K, Kawata M (1996) Distribution of glucocorticoid receptor immunoreactivity and mRNA in the rat brain: an immunohistochemical and in situ hybridization study. Neurosci Res 26(3):235–269. https://doi.org/10.1016/S0168-0102(96)01105-4

Mortimer JE, Dehdashti F, Siegel BA, Katzenellenbogen JA, Fracasso P, Welch MJ (1996) Positron emission tomography with 2-[18F]Fluoro-2-deoxy-D-glucose and 16alpha-[18F]fluoro-17beta-estradiol in breast cancer: correlation with estrogen receptor status and response to systemic therapy. Clin Cancer Res 2(6):933–939

Nachar O, Rousseau JA, Lefebvre B, Ouellet R, Ali H, van Lier JE (1999) Biodistribution, dosimetry and metabolism of 11beta-methoxy-(17alpha,20E/Z)-[123I]iodovinylestradiol in healthy women and breast cancer patients. J Nucl Med 40(10):1728–1736

Nayak TK, Hathaway HJ, Ramesh C, Arterburn JB, Dai D, Sklar LA, Norenberg JP, Prossnitz ER (2008) Preclinical development of a neutral, estrogen receptor-targeted, tridentate 99mTc(I)-

estradiol-pyridin-2-yl hydrazine derivative for imaging of breast and endometrial cancers. J Nucl Med 49(6):978–986. https://doi.org/10.2967/jnumed.107.048546

Nayak TK, Ramesh C, Hathaway HJ, Norenberg JP, Arterburn JB, Prossnitz ER (2014) GPER-targeted, 99m Tc-labeled, nonsteroidal ligands demonstrate selective tumor imaging and in vivo estrogen binding. Mol Cancer Res 12(11):1635–1643. https://doi.org/10.1158/1541-7786.MCR-14-0289

O'Connor CA, Cernak I, Vink R (2005) Both estrogen and progesterone attenuate edema formation following diffuse traumatic brain injury in rats. Brain Res 1062(1–2):171–174. https://doi.org/10.1016/j.brainres.2005.09.011

Ogino Y, Tohyama S, Kohno S, Toyota K, Yamada G, Yatsu R, Kobayashi T, Tatarazako N, Sato T, Matsubara H, Lange A, Tyler CR, Katsu Y, Iguchi T, Miyagawa S (2018) Functional distinctions associated with the diversity of sex steroid hormone receptors ESR and AR. J Steroid Biochem Mol Biol 184(November 2017):38–46. https://doi.org/10.1016/j.jsbmb.2018.06.002

Okamoto M, Naka K, Ishiwata K, Shimizu I, Toyohara J (2017) Synthesis and basic evaluation of 7α-(3-[18F]fluoropropyl)-testosterone and 7α-(3-[18F]fluoropropyl)-dihydrotestosterone. Ann Nucl Med 31(1):53–62. https://doi.org/10.1007/s12149-016-1130-7

Ooishi Y, Kawato S, Hojo Y, Hatanaka Y, Higo S, Murakami G, Komatsuzaki Y, Ogiue-Ikeda M, Kimoto T, Mukai H (2012) Modulation of synaptic plasticity in the hippocampus by hippocampus-derived estrogen and androgen. J Steroid Biochem Mol Biol 131(1–2):37–51. https://doi.org/10.1016/j.jsbmb.2011.10.004

Östlund H, Keller E, Hurd YL (2003) Estrogen receptor gene expression in relation to neuropsychiatric disorders. Ann N Y Acad Sci 1007(1):54–63. https://doi.org/10.1196/annals.1286.006

Owen D (2002) From the womb to adulthood: programming glucocorticoid and mineralocorticoid receptor expression in the brain. Clin Invest Med 25(3):97–101

Paquette M, Phoenix S, Ouellet R, Langlois R, van Lier JE, Turcotte ÉE, Bénard F, Lecomte R (2013) Assessment of the novel estrogen receptor PET tracer 4-Fluoro-11β-methoxy-16α-[18F]fluoroestradiol (4FMFES) by PET imaging in a breast cancer murine model. Mol Imaging Biol 15(5):625–632. https://doi.org/10.1007/s11307-013-0638-7

Paquette M, Lavallée É, Phoenix S, Ouellet R, Senta H, van Lier JE, Guérin B, Lecomte R, Turcotte ÉE (2018) Improved estrogen receptor assessment by PET using the novel radiotracer 18 F-4FMFES in estrogen receptor–positive breast cancer patients: an ongoing phase II clinical trial. J Nucl Med 59(2):197–203. https://doi.org/10.2967/jnumed.117.194654

Parent EE, Jenks C, Sharp T, Welch MJ, Katzenellenbogen JA (2006) Synthesis and biological evaluation of a nonsteroidal bromine-76-labeled androgen receptor ligand 3-[76Br]bromo-hydroxy-flutamide. Nucl Med Biol 33(6):705–713. https://doi.org/10.1016/j.nucmedbio.2006.05.009

Parent EE, Dence CS, Jenks C, Sharp TL, Welch MJ, Katzenellenbogen JA (2007) Synthesis and biological evaluation of [18 F]bicalutamide, 4-[76 Br]bromobicalutamide, and 4-[76 Br]bromo-thiobicalutamide as non-steroidal androgens for prostate cancer imaging. J Med Chem 50(5):1028–1040. https://doi.org/10.1021/jm060847r

Pareto D, Alvarado M, Hanrahan SM, Biegon A (2004) In vivo occupancy of female rat brain estrogen receptors by 17β-estradiol and tamoxifen. Neuroimage 23(3):1161–1167. https://doi.org/10.1016/j.neuroimage.2004.07.036

Pavlik EJ, Nelson K, Gallion HH, van Nagell JR, Donaldson ES, Shih WJ, Spicer JA, Preston DF, Baranczuk RJ, Kenady DE (1990) Characterization of high specific activity [16 alpha-123I]Iodo-17 beta-estradiol as an estrogen receptor-specific radioligand capable of imaging estrogen receptor-positive tumors. Cancer Res 50(24):7799–7805

Pelletier G, Labrie C, Labrie F (2000) Localization of oestrogen receptor alpha, oestrogen receptor beta and androgen receptors in the rat reproductive organs. J Endocrinol 165(2):359–370. https://doi.org/10.1677/joe.0.1650359

Perlman WR, Webster MJ, Kleinman JE, Weickert CS (2004) Reduced glucocorticoid and estrogen receptor alpha messenger ribonucleic acid levels in the amygdala of patients with major mental illness. Biol Psychiatry 56(11):844–852. https://doi.org/10.1016/j.biopsych.2004.09.006

Perlman WR, Webster MJ, Herman MM, Kleinman JE, Weickert CS (2007) Age-related differences in glucocorticoid receptor mRNA levels in the human brain. Neurobiol Aging 28(3):447–458. https://doi.org/10.1016/j.neurobiolaging.2006.01.010

Peterson LM, Mankoff DA, Lawton T, Yagle K, Schubert EK, Stekhova S, Gown A, Link JM, Tewson T, Krohn KA (2008) Quantitative imaging of estrogen receptor expression in breast cancer with PET and 18F-fluoroestradiol. J Nucl Med 49(3):367–374. https://doi.org/10.2967/jnumed.107.047506

Pike CJ, Carroll JC, Rosario ER, Barron AM (2009) Protective actions of sex steroid hormones in Alzheimer's disease. Front Neuroendocrinol 30(2):239–258. https://doi.org/10.1016/j.yfrne.2009.04.015

Pomper MG, Katzenellenbogen JA, Welch MJ, Brodack JW, Mathias CJ (1988) 21-[18F]fluoro-16 alpha-ethyl-19-norprogesterone: synthesis and target tissue selective uptake of a progestin receptor based radiotracer for positron emission tomography. J Med Chem 31(7):1360–1363. https://doi.org/10.1021/jm00402a019

Pomper MG, Kochanny MJ, Thieme AM, Carlson KE, VanBrocklin HF, Mathias CJ, Welch MJ, Katzenellenbogen JA (1992) Fluorine-substituted corticosteroids: synthesis and evaluation as potential receptor-based imaging agents for positron emission tomography of the brain. International Journal of Radiation Applications and Instrumentation. Part B, Nuclear Medicine and Biology 19(4):461–480

Pompili M, Serafini G, Innamorati M, Möller-Leimkühler AM, Giupponi G, Girardi P, Tatarelli R, Lester D (2010) The hypothalamic-pituitary-adrenal axis and serotonin abnormalities: a selective overview for the implications of suicide prevention. Eur Arch Psychiatry Clin Neurosci 260(8):583–600. https://doi.org/10.1007/s00406-010-0108-z

Porcu P, Barron AM, Frye CA, Walf AA, Yang S-Y, He X-Y, Morrow AL, Panzica GC, Melcangi RC (2016) Neurosteroidogenesis today: novel targets for neuroactive steroid synthesis and action and their relevance for translational research. J Neuroendocrinol 28(2):12351. https://doi.org/10.1111/jne.12351

Ramesh C, Bryant B, Nayak T, Revankar CM, Anderson T, Carlson KE, Katzenellenbogen JA, Sklar LA, Norenberg JP, Prossnitz ER, Arterburn JB (2006) Linkage effects on binding affinity and activation of GPR30 and estrogen receptors ERα/β with tridentate pyridin-2-yl hydrazine tricarbonyl−re/99m Tc(I) chelates. J Am Chem Soc 128(45):14476–14477. https://doi.org/10.1021/ja066360p

Resnick SM, Henderson VW (2002) Hormone therapy and risk of Alzheimer disease: a critical time. JAMA 288(17):2170–2172. https://doi.org/10.1001/jama.288.17.2170

Rijks LJ, Bakker PJ, van Tienhoven G, Noorduyn LA, Boer GJ, Rietbroek RC, Taat CW, Janssen AG, Veenhof CH, van Royen EA (1997a) Imaging of estrogen receptors in primary and metastatic breast cancer patients with iodine-123-labeled Z-MIVE. J Clin Oncol 15(7):2536–2545. https://doi.org/10.1200/JCO.1997.15.7.2536

Rijks LJ, Boer GJ, Endert E, de Bruin K, Janssen AG, van Royen EA (1997b) The Z-isomer of 11 beta-methoxy-17 alpha-[123I]iodovinylestradiol is a promising radioligand for estrogen receptor imaging in human breast cancer. Nucl Med Biol 24(1):65–75

Rijks LJ, Busemann Sokole E, Stabin MG, de Bruin K, Janssen AG, van Royen EA (1998a) Biodistribution and dosimetry of iodine-123-labelled Z-MIVE: an oestrogen receptor radioligand for breast cancer imaging. Eur J Nucl Med 25(1):40–47

Rijks LJ, van den Bos JC, van Doremalen PA, Boer GJ, de Bruin K, Janssen AG, van Royen EA (1998b) New iodinated progestins as potential ligands for progesterone receptor imaging in breast cancer. Part 2: in vivo pharmacological characterization. Nucl Med Biol 25(8):791–798

Rubinow D, Schmidt P (2006) Gonadal steroid regulation of mood: the lessons of premenstrual syndrome☆. Front Neuroendocrinol 27(2):210–216. https://doi.org/10.1016/j.yfrne.2006.02.003

Rupprecht R (2003) Neuroactive steroids: mechanisms of action and neuropsychopharmacological properties. Psychoneuroendocrinology 28(2):139–168. https://doi.org/10.1016/S0306-4530(02)00064-1

Salem K, Kumar M, Kloepping KC, Michel CJ, Yan Y, Fowler AM (2018) Determination of binding affinity of molecular imaging agents for steroid hormone receptors in breast cancer. Am J Nucl Med Mol Imaging 8(2):119–126

Salem K, Kumar M, Yan Y, Jeffery JJ, Kloepping KC, Michel CJ, Powers GL, Mahajan AM, Fowler AM (2019) Sensitivity and isoform specificity of 18 F-fluorofuranylnorprogesterone for measuring progesterone receptor protein response to estradiol challenge in breast cancer. J Nucl Med 60(2):220–226. https://doi.org/10.2967/jnumed.118.211516

Sapolsky RM (2000) How do glucocorticoids influence stress responses? Integrating permissive, suppressive, stimulatory, and preparative actions. Endocr Rev 21(1):55–89. https://doi.org/10.1210/er.21.1.55

Sapolsky RM (2004) Is impaired neurogenesis relevant to the affective symptoms of depression? Biol Psychiatry 56(3):137–139. https://doi.org/10.1016/j.biopsych.2004.04.012

Sasaki M, Fukumura T, Kuwabara Y, Yoshida T, Nakagawa M, Ichiya Y, Masuda K (2000) Biodistribution and breast tumor uptake of 16alpha-[18F]-fluoro-17beta-estradiol in rat. Ann Nucl Med 14(2):127–130

Scheidhauer K, Müller S, Smolarz K, Bräutigam P, Briele B (1991) Tumor scintigraphy using 123I-labeled estradiol in breast cancer—receptor scintigraphy. Nuklearmedizin 30(3):84–99

Schober O, Scheidhauer K, Jackisch C, Schicha H, Smolarz K, Bolte A, Reiners C, Höffken K, Biersack HJ, Briele B (1990) Breast cancer imaging with radioiodinated oestradiol. Lancet (London, England) 335(8704):1522. https://doi.org/10.1016/0140-6736(90)93056-u

Schumacher M, Hussain R, Gago N, Oudinet J-P, Mattern C, Ghoumari AM (2012) Progesterone synthesis in the nervous system: implications for myelination and myelin repair. Front Neurosci 6:1–22. https://doi.org/10.3389/fnins.2012.00010

Schwartz N, Verma A, Bivens CB, Schwartz Z, Boyan BD (2016) Rapid steroid hormone actions via membrane receptors. Biochim Biophys Acta 1863(9):2289–2298. https://doi.org/10.1016/j.bbamcr.2016.06.004

Scovell JM, Khera M (2018) Testosterone replacement therapy versus clomiphene citrate in the Young Hypogonadal male. Eur Urol Focus 4(3):321–323. https://doi.org/10.1016/j.euf.2018.07.033

Seimbille Y, Bénard F, Rousseau J, Pepin E, Aliaga A, Tessier G, van Lier JE (2004) Impact on estrogen receptor binding and target tissue uptake of [18F]fluorine substitution at the 16α-position of fulvestrant (faslodex; ICI 182,780). Nucl Med Biol 31(6):691–698. https://doi.org/10.1016/j.nucmedbio.2004.02.010

Sherman S, Miller H, Nerurkar L, Schiff I (2005) Research opportunities for reducing the burden of menopause-related symptoms. Am J Med 118(12):166–171. https://doi.org/10.1016/j.amjmed.2005.12.004

Shughrue PJ, Stumpf WE, MacLusky NJ, Zielinski JE, Hochberg RB (1990) Developmental changes in estrogen receptors in mouse cerebral cortex between birth and postweaning: studied by autoradiography with 11 beta-methoxy-16 alpha-[125I]iodoestradiol. Endocrinology 126(2):1112–1124. https://doi.org/10.1210/endo-126-2-1112

Singh M, Su C (2013) Progesterone, brain-derived neurotrophic factor and neuroprotection. Neuroscience 239:84–91. https://doi.org/10.1016/j.neuroscience.2012.09.056

Skolnick BE, Maas AI, Narayan RK, van der Hoop RG, MacAllister T, Ward JD, Nelson NR, Stocchetti N (2014) A clinical trial of progesterone for severe traumatic brain injury. N Engl J Med 371(26):2467–2476. https://doi.org/10.1056/NEJMoa1411090

Spritzer MD, Galea LAM (2007) Testosterone and dihydrotestosterone, but not estradiol, enhance survival of new hippocampal neurons in adult male rats. Dev Neurobiol 67(10):1321–1333. https://doi.org/10.1002/dneu.20457

Steiner J, Brisch R, Mawrin C, Bernstein H-G, Ullrich O, Bogerts B, Mawrin C, Bielau H (2006) Immunological aspects in the neurobiology of suicide: elevated microglial density in schizophrenia and depression is associated with suicide. J Psychiatr Res 42(2):151–157. https://doi.org/10.1016/j.jpsychires.2006.10.013

Stratakis CA, Chrousos GP (1995) Neuroendocrinology and pathophysiology of the stress system. Ann N Y Acad Sci 771(1 Stress):1–18. https://doi.org/10.1111/j.1749-6632.1995.tb44666.x

Stumpf WE, Morin JK, Ennis BW, Zielinski JE, Hochberg RB (1987) Utility of [16 alpha-125I] iodoestradiol for autoradiography for the study of cellular and regional distribution of receptors. J Histochem Cytochem 35(1):87–92. https://doi.org/10.1177/35.1.3794310

Takahashi K, Hallberg M, Magnusson K, Nyberg F, Watanabe Y, Långström B, Bergström M (2007a) Increase in [11C]vorozole binding to aromatase in the hypothalamus in rats treated with anabolic androgenic steroids. Neuroreport 18(2):171–174. https://doi.org/10.1097/WNR.0b013e328010ff14

Takahashi N, Yang DJ, Kurihara H, Borne A, Kohanim S, Oh C-S, Mawlawi O, Kim EE (2007b) Functional imaging of estrogen receptors with radiolabeled-GAP-EDL in rabbit endometriosis model. Acad Radiol 14(9):1050–1057. https://doi.org/10.1016/j.acra.2007.05.020

Talih F, Fattal O, Malone D (2007) Anabolic steroid abuse: psychiatric and physical costs. Cleve Clin J Med 74(5):341–344, 346, 349–352

Tarle M, Padovan R, Spaventi S (1981) The uptake of radioiodinated 5 alpha-dihydrotestosterone by the prostate of intact and castrated rats. Eur J Nucl Med 6(2):79–83. https://doi.org/10.1007/BF00253718

Tewson TJ, Mankoff DA, Peterson LM, Woo I, Petra P (1999) Interactions of 16alpha-[18F]-fluoroestradiol (FES) with sex steroid binding protein (SBP). Nucl Med Biol 26(8):905–913

Tonn Eisinger KR, Larson EB, Boulware MI, Thomas MJ, Mermelstein PG (2018) Membrane estrogen receptor signaling impacts the reward circuitry of the female brain to influence motivated behaviors. Steroids 133:53–59. https://doi.org/10.1016/j.steroids.2017.11.013

Toran-Allerand CD, Miranda RC, Hochberg RB, MacLusky NJ (1992) Cellular variations in estrogen receptor mRNA translation in the developing brain: evidence from combined [125I]estrogen autoradiography and non-isotopic in situ hybridization histochemistry. Brain Res 576(1):25–41. https://doi.org/10.1016/0006-8993(92)90606-A

Truillet C, Parker MFL, Huynh LT, Wei J, Jami KM, Wang Y, Shen YS, Sriram R, Wilson DM, Kurhanewicz J, Evans MJ (2018) Measuring glucocorticoid receptor expression in vivo with PET. Oncotarget 9(29):20399–20408. https://doi.org/10.18632/oncotarget.24911

Van de Wiele C, Cocquyt V, VandenBroecke R, De Vos F, Van Belle S, Dhaene K, Slegers G, Dierckx RA (2001) Iodine-labeled tamoxifen uptake in primary human breast carcinoma. J Nucl Med 42(12):1818–1820

VanBrocklin HF, Pomper MG, Carlson KE, Welch MJ, Katzenellenbogen JA (1992) Preparation and evaluation of 17-ethynyl-substituted 16 alpha-[18F]fluoroestradiols: selective receptor-based PET imaging agents. Int J Rad Appl Instrum B 19(3):363–374

VanBrocklin HF, Rocque PA, Lee HV, Carlson KE, Katzenellenbogen JA, Welch MJ (1993a) 16 beta-[18F]fluoromoxestrol: a potent, metabolically stable positron emission tomography imaging agent for estrogen receptor positive human breast tumors. Life Sci 53(10):811–819. https://doi.org/10.1016/0024-3205(93)90503-u

VanBrocklin HF, Carlson KE, Katzenellenbogen JA, Welch MJ (1993b) 16 beta-([18F]Fluoro)estrogens: systematic investigation of a new series of fluorine-18-labeled estrogens as potential imaging agents for estrogen-receptor-positive breast tumors. J Med Chem 36(11):1619–1629. https://doi.org/10.1021/jm00063a012

VanBrocklin HF, Liu A, Welch M, Oneil J, Katzenellenbogen J (1994) The synthesis of 7α-methyl-substituted estrogens labeled with fluorine-18: potential breast tumor imaging agents. Steroids 59(1):34–45. https://doi.org/10.1016/0039-128X(94)90043-4

Vegeto E, Benedusi V, Maggi A (2008) Estrogen anti-inflammatory activity in brain: A therapeutic opportunity for menopause and neurodegenerative diseases. Front Neuroendocrinol 29(4):507–519. https://doi.org/10.1016/j.yfrne.2008.04.001

Venema CM, Mammatas LH, Schröder CP, Van Kruchten M, Apollonio G, Glaudemans AWJM, Bongaerts AHH, Hoekstra OS, Verheul HMW, Boven E, van der Vegt B, de Vries EFJ, de Vries EGE, Boellaard R, van der Houven van Oordt CWM, Hospers GAP (2017) Androgen and estrogen receptor imaging in metastatic breast cancer patients as a surrogate for tissue biopsies. J Nucl Med 58(12):1906–1912. https://doi.org/10.2967/jnumed.117.193649

Verhagen A, Luurtsema G, Pesser JW, de Groot TJ, Wouda S, Oosterhuis JW, Vaalburg W (1991a) Preclinical evaluation of a positron emitting progestin ([18F]fluoro-16α-methyl-19-norprogesterone) for imaging progesterone receptor positive tumours with positron emission tomography. Cancer Lett 59(2):125–132. https://doi.org/10.1016/0304-3835(91)90176-I

Verhagen A, Elsinga PH, de Groot TJ, Paans AM, de Goeij CJ, Sluyser M, Vaalburg W (1991b) A fluorine-18 labeled progestin as an imaging agent for progestin receptor positive tumors with positron emission tomography. Cancer Res 51(7):1930–1933

Verhagen A, Studeny M, Luurtsema G, Visser GM, De Goeij CCJ, Sluyser M, Nieweg OE, Van der Ploeg E, Go KG, Vaalburg W (1994) Metabolism of a [18F]fluorine labeled progestin (21 -[18F]fluoro-16α -ethyl-19-norprogesterone) in humans: a clue for future investigations. Nucl Med Biol 21(7):941–952. https://doi.org/10.1016/0969-8051(94)90083-3

Vijaykumar D, Mao W, Kirschbaum KS, Katzenellenbogen JA (2002) An efficient route for the preparation of a 21-fluoro progestin-16α,17α-dioxolane, a high-affinity ligand for PET imaging of the progesterone receptor. J Org Chem 67(14):4904–4910. https://doi.org/10.1021/jo020190r

Visser GM, Krugers HJ, Luurtsema G, van Waarde A, Elsinga PH, DeKloet ER, Groen MB, Bohus B, Go KG, Paans AM (1995) Synthesis and organ distribution of [18F]fluoro-Org 6141 in the rat: a potential glucocorticoid receptor ligand for positron emission tomography. Nucl Med Biol 22(7):915–920

de Vries EF, Rots MG, Hospers GA (2007) Nuclear imaging of hormonal receptor status in breast cancer: a tool for guiding endocrine treatment and drug development. Curr Cancer Drug Targets 7(6):510–519

Wright DW, Kellermann AL, Hertzberg VS, Clark PL, Frankel M, Goldstein FC, Salomone JP, Dent LL, Harris OA, Ander DS, Lowery DW, Patel MM, Denson DD, Gordon AB, Wald MM, Gupta S, Hoffman SW, Stein DG (2007) ProTECT: a randomized clinical trial of progesterone for acute traumatic brain injury. Ann Emerg Med 49(4):391–402.e2. https://doi.org/10.1016/j.annemergmed.2006.07.932

Wuest F, Kniess T, Bergmann R, Henry B, Pietzsch J (2007) Synthesis and radiopharmacological characterization of [11C]AL-438 as a nonsteroidal ligand for imaging brain glucocorticoid receptors. Bioorg Med Chem Lett 17(14):4035–4039. https://doi.org/10.1016/j.bmcl.2007.04.094

Wuest F, Kniess T, Henry B, Peeters BWMM, Wiegerinck PHG, Pietzsch J, Bergmann R (2009) Radiosynthesis and radiopharmacological evaluation of [N-methyl-11C]org 34850 as a glucocorticoid receptor (GR)-binding radiotracer. Appl Radiat Isot 67(2):308–312. https://doi.org/10.1016/j.apradiso.2008.10.014

Wüst F, Carlson KE, Katzenellenbogen JA (2003) Synthesis of novel arylpyrazolo corticosteroids as potential ligands for imaging brain glucocorticoid receptors. Steroids 68(2):177–191. https://doi.org/10.1016/S0039-128X(02)00171-X

Wüst F, Kniess T, Kretzschmar M, Bergmann R (2005) Synthesis and radiopharmacological evaluation of 2′-(4-fluorophenyl)-21-[18F]fluoro-20-oxo-11β,17α-dihydroxy-pregn-4-eno[3,2-c]pyrazole as potential glucocorticoid receptor ligand for positron emission tomography (PET). Bioorg Med Chem Lett 15(5):1303–1306. https://doi.org/10.1016/j.bmcl.2005.01.033

Xia X, Feng H, Li C, Qin C, Song Y, Zhang Y, Lan X (2016) 99m Tc-labeled estradiol as an estrogen receptor probe: preparation and preclinical evaluation. Nucl Med Biol 43(1):89–96. https://doi.org/10.1016/j.nucmedbio.2015.09.006

Xing G, Russell S, Webster MJ, Post RM (2004) Decreased expression of mineralocorticoid receptor mRNA in the prefrontal cortex in schizophrenia and bipolar disorder. Int J Neuropsychopharmacol 7(2):143–153. https://doi.org/10.1017/S1461145703004000

Yang DJ, Li C, Kuang LR, Price JE, Buzdar AU, Tansey W, Gretzer M, Kim EE, Wallace S (1994) Imaging, biodistribution and therapy potential of halogenated tamoxifen analogues. Life Sci 55(1):53–67. https://doi.org/10.1016/0024-3205(94)90081-7

Yoo J, Dence CS, Sharp TL, Katzenellenbogen JA, Welch MJ (2005) Synthesis of an estrogen receptor β-selective radioligand: 5-[18 F]Fluoro-(2 R* ,3 S*)-2,3-bis(4-hydroxyphenyl)pentanenitrile and comparison of in vivo distribution with 16α-[18 F]fluoro-17β-estradiol. J Med Chem 48(20):6366–6378. https://doi.org/10.1021/jm050121f

Young EA, Lopez JF, Murphy-Weinberg V, Watson SJ, Akil H (2003) Mineralocorticoid receptor function in major depression. Arch Gen Psychiatry 60(1):24–28. https://doi.org/10.1001/archpsyc.60.1.24

Yurt A, Muftuler FZB, Unak P, Yolcular S, Acar C, Enginar H (2009) Synthesis of a novel antiestrogen radioligand (99m Tc-TOR-DTPA). Cancer Biother Radiopharm 24(6):707–716. https://doi.org/10.1089/cbr.2009.0656

Zalachoras I, Houtman R, Meijer OC (2013) Understanding stress-effects in the brain via transcriptional signal transduction pathways. Neuroscience 242:97–109. https://doi.org/10.1016/j.neuroscience.2013.03.038

Zanzonico PB, Finn R, Pentlow KS, Erdi Y, Beattie B, Akhurst T, Squire O, Morris M, Scher H, McCarthy T, Welch M, Larson SM, Humm JL (2004) PET-based radiation dosimetry in man of 18F-fluorodihydrotestosterone, a new radiotracer for imaging prostate cancer. J Nucl Med 45(11):1966–1971

Zhang Z, Yang R, Zhou R, Li L, Sokabe M, Chen L (2009) Progesterone promotes the survival of newborn neurons in the dentate gyrus of adult male mice. Hippocampus 20(3):402–412. https://doi.org/10.1002/hipo.20642

Zhang X, Yang J, Li Y, Ma X, Li R (2017) Sex chromosome abnormalities and psychiatric diseases. Oncotarget 8(3):3969–3979. https://doi.org/10.18632/oncotarget.13962

Zhou D, Carlson KE, Katzenellenbogen JA, Welch MJ (2006) Bromine- and iodine-substituted 16α,17α-Dioxolane Progestins for breast tumor imaging and radiotherapy: synthesis and receptor binding affinity. J Med Chem 49(15):4737–4744. https://doi.org/10.1021/jm060348q

Zhou H-B, Lee JH, Mayne CG, Carlson KE, Katzenellenbogen JA (2010) Imaging progesterone receptor in breast tumors: synthesis and receptor binding affinity of fluoroalkyl-substituted analogues of Tanaproget. J Med Chem 53(8):3349–3360. https://doi.org/10.1021/jm100052k

Zhu H, Huang L, Zhang Y, Xu X, Sun Y, Shen Y-M (2010) Design, synthesis, and evaluation of cyclofenil derivatives for potential SPECT imaging agents. J Biol Inorg Chem 15(4):591–599. https://doi.org/10.1007/s00775-010-0627-0

Zielinski JE, Yabuki H, Pahuja SL, Larner JM, Hochberg RB (1986) 16 alpha-[125I]iodo-11 beta-methoxy-17 beta-estradiol: a radiochemical probe for estrogen-sensitive tissues. Endocrinology 119(1):130–139. https://doi.org/10.1210/endo-119-1-130

PET Imaging of Monoamine Oxidase B

15

Elena Rodriguez-Vieitez

Contents

Abstract

The monoamine oxidase B (MAO-B) enzyme has a prominent role in brain function, being involved in the breakdown of monoaminergic neurotransmitters. Abnormally high MAO-B levels in the brain, found across different neurological and neurodegenerative disorders including Alzheimer's disease (AD) and Parkinson's disease (PD), are associated with deleterious effects involving reduc-

E. Rodriguez-Vieitez (✉)
Division of Clinical Geriatrics, Department of Neurobiology, Care Sciences and Society, Center for Alzheimer Research, Karolinska Institutet, Stockholm, Sweden
e-mail: elena.rodriguez-vieitez@ki.se

tions in dopamine levels and increased oxidative stress, astrocytosis, and neuro-inflammation. Recent advances in positron emission tomography (PET) using radiotracers specific to MAO-B have allowed the in vitro and in vivo investigation of the brain regional and temporal patterns of MAO-B in normal aging and brain disorders including depression, AD, PD, and amyotrophic lateral sclerosis (ALS). Multiple MAO-B tracers, characterized by either irreversible or reversible binding kinetics, have been under development and validation over the past ~30 years. Recent multimodal MRI-PET studies have allowed investigating MAO-B in relation to other pathophysiological changes including amyloid-β and tau deposition, glucose metabolism, and brain structural changes. PET imaging of MAO-B is also useful for the monitoring of clinical trials of MAO-B inhibitors. This chapter presents a review of in vivo PET imaging studies of MAO-B from preclinical to clinical applications as well as in vitro autoradiography investigations, highlighting recent progress in the field and future prospects.

Abbreviations

AD	Alzheimer's disease
ALS	Amyotrophic lateral sclerosis
CJD	Creutzfeldt-Jakob disease
DWI	Diffusion-weighted imaging
FDG	Fluorodeoxyglucose
GABA	γ-aminobutyric acid
GFAP	Glial fibrillary acidic protein
MAO-A	Monoamine oxidase A
MAO-B	Monoamine oxidase B
MRI	Magnetic resonance imaging
PD	Parkinson's disease
PET	Positron emission tomography
PiB	Pittsburgh compound B
SUVR	Standardized uptake value ratio
TSPO	Translocator protein

15.1 Neurobiology and Clinical Relevance of MAO-B

Monoamine oxidases (MAOs) are flavin-containing enzymes that regulate the levels of monoaminergic neurotransmitters, with critical implications for the maintenance of healthy brain function. From a neurochemical perspective, the MAO enzymes catalyze the oxidative deamination of endogenous monoamine neurotransmitters as well as of amines of exogenous origin. As a by-product of this oxidation reaction, reactive oxygen species such as hydrogen peroxide are released, and their excess

has been linked to oxidative stress and neuroinflammation (Ramsay 2016; Youdim et al. 2006). There are two types of MAO, MAO-A and MAO-B, both located in the mitochondrial outer membrane, but with distinct substrate specificities and regional distributions in the brain and peripheral organs (Saura et al. 1996).

15.1.1 Neurobiology of MAO-B

MAO-B has high clinical relevance, being the major enzyme responsible for metabolizing dopamine in the human brain, a neurotransmitter that is essential to multiple brain functions including movement, mood, motivation, and cognition. The accumulation of data from in vitro and in vivo studies, as reviewed in Sections 15.4 and 15.5, has shown that brain MAO-B levels are elevated in a range of neurodegenerative and other neurological and neuropsychiatric disorders, including depression, Parkinson's disease (PD) and Parkinsonian disorders, amyotrophic lateral sclerosis (ALS), and Alzheimer's disease (AD) (Fowler et al. 2015; Ramsay 2016). In these disorders, the abnormal upregulation of MAO-B leads to declining levels of dopamine and other neurotransmitters, together with excess neurotoxic byproducts, oxidative stress, and neuroinflammation, all of which promote neuronal dysfunction and neurodegeneration (Arranz and De Strooper 2019; De Strooper and Karran 2016). MAO-B is abundantly located in astrocytes, and overexpressed under certain pathological conditions associated to astrocytosis (De Strooper and Karran 2016). Preclinical studies in a transgenic mouse model of AD reported MAO-B upregulation in astrocytes, resulting in excess γ-aminobutyric acid (GABA) production and cognitive deficits (Jo et al. 2014). Suppressing GABA synthesis by inhibiting MAO-B improved synaptic plasticity and reduced astrocytosis in the brains of transgenic AD mice (Park et al. 2019). Therefore, there is a growing interest in the investigation of reactive astrocytes as a promising therapeutic target (Arranz and De Strooper 2019; Boche et al. 2019), and PET imaging of MAO-B could play a major role toward the quantification of astrocytosis in the context of the pathological cascade in neurodegenerative and other brain disorders. Further studies have shown that MAO-B overexpression is associated to increased γ-secretase-mediated amyloid-β production in the hypothalamus and frontal cortex in AD, being found both in astrocytes and in neurons (Schedin-Weiss et al. 2017). Building on all the available preclinical evidence, there has been a long-standing effort to unravel the biological mechanisms underlying MAO-B overexpression and to explore its regulation as a potential therapeutic target in a range of brain disorders.

15.1.2 Molecular Neuroanatomy of MAO-B

Knowledge about the neuroanatomical distribution and cellular localization of MAO-B has been gained through in vitro studies in human and animal models using biochemical techniques such as immunoblotting, immunohistochemistry, and immunocytochemistry. While animal models have provided a wealth of valuable

data, interspecies differences are a limitation of translational research. For example, the human brain has substantially higher tissue concentrations of MAO-B than are found in rodents (Saura et al. 1996). This means that while animal models are helpful for initial testing of radiotracers, in vitro and in vivo studies in human brain are needed before tracers can be validated for use in clinical studies.

Early studies determined that MAO-B is located both in neurons and astrocytes, but with different predominance across brain regions. Studies in normal aging and across neurodegenerative diseases are converging to the finding that MAO-B is abundantly expressed in glial cells, particularly in the outer wall of mitochondria in astrocytes (Saura et al. 1996). The astrocytic localization of MAO-B has been revealed experimentally using immunohistochemical staining for glial fibrillary acidic protein (GFAP), an intermediate filament expressed by reactive astrocytes, as well as using markers for other astrocytic filaments such as vimentin and nestin. Early immunocytochemistry studies in the rat brain (Levitt et al. 1982) using a double immunofluorescence technique by means of antisera to MAO-B and either GFAP as a marker of astrocytes or serotonin as a marker of serotonergic neurons, determined that MAO-B was overexpressed in astrocytes. In certain areas of the rat brain, MAO-B was also expressed in serotonin-containing neurons, in particular in the brainstem raphe nuclei and the hypothalamus, i.e., regions rich in serotonergic cell groups. In postmortem spinal cord tissue from ALS patients, double-staining studies using MAO-B and GFAP determined that MAO-B was co-located with astrocytes as measured by GFAP; high MAO-B was also observed in serotonergic and histaminergic neurons (Ekblom et al. 1993, 1994). The astrocytes displayed a high level of phenotypic heterogeneity, whereby not all types of astrocytes overexpressed MAO-B, so that the correlation between MAO-B and GFAP was only moderate.

More recently, quantitative immunoblotting analyses of MAO-B antibodies in postmortem human control brain tissue with an average age of 48 years have shown that the MAO-B distribution in the brain is heterogeneous. Highest levels of MAO-B were observed in the hypothalamus, nucleus basalis, and hippocampal uncus, followed by rather high levels in the striatum and globus pallidus, and somewhat lower levels in other cortical regions including frontal and cingulate cortices; lowest levels were measured in the cerebellum (Tong et al. 2013). When focusing on the frontal cortices, MAO-B was positively associated with age showing an ~18% increase in MAO-B per decade from 18 to 99 years (Tong et al. 2013). Besides age, a number of other factors influence MAO-B expression in the human brain, including smoking, depressive symptoms, neuroinflammation, and medications such as the use of MAO-B inhibitors (Fowler et al. 2015).

Compared to control subjects, MAO-B levels were high in PD and Parkinsonian disorders including multiple system atrophy and progressive supranuclear palsy (Tong et al. 2017). Also, MAO-B levels were positively correlated with standard astrocyte markers including GFAP, vimentin, and nestin across PD and Parkinsonian disorders. These findings provide additional evidence that levels of MAO-B protein may serve as a biochemical marker of astrocyte activation, with the limitation that

MAO-B may not be entirely specific for astrocytosis (Tong et al. 2017). Overall, the elevation in MAO-B levels was less prominent than that measured with standard astrocytic markers (Tong et al. 2017), which highlights that MAO-B and GFAP, while moderately correlated, are not measuring exactly the same processes. More detailed findings from in vitro autoradiography studies are reviewed in Sect. 15.4.

15.1.3 MAO-B as Therapeutic Target

From a therapeutic point of view, there are a number of treatment strategies and clinical trials aiming at inhibiting MAO-B levels in the brain. Based on accumulated neurobiological knowledge about the role of MAO-B in brain function, the inhibition of this enzyme would dampen the metabolism of dopamine, leading to increased levels of endogenous dopamine and reduced neuroinflammation. To date, many clinical trials of MAO-B inhibitors have been conducted or are underway toward the treatment of depression, PD, and more recently AD, partly due to the growing interest in neuroinflammation as a therapeutic target (Ramsay 2016; Schapira et al. 2006; Youdim et al. 2006). The FDA (US Food and Drug Administration) approved the irreversible MAO-B inhibitors selegiline and rasagiline for the symptomatic treatment of motor dysfunction in PD. More recently, reversible MAO-B inhibitors are undergoing clinical trials, but their efficacy is still uncertain.

15.2 Requirements to Develop PET Tracers for Imaging MAO-B

Positron emission tomography (PET) is a molecular imaging technique that allows measuring molecular changes in the brain with very high sensitivity. With a growing recognition of the role of neuroinflammation across multiple brain disorders, PET imaging of MAO-B is a promising tool to quantify astrocytosis and as an outcome measure in clinical trials for evaluating the efficacy and optimize the dosage of MAO-B inhibitors (Fowler et al. 2015, 2005; Narayanaswami et al. 2019). The main challenges in the development of radiotracers for MAO-B have been to produce chemical compounds with high specificity and sensitivity for MAO-B and with appropriate pharmacokinetics so that the quantitative PET binding measures are reliable estimates of the actual concentrations of MAO-B enzyme in the brain. The radiotracers should be sufficiently lipophilic to cross the blood-brain barrier, but their lipophilicity should be limited to minimize their non-specific binding to white matter. It is also important to minimize the amounts of radioactive metabolites entering the brain, which may confound the MAO-B PET signal.

Despite active research into MAO-B tracers for the past ~30 years, to date only a limited number of radiotracers have met the required qualities for potential translation to human. A summary of the radiotracers that will be reviewed in this chapter is presented in Table 15.1; the corresponding chemical structures of these tracers are

Table 15.1 Schematic summary of MAO-B PET tracers applied in in vivo imaging studies

PET tracers	Pharmacokinetic modelling studies	In vivo PET imaging studies in animal models	In vivo PET imaging studies in human
Irreversible binding tracers			
¹¹C-L-deprenyl	*2-tissue-compartment model with plasma input:* Lammertsma et al. (1991) (human) Fowler et al. (1995) (human) *Graphical Patlak analysis with plasma input:* Fowler et al. (1987) (human) Lammertsma et al. (1991) (human)	*Mouse:* MacGregor et al. (1985) *Baboon:* Fowler et al. (1988)	*Test-retest studies:* Logan et al. (2000) *Clinical trials of MAO-B inhibitors:* Bench et al. (1991) Fowler et al. (1994) Freedman et al. (2005)
¹¹C-L-deprenyl-D₂ (also known as ¹¹C-deuterium-L-deprenyl)	*2-tissue-compartment model with plasma input:* Fowler et al. (1988) (baboon) Fowler et al. (1995) (human) *Graphical Patlak analysis with plasma input:* Fowler et al. (1995) (human) *Modified reference Patlak analysis:* Bergström et al. (1998) (human) Johansson et al. (2007) (human)	*Baboon:* Fowler et al. (1988) *Transgenic mouse models of Alzheimer's disease:* Rodriguez-Vieitez et al. (2015) Olsen et al. (2018)	*Test-retest studies:* Logan et al. (2000) Arakawa et al. (2017) *Aging:* Fowler et al. (1997) *Effects of smoking:* Fowler et al. (1996) *Alzheimer's disease:* Carter et al. (2012), Carter et al. (2019a, 2019b) Rodriguez-Vieitez et al. (2016a, 2016b) Vilaplana et al. (2020) *Amyotrophic lateral sclerosis:* Johansson et al. (2007) *Creutzfeldt-Jakob disease:* Engler et al. (2003, 2012) *Epilepsy:* Bergström et al. (1998) *Fibromyalgia:* Albrecht et al. (2019) *Clinical trials of MAO-B inhibitors:* Hirvonen et al. (2009) Sturm et al. (2017)
¹⁸F-fluorodeprenyl	Not available	*Cynomolgus monkey:* Nag et al. (2012b)	Not available

Table 15.1 (continued)

PET tracers	Pharmacokinetic modelling studies	In vivo PET imaging studies in animal models	In vivo PET imaging studies in human
[18]F-fluorodeprenyl-D[2]	*2-tissue-compartment model with plasma input:* Nag et al. (2016) (cynomolgus monkey)	*Cynomolgus monkey:* Nag et al. (2016)	Not available
[18]F-fluororasagiline	Not available	*Cynomolgus monkey:* Nag et al. (2012a)	Not available
[18]F-fluororasagiline-D[2]	Not available	*Cynomolgus monkey:* Nag et al. (2013)	Not available
[11]C-Cou	*2-tissue-compartment model with plasma input:* Drake et al. (2018) (rhesus monkey)	*Rhesus monkey:* Drake et al. (2018)	Not available
Reversible binding tracers			
[11]C-SL25.1188	*1-tissue-compartment model with plasma input:* Saba et al. (2010) (baboon) Rusjan et al. (2014) (human) *2-tissue-compartment model with plasma input:* Saba et al. (2010) (baboon) Rusjan et al. (2014) (human) *Graphical Logan analysis with plasma input:* Saba et al. (2010) (baboon) Rusjan et al. (2014) (human)	*Baboon:* Saba et al. (2010)	*Healthy human brain:* Rusjan et al. (2014) *Depression:* Moriguchi et al. (2019)
^{18}F-FSL25.1188	*Graphical Logan analysis with plasma input:* Dahl et al. (2019) (cynomolgus monkey)	*Cynomolgus monkey:* Dahl et al. (2019)	Not available
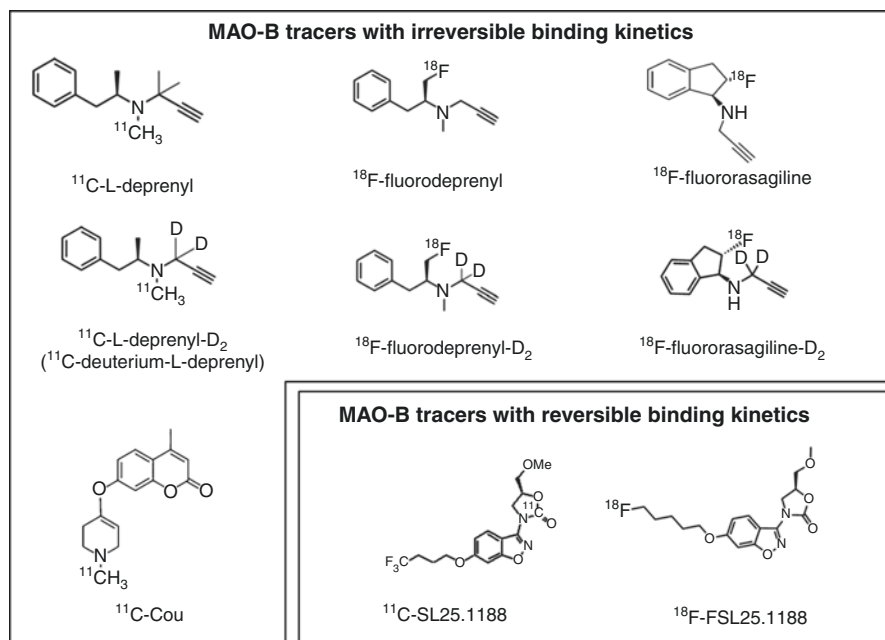
Fig. 15.1 Chemical structures of PET tracers for imaging MAO-B

illustrated in Fig. 15.1. From a pharmacokinetic point of view, tracers are classified into those that are best described by either irreversible or reversible binding kinetics. Most MAO-B tracers that have reached application in human PET studies have been labelled with carbon-11 (half-life of 20.4 min), which is useful when repeated scans are needed in the same subjects over a short period of time, for example, in drug dosing studies. More recently, there is an intense research effort to develop fluorine-18 (half-life of 110 min)-labelled radiotracers, which have other advantages, in particular greater clinical utility for administration in facilities that do not have a cyclotron on site. Full pharmacokinetic modelling with arterial sampling is used for newly developed MAO-B tracers, followed by validation of simplified models using reference regions that obviate the need for arterial sampling, and therefore have greater potential for clinical application.

15.3   Development and Pharmacokinetic Characterization of MAO-B PET Tracers

15.3.1 Tracers with Irreversible Binding Kinetics

15.3.1.1   Carbon-11-Labelled Tracers

Originally developed in the 1980s, the most widely investigated PET tracers for MAO-B have been the irreversible binding tracers ^{11}C-L-deprenyl and its deuterated analog, ^{11}C-L-deprenyl-D$_2$—also referred to as ^{11}C-deuterium-L-deprenyl (Fowler

et al. 2015); these tracers are stereoselective, so that only the L enantiomers (but not the D) are active toward MAO-B. In these tracers, also known as "suicide enzyme inhibitors," the propargylamine chemical structure forms a covalent bond to the flavin cofactor of the MAO-B enzyme. This covalent bond is formed via the cleavage of the carbon-hydrogen or carbon-deuterium bonds on the methylene carbon of the propargyl group. As the tracers bind to the catalytically active MAO-B enzyme molecules, the signal intensity recorded by the PET scanner reflects the concentration of MAO-B in brain tissue. The carbon-deuterium bonds are stronger and thus require more energy to be cleaved compared to the carbon-hydrogen bonds. As a result, the deuterated tracers have lower binding rates to MAO-B compared to the respective non-deuterated forms—also known as the "deuterium effect"—and thus the deuterated tracers have enhanced sensitivity to MAO-B.

Early in vivo PET investigations showed that ^{11}C-L-deprenyl has a high level of specificity to MAO-B in mouse brain (MacGregor et al. 1985), as well as in human brain (Fowler et al. 1987)—where it was blocked by the administration of unlabelled L-deprenyl and the non-selective MAO inhibitor phenelzine. A subsequent pharmacokinetic study of ^{11}C-L-deprenyl using experimental data with arterial plasma input in normal subjects compared irreversible vs. reversible 2-tissue-compartment models (Lammertsma et al. 1991) where the brain tissue is divided into two compartments: (1) free and non-specific binding in tissue and (2) specific binding in tissue. The ^{11}C-L-deprenyl binding data were well fitted by the 2-tissue-compartment model, using rate constants for the transfer from plasma to tissue (K_1) and viceversa (k_2), and with k_3 as the rate of irreversible binding to MAO-B. The inclusion of a k_4 constant to simulate reversible binding kinetics to MAO-B did not significantly improve the model fit, thus supporting the irreversible model. The data were also well fitted by a graphical Patlak model for irreversible binding (Patlak and Blasberg 1985), where the concentration of MAO-B in brain is quantified by K_i, the rate of net influx to the specifically bound compartment. Of note, the influence of cerebral blood flow on the Patlak-derived K_i net influx rate and on k_3 as obtained from the 2-tissue-compartment model was examined by using data from one subject with both ^{11}C-L-deprenyl and ^{15}O-water PET scans available. The analyses showed that the regional Patlak-derived net influx rates (K_i) for ^{11}C-L-deprenyl were positively correlated to cerebral blood flow. Using various doses of the reversible MAO-B inhibitor Ro 19–6327, Lammertsma et al. (1991) showed that the inhibition of MAO-B cannot be reliably measured using the Patlak-derived K_i constant because of variations in cerebral blood flow. In contrast, the rate of binding to MAO-B derived from the 2-tissue-compartment model (k_3) was not strongly influenced by cerebral blood flow, and therefore this study suggests that the full kinetic modelling (k_3 constant) is a more reliable method for MAO-B quantification compared to the Patlak analysis (K_i) for the ^{11}C-L-deprenyl tracer, especially for the evaluation of drug trials.

The pharmacokinetic properties of ^{11}C-L-deprenyl-D$_2$ and ^{11}C-L-deprenyl were compared to investigate the deuterium effect in the baboon brain (Fowler et al. 1988) and in human volunteers (Fowler et al. 1995). Both tracers were modelled by a 2-tissue-compartment model with arterial plasma input as previously described (Lammertsma et al. 1991), as well as by graphical analysis for irreversible tracers in

the study in humans (Fowler et al. 1995). Using the compartmental model, it was found that λk_3 (with $\lambda = K_1/k_2$) is a more robust measure of radiotracer binding than k_3, being less influenced by cerebral blood flow. Importantly, the deuterated compound (^{11}C-L-deprenyl-D_2) had slower rate of trapping in human brain as measured by λk_3 compared to ^{11}C-L-deprenyl, leading to increased sensitivity to changes in MAO-B, and lower influence of brain perfusion on tracer binding. Test-retest investigations with ^{11}C-L-deprenyl-D_2 indicated that λk_3 had a low test-retest variability with an absolute value of less than ~10% in healthy subjects (Logan et al. 2000; Arakawa et al. 2017); further test-retest investigations in patients would be valuable. Due to its improved pharmacokinetic properties, subsequent studies focused on the ^{11}C-L-deprenyl-D_2 tracer only, where a modified reference Patlak model using the cerebellum gray matter as reference allowed estimating tracer binding by means of parametric Patlak slope images, a simplified approach with greater potential for clinical application as it obviates the need for arterial sampling (Bergström et al. 1998; Johansson et al. 2007; Rodriguez-Vieitez and Nordberg 2018; Patlak and Blasberg 1985).

During the past few years, a new family of metabolically trapped compounds with irreversible binding kinetics has been under development (Narayanaswami et al. 2019). A metabolically trapped tracer for MAO-B is a compound that serves as substrate for the MAO-B enzyme, and which is selectively metabolized and trapped within the brain tissue, but without forming a covalent bond (the most well-known metabolically trapped tracer is ^{18}F-FDG, an analog of glucose that is trapped in highly metabolic regions in the brain). Preliminary studies on tetrahydropyridine compounds showed that they are metabolically trapped by MAO-B enzyme in brain tissue of rhesus monkey brain, but not substantially trapped in rat brain, pointing to species differences and the need to perform tests in human brain. The tracer ^{11}C-Cou is a tetrahydropyridine, which is a metabolically trapped PET tracer for MAO-B, showing rapid and irreversible retention in the primate brain. Since ^{11}C-Cou demonstrated quite rapid rate of trapping, a deuterated analog was developed, but it did not show suitable pharmacokinetics in rhesus monkey brain (Drake et al. 2018). MAO-B mouse models of PD (Chamoli et al. 2018; Mallajosyula et al. 2008; Siddiqui et al. 2011) are being considered for the testing of newly developed compounds prior to potential translation to human PET application.

15.3.1.2 Fluorine-18-Labelled Tracers

Recent advances in the chemical organic synthesis of fluorinated L-deprenyl compounds have allowed developing various tracers that incorporate fluorine-18 in different positions on the aliphatic chain rather than in the aromatic ring (Nag et al. 2011), resulting in compounds with high MAO-B affinity and selectivity as shown by autoradiography in postmortem human brain tissue. PET studies with ^{18}F-fluorodeprenyl in the cynomolgus monkey brain showed the expected in vivo MAO-B distribution in the brain as illustrated in Fig. 15.2, and irreversible pharmacokinetic behavior (Nag et al. 2012b). Subsequently, the same research group developed the respective deuterated analog, ^{18}F-fluorodeprenyl-D_2, which showed the
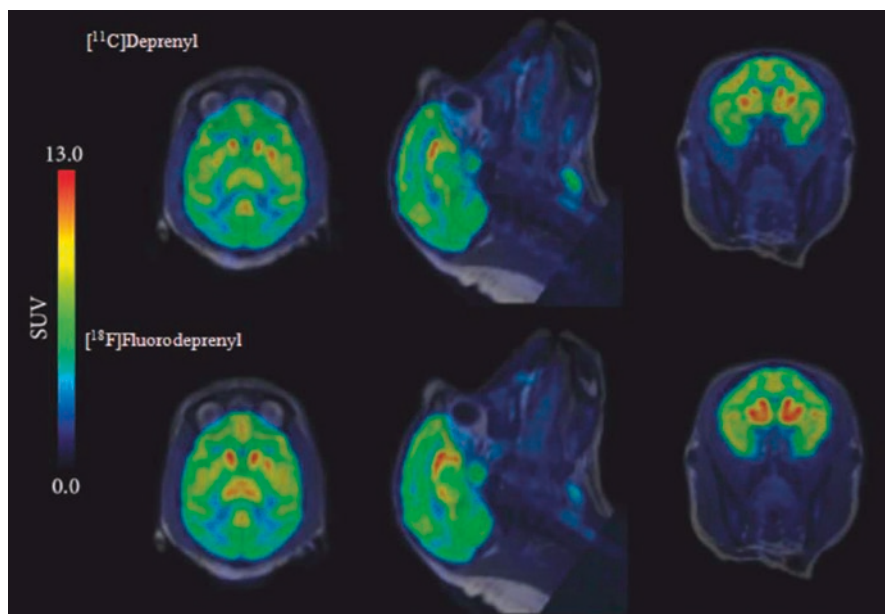
Fig. 15.2 Illustrative PET scans using MAO-B tracers ^{11}C-L-deprenyl and ^{18}F-fluorodeprenyl co-registered with MRI and averaged between 9 and 120 min in cynomolgus monkey brain. Reprinted from Nag et al. (2012b), with permission from John Wiley & Sons Inc. © 1999–2020. *SUV* standardized uptake value

expected in vivo MAO-B regional distribution in cynomolgus monkey brain, and decreased tracer uptake after administration of MAO-B inhibitor L-deprenyl (Nag et al. 2016). Kinetic modeling of the in vivo ^{18}F-fluorodeprenyl-D_2 uptake in cynomolgus monkey brain using a 2-tissue-compartment model with 4 rate constants fitted the data better than the corresponding model with 3 rate constants, providing evidence for a certain degree of reversibility of this tracer. Also, a head-to-head comparison in cynomolgus monkey brain showed that ^{18}F-fluorodeprenyl-D_2 has more reversible kinetic behavior than ^{11}C-L-deprenyl-D_2 (Nag et al. 2016); despite these encouraging findings and that ^{18}F-fluorodeprenyl-D_2 has shown the expected MAO-B regional distribution by in vitro autoradiography in human brain tissue, this tracer has not yet been translated to in vivo human PET studies.

Continuing on the path toward developing fluorinated MAO-B tracers for clinical use, the same research group developed and evaluated fluorine-18-labelled derivatives of rasagiline, also known as ^{18}F-fluororasagiline (Nag et al. 2012a), but this tracer showed significant levels of radioactive metabolites entering the brain. With the motivation to develop a tracer with a certain degree of reversibility, the deuterated analog ^{18}F-fluororasagiline-D_2 was subsequently synthesized (Nag et al. 2013). The ^{18}F-fluororasagiline-D_2 tracer showed suitable kinetics in cynomolgus monkey brain; however, its translation to human in vivo studies is still pending.

15.3.2 Tracers with Reversible Binding Kinetics

While the irreversibly binding tracers reviewed above (Sect. 15.3.1) have provided good correlations with in vitro MAO-B protein concentrations in the brain (Tong et al. 2013), their rate of binding is partly influenced by cerebral blood flow and some radiotracers present with undesirable radioactive metabolites entering the brain. To overcome these limitations, there has been a recent effort to develop reversible tracers.

15.3.2.1 Carbon-11-Labelled Tracers

A reversible carbamate inhibitor of MAO-B, ^{11}C-SL25.1188, was synthesized via ^{11}C-phosgene as a carbon-11 precursor. In vivo data on ^{11}C-SL25.1188 tracer binding in baboon brain were appropriately fitted to 1-tissue-compartment or 2-tissue-compartment reversible models as well as by the graphical Logan approach (Logan 2000), and tracer binding could be blocked by pretreatment with L-deprenyl (Saba et al. 2010). Despite these promising findings, the need for ^{11}C-phosgene as a precursor poses a limitation toward clinical application. To avoid the use of ^{11}C-phosgene, a new technique using a direct [11]CO_2 fixation method was recently developed (Vasdev et al. 2011); the newly synthesized ^{11}C-SL25.1188 tracer was subsequently tested in healthy human brain (Rusjan et al. 2014). In this paper, the pharmacokinetic evaluation of ^{11}C-SL25.1188 in human brain revealed that the tracer has excellent properties including high reversibility, selectivity for MAO-B, and absence of metabolites entering the brain. The time-activity data including arterial sampling were well fitted by a 2-tissue-compartment model and by the graphical Logan approach for reversible binding. Being the first reversible tracer to be used in human for imaging MAO-B, the ^{11}C-SL25.1188 tracer binding as measured by the distribution volume V_T derived from the Logan graphical approach provided a robust measure of MAO-B binding in the human brain, which was well correlated with the known regional distribution of MAO-B from postmortem studies (Rusjan et al. 2014). The ^{11}C-SL25.1188 tracer was recently applied for the first time in a human brain disorder, being evaluated in a cohort of patients with major depressive disorder (Moriguchi et al. 2019), as further described in Sect. 15.5.

15.3.2.2 Fluorine-18-Labelled Tracers

Current efforts are being directed at developing fluorinated reversible tracers, which would have clear advantages from a clinical perspective. A fluorinated version of SL25.1188, ^{18}F-FSL25.1188, showed reversible in vivo binding kinetics in cynomolgus monkey brain with highest uptake in the thalamus and striatum, moderate in cortical regions, and lowest in the cerebellum; the expected MAO-B regional distribution was also observed by autoradiography in postmortem human brain sections (Dahl et al. 2019). As a potential limitation, the ^{18}F-FSL25.1188 tracer showed some level of uptake in the skull at late time frames (from 50 to 90 min) due to in vivo defluorination, which could affect its accurate quantification in regions such as the temporal cortex. Research aimed at clinical translation of ^{18}F-FSL25.1188 to human brain imaging is still at an early stage.

15.4   In Vitro Molecular Imaging of MAO-B by Autoradiography

In parallel with the development of novel MAO-B PET tracers, in vitro autoradiography studies in postmortem human brain tissue have been performed to test the specificity and binding properties of the tracers (Tong et al. 2013). More detailed in vitro autoradiography investigations are also performed to compare the regional and laminar distributions of MAO-B PET tracers vs. other tracers specific to amyloid-β or tau in adjacent brain sections, often in combination with immunohistochemical measures to gain greater understanding of the types of neuropathological features associated with tracer binding. Despite the fact that in vitro autoradiography is an active field of research, antemortem vs. postmortem comparisons of MAO-B PET tracers are still rare.

Autoradiography studies of MAO-B began in the 1980s using ^{11}C-labelled L-deprenyl in whole-hemisphere frozen sections from postmortem healthy human brain tissue. This tracer showed a pattern of high binding in the basal ganglia, thalamus, and hippocampus and moderate binding in the cerebral cortex; non-specific binding was low, amounting to ~20% of the total binding (Jossan et al. 1989). Quantitative autoradiography using either ^{3}H-L-deprenyl (Jossan et al. 1991) or the reversible MAO-B tracer ^{3}H-lazabemide (Saura et al. 1994) showed higher binding in AD compared to control cases. ^{3}H-L-deprenyl was elevated in spinal cord, motor cortex, and white matter in ALS compared to control cases (Jossan et al. 1994).

Frequently, autoradiography studies are performed in combination with immunohistochemical staining in adjacent sections. A positive correlation was observed between ^{3}H-L-deprenyl binding and GFAP staining in ALS patients (Ekblom et al. 1993, 1994; Jossan et al. 1994), in support of the astroglial localization of MAO-B. Similarly, ^{3}H-lazabemide binding was correlated with plaque-associated astrogliosis as measured by GFAP staining in AD brain tissue (Saura et al. 1994). Also using ^{3}H-lazabemide autoradiography, Saura et al. (Saura et al. 1997) reported an overall positive association between MAO-B and age in control brains, which followed a biphasic trajectory characterized by a negligible change in MAO-B up to age 50, and a significant increase in MAO-B after 50 years, likely reflecting age-associated neuroinflammation.

These early autoradiography findings, together with a recently renewed interest in neuroinflammation as a therapeutic target in neurodegenerative diseases, have motivated further autoradiography studies using ^{11}C-L-deprenyl combined with GFAP immunohistochemical staining in AD brain tissue. ^{11}C-L-deprenyl binding showed the highest intensity in correlation with GFAP staining at early Braak stages of AD compared to that in more advanced disease stages, suggesting that astrocytosis plays an early role in disease progression (Gulyás et al. 2011). Subsequently, multitracer autoradiography studies (Lemoine et al. 2017; Marutle et al. 2013) were designed to investigate MAO-B in relation to other relevant pathological features in the AD brain including amyloid-β and tau deposition. Both studies revealed similar laminar patterns of ^{3}H-L-deprenyl binding in AD, which differed from the laminar distribution of fibrillar amyloid-β deposition as measured by ^{3}H-PiB (Lemoine et al. 2017; Marutle et al. 2013). In the frontal cortex, ^{3}H-L-deprenyl binding was highest
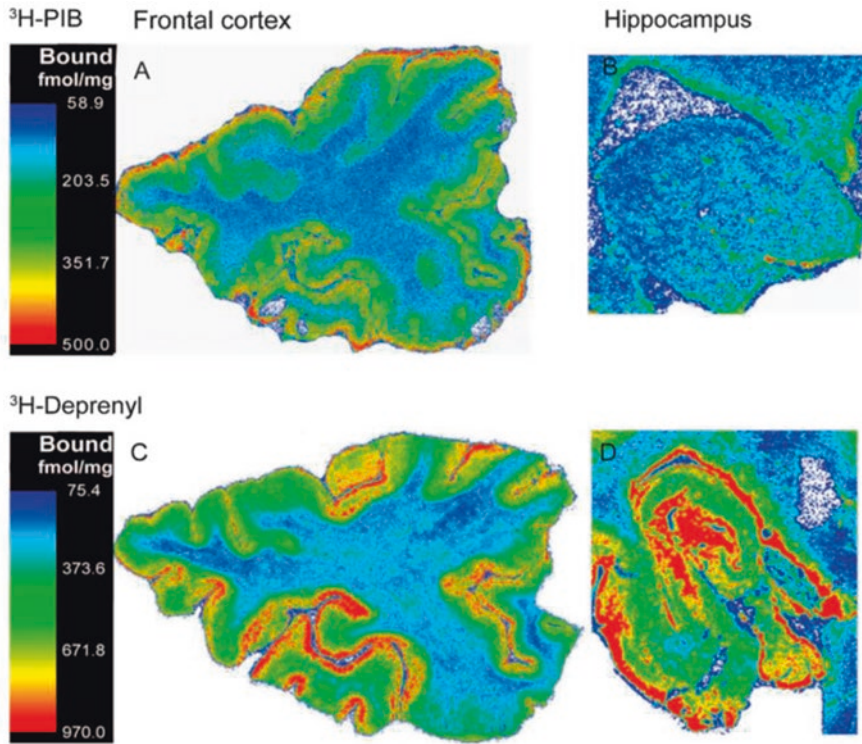
Fig. 15.3 In vitro autoradiography studies in Alzheimer's disease postmortem brain tissue using ^{3}H-PiB in frontal cortex (**a**) and hippocampus (**b**), compared to ^{3}H-L-deprenyl in frontal cortex (**c**) and hippocampus (**d**). Figure adapted from Marutle et al. (2013), under the terms of the Creative Commons CC BY license

in superficial layers, while ^{3}H-PiB binding was elevated in all layers; in contrast, the hippocampus showed low ^{3}H-PiB binding to fibrillar amyloid-β but intense ^{3}H-L-deprenyl binding in all layers, as illustrated in Fig. 15.3 (Marutle et al. 2013). GFAP staining confirmed abundant reactive astrocytes surrounding amyloid-β plaques in correlation with ^{3}H-L-deprenyl binding in superficial layers of the frontal cortex (Marutle et al. 2013). The laminar pattern of ^{3}H-L-deprenyl was more closely associated with tau deposition as measured by ^{3}H-THK5117 than it was to ^{3}H-PiB (Lemoine et al. 2017), suggesting a close association between astrocytosis and tau pathology (Lemoine et al. 2017). Of note, early-generation tau tracers such as ^{3}H-THK5117 have limitations due a certain amount of off-target binding to MAO-B most prominently in the basal ganglia (Lemoine et al. 2018). Therefore, the correlations between ^{3}H-L-deprenyl and ^{3}H-THK5117 PET tracers in these subcortical regions should be taken with a degree of caution (Lemoine et al. 2017; Murugan et al. 2019). Overall, there was a close association between ^{3}H-L-deprenyl binding and GFAP in AD brain indicating a good level of correspondence between MAO-B and activated astrocytes; adjacent paraffin sections showed similar staining patterns for the tau marker AT8 and GFAP, adding support to the observed association between tau deposits and activated astrocytes (Lemoine et al. 2017).

There are also some challenges and limitations in the autoradiography studies of MAO-B. As pointed out in early studies (Fowler et al. 1987), the procedures for the isolation of MAO-B from its native environment within a tissue that are necessary for performing in vitro studies may change some properties of the enzyme, so differences in MAO-B activity may be observed when comparing in vivo and in vitro analyses. For example, while elevated in vivo ^{11}C-deuterium-L-deprenyl binding was observed in a transgenic mouse model of AD compared to age-matched controls, no differences were observed by in vitro autoradiography with ^{3}H-L-deprenyl (Rodriguez-Vieitez et al. 2015), which may point to limitations of the in vitro imaging technique in mouse brains. Finally, while there are some isolated case studies (Engler et al. 2012), no systematic comparisons between antemortem and postmortem MAO-B activity in human brain have been performed; these types of studies would be informative to validate the in vivo findings against in vitro data in the same individuals and to unravel the biological mechanisms and pathological changes underlying the in vivo PET signal.

15.5 Applications of In Vivo PET Imaging of MAO-B in Health and Disease

15.5.1 Aging

An in vivo PET study with ^{11}C-L-deprenyl-D$_2$ in healthy human brain (21 participants, age range 23–86 years) using arterial plasma sampling and a 2-tissue-compartment irreversible kinetic model showed an increase in ^{11}C-L-deprenyl-D$_2$ binding (λk_3) with age of about 7% per decade in all brain regions except the cingulate gyrus, likely due to age-related neuroinflammation (Fowler et al. 1997). In contrast to the age-associated increase in MAO-B, subjects showed the expected decline in cerebral blood flow with age, as measured by the blood-to-brain influx constant K_1, as well as in glucose metabolism in 15 participants for whom both ^{11}C-L-deprenyl-D$_2$ and ^{18}F-FDG PET were available. Of note, the age-related increase in MAO-B observed in vivo was smaller than that previously reported by in vitro biochemical methods to determine MAO-B protein concentrations in brain tissues, thus pointing to some discrepancies between in vivo and in vitro findings.

15.5.2 Effects of Smoking

Previous studies have reported that smokers have reduced platelet MAO-B levels (Fowler et al. 2003). While the reasons for the observed reduction in MAO-B levels were unknown, it was hypothesized as due to either slower rates of MAO-B synthesis in smokers compared to non-smokers or to MAO-B inhibition caused by substances present in the tobacco, without excluding the possibility that low MAO-B individuals may be more vulnerable to smoking. PET studies with ^{11}C-L-deprenyl-D$_2$ revealed that smokers had up to 40% reduction in MAO-B levels in the brain compared to non-smokers or former smokers (Fowler et al. 1996), while blood-to-brain flow (K_1) and glucose metabolism (^{18}F-FDG) in smokers were not different from those in non-smokers.

15.5.3 Neuroinflammation in Neurodegenerative Diseases

Among the few PET tracers available to quantify astrocytosis in vivo in human brain, the most commonly used has been ^{11}C-deuterium-L-deprenyl, as highlighted in recent reviews (Albrecht et al. 2016; Boche et al. 2019; Carter et al. 2019b; Narayanaswami et al. 2018; Varrone and Nordberg 2015). Elevated ^{11}C-deuterium-L-deprenyl PET binding has been reported in a range of neurodegenerative diseases including AD (Carter et al. 2012; Rodriguez-Vieitez et al. 2016a), ALS (Johansson et al. 2007), and Creutzfeldt-Jakob disease (CJD) (Engler et al. 2003, 2012), as well as and in the affected hemisphere of epileptic patients (Bergström et al. 1998). A multitracer PET study in patients with probable CJD (Engler et al. 2003) revealed both high ^{11}C-deuterium-L-deprenyl and low ^{18}F-FDG uptake in several cortical regions, indicating the presence of astrocytosis and neuronal dysfunction.

Using a multitracer PET imaging study design including ^{11}C-deuterium-L-deprenyl, ^{11}C-PiB and ^{18}F-FDG in sporadic AD patients (Rodriguez-Vieitez and Nordberg 2018), significantly increased ^{11}C-deuterium-L-deprenyl binding was observed in prodromal stages of AD in comparison to healthy controls or to patients with AD dementia (Carter et al. 2012), as illustrated in Fig. 15.4. In addition, the 1–4 min early phase of ^{11}C-deuterium-L-deprenyl standardized uptake value ratio (SUVR) was used as a surrogate marker of brain perfusion, being highly correlated

Fig. 15.4 Representative in vivo multitracer PET scans of ^{11}C-deuterium-L-deprenyl (^{11}C-DED), in comparison with ^{18}F-FDG and ^{11}C-PiB. *AD* Alzheimer's disease, *HC* healthy controls, *MCI* mild cognitive impairment, *PiB+ (−)* Pittsburgh compound B positive (negative), *SUVR* standardized uptake value ratio. Figure adapted from Rodriguez-Vieitez et al. (2016a), with permission © SNMMI
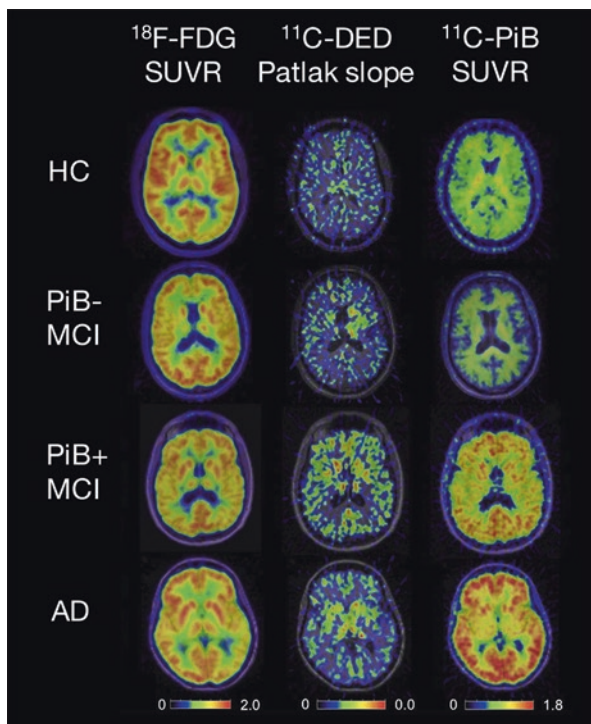
with glucose metabolism (^{18}F-FDG) (Rodriguez-Vieitez et al. 2016a); a limitation of this study was however the lack of an independent measure of brain perfusion such as ^{15}O-water PET. The same multitracer PET paradigm investigated in familial autosomal dominant AD, in which mutation carriers develop symptomatic AD at a rather predictable age of onset, revealed that the most prominent elevation in ^{11}C-deuterium-L-deprenyl binding occurs at the presymptomatic stage, up to two decades prior to symptom onset (Schöll et al. 2015). The longitudinal follow-up of this cohort showed increasing amyloid-β plaque deposition (^{11}C-PiB) together with declining levels of both astrocytosis (^{11}C-deuterium-L-deprenyl) and glucose metabolism (^{18}F-FDG) in mutation carriers along disease progression (Carter et al. 2019a; Rodriguez-Vieitez et al. 2016b). ^{11}C-deuterium-L-deprenyl was also found to be elevated from early disease stages in two different transgenic mouse models of AD (Olsen et al. 2018; Rodriguez-Vieitez et al. 2015); in both studies the astrocytic marker GFAP was observed to peak at late stages and not being well correlated to ^{11}C-deuterium-L-deprenyl, suggesting that the two markers measure different aspects or stages of astrocytosis. Overall, these studies showing elevation of ^{11}C-deuterium-L-deprenyl in neurodegenerative diseases suggest that the modulation of astrocytosis is a promising early therapeutic target, but further research is needed (Schott and Fox 2016).

More recently, multimodal MRI-PET imaging studies have allowed interrogating the relationships between structural and molecular changes in the brain. Molecular biology studies have shown that astrocytes and microglia interact in neurodegenerative diseases and that their activation is accompanied by morphological remodelling such as early hypertrophy of astrocytes followed by atrophy and astrodegeneration, while microglia undergo morphological changes toward ameboid-like forms (Arranz and De Strooper 2019; Boche et al. 2019; De Strooper and Karran 2016). An emerging field of research proposes using MRI sequences such as diffusion-weighted imaging (DWI) toward investigating microstructural brain changes that may be sensitive to glial morphological changes. Using a DWI approach to assess cortical microstructural changes in the gray matter, a negative association was observed between cortical mean diffusivity and ^{11}C-deuterium-L-deprenyl PET in autosomal dominant AD, and a positive association with cortical thickness, suggesting that astrocytosis may be linked to macrostructural and microstructural changes in the gray matter (Vilaplana et al. 2020). Further developments using longitudinal, multimodal imaging will contribute to characterizing the complex molecular and morphological changes associated with neuroinflammation in different brain diseases.

15.5.4 Neuroinflammation in Other Neurological Diseases

PET imaging of MAO-B can be used to investigate neuroinflammatory aspects in other neurological diseases. While neuroinflammation is believed to play an important role in diseases characterized by chronic pain, its underlying molecular mechanisms are not well-known. An in vivo PET study combining ^{11}C-deuterium-L-deprenyl

and TSPO (translocator protein) tracer ^{11}C-PBR28, a marker of microgliosis, sought to investigate neuroinflammatory mechanisms in fibromyalgia, a chronic disorder characterized by musculoskeletal pain, fatigue, and cognitive difficulties, which is still poorly understood (Albrecht et al. 2019). Fibromyalgia patients had elevated fronto-parietal ^{11}C-PBR28 binding, but no difference in ^{11}C-deuterium-L-deprenyl compared to a control group, therefore suggesting that microgliosis is the main mechanism driving neuroinflammation in this disease. These types of studies will be useful to clarify whether astrocytes and/or microglia are major players in disease initiation or progression and to design therapies aiming at the modulation of the relevant glial cell types and neuroinflammatory phenotypes in the disease of interest.

15.5.5 Depression

The monoamine hypothesis of depression proposes that the underlying pathophysiological mechanisms for depression are the deficits in monoamine neurotransmitters including dopamine, norepinephrine and serotonin, which are involved in arousal, mood, motivation, and reward (Pitsillou et al. 2020). Individuals with depression have high levels of MAO-A and MAO-B in the brain. While existing therapeutic strategies have aimed mostly at inhibiting MAO-A, there is a recent interest in exploring also MAO-B as a therapeutic target in depression. The ^{11}C-SL25.1188 tracer was recently translated for in vivo human PET studies to investigate depression (Moriguchi et al. 2019). In this study, the MAO-B distribution volume (V_T) was higher in a group of 20 patients with major depressive disorder compared to an age-matched group of controls, most prominently in the prefrontal cortices, which was also positively correlated with duration of illness; other cortical regions and the thalamus also had high MAO-B expression in patients. However, more PET imaging studies with tracers for MAO-B or other relevant targets would be needed to better characterize the neuroinflammatory underpinnings of depression.

15.5.6 Evaluation of Clinical Trials of MAO-B Inhibitors

MAO-B inhibition has been investigated as a potential therapeutic approach in neurodegenerative diseases including AD and PD (Schapira et al. 2006; Thomas 2000; Youdim et al. 2006). In the context of clinical trials, PET imaging of MAO-B is a promising tool to evaluate whether MAO-B inhibitors cross the blood-brain barrier, how they distribute in the brain, and for optimization of drug dosing and to quantify trial outcomes. In clinical trials, PET scans have been performed using ^{11}C-labelled tracers, in which a scan can be repeated in the same individual before and after administration of the drug. Early studies used ^{11}C-L-deprenyl PET to find the dose of reversible MAO-B inhibitor lazabemide (Ro 19–6327) that achieved >90% inhibition of MAO-B activity in normal subjects (Bench et al. 1991). This study also showed that brain MAO-B activity was correlated with platelet MAO-B

peripherally, suggesting the potential utility of platelet MAO-B activity as a marker to monitor trial outcomes. A study using serial ^{11}C-L-deprenyl PET scans in the same individuals investigated the dynamic trajectory of MAO-B after withdrawal from treatment with MAO-B irreversible inhibitor L-deprenyl until recovery to baseline MAO-B levels (Fowler et al. 1994). The half-life of recovery to baseline levels of MAO-B was determined to be 40 days, and because the binding of L-deprenyl to MAO-B involves covalent modification of the enzyme, the 40-day half-life for recovery of brain MAO-B activity can be interpreted as a measure of how long it takes for the brain to synthesize new MAO-B molecules. From a therapeutic point of view, this slow turnover of MAO-B also indicates that a reduced dose of L-deprenyl could have a good therapeutic effect, which would avoid excessive drug use and potential associated side effects. A similar PET imaging study with ^{11}C-L-deprenyl was used to evaluate the MAO-B inhibitory effect of irreversible inhibitor rasagiline in the brain, and this study also showed a gradual recovery of brain MAO-B activity after withdrawal from drug treatment (Freedman et al. 2005).

Irreversible MAO-B inhibitor drugs have shown certain limitations, such as that in some cases the effects were short-term. Therefore, reversible MAO-B inhibitors have been explored as potential treatment for PD and more recently AD (Borroni et al. 2017). A PET study with ^{11}C-L-deprenyl-D_2 was used to find the dose of reversible MAO-B inhibitor EVT-301 that resulted in near complete occupancy of brain MAO-B (Hirvonen et al. 2009). More recently, a PET study with ^{11}C-L-deprenyl-D_2 was applied to optimize the dose of reversible inhibitor sembragiline (also known as EVT-302) leading to the maximum inhibition of brain MAO-B (Sturm et al. 2017), as shown in Fig. 15.5. Novel reversible MAO-B inhibitors are being further investigated as potential treatments for AD (Park et al. 2019).

15.6 Conclusions and Future Prospects

PET studies of brain MAO-B in healthy volunteers and in patients with different brain disorders have evolved over the past ~30 years since the first MAO-B specific radiotracers were developed and investigated in preclinical and clinical studies. Different factors such as age, smoking, or depressive symptoms have been found to affect the levels of MAO-B in the brain. While the available radiotracers reviewed in this chapter have shown many properties that make them suitable for MAO-B quantification, radiochemists continue to develop novel radiotracers with improved properties, especially focusing on reversible radiotracers and more recently fluorine-18-labelled compounds for more widespread clinical application in centers without on-site cyclotron.

Many scientific questions remain to be investigated using in vivo and in vitro studies. Translational in vitro studies combining autoradiography and immunohistochemical analyses are critically needed to determine exactly what the MAO-B tracers are binding to and their relationship to other pathological markers such as amyloid-β and tau. In particular, there is a paucity of antemortem/postmortem

Fig. 15.5 Illustration of MAO-B inhibition in the brain following treatment with 1 mg sembragiline once a day for 2 weeks, as visualized using ^{11}C-L-deprenyl-D$_2$ PET before treatment (baseline PET) and after treatment (post-dose PET). *SUV* standardized uptake value. Reprinted from Sturm et al. (2017), under the terms of the Creative Commons CC BY license
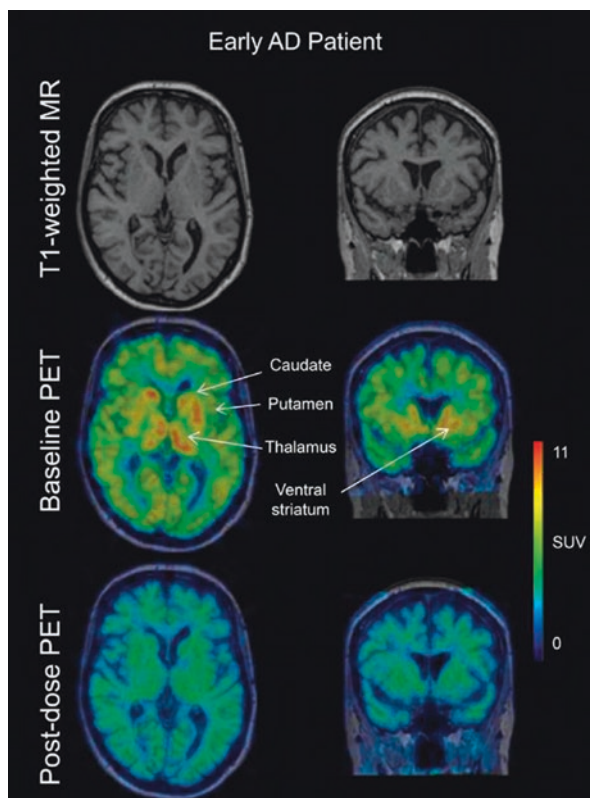
investigations, which would be highly informative to further validate the in vivo findings and understand what the MAO-B PET signal means biologically. Multimodal and multitracer MRI-PET imaging approaches have provided unique information on the comparative regional and temporal patterns of in vivo brain astrocytosis, amyloid-β deposition, glucose metabolism, and brain structure. There are still very few in vivo longitudinal studies with MAO-B PET tracers, or to investigate the relationships between astrocytosis and microgliosis by either imaging or using glial markers in the plasma or CSF (e.g., GFAP as a biofluid marker of astrocytosis). Given the heterogeneity of the astrocytic response, there is a need to develop novel PET radiotracers specifically targeting the multiple biological changes associated with astrocytosis. Along these lines, future translational MRI-PET imaging investigations in combination with fluid biomarkers will be needed to advance the understanding of glial cells as therapeutic targets, with a view toward clinical applications.

Disclosure: The author declares that she has no competing interests.

References

Albrecht DS, Granziera C, Hooker JM, Loggia ML (2016) In vivo imaging of human Neuroinflammation. ACS Chem Neurosci 7(4):470–483. https://doi.org/10.1021/acschemneuro.6b00056

Albrecht DS, Forsberg A, Sandstrom A, Bergan C, Kadetoff D, Protsenko E et al (2019) Brain glial activation in fibromyalgia - A multi-site positron emission tomography investigation. Brain Behav Immun 75:72–83. https://doi.org/10.1016/j.bbi.2018.09.018

Arakawa R, Stenkrona P, Takano A, Nag S, Maior RS, Halldin C (2017) Test-retest reproducibility of [(11)C]-L-deprenyl-D2 binding to MAO-B in the human brain. EJNMMI Res 7(1):54. https://doi.org/10.1186/s13550-017-0301-4

Arranz AM, De Strooper B (2019) The role of astroglia in Alzheimer's disease: pathophysiology and clinical implications. Lancet Neurol 18(4):406–414. https://doi.org/10.1016/S1474-4422(18)30490-3

Bench CJ, Price GW, Lammertsma AA, Cremer JC, Luthra SK, Turton D et al (1991) Measurement of human cerebral monoamine oxidase type B (MAO-B) activity with positron emission tomography (PET): a dose ranging study with the reversible inhibitor Ro 19-6327. Eur J Clin Pharmacol 40(2):169–173. https://doi.org/10.1007/bf00280072

Bergström M, Kumlien E, Lilja A, Tyrefors N, Westerberg G, Langstrom B (1998) Temporal lobe epilepsy visualized with PET with 11C-L-deuterium-deprenyl—Analysis of kinetic data. Acta Neurol Scand 98(4):224–231. https://doi.org/10.1111/j.1600-0404.1998.tb07300.x

Boche D, Gerhard A, Rodriguez-Vieitez E, Faculty M (2019) Prospects and challenges of imaging neuroinflammation beyond TSPO in Alzheimer's disease. Eur J Nucl Med Mol Imaging 46(13):2831–2847. https://doi.org/10.1007/s00259-019-04462-w

Borroni E, Bohrmann B, Grueninger F, Prinssen E, Nave S, Loetscher H et al (2017) Sembragiline: a novel, selective monoamine oxidase type B inhibitor for the treatment of Alzheimer's disease. J Pharmacol Exp Ther 362(3):413–423. https://doi.org/10.1124/jpet.117.241653

Carter SF, Scholl M, Almkvist O, Wall A, Engler H, Langstrom B et al (2012) Evidence for astrocytosis in prodromal Alzheimer disease provided by 11C-deuterium-L-deprenyl: a multitracer PET paradigm combining 11C-Pittsburgh compound B and 18F-FDG. J Nucl Med 53(1):37–46. https://doi.org/10.2967/jnumed.110.087031

Carter SF, Chiotis K, Nordberg A, Rodriguez-Vieitez E (2019a) Longitudinal association between astrocyte function and glucose metabolism in autosomal dominant Alzheimer's disease. Eur J Nucl Med Mol Imaging 46(2):348–356. https://doi.org/10.1007/s00259-018-4217-7

Carter SF, Herholz K, Rosa-Neto P, Pellerin L, Nordberg A, Zimmer ER (2019b) Astrocyte biomarkers in Alzheimer's disease. Trends Mol Med 25(2):77–95. https://doi.org/10.1016/j.molmed.2018.11.006

Chamoli M, Chinta SJ, Andersen JK (2018) An inducible MAO-B mouse model of Parkinson's disease: a tool towards better understanding basic disease mechanisms and developing novel therapeutics. J Neural Transm (Vienna) 125(11):1651–1658. https://doi.org/10.1007/s00702-018-1887-z

Dahl K, Bernard-Gauthier V, Nag S, Varnas K, Narayanaswami V, Mahdi Moein M et al (2019) Synthesis and preclinical evaluation of [(18)F]FSL25.1188, a reversible PET radioligand for monoamine oxidase-B. Bioorg Med Chem Lett 29(13):1624–1627. https://doi.org/10.1016/j.bmcl.2019.04.040

De Strooper B, Karran E (2016) The cellular phase of Alzheimer's disease. Cell 164(4):603–615. https://doi.org/10.1016/j.cell.2015.12.056

Drake LR, Brooks AF, Mufarreh AJ, Pham JM, Koeppe RA, Shao X et al (2018) Deuterium kinetic isotope effect studies of a potential in vivo metabolic trapping agent for monoamine oxidase B. ACS Chem Neurosci 9(12):3024–3027. https://doi.org/10.1021/acschemneuro.8b00219

Ekblom J, Jossan SS, Bergstrom M, Oreland L, Walum E, Aquilonius SM (1993) Monoamine oxidase-B in astrocytes. Glia 8(2):122–132. https://doi.org/10.1002/glia.440080208

Ekblom J, Jossan SS, Oreland L, Walum E, Aquilonius SM (1994) Reactive gliosis and monoamine oxidase B. J Neural Transm Suppl 41:253–258

Engler H, Lundberg PO, Ekbom K, Nennesmo I, Nilsson A, Bergstrom M et al (2003) Multitracer study with positron emission tomography in Creutzfeldt-Jakob disease. Eur J Nucl Med Mol Imaging 30(1):85–95. https://doi.org/10.1007/s00259-002-1008-x

Engler H, Nennesmo I, Kumlien E, Gambini JP, Lundberg P, Savitcheva I et al (2012) Imaging astrocytosis with PET in Creutzfeldt-Jakob disease: case report with histopathological findings. Int J Clin Exp Med 5(2):201–207

Fowler JS, MacGregor RR, Wolf AP, Arnett CD, Dewey SL, Schlyer D et al (1987) Mapping human brain monoamine oxidase A and B with 11C-labeled suicide inactivators and PET. Science 235(4787):481–485

Fowler JS, Wolf AP, MacGregor RR, Dewey SL, Logan J, Schlyer DJ et al (1988) Mechanistic positron emission tomography studies: demonstration of a deuterium isotope effect in the monoamine oxidase-catalyzed binding of [11C]L-deprenyl in living baboon brain. J Neurochem 51(5):1524–1534. https://doi.org/10.1111/j.1471-4159.1988.tb01121.x

Fowler JS, Volkow ND, Logan J, Wang GJ, MacGregor RR, Schyler D et al (1994) Slow recovery of human brain MAO B after L-deprenyl (Selegeline) withdrawal. Synapse 18(2):86–93. https://doi.org/10.1002/syn.890180203

Fowler JS, Wang GJ, Logan J, Xie S, Volkow ND, MacGregor RR et al (1995) Selective reduction of radiotracer trapping by deuterium substitution: comparison of carbon-11-L-deprenyl and carbon-11-deprenyl-D2 for MAO B mapping. J Nucl Med 36(7):1255–1262

Fowler JS, Volkow ND, Wang GJ, Pappas N, Logan J, MacGregor R et al (1996) Inhibition of monoamine oxidase B in the brains of smokers. Nature 379(6567):733–736. https://doi.org/10.1038/379733a0

Fowler JS, Volkow ND, Wang GJ, Logan J, Pappas N, Shea C et al (1997) Age-related increases in brain monoamine oxidase B in living healthy human subjects. Neurobiol Aging 18(4):431–435. https://doi.org/10.1016/s0197-4580(97)00037-7

Fowler JS, Logan J, Wang GJ, Volkow ND (2003) Monoamine oxidase and cigarette smoking. Neurotoxicology 24(1):75–82. https://doi.org/10.1016/s0161-813x(02)00109-2

Fowler JS, Logan J, Volkow ND, Wang GJ (2005) Translational neuroimaging: positron emission tomography studies of monoamine oxidase. Mol Imaging Biol 7(6):377–387. https://doi.org/10.1007/s11307-005-0016-1

Fowler JS, Logan J, Shumay E, Alia-Klein N, Wang GJ, Volkow ND (2015) Monoamine oxidase: radiotracer chemistry and human studies. J Labelled Comp Radiopharm 58(3):51–64. https://doi.org/10.1002/jlcr.3247

Freedman NM, Mishani E, Krausz Y, Weininger J, Lester H, Blaugrund E et al (2005) In vivo measurement of brain monoamine oxidase B occupancy by rasagiline, using (11)C-l-deprenyl and PET. J Nucl Med 46(10):1618–1624

Gulyas B, Pavlova E, Kasa P, Gulya K, Bakota L, Varszegi S et al (2011) Activated MAO-B in the brain of Alzheimer patients, demonstrated by [11C]-L-deprenyl using whole hemisphere autoradiography. Neurochem Int 58(1):60–68. https://doi.org/10.1016/j.neuint.2010.10.013

Hirvonen J, Kailajarvi M, Haltia T, Koskimies S, Nagren K, Virsu P et al (2009) Assessment of MAO-B occupancy in the brain with PET and [11C]-L-deprenyl-D2: a dose-finding study with a novel MAO-B inhibitor, EVT 301. Clin Pharmacol Ther 85(5):506–512. https://doi.org/10.1038/clpt.2008.241

Jo S, Yarishkin O, Hwang YJ, Chun YE, Park M, Woo DH et al (2014) GABA from reactive astrocytes impairs memory in mouse models of Alzheimer's disease. Nat Med 20(8):886–896. https://doi.org/10.1038/nm.3639

Johansson A, Engler H, Blomquist G, Scott B, Wall A, Aquilonius SM et al (2007) Evidence for astrocytosis in ALS demonstrated by [11C](L)-deprenyl-D2 PET. J Neurol Sci 255(1–2):17–22. https://doi.org/10.1016/j.jns.2007.01.057

Jossan SS, d'Argy R, Gillberg PG, Aquilonius SM, Langstrom B, Halldin C et al (1989) Localization of monoamine oxidase B in human brain by autoradiographical use of 11C-labelled L-deprenyl. J Neural Transm 77(1):55–64. https://doi.org/10.1007/bf01255819

Jossan SS, Gillberg PG, Gottfries CG, Karlsson I, Oreland L (1991) Monoamine oxidase B in brains from patients with Alzheimer's disease: a biochemical and autoradiographical study. Neuroscience 45(1):1–12. https://doi.org/10.1016/0306-4522(91)90098-9

Jossan SS, Ekblom J, Aquilonius SM, Oreland L (1994) Monoamine oxidase-B in motor cortex and spinal cord in amyotrophic lateral sclerosis studied by quantitative autoradiography. J Neural Transm Suppl 41:243–248

Lammertsma AA, Bench CJ, Price GW, Cremer JE, Luthra SK, Turton D et al (1991) Measurement of cerebral monoamine oxidase B activity using L-[11C]deprenyl and dynamic positron emission tomography. J Cereb Blood Flow Metab 11(4):545–556. https://doi.org/10.1038/jcbfm.1991.103

Lemoine L, Saint-Aubert L, Nennesmo I, Gillberg PG, Nordberg A (2017) Cortical laminar tau deposits and activated astrocytes in Alzheimer's disease visualised by 3H-THK5117 and 3H-deprenyl autoradiography. Sci Rep 7:45496. https://doi.org/10.1038/srep45496

Lemoine L, Leuzy A, Chiotis K, Rodriguez-Vieitez E, Nordberg A (2018) Tau positron emission tomography imaging in tauopathies: the added hurdle of off-target binding. Alzheimers Dement (Amst) 10:232–236. https://doi.org/10.1016/j.dadm.2018.01.007

Levitt P, Pintar JE, Breakefield XO (1982) Immunocytochemical demonstration of monoamine oxidase B in brain astrocytes and serotonergic neurons. Proc Natl Acad Sci U S A 79(20):6385–6389

Logan J (2000) Graphical analysis of PET data applied to reversible and irreversible tracers. Nucl Med Biol 27(7):661–670. https://doi.org/10.1016/s0969-8051(00)00137-2

Logan J, Fowler JS, Volkow ND, Wang GJ, MacGregor RR, Shea C (2000) Reproducibility of repeated measures of deuterium substituted [11C]L-deprenyl ([11C]L-deprenyl-D2) binding in the human brain. Nucl Med Biol 27(1):43–49. https://doi.org/10.1016/s0969-8051(99)00088-8

MacGregor RR, Halldin C, Fowler JS, Wolf AP, Arnett CD, Langstrom B et al (1985) Selective, irreversible in vivo binding of [11C]clorgyline and [11C]-L-deprenyl in mice: potential for measurement of functional monoamine oxidase activity in brain using positron emission tomography. Biochem Pharmacol 34(17):3207–3210. https://doi.org/10.1016/0006-2952(85)90173-x

Mallajosyula JK, Kaur D, Chinta SJ, Rajagopalan S, Rane A, Nicholls DG et al (2008) MAO-B elevation in mouse brain astrocytes results in Parkinson's pathology. PLoS One 3(2):e1616. https://doi.org/10.1371/journal.pone.0001616

Marutle A, Gillberg PG, Bergfors A, Yu W, Ni R, Nennesmo I et al (2013) (3)H-deprenyl and (3)H-PIB autoradiography show different laminar distributions of astroglia and fibrillar beta-amyloid in Alzheimer brain. J Neuroinflammation 10:–90. https://doi.org/10.1186/1742-2094-10-90

Moriguchi S, Wilson AA, Miler L, Rusjan PM, Vasdev N, Kish SJ et al (2019) Monoamine oxidase B Total distribution volume in the prefrontal cortex of major depressive disorder: an [11C]SL25.1188 positron emission tomography study. JAMA Psychiat 76(6):634–641. https://doi.org/10.1001/jamapsychiatry.2019.0044

Murugan NA, Chiotis K, Rodriguez-Vieitez E, Lemoine L, Agren H, Nordberg A (2019) Cross-interaction of tau PET tracers with monoamine oxidase B: evidence from in silico modelling and in vivo imaging. Eur J Nucl Med Mol Imaging 46(6):1369–1382. https://doi.org/10.1007/s00259-019-04305-8

Nag S, Lehmann L, Heinrich T, Thiele A, Kettschau G, Nakao R et al (2011) Synthesis of three novel fluorine-18 labeled analogues of L-deprenyl for positron emission tomography (PET) studies of monoamine oxidase B (MAO-B). J Med Chem 54(20):7023–7029. https://doi.org/10.1021/jm200710b

Nag S, Lehmann L, Kettschau G, Heinrich T, Thiele A, Varrone A et al (2012a) Synthesis and evaluation of [(1)(8)F]fluororasagiline, a novel positron emission tomography (PET) radioligand for monoamine oxidase B (MAO-B). Bioorg Med Chem 20(9):3065–3071. https://doi.org/10.1016/j.bmc.2012.02.056

Nag S, Varrone A, Toth M, Thiele A, Kettschau G, Heinrich T et al (2012b) In vivo evaluation in cynomolgus monkey brain and metabolism of [(1)(8)F]fluorodeprenyl: a new MAO-B pet radioligand. Synapse 66(4):323–330. https://doi.org/10.1002/syn.21514

Nag S, Lehmann L, Kettschau G, Toth M, Heinrich T, Thiele A et al (2013) Development of a novel fluorine-18 labeled deuterated fluororasagiline ([(18)F]fluororasagiline-D2) radioligand for PET studies of monoamino oxidase B (MAO-B). Bioorg Med Chem 21(21):6634–6641. https://doi.org/10.1016/j.bmc.2013.08.019

Nag S, Fazio P, Lehmann L, Kettschau G, Heinrich T, Thiele A et al (2016) In vivo and in vitro characterization of a novel MAO-B inhibitor radioligand, 18F-labeled deuterated fluorodeprenyl. J Nucl Med 57(2):315–320. https://doi.org/10.2967/jnumed.115.161083

Narayanaswami V, Dahl K, Bernard-Gauthier V, Josephson L, Cumming P, Vasdev N (2018) Emerging PET radiotracers and targets for imaging of neuroinflammation in neurodegenerative diseases: outlook beyond TSPO. Mol Imaging 17:1536012118792317. https://doi.org/10.1177/1536012118792317

Narayanaswami V, Drake LR, Brooks AF, Meyer JH, Houle S, Kilbourn MR et al (2019) Classics in neuroimaging: development of PET tracers for imaging monoamine oxidases. ACS Chem Neurosci 10(4):1867–1871. https://doi.org/10.1021/acschemneuro.9b00081

Olsen M, Aguilar X, Sehlin D, Fang XT, Antoni G, Erlandsson A et al (2018) Astroglial responses to amyloid-Beta progression in a mouse model of Alzheimer's disease. Mol Imaging Biol 20(4):605–614. https://doi.org/10.1007/s11307-017-1153-z

Park JH, Ju YH, Choi JW, Song HJ, Jang BK, Woo J et al (2019) Newly developed reversible MAO-B inhibitor circumvents the shortcomings of irreversible inhibitors in Alzheimer's disease. Sci Adv 5(3):eaav0316. https://doi.org/10.1126/sciadv.aav0316

Patlak CS, Blasberg RG (1985) Graphical evaluation of blood-to-brain transfer constants from multiple-time uptake data. Generalizations J Cereb Blood Flow Metab 5(4):584–590. https://doi.org/10.1038/jcbfm.1985.87

Pitsillou E, Bresnehan SM, Kagarakis EA, Wijoyo SJ, Liang J, Hung A et al (2020) The cellular and molecular basis of major depressive disorder: towards a unified model for understanding clinical depression. Mol Biol Rep 47(1):753–770. https://doi.org/10.1007/s11033-019-05129-3

Ramsay RR (2016) Molecular aspects of monoamine oxidase B. Prog Neuro-Psychopharmacol Biol Psychiatry 69:81–89. https://doi.org/10.1016/j.pnpbp.2016.02.005

Rodriguez-Vieitez E, Nordberg A (2018) Imaging neuroinflammation: quantification of astrocytosis in a multitracer PET approach. Methods Mol Biol 1750:231–251. https://doi.org/10.1007/978-1-4939-7704-8_16

Rodriguez-Vieitez E, Ni R, Gulyas B, Toth M, Haggkvist J, Halldin C et al (2015) Astrocytosis precedes amyloid plaque deposition in Alzheimer APPswe transgenic mouse brain: a correlative positron emission tomography and in vitro imaging study. Eur J Nucl Med Mol Imaging 42(7):1119–1132. https://doi.org/10.1007/s00259-015-3047-0

Rodriguez-Vieitez E, Carter SF, Chiotis K, Saint-Aubert L, Leuzy A, Scholl M et al (2016a) Comparison of early-phase 11C-deuterium-l-deprenyl and 11C-Pittsburgh compound B PET for assessing brain perfusion in Alzheimer disease. J Nucl Med 57(7):1071–1077. https://doi.org/10.2967/jnumed.115.168732

Rodriguez-Vieitez E, Saint-Aubert L, Carter SF, Almkvist O, Farid K, Scholl M et al (2016b) Diverging longitudinal changes in astrocytosis and amyloid PET in autosomal dominant Alzheimer's disease. Brain 139(Pt 3):922–936. https://doi.org/10.1093/brain/awv404

Rusjan PM, Wilson AA, Miler L, Fan I, Mizrahi R, Houle S et al (2014) Kinetic modeling of the monoamine oxidase B radioligand [(1)(1)C]SL25.1188 in human brain with high-resolution positron emission tomography. J Cereb Blood Flow Metab 34(5):883–889. https://doi.org/10.1038/jcbfm.2014.34

Saba W, Valette H, Peyronneau MA, Bramoulle Y, Coulon C, Curet O et al (2010) [(11)C]SL25.1188, a new reversible radioligand to study the monoamine oxidase type B with PET: preclinical characterisation in nonhuman primate. Synapse 64(1):61–69. https://doi.org/10.1002/syn.20703

Saura J, Luque JM, Cesura AM, Da Prada M, Chan-Palay V, Huber G et al (1994) Increased monoamine oxidase B activity in plaque-associated astrocytes of Alzheimer brains revealed by quantitative enzyme radioautography. Neuroscience 62(1):15–30

Saura J, Bleuel Z, Ulrich J, Mendelowitsch A, Chen K, Shih JC et al (1996) Molecular neuroanatomy of human monoamine oxidases A and B revealed by quantitative enzyme radioautography and in situ hybridization histochemistry. Neuroscience 70(3):755–774. https://doi.org/10.1016/s0306-4522(96)83013-2

Saura J, Andres N, Andrade C, Ojuel J, Eriksson K, Mahy N (1997) Biphasic and region-specific MAO-B response to aging in normal human brain. Neurobiol Aging 18(5):497–507. https://doi.org/10.1016/s0197-4580(97)00113-9

Schapira AH, Bezard E, Brotchie J, Calon F, Collingridge GL, Ferger B et al (2006) Novel pharmacological targets for the treatment of Parkinson's disease. Nat Rev Drug Discov 5(10):845–854. https://doi.org/10.1038/nrd2087

Schedin-Weiss S, Inoue M, Hromadkova L, Teranishi Y, Yamamoto NG, Wiehager B et al (2017) Monoamine oxidase B is elevated in Alzheimer disease neurons, is associated with gamma-secretase and regulates neuronal amyloid beta-peptide levels. Alzheimers Res Ther 9(1):57. https://doi.org/10.1186/s13195-017-0279-1

Schöll M, Carter SF, Westman E, Rodriguez-Vieitez E, Almkvist O, Thordardottir S et al (2015) Early astrocytosis in autosomal dominant Alzheimer's disease measured in vivo by multi-tracer positron emission tomography. Sci Rep 5:16404. https://doi.org/10.1038/srep16404

Schott JM, Fox NC (2016) Inflammatory changes in very early Alzheimer's disease: friend, foe, or don't know? Brain 139(Pt 3):647–650. https://doi.org/10.1093/brain/awv405

Siddiqui A, Mallajosyula JK, Rane A, Andersen JK (2011) Ability to delay neuropathological events associated with astrocytic MAO-B increase in a parkinsonian mouse model: implications for early intervention on disease progression. Neurobiol Dis 43(2):527–532. https://doi.org/10.1016/j.nbd.2010.12.014

Sturm S, Forsberg A, Nave S, Stenkrona P, Seneca N, Varrone A et al (2017) Positron emission tomography measurement of brain MAO-B inhibition in patients with Alzheimer's disease and elderly controls after oral administration of sembragiline. Eur J Nucl Med Mol Imaging 44(3):382–391. https://doi.org/10.1007/s00259-016-3510-6

Thomas T (2000) Monoamine oxidase-B inhibitors in the treatment of Alzheimer's disease. Neurobiol Aging 21(2):343–348. https://doi.org/10.1016/s0197-4580(00)00100-7

Tong J, Meyer JH, Furukawa Y, Boileau I, Chang LJ, Wilson AA et al (2013) Distribution of monoamine oxidase proteins in human brain: implications for brain imaging studies. J Cereb Blood Flow Metab 33(6):863–871. https://doi.org/10.1038/jcbfm.2013.19

Tong J, Rathitharan G, Meyer JH, Furukawa Y, Ang LC, Boileau I et al (2017) Brain monoamine oxidase B and A in human parkinsonian dopamine deficiency disorders. Brain 140(9):2460–2474. https://doi.org/10.1093/brain/awx172

Varrone A, Nordberg A (2015) Molecular imaging of neuroinflammation in Alzheimer's disease. Clin Transl Imaging 3:437–447

Vasdev N, Sadovski O, Moran MD, Parkes J, Meyer JH, Houle S et al (2011) Development of new radiopharmaceuticals for imaging monoamine oxidase B. Nucl Med Biol 38(7):933–943. https://doi.org/10.1016/j.nucmedbio.2011.03.003

Vilaplana E, Rodriguez-Vieitez E, Ferreira D, Montal V, Almkvist O, Wall A et al (2020) Cortical microstructural correlates of astrocytosis in autosomal dominant Alzheimer disease. Neurology 94:e2026. https://doi.org/10.1212/WNL.0000000000009405

Youdim MB, Edmondson D, Tipton KF (2006) The therapeutic potential of monoamine oxidase inhibitors. Nat Rev Neurosci 7(4):295–309. https://doi.org/10.1038/nrn1883

Attempts to Image MRP1 Function in the Blood-Brain Barrier Using the Metabolite Extrusion Method

16

Toshimitsu Okamura, Tatsuya Kikuchi, and Ming-Rong Zhang

Contents

Abstract

Multidrug resistance-associated protein 1 (MRP1) is a member of the adenosine triphosphate-binding cassette superfamily of transporters and plays an important role in limiting the permeation of xenobiotics and exporting endogenous sub-

T. Okamura (✉) · T. Kikuchi · M.-R. Zhang
National Institute of Radiological Sciences, National Institutes for Quantum and Radiological Science and Technology, Chiba, Japan
e-mail: okamura.toshimitsu@qst.go.jp; kikuchi.tatsuya@qst.go.jp; zhang.ming-rong@qst.go.jp

547

stances across the blood-brain and blood-cerebrospinal fluid barriers and across brain parenchymal cells in the central nervous system. In addition to multidrug resistance, changes in activity or expression of cerebral MRP1 occur in several brain diseases. Therefore, noninvasive and quantitative assessment of MRP1 activity in the brain is valuable for investigating the changes in MRP1 related to brain diseases, toward an understanding of the underlying molecular mechanisms. In this chapter, we will focus on 6-bromo-7-[^{11}C]methylpurine for imaging MRP1 activity, as well as the concept of the metabolite extrusion method (MEM) for measuring efflux transporter activity. Several positron emission tomography (PET) and single-photon emission computed tomography (SPECT) imaging studies of MRPs activity are also reviewed. Finally, we discuss our recent findings regarding the contribution of Mrp1 in brain parenchymal cells to tracer efflux and the sensitivity of 6-bromo-7-[^{11}C]methylpurine for measuring MRP1 activity.

Abbreviations

[^{18}F]FEP-4MA	*N*-[^{18}F]Fluoroethylpiperidin-4ylmethyl acetate
15*R*-[^{11}C]TIC-Me	(15*R*)-16-m-[^{11}C]tolyl-17,18,19,20-tetranorisocarbacyclin methyl ester
^{99m}Tc-ECD	*N*,*N*′-1,2-ethylenediylbis-L-cysteine diethyl ester
^{99m}Tc-HIDA	^{99m}Tc-*N*-(2,6-dimethylphenylcarbamoylmethyl)-iminodiacetic acid
^{99m}Tc-MIBI	^{99m}Tc-hexakis-2-methoxyisobutylisonitrile
ABC	Adenosine triphosphate-binding cassette
BBB	Blood-brain barrier
BCECs	Brain capillary endothelial cells
BEI	Brain efflux index
GSH	Glutathione
GSTs	Glutathione *S*-transferases
ICI	Intracerebral injection
ID	Injected dose
LT	Leukotriene
MDR	Multidrug resistance
MEM	Metabolite extrusion method
MRP	Multidrug resistance-associated protein
OAT3	Organic anion transporter 3
PET	Positron emission tomography
SPECT	Single-photon emission computed tomography
WT	Wild type

16.1 Introduction

Multidrug resistance-associated protein 1 (MRP1), also denoted as ABCC1, is a member of the adenosine triphosphate-binding cassette (ABC) superfamily of transporters and transports a wide range of compounds, including xenobiotics and physiological substances, from cells in an energy-dependent manner (Bakos and Homolya 2007; Cole et al. 1992). The significance of MRP1 in human health and disease has been accepted, and the preclinical and clinical interest has increased, primarily because of its extraordinary transport properties. In the central nervous system, MRP1 is expressed at the blood-brain barrier (BBB) and blood-cerebrospinal fluid barrier (Dallas et al. 2006). In addition to multidrug resistance (MDR) (Loscher and Potschka 2005; Leslie et al. 2005), changes in activity or expression of cerebral MRP1 occur in several brain diseases (Qosa et al. 2015; Krohn et al. 2015; Krohn et al. 2011). In the adult and the developing human brain, MRP1 is also expressed in nonendothelial cells such as astrocytes and neurons (Bernstein et al. 2014; Daood et al. 2008).

Furthermore, a recent meta-analysis suggested that MRP1 is overexpressed in neurons and astrocytes of intractable epilepsy patients (Sun et al. 2016). Moreover, MRP1 expression was increased in samples from traumatic brain injury patients compared with controls, while cells with the morphological appearance of neurons or astrocytes are MRP1-immunoreactive (Willyerd et al. 2016). Therefore, noninvasive and quantitative assessment of MRP1 activity in the brain is valuable for investigating changes in MRP1 related to brain diseases, toward an understanding of the underlying molecular mechanisms.

Here, we will focus on 6-bromo-7-[^{11}C]methylpurine for imaging of MRP1 activity and the concept of the metabolite extrusion method (MEM) for measuring the activity of an efflux transporter. Several studies which imaged the activity of MRPs, including MRP1, MRP2, and MRP4, using PET and SPECT are also reviewed. Finally, we discuss our recent findings suggesting that Mrp1 in brain parenchymal cells, but not at the BBB, may contribute to the efflux of the glutathione (GSH) conjugate of 6-bromo-7-[^{11}C]methylpurine from the brain and the sensitivity of 6-bromo-7-[^{11}C]methylpurine for measuring MRP1 activity.
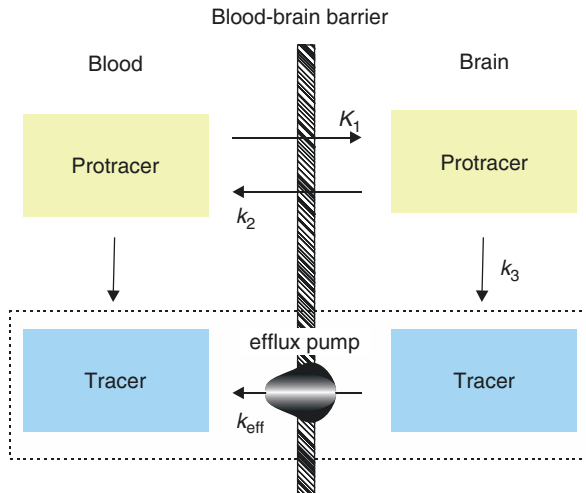
16.2 Metabolite Extrusion Method (MEM)

16.2.1 Concept of the MEM

The blood-brain barrier (BBB) consists of a monolayer of brain capillary endothelial cells (BCECs) and limits the entry of large or hydrophilic substances into the brain, except for nutrients such as amino acids and glucose (Pardridge 1998; Bradbury 1993; Reese and Karnovsky 1967). For assessment of efflux transporter activity, it would thus be challenging to deliver radiolabeled hydrophilic substrates into the brain via intravenous administration. One of the methods to overcome this problem is intracerebral injection (Cserr and Berman 1978) or the brain efflux index

(BEI) (Kakee et al. 1996; Kusuhara et al. 2003). In the BEI, a radiolabeled substrate is microinjected into the brain, and elimination of the substrate from the brain is measured over time. The efflux rate can then be determined from the slope of a semilogarithmic plot of the percentage of the substrate remaining in the brain against time. Apart from the disadvantage of invasiveness, the BEI provides an ideal situation where the decrease in brain radioactivity depends on the clearance of a single radioactive substrate.

The MEM is a method for the noninvasive measurement of efflux transporter activity (not limited to MRP1) and provides the same situation as the BEI without intracerebral injection (Kikuchi et al. 2016; Okamura et al. 2010; Okamura et al. 2009a; Okamura et al. 2007). In this chapter, we use the term "protracer" to denote the radiolabeled lipophilic compound for the delivery of a radiolabeled hydrophilic substrate for an efflux transporter into the brain, while we use the term "tracer" to denote a radiolabeled hydrophilic substrate resulting from the brain metabolism of the protracer, where the tracer provides information regarding the activity of an efflux transporter. To clearly distinguish an MEM tracer from a non-MEM tracer such as [^{11}C]verapamil or [^{11}C]loperamide, we also use the term "probe" to denote a non-MEM radiolabeled compound for imaging an efflux transporter. The schematic explanation for the MEM is shown in Fig. 16.1. A protracer in the blood enters the brain through the BBB after intravenous administration. The protracer in the brain diffuses back into the blood and also becomes converted into a tracer that

Fig. 16.1 Diagrammatic representation of the metabolite extrusion method (MEM). The terms of "protracer" and "tracer" are defined in Sect. 16.2.1. A protracer readily enters the brain after intravenous administration and undergoes rapid conversion into a tracer. After the protracer has been completely converted into the tracer, the time course of radioactivity in the brain can be considered one-tissue compartment model inside the dotted box. K_1 and k_2 represent the transport rate constants of the protracer across the BBB, while k_3 denotes the conversion rate of the protracer into the tracer, and k_{eff} shows the efflux rate of the tracer from the brain to the blood

is then eliminated by an efflux transporter of interest. The decreased brain radioactivity after the disappearance of the protracer can be considered the elimination of the tracer from the brain. Thus, the efflux rate (k_{eff}) of the tracer can be noninvasively determined from the time course of brain radioactivity.

In the MEM, the conversion rate of a protracer to a tracer (hydrophilic substrate) is crucial for measuring the activity of an efflux transporter of interest. If the conversion rate is slow, the complete disappearance of the protracer is delayed, resulting in the low concentration of the tracer in the brain. These issues may compromise the accurate measurement of the efflux rate.

16.2.2 Design of a Protracer and Tracer for Imaging MRP1 Activity

To obtain an accurate measurement of k_{eff} by the MEM, a protracer should meet the following criteria: (1) high extraction to the brain tissue from the blood and (2) rapid conversion into a tracer ($k_2 << k_3$). Moreover, an easily modified protracer platform is desirable for introducing a lipophilic group, radiolabeling, and adjusting the conversion rate for application to different species including humans. In addition, if the tracer satisfies the kinetic condition of $k_{eff} << (k_2 + k_3)$ (see below), the MEM provides a monoexponential curve of the tracer after a short lag time, thereby allowing the simple measurement of k_{eff}.

In the two-tissue compartment model, the measured brain concentration (Cb) is equal to the integral of the arterial plasma input curve (input function) convolved with a term called the tissue impulse response function (R):

$$Cb(t) = \text{Input Function} \otimes R(t)$$

In the MEM, however, an efflux rate is determined from the time-activity curve following the conversion of a protracer to a tracer, and the input function can thus be considered a constant value. As described in a previous review (Okamura et al. 2010), the response function (R) with respect to time (t) is given by:

$$R(t) = Ae^{-(k_2 + k_3)t} + Be^{-k_{eff}t}$$

$$A = \frac{k_2 - k_{eff}}{k_2 + k_3 - k_{eff}}, \quad B = \frac{k_3}{k_2 + k_3 - k_{eff}}$$

where k_2 and k_3 are the rate parameters describing the diffusional transport of a protracer through the BBB and the conversion of a protracer to a tracer, respectively, and k_{eff} (an index of the activity of an efflux transporter) is the parameter describing the rate of the tracer clearance from the brain by an efflux transporter. The condition $k_{eff} << (k_2 + k_3)$ is required to obtain a monoexponential curve of a tracer after a short lag time.

Based on these requirements, we describe the design of a protracer and tracer for imaging of MRP1 activity. The substrates of MRP1 comprise many lipophilic compounds, conjugated organic anions, and nonconjugated organic

anions, and typical substrates include GSH, glucuronate, and sulfate conjugates (Bakos and Homolya 2007). Initially, we selected GSH conjugates as a candidate tracer, although glucuronide or sulfate conjugates may be candidates. According to the requirements mentioned above, a protracer should be efficiently converted to a tracer (a GSH conjugate). Since 6-chloropurine is converted to *S*-(6-purinyl)glutathione by hepatic and renal glutathione *S*-transferases (GSTs) (Hwang and Elfarra 1993), 6-chloropurine was selected as the basic skeleton of the protracer. Then, 6-chloropurine was methylated with [14C]methyl iodide, providing the two candidate protracers, 6-chloro-9-[14C]methylpurine and 6-chloro-7-[14C]methylpurine. The reaction rate (in vitro k_3) of 6-chloro-7-[14C]methylpurine with GSH in rat brain homogenates was much higher than that of 6-chloro-9-[14C]methylpurine (Okamura et al. 2007). The difference in the reaction rate between these candidate protracers unambiguously accounted for a fraction of each protracer remaining in the in vivo brain. 6-Chloro-9-[14C]methylpurine did not satisfy the requirements as a protracer, whereas 6-chloro-7-[14C]methylpurine was a promising protracer. The GSH conjugate of 6-chloro-7-methylpurine, *S*-(7-methylpurin-6-yl)glutathione, was shown to be a substrate for MRP1 in vitro (Okamura et al. 2007). Replacement of chlorine by bromine in the 6-chloro-7-[14C]methylpurine increased the reaction rate with GSH in mouse brain homogenates (Okamura et al. 2009b). We thus evaluated 6-bromo-7-methylpurine as a protracer for imaging of MRP1 activity in the brain (Okamura et al. 2009c). The structure of 6-bromo-7-[11C]methylpurine is shown in Fig. 16.2.

16.2.3 Imaging of MRP1 Activity in the Brain Using 6-Bromo-7-[11C]Methylpurine

The protracer 6-bromo-7-[11C]methylpurine showed high uptake in the brain of wild-type (WT) and *Mrp1*−/− mice 1.5 min after intravenous administration (approximately 6% injected dose/g) and then a rapid decrease in the brain radioactivity. After intravenous administration, 6-bromo-7-[14C]methylpurine was converted to its GSH conjugate in the brains of WT and *Mrp1*−/− mice by 15 min, and therefore, the washout rate of the brain radioactivity from 15 to 60 min after the injection of 6-bromo-7-[11C]methylpurine reflects the efflux rate of *S*-(7-[11C]methylpurin-6-yl)glutathione from the brain. In addition, the efflux rate was approximately tenfold lower in *Mrp1*−/− (0.15 h−1 or 0.0025 min−1) than WT mice (1.4 h−1 or 0.023 min−1) (Okamura et al. 2009c). Moreover, the influx of *S*-(7-[11C]methylpurin-6-yl)glutathione from the blood to the brain in WT and *Mrp1*−/− mice was extremely low for 60 min after intravenous injection, indicating that this tracer in the blood cannot cross the BBB (Okamura et al. 2020). Thus, 6-bromo-7-[11C]methylpurine allows noninvasive and quantitative measurement of MRP1 activity in the brain. However, recent findings showed that multiple efflux transporters contribute to the efflux of the GSH conjugate from the mouse brain. We will address this in Sect. 16.4.
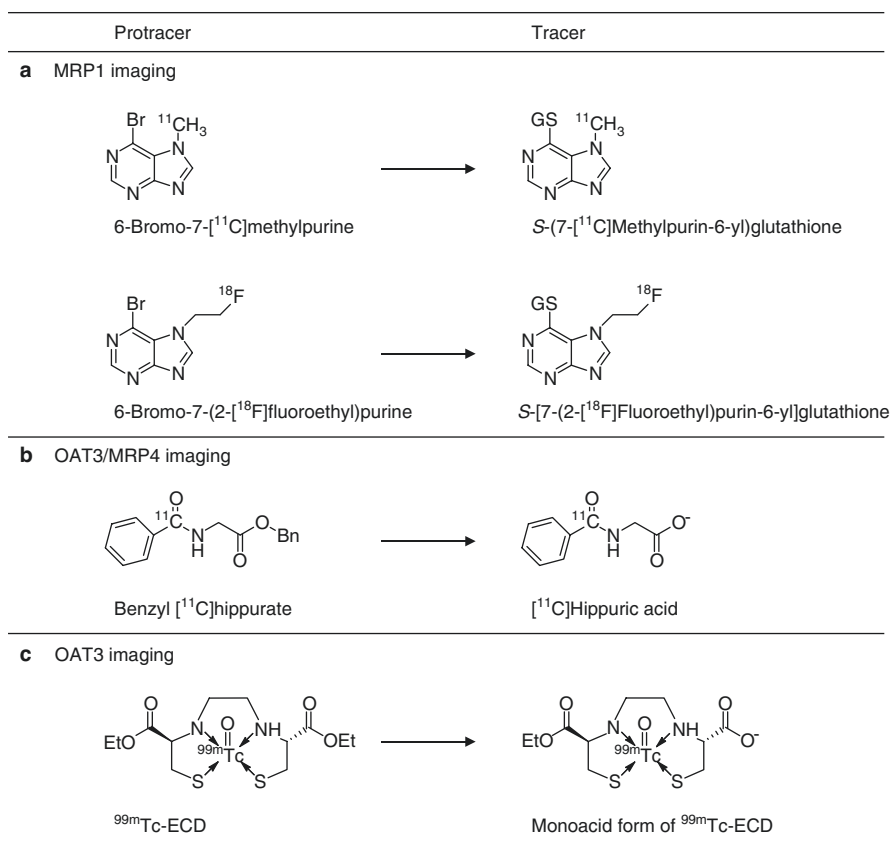
Fig. 16.2 Structures of MEM tracers. (**a**) The efflux rate of *S*-(7-[^{11}C]methylpurin-6-yl)glutathione from the brain after intravenous administration of 6-bromo-7-[^{11}C]methylpurine was reduced to nearly zero in *Mrp1*$^{-/-}$ mice compared with WT mice, and thus the protracer allows noninvasive and quantitative measurement of Mrp1 activity in the brain. However, recent studies show that the efflux process of *S*-(7-[^{11}C]methylpurin-6-yl)glutathione from the brain via Mrp1 would not be the rate-limiting step in mice and that Mrp4 and Oat3 contribute to the efflux of the tracer (see Sect. 16.4). The ^{18}F-labeled derivative may be transported from the brain by the same mechanisms as the ^{11}C-labeled tracer. GS denotes a glutathionyl group. (**b**) Benzyl [^{11}C]hippurate is a potential protracer for imaging the activities of Oat3 in the brains and Mrp4 in the hearts of mice. (**c**) ^{99m}Tc-ECD can be used as a protracer for imaging of Oat3 activity in the mouse brain, but not in primates, including humans

16.2.4   MRP1 Imaging in Peripheral Tissues Using 6-Bromo-7-[^{11}C]Methylpurine

MRP1 is ubiquitously expressed in normal tissues, including the brain, lung, heart, and kidney (Bakos and Homolya 2007; Flens et al. 1996). The change of MRP1 expression is associated with certain lung diseases (van der Deen et al. 2006), and the noninvasive measurement of pulmonary MRP1 activity would thus help

elucidate pathological conditions and diagnoses of lung diseases. We examined the feasibility of imaging pulmonary MRP1 activity using 6-bromo-7-[^{11}C]methylpurine (Okamura et al. 2013). The radioactivity in the lungs of WT and $Mrp1^{-/-}$ mice reached a maximum level immediately after the intravenous administration of 6-bromo-7-[^{11}C]methylpurine. Thereafter, the radioactivity in the lungs of WT mice was rapidly reduced, whereas in $Mrp1^{-/-}$ mice, the radioactivity was mostly retained. In addition, radioactive compounds in the lungs of $Mrp1^{-/-}$ mice 5 min after the intravenous administration of 6-bromo-7-[^{11}C]methylpurine almost entirely consisted of S-(7-methylpurin-6-yl)glutathione (MRP1 substrate), although 27% of the radioactivity in the lungs of WT mice was present as an unknown metabolite. Thus, this protracer showed a kinetic behavior according to the MEM model: 6-bromo-7-[^{11}C]methylpurine diffuses into the lung tissue after administration and undergoes conversion into the tracer, its GSH conjugate, which is then specifically effluxed by Mrp1. This finding suggests that 6-bromo-7-[^{11}C]methylpurine can be used to measure MRP1 activity in the lungs (Okamura et al. 2013).

Zoufal et al. have recently investigated whether the activity of MRPs in excretory organs can be measured with 6-bromo-7-[^{11}C]methylpurine (Zoufal et al. 2019). The elimination rate constant of 6-bromo-7-[^{11}C]methylpurine-derived radioactivity was significantly decreased in the kidneys of $Mrp1^{-/-}$ mice compared with WT mice. Loss of $Mrp4^{-/-}$ also significantly decreased the elimination rate constant in the kidney. These results suggest that 6-bromo-7-[^{11}C]methylpurine may be useful for assessing the activity of MRPs in the kidneys. However, further studies are required to identify the MRP subtypes involved in the renal excretion.

MRP1 is highly expressed in the heart (Flens et al. 1996), and it has been shown that MRP1 polymorphisms are related to anthracycline-induced cardiotoxicity in cancer patients (Semsei et al. 2012; Wojnowski et al. 2005). To our knowledge, thus far, no studies are available regarding PET tracers or probes for the measurement of MRP1 activity in the heart. However, based on previous reports, we would like to suggest the possibility of MRP1 imaging in the heart using 6-bromo-7-[^{11}C]methylpurine. Zoufal et al. investigated whether the activity of MRPs in excretory organs can be measured with 6-bromo-7-[^{11}C]methylpurine (Zoufal et al. 2019). In their study, a region of interest was drawn around the left ventricle of the heart of mice to obtain image-derived blood concentration-time curves. Similar to the kinetics in the lungs, the radioactivity clearance rate in the blood of $Mrp1^{-/-}$ mice, which was determined by regression analysis from 17.5 to 80 min, was significantly decreased compared with that of WT mice (Zoufal et al. 2019). In contrast to the image-derived concentration-time curves in the blood, we examined the time course of radioactivity in the blood collected from the stump following decapitation (Okamura et al. 2013). Consequently, the radioactivity in the blood of $Mrp1^{-/-}$ mice was 1.4% injected dose (ID)/g at 1 min, 1.1% ID/g at 15 min, and 0.84% ID/g at 60 min, while that of WT mice was 5.8% ID/g at 1 min, 1.1% ID/g at 15 min, and 0.27% ID/g at 60 min. The time course of radioactivity in the blood was inconsistent between the collected blood and the image-derived blood. Given that MRP1 is highly expressed in the heart (Flens et al. 1996), we believe that the elimination rate of the radioactivity in the image-derived blood of $Mrp1^{-/-}$ mice would be strongly affected by the

loss of Mrp1 in the heart tissue, hinting a possibility of MRP1 imaging in the heart using 6-bromo-7-[^{11}C]methylpurine. However, further studies in a large animal model are needed.

## 16.3   Other Potential Tracers or Probes for the Imaging of MRP1, MRP2, and MRP4

Except for 6-bromo-7-[^{11}C]methylpurine, few reports are available regarding PET protracers or probes for imaging of MRP1 activity. Since ^{18}F has a longer half-life than ^{11}C (110 vs. 20 min), a ^{18}F-labeled derivative of 6-bromo-7-[^{11}C]methylpurine has advantages over 6-bromo-7-[^{11}C]methylpurine such as better image quality and applications in species that show lower rates of GSH conjugation. Thus, a series of ^{18}F-labeled 6-halopurines were synthesized and evaluated as a protracer for imaging of MRP1 activity in the brain. As a consequence, 6-bromo-7-(2-[^{18}F]fluoroethyl) purine (Fig. 16.2) was suggested to be a promising protracer for noninvasive measurement of MRP1 activity in the brain (Galante et al. 2014).

The SPECT probes ^{99m}Tc-hexakis-2-methoxyisobutylisonitrile (^{99m}Tc-MIBI) and ^{99m}Tc-tetrofosmin, which function as myocardial perfusion imaging agents (Higley et al. 1993; Wackers et al. 1989), have been suggested to serve as substrates for MRP1 (Li et al. 2001; Hendrikse et al. 1998). Therefore, the SPECT probes may be used for visualization of MRP1 activity in a tissue of interest. For ^{99m}Tc-MIBI, the elimination rate from the lungs corresponded to the alteration of MRP1 expression: the rate of inhaled ^{99m}Tc-MIBI from the lungs in smokers with high levels of MRP1 expression was slower compared with that in nonsmokers with low levels of MRP1 expression (Mohan et al. 2019; Mohan et al. 2016). However, the use of ^{99m}Tc-MIBI for MRP1 imaging in the brain would be difficult because the positive charge of ^{99m}Tc-MIBI is unfavorable for the ingress into the brain. It should also be noted that ^{99m}Tc-MIBI and ^{99m}Tc-tetrofosmin are substrates for the ABC transporter P-glycoprotein (Ballinger et al. 1996; Piwnica-Worms et al. 1993).

A series of flavone derivatives were synthesized and evaluated as probes to visualize MRP1 (Mavel et al. 2006). In vitro experiments using Pgp- or MRP1-overexpressing cell lines showed these compounds to be selective for MRP1-expressing cells and enhanced the sensitivity of MRP1-mediated MDR cell lines to doxorubicin toxicity, suggesting that halogen-substituted flavone derivatives are potential PET and SPECT probes for imaging MRP1-mediated MDR phenomena. However, to date, the radiolabeling for PET or SPECT imaging or the in vivo evaluation of these candidates has not been reported.

MRP2 mainly mediates the hepatobiliary transport of many drugs and endogenous conjugated metabolites, and MRP2 deficiency leads to Dubin-Johnson syndrome, an inherited disorder characterized by conjugated hyperbilirubinemia (Nies and Keppler 2007). Compared with MRP1, there are relatively many studies focusing on the imaging of MRP2 in the liver. Hendrikse et al. examined the substrate specificities of ^{99m}Tc-N-(2,6-dimethylphenylcarbamoylmethyl)-iminodiacetic acid (^{99m}Tc-HIDA), a hepatobiliary agent (Wistow et al. 1977), for MRP1, MRP2, and
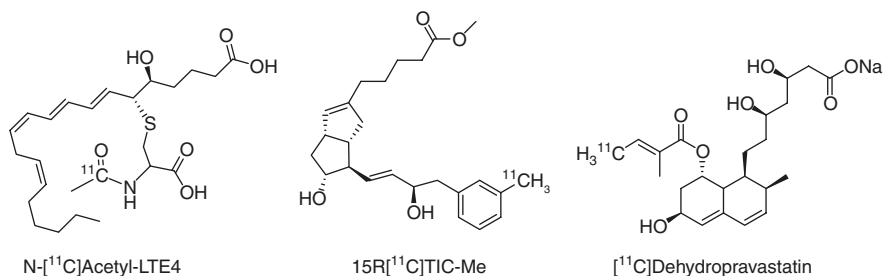
Fig. 16.3 Structures of potential PET probes for MRP2 imaging

P-glycoprotein and examined the kinetics of ^{99m}Tc-HIDA in normal and Mrp2-deficient GY/TR$^-$ rats (Hendrikse et al. 2004). The results showed that ^{99m}Tc-HIDA was transported by MRP1 and MRP2, but not by P-glycoprotein, and the elimination rate for radioactivity from the liver of control rats (half-life: 7 min) was faster than that of GY/TR$^-$ rats (half-life: 40 min). Thus, ^{99m}Tc-HIDA might be useful for assessing the in vivo activity of MRP2 in the liver.

The structures of the potential PET probes for imaging MRP2 are displayed in Fig. 16.3. It has been shown that the inflammatory cytokine leukotriene C_4 (LTC$_4$) and its metabolites, LTD$_4$ and LTE$_4$, are substrates for both MRP1 and MRP2 (Ito et al. 2001; Leier et al. 1994). The leukotriene derivatives labeled with a positron emitter could thus be a potential probe for assessing MRP1 or MRP2 activity. Furthermore, N-[^{11}C]acetyl-LTE$_4$ was synthesized, and its kinetic behavior was investigated in normal rats, in cholestatic rats, and in Mrp2-deficient GY/TR$^-$ rats using PET (Hendrikse 2000; Guhlmann et al. 1995). After injection of N-[^{11}C]acetyl-LTE$_4$, a fast clearance from the blood and a transient accumulation in the liver were observed in normal rats, whereas N-[^{11}C]acetyl-LTE$_4$ showed a delayed washout from the blood in cholestatic and GY/TR$^-$ rats. Moreover, there was a delayed decrease in hepatic N-[^{11}C]acetyl-LTE$_4$ and negligible amounts of radioactivity in the intestine in GY/TR$^-$ rats, compared with normal rats. The findings imply that N-[^{11}C]acetyl-LTE$_4$ might enable the noninvasive assessment of Mrp2-mediated transport in the liver.

The probe (15R)-16-m-[^{11}C]tolyl-17,18,19,20-tetranorisocarbacyclin methyl ester (15R-[^{11}C]TIC-Me) was converted in the blood into its acid form, 15R-[^{11}C]TIC, which was, in turn, converted to at least three metabolites (M1, M2, and M3) (Takashima et al. 2010). An in vitro transport assay using Mrp2-expressing membrane vesicles suggested that the major metabolites (M2 in the plasma and M3 in the bile) were good substrates for Mrp2. Moreover, the intrinsic canalicular efflux clearance of M2 and M3 in Mrp2-deficient rats was reduced compared with controls. Thus, the authors of this study conclude that 15R-[^{11}C]TIC-Me might be useful for in vivo analyses of Mrp2-mediated hepatobiliary transport.

A recent study suggested that [^{11}C]dehydropravastatin can assess the hepatobiliary transport by MRP2 and organic anion-transporting polypeptides in rats and

humans (Kaneko et al. 2018; Shingaki et al. 2013). Rifampicin-treated and Mrp2-defective rats decreased the canalicular efflux clearance of [^{11}C]dehydropravastatin (Shingaki et al. 2013). Similarly, the decrease in the canalicular efflux clearance in rifampicin-treated subjects was observed compared with that in control subjects, and the canalicular efflux clearance in a patient with Dubin-Johnson syndrome, caused by hereditary MRP2 deficiency, was also lower than that in control subjects (Kaneko et al. 2018).

MRP4 is thought to play a crucial role in homeostasis since this protein contributes to the transport of several important endogenous substances such as cAMP, cGMP, ADP, prostaglandins, and leukotrienes (Wen et al. 2015), whose alteration is probably responsible for pathophysiological processes. In addition, MRP4 controls cAMP levels in cardiac myocytes by extruding cAMP (Sassi et al. 2012). Noninvasive measurement of MRP4 activity may thus be useful for the understanding of the relationship between MRP4 and certain diseases. To our knowledge, there is only one study that investigated the feasibility of imaging MRP4 activity in vivo using PET (Kikuchi et al. 2016). Benzyl [^{11}C]hippurate is a potential protracer for estimating the activities of MRP4 in the mouse heart and organic anion transporter 3 (OAT3) in the brain (see also Sect. 16.5), and the structure of the protracer is shown in Fig. 16.2. Benzyl [^{11}C]hippurate is converted into [^{11}C]hippuric acid, which is thought to be a substrate of MRP4 (Mutsaers et al. 2011), in the heart. The efflux rate of the [^{11}C]hippuric acid formed in the heart of $Mrp4^{-/-}$ mice (0.043 min^{-1}) after administration of benzyl [^{11}C]hippurate was approximately 60% lower than that of control mice (0.11 min^{-1}). The protracer benzyl [^{11}C]hippurate might thus be used to assess MRP4 activity in the mouse heart, although further studies are needed for evaluating MRP4 specificity for [^{11}C]hippuric acid elimination from the heart (Kikuchi et al. 2016).

16.4   Feasibility of MRP1 Imaging in the Blood-Brain Barrier

16.4.1 Type of Protracer

As shown in Fig. 16.1, the MEM is described by the simple compartment model, and thus the activity of an efflux transporter at the BBB appears to be assessed from the brain kinetics of a tracer. This would be true for a protracer that can be metabolized to a tracer only in BCECs because a single efflux transporter at the luminal side of BCECs contributes to the efflux of the tracer to the blood. However, the brain has different kinds of cells such as BCECs, neurons, and glial cells, and thus, a protracer that is metabolized in these cells would not always provide information of the activity of an efflux transporter at the BBB. Unfortunately, a protracer that can be metabolized only in BCECs has not been developed yet.

Since 6-bromo-7-[^{11}C]methylpurine can easily enter the brain because of its hydrophobicity, the protracer should be able to diffuse into not only BCECs but also brain parenchymal cells, including neurons and nonneuronal cells. Moreover, GSTs, which catalyze GSH conjugation, are found in neurons, glial cells, and

endothelial cells in the rodent brain (Beiswanger et al. 1995; Johnson et al. 1993; Cammer et al. 1989). Therefore, *S*-(7-[^{11}C]methylpurin-6-yl)glutathione would be produced within brain parenchymal cells as well as BCECs. The tracer, *S*-(7-[^{11}C]methylpurin-6-yl)glutathione, formed in brain parenchymal cells, must penetrate three membranes to be eliminated from the brain to the blood. In other words, at least three transporters, an efflux transporter at the luminal side (blood side), an uptake transporter at the abluminal side (brain side) of BCECs, and an efflux transporter in brain parenchymal cells, are required for the efflux of *S*-(7-[^{11}C]methylpurin-6-yl)glutathione from brain parenchymal cells to the blood through the BBB (BCECs).

16.4.2 MRP1 at the Blood-Brain Barrier Versus Brain Parenchymal Cells

In the central nervous system, MRP1 is expressed not only at the BBB and blood-cerebrospinal fluid barrier (Dallas et al. 2006) but also in nonendothelial cells such as astrocytes and neurons in the adult and developing human brain (Bernstein et al. 2014; Daood et al. 2008). As described above, 6-bromo-7-[^{11}C]methylpurine allows noninvasive and quantitative measurement of MRP1 activity in the brain. However, the protracer cannot discriminate between the washout of *S*-(7-[^{11}C]methylpurin-6-yl)glutathione from brain parenchymal cells and through the BBB (Fig. 16.4); we thus investigated the involvement of MRP1 at the BBB in the tracer efflux using the intracerebral injection method, which is similar to the BEI for analyzing efflux at the BBB (Kakee et al. 1996). In our recent study, no significant differences in the efflux rate of *S*-(7-[^{11}C]methylpurin-6-yl)glutathione was observed between WT and *Mrp1*$^{-/-}$ mice after intracerebral injection (Okamura et al. 2020). This result shows that intracerebrally injected *S*-(7-[^{11}C]methylpurin-6-yl)glutathione was cleared from the brain, presumably through the BBB, but the tracer efflux was not mediated by Mrp1. By contrast, the tracer produced in the brain following administration of 6-bromo-7-[^{11}C]methylpurine was almost completely trapped in the brain of *Mrp1*$^{-/-}$ mice (Okamura et al. 2020). Therefore, Mrp1 in brain parenchymal cells, but not the BBB, may contribute to the extrusion of *S*-(7-[^{11}C]methylpurin-6-yl)glutathione from the brain to the blood.

16.4.3 Involvement of MRP4 and OAT3 in the Efflux of *S*-(7-[^{11}C] Methylpurin-6-Yl)Glutathione

In addition to Mrp1, Mrp4 and Oat3 contribute to the efflux of *S*-(7-[^{11}C]methylpurin-6-yl)glutathione produced in the brain after intravenous administration of 6-bromo-7-[^{11}C]methylpurine (Okamura et al. 2020). In mice, Mrp4 and Oat3 are localized at the luminal and abluminal membrane of BCECs, respectively (Ohtsuki et al. 2004; Leggas et al. 2004). It has also been reported
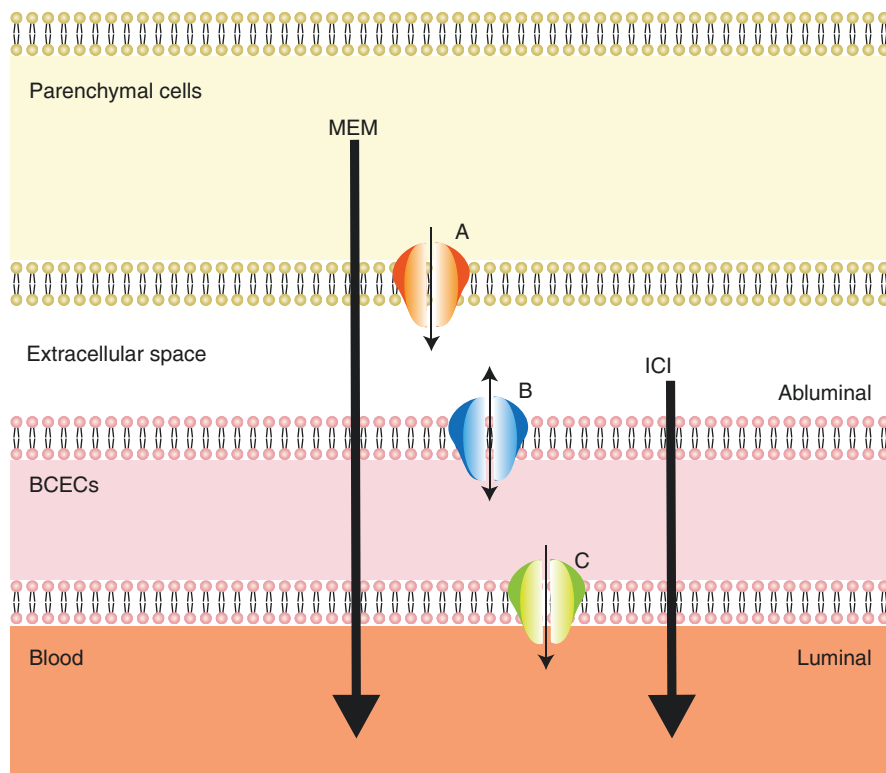
Fig. 16.4 Putative mechanism for the efflux of S-(7-[^{11}C]methylpurin-6-yl)glutathione from the brain. In the MEM, S-(7-[^{11}C]methylpurin-6-yl)glutathione would be formed within glial cells, neurons, and BCECs. S-(7-[^{11}C]Methylpurin-6-yl)glutathione produced within parenchymal cells is therefore effluxed to the extracellular space by transporter A and then is taken up into BCECs by transporter B. Finally, the tracer is extruded into the blood by transporter C at the luminal side of BCECs. A recent study using the MEM and the intracerebral injection (ICI) method, which is similar to the BEI for analyzing efflux at the BBB, suggests that transporters A, B, and C contributing to the tracer efflux from the mouse brain are Mrp1, Oat3, and Mrp4, respectively. Note that this figure shows only three transporters; however, we cannot exclude the possibility that other transporters mediate the transport of S-(7-[^{11}C]methylpurin-6-yl)glutathione from the brain

that the interplay between Oat3 and Mrp4 at the BBB may allow vectorial transport of prostaglandins, fatty acids derived from arachidonic acid metabolism, from the brain interstitial fluid to the blood across BCECs (Tachikawa et al. 2014); that is, Oat3 takes up prostaglandins from the interstitial fluid into BCECs, and subsequently, Mrp4 eliminates them from BCECs into the blood. Based on this observation, S-(7-[^{11}C]methylpurin-6-yl)glutathione in the extracellular space may be incorporated into BCECs by Oat3 and then effluxed from the cells to the blood by Mrp4 to be cleared from the brain. Nonetheless, we cannot rule out the possibility that other pumps are involved in the transport of the tracer into and out of BCECs.

### 16.4.4	The Efflux Process Via Mrp1 Is Not the Rate-Limiting Step in the Mouse Brain

6-Bromo-7-[^{11}C]methylpurine allows the assessment of a transporter either at the luminal side or the abluminal side of the BBB, or in brain parenchymal cells, probably Mrp4, Oat3, or Mrp1. The determined efflux rate of S-(7-[^{11}C]methylpurin-6-yl) glutathione would reflect the slowest step of the efflux processes, i.e., the rate-limiting step. Unfortunately, no methods are available for determining the rate-limiting step of the efflux process in the brain. However, in control mice, we found that the efflux rate of intracerebrally injected S-(7-[^{11}C]methylpurin-6-yl)glutathione was comparable to that of the tracer formed in the brain after intravenous injection of 6-bromo-7-[^{11}C]methylpurine (Okamura et al. 2020). This finding shows that the efflux process of the tracer via Mrp1 from brain parenchymal cells to the extracellular space would not be the rate-limiting step, but either the uptake or efflux process at the BBB, partly via Oat3 and Mrp4, is the rate-limiting step. As a result, it is difficult to assess Mrp1 activity in the mouse brain using 6-bromo-7-[^{11}C]methylpurine, unless Mrp1 activity markedly changes, such as in gene knockout animals. After the protracer injection, there was only a moderate reduction in the washout rate of brain radioactivity in heterozygous $Mrp1^{+/-}$ mice, which are expected to have a 50% reduction in Mrp1 expression, compared with WT mice (Zoufal et al. 2019). This finding implies that the transport system is very high capacity, e.g., possesses a high ratio of maximal transport rate to the Michaelis-Menten constant.

6-Bromo-7-[^{11}C]methylpurine was shown to possess limited sensitivity for measuring moderate changes in MRP1 activity in the mouse brain (Zoufal et al. 2019); however, the same research group has further investigated whether MRP1 activity in the brain differs between a beta-amyloidosis mouse model (APP/PS1–21) and control mice using the protracer (Zoufal et al. 2020). They partially inhibited MRP1 in the brain with MK571 (300 mg/kg, i.p.), an MRP1 inhibitor, to reduce the transport capacity of MRP1, thereby increasing the sensitivity of 6-bromo-7-[^{11}C]methylpurine to detect small changes in MRP1 activity. They found a significant positive correlation between the efflux rate and MRP1 levels in the brain. However, the sensitivity was still poor: when values were roughly read from the figure, Mrp1 levels were increased from 0.5 to 5.5, whereas the elimination rate was slightly increased from 0.9 h^{-1} to 1.1 h^{-1}, i.e., from 0.015 min^{-1} to 0.018 min^{-1} (Zoufal et al. 2020). Zoufal et al. speculated that astrocytes were involved in the increases in the efflux parameter based on their strong expression of MRP1 and GSTs and their uniform distribution through the brain. Furthermore, they posited that 6-bromo-7-[^{11}C]methylpurine may be used in future studies as a marker of astrocyte function (Zoufal et al. 2020). Considering our findings regarding the rate-limiting step (Okamura et al. 2020) and recent reports regarding the limited sensitivity (Zoufal et al. 2019; Zoufal et al. 2020), however, we posit that 6-bromo-7-[^{11}C]methylpurine cannot quantitatively assess Mrp1 activity in either astrocytes or the brains of mice, even if astrocytes among brain parenchymal cells mainly contribute to the efflux of the GSH conjugate from the brain. This question deserves further studies.

16.5   Application of the MEM to Other Efflux Transporters

The MEM would apply to noninvasive and quantitative measurement of the activity of other efflux transporters. We have recently developed a protracer, benzyl [^{11}C]hippurate, for measuring the activity of OAT3 in the mouse brain (Kikuchi et al. 2016). The protracer showed moderate brain uptake 0.5 min after intravenous injection and became converted into [^{11}C]hippuric acid, which is thought of as a substrate of MRP4 and OAT3 (Mutsaers et al. 2011; Deguchi et al. 2006), after 5-min postinjection. Moreover, the efflux rate of [^{11}C]hippuric acid in the brain of *Oat*3$^{-/-}$ mice was approximately 20% of that of the control mice, indicating that the efflux rate primarily reflected the activity of OAT3 in the brain. Interestingly, MRP4 did not contribute to the elimination of [^{11}C]hippuric acid from the brain although MRP4 is expressed in BCECs (Leggas et al. 2004) and [^{11}C]hippuric acid was retained in the heart of *Mrp*4$^{-/-}$ mice (Kikuchi et al. 2016). Given the localization of OAT3 in BCECs, [^{11}C]hippuric acid formed in the mouse brain would be cleared by other transporters (excluding MRP4) after [^{11}C]hippuric acid had been taken up into BCECs mainly via OAT3.

Technetium-99m complex with *N,N′*-1,2-ethylenediylbis-L-cysteine diethyl ester (^{99m}Tc-ECD), whose structure is shown in Fig. 16.2, has been clinically used for brain perfusion imaging (Kapucu et al. 2009). Injected, ^{99m}Tc-ECD enters the brain and becomes metabolized into a monoacid in the brain (Walovitch et al. 1994; Walovitch et al. 1991). In mice, Oat3 mediates the efflux of the ^{99m}Tc-ECD metabolite from the brain to the blood (Kikuchi et al. 2014), and thus ^{99m}Tc-ECD is a potential protracer for the assessment of Oat3 activity in the mouse brain. Indeed, ^{99m}Tc-ECD was used to analyze the efflux transport function of Oat3 at the BBB (Kuwahara et al. 2018). However, we should note that ^{99m}Tc-ECD as an OAT3 protracer would apply to rodents but not primates because OAT3 is poorly expressed in BCEC in primates, including humans, but highly expressed in mice (Deo et al. 2013). In primates, radioactivity remained trapped in the brain long after the administration of ^{99m}Tc-ECD (Walovitch et al. 1994; Walovitch et al. 1991), which is necessary for imaging of cerebral blood flow.

The protracer 6-[^{125}I]iodo-9-pentylpurine was designed for the assessment of the efflux transport of iodide from the brain (Okamura et al. 2009a). The protracer readily entered the brain and showed the almost complete conversion to [^{125}I]$^-$ by 10 min after intravenous administration into mice, whereas the influx of [^{125}I]$^-$ from the blood to the brain was extremely low for 20 min after intravenous administration. In addition, dose-dependent inhibition of [^{125}I]$^-$ efflux from the brain was observed in mice pretreated with perchlorate, an inhibitor of iodide transport. Thus, the protracer labeled with ^{124}I for PET may be able to assess the I$^-$ efflux from the brain noninvasively, although further studies are needed to identify a carrier protein involved in the efflux of iodide.

N-[^{18}F]Fluoroethylpiperidin-4ylmethyl acetate ([^{18}F]FEP-4MA) was developed for measuring the activity of acetylcholinesterase in the brain and was shown to be hydrolyzed by this enzyme to its metabolite *N*-[^{18}F]fluoroethyl-4-piperidinemethanol (Kikuchi et al. 2010; Kikuchi et al. 2005). In contrast to [^{18}F]FEP-4MA, the influx

of the hydrophilic alcohol metabolite from the blood to the brain was negligible after intravenous administration, and the metabolite generated in the brain after [^{18}F]FEP-4MA administration might thus be retained. However, the alcohol metabolite formed in the brain was slowly washed out from the brain (Kikuchi et al. 2010), suggesting that certain transporters may mediate the efflux of the alcohol metabolite from the brain. Thus, [^{18}F]FEP-4MA may be a potential protracer for imaging of the efflux systems, although the carriers that export the alcohol metabolite are currently unknown.

16.6 Conclusions and Perspectives

Our studies using the MEM with 6-bromo-7-[^{11}C]methylpurine and the intracerebral injection method with *S*-(7-[^{11}C]methylpurin-6-yl)glutathione in transgenic mice revealed that Mrp1, Oat3, and Mrp4 mediate tracer efflux from the brain. Mrp1 may contribute to the efflux of *S*-(7-[^{11}C]methylpurin-6-yl)glutathione from brain parenchymal cells, while the tracer in the extracellular space of the brain is likely cleared in part by transport across the BBB by the combination of Oat3 and Mrp4. Although 6-bromo-7-[^{11}C]methylpurine would not allow the imaging of Mrp1 activity in the mouse brain, it should be noted that the protracer is not always unusable for evaluating MRP1 activity in human brain (parenchymal cells) because there may be species difference in the rate-limiting step of the efflux process via MRP1 between humans and mice. Despite reports suggesting the pathophysiological importance of MRP1 in brain parenchymal cells as described in the Introduction section, past studies have exclusively focused on the in vivo role or function of MRP1 at the blood-brain or blood-cerebrospinal fluid interfaces (Lee et al. 2004; Sugiyama et al. 2003; Cisternino et al. 2003; Wijnholds et al. 2000). Methods for noninvasively assessing MRP1 activity in humans have not been developed yet, and hence 6-bromo-7-[^{11}C]methylpurine is expected to be a potential protracer for the assessment in human brain parenchymal cells, although further clinical studies are needed.

References

Bakos E, Homolya L (2007) Portrait of multifaceted transporter, the multidrug resistance-associated protein 1 (MRP1/ABCC1). Pflugers Arch 453(5):621–641

Ballinger JR, Bannerman J, Boxen I, Firby P, Hartman NG, Moore MJ (1996) Technetium-99m-tetrofosmin as a substrate for P-glycoprotein: in vitro studies in multidrug-resistant breast tumor cells. J Nucl Med 37(9):1578–1582

Beiswanger CM, Diegmann MH, Novak RF, Philbert MA, Graessle TL, Reuhl KR, Lowndes HE (1995) Developmental changes in the cellular distribution of glutathione and glutathione S-transferases in the murine nervous system. Neurotoxicology 16(3):425–440

Bernstein HG, Hölzl G, Dobrowolny H, Hildebrandt J, Trubner K, Krohn M, Bogerts B, Pahnke J (2014) Vascular and extravascular distribution of the ATP-binding cassette transporters ABCB1 and ABCC1 in aged human brain and pituitary. Mech Ageing Dev 141-142:12–21

Bradbury MW (1993) The blood-brain barrier. Exp Physiol 78(4):453–472

Cammer W, Tansey F, Abramovitz M, Ishigaki S, Listowsky I (1989) Differential localization of glutathione-S-transferase Yp and Yb subunits in oligodendrocytes and astrocytes of rat brain. J Neurochem 52(3):876–883

Cisternino S, Rousselle C, Lorico A, Rappa G, Scherrmann JM (2003) Apparent lack of Mrp1-mediated efflux at the luminal side of mouse blood-brain barrier endothelial cells. Pharm Res 20(6):904–909

Cole SP, Bhardwaj G, Gerlach JH, Mackie JE, Grant CE, Almquist KC, Stewart AJ, Kurz EU, Duncan AM, Deeley RG (1992) Overexpression of a transporter gene in a multidrug-resistant human lung cancer cell line. Science 258(5088):1650–1654

Cserr HF, Berman BJ (1978) Iodide and thiocyanate efflux from brain following injection into rat caudate nucleus. Am J Phys 235(4):F331–F337

Dallas S, Miller DS, Bendayan R (2006) Multidrug resistance-associated proteins: expression and function in the central nervous system. Pharmacol Rev 58(2):140–161

Daood M, Tsai C, Ahdab-Barmada M, Watchko JF (2008) ABC transporter (P-gp/ABCB1, MRP1/ABCC1, BCRP/ABCG2) expression in the developing human CNS. Neuropediatrics 39(4):211–218

van der Deen M, Marks H, Willemse BW, Postma DS, Muller M, Smit EF, Scheffer GL, Scheper RJ, de Vries EG, Timens W (2006) Diminished expression of multidrug resistance-associated protein 1 (MRP1) in bronchial epithelium of COPD patients. Virchows Arch 449(6):682–688

Deguchi T, Isozaki K, Yousuke K, Terasaki T, Otagiri M (2006) Involvement of organic anion transporters in the efflux of uremic toxins across the blood-brain barrier. J Neurochem 96(4):1051–1059

Deo AK, Theil FP, Nicolas JM (2013) Confounding parameters in preclinical assessment of blood-brain barrier permeation: an overview with emphasis on species differences and effect of disease states. Mol Pharm 10(5):1581–1595

Flens MJ, Zaman GJ, van der Valk P, Izquierdo MA, Schroeijers AB, Scheffer GL, van der Groep P, de Haas M, Meijer CJ, Scheper RJ (1996) Tissue distribution of the multidrug resistance protein. Am J Pathol 148(4):1237–1247

Galante E, Okamura T, Sander K, Kikuchi T, Okada M, Zhang MR, Robson M, Badar A, Lythgoe M, Koepp M, Arstad E (2014) Development of purine-derived 18F-labeled pro-drug tracers for imaging of MRP1 activity with PET. J Med Chem 57(3):1023–1032

Guhlmann A, Krauss K, Oberdorfer F, Siegel T, Scheuber PH, Muller J, Csuk-Glanzer B, Ziegler S, Ostertag H, Keppler D (1995) Noninvasive assessment of hepatobiliary and renal elimination of cysteinyl leukotrienes by positron emission tomography. Hepatology 21(6):1568–1575

Hendrikse NH (2000) Monitoring interactions at ATP-dependent drug efflux pumps. Curr Pharm Des 6(16):1653–1668

Hendrikse NH, Franssen EJ, van der Graaf WT, Meijer C, Piers DA, Vaalburg W, de Vries EG (1998) 99mTc-sestamibi is a substrate for P-glycoprotein and the multidrug resistance-associated protein. Br J Cancer 77(3):353–358

Hendrikse NH, Kuipers F, Meijer C, Havinga R, Bijleveld CM, van der Graaf WT, Vaalburg W, de Vries EG (2004) In vivo imaging of hepatobiliary transport function mediated by multidrug resistance associated protein and P-glycoprotein. Cancer Chemother Pharmacol 54(2):131–138

Higley B, Smith FW, Smith T, Gemmell HG, Das Gupta P, Gvozdanovic DV, Graham D, Hinge D, Davidson J, Lahiri A (1993) Technetium-99m-1,2-bis[bis(2-ethoxyethyl) phosphino]ethane: human biodistribution, dosimetry and safety of a new myocardial perfusion imaging agent. J Nucl Med 34(1):30–38

Hwang IY, Elfarra AA (1993) Detection and mechanisms of formation of S-(6-purinyl)glutathione and 6-mercaptopurine in rats given 6-chloropurine. J Pharmacol Exp Ther 264(1):41–46

Ito K, Suzuki H, Sugiyama Y (2001) Charged amino acids in the transmembrane domains are involved in the determination of the substrate specificity of rat Mrp2. Mol Pharmacol 59(5):1077–1085

Johnson JA, el Barbary A, Kornguth SE, Brugge JF, Siegel FL (1993) Glutathione S-transferase isoenzymes in rat brain neurons and glia. J Neurosci 13(5):2013–2023

Kakee A, Terasaki T, Sugiyama Y (1996) Brain efflux index as a novel method of analyzing efflux transport at the blood-brain barrier. J Pharmacol Exp Ther 277(3):1550–1559

Kaneko K, Tanaka M, Ishii A, Katayama Y, Nakaoka T, Irie S, Kawahata H, Yamanaga T, Wada Y, Miyake T, Toshimoto K, Maeda K, Cui Y, Enomoto M, Kawamura E, Kawada N, Kawabe J, Shiomi S, Kusuhara H, Sugiyama Y, Watanabe Y (2018) A clinical quantitative evaluation of hepatobiliary transport of [(11)C]dehydropravastatin in humans using positron emission tomography. Drug Metab Dispos 46(5):719–728

Kapucu OL, Nobili F, Varrone A, Booij J, Vander Borght T, Nagren K, Darcourt J, Tatsch K, Van Laere KJ (2009) EANM procedure guideline for brain perfusion SPECT using 99mTc-labelled radiopharmaceuticals, version 2. Eur J Nucl Med Mol Imaging 36(12):2093–2102

Kikuchi T, Zhang MR, Ikota N, Fukushi K, Okamura T, Suzuki K, Arano Y, Irie T (2005) N-[18F]fluoroethylpiperidin-4ylmethyl acetate, a novel lipophilic acetylcholine analogue for PET measurement of brain acetylcholinesterase activity. J Med Chem 48(7):2577–2583

Kikuchi T, Okamura T, Zhang MR, Fukushi K, Irie T (2010) In vivo evaluation of N-[(18)F]fluoroethylpiperidin-4ylmethyl acetate in rats compared with MP4A as a probe for measuring cerebral acetylcholinesterase activity. Synapse 64(3):209–215

Kikuchi T, Okamura T, Wakizaka H, Okada M, Odaka K, Yui J, Tsuji AB, Fukumura T, Zhang MR (2014) OAT3-mediated extrusion of the ^{99m}Tc-ECD metabolite in the mouse brain. J Cereb Blood Flow Metab 34(4):585–588

Kikuchi T, Okamura T, Okada M, Ogawa M, Suzuki C, Wakizaka H, Yui J, Fukumura T, Gee AD, Zhang MR (2016) Benzyl [^{11}C]hippurate as an agent for measuring the activities of organic anion transporter 3 in the brain and multidrug resistance-associated protein 4 in the heart of mice. J Med Chem 59(12):5847–5856

Krohn M, Lange C, Hofrichter J, Scheffler K, Stenzel J, Steffen J, Schumacher T, Bruning T, Plath AS, Alfen F, Schmidt A, Winter F, Rateitschak K, Wree A, Gsponer J, Walker LC, Pahnke J (2011) Cerebral amyloid-beta proteostasis is regulated by the membrane transport protein ABCC1 in mice. J Clin Invest 121(10):3924–3931

Krohn M, Bracke A, Avchalumov Y, Schumacher T, Hofrichter J, Paarmann K, Frohlich C, Lange C, Bruning T, von Bohlen Und Halbach O, Pahnke J (2015) Accumulation of murine amyloid-beta mimics early Alzheimer's disease. Brain 138(Pt 8):2370–2382

Kusuhara H, Terasaki T, Sugiyama Y (2003) Brain efflux index method. Characterization of efflux transport across the blood-brain barrier. Methods Mol Med 89:219–231

Kuwahara H, Song J, Shimoura T, Yoshida-Tanaka K, Mizuno T, Mochizuki T, Zeniya S, Li F, Nishina K, Nagata T, Ito S, Kusuhara H, Yokota T (2018) Modulation of blood-brain barrier function by a heteroduplex oligonucleotide in vivo. Sci Rep 8(1):4377

Lee YJ, Kusuhara H, Sugiyama Y (2004) Do multidrug resistance-associated protein-1 and -2 play any role in the elimination of estradiol-17 beta-glucuronide and 2,4-dinitrophenyl-S-glutathione across the blood-cerebrospinal fluid barrier? J Pharm Sci 93(1):99–107

Leggas M, Adachi M, Scheffer GL, Sun D, Wielinga P, Du G, Mercer KE, Zhuang Y, Panetta JC, Johnston B, Scheper RJ, Stewart CF, Schuetz JD (2004) Mrp4 confers resistance to topotecan and protects the brain from chemotherapy. Mol Cell Biol 24(17):7612–7621

Leier I, Jedlitschky G, Buchholz U, Cole SP, Deeley RG, Keppler D (1994) The MRP gene encodes an ATP-dependent export pump for leukotriene C4 and structurally related conjugates. J Biol Chem 269(45):27807–27810

Leslie EM, Deeley RG, Cole SP (2005) Multidrug resistance proteins: role of P-glycoprotein, MRP1, MRP2, and BCRP (ABCG2) in tissue defense. Toxicol Appl Pharmacol 204(3):216–237

Li XF, Kinuya S, Yokoyama K, Konishi S, Ma YY, Watanabe N, Shuke N, Bunko H, Michigishi T, Tonami N (2001) Technetium-99m-tetrofosmin would be a substrate for multidrug resistance-associated protein (MRP): comparison between a leukemia cell line with high MRP gene expression and its parental cell line. Cancer Biother Radiopharm 16(1):17–23

Loscher W, Potschka H (2005) Drug resistance in brain diseases and the role of drug efflux transporters. Nat Rev Neurosci 6(8):591–602

Mavel S, Dikic B, Palakas S, Emond P, Greguric I, de Gracia AG, Mattner F, Garrigos M, Guilloteau D, Katsifis A (2006) Synthesis and biological evaluation of a series of flavone derivatives as

potential radioligands for imaging the multidrug resistance-associated protein 1 (ABCC1/MRP1). Bioorg Med Chem 14(5):1599–1607

Mohan HK, Routledge T, Cane P, Livieratos L, Ballinger JR, Peters AM (2016) Does the clearance of inhaled (99m)Tc-Sestamibi correlate with multidrug resistance protein 1 expression in the human lung? Radiology 280(3):924–930

Mohan HK, Livieratos L, Peters AM (2019) Lung clearance of inhaled aerosol of Tc-99m-methoxyisobutyl isonitrile: relationships with cigarette smoking, age and gender. Clin Physiol Funct Imaging 39(4):236–239

Mutsaers HA, van den Heuvel LP, Ringens LH, Dankers AC, Russel FG, Wetzels JF, Hoenderop JG, Masereeuw R (2011) Uremic toxins inhibit transport by breast cancer resistance protein and multidrug resistance protein 4 at clinically relevant concentrations. PLoS One 6(4):e18438

Nies AT, Keppler D (2007) The apical conjugate efflux pump ABCC2 (MRP2). Pflugers Arch 453(5):643–659

Ohtsuki S, Kikkawa T, Mori S, Hori S, Takanaga H, Otagiri M, Terasaki T (2004) Mouse reduced in osteosclerosis transporter functions as an organic anion transporter 3 and is localized at abluminal membrane of blood-brain barrier. J Pharmacol Exp Ther 309(3):1273–1281

Okamura T, Kikuchi T, Fukushi K, Arano Y, Irie T (2007) A novel noninvasive method for assessing glutathione-conjugate efflux systems in the brain. Bioorg Med Chem 15(9):3127–3133

Okamura T, Igarashi J, Kikuchi T, Fukushi K, Arano Y, Irie T (2009a) A radiotracer method to study efflux transport of iodide liberated from thyroid hormones via deiodination metabolism in the brain. Life Sci 84(23–24):791–795

Okamura T, Kikuchi T, Fukushi K, Irie T (2009b) Reactivity of 6-halopurine analogs with glutathione as a radiotracer for assessing function of multidrug resistance-associated protein 1. J Med Chem 52(22):7284–7288

Okamura T, Kikuchi T, Okada M, Toramatsu C, Fukushi K, Takei M, Irie T (2009c) Noninvasive and quantitative assessment of the function of multidrug resistance-associated protein 1 in the living brain. J Cereb Blood Flow Metab 29(3):504–511

Okamura T, Kikuchi T, Irie T (2010) PET imaging of MRP1 function in the living brain: method development and future perspectives. Curr Top Med Chem 10(17):1810–1819

Okamura T, Kikuchi T, Okada M, Wakizaka H, Zhang MR (2013) Imaging of activity of multidrug resistance-associated protein 1 in the lungs. Am J Respir Cell Mol Biol 49(3):335–340

Okamura T, Okada M, Kikuchi T, Wakizaka H, Zhang MR (2020) Mechanisms of glutathione-conjugate efflux from the brain into blood: involvement of multiple transporters in the course. J Cereb Blood Flow Metab 40(1):116–125

Pardridge WM (1998) CNS drug design based on principles of blood-brain barrier transport. J Neurochem 70(5):1781–1792

Piwnica-Worms D, Chiu ML, Budding M, Kronauge JF, Kramer RA, Croop JM (1993) Functional imaging of multidrug-resistant P-glycoprotein with an organotechnetium complex. Cancer Res 53(5):977–984

Qosa H, Miller DS, Pasinelli P, Trotti D (2015) Regulation of ABC efflux transporters at blood-brain barrier in health and neurological disorders. Brain Res 1628(Pt B):298–316

Reese TS, Karnovsky MJ (1967) Fine structural localization of a blood-brain barrier to exogenous peroxidase. J Cell Biol 34(1):207–217

Sassi Y, Abi-Gerges A, Fauconnier J, Mougenot N, Reiken S, Haghighi K, Kranias EG, Marks AR, Lacampagne A, Engelhardt S, Hatem SN, Lompre AM, Hulot JS (2012) Regulation of cAMP homeostasis by the efflux protein MRP4 in cardiac myocytes. FASEB J 26(3):1009–1017

Semsei AF, Erdelyi DJ, Ungvari I, Csagoly E, Hegyi MZ, Kiszel PS, Lautner-Csorba O, Szabolcs J, Masat P, Fekete G, Falus A, Szalai C, Kovacs GT (2012) ABCC1 polymorphisms in anthracycline-induced cardiotoxicity in childhood acute lymphoblastic leukaemia. Cell Biol Int 36(1):79–86

Shingaki T, Takashima T, Ijuin R, Zhang X, Onoue T, Katayama Y, Okauchi T, Hayashinaka E, Cui Y, Wada Y, Suzuki M, Maeda K, Kusuhara H, Sugiyama Y, Watanabe Y (2013) Evaluation of Oatp and Mrp2 activities in hepatobiliary excretion using newly developed positron emission tomography tracer [11C]dehydropravastatin in rats. J Pharmacol Exp Ther 347(1):193–202

Sugiyama D, Kusuhara H, Lee YJ, Sugiyama Y (2003) Involvement of multidrug resistance associated protein 1 (Mrp1) in the efflux transport of 17beta estradiol-D-17beta-glucuronide (E217betaG) across the blood-brain barrier. Pharm Res 20(9):1394–1400

Sun Y, Luo X, Yang K, Sun X, Li X, Zhang C, Ma S, Liu Y, Yin J (2016) Neural overexpression of multidrug resistance-associated protein 1 and refractory epilepsy: a meta-analysis of nine studies. Int J Neurosci 126(4):308–317

Tachikawa M, Hosoya K, Terasaki T (2014) Pharmacological significance of prostaglandin E2 and D2 transport at the brain barriers. Adv Pharmacol 71:337–360

Takashima T, Nagata H, Nakae T, Cui Y, Wada Y, Kitamura S, Doi H, Suzuki M, Maeda K, Kusuhara H, Sugiyama Y, Watanabe Y (2010) Positron emission tomography studies using (15R)-16-m-[11C]tolyl-17,18,19,20-tetranorisocarbacyclin methyl ester for the evaluation of hepatobiliary transport. J Pharmacol Exp Ther 335(2):314–323

Wackers FJ, Berman DS, Maddahi J, Watson DD, Beller GA, Strauss HW, Boucher CA, Picard M, Holman BL, Fridrich R, Inglese E, Delaloye B, Bischof-Delaloye A, Camin L, McKusick K (1989) Technetium-99m hexakis 2-methoxyisobutyl isonitrile: human biodistribution, dosimetry, safety, and preliminary comparison to thallium-201 for myocardial perfusion imaging. J Nucl Med 30(3):301–311

Walovitch RC, Franceschi M, Picard M, Cheesman EH, Hall KM, Makuch J, Watson MW, Zimmerman RE, Watson AD, Ganey MV et al (1991) Metabolism of 99mTc-L,L-ethyl cysteinate dimer in healthy volunteers. Neuropharmacology 30(3):283–292

Walovitch RC, Cheesman EH, Maheu LJ, Hall KM (1994) Studies of the retention mechanism of the brain perfusion imaging agent 99mTc-bicisate (99mTc-ECD). J Cereb Blood Flow Metab 14(Suppl 1):S4–S11

Wen J, Luo J, Huang W, Tang J, Zhou H, Zhang W (2015) The pharmacological and physiological role of multidrug-resistant protein 4. J Pharmacol Exp Ther 354(3):358–375

Wijnholds J, deLange EC, Scheffer GL, van den Berg DJ, Mol CA, van der Valk M, Schinkel AH, Scheper RJ, Breimer DD, Borst P (2000) Multidrug resistance protein 1 protects the choroid plexus epithelium and contributes to the blood-cerebrospinal fluid barrier. J Clin Invest 105(3):279–285

Willyerd FA, Empey PE, Philbrick A, Ikonomovic MD, Puccio AM, Kochanek PM, Okonkwo DO, Clark RS (2016) Expression of ATP-binding cassette transporters B1 and C1 after severe traumatic brain injury in humans. J Neurotrauma 33(2):226–231

Wistow BW, Subramanian G, Heertum RL, Henderson RW, Gagne GM, Hall RC, McAfee JG (1977) An evaluation of 99mTc-labeled hepatobiliary agents. J Nucl Med 18(5):455–461

Wojnowski L, Kulle B, Schirmer M, Schluter G, Schmidt A, Rosenberger A, Vonhof S, Bickeboller H, Toliat MR, Suk EK, Tzvetkov M, Kruger A, Seifert S, Kloess M, Hahn H, Loeffler M, Nurnberg P, Pfreundschuh M, Trumper L, Brockmoller J, Hasenfuss G (2005) NAD(P)H oxidase and multidrug resistance protein genetic polymorphisms are associated with doxorubicin-induced cardiotoxicity. Circulation 112(24):3754–3762

Zoufal V, Mairinger S, Krohn M, Wanek T, Filip T, Sauberer M, Stanek J, Traxl A, Schuetz JD, Kuntner C, Pahnke J, Langer O (2019) Influence of multidrug resistance-associated proteins on the excretion of the ABCC1 imaging probe 6-Bromo-7-[(11)C]methylpurine in mice. Mol Imaging Biol 21(2):306–316

Zoufal V, Mairinger S, Krohn M, Wanek T, Filip T, Sauberer M, Stanek J, Kuntner C, Pahnke J, Langer O (2020) Measurement of cerebral ABCC1 transport activity in wild-type and APP/PS1-21 mice with positron emission tomography. J Cereb Blood Flow Metab 40(5):954-965.

Neuroinflammation: From Target Selection to Preclinical and Clinical Studies

17

Bastian Zinnhardt, Cristina Barca, Claudia Foray, Inga B. Fricke, Thomas Viel, Alexandra Winkeler, Albert D. Windhorst, and Andreas H. Jacobs

Contents

B. Zinnhardt
European Institute for Molecular Imaging (EIMI), University of Münster, Münster, Germany

Department of Nuclear Medicine, University Hospital Münster, Münster, Germany

Biomarkers and Translational Technologies (BTT), Pharma Research and Early Development (pRED), F. Hoffmann-La Roche Ltd, Basel, Switzerland
e-mail: bastian.zinnhardt@roche.com

C. Barca · C. Foray
European Institute for Molecular Imaging (EIMI), University of Münster, Münster, Germany
e-mail: cristina.barca@uni-muenster.de; claudia.foray@uni-muenster.de

I. B. Fricke
European Institute for Molecular Imaging (EIMI), University of Münster, Münster, Germany

Bruker BioSpin MRI GmbH, Ettlingen, Germany
e-mail: inga.fricke@bruker.com

T. Viel
Paris Centre de Recherche Cardiovasculaire, INSERM-U970, Université Paris Descartes, Paris, France
e-mail: thomas.viel@inserm.fr

A. Winkeler
UMR 1023, IMIV, Service Hospitalier Frédéric Joliot, CEA, Inserm, Université Paris Sud, CNRS, Université Paris-Saclay, Orsay, France

A. D. Windhorst
Department of Radiology and Nuclear Medicine, Amsterdam Neuroscience, VU University Medical Center, Amsterdam, The Netherlands

A. H. Jacobs (✉)
Department of Geriatrics, Johanniter Hospital, Evangelische Kliniken, Bonn, Germany
e-mail: ahjacobs@uni-muenster.de

Abstract

Inflammation is a highly dynamic and complex adaptive process to preserve and restore tissue homeostasis in neurological disorders and often serves as a prognostic marker for disease outcome. The underlying cellular and factorial heterogeneity represents an opportunity in the development of disease-modifying therapies.

Molecular imaging of neuroinflammation (NI) may support the characterization of key aspects of the dynamic interplay of various inducers, sensors, transducers, and effectors of the multifactorial inflammatory response in vivo in animal models and patients. The characterization of the NI response by molecular imaging will (i) support early diagnosis and disease follow-up, (ii) guide (stereotactic) biopsy sampling, (iii) highlight the dynamic changes during disease pathogenesis in a noninvasive manner, (iv) help monitoring existing therapies, (v) support the development of novel NI-modifying therapies, and (vi) aid stratification of patients, according to their individual NI profile.

This book chapter will review the basic principles of NI, recent developments and applications of novel molecular imaging targets, key considerations for the selection and development of imaging targets, as well as examples of successful clinical translation of NI imaging.

17.1   Introduction

Inflammation is a highly dynamic and complex process combining local and systemic reactions of multiple cell types, chemical signals, and signaling pathways.

Depending on the inflammatory stimulus and the unique tissue- and disease-specific microenvironment, inflammation can support repair and regeneration processes and, on the opposite, worsen tissue injury (e.g., allergy, chronic infections, neurodegeneration).

The type (mechanical, chemical, infectious, tumoral) of inflammatory stimuli determines the degree and nature of the inflammatory response. However, neuroinflammation (NI) contains unique features, i.e., (i) the CNS has efficient natural

protection from mechanical aggressions by the skull and from biological and chemical aggressions by the blood-brain barrier (BBB); (ii) the CNS has limited regenerative capacities; and (iii) any local impairment of its spatial organization can lead to a definite loss of function.

During NI, resident microglia and infiltrating peripheral immune cells induce a neuroinflammatory response with the overall goal to limit the extent of the disease, to clear tissue damage, and to support repair and regeneration. However, in several cases NI may contribute to the disease process itself, depending on the pathological mechanism.

To improve our understanding of the heterogeneity and dynamics of the disease-specific neuroinflammatory response, including the variety of cells and factors induced and the subsequent changes in tissue organization, exploration methods must take "time" and "space" into account. Molecular, anatomical, and functional in vivo imaging methods are essential for (i) early diagnosis and disease follow-up, (ii) investigating dynamic changes during NI noninvasively, (iii) guiding (stereotactic) biopsy sampling, (iv) monitoring existing therapies, (v) supporting the development of novel NI-modifying therapies, and (vi) stratification of patients, according to their specific cellular and molecular composition of NI in correlation to their therapy response. Dedicated imaging paradigms thus have a major impact on patient care (Villa et al. 2018; Zinnhardt et al. 2018). Moreover, in vivo imaging technologies are of importance to decipher the molecular mechanisms and functional consequences of neuroinflammatory processes at various disease stages.

It will be important, however, to cross-correlate imaging findings of NI with functional parameters and to integrate imaging data with detailed immunophenotyping by, e.g., flow cytometry and omics data for clinical decision-making. This will allow to gain a holistic understanding of the patients' individual NI profile and to understand the dynamic interplay of NI and the molecular mechanisms inducing cellular damage.

This book chapter will review the process of target selection and tracer development, as well as current NI imaging strategies in experimental and clinical application.

We describe and discuss the current status and possible future developments of (i) molecular targets for NI, (ii) imaging methods and technologies, and (iii) a variety of neurological diseases. This review will complement other book chapters focusing on dedicated molecular targets of NI.

The focus will be on particular requirements for target selection, molecular mechanisms, and possible targets for imaging in NI, assuming that the reader is familiar with the basic principles of the major imaging technologies, such as optical [OI], radionuclide (positron emission tomography [PET] and single photon emission computed tomography [SPECT]), and magnetic resonance imaging [MRI], as their different strengths and weaknesses have already been extensively commented upon, i.e., a high sensitivity and high spatial resolution for OI; high sensitivity and possibility for true signal quantification for radionuclide imaging; and high spatial resolution and physiological and biochemical imaging for MRI.

This book chapter is divided into three parts. The basic principles of NI are briefly summarized and potential targets for molecular imaging are reviewed in the first part.

In the second part, particular requirements as well as decision points for molecular imaging targets and tracer development are discussed. The third part highlights the application of the concepts of the second part in clinical and experimental molecular imaging of NI.

17.2 Basic Principles of Neuroinflammation

The term "inflammation" describes a multicellular and multifactorial process, characterized by (i) changes in local vasculature (increased blood flow and vascular permeability), (ii) activation of resident immune cells, (iii) infiltration of peripheral immune cells (neutrophils, macrophages, lymphocytes), and (iv) cytokine production (Graeber et al. 2011). During NI, a certain stimulus (environmental, toxic, hypoxic, viral, bacterial, mechanical, protein deposits, etc.) leads to an immune activation in the CNS, potentially contributing to tissue damage, loss of neurons and dysfunction, and on the other hand neuroregeneration and tissue repair (Graeber et al. 2011).

The underlying mechanisms include:

1. Activation of damage-associated molecular patterns (DAMPs, e.g., high-mobility group box 1 [HMGB1] proteins, heat-shock proteins [HSPs], histones, oxidized lipids, ATP, amyloid-ß) by tissue injury or of pathogen-associated molecular patters (PAMPs) by exogenous pathogens
2. Activation of Toll-like receptors (TLR) of various subtypes and of the receptor for advanced glycation end products (RAGE) with subsequent release of adhesion molecules, cytokines, and chemokines directing activation and targeted migration of effector cells (microglia, macrophages, lymphocytes)
3. Activation and recruitment of microglial cells
4. Infiltration of macrophages and T-lymphocytes of various subtypes (CD4+, CD8+, Th1, Th2, Th17, regulatory T cells)
5. Alteration of blood-brain barrier (BBB) integrity
6. Activation and recruitment of astrocytes
7. Release or expression of a variety of signaling factors, including neuron-derived neuropeptides, membrane proteins (e.g., fractalkine, cannabinoid receptors, major histocompatibility complex [MHC] molecules), semaphorins, and lectins which all take part in the regulation of NI (Jacobs et al. 2012; Stephenson et al. 2018)

In summary, the heterogeneous nature of NI and the pleiotropic functions of different immune cells during the course of NI render NI as attractive source of targets for therapeutic modulation in the treatment of neurological diseases. Molecular imaging of NI has greatly enhanced our understanding of the dynamics of immune
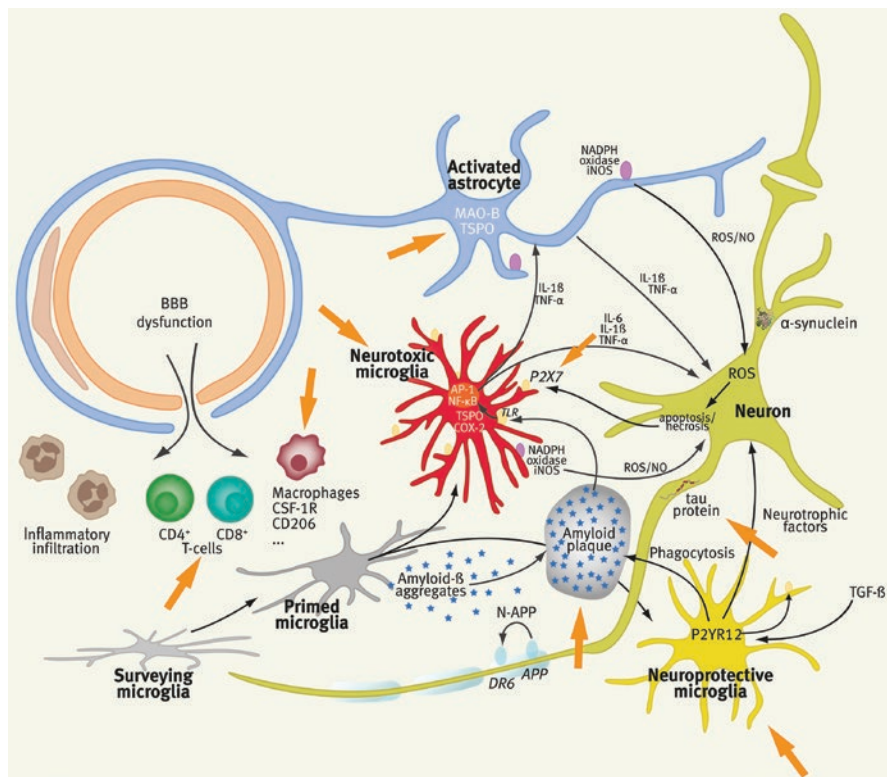
Fig. 17.1 Overview of selected imaging targets within the neurovascular unit. Abbreviations: *MAO-B* monoamine oxidase B, *TSPO* translocator protein, *IL* interleukin, *TNF-a* tumor necrosis factor alpha, *ROS* reactive oxygen species, *TGF-β* transforming growth factor beta, *APP* amyloid precursor protein, *CSF-1R* colony-stimulating factor 1 receptor, *TLR* Toll-like receptor, *BBB* blood-brain barrier (modified from Jacobs et al. 2012 and Perani et al. 2019)

cells and factors in neurological diseases. The following paragraphs will highlight examples of imaging targets in NI (Fig. 17.1).

17.3   Potential Imaging Targets

17.3.1 DAMPs

Damage-associated molecular patterns (DAMPs) represent a heterogeneous group of nuclear or cytosolic proteins released in response to a pathological stimulus, including the high-mobility group protein B1 (HMGB1), S100 proteins, heat-shock proteins (HSPs), chromogranin A, and chromogranin Aβ. In addition, nucleic acids and nucleotide derivatives, such as mitochondrial DNA (mt-DNA), DNA, and adenosine triphosphate (ATP), may serve as DAMPs (Ardura-Fabregat et al. 2017).

An excellent example of in vivo molecular imaging of DAMPs has been the direct visualization of amyloid-ß (the DAMP of AD) using radiolabeled thioflavine derivatives (e.g., Pittsburgh compound B; [¹¹C]PIB). Next-generation tracers include [¹⁸F]florbetapir, [¹⁸F]florbetaben, and [¹⁸F]flutemetamol, which are currently approved by the Food and Drug Administration and the European Medicines Agency (for review, see Perani et al. 2019).

Another DAMP of interest in NI is the appearance of hyperphosphorylated tau protein. Several classes of tau tracers have been described, including the [¹⁸F]THK family, [¹⁸F]flortaucipir (formerly known as [¹⁸F]AV1451 and [¹⁸F]T807), and [¹¹C]PBB3 (for review, see Perani et al. 2019). Recently, tracers with improved characteristics and hence improved selectivity and specificity were introduced (Honer et al. 2017; Kuwabara et al. 2018; Wong et al. 2018). Other DAMP-targeting tracers for neurodegenerative diseases are reviewed elsewhere (Perani et al. 2019).

17.3.2 Chemokines

Chemokines and their receptors comprise approximately 50 peptides and 20 receptors in humans, with homologs, orthologs, and related peptides in other vertebrate species. In NI, chemokines and their receptors fulfill multiple roles. They are involved in guiding movement of (immuno-) cells (chemoattraction), modulating the chemokine environment, activation of glial cells, and coordination of complex tissue responses (Ransohoff 2009).

Among the most intensively studied chemokines in AD are CX3C chemokine ligand 1 (CX3CL1, fractalkine) and chemokine ligand 2 (CCL2).

CX3CL1 and CX3CR1 may have a bimodal function in AD, depending on the underlying pathology. CX3CL1 and CX3CR1 play a beneficial role in the context of tau pathology while exerting detrimental functions in amyloid pathology (Ardura-Fabregat et al. 2017). No PET ligands were described for imaging the CX3CL1 and CX3CR1 system. In contrast, the CCL2-CCR2 pathway seems to be positively associated with AD disease severity. Recently, a PET probe for CCR2-directed inflammation was successfully introduced (Liu et al. 2017). However, validation in the context of NI is still missing.

Another chemokine of interest is C-X-C motif chemokine receptor 4 (CXCR4) involved in the regulation of leukocyte trafficking (Jacobson and Weiss 2013). CXCR4 can be visualized by PET using the probe [⁶⁸Ga]pentixafor (Buck et al. 2017).

17.3.3 Microglia/Macrophages

Microglia play an important role in tissue homeostasis and response to pathological stimuli (Hickman et al. 2018). Their responsiveness to injury suggests microglia as diagnostic markers of disease onset or progression. Microglia and their counterparts outside of the CNS, macrophages, represent an interesting target for imaging NI.

Various cell surface and mitochondrial receptors expressed in microglia/macrophage cells are involved in the regulation and function of microglia and macrophages, and some of these receptors were used for the development of ligands for imaging. One of the most studied targets is the 18 kDa translocator protein (TSPO, formerly called peripheral benzodiazepine receptor or PBR), which is upregulated in response to neuroinflammatory stimuli. TSPO will be further discussed later in this chapter as well as in another book chapter (Chap. 33). Besides TSPO, new targets for microglia/macrophage imaging are evolving, as TSPO PET in clinical applications is limited by (i) low target density in neurodegeneration, (ii) lack of selectivity for microglia (astrocytes, peripheral macrophages, endothelial cells), (iii) varying binding affinity due to a genetic polymorphism, and (iv) lack of selectivity for various microglia subtypes (Tronel et al. 2017).

New microglia targets include receptor-based ligands (purinergic receptors P2X7 and P2YR12, colony-stimulating factor receptor 1 (CSF-1R), cannabinoid receptors (α7 and α4β2), nicotinic acetylcholine receptors, adenosine 2A receptor, folate receptor β) and enzyme-targeting ligands (cyclooxygenase, nitric oxide synthase, matrix metalloproteinase, β-glucuronidase, and enzymes of the kynurenine pathway) (Wagner et al. 2007; de Vries et al. 2008; Martín et al. 2015; Tronel et al. 2017; Colás et al. 2018; Janssen et al. 2018; Villa et al. 2018; Horti et al. 2019).

Macrophages can be imaged, e.g., with the radiolabeled macrophage mannose receptor (MMR, CD206)-targeting [68Ga]NOTA-anti-MMR nanobodies (Movahedi et al. 2012; Varasteh et al. 2019).

17.3.4 Lymphocytes

Lymphocytes are important mediators of the NI response in neurological disorders but fulfill also physiological functions, including memory consolidation, hippocampal long-term potentiation, and neurogenesis, and they also contribute to psychological stress resilience. In response to NI, lymphocytes infiltrate into the CNS where they enhance and perpetuate neuroinflammatory processes, e.g., in neurodegeneration (González et al. 2014). The vast heterogeneity of NI-associated lymphocytes makes lymphocytes an attractive but also challenging imaging target.

Two important subsets of T cells, CD4+ and CD8+, can be investigated using single-domain antibody fragments (VHHs) and cys-diabodies (Tavaré et al. 2015; Rashidian et al. 2017). Likewise, first approaches for imaging B cells using ^{64}Cu-rituximab were described (James et al. 2017). The use of these new imaging biomarkers in the context of NI remains to be elucidated. In the context of lymphocyte-targeting immunotherapies, immuno-PET will inform on the presence and localization of the therapeutic target (Zettlitz et al. 2019). Likewise, direct visualization of immune checkpoints may support the identification of cellular target expression, heterogeneity of inflammatory lesions, as well as therapy effects (Niemeijer et al. 2018).

17.3.5 Astrocytes

Astrocytes are a heterogeneous and pleomorphic population of glial cells in the brain. Astrocytes are in direct contact with cerebral blood vessels and neurons, forming the neurovascular unit (NVU). Next to physiological functions as regulators of blood flow, neuronal development and activity, energy metabolism, and circadian rhythm, astrocytes differentially respond to NI stimuli. Depending on the underlying stimulus, astrocytes fulfill beneficial and detrimental functions in NI (González et al. 2014; Boche et al. 2019).

Current astrocyte imaging techniques are limited to ^{11}C-deuterium-L-deprenyl (^{11}C-DED) binding to MAO-B. ^{11}C-DED may be used to image early stages of AD (Boche et al. 2019). Recently, imidazoline-2 binding site (I2BS)-targeting tracers are gaining attention for the assessment of astrocytes (Boche et al. 2019).

To noninvasively investigate the (over-) expression, activation, and/or increase/decrease of factors, gene reporters and cells in response to NI by molecular imaging, targets of interest, and their respective tracers have to fulfill certain requirements, as described below (for review, see Elsinga 2002, Patel and Gibson 2008, and Serdons et al. 2009).

17.3.6 Target Considerations

Before developing and designing novel tracers for the investigation of NI, certain criteria should be considered:

1. Unmet clinical need/specific biological question: The decision on a target for tracer development must be based on recent targets in drug development, a currently unmet medical need and/or a biological question, which could not be answered without noninvasive imaging.
2. Level of expression and maximum concentration of target binding sites (B_{max}): Ideally, the target of interest should be expressed in sufficient amounts to be detected by a tracer. As the level of affinity (K_d) of many radiotracers is usually in the pico-/nanomolar range, the expression level of the target should be at least a factor of 4 higher than the K_d ($Bmax/K_d > 4$–10). Targets with low expression levels require a higher radiotracer affinity, in order to show specific binding in vivo (Zhang and Villalobos 2017).
3. Cellular expression: The cellular sources of a certain marker of interest are often not fully characterized. This is of particular importance in tracer development, as this may lead to difficulties in the interpretation of future imaging results. An ideal target is only expressed by a certain cell type at a certain disease state. However, the plasticity of cells and factors and the dynamics of NI make it difficult to achieve this goal. Dedicated immuno-phenotyping and cross-correlation of preclinical and clinical tissue samples may inform on the cellular substrates of the target of interest.

4. Biological function: In line with the characterization of the cellular sources of the target of interest, the precise function of the target should ideally be determined in advance. However, the particular function of the target may change during the course of NI.

5. Target localization: The localization and biological function of the target determines the molecular structure of the lead radio tracer. Most current tracers are small molecule tracers targeting cellular receptors, transporters, enzymes, as well as intra- and extracellular proteins and protein aggregates (Van de Bittner et al. 2014). However, in the era of immunotherapies, radiolabeled biologicals including antibodies, antibody fragments, and nanobodies are increasingly investigated as radio tracers with longer circulation times and biological half-life.

17.3.7 Tracer Considerations

Next to considerations for target selection, the design of NI tracers needs to take the following points into consideration (for review, see Pike 2009, Serdons et al. 2009, Zhang and Villalobos 2017, and Vermeulen et al. 2019):

1. Blood-brain barrier (BBB) penetration: To reach their target in the brain, novel NI tracers need to be able to cross the BBB while avoiding to be actively transported out of the brain by, e.g., P-glycoprotein (P-gp) efflux pumps and/or multidrug resistance-associated proteins (Pike 2009). Additionally, tracers need to be able to cross the cell membrane for intracellular targets.

2. Structure attribute: Structure of the lead compound allows for high specific activity labeling with short-lived isotopes, including F-18 or C-11.

3. Affinity: The affinity for the target should be ideally in the nano- to picomolar range.

4. Specificity/selectivity: The tracer should have a high specificity and selectivity for the target to avoid off-target tracer binding to, for example, plasma proteins.

5. Binding characteristics: The binding characteristics of the lead structure (e.g., covalent vs. non-covalent, internalization, metabolic trapping, etc.) are of importance for the quantification of the imaging signal.

6. Metabolic stability: The biological half-life and the bioavailability of a tracer are determined by the chemical structure of the lead compound and the tracer environment. Nevertheless, most of the tracers are rapidly metabolized by metabolizing enzymes in blood and tissues. It remains important that the resulting radiometabolites are polar and less lipophilic than the parent tracer for rapid washout from the brain, as radiometabolites are indistinguishable from the parent tracer fraction in PET. Ideally, the parent tracer should not be metabolized at all, allowing for determination of true quantitative measures (e.g., regional values of volumes of distribution (V_T) or binding potentials (BP) of the target) (Pike 2009).

Additionally, the biological half-life should be shorter than for a therapeutic drug, as a fast clearance of the tracer from the blood pool will improve the target-to-background ratio (Serdons et al. 2009).

Next to the biological half-life, the half-life of the chosen radioisotope determines the duration of possible biological investigations. For example, isotopes like C-11 with a half-life of about 20 min do not allow repeated imaging sessions, whereas isotopes with longer half-life (e.g., Zr-89, $T_{1/2}$, 78.4 h) allow repeated imaging sessions with a single injection of tracer. However, isotopes with a longer half-life also bear the risk of longer exposure and higher organ doses for the patient (Van Dongen et al. 2015). For quantification purposes it is essential that no brain-permeable radioactive metabolites occur (Pike 2009).

17.4   Preclinical Imaging and Clinical Imaging in Neurological Diseases

After target selection, lead definition, and initial radiotracer synthesis, tracer candidates undergo further ex vivo and in vivo investigations before entering clinical trials.

First, tracer candidates are screened for stability and ex vivo binding affinities (e.g., cellular binding and autoradiography, competition assays). The most promising tracer candidates are then transferred into small animals (mice and rats), including healthy animals (biodistribution, pharmacokinetics, toxicity, kinetic modeling) and disease models of interest. The candidate tracers are then further tested in larger animals, e.g., nonhuman primates (NHP) before entering first-in-man studies in healthy volunteers (dosimetry) and small patient cohorts (Serdons et al. 2009; Zhang and Villalobos 2017). The general workflow of tracer development is summarized in Fig. 17.2.
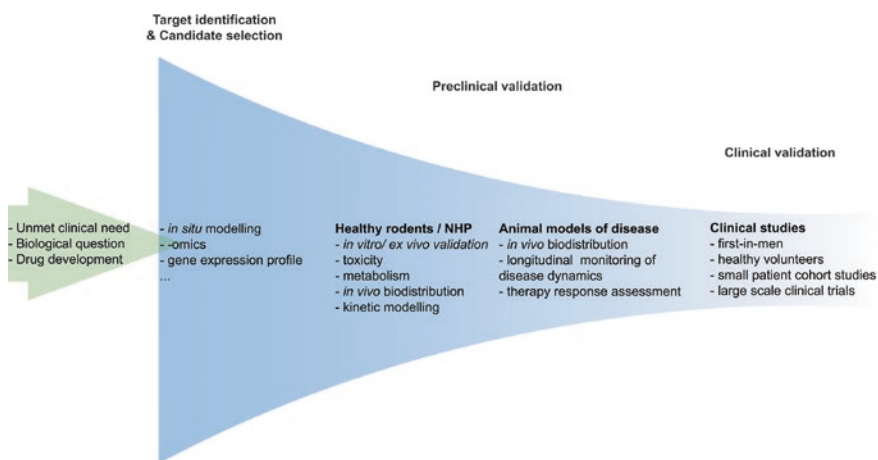
Fig. 17.2 Simplified workflow of tracer development

Along the development of novel imaging biomarkers, important go/no-go decision points have to be taken into consideration. For example, in the initial phase of target selection, tracers are required that have sufficient biological and radiochemical purities (>95%), as well as favorable affinity and in vivo stability (>95%). If one of these points is not met, the target/lead structure should be reconsidered. In accordance, tracers in first in vivo validation not showing favorable pharmacodynamics and pharmacokinetics, target engagement, and sensitivity have to be returned for radiochemical modification. Potential decision points are summarized in Fig. 17.3.

The following paragraphs will highlight examples of NI tracers and their transition from ex vivo to *first-in-patient* applications.
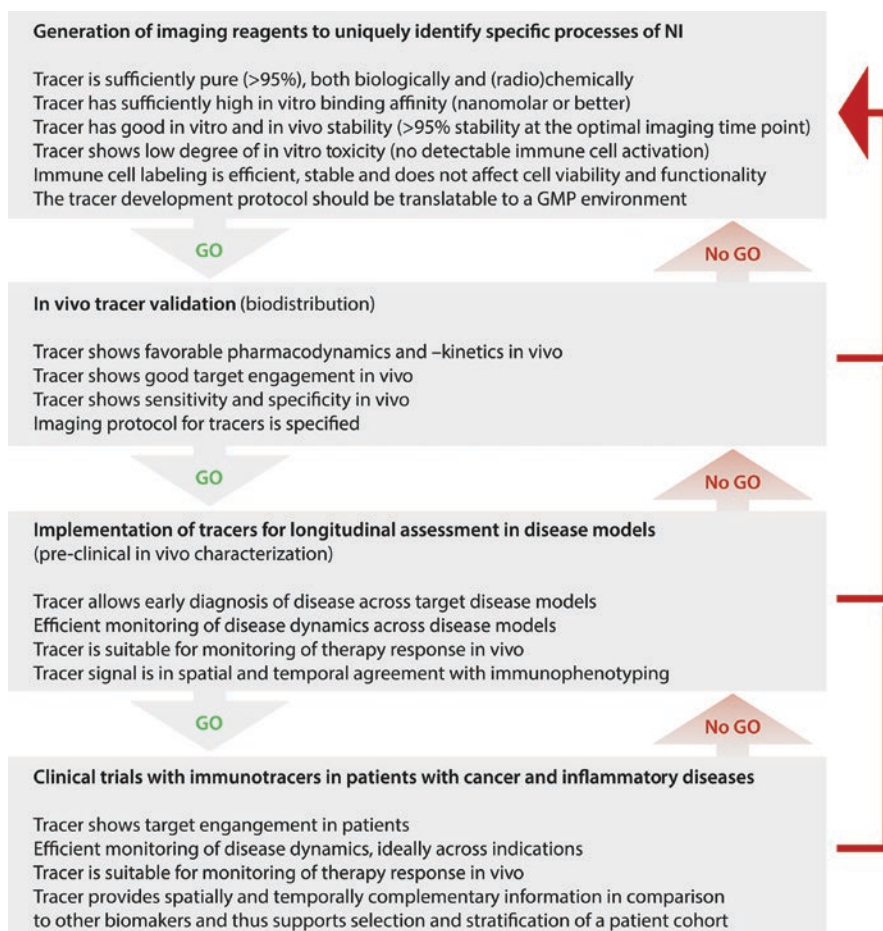
Fig. 17.3 Overview of potential go/no-go decision criteria in the development of imaging biomarkers

17.5   From Ex Vivo Validation to First-in-Man Studies: The Story of [¹⁸F]DPA-714

Upregulation of the 18 kDa translocator protein (TSPO, formerly called peripheral benzodiazepine receptor or PBR) is a hallmark of neuroinflammation. TSPO is located in the outer mitochondrial membrane and involved in the transport of cholesterol into mitochondria. Under physiological conditions, TSPO is expressed by ependymal cells, olfactory bulb neurons, and endothelial cells, but its global expression is low (Rupprecht et al. 2010). In response to neuroinflammatory stimuli, TSPO becomes rapidly and extensively upregulated. However, despite more than 30 years of research, the precise functions of TSPO remain to be elucidated. Initially, TSPO tracers were developed to image microglial activation, highlighting the importance of characterization of cellular sources by immuno-phenotyping. It has to be pointed out that the cellular sources may be depending on the disease context, disease severity, and disease stage (Lavisse et al. 2012; Zinnhardt et al. 2015, 2018; Wiesmann et al. 2017; Villa et al. 2018).

Nevertheless, TSPO meets most of the target criteria for tracer development as described above.

Following the process of target selection, several TSPO tracers were developed. The first-generation TSPO tracer *(R)*-[¹¹C]PK11195 is among them. However, the application of *(R)*- [¹¹C]PK11195 was severely limited by poor signal-to-noise ratios, as well as the short half-life of the ¹¹C-label. Second-generation tracers with improved bioavailability, higher specificity, and favorable signal-to-noise ratios were developed, including [¹⁸F]DPA-714 (Jacobs et al. 2012). Using the example of [¹⁸F]DPA-714, the following paragraphs will exemplary highlight the transition from ex vivo to in vivo applications, including major decision points for transition to the next phase.

The synthesis and first characterization of [¹⁸F]DPA-714 were first described by James et al. (2008). The in vitro binding affinity of the lead molecule DPA-714 for its target TSPO was determined in isolated mitochondria from rat kidneys and C6 glioma cells. Partition coefficients (Log D) were determined by HPLC. In vivo validation was performed in rats after QA-induced excitotoxic damage. For validation of the in vivo biodistribution findings, several brain regions and peripheral organs were harvested and measured ex vivo in a gamma counter. After obtaining encouraging imaging results, pre-dosing with cold DPA-714, DPA-713, and PK11195, respectively, was performed. Pre-dosing led to substantial blocking of the signal, indicating specificity of the tracer.

Biodistribution studies in healthy rats were not performed; instead the biodistribution and specificity of [¹⁸F]DPA-714 were investigated in a more clinically relevant nonhuman primate model after pretreatment with PK11195 5 min before radioligand injection, as well as with a displacement study, where non-labeled DPA-714 was administered 20 min after the injection of [¹⁸F]DPA-714 (James et al. 2008).

Despite an initial validation and proof of specificity, several points remained to be addressed for the ultimate goal of translating [¹⁸F]DPA-714 into clinical

application, including biodistribution in healthy and murine models of disease, histological validation, cross-correlation with other (imaging-) biomarkers, longitudinal studies for the investigation of disease dynamics across various indications, investigations of therapy-induced changes, first-in-man and clinical studies, as well as quantitative modeling of [^{18}F]DPA-714 PET signals.

Consequently, the biodistribution of [^{18}F]DPA-714 was further investigated in mice (Vicidomini et al. 2015) and healthy NHP (Lavisse et al. 2015b). In addition, indispensable for the pharmacodynamic assessment of a lead tracer, the plasma and brain metabolism of [^{18}F]DPA-714 was determined ex vivo and in vivo (Peyronneau et al. 2013).

The in vivo characteristics of [^{18}F]DPA-714 were further analyzed at single time points and longitudinally in various rodent models of NI, including stroke (Fig. 17.4) (Martín et al. 2010; Zinnhardt et al. 2015), glioma (Fig. 17.5) (Tang et al. 2012; Winkeler et al. 2012; Zinnhardt et al. 2017; Pigeon et al. 2019), models of multiple sclerosis (Fig. 17.6) (Abourbeh et al. 2012; Zinnhardt et al. 2019), Alzheimer's disease (AD) (Sérrière et al. 2015; Takkinen et al. 2017; Chaney et al. 2019), Parkinson's disease (Fig. 17.7) (Fricke et al. 2016), ALS (Gargiulo et al. 2016), traumatic brain injury (Wang et al. 2014a; Israel et al. 2016), epilepsy (Harhausen et al. 2013; Nguyen et al. 2018), subarachnoid hemorrhage (Lee et al. 2015), experimental BBB opening (Sinharay et al. 2019), depression and anxiety (Wang et al.
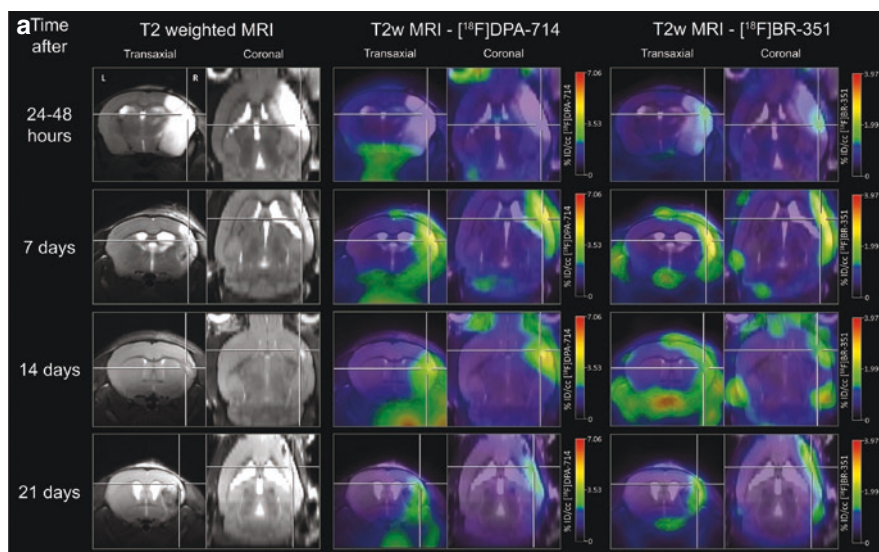
Fig. 17.4 (**a**) Example of a longitudinal study combining two imaging biomarkers of NI [^{18}F]DPA-714 (TSPO) and [^{18}F]BR-351 (MMPs) in the postischemic phase after stroke. (**b**) TSPO PET signals peaked 14 days after stroke, whereas MMP PET preceded peaking 1 week after stroke. (**c**) Histological validation of target expression. The combination of imaging biomarkers and in vivo PET supported the characterization of the reactive postischemic inflammation (modified from Zinnhardt et al. 2015)
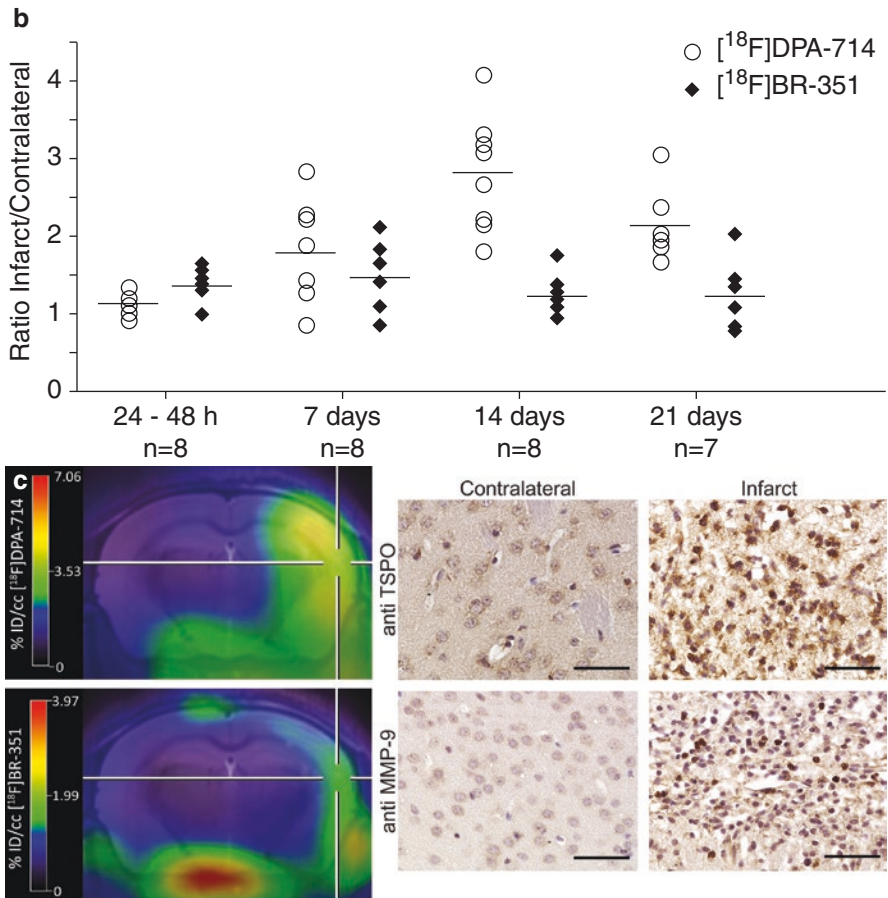
Fig. 17.4 (continued)

2018), alcohol exposure (Saba et al. 2018), morphine exposure (Auvity et al. 2016, 2017), HIV-associated NI (Lee et al. 2015), and Zika virus-associated NI (Lee et al. 2015).

The suitability of [^{18}F]DPA-714 as imaging biomarker to detect therapy-induced changes of disease-modifying therapies was also successfully investigated in various animal models of NI (Martin et al. 2011; Awde et al. 2013; Wang et al. 2014b; Domercq et al. 2016; Wiesmann et al. 2017; Colás et al. 2018; Tan et al. 2018; Zinnhardt et al. 2018).

Importantly, head-to-head comparisons with, for example, first-generation TSPO ligands were performed to understand the relative improvement of tracer
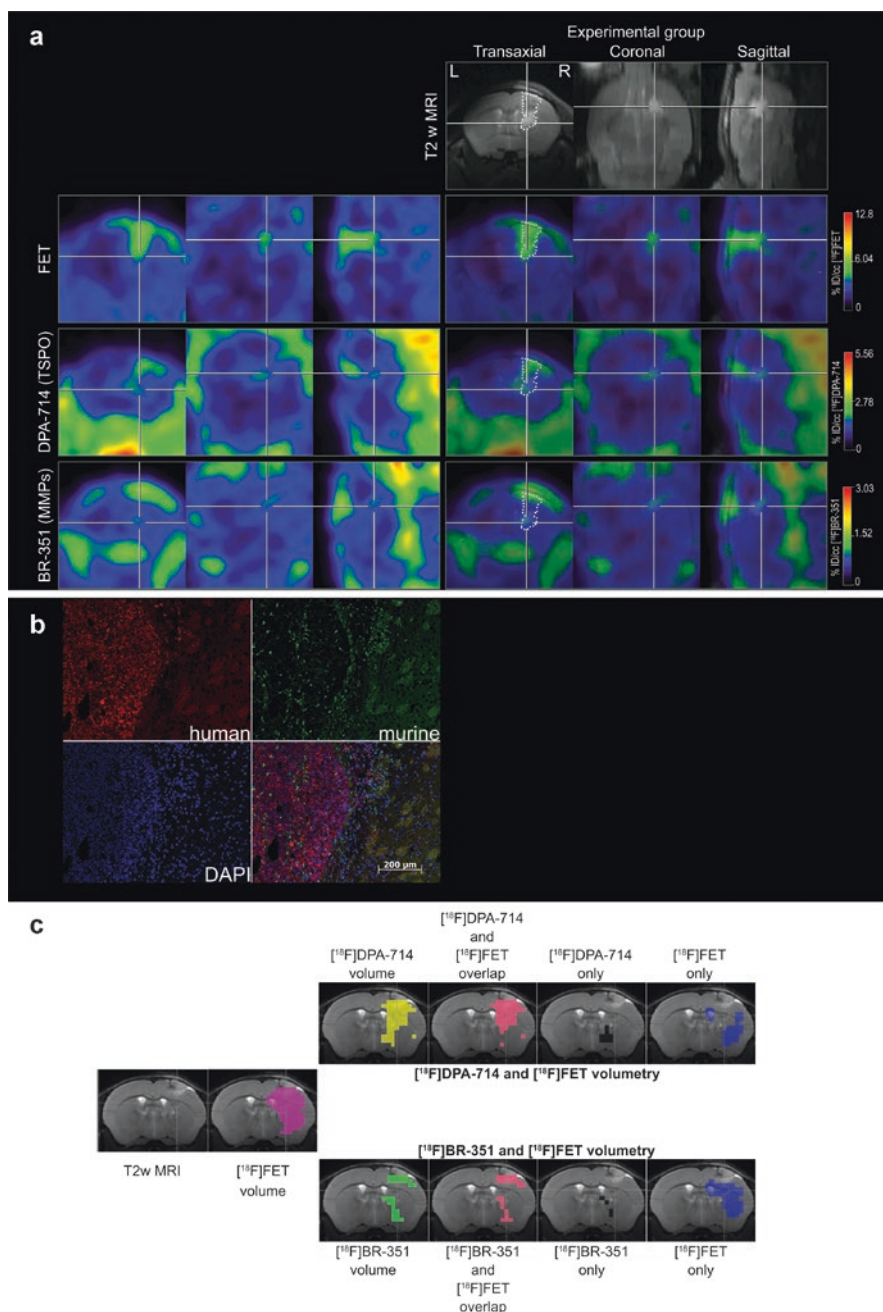
Fig. 17.5 (**a**) The combination of the imaging biomarkers [^{18}F]FET, [^{18}F]DPA-714, and [^{18}F]BR-351 reveals complementary information of the glioma immune microenvironment. (**b**) Histological confirmation of TSPO expression in human glioma cell lines and infiltrating murine immune cells. (**c**) A thresholding-based volumetric analysis reveals distinct areas of tracer uptake, potentially representing areas of tumor infiltration and immune escape (modified from Zinnhardt et al. 2017)
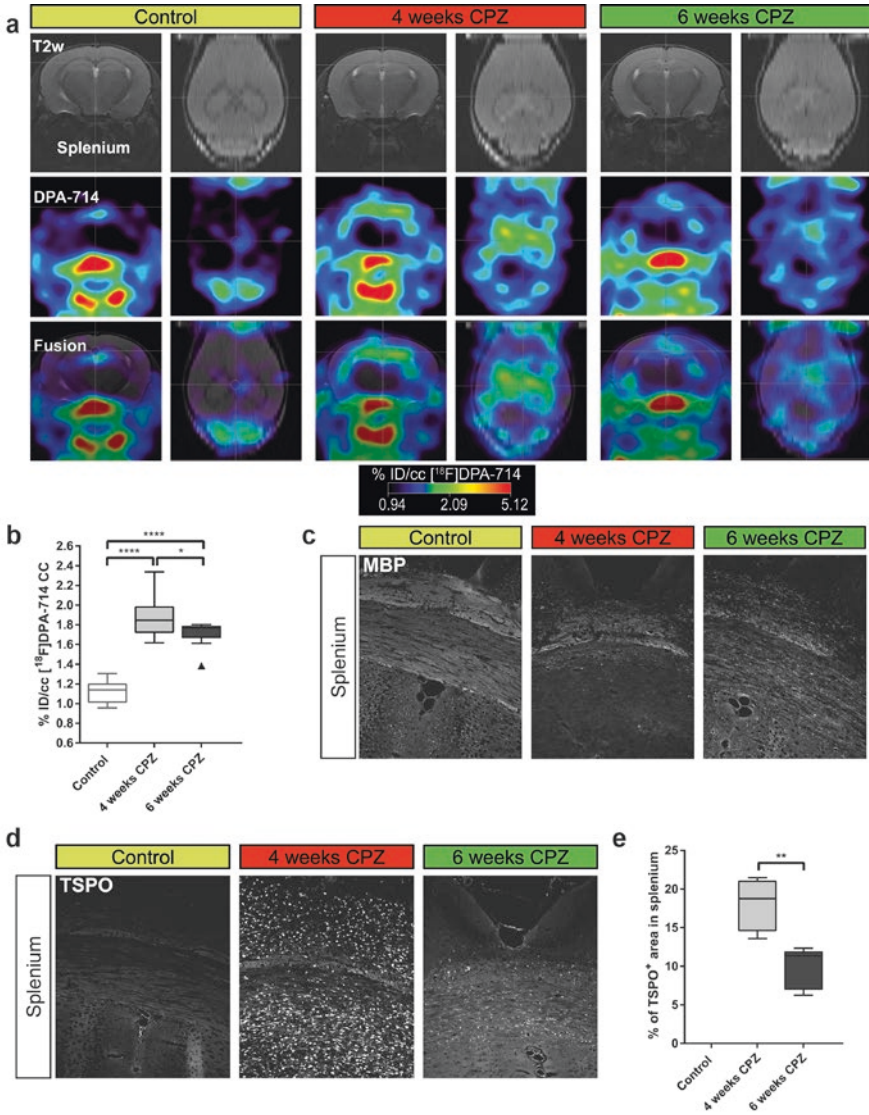
Fig. 17.6 (**a**) [^{18}F]DPA-714 (TSPO) imaging of two distinct disease stages (demyelination at week 4 vs. remyelination at week 6) in the cuprizone model of multiple sclerosis. (**b**) Increased uptake of [^{18}F]DPA-714 was observed during demyelination, whereas uptake levels decreased at remyelination. (**c**) Immunofluorescence for myelin basic protein (MBP) confirmed time-dependent demyelination and remyelination in the cuprizone model. (**d**, **e**) Immunofluorescence confirmed increased TSPO expression in the splenium of the corpus callosum at demyelination (week 4). At remyelination (week 6), TSPO levels decreased again (modified from Zinnhardt et al. 2019)
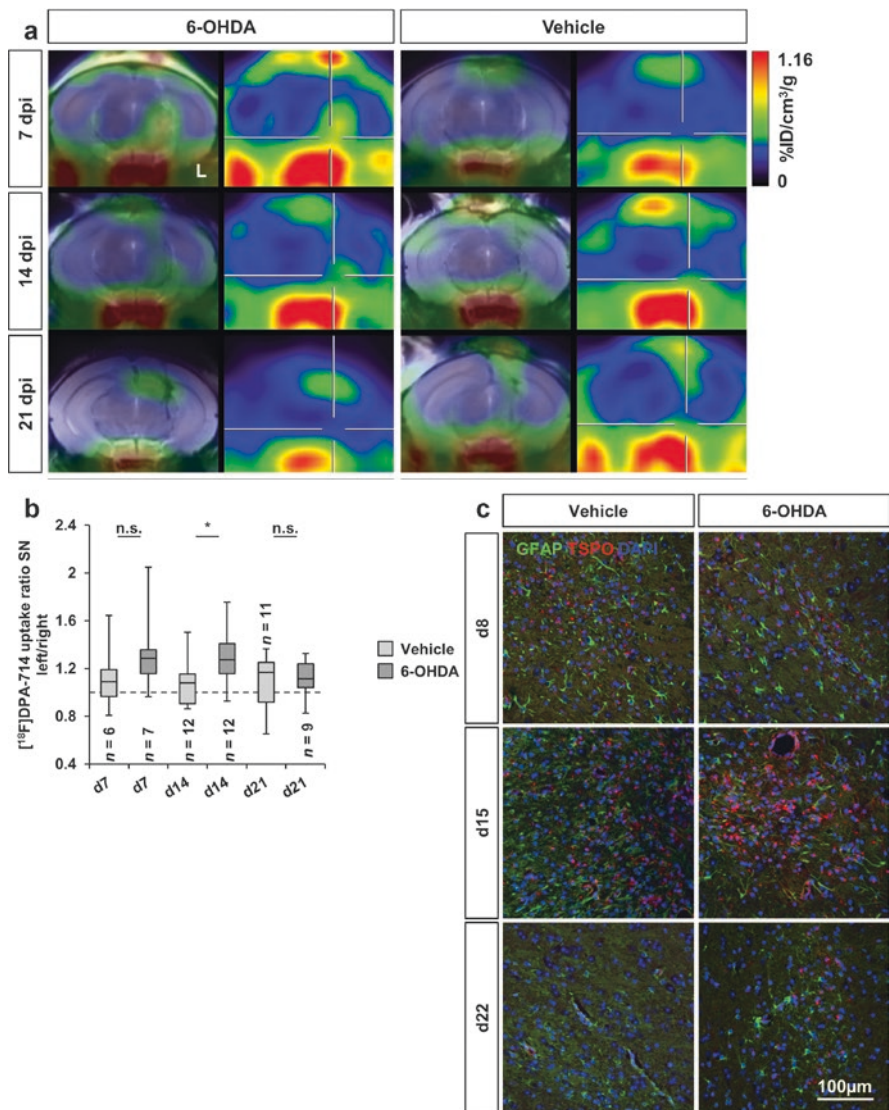
Fig. 17.7 (**a**, **b**) Intranigral 6-OHDA-induced degeneration of the nigrostriatal system is accompanied by increased TSPO levels, measured by [^{18}F]DPA-714 in the substantia nigra. (**c**) Histological markers validate the presence of micro- and astrogliosis in the substantia nigra (modified from Fricke et al. 2016)

characteristics, including an improved higher signal-to-noise ratio (Chauveau et al. 2009; Boutin et al. 2013; Sridharan et al. 2017).

Through histological assessment, most of the studies focusing on NI identified myeloid cells as the major source of TSPO expression (Rupprecht et al. 2010; Jacobs et al. 2012; Chaney et al. 2019). However, the general concept of [^{18}F]DPA-714 as microglia tracer was challenged by Lavisse et al. in Lavisse et al. 2012, highlighting astrocytes as additional source of TSPO expression (Lavisse et al. 2012). Although the expression of TSPO in astrocytes seems to be disease context-dependent and mostly associated with chronic disease stages (Wiesmann et al. 2017; Zinnhardt et al. 2019), these findings again highlight the importance of a detailed characterization of the cellular sources of the target of interest in radiotracer development.

After successful characterization in animal models, another important step toward clinical application was marked with the description of an automated synthesis of [^{18}F]DPA-714 required for manufacturing qualification for clinical production (Kuhnast et al. 2012). Consequently, healthy volunteers were imaged with [^{18}F]DPA-714 including arterial and venous blood sampling to understand the biodistribution characteristics, in vivo stability, and dosimetry of [^{18}F]DPA-714 in humans (Arlicot et al. 2012). [^{18}F]DPA-714 was described with excellent in vivo stability, biodistribution, and acceptable effective dose estimation, paving the way for small cohort studies in patients with neurological diseases, including stroke (Ribeiro et al. 2014), ALS (Corcia et al. 2012), and AD (Hamelin et al. 2016, 2018).

In summary, the development of [^{18}F]DPA-714 as NI tracer represents an excellent example of structured radiotracer development leading to successful clinical applications.

However, the application of [^{18}F]DPA-714 may be complicated by (i) the lack of selectivity of TSPO to distinguish different immune cell subsets, in particular microglia, (ii) the differential binding affinities within the human population (Owen et al. 2010, 2012, 2015), (iii) the intracellular localization of the target, and (iv) challenges in the exact quantification of [^{18}F]DPA-714 signals, due to a lack of a TSPO devoid reference region within the brain (Golla et al. 2015, 2016; Lavisse et al. 2015a; García-Lorenzo et al. 2018; Wimberley et al. 2018).

The challenge to image microglia has led to the identification and investigation of additional targets for imaging NI. In an integrated approach within the EU FP7 framework "Imaging Inflammation in Neurodegenerative diseases," Villa et al. aimed to identify new translational markers of the anti-inflammatory/protective state of microglia for the development of novel PET tracers. Using bioinformatics, genes encoding candidate targets were selected based on the following criteria:

1. The level of expression of the candidate mRNA in the anti-inflammatory state had to be at least twofold higher compared to the resting/surveilling state and to the pro-inflammatory activation state.
2. The genes had to be similarly regulated in rodents and humans.
3. The genes had to be preferentially expressed in microglia.
4. Cell surface expression rather than intracellular expression.

5. Higher expression in microglia versus macrophages (or other neural cell types).
6. Available literature on small molecule compounds binding the encoded proteins (to be used for the development of a PET tracer).

The resulting target candidates were further investigated in human primary macrophage and microglia cultures. Polarization with recombinant IL-4 and LPS is allowed to select markers for anti- and pro-inflammatory microglia, respectively. These candidates were further investigated in microglia isolated from murine brains after intracerebral injection of IL-4 and LPS. The results suggested P2ry12/P2RY12 as a promising translational target for PET imaging of the anti-inflammatory activation state of microglia, due to its high specificity for microglial cells versus other brain cells and macrophages and the high and consistent induction in mouse models of disease in vivo and in human microglia in vitro. Consequently, P2RY12 was chosen for the development of novel PET tracers for application in preclinical and clinical in vivo imaging (Villa et al. 2018).

Together, this study highlights the potential of a rationale-based approach for the identification of new molecular targets for imaging NI and may serve as blueprint for the identification of novel biomarkers in NI.

Currently, several other targets, including the role of purinergic receptors for imaging NI, are under investigation (Jacobs et al. 2012; Janssen et al. 2018; Perani et al. 2019). These will be reviewed elsewhere in this book (e.g., Chap. 26).

17.6   Conclusions

CNS diseases represent a pathophysiologically heterogeneous group of diseases, where neuroinflammation is the common link between cellular stress response, synapse dysfunction, and neuronal damage. Targeting the NI response represents an exciting strategy in drug discovery and patient management to protect neuronal function. However, noninvasive tools to assess the NI response for integration into the drug discovery process and clinical decision-making are still scarce.

Assessing the NI response by molecular imaging remains an important denominator to understand the underlying pathophysiological changes in neurological diseases. In the era of targeted immunotherapies, the detailed characterization of the immuno-environment in neurological diseases is of great fundamental and clinical interest. Novel tracers will provide quantifiable endpoints for the development and early assessment of therapeutic efficacy in various neurological diseases and may support decision-making in drug development. It will be important to cross-correlate imaging findings with in-depth immuno-phenotyping as well as benchmark novel tracer developments against existing NI and clinical standard tracers. The applicability of novel NI tracers in clinical studies will also be strongly dependent on the availability of improved methodology, including the level of standardization, harmonization across centers, and available quantification tools.

Additionally, the application of a single tracer will likely not be sufficient to image the complexity of NI, suggesting that multi-tracer and multi-modality

combinations may be the method of choice to cope with and disentangle the complexity of neurological diseases. To be successful, an integrated, multidisciplinary approach is necessary to facilitate the transition of novel tracers targeting the NI response into clinical application.

References

Abourbeh G, Thézé B, Maroy R, Dubois A, Brulon V, Fontyn Y, Dollé F, Tavitian B, Boisgard R (2012) Imaging microglial/macrophage activation in spinal cords of experimental autoimmune encephalomyelitis rats by positron emission tomography using the mitochondrial 18 kDa translocator protein radioligand [^{18}F]DPA-714. J Neurosci 32:5728–5736

Ardura-Fabregat A, Boddeke EWGM, Boza-Serrano A, Brioschi S, Castro-Gomez S, Ceyzériat K, Dansokho C, Dierkes T, Gelders G, Heneka MT, Hoeijmakers L, Hoffmann A, Iaccarino L, Jahnert S, Kuhbandner K, Landreth G, Lonnemann N, Löschmann PA, McManus RM, Paulus A, Reemst K, Sanchez-Caro JM, Tiberi A, Van der Perren A, Vautheny A, Venegas C, Webers A, Weydt P, Wijasa TS, Xiang X, Yang Y (2017) Targeting neuroinflammation to treat Alzheimer's disease. CNS Drugs 31:1057–1082

Arlicot N, Vercouillie J, Ribeiro M-J, Tauber C, Venel Y, Baulieu J-L, Maia S, Corcia P, Stabin MG, Reynolds A, Kassiou M, Guilloteau D (2012) Initial evaluation in healthy humans of [18F]DPA-714, a potential PET biomarker for neuroinflammation. Nucl Med Biol 39:570–578

Auvity S, Saba W, Goutal S, Leroy C, Buvat I, Cayla J, Caillé F, Bottlaender M, Cisternino S, Tournier N (2016) Acute morphine exposure increases the brain distribution of [^{18} F]DPA-714, a PET biomarker of glial activation in nonhuman Primates. Int J Neuropsychopharmacol 20:pyw077

Auvity S, Goutal S, Thézé B, Chaves C, Hosten B, Kuhnast B, Saba W, Boisgard R, Buvat I, Cisternino S, Tournier N (2017) Evaluation of TSPO PET imaging, a marker of glial activation, to study the neuroimmune footprints of morphine exposure and withdrawal. Drug Alcohol Depend 170:43–50

Awde AR, Boisgard R, Thézé B, Dubois A, Zheng J, Dollé F, Jacobs AH, Tavitian B, Winkeler A (2013) The translocator protein radioligand 18F-DPA-714 monitors antitumor effect of erufosine in a rat 9L intracranial glioma model. J Nucl Med 54:2125–2131

Boche D, Gerhard A, Rodriguez-Vieitez E, Faculty, on behalf of the M (2019) Prospects and challenges of imaging neuroinflammation beyond TSPO in Alzheimer's disease. Eur J Nucl Med Mol Imaging 46(13):2831–2847

Boutin H, Prenant C, Maroy R, Galea J, Greenhalgh AD, Smigova A, Cawthorne C, Julyan P, Wilkinson SM, Banister SD, Brown G, Herholz K, Kassiou M, Rothwell NJ (2013) [18F]DPA-714: direct comparison with [11C]PK11195 in a model of cerebral ischemia in rats. PLoS One 8:e56441

Buck AK, Stolzenburg A, Hänscheid H, Schirbel A, Lückerath K, Schottelius M, Wester H-J, Lapa C (2017) Chemokine receptor – directed imaging and therapy. Methods 130:63–71

Chaney A, Williams SR, Boutin H (2019) In vivo molecular imaging of neuroinflammation in Alzheimer's disease. J Neurochem 149:438–451

Chauveau F, Van Camp N, Dollé F, Kuhnast B, Hinnen F, Damont A, Boutin H, James M, Kassiou M, Tavitian B (2009) Comparative evaluation of the translocator protein radioligands 11C-DPA-713, 18F-DPA-714, and 11C-PK11195 in a rat model of acute neuroinflammation. J Nucl Med 50:468–476

Colás L, Domercq M, Ramos-Cabrer P, Palma A, Gómez-Vallejo V, Padro D, Plaza-García S, Pulagam KR, Higuchi M, Matute C, Llop J, Martín A (2018) In vivo imaging of A7 nicotinic receptors as a novel method to monitor neuroinflammation after cerebral ischemia. Glia 66:1611–1624

Corcia P, Tauber C, Vercoullie J, Arlicot N, Prunier C, Praline J, Nicolas G, Venel Y, Hommet C, Baulieu J-L, Cottier J-P, Roussel C, Kassiou M, Guilloteau D, Ribeiro M-J (2012) Molecular imaging of microglial activation in amyotrophic lateral sclerosis. PLoS One 7:e52941

Domercq M, Szczupak B, Gejo J, Gómez-Vallejo V, Padro D, Gona KB, Dollé F, Higuchi M, Matute C, Llop J, Martín A (2016) PET imaging with [18 F]FSPG evidences the role of system xc - on brain inflammation following cerebral ischemia in rats. Theranostics 6:1753–1767

Elsinga PH (2002) Radiopharmaceutical chemistry for positron emission tomography. Methods 27:208–217

Fricke IB, Viel T, Worlitzer MM, Collmann FM, Vrachimis A, Faust A, Wachsmuth L, Faber C, Dollé F, Kuhlmann MT, Schäfers K, Hermann S, Schwamborn JC, Jacobs AH (2016) 6-hydroxydopamine-induced Parkinson's disease-like degeneration generates acute micro- and astrogliosis in the nigrostriatal system but no bioluminescence imaging detectable alteration in adult neurogenesis. Eur J Neurosci 43:1352

García-Lorenzo D, Lavisse S, Leroy C, Wimberley C, Bodini B, Remy P, Veronese M, Turkheimer F, Stankoff B, Bottlaender M (2018) Validation of an automatic reference region extraction for the quantification of [18 F]DPA-714 in dynamic brain PET studies. J Cereb Blood Flow Metab 38:333–346

Gargiulo S, Anzilotti S, Coda ARD, Gramanzini M, Greco A, Panico M, Vinciguerra A, Zannetti A, Vicidomini C, Dollé F, Pignataro G, Quarantelli M, Annunziato L, Brunetti A, Salvatore M, Pappatà S (2016) Imaging of brain TSPO expression in a mouse model of amyotrophic lateral sclerosis with 18F-DPA-714 and micro-PET/CT. Eur J Nucl Med Mol Imaging 43:1348–1359

Golla SSV, Boellaard R, Oikonen V, Hoffmann A, van Berckel BNM, Windhorst AD, Virta J, Haaparanta-Solin M, Luoto P, Savisto N, Solin O, Valencia R, Thiele A, Eriksson J, Schuit RC, Lammertsma AA, Rinne JO (2015) Quantification of [18F]DPA-714 binding in the human brain: initial studies in healthy controls and Alzheimer's disease patients. J Cereb Blood Flow Metab 35:766–772

Golla SSV, Boellaard R, Oikonen V, Hoffmann A, van Berckel BNM, Windhorst AD, Virta J, Te Beek ET, Groeneveld GJ, Haaparanta-Solin M, Luoto P, Savisto N, Solin O, Valencia R, Thiele A, Eriksson J, Schuit RC, Lammertsma AA, Rinne JO (2016) Parametric binding images of the TSPO ligand 18F-DPA-714. J Nucl Med 57:1543–1547

González H, Elgueta D, Montoya A, Pacheco R (2014) Neuroimmune regulation of microglial activity involved in neuroinflammation and neurodegenerative diseases. J Neuroimmunol 274:1–13

Graeber MB, Li W, Rodriguez ML (2011) Role of microglia in CNS inflammation. FEBS Lett 585:3798–3805

Hamelin L, Lagarde J, Dorothée G, Leroy C, Labit M, Comley RA, de Souza LC, Corne H, Dauphinot L, Bertoux M, Dubois B, Gervais P, Colliot O, Potier MC, Bottlaender M, Sarazin M (2016) Early and protective microglial activation in Alzheimer's disease: a prospective study using 18 F-DPA-714 PET imaging. Brain 139:1252–1264

Hamelin L, Lagarde J, Dorothée G, Potier MC, Corlier F, Kuhnast B, Caillé F, Dubois B, Fillon L, Chupin M, Bottlaender M, Sarazin M (2018) Distinct dynamic profiles of microglial activation are associated with progression of Alzheimer's disease. Brain 141:1855–1870

Harhausen D, Sudmann V, Khojasteh U, Muller J, Zille M, Graham K, Thiele A, Dyrks T, Dirnagl U, Wunder A (2013) Specific imaging of inflammation with the 18kDa translocator protein ligand DPA-714 in animal models of epilepsy and stroke. PLoS One 8:e69529

Hickman S, Izzy S, Sen P, Morsett L, El Khoury J (2018) Microglia in neurodegeneration. Nat Neurosci 21:1359–1369

Honer M, Gobbi L, Knust H, Kuwabara H, Muri D, Koerner M, Valentine H, Dannals RF, Wong DF, Borroni E (2017) Preclinical evaluation of 18 F-RO6958948, 11 C-RO6931643 and 11 C-RO6924963 as novel radiotracers for imaging aggregated tau in Alzheimer's disease with positron emission tomography. J Nucl Med

Horti AG, Naik R, Foss CA, Minn I, Misheneva V, Du Y, Wang Y, Mathews WB, Wu Y, Hall A, LaCourse C, Ahn H-H, Nam H, Lesniak WG, Valentine H, Pletnikova O, Troncoso JC, Smith MD, Calabresi PA, Savonenko AV, Dannals RF, Pletnikov MV, Pomper MG (2019) PET imaging of microglia by targeting macrophage colony-stimulating factor 1 receptor (CSF1R). Proc Natl Acad Sci U S A 116:1686–1691

Israel I, Ohsiek A, Al-Momani E, Albert-Weissenberger C, Stetter C, Mencl S, Buck AK, Kleinschnitz C, Samnick S, Sirén A-L (2016) Combined [18F]DPA-714 micro-positron emission tomography and autoradiography imaging of microglia activation after closed head injury in mice. J Neuroinflammation 13:140

Jacobs AH, Tavitian B, Consortium, Inm (2012) Noninvasive molecular imaging of neuroinflammation. J Cereb Blood Flow Metab 32:1393–1415

Jacobson O, Weiss ID (2013) CXCR4 chemokine receptor overview: biology, pathology and applications in imaging and therapy. Theranostics 3:1–2

James ML, Fulton RR, Vercoullie J, Henderson DJ, Garreau L, Chalon S, Dolle F, Selleri S, Guilloteau D, Kassiou M (2008) DPA-714, a new translocator protein–specific ligand: synthesis, radiofluorination, and pharmacologic characterization. J Nucl Med 49:814–822

James ML, Hoehne A, Mayer AT, Lechtenberg K, Moreno M, Gowrishankar G, Ilovich O, Natarajan A, Johnson EM, Nguyen J, Quach L, Han M, Buckwalter M, Chandra S, Gambhir SS (2017) Imaging B cells in a mouse model of multiple sclerosis using 64 cu-rituximab PET. J Nucl Med 58:1845–1851

Janssen B, Vugts DJ, Windhorst AD, Mach RH (2018) PET imaging of microglial activation-beyond targeting TSPO. Molecules 23:607

Kuhnast B, Damont A, Hinnen F, Catarina T, Demphel S, Le Helleix S, Coulon C, Goutal S, Gervais P, Dollé F (2012) [18F]DPA-714, [18F]PBR111 and [18F]FEDAA1106—selective radioligands for imaging TSPO 18kDa with PET: automated radiosynthesis on a TRACERLAb FX-FN synthesizer and quality controls. Appl Radiat Isot 70:489–497

Kuwabara H, Comley RA, Borroni E, Honer M, Kitmiller K, Roberts J, Gapasin L, Mathur A, Klein G, Wong DF (2018) Evaluation of18F-RO-948 PET for quantitative assessment of tau accumulation in the human brain. J Nucl Med 59:1877–1884

Lavisse S, Guillermier M, Herard AS, Petit F, Delahaye M, Van Camp N, Ben Haim L, Lebon V, Remy P, Dolle F, Delzescaux T, Bonvento G, Hantraye P, Escartin C (2012) Reactive astrocytes overexpress TSPO and are detected by TSPO positron emission tomography imaging. J Neurosci 32:10809–10818

Lavisse S, García-Lorenzo D, Peyronneau M-A, Bodini B, Thiriez C, Kuhnast B, Comtat C, Remy P, Stankoff B, Bottlaender M (2015a) Optimized quantification of translocator protein radioligand ^{18}F-DPA-714 uptake in the brain of genotyped healthy volunteers. J Nucl Med 56:1048–1054

Lavisse S, Inoue K, Jan C, Peyronneau MA, Petit F, Goutal S, Dauguet J, Guillermier M, Dollé F, Rbah-Vidal L, Van Camp N, Aron-Badin R, Remy P, Hantraye P (2015b) [18F]DPA-714 PET imaging of translocator protein TSPO (18 kDa) in the normal and excitotoxically-lesioned nonhuman primate brain. Eur J Nucl Med Mol Imaging 42:478–494

Lee DE, Yue X, Ibrahim WG, Lentz MR, Peterson KL, Jagoda EM, Kassiou M, Maric D, Reid WC, Hammoud DA (2015) Lack of neuroinflammation in the HIV-1 transgenic rat: an [18F]-DPA714 PET imaging study. J Neuroinflammation 12:171

Liu Y, Gunsten SP, Sultan DH, Luehmann HP, Zhao Y, Blackwell TS, Bollermann-Nowlis Z, Pan J, Byers DE, Atkinson JJ, Kreisel D, Holtzman MJ, Gropler RJ, Combadiere C, Brody SL (2017) PET-based imaging of chemokine receptor 2 in experimental and disease-related lung inflammation. Radiology 283:758–768

Martín A, Boisgard R, Thézé B, Van Camp N, Kuhnast B, Damont A, Kassiou M, Dollé F, Tavitian B (2010) Evaluation of the PBR/TSPO radioligand [(18)F]DPA-714 in a rat model of focal cerebral ischemia. J Cereb Blood Flow Metab 30:230–241

Martin A, Boisgard R, Kassiou M, Dolle F, Tavitian B (2011) Reduced PBR/TSPO expression after minocycline treatment in a rat model of focal cerebral ischemia: a PET study using [(18) F]DPA-714. Mol Imaging Biol 13:10–15

Martín A, Szczupak B, Gómez-Vallejo V, Domercq M, Cano A, Padro D, Muñoz C, Higuchi M, Matute C, Llop J (2015) In vivo PET imaging of the α4β2 nicotinic acetylcholine receptor as a marker for brain inflammation after cerebral ischemia. J Neurosci 35:5998–6009

Movahedi K, Schoonooghe S, Laoui D, Houbracken I, Waelput W, Breckpot K, Bouwens L, Lahoutte T, De Baetselier P, Raes G, Devoogdt N, Van Ginderachter JA (2012) Nanobody-based targeting of the macrophage mannose receptor for effective in vivo imaging of tumor-associated macrophages. Cancer Res 72:4165–4177

Nguyen D-L, Wimberley C, Truillet C, Jego B, Caillé F, Pottier G, Boisgard R, Buvat I, Bouilleret V (2018) Longitudinal positron emission tomography imaging of glial cell activation in a mouse model of mesial temporal lobe epilepsy: toward identification of optimal treatment windows. Epilepsia 59:1234–1244

Niemeijer AN, Leung G, Huisman MC, Bahce I, Hoekstra OS, van Dongen GAMS, Boellaard R, Du S, Hayes W, Smith R, Windhorst AD, Hendrikse NH, Poot A, Vugts DJ, Thunnissen E, Morin P, Lipovsek D, Donnelly DJ, Bonacorsi SJ, Velasquez LM, de Gruijl TD, Smit EF, de Langen AJ (2018) Whole body PD-1 and PD-L1 positron emission tomography in patients with non-small-cell lung cancer. Nat Commun 9:4664

Owen DR, Howell OW, Tang S-P, Wells LA, Bennacef I, Bergstrom M, Gunn RN, Rabiner EA, Wilkins MR, Reynolds R, Matthews PM, Parker CA (2010) Two binding sites for [3H]PBR28 in human brain: implications for TSPO PET imaging of neuroinflammation. J Cereb Blood Flow Metab 30:1608–1618

Owen DR, Yeo AJ, Gunn RN, Song K, Wadsworth G, Lewis A, Rhodes C, Pulford DJ, Bennacef I, Parker CA, StJean PL, Cardon LR, Mooser VE, Matthews PM, Rabiner EA, Rubio JP (2012) An 18-kDa translocator protein (TSPO) polymorphism explains differences in binding affinity of the PET radioligand PBR28. J Cereb Blood Flow Metab 32:1–5

Owen DR, Guo Q, Rabiner EA, Gunn RN (2015) The impact of the rs6971 polymorphism in TSPO for quantification and study design. Clin Transl Imaging 3:417–422

Patel S, Gibson R (2008) In vivo site-directed radiotracers: a mini-review. Nucl Med Biol 35:805–815

Perani D, Iaccarino L, Lammertsma AA, Windhorst AD, Edison P, Boellaard R, Hansson O, Nordberg A, Jacobs AH, Bottlaender M, Brooks D, Carroll MA, Chalon S, Gee A, Gerhard A, Halldin C, Herholz K, Herth MM, Hinz R, Knudsen GM, Kuhnast B, López-Picón F, Moresco RM, Pappata S, Rinne JO, Rodriguez-Vieitez E, Santiago-Ribeiro MJ, Turkheimer FE, Van Laere K, Varrone A, Vercouillie J, Winkeler A (2019) A new perspective for advanced positron emission tomography–based molecular imaging in neurodegenerative proteinopathies. Alzheimers Dement 15:1081–1103

Peyronneau M-A, Saba W, Goutal S, Damont A, Dollé F, Kassiou M, Bottlaender M, Valette H (2013) Metabolism and quantification of [18 F]DPA-714, a new TSPO positron emission tomography Radioligand. Drug Metab Dispos 41:122–131

Pigeon H, Pérès EA, Truillet C, Jego B, Boumezbeur F, Caillé F, Zinnhardt B, Jacobs AH, Le Bihan D, Winkeler A (2019) TSPO-PET and diffusion-weighted MRI for imaging a mouse model of infiltrative human glioma. Neuro Oncol 21:755

Pike VW (2009) PET radiotracers: crossing the blood–brain barrier and surviving metabolism. Trends Pharmacol Sci 30:431–440

Ransohoff RM (2009) Chemokines and chemokine receptors: standing at the crossroads of Immunobiology and neurobiology. Immunity 31:711–721

Rashidian M, Ingram JR, Dougan M, Dongre A, Whang KA, LeGall C, Cragnolini JJ, Bierie B, Gostissa M, Gorman J, Grotenbreg GM, Bhan A, Weinberg RA, Ploegh HL (2017) Predicting

the response to CTLA-4 blockade by longitudinal noninvasive monitoring of CD8 T cells. J Exp Med 214:2243–2255

Ribeiro M-J, Vercouillie J, Debiais S, Cottier J-P, Bonnaud I, Camus V, Banister S, Kassiou M, Arlicot N, Guilloteau D (2014) Could (18)F-DPA-714 PET imaging be interesting to use in the early post-stroke period? EJNMMI Res 4:28

Rupprecht R, Papadopoulos V, Rammes G, Baghai TC, Fan J, Akula N, Groyer G, Adams D, Schumacher M (2010) Translocator protein (18 kDa) (TSPO) as a therapeutic target for neurological and psychiatric disorders. Nat Rev Drug Discov 9:971–988

Saba W, Goutal S, Auvity S, Kuhnast B, Coulon C, Kouyoumdjian V, Buvat I, Leroy C, Tournier N (2018) Imaging the neuroimmune response to alcohol exposure in adolescent baboons: a TSPO PET study using ^{18} F-DPA-714. Addict Biol 23:1000–1009

Serdons K, Verbruggen A, Bormans GM (2009) Developing new molecular imaging probes for PET. Methods 48:104–111

Sérrière S, Tauber C, Vercouillie J, Mothes C, Pruckner C, Guilloteau D, Kassiou M, Doméné A, Garreau L, Page G, Chalon S (2015) Amyloid load and translocator protein 18 kDa in APPswePS1-dE9 mice: a longitudinal study. Neurobiol Aging 36:1639–1652

Sinharay S, Tu T-W, Kovacs ZI, Schreiber-Stainthorp W, Sundby M, Zhang X, Papadakis GZ, Reid WC, Frank JA, Hammoud DA (2019) In vivo imaging of sterile microglial activation in rat brain after disrupting the blood-brain barrier with pulsed focused ultrasound: [18F]DPA-714 PET study. J Neuroinflammation 16:155

Sridharan S, Lepelletier F-X, Trigg W, Banister S, Reekie T, Kassiou M, Gerhard A, Hinz R, Boutin H (2017) Comparative evaluation of three TSPO PET radiotracers in a LPS-induced model of mild Neuroinflammation in rats. Mol Imaging Biol 19:77–89

Stephenson J, Nutma E, van der Valk P, Amor S (2018) Inflammation in CNS neurodegenerative diseases. Immunology 154:204–219

Takkinen JS, López-Picón FR, Al Majidi R, Eskola O, Krzyczmonik A, Keller T, Löyttyniemi E, Solin O, Rinne JO, Haaparanta-Solin M (2017) Brain energy metabolism and neuroinflammation in ageing APP/PS1-21 mice using longitudinal ^{18} F-FDG and ^{18} F-DPA-714 PET imaging. J Cereb Blood Flow Metab 37:2870–2882

Tan C, Zhao S, Higashikawa K, Wang Z, Kawabori M, Abumiya T, Nakayama N, Kazumata K, Ukon N, Yasui H, Tamaki N, Kuge Y, Shichinohe H, Houkin K (2018) [18F]DPA-714 PET imaging shows immunomodulatory effect of intravenous administration of bone marrow stromal cells after transient focal ischemia. EJNMMI Res 8:35

Tang D, Hight MR, McKinley ET, Fu A, Buck JR, Smith RA, Tantawy MN, Peterson TE, Colvin DC, Ansari MS, Nickels M, Manning HC (2012) Quantitative preclinical imaging of TSPO expression in glioma using N,N-diethyl-2-(2-(4-(2-18F-fluoroethoxy)phenyl)-5,7-dimethylpyrazolo[1,5-a]pyrimidin-3-yl)acetamide. J Nucl Med 53:287–294

Tavaré R, McCracken MN, Zettlitz KA, Salazar FB, Olafsen T, Witte ON, Wu AM (2015) Immuno-PET of murine T cell reconstitution postadoptive stem cell transplantation using anti-CD4 and anti-CD8 Cys-diabodies. J Nucl Med 56:1258–1264

Tronel C, Largeau B, Santiago Ribeiro MJ, Guilloteau D, Dupont A-C, Arlicot N (2017) Molecular targets for PET imaging of activated microglia: the current situation and future expectations. Int J Mol Sci 18:802

Van de Bittner GC, Ricq EL, Hooker JM (2014) A philosophy for CNS radiotracer design. Acc Chem Res 47:3127–3134

Van Dongen GA, Huisman MC, Boellaard R, Harry Hendrikse N, Windhorst AD, Visser GW, Molthoff CF, Vugts DJ (2015) 89Zr-immuno-PET for imaging of long circulating drugs and disease targets: why, how and when to be applied? Q J Nucl Med Mol Imaging 59:18–38

Varasteh Z, Mohanta S, Li Y, López Armbruster N, Braeuer M, Nekolla SG, Habenicht A, Sager HB, Raes G, Weber W, Hernot S, Schwaiger M (2019) Targeting mannose receptor expression on macrophages in atherosclerotic plaques of apolipoprotein E-knockout mice using 68Ga-NOTA-anti-MMR nanobody: non-invasive imaging of atherosclerotic plaques. EJNMMI Res 9:5

Vermeulen K, Vandamme M, Bormans G, Cleeren F (2019) Design and challenges of radiopharmaceuticals. Semin Nucl Med 49:339

Vicidomini C, Panico M, Greco A, Gargiulo S, Coda ARD, Zannetti A, Gramanzini M, Roviello GN, Quarantelli M, Alfano B, Tavitian B, Dollé F, Salvatore M, Brunetti A, Pappatà S (2015) In vivo imaging and characterization of [18F]DPA-714, a potential new TSPO ligand, in mouse brain and peripheral tissues using small-animal PET. Nucl Med Biol 42:309–316

Villa A, Klein B, Janssen B, Pedragosa J, Pepe G, Zinnhardt B, Vugts DJ, Gelosa P, Sironi L, Beaino W, Damont A, Dollé F, Jego B, Winkeler A, Ory D, Solin O, Vercouillie J, Funke U, Laner-Plamberger S, Blomster LV, Christophersen P, Vegeto E, Aigner L, Jacobs A, Planas AM, Maggi A, Windhorst AD (2018) Identification of new molecular targets for PET imaging of the microglial anti-inflammatory activation state. Theranostics 8:5400–5418

de Vries EFJ, Doorduin J, Dierckx RA, van Waarde A (2008) Evaluation of [11C]rofecoxib as PET tracer for cyclooxygenase 2 overexpression in rat models of inflammation. Nucl Med Biol 35:35–42

Wagner S, Breyholz HJ, Law MP, Faust A, Höltke C, Schröer S, Haufe G, Levkau B, Schober O, Schäfers M, Kopka K (2007) Novel fluorinated derivatives of the broad-spectrum MMP inhibitors N-hydroxy-2(R)-[[(4-methoxyphenyl)sulfonyl](benzyl)- and (3-picolyl)-amino]-3-methyl-butanamide as potential tools for the molecular imaging of activated MMPs with PET. J Med Chem 50:5752–5764

Wang Y, Yue X, Kiesewetter DO, Niu G, Teng G, Chen X (2014a) PET imaging of neuroinflammation in a rat traumatic brain injury model with radiolabeled TSPO ligand DPA-714. Eur J Nucl Med Mol Imaging 41:1440–1449

Wang Y, Yue X, Kiesewetter DO, Wang Z, Lu J, Niu G, Teng G, Chen X (2014b) [(18)F]DPA-714 PET imaging of AMD3100 treatment in a mouse model of stroke. Mol Pharm 11:3463–3470

Wang Y-L, Han Q-Q, Gong W-Q, Pan D-H, Wang L-Z, Hu W, Yang M, Li B, Yu J, Liu Q (2018) Microglial activation mediates chronic mild stress-induced depressive- and anxiety-like behavior in adult rats. J Neuroinflammation 15:21

Wiesmann M, Zinnhardt B, Reinhardt D, Eligehausen S, Wachsmuth L, Hermann S, Dederen PJ, Hellwich M, Kuhlmann MT, Broersen LM, Heerschap A, Jacobs AH, Kiliaan AJ (2017) A specific dietary intervention to restore brain structure and function after ischemic stroke. Theranostics 7:493–512

Wimberley C, Lavisse S, Brulon V, Peyronneau M-A, Leroy C, Bodini B, Remy P, Stankoff B, Buvat I, Bottlaender M (2018) Impact of endothelial 18-kDa translocator protein on the quantification of 18F-DPA-714. J Nucl Med 59:307–314

Winkeler A, Boisgard R, Awde AR, Dubois A, Thézé B, Zheng J, Ciobanu L, Dollé F, Viel T, Jacobs AH, Tavitian B (2012) The translocator protein ligand [18F]DPA-714 images glioma and activated microglia in vivo. Eur J Nucl Med Mol Imaging 39:811–823

Wong DF, Comley RA, Kuwabara H, Rosenberg PB, Resnick SM, Ostrowitzki S, Vozzi C, Boess F, Oh E, Lyketsos CG, Honer M, Gobbi L, Klein G, George N, Gapasin L, Kitzmiller K, Roberts J, Sevigny J, Nandi A, Brasic J, Mishra C, Thambisetty M, Mogekar A, Mathur A, Albert M, Dannals RF, Borroni E (2018) Characterization of 3 novel tau radiopharmaceuticals, 11C-RO-963, 11C-RO-643, and 18F-RO-948, in healthy controls and in Alzheimer subjects. J Nucl Med 59:1869–1876

Zettlitz KA, Tavaré R, Tsai W-TK, Yamada RE, Ha NS, Collins J, van Dam RM, Timmerman JM, Wu AM (2019) 18F-labeled anti-human CD20 cys-diabody for same-day immunoPET in a model of aggressive B cell lymphoma in human CD20 transgenic mice. Eur J Nucl Med Mol Imaging 46:489–500

Zhang L, Villalobos A (2017) Strategies to facilitate the discovery of novel CNS PET ligands. EJNMMI Radiopharm Chem 1:13

Zinnhardt B, Viel T, Wachsmuth L, Vrachimis A, Wagner S, Breyholz H-JH-J, Faust A, Hermann S, Kopka K, Faber C, Dollé F, Pappata S, Planas AMAM, Tavitian B, Schäfers M, Sorokin LMLM, Kuhlmann MTMT, Jacobs AHAH (2015) Multimodal imaging reveals temporal and spatial microglia and matrix metalloproteinase activity after experimental stroke. J Cereb Blood Flow Metab 35:1711–1721

Zinnhardt B, Pigeon H, Thézé B, Viel T, Wachsmuth L, Fricke IB, Schelhaas S, Honold L, Schwegmann K, Wagner S, Faust A, Faber C, Kuhlmann MT, Hermann S, Schäfers M, Winkeler A, Jacobs AH (2017) Combined PET imaging of the inflammatory tumor microenvironment identifies margins of unique radiotracer uptake. Cancer Res 77:1831–1841

Zinnhardt B, Wiesmann M, Honold L, Barca C, Schäfers M, Kiliaan AJ, Jacobs AH (2018) In vivo imaging biomarkers of neuroinflammation in the development and assessment of stroke therapies - towards clinical translation. Theranostics 8:2603

Zinnhardt B, Belloy M, Fricke IB, Orije J, Guglielmetti C, Hermann S, Wagner S, Schäfers M, Van Der Linden A, Jacobs AH (2019) Molecular imaging of immune cell dynamics during De- and remyelination in the cuprizone model of multiple sclerosis by [18F]DPA-714 PET and MRI. Theranostics 9:1523

Preclinical and Clinical Aspects of Nicotinic Acetylcholine Receptor Imaging

18

Peter Brust, Winnie Deuther-Conrad, Cornelius Donat,
Henryk Barthel, Patrick Riss, Louise Paterson,
Alexander Hoepping, Osama Sabri, and Paul Cumming

Contents

P. Brust (✉) · W. Deuther-Conrad · C. Donat
Department of Neuroradiopharmaceuticals, Helmholtz-Zentrum Dresden-Rossendorf,
Research Site Leipzig, Institute of Radiopharmaceutical Cancer Research, Leipzig, Germany
e-mail: p.brust@hzdr.d; w.deuther-conrad@hzdr.de; c.donat@imperial.ac.uk

H. Barthel · O. Sabri
Department of Nuclear Medicine, University of Leipzig, Leipzig, Germany
e-mail: Henryk.Barthel@medizin.uni-leipzig.de; osama.sabri@medizin.uni-leipzig.de

P. Riss
Department of Chemistry, University of Oslo, Oslo, Norway
e-mail: patrick.riss@kjemi.uio.no

L. Paterson
Division of Brain Sciences, Imperial College London, London, UK
e-mail: l.paterson@imperial.ac.uk

A. Hoepping
ABX Pharmaceuticals, Radeberg, Germany
e-mail: hoepping@abx.de

P. Cumming
Department of Nuclear Medicine, Inselspital, Bern University, Bern, Switzerland

School of Psychology and Counselling and IHBI, Queensland University of Technology,
Brisbane, Australia

593

Abstract

Innovations in radiochemistry and pharmacology are opening new vistas for studies of nicotinic acetylcholine receptors (nAChRs) in human brain by positron emission tomography (PET) and by single-photon emission computed tomography (SPECT). In parallel, instrumentation optimized for molecular imaging in rodents facilitates preclinical studies in models of human diseases with perturbed nAChR signalling, notably Alzheimer's disease and other neurodegenerative conditions, schizophrenia and other neuropsychiatric disorders, substance abuse and traumatic brain injury. The nAChRs are ligand-gated ion channels composed of five subunits forming a central pore for cation flux. The most abundant nAChRs in the central nervous system are heteropentamers (designated $\alpha 4 \beta 2$), followed by the $\alpha 7$ homopentamer. We present a systematic review of published findings with the various nAChR ligands using imaging techniques in vivo, emphasizing preclinical models and human studies. Molecular PET imaging of the $\alpha 4 \beta 2$ nAChR subtype with the antagonist 2-[^{18}F]fluoro-A-85380 is hampered by the long acquisition times. Newer agents such as $(-)$-[^{18}F]flubatine, [^{18}F]XTRA or [^{18}F]nifene permit quantitation of $\alpha 4 \beta 2$ receptors with PET recordings lasting 90 min or less and without the toxicity risk of earlier epibatidine derivatives. The early PET studies of $\alpha 7$ nAChRs suffered from low pharmacological specificity, further hampered by low natural abundance of the receptor. However, several good $\alpha 7$ nAChR ligands such as [^{18}F]ASEM and [^{18}F]DBT10 have emerged in the past few years. There are still no ligands selective for $\alpha 6$-containing nAChRs, despite their importance for nicotine-induced dopamine release in striatum. Selective $\alpha 3 \beta 4$ nAChR radioligands are under development but remain untested in clinical studies of depression and addiction. Several nAChR ligands find use for pharmacological occupancy studies, and competition from endogenous acetylcholine reduces $\alpha 4 \beta 2$ binding site availability, a property that enables monitoring by PET of acetylcholine release in living brain.

18.1   Introduction

Nicotine is an addictive drug named after the French diplomat Jean Nicot, who introduced cultivation of the tobacco plant (*Nicotiana tabacum*) in Europe. As early as 1828, nicotine was characterized as the major pharmacologically active substance of this solanaceous herb (Posselt and Reimann 1828). Elucidation of its chemical structure followed 60 years later (Pinner and Wolffenstein 1891; Pinner 1893), and soon thereafter Amé Pictet obtained the first successful synthesis (Pictet 1903). The stimulation of sympathetic ganglia by nicotine, first observed by John Newport Langley in Cambridge (Langley 1901), led to the concept that receptors mediate drug actions (Langley 1905; Bennett 2000) and ultimately to the modern concept of molecular neurotransmission.

Nicotine and related alkaloids are present in other *Solanaceae*, such as tomato, potato, peppers and eggplant, and also in tea leaves (Schep et al. 2009), such that the mean daily dietary nicotine intake is about 1.4 μg per day (Siegmund et al. 1999). Nicotine absorption in the gut is rapid, and it is highly permeable to the blood-brain barrier (Oldendorf et al. 1979; Allen and Lockman 2003). Indeed, inhaled nicotine enters the brain within seconds (Rose et al. 2010), which may account for the perniciousness of smoking as a vehicle for nicotine self-administration. Within the brain, nicotine binds with high affinity to heteromeric (mainly the α4β2 subtype) and homomeric (mainly the α7 subtype) nicotinic acetylcholine receptors (nAChRs) (Changeux 2010; Bouzat and Sine 2018), which are the focus of this chapter. Signalling by the endogenous agonist acetylcholine via cerebral nAChRs is critically involved in attention, vigilance and cognition, as well as locomotion and reward mechanisms (Changeux 2010; Graef et al. 2011). Activation of nAChRs stimulates dopamine release in the basal ganglia, especially in the ventral striatum (Pradhan et al. 2002; Cumming et al. 2003), which almost certainly underlies the addictive potential of nicotine and tobacco smoking (Hogg et al. 2003). Furthermore, nAChRs play a major role in brain development (Hruska et al. 2009; Ross et al. 2010). Recently allosteric modulators of nAChRs are undergoing intensive consideration for drug development (Chatzidaki and Millar 2015; Wang and Lindstrom 2018).

Nicotinic receptors, in particular the α7 subtype, are expressed by many classes of neurons and indeed by virtually all cell types of the brain, including astrocytes (Sharma and Vijayaraghavan 2001), microglia (De Simone et al. 2005; Suzuki et al. 2006), oligodendrocyte precursor cells (Sharma and Vijayaraghavan 2002) and endothelial cells (Hawkins et al. 2005). Perhaps consistent with this protean cellular distribution, there is evidence for dysfunction of nAChRs in diverse human neurological and psychiatric diseases (Jasinska et al. 2014; Bertrand et al. 2015; Dineley et al. 2015), which motivates the present search for optimal molecular imaging agents.

The nAChRs belong to the Cys-loop superfamily of pentameric ligand-gated ion channels, which also includes the serotonin 5-HT$_3$, γ-aminobutyric acid (GABA$_A$ and GABA$_C$) and glycine receptors, as has been reviewed in detail (Paterson and Nordberg 2000; Taly et al. 2009; Plested 2016). Functional nAChRs consist of

pentamers of homologous or heterologous subunits forming a central cation channel permeable for Na^+, K^+ and Ca^{2+} ions. There are at least 17 genes encoding the following subunits: α1–10, β1–4, δ ε and γ (Karlin 2002), all of which occur in mammals except for the avian α8 subunit. Each monomer possesses an extracellular N-terminal domain, four transmembrane helices and a small cytoplasmic region (Karlin 2002). Also, the 1.76 Å resolution X-ray structure of a nAChR homologue, the prokaryotic acetylcholine-binding protein (AChBP), has been reported (Brejc et al. 2001; Bourne et al. 2005; Hibbs et al. 2009), and a refined model of the membrane-associated nAChR from Torpedo electric organ based on 4 Å resolution electron microscopy data has been presented (Unwin 2005). An X-ray crystal structure is now available for the human α4β2 subtype, bound to nicotine (Giastas et al. 2018).

The consensus nomenclature for nAChRs is based on the predominant subunit composition of the receptor (Alexander et al. 2017). Although most functional receptors are heteromers, the α7–10 subunits form functional homomers in vivo. Most neuronal nAChRs contain α- and β-subunits only (δ, ε and γ are expressed in peripheral tissues). Of the various possible αβ permutations, nAChRs with six of the α-subunits (2–7) and three of the β-subunits (2–4) have been identified in mammalian brain, with heteromeric α4β2 nAChRs predominating (Gotti et al. 2006). The next most abundant cerebral nAChR is the homomeric α7 subtype, which is functionally distinct from the heteromeric nAChRs due to its lower affinity for the agonists acetylcholine and nicotine and higher affinity for α-bungarotoxin, an antagonistic derived from snake venom. Indeed, radiolabelled α-bungarotoxin serves admirably for selective α7 autoradiography in vitro (Clarke et al. 1984). The α7 nAChRs show relatively fast activation and have the highest permeability to Ca^{2+} of all nAChR subtypes, whereas the α4β2 hetero-oligomer is characterized by a high affinity for ACh and slow desensitization (Changeux 2010). A recent study indicates that heteromeric α7β2 nAChRs are also naturally present in the brain and are functionally distinct from the α7 nAChR (Wu et al. 2016).

In general, activation of nAChRs requires cooperativity between subunits, with the agonist binding sites being located at subunit interfaces (Taylor et al. 1994). Activation of nAChR heteromers requires binding of two ACh molecules at orthosteric binding sites, which are formed within the hydrophilic extracellular domain from three peptide domains on the α-subunit and three domains on the adjacent subunits (β or other) (Kalamida et al. 2007). Homomers have five acetylcholine binding sites, one between each α-α-subunit interface (Millar and Harkness 2008).

As noted above, the nAChRs can shift between functionally distinct conformational states. Four such states have been identified: resting (R), activated (A) with rapid opening within 1 ms and low affinity (μM to mM) for agonists, and two desensitized, which are closed channel states refractory to opening for intervals lasting ms (I, insensitive) or minutes (D, desensitized), although still possessing high affinity (pM to nM) for receptor agonists (Decker et al. 2000; Auerbach 2015). Thus, binding of ligands either at the orthosteric site or any of several allosteric sites alters the functional state of nAChRs by favouring particular conformational states, consequently modifying the equilibrium between the four states of the receptor (Taly

et al. 2009). Activation of nAChRs increases cation influx. This has a spectrum of consequences, including (i) immediate effects, such as neurotransmitter release; (ii) short-term effects, such as receptor desensitization and recovery; and (iii) long-lasting adaptive effects, such as neuroprotection or brain plasticity via altered gene expression (Radcliffe and Dani 1998; Leonard 2003; Shen and Yakel 2009). The particular pathways of intracellular signalling evoked by activation of nAChRs are complex and cell-specific (Frazier et al. 1998; Schilström et al. 2000; Berg and Conroy 2002).

Neuronal nAChRs in the brain are localized at post-, pre-, peri- and extrasynaptic sites of cholinergic or other neurones, affording multiple ways in which to modulate brain function. Prolonged exposure of nAChRs to agonists (e.g. nicotine) results in upregulation of functional receptors (i.e. an increase in the number of [^{3}H]nicotine binding sites) rather than the downregulation typically seen with G-protein-coupled metabotropic receptors. This upregulation is thought to occur via altered nAChR turnover, resulting in increased insertion of receptors into the cell membrane, or decreased removal via altered endocytotic trafficking or degradation rates (Peng et al. 1994; Darsow et al. 2005). The predominant nAChRs in the brain, α4β2 and α7, seem particularly sensitive to this form of post-translational regulation. In analogy to dopamine receptors (Cumming 2011), multiple affinity states of nAChRs are differentially sensitive to agonist and antagonist ligands. Exposure to acetylcholine, other agonists and pharmacological chaperones can alter the affinity states of the nAChRs receptor to influence receptor translocation and modulate the cell surface expression of nAChR subtypes (Darsow et al. 2005; Kumari et al. 2008; Govind et al. 2009; Lester et al. 2009; Crespi et al. 2018).

The total concentration of nAChRs in membrane homogenates from rodent brain is between 8 and 15 pmol/g tissue (Wang et al. 2011), and in human brain up to 10 pmol/g tissue (Shimohama et al. 1985; Marutle et al. 1998), which is similar to the abundance of dopamine receptors in striatum (Cumming 2011). The predominant heteromeric α4β2 nAChRs receptors account for some 80% of the total abundance of brain nAChRs (Wang et al. 2011). For the less abundant α7 nAChRs, a B_{max} of 5 pmol/g tissue has been described in mice (Whiteaker et al. 1999), while levels of [^{125}I]α-bungarotoxin binding in the temporal cortex were only 1 pmol/g tissue for human and monkey (Gotti et al. 2006). Notably, these studies are based on tissue homogenates. However, the native environment of nAChRs is important for accurate quantitation of nAChRs in the brain (Wang et al. 2011); a very similar phenomenon has been described for other receptors, e.g. dopamine (Cumming 2011) and opioid receptors (Quelch et al. 2014), suggesting that many receptors may be lost during the preparation of membranes or that not all receptors are externalized in the plasma membrane. Therefore, to predict the potential of nAChR radioligands for molecular imaging, binding to nAChRs should in general be tested by autoradiographic analysis of sections from frozen, intact brain.

The relatively few quantitative autoradiographic studies consistently report higher nAChR densities than homogenate-based studies. Autoradiographic studies with ligands for heteromeric α4β2 nAChRs characteristically reveal particularly intense binding in the thalamus (Fig. 18.1). Using [^{18}F]FNEP, the B_{max} for
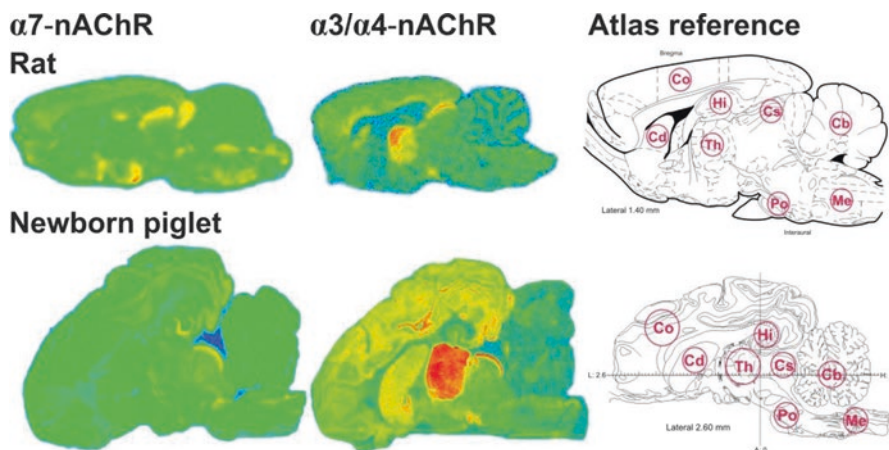
Fig. 18.1 Representative autoradiograms of rat (*upper row*) and neonate pig brains (*lower row*) obtained with an α7 nAChR ligand ([^{125}I]α-bungarotoxin) and the semi-selective α4β2 ligand [^{3}H]epibatidine. For anatomic reference, the right-hand side of the figure shows comparable sagittal planes modified from the rat brain atlas (Paxinos and Watson 1998) and the pig brain atlas (Felix et al. 1999). Structures marked in the references atlases are *Co* cerebral cortex, *Cd* caudate nucleus, *Cs* superior colliculus, *Cb* cerebellum, *Hi* hippocampus, *Th* thalamus, *Po* pons, *Me* medulla oblongata

heteromeric nAChRs in human thalamus autoradiograms was 20 pmol/g tissue (Gatley et al. 1998), which is comparable to the density of binding sites of 2-[^{18}F]fluoro-A-85380 in porcine thalamus, i.e. 46 pmol/g tissue (Deuther-Conrad et al. 2006). In quantitative receptor autoradiographic studies with the α7 selective ligands [^{3}H]MLA and [^{125}I]α-bungarotoxin, densities were as high as 40 pmol/g tissue in mouse brain (Whiteaker et al. 1999), whereas other studies with [^{125}I]α-bungarotoxin have indicated densities of 4–20 pmol/g tissue in rat and 2–10 pmol/g tissue in neonate pig (Hoffmeister et al. 2011). Across species, autoradiographic studies have revealed a characteristic distribution pattern for α7 nAChRs (Fig. 18.1), which is rather diffuse, but with focally high density in the hippocampus, the colliculi and the hypothalamus (except in newborn piglet), with moderate radiotracer binding in thalamus and low expression in the cerebellum (Breese et al. 1997; Whiteaker et al. 1999; Hoffmeister et al. 2011). The regional distribution of the α7 nAChR ligand [^{3}H]AZ11637326 in rat brain by autoradiography ex vivo (in which the tracer had been administered while the animal was alive) was consistent with autoradiography findings in vitro (Maier et al. 2011).

Molecular brain imaging of nAChRs in general refers to the use of radiolabelled receptor ligands, although optical imaging has been used to investigate the cholinergic system (Prakash and Frostig 2005). Furthermore, clinical imaging of α4β2 nAChR in Alzheimer's disease is reviewed elsewhere (see Sabri et al. in PET and SPECT in Neurology). Therefore, the current review is focussed primarily, albeit not exclusively, on preclinical aspects of PET and SPECT brain imaging of the

nAChR in vivo, along with a presentation on instrumentation and radiotracer development. This review is updated and extended from an earlier chapter on the same topic (Brust et al. 2014).

18.2   Advances in Animal PET and SPECT Technology

As noted above, studies of nAChRs abundance in vitro and ex vivo use selective radioligands in conjunction with quantitative autoradiography. However, molecular imaging with positron emission tomography (PET) or single-photon emission computed tomography (SPECT) enables the detection of neuroreceptors in the living brain. Contrary to autoradiography in vitro, imaging procedures in vivo allow for longitudinal studies in individual animals, thereby reducing intersubject variability and allowing intervention or challenge studies. Animal PET studies using clinical scanners, most having a spatial resolution of approximately 5 mm, are barely adequate for resolution of structures within mouse brain, which measures only 10 mm along its longest axis.

Although dedicated small-animal PET systems such as the Focus series (Siemens), microPET P4 (Concorde Microsystems) or ClearPET (Raytest) enable microPET imaging in rodents and small non-human primates with high resolution and sensitivity, these instruments are no longer commercially available. However, current efforts aim to improve the performance of stand-alone small-animal PET scanners by using detector systems approaching the physical limits of spatial resolution (circa 1 mm) with optimized reconstruction algorithms (Yang et al. 2016). Other approaches are to improve the spatial resolution of commercially available systems by optimizing the arrangement of detectors (Bolwin et al. 2017), or applying new detector material (Abbaszadeh and Levin 2017). Commercial stand-alone PET systems designed for small-animal imaging include the beta-CUBE (Molecubes) or VECTor (MILabs). Contemporary small-animal PET scanners increasingly combine the PET and MRI imaging modalities in one instrument. Sequential PET and MR measurements can be realized with instruments such as the nanoScan PET/MRI systems (Mediso). The PET CLIP-ON system (MR Solutions). The PET/MR 3T system (Bruker) or the PET INSERT system (MR Solutions) give simultaneous multimodal acquisitions.

Despite spatial resolution approaching 1 mm, images from small-animal PET and SPECT instruments suffer from a lack of anatomic information. In common practice, the emission images are registered to digitized brain atlases, based on histology or magnetic resonance imaging (MRI) atlases for rodent brain (Jupp et al. 2007; Rominger et al. 2010). Contemporary multimodal imaging systems combine small-animal PET with SPECT, X-ray computed tomography (CT) and/or MRI. PET-CT presents a great advantage for brain studies in that a high-resolution structural brain image in perfect registration with the PET image is obtained for each individual animal, without resorting to some standard atlas. In addition, the CT scan serves to correct the PET images for attenuation by tissue, thus providing

absolute quantitation of radioactivity concentrations in the brain without requiring an additional time-consuming transmission scan. MRI offers better tissue contrast than CT, but the combining of PET and MRI instrumentation initially presented a greater technical challenge.

Initially, the instrumentation for simultaneous small-animal imaging entailed the development of PET inserts, with special efforts made by research teams in academia and industry to improve the PET detector technology with regard to MRI compatibility. An early prototype PET/MRI scanner developed at the University of Cambridge (Lucas et al. 2007) was followed by the commercial PET/MRI system for rodents developed by Mediso; its 1 tesla permanent magnet limits MRI applications but offers great flexibility for animal PET studies. PET inserts using silicone-based photoelectron multipliers are compatible with magnetic fields (Wehner et al. 2015), and a recently developed PET insert can operate within the bore of a 7 T magnet (Thiessen et al. 2016). Likewise, a SPECT camera that can be placed within an MRI magnet has recently been developed for small-animal studies (Meier et al. 2011). Whereas PET attenuation correction is usually obtained by CT scanning, MR-based attenuation correction has been demonstrated for PET and SPECT imaging using clinical scanners (Marshall et al. 2011) and has recently successfully been proven for small-animal studies (Kranz et al. 2014, 2016; Sattler et al. 2014). Despite considerable progress, simultaneous PET/MRI scanners have lower detection sensitivity in comparison with dedicated PET scanners (Cabello and Ziegler 2018; Hallen et al. 2018). However, in recent years the focus has shifted towards the development of fully integrated scanners (Ko et al. 2016; Parl et al. 2019).

Most animal PET studies are confounded by the need to use anaesthesia, which can profoundly alter radiotracer pharmacokinetics. Monkeys are trained to tolerate head fixation during PET recordings lasting as long as 30 min (Sandiego et al. 2013). The "rat conscious animal PET" (ratCAP) with a head-mounted PET detector was developed at Brookhaven for imaging in awake, behaving rats (Schulz et al. 2011). While this technology has been slow to mature, there is a recent report of FDG PET recordings in awake, behaving chickens and rats (Gold et al. 2018).

18.3 PET and SPECT Radioligands Targeting nAChR

Many autoradiographic studies of nAChRs in human post-mortem brain specimens have employed rather non-selective agonist ligands such as [^{3}H]acetylcholine, [^{3}H]nicotine, [^{3}H/^{125}I]epibatidine or [^{3}H]cytisine, or alternately the antagonist ligand [^{3}H/^{125}I]α-bungarotoxin (Paterson and Nordberg 2000). These studies suggested the existence of at least three native receptor subtypes, i.e. α-bungarotoxin binding at homomeric α7 nAChRs and acetylcholine/nicotine binding mainly at heteromeric α4β2 nAChRs, plus a relatively small population of heteromeric receptors containing the α3 subunit. Given the predominance of α4β2 and the α7 subtypes in the brain as documented above, they have presented the main targets for molecular imaging of nAChRs. The available information on the distribution, density and functional role of other subtypes in the brain is relatively sparse (Gotti et al. 2006; Sharma and

Vijayaraghavan 2008; Zoli et al. 2015). Furthermore, the current emphasis on α4β2 and the α7 subtypes as targets for pharmaceutical development may account for the paucity of selective high-affinity drugs for the other subtypes (Gündisch and Eibl 2011) due to a kind of circularity.

18.3.1 Radioligands for α4β2 nAChRs

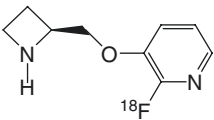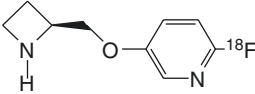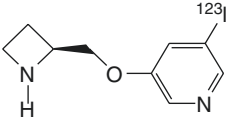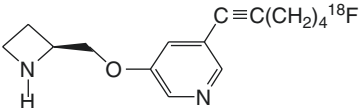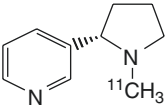Reviews summarizing the history of ligand development for the nAChRs (Sihver et al. 2000a, b; Ding and Fowler 2005; Horti and Villemagne 2006; Horti et al. 2010) have helped galvanize research groups to generate new lead compounds for molecular imaging and therapeutics. Selectivity and high affinity (nM) in vitro are necessary but not sufficient for successful visualization of nAChRs. In general, PET and SPECT tracers, if they are to be successful, must fulfil a multitude of additional criteria. Chief among these are (1) low non-specific binding and absence of brain-penetrating radiometabolites, (2) rapid clearance from non-specific brain regions and plasma to reduce background in the target tissue, (3) high membrane permeability, (4) high permeability and low efflux at the blood-brain barrier (BBB) and (5) attainment of equilibrium binding with a tolerable time interval. Settling upon optimal tracers is often a matter of fierce competition.

The vast majority of novel tracers for α4β2 nAChRs derive from three compounds: nicotine, epibatidine and 3-pyridyl ether. Seven of these tracers have so far been used successfully to image α4β2 receptors in human brain: S-[^{11}C]nicotine (Nordberg 1993); the two halogen-substituted derivatives of A-85380, namely, 2-[^{18}F]fluoro-A-85380 (Kimes et al. 2003) and 6-[^{18}F]fluoro-A-85380 (Ding et al. 2000a; Horti et al. 2000); the two epibatidine derivatives (−)-[^{18}F]flubatine and (+)-[^{18}F]flubatine (Sabri et al. 2018; Tiepolt et al. 2018); [^{18}F]nifene (Betthauser et al. 2017); and [^{18}F]XTRA (Coughlin et al. 2018c). Receptor-ligand interactions frequently entail stereoselective features (Smith and Jakobsen 2007), as has been formally demonstrated for the case of nAChRs in human PET studies with the two stereoisomers of [^{11}C]nicotine (Nordberg et al. 1991, 1992), and also several of the radioligands discussed below. A summary of the compounds that have been investigated for imaging of α4β2 nAChRs with PET and SPECT, their associated references, binding affinities and results of biodistribution ex vivo and PET imaging studies is given in Table 18.1.
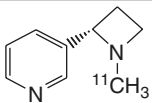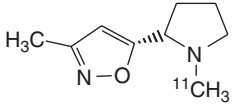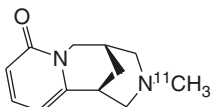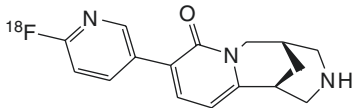
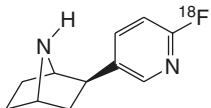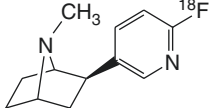#### 18.3.1.1 Nicotine Derivatives

The tracer S-[^{11}C]nicotine, one of the very first positron-emitting receptor ligands (Maziere et al. 1976), was initially developed to investigate the biodistribution of nicotine in the context of tobacco addiction and for investigation of diabetes insipidus and for insecticide research (Soloway 1976; Gündisch 2000). With the advent of PET, S-[^{11}C]nicotine was tested for imaging nAChRs in human brain (Nordberg 1993). However, co-administration of unlabelled nicotine failed to displace much of the radioligand, indicating that the PET signal did not sensitively reveal specific binding to α4β2 nAChRs (Nybäck et al. 1994); cerebral S-[^{11}C]nicotine uptake

Table 18.1 Molecular structures, IUPAC names, binding affinities and results of biodistribution ex vivo and PET imaging studies in vivo of the cerebral binding of α4β2 nAChR-selective radioligands

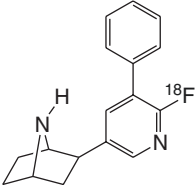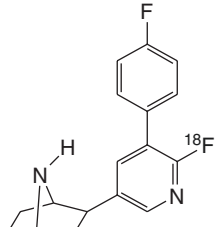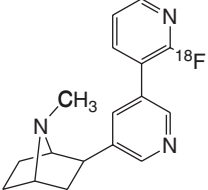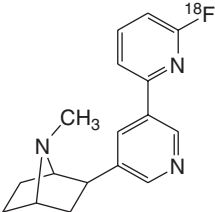|	Main findings
 2-[^{18}F]fluoro-A-85380 ((S)-3-(azetidin-2-ylmethoxy)-2-[^{18}F]fluoropyridine)	Thalamic uptake of radioactivity in rat and baboon peaked at 60 min. In humans, cerebral uptake pattern was consistent with the known distribution of α4β2 nAChRs. The total distribution volume was significantly higher in smokers than in non-smokers, except in the thalamus. Radioactivity in the brain reached steady state by 6 h. K_i = 0.061 nM (Dollé et al. 1999; Kimes et al. 2003, 2008; Mukhin et al. 2008)
 6-[^{18}F]fluoro-A-85380 ((S)-3-(azetidin-2-ylmethoxy)-6-[^{18}F]fluoropyridine)	In baboon dynamic PET, faster peak uptake and clearance as well as higher thalamus-to-cerebellum ratios than obtained for 2-[^{18}F]fluoro-A-85380. K_i = 0.025 nM (Ding et al. 2000a, Horti et al. 2000)
 5-[$^{123/125}$I]iodo-A-85380 (((S)-3-(azetidin-2-ylmethoxy)-5-[$^{123/125}$I]iodopyridine)	In rhesus dynamic PET, regional distribution in brain consistent with the known nAChR distribution pattern. Relatively slow kinetics, with maximal binding ratios at more than 4 h. In baboon, significant displacement of radioactivity from cerebellum by cytosine, indicating this region inappropriate as reference region. K_d (rat) = 10 pM, K_d (human) = 12 pM (Chefer et al. 1998; Fujita et al. 2000)
 [^{18}F]ZW-104 ((S)-3-(azetidin-2-ylmethoxy)-5-(6-[^{18}F]fluorohex-1-yn-1-yl)pyridine)	In baboon dynamic PET, rather slow kinetics in thalamus. High affinity towards multiple β2-containing nAChR subtypes. K_i = 0.21 nM (Valette et al. 2009)
 S-[^{11}C]nicotine ((S)-3-(1-[^{11}C]methylpyrrolidin-2-yl)pyridine)	In human and rhesus monkey dynamic PET studies, binding was less selective for nAChR subtypes than in the case of [^{11}C]MPA. K_i = 10 nM (Sihver et al. 1999b)

Table 18.1 (continued)

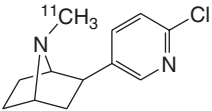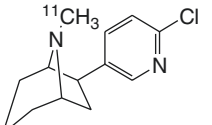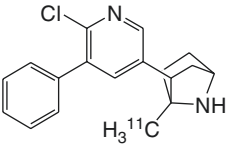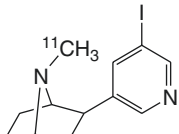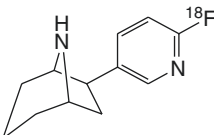|	Main findings
[¹¹C]MPA ((S)-3-(1-[¹¹C]methylazetidin-2-yl)pyridine)	Specific binding in rhesus monkey proven by nicotine displacement in dynamic PET studies, but specific binding was found to be rather low. $K_d = 0.011$ nM (Sihver et al. 1999b)
[¹¹C]ABT418 ((S)-3-[¹¹C]methyl-5-(1-methylpyrrolidin-2-yl) isoxazole)	In rhesus dynamic PET, low uptake and rapid washout, with no evidence for displacement by unlabelled ABT-418. Increased uptake following S-(−)-nicotine pretreatment. $K_i = 3$ nM. (Arneric et al. 1994; Valette et al. 1997; Sihver et al. 1999b)
N-[¹¹C]methylcytisine ([¹¹C]caulophylline) ((1R,5S)-3-[¹¹C]methyl-2,3,4,5-tetrahydro-1,5-methanopyrido[1,2-d][1,4] diazepin-7(1H)-one)	No evidence of specific binding in rhesus monkey brain by dynamic PET. $K_i = 5.7$ nM (Valette et al. 1997; Imming et al. 2001)
[¹⁸F]FPyCYT ((1R,5S)-8-(6-[¹⁸F]fluoropyridin-3-yl)-2,3,4,5-tetrahydro-1,5-methanopyrido[1,2-d][1,4] diazepin-7(1H)-one)	In rat biodistribution study, low (0.3% ID/g) and uniform brain uptake, with little evidence of specific binding. $K_i = 24$ nM (Roger et al. 2003)
[¹⁸F]NFEP ((1R,2R,4S)-2-(6-[¹⁸F]fluoropyridin-3-yl)-7-azabicyclo[2.2.1]heptane)	High brain uptake by mouse biodistribution and baboon PET studies and clear indication of specific binding. Applications in humans limited by high toxicity. $K_{app} = 0.02$ nM (Ding et al. 1996, 1999; Liang et al. 1997; Villemagne et al. 1997; Dolci et al. 1999)
[¹⁸F]N-methyl-NFEP ((1R,2R,4S)-2-(6-[¹⁸F]fluoropyridin-3-yl)-7-methyl-7-azabicyclo[2.2.1]heptane)	In baboon dynamic PET, higher peak uptake in all brain regions than for [¹⁸F] NFEP. Despite milder toxicity than [¹⁸F] NFEP, evidence against safe use in humans. $K_d = 0.028$ nM (Ding et al. 1999)

Table 18.1 (continued)

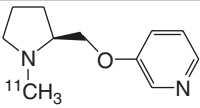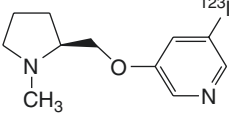|	Main findings
 [18F]FphEP ((1R,2R,4S)-2-(6-[18F]fluoro-5-phenylpyridin-3-yl)-7-azabicyclo[2.2.1]heptane)	In baboon dynamic PET; more favourable kinetics than 2-[18F]fluoro-A-85380. Peak uptake at 20 min, but no evidence for displacement by nicotine challenge. K_d = 0.66 nM (Roger et al. 2006; Valette et al. 2007)
 [18F]F₂PhEP ((1R,2R,4S)-2-(6-[18F]fluoro-5-(4-fluorophen-1-yl)pyridin-3-yl)-7-azabicyclo[2.2.1]heptane)	Dynamic PET in baboon did not indicate reduction in brain distribution volume following pretreatment with nicotine. K_i = 0.029 nM (Valette et al. 2007)
 [18F]XTRA, JHU86428 ((1R,2R,4S)-2-(2′-[18F]fluoro-[3,3′-bipyridin]-5-yl)-7-methyl-7-azabicyclo[2.2.1]heptane)	Dynamic PET showed peak activity in baboon thalamus at 75 min after bolus, requiring several hours for steady-state measurement. K_i = 0.058 nM (Horti and Wong 2009; Coughlin et al. 2018c)
 [18F]AZAN, JHU87522 ((1R,2R,4S)-2-(6-[18F]fluoro-[2,3′-bipyridin]-5′-yl)-7-methyl-7-azabicyclo[2.2.1]heptane)	Baboon dynamic PET showed rapid brain kinetics, favourable metabolic profile and high BP$_{ND}$, reliably measured with 90 min scans. However, part of in vivo binding could be related to other nAChRs with β-subunits. K_i = 0.26 nM (Gao et al. 2008b, Kuwabara et al. 2012)

Table 18.1 (continued)

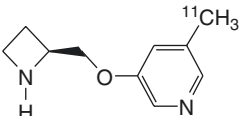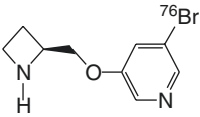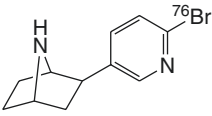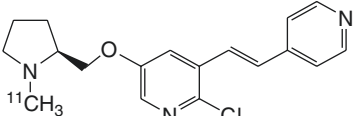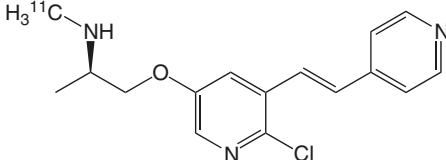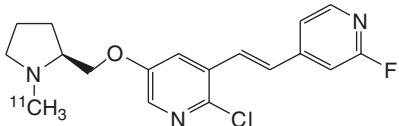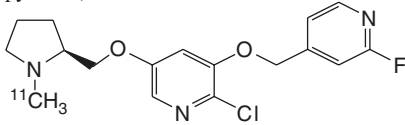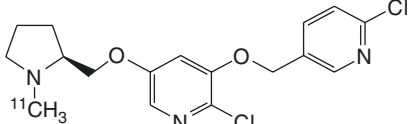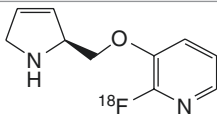|	Main findings
N-[^{11}C]methyl-epibatidine ((1R,2R,4S)-2-(6-chloropyridin-3-yl)-7-[^{11}C]methyl-7-azabicyclo[2.2.1]heptane)	Different kinetics of brain uptake and washout seen for the stereoisomers in rats and mice. Dynamic PET showed high enrichment of radioactivity in the thalamus of the pig, but steady-state not attained during 60 min scans. Applications in humans limited by high toxicity. K_i = 0.027 nM (Patt et al. 1999; Spang et al. 2000)
N-[^{11}C]methyl-homoepibatidine ((1S,5R,6R)-6-(6-chloropyridin-3-yl)-8-[^{11}C]methyl-8-azabicyclo[3.2.1]octane)	In pig dynamic PET, the (−)-enantiomer showed a regional distribution high accumulation in the thalamus consistent with representative for the aα4bβ2 nAChR, which could be displaced cytisine. Distribution of the (+)-enantiomer non-specific. Applications in humans limited by high toxicity. K_i = 0.13 nM (Malpass et al. 2001; Patt et al. 2001)
2-(6-chloro-5-phenylpyridin-3-yl)-7-[^{11}C]methyl-7-azabicyclo[2.2.1]heptane	Rat biodistribution study showed high displaceable binding. Dynamic baboon PET showed rapid peak in thalamus but increasing ratio relative to cerebellum over at least 2 h. K_i = 0.032 nM (Huang et al. 2004, 2005)
[^{11}C]NMI-EPB ((1R,2R,4S)-2-(5-iodopyridin-3-yl)-7-[^{11}C]methyl-7-azabicyclo[2.2.1]heptane)	Baboon dynamic PET showed high uptake and displaceable thalamic binding. Higher uptake and faster kinetics than 2-[^{18}F]fluoro-A-85380; however, (−)-enantiomer did not reach steady state within 90 min post-injection. K_i = 0.068 nM (Ding et al. 2006; Gao et al. 2008a)
[^{18}F]flubatine ((((1R,2R,4S)-2-(6-[^{18}F]fluoropyridin-3-yl)-7-azabicyclo[2.2.1]heptane))	Higher uptake of radioactivity in mouse than for 2-[^{18}F]fluoro-A-85380. Binding equilibrium of the (−)-enantiomer was reached significantly earlier (~60 min p.i.) than that of the (+)-enantiomer. K_i(+) = 0.064 nM, K_i(−) = 0.112 nM (Brust et al. 2008; Deuther-Conrad et al. 2008)

(continued)

Table 18.1 (continued)
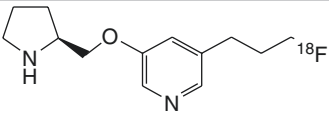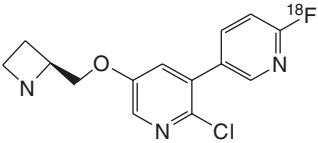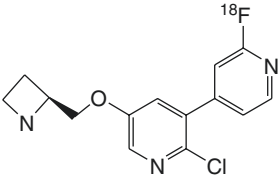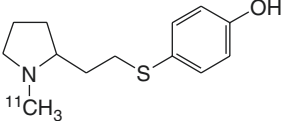
	Main findings
[^{11}C]A-84543 ((S)-3-((1-[^{11}C]methylpyrrolidin-2-yl)methoxy) pyridine)	Mouse biodistribution showed high brain uptake and a distribution consistent with the density of α4β2 nAChRs. $K_i = 0.38$ nM (Kassiou et al. 1998)
5-[^{123}I]iodo-A-84543 ((S)-3-((1-methylpyrrolidin-2-yl)methoxy)-5-[^{123}I]iodopyridine)	Nearly homogeneous distribution in mouse brain, likewise seen in baboon dynamic SPECT. $K_i = 0.016$ nM (Fan et al. 2001; Henderson et al. 2004)
5-[^{11}C]methyl-A-85380, 5-MA ((S)-3-((azetidin-2-yl)methoxy)-5-[^{11}C] methylpyridine)	Mouse biodistribution consistent with α4β2 nAChRs. Rhesus monkey dynamic PET showed high non-specific binding. $K_i = 0.27$ nM (Iida et al. 2004)
[^{76}Br]BAP ((S)-3-((azetidin-2-yl)methoxy)-5-[^{76}Br] bromopyridine)	In comparison with rat biodistribution, baboon dynamic PET showed higher non-specific binding with nicotine or cystine displacement. $K_i = 0.023$ nM (Sihver et al. 1999a)
[^{76}Br]BrPH ((1R,2R,4S)-2-(6-[^{67}Br]bromopyridin-3-yl)-7-azabicyclo[2.2.1]heptane)	Rat biodistribution and baboon dynamic PET showed binding to nAChRs but without subtype selectivity. $K_d = 0.008$ nM (Kassiou et al. 2002)
[^{11}C]Me-p-PVC ((S,E)-2-chloro-5-((1-[^{11}C]methylpyrrolidin-2-yl) methoxy)-3-(2-(pyridin-4-yl)vinyl)pyridine)	Rapid accumulation in mice ex vivo, and rhesus PET studies, thus quantifiable with 2 h recordings, but BP$_{ND}$ slightly lower than for 2-[^{18}F]fluoro-A-85380. $K_i = 0.028$ nM (Brown et al. 2004)

Table 18.1 (continued)

	Main findings
 [¹¹C]*p*-PVP-MEMA, (*R*,*E*)-1-(6-chloro-5-(2-(pyridin-4-yl)vinyl) pyridin-3-yloxy)-*N*-[¹¹C]methylpropan-2-amine.	In dynamic PET studies in baboon, [¹¹C]*p*-PVP-MEMA entered the brain rapidly with a peak concentration of 0.5% ID/mL 2 min p.i. but with a low thalamus/cerebellum ratio of about 1 at 1 h p.i., possibly due to low metabolic stability of the parent compound. $K_i = 0.077$ nM) (Dolle et al. 2008)
 [¹¹C]JHU85270 ((*S*,*E*)-2-chloro-3-(2-(2-fluoropyridin-4-yl) vinyl)-5-((1-[¹¹C]methylpyrrolidin-2-yl)methoxy) pyridine) [¹¹C]JHU85208 ((*S*)-2-chloro-3-((2-fluoropyridin-4-yl)methoxy)- 5-((1-[¹¹C]methylpyrrolidin-2-yl)methoxy) pyridine) [¹¹C]JHU85157 ((*S*,*E*)-2-chloro-3-(2-(6-chloropyridin-3-yl) vinyl)-5-((1-[¹¹C]methylpyrrolidin-2-yl)methoxy) pyridine)	In baboon dynamic PET, thalamic BP_{ND} lower than that of 2-[¹⁸F]fluoro-A-85380 due to rapid metabolism to brain-penetrating metabolites. K_i(JHU85270) = 0.09 nM, K_i(JHU85208) = 0.05 nM, K_i(JHU85157) = 0.02 nM (Gao et al. 2009)
 [¹⁸F]nifene ((*S*)-3-((2,5-dihydro-1*H*-pyrrol-2-yl)methoxy)-2- [¹⁸F]fluoropyridine)	In rhesus dynamic PET, fast kinetics with peak thalamic binding at less than 10 min, thalamus to cerebellum ratio of ~2. $K_i = 0.5$ nM (Pichika et al. 2006)

(continued)

Table 18.1 (continued)

	Main findings
 [18F]nifrolidine ((S)-3-((2,5-dihydro-1H-pyrrol-2-yl)methoxy)-5-(3-[18F]fluoroprop-1-yl)pyridine)	In rhesus dynamic PET, good labelling of thalamus, with slightly faster kinetics than for 2-[18F]fluoro-A-85380, with maximal binding at 70 min, and plateau thalamus-to-cerebellum ratio of 1.7 at 2 h. K_i = 0.8 nM (Chattopadhyay et al. 2005)
 [18F]NIDA52189 ((S)-2-chloro-6′-[18F]fluoro-5-((1-methylazetidin-2-yl)methoxy)-3,3′-bipyridine)	In rhesus dynamic PET, distribution consistent with α4β2 nAChRs, but BP_{ND} 2.5 times higher than for 2-[18F]fluoro-A-85380. K_d = 0.005 nM (Zhang et al. 2004)
 [18F]NIDA522131 ((S)-2-chloro-2′-[18F]fluoro-5-((1-methylazetidin-2-yl)methoxy)-3,4′-bipyridine)	In rhesus dynamic PET, BP_{ND} in thalamus 3–4-fold greater than with 2-[18F]fluoro-A-85380 but at least 8 h recordings required for stable estimation. K_d = 0.005 nM (Chefer et al. 2008)
 [11C]SIB-1553A (4-((2-(1-methylpyrrolidin-2-yl)ethyl)thio) phenol)	In rat biodistribution study, 0.5% ID/g at 10 min and 0.25% ID/g at 30 min, but no evidence of specific binding discernible against high background. SIB-1553A was more potent than nicotine on α2β4 (EC_{50} = 0.59 μM, (nicotine) = 1.95 μM) and α3β4 (EC_{50} = 1.10 μM, (nicotine) = 7.50 μM), but no effect on α4β2 and α3β2 receptors was observed potentially explaining the absence of specific binding in brain (Sobrio et al. 2008)

proved mainly to be determined by blood flow, rather than local abundance of nAChRs in vivo (Gündisch 2000), this in keeping with its considerable lipophilicity. Indeed, labelled nicotine serves admirably as a cerebral blood flow tracer.

18.3.1.2 Cytisine Derivatives

The nAChR agonist [3H]cytisine is a useful radioligand for characterization of α4β2 nAChRs in vitro. However, the cytisine derivatives [11C]ABT-418 and N-[11C]methylcytisine (Valette et al. 1997) failed in vivo due to their low cerebral uptake and

rapid washout. Another derivative, [^{11}C]MPA, showed high-affinity binding to α4β2 nAChRs (~10–100-fold higher than [^{11}C]ABT-418 and *S*-[^{11}C]nicotine) in membranes from rat forebrain (Sihver et al. 1998). Furthermore [^{11}C]MPA showed rapid uptake into monkey brain, with similar permeability as [^{11}C]ABT-418 and *S*-[^{11}C]nicotine. Pre-administration of unlabelled *S*-nicotine (0.02 mg/kg) decreased the peak uptake of [^{11}C]MPA in monkey brain by about 20%, indicating the presence of some specific binding to nAChRs (Sihver et al. 1999b), but no further studies have been published with this ligand. [^{18}F]fluoropyridinylcytisine was developed as another candidate radioligand for α4β2 nAChR imaging. However, its distribution in living rat brain did not match the regional distribution of nAChRs, and blocking studies with nicotine failed to demonstrate specific binding of this tracer (Roger et al. 2003).

18.3.1.3 Epibatidine Derivatives

Epibatidine, an alkaloid from the skin of the Ecuadoran poison arrow frog *Epipedobates anthonyi*, has long been known for its high-affinity binding to heteromeric nAChRs (Daly 1998). It has considerable toxicity due to its potent activation of many different neuronal nAChR subtypes (Avalos et al. 2002), notably the α3β4 nAChR (Tomizawa et al. 2001; Avalos et al. 2002). Nonetheless, radiolabelled epibatidine derivatives have found limited use in human PET studies (Bohnen and Frey 2007). Theoretically, subtype-specific analogues of epibatidine might have favourable tracer properties with lesser toxicity (Avalos et al. 2002). Although [^{18}F]NFEP ([^{18}F]FPH, norchlorofluoroepibatidine) and [^{18}F]*N*-Me-NFEP showed good brain uptake and signal-to-background ratios in mouse and baboon brain (Ding et al. 1996; Dolci et al. 1999), their toxicity, even when prepared at high specific activity, was too high for use in man (Horti et al. 1997; Molina et al. 1997; Villemagne et al. 1997; Ding et al. 1999). However, Horti and co-workers successfully synthesized epibatidine derivatives with lesser toxicity (Horti et al. 1998a).

Fluorine-18-labelled FPhEP (Roger et al. 2006), a functional nAChR antagonist with much reduced toxicity, had faster brain kinetics in baboon than did 2-[^{18}F]fluoro-A-85380 (discussed below), whereas its fluorophenyl analogue [^{18}F]F$_2$PhEP had higher specific binding (Valette et al. 2007). Its binding on PET was quantified as *binding potential* (BP_{ND}), which is proportional to the ratio B_{max}/K_d. However, nicotine failed to displace either radioligand, indicating low specific binding. Patt and co-workers developed *N*-[^{11}C]methylepibatidine and *N*-[^{11}C]methylhomoepibatidine (Patt et al. 1999, 2001) and compared the uptake and binding of *N*-[^{11}C]methylepibatidine enantiomers in the brain of living mouse, rat and pig. Whereas the (−)-enantiomer showed slower uptake and gradual accumulation in the brain, the (+)-enantiomer had very rapid uptake and washout, indicating distinct binding mechanisms. Because of its better kinetics and higher selectivity, *N*-[^{11}C]methyl-(−)-epibatidine was investigated in pigs by PET, showing high brain uptake. However, steady-state binding in the highest binding regions (thalamus) was not attained within 1 h recordings, which is a disadvantage for quantitation of carbon-11-labelled tracers, due to the 20 min physical half-life. Furthermore there was high toxicity, precluding its use in humans (Patt et al. 1999). The analogue

N-[¹¹C]methylhomo-epibatidine had a better toxicity profile; as with *N*-[¹¹C]methy-lepibatidine, the (−)-enantiomer of *N*-[¹¹C]methylhomo-epibatidine showed high uptake in pig brain, while the (+)-enantiomer was rapidly washed out. Although findings of *N*-[¹¹C]methyl-(−)-homoepibatidine binding in pig brain suggested suitability for PET imaging, its toxicity in mice and rats was comparable to that of *N*-methylepibatidine, again precluding its safe use in humans (Patt et al. 2001).

Further development of epibatidine derivatives has focussed on maintaining or improving kinetic profiles while reducing toxicity. One such compound, 2-(6-chloro-5-phenylpyridin-3-yl)-7-[¹¹C]methyl-7-aza-bicyclo[2.2.1] heptane, showed a thalamus/cerebellum ratio of 4.2 at 90 min after injection, indicating high specific binding in rat brain, which was displaceable by nicotine treatment (1 mg/kg). A preliminary PET study of this tracer in a baboon revealed fast brain uptake and high thalamic binding consistent with α4β2 nAChR distribution. However binding equilibrium was not reached within 2 h, which is the absolute limit for PET recordings with ¹¹C-labelled radioligands (Huang et al. 2004).

Mu et al. synthesized another series of labelled epibatidine and homoepibatidine analogues (Mu et al. 2006). Of these, the 8-[¹¹C]methyl-8-aza-bicyclo[3.2.1]octane derivative had a double bond conjugated with the pyridine nucleus, thus restricting free rotation of the pyridine ring. It showed high affinity (2 nM) in vitro and at least 100-fold selectivity for α4β4 over α7 nAChRs. Furthermore, its toxicity was 50-fold lower than for epibatidine. Although promising for PET studies, there are no further reports on its evaluation. The antagonistic epibatidine derivative (±)-[¹¹C]NMI-EPB (Ding et al. 2006) had 2.5-fold higher uptake in the baboon brain than did the 3-pyridyl ether 2-[¹⁸F]fluoro-A-85380, which is discussed in more detail below (Ding et al. 2006). Surprisingly, separation of the (±)-[¹¹C]NMI-EPB enantiomers revealed that (+)-[¹¹C]NMI-EPB had fast kinetics and but low affinity, whereas (−)-[¹¹C]NMI-EPB appeared to be suitable for imaging but had a slow kinetics (Gao et al. 2007a).

Two further sets of epibatidine analogues (Gao et al. 2007a, 2008b) were subsequently developed by the group from Johns Hopkins University, including (−)-[¹⁸F]JHU87522 (now termed [¹⁸F]AZAN) (Gao et al. 2008b; Horti et al. 2010), which had promising properties with respect to brain uptake, kinetics, metabolic stability and low toxicity. Results of [¹⁸F]AZAN toxicology and human radiation dosimetry have been reported (Horti et al. 2010). PET studies in baboons confirmed that [¹⁸F]AZAN rapidly enters brain, attaining steady state within 90 min after injection (Kuwabara et al. 2012). Furthermore, blocking experiments with cytisine showed [¹⁸F]AZAN to bind specifically to β2-containing (predominantly α4β2) nAChRs, supporting its suitability for nicotinic drug evaluation. Based on its exceptionally high affinity in vitro and improved lipophilicity over 2-[¹⁸F]FA, another epibatidine analogue, (−)-[¹⁸F]JHU86428 ([¹⁸F]XTRA), was proposed as a potential tracer for the less abundant extrathalamic α4β2 nAChRs (Gao et al. 2008b, Horti et al. 2010). An improved radiosynthesis methodology has been reported (Gao et al. 2010). Following successful imaging in non-human primates (Kuwabara et al. 2017), [¹⁸F]XTRA proved fit for quantitation of α4β2 nAChRs in hippocampus of healthy humans and showed an age-dependent decline (Coughlin et al. 2018c).

Toxicity of epibatidine analogues arises from high affinity for the ganglionic α3β4 receptors. This has motivated the search for derivatives with higher α4β2 selectivity. To this end, ^{18}F-labelled stereoisomers of the chloro-fluoro-substituted homoepibatidine analogue, flubatine (previously called NCFHEB), have been synthesized. The flubatine enantiomers both bind with subnanomolar affinity to membranes from rat thalamus or HEK293 cells expressing the human α4β2 nAChR (Deuther-Conrad et al. 2004), with twofold higher affinity for the (+)-enantiomer. Previous work shows that fluoro- and norchloro-analogues of epibatidine have selectivity for β2-containing receptors (Avalos et al. 2002). Indeed, the affinity of both flubatine enantiomers for α4β2 nAChRs was comparable to that of epibatidine, but affinity to ganglionic α3β4 nAChRs was 20–60-fold lower (Deuther-Conrad et al. 2004). The increased subtype selectivity of flubatine seemingly results in lesser pharmacological side effects compared to epibatidine; injection of 25 μg/kg (+)-flubatine or (−)-flubatine to awake mice was without important pharmacological effects (Deuther-Conrad et al. 2008). The doses encountered in a human PET study with [^{18}F]flubatine was 1000-fold lower (Vaupel et al. 2005), which entails a considerable margin of safety. In addition to its selectivity for α4β2, (−)-flubatine and (+)-flubatine also had considerably better selectivity for α4β2 over α7 receptors than did (−)-epibatidine (Deuther-Conrad et al. 2004).

N-methyl and *N*-ethyl derivatives of flubatine have been synthesized but displayed lower target affinities and were consequently not considered for radiolabelling (Deuther-Conrad et al. 2004). Similar distribution patterns for (+)-[^{18}F]flubatine and (−)-[^{18}F]flubatine were observed in mice, rat and porcine brain (Brust et al. 2008; Deuther-Conrad et al. 2008; Sabri et al. 2008). Allen et al. provided evidence that nicotine analogues are transported into the brain via the blood-brain barrier (BBB) choline transporter (Allen et al. 2003); this mechanism may also be involved in the brain uptake of epibatidine and homoepibatidine derivatives (Deuther-Conrad et al. 2008). Indeed, addition of flubatine to the incubation medium inhibited with an IC$_{50}$ of 370 ± 90 μM the uptake of [^{3}H]choline in immortalized rat brain endothelial cells, which are known to express the blood-brain barrier (BBB) choline transporter (Deuther-Conrad et al. 2008). This result is comparable to the K_i of 65 μM obtained for hemicholinium-3 in the same experimental system (Friedrich et al. 2001). Furthermore, in vivo experiments in rats have confirmed the postulated interaction of flubatine with the BBB choline transporter; 50 μM flubatine reduced the transport rate of [^{3}H]choline by 21%, whereas equimolar epibatidine resulted in a ~ 40% reduction (Deuther-Conrad et al. 2008). The stronger interaction of epibatidine is consistent with its higher uptake in mouse brain (London et al. 1995) compared to (+)-[^{18}F]flubatine or (−)-[^{18}F]flubatine.

PET studies in young pigs were performed to compare the brain uptake and kinetics of (+)-[^{18}F]flubatine and (−)-[^{18}F]flubatine with that of 2-[^{18}F]fluoro-A-85380, a 3-pyridyl ether discussed in detail below. The brain uptake of both enantiomers proved to be two- to threefold higher than that of 2-[^{18}F]fluoro-A-85380. The binding equilibrium of (−)-[^{18}F]flubatine was reached significantly earlier (~ 60 min p.i.) than that of the (+)-enantiomer (Brust et al. 2008), consistent with its lesser affinity in vitro. The specific binding of (−)-[^{18}F]flubatine in porcine brain

was comparable to that of 2-[^{18}F]fluoro-A-85380, but (+)-[^{18}F]flubatine displayed about twofold higher specific binding. Thus, both [^{18}F]flubatine enantiomers may present advantages over 2-[^{18}F]fluoro-A-85380 for application in human PET studies, especially as pertains to the time to equilibrium binding.

The metabolites of (+)-[^{18}F]flubatine in pig urine and plasma have been determined by HPLC-MS (Ludwig et al. 2018). Displaceable binding of (−)-[^{18}F]flubatine in human cerebellum upon smoking (Bhatt et al. 2018) raises a red flag for its quantitation through reference tissue methods, which assume absence of specific binding in the reference region. Nonetheless, (−)-[^{18}F]flubatine PET studies in non-human primate showed complete displacement with nicotine, revealing a non-displaceable distribution volume (V_{ND}) of 6 mg/ml, and BP_{ND} of 4 in the thalamus, 1 in the frontal cortex and putamen and only 0.1 in the cerebellum (Bois et al. 2015), consistent with an earlier semi-quantitative analysis in non-human primate (Hockley et al. 2013). The extensive displaceable binding in human cerebellum might reflect a species difference.

18.3.1.4   3-Pyridyl Ethers

First developed as experimental treatments for Alzheimer's disease, the 3-pyridyl ethers were identified as promising radioligands for nAChRs imaging (Gündisch 2000; Horti and Villemagne 2006; Horti et al. 2010). The 3-pyridyl ethers are equipotent to epibatidine at the mainly α4β2 nAChR [^{3}H]cytisine binding sites in the brain but are 100-fold less potent than epibatidine as agonists at α3β4 nAChRs (Abreo et al. 1996). As noted above, this predicts larger dose safety margins with minimal cardiovascular or other toxic side effects. The prototype compound A-85380 has similar binding affinities at recombinant α2β2, α3β2 and α4β2 nAChRs in vitro (Xiao and Kellar 2004). In addition, the iodinated derivative 5-[^{125}I]iodo-A-85380 binds with high affinity to α6β2β3 nAChRs in monkey and rat striatum (Kulak et al. 2002). Therefore, 3-pyridyl ethers are properly regarded as β2-selective compounds (Jensen et al. 2005; Lai et al. 2005), also considering their lack of affinity for the α7 nAChR (Sullivan et al. 1996).

As noted above, 2-[^{18}F]fluoro-A-85380 and 6-[^{18}F]fluoro-A-85380 (Horti et al. 1998b, 2000) showed early promise for PET imaging, having less toxicity than epibatidine analogues. Of the two, 6-[^{18}F]fluoro-A-85380 (Scheffel et al. 2000) had superior kinetics, characterized by earlier peak and faster clearance from the brain (Ding et al. 2004), and better target-to-background ratios than were obtained with 2-[^{18}F]fluoro-A-85380 in a comparative study in baboon (Ding et al. 2000a). Although 6-[^{18}F]fluoro-A-85380 has nonetheless not yet found wide use, both derivatives proved successful in human brain imaging (see Sabri et al. in PET and SPECT in Neurology). The SPECT analogue 5-[^{123}I]iodo-A-85380 was tested in non-human primates (Chefer et al. 1998), and has also served for nicotine challenge studies in human smokers (Esterlis et al. 2010a), as described below. Although suffering from slow kinetics, 5-[^{123}I]iodo-A-85380 was sensitive to competition from endogenous acetylcholine (Fujita et al. 2003), a property also to be discussed in some detail below. The methyl-substituted derivative 5-[^{123}I]iodo-A-84543 (Henderson et al. 2004) displayed faster kinetics, but homogenous uptake of

radioactivity in baboon brain, in contrast to the spatially heterogeneous pattern of specific binding for the analogue [^{11}C]A-84543 seen in mouse brain (Kassiou et al. 1998). PET studies in pigs with [^{11}C]A-186253, a structurally similar tracer, showed little displacement by cytisine, indicating excessive non-specific binding (Itier et al. 2004).

The comparably low brain uptake of 2-[^{18}F]fluoro-A-85380 was similar to that previously found with 5-[^{11}C]methyl-A-85380 (2.2% ID/g brain tissue at 30 min p.i. (Iida et al. 2004)). This may be related to their rather high polarity (Zhang et al. 2004), which is a critical parameter for brain radiotracer uptake (Waterhouse 2003). Nevertheless 2-[^{18}F]fluoro-A-85380 was successfully used to image nAChRs in non-human primates (Chefer et al. 1999, 2003; Valette et al. 1999; Le Foll et al. 2007) and in rat microPET studies (Vaupel et al. 2007). An optimized radiosynthesis of 2-[^{18}F]fluoro-A-85380 and improved analytical techniques (Mitkovski et al. 2005; Schmaljohann et al. 2005; Kimes et al. 2008) have facilitated its use in human PET studies (Ellis et al. 2009b) (Lotfipour et al. 2012b). Despite the disadvantage of its slow binding kinetics, requiring interrupted or continuous PET recordings lasting at least 6 h (Gallezot et al. 2005; Horti and Villemagne 2006), 2-[^{18}F]fluoro-A-85380 remains the most frequently utilized ligand in human PET studies (see Sabri et al. in PET and SPECT in Neurology); despite its limitations, it remains for the present the standard against which other nAChR PET ligands have been compared.

A series of 5-substituted-6-halogeno derivatives of A-85380 have potentially improved lipophilicity and affinity (Zhang et al. 2004). PET studies in rhesus monkey with two such [^{18}F]-labelled derivatives showed higher lipophilicity than for 2-[^{18}F]fluoro-A-85380, resulting in enhanced target-to-background ratios. Imaging studies with another 5-substituted A-85380 derivative, [^{11}C]5-MA (Iida et al. 2004), demonstrated lower total brain uptake and lower target-to-background ratios than for 2- or 6-[^{18}F]fluoro-A-85380. A further analogue, [^{18}F]ZW-104 has had initial testing (Kozikowski et al. 2005; Valette et al. 2009; Saba et al. 2010). In baboon PET studies, [^{18}F]ZW-104 showed regional radioactivity distribution resembling that of 2-[^{18}F]fluoro-A-85380 and some superior properties, including higher accumulation in the brain, earlier peak uptake in the thalamus and faster washout kinetics. However, it also displayed considerable affinity for α3β2 and α2β2 receptors in vitro (Valette et al. 2009) and rather high non-displaceable (by nicotine) uptake in the striatum, a region with comparably low density of nAChRs.

Many further derivatives have been tested in rodent and non-human primate PET studies: [^{76}Br]BAP (Sihver et al. 1999a); [^{76}Br]BrPH (Kassiou et al. 2002); [^{11}C]Me-p-PVC (Brown et al. 2004) and its analogues [^{11}C]JHU85208, [^{11}C]JHU85157 and [^{11}C]JHU85270 (Gao et al. 2007b, 2009); [^{18}F]nifene (Pichika et al. 2006; Easwaramoorthy et al. 2007); and two carbon-11- and fluorine-18-labelled isotopomers of one pyridine-derived ligand. While some of these ligands had better kinetics than 2-[^{18}F]fluoro-A-85380, their low BP_{ND}, high non-specific binding or non-selectivity discouraged further development for human imaging (Easwaramoorthy et al. 2007). Despite this, specific binding of [^{18}F]nifene was later attributed entirely to α4β2 nAChRs based on studies in β2-knockout mice (Bieszczad

et al. 2012), and subsequent human studies demonstrated the safety and test-retest reliability of [^{18}F]nifene (Betthauser et al. 2017; Lao et al. 2017). This was further supported by a study showing no significant decline in [^{18}F]nifene binding over five decades of healthy human ageing (Mukherjee et al. 2018). Despite the partial selectivity of the tracer for α4β2 nAChRs, there was low binding in human habenula (which contains α3β2 nAChRs) and in the red nucleus (which contains abundant α2β2 nAChRs).

PET imaging of α4β2 nAChRs using the pyridyl ether analogue [^{18}F]nifrolidine has been tested in non-human primate (Chattopadhyay et al. 2005). Although having favourable kinetics, the thalamus-to-cerebellum ratio was lower than that of other α4β2-targeting pyridyl ether analogues (Chattopadhyay et al. 2005), attaining a value of 4 at several hours after administration in non-human primate and showing considerable displaceability by nicotine (Pichika et al. 2013). Similarly, there have been no follow-up reports on the nifrolidine homologue [^{18}F]nifzetidine (Mukherjee et al. 2004), except for a report showing a continuous increase of the thalamus/cerebellum ratio up to 3 h after administration to non-human primates (Pichika et al. 2011). Such slow kinetics is unfavourable for quantitation.

The series of pyridyl ether-based compounds [^{18}F]NIDA52189, [^{18}F]NIDA522131 and [^{18}F]NIDA52289 have been synthesized and evaluated by PET in rhesus monkeys (Horti and Villemagne 2006), especially intended for imaging of the relatively sparse extrathalamic α4β2 nAChRs. Among these, [^{18}F]NIDA52189 (Zhang et al. 2004) and [^{18}F]NIDA522131 (Chefer et al. 2008) were deemed superior to 2-[^{18}F]FA with respect to extrathalamic binding but suffered from slow kinetics in vivo.

18.3.1.5 Non-Epibatidine-and-Non-A-85380-Related Compounds

Carbon-11-labelled Me-*p*-PVC (Brown et al. 2002) and *p*-PVP-MEMA, which were selected from the class of (4-pyridinyl)vinylpyridines developed by Abbott Laboratories, possessed picomolar affinity towards α4β2 receptors. Nevertheless, [^{11}C]Me-*p*-PVC had low BP_{ND} in thalamus of non-human primate (Brown et al. 2004), and [^{11}C]*p*-PVP-MEMA had a low target-to-background ratio in a preliminary PET study (Dollé et al. 2008).

18.3.2 Imaging of Heteromeric β4-Containing nAChR Subtype
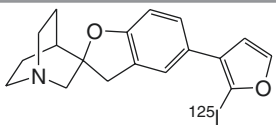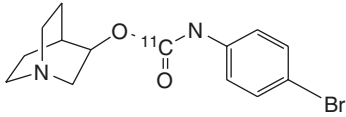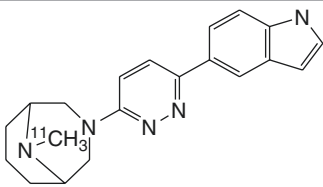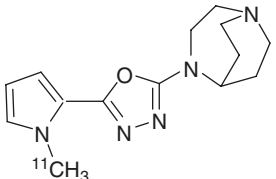
The putative β4-selective agonist [^{11}C]SIB-1553A was assessed by biodistribution and ex vivo brain autoradiography in rats (Sobrio et al. 2008). Its low specific binding did not encourage further development, and there was no attempt made to separate and individually investigate the enantiomers of this racemic radioligand.

18.3.3 Radioligands for α7 nAChRs

Efforts to develop a radiopharmaceutical for PET imaging of α7 nAChR have met with growing success in the past few years. Structurally diverse classes of
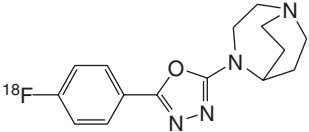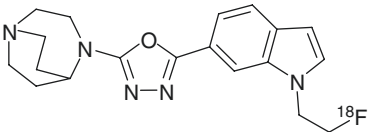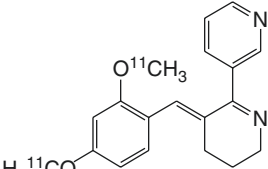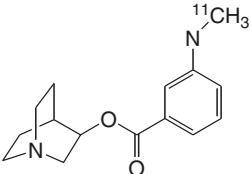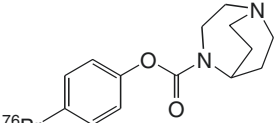
compounds meet the steric and electronic requirements of this binding site, as reviewed recently (Brust et al. 2012; Mo et al. 2014). As noted above, the cerebral expression of α7 nAChR is comparatively low, constituting perhaps one quarter of the density for α4β2 receptors (Spurden et al. 1997; Whiteaker et al. 1999; Hellström-Lindahl and Court 2000). Because of this low natural abundance of α7 sites, high affinity is particularly important for an effective PET tracer. Binding properties of various α7 tracers tested to date are summarized in Table 18.2.

Table 18.2 Results of biodistribution ex vivo and PET imaging studies in vivo of the cerebral binding of α7 nAChR selective radioligands
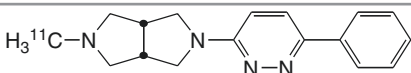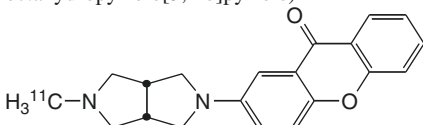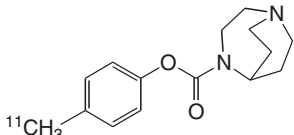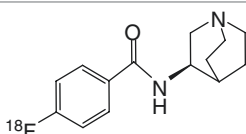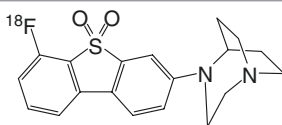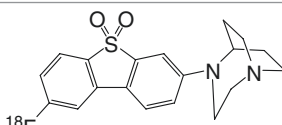
	Main findings
 [125I]**4** ((1′S,2R,4′S)-5-(2-[125I]iodofuran-3-yl)-3H-4′-azaspiro[benzofuran-2,2′-bicyclo[2.2.2]octane])	Biodistribution in CD1 mice showed very limited uptake in brain, and no evidence of displaceable binding. K_i = 0.33 nM (Pomper et al. 2005)
 [11C]**1** ((1S,3R,4S)-quinuclidin-3-yl (4-bromophenyl)[11C]carbamate)	Biodistribution study in rats showed no regionally selective or specific binding. Affinity has not been reported (Dollé et al. 2001)
 [11C]NS12857 ((1R,5S)-3-(6-(1H-indol-5-yl)pyridazin-3-yl)-9-[11C]methyl-3,9-diazabicyclo[3.3.1]nonane)	High uptake in pig brain by dynamic PET but lack of displacement in vivo. K_i = 0.51 nM (Lehel et al. 2009)
 [11C]NS14492 (2-(1,4-diazabicyclo[3.2.2]nonan-4-yl)-5-(1-[11C]methyl-1H-pyrrol-2-yl)-1,3,4-oxadiazole)	Dose-dependent decline in cerebral binding after receptor blockade in pigs. K_i = 2.2 nM (Ettrup et al. 2011)

Table 18.2 (continued)
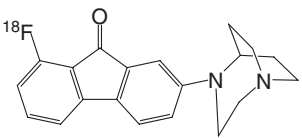
	Main findings
[ ] [^{18}F]NS10743 (2-(1,4-diazabicyclo[3.2.2]nonan-4-yl)-5-(4-[^{18}F]fluorophenyl)-1,3,4-oxadiazole)	High uptake in the pig brain by dynamic PET, with clear evidence of displaceable binding in regions of relatively high tracer accumulation. K_i = 9.27 nM (Deuther-Conrad et al. 2011)
[ ] [^{18}F]NS14490 (((1R,5S)-3-(6-(1-(2-[^{18}F]fluoroethyl) indol-5-yl)pyridazin-3-yl)-9-methyl-3,9-diazabicyclo[3.3.1]nonane))	Moderate uptake in the pig brain by dynamic PET, with clear evidence of displaceable binding in brain and cerebral vasculature. K_i = 2.5 nM (Rötering et al. 2014)
[ ] 2/4-methoxy-[^{11}C]GTS21 ((E)-3-(2,4-dimethoxybenzylidene)-3,4,5,6-tetrahydro-2,3′-bipyridine)	In baboon dynamic PET, very high initial uptake followed by rapid clearance; relatively little evidence for specific α7 nAChR binding. Brain penetrating radiometabolites detected in plasma. K_i = 211 nM (Kim et al. 2007b)
[ ] [^{11}C]MeQAA ((1S,3R,4S)-quinuclidin-3-yl 3-([^{11}C] methylamino)benzoate	In rhesus monkey dynamic PET, the R-enantiomer had high cerebral uptake and distribution consistent with α7 nAChRs. K_i = 41 nM (Ogawa et al. 2010)
[ ] [^{76}Br]SSR180711 (4-[^{76}Br]bromophenyl 1,4-diazabicyclo[3.2.2] nonane-4-carboxylate)	In rhesus monkey dynamic PET, substantial and heterogeneous brain accumulation. Binding globally reduced to level seen in cerebellum by pretreatment with the α7 nAChR agonist SSR180711. Biton et al. (2007) reported K_i values of 22 ± 4 and 14 ± 1 nM in rat and human, respectively (Hashimoto et al. 2008)

Table 18.2 (continued)

	Main findings
 [¹¹C]A-582941 (2-[¹¹C]methyl-5-(6-phenylpyridazin-3-yl) octahydropyrrolo[3,4-c]pyrrole) [¹¹C]A-844606 (2-(5-methylhexahydropyrrolo[3,4-c] pyrrol-2(1H)-yl)-9H-xanthen-9-one)	In rhesus monkey dynamic PET studies, evidence for regional distribution consistent with α7 nAChR expression. K_i (A-582941, rat) = 10.8 nM, K_i (A-582941, human) = 17 nM, IC_{50} (A-844606, rat) = 11 nM (Toyohara et al. 2010)
 [¹¹C]CHIBA-1001 (4-[¹¹C]methylphenyl)-1,4-diazabicyclo[3.2.2] nonane-4-carboxylate)	In a PET study of one healthy human, evidence for preferential binding in the hippocampus, cortex and basal ganglia, with slow washout, and least binding in cerebellum. K_i = 35 nM (Toyohara et al. 2009)
 [¹⁸F]4 (4-[¹⁸F]fluoro-N-((1S,3R,4S)-quinuclidin-3-yl) benzamide)	Low brain uptake in rats, homogenous distribution. K_i = 14 nM (Pin et al. 2014)
 [¹⁸F]ASEM (7-(1,4-diazabicyclo[3.2.2]nonan-4-yl)-4-[¹⁸F]fluorodibenzo[b,d]thiophene 5,5-dioxide)	The radiotracer readily entered the baboon brain and specifically labelled α7-nAChR. SSR180711 blocked the binding in the baboon brain in a dose-dependent manner. K_i = 0.84 nM (Horti et al. 2014; Teodoro et al. 2015)
 [¹⁸F]DBT10 (7-(1,4-diazabicyclo[3.2.2]nonan-4-yl)-2-[¹⁸F]fluorodibenzo[b,d]thiophene 5,5-dioxide)	Uptake of the radiotracer in monkey brain occurred rapidly, reaching SUV values of 2.9–3.7 within 30 min. There was dose-dependent blockade by ASEM throughout the brain. K_i = 0.60 nM (Hillmer et al. 2016b)

Table 18.2 (continued)

	Main findings
 [^{18}F]FLN28 (7-(1,4-diazabicyclo[3.2.2]nonan-4-yl)-1-[^{18}F]fluoro-9*H*-fluoren-9-one)	A fluoren-9-one derived α7 nAChR selective PET ligand (Teodoro et al. 2018) with high brain uptake in mice and rats. K_i = 2.98 nM (Wang et al. 2018)

18.3.3.1 Quinuclidine-Based Ligands

The lead compound of a series of azabicycle carbamate α7 receptor agonists developed by Astra Laboratories has been labelled with carbon-11 and evaluated in rats (Dollé et al. 2001). Despite having relatively good brain uptake, no regionally selective or specific binding could be seen. Another series of potential α7-selective imaging agents based on the quinuclidine moiety has been labelled with carbon-11 and iodine-125 (Pomper et al. 2005). Target selectivities of these compounds were modest, and the most affine compounds had significant binding to the 5-HT$_3$ receptor, a structural homologue of α7 nAChR (Zwart et al. 2004).

18.3.3.2 GTS-21

Other potential α7 ligands originate from benzylidene anabasein compounds such as GTS-21 (de Fiebre et al. 1995; Meyer et al. 1998). Indeed, GTS-21 (3-(2,4-dimethoxybenzylidene)-anabaseine) showed early promise as a α7 nAChR agonist medication for improving cognition in patients with schizophrenia (Freedman et al. 2008; Tregellas et al. 2011). It has been labelled with iodine-123 (Zhang et al. 2001) and carbon-11 (Kim et al. 2007b). Consistent with the relatively low affinity and specificity of GTS-21 for α7 nAChRs, the distribution and kinetics of 5- [^{123}I]GTS-21 and 2- [^{11}C]GTS-21 in the brain of living baboon and mice were dominated by non-specific binding (Kim et al. 2007a).

18.3.3.3 Diazabicyclononane Derivatives

The 1,4-diazabicyclo-[3.2.2]nonane skeleton (Bunnelle et al. 2004) was identified as a motif for α7 nAChR ligands, and the two novel diazabicyclononane-derived PET ligands [^{76}Br]SSR180711 and [^{11}C]CHIBA-1001 were evaluated by PET in conscious non-human primates, with testing in a model of schizophrenia (Hashimoto et al. 2008). Of the two tracers, [^{11}C]CHIBA-1001 demonstrated superior accumulation in the brain, revealing a heterogeneous regional distribution consistent with the localization of α7 in the brain; specific binding was blocked by selective α7 but not α4β2 agonists revealing some potential for measuring occupancy by pharmaceuticals at α7 nAChRs. A first clinical PET study confirmed the suitability of [^{11}C]CHIBA-1001, although the regional binding differences were small in the human brain (Toyohara et al. 2009). Notably, α7-specific binding could not be demonstrated in vitro: there was no displacement of 30 nM [^{3}H]CHIBA binding from rat

brain membranes by 1 μM α-bungarotoxin (Tanibuchi et al. 2010). Another rodent study reported low in vitro binding affinity of [^{3}H]CHIBA and poor in vivo selectivity to α7 nAChRs in rodent brain (Ding et al. 2012). Furthermore, differences in the regional distribution of the binding sites of CHIBA-1001 relative to [^{125}I]α-bungarotoxin were evident in monkey and human brain samples (Tanibuchi et al. 2010).

The 1,4-diazabicyclo[3.2.2]nonane derivatives developed by NeuroSearch emerged as promising PET ligands for imaging of cerebral α7 nAChR (Peters et al. 2007). Two carbon-11 radioligands were developed, [^{11}C]NS12857 (Lehel et al. 2009) and [^{11}C]NS14492 (Ettrup et al. 2011), along with the fluorine-18 compounds [^{18}F]NS10743 (Deuther-Conrad et al. 2009) and [^{18}F]NS14490 (Rötering et al. 2014). The cerebral uptake of these three 1,4-diazabicyclo[3.2.2]nonane derivatives exceeded that of [^{11}C]CHIBA-1001. Although the uptake of [^{11}C]NS12857 was not displaced by α7 nAChR-selective compounds, specific binding was clearly evident for [^{11}C]NS14492, [^{18}F]NS14490 and [^{18}F]NS10743, the ligands with higher target affinity (Brust et al. 2012).

NS14492 has been labelled with tritium to allow in vitro autoradiographic studies on α7 nAChR assessing α7 nAChR density in the porcine brain and by extension other species (Magnussen et al. 2015). Figure 18.2 shows the autoradiographic comparison of a saturating concentration of [^{125}I]α-bungarotoxin and [^{3}H]NS14492 in whole brain sections from newborn piglets. Brain region-specific binding pattern of [^{3}H]NS14492 is very similar to that of [^{125}I]α-bungarotoxin, with the non-specific binding being considerably lower. Furthermore, the use of [^{3}H]NS14492 provides a higher resolution, which is especially noticeable in the laminar layers of the neocortex. [^{3}H]NS14492 therefore is an interesting alternative to [^{125}I]α-bungarotoxin when assessing α7 nAChR density in the porcine brain and by extension other species.

The general suitability of the diazabicyclononane derivatives for PET imaging of α7 nAChRs was shown by preclinical PET studies in pigs (Lehel et al. 2009; Deuther-Conrad et al. 2011; Ettrup et al. 2011), although the magnitude of BP_{ND}, about 0.5, is rather low for a useful PET tracer. In view of the low natural abundance

5 nMol/L [^{125}I]-α-BTX   5 nMol/L [^{3}H]NS14492
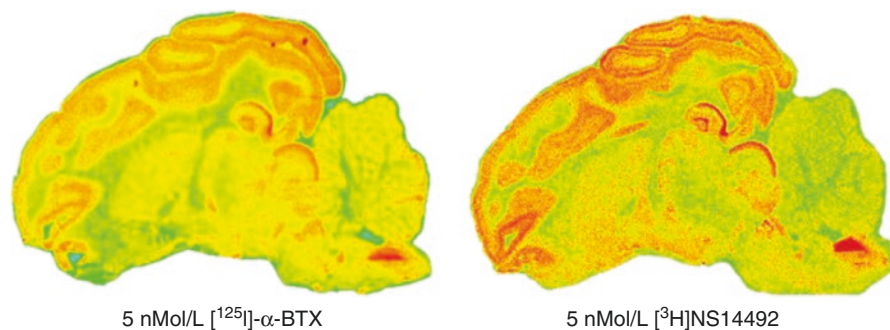
Fig. 18.2 Autoradiographic comparison of [^{125}I]α-bungarotoxin and [^{3}H]NS14492 binding to brain sections from newborn piglets. For anatomic reference see Fig. 18.1

of the α7 nAChR in the brain, a substantial increase in α7 affinity of PET radiotracers may be required for sensitive quantitation (Brust et al. 2012); target affinities of [^{11}C]CHIBA-1001 (K_i ~ 35 nM) (Hashimoto et al. 2008; Toyohara et al. 2009) and [^{18}F]NS10743 (K_i ~ 10 nM) (Deuther-Conrad et al. 2009) do not predict adequate specific signal in vivo, given the low B_{max} (Koeppe 2001). NS14490, a novel diazabicyclononane derivative, with a K_i of 3 nM may be more promising in this regard (Brust and Deuther-Conrad 2012). The distribution of [^{18}F]NS14490 binding in mouse brain autoradiograms correlated with the known pattern of α7 nAChR expression and was displaced with the α7 nAChR ligand methyllycaconitine (Brust and Deuther-Conrad 2012).

With tilorone, an amphiphilic molecule possessing high interferon-inducing potential, a novel α7 nAChR pharmacophore has been identified (Briggs et al. 2008; Schrimpf et al. 2012), leading to a new series of diazabicyclononane-substituted dibenzothiophene derivatives for PET imaging developed independently by two groups (Gao et al. 2013; Scheunemann et al. 2014). The 2-fluoro dibenzothiophene sulfone derivative (DBT10) and 4-fluoro dibenzothiophene sulfone derivative (ASEM) have been identified as potential α7 nAChR imaging agents, as shall be discussed in more detail below. In addition, a small library of further tilorone-based derivatives was synthesized to explore further the impact of the isomeric effect and effects of different cationic centres on the ligand features. However, an isomer, substituted with fluorine and the cationic centre in the same benzo ring, did not achieve criteria for further ^{18}F-labelling. Increased flexibility of the tertiary amine of the cationic centre 9-methyl-3,9-diazabicyclo[3.3.1]nonane and 3-methyl-3,8-diazabicyclo[3.2.1]octane resulted in a remarkable loss of binding affinity (Teodoro et al. 2015). Most recently, a series of novel fluoren-9-one-based diazabicyclononane derivatives has been developed, showing low nM affinity towards the α7 nAChR and >1000-fold selectivity over the α4β2 nAChR (Teodoro et al. 2018; Wang et al. 2018). Two derivatives were radiolabelled leading to the corresponding carbonyl bioisosteres of [^{18}F]DBT10 and [^{18}F]ASEM. The carbonyl derivative of [^{18}F]DBT10 exhibited high initial brain uptake (12% ID/g at 15 min post-injection) and displaceable binding (Wang et al. 2018).

Both [^{18}F]DBT10 and [^{18}F]ASEM have been investigated as PET tracers in non-human primates, showing a favourable kinetic profile for quantitation of the α7 nAChR in living brain (Horti et al. 2014; Hillmer et al. 2016b). Recently, a direct comparison in rhesus monkey of [^{18}F]DBT10 and [^{18}F]ASEM indicated very similar pharmacokinetics (Hillmer et al. 2017). A blocking study with [^{18}F]DBT10 in pigs revealed a 75% decrease of the binding potential BP_{ND} after treatment with 3 mg•kg^{-1} i.v. of the α7 nAChR partial agonist NS6740 (Fig. 18.3) (Teodoro et al. 2015). The total distribution volume (V_T; ml g^{-1}) of [^{18}F]ASEM has been quantified in non-smoking healthy volunteers over a broad range of ages, showing a positive correlation between [^{18}F]ASEM V_T and age in various brain regions of interest, with V_T increasing from 20 to 30 ml g^{-1} (Coughlin et al. 2018b). Occupancy by the experimental drug DMXB-A at central α7 nAChRs could be estimated from [^{18}F]ASEM binding changes in the brain of healthy volunteers (Wong et al. 2018).
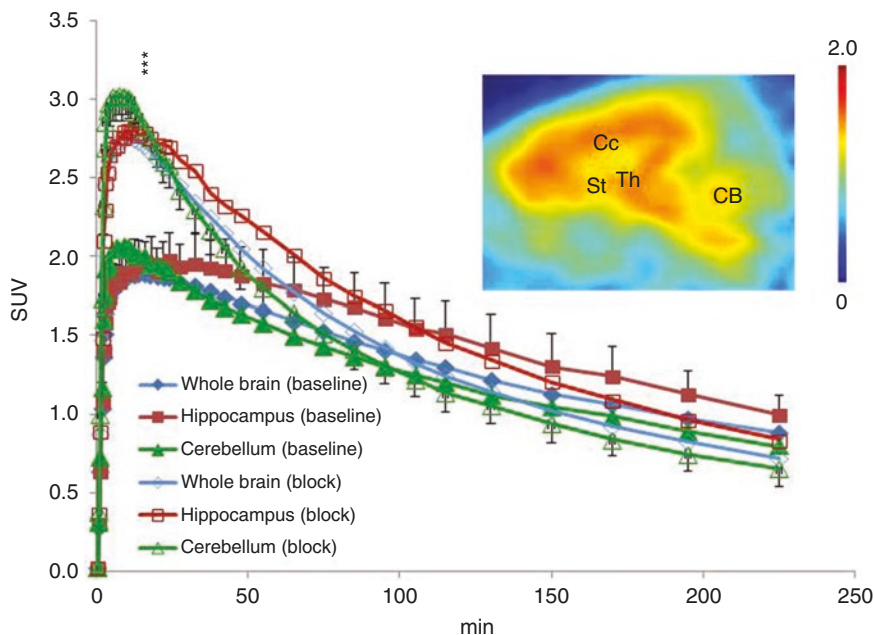
Fig. 18.3 Specific uptake values (SUV) of [^{18}F]DBT10 in porcine brain under baseline and blocking (3 mg·kg^{-1} NS6740 i.v.) conditions

Given this success and in expectation of future human applications, an automated cGMP-compliant radiosynthesis of [^{18}F]DBT10 was established, and toxicity and radiation dosimetry studies were performed. The single-dose toxicity in rats (No-Observed-Effect-Level = 620 μg·kg^{-1}) and the effective dose estimated from mouse and pig studies (12.7 and 13.7 μSv/MBq, resp.) indicated the safe use of [^{18}F]DBT10 in human PET studies ((Kranz et al. 2014; Teodoro et al. 2015).

18.3.3.4   [^{11}C]A-582941 and [^{11}C]A-844606

A new series of octahydropyrrolo[3,4-c]pyrrole derivatives was described by Abbott Laboratories, two of which were selected for labelling with carbon-11 (Toyohara et al. 2010). Whereas no regional heterogeneity or displaceable binding was evident in mouse brain ex vivo, pretreatment with an α7-specific agonist decreased the total distribution volumes of both tracers in conscious monkey PET studies, indicative of a BP$_{ND}$ close to 0.5, as with the NeuroSearch (NS) compounds cited above.

18.3.3.5   [^{125}I]I-TSA

A diazabicyclooctane-derived PET ligand with high affinity and selectivity has been radiolabelled and evaluated in mice (Ogawa et al. 2006). Despite a subnanomolar affinity, the high non-specific binding made [^{125}I]I-TSA inadequate for imaging of brain α7 receptors.

18.3.3.6 *R*-[¹¹C]MeQAA

The two enantiomers of [¹¹C]MeQAA, an azabicyclooctylester-derived compound, were evaluated in mice and conscious monkey PET studies (Ogawa et al. 2009). Although *(R)*-[¹¹C]MeQAA showed target-specific accumulation, the in vivo selectivity was insufficient due to binding to the serotonin 5HT₃-R. Nonetheless, the tracer was used more recently in a multitracer study of aged monkeys (Nishiyama et al. 2015). The hippocampal binding of *(R)*-[¹¹C]MeQAA correlated inversely with binding of a marker for mitochondrial complex I and positively with the binding of a marker for beta-amyloid deposition in the aged animals. The authors interpreted their results to indicate a significant (adaptive?) upregulation of α7 nAChRs in metabolically compromised and degenerating brain tissue.

18.3.4 Radioligands for α3β4 nAChRs

Recently, a series of quinuclidine *anti*-1,2,3-triazole derivatives was synthetized with the aim of developing an ¹⁸F-labelled radioligand for imaging the α3β4 nAChR in the brain. This subtype attracts interest because of its involvement in drug addiction and depression pathways (Rahman et al. 2015). In contrast to α4β2 and α7, the α3β4 subtype expression is mainly in the autonomic ganglia (hence the toxicity of epibatidine) but also in some specific brain regions and neuronal subpopulations. These regions notably include the medial habenula, nucleus interpeduncularis, dorsal medulla, pineal gland and retina (Gotti et al. 2009). Binding studies in vitro revealed that stereochemistry at the C3 position of the quinuclidine scaffold plays an important role in the nAChR subtype selectivity (Sarasamkan et al. 2016). Whereas the *(R)*-enantiomers are selective to α7 over α4β2 (by factors of 44–225) and to a smaller degree over α3β4 (3–33), their *(S)*-counterparts prefer α3β4 over α4β2 (62–237) as well as over α7 (5–294). Two potent compounds *(S)*-T1 and *(S)*-T2 were identified that bind selectively to α3β4 nAChR over α7 nAChR. The compound *(S)*-T1 was chosen for radiolabelling and first preclinical evaluation (Sarasamkan et al. 2017). The brain uptake and the brain-to-blood ratio of *(S)*-[¹⁸F]T1 in mice at 30 min post-injection were 2.02 (SUV) and 6.1, respectively. According to an ex vivo analysis, the tracer remained intact (>99%) in the brain. Only one major radiometabolite was detected in plasma and urine samples. In vitro autoradiography on pig brain slices revealed binding of *(S)*-[¹⁸F]T1 to brain regions associated with the expression of α3β4 nAChRs, which could be reduced by the α3β4 nAChR selective drug AT-1001. These findings suggest *(S)*-[¹⁸F]T1 as a promising tool for non-invasive PET imaging of α3β4 nAChRs in the brain.

18.4 nAChR Imaging of Neurodegenerative Diseases

Reductions in cortical nAChR binding have been found in patients with diverse forms of neurodegeneration, including Alzheimer's disease, Parkinson's disease, Lewy body disease, progressive supranuclear palsy and Down's syndrome (Perry

et al. 1986; Picciotto and Zoli 2002) (see also Sabri et al. in PET and SPECT in Neurology). However, there have been few preclinical PET and SPECT studies of nAChRs in animal models of neurodegenerative disease. This is attributable to two considerations: First, models in transgenic mice have only recently become available for some of these diseases, while remaining lacking for others, and second, the spatial resolution of small-animal PET and SPECT instruments has until recently been inadequate for regional analysis of neuroreceptors in rodent brain, as noted in the instrumentation section above. Therefore, the majority of such investigations use autoradiography in vitro. Furthermore, the occurrence of species differences is a hindrance to the interpretation of preclinical imaging studies (Pauly et al. 1989; Quik et al. 2000; Han et al. 2003). Despite these limitations, molecular imaging is emerging as a powerful tool for investigating pathophysiological changes in animal models of neurodegenerative diseases, especially when conducted in conjunction with techniques such as in vivo microdialysis, electrophysiology and histopathology (Higuchi et al. 2012).

18.4.1 Alzheimer's Disease

A link between cognitive performance and α4β2 nAChR expression in the forebrain of healthy rats has been demonstrated in a PET study using the ligand [^{18}F]nifene (Bieszczad et al. 2012), as confirmed by autoradiography ex vivo and in vitro. The three imaging methods showed the same rank order of specific binding by brain region. We anticipate that [^{18}F]nifene PET should allow tracking of dynamic changes in nAChRs during learning acquisition and memory consolidation, in rodents and also in large-brained animals. In contrast to the case for humans (Zanardi et al. 2002), normal ageing does not seem to reduce nAChR density in rat brain (Picciotto and Zoli 2002; Schliebs and Arendt 2011).

The hallmark histopathological features of Alzheimer's disease are extraneuronal amyloid plaques composed of aggregated amyloid-β peptides (Aβ), and intraneuronal neurofibrillary tangles, which are composed largely of hyperphosphorylated forms of tau, a microtubule-associated protein (Thal and Braak 2005). Molecular imaging studies in animal models have primarily targeted fibrillar protein assemblies such as β-amyloid and tau depositions, neuroinflammatory processes and cerebral glucose metabolism (Higuchi et al. 2012). However, these features are closely related to cholinergic hypofunction found in Alzheimer's disease and relevant animal models (Schliebs and Arendt 2011).

Cognitive impairment in Alzheimer's disease is at least partially associated with loss of cortical nAChRs, which may arise due to toxicity of soluble β-amyloid (Zanardi et al. 2002; Schliebs 2005; Schliebs and Arendt 2011). Nicotine treatment in a transgenic mouse model (3xTg-AD) can mediate increased tau phosphorylation and decrease β-amyloid load (Rubio et al. 2006). Impaired cholinergic neurotransmission has been described in the brain of Tg2576 mice, which express the Swedish mutation of human β-amyloid precursor protein (Apelt et al. 2002). Enzyme activities for acetylcholine synthesis (choline acetyltransferase) and degradation

(acetylcholine esterase; AChE) did not differ between transgenic mice and non-transgenic littermates. However, a reduction of high-affinity choline uptake and M_1-muscarinic receptor density was observed. Autoradiography with [³H]cytisine revealed a significant 20% loss of α4-containing nAChRs in cingulate and parietal cortices of these animals at an age of 17 months. However, there was no change in the number of basal forebrain cholinergic neurons in the transgenic mice, compared to age-matched wild-type animals.

Evidence for an involvement of α7 nAChR in Alzheimer's disease was first presented three decades ago (Davies and Feisullin 1981). More recently, a very high-affinity binding of (soluble) β-amyloid to α7 nAChRs has been described in vitro (Wang et al. 2000), supporting the hypothesis that β-amyloid at very low concentrations may initiate neuronal degeneration via an α7 nAChR-mediated inflammatory process (Bencherif and Lippiello 2010). A 20% reduction in α7 nAChRs labelled with [125I]α-bungarotoxin was evident in the hippocampus, retrosplenial and parietal cortices and thalamus of 3xTg-AD mice at 6 months of age. There was a significant correlation between intraneuronal β-amyloid and reduced α7 nAChR binding in the same mouse model (Oddo et al. 2005). Whereas chronic nicotine administration did not alter α7 nAChR levels in these mice, there was an increase in α4β2 nAChRs labelled with [125I]epibatidine (Oddo et al. 2005). In contrast to the earlier report, no alteration in α7 nAChR binding was noted in a subsequent study of the triple transgenic 3xTg-AD mice, which closely emulate several features of natural Alzheimer's disease (Hedberg et al. 2010); this unexpected negative finding was attributed to unknown environmental and/or genetic factors.

The abundance of α7 nAChRs was determined using nanogold-conjugated α-bungarotoxin in the APP(SWE) mouse model of Alzheimer's disease (Jones et al. 2004). Interestingly, the α7 nAChR binding increased in the transgenic animals until 9 months of age but had declined at 12 months, most notably in areas of gliosis associated with β-amyloid plaques (Jones et al. 2006). Also [125I]α-bungarotoxin binding decreased in APP(SWE) mice between 9 months of age and 16 months (Hellström-Lindahl et al. 2004).

With the establishment of reliable cholinergic PET tracers, a number of molecular imaging studies of Alzheimer's disease have appeared in recent years. The first phase of this research consisted of studies of the $\alpha_4\beta_2$ subtype of nAChR with 2-[¹⁸F]fluoro-A-85380 (2-FA). One such quantitative PET study of 14 early AD patients showed no difference in V_T compared to healthy controls, nor was there any relationship between tracer uptake and cognitive scores (Ellis et al. 2008). The same research group did not detect any reduction in binding with healthy ageing (Ellis et al. 2009a), and did not find any effect of precognitive treatment with galantamine on 2-FA binding in Alzheimer's disease patients (Ellis et al. 2009b). Another study with 2-FA using a white matter reference tissue calculation of binding potential (BP_{ND}) found a 40% reduction in cerebral cortex of a group of nine patients with moderate Alzheimer's disease, but no such change in the thalamus (Kendziorra et al. 2011). Similar findings in a group of mild cognitive impairment (MCI) patients suggested that the loss of $\alpha_4\beta_2$ sites was already complete at the prodromal state of the disease. Others reported a 20–40% decline in 2-FA V_T/f_p (i.e. the distribution

volume corrected for the plasma free fraction) in the thalamus, caudate, hippocampus anterior cingulate cortex and insula in a group of 24 Alzheimer's disease patients compared to a healthy control group (Sultzer et al. 2017). Similarly, a dual tracer study with 2-FA and the beta-amyloid tracer [^{11}C]PiB showed an inverse relationship between the binding ratio of $\alpha_4\beta_2$ tracer and the amyloid BP_{ND} in the medial frontal cortex and basal forebrain of Alzheimer's disease patients (Okada et al. 2013). While the preponderance of such studies indicates a widespread loss of $\alpha_4\beta$ binding sites in Alzheimer's disease, there is a certain lack of congruence about its spatial extent and magnitude. This may reflect the various endpoints used for quantitation and the very long interval of 4–6 h required for attainment of equilibrium binding with 2-FA. Another PET study with (−)-[^{18}F]flubatine PET in patients with early Alzheimer's disease showed the reductions in $\alpha_4\beta_2$ nAChR mainly in target regions of the basal forebrain-cortical and septohippocampal cholinergic projections. The same study showed relationship between lower $\alpha_4\beta_2$ nAChR availability and impairment of distinct cognitive domains, notably episodic memory and executive function/working memory (Sabri et al. 2018). Further details, in particular related to the $\alpha_4\beta_2$ radioligands (−)-[^{18}F]flubatine and (+)-[^{18}F]flubatine, are reviewed elsewhere (Sabri et al. 2014).

Very recently, uptake of the $\alpha7$ nAChR ligand [^{11}C]-*(R)*-MeQAA was measured in groups of 20 Alzheimer's disease patients and 10 healthy age-matched controls. In the nucleus basalis magnocellularis and medial prefrontal cortex, the $\alpha7$ nAChR binding correlated positively with individual beta-amyloid PET results. Furthermore, the $\alpha7$ nAChR binding correlated positively with memory and executive function (Nakaizumi et al. 2018). This stands in agreement with findings in aged monkeys cited above, where [^{11}C]-*(R)*-MeQAA binding, ostensibly to $\alpha7$ NAChR, was associated with increased beta-amyloid binding (Nishiyama et al. 2015). Similar increases in Alzheimer's disease mice were attributed to microglial activation (Matsumura et al. 2015) at sites of amyloid deposition. At time of writing, the jury is out whether this might represented a compensatory and salutogenic reaction, or another aspect of pathology.

[^{18}F]fluoroethoxybenzovesamicol (FEOBV) is a novel PET radiotracer, which binds selectively to the vesicular acetylcholine transporter in terminals of basal forebrain neurons. SUVR analysis of this tracer showed widespread decreases in tracer binding in a group of Alzheimer's disease patients (Aghourian et al. 2017). Together with findings reported above, this suggests pre- and postsynaptic elements of basal-forebrain cholinergic pathways are compromised in Alzheimer's disease.

18.4.2 Movement Disorders

Parkinson's disease is, after Alzheimer's disease, the second most common neurodegenerative disorder. The hallmark neuropathology of Parkinson's disease is selective degeneration of midbrain dopaminergic neurons of the substantia nigra pars compacta (SNpc) and the presence of intra-cytoplasmic inclusions (Lewy bodies) consisting of aggregated α-synuclein (Spillantini et al. 1997) in surviving dopamine

neurons. Neurotoxins such as MPTP and 6-hydroxydopamine have been used in animal models emulating the nigrostriatal degeneration of Parkinson's disease (Quik 2004). Lesions of the nigrostriatal pathway in rats reveal a population of [³H]nicotine binding sites on dopamine terminals, where they are positioned to influence dopamine release (Clarke and Pert 1985). More recently, the stimulation of striatal dopamine release by nicotine has been linked specifically to α6β2β3 and α6α4β2β3 nAChRs, which predominate in the basal ganglia (Quik et al. 2011). Quantitative analysis with the α6β2 nAChR subtype ligand [¹²⁵I]α-conotoxin MII in conjunction with plasma membrane dopamine transporter measurements in MPTP-lesioned mice shows an association with presynaptic nigrostriatal terminals (Quik et al. 2003). In that study, much smaller reductions in the binding of [¹²⁵I]epibatidine (multiple sites) and 5-[¹²⁵I]iodo-A-85380 (β2-sites) were noted after dopamine lesioning, while no change was detected in α7 nAChRs measured with [¹²⁵I]α-bungarotoxin binding after nigrostriatal lesions. Displacement of [¹²⁵I]α-conotoxin MII binding with the analogue E11A was biphasic, allowing resolution of the α6β2β3 and α6α4β2β3 components (Bordia et al. 2007); autoradiographic studies in MPTP-treated mouse and non-human primates, as well as in material from idiopathic Parkinson's disease patients, revealed the α6α4β2β3 nAChR subtype population to be selectively vulnerable to nigrostriatal damage. Chronic oral nicotine administration was able to protect nicotinic receptors and dopaminergic markers in MPTP-treated monkeys (Bordia et al. 2006; Quik et al. 2006). Treatment of rats with a selective α7 nAChR agonist protected against nigrostriatal degeneration in the 6-OHDA model of parkinsonism, an effect that was linked to attenuated microglial activation (Serriere et al. 2015).

In a 2-[¹⁸F]fluoro-A-85380 PET study, the density of α4β2 nAChRs was slightly reduced in the basal ganglia of non-smoking Parkinson's disease patients (Kas et al. 2009). Another 2-[¹⁸F]fluoro-A-85380 PET study of Parkinson's disease patients reported a widespread reduction of α4β2 nAChR availability in cortical and subcortical regions, which correlated with the severity of mild cognitive or depressive symptoms (Meyer et al. 2009). There have been no α7 nAChR studies in Parkinson's disease, despite the preclinical evidence suggesting a role for these receptors in protecting against nigrostriatal degeneration. There is a current lack of agents for molecular imaging of the particular α6-containing nAChRs subtypes present in the basal ganglia, which may be of great relevance to Parkinson's disease given their involvement in dopamine release.

Huntington's disease is an autosomal dominant hereditary disorder proceeding to severe cognitive impairment and motor symptoms, notably hyperkinetic involuntary movements (chorea) (Roos 2010). A transgenic rat model of HD, which carries a truncated huntingtin cDNA fragment with 51 CAG repeats under control of the native rat huntingtin promoter, has been developed (von Horsten et al. 2003). Early investigations of nicotinic receptors in *post-mortem* brain from Huntington's disease patients did not reveal any significant changes (Perry et al. 1987; Whitehouse and Kellar 1987). However, autoradiographic assessment of 2-year-old transgenic rats revealed significant increase of nAChR in various regions in heterozygous but not homozygous animals (Bauer et al. 2005). There have not yet been any PET studies of nAChR in patients with Huntington's disease.

18.5   Epilepsy

Some forms of epilepsy have recently been associated with alterations of α4 nAChR subtype expression (Raggenbass and Bertrand 2002), and there is experimental evidence that the α7 nAChR may play a role in epileptogenesis (Dobelis et al. 2003). The autosomal dominant nocturnal frontal lobe epilepsy (ADNFLE) can be caused by mutations in the neuronal nicotinic acetylcholine receptor (nAChR) subunit genes CHRNA4 and CHRNB2 (Steinlein et al. 1995; Phillips et al. 2001). Relative to age-matched non-smoking subjects, there was a 10–20% increase in the binding of 2-[^{18}F]fluoro-A-85380 to α4β2 receptors in the brain of patients with ADNFLE (Picard et al. 2006); knock-in mice bearing a culprit mutant α4 gene have been prepared (Lipovsek et al. 2008), but have not been investigated by receptor autoradiography or PET. A recent clinical PET study of patients with idiopathic generalized epilepsy using the α4β2 nAChR ligand [^{18}F]A-85380 showed focal 25% increases in the binding ratio within the anterior cingulate cortex (ACC), which could distinguish individual patients from healthy controls (Garibotto et al. 2019).

18.6   nAChR Imaging of Stroke and Neuroinflammation

Stroke is the leading cause of adult disability in the United States and Europe and the second leading cause of death worldwide. Stroke is characterized by a loss of brain functions due to rapid disturbances in cerebral blood supply, either as reduced blood flow by thrombosis or embolism (ischemic stroke) or bleeding (haemorrhagic stroke). Hyperacute mechanisms of stroke-related brain tissue damage, such as excitotoxicity, can be discriminated from delayed factors such as inflammation and apoptosis. All cellular components of the so-called neurovascular unit, which includes neurons, astrocytes and endothelial cells, express nAChRs (Paulson et al. 2010). Insofar as long-term tobacco smoking is a risk factor for ischemic stroke (Hawkins et al. 2002), it may be relevant that nAChRs were altered in a *postmortem* study of smokers; α4 expression was increased in neurons and dendritic processes, and α7 expression was decreased in hippocampal neurons and astrocytes (Teaktong et al. 2004). In hypertensive stroke-prone rats, cortical α7 nAChRs are reduced, without concomitant changes in the α4β2 nAChRs (Ferrari et al. 1999). Activation of nAChRs by nicotine promotes endothelial cell proliferation (Villablanca 1998) and leucocyte migration (Yong et al. 1997), which together may increase thrombotic risk. However, nAChR agonism was neuroprotective against excitotoxicity in vitro, an effect mediated by growth factors (Belluardo et al. 1998) and also by inactivation of the toxins (O'Neill et al. 2002). These effects were blocked by the α7 nAChR antagonist α-bungarotoxin (Donnelly-Roberts et al. 1996). Interestingly, nicotine increased oedema/infarct size in a rodent stroke model (Paulson et al. 2010). A particular contribution of α7 nAChRs to stroke-related excitotoxicity might reflect their high Ca^{2+} permeability, especially under depolarizing conditions. Treatment with the acetylcholinesterase inhibitor methanesulfonyl fluoride attenuated stroke-induced learning and memory deficits in rats (Borlongan et al. 2005).

These rather discordant findings of effects of nAChR agonism in stroke models may reflect the different contributions of excitotoxicity and neuroinflammatory processes. The α7 nAChRs expressed on microglia (Shytle et al. 2004a) seem particularly poised to mediate inflammatory responses. Nicotinic agonism at these sites suppressed inflammation by decreasing TNF-α production, while nicotine antagonists had the opposite effect (Shytle et al. 2004a). In addition to central mechanisms, cholinergic signalling in the "cholinergic anti-inflammatory pathway" involving the vagus nerve may suppress the release of pro-inflammatory cytokines and influence migration of T cells from the periphery to brain areas affected by stroke or multiple sclerosis (Borovikova et al. 2000) by a mechanism sensitive to α–bungarotoxin (Pavlov et al. 2003).

Despite this extensive background, there have been very few molecular imaging studies of nAChRs in relevant neuroinflammation models. We have undertaken PET studies to assess α7 nAChR alterations in the sheep stroke model (Boltze et al. 2008). Here, we measured [^{18}F]DBT10 binding at different time points after permanent medial cerebral artery occlusion (pMCAO) by dynamic imaging using a clinical hybrid PET/MRI system. We found increased tracer uptake in the stroke-border zone 14 days after pMCAO. In these areas, microglia activation and macrophage infiltration were histologically confirmed. Ongoing studies aim to establish better the time course and histological correlates of the α7 nAChR changes in our stroke model. A recent dual tracer study monitored longitudinal changes in 2-[^{18}F]fluoro-A85380 and [^{11}C]PK11195 binding during a month after middle cerebral artery occlusion (MCAO) in rats. In the ischemic territory, both ligands showed progressive binding increase from day 3 to 7 post-injury, followed by a progressive decrease (Martin et al. 2015). *Post-mortem* analysis linked the changes to increased α4β2 nAChR and TSPO expression on microglia and macrophages.

In PET studies in a rat stroke model with transient MCAO occlusion, the PET signal from the α7 nAChR ligand [^{11}C]NS14492 increased around the core of the infarct, consistent with activation of microglia and astrocytes following the injury (Colas et al. 2018). In that study, treatment with the α7 agonist PHA 568487 1 week after the stroke lowered TSPO binding (suggesting a rescue from microgliosis) while diminishing the ultimate infarct volume. Thus, the α7 nAChR is a promising target for disease-altering interventions against stroke.

Atherosclerosis is a kind of chronic inflammatory condition that brings a high risk of cardiovascular events. Especially the "vulnerable" atherosclerotic plaques have a high risk of rupture, which is predictable from their avidity on FDG PET, as an index of macrophage infiltration into the vessel wall. As such, α7 nAChR PET presents an unexplored channel for investigating inflammatory changes in atherosclerosis (Boswijk et al. 2017). This follows also for a wide range of chronic inflammatory conditions such as rheumatoid arthritis, Crohn's disease, etc.

18.7   nAChR Imaging of Traumatic Brain Injury

Traumatic brain injury is a permanent or temporary impairment of brain functions with an associated diminished or altered state of consciousness caused by external mechanical force transferring kinetic energy to the brain tissue. In developed

countries, TBI is the most important cause of death and disability in young adults, in both civilian and military contexts (Olesen and Leonardi 2003) (Dewan et al. 2018). Indeed, TBI causes some 30–50% of all injury-related deaths (de Ramirez et al. 2012; Kamal et al. 2016). Apart from the distinct acute injuries, TBI is a continuous disease process (Masel and DeWitt 2010), with survivors often suffering from persistent or permanent physical and cognitive impairments (Fleminger and Ponsford 2005) occurring as long-term sequelae of the initial injury. This profile imposes a considerable socio-economic burden (Humphreys et al. 2013), which is further exacerbated by the failure of clinical trials aiming to improve outcomes (Loane and Faden 2010; Gruenbaum et al. 2016).

18.7.1 Animal Models of TBI

Experimental animal models of TBI provide a solid body of evidence for specific cholinergic alterations. A plethora of different TBI models has been developed since the late 1940s. There is a distinction to be made between closed head injuries and open-head models, whereby in the former model the underlying cortical tissue is damaged by impact on the intact *dura mater*. Most animal studies of cholinergic responses to TBI make use of fluid-percussion injuries (FPI), weight drop and controlled cortical impact (CCI) (Xiong et al. 2013) (O'Connor et al. 2011). This can be performed either through a fluidic wave, as in the FPI models (Thompson et al. 2005), rigid impactors such as weight drop (Marmarou et al. 1994) or CCI models (Lighthall 1988). Unfortunately, there is little data on cholinergic alterations provoked by the more clinically relevant (repeated) closed-head or concussive models. The CCI model, which was first developed in small animals (Lighthall 1988) and later used in pigs (Duhaime et al. 2000; Alessandri et al. 2003; Manley et al. 2006), entails a piston strike, which results in more focal brain injury than is afforded by the FPI model.

Early evidence of the involvement of the cholinergic system in TBI was obtained in dogs and cats, in which increased acetylcholine concentration was noted in cerebrospinal fluid up to 48 h post-injury (Bornstein 1946). In subsequent years, studies of TBI implicate diverse aspects of cholinergic neurotransmissions, including muscarinic and nicotinic receptors, enzymatic pathways and vesicular transporters (Hayes et al. 1992; Arciniegas 2011; Kelso and Oestreich 2012; Shin and Dixon 2015). In an autoradiographic study of rats with TBI, there were widespread and substantial bilateral reductions in cortical and hippocampal α7 nAChRs labelled with [^{125}I]α-bungarotoxin, in contrast to lesser, more focal and ipsilateral effects on heteromeric nAChRs labelled with [^{3}H]epibatidine (Verbois et al. 2000). We have seen a similar decline in α7 binding in the brain of rats and neonate piglets following FP injuries (Donat et al. 2008, 2010a, b; Hoffmeister et al. 2011). In a saturation binding study, the reductions were linked to declines in B_{max}, rather than affinity changes (Verbois et al. 2002), an issue that must always be considered in autoradiographic or PET studies performed with a single ligand concentration. Peak effects occurred at 2 days post-injury but persisted for as long as 2 weeks. Brain regions not directly subjected to mechanical damage, such as the thalamus, were found to

exhibit reduced density of α7 and α3/4 nAChR, indicating retrograde and antero-grade changes.

Most interestingly, brain areas showing reduced nAChR binding after TBI also showed delayed neuroinflammation, as indicated by increased binding of a tracer for the 18 kDA translocator protein, a marker of microglial activation (Donat et al. 2016), suggesting that nAChRs regulate neuroinflammatory responses (Egea et al. 2015). Indeed, in a model of blast-induced TBI, midbrain structures showed low-ered gene transcripts of muscarinic and α7 nAChR, accompanied by increased gene transcripts of pro-inflammatory markers (Valiyaveettil et al. 2013). Treatments with agonists and positive allosteric modulators of α7 nAChR attenuated microglia acti-vation after TBI while rescuing blood-brain barrier permeability increases and reducing motor deficits (Gatson et al. 2015; Dash et al. 2016). This is consistent with anti-inflammatory effects α7 nAChR activation on microglia and potentially endothelial cells (Kimura, Dohgu et al. 2018), as indicated before (Cortes et al. 2017; Zhang et al. 2017).

Cognitive impairment was demonstrated in the rat FPI model (Scheff et al. 1997), suggesting that the α7 nAChR reductions may contribute to these cognitive deficits caused by brain trauma. Also in the FPI paradigm, prolonged treatment with nico-tine partially attenuated the cognitive deficits seen in the Morris water maze perfor-mance and reduced the magnitude and spatial extent of the α7 changes (Verbois et al. 2003a, b). Indeed, nicotine has been effective in a number of other brain lesion models (Visanji et al. 2006; Huang et al. 2009; Zafonte et al. 2009; Quik et al. 2010), even though human patients who are smokers do not show improved out-come after TBI (Ostberg and Tenovuo 2014), because of smoking-associated health impairments such as vascular diseases. Furthermore, investigations in α7 knockout mice failed to show much effect of α7 receptor expression on lesion volume or microglia activation (Kelso et al. 2006), which could be confounded by compensa-tory mechanisms (Smith et al. 2014). Nonetheless, dietary choline supplements par-tially rescued the spatial memory deficits and α7 receptor deficits after CCI (Guseva et al. 2008; Guseva et al. 2013).

18.7.2 Human TBI Studies

Neuroinflammation, a process mediated primarily by glia cells, i.e. microglia and astrocytes, is not just a hallmark pathology of TBI, but also a potential avenue of intervention (Morganti-Kossmann et al. 2019). Activated microglia, which are the resident macrophages of the brain, can assume many different roles post-injury, as characterized by diverse morphologies and molecular expression patterns. The dichotomy of pro-inflammatory M1 microglial phenotype versus anti-inflammatory M2 phenotype (Donat et al. 2017) may be an oversimplification (Ransohoff 2016), but it should not be assumed that all microglia are equal. A similar model of func-tions and phenotypes has been recently reported for astrocytes (Liddelow et al. 2017).

Glial activation can persist for many years after TBI (Ramlackhansingh et al. 2011). TBI is a risk factor for neurodegenerative diseases including chronic

traumatic encephalopathy (McKee et al. 2016) and dementias, including Alzheimer's disease (AD) (LoBue et al. 2018). The link between TBI and dementia may be mediated either by tau pathology or by altered cholinergic neurotransmission particularly involving hetero- and homomeric nAChR, as proposed for AD in the 1980s (Shimohama et al. 1986), in association with the cholinergic hypothesis of AD (Bohnen et al. 2018; Hampel et al. 2018). Historically, nAChR changes were linked to cognitive symptoms (Wallace and Bertrand 2013), as most α7 and α4/3β2/4 nAChR are expressed on cortical neurons. However, cholinergic enzymes and receptors are also implicated in central and peripheral inflammatory response (Fujii et al. 2017), pointing to the above-mentioned cholinergic anti-inflammatory pathway (Martelli et al. 2014). Acetylcholine receptors may be essential mediators of this pathway and are likely involved in the neuroinflammatory response after TBI (Ren et al. 2017). Indeed, microglia express α7 nAChR (Shytle et al. 2004b), as do astrocytes (Shen and Yakel 2012), where they seem to be directly involved in regulating glia activation. Reduced α7 nAChR expression or antagonist exposure can promote the pro-inflammatory phenotype, while treatment with agonists may shift microglia towards an anti-inflammatory phenotype (Cortes et al. 2017; Zhang et al. 2017).

Several studies have investigated key players of the cholinergic neurotransmission following TBI. However, only very few studies investigated human patients or tissue samples. In a human *post-mortem* study, performed after traumatic brain injury, reduced choline acetyl transferase activity and synaptophysin immunoreactivity in cerebral cortex were found, indicating damage of the cholinergic innervation, but nAChR binding determined by either [^{3}H]nicotine or [^{125}I]α-bungarotoxin was unchanged (Murdoch et al. 1998), suggesting mainly presynaptic mechanisms. *Post-mortem* cortical tissue from patients acquired between 1 and 300 h after injury showed a reduction in choline acetyltransferase activity, but no change in muscarinic (M1 and M2 receptors) or nicotinic receptors, determined by either [^{3}H]nicotine or [^{125}I]α-bungarotoxin (Dewar and Graham 1996; Murdoch et al. 1998). Reduced synaptophysin immunoreactivity was seen as an indicator of mainly presynaptic pathomechanisms, even though a follow-up study showed extensive damage in basal forebrain cholinergic neurons (Murdoch et al. 2002). Interestingly, diffusion tensor imaging indicated axonal injury in the same areas (Hong et al. 2012). More importantly, recent studies of CTE showed a gradual emergence of pretangle pathology and oligomeric tau accumulation in cholinergic neurons of the basal forebrain, which might directly relate to cholinergic impairments and ultimately to cognitive dysfunction and immune dysregulation (Mufson et al. 2016). Laser capture microdissection and gene profiling of these neurons showed, among other findings, a reduction in CHRNB2 transcripts, encoding the nAChR β2 subunit (Mufson et al. 2018). Another potential factor in TBI is autoimmune consequences (Raad et al. 2014). One study reported a significant increase in blood autoantibodies to regions of the α7 subunit in children with TBI, which correlated to severity (Sorokina et al. 2012).

In vivo molecular imaging with nAChR subtype-specific tracers is still lacking in clinical TBI. However, PET imaging with [^{11}C]MP4A in chronic TBI patients

indicated loss of AChE activity (Östberg et al. 2011; Ostberg et al. 2018). Treatment of post-traumatic cognitive deficits using cholinergic compounds, e.g. acetylcholinesterase inhibitors, has been attempted in several studies of small patient groups. However, most of these exploratory studies did not meet their endpoints justifying larger randomized placebo-controlled studies, and systematic reviews therefore concluded only weak evidence of efficacy (Wheaton et al. 2011; Bengtsson and Godbolt 2016).

18.8   nAChR Imaging of Addiction and Psychiatric Disorders

18.8.1 Physiological Effects of Nicotine in the Context of Addiction

Whereas acetylcholine is rapidly inactivated by AChE, nicotine exerts prolonged agonism due to its metabolic stability. This property accounts for the well-known phenomenon of desensitization of nicotinic receptors by nicotine (Govind et al. 2012), in which inactivated receptors concentrate in the plasma membrane due first to agonist-evoked conformational changes, which is followed by decreased degradation of subunits (Govind et al. 2012). In the case of α4β2 nAChRs, upregulation is mediated by activation of protein kinase C, which results in phosphorylation of the α4 subunit (Wecker et al. 2010). This mechanism is supported by studies in rats and 3xTd-AD mice showing upregulation of α4β2 nAChR after chronic nicotine administration (Flores et al. 1992; Oddo et al. 2005). Chronic nicotine treatment persistently increased the binding of the α4β2 ligand 5-[^{123}I]iodo-A-85380 by approximately 50% in the brain of baboons (Kassiou et al. 2001). Similarly, a 2-[^{18}F]fluoro-A-85380 PET study in chronic smokers abstinent for at least 24 h revealed persistent upregulation of α4β2 nAChR throughout the brain (Mukhin et al. 2008); these findings stress the requirement for strict control of exposure to nicotine in the design of clinical and preclinical imaging studies of nAChRs. Thus, exposure of rats to tobacco smoke not only induced nicotine dependence but also increased the α7 nAChR density in the CA2/3 area (+ 25%) and the stratum oriens (+ 18%) of the hippocampus (Small et al. 2010).

Since the nAChRs are ligand-gated cation channels, their activation facilitates depolarization and enhances the release of dopamine and other neurotransmitters. Consistent with the increased energy demands associated with depolarization, acute challenge with nicotine increases the cerebral metabolic rate for glucose (CMRglc) as measured by [^{14}C]-deoxyglucose autoradiography; these effects are most notable in the thalamus and other rat brain regions in which nicotinic receptors are most abundant (London et al. 1988; Marenco et al. 2000). Despite the phenomenon of upregulation/desensitization of nAChRs, stimulation of CMRglc in rat brain was still evident after reinstatement of nicotine following a period of withdrawal (Schröck and Kuschinsky 1991). Effects of nicotine on CMRglc are poorly documented in human brain, but one PET study showed that nicotine-evoked stimulation of 2-[^{18}F]fluorodeoxyglucose uptake in non-smokers was dependent on the hostility

trait, as was also seen in smoking subjects treated with a higher dose of nicotine (Fallon et al. 2004). The latter finding seems consistent with desensitization of the cerebrometabolic response to nicotine challenge in the smoking group. Smoking provoked a delayed increased in the cerebral consumption of oxygen in the brain of acutely withdrawn smokers, suggesting a global effect of nicotine or other constituents of tobacco smoke on mitochondrial respiration as distinct from glycolysis (Vafaee et al. 2015).

Baseline levels of 2-[^{18}F]fluoro-A-85380 binding in the brainstem of healthy squirrel monkeys predicted their motivation to subsequently self-administer nicotine, as indicated by number of bar presses (Le Foll et al. 2009), suggesting that nAChRs mediate a trait vulnerability specifically for nicotine abuse. It is unclear whether this association with nicotine addiction generalizes to other addictive drugs. However, activation of nAChRs on dopamine neurons and terminals is central to the reinforcing and addictive properties of nicotine. Stimulation of striatal dopamine release by nicotine has recently been linked to α6β2β3 and α6α4β2β3 nAChRs, which predominate in the basal ganglia (Quik et al. 2011). Activation of these receptors increases the firing rate and augments phasic bursting of midbrain dopamine neurons (De Biasi and Dani 2011). The α7 nAChRs in the ventral tegmental area may mediate nicotine's stimulatory effect on mesolimbocortical dopaminergic function and consequently its reinforcing and dependence-producing properties (Nomikos et al. 2000).

In an early molecular imaging study of nAChRs, binding of the SPECT tracer 5-[^{123}I]-A-85380 at α4β2 sites was increased by one third in the cortex and striatum of smokers with confirmed abstinence for 1 week (Staley et al. 2006). This study recapitulated in human smokers the well-known upregulation and inactivation of nAChRs following repeated nicotine exposure seen in experimental animals. The same group showed normalization of nAChR availability after 6 weeks of abstinence (Cosgrove et al. 2009). The competition paradigm affords the possibility of detecting occupancy by exogenous nicotine or other drugs at nAChR in living individuals. Here, comparison of molecular imaging results at baseline and after drug challenge reveals the percentage of receptors occupied by the drug. In one such 5-[^{123}I]-A-85380 SPECT study, smoking to satiety (about two cigarettes) induced a 67% reduction in their chosen endpoint, V_T/f_p (Esterlis et al. 2010a). Occupancy after use of a nicotine inhaler (56%) was significantly lower than after smoking cigarettes to satiety (Esterlis et al. 2010b).

These nAChR occupancies may be underestimated due to the slow kinetics of the SPECT tracer relative to the pharmacodynamics of nicotine. Corresponding PET studies with 2-[^{18}F]fluoro-A-85380 showed 79% occupancy after smoking a low-nicotine cigarette and 26% after smoking a denicotinized cigarette (Brody et al. 2009). In another 2-[^{18}F]fluoro-A-85380 PET study, a few puffs on a normal cigarette induced 50% occupancy persisting 3 h later, whereas an entire cigarette provoked 88% occupancy (Brody et al. 2006). Even exposure to second-hand smoke led to 20% occupancy (Brody et al. 2011). A single low dose (0.5 mg) of varenicline provoked complete saturation of 2-[^{18}F]fluoro-A-85380 binding sites in human brain (Lotfipour et al. 2012a). Thus, varencline is apt to evoke full agonism at α7

nAChRs, with partial agonism at other sites, i.e. α4β2, as well as α3β4, and α6β2 subtypes.

Altered dopamine release can be detected in PET studies with [^{11}C]raclopride and other benzamide antagonists of $D_{2/3}$ receptors, wherein ligand binding is reduced by competition from endogenous dopamine (Laruelle 2000; Cumming et al. 2003). Whereas powerful psychostimulants such as amphetamine can evoke 30% decreases in striatal [^{11}C]raclopride binding, challenge with nicotine reduced this binding by only 5–10% in striatum of anaesthetized pigs, most notably in the ventral striatum (Cumming et al. 2003). There were effects of similar magnitude in the brain of non-human primates (Marenco et al. 2004), although others saw no such effects in PET scans of awake monkeys (Tsukada et al. 2002), suggesting a confounding effect of general anaesthesia. Similarly, intranasal administration of nicotine did not greatly reduce striatal [^{11}C]raclopride binding in healthy habitual smokers, although baseline binding correlated with scores of nicotine dependence, and there was a positive relationship between binding changes and individual reports of pleasant subjective experience (Montgomery et al. 2007), as likewise seen in another [^{11}C]raclopride PET study of smokers (Barrett et al. 2004). In general, preclinical studies with non-contingent pharmacological challenge may not replicate the motivational aspects of self-administered nicotine.

Dopamine synthesis capacity in living striatum can be measured by PET studies with DOPA decarboxylase substrates such as [^{11}C]DOPA or 6-[^{18}F]fluoro-DOPA (FDOPA). Whereas acute nicotine treatment had no effect on [^{11}C]DOPA utilization in striatum of awake monkeys, this utilization was reduced by one third after overnight abstinence in monkey habituated to nicotine and normalized rapidly following reinstatement of nicotine treatment (Domino et al. 2009). On the other hand, in an isolated clinical PET finding, FDOPA utilization was 20–30% higher in striatum of human smokers (Salokangas et al. 2000). Another study showed a 20% reduction in the striatal utilization of FDOPA in a larger group of dependent smokers (Rademacher et al. 2016), which may have greater face validity as an adaptive response to chronic nicotine exposure.

18.8.2 Alcohol Dependence

There is very high comorbidity between nicotine and alcohol dependence, and considerable overlap between their neural mechanisms of addiction (Larsson and Engel 2004). Indeed, a possible role for nAChR in alcohol addiction has been proposed (Meyerhoff et al. 2006). Altered nACh receptor density in vitro has been observed in rats in response to ethanol using a combination of [^{3}H]nicotine, [^{3}H]MLA and [^{125}I]alpha-bungarotoxin, but the direction of change was inconsistent and region-specific (Yoshida et al. 1982; Booker and Collins 1997; Robles and Sabria 2008). In vivo, binding of the SPECT radioligand [^{123}I]5-IA-85380 in rhesus monkey was unaltered following chronic alcohol self-administration, although decreases in cortical and thalamic binding were observed following abstinence (Cosgrove et al. 2010). More recently, using [^{18}F]nifene in a PET study in non-human primates,

reductions in nACh receptor density were observed following chronic alcohol exposure (Hillmer et al. 2014). Further validation work is required in human subjects to resolve these inconsistencies.

18.8.3 Schizophrenia and Depression

Nicotine addiction is notoriously prevalent among patients with schizophrenia (Lohr and Flynn 1992), a chronic psychiatric disease characterized by behavioural changes, which are difficult to model in experimental animals. The DSM-IV criteria for schizophrenia consist of positive symptoms (such as agitation, paranoia and hallucinations), negative symptoms (including emotional blunting, avolition and social withdrawal) and specific cognitive and psychomotor deficits (Goldman-Rakic and Selemon 1997). An increasing appreciation of the importance of cognitive deterioration has motivated a search for treatments to improve processing speed, attention/vigilance and working memory (Nuechterlein et al. 2004; Heinrichs 2005). This has emerged in the context of a hypothesis implicating gene-mediated dysfunction of α7 nAChRs (Freedman et al. 1997; Stephens et al. 2009; Dome et al. 2010) in the cognitive impairments of schizophrenia (Nomikos et al. 2000). Indeed, in one *post-mortem* study, the hippocampal [^{125}I]α-bungarotoxin binding was decreased in a schizophrenic patient population consisting mainly of smokers (Freedman et al. 1995). Furthermore there were significant differences in α7 nAChR (*CHRNA7*) expression at both mRNA and protein levels between smokers and non-smokers with schizophrenia (Mexal et al. 2010).

Nicotinic receptors and treatments have been investigated in a number of murine models emulating some behaviour aspects of schizophrenia. An auditory gating defect in dilute brown non-Agouti (DBA/2) mice is rectified by treatment with an α4β2 agonist (Wildeboer and Stevens 2008), but other nAChR subtypes such as α7 may also mediate sensory gating in these mice (Radek et al. 2006). Mice lacking the plasma membrane dopamine transporter show hyperactivity and cognitive deficits, and are hypersensitive to the locomotor stimulant effect of nicotine, which models schizophrenia. Treatment of these mice with nicotine improved their performance in spatial and cued learning tasks (Weiss et al. 2007a), whereas autoradiography showed a small decline in the β2 subunit, a large decrease in β6 and substantially increased α7 nAChR expression (Weiss et al. 2007b). Deficiency of the microtubule-stabilizing protein STOP results in impaired hippocampal plasticity and behavioural hypersensitivity to psychostimulants, likewise associated with a decrease in β6, and a substantial increase in α7 nAChRs (Bouvrais-Veret et al. 2007), suggesting a common nicotinergic pathway in these two models of schizophrenia.

A preliminary study with the α7-nAChR ligand [^{18}F]ASEM showed a moderate reduction of binding in the brain of a group of patients with schizophrenia (Wong et al. 2018). This finding was recapitulated in another study of recent onset psychosis (Coughlin et al. 2018a). Given the association of α7 nAChR expression with microglia, the resident brain macrophage, it is a matter of interest if there are changes in inflammatory pathways in association with schizophrenia. A recent

meta-analysis of many PET TSPO studies in patients with schizophrenia showed an overall finding of reduced microglial activation (Plaven-Sigray et al. 2018). While this was contrary to general expectation of an active inflammatory process during schizophrenia, it may be consistent with the α7-nAChR findings.

Availability of α4β2 nAChR binding sites was globally reduced in a 5-[¹²³I]iodo-A-85380 SPECT study of patients with major depression (Saricicek et al. 2012). Changes in behaviour, and in endocrine, and immune and neurotransmitter systems, modelling symptoms of patients with major depression have been described in rats following bilateral olfactory bulbectomy (Song and Leonard 2005). Such rats present characteristic alterations in cholinergic function (Hozumi et al. 2003). Although degeneration of cholinergic neurons may well underlie the impairments of learning and memory-related behaviour in olfactory bulbectomy rats, densities of nAChRs have not yet been investigated in this model. Interestingly, a recent TSPO PET study showed globally increased microglial expression in cortex of patients with major depression and an association with cognitive deficits (Li et al. 2018). However, there has hitherto been no PET study of α7-nAChR depressed (non-smoking) patients.

18.9 nAChR Imaging for Measurement of Endogenous Acetylcholine

The competition model for measuring dopamine release by molecular imaging, i.e. the [¹¹C]raclopride binding model described above, has delivered substantial insights into the role of dopamine in the pathophysiologies of schizophrenia and nicotine addiction. However, attempts to generalize the dopamine competition model to other neurotransmitter systems have met with mixed success (Paterson et al. 2010; Finnema et al. 2015). A molecular imaging assay for fluctuations in extracellular acetylcholine would be a useful tool for evaluating new pharmacologic treatments for Alzheimer's disease and other conditions, and the first demonstration of an acetylcholine sensitive α4β2 PET tracer was recently published (Hillmer et al. 2016a). Competition between endogenous acetylcholine and radioligands targeting muscarinic acetylcholine receptors is reported in the literature (Dewey et al. 1993; Suhara et al. 1994; Ma et al. 2004; Eckelman 2006), but the case is better established for nAChR ligands, the details of which are presented here.

Preclinical studies in rodents suggest that treatment with AChE inhibitors may raise acetylcholine levels sufficiently to elicit changes in binding potential with PET. Treatment with AChE inhibitors, an important class of compounds used for alleviation of Alzheimer's disease symptoms, affords a convenient way of enhancing acetylcholine levels in living brain in tests of the competition model. In the first such study, the uptake of 2-[¹⁸F]fluoro-A-85380 in rat thalamus measured ex vivo was 45% reduced by the AChE inhibitor physostigmine (Dollé et al. 1999); decreases of similar magnitude were seen in animals treated with typical α4β2 agonist ligands (2-fluoro-A-85380, nicotine, epibatidine and cytisine) but not by α7- or 5-HT₃-specific antagonists. Previous microdialysis studies had confirmed that the same

dose of physostigmine (300 µg/kg) caused large increases in interstitial acetylcholine (Cuadra et al. 1994), thus substantiating the competition model.

In a non-human primate PET study, Ding et al. investigated whether modulation of acetylcholine levels could modulate [^{18}F]NFEP binding (Ding et al. 2000b). As predicted, binding was 25% lower in the thalamus and striatum following physostigmine administration. Furthermore, treatment with the dopamine $D_{2/3}$ antagonist raclopride reduced the striatal binding of [^{18}F]NFEP by 22%, and the agonist quinpirole increased striatal binding by 26%, but selective dopamine D_1 drugs had no such effects. These findings were consistent with results of cerebral microdialysis studies showing that dopamine $D_{2/3}$ receptors tonically inhibit acetylcholine release in the striatum (Damsma et al. 1991; DeBoer et al. 1996).

In a 5-[^{123}I]iodo-A-85380 SPECT study in non-human primate, a bolus plus constant infusion paradigm was used to obtain equilibrium binding prior to physostigmine treatment (Fujita et al. 2003). Due to instability of the plasma 5-[^{123}I]iodo-A-85380 concentration following physostigmine, the BP_{ND} was not calculated, but there was a 14–17% decrease in thalamic tracer uptake. This decline was independent of the physostigmine dose administered, suggesting a ceiling effect in the competition from endogenous acetylcholine. In a subsequent 2-[^{18}F]fluoro-A-85380 study, a more prolonged infusion of physostigmine evoked a 40% reduction in 2-[^{18}F]fluoro-A-85380 V_T in putamen and more modest reduction in cerebral cortex (Valette et al. 2005). The effect was dose-dependent, and infusion of galantamine, a weaker AChE inhibitor, did not alter 2-[^{18}F]fluoro-A-85380 binding, which again suggests a fairly narrow relationship between interstitial acetylcholine concentration and increased competition.

In PET studies in rats, cortical and thalamic [^{18}F]nifene binding was found to be significantly reduced (3–10%) following physostigmine and galantamine administration (Hillmer et al. 2013) suggesting this ligand may also be sensitive to changes in endogenous acetylcholine. In vitro binding studies with [^{18}F]nifene and [^{3}H]cytosine showed displacement of both ligands upon addition of an AChE inhibitor to the medium (Easwaramoorthy et al. 2007). This highlights the rapid hydrolysis of endogenous acetylcholine in the presence of native AChE and raises the consideration that inactivation/upregulation of nAChRs may arise from "supernormal" activation during AChE inhibition, or during exposure to nicotine or other long-lived agonists. Breakdown of released acetylcholine is usually complete within a matter of seconds (Bruno et al. 2006). As such, the PET observations described above cannot unambiguously be ascribed to the competition model; some of the decreases in receptor binding after treatment with AChE inhibitors might rather be attributable to transition of the receptors to a low-affinity state or to trafficking mechanisms. This is especially a consideration in studies with ligands with slow kinetics, such as in the above reports.

More recently, (−)-[^{18}F]flubatine ((−)-[^{18}F]NCFHEB) was shown to be sensitive to displacement by endogenous acetylcholine in non-human primates. Treatment with AChE inhibitors donepezil and physostigmine led to dose-dependent, significant reductions (10–34%) in V_T in bolus and bolus-infusion protocols, respectively (Gallezot et al. 2014). This finding was soon followed by a similar study in human

subjects (Hillmer et al. 2016a), in which a bolus and bolus-infusion protocol with [^{18}F]flubatine revealed small but significant reductions in V_T in cortical regions following physostigmine administration.

Overall these data suggest that measuring acetylcholine changes using selective α4β2 nAChR radioligands may be possible and that we should expect future applications of this methodology in clinical populations such as Alzheimer's disease, substance dependence and schizophrenia.

18.10 Conclusion

The development of selective ligands for nAChRs has been challenging due to the diversity of subtypes existing in the brain and due to the unfavourable kinetics and toxicity profiles of some lead compounds. Promising novel tracers targeting α4β2 nAChRs include [^{18}F]AZAN, [^{18}F]nifene, [^{18}F]XTRA and both the (−) and (+) enantiomers of [^{18}F]flubatine. For the α7 nAChR, [^{18}F]DBT10 and [^{18}F]ASEM are promising candidates. Despite the importance of α6 nAChRs in the action of nicotine on dopamine release, selective tracers for this target remain elusive.

References

Abbaszadeh S, Levin CS (2017) New-generation small animal positron emission tomography system for molecular imaging. J Med Imaging (Bellingham) 4:011008

Abreo MA, Lin NH, Garvey DS et al (1996) Novel 3-pyridyl ethers with subnanomolar affinity for central neuronal nicotinic acetylcholine receptors. J Med Chem 39:817–825

Aghourian M, Legault-Denis C, Soucy JP et al (2017) Quantification of brain cholinergic denervation in Alzheimer's disease using PET imaging with [^{18}F]-FEOBV. Mol Psychiatry 22:1531–1538

Alessandri B, Heimann A, Filippi R et al (2003) Moderate controlled cortical contusion in pigs: effects on multi-parametric neuromonitoring and clinical relevance. J Neurotrauma 20:1293–1305

Alexander SP, Peters JA, Kelly E et al (2017) The concise guide to pharmacology 2017/18: Ligand-gated ion channels. Br J Pharmacol 174(Suppl 1):S130–S159

Allen DD, Lockman PR (2003) The blood-brain barrier choline transporter as a brain drug delivery vector. Life Sci 73:1609–1615

Allen DD, Lockman PR, Roder KE et al (2003) Active transport of high-affinity choline and nicotine analogs into the central nervous system by the blood-brain barrier choline transporter. J Pharmacol Exp Ther 304:1268–1274

Apelt J, Kumar A, Schliebs R (2002) Impairment of cholinergic neurotransmission in adult and aged transgenic Tg2576 mouse brain expressing the Swedish mutation of human beta-amyloid precursor protein. Brain Res 953:17–30

Arciniegas DB (2011) Cholinergic dysfunction and cognitive impairment after traumatic brain injury. Part 2: evidence from basic and clinical investigations. J Head Trauma Rehabil 26:319–323

Arneric SP, Sullivan JP, Briggs CA et al (1994) (S)-3-methyl-5-(1-methyl-2-pyrrolidinyl) isoxazole (ABT 418): a novel cholinergic ligand with cognition-enhancing and anxiolytic activities: I. In vitro characterization. J Pharmacol Exp Ther 270:310–318

Auerbach A (2015) Agonist activation of a nicotinic acetylcholine receptor. Neuropharmacology 96:150–156

Avalos M, Parker MJ, Maddox FN et al (2002) Effects of pyridine ring substitutions on affinity, efficacy, and subtype selectivity of neuronal nicotinic receptor agonist epibatidine. J Pharmacol Exp Ther 302:1246–1252

Barrett SP, Boileau I, Okker J et al (2004) The hedonic response to cigarette smoking is proportional to dopamine release in the human striatum as measured by positron emission tomography and [^{11}C]raclopride. Synapse 54:65–71

Bauer A, Zilles K, Matusch A et al (2005) Regional and subtype selective changes of neurotransmitter receptor density in a rat transgenic for the Huntington's disease mutation. J Neurochem 94:639–650

Belluardo N, Blum M, Mudo G et al (1998) Acute intermittent nicotine treatment produces regional increases of basic fibroblast growth factor messenger RNA and protein in the tel- and diencephalon of the rat. Neuroscience 83:723–740

Bencherif M, Lippiello PM (2010) Alpha7 neuronal nicotinic receptors: the missing link to understanding Alzheimer's etiopathology? Med Hypotheses 74:281–285

Bengtsson M, Godbolt AK (2016) Effects of acetylcholinesterase inhibitors on cognitive function in patients with chronic traumatic brain injury: a systematic review. J Rehabil Med 48:1–5

Bennett MR (2000) The concept of transmitter receptors: 100 years on. Neuropharmacology 39:523–546

Berg DK, Conroy WG (2002) Nicotinic α7 receptors: synaptic options and downstream signaling in neurons. J Neurobiol 53:512–523

Bertrand D, Lee CH, Flood D et al (2015) Therapeutic potential of α7 nicotinic acetylcholine receptors. Pharmacol Rev 67:1025–1073

Betthauser TJ, Hillmer AT, Lao PJ et al (2017) Human biodistribution and dosimetry of [^{18}F]nifene, an α4β2* nicotinic acetylcholine receptor PET tracer. Nucl Med Biol 55:7–11

Bhatt S, Hillmer AT, Nabulsi N et al (2018) Evaluation of (−)-[^{18}F]flubatine-specific binding: Implications for reference region approaches. Synapse 72

Bieszczad KM, Kant R, Constantinescu CC et al (2012) Nicotinic acetylcholine receptors in rat forebrain that bind ^{18}F-nifene: relating PET imaging, autoradiography, and behavior. Synapse 66:418–434

Biton B, Bergis OE, Galli F et al (2007) SSR180711, a novel selective alpha7 nicotinic receptor partial agonist: (1) binding and functional profile. Neuropsychopharmacology 32:1–16

Bohnen NI, Frey KA (2007) Imaging of cholinergic and monoaminergic neurochemical changes in neurodegenerative disorders. Mol Imaging Biol 9(4):243–257

Bohnen NI, Grothe MJ, Ray NJ et al (2018) Recent advances in cholinergic imaging and cognitive decline-Revisiting the cholinergic hypothesis of dementia. Curr Geriatr Rep 7:1–11

Bois F, Gallezot JD, Zheng MQ et al (2015) Evaluation of [^{18}F]-(−)-norchlorofluorohomoepibatidine ([^{18}F]-(−)-NCFHEB) as a PET radioligand to image the nicotinic acetylcholine receptors in non-human primates. Nucl Med Biol 42:570–577

Boltze J, Forschler A, Nitzsche B et al (2008) Permanent middle cerebral artery occlusion in sheep: a novel large animal model of focal cerebral ischemia. J Cereb Blood Flow Metab 28:1951–1964

Bolwin K, Vernekohl D, Luhder J et al (2017) Development of a clear sub-millimeter small animal PET scanner by reducing the influence of the non-collinearity effect. J Instrum 12

Booker TK, Collins AC (1997) Long-term ethanol treatment elicits changes in nicotinic receptor binding in only a few brain regions. Alcohol 14:131–140

Bordia T, Grady SR, McIntosh JM et al (2007) Nigrostriatal damage preferentially decreases a subpopulation of alpha6beta2* nAChRs in mouse, monkey, and Parkinson's disease striatum. Mol Pharmacol 72:52–61

Bordia T, Parameswaran N, Fan H et al (2006) Partial recovery of striatal nicotinic receptors in 1-methyl-4-phenyl-1,2,3,6-tetrahydropyridine (MPTP)-lesioned monkeys with chronic oral nicotine. J Pharmacol Exp Ther 319:285–292

Borlongan CV, Sumaya IC, Moss DE (2005) Methanesulfonyl fluoride, an acetylcholinesterase inhibitor, attenuates simple learning and memory deficits in ischemic rats. Brain Res 1038:50–58

Bornstein MB (1946) Presence and action of acetylcholine in experimental brain trauma. J Neurophysiol 9:349–366

Borovikova LV, Ivanova S, Zhang M et al (2000) Vagus nerve stimulation attenuates the systemic inflammatory response to endotoxin. Nature 405:458–462

Boswijk E, Bauwens M, Mottaghy FM et al (2017) Potential of α7 nicotinic acetylcholine receptor PET imaging in atherosclerosis. Methods

Bourne Y, Talley TT, Hansen SB et al (2005) Crystal structure of a Cbtx-AChBP complex reveals essential interactions between snake α-neurotoxins and nicotinic receptors. EMBO J 24:1512–1522

Bouvrais-Veret C, Weiss S, Andrieux A et al (2007) Sustained increase of alpha7 nicotinic receptors and choline-induced improvement of learning deficit in STOP knock-out mice. Neuropharmacology 52:1691–1700

Bouzat C, Sine SM (2018) Nicotinic acetylcholine receptors at the single-channel level. Br J Pharmacol 175:1789–1804

Breese CR, Adams C, Logel J et al (1997) Comparison of the regional expression of nicotinic acetylcholine receptor alpha7 mRNA and [^{125}I]-α-bungarotoxin binding in human postmortem brain. J Comp Neurol 387:385–398

Brejc K, van Dijk WJ, Klaassen RV et al (2001) Crystal structure of an ACh-binding protein reveals the ligand-binding domain of nicotinic receptors. Nature 411:269–276

Briggs CA, Schrimpf MR, Anderson DJ et al (2008) α7 nicotinic acetylcholine receptor agonist properties of tilorone and related tricyclic analogues. Br J Pharmacol 153:1054–1061

Brody AL, Mandelkern MA, Costello MR et al (2009) Brain nicotinic acetylcholine receptor occupancy: effect of smoking a denicotinized cigarette. Int J Neuropsychopharmacol 12:305–316

Brody AL, Mandelkern MA, London ED et al (2011) Effect of secondhand smoke on occupancy of nicotinic acetylcholine receptors in brain. Arch Gen Psychiatry 68:953–960

Brody AL, Mandelkern MA, London ED et al (2006) Cigarette smoking saturates brain α4β2 nicotinic acetylcholine receptors. Arch Gen Psychiatry 63:907–915

Brown L, Chefer S, Pavlova O et al (2004) Evaluation of 5-(2-(4-pyridinyl)vinyl)-6-chloro-3-(1-methyl-2-(S)-pyrrolidinylmethoxy)py ridine and its analogues as PET radioligands for imaging nicotinic acetylcholine receptors. J Neurochem 91:600–612

Brown LL, Kulkarni S, Pavlova OA et al (2002) Synthesis and evaluation of a novel series of 2-chloro-5-((1-methyl-2-(S)-pyrrolidinyl)methoxy)-3-(2-(4-pyridinyl)vinyl) pyridine analogues as potential positron emission tomography imaging agents for nicotinic acetylcholine receptors. J Med Chem 45:2841–2849

Bruno JP, Gash C, Martin B et al (2006) Second-by-second measurement of acetylcholine release in prefrontal cortex. Eur J Neurosci 24:2749–2757

Brust P, Deuther-Conrad W (2012) Molecular imaging of α7 nicotinic acetylcholine receptors in vivo: current status and perspectives. In: Bright P (ed) Neuroimaging - clinical applications. InTech, Rijeka, Croatia

Brust P, Deuther-Conrad W, Donat CK et al (2014) Preclinical aspects of nicotinic acetylcholine receptor imaging. In: Dierckx RAJO (ed) PET and SPECT of neurobiological systems. Springer, Berlin, Heidelberg

Brust P, Patt JT, Deuther-Conrad W et al (2008) In vivo measurement of nicotinic acetylcholine receptors with [^{18}F]norchloro-fluoro-homoepibatidine. Synapse 62:205–218

Brust P, Peters D, Deuther-Conrad W (2012) Development of radioligands for the imaging of α7 nicotinic acetylcholine receptors with positron emission tomography. Curr Drug Targets 13:594–601

Bunnelle WH, Dart MJ, Schrimpf MR (2004) Design of ligands for the nicotinic acetylcholine receptors: the quest for selectivity. Curr Top Med Chem 4:299–334

Cabello J, Ziegler SI (2018) Advances in PET/MR instrumentation and image reconstruction. Br J Radiol 91:20160363

Changeux JP (2010) Nicotine addiction and nicotinic receptors: lessons from genetically modified mice. Nat Rev Neurosci 11:389–401

Chattopadhyay S, Xue B, Collins D et al (2005) Synthesis and evaluation of nicotine α4β2 receptor radioligand, 5-(3'-^{18}F-fluoropropyl)-3-(2-(S)-pyrrolidinylmethoxy)pyridine, in rodents and PET in nonhuman primate. J Nucl Med 46:130–140

Chatzidaki A, Millar NS (2015) Allosteric modulation of nicotinic acetylcholine receptors. Biochem Pharmacol 97:408–417

Chefer SI, Horti AG, Koren AO et al (1999) 2-[^{18}F]F-A-85380: a PET radioligand for α4β2 nicotinic acetylcholine receptors. Neuroreport 10:2715–2721

Chefer SI, Horti AG, Lee KS et al (1998) In vivo imaging of brain nicotinic acetylcholine receptors with 5-[^{123}I]iodo-A-85380 using single photon emission computed tomography. Life Sci 63:PL355–PL360

Chefer SI, London ED, Koren AO et al (2003) Graphical analysis of 2-[^{18}F]FA binding to nicotinic acetylcholine receptors in rhesus monkey brain. Synapse 48:25–34

Chefer SI, Pavlova OA, Zhang Y et al (2008) NIDA522131, a new radioligand for imaging extrathalamic nicotinic acetylcholine receptors: in vitro and in vivo evaluation. J Neurochem 104:306–315

Clarke PB, Pert A (1985) Autoradiographic evidence for nicotine receptors on nigrostriatal and mesolimbic dopaminergic neurons. Brain Res 348:355–358

Clarke PB, Pert CB, Pert A (1984) Autoradiographic distribution of nicotine receptors in rat brain. Brain Res 323:390–395

Colas L, Domercq M, Ramos-Cabrer P et al (2018) In vivo imaging of α7 nicotinic receptors as a novel method to monitor neuroinflammation after cerebral ischemia. Glia

Cortes M, Cao M, Liu HL et al (2017) alpha7 nicotinic acetylcholine receptor signaling modulates the inflammatory phenotype of fetal brain microglia: first evidence of interference by iron homeostasis. Sci Rep 7:10645

Cosgrove KP, Batis J, Bois F et al (2009) beta2-Nicotinic acetylcholine receptor availability during acute and prolonged abstinence from tobacco smoking. Arch Gen Psychiatry 66:666–676

Cosgrove KP, Kloczynski T, Bois F et al (2010) Decreased Beta$_2$*-nicotinic acetylcholine receptor availability after chronic ethanol exposure in nonhuman primates. Synapse 64:729–732

Coughlin J, Du Y, Crawford JL et al (2018a) The availability of the α7 nicotinic acetylcholine receptor in recent-onset psychosis: a study using ^{18}F-ASEM PET. J Nucl Med

Coughlin JM, Du Y, Rosenthal HB et al (2018b) The distribution of the alpha7 nicotinic acetylcholine receptor in healthy aging: an in vivo positron emission tomography study with [^{18}F]ASEM. NeuroImage 165:118–124

Coughlin JM, Slania S, Du Y et al (2018c) ^{18}F-XTRA PET for enhanced imaging of the extrathalamic alpha4beta2 nicotinic acetylcholine receptor. J Nucl Med 59:1603–1608

Crespi A, Colombo SF, Gotti C (2018) Proteins and chemical chaperones involved in neuronal nicotinic receptor expression and function: an update. Br J Pharmacol 175:1869–1879

Cuadra G, Summers K, Giacobini E (1994) Cholinesterase inhibitor effects on neurotransmitters in rat cortex in vivo. J Pharmacol Exp Ther 270:277–284

Cumming P (2011) Absolute abundances and affinity states of dopamine receptors in mammalian brain: a review. Synapse 65:892–909

Cumming P, Rosa-Neto P, Watanabe H et al (2003) Effects of acute nicotine on hemodynamics and binding of [^{11}C]raclopride to dopamine D$_{2,3}$ receptors in pig brain. NeuroImage 19:1127–1136

Daly JW (1998) Thirty years of discovering arthropod alkaloids in amphibian skin. J Nat Prod 61:162–172

Damsma G, Robertson GS, Tham CS et al (1991) Dopaminergic regulation of striatal acetylcholine release: importance of D1 and N-methyl-D-aspartate receptors. J Pharmacol Exp Ther 259:1064–1072

Darsow T, Booker TK, Pina-Crespo JC et al (2005) Exocytic trafficking is required for nicotine-induced up-regulation of α4β2 nicotinic acetylcholine receptors. J Biol Chem 280:18311–18320

Dash PK, Zhao J, Kobori N et al (2016) Activation of alpha 7 cholinergic nicotinic receptors reduce blood-brain barrier permeability following experimental traumatic brain injury. J Neurosci 36:2809–2818

Davies P, Feisullin S (1981) Postmortem stability of α-bungarotoxin binding sites in mouse and human brain. Brain Res 216:449–454

De Biasi M, Dani JA (2011) Reward, addiction, withdrawal to nicotine. Annu Rev Neurosci 34:105–130

de Fiebre CM, Meyer EM, Henry JC et al (1995) Characterization of a series of anabaseine-derived compounds reveals that the 3-(4)-dimethylaminocinnamylidine derivative is a selective agonist at neuronal nicotinic α7/^{125}I-alpha-bungarotoxin receptor subtypes. Mol Pharmacol 47:164–171

de Ramirez SS, Hyder AA, Herbert HK et al (2012) Unintentional injuries: magnitude, prevention, and control. Annu Rev Public Health 33:175–191

De Simone R, Ajmone-Cat MA, Carnevale D et al (2005) Activation of α7 nicotinic acetylcholine receptor by nicotine selectively up-regulates cyclooxygenase-2 and prostaglandin E2 in rat microglial cultures. J Neuroinflammation 2:1–10

DeBoer P, Heeringa MJ, Abercrombie ED (1996) Spontaneous release of acetylcholine in striatum is preferentially regulated by inhibitory dopamine D2 receptors. Eur J Pharmacol 317:257–262

Decker MW, Sullivan JP, Arneric SP et al (2000) Neuronal nicotinic acetylcholine receptors: novel targets for CNS therapeutics. In: Bloom FE, Kupfer DJ (eds) Psychopharmacology: fourth generation of progress. American College of Neuropsychopharmacology, New York. http://www.acnp.org/g4/gn401000009/default.htm

Deuther-Conrad W, Fischer S, Hiller A et al (2011) Assessment of α7 nicotinic acetylcholine receptor availability in juvenile pig brain with [^{18}F]NS10743. Eur J Nucl Med Mol Imaging 38:1541–1549

Deuther-Conrad W, Fischer S, Hiller A et al (2009) Molecular imaging of α7 nicotinic acetylcholine receptors: design and evaluation of the potent radioligand [^{18}F]NS10743. Eur J Nucl Med Mol Imaging 36:791–800

Deuther-Conrad W, Patt JT, Feuerbach D et al (2004) Norchloro-fluoro-homoepibatidine: specificity to neuronal nicotinic acetylcholine receptor subtypes in vitro. Farmacoterapia 59:785–792

Deuther-Conrad W, Patt JT, Lockman PR et al (2008) Norchloro-fluoro-homoepibatidine (NCFHEB) - a promising radioligand for neuroimaging nicotinic acetylcholine receptors with PET. Eur Neuropsychopharmacol 18:222–229

Deuther-Conrad W, Wevers A, Becker G et al (2006) Autoradiography of 2-[^{18}F]F-A-85380 on nicotinic acetylcholine receptors in the porcine brain in vitro. Synapse 59:201–210

Dewan MC, Rattani A, Gupta S et al (2018) Estimating the global incidence of traumatic brain injury. J Neurosurg:1–18

Dewar D, Graham DI (1996) Depletion of choline acetyltransferase activity but preservation of M1 and M2 muscarinic receptor binding sites in temporal cortex following head injury: a preliminary human postmortem study. J Neurotrauma 13:181–187

Dewey SL, Smith GS, Logan J et al (1993) Modulation of central cholinergic activity by GABA and serotonin: PET studies with 11C-benztropine in primates. Neuropsychopharmacology 8:371–376

Dineley KT, Pandya AA, Yakel JL (2015) Nicotinic ACh receptors as therapeutic targets in CNS disorders. Trends Pharmacol Sci 36:96–108

Ding M, Ghanekar S, Elmore CS et al (2012) [^{3}H]Chiba-1001(methyl-SSR180711) has low in vitro binding affinity and poor in vivo selectivity to nicotinic alpha-7 receptor in rodent brain. Synapse 66:315–322

Ding Y, Liu N, Wang T et al (2000a) Synthesis and evaluation of 6-[^{18}F]fluoro-3-(2(S)-azetidinylmethoxy)pyridine as a PET tracer for nicotinic acetylcholine receptors. Nucl Med Biol 27:381–389

Ding YS, Fowler J (2005) New-generation radiotracers for nAChR and NET. Nucl Med Biol 32:707–718

Ding YS, Fowler JS, Logan J et al (2004) 6-[^{18}F]Fluoro-A-85380, a new PET tracer for the nicotinic acetylcholine receptor: studies in the human brain and in vivo demonstration of specific binding in white matter. Synapse 53:184–189

Ding YS, Gatley SJ, Fowler JS et al (1996) Mapping nicotinic acetylcholine receptors with PET. Synapse 24:403–407

Ding YS, Kil KE, Lin KS et al (2006) A novel nicotinic acetylcholine receptor antagonist radioligand for PET studies. Bioorg Med Chem Lett 16:1049–1053

Ding YS, Logan J, Bermel R et al (2000b) Dopamine receptor-mediated regulation of striatal cholinergic activity: positron emission tomography studies with norchloro[^{18}F]fluoroepibatidine. J Neurochem 74:1514–1521

Ding YS, Molina PE, Fowler JS et al (1999) Comparative studies of epibatidine derivatives [^{18}F]NFEP and [^{18}F]N-methyl-NFEP: kinetics, nicotine effect, and toxicity. Nucl Med Biol 26:139–148

Dobelis P, Hutton S, Lu Y et al (2003) GABAergic systems modulate nicotinic receptor-mediated seizures in mice. J Pharmacol Exp Ther 306:1159–1166

Dolci L, Dolle F, Valette H et al (1999) Synthesis of a fluorine-18 labeled derivative of epibatidine for in vivo nicotinic acetylcholine receptor PET imaging. Bioorg Med Chem 7:467–479

Dollé F, Dolci L, Valette H et al (1999) Synthesis and nicotinic acetylcholine receptor in vivo binding properties of 2-fluoro-3-[2(S)-2-azetidinylmethoxy]pyridine: a new positron emission tomography ligand for nicotinic receptors. J Med Chem 42:2251–2259

Dollé F, Langle S, Roger G et al (2008) Synthesis and in-vivo evaluation of [(11)C]p-PVP-MEMA as a PET radioligand for imaging nicotinic receptors. Aust J Chem 61:438–445

Dollé F, Valette H, Hinnen F et al (2001) Synthesis and preliminary evaluation of a carbon-11-labelled agonist of the α7 nicotinic acetylcholine receptor. J Label Compd Radiopharm 44:785–795

Dolle RE, Le Bourdonnec B, Goodman AJ et al (2008) Comprehensive survey of chemical libraries for drug discovery and chemical biology: 2007. J Comb Chem 10:753–802

Dome P, Lazary J, Kalapos MP et al (2010) Smoking, nicotine and neuropsychiatric disorders. Neurosci Biobehav Rev 34:295–342

Domino EF, Tsukada H, Harada N (2009) Positron emission tomographic measure of brain dopamine dependence to nicotine as a model of drugs of abuse. Psychopharmacology 204:149–153

Donat CK, Gaber K, Meixensberger J et al (2016) Changes in binding of [^{123}I]CLINDE, a high-affinity translocator protein 18 kDa (TSPO) selective radioligand in a rat model of traumatic brain injury. NeuroMolecular Med 18:158–169

Donat CK, Schuhmann MU, Voigt C et al (2008) Time-dependent alterations of cholinergic markers after experimental traumatic brain injury. Brain Res 1246:167–177

Donat CK, Scott G, Gentleman SM et al (2017) Microglial activation in traumatic brain injury. Front Aging Neurosci 9:208

Donat CK, Walter B, Deuther-Conrad W et al (2010a) Alterations of cholinergic receptors and the vesicular acetylcholine transporter after lateral fluid percussion injury in newborn piglets. Neuropathol Appl Neurobiol 36:225–236

Donat CK, Walter B, Kayser T et al (2010b) Effects of lateral fluid percussion injury on cholinergic markers in the newborn piglet brain. Int J Dev Neurosci 28:31–38

Donnelly-Roberts DL, Xue IC, Arneric SP et al (1996) In vitro neuroprotective properties of the novel cholinergic channel activator (ChCA), ABT-418. Brain Res 719:36–44

Duhaime AC, Margulies SS, Durham SR et al (2000) Maturation-dependent response of the piglet brain to scaled cortical impact. J Neurosurg 93:455–462

Easwaramoorthy B, Pichika R, Collins D et al (2007) Effect of acetylcholinesterase inhibitors on the binding of nicotinic α$_4$β$_2$ receptor PET radiotracer, ^{18}F-nifene: a measure of acetylcholine competition. Synapse 61:29–36

Eckelman WC (2006) Imaging of muscarinic receptors in the central nervous system. Curr Pharm Des 12:3901–3913

Egea J, Buendia I, Parada E et al (2015) Anti-inflammatory role of microglial alpha7 nAChRs and its role in neuroprotection. Biochem Pharmacol

Ellis JR, Nathan PJ, Villemagne VL et al (2009a) The relationship between nicotinic receptors and cognitive functioning in healthy aging: an in vivo positron emission tomography (PET) study with 2-[(18)F]fluoro-A-85380. Synapse 63:752–763

Ellis JR, Nathan PJ, Villemagne VL et al (2009b) Galantamine-induced improvements in cognitive function are not related to alterations in α4β2 nicotinic receptors in early Alzheimer's disease as measured in vivo by 2-[^{18}F]Fluoro-A-85380 PET. Psychopharmacology 202:79–91

Ellis JR, Villemagne VL, Nathan PJ et al (2008) Relationship between nicotinic receptors and cognitive function in early Alzheimer's disease: A 2-[F-18]fluoro-A-85380 PET study. Neurobiol Learn Mem 90:404–412

Esterlis I, Cosgrove KP, Batis JC et al (2010a) Quantification of smoking-induced occupancy of beta2-nicotinic acetylcholine receptors: estimation of nondisplaceable binding. J Nucl Med 51:1226–1233

Esterlis I, Mitsis EM, Batis JC et al (2010b) Brain beta2*-nicotinic acetylcholine receptor occupancy after use of a nicotine inhaler. Int J Neuropsychopharmacol:1–10

Ettrup A, Mikkelsen JD, Lehel S et al (2011) [^{11}C]NS14492 as a novel PET ligand for imaging cerebral α7 nicotinic receptors: in vivo evaluation and drug occupancy measurements. J Nucl Med 52:1449–1456

Fallon JH, Keator DB, Mbogori J et al (2004) Hostility differentiates the brain metabolic effects of nicotine. Brain Res Cogn Brain Res 18:142–148

Fan H, Scheffel UA, Rauseo P et al (2001) [^{125}/ ^{123}I] 5-Iodo-3-pyridyl ethers. syntheses and binding to neuronal nicotinic acetylcholine receptors. Nucl Med Biol 28:911–921

Felix B, Leger ME, Albe-Fessard D et al (1999) Stereotaxic atlas of the pig brain. Brain Res Bull 49:1–137

Ferrari R, Frasoldati A, Leo G et al (1999) Changes in nicotinic acetylcholine receptor subunit mRNAs and nicotinic binding in spontaneously hypertensive stroke prone rats. Neurosci Lett 277:169–172

Finnema SJ, Scheinin M, Shahid M et al (2015) Application of cross-species PET imaging to assess neurotransmitter release in brain. Psychopharmacology 232:4129–4157

Fleminger S, Ponsford J (2005) Long term outcome after traumatic brain injury. BMJ (Clin Res ed) 331:1419–1420

Flores CM, Rogers SW, Pabreza LA et al (1992) A subtype of nicotinic cholinergic receptor in rat brain is composed of α4 and β2 subunits and is up-regulated by chronic nicotine treatment. Mol Pharmacol 41:31–37

Frazier CJ, Rollins YD, Breese CR et al (1998) Acetylcholine activates an α-bungarotoxin-sensitive nicotinic current in rat hippocampal interneurons, but not pyramidal cells. J Neurosci 18:1187–1195

Freedman R, Coon H, Myles-Worsley M et al (1997) Linkage of a neurophysiological deficit in schizophrenia to a chromosome 15 locus. Proc Natl Acad Sci U S A 94:587–592

Freedman R, Hall M, Adler LE et al (1995) Evidence in postmortem brain tissue for decreased numbers of hippocampal nicotinic receptors in schizophrenia. Biol Psychiatry 38:22–33

Freedman R, Olincy A, Buchanan RW et al (2008) Initial phase 2 trial of a nicotinic agonist in schizophrenia. Am J Psychiatry 165:1040–1047

Friedrich A, George RL, Bridges CC et al (2001) Transport of choline and its relationship to the expression of the organic cation transporters in a rat brain microvessel endothelial cell line (RBE4). Biochim Biophys Acta 1512:299–307

Fujii T, Mashimo M, Moriwaki Y et al (2017) Expression and function of the cholinergic system in immune cells. Front Immunol 8:1085

Fujita M, Al-Tikriti MS, Tamagnan G et al (2003) Influence of acetylcholine levels on the binding of a SPECT nicotinic acetylcholine receptor ligand [^{123}I]5-I-A-85380. Synapse 48:116–122

Fujita M, Tamagnan G, Zoghbi SS et al (2000) Measurement of α4β2 nicotinic acetylcholine receptors with [^{123}I]5-I-A-85380 SPECT. J Nucl Med 41:1552–1560

Gallezot JD, Bottlaender M, Gregoire MC et al (2005) In vivo imaging of human cerebral nicotinic acetylcholine receptors with 2-[^{18}F]-fluoro-A-85380 and PET. J Nucl Med 46:240–247

Gallezot JD, Esterlis I, Bois F et al (2014) Evaluation of the sensitivity of the novel α4β2* nicotinic acetylcholine receptor PET radioligand ^{18}F-(−)-NCFHEB to increases in synaptic acetylcholine levels in rhesus monkeys. Synapse 68:556–564

Gao Y, Horti AG, Kuwabara H et al (2007a) Derivatives of (−)-7-methyl-2-(5-(pyridinyl) pyridin-3-yl)-7-azabicyclo[2.2.1]heptane are potential ligands for positron emission tomography imaging of extrathalamic nicotinic acetylcholine receptors. J Med Chem 50:3814–3824

Gao Y, Horti AG, Kuwabara H et al (2008a) New synthesis and evaluation of enantiomers of 7-methyl-2-exo-(3′-iodo-5′-pyridinyl)-7-azabicyclo[2.2.1]heptane as stereoselective ligands for PET imaging of nicotinic acetylcholine receptors. Bioorg Med Chem Lett 18:6168–6170

Gao Y, Kellar KJ, Yasuda RP et al (2013) Derivatives of dibenzothiophene for positron emission tomography imaging of alpha7-nicotinic acetylcholine receptors. J Med Chem

Gao Y, Kuwabara H, Spivak CE et al (2008b) Discovery of (−)-7-methyl-2-exo-[3′-(6-[^{18}F]fluoropyridin-2-yl)-5′-pyridinyl]-7-azabicyclo[2.2 .1]heptane, a radiolabeled antagonist for cerebral nicotinic acetylcholine receptor (α4β2-nAChR) with optimal positron emission tomography imaging properties. J Med Chem 51:4751–4764

Gao Y, Ravert HT, Holt D et al (2007b) 6-Chloro-3-(((1-[^{11}C]methyl)-2-(S)-pyrrolidinyl) methoxy)-5-(2-fluoropyri din-4-yl)pyridine ([^{11}C]JHU85270), a potent ligand for nicotinic acetylcholine receptor imaging by positron emission tomography. Appl Radiat Isot 65:947–951

Gao Y, Ravert HT, Kuwabara H et al (2009) Synthesis and biological evaluation of novel carbon-11 labeled pyridyl ethers: candidate ligands for in vivo imaging of α4β2 nicotinic acetylcholine receptors (α4β2-nAChRs) in the brain with positron emission tomography. Bioorg Med Chem 17:4367–4377

Gao Y, Wang H, Mease RC et al (2010) Improved syntheses of precursors for PET radioligands [^{18}F]XTRA and [^{18}F]AZAN. Tetrahedron Lett 51:5333–5335

Garibotto V, Wissmeyer M, Giavri Z et al (2019) Nicotinic receptor abnormalities as a biomarker in idiopathic generalized epilepsy. Eur J Nucl Med Mol Imaging 46:385–395

Gatley SJ, Ding YS, Brady D et al (1998) In vitro and ex vivo autoradiographic studies of nicotinic acetylcholine receptors using ^{18}F fluoronochloroepibatidine in rodent and human brain. Nucl Med Biol 25:449–454

Gatson JW, Simpkins JW, Uteshev VV (2015) High therapeutic potential of positive allosteric modulation of alpha7 nAChRs in a rat model of traumatic brain injury: proof-of-concept. Brain Res Bull 112:35–41

Giastas P, Zouridakis M, Tzartos SJ (2018) Understanding structure-function relationships of the human neuronal acetylcholine receptor: insights from the first crystal structures of neuronal subunits. Br J Pharmacol 175:1880–1891

Gold MEL, Norell MA, Budassi M et al (2018) Rapid ^{18}F-FDG uptake in brain of awake, behaving rat and anesthetized chicken has implications for behavioral PET studies in species with high metabolisms. Front Behav Neurosci 12:115

Goldman-Rakic PS, Selemon LD (1997) Functional and anatomical aspects of prefrontal pathology in schizophrenia. Schizophr Bull 23:437–458

Gotti C, Clementi F, Fornari A et al (2009) Structural and functional diversity of native brain neuronal nicotinic receptors. Biochem Pharmacol 78:703–711

Gotti C, Zoli M, Clementi F (2006) Brain nicotinic acetylcholine receptors: native subtypes and their relevance. Trends Pharmacol Sci 27:482–491

Govind AP, Vezina P, Green WN (2009) Nicotine-induced upregulation of nicotinic receptors: underlying mechanisms and relevance to nicotine addiction. Biochem Pharmacol 78:756–765

Govind AP, Walsh H, Green WN (2012) Nicotine-induced upregulation of native neuronal nicotinic receptors is caused by multiple mechanisms. J Neurosci 32:2227–2238

Graef S, Schönknecht P, Sabri O et al (2011) Cholinergic receptor subtypes and their role in cognition, emotion, and vigilance control: an overview of preclinical and clinical findings. Psychopharmacology 215:205–229

Gruenbaum SE, Zlotnik A, Gruenbaum BF et al (2016) Pharmacologic neuroprotection for func-
    tional outcomes after traumatic brain injury: a systematic review of the clinical literature. CNS
    Drugs 30:791–806

Gündisch D (2000) Nicotinic acetylcholine receptors and imaging. Curr Pharm Des 6:1143–1157

Gündisch D, Eibl C (2011) Nicotinic acetylcholine receptor ligands, a patent review (2006-2011).
    Expert Opin Ther Pat 21:1867–1896

Guseva MV, Hopkins DM, Scheff SW et al (2008) Dietary choline supplementation improves
    behavioral, histological, and neurochemical outcomes in a rat model of traumatic brain injury.
    J Neurotrauma 25:975–983

Guseva MV, Kamenskii AA, Gusev VB (2013) Optimization of choline administration regi-
    men for correction of cognitive functions in rats after brain injury. Bull Exp Biol Med. 2013
    155(2):197–9

Hallen P, Schug D, Weissler B et al (2018) PET performance evaluation of the small-animal
    Hyperion II(D) PET/MRI insert based on the NEMA NU-4 standard. Biomed Phys Eng
    Express 4:065027

Hampel H, Mesulam MM, Cuello AC et al (2018) The cholinergic system in the pathophysiology
    and treatment of Alzheimer's disease. Brain 141:1917–1933

Han ZY, Zoli M, Cardona A et al (2003) Localization of [^{3}H]nicotine, [^{3}H]cytisine, [^{3}H]epibati-
    dine, and [^{125}I]alpha-bungarotoxin binding sites in the brain of Macaca mulatta. J Comp Neurol
    461:49–60

Hashimoto K, Nishiyama S, Ohba H et al (2008) [^{11}C]CHIBA-1001 as a novel PET ligand for α7
    nicotinic receptors in the brain: a PET study in conscious monkeys. PLoS One 3:e3231

Hawkins BT, Brown RC, Davis TP (2002) Smoking and ischemic stroke: a role for nicotine?
    Trends Pharmacol Forensic Sci 23:78–82

Hawkins BT, Egleton RD, Davis TP (2005) Modulation of cerebral microvascular permeability by
    endothelial nicotinic acetylcholine receptors. Am J Physiol Heart Circ Physiol 289:H212–H219

Hayes RL, Jenkins LW, Lyeth BG (1992) Neurotransmitter-mediated mechanisms of traumatic
    brain injury: acetylcholine and excitatory amino acids. J Neurotrauma 9(Suppl 1):S173–S187

Hedberg MM, Clos MV, Ratia M et al (2010) Effect of huprine X on β-amyloid, synaptophysin and
    α7 neuronal nicotinic acetylcholine receptors in the brain of 3xTg-AD and APPswe transgenic
    mice. Neurodegener Dis 7:379–388

Heinrichs RW (2005) The primacy of cognition in schizophrenia. Am Psychol 60:229–242

Hellström-Lindahl E, Court J, Keverne J et al (2004) Nicotine reduces Abeta in the brain and cere-
    bral vessels of APPsw mice. Eur J Neurosci 19:2703–2710

Hellström-Lindahl E, Court JA (2000) Nicotinic acetylcholine receptors during prenatal develop-
    ment and brain pathology in human aging. Behav Brain Res 113:159–168

Henderson DJ, Eberl S, Thomson S et al (2004) 3-Pyridyl ethers as SPECT radioligands for imag-
    ing nicotinic acetylcholine receptors. Appl Radiat Isot 60:669–676

Hibbs RE, Sulzenbacher G, Shi J et al (2009) Structural determinants for interaction of partial
    agonists with acetylcholine binding protein and neuronal α7 nicotinic acetylcholine receptor.
    EMBO J 28:3040–3051

Higuchi M, Maeda J, Ji B et al (2012) PET applications in animal models of neurodegenerative and
    neuroinflammatory disorders. Curr Top Behav Neurosci 11:45–64

Hillmer AT, Esterlis I, Gallezot JD et al (2016a) Imaging of cerebral α4β2* nicotinic acetylcholine
    receptors with (−)-[^{18}F]Flubatine PET: Implementation of bolus plus constant infusion and
    sensitivity to acetylcholine in human brain. NeuroImage 141:71–80

Hillmer AT, Li S, Zheng MQ et al (2017) PET imaging of α7 nicotinic acetylcholine receptors: a
    comparative study of [^{18}F]ASEM and [^{18}F]DBT-10 in nonhuman primates, and further evalua-
    tion of [^{18}F]ASEM in humans. Eur J Nucl Med Mol Imaging

Hillmer AT, Tudorascu DL, Wooten DW et al (2014) Changes in the α4β2* nicotinic acetylcho-
    line system during chronic controlled alcohol exposure in nonhuman primates. Drug Alcohol
    Depend 138:216–219

Hillmer AT, Wooten DW, Farhoud M et al (2013) PET imaging of acetylcholinesterase inhibitor
    induced effects on α4β2 nicotinic acetylcholine receptor binding. Synapse 67:882–886

Hillmer AT, Zheng MQ, Li S et al (2016b) PET imaging evaluation of [^{18}F]DBT-10, a novel radio-ligand specific to α7 nicotinic acetylcholine receptors, in nonhuman primates. Eur J Nucl Med Mol Imaging 43:537–547

Hockley BG, Stewart MN, Sherman P et al (2013) (−)-[^{18}F]Flubatine: evaluation in rhesus monkeys and a report of the first fully automated radiosynthesis validated for clinical use. PETSerotoninpdf 56:595–599

Hoffmeister PG, Donat CK, Schuhmann MU et al (2011) Traumatic brain injury elicits similar alter-ations in α7 nicotinic receptor density in two different experimental models. NeuroMolecular Med 13:44–53

Hogg RC, Raggenbass M, Bertrand D (2003) Nicotinic acetylcholine receptors: from structure to brain function. Rev Physiol Biochem Pharmacol 147:1–46

Hong JH, Jang SH, Kim OL et al (2012) Neuronal loss in the medial cholinergic pathway from the nucleus basalis of Meynert in patients with traumatic axonal injury: a preliminary diffusion tensor imaging study. J Head Trauma Rehabil 27:172–176

Horti A, Scheffel U, Stathis M et al (1997) Fluorine-18-FPH for PET imaging of nicotinic acetyl-choline receptors. J Nucl Med 38:1260–1265

Horti AG, Chefer SI, Mukhin AG et al (2000) 6-[^{18}F]fluoro-A-85380, a novel radioligand for in vivo imaging of central nicotinic acetylcholine receptors. Life Sci 67:463–469

Horti AG, Gao Y, Kuwabara H et al (2010) Development of radioligands with optimized imaging properties for quantification of nicotinic acetylcholine receptors by positron emission tomog-raphy. Life Sci 86:575–584

Horti AG, Gao Y, Kuwabara H et al (2014) ^{18}F-ASEM, a radiolabeled antagonist for imaging the α7-nicotinic acetylcholine receptor with PET. J Nucl Med 55:672–677

Horti AG, Scheffel U, Kimes AS et al (1998a) Synthesis and evaluation of N-[^{11}C]methylated analogues of epibatidine as tracers for positron emission tomographic studies of nicotinic ace-tylcholine receptors. J Med Chem 41:4199–4206

Horti AG, Scheffel U, Koren AO et al (1998b) 2-[^{18}F]Fluoro-A-85380, an in vivo tracer for the nicotinic acetylcholine receptors. Nucl Med Biol 25:599–603

Horti AG, Villemagne VL (2006) The quest for Eldorado: development of radioligands for in vivo imaging of nicotinic acetylcholine receptors in human brain. Curr Pharm Des 12:3877–3900

Horti AG, Wong DF (2009) Clinical perspective and recent development of pet radioligands for imaging cerebral nicotinic acetylcholine receptors. PET Rev 4:89–100

Hozumi S, Nakagawasai O, Tan-No K et al (2003) Characteristics of changes in cholinergic func-tion and impairment of learning and memory-related behavior induced by olfactory bulbec-tomy. Behav Brain Res 138:9–15

Hruska M, Keefe J, Wert D et al (2009) Prostate stem cell antigen is an endogenous lynx1-like prototoxin that antagonizes α7-containing nicotinic receptors and prevents programmed cell death of parasympathetic neurons. J Neurosci 29:14847–14854

Huang LZ, Parameswaran N, Bordia T et al (2009) Nicotine is neuroprotective when administered before but not after nigrostriatal damage in rats and monkeys. J Neurochem 109:826–837

Huang Y, Zhu Z, Narendran R et al (2004) Pharmacological evaluation of [C-11]2-[3-(6-chloro-5-phenyl)pyridinyl]-7-methyl-7-aza-bicyclo[2.2.1]heptane, a new PET radioligand for the nico-tinic acetylcholine receptors. NeuroImage 22:S2–T113

Huang Y, Zhu Z, Xiao Y et al (2005) Epibatidine analogues as selective ligands for the α(x) β2-containing subtypes of nicotinic acetylcholine receptors. Bioorg Med Chem Lett 15:4385–4388

Humphreys I, Wood RL, Phillips CJ et al (2013) The costs of traumatic brain injury: a literature review. Clinicoecon Outcomes Res 5:281–287

Iida Y, Ogawa M, Ueda M et al (2004) Evaluation of 5-^{11}C-methyl-A-85380 as an imaging agent for PET investigations of brain nicotinic acetylcholine receptors. J Nucl Med 45:878–884

Imming P, Klaperski P, Stubbs MT et al (2001) Syntheses and evaluation of halogenated cytisine derivatives and of bioisosteric thiocytisine as potent and selective nAChR ligands. Eur J Med Chem 36:375–388

Itier V, Schonbachler R, Tribollet E et al (2004) A-186253, a specific antagonist of the alpha4beta2 nAChRs: its properties and potential to study brain nicotinic acetylcholine receptors. Neuropharmacology 47:538–557

Jasinska AJ, Zorick T, Brody AL et al (2014) Dual role of nicotine in addiction and cognition: a review of neuroimaging studies in humans. Neuropharmacology 84:111–122

Jensen AA, Frolund B, Liljefors T et al (2005) Neuronal nicotinic acetylcholine receptors: structural revelations, target identifications, and therapeutic inspirations. J Med Chem 48:4705–4745

Jones IW, Barik J, O'Neill MJ et al (2004) Alpha bungarotoxin-1.4 nm gold: a novel conjugate for visualising the precise subcellular distribution of α7* nicotinic acetylcholine receptors. J Neurosci Methods 134:65–74

Jones IW, Westmacott A, Chan E et al (2006) α7 nicotinic acetylcholine receptor expression in Alzheimer's disease: receptor densities in brain regions of the APP(SWE) mouse model and in human peripheral blood lymphocytes. J Mol Neurosci 30:83–84

Jupp B, Williams J, Binns D et al (2007) Imaging small animal models of epileptogenesis. Neurol Asia 12(Suppl. 1):51–54

Kalamida D, Poulas K, Avramopoulou V et al (2007) Muscle and neuronal nicotinic acetylcholine receptors. Structure, function and pathogenicity. FEBS J 274:3799–3845

Kamal VK, Agrawal D, Pandey RM (2016) Epidemiology, clinical characteristics and outcomes of traumatic brain injury: Evidences from integrated level 1 trauma center in India. J Neurosci Rural Pract 7:515–525

Karlin A (2002) Emerging structure of the nicotinic acetylcholine receptors. Nat Rev Neurosci 3:102–114

Kas A, Bottlaender M, Gallezot JD et al (2009) Decrease of nicotinic receptors in the nigrostriatal system in Parkinson's disease. J Cereb Blood Flow Metab 29:1601–1608

Kassiou M, Bottlaender M, Loc'h C et al (2002) Pharmacological evaluation of a Br-76 analog of epibatidine: a potent ligand for studying brain nicotinic acetylcholine receptors. Synapse 45:95–104

Kassiou M, Eberl S, Meikle SR et al (2001) In vivo imaging of nicotinic receptor upregulation following chronic (−)-nicotine treatment in baboon using SPECT. Nucl Med Biol 28:165–175

Kassiou M, Scheffel UA, Ravert HT et al (1998) Pharmacological evaluation of [^{11}C]A-84543: an enantioselective ligand for in vivo studies of neuronal nicotinic acetylcholine receptors. Life Sci 63:PL13–PL18

Kelso ML, Oestreich JH (2012) Traumatic brain injury: central and peripheral role of alpha7 nicotinic acetylcholine receptors. Curr Drug Targets 13:631–636

Kelso ML, Wehner JM, Collins AC et al (2006) The pathophysiology of traumatic brain injury in alpha7 nicotinic cholinergic receptor knockout mice. Brain Res 1083:204–210

Kendziorra K, Wolf H, Meyer PM et al (2011) Decreased cerebral α4β2* nicotinic acetylcholine receptor availability in patients with mild cognitive impairment and Alzheimer's disease assessed with positron emission tomography. Eur J Nucl Med Mol Imaging 38:515–525

Kim SW, Ding YS, Alexoff D et al (2007a) Synthesis and positron emission tomography studies of C-11-labeled isotopomers and metabolites of GTS-21, a partial α7 nicotinic cholinergic agonist drug. Nucl Med Biol 34:541–551

Kim SW, Ding YS, Alexoff D et al (2007b) Synthesis and positron emission tomography studies of C-11-labeled isotopomers and metabolites of GTS-21, a partial alpha7 nicotinic cholinergic agonist drug. Nucl Med Biol 34:541–551

Kimes AS, Chefer SI, Matochik JA et al (2008) Quantification of nicotinic acetylcholine receptors in the human brain with PET: bolus plus infusion administration of 2-[^{18}F]F-A85380. NeuroImage 39:717–727

Kimes AS, Horti AG, London ED et al (2003) 2-[^{18}F]F-A-85380: PET imaging of brain nicotinic acetylcholine receptors and whole body distribution in humans. FASEB J 17:1331–1333

Ko GB, Yoon HS, Kim KY et al (2016) Simultaneous multiparametric PET/MRI with silicon photo-multiplier PET and ultra-high-field MRI for small-animal imaging. J Nucl Med 57:1309–1315

Koeppe RA (2001) A panel discussion on the future of pharmacology and experimental tomography. In: Gjedde A, Hansen SB, Knudsen GM, Paulson OB (eds) Physiological imaging of the brain with PET. Academic Press, New York

Kozikowski A, Musachio J, Kellar K et al (2005) Ligands for nicotinic acetylcholine receptors, and methods of making and using them. Georgetetown University

Kranz M, Sattler B, Deuther-Conrad W et al (2014) Preclinical dose assessment and biodistribution of [^{18}F]DBT10, a new α7 nicotinic acetylcholine receptor (α7-nAChR) imaging ligand. J Nucl Med 55(Suppl. 1):1143

Kranz M, Sattler B, Wüst N et al (2016) Evaluation of the enantiomer specific biokinetics and radiation doses of [^{18}F]fluspidine-a new tracer in clinical translation for imaging of σ$_1$ receptors. Molecules 21:1164

Kulak JM, Sum J, Musachio JL et al (2002) 5-Iodo-A-85380 binds to α-conotoxin MII-sensitive nicotinic acetylcholine receptors (nAChRs) as well as α4β2 subtypes. J Neurochem 81:403–406

Kumari S, Borroni V, Chaudhry A et al (2008) Nicotinic acetylcholine receptor is internalized via a Rac-dependent, dynamin-independent endocytic pathway. J Cell Biol 181:1179–1193

Kuwabara H, Gao Y, Stabin M et al (2017) Imaging α4β2 nicotinic acetylcholine receptors (nAChRs) in baboons with [^{18}F]XTRA, a radioligand with improved specific binding in extrathalamic regions. Mol Imaging Biol 19:280–288

Kuwabara H, Wong DF, Gao Y et al (2012) PET Imaging of nicotinic acetylcholine receptors in baboons with 18F-AZAN, a radioligand with improved brain kinetics. J Nucl Med 53:121–129

Lai A, Parameswaran N, Khwaja M et al (2005) Long-term nicotine treatment decreases striatal α6* nicotinic acetylcholine receptor sites and function in mice. Mol Pharmacol 67:1639–1647

Langley JN (1901) On the stimulation and paralysis of nerve-cells and of nerve-endings: Part I. J Physiol 27:224–236

Langley JN (1905) On the reaction of cells and of nerve-endings to certain poisons, chiefly as regards the reaction of striated muscle to nicotine and to curari. J Physiol 33:374–413

Lao PJ, Betthauser TJ, Tudorascu DL et al (2017) [^{18}F]Nifene test-retest reproducibility in first-in-human imaging of α4β2* nicotinic acetylcholine receptors. Synapse 71. https://doi.org/10.1002/syn.21981

Larsson A, Engel JA (2004) Neurochemical and behavioral studies on ethanol and nicotine interactions. Neurosci Biobehav Rev 27:713–720

Laruelle M (2000) Imaging synaptic neurotransmission with in vivo binding competition techniques: a critical review. J Cereb Blood Flow Metab 20:423–451

Le Foll B, Chefer SI, Kimes AS et al (2007) Validation of an extracerebral reference region approach for the quantification of brain nicotinic acetylcholine receptors in squirrel monkeys with PET and 2-18F-fluoro-A-85380. J Nucl Med 48:1492–1500

Le Foll B, Chefer SI, Kimes AS et al (2009) Baseline expression of α4β2* nicotinic acetylcholine receptors predicts motivation to self-administer nicotine. Biol Psychiatry 65:714–716

Lehel S, Madsen J, Ettrup A et al (2009) [^{11}C]NS-12857: a novel PET ligand for α7-nicotinergic receptors. J Labelled Compd Rad 52:S379–S379

Leonard S (2003) Consequences of low levels of nicotinic acetylcholine receptors in schizophrenia for drug development. Drug Dev Res 60:127–136

Lester HA, Xiao C, Srinivasan R et al (2009) Nicotine is a selective pharmacological chaperone of acetylcholine receptor number and stoichiometry. Implications for drug discovery. AAPS J 11:167–177

Li H, Sagar AP, Keri S (2018) Microglial markers in the frontal cortex are related to cognitive dysfunctions in major depressive disorder. J Affect Disord 241:305–310

Liang F, Navarro HA, Abraham P et al (1997) Synthesis and nicotinic acetylcholine receptor binding properties of exo-2-(2′-fluoro-5′-pyridinyl)-7-azabicyclo- 2.2.1 heptane: a new positron emission tomography ligand for nicotinic receptors. J Med Chem 40:2293–2295

Liddelow SA, Guttenplan KA, Clarke LE et al (2017) Neurotoxic reactive astrocytes are induced by activated microglia. Nature 541:481–487

Lighthall JW (1988) Controlled cortical impact: a new experimental brain injury model. J Neurotrauma 5:1–15

Lipovsek M, Plazas P, Savino J et al (2008) Properties of mutated murine α4β2 nicotinic receptors linked to partial epilepsy. Neurosci Lett 434:165–169

Loane DJ, Faden AI (2010) Neuroprotection for traumatic brain injury: translational challenges and emerging therapeutic strategies. Trends Pharmacol Sci 31:596–604

LoBue C, Cullum CM, Didehbani N et al (2018) Neurodegenerative dementias after traumatic brain injury. J Neuropsychiatry Clin Neurosci 30:7–13

Lohr JB, Flynn K (1992) Smoking and schizophrenia. Schizophr Res 8:93–102

London ED, Connolly RJ, Szikszay M et al (1988) Effects of nicotine on local cerebral glucose utilization in the rat. J Neurosci 8:3920–3928

London ED, Scheffel U, Kimes AS et al (1995) In vivo labeling of nicotinic acetylcholine receptors in brain with [³H]epibatidine. Eur J Pharmacol 278:R1–R2

Lotfipour S, Mandelkern M, Alvarez-Estrada M et al (2012a) A single administration of low-dose varenicline saturates α4β2* nicotinic acetylcholine receptors in the human brain. Neuropsychopharmacology 37:1738–1748

Lotfipour S, Mandelkern M, Alvarez-Estrada M et al (2012b) A single administration of low-dose varenicline saturates alpha4beta2(*) nicotinic acetylcholine receptors in the human brain. Neuropsychopharmacology 37:1738–1748

Lucas A, Hawkes R, Ansorge R et al (2007) Development of a combined microPET(R)MR system. Workshop on Medical Instrumentation Signal and Imaging, 11-12 April 2007 Aveiro. Portugal 827

Ludwig FA, Fischer S, Smits R et al (2018) Exploring the metabolism of (+)-[¹⁸F]flubatine in vitro and in vivo: LC-MS/MS aided identification of radiometabolites in a clinical PET study. Molecules 23(2):464

Ma B, Sherman PS, Moskwa JE et al (2004) Sensitivity of [¹¹C]N-methylpyrrolidinyl benzilate ([¹¹C]NMPYB) to endogenous acetylcholine: PET imaging vs tissue sampling methods. Nucl Med Biol 31:393–397

Magnussen JH, Ettrup A, Donat CK et al (2015) Radiosynthesis and in vitro validation of ³H-NS14492 as a novel high affinity alpha7 nicotinic receptor radioligand. Eur J Pharmacol 762:35–41

Maier DL, Hill G, Ding M et al (2011) Pre-clinical validation of a novel alpha-7 nicotinic receptor radiotracer, [³H]AZ11637326: target localization, biodistribution and ligand occupancy in the rat brain. Neuropharmacology 61:161–171

Malpass JR, Hemmings DA, Wallis AL et al (2001) Synthesis and nicotinic acetylcholine-binding properties of epibatidine homologues: homoepibatidine and dihomoepibatidine. Nicotin1 2001:1044–1050

Manley GT, Rosenthal G, Lam M et al (2006) Controlled cortical impact in swine: pathophysiology and biomechanics. J Neurotrauma 23:128–139

Marenco S, Carson RE, Berman KF et al (2004) Nicotine-induced dopamine release in primates measured with [¹¹C]raclopride PET. Neuropsychopharmacology 29:259–268

Marenco T, Bernstein S, Cumming P et al (2000) Effects of nicotine and chlorisondamine on cerebral glucose utilization in immobilized and freely-moving rats. Br J Pharmacol 129:147–155

Marmarou A, Foda MA, van den Brink W et al (1994) A new model of diffuse brain injury in rats. Part I: Pathophysiology and biomechanics. J Neurosurg 80:291–300

Marshall HR, Stodilka RZ, Theberge J et al (2011) A comparison of MR-based attenuation correction in PET versus SPECT. Phys Med Biol 56:4613–4629

Martelli D, McKinley MJ, McAllen RM (2014) The cholinergic anti-inflammatory pathway: a critical review. Auton Neurosci 182:65–69

Martin A, Szczupak B, Gomez-Vallejo V et al (2015) In vivo PET imaging of the alpha4beta2 nicotinic acetylcholine receptor as a marker for brain inflammation after cerebral ischemia. J Neurosci 35:5998–6009

Marutle A, Warpman U, Bogdanovic N et al (1998) Regional distribution of subtypes of nicotinic receptors in human brain and effect of aging studied by (+/−)- ³H epibatidine. Brain Res 801:143–149

Masel BE, DeWitt DS (2010) Traumatic brain injury: a disease process, not an event. J Neurotrauma 27:1529–1540

Matsumura A, Suzuki S, Iwahara N et al (2015) Temporal changes of CD68 and α7 nicotinic acetylcholine receptor expression in microglia in Alzheimer's disease-like mouse models. J Alzheimers Dis 44:409–423

Maziere M, Comar D, Marazano C et al (1976) Nicotine-11C: synthesis and distribution kinetics in animals. Eur J Nucl Med 1:255–258

McKee AC, Alosco ML, Huber BR (2016) Repetitive head impacts and chronic traumatic encephalopathy. Neurosurg Clin N Am 27:529–535

Meier D, Wagenaar DJ, Chen S et al (2011) A SPECT camera for combined MRI and SPECT for small animals. Nucl Instrum Methods Phys Res 652:731–734

Mexal S, Berger R, Logel J et al (2010) Differential regulation of α7 nicotinic receptor gene (*CHRNA7*) expression in schizophrenic smokers. J Mol Neurosci 40:185–195

Meyer EM, Kuryatov A, Gerzanich V et al (1998) Analysis of 3-(4-hydroxy, 2-methoxybenzylidene) anabaseine selectivity and activity at human and rat α7 nicotinic receptors. J Pharmacol Exp Ther 287:918–925

Meyer PM, Strecker K, Kendziorra K et al (2009) Reduced α4β2*-nicotinic acetylcholine receptor binding and its relationship to mild cognitive and depressive symptoms in Parkinson disease. Arch Gen Psychiatry 66:866–877

Meyerhoff DJ, Tizabi Y, Staley JK et al (2006) Smoking comorbidity in alcoholism: neurobiological and neurocognitive consequences. Alcohol Clin Exp Res 30:253–264

Millar NS, Harkness PC (2008) Assembly and trafficking of nicotinic acetylcholine receptors (Review). Mol Membr Biol 25:279–292

Mitkovski S, Villemagne VL, Novakovic KE et al (2005) Simplified quantification of nicotinic receptors with 2[^{18}F]F-A-85380 PET. Nucl Med Biol 32:585–591

Mo YX, Yin YF, Li YM (2014) Neural nAChRs PET imaging probes. Nucl Med Commun 35:135–143

Molina PE, Ding YS, Carroll FI et al (1997) Fluoro-norchloroepibatidine: preclinical assessment of acute toxicity. Nucl Med Biol 24:743–747

Montgomery AJ, Lingford-Hughes AR, Egerton A et al (2007) The effect of nicotine on striatal dopamine release in man: A [^{11}C]raclopride PET study. Synapse 61:637–645

Morganti-Kossmann MC, Semple BD, Hellewell SC et al (2019) The complexity of neuroinflammation consequent to traumatic brain injury: from research evidence to potential treatments. Acta Neuropathol 137:731–755

Mu L, Drandarov K, Bisson WH et al (2006) Synthesis and binding studies of epibatidine analogues as ligands for the nicotinic acetylcholine receptors. Eur J Med Chem 41:640–650

Mufson EJ, He B, Ginsberg SD et al (2018) Gene profiling of nucleus basalis tau containing neurons in chronic traumatic encephalopathy: a chronic effects of neurotrauma consortium study. J Neurotrauma 35:1260–1271

Mufson EJ, Perez SE, Nadeem M et al (2016) Progression of tau pathology within cholinergic nucleus basalis neurons in chronic traumatic encephalopathy: a chronic effects of neurotrauma consortium study. Brain Inj 30:1399–1413

Mukherjee J, Lao PJ, Betthauser TJ et al (2018) Human brain imaging of nicotinic acetylcholine α4β2* receptors using [^{18}F]Nifene: Selectivity, functional activity, toxicity, aging effects, gender effects, and extrathalamic pathways. J Comp Neurol 526:80–95

Mukherjee J, Pichika R, Leslie FM et al (2004) Design and development of novel new PET imaging agents for α4β2 nicotinic recpetors: 18F-nifrolidine and 18F-nifzetidine. NeuroImage 22:S2–T124

Mukhin AG, Kimes AS, Chefer SI et al (2008) Greater nicotinic acetylcholine receptor density in smokers than in nonsmokers: a PET study with 2-18F-FA-85380. J Nucl Med 49:1628–1635

Murdoch I, Nicoll JAR, Graham DI et al (2002) Nucleus basalis of Meynert pathology in the human brain after fatal head injury. J Neurotrauma 19:279–284

Murdoch I, Perry EK, Court JA et al (1998) Cortical cholinergic dysfunction after human head injury. J Neurotrauma 15:295–305

Nakaizumi K, Ouchi Y, Terada T et al (2018) In vivo depiction of α7 nicotinic receptor loss for cognitive decline in Alzheimer's disease. J Alzheimers Dis 61:1355–1365

Nishiyama S, Ohba H, Kanazawa M et al (2015) Comparing α7 nicotinic acetylcholine receptor binding, amyloid-β deposition, and mitochondria complex-I function in living brain: a PET study in aged monkeys. Synapse 69:475–483

Nomikos GG, Schilström B, Hildebrand BE et al (2000) Role of α7 nicotinic receptors in nicotine dependence and implications for psychiatric illness. Behav Brain Res 113:97–103

Nordberg A (1993) Clinical studies in Alzheimer patients with positron emission tomography. Behav Brain Res 57:215–224

Nordberg A, Hartvig P, Lilja A et al (1991) Nicotine receptors in the brain of patients with Alzheimer's disease. Studies with ^{11}C-nicotine and positron emission tomography. Acta Radiol Suppl 376:165–166

Nordberg A, Lilja A, Lundqvist H et al (1992) Tacrine restores cholinergic nicotinic receptors and glucose metabolism in Alzheimer patients as visualized by positron emission tomography. Neurobiol Aging 13:747–758

Nuechterlein KH, Barch DM, Gold JM et al (2004) Identification of separable cognitive factors in schizophrenia. Schizophr Res 72:29–39

Nybäck H, Halldin C, Ahlin A et al (1994) PET studies of the uptake of (*S*)- and (*R*)-[^{11}C]nicotine in the human brain: difficulties in visualizing specific receptor binding in vivo. Psychopharmacology 115:31–36

O'Connor WT, Smyth A, Gilchrist MD (2011) Animal models of traumatic brain injury: a critical evaluation. Pharmacol Ther 130:106–113

O'Neill MJ, Murray TK, Lakics V et al (2002) The role of neuronal nicotinic acetylcholine receptors in acute and chronic neurodegeneration. Curr Drug Targets CNS Neurol Disord 1:399–411

Oddo S, Caccamo A, Green KN et al (2005) Chronic nicotine administration exacerbates tau pathology in a transgenic model of Alzheimer's disease. Proc Natl Acad Sci U S A 102:3046–3051

Ogawa M, Nishiyama S, Tsukada H et al (2010) Synthesis and evaluation of new imaging agent for central nicotinic acetylcholine receptor α7 subtype. Nucl Med Biol 37:347–355

Ogawa M, Tatsumi R, Fujio M et al (2006) Synthesis and evaluation of [^{125}I]I-TSA as a brain nicotinic acetylcholine receptor α7 subtype imaging agent. Nucl Med Biol 33:311–316

Ogawa M, Tsukada H, Hatano K et al (2009) Central in vivo nicotinic acetylcholine receptor imaging agents for positron emission tomography (PET) and single photon emission computed tomography (SPECT). Biol Pharm Bull 32:337–340

Okada H, Ouchi Y, Ogawa M et al (2013) Alterations in α4β2 nicotinic receptors in cognitive decline in Alzheimer's aetiopathology. Brain 136:3004–3017

Oldendorf W, Braun L, Cornford E (1979) pH dependence of blood-brain barrier permeability to lactate and nicotine. Stroke 10:577–581

Olesen J, Leonardi M (2003) The burden of brain diseases in Europe. Eur J Neurol 10:471–477

Ostberg A, Tenovuo O (2014) Smoking and outcome of traumatic brain injury. Brain Inj 28:155–160

Ostberg A, Virta J, Rinne JO et al (2018) Brain cholinergic function and response to rivastigmine in patients with chronic sequels of traumatic brain injury: A PET study. J Head Trauma Rehabil 33:25–32

Östberg A, Virta J, Rinne JO et al (2011) Cholinergic dysfunction after traumatic brain injury: preliminary findings from a PET study. Neurology 76:1046–1050

Parl C, Kolb A, Stricker-Shaver D et al (2019) Dual layer doI detector modules for a dedicated mouse brain PET/MRI. Phys Med Biol 64:055004

Paterson D, Nordberg A (2000) Neuronal nicotinic receptors in the human brain. Prog Neurobiol 61:75–111

Paterson LM, Tyacke RJ, Nutt DJ et al (2010) Measuring endogenous 5-HT release by emission tomography: promises and pitfalls. J Cereb Blood Flow Metab 30:1682–1706

Patt JT, Spang JE, Buck A et al (2001) Synthesis and in vivo studies of the stereoisomers of N-[^{11}C]methyl-homoepibatidine. Nucl Med Biol 28:645–655

Patt JT, Spang JE, Westera G et al (1999) Synthesis and in Vivo studies of [C-11]N-methylepibatidine: comparison of the stereoisomers. Nucl Med Biol 26:165–173

Paulson JR, Yang T, Selvaraj PK et al (2010) Nicotine exacerbates brain edema during in vitro and in vivo focal ischemic conditions. J Pharmacol Exp Ther 332:371–379

Pauly JR, Stitzel JA, Marks MJ et al (1989) An autoradiographic analysis of cholinergic receptors in mouse brain. Brain Res Bull 22:453–459

Pavlov VA, Wang H, Czura CJ et al (2003) The cholinergic anti-inflammatory pathway: a missing link in neuroimmunomodulation. Mol Med 9:125–134

Paxinos G, Watson C (1998) The rat brain in stereotaxic coordinates. Academic Press, New York

Peng X, Gerzanich V, Anand R et al (1994) Nicotine-induced increase in neuronal nicotinic receptors results from a decrease in the rate of receptor turnover. Mol Pharmacol 46:523–530

Perry EK, Perry RH, Smith CJ et al (1987) Nicotinic receptor abnormalities in Alzheimer's and Parkinson's diseases. J Neurol Neurosurg Psychiatry 50:806–809

Perry EK, Perry RH, Smith CJ et al (1986) Cholinergic receptors in cognitive disorders. Can J Neurol Sci 13:521–527

Peters D, Olsen GM, Nielsen EO et al (2007) Novel 1,4-diaza-bicyclo[3.2.2]nonyl oxadiazolyl derviatives and their medical use, WO/2007/138037.

Phillips HA, Favre I, Kirkpatrick M et al (2001) CHRNB2 is the second acetylcholine receptor subunit associated with autosomal dominant nocturnal frontal lobe epilepsy. Am J Hum Genet 68:225–231

Picard F, Bruel D, Servent D et al (2006) Alteration of the in vivo nicotinic receptor density in ADNFLE patients: a PET study. Brain 129:2047–2060

Picciotto MR, Zoli M (2002) Nicotinic receptors in aging and dementia. J Neurobiol 53:641–655

Pichika R, Easwaramoorthy B, Christian BT et al (2011) Nicotinic alpha4beta2 receptor imaging agents. Part III. Synthesis and biological evaluation of 3-(2-(S)-azetidinylmethoxy)-5-(3′-(18)F-fluoropropyl)pyridine ((18)F-nifzetidine). Nucl Med Biol 38:1183–1192

Pichika R, Easwaramoorthy B, Collins D et al (2006) Nicotinic α4β2 receptor imaging agents Part II. Synthesis and biological evaluation of 2-[18F]fluoro-3-[2-((S)-3-pyrrolinyl)methoxy]pyridine (18F-nifene) in rodents and imaging by PET in nonhuman primate. Nucl Med Biol 33:295–304

Pichika R, Kuruvilla SA, Patel N et al (2013) Nicotinic α4β2 receptor imaging agents. Part IV. Synthesis and Biological Evaluation of 3-(2-(S)-3,4-dehydropyrrolinyl methoxy)-5-(3′-18F-Fluoropropyl)pyridine (18F-Nifrolene) using PET. Nucl Med Biol 40:117–125

Pictet A (1903) Synthese de la nicotine. Nicotin7 137:860–862

Pin F, Vercouillie J, Ouach A et al (2014) Design of α7 nicotinic acetylcholine receptor ligands in quinuclidine, tropane and quinazoline series. Chemistry, molecular modeling, radiochemistry, in vitro and in rats evaluations of a [18F] quinuclidine derivative. Eur J Med Chem 82:214–224

Pinner A (1893) Ueber Nicotin. Die Constitution des Alkaloids V Mittheilung Berichte der deutschen chemischen Gesellschaft 26:292–305

Pinner A, Wolffenstein R (1891) Ueber Nicotin. Ber Dtsch Chem Ges 24:61–67

Plaven-Sigray P, Matheson GJ, Collste K et al (2018) Positron emission tomography studies of the glial cell marker translocator protein in patients with psychosis: a meta-analysis using individual participant data. Biol Psychiatry 84:433–442

Plested AJ (2016) Structural mechanisms of activation and desensitization in neurotransmitter-gated ion channels. Nat Struct Mol Biol 23:494–502

Pomper MG, Phillips E, Fan H et al (2005) Synthesis and biodistribution of radiolabeled α7 nicotinic acetylcholine receptor ligands. J Nucl Med 46:326–334

Posselt W, Reimann L (1828) Chemische Untersuchungen des Tabaks und Darstellung des eigenthümlichen wirksamen Princips dieser Pflanze. Nicotin6 24:138–161

Pradhan AA, Cumming P, Clarke PB (2002) [125I]Epibatidine-labelled nicotinic receptors in the extended striatum and cerebral cortex: lack of association with serotonergic afferents. Brain Res 954:227–236

Prakash N, Frostig RD (2005) What has intrinsic signal optical imaging taught us about NGF-induced rapid plasticity in adult cortex and its relationship to the cholinergic system? Mol Imaging Biol 7:14–21

Quelch DR, Katsouri L, Nutt DJ et al (2014) Imaging endogenous opioid peptide release with [11C]carfentanil and [3H]diprenorphine: influence of agonist-induced internalization. J Cereb Blood Flow Metab 34:1604–1612

Quik M (2004) Smoking, nicotine and Parkinson's disease. Trends Neurosci 27:561–568

Quik M, Campos C, Parameswaran N et al (2010) Chronic nicotine treatment increases nAChRs and microglial expression in monkey substantia nigra after nigrostriatal damage. J Mol Neurosci 40:105–113

Quik M, Parameswaran N, McCallum SE et al (2006) Chronic oral nicotine treatment protects against striatal degeneration in MPTP-treated primates. J Neurochem 98:1866–1875

Quik M, Perez XA, Grady SR (2011) Role of alpha6 nicotinic receptors in CNS dopaminergic function: relevance to addiction and neurological disorders. Biochem Pharmacol 82:873–882

Quik M, Polonskaya Y, Gillespie A et al (2000) Localization of nicotinic receptor subunit mRNAs in monkey brain by in situ hybridization. J Comp Neurol 425:58–69

Quik M, Sum JD, Whiteaker P et al (2003) Differential declines in striatal nicotinic receptor subtype function after nigrostriatal damage in mice. Mol Pharmacol 63:1169–1179

Raad M, Nohra E, Chams N et al (2014) Autoantibodies in traumatic brain injury and central nervous system trauma. Neuroscience 281:16–23

Radcliffe KA, Dani JA (1998) Nicotinic stimulation produces multiple forms of increased glutamatergic synaptic transmission. J Neurosci 18:7075–7083

Radek RJ, Miner HM, Bratcher NA et al (2006) Alpha4beta2 nicotinic receptor stimulation contributes to the effects of nicotine in the DBA/2 mouse model of sensory gating. Psychopharmacology 187:47–55

Rademacher L, Prinz S, Winz O et al (2016) Effects of smoking cessation on presynaptic dopamine function of addicted male smokers. Biol Psychiatry 80:198–206

Raggenbass M, Bertrand D (2002) Nicotinic receptors in circuit excitability and epilepsy. J Neurobiol 53:580–589

Rahman S, Engleman EA, Bell RL (2015) Nicotinic receptor modulation to treat alcohol and drug dependence. Front Neurosci 8:426

Ramlackhansingh AF, Brooks DJ, Greenwood RJ et al (2011) Inflammation after trauma: microglial activation and traumatic brain injury. Ann Neurol 70:374–383

Ransohoff RM (2016) A polarizing question: do M1 and M2 microglia exist? Nat Neurosci 19:987–991

Ren C, Tong YL, Li JC et al (2017) The protective effect of alpha 7 nicotinic acetylcholine receptor activation on critical illness and its mechanism. Int J Biol Sci 13:46–56

Robles N, Sabria J (2008) Effects of moderate chronic ethanol consumption on hippocampal nicotinic receptors and associative learning. Neurobiol Learn Mem 89:497–503

Roger G, Lagnel B, Rouden J et al (2003) Synthesis of a [2-pyridinyl-^{18}F]-labelled fluoro derivative of (−)-cytisine as a candidate radioligand for brain nicotinic α4β2 receptor imaging with PET. Bioorg Med Chem 11:5333–5343

Roger G, Saba W, Valette H et al (2006) Synthesis and radiosynthesis of [^{18}F]FPhEP, a novel α4β2-selective, epibatidine-based antagonist for PET imaging of nicotinic acetylcholine receptors. Bioorg Med Chem 14:3848–3858

Rominger A, Wagner E, Mille E et al (2010) Endogenous competition against binding of [^{18}F]DMFP and [^{18}F]fallypride to dopamine D$_{2/3}$ receptors in brain of living mouse. Synapse 64:313–322

Roos RA (2010) Huntington's disease: a clinical review. Orphanet J Rare Dis 5:40

Rose JE, Mukhin AG, Lokitz SJ et al (2010) Kinetics of brain nicotine accumulation in dependent and nondependent smokers assessed with PET and cigarettes containing ^{11}C-nicotine. Proc Natl Acad Sci U S A 107:5190–5195

Ross RG, Stevens KE, Proctor WR et al (2010) Research review: cholinergic mechanisms, early brain development, and risk for schizophrenia. J Child Psychol Psychiatry 51:535–549

Rötering S, Deuther-Conrad W, Cumming P et al (2014) Imaging of α7 nicotinic acetylcholine receptors in brain and cerebral vasculature of juvenile pigs with [^{18}F]NS14490. EJNMMI Res 4:43

Rubio A, Perez M, Avila J (2006) Acetylcholine receptors and tau phosphorylation. Curr Mol Med 6:423–428

Saba W, Valette H, Granon S et al (2010) [^{18}F]ZW-104, a new radioligand for imaging α2-α3-α4/β2 central nicotinic acetylcholine receptors: Evaluation in mutant mice. Synapse 64:570–572

Sabri O, Kendziorra K, Wolf H et al (2008) Acetylcholine receptors in dementia and mild cognitive impairment. Eur J Nucl Med Mol Imaging 35(Suppl 1):S30–S45

Sabri O, Meyer PM, Gertz H-J et al (2014) PET imaging of the α4β2* nicotinic acetylcholine receptors in Alzheimer's disease. In: Dierckx RAJO (ed) PET and SPECT in neurology. Springer, Berlin Heidelberg

Sabri O, Meyer PM, Graf S et al (2018) Cognitive correlates of α4β2 nicotinic acetylcholine receptors in mild Alzheimer's dementia. Brain 141:1840–1854

Salokangas RK, Vilkman H, Ilonen T et al (2000) High levels of dopamine activity in the basal ganglia of cigarette smokers. Am J Psychiatry 157:632–634

Sandiego CM, Jin X, Mulnix T et al (2013) Awake nonhuman primate brain PET imaging with minimal head restraint: evaluation of GABAA-benzodiazepine binding with ^{11}C-flumazenil in awake and anesthetized animals. J Nucl Med 54:1962–1968

Sarasamkan J, Fischer S, Deuther-Conrad W et al (2017) Radiosynthesis of (S)-[18F]T1: The first PET radioligand for molecular imaging of α3β4 nicotinic acetylcholine receptors. Appl Radiat Isot 124:106–113

Sarasamkan J, Scheunemann M, Apaijai N et al (2016) Varying chirality across nicotinic acetylcholine receptor subtypes: selective binding of quinuclidine triazole compounds. ACS Med Chem Lett 7:890–895

Saricicek A, Esterlis I, Maloney KH et al (2012) Persistent beta2*-nicotinic acetylcholinergic receptor dysfunction in major depressive disorder. Am J Psychiatry 169:851–859

Sattler B, Kranz M, Starke A et al (2014) Internal dose assessment of (−)-^{18}F-flubatine, comparing animal model datasets of mice and piglets with first-in-human results. J Nucl Med 55:1885–1892

Scheff SW, Baldwin SA, Brown RW et al (1997) Morris water maze deficits in rats following traumatic brain injury: lateral controlled cortical impact. J Neurotrauma 14:615–627

Scheffel U, Horti AG, Koren AO et al (2000) 6-[18F]Fluoro-A-85380: an in vivo tracer for the nicotinic acetylcholine receptor. Nucl Med Biol 27:51–56

Schep LJ, Slaughter RJ, Beasley DM (2009) Nicotinic plant poisoning. Clin Toxicol (Phila) 47:771–781

Scheunemann M, Teodoro R, Wenzel B et al (2014) Synthesis and F-18 labeling of a 2-fluoro dibenzothiophene sulfone derivative, as a potential alpha-7 nicotinic acetylcholine receptor (α7 nAChR) imaging agent. Nuklearmedizin 53:A26

Schilström B, Fagerquist MV, Zhang X et al (2000) Putative role of presynaptic α7* nicotinic receptors in nicotine stimulated increases of extracellular levels of glutamate and aspartate in the ventral tegmental area. Synapse 38:375–383

Schliebs R (2005) Basal forebrain cholinergic dysfunction in Alzheimer's disease—interrelationship with beta-amyloid, inflammation and neurotrophin signaling. Neurochem Res 30:895–908

Schliebs R, Arendt T (2011) The cholinergic system in aging and neuronal degeneration. Behav Brain Res 221:555–563

Schmaljohann J, Gundisch D, Minnerop M et al (2005) A simple and fast method for the preparation of n.c.a. 2-[18F]F-A85380 for human use. Appl Radiat Isot 63:433–435

Schrimpf MR, Sippy KB, Briggs CA et al (2012) SAR of α7 nicotinic receptor agonists derived from tilorone: exploration of a novel nicotinic pharmacophore. Bioorg Med Chem Lett 22:1633–1638

Schröck H, Kuschinsky W (1991) Effects of nicotine withdrawal on the local cerebral glucose utilization in conscious rats. Brain Res 545:234–238

Schulz D, Southekal S, Junnarkar SS et al (2011) Simultaneous assessment of rodent behavior and neurochemistry using a miniature positron emission tomograph. Nat Methods 8:347–352

Serriere S, Domene A, Vercouillie J et al (2015) Assessment of the protection of dopaminergic neurons by an alpha7 nicotinic receptor agonist, PHA 543613 using [(18)F]LBT-999 in a Parkinson's disease rat model. Front Med (Lausanne) 2:61

Sharma G, Vijayaraghavan S (2001) Nicotinic cholinergic signaling in hippocampal astrocytes involves calcium-induced calcium release from intracellular stores. Proc Natl Acad Sci U S A 98:4148–4153

Sharma G, Vijayaraghavan S (2002) Nicotinic receptor signaling in nonexcitable cells. J Neurobiol 53:524–534

Sharma G, Vijayaraghavan S (2008) Nicotinic receptors: role in addiction and other disorders of the brain. Subst Abus 2008:81

Shen JX, Yakel JL (2009) Nicotinic acetylcholine receptor-mediated calcium signaling in the nervous system. Acta Pharmacol Sin 30:673–680

Shen JX, Yakel JL (2012) Functional alpha7 nicotinic ACh receptors on astrocytes in rat hippocampal CA1 slices. J Mol Neurosci 48:14–21

Shimohama S, Taniguchi T, Fujiwara M et al (1985) Biochemical characterization of the nicotinic cholinergic receptors in human brain: binding of (−)-[^{3}H]nicotine. J Neurochem 45:604–610

Shimohama S, Taniguchi T, Fujiwara M et al (1986) Changes in nicotinic and muscarinic cholinergic receptors in Alzheimer-type dementia. J Neurochem 46:288–293

Shin SS, Dixon CE (2015) Alterations in cholinergic pathways and therapeutic strategies targeting cholinergic system after traumatic brain injury. J Neurotrauma 32:1429–1440

Shytle RD, Mori T, Townsend K et al (2004a) Cholinergic modulation of microglial activation by α7 nicotinic receptors. J Neurochem 89:337–343

Shytle RD, Mori T, Townsend K et al (2004b) Cholinergic modulation of microglial activation by alpha 7 nicotinic receptors. J Neurochem 89:337–343

Siegmund B, Leitner E, Pfannhauser W (1999) Determination of the nicotine content of various edible nightshades (Solanaceae) and their products and estimation of the associated dietary nicotine intake. J Agric Food Chem 47:3113–3120

Sihver W, Fasth KJ, Horti AG et al (1999a) Synthesis and characterization of binding of 5-[^{76}Br]bromo-3-[[2(S)-azetidinyl]methoxy]pyridine, a novel nicotinic acetylcholine receptor ligand, in rat brain. J Neurochem 73:1264–1272

Sihver W, Fasth KJ, Ögren M et al (1998) In vitro evaluation of ^{11}C-labeled (S)-nicotine, (S)-3-methyl-5-(1-methyl-2-pyrrolidinyl)isoxazole, and (R,S)-1-methyl-2-(3-pyridyl)azetidine as nicotinic receptor ligands for positron emission tomography studies. J Neurochem 71:1750–1760

Sihver W, Fasth KJ, Ögren M et al (1999b) In vivo positron emission tomography studies on the novel nicotinic receptor agonist [^{11}C]MPA compared with [^{11}C]ABT-418 and (S)(−) [^{11}C]nicotine in rhesus monkeys. Nucl Med Biol 26:633–640

Sihver W, Langström B, Nordberg A (2000a) Ligands for in vivo imaging of nicotinic receptor subtypes in Alzheimer brain. Acta Neurol Scand Suppl 176:27–33

Sihver W, Nordberg A, Langström B et al (2000b) Development of ligands for in vivo imaging of cerebral nicotinic receptors. Behav Brain Res 113:143–157

Small E, Shah HP, Davenport JJ et al (2010) Tobacco smoke exposure induces nicotine dependence in rats. Psychopharmacology 208:143–158

Smith DF, Jakobsen S (2007) Stereoselective neuroimaging in vivo. Eur Neuropsychopharmacol 17:507–522

Smith ML, Souza FG, Bruce KS et al (2014) Acetylcholine receptors in the retinas of the alpha7 nicotinic acetylcholine receptor knockout mouse. Mol Vis 20:1328–1356

Sobrio F, Quentin T, Dhilly M et al (2008) Radiosynthesis and ex vivo evaluation of [^{11}C]-SIB-1553A as a PET radiotracer for β4 selective subtype nicotinic acetylcholine receptor. Nucl Med Biol 35:377–385

Soloway SB (1976) Naturally occurring insecticides. Environ Health Perspect 14:109–117

Song C, Leonard BE (2005) The olfactory bulbectomised rat as a model of depression. Neurosci Biobehav Rev 29:627–647

Sorokina EG, Vol'pina OM, Semenova Zh B et al (2012) Autoantibodies to the α7 subunit of the neuronal acetylcholine receptor in craniocerebral trauma in children. Neurosci Behav Physiol 42:740–744

Spang JE, Patt JT, Westera G et al (2000) Comparison of N-[^{11}C]methyl-norchloroepibatidine and N-[^{11}C]methyl-2-(2-pyridyl)-7-azabicyclo[2.2.1]heptane with N-[^{11}C]methyl-epibatidine in small animal PET studies. Nucl Med Biol 27:239–247

Spurden DP, Court JA, Lloyd S et al (1997) Nicotinic receptor distribution in the human thalamus: autoradiographical localization of [^{3}H]nicotine and [^{125}I] alpha-bungarotoxin binding. J Chem Neuroanat 13:105–113

Spillantini MG, Schmidt ML, Lee VM, Trojanowski JQ, Jakes R, Goedert M (1997) Alpha-synuclein in Lewy bodies. Nature 388(6645):839–40

Staley JK, Krishnan-Sarin S, Cosgrove KP et al (2006) Human tobacco smokers in early abstinence have higher levels of β2* nicotinic acetylcholine receptors than nonsmokers. J Neurosci 26:8707–8714

Steinlein OK, Mulley JC, Propping P et al (1995) A missense mutation in the neuronal nicotinic acetylcholine receptor alpha 4 subunit is associated with autosomal dominant nocturnal frontal lobe epilepsy. Nat Genet 11:201–203

Stephens SH, Logel J, Barton A et al (2009) Association of the 5′-upstream regulatory region of the α7 nicotinic acetylcholine receptor subunit gene (CHRNA7) with schizophrenia. Schizophr Res 109:102–112

Suhara T, Inoue O, Kobayashi K et al (1994) An acute effect of triazolam on muscarinic cholinergic receptor binding in the human brain measured by positron emission tomography. Psychopharmacology 113:311–317

Sullivan JP, Donnelly-Roberts D, Briggs CA et al (1996) A-85380 [3-(2(S)-azetidinylmethoxy) pyridine]: in vitro pharmacological properties of a novel, high affinity α4β2 nicotinic acetylcholine receptor ligand. Neuropharmacology 35:725–734

Sultzer DL, Melrose RJ, Riskin-Jones H et al (2017) Cholinergic receptor binding in alzheimer disease and healthy aging: assessment in vivo with positron emission tomography imaging. Am J Geriatr Psychiatry 25:342–353

Suzuki T, Hide I, Matsubara A et al (2006) Microglial α7 nicotinic acetylcholine receptors drive a phospholipase C/IP3 pathway and modulate the cell activation toward a neuroprotective role. J Neurosci Res 83:1461–1470

Taly A, Corringer PJ, Guedin D et al (2009) Nicotinic receptors: allosteric transitions and therapeutic targets in the nervous system. Nat Rev Drug Discov 8:733–750

Tanibuchi Y, Wu J, Toyohara J et al (2010) Characterization of [^{3}H]CHIBA-1001 binding to α7 nicotinic acetylcholine receptors in the brain from rat, monkey, and human. Brain Res 1348:200–208

Taylor P, Radic Z, Kreienkamp HJ et al (1994) Expression and ligand specificity of acetylcholinesterase and the nicotinic receptor: a tale of two cholinergic sites. Biochem Soc Trans 22:740–745

Teaktong T, Graham AJ, Johnson M et al (2004) Selective changes in nicotinic acetylcholine receptor subtypes related to tobacco smoking: an immunohistochemical study. Neuropathol Appl Neurobiol 30:243–254

Teodoro R, Scheunemann M, Deuther-Conrad W et al (2015) A promising PET tracer for imaging of α7 nicotinic acetylcholine receptors in the brain: design, synthesis, and in vivo evaluation of a dibenzothiophene-based radioligand. Molecules 20:18387–18421

Teodoro R, Scheunemann M, Wenzel B et al (2018) Synthesis and radiofluorination of novel fluoren-9-one based derivatives for the imaging of α7 nicotinic acetylcholine receptor with PET. Bioorg Med Chem Lett 28:1471–1475

Thal DR, Braak H (2005) Post-mortem diagnosis of Alzheimer's disease (in German). Pathologe 26:201–213

Thiessen JD, Shams E, Stortz G et al (2016) MR-compatibility of a high-resolution small animal PET insert operating inside a 7 T MRI. Phys Med Biol 61:7934–7956

Thompson HJ, Lifshitz J, Marklund N et al (2005) Lateral fluid percussion brain injury: a 15-year review and evaluation. J Neurotrauma 22:42–75

Tiepolt S, Becker GA, Wilke S et al (2018) (+)-[^{18}F]flubatine ein neuer α4β2* nikotinischer acetylcholin-rezeptor (nAChR) PET radioligand - ergebnisse der first-In-Human Studie bei Patienten mit Alzheimer Demenz (AD) und gesunden Probanden (HC). Nuklearmedizin 57:A37

Tomizawa M, Cowan A, Casida JE (2001) Analgesic and toxic effects of neonicotinoid insecticides in mice. Toxicol Appl Pharmacol 177:77–83

Toyohara J, Ishiwata K, Sakata M et al (2010) In vivo evaluation of α7 nicotinic acetylcholine receptor agonists [^{11}C]A-582941 and [^{11}C]A-844606 in mice and conscious monkeys. PLoS One 5:e8961

Toyohara J, Sakata M, Wu J et al (2009) Preclinical and the first clinical studies on [¹¹C]CHIBA-1001 for mapping α7 nicotinic receptors by positron emission tomography. Ann Nucl Med 23:301–309

Tregellas JR, Tanabe J, Rojas DC et al (2011) Effects of an alpha 7-nicotinic agonist on default network activity in schizophrenia. Biol Psychiatry 69:7–11

Tsukada H, Miyasato K, Kakiuchi T et al (2002) Comparative effects of methamphetamine and nicotine on the striatal [¹¹C]raclopride binding in unanesthetized monkeys. Synapse 45:207–212

Unwin N (2005) Refined structure of the nicotinic acetylcholine receptor at 4A resolution. J Mol Biol 346:967–989

Vafaee MS, Gjedde A, Imamirad N et al (2015) Smoking normalizes cerebral blood flow and oxygen consumption after 12-hour abstention. J Cereb Blood Flow Metab 35:699–705

Valette H, Bottlaender M, Dollé F et al (2005) Acute effects of physostigmine and galantamine on the binding of [¹⁸F]fluoro-A-85380: A PET study in monkeys. Synapse 56:217–221

Valette H, Bottlaender M, Dollé F et al (1997) An attempt to visualize baboon brain nicotinic receptors with N-[¹¹C]ABT-418 and N-[¹¹C]methyl-cytisine. Nucl Med Commun 18:164–168

Valette H, Bottlaender M, Dollé F et al (1999) Imaging central nicotinic acetylcholine receptors in baboons with [¹⁸F]fluoro-A-85380. J Nucl Med 40:1374–1380

Valette H, Dollé F, Saba W et al (2007) [¹⁸F]FPhEP and [¹⁸F]F2PhEP, two new epibatidine-based radioligands: evaluation for imaging nicotinic acetylcholine receptors in baboon brain. Synapse 61:764–770

Valette H, Xiao Y, Peyronneau MA et al (2009) ¹⁸F-ZW-104: a new radioligand for imaging neuronal nicotinic acetylcholine receptors—In vitro binding properties and PET studies in baboons. J Nucl Med 50:1349–1355

Valiyaveettil M, Alamneh YA, Miller SA et al (2013) Modulation of cholinergic pathways and inflammatory mediators in blast-induced traumatic brain injury. Chem Biol Interact 203:371–375

Vaupel DB, Stein EA, Mukhin AG (2007) Quantification of α4β2* nicotinic receptors in the rat brain with microPET(R) and 2-[¹⁸F]F-A-85380. NeuroImage 34:1352–1362

Vaupel DB, Tella SR, Huso DL et al (2005) Pharmacological and toxicological evaluation of 2-fluoro-3-(2(S)-azetidinylmethoxy)pyridine (2-F-A-85380), a ligand for imaging cerebral nicotinic acetylcholine receptors with positron emission tomography. J Pharmacol Exp Ther 312:355–365

Verbois SL, Hopkins DM, Scheff SW et al (2003a) Chronic intermittent nicotine administration attenuates traumatic brain injury-induced cognitive dysfunction. Neuroscience 119:1199–1208

Verbois SL, Scheff SW, Pauly JR (2002) Time-dependent changes in rat brain cholinergic receptor expression after experimental brain injury. J Neurotrauma 19:1569–1585

Verbois SL, Scheff SW, Pauly JR (2003b) Chronic nicotine treatment attenuates alpha 7 nicotinic receptor deficits following traumatic brain injury. Neuropharmacology 44:224–233

Verbois SL, Sullivan PG, Scheff SW et al (2000) Traumatic brain injury reduces hippocampal alpha7 nicotinic cholinergic receptor binding. J Neurotrauma 17:1001–1011

Villablanca AC (1998) Nicotine stimulates DNA synthesis and proliferation in vascular endothelial cells in vitro. J Appl Physiol 84:2089–2098

Villemagne VL, Horti A, Scheffel U et al (1997) Imaging nicotinic acetylcholine receptors with fluorine-18-FPH, an epibatidine analog. J Nucl Med 38:1737–1741

Visanji NP, O'Neill MJ, Duty S (2006) Nicotine, but neither the alpha4beta2 ligand RJR2403 nor an alpha7 nAChR subtype selective agonist, protects against a partial 6-hydroxydopamine lesion of the rat median forebrain bundle. Neuropharmacology 51:506–516

von Horsten S, Schmitt I, Nguyen HP et al (2003) Transgenic rat model of Huntington's disease. Hum Mol Genet 12:617–624

Wallace TL, Bertrand D (2013) Importance of the nicotinic acetylcholine receptor system in the prefrontal cortex. Biochem Pharmacol 85:1713–1720

Wang HY, Lee DH, D'Andrea MR et al (2000) β-Amyloid(1-42) binds to α7 nicotinic acetylcholine receptor with high affinity. Implications for Alzheimer's disease pathology. J Biol Chem 275:5626–5632

Wang J, Lindstrom J (2018) Orthosteric and allosteric potentiation of heteromeric neuronal nicotinic acetylcholine receptors. Br J Pharmacol 175:1805–1821

Wang MH, Yoshiki H, Anisuzzaman AS et al (2011) Re-evaluation of nicotinic acetylcholine receptors in rat brain by a tissue-segment binding assay. Front Pharmacol 2:65

Wang S, Fang Y, Wang H et al (2018) Design, synthesis and biological evaluation of 1,4-diazobicylco[3.2.2]nonane derivatives as α7-nicotinic acetylcholine receptor PET/CT imaging agents and agonists for Alzheimer's disease. Eur J Med Chem 159:255–266

Waterhouse RN (2003) Determination of lipophilicity and its use as a predictor of blood-brain barrier penetration of molecular imaging agents. Mol Imaging Biol 5:376–389

Wecker L, Pollock VV, Pacheco MA et al (2010) Nicotine-induced up regulation of alpha4beta2 neuronal nicotinic receptors is mediated by the protein kinase C-dependent phosphorylation of alpha4 subunits. Neuroscience 171:12–22

Wehner J, Weissler B, Dueppenbecker PM et al (2015) MR-compatibility assessment of the first preclinical PET-MRI insert equipped with digital silicon photomultipliers. Phys Med Biol 60:2231–2255

Weiss S, Nosten-Bertrand M, McIntosh JM et al (2007a) Nicotine improves cognitive deficits of dopamine transporter knockout mice without long-term tolerance. Neuropsychopharmacology 32:2465–2478

Weiss S, Tzavara ET, Davis RJ et al (2007b) Functional alterations of nicotinic neurotransmission in dopamine transporter knock-out mice. Neuropharmacology 52:1496–1508

Wheaton P, Mathias JL, Vink R (2011) Impact of pharmacological treatments on cognitive and behavioral outcome in the postacute stages of adult traumatic brain injury: a meta-analysis. J Clin Psychopharmacol 31:745–757

Whiteaker P, Davies AR, Marks MJ et al (1999) An autoradiographic study of the distribution of binding sites for the novel α7-selective nicotinic radioligand [³H]-methyllycaconitine in the mouse brain. Eur J Neurosci 11:2689–2696

Whitehouse PJ, Kellar KJ (1987) Nicotinic and muscarinic cholinergic receptors in Alzheimer's disease and related disorders. J Neural Transm Suppl 24:175–182

Wildeboer KM, Stevens KE (2008) Stimulation of the alpha4beta2 nicotinic receptor by 5-I A-85380 improves auditory gating in DBA/2 mice. Brain Res 1224:29–36

Wong DF, Kuwabara H, Horti AG et al (2018) Brain PET imaging of α7-nAChR with [¹⁸F]ASEM: reproducibility, occupancy, receptor density, and changes in schizophrenia. Int J Neuropsychopharmacol 21:656–667

Wu J, Liu Q, Tang P et al (2016) Heteromeric α7β2 nicotinic acetylcholine receptors in the brain. Trends Pharmacol Sci 37:562–574

Xiao Y, Kellar KJ (2004) The comparative pharmacology and up-regulation of rat neuronal nicotinic receptor subtype binding sites stably expressed in transfected mammalian cells. J Pharmacol Exp Ther 310:98–107

Xiong Y, Mahmood A, Chopp M (2013) Animal models of traumatic brain injury. Nat Rev 14:128–142

Yang Y, Bec J, Zhou J et al (2016) A prototype high resolution small-animal PET scanner dedicated to mouse brain imaging. J Nucl Med 57:1130–1135

Yong T, Zheng MQ, Linthicum DS (1997) Nicotine induces leukocyte rolling and adhesion in the cerebral microcirculation of the mouse. J Neuroimmunol 80:158–164

Yoshida K, Engel J, Liljequist S (1982) The effect of chronic ethanol administration of high affinity ³H-nicotinic binding in rat brain. Naunyn Schmiedeberg's Arch Pharmacol 321:74–76

Zafonte R, Friedewald WT, Lee SM et al (2009) The citicoline brain injury treatment (COBRIT) trial: design and methods. J Neurotrauma 26:2207–2216

Zanardi A, Leo G, Biagini G et al (2002) Nicotine and neurodegeneration in ageing. Toxicol Lett 127:207–215

Zhang JH, Akula MR, Kabalka GW (2001) 3-((2,4-dimethyl-5-[¹²³I]iodo)benzylidene)-anabaseine: a potent SPECT agent for imaging lung cancer. J Label Compd Radiopharm 44:S359–S361

Zhang Q, Lu Y, Bian H et al (2017) Activation of the alpha7 nicotinic receptor promotes lipopolysaccharide-induced conversion of M1 microglia to M2. Am J Transl Res 9:971–985

Zhang Y, Pavlova OA, Chefer SI et al (2004) 5-substituted derivatives of 6-halogeno-3-((2-(S)-azetidinyl)methoxy)pyridine and 6-halogeno-3-((2-(S)-pyrrolidinyl)methoxy)pyridine with low picomolar affinity for α4β2 nicotinic acetylcholine receptor and wide range of lipophilicity: potential probes for imaging with positron emission tomography. J Med Chem 47:2453–2465

Zoli M, Pistillo F, Gotti C (2015) Diversity of native nicotinic receptor subtypes in mammalian brain. Neuropharmacology 96:302–311

Zwart R, Bodkin M, Broad LM et al (2004) Common structural and pharmacological properties of 5-HT$_3$ receptors and α7 nicotinic acetylcholine receptors. In: Silman I, Soreq H, Anglister L, Michaelson D, Fisher A (eds) Cholinergic mechanisms: function and dysfunction. Tylor & Francis, London

Development of PET and SPECT Radioligands for In Vivo Imaging of NMDA Receptors

19

Takeshi Fuchigami, Morio Nakayama, and Yasuhiro Magata

Contents

Abstract

N-Methyl-d-aspartate receptors (NMDARs) play an important role in the neuro-transmission of the central nervous system (CNS). On the other hand, aberrant functioning of the NMDARs has been implicated in various CNS disorders. Positron emission tomography (PET) and single photon emission computed tomography (SPECT) imaging of NMDARs may provide novel insights on CNS functions and various CNS disorders that could lead to the discovery of potential drug therapies. Despite numerous efforts to develop a number of radioligands for NMDARs since the late 1980s, there are no clinically useful in vivo imaging probes. However, recent continuous efforts have provided several promising

T. Fuchigami · M. Nakayama
Graduate School of Biomedical Sciences, Nagasaki University, Nagasaki, Japan
e-mail: t-fuchi@nagasaki-u.ac.jp; morio@nagasaki-u.ac.jp

Y. Magata (✉)
Preeminent Medical Photonics Education and Research Center, Hamamatsu University School of Medicine, Hamamatsu, Japan
e-mail: ymagata@hama-med.ac.jp

661

radiotracers for NMDARs, such as 3-benzazepine derivatives targeting GluN2B. In this chapter, we summarize the progress in the development of PET and SPECT imaging agents for NMDARs and discuss the prospects in this field.

Abbreviations

% ID/g	Percent injected dose per gram of tissue
% ID/mL	Percent injected dose per milliliter of tissue
3MPICA	3-[2-[(3-methoxyphenylamino)carbonyl]ethenyl]-4,6-dichloro-indole-2- carboxylic acid
AD	Alzheimer's diseases
BBB	Blood-brain barrier
BP	Binding potential
CBZ	Benzyloxycarbonyl
cis-HPTC	*cis*-2-Hydroxymethyl-*r*-1-(*N*-piperidyl)-1-(2-thienyl)cyclohexane
CNS 1261	*N*-(1-Naphthyl)-*N*′-(3-iodophenyl)-*N*′-methylguanidine
CNS 5161	*N*-(2-Chloro-5-(methylmercapto)phenyl)-*N*′-methylguanidine monohydrochloride
CNS PET MPO	Central nervous system PET multiparameter optimization
CNS	Central nervous system
CP-101,606	(*1S,2S*)-1-(4-Hydroxyphenyl)-2-(4-hydroxy-4-phenylpiperidino)-1-propanol
DAO	D-Amino acid oxidase
DCKA	5,7-Dichlorokynurenic acid
DTG	1,3-Di-*o*-tolylguanidine
EMD-95885	6-3-4-(4-Fluorobenzyl)piperidinopropionyl-3H-benzoxazol-2-one
GE-179	*N*-(2-Chloro-5-(2-fluoroethylthiophenyl)-*N*′-(3-thiomethylphenyl)-*N*′-methylguanidine
GMOM	*N*-(2-Chloro-5-thiomethylphenyl)-*N*′-(3-methoxy-phenyl)-*N*′-methylguanidine
GV150526A	3-(2-((Phenylamino)carbonyl)ethyenyl)-4,6-dichloroindol-2-carboxylic acid
HACH242	*N*-((5-(4-Fluoro-2-methoxyphenyl)pyridin-3-yl)methyl)cyclopentanamine
HON0001	7-Hydroxy-6-methoxy-2-methyl-1-(2-(4-(trifluoromethyl)phenyl)ethyl)-1,2,3,4-tetrahydroisoquinoline hydrochloride
HPLC	High-performance liquid chromatography
Ifenprodil	4-[2-(4-Benzylpiperidin-1-yl)-1-hydroxypropyl]phenol
Ketamine	(R,S)-2-(2-Chlorophenyl)-2-(methylamino)cyclohexanone
Kryptofix 2.2.2	4, 7,13,16,21,24-Hexaoxa-1,10-diazabicyclo[8.8.8]-hexacosane
L-689,560	trans-2-Carboxy-5,7-dichloro-4-phenylaminocarbonylamino-1,2,3,4-tetrahydroquinoline

L-703,717	3-[3-(4-Methoxybenzyl)phenyl]-4-hydroxy-7-chloroquinolin-2(1H)-one
MDL-104,653	3-Phenyl-4-hydroxy-7-chloro-quinolin-2(1H)-one
MDL-105519	(Z)-2-Carboxy-4,6-dichloroindole-3-(2′-phenyl-2′-carboxy)-ene
MEM	1-Amino-3-fluoromethyl-5-methyl-adamantane
Memantine	3,5-Dimethyladamantan-1-amine
MK-0657	(3S,4R)-4-Methylbenzyl 3-fluoro-4-((pyrimidin-2-yl-amino)methyl) piperidine-1-carboxylate
MK-801	Dizocilpine maleate {(+)-10,11-dihydro-5-methyl-5H-dibenzo[a,d] cyclohepten-5,10-diyldiammonium maleate}
N2B-05182	((1-(4-Fluoro-3-methylphenyl)-1H-1,2,3-triazol-4-yl)methoxy)-5-methoxypyrimidine
NCAM	N-[2-(N-(2-Mercaptoethyl))aminoethyl]-N-(2-mercaptoethyl)-3.5-dimethyl acetamide amantadine
NHAM	[1-[N-[N-(2-Mercaptoethyl)]-N-[2-(2-mercaptoethyl)amino] amino ethyl] amino-3,5-dimethyladamantane
NMDAR	N-Methyl-d-aspartate receptors
NPS 1506	[3-Fluoro-γ-(3-fluorophenyl)-N-methylbenzenepropamine]
PAMQX	(D)-7-Iodo-N-(1-phosphonoethyl)-5-aminomethylquinoxaline-2,3-dione
PCP	Phencyclidine {1-(1-phenylcyclohexyl) piperidine}
PD	Parkinson's disease
PET	Positron emission tomography
PK-209	(3-(2-Chloro-5-(methylthio)phenyl)-1-(3-(fluoromethoxy)phenyl)-1-methylguanidine)
RGH-896	2-[4-[(4-Fluorophenyl)methyl]piperidin-1-yl]-2-oxo-N-(2-oxo-3H-1,3-benzoxazol-6-yl)acetamide
Ro 25-6981	[(±)-(R*,S*)]-a-(4-Hydroxyphenyl)-b-methyl]-4-(phenylmethyl)-1-piperidine propanol
Ro-647312	[2-(3,4-Dihydro-1H-isoquinolin-2-yl)-pyridin-4-yl]-imethylamine
SAR	Structure-activity relationship
SPECT	Single photon emission computed tomography
ST3	{(S)-5-[(R)-2-Amino-2-carboxyethyl]-1-[4-(3-fluoropropyl)phenyl]-4,5-dihydro-1H-pyrazole-3-carboxylic acid
TCP	N-(1-[2-Thienylcyclohexyl)-3,4-piperidine
TLC	Thin-layer chromatography
V_T	Total volume of distribution
WMS-1405 (Me-NB1)	7-Methoxy-3-(4-phenylbutyl)-2,3,4,5,-tetrahydro-1H-3-benzazepin-1-ol

19.1   Introduction

N-Methyl-d-aspartate receptors (NMDARs) are glutamate-gated ion channels that play a central role in excitatory neurotransmission and are known to be involved in learning, memory, and synaptic plasticity (Riedel et al. 2003; Lau and Zukin 2007; Traynelis et al. 2010). On the other hand, excessive glutamate causes overactivation of NMDARs, which results in an increase of intracellular calcium. Subsequent downstream events, including activation of nitric oxide synthase, calcium-sensitive proteases, and mitochondrial damage, can induce neuronal death. This glutamate excitotoxicity is thought to be implicated in the pathophysiology of various neurological diseases, including epilepsy, ischemia, stroke, and neurodegenerative disorders, such as Parkinson's disease (PD), Alzheimer's disease (AD), and Huntington's disease. Hypofunction of NMDARs has been suggested to be related to the pathology of schizophrenia. Therefore, NMDARs have been considered to be attractive therapeutic targets for these diseases (Kemp and McKernan 2002; Kalia et al. 2008; Lau and Tymianski 2010; Paoletti et al. 2013).

NMDARs are unique ligand-gated ion channels. Activation of the receptors not only requires simultaneous binding of two amino acids, glycine and glutamate, but also removal of magnesium (Mg^{2+}) blockade by membrane depolarization. These events lead to the opening of the receptor pore, followed by calcium influx into cells. Consequently, Ca^{2+}-dependent signal transduction cascades trigger the modulation of many aspects of neuronal function (Dingledine et al. 1999; Traynelis et al. 2010). The functional NMDARs require assembly of two GluN1 subunits (previously named NR1 subunits) together with either two GluN2 (previously named NR2 subunits) or a combination of GluN2 and GluN3 (previously named NR3 subunits) (Laube et al. 1998; Furukawa et al. 2005; Ulbrich and Isacoff 2008; Paoletti et al. 2013). GluN1 have only one gene (eight splice variants) with ubiquitous distribution in the brain. GluN2 are divided into four types (GluN2A–D). These subunits show distinct anatomical distributions in the brain which determine the biophysical and pharmacological properties of the NMDARs (Köhr 2006; Paoletti and Neyton 2007). GluN3 have glycine-binding sites, and glycine alone is sufficient to activate GluN1/GluN3 receptors. However, the function of GluN3-containing NMDARs remains to be fully elucidated (Low and Wee 2010).

The NMDAR's architecture has been reported to be clamshell-like with several binding sites for endogenous and exogenous ligands as shown in Fig. 19.1. While the glutamate-binding site is exhibited on the GluN2, the glycine-binding site is located on the GluN1 or GluN3 (Furukawa and Gouaux 2003; Furukawa et al. 2005; Yao et al. 2008). Zinc (Zn^{2+}) has been reported to bind to GluN2A or GluN2B and inhibits the ion channel activity in a non-competitive manner (Rachline et al. 2005; Karakas et al. 2009). Polyamines are allosteric potentiators of GluN2B-containing NMDARs, presumably through recognition of the dimer interface of GluN1 and GluN2B (Mony et al. 2009). A number of exogenous ligands for the several binding sites of NMDARs have been developed as neuroprotective agents. Numerous small compounds have been identified to exhibit binding on the glutamate-binding sites or glycine-binding sites in a competitive manner (Danysz and Parsons 1998; Dingledine et al. 1999). Aliphatic cyclic amines, such as dizocilpine maleate (MK-801) and phencyclidine (PCP), have been reported to inhibit NMDARs strongly in a non-competitive and
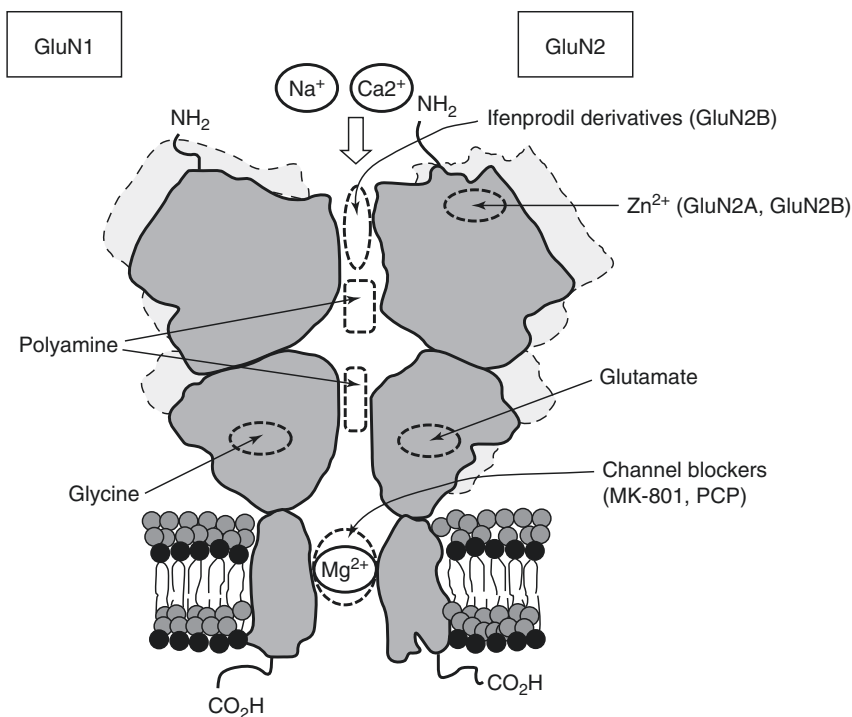
Fig. 19.1 Structure of NMDARs and location of ligand binding site

voltage-dependent manner (Anis et al. 1983; Foster and Wong 1987). These compounds are called open channel blockers because the blocking effect on NMDARs is caused by binding to the channel pore region near the Mg^{2+} binding site (Kashiwagi et al. 1997). Recently, ifenprodil and related compounds, which are GluN2B-selective antagonists, have been identified to bind at the interface between GluN1 and GluN2B (Karakas et al. 2011).

Positron emission tomography (PET) and single photon emission computed tomography (SPECT) imaging for NMDARs could be powerful tools for obtaining information about the functional mechanism of the NMDA ion channel in the living brain, the pathophysiology of related neurological disorders, and in vivo occupancy of agonists or antagonists of NMDARs. Although a conclusive relationship between NMDAR expression and neurodegenerative disease has yet be elucidated, several reports suggested that NMDAR expression is deregulated in neurological patients. It is reported that mRNA and protein levels of NMDAR GluN2A and GluN2B were decreased in AD patients (Hynd et al. 2004; Jacob et al. 2007). In addition, [^{3}H]Ro 25-6981 (GluN2B-selective ligand as described below) binding was increased in the putamen of PD patients experiencing motor complications (Calon et al. 2003), and protein levels of the GluN1 were decreased in the postmortem left hippocampus in schizophrenic patients (Vrajová et al. 2010). Therefore, nuclear medicine imaging of NMDARs could lead to characterization of disease progression and early diagnosis of such diseases.

Development of imaging agents for NMDARs has been extensively reviewed previously (Sobrio et al. 2010; Fuchigami et al. 2015; Gruber and Ametamey 2017; Fu et al. 2019a). General strategies for the development of radioligands for NMDARs have been based on the structural modification of NMDAR antagonists for application in PET or SPECT imaging. Thus, the target sites for the radioligands could be divided into four classes as follows: (1) PCP-binding site (channel blocker binding site), (2) glutamate-binding site, (3) glycine-binding site, and (4) ifenprodil-binding site (GluN2B negative modulator binding site). Despite enormous efforts, there are still no satisfactory radioligands for the visualization of NMDARs in the living brain. In this chapter, we summarize the history and present status of radioligands for these four sites.

19.1.1 Radioligands for PCP-Binding Site

Open channel blockers of NMDARs, such as MK-801 and PCP derivatives (Fig. 19.2), have been reported to bind to NMDARs in a receptor activation-dependent manner (Loo et al. 1986; Foster and Wong 1987; Wong et al. 1988). Thus, in vivo imaging of the PCP-binding site of NMDARs would not only provide quantification of NMDAR density in the living brain but also allow receptor activation under normal and pathophysiological conditions to be monitored. In recent decades, a number of reports have emerged regarding the development of radioligands based on dissociative anesthetics (PCP, MK-801, ketamine, memantine derivatives, diarylguanidines) as shown in Fig. 19.2.
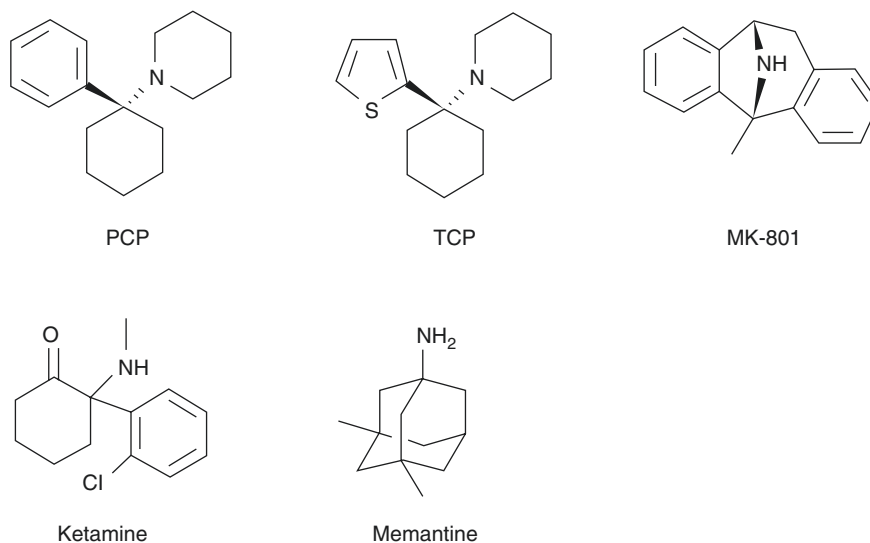
Fig. 19.2 Chemical structure of open channel blockers of NMDARs

19.1.1.1   Dissociative Anesthetic Derivatives

PCP and TCP Derivatives

PCP, one of the dissociative anesthetics, has been found to inhibit the actions of NMDARs by blocking the ion channel (Anis et al. 1983). On the other hand, TCP ([2-thienyl]-cyclohexyl-PCP), one of the PCP derivatives, has been reported to show severalfold higher affinity than PCP itself toward the PCP-binding site (Vincent et al. 1979; Tsukiyama et al. 1991).

In structure-activity relationship (SAR) studies of PCP derivatives, the binding affinity of the compounds was expressed as $K_{0.5}$, which means the half maximal (50%) inhibitory concentration of [^{3}H]PCP binding. Methoxy analogs **1** and **2** (Fig. 19.3) showed a higher binding affinity (**1**; $K_{0.5} = 90$ nM, **2**; $K_{0.5} = 58$ nM) than PCP itself (PCP; $K_{0.5} = 250$ nM) (Chaudieu et al. 1989). The IC_{50} value of methoxy-methyl analog of TCP (**3**, Fig. 19.3) for the [^{3}H]TCP-binding site was 16 nM, which was slightly weaker than TCP ($IC_{50} = 7.9$ nM) but stronger than PCP ($IC_{50} = 52$ nM) (Tsukiyama et al. 1991). These compounds were labeled with C-11 and then evaluated as PET radioligands for the PCP-binding site of NMDARs (Haradahira et al. 1998). The [^{11}C]-radiotracers were prepared from hydroxyl precursors reacting with [^{11}C]CH_3I to reach a specific activity of more than 41 GBq/μmol. In the biodistribution studies in mice, initial uptake of the TCP analog [^{11}C]**3** was twofold higher (2.6–2.9% ID/g at 1 min) than the PCP analogs [^{11}C]**1** (1.4–1.6% ID/g at 1 min) and [^{11}C]**2** (1.1–1.5%ID/g at 1 min). On the other hand, [^{11}C]**3** showed faster clearance in the brain than [^{11}C]**1** and [^{11}C]**2**. However, there was no significant difference in
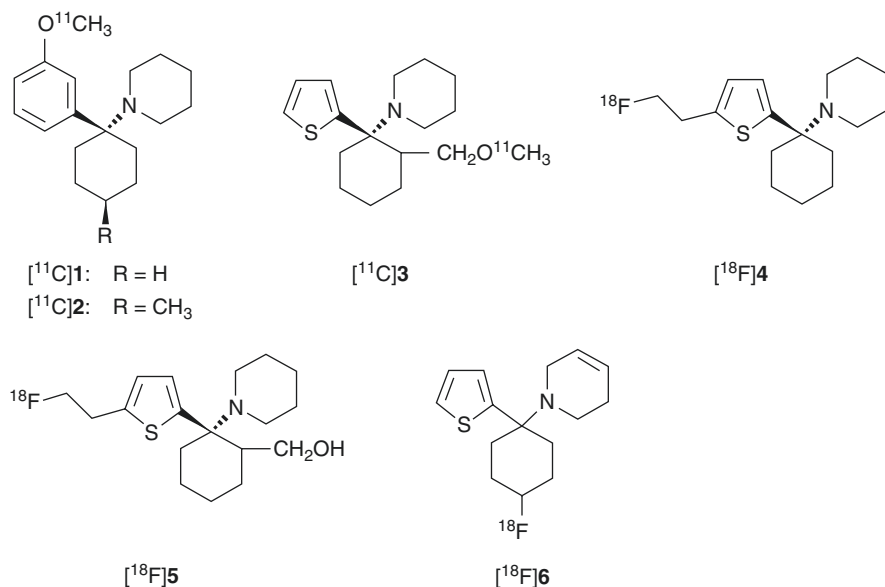
Fig. 19.3 Chemical structure of radiolabeled PCP and TCP derivatives

Fig. 19.4 Regional brain distribution of radioactivity in rats at 15 min after injection of [^{18}F]**4**. In the blocking study, *cis*-HPTC (1.7 mmol/kg) was pre-injected 5 min before administration of [^{18}F]**4**. Student's t-test with respect to the control, (**a**) $P < 0.01$, (**b**) not significant (Orita et al. 1993)
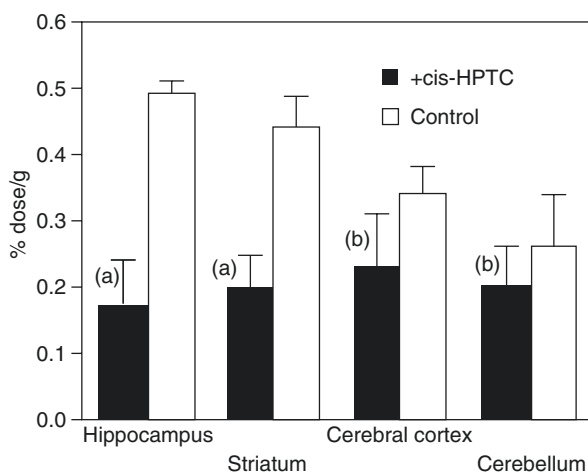
the accumulated radioactivity level between the NMDAR-rich regions and NMDAR-poor regions. These results indicated that the radioligands had no small binding interaction with brain components other than PCP-binding site. Since no blocking studies using the PCP-binding site antagonists were performed, it is unclear whether these radioligands bound specifically in certain brain regions (Haradahira et al. 1998).

Orita et al. developed [^{18}F]fluoroethyl analog of TCP ([^{18}F]**4**, Fig. 19.3) with IC$_{50}$ values of 61 nM for the PCP-binding site of NMDARs. The [^{18}F]**4** showed heterogeneous in vivo distribution that was similar to NMDAR expression. In addition, co-injection of high-affinity ion channel blocker *cis*-HPTC (1.7 μmol/kg) yielded reduction of regional cerebral distribution of [^{18}F]**4** (Fig. 19.4). However, this tracer may be an unsuitable PET radioligand for NMDARs because of the high non-specific binding in brain tissues (Orita et al. 1993).

Another [^{18}F]fluoroethyl analog of TCP ([^{18}F]**5**, Fig. 19.3) has been synthesized, and biodistribution analysis in rats revealed that this tracer exhibited peak uptake (0.25% ID/g) in the brain at 10 min. However, no regional difference was observed in the brain tissues, and blocking effect of *cis*-HPTC (1.7 μmol/kg) was not observed for all the tissues investigated. Non-specific brain distribution of [^{18}F]**5** could be attributed to the hydrophobic property and low affinity for NMDARs (IC$_{50}$ = 1.5 μM vs [^{3}H]TCP) of these ligands (Shibayama et al. 1996).

Ouyang et al. have reported a fluorocyclohexyl analog of TCP ([^{18}F]**6**, Fig. 19.3) with IC$_{50}$ value of 97 nM for the PCP-binding site (vs [^{3}H]MK-801). In PET studies in the rhesus monkey, [^{18}F]**6** showed up to 0.08%ID/mL of brain uptake, but the radioactivity was cleared rapidly from all regions of the brain indicative of little or no retention of the radiotracer in the receptor-rich regions (Fig. 19.5) (Ouyang et al. 1996). Because [^{18}F]**6** has only moderate affinity and the specificity for NMDARs has not been confirmed, new radioligands with significant improvement of binding affinity and target specificity have to be developed.

Fig. 19.5 PET data on the binding of [^{18}F]**6** in a rhesus monkey brain. (Ouyang et al. 1996)
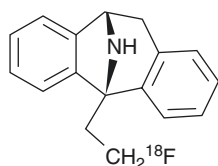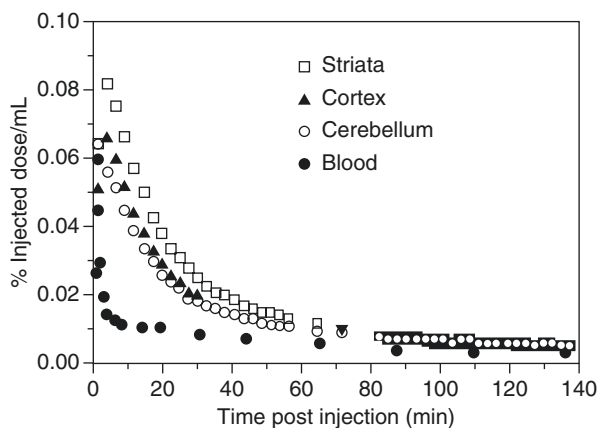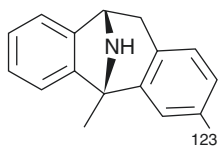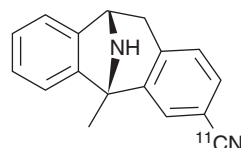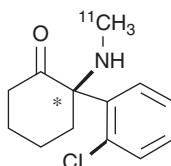
Fig. 19.6 Chemical structure of radiolabeled MK-801 derivatives and [^{11}C]ketamine

MK-801 Derivatives

The anticonvulsant MK-801 (Fig. 19.2) has been identified as a potent and selective non-competitive NMDAR antagonist (Wong et al. 1986). Because MK-801 has high binding affinity for the PCP-binding site of NMDARs (Wong et al. 1988) and easy penetrability into the brain (Clineschmidt et al. 1982), MK-801 analogs were expected to be suitable as in vivo imaging probes for NMDARs. Several MK-801 derivatives labeled with ^{11}C, ^{18}F, or ^{123}I have been synthesized and evaluated as PET or SPECT radioligands for NMDARs.

Blin et al. reported the preparation of [^{18}F]fluoromethyl analog of MK-801 ([^{18}F]FMM, Fig. 19.6) and PET studies on baboons (Blin et al. 1991). In the baseline PET studies, initial accumulation into the brain of [^{18}F]FMM was marked with peak uptake values as high as 0.03% ID/mL. However, the ratios of [^{18}F]FMM in the

cerebral cortex and striatum (NMDAR-rich regions) to the cerebellum (NMDAR-poor regions) were only minimal (maximal ratios ranging from 1.1 to 1.6 during the first 20–40 min). In addition, there was no clear reduction in the brain uptake and target to non-target ratios by pretreatment of the open channel blockers (PCP or MK-801). Because binding of [^{3}H]MK-801 to the PCP-binding site has been enhanced severalfold in the presence of high amount of glutamate (Wong et al. 1988), the authors investigated further using PET studies of [^{18}F]FMM on ischemic baboons with excessive glutamate activation. However, the brain kinetics of [^{18}F]FMM was not significantly different between the ischemic and control groups. It can be concluded that [^{18}F]FMM is an unsuitable radioligand for the PCP-binding site of NMDARs (Blin et al. 1991). Ransom et al. developed the 3-[^{123}I]iodo analog of MK-801 ([^{123}I]3-iodo-MK-801, Fig. 19.6) as a SPECT imaging agent. Over 95% of [^{123}I]3-iodo-MK-801 binding was specific in rat brain homogenates. MK-801 derivatives were shown to bind with high affinity for the [^{123}I]3-iodo-MK-801 binding site (3-iodo-MK-801, IC$_{50}$ = 3.4 nM; (+)-MK-801, IC$_{50}$ = 5.6 nM) indicating excellent binding affinity of this tracer for the PCP-binding site (Ransom et al. 1990). These positive in vitro results prompted further in vivo imaging studies. Owens et al. reported the clinical SPECT investigation of [^{123}I]3-iodo-MK-801. In normal subjects, [^{123}I]3-iodo-MK-801 showed rapid uptake into the brain, but the tracer has a high non-specific retention in the brain tissues probably due to its high lipophilicity (Owens et al. 1997). Brown et al. reported the clinical SPECT studies of [^{123}I]3-iodo-MK-801 in Alzheimer's diseases (AD) and healthy subjects. There were slight differences in the brain uptake/rCBF (regional cerebral blood flow) ratio and washout of [^{123}I]3-iodo-MK-801 between the AD patients and control groups, which suggested that the binding of this tracer in the brain was increased in AD patients. However, the authors concluded that [^{123}I]3-iodo-MK-801 did not provide accurate measurement of NMDARs since the alteration was not significant, and the brain distribution of this tracer was homogeneous in both AD and control groups (Brown et al. 1997).

Andersson et al. successfully synthesized 3-[^{11}C]cyano analog of MK-801 ([^{11}C]MKC, Fig. 19.6) with high specific activity (220–600 GBq/μmol) from 3-iodo precursor using palladium(0)-promoted [^{11}C]-cyanation (Andersson et al. 1998). Saturation assay in rat cortical membranes revealed that [^{11}C]MKC had a single high-affinity binding site with a K_d of 8.2 nM and a B_{max} of 1.6 pmol/mg protein (Sihver et al. 1998). In vitro autoradiography demonstrated that the highest specific binding in rat slices of [^{11}C]MKC was observed in the hippocampus and frontal cortex. Moderate binding was found in the caudate putamen and thalamus. Low-density binding sites were observed in the cerebellum, pons, midbrain, and brainstem (Fig. 19.7). This correlated with the distribution of [^{3}H]MK-801 (Bowery et al. 1988). The in vivo PET studies demonstrated that [^{11}C]MKC showed a rapid and high uptake in the brain tissues. In addition, the radioactivity level was higher in the frontal cortex than cerebellar cortex, but the brain distribution pattern was well correlated with the rCBF (Fig. 19.8). Neither MK801 (0.1 mg/kg) nor ketamine (2.5 mg/kg) as pretreatment dose caused a significant change in regional brain
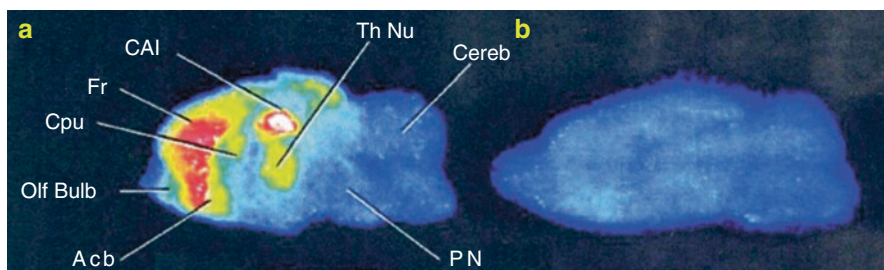
Fig. 19.7 In vitro autoradiography of [^{11}C]MKC in the rat brain slices. Total binding (A) and non-specific binding (B) are shown in sagittal planes. Non-specific binding was measured in the presence of MK-801 (1 mM). Abbreviations: *Acb* accumbens nucleus, *CA1* CA1 of hippocampus, *Cereb* cerebellum, *Cpu* caudate putamen, *Fr* frontal cortex, *Olf bulb* olfactory bulb, *PN* pontine nuclei, *Th Nu* thalamic nuclei. Sihver et al. (1998)
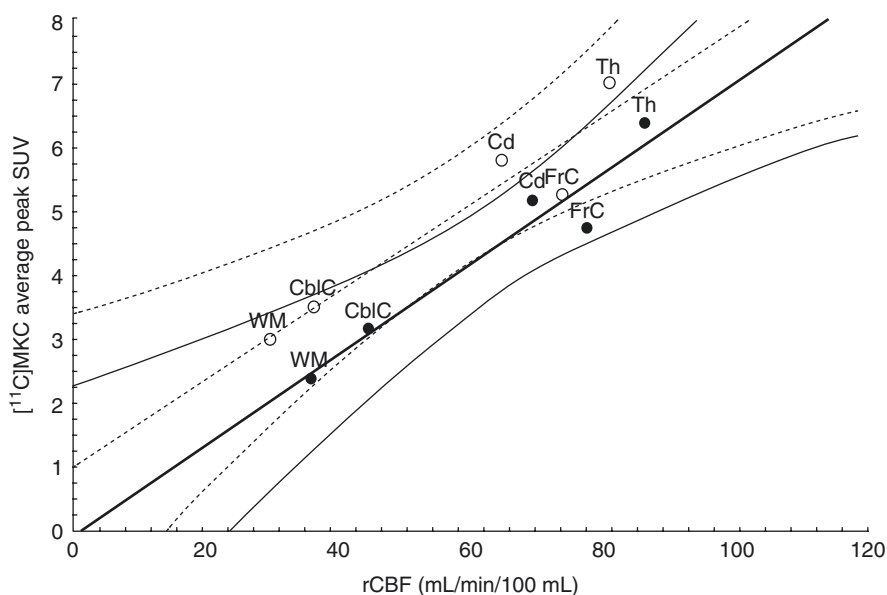
Fig. 19.8 Typical graph presenting the relation between peak [^{11}C]MKC uptake and rCBF in the same regions in the baseline measurement (open circles and dotted lines) and ketamine-pretreatment measurement (closed circles and continuous lines). Curved lines indicate 95% confidence. Abbreviations: *FrC* frontal cortex, *Cd* right caudate nucleus, *Th* thalamic nuclei, *CblC* cerebellar cortex, *TM* white matter. Sihver et al. (1998)

kinetics. These results could be caused by the very low specific binding fraction of [^{11}C]MKC under in vivo conditions (Sihver et al. 1998). Development of new radio-ligands with lower lipophilicity and higher NMDAR selectivity should be tried to reduce non-specific binding.

[^{11}C]Ketamine

Ketamine (Fig. 19.2) is known as a PCP-like anesthetic drug which has a weak binding affinity for the PCP-binding site of NMDARs (Lodge and Johnson 1990). In the displacement assay using pig brain homogenates, the K_i values of (*S*)-ketamine and (*R*)-ketamine for [^{3}H]MK-801 binding site of NMDARs were 1.2 and 5.0 μM, respectively (Oye et al. 1992). [^{11}C]-labeled (R,S)-ketamine ([^{11}C]ketamine, Fig. 19.6) and its enantiomers were synthesized, and then in vivo evaluation was performed (Hartvig et al. 1994; Shiue et al. 1997). Although [^{11}C]ketamine showed high blood-brain barrier (BBB) permeability (2.80% ID/g at 5 min after injection) in mice brain, unchanged [^{11}C]ketamine was only 50% at 5 min. PET studies in a baboon demonstrated that the influx of [^{11}C]ketamine and its enantiomers into the brain were high for the first few minutes, but radioactivity then declined rapidly and a similar uptake in the striatum and cerebellum was observed. In addition, these three tracers were also metabolized rapidly in the baboon plasma. Because [^{11}C]ketamine and its enantiomers were revealed to be metabolically unstable and had inconsistent binding with NMDAR expression, these tracers failed to act as useful radioligands for in vivo imaging of NMDARs (Shiue et al. 1997).

Memantine Derivatives

Memantine (Fig. 19.2) is a drug used in the treatment of various neurological and psychiatric disorders, including Parkinson's disease and Alzheimer's disease. Memantine has been identified as a non-competitive open channel blocker of NMDARs with good BBB permeability (Parsons et al. 1993; Lipton 2004). Therefore, several radiolabeled memantine derivatives have been developed as imaging agents for NMDARs.

In 1998, Samnick et al. reported the development of 3-[^{18}F]fluoromethyl analog of memantine ([^{18}F]MEM, Fig. 19.9) for PET imaging of ion channel site. The MEM showed a slightly weaker inhibitory activity to the current response to NMDARs ($IC_{50} = 6.0$ μM) than memantine ($IC_{50} = 2.9$ μM) and PCP ($IC_{50} = 1.0$ μM). In the biodistribution studies in mice, [^{18}F]MEM showed an excellent brain uptake (3.6% ID/g at 60 min), and the accumulation in the frontal cortex and hippocampus was higher than in the cerebellum. In addition, co-injection of MK-801 (0.10 mg/kg) led to 25–36% reduction of radioactivity in NMDAR-rich regions. PET studies
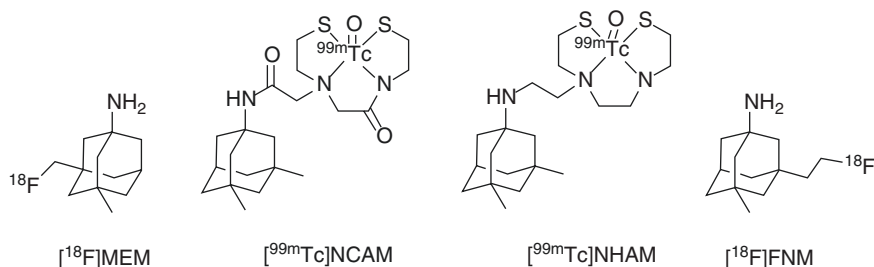
Fig. 19.9 Chemical structure of radiolabeled memantine derivatives

in a rhesus monkey revealed that [^{18}F]MEM displayed high brain uptake and low clearance of the radiotracer from the brain tissues. Pretreatment with memantine (0.50 and 1 mg/kg) yielded a reduction of uptake of up to 32% from 60 min in the examined brain regions. However, the highest uptake was observed in the cerebellum, which is an NMDAR-poor region. In addition, pretreatment with haloperidol, which is a ligand with high affinity for dopamine D2 and sigma receptors, also caused similar reduction of radioactivity in the brain (Samnick et al. 1998). In clinical PET studies, [^{18}F]MEM showed perfusion-dependent uptake in the brain rather than NMDAR expression (Ametamey et al. 2002). Because of inconsistent binding with NMDAR expression and low specificity for NMDARs, it would appear that [^{18}F]MEM is an unsuitable radioligand (Samnick et al. 1998; Ametamey et al. 2002). However, the different brain distribution pattern of [^{18}F]MEM observed among species was noteworthy. New technetium-labeled memantine derivatives such as [^{99m}Tc]NCAM and, in 2012, [^{99m}Tc]NHAM have been reported as novel SPECT imaging probes (Fig. 19.9). The [^{99m}Tc]NCAM had a single binding site with a K_d of 701 nM. Furthermore, the in vitro binding of [^{99m}Tc]NCAM was blocked by ketamine and MK-801 in a competitive manner. In the biodistribution studies in mice, [^{99m}Tc]NCAM showed 1.2% ID/g brain uptake at 5 min, and the target (frontal cortex, hippocampus) to non-target (cerebellum) ratio of radioactivity reached 2.5–3.0 at 60 min. The in vivo blocking studies were not so far reported in the literature (Zhou et al. 2012).

[^{18}F]Fluoroethylnormemantine ([^{18}F]FNM) has been developed as a moderately lipophilic PET tracer (LogD$_{7.4}$ = 1.93). Although [^{18}F]FNM showed a high BBB permeability and good in vivo metabolic stability, this tracer exhibited low affinity to NMDAR (IC$_{50}$ = 5 μM vs [^{3}H]TCP binding to rat brain slices), homogeneous in vivo brain distribution, and unclear specificity to NMDAR (Salabert et al. 2015, 2018).

19.1.1.2   Diarylguanidine Derivatives

Initially reported imaging probes, such as PCP and MK-801 analogs, suffered from high non-specific in vivo accumulation, which was probably due to the high lipophilicity and lack of selectivity for NMDARs. Diarylguanidine derivatives were discovered as NMDAR open channel blockers with high potency and selectivity. These compounds showed therapeutic effect in various v v of brain disease (Reddy et al. 1994; Hu et al. 1997). Because most diarylguanidines are more hydrophilic than PCP and MK-801, several radiolabeled diarylguanidine analogs were developed for PET or SPECT imaging of NMDARs. In the first study, [^{125}I]CNS 1261 (Fig. 19.10) was developed as a high-affinity imaging agent for NMDARs with a K_i value of 4.2 nM for the [^{3}H]MK-801 binding site with moderate lipophilicity (Log D = 2.19). Binding assays to other neurotransmitter receptors demonstrated that CNS 1261 had a weaker binding affinity for the other 41 neurotransmitter receptors. Ex vivo autoradiography studies with normal rats showed that the [^{125}I]CNS 1261 uptake in the hippocampus was 2.4–2.9-fold higher than that in the cerebellum, in which the accumulation matched the distribution of NMDARs. In the ischemic rat brain, [^{125}I]CNS 1261 uptake was considerably increased in the neocortex and striatum,
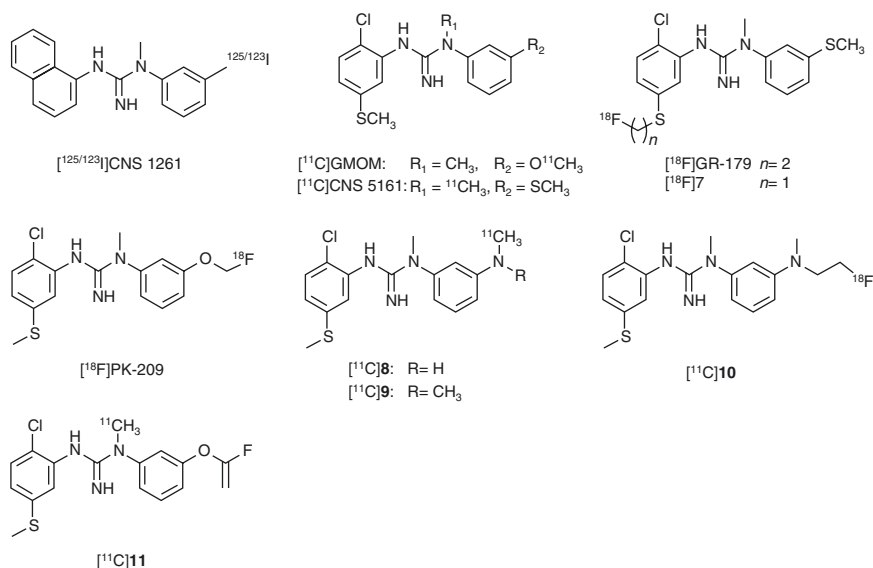
Fig. 19.10 Chemical structure of radiolabeled diarylguanidine derivatives
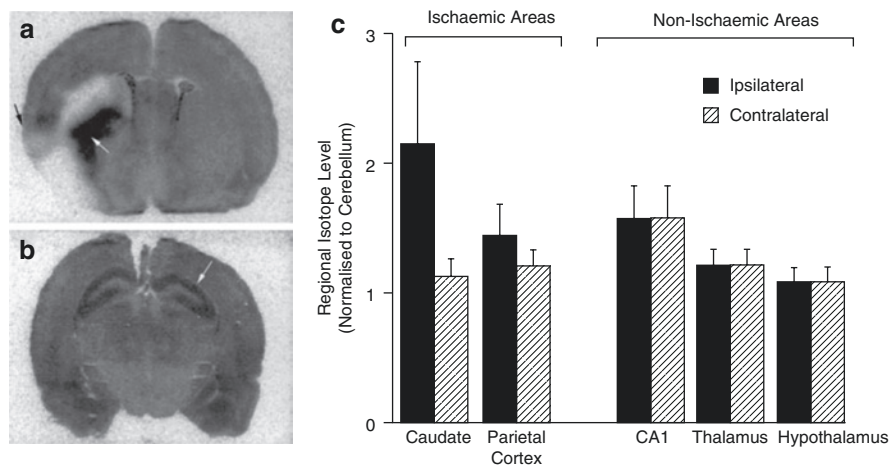
Fig. 19.11 Ex vivo autoradiography of [125I]CNS 1261 in coronal sections of rat brain at the level of (**a**) the caudate nucleus (white arrow) and circumscribed zones of the cerebral cortex (**b**) and CA1 region of the hippocampus (white arrow). The animals were injected with [125I]CNS 1261 15 min after permanent occlusion of the middle cerebral artery (left hemisphere) and sacrificed 120 min after tracer injection. (**c**) Accumulated radioactivity levels in ROIs to the cerebellum. Owens et al. (2000)

with a twofold higher uptake in the ischemic hemisphere of the caudate nucleus uptake than the same regions on the contralateral non-ischemic hemisphere (Fig. 19.11). This suggested that [125I]CNS 1261 could recognize the areas of
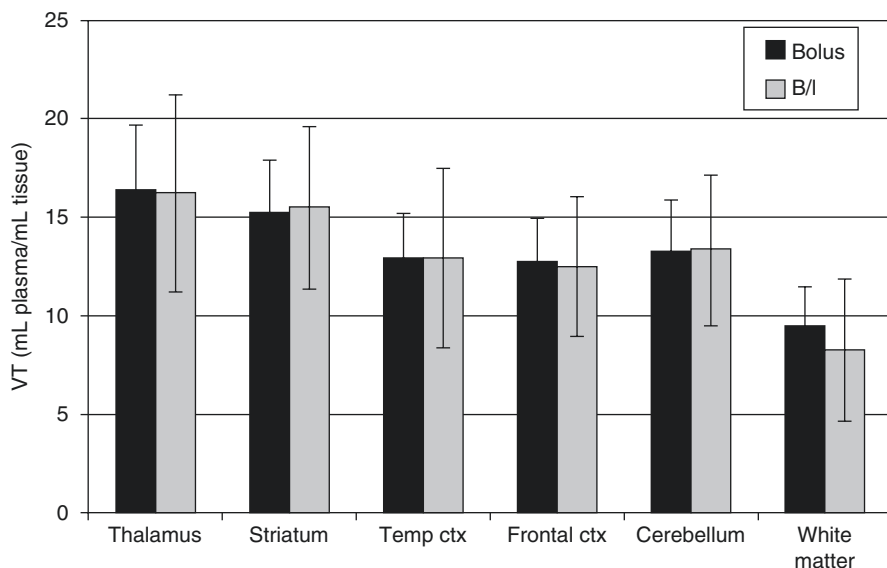
Fig. 19.12 The mean V_T values (±SD) of [^{125}I]CNS 1261 for ROIs from healthy volunteers scanned with the bolus protocol ($n = 7$) (dark bars) and with the bolus/infusion protocol ($n = 6$) (light bars). Bressan et al. (2004)

NMDAR activation (Owens et al. 2000). Based on these results, several clinical SPECT studies of [^{123}I]CNS 1261 were conducted. SPECT imaging of [^{123}I]CNS 1261 in healthy volunteers was conducted by using both bolus and bolus plus constant infusion paradigms. Total volume of distribution (V_T) values were approximately the same in the NMDAR-rich regions (striatum, hippocampus, frontal cortex) and NMDAR-poor region (cerebellum). The V_T value in the thalamus, which is a region with considerably high expression of NMDARs, was slightly higher than in other regions (Fig. 19.12) (Erlandsson et al. 2003; Bressan et al. 2004). Bolus plus infusion of ketamine in healthy volunteers caused a global reduction in V_T of [^{123}I]CNS 1261 compared with placebo in most brain regions, including the putamen, temporal, and pericallosal regions (Stone et al. 2006). Subsequent work by the same group demonstrated that the degree of reduction in the V_T values of [^{123}I]CNS 1261 correlated with the negative symptoms of schizophrenia in all brain regions examined (Stone et al. 2008). In addition, they reported that drug-free patients with schizophrenia had reduced binding of [^{123}I]CNS 1261 in the left hippocampus relative to the whole cortex compared with healthy controls (Pilowsky et al. 2006). In contrast, the same group found that the V_T values of [^{123}I]CNS 1261 did not differ between healthy normal volunteers and drug-free or typical antipsychotic-treated schizophrenia patients. On the other hand, clozapine-treated patients showed a significant reduction of V_T in all brain regions examined, which indicated a decrease of NMDAR activation in this group. However, the regional brain distribution of [^{123}I]CNS 1261 was almost homogeneous in all groups (Bressan et al. 2005). Although there was no conclusive evidence that [^{123}I]CNS 1261 could recognize

NMDAR activation, these reports suggested that protein expression levels of NMDARs could be reduced in the brain of schizophrenia patients. Numerous reports indicated the involvement of NMDAR hypofunction in the pathophysiology of positive and negative symptoms of schizophrenia (Kantrowitz and Javitt 2010; Lin et al. 2012). Recently, Knol et al. reported further in vivo studies of [^{123}I]CNS 1261 using rats. This tracer showed higher accumulation in the NMDAR-rich regions such as the hippocampus and frontal cortex than that of NMDAR-poor cerebellum, in which the ratio was maximum (about 1.4) at 2 h post-injection. Pretreatment with the NMDAR co-agonist, d-serine (10 mg/kg), led to no significant change in the hippocampus/cerebellar ratio. On the other hand, treatment with d-serine and MK-801 resulted in a significantly lower hippocampus/cerebellar ratio, which indicated the existence of specific trapping of a certain amount of [^{123}I]CNS 1261 in the NMDAR-rich regions. However, the authors concluded that the use of [^{123}I]CNS 1261 would be limited in terms of quantification and detection of small changes in receptor availability because of a considerable amount of non-specific binding of this tracer (Knol et al. 2009).

To provide potential PET radioligands for the PCP-binding site, [^{11}C]-labeled diarylguanidine derivatives have been synthesized and evaluated. [^{11}C]GMOM (Fig. 19.10) has been found to exhibit a strong binding affinity for NMDARs (K_i = 5.2 nM). In rats, brain uptake of [^{11}C]GMOM was high and peaked during the early part of the study. Regional brain distribution at 10 min was 1.23, 0.93, and 0.74% ID/g for the frontal cortex, hippocampus, and cerebellum, respectively, as regards the appearance of contrast in the NMDAR-rich and NMDAR-poor regions. Pretreatment with the open channel blockers GMOM or MK-801 (1 mg/kg) or the NB2B-selective NMDAR modulator Ro 25-6981 led to a moderate and uniform decrease of [^{11}C]GMOM uptake in brain regions. On the other hand, the NMDAR co-agonist d-serine increased [^{11}C]GMOM binding in all regions. PET imaging in baboons revealed that [^{11}C]GMOM exhibited high BBB penetration. However, the brain distribution of [^{11}C]GMOM was almost homogeneous, and pre-administration of MK801 did not reduce regional VT's or regional V_T ratios. The authors hypothesized that these inconsistent results could be caused by the blocking effect of anesthesia (ketamine and isoflurane) to NMDAR activity. Further PET investigations of [^{11}C]GMOM in other conditions, such as in a conscious state, have not been reported so far (Waterhouse et al. 2004). In clinical studies, [^{11}C]GMOM showed high brain uptake and relatively consistent localization with NMDAR expression. Treatment with ketamine led to a significant reduction in the net influx rate constant (K_i) in the gray matter. As mentioned above, [^{11}C]GMOM has been rapidly metabolized, and the brain kinetics of the metabolites should be taken into consideration. Further investigation would be required in a larger number of subjects with test-retest studies (van der Doef et al. 2016). The limitation of such clinical studies is that the available blockers are restricted because of the high toxicity of ion channel blockers with the NMDARs.

Another diarylguanidine derivative, CNS 5161 (Fig. 19.10), has been shown to exhibit high affinity for the PCP-binding site (K_i = 1.9 nM) (Hu et al. 1997; Dumont et al. 2002). Clinical trials using CNS 5161 have been evaluated in the treatment of

neuropathic pain (Walters et al. 2002; Forst et al. 2007). [³H]CNS 5161 showed a heterogeneous in vivo brain distribution in rats and a cortex/cerebellum ratio of 1.4. Pretreatment with NMDA increased the ratio in the hippocampus/cerebellum to 1.6–1.9, while MK801 diminished this increase that resulted in ratios close to 1. [³H]CNS 5161 appeared to be unstable in arterial blood, as 65% of the parent compound was metabolized to several more hydrophilic compounds even 20 min after tracer injection (Biegon et al. 2007). The [¹¹C]CNS 5161 was synthesized by [¹¹C]methylation of the desmethyl guanidine precursor with low specific activity (41 GBq/mmol) (Zhao et al. 2006). In human PET studies, [¹¹C]CNS 5161 exhibited the largest uptake in the putamen and thalamus and the lowest uptake in the cerebellum, but relatively lower radioactivity was observed in the hippocampus compared with other gray matter regions. Similar to rats, the metabolism of [¹¹C]CNS 5161 was rapid in human plasma. No blocking studies were reported in the literature (Asselin et al. 2004). Recently, clinical PET studies of [¹¹C]CNS 5161 were carried out to assess the effect of levodopa on striatal and cortical NMDAR activity in patients with Parkinson's disease with and without dyskinesias (Ahmed et al. 2011). The levodopa-treated dyskinetic patients had higher [¹¹C]CNS 5161 uptake in the caudate, putamen, and precentral gyrus compared with patients without dyskinesias. These results are consistent with reports that upregulation of NMDARs has been associated with the development of levodopa-induced dyskinesias in animal models of Parkinsonism (Oh et al. 1998). However, no significant increase in [¹¹C]CNS 5161 uptake was observed in patients with Parkinson's disease when compared with control subjects. In addition, relatively high uptake of [¹¹C]CNS 5161 in the cerebellum was observed, which was inconsistent with the brain distribution of [¹¹C]CNS 5161 in a previous clinical PET study reported by Asselin et al. (Asselin et al. 2004). Further investigations are necessary in order to prove the usefulness of these diarylguanidines as radioligands for measuring NMDAR function by PET or SPECT.

Recently, ¹⁸F-labeled *S*-fluoroalkyl diarylguanidines were synthesized and used for in vitro evaluation. Among them, [¹⁸F]GE-179 and [¹⁸F]**7** (Fig. 19.10) showed high affinity for the PCP-binding site (K_d = 2.4 nM for [¹⁸F]GE-179 and K_d = 1.4 nM for [¹⁸F]**7**). Further studies could not be performed on [¹⁸F]**7** owing to low stability of this ligand. A broad receptor binding assay for 60 receptors demonstrated that [¹⁸F]GE-179 had high selectivity for the PCP-binding site of NMDARs (Robins et al. 2010). Although this tracer showed high brain uptake, the V_T of each region was correlated to cerebral blood flow rather than the levels of NMDAR expression. However, the distribution of the radioactivity of [¹⁸F]GE-179 might be explained by subunit composition as the channel open probability of GluN2A is reported to be higher than that of the other subunits. No blocking studies using unlabeled GE-179 or other channel blockers were feasible in this clinical study (McGinnity et al. 2014). In studies by other groups, PET/CT imaging of [¹⁸F]GE-179 along with drug competition in rats demonstrated that none of the ion channel blockers (GE-179, MK801, PCP, and ketamine), allosteric inhibitor (ifenprodil), and NMDAR activator (methamphetamine) significantly altered the PET signals in the brain. PET/MR in rhesus macaques exhibited that pretreatment with GE-179 led to no meaningful

reduction in the PET signal. These results indicated that a large part of the [^{18}F]GE-179 signals seems to be non-specific (Schoenberger et al. 2018; Sander et al. 2019). However, it cannot be excluded that anesthesia reduced B_{max} of [^{18}F]GE-179 in the brain, which abolished the accessibility of this tracer to the target site (McGinnity et al. 2019). Golla et al. reported [^{18}F]PK-209 (Fig. 19.10) as a high-affinity PET tracer for the ion channel site (K_i = 18 nM vs [^{3}H]MK-801). In line with the moderate lipophilicity ($\log D_{7.4}$ = 1.45), this tracer entered the brain easily. However, over 70% of the parent compound was metabolized, and the distribution was inconsistent with the expression patterns of NMDA receptors (Golla et al. 2015). Klein et al. developed three new meta-substituted GMOM analogs, [^{11}C]**8**, [^{11}C]**9**, and [^{11}C]**10**, with favorable K_i values for the ion channel of the NMDAR (19.1, 1.35, and 4.81 nM, respectively). Although ex vivo studies of these tracers in awake rats demonstrated good brain uptake, pretreatment of animals with MK-801 increased the brain uptake. Over 38% of the radioactivity in the brain tissue represents metabolites, which may obscure specific binding of these tracers (Klein et al. 2016). In order to overcome the low metabolic stability of guanidine derivatives, Klein et al. developed the fluorovinyloxy analog [^{11}C]**11** with a high affinity for the ion channel site of NMDAR. However, pretreatment with MK-801 showed no significant inhibitory effect on [^{11}C]**11**, and only a small improvement in the metabolic stability was achieved (Klein et al. 2017).

19.1.1.3 Other Open Channel Blocker Derivatives

The 6,11-ethanobenzo[b]quinolizinium derivatives are highly hydrophilic compounds reported to exhibit high affinity and specificity to the PCP-binding site of the NMDARs (Mallamo et al. 1994). Based on the SAR studies, new fluorine-18 radioligands ([^{18}F]**12** and [^{18}F]**13**) and a carbon-11 ligand ([^{11}C]**14**) have been developed as novel PET radioligands for the PCP-binding site of NMDARs as shown in Fig. 19.13 (Sasaki et al. 1998; Ishibashi et al. 2000). These compounds showed moderate binding affinity for the PCP-binding site (**12**, IC$_{50}$ = 47 nM; **13**, IC$_{50}$ = 89 nM; **14**, IC$_{50}$ = 19 nM vs [^{3}H]TCP) (Sasaki et al. 1998). In vivo biodistribution studies demonstrated that these three radioligands showed a quite low BBB permeability (0.02–0.05% ID/g at 15 min) presumably because of their cationic property and extremely low lipophilicity (Ishibashi et al. 2000). To improve brain uptake and receptor specificity, the reduced derivative [^{11}C]**15** was developed as a prodrug for [^{11}C]**14**. In the preliminary in vivo studies, cationic [^{14}C]**15** was easily metabolized to neutral [^{14}C]**14** at 15 min after injection. However, most of [^{14}C]**14** was cleared from the brain at 45 min. Although [^{11}C]**15** showed a higher BBB penetration (0.7–0.8% ID/g at 15 min) than that of [^{14}C]**14**, no regional difference was observed between the forebrain regions and cerebellum (Sasaki et al. 2001). Although [^{11}C]**15** was not confirmed to be a useful PET ligand for NMDARs, this prodrug strategy can be applied to the development of in vivo imaging agents.

BIII277CL (Fig. 19.13), a potent anticonvulsant and neuroprotective agent, has been reported to have high affinity (K_i = 4.5 nM vs [^{3}H]MK-801) at the PCP-binding site of NMDARs (Grauert et al. 1997, 1998). Kokic et al. have developed a methyl analog of BIII277CL (**16**, Fig. 19.13) with substantial affinity for the PCP-binding
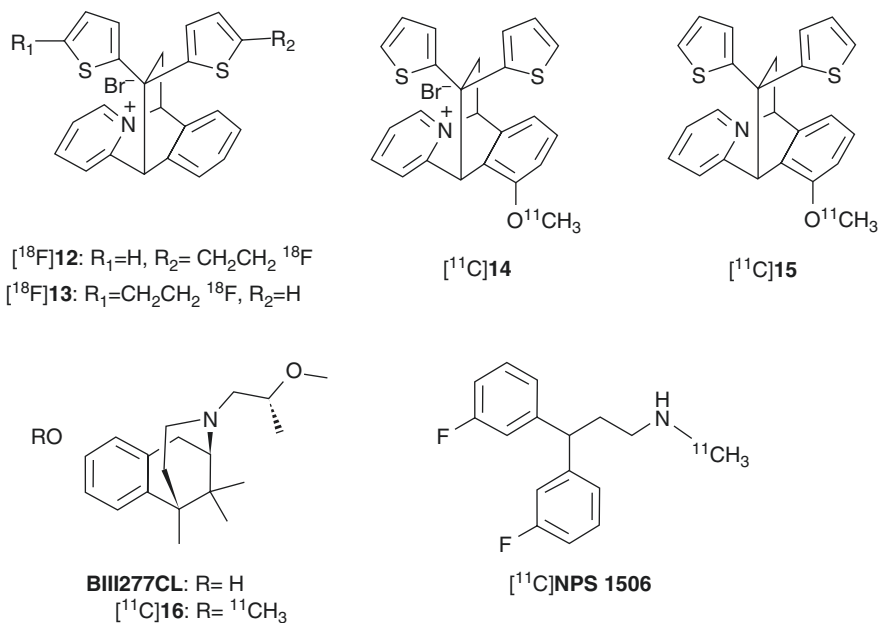
Fig. 19.13 Chemical structure of other radiolabeled open channel blocker derivatives

site ($K_i = 49$ nM vs [³H]TCP) as a candidate imaging agent for NMDARs. PET studies of [¹¹C]**16** in pigs revealed homogeneous localization in the cortex and cerebellum. The kinetic analysis using one-tissue compartment model revealed that V_T of [¹¹C]**16** was approximately 1 in both the cortex and cerebellum. These results indicated a lack of specific binding of [¹¹C]**16** for NMDARs (Kokic et al. 2002).

NPS 1506 (Fig. 19.13) has been reported as a non-competitive NMDAR antagonist with moderate affinity ($IC_{50} = 664$ nM vs [³H]MK-801). NPS 1506 is neuroprotective in a variety of animal models of stroke and head injury with no PCP-like psychotomimetic effects at doses between 1 and 5 mg/kg i.p. in rats (Mueller et al. 1999). Considering such a pharmacological profile, which is different from the previous NMDAR antagonists, NPS 1506 was labeled with carbon-11 and evaluated as a novel PET tracer for the PCP-binding site of NMDARs. Biodistribution of [¹¹C]NPS 1506 in mice and rat demonstrated that uptake into the brain was rapid and occurred at high levels. However, the regional brain distribution was fairly uniform and did not clearly reflect the known localization of NMDARs in the rodent brain. In addition, treatment with unlabeled NPS 1506 did not cause any change in uptake in the mouse brain compared with the control group. An activator of NMDARs, 3-nitropropionic acid (20 mg/kg), did not produce any change in the regional uptake in the hippocampus nor the striatum. Therefore, [¹¹C]NPS 1506 may be an unsuitable in vivo tracer for NMDARs because of its large non-specific binding fraction and low in vitro binding affinity for NMDARs (Fuchigami et al. 2003).

19.1.2 Radioligands for Glutamate-Binding Site

Most competitive antagonists for the glutamate-binding site have an acid moiety that may cause low brain uptake and have demonstrated low selectivity for NMDAR against the other glutamate receptors. Therefore, few radioligands for this site have been published in the literature. Considerable effort has been devoted to developing GluN1/2A-selective NMDA receptor ligands targeting the glutamate-binding site for treatment and imaging of GluN1/2A-related CNS disorders, including schizophrenia, mood disorder, PD, and AD (He et al. 2019). Tamborini et al. reported a radiotracer targeting the competitive glutamate site with the aim of imaging GluN1/2A-containing NMDAR. They discovered compounds **17** and **18** (Fig. 19.14) with K_i values of 250 and 48.3 nM for GluN1/2A/NMDAR, respectively. Although ex vivo autoradiography of [125I]**19** (Fig. 19.14), a prodrug of [125I]**17**, in mice was consistent with the distribution of GluN1/2A subtype receptor mRNA expression, the BBB permeability of this tracer may not be enough to visualize the target. Compound **18** with more GluN1/2A selectivity has been derivatized to prodrug [11C]**20** (Fig. 19.14); however, ex vivo studies showed still poor brain uptake of [11C]**20**, and its localization suggested binding to both GluN1/2B and GluN1/2C (Tamborini et al. 2016). Recently, Lind et al. developed ST3 {(*S*)-5-[(*R*)-2-amino-2-carboxyethyl]-1-[4-(3-fluoropropyl)phenyl]-4,5-dihydro-1H-pyrazole-3-carboxylic acid}, which has high affinity for GluN1/2A (K_i = 52 nM) (Fig. 19.14) with a 15-fold selectivity over GluN1/2B (Lind et al. 2017). It is expected that continuous efforts lead to the development of prospective selective radioligands for the glutamate site of GluN1/2A-containing NMDAR.

17: R = I
[125I]**17**: R = 125I
18: R = CH$_3$

[125I]**19**: R = 125I
[11C]**20**: R = 11CH$_3$

ST3
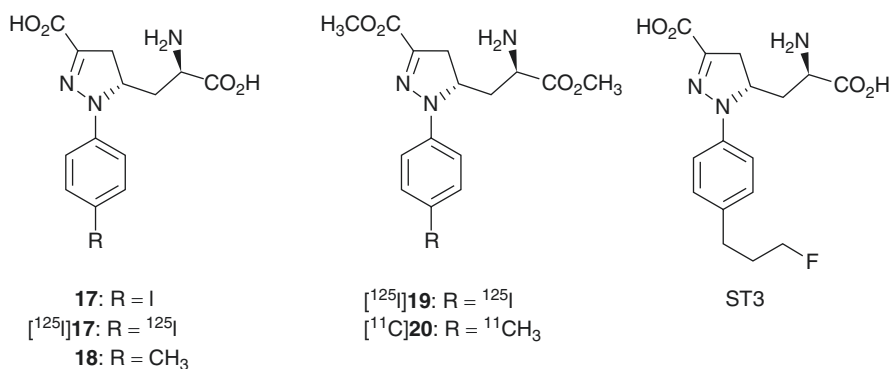
Fig. 19.14 Chemical structure of antagonists and radioligands for glutamate-binding site
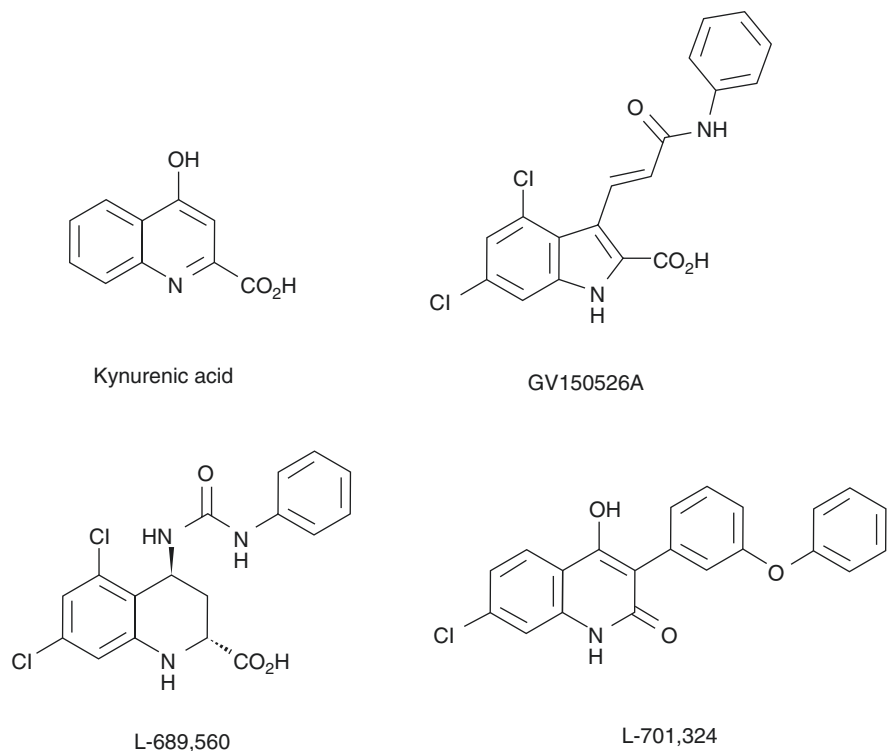
Fig. 19.15 Chemical structure of glycine-binding site antagonists

19.1.3 Radioligands for Glycine-Binding Site

Because glycine and d-serine are essential co-agonists for NMDA ion channel activation, various classes of glycine-binding site antagonists (Fig. 19.15) have been reported as anticonvulsants and neuroprotective agents (Danysz and Parsons 1998). Hypofunction of NMDARs is considered to be associated with the pathophysiology of schizophrenia. Indeed, it was reported that the enhancement of NMDAR activity via the glycine site was efficacious in the treatment of schizophrenia (Millan 2005). Imaging of the glycine site of NMDARs was considered useful for obtaining information about the functional mechanism of the glycine site in the living brain and in the diagnosis of various neurological disorders.

19.1.3.1 Radioligands Based on Cyclic Amino Acids

7-Chloro-5-iodokynurenic acid (**21**, Fig. 19.16) has been identified as a potent (IC_{50} vs [³H]glycine binding, 32 nM) and selective antagonist for the glycine site of NMDARs (Leeson et al. 1991). [¹²³I]**21** was successfully synthesized by halogen exchange reaction of a mixture of 5-bromo-7-chloro- and 7-bromo-5-chlorokynurenic acid at a specific activity of 37 GBq/μmol. In the biodistribution studies in
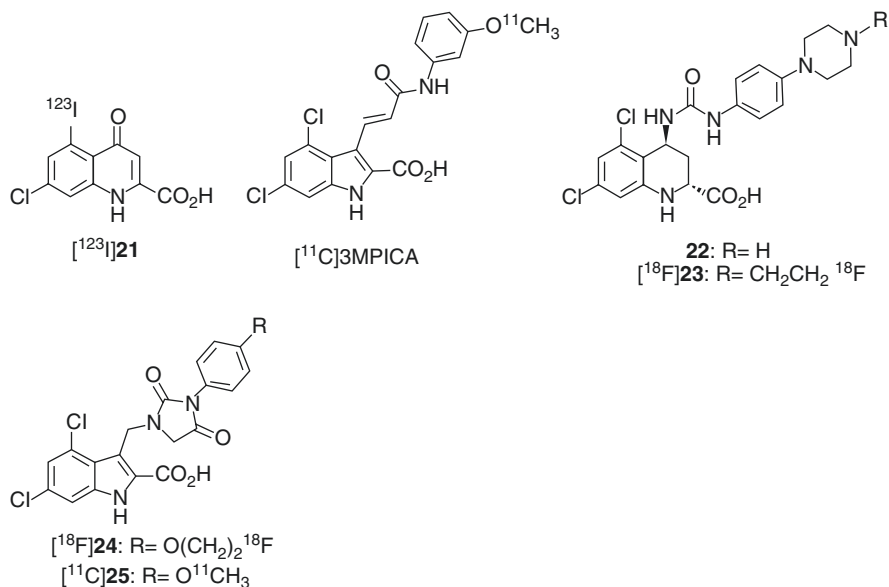
Fig. 19.16 Chemical structure of radiolabeled cyclic amino acid derivatives

mice, [^{123}I]**21** showed fast deiodination (85% of parent compound was changed to ^{123}I$^-$) and low brain uptake (0.61% ID/g at 5 min). Thus, [^{123}I]**21** had been demonstrated to be an unsuitable in vivo tracer (Dumont and Slegers 1997).

GV150526A (Fig. 19.15) is one of the most potent glycine site antagonists (K_i = 3.2 nM vs [^{3}H]glycine) with reasonable lipophilicity (log P = 2.24) (Di Fabio et al. 1997). Based on the report, Waterhouse et al. developed a meta-methoxy derivative [^{11}C]3MPICA (Fig. 19.16) with high affinity for the glycine site (K_i = 4.8 nM vs [^{3}H]MDL 105,519) (Waterhouse et al. 2002a). In the biodistribution studies in rats, regional uptake of [^{11}C]3MPICA at 2 min ranged from 0.11% ID/g to 0.18% ID/g. The radioactivity was cleared rapidly from all brain regions examined. Blocking studies using unlabeled compound (1 mg/kg) did not cause a marked reduction in the ratio of the brain tissues/blood. Treatment with warfarin (100 mg/kg) led to reduction in blood radioactivity concentrations, while brain uptake was not changed significantly, which indicated that factors other than binding to serum albumin could prevent BBB penetration of [^{11}C]3MPICA (Waterhouse et al. 2002b).

trans-5,7-Dichloro-4-substituted-2-carboxytetrahydroquinolines such as **22** (Fig. 19.16) showed high affinities (K_i = 6.0 nM vs [^{3}H]5,7-dichlorokynurenic acid) for the glycine site of NMDARs (Leeson et al. 1992). Based on the SAR studies, fluoroethyl derivative [^{18}F]**23** (Fig. 19.16) was designed, synthesized, and evaluated as a PET radioligand for glycine site. Component **23** had a relatively low lipophilicity (log$D$ = 1.3) and high affinity (K_i = 12 nM vs [^{3}H]MDL 105,519) for the glycine-binding site. Biodistribution studies revealed that [^{18}F]**23** showed homogeneous low levels of accumulation in all considered brain regions. Because regional differences

Fig. 19.17 Chemical structure of PAMQX
and radioiodinated PAMQX derivative

PAMQX: X= Br
[^{131}I]**26**: X= ^{131}I
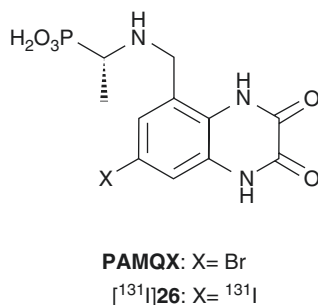
in the brain distribution of [^{18}F]**23** could not be detected, no blocking experiments were performed (Piel et al. 2003). Recently, hydantoin-substituted indole carboxylic acids were developed as novel PET ligands for the glycine-binding site with a higher lipophilicity than **23**. Compounds **24** and **25** showed moderate affinity for the glycine site (K_i = 53 nM for **24** and K_i = 31 for **25** in [^{3}H]MDL 105,519 binding assay). The logD values of **17** and **18** were 2.07 and 2.26, respectively. [^{18}F]**24** and [^{11}C]**25** were synthesized with poor overall decay-corrected radiochemical yields of 5–7% and 6–9% and specific activities of 24–67 GBq/µmol and 8–26 GBq/µmol, respectively (Bauman et al. 2011). No further in vivo evaluations of these radioligands have been reported so far.

19.1.3.2 5-Aminomethylquinoxaline-2,3-Dione Derivative

(D)-7-Bromo-*N*-(1-phosphonoethyl)-5-aminomethylquinoxaline-2,3-dione (PAMQX, Fig. 19.17) has been discovered as a selective and high-affinity glycine site antagonist with an IC$_{50}$ value of 6 nM against [^{3}H]MDL-105519 binding (Auberson et al. 1999). The 7-iodo derivative of PAMQX (**26**, Fig. 19.17) exhibited comparable affinity (IC$_{50}$ = 8 nM vs [^{3}H]MDL-105,519) for the glycine site with PAMQX (Ametamey et al. 2000). Radiosynthesis of [^{131}I]**26** was achieved by iododestannylation of *N*-CBZ-protected tributylstannyl precursor followed by deprotection of CBZ group. Biodistribution studies of [^{123}I]**26** in mice revealed an extremely low BBB permeability of [^{123}I]**26** (0.03% ID/g at 30 min) probably due to its high polarity and low log *D* value (log$D_{7.4}$ = −2.5) (Ametamey et al. 2000).

19.1.3.3 4-Hydroxyquinolone Derivatives

The radioligands consisting of carboxylic acids showed poor brain penetration due to the highly polar nature of the charged carboxylate. The 4-hydroxyquinolones (4-HQs)-devised carboxylic bioisostere had been developed as one of the most potent antagonists for the glycine-binding site of NMDARs. As expected, this series showed in vivo anticonvulsant activity, which suggested an ability to penetrate the BBB (Kulagowski et al. 1994; Rowley et al. 1997). In line with this, Haradahira et al. synthesized and evaluated [^{11}C]L-703,717 (Fig. 19.18), one of the most potent glycine site antagonists (IC$_{50}$ = 4.5 nM vs [^{3}H]L-689,560), as a PET radioligand for the glycine-binding site. In a biodistribution study in mice, [^{11}C]L-703,717 demonstrated a low BBB permeability (0.32–0.36% ID/g at 1 min) and extremely high
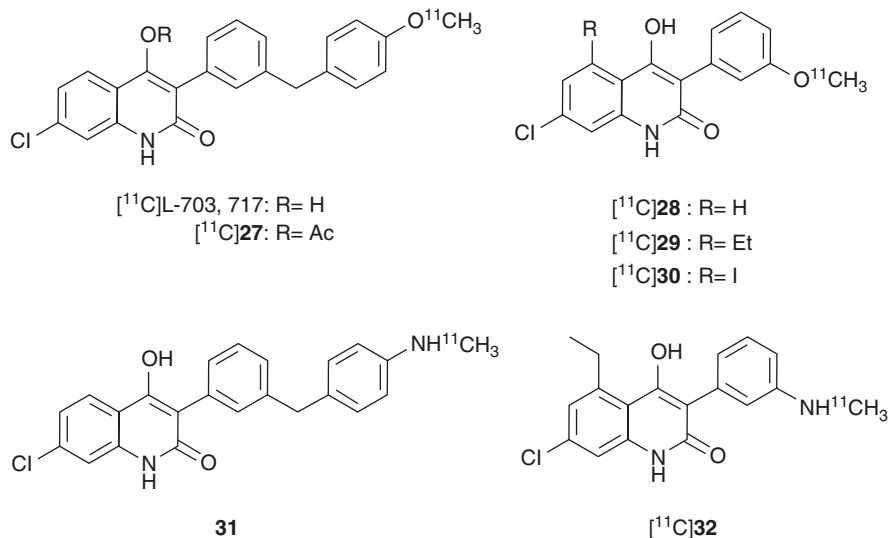
Fig. 19.18 Chemical structure of radiolabeled 4-hydroxyquinolone derivatives

blood concentration presumably due to the high affinity for the warfarin-binding site of the plasma protein. Indeed, warfarin led to a dose-dependent enhancement of the initial brain uptake of [^{11}C]L-703,717 that resulted in a fivefold increase in the brain radioactivity at the dose of 200 mg of warfarin. However, the radioactivity in the cerebrum was rapidly decreased (0.2% ID/g) with some retention observed in the cerebellum (0.65% ID/g) at 30 min after injection. This suggested inconsistent binding with known distribution of NMDARs. In addition, a significant blocking effect by non-radioactive L-703,717 (2 mg/kg) was observed only in the cerebellum (Haradahira and Suzuki 1999; Haradahira et al. 2000). To improve brain penetration of [^{11}C] L-703,717, the acetyl derivative of L-703,717 ([^{11}C]**27**, Fig. 19.18) was prepared and evaluated as prodrug of [^{11}C]L-703,717. Initial brain uptake of [^{11}C]**27** (0.71% ID/g) was twofold higher than that of [^{11}C]L-703,717 (0.36% ID/g). Metabolism experiments of [^{11}C]**27** in rat brain homogenates confirmed that about 80% of [^{11}C]**27** was converted to [^{11}C]L-703,717 at 20 min after injection. Ex vivo autoradiography demonstrated that [^{11}C]**27** exhibited similar cerebellar localization of radioactivity to [^{11}C] L-703,717 (Haradahira et al. 2001). Further in vivo evaluation revealed that the specific cerebellar binding of [^{11}C]L-703,717 was abolished in NR2C-deficient mice as shown in Fig. 19.19 (A–C). This result suggested that the in vivo cerebellar localization of [^{11}C]L-703,717 could be caused by preferential binding to the NR2C subunit-containing NMDARs predominantly expressed in the cerebellum. However, [^{11}C]L-703,717 exhibited high specific localization in the hippocampus and cerebral cortex under in vitro condition as shown in Fig. 19.19 (D–F), indicative of the absence of intrinsic selectivity for the NR2C subunit-containing NMDARs in the cerebellum (Haradahira et al. 2002b). Thus, the authors next hypothesized that endogenous NMDAR co-agonists might play a key role in
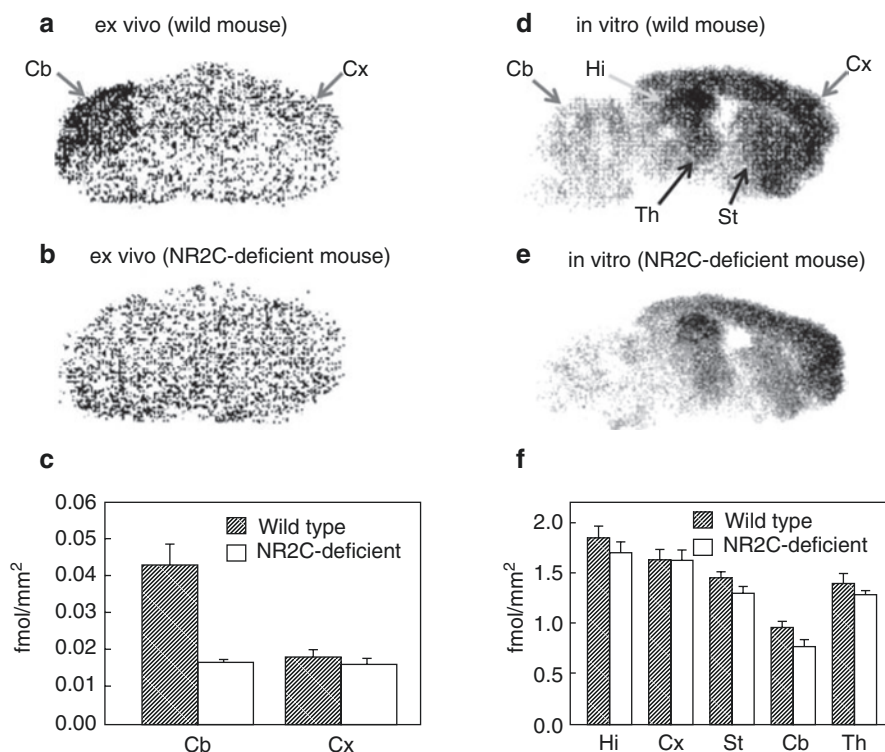
Fig. 19.19 Ex vivo and in vitro autoradiograms of [¹¹C]L-703,717 in sagittal sections of wild-type and NR2C-deficient mice brain. (**a**, **b**) Ex vivo images obtained at 20 min after injection of [¹¹C]L-703,717 and warfarin (60 mg/kg). (**c**) Quantified values of the ex vivo binding in the cerebral cortex (Cx) and cerebellum (Cb). (**d**, **e**): In vitro images of [¹¹C]L-703,717. (**f**) Quantified values of the in vitro binding in the hippocampus (Hi), cerebral cortex (Cx), striatum (St), cerebellum (Cb), and thalamus (Th). Haradahira et al. (2002b)

the unusual localization in the cerebellum of [¹¹C]L-703,717. Both glycine and d-serine are known as co-agonists of NMDARs and exist at micromolar level in the living brain. Glycine is distributed throughout the brain, while d-serine is localized only in the forebrain regions (Hashimoto et al. 1993; Schell et al. 1997). d-Serine is reported to be nearly undetectable in the cerebellum due to the highest level of d-amino acid oxidase (DAO) activity (Schell et al. 1995). Haradahira et al. demonstrated that the cerebellar localization of [¹¹C]L-703,717 was abolished in mutant ddY/DAO⁻ mice, in which the d-serine level in the cerebellum was markedly increased (Fig. 19.20). Hence, the authors proposed that the low level of [¹¹C]L-703,717 binding in forebrain regions could be explained by the strong inhibition of high amount of endogenous d-serine, whereas specific localization in the cerebellum might be due to the lack of d-serine (Haradahira et al. 2003). Considering that [¹¹C]L-703,717 has been demonstrated to recognize cerebellar NMDARs to some extent, clinical PET studies of [¹¹C]**27** (a prodrug of [¹¹C] L-703,717) were

Fig. 19.20 Ex vivo autoradiogram of [¹¹C]L-703,717 in the brain of normal ddY/DAO⁺ and mutant ddY/DAO⁻ mice. The brain slices (50 μm) were obtained at 30 min after injection of [¹¹C]L-703,717 and warfarin (60 mg/kg). Haradahira et al. (2003)
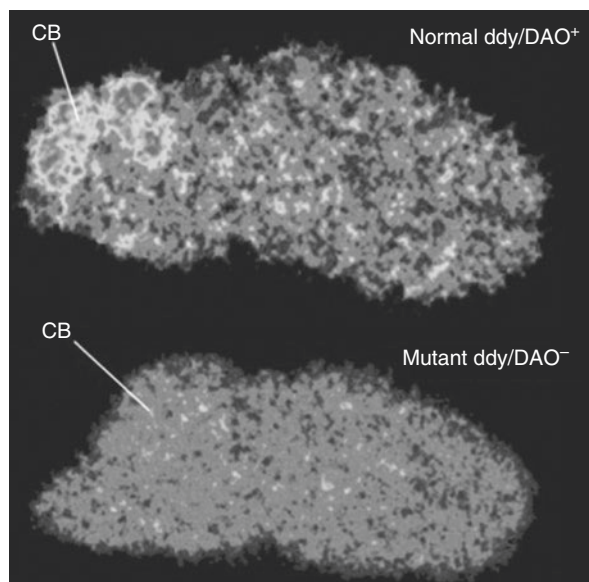
performed for the visualization of NMDARs in the cerebellum (Matsumoto et al. 2007). Binding potential (BP) calculated from white matter as a reference region in the cerebellar cortex was twofold higher than in the cerebral cortices (cerebellar cortex, BP = 2.2; cerebral cortices, BP = 1.1). Regional brain distributions were consistent with previous reports of rodents (Haradahira et al. 2001). However, the brain uptake of [¹¹C]**27** was too low for the visualization of the cerebellar NMDAs by PET (Matsumoto et al. 2007).

3-Methoxy-MDL-104,653 (**28**, Fig. 19.18) has been reported as a weak antagonist (IC$_{50}$ = 204 nM vs [³H]L-689,560) for the glycine site of NMDARs (Rowley et al. 1997). PET studies on monkeys demonstrated that [¹¹C]**28** exhibited higher localization in the cortex regions than in the cerebellum, in which binding was not blocked by glycine site agonists (Haradahira et al. 2002c). It is reported that glycine site agonists and antagonists bind to overlapping but different sites on the NMDARs (Kuryatov et al. 1994; Wafford et al. 1995). Previous studies on [¹¹C]L-703,717 suggested that most radioligands for the glycine site were susceptible to inhibition by endogenous agonists (agonist-sensitive) which resulted in strong inhibition of in vivo binding by agonists (Haradahira et al. 2002b, 2003). On the other hand, [¹¹C]**27** might be an atypical glycine site antagonist, in which the binding site overlaps with the glycine antagonist-binding site, but not with the agonist-binding site, namely, agonist-insensitive ligand. Although insufficient BBB permeability and high non-specific binding limited further investigations of [¹¹C]**28**, structural optimization of [¹¹C]**28** in order to increase BBB permeability as well as improved in vivo specificity would produce a useful agonist-insensitive radioligand for the glycine site of NMDARs, especially in the forebrain regions which play crucial roles in various brain functions. On the basis of SAR studies, we developed 5-ethyl
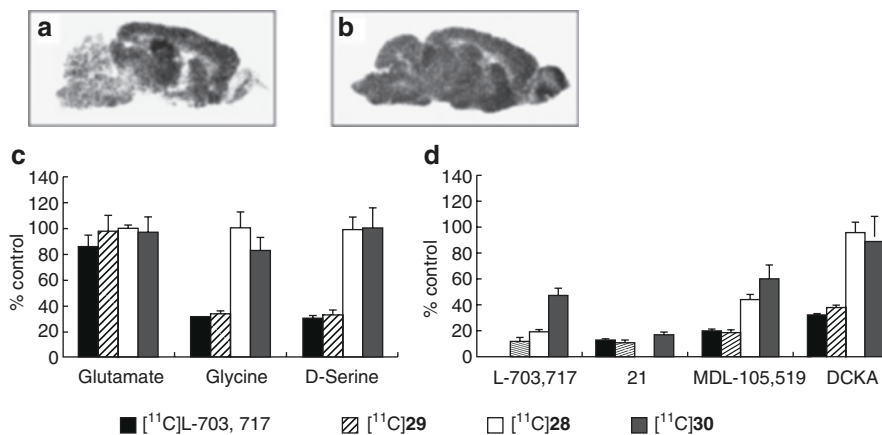
Fig. 19.21 Typical autoradiogram of in vitro binding of [¹¹C]**28** (**a**) and [¹¹C]**29** (**b**). Effect of NMDAR agonists (**c**) and antagonists (**d**) on in vitro specific [¹¹C]4-hydroxyquinolones binding to the hippocampus. Abbreviations: *DCKA* 5,7-dichlorokynurenic acid. Fuchigami et al. (2008)

(**29**) and 5-iodine (**30**) derivative of [¹¹C]**28** (Fig. 19.18) with high affinity for the glycine site (K_i = 7.2 and 10.3 nM vs [³H]MDL-105,519, respectively). In vitro autoradiography demonstrated that [¹¹C]**29** and [¹¹C]**30** displayed quite different binding properties**.** [¹¹C]**29** showed high accumulation in the forebrain regions but lowest in the cerebellum. The binding was inhibited both by glycine site antagonists and agonists as shown in Fig. 19.21 (a, c, and d) which suggested that [¹¹C]**29** is an agonist-sensitive ligand. On the other hand, [¹¹C]**30** exhibited homogeneous accumulation throughout the brain, and the binding was inhibited by glycine site antagonists but not by agonists as shown in Fig. 19.21 (b, c, and d) which suggested that [¹¹C]**30** is an agonist-insensitive ligand (Fuchigami et al. 2008). These results indicated that 4-HQs could be divided into two groups "agonist-sensitive ligands ([¹¹C]L-703,717 and [¹¹C]**29**)" and "agonist-insensitive ligands ([¹¹C]**28** and [¹¹C]**30**)." It is possible that the agonist-insensitive ligands can bind the glycine antagonist-preferring site, such as homomeric GluN1 or inactivated GluN1/GluN2 site, of the NMDARs. On the other hand, the agonist-sensitive ligand can preferentially bind to the functional and heteromeric NMDARs, which are localized in the forebrain regions rather than in the cerebellum, and therefore is sensitive to agonist binding. Unfortunately, [¹¹C]**29** and [¹¹C]**30** did not exhibit a significant increase in brain uptake compared with [¹¹C] L-703,717 and [¹¹C]**28**, although [¹¹C]**29** and [¹¹C]**30** had moderate lipophilicity (log P = 2.25 for **29** and 1.81 for **30**). Consistent with previous reports (Haradahira et al. 2002c), agonist-sensitive [¹¹C]**29** showed higher localization in the cerebellum, whereas agonist-insensitive [¹¹C]**30** showed homogeneous brain uptake. However, poor brain uptake and high non-specific binding of [¹¹C]**29** and [¹¹C]**30** limited further detailed in vivo investigations. Because warfarin increased brain uptake of [¹¹C]**29** and [¹¹C]**30**, the binding of these tracers for serum albumin should have considerable effect on in vivo brain uptake (Fuchigami et al. 2008). The 4-HQs are all acidic with pKa values of around 5 or

below (Rowley et al. 1997) and more amenable to binding with plasma proteins than non-acidic compounds, which result in poor BBB permeability. Introduction of the basic amino group into 4-HQs was expected to increase the pKa value and reduce unsuitable protein binding, which could increase brain uptake. We synthesized and evaluated several amino 4-HQ derivatives as new PET radioligand candidates for the glycine site. Among these ligands, methylamino derivatives of 4-HQs (**31** and **32**, Fig. 19.18) have been identified as high-affinity glycine site ligands (K_i values, 11.7 nM for **31** and 11.8 nM for **32**). In vitro autoradiography experiments demonstrated that both [^{11}C]**31** and [^{11}C]**32** showed higher accumulation in the forebrain regions than cerebellum, which was consistent with known NMDAR distribution. Furthermore, the in vitro binding of [^{11}C]**31** and [^{11}C]**32** was strongly inhibited by both glycine agonists and antagonists, which suggests that these tracers are agonist-sensitive glycine site ligands. Although no agonist-insensitive ligands for glycine site were obtained, further in vivo characterization of [^{11}C]**31** and [^{11}C]**32** was performed. In the biodistribution studies in mice, cerebellum to blood ratio of both [^{11}C]**31** and [^{11}C]**32** at 30 min was about 0.06 at 30 min after injection, which indicated poor BBB penetration of these radioligands. Although the plasma protein-binding ratio of [^{11}C]**32** was much lower than that of methoxy analogs (71% vs 94–98%, respectively), [^{11}C]**32** still bound with plasma protein strongly (Fuchigami et al. 2009). Further SAR studies are required for developing favorable PET ligands for the glycine site of NMDARs with improved BBB permeability.

19.1.4 Development of Radioligands for Ifenprodil-Binding Site

In the adult brain, GluN2B expression has been reported to be restricted to the forebrain areas, including the cortex, hippocampus, striatum, thalamus, and olfactory bulb (Akazawa et al. 1994; Monyer et al. 1994). Since GluN2B has been suggested to play a key role in various diseases such as ischemic stroke, Parkinson's disease, Alzheimer's disease, and neuropathic pain, a number of organic compounds that target the GluN2B have been developed for the treatment of such diseases (Gogas 2006; Mony et al. 2009). Ifenprodil was initially discovered as a GluN2B-selective negative modulator of NMDARs (K_d = 34 nM for GluN1a/2B receptors); however, it showed poor selectivity for NMDARs over other receptors such as α1-adrenergic and σ receptors (Contreras et al. 1990; Karbon et al. 1990; Williams 1993; Hashimoto and London 1995; Grimwood et al. 2000). Accordingly, several series of GluN2B antagonists with improved selectivity and affinity for GluN2B-containing NMDARs have been developed (Chazot 2004; Gogas 2006; Mony et al. 2009). These compounds are divided into two classes, the "ifenprodil derivatives" and the "non ifenprodil-related compounds" as shown in Fig. 19.22. Ifenprodil derivatives are likely to share the same site with ifenprodil on the interlobe cleft of the GluN2B subunit (Malherbe et al. 2003). However, whether non-ifenprodil-related GluN2B-selective antagonists have a similar binding mode to ifenprodil is unclear.

In vivo imaging of GluN2B-containing NMDARs is considered useful for obtaining information about various psychiatric diseases and facilitating drug

Ifenprodil derivatives

Ifenprodil

CP-101,606

RGH-896

WMS-1405 (Me-NB1)

Non ifenprodil-related compounds

Benzylamidine derivative

MK-0657

HON0001
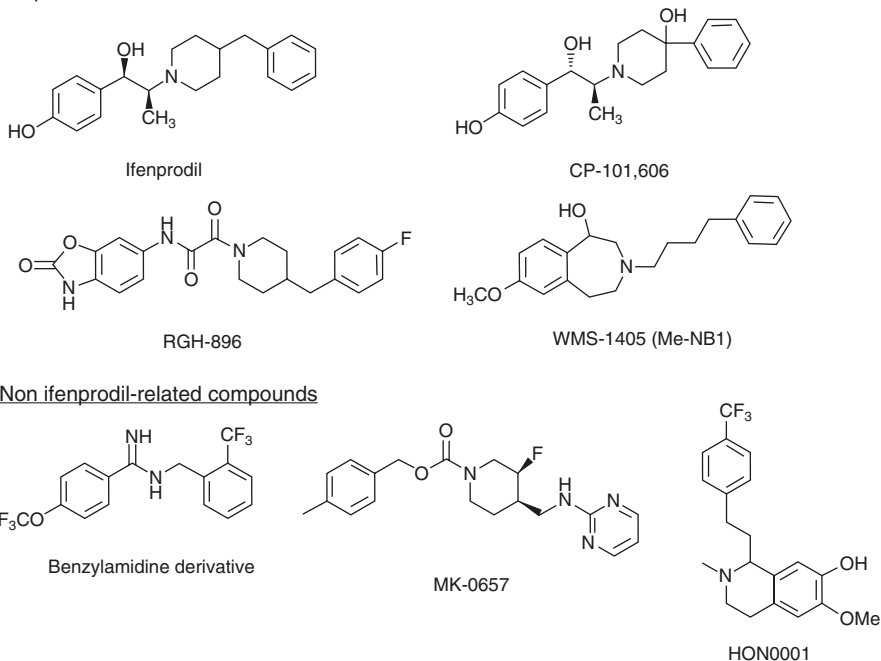
Fig. 19.22 Chemical structure of GluN2B-selective NMDAR antagonists

development, as well as in vivo occupancy. Development of PET or SPECT imaging probes for GluN2B has been conducted based on these GluN2B-selective antagonists as described below.

19.1.4.1 Ifenprodil Derivatives

It has been shown that CP-101,606 is a potent NMDAR antagonist highly selective for GluN2B-containing receptors with K_d values of 10 nM (Menniti et al. 1997). A carbon-11-labeled methoxy analog of CP-101,606 ([^{11}C]**33**, Fig. 19.23) was developed for PET imaging of the GluN2B-containing NMDARs (Haradahira et al. 2002a). In vitro autoradiography in rat brain slices revealed an extremely high localization of [^{11}C]**33** in the forebrain regions and very low in the cerebellum as shown in Fig. 19.24a. The in vitro distribution pattern of [^{11}C]**33** matched previously reported [^{3}H]CP-101,606 binding (Menniti et al. 1997) and GluN2B expression (Mori and Mishina 1995). Non-specific binding of [^{11}C]**33** was found to be less than 5% as shown in Fig. 19.24b. The binding of [^{11}C]**33** was displaced by CP-101,606 and ifenprodil in a competitive manner. Treatment of spermine and Zn^{2+} (1 mM) markedly decreased in vitro binding of [^{11}C]**33** (74–82%). It is suggested that ifenprodil and Zn^{2+} share the binding site on the interlobe cleft of GluN2B (Rachline et al. 2005). These results indicated that this tracer recognizes the ifenprodil-binding site on the GluN2B under in vitro condition. In contrast, in vivo biodistribution
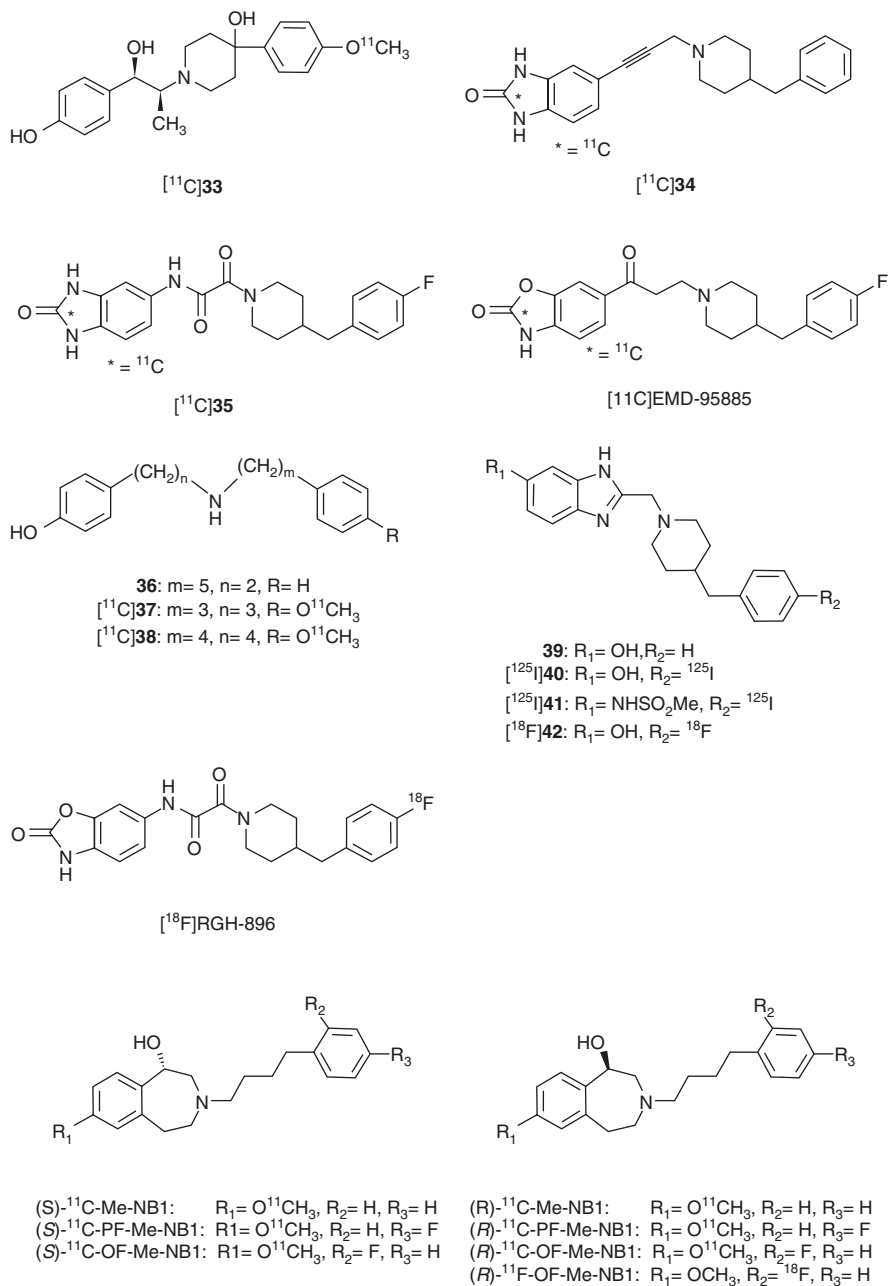
Fig. 19.23 Chemical structure of radiolabeled ifenprodil derivatives and bis(phenylalkyl)-amines
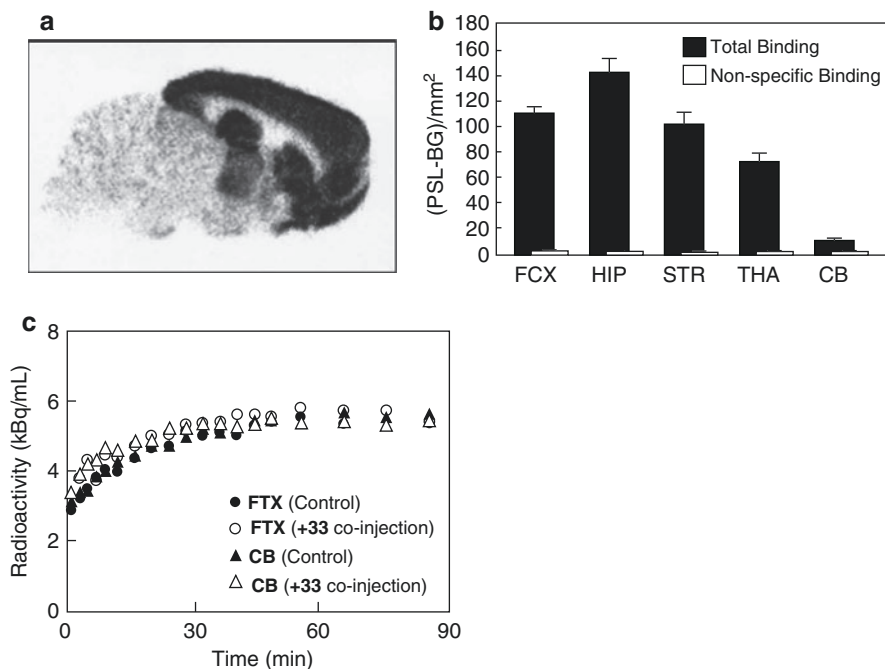
Fig. 19.24 (**a**) In vitro autoradiogram of [^{11}C]**33** in sagittal sections of rat brain. (**b**) Quantified values of the autoradiogram in the frontal cortex (FCX), hippocampus (HIP), striatum (STR), thalamus (THA), and cerebellum (CB). Non-specific binding was determined in the presence of (+)CP-101,606 (10 μM). (PSL-BG)/mm^2 means photostimulated luminescence (PSL) values per mm^2. Background PSL values (BG) were subtracted from the total PSL values on ROIs. (**c**) Time radioactivity curves in the frontal cortex (FCX) and cerebellum (CB) after i.v. injection of [^{11}]**33** into monkey. Non-radioactive **33** (2 mg/kg) was injected simultaneously with [^{11}C]**33** into the same monkey. Haradahira et al. (2002a)

studies on mice and PET studies on monkeys demonstrated that this tracer exhibited a moderate brain uptake, but no apparent specific localization of the radioactivity was observed in any of the brain regions as shown in Fig. 19.24c (Haradahira et al. 2002a).

The 1-(arylalkynyl)-4-benzylpiperidine derivative **34** (Fig. 19.23) has been discovered as highly potent (IC$_{50}$ = 5.3 nM) GluN2B-selective NMDAR antagonist (Wright et al. 2000). The in vivo brain uptake of [^{11}C]**34** in rats was fairly low (0.07% ID/g at 30 min), and localization was inconsistent with known GluN2B expression with highest uptake in the cerebellum and lowest in the striata. Pretreatment with ifenprodil (20 mg/kg, i.p.) did not cause a prominent change in brain tissues/plasma ratio of radioactivity, which suggested a high non-specific binding of [^{11}C]**34** (Roger et al. 2003). Barta-Szalai et al. developed oxamides derived from indole-2-carboxamides as potent GluN2B-selective NMDA receptor antagonists. Among them, compound **35** showed the best affinity in this series with an IC$_{50}$ of 5 nM in the [^{3}H]Ro-25,6981 binding assay (Barta-Szalai et al. 2004).

Recently, [11C]**35** was synthesized using [11C]phosgene. [11C]**35** was obtained with a radiochemical yield of 30–40% with high specific radioactivity (72–127 GBq/μmol) (Labas et al. 2010). Further in vitro and in vivo studies of [11C]**35** have not yet been published. Another 4-benzylpiperidine derivative, EMD-95885 (Fig. 19.23), has been reported to exhibit high affinity (IC_{50} = 3.9 nM) and is a selective GluN2B antagonist (Leibrock et al. 1997). [11C] EMD-95885 was prepared by a similar method as used for [11C]**34** using [11C]COCl$_2$ with a specific activity of 37–74 GBq/μmol. Radiosensitive β-microprobe acquisition and biodistribution studies in rats revealed that [11C]EMD-95885 displayed five- to ninefold higher BBB penetration than [11C]**34**. However, the distribution was almost homogeneous in all brain structures studied. Pretreatment with non-radioactive **34** or ifenprodil led to a considerable reduction in brain uptake of [11C]EMD-95885, whereas other site ligands such as MK-801, MDL-105,519, and DTG (1,3-di-*o*-tolylguanidine) had no blocking effect (Fig. 19.25), suggesting some specific binding in the brain tissues (Roger et al. 2004). It should be taken into consideration that the blocking effects of [11C]EMD-95885 binding were observed not only in GluN2B-rich regions, such as the hippocampus and frontal cortex, but also in GluN2B-poor region, such as the cerebellum. Although treatment with ifenprodil-like compounds resulted in a decrease of in vivo [11C]EMD-95885 binding, this tracer was not a promising PET radioligand for the GluN2B-containing NMDARs.

The bis(phenylalkyl)amines were reported to be selective antagonists of GluN1a/2B receptors. The most potent of this series, compound **36** (Fig. 19.23), has an IC_{50} value of 8 nM and > 1000-fold selectivity for GluN1a/2B receptors over other subunit-containing receptors (Tamiz et al. 1998). Thus, two 11C-labeled analogs of bis(phenylalkyl) amine, bis(phenylpropyl)amine ([11C]**37**) and bis(phenylbutyl)amine ([11C]**38**), were
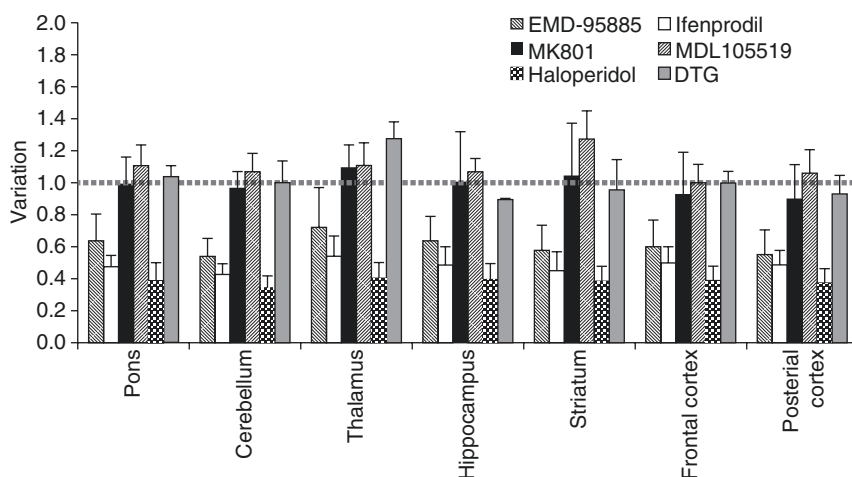
Fig. 19.25 Effect of various drugs on in vivo localization of [11C]EMD-95885 in rat brain. The y-axis labeled as "Variation" means ratio of the binding in the presence of blocker to the binding in the absence of blocker in each brain region. Roger et al. (2004)

synthesized and evaluated by Sasaki et al. These [^{11}C]-ligands were prepared by *O*-methylation on the corresponding diphenol precursors with [^{11}C]CH$_3$I with a specific activity of around 75 GBq/μmol. In the in vitro autoradiography studies, both [^{11}C]**37** and [^{11}C]**38** displayed almost homogeneous distribution throughout the brain. Treatment with non-radioactive **37** and **38** led to only 50% and 40% reduction in the in vitro binding of [^{11}C]**37** and [^{11}C]**38**, respectively. Both spermine and ifenprodil caused 30–40% reduction of these tracers, which indicated that these bis(phenylalkyl) amines shared the binding site with ifenprodil. Further in vivo studies in rodents demonstrated that [^{11}C]**37** exhibited homogeneous accumulation and non-labeled **37** increased the brain uptake. Because of the high non-specific binding both in vitro and in vivo, [^{11}C]**37** and [^{11}C]**38** are unsuitable radiotracers for GluN1a/2B receptors (Sasaki et al. 2004). A new series of benzimidazole derivatives such as compound **39** [K_i = 1.5 nM vs [^{3}H]{(*E*)-*N*^{1}-(2-methoxybenzyl) cinnamamidine (compound **43** as described below)}] was developed as highly potent GluN2B antagonists (McCauley et al. 2004). Based on the article, we developed 4′-radioiodinated benzimidazoles as SPECT imaging agents for the GluN2B. The compounds **40** and **41** showed high affinity for GluN2B with K_i values of 7.3 nM and 5.8 nM, respectively (vs [^{3}H]ifenprodil). In vitro autoradiography revealed that both [^{125}I]**40** and [^{125}I]**41** exhibited high accumulation in the forebrain regions but low in the cerebellum as shown in Fig. 19.26a. These regional distributions of the radioligands were consistent with the expression of the
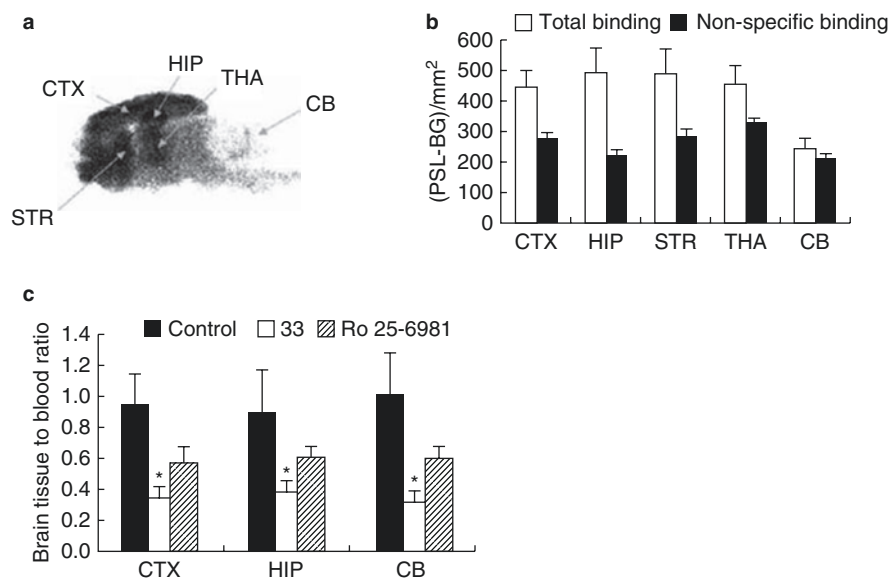
Fig. 19.26 (**a**) In vitro autoradiogram of [^{125}I]**40** in sagittal sections of rat brain. (**b**) Quantified values of the autoradiogram in the cerebral cortex (CTX), hippocampus (HIP), striatum (STR), thalamus (THA), and cerebellum (CB). Non-specific binding was determined in the presence of non-radioactive **40** (10 μM). (**c**) Effect of non-radioactive **40** and Ro 25-6981 (GluN2B antagonist) on the brain tissue to blood ratio in mice at 180 min after intravenous injection of [^{125}I]**40**. Drugs were pretreated 30 min before the tracer injection. *$P < 0.01$ in comparison to the control group. Fuchigami et al. (2010)

GluN2B. The in vitro binding of these tracers was blocked by GluN2B antagonist but not by other site ligands, which suggested the high selectivity of [^{125}I]**40** and [^{125}I]**41** for the GluN2B subunit. However the specific binding of these [^{125}I]benzimidazoles was lower than CP-101,606 analog [^{11}C]**33** as shown in Fig. 19.26b probably due to high lipophilicity of these [^{125}I]ligands. In mice, [^{125}I]**40** and [^{125}I]**41** showed moderate brain uptake at 5–180 min after administration (0.42–0.56% and 0.44–0.67% ID/g, respectively). The brain-to-blood ratio of [^{125}I]**40** led to 34% reduction in the presence of non-radioactive **40** and 59% reduction in the presence of the GluN2B ligand Ro 25-6981 as shown in Fig. 19.26c. Although these radioligands showed poor BBB permeability and inconsistent distribution with GluN2B, [^{125}I]**40** may be partially bound to the GluN2B subunit under in vivo conditions. Compound **40** may be a potential scaffold for further structural modification in order to develop potential imaging probes for the GluN2B-containing NMDARs (Fuchigami et al. 2010). More recently, high-affinity GluN2B antagonists benzimidazole derivative (**42**, Fig. 19.23) and RGH-896 (Fig. 19.23) were successfully labeled with ^{18}F by an aromatic nucleophilic radiofluorination followed by a reduction of the para-position carbonyl function (Labas et al. 2011). Despite modification of synthetic conditions, both [^{18}F]**42** and [^{18}F]RGH-896 were obtained with poor specific activities of 1.7 GBq/μmol and 1.2 GBq/μmol, respectively. In vivo brain uptakes of [^{18}F]**42** or [^{18}F]RGH-896 in rats were quite low at 120 min after injection of radiotracers (0.035% ID/g and 0.054% ID/g, respectively). High accumulation of radioactivity in the bone and further metabolic analysis of [^{18}F]fluorobenzyl piperidine fragment implicated that [^{18}F]**42** and [^{18}F]RGH-896 seemed to be rapidly defluorinated by hydroxylation in the benzyl ring followed by glucuronidation (Labas et al. 2011). It is reported that cleavage and reconstitution of a bond in the piperidine ring of ifenprodil led to 3-benzazepine derivatives as selective GluN1/GluN2B antagonists (Tewes et al. 2010; Szermerski et al. 2018). In particular, WMS-1405 showed the most potent binding affinity (K_i = 5.4 nM) for GluN1/GluN2B NMDA receptors with poor interaction with σ1 and σ2 receptors (K_i = 182 and 554 nM, respectively). In 2018, Krämer et al. labeled WMS-1405 with C-11 to yield ^{11}C-Me-NB1 as a PET tracer of GluN1/GluN2B. In vitro autoradiography demonstrated that ^{11}C-Me-NB1 showed homogeneous distribution throughout the rat brain slices. The binding was blocked by GluN2B antagonists, eliprodil (54 nM and 10 μM) and Ro-25-6981 (100 μM). However, haloperidol (10 μM), an antagonist of D_2, D_3, and D_4 receptors and an inverse agonist of σ1 receptor, reduced the binding of ^{11}C-Me-NB1. In ex vivo studies in rat, high brain SUVs were shown in the cortex with high expression of GluN2B (3.7 ± 1.0), whereas a relatively high SUV value was observed in the midbrain and cerebellum with the GluN2B-poor region (3.8 ± 1.2 and 2.8 ± 0.8, respectively). In addition, treatment with eliprodil (2 mg/kg) led to a reduction in ^{11}C-Me-NB1 binding in all the brain regions. These results indicated that ^{11}C-Me-NB1 binds not only to GluN2B but also in off-target regions (Krämer et al. 2018). Next, the same group separately synthesized the enantiopure (*R*)- and (*S*)-^{11}C-Me-NB1, respectively. Interestingly, these tracers showed quite different properties. In vitro autoradiography with rat brain slices demonstrated the heterogeneous brain distribution of (*R*)-^{11}C-Me-NB1 with high selectivity for the GluN2B-rich forebrain, whereas (*S*)-^{11}C-Me-NB1 displayed a homogeneous accumulation in all brain regions and predominantly

exhibited σ_1-receptor binding. Similar results were observed in the postmortem human brain tissues. In PET imaging with rodents, (R)-^{11}C-Me-NB1 displayed consistent accumulation in the GluN2B-expression pattern. Eliprodil led to the dose-dependent reduction in (R)-^{11}C-Me-NB1 accumulation in the GluN2B-rich regions. These results indicated that (R)-^{11}C-Me-NB1 is a promising PET tracer for imaging the GluN2B subunit of the NMDA receptor (Haider et al. 2019). Introduction of fluoride at the para position of the phenyl moiety in (R)-Me-NB1 abolished specific binding for GluN2B, whereas (R)-OF-Me-NB1 which introduced fluorine atom at the ortho position maintained binding affinity and specificity to GluN2B as demonstrated both by in vitro and in vivo studies. PET imaging studies of (R)-^{18}F-OF-Me-NB1 in rats showed consistent brain accumulation in the known GluN2B distribution with high specific binding to GluN2B as determined by blocking studies with CP101,606 (Haider et al. 2018). (R)-^{18}F-OF-Me-NB1 may be superior to (R)-^{11}C-Me-NB1 in that ^{18}F has a longer half-life than [11]C (109.8 vs 20.3 min) and can be easy to handle and evaluate because of a better pharmacokinetic profile. However, further detailed in vivo studies, including clinical studies, would be needed to confirm the feasibility of these PET tracers.

19.1.4.2 Non-ifenprodil-Related GluN2B Antagonist Derivatives

A series of 2-(3,4-dihydro-1H-isoquinolin-2yl)-pyridines have been identified as a new class of selective antagonists of GluN1/GluN2B-containing NMDARs. Among them, Ro-647312 (Fig. 19.27) displayed high affinity and selectivity for
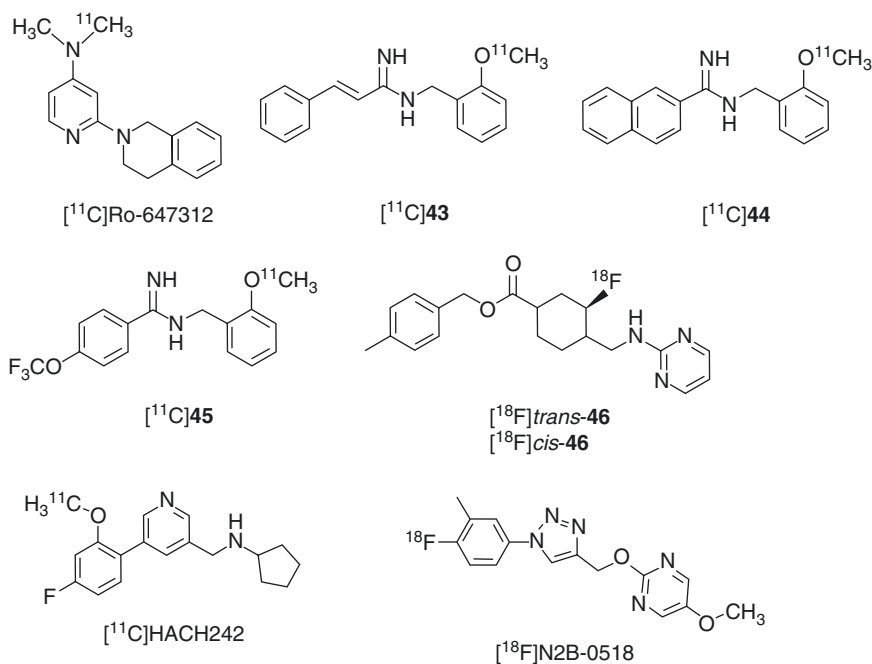
Fig. 19.27 Chemical structure of radiolabeled non-ifenprodil-related derivatives

GluN2B-containing NMDARs (K_i = 8 nM vs [³H]Ro 25-6981) (Büttelmann et al. 2003). The [¹¹C]Ro-647312 was synthesized using [¹¹C]methyl triflate from the nor-methyl compound with a specific activity of 37–129 GBq/µmol. Biodistribution studies of [¹¹C]Ro-647312 in rats demonstrated that the distribution of radioactivity was homogeneous in all brain structures and correlated poorly with known distribution of GluN2B (Dollé et al. 2004). Benzylamidines were discovered as novel series of highly potent GluN2B-selective NMDAR antagonists. From this series, (*E*)-styrene derivative (**43**, Fig. 19.27) and 2-naphthyl derivative (**44**, Fig. 19.27) displayed excellent high affinity for GluN2B with K_i value of 0.7 nM and 1.3 nM (vs [³H]ifenprodil), respectively (Claiborne et al. 2003; Curtis et al. 2003). The 4-tri-fluoromethoxyphenyl derivative (**45**, Fig. 19.27) was identified as a highly potent GluN2B antagonist with K_i value of 5.7 nM as determined by patch-clamp experiments of GluN1a/GluN2B receptors (Claiborne et al. 2003). In vitro autoradiography studies showed consistent brain localization of [¹¹C]**45** with distribution of GluN2B. In addition, the in vitro binding of [¹¹C]**45** was strongly inhibited (over 75%) by non-radioactive **45** and ifenprodil (100 µM) (Fig. 19.28), which suggested the high specific binding toward GluN2B-containing NMDARs. [¹¹C]**43** and [¹¹C]**44** showed moderate initial brain uptake (about 1.0% ID/g at 5 min), while [¹¹C]**45** exhibited higher brain uptake with 1.8% ID/g. Metabolite analysis demonstrated that only 31% and 37% of intact [¹¹C]**43** and [¹¹C]**44**, respectively, were detected in the brain, whereas 49% of authentic [¹¹C]**45** remained in the brain at 40 min. Because of metabolic instability, it can be stated that these radiotracers are unsuitable imaging agents for the GluN2B (Arstad et al. 2006). Our independent studies of [¹¹C]**43** and [¹¹C]**44** agreed with the study by Arstad et al. The percentage of unchanged radioligands was very low not only in the blood but also in the brain. These data implicated that the metabolite of the radiotracers could enter the brain tissue. Indeed, radio TLC analysis of [¹¹C]**44** in the whole brain demonstrated that the metabolite deemed as the amide derivative of [¹¹C]**44**, which could pass easily through BBB, was detected (Fuchigami et al. 2018). MK-0657 (Fig. 19.27) was reported as a highly potent GluN2B antagonist (IC_{50} = 3.6 nM). Clinical trial of MK-0657 has begun for the treatment of neuropathic pain, Parkinson's disease, and major depression (Addy et al. 2009; Mony et al. 2009). Two radiofluorinated diaste-reoisomers of MK-0657 ([¹⁸F]*trans*-**46** and [¹⁸F]*cis*-**46**) have been developed as PET radioligands for GluN2B-containing NMDARs. Both ligands displayed high affinity for GluN2B with K_d values ranging from 1.9 to 7.1 nM for [¹⁸F]*trans*-**46** and 5.9–15.2 nM for [¹⁸F]*cis*-**46**, respectively. In vitro autoradiography experiments on rat brain slices showed similar localization of [¹⁸F]*trans*-**46** and [¹⁸F]*cis*-**46** to the known distribution pattern of GluN2B as shown in Fig. 19.29a, b. The in vitro binding of these ligands was strongly inhibited by Ro 25-6981 (10 µM), which led to low non-specific binding in all brain regions as shown in Fig. 19.29c (Koudih et al. 2012). These promising in vitro results could lead to further in vivo evaluation of [¹⁸F]*trans*-**46** and [¹⁸F]*cis*-**46** in the future. Christiaans et al. reported a high-affinity PET probe *N*-((5-(4-fluoro-2-[¹¹C]methoxyphenyl)pyridin-3-yl)methyl) cyclopen-tanamine ([¹¹C]HACH242) for the GluN2B subunit (K_i = 12.4 nM vs [³H]ifenprodil assay). This probe showed consistent in vitro binding with GluN2B expression in the rat brain sections. However, [¹¹C]HACH242 revealed inconsistent ex vivo brain
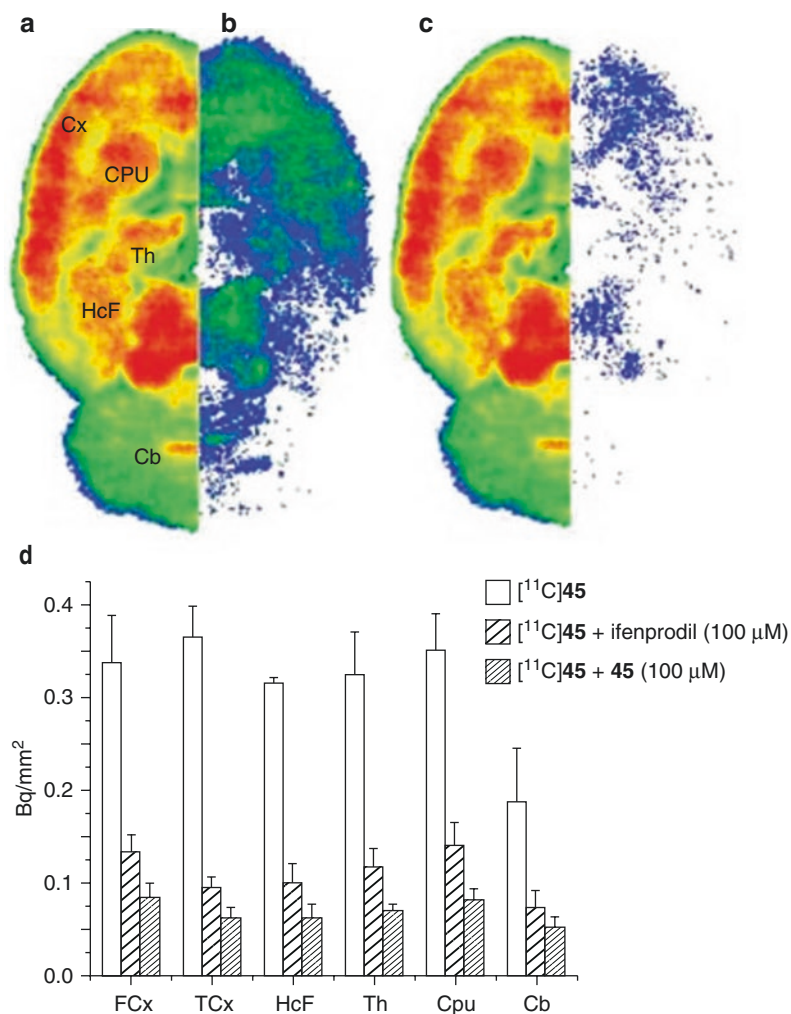
Fig. 19.28 In vitro autoradiogram of [¹¹C]**45** in sagittal sections of rat brain, under control conditions (**a**), in the presence of 100 μM ifenprodil (**b**) or non-radioactive 49 (**c**), and quantified values of the autoradiogram under the above three conditions (**d**). Abbreviations: *Cx* cortex, *FCx* frontal cortex, *TCx* temporal cortex, *Cpu* caudate putamen, *Th* thalamus, *HcF* hippocampal formation, *Cb* cerebellum. Arstad et al. (2006)

distribution with the expression level of the GluN2B subunit presumably due to non-specific binding to the σ1 receptors (Christiaans et al. 2014). PET imaging of [¹¹C]HACH242 in the primate brain demonstrated a high brain uptake but homogeneous distribution. No significant reduction in the brain [¹¹C]HACH242 SUV values was observed after intravenous infusion of radiprodil. Metabolism experiments indicated that only 26% of the parent fraction of [¹¹C]HACH242 remained till 20 min post-injection (van der Aart et al. 2019).
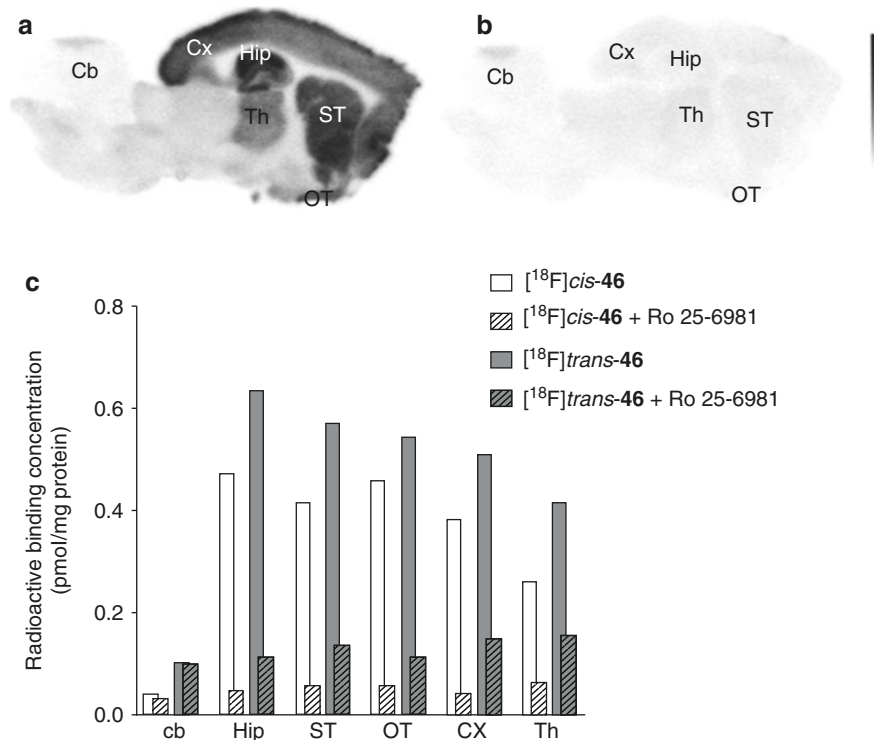
Fig. 19.29 In vitro autoradiogram of [^{18}F]*cis*-**46** in sagittal sections of rat brain, under control conditions (**a**), in the presence of 10 μM Ro 25-6981 (**b**). Radioligands concentration in brain structure after in vitro binding of [^{18}F]*cis*-**46** or [^{18}F]*trans*-**46** alone or co-incubation with Ro 25-6981 (10 μM) on rat brain sections (**c**). Abbreviations: *Cb* cerebellum, *Cx* cortex, *Hip* hippocampus, *ST* striatum, *OT* olfactory tubercle, *Th* thalamus. Koudih et al. (2012)

Recently, Fu et al. reported several ^{18}F-labeled methoxypyrimidines as PET tracers for GluN2B. The 2-((1-(4-[^{18}F]fluoro-3-methylphenyl)-1H-1,2,3-triazol-4-yl) methoxy)-5-methoxypyrimidine ([^{18}F]N2B-0518) strongly inhibited the current responses of the GluN1/GluN2B receptors with an IC$_{50}$ value of 28 nM. In vitro autoradiography demonstrated that the localization of [^{18}F]N2B-0518 was consistent with the expression of the GluN2B subunit. In vivo biodistribution study showed that [^{18}F]N2B-0518 showed moderate brain uptake (3.60% ID/g at 2 min); however, no detailed brain distribution studies have been reported (Fu et al. 2019b).

19.1.5 Conclusion and Perspectives

Despite considerable efforts, no radioligands have been confirmed as potential in vivo imaging agents for NMDARs by PET or SPECT imaging. Because NMDARs form complex systems with ligand-gated ion channels including two

agonist-binding sites, a transmembrane ion permeation pore, and various allosteric modulator binding sites, it may be difficult to apply the strategy of developing radioligands for other neurotransmitter receptors that can be successfully visualized by PET or SPECT imaging.

Initially developed radiolabeled dissociative anesthetic derivatives, which are non-competitive NMDAR open channel blockers, were shown to exhibit high non-specific in vivo accumulation probably due to high lipophilicity and/or lack of selectivity for NMDARs. Among these dissociative anesthetics, only MK-801 has been confirmed as an NMDAR specific ligand (Wong et al. 1986). Although several radiolabeled MK-801 derivatives showed in vitro brain localization consistent with NMDAR expression, these ligands exhibited high non-specific binding under in vivo conditions. It should be noted that [^{3}H]MK-801 exhibited high specific binding (78%) in vivo if the brain tissue was homogenized, filtered, and washed. In addition, the specific binding was abolished by omission of the washing procedures (Price et al. 1988). These results indicated that although [^{3}H]MK-801 has a certain in vivo specific binding component to NMDARs, the high adsorption property of this ligand on brain tissue may hamper in vivo imaging of NMDARs, probably owing to high lipophilicity of [^{3}H]MK-801. Radiolabeled MK-801 derivatives with optimized lipophilicity and binding affinity for the PCP-binding site may be potential imaging agents for NMDARs. Radiolabeled diarylguanidine derivatives were developed as more hydrophilic imaging agents for the PCP-binding site of NMDARs. In vivo studies of ischemic rats demonstrated that pathological activation of NMDARs led to an increase in [^{125}I]CNS 1261 binding (Owens et al. 2000). However, the possibility that this change was caused by change in cerebral blood flow and/or input function of these tracers could not be excluded. In vivo displacement effect of open channel blockers for [$^{123/125}$I]CNS 1261 binding in the brain tissues has not yet been confirmed. In addition, rapid in vivo metabolism of [^{125}I]CNS 1261 (half-life, 2.2 min in rat plasma) should be taken into consideration (Owens et al. 2000). Nevertheless, altered in vivo pharmacokinetics of [^{123}I]CNS 1261 in patients with schizophrenia compared with healthy controls was noteworthy (Pilowsky et al. 2006). On the other hand, there are several prospective reports regarding the development of PET tracers for the ion channel site. ^{18}F-GE-179 showed high affinity and selectivity for the ion channel site, although in vivo pharmacokinetic studies have not yet been optimized (Robins et al. 2010; McGinnity et al. 2014; Schoenberger et al. 2018). One limitation of this chemical backbone is the rapid metabolism which could not be ignored for specific PET imaging. Attempts to improve the metabolic stability, such as reports on the fluorovinyloxy analogs (Klein et al. 2017), could facilitate the development of promising PET tracers for this site. Because it is suggested that only 30% NMDARs are under open states (Jahr 1992), imaging PCP-binding site by such activity-dependent-binding radioligands would be difficult. Nonetheless, further studies on the development of new imaging probes for the PCP-binding site should be undertaken. Radioligands for this site could detect activated NMDARs in the living brain including various brain disorders. Indeed, PET signals of ^{18}F-GE-179 increased in the disease states, such as focal epilepsies (McGinnity et al. 2015) and brain ischemia (Zhou et al. 2018).

Another possibility is that the poor in vivo results of radioligands for the PCP-binding site could be caused by their restricted in vivo access to the inside of the ion channel. Compared with the PCP-binding site, glycine- and ifenprodil- binding sites were reported to be located outside of the receptor. Accordingly, these two sites have been considered as attractive targets for visualization of NMDARs by PET or SPECT imaging.

Several radioligands for the glycine-binding site showed promising in vitro results. In contrast, in vivo results revealed quite low brain uptake and unusual cerebellar localization of these tracers. The difference between in vitro and in vivo studies could be explained by the influence by endogenous glycine site agonists. The in vivo binding of [^{11}C]L-703,717 was strongly affected by endogenous d-serine concentration (Haradahira et al. 2003). On the other hand, in most of the in vitro experiments, brain slices or homogenates were well washed, which resulted in the removal of endogenous glycine and d-serine. Considering these results, we hypothesized that the agonist-insensitive radioligands with high affinity for glycine site radioligands could be useful for in vivo imaging of NMDARs. Fuchigami and Magata et al. developed high-affinity "agonist-insensitive" glycine site ligand [^{11}C]**23**, but BBB passage was too low to obtain reliable in vivo results (Fuchigami et al. 2008). Further investigations should be carried out for the development of new imaging probes with high BBB penetration to allow for the binding mechanism of glycine antagonists to be identified.

Radioligands for the ifenprodil-binding site showed consistent localization with the expression of GluN2B and high specificity to GluN2B-rich region only under in vitro condition but not in vivo. It is suggested that ifenprodil could exhibit higher affinity for the agonist-bound activated or desensitized state of NMDARs relative to the agonist-unbound state (Kew et al. 1996). It is demonstrated that neuroprotective effects of GluN2B antagonists were much more potent at pH = 6.5 than at pH = 7.5 (Mott et al. 1998). In the ischemic tissue with NMDAR activated state, pH value was reported to be around 6.5 (Silver and Erecińska 1992). Therefore, it is possible that the radioligands for the ifenprodil-binding site could recognize only agonist-bound and/or activated NMDAR like PCP-binding site ligands. Nonetheless, new radioligands with optimized lipophilicity, metabolic stability, and binding affinity could show different pharmacokinetics from reported radioligands. Continuous efforts should be undertaken in order to develop promising in vivo imaging agents for the ifenprodil-binding site. Although benzimidazole derivative [^{125}I]**33** showed inconsistent in vivo localization with GluN2B expression, this tracer could exhibit partial specific binding for GluN2B (Fuchigami et al. 2010). Further SAR studies of benzimidazoles could provide promising radioligands for the ifenprodil-binding site of NMDARs. Radiolabeled benzylamidines showed excellent high specific binding for the GluN2B under in vitro conditions (Arstad et al. 2006). Optimized benzylamidine derivatives with high metabolic stability and moderate lipophilicity could be attractive imaging probe candidates for the ifenprodil-binding site of NMDARs. Recently, new series of antagonists for the ifenprodil-binding site, such as MK-0657 and HON0001, were reported (Suetake-Koga et al. 2006; Addy et al. 2009). Indeed, [^{18}F]-labeled MK-0657 derivatives showed promising in vitro results

(Koudih et al. 2012). More recently, there are several innovative reports on the development of PET tracers for imaging of GluN2B. Two enantiopure 3-benzazepine derivatives, (R)-^{11}C-Me-NB1 and (R)-^{18}F-OF-Me-NB1, were demonstrated to be promising radioligands for the specific imaging of GluN2B receptors as confirmed both by in vitro and in vivo studies (Haider et al. 2019). Further investigations are needed to confirm the feasibility of these compounds as clinically useful PET tracers.

In general, higher B_{max}/K_d of radioligands could give higher target-to-non-target (T/N) binding ratios. Eckelman et al. suggested that PET tracers should have B_{max}/K_d ratio greater than 10 to provide a useful specific in vivo signal (Eckelman et al. 1979, 2006). B_{max} values of the PCP-binding site in the dentate gyrus of the rat brain and CA1 stratum radiatum of the human brain using [^{3}H]MK-801 were demonstrated to be 173 fmol/mg and 141 fmol/mg protein, respectively (Bowery et al. 1988). Accordingly, K_d values below 1.73 and 1.41 nM may be required for PCP-binding site ligands in the rat and human brain, respectively, to obtain a B_{max}/K_d ratio over 10. The B_{max} value of the glycine-binding site in rat brain membranes using [^{3}H]MDL 105,519 was calculated to be 12.1 pmol/mg protein (Baron et al. 1996). Therefore, a K_d below 121 nM may be required for glycine-binding site ligands in the rat brain to obtain a B_{max}/K_d ratio over 10. The B_{max} value of the ifenprodil-binding site in rat brain membranes using [^{3}H]Ro 25-6981 was estimated to be 1.6 pmol/mg protein (Mutel et al. 1998). Thus, a K_d below 16 nM may be required for glycine-binding site ligands in the rat brain to obtain a B_{max}/K_d ratio over 10. Although several radioligands for NMDARs meet the above conditions, numerous factors decrease the reliability of in vivo images such as the low plasma-free fraction of radioligands and PgP efflux. It has been suggested that radiotracers with low molecular weight (MW) (<500 Da) and moderate lipophilicity (logD$_{7.4}$ values; 2.0–3.5) could have optimal BBB permeability (Waterhouse 2003; Pike 2009). Recently, a central nervous system PET multiparameter optimization (CNS PET MPO) algorithm has been developed for the prediction of the required physicochemical properties of the clinically useful CNS PET agents (Wager et al. 2010; Zhang et al. 2013). The researchers have used a set of six parameters, including ClogP (calculated logP), ClogD (calculated distribution coefficient at pH = 7.4), MW, TPSA (topological polar surface area), HBD (number of hydrogen bond donors), and pKa (ionization constant of the most basic center) as important factors for CNS PET agents. In their algorithm, desirable ranges were set as ClogP ≤2.8, ClogD ≤1.7, MW ≤ 305.3, 44.8 < TPSA ≤63.3, HBD ≤ 1, and pKa ≤ 7.2. The scores of each parameter can be calculated ranging from 0.0 to 1.0. The most successful CNS PET tracers in the previous database had CNS PET MPO scores of >3 (Zhang et al. 2013). Therefore, it would be desirable that the newly developed radioligands fulfill such conditions. Furthermore, exhaustive binding assays of these ligands for various receptors and transporters expressed in the brain should be carried out to screen NMDAR-specific radioligands.

Another interpretation is that the discrepancy between the in vitro and in vivo brain localization of radioligands for NMDARs could be caused by dynamic plasticity of NMDARs. It has been suggested that considerable structural change of

NMDARs occurs following binding of both endogenous agonists and exogenous ligands (Traynelis et al. 2010). It is reported that the number of NMDARs on the cell surface is frequently changed by tyrosine phosphorylation and/or cysteine palmitoylation of C-terminus of NMDARs with an alteration in subunit composition (Vallano et al. 1996; Roche et al. 2001; Hayashi et al. 2009). Further investigations such as in vivo imaging studies of genetically modified or drug-treated animals with various conditions of NMDARs would be needed to clarify the discrepancy between the in vitro and in vivo experiments. In addition, novel screening systems other than traditional in vitro assays should be used. Using living brain slices as a screening method (Matsumura et al. 1995) may lead to the development of promising radioligands for NMDARs.

References

van der Aart J, Yaqub M, Kooijman EJM et al (2019) Evaluation of the novel PET tracer [11C]HACH242 for imaging the GluN2B NMDA receptor in non-human primates. Mol Imaging Biol 21:676–685

Addy C, Assaid C, Hreniuk D et al (2009) Single-dose administration of MK-0657, an NR2B-selective NMDA antagonist, does not result in clinically meaningful improvement in motor function in patients with moderate Parkinson's disease. J Clin Pharmacol 49:856–864

Ahmed I, Bose SK, Pavese N et al (2011) Glutamate NMDA receptor dysregulation in Parkinson's disease with dyskinesias. Brain 134:979–986

Akazawa C, Shigemoto R, Bessho Y et al (1994) Differential expression of five N-methyl-d-aspartate receptor subunit mRNAs in the cerebellum of developing and adult rats. J Comp Neurol 347:150–160

Ametamey SM, Kokic M, Carrey-Rémy N et al (2000) Synthesis, radiolabelling and biological characterization of (D)-7-iodo- N-(1-phosphonoethyl)-5- aminomethylquinoxaline-2,3-dione, a glycine-binding site antagonist of NMDA receptors. Bioorg Med Chem Lett 10:75–78

Ametamey SM, Bruehlmeier M, Kneifel S et al (2002) PET studies of 18F-memantine in healthy volunteers. Nucl Med Biol 29:227–231

Andersson Y, Tyrefors N, Sihver S et al (1998) Synthesis of a 11C-labelled derivative of the N-methyl-d-aspartate receptor antagonist MK-801. J Label Compd Radiopharm 41:567–576

Anis NA, Berry SC, Burton NR, Lodge D (1983) The dissociative anaesthetics, ketamine and phencyclidine, selectively reduce excitation of central mammalian neurones by N-methyl-aspartate. Br J Pharmacol 79:565–575

Arstad E, Platzer S, Berthele A et al (2006) Towards NR2B receptor selective imaging agents for PET-synthesis and evaluation of N-[11C]-(2-methoxy)benzyl (E)-styrene-, 2-naphthyl- and 4-trifluoromethoxyphenylamidine. Bioorg Med Chem 14:6307–6313

Asselin MC, Hammer A, Turton D et al (2004) Initial kinetic analysis of the in vivo binding of the putative NMDA receptor ligand [11C]CNS 5161 in humans. NeuroImage 22:T137

Auberson YP, Acklin P, Bischoff S et al (1999) N-phosphonoalkyl-5- aminomethylquinoxaline-2,3-diones: in vivo active AMPA and NMDA(glycine) antagonists. Bioorg Med Chem Lett 9:249–254

Baron BM, Siegel BW, Harrison BL et al (1996) [3H]MDL 105,519, a high-affinity radioligand for the N-methyl-d-aspartate receptor-associated glycine recognition site. J Pharmacol Exp Ther 279:62–68

Barta-Szalai G, Borza I, Bozó E et al (2004) Oxamides as novel NR2B selective NMDA receptor antagonists. Bioorg Med Chem Lett 14:3953–3956

Bauman A, Piel M, Höhnemann S et al (2011) Synthesis, labelling and evaluation of hydantoin-substituted indole carboxylic acids as potential ligands for positron emission tomography

imaging of the glycine binding site of the N-methyl-d-aspartate receptor. J Label Compd Radiopharm 54:645–656

Biegon A, Gibbs A, Alvarado M et al (2007) In vitro and in vivo characterization of [³H]CNS-5161-a use-dependent ligand for the *N*-methyl-d-aspartate receptor in rat brain. Synapse 61:577–586

Blin J, Denis A, Yamaguchi T et al (1991) PET studies of [¹⁸F]methyl-MK-801, a potential NMDA receptor complex radioligand. Neurosci Lett 121:183–186

Bowery NG, Wong EH, Hudson AL (1988) Quantitative autoradiography of [³H]-MK-801 binding sites in mammalian brain. Br J Pharmacol 93:944–954

Bressan RA, Erlandsson K, Mulliganb RS et al (2004) A bolus/infusion paradigm for the novel NMDA receptor SPET tracer [¹²³I]CNS 1261. Nucl Med Biol 31:155–164

Bressan RA, Erlandsson K, Stone JM et al (2005) Impact of schizophrenia and chronic antipsychotic treatment on [¹²³I]CNS-1261 binding to *N*-methyl-d-aspartate receptors in vivo. Biol Psychiatry 58:41–46

Brown DR, Wyper DJ, Owens J et al (1997) ¹²³Iodo-MK-801: a SPECT agent for imaging the pattern and extent of glutamate (NMDA) receptor activation in Alzheimer's disease. J Psychiatr Res 31:605–619

Büttelmann B, Alanine A, Bourson A et al (2003) 2-(3,4-Dihydro-1H-isoquinolin-2yl)-pyridines as a novel class of NR1/2B subtype selective NMDA receptor antagonists. Bioorg Med Chem Lett 13:829–832

Calon F, Rajput AH, Hornykiewicz O et al (2003) Levodopa-induced motor complications are associated with alterations of glutamate receptors in Parkinson's disease. Neurobiol Dis 14:404–416

Chaudieu I, Vignon J, Chicheportiche M et al (1989) Role of the aromatic group in the inhibition of phencyclidine binding and dopamine uptake by PCP analogs. Pharmacol Biochem Behav 32:699–705

Chazot PL (2004) The NMDA receptor NR2B subunit: a valid therapeutic target for multiple CNS pathologies. Curr Med Chem 11:389–396

Christiaans JA, Klein PJ, Metaxas A et al (2014) Synthesis and preclinical evaluation of carbon-11 labelled *N*-((5-(4-fluoro-2-[¹¹C]methoxyphenyl)pyridin-3-yl)methyl)cyclopentanamine as a PET tracer for NR2B subunit-containing NMDA receptors. Nucl Med Biol 41:670–680

Claiborne CF, McCauley JA, Libby BE et al (2003) Orally efficacious NR2B-selective NMDA receptor antagonists. Bioorg Med Chem Lett 13:697–700

Clineschmidt BV, Martin GE, Bunting PR (1982) Anticonvulsant activity of (+)-5-methyl-10, 11-dihydro-5H-dibenzo[a, d]cyclohepten-5, 10-imine (MK-801), a substance with potent anticonvulsant, central sympathomimetic, and apparent anxiolytic properties. Drug Dev Res 2:123–134

Contreras PC, Bremer ME, Gray NM (1990) Ifenprodil and SL 82.0715 potently inhibit binding of [³H](+)-3-PPP to sigma binding sites in rat brain. Neurosci Lett 116:190–193

Curtis NR, Diggle HJ, Kulagowski JJ et al (2003) Novel *N*¹-(benzyl)cinnamamidine derived NR2B subtype-selective NMDA receptor antagonists. Bioorg Med Chem Lett 13:693–696

Danysz W, Parsons CG (1998) Glycine and *N*-methyl-d-aspartate receptors: physiological significance and possible therapeutic applications. Pharmacol Rev 50:597–664

Di Fabio R, Capelli AM, Conti N et al (1997) Substituted indole-2-carboxylates as in vivo potent antagonists acting as the strychnine-insensitive glycine binding site. J Med Chem 40:841–850

Dingledine R, Borges K, Bowie D, Traynelis SF (1999) The glutamate receptor ion channels. Pharmacol Rev 51:7–61

van der Doef TF, Golla SSV, Klein PJ et al (2016) Quantification of the novel N-methyl-d-aspartate receptor ligand [¹¹C]GMOM in man. J Cereb Blood Flow Metab 36:1111–1121

Dollé F, Valette H, Demphel S et al (2004) Radiosynthesis and in vivo evaluation of [¹¹C]Ro-647312: a novel NR1/2B subtype selective NMDA receptor radioligand. J Label Compd Radiopharm 47:911–920

Dumont F, Slegers G (1997) Synthesis and in vivo evaluation of 7-chloro-5-[¹²³I]iodo-4-oxo-1,4-dihydroquinoline-2-carboxylic acid. Appl Radiat Isot 48:1173–1177

Dumont F, Sultana A, Waterhouse RN (2002) Synthesis and in vitro evaluation of *N*,*N*′-diphenyl and *N*-naphthyl-*N*'-phenylguanidines as *N*-methyl-d-aspartate receptor ion-channel ligands. Bioorg Med Chem Lett 12:1583–1586

Eckelman WC, Gibson RE, Rzeszotarski WJ et al (1979) The design of receptor binding radiotracers. Principles of Radiopharmacology. CRC Press, New York, pp 251–274

Eckelman WC, Kilbourn MR, Mathis CA (2006) Discussion of targeting proteins in vivo: in vitro guidelines. Nucl Med Biol 33:449–451

Erlandsson K, Bressan RA, Mulligan RS et al (2003) Kinetic modelling of [^{123}I]CNS 1261—a potential SPET tracer for the NMDA receptor. Nucl Med Biol 30:441–454

Forst T, Smith T, Schütte K et al (2007) Dose escalating safety study of CNS 5161 HCl, a new neuronal glutamate receptor antagonist (NMDA) for the treatment of neuropathic pain. Br J Clin Pharmacol 64:75–82

Foster AC, Wong EH (1987) The novel anticonvulsant MK-801 binds to the activated state of the *N*-methyl-d-aspartate receptor in rat brain. Br J Pharmacol 91:403–409

Fu H, Chen Z, Josephson L et al (2019a) Positron emission tomography (PET) ligand development for ionotropic glutamate receptors: challenges and opportunities for radiotracer targeting N-methyl-d-aspartate (NMDA), α-amino-3-hydroxy-5-methyl-4-isoxazolepropionic acid (AMPA), and kainate receptors. J Med Chem 62:403–419

Fu H, Tang W, Chen Z et al (2019b) Synthesis and preliminary evaluations of a triazole-cored antagonist as a PET imaging probe ([^{18}F]N2B-0518) for GluN2B subunit in the brain. ACS Chem Neurosci 10:2263–2275

Fuchigami T, Haradahira T, Arai T et al (2003) Synthesis and brain regional distribution of [^{11}C]NPS 1506 in mice and rat: an N-methyl-d-aspartate (NMDA) receptor antagonist. Biol Pharm Bull 26:1570–1573

Fuchigami T, Haradahira T, Fujimoto N et al (2008) Difference in brain distributions of carbon 11-labeled 4-hydroxy-2(1H)-quinolones as PET radioligands for the glycine-binding site of the NMDA ion channel. Nucl Med Biol 35:203–212

Fuchigami T, Haradahira T, Fujimoto N et al (2009) Development of N-[^{11}C] methylamino 4-hydroxy-2(1H)-quinolone derivatives as PET radioligands for the glycine-binding site of NMDA receptors. Bioorg Med Chem 17:5665–5675

Fuchigami T, Yamaguchi H, Ogawa M et al (2010) Synthesis and biological evaluation of radio-iodinated benzimidazoles as SPECT imaging agents for NR2B subtype of NMDA receptor. Bioorg Med Chem 18:7497–7506

Fuchigami T, Nakayama M, Yoshida S (2015) Development of PET and SPECT probes for glutamate receptors. ScientificWorldJournal 2015:716514

Fuchigami T, Fujimoto N, Haradahira T et al (2018) Synthesis and characterization of 11 C-labeled benzyl amidine derivatives as PET radioligands for GluN2B subunit of the NMDA receptors. J Label Comp Radiopharm 61:1095–1105

Furukawa H, Gouaux E (2003) Mechanisms of activation, inhibition and specificity: crystal structures of the NMDA receptor NR1 ligand-binding core. EMBO J 22:2873–2885

Furukawa H, Singh SK, Mancusso R, Gouaux E (2005) Subunit arrangement and function in NMDA receptors. Nature 438:185–192

Gogas KR (2006) Glutamate-based therapeutic approaches: NR2B receptor antagonists. Curr Opin Pharmacol 6:68–74

Golla SS, Klein PJ, Bakker J (2015) Preclinical evaluation of [^{18}F]PK-209, a new PET ligand for imaging the ion-channel site of NMDA receptors. Nucl Med Biol 42:205–212

Grauert M, Bechtel WD, Ensinger HA et al (1997) Synthesis and structure–activity relationships of 6,7-benzomorphan derivatives as antagonists of the NMDA receptor-channel complex. J Med Chem 40:2922–2930

Grauert M, Rho JM, Subramaniam S, Rogawski MA (1998) *N*-methyl-d-aspartate receptor channel block by the enantiomeric 6,7-benzomorphans BIII 277 CL and BIII 281 CL. J Pharmacol Exp Ther 285:767–776

Grimwood S, Richards P, Murray F et al (2000) Characterisation of N-methyl-d-aspartate receptor-specific [^{3}H]ifenprodil binding to recombinant human NR1a/NR2B receptors compared with native receptors in rodent brain membranes. J Neurochem 75:2455–2463

Gruber S, Ametamey SM (2017) Imaging the glutamate receptor subtypes-much achieved, and still much to do. Drug Discov Today Technol 25:27–36

Haider A, Iten I, Ahmed H et al (2018) Identification and preclinical evaluation of a radiofluorinated benzazepine derivative for imaging the GluN2B subunit of the ionotropic NMDA receptor. J Nucl Med 60:259–266

Haider A, Herde AM, Krämer SD et al (2019) Preclinical evaluation of benzazepine-based PET radioligands (R)- and (S)-^{11}C-me-NB1 reveals distinct enantiomeric binding patterns and a tightrope walk between GluN2B- and σ1-receptor-targeted PET imaging. J Nucl Med 60:1167–1173

Haradahira T, Suzuki K (1999) An improved synthesis of [11C]L-703,717 as a radioligand for the glycine site of the NMDA receptor. Nucl Med Biol 26:245–247

Haradahira T, Sasaki S, Maeda M et al (1998) Synthesis and brain distribution of carbon-11 labeled analogs of antagonists for the NMDA receptor coupled PCP-binding site. J Label Compd Radiopharm 41:843–858

Haradahira T, Zhang M, Maeda J et al (2000) A strategy for increasing the brain uptake of a radioligand in animals: use of a drug that inhibits plasma protein binding. Nucl Med Biol 27:357–360

Haradahira T, Zhang MR, Maeda J et al (2001) A prodrug of NMDA/glycine site antagonist, L-703,717, with improved BBB permeability: 4-acetoxy derivative and its positron-emitter labeled analog. Chem Pharm Bull (Tokyo) 49:147–150

Haradahira T, Maeda J, Okauchi T et al (2002a) Synthesis, in vitro and in vivo pharmacology of a C-11 labeled analog of CP–101,606, (±)threo-1-(4-hydroxyphenyl) −2-[4-hydroxy-4-(p-[11C]methoxyphenyl)piperidino]-1-propanol, as a PET tracer for NR2B subunit-containing NMDA receptors. Nucl Med Biol 29:517–525

Haradahira T, Okauchi T, Maeda J et al (2002b) A positron-emitter labeled glycine(B) site antagonist, [11C]L-703,717, preferentially binds to a cerebellar NMDA receptor subtype consisting of GluR epsilon 3 subunit in vivo, but not in vitro. Synapse 43:131–133

Haradahira T, Suhara S, Okauchi T et al (2002c) Developments of PET radioligands for NMDA receptors. World J Nucl Med 1:S183–S184

Haradahira T, Okauchi T, Maeda J et al (2003) Effects of endogenous agonists, glycine and d-serine, on in vivo specific binding of [11C]L-703,717, a PET radioligand for the glycine-binding site of NMDA receptors. Synapse 50:130–136

Hartvig P, Valtysson J, Antoni G et al (1994) Brain kinetics of (R)- and (S)-[N-methyl-11C]ketamine in the rhesus monkey studied by positron emission tomography (PET). Nucl Med Biol 21:927–934

Hashimoto K, London ED (1995) Interactions of erythro-ifenprodil, threo-ifenprodil, erythro-iodoifenprodil, and eliprodil with subtypes of sigma receptors. Eur J Pharmacol 273:307–310

Hashimoto A, Nishikawa T, Oka T, Takahashi K (1993) Endogenous d-serine in rat brain: N-methyl-d-aspartate receptor-related distribution and aging. J Neurochem 60:783–786

Hayashi T, Thomas GM, Huganir RL (2009) Dual palmitoylation of NR2 subunits regulates NMDA receptor trafficking. Neuron 64:213–226

He Y, Mu L, Ametamey SM, Schibli R (2019) Recent progress in allosteric modulators for GluN2A subunit and development of GluN2A-selective nuclear imaging probes. J Label Comp Radiopharm 62:552–560

Hu LY, Guo J, Magar SS et al (1997) Synthesis and pharmacological evaluation of N-(2,5-disubstituted phenyl)-N′-(3-substituted phenyl)-N'-methylguanidines as N-methyl −d-aspartate receptor ion-channel blockers. J Med Chem 40:4281–4289

Hynd MR, Scott HL, Dodd PR (2004) Differential expression of N-methyl-d-aspartate receptor NR2 isoforms in Alzheimer's disease. J Neurochem 90:913–919

Ishibashi N, Kuwamura T, Sano H et al (2000) Synthesis and evaluation of 18F- and 11C-labelled 9,10-ethanobenzo[b]quinolizinium derivatives for imaging of the NMDA receptor at the TCP-binding site. J Label Compd Radiopharm 43:375–383

Jacob CP, Koutsilieri E, Bartl J et al (2007) Alterations in expression of glutamatergic transporters and receptors in sporadic Alzheimer's disease. J Alzheimers Dis 11:97–116

Jahr CE (1992) High probability opening of NMDA receptor channels by l-glutamate. Science 255:470–472

Kalia LV, Kalia SK, Salter MW (2008) NMDA receptors in clinical neurology: excitatory times ahead. Lancet Neurol 7:742–755

Kantrowitz JT, Javitt DC (2010) N-methyl-d-aspartate (NMDA) receptor dysfunction or dysregulation: the final common pathway on the road to schizophrenia? Brain Res Bull 83:108–121

Karakas E, Simorowski N, Furukawa H (2009) Structure of the zinc-bound amino-terminal domain of the NMDA receptor NR2B subunit. EMBO J 28:3910–3920

Karakas E, Simorowski N, Furukawa H (2011) Subunit arrangement and phenylethanolamine binding in GluN1/GluN2B NMDA receptors. Nature 475:249–253

Karbon EW, Patch RJ, Pontecorvo MJ, Ferkany JW (1990) Ifenprodil potently interacts with [3H](+)-3-PPP-labeled sigma binding sites in Guinea pig brain membranes. Eur J Pharmacol 176:247–248

Kashiwagi K, Pahk AJ, Masuko T et al (1997) Block and modulation of N-methyl-d-aspartate receptors by polyamines and protons: role of amino acid residues in the transmembrane and pore-forming regions of NR1 and NR2 subunits. Mol Pharmacol 52:701–713

Kemp JA, McKernan RM (2002) NMDA receptor pathways as drug targets. Nat Neurosci 5(Suppl):1039–1042

Kew JN, Trube G, Kemp JA (1996) A novel mechanism of activity-dependent NMDA receptor antagonism describes the effect of ifenprodil in rat cultured cortical neurones. J Physiol 497:761–772

Klein PJ, Chomet M, Metaxas A et al (2016) Synthesis, radiolabeling and evaluation of novel amine guanidine derivatives as potential positron emission tomography tracers for the ion channel of the N-methyl-d-aspartate receptor. Eur J Med Chem 118:143–160

Klein PJ, Schuit RC, Metaxas A et al (2017) Synthesis, radiolabeling and preclinical evaluation of a [11C]GMOM derivative as PET radiotracer for the ion channel of the N-methyl-d-aspartate receptor. Nucl Med Biol 51:25–32

Knol RJ, de Bruin K, van Eck-Smit BL et al (2009) In vivo [123I]CNS-1261 binding to d-serine-activated and MK801-blocked NMDA receptors: a storage phosphor imaging study in rats. Synapse 63:557–564

Köhr G (2006) NMDA receptor function: subunit composition versus spatial distribution. Cell Tissue Res 326:439–446

Kokic M, Honer M, Kessler LJ et al (2002) Synthesis and in vitro and in vivo evaluation of [11C]methyl-BIII277CL for imaging the PCP-binding site of the NMDA receptor by PET. J Recept Signal Transduct Res 22:123–139

Koudih R, Gilbert G, Dhilly M et al (2012) Synthesis and in vitro characterization of trans- and cis-[18F]-4-methylbenzyl 4-[(pyrimidin-2-ylamino)methyl]-3- fluoropiperidine-1-carboxylates as new potential PET radiotracer candidates for the NR2B subtype N-methyl-d-aspartate receptor. Eur J Med Chem 53:408–415

Krämer SD, Betzel T, Mu L et al (2018) Evaluation of 11C-Me-NB1 as a potential PET radioligand for measuring GluN2B-containing NMDA receptors, drug occupancy, and receptor cross talk. J Nucl Med 59:698–703

Kulagowski JJ, Baker R, Curtis NR et al (1994) 3′-(Arylmethyl)- and 3′-(aryloxy)-3-phenyl-4-hydroxyquinolin-2(1H)-ones: orally active antagonists of the glycine site on the NMDA receptor. J Med Chem 37:1402–1405

Kuryatov A, Laube B, Betz H, Kuhse J (1994) Mutational analysis of the glycine-binding site of the NMDA receptor: structural similarity with bacterial amino acid-binding proteins. Neuron 12:1291–1300

Labas R, Sobrio F, Bramoullé Y et al (2010) Radiosynthesis of N-[4-(4-fluorobenzyl) piperidin-1-yl]-N′-(2-[11C]oxo-1,3-dihydrobenzimidazol-5-yl)oxamide, a NR2B- selective NMDA receptor antagonist. J Label Compd Radiopharm 53:63–67

Labas R, Gilbert G, Nicole O et al (2011) Synthesis, evaluation and metabolic studies of radiotracers containing a 4-(4-[18F]-fluorobenzyl)piperidin-1-yl moiety for the PET imaging of NR2B NMDA receptors. Eur J Med Chem 46:2295–2309

Lau A, Tymianski M (2010) Glutamate receptors, neurotoxicity and neurodegeneration. Pflugers Arch 460:525–542

Lau CG, Zukin RS (2007) NMDA receptor trafficking in synaptic plasticity and neuropsychiatric disorders. Nat Rev Neurosci 8:413–426

Laube B, Kuhse J, Betz H (1998) Evidence for a tetrameric structure of recombinant NMDA receptors. J Neurosci 18:2954–2961

Leeson PD, Baker R, Carling RW et al (1991) Kynurenic acid derivatives. Structure–activity relationships for excitatory amino acid antagonism and identification of potent and selective antagonists at the glycine site on the N-methyl-d-aspartate receptor. J Med Chem 34:1243–1252

Leeson PD, Carling RW, Moore KW et al (1992) 4-Amido-2- carboxytetrahydroquinolines. Structure–activity relationships for antagonism at the glycine site of the NMDA receptor. J Med Chem 35:1954–1968

Leibrock J, Prücher H, Rautenberg W (1997) EMD 95885, a new eliprodil analogue with higher affinity for the N-methyl-d-aspartate (NMDA) receptor. Pharmazie 52:479–480

Lin CH, Lane HY, Tsai GE (2012) Glutamate signaling in the pathophysiology and therapy of schizophrenia. Pharmacol Biochem Behav 100:665–677

Lind GE, Mou TC, Tamborini L et al (2017) Structural basis of subunit selectivity for competitive NMDA receptor antagonists with preference for GluN2A over GluN2B subunits. Proc Natl Acad Sci U S A 114:E6942–E6951

Lipton SA (2004) Paradigm shift in NMDA receptor antagonist drug development: molecular mechanism of uncompetitive inhibition by memantine in the treatment of Alzheimer's disease and other neurologic disorders. J Alzheimers Dis 6(6 Suppl):S61–S74

Lodge D, Johnson KM (1990) Noncompetitive excitatory amino acid receptor antagonists. Trends Pharmacol Sci 11:81–86

Loo P, Braunwalder A, Lehmann J, Williams M (1986) Radioligand binding to central phencyclidine recognition sites is dependent on excitatory amino acid receptor agonists. Eur J Pharmacol 123:467–468

Low CM, Wee KS (2010) New insights into the not-so-new NR3 subunits of N-methyl-d-aspartate receptor: localization, structure, and function. Mol Pharmacol 78:1–11

Malherbe P, Mutel V, Broger C et al (2003) Identification of critical residues in the amino terminal domain of the human NR2B subunit involved in the RO 25-6981 binding pocket. J Pharmacol Exp Ther 307:897–905

Mallamo JP, Earley WG, Kumar V et al (1994) Identification, synthesis, and characterization of a unique class of N-methyl-d-aspartate antagonists. The 6,11-Ethanobenzo[b]quinolizinium cation. J Med Chem 37:4438–4448

Matsumoto R, Haradahira T, Ito H et al (2007) Measurement of glycine binding site of N-methyl-d-asparate receptors in living human brain using 4-acetoxy derivative of L-703,717, 4-acetoxy-7-chloro-3-[3-(4-[^{11}C] methoxybenzyl) phenyl]-2(1H)-quinolone (AcL703) with positron emission tomography. 61(10):795–800

Matsumura K, Bergström M, Onoe H et al (1995) In vitro positron emission tomography (PET): use of positron emission tracers in functional imaging in living brain slices. Neurosci Res 22:219–229

McCauley JA, Theberge CR, Romano JJ et al (2004) NR2B-selective N-methyl-d-aspartate antagonists: synthesis and evaluation of 5-substituted benzimidazoles. J Med Chem 47:2089–2096

McGinnity CJ, Hammers A, Riaño Barros DAR et al (2014) Initial evaluation of ^{18}F-GE-179, a putative PET tracer for activated N-methyl d-aspartate receptors. J Nucl Med 55:423–430

McGinnity CJ, Koepp MJ, Hammers A et al (2015) NMDA receptor binding in focal epilepsies. J Neurol Neurosurg Psychiatry 86:1150–1157

McGinnity CJ, Årstad E, Beck K et al (2019) Comment on " In vivo [^{18}F]GE-179 brain signal does not show NMDA-specific modulation with drug challenges in rodents and nonhuman primates". ACS Chem Neurosci 10:768–772

Menniti F, Chenard B, Collins M et al (1997) CP−101,606, a potent neuroprotectant selective for forebrain neurons. Eur J Pharmacol 331:117–126

Millan MJ (2005) N-methyl-d-aspartate receptors as a target for improved antipsychotic agents: novel insights and clinical perspectives. Psychopharmacology 179:30–53

Mony L, Kew JN, Gunthorpe MJ, Paoletti P (2009) Allosteric modulators of NR2B-containing NMDA receptors: molecular mechanisms and therapeutic potential. Br J Pharmacol 157:1301–1317

Monyer H, Burnashev N, Laurie DJ et al (1994) Developmental and regional expression in the rat brain and functional properties of four NMDA receptors. Neuron 12:529–540

Mori H, Mishina M (1995) Structure and function of the NMDA receptor channel. Neuropharmacology 34:1219–1237

Mott DD, Doherty JJ, Zhang S et al (1998) Phenylethanolamines inhibit NMDA receptors by enhancing proton inhibition. Nat Neurosci 1:659–667

Mueller AL, Artman LD, Balandrin MF et al (1999) NPS 1506, a novel NMDA receptor antagonist and neuroprotectant. Review of preclinical and clinical studies. Ann N Y Acad Sci 890:450–457

Mutel V, Buchy D, Klingelschmidt A et al (1998) *In vitro* binding properties in rat brain of [^{3}H]RO 25–6981, a potent and selective antagonist of NMDA receptors containing NR2B subunits. J Neurochem 70:2147–2155

Oh JD, Russell DS, Vaughan CL et al (1998) Enhanced tyrosine phosphorylation of striatal NMDA receptor subunits: effect of dopaminergic denervation and L-DOPA administration. Brain Res 813:150–159

Orita K, Sasaki S, Maeda M et al (1993) Synthesis and evaluation of 1-(1-[5-(2′-[^{18}F]fluoroethyl)-2-thienyl]-cyclohexyl)piperidine as a potential in vivo radioligand for the NMDA receptor-channel complex. Nucl Med Biol 20:865–873

Ouyang X, Mukherjee J, Yang ZY (1996) Synthesis, radiosynthesis, and biological evaluation of fluorinated thienylcyclohexyl piperidine derivatives as potential radiotracers for the NMDA receptor-linked calcium ionophore. Nucl Med Biol 23:315–324

Owens J, Wyper DJ, Patterson J et al (1997) First SPET images of glutamate (NMDA) receptor activation in vivo in cerebral ischaemia. Nucl Med Commun 18:149–158

Owens J, Tebbutt AA, McGregor AL et al (2000) Synthesis and binding characteristics of *N*-(1-naphthyl)-*N*′-(3-[^{125}I]-iodophenyl)-*N*′-methylguanidine ([^{125}I]-CNS 1261): a potential SPECT agent for imaging NMDA receptor activation. Nucl Med Biol 27:557–564

Oye I, Paulsen O, Maurset A (1992) Effects of ketamine on sensory perception: evidence for a role of *N*-methyl-d-aspartate receptors. J Pharmacol Exp Ther 260:1209–1213

Paoletti P, Neyton J (2007) NMDA receptor subunits: function and pharmacology. Curr Opin Pharmacol 7:39–47

Paoletti P, Bellone C, Zhou Q (2013) NMDA receptor subunit diversity: impact on receptor properties, synaptic plasticity and disease. Nat Rev Neurosci 14:383–400

Parsons CG, Gruner R, Rozental J et al (1993) Patch clamp studies on the kinetics and selectivity of *N*-methyl-d-aspartate receptor antagonism by memantine (1-amino-3,5-dimethyladamantane). Neuropharmacology 32:1337–1350

Piel M, Schirrmacher R, Höhnemann S et al (2003) Synthesis and evaluation of 5,7-dichloro-4-(3-{4-[4-(2-[^{18}F]fluoroethyl)-piperazin-1-yl]-phenyl}-ureido)-1,2,3,4-tetrahydroquinoline-2-carboxylic acid as a potential NMDA ligand to study glutamatergic neurotransmission *in vivo*. J Label Compd Radiopharm 46:645–659

Pike VW (2009) PET radiotracers: crossing the blood–brain barrier and surviving metabolism. Trends Pharmacol Sci 30:431–440

Pilowsky LS, Bressan RA, Stone JM et al (2006) First in vivo evidence of an NMDA receptor deficit in medication-free schizophrenic patients. Mol Psychiatry 11:118–119

Price GW, Ahier RG, Middlemiss DN et al (1988) In vivo labelling of the NMDA receptor channel complex by [^{3}H]MK-801. Eur J Pharmacol 158:279–282

Rachline J, Perin-Dureau F, Le Goff A et al (2005) The micromolar zinc-binding domain on the NMDA receptor subunit NR2B. J Neurosci 25:308–317

Ransom RW, Eng WS, Burns HD et al (1990) (+)-3-[^{123}I]Iodo-MK-801: synthesis and characterization of binding to the *N*-methyl-d-aspartate receptor complex. Life Sci 46:1103–1110

Reddy NL, Hu LY, Cotter RE et al (1994) Synthesis and structure–activity studies of *N*,*N*′-diarylguanidine derivatives *N*-(1-naphthyl)-*N*′-(3-ethylphenyl)-*N*′- methylguanidine: a new, selective noncompetitive NMDA receptor antagonist. J Med Chem 37:260–267

Riedel G, Platt B, Micheau J (2003) Glutamate receptor function in learning and memory. Behav Brain Res 140:1–47

Robins EG, Zhao Y, Khan I et al (2010) Synthesis and in vitro evaluation of ^{18}F-labelled S-fluoroalkyl diarylguanidines: novel high-affinity NMDA receptor antagonists for imaging with PET. Bioorg Med Chem Lett 20:1749–1751

Roche KW, Standley S, McCallum J et al (2001) Molecular determinants of NMDA receptor internalization. Nat Neurosci 4:794–802

Roger G, Lagnel B, Besret L et al (2003) Synthesis, radiosynthesis and in vivo evaluation of 5-[3-(4-benzylpiperidin-1-yl)prop-1-ynyl]-1,3-dihydrobenzoimidazol-2- [^{11}C] one, as a potent NR$_{1A}$/2B subtype selective NMDA PET radiotracer. Bioorg Med Chem 11:5401–5408

Roger G, Dollé F, De Bruin B et al (2004) Radiosynthesis and pharmacological evaluation of [^{11}C]EMD-95885: a high affinity ligand for NR2B-containing NMDA receptors. Bioorg Med Chem 12:3229–3237

Rowley M, Kulagowski JJ, Watt AP et al (1997) Effect of plasma protein binding on in vivo activity and brain penetration of glycine/NMDA receptor antagonists. J Med Chem 40:4053–4068

Salabert AS, Fonta C, Fontan C et al (2015) Radiolabeling of [^{18}F]-fluoroethylnormemantine and initial in vivo evaluation of this innovative PET tracer for imaging the PCP sites of NMDA receptors. Nucl Med Biol 42:643–653

Salabert AS, Mora-Ramirez E, Beaurain M et al (2018) Evaluation of [18F]FNM biodistribution and dosimetry based on whole-body PET imaging of rats. Nucl Med Biol 59:1–8

Samnick S, Ametamey S, Leenders KL et al (1998) Electrophysiological study, biodistribution in mice, and preliminary PET evaluation in a rhesus monkey of 1-amino-3-[^{18}F]fluoromethyl-5-methyl-adamantane (18]F-MEM): a potential radioligand for mapping the NMDA-receptor complex. Nucl Med Biol 25:323–330

Sander CY, Schoenberger M, Hooker JM (2019) Response to comment on "in vivo [^{18}F]GE-179 brain signal does not show NMDA-specific modulation with drug challenges in rodents and nonhuman primates". ACS Chem Neurosci 10:773–775

Sasaki S, Ishibashi N, Kuwamura T et al (1998) Excellent acceleration of the Diels–Alder reaction by microwave irradiation for the synthesis of new fluorine-substituted ligands of NMDA receptor. Bioorg Med Chem Lett 8:2983–2986

Sasaki S, Kanda T, Ishibashi N et al (2001) 4,5,9,10-tetrahydro-1,4-ethanobenz[b] quinolizine as a prodrug for its quinolizinium cation as a ligand to the open state of the TCP-binding site of NMDA receptors. Bioorg Med Chem Lett 11:519–521

Sasaki S, Kurosaki F, Haradahira T et al (2004) Synthesis of ^{11}C-labelled bis(phenylalkyl)amines and their in vitro and in vivo binding properties in rodent and monkey brains. Biol Pharm Bull 27:531–537

Schell MJ, Molliver ME, Snyder SH (1995) d-serine, an endogenous synaptic modulator: localization to astrocytes and glutamate-stimulated release. Proc Natl Acad Sci U S A 92:3948–3952

Schell MJ, Brady RO Jr, Molliver ME, Snyder SH (1997) d-serine as a neuromodulator: regional and developmental localizations in rat brain glia resemble NMDA receptors. J Neurosci 17:1604–1615

Schoenberger M, Schroeder FA, Placzek MS et al (2018) In vivo [18F]GE-179 brain signal does not show NMDA-specific modulation with drug challenges in rodents and nonhuman primates. ACS Chem Neurosci 9:298–305

Shibayama Y, Sasaki S, Tomita U et al (1996) Synthesis and evaluation of new ^{18}F-labelled thienylcyclohexylpiperidine (TCP) analogues as radioligands for the NMDA receptor-channel complex. J Label Compd Radiopharm 38:77–86

Shiue CY, Vallabhahosula S, Wolf AP et al (1997) Carbon-11 labelled ketamine-synthesis, distribution in mice and PET studies in baboons. Nucl Med Biol 24:145–150

Sihver S, Sihver W, Andersson Y et al (1998) In vitro and in vivo characterization of (+)-3-[^{11}C]cyano-dizocilpine. J Neural Transm 105:117–131

Silver IA, Erecińska M (1992) Ion homeostasis in rat brain in vivo: intra- and extracellular [Ca^{2+}] and [H$^+$] in the hippocampus during recovery from short-term, transient ischemia. J Cereb Blood Flow Metab 12:759–772

Sobrio F, Gilbert G, Perrio C et al (2010) PET and SPECT imaging of the NMDA receptor system: an overview of radiotracer development. Mini Rev Med Chem 10:870–886

Stone JM, Erlandsson K, Arstad E et al (2006) Ketamine displaces the novel NMDA receptor SPET probe [^{123}I]CNS-1261 in humans *in vivo*. Nucl Med Biol 33:239–243

Stone JM, Erlandsson K, Arstad E et al (2008) Relationship between ketamine-induced psychotic symptoms and NMDA receptor occupancy: a [^{123}I]CNS-1261 SPET study. Psychopharmacology 197:401–408

Suetake-Koga S, Shimazaki T, Takamori K et al (2006) *In vitro* and antinociceptive profile of HON0001, an orally active NMDA receptor NR2B subunit antagonist. Pharmacol Biochem Behav 84:134–141

Szermerski M, Börgel F, Schepmann D et al (2018) Fluorinated GluN2B receptor antagonists with a 3-benzazepine scaffold designed for PET studies. ChemMedChem 13:1058–1068

Tamborini L, Chen Y, Foss CA et al (2016) Development of radiolabeled ligands targeting the glutamate binding site of the N-methyl-d-aspartate receptor as potential imaging agents for brain. J Med Chem 59:11110–11119

Tamiz AP, Whittemore ER, Zhou ZL et al (1998) Structure–activity relationships for a series of bis(phenylalkyl)amines: potent subtype-selective inhibitors of *N*-methyl-d-aspartate receptors. J Med Chem 41:3499–3506

Tewes B, Frehland B, Schepmann D et al (2010) Design, synthesis, and biological evaluation of 3-benzazepin-1-ols as NR2B-selective NMDA receptor antagonists. ChemMedChem 5:687–695

Traynelis SF, Wollmuth LP, McBain CJ et al (2010) Glutamate receptor ion channels: structure, regulation, and function. Pharmacol Rev 62:405–496

Tsukiyama S, Hashimoto A, Katayama S et al (1991) Fluoromethylated and hydroxymethylated derivatives of *N*-methyl-d-aspartate receptor antagonist 1-[1-(2-thienyl)cyclohexyl]piperidine. Chem Pharm Bull (Tokyo) 39:1581–1584

Ulbrich MH, Isacoff EY (2008) Rules of engagement for NMDA receptor subunits. Proc Natl Acad Sci U S A 105:14163–14168

Vallano ML, Lambolez B, Audinat E, Rossier J (1996) Neuronal activity differentially regulates NMDA receptor subunit expression in cerebellar granule cells. J Neurosci 16:631–639

Vincent JP, Kartalovski B, Geneste P et al (1979) Interaction of phencyclidine ('angel dust') with a specific receptor in rat brain membranes. Proc Natl Acad Sci U S A 76:4678–4682

Vrajová M, Stastný F, Horácek J et al (2010) Expression of the hippocampal NMDA receptor GluN1 subunit and its splicing isoforms in schizophrenia: postmortem study. Neurochem Res 35:994–1002

Wafford KA, Kathoria M, Bain CJ et al (1995) Identification of amino acids in the *N*-methyl-d-aspartate receptor NR1 subunit that contribute to the glycine-binding site. Mol Pharmacol 47:374–380

Wager TT, Hou X, Verhoest PR et al (2010) Moving beyond rules: the development of a central nervous system multiparameter optimization (CNS MPO) approach to enable alignment of druglike properties. ACS Chem Neurosci 1:435–449

Walters MR, Bradford AP, Fischer J et al (2002) Early clinical experience with the novel NMDA receptor antagonist CNS 5161. Br J Clin Pharmacol 53:305–311

Waterhouse RN (2003) Determination of lipophilicity and its use as a predictor of blood–brain barrier penetration of molecular imaging agents. Mol Imaging Biol 5:376–389

Waterhouse RN, Sultana A, Guo N et al (2002a) Synthesis and characterization of 4,6-dichloroindole-based radioligands for imaging the glycine site of the NMDA ion channel. J Labelled Cpd Radiopharm 45:91–102

Waterhouse RN, Sultana A, Laruelle M (2002b) *In vivo* evaluation of [^{11}C]-3-[2-[(3-methoxyphenylamino)carbonyl]ethenyl]-4,6-dichloroindole-2-carboxylic acid ([^{11}C]3MPICA) as a PET radiotracer for the glycine site of the NMDA ion channel. Nucl Med Biol 29:791–794

Waterhouse RN, Slifstein M, Dumont F et al (2004) *In vivo* evaluation of [^{11}C]*N*-(2-chloro-5-thiomethylphenyl)-N'-(3-methoxy-phenyl)-*N*'-methylguanidine ([^{11}C] GMOM) as a potential PET radiotracer for the PCP/NMDA receptor. Nucl Med Biol 31:939–948

Williams K (1993) Ifenprodil discriminates subtypes of the *N*-methyl-d-aspartate receptor: selectivity and mechanisms at recombinant heteromeric receptors. Mol Pharmacol 44:851–859

Wong EH, Kemp JA, Priestley T et al (1986) The anticonvulsant MK-801 is a potent *N*-methyl-d-aspartate antagonist. Proc Natl Acad Sci U S A 83:7104–7108

Wong EH, Knight AR, Woodruff GN (1988) [³H]MK-801 labels a site on the *N*-methyl-d-aspartate receptor channel complex in rat brain membranes. J Neurochem 50:274–281

Wright JL, Gregory TF, Kesten SR et al (2000) Subtype-selective *N*-methyl-d-aspartate receptor antagonists: synthesis and biological evaluation of 1-(heteroarylalkynyl)- 4-benzylpiperidines. J Med Chem 43:3408–3419

Yao Y, Harrison CB, Freddolino PL et al (2008) Molecular mechanism of ligand recognition by NR3 subtype glutamate receptors. EMBO J 27:2158–2170

Zhang L, Villalobos A, Beck EM et al (2013) Design and selection parameters to accelerate the discovery of novel central nervous system positron emission tomography (PET) ligands and their application in the development of a novel phosphodiesterase 2A PET ligand. J Med Chem 56:4568–4579

Zhao Y, Robins E, Turton D et al (2006) Synthesis and characterization of *N*-(2-chloro-5-methylthiophenyl)-N′-(3-methylthiophenyl)-N′-[¹¹C]methylguanidine [¹¹C]CNS 5161, a candidate PET tracer for functional imaging of NMDA receptors. J Label Compd Radiopharm 49:163–170

Zhou X, Zhang J, Yan C et al (2012) Preliminary studies of ⁹⁹ᵐTc-memantine derivatives for NMDA receptor imaging. Nucl Med Biol 9:1034–1041

Zhou W, Bao W, Jiang D et al (2018) [¹⁸F]-GE-179 positron emission tomography (PET) tracer for N-methyl-d-aspartate receptors: one-pot synthesis and preliminary micro-PET study in a rat model of MCAO. Nucl Med Biol 61:45–55

Progress in PET Imaging of the Norepinephrine Transporter System

Yu-Shin Ding

Contents

Abstract

The norepinephrine transporter (NET) has long been recognized to play a role in various neurological and psychiatric disorders, e.g., ADHD, substance abuse, depression, alcoholism, obesity, addiction, and Alzheimer's and Parkinson's diseases. However, many of the important findings resulting from studies in vitro

Y.-S. Ding (✉)

Departments of Radiology, Psychiatry and Chemistry, New York University School of Medicine, New York, NY, USA
e-mail: Yu-Shin.Ding@nyulangone.org

713

using postmortem tissues have never been verified via in vivo methods due to the lack of suitable radioligands, preventing the brain imaging of NET in living systems. We have identified the superiority of *(S,S)*-[¹¹C]MRB and the suitability of the MRB analogs as potential NET ligands for PET translational studies from preclinical investigation in animals to clinical research in humans. In this review article, progress in these translational research studies will be discussed, including the role of NET in ADHD, substance abuse, depression, post -traumatic stress disorder (PTSD), alcohol dependence, obesity, aging, Parkinson's disease, and Alzheimer's disease.

20.1   Introduction

In a previous review article (Ding et al. 2006), we provided background and clinical relevance of the norepinephrine transporter (NET) to support the need to develop novel radiotracers to study the brain NET system in order to better understand its role in brain function and diseases. We also discussed the design and biological evaluation of several radioligands for imaging the brain NET system with PET. Based on these characterization studies (Ding et al. 2003, 2005; Lin et al. 2005), including C-11 labeled desipramine (DMI), 2-hydroxy-desipramine (HDMI), talopram, talsupram, nisoxetine (Nis), oxaprotiline (Oxap), and lortalamine, and C-11 and F-18 derivatives of reboxetine, methylreboxetine (MRB), and their individual *(R,R)* and *(S,S)* enantiomers, in conjunction with studies using radiolabeled 4-iodo-tomoxetine and 2-iodo-nisoxetine, we have identified the superiority of *(S,S)*-[¹¹C]MRB and the suitability of the MRB analogs as potential NET ligands for PET translational studies from preclinical investigation in animals to clinical research in humans. In this review article, progress in this translational research will be discussed.

20.2   Challenges in NET Imaging of the Brain

NET possesses several intrinsic disadvantages as a molecular imaging target as compared to the other monoamine transporters (dopamine transporter (DAT) and serotonin transporter). These disadvantages have presented drawbacks, described below, and hindered for decades of progress in ligand development and imaging of NET in the living human brain.

20.2.1 NET Has a Relatively Low Density in the Brain

Bmax for NET is ~5–150 fmol/mg tissue (Smith et al. 2006; Tejani-Butt 1992); however, DAT has a more than 50-fold higher density, and SERT is over five- ten-fold higher (Kaufman et al. 1991; Zeng et al. 2006).

20.2.2   NET Has a Widespread Distribution in the Brain

Studies in rodents, cats, non-human primates, and humans have indicated that nor-adrenergic terminals in the central nervous system (CNS) are widespread. Highest levels occur in the locus coeruleus complex (LC) and raphe nuclei, with moderate density in the hypothalamus, midline thalamic nuclei, bed nucleus of the stria terminalis, and central nucleus of the amygdala and brainstem nuclei, with lowest levels in basolateral amygdala and cortical and striatal regions (Ding et al. 2003, 2010; Tejani-Butt 1992; Charnay et al. 1995; Ding and Fowler 2005; Gallezot et al. 2007, 2010; Hannestad et al. 2010a)..

20.2.3   NET Has a Lower Contrast Between NET-Poor and NET-Rich Regions

Two detrimental effects on NET imaging as the result of the widespread distribution of NET in the brain are (1) lower contrast and (2) lack of an obvious reference region. In contrast, a significant difference in the density between the transporter-rich and transporter-poor regions for both DAT and SERT systems offers much better contrast for PET imaging of DAT/SERT and simplifies data analysis methods by using a reference region approach.

20.2.4   The Locus Coeruleus (LC), the Highest NET Density Region, Has a Small Structure That Makes It Difficult to Be Delineated and Quantitated

We and other research groups have been making progress toward ligand development for PET imaging of NET. After over two decades of effort, *(S,S)*-[11C]MRB and its analogs are considered by far the most promising NET ligands for PET imaging (Ding et al. 2006). This ligand has been used to study the role of NET in humans. How best to carry out these translational research studies and how best to normalize data from the NET-PET studies to obtain a measure related to NET availability have been the subject of our recent work. Specific examples of tracer applications in the neurosciences (mainly in the brain) are given in the following sections.

20.3   Translational PET Imaging Studies of NET

The NET has been suggested to play a role in numerous disorders such as substance abuse and withdrawal, ADHD, depression, schizophrenia, Alzheimer's disease, Parkinson's Disease, as well as aging; however, in vivo brain imaging studies of NET have not been possible due to the lack of suitable radioligands (Ding et al. 2006). We have evaluated the suitability of *(S,S)*-[11C]MRB in preclinical models and further evaluated it in humans. The results show that *(S,S)*-[11C]MRB possesses

properties that are highly favorable for the imaging of brain NET as a PET tracer, including (a) a regional distribution consistent with the known distribution of NET in the brain; (b) high test/retest reproducibility in nonhuman primates and humans; (c) excellent specificity and selectivity for NET over other monoamine transporters, namely, DAT and SERT; and (d) the short half-life of its ^{11}C label ($t_{1/2} = 20$ min), enabling multiple assessments (e.g., baseline and drug intervention) in the same subject on the same day. So far, we have carried out over 300 scans using *(S,S)*-[^{11}C]MRB, including preclinical and clinical studies, to investigate cocaine abuse, alcoholism, depression, post-traumatic stress disorder (PTSD), obesity, brown adipose tissue (brown fat), and diabetes-related studies (studies related to drug occupancy of several novel pharmaceuticals targeting the NET system during their Phase I clinical trials are not included). These studies have facilitated our better understanding of the role of NET in brain function and diseases. Furthermore, the use of PET with a suitable NET ligand to study drug occupancy and drug mechanisms will assist in the development of the next generation of effective drugs for the treatment of various NET-related disorders. Here are presented a few examples to illustrate the progress in PET imaging of the NET system using *(S,S)*-[^{11}C]MRB (abbreviated henceforth as [^{11}C]MRB).

20.3.1 NET Imaging in Substance Abuse

Cocaine inhibits neurotransmitter uptake of human monoamine transporters, including the NET, DAT, and SERT, with comparable potency. Alterations in NET concentration in the CNS following cocaine exposure have been identified in rats, nonhuman primate models, and postmortem human studies in cocaine users (Beveridge et al. 2005; Macey et al. 2003; Mash et al. 2005). Although these observations point to potentially important dysregulations in NET and NET-mediated neuroenergetics in response to chronic cocaine use (Weinshenker and Schroeder 2007), in vivo studies of NET regulation in clinical populations have yet to be explored. Thus, our aim was to use [^{11}C]MRB to determine the alterations in brain NET concentration in chronic cocaine users (Ding et al. 2010).

20.3.1.1 NET Abnormalities in Cocaine Dependence

In a pilot study, 12 healthy control subjects (HC) (6 M and 6 F; range 25–54) and 10 cocaine-dependent individuals (COC) (7 M, 3F; range 39–49) were recruited (Ding et al. 2010). COC subjects were studied either as inpatients or outpatients, with cocaine abstinence at the time of PET scanning established by 24-h inpatient supervision and/or negative urine toxicology testing, respectively. All subjects participated in magnetic resonance imaging (structural MRI, 3 T) and PET scanning (high-resolution research tomograph, HRRT, 207 slices, resolution ~2.5 mm FWHM in 3D acquisition mode) on two different days. Binding potential (BP_{ND}) parametric images were computed using the simplified reference tissue model (SRTM2) with the occipital cortex as reference region. BP_{ND} values were compared between the two groups.

High-resolution imaging of brain NET using [^{11}C]MRB and HRRT clearly delineated the fine-scale regional distribution of [^{11}C]MRB in small brain regions known to have high NET concentrations, including the hypothalamus, red nucleus, midbrain raphe, pontine raphe, thalamus and its subnuclei (dorsomedial thalamic nucleus, ventrolateral thalamic nucleus, pulvinar), and the area of locus coeruleus (LC). The BP_{ND} was significantly increased in the thalamus (27%; $P < 0.02$) and dorsomedial thalamic nuclei (30%; $P < 0.03$) in COC as compared to HC. We also found that there was an age effect on NET concentrations in HC. Thus, group comparison in a covariance analysis to account for the differences in age between groups was also performed. Upon age normalization, the upregulation of NET in COC also reached significance in LC (63%, $P < 0.01$) and pulvinar (55%, $P < 0.02$) regions (Fig. 20.1).

20.3.1.2 Duration of Abstinence Effect on NET Binding

In a subsequent study, we looked into the duration of the effect of abstinence on NET binding. Regional brain NET binding potential ($BP_{ND,}$ MRTM2) was measured with [^{11}C]-MRB PET scanning in healthy controls ($n = 12$, 38 ± 11 years) and patients with chronic cocaine dependence (total $n = 15$, 43 ± 6 years, with 22 ± 7 years of cocaine use) after 1 week ($n = 4$), 2 week ($n = 6$), 3 to 5 weeks ($n = 5$) of abstinence.

Our results served to reproduce our previous finding that NET is upregulated in chronic cocaine users after recent abstinence, as compared with controls. In addition, we found that subjects with cocaine dependence had higher NET BP_{ND} values in the ventral lateral thalamus (70%; $p < 0.05$) after 1 week of abstinence; that level
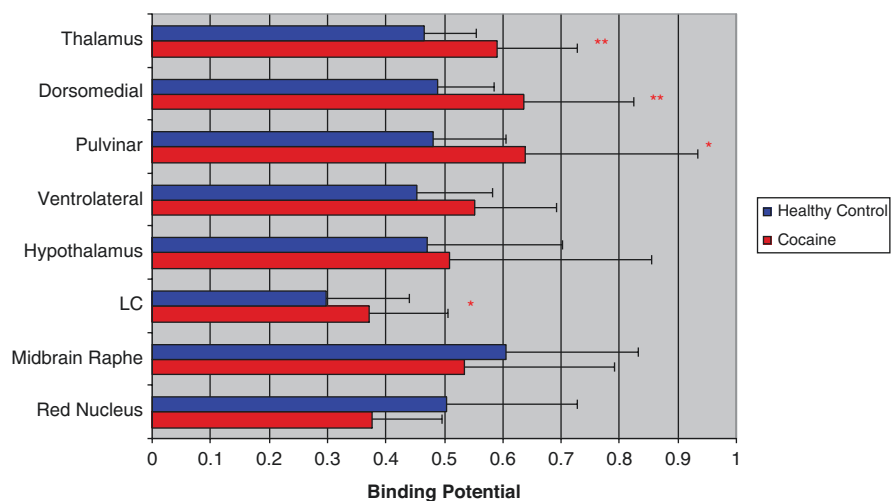
** Reached statistically significant

 * Reached statistically significant upon age-normalization

Fig. 20.1 Effect of cocaine dependence on [^{11}C]MRB binding in humans. BP_{ND} values (binding potential) were compared between healthy control and cocaine-dependent individuals

remained elevated (85%; $p < 0.01$) during the second week of abstinence. By the third week, NET levels slowly declined (11%; $p = 0.60$) (Li et al. 2006). Similar significant patterns were observed in the measurement of the whole thalamus and the midbrain raphe nuclei.

The observations of an increased binding of $[^{11}C]MRB$ in our in vivo PET imaging studies of chronic COC subjects is consistent with previously published in vitro data in rodents, rhesus monkeys, and postmortem human brains (Beveridge et al. 2005; Macey et al. 2003; Mash et al. 2005). Our results are also in agreement with an in vitro study in which an upregulation of NET mRNA in the LC was observed in rats following chronic binge administration of cocaine (Burchett and Bannon 1997). Interestingly, in this rat study, an alteration was observed in an opposite direction for the other two monoamine transporters, i.e., a decrease in SERT mRNA (in raphe) and DAT mRNA (in midbrain) following a binge regimen of chronic COC.

20.3.2 NET Imaging in ADHD

Attention deficit hyperactivity disorder (ADHD), a complex developmental behavioral and cognitive disorder that affects approximately 3–7% of school-aged boys and 2–4% of adults, is associated with impaired academic and occupational achievements, problem behaviors, increased risk for accidents, and substance abuse. (Dopheide and Pliszka 2009; Barkley 1997) The core features of ADHD—inattention, hyperactivity, and impulsivity—can be attributed to dysfunction in neural systems that regulate attention, executive function, motor control, and reward (Bush 2010; Makris et al. 2009); however, effective treatments remain elusive, and the neurochemical mechanisms of this disorder are poorly understood (Bush 2010; Makris et al. 2009). The three therapeutic classes of pharmacologic treatments for ADHD—(a) psychostimulants (e.g., methylphenidate hydrochloride; MPH); (b) non-stimulant catecholamine reuptake inhibitors (e.g., atomoxetine, ATX); and (c) α2 adrenergic receptor agonists (e.g., guanfacine)—all modulate DA and NE neurotransmission (Makris et al. 2009; Madras et al. 2005). Small changes in extracellular NE or DA concentration affect networks of pyramidal cells in the prefrontal cortex (PFC) which regulates and sustains attention. The beneficial effects of DA occur at D1 receptors, while those of NE are believed to occur at α2 receptors (Arnsten 2009). Here we present several of our translational research studies of drug occupancy designed directly toward developing a better understanding of the mechanisms that contribute to the therapeutic effects of pharmacologic treatments for ADHD.

20.3.2.1 ATX Occupancy Study on NET in Humans and Nonhuman Primates

Atomoxetine (ATX, Strattera), a potent NET reuptake inhibitor ($K_i \sim 5$ nM), is the first non-stimulant drug that was approved for the treatment of ADHD (Arnsten 2006; Bymaster et al. 2002; Chamberlain et al. 2007a; Del Campo et al. 2011; Michelson et al. 2001; Spencer et al. 2002; Swanson and Volkow 2009; Volkow

et al. 2001). When [^{11}C]MRB was initially tested in a drug occupancy study in humans using atomoxetine (ATX), a reduction in [^{11}C]MRB binding was observed, but there was no obvious dose-dependent effect (Logan et al. 2007). One hypothesis was that the doses of ATX examined in the human PET study (oral, 25, 50 or 100 mg), though clinically relevant, were too high. That is, the three tested doses all reached saturation, the plateau portion of the corresponding dose-occupancy curve, and as a result there was no obvious dose-dependent effect. Another occupancy study of ATX using [^{18}F]F-MeNER-D2 in rhesus monkeys showed a reasonable dose-dependent occupancy, though only in one of the two monkeys studied and the IC_{50} (or ED_{50}) was not determined (Seneca et al. 2006).

Thus, the suitability of [^{11}C]MRB for occupancy studies was further evaluated by carrying out investigations in a nonhuman primate model (rhesus macaque) using lower doses of ATX than those used in the previous PET study with [^{11}C]MRB (Logan et al. 2007) and with a continuous ATX infusion paradigm to maintain a constant concentration of ATX in the plasma during the PET acquisition time (120 min). Ten PET studies were performed in three anesthetized rhesus monkeys following an infusion of ATX or placebo.

For each PET study, two infusion rates were used: ATX infusion at a "loading" rate was first given for 1 h starting at 2 h before the injection of [^{11}C]MRB; then ATX was given at a "maintenance" rate (37.5% lower than the "loading" rate) at 1 h before the injection of [^{11}C]MRB. This infusion rate was maintained until the end of the 2-h PET scan (i.e., 3 h at "maintenance" rate) (Fig. 20.2). Three doses of "maintenance" rate were used: 0.01 mg/kg/h (low dose), 0/03 mg/kg/h (medium dose), and 0.09 mg/kg/h (high dose) mg/kg/h (i.e., each monkey had four PET scans, including the baseline scan with placebo). The design was to have each monkey have four PET scans on 2 study days. These 2 study days were scheduled at least

Study Design:

Each monkey was scanned four times, twice a day
Day 1: baseline and medium dose scans
Day 2: low and high dose scans

t_0
Start
ATX infusion
at "loading" rate

t_0 + 60 min
Reduce infusion
to "sustain" rate
(0.625 x loading rate)

● PK sample to quantify
ATX plasma levels

t_0 + 120 min
[C-11]MRB injection
& start scan

t_0 + 240 min
End scan
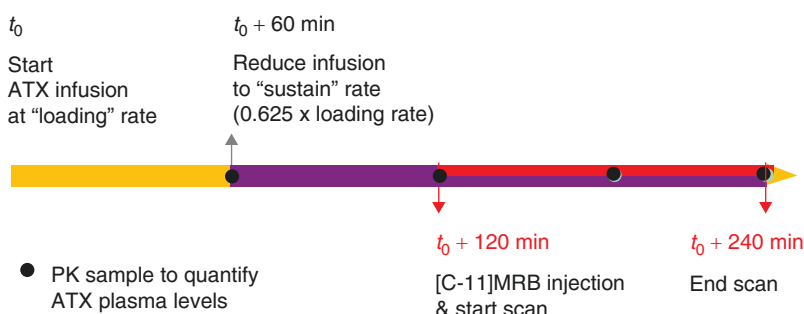
Fig. 20.2 Study design for the two-day, four-dose studies to measure ATX occupancy of NET in non-human primates using [^{11}C]MRB

3 weeks apart to allow recovery from the effect of the anesthesia and blood drawing. On each study day, two PET scans were acquired, beginning 4 h apart. The first study day consisted of the baseline and medium-dose scans, and the second study day consisted of the low- and high-dose scans.

A dose-dependent reduction of [^{11}C]MRB volume of distribution was observed after correction for [^{11}C]MRB plasma free fraction. Although the slow clearance of [^{11}C]MRB in NET-rich regions such as the thalamus posed a concern for kinetic modeling, the combination of the suitably designed infusion study paradigm and refined kinetic modeling methods an unequivocal dose-dependent occupancy of atomoxetine was obtained (Fig. 20.3) clearly demonstrating the suitability of [^{11}C]MRB for drug occupancy studies of the NET (Gallezot et al. 2010).

Based on this study, ATX IC_{50} was estimated to be 32 ± 13 ng/mL plasma, corresponding to an effective dose (ED_{50}) of 0.13 mg/kg, which is much lower than the therapeutic dose of ATX in ADHD (1.0–1.5 mg/kg). In the previous ATX occupancy study in humans, three clinically relevant doses were used (oral, 25, 50, and 100 mg), and the blood levels of ATX (in ng/mL plasma) averaged over subjects were 116 (25 mg ATX), 206 (50 mg ATX), and 421 (100 mg ATX), which was significantly higher than the estimated IC_{50} for ATX in plasma (~30 ng/mL). This suggests that the lack of an obvious dose-dependent effect in the previous study was indeed because the three clinically relevant doses all reached saturation with over 78–93% occupancy, i.e., the plateau portion of the corresponding dose-occupancy curve (Logan et al. 2007). Taken together, our results clearly indicate the importance of dose selection for PET occupancy studies, especially when observation of dose-dependency of the study drug is one of the goals for the outcome measurement.
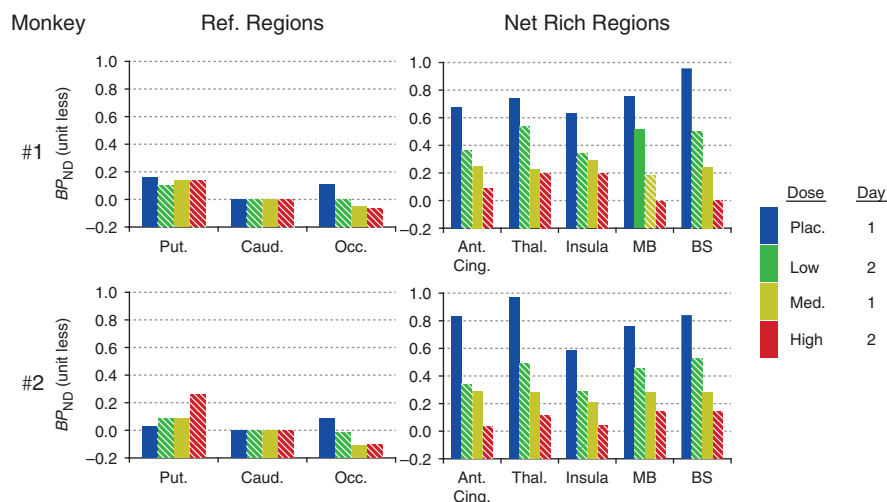
Fig. 20.3 Dose-dependent occupancy of ATX in NET-rich regions in two monkeys using [^{11}C]MRB after the placebo (Plac.), low, medium, and high ATX doses. BP_{ND} values were measured for NET-poor regions [putamen (put.) and occipital cortex (Occ.)] and NET-rich regions [anterior cingulate (Ant. Cing.), thalamus (Thal.), Insular, mid brain (MB) and brain stem (BS)], using caudate as a reference region

20.3.2.2 ATX Occupancy Study on SERT: Implications for Treatment of Depression and ADHD

The development of ATX and its approval for the treatment of ADHD by the Food and Drug Administration (Faraone et al. 2005) was based on the rationale that it selectively blocks the NET (Barton 2005) and increases the availability of intrasynaptic NE, resulting in the improvement of high-level cognitive functions that are often impaired in ADHD, such as working memory and inhibitory response control (Robbins and Arnsten 2009). In principle, ATX may offer clinical advantages by virtue of its limited effects on subcortical dopamine, which is thought to be responsible for the abuse potential of psychostimulant treatment (Volkow 2006). Furthermore, this single NE pathway of drug mechanism may facilitate further drug research and development.

The noradrenergic action also exerts important clinical effects in different antidepressants such as desipramine and nortriptyline (tricyclics with prevalent noradrenergic effects). Thus, ATX has also been used to improve responses to treatment of depression (Dell'Osso et al. 2010; O'Sullivan et al. 2009).

Serendipitously, we discovered that ATX displayed a blocking effect similar to fluoxetine (a selective SERT inhibitor) (Ding and Fowler 2005) on binding of [^{11}C]DASB, a selective SERT ligand (Houle et al. 2000) (Fig. 20.4). These results suggested that ATX not only binds to NET but also binds to SERT with high affinity. To date, whether the therapeutic effects of ATX in the treatment of either ADHD or depression are due to inhibitory effects on one (NET) or two transporters (NET and SERT) is not known. Therefore, we took on this investigation by carrying out comparative occupancy studies with [^{11}C]MRB (a NET ligand, as described above

Is ATX a Selective NET Inhibitor?

Evaluation of [^{11}C]DASB, a SERT Ligand
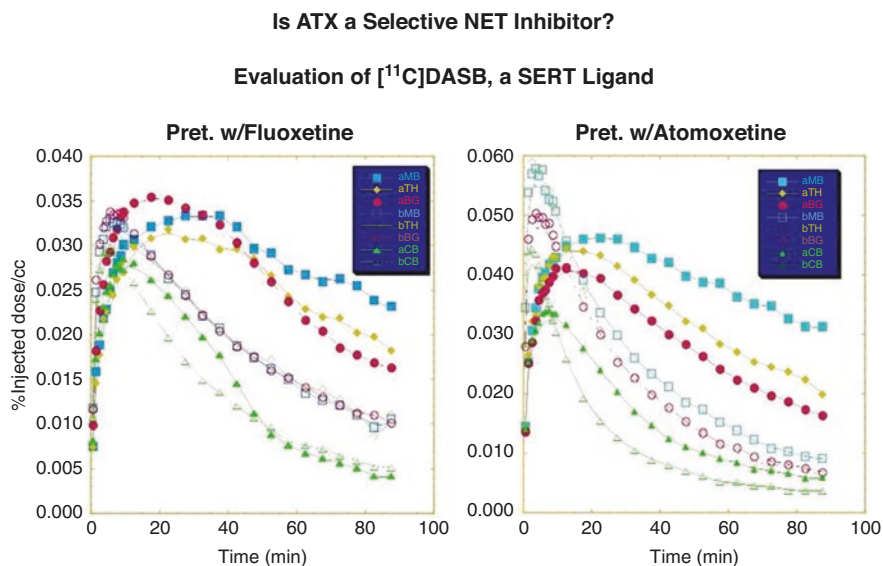
Fig. 20.4 ATX displayed a blocking effect similar to fluoxetine (a selective SERT inhibitor) on binding of [^{11}C]DASB (a selective SERT ligand), questioning the in vivo selectivity of ATX

(Gallezot, 2007 #11;Gallezot, 2010 #12) and [^{11}C]AFM (a SERT ligand) (Huang et al. 2002) to evaluate the in vivo IC_{50} of ATX for both NET and SERT in nonhuman primates using PET.

The continuous infusion protocol with [^{11}C]AFM was similar to our previous study with [^{11}C]MRB (see above) (Gallezot et al. 2007, 2010). Two monkeys were scanned at different maintenance rates: 0.045 mg/kg/h (low dose), 0.135 mg/kg/h (medium dose), and 0.405 mg/kg/h (high dose). One monkey was scanned with the higher maintenance rates: 0.135 mg/kg/h (medium dose), 0.405 mg/kg/h (high dose), and 1.054 mg/kg/h (very high dose) (details of this study will be published elsewhere).

20.3.2.3 Summary of the Comparative Occupancy Studies of ATX for NET (Using [^{11}C]MRB) and SERT (Using [^{11}C]AFM)

ATX displayed dose-dependent occupancy of both NET and SERT, with a higher occupancy of NET: IC_{50} of 31 ± 10 and 99 ± 21 ng/mL plasma for NET and SERT, respectively. At a clinically relevant dose (1.8 mg/kg, ~600 ng/mL plasma), ATX would occupy >95% of NET and occupy >85% of SERT. It is worth noting that this value of 3.2 for the selectivity ratio of ATX toward NET vs. SERT measured via in vivo PET imaging in non-human primates (NHP) is similar to a value of 4.5 for the selectivity ratio derived from the previously reported in vitro K_d values using human NET and SERT tissue homogenates (8.9 and 2 nM for SERT and NET, respectively) (Tatsumi et al. 1997). Based on these data, we propose that ATX at clinically relevant doses occupies high proportions of both NET and SERT. Thus, the interpretation of the therapeutic mode of action of ATX for treatment of depression and ADHD may be more complex than selective blockade of the NET.

20.3.2.4 The Mechanisms of Action of ATX in ADHD and Depression

It has been shown that response inhibition (the ability to exert high-level inhibitory control over motor responses so as to suppress unwanted actions) is impaired in subjects with ADHD and is one of the most robust cognitive findings in ADHD research (Lijffijt et al. 2005). Response inhibition (a.k.a. impulsivity) can be measured by the stop-signal task (SST) and quantified by the stop-signal reaction time (SSRT), an estimate of the time taken to inhibit the prepotent motor response (Aron et al. 2003a). The research group at Cambridge, UK, found that single doses of atomoxetine (60 mg) were able to improve response inhibition in humans and in rats (Chamberlain et al. 2006, 2007a; Bari et al. 2009; Eagle et al. 2008). By contrast, serotonin manipulations with citalopram, a SERT blocker (Del Campo et al. 2011; Chamberlain et al. 2006), or with buspirone, a serotonin 5-HT1A receptor agonist (Chamberlain et al. 2006, 2007b), appear to have no behavioral effects on the SSRT. These results suggest that atomoxetine enhances stopping selectively via actions on NE uptake and that NET drugs may be more suited to ameliorating impaired response inhibition as an ADHD therapeutic target.

Taken together, the inhibitory effect of ATX on NET plays a crucial role in its therapeutic effect on ADHD, while the inhibitory effect of ATX on SERT may play a more important role in its therapeutic effect on depression. Further studies to

elucidate the actual relationship between the drug mechanisms and drug therapeutic effects are needed.

20.3.2.5 MPH Occupancy Study on NET in Humans

The effects of MPH on the DA system have been studied extensively. Our previous PET studies have demonstrated that MPH's pharmacological effects reside in *d-threo*-MPH, the active enantiomer (Ding et al. 1997), and that at clinical doses, MP significantly occupies DAT in vivo in humans (Swanson and Volkow 2009; Volkow et al. 1998), suggesting that DA reuptake inhibition may be an important therapeutic mechanism in ADHD. However, MPH has shown higher in vitro affinity for NET than DAT ($K_i = 38$ nM vs. 193 nM) (Eshleman et al. 1999). The potential role of NE in ADHD was supported by animal and human data (Biederman et al. 2008). Low doses of MPH increase levels of NE in the PFC in animals (Berridge et al. 2006), and low doses of MPH improve performance of PFC tasks in subjects with ADHD (Aron et al. 2003b). The absence of a suitable NET tracer has delayed similar in vivo PET studies of NET until now.

We used [^{11}C]MRB to determine the effective dose 50 (ED$_{50}$) of MPH for NET (Hannestad et al. 2010b). We first conducted a preliminary duration study to determine how much time it takes from oral MPH administration to maximum occupancy of the brain NET. As peak displacement of [^{11}C]MRB by MPH (oral 40 mg, i.e., 0.35–0.55 mg/kg, the average clinical maintenance dose of MPH) was achieved by 75 min, we chose 75 min as the time between oral MPH dosing and [^{11}C]MRB injection for the subsequent occupancy study. Based on our previous experience with ATX occupancy studies in humans, dose selection is critical if dose-dependent occupancy is one of the goals to be achieved. Thus, in this within-subject design study, healthy subjects ($n = 11$) received oral, single-blind placebo and 2.5 mg, 10 mg, and 40 mg of MPH 75 min prior to [^{11}C]MRB injection. Dynamic PET imaging was performed for 2 h with HRRT. Three regions with known lowest density of NET (occipital cortex, caudate and putamen) were investigated (Logan 2005) further as reference regions by comparing the distribution volume (V_T) in these three regions between the placebo and 40 mg MPH conditions (Hannestad et al. 2010b). We found no significant change of V_T (or V_T/f_P, where f_P = plasma free fraction) in these three regions between the placebo and 40 mg MPH conditions, and the putamen and occipital had similar V_T values. Thus, the multilinear reference tissue model with occipital cortex as the reference region was used to estimate binding potential (BP$_{ND}$) in the thalamus and other NET-rich regions.

We found that BP$_{ND}$ was reduced by MPH in a dose-dependent manner in thalamus and other NET-rich regions (Fig. 20.5). The global ED$_{50}$ was estimated to be 0.14 mg/kg; therefore the average clinical maintenance dose of MPH (0.35–0.55 mg/kg) produces 70–80% occupancy of NET. This is the first in vivo study in humans showing that clinically relevant doses of MPH occupy significant levels of NET, despite the fact that MPH has been used for the treatment of ADHD for decades. The ED$_{50}$ is lower than that for DAT (0.25 mg/kg), suggesting the potential relevance of NET inhibition in the therapeutic effects of MPH in ADHD.
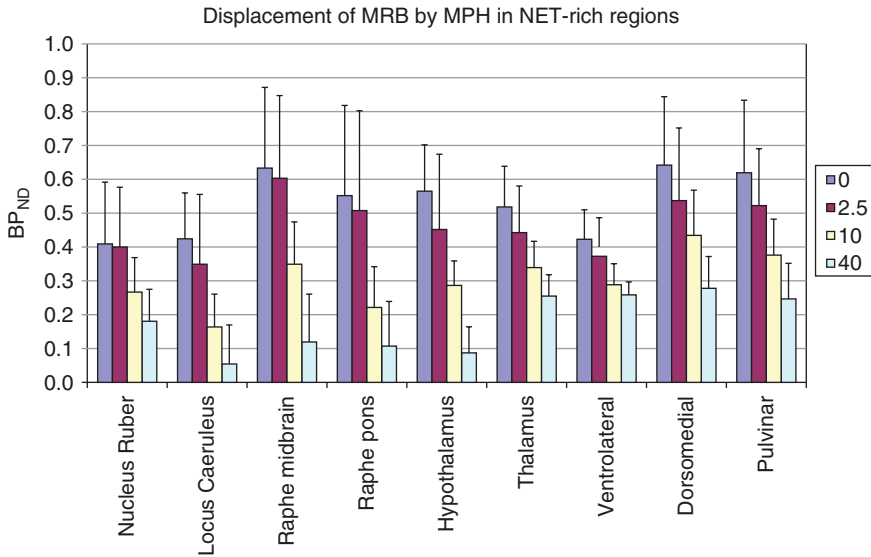
Fig. 20.5 BP$_{ND}$ values were reduced by methylphenidate in a dose-dependent manner in NET-rich regions after four doses of oral methylphenidate (0, 2.5, 10, 40 mg)
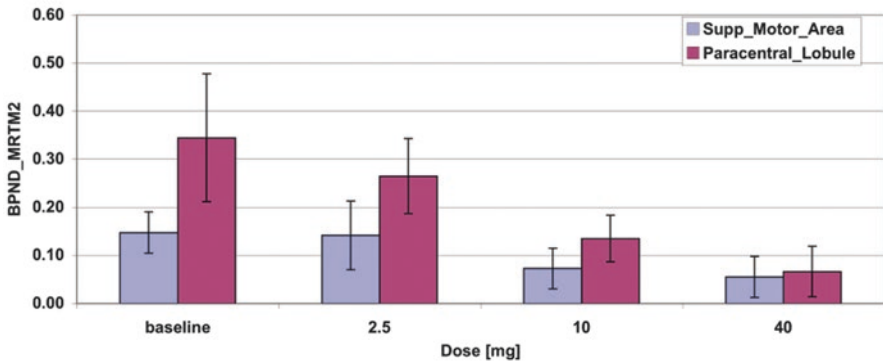
Fig. 20.6 Dose-dependent displacement of [^{11}C]MRB by methylphenidate in two cortical regions (paracentral lobule and the supplementary motor area (SMA)) were also detected after four doses of oral methylphenidate (0, 2.5, 10, 40 mg)

Previous studies also suggested that effects on delayed responding and working memory are mediated by noradrenergic afferents from LC (the highest NET density region) to PFC (Biederman et al. 2008; Solanto 1998). However, limited studies were able to link brain processes with attention and ADHD. It has also been shown that the temporal, parietal, and prefrontal (PFC) association cortices mediate different aspects of attention and that treatments for ADHD enhance catecholamine actions in PFC and improve PFC functions (Arnsten 2009). Although the density of NET in PFC is very low, we were able to detect dose-dependent displacement of [^{11}C]MRB by MP in two cortical regions in which NET densities were high enough: paracentral lobule and the supplementary motor area (SMA) (Fig. 20.6), which are

areas involved in the response to MPH and inhibition control during cognitive tasks, respectively (Li et al. 2006; Hannestad et al. 2010b; Volkow et al. 2008). Although we cannot assess the effect of MPH in the PFC directly, our assumption is that the global ED_{50} calculated using NET-rich regions, including the neocortical paracentral lobule, is similar to the ED_{50} in regions with lower NET density, such as the PFC. It is also important to fill the gap by combining PET (offers specificity) and other modality such as fMRI (offers spatial and temporal resolution) to explore the underlying molecular processes.

20.3.3 NET Imaging in PTSD

Termination of the action of NE on adrenergic receptors is accomplished primarily by NE reuptake into the presynaptic terminal via the NE transporters (NET). Animal studies and postmortem studies in humans have implicated reductions in NET expression in depression, which is often comorbid with PTSD. While acute stress does not alter NET density, there is evidence from rodent studies that repeated stress decreases NET density in the locus coeruleus (LC) and limbic brain regions (Zafar et al. 1997). These important findings, however, have not yet been confirmed in humans using in vivo methods because brain imaging of NET in living humans has been hampered for over 20 years by the lack of suitable radioligands. Given that the NET is a suitable target for antidepressants and the established role of noradrenergic mechanisms in PTSD, additional research on the distribution and function of NET in the brain of patients with PTSD is important to better understand the hypothesized dysregulations in NE function in PTSD. Thus, the hypothesis that lower NET density may be related to the development of mood and anxiety disorders (Arnsten and Li 2005; Liprando et al. 2004; Miner et al. 2006; Moron et al. 2002) was investigated using the most promising NET ligand, $[^{11}C]MRB$. In order to evaluate whether trauma exposure and PTSD would be associated with lower NET density in the locus coeruleus (LC), we conducted PET studies using $[^{11}C]MRB$ in three groups of individuals: 18 healthy adults (healthy controls: HC); 16 adults exposed to trauma who did not develop PTSD (trauma control: TC), and 22 adults exposed to trauma who developed PTSD. As a secondary aim, we evaluated the relation between NET availability in LC and a contemporary phenotypic model of PTSD symptomatology, namely, a five-factor model comprised of reexperiencing, avoidance, numbing, dysphoric arousal, and anxious arousal (Armour et al. 2012; Elhai et al. 2011; Pietrzak et al. 2012). Our study results revealed that both the PTSD group and the TC group had significantly lower NET density than the HC group (41% lower with Cohen's $d = 1.04$ for the PTSD group, and 31% lower with Cohen's $d = 0.77$ for the TC group, respectively), while NET density was not significantly different between the TC and PTSD groups (15% lower in PTSD versus TC group; Cohen's $d = 0.27$). In the PTSD group, NET density in the LC was independently positively associated with severity of anxious arousal (i.e., hypervigilance symptoms, $r = 0.52$), but not
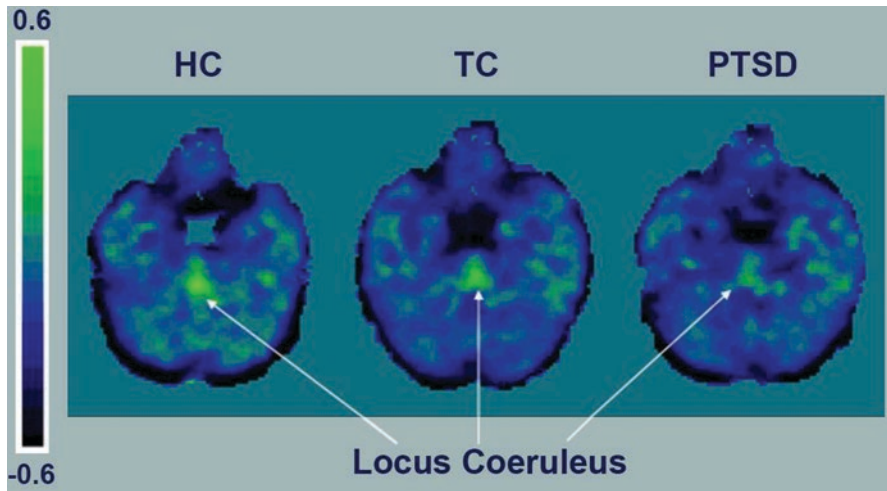
Fig. 20.7 Three representative participants were chosen with binding potential (BP) values similar to the mean of each study group. PET images are in Montreal Neurological Institute space. HC indicates healthy adults; PTSD, adults exposed to trauma who developed posttraumatic stress disorder; and TC, adults exposed to trauma who did not develop PTSD

with any of the other symptom clusters. Results of this study suggest that TC and PTSD are associated with significant reductions in NET availability in LC and that NET density in this brain region is associated with increased severity of anxious arousal symptoms among individuals with PTSD (Pietrzak et al. 2013) (Fig. 20.7).

20.3.4 NET Imaging in Alcohol Dependence

We investigated the role of NET in alcohol dependence in human subjects, in vivo, using [^{11}C]MRB and PET. Unmedicated, recently abstinent (4–6 weeks abstinent to compensate for acute alcohol withdrawal effects) nonobese men and women meeting DSM-IV (Pincus et al. 1996) [72] criteria for current alcohol dependence ($n = 15$) and age- and sex-matched healthy control subjects ($n = 15$) were studied and compared. Our hypothesis was that in areas of highest NET density, we would detect lower ligand binding commensurate with NET downregulation due to chronic alcohol exposure. We identified two brain regions in alcoholics, thalamus and locus coeruleus, that exhibited reduced NET binding potential (BP$_{ND}$). We have postulated that these regions are involved in alcohol craving, acquisition, and ingestion and that they may serve as biomarkers of altered NET expression in alcohol dependence disorders and as potential therapeutic targets for drug development (unpublished results; details of this study will be published elsewhere).

20.3.5 NET Imaging in Brown Adipose Tissue (Brown Fat)

We have conducted studies in humans to investigate the role of NET in obesity. The preliminary data suggest that there is lower NET binding in the thalamus (including pulvinar) in obese subjects (body mass index (BMI) of 34.7 ± 2.6) as compare to matched lean subjects (BMI of 23.1 ± 1.4) (unpublished results, details of this study will be published elsewhere).

Obesity is characterized by impaired energy expenditure associated with adaptive thermogenesis (Camastra et al. 1999; Golay et al. 1986; Jequier and Schutz 1985; Yeckel et al. 2009). Brown adipose tissue (BAT, brown fat), one of the primary tissues responsible for adaptive non-shivering thermogenesis in mammals (Wijers et al. 2009), was previously thought to disappear in humans as part of development into adulthood. The recent confirmation that BAT still exists in adult humans provides a renewed interest in this tissue; however, the relative importance of BAT activity to adult human whole body energy expenditure is still unknown. Lessons learned from steps taken to reduce undesirable FDG-labeling during many false-positive clinical scans (Christensen et al. 2006; Hany et al. 2002; Nedergaard et al. 2007) demonstrate that repeat scans after beta-adrenergic blockade eliminate the interfering BAT signal (Agrawal et al. 2009). These data suggest the presence of strong sympathetic nervous system (SNS) activation of BAT in humans and the potential involvement of noradrenergic system in the regulation of BAT activity. Thus, in addition to a NET obesity study in the brain, we also carried out a pilot study to look into the NET involvement in both central and peripheral SNS function and to determine whether BAT can be visualized with NET-PET imaging and whether NET binding in BAT can be quantified under both basal and activated conditions in humans.

Based on [^{18}F]FDG-PET imaging data, [^{18}F]FDG-imaging requires subjects under cold stimulation during the PET imaging, and BAT does not appear to be visualized with [^{18}F]FDG-PET at room temperature (Saito et al. 2009; van Marken Lichtenbelt et al. 2009). The BAT metabolic activity is related to age, gender, BMI, cold exposure, and medications (Cypess et al. 2009). Thus, the [^{18}F]FDG-PET approach may not be suitable for imaging BAT at the basal state, i.e., room temperature. Since BAT activation appears to be dynamic, expressing large variability due to thermal sensitivity, individual differences in BAT activation due to variations in thermal response are likely to make comparisons between obese and normal-weight subjects difficult. Moreover, [^{18}F]FDG is not specific to BAT, nor is glucose the primary substrate for BAT heat production. The [^{18}F]FDG-PET strategy will not address regulatory mechanisms that are related to the specific SNS modulation features of BAT, which are likely to be key features to understanding potential dysfunction. Therefore, it is important to develop new and more specific methods to address both the plasticity of BAT activation and basal characteristics that do not require stimulation or that could alternatively be used in combination with strategies that highlight BAT stimulated activity.

20.3.5.1   Novel Strategy to Imaging BAT in the Basal State Using NET-[¹¹C]MRB: Preclinical Evaluation

We first conducted both ex vivo and in vivo evaluation in rats using [^{11}C]MRB to determine BAT imaging in the basal state of BAT (at room temperature; r.t.), which is not achievable with [^{18}F]FDG (Lin et al. 2012). In the ex vivo study, awake male Sprague-Dawley rats were administered intravenous [^{18}F]FDG or [^{11}C]MRB after exposure to cold (4 °C for 4 h, $n = 9$) or remaining at r.t. ($n = 9$) and were sacrificed at 20, 40, and 60 min postinjection. The results demonstrate that the uptake of [^{11}C]MRB in BAT was three times higher than [^{18}F]FDG at r.t. ($P = 0.0088$), and the cold exposure increased [^{18}F]FDG uptake in BAT tenfold compared to the r.t. control (1.6 ± 0.3 vs. 0.2 ± 0.05%ID/g, $P = 0.0009$), while no significant thermal effect was observed with [^{11}C]MRB BAT uptake (0.87 ± 0.18 vs. 0.63 ± 0.09%ID/g, $P = 0.082$). In addition to the brain and heart, BAT exhibited specific [^{11}C]MRB uptake that was significantly reduced to near baseline levels ($P = 0.0013$) by pre-treatment with unlabeled MRB or nisoxetine. These results were concordant with the in vivo PET imaging of anesthetized rats, which clearly demonstrated intense [^{11}C]MRB uptake in the interscapular BAT of both r.t. and cold-exposed rats; in contrast, [^{18}F]FDG in BAT was only detected in rats treated with cold (Fig. 20.8).

HPLC analysis revealed that 94–99% of total radioactivity in BAT represented unchanged [^{11}C]MRB, which further supports the NET-PET strategy for imaging BAT in humans at basal conditions. This NET-PET imaging strategy for BAT will

[^{18}F]FDG   **[^{18}F]FDG**   **[^{11}C]MRB**   **[^{11}C]MRB**   **[^{11}C]MRB**
r.t.   **cold**   **r.t.**   **cold**   **blocked**
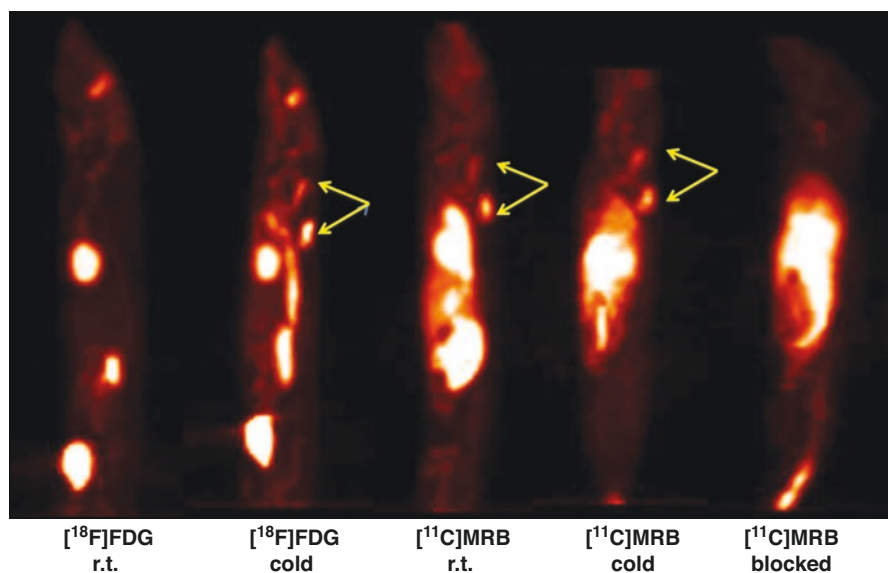
Fig. 20.8 PET images (50–70 min post-injection) on isoflurane-anesthetized rats from left to right: [^{18}F]FDG room temperature control, [^{18}F]FDG cold-exposed rat, [^{11}C]MRB room temperature control, [^{11}C]MRB cold-exposed rat, and [^{11}C]MRB following blockade by unlabeled MRB. Brown adipose tissue (BAT) is denoted by arrows

help to provide insight into whether BAT is a pivotal target tissue for therapeutic interventions designed to reduce human obesity and will also help to elucidate mechanisms related to its function/dysfunction. Our choice of the [^{11}C]MRB ligand also has other specific advantages. Studies have shown that disruption of NET function directly impacts both autonomic function and mental health (Esler et al. 1991; Ganguly et al. 1986; Haenisch et al. 2009; Hahn et al. 2008, 2005, 2003, 2009) and that NET function is regulated both centrally and peripherally by insulin (Robertson et al. 2010). Unlike many other NET ligands, [^{11}C]MRB is able to cross the blood-brain barrier, allowing for simultaneous central and peripheral imaging. Thus, using [^{11}C]MRB may help to further elucidate mechanisms of BAT action and the role of NET in energy balance of obesity and insulin resistance by simultaneously correlating the CNS and peripheral SNS functions.

20.3.5.2   Novel Strategy to Imaging BAT in the Basal State Using NET-[^{11}C]MRB in Humans

Ten healthy, Caucasian subjects (5 M, age 24.6 ± 2.6, BMI 21.6 ± 2.7 kg/m^2; 5 F, age 25.4 ± 2.1, BMI 22.1 ± 1.0 kg/m^2) underwent ^{11}C-MRB PET-CT imaging (mCT PET/CT scanner, Siemens/CTI, USA) for cervical/supraclavicular BAT under r.t. and cold-stimulated conditions (RPCM Cool Vest; enthalpy 15 °C) compared to [^{18}F]FDG PET-CT imaging (Hwang et al. 2015). Cold condition scans were performed while subjects wore a climate vest loaded with cold packs, whereas room temperature scans were conducted using the same climate vest loaded with room temperature packs, to avoid potential biases from changes in attenuation between the two conditions. For [^{18}F]FDG studies, subjects wore the climate vest for half an hour before [^{18}F]FDG injection, during the 60-min period between the injection and scan, and during the 25–30 min scan. For [^{11}C]MRB PET-CT scans, the climate vest was placed on the subjects 30 min prior to intravenous [^{11}C]MRB administration and remained on the subject for the duration of the 120–125 min dynamic scan. PET-CT scanning began with the administration of [^{11}C]MRB. All scans were performed under fasting conditions.

For analysis of tracer uptake, we chose an [^{18}F]FDG SUV >1.5 and Hounsfield units (−200 to −50) as has been used by others (Blondin et al. 2014; Lee et al. 2014) to define BAT tissue. Uptake of [^{11}C]MRB was quantified as the distribution volume ratio (DVR) using the occipital cortex as the reference region since the tracer binding has been well characterized in our previous brain studies in humans (Ding et al. 2010; Hannestad et al. 2010a; Pietrzak et al. 2013; Li et al. 2014), and uptake of metabolites of [^{11}C]MRB was minimal in rodent BAT. Muscle was also chosen as a peripheral reference, and a ratio of BAT-DVR to muscle-DVR (BAT/muscle) was compared. Total body fat and lean body mass were assessed via bioelectrical impedance analysis.

Consistent with previous studies, we found [^{18}F]FDG uptake in BAT was difficult to identify at r.t. but easily detected with cold stimulation ($p = 0.01$). In contrast, BAT [^{11}C]MRB uptake (also normalized for muscle) was equally evident under both r.t. and cold conditions (BAT DVR, r.t. 1.0 ± 0.3 vs. cold 1.1 ± 0.3, $p = 0.31$; BAT/muscle DVR, r.t. 2.3 ± 0.7 vs. cold 2.5 ± 0.5, $p = 0.61$) (Fig. 20.9). Importantly, BAT
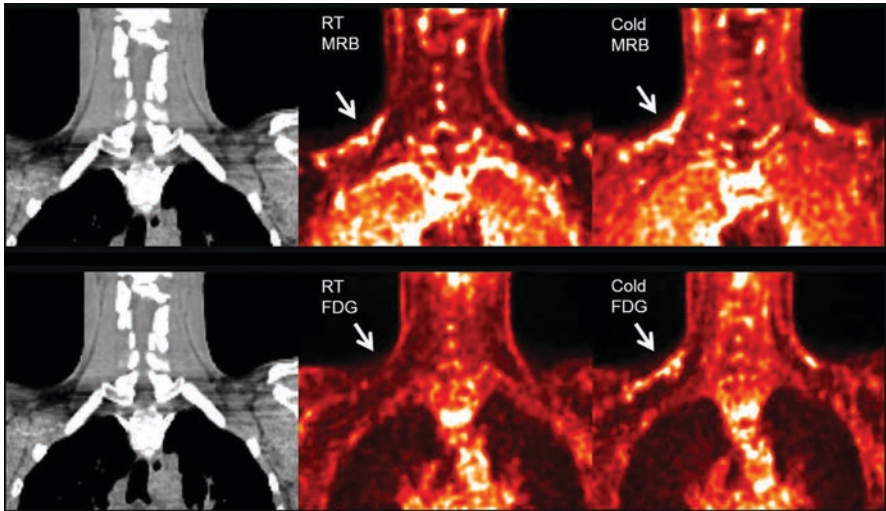
Fig. 20.9 PET and CT images in one representative male subject showed that [18F]FDG uptake in BAT was observed under mild cold conditions but not at room temperature, while [11C]MRB uptake in BAT was observed under both room temperature and cold conditions. [18F]FDG and [11C]MRB are scaled from SUV 0 (black) to SUV 2 (white). [11C]MRB images are computed from the average of frames acquired between 40 to 60 min post-injection

DVR and BAT/muscle DVR of [11C]MRB at r.t. correlated positively with core body temperature ($r = 0.76$, $p = 0.05$ and $r = 0.92$, $p = 0.004$, respectively), a relationship not observed with [18F]FDG ($p = 0.63$). There were no relationships between [11C]MRB uptake and heart rate or BMI. However, the magnitude of change in 11C-MRB BAT uptake in response to cold correlated negatively with percent body fat ($r = -0.74$, $p = 0.04$) and positively with lean mass ($r = 0.71$, $p = 0.05$), which showed a gender difference (Fig. 20.10). This gender difference most likely reflected the difference in body composition and body temperature between men and women. There were no relationships between the change in [18F]FDG uptake in response to cold and body composition, BMI, body temperature, heart rate, or blood pressure.

We recently assessed BAT using a state-of-the-art PET/MR combined scanner with simultaneous acquisition (Biograph mMR, Siemens). Representative images of the overlaid PET data on MR fat images acquired with a 3D two-point Dixon sequence showed excellent co-localization of BAT area from the two imaging modalities (Fig. 20.11). The simultaneously acquired PET and MR-fat images significantly facilitated the localization and quantification of BAT. Further, using a 3D multiple gradient echo sequence, MR quantification of BAT allows mapping of percentage water for quantifying fat, water, and R2* (= 1/T2*) in BAT. The fat fraction (FF) can be calculated from PDFF = F/(F + W), where PDFF is the proton density FF, F is the fat signal, and W is the water signal. The FF is known to be lower in BAT than in WAT (Hu et al. 2013), while R2* is expected to be higher. Using this strategy, the changes in fat fraction and fat volume in BAT, measured with MR, can be

Fig. 20.10 Relationship between change in MRB uptake in response to cold and (**a**) body temperature after cold; (**b**) percentage body fat; (**c**) lean body mass (open circle = men; closed circle = women)
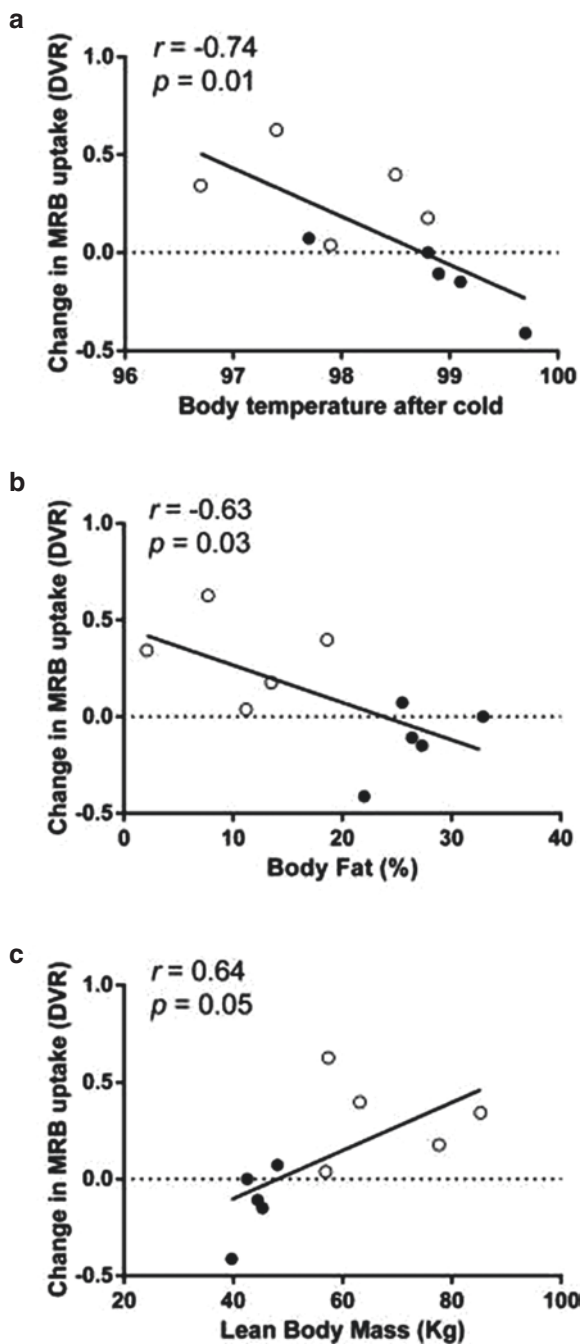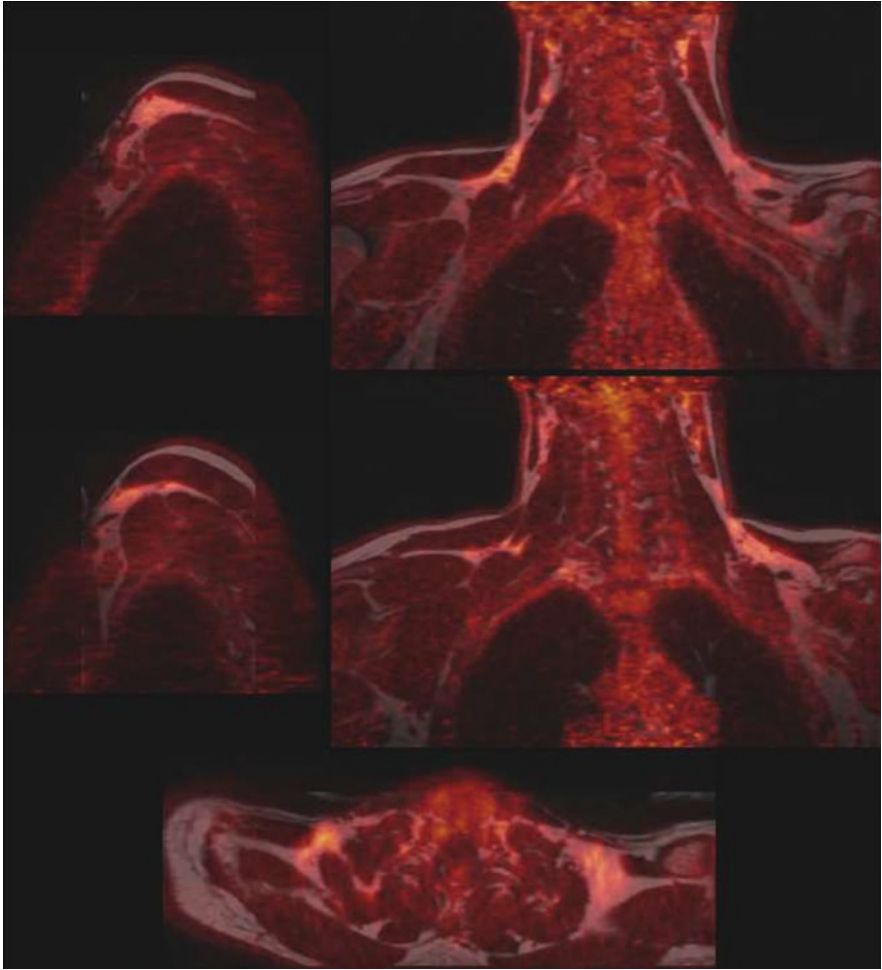
Fig. 20.11 PET-BAT image overlaid on MR-fat images acquired with a 3D two-point Dixon sequence. Images have been reformatted into three planes: sagittal through each shoulder (left), coronal (right), and axial (bottom)

correlated with the BAT activation measured with PET after various interventions. Combination of the high specificity of PET and high spatial resolution of MR will provide unique information on BAT quantification.

20.3.6 NET Imaging in Obesity

In collaboration with University Medical Centre in Leipzig, the central NET system was investigated using [^{11}C]MRB, including NET imaging in obesity.

20.3.6.1 Linking NET to Emotional Distress and Obesity

In a group of lean to morbidly obese individuals ($n = 20$), Melasch et al. (Melasch et al. 2016) showed that an increased body mass index (BMI) is related to a lowered NET availability within the hypothalamus, known as the brain's homeostatic control site. The hypothalamus displayed a strengthened connectivity in relation to the individual hypothalamic NET availability to the anterior insula/frontal operculum, as well as the medial orbitofrontal cortex, assumed to host the primary and secondary gustatory cortex, respectively ($n = 19$). The resting-state activity in these two regions was correlated positively to the BMI and the scores of IWQOL-Lite (the impact of weight on quality of life-Lite questionnaire) (Fig. 20.12), but not to the Beck depression inventory (Pattinson et al. 2009), suggesting that the higher the resting-state activity in these regions, and hence the higher the BMI, the stronger the negative impact of the body weight on the individual's emotional well-being was. This pilot study suggests that the loss in emotional well-being with weight is embedded within the central norepinephrine network.

NET-Dependent Changes and Neurobehaviour in Obesity
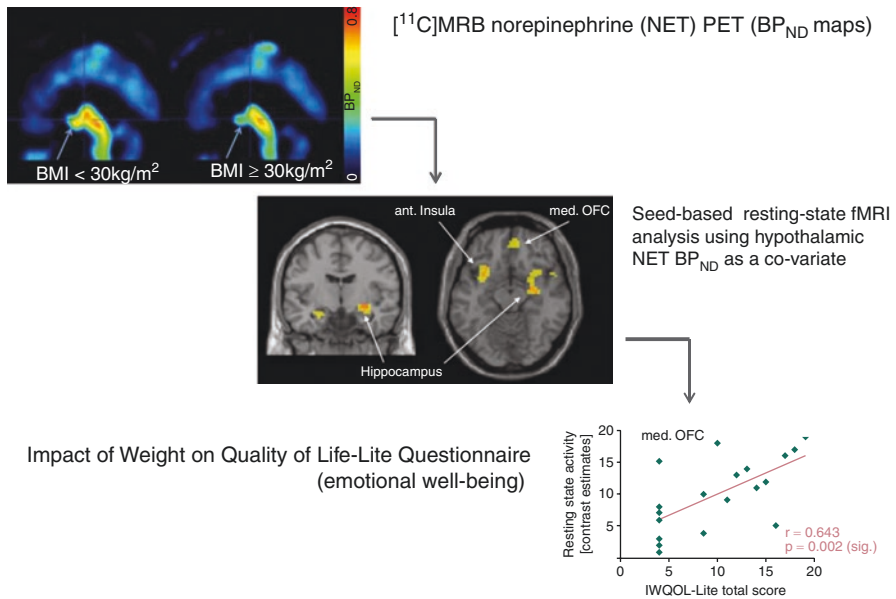
Fig. 20.12 NET-Dependent Changes and Neurobehaviour in Obesity: Seed-based resting-state fMRI analysis using hypothalamic NET BP_{ND} as a co-variate showing stronger connectivity between the hypothalamus and limbic brain areas that determines emotional well-being

20.3.6.2 Central In Vivo NET Availability Is Altered in Emotional Eating of Individuals with Obesity

Our previous studies in cocaine abuse using [^{11}C]MRB indicated significant upregulation of NET in the thalamus of cocaine users, as compared to healthy controls (Ding et al. 2010). However, when comparing PET imaging using [^{11}C]MRB for healthy controls and morbidly obese subjects, a decrease in NET availability was found in the thalamus in obese subjects (Li et al. 2014). These findings present a notable difference in neurotransmission between individuals with substance use disorder and those with obesity. To investigate an association between NET availability in obese individuals and emotional eating (EE), Bresch et al. (Bresch et al. 2017) sought to measure EE through the EE subscale of the Dutch Eating Behavior Questionnaire for obese subjects and healthy controls before performing PET scans with [^{11}C]MRB. This study did not find significant differences in EE scores and regional NET levels between healthy controls (BMI 23.9 ± 2.5 kg/m^2) and obese participants (BMI 42.4 ± 3.7 kg/m^2). However, for obese individuals only, correlative data analyses pointed to a sinoidal distribution pattern as a higher degree of EE related to lower NET availability in the locus coeruleus and to higher NET availability in the left thalamus (Fig. 20.13) Collectively, these studies suggest that NE transmission is regionally impaired in substance use disorder, obese, and EE populations and that regional fluctuations in NET availability determine the deviations in motivated behavior, such as emotional eating, which are seen in substance use disorder and obesity (Lindgren et al. 2018).
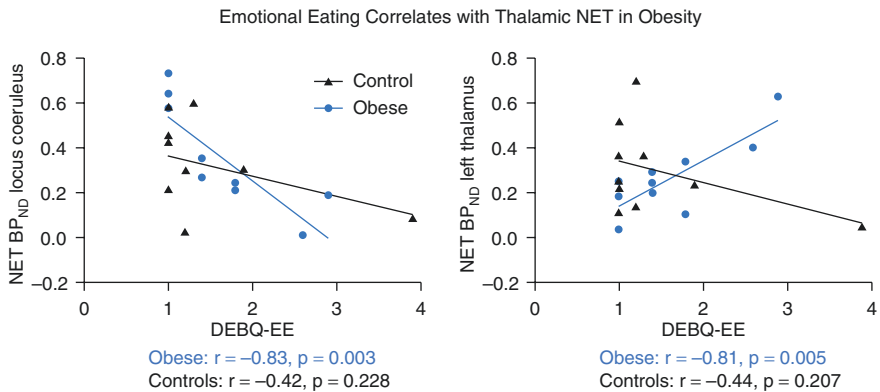
Fig. 20.13 Emotional Eating Correlates with Thalamic NET in Obesity: for obese individuals higher EE scores correlated with lower NET availability in the locus coeruleus and higher NET availability in the left thalamus

20.3.6.3 NET Availability and Success of Weight Loss in Obese Individuals

A recent study was carried out by Vettermann et al. to compare central NET availability in ten obese, otherwise healthy individuals with a body mass index (BMI) of 42.4 ± 3.7 kg/m^2 (age 34 ± 9 years, four women) and ten matched nonobese, healthy controls (BMI 23.9 ± 2.5 kg/m^2, age 33 ± 10 years, four women) using [^{11}C]MRB before and 6 months after dietary intervention. The results indicated that an increase in binding potential (BP$_{ND}$) in the insula and the hippocampus of obese individuals correlated well with changes in BMI ($-3.3 \pm 5.3\%$; $p = 0.03$) following completion of the 6-mo dietary intervention. Furthermore, NET availability before intervention could help to predict the amount and success of weight loss in obese individuals. Lower BP$_{ND}$ in these regions (but also in the midbrain and the prefrontal cortex) at baseline was associated with higher achieved weight loss (e.g., hippocampal area R2 = 0.80; $p < 0.0001$) (Fig. 20.14).

NET Availability Predicts Weight Loss in Obesity
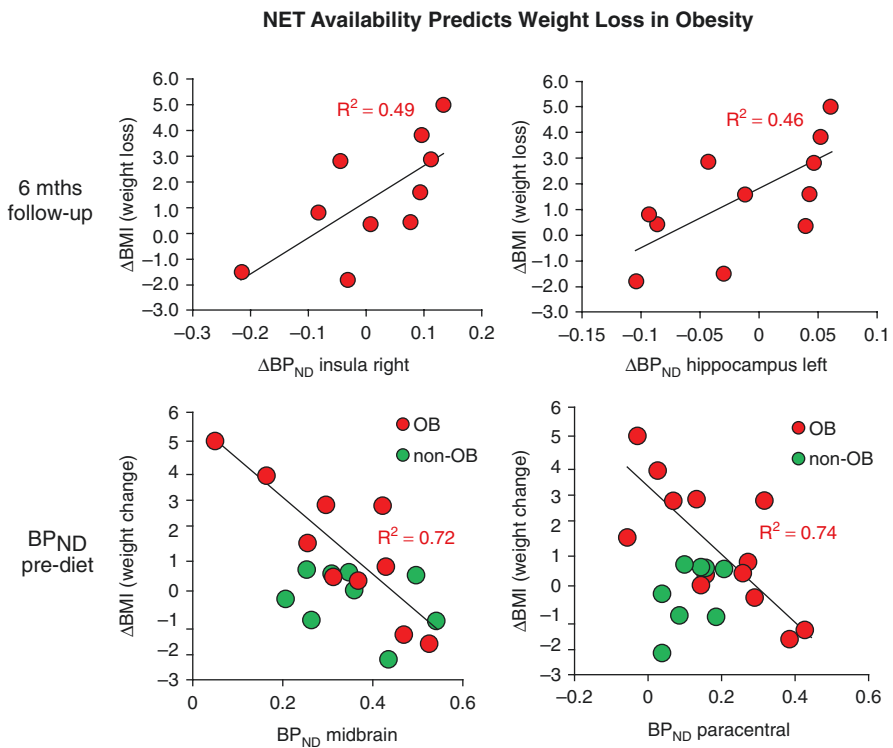
Vettermann F, et al. Eur J Nucl Med Mo Imaging. 2018 Jul;45(9):1618-1625.

Fig. 20.14 NET Availability Predicts Weight Loss in Obesity: NET availability before intervention could help predict the amount and success of weight loss in obese individuals

These first longitudinal interventional data on NET availability in highly obese individuals indicate that the central NA system is modifiable and that weight loss may be predicted by measuring regional NAT availability prior to intervention. If confirmed, such measurement of NAT availability with PET may serve as an individual biomarker to predict the likelihood of achieving weight loss after dietary intervention and offer the possibility of identifying patients who will or will not benefit from dietary intervention. Whether measurement of NET availability with PET is also able to predict the success of other anti-obesity treatments such as bariatric surgery and might therefore be used in the future in formulating personalized interventional strategies in individuals with obesity needs to be evaluated in prospective comparative studies.

20.3.7 NET in Parkinson's Disease (PD)

Although postmortem studies have detected a substantial noradrenergic deficit in Parkinson's disease patients (Kish et al. 1984), in vivo assessment of the noradrenergic system has been hampered by the lack of suitable imaging tools. Through our extensive development and validation studies in both nonhuman primates and humans, [^{11}C]MRB has now been adopted by many other researchers for NET imaging, including in PD research (Nahimi et al. 2018; Sommerauer et al. 2018a, b).

Rapid eye movement sleep behavior disorder (RBD) accompanies Parkinson's disease and its presence predicts an unfavorable disease course with a higher propensity to cognitive impairment and orthostatic hypotension. Noradrenergic innervation of the brain arises almost exclusively from the neuromelanin-containing cells of the locus coeruleus. Using the neuromelanin-sensitive MR and NET availability biomarker ([^{11}C]MRB), the association of RBD, cognition, and autonomic dysfunction in PD with loss of noradrenergic function was examined (Sommerauer et al. 2018a). The authors found that Parkinson's disease patients with RBD showed decreased locus coeruleus neuromelanin signal on MRI ($P < 0.001$) and widespread reduced binding of [^{11}C]MRB ($P < 0.001$), which correlated with amount of REM sleep without atonia. Parkinson's disease with RBD was also associated with a higher incidence of cognitive impairment, slowed EEG activity, and orthostatic hypotension.

Another recent study (Nahimi et al. 2018) using [^{11}C]MRB showed reduced NET binding in patients with PD, as compared to controls, with significant declines in red nucleus and thalamus. They found no associations between [^{11}C]MRB BP$_{ND}$ estimates and disease severity in terms of disease duration, disease stage, or severity of motor symptoms. However, tremor symptoms in PD patients were associated with higher [^{11}C]MRB BP$_{ND}$ in the thalamus compared to patients without tremor. It is known that PD patients with tremor-dominant disease represent a subgroup of a more benign course of disease with slower progression of motor and non-motor symptoms and lower frequency of cognitive impairment. So this better-preserved NET availability (noradrenergic neurons) when compared to the akinetic-rigid subtype could be potentially an important biomarker, though a larger sample size is needed to reproduce this interesting result.

20.3.8 NET in Aging and Alzheimer's Disease (AD)

There is little published data on how in vivo NET availability varies with age, but our preliminary data have documented declines in NET availability in healthy adults in the pulvinar, hypothalamus, and LC (P = 0.03, 0.009, 0.04, respectively; age range = 25–54) (Fig. 20.15). Similar results were reproduced in a collaborative project with a Vancouver group (Yatham et al. 2018) and in a recent study (Vanicek et al. 2014). According to our previous study, the % BP_{ND} change for DAT was approx. 0.7% per year (Volkow et al. 1996); however, the % BP_{ND} decline per year for NET was about threefold faster based on our pilot study (Ding et al. 2010). These intriguing results warrant further investigation with a larger sample size.

Alzheimer's disease (AD) is a major health challenge in our aging society. An improved understanding of its underlying pathological mechanisms is urgently needed to enable the development of effective treatments. Postmortem findings indicate that tau pathology emerges decades before amyloid pathology, appearing first in the brainstem—in particular in the locus coeruleus (LC, the major source of the brain's norepinephrine [NE]) (Baker et al. 1989; Sharma et al. 2010; Aston et al. 1986)—before slowly spreading to the entorhinal cortex and other LC targets, including hippocampus (Braak et al. 2011). The LC is particularly vulnerable to toxins and infection and is often the first place AD pathology appears. Postmortem studies suggest that loss of LC neurons predicts onset and severity of AD symptoms better than Aβ/neurofibrillary tangle pathology or cell loss in any other brain region implicated in AD (Bondareff et al. 1981, 1987; Burke et al. 1988; Busch et al. 1997; Chan-Palay and Asan 1989; Gannon et al. 2015; German et al. 1992; Hardy et al. 1985; Iversen et al. 1983; Mann et al. 1982; Marcyniuk et al. 1986; Strong et al.
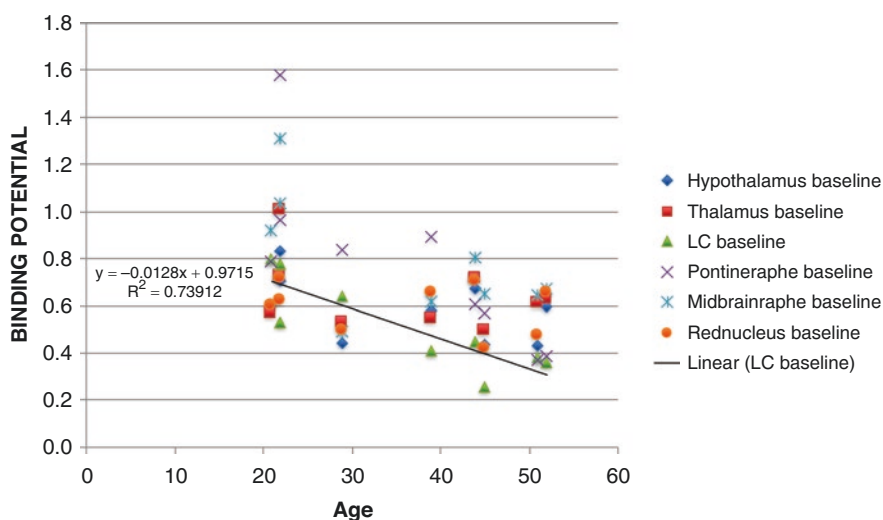
Fig. 20.15 Age effect on NET availability (binding potential) in HC

1991; Wilson et al. 2013). However, *it is not yet possible to measure the early progression of tau pathology in the LC of living humans* due to the off-target binding of the current tau radioligands to neuromelanin, which is found at high levels in the LC (Hansen et al. 2016) (Lemoine et al. 2018; Saint-Aubert et al. 2017).

Our studies in humans using NET-[^{11}C]MRB imaging demonstrated a special vulnerability of LC to aging and stress (PTSD), suggesting that NET dysfunction plays an important role in aging. We and others have recently implemented a specific neuromelanin-MR sequence (Clewett et al. 2016; Keren et al. 2009, 2015; Sasaki et al. 2006) that makes it possible to reliably delineate and quantitate the NET-MRB binding (NET availability) and MR (neuromelanin) signal intensities in LC (indexing functional and structural integrity) by using state-of-the-art PET-MR combined imaging with simultaneous acquisition. We hypothesize that NET-MRB imaging may provide a new noninvasive approach for preclinical diagnosis, staging, and assessment of therapeutic interventions in AD.

20.3.9 Kinetic Modeling for NET Imaging Studies in the Brain

It is important to point out that arterial input function measurement was conducted for almost all of our PET-NET brain imaging studies using [^{11}C]MRB (Ding et al. 2010; Gallezot et al. 2007, 2010; Logan et al. 2007, 2005; Hannestad et al. 2010b; Li et al. 2005). This made it possible to quantify the volume of distribution (V_T) of [^{11}C]MRB using multilinear analysis MA1 (Ichise et al. 2002) and a direct comparison of the quantification of [^{11}C]MRB binding potential (BP_{ND}) without arterial blood sampling using either MRTM2 or SRTM2 (Ichise et al. 2002; Innis et al. 2007). With these validation techniques (Gallezot et al. 2010; Hannestad et al. 2010b), we evaluated several candidate reference regions so that placement of arterial lines may not be needed for future NET imaging studies using [^{11}C]MRB.

As described above, one of the intrinsic challenges for imaging NET is its wide distribution throughout the brain, with relatively low contrast between transporter-poor and transporter-rich regions. It has been shown that the lowest NET densities measured by autoradiography in rhesus monkeys were in the putamen and caudate (Smith et al. 2006), while the lowest concentration of NET in humans was found in the occipital cortex, based on one in vitro autoradiography study in humans using [^{18}F]F-MeNER-D2 (Schou et al. 2005). Thus, evaluation of caudate, putamen, and occipital cortex as potential reference regions was conducted in both rhesus monkeys and humans.

Based on our [^{11}C]MRB studies in nonhuman primates (NHP), we found that the use of caudate as the reference region in NHP leads to the least bias. This bias is not significant as compared to the "gold standard" IC_{50} estimate obtained using only V_T or V_T/f_P values (Gallezot et al. 2010). Moreover, similar results were obtained while using the binding potentials BP_F and BP_{ND} (Innis et al. 2007). The latter could be estimated without arterial blood sampling by using MRTM2 and provided results equivalent to those obtained with the arterial data, i.e., without introducing further bias. Based on our [^{11}C]MRB studies in both NHP and humans, it seems that the

fraction of displaceable binding in the occipital cortex for [^{11}C]MRB is higher in rhesus monkeys than in humans.

Interestingly, the issue of selecting a reference region seems to be less troublesome in humans since all three NET-poor regions (caudate, putamen and occipital) were considered as reasonable reference regions based on the results of our occupancy study of methylphenidate in humans (Hannestad et al. 2010b) (see above discussion). The occipital cortex has lower levels of NET than the striatum (Schou et al. 2005) and is a relatively bigger region with a simpler shape than the caudate and putamen, making it more suitable as the reference region for human studies, especially when ROIs are delineated with an automated template. Thus, using MRTM2 with a reference region to quantify [^{11}C]MRB binding without arterial sampling for occupancy studies is feasible in nonhuman primates and adequate in humans.

20.4   Summary and Outlook

The main purpose of this review article is to outline the progress that has been made on PET imaging of the NET system during the past decade, starting from ligand development, ligand characterization, toxicology evaluation, and ligand validation and approval for human studies (Ding et al. 2006), leading to translational research in humans. A few specific applications using [^{11}C]MRB in the scope of evaluation of disease abnormality, determination of drug occupancy, understanding biological processes, and interpretation of drug mechanisms have been explored. Our pilot investigations clearly indicated how little we know about the role of NET in various CNS disorders. As previously mentioned, many of the important findings resulted from studies in vitro using postmortem tissues and have suggested the implication of NET in various neurological and psychiatric disorders, but they have never been verified via in vivo methods due to the lack of suitable radioligands.

We have just begun to learn the role of NET in the pathophysiology and the treatment of several disorders, including cocaine abuse, ADHD, depression, PTSD, alcohol dependence, obesity, and also in normal aging. For example, cocaine is the most abused drug with the highest reinforcing ability. Its effect on the dopamine system has been well characterized; however, its effect on NET in humans has never been investigated. Our studies on cocaine abusers and the effect of duration of abstinence on NET binding provide the first evidence of NET abnormalities in cocaine dependence.

Our occupancy studies of MPH demonstrate that clinically relevant doses block 70% to 80% of NET, whereas only 60% to 70% of DAT is blocked at similar doses. Despite of the fact that MPH has been the most prescribed drug for the treatment of ADHD over the last 50 years, our study provides the first evidence questioning the traditional thinking that the therapeutic effect of MPH is mainly due to its inhibition of DAT.

Our PET imaging studies on ATX unveiled its high in vivo affinity toward both NET and SERT, questioning the traditional thinking that ATX is a selective NET inhibitor. These results suggest a cautious interpretation of the therapeutic mode of

action of ATX for treatment of depression and ADHD, as the therapeutic effect of ATX may be more complex than selective blockade of the NET.

It is important to point out that most of our investigations to evaluate disease abnormality are pilot studies with relatively small sample sizes. Further studies employing larger samples are needed to confirm the results. Furthermore, other important aspects (e.g., gender) that have been linked to various disorders may be revealed.

Though the major focus of this chapter is on our translational research using [^{11}C]MRB, its F-18 analogues, such as [^{18}F]fluoromethyl (*(S,S)*-[F]FMeNER) (Schou et al. 2004) and [^{18}F]fluoroethyl analogs, (*(S,S)*-[^{18}F]FRB) (Ding et al. 2006, 2005; Lin et al. 2005), also showed promising results. Unfortunately, their relatively lower binding affinity and defluorination problems precluded their further translational research in humans (Ding et al. 2006; Takano et al. 2008a, b). NET ligand development work is ongoing. Future studies using PET ligands with greater affinity and specificity toward NET may help to further examine the role of noradrenergic function in various CNS disorders and facilitate our understanding of the role of NET in living humans, without having to rely solely on results from postmortem studies.

New strategies are being developed for synergistic PET/MR imaging using the simultaneous data acquisition capabilities of a combined PET/MR scanner (e.g., Siemens mMR) in order to take advantage of the spatial resolution of MRI with the biochemical and functional information from PET. This state-of-the-art PET/MR combined modality would facilitate co-registration; for example, the locus coeruleus (LC), which plays an important role in various CNS disorders and is the region of highest NET density, has a very small structure that poses a challenge to NET imaging due to difficulties encountered during PET and MRI co-registration when separate PET and MRI scans are collected—a problem that can be addressed by simultaneous MR and PET data acquisition. Furthermore, it would permit simultaneous imaging of physiologic and pathophysiologic processes and avoid the potential confounding effects of day-to-day and status variations. It would also provide an unprecedented opportunity to correlate PET measures with MR-detected patterns of neural synchrony in both cortical and subcortical regions, facilitating the search process for optimal biomarkers for various CNS disorders. For example, we have demonstrated the dose-dependent occupancy of MPH in LC, subcortical and cortical regions by using NET-PET imaging (see above Sect. 3.2.5). The use of PET/MR with simultaneous acquisition after the treatment with MPH may facilitate our understanding of the functional connectivity among the brain regions by linking the effect of MPH from LC to its projection into cortical regions, including PFC.

Further, NET imaging in PD and AD may provide a new noninvasive approach for preclinical diagnosis, staging, and assessment of therapeutic interventions in these neurodegenerative diseases.

References

Ding YS, Lin KS, Logan J (2006) PET imaging of norepinephrine transporters. Curr Pharm Des 12:3831–3845

Ding YS, Lin KS, Garza V, Carter P, Alexoff D, Logan J et al (2003) Evaluation of a new norepinephrine transporter PET ligand in baboons, both in brain and peripheral organs. Synapse 50:345–352

Ding YS, Lin KS, Logan J, Benveniste H, Carter P (2005) Comparative evaluation of positron emission tomography radiotracers for imaging the norepinephrine transporter: (S,S) and (R,R) enantiomers of reboxetine analogs (11C methylreboxetine, 3-Cl- 11C methylreboxetine and 18F fluororeboxetine), (R)- 11C nisoxetine, 11C oxaprotiline and 11C lortalamine. J Neurochem 94:337–351

Lin KS, Ding YS, Kim SW, Kil KE (2005) Synthesis, enantiomeric resolution, F-18 labeling and biodistribution of reboxetine analogs: promising radioligands for imaging the norepinephrine transporter with positron emission tomography. Nucl Med Biol 32:415–422

Smith HR, Beveridge TJ, Porrino LJ (2006) Distribution of norepinephrine transporters in the non-human primate brain. Neuroscience 138:703–714

Tejani-Butt SM (1992) 3H nisoxetine: a radioligand for quantitation of norepinephrine uptake sites by autoradiography or by homogenate binding. J Pharmacol Exp Ther 260:427–436

Kaufman MJ, Spealman RD, Madras BK (1991) Distribution of cocaine recognition sites in monkey brain: I. in vitro autoradiography with [3H]CFT. Synapse 9:177–187

Zeng Z, Chen TB, Miller PJ, Dean, Tang, Ys, et al. The serotonin transporter in rhesus monkey brain: comparison of DASB and citalopram binding sites. Nucl Med Biol 2006;33:555–563.

Charnay Y, Leger L, Vallet PG, Hof PR, Jouvet M, Bouras C (1995) 3H nisoxetine binding sites in the cat brain: an autoradiographic study. Neuroscience 69:259–270

Ding Y-S, Fowler J (2005) New-generation radiotracers for nAChR and NET. Nucl Med Biol 32(7):707–718

Ding YS, Singhal T, Planeta-Wilson B et al (2010) PET imaging of the effects of age and cocaine on the norepinephrine transporter in the human brain using (S,S)- (11)C O-methylreboxetine and HRRT. Synapse 64(1):30–38

Gallezot JD, Planeta-Wilson B, Wang GK, Carson RE, Ding YS (2007) Parametric imaging of the NET radioligand C-11 MRB in humans: a test-retest study. J Nucl Med 48:159P

Gallezot JD, Weinzimmer D, Nabulsi N, Lin SF, Fowles K, Sandiego C et al (2010) Evaluation of 11C MRB for assessment of occupancy of norepinephrine transporters: studies with atomoxetine in non-human primates. NeuroImage 56:268–279

Hannestad J, Gallezot JD, Planeta-Wilson B et al (2010a) Clinically relevant doses of methylphenidate significantly occupy norepinephrine transporters in humans in vivo. Biol Psychiatry 68:854–860

Beveridge TJ, Smith HR, Nader MA, Porrino LJ (2005) Effects of chronic cocaine self-administration on norepinephrine transporters in the nonhuman primate brain. Psychopharmacology 180:781–788

Macey DJ, Smith HR, Nader MA, Porrino LJ (2003) Chronic cocaine self-administration upregulates the norepinephrine transporter and alters functional activity in the bed nucleus of the stria terminalis of the rhesus monkey. J Neurosci 23:12–16

Mash DC, Ouyang Q, Qin Y, Pablo J (2005) Norepinephrine transporter immunoblotting and radioligand binding in cocaine abusers. J Neurosci Methods 143:79–85

Weinshenker D, Schroeder JP (2007) There and back again: a tale of norepinephrine and drug addiction. Neuropsychopharmacology 32:1433–1451

Li CSR, Huang C, Constable RT, Sinha R (2006) Imaging response inhibition in a stop signal task – neural correlates independent of signal monitoring and post-response processing. J Neurosci 26:186–192

Burchett SA, Bannon MJ (1997) Serotonin, dopamine and norepinephrine transporter mRNAs: heterogeneity of distribution and response to "binge" cocaine administration. Brain 49:95–102

Dopheide JA, Pliszka SR (2009) Attention-deficit-hyperactivity disorder: an update. Pharmacotherapy 29:656–679

Barkley RA (1997) Behavioral inhibition, sustained attention, and executive functions: constructing a unifying theory of ADHD. Psychol Bull 121(1):65–94

Bush G (2010) Attention-deficit/hyperactivity disorder and attention networks. Neuropsychopharmacology 35:278–300

Makris N, Biederman J, Monuteaux MC, Seidman LJ (2009) Towards conceptualizing a neural systems-based anatomy of attention-deficit/hyperactivity disorder. Dev Neurosci 31:36–49

Madras BK, Miller GM, Fischman AJ (2005) The dopamine transporter and attention-deficit/hyperactivity disorder. Biol Psychiatry 57:1397–1409

Arnsten AF (2009) Toward a new understanding of attention-deficit hyperactivity disorder pathophysiology: an important role for prefrontal cortex dysfunction. CNS Drugs 23(Suppl 1):33–41

Arnsten AF (2006) Fundamentals of attention-deficit/hyperactivity disorder: circuits and pathways. J Clin Psychiatry 67(suppl 8):7–12

Bymaster FP, Katner JS, Nelson DL, Hemrick-Luecke SK, Threlkeld PG, Heiligenstein JH et al (2002) Atomoxetine increases extracellular levels of norepinephrine and dopamine in prefrontal cortex of rat: a potential mechanism for efficacy in attention deficit/hyperactivity disorder. Neuropsychopharmacology 27:699–711

Chamberlain SR, Del Campo N, Dowson J, Müller U, Clark L, Robbins TW et al (2007a) Atomoxetine improved response inhibition in adults with attention deficit/hyperactivity disorder. Biol Psychiatry 62:977–984

Del Campo N, Chamberlain SR, Sahakian BJ, Robbins TW (2011) The roles of dopamine and noradrenaline in the pathophysiology and treatment of attention-deficit/hyperactivity disorder. Biol Psychiatry 69:e145–e157

Michelson D, Faries D, Wernicke J, Kelsey D, Kendrick K, Sallee FR et al (2001) Atomoxetine in the treatment of children and adolescents with attention-deficit/hyperactivity disorder: a randomized, placebo-controlled, dose-response study. Pediatrics 108:E83

Spencer TJ, Biederman J, Wilens TE, Faraone SV (2002) Novel treatments for attention deficit/hyperactivity disorder in children. J Clin Psychiatry 63(Suppl 12):16–22

Swanson JM, Volkow ND (2009) Psychopharmacology: concepts and opinions about the use of stimulant medications. J Child Psychol Psychiatry 50:180–193

Volkow ND, Wang GW, Fowler JS, Logan J, Gerasimov M, Maynard L et al (2001) Therapeutic doses of oral methylphenidate significantly increase extracellular dopamine in the human brain. J Neurosci 21:RC121

Logan J, Wang GJ, Telang F, Fowler JS, Alexoff D, Zabroski J et al (2007) Imaging the norepinephrine transporter in humans with (S, S)- 11C O-methyl reboxetine and PET: problems and progress. Nucl Med Biol 34:667–679

Seneca N, Gulyás B, Varrone A, Schou M, Airaksinen A, Tauscher J et al (2006) Atomoxetine occupies the norepinephrine transporter in a dose-dependent fashion: a PET study in nonhuman primate brain using (S, S)- 18F FMeNER-D2. Psychopharmacology 188:119–127

Faraone SV, Biederman J, Spencer T, Michelson D, Adler L, Reimherr F et al (2005) Efficacy of atomoxetine in adult attention-deficit/hyperactivity disorder: a drug-placebo response curve analysis. Behav Brain Funct 1:16

Barton J (2005) Atomoxetine: a new pharmacotherapeutic approach in the management of attention deficit/hyperactivity disorder. Arch Dis Child 90(Supp 1):i26–ii9

Robbins TW, Arnsten AF (2009) The neuropsychopharmacology of fronto-executive function: monoaminergic modulation. Annu. Rev. Neurosci 32:267–287

Volkow ND (2006) Stimulant medications: how to minimize their reinforcing effects? Am J Psychiatry 163(3):359–361

Dell'Osso B, Palazzo MC, Oldani L, Altamura AC (2010) The noradrenergic action in antidepressant treatments: pharmacological and clinical aspects. CNS Neurosci Ther 17:723–732

O'Sullivan JB, Ryan KM, Curtin NM, Harkin A, Connor TJ (2009) Noradrenaline reuptake inhibitors limit neuroinflammation in rat cortex following a systemic inflammatory challenge: implications for depression and neurodegeneration. Int J Neuropsychopharmacol 12(5):687–699

Houle S, Ginovart N, Hussey D, Meyer JH, Wilson AA (2000) Imaging the serotonin transporter with positron emission tomography: initial human studies with 11C DAPP and 11C DASB. Eur J Nucl Med 27:1719–1722

Huang Y, Hwang DR, Narendran R, Sudo Y, Chatterjee R, Bae SA et al (2002) Comparative evaluation in nonhuman primates of five PET radiotracers for imaging the serotonin transporters: 11C McN 5652, 11C ADAM, 11C DASB, 11C DAPA, and 11C AFM. J Cereb Blood Flow Metab 22:1377–1398

Tatsumi M, Groshan K, Blakely RD, Richelson E (1997) Pharmacological profile of antidepressants and related compounds at human monoamine transporters. Eur J Pharmacol 340:249–258

Lijffijt M, Kenemans JL, Verbaten MN, van Engeland H (2005) A meta-analytic review of stopping performance in attention-deficit/hyperactivity disorder: deficient inhibitory motor control? J Abnorm Psychol 114(2):216–222

Aron AR, Fletcher PC, Bullmore ET, Sahakian BJ, Robbins TW (2003a) Stop-signal inhibition disrupted by damage to right inferior frontal gyrus in humans. Nat Neurosci 6:115–116

Bari A, Eagle DM, Mar AC, Robinson ES, Robbins TW (2009) Dissociable effects of noradrenaline, dopamine, and serotonin uptake blockade on stop task performance in rats. Psychopharmacology 205(2):273–283

Chamberlain SR, Müller U, Blackwell AD, Clark L, Robbins TW, Sahakian BJ (2006) Neurochemical modulation of response inhibition and probabilistic learning in humans. Science 311(5762):861–863

Eagle DM, Bari A, Robbins TW (2008) The neuropsychopharmacology of action inhibition: cross-species translation of the stop-signal and go/no-go tasks. Psychopharmacology 199(3):439–456

Chamberlain SR, Müller U, Deakin JB, Corlett PR, Dowson J, Cardinal RN et al (2007b) Lack of deleterious effects of buspirone on cognition in healthy male volunteers. J Psychopharmacol 21:210–215

Ding YS, Fowler JS, Volkow ND, Dewey SL, Wang GJ, Logan J et al (1997) Chiral drugs: comparison of the pharmacokinetics of [11C]d-threo and L-threo-methylphenidate in the human and baboon brain. Psychopharmacology 131(1):71–78

Volkow ND, Wang GJ, Fowler JS, Gatley SJ, Logan J, Ding YS et al (1998) Dopamine transporter occupancies in the human brain induced by therapeutic doses of oral methylphenidate. Am J Psychiatry 155:1325–1331

Eshleman AJ, Carmolli M, Cumbay M, Martens CR, Neve KA, Janowsky A (1999) Characteristics of drug interactions with recombinant biogenic amine transporters expressed in the same cell type. J Pharmacol Exp Ther 289:877–885

Biederman J, Melmed RD, Patel A et al (2008) A randomized, double-blind, placebo-controlled study of guanfacine extended release in children and adolescents with attention-deficit/hyperactivity disorder. Pediatrics 121(1):e73–e84

Berridge CW, Devilbiss DM, Andrzejewski ME et al (2006) Methylphenidate preferentially increases catecholamine neurotransmission within the prefrontal cortex at low doses that enhance cognitive function. Biol Psychiatry 60(10):1111–1120

Aron AR, Dowson JH, Sahakian BJ, Robbins TW (2003b) Methylphenidate improves response inhibition in adults with attention-deficit/hyperactivity disorder. Biol Psychiatry 54:1465–1468

Hannestad J, Gallezot JD, Planeta-Wilson B, Lin SF, Williams WA, van Dyck CH et al (2010b) Clinically relevant doses of methylphenidate significantly occupy the norepinephrine transporter in humans in vivo. Biol Psychiatry 6:854–860

Solanto MV (1998) Neuropsychopharmacological mechanisms of stimulant drug action in attention-deficit hyperactivity disorder: a review and integration. Behav Brain Res 94(1):127–152

Volkow ND, Fowler JS, Wang GJ et al (2008) Methylphenidate decreased the amount of glucose needed by the brain to perform a cognitive task. PLoS One 3:e2017

Zafar HM, Pare WP, Tejani-Butt SM (1997) Effect of acute or repeated stress on behavior and brain norepinephrine system in Wistar-Kyoto (WKY) rats. Brain 44:289–295

Arnsten AF, Li BM (2005) Neurobiology of executive functions: catecholamine influences on prefrontal cortical functions. Biol Psychiatry 57(11):1377–1384

Liprando LA, Miner LH, Blakely RD, Lewis DA, Sesack SR (2004) Ultrastructural interactions between terminals expressing the norepinephrine transporter and dopamine neurons in the rat and monkey ventral tegmental area. Synapse 54:233–244

Miner LH, Jedema HP, Moore FW, Blakely RD, Grace AA, Sesack SR (2006) Chronic stress increases the plasmalemmal distribution of the norepinephrine transporter and the coexpression of tyrosine hydroxylase in norepinephrine axons in the prefrontal cortex. J Neurosci 26:1571–1578

Moron JA, Brockington A, Wise RA, Rocha BA, Hope BT (2002) Dopamine uptake through the norepinephrine transporter in brain regions with low levels of the dopamine transporter: evidence from knock-out mouse lines. J Neurosci 22:389–395

Armour C, Elhai JD, Richardson D, Ractliffe K, Wang L, Elklit A (2012) Assessing a five factor model of PTSD: is dysphoric arousal a unique PTSD construct showing differential relationships with anxiety and depression? J Anxiety Disord 26(2):368–376

Elhai JD, Biehn TL, Armour C, Klopper JJ, Frueh BC, Palmieri PA (2011) Evidence for a unique PTSD construct represented by PTSD's D1-D3 symptoms. J Anxiety Disord 25:340–345

Pietrzak RH, Tsai J, Harpaz-Rotem I, Whealin JM, Southwick SM (2012) Support for a novel five-factor model of posttraumatic stress symptoms in three independent samples of Iraq/Afghanistan veterans: a confirmatory factor analytic study. J Psychiatr Res 46:317–322

Pietrzak RH, Gallezot JD, Ding YS et al (2013) Association of posttraumatic stress disorder with reduced in vivo norepinephrine transporter availability in the locus coeruleus. JAMA 70:1199–1205

Pincus HA, First M, Frances A, McQueen L (1996) Reviewing DSM-IV. Am J Psychiatry 153(6):850

Camastra S, Bonora E, Del Prato S, Rett K, Weck M, Ferrannini E (1999) Effect of obesity and insulin resistance on resting and glucose-induced thermogenesis in man. Int J Obes Relat Metab Disord 23:1307–1313

Golay A, Schutz Y, Felber JP, de Fronzo RA, Jequier E (1986) Lack of thermogenic response to glucose/insulin infusion in diabetic obese subjects. Int J Obes 10:107–116

Jequier E, Schutz Y (1985) New evidence for a thermogenic defect in human obesity. Int J Obes 9(Suppl 2):1–7

Yeckel CW, Gulanski B, Zgorski ML, Dziura J, Parish R, Sherwin RS (2009) Simple exercise recovery index for sympathetic overactivity is linked to insulin resistance. Med Sci Sports Exerc 41:505–515

Wijers SL, Saris WH, van Marken Lichtenbelt WD (2009) Recent advances in adaptive thermogenesis: potential implications for the treatment of obesity. Obes Rev 10:218–226

Christensen CR, Clark PB, Morton KA (2006) Reversal of hypermetabolic brown adipose tissue in F-18 FDG PET imaging. Clin Nucl Med 31:193–196

Hany TF, Gharehpapagh E, Kamel EM, Buck A, Himms-Hagen J, von Schulthess GK (2002) Brown adipose tissue: a factor to consider in symmetrical tracer uptake in the neck and upper chest region. Eur J Nucl Med Mol Imaging 29:1393–1398

Nedergaard J, Bengtsson T, Cannon B (2007) Unexpected evidence for active brown adipose tissue in adult humans. Am J Physiol Endocrinol Metab 293:E444–E452

Agrawal A, Nair N, Baghel NS (2009) A novel approach for reduction of brown fat uptake on FDG PET. Br J Radiol 82:626–631

Saito M, Okamatsu-Ogura Y, Matsushita M, Watanabe K, Yoneshiro T, Nio-Kobayashi J et al (2009) High incidence of metabolically active brown adipose tissue in healthy adult humans: effects of cold exposure and adiposity. Diabetes 58:1526–1531

van Marken Lichtenbelt WD, Vanhommerig JW, Smulders NM, Drossaerts JM, Kemerink GJ, Bouvy ND et al (2009) Cold-activated brown adipose tissue in healthy men. N Engl J Med 360(15):1500–1508

Cypess AM, Lehman S, Williams G, Tal I, Rodman D, Goldfine AB et al (2009) Identification and importance of brown adipose tissue in adult humans. N Engl J Med 360:1509–1517

Lin SF, Fan X, Yeckel CW, Weinzimmer D, Mulnix T, Gallezot JD et al (2012) Ex vivo and in vivo evaluation of the norepinephrine transporter ligand 11C MRB for brown adipose tissue imaging. Nucl Med Biol 39:1081–1086

Esler MD, Wallin G, Dorward PK et al (1991) Effects of desipramine on sympathetic nerve firing and norepinephrine spillover to plasma in humans. Am J Phys 260:R817–R823

Ganguly PK, Dhalla KS, Innes IR, Beamish RE, Dhalla NS (1986) Altered norepinephrine turnover and metabolism in diabetic cardiomyopathy. Circ Res 59:684–693

Haenisch B, Linsel K, BruÆss M, Gilsbach R, Propping P, NoÆthen MM et al (2009) Association of major depression with rare functional variants in norepinephrine transporter and serotonin1A receptor genes. Am J Med Genet B Neuropsychiatr Genet 150B:1013–1016

Hahn MK, Blackford JU, Haman K, Mazei-Robison M, English BA, Prasad HC et al (2008) Multivariate permutation analysis associates multiple polymorphisms with subphenotypes of major depression. Genes Brain Behav 7:487–495

Hahn MK, Mazei-Robison MS, Blakely RD (2005) Single nucleotide polymorphisms in the human norepinephrine transporter gene affect expression, trafficking, antidepressant interaction, and protein kinase C regulation. Mol Pharmacol 68:457–466

Hahn MK, Robertson D, Blakely RD (2003) A mutation in the human norepinephrine transporter gene (SLC6A2) associated with orthostatic intolerance disrupts surface expression of mutant and wild-type transporters. J Neurosci 23:4470–4478

Hahn MK, Steele A, Couch RS, Stein MA, Krueger JJ (2009) Novel and functional norepinephrine transporter protein variants identified in attention deficit hyperactivity disorder. Neuropharmacology 57:694–701

Robertson SD, Matthies HJG, Owens WA, Sathananthan V, Christianson NSB, Kennedy JP et al (2010) Insulin reveals Akt signaling as a novel regulator of norepinephrine transporter trafficking and norepinephrine homeostasis. J Neurosci 30:11305–11316

Hwang JJ, Yeckel CW, Gallezot JD et al (2015) Imaging human brown adipose tissue under room temperature conditions with (11)C-MRB, a selective norepinephrine transporter PET ligand. Metabolism 64:747–755

Blondin DP, Labbe SM, Tingelstad HC, Noll C, Kunach M, Phoenix S et al (2014) Increased brown adipose tissue oxidative capacity in cold-acclimated humans. J Clin Endocrinol Metab 99(3):E438–E446

Lee P, Smith S, Linderman J, Courville AB, Brychta RJ, Dieckmann W et al (2014) Temperature-acclimated brown adipose tissue modulates insulin sensitivity in humans. Diabetes 63(11):3686–3698

Li CS, Potenza MN, Lee DE et al (2014) Decreased norepinephrine transporter availability in obesity: Positron Emission Tomography imaging with (S,S)- (11)C O-methylreboxetine. NeuroImage 86:306–310

Hu HH, Perkins TG, Chia JM, Gilsanz V (2013) Characterization of human brown adipose tissue by chemical-shift water-fat MRI. AJR Am J Roentgenol 200(1):177–183

Melasch J, Rullmann M, Hilbert A, Luthardt J, Becker GA, Patt M et al (2016) The central nervous norepinephrine network links a diminished sense of emotional Well-being to an increased body weight. Int J Obes 40(5):779–787

Pattinson KTS, Mitsis GD, Harvey AK, Jbabdi S, Dirckx S, Mayhew SD et al (2009) Determination of the human brainstem respiratory control network and its cortical connections in vivo using functional and structural imaging. NeuroImage 44(2):295–305

Bresch A, Rullmann M, Luthardt J, Becker GA, Reissig G, Patt M et al (2017) Emotional eating and in vivo norepinephrine transporter availability in obesity: a [(11) C]MRB PET pilot study. Int J Eat Disord 50(2):152–156

Lindgren E, Gray K, Miller G, Tyler R, Wiers CE, Volkow ND et al (2018) Food addiction: A common neurobiological mechanism with drug abuse. Front Biosci (Landmark Ed) 23:811–836

Kish SJ, Shannak KS, Rajput AH, Gilbert JJ, Hornykiewicz O (1984) Cerebellar norepinephrine in patients with Parkinson's disease and control subjects. Arch Neurol 41(6):612–614

Nahimi A, Sommerauer M, Kinnerup MB, Ostergaard K, Winterdahl M, Jacobsen J et al (2018) Noradrenergic deficits in Parkinson disease imaged with (11)C-MeNER. J Nucl Med 59(4):659–664

Sommerauer M, Fedorova TD, Hansen AK, Knudsen K, Otto M, Jeppesen J et al (2018a) Evaluation of the noradrenergic system in Parkinson's disease: an 11C-MeNER PET and neuromelanin MRI study. Brain 141(2):496–504

Sommerauer M, Hansen AK, Parbo P, Fedorova TD, Knudsen K, Frederiksen Y et al (2018b) Decreased noradrenaline transporter density in the motor cortex of Parkinson's disease patients. Mov Disord 33(6):1006–1010

Yatham LN, Sossi V, Ding YS, Vafai N, Arumugham SS, Dhanoa T et al (2018) A positron emission tomography study of norepinephrine transporter occupancy and its correlation with symptom response in depressed patients treated with quetiapine XR. Int J Neuropsychopharmacol 21(2):108–113

Vanicek T, Spies M, Rami-Mark C, Savli M, Hoflich A, Kranz GS et al (2014) The norepinephrine transporter in attention-deficit/hyperactivity disorder investigated with positron emission tomography. JAMA Psychiat 71(12):1340–1349

Volkow ND, Ding YS, Fowler JS, Wang GJ, Logan J, Gatley SJ et al (1996) Dopamine transporters decrease with age. J Nucl Med 37(4):554–559

Baker KG, Tork I, Hornung JP, Halasz P (1989) The human locus coeruleus complex: an immunohistochemical and three dimensional reconstruction study. Exp Brain Res 77(2):257–270

Sharma Y, Xu T, Graf WM, Fobbs A, Sherwood CC, Hof PR et al (2010) Comparative anatomy of the locus coeruleus in humans and nonhuman primates. J Comp Neurol 518(7):963–971

Aston-Jones G, Ennis M, Pieribone VA, Nickell WT, Shipley MT. The brain nucleus locus coeruleus: restricted afferent control of a broad efferent network. Science 1986;234(4777):734–7.

Braak H, Thal DR, Ghebremedhin E, Del Tredici K (2011) Stages of the pathologic process in Alzheimer disease: age categories from 1 to 100 years. J Neuropathol Exp Neurol 70(11):960–969

Bondareff W, Mountjoy CQ, Roth M (1981) Selective loss of neurones of origin of adrenergic projection to cerebral cortex (nucleus locus coeruleus) in senile dementia. Lancet (London, England) 1(8223):783–784

Bondareff W, Mountjoy CQ, Roth M, Rossor MN, Iversen LL, Reynolds GP et al (1987) Neuronal degeneration in locus ceruleus and cortical correlates of Alzheimer disease. Alzheimer Dis Assoc Disord 1(4):256–262

Burke WJ, Chung HD, Huang JS, Huang SS, Haring JH, Strong R et al (1988) Evidence for retrograde degeneration of epinephrine neurons in Alzheimer's disease. Ann Neurol 24(4):532–536

Busch C, Bohl J, Ohm TG (1997) Spatial, temporal and numeric analysis of Alzheimer changes in the nucleus coeruleus. Neurobiol Aging 18(4):401–406

Chan-Palay V, Asan E (1989) Alterations in catecholamine neurons of the locus coeruleus in senile dementia of the Alzheimer type and in Parkinson's disease with and without dementia and depression. J Comp Neurol 287(3):373–392

Gannon M, Che P, Chen Y, Jiao K, Roberson ED, Wang Q (2015) Noradrenergic dysfunction in Alzheimer's disease. Front Neurosci 9:220

German DC, Manaye KF, White CL 3rd, Woodward DJ, McIntire DD, Smith WK et al (1992) Disease-specific patterns of locus coeruleus cell loss. Ann Neurol 32(5):667–676

Hardy J, Adolfsson R, Alafuzoff I, Bucht G, Marcusson J, Nyberg P et al (1985) Transmitter deficits in Alzheimer's disease. Neurochem Int 7(4):545–563

Iversen LL, Rossor MN, Reynolds GP, Hills R, Roth M, Mountjoy CQ et al (1983) Loss of pigmented dopamine-beta-hydroxylase positive cells from locus coeruleus in senile dementia of Alzheimer's type. Neurosci Lett 39(1):95–100

Mann DM, Yates PO, Hawkes J (1982) The noradrenergic system in Alzheimer and multi-infarct dementias. J Neurol Neurosurg Psychiatry 45(2):113–119

Marcyniuk B, Mann DM, Yates PO (1986) The topography of cell loss from locus caeruleus in Alzheimer's disease. J Neurol Sci 76(2–3):335–345

Strong R, Huang JS, Huang SS, Chung HD, Hale C, Burke WJ (1991) Degeneration of the cholinergic innervation of the locus ceruleus in Alzheimer's disease. Brain Res 542(1):23–28

Wilson RS, Nag S, Boyle PA, Hizel LP, Yu L, Buchman AS et al (2013) Neural reserve, neuronal density in the locus ceruleus, and cognitive decline. Neurology 80(13):1202–1208

Hansen AK, Knudsen K, Lillethorup TP, Landau AM, Parbo P, Fedorova T et al (2016) In vivo imaging of neuromelanin in Parkinson's disease using 18 F-AV-1451 PET. Brain 139(7):2039–2049

Lemoine L, Leuzy A, Chiotis K, Rodriguez-Vieitez E, Nordberg A (2018) Tau positron emission tomography imaging in tauopathies: the added hurdle of off-target binding. Alzheimers Dement (Amst) 10:232–236

Saint-Aubert L, Lemoine L, Chiotis K, Leuzy A, Rodriguez-Vieitez E, Nordberg A (2017) Tau PET imaging: present and future directions. Mol Neurodegener 12(1):19

Clewett D, Lee TH, Greening SG, Ponzio A, Margalit E, Mather M (2016) Neuromelanin marks the spot: identifying a locus coeruleus biomarker of cognitive reserve in healthy aging. Neurobiol Aging 37:117–126

Keren NI, Lozar CT, Harris KC, Morgan PS, Eckert MA (2009) In vivo mapping of the human locus coeruleus. NeuroImage 47(4):1261–1267

Keren NI, Taheri S, Vazey EM, Morgan PS, Granholm A-CE, Aston-Jones GS et al (2015) Histologic validation of locus coeruleus MRI contrast in post-mortem tissue. NeuroImage 113:235–245

Sasaki M, Shibata E, Tohyama K, Takahashi J, Otsuka K, Tsuchiya K et al (2006) Neuromelanin magnetic resonance imaging of locus ceruleus and substantia nigra in Parkinson's disease. Neuroreport 17(11):1215–1218

Li CS, Kosten TR, Sinha R (2005) Sex differences in brain activation during stress imagery in abstinent cocaine users: a functional magnetic resonance imaging study. Biol Psychiatry 57(5):487–494

Logan J, Ding YS, Lin KS, Pareto D, Fowler J, Biegon A (2005) Modeling and analysis of PET studies with norepinephrine transporter ligands: the search for a reference region. Nucl Med Biol 32:531–542

Ichise M, Toyama H, Innis RB, Carson RE (2002) Strategies to improve neuroreceptor parameter estimation by linear regression analysis. J Cereb Blood Flow Metab 22:1271–1281

Innis RB, Cunningham VJ, Delforge J, Fujita M, Gjedde A, Gunn RN et al (2007) Consensus nomenclature for in vivo imaging of reversibly binding radioligands. J Cereb Blood Flow Metab 27:1533–1539

Schou M, Halldin C, Pike VW, Mozley PD, Dobson D, Innis RB et al (2005) Post-mortem human brain autoradiography of the norepinephrine transporter using (S,S)- 18F FMeNER-D2. Eur Neuropsychopharmacol 15:517–520

Schou M, Halldin C, Sovago J, Pike VW, Hall H, Gulyas B et al (2004) PET evaluation of novel radiofluorinated reboxetine analogs as norepinephrine transporter probes in the monkey brain. Synapse 53:57–67

Takano A, Halldin C, Varrone A, Karlsson P, Sjoholm N, Stubbs JB et al (2008a) Biodistribution and radiation dosimetry of the norepinephrine transporter radioligand (S,S)-[18F]FMeNER-D2: a human whole-body PET study. Eur J Nucl Med Mol Imaging 35(3):630–636

Takano A, Varrone A, Gulyas B, Karlsson P, Tauscher J, Halldin C (2008b) Mapping of the norepinephrine transporter in the human brain using PET with (S,S)-[18F]FMeNER-D2. NeuroImage 42(2):474–482

Positron Emission Tomography (PET) Imaging of Opioid Receptors

21

Aren van Waarde, Anthony R. Absalom, Anniek K. D. Visser, and Rudi A. J. O. Dierckx

Contents

A. van Waarde (✉) · A. K. D. Visser
Department of Nuclear Medicine and Molecular Imaging, University Medical Center Groningen, University of Groningen, Groningen, The Netherlands
e-mail: a.van.waarde@umcg.nl

A. R. Absalom
Department of Anaesthesiology, University Medical Center Groningen, University of Groningen, Groningen, The Netherlands
e-mail: a.r.absalom@umcg.nl

R. A. J. O. Dierckx
Department of Nuclear Medicine and Molecular Imaging, University Medical Center Groningen, University of Groningen, Groningen, The Netherlands

Department of Nuclear Medicine, University Hospital Gent, University of Gent, Ghent, Belgium
e-mail: r.a.dierckx@umcg.nl

Abstract

The opioid system consists of opioid receptors (which mediate the actions of opium), their endogenous ligands (the enkephalins, endorphins, endomorphins, dynorphin, and nociceptin), and the proteins involved in opioid production, transport, and degradation. PET tracers for the various opioid receptor subtypes are available, and changes in regional opioidergic activity have been assessed during both sensory and affective processing in healthy individuals and in various disease conditions such as chronic pain, neurodegeneration, epilepsy, eating disorders, behavioral addiction, and substance abuse. It is not always clear whether observed changes of tracer binding reflect altered release of endogenous opioids or altered opioid receptor expression. This issue may be resolved by studies in experimental animals that combine in vivo PET imaging with ex vivo immunohistochemistry. Some radioligands for opioid receptors have suboptimal kinetics (i.e., slow dissociation from their target protein) or can induce undesired side effects even at low administered doses (sedation, respiratory arrest). Yet, PET offers the unique opportunity of quantifying opioid receptor-mediated signaling in the living human brain. PET imaging has provided evidence for a link between opioid neurotransmission and peripheral immune activation.

21.1 Introduction

The term "opioid" is derived from opium: dried latex from the opium poppy (*Papaver somniferum*) which has been used since ancient times as an analgesic and recreational drug (Kalant 1997). An opioid is either a synthetic narcotic that has similar activities as opium or a naturally occurring peptide that has such activities. Several classes of endogenous opioids have been discovered, viz., the enkephalins

(Hughes et al. 1975), endorphins (Cox et al. 1976; Simantov and Snyder 1976), endomorphins (Zadina et al. 1997), dynorphins (Goldstein et al. 1979), and nociceptin (Meunier et al. 1995; Reinscheid et al. 1995). These messenger substances bind to G-protein-coupled opioid receptors in the brain, the spinal cord, and the digestive tract. Agonist binding to opioid receptors results in a decrease of the activity of adenylyl cyclase (Snyder and Pasternak 2003; Trescot et al. 2008; Waldhoer et al. 2004).

At least four broad subclasses of opioid receptors have been identified by the use of selective ligands (Dhawan et al. 1996). Assessment of antagonist potencies against the actions of various opioid agonists in different tissue preparations resulted in the identification of the mu, delta, and kappa subclasses (Lord et al. 1977; Martin et al. 1976). Later, mRNAs for these three subtypes were cloned and characterized (Chen et al. 1993; Evans et al. 1992; Kieffer et al. 1992; Yasuda et al. 1993). Mu opioid receptors (μOR) are named after morphine, the alkaloid which is the active compound in opium (Martin et al. 1976). Kappa opioid receptors (κOR) derive their name from the drug ketocyclazocine (Martin et al. 1976). Delta opioid receptors (δOR) were initially characterized in the murine vas deferens (Lord et al. 1977). μOR are ß-endorphin preferring, κOR dynorphin preferring, and δOR enkephalin preferring (Minami and Satoh 1995). Nonclassical, nociceptin- or opiate-like receptors 1 (ORL1) bind nociceptin (Meunier et al. 1995; Reinscheid et al. 1995).

ß-Endorphin binds with nM affinity to μOR and δOR (K_i about 1 nM) but with low affinity to κOR ($K_i = 52$ nM) (Raynor et al. 1994). In contrast, dynorphin A has sub-nM affinity to κOR ($K_i = 0.5$ nM), low affinity to μOR ($K_i = 32$ nM), and negligible affinity to δOR ($K_i > 1$ μM) (Raynor et al. 1994). Enkephalins have sub-nM or nM affinity to δOR and μOR (K_i values 0.6–4 nM) but negligible affinity to κOR ($K_i > 1$ μM) (Raynor et al. 1994). Endomorphins are very potent and selective μOR agonists ($K_i = 0.3–0.7$ nM) (Hackler et al. 1997). Stimulation of μOR or δOR generally results in analgesia and reward, whereas κOR stimulation may have negative consequences, such as dysphoria and hallucinations.

Opioids and their receptors play important roles in a large spectrum of physiological processes, including learning and memory, reward, mood, appetite, circadian rhythms, sexual activity, pregnancy, locomotion, cardiovascular, gastrointestinal, renal and hepatic function, respiration, regulation of body temperature, and immunological response (Vaccarino and Kastin 2001). Well known is their involvement in regulating the sensation of pain; opiates are clinically employed to produce analgesia.

21.2 Opioid Receptor Ligands for PET: A Historical Overview

Several radioligands for PET imaging of opioid receptors have been prepared. These include subtype-selective and non-subtype-selective agonists and antagonists (see Table 21.1). Many comprehensive reviews on opioid receptor imaging were published between 2000 and 2008 (Frost 2001; Hammers and Lingford-Hughes

Table 21.1 PET probes for the opioid system

Name	Action	Abbreviation	Initial publication
[^{18}F]Cyclofoxy	Antagonist, μOR, and κOR	–	Pert et al. (1984)
[^{11}C]Diprenorphine	Antagonist, non-subtype selective	DPN	Luthra et al. (1985)
[^{18}F]Diprenorphine	Antagonist, non-subtype selective	FDPN	Wester et al. (2000)
[^{11}C]Buprenorphine	Mixed agonist/antagonist, non-subtype selective	BPN	Luthra et al. (1987)
[^{18}F]-FE-PEO	Full agonist, non-subtype selective	–	Riss et al. (2013)
[^{11}C]Carfentanil	Agonist, μOR	CFN	Dannals et al. (1985)
[^{11}C]AH7921	Agonist, μOR	–	Rafique et al. (2017)
[^{11}C]Methylnaltrindole	Antagonist, δOR	MeNTI	Lever et al. (1992)
[^{64}Cu]TIPP conjugate	Antagonist, δOR	–	Pirisedigh et al. (2017)
[^{11}C]GR103545	Agonist, κOR	–	Talbot et al. (2005)
[^{11}C]EKAP	Agonist, κOR	–	Li et al. (2019a)
[^{11}C]FEKAP	Agonist, κOR	–	Li et al. (2019b)
[^{11}C]MeJDTic	Antagonist, κOR	–	Poisnel et al. (2008)
[^{11}C]LY2795050	Antagonist, κOR	–	Zheng et al. (2013)
[^{11}C]LY2459989	Antagonist, κOR	–	Zheng et al. (2014)
[^{18}F]LY2459989	Antagonist, κOR	–	Cai et al. (2017), Li et al. (2018)
[^{11}C]NOP-1A	Antagonist, ORL1	–	Pike et al. (2011)
[^{18}F]MK-0911	Antagonist, ORL1	–	Hostetler et al. (2013)

2006; Henriksen and Willoch 2008; Koepp and Duncan 2000; Lever 2007; Ravert et al. 2004; Sprenger et al. 2005).

The first attempt at in vivo labeling of opioid receptors was made in 1975. Investigators at Johns Hopkins University administered a labeled opioid receptor antagonist, [^{3}H]naloxone, to living rats. In the excised brain tissue of these animals, they observed a regional distribution of radioactivity which corresponded to the known distribution of opioid receptors in the rodent brain (striatum > hindbrain > cerebellum). Because of strong nonspecific binding of [^{3}H]naloxone, acceptable target-to-nontarget ratios of radioactivity could only be reached after ex vivo washing of brain slices to remove nonspecifically bound tracer. Yet, this seminal study paved the way for all later imaging of neuroreceptors in the living brain (Pert and Snyder 1975).

The first successful PET probe for opioid receptors was prepared in 1984 (Pert et al. 1984; Channing et al. 1985). After intravenous administration of [^{18}F]3-acetylcyclofoxy (3-acetyl-6-deoxy-6-ß-[^{18}F]-fluoronaltrexone), a regional distribution of radioactivity was observed which corresponded to the regional distribution of opioid receptors in the rat and baboon brain. Bound tracer in the baboon brain was completely displaced by the active (−)enantiomer of naloxone, whereas an

identical dose of the inactive (+)enantiomer (0.13 mg/kg) had no effect (Pert et al. 1984).

Since [^{3}H]naloxone showed a low ratio of specific-to-nonspecific binding, an antagonist with a higher affinity ([^{3}H]diprenorphine, [^{3}H]DPN) was prepared and successfully applied in autoradiography (review in (Frost 2001)). However, labeling DPN with ^{11}C proved difficult. Because of these difficulties, radiochemists focused their attention on other opioid ligands, and a method was developed to label carfentanil (CFN) with ^{11}C, using a carboxylic acid analog of carfentanil as a precursor (Dannals et al. 1985). The resulting tracer, [^{11}C]CFN, was used to acquire the very first images of opioid receptors in the human brain (Frost et al. 1985). At baseline, a regional distribution of radioactivity was observed which corresponded to the known regional densities of μOR. After treatment of the volunteer with naloxone (1 mg/kg), cerebral uptake of the tracer was strongly suppressed, indicating that [^{11}C]CFN binds to μOR in the living brain in vivo (Frost et al. 1985). A regional distribution of radioactivity consistent with μOR binding and blockade of tracer uptake by naloxone were also observed in the mouse brain. Thus, [^{11}C]CFN is suitable for studies of μOR in rodents (Saji et al. 1992).

In the same year that the first images of opioid receptors in the human brain were acquired, radiochemists developed a method for preparation of [^{11}C]DPN. The compound was labeled at the N-carbon atom of its cyclopropylmethyl group (Luthra et al. 1985). A study with [^{11}C]DPN in four healthy volunteers indicated that the tracer is rapidly washed out from brain regions with a low density of opioid receptors, whereas activity is retained in receptor-rich target areas. Eighty to ninety percent of tracer binding in target regions is naloxone reversible, suggesting that [^{11}C]DPN is suitable for studies of opioid receptors in man (Jones et al. 1988).

A different method to prepare [^{11}C]DPN was later published. That method involves [^{11}C]-*O*-methylation of 3-*O*-*t*-butyldimethylsilyl-(6-*O*-desmethyl) diprenorphine with [^{11}C]methyl iodide, followed by acidic deprotection of the reaction product (Lever et al. 1987). The advantage of this approach compared to the previously published method is its greater radiochemical yield.

The non-subtype-selective opioid ligand buprenorphine (BPN) has also been labeled with ^{11}C. The first published method involved the reaction of an *N*-(decyclopropylmethyl) precursor of buprenorphine with [^{11}C]cyclopropanecarbonyl chloride followed by reduction with lithium aluminum hydride (Luthra et al. 1987). Later, a more facile synthesis of [^{11}C]BPN was reported, in which the drug was labeled with ^{11}C at the 6-methoxy position, using a methylation reaction with [^{11}C]iodomethane (Lever et al. 1990). In a preclinical study in a baboon, the cerebral kinetics of [^{11}C]BPN and [^{11}C]DPN were directly compared. (−)Naloxone-sensitive binding of both ligands was observed in the striatum but not in the cerebellum. Uptake values and time courses in the target region were similar. The investigators concluded that [^{11}C]DPN shows better kinetics than [^{11}C]BPN since [^{11}C]DPN is cleared more rapidly from brain areas devoid of opioid receptors (Shiue et al. 1991). [^{11}C]BPN shows a regional distribution in the baboon brain consistent with regional opioid receptor density, whereas bound radioactivity in target areas can be displaced

by naloxone. Moreover, [¹¹C]BPN binding in the striatum shows a good (~10%) short-term test-retest variability (Galynker et al. 1996).

A non-subtype-selective agonist radioligand for opioid receptor imaging has become available. This compound, called [¹⁸F]FE-PEO, binds with K_i values of 0.4–1.6 nM to all opioid receptor subtypes. The distribution of radioactivity in the rat brain corresponds to regional opioid receptor levels, but nonspecific binding is rather high (≥33% even in target areas). [¹⁸F]FE-PEO is relatively slowly metabolized (60% parent in rat plasma after 3 h), and radioactive metabolites do not enter the brain (Riss et al. 2013).

A benzamide radioligand for μ-opioid receptors with agonist activity ([¹¹C]AH7921) was recently labeled with ¹¹C and tested in rats as a potential alternative to [¹¹C]CFN (Rafique et al. 2017). Although this agent showed several drawbacks, such as a low binding potential and entry of a radioactive metabolite in the brain, the authors claim that it may be used for quantitative imaging of μOR availability and competition with endogenous opioids.

The first successful radioligand for δOR was the antagonist N1′-([¹¹C]methyl) naltrindole ([¹¹C]MeNTI). [¹¹C]MeNTI was synthesized by alkylation of 3-O-benzylnaltrindole with [¹¹C]methyl iodide followed by removal of the protecting benzyl moiety. [¹¹C]MeNTI binding in the brain of living mice was blocked (up to 75%) by naltrindole (δOR antagonist), but not by cyprodine (μOR antagonist) nor by U50,488 (κOR agonist). Regional tracer uptake showed a linear, close correlation to δOR densities known from autoradiography. These data indicated that [¹¹C]MeNTI binds selectively to δOR in the mouse brain in vivo (Lever et al. 1992).

An attempt to label the delta-1 subtype of δOR in the mouse brain with the selective ligand [³H]benzylidenenaltrexone (BNTX) was only partially successful. Although some specific binding of the compound was observed in vivo and tracer uptake could be blocked with the appropriate compounds, ratios of specific-to-nonspecific binding were very poor (Lever et al. 1996). Fluorinated analogs of naltrindole (N1′-fluoroethyl-naltrindole or BU97001 and N1′-fluoroethyl-(14-formylamino)-naltrindole or BU97018) have been proposed for PET imaging. BU97001 has been tritiated and used successfully for autoradiography of the rat brain; it shows sub-nM affinity to δOR (K_d 0.42 nM) (Tyacke et al. 2002). However, PET data for [¹⁸F]BU97001 have not yet been reported.

A ¹¹C-labeled N-substituted quinolinimide derivative with much higher subtype selectivity than [¹¹C]MeNTI has been tested as a potential ligand for in vivo imaging of δOR. The compound was rapidly degraded in both plasma and brain tissue after intravenous injection in rats, and specific binding could not be detected in vivo (Bourdier et al. 2007). A radiofluorinated δOR antagonist based on the Dmt-Tic pharmacophore has also been prepared. Although the compound showed significant binding to δOR in brain slices, it failed to cross the blood–brain barrier in living rats (Ryu et al. 2008). Three benzamide δOR agonists have been labeled with ¹¹C and subjected to preclinical testing. All compounds showed a very low brain uptake and no regional specific binding in mice. One of the compounds, called [¹¹C]SNC80, was also tested in a monkey. Results in this primate were similar to those seen

previously in mice, i.e., low blood–brain barrier permeability and a uniform distribution of radioactivity throughout the brain, indicating nonspecific binding (Pichika et al. 2010).

Recently, a conjugate of the δOR antagonist TIPP was labeled with ^{64}Cu (Pirisedigh et al. 2017). This tracer was only tested by ex vivo autoradiography in rat brain sections. It showed a regional distribution corresponding to the known expression levels of the δOR.

Initial attempts at developing subtype-selective radioligands for κOR were not successful. ^{18}F-labeled analogs of U-50488 were prepared by fluoroalkyl substitution, but the labeling procedure resulted in a very strong (≥100-fold) loss of affinity with reference to the parent compound (Chesis and Welch 1990). A successful agonist radioligand for κOR, [^{11}C]GR89696, was finally prepared in 1999 (Ravert et al. 1999). The R enantiomer, later called [^{11}C]GR103545, shows an excellent hypothalamus/cerebellum ratio of 11.4 in the mouse brain at 90 min after injection, in contrast to the S enantiomer which is inactive (target/nontarget ratio = 1) (Ravert et al. 2002). Using subtype-selective opioid receptor ligands in blocking studies, the binding of [^{11}C]GR103545 was shown to be κOR selective and saturable. Preclinical evaluation in baboons also indicated that [^{11}C]GR103545 is a promising tracer for imaging of κOR. A regional distribution of radioactivity is observed that is consistent with the regional density of κOR. Naloxone pretreatment reduces tracer uptake in all brain regions to the level observed in the cerebellum. In vivo binding of the tracer is stereoselective, and significant washout occurs within the time frame of a PET scan (Talbot et al. 2005). A one-pot radiosynthesis for preparation of [^{11}C]GR103545 with high specific radioactivity has recently been described (Nabulsi et al. 2011). Two other agonist radioligands for κOR, FEKAP and EKAP, have recently been labeled with ^{11}C and evaluated in non-human primates (Li et al. 2019a; Li et al. 2019b). Both ligands show sub-nM affinity to κOR, reasonable to excellent selectivity for κOR over μOR and δOR, a fairly rapid metabolism in monkey plasma, fast and reversible kinetics in the brain and regional binding potential values consistent with binding to κOR. Blocking and receptor occupancy studies were also performed, using the opioid drugs naloxone, LY2795050 and LY2456302. Thus, these ligands seem suitable for in vivo studies of cerebral κOR.

Antagonist radioligands for κOR have also been proposed. [^{11}C]MeJDTic was prepared by methylation of the precursor JDTic with [^{11}C]methyl triflate. In a preclinical study in mice, high uptake of the tracer was noted in target organs (lung, hypothalamus). Blocking and displacement studies with nonradioactive kappa, mu, and delta ligands suggested that [^{11}C]MeJDTic binds specifically to κOR in the brain of living mice in vivo (Poisnel et al. 2008). Yet, no follow-up studies with [^{11}C]MeJDTic have been reported. A fluoropropyl derivative of JDtTic was later labeled with ^{18}F and evaluated in intact mice. This tracer failed because radioactive metabolites were formed that entered the brain and significant specific binding in target regions could not be detected (Schmitt et al. 2017). Another antagonist, [^{11}C]LY2795050, was evaluated in Sprague–Dawley rats, wild-type and κOR knockout mice, and rhesus monkeys. Specific binding of the probe to cerebral κOR

was observed; this binding was completely blocked by pretreatment of monkeys with naloxone (1 mg/kg) and dose-dependently inhibited by the selective κOR antagonist LY2456302. Tracer metabolism in primates is moderate (40% parent remaining in monkey plasma at 30 min), and tracer pharmacokinetics appears favorable; thus, [^{11}C]LY2795050 is the first successful antagonist radioligand for κOR (Zheng et al. 2013).

Still another κOR antagonist, LY2459989, was labeled in recent years, both with ^{11}C (Zheng et al. 2014) and ^{18}F (Li et al. 2018). The two tracers show sub-nM affinity to κOR and high selectivity for κOR over μOR and δOR. They have been evaluated in rats and rhesus monkeys. A rapid uptake in the brain is observed and regional binding potential values are consistent with the known distribution of κOR in primates. Pretreatment of animals with naloxone results in a homogeneous background radioactivity throughout the brain, and tracer uptake in target regions is dose-dependently reduced by the selective κOR antagonists LY2456302 and unlabeled LY2459989. Thus, [^{11}C]- and [^{18}F]LY2459989 should also be considered as useful κOR ligands.

The last subclass of the opioid system for which imaging probes have been developed is the nociceptin/orphanin or opiate-like receptor (ORL1). [^{11}C]Methyl-Ro64–6198 failed as a radioligand for this subtype since its in vivo binding in the mouse brain was largely nonspecific (Ogawa et al. 2001). A second probe, [^{11}C]CPEB, showed some saturable in vivo binding but lack of specificity to ORL1 (Ogawa et al. 2003).

The first successful ORL1 ligand was [^{11}C]NOP-1A, a specific antagonist with sub-nM affinity (0.15 nM). This compound was selected from a library of ORL1 antagonists developed by Eli Lilly & Co. (Pedregal et al. 2012). After intravenous administration of [^{11}C]NOP-1A to rhesus monkeys, a regional cerebral distribution of radioactivity is observed consistent with binding of the probe to its target. Brain uptake is reduced by 50–70% after pretreatment of animals with the ORL1 antagonist SB-612111 (Pike et al. 2011; Kimura et al. 2011). The regional distribution of [^{11}C]NOP-1A in the human brain resembles that in the monkey brain. Regional distribution volume of the tracer can be reliably estimated using a two-tissue compartment model with arterial sampling or Ichise's noncompartmental bilinear analysis (Lohith et al. 2012).

Another ORL1 antagonist for PET imaging has been developed by Merck. Their compound [^{18}F]MK-0911 shows a regional distribution in the monkey and human brain consistent with the regional expression of ORL1. Binding in the monkey brain is inhibited after pretreatment of animals with several structurally diverse ORL1 antagonists (MK-0584, MK-0337, MK-5757). Dose-dependent occupancy of ORL1 in the human brain by nonradioactive MK-5757 could be assessed with [^{18}F]MK-0911 and PET (Hostetler et al. 2013).

21.3   Characteristics of Widely Used Radioligands

21.3.1 Cyclofoxy

[³H]Cyclofoxy (Fig. 21.1), the parent compound of [¹⁸F]cyclofoxy, labels both μOR and κOR in autoradiography of the rat and guinea pig brain (McLean et al. 1987; Rothman and McLean 1988). The regional pattern of radioactivity in the rat brain after in vivo injection of [³H]cyclofoxy corresponds to the regional distribution of these opioid receptor subtypes (Rothman and McLean 1988; Ostrowski et al. 1987), and brain radioactivity is reduced to background levels after pretreatment of animals with unlabeled naloxone (Ostrowski et al. 1987). K_i values of (−)cyclofoxy for μOR, κOR, and δOR in rat brain membranes are 2.6, 9.3, and 89 nM, respectively, whereas the (+)enantiomer is essentially inactive (K_i values > 10 μM) (Rothman et al. 1988). Consistent with these in vitro data, uptake of the radiofluorinated (−) enantiomer in the rat brain shows striking regional differences consistent with tracer
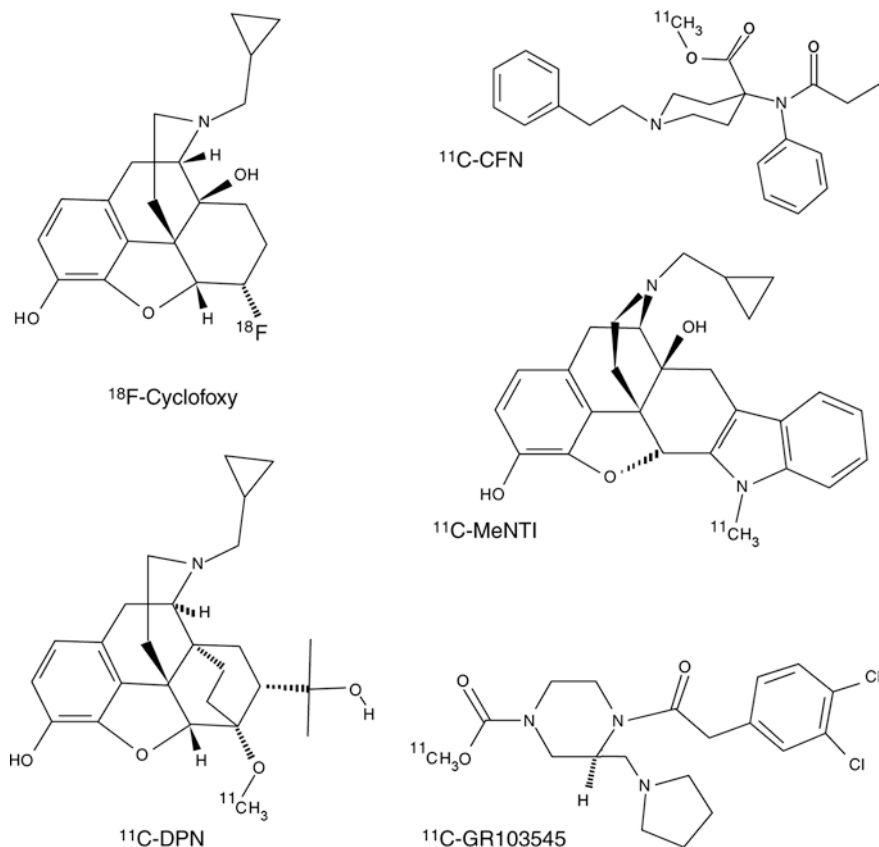
Fig. 21.1 Chemical structures of widely used opioid radioligands

binding to opioid receptors, whereas the tritiated (+)enantiomer is rather homogeneously distributed and shows low brain uptake. Pretreatment of animals with unlabeled (−)cyclofoxy reduces the uptake of [^{18}F](−)cyclofoxy in all regions to the level of the tritiated (+) enantiomer (Kawai et al. 1990). Thus, [^{18}F]cyclofoxy visualizes μOR and κOR in the living brain.

Kinetic analysis of [^{3}H]cyclofoxy uptake in the rat brain suggested an in vivo K_d of 2.1–5.2 nM in different brain areas and a B_{max} ranging from 1 pmol/g in the cerebellum to 78 pmol/g in the thalamus. Binding was reversible on a PET time scale (Sawada et al. 1991). In a follow-up study, a combination of bolus injection and constant infusion of [^{18}F]cyclofoxy was applied to estimate the receptor-ligand parameters in a condition of "true" tissue-blood equilibrium, which was reached after 60 min. K_d values of 1.4–2.9 nM were measured and B_{max} in target areas ranged from 15 to 74 pmol/g tissue. Rodent cerebellum could not be used as a reference region since the level of nonspecific binding in the cerebellum was different from that in other parts of the brain (Kawai et al. 1991). Bolus plus continuous infusion of [^{18}F]cyclofoxy was also advantageous in baboons, as it resulted in shorter scan times, a simplified protocol for blood sampling, and more accurate receptor measurements (Carson et al. 1993).

21.3.2 CFN (Fig. 21.1)

In vitro binding assays in human thalamic membranes indicated a K_d of 0.08 nM for [^{3}H]CFN (Titeler et al. 1989). In the rat brain, K_i values of 0.051, 4.7, and 13 nM were measured at μOR, δOR, and κOR, respectively (Frost et al. 1985). For the guinea pig brain, the corresponding values were 0.024, 3.28, and 43.1 nM (Cometta-Morini et al. 1992). In vitro competition studies using opioid ligands with a wide range of subtype selectivities confirmed that [^{3}H]CFN selectively labels μOR, in both the rat and human brain (Titeler et al. 1989). Thus, CFN is a potent and selective μOR agonist. Later in vitro binding studies on rat brain sections demonstrated that [^{11}C]CFN has higher affinity for the μ$_1$ subtype than for μ$_2$. Small animal imaging studies in which the μOR ligand cyprodime and the μ$_1$-subtype-selective ligand naloxonazine were used have indicated that the in vivo binding of [^{11}C]CFN involves only the μ$_1$ subtype, whereas binding to μ$_2$ receptors cannot be detected (Eriksson and Antoni 2015). Thus, [^{11}C]CFN images of the human brain may primarily show the distribution of the μ$_1$ subtype.

A study which applied compartment modeling for the analysis of [^{11}C]CFN binding in the human brain showed that the occipital cortex can be considered as a region with low or negligible receptor density. Target region-to-occipital cortex ratios of radioactivity at late time points can be used instead of ratios of k_3/k_4 when tracer kinetic modeling is not feasible, e.g., in clinical research protocols (Frost et al. 1989). However, Logan graphical analysis or a simplified reference tissue model approach can provide more accurate estimates of [^{11}C]CFN binding to μOR in the human brain than the ratio method (Endres et al. 2003). A test-retest study which assessed [^{11}C]CFN binding in the brain of healthy volunteers twice, on a

single day, indicated that both the regional two-tissue compartment model distribution volume (V_T) of the tracer and binding potential (BP_{ND}) are reproducible (variability <6 and <10%, respectively) (Hirvonen et al. 2009).

Administration of [^{11}C]CFN can induce somnolence and sedation and, at higher dose, respiratory arrest. These pharmacological effects are related to the fact that CFN is an opioid agonist. The upper limit for the administered mass of CFN is about 0.1 µg/kg (Frost 2001). [^{11}C]CFN binding in the human brain is affected by polymorphisms of the µOR gene. Carriers of the G allele (Asn40Asp variant, which may contribute to the development of alcohol dependence) have lower global binding potential than subjects homozygous for the A allele (Weerts et al. 2013).

Radiofluorinated analogs of carfentanil with subnanomolar affinities to µOR have been prepared (Henriksen et al. 2005a). *N*-[4-(methoxymethyl)-1-[2-(2-thienyl)ethyl]-4-piperidinyl]-*N*-phenyl-2-(±)-[^{18}F]fluoropropan-amide ([^{18}F]sufentanil) showed a high brain uptake in living mice and a distribution of radioactivity corresponding to regional µOR expression. The compound was rapidly metabolized in plasma (only 21% parent remaining at 40 min), but the metabolites appeared to not enter the brain in significant amounts (Henriksen et al. 2005b).

An updated (modernized) synthetic procedure for the preparation of [^{11}C]CFN (by reaction of a carboxylate precursor with [^{11}C]methyltriflate) has recently been described (Blecha et al. 2017). This procedure has the additional advantage that organic solvents could be replaced by ethanol.

21.3.3 DPN (Fig. 21.1)

Another widely applied radioligand for opioid receptor mapping is [^{11}C]DPN. [^{3}H]DPN binds with subnanomolar (K_d 0.22–0.23 nM) affinity to opioid receptors in the rat brain (Chang et al. 1981) and in the human frontal cortex (Pfeiffer et al. 1982). K_i values of DPN for µOR, δOR, and κOR in the rat brain are 0.20, 0.18, and 0.47 nM, respectively (Chang et al. 1981). Thus DPN is a non-subtype-selective opioid antagonist. Automated procedures for radiosynthesis of [^{18}F]FDPN and [^{11}C]DPN have been described (Schoultz et al. 2013; Fairclough et al. 2014).

Using RB101, an inhibitor of enkephalin-degrading enzymes, the in vivo binding of [^{3}H]DPN to opioid receptors in the mouse brain was shown to be sensitive to competition by endogenous enkephalins. Although RB101 is devoid of affinity to opioid receptors, the compound dose-dependently inhibits [^{3}H]DPN binding in the unstressed mouse brain up to a maximum of 30%. When mice were stressed by a warm-swim test, a greater inhibition of [^{3}H]DPN binding by RB101 was observed (maximally 45%). These effects of RB101 are probably related to increased levels of endogenous enkephalins (Ruiz-Gayo et al. 1992).

A validation study using [^{3}H]DPN in rats showed that compartment modeling of PET data with the cerebellum as reference region can provide accurate measurements of regional opioid receptor B_{max} and K_d, although K_d values estimated in vivo are an order of magnitude higher than those determined in vitro, probably due to diffusion gradients in tissue or protein binding of the radioligand (Cunningham

et al. 1991). However, the cerebellum cannot be considered as a region devoid of opioid receptors in human studies since μOR and κOR are expressed at low levels in this area of the human brain (Schadrack et al. 1999).

The kinetics of [^{11}C]DPN and [^{11}C]CFN in the brain of human volunteers have been directly compared (Frost et al. 1990; Villemagne et al. 1994). Binding of both ligands in the thalamus (an area containing mainly μOR) was not significantly different, but [^{11}C]DPN showed significantly greater binding than [^{11}C]CFN in the striatum, cingulate, and frontal cortex. Dissociation of [^{11}C]CFN from its binding sites was observed, but dissociation of [^{11}C]DPN was hardly noticeable. [^{11}C]CFN binding reached a plateau, whereas [^{11}C]DPN uptake showed a steady increase (Frost et al. 1990). Total radioactivity in the human brain (SUV) and the ratio of total/nonspecific binding were twice as great after administration of [^{11}C]DPN than [^{11}C]CFN. The dose of naloxone required to fully block [^{11}C]DPN binding was ten times greater than that required for [^{11}C]CFN (Villemagne et al. 1994). Thus, [^{11}C]DPN appeared to label δOR and KOR in addition to the μOR which are selectively labeled by [^{11}C]CFN. In a later animal study, the sensitivity of [^{11}C]CFN and [^{3}H]DPN binding to endogenous opioid release was directly compared, opioid release being stimulated by administering amphetamine and methadone to rats. The binding of [^{11}C]CFN but not [^{3}H]DPN was significantly reduced after such challenges. In vitro binding and subcellular fractionation studies indicated that this may be due to the fact that [^{11}C]CFN binds preferentially to receptors on the cell surface, whereas [^{3}H]DPN binds to both surface and internalized receptors. Thus, [^{11}C]CFN may be a better ligand than [^{11}C]DPN for in vivo imaging of endogenous opioid peptide release (Quelch et al. 2014).

Both the regional density (B_{max}) and radioligand affinity (K_d) of opioid receptors can be assessed by applying a two-injection protocol, in which [^{11}C]DPN is administered at high (20–160 TBq/mmol) and low (1–3 TBq/mmol) specific radioactivities (Sadzot et al. 1991) or by a pulse-chase protocol (Jones et al. 1994a). Parametric images of [^{11}C]DPN binding can be prepared, using both conventional spectral analysis and rank shaping (Hammers et al. 2007a).

Radiofluorinated analogs of DPN have been prepared. *N*-(3-[^{18}F]Fluoropropyl)-*N*-nordiprenorphine (FPND) showed rather limited brain uptake (Bai et al. 1990) but a striatum/cerebellum ratio of 3.3 ± 0.7 at 30 min postinjection which was reduced to unity after pretreatment of animals with naloxone (1 mg/kg). The tracer was extensively metabolized (<25% parent remaining in blood at 30 min), but not significantly defluorinated (Chesis et al. 1990). 6-*O*-(3-[^{18}F]Fluoroethyl)-6-O-desmethyldiprenorphine ([^{18}F]DPN) showed a regional binding pattern in the human brain similar to that of [^{11}C]DPN (Wester et al. 2000). FDPN binds to μOR, δOR, and κOR in rat brain slices like the parent tracer, DPN (Wester et al. 2000). A scan duration of at least 90 min is required for reliable estimates of tracer distribution volume (Boecker et al. 2005). If metabolite-corrected plasma data are used as input function, individualized metabolite correction should be performed since women metabolize FDPN significantly faster than men (Henriksen et al. 2006).

21.3.4 MeNTI

K_i values of MeNTI (Fig. 21.1) at δOR, μOR, and κOR in guinea pig brain membranes are 0.02, 14, and 65 nM, respectively (Portoghese et al. 1990). Thus, MeNTI is a very potent and subtype-selective δOR antagonist.

In the human brain, [11C]MeNTI shows regional kinetics concordant with selective binding of the tracer to δOR. Prolonged retention of radioactivity is observed in receptor-rich areas, whereas the ligand is rapidly washed out from nontarget areas of the brain. The regional distribution of radioactivity is closely correlated with local δOR densities but not with regional densities of μ or κ binding sites. Tracer uptake is blocked after pretreatment of volunteers with naltrexone (up to 73%) (Madar et al. 1996).

[11C]MeNTI shows irreversible binding characteristics in the human brain during a 90-min scanning period. A constrained three-compartment kinetic model is superior to other data-analytical techniques for quantification of the in vivo binding of the tracer to δOR (Smith et al. 1999).

21.3.5 GR103545

The subtype selectivity of [11C]GR103545 (Fig. 21.1) has been determined in HEK-239 cells expressing human κOR, CHO-K1 cells expressing human μOR, and CHO cells expressing human δOR. K_i values at the three OR subtypes were 0.02, 16.2, and 536 nM, respectively (Schoultz et al. 2010). Thus, [11C]GR103545 is an extremely potent and subtype-selective κOR agonist.

In a preclinical study in awake rhesus macaques, [11C]GR103545 showed a regional volume of distribution in the brain which corresponded to regional κOR densities (Schoultz et al. 2010). In a more recent study, the use of a bolus-plus-continuous-infusion protocol was shown to permit estimation of both B_{max} and K_d of κOR in the monkey brain in vivo (Tomasi et al. 2013). The cerebellum was used as the reference region in kinetic analysis.

A low injected mass of [11C]GR103545 is essential since this κOR agonist can induce respiratory depression, reductions of heart rate, and sedation even at very low administered doses of 0.3 μg/kg. Based on the K_d value estimated for the radioligand in nonhuman primates, a dose of 1.4 μg (3.38 nmol) was estimated as an acceptable dose limit in human studies for subjects with a body mass of 70 kg (Tomasi et al. 2013). In a preclinical study in rats, [11C]GR103545 was found to be suitable for estimation of the dose-dependent occupancy of the cerebral κOR population by salvinorin A (Placzek et al. 2015).

A first-in-man study with [11C]GR103545 has been performed. All subjects were scanned at baseline. Seven subjects were also scanned 75 min after oral administration of naltrexone and six subjects at two time points (1.5 h and 8 h) after intake of the selective κOR antagonist PF-04455242. Drug treatment resulted in a decrease of tracer distribution volume (V_T) in all brain regions. A two-tissue compartment model with multilinear analysis method was identified as the method of choice for

estimation of V_T. The in vivo affinity of the radiotracer for its target was estimated as 0.069 nM. [^{11}C]GR103545 seems suitable for quantification of regional κOR density and κOR occupancy in the human brain, although the radioligand has slow kinetics and variability in the estimated model parameters is rather high (Naganawa et al. 2014a).

21.3.6 LY2795050

LY2795050 (Fig. 21.2) is an opioid antagonist with K_i values of 0.72, 25.8 and 153 nM at cloned human κ, μ and δ receptors (Zheng et al. 2013). In vivo competition studies in the monkey brain confirmed that [^{11}C]LY2795050 binds specifically and selectively to κOR. Although the in vivo selectivity of the ligand for κOR over μOR is smaller than that observed in vitro (7.6 rather than 36), the PET signal of a region expressing similar densities of κOR and μOR will predominantly (for 88%) reflect the presence of the κOR (Kim et al. 2013).

Blocking and kinetic modeling studies of [^{11}C]LY2795050 binding in the human brain indicated regional distribution volume (V_T) values corresponding to known regional densities of the κOR (Naganawa et al. 2014b). Since a reference region without specific binding is lacking in human brain, the authors proposed the use of a fixed value for V_T in cerebellum in model fits. This approach assumes that binding of the ligand in cerebellum is unaltered under the study conditions. A later
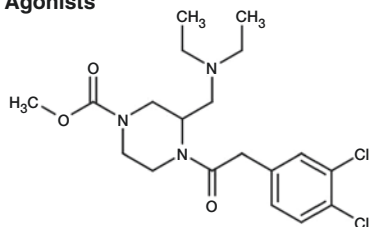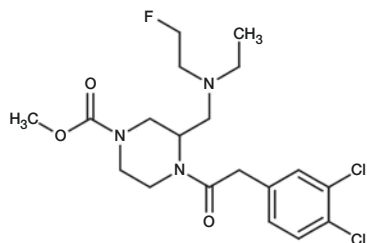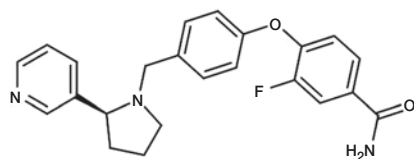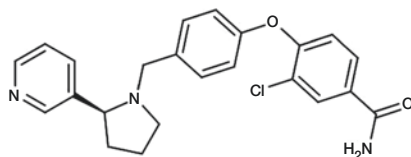
Fig. 21.2 Structures of some κOR agonists and antagonists that have been radiolabeled for PET imaging

publication examined the reproducibility of [¹¹C]LY2795050 scans in human brain, using a two-tissue compartment model fit with fixing of cerebellar V_T. The test-retest reproducibility of V_T in all brain regions was better than 10% with exception of the amygdala where it was 12%. In contrast to V_T, binding potential values showed a good reproducibility in regions with moderate or high receptor densities ($BP_{ND} > 0.4$) but a poor reproducibility in areas with small receptor populations (Naganawa et al. 2015).

An automated GMP procedure for preparation of [¹¹C]LY2795050 has been described (Yang et al. 2018).

21.3.7 LY2459989

LY2459989 (Fig. 21.2) is an opioid antagonist with K_i values of 0.18, 7.68, and 91.3 nM at cloned human κ, μ, and δ receptors (Zheng et al. 2014). Ex vivo biodistribution studies in rodents and imaging studies in monkeys have confirmed that [¹¹C]LY2459989 binds specifically to κOR. Pretreatment of monkeys with naloxone (1 mg/kg) results in a uniform distribution of radioactivity in the brain and tracer uptake is dose-dependently reduced after pretreatment of animals with the subtype-selective κOR antagonists LY2456302 and unlabeled LY2459989. The observed binding potential values of the tracer are high, and regional binding potential is an accurate reflection of known expression levels of the κOR (Zheng et al. 2014).

In a recent paper, sensitivities of the binding of [¹¹C]GR103545 and [¹¹C]LY2459989 in rat brain to competition by unlabeled κOR antagonists and agonists were directly compared. The binding potential values of both tracers were similarly affected when animals were pretreated with kappa antagonists (naloxone, naltrexone, LY2795050, JDTic, nor-BNI) and also after treatment of rats with the kappa agonists butorphan and GR89696. However, pretreatment of animals with the κOR agonists salvinorin A and U-50488 resulted in a strong decrease of [¹¹C]GR103545 binding, but did not affect the binding potential of [¹¹C]LY2459989 (Placzek et al. 2019). This surprising discrepancy suggests that agonists may interact in different ways with κOR and the target occupancy of some κOR agonists cannot be detected with [¹¹C]LY2459989.

21.4 PET Studies in Healthy Volunteers

21.4.1 Influence of Gender, Hormonal Status, and Age

[¹¹C]-CFN-PET has been applied for the study of changes of opioid receptor binding in the brain of women during the menstrual cycle. No significant differences in tracer binding were noted between the follicular and luteal phases of the cycle, but follicular levels of estradiol in the circulation were negatively correlated with [¹¹C]CFN binding potential in the amygdala and hypothalamus. These results, combined with measurements of luteinizing hormone pulse, suggested that μOR in the

amygdala modulate gonadal steroid hormone pulsatility, whereas circulating estradiol regulates μOR function in the brain (Smith et al. 1998). Neuroimaging has shown that black cohosh, a herbal extract used to treat menopausal symptoms, affects the endogenous opioid receptor system. Significant increases in [^{11}C]CFN binding potential (10–61%) were noted in the cortical areas, thalamus, and nucleus accumbens of the brain of postmenopausal women (Reame et al. 2008). In the thalamus and nucleus accumbens, similar effects were observed after estrogen replacement therapy (Smith et al. 2006).

A PET study with [^{11}C]CFN, involving 50 subjects, indicated that the cerebral binding of [^{11}C]CFN is affected both by gender and by age. Binding potential of the radioligand increased with age in the neocortex and putamen. Women showed higher [^{11}C]CFN binding than men of the same age in several cortical and subcortical areas; however, in postmenopausal women, μOR binding in the thalamus and amygdala declined to levels lower than in age-matched men (Zubieta et al. 1999). A PET study with [^{18}F]cyclofoxy confirmed that opioid receptor binding in the thalamus of females is lower than in males, both in healthy aged subjects and in patients with Alzheimer disease (Cohen et al. 2000). MRI-based partial volume correction is required for the accurate assessment of receptor densities in small structures of the human brain. Applying such correction to [^{11}C]CFN data for the left temporal cortex, binding of the radioligand appeared to increase with age (0.9% per year), consistent with B_{max} values from postmortem autoradiography. Without partial volume correction, the effect of aging could not be observed (Bencherif et al. 2004a).

Correlations between regional serotonin transporter and μOR binding were examined in a PET study involving 21 healthy volunteers. The subjects were first injected with the 5-HT transporter tracer [^{11}C]MADAM. When radioactivity from the first injection had decayed, the μOR tracer [^{11}C]carfentanil was injected and a second PET scan was made, with the subject's brain in exactly the same position in the camera. Voxel-based correlation analysis was used to identify brain regions with positive correlations between serotonin transporter and μOR binding. Significant correlations were observed in anteromedial thalamus, dorsal anterior cingulate cortex, dorsolateral prefrontal cortex, amygdala, left parietal cortex, and medial temporal cortex. This finding may indicate that in these regions, endogenous opioids are modulating serotonin release from nerve endings (Tuominen et al. 2014).

A PET study with the κOR ligand [^{11}C]LY2795050 in 27 healthy volunteers reported opposite sex differences in κOR availability as were reported for total opioid receptor binding with [^{11}C]CFN. Men had significantly higher V_T values than women in several brain regions (Vijay et al. 2016).

21.4.2 Feeding

An interesting PET study in ten healthy male volunteers examined whether feeding releases endogenous opioids in the brain and if the magnitude of this response is related to the pleasure of eating. Each volunteer was scanned three times with [^{11}C]CFN: (i) after an overnight fast, (ii) after an overnight fast followed by a

pleasant meal (preferred type of pizza), and (iii) after an overnight fast plus the consumption of an unpleasant meal (nutrient drink). Feeding was associated with a significant release of endogenous opioids (a decrease of radioligand binding potential throughout the brain), but this release was more pronounced after the unpleasant than after the pleasant meal. Thus, opioid release appears to be not directly related to the subjective pleasure but rather to metabolic and homeostatic responses of the body to food consumption (Tuulari et al. 2017).

21.4.3 Personality Traits

Several PET studies have explored relationships between opioid receptor availability in the human brain and personality traits. Using the tracer [^{18}F]DPN, German investigators scanned 23 healthy male volunteers under resting conditions. Subsequently, the subjects were psychologically tested for novelty seeking, harm avoidance, reward dependence, and persistence. A significant correlation was detected between the score for reward dependence (a personality trait predisposing for addictive behavior) and tracer binding potential in the bilateral ventral striatum with nucleus accumbens (Schreckenberger et al. 2008).

A later study from the USA involved scanning of 19 young healthy male volunteers with the μOR ligand [^{11}C]CFN and PET. Subjects were scanned both at baseline and during receipt of a painful stress challenge (infusion of hypertonic saline solution in the left masseter muscle). High scores for impulsiveness and low deliberation scores were associated with significantly higher baseline μOR availability and greater stress-induced endogenous opioid system activation, measured as a reduction of [^{11}C]CFN binding potential. These differences were noted in several brain areas (prefrontal and orbitofrontal cortices, anterior cingulate, thalamus, nucleus accumbens, and basolateral amygdala). Thus, μOR binding potential appears to predict an individual's vulnerability to risky behaviors, such as the development of substance abuse (Love et al. 2009).

A study from Finland measured brain μOR availability with [^{11}C]CFN under resting conditions in 22 healthy volunteers: 10 individuals scoring in the upper and 12 individuals scoring in the lowest quartile for harm avoidance. A high score for harm avoidance (particularly in the subscales shyness with strangers, fatigability, and asthenia) was associated with high μOR availability (or low endogenous μ-opioid drive) in the anterior cingulate cortex, ventromedial and dorsolateral prefrontal cortices, and anterior insular cortex. Thus, high μOR availability may be related to vulnerability for affective disorders (Tuominen et al. 2012). In a later study from the same group, 49 healthy volunteers were scanned with [^{11}C]CFN, and the avoidance and anxiety dimensions of their attachment were measured with the Experiences in Close Relationships-Revised scale. In this study, the avoidance dimension was found to be negatively (not positively) correlated with μOR availability (i.e., [^{11}C]CFN binding potential) in the thalamus, anterior cingulate cortex, frontal cortex, amygdala, and insula, whereas the anxiety dimension was not correlated with μOR availability in any brain region. The authors suggested that

inter-individual differences in µOR availability may be related to differences in avoidant attachment style (Nummenmaa et al. 2015). In a study from the following year, measured [¹¹C]CFN binding potentials were compared to individual differences in behavioral dispositions when subjects encountered signals of reward and harm. Sensitivity of the behavioral activation system but not the behavioral inhibition system was found to be positively associated with [¹¹C]CFN binding potential in frontal cortex, amygdala, ventral striatum, brainstem, cingulate cortex, and insula. Particularly the score for "fun seeking" was strongly associated with µOR availability (Karjalainen et al. 2016).

In an American PET study with [¹¹C]DPN in 12 healthy subjects, a high score of neuroticism was found to be associated with high opioid receptor binding in the right anterior insula. On the other hand, a high score of extraversion was associated with low tracer binding in the left posterior insula (Rodman et al. 2017).

21.4.4 Affective Responses

The opioid system appears to play an important role in the regulation of affective responses. An initial PET study examined [¹¹C]CFN binding and blood flow (uptake of ¹⁵O-water) in the brain of 12 healthy male volunteers, which viewed either aversive images (facial mutilation, wounds, dead bodies) or neutral images (common objects, benign scenes, normal faces). Higher baseline µOR binding potential in the left temporal pole of the subjects was associated with lower blood flow in this region during presentation of the aversive emotional stimuli. This finding was interpreted as evidence for an inhibitory or anxiolytic role of the opioid system in limbic regions of the brain (Liberzon et al. 2002).

A second study examined healthy female volunteers, using [¹¹C]CFN and PET. Sustained neutral and sadness states were elicited by the recall of an autobiographical event associated with these emotions. Sustained sadness caused an increase of µOR availability in the rostral anterior cingulate, ventral pallidum, amygdala, and inferior temporal cortex which was interpreted as reflecting a reduction of the release of endogenous opioids due to deactivation of opioid neurotransmission (Zubieta et al. 2003).

Whereas sustained sadness in healthy volunteers is associated with a reduction in the release of endogenous opioids, positive emotion appears to be associated with an increase of that release. An interesting study from London scanned 25 healthy male volunteers with [¹¹C]DPN and PET, both during positive mood induction (sexually oriented video clip, listening to favorite music, reading positive statements, unexpected gift of 30 GBP) and during neutral mood (nature movie, listening to unknown classical music, reading neutral statements, no gift). Significant reductions of [¹¹C]DPN binding were noted in the hippocampus during positive mood induction, and the magnitude of positive mood change was negatively correlated with DPN binding in the amygdala (Koepp et al. 2009). An interesting PET study with [¹¹C]CFN evaluated the response of the µ-opioid system to social feedback. Eighteen subjects selected at least 40 profiles of preferred sex-individuals from a

database of 500. During a subsequent scanning session with [^{11}C]CFN, images of the faces of these individuals and their responses to the question: Would you like me? (Definitely no, or very likely yes) were presented to them on a computer screen (35 min of acceptance followed by 35 min of rejection, or vice versa, in counterbalanced order). During a separate scanning session with [^{11}C]CFN, the same subjects were scanned at baseline. The human faces on the screen were then replaced by gray blocks and in stead of feedback, the screen said: "non applicable." Social rejection was found to be associated with significant opioid release in the ventral striatum, amygdala, midline thalamus, and periaqueductal gray, a response that may be aimed at reducing the experience of social pain. This interpretation was supported by the observation that a higher score for the character trait resiliency was associated with greater opioid release in the amygdala, periaqueductal gray and subgenual anterior cingulate cortex (ACC), whereas reduced negative feelings during rejection were associated with greater opioid release in the pregenual ACC. In contrast to social rejection, acceptance resulted in activation of opioid release in the amygdala and anterior insula but deactivation in the midline thalamus and subgenual ACC. Opioid release in the left ventral striatum during acceptance was associated with the desire for social interaction. Thus, neurotransmission via μOR may be involved in the preservation and promotion of emotional well-being of human subjects in their social environment (Hsu et al. 2013).

A PET study with [^{11}C]CFN examined the effect of social touch on the activity of the endogenous opioid system. Eighteen male volunteers were scanned twice with this tracer. During the baseline scan, the subjects were left alone, whereas during the social touch scan, their partners were present and were caressing them in a non-sexual way. The scans were separated by an interval of 2 h, and the order of the scans was counterbalanced, i.e., in half of the subjects, the baseline scan was made first, whereas in the other half, it was made last. The subjects reported pleasant sensations during the social touch scan, and the binding potential of the tracer was increased in various regions of the cortex (frontal, cingulate, insular), the thalamus, and the striatum, indicating deactivation of the endogenous opioid system (Nummenmaa et al. 2016).

Another study from the same group focused on the impact of social laughter on the opioid system. Twelve male volunteers were scanned twice with [^{11}C]CFN. Before the test scan, their closest friends were present in the room and they were watching laughter-inducing comedy clips together, but before the baseline scan the subjects spent 30 min alone in the testing room. After the laughing session, the binding potential of the tracer was decreased in the thalamus, caudate nucleus, and anterior insula. In cingulate and orbitofrontal cortex, the magnitude of this decrease was correlated to the rate of social laughter. These data suggest that endogenous opioids are released after social laughter (Manninen et al. 2017).

In a study with the PET tracers [^{11}C]CFN and [^{11}C]raclopride, regional μOR and D$_2$R availabilities were quantified in the brains of 35 healthy adult females. During subsequent fMRI sessions, the subjects watched movie scenes with varying emotional content, ranging from very pleasant to vary scary, and regional increases of cerebral blood flow were quantified. The availability of μOR in the brain was found

to be negatively correlated to fMRI-quantified blood flow responses to arousing scenes in amygdala, hippocampus, thalamus, and hypothalamus. Measured binding potentials of D_2R were not correlated with arousal or pleasantness in any brain region. Thus, emotional arousal appears to be regulated by the μOR system (Karjalainen et al. 2019).

A PET study with the κOR ligand [¹¹C]EKAP in a group of 18 healthy middle-aged volunteers examined the relationship between social status (measured with the Barratt Simplified Measure of Social Status test) and tracer volume of distribution in various areas of the brain. Social status was found to be inversely correlated to regional κOR levels in amygdala, anterior cingulate cortex, caudate, frontal cortex, hippocampus, pallidum, putamen, and ventral striatum, i.e., in regions related to reward and aversion, whereas in other brain regions, no correlation was observed (Matuskey et al. 2019). This finding was interpreted as evidence for the hypothesis that κOR may mediate the negative effects of social behaviors.

21.4.5 Physical Exercise

Long-distance runners have often reported to enter a state of euphoria while running, commonly referred to as "runner's high." In order to examine possible mechanisms underlying this phenomenon, ten athletes were scanned with [¹⁸F]DPN and PET, both at rest and after 2 h of endurance running (in random order). By SPM2 analysis, reductions of tracer binding were noted in several brain areas after exercise. Reported levels of euphoria were inversely correlated with [¹⁸F]DPN binding in the prefrontal/orbitofrontal cortices, anterior cingulate cortex, bilateral insula, parainsular cortex, and temporoparietal regions. These findings support the idea that running is associated with increased release of endorphins, resulting in positive mood changes (Boecker et al. 2008).

A more recent PET study with [¹¹C]CFN in seven healthy male subjects performing cycling exercise has indicated that the pattern and emotional impact of μOR activation in the human brain is dependent on the intensity of the workload. Subjects performed either heavy or severe exercise. After both forms of exercise, reduced tracer binding was noted in several brain regions (particularly insular cortex and cerebellum), indicating activation of the opioid system. In heavy exercise, such decreases were correlated with increased positive sensations. However, in severe exercise, they were correlated with negative sensations. In severe but not in heavy exercise, an increase of tracer binding was noted in the pituitary gland, indicating deactivation of the μOR system in that organ. This last finding may be related to the development of fatigue and exhaustion in exercising subjects (Hiura et al. 2017). Similar findings were reported in a later PET study with [¹¹C]CFN. In that study, 22 healthy subjects were scanned on 3 different occasions: after rest, a 60 min session of moderate exercise and a 60 min session of high-intensity exercise, using a bicycle ergometer. Moderate exercise did not result in significant changes of μOR binding, although increased euphoria was associated with decreased μOR availability. High-intensity exercise resulted in a significant decrease of μOR binding in thalamus,

insula, orbitofrontal cortex, hippocampus, and anterior cingulate, i.e., in brain regions involved in pain, reward, and emotional processing. These regional decreases were associated with increased negative emotions, such as irritation, exhaustion, and dissatisfaction (Saanijoki et al. 2018a).

Since the endogenous opioid system is involved in the rewarding aspects of both food and physical exercise, a combined PET-fMRI study in 24 healthy lean male volunteers examined the interaction between endogenous opioid release following exercise and anticipatory food reward. Two [^{11}C]CFN-PET scans were made of each subject on separate days: after 1 h of rest and after 1 h of moderate-intensity aerobic cycling exercise. Immediately after each PET scan, a fMRI scan was made during which images of palatable food and of nonpalatable items (cars) were presented to the subjects. The order of the rest and exercise scans was counterbalanced among the participants, and all participants fasted 3 h before each PET scan. Changes of μOR availability after exercise showed a large variability among subjects. A larger exercise-induced decrease of μOR binding was associated with larger increases in anticipatory food reward responses (food-induced increases of cerebral blood flow) following exercise. Thus, differences in μOR activation following exercise may contribute to inter-individual variation in food craving and food consumption (Saanijoki et al. 2018b).

21.4.6 Pain

Opioid receptor expression ([^{11}C]DPN or [^{18}F]DPN binding) is high in projections of the medial and part of the lateral pain system of the human brain (Baumgartner et al. 2006; Jones et al. 1991). The lateral network is believed to be associated with the sensory aspects and the medial network with the affective aspects of pain perception. Reductions in receptor availability have been observed in healthy volunteers suffering pain. These data can be interpreted as decreases of regional receptor availability because of release of endogenous opioids, although internalization or downregulation of opioid receptors can also occur. Released opioids may mediate antinociception.

Sustained masseter muscle pain in 20 healthy volunteers was associated with significant declines of the binding of [^{11}C]CFN in several cortical and subcortical brain regions (Zubieta et al. 2001). When capsaicin was applied to the dorsal side of the left hand of eight healthy volunteers, a pain-related decrease in [^{11}C]CFN binding was measured in the contralateral thalamus (Bencherif et al. 2002). In eight healthy volunteers who received painful heat stimulation through the right forearm, a significant reduction of [^{18}F]DPN binding was noted in the limbic and paralimbic areas of the brain, including the rostral anterior cingulate cortex and the insula (Sprenger et al. 2006a).

The duration of pain-induced changes in μOR binding potential has been examined in a PET study with [^{11}C]CFN. Three subsequent 90-min scans were made in 14 healthy male volunteers; the first scan consisted of two 45-min baseline intervals, the second scan involved a 45-min period of sustained muscle pain followed by a

45-min baseline interval, and the third scan consisted again of two 45-min baseline intervals. Robust decreases of [¹¹C]CFN binding were noted in several cortical and subcortical regions during the pain challenge. However, these changes did not persist in a subsequent scan. Pain-induced alterations of opioid release and/or μOR internalization are therefore short lasting (Scott et al. 2007a).

In a study involving 14 male and 14 female healthy individuals subjected to sustained masseter muscle pain (infusion of hypertonic saline), men demonstrated larger declines of [¹¹C]CFN binding in the anterior thalamus, ventral basal ganglia, and amygdala. Conversely, women showed greater declines of the PET signal in the nucleus accumbens. Thus, opioid receptor-mediated antinociceptive responses show gender differences (Zubieta et al. 2002).

Opioid release is also involved in placebo analgesia. In a PET study with [¹¹C]CFN, healthy subjects were scanned under four different conditions: painful skin heat with placebo cream, painful skin heat under control conditions, nonpainful warmth with placebo cream, and nonpainful warmth under control conditions. In all cases, the volunteers were told that the placebo cream was a powerful analgesic. Placebo treatment resulted in significant decreases of [¹¹C]CFN binding in several brain regions known to be involved in pain and affect; thus, endogenous opioid release appears to be part of the mechanism by which expectancies regulate the perception of pain (Wager et al. 2007). A later study from the same group examined placebo and nocebo effects, i.e., the subjects expected the placebo cream to either ameliorate or exacerbate their pain. Placebo and nocebo effects were found to be associated with opposite opioid and dopaminergic responses. A placebo activated opioid neurotransmission in the anterior cingulate, orbitofrontal and insular cortices, nucleus accumbens, amygdala, and periaqueductal gray, whereas dopaminergic neurotransmission was activated in the ventral basal ganglia including the nucleus accumbens. Nocebo responses consisted of a deactivation of opioid and dopamine release. The magnitude of opioid and dopamine activation was correlated with the anticipated and subjectively perceived placebo effect (Scott et al. 2008). However, a subsequent [¹¹C]CFN-PET study in a large number of healthy volunteers ($n = 48$) indicated that a priori expectations (anticipations) are not correlated with placebo-induced decreases in pain ratings during placebo administration. Subjects with higher expectations showed greater μOR activation in the dorsolateral prefrontal cortex after placebo administration, but this did not correspond to subjective analgetic effects. The largest placebo responses were noted in individuals with low expectations and high subjective effectiveness. Activation of μOR in anterior cingulate cortex was correlated with the effectiveness of the placebo. In subjects with high expectations but low reported effectiveness of the placebo, placebo administration resulted in a nocebo, hyperalgesic response (Pecina et al. 2014).

A PET study in an animal model of placebo analgesia has confirmed that the intrinsic μOR system in the medial prefrontal cortex is involved in the placebo effect (Zeng et al. 2018).

When heat pain was combined with either acupuncture or placebo needle stimulation in healthy volunteers, acupuncture was shown to result in altered binding of [¹¹C]DPN (mainly decreases) in the orbitofrontal cortex, medial prefrontal cortex, insula, thalamus, and anterior cingulate cortex (Dougherty et al. 2008).

Opioid receptor availability at baseline conditions appears to be a predictor of human sensitivity to both painful (cold pressor test) and mechanical stimuli (touch, vibration). Greater sensitivity was associated with a lower BP of [^{18}F]DPN in various cortical areas (Mueller et al. 2010). In a later study on 12 healthy male volunteers, a significant correlation was observed between baseline binding potential of [^{11}C]CFN (μOR binding) in the striatum and the cold pressor pain threshold (Hagelberg et al. 2012).

A Japanese study examined opioid mechanisms underlying heterotopic nociceptive counter-stimulation (HCNS). HCNS aims to activate endogenous pain inhibition processes, which can be beneficial in pain treatment. The right sural nerve of eight healthy volunteers was transcutaneously stimulated, resulting in leg pain. Immersion of the left hand in cold water was applied as HCNS. A late component of somatosensory evoked potentials, reflecting activity of the anterior cingulate cortex, was reduced by HCNS, and this reduction was associated with a higher binding potential of [^{11}C]CFN in the right amygdala at baseline. Activation of μOR in the amygdala may thus be involved in the anti-nociceptive effects of HCNS (Piché et al. 2014).

Since peripheral inflammatory factors can influence central nervous system functioning, and, on the other hand, central mechanisms such as neural activity can modulate peripheral immune function, an American study examined relationships between IL-I family cytokine levels in plasma and μOR availability in human brain. Thirty-four healthy volunteers (22 female, 12 male) were scanned with [^{11}C]CFN in the presence and absence of a standardized pain challenge (intramuscular infusion of hypertonic saline by a computer-controlled pump). Cytokine levels in plasma were measured during both conditions. Higher baseline levels of IL-Iß were shown to be associated with lower binding potentials of [^{11}C]CFN in the amygdala and greater sensitivity to pain. Subjects with a greater pain-induced increase in IL-Iß experienced less endogenous opioid analgesia. Activation of μORs in ventral caudate and nucleus accumbens during the pain challenge was significantly associated with levels of IL-Ira, an anti-nociceptive cytokine. Thus, cytokine levels in human plasma and the endogenous opioid neurotransmitter system seem to interact (Prossin et al. 2015).

A PET study from Finland has indicated that vicarious pain (i.e., seeing others in pain) activates specific regions in the human brain and that μOR but not D_2R are involved in this response. Thirty-five healthy subjects were scanned, using the μOR tracer [^{11}C]CFN and the D_2R tracer [^{11}C]raclopride. Functional MRI scans of their brains were also made, during the watching of videoclips that depicted humans in painful or painless situations. The fMRI scans demonstrated increases of blood flow in various brain regions when the subjects watched painful scenes. In anterior and posterior insulae, thalamus, secondary and primary somatosensory cortrices, primary motor cortex and superior temporal sulci, the magnitude of these increases was negatively correlated to measured [^{11}C]CFN binding potentials, whereas the response in orbitofrontal cortex showed a positive correlation to μOR avaibility. In contrast to μOR. dopamine D_2R availability was not correlated to the blood flow response in any brain region (Karjalainen et al. 2017). Thus, inter-individual differences in μOR availability may explain why some humans react more strongly than others to the seeing of pain.

21.4.7 Vestibular Processing

An interesting study examined involvement of the opioid system in vestibular neu-rotransmission in humans. Ten right-handed healthy volunteers were scanned with the ligand [^{18}F]DPN, both under baseline conditions and during caloric stimulation of the right ear. Each 90-min scan session consisted of three subsequent phases: a prestimulation period (30 min), a stimulation or sham period (30 min), and a follow-up period (30 min). During the stimulation period, warm (44 °C) and cold (30 °C) air were alternated at 5-min intervals in order to avoid habituation; during the sham period, the tubing was fixed to the subjects head in such a way that the air flow passed beside the ear. A decrease in tracer binding was noted in the right posterior insular cortex and the postcentral region during stimulation, indicating release of endogenous opioids and involvement of the opioid system in vestibular processing (Baier et al. 2010).

21.4.8 Myocardial Opioid Receptors

Both [^{11}C]*N*-methyl-naltrindole ([^{11}C]MeNTI) and [^{11}C]CFN show specific binding in the human heart. However, the reduction of myocardial distribution volume and binding potential of these opioid ligands after pretreatment of volunteers with nal-oxone is only minor (14–21 and 19–25%, respectively), suggesting low levels of δOR and μOR expression and poor signal-to-noise ratios in PET (Villemagne et al. 2002).

21.4.9 Occupancy Studies

PET offers the unique opportunity of measuring the fraction of receptor populations occupied by nonradioactive drugs in the living brain and relating measured levels of occupancy to the magnitude of the therapeutic effect or to unwanted side effects. Receptor occupancy is estimated by assessing competition of a nonradioactive drug with the radioligand for the same binding sites. The basic idea was already pub-lished in 1980 (Homcy et al. 1980).

Using the radioligand [^{11}C]CFN, a half-life of μOR blockade of 72–108 h was measured in the brain of healthy volunteers after a single oral dosing of naltrexone, corresponding to the duration of pharmacological effects when the drug is used for treatment of heroin dependence (Lee et al. 1988).

A later study with [^{11}C]CFN compared the duration of occupancy of μOR in the human brain by the antagonists nalmefene and naloxone. Clearance half-lives were 28.7 h after administration of 1 mg of nalmefene and 2.0 h for 2 mg of naloxone. The longer blockade by nalmefene could represent an advantage in the clinical use of this compound for reversal of opioid anesthesia or for treatment of drug addicts after an opioid overdose (Kim et al. 1997). Nalmefene has also been proposed for treatment of alcoholism. The decline of μOR occupancy in the human brain after single or repeated nalmefene dosing was found to be slower than the decline in

plasma concentration of the drug or its metabolites, indicating slow dissociation of receptor-bound nalmefene in vivo (Ingman et al. 2005).

Buprenorphine is used for the treatment of heroin dependence. Buprenorphine occupancy of μOR in the human brain has been examined, using [11C]CFN and PET. Four hours after administration of 2 mg buprenorphine, receptor occupancy ranged from 36 to 50%. When the buprenorphine dose was raised to 16 mg, levels of occupancy increased to 79–95%. Placebo-treated heroin abusers had greater μOR binding potential in the inferofrontal and anterior cingulate cortex compared to matched healthy controls (Zubieta et al. 2000). Increasing doses of buprenorphine were associated both with decreased μOR availability and with decreased withdrawal symptoms. The highest dose of buprenorphine (32 mg) caused virtually complete μOR occupancy (Greenwald et al. 2003). The duration of action of buprenorphine was examined in ten heroin-dependent subjects after termination of a 16 mg/day dose of the drug. Relative to a control group of heroin-dependent subjects maintained on placebo, μOR occupancy was 70, 46, 33, and 18% at 4, 28, 52, and 76 h after last use of the drug. Receptor occupancy was correlated with withdrawal symptoms; an occupancy of 50–60% appeared necessary for adequate symptom suppression (Greenwald et al. 2007).

Nasal spray formulations of naloxone may be useful in the treatment of victims of opioid overdose and may also be used for treating subjects with gambling disorder and alcohol addicts. Occupancy of the μOR population in the human brain after intranasal spray dosing of naloxone has been assessed in healthy volunteers with [11C]CFN and PET. Naloxone levels in the brain were found to peak within half an hour, a bit later than levels in plasma which peaked at 20 min. Receptor occupancies after intranasal administration of 2 and 4 mg naloxone were 67 and 85%, respectively, whereas the clearance half-life of the bound drug was about 100 min (Johansson et al. 2019).

The κOR antagonist LY2456302 has been developed for treating neuropsychiatric disorders and substance abuse. Dose-dependent target occupancy by this drug has been measured in a PET study with [11C]LY2795050 in 30 healthy volunteers. An oral dose of 10 mg resulted in virtually complete κOR occupancy and was well-tolerated (Naganawa et al. 2016).

Although the dose- and time-dependent opioid receptor occupancy by antagonists and partial agonists can be assessed with PET, measurements of receptor occupancy by full agonists may be problematic. No difference in [11C]DPN binding was found in the brain of opioid-dependent subjects stable on methadone (18–90 mg daily, PET scan performed at peak plasma levels of the agonist) as compared to healthy controls. In rats receiving increased doses of methadone, no dose-dependent reduction of the cerebral binding of [11C]DPN was observed. These negative findings were explained by assuming that methadone is already efficacious at very low levels of receptor occupancy (<10%, i.e., below the detection limit of PET) (Melichar et al. 2005). In a subsequent preclinical study, rats were pretreated with antinociceptive doses of oxycodone (μOR and κOR agonist), morphine (μOR agonist), and buprenorphine (δOR and κOR antagonist, μOR partial agonist). Full agonists did not reduce the brain uptake of [11C]DPN at all, whereas buprenorphine administration resulted in a strong reduction (up to 90%) of tracer binding (Hume et al. 2007).

Opioid receptor occupancy by the antagonist naloxone could also be measured with [^{11}C]DPN and PET, a drug dose of 13 µg/kg resulting in 50% occupancy (Melichar et al. 2003). The reason for the negative findings with exogenous full agonists is not clear, since endogenous enkephalins have been shown to compete with [^{11}C]DPN for OR binding in the human brain (Ruiz-Gayo et al. 1992). Moreover, an early PET study reported 19–32% lower binding of [^{18}F]cyclofoxy in various brain regions of long-term methadone-treated former heroin addicts as compared to controls (22 h after the last dose), and the reduction of tracer binding in caudate and putamen correlated with levels of methadone in plasma (Kling et al. 2000). Since the observed competition is both tracer and agonist dependent, these PET data may indicate the presence of multiple, different agonist binding sites on opioid receptor proteins or upregulation of subclasses of opioid receptors in heroin-dependent subjects.

Opioid receptor (particularly µOR) agonists increase and antagonists decrease feeding and other rewarding behaviors in animal models. A [^{11}C]CFN-PET study examined cerebral µOR occupancy in 26 healthy male volunteers after single oral doses of either GSK1521498 (µOR inverse agonist, candidate drug for the treatment of overeating) or naltrexone (µOR and κOR antagonist). Activation of the amygdala by a palatable food stimulus (fruit drink) was examined in the same volunteers, using fMRI. Although a dose-dependent occupancy of µOR was observed for both compounds, GSK1521498 significantly attenuated activation of the amygdala by the food stimulus, in contrast to naltrexone. This difference may be related to the fact that µOR and κOR signaling have different effects on feeding behavior and reward processing (Rabiner et al. 2011).

Naloxone administration triggers activity of the hypothalamic-pituitary-adrenal (HPA) axis by blocking opioid inhibitory tone at corticotropin-releasing factor (CRF) neurons in the paraventricular nucleus of the hypothalamus. These neurons regulate the secretion of adrenocorticotropic hormone (ACTH) and cortisol. An interesting study measured µOR binding potential in the brain of 18 healthy subjects using [^{11}C]CFN and PET. The following day, ACTH and cortisol responses to an incremental naloxone challenge were tested in the same subject group. Cortisol responses to naloxone were negatively correlated to [^{11}C]CFN binding potential in several brain areas (ventral striatum, putamen, caudate, hypothalamus). Apparently, subjects with higher binding potential have lower endogenous occupancy of µOR by ß-endorphin and thus place less inhibitory tone on the HPA axis; therefore these subjects show a smaller cortisol response to naloxone (Wand et al. 2011).

21.5 PET Studies in Patients and Drug Addicts

21.5.1 Major Depressive, Borderline Personality, and Posttraumatic Stress Disorder

Using the sustained neutral and sadness state paradigm, µOR availability in the brain of healthy female volunteers and patients with major depressive disorder (MDD) has been compared. Healthy controls showed an increase of µOR

availability in the anterior cingulate during the sustained sadness condition indicating deactivation of μOR-mediated neurotransmission, but in patients who did not respond to antidepressant treatment after PET imaging, sustained sadness was associated with a *decreased* binding of [^{11}C]CFN in this region, i.e., activation of the opioid system. Patients with MDD showed significantly lower μOR binding potential in the posterior thalamus than healthy controls during the neutral state. These PET data indicated that endogenous opioid neurotransmission is altered in MDD (Kennedy et al. 2006). A later study from the same group showed that in MDD patients but not in healthy subjects, plasma levels of the inflammatory cytokine IL-18 are positively correlated with baseline μOR binding potential and with activation of μOR-mediated neurotransmission during a sadness challenge (Prossin et al. 2011). Thus, there may be a link between peripheral stress-activated proinflammatory mechanisms and central stress-activated neurotransmitter systems, such as the opioid system.

A study from the same group examined responses of the μOR system to sustained sadness in patients with borderline personality disorder. During the baseline (neutral) state, patients showed greater [^{11}C]CFN binding than healthy controls in the bilateral orbitofrontal cortex, caudate, and nucleus accumbens besides the left amygdala but lower binding in the posterior thalamus. Induction of sadness caused greater declines of [^{11}C]CFN binding potential in the pregenual anterior cingulate, left orbitofrontal cortex, left ventricular pallidum, left amygdala, and left inferior prefrontal cortex of the patients than of healthy controls and greater increases of binding potential in the left nucleus accumbens, the hypothalamus, and the right hippocampus/parahippocampus. Apparently, the opioid system of patients with borderline personality disorder differs from healthy, age- and sex-matched control subjects both at baseline and in its response to a negative emotional challenge (Prossin et al. 2010). Altered opioid neurotransmission may also be a mechanism underlying modified limbic system activity and mood disorders in polycystic ovary syndrome (PCOS). Insulin-resistant women with PCOS showed a greater blood flow response in limbic regions of the brain to unpleasant images than healthy controls, and the extent of this limbic activation was positively correlated to μOR availability in the right amygdala and left ventral anterior cingulate (Marsh et al. 2013).

An interesting study compared μOR binding in the brain of 14 healthy male volunteers, 15 males with combat exposure but without posttraumatic stress disorder (PTSD), and 16 male patients with PTSD, using [^{11}C]CFN and PET. The two groups which had been exposed to war trauma showed lower μOR binding in the amygdala, nucleus accumbens, dorsal frontal cortex, and insular cortex than healthy volunteers but higher μOR binding in the orbitofrontal cortex. PTSD patients showed a significant reduction of μOR binding in the anterior cingulate cortex compared to both other groups. Combat-exposed subjects without PTSD had lower μOR binding in the amygdala but higher binding in the orbitofrontal cortex than either PTSD patients or healthy controls. Thus, the opioid system of the brain shows specific changes both after trauma and in PTSD (Liberzon et al. 2007).

Preclinical data have suggested that the dynorphin/κOR system may be related to symptoms of fear and depression after exposure to trauma. An American study used

the κOR ligand [¹¹C]LY2795050 to scan the brains of 35 subjects with a wide range of exposure to trauma (ranging from healthy controls to subjects with PTSD, MDD, and generalized anxiety disorder). Measured distribution volumes of the tracer in amygdala, anterior cingulate cortex, and ventral striatum were significantly and negatively correlated with 24-h urinary cortisol levels and severity of loss (i.e., dysphoria, depressive symptoms, emotional numbing), but not with feelings of threat (i.e., fear) in the subject group (Pietrzak et al. 2014). In contrast to the findings of this initial study, a later pilot study with [¹¹C]GR103545 did not observe any significant difference of regional tracer distribution volume (i.e., κOR availability) between 10 patients with MDD and 13 healthy volunteers (Miller et al. 2018).

If medication-free patients with MDD and healthy controls were scanned with [¹¹C]CFN and subjected to a social rejection and acceptance protocol (as described above, Sect. 21.4.3 (Hsu et al. 2013)), the patients showed a reduced release of opioids in various brain regions in response to rejection and a slower emotional recovery than the healthy subjects. During acceptance, only the healthy controls reported an increase in self-esteem and an increased desire for social interaction, which was correlated with release of endogenous opioids in the nucleus accumbens. A reduced activity of the endogenous opioid system may thus be involved in the pathophysiology of MDD, resulting in a less effective recovery from negative and a decreased pleasure from positive social interactions (Hsu et al. 2015).

Another PET study from the same group examined changes of the regional binding potential of [¹¹C]CFN and plasma levels of interleukin-18 in 28 human volunteers during the induction of sad or neutral mood, using a standard protocol. The subject group consisted of 15 healthy controls and 13 patients with unmedicated MDD. All subjects were female. IL-18 levels were increased during sadness, indicating peripheral immune activation and were reduced during neutral mood. IL-18 increases in the patients were significantly greater than in the control group. Moreover, these increases were found to be linearly proportional to sadness-induced μOR activation (i.e., reductions of tracer binding potential) in left ventral pallidum, bilateral anterior cingulate cortices, right hypothalamus, and bilateral amygdala. Apparently, changes in mood regulate human immune function, and this regulation may be related to central opioid neurotransmission (Prossin et al. 2016).

An interesting study with [¹¹C]CFN examined the impact of placebo and antidepressant treatment in 35 medication-free patients with MDD. All subjects were treated with a placebo during two periods of 1 week. They were either informed that the placebo was a fast-acting antidepressant drug or that it was an inactive control. After each week of treatment, a [¹¹C]CFN-PET scan was made. In half of the subjects, the "active" placebo was given first and was followed by the "inactive" placebo, whereas in the other half, the order of treatments was reversed. After both PET scans and placebo treatments, all subjects were treated for 10 weeks with a real antidepressant, in most cases a selective serotonin reuptake inhibitor.

Higher μOR binding in the nucleus accumbens at baseline was associated with better antidepressant response. A decrease of tracer binding potential in subgenual anterior cingulate cortex, nucleus accumbens, thalamus, and amygdala after 1 week of "active" placebo (compared to the amount of binding after 1 week of "inactive"

placebo) was associated with placebo-induced reductions in depressive symptoms and also with a better response to the real antidepressant at the end of the trial. Thus, a placebo is capable of activating the endogenous μ-opioid system in patients with MDD and this system is also involved in the response of such patients to an antidepressant drug (Pecina et al. 2015).

21.5.2 Pain

In a group of four patients with rheumatoid arthritis, regional cerebral opioid receptor binding of [11C]DPN was quantified both during a period of pain and during a period when the subjects were out of pain. Significant decreases of [11C]DPN binding were seen in many brain areas when subjects suffered pain (particularly straight gyrus and frontal, cingulate, and temporal cortex) (Jones et al. 1994b). In a patient with central poststroke pain which developed after a small pontine hemorrhagic infarction, a reduction of the binding of [11C]DPN was also noted, and this reduction was more striking than the hypometabolism of [18F]FDG on the lateral cortical surface contralateral to the symptoms (Willoch et al. 1999).

Changes of [11C]DPN binding in the brain of six patients after surgical relief of trigeminal neuralgia pain were examined in a later study. The volume of distribution of the tracer in several cortical areas (prefrontal, insular, perigenual, midcingulate, inferior parietal), basal ganglia, and the thalamus was found to be significantly increased after surgery (Jones et al. 1999). These data and the findings in the previous studies were interpreted as evidence for the release of opioid peptides during various forms of pain resulting in a reduction of the fraction of the receptor population available for ligand binding. However, changes of opioid receptor numbers (upregulation after surgery or after the disappearance of pain) could not be ruled out.

In a later study involving four patients with central neuropathic pain (mainly poststroke) and age-matched controls, patients were found to have significantly less [11C]DPN binding in the dorsolateral, anterior cingulate, and insula cortices, the thalamus, and the inferior parietal cortex. These reductions were not a direct consequence of their cerebral lesions, since these were located in other brain areas. The authors interpreted the PET data as evidence for reduced damping of nociceptor activity in the patients and as a possible explanation for the fact that high doses of opiates are frequently required to achieve optimal analgesia in subjects with central neuropathic pain (Jones et al. 2004). Essentially similar findings were reported in a study from another institution, using the same tracer and involving 5 patients with central poststroke pain and 12 healthy volunteers (Willoch et al. 2004).

An interesting study compared changes of [11C]DPN binding in the brain of patients with peripheral neuropathic pain and central poststroke pain. Peripheral neuropathic pain patients showed bilateral and symmetric decreases of [11C]DPN binding, in contrast to central poststroke pain patients where an asymmetric decrease was noted, which was most prominent in the contralateral hemisphere. The symmetric and bilateral decline in the former patient group may reflect endogenous opioid release, whereas the lateralized decrease in the latter group suggests a loss of

opioid receptors (Maarrawi et al. 2007a). Thus, central and peripheral forms of neuropathic pain may have different effects on the opioid system of the brain.

In a group of ten patients with restless legs syndrome (RLS), significant negative correlations were observed between [^{11}C]DPN binding in areas serving the medial pain system and RLS severity or pain scores. These findings suggested release of endogenous opioids within the medial pain system related to the severity of the syndrome (von Spiczak et al. 2005).

Changes of the opioid system in patients with cluster headache were also examined, using the tracer [^{11}C]DPN and PET. When patients as a group were compared with healthy volunteers, a striking (>50%) decrease of tracer binding was noted in the pineal gland but not in any other brain area. Within the patient group, opioid receptor availability in the ipsilateral hypothalamus and anterior cingulate cortex was negatively correlated to the duration of the headache disorder. The patients did not experience acute pain during or immediately before the study; thus, the observed alterations of [^{11}C]DPN binding appear to not represent an effect of acute pain processing but rather alterations in the opioid system related to the development of the disease. Opioidergic dysfunction in circuitries generating the biologic clock may be a mechanism underlying cluster headache (Sprenger et al. 2006b).

In patients with complex regional pain syndrome (CRPS), a chronic pain condition which can develop after limb trauma, binding of the non-subtype-selective OR ligand [^{18}F]DPN was found to be reduced in the contralateral amygdala and parahippocampal gyri but increased in the contralateral prefrontal cortical areas. Ligand binding in the ipsilateral temporal cortex and midcingulate cortex was negatively correlated with pain scores, but ligand binding in the contralateral temporal cortex was positively correlated with anxiety and depression scales (Klega et al. 2010). These findings suggest that the endogenous opioid system is implied in both chronic pain and its psychiatric comorbidity.

A study with the tracer [^{11}C]CFN compared μOR binding in the brain of four patients with trigeminal neuropathic pain and eight gender- and age-matched healthy controls. Patients showed reduced tracer binding in the left nucleus accumbens, and binding potential in this area was negatively correlated with their pain ratings. This finding was interpreted as evidence for downregulation of μOR after persistent activation of opioid neurotransmission in chronic pain (DosSantos et al. 2012a). A recent PET study in experimental animals has proven that reduced μOR availability in chronic neuropathic pain (measured with [^{18}F]DPN and PET) reflects reduced μOR expression. In this study, μOR expression in various brain areas was quantified by ex vivo immunohistochemistry (Thompson et al. 2018).

Another PET study with [^{11}C]CFN examined regional μOR binding potential values in the human brain during experimentally induced pain (application of 0.35 g of 10% capsaicin cream on a 6.25 cm^2 area of the left hand). The data from the PET study were compared to evaluations of the sleep quality of the subjects ($n = 14$) during the previous month, using the Pittsburgh Sleep Quality Index. Poor sleep quality was significantly and positively correlated to greater μOR binding potential in the frontal lobes, and sleep duration was negatively associated with binding potential in these lobes, the temporal lobe and the anterior cingulate. Thus, individual variation

in the quality and duration of sleep appear to be associated with variation in cerebral μOR binding during tonic pain. Poor sleep may be related to impaired pain-suppressing mechanisms (less release of endogenous opioids in response to a painful stimulus) and an increased perception of pain (Campbell et al. 2013).

A more complicated study with [^{11}C]CFN provided evidence for the hypothesis that both alterations in μOR availability and a reduced release of endogenous opioids contribute to the clinical symptoms of patients suffering from chronic back pain. Tracer binding potential was measured in 16 patients with chronic back pain and 16 age- and gender-matched healthy volunteers under three different conditions: at baseline, during pain expectation (intramuscular injection of isotonic saline), and during sustained moderate pain (intramuscular injection of hypertonic saline). Baseline μOR binding in the thalamus proved to be higher in the patients than in the control subjects, and the patients showed smaller reductions in μOR binding in several brain areas, both during the painful condition and the expectation of pain (Martikainen et al. 2013).

PET with the μOR tracer [^{11}C]CFN has also been used to examine activity of the opioid system during migraine attacks. Seven patients with frequent migraine were scanned both during the ictal and interictal phase. μOR binding in the ipsilateral medial prefrontal cortex was found to be significantly reduced during the ictal phase, possibly due to increased release of endogenous opioids, in order to fight the ongoing pain. The magnitude of this reduction was negatively correlated to the combined extension and severity of the migraine attack (Dasilva et al. 2014).

Migraine, particularly in patients that have used opioids to suppress their pain, is frequently associated with allodynia, i.e., an increased sensitivity of the skin to stimuli that should not cause pain. Normal activities, such as washing the skin with warm water, or combing the hair, are painful for subjects suffering from allodynia. A report following on the previous PET study examined changes of [^{11}C]CFN in patient's brains during migraine-associated allodynia. The skin was thermally challenged by a device that provided heat pulses every 10s during a period of 20 min. Patients were challenged and scanned both during the ictal and interictal phase of their migraine. A decrease of μOR binding potential was observed in the ventrolateral periaqueductal gray matter and the red nucleus area of the midbrain, when patients were thermally challenged and showed allodynia. The magnitude of this decrease was positively correlated to allodynic severity during a migraine attack (Nascimento et al. 2014).

Simultaneous PET (with the opioid receptor ligand [^{11}C]DPN) and functional MRI (fMRI) has been used to examine the opioidergic pain system in the human brain. Eight healthy volunteers were scanned twice on the same day, during the application of a painful and a non-painful stimulus (pressure). The order of the scans was randomized. Pain-related activation of several brain regions was observed in fMRI, but in most of these regions, opioid receptor binding was not significantly altered. Co-localized fMRI and PET signal changes were noticed only in the ipsilateral thalamus and the contralateral striatum. Decreases of tracer binding potential and increases of blood flow (fMRI BOLD signal) were significantly correlated in the thalamus, suggesting that in this area of the brain, enhanced opioid

neurotransmission is a major cause of the increases of flow, i.e., of neuronal activation. However, no correlation was observed between the PET and fMRI signal changes in the striatum, suggesting that in this region, additional receptor systems were contributing to the observed flow changes (Wey et al. 2014).

A British study used the PET tracer [^{11}C]DPN to relate opioid receptor availability in the human brain to pain perception in arthritis. Within the patient group with arthritis ($n = 17$), the perception of higher levels of chronic pain in the week before the scan was associated with higher OR availability, particularly in the caudate, nucleus accumbens, and subcallosal area. This observation suggests that opioid receptors are upregulated in individuals experiencing greater chronic pain. Higher OR availability was associated with higher acute thermal pain thresholds, suggesting that OR upregulation is an adaptive response aimed at dampening the pain perception. When the entire patient group was considered, OR availability in the patients caudate nucleus was reduced in comparison to healthy controls ($n = 9$), suggesting a greater release of endogenous opioid ligands and greater occupancy of ORs in the arthritis group (Brown et al. 2015).

Patients with fibromyalgia report widespread pain in muscles and connective tissue, whereas no pathology can be identified in the painful body areas. The central nervous system of these patients may have become overly sensitive to painful stimuli. In order to test this hypothesis, pain-evoked increases of cerebral blood flow were quantified with fMRI and regional μOR availability was quantified in 18 female patients with fibromyalgia, using PET and [^{11}C]CFN. Patients showed a lower μOR availability in dorsolateral prefrontal and anterior cingulate cortex than healthy controls, and this was associated with a lower blood flow response to painful stimuli. Thus, the endogenous opioid system appears to be dysregulated in fibromyalgia, resulting in lower activation of antinoceptive brain regions after incoming painful stimuli and abnormal sensitivity to pain (Schrepf et al. 2016).

21.5.3 Pain Treatment

Monitoring the relationship between opioid receptor occupancy and pain relief could be useful in the development of improved techniques for the treatment of pain (Sadzot et al. 1990; Sadzot and Frost 1990). This study paradigm has been employed in several reports.

An initial study examined the contribution of the endogenous opioid system to pain relief induced by motor cortex stimulation (MCS). Eight patients with refractory neuropathic pain were scanned three times with [^{11}C]DPN and PET: twice preoperatively with a 2-week interval and once after 7 months of chronic MCS. The preoperative test-retest scans did not show any significant differences, but comparison of the last scan with the two preoperative scans revealed significant decreases of tracer binding in the anterior middle cingulate cortex, periaqueductal gray, prefrontal cortex, and cerebellum. The magnitude of the changes in the first two brain areas was significantly correlated with pain relief. These findings were interpreted as

evidence for the release of endogenous opioids in brain structures involved in pain processing after MCS (Maarrawi et al. 2007b).

The effects of traditional Chinese acupuncture and placebo needle stimulation have been compared in chronic pain patients diagnosed with fibromyalgia. [^{11}C]CFN-PET scans were made at both the beginning and the end of the 4-week treatment period. Acupuncture was shown to result in both short- and long-term increases in [^{11}C]CFN binding potential in multiple pain and sensory processing regions. In the sham group, small reductions of [^{11}C]CFN binding were observed, consistent with previously reported placebo effects. The long-term increases after acupuncture were correlated with reductions in clinical pain. Thus, acupuncture and sham acupuncture may have different effects on cerebral μOR binding and alterations of μOR binding potential may be involved in the analgesic effect of acupuncture (Harris et al. 2009).

A case study reported that transcranial direct current stimulation (tDCS) of the motor cortex in a trigeminal neuropathic pain patient considerably decreased the binding potential of [^{11}C]CFN in several brain areas compared to sham tDCS. The effect was particularly striking in the posterior thalamus. tDCS increased the threshold for experimental cold pain in the patient but did not improve her clinical pain. The authors suggested that the release of endogenous opioids is immediately increased by tDCS, but repetitive tDCS sessions are required to revert neuroplastic changes related to the neuropathic pain (DosSantos et al. 2012b). A follow-up study from the same group examined the mechanisms underlying tDCS. Nine healthy volunteers were scanned with [^{11}C]CFN on two different occasions: at baseline and during application of tDCS. The last scan comprised a placebo phase (in which tDCS electrodes were present but no stimulation was applied) and a real stimulation phase. The placebo phase was associated with a decrease of tracer binding potential in the periaqueductal gray, precuneus, and thalamus, indicating release of endogenous opioids in response to the placebo. Real tDCS was associated with similar changes in periaqueductal gray and precuneus and an additional decrease of tracer binding in the left prefrontal cortex. Significant analgesic effects (increases of pain thresholds) were only observed after real tDCS. Thus, the endogenous μOR system is already activated by a placebo, and the placebo effect seems to be extended and optimized by real tDCS (DosSantos et al. 2014).

A PET study with [^{11}C]DPN examined OR availability in 15 patients suffering from refractory neuropathic pain. The patients were subsequently treated by receiving chronically implanted motor cortex stimulation. Preoperative levels of opioid binding in several brain regions (insula, thalamus, periaqueductal grey, anterior cingulate, and orbitofrontal cortex) were found to be significantly and positively correlated with postoperative pain relief after 7 months. Thus, PET scans with an opioid receptor ligand may help clinicians to select patients with neuropathic pain, who are likely to benefit from motor cortex stimulation (Maarrawi et al. 2013).

A Chinese study evaluated the impact of 30 min of transcutaneous electrical acupoint stimulation (TEAS) on μOR availability in the brain of anaesthetized rhesus monkeys, using [^{11}C]CFN and PET. The study showed that 2 Hz but not 100 Hz stimulation resulted in a significant increase of tracer binding potential in the

anterior cingulate cortex, caudate nucleus, putamen, temporal lobe, somatosensory cortex, and amygdala (compared to a 0 Hz control scan). These results suggest that not only the release of endogenous opioid peptides, but also an upregulation of µOR plays a role in the mechanism of action of TEAS (Xiang et al. 2014).

A decreased availability of µOR in the human brain (suggesting the release of endogenous opioids) has also been observed in healthy volunteers ($n = 10$) after transcranial magnetic stimulation (TMS). After active but not sham TMS, the binding potential values of [^{11}C]CFN were lowered in the right ventral striatum, medial orbitofrontal, prefrontal and anterior cingulate cortices, left insula, superior temporal gyrus, dorsolateral prefrontal cortex, and precentral gyrus. In contrast to these changes of µOR, dopamine D2R availability was not altered after TMS (Lamusuo et al. 2017).

21.5.4 Substance Abuse

21.5.4.1 Cocaine Dependence

The endogenous opioid system appears to play a role in the reinforcing actions of non-opioid drugs. American investigators examined µOR binding in the brain of cocaine addicts, 1–4 days after their last use of cocaine, using [^{11}C]CFN and PET. An increase of tracer binding was observed, particularly in the frontal cortex and caudate nucleus, and this increase persisted even after 4 weeks of drug abstinence. The magnitude of [^{11}C]CFN uptake was positively correlated with the severity of cocaine craving experienced by the subjects. These findings confirmed the involvement of the opioid system in cocaine dependence (Zubieta et al. 1996).

Increases of µOR binding potential in the anterior cingulate and anterior frontal cortex of cocaine users during abstinence are not only positively correlated with the intensity of cocaine craving, but the elevation of [^{11}C]CFN binding in these areas is also correlated with the percentage of days with cocaine use and the amount of cocaine used per day before the study period (Gorelick et al. 2005).

Regional increases of µOR binding appear to be related not only to the intensity of cocaine craving but also to the time interval before relapse to cocaine use after discharge from a closed research ward. In an interesting study, 15 cocaine-dependent subjects were housed in this ward for 12 weeks of monitored abstinence. During this period, regional brain µOR binding was measured at 1 and 12 weeks, using [^{11}C]CFN and PET. A shorter time interval before relapse was associated with increased µOR binding in the frontal and temporal cortex in both PET scans and with a lesser decrease in binding between 1 and 12 weeks. The significance of this correlation persisted even after accounting for clinical variables. Thus, increased µOR binding in the frontal and temporal cortex is a predictor of time to relapse to cocaine use (Gorelick et al. 2008).

A PET study examined regional µOR ([^{11}C]CFN) binding in the brain of treatment-seeking cocaine users before the onset of treatment and correlated this parameter with subsequent treatment outcome. Elevated µOR binding in brain regions associated with reward sensitivity correlated with greater cocaine use

during treatment and shorter duration of cocaine abstinence. Thus, μOR binding in these brain areas was a significant independent predictor of treatment outcome (Ghitza et al. 2010).

The mechanism of action of psychostimulant drugs in the mammalian brain appears to involve the release of endogenous opioids (endorphins) in the reward system. Two recent PET studies have attempted to obtain experimental proof for this mechanism by administering d-amphetamine to healthy volunteers (i.v.) and examining the impact of this challenge on [11C]CFN binding in the brain. A Swedish study in which ten subjects were scanned under three conditions (baseline, placebo, amphetamine 0.3 mg/kg) could not detect any significant differences in the binding potential of [11C]CFN after the amphetamine challenge (Guterstam et al. 2013). However, another study in which 12 subjects were scanned before and 3 h after an amphetamine challenge (either a high dose, 0.5 mg/kg, or an ultralow dose 0.017 mg/kg) reported that [11C]CFN binding was reduced after the high but not the ultralow dose in the frontal cortex, putamen, caudate, thalamus, anterior cingulate cortex, and insula (Colasanti et al. 2012).

21.5.4.2 Opioid Dependence

Similar changes of opioid receptor binding as were reported for cocaine addicts have also been observed in early abstinence from opioid (heroin) dependence. Compared with 20 healthy controls, ten subjects with opioid dependence who had completed inpatient detoxification showed increased [11C]DPN binding in the whole brain and in 15 out of 21 studied brain areas (Williams et al. 2007).

21.5.4.3 Alcohol Dependence

Whereas studies in cocaine and heroin addicts suggest increases of opioid receptor binding during abstinence, studies in alcohol dependence have produced conflicting results. In an early PET study with [11C]CFN, μOR binding potential was measured in eight male alcohol-dependent subjects during alcohol withdrawal and eight matched healthy controls. Contrary to the findings in cocaine abusers, alcoholics showed *reductions* of μOR binding potential in the right dorsal lateral prefrontal cortex, right anterior frontal cortex, and right parietal cortex. Lower μOR binding potential was associated with higher craving and with depressive symptoms in the subjects (Bencherif et al. 2004b). Based on the findings in subsequent studies, one could speculate that alcohol abstinence and depression have different effects on μOR binding (an increase and a decrease, respectively), the latter effect predominating in this early investigation.

Opposite results were reported in a German study. The authors examined [11C]CFN binding in the brain of alcoholics after 1–3 weeks of abstinence. Significantly *higher* binding was observed in the ventral striatum of the patients compared with healthy controls. This increase persisted up to 5 weeks, and its magnitude was significantly correlated with the intensity of alcohol craving. Elevated availability of μOR in the striatum was considered as a neuronal correlate of alcohol urge since the ventral striatum is known to be an important part of the reward system in the human brain (Heinz et al. 2005). Similar results were reported in a large study

involving 25 alcohol-dependent subjects who were scanned on day 5 of abstinence and 30 healthy controls. Alcohol-dependent subjects had a significantly higher binding potential of [^{11}C]CFN in many brain regions. There was a significant inverse relationship between [^{11}C]CFN binding in several brain regions and the intensity of craving in the alcohol-dependent group. No significant group differences in binding of the δOR ligand [^{11}C]MeNTI were observed, but the binding potential of this ligand in the caudate nucleus was positively correlated with recent drinking in alcohol-dependent subjects (Weerts et al. 2011).

In alcohol-dependent subjects completing a 19-day inpatient protocol (alcohol abstinence followed by naltrexone treatment, 50 mg daily, on days 15–19), a virtually complete (95%) occupancy of μOR by naltrexone was observed, using [^{11}C]CFN and PET. However, a much lower and highly variable (0–50%) occupancy of δOR was detected in [^{11}C]MeNTI scans. The relationship between δOR occupancy and treatment outcome could be explored in future studies (Weerts et al. 2008).

A British study with the non-subtype-selective opioid ligand [^{11}C]DPN reported a trend toward increased tracer binding in 11 alcohol-dependent subjects during early abstinence, compared to healthy controls, although this trend did not reach statistical significance. A significant correlation between alcohol craving and the global and regional distribution volume of [^{11}C]DPN was noted in the alcohol-dependent subjects (Williams et al. 2009).

A recent study examined [^{11}C]CFN binding in the human brain before and immediately after alcohol consumption in 13 heavy drinkers and an age-matched control group of 12 healthy subjects. Drinking alcohol reduced tracer binding in the nucleus accumbens and orbitofrontal cortex, indicating release of endogenous opioids in brain areas involved in the valuation of reward. The magnitude of change in the orbitofrontal cortex was significantly correlated with problem alcohol use and with subjective high in the drinker group. Thus, the release of endogenous opioids by ethanol promotes further alcohol consumption, and altered function of the opioid system appears to contribute to alcohol abuse (Mitchell et al. 2012).

Increases of the plasma level of the hormone cortisol after administration of an opioid antagonist (such as the drug naloxone) are supposed to provide information about opioid receptor activity. In an American study, naloxone was administered to 18 healthy control and 25 alcohol-dependent subjects (after 5 days of medically supervised alcohol withdrawal). The dose of naloxone required to induce a peak cortisol response was two times higher in the alcohol-dependent group. PET scans with [^{11}C]CFN were made in all subjects, and the relationship between tracer binding potential and rising slope of the cortisol response was examined. Alcohol-dependent subjects showed a significantly higher tracer binding potential in several brain regions than healthy controls, as was previously reported (Weerts et al. 2011). In healthy controls, there was a significant negative correlation between cortisol slope and regional binding potentials of the tracer, but in alcohol-dependent subjects, these parameters were not correlated. Thus, in healthy subjects, the naloxone test can provide information about individual differences in μOR availability, but in shortly abstinent alcohol-dependent subjects, the relationship between naloxone-induced cortisol response and μOR availability is disrupted (Wand et al. 2012).

In a follow-up study from the same group, PET scans with the δOR ligand [^{11}C]methylnantrindole were made in 15 healthy control and 20 shortly abstinent alcohol-dependent subjects, and δOR binding potential in various regions of the brain was correlated to cortisol area under the curve (AUC) after administration of naloxone. Similar to the findings for μOR, significant negative correlations were observed between cortisol AUC and δOR binding potential in several brain regions of healthy subjects. However, in alcohol-dependent subjects, such correlations were not observed. Thus, in healthy subjects, the naloxone test provides information about indivual differences in δOR availability, but in alcohol-dependent subjects, the close relationship between opioidergic neurotransmission and hormonal response is lost (Wand et al. 2013).

A PET study with the μOR tracer [^{11}C]CFN examined the relationship between opioid release in the human brain after alcohol consumption and the catechol-O-methyltransferase genotype. Thirteen heavy drinkers and 12 matched healthy control subjects were scanned twice with [^{11}C]CFN: first at baseline and then after the consumption of a standard drink of alcohol. Independent of their drinking history (or gender), individuals with the Val158 variant of the enzyme showed greater opioid release in the right nucleus accumbens and less release in medial orbital frontal cortex. The Val158 variant results in greater activity of catecholamine-O-methyltransferase in the human brain and, consequently, lower dopamine levels in the frontal cortex. Apparently, genetic differences in endogenous dopamine levels can modulate endogenous opioid release in brain regions that contribute to the rewarding effects of alcohol. The Val158 variant could make individuals more prone to impulsive decision-making (Mitchell et al. 2013).

The higher binding potential values of [^{11}C]CFN in the brain of alcohol-dependent subjects that have been reported by various research groups may either reflect increased expression of μOR, or a reduced concentration of endogenous, competing opioid ligands. In order to differentiate between these possible explanations, a German study examined post-mortem brain tissue of 43 alcohol-dependent subjects and 43 healthy controls. The density of μOR in tissue samples was determined by in vitro assays, using the ligand [^{3}H]DAMGO. Tracer binding in the brain of alcohol-dependent subjects was 23–51% lower than in healthy controls. Thus, increased binding potential values of [^{11}C]CFN in the brains of alcoholics seem to reflect reduced competition of endogenous opioids rather than increased receptor expression (Hermann et al. 2017).

Addiction (to alcohol or other substances of abuse) may be considered as a state of "reward deficiency." Addicts take a rewarding substance to compensate for their deficient reward. If this interpretation of addiction is correct, drug addicts should show a reduced release of endogenous opioids after a release-inducing stimulus compared to healthy controls. In a British PET study, 13 abstinent alcohol-dependent male subjects and 15 healthy volunteers were scanned twice with [^{11}C]CFN, before and 3 h after an oral dose of dexamphetamine. Consistent with the hypothesis, the healthy volunteers showed a significant decline of tracer binding potential in many areas of the brain after the amphetamine challenge, but in alcohol-dependent subjects, this response was reduced, particularly in frontal lobe, insula, thalamus,

anterior cingulate, nucleus accumbens, and putamen (Turton et al. 2018). In pathological gambling, a behavioral addiction with similarities to substance abuse, a similar "blunted" response of the opioid system to amphetamine was noted, although baseline μOR availability was not different in pathological gamblers and healthy volunteers (Mick et al. 2016).

In an extensive PET study with the novel PET tracer [¹¹C]LY2795050, κOR availability was measured in the brain of 36 alcohol-dependent subjects and 28 healthy controls. Tracer distribution volume in the amygdala and pallidum was significantly lower in the alcohol-dependent group than in the healthy control group. An age effect on tracer binding could not be observed in any brain region (Vijay et al. 2018). These observations for κOR are in contrast with findings for μOR or total OR that have been reported to be either increased or unchanged in alcohol-dependent subjects. Also, human μOR show an age-related decline, whereas κOR appear to be preserved in the aging human brain.

21.5.4.4 Nicotine Dependence

Several PET studies have examined the relationship between opioid neurotransmission and smoking. In an initial, groundbreaking publication, six healthy male smokers and six age- and sex-matched nonsmokers were scanned with both [¹¹C]CFN and the dopamine receptor ligand [¹¹C]raclopride. Smokers abstained from smoking for 12 h prior to the study. They first smoked a denicotinized cigarette, 2 and 12 min after scan onset, followed by a normal cigarette after 40 and 50 min. Total scan duration was 90 min. Thus, each scan period consisted of an initial, denicotinized phase and a later, average nicotine phase. Nonsmokers were subjected to the same scanning protocol but were only scanned at baseline (i.e., they did not smoke anything). In the smoker group, significant declines of [¹¹C]CFN binding in the right anterior cingulate cortex were noted during transition from the first to the second phase of the scan, indicating activation of opioid neurotransmission by nicotine. A simultaneous decline of [¹¹C]raclopride binding was noted in the ventral basal ganglia, and the magnitude of this decline correlated with nicotine dependence score. Increases of the release of endogenous opioids and dopamine are probably involved in the rewarding effect of nicotine. Smokers had lower μOR binding potential in the cingulate cortex, thalamus, ventral basal ganglia, and amygdala compared to nonsmokers during the first phase of the scan; these reductions were reversed in the thalamus, ventral basal ganglia, and amygdala after nicotine smoking (Scott et al. 2007b). Greater μOR availability in the basal ganglia and thalamus of nonsmokers compared to overnight abstinent smokers was also observed in a later study (Nuechterlein et al. 2016).

In contrast to the observations of Scott and Nuchterlein et al., another PET study with [¹¹C]CFN did not observe any significant change in tracer binding potential between placebo and active cigarette smoking and also no significant difference in μOR availability between smokers and nonsmokers (Kuwabara et al. 2014). The discrepancy between this and the initial study led to the hypothesis that the expectancy of a smoker, or the sensorimotor effects of denicotinized cigarettes may contribute to the observed release of endogenous opioids. However, a negative

correlation was observed between µOR availability in bilateral superior temporal cortices during placebo smoking and scores for nicotine dependence. Thus, µOR in this area may play a role in nicotine addiction, and stimulation of these receptors by endogenous opioids may be involved in nicotine reward (Kuwabara et al. 2014).

Two recent PET studies showed that psychological and behavioral factors can indeed exert important actions on the µ-opioid system. In the first study, smokers showed a reduction of [11C]CFN binding potential in the thalamus and nucleus accumbens after smoking a denicotinized (placebo) cigarette, indicating µOR activation. No further activation was observed after the smoking of a normal cigarette (Nuechterlein et al. 2016). In the last study, 20 chronic tobacco smokers (males) were asked to abstain for one night from smoking. The next morning, they first smoked a denicotinized cigarette (at 8.00 h) and, subsequently, a normal cigarette with an average dose of nicotine (at 10.00 h). PET scans with [11C]CFN were made either during the placebo or the nicotine smoking session (on two different days), using a bolus plus infusion protocol. The very low nicotine peak levels in plasma after smoking a denicotinized cigarette were significantly correlated with tracer binding potential after the smoking session, but no correlation was observed between the high peak levels after smoking of the normal cigarette and tracer binding potential (Domino and Hirasawa-Fujita 2019). Thus, "placebo" effects seem to have a major impact on [11C]CFN binding in the smoker's brain.

Another study with [11C]CFN examined the relationship between smoking and the relief of negative affect. Twenty-two smokers were scanned after overnight abstinence, once after smoking a denicotinized cigarette and at another scanning day after smoking a normal cigarette. Higher µOR availability in the amygdala was correlated with greater motivation to smoke in order to relieve negative affect, but not with changes in affect after smoking (Falcone et al. 2012). A positive correlation between the craving to smoke and µOR binding potential in several brain regions (amygdala, hippocampus, insula, nucleus accumbens, putamen, and ventral striatum) was also reported in a later study (Domino and Hirasawa-Fujita 2019).

Polymorphisms of the µOR gene affect both the levels of µOR expression in the human brain and smoking behavior. Smokers homozygous for the wild-type *OPRM1* A allele show significantly higher [11C]CFN binding in the bilateral amygdala, left thalamus, and left anterior cingulate cortex than smokers carrying the *OPRM1* A118G allele. In bearers of the G polymorphism, the extent of reward difference between smoking a normal and a denicotinized cigarette was significantly associated with the change of [11C]CFN binding potential in the right amygdala, caudate, anterior cingulate cortex, and thalamus, but in smokers homozygous for the wild-type gene, this association could not be observed (Ray et al. 2011). Later PET studies in µOR-genotyped overnight abstinent smokers confirmed that smokers bearing the G polymorphism have less free µORs in some brain areas (amygdala and nucleus accumbens) than carriers of the AA wildtype (Nuechterlein et al. 2016; Domino et al. 2015). In one of these studies, GG carriers were found to show also a less extensive decrease of [11C]CFN binding potential after the smoking of a "real" cigarette than AA carriers, i.e., a blunted response of the µ-opioid system (Domino et al. 2015).

Another PET study examined whether individual differences in µOR availability in alcohol-dependent subjects are associated with tobacco use, nicotine dependence, and level of nicotine craving. Subjects had withdrawn from alcohol use under medical supervision. They were not allowed to smoke but received transdermal nicotine maintenance (21 mg/day). Higher scores in a nicotine dependence test were found to be associated with a lower binding potential of [^{11}C]CFN in the amygdala, cingulate, globus pallidus, thalamus, and insula. The number of cigarettes which subjects had used per day prior to the study was also negatively correlated with [^{11}C]CFN binding potential in these areas. Thus, smoking intensity and severity of nicotine dependence appear to be related to reduced µOR binding potential in several brain regions of alcohol-dependent subjects (Weerts et al. 2014).

21.5.5 Eating Disorders

Bulimia nervosa, a disorder characterized by cycles of food restriction, binge eating, and vomiting, shares certain phenomena with addiction and substance abuse. Compared with controls, bulimic individuals show significantly decreased µOR binding in the left insular cortex, a brain area involved in taste discrimination and eating reward. This finding may reflect either downregulation of µOR in the bulimic state as a consequence of chronically increased release of opioid peptides or a personality trait that increases the reward value of dieting (Bencherif et al. 2005).

In another PET study, 7 subjects with binge eating disorder, 15 subjects with pathological gambling, and 17 healthy control subjects were scanned with [^{11}C]CFN and [^{18}F]DOPA. Patients with binge eating disorder showed reductions of µOR binding potential in many cortical and subcortical areas of the brain and a significant decrease of the striatal influx constant of [^{18}F]DOPA. However, in subjects with pathological gambling, µOR binding potential was decreased mainly in the anterior cingulate, and the striatal influx of [^{18}F]DOPA was not significantly altered compared to healthy controls. Thus, two forms of addiction (to eating and to gambling) displayed different patterns of neurobiological changes (Majuri et al. 2017). A later study from the same group used [^{11}C]CFN to measure µOR binding potential in the brains of patients with binge eating disorder, patients with morbid obesity and healthy controls. Both eating disorders were associated with similar, widespread reductions of µOR binding potential. Thus, these two eating disorders shared a common opioid abnormality (Joutsa et al. 2018). In a third study from the same group, 13 pathological gamblers and 15 age-, sex-, and weight-matched healthy control subjects were scanned with [^{11}C]CFN and [^{18}F]DOPA. In both groups, a similar correlation was observed between µOR availability in the basal ganglia (putamen, caudate nucleus and globus pallidus) and the presynaptic capacity for dopamine synthesis. Thus, presynaptic dopamine neurotransmission and opioid receptor function in the basal ganglia appear to be linked and this link is not affected by behavioral addiction (Majuri et al. 2018).

21.5.6 Obesity

An initial PET study on the involvement of endogenous opioid systems in obesity scanned seven chronically obese men with [^{11}C]CFN in the fasted and fed condition, at the onset of therapy and after 15% weight loss had been achieved by a low-calorie diet. Seven age- and ethnicity-matched lean control subjects were scanned only once, in the fasted and fed condition. Thus, four PET scans were made in the obese subjects and two scans in the healthy controls. In the initial scans, obese subjects showed lower μOR binding potentials in several brain regions than lean subjects or obese subjects after weight loss. In healthy controls, the observed decline of tracer binding potential in the right temporal pole after feeding was highly correlated to reductions in negative affect, but this correlation was not observed in the patient group. In patients, the magnitude of this decline at the onset of treatment tended to be associated with weight regain, 1 year after treatment. Thus, the magnitude of μOR activation in the right temporal pole after an acute meal may predict the risk of weight regain of obese subjects after therapy (Burghardt et al. 2015).

Since both the endogenous opioid system and the dopaminergic system are involved in the regulation of food intake and reward processing, a Finnish study examined pathological changes in μOR and dopamine D$_2$R availability in obese subjects. Thirteen obese (mean BMI 42 kg/m^2) and 14 age-matched healthy women were scanned with the PET tracers [^{11}C]CFN and [^{11}C]raclopride. Obese subjects had significantly lower μOR binding potentials in ventral striatum, orbitofrontal cortex, amygdala, putamen, insula, and anterior cingulate. [^{11}C[CFN binding potential in such areas was negatively correlated with BMI and self-reported food addiction. However, there were no significant differences between healthy and obese subjects concerning the regional binding potentials of [^{11}C]raclopride (Karlsson et al. 2015). These results can be interpreted as evidence for downregulation of μOR in the human brain as a consequence of excessive stimulation by endogenous opioids, related to persistent overeating. However, a low density of μOR could also be a neurochemical trait that predisposes subjects to becoming obese.

In a follow-up study from the same year, group sizes were expanded to 25 obese and 20 healthy female subjects, and the correlation between regional μOR and D$_2$R binding potentials was examined (Tuominen et al. 2015). In healthy subjects, μOR and D$_2$R availabilities in ventral striatum and dorsal caudate nucleus were positively associated, and D$_2$R availability in ventral striatum was also associated with μOR availability in the ventral tegmental area. In obese subjects, an association between μOR and D$_2$R binding was observed in the caudate nucleus, but the association in the ventral striatum was much weaker than in lean subjects and the association between striatal D$_2$R and tegmental μOR binding was abolished. Thus, the interaction between the opioid and dopaminergic systems may be altered in obesity.

A second follow-up study addressed the question whether reduced μOR availability is a state or a trait in obesity. Sixteen obese women were scanned twice with [^{11}C]CFN and [^{11}C]raclopride, both before and 6 months after bariatric surgery (gastric bypass or sleeve gastrectomy). Measured binding potentials were compared to those of an age-matched healthy control group ($n = 14$). A reduced availability of

μOR in ventral striatum, insula, amygdala, and thalamus was initially observed, but the binding potential of [^{11}C]CFN in these areas normalized after gastric surgery and weight loss (26.1 ± 7.6 kg). Apparently, the reduced availability of μOR in the patient group was associated with the obese phenotype and was not a persistent neurochemical trait. In contrast to μOR, the binding potential of D$_2$R was not altered after surgery (Karlsson et al. 2016).

21.5.7 Epilepsy

Opioid receptors and endogenous opioid peptides are known to play a role in the mechanisms underlying seizures. Many PET studies with opioid receptor ligands have been performed in patients with epilepsy. The first of these involved [^{11}C]CFN and subjects with complex partial seizures due to unilateral temporal seizure foci. [^{11}C]CFN binding in the temporal neocortex was greater on the side of the focus than on the contralateral side. This increase was interpreted as evidence for involvement of μOR in a tonic anticonvulsant system that limits the spread of electrical activity (Frost et al. 1988). In contrast to [^{11}C]CFN binding, [^{11}C]DPN uptake (Mayberg et al. 1991) and [^{18}F]cyclofoxy (Theodore et al. 1992) uptake in the ipsilateral and contralateral lobes were not significantly different, suggesting that opioid receptor subtypes are differentially regulated in temporal lobe epilepsy. Evidence for differential regulation was obtained in a later study in which subjects with temporal lobe epilepsy were scanned both with the δOR ligand [^{11}C]methylnaltrindole ([^{11}C]MeNTI) and with the μOR ligand [^{11}C]CFN. Binding of both ligands was increased in the ipsilateral temporal cortex, but the regional pattern of the changes was different (more extended for [^{11}C]MeNTI than for [^{11}C]CFN). Upregulation of δOR may indicate an anticonvulsant action for this receptor subtype (Madar et al. 1997). A more recent study examined [^{11}C]DPN binding in the brain of patients with temporal lobe epilepsy both shortly (within a few hours) after spontaneous epileptic seizures and interictally. In 14 healthy controls, no changes of [^{11}C]DPN binding were observed as a function of time, but in the patients, an increase of tracer binding was noted in the ipsilateral temporal pole and fusiform gyrus, shortly after seizures. The magnitude of this increase was inversely correlated to the interval that had elapsed since the last seizure, suggesting an increase of receptor binding during seizures followed by a gradual return to baseline (Hammers et al. 2007b). A follow-up article that was published after 6 years pointed out that in order to correctly quantify opioid receptor availability after spontaneous epileptic seizures, [^{11}C]DPN data need to be corrected for the partial volume effect. After such correction, postictal increases in tracer distribution volume could also be detected in the hippocampus (McGinnity et al. 2013). Thus, results from PET studies with three different ligands ([^{11}C]CFN, [^{11}C]MeNTI, and [^{11}C]DPN) have supported the idea that the opioid system is involved in seizure control.

The interictal distribution volume of [^{11}C]DPN in the cortex and thalamus of eight patients with childhood and juvenile absence epilepsy was found to be not significantly different from values in healthy age-matched controls; thus, there

appeared to be no overall abnormality of opioid receptors in this patient group (Prevett et al. 1994). To examine whether absence seizures are associated with release of endogenous opioids, investigators scanned eight patients with primary generalized epilepsy and eight control subjects with [^{11}C]DPN and PET. Serial absences were precipitated in the patients by hyperventilation for 10 min, starting 30–40 min after injection of the tracer. Increased washout of DPN was observed in the association cortex but not in other brain areas during seizures, as compared with control subjects and patients scanned without provocation of absences. Pharmacokinetic modeling suggested that absence seizures resulted in a significant, 15–41% decrease in the rate constant of association (k_3) of the tracer. These data were interpreted as evidence for the release of endogenous opioids in the association cortex at the time of absences, leading to increased opioid receptor occupancy (Bartenstein et al. 1993).

A later study involved five patients with reading epilepsy who were scanned both at baseline (reading a string of symbols) and during seizure activation (reading a scientific paper). The latter condition was associated with significantly lower binding of [^{11}C]DPN in the left parietotemporal-occipital cortex of the patients as compared with six healthy controls, suggesting release of endogenous opioids as part of a mechanism to terminate reading-induced seizures (Koepp et al. 1998).

Two patients with mesobasal temporal lobe epilepsy have been scanned with [^{11}C]DPN, before and after selective amygdalohippocampectomy. After removal of the epileptic focus, [^{11}C]DPN binding in the ipsilateral frontal cortex was found to be reduced, suggesting either downregulation of opioid receptors in the absence of seizures or postoperative neuronal dysfunction (Bartenstein et al. 1994).

21.5.8 Neurodegenerative Diseases

Losses of opioid receptors with different regional patterns have been observed in several neurodegenerative diseases.

21.5.8.1 Huntington's Disease

Significant decreases of [^{11}C]DPN binding (24–40%) were noted in the caudate and putamen of Huntington's disease (HD) patients using striatum-to-occipital cortex uptake ratios, spectral analysis, voxelwise parametric analysis, and statistical parametric mapping (SPM) for quantification (Weeks et al. 1997).

21.5.8.2 Alzheimer Disease

Decreases of opioid receptor binding (up to 40%) have been detected in the brain of Alzheimer disease (AD) patients using the tracer [^{18}F]cyclofoxy, and these changes were not correlated with decreases in regional cerebral blood flow (Cohen et al. 1997).

21.5.8.3 Parkinson Disease and Related Disorders

An initial study on eight clinically defined Parkinson disease (PD) patients, seven subjects with the striatonigral degeneration type of multiple system atrophy and six subjects with Steele-Richardson-Olszewski (SRO) syndrome examined opioid receptor binding in the human striatum with the tracer [^{11}C]DPN and PET. In the PD patient group, tracer binding was not significantly altered compared to healthy controls. Striatonigral degeneration was associated with reduced binding of [^{11}C]DPN in the putamen, but not in the caudate. In the SRO syndrome group, both caudate and putamen opioid receptor binding were significantly reduced. The binding pattern of [^{11}C]DPN may thus help to differentiate between various akinetic-rigid syndromes (Burn et al. 1995). In ten patients with the olivopontocerebellar variant of multiple system atrophy, a significant 12% reduction of the caudate-occipital ratio and a 15% reduction of the putamen-occipital uptake ratio of [^{11}C]DPN were noted. The latter decline was correlated to loss of [^{18}F]DOPA uptake in the putamen (average reduction 29%) (Rinne et al. 1995).

Using [^{11}C]DPN-PET and either a region-of-interest (ROI) or an SPM approach, a significantly reduced opioid receptor binding was later noted in the striatum and thalamus of PD patients with levodopa-induced dyskinesias but not in non-dyskinetic subjects (Piccini et al. 1997). No difference in striatal dopamine D_1 or D_2 receptor binding was found between the two subgroups, and measurements with PET and [^{15}O]water showed that rCBF after oral administration of levodopa was increased during dyskinesias in lentiform nuclei and motor, premotor, and dorsal prefrontal cortex. Thus, dyskinesias appear to arise not from a disturbance of dopamine receptor availability but rather from overactivity of opioid transmission, particularly the basal ganglia-frontal projections (Brooks et al. 2000).

In bilaterally 1-methyl-4-phenyl-1,2,3,6-tetrahydropyridine (MPTP)-lesioned monkeys which had clinically recovered from the acute motor effects of dopaminergic neuron lesioning, a 65% decrease in the accumulation of [^{18}F]DOPA was noted in the basal ganglia. This decrease was associated with a 30–35% decline of [^{18}F]cyclofoxy binding in the caudate, anterior putamen, thalamus, and amygdala. The authors concluded that altered opioid receptor signaling (probably increased levels of Met-enkephalin) had contributed to the behavioral changes which were observed in the animals, i.e., the masking of their motor symptoms (Cohen et al. 1998). A later study from the same group showed that in unilaterally MPTP-lesioned monkeys with parkinsonian symptoms, opioid receptor availability is reduced by 30–35% on both the lesioned and the non-lesioned sides of the brain (Cohen et al. 1999).

In contrast to the decreases of opioid receptor binding which were observed in akinetic-rigid syndromes and PD patients with dyskinesias, no abnormalities of [^{11}C]DPN binding were noted in patients with primary torsion dystonia (carriers of the DYT1 gene), and no correlation between the severity of dystonia and opioid binding could be detected (Whone et al. 2004).

21.5.9 Opioid Receptor Expression in Lung Tumors

A pilot PET study involving seven patients with lung carcinomas examined the feasibility of tumor imaging with the radioligands [^{11}C]MeNTI and [^{11}C]CFN. Four of these patients were also scanned with [^{18}F]FDG for clinical indications. All tumors showed an accumulation of opioid receptor ligands above background. The tumor-to-nontumor binding ratio of the δOR ligand [^{11}C]MeNTI (4.3 ± 1.3) was greater than that of the μOR ligand [^{11}C]CFN (2.4 ± 1.2) but lower than that of [^{18}F]FDG (7.7 ± 0.5). About 50% of [^{11}C]MeNTI uptake and 44% of [^{11}C]CFN uptake in the tumors could be blocked by naloxone. Particularly [^{11}C]MeNTI appears suitable for investigation of lung carcinoma biology, since δOR may be involved in tumor invasion and metastasis (Madar et al. 2007). A ligand targeting μOR and δOR was tested in tumor-bearing mice as a strategy for delivering cytotoxic drugs to lung cancer, but unfortunately, this strategy failed since the specificity of payload delivery was inadequate (Li and Low 2017).

21.6 Conclusion

PET imaging has provided insight in the involvement of opioid system in affective and sensory processing. Changes of opioid receptor expression related to increasing age and altered hormonal status have also been reported. Moreover, OR imaging has been successfully applied in the study of the pharmacokinetics and pharmacodynamics of novel and existing drugs.

Regional changes of OR availability have been observed in psychiatric and neurodegenerative disorders, epilepsy, pain, bulimia nervosa, behavioral addiction, and substance abuse. PET imaging may contribute to the development of improved techniques for the treatment of pain (and addiction) by monitoring the relationship between OR occupancy and symptom relief.

References

Bai LQ, Teng RR, Shiue CY, Wolf AP, Dewey SL, Holland MJ et al (1990) No-carrier-added (NCA) N-(3-[18F]fluoropropyl)-N-norbuprenorphine and N-(3-[18F]fluoropropyl)-N-nordiprenorphine--synthesis, anatomical distribution in mice and rats, and tomographic studies in a baboon. Int J Rad Appl Instrum B 17:217–227

Baier B, Bense S, Birklein F, Buchholz HG, Mischke A, Schreckenberger M et al (2010) Evidence for modulation of opioidergic activity in central vestibular processing: A [(18)F] diprenorphine PET study. Hum Brain Mapp 31:550–555

Bartenstein PA, Duncan JS, Prevett MC, Cunningham VJ, Fish DR, Jones AK et al (1993) Investigation of the opioid system in absence seizures with positron emission tomography. J Neurol Neurosurg Psychiatry 56:1295–1302

Bartenstein PA, Prevett MC, Duncan JS, Hajek M, Wieser HG (1994) Quantification of opiate receptors in two patients with mesiobasal temporal lobe epilepsy, before and after selective amygdalohippocampectomy, using positron emission tomography. Epilepsy Res 18:119–125

Baumgartner U, Buchholz HG, Bellosevich A, Magerl W, Siessmeier T, Rolke R et al (2006) High opiate receptor binding potential in the human lateral pain system. NeuroImage 30:692–699

Bencherif B, Fuchs PN, Sheth R, Dannals RF, Campbell JN, Frost JJ (2002) Pain activation of human supraspinal opioid pathways as demonstrated by [11C]-carfentanil and positron emission tomography (PET). Pain 99:589–598

Bencherif B, Stumpf MJ, Links JM, Frost JJ (2004a) Application of MRI-based partial-volume correction to the analysis of PET images of mu-opioid receptors using statistical parametric mapping. J Nucl Med 45:402–408

Bencherif B, Wand GS, McCaul ME, Kim YK, Ilgin N, Dannals RF et al (2004b) Mu-opioid receptor binding measured by [11C]carfentanil positron emission tomography is related to craving and mood in alcohol dependence. Biol Psychiatry 55:255–262

Bencherif B, Guarda AS, Colantuoni C, Ravert HT, Dannals RF, Frost JJ (2005) Regional mu-opioid receptor binding in insular cortex is decreased in bulimia nervosa and correlates inversely with fasting behavior. J Nucl Med 46:1349–1351

Blecha JE, Henderson BD, Hockley BG, VanBrocklin HF, Zubieta JK, Dasilva AF et al (2017) An updated synthesis of [(11) C]carfentanil for positron emission tomography (PET) imaging of the mu-opioid receptor. J Labelled Comp Radiopharm 60:375–380

Boecker H, Sprenger T, Henriksen G, Toelle TR, Spilker ME (2005) Optimal duration of PET studies with 18F-fluoroethyl-diprenorphine. J Nucl Med 46:2092–2096

Boecker H, Sprenger T, Spilker ME, Henriksen G, Koppenhoefer M, Wagner KJ et al (2008) The runner's high: opioidergic mechanisms in the human brain. Cereb Cortex 18:2523–2531

Bourdier T, Poisnel G, Dhilly M, Delamare J, Henry J, Debruyne D et al (2007) Synthesis and biological evaluation of N-substituted quinolinimides, as potential ligands for in vivo imaging studies of delta-opioid receptors. Bioconjug Chem 18:538–548

Brooks DJ, Piccini P, Turjanski N, Samuel M (2000) Neuroimaging of dyskinesias. Ann Neurol 47:S154–S158

Brown CA, Matthews J, Fairclough M, McMahon A, Barnett E, Al-Kaysi A et al (2015) Striatal opioid receptor availability is related to acute and chronic pain perception in arthritis: does opioid adaptation increase resilience to chronic pain? Pain 156:2267–2275

Burghardt PR, Rothberg AE, Dykhuis KE, Burant CF, Zubieta JK (2015) Endogenous opioid mechanisms are implicated in obesity and weight loss in humans. J Clin Endocrinol Metab 100:3193–3201

Burn DJ, Rinne JO, Quinn NP, Lees AJ, Marsden CD, Brooks DJ (1995) Striatal opioid receptor binding in Parkinson's disease, striatonigral degeneration and Steele-Richardson-Olszewski syndrome, A [11C]diprenorphine PET study. Brain 118(Pt 4):951–958

Cai Z, Li S, Pracitto R, Navarro A, Shirali A, Ropchan J et al (2017) Fluorine-18-labeled antagonist for PET imaging of kappa opioid receptors. ACS Chem Neurosci 8:12–16

Campbell CM, Bounds SC, Kuwabara H, Edwards RR, Campbell JN, Haythornthwaite JA et al (2013) Individual variation in sleep quality and duration is related to cerebral mu opioid receptor binding potential during tonic laboratory pain in healthy subjects. Pain Med 14:1882–1892

Carson RE, Channing MA, Blasberg RG, Dunn BB, Cohen RM, Rice KC et al (1993) Comparison of bolus and infusion methods for receptor quantitation: application to [18F]cyclofoxy and positron emission tomography. J Cereb Blood Flow Metab 13:24–42

Chang KJ, Hazum E, Cuatrecasas P (1981) Novel opiate binding sites selective for benzomorphan drugs. Proc Natl Acad Sci U S A 78:4141–4145

Channing MA, Eckelman WC, Bennett JM, Burke TR Jr, Rice KC (1985) Radiosynthesis of [18F]3-acetylcyclofoxy: a high affinity opiate antagonist. Int J Appl Radiat Isot 36:429–433

Chen Y, Mestek A, Liu J, Hurley JA, Yu L (1993) Molecular cloning and functional expression of a mu-opioid receptor from rat brain. Mol Pharmacol 44:8–12

Chesis PL, Welch MJ (1990) Synthesis and in vitro characterization of fluorinated U-50488 analogs for PET studies of kappa opioid receptors. Int J Rad Appl Instrum A 41:267–273

Chesis PL, Griffeth LK, Mathias CJ, Welch MJ (1990) Sex-dependent differences in N-(3-[18F]fluoropropyl)-N-nordiprenorphine biodistribution and metabolism. J Nucl Med 31:192–201

Cohen RM, Andreason PJ, Doudet DJ, Carson RE, Sunderland T (1997) Opiate receptor avidity and cerebral blood flow in Alzheimer's disease. J Neurol Sci 148:171–180

Cohen RM, Carson RE, Aigner TG, Doudet DJ (1998) Opiate receptor avidity is reduced in non-motor impaired MPTP-lesioned rhesus monkeys. Brain Res 806:292–296

Cohen RM, Carson RE, Wyatt RJ, Doudet DJ (1999) Opiate receptor avidity is reduced bilaterally in rhesus monkeys unilaterally lesioned with MPTP. Synapse 33:282–288

Cohen RM, Carson RE, Sunderland T (2000) Opiate receptor avidity in the thalamus is sexually dimorphic in the elderly. Synapse 38:226–229

Colasanti A, Searle GE, Long CJ, Hill SP, Reiley RR, Quelch D et al (2012) Endogenous opioid release in the human brain reward system induced by acute amphetamine administration. Biol Psychiatry 72:371–377

Cometta-Morini C, Maguire PA, Loew GH (1992) Molecular determinants of mu receptor recognition for the fentanyl class of compounds. Mol Pharmacol 41:185–196

Cox BM, Goldstein A, Hi CH (1976) Opioid activity of a peptide, beta-lipotropin-(61-91), derived from beta-lipotropin. Proc Natl Acad Sci U S A 73:1821–1823

Cunningham VJ, Hume SP, Price GR, Ahier RG, Cremer JE, Jones AK (1991) Compartmental analysis of diprenorphine binding to opiate receptors in the rat in vivo and its comparison with equilibrium data in vitro. J Cereb Blood Flow Metab 11:1–9

Dannals RF, Ravert HT, Frost JJ, Wilson AA, Burns HD, Wagner HN Jr (1985) Radiosynthesis of an opiate receptor binding radiotracer: [11C]carfentanil. Int J Appl Radiat Isot 36:303–306

Dasilva AF, Nascimento TD, DosSantos MF, Lucas S, van HolsbeecK H, DeBoer M et al (2014) Association of mu-opioid activation in the prefrontal cortex with spontaneous migraine attacks - brief report I. Ann Clin Transl Neurol 1:439–444

Dhawan BN, Cesselin F, Raghubir R, Reisine T, Bradley PB, Portoghese PS et al (1996) International union of pharmacology. XII. Classification of opioid receptors. Pharmacol Rev 48:567–592

Domino EF, Hirasawa-Fujita M (2019) Tobacco smoking and brain endogenous opioid release: more than nicotine alone. Nicotine Tob Res 21(6):772–777

Domino EF, Hirasawa-Fujita M, Ni L, Guthrie SK, Zubieta JK (2015) Regional brain [(11)C]carfentanil binding following tobacco smoking. Prog Neuro-Psychopharmacol Biol Psychiatry 59:100–104

DosSantos MF, Martikainen IK, Nascimento TD, Love TM, Deboer MD, Maslowski EC et al (2012a) Reduced basal ganglia mu-opioid receptor availability in trigeminal neuropathic pain: a pilot study. Mol Pain 8:74

DosSantos MF, Love TM, Martikainen IK, Nascimento TD, Fregni F, Cummiford C et al (2012b) Immediate effects of tDCS on the mu-opioid system of a chronic pain patient. Front Psych 3:93

DosSantos MF, Martikainen IK, Nascimento TD, Love TM, Deboer MD, Schambra HM et al (2014) Building up analgesia in humans via the endogenous mu-opioid system by combining placebo and active tDCS: a preliminary report. PLoS One 9:e102350

Dougherty DD, Kong J, Webb M, Bonab AA, Fischman AJ, Gollub RL (2008) A combined [11C]diprenorphine PET study and fMRI study of acupuncture analgesia. Behav Brain Res 193:63–68

Endres CJ, Bencherif B, Hilton J, Madar I, Frost JJ (2003) Quantification of brain mu-opioid receptors with [11C]carfentanil: reference-tissue methods. Nucl Med Biol 30:177–186

Eriksson O, Antoni G (2015) [11C]Carfentanil Binds preferentially to mu-opioid receptor subtype 1 compared to subtype 2. Mol Imaging 14:476–483

Evans CJ, Keith DE Jr, Morrison H, Magendzo K, Edwards RH (1992) Cloning of a delta opioid receptor by functional expression. Science 258:1952–1955

Fairclough M, Prenant C, Brown G, McMahon A, Lowe J, Jones A (2014) The automated radiosynthesis and purification of the opioid receptor antagonist, [6-O-methyl-11C]diprenorphine on the GE TRACERlab FXFE radiochemistry module. J Labelled Comp Radiopharm. 57:388–396

Falcone M, Gold AB, Wileyto EP, Ray R, Ruparel K, Newberg A et al (2012) mu-Opioid receptor availability in the amygdala is associated with smoking for negative affect relief. Psychopharmacology 222:701–708

Frost JJ (2001) PET imaging of the opioid receptor: the early years. Nucl Med Biol 28:509–513

Frost JJ, Wagner HN Jr, Dannals RF, Ravert HT, Links JM, Wilson AA et al (1985) Imaging opiate receptors in the human brain by positron tomography. J Comput Assist Tomogr 9:231–236

Frost JJ, Mayberg HS, Fisher RS, Douglass KH, Dannals RF, Links JM et al (1988) Mu-opiate receptors measured by positron emission tomography are increased in temporal lobe epilepsy. Ann Neurol 23:231–237

Frost JJ, Douglass KH, Mayberg HS, Dannals RF, Links JM, Wilson AA et al (1989) Multicompartmental analysis of [11C]-carfentanil binding to opiate receptors in humans measured by positron emission tomography. J Cereb Blood Flow Metab 9:398–409

Frost JJ, Mayberg HS, Sadzot B, Dannals RF, Lever JR, Ravert HT et al (1990) Comparison of [11C]diprenorphine and [11C]carfentanil binding to opiate receptors in humans by positron emission tomography. J Cereb Blood Flow Metab 10:484–492

Galynker I, Schlyer DJ, Dewey SL, Fowler JS, Logan J, Gatley SJ et al (1996) Opioid receptor imaging and displacement studies with [6-O-[11C] methyl]buprenorphine in baboon brain. Nucl Med Biol 23:325–331

Ghitza UE, Preston KL, Epstein DH, Kuwabara H, Endres CJ, Bencherif B et al (2010) Brain mu-opioid receptor binding predicts treatment outcome in cocaine-abusing outpatients. Biol Psychiatry 68:697–703

Goldstein A, Tachibana S, Lowney LI, Hunkapiller M, Hood L (1979) Dynorphin-(1-13), an extraordinarily potent opioid peptide. Proc Natl Acad Sci U S A 76:6666–6670

Gorelick DA, Kim YK, Bencherif B, Boyd SJ, Nelson R, Copersino M et al (2005) Imaging brain mu-opioid receptors in abstinent cocaine users: time course and relation to cocaine craving. Biol Psychiatry 57:1573–1582

Gorelick DA, Kim YK, Bencherif B, Boyd SJ, Nelson R, Copersino ML et al (2008) Brain mu-opioid receptor binding: relationship to relapse to cocaine use after monitored abstinence. Psychopharmacology 200:475–486

Greenwald MK, Johanson CE, Moody DE, Woods JH, Kilbourn MR, Koeppe RA et al (2003) Effects of buprenorphine maintenance dose on mu-opioid receptor availability, plasma concentrations, and antagonist blockade in heroin-dependent volunteers. Neuropsychopharmacology 28:2000–2009

Greenwald M, Johanson CE, Bueller J, Chang Y, Moody DE, Kilbourn M et al (2007) Buprenorphine duration of action: mu-opioid receptor availability and pharmacokinetic and behavioral indices. Biol Psychiatry 61:101–110

Guterstam J, Jayaram-Lindstrom N, Cervenka S, Frost JJ, Farde L, Halldin C et al (2013) Effects of amphetamine on the human brain opioid system--a positron emission tomography study. Int J Neuropsychopharmacol 16:763–769

Hackler L, Zadina JE, Ge LJ, Kastin AJ (1997) Isolation of relatively large amounts of endomorphin-1 and endomorphin-2 from human brain cortex. Peptides 18:1635–1639

Hagelberg N, Aalto S, Tuominen L, Pesonen U, Nagren K, Hietala J et al (2012) Striatal mu-opioid receptor availability predicts cold pressor pain threshold in healthy human subjects. Neurosci Lett 521:11–14

Hammers A, Lingford-Hughes A (2006) Opioid imaging. Neuroimaging Clin N Am 16:529–552, vii

Hammers A, Asselin MC, Turkheimer FE, Hinz R, Osman S, Hotton G et al (2007a) Balancing bias, reliability, noise properties and the need for parametric maps in quantitative ligand PET: [(11)C]diprenorphine test-retest data. NeuroImage 38:82–94

Hammers A, Asselin MC, Hinz R, Kitchen I, Brooks DJ, Duncan JS et al (2007b) Upregulation of opioid receptor binding following spontaneous epileptic seizures. Brain 130:1009–1016

Harris RE, Zubieta JK, Scott DJ, Napadow V, Gracely RH, Clauw DJ (2009) Traditional Chinese acupuncture and placebo (sham) acupuncture are differentiated by their effects on mu-opioid receptors (MORs). NeuroImage 47:1077–1085

Heinz A, Reimold M, Wrase J, Hermann D, Croissant B, Mundle G et al (2005) Correlation of stable elevations in striatal mu-opioid receptor availability in detoxified alcoholic patients with alcohol craving: a positron emission tomography study using carbon 11-labeled carfentanil. Arch Gen Psychiatry 62:57–64

Henriksen G, Willoch F (2008) Imaging of opioid receptors in the central nervous system. Brain 131:1171–1196

Henriksen G, Platzer S, Marton J, Hauser A, Berthele A, Schwaiger M et al (2005a) Syntheses, biological evaluation, and molecular modeling of 18F-labeled 4-anilidopiperidines as mu-opioid receptor imaging agents. J Med Chem 48:7720–7732

Henriksen G, Platzer S, Hauser A, Willoch F, Berthele A, Schwaiger M et al (2005b) 18F-labeled sufentanil for PET-imaging of mu-opioid receptors. Bioorg Med Chem Lett 15:1773–1777

Henriksen G, Spilker ME, Sprenger T, Hauser AI, Platzer S, Boecker H et al (2006) Gender dependent rate of metabolism of the opioid receptor-PET ligand [18F]fluoroethyldiprenorphine. Nuklearmedizin 45:197–200

Hermann D, Hirth N, Reimold M, Batra A, Smolka MN, Hoffmann S et al (2017) Low mu-opioid receptor status in alcohol dependence identified by combined positron emission tomography and post-mortem brain analysis. Neuropsychopharmacology 42:606–614

Hirvonen J, Aalto S, Hagelberg N, Maksimow A, Ingman K, Oikonen V et al (2009) Measurement of central mu-opioid receptor binding in vivo with PET and [11C]carfentanil: a test-retest study in healthy subjects. Eur J Nucl Med Mol Imaging 36:275–286

Hiura M, Sakata M, Ishii K, Toyohara J, Oda K, Nariai T et al (2017) Central mu-opioidergic system activation evoked by heavy and severe-intensity cycling exercise in humans: a pilot study using positron emission tomography with 11C-CARFENTANIL. Int J Sports Med 38:19–26

Homcy CJ, Strauss HW, Kopiwoda S (1980) Beta receptor occupancy. Assessment in the intact animal. J Clin Invest 65:1111–1118

Hostetler ED, Sanabria-Bohorquez S, Eng W, Joshi AD, Patel S, Gibson RE et al (2013) Evaluation of [18F]MK-0911, a positron emission tomography (PET) tracer for opioid receptor-like 1 (ORL1), in rhesus monkey and human. NeuroImage 68:1–10

Hsu DT, Sanford BJ, Meyers KK, Love TM, Hazlett KE, Wang H et al (2013) Response of the mu-opioid system to social rejection and acceptance. Mol Psychiatry 18:1211–1217

Hsu DT, Sanford BJ, Meyers KK, Love TM, Hazlett KE, Walker SJ et al (2015) It still hurts: altered endogenous opioid activity in the brain during social rejection and acceptance in major depressive disorder. Mol Psychiatry 20:193–200

Hughes J, Smith TW, Kosterlitz HW, Fothergill LA, Morgan BA, Morris HR (1975) Identification of two related pentapeptides from the brain with potent opiate agonist activity. Nature 258:577–580

Hume SP, Lingford-Hughes AR, Nataf V, Hirani E, Ahmad R, Davies AN et al (2007) Low sensitivity of the positron emission tomography ligand [11C]diprenorphine to agonist opiates. J Pharmacol Exp Ther 322:661–667

Ingman K, Hagelberg N, Aalto S, Nagren K, Juhakoski A, Karhuvaara S et al (2005) Prolonged central mu-opioid receptor occupancy after single and repeated nalmefene dosing. Neuropsychopharmacology 30:2245–2253

Johansson J, Hirvonen J, Lovro Z, Ekblad L, Kaasinen V, Rajasilta O et al (2019) Intranasal naloxone rapidly occupies brain mu-opioid receptors in human subjects. Neuropsychopharmacology 44(9):1667–1673

Jones AK, Luthra SK, Maziere B, Pike VW, Loc'h C, Crouzel C et al (1988) Regional cerebral opioid receptor studies with [11C]diprenorphine in normal volunteers. J Neurosci Methods 23:121–129

Jones AK, Qi LY, Fujirawa T, Luthra SK, Ashburner J, Bloomfield P et al (1991) In vivo distribution of opioid receptors in man in relation to the cortical projections of the medial and lateral pain systems measured with positron emission tomography. Neurosci Lett 126:25–28

Jones AK, Cunningham VJ, Ha-Kawa SK, Fujiwara T, Liyii Q, Luthra SK et al (1994a) Quantitation of [11C]diprenorphine cerebral kinetics in man acquired by PET using presaturation, pulse-chase and tracer-only protocols. J Neurosci Methods 51:123–134

Jones AK, Cunningham VJ, Ha-Kawa S, Fujiwara T, Luthra SK, Silva S et al (1994b) Changes in central opioid receptor binding in relation to inflammation and pain in patients with rheumatoid arthritis. Br J Rheumatol 33:909–916

Jones AK, Kitchen ND, Watabe H, Cunningham VJ, Jones T, Luthra SK et al (1999) Measurement of changes in opioid receptor binding in vivo during trigeminal neuralgic pain using [11C] diprenorphine and positron emission tomography. J Cereb Blood Flow Metab 19:803–808

Jones AK, Watabe H, Cunningham VJ, Jones T (2004) Cerebral decreases in opioid receptor binding in patients with central neuropathic pain measured by [11C]diprenorphine binding and PET. Eur J Pain 8:479–485

Joutsa J, Karlsson HK, Majuri J, Nuutila P, Helin S, Kaasinen V et al (2018) Binge eating disorder and morbid obesity are associated with lowered mu-opioid receptor availability in the brain. Psychiatry Res Neuroimaging 276:41–45

Kalant H (1997) Opium revisited: a brief review of its nature, composition, non-medical use and relative risks. Addiction 92:267–277

Karjalainen T, Tuominen L, Manninen S, Kalliokoski KK, Nuutila P, Jaaskelainen IP et al (2016) Behavioural activation system sensitivity is associated with cerebral mu-opioid receptor availability. Soc Cogn Affect Neurosci 11:1310–1316

Karjalainen T, Karlsson HK, Lahnakoski JM, Glerean E, Nuutila P, Jaaskelainen IP et al (2017) Dissociable roles of cerebral mu-opioid and type 2 dopamine receptors in vicarious pain: a combined PET-fMRI study. Cereb Cortex 27:4257–4266

Karjalainen T, Seppala K, Glerean E, Karlsson HK, Lahnakoski JM, Nuutila P et al (2019) Opioidergic regulation of emotional arousal: a combined PET-fMRI study. Cereb Cortex 29(9):4006–4016

Karlsson HK, Tuominen L, Tuulari JJ, Hirvonen J, Parkkola R, Helin S et al (2015) Obesity is associated with decreased mu-opioid but unaltered dopamine D2 receptor availability in the brain. J Neurosci 35:3959–3965

Karlsson HK, Tuulari JJ, Tuominen L, Hirvonen J, Honka H, Parkkola R et al (2016) Weight loss after bariatric surgery normalizes brain opioid receptors in morbid obesity. Mol Psychiatry 21:1057–1062

Kawai R, Sawada Y, Channing M, Dunn B, Newman AH, Rice KC et al (1990) Kinetic analysis of the opiate antagonist cyclofoxy in rat brain: simultaneous infusion of active and inactive enantiomers. J Pharmacol Exp Ther 255:826–835

Kawai R, Carson RE, Dunn B, Newman AH, Rice KC, Blasberg RG (1991) Regional brain measurement of Bmax and KD with the opiate antagonist cyclofoxy: equilibrium studies in the conscious rat. J Cereb Blood Flow Metab 11:529–544

Kennedy SE, Koeppe RA, Young EA, Zubieta JK (2006) Dysregulation of endogenous opioid emotion regulation circuitry in major depression in women. Arch Gen Psychiatry 63:1199–1208

Kieffer BL, Befort K, Gaveriaux-Ruff C, Hirth CG (1992) The delta-opioid receptor: isolation of a cDNA by expression cloning and pharmacological characterization. Proc Natl Acad Sci U S A 89:12048–12052

Kim S, Wagner HN Jr, Villemagne VL, Kao PF, Dannals RF, Ravert HT et al (1997) Longer occupancy of opioid receptors by nalmefene compared to naloxone as measured in vivo by a dual-detector system. J Nucl Med 38:1726–1731

Kim SJ, Zheng MQ, Nabulsi N, Labaree D, Ropchan J, Najafzadeh S et al (2013) Determination of the in vivo selectivity of a new kappa-opioid receptor antagonist PET tracer 11C-LY2795050 in the rhesus monkey. J Nucl Med 54:1668–1674

Kimura Y, Fujita M, Hong J, Lohith TG, Gladding RL, Zoghbi SS et al (2011) Brain and whole-body imaging in rhesus monkeys of 11C-NOP-1A, a promising PET radioligand for nociceptin/orphanin FQ peptide receptors. J Nucl Med 52:1638–1645

Klega A, Eberle T, Buchholz HG, Maus S, Maihofner C, Schreckenberger M et al (2010) Central opioidergic neurotransmission in complex regional pain syndrome. Neurology 75:129–136

Kling MA, Carson RE, Borg L, Zametkin A, Matochik JA, Schluger J et al (2000) Opioid receptor imaging with positron emission tomography and [(18)F]cyclofoxy in long-term, methadone-treated former heroin addicts. J Pharmacol Exp Ther 295:1070–1076

Koepp MJ, Duncan JS (2000) PET: opiate neuroreceptor mapping. Adv Neurol 83:145–156

Koepp MJ, Richardson MP, Brooks DJ, Duncan JS (1998) Focal cortical release of endogenous opioids during reading-induced seizures. Lancet 352:952–955

Koepp MJ, Hammers A, Lawrence AD, Asselin MC, Grasby PM, Bench CJ (2009) Evidence for endogenous opioid release in the amygdala during positive emotion. NeuroImage 44:252–256

Kuwabara H, Heishman SJ, Brasic JR, Contoreggi C, Cascella N, Mackowick KM et al (2014) Mu opioid receptor binding correlates with nicotine dependence and reward in smokers. PLoS One 9:e113694

Lamusuo S, Hirvonen J, Lindholm P, Martikainen IK, Hagelberg N, Parkkola R et al (2017) Neurotransmitters behind pain relief with transcranial magnetic stimulation - positron emission tomography evidence for release of endogenous opioids. Eur J Pain 21:1505–1515

Lee MC, Wagner HN Jr, Tanada S, Frost JJ, Bice AN, Dannals RF (1988) Duration of occupancy of opiate receptors by naltrexone. J Nucl Med 29:1207–1211

Lever JR (2007) PET and SPECT imaging of the opioid system: receptors, radioligands and avenues for drug discovery and development. Curr Pharm Des 13:33–49

Lever JR, Dannals RF, Wilson AA, Ravert HT, Wagner HN Jr (1987) Synthesis of carbon-11 labeled diprenorphine: a radioligand for positron emission tomographic studies of opiate receptors. Tetrahedron Lett 28:4015–4018

Lever JR, Mazza SM, Dannals RF, Ravert HT, Wilson AA, Wagner HN Jr (1990) Facile synthesis of [11C]buprenorphine for positron emission tomographic studies of opioid receptors. Int J Rad Appl Instrum A 41:745–752

Lever JR, Scheffel U, Kinter CM, Ravert HT, Dannals RF, Wagner HN Jr et al (1992) In vivo binding of N1'-([11C]methyl)naltrindole to delta-opioid receptors in mouse brain. Eur J Pharmacol 216:459–460

Lever JR, Stathis M, Kinter CM, Scheffel U (1996) In vivo labeling of delta opioid receptors in mouse brain by [3H]benzylidenenaltrexone, a ligand selective for the delta 1 subtype. Life Sci 58:L331–L336

Li G, Low PS (2017) Synthesis and evaluation of a ligand targeting the mu and delta opioid receptors for drug delivery to lung cancer. Bioorg Med Chem Lett 27:2074–2078

Li S, Cai Z, Zheng MQ, Holden D, Naganawa M, Lin SF et al (2018) Novel (18)F-labeled kappa-opioid receptor antagonist as PET radiotracer: synthesis and in vivo evaluation of (18) F-LY2459989 in nonhuman primates. J Nucl Med 59:140–146

Li S, Zheng MQ, Naganawa M, Kim S, Gao H, Kapinos M et al (2019a) Development and in vivo evaluation of a novel kappa opioid receptor agonist as PET radiotracer with superior imaging characteristics. J Nucl Med s(7):1023–1030

Li S, Zheng MQ, Naganawa M, Gao H, Pracitto R, Shirali A et al (2019b) Novel kappa opioid receptor agonist as improved PET radiotracer: development and in vivo evaluation. Mol Pharm 16:1523–1531

Liberzon I, Zubieta JK, Fig LM, Phan KL, Koeppe RA, Taylor SF (2002) mu-Opioid receptors and limbic responses to aversive emotional stimuli. Proc Natl Acad Sci U S A 99:7084–7089

Liberzon I, Taylor SF, Phan KL, Britton JC, Fig LM, Bueller JA et al (2007) Altered central micro-opioid receptor binding after psychological trauma. Biol Psychiatry 61:1030–1038

Lohith TG, Zoghbi SS, Morse CL, Araneta MF, Barth VN, Goebl NA et al (2012) Brain and whole-body imaging of nociceptin/orphanin FQ peptide receptor in humans using the PET ligand 11C-NOP-1A. J Nucl Med 53:385–392

Lord JA, Waterfield AA, Hughes J, Kosterlitz HW (1977) Endogenous opioid peptides: multiple agonists and receptors. Nature 267:495–499

Love TM, Stohler CS, Zubieta JK (2009) Positron emission tomography measures of endogenous opioid neurotransmission and impulsiveness traits in humans. Arch Gen Psychiatry 66:1124–1134

Luthra SK, Pike VW, Brady F (1985) The preparation of carbon-11 labeled diprenorphine: A new radioligand for the study of the opiate receptor system in vivo. J Chem Soc Chem Commun:1423–1425

Luthra SK, Pike VW, Brady F, Horlock PL, Prenant C, Crouzel C (1987) Preparation of [11C]buprenorphine--a potential radioligand for the study of the opiate receptor system in vivo. Int J Rad Appl Instrum A 38:65–66

Maarrawi J, Peyron R, Mertens P, Costes N, Magnin M, Sindou M et al (2007a) Differential brain opioid receptor availability in central and peripheral neuropathic pain. Pain 127:183–194

Maarrawi J, Peyron R, Mertens P, Costes N, Magnin M, Sindou M et al (2007b) Motor cortex stimulation for pain control induces changes in the endogenous opioid system. Neurology 69:827–834

Maarrawi J, Peyron R, Mertens P, Costes N, Magnin M, Sindou M et al (2013) Brain opioid receptor density predicts motor cortex stimulation efficacy for chronic pain. Pain 154:2563–2568

Madar I, Lever JR, Kinter CM, Scheffel U, Ravert HT, Musachio JL et al (1996) Imaging of delta opioid receptors in human brain by N1'-([11C]methyl)naltrindole and PET. Synapse 24:19–28

Madar I, Lesser RP, Krauss G, Zubieta JK, Lever JR, Kinter CM et al (1997) Imaging of delta- and mu-opioid receptors in temporal lobe epilepsy by positron emission tomography. Ann Neurol 41:358–367

Madar I, Bencherif B, Lever J, Heitmiller RF, Yang SC, Brock M et al (2007) Imaging delta- and mu-opioid receptors by PET in lung carcinoma patients. J Nucl Med 48:207–213

Majuri J, Joutsa J, Johansson J, Voon V, Alakurtti K, Parkkola R et al (2017) Dopamine and opioid neurotransmission in behavioral addictions: a comparative PET study in pathological gambling and binge eating. Neuropsychopharmacology 42:1169–1177

Majuri J, Joutsa J, Arponen E, Forsback S, Kaasinen V (2018) Dopamine synthesis capacity correlates with micro-opioid receptor availability in the human basal ganglia: a triple-tracer PET study. NeuroImage 183:1–6

Manninen S, Tuominen L, Dunbar RI, Karjalainen T, Hirvonen J, Arponen E et al (2017) Social laughter triggers endogenous opioid release in humans. J Neurosci 37:6125–6131

Marsh CA, Berent-Spillson A, Love T, Persad CC, Pop-Busui R, Zubieta JK et al (2013) Functional neuroimaging of emotional processing in women with polycystic ovary syndrome: a case-control pilot study. Fertil Steril 100:200–207

Martikainen IK, Pecina M, Love TM, Nuechterlein EB, Cummiford CM, Green CR et al (2013) Alterations in endogenous opioid functional measures in chronic back pain. J Neurosci 33:14729–14737

Martin WR, Eades CG, Thompson JA, Huppler RE, Gilbert PE (1976) The effects of morphine- and nalorphine- like drugs in the nondependent and morphine-dependent chronic spinal dog. J Pharmacol Exp Ther 197:517–532

Matuskey D, Dias M, Naganawa M, Pittman B, Henry S, Li S et al (2019) Social status and demographic effects of the kappa opioid receptor: a PET imaging study with a novel agonist radiotracer in healthy volunteers. Neuropsychopharmacology 44(10):1714–1719

Mayberg HS, Sadzot B, Meltzer CC, Fisher RS, Lesser RP, Dannals RF et al (1991) Quantification of mu and non-mu opiate receptors in temporal lobe epilepsy using positron emission tomography. Ann Neurol 30:3–11

McGinnity CJ, Shidahara M, Feldmann M, Keihaninejad S, Riano Barros DA, Gousias IS et al (2013) Quantification of opioid receptor availability following spontaneous epileptic seizures: correction of [11C]diprenorphine PET data for the partial-volume effect. NeuroImage 79:72–80

McLean S, Rice KC, Lessor R, Rothman RB (1987) [3H]cyclofoxy, a ligand suitable for positron emission tomography, labels mu and kappa opioid receptors. Neuropeptides 10:235–239

Melichar JK, Nutt DJ, Malizia AL (2003) Naloxone displacement at opioid receptor sites measured in vivo in the human brain. Eur J Pharmacol 459:217–219

Melichar JK, Hume SP, Williams TM, Daglish MR, Taylor LG, Ahmad R et al (2005) Using [11C]diprenorphine to image opioid receptor occupancy by methadone in opioid addiction: clinical and preclinical studies. J Pharmacol Exp Ther 312:309–315

Meunier JC, Mollereau C, Toll L, Suaudeau C, Moisand C, Alvinerie P et al (1995) Isolation and structure of the endogenous agonist of opioid receptor-like ORL1 receptor. Nature 377:532–535

Mick I, Myers J, Ramos AC, Stokes PR, Erritzoe D, Colasanti A et al (2016) Blunted endog-
    enous opioid release following an oral amphetamine challenge in pathological gamblers.
    Neuropsychopharmacology 41:1742–1750

Miller JM, Zanderigo F, Purushothaman PD, DeLorenzo C, Rubin-Falcone H, Ogden RT et al
    (2018) Kappa opioid receptor binding in major depression: A pilot study. Synapse 72:e22042

Minami M, Satoh M (1995) Molecular biology of the opioid receptors: structures, functions and
    distributions. Neurosci Res 23:121–145

Mitchell JM, O'Neil JP, Janabi M, Marks SM, Jagust WJ, Fields HL (2012) Alcohol consumption
    induces endogenous opioid release in the human orbitofrontal cortex and nucleus accumbens.
    Sci Transl Med 4:116ra6

Mitchell JM, O'Neil JP, Jagust WJ, Fields HL (2013) Catechol-O-methyltransferase genotype
    modulates opioid release in decision circuitry. Clin Transl Sci 6:400–403

Mueller C, Klega A, Buchholz HG, Rolke R, Magerl W, Schirrmacher R et al (2010) Basal opioid
    receptor binding is associated with differences in sensory perception in healthy human sub-
    jects: a [18F]diprenorphine PET study. NeuroImage 49:731–737

Nabulsi NB, Zheng MQ, Ropchan J, Labaree D, Ding YS, Blumberg L et al (2011) [11C]GR103545:
    novel one-pot radiosynthesis with high specific activity. Nucl Med Biol 38:215–221

Naganawa M, Jacobsen LK, Zheng MQ, Lin SF, Banerjee A, Byon W et al (2014a) Evaluation of
    the agonist PET radioligand [(1)(1)C]GR103545 to image kappa opioid receptor in humans:
    kinetic model selection, test-retest reproducibility and receptor occupancy by the antagonist
    PF-04455242. NeuroImage 99:69–79

Naganawa M, Zheng MQ, Nabulsi N, Tomasi G, Henry S, Lin SF et al (2014b) Kinetic model-
    ing of (11)C-LY2795050, a novel antagonist radiotracer for PET imaging of the kappa opioid
    receptor in humans. J Cereb Blood Flow Metab 34:1818–1825

Naganawa M, Zheng MQ, Henry S, Nabulsi N, Lin SF, Ropchan J et al (2015) Test-retest repro-
    ducibility of binding parameters in humans with 11C-LY2795050, an antagonist PET radio-
    tracer for the kappa opioid receptor. J Nucl Med 56:243–248

Naganawa M, Dickinson GL, Zheng MQ, Henry S, Vandenhende F, Witcher J et al (2016) Receptor
    occupancy of the kappa-opioid antagonist LY2456302 measured with positron emission
    tomography and the novel radiotracer 11C-LY2795050. J Pharmacol Exp Ther 356:260–266

Nascimento TD, DosSantos MF, Lucas S, van HH DBM, Maslowski E et al (2014) mu-Opioid
    activation in the midbrain during migraine allodynia - brief report II. Ann Clin Transl Neurol
    1:445–450

Nuechterlein EB, Ni L, Domino EF, Zubieta JK (2016) Nicotine-specific and non-specific effects
    of cigarette smoking on endogenous opioid mechanisms. Prog Neuro-Psychopharmacol Biol
    Psychiatry 69:69–77

Nummenmaa L, Manninen S, Tuominen L, Hirvonen J, Kalliokoski KK, Nuutila P et al (2015)
    Adult attachment style is associated with cerebral mu-opioid receptor availability in humans.
    Hum Brain Mapp 36:3621–3628

Nummenmaa L, Tuominen L, Dunbar R, Hirvonen J, Manninen S, Arponen E et al (2016) Social
    touch modulates endogenous mu-opioid system activity in humans. NeuroImage 138:242–247

Ogawa M, Hatano K, Kawasumi Y, Wichmann J, Ito K (2001) Synthesis and in vivo evaluation
    of [11C]methyl-Ro 64-6198 as an ORL1 receptor imaging agent. Nucl Med Biol 28:941–947

Ogawa M, Hatano K, Kawasumi Y, Ishiwata K, Kawamura K, Ozaki S et al (2003) Synthesis and
    evaluation of 1-[(3R,4R)-1-cyclooctylmethyl-3-hydroxymethyl-4-piperidyl]-3-[11C]ethyl-1,3-
    dihyd ro-2H-benzimidazol-2-one as a brain ORL1 receptor imaging agent for positron emis-
    sion tomography. Nucl Med Biol 30:51–59

Ostrowski NL, Burke TR Jr, Rice KC, Pert A, Pert CB (1987) The pattern of [3H]cyclofoxy reten-
    tion in rat brain after in vivo injection corresponds to the in vitro opiate receptor distribution.
    Brain Res 402:275–286

Pecina M, Stohler CS, Zubieta JK (2014) Neurobiology of placebo effects: expectations or learn-
    ing? Soc Cogn Affect Neurosci 9:1013–1021

Pecina M, Bohnert AS, Sikora M, Avery ET, Langenecker SA, Mickey BJ et al (2015) Association between placebo-activated neural systems and antidepressant responses: neurochemistry of placebo effects in major depression. JAMA Psychiat 72:1087–1094

Pedregal C, Joshi EM, Toledo MA, Lafuente C, Diaz N, Martinez-Grau MA et al (2012) Development of LC-MS/MS-based receptor occupancy tracers and positron emission tomography radioligands for the nociceptin/orphanin FQ (NOP) receptor. J Med Chem 55:4955–4967

Pert CB, Snyder SH (1975) Identification of opiate receptor binding in intact animals. Life Sci 16:1623–1634

Pert CB, Danks JA, Channing MA, Eckelman WC, Larson SM, Bennett JM et al (1984) 3-[18F]Acetylcyclofoxy: a useful probe for the visualization of opiate receptors in living animals. FEBS Lett 177:281–286

Pfeiffer A, Pasi A, Mehraein P, Herz A (1982) Opiate receptor binding sites in human brain. Brain Res 248:87–96

Piccini P, Weeks RA, Brooks DJ (1997) Alterations in opioid receptor binding in Parkinson's disease patients with levodopa-induced dyskinesias. Ann Neurol 42:720–726

Piché M, Watanabe N, Sakata M, Oda K, Toyohara J, Ishii K et al (2014) Basal mu-opioid receptor availability in the amygdala predicts the inhibition of pain-related brain activity during heterotopic noxious counter-stimulation. Neurosci Res 81-82:78–84

Pichika R, Jewett DM, Sherman PS, Traynor JR, Husbands SM, Woods JH et al (2010) Synthesis and in vivo brain distribution of carbon-11-labeled delta-opioid receptor agonists. Nucl Med Biol 37:989–996

Pietrzak RH, Naganawa M, Huang Y, Corsi-Travali S, Zheng MQ, Stein MB et al (2014) Association of in vivo kappa-opioid receptor availability and the transdiagnostic dimensional expression of trauma-related psychopathology. JAMA Psychiat 71:1262–1270

Pike VW, Rash KS, Chen Z, Pedregal C, Statnick MA, Kimura Y et al (2011) Synthesis and evaluation of radioligands for imaging brain nociceptin/orphanin FQ peptide (NOP) receptors with positron emission tomography. J Med Chem 54:2687–2700

Pirisedigh A, Blais V, it-Mohand S, Abdallah K, Holleran BJ, Leduc R et al (2017) Synthesis and evaluation of a (64)Cu-conjugate, a selective delta-opioid receptor positron emission tomography imaging agent. Org Lett 19:2018–2021

Placzek MS, Van de Bittner GC, Wey HY, Lukas SE, Hooker JM (2015) Immediate and persistent effects of salvinorin A on the kappa opioid receptor in rodents, monitored in vivo with PET. Neuropsychopharmacology 40:2865–2872

Placzek MS, Schroeder FA, Che T, Wey HY, Neelamegam R, Wang C et al (2019) Discrepancies in kappa opioid agonist binding revealed through PET imaging. ACS Chem Neurosci 10:384–395

Poisnel G, Oueslati F, Dhilly M, Delamare J, Perrio C, Debruyne D et al (2008) [11C]-MeJDTic: a novel radioligand for kappa-opioid receptor positron emission tomography imaging. Nucl Med Biol 35:561–569

Portoghese PS, Sultana M, Takemori AE (1990) Design of peptidomimetic delta opioid receptor antagonists using the message-address concept. J Med Chem 33:1714–1720

Prevett MC, Cunningham VJ, Brooks DJ, Fish DR, Duncan JS (1994) Opiate receptors in idiopathic generalised epilepsy measured with [11C]diprenorphine and positron emission tomography. Epilepsy Res 19:71–77

Prossin AR, Love TM, Koeppe RA, Zubieta JK, Silk KR (2010) Dysregulation of regional endogenous opioid function in borderline personality disorder. Am J Psychiatry 167:925–933

Prossin AR, Koch AE, Campbell PL, McInnis MG, Zalcman SS, Zubieta JK (2011) Association of plasma interleukin-18 levels with emotion regulation and mu-opioid neurotransmitter function in major depression and healthy volunteers. Biol Psychiatry 69:808–812

Prossin AR, Zalcman SS, Heitzeg MM, Koch AE, Campbell PL, Phan KL et al (2015) Dynamic interactions between plasma IL-1 family cytokines and central endogenous opioid neurotransmitter function in humans. Neuropsychopharmacology 40:554–565

Prossin AR, Koch AE, Campbell PL, Barichello T, Zalcman SS, Zubieta JK (2016) Acute experimental changes in mood state regulate immune function in relation to central opioid neuro-

transmission: a model of human CNS-peripheral inflammatory interaction. Mol Psychiatry 21:243–251

Quelch DR, Katsouri L, Nutt DJ, Parker CA, Tyacke RJ (2014) Imaging endogenous opioid peptide release with [11C]carfentanil and [3H]diprenorphine: influence of agonist-induced internalization. J Cereb Blood Flow Metab 34:1604–1612

Rabiner EA, Beaver J, Makwana A, Searle G, Long C, Nathan PJ et al (2011) Pharmacological differentiation of opioid receptor antagonists by molecular and functional imaging of target occupancy and food reward-related brain activation in humans. Mol Psychiatry 16:826–835, 785

Rafique W, Khanapur S, Spilhaug MM, Riss PJ (2017) Reaching out for sensitive evaluation of the Mu opioid receptor in vivo: positron emission tomography imaging of the agonist [(11)C]AH7921. ACS Chem Neurosci 8:1847–1852

Ravert HT, Mathews WB, Musachio JL, Scheffel U, Finley P, Dannals RF (1999) [11C]-methyl 4-[(3,4-dichlorophenyl)acetyl]-3-[(1-pyrrolidinyl)-methyl]-1-   piperazinecarboxylate ([11C]GR89696): synthesis and in vivo binding to kappa opiate receptors. Nucl Med Biol 26:737–741

Ravert HT, Scheffel U, Mathews WB, Musachio JL, Dannals RF (2002) [(11)C]-GR89696, a potent kappa opiate receptor radioligand; in vivo binding of the R and S enantiomers. Nucl Med Biol 29:47–53

Ravert HT, Bencherif B, Madar I, Frost JJ (2004) PET imaging of opioid receptors in pain: progress and new directions. Curr Pharm Des 10:759–768

Ray R, Ruparel K, Newberg A, Wileyto EP, Loughead JW, Divgi C et al (2011) Human Mu opioid receptor (OPRM1 A118G) polymorphism is associated with brain mu-opioid receptor binding potential in smokers. Proc Natl Acad Sci U S A 108:9268–9273

Raynor K, Kong H, Chen Y, Yasuda K, Yu L, Bell GI et al (1994) Pharmacological characterization of the cloned kappa-, delta-, and mu-opioid receptors. Mol Pharmacol 45:330–334

Reame NE, Lukacs JL, Padmanabhan V, Eyvazzadeh AD, Smith YR, Zubieta JK (2008) Black cohosh has central opioid activity in postmenopausal women: evidence from naloxone blockade and positron emission tomography neuroimaging. Menopause 15:832–840

Reinscheid RK, Nothacker HP, Bourson A, Ardati A, Henningsen RA, Bunzow JR et al (1995) Orphanin FQ: a neuropeptide that activates an opioidlike G protein-coupled receptor. Science 270:792–794

Rinne JO, Burn DJ, Mathias CJ, Quinn NP, Marsden CD, Brooks DJ (1995) Positron emission tomography studies on the dopaminergic system and striatal opioid binding in the olivopontocerebellar atrophy variant of multiple system atrophy. Ann Neurol 37:568–573

Riss PJ, Hong YT, Marton J, Caprioli D, Williamson DJ, Ferrari V et al (2013) Synthesis and evaluation of 18F-FE-PEO in rodents: an 18F-labeled full agonist for opioid receptor imaging. J Nucl Med 54:299–305

Rodman AM, Deckersbach T, Chou T, Kong J, Gollub RL, Dougherty DD (2017) A preliminary study of the opioid system and personality traits using positron emission tomography. Mol Neuropsychiatry 3:12–18

Rothman RB, McLean S (1988) An examination of the opiate receptor subtypes labeled by [3H]cycloFOXY: an opiate antagonist suitable for positron emission tomography. Biol Psychiatry 23:435–458

Rothman RB, Bykov V, Reid A, De Costa BR, Newman AH, Jacobson AE et al (1988) A brief study of the selectivity of norbinaltorphimine, (−)-cyclofoxy, and (+)-cyclofoxy among opioid receptor subtypes in vitro. Neuropeptides 12:181–187

Ruiz-Gayo M, Baamonde A, Turcaud S, Fournie-Zaluski MC, Roques BP (1992) In vivo occupation of mouse brain opioid receptors by endogenous enkephalins: blockade of enkephalin degrading enzymes by RB 101 inhibits [3H]diprenorphine binding. Brain Res 571:306–312

Ryu EK, Wu Z, Chen K, Lazarus LH, Marczak ED, Sasaki Y et al (2008) Synthesis of a potent and selective (18)F-labeled delta-opioid receptor antagonist derived from the Dmt-Tic pharmacophore for positron emission tomography imaging. J Med Chem 51:1817–1823

Saanijoki T, Tuominen L, Tuulari JJ, Nummenmaa L, Arponen E, Kalliokoski K et al (2018a) Opioid release after high-intensity interval training in healthy human subjects. Neuropsychopharmacology 43:246–254

Saanijoki T, Nummenmaa L, Tuulari JJ, Tuominen L, Arponen E, Kalliokoski KK et al (2018b) Aerobic exercise modulates anticipatory reward processing via the mu-opioid receptor system. Hum Brain Mapp 39:3972–3983

Sadzot B, Frost JJ (1990) Pain and opiate receptors: considerations for the design of positron emission tomography studies. Anesth Prog 37:113–120

Sadzot B, Mayberg HS, Frost JJ (1990) Detection and quantification of opiate receptors in man by positron emission tomography. Potential applications to the study of pain. Neurophysiol Clin 20:323–334

Sadzot B, Price JC, Mayberg HS, Douglass KH, Dannals RF, Lever JR et al (1991) Quantification of human opiate receptor concentration and affinity using high and low specific activity [11C]diprenorphine and positron emission tomography. J Cereb Blood Flow Metab 11:204–219

Saji H, Tsutsumi D, Magata Y, Iida Y, Konishi J, Yokoyama A (1992) Preparation and biodistribution in mice of [11C]carfentanil: a radiopharmaceutical for studying brain mu-opioid receptors by positron emission tomography. Ann Nucl Med 6:63–67

Sawada Y, Kawai R, McManaway M, Otsuki H, Rice KC, Patlak CS et al (1991) Kinetic analysis of transport and opioid receptor binding of [3H](−)-cyclofoxy in rat brain in vivo: implications for human studies. J Cereb Blood Flow Metab 11:183–203

Schadrack J, Willoch F, Platzer S, Bartenstein P, Mahal B, Dworzak D et al (1999) Opioid receptors in the human cerebellum: evidence from [11C]diprenorphine PET, mRNA expression and autoradiography. Neuroreport 10:619–624

Schmitt S, Delamare J, Tirel O, Fillesoye F, Dhilly M, Perrio C (2017) N-[(18)F]-FluoropropylJDTic for kappa-opioid receptor PET imaging: radiosynthesis, pre-clinical evaluation, and metabolic investigation in comparison with parent JDTic. Nucl Med Biol 44:50–61

Schoultz BW, Hjornevik T, Willoch F, Marton J, Noda A, Murakami Y et al (2010) Evaluation of the kappa-opioid receptor-selective tracer [(11)C]GR103545 in awake rhesus macaques. Eur J Nucl Med Mol Imaging 37:1174–1180

Schoultz BW, Reed BJ, Marton J, Willoch F, Henriksen G (2013) A fully automated radiosynthesis of [18F]fluoroethyl-diprenorphine on a single module by use of SPE cartridges for preparation of high quality 2-[18F]fluoroethyl tosylate. Molecules 18:7271–7278

Schreckenberger M, Klega A, Grunder G, Buchholz HG, Scheurich A, Schirrmacher R et al (2008) Opioid receptor PET reveals the psychobiologic correlates of reward processing. J Nucl Med 49:1257–1261

Schrepf A, Harper DE, Harte SE, Wang H, Ichesco E, Hampson JP et al (2016) Endogenous opioidergic dysregulation of pain in fibromyalgia: a PET and fMRI study. Pain 157:2217–2225

Scott DJ, Stohler CS, Koeppe RA, Zubieta JK (2007a) Time-course of change in [11C]carfentanil and [11C]raclopride binding potential after a nonpharmacological challenge. Synapse 61:707–714

Scott DJ, Domino EF, Heitzeg MM, Koeppe RA, Ni L, Guthrie S et al (2007b) Smoking modulation of mu-opioid and dopamine D2 receptor-mediated neurotransmission in humans. Neuropsychopharmacology 32:450–457

Scott DJ, Stohler CS, Egnatuk CM, Wang H, Koeppe RA, Zubieta JK (2008) Placebo and nocebo effects are defined by opposite opioid and dopaminergic responses. Arch Gen Psychiatry 65:220–231

Shiue CY, Bai LQ, Teng RR, Arnett CD, Dewey SL, Wolf AP et al (1991) A comparison of the brain uptake of N-(cyclopropyl[11C]methyl)norbuprenorphine ([11C]buprenorphine) and N-(cyclopropyl[11C]methyl)nordiprenorphine ([11C]diprenorphine) in baboon using PET. Int J Rad Appl Instrum B 18:281–288

Simantov R, Snyder SH (1976) Morphine-like peptides in mammalian brain: isolation, structure elucidation, and interactions with the opiate receptor. Proc Natl Acad Sci U S A 73:2515–2519

Smith YR, Zubieta JK, del Carmen MG, Dannals RF, Ravert HT, Zacur HA et al (1998) Brain opioid receptor measurements by positron emission tomography in normal cycling women: rela-

tionship to luteinizing hormone pulsatility and gonadal steroid hormones. J Clin Endocrinol Metab 83:4498–4505

Smith JS, Zubieta JK, Price JC, Flesher JE, Madar I, Lever JR et al (1999) Quantification of delta-opioid receptors in human brain with N1'-([11C]methyl) naltrindole and positron emission tomography. J Cereb Blood Flow Metab 19:956–966

Smith YR, Stohler CS, Nichols TE, Bueller JA, Koeppe RA, Zubieta JK (2006) Pronociceptive and antinociceptive effects of estradiol through endogenous opioid neurotransmission in women. J Neurosci 26:5777–5785

Snyder SH, Pasternak GW (2003) Historical review: Opioid receptors. Trends Pharmacol Sci 24:198–205

von Spiczak S, Whone AL, Hammers A, Asselin MC, Turkheimer F, Tings T et al (2005) The role of opioids in restless legs syndrome: an [11C]diprenorphine PET study. Brain 128:906–917

Sprenger T, Berthele A, Platzer S, Boecker H, Tolle TR (2005) What to learn from in vivo opioi-dergic brain imaging? Eur J Pain 9:117–121

Sprenger T, Valet M, Boecker H, Henriksen G, Spilker ME, Willoch F et al (2006a) Opioidergic activation in the medial pain system after heat pain. Pain 122:63–67

Sprenger T, Willoch F, Miederer M, Schindler F, Valet M, Berthele A et al (2006b) Opioidergic changes in the pineal gland and hypothalamus in cluster headache: a ligand PET study. Neurology 66:1108–1110

Talbot PS, Narendran R, Butelman ER, Huang Y, Ngo K, Slifstein M et al (2005) 11C-GR103545, a radiotracer for imaging kappa-opioid receptors in vivo with PET: synthesis and evaluation in baboons. J Nucl Med 46:484–494

Theodore WH, Carson RE, Andreasen P, Zametkin A, Blasberg R, Leiderman DB et al (1992) PET imaging of opiate receptor binding in human epilepsy using [18F]cyclofoxy. Epilepsy Res 13:129–139

Thompson SJ, Pitcher MH, Stone LS, Tarum F, Niu G, Chen X et al (2018) Chronic neuropathic pain reduces opioid receptor availability with associated anhedonia in rat. Pain 159:1856–1866

Titeler M, Lyon RA, Kuhar MJ, Frost JF, Dannals RF, Leonhardt S et al (1989) Mu opiate recep-tors are selectively labelled by [3H]carfentanil in human and rat brain. Eur J Pharmacol 167:221–228

Tomasi G, Nabulsi N, Zheng MQ, Weinzimmer D, Ropchan J, Blumberg L et al (2013) Determination of in vivo Bmax and Kd for 11C-GR103545, an Agonist PET tracer for kappa-opioid receptors: a study in nonhuman primates. J Nucl Med 54:1–9

Trescot AM, Datta S, Lee M, Hansen H (2008) Opioid pharmacology. Pain Physician 11:S133–S153

Tuominen L, Salo J, Hirvonen J, Nagren K, Laine P, Melartin T et al (2012) Temperament trait harm avoidance associates with mu-opioid receptor availability in frontal cortex: a PET study using [(11)C]carfentanil. NeuroImage 61:670–676

Tuominen L, Nummenmaa L, Keltikangas-Jarvinen L, Raitakari O, Hietala J (2014) Mapping neurotransmitter networks with PET: an example on serotonin and opioid systems. Hum Brain Mapp 35:1875–1884

Tuominen L, Tuulari J, Karlsson H, Hirvonen J, Helin S, Salminen P et al (2015) Aberrant meso-limbic dopamine-opiate interaction in obesity. NeuroImage 122:80–86

Turton S, Myers JF, Mick I, Colasanti A, Venkataraman A, Durant C et al (2018) Blunted endog-enous opioid release following an oral dexamphetamine challenge in abstinent alcohol-dependent individuals. Mol Psychiatry. https://doi.org/10.1038/s41380-018-0107-4

Tuulari JJ, Tuominen L, de Boer FE, Hirvonen J, Helin S, Nuutila P et al (2017) Feeding releases endogenous opioids in humans. J Neurosci 37:8284–8291

Tyacke RJ, Robinson ES, Schnabel R, Lewis JW, Husbands SM, Nutt DJ et al (2002) N1'-fluoroethyl-naltrindole (BU97001) and N1'-fluoroethyl-(14-formylamino)-naltrindole (BU97018) potential delta-opioid receptor PET ligands. Nucl Med Biol 29:455–462

Vaccarino AL, Kastin AJ (2001) Endogenous opiates: 2000. Peptides 22:2257–2328

Vijay A, Wang S, Worhunsky P, Zheng MQ, Nabulsi N, Ropchan J et al (2016) PET imaging reveals sex differences in kappa opioid receptor availability in humans, in vivo. Am J Nucl Med Mol Imaging 6:205–214

Vijay A, Cavallo D, Goldberg A, de Latt B, Nabulsi N, Huang Y et al (2018) PET imaging reveals lower kappa opioid receptor availability in alcoholics but no effect of age. Neuropsychopharmacology 43:2539–2547

Villemagne VL, Frost JJ, Dannals RF, Lever JR, Tanada S, Natarajan TK et al (1994) Comparison of [11C]diprenorphine and [11C]carfentanil in vivo binding to opiate receptors in man using a dual detector system. Eur J Pharmacol 257:195–197

Villemagne PS, Dannals RF, Ravert HT, Frost JJ (2002) PET imaging of human cardiac opioid receptors. Eur J Nucl Med Mol Imaging 29:1385–1388

Wager TD, Scott DJ, Zubieta JK (2007) Placebo effects on human mu-opioid activity during pain. Proc Natl Acad Sci U S A 104:11056–11061

Waldhoer M, Bartlett SE, Whistler JL (2004) Opioid receptors. Annu Rev Biochem 73:953–990

Wand GS, Weerts EM, Kuwabara H, Frost JJ, Xu X, McCaul ME (2011) Naloxone-induced cortisol predicts mu opioid receptor binding potential in specific brain regions of healthy subjects. Psychoneuroendocrinology 36:1453–1459

Wand GS, Weerts EM, Kuwabara H, Wong DF, Xu X, McCaul ME (2012) The relationship between naloxone-induced cortisol and mu opioid receptor availability in mesolimbic structures is disrupted in alcohol dependent subjects. Alcohol 46:511–517

Wand GS, Weerts EM, Kuwabara H, Wong DF, Xu X, McCaul ME (2013) The relationship between naloxone-induced cortisol and delta opioid receptor availability in mesolimbic structures is disrupted in alcohol-dependent subjects. Addict Biol 18:181–192

Weeks RA, Cunningham VJ, Piccini P, Waters S, Harding AE, Brooks DJ (1997) 11C-diprenorphine binding in Huntington's disease: a comparison of region of interest analysis with statistical parametric mapping. J Cereb Blood Flow Metab 17:943–949

Weerts EM, Kim YK, Wand GS, Dannals RF, Lee JS, Frost JJ et al (2008) Differences in delta- and mu-opioid receptor blockade measured by positron emission tomography in naltrexone-treated recently abstinent alcohol-dependent subjects. Neuropsychopharmacology 33:653–665

Weerts EM, Wand GS, Kuwabara H, Munro CA, Dannals RF, Hilton J et al (2011) Positron emission tomography imaging of mu- and delta-opioid receptor binding in alcohol-dependent and healthy control subjects. Alcohol Clin Exp Res 35:2162–2173

Weerts EM, McCaul ME, Kuwabara H, Yang X, Xu X, Dannals RF et al (2013) Influence of OPRM1 Asn40Asp variant (A118G) on [11C]carfentanil binding potential: preliminary findings in human subjects. Int J Neuropsychopharmacol 16:47–53

Weerts EM, Wand GS, Kuwabara H, Xu X, Frost JJ, Wong DF et al (2014) Association of smoking with mu-opioid receptor availability before and during naltrexone blockade in alcohol-dependent subjects. Addict Biol 19:733–742

Wester HJ, Willoch F, Tolle TR, Munz F, Herz M, Oye I et al (2000) 6-O-(2-[18F]fluoroethyl)-6-O-desmethyldiprenorphine ([18F]DPN): synthesis, biologic evaluation, and comparison with [11C]DPN in humans. J Nucl Med 41:1279–1286

Wey HY, Catana C, Hooker JM, Dougherty DD, Knudsen GM, Wang DJ et al (2014) Simultaneous fMRI-PET of the opioidergic pain system in human brain. NeuroImage 102(Pt 2):275–282

Whone AL, von Spiczak S, Edwards M, Valente EM, Hammers A, Bhatia KP et al (2004) Opioid binding in DYT1 primary torsion dystonia: an 11C-diprenorphine PET study. Mov Disord 19:1498–1503

Williams TM, Daglish MR, Lingford-Hughes A, Taylor LG, Hammers A, Brooks DJ et al (2007) Brain opioid receptor binding in early abstinence from opioid dependence: positron emission tomography study. Br J Psychiatry 191:63–69

Williams TM, Davies SJ, Taylor LG, Daglish MR, Hammers A, Brooks DJ et al (2009) Brain opioid receptor binding in early abstinence from alcohol dependence and relationship to craving: an [11C]diprenorphine PET study. Eur Neuropsychopharmacol 19:740–748

Willoch F, Tolle TR, Wester HJ, Munz F, Petzold A, Schwaiger M et al (1999) Central pain after pontine infarction is associated with changes in opioid receptor binding: a PET study with 11C-diprenorphine. AJNR Am J Neuroradiol 20:686–690

Willoch F, Schindler F, Wester HJ, Empl M, Straube A, Schwaiger M et al (2004) Central poststroke pain and reduced opioid receptor binding within pain processing circuitries: a [11C]diprenorphine PET study. Pain 108:213–220

Xiang XH, Chen YM, Zhang JM, Tian JH, Han JS, Cui CL (2014) Low- and high-frequency transcutaneous electrical acupoint stimulation induces different effects on cerebral mu-opioid receptor availability in rhesus monkeys. J Neurosci Res 92:555–563

Yang L, Brooks AF, Makaravage KJ, Zhang H, Sanford MS, Scott PJH et al (2018) Radiosynthesis of [(11)C]LY2795050 for preclinical and clinical PET imaging using Cu(II)-mediated cyanation. ACS Med Chem Lett 9:1274–1279

Yasuda K, Raynor K, Kong H, Breder CD, Takeda J, Reisine T et al (1993) Cloning and functional comparison of kappa and delta opioid receptors from mouse brain. Proc Natl Acad Sci U S A 90:6736–6740

Zadina JE, Hackler L, Ge LJ, Kastin AJ (1997) A potent and selective endogenous agonist for the mu-opiate receptor. Nature 386:499–502

Zeng Y, Hu D, Yang W, Hayashinaka E, Wada Y, Watanabe Y et al (2018) A voxel-based analysis of neurobiological mechanisms in placebo analgesia in rats. NeuroImage 178:602–612

Zheng MQ, Nabulsi N, Kim SJ, Tomasi G, Lin SF, Mitch C et al (2013) Synthesis and evaluation of 11C-LY2795050 as a kappa-opioid receptor antagonist radiotracer for PET imaging. J Nucl Med 54:455–463

Zheng MQ, Kim SJ, Holden D, Lin SF, Need A, Rash K et al (2014) An improved antagonist radiotracer for the kappa-opioid receptor: synthesis and characterization of (11)C-LY2459989. J Nucl Med 55:1185–1191

Zubieta JK, Gorelick DA, Stauffer R, Ravert HT, Dannals RF, Frost JJ (1996) Increased mu opioid receptor binding detected by PET in cocaine-dependent men is associated with cocaine craving. Nat Med 2:1225–1229

Zubieta JK, Dannals RF, Frost JJ (1999) Gender and age influences on human brain mu-opioid receptor binding measured by PET. Am J Psychiatry 156:842–848

Zubieta J, Greenwald MK, Lombardi U, Woods JH, Kilbourn MR, Jewett DM et al (2000) Buprenorphine-induced changes in mu-opioid receptor availability in male heroin-dependent volunteers: a preliminary study. Neuropsychopharmacology 23:326–334

Zubieta JK, Smith YR, Bueller JA, Xu Y, Kilbourn MR, Jewett DM et al (2001) Regional mu opioid receptor regulation of sensory and affective dimensions of pain. Science 293:311–315

Zubieta JK, Smith YR, Bueller JA, Xu Y, Kilbourn MR, Jewett DM et al (2002) mu-opioid receptor-mediated antinociceptive responses differ in men and women. J Neurosci 22:5100–5107

Zubieta JK, Ketter TA, Bueller JA, Xu Y, Kilbourn MR, Young EA et al (2003) Regulation of human affective responses by anterior cingulate and limbic mu-opioid neurotransmission. Arch Gen Psychiatry 60:1145–1153

A. van Waarde
Department of Nuclear Medicine and Molecular Imaging, University of Groningen, University Medical Center Groningen, Groningen, The Netherlands

Abstract

The function of ATP-binding cassette (ABC) transporters at the blood-brain barrier (BBB) is to protect the brain from toxic compounds. Additionally, they play a crucial role in the onset and progression of several central nervous system (CNS) diseases as well as in drug resistance. Many compounds were identified as substrates, inhibitors, inducers, or activators for ABC transporters, causing important drug-drug interactions. PET imaging represents an excellent tool for assessing the function and expression of ABC transporters. Over the last years, many PET tracers with different characteristics have been developed, mainly for measuring P-glycoprotein (P-gp) function at the BBB. Although (R)-[11C]verapamil or [11C]N-desmethyl-loperamide are considered as the "gold standard" P-gp tracers, they have several drawbacks such as its high affinity to P-gp which limits its use for assessing P-gp increased function. Therefore, PET tracers with lower affinity to the transporter have been developed and studied in different species. The assessment of ABC transporters by PET imaging can provide new insight into the physiology and pathophysiology of different CNS diseases and may open new avenues for therapies. Moreover, PET can be used for screening the affinity of new entities toward various ABC transporters and thus enhance the development of CNS drugs.

22.1 ABC Transporter Expression at the Blood-Brain Barrier in Neurological Diseases

22.1.1 Blood-Brain Barrier

The function of the human brain requires a strictly controlled environment. The blood-brain barrier (BBB) plays an important role in maintaining homeostasis of this micro-environment by protecting the brain from neurotoxic substances since it functions as a biochemical and physical barrier (Hawkins and Davis 2005). This barrier was first described by Paul Ehrlich, who found that trypan blue injections in the peripheral blood circulation did not reach the spinal cord and brain in rabbits (Templeton et al. 1997). Nowadays, we know the BBB consists of a monolayer of non-fenestrated brain microvessel endothelial cells connected by tight junctions, which limits transport by passive diffusion across the BBB. Only small lipophilic molecules and drugs with molecular weights less than 400 Da and less than eight hydrogen bonds can cross the barrier by passive diffusion (Morris et al. 2017).

For compounds that cannot enter the brain by passive diffusion due to their ionization, hydrophilicity, or size, membrane transporters at the endothelial cells can facilitate the transport across the BBB (Zhao et al. 2015). Apart from the limited transport by passive diffusion, the BBB also presents numerous efflux transporters that carry a wide variety of molecules from the brain to the blood. The best-known efflux transporters are the ATP-binding cassette transporters (ABC transporters). These transporters play an important role in protecting the central nervous system (CNS). In this chapter, we will focus on the ABC transporters, with a particular emphasis on P-glycoprotein and its involvement in several neurological disorders, such as Alzheimer's disease, Parkinson's disease, and epilepsy.

22.1.2 ABC Transporters

The ABC transporter superfamily represents the largest family of transmembrane proteins and consists of about 50 members classified into 7 different subfamilies. These transporters are ATP-dependent and use this energy to drive the transport of various endogenous and exogenous molecules across cell membranes (Dean and Allikmets 2001; Dean et al. 2001). They play a significant role in various CNS disorders and their pharmaceutical treatments in two different ways: First, many pharmaceuticals used as therapeutic drugs in CNS diseases are substrates of ABC transporters, which limits their access to the brain; and second, the expression and function of ABC transporters may be altered in certain CNS diseases, either as a cause or a consequence of the disease, resulting in altered drug entry in the CNS (see Table 22.1).

P-gp, also known as ABCB1, was the first ABC transporter described and has by far been the most studied. This transporter is found at the luminal side of the endothelial cells at the BBB and acts as an efflux transporter for various structurally

Table 22.1 CNS diseases involving impairments in ABC transporters

CNS disease	ABC transporter involved	The main change in ABC transporters activity	References
Alzheimer's disease	ABCA1, ABCA2, ABCB1, ABCG2	Decreased P-gp, BCRP, and MRP1 expression and function	Wolf et al. (2012), Macé et al. (2005), Xiong et al. (2009), Lam et al. (2001), Krohn et al. (2011), Kuhnke et al. (2007), Riddell et al. (2007))
Parkinson's disease	ABCB1	Decreased P-gp expression and function	Kortekaas et al. (2005), Westerlund et al. (2008), Zschiedrich et al. (2009), Liu et al. (2013)
Epilepsy	ABCC1, ABCCs, ABCG2	Increased P-gp, BCRP, MRP1, and MRP2 expression and function	Löscher and Potschka (2005a), Wang et al. (2016), Summers et al. (2004), Löscher and Potschka (2005b), Hartz et al. (2017), van Vliet et al. (2005), Syvänen et al. (2013), Feldmann and Koepp (2012), Aronica et al. (2012)
Brain tumors	ABCA1, ABCB1, ABCC1, ACC4, ABCG2	Increased P-gp, BCRP, and MRP1 function and expression	Haber et al. (2006), Agarwal et al. (2011), Porro et al. (2010), Parrish et al. (2015), Liu et al. (2015), Deeken and Loscher (2007), Sane et al. (2014)
Ischemic stroke	ABCB1, ABCG2, ABCC1, ABCC5	Increased P-gp, BCRP, and MRP1 expression	ElAli and Hermann (2010), Kilic et al. (2008), Dazert et al. (2006), Ueno et al. (2009)
Multiple sclerosis	ABCB1, ABCD3, ABCG2	Decreased P-gp expression	Kooij et al. (2011), Kooij et al. (2010), Gray et al. (2014)
Amyotrophic lateral sclerosis	ABCB1, ABCG2	Increased P-gp and BCRP activity	Milane et al. (2010), Jablonski et al. (2012, 2014)
HIV-encephalitis	ABCB1, ABCC1, BCC4, BCC5, ABCG2	Increased BCRP and MRP1 expression	Robillard et al. (2014), Hayashi et al. (2005)
Lysosomal storage diseases	ABCC4	Increased MRP4 function	Schaheen (2006)
Depression	ABCB1	Increased P-gp function	de Klerk et al. (2009), Brzozowska et al. (2017)
Schizophrenia	ABCB1	Decreased P-gp expression	Bernstein et al. (2016)
Creutzfeldt-Jakob disease	ABCB1	Decreased P-gp expression	Vogelgesang et al. (2006)

different substrates (see Table 22.2). Besides P-glycoprotein, other ABC transporters with a similar function exist. ABCG2 (or breast cancer resistance protein BCRP), ABCC1 (or multidrug resistance protein MRP1), ABCC4, and ABCC5 are also localized at the luminal side of the human brain capillary endothelial cells of the

Table 22.2 Examples of drugs that act as substrates of P-gp, BRCP, and MRP1 transporters (updated from (Mahringer and Fricker 2016; Qosa et al. 1628))

ABC transporter	Drug class	Substrates drugs
P-gp	Cytostatic	Vinblastine, vincristine, doxorubicin, paclitaxel, methotrexate
	Immunosuppressant	Cyclosporine A, tacrolimus
	Corticoids	Dexamethasone, aldosterone, cortisol
	Analgesics	Morphine, methadone, fentanyl
	Antiretroviral HIV	Ritonavir, indinavir
	Anthelminthic	Ivermectin
	Antidiarrheal	Loperamide
	Antiemetic	ondansetron
	Antibiotic	Erythromycin, tetracyclines, rifampicin
	Antiarrhythmic	Amiodarone
	Cardiac glycoside	Digoxin
	Calcium channel blocker	Verapamil, nifedipine, diltiazem
	Beta-blocker	Propranolol
	Statin	Lovastatin, simvastatin
	Antiepileptic	Phenytoin, carbamazepine, phenobarbital
	Antipsychotic	Chlorpromazine
	Antidepressant	Paroxetine, amitriptyline, venlafaxine
BCRP	Cytostatic	Anthracyclines, mitoxantrone, etoposide, erlotinib, gefitinib
	Antiretroviral HIV	Zidovudine, lamivudine
	Antibiotics	Ciprofloxacin, norfloxacin
	Immunosuppressant	Cyclosporine A, tacrolimus
MRP1	Cytostatic	Etoposide, vincristine, doxorubicin, methotrexate
	Immunosuppressant	Tacrolimus, cyclosporine A
	Antiretroviral HIV	Saquinavir, ritonavir
	Antiepileptic	Levetiracetam, phenobarbital
	Antibiotic	Azithromycin, ciprofloxacin

BBB (see Fig. 22.1). ABCC6, ABCC11, and ABCC12 are also present in the microvasculature of the brain, albeit at lower expression levels (Dauchy et al. 2008).

22.1.3 P-Glycoprotein

P-glycoprotein (P-gp) or ABCB1, encoded by the MDR1 gene, was the first ABC transporter discovered and remains the most studied one. This 170 kDa membrane protein is located between the cytoplasm and the periplasm and consists of a single chain with two homologous parts. At the intracellular side of the two homologous parts, six transmembrane (TM) helices and two ATP nucleotide-binding domains (NBDs) are present. During the efflux of a substrate, translational and rotational

Fig. 22.1 ABC transporters in the human endothelial cell at the BBB update from (Mahringer and Fricker 2016; Liu 2019)
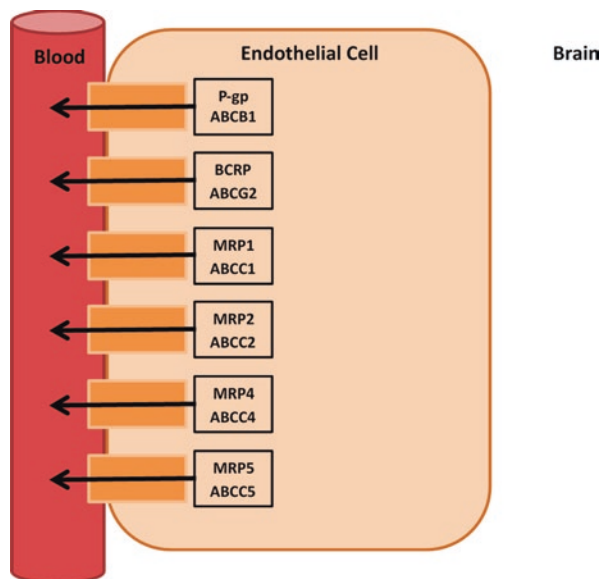
motions in P-gp take place: ATP causes a change in the TM helix, which will cata-
lyze the efflux of the P-gp substrate through the transmembrane domain (TMD) and
lipid bilayer.

P-gp is involved in the efflux of a broad range of structurally different substrates
including analgesics, antihistamines, and antibiotics and is therefore thought to play
an important role in drug resistance (Tamaki et al. 2011) (see Table 22.2). Besides
the efflux of many pharmaceuticals, P-gp transports also endogenous compounds
such as amyloid-β and, therefore, may play an important role in the pathophysiol-
ogy of Alzheimer's disease.

22.1.4 BCRP

BCRP is encoded by the ABCG2 gene located on chromosome 4q22. This trans-
porter was first discovered in 1998 by Doyle and colleagues in a multidrug-resis-
tant human breast cancer cell line (Doyle et al. 1998). BCRP consists of a polytopic
TM protein with 655 amino acids. It differs from P-gp in its structure since it is a
half ABC transporter, consisting of only one NBD and one membrane-spanning
domain (MSD) (Ni et al. 2010). BCRP is responsible for the efflux of more than
200 different substrates, including chemotherapeutics, tyrosine kinase inhibitors,
antivirals, carcinogens (see Table 22.2) and also physiological substances, such as
uric acid and estrone-3-sulfate. This makes BCRP one of the most important efflux
transporters at the BBB. Although the substrate and inhibitor specificity of BCRP
show some overlap with P-gp and MDR1, they are not completely identical, as can
be explained by the different protein structures and working mechanisms (Mao and
Unadkat 2015).

22.1.4.1 MRP Family and MRP1

Besides P-gp and BCRP, members of the multidrug resistance protein (MRP) family are efflux transporters at the BBB. The transporters in this family are less studied and characterized than P-gp and BCRP, and their function at the BBB is less clear, although it is known that the MRP family is responsible for the efflux of a diverse range of compounds including xenobiotics and endogenous substrates. Subfamily ABCC, which expresses the MRP transporters, contains 12 proteins, and 9 of these are known to be involved in ATP-dependent transmembrane efflux of drugs in various cells and tissue types in the human body. Proteins in the MRP subfamily share common structural features including multiple TM helices in MSDs and NBDs at the intracellular side for the binding of ATP. MRP1, MRP2, MRP3, MRP6, and MRP7 have an additional NH_2-proximal MSD, and therefore they are called the "long MRPs" (Haimeur et al. 2004). The first of the nine drug-transporting MRPs is MRP1, which is encoded by the ABCC1 gene on chromosome 16p13.1 and is the most studied and best-known MRP family member. It was discovered by Cole et al. in 1992 as a cause of multidrug resistance in a drug-selected human lung cancer cell line (Cole et al. 1992) and it is because of this broad substrate specificity (Table 22.2) that MRP1 continues to be of considerable interest in preclinical and clinical studies.

22.1.4.2 Alzheimer's Disease

The incidence of neurodegenerative diseases has increased significantly over the past few decades because the life expectancy of the human population has increased. In 1906 Alzheimer's disease was first described by Alois Alzheimer as a particularly severe disease process of the cerebral cortex (Alzheimer 1906; Hippius and Neundörfer 2003). Clinically Alzheimer's disease is characterized by a decline in memory, language, and cognitive skills, which affects the patient's ability to perform everyday activities (Ballard et al. 2011). Alzheimer's disease is an irreversible and incurable condition. The underlying cause of these symptoms can be found in the destruction of neurons in brain regions involved in the cognitive function. Although the exact pathogenesis of Alzheimer's remains unclear, hallmarks of AD are the accumulation of neurotoxic amyloid-β (Aβ) plaques in the extracellular compartment of the brain, inflammation, accumulation of hyper phosphorylated tau in intracellular neurofibrillary tangles and neuronal loss (Zlokovic 2011). The amyloid hypothesis suggests that this accumulation of Aβ is caused by an imbalance of overproduction and impaired clearance, and this may be the key element triggering neuronal degeneration (Hardy and Allsop 1991). Although no significant association was found between ABCB1 polymorphisms and the risk of developing AD in humans, P-gp is thought to play an important role in the pathophysiology of AD since this efflux transporter facilitates transport of Aβ out of the brain (Vogelgesang and Jedlitschky 2014; Cirrito et al. 2005). Various studies have reported an inverse correlation between Aβ deposition and cerebrovascular ABCB1 expression (Pereira et al. 2017; Zhao et al. 2017).

22.1.4.3 Parkinson's Disease

Parkinson's disease (PD) is a neurodegenerative disorder characterized by clinical symptoms of uncontrolled movement and in a later stage by dementia. The symptoms of this disease are caused by the death of dopamine generating cells in the substantia nigra. The reason for this cell death is unknown, although it is known that exposure to neurotoxic pesticides is a risk factor for the development of PD (Steece-Collier et al. 2002; Wirdefeldt et al. 2011; Pezzoli and Cereda 2013). Pesticides are a group of compounds with various mechanisms of action and pharmacokinetic properties, including fungicides, herbicides, and insecticides. In epidemiologic studies in humans, toxicity models in animals, and in vitro studies, exposure to pesticides was shown to be associated with an increased risk of the development of PD. An alteration of the BBB transport of such neurotoxic pesticides has been proposed as an underlying pathophysiological mechanism that may lead to PD. Since P-gp has an extensive range of substrates, P-gp may be involved in the removal of neurotoxic pesticides out of the brain. However, it is still unknown if P-gp is truly involved in this transport, although multiple studies did investigate the association between ABCB1 and PD. In only a few studies, an association between ABCB1 alterations and Parkinson's disease was found, especially in later stages of the disease (Droździk et al. 2003; Marzolini et al. 2004; Westerlund et al. 2009; Bartels et al. 2008a, b).

22.1.4.4 Epilepsy and Antiepileptic Drugs

Epilepsy is known as a serious neurological disorder characterized by unpredictable seizures. Epilepsy is affecting more than 60 million people worldwide. Intractable epilepsy (IE), in which a patient's seizures fail to come under control with pharmacotherapeutics, is a severe form of epilepsy, occurring in 20–30% of patients diagnosed with epilepsy. The underlying mechanisms of IE are not fully clear, although there are several explanations found in the literature. One of these focuses on overexpression of P-gp transporters, MDR transporters, and other efflux transporters at the BBB in the cerebrovascular endothelium around the epileptic focus in the brain (Wang et al. 2016; Feldmann et al. 2013). However, it is not clear whether this upregulation of P-gp is caused by epilepsy, by uncontrolled recurrent seizures, by drug-associated induction of efflux transporters, by genetic polymorphisms, or by a combination of all of these factors (Tang et al. 2017).

22.1.4.5 Ischemic Stroke

During ischemic stroke, the blood flow is locally disrupted leading to deprivation of brain tissue from oxygen and glucose. Subsequently, a lack of sufficient oxygen activates hypoxia-inducible factor 1-alpha (HIF-1α) and nuclear factor κB, leading to a time-dependent increase in P-gp expression (Wang et al. 1995; Koong et al. 1994; Cen et al. 2013). This increase is thought to be an attempt of the ischemic brain to maintain a functional barrier between the blood and the brain when the BBB is compromised (Spudich et al. 2006; Lazarowski et al. 2007). However, an increase in P-gp function might cause a reduced uptake of therapeutic drugs in the brain after ischemic stroke.

22.1.4.6 Aging

Since aging is the most important risk factor for the development of AD, and P-gp is a known efflux transporter of Aβ, there is an increasing interest in the function of P-gp in normal aging and Alzheimer's disease. Aβ transport at the BBB is significantly altered with increasing age. In 2002, Vogelgesang et al. studied brain tissue samples of 243 non-demented subjects and found there was an age-related decrease in P-gp in association with an increase of amyloid deposition (Vogelgesang et al. 2002a). A later PET study with the tracer (R)-[11C]verapamil also reported a decrease of P-gp function with increasing aging (Bauer et al. 2009). Chiu et al. showed a trend of reduced P-gp function with advancing age and also a significant reduction in P-gp function in Alzheimer's disease patients compared with healthy elderly controls (Chiu et al. 2015). Amyloid transporter gene expression is age-dependent, which may result in changes in protein expression at the BBB (Osgood et al. 2017). Besides a reduction in P-gp function, a reduction in lipoprotein receptor-related protein 1 (LRP-1) efflux transporter function and an increase in the function of receptors for advanced glycation end products (RAGE) were found in animal studies. The latter changes may result in an increased influx of Aβ into the brain (Church et al. 2014).

22.1.4.7 Polymorphism, Genotyping, and Individualized Medicine

The ABCB1 gene, which codes for P-gp, displays more than 50 single nucleotide polymorphisms (SNPs) (Sharom 2008). Variability in pharmacogenes can influence the metabolism, transport, and elimination of drugs. This makes the variability in pharmacogenes an interesting field of research since it may alter the response of patients to specific pharmaceuticals. Different forms of such genes may be associated with interindividual variations in drug efficacy or the severity of unwanted side effects. Pharmacogenetic data is also of great value in the prediction of neurological diseases. Since ABC transporters influence the uptake of many CNS pharmaceuticals, the question arises whether polymorphisms may predict therapy outcome. The hypothesis that variation in the ABCB1 gene is associated with antidepressant treatment outcome has been tested in various clinical studies, and the results were inconclusive. In a meta-analysis of 16 studies in which the association between ABCB1 polymorphisms and antidepressant treatment outcome was analyzed, Breitenstein et al. found that SNP rs2032583 and rs2235015 have a significant influence on treatment outcome and could possibly be used as predictors of treatment outcome in depression (Breitenstein et al. 2015). However, despite the extensive number of studies performed, no unambiguous answer to the question of the predictive value of ABCB1 polymorphisms was reached. Multiple studies have found an association between MDR1 C3435T polymorphism and antiepileptic drug resistance (Wang 2015; Keangpraphun et al. 2015).

22.1.4.8 Drug Resistance and ABC Transporters

Pharmaceuticals can cross the BBB and enter the brain via six major pathways: paracellular transport, passive transcellular diffusion, carrier-mediated transport, receptor-mediated transcytosis, adsorptive-mediated transcytosis, and cell-mediated transport. In various diseases including CNS disorders, oncologic diseases,

and infectious diseases, the effect of treatment is limited because of drug resistance. A prerequisite for adequate distribution of the drug to its target is adequate transport between various tissues and compartments. Distribution of drugs to the brain is dependent on both the properties of the BBB and the properties of the drug (Yamamoto et al. 2018; Elsinga et al. 2004). An efflux transporter as P-glycoprotein can have a great impact on the distribution of various drugs and is thought to be responsible for drug resistance in cancer, epilepsy, Alzheimer's disease, and schizophrenia (Bartels 2011; Loscher et al. 2012; Rosenhagen and Uhr 2011). Drug resistance may be due to two underlying causes: First, the drugs used in the treatment of those diseases are substrates of ABC transporters and second, the expression of the ABC transporters involved in drug efflux can be altered by the disease itself. Studies in the field of drug resistance have led to important new developments, such as specific transport inhibitors, specific antibodies for the transporters, and new in vivo imaging techniques (e.g., novel PET tracers). However, drug resistance is still a major therapeutic obstacle, and further studies are required.

22.2   Mechanism of Action of ABC Transporter-Binding Substances

Typically, the ABC transporters consist of a pair of NBDs, present on the membrane side in contact with the cytoplasm and two TMDs. There exist ABC transporters with a different number of TMDs and NBDs. The NBDs are responsible for the ATP binding and hydrolysis, and thus they provide the energy for the active transport of substances. The TMDs are the substrate-binding site which contributes to the transport specificity (Linton and Higgins 2007).

It was initially thought that the P-gp transporter possessed two binding sites (Shapiro and Ling 1997). Then, a third ligand-binding site was discovered (Shapiro et al. 2001). And later on, Martin et al. suggested that the P-gp transporter contained four ligand-binding sites (Martin et al. 2000). Sites I, II, and III work as transport sites because they interact with substrates (such as paclitaxel, vinblastine) and modulators (tariquidar). Site IV, on the other hand, acts as a regulatory site. Since a wide number of compounds can also interact with BCRP and MRP1, these transporters may also have several ligand-binding sites similar to the P-gp transporter (Gameiro et al. 2017; Colabufo et al. 2010).

The compounds that interact with the ABC transporters can behave as substrates, inhibitors, inducers, or activators. Substrates are pumped out of the cell in an ATP-dependent manner, inhibitors reduce the ABC transporter function, inducers increase the transporter expression, and activators enhance the transporter function. Notice that one compound can have different modes of action (depending on the administered dose): drugs that are P-gp substrates can also act as P-gp inhibitors or inducers (Zhou 2008). It is important to mention that induction and activation are not always related. A compound can increase the expression level of the transporter but not increase its functionality and vice versa (Gameiro et al. 2017).

Different hypotheses try to explain how inhibitors interfere with the transporter. The inhibitor may act by blocking the ligand-binding site, by preventing the ATP hydrolysis or by modifying the integrity of the lipid membrane. There are different types of inhibitors, classified by their potency and selectivity (Silva et al. 2015). Some P-gp inhibitors are used as therapeutic agents and are co-administrated with chemotherapeutic agents or antiepileptic drugs to overcome drug resistance in cancer or epilepsy (Zhou 2008).

An inducer promotes upregulation of the protein expression (Gameiro et al. 2017). Many structurally unrelated compounds have been reported as P-gp inducers such as abacavir, aldosterone, hypericin, morphine, and rifampicin (Silva et al. 2015). Numerous routes can regulate the transcription of the MDR1 (ABCB1) gene, which highlights the ability of P-gp to respond to a wide variety of stimuli. Upregulation of the MDR1 gene depends on different transcription factors (pregnane X receptor (PXR), heat-shock transcription factor 1 (HSF-1), nuclear factor Y (NF-Y), and early growth response protein 1 (EGR-1)) that do not bind directly to P-gp (Silva et al. 2015). The nuclear factor PXR can be activated by diverse compounds such as rifampicin, phenobarbital, and mifepristone. PXR upregulates the MDR1 expression, which subsequently leads to an increased expression of P-gp (Zhou 2008; Miller et al. 2008).

Activators bind to the protein and induce a conformational change that enhances the transport of other substrates bound to a different ligand-binding site (Gameiro et al. 2017). These compounds increase the P-gp function without increasing the protein expression. Therefore, activators induce the P-gp function as long as they are present. This is a more rapid mechanism than the action of P-gp inducers (Silva et al. 2015).

Since many compounds can modify the function of the ABC transporters (in particular P-gp and BCRP), the Food and Drug Administration (FDA) and the European Medicine Agency (EMA) developed guidelines for the screening of drugs that cause transporter-mediated drug-drug interactions (DDI) (Colabufo et al. 2010; Clinical Drug Interaction Studies — Study Design, Data Analysis, and Clinical Implications Guidance for Industry 2017; Guideline on the Investigation of Drug Interactions 2012). Concomitant administration of drugs that can interfere with ABC transporters may cause alterations of drug concentrations and, therefore, may lead to decreases in drug efficacy or to toxicity. Appropriate measures should be taken to prevent the clinical implications of transport-mediated DDI. Treatment effects should be monitored, administered dose should be adjusted if necessary, and alternative therapies may have to be sought (Lund et al. 2017).

22.3 Use of P-gp Modulators to Treat Drug Resistance, Neurological Disorders, and Other Conditions

Since P-gp dysfunctions are encountered in many different diseases of the CNS, P-gp modulators may restore the proper function and may improve the disease condition.

22.3.1 P-gp Inhibitors and Drug Resistance

Resistance to drug treatment is a common clinical issue in cancer and infectious diseases, and it also occurs in rheumatoid arthritis, epilepsy, depression, and other psychiatric disorders. The role of P-gp and other ABC transporters in drug resistance has gained increasing attention (Löscher and Potschka 2005c).

P-gp inhibitors have been developed and used to overcome drug resistance in a wide variety of diseases. P-gp inhibitors can be classified into four generations (Silva et al. 2015; Li et al. 2016): The first generation of P-gp inhibitors includes verapamil and cyclosporine A. These inhibitors are characterized by their low therapeutic response and high toxicity (cardiovascular toxicity). The second generation (e.g., valspodar) was developed in order to achieve higher potency and reduced toxicity. However, these compounds also inhibit cytochrome P450, and many DDIs were encountered when the inhibitors were co-administrated with chemotherapeutic agents. Thus, a third generation of P-gp inhibitors was developed. These compounds were 200-fold more potent than the first and second generation of inhibitors (Li et al. 2016). Some of these inhibitors (e.g., tariquidar) were evaluated in clinical trials (Li et al. 2016; Fox and Bates 2007). Recently, natural substances have been proposed to reverse drug resistance. These compounds, which represent the fourth generation of P-gp inhibitors (Silva et al. 2015), are obtained from different natural sources. They include alkaloids, flavonoids, coumarins, resins, etc. and are characterized by low cytotoxicity and increased oral bioavailability (Li et al. 2016; Dewanjee et al. 2017).

In cancer drug resistance, it has been suggested that the overexpression of efflux transporters in tumors reduces the drug concentration in the target tissue and consequently limits the treatment efficacy (Juliano and Ling 1976; Fletcher et al. 2016). P-gp, MRP1, and BCRP are the most relevant efflux transporters related to drug resistance. A wide variety of anticancer drugs such as vinca alkaloids (vincristine), taxanes (docetaxel and paclitaxel), anthracyclines (doxorubicin), topoisomerase inhibitors such as topotecan, and tyrosine kinase inhibitors (gefitinib) are substrates of the P-gp transporter (Waghray and Zhang 2018).

To date, clinical trials with P-gp inhibitors in combination with anticancer drugs were unsuccessful. Several causes may explain the failures. First, the low affinity of early-generation inhibitors required the use of high drug doses which led to severe side effects and toxicity. Moreover, the concomitant administration of P-gp inhibitors and anticancer drugs reduces the metabolism and excretion of the chemotherapeutic agents and increases their concentration in plasma (Waghray and Zhang 2018). Contradictory conclusions were obtained with regard to tariquidar. Some studies identified tariquidar as a P-gp inhibitor and P-gp substrate depending on the used dose. Others reported that tariquidar can also act as a BCRP inhibitor and substrate (Kannan et al. 2011a). The structure of the binding pocket of the P-gp transporter is not well-known, which precludes the development of potent and highly specific P-gp inhibitors (Waghray and Zhang 2018).

The P-gp transporter located at the BBB also decreases the concentration of numerous unrelated drugs in the CNS. For instance, it has been shown that

antiepileptic drugs such as phenytoin, carbamazepine, phenobarbital, lamotrigine, and gabapentin are substrates of P-gp (Wang et al. 2016). Therefore, it has been suggested that P-gp plays an important role in drug-resistant epilepsy or IE (Wang et al. 2016; Schmidt and Schachter 2014). Many scientific publications support the role of P-gp in drug-resistant epilepsy. Preclinical studies have found that phenobarbital-resistant rats showed higher P-gp expression levels at the BBB than phenobarbital responsive rats (Volk and Löscher 2005). Moreover, chronic administration of phenobarbital caused a reduction of phenobarbital concentration in the hippocampus and an increase of P-gp expression (Yang et al. 2008). Despite the unsuccessful strategy of using P-gp inhibitors to overcome cancer drug resistance, it has been proposed that the co-administration of P-gp inhibitors and antiepileptic drugs could restore the antiepileptic efficacy. In support of this idea, the administration of tariquidar together with phenobarbital to phenobarbital-resistant rats counteracted the phenobarbital resistance (Brandt et al. 2006). Moreover, the co-administration of verapamil and carbamazepine to patients with IE improved the efficacy of the antiepileptic drug (Summers et al. 2004). Therefore, modulation of the P-gp function using P-gp inhibitors may be a new approach to overcome drug resistance in epilepsy.

The use of P-gp inhibitors in treatment-resistant depression has also been suggested. Around 60% of patients with depression do not show a satisfactory response to their medication and again the P-gp transporter may play a role in limiting the brain penetration of the applied antidepressant drugs (O'Brien et al. 2012). In vivo studies performed in mice demonstrated that co-administration of the P-gp inhibitor verapamil and the antidepressant escitalopram for 22 days increased the brain concentration of the antidepressant (O'Brien et al. 2015). However, further studies are needed to elucidate the relationship between P-gp function and treatment-resistant depression.

New strategies to overcome drug resistance in cancer and other pathologies have been explored such as the development of drugs that do not show affinity to the ABC transporters and the use of advanced delivery systems such as liposomes or gold nanoparticles as well as the use of antibody-drug conjugates. These new approaches aim to bypass the P-gp efflux action, to target the drug delivery to a specific tissue, and to reduce the toxic side effects of the drug (Löscher and Potschka 2005c; Li et al. 2016; Waghray and Zhang 2018).

22.3.2 P-gp Inducers and Activators to Treat Neurodegenerative Disease and Intoxications

P-gp inducers and activators (such as St. John's wort (*Hypericum perforatum*), dexamethasone, vinblastine, and rifampicin (Silva et al. 2015)) increase P-gp function and/or expression, and they may be used to reduce the brain penetration of harmful substances (Gameiro et al. 2017). The use of P-gp inducers or activators can be important in the treatment of intoxications (Silva et al. 2014; Dinis-Oliveira et al. 2006). For instance, the administration of dexamethasone to paraquat-exposed

rats decreased paraquat accumulation in the lungs and reduced the lung damage (Dinis-Oliveira et al. 2006).

Another potential use of inducers and activators was suggested by Haslam et al. based on the finding that the upregulation of ABC transporters in the hair follicle prevents alopecia induced by chemotherapy. This strategy may reduce hair loss in cancer patients (Haslam et al. 2013, 2015).

Additionally, inducers have been proposed as a potential treatment for Alzheimer's and Parkinson's disease. In the case of Alzheimer's disease, Aβ has been identified as a substrate of the P-gp transporter (Lam et al. 2001). Vogelgesang et al. found an inverse correlation between the deposition of Aβ in the brain of elderly humans and the P-gp expression in endothelial cells of the cerebral vasculature (Vogelgesang et al. 2002b). Recent research also highlighted the relationship between the MDR1 gene, which is encoding P-gp, and the risk of developing Parkinson's disease (Droździk et al. 2003). It has been suggested that repeated contact with pesticides is associated with the development of Parkinson's disease in patients carrying a c3435T polymorphism of the MDR1 gene (Kortekaas et al. 2005; Lai et al. 2002; Kamel and Hoppin 2004). Furthermore, PET studies have indicated that the P-gp function is decreased in Alzheimer's and Parkinson's disease (Kortekaas et al. 2005; van Assema et al. 2012); thus the use of P-gp inducers may help to treat the disease.

Some preclinical studies have already demonstrated that P-gp inducers such as pregnenolone-16α-carbonitrile can restore the P-gp function at the BBB and reduce the Aβ deposition in the brain (Hartz et al. 2010). Similar results were obtained in mice models of Alzheimer's disease after treatment with St. John's wort. Animals receiving St. John's wort showed a reduction of Aβ accumulation and an increase in the cerebrovascular expression of P-gp (Brenn et al. 2014).

Many efforts have been made to find new molecules able to induce or activate the P-gp function, which could be applied to treat intoxication or neurodegenerative disease. Recently, MC111 was identified as a promising candidate, due to its capacity to induce P-gp and BCRP expression in SW480 human colon adenocarcinoma cells (Colabufo et al. 2018). In vivo studies using rats and the PET tracer [^{18}F]MC225 are ongoing to confirm these findings.

22.4 PET

Positron-emission tomography (PET) and single-photon emission computed tomography (SPECT) together with magnetic resonance imaging (MRI) and computed tomography (CT) are imaging techniques that allow noninvasive tracking of pathophysiological processes in various neuropsychiatric disorders. Molecular imaging has also been used in various aspects of drug development (Willmann et al. 2008). For an efficient visualization, characterization, and measurement of biological processes at the molecular, cellular, whole organ, or body level, specific imaging probes are needed. These probes are also known as tracers and provide functional information, like the magnitude of regional blood flow, glucose metabolism, or receptor

density which can be presented either as a two- or three-dimensional image. PET is the most sensitive technique for in vivo imaging and quantification of biological and pathophysiological processes. However, the spatial resolution of PET is relatively low, and the additional use of CT or MRI imaging is required to provide high-resolution structural images that can be fused with the functional PET image. PET/CT or PET/MRI scanners provide both anatomical and functional information in a single scanning session.

The decay of radionuclides for PET imaging occurs by the emission of a positively charged particle called positron. When emitted from the nucleus, the positron travels a very short distance (positron range, 3–5 mm) in the surrounding tissue before it annihilates by combining with an electron. The mass of the positron and electron is then converted to energy resulting in two 511 keV γ-photons which are emitted simultaneously at an angle of approximately 180°. The pair of photons is detected by rings of detectors in the PET scanner. The acquisition of a large number of coincident events provides data that can be reconstructed to an image with information on the spatial distribution of radioactivity as a function of time.

Traditionally, PET tracers for imaging of ABC transporters are evaluated using a dual-scan protocol. This protocol involves a baseline PET scan where the efflux transporters are working adequately and an after-treatment scan where the function of these transporters is either inhibited or induced. An inhibitor is usually used for the challenge, which will reduce the transporter function and, therefore, increase the brain uptake of the tracer (Syvänen and Eriksson 2013; Kannan et al. 2009). By contrast, if an inducer is used, the cerebral uptake of the tracer will decrease. Since the majority of the ABC transporter tracers behave as strong transporter substrates, their baseline uptake of radioactivity in the brain is very low; thus measuring decreases of this uptake is complicated. For this reason, inhibitors are commonly used to validate PET tracers for ABC transporters. Once, an appropriate and specific tracer is found, PET imaging allows to assess the function of that particular ABC transporter in the healthy or diseased human brain and to evaluate the impact of treatments on the function of this transporter.

Recently, the introduction of whole-body PET, which allows simultaneous assessment of tracer uptake in all organs and tissues of the human body, has roused interest in studying the connection among different systems that may play a role in a particular disease (Rahmim et al. 2019). Using this technique, it may, for instance, be possible to study the role of the gut-brain axis in CNS diseases. It has been pointed out that the microbiota present in the gastrointestinal tract has an important impact on the brain. The gut flora not only affects the enteric nervous system but also the CNS via neuroendocrine and metabolic pathways (Carabotti et al. 2009). Changes in the microbiota are related to anxiety and depression (Foster and McVey Neufeld 2013). The onset of other brain disorders such as schizophrenia, autism, and Parkinson's disease has also been related to dysfunction of the gut-brain axis (Cherry et al. 2018). Recent publications suggest that the gut microbiota can affect the integrity of the BBB and may contribute to the development or the progression of neurodegenerative diseases (Parker et al. 2019). The microbiome of Alzheimer's disease patients may also cause a reduction of P-glycoprotein expression in the

intestinal epithelial cells (Haran et al. 2019). Dynamic whole-body PET may bring the opportunity to explore and compare the functionality of the P-gp transporters at the BBB and the intestinal tract. This new approach may broaden insight in the gut-brain axis and its implication in the onset of neurodegenerative diseases.

22.5 PET Tracers for Imaging of ABC Transporter Function and Expression in the BBB: Background

The function of the ABC transporters can be assessed by positron-emission tomography. Since PET is a noninvasive technique, it allows studying the same subject at different time points, e.g., before and after treatment, or at different stages of a disease. Moreover, since longitudinal studies can be performed, the number of subjects required to reach statistical significance is reduced (Willmann et al. 2008). Specific tracers should be designed in order to explore the function of ABC transporters.

In 1998, Hendrikse et al. used [^{11}C]verapamil to image the P-gp function for the first time (Hendrikse et al. 1998). Since then, many other compounds have been radiolabeled with carbon-11 or fluorine-18 to explore the function of P-gp and other ABC transporters at the BBB (Saidijam et al. 2018): *(R)*-[^{11}C]verapamil (Luurtsema et al. 2005a), [^{11}C]-*N*-desmethyl-loperamide ([^{11}C]dLop) (Zoghbi et al. 2008), [^{11}C]phenytoin (Verbeek et al. 2012a), [^{18}F]paclitaxel (Hsueh et al. 2006), [^{11}C]laniquidar (Luurtsema et al. 2009), [^{11}C]tariquidar(Bauer et al. 2010), [^{18}F]MC225 (Savolainen et al. 2015), and [^{11}C]metoclopramide (Pottier et al. 2016). Although numerous research studies have been performed with these tracers, none of the tracers was incorporated into the routine medical practice.

The majority of the ABC transporter tracers have been aimed at the imaging of P-gp. Several attempts have been made to develop PET tracers for other ABC transporters, with limited success. Most BCRP and MRP1 substrates proved to show also affinity toward the P-gp transporter. Because of this lack of specificity, the function of a particular transporter cannot be distinguished from the action of other systems (Saidijam et al. 2018; Wanek et al. 2013).

PET studies with "BCRP-selective compounds" did not show differences of uptake in wild-type and BCRP knockout mice or rats (Tournier et al. 2018; Hosten et al. 2013; Mairinger et al. 2010). Since BCRP is the most abundant ABC transporter in the human brain, Wanek et al. designed a protocol for visualizing this transporter at the BBB. The protocol consists of using the dual P-gp/BCRP tracer [^{11}C]tariquidar in combination with cold tariquidar or in P-gp knockout mice. P-gp function is then inhibited or absent, and therefore, the function of BCRP can be assessed (Wanek et al. 2012).

Two PET tracers have been developed for the MRP1 transporter: 6-bromo-7-[^{11}C]methylpurine (Okamura et al. 2009) and 6-bromo-7-(2-[^{18}F]fluoroethyl)purine (Galante et al. 2014). Both are prodrugs that after entering the brain are conjugated with glutathione, and as a result, become substrates for MRP1. In vivo experiments showed significant differences in the brain clearance of both tracers between wild-type and MRP1 knockout mice (Okamura et al. 2009; Galante et al. 2014). Since a relationship between the MRP1 transporter and Aβ clearance from the brain has

been proposed, additional studies were performed in a beta-amyloidosis mouse model (APP/PSI-21) using 6-bromo-7-[^{11}C]methylpurine ([^{11}C]BMP). The study evaluated the MRP1 function in APP/PSI-21 mice and in wild-type mice. The study revealed a significantly higher value of the elimination constant (k_{elim}) after the treatment with the MRP1 inhibitor MK571 in the APP/PSI-21 mice compared to the wild-type mice, which represents an increase of MRP1 expression in the astrocytes. Moreover, Western blot results showed an increase in MRP1 levels which was positively correlated with the induction of the MPR1 activity (Zoufal et al. 2020). This study suggests that [^{11}C]BMP may be used to measure the astrocyte MRP1 function (Zoufal et al. 2020). Unfortunately, species differences in the expression levels of MRP1 hamper the translation of preclinical data to humans (Uchida et al. 2011).

To date, the most commonly used PET tracers for imaging P-gp function at the BBB are *(R)*-[^{11}C]verapamil and [^{11}C]dLop. Although these tracers have been extensively used in small animals and humans, both tracers have some important drawbacks (Wanek et al. 2013). They act as strong substrates of the P-gp transporter which means that the tracers have a high affinity for the transporter protein. Consequently, the tracers are pumped out from the brain to the blood with very high efficiency and low uptake of the tracer is observed at baseline conditions, when the transporter is fully functional (Langer 2016; Luurtsema et al. 2016). Due to the low uptake at baseline, these PET tracers are not able to measure increases in the P-gp function as occur in drug-resistant epilepsy (Wang et al. 2016). However, *(R)*-[^{11}C]verapamil and [^{11}C]dLop can detect decreases in the P-gp function. Such decreases will result in higher uptake of radioactivity in the brain. Thus, these tracers can be used to study diseases characterized by a decline in P-gp function, such as Alzheimer's disease (van Assema and van Berckel 2016).

Another important disadvantage of *(R)*-[^{11}C]verapamil is its extensive in vivo metabolism resulting in the formation of radioactive metabolites (dealkylation fragments and polar metabolites) that can cross the BBB. Some of these metabolites are also P-gp substrates (Luurtsema et al. 2005b). A PET study radiolabeled the main metabolite of *(R)*-[^{11}C]verapamil, called D617 (Verbeek et al. 2012b). This study evaluated the kinetics of [^{11}C]D617 to investigate whether the kinetics of *(R)*-[^{11}C]verapamil and [^{11}C]D617 are similar, and [^{11}C]D617 can be used as an alternative tracer to measure the P-gp function (Verbeek et al. 2012b). However, although the kinetics of [^{11}C]D617 were comparable to that of *(R)*-[^{11}C]verapamil at baseline, the increase of the brain uptake of [^{11}C]D617 after P-gp inhibition was lower. A similar approach was more successful in the case of loperamide. [^{11}C]dLop which is the main metabolite of [^{11}C]loperamide became the preferred P-gp tracer, as its imaging data were more easily interpreted than those of the parent compound (Lazarova et al. 2008).

In the case of *(R)*-[^{11}C]verapamil, the presence of radioactive metabolites can lead to quantification errors. Even though the radioactivity in blood samples can be corrected for the metabolite fraction, the radioactivity in tissue cannot be corrected, and metabolites will contribute to the tissue signal (Wanek et al. 2013; Tournier et al. 2018). This issue can be solved by using short PET acquisition times because metabolism is negligible shortly after radiotracer injection (Muzi et al. 2009).

Radiolabeling with carbon-11 has the disadvantage of a short physical half-life of the radiotracer (20.4 min) and a low spatial resolution of PET images (because of the long-range of the ^{11}C positron ($^+\beta$)). The use of fluorine-18 for radiolabeling allows the distribution of the resulting PET tracer to remote imaging centers and allows using longer scan times because of the longer physical half-life of ^{18}F (109.8 min) (Luurtsema et al. 2016; Raaphorst et al. 2017a).

Since the perfect tracer to measure the P-gp function does not yet exist, new tracers for ABC transporters are needed. Ideal PET tracers should be produced in high overall yields and with high molar activities. They should display a lipophilicity above 2 and below 3.5 to ensure adequate brain penetration and limited nonspecific binding (Pike 2009). Moreover, these molecules should show a high specificity for the desired ABC transporter. They should be slowly metabolized, and their metabolites should not cross the BBB and not be substrates for ABC transporters. The parent tracers should show a moderate affinity to the ABC transporter of interest, resulting in a moderate brain uptake at baseline. They would then be able to measure decreases as well as increases of the transporter function at the BBB. Radiolabeling should be done with fluorine-18, to obtain high-quality images (Kannan et al. 2009; Wanek et al. 2013; Luurtsema et al. 2016).

Many strategies have been explored to overcome a low baseline uptake of radioactivity in the brain. The first approach was to develop PET tracers with greater lipophilicity to enhance their passive diffusion to the brain; however, high lipophilicity may lead to increased nonspecific binding (Syvänen and Eriksson 2013; Toyohara 2016). Next, well-known P-gp inhibitors such as tariquidar, elacridar, and laniquidar were radiolabeled with carbon-11 to obtain radiotracers that would bind to P-gp but not be transported. In theory, this approach would provide a higher brain uptake at baseline and would allow measurement of P-gp expression in the brain. Unfortunately, at low concentrations, these inhibitors were recognized as substrates by P-gp and BCRP at the BBB of rats. Therefore, these tracers were transported out of the brain, resulting in a low baseline uptake. This strategy of inhibitor labeling proved to be unsuccessful (Wanek et al. 2013). A third approach to increase the baseline uptake of PET tracers for P-gp consists of the development of lower avidity substrates. This approach using weak P-gp substrates aimed at higher baseline uptake in the brain which facilitates the measurement of increases in the P-gp function. Several radiotracers have already been identified as weak P-gp substrates and their kinetics are being evaluated (Verbeek et al. 2012a; Pottier et al. 2016; Toyohara et al. 2016; Savolainen et al. 2017a).

Recently, it has been noticed that *(R)*-[^{11}C]verapamil and [^{11}C]dLop possess limited sensitivity to detect small changes in the P-gp function. The brain distribution of *(R)*-[^{11}C]verapamil and [^{11}C]dLop was not significantly increased in heterozygous mice (+/−), which have 50% lower P-gp levels, compared to wild-type mice. These results indicate that the P-gp function should be reduced by more than 50% to effectively limit the entrance of P-gp substrates in the brain (Wanek et al. 2015). The limited sensitivity of the existing PET tracers may be due to their high affinity to the transporter. It has been proposed that PET imaging with weak P-gp substrates may result in higher sensitivity for detecting small variations in the P-gp function, as may occur in several diseases (Langer 2016; Bauer et al. 2019).

22.6 Substrates as Tracers for Measuring P-gp Function

22.6.1 Strong Substrates (Fig. 22.2)

22.6.1.1 [^{11}C]Verapamil

The L-type calcium channel blocker verapamil [2,8-bis(3,4-dimethoxyphenyl)-6-methyl-2-isopropyl-6-azaoctanitrile] is widely used in the treatment of hypertension (McTavish and Sorkin 1989), angina pectoris, and cardiac arrhythmias. Verapamil metabolizes preferentially to norverapamil via *N*-demethylation (Kroemer et al. 1993). After oral administration, the *(S)*-enantiomer of verapamil is
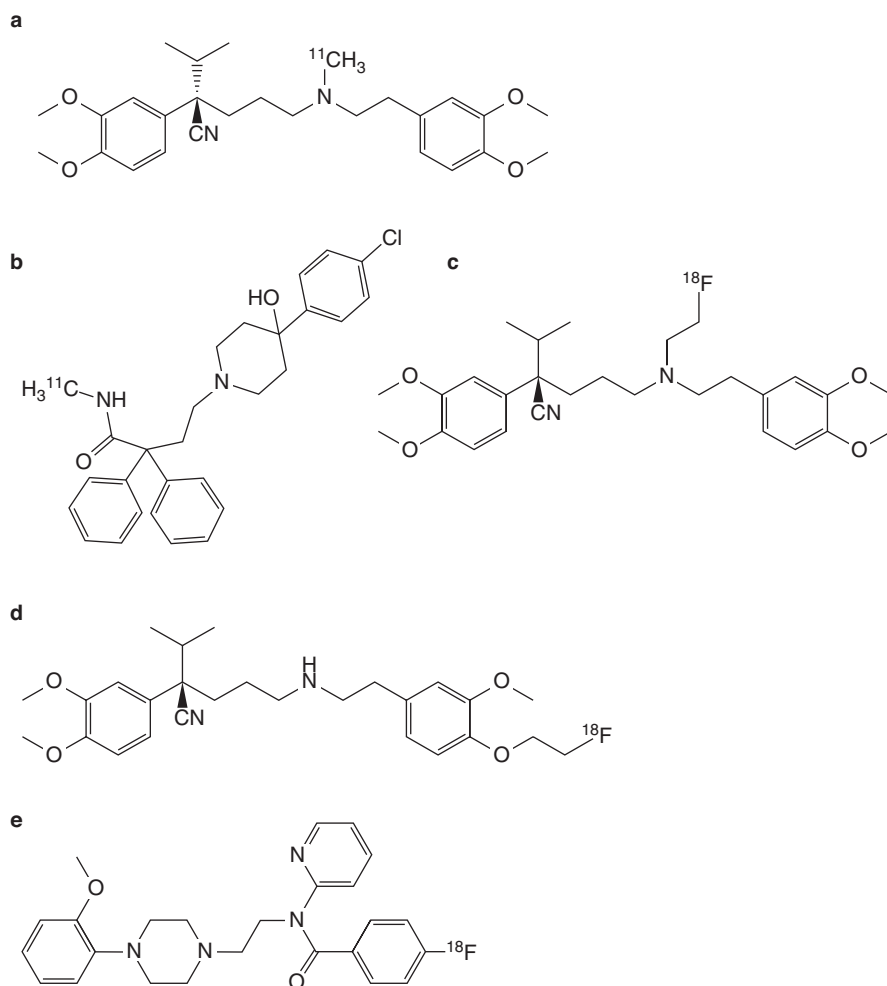
Fig. 22.2 Structures of strong P-gp substrates: *(R)*-[^{11}C]verapamil (**a**), [^{11}C]dLop (**b**), [*(R)-N*-[^{18}F]fluoroethylverapamil (**c**), *(R)*-O-[^{18}F]fluoroethylnorverapamil (**d**), and [^{18}F]MPPF (**e**)

metabolized more actively than *(R)*-verapamil in humans, resulting in a 2.5 times higher concentration of the *(R)*-enantiomer in plasma (Häussermann et al. 1991). *(R)*-verapamil has only 5–10% of the calcium channel blocking activity of the *(S)*-enantiomer. However, the *(R)*-enantiomer is equipotent to racemic verapamil and *(S)*-verapamil in its efficacy to inhibit P-gp. Verapamil is metabolized by cytochrome P450 enzymes, and some of the radioactive metabolites are themselves substrates and inhibitors of P-gp (Pauli-Magnus et al. 2000) In addition, polar radiolabeled metabolites are formed, which result in a non-P-gp-mediated signal (Luurtsema et al. 2005b). Quantification of racemic [¹¹C]verapamil is difficult because the enantiomers have different pharmacokinetic properties (Laberge et al. 2001). Therefore, PET studies need to be performed with an optically pure enantiomer. *(R)*- and *(S)*-[¹¹C]verapamil were prepared from *(R)*- and *(S)*-desmethylverapamil by methylation with no-carrier added [¹¹C]methyl iodide or [¹¹C]methyl triflate (Luurtsema et al. 2002). Although no difference in P-gp-mediated transport selectivity between *(R)*- and *(S)*-verapamil was found (Luurtsema et al. 2003), *(R)*-[¹¹C]verapamil was selected as the most appropriate tracer for measuring P-gp function with PET because the *(R)*-enantiomer was less metabolized in humans and showed a lower affinity for calcium channels. This tracer showed a low brain uptake at baseline both in humans and other vertebrate species, but co-administration with P-gp inhibitors as cyclosporine A (CsA) or tariquidar increased its volume of distribution (V_T) and kinetic constant k_1 (Muzi et al. 2009; Bankstahl et al. 2008). The increase in brain V_T after administration of tariquidar was approximately +300% in rats and + 24 ± 15% in humans (Kuntner et al. 2010; Wagner et al. 2009), which points to a pronounced species difference regarding the tariquidar effect.

22.6.1.2 [¹¹C]*N*-Desmethyl-Loperamide

Loperamide is an antidiarrheal agent that acts through agonism at *μ*-opioid receptors in the gut (Awouters et al. 1993). This drug is normally without harmful central effects because P-gp expels it from the brain. [¹¹C]loperamide is avidly metabolized to [¹¹C]dLop via demethylation (Zoghbi et al. 2008). This metabolite is also a substrate for P-gp, and it has been used as a PET tracer instead of [¹¹C]loperamide. Demethylation of [¹¹C]dLop may occur, but it will lead only to the formation of single-carbon radiometabolites such as [¹¹C]methanol. These metabolites will be oxidized and ultimately expired as [¹¹C]carbon dioxide. They should not accumulate in brain tissue and will therefore not cause problems in the kinetic analysis of the acquired PET data. The uptake of [¹¹C]dLop 30 min after its injection was about 3.5-fold higher in the forebrain of P-gp knockout mice compared to wild-type mice supporting the results from previous studies which indicate that [¹¹C]dLop is a substrate of P-gp (Lazarova et al. 2008). Similar results were acquired in monkeys. [¹¹C]dLop was found to be selective for P-gp when tested in human cell lines that overexpress P-gp, MRP1, or BCRP and also in P-gp knockout mice (Kannan et al. 2010). At low concentrations (≤1 nM), dLop acts only as a substrate, but at higher concentrations (≥20 μM), it acts both as a substrate and an inhibitor. Because low concentrations of radiotracer are used in PET imaging, [¹¹C]dLop will act only as a selective substrate for P-gp at the BBB. Pretreatment with the inhibitor tariquidar

increases the brain uptake of [^{11}C]dLop markedly in monkeys and humans (Kreisl et al. 2010). After entry of [^{11}C]dLop into the brain, it is trapped and does not wash out. Although dLop is an opiate agonist, its trapping is not a result of high-affinity binding to the opiate receptor. Brain uptake of [^{11}C]dLop cannot be displaced by receptor-saturating doses of an opiate agonist or antagonist (Lazarova et al. 2008). This irreversible trapping amplifies the PET signal, so it is advantageous from an imaging perspective. dLop has a pK_a of 7.3 and may be trapped by passive diffusion into acidic organelles, mainly lysosomes, followed by protonation within the organelle (Kaufmann and Krise 2007; Macintyre and Cutler 1988). To test this hypothesis, the accumulation of [^{3}H]dLop was measured in human cell lines and compared to the uptake of other weak bases (Kannan et al. 2011b). [^{11}C]dLop was found to be ionically trapped in acidic lysosomes and tariquidar competed for lysosomal accumulation, both in vitro and in vivo. This interaction is problematic in peripheral organs but not in the brain. Thus [^{11}C]dLop can still be used, either alone or in combination with tariquidar, to measure the function of P-gp at the BBB. However, the low brain uptake of [^{11}C]dLop at baseline conditions complicates the evaluation of increases in the P-gp function, as is also the case with *(R)*-[^{11}C]verapamil.

22.6.1.3   Fluorine-18 Verapamil Analogs

The synthesis of two fluorine-18 *(R)*-verapamil analogs has also been reported: *(R)*-*N*-[^{18}F]fluoroethylverapamil and *(R)*-O-[^{18}F]fluoroethylnorverapamil. Since *(R)*-[^{11}C]verapamil is considered as the gold standard for measuring the P-gp function until now, these two candidates were proposed as promising radiofluorinated analogs. *(R)*-*N*-[^{18}F]fluoroethylverapamil was obtained as follows: first, [^{18}F]fluoroethyl triflate was obtained from bromoethyltosylate using a silver triflate column, and secondly, [^{18}F]fluoroethyl triflate was distilled into a vial containing the precursor *(R)*-norverapamil. The synthesis of *(R)*-O-[^{18}F]fluoroethylnorverapamil was simpler. The precursor contained a tosyl group which allows direct fluorination, but Boc deprotection was also required. Preclinical studies carried out in rats showed that after administration of the P-gp inhibitor tariquidar, the brain uptake of *(R)*-*N*-[^{18}F]fluoroethylverapamil and *(R)*-O-[^{18}F]fluoroethylnorverapamil was increased by 3.6- and 2.4-fold, respectively. A PET study using P-gp knockout and P-gp and BCRP double-knockout mice showed that *(R)*-O-[^{18}F]fluoroethylnorverapamil was more specific for P-gp than *(R)*-*N*-[^{18}F]fluoroethylverapamil; thus, this analog was selected as the best tracer candidate (Raaphorst et al. 2017a).

22.6.1.4   [^{18}F]MPPF

The radiosynthesis of 4-(2′-methoxyphenyl)-1-[2′-(*N*-2″-pyridinyl)-p-[^{18}F]fluoro-benzamido] ethylpiperazine ([^{18}F]MPPF) comprises nucleophilic aromatic substitution of a para-nitro compound. The synthesis was performed in the presence of K_2CO_3 and Kryptofix$_{222}$ and under microwave heating (Le Bars et al. 1998). [^{18}F]MPPF is a PET tracer aimed at the imaging of the serotonin 5-HT$_{1A}$ receptor; however, it was discovered to be also a substrate of P-gp. Administration of the P-gp inhibitor cyclosporine A increased the tracer uptake in rat hippocampus (Laćan et al. 2008). This observation was confirmed by biodistribution studies performed in

P-gp knockout mice. The tracer uptake in the brain of P-gp knockout animals was two- to threefold higher than in wild-type mice (Passchier et al. 2000). However, in cells transfected with human P-gp or BCRP genes, [18F]MPPF efflux was not reduced by the P-gp inhibitor valspodar, and, thus, [18F]MPPF may not be transported by the human P-gp. A study performed in nonhuman primates showed an increase in the uptake of [18F]MPPF in the brain after the treatment with cyclosporine; however, this increase was attributable to an increase of the free fraction of the tracer in plasma. This study noted that cyclosporine A binds to plasma proteins and displaces other compounds (such as [18F]MPPF) from its plasma protein binding sites (Tournier et al. 2012). All these findings restrict the use of [18F]MPPF as a PET tracer for measuring the function of P-gp at the BBB.

22.6.2 Weak P-gp Substrates (Fig. 22.3)

22.6.2.1   [11C]Phenytoin

In 2010, an in vitro study showed that phenytoin and phenobarbital (antiepileptic drugs) are transported by the human P-gp, which strengthens the hypothesis that P-gp is involved in antiepileptic drug resistance (Zhang et al. 2010). In rhesus monkeys [11C]phenytoin showed a high brain uptake (Stavchansky et al. 1978), which suggests that phenytoin behaves as a weak P-gp substrate (Verbeek et al. 2012a). [11C]Phenytoin was synthesized via [11C]CO using a high-pressure autoclave (Verbeek et al. 2012a). In rats, the baseline uptake of [11C]phenytoin was higher than that of [11C]verapamil. After administration of 15 mg/kg of tariquidar, the brain
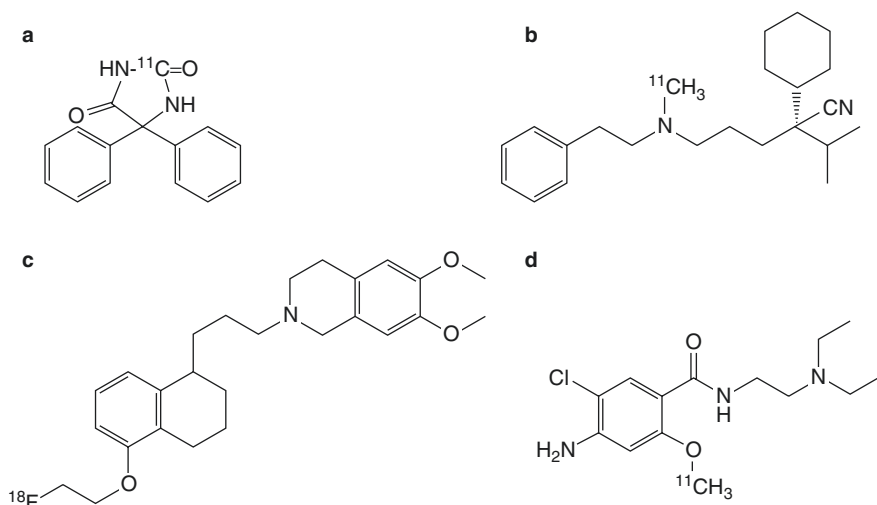
Fig. 22.3 Structure of weak P-gp substrates: [11C]Phenytoin (**a**), *(R)*-[11C]emopamil (**b**), [18F]MC225 (**c**), and [11C]metoclopramide (**d**)

uptake of [^{11}C]phenytoin showed a smaller increase compared to avid substrates tracers such as [^{11}C]verapamil. This observation also indicates a moderate affinity of [^{11}C]phenytoin to P-gp (Verbeek et al. 2012a). Quantification of the brain uptake of [^{11}C]phenytoin in humans was assessed by different kinetic models. The results of this study indicated that the tissue-tissue compartment model (1-TCM) is the preferred technique to analyze the data, and K_1 and V_T can be used for measuring the P-gp function (Mansor et al. 2015). Although [^{11}C]phenytoin seems to be a good tracer candidate to measure increases in the function of P-gp, further studies performed under pathologic conditions are still required.

22.6.2.2 [^{11}C]Emopamil

2-Isopropyl-5-[methyl-(2-phenylethyl)amino]-2-phenylpentanenitrile (emopamil) is a calcium channel blocker. Its chemical structure is similar to verapamil. A study evaluated the brain penetration of emopamil, verapamil, and gallopamil in rats and concluded that the cerebral availability and BBB permeability were higher for emopamil than for verapamil and gallopamil (Szabo 1989). The rather high brain penetration of emopamil at baseline condition encouraged the development of [^{11}C]emopamil as a weak substrate tracer for P-gp (Toyohara et al. 2016). *(R)*- and *(S)*-[^{11}C]emopamil were synthesized via methylation of the precursors, *(R)*- and *(S)*-noremopamil, with [^{11}C]methyl triflate. From mice experiments, it was concluded that *(R)*-[^{11}C]emopamil provides higher uptake than *(S)*-[^{11}C]emopamil. *(R)*-[^{11}C]emopamil showed a twofold higher area-under-the-curve (AUC) of the brain radioactivity in baseline scans than *(R)*-[^{11}C]verapamil. However, after the administration of cyclosporine A, the AUCs of the brain radioactivity of both tracers were similar. Unfortunately, both *(R)*- and *(S)*-[^{11}C]emopamil are rapidly metabolized (Toyohara et al. 2016). To verify that *(R)*-[^{11}C]emopamil is suitable for measuring P-gp upregulation, additional experiments in animal models are needed.

22.6.2.3 [^{18}F]MC225

Savolainen et al. evaluated three fluorine-18 compounds that shared the same moiety: 6,7-dimethoxytetrahydroisoquinoline, which is also present in tariquidar and elacridar (Savolainen et al. 2015). The compounds were assessed in vitro and in vivo with PET imaging, using P-gp and BCRP knockout mice. The results were compared to those obtained with [^{11}C]verapamil. From this experiment, [^{18}F]MC225 was selected as the most appropriate candidate to measure P-gp function at the BBB. The synthesis of [^{18}F]MC225 consists of two steps: First, [^{18}F]bromomethyl-fluorine is synthesized from 2-bromoethlyltosylate by heating at 90 °C for 15 min in dichlorobenzene. Afterward, the distilled [^{18}F]fluorethyl bromide is trapped in a vial containing sodium hydride and the phenol precursor of MC225 in dimethylformamide (DMF), and the vial is heated at 80 °C for 5 min. PET studies demonstrated that the baseline uptake of [^{18}F]MC225 was higher than that of [^{11}C]verapamil in rats. Baseline V_T values of [^{11}C]Verapamil ranged from 1.1 to 2.3 (Kuntner et al. 2010), whereas values for [^{18}F]MC225 varied from 6.6 to 11 (Savolainen et al. 2017a). The brain uptake of [^{18}F]MC225 was also higher in P-gp and BCRP knockout mice than in the wild-type, and in addition, [^{18}F]MC225 showed greater

metabolic stability (Savolainen et al. 2015). [^{18}F]MC225 showed specificity for P-gp over BCRP or MRP1 (Savolainen et al. 2015; Fusi et al. 2017). Rat experiments confirmed that [^{18}F]MC225 is transported by P-gp and not by BCRP. Inhibition of P-gp increased the brain uptake of the tracer, but inhibition of BCRP did not affect this uptake (Savolainen et al. 2017a). At 30 min after tracer injection, only 24% of the plasma radioactivity represented the parent compound. Different kinetic models were fitted to the data, and it was concluded that a 1-TCM was the preferred model for [^{18}F]MC225 in rats. After inhibition of P-gp, the changes in the influx rate constant K_1 were higher than the changes in V_T; for this reason, K_1 was proposed as the best parameter to measure the P-gp function (Savolainen et al. 2017a), as has also been suggested for analysis of the data of *(R)*-[^{11}C]verapamil (Muzi et al. 2009). PET studies with [^{18}F]MC225 are ongoing to demonstrate that this tracer is able to measure increases and decreases of the P-gp function at the BBB.

22.6.2.4　[^{11}C]Metoclopramide

Metoclopramide is a dopamine D2 receptor antagonist that is used as antiemetic. The drug was not identified as a P-gp substrate during in vitro experiments; however, in vivo studies in mice revealed increased (6.6-fold) brain concentration of metoclopramide in P-gp knockout compared to wild-type mice (Feng et al. 2008). Patients treated with metoclopramide reported CNS effects, which suggest that metoclopramide crosses the BBB (Pottier et al. 2016). Therefore, [^{11}C]metoclopramide was synthesized by radiomethylation of the methoxy phenol moiety of nor-metoclopramide using [^{11}C]methyl triflate (Pottier et al. 2016). In vitro assays using P-gp and BCRP, overexpressing cells demonstrated that [^{11}C]metoclopramide is specific for P-gp over BCRP. Moreover, the brain uptake of the tracer in rats increases after P-gp inhibition, resulting in an increase of K_1 and the binding potential (BP) in the two-tissue compartment model (2-TCM). At 30 min after tracer injection, only 20% of plasma radioactivity represented the parent compound in rats (Pottier et al. 2016). The kinetics of [^{11}C]metoclopramide were also evaluated in nonhuman primates; P-gp inhibition increased the brain distribution in these animals. In this case, a 1-TCM was used to fit the data, and the most sensitive parameter was the V_T which increased by 2.02-fold. The inhibition also caused an increase in K_1 (1.28-fold) and a decrease in k_2 (1.64-fold). However, the metabolism of [^{11}C]metoclopramide in nonhuman primates was more rapid than in rats, and 30 min after tracer injection, the fraction of the parent [^{11}C]metoclopramide in plasma was below the limit of detection (Auvity et al. 2018). Recently, the kinetics of this tracer was also assessed in humans. Here, the kinetic analysis showed a significant increase in V_T by 29 ± 17% after P-gp inhibition, mainly due to a significant 15 ± 5% decrease in k_2. K_1 was slightly increased after the treatment' however, this increase was significant in only a few regions compared to the baseline scan (Tournier et al. 2019). Further studies in pharmacoresistant patients are needed to demonstrate that [^{11}C]metoclopramide can visualize the increase of the P-gp function in these patients.

22.7   P-gp Inhibitors as Tracers for Measuring P-gp Expression

22.7.1 [¹¹C]Elacridar, [¹¹C]Tariquidar, and [¹¹C]Laniquidar

Many well-known P-gp inhibitors such as elacridar, tariquidar, and laniquidar were radiolabeled with carbon-11 (Fig. 22.4) and later also with fluorine-18. Elacridar, tariquidar, and laniquidar belong to the third generation of P-gp inhibitors. Tariquidar is described as a noncompetitive P-gp inhibitor which shows good selectivity toward the P-gp transporter over other efflux transporters, although it also inhibits BCRP transporter but with less potency. Elacridar is considered as a P-gp and BCRP inhibitor. Laniquidar is a noncompetitive inhibitor less potent that tariquidar and elacridar and is highly selective for P-gp (Wanek et al. 2013). Preclinical studies performed in rats showed that elacridar and tariquidar can increase the uptake of [¹¹C]verapamil in the brain up to 11-fold, with half-maximum effective doses of 1.2 ± 0.1 and 3.0 ± 0.2 mg/kg, respectively. The results also showed that elacridar is three times more potent than tariquidar (Kuntner et al. 2009).
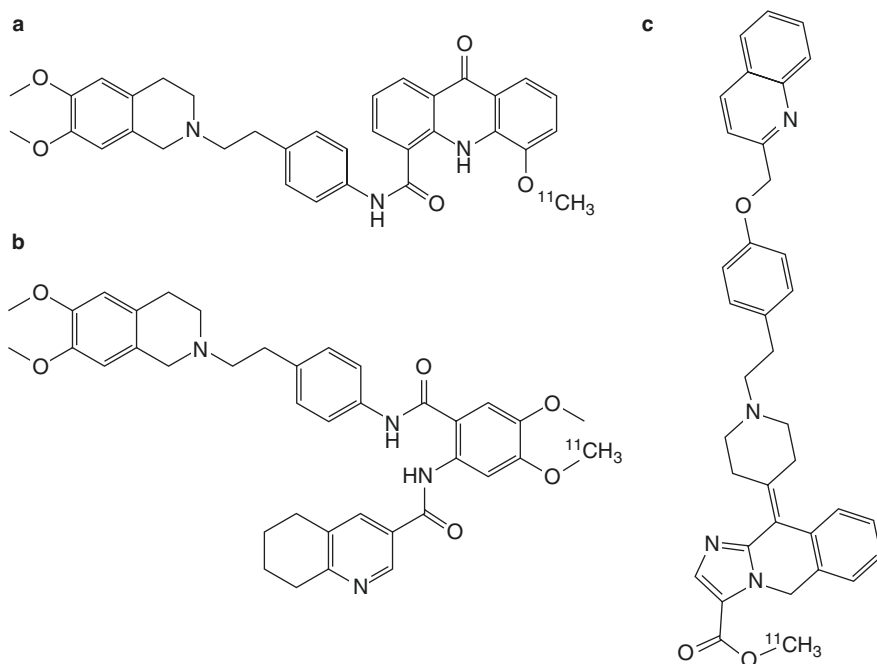
Fig. 22.4 Structure of P-gp inhibitors: [¹¹C]elacridar (**a**), [¹¹C]tariquidar (**b**), and [¹¹C]laniquidar (**c**)

For the [^{11}C]elacridar synthesis, the O-desmethyl-elacridar was reacted with [^{11}C]-methyl triflate in acetone containing NaOH. [^{11}C]elacridar was administrated to mice and rats to evaluate its kinetics. The brain uptake in P-gp knockout mice was 2.5-fold higher, and in BCRP knockout mice was 1.3-fold higher compared to wild-type mice. The co-administration of [^{11}C]elacridar with the unlabeled compound also increased the brain uptake in rats (Dörner et al. 2009). Another PET study found increased K_1 values of [^{11}C]elacridar in P-gp and BCRP knockout mice compared to wild-type mice, suggesting the brain penetration of [^{11}C]elacridar is limited by these two transporters (Kawamura et al. 2010a). In conclusion, [^{11}C]elacridar is not specific for P-gp, and its radioactive signal in baseline scans is very low.

O-desmethyl-tariquidar was reacted with [^{11}C]methyl iodide or [^{11}C]methyl triflate to obtain [^{11}C]tariquidar (Bauer et al. 2010; Kawamura et al. 2010b). In vivo studies performed in mice showed an increase of [^{11}C]tariquidar brain uptake after the administration of unlabeled tariquidar (Kawamura et al. 2010b). Moreover, the brain uptake of [^{11}C]tariquidar was higher in P-gp knockout mice and BCRP knockout mice than in wild-type mice (Bauer et al. 2010; Kawamura et al. 2010b). PET experiments performed in rats also found an increase in the brain uptake of [^{11}C]tariquidar after the administration of tariquidar and elacridar (Bauer et al. 2010). The studies revealed a high metabolic stability of the tracer in the brain and plasma (Kawamura et al. 2010b). In tumor cells, the uptake of [^{11}C]tariquidar and [^{11}C]elacridar increased after the administration of unlabeled tariquidar and this increase was similar to the one observed for [^{11}C]verapamil (Wanek et al. 2011). The kinetics of [^{11}C]tariquidar and [^{11}C]elacridar were also evaluated in healthy human subjects. The brain uptake at baseline condition was very low for both tracers; however, after the administration of unlabeled tariquidar, the brain uptake of [^{11}C]tariquidar increased by 27 ± 15% and by 21 ± 15% in the case of [^{11}C]elacridar. Both tracers showed a low amount of radiometabolites in plasma, 60 min after injection. The results indicate that [^{11}C]tariquidar and [^{11}C]elacridar behave as P-gp and BCRP substrates in vivo and therefore are unable to visualize P-gp expression at the BBB (Bauer et al. 2013).

The radiosynthesis of [^{11}C]laniquidar involved methylation of a precursor with [^{11}C]methyl iodide in DMSO containing tetrabutylammonium hydroxide (Luurtsema et al. 2009). [^{11}C]laniquidar was injected via the tail vein, and rats were sacrificed at different time points to count radioactivity in various tissues. Moreover, rats were also pretreated with cyclosporine A, and the brain concentration of [^{11}C]laniquidar was determined 30 min after injection. The brain uptake of [^{11}C]laniquidar was low and was increased after treatment with cyclosporine A. The metabolism of the tracer was slow, resulting in a parent fraction of 68% in plasma, 30 min after injection. However, the results suggest that laniquidar may act as a P-gp substrate instead of as a P-gp inhibitor at tracer concentrations (Luurtsema et al. 2009). Co-administration of [^{11}C]laniquidar and unlabeled laniquidar in mice confirmed that laniquidar may act as a P-gp substrate at low doses and as a P-gp inhibitor at high doses (Moerman et al. 2012).

22.7.2 [^{18}F]Fluoroelacridar, [^{18}F]Fluoroethlyelacridar, and [^{18}F] Fluoroethyltariquidar

The synthesis of fluorine-18-labeled analogs of elacridar and tariquidar has been reported. These tracers showed similar properties to their carbon-11 analogs (Dörner et al. 2011; Kawamura et al. 2011). [^{18}F]Fluoroelacridar was synthesized by nucleophilic aromatic substitution of the 1-nitro precursor. The reaction was done in the presence of dried krytofix$_{222}$ and K$_2$CO$_3$ complex together with the precursor dissolved in dimethyl sulfoxide (DMSO), and the reaction mixture was heated for 60 min at 175 °C. Preclinical studies performed in rats showed a significant increase in brain uptake of the tracer after the administration of the P-gp and BCRP inhibitor elacridar. Brain uptake was also higher in P-gp and BCRP knockout than in wild-type mice (Dörner et al. 2011). Although [^{18}F]fluoroelacridar behaved similarly to [^{11}C]elacridar, both tracers are substrates of P-gp and BCRP which hampers the quantification of a specific transporter. [^{18}F]Fluoroelacridar also showed an intense defluorination in vivo, which limits its use as a PET tracer (Dörner et al. 2011).

[^{18}F]fluoroethylelacridar and [^{18}F]fluoroethyltariquidar were synthesized by alkylation of its O-desmethyl precursors with [^{18}F]2-fluoroethyl bromide. These precursors were heated at 90–120 °C for 10 min in DMF containing tetrabutylammonium hydroxide and [^{18}F]2-fluoroethyl bromide. Preclinical studies performed in wild-type and knockout mice revealed that these fluorine-18 tracers present similar kinetics and biodistribution as their carbon-11 analogs. An increase in the brain uptake was observed after the administration of tariquidar or elacridar to wild-type mice, and a higher uptake of the tracer was found in P-gp/BCRP knockout mice compared to wild-type (Kawamura et al. 2011). Both tracers were again substrates of P-gp and BCRP; therefore, they cannot be used to measure only the P-gp function (Raaphorst et al. 2017a; Kawamura et al. 2011).

The radiolabeling of P-gp inhibitors to measure the P-gp expression turned to be an unsuccessful strategy. The results provided by the preclinical and clinical studies were unexpected. First, the baseline brain uptake of these tracers was very low, and, second, the treatment with P-gp inhibitors caused an increase in the brain uptake. At tracer concentrations, these compounds may act as P-gp substrates rather than P-gp inhibitors. (Luurtsema et al. 2016). Therefore, [^{11}C]elacridar, [^{11}C]tariquidar, and [^{11}C]laniquidar as well as their fluorine-18 analogs fail to measure P-gp expression at the BBB (Wanek et al. 2013).

22.7.3 Novel P-gp Inhibitors as PET Tracers

Until now, most radiolabeled inhibitors aimed to quantify the expression of the P-gp transporter have not been successful. However, Verbeek and colleges have recently published the synthesis of two novel PET tracers for measuring P-gp expression, [^{18}F]2-(4-fluoro-2-oxoindolin-3-ylidene)-N-(4-methoxyphenyl)hydrazine-carbothioamide ([^{18}F]5) and [^{18}F]2-(6-fluoro-2-oxoindolin-3-ylidene)-N-(4-methoxyphenyl) hydrazine-carbothioamide ([^{18}F]6) (Verbeek et al. 2018). The

kinetics of both tracers were evaluated in P-gp knockout mice and rats before and after administration of the P-gp inhibitor tariquidar. [^{18}F]5 showed greater metabolic stability than [^{18}F]6. PET studies performed in P-gp knockout mice revealed a significantly lower uptake of [^{18}F]5 compared to wild-type mice. Additionally, the administration of tariquidar did not modify the uptake of the tracer in the rat brain. Thus, this study suggested that [^{18}F]5 may be a promising radiotracer that binds to the P-gp transporter and may allow measurement of P-gp expression levels in vivo (Verbeek et al. 2018). However, additional experiments are needed to prove if [^{18}F]5 behaves as a P-gp inhibitor.

22.8   Kinetic Modeling of the P-gp Function

As has been explained before, PET is a functional imaging technique that measures the radioactivity concentration of a tracer in a specific target. This technique allows monitoring of the interactions of a radiotracer with its target(s) and quantification of the effects of a drug on physiological processes (Morris et al. 2004). Quantitative analysis of the PET data can involve the normalizing of average values from a region of interest using, for instance, standardized uptake values (SUV) or kinetic modeling methods. Kinetic modeling usually requires the acquisition of dynamic images, which give information about the concentration of the tracer in the target tissue as a function of time, as well as measurements of radioactivity in blood or plasma of the subject at different time points to acquire an arterial input function (Kuntner and Stout 2014; Kuntner 2014; Gunn et al. 2001). Moreover, since radiotracers can be extensively metabolized, the radioactivity concentration in plasma should be corrected for the fraction of metabolites. Reference tissue models have also been developed in order to avoid the need for blood sampling. In this case, the time-activity curve of the radiotracer in the tissue of interest is related to the time-activity curve in a reference tissue that lacks the tracer target (Gunn et al. 2001; Lammertsma and Hume 1996). Compartmental models are frequently used to describe the tracer kinetics, in order to analyze the delivery and elimination of the tracer in the tissue of interest. These methods can be used to calculate the mean transfer rate constants, which describe the movement of the tracer through different compartments, and the volume of distribution (V_T) or the binding potential of the tracer to the target (Carson 2003). Kinetic modeling can also be used to determine which parameter describes most adequately the function under study or which parameter is most sensitive to changes in this function (Kuntner 2014).

The P-gp transporter is mainly located at the luminal side of the endothelial cells at the BBB. Thus, the rate constants K_1 and k_2, which describe the movement of the tracer from the blood to the brain (or first tissue compartment), have been proposed as the best parameters to measure the P-gp function (Tournier et al. 2018). Since the P-gp transporter is an efflux pump, it is expected that the efflux rate constant k_2 would be the parameter which is most affected by a P-gp inhibition, and thus, it would be the best parameter to measure the P-gp function. However, several PET studies with P-gp tracers found a significant increase in K_1

and V_T after administration of P-gp inhibitors, but no changes in k_2. Thus, it was suggested that P-gp tracers pass from the blood to the endothelial cells and from there back to the blood by a very rapid P-gp-mediated transport. This transport is much more rapid than the PET acquisition, and therefore, the P-gp function is reflected in the value of K_1, instead of the value of k_2. A review of the kinetics of several P-gp PET tracers concluded that K_1 corrected for changes in the blood flow is the preferred parameter to measure P-gp function at the BBB (Lubberink 2016). However, recent studies performed with [11C]metoclopramide in nonhuman primates observed a significant decrease in k_2 after intravenous co-infusion of tariquidar. The results of these studies suggested that the most sensitive parameter to measure P-gp inhibition was V_T (Auvity et al. 2018). Similar results were obtained in humans where a significant increase in V_T was found during the infusion of cyclosporine A. In that study, K_1 showed a significant increase in only a few brain regions after P-gp inhibition (Tournier et al. 2019). These publications have reopened the debate about the question which kinetic parameter represents most adequately the P-gp function.

22.9 The Use of P-gp Tracers and PET to Assess Brain Disorders in Humans

The association between Alzheimer's disease and an impaired function of P-gp is an interesting field of research and was studied by various research groups. In the last decade, several radiotracers have been developed to evaluate the function of P-gp in Alzheimer's disease (Leopoldo et al. 2014). Only a few of these tracers survived the in vitro and animal tests and were employed in humans. Until now, *(R)*-[11C]verapamil is the gold standard to measure the function of P-gp in patient brains. This tracer revealed a significant decline of P-gp function in AD patients compared to healthy controls (van Assema et al. 2012). However, *(R)*-[11C]verapamil does not allow assessment of the efficacy of P-gp inducers which are considered as promising drugs for the treatment of AD. For this purpose, weak P-gp substrates are intensively studied and validated in rodents and nonhuman primates. The fact that these compounds have shown a higher uptake at baseline and a higher sensitivity to changes of P-gp function compared to avid substrates is encouraging (Fusi et al. 2017; Raaphorst et al. 2017b; Savolainen et al. 2017b).

In PD, a decreased P-gp function in frontal regions of the brain was seen only in advanced stages of the disease, using *(R)*-[11C]verapamil. In the early stages of PD, no significant reduction of P-gp function was found, which makes P-gp dysfunction at the BBB less likely to be the primary cause of the disease (Bartels et al. 2008a, b).

In epilepsy, the function of P-gp is thought to be increased, which leads to insufficient uptake of antiepileptic drugs in the brain. Although [11C]verapamil alone cannot accurately assess increases of P-gp in patients with epilepsy, [11C]verapamil can be used in combination with tariquidar. This combination indicated that patients suffering from drug-resistant epilepsy show a higher P-gp function in some regions of the brain than drug-sensitive patients or healthy controls (Feldmann et al. 2013).

Additionally, Langer and colleagues studied the P-gp function in a small group of patients suffering from drug-resistant epilepsy, and they found some asymmetries in the kinetic parameters of [^{11}C]verapamil in the parahippocampal and ambient gyrus (PAHG), amygdala, and medial and lateral anterior temporal lobe. However, these regional differences were not statistically significant (Langer et al. 2007). [^{11}C]Phenytoin, a weak substrate for P-gp, is under investigation as a hopefully better technique to evaluate the function of P-gp in patients suffering from drug-resistant epilepsy.

22.10 The Use of P-gp Tracers to Evaluate the Clinical Implications of Drug-Drug Interaction

ABC transporter-mediated drug-drug interactions (DDIs) have gained attention since numerous compounds can interact with these transporters.

On one hand, concomitant administration of drugs can culminate in adverse drug events which can cause patient hospitalization and increased patient morbidity as well as increased treatment costs. Interaction of a drug with ABC transporters can modify the pharmacokinetics of a co-administered drug by changing its absorption, distribution, metabolism, and/or elimination. DDIs can lead to unexpected toxicity or reduced drug effectiveness (Lund et al. 2017; Zhang et al. 2008). For instance, a drug that inhibits the P-gp function can increase the concentration of a concurrently administered drug in the target tissue and can thus increase the risk of an adverse drug event. In the case of drugs with a narrow therapeutic index such as digoxin, which is a P-gp substrate, it is essential to study potential DDIs (Zhang et al. 2008). However, it should be noted that not all DDIs will be clinically relevant (Lund et al. 2017).

On the other hand, transporter-mediated DDIs are crucial in the drug development process. The FDA and EMA have already advised in vitro assays to screen whether a new compound is a P-gp substrate, inhibitor, or inducer (Clinical Drug Interaction Studies — Study Design, Data Analysis, and Clinical Implications Guidance for Industry 2017; Guideline on the Investigation of Drug Interactions 2012). However, such in vitro methods have disadvantages. They are not yet standardized among laboratories, and P-gp inducers are difficult to recognize in vitro (Lund et al. 2017; Zhang et al. 2008). Furthermore, for ABC transporters other than P-gp, in vitro methods have not yet been fully developed (Zhang et al. 2008). In addition, if in vitro studies show that a new compound may interact with an ABC transporter, in vivo studies need to be performed to confirm this finding (Langer 2016; Zhang et al. 2008).

In clinical studies, the drug concentration in the blood of the subjects is usually measured. However, it is known that some DDIs mediated by ABC transporters do not result in a change of drug concentration in the blood, but changes in tissue pharmacokinetics. For example, P-gp inhibition at the BBB is usually not accompanied by changes in the plasma concentration of the drug, but it causes an increase in brain concentration (Langer 2016; Wulkersdorfer et al. 2014).

Since PET allows quantification of the concentration of the drug in the target tissue, imaging represents an interesting technique to study the DDIs mediated by ABC transporters. PET images can be used to quantify several pharmacokinetic parameters of a test drug, such as the tissue and blood concentrations during the scanning time. This usually requires the use of dynamic PET scans and blood sampling. By applying pharmacokinetic models to the data, different kinetic parameters are estimated which may help to interpret some physiological processes (Langer 2016).

PET studies are commonly applied in drug development to measure the binding of a new drug to its target receptor (Matthews et al. 2012; Cunningham et al. 2005; Lee and Farde 2006). Moreover, as many drugs can be affected by the efflux action of ABC transporters and, therefore, do not reach the desired target, PET studies of ABC transporters may be used to predict which drug can reach the CNS in appropriate concentrations.

These PET studies require the administration of a radiotracer to image the function of a specific ABC transporter. Each study consists of a dual-scan protocol where the radiotracer is administrated under two different conditions. One scan will be performed without the administration of the test drug. It will provide information about the normal distribution of the tracer. This scan will be referred to as the baseline scan. The second scan will be performed after (or during) administration of the newly developed drug. Changes in the distribution of the radiotracer with regard to the baseline scan will show how the test drug affects the function of the specific ABC transporter. If the drug under study is expected to be a substrate of the ABC transporter, a different study protocol may be used. In this case, the drug under study could be radiolabeled with fluorine-18 or carbon-11. After studying the normal distribution of the test drug, a second PET scan should be performed in combination with a well-known inhibitor or inducer of the specific ABC transporter. This approach will show how changes in ABC transporter function affect the distribution of the test drug (Langer 2016; Wulkersdorfer et al. 2014).

PET studies of ABC transporters play now an important role in the assessment of drug disposition in target tissues, in particular, the CNS. Therefore, the search for improved tracers for PET imaging of ABC transporters has been intensified (Kannan et al. 2009; Wanek et al. 2013; Luurtsema et al. 2016).

22.11 Discussion and Concluding Remarks

The implication of ABC transporters in the onset of neurodegenerative disease as well as in the deposition of CNS drugs makes these efflux transporters an interesting therapeutic target. Since PET imaging allows the in vivo assessment of biochemical processes, this technique is well-suited for evaluation of the ABC transporter function under different conditions or at different stages of a disease. Therefore, many research groups are developing novel PET tracers for improved assessment of ABC transporter function in vivo. Current research focuses on the development of weak substrates for P-gp which can be used to measure both increases and decreases of the efflux function.

PET imaging of ABC transporters may expand our knowledge regarding their involvement in the onset and progression of several neurodegenerative diseases. Novel treatment approaches for Alzheimer's or Parkinson's disease, such as treatment with P-gp inducers, can also be tested in experimental animals and humans, using PET. Moreover, PET imaging may be a useful tool to evaluate the affinity of novel CNS drugs toward various ABC transporters. This technique may predict the biodistribution and, in particular, the brain penetration of new drug candidates at an early stage in the drug development process, and may thus enhance the success rate of drug development.

It is expected that the use of novel and specific tracers for ABC transporters will increase our understanding regarding the diagnosis and treatment of neurodegenerative disease as well as our insight into potential transporter-mediated DDIs.

References

Agarwal S, Hartz AMS, Elmquist WF, Bauer B (2011) Breast cancer resistance protein and P-glycoprotein in brain cancer: two gatekeepers team up. Curr Pharm Des 17:2793–2802

Alzheimer A (1906) Über einen eigenartigen schweren Erkrankungsprozeß der Hirnrinde. Neurol Zentralblatt

Aronica E, Sisodiya SM, Gorter JA (2012) Cerebral expression of drug transporters in epilepsy. Adv Drug Deliv Rev 64:919–929

van Assema DME, van Berckel BNM (2016) Blood-brain barrier ABC-transporter P-glycoprotein in Alzheimer's disease: still a suspect? Curr Pharm Des 22:1–8

van Assema DME, Lubberink M, Bauer M et al (2012) Blood–brain barrier P-glycoprotein function in Alzheimer's disease. Brain 135:181–189

Auvity S, Caillé F, Marie S et al (2018) P-glycoprotein (ABCB1) inhibits the influx and increases the efflux of 11 C-metoclopramide across the blood-brain barrier: a PET study on non-human primates. J Nucl Med 59(10):1609–1615

Awouters F, Megens A, Verlinden M, Schuurkes J, Niemegeers C, Janssen PAJ (1993) Loperamide. Dig Dis Sci 38:977–995

Ballard C, Gauthier S, Corbett A, Brayne C, Aarsland D, Jones E (2011) Alzheimer's disease. Lancet (London, England) 377(9770):1019–1031

Bankstahl JP, Kuntner C, Abrahim A et al (2008) Tariquidar-induced P-glycoprotein inhibition at the rat blood-brain barrier studied with (R)-11C-verapamil and {PET}. J Nucl Med 49:1328–1335

Bartels AL (2011) Blood-brain barrier P-glycoprotein function in neurodegenerative disease. Curr Pharm Des 17:2771–2777

Bartels AL, van Berckel BNM, Lubberink M, Luurtsema G, Lammertsma AA, Leenders KL (2008a) Blood-brain barrier P-glycoprotein function is not impaired in early Parkinson's disease. Park Relat Disord 115(7):1001–1009

Bartels AL, Willemsen ATM, Kortekaas R et al (2008b) Decreased blood-brain barrier P-glycoprotein function in the progression of Parkinson's disease, PSP and MSA. J Neural Transm 115:1001–1009

Bauer F, Kuntner C, Bankstahl JP et al (2010) Synthesis and in vivo evaluation of [11C]tariquidar, a positron emission tomography radiotracer based on a third-generation P-glycoprotein inhibitor. Bioorg Med Chem 18:5489–5497

Bauer M, Karch R, Neumann F, et al (2009) Age dependency of cerebral P-gp function measured with (R)-[11C]verapamil and PET. Eur J Clin Pharmacol 65:941–946

Bauer M, Karch R, Zeitlinger M et al (2013) Interaction of 11C-tariquidar and 11C-elacridar with P-glycoprotein and breast cancer resistance protein at the human blood-brain barrier. J Nucl Med 54:1181–1187

Bauer M, Tournier N, Langer O (2019) Imaging P-glycoprotein function at the blood–brain barrier as a determinant of the variability in response to central nervous system drugs. Clin Pharmacol Ther 105:1061–1064

Bernstein H-G, Hildebrandt J, Dobrowolny H, Steiner J, Bogerts B, Pahnke J (2016) Morphometric analysis of the cerebral expression of ATP-binding cassette transporter protein ABCB1 in chronic schizophrenia: Circumscribed deficits in the habenula. Schizophr Res 177:52–58

Brandt C, Bethmann K, Gastens AM, Löscher W (2006) The multidrug transporter hypothesis of drug resistance in epilepsy: proof-of-principle in a rat model of temporal lobe epilepsy. Neurobiol Dis 24:202–211

Breitenstein B, Brückl TM, Ising M, Müller-Myhsok B, Holsboer F, Czamara D (2015) ABCB1 gene variants and antidepressant treatment outcome: a meta-analysis. Am J Med Genet Part B Neuropsychiatr Genet

Brenn A, Grube M, Jedlitschky G et al (2014) St. John's wort reduces beta-amyloid accumulation in a double transgenic Alzheimer's disease mouse model - role of P-glycoprotein. Brain Pathol 24:18–24

Brzozowska NI, Smith KL, Zhou C et al (2017) Genetic deletion of P-glycoprotein alters stress responsivity and increases depression-like behavior, social withdrawal and microglial activation in the hippocampus of female mice. Brain Behav Immun 65:251–261

Carabotti M, Scirocco A, Maselli MA, Severi C (2009) The gut-brain axis: interactions between enteric microbiota, central and enteric nervous systems. Ann Gastroenterol 28:203–209

Carson RE (2003) Tracer kinetic modeling in PET. In: Positron emission tomography. Springer-Verlag, London, pp 127–159

Cen J, Liu L, Li M-S et al (2013) Alteration in P-glycoprotein at the blood-brain barrier in the early period of MCAO in rats. J Pharm Pharmacol 65:665–672

Cherry SR, Jones T, Karp JS, Qi J, Moses WW, Badawi RD (2018) Total-body PET: maximizing sensitivity to create new opportunities for clinical research and patient care. J Nucl Med 59:3–12

Chiu C, Miller MC, Monahan R, Osgood DP, Stopa EG, Silverberg GD (2015) P-glycoprotein expression and amyloid accumulation in human aging and Alzheimer's disease: preliminary observations. Neurobiol Aging 36:2475–2482

Church RM, Miller MC, Freestone D et al (2014) Amyloid-beta accumulation, neurogenesis, behavior, and the age of rats. Behav Neurosci

Cirrito JR, Deane R, Fagan AM et al (2005) P-glycoprotein deficiency at the blood-brain barrier increases amyloid-beta deposition in an Alzheimer disease mouse model. J Clin Invest 115:3285–3290

Clinical Drug Interaction Studies — Study Design, Data Analysis, and Clinical Implications Guidance for Industry. 2017. https://www.fda.gov/downloads/drugs/guidances/ucm292362.pdf

Colabufo NA, Berardi F, Cantore M et al (2010) Perspectives of P-glycoprotein modulating agents in oncology and neurodegenerative diseases: Pharmaceutical, biological and diagnostic potentials. J Med Chem 53:1883–1897

Colabufo NA, Contino M, Cantore M et al (2018) An innovative small molecule for promoting neuroreparative strategies. RSC Adv 8:5451–5458

Cole S, Bhardwaj G, Gerlach J et al (1992) Overexpression of a transporter gene in a multidrug-resistant human lung cancer cell line. Science (80-) 258:1650–1654

Cunningham VJ, Parker CA, Rabiner EA, Gee AD, Gunn RN (2005) PET studies in drug development: methodological considerations. Drug Discov Today Technol 2:311–315

Dauchy S, Dutheil F, Weaver RJ et al (2008) {ABC} transporters, cytochromes P450 and their main transcription factors: expression at the human blood-brain barrier. J Neurochem 107:1518–1528

Dazert P, Suofu Y, Grube M et al (2006) Differential regulation of transport proteins in the peri-infarct region following reversible middle cerebral artery occlusion in rats. Neuroscience 142:1071–1079

Dean M, Allikmets R (2001) Complete characterization of the human ABC gene family. J Bioenerg Biomembr 33(6):475–479

Dean M, Hamon Y, Chimini G (2001) The human ATP-binding cassette transporter superfamily. Genome Res

Deeken JF, Loscher W (2007) The blood-brain barrier and cancer: transporters, treatment, and Trojan horses. Clin Cancer Res 13:1663–1674

Dewanjee S, Dua T, Bhattacharjee N et al (2017) Natural products as alternative choices for P-glycoprotein (P-gp) inhibition. Molecules 22:871

Dinis-Oliveira RJ, Duarte JA, Remião F, Sánchez-Navarro A, Bastos ML, Carvalho F (2006) Single high dose dexamethasone treatment decreases the pathological score and increases the survival rate of paraquat-intoxicated rats. Toxicology 227:73–85

Dörner B, Kuntner C, Bankstahl JP et al (2009) Synthesis and small-animal positron emission tomography evaluation of [11C]-elacridar as a radiotracer to assess the distribution of P-glycoprotein at the blood-brain barrier. J Med Chem 52:6073–6082

Dörner B, Kuntner C, Bankstahl JP et al (2011) Radiosynthesis and in vivo evaluation of 1-[18F]fluoroelacridar as a positron emission tomography tracer for P-glycoprotein and breast cancer resistance protein. Bioorganic Med Chem 19:2190–2198

Doyle LA, Yang W, Abruzzo LV et al (1998) A multidrug resistance transporter from human MCF-7 breast cancer cells. Proc Natl Acad Sci U S A 95:15665–15670

Droździk M, Białecka M, Myśliwiec K, Honczarenko K, Stankiewicz J, Sych Z (2003) Polymorphism in the P-glycoprotein drug transporter MDR1 gene: a possible link between environmental and genetic factors in Parkinson's disease. Pharmacogenetics 13:259–263

ElAli A, Hermann DM (2010) Apolipoprotein E controls {ATP}-binding cassette transporters in the ischemic brain. Sci Signal 3:ra72–ra72

Elsinga P, Hendrikse N, Bart J, Vaalburg W, Waarde A (2004) PET studies on P-glycoprotein function in the blood-brain barrier: how it affects uptake and binding of drugs within the CNS. Curr Pharm Des

Feldmann M, Koepp M (2012) P-glycoprotein imaging in temporal lobe epilepsy: In vivo PET experiments with the Pgp substrate [11 C]-verapamil. Epilepsia 53:60–63

Feldmann M, Asselin MC, Liu J et al (2013) P-glycoprotein expression and function in patients with temporal lobe epilepsy: a case-control study. Lancet Neurol

Feng B, Mills JB, Davidson RE et al (2008) In vitro P-glycoprotein assays to predict the in vivo interactions of P-glycoprotein with drugs in the central nervous system. Drug Metab Dispos 36:268–275

Fletcher JI, Williams RT, Henderson MJ, Norris MD, Haber M (2016) ABC transporters as mediators of drug resistance and contributors to cancer cell biology. Drug Resist Updat 26:1–9

Foster JA, McVey Neufeld K-A (2013) Gut–brain axis: how the microbiome influences anxiety and depression. Trends Neurosci 36:305–312

Fox E, Bates SE (2007) Tariquidar (XR9576): a P-glycoprotein drug efflux pump inhibitor. Expert Rev Anticancer Ther 7:447–459

Fusi F, Durante M, Gorelli B, Perrone MG, Nicola Antonio C, Saponara S (2017) MC225, a novel probe for P-glycoprotein PET Imaging at the blood-brain barrier. J Cardiovasc Pharmacol 70:1

Galante E, Okamura T, Sander K et al (2014) Development of purine-derived 18F-labeled pro-drug tracers for imaging of MRP1 activity with PET. J Med Chem 57:1023–1032

Gameiro M, Silva R, Rocha-Pereira C et al (2017) Cellular models and in vitro assays for the screening of modulators of P-gp, MRP1 and BCRP. Molecules 22:4–6

Gray E, Rice C, Hares K et al (2014) Reductions in neuronal peroxisomes in multiple sclerosis grey matter. Mult Scler J 20:651–659

Guideline on the Investigation of Drug Interactions. 2012. http://www.ema.europa.eu/docs/en_GB/document_library/Scientific_guideline/2012/07/WC500129606.pdf

Gunn RN, Gunn SR, Cunningham VJ (2001) Positron emission tomography compartmental models. J Cereb Blood Flow Metab 21:635–652

Haber M, Smith J, Bordow SB et al (2006) Association of high-level MRP1 expression with poor clinical outcome in a large prospective study of primary neuroblastoma. J Clin Oncol 24:1546–1553

Haimeur A, Conseil G, Deeley RG, Cole SPC (2004) The MRP-related and BCRP/ABCG2 multi-drug resistance proteins: biology, substrate specificity and regulation. Curr Drug Metab 5:21–53

Haran JP, Bhattarai SK, Foley SE et al (2019) Alzheimer's disease microbiome is associated with dysregulation of the anti-inflammatory P-glycoprotein pathway. Pettigrew MM, ed. MBio 10:1–14

Hardy J, Allsop D (1991) Amyloid deposition as the central event in the aetiology of Alzheimer's disease. Trends Pharmacol Sci 12(10):383–388

Hartz AMS, Miller DS, Bauer B (2010) Restoring blood-brain barrier P-glycoprotein reduces brain amyloid-β in a mouse model of Alzheimer 's disease. Mol Pharmacol 77:715–723

Hartz AMS, Pekcec A, Soldner ELB, Zhong Y, Schlichtiger J, Bauer B (2017) P-gp protein expression and transport activity in rodent seizure models and human epilepsy. Mol Pharm 14:999–1011

Haslam IS, Pitre A, Schuetz JD, Paus R (2013) Protection against chemotherapy-induced alopecia: targeting ATP-binding cassette transporters in the hair follicle? Trends Pharmacol Sci 34:599–604

Haslam IS, El-Chami C, Faruqi H, Shahmalak A, O'Neill CA, Paus R (2015) Differential expression and functionality of ATP-binding cassette transporters in the human hair follicle. Br J Dermatol 172:1562–1572

Häussermann K, Benz B, Gekeler V, Schumacher K, Eichelbaum M (1991) Effects of verapamil enantiomers and major metabolites on the cytotoxicity of vincristine and daunomycin in human lymphoma cell lines. Eur J Clin Pharmacol 40:53–59

Hawkins BT, Davis TP (2005) The blood-brain barrier/neurovascular unit in health and disease. Pharmacol Rev 57:173–185

Hayashi K, Pu H, Tian J et al (2005) HIV-Tat protein induces P-glycoprotein expression in brain microvascular endothelial cells. J Neurochem 93:1231–1241

Hendrikse NH, Schinkel AH, De Vries EGE et al (1998) Complete in vivo reversal of P-glycoprotein pump function in the blood-brain barrier visualized with positron emission tomography. Br J Pharmacol 124:1413–1418

Hippius H, Neundörfer G (2003) The discovery of Alzheimer's disease. Dialogues Clin Neurosci 5(1):101–108

Hosten B, Boisgard R, Jacob A et al (2013) [11C]befloxatone brain kinetics is not influenced by Bcrp function at the blood–brain barrier: a PET study using Bcrp TGEM knockout rats. Eur J Pharm Sci 50:520–525

Hsueh W, Kesner AL, Gangloff A et al (2006) Predicting chemotherapy response to paclitaxel with 18F-Fluoropaclitaxel and PET. J Nucl Med 47:1995–1999

Jablonski MR, Jacob DA, Campos C et al (2012) Selective increase of two ABC drug efflux transporters at the blood–spinal cord barrier suggests induced pharmacoresistance in ALS. Neurobiol Dis 47:194–200

Jablonski MR, Markandaiah SS, Jacob D et al (2014) Inhibiting drug efflux transporters improves efficacy of ALS therapeutics. Ann Clin Transl Neurol 1:996–1005

Juliano RL, Ling V (1976) A surface glycoprotein modulating drug permeability in Chinese hamster ovary cell mutants. Biochim Biophys Acta 455:152–162

Kamel F, Hoppin JA (2004) Association of pesticide exposure with neurologic dysfunction and disease. Environ Health Perspect 112:950–958

Kannan P, John C, Zoghbi SS et al (2009) Imaging the function of P-glycoprotein with radiotracers: pharmacokinetics and in vivo applications. Clin Pharmacol Ther 86:368–377

Kannan P, Brimacombe KR, Zoghbi SS et al (2010) N-desmethyl-loperamide is selective for P-glycoprotein among three ATP-binding cassette transporters at the blood-brain barrier. Drug Metab Dispos 38:917–922

Kannan P, Telu S, Shukla S et al (2011a) The "specific" P-glycoprotein inhibitor tariquidar is also a substrate and an inhibitor for breast cancer resistance protein (BCRP/ABCG2). ACS Chem Neurosci 2:82–89

Kannan P, Brimacombe KR, Kreisl WC et al (2011b) Lysosomal trapping of a radiolabeled substrate of P-glycoprotein as a mechanism for signal amplification in {PET}. Proc Natl Acad Sci 108:2593–2598

Kaufmann AM, Krise JP (2007) Lysosomal sequestration of amine-containing drugs: analysis and therapeutic implications. J Pharm Sci 96:729–746

Kawamura K, Yamasaki T, Konno F et al (2010a) Evaluation of limiting brain penetration related to P-glycoprotein and breast cancer resistance protein using [11C]{GF}120918 by {PET} in mice. Mol Imaging Biol 13:152–160

Kawamura K, Konno F, Yui J et al (2010b) Synthesis and evaluation of [11C]{XR}9576 to assess the function of drug efflux transporters using {PET}. Ann Nucl Med 24:403–412

Kawamura K, Yamasaki T, Konno F et al (2011) Synthesis and in vivo evaluation of 18F-fluoroethyl GF120918 and XR9576 as positron emission tomography probes for assessing the function of drug efflux transporters. Bioorg Med Chem 19:861–870

Keangpraphun T, Towanabut S, Chinvarun Y, Kijsanayotin P (2015) Association of ABCB1 C3435T polymorphism with phenobarbital resistance in Thai patients with epilepsy. J Clin Pharm Ther

Kilic E, Spudich A, Kilic Ü et al (2008) ABCC1: a gateway for pharmacological compounds to the ischaemic brain. Brain 131:2679–2689

de Klerk OL, Willemsen ATM, Roosink M et al (2009) Locally increased P-glycoprotein function in major depression: a PET study with [11C]verapamil as a probe for P-glycoprotein function in the blood-brain barrier. Int J Neuropsychopharmacol 12:895–904

Kooij G, van Horssen J, de Lange ECM et al (2010) T lymphocytes impair P-glycoprotein function during neuroinflammation. J Autoimmun 34:416–425

Kooij G, Mizee MR, van Horssen J et al (2011) Adenosine triphosphate-binding cassette transporters mediate chemokine (C-C motif) ligand 2 secretion from reactive astrocytes: relevance to multiple sclerosis pathogenesis. Brain 134:555–570

Koong AC, Chen EY, Giaccia AJ (1994) Hypoxia causes the activation of nuclear factor kB through the phosphorylation of IkBα on tyrosine residues1. Cancer Res

Kortekaas R, Leenders KL, van Oostrom JCH et al (2005) Blood-brain barrier dysfunction in parkinsonian midbrain in vivo. Ann Neurol 57:176–179

Kreisl WC, Liow JS, Kimura N et al (2010) P-glycoprotein function at the blood-brain barrier in humans can be quantified with the substrate radiotracer 11C-N-desmethyl-loperamide. J Nucl Med 51:559–566

Kroemer H, Gautier J-C, Beaune P, Henderson C, Wolf CR, Eichelbaum M (1993) Identification of P450 enzymes involved in metabolism of verapamil in humans. Naunyn-Schmiedeberg{\textquotesingle}s Arch Pharmacol 348(3):332–337

Krohn M, Lange C, Hofrichter J et al (2011) Cerebral amyloid-β proteostasis is regulated by the membrane transport protein ABCC1 in mice. J Clin Invest 121:3924–3931

Kuhnke D, Jedlitschky G, Grube M et al (2007) MDR1-P-glycoprotein (ABCB1) mediates transport of Alzheimer's amyloid-β peptides—implications for the mechanisms of Aβ clearance at the blood–brain barrier. Brain Pathol 17:347–353

Kuntner C (2014) Kinetic modeling in pre-clinical positron emission tomography. Z Med Phys 24:274–285

Kuntner C, Stout D (2014) Quantitative preclinical PET imaging: opportunities and challenges. Front Phys 2:1–12

Kuntner C, Bankstahl JP, Bankstahl M et al (2009) Dose-response assessment of tariquidar and elacridar and regional quantification of P-glycoprotein inhibition at the rat blood-brain barrier using (R)-[11C]verapamil {PET}. Eur J Nucl Med Mol Imaging 37:942–953

Kuntner C, Bankstahl JP, Bankstahl M et al (2010) Dose-response assessment of tariquidar and elacridar and regional quantification of P-glycoprotein inhibition at the rat blood-brain barrier using (R)-[11C]verapamil PET. Eur J Nucl Med Mol Imaging 37:942–953

Laberge P, Martineau P, Sebajang H, Lalonde G (2001) Verapamil intoxication after substitution of immediate-release for extended-release verapamil. Am J Heal Pharm 58:402–405

Laćan G, Plenevaux A, Rubins DJ et al (2008) Cyclosporine, a P-glycoprotein modulator, increases [18F]MPPF uptake in rat brain and peripheral tissues: microPET and ex vivo studies. Eur J Nucl Med Mol Imaging 35:2256–2266

Lai BCL, Marion SA, Teschke K, Tsui JKC (2002) Occupational and environmental risk factors for Parkinson's disease. Parkinsonism Relat Disord 8:297–309

Lam FC, Liu R, Lu P et al (2001) β-Amyloid efflux mediated by p-glycoprotein. J Neurochem 76:1121–1128

Lammertsma AA, Hume SP (1996) Simplified reference tissue model for PET receptor studies. NeuroImage 4:153–158

Langer O (2016) Use of PET imaging to evaluate transporter-mediated drug-drug interactions. J Clin Pharmacol:S143–S156

Langer O, Bauer M, Hammers A et al (2007) Pharmacoresistance in epilepsy: a pilot PET study with the P-glycoprotein substrate R -[11 C]verapamil. Epilepsia 48:1774–1784

Lazarova N, Zoghbi SS, Hong J et al (2008) Synthesis and evaluation of [N-methyl-11C]N-desmethyl-loperamide as a new and improved {PET} radiotracer for imaging P-gp function. J Med Chem 51:6034–6043

Lazarowski A, Caltana L, Merelli A, Rubio MD, Ramos AJ, Brusco A (2007) Neuronal mdr-1 gene expression after experimental focal hypoxia: A new obstacle for neuroprotection? J Neurol Sci 258(1–2):84–92

Le Bars D, Lemaire C, Ginovart N et al (1998) High-yield radiosynthesis and preliminary in vivo evaluation of p-[18F]MPPF, a fluoro analog of WAY-100635. Nucl Med Biol 25:343–350

Lee C-M, Farde L (2006) Using positron emission tomography to facilitate CNS drug development. Trends Pharmacol Sci 27:310–316

Leopoldo M, Contino M, Berardi F, Perrone R, Colabufo NA (2014) PET radiotracers for imaging P-glycoprotein: the challenge for early diagnosis in AD. ChemMedChem 9:38–42

Li W, Zhang H, Assaraf YG et al (2016) Overcoming ABC transporter-mediated multidrug resistance: molecular mechanisms and novel therapeutic drug strategies. Drug Resist Updat 27:14–29

Linton KJ, Higgins CF (2007) Structure and function of ABC transporters: the ATP switch provides flexible control. Pflügers Arch - Eur J Physiol 453:555–567

Liu X (2019) ABC family transporters. In: Liu X, Pan G (eds) Drug transporters in drug disposition, effects and Toxicity. Springer Singapore, Singapore, pp 13–100

Liu X, Ma T, Qu B, Ji Y, Liu Z (2013) Pesticide-induced gene mutations and Parkinson disease risk: a meta-analysis. Genet Test Mol Biomarkers 17:826–832

Liu J, Chi N, Zhang JY, Zhu W, Bian YS, Chen HG (2015) Isolation and characterization of cancer stem cells from medulloblastoma. Genet Mol Res 14:3355–3361

Löscher W, Potschka H (2005a) Drug resistance in brain diseases and the role of drug efflux transporters. Nat Rev Neurosci 6:591–602

Löscher W, Potschka H (2005b) Blood-brain barrier active efflux transporters: ATP-binding cassette gene family. NeuroRx 2:86–98

Löscher W, Potschka H (2005c) Role of drug efflux transporters in the brain for drug disposition and treatment of brain diseases. Prog Neurobiol 76:22–76

Loscher W, Luna-Tortos C, Romermann K, Fedrowitz M (2012) Do ATP-binding cassette transporters cause pharmacoresistance in epilepsy? Problems and approaches in determining which antiepileptic drugs are affected. Curr Pharm Des 17(26):2808–2828

Lubberink M (2016) Kinetic models for measuring P-glycoprotein function at the blood-brain barrier with positron emission tomography. Curr Pharm Des 22:5786–5792

Lund M, Petersen TS, Dalhoff KP (2017) Clinical implications of P-glycoprotein modulation in drug-drug interactions. Drugs 77:859–883

Luurtsema G, Windhorst AD, Mooijer MPJ, Herscheid JDM, Lammertsma AA, Franssen EJF (2002) Fully automated high yield synthesis of (R)- and (S)-[11C]verapamil for measuring P-glycoprotein function with positron emission tomography. J Label Compd Radiopharm 45:1199–1207

Luurtsema G, Molthoff CFM, Windhorst AD et al (2003) (R)- and (S)-[11C]verapamil as {PET}-tracers for measuring P-glycoprotein function: in vitro and in vivo evaluation. Nucl Med Biol 30:747–751

Luurtsema G, Molthoff CFM, Schuit RC, Windhorst AD, Lammertsma AA, Franssen EJF (2005a) Evaluation of (R)-[11C]verapamil as {PET} tracer of P-glycoprotein function in the blood{\textendash}brain barrier: kinetics and metabolism in the rat. Nucl Med Biol 32:87–93

Luurtsema G, Molthoff CFM, Schuit RC, Windhorst AD, Lammertsma AA, Franssen EJF (2005b) Evaluation of (R)-[11C]verapamil as PET tracer of P-glycoprotein function in the blood-brain barrier: kinetics and metabolism in the rat. Nucl Med Biol 32:87–93

Luurtsema G, Schuit RC, Klok RP et al (2009) Evaluation of [11C]laniquidar as a tracer of P-glycoprotein: radiosynthesis and biodistribution in rats. Nucl Med Biol 36:643–649

Luurtsema G, Elsinga P, Dierckx R, Boellaard R, Waarde A (2016) PET tracers for imaging of ABC transporters at the blood-brain barrier: principles and strategies. Curr Pharm Des 22:5779–5785

Macé S, Cousin E, Ricard S et al (2005) ABCA2 is a strong genetic risk factor for early-onset Alzheimer's disease. Neurobiol Dis 18:119–125

Macintyre AC, Cutler DJ (1988) The potential role of lysosomes in tissue distribution of weak bases. Biopharm Drug Dispos 9:513–526

Mahringer A, Fricker G (2016) ABC transporters at the blood-brain barrier. Expert Opin Drug Metab Toxicol 12:499–508

Mairinger S, Langer O, Kuntner C et al (2010) Synthesis and in vivo evaluation of the putative breast cancer resistance protein inhibitor [11C]methyl 4-((4-(2-(6,7-dimethoxy-1,2,3,4-tetrahydroisoquinolin-2-yl)ethyl)phenyl)amino-carbonyl)-2-(quinoline-2-carbonylamino) benzoate. Nucl Med Biol 37:637–644

Mansor S, Boellaard R, Froklage FE et al (2015) Quantification of dynamic 11C-phenytoin PET studies. J Nucl Med 56:1372–1377

Mao Q, Unadkat JD (2015) Role of the breast cancer resistance protein (BCRP/ABCG2) in drug transport--an update. AAPS J 17:65–82

Martin C, Berridge G, Higgins CF, Mistry P, Charlton P, Callaghan R (2000) Communication between multiple drug binding sites on P-glycoprotein. Mol Pharmacol 58:624–632

Marzolini C, Paus E, Buclin T, Kim RB (2004) Polymorphisms in human MDR1 (P-glycoprotein): Recent advances and clinical relevance. Clin Pharmacol Ther

Matthews PM, Rabiner EA, Passchier J, Gunn RN (2012) Positron emission tomography molecular imaging for drug development. Br J Clin Pharmacol 73:175–186

McTavish D, Sorkin EM (1989) Verapamil. Drugs 38:19–76

Milane A, Fernandez C, Dupuis L et al (2010) P-glycoprotein expression and function are increased in an animal model of amyotrophic lateral sclerosis. Neurosci Lett 472:166–170

Miller DS, Bauer B, Hartz AMS (2008) Modulation of P-glycoprotein at the blood-brain barrier: opportunities to improve central nervous system pharmacotherapy. Pharmacol Rev 60:196–209

Moerman L, Dumolyn C, Boon P, De Vos F (2012) The influence of mass of [11C]-laniquidar and [11C]-N-desmethyl-loperamide on P-glycoprotein blockage at the blood{\textendash}brain barrier. Nucl Med Biol 39:121–125

Morris ED, Endres CJ, Schmidt KC, Christian BT, Muzic RF, Fisher RE. Kinetic modeling in positron emission tomography. In: Emission tomography. 46. Elsevier; Amsterdam 2004:499–540

Morris ME, Rodriguez-Cruz V, Felmlee MA (2017) SLC and ABC transporters: expression, localization, and species differences at the blood-brain and the blood-cerebrospinal fluid barriers. AAPS J 19(5):1317–1331

Muzi M, Mankoff DA, Link JM et al (2009) Imaging of cyclosporine inhibition of P-glycoprotein activity using 11C-verapamil in the brain: studies of healthy humans. J Nucl Med 50:1267–1275

Ni Z, Bikadi Z, Rosenberg MF, Mao Q (2010) Structure and function of the human breast cancer resistance protein (BCRP/ABCG2). Curr Drug Metab 11:603

O'Brien FE, Dinan TG, Griffin BT, Cryan JF (2012) Interactions between antidepressants and P-glycoprotein at the blood-brain barrier: clinical significance of in vitro and in vivo findings. Br J Pharmacol 165:289–312

O'Brien FE, Moloney GM, Scott KA et al (2015) Chronic P-glycoprotein inhibition increases the brain concentration of escitalopram: potential implications for treating depression. Pharmacol Res Perspect 3:1–11

Okamura T, Kikuchi T, Okada M et al (2009) Noninvasive and quantitative assessment of the function of multidrug resistance-associated protein 1 in the living brain. J Cereb Blood Flow Metab 29:504–511

Osgood D, Miller MC, Messier AA, Gonzalez L, Silverberg GD (2017) Aging alters mRNA expression of amyloid transporter genes at the blood-brain barrier. Neurobiol Aging 57:178–185

Parker A, Fonseca S, Carding SR. Gut microbes and metabolites as modulators of blood-brain barrier integrity and brain health. Gut Microbes 2019;0:1–23

Parrish K, Sarkaria J, Elmquist W (2015) Improving drug delivery to primary and metastatic brain tumors: Strategies to overcome the blood-brain barrier. Clin Pharmacol Ther 97:336–346

Passchier J, van Waarde A, Doze P, Elsinga PH, Vaalburg W (2000) Influence of P-glycoprotein on brain uptake of [18F]MPPF in rats. Eur J Pharmacol 407:273–280

Pauli-Magnus C, von Richter O, Burk O et al (2000) Characterization of the major metabolites of verapamil as substrates and inhibitors of P-glycoprotein. J Pharmacol Exp Ther 293:376–382

Pereira CD, Martins F, Wiltfang J, da Cruz e Silva OAB, Rebelo S (2017) ABC transporters are key players in Alzheimer's disease. J Alzheimers Dis 61:463–485

Pezzoli G, Cereda E (2013) Exposure to pesticides or solvents and risk of Parkinson disease. Neurology 80:2035–2041

Pike VW (2009) PET radiotracers: crossing the blood–brain barrier and surviving metabolism. Trends Pharmacol Sci 30:431–440

Porro A, Haber M, Diolaiti D et al (2010) Direct and coordinate regulation of ATP-binding cassette transporter genes by Myc factors generates specific transcription signatures that significantly affect the chemoresistance phenotype of cancer cells. J Biol Chem 285:19532–19543

Pottier G, Marie S, Goutal S et al (2016) Imaging the impact of the P-glycoprotein (ABCB1) function on the brain kinetics of metoclopramide. J Nucl Med 57:309–314

Qosa H, Miller DS, Pasinelli P, Trotti D (1628) Regulation of ABC efflux transporters at blood-brain barrier in health and neurological disorders. Brain Res 2015:298–316

Raaphorst RM, Luurtsema G, Schuit RC et al (2017a) Synthesis and evaluation of new fluorine-18 labeled verapamil analogs to investigate the function of P-glycoprotein in the blood–brain barrier. ACS Chem Neurosci 8:1925–1936

Raaphorst RM, Savolainen H, Cantore M et al (2017b) Comparison of in vitro assays in selecting radiotracers for in vivo P-glycoprotein PET imaging. Pharmaceuticals (Basel) 10:1–25

Rahmim A, Lodge MA, Karakatsanis NA et al (2019) Dynamic whole-body PET imaging: principles, potentials and applications. Eur J Nucl Med Mol Imaging 46:501–518

Riddell DR, Zhou H, Comery TA et al (2007) The LXR agonist TO901317 selectively lowers hippocampal Aβ42 and improves memory in the Tg2576 mouse model of Alzheimer's disease. Mol Cell Neurosci 34:621–628

Robillard KR, Hoque MT, Bendayan R (2014) Expression of ATP-binding cassette membrane transporters in a HIV-1 transgenic rat model. Biochem Biophys Res Commun 444:531–536

Rosenhagen MC, Uhr M (2011) The clinical impact of ABCB1 polymorphisms on the treatment of psychiatric diseases. Curr Pharm Des 17:2843–2851

Saidijam M, Karimi Dermani F, Sohrabi S, Patching SG (2018) Efflux proteins at the blood–brain barrier: review and bioinformatics analysis. Xenobiotica 48:506–532

Sane R, Wu S-P, Zhang R, Gallo JM (2014) The effect of ABCG2 and ABCC4 on the pharmacokinetics of methotrexate in the brain. Drug Metab Dispos 42:537–540

Savolainen H, Cantore M, Colabufo NA, Elsinga PH, Windhorst AD, Luurtsema G (2015) Synthesis and preclinical evaluation of three novel fluorine-18 labeled radiopharmaceuticals for P-glycoprotein PET imaging at the blood-brain barrier. Mol Pharm 12:2265–2275

Savolainen H, Windhorst AD, Elsinga PH et al (2017a) Evaluation of [18 F]MC225 as a PET radiotracer for measuring P-glycoprotein function at the blood–brain barrier in rats: Kinetics, metabolism, and selectivity. J Cereb Blood Flow Metab 37:1286–1298

Savolainen H, Windhorst AD, Elsinga PH et al (2017b) Evaluation of [18F]MC225 as a PET radiotracer for measuring P-glycoprotein function at the blood-brain barrier in rats: kinetics, metabolism, and selectivity. J Cereb Blood Flow Metab 37:1286–1298

Schaheen L (2006) Suppression of the cup-5 mucolipidosis type IV-related lysosomal dysfunction by the inactivation of an ABC transporter in C. elegans. Development 133:3939–3948

Schmidt D, Schachter SC (2014) Drug treatment of epilepsy in adults. BMJ 348:g254–g254

Shapiro AB, Ling V (1997) Positively cooperative sites for drug transport by P-glycoprotein with distinct drug specificities. Eur J Biochem 250:130–137

Shapiro AB, Fox K, Lam P, Ling V (2001) Stimulation of P-glycoprotein-mediated drug transport by prazosin and progesterone. Eur J Biochem 259:841–850

Sharom FJ (2008) {ABC} multidrug transporters: structure, function and role in chemoresistance. Pharmacogenomics 9:105–127

Silva R, Sousa E, Carmo H et al (2014) Induction and activation of P-glycoprotein by dihydroxylated xanthones protect against the cytotoxicity of the P-glycoprotein substrate paraquat. Arch Toxicol 88:937–951

Silva R, Vilas-Boas V, Carmo H et al (2015) Modulation of P-glycoprotein efflux pump: induction and activation as a therapeutic strategy. Pharmacol Ther 149:1–123

Spudich A, Kilic E, Xing H et al (2006) Inhibition of multidrug resistance transporter-1 facilitates neuroprotective therapies after focal cerebral ischemia. Nat Neurosci 9:487–488

Stavchansky SA, Tilbury RS, McDonald JM, Ting CT, Kostenbauder HB (1978) In vivo distribution of carbon-11 phenytoin and its major metabolite, and their use in scintigraphic imaging. J Nucl Med 19:936–941

Steece-Collier K, Maries E, Kordower JH (2002) Etiology of Parkinson's disease: genetics and environment revisited. Proc Natl Acad Sci U S A 99:13972–13974

Summers MA, Moore JL, McAuley JW (2004) Use of verapamil as a potential P-glycoprotein inhibitor in a patient with refractory epilepsy. Ann Pharmacother 38:1631–1634

Syvänen S, Eriksson J (2013) Advances in PET imaging of P-glycoprotein function at the blood-brain barrier. ACS Chem Neurosci 4:225–237

Syvänen S, Russmann V, Verbeek J et al (2013) [11C]quinidine and [11C]laniquidar PET imaging in a chronic rodent epilepsy model: Impact of epilepsy and drug-responsiveness. Nucl Med Biol 40:764–775

Szabo L (1989) (S)-emopamil, a novel calcium and serotonin antagonist for the treatment of cerebrovascular disorders. 2nd communication: brain penetration, cerebral vascular and metabolic effects. Arzneimittelforschung 39:309–314

Tamaki A, Ierano C, Szakacs G, Robey RW, Bates SE (2011) The controversial role of ABC transporters in clinical oncology. Essays Biochem 50(1):209–232

Tang F, Hartz AMS, Bauer B (2017) Drug-resistant epilepsy: multiple hypotheses, few answers. Front Neurol

Templeton NS, Lasic DD, Frederik PM, Strey HH, Roberts DD, Pavlakis GN (1997) Improved DNA: liposome complexes for increased systemic delivery and gene expression. Nat Biotechnol 15:647–652

Tournier N, Cisternino S, Peyronneau M-A et al (2012) Discrepancies in the P-glycoprotein-mediated transport of 18F-MPPF: a pharmacokinetic study in mice and non-human primates. Pharm Res 29:2468–2476

Tournier N, Stieger B, Langer O (2018) Imaging techniques to study drug transporter function in vivo. Pharmacol Ther 189:104–122

Tournier N, Bauer M, Pichler V et al (2019) Impact of P-glycoprotein function on the brain kinetics of the weak substrate 11 C-metoclopramide assessed with PET imaging in humans. J Nucl Med 60:985–991

Toyohara J (2016) Importance of P-gp PET imaging in pharmacology. Curr Pharm Des 22:5830–5836

Toyohara J, Okamoto M, Aramaki H, Zaitsu Y, Shimizu I, Ishiwata K (2016) (R)-[11 C]Emopamil as a novel tracer for imaging enhanced P-glycoprotein function. Nucl Med Biol 43:52–62

Uchida Y, Ohtsuki S, Katsukura Y et al (2011) Quantitative targeted absolute proteomics of human blood-brain barrier transporters and receptors. J Neurochem 117:333–345

Ueno M, Nakagawa T, Huang C-l et al (2009) The expression of P-glycoprotein is increased in vessels with blood-brain barrier impairment in a stroke-prone hypertensive model. Neuropathol Appl Neurobiol 35:147–155

Verbeek J, Eriksson J, Syvänen S et al (2012a) [11C]phenytoin revisited: synthesis by [11C]CO carbonylation and first evaluation as a P-gp tracer in rats. EJNMMI Res 2:36

Verbeek J, Syvänen S, Schuit RC et al (2012b) Synthesis and preclinical evaluation of [11C]D617, a metabolite of (R)-[11C]verapamil. Nucl Med Biol 39:530–539

Verbeek J, Eriksson J, Syvänen S et al (2018) Synthesis and preliminary preclinical evaluation of fluorine-18 labelled isatin-4-(4-methoxyphenyl)-3-thiosemicarbazone ([18F]4FIMPTC) as a novel PET tracer of P-glycoprotein expression. EJNMMI Radiopharm Chem 3:11

van Vliet EA, Redeker S, Aronica E, Edelbroek PM, Gorter JA (2005) Expression of multidrug transporters MRP1, MRP2, and BCRP shortly after status epilepticus, during the latent period, and in chronic epileptic rats. Epilepsia 46:1569–1580

Vogelgesang S, Jedlitschky G (2014) In vitro models of the human blood-brain barrier and the impact of efflux transporters on neurological disorders: the work of Cioni et al. (2012). Front Psych 5:128

Vogelgesang S, Cascorbi I, Schroeder E et al (2002a) Deposition of Alzheimer's beta-amyloid is inversely correlated with P-glycoprotein expression in the brains of elderly non-demented humans. Pharmacogenetics 12:535–541

Vogelgesang S, Cascorbi I, Schroeder E et al (2002b) Deposition of Alzheimer{\textquotesingle}s ??-amyloid is inversely correlated with P-glycoprotein expression in the brains of elderly non-demented humans. Pharmacogenetics 12:535–541

Vogelgesang S, Glatzel M, Walker LC, Kroemer HK, Aguzzi A, Warzok RW (2006) Cerebrovascular P-glycoprotein expression is decreased in Creutzfeldt–Jakob disease. Acta Neuropathol 111:436–443

Volk HA, Löscher W (2005) Multidrug resistance in epilepsy: rats with drug-resistant seizures exhibit enhanced brain expression of P-glycoprotein compared with rats with drug-responsive seizures. Brain 128:1358–1368

Waghray D, Zhang Q (2018) Inhibit or evade multidrug resistance P-glycoprotein in cancer treatment. J Med Chem 61:5108–5121

Wagner CC, Bauer M, Karch R et al (2009) A pilot study to assess the efficacy of tariquidar to inhibit P-glycoprotein at the human blood-brain barrier with (R)-11C-verapamil and {PET}. J Nucl Med 50:1954–1961

Wanek T, Kuntner C, Bankstahl JP et al (2011) A comparative small-animal {PET} evaluation of [11C]tariquidar, [11C]elacridar and (R)-[11C]verapamil for detection of P-glycoprotein-expressing murine breast cancer. Eur J Nucl Med Mol Imaging 39:149–159

Wanek T, Kuntner C, Bankstahl JP et al (2012) A novel PET protocol for visualization of breast cancer resistance protein function at the blood-brain barrier. J Cereb Blood Flow Metab 32:2002–2011

Wanek T, Mairinger S, Langer O (2013) Radioligands targeting P-glycoprotein and other drug efflux proteins at the blood-brain barrier. J Label Compd Radiopharm 56:68–77

Wanek T, Römermann K, Mairinger S et al (2015) Factors governing P-glycoprotein-mediated drug-drug interactions at the blood-brain barrier measured with positron emission tomography. Mol Pharm 12:3214–3225

Wang Q (2015) ABCB1 gene C3435T polymorphism and drug resistance in epilepsy: evidence based on 8604 subjects. Med Sci Monit

Wang GL, Jiang BH, Rue EA, Semenza GL (1995) Hypoxia-inducible factor 1 is a basic-helix-loop-helix-PAS heterodimer regulated by cellular O2 tension. Proc Natl Acad Sci

Wang G-X, Wang D-W, Liu Y, Ma Y-H (2016) Intractable epilepsy and the P-glycoprotein hypothesis. Int J Neurosci 126:385–392

Westerlund M, Belin AC, Olson L, Galter D (2008) Expression of multi-drug resistance 1 mRNA in human and rodent tissues: reduced levels in Parkinson patients. Cell Tissue Res 334:179–185

Westerlund M, Belin AC, Anvret A et al (2009) Association of a polymorphism in the ABCB1 gene with Parkinson's disease. Park Relat Disord

Willmann JK, van Bruggen N, Dinkelborg LM, Gambhir SS (2008) Molecular imaging in drug development. Nat Rev Drug Discov 7:591–607

Wirdefeldt K, Adami HO, Cole P, Trichopoulos D, Mandel J (2011) Epidemiology and etiology of Parkinson's disease: a review of the evidence. Eur J Epidemiol 26

Wolf A, Bauer B, Hartz AMS (2012) ABC transporters and the Alzheimer's disease enigma. Front Psych 3:1–14

Wulkersdorfer B, Wanek T, Bauer M, Zeitlinger M, Müller M, Langer O (2014) Using positron emission tomography to study transporter-mediated drug–drug interactions in tissues. Clin Pharmacol Ther 96:206–213

Xiong H, Callaghan D, Jones A et al (2009) ABCG2 is upregulated in Alzheimer's brain with cerebral amyloid angiopathy and may act as a gatekeeper at the blood-brain barrier for A 1-40 peptides. J Neurosci 29:5463–5475

Yamamoto Y, Välitalo PA, Wong YC et al (2018) Prediction of human CNS pharmacokinetics using a physiologically-based pharmacokinetic modeling approach. Eur J Pharm Sci 112:168–179

Yang H, Liu H, Liu X et al (2008) Increased P-glycoprotein function and level after long-term exposure of four antiepileptic drugs to rat brain microvascular endothelial cells in vitro. Neurosci Lett 434:299–303

Zhang L, Zhang YD, Strong JM, Reynolds KS, Huang S-M (2008) A regulatory viewpoint on transporter-based drug interactions. Xenobiotica 38:709–724

Zhang C, Kwan P, Zuo Z, Baum L (2010) In vitro concentration dependent transport of phenytoin and phenobarbital, but not ethosuximide, by human P-glycoprotein. Life Sci 86:899–905

Zhao Z, Nelson AR, Betsholtz C, Zlokovic BV (2015) Establishment and dysfunction of the blood-brain barrier. Cell 163:1064–1078

Zhao Y, Hou D, Feng X, Lin F, Luo J (2017) Role of ABC transporters in the pathology of Alzheimer's disease. Rev Neurosci 28(2):155–159

Zhou S-F (2008) Structure, function and regulation of P-glycoprotein and its clinical relevance in drug disposition. Xenobiotica 38:802–832

Zlokovic BV (2011) Neurovascular pathways to neurodegeneration in Alzheimer's disease and other disorders. Nat Rev Neurosci

Zoghbi SS, Liow J-S, Yasuno F et al (2008) 11C-loperamide and its N-desmethyl radiometabolite are avid substrates for brain permeability-glycoprotein efflux. J Nucl Med 49:649–656

Zoufal V, Mairinger S, Krohn M et al (2020) Measurement of cerebral ABCC1 transport activity in wild-type and APP/PS1-21 mice with positron emission tomography. J Cereb Blood Flow Metab 40(5):954–965

Zschiedrich K, König IR, Brüggemann N et al (2009) MDR1 variants and risk of Parkinson disease. J Neurol 256:115–120

PET Imaging of Phosphodiesterases in Brain

23

Maarten Ooms and Guy Bormans

Contents

Abstract

Phosphodiesterases (PDEs) regulate the intracellular concentration of the secondary messengers cGMP and cAMP thereby modulating a variety of cellular activities in brain. Eleven different families of PDEs have been identified of which at least six show significant expression in brain. Phosphodiesterase inhibitors have been evaluated clinically as potential drugs for treatment of different CNS diseases but so far, no PDE inhibitor has been registerered as a drug for

M. Ooms
SCK CEN, Belgian Nuclear Research Centre, Institute for Nuclear Materials Science, Mol, Belgium
e-mail: maarten.ooms@sckcen.be

G. Bormans (✉)
Radiopharmaceutical Research, Department of Pharmacological and Pharmaceutical Sciences, KU Leuven, Leuven, Belgium
e-mail: guy.bormans@kuleuven.be

treatment of a CNS disease. PET ligands have been developed and evaluated targeting PDE2,4,5, and 10 and clinical PET studies were conducted with radio-labeled PDE2, 4, and 10 inhibitors. PDEs are interesting targets for in vivo imaging with PET as both their expression level and affinity for inhibitors can be modulated. This chapter provides an overview of the development of PDE PET tracers and their application in preclinical and clinical research.

23.1 Introduction Phosphodiesterases

Phosphodiesterases (PDEs) are a group of 11 families of ubiquitous intracellular enzymes that hydrolyze the cyclic nucleotides 3′,5′-cyclic adenosine monophosphate (cAMP) and/or 3′,5′-cyclic guanosine monophosphate (cGMP) to the corresponding 5′ monophosphates (Maurice et al. 2014).

The different families of PDEs are grouped based on their C-terminal catalytic domain homology. PDEs can be selective for cAMP or cGMP but can also have dual cGMP and cAMP selectivity (Table 23.1). Isoforms within a PDE family differ with regard to their N-terminal regulatory domain which is important for subcellular localization or modulation of catalytic activity.

Both cAMP and cGMP are important intracellular second messenger molecules for G-protein coupled receptors. Both cyclic nucleotides accomplish phosphorylation of a multitude of downstream targets including CREB (cAMP response element binding protein). cAMP activates protein kinase A (PKA), exchange protein activated by cAMP (Epac) (Bos 2006), and popeye domain-containing (POPDC) proteins (Schindler and Brand 2016). cGMP on the other hand stimulates protein kinase G. Both cAMP and cGMP activate cyclic nucleotide gated channels (CNGs).

The simultaneous use of cGMP and/or cAMP as second messengers in various cellular pathways is possible by compartmentalization, i.e., spatial separation of these signalling pathways as was observed in cardiac myocytes (Zaccolo 2011). PDEs can also be largely confined to specific subcellular pools in order to control local cAMP and/or cGMP levels (Mongillo et al. 2004).

The synthesis of cAMP is managed by both transmembrane adenylyl cyclases (tACs) and soluble adenylyl cyclases (sACs). The synthesis of cGMP is controlled by particulate and soluble guanylyl cyclases (pGCs). The concentration and compartmentalization of both cAMP and cGMP is tightly regulated by synthesis and hydrolysis through PDE activity although the hydrolysis outperforms the synthesis capacity (Baillie et al. 2019).

Both the catalytic function (V_{max}) and the affinity of PDEs can be modulated by different mechanisms including oligomerization, modulation by regulatory domains, and post translational modifications such as phosphorylation, ubiquitylation, SUMOylation, S-nitrosylation, and proline hydroxylation (Baillie et al. 2019).

PDEs exist as homodimers except for PDE1 and 6 which occur as heterotetramers (Bender and Beavo 2006). The conformation of the homodimer can change

Table 23.1 Overview of characteristics of different phosphodiesterase families

PDE family (members)	Substrate	N-terminal regulatory/ localization domain	Relative expression in brain (Lakics et al. 2010) (expression in other organs)	Clinical trial with CNS target	PET tracers for CNS
PDE1 (1A, 1B, 1C)	cGMP, cAMP	Calmodulin	1B caudate and nucleus accumbens, 1C substantia nigra	Schizophrenia, PD, cognition enhancement	–
PDE2 (2A)	cGMP, cAMP	GAFA/B-cGMP stimulated	Hippocampus, cortical regions	Schizophrenia	+
PDE3 (3A, 3B)	cGMP, cAMP	Transmembrane domain	3A cerebellum	Tinnitus, AD, MCI	–
PDE4 (4A, 4B, 4C, 4D)	cAMP	UCR	4A, B, and D all brain regions. 4C cortex, thalamic nuclei and cerebellum	AD, Fragile X, HD, dementia	+
PDE5 (5A)	cGMP	GAFA/B cGMP stimulated	Low levels in vasculature	Migraine, mild TBI	–
PDE6 (6A, 6B, 6C)	cGMP	GAFA/B cGMP stimulated	(PDE6A retina)	–	–
PDE7 (7A, 7B)	cAMP		PDE7B caudate, nucleus accumbens, cortex, hippocampus	–	–
PDE8 (8A, 8B)	cAMP	Per-ARNT-Sim (PAS) domain	(PDE8B thyroid) 8A and 8B low brain levels	–	–
PDE9 (9A)	cGMP	Nuclear localization domain	Dorsal root ganglia, cerebellum	AD, schizophrenia	–
PDE10 (10A)	cGMP, cAMP	GAFA/B cAMP stimulated	Caudate nucleus, nucleus accumbens	Schizophrenia	++
PDE11 (11A)	cGMP, cAMP	GAFA/B cGMP stimulated	Dorsal root ganglia Substantia nigra	–	–

due to activation of the regulatory domain from a low activity conformation with (partially) blocked access to the catalytic site to a highly active conformation with fully accessible catalytic site in a high affinity state.

PDEs have regulatory domains including calcium/calmodulin-binding domains (PDE1), GAF domains (cGMP-binding PDEs, Anabaena adenylyl cyclase, and *Escherichia coli* FhlA; PDE2, PDE5, PDE6, PDE10, and PDE11), PAS domains (Per-ARNT-Sim; PDE8), UCR domains (upstream conserved regulatory domains; PDE4), and autoinhibitory domains. The GAF and UCR domains are unique regulatory domains that only occur in PDEs in mammals.

The GAF domains of PDE2,5,6, and 11 allosterically bind cGMP, whereas the GAF domain of PDE10 allosteric binds cAMP. This allosteric binding causes

structural changes relieving autoinhibition of the PDEs (Francis et al. 2011). GAF domains can also provide contacts for dimerization8. cGMP binding the GAF-A domain of PDE6 enhances protein–protein interactions that inhibit PDE6 catalytic activity. Allosteric binding of cGMP to the GAF-B domain of PDE2A increases hydrolysis rate of cAMP with a factor of 10 thereby cross-regulating the concentration of both cyclic nucleotides (Wu et al. 2018).

23.1.1 Drugs Targeting PDEs

Major marketed PDE inhibitors include non-specific PDE inhibitors used since 1970s for treatment of asthma; PDE3 inhibitors for treatment of heart failure and claudication; PDE4 inhibitors for treatment of chronic obstructive pulmonary disease, psorias, dermatitis, and bowel disorders and PDE5 inhibitors for treatment of erectile dysfunction and pulmonary arterial hypertension (Baillie et al. 2019).

Most PDEs are (also) expressed in the brain, and a large number of clinical studies have investigated the use of PDE inhibitors for treatment of various neurological diseases (Table 23.1). Most if not all of these clinical studies however failed due to safety concerns or a lack of efficacy. In some of these clinical trials PET was used to determine the PDE occupancy level of the drug candidate (see below).

Besides PDE inhibitors targeting the catalytic site also allosteric modulators targeting the regulatory domain (which can also activate the PDE activity) are being pursued preclinically for PDE4D (Sutcliffe et al. 2014; Burgin et al. 2010; Omar et al. 2019; Titus et al. 2018), PDE5 (Weeks et al. 2005), PDE10 (García et al. 2017; Jäger et al. 2012), and PDE11 (Weeks et al. 2005).

23.2   PET Studies Targeting Phosphodiesterases

Phosphodiesterases are an interesting target for PET but the binding potential of PET tracers depends both on expression levels and affinity and both parameters can be modulated for PDEs in CNS pathologies. Especially phosphodiesterases with a GAF domain are subject to cGMP and/or cAMP modulation of the affinity of PET tracers directed to the C-terminal catalytic domain. The specific cause for a changed PET binding potential in a studied pathology may therefore be caused by local cGMP and/or cAMP concentration induced PDE affinity modulation vs. PDE expression. The PET binding potential may however provide a more physiologically relevant readout for global PDE activity compared to techniques that only rely on quantifying protein expression levels. On the other hand, PET has only a limited resolution which does not allow to identify potential changes in subcellular compartmentalization of PDEs which have been reported to be important in different CNS pathologies. The existence of 11 different PDE families, each consisting of a number of subtypes requires PET tracers to have high selectivity for the PDE type that is studied as different PDE subtypes will likely be present in the same brain region, cells, and cell compartments.

Different PET tracers for phosphodiesterases have been reviewed extensively (Andrés et al. 2012; Schröder et al. 2016), so in this chapter we will focus on novel developments reported since 2016.

23.2.1 PDE1

The PDE1 family consists of PDE1A, PDE1B, and PDE1C isoforms and is the only mammalian PDEs that are transiently activated by the calcium/calmodulin complex. They thus provide intracellular cross-talk between calcium and cyclic nucleotide signaling. PDE1B has the highest expression in brain and co-localizes with dopaminergic D_1 and D_2 receptors in striatal and cortical neurons (Pekcec et al. 2018). Several PDE1 inhibitors have been developed (Chen et al. 2019; Li et al. 2016; Dyck et al. 2017; Khammy et al. 2017; Enomoto et al. 2019) of which ITI-214 (Fig. 23.1) was tested in a clinical study for treatment of schizophrenia (NCT01900522). So far however, no PET tracers targeting PDE1A were reported.

23.2.2 PDE2A

PDE2A hydrolyzes both cAMP and cGMP and shows high expression in cortex, amygdala, and hippocampus. Several PDE2A specific inhibitors were developed (Trabanco et al. 2016) and some were evaluated in clinical studies for anxiety, cognition enhancement, schizophrenia, and/or depression including ND-7001 (Gomez and Breitenbucher 2013), PF-05180999 (Fig. 23.2) (Helal et al. 2018) (NCT01981486 and NCT01981499), and TAK-915 (Fig. 23.2) (Mikami et al. 2017) (NCT02461160, NCT02584569).

Fig. 23.1 Structure of PDE1inhibiotor ITI-214
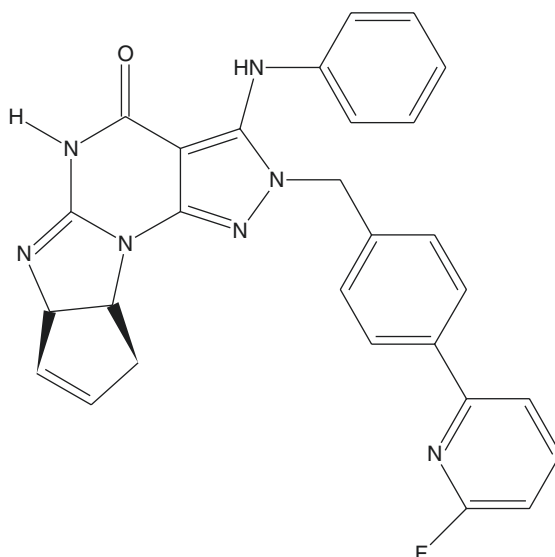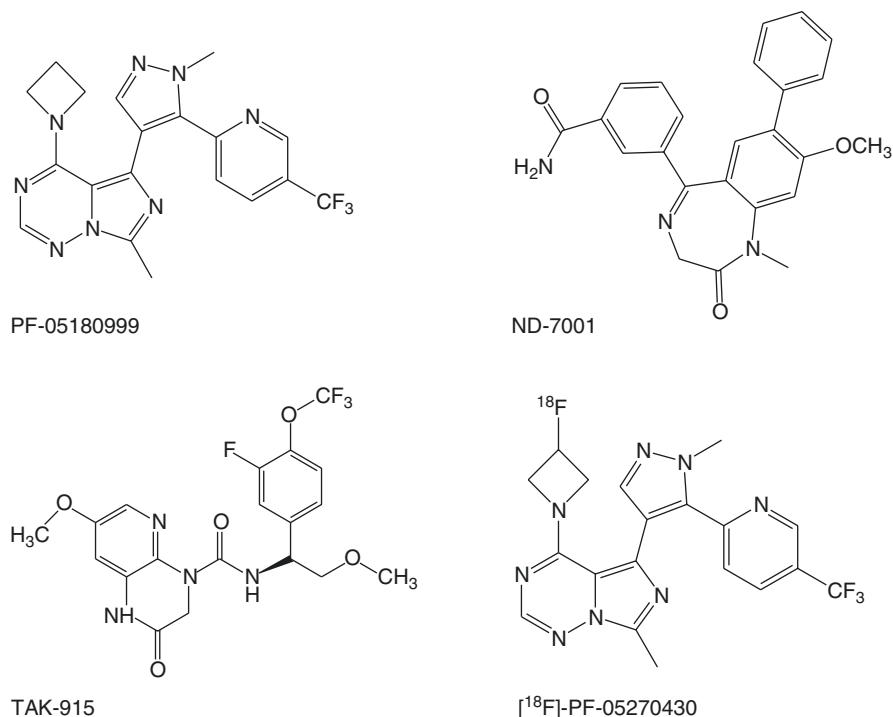
Fig. 23.2 Chemical structures of PDE2 inhibvitors PF-05180999, ND-7001, TAK-915, and PDE2A PET tracer [^{18}F]PF-05270430

Several PDE2A PET tracers have been developed and evaluated preclinically (Chen et al. 2016; Schröder et al. 2015, 2018; Ritawidya et al. 2019) but only two tracers ([^{18}F]PF-05270430 and [^{18}F]MNI-794, Fig. 23.2) were evaluated clinically. [^{18}F]PF-05270430 displayed fast and reversible kinetics in nonhuman primates, as well as PDE2A specific binding blockable by a PDE2A inhibitor. First in human evaluation of [^{18}F]PF-05270430 (Naganawa et al. 2016) demonstrated highest uptake in striatum, followed by neocortical regions and white matter, and lowest in the cerebellum. Binding potential relative to the nondisplaceable tracer (BP_{ND}) were determined with the simplified reference tissue model and a 70 min scan using cerebellum as reference tissue. BP_{ND} values ranging from 0.3 (parietal cortex) to 0.8 (putamen) were obtained with a test-retest variability of 16%.

[^{18}F]MNI-794 was used to quantify the occupancy of TAK-915 (NCT02584569, Fig. 23.2), but no detailed reports on this PET tracer have been published.

Unfortunately no preclinical nor clinical studies using PET to investigate the expression levels of PDE2A in CNS pathologies have been published so far. Interestingly, at low dose, PDE2A inhibition produced a paradoxal increase of PDE2A autoradiography binding probably due to release of cGMP activating a dormant pool of PDE2A enzymes via binding to the GAF-B domain (Pandit et al. 2009;

Gu et al. 2019). A loss of function mutation in PDE2A was found to be associated with chorea suggesting a role of PDE2A in hyperkinetic movement disorders (Salpietro et al. 2018).

23.2.3 PDE4

PDE4 is a highly disperse family of phosphodiesterases which exclusively hydrolyzes cAMP. The family is encoded by four sub-family genes (PDE4A to D) which generate over 16 different splice variants with each a unique N-Terminal regulatory domain. These splice variants can generally be divided into three major categories: long form, short form, and super-short form (Omori and Kotera 2007). The N-Terminal domain of the long form splice variants contains two Upstream Conserved Regions (UCR1 and UCR2) which are conserved in all PDE4 subfamilies. Short and super-short isoforms however only express one or even only a part of one UCR (Francis et al. 2011). It is generally accepted that UCR 1 is required for dimerization, while UCR2 plays an important role in the regulation of enzymatic activity and intracellular targeting (Richter and Conti 2002). PDE4 also has a phosphorylation site for PKA that regulates PDE4 activity and activates PDE4 when cAMP levels are high.

The expression of PDE4 is rather ubiquitous; however high expression in immune cells, brain, and cardiovascular tissues have been reported (Richter et al. 2011; Lakics et al. 2010; Tenor et al. 1996). Among all PDE families, PDE4 is the most abundant in the brain, accounting for 30–70% of all PDE activity in the central nervous system (Lakics et al. 2010). Due to the importance of cAMP signaling in the brain physiology, it is generally accepted that PDE4, as the major cAMP hydrolyzing enzyme in the brain, plays a decisive role in normal functioning of the brain. Alterations in cAMP signaling are believed to be a key element in the pathophysiology of multiple psychiatric and neurological disorders such as depression, Alzheimers Disease, and Parkinson's disease (Missale et al. 1998; Reiach et al. 1999; Martínez et al. 1999; Casacchia et al. 1983). Therefore, it is believed that stabilizing cAMP levels using PDE4 inhibitors can have beneficial effects on emotional and cognitive behaviors in such diseases (Zhu et al. 2001; Li et al. 2009; O'Donnell 1993; O'Donnell and Frith 1999; Zhang and O'Donnell 2000; Zhang 2009). Additionally, PDE4 is highly expressed in inflammatory cells and lung smooth muscle cells. Therefore, it is believed that PDE4 is also an important regulator of the inflammatory response in several lung diseases such as asthma and Chronic Obstructive Pulmonary Disease (COPD). Inhibition of PDE4 could therefore also have beneficial effects on the symptoms of these diseases (Hatzelmann et al. 2010).

Rolipram is a non-subtype selective PDE4 inhibitor which has been used for treatment on regular basis in preclinical and clinical trials (Casacchia et al. 1983; Renau 2004). In a number of single-arm (phase I) trials and in several randomized phase III trials, rolipram demonstrated clinical activity in reducing symptoms of depression. Also in COPD, rolipram was found to be an efficient treatment option.

The application of rolipram was however limited due to dose-limiting side effects including headache, gastric hyper secretion, and emesis (Hebenstreit et al. 1989; Scott et al. 1991; Bobon et al. 1988; Fleischhacker et al. 1992; Krause et al. 1990). Especially the emetic effects have put a serious hold on the further development of rolipram and other related PDE4 inhibitors. It is believed that the lack of selectivity of rolipram toward the different PDE4 subtypes may account for some of the side effects observed. Several studies indicate that the emetic effects of rolipram might be caused by the PDE4D inhibition in the area postrema and nucleus of the solitary tract (Halpin 2008; Lamontagne et al. 2001; Mori et al. 2010; Cherry and Davis 1999; Robichaud et al. 2002), while PDE4B inhibition would be responsible for the anti-depressant effect of rolipram (Zhang et al. 2017).

For the treatment of COPD, the problem of emesis was reduced by the development of a PDE4 inhibitor with limited brain penetration to avoid central inhibition of PDE4D. This PDE4 inhibitor, roflumilast has now been approved for the treatment of COPD (Rabe 2011). When treating neuropsychiatric disorders such as depression, brain penetration is however crucial for its pharmacological activity. Therefore, more efforts are invested on developing subtype specific inhibitors to avoid the emesis problem (Azam and Tripuraneni 2014). Since mice deficient in PDE4B showed anxiogenic and antidepressant effects, PDE4B is believed to be an important target for depression (Zhang et al. 2008). Several PDE4B selective inhibitors have been developed showing similar anti-depressant activities as rolipram (Azam and Tripuraneni 2014). Although PDE4D inhibition has been linked to the emetic effects of nonselective PDE4 inhibitors, it is still believed that PDE4D inhibitors could have therapeutic potential as PDE4D is attributed to play an important role in cognition. Indeed, animal models deficient of the PDE4D gene show increased cognitive performance (Li et al. 2011; Ricciarelli et al. 2017). Therefore, a lot of effort is also put in the development of PDE4D-selective inhibitors as a treatment for Alzheimer's disease and cognitive brain disorders. For example, PDE4D inhibitors such as BPN14770 are currently under development for the treatment of Fragile X Syndrome and other brain disorders (Gurney et al. 2019; Cui et al. 2019).

The majority of the information on PDE4 comes from ex vivo data. Enzymatic activity of PDE4 is however highly dependent on the phosphorylation state of the enzyme (MacKenzie et al. 2002). Since dephosphorylation occurs rapidly after death, caution is required when interpreting ex vivo measurements of PDE4 activity. Therefore, the availability of PDE4 PET imaging is crucial to quantify PDE4 alterations in vivo. The non-PDE4 selective inhibitor Rolipram has 2 enantiomers who have both been radiolabelled with carbon-11 for PET imaging. [^{11}C](R)-Rolipram (Fig. 23.3) has a high affinity for PDE4 and PET imaging with [^{11}C](R)-Rolipram has been shown to allow monitoring of PDE4 activity and expression in vivo (Lourenco et al. 2001, 1999). Since its development, [^{11}C](R)-Rolipram has been used to explore PDE4 levels in several preclinical models of disease as well as in patient populations. [^{11}C](S)-Rolipram on the other hand has a 20-fold lower affinity toward PDE4 compared to its R-entantiomer. Due to its much lower affinity however, [^{11}C](S)-Rolipram can be used to quantify non-displacable binding or changes in tracer brain delivery caused by disease or treatment (Fujita et al. 2005; Itoh et al. 2010).
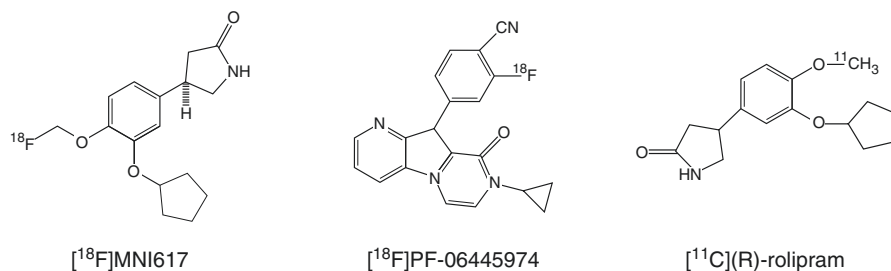
Fig. 23.3 Chemical structures of PDE4 tracers [¹⁸F]MNI617, [¹⁸F]PF-06445974, and [¹¹C](R)-rolipram

A recent study in conscious rats showed that PKA-mediated phosphorylation of PDE4 increased the in vivo binding of [¹¹C](R)-Rolipram, consistent with the increased affinity of rolipram toward the phosphorylated PDE4 enzyme (Itoh et al. 2010; Takano et al. 2018). This study was the first to indicate that [¹¹C](R)-Rolipram binding was dependent on the phosphorylation state of PDE4. A further study building upon these results showed that [¹¹C](R)-Rolipram was also sensitive to changes in PDE4 activity due to protein–protein interaction. This study used [¹¹C] (R)-Rolipram PET to investigate the interaction between disrupted in schizophrenia protein 1 (DISC1) and PDE4 (Ooms et al. 2019). The fact that PDE4 activity was increased in absence of critical DISC1 protein isoforms suggests a complex regulatory system for PDE4 activity. Additionally, it potentially links PDE4 activity to multiple neurological disorders such as schizophrenia and even Huntington's disease.

Apart from the preclinical exploratory studies investigating PDE4 activation, [¹¹C](R)-Rolipram PET can also be used to evaluate targeting properties in the development of novel PDE4 inhibitors. For example, brain PDE4 occupancy of Roflumilast was assessed in non-human primates using [¹¹C](R)-Rolipram PET (Takano et al. 2018). Also in human subjects, [¹¹C](R)-Rolipram was used to assess brain occupancy of multiple PDE4 inhibitors such as GSK356278 (van der Aart et al. 2018) and HT-0712 (NCT01215552).

Despite the necessity of preclinical models, they do have their limitations, especially when it comes to evaluating neuropsychiatric disorders. The first-in-man studies using [¹¹C](R)-Rolipram PET imaging in healthy volunteers have been conducted already quite some time ago (DaSilva et al. 2002). Since then, [¹¹C] (R)-Rolipram PET has been used in multiple studies to investigate the role of PDE4 in neurological and psychiatric disorders.

Dysregulations in the cAMP pathway have been thought to be an important contributing factor to the symptoms of major depressive disorder (MDD). As the brain's major cAMP hydrolyzing PDE, PDE4 is therefore hypothesized to be a key player in the pathogenesis of MDD. Initial studies using [¹¹C](R)-Rolipram to investigate PDE4 activity in a small population of unmedicated patients with MDD have found a significant downregulation of PDE4 activity (Fujita et al. 2012). The decline in PDE4 activity could however be reversed by a treatment using selective serotonine reuptake inhibitors. These studies confirm that PDE4 and the cAMP signaling

pathway play an important role in the pathology of MDD. The lack of correlation between [^{11}C](R)-Rolipram binding and symptoms of MDD however indicate a complexity of the disease beyond PDE4 (Fujita et al. 2017).

As stated previously, PDE4 is also believed to be involved in the pathophysiology of several other disorders. Several recent studies have used [^{11}C](R)-Rolipram PET to evaluate PDE4 levels in patient populations with Parkinson's disease. [^{11}C](R)-Rolipram binding was decreased in several brain regions of the striato-thalamo-cortical circuit. The loss of PDE4 expression correlated to the performance in spatial working memory (Niccolini et al. 2017). Additionally, a correlation with excessive daytime sleepiness was found suggesting a role of PDE4 in the pathophysiology of Parkinson's disease (Wilson et al. 2019).

Finally a recent study has been started in which [^{11}C](R)-Rolipram PET is being used to evaluate PDE4 levels in brain and peripheral tissues of patients with McCune-Albright syndrome (NCT02743377). This rare genetic disorder is a mosaic disorder arising from a spontaneous mutation of the GNAS complex locus (Guanine Nucleotide binding protein, Alpha Stimulating complex), which encodes the cAMP pathway-associated G-protein, Gsα. The resulting local dysregulation in cAMP signaling is believed to cause a disperse pattern of fibrous dysplasia. The preliminary data of their study in two patients showed a [^{11}C](R)-Rolipram distribution pattern that correlates with the known locations of fibrous dysplasia in patients with McCune-Albright syndrome (Lora et al. 2019).

In all these clinical trials, determination of [^{11}C](R)-Rolipram distribution volumes is crucial for the correct quantification and interpretation of PET images. Due to the lack of a suitable reference region, quantification of the concentration of [^{11}C](R)-Rolipram in the brain requires arterial sampling. In order to decrease the invasiveness of the procedure and hence increasing clinical applicability, several studies looked for alternative methods for quantification of brain [^{11}C](R)-Rolipram uptake. Both image derived input function using time activity curves from the carotid artery (Lyoo et al. 2014) and a population-based input curve have been shown to be a valuable alternative to avoid arterial sampling (Zanotti-Fregonara et al. 2012).

Despite the success of [^{11}C](R)-Rolipram, the quest for an improved PDE4 PET tracer continues. Recently a fluorine-18-radiolabeled alternative for rolipram, [^{18}F]MNI-617 (Fig. 23.3), was successfully radiolabeled and evaluated in non-human primates. It rapidly entered the brain with brain uptake similar to [^{11}C](R)-Rolipram and a distribution pattern consistent with that of PDE4 expression (Thomae et al. 2016). Together with the increased interest in PDE4 subtype selective inhibitors, also the quest for PDE4 subtype selective PET tracer was engaged. PF-06445974 (Fig. 23.3) is a tricyclic pyrrolopyridine compound with a sub-nanomolar affinity for PDE4B and a good selectivity toward PDE4D (>36×). As a PET tracer, [^{18}F]PF-06445974 showed rapid brain uptake and high target specificity. Clinical trials are currently ongoing to evaluate the feasibility of this radiopharmaceutical for PDE4B visualization in a healthy patient population (NCT03030391).

Parallel to the development of BPN14770 as a PDE4D selective inhibitor for the treatment of several brain disorders including fragile X syndrome and

Alzheimer's disease (Gurney et al. 2019), several PDE4D selective PET radioligands were developed. In a recent study, [11C]T1650 was evaluated as a PDE4D specific PET ligand. Studies in non-human primates indicated that [11C]T1650 showed good brain uptake that could be blocked after co-injection with BPN14477056. Currently, clinical trials using [11C]T1650 and [11C]T2310 (undisclosed structures) combined with BPN144770 blocking (NCT03861000, NCT04044781) are ongoing.

23.2.4 PDE5

PDE5 is notorious for its regulation of blood flow in the corpus cavernosum through hydrolysis of cGMP. Several PDE5 inhibitors have been marketed for treatment of erectile dysfunction, and some are being investigated for the treatment of pulmonary hypertension (Ahmed 2018).

PDE5 was however also reported to be expressed in the brain, and PDE5 inhibition was suggested to be neuroprotective (Teich et al. 2016; Gulisano et al. 2018; Heckman et al. 2017).

Several PDE5 PET tracers have been evaluated preclinically but so far none of the PET tracers were able to visualize PDE5 in brain. Several vardenafil derivatives, ethoxyethyl pyrazolopyrimidine derivatives, and carbon-11 labelled sildenafil (Fig. 23.4) have relatively high PSA values and showed low brain uptake (Chekol et al. 2014). PDE5-specific retention in the lungs of mice in relation with the PDE5 affinity of the different evaluated tracers was observed.
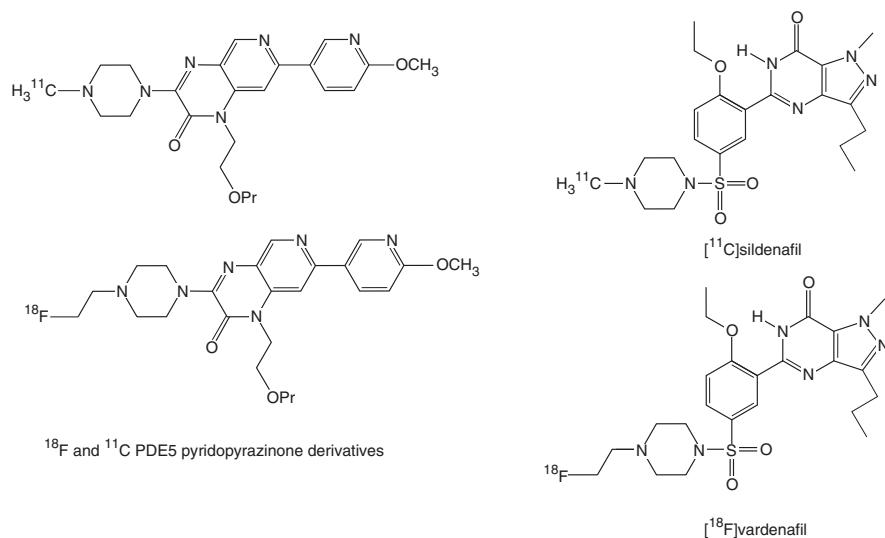
Fig. 23.4 Chemical structures of PDE5 PET tracers: 18F and 11C PDE5 pyridopyrazinone derivatives, [11C]sildenafil and [18F]vardenafil

Although no PDE5-specific binding was observed for ^{11}C-sildenafil, therapeutic doses of sildenafil resulted in pharmacologically relevant CSF levels and increased CSF cGMP levels in a non-human primate (Gómez-Vallejo et al. 2016).

A fluorinated quinolone was synthesized and tested in vitro and in vivo but the tracer was quickly metabolized in vivo generating brain permeable radiometabolites (Liu et al. 2016; Wenzel et al. 2019). Other quinolone derivatives were evaluated in vitro for their PDE5 affinity and selectivity, but their radiolabelling and in vivo evaluation has not yet been reported (Liu et al. 2017).

High affinity fluorine-18- and carbon-11-labelled pyridopyrazinone derivatives (Fig. 23.4) were found to efficiently cross the blood–brain barrier but no PDE5-specific retention was observed in rat brain (Chekol et al. 2017).

23.2.5 PDE7

Both PDE7 gene silencing (Morales-Garcia et al. 2015a) and pharmacological PDE7 inhibition (Morales-Garcia et al. 2015b, 2017) were reported to attenuate neurodegeneration in Parkinson model mice.

No clinical studies targeting PDE7 have been reported so far, and only few PDE7-specific inhibitors were reported (Safavi et al. 2013; Paterniti et al. 2011).

The spiroquinazolinone [18F]MICA-003 (Fig. 23.5) was evaluated as a PET tracer for PDE7 in the brain, but although the tracer showed good brain entry and fast wash-out, the tracer was found to quickly metabolize generating radiometabolites that accumulated in brain (Thomae et al. 2015). Also, no blocking studies were reported so that is not clear whether brain uptake and retention was (in part) PDE7 specific.

23.2.6 PDE9

PDE9 selctively hydrolyzes cGMP with high affinity. In situ hybridizations studies indicate that more than 20 different splice variants of PDE9A exist. PDE9 is

Fig. 23.5 Structure of [18F]MICA-003
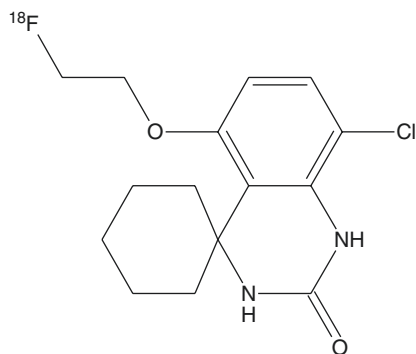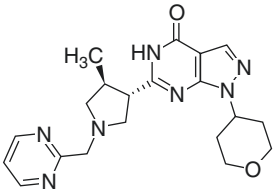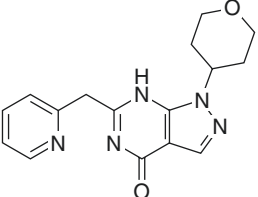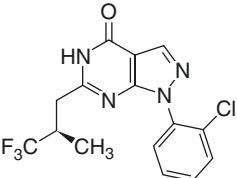
expressed in proximal dendrites and cell bodies of neurons throughout the whole brain (Patel et al. 2018). Different PDE9A inhibitors were advanced to clinical studies for treatment of Alzheimer's disease, schizophrenia and attenuated psychosis syndrome (Boland et al. 2017; Moschetti et al. 2018) (Table 23.2).

No PET radioligands have however been reported so far.

23.2.7 PDE10A

PDE10A is a dual substrate (although with a mugh higher affinity but lower V_{max} for cAMP than for cGMP) phosphodiesterase with brain expression limited to the basal ganglia and mainly in the axons of the medium spiny neurons in the striatum. PDE10A modulates the cAMP/PKA/DARP-32 signalling cascade and the phosphorylation of many downstream effector molecules. Twelve splice variants of PDE10 were identified but the predominant forms in brain are PDE10A1 that localizes in the cytosol, whereas palmytoylated PDE10A2 is associated with plasma membranes (Jäger et al. 2012). Recently, PDE10A19 was identified as an isoform which is exclusively expressed in primates and also localizes in the cytosol (MacMullen et al. 2017). PDE10 can be modulated via its GAF-B domain that binds

Table 23.2 Chemical structure of PDE9A inhibitors and pathologies for which they were evaluated clinically

Name	Structure	Clinical trials
PF-04447943		Alzheimer's disease (NCT00930059, NCT00988598), sickle cell disease (NCT02114203)
BI 409306		Schizophrenia (NCT03351244, NCT01892384, NCT02281773), Alzheimers disease (NCT02392468, NCT02337907, NCT02240693), Attenuated Psychosis Syndrome (NCT03230097).
Eisai E2027	Undisclosed structure	Dementia with Lewy bodies (NCT03467152)
BAY 73-6691		–

cAMP with high affinity and effectively stimulates PDE10A hydrolysis of cAMP. GAF-B stimulates cGMP hydrolysing activity at low cAMP concentration but completely inhibits cGMP hydrolysis at high cAMP concentration (Thomae et al. 2015).

PDE10A has been associated with Huntington's disease, Parkinson's disease (García et al. 2014), and schizophrenia (Świerczek et al. 2019). MacMullen et al. also identified an association between PDE10A single-nucleotide polymorphisms within the first large intron and bipolar disorder (Patel et al. 2018).

A clinical study with PF-02545920 (aka MP10) did not reveal significant differences in efficacy compared to placebo, challenging the use of PDE10A inhibitors as antipsychotic agents for schizophrenia (DeMartinis 3rd et al. 2019). Also in the treatment of Huntington's disease PF-02545920 did not perform significantly better than placebo (NCT02342548).

The efficacy and safety of TAK-063 was evaluated in schizophrenic patients. Although this study did not meet the primary endpoint, the effects of TAK-063 may be suggestive of antipsychotic activity (Macek et al. 2019). TAK-063 was also evaluated for prevention of ketamine-induced brain activity changes and psychotic-like symptoms using fMRI BOLD (NCT01892189). In rats and monkeys, TAK-063 increased fMRI BOLD signal in striatum and amygdala and reversed ketamine-induced BOLD signals in the cortex (Tomimatsu et al. 2016), but the full results of this clinical study have not yet been reported.

OMS643762 (NCT01952132) and EVP-6308 (NCT02037074) were also evaluated in schizophrenic patients, but results of these clinical studies have yet to be disclosed.
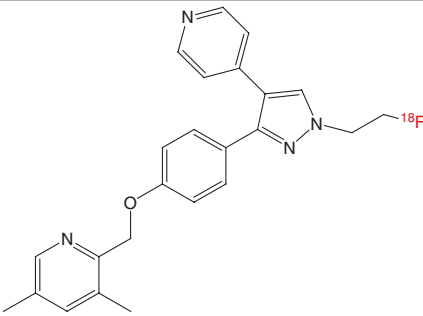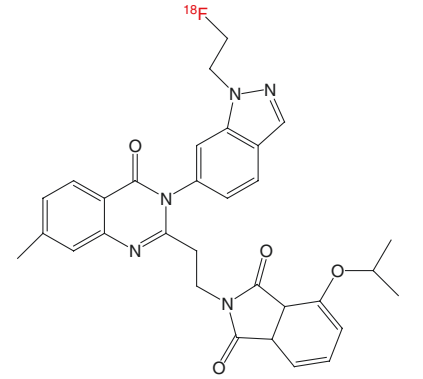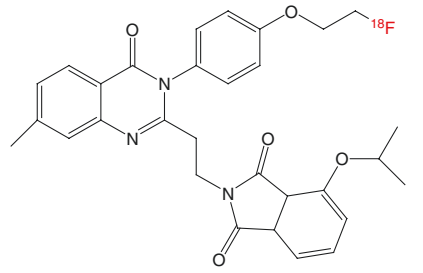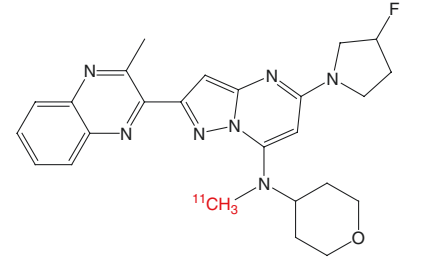
A multitude of PDE10A radioligands have been evaluated preclinically and at least six PDE10A tracers (Table 23.3) were advanced to clinical studies. High specific binding of PDE10A tracers is observed in striatum and globus pallidus and low binding in other brain regions.

In vivo PET studies in rats showed higher striatal binding of [^{18}F]JNJ42259152 after pretreatment with the PDE4 inhibitor rolipram or the PDE2 inhibitor JNJ49137530 demonstrating profound interactions and cooperation between different PDEs in brain in vivo (Ooms et al. 2016).

In preclinical PET studies on rodents no modulation of PDE10A binding potential was identified after chronic treatment with haloperidol (Natesan et al. 2014). Repeated D-amphetamine treatment however significantly increases PDE10A binding in rats, but this effect can be abolished by selective D_1 receptor blocking (Ooms et al. 2017). Early decrease of PDE10A binding was observed in R6/2 (Ooms et al. 2014) and Q175 (Bertoglio et al. 2018; Häggkvist et al. 2017) Huntington mice.

After careful comparison, Bioscutti et al. concluded that [^{11}C]IMA107, [^{18}F]MNI659, and [^{11}C]Lu AE92686 have the most appropriate characteristics as PDE10A PET ligands for clinical application, based on brain kinetics, test-retest variability, and specific signal considerations (Boscutti et al. 2019). Since expression of PDE10A is very low in the cerebellum, a dynamic scanning protocol using the simplified reference tissue approach can be used to quantify the BP_{ND}.

Table 23.3 PDE10A PET tracers that were advanced to clinical studies

Name	Structure	Clinical studies
[18F]JNJ42249152		Dosimetry (Van Laere et al. 2013a) test-retest (Van Laere et al. 2013b), Huntington (Ahmad et al. 2014)
[18F]MNI654		First-in-man and dosimetry (Barret et al. 2014)
[18F]MNI659		First-in-man and dosimetry (Häggkvist et al. 2017), Huntington (Russell et al. 2016), age and gender (Fazio et al. 2017a), occupancy of PF-02545920 (Delnomdedieu et al. 2017), occupancy of EVP-6308 (NCT02001389)
[11C]IMA107		First in man (Plisson et al. 2014) Huntington (Niccolini et al. 2015a), Parkinson (Niccolini et al. 2015b), schizophrenia (Marques et al. 2016) PDE10A p.Tyr107Cys mutation (Diggle et al. 2016) Cocaine users (Tollefson et al. 2019), premanifest Huntingtons (Wilson et al. 2016), occupancy of RO5545965 (NCT01923025)

(continued)

Table 23.3 (continued)

Name	Structure	Clinical studies
[^{11}C]T-773		Occupancy TAK-063 (Takano et al. 2016)
[^{11}C]Lu AE92686		First in man (Kehler et al. 2014), schizophrenia (Bodén et al. 2017)

Loss of PDE10A levels (quantified as BP_{ND}) in caudate (−28%), putamen (−26%) and globus pallidus (−19%) were found to correlate well with the gradual and progressive increase of motor symptoms in patients with Parkinsons disease, indicating that PDE10A imaging provides a similar potential as dopamine transporter imaging to monitor Parkinsons disease progression (Niccolini et al. 2015b). No difference was found in the BP_{ND} of patients responding to levodopa and patients with levodopa-induced dyskinesias (Takano et al. 2016).

In line with preclinical findings, significantly lower levels (−50 to −70%) of PDE10A were also detected in striatum and globus pallidus of patients with manifest Huntington's disease (Ahmad et al. 2014; Russell et al. 2016; Wilson et al. 2017). Also in premanifest Huntington's disease gene expansion carriers (HDGECs), a decrease in PDE10A binding was observed correlating with worse UHDRS (Unified Huntington's Disease Rating Scale) motor scores, disease burden pathology, and regional atrophy (Russell et al. 2014). In far-onset premanifest HDGECs (predicted on average 25 years from symptomatic onset), striatal and pallidal PDE10A tracer binding was reduced by about 30%, whereas a 35% increase was observed in the motor thalamic nuclei (Niccolini et al. 2015c). Overall PDE10A alterations seem to be one of the earlierst biochemical changes in HD identified to date, and PDE10A PET likely can be used to monitor HD progression and follow up efficacy of novel treatments (Boscutti et al. 2019).

In patients with PDE10A mutations associated with a hyperkinetic movement disorder, PDE10A PET also demonstrated loss of striatal PDE10A tracer binding (Diggle et al. 2016). Interestingly, these mutations are located in the regulatory allosteric GAF-A or GAF-B domains, and the results of this study thus indicate that these patients would benefit from strategies aiming to increase PDE10A function (Whiteley et al. 2019).

Patients with schizophrenia showed in one study similar (Marques et al. 2016) but in another study lower PDE10A BP_{ND} in striatum compared to healthy controls. The striatal PDE10A binding potential was found to correlate with the prefrontal cortical thickness (Bodén et al. 2017), and a combined PET/MR study further demonstrated that PDE10A levels correlate with striatal function in schizophrenia (Persson et al. 2019).

Considerable loss (about 8% per decade) of PDE10A binding potential in striatum but less (about 4%) in the globus pallidus as a function of age was found together with a trend of higher binding potential in women compared to man (Fazio et al. 2017b). In studies comparing PDE10A binding in patients and healthy controls, it is therefore important to assure age-matching. PDE10A BP_{ND} correlated with $D_{2/3}$ receptor BP_{ND} in the striatum but not in the globus pallidus (Whiteley et al. 2019).

23.3 Conclusions

Phosphodiesterases are an intriguing family of intracellular enzymes of which several subtypes show high expression in the brain. Not only expression of PDEs can be altered, but also their affinity for inhibitors can be allosterically modulated. This modulation can be quite different in vivo compared to in vitro, e.g., because of postmortem degradation of allosteric cAMP and/or cGMP or because of dephosphorylation of PDE4. Successful PET radioligands were developed and translated to clinical application for visualization of PDE2A, PDE4, and PDE10A in the brain. Especially for the latter two subtypes, many (pre)clinical studies have been performed to investigate their role in different CNS diseases. It can be expected that novel PET radioligands for so far unexplored PDEs (e.g., PDE1 and PDE7) will be available in the future to enable new clinical studies looking at phosphodiesterase function and interplay in brain in health and disease.

References

van der Aart J, Salinas C, Dimber R, Pampols-Maso S, Weekes AA, Tonkyn J, Gray FA, Passchier J, Gunn RN, Rabiner EA (2018) Quantification of human brain PDE4 occupancy by GSK356278: A [11C](R)-rolipram PET study. J Cereb Blood Flow Metab 38(11):2033–2040. https://doi.org/10.1177/0271678X17720868. Epub 2017 Jul 24

Ahmad R, Bourgeois S, Postnov A, Schmidt ME, Bormans G, Van Laere K, Vandenberghe W (2014) PET imaging shows loss of striatal PDE10A in patients with Huntington disease. Neurology 82(3):279–281. https://doi.org/10.1212/WNL.0000000000000037. Epub 2013 Dec 18

Ahmed NS (2018) Tadalafil: 15 years' journey in male erectile dysfunction and beyond. Drug Dev Res. https://doi.org/10.1002/ddr.21493. [Epub ahead of print]

Andrés JI, De Angelis M, Alcázar J, Celen S, Bormans G (2012) Recent advances in positron emission tomography (PET) radiotracers for imaging phosphodiesterases. Curr Top Med Chem 12(11):1224–1236. Review

Azam MA, Tripuraneni NS (2014) Selective phosphodiesterase 4B inhibitors: a review. Sci Pharm 82(3):453–481. https://doi.org/10.3797/scipharm.1404-08

Baillie GS, Tejeda GS, Kelly MP (2019) Therapeutic targeting of 3′,5′-cyclic nucleotide phosphodiesterases: inhibition and beyond. Nat Rev Drug Discov. https://doi.org/10.1038/s41573-019-0033-4. [Epub ahead of print]. Review

Barret O, Thomae D, Tavares A, Alagille D, Papin C, Waterhouse R, McCarthy T, Jennings D, Marek K, Russell D, Seibyl J, Tamagnan G (2014) In vivo assessment and dosimetry of 2 novel PDE10A PET radiotracers in humans: 18F-MNI-659 and 18F-MNI-654. J Nucl Med 55(8):1297–1304. https://doi.org/10.2967/jnumed.113.122895. Epub 2014 Jun 4

Bender AT, Beavo JA (2006) Cyclic nucleotide phosphodiesterases: molecular regulation to clinical use. Pharmacol Rev 58(3):488–520. Review

Bertoglio D, Verhaeghe J, Kosten L, Thomae D, Van der Linden A, Stroobants S, Wityak J, Dominguez C, Mrzljak L, Staelens S (2018) MR-based spatial normalization improves [18F]MNI-659 PET regional quantification and detectability of disease effect in the Q175 mouse model of Huntington's disease. PLoS One 13(10):e0206613. eCollection 2018. https://doi.org/10.1371/journal.pone.0206613

Bobon D, Breulet M, Gerard-Vandenhove MA, Guiot-Goffioul F, Plomteux G, Sastre-y-Hernández M, Schratzer M, Troisfontaines B, von Frenckell R, Wachtel H (1988) Is phosphodiesterase inhibition a new mechanism of antidepressant action? A double blind double-dummy study between rolipram and desipramine in hospitalized major and/or endogenous depressives. Eur Arch Psychiatry Neurol Sci 238(1):2–6

Bodén R, Persson J, Wall A, Lubberink M, Ekselius L, Larsson EM, Antoni G (2017) Striatal phosphodiesterase 10A and medial prefrontal cortical thickness in patients with schizophrenia: a PET and MRI study. Transl Psychiatry 7(3):e1050. https://doi.org/10.1038/tp.2017.11

Boland K, Moschetti V, Dansirikul C, Pichereau S, Gheyle L, Runge F, Zimdahl-Gelling H, Sand M (2017) A phase I, randomized, proof-of-clinical-mechanism study assessing the pharmacokinetics and pharmacodynamics of the oral PDE9A inhibitor BI 409306 in healthy male volunteers. Hum Psychopharmacol 32(1). https://doi.org/10.1002/hup.2569

Bos JL (2006) Epac proteins: multi-purpose cAMP targets. Trends Biochem Sci 31(12):680–686. Epub 2006 Nov 2. Review. Erratum in: Trends Biochem Sci. 2007 Jan;32(1):5

Boscutti G, Rabiner EA, Plisson C (2019) PET Radioligands for imaging of the PDE10A in human: current status. Neurosci Lett 691:11–17. https://doi.org/10.1016/j.neulet.2018.08.006. Epub 2018 Aug 10. Review

Burgin AB, Magnusson OT, Singh J, Witte P, Staker BL, Bjornsson JM, Thorsteinsdottir M, Hrafnsdottir S, Hagen T, Kiselyov AS, Stewart LJ, Gurney ME (2010) Design of phosphodiesterase 4D (PDE4D) allosteric modulators for enhancing cognition with improved safety. Nat Biotechnol 28(1):63–70. https://doi.org/10.1038/nbt.1598. Epub 2009 Dec 27

Casacchia M, Meco G, Castellana F, Bedini L, Cusimano G, Agnoli A (1983) Therapeutic use of a selective cAMP phosphodiesterase inhibitor (Rolipram) in Parkinson's disease. Pharmacol Res Commun 15(3):329–334

Chekol R, Gheysens O, Cleynhens J, Pokreisz P, Vanhoof G, Ahamed M, Janssens S, Verbruggen A, Bormans G (2014) Evaluation of PET radioligands for in vivo visualization of phosphodiesterase 5 (PDE5). Nucl Med Biol 41(2):155–162. https://doi.org/10.1016/j.nucmedbio.2013.10.007. Epub 2013 Oct 30

Chekol R, Gheysens O, Ahamed M, Cleynhens J, Pokreisz P, Vanhoof G, Janssens S, Verbruggen A, Bormans G (2017) Carbon-11 and fluorine-18 radiolabeled pyridopyrazinone derivatives for positron emission tomography (PET) imaging of phosphodiesterase-5 (PDE5). J Med Chem 60(1):486–496. https://doi.org/10.1021/acs.jmedchem.6b01666. Epub 2016 Dec 23

Chen L, Nabulsi N, Naganawa M, Zasadny K, Skaddan MB, Zhang L, Najafzadeh S, Lin SF, Helal CJ, Boyden TL, Chang C, Ropchan J, Carson RE, Villalobos A, Huang Y (2016) Preclinical evaluation of 18F-PF-05270430, a novel PET radioligand for the phosphodiesterase 2A enzyme. J Nucl Med 57(9):1448–1453. https://doi.org/10.2967/jnumed.115.171454. Epub 2016 May 19

Chen J, Zook D, Crickard L, Tabatabaei A (2019) Effect of phosphodiesterase (1B, 2A, 9A and 10A) inhibitors on central nervous system cyclic nucleotide levels in rats and mice. Neurochem Int 129:104471. https://doi.org/10.1016/j.neuint.2019.104471. Epub 2019 May 20

Cherry JA, Davis RL (1999) Cyclic AMP phosphodiesterases are localized in regions of the mouse brain associated with reinforcement, movement, and affect. J Comp Neurol 407(2):287–301

Cui SY, Yang MX, Zhang YH, Zheng V, Zhang HT, Gurney ME, Xu Y, O'Donnell JM (2019) Design and synthesis of selective phosphodiesterase 4D (PDE4D) allosteric inhibitors for the treatment of Fragile X syndrome and other brain disorders. J Pharmacol Exp Ther 371(2):250–259. https://doi.org/10.1124/jpet.119.259986. Epub 2019 Sep 5

DaSilva JN, Lourenco CM, Meyer JH, Hussey D, Potter WZ, Houle S (2002) Imaging cAMP-specific phosphodiesterase-4 in human brain with R-[11C]rolipram and positron emission tomography. Eur J Nucl Med Mol Imaging 29(12):1680–1683. Epub 2002 Oct 2

Delnomdedieu M, Forsberg A, Ogden A, Fazio P, Yu CR, Stenkrona P, Duvvuri S, David W, Al-Tawil N, Vitolo OV, Amini N, Nag S, Halldin C, Varrone A (2017) In vivo measurement of PDE10A enzyme occupancy by positron emission tomography (PET) following single oral dose administration of PF-02545920 in healthy male subjects. Neuropharmacology 117:171–181. https://doi.org/10.1016/j.neuropharm.2017.01.016. Epub 2017 Jan 22

DeMartinis N 3rd, Lopez RN, Pickering EH, Schmidt CJ, Gertsik L, Walling DP, Ogden A (2019) A proof-of-concept study evaluating the phosphodiesterase 10a inhibitor PF-02545920 in the adjunctive treatment of suboptimally controlled symptoms of schizophrenia. J Clin Psychopharmacol 39(4):318–328. https://doi.org/10.1097/JCP.0000000000001047

Diggle CP, Sukoff Rizzo SJ, Popiolek M, Hinttala R, Schülke JP, Kurian MA, Carr IM, Markham AF, Bonthron DT, Watson C, Sharif SM, Reinhart V, James LC, Vanase-Frawley MA, Charych E, Allen M, Harms J, Schmidt CJ, Ng J, Pysden K, Strick C, Vieira P, Mankinen K, Kokkonen H, Kallioinen M, Sormunen R, Rinne JO, Johansson J, Alakurtti K, Huilaja L, Hurskainen T, Tasanen K, Anttila E, Marques TR, Howes O, Politis M, Fahiminiya S, Nguyen KQ, Majewski J, Uusimaa J, Sheridan E, Brandon NJ (2016) Biallelic mutations in PDE10A lead to loss of striatal PDE10A and a hyperkinetic movement disorder with onset in infancy. Am J Hum Genet 98(4):735–743. https://doi.org/10.1016/j.ajhg.2016.03.015

Dyck B, Branstetter B, Gharbaoui T, Hudson AR, Breitenbucher JG, Gomez L, Botrous I, Marrone T, Barido R, Allerston CK, Cedervall EP, Xu R, Sridhar V, Barker R, Aertgeerts K, Schmelzer K, Neul D, Lee D, Massari ME, Andersen CB, Sebring K, Zhou X, Petroski R, Limberis J, Augustin M, Chun LE, Edwards TE, Peters M, Tabatabaei A (2017) Discovery of selective phosphodiesterase 1 inhibitors with memory enhancing properties. J Med Chem 60(8):3472–3483. https://doi.org/10.1021/acs.jmedchem.7b00302. Epub 2017 Apr 13

Enomoto T, Tatara A, Goda M, Nishizato Y, Nishigori K, Kitamura A, Kamada M, Taga S, Hashimoto T, Ikeda K, Fujii Y (2019. pii: jpet.119.260869) A novel phosphodiesterase 1 inhibitor DSR-141562 exhibits efficacies in animal models for positive, negative, and cognitive symptoms associated with schizophrenia. J Pharmacol Exp Ther. https://doi.org/10.1124/jpet.119.260869. [Epub ahead of print]

Fazio P, Schain M, Mrzljak L, Amini N, Nag S, Al-Tawil N, Fitzer-Attas CJ, Bronzova J, Landwehrmeyer B, Sampaio C, Halldin C, Varrone A (2017a) Patterns of age related changes for phosphodiesterase type-10A in comparison with dopamine $D_{2/3}$ receptors and sub-cortical volumes in the human basal ganglia: A PET study with ^{18}F-MNI-659 and ^{11}C-raclopride with correction for partial volume effect. NeuroImage 152:330–339. https://doi.org/10.1016/j.neuroimage.2017.02.047. Epub 2017 Feb 28

Fazio P, Schain M, Mrzljak L, Amini N, Nag S, Al-Tawil N, Fitzer-Attas CJ, Bronzova J, Landwehrmeyer B, Sampaio C, Halldin C, Varrone A (2017b) Phosphodiesterase 10A levels are related to striatal function in schizophrenia: a combined positron emission tomography and functional magnetic resonance imaging study. NeuroImage 152:330–339. https://doi.org/10.1016/j.neuroimage.2017.02.047. Epub 2017 Feb 28

Fleischhacker WW, Hinterhuber H, Bauer H, Pflug B, Berner P, Simhandl C, Wolf R, Gerlach W, Jaklitsch H, Sastre-y-Hernández M et al (1992) A multicenter double-blind study of three different doses of the new cAMP-phosphodiesterase inhibitor rolipram in patients with major depressive disorder. Neuropsychobiology 26(1–2):59–64

Francis SH, Blount MA, Corbin JD (2011) Mammalian cyclic nucleotide phosphodiesterases: molecular mechanisms and physiological functions. Physiol Rev 91(2):651–690. https://doi.org/10.1152/physrev.00030.2010. Review

Fujita M, Zoghbi SS, Crescenzo MS, Hong J, Musachio JL, Lu JQ, Liow JS, Seneca N, Tipre DN, Cropley VL, Imaizumi M, Gee AD, Seidel J, Green MV, Pike VW, Innis RB (2005) Quantification of brain phosphodiesterase 4 in rat with (R)-[11C]rolipram-PET. NeuroImage 26(4):1201–1210

Fujita M, Hines CS, Zoghbi SS, Mallinger AG, Dickstein LP, Liow JS, Zhang Y, Pike VW, Drevets WC, Innis RB, Zarate CA Jr (2012) Downregulation of brain phosphodiesterase type IV measured with 11C-(R)-rolipram positron emission tomography in major depressive disorder. Biol Psychiatry 72(7):548–554. https://doi.org/10.1016/j.biopsych.2012.04.030. Epub 2012 Jun 5

Fujita M, Richards EM, Niciu MJ, Ionescu DF, Zoghbi SS, Hong J, Telu S, Hines CS, Pike VW, Zarate CA, Innis RB (2017) cAMP signaling in brain is decreased in unmedicated depressed patients and increased by treatment with a selective serotonin reuptake inhibitor. Mol Psychiatry 22(5):754–759. https://doi.org/10.1038/mp.2016.171. Epub 2016 Oct 11

García AM, Redondo M, Martinez A, Gil C (2014) Phosphodiesterase 10 inhibitors: new disease modifying drugs for Parkinson's disease? Curr Med Chem 21(10):1171–1187. Review

García AM, Brea J, González-García A, Pérez C, Cadavid MI, Loza MI, Martinez A, Gil C (2017) Targeting PDE10A GAF domain with small molecules: a way for allosteric modulation with anti-inflammatory effects. Molecules 22(9). pii: E1472. https://doi.org/10.3390/molecules22091472

Gomez L, Breitenbucher JG (2013) PDE2 inhibition: potential for the treatment of cognitive disorders. Bioorg Med Chem Lett 23(24):6522–6527. https://doi.org/10.1016/j.bmcl.2013.10.014. Epub 2013 Oct 24. Review

Gómez-Vallejo V, Ugarte A, García-Barroso C, Cuadrado-Tejedor M, Szczupak B, Dopeso-Reyes IG, Lanciego JL, García-Osta A, Llop J, Oyarzabal J, Franco R (2016) Pharmacokinetic investigation of sildenafil using positron emission tomography and determination of its effect on cerebrospinal fluid cGMP levels. J Neurochem 136(2):403–415. https://doi.org/10.1111/jnc.13454

Gu G, Scott T, Yan Y, Warren N, Zhang A, Tabatabaei A, Xu H, Aertgeerts K, Gomez L, Morse A, Li YW, Breitenbucher JG, Massari E, Vivian J, Danks A (2019) Target engagement of a phosphodiesterase 2A inhibitor affecting long-term memory in the rat. J Pharmacol Exp Ther 370(3):399–407. https://doi.org/10.1124/jpet.118.255851. Epub 2019 Jun 28

Gulisano W, Tropea MR, Arancio O, Palmeri A, Puzzo D (2018) Sub-efficacious doses of phosphodiesterase 4 and 5 inhibitors improve memory in a mouse model of Alzheimer's disease. Neuropharmacology 138:151–159. https://doi.org/10.1016/j.neuropharm.2018.06.002. Epub 2018 Jun 6

Gurney ME, Nugent RA, Mo X, Sindac JA, Hagen TJ, Fox D 3rd, O'Donnell JM, Zhang C, Xu Y, Zhang HT, Groppi VE, Bailie M, White RE, Romero DL, Vellekoop AS, Walker JR, Surman MD, Zhu L, Campbell RF (2019) Design and synthesis of selective phosphodiesterase 4D (PDE4D) allosteric inhibitors for the treatment of Fragile X syndrome and other brain disorders. J Med Chem 62(10):4884–4901. https://doi.org/10.1021/acs.jmedchem.9b00193. Epub 2019 Apr 23

Häggkvist J, Tóth M, Tari L, Varnäs K, Svedberg M, Forsberg A, Nag S, Dominguez C, Munoz-Sanjuan I, Bard J, Wityak J, Varrone A, Halldin C, Mrzljak L (2017) Longitudinal small-animal PET imaging of the zQ175 mouse model of Huntington disease shows in vivo changes of molecular targets in the striatum and cerebral cortex. J Nucl Med 58(4):617–622. https://doi.org/10.2967/jnumed.116.180497. Epub 2016 Nov 10

Halpin DM (2008) ABCD of the phosphodiesterase family: interaction and differential activity in COPD. Int J Chron Obstruct Pulmon Dis 3(4):543–561. Review

Hatzelmann A, Morcillo EJ, Lungarella G, Adnot S, Sanjar S, Beume R, Schudt C, Tenor H (2010) The preclinical pharmacology of roflumilast—A selective, oral phosphodiesterase 4 inhibitor in development for chronic obstructive pulmonary disease. Pulm Pharmacol Ther 23(4):235–256. https://doi.org/10.1016/j.pupt.2010.03.011. Epub 2010 Apr 7. Review

Hebenstreit GF, Fellerer K, Fichte K, Fischer G, Geyer N, Meya U, Sastre-y-Hernández M, Schöny W, Schratzer M, Soukop W et al (1989) Rolipram in major depressive disorder: results of a double-blind comparative study with imipramine. Pharmacopsychiatry 22(4):156–160

Heckman PRA, Blokland A, Prickaerts J (2017) From age-related cognitive decline to Alzheimer's disease: a translational overview of the potential role for phosphodiesterases. Adv Neurobiol 17:135–168. https://doi.org/10.1007/978-3-319-58811-7_6. Review

Helal CJ, Arnold E, Boyden T, Chang C, Chappie TA, Fisher E, Hajos M, Harms JF, Hoffman WE, Humphrey JM, Pandit J, Kang Z, Kleiman RJ, Kormos BL, Lee CW, Lu J, Maklad N, McDowell L, McGinnis D, O'Connor RE, O'Donnell CJ, Ogden A, Piotrowski M, Schmidt CJ, Seymour PA, Ueno H, Vansell N, Verhoest PR, Yang EX (2018) Identification of a potent, highly selective, and brain penetrant phosphodiesterase 2A inhibitor clinical candidate. J Med Chem 61(3):1001–1018. https://doi.org/10.1021/acs.jmedchem.7b01466. Epub 2018 Jan 16

Itoh T, Abe K, Hong J, Inoue O, Pike VW, Innis RB, Fujita M (2010) Quantification of brain phosphodiesterase 4 in rat with (R)-[11C]rolipram-PET. Synapse 64(2):172–176. https://doi.org/10.1002/syn.20728

Jäger R, Russwurm C, Schwede F, Genieser HG, Koesling D, Russwurm M (2012) Activation of PDE10 and PDE11 phosphodiesterases. J Biol Chem 287(2):1210–1219. https://doi.org/10.1074/jbc.M111.263806. Epub 2011 Nov 21

Kehler J, Kilburn JP, Estrada S, Christensen SR, Wall A, Thibblin A, Lubberink M, Bundgaard C, Brennum LT, Steiniger-Brach B, Christoffersen CT, Timmermann S, Kreilgaard M, Antoni G, Bang-Andersen B, Nielsen J (2014) Discovery and development of 11C-Lu AE92686 as a radioligand for PET imaging of phosphodiesterase10A in the brain. J Nucl Med 55(9):1513–1518. https://doi.org/10.2967/jnumed.114.140178. Epub 2014 Jul 3

Khammy MM, Dalsgaard T, Larsen PH, Christoffersen CT, Clausen D, Rasmussen LK, Folkersen L, Grunnet M, Kehler J, Aalkjaer C, Nielsen J (2017) PDE1A inhibition elicits cGMP-dependent relaxation of rat mesenteric arteries. Br J Pharmacol 174(22):4186–4198. https://doi.org/10.1111/bph.14034. Epub 2017 Oct 15

Krause W, Kühne G, Sauerbrey N (1990) Pharmacokinetics of (+)-rolipram and (−)-rolipram in healthy volunteers. Eur J Clin Pharmacol 38(1):71–75

Lakics V, Karran EH, Boess FG (2010) Quantitative comparison of phosphodiesterase mRNA distribution in human brain and peripheral tissues. Neuropharmacology 59(6):367–374. https://doi.org/10.1016/j.neuropharm.2010.05.004. Epub 2010 May 21. Erratum in: Neuropharmacology. 2013 Apr;67:532

Lamontagne S, Meadows E, Luk P, Normandin D, Muise E, Boulet L, Pon DJ, Robichaud A, Robertson GS, Metters KM, Nantel F (2001) Localization of phosphodiesterase-4 isoforms in the medulla and nodose ganglion of the squirrel monkey. Brain Res 920(1–2):84–96

Li YF, Huang Y, Amsdell SL, Xiao L, O'Donnell JM, Zhang HT (2009) Antidepressant- and anxiolytic-like effects of the phosphodiesterase-4 inhibitor rolipram on behavior depend on cyclic AMP response element binding protein-mediated neurogenesis in the hippocampus. Neuropsychopharmacology 34(11):2404–2419. https://doi.org/10.1038/npp.2009.66. Epub 2009 Jun 10

Li YF, Cheng YF, Huang Y, Conti M, Wilson SP, O'Donnell JM, Zhang HT (2011) Phosphodiesterase-4D knock-out and RNA interference-mediated knock-down enhance memory and increase hippocampal neurogenesis via increased cAMP signaling. J Neurosci 31(1):172–183. https://doi.org/10.1523/JNEUROSCI.5236-10.2011

Li P, Zheng H, Zhao J, Zhang L, Yao W, Zhu H, Beard JD, Ida K, Lane W, Snell G, Sogabe S, Heyser CJ, Snyder GL, Hendrick JP, Vanover KE, Davis RE, Wennogle LP (2016) Discovery of potent and selective inhibitors of phosphodiesterase 1 for the treatment of cognitive impairment associated with neurodegenerative and neuropsychiatric diseases. J Med Chem 59(3):1149–1164. https://doi.org/10.1021/acs.jmedchem.5b01751. Epub 2016 Feb 2

Liu J, Wenzel B, Dukic-Stefanovic S, Teodoro R, Ludwig FA, Deuther-Conrad W, Schröder S, Chezal JM, Moreau E, Brust P, Maisonial-Besset A (2016) Development of a new radio-fluorinated quinoline analog for PET imaging of phosphodiesterase 5 (PDE5) in brain. Pharmaceuticals (Basel) 9(2). pii: E22. https://doi.org/10.3390/ph9020022

Liu J, Maisonial-Besset A, Wenzel B, Canitrot D, Baufond A, Chezal JM, Brust P, Moreau E (2017) Synthesis and in vitro evaluation of new fluorinated quinoline derivatives with high affinity for PDE5: Towards the development of new PET neuroimaging probes. Eur J Med Chem 136:548–560. https://doi.org/10.1016/j.ejmech.2017.03.091. Epub 2017 Apr 19

Lora W et al (2019) PET imaging of phosphodiesterase 4 in brain and peripheral organs of McCune-Albright syndrome. J Nucl Med 60:506

Lourenco CM, DaSilva JN, Warsh JJ, Wilson AA, Houle S (1999) Imaging of cAMP-specific phosphodiesterase-IV: comparison of [11C]rolipram and [11C]Ro 20-1724 in rats. Synapse 31(1):41–50

Lourenco CM, Houle S, Wilson AA, DaSilva JN (2001) Characterization of r-[11C]rolipram for PET imaging of phosphodieterase-4: in vivo binding, metabolism, and dosimetry studies in rats. Nucl Med Biol 28(4):347–358

Lyoo CH, Zanotti-Fregonara P, Zoghbi SS, Liow JS, Xu R, Pike VW, Zarate CA Jr, Fujita M, Innis RB (2014) Image-derived input function derived from a supervised clustering algorithm: methodology and validation in a clinical protocol using [11C](R)-rolipram. PLoS One 9(2):e89101. eCollection 2014. https://doi.org/10.1371/journal.pone.0089101

Macek TA, McCue M, Dong X, Hanson E, Goldsmith P, Affinito J, Mahableshwarkar AR (2019) A proof-of-concept study evaluating the phosphodiesterase 10A inhibitor PF-02545920 in the adjunctive treatment of suboptimally controlled symptoms of schizophrenia. Schizophr Res 204:289–294. https://doi.org/10.1016/j.schres.2018.08.028. Epub 2018 Sep 3

MacKenzie SJ, Baillie GS, McPhee I, MacKenzie C, Seamons R, McSorley T, Millen J, Beard MB, van Heeke G, Houslay MD (2002) Long PDE4 cAMP specific phosphodiesterases are activated by protein kinase A-mediated phosphorylation of a single serine residue in upstream conserved region 1 (UCR1). Br J Pharmacol 136(3):421–433

MacMullen CM, Fallahi M, Davis RL (2017) Novel PDE10A transcript diversity in the human striatum: Insights into gene complexity, conservation and regulation. Gene 606:17–24. https://doi.org/10.1016/j.gene.2016.12.033. Epub 2016 Dec 30

Marques TR, Natesan S, Niccolini F, Politis M, Gunn RN, Searle GE, Howes O, Rabiner EA, Kapur S (2016) Phosphodiesterase 10A in schizophrenia: a PET study using [(11)C]IMA107. Am J Psychiatry 173(7):714–721. https://doi.org/10.1176/appi.ajp.2015.15040518. Epub 2016 Feb 19

Martínez M, Fernández E, Frank A, Guaza C, de la Fuente M, Hernanz A (1999) Increased cerebrospinal fluid cAMP levels in Alzheimer's disease. Brain Res 846(2):265–267

Maurice DH, Ke H, Ahmad F, Wang Y, Chung J, Manganiello VC (2014) Advances in targeting cyclic nucleotide phosphodiesterases. Nat Rev Drug Discov 13(4):290–314. https://doi.org/10.1038/nrd4228. Review

Mikami S, Nakamura S, Ashizawa T, Nomura I, Kawasaki M, Sasaki S, Oki H, Kokubo H, Hoffman ID, Zou H, Uchiyama N, Nakashima K, Kamiguchi N, Imada H, Suzuki N, Iwashita H, Taniguchi T (2017) Discovery of clinical candidate N-((1S)-1-(3-fluoro-4-(trifluoromethoxy)phenyl)-2-methoxyethyl)-7-methoxy-2-oxo-2,3-dihydropyrido[2,3-b]pyrazine-4(1H)-carboxamide (TAK-915): a highly potent, selective, and brain-penetrating phosphodiesterase 2A inhibitor for the treatment of cognitive disorders. J Med Chem 60(18):7677–7702. https://doi.org/10.1021/acs.jmedchem.7b00807. Epub 2017 Sep 5

Missale C, Nash SR, Robinson SW, Jaber M, Caron MG (1998) Dopamine receptors: from structure to function. Physiol Rev 78(1):189–225. Review

Mongillo M, McSorley T, Evellin S, Sood A, Lissandron V, Terrin A, Huston E, Hannawacker A, Lohse MJ, Pozzan T, Houslay MD, Zaccolo M (2004) Fluorescence resonance energy transfer-based analysis of cAMP dynamics in live neonatal rat cardiac myocytes reveals distinct functions of compartmentalized phosphodiesterases. Circ Res 95(1):67–75. Epub 2004 Jun 3

Morales-Garcia JA, Aguilar-Morante D, Hernandez-Encinas E, Alonso-Gil S, Gil C, Martinez A, Santos A, Perez-Castillo A (2015a) Silencing phosphodiesterase 7B gene by lentiviral-shRNA interference attenuates neurodegeneration and motor deficits in hemiparkinsonian mice. Neurobiol Aging 36(2):1160–1173. https://doi.org/10.1016/j.neurobiolaging.2014.10.008. Epub 2014 Oct 13

Morales-Garcia JA, Alonso-Gil S, Gil C, Martinez A, Santos A, Perez-Castillo A (2015b) Phosphodiesterase 7 inhibition induces dopaminergic neurogenesis in hemiparkinsonian rats. Stem Cells Transl Med 4(6):564–575. https://doi.org/10.5966/sctm.2014-0277. Epub 2015 Apr 29

Morales-Garcia JA, Echeverry-Alzate V, Alonso-Gil S, Sanz-SanCristobal M, Lopez-Moreno JA, Gil C, Martinez A, Santos A, Perez-Castillo A (2017) Phosphodiesterase7 inhibition activates adult neurogenesis in hippocampus and subventricular zone in vitro and in vivo. Stem Cells 35(2):458–472. https://doi.org/10.1002/stem.2480. Epub 2016 Sep 16

Mori F, Pérez-Torres S, De Caro R, Porzionato A, Macchi V, Beleta J, Gavaldà A, Palacios JM, Mengod G (2010) The human area postrema and other nuclei related to the emetic reflex express cAMP phosphodiesterases 4B and 4D. J Chem Neuroanat 40(1):36–42. https://doi.org/10.1016/j.jchemneu.2010.03.004. Epub 2010 Mar 27

Moschetti V, Kim M, Sand M, Wunderlich G, Andersen G, Feifel U, Jang IJ, Timmer W, Rosenbrock H, Boland K (2018) The safety, tolerability and pharmacokinetics of BI 409306, a novel and potent PDE9 inhibitor: Overview of three Phase I randomised trials in healthy volunteers. Eur Neuropsychopharmacol 28(5):643–655. https://doi.org/10.1016/j.euroneuro.2018.01.003. Epub 2018 Mar 19

Naganawa M, Waterhouse RN, Nabulsi N, Lin SF, Labaree D, Ropchan J, Tarabar S, DeMartinis N, Ogden A, Banerjee A, Huang Y, Carson RE (2016) First-in-human assessment of the novel PDE2A PET radiotracer 18F-PF-05270430. J Nucl Med 57(9):1388–1395. https://doi.org/10.2967/jnumed.115.166850. Epub 2016 Apr 21

Natesan S, Ashworth S, Nielsen J, Tang SP, Salinas C, Kealey S, Lauridsen JB, Stensbøl TB, Gunn RN, Rabiner EA, Kapur S (2014) Effect of chronic antipsychotic treatment on striatal phosphodiesterase 10A levels: a [11C]MP-10 PET rodent imaging study with ex vivo confirmation. Transl Psychiatry 4:e376. https://doi.org/10.1038/tp.2014.17

Niccolini F, Haider S, Reis Marques T, Muhlert N, Tziortzi AC, Searle GE, Natesan S, Piccini P, Kapur S, Rabiner EA, Gunn RN, Tabrizi SJ, Politis M (2015a) Altered PDE10A expression detectable early before symptomatic onset in Huntington's disease. Brain 138(Pt 10):3016–3029. https://doi.org/10.1093/brain/awv214. Epub 2015 Jul 21

Niccolini F, Foltynie T, Reis Marques T, Muhlert N, Tziortzi AC, Searle GE, Natesan S, Kapur S, Rabiner EA, Gunn RN, Piccini P, Politis M (2015b) Loss of phosphodiesterase 10A expression is associated with progression and severity in Parkinson's disease. Brain 138(Pt 10):3003–3015. https://doi.org/10.1093/brain/awv219. Epub 2015 Jul 25

Niccolini F, Haider S, Reis Marques T, Muhlert N, Tziortzi AC, Searle GE, Natesan S, Piccini P, Kapur S, Rabiner EA, Gunn RN, Tabrizi SJ, Politis M (2015c) The phosphodiesterase 10 positron emission tomography tracer, [18F]MNI-659, as a novel biomarker for early Huntington disease. Brain 138(Pt 10):3016–3029. https://doi.org/10.1093/brain/awv214. Epub 2015 Jul 21

Niccolini F, Wilson H, Pagano G, Coello C, Mehta MA, Searle GE, Gunn RN, Rabiner EA, Foltynie T, Politis M (2017) Loss of phosphodiesterase 4 in Parkinson disease: Relevance to cognitive deficits. Neurology 89(6):586–593. https://doi.org/10.1212/WNL.0000000000004201. Epub 2017 Jul 12

O'Donnell JM (1993) Antidepressant-like effects of rolipram and other inhibitors of cyclic adenosine monophosphate phosphodiesterase on behavior maintained by differential reinforcement of low response rate. J Pharmacol Exp Ther 264(3):1168–1178

O'Donnell JM, Frith S (1999) Behavioral effects of family-selective inhibitors of cyclic nucleotide phosphodiesterases. Pharmacol Biochem Behav 63(1):185–192

Omar F, Findlay JE, Carfray G, Allcock RW, Jiang Z, Moore C, Muir AL, Lannoy M, Fertig BA, Mai D, Day JP, Bolger G, Baillie GS, Schwiebert E, Klussmann E, Pyne NJ, Ong ACM, Bowers K, Adam JM, Adams DR, Houslay MD, Henderson DJP (2019) Small-molecule allosteric activators of PDE4 long form cyclic AMP phosphodiesterases. Proc Natl Acad Sci U S A 116(27):13320–13329. https://doi.org/10.1073/pnas.1822113116. Epub 2019 Jun 17

Omori K, Kotera J (2007) Overview of PDEs and their regulation. Circ Res 100(3):309–327. Review

Ooms M, Rietjens R, Rangarajan JR, Vunckx K, Valdeolivas S, Maes F, Himmelreich U, Fernandez-Ruiz J, Bormans G, Van Laere K, Casteels C (2014) Early decrease of type 1 canna-

binoid receptor binding and phosphodiesterase 10A activity in vivo in R6/2 Huntington mice. Neurobiol Aging 35(12):2858–2869. https://doi.org/10.1016/j.neurobiolaging.2014.06.010. Epub 2014 Jun 16

Ooms M, Attili B, Celen S, Koole M, Verbruggen A, Van Laere K, Bormans G (2016) [18F]JNJ42259152 binding to phosphodiesterase 10A, a key regulator of medium spiny neuron excitability, is altered in the presence of cyclic AMP. J Neurochem 139(5):897–906. https://doi.org/10.1111/jnc.13855. Epub 2016 Nov 4

Ooms M, Celen S, De Hoogt R, Lenaerts I, Liebregts J, Vanhoof G, Langlois X, Postnov A, Koole M, Verbruggen A, Van Laere K, Bormans G (2017) Striatal phosphodiesterase 10A availability is altered secondary to chronic changes in dopamine neurotransmission. EJNMMI Radiopharm Chem 1(1):3. https://doi.org/10.1186/s41181-016-0005-5. Epub 2016 Mar 21. Erratum in: EJNMMI Radiopharm Chem. 2018;3:13

Ooms M, Tsujikawa T, Lohith TG, Mabins SN, Zoghbi SS, Sumitomo A, Jaaro-Peled H, Kimura Y, Telu S, Pike VW, Tomoda T, Innis RB, Sawa A, Fujita M (2019) A nonhuman primate PET study: measurement of brain PDE4 occupancy by roflumilast using (R)-[11C]rolipram. J Cereb Blood Flow Metab 39(7):1306–1313. https://doi.org/10.1177/0271678X18758997. Epub 2018 Feb 12

Pandit J, Forman MD, Fennell KF, Dillman KS, Menniti FS (2009) Mechanism for the allosteric regulation of phosphodiesterase 2A deduced from the X-ray structure of a near full-length construct. Proc Natl Acad Sci U S A 106(43):18225–18230. https://doi.org/10.1073/pnas.0907635106. Epub 2009 Oct 14

Patel NS, Klett J, Pilarzyk K, Lee DI, Kass D, Menniti FS, Kelly MP (2018) Identification of new PDE9A isoforms and how their expression and subcellular compartmentalization in the brain change across the life span. Neurobiol Aging 65:217–234. https://doi.org/10.1016/j.neurobiolaging.2018.01.019. Epub 2018 Feb 5

Paterniti I, Mazzon E, Gil C, Impellizzeri D, Palomo V, Redondo M, Perez DI, Esposito E, Martinez A, Cuzzocrea S (2011) New methods for the discovery and synthesis of PDE7 inhibitors as new drugs for neurological and inflammatory disorders. PLoS One 6(1):e15937. https://doi.org/10.1371/journal.pone.0015937

Pekcec A, Schülert N, Stierstorfer B, Deiana S, Dorner-Ciossek C, Rosenbrock H (2018) Targeting the dopamine D_1 receptor or its downstream signalling by inhibiting phosphodiesterase-1 improves cognitive performance. Br J Pharmacol 175(14):3021–3033. https://doi.org/10.1111/bph.14350. Epub 2018 Jun 3

Persson J, Szalisznyó K, Antoni G, Wall A, Fällmar D, Zora H, Bodén R (2019) Phosphodiesterase 10A levels are related to striatal function in schizophrenia: a combined positron emission tomography and functional magnetic resonance imaging study. Eur Arch Psychiatry Clin Neurosci. https://doi.org/10.1007/s00406-019-01021-0. [Epub ahead of print]

Plisson C, Weinzimmer D, Jakobsen S, Natesan S, Salinas C, Lin SF, Labaree D, Zheng MQ, Nabulsi N, Marques TR, Kapur S, Kawanishi E, Saijo T, Gunn RN, Carson RE, Rabiner EA (2014) Phosphodiesterase 10A PET radioligand development program: from pig to human. J Nucl Med 55(4):595–601. https://doi.org/10.2967/jnumed.113.131409. Epub 2014 Mar 10

Rabe KF (2011) Update on roflumilast, a phosphodiesterase 4 inhibitor for the treatment of chronic obstructive pulmonary disease. Br J Pharmacol 163(1):53–67. https://doi.org/10.1111/j.1476-5381.2011.01218.x. Review

Reiach JS, Li PP, Warsh JJ, Kish SJ, Young LT (1999) Reduced adenylyl cyclase immunolabeling and activity in postmortem temporal cortex of depressed suicide victims. J Affect Disord 56(2–3):141–151

Renau TE (2004) The potential of phosphodiesterase 4 inhibitors for the treatment of depression: opportunities and challenges. Curr Opin Investig Drugs 5(1):34–39. Review

Ricciarelli R, Brullo C, Prickaerts J, Arancio O, Villa C, Rebosio C, Calcagno E, Balbi M, van Hagen BT, Argyrousi EK, Zhang H, Pronzato MA, Bruno O, Fedele E (2017) Memory-enhancing effects of GEBR-32a, a new PDE4D inhibitor holding promise for the treatment of Alzheimer's disease. Sci Rep 7:46320. https://doi.org/10.1038/srep46320

Richter W, Conti M (2002) Dimerization of the type 4 cAMP-specific phosphodiesterases is mediated by the upstream conserved regions (UCRs). J Biol Chem 277(43):40212–40221. Epub 2002 Aug 12

Richter W, Xie M, Scheitrum C, Krall J, Movsesian MA, Conti M (2011) Conserved expression and functions of PDE4 in rodent and human heart. Basic Res Cardiol 106(2):249–262. https://doi.org/10.1007/s00395-010-0138-8. Epub 2010 Dec 16

Ritawidya R, Ludwig FA, Briel D, Brust P, Scheunemann M (2019) Synthesis and in vitro evaluation of 8-pyridinyl-substituted benzo[*e*]imidazo[2,1-*c*][1,2,4]triazines as phosphodiesterase 2A inhibitors. Molecules 24(15). pii: E2791. https://doi.org/10.3390/molecules24152791

Robichaud A, Stamatiou PB, Jin SL, Lachance N, MacDonald D, Laliberté F, Liu S, Huang Z, Conti M, Chan CC (2002) Deletion of phosphodiesterase 4D in mice shortens alpha(2)-adrenoceptor-mediated anesthesia, a behavioral correlate of emesis. J Clin Invest 110(7):1045–1052

Russell DS, Barret O, Jennings DL, Friedman JH, Tamagnan GD, Thomae D, Alagille D, Morley TJ, Papin C, Papapetropoulos S, Waterhouse RN, Seibyl JP, Marek KL (2014) The phosphodiesterase 10 positron emission tomography tracer, [18F]MNI-659, as a novel biomarker for early Huntington disease. JAMA Neurol 71(12):1520–1528. https://doi.org/10.1001/jamaneurol.2014.1954

Russell DS, Jennings DL, Barret O, Tamagnan GD, Carroll VM, Caillé F, Alagille D, Morley TJ, Papin C, Seibyl JP, Marek KL (2016) Change in PDE10 across early Huntington disease assessed by [18F]MNI-659 and PET imaging. Neurology 86(8):748–754. https://doi.org/10.1212/WNL.0000000000002391. Epub 2016 Jan 22

Safavi M, Baeeri M, Abdollahi M (2013) New methods for the discovery and synthesis of PDE7 inhibitors as new drugs for neurological and inflammatory disorders. Expert Opin Drug Discov 8(6):733–751. https://doi.org/10.1517/17460441.2013.787986. Epub 2013 Apr 9. Review

Salpietro V, Perez-Dueñas B, Nakashima K, San Antonio-Arce V, Manole A, Efthymiou S, Vandrovcova J, Bettencourt C, Mencacci NE, Klein C, Kelly MP, Davies CH, Kimura H, Macaya A, Houlden H (2018) A homozygous loss-of-function mutation in PDE2A associated to early-onset hereditary chorea. Mov Disord 33(3):482–488. https://doi.org/10.1002/mds.27286. Epub 2018 Feb 2

Schindler RF, Brand T (2016) The Popeye domain containing protein family—A novel class of cAMP effectors with important functions in multiple tissues. Prog Biophys Mol Biol 120(1–3):28–36. https://doi.org/10.1016/j.pbiomolbio.2016.01.001. Epub 2016 Jan 7. Review

Schröder S, Wenzel B, Deuther-Conrad W, Teodoro R, Egerland U, Kranz M, Scheunemann M, Höfgen N, Steinbach J, Brust P (2015) Synthesis, 18F-radiolabelling and biological characterization of novel fluoroalkylated triazine derivatives for in vivo imaging of phosphodiesterase 2A in brain via positron emission tomography. Molecules 20(6):9591–9615. https://doi.org/10.3390/molecules20069591

Schröder S, Wenzel B, Deuther-Conrad W, Scheunemann M, Brust P (2016) Novel radioligands for cyclic nucleotide phosphodiesterase imaging with positron emission tomography: an update on developments since 2012. Molecules 21(5). pii: E650. https://doi.org/10.3390/molecules21050650. Review

Schröder S, Wenzel B, Deuther-Conrad W, Teodoro R, Kranz M, Scheunemann M, Egerland U, Höfgen N, Briel D, Steinbach J, Brust P (2018) Investigation of an ^{18}F-labelled imidazopyridotriazine for molecular imaging of cyclic nucleotide phosphodiesterase 2A. Molecules 23(3). pii: E556. https://doi.org/10.3390/molecules23030556

Scott AI, Perini AF, Shering PA, Whalley LJ (1991) In-patient major depression: is rolipram as effective as amitriptyline? Eur J Clin Pharmacol 40(2):127–129

Sutcliffe JS, Beaumont V, Watson JM, Chew CS, Beconi M, Hutcheson DM, Dominguez C, Munoz-Sanjuan I (2014) Efficacy of selective PDE4D negative allosteric modulators in the object retrieval task in female cynomolgus monkeys (Macaca fascicularis). PLoS One 9(7):e102449. eCollection 2014. https://doi.org/10.1371/journal.pone.0102449

Świerczek A, Jankowska A, Chłoń-Rzepa G, Pawłowski M, Wyska E (2019) Advances in discovery of PDE10A inhibitors for CNS-related disorders. Part 2: focus on schizophrenia. Curr Drug Targets. https://doi.org/10.2174/1389450120666190801114210. [Epub ahead of print]

Takano A, Stenkrona P, Stepanov V, Amini N, Martinsson S, Tsai M, Goldsmith P, Xie J, Wu J, Uz T, Halldin C, Macek TA (2016) A human [(11)C]T-773 PET study of PDE10A binding after oral administration of TAK-063, a PDE10A inhibitor. NeuroImage 141:10–17. https://doi.org/10.1016/j.neuroimage.2016.06.047. Epub 2016 Jul 15

Takano A, Uz T, Garcia-Segovia J, Tsai M, Lahu G, Amini N, Nakao R, Jia Z, Halldin C (2018) A nonhuman primate PET study: measurement of brain PDE4 occupancy by roflumilast using (R)-[^{11}C]rolipram. Mol Imaging Biol 20(4):615–622. https://doi.org/10.1007/s11307-018-1168-0

Teich AF, Sakurai M, Patel M, Holman C, Saeed F, Fiorito J, Arancio O (2016) PDE5 exists in human neurons and is a viable therapeutic target for neurologic disease. J Alzheimers Dis 52(1):295–302. https://doi.org/10.3233/JAD-151104

Tenor H, Hatzelmann A, Church MK, Schudt C, Shute JK (1996) Effects of theophylline and rolipram on leukotriene C4 (LTC4) synthesis and chemotaxis of human eosinophils from normal and atopic subjects. Br J Pharmacol 118(7):1727–1735

Thomae D, Servaes S, Vazquez N, Wyffels L, Dedeurwaerdere S, Van der Veken P, Joossens J, Augustyns K, Stroobants S, Staelens S (2015) Synthesis and preclinical evaluation of an 18F labeled PDE7 inhibitor for PET neuroimaging. Nucl Med Biol 42(12):975–981. https://doi.org/10.1016/j.nucmedbio.2015.07.007. Epub 2015 Jul 29

Thomae D, Morley TJ, Lee HS, Barret O, Constantinescu C, Papin C, Baldwin RM, Tamagnan GD, Alagille D (2016) Identification and in vivo evaluation of a fluorine-18 rolipram analogue, [(18) F]MNI-617, as a radioligand for PDE4 imaging in mammalian brain. J Labelled Comp Radiopharm 59(5):205–213. https://doi.org/10.1002/jlcr.3389. Epub 2016 Mar 22

Titus DJ, Wilson NM, Alcazar O, Calixte DA, Dietrich WD, Gurney ME, Atkins CM (2018) A negative allosteric modulator of PDE4D enhances learning after traumatic brain injury. Neurobiol Learn Mem 148:38–49. https://doi.org/10.1016/j.nlm.2017.12.008. Epub 2017 Dec 30

Tollefson S, Gertler J, Himes ML, Paris J, Kendro S, Lopresti B, Scott Mason N, Narendran R (2019) Imaging phosphodiesterase-10a availability in cocaine use disorder with [^{11} C]IMA107 and PET. Synapse 73(1):e22070. https://doi.org/10.1002/syn.22070. Epub 2018 Sep 27

Tomimatsu Y, Cash D, Suzuki M, Suzuki K, Bernanos M, Simmons C, Williams SC, Kimura H (2016) TAK-063, a phosphodiesterase 10A inhibitor, modulates neuronal activity in various brain regions in phMRI and EEG studies with and without ketamine challenge. Neuroscience 339:180–190. https://doi.org/10.1016/j.neuroscience.2016.10.006. Epub 2016 Oct 8

Trabanco AA, Buijnsters P, Rombouts FJ (2016) Towards selective phosphodiesterase 2A (PDE2A) inhibitors: a patent review (2010 - present). Expert Opin Ther Pat 26(8):933–946. https://doi.org/10.1080/13543776.2016.1203902. Epub 2016 Jun 30. Review

Van Laere K, Ahmad RU, Hudyana H, Celen S, Dubois K, Schmidt ME, Bormans G, Koole M (2013a) Human biodistribution and dosimetry of 18F-JNJ42259152, a radioligand for phosphodiesterase 10A imaging. Eur J Nucl Med Mol Imaging 40(2):254–261. https://doi.org/10.1007/s00259-012-2270-1. Epub 2012 Nov 16

Van Laere K, Ahmad RU, Hudyana H, Dubois K, Schmidt ME, Celen S, Bormans G, Koole M (2013b) Quantification of 18F-JNJ-42259152, a novel phosphodiesterase 10A PET tracer: kinetic modeling and test-retest study in human brain. J Nucl Med 54(8):1285–1293. https://doi.org/10.2967/jnumed.112.118679. Epub 2013 Jul 10

Weeks JL, Blount MA, Beasley A, Zoraghi R, Thomas MK, Sekhar KR, Corbin JD, Francis SH (2005) Radiolabeled ligand binding to the catalytic or allosteric sites of PDE5 and PDE11. Methods Mol Biol 307:239–262

Wenzel B, Liu J, Dukic-Stefanovic S, Deuther-Conrad W, Teodoro R, Ludwig FA, Chezal JM, Moreau E, Brust P, Maisonial-Besset A (2019) Targeting cyclic nucleotide phosphodiesterase 5 (PDE5) in brain: toward the development of a PET radioligand labeled with fluorine-18. Bioorg Chem 86:346–362. https://doi.org/10.1016/j.bioorg.2019.01.037. Epub 2019 Jan 28

Whiteley EL, Tejeda GS, Baillie GS, Brandon NJ (2019) PDE10A mutations help to unwrap the neurobiology of hyperkinetic disorders. Cell Signal 60:31–38. https://doi.org/10.1016/j.cellsig.2019.04.001. Epub 2019 Apr 2. Review

Wilson H, Niccolini F, Haider S, Marques TR, Pagano G, Coello C, Natesan S, Kapur S, Rabiner EA, Gunn RN, Tabrizi SJ, Politis M (2016) Loss of extra-striatal phosphodiesterase 10A expression in early premanifest Huntington's disease gene carriers. J Neurol Sci 368:243–248. https://doi.org/10.1016/j.jns.2016.07.033. Epub 2016 Jul 15

Wilson H, De Micco R, Niccolini F, Politis M (2017) Molecular imaging markers to track Huntington's disease pathology. Front Neurol 8:11. eCollection 2017. Review. https://doi.org/10.3389/fneur.2017.00011

Wilson H, Pagano G, Niccolini F, Muhlert N, Mehta MA, Searle G, Gunn RN, Rabiner EA, Foltynie T, Politis M (2019. pii: S1353-8020(19)30073-2) The role of phosphodiesterase 4 in excessive daytime sleepiness in Parkinson's disease. Parkinsonism Relat Disord. https://doi.org/10.1016/j.parkreldis.2019.02.027. [Epub ahead of print]

Wu Y, Li Z, Huang YY, Wu D, Luo HB (2018) Novel phosphodiesterase inhibitors for cognitive improvement in Alzheimer's disease. J Med Chem 61(13):5467–5483. https://doi.org/10.1021/acs.jmedchem.7b01370. Epub 2018 Feb 5. Review

Zaccolo M (2011) Spatial control of cAMP signalling in health and disease. Curr Opin Pharmacol 11(6):649–655. https://doi.org/10.1016/j.coph.2011.09.014. Epub 2011 Oct 13. Review

Zanotti-Fregonara P, Hines CS, Zoghbi SS, Liow JS, Zhang Y, Pike VW, Drevets WC, Mallinger AG, Zarate CA Jr, Fujita M, Innis RB (2012) Population-based input function and image-derived input function for [^{11}C](R)-rolipram PET imaging: methodology, validation and application to the study of major depressive disorder. NeuroImage 63(3):1532–1541. https://doi.org/10.1016/j.neuroimage.2012.08.007. Epub 2012 Aug 10

Zhang HT (2009) Cyclic AMP-specific phosphodiesterase-4 as a target for the development of antidepressant drugs. Curr Pharm Des 15(14):1688–1698. Review

Zhang HT, O'Donnell JM (2000) Behavioral effects of family-selective inhibitors of cyclic nucleotide phosphodiesterases. Psychopharmacology 150(3):311–316

Zhang HT, Huang Y, Masood A, Stolinski LR, Li Y, Zhang L, Dlaboga D, Jin SL, Conti M, O'Donnell JM (2008) Anxiogenic-like behavioral phenotype of mice deficient in phosphodiesterase 4B (PDE4B). Neuropsychopharmacology 33(7):1611–1623. Epub 2007 Aug 15

Zhang C, Xu Y, Zhang HT, Gurney ME, O'Donnell JM (2017) Comparison of the pharmacological profiles of selective PDE4B and PDE4D inhibitors in the central nervous system. Sci Rep 7:40115. https://doi.org/10.1038/srep40115

Zhu J, Mix E, Winblad B (2001) Therapeutic use of a selective cAMP phosphodiesterase inhibitor (Rolipram) in Parkinson's disease. CNS Drug Rev 7(4):387–398. Review

PET Imaging of Purinergic Receptors

24

Bieneke Janssen, Danielle J. Vugts,
and Albert D. Windhorst

Contents

Abstract

Over the recent years, interest in the purinergic signaling system has sparked in the field of positron emission tomography (PET). Purinergic receptors play key roles in physiological and pathological processes, although the exact role in these processes is not always fully understood. PET provides an excellent imaging technique to study (patho)physiological processes in the living brain, and therefore radiopharmaceuticals (or tracers) targeting different purinergic receptors have been developed recently. This chapter will discuss the state of the art of PET tracer development for the P2 family of purinergic receptors, which is especially of interest for visualization of neuroinflammation, more specifically microglial activation.

B. Janssen (✉)
Department of Radiology, Perelman School of Medicine, University of Pennsylvania, Philadelphia, PA, USA
e-mail: Bieneke.Janssen@pennmedicine.upenn.edu

D. J. Vugts · A. D. Windhorst
Department of Radiology and Nuclear Medicine, Amsterdam UMC, Vrije Universiteit Amsterdam, Amsterdam, The Netherlands
e-mail: d.vugts@amsterdamumc.nl; ad.windhorst@amsterdamumc.nl

24.1   Introduction

The involvement of purinergic signaling in the modulation of many physiological processes is more and more recognized, although the exact role of some of the purinergic receptors is still not fully understood. Physiological processes involving these receptors include (neuro)inflammation, immune cell recruitment, neurotransmission, and pain perception (Woods et al. 2016). The two families of purinergic receptors are classified in P1 and P2 receptors, natural ligands mainly being adenosine and adenosine 5′-triphosphate (ATP), respectively (Woods et al. 2016). As adenosine (P1) receptor imaging is already described in Chap. 8 (Elmenhorst et al) of this book, this chapter will focus on purinergic P2 receptor imaging. P2 receptors are subdivided in P2X and P2Y receptor families, where the seven P2X receptors ($P2X_{1-7}$) are ATP-gated cation channels and the eight P2Y receptors ($P2Y_1$, $P2Y_2$, $P2Y_4$, $P2Y_6$, $P2Y_{11-14}$) are G-protein coupled receptors (Woods et al. 2016; Burnstock 2016). Upon damage to the cell membrane, e.g., caused by pathological insults, the extracellular concentration of ATP significantly increases, activating P2X receptors, while P2Y receptors are activated by ATP but also by adenosine 5′-diphosphate (ADP), uridine triphosphate, uridine diphosphate (UDP), and UDP-glucose (Calovi et al. 2019). In the central nervous system (CNS), ATP degradation and signaling is mainly regulated by microglia, the resident immune cells in the CNS. More specifically, microglia status determines ATP release and degradation and influences microglia behavior, ranging from restoration of cell viability to induction of cell death (Calovi et al. 2019). Hence, tracers targeting purinergic P2 receptors are predominantly developed for imaging of the neuroinflammatory response in CNS pathologies. The most significantly expressed P2 receptors on microglia are $P2X_4$, $P2X_7$, $P2Y_6$, $P2Y_{12}$, and $P2Y_{13}$. Expression of the different receptors varies and is related to factors like biological function, sex, and age (Calovi et al. 2019). This chapter will discuss the P2 targeting tracers developed to date, which are limited to ligands for receptors $P2X_4$, $P2X_7$, $P2Y_1$, and $P2Y_{12}$.

24.2   The P2X₄ Receptor

Although the precise role and mechanism of activation of the $P2X_4$ receptor ($P2X_4R$) are largely unknown (Suurväli et al. 2017), it likely plays a role in cellular processes under physiological conditions, since activation of the receptor only requires low concentrations (nM) of extracellular ATP (Calovi et al. 2019), unlike, e.g., the $P2X_7$ receptor ($P2X_7R$). Nevertheless, the current hypothesis is that $P2X_4R$ primes microglia toward a pro-inflammatory state associated with neuropathic pain and brain injury (Calovi et al. 2019; Suurväli et al. 2017), making it a potential target of interest for PET imaging. The only tracers targeting $P2X_4R$ to date have been developed by Wang et al., and all are analogues of 5-(3-bromophenyl)-1,3-dihydro-2*H*-benzofuro[3,2-*e*][1,4]diazepin-2-one (5-BDBD, IC_{50} = 1.2 μM (Balázs et al. 2013)) (Wang et al. 2017). Some of the analogues were successfully radiolabeled (Fig. 24.1); however, in vivo evaluation of these ligands has not been reported thus

Fig. 24.1 Radiolabeled
5-BDBD analogues
targeting the P2X$_4$ receptor
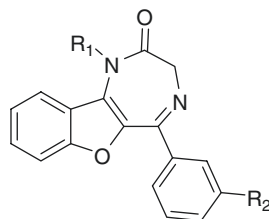
$[^{11}C]8c$ R$_1$ = $^{11}CH_3$, R$_2$ = Br

$[^{11}C]9$ R$_1$ = $^{11}CH_3$, R$_2$ = OH

$[^{18}F]5a$ R$_1$ = H, R$_2$ = ^{18}F

$[^{18}F]11$ R$_1$ = H, R$_2$ = OCH$_2$CH$_2$$^{18}F$

far, nor have in vitro experiments in tissue of animal models of neuroinflammation or postmortem tissue of human patients. All analogues displayed similar affinity toward P2X$_4$R as the lead compound 5-BDBD, and so it remains questionable if this affinity is high enough for in vivo imaging of P2X$_4$R.

24.3   The P2X$_7$ Receptor

The most studied target in the field of purinergic signaling and thus, not surprisingly, also in PET imaging to date is P2X$_7$R. P2X$_7$R is expressed in cells of the myeloid lineage, and in CNS P2X$_7$R is mostly expressed on microglia cells, but receptor expression has also been shown in other brain cells like astrocytes and sometimes neurons (Bartlett et al. 2014). P2X$_7$R is regarded silent in normal physiology, since high (mM) concentrations of its natural agonist ATP are required for activation and functional upregulation of the receptor (Bhattacharya and Biber 2016). The activation of P2X$_7$R is associated with multiple signaling pathways, including the activation of the inflammasome leading to release of pro-inflammatory cytokines and reactive oxygen species, and P2X$_7$R is therefore strongly linked to neuroinflammation (Bartlett et al. 2013, 2014; Bhattacharya and Biber 2016). Due to this association with the pro-inflammatory activation of microglia, the P2X$_7$R is of interest for both PET imaging and drug development in CNS disease. This is exemplified by the fact that quite a number of PET tracers targeting P2X$_7$R have been developed in recent years (Fig. 24.2). Two of the reported tracers, $[^{11}C]$A-740003 and $[^{18}F]$EFB, both bearing a cyanoguanidine moiety, have limited application in CNS disease due to poor brain uptake (Fantoni et al. 2017; Janssen et al. 2014). However, by using $[^3H]$A-740003 in in vitro autoradiography experiments on brains of rats suffering from experimental autoimmune encephalomyelitis (EAE, an animal model of multiple sclerosis (MS), as well as on human postmortem brain tissue of MS patients, tracking neuroinflammation by targeting P2X$_7$R was shown to be feasible, since higher tracer binding was observed at the peak of the disease (EAE)
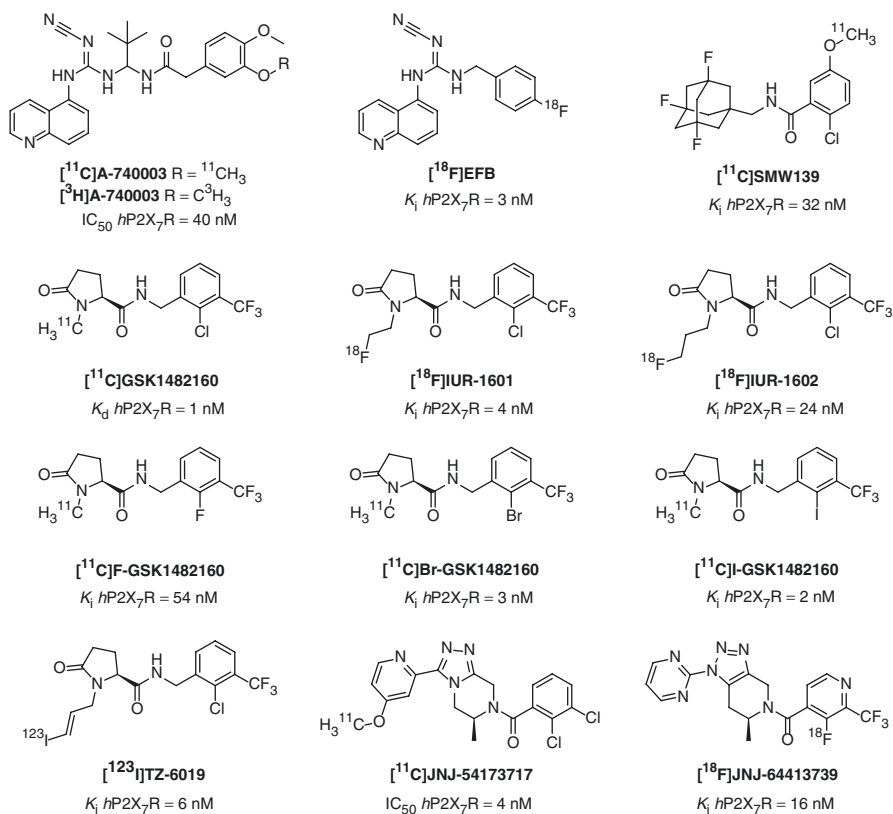
Fig. 24.2 Tracers targeting the P2X$_7$ receptor

and in active MS lesions in human tissue (Beaino et al. 2017). The results in the EAE rat model were further confirmed by a different group using [^{11}C]GSK1482160, with which increased tracer binding was observed in lumbar spinal cord of EAE rats at the peak of the disease (12–14 days post immunization) (Han et al. 2017). Unfortunately, due to too low affinity of [^{11}C]GSK1482160 for rat P2X$_7$R, this effect could not be observed in vivo. Using the same tracer, Territo et al. demonstrated a 3.6-fold higher uptake in the brain of mice treated with lipopolysaccharide (LPS) 72 h prior to PET scanning, compared with saline-treated animals (Territo et al. 2017). Interestingly, other groups reported peak expression of P2X$_7$R and Iba1 12 and 24 h after treatment with LPS (Fantoni et al. 2017; Berdyyeva et al. 2019; Choi et al. 2007), a variation that is likely due to high variability observed in LPS-induced neuroinflammation (Catorce and Gevorkian 2016). In addition to the promising results in rodent neuroinflammation models, [^{11}C]GSK1482160 also entered brain of nonhuman primates with a maximum standard uptake value (SUV) of 2.7 at 70 min postinjection (Han et al. 2017). Likewise, first-in-human results showed a brain uptake of 2% of the total injected dose (SUV 1.0) in healthy volunteers at

20 min postinjection (Green et al. 2018). Despite the observed high liver uptake in human, clearance of [¹¹C]GSK1482160 seems suited for further clinical evaluation. Attempts to synthesize two radiofluorinated analogues of GSK1482160 ([¹⁸F]IUR-1601 (Gao et al. 2018) and [¹⁸F]IUR-1602 (Gao et al. 2019a)) were so far unsuccessful; both compounds were found to be unstable; therefore radiochemical yields were too low to enable preclinical evaluation of these analogues. Three more carbon-11-labeled halogenated analogues of GSK1482160 have been developed, but these have not been biologically evaluated yet (Gao et al. 2019b). An iodinated analogue of GSK1482160, [¹²³I]TZ-6019, showed significantly higher binding in the brain of a P301S mouse model of Alzheimer's disease (AD) compared with wild-type mouse brain (1.3-, 1.7- and 2.4-fold increase in the whole brain, hippocampus, and cortex, respectively) (Jin et al. 2018).

A study using the adamantane benzamide [¹¹C]SMW139 showed that tracer binding in postmortem brain tissue of AD patients and healthy controls was not significantly different (Janssen et al. 2018). However, in a rat model locally overexpressing human P2X₇R unilaterally in striatum (Ory et al. 2016), binding of [¹¹C]SMW139 to P2X₇R could be demonstrated in vivo *(*Janssen et al. 2018*)*. In addition, first in vivo results in the EAE rat model using [¹¹C]SMW139 look promising (Beaino et al. 2019), as significantly increased tracer uptake was observed at the peak of the disease, similar to previous in vitro results with [³H]A-740003 and [¹¹C]GSK1482160 (Beaino et al. 2017; Han et al. 2017). Very recently in a first-in-human study in a small set of MS patients and healthy subjects, [¹¹C]SMW139 showed good pharmacokinetics and quantifiable uptake in the brain (Hagens et al. 2020). Additionally, for all brain regions investigated, V_T and BP_{ND} were elevated in MS patients compared with healthy controls, with only V_T differences reaching statistical significance (Hagens et al. 2020). The previously mentioned rat model of local human P2X₇R expression has also been used to evaluate the imaging potential of [¹¹C]JNJ-54173717, and specific uptake of this tracer in the P2X₇R-expressing striatum was confirmed (Ory et al. 2016). An in vitro autoradiography study with the same tracer showed a time-dependent increase in tracer binding in the brain of rats treated with 6-hydroxydopamine (6-OHDA), an acute model of Parkinson's disease (PD), with highest P2X₇R expression 14 days after 6-OHDA injection, which co-localized with Iba1 immunohistochemical staining (Crabbé et al. 2019). On the contrary, in the same study no differences in P2X₇R binding between the different time points were observed in a chronic A53T viral vector model of PD. [¹¹C]JNJ-54173717 readily crossed the blood-brain barrier in nonhuman primates (Ory et al. 2016), and in a first-in-human study, the tracer was found to be suitable for quantification of P2X₇R in human brain (Van Weehaeghe et al. 2019a). However, no differences in brain uptake of the tracer were observed between PD patients and healthy volunteers (Van Weehaeghe et al. 2019a), which is in line with the findings in the chronic animal model of PD. In addition, a possible genotype effect (polymorphism rs3751143) on tracer binding was detected, which should be further explored. Similar to the results in PD patients, no difference was observed between healthy

volunteers and patients with amyotrophic lateral sclerosis (ALS) (Van Weehaeghe et al. 2019b). The lack of difference between volunteers and patients in both studies may be due to time dependence of $P2X_7R$ expression, as it might be most prominent in early stages or acute neuroinflammation, since microglial activation is driven by $P2X_7R$ activation. Another Janssen R&D compound, $[^{18}F]JNJ\text{-}64413739$, showed a significant increase in $P2X_7R$ binding in the ipsilateral, LPS-treated side of rat brains 2 days posttreatment compared with the contralateral hemisphere, both in vivo with PET and ex vivo with autoradiography (Berdyyeva et al. 2019). $P2X_7R$ binding levels also correlated with Iba1 immunohistochemical staining. Interestingly, this increase was not observed in in vitro autoradiography with $[^{18}F]JNJ\text{-}64413739$, which might be indicative of a difference in binding mechanism in vitro and in vivo (Berdyyeva et al. 2019). Brain uptake of $[^{18}F]JNJ\text{-}64413739$ peaked in nonhuman primates within 10 min postinjection, and a relatively fast metabolic rate (40% intact tracer at 30 min postinjection) but no defluorination was observed (Kolb et al. 2019). A first-in-human study in healthy volunteers showed limited bias, good test-retest variability and excellent reliability with a dynamic 90 min acquisition (Koole et al. 2018). No appropriate reference region could be determined in both nonhuman primates and humans (Kolb et al. 2019; Koole et al. 2018). In human subjects, high interindividual signal variability was observed, which is possibly due to a binding effect of a $P2X_7R$ polymorphism (Koole et al. 2018), as was also observed for $[^{11}C]JNJ\text{-}54173717$ (Van Weehaeghe et al. 2019a).

24.4   The P2Y₁ Receptor

There is limited knowledge about the expression of the $P2Y_1$ receptor ($P2Y_1R$) in normal and diseased brain; however, alterations in its activity or expression are suggested to play a pathophysiological role in, e.g., neurodegeneration, neuroprotection, and neuroregeneration (Moldovan et al. 2019). $P2Y_1R$ binds preferentially ADP over ATP and was shown to be involved in microglial migration together with the $P2Y_{12}$ receptor ($P2Y_{12}R$) (De Simone et al. 2010). Only a limited number of non-nucleotidic compounds with high affinity for $P2Y_1R$ have been reported, one of which is a highly selective $P2Y_1R$ antagonist developed by Bristol-Myers Squibb ($K_i = 6$ nM) (Chao et al. 2013). In order to make an analogue amenable to radiolabeling, Moldovan et al. pursued the synthesis of fluoro-substituted analogues (Moldovan et al. 2019). In vitro evaluation of their small compound library led to the selection of compound **18** (Fig. 24.3, $IC_{50} = 10$ nM vs. $IC_{50} = 180$ nM for the lead compound in the same assay). Metabolism of $[^{18}F]$**18** was studied in CD-1 mice at 30 min postinjection, and only minor amounts of intact tracer were observed, with the main metabolite (85%) being $[^{18}F]$fluoride. The rather unexpected but extensive defluorination of $[^{18}F]$**18** hampers any future use in vivo, and the authors are currently focusing on more metabolically stable analogues of selective $P2Y_1R$ antagonist **18** (Moldovan et al. 2019).

Fig. 24.3 P2Y$_1$
receptor tracer

$[^{18}F]18$

IC$_{50}$ P2Y$_1$R = 10 nM
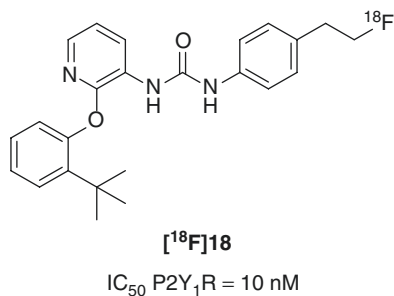
Fig. 24.4 Non-brain
penetrant P2Y$_{12}$
receptor tracer

$[^{11}C]5$

IC$_{50}$ P2Y$_{12}$R = 6 nM
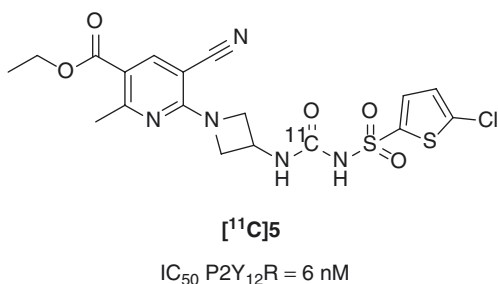
24.5 The P2Y$_{12}$ Receptor

P2Y$_{12}$R is involved in chemotaxis and directs the microglia to move toward higher
ATP concentrations, e.g., to a site of injury. P2Y$_{12}$R is exclusively expressed by
microglia in the CNS and is used as a microglial marker; however, its expression is
downregulated in pro-inflammatory conditions (Calovi et al. 2019; Haynes et al.
2006). One potential PET tracer has been developed to date ($[^{11}C]5$, IC$_{50}$ = 6 nM
(Bach et al. 2013), Fig. 24.4), but unfortunately it did not cross the blood-brain bar-
rier (Villa et al. 2018) and therefore has not been evaluated in vivo in neuroinflam-
mation models. Villa et al. did show that while P2Y$_{12}$R is downregulated in
pro-inflammatory microglia, in contrast it is highly upregulated in the anti-inflam-
matory microglial phenotype (Villa et al. 2018). In addition, $[^{11}C]5$ could be used in
in vitro autoradiography studies using brain tissues of both a mouse model of stroke
and postmortem human brain tissue of a patient deceased after stroke. Indeed,
decreased tracer binding was observed in both human and mouse affected tissue
compared with the non-affected hemispheres, and tracer binding corresponded to
immunohistochemical staining for P2Y$_{12}$R (Villa et al. 2018). Similarly, in an EAE
rat model and human brain tissue of MS patients, $[^{11}C]5$ showed downregulation of
P2Y$_{12}$R at the peak of the disease in EAE rats and in human MS lesions (Beaino
et al. 2017). In addition, in the EAE rat model, P2Y$_{12}$R expression came back up to
baseline levels in the EAE recovery phase and was also shown to be complementary
to expression of P2X$_7$R, a pro-inflammatory microglial marker. These results show

that P2Y$_{12}$R could be a promising target for PET imaging of the anti-inflammatory microglia, provided that a brain penetrant P2Y$_{12}$R ligand can be identified.

24.6   Concluding Remarks

The interest in purinergic P2 receptor imaging has only relatively recently emerged, and thus there is still much to gain in this field. Thus far, P2X$_7$R has been the most investigated target and has been identified as a viable target for imaging of pro-inflammatory microglia. First-in-human studies have been conducted; however, no significant differences in tracer uptake have been found between PD or ALS patients and healthy volunteers. In contrast, albeit only in a small set of subjects, higher tracer uptake was demonstrated in MS patients as compared with healthy volunteers. Taken together, these first-in-human results warrant additional clinical evaluation for P2X$_7$R imaging, especially since animal studies in both chronic and acute PD models show that P2X$_7$R expression is highly time-dependent and may peak in human disease in earlier stages as well, compared with receptor expression in chronic disease. Currently the only purinergic target under investigation for imaging of the anti-inflammatory microglial phenotype is P2Y$_{12}$R, and, once a brain penetrant tracer can be identified, such a tracer could be used as a complementary method to pro-inflammatory microglia imaging (e.g., TSPO, P2X$_4$R, P2X$_7$R) to study the dynamics of microglial activation in vivo. This could be of incredible importance in a deeper understanding of neurological diseases involving neuroinflammation, as well as be a meaningful aid in drug development and follow-up of anti-inflammatory treatment strategies.

References

Bach P, Bostrom J, Brickmann K, van Giezen JJ, Groneberg RD, Harvey DM, O'Sullivan M, Zetterberg F (2013) Synthesis, structure-property relationships and pharmacokinetic evaluation of ethyl 6-aminonicotinate sulfonylureas as antagonists of the P2Y(1)(2) receptor. Eur J Med Chem 65:360–375. https://doi.org/10.1016/j.ejmech.2013.04.007

Balázs B, Dankó T, Kovács G, Köles L, Hediger MA, Zsembery Á (2013) Investigation of the inhibitory effects of the benzodiazepine derivative, 5-BDBD on P2X$_4$ purinergic receptors by two complementary methods. Cell Physiol Biochem 32(1):11–24. https://doi.org/10.1159/000350119

Bartlett R, Yerbury JJ, Sluyter R (2013) P2X7 receptor activation induces reactive oxygen species formation and cell death in murine EOC13 microglia. Mediat Inflamm 2013:271813. https://doi.org/10.1155/2013/271813

Bartlett R, Stokes L, Sluyter R (2014) The P2X7 receptor channel: recent developments and the use of P2X7 antagonists in models of disease. Pharmacol Rev 66(3):638. https://doi.org/10.1124/pr.113.008003

Beaino W, Janssen B, Kooij G, van der Pol SMA, Hof BV, van Horssen J, Windhorst AD, de Vries HE (2017) Purinergic receptors P2Y12R and P2X7R: potential targets for PET imaging of microglia phenotypes in multiple sclerosis. J Neuroinflammation 14:259. https://doi.org/10.1186/s12974-017-1034-z

Beaino W, Janssen B, Kooijman E, Vos R, Schuit R, Kassiou M, Vugts D, de Vries H, Windhorst A (2019) Neuroinflammation imaging with the P2X(7)R PET tracer C-11 SMW139 in the experimental autoimmune encephalomyelitis (EAE) model. J Labelled Comp Radiopharm 62:S73–S74

Berdyyeva T, Xia C, Taylor N, He Y, Chen G, Huang C, Zhang W, Kolb H, Letavic M, Bhattacharya A, Szardenings AK (2019) PET imaging of the P2X7 Ion Channel with a novel tracer [18F]JNJ-64413739 in a rat model of Neuroinflammation. Mol Imaging Biol 21:871. https://doi.org/10.1007/s11307-018-01313-2

Bhattacharya A, Biber K (2016) The microglial ATP-gated ion channel P2X7 as a CNS drug target. Glia 64(10):1772–1787. https://doi.org/10.1002/glia.23001

Burnstock G (2016) An introduction to the roles of purinergic signalling in neurodegeneration, neuroprotection and neuroregeneration. Neuropharmacology 104:4–17. https://doi.org/10.1016/j.neuropharm.2015.05.031

Calovi S, Mut-Arbona P, Sperlágh B (2019) Microglia and the purinergic signaling system. Neuroscience 405:137–147. https://doi.org/10.1016/j.neuroscience.2018.12.021

Catorce MN, Gevorkian G (2016) LPS-induced murine Neuroinflammation model: Main features and suitability for pre-clinical assessment of nutraceuticals. Curr Neuropharmacol 14(2):155–164

Chao H, Turdi H, Herpin TF, Roberge JY, Liu Y, Schnur DM, Poss MA, Rehfuss R, Hua J, Wu Q, Price LA, Abell LM, Schumacher WA, Bostwick JS, Steinbacher TE, Stewart AB, Ogletree ML, Huang CS, Chang M, Cacace AM, Arcuri MJ, Celani D, Wexler RR, Lawrence RM (2013) Discovery of 2-(Phenoxypyridine)-3-phenylureas as small molecule P2Y1 antagonists. J Med Chem 56(4):1704–1714. https://doi.org/10.1021/jm301708u

Choi HB, Ryu JK, Kim SU, McLarnon JG (2007) Modulation of the purinergic P2X7 receptor attenuates lipopolysaccharide-mediated microglial activation and neuronal damage in inflamed brain. J Neurosci 27(18):4957–4968. https://doi.org/10.1523/jneurosci.5417-06.2007

Crabbé M, Van der Perren A, Bollaerts I, Kounelis S, Baekelandt V, Bormans G, Casteels C, Moons L, Van Laere K (2019) Increased P2X7 receptor binding is associated with neuroinflammation in acute but not chronic rodent models for Parkinson's disease. Front Neurosci 13(799). https://doi.org/10.3389/fnins.2019.00799

De Simone R, Niturad CE, De Nuccio C, Ajmone-Cat MA, Visentin S, Minghetti L (2010) TGF-β and LPS modulate ADP-induced migration of microglial cells through P2Y1 and P2Y12 receptor expression. J Neurochem 115(2):450–459. https://doi.org/10.1111/j.1471-4159.2010.06937.x

Fantoni ER, Dal Ben D, Falzoni S, Di Virgilio F, Lovestone S, Gee A (2017) Design, synthesis and evaluation in an LPS rodent model of neuroinflammation of a novel (18)F-labelled PET tracer targeting P2X7. EJNMMI Res 7(1):31. https://doi.org/10.1186/s13550-017-0275-2

Gao M, Wang M, Glick-Wilson BE, Meyer JA, Peters JS, Territo PR, Green MA, Hutchins GD, Zarrinmayeh H, Zheng Q-H (2018) Synthesis and preliminary biological evaluation of a novel P2X7R radioligand [18F]IUR-1601. Bioorg Med Chem Lett 28(9):1603–1609. https://doi.org/10.1016/j.bmcl.2018.03.044

Gao M, Wang M, Glick-Wilson BE, Meyer JA, Peters JS, Territo PR, Green MA, Hutchins GD, Zarrinmayeh H, Zheng Q-H (2019a) Synthesis and initial in vitro characterization of a new P2X7R radioligand [18F]IUR-1602. Appl Radiat Isot 144:10–18. https://doi.org/10.1016/j.apradiso.2018.11.006

Gao MZ, Wang M, Meyer JA, Territo PR, Hutchins GD, Zarrinmayeh H, Zheng QH (2019b) Synthesis and in vitro biological evaluation of new P2X7R radioligands C-11 halo-GSK1482160 analogs. Bioorg Med Chem Lett 29(12):1476–1480. https://doi.org/10.1016/j.bmcl.2019.04.018

Green M, Hutchins G, Fletcher J, Territo W, Polson H, Trussell H, Wissmann C, Zheng Q-H, Gao M, WANG M, Glick-WIlson B (2018) Distribution of the P2X7-receptor-targeted [11C]GSK1482160 radiopharmaceutical in normal human subjects. J Nucl Med 59(Suppl 1):1009

Hagens MHJ, Golla SSV, Janssen B, Vugts DJ, Beaino W, Windhorst AD, O'Brien-Brown J, Kassiou M, Schuit RC, Schwarte LA, de Vries HE, Killestein J, Barkhof F, van Berckel BNM,

Lammertsma AA (2020) The P2X7 receptor tracer [11C]SMW139 as an in vivo marker of neuroinflammation in multiple sclerosis: a first in man study. Eur J Nucl Med Mol Imaging 47(2):379–389

Han J, Liu H, Liu C, Jin H, Perlmutter JS, Egan TM, Tu Z (2017) Pharmacologic characterizations of a P2X7 receptor-specific radioligand, [11C]GSK1482160 for neuroinflammatory response. Nucl Med Commun 38(5):372–382. https://doi.org/10.1097/mnm.0000000000000660

Haynes SE, Hollopeter G, Yang G, Kurpius D, Dailey ME, Gan W-B, Julius D (2006) The P2Y12 receptor regulates microglial activation by extracellular nucleotides. Nat Neurosci 9(12):1512–1519. https://doi.org/10.1038/nn1805

Janssen B, Vugts DJ, Funke U, Spaans A, Schuit RC, Kooijman E, Rongen M, Perk LR, Lammertsma AA, Windhorst AD (2014) Synthesis and initial preclinical evaluation of the P2X(7) receptor antagonist C-11 A-740003 as a novel tracer of neuroinflammation. J Labelled Comp Radiopharm 57(8):509–516. https://doi.org/10.1002/jlcr.3206

Janssen B, Vugts DJ, Wilkinson SM, Ory D, Chalon S, Hoozemans JJM, Schuit RC, Beaino W, Kooijman EJM, van den Hoek J, Chishty M, Doméné A, Van der Perren A, Villa A, Maggi A, Molenaar GT, Funke U, Shevchenko RV, Baekelandt V, Bormans G, Lammertsma AA, Kassiou M, Windhorst AD (2018) Identification of the allosteric P2X7 receptor antagonist [11C]SMW139 as a PET tracer of microglial activation. Sci Rep 8(1):6580. https://doi.org/10.1038/s41598-018-24814-0

Jin H, Han J, Resing D, Liu H, Yue X, Miller RL, Schoch KM, Miller TM, Perlmutter JS, Egan TM, Tu Z (2018) Synthesis and in vitro characterization of a P2X7 radioligand [123I]TZ6019 and its response to neuroinflammation in a mouse model of Alzheimer disease. Eur J Pharmacol 820:8–17. https://doi.org/10.1016/j.ejphar.2017.12.006

Kolb H, Barret O, Bhattacharya A, Chen G, Constantinescu C, Huang C, Letavic M, Tamagnan G, Xia C, Zhang W, Szardenings AK (2019) Preclinical evaluation and non-human primate receptor occupancy study of (18)F-JNJ-64413739, a novel PET radioligand for P2X7 receptors. Nucl Med 60:1154. https://doi.org/10.2967/jnumed.118.212696

Koole M, Schmidt M, Hijzen A, Ravenstijn P, Vandermeulen C, Van Weehaeghe D, Serdons K, Celen S, Bormans G, Ceusters M, Zhang W, Van Nueten L, Kolb H, de Hoon J, Van Laere K (2018) 18F-JNJ-64413739, a novel PET ligand for the P2X7 ion channel: radiation dosimetry, kinetic modeling, test-retest variability and occupancy of the P2X7 antagonist JNJ-54175446. J Nucl Med 60:683. https://doi.org/10.2967/jnumed.118.216747

Moldovan RP, Wenzel B, Teodoro R, Neumann W, Dukic-Stefanovic S, Kraus W, Rong PJ, Deuther-Conrad W, Hey-Hawkins E, Krugel U, Brust P (2019) Studies towards the development of a PET radiotracer for imaging of the P2Y(1) receptors in the brain: synthesis, F-18-labeling and preliminary biological evaluation. Eur J Med Chem 165:142–159. https://doi.org/10.1016/j.ejmech.2019.01.006

Ory D, Celen S, Gijsbers R, Van Den Haute C, Postnov A, Koole M, Vandeputte C, Andres JI, Alcazar J, De Angelis M, Langlois X, Bhattacharya A, Schmidt M, Letavic MA, Vanduffel W, Van Laere K, Verbruggen A, Debyser Z, Bormans G (2016) Preclinical evaluation of a P2X7 receptor-selective radiotracer: PET studies in a rat model with local overexpression of the human P2X7 receptor and in nonhuman Primates. J Nucl Med 57(9):1436–1441. https://doi.org/10.2967/jnumed.115.169995

Suurväli J, Boudinot P, Kanellopoulos J, Rüütel Boudinot S (2017) P2X4: a fast and sensitive purinergic receptor. Biom J 40(5):245–256. https://doi.org/10.1016/j.bj.2017.06.010

Territo PR, Meyer JA, Peters JS, Riley AA, McCarthy BP, Gao M, Wang M, Green MA, Zheng QH, Hutchins GD (2017) Characterization of (11)C-GSK1482160 for targeting the P2X7 receptor as a biomarker for neuroinflammation. J Nucl Med 58(3):458–465. https://doi.org/10.2967/jnumed.116.181354

Van Weehaeghe D, Koole M, Schmidt ME, Deman S, Jacobs AH, Souche E, Serdons K, Sunaert S, Bormans G, Vandenberghe W, Van Laere K (2019a) [11C]JNJ54173717, a novel P2X7 receptor radioligand as marker for neuroinflammation: human biodistribution, dosimetry, brain kinetic modelling and quantification of brain P2X7 receptors in patients with Parkinson's disease and

healthy volunteers. Eur J Nucl Med Mol Imaging 46(10):2051–2064. https://doi.org/10.1007/s00259-019-04369-6

Van Weehaeghe D, Van Schoor E, Koole M, De Vocht J, Ceelen S, Declercq L, Thal DR, Van Damme P, Bormans G, Van Laere K (2019b) C-11 JNJ717 P2X7 receptor PET as a novel neuroinflammation target: ex vivo and in vivo comparison with F-18 DPA714 in human ALS. J Cereb Blood Flow Metab 39:120–121

Villa A, Klein B, Janssen B, Pedragosa J, Pepe G, Zinnhardt B, Vugts DJ, Gelosa P, Sironi L, Beaino W, Damont A, Dolle F, Jego B, Winkeler A, Ory D, Solin O, Vercouillie J, Funke U, Laner-Plamberger S, Blomster LV, Christophersen P, Vegeto E, Aigner L, Jacobs A, Planas AM, Maggi A, Windhorst AD (2018) Identification of new molecular targets for PET imaging of the microglial anti-inflammatory activation state. Theranostics 8(19):5400–5418. https://doi.org/10.7150/thno.25572

Wang M, Gao M, Meyer JA, Peters JS, Zarrinmayeh H, Territo PR, Hutchins GD, Zheng Q-H (2017) Synthesis and preliminary biological evaluation of radiolabeled 5-BDBD analogs as new candidate PET radioligands for P2X4 receptor. Bioorg Med Chem 25(14):3835–3844. https://doi.org/10.1016/j.bmc.2017.05.031

Woods LT, Ajit D, Camden JM, Erb L, Weisman GA (2016) Purinergic receptors as potential therapeutic targets in Alzheimer's disease. Neuropharmacology 104:169–179. https://doi.org/10.1016/j.neuropharm.2015.10.031

Imaging of the Serotonin System: Radiotracers and Applications in Memory Disorders

25

Gitte Moos Knudsen and Steen G. Hasselbalch

Contents

G. M. Knudsen
Neurobiology Research Unit, Center for Experimental Medicine Neuropharmacology (NeuroPharm), Rigshospitalet, University of Copenhagen, Copenhagen, Denmark
e-mail: gmk@nru.dk

S. G. Hasselbalch (✉)
Neurobiology Research Unit, Center for Experimental Medicine Neuropharmacology (NeuroPharm), Rigshospitalet, University of Copenhagen, Copenhagen, Denmark

Danish Dementia Research Centre, Rigshospitalet, University of Copenhagen, Copenhagen, Denmark
e-mail: steen.gregers.hasselbalch@regionh.dk

Abstract

The serotonergic system plays a key modulatory role in the brain and is the target for many drug treatments for brain disorders either through reuptake blockade or via interactions at the 14 subtypes of serotonin (5-HT) receptors. This chapter provides the current status of radioligands used for positron emission tomography (PET) and single-photon emission computerised tomography (SPECT) imaging of the human brain 5-HT receptors and the 5-HT transporter (SERT) with particular emphasis on the applications in Alzheimer's disease (AD).

Currently available radioligands for in vivo brain imaging of the 5-HT system in humans include radiolabelled compounds for the 5-HT$_{1A}$, 5-HT$_{1B}$, 5-HT$_{2A}$, 5-HT$_4$ and to some extent 5-HT$_6$ receptors and for SERT. Imaging of serotonergic targets in humans has given invaluable insight into the normal brain function and into brain disorders where the serotonergic system is perturbed.

Imaging studies show that the 5-HT$_{1A}$ receptor binding is increased, and 5-HT$_{2A}$ receptor binding is decreased in mild cognitive impairment (MCI). In early AD, 5-HT$_4$ receptor binding is increased, whereas in early and more advanced AD, SERT and the 5-HT$_{1A}$ and 5-HT$_{2A}$ receptor binding are reduced in a region-specific manner. Future studies should focus on the association between serotonergic dysfunction and symptomatology in order to increase our understanding of the neurobiological background for neuropsychiatric symptoms in neurodegenerative and neuropsychiatric disorders.

25.1   Introduction

The serotonergic (5-HT) system plays a key modulatory role in many brain functions. The serotonin transporter and 14 serotonergic receptor subtypes result in a complex pattern of modulatory control over various physiological, emotional and cognitive processes. These include, e.g. mood, sleep, diurnal rhythms, cognition, learning, memory and appetite. Serotonergic dysfunction has been implicated in the aetiology of many psychiatric and neurological disorders, e.g. affective disorders, anxiety, schizophrenia, Alzheimer's disease, migraine and epilepsy. The development of in vivo brain imaging techniques, such as positron emission tomography (PET) and single-photon emission computerised tomography (SPECT), increasingly allows the study of the serotonergic system in the human brain; for review, see Paterson et al. (2013) and Kumar and Mann (2014).

This review covers the current status of which PET and SPECT radioligands are available for imaging serotonergic targets within the brain. Secondly, as an example of one of the applications of PET imaging, the current knowledge about disturbances of the serotonergic system in Alzheimer's disease is given.

25.1.1 5-HT Targets for PET and SPECT

The 5-HT receptors are amongst the most diverse group of neurotransmitter receptors in the human genome, and the 5-HT system is also one of the phylogenetically oldest systems. Currently, 14 structurally and pharmacologically distinct mammalian 5-HT receptor subtypes have been described. Based on their structure, affinity for different ligands and second messenger pathway, they are assigned to one of seven families, 5-HT$_{1-7}$ (Hoyer et al. 2002). All 5-HT receptors, except the 5-HT$_3$ receptor, are G-protein-coupled seven transmembrane-spanning receptors (GPCRs). The 5-HT$_3$ receptor is a ligand-gated sodium ion channel. In addition, the 5-HT transporters (SERTs) responsible for 5-HT reuptake and 5-HT synthetic enzymes, especially tryptophan hydroxylase, are also targets for tracer development. Significant discoveries of the 5-HT system in the human brain have been made following the development of selective PET and SPECT radioligands; some examples are given in (Jones and Rabiner 2012; Rebholz et al. 2018; Spies et al. 2015).

25.2 Current Radioligands for In Vivo Brain Imaging of the 5-HT System

A multitude of radioligands exist for in vitro studies of serotonergic targets, and over the last decade, we have seen an impressive increase in the number of useful PET and SPECT radioligands. Based on PET neuroimaging studies, a high-resolution human brain atlas of the 5-HT$_{1A}$, 5-HT$_{1B}$, 5-HT$_{2A}$ and 5-HT$_4$ receptors, and the 5-HT transporter has recently been made available (Beliveau et al. 2017), downloadable from https://nru.dk/index.php/misc/category/90-nru-serotonin-atlas. Published PET and SPECT radioligands for imaging the serotonergic system are extensively reviewed in (Paterson et al. 2013), but here, we will only summarise some of the to date most utilised radiotracers.

25.2.1 5-HT$_{1A}$ Receptor

The 5-HT$_{1A}$ receptor is one of the best characterised receptors in the serotonergic family; its role as an inhibitory autoreceptor in the raphe nuclei and the possible implications of this role for the treatment of depression and anxiety with serotonin reuptake inhibitors are well-known (King et al. 2008).

Many of the 5-HT$_{1A}$ radioligands were based on WAY-100635 (*N*-[2-[4-(2-methoxyphenyl)piperazin-1-yl]ethyl]-*N*-pyridin-2-ylcyclohexanecarboxamide), which in its *carbonyl*-^{11}C-labelled form is widely used for 5-HT$_{1A}$ receptor imaging. Currently, four radioligands are used for PET studies of the 5-HT$_{1A}$ receptor in humans: [*carbonyl*-^{11}C]WAY-100635, [^{18}F]MPPF, [^{18}F]FCWAY and [^{11}C]CUMI-101. [*carbonyl*-^{11}C]WAY-100635 (Pike et al. 1995) is so far the most widely used 5-HT$_{1A}$ receptor radioligand. It has a high target-to-background ratio,

but its fast systemic metabolism makes it difficult to quantify accurately. [18F]MPPF has the advantage of the longer lived 18F-label, and it also selectively labels the 5-HT$_{1A}$ receptors with a low non-specific binding. Its major disadvantage is its low brain uptake. [18F]FCWAY is rarely used, probably because of issues with defluorination of the parent compound which leads to high bone uptake of radioactivity (Ryu et al. 2007). [11C]CUMI-101 is a high-affinity partial agonist 5-HT$_{1A}$ radioligand that displays high specific binding and seems suitable for imaging the high-affinity site within the human brain (Milak et al. 2008; Pinborg et al. 2012). More recently, however, it has been found that [11C]CUMI-101 has significant binding to α1-adrenoceptors in humans (Shrestha et al. 2014, 2016)

25.2.2 5-HT$_{1B}$ Receptor

The 5-HT$_{1B}$ receptor is of particular interest in relation to obesity (Halford et al. 2007) and migraine (Tfelt-Hansen 2012). No less than two PET radiotracers for imaging the 5-HT$_{1B}$ receptor are now available for use in humans: [11C]AZ10419369 and [11C]P943. [11C]AZ10419369 (5-methyl-8-(4-[11C]methyl-piperazin-1-yl)-4-oxo-4H-chromene-2-carboxylic acid(4-morpholin-4-yl-phenyl)-amide) is a 5-HT$_{1B}$ partial agonist used in humans (Varnas et al. 2011); it has a slow systemic metabolism. The high-affinity 5-HT$_{1B}$ antagonist radioligand, [11C]P943 (R-1-[4-(2-methoxy-isopropyl)-phenyl]-3-[2-(4-methyl-piperazin-1-yl)benzyl]-pyrrolidin-2-one), also shows good properties for quantification in the human brain (Gallezot et al. 2010). For both radiotracers, the cerebellum constitutes an acceptable reference region, and there is evidence that the radiotracers are sensitive to displacement by endogenous 5-HT in non-human primates (Finnema et al. 2010; Ridler et al. 2011) and in pigs (Jørgensen et al. 2018a, b). Normative data from healthy individuals show an 8% decline in 5-HT$_{1B}$ receptor binding per decade (Savli et al. 2012), but no gender-related differences have been reported (Matuskey et al. 2012).

25.2.3 5-HT$_{2A}$ Receptor

5-HT$_{2A}$ receptors are of interest for many reasons: they are a primary target of psychedelic compounds (Lee and Roth 2012), contribute to the efficacy of antipsychotic medications and are involved in the aetiology or treatment of various psychiatric disorders (Leysen 2004).

Several different radioligands for imaging the brain 5-HT$_{2A}$ receptor have successfully been used in human PET studies, e.g. [18F]altanserin; [18F]setoperone; [11C]NMSP; [11C]MDL 100,907; and [11C]Cimbi-36. In addition, the SPECT tracer [123I]-R91150 is used in imaging studies, but the radiotracer displays a lower signal-to-noise ratio compared to the available PET radioligands.

Despite its lipophilic radiometabolite, [18F]altanserin has been widely used as a PET radiotracer. Because of its longer half-life, the 18F-labelling facilitates the

application of a bolus/infusion paradigm that in turn enables subtraction of the lipophilic brain metabolite (Pinborg et al. 2003). Imaging data obtained from [^{18}F]altanserin binding in the human brain are highly reproducible (Haugbol et al. 2007). [^{18}F]altanserin was used to determine changes in 5-HT$_{2A}$ receptor density in relation to ageing (Adams et al. 2004), and it has been reported that binding in healthy subjects correlates with the body mass index (Erritzoe et al. 2009) but does not vary with gender (Frokjaer et al. 2009). Furthermore, twin studies have shown that [^{18}F]altanserin binding is strongly genetically determined (Pinborg et al. 2008).

[^{11}C]NMSP   (*N*-methylspiperone,   8-[4-(4-fluorophenyl)-4-oxobutyl]-2-methyl-4-phenyl-2,4,8-triazaspiro[4.5]decan-1-one) is a dual D$_2$/5-HT$_2$ receptor ligand (Wong et al. 1984). As [^{18}F]setoperone, NMSP has high affinity for both receptors, but since the density of D$_2$ receptors is low and that of 5-HT$_2$ receptors is high in the cortical brain regions, then the majority of specific binding in the neocortex is due to 5-HT$_2$ receptor binding. For subcortical brain regions, the reverse is true (Lyon et al. 1986). Because of its non-selectivity, [^{11}C]NMSP is no longer in common use. The same applies for the radioligand [^{18}F]setoperone (6-[2-[4-(4-[^{18}F]fluorobenzoyl)piperidin-1-yl]ethyl]-7-methyl-2,3-di-hydro-[1,3]thiazolo[3,2-a]pyrimidin-5-one.

The 5-HT2A receptor-selective tracer 11C-MDL100907 has been characterised in humans (Talbot et al. 2012). Based on in vitro data (Kristiansen et al. 2005), [^{11}C]MDL 100907 is more selective for the 5-HT$_{2A}$ receptor than [^{18}F]altanserin, but it is questionable if this has any practical implications because of the scarcity of 5-HT$_{2B}$ and to some extent 5-HT$_{2C}$ receptors. Another promising radioligand is [^{11}C]Cimbi-36 (Ettrup et al. 2014a, b) which is so far the only 5-HT$_{2A}$ receptor agonist radioligand that has proven successful in humans. [^{11}C]Cimbi-36 has excellent test-retest reproducibility properties, and head-to-head comparisons with [^{18}F]altanserin suggest that in brain regions with high 5-HT$_{2C}$ receptor density, choroid plexus and hippocampus, [^{11}C]Cimbi-36 likely represents binding to both 5-HT$_{2A}$ and 5-HT$_{2C}$ receptors (Ettrup et al. 2016). In the pig brain, cerebral 5-HT release correlates with [^{11}C]Cimbi-36 PET measures of 5-HT$_{2A}$ receptor occupancy, and likewise, [^{11}C]Cimbi-36 binding is reduced in response to a fenfluramine challenge in non-human primates (Yang et al. 2017). Acute SSRI intervention in human leads to variable changes in the brain [^{11}C]Cimbi-36 binding (da Cunha-Bang et al. 2019), possibly due to interindividual variability of the SSRI 5-HT release response. Preliminary data suggest that a stronger 5-HT challenge, such as dexamphetamine, is associated with a reduction in the brain [^{11}C]Cimbi-36 binding (Erritzoe, in prep).

25.2.4 5-HT$_{2B}$ and 5-HT$_{2C}$ Receptors

To date, it is questionable if 5-HT$_{2B}$ receptors are expressed in the brain in sufficient amounts to allow for imaging. This is not the case for 5-HT$_{2C}$ receptors, but currently, all radiolabelled 5-HT$_{2C}$ receptor ligands have shared pharmacology with other receptors. No radiotracers have been developed for SPECT or PET imaging of 5-HT$_{2B}$ or 5-HT$_{2C}$ receptors.

25.2.5 5-HT₃ Receptors

Despite a number of research centres undertaking a concerted effort to develop 5-HT$_3$-selective PET and SPECT tracers, it seems that the very discrete localisation and relatively low levels of 5-HT$_3$ receptors that are localised with highest densities in the brainstem (Parker et al. 1996) make it a very difficult target to image in vivo.

25.2.6 5-HT₄ Receptors

5-HT$_4$ receptors are involved in learning and memory and are potential targets for the treatment of Alzheimer's disease (for a review, see Bockaert et al. (2004)). So far, one PET ligand, [^{11}C]SB207145 (8-amino-7-chloro-(*N*-[^{11}C]methyl-4-piperidylmethyl)-1,4-benzodioxan-5-carboxylate), has been successfully evaluated and used in humans.

The 5-HT$_4$ receptor antagonist SB207145 was initially radiolabelled with C-11 (Gee et al. 2008) and evaluated for its potential as a PET radioligand for 5-HT$_4$ imaging. [^{11}C]SB207145 was subsequently successfully quantified for use in human brain studies (Marner et al. 2009). In this study, a comprehensive quantification of the binding of [^{11}C]SB207145 to cerebral 5-HT$_4$ receptors in the human brain in vivo was further provided. Distribution volumes and binding potentials of [^{11}C]SB207145 showed good test-retest reproducibility and time stability. The blocking study with piboserod confirmed that the cerebellum is a suitable reference region devoid of specific binding and that reference tissue models apply. Subsequently, it was shown that [^{11}C]SB207145 is not to any significant degree displaceable by acutely increased levels of endogenous 5-HT (Marner et al. 2010), but cautions need to be taken to ensure that the injected mass of SB207145 does not exceed 4.5 μg (Madsen et al. 2011c). Clinical data (Fisher et al. 2015a, b; Haahr et al. 2014) suggest, however, that [^{11}C]SB207145 serves as a proxy for changes in brain 5-HT levels and this feature needs to be considered when interpreting clinical studies. Normative data on age- and sex-related variations have been published (Madsen et al. 2011b).

25.2.7 5-HT₅ Receptors

The 5-HT$_5$ receptor has two subtypes, the 5-HT$_{5A}$ and the 5-HT$_{5B}$ receptors. The 5-HT$_{5A}$ receptor has been identified in the human brain, but the 5-HT$_{5B}$ receptor is not expressed in humans because the coding sequence is interrupted by stop codons (Nelson 2004). The 5-HT$_{5A}$ receptor shows a particularly high presence in raphe and other brainstem and pons nuclei (Volk et al. 2010). There are no available radioligands for either of the 5-HT$_5$ receptors.

25.2.8 5-HT$_6$ Receptors

5-HT$_6$ receptors are found exclusively in the CNS and are predominantly expressed in the striatum, limbic system and cortex (Woolley et al. 2004). They are of particular interest because of their involvement in learning and memory (King et al. 2008), and the receptor shows a significant age-related decline in healthy subjects, primarily in basal ganglia (Radhakrishnan et al. 2018). So far, only one non-selective radioligand for PET imaging of the 5-HT$_6$ receptor has made its way into humans, namely,   [^{11}C]GSK215083   (3-[(3-fluorophenyl)sulfonyl]-8-(4-[^{11}C]methyl-1-piperazinyl)quinoline (Parker et al. 2012). GSK215083 has high affinity for 5-HT$_6$ (in vitro K_i, 0.16 nM) but also has high 5-HT$_{2A}$ affinity (in vitro K_i, 0.79 nM). However, the differential localisation of 5-HT$_{2A}$ and 5-HT$_6$ receptors (predominantly cortical and striatal, respectively) combined with the ~fivefold difference in affinity means that discrimination between these two receptor types can be done to some extent.

25.2.9 5-HT$_7$ Receptors

In spite of many attempts to develop 5-HT$_7$-selective PET and SPECT tracers, none of these have yet made their way into human use. The so far most promising radiotracer is [^{11}C]Cimbi-717 which in pigs displayed the most promising results for selective 5-HT$_7$ receptor PET imaging (Hansen et al. 2014), because it is displaceable with 5-HT$_7$ receptor selective compounds. See also review by L'Estrade et al. (2020).

25.2.10 SERT

SERT is the serotonin transporter, and it receives considerable interest, not the least due to the success of its inhibitors in the treatment of depression and anxiety disorders. Several PET and SPECT ligands have been developed for this purpose, and a detailed review of SERT imaging by PET and SPECT can be found in Huang et al. (2010).

Initially, images of SERT in the human brain came from the non-selective cocaine derivative SPECT ligand [^{123}I]β-CIT and later with the selective but kinetically irreversible PET ligand [^{11}C](+)McN5652. Today, the most successful line of SERT radioligands is that developed from diarylsulfides such as [^{123}I]ADAM and especially [^{11}C]MADAM and [^{11}C]DASB.

The so far best SPECT radioligand for SERT imaging is [^{123}I]ADAM (2-((2-((dimethylamino)methyl)phenyl)thio)-5-iodophenylamine), which is potent and selective and has a high target-to-background ratio in human studies (Newberg et al. 2004). Quantification of the SERT binding with [^{123}I]ADAM SPECT is most often done with a ratio method, based on data acquired from 200 to 240 min. This has, however, been shown to overestimate the specific binding by about 10%. The

most reliable outcome is based on a 0–120 min SPECT acquisition followed by Logan non-invasive modelling (Frokjaer et al. 2008).

The first selective PET radioligand for imaging SERT in the human brain was [11C](+)McN5652 (*trans*-1,2,3,5,6,10-β-hexahydro-6-[4-(methylthio)phenyl]pyrrolo-[2,1-*a*]isoquinoline) (Szabo et al. 1995). Its use has been limited by a relatively low target-to-background ratio in vivo, as well as a slow brain uptake and irreversible kinetics that complicate quantification in high-binding regions (Frankle et al. 2004).

[11C]DASB (3-amino-4-(2-dimethylamino-methyl-phenylsulfanyl)-benzonitrile) is one of a series of 11C-labelled arylthiobenzylamines developed by Wilson and Houle (1999). [11C]DASB displays good selectivity and high affinity and is today the most widely used radiotracer for in vivo imaging of SERT. [11C]DASB PET can be quantified with reference tissue models (Ginovart et al. 2001); this is the most frequently used way of quantifying [11C]DASB. Furthermore, test-retest data show high reproducibility and reliability (Kim et al. 2006). [11C]DASB PET normative data are available (Erritzoe et al. 2009, 2010), and apart from a multitude of patient studies, it has also been used to measure SERT occupancy at clinical doses of selective reuptake inhibitors, e.g. citalopram and paroxetine (Meyer et al. 2004).

[11C]MADAM (*N,N*-dimethyl-2-(2-amino-4-methylphenylthio)-benzylamine) is yet another PET radioligand that has made its way into humans (Lundberg et al. 2005). When done several weeks apart, test-retest reproducibility of [11C]MADAM is excellent (Lundberg et al. 2006). As for [11C]DASB, [11C]MADAM has been used to estimate relative SERT occupancy of citalopram and escitalopram (Lundberg et al. 2007) and to investigate the relationship between 5-HT$_{1A}$ and SERT binding in healthy young men and women (Henningsson et al. 2009; Jovanovic et al. 2008). [11C]DASB and [11C]MADAM seem comparable in terms of their pharmacological and kinetic profile; the majority of clinical studies have, however, been done with [11C]DASB.

25.3 PET Imaging of the Serotonergic System in Alzheimer's Disease

As an example of the application of PET imaging in neurology and psychiatry, studies of the serotonergic system in Alzheimer's disease (AD) will be reviewed in this section. With increasing incidence and prevalence worldwide, AD presents a unique challenge to researchers in order to provide better diagnostic tools, as well as a better understanding of the pathophysiology of the disease. Biomarkers such as medial temporal lobe atrophy on magnetic resonance imaging, glucose metabolism measured with PET or beta-amyloid and tau in cerebrospinal fluid become increasingly incorporated into the diagnostic process (Dubois et al. 2010; Jack Jr et al. 2018). Therefore, the focus of neuroreceptor imaging with PET has changed in the direction of better understanding the pathophysiology behind the symptomatology of AD (Xu et al. 2012). The ultimate goal of this research is better and more specific treatment options.

Postmortem and clinical studies have shown widespread dysfunction of the serotonergic transmitter system in AD. Thus, postmortem brain studies have consistently found significant loss of serotonin-producing neurons or reductions in the presynaptically located serotonin transporter (SERT) in the raphe nuclei (Aletrino et al. 1992; Halliday et al. 1992; Hendricksen et al. 2004; Tejani-Butt et al. 1995) and in serotonergic neuronal projections (Tejani-Butt et al. 1995; Thomas et al. 2006; Tsang et al. 2003). Also, in several postmortem studies, pre- and postsynaptic receptor subtypes have been found reduced: $5\text{-}HT_{1A}$ (Becker et al. 2014; Lai et al. 2003b; Vidal et al. 2016), $5\text{-}HT_{1B}$ (Garcia-Alloza et al. 2004), $5\text{-}HT_{2A}$ (Bowen et al. 1989; Cheng et al. 1991; Lai et al. 2005; Lorke et al. 2006) and $5\text{-}HT_6$ receptors (Garcia-Alloza et al. 2004; Lorke et al. 2006). Since serotonergic dysfunction and neuropsychiatric symptoms have been linked to mood disorders, disturbances in the serotonergic system could be related to the presence of neuropsychiatric symptoms in AD. This would be especially relevant for depressive symptoms, which are frequent in AD (Ballard et al. 1996; Lyketsos et al. 2002). Serotonin may, however, also play a role in normal cognitive functions (for review, see Schmitt and co-workers (Schmitt et al. 2006). More recently, the involvement of serotonin in cognition has further been substantiated by studies in healthy young subjects, showing an association between high SERT binding in fronto-striatal regions and better performance on tasks involving executive function and logical reasoning (Madsen et al. 2011a) and an inverse association between $5\text{-}HT_4$ receptor binding in the hippocampus and memory performance (Haahr et al. 2013). As $5\text{-}HT_4$ receptor binding is suggested to be a biomarker of serotonergic tonus in human (Haahr et al. 2014), low levels of central 5-HT could partly be responsible for not only neuropsychiatric symptomatology but also cognitive impairment in patients with AD.

25.3.1 $5\text{-}HT_{1A}$ Receptor Binding in AD

Using [^{18}F]MPPF, Kepe and co-workers found significant reductions in $5\text{-}HT_{1A}$ receptor densities in both the hippocampus and raphe nuclei in patients with mild cognitive impairment (MCI) (24%) and AD patients (49%) (Kepe et al. 2006). They interpreted their findings as secondary to neocortical degeneration of synapses and neurons, because a positive association of $5\text{-}HT_{1A}$ receptor binding with glucose metabolism was found in the hippocampus. Further, $5\text{-}HT_{1A}$ receptor binding was negatively correlated with [^{18}F]FDDNP, a marker of tau pathology (Kepe et al. 2006). Interestingly, using the same tracer, Truchot and co-workers found a biphasic change in $5\text{-}HT_{1A}$ receptor binding in the hippocampus, parahippocampus and inferior temporal cortex with upregulation in MCI and a marked reduction (approx. 50%) in AD (Truchot et al. 2007) which may suggest a compensatory upregulation due to lower serotonin levels in the pre-dementia stage of AD. Following this upregulation, $5\text{-}HT_{1A}$ receptor binding may eventually decrease in early-to-moderate stages of AD due to neurodegeneration, as suggested by Kepe et al. (2006).

25.3.2 5-HT$_{2A}$ Receptor Binding in AD

Several studies have found widespread reduction in 5-HT$_{2A}$ receptor binding in mild-to-moderate AD. Using PET and [^{18}F]setoperone in patients with AD, Blin and colleagues found a 35–69% reduction in temporoparietal cortical 5-HT$_2$ receptor binding (Blin et al. 1993). In a similar patient group (mean MMSE 20) but using [^{18}F]altanserin, Meltzer and colleagues found reductions of approximately 30% in the anterior cingulate, prefrontal and sensorimotor cortices (Meltzer et al. 1999). In two consecutive [^{18}F]altanserin studies in MCI and AD patients, these findings were corroborated by widespread neocortical reductions in receptor binding (MCI: 22–29% and AD: 28–39%) (Hasselbalch et al. 2008; Marner et al. 2011). Importantly, all three [^{18}F]altanserin studies employed correction for partial volume error due to atrophy, and atrophy did not explain the findings.

In contrast to the 5-HT$_{1A}$ receptor findings above, the reductions in 5-HT$_{2A}$ receptor are widespread and occur early in the course of the disease (Hasselbalch et al. 2008), but the reason for this reduction is largely unexplained. It is unlikely that loss of serotonergic neurons projecting to neocortex has any major impact on the post-synaptic 5-HT$_{2A}$ receptor reductions, since reductions in 5-HT$_{2A}$ receptors are not accompanied by similar reductions in presynaptic serotonin transporter binding (Marner et al. 2012). One plausible explanation for the diffuse neocortical 5-HT$_{2A}$ receptor reductions could be that local AD pathology, especially in the form of widespread beta-amyloid accumulation, is responsible for the reduction in 5-HT$_{2A}$ receptors. Beta-amyloid accumulation has a spatial distribution similar to the reduction in 5-HT$_{2A}$ receptor binding, whereas neurodegeneration in the form of tau accumulation follows a different pattern (Braak and Braak 1991). As an indirect support of the proposed beta-amyloid/5HT$_{2A}$ receptor association, Marner and co-workers found a nonsignificant 5–10% reduction in ^{18}F-altanserin binding in neocortical regions in a 2-year follow-up study of 15 MCI patients (Marner et al. 2011). This reduction inversely mirrors the small increase in beta-amyloid accumulation found in early AD in most studies (Jack Jr et al. 2010). Further, experimental studies have shown an association between increased beta-amyloid load and decreased 5-HT$_{2A}$ receptor binding (Christensen et al. 2008; Holm et al. 2010). Thus, 5-HT$_{2A}$ receptor may be especially sensitive to beta-amyloid pathology, but the nature of this interaction needs to be clarified in future studies.

25.3.3 5-HT$_4$ Receptor Binding in AD

The 5-HT$_4$ receptor is especially interesting in AD as it is both linked to memory function and beta-amyloid accumulation. There is ample evidence for pro-cognitive actions of agonists to the 5-HT$_4$ receptor. Thus, in animals, pre-task systemic injections of 5-HT$_4$ receptor agonists have shown to improve performance in a variety of memory tasks such as olfactory associative learning (Marchetti et al. 2000; Marchetti-Gauthier et al. 1997), place and object recognition (Lamirault and Simon 2001), the Morris water maze (Lelong et al. 2001) and matching to sample (Terry Jr et al. 1998). In the only study in healthy humans, using [^{11}C]SB207145 and Rey's

Auditory Verbal Learning Test in healthy young subjects, Haahr and co-workers found significant negative associations between the immediate and delayed recall scores and hippocampal $5\text{-}HT_4$ receptor binding (Haahr et al. 2013). This paradoxical finding was explained by upregulation of $5\text{-}HT_4$ receptor levels to partially compensate for lower hippocampal 5-HT levels in subjects with poorer memory function (Haahr et al. 2013). This explanation has been corroborated by findings of a reduction in $5\text{-}HT_4$ receptor binding following a 3-week administration of a selective 5-HT reuptake inhibitor (Haahr et al. 2014). In early AD, Madsen and co-workers found some support for this hypothesis: In mild stage AD patients, beta-amyloid imaging with $[^{11}C]PiB$ and $5\text{-}HT_4$ receptor imaging using $[^{11}C]SB207145$ was performed in the same subjects (Madsen et al. 2011d). PiB-positive individuals had 13% higher $5\text{-}HT_4$ receptor binding compared to PiB-negative individuals. The $5\text{-}HT_4$ receptor binding was positively correlated to beta-amyloid burden and negatively to the MMSE score (Mini-Mental State Examination—a measure of global cognitive function) of the AD patients. These findings suggest that cerebral $5\text{-}HT_4$ receptor upregulation starts at a preclinical stage of AD and continues, while dementia is still at a mild stage, which contrasts other receptor subtypes. As in the study of healthy subjects mentioned above, it was speculated that the upregulation was a compensatory effect of decreased levels of interstitial 5-HT in early AD (Madsen et al. 2011d). Further, agonism of the $5\text{-}HT_4$ receptor increases alpha-secretase activity and thus promotes non-amyloidogenic degradation of the amyloid precursor protein (APP) (Cachard-Chastel et al. 2007). Therefore, an upregulation of the $5\text{-}HT_4$ receptor level in early AD may serve to counteract beta-amyloid accumulation, but further studies are needed to elucidate these rather speculative interactions.

25.3.4 $5\text{-}HT_6$ Receptor Binding in AD

The $5\text{-}HT_6$ receptor has been implicated in memory functions, as $5\text{-}HT_6$ antagonism can reverse scopolamine-induced episodic memory dysfunction (de Bruin et al. 2011), although the effect may be strongest for working memory and aversive learning (Da Silva et al. 2012). The pro-cognitive effects of $5\text{-}HT_6$ antagonism have been investigated in clinical trials of mild-to-moderate AD but have failed to show clinical effects (Maher-Edwards et al. 2010; Atri et al. 2018). In the postmortem AD brains, reductions in $5\text{-}HT_6$ binding have been found in frontal as well as temporal cortical areas (Garcia-Alloza et al. 2004; Lorke et al. 2006). As described above, a PET tracer non-selective for the $5\text{-}HT_6$ receptor is being used, but so far, no studies examining patients with AD have been published.

25.3.5   SERT Binding in AD

As described above, several studies in the postmortem AD brains have shown significant losses of serotonin-producing neurons or reductions in the presynaptically located SERT in the raphe nuclei and in serotonergic neuronal projections (Aletrino et al. 1992; Halliday et al. 1992; Hendricksen et al. 2004; Tejani-Butt et al. 1995;

Thomas et al. 2006; Tsang et al. 2003). Three studies have investigated the SERT binding in AD in vivo by PET in AD. Ouchi and co-workers used [^{11}C]DASB in 15 mild to moderately demented AD patients, of whom 7 also had depressive symptoms (Ouchi et al. 2009). They found that [^{11}C]DASB binding in the dense SERT regions (the midbrain, including the raphe nuclei, nucleus accumbens, putamen, and thalamus) of the depressed AD group was significantly lower than that in an age-matched control group (Ouchi et al. 2009). In the midbrain, the reduction amounted to 33%. In the nondepressed group, a significant SERT reduction was found only in the putamen. In contrast, in 12 mild-to-moderate AD patients, Marner and co-workers did not find reductions in [^{11}C]DASB binding in the raphe nuclei (Marner et al. 2012). In this study, SERT binding was reduced in mesial temporal lobe only, whereas 5-HT$_{2A}$ receptor binding measured using ^{18}F-altanserin was globally reduced by 28–39% in the same subjects. Finally, in 28 MCI subjects, Smith et al. found widespread reductions in SERT binding in cortical and limbic regions, as well as in the raphe nuclei, which were associated with both verbal and visual memory scores (Smith et al. 2017).The discrepancies between these studies may arise from methodological differences and also from patient selection, and all three studies document early disruption of serotonergic transmission in AD. In conclusion, in end-stage AD, postmortem studies clearly show degeneration of serotonergic neurons in the raphe and in serotonergic neuronal projections, and PET studies corroborate these findings with serotonergic neurons and projections being affected even in early stages of the disease.

25.4　Can Serotonergic Dysfunction Explain AD Symptomatology?

As described above, dysfunction of the serotonergic transmitter system is well-documented in AD. The important question is whether this dysfunction explains part of the symptomatology of the disorder. In postmortem studies of AD, low densities of neocortical SERT and 5-HT$_{1A}$ receptors have been associated with depression and aggression, respectively (Chen et al. 1996; Lai et al. 2003a). Also, Garcia-Alloza et al. found associations between cognition and frontal cortex 5-HT$_{1B}$ binding and between behavioural symptoms and temporal 5-HT$_6$ binding (Garcia-Alloza et al. 2004). Postmortem studies are associated with problems regarding time interval between symptom evaluation and receptor binding analyses, and also, they represent an end stage of the disease. But in vivo studies have so far not been able to give a clear answer to the question. Although Kepe et al. (2006) demonstrated a correlation between hippocampal 5-HT$_{1A}$ receptor binding and MMSE, they interpreted this association as secondary to the well-known correlation between neurodegeneration and cognitive function. No correlation between MMSE score and 5-HT$_{2A}$ receptor binding was found in two studies of MCI and AD patients (Meltzer et al. 1999; Hasselbalch et al. 2008). However, these studies included rather small sample sizes, and also, the limited range of cognitive dysfunction may have made it difficult to determine correlations between serotonergic and cognitive dysfunction. In a SPECT study of AD patients

(Versijpt et al. 2003), a correlation between MMSE scores and 5-HT$_{2A}$ receptor binding in the left orbitofrontal region was found, but the relevance of this finding is not clear. Patients with significant neuropsychiatric symptoms can be very difficult to include in PET studies, and generally, patients covering the spectrum from mild to severe neuropsychiatric symptoms are lacking in in vivo studies. Meltzer and co-workers found no difference in 5-HT$_{2A}$ receptor binding in AD subjects with depression compared to AD subjects without depression. Further, in the depressed patients, there was no correlation between 5-HT$_{2A}$ receptor binding and Hamilton depression scale score (Meltzer et al. 1999). Likewise, an inverse correlation between neuropsychiatric symptoms scored by the Neuropsychiatric Inventory (NPI) and striatal 5-HT$_{2A}$ receptor binding observed in MCI (Hasselbalch et al. 2008; Marner et al. 2011) could not be corroborated in with the same methodology in a sample of AD patients (Marner et al. 2012). Similarly, SERT findings have been controversial with regard to neuropsychiatric symptoms: In a postmortem study of depressive versus nondepressive AD patients, Hendricksen et al. (Hendricksen et al. 2004) found no differences in raphe pathology. In contrast, Ouchi and co-workers found significant correlations between SERT high-binding regions (the midbrain, striatum and thalamus) and geriatric depressions scores when grouping depressed and nondepressed AD patients (Ouchi et al. 2009). However, Marner and co-workers did not find significant associations between measures of depression and SERT binding in AD patients, but in this study, patients had less cognitive and neuropsychiatric symptoms (Marner et al. 2012) as compared to Ouchi et al. (2009). Thus, postmortem and in vivo imaging data are only consistent when it comes to the association between reduced SERT expression in the midbrain and depressive symptoms in AD (Ouchi et al. 2009; Chen et al. 1996). In the study by Smith et al. (Smith et al. 2017), SERT binding was positively correlated with performance on tests of visual and verbal memory and to a greater extent than a reduction in regional cerebral blood flow and grey matter volume. These findings may suggest a specific role of 5-HT transmission in cognitive dysfunction in AD, but future in vivo studies need to include larger samples of patients with a spectrum of cognitive and neuropsychiatric symptoms. Even when doing so, the complex neuropathology and the interaction between several affected transmitter systems may make the aim of establishing associations between serotonin receptor subtypes and symptomatology too simplistic. However, once the pathophysiology of AD symptoms is further elucidated, in vivo imaging studies may help us to determine available drug targets.

References

Adams KH, Pinborg LH, Svarer C, Hasselbalch SG, Holm S, Haugbol S, Madsen K, Frokjaer V, Martiny L, Paulson OB, Knudsen GM (2004) A database of [(18)F]-altanserin binding to 5-HT(2A) receptors in normal volunteers: normative data and relationship to physiological and demographic variables. NeuroImage 21:1105–1113

Aletrino MA, Vogels OJ, Van Domburg PH, Ten Donkelaar HJ (1992) Cell loss in the nucleus raphes dorsalis in Alzheimer's disease. Neurobiol Aging 13:461–468

Atri A, Frölich L, Ballard C, Tariot PN, Molinuevo JL, Boneva N, Windfeld K, Raket LL, Cummings JL (2018) Effect of idalopirdine as adjunct to cholinesterase inhibitors on change in cognition in patients with Alzheimer disease: three randomized clinical trials. JAMA 319((2):130–142

Ballard C, Bannister C, Solis M, Oyebode F, Wilcock G (1996) The prevalence, associations and symptoms of depression amongst dementia sufferers. J Affect Disord 36:135–144

Becker G, Streichenberger N, Billard T, Newman-Tancredi A, Zimmer L (2014) A postmortem study to compare agonist and antagonist 5-HT1A receptor-binding sites in Alzheimer's disease. CNS Neurosci Ther 20(10):930–949

Beliveau V, Ganz M, Feng L, Ozenne B, Højgaard L, Fisher PM, Svarer C, Greve DN, Knudsen GM (2017) A high-resolution in vivo atlas of the human Brain's serotonin system. J Neurosci. 37(1):120–128

Blin J, Baron JC, Dubois B, Crouzel C, Fiorelli M, Ttar-Levy D, Pillon B, Fournier D, Vidailhet M, Agid Y (1993) Loss of brain 5-HT2 receptors in Alzheimer's disease. In vivo assessment with positron emission tomography and [18F]setoperone. Brain 116(Pt 3):497–510

Bockaert J, Claeysen S, Compan V, Dumuis A (2004) 5-HT4 receptors. Curr Drug Targets CNS Neurol Disord 3:39–51

Bowen DM, Najlerahim A, Procter AW, Francis PT, Murphy E (1989) Circumscribed changes of the cerebral cortex in neuropsychiatric disorders of later life. Proc Natl Acad Sci U S A 86:9504–9508

Braak H, Braak E (1991) Neuropathological staging of Alzheimer-related changes. Acta Neuropathol 82:239–259

de Bruin NM, Prickaerts J, van Loevezijn A, Venhorst J, de Groote L, Houba P, Reneerkens O, Akkerman S, Kruse CG (2011) Two novel 5-HT6 receptor antagonists ameliorate scopolamine-induced memory deficits in the object recognition and object location tasks in Wistar rats. Neurobiol Learn Mem 96:392–402

Cachard-Chastel M, Lezoualc'h F, Dewachter I, Delomenie C, Croes S, Devijver H, Langlois M, Van LF, Sicsic S, Gardier AM (2007) 5-HT4 receptor agonists increase sAPPalpha levels in the cortex and hippocampus of male C57BL/6j mice. Br J Pharmacol 150:883–892

Chen CP, Alder JT, Bowen DM, Esiri MM, McDonald B, Hope T, Jobst KA, Francis PT (1996) Presynaptic serotonergic markers in community-acquired cases of Alzheimer's disease: correlations with depression and neuroleptic medication. J Neurochem 66:1592–1598

Cheng AV, Ferrier IN, Morris CM, Jabeen S, Sahgal A, McKeith IG, Edwardson JA, Perry RH, Perry EK (1991) Cortical serotonin-S2 receptor binding in Lewy body dementia, Alzheimer's and Parkinson's diseases. J Neurol Sci 106:50–55

Christensen R, Marcussen AB, Wortwein G, Knudsen GM, Aznar S (2008) Abeta(1-42) injection causes memory impairment, lowered cortical and serum BDNF levels, and decreased hippocampal 5-HT(2A) levels. Exp Neurol 210:164–171

da Cunha-Bang S, Ettrup A, Mc Mahon B, Skibsted AP, Schain M, Lehel S, Dyssegaard A, Jørgensen LM, Møller K, Gillings N, Svarer C, Knudsen GM (2019) Measuring endogenous changes in serotonergic neurotransmission with [11C]Cimbi-36 positron emission tomography in humans. Transl Psychiatry 9(1):134

Da Silva C-AV, Quiedeville A, Boulouard M, Dauphin F (2012) 5-HT6 receptor blockade differentially affects scopolamine-induced deficits of working memory, recognition memory and aversive learning in mice. Psychopharmacology 222:99–115

Dubois B, Feldman HH, Jacova C, Cummings JL, Dekosky ST, Barberger-Gateau P, Delacourte A, Frisoni G, Fox NC, Galasko D, Gauthier S, Hampel H, Jicha GA, Meguro K, O'Brien J, Pasquier F, Robert P, Rossor M, Salloway S, Sarazin M, de Souza LC, Stern Y, Visser PJ, Scheltens P (2010) Revising the definition of Alzheimer's disease: a new lexicon. Lancet Neurol 9:1118–1127

Erritzoe D, Frokjaer VG, Haugbol S, Marner L, Svarer C, Holst K, Baare WF, Rasmussen PM, Madsen J, Paulson OB, Knudsen GM (2009) Brain serotonin 2A receptor binding: relations to body mass index, tobacco and alcohol use. NeuroImage 46:23–30

Erritzoe D, Holst K, Frokjaer VG, Licht CL, Kalbitzer J, Nielsen FA, Svarer C, Madsen J, Knudsen G (2010) A nonlinear relationship between cerebral serotonin transporter and 5-HT2A receptor binding: an in vivo molecular imaging study in humans. J Neurosci 30:3391–3397

Ettrup A, da Cunha-Bang S, McMahon B, Lehel S, Dyssegaard A, Skibsted AW, Jørgensen LM, Hansen M, Baandrup AO, Bache S, Svarer C, Kristensen JL, Gillings N, Madsen J, Knudsen GM (2014a) Serotonin 2A receptor agonist binding in the human brain with [^{11}C]Cimbi-36. J Cereb Blood Flow Metab 34(7):1188–1196

Ettrup A, da Cunha-Bang S, McMahon B, Lehel S, Dyssegaard A, Skibsted AW, Jørgensen LM, Hansen M, Baandrup AO, Bache S, Svarer C, Kristensen JL, Gillings N, Madsen J, Knudsen GM (2014b Jul) Serotonin 2A receptor agonist binding in the human brain with [11C]Cimbi-36. J Cereb Blood Flow Metab 34(7):1188–1196

Ettrup A, Svarer C, McMahon B, da Cunha-Bang S, Lehel S, Møller K, Dyssegaard A, Ganz M, Beliveau V, Jørgensen LM, Gillings N, Knudsen GM (2016) Serotonin 2A receptor agonist binding in the human brain with [(11)C]Cimbi-36: test-retest reproducibility and head-to-head comparison with the antagonist [(18)F]altanserin. Neuroimage 130:167–174

Finnema SJ, Varrone A, Hwang TJ, Gulyas B, Pierson ME, Halldin C, Farde L (2010) Fenfluramine-induced serotonin release decreases [11C]AZ10419369 binding to 5-HT1B-receptors in the primate brain. Synapse 64:573–577

Fisher PM, Holst KK, Adamsen D, Klein AB, Frokjaer VG, Jensen PS, Svarer C, Gillings N, Baare WF, Mikkelsen JD, Knudsen GM (2015a) BDNF Val66met and 5-HTTLPR polymorphisms predict a human in vivo marker for brain serotonin levels. Hum Brain Mapp 36(1):313–323

Fisher PM, Holst KK, Adamsen D, Klein AB, Frokjaer VG, Jensen PS, Svarer C, Gillings N, Baare WFC, Mikkelsen JD, Knudsen GM (2015b Jan) BDNF val66met and 5-HTTLPR polymorphisms predict a human in vivo marker for brain serotonin levels. Hum Brain Mapp 36(1):313–323

Frankle WG, Huang Y, Hwang DR, Talbot PS, Slifstein M, Van HR, bi-Dargham A, Laruelle M (2004) Comparative evaluation of serotonin transporter radioligands 11C-DASB and 11C-McN 5652 in healthy humans. J Nucl Med 45:682–694

Frokjaer VG, Pinborg LH, Madsen J, de Nijs R, Svarer C, Wagner A, Knudsen GM (2008) Evaluation of the serotonin transporter ligand 123I-ADAM for SPECT studies on humans. J Nucl Med 49:247–254

Frokjaer VG, Erritzoe D, Madsen J, Paulson OB, Knudsen GM (2009) Gender and the use of hormonal contraception in women are not associated with cerebral cortical 5-HT 2A receptor binding. Neuroscience 163:640–645

Gallezot JD, Nabulsi N, Neumeister A, Planeta-Wilson B, Williams WA, Singhal T, Kim S, Maguire RP, McCarthy T, Frost JJ, Huang Y, Ding YS, Carson RE (2010) Kinetic modeling of the serotonin 5-HT(1B) receptor radioligand [(11)C]P943 in humans. J Cereb Blood Flow Metab 30:196–210

Garcia-Alloza M, Hirst WD, Chen CP, Lasheras B, Francis PT, Ramirez MJ (2004) Differential involvement of 5-HT(1B/1D) and 5-HT6 receptors in cognitive and non-cognitive symptoms in Alzheimer's disease. Neuropsychopharmacology 29:410–416

Gee AD, Martarello L, Passchier J, Wishart M, Parker C, Matthews J, Comley R, Hopper R, Gunn R (2008) Synthesis and evaluation of [11C]SB207145 as the first in vivo serotonin 5-HT4 receptor radioligand for PET imaging in man. Curr Radiopharm 1:110–114

Ginovart N, Wilson AA, Meyer JH, Hussey D, Houle S (2001) Positron emission tomography quantification of [(11)C]-DASB binding to the human serotonin transporter: modeling strategies. J Cereb Blood Flow Metab 21:1342–1353

Haahr ME, Fisher P, Holst K, Madsen K, Jensen CG, Marner L, Lehel S, Baare W, Knudsen G, Hasselbalch S (2013) The 5-HT(4) receptor levels in hippocampus correlates inversely with memory test performance in humans. Hum Brain Mapp 34:3066–3074

Haahr ME, Fisher PM, Jensen CG, Frokjaer VG, Mahon BM, Madsen K, Baaré WF, Lehel S, Norremolle A, Rabiner EA, Knudsen GM (2014) Central 5-HT4 receptor binding as biomarker of serotonergic tonus in humans: a [11C]SB207145 PET study. Mol Psychiatry 19(4):427–432

Halford JC, Harrold JA, Boyland EJ, Lawton CL, Blundell JE (2007) Serotonergic drugs: effects on appetite expression and use for the treatment of obesity. Drugs 67:27–55

Halliday GM, McCann HL, Pamphlett R, Brooks WS, Creasey H, McCusker E, Cotton RG, Broe GA, Harper CG (1992) Brain stem serotonin-synthesizing neurons in Alzheimer's disease: a clinicopathological correlation. Acta Neuropathol 84:638–650

Hansen HD, Herth MM, Ettrup A, Andersen VL, Lehel S, Dyssegaard A, Kristensen JL, Knudsen GM (2014) Radiosynthesis and in vivo evaluation of novel radioligands for PET imaging of cerebral 5-HT7 receptors. J Nucl Med 55(4):640–646

Hasselbalch SG, Madsen K, Svarer C, Pinborg LH, Holm S, Paulson OB, Waldemar G, Knudsen GM (2008) Reduced 5-HT2A receptor binding in patients with mild cognitive impairment. Neurobiol Aging 29:1830–1838

Haugbol S, Pinborg LH, Arfan HM, Frokjaer VM, Madsen J, Dyrby TB, Svarer C, Knudsen GM (2007) Reproducibility of 5-HT2A receptor measurements and sample size estimations with [18F]altanserin PET using a bolus/infusion approach. Eur J Nucl Med Mol Imaging 34:910–915

Hendricksen M, Thomas AJ, Ferrier IN, Ince P, O'Brien JT (2004) Neuropathological study of the dorsal raphe nuclei in late-life depression and Alzheimer's disease with and without depression. Am J Psychiatry 161:1096–1102

Henningsson S, Borg J, Lundberg J, Bah J, Lindstrom M, Ryding E, Jovanovic H, Saijo T, Inoue M, Rosen I, Traskman-Bendz L, Farde L, Eriksson E (2009) Genetic variation in brain-derived neurotrophic factor is associated with serotonin transporter but not serotonin-1A receptor availability in men. Biol Psychiatry 66:477–485

Holm P, Ettrup A, Klein AB, Santini MA, El-Sayed M, Elvang AB, Stensbol TB, Mikkelsen JD, Knudsen GM, Aznar S (2010) Plaque deposition dependent decrease in 5-HT2A serotonin receptor in AbetaPPswe/PS1dE9 amyloid overexpressing mice. J Alzheimers Dis 20:1201–1213

Hoyer D, Hannon JP, Martin GR (2002) Molecular, pharmacological and functional diversity of 5-HT receptors. Pharmacol Biochem Behav 71:533–554

Huang Y, Zheng MQ, Gerdes JM (2010) Development of effective PET and SPECT imaging agents for the serotonin transporter: has a twenty-year journey reached its destination? Curr Top Med Chem 10:1499–1526

Jack CR Jr, Knopman DS, Jagust WJ, Shaw LM, Aisen PS, Weiner MW, Petersen RC, Trojanowski JQ (2010) Hypothetical model of dynamic biomarkers of the Alzheimer's pathological cascade. Lancet Neurol 9:119–128

Jack CR Jr, Bennett DA, Blennow K, Carrillo MC, Dunn B, Haeberlein SB, Holtzman DM, Jagust W, Jessen F, Karlawish J, Liu E, Molinuevo JL, Montine T, Phelps C, Rankin KP, Rowe CC, Scheltens P, Siemers E, Snyder HM, Sperling R (2018) NIA-AA research framework: toward a biological definition of Alzheimer's disease. Alzheimers Dement 14(4):535–562

Jones T, Rabiner EA (2012) The development, past achievements, and future directions of brain PET. J Cereb Blood Flow Metab 32:1426–1454

Jørgensen LM, Weikop P, Svarer C, Feng L, Keller SH, Knudsen GM (2018a) Cerebral serotonin release correlates with [(11)C]AZ10419369 PET measures of 5-HT(1B) receptor binding in the pig brain. J Cereb Blood Flow Metab 38(7):1243–1252

Jørgensen LM, Weikop P, Svarer C, Feng L, Keller SH, Knudsen GM (2018b Jul) Cerebral serotonin release correlates with [11C]AZ10419369 PET measures of 5-HT1B receptor binding in the pig brain. J Cereb Blood Flow Metab 38(7):1243–1252

Jovanovic H, Lundberg J, Karlsson P, Cerin A, Saijo T, Varrone A, Halldin C, Nordstrom AL (2008) Sex differences in the serotonin 1A receptor and serotonin transporter binding in the human brain measured by PET. NeuroImage 39:1408–1419

Kepe V, Barrio JR, Huang SC, Ercoli L, Siddarth P, Shoghi-Jadid K, Cole GM, Satyamurthy N, Cummings JL, Small GW, Phelps ME (2006) Serotonin 1A receptors in the living brain of Alzheimer's disease patients. Proc Natl Acad Sci U S A 103:702–707

Kim JS, Ichise M, Sangare J, Innis RB (2006) PET imaging of serotonin transporters with [11C]DASB: test-retest reproducibility using a multilinear reference tissue parametric imaging method. J Nucl Med 47:208–214

King MV, Marsden CA, Fone KC (2008) A role for the 5-HT(1A), 5-HT4 and 5-HT6 receptors in learning and memory. Trends Pharmacol Sci 29:482–492

Kristiansen H, Elfving B, Plenge P, Pinborg LH, Gillings N, Knudsen GM (2005) Binding characteristics of the 5-HT2A receptor antagonists altanserin and MDL 100907. Synapse 58:249–257

Kumar JS, Mann JJ (2014) PET tracers for serotonin receptors and their applications. Cent Nerv Syst Agents Med Chem 14(2):96–112

Lai MK, Tsang SW, Francis PT, Esiri MM, Hope T, Lai OF, Spence I, Chen CP (2003a) [H-3]GR113808 binding to serotonin 5-HT4 receptors in the postmortem neocortex of Alzheimer disease: a clinicopathological study. J Neural Transm 110:779–788

Lai MK, Tsang SW, Francis PT, Esiri MM, Keene J, Hope T, Chen CP (2003b) Reduced serotonin 5-HT1A receptor binding in the temporal cortex correlates with aggressive behavior in Alzheimer disease. Brain Res 974:82–87

Lai MK, Tsang SW, Alder JT, Keene J, Hope T, Esiri MM, Francis PT, Chen CP (2005) Loss of serotonin 5-HT2A receptors in the postmortem temporal cortex correlates with rate of cognitive decline in Alzheimer's disease. Psychopharmacology 179:673–677

Lamirault L, Simon H (2001) Enhancement of place and object recognition memory in young adult and old rats by RS 67333, a partial agonist of 5-HT4 receptors. Neuropharmacology 41:844–853

Lee HM, Roth BL (2012) Hallucinogen actions on human brain revealed. Proc Natl Acad Sci U S A 109:1820–1821

Lelong V, Dauphin F, Boulouard M (2001) RS 67333 and D-cycloserine accelerate learning acquisition in the rat. Neuropharmacology 41:517–522

L'Estrade ET, Erlandsson M, Edgar FG, Ohlsson T, Knudsen GM, Herth MM (2020) Towards selective CNS PET imaging of the 5-HT7 receptor system: past, present and future. Neuropharmacology. [Epub ahead of print] 172:107830

Leysen JE (2004) 5-HT2 receptors. Curr Drug Targets CNS Neurol Disord 3:11–26

Lorke DE, Lu G, Cho E, Yew DT (2006) Serotonin 5-HT2A and 5-HT6 receptors in the prefrontal cortex of Alzheimer and normal aging patients. BMC Neurosci 7:36

Lundberg J, Odano I, Olsson H, Halldin C, Farde L (2005) Quantification of 11C-MADAM binding to the serotonin transporter in the human brain. J Nucl Med 46:1505–1515

Lundberg J, Halldin C, Farde L (2006) Measurement of serotonin transporter binding with PET and [11C]MADAM: a test-retest reproducibility study. Synapse 60:256–263

Lundberg J, Christophersen JS, Petersen KB, Loft H, Halldin C, Farde L (2007) PET measurement of serotonin transporter occupancy: a comparison of escitalopram and citalopram. Int J Neuropsychopharmacol 10:777–785

Lyketsos CG, Lopez O, Jones B, Fitzpatrick AL, Breitner J, DeKosky S (2002) Prevalence of neuropsychiatric symptoms in dementia and mild cognitive impairment: results from the cardiovascular health study. JAMA 288:1475–1483

Lyon RA, Titeler M, Frost JJ, Whitehouse PJ, Wong DF, Wagner HN Jr, Dannals RF, Links JM, Kuhar MJ (1986) 3H-3-N-methylspiperone labels D2 dopamine receptors in basal ganglia and S2 serotonin receptors in cerebral cortex. J Neurosci 6:2941–2949

Madsen K, Erritzoe D, Mortensen EL, Gade A, Madsen J, Baare W, Knudsen GM, Hasselbalch SG (2011a) Cognitive function is related to fronto-striatal serotonin transporter levels – a brain PET study in young healthy subjects. Psychopharmacology 213:573–581

Madsen K, Haahr MT, Marner L, Keller SH, Baare WF, Svarer C, Hasselbalch SG, Knudsen GM (2011b) Age and sex effects on 5-HT(4) receptors in the human brain: a [(11)C]SB207145 PET study. J Cereb Blood Flow Metab 31:1475–1481

Madsen K, Marner L, Haahr M, Gillings N, Knudsen GM (2011c) Mass dose effects and in vivo affinity in brain PET receptor studies – a study of cerebral 5-HT(4) receptor binding with [(11)C]SB207145. Nucl Med Biol 38:1085–1091

Madsen K, Neumann WJ, Holst K, Marner L, Haahr MT, Lehel S, Knudsen GM, Hasselbalch SG (2011d) Cerebral serotonin 4 receptors and amyloid-beta in early Alzheimer's disease. J Alzheimers Dis 26:457–466

Maher-Edwards G, Zvartau-Hind M, Hunter AJ, Gold M, Hopton G, Jacobs G, Davy M, Williams P (2010) Double-blind, controlled phase II study of a 5-HT6 receptor antagonist, SB-742457, in Alzheimer's disease. Curr Alzheimer Res 7:374–385

Marchetti E, Dumuis A, Bockaert J, Soumireu-Mourat B, Roman FS (2000) Differential modulation of the 5-HT(4) receptor agonists and antagonist on rat learning and memory. Neuropharmacology 39:2017–2027

Marchetti-Gauthier E, Roman FS, Dumuis A, Bockaert J, Soumireu-Mourat B (1997) BIMU1 increases associative memory in rats by activating 5-HT4 receptors. Neuropharmacology 36:697–706

Marner L, Gillings N, Comley RA, Baare WF, Rabiner EA, Wilson AA, Houle S, Hasselbalch SG, Svarer C, Gunn RN, Laruelle M, Knudsen GM (2009) Kinetic modeling of 11C-SB207145 binding to 5-HT4 receptors in the human brain in vivo. J Nucl Med 50:900–908

Marner L, Gillings N, Madsen K, Erritzoe D, Baare WF, Svarer C, Hasselbalch SG, Knudsen GM (2010) Brain imaging of serotonin 4 receptors in humans with [11C]SB207145-PET. NeuroImage 50:855–861

Marner L, Knudsen GM, Madsen K, Holm S, Baare W, Hasselbalch SG (2011) The reduction of baseline serotonin 2A receptors in mild cognitive impairment is stable at two-year follow-up. J Alzheimers Dis 23:453–459

Marner L, Frokjaer VG, Kalbitzer J, Lehel S, Madsen K, Baare WF, Knudsen GM, Hasselbalch SG (2012) Loss of serotonin 2A receptors exceeds loss of serotonergic projections in early Alzheimer's disease: a combined [11C]DASB and [18F]altanserin-PET study. Neurobiol Aging 33:479–487

Matuskey D, Pittman B, Planeta-Wilson B, Walderhaug E, Henry S, Gallezot JD, Nabulsi N, Ding YS, Bhagwagar Z, Malison R, Carson RE, Neumeister A (2012) Age effects on serotonin receptor 1B as assessed by PET. J Nucl Med 53:1411–1414

Meltzer CC, Price JC, Mathis CA, Greer PJ, Cantwell MN, Houck PR, Mulsant BH, Ben-Eliezer D, Lopresti B, Dekosky ST, Reynolds CF III (1999) PET imaging of serotonin type 2A receptors in late-life neuropsychiatric disorders. Am J Psychiatry 156:1871–1878

Meyer JH, Wilson AA, Sagrati S, Hussey D, Carella A, Potter WZ, Ginovart N, Spencer EP, Cheok A, Houle S (2004) Serotonin transporter occupancy of five selective serotonin reuptake inhibitors at different doses: an [11C]DASB positron emission tomography study. Am J Psychiatry 161:826–835

Milak MS, Severance AJ, Ogden RT, Prabhakaran J, Kumar JS, Majo VJ, Mann JJ, Parsey RV (2008) Modeling considerations for 11C-CUMI-101, an agonist radiotracer for imaging serotonin 1A receptor in vivo with PET. J Nucl Med 49:587–596

Nelson DL (2004) 5-HT5 receptors. Curr Drug Targets CNS Neurol Disord 3:53–58

Newberg AB, Plossl K, Mozley PD, Stubbs JB, Wintering N, Udeshi M, Alavi A, Kauppinen T, Kung HF (2004) Biodistribution and imaging with (123)I-ADAM: a serotonin transporter imaging agent. J Nucl Med 45:834–841

Ouchi Y, Yoshikawa E, Futatsubashi M, Yagi S, Ueki T, Nakamura K (2009) Altered brain serotonin transporter and associated glucose metabolism in Alzheimer disease. J Nucl Med 50:1260–1266

Parker RM, Barnes JM, Ge J, Barber PC, Barnes NM (1996) Autoradiographic distribution of [3H]-(S)-zacopride-labelled 5-HT3 receptors in human brain. J Neurol Sci 144:119–127

Parker CA, Gunn RN, Rabiner EA, Slifstein M, Comley R, Salinas C, Johnson CN, Jakobsen S, Houle S, Laruelle M, Cunningham VJ, Martarello L (2012) Radiosynthesis and characterization of 11C-GSK215083 as a PET radioligand for the 5-HT6 receptor. J Nucl Med 53:295–303

Paterson LM, Kornum BR, Nutt DJ, Pike VW, Knudsen GM (2013) 5-HT radioligands for human brain imaging with PET and SPECT. Med Res Rev 33:54–111

Pike VW, McCarron JA, Lammerstma AA, Hume SP, Poole K, Grasby PM, Malizia A, Cliffe IA, Fletcher A, Bench CJ (1995) First delineation of 5-HT1A receptors in human brain with PET and [11C]WAY-100635. Eur J Pharmacol 283:R1–R3

Pinborg LH, Adams KH, Svarer C, Holm S, Hasselbalch SG, Haugbol S, Madsen J, Knudsen GM (2003) Quantification of 5-HT2A receptors in the human brain using [18F]altanserin-PET and the bolus/infusion approach. J Cereb Blood Flow Metab 23:985–996

Pinborg LH, Arfan H, Haugbol S, Kyvik KO, Hjelmborg JV, Svarer C, Frokjaer VG, Paulson OB, Holm S, Knudsen GM (2008) The 5-HT2A receptor binding pattern in the human brain is strongly genetically determined. NeuroImage 40:1175–1180

Pinborg LH, Feng L, Haahr ME, Gillings N, Dyssegaard A, Madsen J, Svarer C, Yndgaard S, Kjaer TW, Parsey RV, Hansen HD, Ettrup A, Paulson OB, Knudsen GM (2012) No change in [(1)(1) C]CUMI-101 binding to 5-HT(1A) receptors after intravenous citalopram in human. Synapse 66:880–884

Radhakrishnan R, Nabulsi N, Gaiser E, Gallezot JD, Henry S, Planeta B, Lin SF, Ropchan J, Williams W, Morris E, D'Souza DC, Huang Y, Carson RE, Matuskey D (2018) Age-related change in 5-HT(6) receptor availability in healthy male volunteers measured with (11) C-GSK215083 PET. J Nucl Med 59(9):1445–1450

Rebholz H, Friedman E, Castello J (2018) Alterations of expression of the serotonin 5-HT4 receptor in brain disorders. Int J Mol Sci 13:19(11)

Ridler K, Plisson C, Rabiner EA, Gunn RN, Easwaramoorthy B, bi-Dargham A, Laruelle M, Slifstein M (2011) Characterization of in vivo pharmacological properties and sensitivity to endogenous serotonin of [11C] P943: a positron emission tomography study in Papio anubis. Synapse 65:1119–1127

Ryu YH, Liow JS, Zoghbi S, Fujita M, Collins J, Tipre D, Sangare J, Hong J, Pike VW, Innis RB (2007) Disulfiram inhibits defluorination of (18)F-FCWAY, reduces bone radioactivity, and enhances visualization of radioligand binding to serotonin 5-HT1A receptors in human brain. J Nucl Med 48:1154–1161

Savli M, Bauer A, Mitterhauser M, Ding YS, Hahn A, Kroll T, Neumeister A, Haeusler D, Ungersboeck J, Henry S, Isfahani SA, Rattay F, Wadsak W, Kasper S, Lanzenberger R (2012) Normative database of the serotonergic system in healthy subjects using multi-tracer PET. NeuroImage 63:447–459

Schmitt JA, Wingen M, Ramaekers JG, Evers EA, Riedel WJ (2006) Serotonin and human cognitive performance. Curr Pharm Des 12:2473–2486

Shrestha SS, Liow JS, Lu S, Jenko K, Gladding RL, Svenningsson P, Morse CL, Zoghbi SS, Pike VW, Innis RB (2014) (11)C-CUMI-101, a PET radioligand, behaves as a serotonin 1A receptor antagonist and also binds to α(1) adrenoceptors in brain. J Nucl Med 55(1):141–146

Shrestha SS, Liow JS, Jenko K, Ikawa M, Zoghbi SS, Innis RB (2016) The 5-HT1A receptor PET radioligand 11C-CUMI-101 has significant binding to α1-adrenoceptors in human cerebellum, limiting its use as a reference region. J Nucl Med 57(12):1945–1948

Smith GS, Barrett FS, Joo JH, Nassery N, Savonenko A, Sodums DJ, Marano CM, Munro CA, Brandt J, Kraut MA, Zhou Y, Wong DF, Workman CI (2017) Molecular imaging of serotonin degeneration in mild cognitive impairment. Neurobiol Dis 105:33–41

Spies M, Knudsen GM, Lanzenberger R, Kasper S (2015) The serotonin transporter in psychiatric disorders: insights from PET imaging. Lancet Psychiatry 2(8):743–755

Szabo Z, Kao PF, Scheffel U, Suehiro M, Mathews WB, Ravert HT, Musachio JL, Marenco S, Kim SE, Ricaurte GA (1995) Positron emission tomography imaging of serotonin transporters in the human brain using [11C](+)McN5652. Synapse 20:37–43

Talbot PS, Slifstein M, Hwang DR, Huang Y, Scher E, bi-Dargham A, Laruelle M (2012) Extended characterisation of the serotonin 2A (5-HT2A) receptor-selective PET radiotracer 11C-MDL100907 in humans: quantitative analysis, test-retest reproducibility, and vulnerability to endogenous 5-HT tone. NeuroImage 59:271–285.

Tejani-Butt SM, Yang J, Pawlyk AC (1995) Altered serotonin transporter sites in Alzheimer's disease raphe and hippocampus. Neuroreport 6:1207–1210

Terry AV Jr, Buccafusco JJ, Jackson WJ, Prendergast MA, Fontana DJ, Wong EH, Bonhaus DW, Weller P, Eglen RM (1998) Enhanced delayed matching performance in younger and older macaques administered the 5-HT4 receptor agonist, RS 17017. Psychopharmacology 135:407–415

Tfelt-Hansen P (2012) Clinical pharmacology of current and future drugs for the acute treatment of migraine: a review and an update. Curr Clin Pharmacol 7:66–72

Thomas AJ, Hendriksen M, Piggott M, Ferrier IN, Perry E, Ince P, O'Brien JT (2006) A study of the serotonin transporter in the prefrontal cortex in late-life depression and Alzheimer's disease with and without depression. Neuropathol Appl Neurobiol 32:296–303

Truchot L, Costes SN, Zimmer L, Laurent B, Le BD, Thomas-Anterion C, Croisile B, Mercier B, Hermier M, Vighetto A, Krolak-Salmon P (2007) Up-regulation of hippocampal serotonin metabolism in mild cognitive impairment. Neurology 69:1012–1017

Tsang SW, Lai MK, Francis PT, Wong PT, Spence I, Esiri MM, Keene J, Hope T, Chen CP (2003) Serotonin transporters are preserved in the neocortex of anxious Alzheimer's disease patients. Neuroreport 14:1297–1300

Varnas K, Nyberg S, Halldin C, Varrone A, Takano A, Karlsson P, Andersson J, McCarthy D, Smith M, Pierson ME, Soderstrom J, Farde L (2011) Quantitative analysis of [11C]AZ10419369 binding to 5-HT1B receptors in human brain. J Cereb Blood Flow Metab 31:113–123

Versijpt J, Van Laere KJ, Dumont F, Decoo D, Vandecapelle M, Santens P, Goethals I, Audenaert K, Slegers G, Dierckx RA, Korf J (2003) Imaging of the 5-HT2A system: age-, gender-, and Alzheimer's disease-related findings. Neurobiol Aging 24:553–561

Vidal B, Sebti J, Verdurand M, Fieux S, Billard T, Streichenberger N, Troakes C, Newman-Tancredi A, Zimmer L (2016) Agonist and antagonist bind differently to 5-HT1A receptors during Alzheimer's disease: a post-mortem study with PET radiopharmaceuticals. Neuropharmacology 109:88–95

Volk B, Nagy BJ, Vas S, Kostyalik D, Simig G, Bagdy G (2010) Medicinal chemistry of 5-HT5A receptor ligands: a receptor subtype with unique therapeutical potential. Curr Top Med Chem 10:554–578

Wilson AA, Houle S (1999) Radiosynthesis of carbon-11 labelled N-methyl-2-(arylthio)benzyl-amines; potential radiotracers for the serotonin reuptake receptor. J Label Compd Radiopharm 42:1277–1288

Wong DF, Wagner HN Jr, Dannals RF, Links JM, Frost JJ, Ravert HT, Wilson AA, Rosenbaum AE, Gjedde A, Douglass KH (1984) Effects of age on dopamine and serotonin receptors measured by positron tomography in the living human brain. Science 226:1393–1396

Woolley ML, Marsden CA, Fone KC (2004) 5-ht6 receptors. Curr Drug Targets CNS Neurol Disord 3:59–79

Xu Y, Yan J, Zhou P, Li J, Gao H, Xia Y, Wang Q (2012) Neurotransmitter receptors and cognitive dysfunction in Alzheimer's disease and Parkinson's disease. Prog Neurobiol 97:1–13

Yang KC, Stepanov V, Martinsson S, Ettrup A, Takano A, Knudsen GM, Halldin C, Farde L, Finnema SJ (2017) Fenfluramine reduces [11C]Cimbi-36 binding to the 5-HT2A receptor in the nonhuman primate brain. Int J Neuropsychopharmacol 20(9):683–691

Monoamine Oxidase A and Serotonin Transporter Imaging with Positron Emission Tomography

26

Jeffrey H. Meyer

Contents

Abstract

Serotonin has a major role in neural circuits of mood regulation, substance abuse, and neurodevelopment. Although they differ in cellular and anatomical location, the two brain proteins most strongly implicated in influencing serotonin levels are monoamine oxidase A and the serotonin transporter. The advances in positron emission tomography (PET) radioligand development to image these two

J. H. Meyer (✉)
Department of Psychiatry, Center for Addiction and Mental Health, University of Toronto, Toronto, ON, Canada
e-mail: jeff.meyer@camhpet.ca

proteins have been applied considerably over the past 15 years, greatly increasing our knowledge about fundamental processes in many important, impactful conditions including major depressive disorder, early postpartum, perimenopause, cigarette smoking, alcohol dependence, aggressive behavior, antidepressant development, ecstasy abuse, obsessive compulsive disorder, and seasonal affective disorder as reviewed in this chapter.

26.1   Why Image Indices of Monoamine Oxidase A Density?

Monoamine oxidase A (MAO-A) is an enzyme that metabolizes three major monoamines (serotonin, norepinephrine, dopamine) in the brain and has a role in creating oxidative stress and predisposition to apoptosis (Youdim et al. 2006). Monoamine levels influence mood (Freis 1954; Ruhe et al. 2007), and oxidative stress and apoptosis influence brain development (Bortolato et al. 2008). Hence MAO-A is a logical target for investigations in mood disorders, substance abuse (during which markers of dysregulated monoamine levels occur (Stockmeier 2003; Meyer 2008)), and aggression for which abnormal neurodevelopment is implicated (Buckholtz and Meyer-Lindenberg 2008). Illnesses and conditions for which dysregulation of monoamine levels is implicated include major depressive disorder, substance abuse, neurodegenerative diseases, and aggression (Youdim et al. 2006; Meyer et al. 2006; Fowler et al. 1996; Bacher et al. 2011). MAO-A is predominantly located on outer mitochondria membranes in neurons (as well as astrocytes and glia) and has a high density in brain regions that influence mood (Saura et al. 1992) although the cellular distribution varies by region (Saura et al. 1992, 1996; Finberg 2012). MAO-A density is highest in the brainstem (within the locus coeruleus); moderately high in the cortex, hippocampus, and striatum; lower in cerebellar cortex; and minimal in white matter tissue (Saura et al. 1992, 1996).

The density of MAO-A correlates highly with the level of its metabolic activity (Saura et al. 1992; Nelson et al. 1979); hence, neuroimaging of measures of MAO-A binding can be interpreted as having functional implications (Saura et al. 1992). This approach represents an optimal practical method for applying positron emission tomography (PET) neuroimaging toward a strongly functional index of MAO-A activity. Another imaging approach would be to measure a radiotracer which is metabolized by MAO-A and trapped to some extent in the brain, but this is extremely difficult because the potential brain radiotracer would require kinetics in which the dominant, separable, measurable effect is its metabolism by MAO-A, rather than its crossing of the blood-brain barrier or impairment of removal of trapped radiometabolites. Most radiotracers that assess metabolism accumulate as a product in the

brain which can be a disadvantageous strategy in radiotracer development because such radiotracers are less likely to exhibit reversible time activity curves, and irreversible time activity curves are usually subject to bias from blood flow. Hence, the most optimal, practical neuroimaging approach toward quantitating MAO-A function with PET or SPECT is radioligands that bind to MAO-A as reversible inhibitors.

26.2 Radioligands Available for Neuroimaging Monoamine Oxidase A

There are three PET radiotracers that have been applied for measurement of available monoamine oxidase A in a human study, and a fourth promising radiotracer is in development (see Table 26.1). The first radiotracer developed [^{11}C]clorgyline, demonstrated adequate brain penetration and selectivity, but did not have reversible time activity curves (Fowler et al. 1987). A deuterium-labeled version of [^{11}C]clorgyline was created to attempt to improve reversibility, but it is also not optimally reversible (Fowler et al. 1996). More recently [^{11}C]befloxatone and [^{11}C]harmine were developed. [^{11}C]befloxatone shows promising radiotracer qualities of selectivity and reversibility (Bottlaender et al. 2010; Curet et al. 1998; Dolle et al. 2003) and has been modeled in humans (Bottlaender et al. 2010; Curet et al. 1998; Dolle et al. 2003; Zanotti-Fregonara et al. 2014, 2013). However, test-retest reliability in humans is not known, and it hasn't been studied under blocking conditions in humans.

[^{11}C]Harmine demonstrates the properties of an excellent PET radiotracer for an index of available MAO-A density in humans. Harmine has high affinity for the MAO-A enzyme, ($K_i = 2$ nM), has high brain uptake in humans, and is selective for MAO-A (Meyer et al. 2006; Bergstrom et al. 1997a; Ginovart et al. 2006): The affinity of [^{11}C]harmine is three orders of magnitude higher for MAO-A than MAO-B (Bergstrom et al. 1997a). Displacement studies in baboons using MAO-A selective inhibitors show complete displacement of [^{11}C]harmine in regions with high density of MAO-A (Bergstrom et al. 1997b). The uptake is specific to the parent compound as metabolites of harmine are polar and do not cross the blood-brain barrier (Tweedie and Burke 1987). The uptake of [^{11}C]harmine is highest in brain regions with greater MAO-A density such as the cortex and lowest in regions with low MAO-A density such as white matter (Bergstrom et al. 1997c). The MAO-A V_T (MAO-A distribution volume) is primarily an index of specifically bound [^{11}C]harmine at equilibrium since 80 to 85% represents specific binding and the levels of free and nonspecific binding are similar among different people (Ginovart et al. 2006; Sacher et al. 2011). The modeling of this compound in humans best fits a two tissue compartment model, and negligible bias is found when the Logan model is applied (Ginovart et al. 2006).

Table 26.1 Comparison of PET radiotracers for monoamine oxidase A (from Meyer (2014))

	[11C]Clorgyline	[11C]Harmine	[11C]Befloxatone	[18F] Fluoroethyl-harmol
Selectivity	Excellent (Fowler et al. 1987)	Excellent (Bergstrom et al. 1997a)	Excellent (Dolle et al. 2003)	Excellent (Schieferstein et al. 2015)
Reversibility	Not reversible (Fowler et al. 1987)	Highly reversible (Ginovart et al. 2006)	Highly reversible (Bottlaender et al. 2010)	Moderate in rodent (Schieferstein et al. 2015; Maschauer et al. 2015)
Brain uptake	Very good (Fowler et al. 1987)	High (Ginovart et al. 2006)	High (Zanotti-Fregonara et al. 2013)	Very good (Schieferstein et al. 2015; Maschauer et al. 2015)
Modeling	2 tissue compartment (Fowler et al. 1987)	2 tissue compartment (Ginovart et al. 2006)	2 tissue compartment (Zanotti-Fregonara et al. 2013)	Not yet completed in humans
Specific binding to free and nonspecific binding ratio	Very good but limited assessment (Fowler et al. 1987)	High ~4 (Ginovart et al. 2006; Chiuccariello et al. 2015)	High in baboon (Bottlaender et al. 2010) Unclear in human (Zanotti-Fregonara et al. 2014, 2013)	High in rodent (Schieferstein et al. 2015; Maschauer et al. 2015)
Reliability in humans	Very good (Fowler et al. 1996)	Excellent (Sacher et al. 2012)	Not reported	Not yet completed
Brain-penetrant radioactive metabolites?	Unlikely	No brain-penetrant metabolites (Wilson et al. 2003)	Unlikely	No brain-penetrant metabolites (Maschauer et al. 2015)
Measureable in diverse regions?	Gray matter (Fowler et al. 1987)	Gray matter (Ginovart et al. 2006)	Gray matter (Zanotti-Fregonara et al. 2013)	Gray matter in rodent (Schieferstein et al. 2015; Maschauer et al. 2015)

26.3 Major Depressive Disorder

The in vivo aspect of neuroimaging offers the ability to readily sample medication-free subjects and to selectively choose early-onset major depressive disorder (MDD) which is the most common form (World_Health_Organization 2008). Late-onset

MDD is often attributable to neurodegenerative diseases such as Parkinson's disease and Alzheimer's disease (Krishnan 2002), which would be expected to have very different pathologies from early-onset MDD. Since postmortem studies often preferentially sample older subjects, sometimes they are not targeted toward early-onset MDD. The first three postmortem studies of MAO-A levels and activity had not selectively targeted early-onset MDD, and the early perspective of the field was that there was no abnormality of MAO-A level or activity in MDD (Mann and Stanley 1984; Ordway et al. 1999; Sherif et al. 1991).

In 2006 MAO-A V_S, an index of MAO-A density was measured using [^{11}C] harmine PET in medication-free major depressive episodes (MDE) secondary to early-onset MDD (Meyer et al. 2006). Subjects with MDE were drug-free for at least 5 months, and most were antidepressant naive. All MDE subjects and controls were otherwise healthy. The MAO-A V_S was highly significantly elevated ($p < 0.001$ each region, average magnitude 34% (or two standard deviations)) during MDE (see Fig. 26.1). This was the first definitive study of MAO-A binding in MDE from early-onset MDD: The samples excluded comorbidity, thereby focusing on the differences between this common, early-onset type of MDD and health. The effect size was large and the radiotracer has outstanding qualities for measuring MAO-A binding. In 2008, Barton et al. reported a consistent finding of elevated brain serotonin turnover in unmedicated depressed patients (Barton et al. 2008). In 2009, the finding of greater MAO-A binding in MDE was replicated with [^{11}C]harmine PET, and in 2011 the finding was replicated in antidepressant-free MDE subjects in postmortem study of orbitofrontal cortex applying Western blot (Meyer et al. 2009a; Johnson et al. 2011). The replication finding of [^{11}C]harmine PET was extended to 42 MDE subjects and 37 healthy controls, demonstrating the greatest levels of MAO-A in those with greater severity and/or reversed neurovegetative symptoms (hypersomnia, hyperphagia, or weight gain); an interesting finding since MDE with these
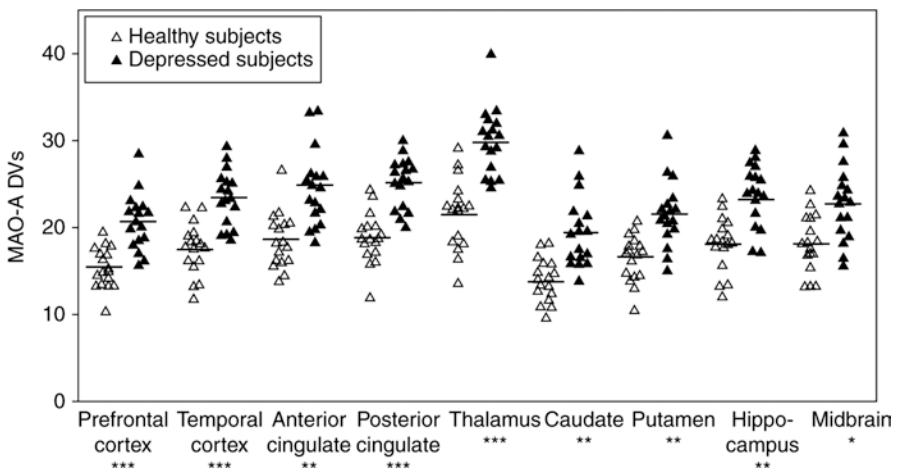
Fig. 26.1 On average, MAO-A DV$_S$ was elevated by 34% or 2 SDs in depressed individuals. The hippocampal region also samples the parahippocampus. Differences between groups were highly statistically significant in each region. *p < 1 × 10^{-5}; †p < 1 × 10^{-4}; ‡p = 0.001

particular symptoms is well known to be more likely to respond to MAO inhibitors (Chiuccariello et al. 2014). It was further demonstrated in a comparison among MDE with comorbid severe borderline personality disorder, MDE with moderate borderline personality disorder, and the healthy that MAO-V_T was considerably elevated, particularly in the prefrontal and anterior cingulate cortex in the most severe group (by 43% and 42%, respectively) but also to a lesser extent in the moderate group (by 23 and 21%, respectively). Interestingly, in the overall group of patients in this study, there was also a positive correlation between current suicidality and prefrontal cortex (PFC) MAO-A V_T (Kolla et al. 2016).

Greater MAO-A binding in affect-modulating regions has important implications for understanding the pathophysiology of MDD. A key longstanding theory concerning MDD is that monoamines were low, but no clear mechanism of monoamine loss had been previously identified, and this finding represents the clearest mechanism to support this theory (Meyer et al. 2006). In addition, since MAO-A has multiple functions, metabolizing serotonin, norepinephrine, and dopamine, oxidizing, and facilitating apoptosis (Youdim et al. 2006), it suggests that new antidepressants should optimally target these additional functions rather than solely raise extracellular serotonin. Such approaches have notable potential to address the issue that at least 40% of MDE does not respond to the common first-line treatment of selective serotonin reuptake inhibitors (Trivedi et al. 2006).

Investigations of MAO-A V_T, or monoamine oxidase distribution volume, were subsequently extended into different states of MDD, an approach which is readily feasible with positron emission tomography. While it might be expected that MAO-A levels would normalize with euthymic mood, the recovered state of MDD is also a state of high risk for another MDE. The risk for a recurrent MDE over 2 years is 20–50% depending upon treatment conditions (Frank et al. 1990; Fava et al. 2004). Elevated MAO-A V_T may be considered an index of a monoamine-lowering process, and in the 1950s during treatment with reserpine-based antihypertensives, it was discovered that chronic monoamine lowering is associated with subsequent onset of MDEs which typically occurred 2 weeks to 4 months later (Freis 1954). In recovered MDD, MAO-A V_T was significantly elevated in the PFC, anterior cingulate cortex (ACC), striatum, hippocampus, thalamus, and midbrain in a sample of 18 medication-free recovered MDD subjects compared to 28 healthy controls (Meyer et al. 2009a). Recovered MDD subjects who had recurrence of their MDE in the subsequent 6 months had the highest levels of MAO-A binding in the prefrontal and anterior cingulate cortex at the time of scanning (Meyer et al. 2009a). The prefrontal cortex and anterior cingulate cortex were of particular interest because these regions (and/or subregions of these structures) are activated in mood induction studies (Liotti et al. 2002) and during cognitive functions like pessimistic perspective that generate sad mood (Sharot et al. 2007; Tom et al. 2007). To address the possibility that other factors related to risk of recurrence did not contribute to the finding, subjects were medication-free for at least a year, had no cognitive behavioral therapy within 3 years, were currently asymptomatic, and had no comorbid medical, psychiatric, or substance abuse illnesses. Given the link between elevated MAO-A binding in prefrontal and anterior cingulate cortex and subsequent MDE, this argues that new interventions are needed to decrease MAO-A levels in these

brain regions even beyond the duration of a therapeutic intervention so as to prevent recurrence.

26.4 Early Postpartum and Perimenopause

Both early postpartum and perimenopause are high-risk points for MDE with a 13% prevalence for a MDE over the first 6 months postpartum and a 17% prevalence rate for new-onset MDE during perimenopause (reviewed (Mann and Stanley 1984; Ordway et al. 1999)). It is known that estrogen levels decline more than 100-fold over the first several days postpartum in humans (O'Hara et al. 1991), and changes in estrogen levels across the menstrual cycle heighten approximately fivefold during perimenopause (reviewed (Mann and Stanley 1984; Ordway et al. 1999)). While several studies reported an inverse relationship between decline in estrogen and rise in MAO-A levels, mRNA and activity (Luine et al. 1975; Ma et al. 1993, 1995; Holschneider et al. 1998), prior to PET imaging studies in 2010 and 2014, MAO-A binding, and mRNA or activity had never been studied in any species in early postpartum, nor during perimenopause.

A [^{11}C]harmine PET study measured MAO-A binding during early postpartum (days 4–6) (Sacher et al. 2010). A highly significant elevation of MAO-A binding was found, which was, on average, 43% greater across the brain regions assayed (prefrontal cortex, anterior cingulate cortex, striatum, thalamus, hippocampus, midbrain) as compared to women not recently pregnant (Sacher et al. 2010). A voxel-based analysis demonstrated that the elevation in MAO-A binding was present throughout the gray matter of the brain (see Fig. 26.2) (Sacher et al. 2010). A subsequent [^{11}C]harmine PET study completed several years later demonstrated a 34% elevation in MAO-A V_T across gray matter regions sampled in perimenopause, including the PFC and ACC (Sacher et al. 2010; Rekkas et al. 2014) (see Fig. 26.3).
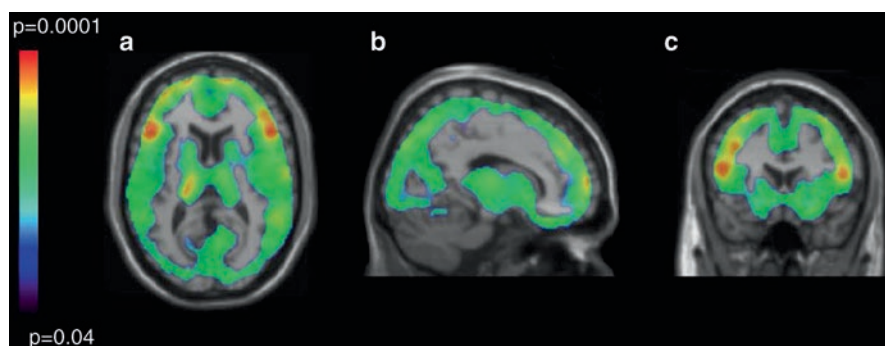
Fig. 26.2 Parametric maps of elevated monoamine oxidase A binding in the postpartum group versus the control group. Maps are superimposed on a T1-weighted magnetic resonance image that is normalized to the T1-weighted template (SPM2; Department of Cognitive Neurology, Wellcome Trust Centre for Neuroimaging, London, England). (a) Transverse. (b) Sagittal. (c) Coronal. The individual voxel threshold was set at p < 0.05; a total of 86,412 voxels comprised a single cluster, which had a cluster-corrected significance of p = 0.03

On average, MAO-A V_T in perimenopausal age was 34% greater compared with reproductive age and 16% greater compared with mehopause (multivariate analysis of variance, group effect, $F_{16.94} = 3.03; P < .001$). Horizontal lines indicate mean MAO-A V_T.
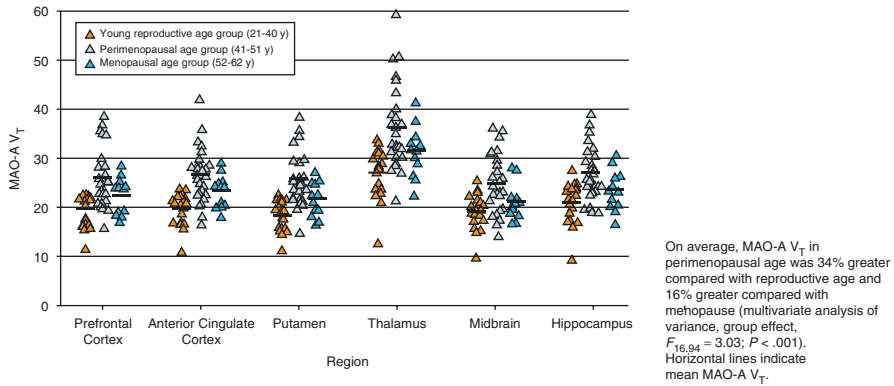
Fig. 26.3 Monoamine oxidase A total distribution volume in women of young reproductive age, women of perimenopausal age, and older women in menopause

These studies, which identify elevation in MAO-A V_T during high-risk states for MDE, have intriguing potential for developing strategies of dietary supplementation to counter the effect of elevated MAO-A level. For example, early postpartum is a time of greater risk for a couple of common, intertwined mood disturbances (O'Hara and Swain 1996). The first is the common, postpartum blues, present in up to 75% of women involving mild sadness, and can be accompanied by some trouble sleeping, irritability, desire for isolation, and difficulty concentrating (O'Hara and Swain 1996). It is considered within the healthy range of experience, typically starting on day 4 postpartum and finishing within the first week. The second is postpartum depression, which is a MDE that occurs within the first 4 weeks after giving birth, although some definitions include onset within the first 3 months after giving birth (O'Hara and Swain 1996; Association AP 1994). When postpartum blues is severe, the risk for MDE is fourfold greater. A dietary supplement strategy composed of blueberry antioxidants (which contain anthocyanins detectable in the brain of rodents), oral tryptophan given the evening of postpartum day 4, and tyrosine given the morning of day 5 was created to counter effects of elevated MAO-A level consisting of greater H_2O_2 production, greater metabolism of serotonin, and greater metabolism of norepinephrine and dopamine. This dietary supplement was shown to prevent depressed mood during early postpartum, assessed with depressed mood induction, in an open trial with a robust effect size of 2.9 (Dowlati et al. 2017) The dietary strategy is also compatible with breastfeeding because tryptophan and tyrosine are already found in breast milk, so the overall concentration of these amino acids in breast milk is not affected by oral administration of these amino acids (Dowlati et al. 2015, 2014).

26.5   Cigarette Smoking

The first study of MAO-A binding applying [^{11}C] clorgyline PET reported available MAO-A binding is reduced in those who smoke cigarettes in the active smoking state (Fowler et al. 1996). Given that the plasma half-life of the key MAO-A-binding

substances found in cigarette smoke (harman and norharman) is only an hour (Rommelspacher et al. 2002), there was reason to specifically assess MAO-A V_T during both active smoking and withdrawal conditions. When MAO-A V_T was assessed in both conditions, it was discovered that prefrontal and anterior cingulate cortex MAO-A V_T (as well as the other brain regions assessed) rose during withdrawal in those who smoke heavily, that is, more than one pack of cigarettes per day, but not in those who smoke more moderately at less than one pack per day and that during withdrawal from heavy smoking, MAO-A V_T was greater than in health in all regions assessed (Bacher et al. 2011).

The elevation in MAO-A V_T has important implications for the problem of sad mood in people who smoke cigarettes. There is a very high comorbidity between cigarette smoking and major depressive disorder with 50% of people with MDD also smoking cigarettes, and the pattern is such that cigarette smoking predisposes to MDD and vice versa (Anda et al. 1990; Breslau et al. 1998). It is the heavy cigarette smoking group who are at much greater risk for MDD (Pratt and Brody 2010), and this group had a 25% elevated MAO-A V_T in the prefrontal and anterior cingulate cortex during withdrawal as compared to healthy controls, arguing for a process of elevated MAO-A level during withdrawal as a mechanism to create risk for MDD (Bacher et al. 2011). Hence repeated exposure of elevated MAO-A level, in the prefrontal and anterior cingulate cortex, a mechanism associated with onset and maintenance of MDE state, occurring after a short period of 8 hours withdrawal could explain the predisposition to MDE in people who smoke cigarettes heavily.

A second problem with mood in people who smoke cigarettes is the depressed mood of acute withdrawal (Carey et al. 1993; Kenford et al. 2002). In the imaging study of MAO-A during cigarette withdrawal, in those who smoked heavily, the magnitude of rise in MAO-A V_T in prefrontal and anterior cingulate cortex during withdrawal was significantly correlated with the shift in visual analogue scales toward depressed mood (Bacher et al. 2011). This rise in MAO-A V_T also correlated with the decline in harman in those who smoke heavily. Harman is the chemical in cigarette smoke that has the highest affinity for MAO-A (Herraiz and Chaparro 2005; Hauptmann and Shih 2001). These results suggest that rapid removal of harman from occupying MAO-A sites leaves a high level of available MAO-A for metabolizing monoamines in prefrontal and anterior cingulate cortex resulting in depressed mood. This argues for testing of MAO-A inhibitor treatments in people who experience sad mood during early cigarette withdrawal as a strategy to assist in quitting, an important issue since 50% of people tend to relapse in the first few days of trying to quit cigarette smoking (Garvey et al. 1992; Law and Tang 1995).

26.6   Alcohol Dependence (AD)

While the mechanism by which MAO-A elevation occurs during early withdrawal from cigarette smoking is not known, mechanisms involving oxidative stress and mitochondrial toxicity are associated with greater expression of MAO-A in glioblastoma and neuroblastoma cell lines (Youdim et al. 2006; Fitzgerald et al.

2007a, b; Ou et al. 2006). The first investigations of MAO-A activity in the post-mortem brain of AD were primarily negative, with no change reported in prefrontal cortex, and a decrease in the hypothalamus and caudate (Oreland et al. 1983; Major et al. 1985). However, none of these studies controlled for factors that influence MAO-A levels, such as cigarette smoking (Fowler et al. 1996; Bacher et al. 2011), exposure to current or past major depressive episodes (Meyer et al. 2006, 2009b; Johnson et al. 2011), and impulsive/aggressive personality traits (Alia-Klein et al. 2008; Soliman et al. 2011). In a [^{11}C] harmine PET study controlling for these factors, MAO-A V_T was significantly greater in the PFC (37%, independent samples t-test, $t_{30} = 3.93$, $p < 0.001$) and all brain regions analyzed (mean 32%, multivariate analysis of variance, $F_{7,24} = 3.67$, $p = 0.008$) (Matthews et al. 2014). Moreover, greater duration of heavy drinking correlated positively with greater MAO-A V_T in the PFC ($R = 0.67$, $p = 0.005$) and all brain regions analyzed ($R = 0.73$–0.57, $p = 0.001$–0.02). A subsequent study of chronic ethanol vapor exposure achieving high levels of ethanol in Sprague Dawley rats comparable to human exposure demonstrated that exposure to alcohol was associated with greater MAO-A activity and protein level in the PFC and ACC (Matthews et al. 2018).

26.6.1 Aggression

Aggression is associated with major social costs since 50% of prisoners have problems with aggression (Fazel and Danesh 2002). Substantial evidence has accumulated to suggest that inherited levels of MAO-A may also have influence upon neurodevelopment and lead to impulsive behavior: MAO-A knockout (KO) mice and wild-type given MAO-A inhibitors during development demonstrate elevated brain serotonin during development, which disrupts the organization of somatosensory thalamocortical afferents and abnormalities in the somatosensory cortex barrel fields (Cases et al. 1996; Vitalis et al. 1998; Mejia et al. 2002). It has been proposed that impulsive aggression observed in MAO-A KO mice and mice given MAO-A inhibitors during development is consequent to impairment in organizing sensory input secondary to these abnormalities (Bortolato et al. 2008). Men who are deficient in MAO-A, consequent to an X-chromosome mutation that impairs function of the MAO-A gene, demonstrate frequent aggressive behavior (Brunner et al. 1993). Consistent with this, people with a genotype associated with low levels of MAO-A in an in vitro assay have been associated with greater risk of developing antisocial behavior (Caspi et al. 2002; Kim-Cohen et al. 2006).

However, a critical gap in the literature is that until 2015, it was unknown whether brain MAO-A levels are low in more severe, clinical disorders of impulsivity, such as antisocial personality disorder (ASPD). To address this, [^{11}C]harmine PET was applied to measure MAO-A V_T, in 18 male ASPD participants and 18 age- and sex-matched controls. Orbitofrontal cortex (OFC) and ventral striatal (VS) MAO-A V_T were lower in ASPD compared to controls (MANOVA group effect: $F_{2,33} = 6.8$, $p = 0.003$; OFC and VS MAO-A V_T each reduced 19%). Similar effects were seen

in other brain regions: anterior cingulate cortex, dorsal putamen, thalamus, hippocampus, and midbrain (MANOVA group effect: $F_{7,28} = 2.9$, $p = 0.022$). In ASPD, VS MAO-A V_T was consistently negatively correlated with measures linked to impulsivity including the Iowa gambling task, the psychopathy checklist revised, and the NEO Personality Inventory-Revised ($r = −0.50$ to $−0.52$, all p-values < 0.05) (Kolla et al. 2015).

Two PET imaging studies of MAO-A in relation to aggressive personality traits also show consistent results. First, a [^{11}C]clorgyline PET study reported a positive correlation between reduced MAO-A binding in prefrontal cortex and subregions of the prefrontal cortex such as the orbitofrontal cortex, with self-reported aggression in healthy men (Fig. 26.4) (Alia-Klein et al. 2008). The second study, which applied [^{11}C]-harmine positron emission tomography with the Revised NEO Personality Inventory, found that prefrontal cortex and subregions of the prefrontal cortex (such as the orbitofrontal cortex) correlated strongly with personality facets angry-hostility negatively ($r = −0.515$, $p = 0.001$) and deliberation facets positively ($r = 0.514$, $p = 0.001$) (Soliman et al. 2011). In a 2-factor regression model, these facets explained 38% of variance in prefrontal cortex MAO-A binding. In both studies, the MAO-A-binding measures among different regions were intercorrelated, so the correlations of MAO-A binding with aggression-related measures were also present in all brain regions sampled which included both cortical and subcortical regions.

Currently this neuroimaging direction is still progressing toward creating impactful information for society. Given that reduced MAO-A binding is related to pathological aggression, a longer-term strategy could be to identify whether harmful environmental influences predispose to this low MAO-A level phenotype in the prefrontal cortex during neurodevelopment so as to develop novel prevention strategies against harmful neurodevelopment.
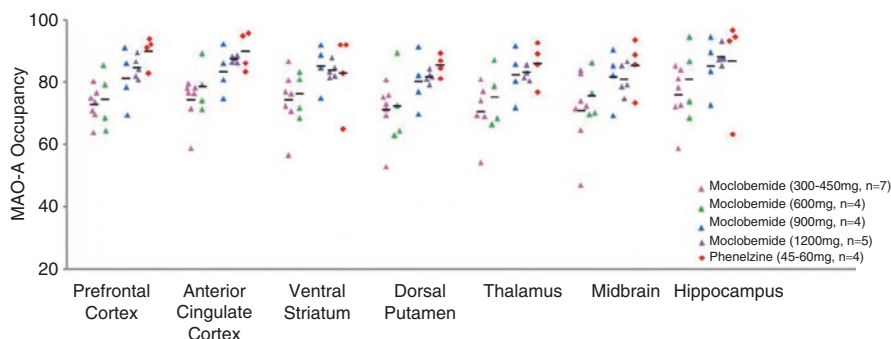
Fig. 26.4 Monoamine oxidase-A occupancy higher in high doses of moclobemide (900–1200 mg) and phenelzine (45–60 mg) than low doses of moclobemide (300–600 mg). There was a significant main effect of doses of moclobemide (1200 and 900 mg) and phenelzine (45 and 60 mg) on occupancy across brain regions sampled when compared to the average clinical doses of moclobemide [300, 450, and 600 mg; MANOVA, $F(7,16) = 3.94$, $p = 0.01$]

26.7   Monoamine Oxidase A Occupancy

Increasingly it is established that clear definitions of target occupancy are key for developing novel therapeutics and occupancy data is now available for two monoamine oxidase inhibitors (MAOI). The irreversible MAOI phenelzine potently reduces MAO-A V_T by 82–93% after a 6-week clinical trial (Chiuccariello et al. 2015) (see Fig. 26.4). Moclobemide, a selective MAO-A inhibitor with a superior tolerability profile, has a lower occupancy at standard treating doses but can reduce MAO-A V_T to a similar extent if the dose is double the usual maximum recommended daily dose (Sacher et al. 2011; Chiuccariello et al. 2015) (also see Fig. 26.4). The degree of inhibition associated with therapeutic effect in these trials exceeds the level of disease effect. However, there are several potential explanations for this: It is plausible that the disease effect is present for months to years prior to treatment, and it is possible that downstream consequences of chronically elevated MAO-A are more likely to be targeted after a greater degree of reversal. Furthermore, some antidepressant mechanisms like inducing signal transduction effects and inducing hippocampal neurogenesis are associated with treatments that raise monoamine levels beyond healthy state (Sacher et al. 2011).

26.8   Why Image Indices of Serotonin Transporter Density?

The serotonin transporter (5-HTT) is a 630 amino acid long protein with 12 transmembrane domains (Lesch et al. 1993a, b) and is mainly found in the soma, dendrites, and terminals of serotonin-releasing neurons (Zhou et al. 1998; Tao-Cheng and Zhou 1999). Most 5-HTT are located on plasma cell membranes, mainly perisynaptically or along axons (Zhou et al. 1998; Tao-Cheng and Zhou 1999). In the human brain, there is a wide variation in regional 5-HTT density: Superior and inferior raphe nuclei > hypothalamus > thalamus (depending upon nucleus) ≈ amygdala > putamen > caudate ≈ hippocampus > insular cortex > prefrontal cortex > white matter > cerebellar cortex (except vermis) (Cortes et al. 1988; Kish et al. 2005; Laruelle et al. 1988). The serotonin transporter is coupled to sodium, chlorine, and potassium transport (Blakely et al. 1997), but the physiological role of greatest interest of 5-HTT in the brain is its influence upon extracellular serotonin levels. Antidepressants which bind to the serotonin transporter raise extracellular serotonin, and 5-HTT knockout mice have elevated extracellular serotonin, confirming the role of the serotonin transporter in modulating extracellular serotonin levels in vivo (Blier and De Montigny 1983; Bel and Artigas 1992, 1993, 1995; Dreshfield et al. 1996; Moret and Briley 1996; Mathews et al. 2000).

Neuroimaging studies of the 5-HTT offer the opportunity to measure an index of total 5-HTT density, the 5-HTT BP_{ND}. This marker is useful for determining therapeutic occupancy of antidepressants as well as several different models of 5-HTT dysregulation in disease. Most disease investigations focus upon potential mechanisms for lowering brain serotonin, and there are at least four models to explain how 5-HTT BP_{ND} could be altered in a disease that lowers brain monoamines (Meyer

2007). The first model is a lesion model in which the density of serotonin-releasing neurons is reduced and reductions in 5-HTT BP_{ND} occur. The second model is a secondary change in transporter binding consequent to serotonin lowering via a different process. However, available evidence suggests that the different monoamine transporters do not regulate in the same fashion after chronic depletion of their endogenous monoamine. Acute reductions in serotonin lead to reductions in 5-HTT mRNA (Yu et al. 1995), but long-term reductions or elevations in serotonin typically show no effect upon regional 5-HTT density (Benmansour et al. 1999; Dewar et al. 1992; Graham et al. 1987). The third model is increased clearance of extracellular monoamine via greater serotonin transporter density since some radiotracers like [^{11}C]DASB preferentially bind to 5-HTT adjacent to extracellular fluid (Quelch et al. 2012). In the third model, greater total available 5-HTT BP_{ND} is interpreted as representative of greater functional 5-HTT density. The fourth model is endogenous displacement and is dependent upon the properties of the radioligand: Endogenous displacement is the property of a few radioligands to express different bindings after short-term manipulations of their endogenous neurotransmitter. Available evidence suggests that this fourth model is unlikely to be relevant in humans with [^{11}C]DASB (Talbot et al. 2005; Praschak-Rieder et al. 2005), but the issue has not been investigated for other radioligands. Abnormalities in 5-HTT BP_{ND} may be discussed in the context of these models.

26.9 Radioligands Available for Imaging Serotonin Transporters

There are at least six different radiotracer imaging protocols for imaging serotonin transporters, and the quality of technique varies widely. Originally, the only two radiotracer techniques were 2-beta-carbomethoxy-3-beta-(4-iodophenyl)-tropane (β-CIT) single-photon emission tomography (SPECT) and [^{11}C](+)McN5652 PET, but both of these methods have significant limitations for quantitation (Kuikka et al. 1993). β-CIT has almost equal affinity for the dopamine transporter as compared to the serotonin transporter (Laruelle et al. 1994). As dopamine transporter density is high in the substantia nigra (Ciliax et al. 1999), the relative contributions of dopamine and serotonin transporter binding to the measure of specific binding cannot be separated in the midbrain, the location where this radiotracer technique is applied. The other early radiotracer, [^{11}C](+)McN5652, has a low ratio of specific binding relative to free and nonspecific binding, which, in combination with modest reversibility, makes valid and reliable quantitation difficult in regions other than the thalamus and impossible in the human cortex (Kent et al. 2002; Buck et al. 2000).

The radiotracer [^{11}C](DASB, 3-amino-4-(2-dimethylaminomethylphenylsulfanyl)-benzonitrile) was a major advance as a result of its selectivity, reversibility, greater specific binding, and reliability (Praschak-Rieder et al. 2005; Ginovart et al. 2001; Meyer et al. 2001, 2004a, b; Wilson et al. 2000, 2002). This radiotracer was three orders of magnitude more selective for the 5-HTT over other monoamine

transporters and highly selective for the 5-HTT in comparison to a number of other targets screened (Wilson et al. 2000, 2002). Selectivity was also demonstrated when 94% of the specific binding was displaceable by 5-HTT binding medications in animal models (Wilson et al. 2000, 2002). [^{11}C]DASB has very good brain uptake in humans (Ginovart et al. 2001). In humans, its ratio of specific binding relative to free and nonspecific is good, and its free and nonspecific binding has low between-subject variability (Ginovart et al. 2001; Ichise et al. 2003). Multiple brain regions may be assessed (Praschak-Rieder et al. 2005; Ginovart et al. 2001; Meyer et al. 2001, 2004a, b; Wilson et al. 2000, 2002), and reliability of regional 5-HTT BP_{ND} measures is very good (Praschak-Rieder et al. 2005; Meyer et al. 2001, 2004b). The 5-HTT BP_{ND} measures are low in cortex, but with a standardized region of interest methods, very good reliability of 5-HTT BP_{ND} in the human cortex is achievable (Praschak-Rieder et al. 2005; Meyer et al. 2001, 2004b). Thus, the discovery of [^{11}C]DASB PET imaging created a new opportunity for validly quantifying 5-HTT binding in humans.

Subsequent to the development of [^{11}C]DASB, several new similarly structured radiotracers were created for imaging techniques of [^{123}I]ADAM SPECT, [^{11}C]MADAM PET, and [^{11}C]HOMADAM PET (see Table 26.2 for a comparison). [^{123}I]ADAM SPECT is superior to β-CIT SPECT; however, [^{123}I]ADAM SPECT is not as useful a technique as the other methods because of its limited specific binding to free and nonspecific binding signal and lack of formal modeling development. [^{11}C]MADAM PET approaches the quality of [^{11}C]DASB PET, but [^{11}C]MADAM has substantially less brain uptake which would be expected to increase the variability of the measurement, especially in regions of lower 5-HTT density (Lundberg et al. 2006). However, it is clear that [^{11}C] MADAM is superior to [^{11}C](+)McN5652 in terms of the reversibility of time activity curves and specific binding signal relative to free and nonspecific binding signal. [^{11}C]HOMADAM PET shows some advantage over [^{11}C]DASB PET (and the other radiotracers) in that it has a more reversible time activity curve and a somewhat greater specific binding to free and nonspecific binding signal (Ginovart et al. 2001; Nye et al. 2008), but there are still key areas of development for [^{11}C]HOMADAM PET, including a reliability assessment of binding measures and assessment of its sensitivity to endogenous serotonin.

26.10 Developing New Antidepressants with Serotonin Transporter Neuroimaging

In two seminal studies published in 2001 and 2004 applying [^{11}C]DASB PET, it was demonstrated across five different selective serotonin reuptake inhibitors (SSRI) that after 4 weeks of treatment, for doses which clinically distinguish from placebo, an 80% occupancy occurs in most brain regions (Meyer et al. 2001, 2004b) (see Fig. 26.5). These SSRI are defined as such by the property of having at least two orders of magnitude preferential affinity for the serotonin transporter over other target sites. Within the datasets, there was increasing occupancy with increasing dose (and plasma level), with plateauing at the higher doses and higher plasma levels. The dose-occupancy relationships consistently demonstrated that the threshold of reaching 80% occupancy was important. Even though these SSRI have a 100-fold range in

Table 26.2 Comparison of PET radiotracers for the serotonin transporter (from Meyer (2014))

	[123I]β-CIT SPECT	[11C]McN5652 PET	[11C]DASB PET	[123I]ADAM SPECT	[11C]MADAM PET	[11C]HOMADAM PET
Selectivity	Non-selective – near 1:1 affinity for 5-HTT to DAT (Laruelle et al. 1994; Carroll et al. 1995)	Likely selective 10:1 to 100:1 affinity for 5-HTT over NET (Shank et al. 1988; Kung et al. 1999)	Highly selective 1000:1 affinity for 5-HTT over NET or DAT; negligible affinity for many other targets (Wilson et al. 2000, 2002)	Highly selective 1000:1 affinity for 5-HTT over NET or DAT (Choi et al. 2000; Oya et al. 2000)	Highly selective (Halldin et al. 2005; Chalon et al. 2003)	Highly selective (Jarkas et al. 2005)
Displaceability of specific binding	Incomplete (Pirker et al. 1995; Tauscher et al. 1999)	In most, reports (Kent et al. 2002; Parsey et al. 2000; Suhara et al. 2003)	Highly displaceable (Meyer et al. 2001, 2004b; Wilson et al. 2000, 2002)	Highly displaceable (Choi et al. 2000; Oya et al. 2000; Erlandsson et al. 2005)	Highly displaceable (Halldin et al. 2005; Chalon et al. 2003; Lundberg et al. 2007)	Highly displaceable (Jarkas et al. 2005)
Reversibility (in human imaging)	Good (Kuikka et al. 1993; Brucke et al. 1993)	Not adequate to adequate, depending upon region (Buck et al. 2000; Parsey et al. 2000; Ikoma et al. 2002)	Adequate in the midbrain, good to very good in other regions (Ginovart et al. 2001; Ichise et al. 2003; Houle et al. 2000)	Adequate in the midbrain (Erlandsson et al. 2005; Catafau et al. 2005)	Adequate in the midbrain, good to very good in other regions	Very reversible in all regions (Nye et al. 2008)
Brain uptake	Adequate (Kuikka et al. 1993; Brucke et al. 1993)	Good (Parsey et al. 2000; Ikoma et al. 2002)	Very good (Ginovart et al. 2001; Ichise et al. 2003; Houle et al. 2000)	Adequate (Erlandsson et al. 2005; Catafau et al. 2005)	Good (Lundberg et al. 2006)	Very good (Nye et al. 2008)

(continued)

Table 26.2 (continued)

	[123I]β-CIT SPECT	[11C]McN5652 PET	[11C]DASB PET	[123I]ADAM SPECT	[11C]MADAM PET	[11C]HOMADAM PET
Sensitivity to endogenous serotonin	Not known	Not known	Negligible (Talbot et al. 2005; Praschak-Rieder et al. 2005)	Not known	Not known	Not known
Specific binding to free and nonspecific binding ratio**	Good	Not adequate in most regions; adequate in the thalamus (Ikoma et al. 2002; Frankle et al. 2005)	Adequate to very good, depending upon region (Ginovart et al. 2001; Ichise et al. 2003)	Not adequate in most regions; adequate in the midbrain (Erlandsson et al. 2005; Catafau et al. 2005)	Adequate to very good (Lundberg et al. 2006, 2005)	Adequate to very good (Nye et al. 2008)
Reliability of 5-HTT BP**	Not measured	Modest (Kent et al. 2002)	Very good to excellent (Praschak-Rieder et al. 2005; Meyer et al. 2001)	Most regions reasonable (Catafau et al. 2005)	Good to very good (Lundberg et al. 2006)	Not yet reported
5-HTT BP measurable in multiple regions?	Brainstem only (Kuikka et al. 1993; Brucke et al. 1993)	Measurable in the thalamus (Ikoma et al. 2002), not measurable in the cortex (Parsey et al. 2000)	Yes (Ginovart et al. 2001; Ichise et al. 2003)	Measurable in the midbrain; unclear for other regions (Erlandsson et al. 2005; Catafau et al. 2005)	Yes (Lundberg et al. 2006)	Yes (Nye et al. 2008)
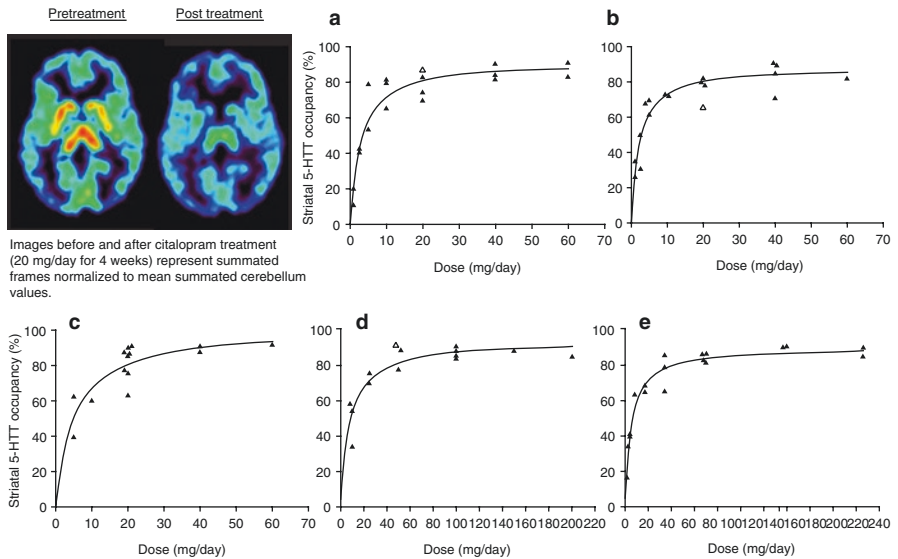
Fig. 26.5 The data was fit using an equation of form $f(x) = a \times x/(b + x)$. Each fit was highly significant ($p < 0.0002$ for all). Scanning occurred before treatment after four weeks of the treating dose. Medication type and dosage that differentiates from placebo are listed as follows: A-citalopram (20–40 mg), B-fluoxetine (20 mg), C-paroxetine (20 mg), D-sertraline (50–100 mg), E-venlafaxineXR (75 mg). Occupancy is the per cent reduction in binding potential (BP_{ND}) i.e., Occupancy = (baseline BP_{ND} − treatment BP_{ND})/baseline BP_{ND}

affinity for the serotonin transporter, an 80% striatal 5-HTT occupancy occurs at minimum clinical dose, thereby demonstrating an additional, important predictive value of the 5-HTT occupancy data in relation to clinical trial development. Furthermore, the added information from occupancy measurement is clear because the in vivo EC_{50} does not correlate with affinity (Meyer et al. 2004b). This association of 80% occupancy with doses of SSRI that distinguish from placebo in clinical trial is consistently reported (Kent et al. 2002; Suhara et al. 2003). Hence, while affinity is an essential piece of information regarding an antidepressant, it cannot predict occupancy, even when plasma levels are known (Meyer et al. 2004b). Given the association between the clinically relevant dose and 5-HTT occupancy for SSRIs, it is now generally believed that an 80% 5-HTT occupancy is a therapeutic threshold for new antidepressants. This technique is frequently applied during phase I trials to assess whether new antidepressants in development are adequately brain penetrant and to guide dosing selection for subsequent phase II clinical trials.

26.11   Major Depressive Disorder

Neuroimaging studies of 5-HTT enable measurement of 5-HTT BP_{ND} in the midst of a MDE, as well as the ability to select more homogeneous subtypes of MDD like early-onset MDD (in contrast to the more heterogenous late-onset MDD). Sampling

early-onset MDD is usually not feasible for postmortem studies of 5-HTT density due to challenges of sampling subjects at older ages. The two postmortem investigations of 5-HTT density in subjects with recent symptoms of MDE evaluated 5-HTT density in the dorsal raphe and locus coeruleus, finding similar levels between MDD and healthy subjects (see review for more details (Stockmeier 2003)).

Neuroimaging studies of 5-HTT binding in untreated MDD exemplify a wide range of sample sizes and quality of techniques. However, there are three studies that focus upon medication-free subjects, with minimum sample sizes of 15 in each group, apply a radioligand of [^{11}C]DASB level quality, and tend to focus upon early-onset MDD. For a broader review of these studies, including smaller studies not meeting these criteria, the reader is referred to Meyer et al. (Meyer 2008). The first study applied [^{11}C]DASB PET to a sample of 20 subjects with early-onset MDE and 20 healthy controls (Meyer et al. 2004a). Subjects were medication-free for at least 3 months, age matched, had no comorbid axis I illnesses, were nonsmoking, and had early-onset MDD. There was no difference in 5-HTT BP_{ND} between MDE and healthy controls, but MDE subjects with severely pessimistic dysfunctional attitudes had significantly higher 5-HTT BP_{ND} (on average 21%) compared to healthy volunteers in brain regions sampling serotonin nerve terminals (prefrontal cortex, anterior cingulate, thalamus, bilateral caudate, bilateral putamen). Consistent with the postmortem studies of MDE, there was no difference in midbrain 5-HTT BP_{ND}. Within the MDE group, greater 5-HTT BP_{ND} was strongly associated with more negativistic dysfunctional attitudes in the same brain regions. An interpretation of the relationship between the functional measure of dysfunctional attitudes and the measure of 5-HTT BP_{ND} is that greater regional 5-HTT levels could provide greater vulnerability to low extracellular 5-HT through excessive clearance of extracellular serotonin, leading to subsequent symptoms of extremely negativistic dysfunctional attitudes. There is particular utility in relating a functional symptom measure to 5-HTT binding because not all neuronal 5-HTT are in a functional location (Zhou et al. 1998; Tao-Cheng and Zhou 1999) although total 5-HTT level correlates with extracellular 5-HT in knockout models in vivo (Mathews et al. 2004)). The second study reported elevated 5-HTT binding in several brain regions (thalamus, striatum, insula) during MDE (Cannon et al. 2007), and the third study reports no difference in remitted MDD (Bhagwagar et al. 2007) (dysfunctional attitudes were not assessed in the latter two studies), demonstrating fairly consistent results across groups.

Among the analyses completed in a recent meta-analysis (Spies et al. 2015), there was a subanalysis of 184 participants who had been studied with radioligands selective for 5-HTT for which the striatum was a suitable region of interest. In this subanalysis, which was restricted to the striatal 5-HTT BP_{ND} due to sample availability, it was interesting that younger samples had relatively higher striatal 5-HTT BP_{ND}, and older samples had relatively lower 5-HTT BP_{ND}. One might speculate that with a longer duration of illness, there is a lower density of 5-HTT BP_{ND}, but this will take further study to determine. As these measures were relative to age-matched controls, the result was not a consequence of simply reductions in 5-HTT BP_{ND} with age (Spies et al. 2015).

26.12 Ecstasy Abuse and Serotonin Transporter Imaging

Ecstasy (3,4-methylenedioxymethamphetamine, MDMA) is a substance that is frequently used in certain social contexts as it enhances emotional well-being, feelings of closeness, and desire to be sociable. Its mechanism, based upon the effects of serotonin transporter blockade and serotonin transporter knockout mice, is likely mainly mediated through binding to the serotonin transporter. Animal models suggest that exposure to MDMA is associated with widespread, persistent loss in serotonin transporter density, raising concern about the safety of exposure to this substance.

PET imaging allows for assessment in regard to the effects of MDMA upon 5-HTT BP_{ND} in vivo including the regional distribution of this effect and its persistence at amounts typically self-administered by people. Neuroimaging results applying [^{11}C]DASB PET have been very consistent across sites with reductions in 5-HTT BP_{ND} in prefrontal, anterior cingulate, parietal, temporal, occipital cortex, insula, and hippocampus but no change in subcortical regions including the striatum, thalamus, and midbrain being typical (McCann et al. 2005, 2008; Urban et al. 2012; Erritzoe et al. 2011; Kish et al. 2010). All studies to date report reductions in 5-HTT BP_{ND} in cortical regions and four out of five reports sparing of subcortical structures (McCann et al. 2005, 2008; Urban et al. 2012; Erritzoe et al. 2011; Kish et al. 2010). The question of persistence of the reduction in 5-HTT BP_{ND} requires further investigations. McCann et al. (McCann et al. 2008) reported no correlation between recency of use and 5-HTT BP_{ND} over the initial 7 months, and Selvaraj et al. (Selvaraj et al. 2009) reported no regional difference in 5-HTT BP_{ND} in people who had abstained on average for 2.7 years suggesting a normalization window in between these two time frames, which ideally should be followed longitudinally.

26.13 Obsessive Compulsive Disorder

Obsessive compulsive disorder is a disabling illness characterized by repeated obsessions and/or compulsions that are distressing and impair function (First et al. 1995). OCD tends to be either relapsing/remitting or chronic (Association AP 1994) affecting 2% of adults (Robins et al. 1984; Weissman et al. 1994). Most likely time of onset is bimodally distributed with an early-onset group in childhood to teenaged years and a late-onset group occurring in the second to third decade. There have been virtually no postmortem investigations into this condition making neuroimaging studies an important source of information toward understanding potential neurochemical abnormalities in this illness.

There have been three investigations of serotonin transporter imaging in obsessive compulsive disorder applying a newer imaging method (all with [^{11}C]DASB PET), and although the individual results focused within each study vary, further scrutiny suggests some consistency (Hesse et al. 2011; Matsumoto et al. 2010; Reimold et al. 2007). Heinz et al. applied a voxel-based analysis and reported decreased 5-HTT BP_{ND} in the midbrain and thalamus in a sample of nine subjects

with OCD (Reimold et al. 2007). In a sample of ten subjects with OCD, Matsumoto reported significantly decreased 5-HTT BP_{ND} within the orbitofrontal and insular cortex (Matsumoto et al. 2010), and in a sample of 19 OCD subjects, divided by early ($n = 6$) and late ($n = 13$) onset, Hesse et al. reported decreased 5-HTT BPND in the medial prefrontal cortex, hippocampus, caudate, putamen, thalamus, occipital cortex, and midbrain, which was primarily driven by reduced 5-HTT BP_{ND} in the late-onset OCD (Hesse et al. 2011). What was reasonably consistent across the studies was a decrease in 5-HTT BP_{ND}, as Matsumoto noted reductions in 5-HTT BP ranging from 6.3% to 42% across all regions studied. The data of Hesse et al. suggests that late-onset OCD is primarily responsible for the differences in 5-HTT BP_{ND} between OCD and health. It is plausible that the studies conducted to date may be underpowered to fully determine the regional extent of the reduction of 5-HTT BP_{ND} in late-onset OCD. The main reasons for being underpowered are that the voxel-based analyses tend to be less sensitive than region of interest-based analyses and the sample sizes may not be large enough to achieve results that are regionally consistent even though the direction of effect is consistent. In support of this perspective, the nonsignificant reductions in OCD across studies suggest a global reduction in 5-HTT BP_{ND}. Based upon the data from these studies, future serotonin transporter imaging investigations should consider larger sample sizes focused upon late-onset OCD.

26.14 Season and Serotonin Transporter Imaging

Seasonal affective disorder, that is, major depressive disorder with regular MDE in winter with full remissions in summer, is an important problem, especially in areas of the world at greater extremes of latitude: Prevalence rates of seasonal affective disorder (SAD) are about 1% at 40′ latitude and 6% at 60′ latitude or greater (Magnusson 2000). The functions of mood, appetite, sleep, and energy which fluctuate with season also are influenced by the serotonin system, and some indicators of serotonin physiology fluctuate with season in humans (Praschak-Rieder et al. 2008).

Prior to serotonin transporter imaging across season, several markers of seasonal fluctuations in serotonin physiology had been reported. In a human postmortem study of serotonin concentrations in the hypothalamus, Carlsson et al. reported lower levels in late winter and higher levels in late summer (Carlsson et al. 1980). Subsequently, Lambert et al. reported seasonal variation in whole brain serotonin turnover in vivo in humans (Lambert et al. 2002). Investigations in rodents find that reduced light exposure is associated with greater 5-HTT density (Rovescalli et al. 1989), lower 5-HT release (Blier et al. 1989), and greater 5-HT clearance (Rovescalli et al. 1989) in the hypothalamus and suprachiasmatic nucleus (two regions with high 5-HT concentration and density) (Tyrer et al. 2016a).

The four largest studies of 5-HTT binding and season have very consistent results. The first study that applied [^{11}C]DASB PET, in 88 healthy, nonsmoking
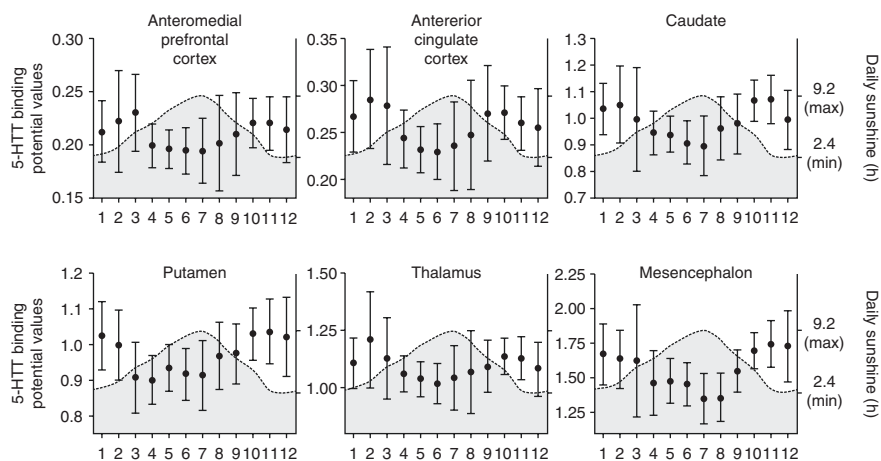
Fig. 26.6 Serotonin transporter binding potential values were measured using the selective serotonin transporter radioligand carbon 11–labeled 3-amino-4-(2-dimethylaminomethyl-phenylsulfanyl)-benzonitrile and positron emission tomography. The serotonin transporter binding potential values were determined in 6 brain regions [anteromedial prefrontal cortex (a), anterior cingulate cortex (b), caudate (c), putamen (d), thalamus (e), and mesencephalon (f)]. Circles represent bimonthly moving average means of serotonin transporter binding potential values; error bars, 95% confidence intervals of the mean. The shaded areas represent the average duration of sunshine in Toronto, Ontario, Canada (range, 2.4–9.2 h a day). There were 38 study participants in the fall and winter seasons and 50 in the spring and summer seasons. The number of study participants for each bimonthly data point was as follows: January, 11; February, 4; March, 6; April, 14; May, 23; June, 24; July, 14; August, 8; September, 13; October, 28; November, 21; and December, 10

humans in Toronto, Canada, found greater 5-HTT binding in the fall/winter as compared to spring/summer in all the brain regions sampled (medial prefrontal cortex, anterior cingulate cortex, thalamus, striatum, and midbrain) (Praschak-Rieder et al. 2008). See Fig. 26.6. The next [11C]DASB PET study of seasonality evaluated 54 subjects in Copenhagen, Denmark, and replicated the same seasonal variation in 5-HTT BP_{ND} (Kalbitzer et al. 2010). Ruhe et al. reported the same relationship between midbrain binding and season in a sample of 49 healthy and 49 depressed subjects applying [123I]B-CIT SPECT (Ruhe et al. 2009). Buchert et al. reported the same seasonal finding in the midbrain but not in the thalamus in a sample of 39 subjects using [11C]McN5652 PET (Buchert et al. 2006). Thus, studies with a large sample size located in more northern latitudes report greater 5-HTT BP_{ND} in the brain regions sampled in fall/winter compared to spring/summer.

More recently two groups evaluated 5-HTT BP_{ND} in both summer and winter in samples with seasonal affective disorder (SAD) and in health (Tyrer et al. 2016a; Mc Mahon et al. 2016). In SAD, with greater severity of symptoms across seasonal change, 5-HTT BP_{ND} was more elevated as compared to those in health or those with more mild SAD symptoms (Tyrer et al. 2016a; Mc Mahon et al. 2016). These findings tended to be global throughout gray matter brain regions including the PFC and ACC. There was a high consistency of findings across the two studies. In

addition, in a single-blind, placebo-controlled, counterbalanced crossover, controlled trial with light therapy in healthy participants, it was shown that 5-HTT BP_{ND} is lowered in the ACC (Harrison et al. 2015). It was also demonstrated that after an open trial of light therapy in SAD, 5-HTT BP_{ND} is lowered in both the PFC and ACC in SAD, as well as throughout other brain regions assayed in SAD, such as the hippocampus, ventral striatum, dorsal putamen, thalamus, and midbrain (Tyrer et al. 2016b).

26.15 Conclusions

Neuroimaging studies applying recently optimized radiotracers for MAO-A (Bergstrom et al. 1997a; Ginovart et al. 2006) and serotonin transporter (Ginovart et al. 2001; Wilson et al. 2000) have created new advances in our knowledge of the relationship of these proteins to mood disorder, aggression, substance abuse, anxiety, and antidepressant development.

Prior to 2006, MAO-A had been viewed as a target for treatment of mood disorders, but neuroimaging studies have led to a new view that elevations in MAO-A level, particularly in the prefrontal and anterior cingulate cortex, occur during major depressive episodes; during high-risk states for major depressive episodes in adults such as in remission prior to recurrence, postpartum, and perimenopause; and during certain commonly comorbid illnesses like alcohol and cigarette dependence disorders and borderline personality disorder (Meyer et al. 2006, 2009a; Bacher et al. 2011; Sacher et al. 2010). New advances in understanding substance abuse are also emerging: During active cigarette smoking, available MAO-A binding is lowered, whereas during acute withdrawal, MAO-A binding is elevated (Fowler et al. 1996; Bacher et al. 2011), and MAO-A binding is highly elevated during early withdrawal from alcohol abuse disorder. These findings suggest that changes in MAO-A availability in adulthood predispose to persistent alterations in mood state. Interestingly, pathologically aggressive behavior and the personality traits of aggression are associated with reduced MAO-A binding, particularly in the prefrontal cortex, and in the context of the relationship of MAO-A levels to these traits in other models, we suggest that this may reflect a marker of a neurodevelopmental influence predisposing to a personality characteristic (Alia-Klein et al. 2008; Soliman et al. 2011).

5-HTT imaging now has a major influence upon novel antidepressant development since an 80% occupancy is predictive of a differential response versus placebo (Meyer et al. 2001, 2004b). 5-HTT imaging has verified that the effects of ecstasy upon reducing 5-HTT density in animal models and postmortem humans apply in vivo (McCann et al. 2005, 2008; Urban et al. 2012; Erritzoe et al. 2011; Kish et al. 2010) and are suggesting that diffuse 5-HTT loss occurs in OCD (Meyer et al. 2001, 2004b). In contrast, greater 5-HTT BP_{ND} in untreated MDD and winter season suggests that a model of predisposition to serotonin loss may contribute toward a similar predisposition toward sad mood (Meyer et al. 2004a; Cannon et al. 2007;

Bhagwagar et al. 2007; Praschak-Rieder et al. 2008; Kalbitzer et al. 2010; Ruhe et al. 2009; Buchert et al. 2006).

References

Alia-Klein N, Goldstein RZ, Kriplani A, Logan J, Tomasi D, Williams B, Telang F, Shumay E, Biegon A, Craig IW, Henn F, Wang GJ, Volkow ND, Fowler JS (2008) Brain monoamine oxidase A activity predicts trait aggression. J Neurosci. 28(19):5099–5104

Anda RF, Williamson DF, Escobedo LG, Mast EE, Giovino GA, Remington PL (1990) Depression and the dynamics of smoking. A national perspective. Jama. 264(12):1541–1545

Association AP (1994) Diagnostic and statistical manual of mental disorders. Vol Fourth Edition. American Psychiatric Association, Washington, DC

Bacher I, Houle S, Xu X, Zawertailo L, Soliman A, Wilson AA, Selby P, George TP, Sacher J, Miler L, Kish SJ, Rusjan P, Meyer JH (2011) Monoamine oxidase a binding in the prefrontal and anterior cingulate cortices during acute withdrawal from heavy cigarette smoking. Arch Gen Psychiatry 68(8):817–826

Barton DA, Esler MD, Dawood T, Lambert EA, Haikerwal D, Brenchley C, Socratous F, Hastings J, Guo L, Wiesner G, Kaye DM, Bayles R, Schlaich MP, Lambert GW (2008) Elevated brain serotonin turnover in patients with depression: effect of genotype and therapy. Arch Gen Psychiatry. 65(1):38–46

Bel N, Artigas F (1992) Fluvoxamine preferentially increases extracellular 5-hydroxytryptamine in the raphe nuclei: an in vivo microdialysis study. Eur J Pharmacol 229:101–103

Bel N, Artigas F (1993) Chronic treatment with fluvoxamine increases extracellular serotonin in frontal cortex but not in raphe nuclei. Synapse 15:243–245

Bel N, Artigas F (1995) In vivo evidence for the reversible action of the monoamine oxidase inhibitor brofaromine on 5-hydroxytryptamine release in rat brain. Naunyn Schmiedebergs Arch Pharmacol. 351(5):475–482

Benmansour S, Cecchi M, Morilak D, Gerhardt G, Javors M, Gould G, Frazer A (1999) Effects of chronic antidepressant treatments on serotonin transporter function, density and mRNA level. J Neurosci. 19(23):10494–10501

Bergstrom M, Westerberg G, Langstrom B (1997a) 11C-harmine as a tracer for monoamine oxidase A (MAO-A): in vitro and in vivo studies. Nucl Med Biol 24(4):287–293

Bergstrom M, Westerberg G, Kihlberg T, Langstrom B (1997b) Synthesis of some 11C-labelled MAO-A inhibitors and their in vivo uptake kinetics in rhesus monkey brain. Nucl Med Biol 24(5):381–388

Bergstrom M, Westerberg G, Nemeth G, Traut M, Gross G, Greger G, Muller-Peltzer H, Safer A, Eckernas SA, Grahner A, Langstrom B (1997c) MAO-A inhibition in brain after dosing with esuprone, moclobemide and placebo in healthy volunteers: in vivo studies with positron emission tomography. Eur J Clin Pharmacol 52(2):121–128

Bhagwagar Z, Murthy N, Selvaraj S, Hinz R, Taylor M, Fancy S, Grasby P, Cowen P (2007) 5-HTT binding in recovered depressed patients and healthy volunteers: a positron emission tomography study with [11C]DASB. Am J Psychiatry. 164(12):1858–1865

Blakely R, Ramamoorthy S, Qian Y, Schroeter S, Bradley C (1997) Regulation of antidepressant-sensitive serotonin transporters. In: Reith M (ed) Neurotransmitter transporters: structure, function, and regulation. Humana Press Inc., Totowa, New Jersey, pp 29–72

Blier P, De Montigny C (1983) Electrophysiological investigations on the effect of repeated zimelidine administration on serotonergic neurotransmission in the rat. J Neuroscience 3(6):1270–1278

Blier P, Galzin AM, Langer SZ (1989) Diurnal variation in the function of serotonin terminals in the rat hypothalamus. J Neurochem. 52(2):453–459

Bortolato M, Chen K, Shih JC (2008) Monoamine oxidase inactivation: from pathophysiology to therapeutics. Adv Drug Deliv Rev 60(13-14):1527–1533

Bottlaender M, Valette H, Delforge J, Saba W, Guenther I, Curet O, George P, Dolle F, Gregoire MC (2010) In vivo quantification of monoamine oxidase A in baboon brain: a PET study using [(11)C]befloxatone and the multi-injection approach. J Cereb Blood Flow Metab 30(4):792–800

Breslau N, Peterson EL, Schultz LR, Chilcoat HD, Andreski P (1998) Major depression and stages of smoking. A longitudinal investigation. Arch Gen Psychiatry. 55(2):161–166

Brucke T, Kornhuber J, Angelberger P, Asenbaum S, Frassine H, Podreka I (1993) SPECT imaging of dopamine and serotonin transporters with [123I]beta-CIT. Binding kinetics in the human brain. J Neural Transm Gen Sect. 94(2):137–146

Brunner HG, Nelen M, Breakefield XO, Ropers HH, van Oost BA (1993) Abnormal behavior associated with a point mutation in the structural gene for monoamine oxidase A. Science. 262(5133):578–580

Buchert R, Schulze O, Wilke F, Berding G, Thomasius R, Petersen K, Brenner W, Clausen M (2006) Is correction for age necessary in SPECT or PET of the central serotonin transporter in young, healthy adults? J Nucl Med 47(1):38–42

Buck A, Gucker PM, Schonbachler RD, Arigoni M, Kneifel S, Vollenweider FX, Ametamey SM, Burger C (2000) Evaluation of serotonergic transporters using PET and [11C](+)McN-5652: assessment of methods. J Cereb Blood Flow Metab. 20(2):253–262

Buckholtz JW, Meyer-Lindenberg A (2008) MAOA and the neurogenetic architecture of human aggression. Trends Neurosci 31(3):120–129

Cannon DM, Ichise M, Rollis D, Klaver JM, Gandhi SK, Charney DS, Manji HK, Drevets WC (2007) Elevated serotonin transporter binding in major depressive disorder assessed using positron emission tomography and [(11)C]DASB; Comparison with bipolar disorder. Biol Psychiatry. 62(8):870–877

Carey MP, Kalra DL, Carey KB, Halperin S, Richards CS (1993) Stress and unaided smoking cessation: a prospective investigation. J Consult Clin Psychol. 61(5):831–838

Carlsson A, Svennerholm L, Winblad B (1980) Seasonal and circadian monoamine variations in human brains examined post mortem. Acta Psychiatr Scand Suppl. 280:75–85

Carroll FI, Kotian P, Dehghani A, Gray JL, Kuzemko MA, Parham KA, Abraham P, Lewin AH, Boja JW, Kuhar MJ (1995) Cocaine and 3 beta-(4'-substituted phenyl)tropane-2 beta-carboxylic acid ester and amide analogues. New high-affinity and selective compounds for the dopamine transporter. J Med Chem. 38(2):379–388

Cases O, Vitalis T, Seif I, De Maeyer E, Sotelo C, Gaspar P (1996) Lack of barrels in the somatosensory cortex of monoamine oxidase A-deficient mice: role of a serotonin excess during the critical period. Neuron. 16(2):297–307

Caspi A, McClay J, Moffitt TE, Mill J, Martin J, Craig IW, Taylor A, Poulton R (2002) Role of genotype in the cycle of violence in maltreated children. Science. 297(5582):851–854

Catafau AM, Perez V, Penengo MM, Bullich S, Danus M, Puigdemont D, Pascual JC, Corripio I, Llop J, Perich J, Alvarez E (2005) SPECT of serotonin transporters using 123I-ADAM: optimal imaging time after bolus injection and long-term test-retest in healthy volunteers. J Nucl Med. 46(8):1301–1309

Chalon S, Tarkiainen J, Garreau L, Hall H, Emond P, Vercouillie J, Farde L, Dasse P, Varnas K, Besnard JC, Halldin C, Guilloteau D (2003) Pharmacological characterization of N,N-dimethyl-2-(2-amino-4-methylphenyl thio)benzylamine as a ligand of the serotonin transporter with high affinity and selectivity. J Pharmacol Exp Ther. 304(1):81–87

Chiuccariello L, Houle S, Miler L, Cooke RG, Rusjan PM, Rajkowska G, Levitan RD, Kish SJ, Kolla NJ, Ou X, Wilson AA, Meyer JH (2014) Elevated monoamine oxidase a binding during major depressive episodes is associated with greater severity and reversed neurovegetative symptoms. Neuropsychopharmacology. 39(4):973–980

Chiuccariello L, Cooke RG, Miler L, Levitan RD, Baker GB, Kish SJ, Kolla NJ, Rusjan PM, Houle S, Wilson AA, Meyer JH (2015) Monoamine oxidase-A occupancy by moclobemide and phenelzine: implications for the development of monoamine oxidase inhibitors. Int J Neuropsychopharmacol 19(1):pyv078

Choi SR, Hou C, Oya S, Mu M, Kung MP, Siciliano M, Acton PD, Kung HF (2000) Selective in vitro and in vivo binding of [(125)I]ADAM to serotonin transporters in rat brain. Synapse. 38(4):403–412

Ciliax BJ, Drash GW, Staley JK, Haber S, Mobley CJ, Miller GW, Mufson EJ, Mash DC, Levey AI (1999) Immunocytochemical localization of the dopamine transporter in human brain. J Comp Neurol. 409(1):38–56

Cortes R, Soriano E, Pazos A, Probst A, Palacios J (1988) Autoradiography of antidepressant binding sites in the human brain: localization using [3H]imipramine and [3H]paroxetine. Neuroscience. 27(2):473–496

Curet O, Damoiseau-Ovens G, Sauvage C, Sontag N, Avenet P, Depoortere H, Caille D, Bergis O, Scatton B (1998) Preclinical profile of befloxatone, a new reversible MAO-A inhibitor. J Affect Disord 51(3):287–303

Dewar KM, Grondin L, Carli M, Lima L, Reader TA (1992) [3H]paroxetine binding and serotonin content of rat cortical areas, hippocampus, neostriatum, ventral mesencephalic tegmentum, and midbrain raphe nuclei region following p-chlorophenylalanine and p-chloroamphetamine treatment. J Neurochem. 58(1):250–257

Dolle F, Valette H, Bramoulle Y, Guenther I, Fuseau C, Coulon C, Lartizien C, Jegham S, George P, Curet O, Pinquier JL, Bottlaender M (2003) Synthesis and in vivo imaging properties of [11C]befloxatone: a novel highly potent positron emission tomography ligand for mono-amine oxidase-A. Bioorg Med Chem Lett 13(10):1771–1775

Dowlati Y, Ravindran AV, Maheux M, Steiner M, Stewart DE, Meyer JH (2014) No effect of oral tyrosine on total tyrosine levels in breast milk: implications for dietary supplementation in early postpartum. Arch Womens Ment Health. 17(6):541–548

Dowlati Y, Ravindran AV, Maheux M, Steiner M, Stewart DE, Meyer JH (2015) No effect of oral L-tryptophan or alpha-lactalbumin on total tryptophan levels in breast milk. Eur Neuropsychopharmacol. 25(6):779–787

Dowlati Y, Ravindran AV, Segal ZV, Stewart DE, Steiner M, Meyer JH (2017) Selective dietary supplementation in early postpartum is associated with high resilience against depressed mood. Proc Natl Acad Sci U S A. 114(13):3509–3514

Dreshfield LJ, Wong DT, Perry KW, Engleman EA (1996) Enhancement of fluoxetine-dependent increase of extracellular serotonin (5-HT) levels by (-)-pindolol, an antagonist at 5-HT1A receptors. Neurochem Res 21(5):557–562

Erlandsson K, Sivananthan T, Lui D, Spezzi A, Townsend CE, Mu S, Lucas R, Warrington S, Ell PJ (2005) Measuring SSRI occupancy of SERT using the novel tracer [123I]ADAM: a SPECT validation study. Eur J Nucl Med Mol Imaging. 32(11):1329–1336

Erritzoe D, Frokjaer VG, Holst KK, Christoffersen M, Johansen SS, Svarer C, Madsen J, Rasmussen PM, Ramsoy T, Jernigan TL, Knudsen GM (2011) In vivo imaging of cerebral serotonin transporter and serotonin(2A) receptor binding in 3,4-methylenedioxymethamphe tamine (MDMA or "ecstasy") and hallucinogen users. Arch Gen Psychiatry. 68(6):562–576

Fava GA, Ruini C, Rafanelli C, Finos L, Conti S, Grandi S (2004) Six-year outcome of cognitive behavior therapy for prevention of recurrent depression. Am J Psychiatry. 161(10):1872–1876

Fazel S, Danesh J (2002) Serious mental disorder in 23000 prisoners: a systematic review of 62 surveys. Lancet. 359(9306):545–550

Finberg J (2012) Role of the organic cation transporter (OCT-3) and monoamine oxidase types A and B in the metabolism of dopamine derived from L-DOPA in rat striatum depleted of dopa-minergic and serotonergic afferent inputs. Tenth International Catecholamine Symposium. Pacific Grove, CA; 82.

First M, Spitzer R, Williams J, Gibbon M (1995) Structured clinical interview for DSM-IV axis i disorders, patient edition (SCID-P), version 2. Biometrics Research, New York

Fitzgerald JC, Ufer C, Billett EE (2007a) A link between monoamine oxidase-A and apoptosis in serum deprived human SH-SY5Y neuroblastoma cells. J Neural Transm. 114(6):807–810

Fitzgerald JC, Ufer C, De Girolamo LA, Kuhn H, Billett EE (2007b) Monoamine oxidase-A modulates apoptotic cell death induced by staurosporine in human neuroblastoma cells. J Neurochem. 103(6):2189–2199

Fowler JS, MacGregor RR, Wolf AP, Arnett CD, Dewey SL, Schlyer D, Christman D, Logan J, Smith M, Sachs H et al (1987) Mapping human brain monoamine oxidase A and B with 11C-labeled suicide inactivators and PET. Science 235(4787):481–485

Fowler JS, Volkow ND, Wang GJ, Pappas N, Logan J, Shea C, Alexoff D, MacGregor RR, Schlyer DJ, Zezulkova I, Wolf AP (1996) Brain monoamine oxidase A inhibition in cigarette smokers. Proc Natl Acad Sci U S A 93(24):14065–14069

Frank E, Kupfer DJ, Perel JM, Cornes C, Jarrett DB, Mallinger AG, Thase ME, McEachran AB, Grochocinski VJ (1990) Three-year outcomes for maintenance therapies in recurrent depression. Arch Gen Psychiatry. 47(12):1093–1099

Frankle WG, Lombardo I, New AS, Goodman M, Talbot PS, Huang Y, Hwang DR, Slifstein M, Curry S, Abi-Dargham A, Laruelle M, Siever LJ (2005) Brain serotonin transporter distribution in subjects with impulsive aggressivity: a positron emission study with [11C]McN 5652. Am J Psychiatry. 162(5):915–923

Freis ED (1954) Mental depression in hypertensive patients treated for long periods with large doses of reserpine. N Engl J Med 251(25):1006–1008

Garvey AJ, Bliss RE, Hitchcock JL, Heinold JW, Rosner B (1992) Predictors of smoking relapse among self-quitters: a report from the Normative Aging Study. Addict Behav. 17(4):367–377

Ginovart N, Wilson AA, Meyer JH, Hussey D, Houle S (2001) Positron emission tomography quantification of [(11)C]-DASB binding to the human serotonin transporter: modeling strategies. J Cereb Blood Flow Metab. 21(11):1342–1353

Ginovart N, Meyer JH, Boovariwala A, Hussey D, Rabiner EA, Houle S, Wilson AA (2006) Positron emission tomography quantification of [11C]-harmine binding to monoamine oxidase-A in the human brain. J Cereb Blood Flow Metab 26(3):330–344

Graham D, Tahraoui L, Langer SZ (1987) Effect of chronic treatment with selective monoamine oxidase inhibitors and specific 5-hydroxytryptamine uptake inhibitors on [3H]paroxetine binding to cerebral cortical membranes of the rat. Neuropharmacology. 26(8):1087–1092

Halldin C, Lundberg J, Sovago J, Gulyas B, Guilloteau D, Vercouillie J, Emond P, Chalon S, Tarkiainen J, Hiltunen J, Farde L (2005) [(11)C]MADAM, a new serotonin transporter radioligand characterized in the monkey brain by PET. Synapse. 58(3):173–183

Harrison SJ, Tyrer AE, Levitan RD, Xu X, Houle S, Wilson AA, Nobrega JN, Rusjan PM, Meyer JH (2015) Light therapy and serotonin transporter binding in the anterior cingulate and prefrontal cortex. Acta Psychiatr Scand 132(5):379–388

Hauptmann N, Shih JC (2001) 2-Naphthylamine, a compound found in cigarette smoke, decreases both monoamine oxidase A and B catalytic activity. Life Sci. 68(11):1231–1241

Herraiz T, Chaparro C (2005) Human monoamine oxidase is inhibited by tobacco smoke: beta-carboline alkaloids act as potent and reversible inhibitors. Biochem Biophys Res Commun. 326(2):378–386

Hesse S, Stengler K, Regenthal R, Patt M, Becker GA, Franke A, Knupfer H, Meyer PM, Luthardt J, Jahn I, Lobsien D, Heinke W, Brust P, Hegerl U, Sabri O (2011) The serotonin transporter availability in untreated early-onset and late-onset patients with obsessive-compulsive disorder. Int J Neuropsychopharmacol. 14(5):606–617

Holschneider DP, Kumazawa T, Chen K, Shih JC (1998) Tissue-specific effects of estrogen on monoamine oxidase A and B in the rat. Life Sci. 63(3):155–160

Houle S, Ginovart N, Hussey D, Meyer J, Wilson A (2000) Imaging the serotonin transporter with positron emission tomography: initial human studies with [11C]DAPP and [11C]DASB. Eur J Nucl Med. 27(11):1719–1722

Ichise M, Liow JS, Lu JQ, Takano A, Model K, Toyama H, Suhara T, Suzuki K, Innis RB, Carson RE (2003) Linearized reference tissue parametric imaging methods: application to [11C]DASB positron emission tomography studies of the serotonin transporter in human brain. J Cereb Blood Flow Metab. 23(9):1096–1112

Ikoma Y, Suhara T, Toyama H, Ichimiya T, Takano A, Sudo Y, Inoue M, Yasuno F, Suzuki K (2002) Quantitative analysis for estimating binding potential of the brain serotonin transporter with [11 C]McN5652. J Cereb Blood Flow Metab. 22(4):490–501

Jarkas N, Votaw JR, Voll RJ, Williams L, Camp VM, Owens MJ, Purselle DC, Bremner JD, Kilts CD, Nemeroff CB, Goodman MM (2005) Carbon-11 HOMADAM: a novel PET radiotracer for imaging serotonin transporters. Nucl Med Biol. 32(3):211–224

Johnson S, Stockmeier CA, Meyer JH, Austin MC, Albert PR, Wang J, May WL, Rajkowska G, Overholser JC, Jurjus G, Dieter L, Johnson C, Sittman DB, Ou XM (2011) The reduction of R1, a novel repressor protein for monoamine oxidase A, in major depressive disorder. Neuropsychopharmacology.

Kalbitzer J, Erritzoe D, Holst KK, Nielsen FA, Marner L, Lehel S, Arentzen T, Jernigan TL, Knudsen GM (2010) Seasonal changes in brain serotonin transporter binding in short serotonin transporter linked polymorphic region-allele carriers but not in long-allele homozygotes. Biol Psychiatry 67(11):1033–1039

Kenford SL, Smith SS, Wetter DW, Jorenby DE, Fiore MC, Baker TB (2002) Predicting relapse back to smoking: contrasting affective and physical models of dependence. J Consult Clin Psychol. 70(1):216–227

Kent JM, Coplan JD, Lombardo I, Hwang DR, Huang Y, Mawlawi O, Van Heertum RL, Slifstein M, Abi-Dargham A, Gorman JM, Laruelle M (2002) Occupancy of brain serotonin transporters during treatment with paroxetine in patients with social phobia: a positron emission tomography study with 11C McN 5652. Psychopharmacology (Berl). 164(4):341–348

Kim-Cohen J, Caspi A, Taylor A, Williams B, Newcombe R, Craig IW, Moffitt TE (2006) MAOA, maltreatment, and gene-environment interaction predicting children's mental health: new evidence and a meta-analysis. Mol Psychiatry. 11(10):903–913

Kish SJ, Furukawa Y, Chang LJ, Tong J, Ginovart N, Wilson A, Houle S, Meyer JH (2005) Regional distribution of serotonin transporter protein in postmortem human brain: is the cerebellum a SERT-free brain region? Nucl Med Biol. 32(2):123–128

Kish SJ, Lerch J, Furukawa Y, Tong J, McCluskey T, Wilkins D, Houle S, Meyer J, Mundo E, Wilson AA, Rusjan PM, Saint-Cyr JA, Guttman M, Collins DL, Shapiro C, Warsh JJ, Boileau I (2010) Decreased cerebral cortical serotonin transporter binding in ecstasy users: a positron emission tomography/[(11)C]DASB and structural brain imaging study. Brain. 133(Pt 6):1779–1797

Kolla NJ, Matthews B, Wilson AA, Houle S, Bagby RM, Links P, Simpson AI, Hussain A, Meyer JH (2015) Lower monoamine oxidase-a total distribution volume in impulsive and violent male offenders with antisocial personality disorder and high psychopathic traits: an [(11)C] harmine positron emission tomography study. Neuropsychopharmacology. 40(11):2596–2603

Kolla NJ, Chiuccariello L, Wilson AA, Houle S, Links P, Bagby RM, McMain S, Kellow C, Patel J, Rekkas PV, Pasricha S, Meyer JH (2016) Elevated monoamine oxidase-a distribution volume in borderline personality disorder is associated with severity across mood symptoms, suicidality, and cognition. Biol Psychiatry. 79(2):117–126

Krishnan KR (2002) Biological risk factors in late life depression. Biol Psychiatry. 52(3):185–192

Kuikka JT, Bergstrom KA, Vanninen E, Laulumaa V, Hartikainen P, Lansimies E (1993) Initial experience with single-photon emission tomography using iodine-123-labelled 2 beta-carbomethoxy-3 beta-(4-iodophenyl) tropane in human brain. Eur J Nucl Med. 20(9):783–786

Kung MP, Hou C, Oya S, Mu M, Acton PD, Kung HF (1999) Characterization of [(123)I]IDAM as a novel single-photon emission tomography tracer for serotonin transporters. Eur J Nucl Med. 26(8):844–853

Lambert GW, Reid C, Kaye DM, Jennings GL, Esler MD (2002) Effect of sunlight and season on serotonin turnover in the brain. Lancet. 360(9348):1840–1842

Laruelle M, Vanisberg M-A, Maloteaux J-M (1988) Regional and subcellular localization in human brain of [3H]paroxetine binding, a marker of serotonin uptake sites. Biol Psych. 24:299–309

Laruelle M, Giddings SS, Zea-Ponce Y, Charney DS, Neumeyer JL, Baldwin RM, Innis RB (1994) Methyl 3 beta-(4-[125I]iodophenyl)tropane-2 beta-carboxylate in vitro binding to dopamine and serotonin transporters under "physiological" conditions. J Neurochem. 62(3):978–986

Law M, Tang JL (1995) An analysis of the effectiveness of interventions intended to help people stop smoking. Arch Intern Med. 155(18):1933–1941

Lesch KP, Wolozin BL, Estler HC, Murphy DL, Riederer P (1993a) Isolation of a cDNA encoding the human brain serotonin transporter. J Neural Transm Gen Sect. 91(1):67–72

Lesch KP, Wolozin BL, Murphy DL, Reiderer P (1993b) Primary structure of the human platelet serotonin uptake site: identity with the brain serotonin transporter. J Neurochem. 60(6):2319–2322

Liotti M, Mayberg HS, McGinnis S, Brannan SL, Jerabek P (2002) Unmasking disease-specific cerebral blood flow abnormalities: mood challenge in patients with remitted unipolar depression. Am J Psychiatry. 159(11):1830–1840

Luine VN, Khylchevskaya RI, McEwen BS (1975) Effect of gonadal steroids on activities of monoamine oxidase and choline acetylase in rat brain. Brain Res. 86(2):293–306

Lundberg J, Odano I, Olsson H, Halldin C, Farde L (2005) Quantification of 11C-MADAM binding to the serotonin transporter in the human brain. J Nucl Med. 46(9):1505–1515

Lundberg J, Halldin C, Farde L (2006) Measurement of serotonin transporter binding with PET and [(11)C]MADAM: A test-retest reproducibility study. Synapse. 60(3):256–263

Lundberg J, Christophersen JS, Petersen KB, Loft H, Halldin C, Farde L (2007) PET measurement of serotonin transporter occupancy: a comparison of escitalopram and citalopram. Int J Neuropsychopharmacol. 10(6):777–785

Ma ZQ, Bondiolotti GP, Olasmaa M, Violani E, Patrone C, Picotti GB, Maggi A (1993) Estrogen modulation of catecholamine synthesis and monoamine oxidase A activity in the human neuroblastoma cell line SK-ER3. J Steroid Biochem Mol Biol. 47(1-6):207–211

Ma ZQ, Violani E, Villa F, Picotti GB, Maggi A (1995) Estrogenic control of monoamine oxidase A activity in human neuroblastoma cells expressing physiological concentrations of estrogen receptor. Eur J Pharmacol. 284(1-2):171–176

Magnusson A (2000) An overview of epidemiological studies on seasonal affective disorder. Acta Psychiatr Scand. 101(3):176–184

Major LF, Hawley RJ, Saini N, Garrick NA, Murphy DL (1985) Brain and liver monoamine oxidase type A and type B activity in alcoholics and controls. Alcohol Clin Exp Res. 9(1):6–9

Mann JJ, Stanley M (1984) Postmortem monoamine oxidase enzyme kinetics in the frontal cortex of suicide victims and controls. Acta Psychiatr Scand. 69(2):135–139

Maschauer S, Haller A, Riss PJ, Kuwert T, Prante O, Cumming P (2015) Specific binding of [(18)F]fluoroethyl-harmol to monoamine oxidase A in rat brain cryostat sections, and compartmental analysis of binding in living brain. J Neurochem 135(5):908–917

Mathews T, Fedele D, Unger E, Lesch KP, Murphy DL, Andrews A (2000) Effects of serotonin transporter inactivation on extracellular 5-HT levels, in vivo microdialysis recovery, and MDMA-induced release of serotonin and dopamine in mouse striatum. Soc Neurosci Abstracts 30:624

Mathews TA, Fedele DE, Coppelli FM, Avila AM, Murphy DL, Andrews AM (2004) Gene dose-dependent alterations in extraneuronal serotonin but not dopamine in mice with reduced serotonin transporter expression. J Neurosci Methods. 140(1-2):169–181

Matsumoto R, Ichise M, Ito H, Ando T, Takahashi H, Ikoma Y, Kosaka J, Arakawa R, Fujimura Y, Ota M, Takano A, Fukui K, Nakayama K, Suhara T (2010) Reduced serotonin transporter binding in the insular cortex in patients with obsessive-compulsive disorder: a [11C]DASB PET study. Neuroimage. 49(1):121–126

Matthews BA, Kish SJ, Xu X, Boileau I, Rusjan PM, Wilson AA, DiGiacomo D, Houle S, Meyer JH (2014) Greater monoamine oxidase a binding in alcohol dependence. Biol Psychiatry. 75(10):756–764

Matthews BA, Tong J, Attwells S, Xu X, Le A, Kish SJ, Meyer JH (2018) Elevated monoamine oxidase A activity and protein levels in rodent brain during acute withdrawal after chronic intermittent ethanol vapor exposure. Drug Alcohol Depend. 185:398–405

Mc Mahon B, Andersen SB, Madsen MK, Hjordt LV, Hageman I, Dam H, Svarer C, da Cunha-Bang S, Baare W, Madsen J, Hasholt L, Holst K, Frokjaer VG, Knudsen GM (2016) Seasonal difference in brain serotonin transporter binding predicts symptom severity in patients with seasonal affective disorder. Brain 139(Pt 5):1605–1614

McCann UD, Szabo Z, Seckin E, Rosenblatt P, Mathews WB, Ravert HT, Dannals RF, Ricaurte GA (2005) Quantitative PET studies of the serotonin transporter in MDMA users and controls using [11C]McN5652 and [11C]DASB. Neuropsychopharmacology. 30(9):1741–1750

McCann UD, Szabo Z, Vranesic M, Palermo M, Mathews WB, Ravert HT, Dannals RF, Ricaurte GA (2008) Positron emission tomographic studies of brain dopamine and serotonin transporters in abstinent (+/-)3,4-methylenedioxymethamphetamine ("ecstasy") users: relationship to cognitive performance. Psychopharmacology (Berl). 200(3):439–450

Mejia JM, Ervin FR, Baker GB, Palmour RM (2002) Monoamine oxidase inhibition during brain development induces pathological aggressive behavior in mice. Biol Psychiatry. 52(8):811–821

Meyer JH (2007) Imaging the serotonin transporter during major depressive disorder and antidepressant treatment. J Psychiatry Neurosci. 32(2):86–102

Meyer JH (2008) Applying neuroimaging ligands to study major depressive disorder. Semin Nucl Med 38(4):287–304

Meyer J. Monoamine Oxidase A and serotonin transporter imaging with positron emission tomography. In: Springer, ed. PET and SPECT of neurobiological systems; 2014:711-739.

Meyer JH, Wilson AA, Ginovart N, Goulding V, Hussey D, Hood K, Houle S (2001) Occupancy of serotonin transporters by paroxetine and citalopram during treatment of depression: a [(11) C]DASB PET imaging study. Am J Psychiatry. 158(11):1843–1849

Meyer JH, Houle S, Sagrati S, Carella A, Hussey DF, Ginovart N, Goulding V, Kennedy J, Wilson AA (2004a) Brain serotonin transporter binding potential measured with carbon 11-labeled DASB positron emission tomography: effects of major depressive episodes and severity of dysfunctional attitudes. Arch Gen Psychiatry. 61(12):1271–1279

Meyer JH, Wilson AA, Sagrati S, Hussey D, Carella A, Potter WZ, Ginovart N, Spencer EP, Cheok A, Houle S (2004b) Serotonin transporter occupancy of five selective serotonin reuptake inhibitors at different doses: an [11C]DASB positron emission tomography study. Am J Psychiatry. 161(5):826–835

Meyer JH, Ginovart N, Boovariwala A, Sagrati S, Hussey D, Garcia A, Young T, Praschak-Rieder N, Wilson AA, Houle S (2006) Elevated monoamine oxidase a levels in the brain: an explanation for the monoamine imbalance of major depression. Arch Gen Psychiatry 63(11):1209–1216

Meyer JH, Wilson AA, Sagrati S, Miler L, Rusjan P, Bloomfield PM, Clark M, Sacher J, Voineskos AN, Houle S (2009a) Brain monoamine oxidase A binding in major depressive disorder: relationship to selective serotonin reuptake inhibitor treatment, recovery, and recurrence. Arch Gen Psychiatry. 66(12):1304–1312

Meyer JH, Wilson A, Sagrati S, Miler L, Rusjan P, Bloomfield PM, Clark M, Sacher J, Voineskos AN, Houle S (2009b) Brain monoamine oxidase A binding in major depressive disorder: relationship to selective serotonin reuptake inhibitor treatment, recovery and recurrence. Archiv Gen Psychiatry 66(12):1304–1312

Moret C, Briley M (1996) Effects of acute and repeated administration of citalopram on extracellular levels of serotonin in rat brain. Eur J Pharmacol 295(2-3):189–197

Nelson DL, Herbet A, Glowinski J, Hamon M (1979) [3H]Harmaline as a specific ligand of MAO A--II. Measurement of the turnover rates of MAO A during ontogenesis in the rat brain. J Neurochem 32(6):1829–1836

Nye JA, Votaw JR, Jarkas N, Purselle D, Camp V, Bremner JD, Kilts CD, Nemeroff CB, Goodman MM (2008) Compartmental modeling of 11C-HOMADAM binding to the serotonin transporter in the healthy human brain. J Nucl Med. 49(12):2018–2025

O'Hara MW, Schlechte JA, Lewis DA, Wright EJ (1991) Prospective study of postpartum blues. Biologic and psychosocial factors. Arch Gen Psychiatry. 48(9):801–806

O'Hara MW, Swain A (1996) Rates and risk of postpartum depression - a meta analysis. International Review of Psychiatry. 8:37–54

Ordway GA, Farley JT, Dilley GE, Overholser JC, Meltzer HY, Balraj EK, Stockmeier CA, Klimek V (1999) Quantitative distribution of monoamine oxidase A in brainstem monoamine nuclei is normal in major depression. Brain Res. 847(1):71–79

Oreland L, Wiberg A, Winblad B, Fowler CJ, Gottfries CG, Kiianmaa K (1983) The activity of monoamine oxidase -A and -B in brains from chronic alcoholics. J Neural Transm. 56(1):73–83

Ou XM, Chen K, Shih JC (2006) Monoamine oxidase A and repressor R1 are involved in apoptotic signaling pathway. Proc Natl Acad Sci U S A. 103(29):10923–10928

Oya S, Choi SR, Hou C, Mu M, Kung MP, Acton PD, Siciliano M, Kung HF (2000) 2-((2-((dimethylamino)methyl)phenyl)thio)-5-iodophenylamine (ADAM): an improved serotonin transporter ligand. Nucl Med Biol. 27(3):249–254

Parsey RV, Kegeles LS, Hwang DR, Simpson N, Abi-Dargham A, Mawlawi O, Slifstein M, Van Heertum RL, Mann JJ, Laruelle M (2000) In vivo quantification of brain serotonin transporters in humans using [11C]McN 5652. J Nucl Med. 41(9):1465–1477

Pirker W, Asenbaum S, Kasper S, Walter H, Angelberger P, Koch G, Pozzera A, Deecke L, Podreka I, Brucke T (1995) beta-CIT SPECT demonstrates blockade of 5HT-uptake sites by citalopram in the human brain in vivo. J Neural Transm Gen Sect. 100(3):247–256

Praschak-Rieder N, Wilson AA, Hussey D, Carella A, Wei C, Ginovart N, Schwarz MJ, Zach J, Houle S, Meyer JH (2005) Effects of tryptophan depletion on the serotonin transporter in healthy humans. Biol Psychiatry. 58(10):825–830

Praschak-Rieder N, Willeit M, Wilson AA, Houle S, Meyer JH (2008) Seasonal variation in human brain serotonin transporter binding. Arch Gen Psychiatry. 65(9):1072–1078

Pratt L, Brody D (2010) Depression and Smoking in the U.S. Household Population Aged 20 and Over, 2005-2008. NCHS Data Brief. 34:1–8

Quelch DR, Parker CA, Nutt DJ, Tyacke RJ, Erritzoe D (2012) Influence of different cellular environments on [(3)H]DASB radioligand binding. Synapse. 66(12):1035–1039

Reimold M, Smolka MN, Zimmer A, Batra A, Knobel A, Solbach C, Mundt A, Smoltczyk HU, Goldman D, Mann K, Reischl G, Machulla HJ, Bares R, Heinz A (2007) Reduced availability of serotonin transporters in obsessive-compulsive disorder correlates with symptom severity - a [11C]DASB PET study. J Neural Transm. 114(12):1603–1609

Rekkas PV, Wilson AA, Lee VW, Yogalingam P, Sacher J, Rusjan P, Houle S, Stewart DE, Kolla NJ, Kish S, Chiuccariello L, Meyer JH (2014) Greater monoamine oxidase a binding in perimenopausal age as measured with carbon 11-labeled harmine positron emission tomography. JAMA Psychiatry. 71(8):873–879

Robins LN, Helzer JE, Weissman MM, Orvaschel H, Gruenberg E, Burke JD Jr, Regier DA (1984) Lifetime prevalence of specific psychiatric disorders in three sites. Arch Gen Psychiatry. 41(10):949–958

Rommelspacher H, Meier-Henco M, Smolka M, Kloft C (2002) The levels of norharman are high enough after smoking to affect monoamineoxidase B in platelets. Eur J Pharmacol. 441(1-2):115–125

Rovescalli AC, Brunello N, Riva M, Galimberti R, Racagni G (1989) Effect of different photoperiod exposure on [3H]imipramine binding and serotonin uptake in the rat brain. J Neurochem. 52(2):507–514

Ruhe HG, Mason NS, Schene AH (2007) Mood is indirectly related to serotonin, norepinephrine and dopamine levels in humans: a meta-analysis of monoamine depletion studies. Mol Psychiatry 12(4):331–359

Ruhe HG, Booij J, Reitsma JB, Schene AH (2009) Serotonin transporter binding with [123I]beta-CIT SPECT in major depressive disorder versus controls: effect of season and gender. Eur J Nucl Med Mol Imaging 36(5):841–849

Sacher J, Wilson A, Houle S, Hassan S, Rusjan P, Bloomfield P, Stewart D, Meyer J (2010) Elevated brain monoamine oxidase A binding in early postpartum. Arch Gen Psychiatry 67(5):468–474

Sacher J, Houle S, Parkes J, Rusjan P, Sagrati S, Wilson AA, Meyer JH (2011) Monoamine oxidase A inhibitor occupancy during treatment of major depressive episodes with moclobemide or St. John's wort: an [(11C]-harmine PET study. J Psychiatry Neurosci 36(6):375–382

Sacher J, Rabiner EA, Clark M, Rusjan P, Soliman A, Boskovic R, Kish SJ, Wilson AA, Houle S, Meyer JH (2012) Dynamic, adaptive changes in MAO-A binding after alterations in substrate availability: an in vivo [(11)C]-harmine positron emission tomography study. J Cereb Blood Flow Metab 32(3):443–446

Saura J, Kettler R, Da Prada M, Richards JG (1992) Quantitative enzyme radioautography with 3H-Ro 41-1049 and 3H-Ro 19- 6327 in vitro: localization and abundance of MAO-A and MAO-B in rat CNS, peripheral organs, and human brain. J Neurosci 12(5):1977–1999

Saura J, Bleuel Z, Ulrich J, Mendelowitsch A, Chen K, Shih JC, Malherbe P, Da Prada M, Richards JG (1996) Molecular neuroanatomy of human monoamine oxidases A and B revealed by quantitative enzyme radioautography and in situ hybridization histochemistry. Neuroscience 70(3):755–774

Schieferstein H, Piel M, Beyerlein F, Luddens H, Bausbacher N, Buchholz HG, Ross TL, Rosch F (2015) Selective binding to monoamine oxidase A: in vitro and in vivo evaluation of (18) F-labeled beta-carboline derivatives. Bioorg Med Chem 23(3):612–623

Selvaraj S, Hoshi R, Bhagwagar Z, Murthy NV, Hinz R, Cowen P, Curran HV, Grasby P (2009) Brain serotonin transporter binding in former users of MDMA ('ecstasy'). Br J Psychiatry. 194(4):355–359

Shank RP, Vaught JL, Pelley KA, Setler PE, McComsey DF, Maryanoff BE (1988) McN-5652: a highly potent inhibitor of serotonin uptake. J Pharmacol Exp Ther. 247(3):1032–1038

Sharot T, Riccardi AM, Raio CM, Phelps EA (2007) Neural mechanisms mediating optimism bias. Nature. 450(7166):102–105

Sherif F, Marcusson J, Oreland L (1991) Brain gamma-aminobutyrate transaminase and mono-amine oxidase activities in suicide victims. Eur Arch Psychiatry Clin Neurosci. 241(3):139–144

Soliman A, Bagby RM, Wilson AA, Miler L, Clark M, Rusjan P, Sacher J, Houle S, Meyer JH (2011) Relationship of monoamine oxidase A binding to adaptive and maladaptive personality traits. Psychol Med. 41(5):1051–1060

Spies M, Knudsen GM, Lanzenberger R, Kasper S (2015) The serotonin transporter in psychiatric disorders: insights from PET imaging. Lancet Psychiatry. 2(8):743–755

Stockmeier CA (2003) Involvement of serotonin in depression: evidence from postmortem and imaging studies of serotonin receptors and the serotonin transporter. J Psychiatr Res 37(5):357–373

Suhara T, Takano A, Sudo Y, Ichimiya T, Inoue M, Yasuno F, Ikoma Y, Okubo Y (2003) High levels of serotonin transporter occupancy with low-dose clomipramine in comparative occu-pancy study with fluvoxamine using positron emission tomography. Arch Gen Psychiatry. 60(4):386–391

Talbot PS, Frankle WG, Hwang DR, Huang Y, Suckow RF, Slifstein M, Abi-Dargham A, Laruelle M (2005) Effects of reduced endogenous 5-HT on the in vivo binding of the serotonin trans-porter radioligand 11C-DASB in healthy humans. Synapse. 55(3):164–175

Tao-Cheng JH, Zhou FC (1999) Differential polarization of serotonin transporters in axons versus soma-dendrites: an immunogold electron microscopy study. Neuroscience. 94(3):821–830

Tauscher J, Pirker W, de Zwaan M, Asenbaum S, Brucke T, Kasper S (1999) In vivo visu-alization of serotonin transporters in the human brain during fluoxetine treatment. Eur Neuropsychopharmacol. 9(1-2):177–179

Tom SM, Fox CR, Trepel C, Poldrack RA (2007) The neural basis of loss aversion in decision-making under risk. Science. 315(5811):515–518

Trivedi MH, Rush AJ, Wisniewski SR, Nierenberg AA, Warden D, Ritz L, Norquist G, Howland RH, Lebowitz B, McGrath PJ, Shores-Wilson K, Biggs MM, Balasubramani GK, Fava M (2006) Evaluation of outcomes with citalopram for depression using measurement-based care in STAR*D: implications for clinical practice. Am J Psychiatry. 163(1):28–40

Tweedie DJ, Burke MD (1987) Metabolism of the beta-carbolines, harmine and harmol, by liver microsomes from phenobarbitone- or 3-methylcholanthrene-treated mice. Identification and quantitation of two novel harmine metabolites. Drug Metab Dispos 15(1):74–81

Tyrer AE, Levitan RD, Houle S, Wilson AA, Nobrega JN, Meyer JH (2016a) Increased Seasonal Variation in Serotonin Transporter Binding in Seasonal Affective Disorder. Neuropsychopharmacology 41(10):2447–2454

Tyrer AE, Levitan RD, Houle S, Wilson AA, Nobrega JN, Rusjan PM, Meyer JH (2016b) Serotonin transporter binding is reduced in seasonal affective disorder following light therapy. Acta Psychiatr Scand 134(5):410–419

Urban NB, Girgis RR, Talbot PS, Kegeles LS, Xu X, Frankle WG, Hart CL, Slifstein M, Abi-Dargham A, Laruelle M (2012) Sustained recreational use of ecstasy is associated with altered pre and postsynaptic markers of serotonin transmission in neocortical areas: a PET study with [(1)(1)C]DASB and [(1)(1)C]MDL 100907. Neuropsychopharmacology 37(6):1465–1473

Vitalis T, Cases O, Callebert J, Launay JM, Price DJ, Seif I, Gaspar P (1998) Effects of monoamine oxidase A inhibition on barrel formation in the mouse somatosensory cortex: determination of a sensitive developmental period. J Comp Neurol. 393(2):169–184

Weissman MM, Bland RC, Canino GJ, Greenwald S, Hwu HG, Lee CK, Newman SC, Oakley-Browne MA, Rubio-Stipec M, Wickramaratne PJ et al (1994) The cross national epidemiology of obsessive compulsive disorder. The Cross National Collaborative Group. J Clin Psychiatry 55(Suppl):5–10

Wilson A, Schmidt M, Ginovart N, Meyer J, Houle S (2000) Novel radiotracers for imaging the serotonin transporter by positron emission tomography: synthesis, radiosynthesis, in vitro and ex vivo evaluation of [11C]-labelled 2-(Phenylthio) araalkylamines. J Med Chem. 43(16):3103–3110

Wilson AA, Ginovart N, Hussey D, Meyer J, Houle S (2002) In vitro and in vivo characterisation of [11C]-DASB: a probe for in vivo measurements of the serotonin transporter by positron emission tomography. Nucl Med Biol. 29(5):509–515

Wilson A, Meyer J, Garcia A, Singh K, Hussey D, Houle S, Ginovart N (2003) Determination of the arterial input function of the MAO-A inhibitor [11C] harmine in human subjects. Neuroreceptor Mapping (abstract).

World_Health_Organization (2008) The Global Burden of Disease: 2004 Update. Department of Health Statistics and Informatics, Information Evidence and Research Cluster, WHO, Switzerland

Youdim MB, Edmondson D, Tipton KF (2006) The therapeutic potential of monoamine oxidase inhibitors. Nat Rev Neurosci 7(4):295–309

Yu A, Yang J, Pawlyk AC, Tejani-Butt SM (1995) Acute depletion of serotonin down-regulates serotonin transporter mRNA in raphe neurons. Brain Res. 688(1-2):209–212

Zanotti-Fregonara P, Leroy C, Roumenov D, Trichard C, Martinot JL, Bottlaender M (2013) Kinetic analysis of [11C]befloxatone in the human brain, a selective radioligand to image monoamine oxidase A. EJNMMI Res 3(1):78

Zanotti-Fregonara P, Leroy C, Rizzo G, Roumenov D, Trichard C, Martinot JL, Bottlaender M (2014) Imaging of monoamine oxidase-A in the human brain with [11C]befloxatone: quantification strategies and correlation with mRNA transcription maps. Nucl Med Commun 35(12):1254–1261

Zhou FC, Tao-Cheng JH, Segu L, Patel T, Wang Y (1998) Serotonin transporters are located on the axons beyond the synaptic junctions: anatomical and functional evidence. Brain Res. 805(1-2):241–254

PET Imaging of Sigma$_1$ Receptors

27

Jun Toyohara, Peter Brust, Hongmei Jia, Muneyuki Sakata, and Kiichi Ishiwata

Contents

J. Toyohara (✉) · M. Sakata · K. Ishiwata
Research Team for Neuroimaging, Tokyo Metropolitan Institute of Gerontology,
Tokyo, Japan
e-mail: toyohara@pet.tmig.or.jp

P. Brust
Department of Neuroradiopharmaceuticals, Helmholtz Zentrum Dresden-Rossendorf,
Leipzig, Germany
e-mail: p.brust@hzdr.de

H. Jia
Key Laboratory of Radiopharmaceuticals, Ministry of Education, College of Chemistry,
Beijing Normal University, Beijing, China
e-mail: hmjia@bnu.edu.cn

Abstract

Sigma receptors are classified into sigma$_1$ and sigma$_2$ subtypes. Sigma$_1$ receptors are widely distributed in the central nervous system (CNS) and in peripheral tissues. Sigma$_1$ receptors play a role in a variety of human CNS diseases, including mood disorders, stroke, neurodegenerative disease and drug addiction. Therefore, there is a great deal of interest in imaging of sigma$_1$ receptors in the living human brain. In contrast, sigma$_2$ receptors have been the focus of tumour imaging studies. A number of radioligands have been developed for imaging of sigma$_1$ receptors in the human brain, and a few, including [^{11}C]SA4503 and (*S*)-(−)-[^{18}F]fluspidine, have been used in clinical studies. Sigma$_1$ receptors are distributed throughout the grey matter of the human brain. A widespread decrease in [^{11}C]SA4503 binding in patients with Alzheimer's disease and a significant decrease in binding on the more affected side of the anterior putamen in patients with Parkinson's disease have been reported. Receptor occupancy studies with [^{11}C]SA4503-PET have shown that some antidepressants and antipsychotics have an affinity for sigma$_1$ receptors in the human brain in addition to their main targets. Recently, it has been reported that the binding of (*S*)-(−)-[^{18}F]fluspidine is increased in patients with untreated major depressive disorder.

Abbreviations

3-PPP	(+)-3-(3-Hydroxyphenyl)-*N*-(1-propyl)piperidine
AChE	Acetylcholinesterase
AD	Alzheimer's disease
BD-1047	*N′*-[2-(3,4-dichlorophenyl)ethyl]-*N*,*N*,*N′*-trimethylethane-1,2-diamine
BDNF	Brain-derived neurotrophic factor
BMY14802 (BMS181100)	1-(4-Fluorophenyl)-4-[4-(5-fluoropyrimidin-2-yl)piperazin-1-yl]butan-1-ol
BP$_{ND}$	Specific binding potential relative to non-displaceable binding
CFT	(1*R*,2*S*,3*S*,5*S*)-3-(4-Fluorophenyl)-8-methyl-8-azabicyclo[3.2.1]octane-2-carboxylate
CNS	Central nervous system
Cutamesine	SA4503 1-[2-(3,4-dimethoxyphenyl)ethyl]-4-(3-phenylpropyl)piperazine
DHEA	Dehydroepiandrosterone
Donepezil	(*RS*)-2-[(1-Benzyl-4-piperidyl)methyl]-5,6-dimethoxy-2,3-dihydroinden-1-one
DTG	1,3-Di(2-tolyl)guanidine
DuP734	2-[1-(Cyclopropylmethyl)piperidin-4-yl]-1-(4-fluorophenyl)ethanonehydrobromide
EBP	Emopamil binding protein (sterol Δ8–Δ7 isomerase)

Eliprodil (SL82.0715)	1-(4-Chlorophenyl)-2-[4-[(4-fluorophenyl) methyl]piperidin-1-yl]ethanol
ER	Endoplasmic reticulum
FDG	2-Deoxy-2-fluoro-D-glucose
Fluspidine	1′-Benzyl-3-(2-fluoroethyl)-3H-spiro[isobenzofuran-1,4′-piperidine]
Fluvoxiamine	(E)-5-Methoxy-1-[4-(trifluoromethyl)phenyl]pentan-1-one O-2-aminoethyl oxime
FM-SA4503	1-[2-(4-Fluoromethoxy-3-methoxyphenyl)ethyl]-4-(3-phenylpropyl)piperazine
f_p	Plasma-free fraction
FPS	1-(3-Fluoropropyl)-4-[(4-cyanophenoxy)methyl]piperidine
Haloperidol	4-[4-(4-Chlorophenyl)-4-hydroxy-1-piperidyl]-1-(4-fluorophenyl)-butan-1-one
HD	Huntington's disease
Ifenprodil	4-[2-(4-Benzylpiperidin-1-yl)-1-hydroxypropyl]phenol
Igmesine (JO1,784)	(E)-N-(Cyclopropylmethyl)-N-ethyl-3,6-diphenylhex-5-en-3-amine
LID	Levodopa-induced dyskinesia
MDD	Major depressive disorder
mI-SA4503	1-[2-(3,4-Dimethoxyphenyl)ethyl]-4-[3-(3-iodophenyl)propyl]piperazine
NE-100	4-[2-(Dipropylamino)ethyl]-2-(2-phenylethoxy)anisole
Nemonapride (YM-09151-2)	N-(1-benzyl-2-methylpyrrolidin-3-yl)-5-chloro-2-methoxy-4-(methylamino)benzamide
NGF	Nerve growth factor
NMDA	N-methyl-D-aspartate
oI-SA4503	1-[2-(3,4-Dimethoxyphenyl)ethyl]-4-[3-(2-iodophenyl)propyl]piperazine
Panamesine	(5S)-5-[[4-(1,3-Benzodioxol-5-yl)-4-hydroxypiperidin-1-yl]methyl]-3-(4-methoxyphenyl)-1,3-oxazolidin-2-one
Paroxetine	(3S,4R)-3-[(2H-1,3-Benzodioxol-5-yloxy)methyl]-4-(4-fluorophenyl)piperidine
PD	Parkinson's disease
Pentazocine (EMD57445)	(2RS,6RS,11RS)-6,11-Dimethyl-3-(3-methylbut-2-en-1-yl)-1,2,3,4,5,6-hexahydro-2,6-methano-3-benzazocin-8-ol
PET	Positron emission tomography
Physostigmine	(3aR,8aS)-1,3a,8-Trimethyl-1H,2H,3H,3aH,8H,8aH- pyrrolo [2,3-b] indol-5-yl N-methylcarbamate
PPBP	4-Phenyl-1-(4-phenylbutyl)piperidine
Raclopride	3,5-Dichloro-N-{[(2S)-1-ethylpyrrolidin-2-yl]methyl}-2-hydroxy-6-methoxybenzamide
rCBF	Regional cerebral blood flow

Rimcazole (BW234U)	9-{3-[(3*R*,5*S*)-3,5-Dimethylpiperazin-1-yl]propyl}-9*H*-carbazole
SFE	WLS1.002 1-(2-fluoroethyl)-4-[(4-cyanophenoxy) methyl]piperidine
SKF 10,047 (N-allylnormetazocine)	(2*R*,6*R*,11*R*)-6,11-dimethyl-3-prop-2-en-1-yl-1,2,3,4,5,6-hexahydro-2,6-methano-3-benzazocin-8-ol
SPECT	Single-photon emission computed tomography
Spiperone	8-[4-(4-Fluorophenyl)-4-oxo-butyl]-1-phenyl-1,3,8-triazaspiro[4.5]decan-4-one
SSRI	Selective serotonin reuptake inhibitor
SUV	Standardised uptake value
TAC	Time-activity curve
Tamoxifen	(*Z*)-2-[4-(1,2-Diphenylbut-1-enyl)phenoxy]-*N*,*N*-dimethylethanamine
TPCNE	1(*Trans*-iodopropen-2-yl)-4-[(4-cyanophenoxy) methyl]piperidine
Trifluoperazine	10-[3-(4-methylpiperazin-1-yl)propyl]-2-(trifluoromethyl)-10*H*-phenothiazine
VAChT	Vesicular acetylcholine transporter
V_T	Total volume of distribution

27.1   Introduction

Sigma receptors were initially categorised as a subtype of opioid receptors, because the effects of a prototypical opioid agonist, SKF10,047 (*N*-allylnormetazocine), were independent from those of other opioid receptor agonists (Martin et al. 1976). Later, it was determined that sigma receptors are unique binding sites that are different from those of other opioid receptors and at least two subtypes (sigma$_1$ and sigma$_2$) were classified based on pharmacological criteria (Bowen et al. 1989). These subtypes display different tissue distributions and distinct physiological and pharmacological profiles in the central and peripheral nervous systems (Hashimoto and Ishiwata 2006). Sigma$_1$ receptors are widely distributed in the central nervous system (CNS) and in peripheral tissues (Hayashi and Su 2004). Peripherally, both subtypes are overexpressed in rapidly proliferating cells, such as those in various types of cancer, and the functional roles of the receptors, especially sigma$_2$, have also been the focus of tumour imaging studies (van Waarde et al. 2010). In the CNS, the sigma$_1$ receptor may function as a modulator of signal transduction through glutamatergic transmitter systems mediated by the *N*-methyl-D-aspartate (NMDA) receptors. Sigma$_1$ agonists show anti-amnesic and neuroprotective effects (van

Waarde et al. 2011), and for that reason, they are attractive novel targets for the treatment of neuropsychiatric diseases (schizophrenia, depression and cognition) and neurodegenerative diseases like ischemic stroke and Alzheimer's disease (AD).

The sigma$_1$ receptor was successfully cloned and characterised as a protein of 233 amino acids with a molecular weight of 25.3 kDa (Hanner et al. 1996). Although the sigma$_1$ receptor is not homologous to any mammalian protein, it shows 30% overlap with yeast Δ8–Δ7 sterol isomerase, also known as emopamil binding protein (EBP). Only recently, the crystal structure of the human sigma$_1$ receptor was elucidated and found to possess a trimeric architecture with only a single transmembrane domain in each protomer (Schmidt et al. 2016).

Sigma$_1$ receptors have been shown to act as ligand-regulated molecular chaperones primarily situated on the mitochondria-associated membrane of the endoplasmic reticulum (ER) (Hayashi and Su 2007). Most recently, the sigma$_2$ receptor was identified as ER-resident transmembrane protein 97 (Alon et al. 2017), which is a sterol response element binding protein target gene.

Endogenous ligands for the sigma$_1$ and sigma$_2$ receptors have not been fully identified, and those for the sigma$_1$ receptor were first proposed to be neurosteroids, including pregnenolone sulphate and progesterone (Su et al. 1988). Recently, the endogenous hallucinogenic trace amine *N,N*-dimethyltryptamine was found to be a potent endogenous ligand for the sigma$_1$ receptor (Fontanila et al. 2009).

In this chapter, investigations related to brain imaging of sigma$_1$ receptors and their role in neurology and psychiatric diseases are reviewed.

27.2 Brain Imaging of Sigma Receptors

27.2.1 Post-mortem Studies

Several post-mortem studies on the distribution and densities of sigma receptors in the human brain have been reported. Weissman et al. (1988) reported that the densities of sigma sites in the brain were highest in the cerebellum, nucleus accumbens and cerebral cortex, using a membrane binding assay with [³H]haloperidol in the presence of spiperone. The binding is moderate in the caudate nucleus and substantia nigra and low in the thalamic and pontine nuclei. Autoradiographic measurements using [³H]DTG showed slightly different results, i.e. high prevalence in the substantia nigra pars compacta and cerebellum with moderate prevalence in the hippocampal dentate granular cells, the striatum and the pineal and pituitary glands (Jansen et al. 1991). In the neocortex, binding was high in the laminae II–IVA and low in the narrow band (5% layer) of midzone. Subtype-selective regional distribution in the brain has been reported in non-human primates but not in humans. Mash and Zabetian (1992) quantified the binding of [³H]3-PPP (sigma$_1$ K_i = 5.1 nM, sigma$_2$/sigma$_1$ = 87; (Walker et al. 1990)) within 36 brain regions in rhesus macaque monkeys (*Macaca mulatta*) and demonstrated marked enrichment of sigma binding

sites over the paralimbic belt cortices, medial and central nuclei of the amygdala and hippocampal formation. Moderate sigma receptor densities were observed in the caudate and putamen.

Several studies reported on the effects of age on sigma receptor expression. Kornhuber et al. (1996) reported an 8.5% decrease per decade in (+)-[^{3}H]pentazocine (sigma$_1$ K_i = 2.0 nM, sigma$_2$/sigma$_1$ = 228; (Walker et al. 1990)) in the frontal cortex. Moreover, altered densities of sigma receptors were observed in patients with schizophrenia and AD (see also Sects. 27.3.1 and 27.3.4).

Most post-mortem examinations of the human brain reported to date measured both sigma$_1$ and sigma$_2$ binding sites using non-selective radioligands. One exception is a previous study of aging effects, which used the sigma$_1$ selective ligand (+)-[^{3}H]pentazocine (Kornhuber et al. 1996).

27.2.2 Radioligands for Imaging of Sigma Receptors

Since the early 1990s, different classes of compounds, such as benzomorphans, phenyl piperidines, *N,N*-disubstituted pyrrolidinylethylamines and *N,N′*-disubstituted piperazines, have been evaluated as radioligands for use in the imaging of sigma receptors by positron emission tomography (PET) and single-photon emission computed tomography (SPECT). A comprehensive overview of the development of radioligands for the different sigma receptor subtypes has been presented in a number of recent reviews (Hashimoto and Ishiwata 2006; Brust et al. 2014a, b; Jia et al. 2019; Mach and Wheeler 2009). The chemical structures of radioligands used clinically for brain imaging of sigma receptors are summarised in Fig. 27.1.

The first radioligand used for imaging sigma$_1$ receptors in the CNS was [^{11}C]SA4503 (Fig. 27.1), which was developed by Ishiwata and co-workers (Ishii et al. 2001). SA4503 has high and selective affinity for the sigma$_1$ receptor (sigma$_1$ IC$_{50}$ = 17.4 nM, sigma$_2$/sigma$_1$ = 103) but low affinity for 36 neuroreceptors, ion channels and second messenger systems (Matsuno et al. 1996; Matsuno and Mita 1998). Later, four groups reinvestigated the binding properties of SA4503 and reported slightly different affinities and selectivities: sigma$_1$ K_i = 3.3–4.6 nM, sigma$_2$/sigma$_1$ = 13.3–55.0 (Hirata et al. 2006; Lever et al. 2006; Shiba et al. 2006; Wang et al. 2014). Density (B_{max}) of the sigma receptor was estimated to be 30–600 fmol/mg protein (approximately 3–60 nM) in the human brain (Weissman et al. 1988; Kornhuber et al. 1996; Jansen et al. 1993). Theoretically, radioligands with nanomolar affinity (1–6 nM) will be suitable for sigma receptor imaging. From this viewpoint, SA4503 has a suitable range of affinity for quantitative in vivo imaging. In human studies, the use of [^{11}C]SA4503-PET allowed successful visualisation of the sigma$_1$ receptor in the brain as described in Sect. 27.2.3.1, but the affinity of [^{11}C]SA4503 was slightly high (i.e. the rate of dissociation of the ligand somewhat low) for measurement of the sigma$_1$ receptor on the time scale of the PET scan using a ^{11}C-labelled tracer with a short half-life (20.4 min) (Sakata et al. 2008).

The second PET ligand that was applied in human studies was [^{18}F]FPS, which was developed by Waterhouse and co-workers (Collier et al. 1996). [^{18}F]FPS was
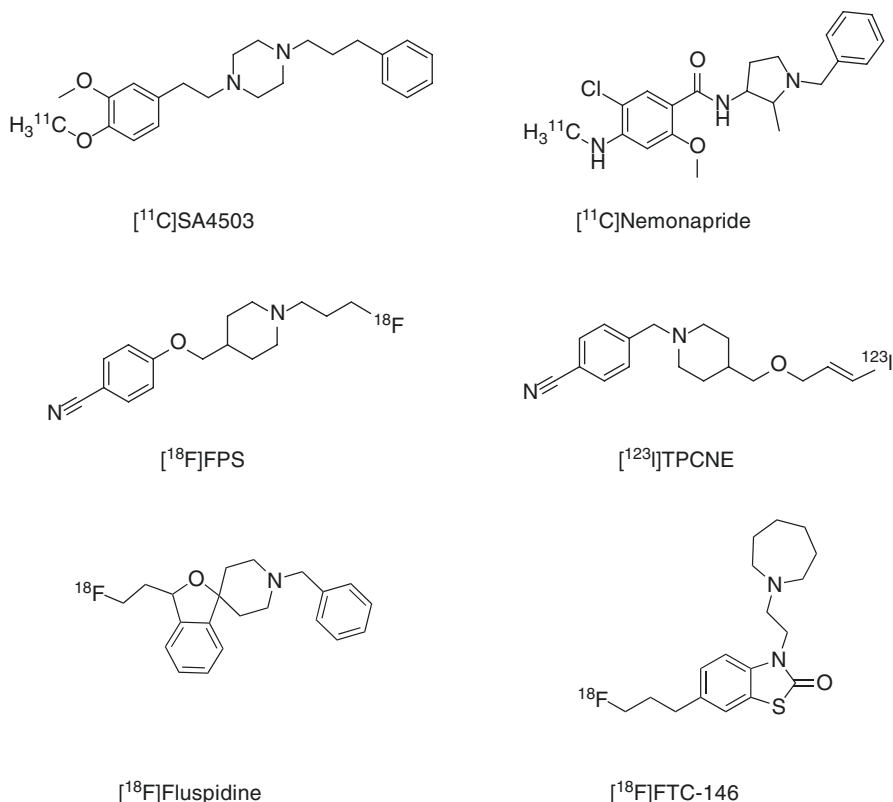
Fig. 27.1 Chemical structures of clinically used sigma ligands for brain imaging

not cleared fast enough from the CNS to reach transient equilibrium by 4 h after administration in healthy volunteers due to its high affinity for the sigma₁ receptor ($K_d = 0.5$ nM) (Waterhouse et al. 2004; Zhao et al. 2005). In an effort to improve the CNS clearance for in vivo PET studies, Zhao et al. (2005) synthesised and evaluated [¹⁸F]SFE (previously designated as [¹⁸F]WLS1.002), a fluoroethyl derivative of [¹⁸F]FPS that exhibits a lower affinity for sigma₁ receptors ($K_d = 5$ nM). A preclinical study showed that [¹⁸F]SFE exhibits very similar regional brain distribution and specific binding in the rodent brain compared to [¹⁸F]FPS. As expected from its lower affinity, [¹⁸F]SFE is cleared much faster from the brain than [¹⁸F]FPS (Waterhouse et al. 2006a). Preclinical toxicity and dosimetry studies of [¹⁸F]SFE suggested that [¹⁸F]SFE will be safe for use in human PET studies (Waterhouse et al. 2006b). However, no further clinical imaging studies have been reported to date.

Carbon-11-labelled nemonapride, which was originally developed as a dopamine D₂-like receptor radioligand (Hatano et al. 1989; Hatazawa et al. 1991), binds not only to D₂-like receptors in the striatum but also to sigma receptors in other regions, such as the cerebral cortex and cerebellum (Ishiwata and Senda 1999), as it

has rather high affinities for both receptors. Nimura et al. (2004) applied [^{11}C]nemonapride to imaging of sigma receptors in the cerebellum of patients suffering from levodopa-induced dyskinesia (LID), a brain area devoid of D$_2$-like receptors.

More recently, Moussa and co-workers developed a series of *N*-(2-benzofuranylmethyl)-*N′*- (alkoxybenzyl)piperazines as selective sigma$_1$ receptor ligands. They found high-affinity sigma$_1$ selective ligands, such as the 4-[^{11}C]methoxy (sigma$_1$ K_i = 2.7 nM, sigma$_2$/sigma$_1$ = 38) and 4-(2-[^{18}F]fluoroethoxy) derivatives (sigma$_1$ K_i = 2.6, sigma$_2$/sigma$_1$ = 187) (Moussa et al. 2010, 2011). These compounds showed good brain uptake and specific binding to sigma$_1$ receptors in the *Papio hamadryas* (baboon) brain. However, these compounds showed irreversible binding profiles during the scan periods because of their high affinities.

The sigma$_1$ receptor-selective ligand [^{123}I]TPCNE (K_i = 0.67 nM, sigma$_2$/sigma$_1$ = 58) was used in a human SPECT study (Stone et al. 2006; Waterhouse et al. 1997). High brain uptake was reduced by haloperidol pretreatment, suggesting the specific binding of [^{123}I]TPCNE to sigma$_1$ receptors. However, the time-activity data were best described by an irreversible model. Thus, no further studies for this ligand have been conducted. Radioiodinated analogues of SA4503 were also prepared for SPECT, i.e. *o*I-SA4503 and *m*I-SA4503 (designated as *o*-BON and *m*-BON, respectively) (Hirata et al. 2006). The affinity and selectivity of *m*I-SA4503 for the sigma$_1$ receptor (sigma$_1$ K_i = 8.9 nM, sigma$_2$/sigma$_1$ = 6.1) were approximately half those of SA4503. Although Hirata et al. (2008) used these compounds in a tumour study on rodents, no clinical studies have been conducted to date.

A review of the clinical trials for a few sigma$_1$ receptor radioligands showed that ligands with affinities (K_i) for the sigma$_1$ receptor of 1–10 nM may be preferable for human studies and that [^{18}F]FM-SA4503 may be more suitable than [^{11}C]SA4503 (Kawamura et al. 2007). However, many sigma receptor ligands have affinity for the vesicular acetylcholine transporter (VAChT) (Efange 2000) and the EBP (Berardi et al. 2001). SA4503 was reported to show affinities for VAChT (K_i = 50 nM, (Shiba et al. 2006)) and EBP (K_i = 1.7 nM, (Berardi et al. 2001)), but [^{11}C]SA4503 did not seem to bind to VAChT in the rat brain in vivo (Ishiwata et al. 2006a). Toyohara et al. (2012) confirmed that the brain uptake of [^{11}C]SA4503 in mice was not blocked by high-affinity EBP blockers tamoxifen (EBP K_i = 2.8 nM, sigma$_1$/EBP = 12) and trifluoperazine (EBP K_i = 3.9 nM, sigma$_1$/EBP = 52).

Selectivity toward VAChT and EBP sites should be taken into consideration when designing new selective ligands, although the relationship between the sigma receptor and EBP has not been clearly elucidated (Brust et al. 2014a, b).

A recently developed innovative compound class of spirocyclic benzofuran derivatives showed weak affinity for VAChT and EBP (Fischer et al. 2011). Wünsch and co-workers started the development of spirocyclic sigma receptor ligands with the 2-benzofuran (Fig. 27.2) (Maier and Wünsch 2002a, b). A very high affinity of **1** to sigma$_1$ receptors (K_i = 1.1 nM) was found while the sigma$_2$ affinity (K_i = 1280 nM) is very low, providing an excellent 1100-fold selectivity for sigma$_1$ receptors over the sigma$_2$ subtype. A screening against more than 60 other receptors, ion channels, transporters and enzymes revealed that there are no cross reactions with other

targets including the hERG channel (Wiese et al. 2009). This is a voltage-gated K$^+$ channel with high expression in the heart, by which potentially new drugs can lead to life-threatening arrhythmia. Generally, during drug development, hERG channel interactions are investigated very early to avoid those problems. Notably, the pharmacophores of sigma$_1$ receptor ligands and hERG channel blockers are very similar (Recanatini et al. 2005). In the mouse capsaicin assay, **1** showed high analgesic activity, which is in the same range as the analgesic activity of S1RA (E-52862), a prototypical benzomorphan sigma$_1$ receptor antagonist which was in Phase II clinical trials for pain (EudraCT Number: 2012-000398-21). Therefore, **1** and fluspidine are regarded as sigma$_1$ receptor antagonists. Incubation with rat liver microsomes provided important information on metabolic transformations. The acetal functional group appeared to be rather sensitive (Wiese et al. 2009).

In order to remove the chemically and metabolically labile acetal functionality and to install a structural element, which allows the introduction of a fluorine atom for potential radiolabelling, the methoxy group of **1** was replaced by homologous fluoroalkyl residues (compounds **2–5** in Fig. 27.2). The homologous fluoroalkyl derivatives **2–5** show low nanomolar up to subnanomolar sigma$_1$ affinity (see Fig. 27.2). Moreover, all four homologs display very high subtype selectivity (Große Maestrup et al. 2009, 2011; Maisonial et al. 2011, 2012; Wiese et al. 2011). The ethyl derivative with the highest sigma$_1$ affinity ($K_i = 0.59$ nM), the highest subtype selectivity (1331-fold), the highest metabolic stability (91% radiotracer remaining in mouse plasma at 30 min p.i), the highest brain-to-plasma ratio and the highest target-to-nontarget ratio in the brain (4.7 at 45 in p.i.) was termed fluspidine and chosen for further preclinical evaluation.

Fig. 27.2 Development of fluorinated spirocyclic benzofuran starting from methoxy derivative **1**
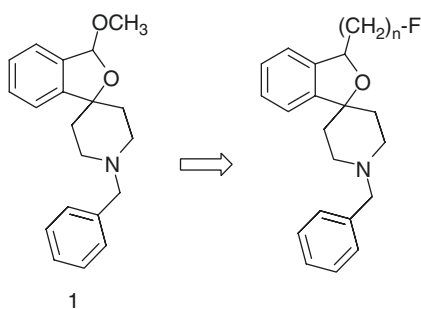
compd.	n	$K_i(\sigma_1)$ (nM)	$K_i(\sigma_2)$ (nM)	selectivity
2	1	0.74	550	743
3	2	0.59	785	1331
4	3	1.4	837	598
5	4	1.2	489	408

Since fluspidine is a chiral compound, enantiomerically pure (*R*)- and (*S*)-fluspidine were synthesized, and their sigma$_1$ affinities, determined in a competitive equilibration binding assay, were 0.57 nM and 2.3 nM, respectively (Holl et al. 2013). Notably, later kinetic analysis revealed an irreversible binding mode of (*R*)-fluspidine which prevented the precise determination of the equilibrium dissociation constant K_D, while for (*S*)-fluspidine, a K_D of 0.1 nM was estimated (Baum et al. 2017). Due to the high sigma$_1$ affinity of both fluspidine enantiomers (*R*)-**13** and (*S*)-**13**, the radiosynthesis was performed by nucleophilic substitution of the (*R*)- and (*S*)-tosylates with K[^{18}F]F complexed with the cryptand Kryptofix$^{(R)}$, and an automated procedure was developed for further preclinical evaluation (Maisonial-Besset et al. 2014). The uptake of (*S*)-(−)-[^{18}F]fluspidine in porcine brain measured with PET was strongly correlated with the uptake in mouse brain measured by ex vivo autoradiography. Furthermore, the PET studies revealed a strong inhibition by SA4503 (see Fig. 27.3).

Both enantiomers of [^{18}F]fluspidine displayed different kinetics in porcine brain (Brust et al. 2014a, b) (Fig. 27.3). Although the initial brain uptake was similar, the accumulation measured at the end of the study was about twofold higher for (*R*)-(+)-[^{18}F]fluspidine. Administration of SA4503 reduced the uptake almost equally for both radiotracers by ~65%. The higher affinity of (*R*)-(+)-[^{18}F]fluspidine found in vitro was clearly translated into higher BP_{ND} values in vivo; however, longer
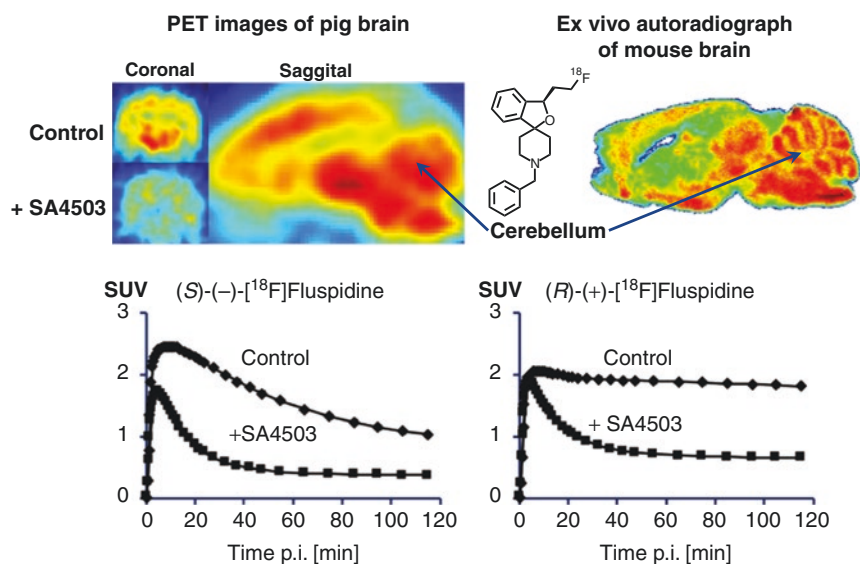
Fig. 27.3 Studies with the PET tracer [^{18}F]fluspidine ([^{18}F](*S*)-**13**): Top left: PET image of whole piglet brain and inhibition study with the sigma$_1$ ligand SA4503. Top right: ex vivo autoradiography of mouse brain; the region of the cerebellum (highest receptor density) is shown exemplarily. Bottom: kinetics of the uptake of (*S*)-(−)-[^{18}F]fluspidine (left) and (*R*)-(+)-[^{18}F]fluspidine in porcine brain without and with preinjection of SA4503 (modified according to Brust P, van den Hoff J, Steinbach J (2014) Development of ^{18}F-labelled radiotracers for neuroreceptor imaging with Positron Emission Tomography. Neurosci Bull 30:777–811)

equilibration periods require longer scanning times. The higher metabolic stability of (S)-(−)-[^{18}F]fluspidine results in a more reliable estimate of the metabolite-corrected plasma input function which is required for kinetic modelling of PET tracers for central sigma$_1$ receptors due to the lack of a receptor-free reference region. For measuring the sigma$_1$ receptor occupancy by either administered drugs or endogenous ligands, also the lower-affine and thus faster dissociating (S)-(−)-[^{18}F]fluspidine seems to be more appropriate due to a higher susceptibility to the competitive compounds (Brust et al. 2014a, b).

Recently, the different brain kinetics of (R)-(+)-[^{18}F]fluspidine and (S)-(−)-[^{18}F]fluspidine was confirmed in monkeys (Baum et al. 2017). SA4503 at the dose of 0.5 mg/kg blocked about 85% of the brain uptake of (S)-(−)-[^{18}F]fluspidine supporting the conclusion that this radiotracer has the kinetic and imaging properties for the investigation of sigma$_1$ receptors in the human brain with PET.

Accordingly, the preclinical dosimetry of (S)-(−)-[^{18}F]fluspidine was investigated based on in vivo and ex vivo data from CD-1 mice. The effective dose (ED) estimations for human application were 14.8 μSv/MBq and 17.3 μSv/MBq, respectively (Kranz et al. 2016). Since toxicity results for (S)-(−)-fluspidine revealed a no observed effect level of 620 μg/kg, more than 10.000-fold above the injected radiotracer amounts, a dosimetry study in human was performed. An ED of 22.1 μSv/MBq was estimated which is similar to that of [^{18}F]FDG (Kranz et al. 2016).

The preclinical studies discussed above provided the scientific data for two ongoing clinical studies using (S)-(−)-[^{18}F]fluspidine in patients with major depressive disorder (MDD) and Huntington's disease (HD) (EudraCT Numbers: 2014-005427-27, 2016-001757-41).

To further develop PET radioligands from the spirocyclic piperidine series of compounds with suitable properties, Jia and co-workers took another approach, i.e. structural modifications on the N-benzyl moiety, while eliminating the substituent on the spirocyclic benzofuran section. Moreover, they replaced the aromatic ring in the N-benzyl moiety with a pyridine group to further reduce the lipophilicity of this series of derivatives (Li et al. 2013). Derivatives **6** and **7** (Fig. 27.4) possessed high sigma$_1$ receptor affinity (subnanomolar and low nanomolar affinity for compounds **6** and **7**, respectively) and excellent sigma$_1$/sigma$_2$ subtype selectivity as well as high sigma$_1$/VAChT selectivity. The corresponding radiotracers [^{18}F]**6** and [^{18}F]**7** showed high initial brain uptakes, high accumulation of the radiotracer in brain areas known to express high levels of sigma$_1$ receptors and specific binding to sigma$_1$ receptors in vivo. Interestingly, the radiotracer [^{18}F]**7** with lower lipophilicity demonstrated higher specificity than [^{18}F]**6**.

Later, four ^{18}F-labelled radioligands including (S)-(−)- and (R)-(+)-[^{18}F]fluspidine, [^{18}F]**6** and [^{18}F]**7** from the same spirocyclic piperidine scaffold were evaluated in non-human primates (Baum et al. 2017). (R)-(+)-[^{18}F]fluspidine and radioligand [^{18}F]**6** with subnanomolar affinity for sigma$_1$ receptors displayed irreversible binding kinetics in the rhesus monkey brain, with no appreciable washout during the 4 h scan sessions. On the other hand, (S)-(−)-[^{18}F]fluspidine and [^{18}F]**7** were found to display fast and reversible kinetics in the monkey brain with good uptake and high specific binding signals. Both are judged to be promising radioligands to image

Fig. 27.4 Novel *para*-aromatic substituted spirocyclic piperidine and piperazine compounds for imaging sigma₁ receptors in the brain
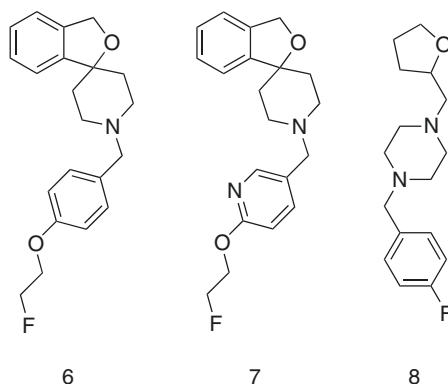
compd.	$K_i(\sigma_1)$ (nM)	$K_i(\sigma_2)$ (nM)	selectivity	Log D
6	0.79	277	351	2.55
7	2.3	327	142	2.50
8	3.2	168	53	0.76

sigma₁ receptors in humans. In rhesus monkeys, [^{18}F]**7** has a tenfold higher plasma-free fraction (f_p), threefold higher BP_{ND} and greater V_T than (S)-(−)-[^{18}F]fluspidine.

Most recently, to develop novel radioligands with high specificity, Jia and co-workers eliminated the aromatic ring in [^{18}F]**6** and got a selective sigma₁ ligand as a tumour imaging agent, 8-(4-(2-[^{18}F]fluoroethoxy)benzyl)-1,4-dioxa-8-azaspiro[4.5]decane (Xie et al. 2015). This radiotracer showed twofold lower lipophilicity than lead compound [^{18}F]**6**. Based on Glennon's pharmacophore model for sigma₁ receptor ligands, the aromatic ring is required as the primary hydrophobic region (Glennon 2005). However, the above results demonstrated that the 'primary hydrophobic region' in the Glennon's pharmacophore model is more flexible. Similar to the design concept of the above tumour radiotracer with low lipophilicity, Jia and co-workers designed the radiotracer 1-(4-[^{18}F]fluorobenzyl)-4-[(tetrahydrofuran-2-yl)methyl]piperidine ([^{18}F]**8**) (Fig. 27.4) constructed from a novel scaffold (He et al. 2017). Interestingly, compound **8** possessed low nanomolar affinity for sigma₁ receptors and high subtype selectivity (K_i = 3.2 nM, sigma₂/sigma₁ = 52). Moreover, this compound displayed negligible affinity for VAChT, adenosine A$_{2A}$, adrenergic α₂, cannabinoid CB₁, dopamine D₁ and D₂, γ-aminobutyric acid A, NMDA, melatonin MT₁ and MT₂ and serotonin 5-HT₁ receptors. The corresponding radiotracer [^{18}F]**8** showed high stability in the mouse brain, i.e. over 95% of the radioactivity signal represented the intact tracer [^{18}F]**8** at 1 h postinjection. Studies in rodents (He et al. 2017) and cynomolgus monkeys (Jia et al. 2018) indicated that this radioligand displayed fast and high brain uptake, suitable kinetics

and high specific binding to sigma$_1$ receptors. Since this tracer possessed low lipophilicity, it showed highest f_p among the sigma$_1$ ligands evaluated to date. Most importantly, this radiotracer displayed higher specific signals (BP_{ND}) than (S)-(−)-[^{18}F]fluspidine. Hence, [^{18}F]**8** warrants further evaluation in humans.

27.2.3   PET Imaging of the Sigma₁ Receptors in the Human Brain

Five radioligands, [^{11}C]SA4503 (Ishii et al. 2001; Sakata et al. 2007), [^{18}F]FPS (Waterhouse et al. 2004), [^{123}I]TPCNE (Stone et al. 2006), (S)-(−)-[^{18}F]fluspidine (Kranz et al. 2016; Becker et al. 2018; Meyer et al. 2018) and [^{18}F]FTC-146 (Hjornevik et al. 2017; Shen et al. 2017), were used for in vivo investigations of the density of the sigma$_1$ receptor in the human brain by PET or SPECT; however, [^{18}F]FPS and [^{123}I]TPCNE showed irreversible binding profiles during the scan periods because of their high affinities. Therefore, no further clinical studies were conducted with those radiotracers.

27.2.3.1   Healthy Subjects

[^{11}C]SA4503 was distributed in all grey matter regions in the human brain (Fig. 27.5). The distribution patterns did not differ between the early and late phases and were similar to those of regional cerebral blood flow (rCBF). The regional tissue time-activity curves (TACs) of [^{11}C]SA4503 in the brain showed a gradual increase in radioactivity over 30 min and then reached a plateau, whereas the radioactivity in plasma decreased very rapidly (Fig. 27.6). These findings suggest that the regional
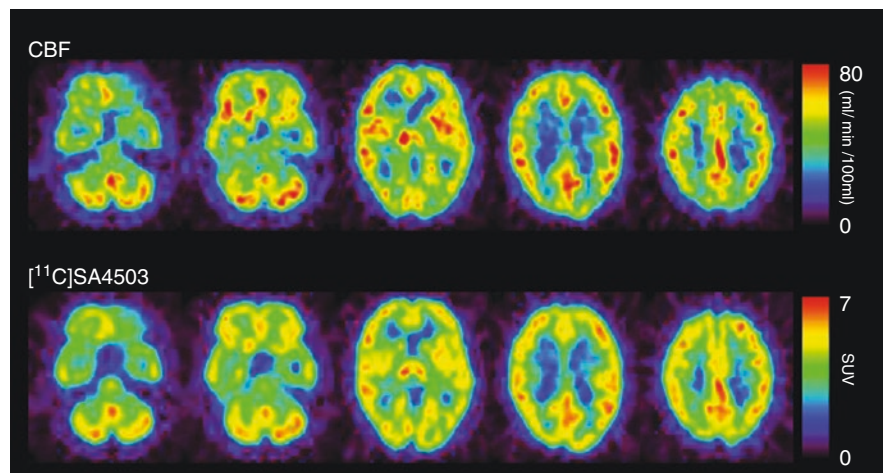
Fig. 27.5   rCBF and sigma$_1$ receptors in the brain of a healthy human subject. rCBF (upper): rCBF was measured using PET and [^{15}O]H$_2$O and calculated as ml/min/100 ml tissue. [^{11}C]SA4503 (lower): static images were acquired 40–60 min after injection of [^{11}C]SA4503 and expressed as standardised uptake value (SUV: regional activity divided by administered dose per body weight)

Fig. 27.6 TACs in the
healthy human brain and
plasma after intravenous
injection of [^{11}C]SA4503
under baseline and
haloperidol-loading (3 mg)
conditions. Decay-
corrected radioactivity was
expressed as
SUV. Haloperidol was
administered orally 18 h
before injection of
[^{11}C]SA4503
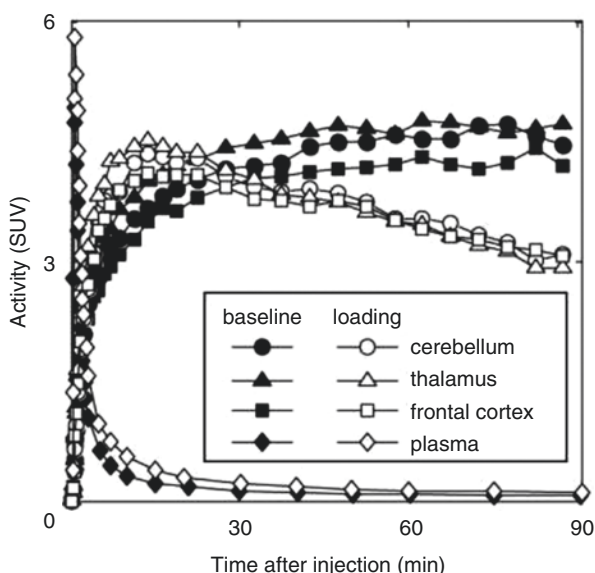
distributions of [^{11}C]SA4503 could depend on the blood flow or permeability rather than receptor density because of its slow dissociation kinetics.

Preclinical studies confirmed age-dependent increases in sigma$_1$ receptors in the brains of non-human primates (Kawamura et al. 2003). These results contrast strikingly with the age-dependent decreases in several other receptors in the primate brain. For investigation of the neuroprotective functions of sigma$_1$ receptors, a PET study with [^{11}C]SA4503 for evaluation of the aging process in the human brain would be of great interest.

27.2.3.2 Kinetic Analysis

In the traditional PET pharmacokinetics analysis for neuroreceptor radioligands, the ratio of k_3 (association constant rate between the free plus nonspecifically and specifically bound compartments) over k_4 (dissociation constant rate between the free plus nonspecifically and specifically bound compartments) in a two-tissue compartmental model (Mintun et al. 1984) is often used as the binding potential, which is currently defined as the specific binding potential relative to non-displaceable binding (BP_{ND}) (Innis et al. 2007). As sigma$_1$ receptors are distributed throughout all brain regions, no suitable reference region with negligible specific binding is available. Therefore, in the kinetic analysis of [^{11}C]SA4503 and (S)-(−)-[^{18}F]fluspidine, arterial blood sampling measurements corrected by metabolite analysis are essential for obtaining the input function. In general, however, the variability of BP_{ND} estimated from direct compartmental analysis without any constraints is clearly larger than that with indirect methods, such as a reference tissue model analysis (Vilkman et al. 2000). In the case of [^{11}C]SA4503, slow kinetics due to its slightly higher

affinity (Fig. 27.6) increased the variability of BP_{ND} in the time scale of the PET scan using a ^{11}C-labelled tracer with a short half-life (20.4 min). An alternative parameter for the evaluation of [^{11}C]SA4503 binding is the total volume of distribution (V_T) estimated by the linear graphical method (Logan et al. 1990), although V_T includes both specific and nonspecific binding (Kimura et al. 2007). The estimation of V_T ($K_1/k_2 \times (1 + k_3/k_4)$) in compartmental analysis tends to be more stable than that of BP_{ND}. Figure 27.7 shows representative V_T images of [^{11}C]SA4503 in a healthy brain. The binding of [^{11}C]SA4503 was high in the cerebellar cortex, moderate in the temporal and parietal cortices and low in the caudate and putamen (Sakata et al. 2007). These distribution patterns resemble the distribution patterns of radioligand binding in primate brains, where sigma receptors were noticed to be widely distributed with regionally different densities, using an in vitro binding assay and autoradiography (Weissman et al. 1988; Mash and Zabetian 1992; Shibuya et al. 1992).

An interaction between sigma$_1$ receptors and steroids has been established (Su et al. 1988; Collier et al. 2007). Currently, no information is available regarding the relationship between plasma hormone levels and [^{11}C]SA4503 binding in the living human brain. If the binding of [^{11}C]SA4503 is sensitive to competition by endogenous steroids, intra-subject variability in BP_{ND} of [^{11}C]SA4503 in women during the menstrual cycle and inter-subject variability in aged subjects, including postmenopausal subjects, may be found. Therefore, plasma steroid levels should be considered in PET studies of patients and healthy volunteers.
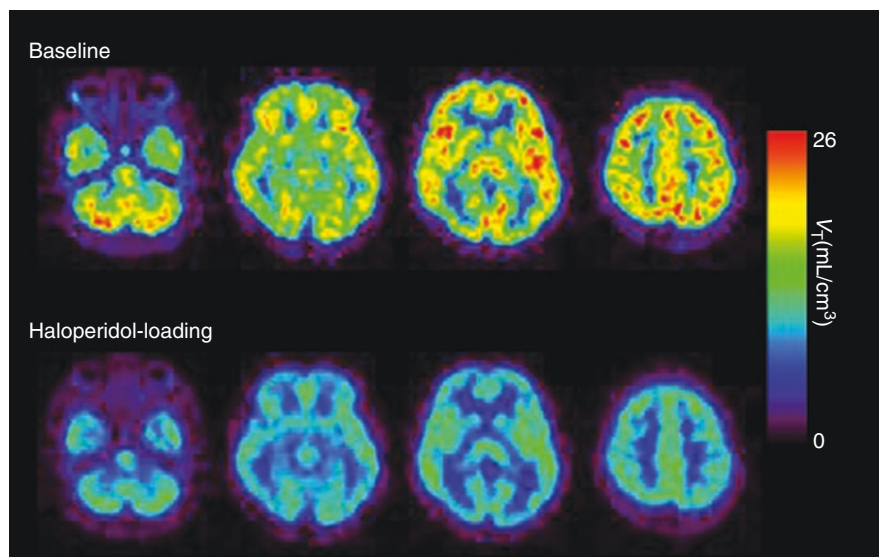

Fig. 27.7 V_T images of [^{11}C]SA4503 in the human brain under baseline (upper) and haloperidol-loading conditions (lower). The binding of [^{11}C]SA4503 was considerably reduced after oral administration of haloperidol (3 mg, 18 h prior to the PET scan)

27.2.3.3   CNS Disease

Mishina et al. (2008) performed [^{11}C]SA4503-PET in AD patients in the early stages of the disease. Figure 27.8 shows representative [^{11}C]SA4503 images compared with those for glucose metabolism evaluated with [^{18}F]FDG-PET. Although the results may have been influenced by atrophy or changes in regional blood flow, a widespread decrease in [^{11}C]SA4503 binding in the brain was found; BP_{ND} for [^{11}C]SA4503 was significantly lower in the cerebellum, thalamus and frontal, temporal and occipital cortices of AD patients than in those of healthy subjects. In other regions of the AD brain, BP_{ND} tended to be reduced. However, the data from these PET studies should be interpreted with caution because donepezil taken by some subjects shows a potent sigma$_1$ receptor agonist activity (see Sects. 2.3.4 and 3.4).

Parkinson's disease (PD) is also a progressive degenerative disorder of the CNS, characterised clinically by resting tremors, sluggish movements, cogwheel rigidity and postural instability. These symptoms are mainly caused by insufficient dopamine synthesis and death of dopaminergic neurons in the substantia nigra. Some studies have suggested that sigma$_1$ receptors are involved in modulating the synthesis and release of dopamine (Chaki et al. 1998). Using [^{11}C]SA4503-PET, Mishina et al. (2005) investigated whether sigma$_1$ receptors were involved in the damage to the dopaminergic system in patients with PD, who showed low densities of dopamine transporters and normal or high densities of dopamine D$_2$ receptors in the putamen using [^{11}C]CFT and [^{11}C]raclopride, respectively. Although the
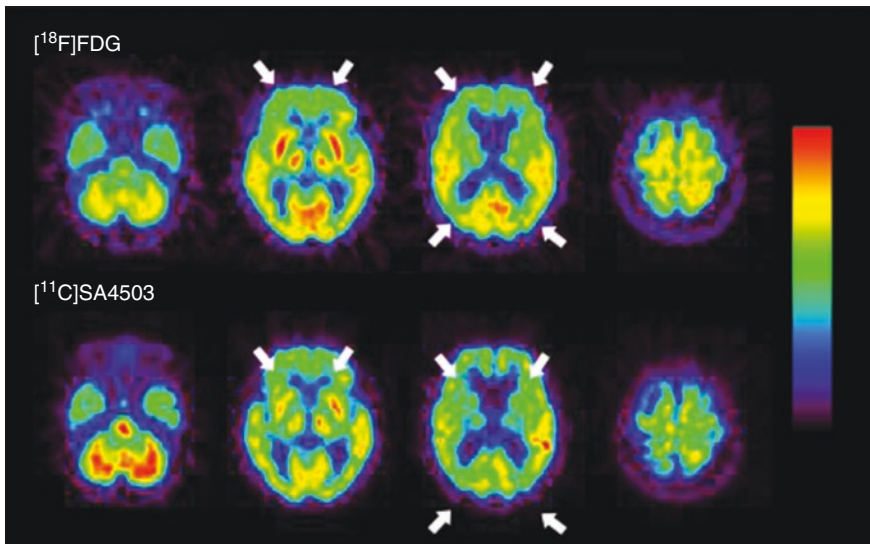
Fig. 27.8 Glucose metabolism and densities of sigma$_1$ receptors in the brain of a patient with AD. Glucose metabolism (upper): static image acquired 45–51 min after injection of [^{18}F]FDG. Sigma$_1$ receptors (lower): V_T derived from Logan graphical analysis of a 90-min dynamic scan of [^{11}C]SA4503. In this patient, uptake of [^{18}F]FDG was primarily decreased in the frontal and parietal cortex, and the distribution of [^{11}C]SA4503 was consistent with this reduction
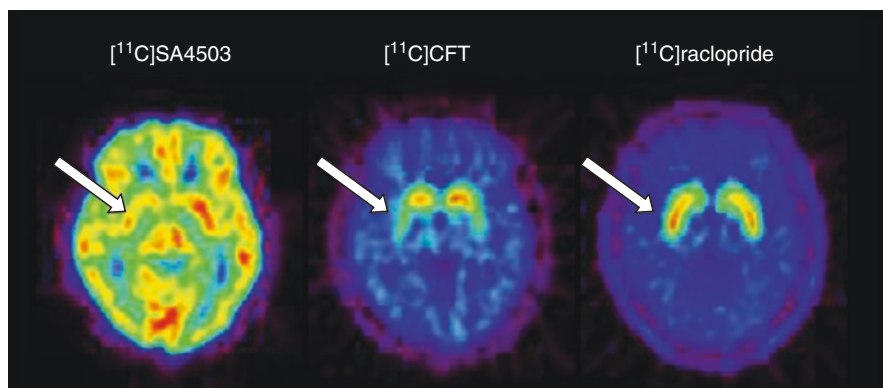
Fig. 27.9 Sigma₁ receptors, dopamine transporters and dopamine D_2 receptors in the brain of a patient with PD. [¹¹C]SA4503 (left), V_T derived from the Logan graphical analysis of a 90-min dynamic scan; [¹¹C]CFT (middle); and [¹¹C]raclopride (right), static image acquired 75–90 min and 40–55 min, respectively, after injection of the radiotracers

differences in BP_{ND} of [¹¹C]SA4503 between normal and PD patients were not clear because of a large inter-subject variability, BP_{ND} in PD patients was significantly lower on the more affected side of the anterior putamen than on the less affected side (Fig. 27.9).

LID in patients with PD mimics acute dystonic reactions induced by antipsychotic drugs, possibly mediated by sigma receptors. A PET study using [¹¹C]nemonapride showed a strong positive correlation between [¹¹C]nemonapride binding and the preoperative LID severity score when the patients were receiving medication (Nimura et al. 2004).

Patients with untreated MDD were investigated with (S)-(−)-[¹⁸F]fluspidine in comparison with age-matched healthy controls. Increased cortico-(para-)limbic sigma₁ receptor availability was found in MDD, which was associated with the severity of acute depressive symptoms (Meyer et al. 2018). Furthermore, Teva Pharmaceutical Industries performed a study to evaluate sigma₁ and dopamine D_2 receptor occupancy by pridopidine in the human brain of healthy volunteers and in patients with HD. No results of that study were published so far.

27.2.3.4 Measurement of Sigma₁ Receptor Occupancy in the Human Brain

While the physiological and pathophysiological roles of sigma receptors remain under investigation, a number of neuropsychiatric drugs are known to have moderate to high affinities for sigma receptors. Moreover, sigma₁ receptor ligands represent a new class of therapeutic agents for neuropsychiatric disorders (Hashimoto and Ishiwata 2006; Ishikawa and Hashimoto 2010). Therefore, levels of sigma receptor occupancy of therapeutic drugs in the living human brain are of great interest. In a feasibility study, Ishiwata et al. (2006b) measured sigma₁ receptor and dopamine D_2 receptor occupancy by haloperidol in the human brain by PET using

[^{11}C]SA4503 and [^{11}C]raclopride, respectively. Sigma$_1$ receptor occupancy was approximately 80% after oral administration of 3 mg haloperidol, whereas dopamine D$_2$ receptor occupancy was approximately 60%.

With respect to studies involving drugs with good potential for high receptor occupancy, a graphical analysis using a Lassen plot (Cunningham et al. 2010; Lassen et al. 1995) may be applicable for the evaluation of specific binding of the radioligand and receptor occupancy by the therapeutic drug, thus providing more stable estimates. The Lassen plot is based on regional changes in V_T between baseline and drug-loaded conditions. The assumptions for the analysis are that nonspecific binding is homogeneous, occupancy is the same in all regions of a regression line and there is a steady state of occupancy for the duration of the scan. A typical Lassen plot for haloperidol-loading study is shown in Fig. 27.10, and the parametric V_T images of [^{11}C]SA4503 for baseline and loading conditions (Fig. 27.7) show that the binding of [^{11}C]SA4503 was globally decreased by haloperidol-loading.

Ishikawa et al. (2007) measured sigma$_1$ receptor occupancy by two therapeutic drugs using [^{11}C]SA4503-PET. Selective serotonin reuptake inhibitor (SSRI) is the
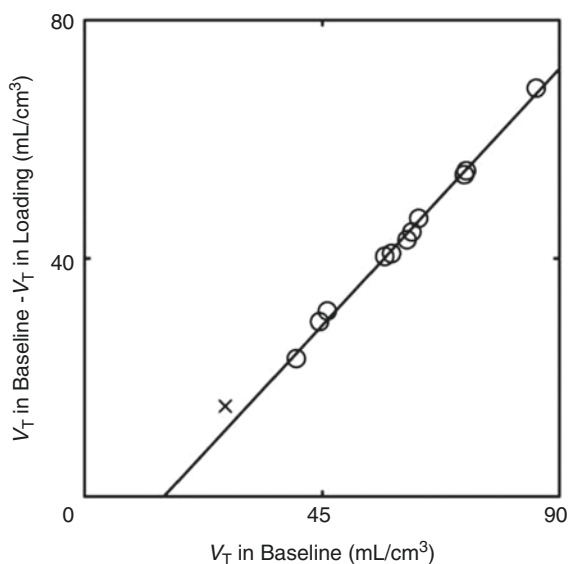
**Fig. 27.10** Typical Lassen plot analysis applied to a haloperidol-loading study. In this plot, the x-axis is V_T under baseline conditions, and the y-axis is the difference between V_T under loading and baseline conditions. The circles represent data from the grey matter regions (cerebral cortices, basal ganglia and cerebellar cortex), and the crosses represent data from the white matter region (centrum semiovale). The clear linear relationship suggests homogeneous nonspecific binding across the grey matter regions investigated, and the x-intercept and gradient of the regression line ($y = 0.96 (x − 15.1)$) represent the volume of free plus nonspecifically bound radioligand (V_{ND}) and the receptor occupancy by nonradioactive haloperidol, respectively. Moreover, the absence of data near the x-axis indicates that no regions, including the white matter, are available as a true reference region devoid of specific binding and that most [^{11}C]SA4503 binding under baseline conditions is specific
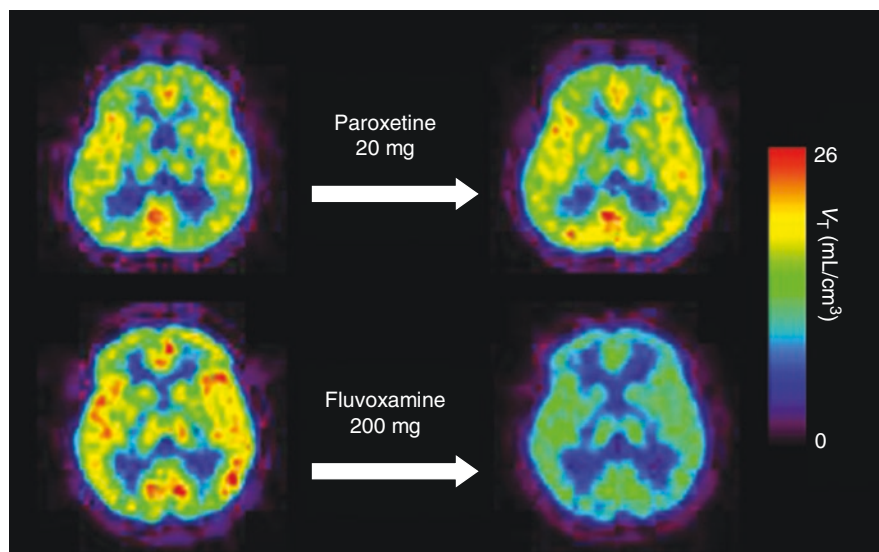
Fig. 27.11 V_T images of [^{11}C]SA4503-PET before and after a single oral administration of an SSRI. The upper pair represents V_T images at baseline (left) and at paroxetine (20 mg)-loading (right) in the same subject. The lower pair shows V_T images at baseline (left) and fluvoxamine (200 mg)-loading (right) in another subject

treatment of choice for many disorders, including major depressive disorder, dysthymia, obsessive–compulsive disorder and obsessive–compulsive spectrum disorders. Fluvoxamine has moderate affinity (K_i = 36 nM) for sigma₁ receptors in addition to the main affinity for serotonin reuptake sites (Narita et al. 1996). A single administration of therapeutic doses of fluvoxamine (50–200 mg) decreased [^{11}C]SA4503 binding in the human brain in a dose-dependent manner, whereas that of paroxetine (20 mg), another SSRI with very low affinity for sigma₁ receptors (K_i = 1893 nM), did not (Fig. 27.11). A similar occupancy study of an antipsychotic drug was also preliminarily described (van Waarde et al. 2011). The second example evaluated was donepezil. This drug has high affinity for sigma receptors (IC_{50} = 14 nM measured with [^{3}H]DTG) (Kato et al. 1999). Figure 27.12 shows that a single administration of donepezil (5 or 10 mg) decreased [^{11}C]SA4503 binding in the human brain in a dose-dependent manner (Ishikawa et al. 2009). The levels of sigma₁ receptor occupancy by fluvoxamine and donepezil were approximately 60% and 75%, respectively. These findings suggest that sigma₁ receptors may be involved in the mechanism of action of fluvoxamine and donepezil.

27.3 Sigma Receptors in CNS Diseases

Since the prototypic sigma₁ receptor ligand SKF10,047 (sigma₁ K_i = 44.8 nM, sigma₂/sigma₁ = 95.1; (Walker et al. 1990)) was found in the 1980s to exhibit psychotomimetic actions, the antipsychotic potential of sigma₁ receptor ligands has
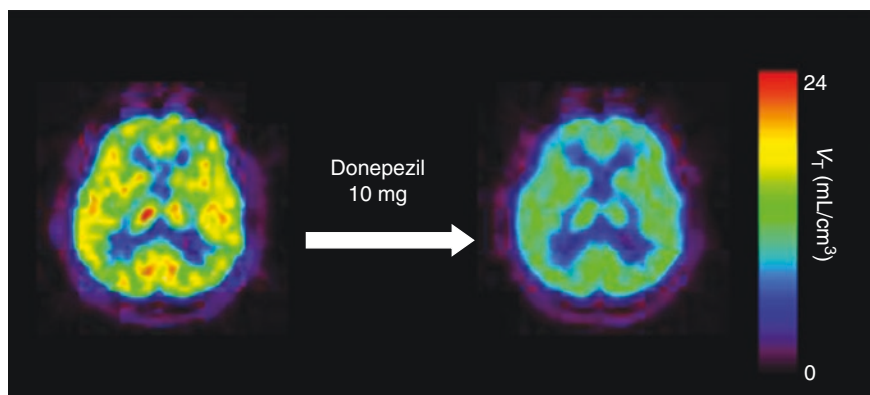
Fig. 27.12 Representative V_T images of [^{11}C]SA4503-PET before and after a single oral administration of donepezil (10 mg) in a healthy subject. Left, image at baseline; right, image after donepezil (10 mg)-loading

been examined extensively. During the 1990s, sigma$_1$ receptor ligands were synthesised mostly to develop new drugs for the treatment of schizophrenia. However, after cloning of the sigma$_1$ receptor gene, molecular biological characterisation indicated relationships between sigma$_1$ receptors and a variety of human diseases, including mood disorders, stroke, neurodegenerative diseases and drug addiction.

27.3.1 Schizophrenia

Five sigma$_1$ receptor ligands, panamesine (EMD57445), eliprodil (SL82.0715), rimcazole (BW234U), BMY14802 (BMS181100) and DuP734, were introduced into clinical trials for the treatment of schizophrenia (Hayashi and Su 2004). The findings of these clinical trials suggest that sigma$_1$ receptor ligands may not possess potent antipsychotic actions against the positive symptoms of schizophrenia, but may be useful for ameliorating certain negative symptoms (Hayashi and Su 2004). Recently, it was reported that fluvoxamine, an SSRI possessing potent sigma$_1$ receptor agonistic activity, improves negative symptoms and cognitive deficits of schizophrenic patients undergoing antipsychotic treatment (Iyo et al. 2008; Niitsu et al. 2010).

Using [^{3}H]haloperidol (sigma$_1$ K_i = 0.3 nM, sigma$_2$/sigma$_1$ = 120; (Walker et al. 1990)) in the presence of spiperone to block binding to dopamine D_2 receptors, Weissman et al. (1991) first reported reductions in the density of sigma binding sites in schizophrenic patients on antipsychotic medication; these reductions were most prominent in the temporal cerebral cortex followed by the parietal cortex. Shibuya et al. (1992) measured sigma receptor binding with [^{3}H]DTG (sigma$_1$ K_i = 11.9 nM, sigma$_2$/sigma$_1$ = 3.2; (Walker et al. 1990)) in 17 areas of the cerebral cortex and

found no significant differences between schizophrenic patients and controls, with exception of the superior parietal cortex in which the binding was significantly increased in the schizophrenic group. In addition, no significant differences were observed between off-drug and on-drug schizophrenic patients in any brain areas. Helmeste et al. (1996) reported no differences in the binding of [³H]nemonapride (previously designated as [³H]YM-09151-2: sigma₁ K_i = 8.4 nM, sigma₂/sigma₁ = 1.1; (Ujike et al. 1996)) in the presence of spiperone in the frontal cortex and cerebellum; however, they observed a decrease in the caudate nucleus. The discrepancies between these results may have been due to differences in schizophrenia types, medication period, quantification methods (receptor binding assay or autoradiography) and radioligands used.

Three out of four case-control association studies failed to find significant associations between alleles of the sigma₁ receptor gene [G-241 T/C-240 T and Gln2Pro (A61C)] and schizophrenia (Uchida et al. 2003).

27.3.2 Mood Disorders

Recent animal and human studies demonstrated a tight link between sigma₁ receptors and higher-order brain functions, such as mood and cognition (Hayashi and Su 2004; Fishback et al. 2010). It is noteworthy that some clinically used antidepressants, such as fluvoxamine (sigma₁ K_i = 36 nM), possess affinities for sigma₁ receptors within the nanomolar concentration range (Narita et al. 1996).

Brain-derived neurotrophic factor (BDNF) plays a critical role in the pathophysiology and in the activity of therapeutic agents in patients with mood disorders (Hashimoto et al. 2004). Furthermore, altered expression of BDNF is considered to be a mechanism of action of antidepressant drugs and mood stabilisers (Hashimoto et al. 2004). Interestingly, cutamesine (SA4503), a selective sigma₁ receptor agonist, was also shown to increase BDNF in the hippocampus of rats (Kikuchi-Utsumi and Nakai 2008). Very recently, Fujimoto et al. (2012) found that cutamesine potentiates the post-translational processing of neurotrophins; in contrast, clinically used antidepressants promote the transcriptional upregulation of BDNF.

The sigma₁ receptor contains binding sites for neurosteroids. It was reported that serum dehydroepiandrosterone (DHEA) and DHEA sulphate levels are altered in patients with depression (Takebayashi et al. 1998). Administration of DHEA is associated with the improvement of symptoms in cases of major depression or dysthymia (van Broekhoven and Verks 2003).

Igmesine (JO1,784) is the first sigma₁ receptor agonist introduced into clinical trials for the treatment of depression. The clinical trial moved into Phase III; however, the antidepressant effect failed to be confirmed in a large sample study (Hayashi et al. 2011). Recently, cutamesine has been introduced into Phase II clinical trials for the treatment of depression (Urfer et al. 2009).

27.3.3 Ischemia

There is substantial experimental evidence that sigma receptors play a role in the modulation of ischemic neuronal injury (Maurice and Lockhart 1997; O'Neill et al. 1995). In vitro studies demonstrated that sigma$_1$ agonists exert potent protective effects in a variety of cell types, such as primary cerebral neurons (Yang et al. 2007), retinal ganglion cells (Ha et al. 2011) and lens cells (Wang and Duncan 2006). Similarly, sigma$_1$ agonists were reported to show robust neuroprotective effects in animal studies. 4-Phenyl-1-(4-phenylbutyl)piperidine (PPBP) prevented early brain injury in rat (Takahashi et al. 1996) and cat (Takahashi et al. 1995) models of transient focal ischemic stroke, suggesting that sigma receptors play an important role in the mechanism of acute injury after transient focal ischemia. Cutamesine has been introduced into Phase II clinical trials for the treatment of post-stroke neurological disturbances (Urfer et al. 2009).

27.3.4 Neurodegenerative Diseases

[^{3}H]DTG binding was measured in seven hippocampal regions in the brains of Alzheimer's disease (AD) patients by autoradiography; an average reduction of 26% was found, which correlated with an average 29% pyramidal cell loss in the same region (Jansen et al. 1993). One study suggested that haplotype TT-241-240P2 of the sigma$_1$ receptor gene, which could lead to a reduction of sigma$_1$ receptor transcription, may be a protective factor against AD (Uchida et al. 2005). However, another study failed to replicate this finding (Maruszak et al. 2007).

Donepezil, an acetylcholinesterase (AChE) inhibitor, is the most widely prescribed drug so far for AD. Donepezil was found to be protective against amyloid β$_{25-35}$ peptide-induced neurotoxicity in mice (Meunier et al. 2006). This effect of donepezil was antagonised by the sigma$_1$ receptor antagonist BD-1047. In vitro studies demonstrated that donepezil, but not the AChE inhibitor physostigmine (also known as eserine), significantly potentiated nerve growth factor (NGF)-induced neurite outgrowth in PC12 cells in a concentration-dependent manner and that the effect of donepezil could be antagonised by NE-100 (Ishima et al. 2008). Furthermore, donepezil, but not physostigmine, significantly improved phencyclidine-induced cognitive impairments in mice, and the effect of donepezil could be antagonised by co-administration of NE-100 (Kunitachi et al. 2009). In summary, it is likely that sigma$_1$ receptors are involved in the mechanism of the neuroprotective pharmacological action of donepezil.

27.3.5 Drug Addiction and Alcoholism

Numerous animal studies have demonstrated a relationship between cocaine dependence and sigma$_1$ receptors (Robson et al. 2012). Many of these studies suggested the potential of sigma$_1$ antagonists to ameliorate cocaine intoxication, dependence and craving, although these effects have not been tested in clinical studies. Cocaine

at clinically relevant concentrations can interact with sigma₁ receptors and upregulate sigma₁ receptors in animals (Liu and Matsumoto 2008).

Despite the fact that substantial preclinical studies demonstrated roles of sigma receptors in drug abuse, only two clinical studies have been published to date in this regard, both of which were gene-association studies. The association of the sigma₁ receptor polymorphism GC-241-240TT or A61C (Gln2Pro) with methamphetamine dependence was examined in a Japanese cohort study of 143 methamphetamine abusers and 181 control subjects (Inada et al. 2004). This study indicated no significant association between sigma₁ receptor polymorphisms and methamphetamine abuse, although the frequency of the CC genotype of A61C tended to be higher in methamphetamine abusers who had experienced spontaneous relapse of methamphetamine psychosis. One gene-association study indicated a link between sigma₁ receptor polymorphisms and alcoholism (Miyatake et al. 2004). The distribution of sigma₁ receptor gene polymorphisms was analysed in 307 alcoholic and 302 control subjects. The frequencies of the A-485 allele and the TT-241-240/Pro2 haplotype in the 5′-upstream region, which lower transcriptional activity of the sigma₁ receptor gene, were significantly higher in control subjects compared with alcoholic subjects. These results suggest that the A-485 allele or TT-241-240/Pro2 haplotype lowers the expression of sigma₁ receptors and may be a possible protective factor against alcoholism.

27.4 Conclusion

Sigma₁ receptors are implicated in the pathophysiology of some neurological and neuropsychiatric disorders. A number of radioligands have been developed and evaluated for imaging of sigma₁ receptors in the CNS by PET and SPECT. [^{11}C]SA4503 was used to generate new findings regarding brain functions in patients with AD and PD, while (S)-(−)-[^{18}F]fluspidine was used in patients with MDD and HD. Moreover, [^{11}C]SA4503-PET demonstrated that some therapeutic drugs for neurological and neuropsychiatric disorders have considerable affinity for sigma₁ receptors in the human brain. Sigma₁ receptor imaging could be useful for pathophysiological studies of the human brain and help in the discovery and validation of potential therapeutic drugs for several CNS disorders. However, clinical sigma₁ receptor imaging is only just beginning to be explored. In view of the recent progress in sigma₁ receptor research and accumulating evidence of the therapeutic potentials of sigma₁ ligands, introduction of new tracers and further clinical studies should be encouraged.

References

Alon A, Schmidt HR, Wood MD et al (2017) Identification of the gene that codes for the σ₂ receptor. Proc Natl Acad Sci U S A 114:7160–7165

Baum EJ, Cai Z, Bois F et al (2017) PET imaging evaluation of four novel σ₁ radiotracers in non-human primates. J Nucl Med 58:982–988

Becker G, Meyer PM, Patt M et al (2018) Kinetic modeling of the new σ1 receptor ligand (−)-[^{18}F]Fluspidine in the human brain. Nuklearmedizin 57:A7

Berardi F, Ferorelli S, Colabufo NA et al (2001) A multireceptorial binding reinvestigation on an extended class of σ ligands: *N*-[ω-(indan-1-yl and tetralin-1-yl)alkyl] derivatives of 3,3-dimethylpiperidine reveal high affinities toward σ$_1$ and EBP sites. Bioorg Med Chem 9:1325–1335

Bowen WD, Hellewell SB, McGarry KA (1989) Evidence for a multi-site model of the rat brain sigma receptor. Eur J Pharmacol 163:309–318

van Broekhoven F, Verks RJ (2003) Neurosteroids in depression: a review. Psychopharmacology 165:97–100

Brust P, Deuther-Conrad W, Lehmkuhl K et al (2014a) Molecular imaging of σ$_1$ receptors in vivo: current status and perspectives. Curr Med Chem 21:35–69

Brust P, van den Hoff J, Steinbach J (2014b) Development of ^{18}F-labelled radiotracers for neuroreceptor imaging with positron emission tomography. Neurosci Bull 30:777–811

Chaki S, Okuyama S, Ogawa S et al (1998) Regulation of NMDA-induced [^{3}H]dopamine release from rat hippocampal slices through sigma-1 binding sites. Neurochem Int 33:29–34

Collier TL, O'Brien JC, Waterhouse RN (1996) Synthesis of [^{18}F]-1-(3-fluoropropyl)-4-(4-cyanophenoxymethyl)piperidine: a potential sigma-1 receptor radioligands for PET. J Label Compd Radiopharm 38:785–794

Collier TL, Waterhouse RN, Kassiou M (2007) Imaging sigma receptors: applications in drug development. Curr Pharm Des 13:51–72

Cunningham VJ, Rabiner EA, Slifstein M et al (2010) Measuring drug occupancy in the absence of a reference region: the Lassen plot re-visited. J Cereb Blood Flow Metab 30:46–50

Efange SMN (2000) *In vivo* imaging of the vesicular acetylcholine transporter and the vesicular monoamine transporter. FASEB J 14:2401–2413

Fischer S, Wiese C, Maestrup EG et al (2011) Molecular imaging of σ receptors: synthesis and evaluation of the potent σ$_1$ selective radioligand [^{18}F]fluspidine. Eur J Nucl Med Mol Imaging 38:540–551

Fishback JA, Robson MJ, Xu YT et al (2010) Sigma receptors: potential targets for a new class of antidepressant drug.

Fontanila D, Johannessen M, Hajipour AR et al (2009) The hallucinogen *N*,*N*-dimethyltryptamine (DMT) is an endogenous sigma1 receptor regulator. Science 323:934–937

Fujimoto M, Hayashi T, Urfer R et al (2012) Sigma-1 receptor chaperones regulate the secretion of brain-derived neurotrophic factor. Synapse 66:630–639

Glennon RA (2005) Pharmacophore identification for sigma-1 (σ$_1$) receptor binding: application of the "deconstruction-reconstruction-elaboration" approach. Mini-Rev Med Chem 5:927–940

Große Maestrup E, Fischer S, Wiese C et al (2009) Evaluation of spirocyclic 3-(3-fluoropropyl)-2-benzofurans as σ$_1$ receptor ligands for neuroimaging with positron emission tomography. J Med Chem 52:6062–6072

Große Maestrup E, Wiese C, Schepmann D et al (2011) Synthesis, pharmacological activity and structure affinity relationships of spirocyclic σ$_1$ receptor ligands with a (2-fluoroethyl) residue in 3-position. Bioorg Med Chem 19:393–405

Ha Y, Dun Y, Thanagaraju M et al (2011) Sigma receptor 1 modulates endoplasmic reticulum stress in retinal neurons. Invest Ophthalmol Vis Sci 52:527–540

Hanner M, Moebius FF, Flandorfer A et al (1996) Purification, molecular cloning, and expression of the mammalian sigma1-binding site. Proc Natl Acad Sci U S A 93:8072–8077

Hashimoto K, Ishiwata K (2006) Sigma receptor ligands: possible application as therapeutic drugs and as radiopharmaceuticals. Curr Pharm Des 12:3857–3876

Hashimoto K, Shimizu E, Iyo M (2004) Critical role of brain-derived neurotrophic factor in mood disorders. Brain Res Brain Res Rev 45:104–114

Hatano K, Ishiwata K, Kawashima K et al (1989) D$_2$-dopamine receptor specific brain uptake of carbon-11-labeled YM-09151-2. J Nucl Med 30:515–522

Hatazawa J, Hatano K, Ishiwata K et al (1991) Measurement of D$_2$ dopamine receptor-specific carbon-11-YM-09151-2 binding in the canine brain by PET: importance of partial volume correction. J Nucl Med 32:713–718

Hayashi T, Su TP (2004) Sigma-1 receptor ligands: potential in the treatment of neuropsychiatric disorders. CNS Drugs 18:269–284

Hayashi T, Su TP (2007) Sigma-1 receptor chaperones at the ER-mitochondrion interface regulate Ca^{2+} signaling and cell survival. Cell 131:596–610

Hayashi T, Tsai S-Y, Mori T et al (2011) Targeting ligand-operated chaperone sigma-1 receptors in the treatment of neuropsychiatric disorders. Expert Opin Ther Targets 15:557–577

He Y, Xie F, Ye J et al (2017) 1-(4-[^{18}F]fluorobenzyl)-4-[(tetrahydrofuran-2-yl)methyl]piperazine: a novel suitable radioligand with low lipophilicity for imaging σ1 receptors in the brain. J Med Chem 60:4161–4172

Helmeste DM, Tang SW, Bunney WE Jr et al (1996) Decrease in sigma but no increase in striatal dopamine D$_4$ sites in schizophrenic brains. Eur J Pharmacol 314(Suppl):R3–R5

Hirata M, Mori T, Soga S et al (2006) Synthesis and in vitro evaluation of iodinated derivatives of piperazine as a new ligand for sigma receptor imaging by single photon emission computed tomography. Chem Pharm Bull 54:407–475

Hirata M, Mori T, Umeda T et al (2008) Evaluation of radioiodinated 1-[2-(3,4-Dimethoxyphenyl) ethyl]-4-(2-iodophenylpropyl)piperazine as a tumor diagnostic agent with functional sigma receptor imaging by single photon emission computed tomography. Biol Pharm Bull 31:879–883

Hjornevik T, Cipriano PW, Shen B et al (2017) Biodistribution and radiation dosimetry of ^{18}F-FTC-146 in humans. J Nucl Med 58:2004–2009

Holl K, Falck E, Köhler J et al (2013) Synthesis, characterization, and metabolism studies of fluspidine enantiomers. Chem Med Chem 12:2047–2056

Inada T, Iijima Y, Uchida N et al (2004) No association found between the type 1 sigma receptor gene polymorphisms and methamphetamine abuse in the Japanese population: a collaborative study by the Japanese genetics initiative for drug abuse. Ann N Y Acad Sci 1025:27–33

Innis RB, Cunningham VJ, Delforge J et al (2007) Consensus nomenclature for in vivo imaging of reversibly binding radioligands. J Cereb Blood Flow Metab 27:1533–1539

Ishii K, Ishiwata K, Kimura Y et al (2001) Mapping of sigma$_1$ receptors in living human brain. Neuroimage 13(Suppl):S984

Ishikawa M, Hashimoto K (2010) The role of sigma-1 receptors in the pathophysiology of neuropsychiatric diseases. J Recept Ligand Channel Res 3:25–36

Ishikawa M, Ishiwata K, Ishii K et al (2007) High occupancy of sigma-1 receptors in the human brain after single oral administration of fluvoxamine: a positron emission tomography study using [^{11}C]SA4503. Biol Psychiatry 62:878–883

Ishikawa M, Sakata M, Ishii K et al (2009) High occupancy of sigma$_1$ receptors in the human brain after single oral administration of donepezil: a positron emission tomography study using [^{11}C]SA4503. Int J Neuropsychopharmacol 12:1127–1131

Ishima T, Nishimura T, Iyo M et al (2008) Potentiation of nerve growth factor-induced neurite outgrowth in PC12 cells by donepezil: role of sigma-1 receptors and IP$_3$ receptors. Prog Neuro-Psychopharmacol Biol Psychiatry 32:1656–1659

Ishiwata K, Senda M (1999) In vivo binding of [^{11}C]nemonapride to sigma receptors in the cortex and cerebellum. Nucl Med Biol 26:627–631

Ishiwata K, Kawamura K, Yajima K et al (2006a) Evaluation of (+)-p-[^{11}C]methylvesamicol for mapping sigma$_1$ receptors: a comparison with [^{11}C]SA4503. Nucl Med Biol 33:543–548

Ishiwata K, Oda K, Sakata M et al (2006b) A feasibility study of [^{11}C]SA4503-PET for evaluating sigma$_1$ receptor occupancy by neuroleptics: the binding of haloperidol to sigma$_1$ and dopamine D$_2$-like receptors. Ann Nucl Med 20:569–573

Iyo M, Shirayama Y, Watanabe H et al (2008) Fluvoxamine as a sigma-1 receptor agonist improved cognitive impairments in a patient with schizophrenia. Prog Neuro-Psychopharmacol Biol Psychiatry 15:1072–1073

Jansen KL, Faull RL, Dragunow M et al (1991) Autoradiographic distribution of sigma receptors in human neocortex, hippocampus, basal ganglia, cerebellum, pineal and pituitary glands. Brain Res 559:17–27

Jansen KL, Faull RL, Storey P et al (1993) Loss of sigma binding sites in the CA1 area of the anterior hippocampus in Alzheimer's disease correlates with CA1 pyramidal cell loss. Brain Res 623:299–302

Jia H, Cai Z, Holden D et al (2018) Evaluation of a simple, ^{18}F-labeled radiotracer as PET imaging agent for sigma-1 receptors in the nonhuman primate brain. J Nucl Med 59(Suppl):617

Jia H, Zhang Y, Huang Y (2019) Imaging sigma receptors in the brain: new opportunities for diagnosis of Alzheimer's disease and therapeutic development. Neurosci Lett 691:3–10

Kato K, Hayako H, Ishihara Y et al (1999) TAK-147, an acetylcholinesterase inhibitor, increases choline acetyltransferase activity in cultured rat septal cholinergic neurons. Neurosci Lett 260:5–8

Kawamura K, Kimura Y, Tsukada H et al (2003) An increase of sigma receptors in the aged monkey brain. Neurobiol Aging 24:745–752

Kawamura K, Tsukada H, Shiba K et al (2007) Synthesis and evaluation of fluorine-18-labeled SA4503 as a selective sigma$_1$ receptor ligand for positron emission tomography. Nucl Med Biol 34:571–577

Kikuchi-Utsumi K, Nakai T (2008) Chronic treatment with a selective ligand for the sigma-1 receptor chaperone, SA4503, up-regulates BDNF protein levels in the rat hippocampus. Neurosci Lett 440:19–22

Kimura Y, Naganawa M, Sakata M et al (2007) Distribution volume as an alternative to the binding potential for sigma$_1$ receptor imaging. Ann Nucl Med 21:533–535

Kornhuber J, Schoppmeyer K, Bendig C et al (1996) Characterization of [^{3}H]pentazocine binding sites in post-mortem human frontal cortex. J Neural Transm 103:45–53

Kranz M, Sattler B, Wüst N et al (2016) Evaluation of the enantiomer specific biokinetics and radiation doses of [^{18}F]Fluspidine-a new tracer in clinical translation for imaging of σ_1 receptors. Molecules 21:1164

Kunitachi S, Fujita Y, Ishima T et al (2009) Phencyclidine-induced cognitive deficits in mice are ameliorated by subsequent subchronic administration of donepezil: role of sigma-1 receptors. Brain Res 71279:189–196

Lassen NA, Bartenstein PA, Lammertsma AA et al (1995) Benzodiazepine receptor quantification in vivo in humans using [^{11}C]flumazenil and PET: application of the steady-state principle. J Cereb Blood Flow Metab 10:740–747

Lever JR, Gustafson JL, Xu R et al (2006) Sigma$_1$ and sigma$_2$ receptor binding affinity and selectivity of SA4503 and fluoroethyl SA4503. Synapse 59:350–358

Li Y, Wang X, Zhang J et al (2013) Synthesis and evaluation of novel ^{18}F-labeled spirocyclic piperidine derivatives as σ_1 receptor ligands for positron emission tomography imaging. J Med Chem 56:3478–3491

Liu Y, Matsumoto RR (2008) Alterations in fos-related antigen 2 and σ_1 receptor gene and protein expression are associated with the development of cocaine-induced behavioral sensitization: time course and regional distribution studies. J Pharmacol Exp Ther 327:187–195

Logan J, Fowler JS, Volkow ND et al (1990) Graphical analysis of reversible radioligand binding from time-activity measurements applied to [N-^{11}C-methyl]-(−)-cocaine PET studies in human subjects. J Cereb Blood Flow Metab 10:740–747

Mach RH, Wheeler KT (2009) Development of molecular probes for imaging sigma-2 receptors in vitro and in vivo. Cent Nerv Syst Agents Med Chem 9:230–245

Maier CA, Wünsch B (2002a) Novel s receptor ligands. Part 2. SAR of spiro[[2]benzopyran-1,4′-piperidines] and spiro[[2]benzofuran-1,4′-piperidines] with carbon substituents in position 3. J Med Chem 45:4923–4930

Maier CA, Wünsch B (2002b) Novel spiropiperidines as highly potent and subtype selective σ receptor ligands. Part 1. J Med Chem 45:438–448

Maisonial A, Grosse Maestrup E, Fischer S et al (2011) A ^{18}F-labeled fluorobutyl-substituted spirocyclic piperidine derivative as a selective radioligand for PET imaging of σ1 receptors. Chem Med Chem 6:1401–1410

Maisonial A, Grosse Maestrup E, Wiese C et al (2012) Synthesis, radiofluorination and pharmacological evaluation of a fluoromethyl spirocyclic PET tracer for central σ$_1$ receptors and comparison with fluoroalkyl homologs. Bioorg Med Chem 20:257–269

Maisonial-Besset A, Funke U, Wenzel B et al (2014) Automation of the radiosynthesis and purification procedures for [^{18}F]fluspidine preparation, a new radiotracer for clinical investigations in PET imaging of σ$_1$ receptors in brain. Appl Radiat Isot 84:1–7

Martin WR, Eades CG, Thompson JA et al (1976) The effects of morphine- and nalorphine-like drugs in the nondependent and morphine-dependent chronic spinal dog. J Pharmacol Exp Ther 197:517–532

Maruszak A, Safranow K, Gacia M et al (2007) Sigma receptor type 1 gene variation in a group of polish patients with Alzheimer's disease and mild cognitive impairment. Dement Geriatr Cogn Disord 23:432–438

Mash DC, Zabetian CP (1992) Sigma receptors are associated with cortical limbic areas in the primate brain. Synapse 12:195–205

Matsuno K, Mita S (1998) SA4503: a novel sigma$_1$ receptor agonist. CNS Drug Rev 4:1–24

Matsuno K, Nakazawa M, Okamoto K et al (1996) Binding properties of SA4503, a novel and selective sigma 1 receptor agonist. Eur J Pharmacol 306:271–279

Maurice T, Lockhart BP (1997) Neuroprotective and anti-amnestic potentials of sigma (σ) receptor ligands. Prog Neuro-Psychopharmacol Biol Psychiatry 21:69–102

Meunier J, Ieni J, Maurice T (2006) The anti-amnestic and neuroprotective effects of donepezil against amyloid β$_{25-35}$ peptide-induced toxicity in mice involve an interaction with the σ$_1$ receptor. Br J Pharmacol 149:998–1012

Meyer PM, Strauß M, Becker G et al (2018) First time in vivo assessment of sigma-1 receptor binding (sig-1R) in the brain of unmedicated acute major depressive disorder (MDD) using the novel sig-1R-specific radioligand (−)-[F-18]Fluspidine and PET. Nuklearmedizin 57:A25

Mintun MA, Raichle ME, Kilbourn MR et al (1984) A quantitative model for the in vivo assessment of drug binding sites with positron emission tomography. Ann Neurol 15:217–227

Mishina M, Ishiwata K, Ishii K et al (2005) Function of sigma$_1$ receptors in Parkinson's disease. Acta Neurol Scand 112:103–107

Mishina M, Ohyama M, Ishii K et al (2008) Low density of sigma$_1$ receptors in early Alzheimer's disease. Ann Nucl Med 22:151–156

Miyatake R, Furukawa A, Matsushita S et al (2004) Functional polymorphisms in the sigma1 receptor gene associated with alcoholism. Biol Psychiatry 55:85–90

Moussa IA, Banister SD, Beinat C et al (2010) Design, synthesis, and structure-affinity relationships of regioisomeric N-benzyl alkyl ether piperazine derivatives as σ-1 receptor ligands. J Med Chem 53:6228–6239

Moussa IA, Banister SD, Giboureau N et al (2011) Synthesis and in vivo evaluation of [^{18}F]N-(2-benzofuranylmethyl)-N′-[4-(2-fluoroethoxy)benzyl]piperazine, a novel σ$_1$ receptor PET imaging agent. Bioorg Med Chem 21:6820–6823

Narita N, Hashimoto K, Tomitaka S et al (1996) Interactions of selective serotonin reuptake inhibitors with subtypes of σ receptors in rat brain. Eur J Pharmacol 307:117–119

Niitsu T, Shirayama Y, Fujisaki M (2010) Fluvoxamine improved cognitive impairments in a patient with schizophrenia. Prog Neuro-Psychopharmacol Biol Psychiatry 34:1345–1346

Nimura T, Ando T, Yamaguchi K et al (2004) The role of σ-receptors in levodopa-induced dyskinesia in patients with advanced Parkinson disease: a positron emission tomography study. J Neurosurg 100:606–610

O'Neill M, Caldwell M, Earley B et al (1995) The sigma receptor ligand JO1784 (igmesine hydrochloride) is neuroprotective in the gerbil model of global cerebral ischemia. Eur J Pharmacol 283:217–225

Recanatini M, Poluzzi E, Masetti M et al (2005) QT prolongation through hERG K(+) channel blockade: current knowledge and strategies for the early prediction during drug development. Med Res Rev 25:133–166

Robson MJ, Noorbakhsh B, Seminerio MJ et al (2012) Sigma-1 receptors: potential targets for the treatment of substance abuse. Curr Pharm Des 18:902–919

Sakata M, Kimura Y, Naganawa M et al (2007) Mapping of human cerebral sigma$_1$ receptors using positron emission tomography and [^{11}C]SA4503. NeuroImage 35:1–8

Sakata M, Kimura Y, Naganawa M et al (2008) Shortened protocol in practical [^{11}C]SA4503-PET studies for sigma$_1$ receptor quantification. Ann Nucl Med 22:143–146

Schmidt HR, Zheng S, Gurpinar E et al (2016) Crystal structure of the human σ_1 receptor. Nature 532:527–530

Shen B, Park JH, Hjornevik T et al (2017) Radiosynthesis and first-in-human PET/MRI evaluation with clinical-grade [^{18}F]FTC-146. Mol Imaging Biol 19:779–186

Shiba K, Ogawa K, Ishiwata K et al (2006) Synthesis and binding affinities of methyl vesamicol analogs for the acetylcholine transporter and sigma receptor. Bioorg Med Chem 14:2620–2626

Shibuya H, Mori H, Toru M (1992) Sigma receptors in schizophrenic cerebral cortices. Neurachem Res 17:983–990

Stone JM, Arstad E, Erlandsson K et al (2006) [^{123}I]TPCNE – a novel SPET tracer for the sigma-1 receptor: first human studies and in vivo haloperidol challenge. Synapse 60:109–117

Su TP, London ED, Jaffe JH (1988) Steroid binding at sigma receptors suggests a link between endocrine, nervous, and immune systems. Science 240:219–221

Takahashi H, Kirsch JR, Hashimoto K et al (1995) PPBP [4-phenyl-1-(4-phenylbutyl)piperidine], a potent sigma-receptor ligand, decreases brain injury after transient focal ischemia in cats. Stroke 26:1676–1682

Takahashi H, Kirsch JR, Hashimoto K et al (1996) PPBP [4-phenyl-1-(4-phenylbutyl)piperidine] decreases brain injuey after transient focal ischemia in rats. Stroke 27:2120–2123

Takebayashi M, Kagaya A, Uchitomi Y et al (1998) Plasma dehydroepiandrosterone sulfate in unipolar major depression. Short Commun J Neural Transm 105:537–542

Toyohara J, Sakata M, Ishiwata K (2009) Imaging of sigma$_1$ receptors in the human brain using PET and [^{11}C]SA4503. Cent Nerv Syst Agents Med Chem 9:190–196

Toyohara K, Sakata M, Ishiwata K (2012) Re-evaluation of in vivo selectivity of [^{11}C]SA4503 to σ_1 receptors in the brain: contributions of emopamil binding protein. Nucl Med Biol 39:1049–1052

Uchida N, Ujike H, Nakata K et al (2003) No association between the sigma receptor type 1 gene and schizophrenia: results of analysis and meta-analysis of case-control studies. BMC Psychiatry 3:13

Uchida N, Ujike H, Tanaka Y et al (2005) A variant of sigma receptor type-1 gene is a protective factor for Alzheimer disease. Am J Geriatr Psychiatry 13:1062–1066

Ujike H, Akiyama K, Kuroda S (1996) [^{3}H]YM-09151-2 (nemonapride), a potent radioligand for both sigma 1 and sigma 2 receptor subtypes. Neuroreport 7:1057–1061

Urfer R, Takao K, Sato W et al (2009) SA4503 is a potent and selective sigma-1 receptor agonist in clinical development for depression and stroke. Soc Neurosci Abstr 496:3

Vilkman H, Kajander J, Nagren K et al (2000) Measurement of extrastriatal D$_2$-like receptor binding with [^{11}C]FLB 457 – a test-retest analysis. Eur J Nucl Med 27:1666–1673

van Waarde A, Rybczynska AA, Ramakrishnan N et al (2010) Sigma receptors in oncology: therapeutic and diagnostic applications of sigma ligands. Curr Pharm Des 16:3519–3537

van Waarde A, Ramakrishnan NK, Rybczynska AA et al (2011) The cholinergic system, sigma-1 receptors and cognition. Behav Brain Res 221:543–554

Walker JM, Bowen WD, Walker FO et al (1990) Sigma receptors: biology and function. Pharmacol Rev 42:355–402

Wang L, Duncan G (2006) Silencing of sigma-1 receptor induces cell death in human lens cells. Exp Cell Res 312:1439–1446

Wang X, Li D, Deuther-Conrad W et al (2014) Novel cyclopentadienyl tricarbonyl ^{99m}Tc complexes containing 1-piperonylpiperazine moiety: potential imaging probes for sigma-1 receptors. J Med Chem 57:7113–7125

Waterhouse RN, Mardon K, Giles KM et al (1997) Halogenated 4-(phenoxymethyl)piperidines as potential radiolabeled probes for sigma-1 receptors: in vivo evaluation of [^{123}I]-1-(iodopropen-2-yl)-4-[(4-cyanophenoxy)methyl]piperidine. J Med Chem 40:1657–1667

Waterhouse RN, Nobler MS, Zhou Y et al (2004) First evaluation of the sigma-1 receptor radio-ligand [^{18}F]1-3-fluoropropyl-4-((4-cyanophenoxy)-methyl)piperidine ([^{18}F]FPS) in humans. Neuroimage 22(Supp. 2):T29–T30

Waterhouse RN, Chang RC, Zhao J et al (2006a) In vivo evaluation in rats of [^{18}F]1-(2-fluoroethyl)-4-[(4-cyanophenoxy)methyl]piperidine as a potential radiotracer for PET assessment of CNS sigma-1 receptors. Nucl Med Biol 33:211–215

Waterhouse RN, Zhao J, Stabin MG et al (2006b) Preclinical acute toxicity studies and dosimetry estimates of the novel sigma-1 receptor radiotracer, [^{18}F]SFE. Mol Imaging Biol 8:284–291

Weissman AD, Su TP, Hedreen JC et al (1988) Sigma receptors in post-mortem human brains. J Pharmacol Exp Ther 247:29–33

Weissman AD, Casanova MF, Kleinman JE et al (1991) Selective loss of cerebral cortical sigma, but not PCP binding sites in schizophrenia. Biol Psychiatry 29:41–54

Wiese C, Grosse Maestrup E, Schepmann D et al (2009) Pharmacological and metabolic characterisation of the potent sigma1 receptor ligand 1′-benzyl-3-methoxy-3H-spiro[[2]benzofuran-1,4′-piperidine]. J Pharm Pharmacol 61:631–640

Wiese C, Maestrup EG, Schepmann D et al (2011) Enantioselective s1 receptor binding and biotransformation of the spirocyclic PET tracer 1′-benzyl-3-(3-fluoropropyl)-3H-spiro[[2]benzofuran-1,4′-piperidine]. Chirality 23:148–154

Xie F, Bergmann R, Kniess T et al (2015) ^{18}F-labeled 1,4-dioxa-8-azaspiro[4.5]decan derivative: synthesis and biological evaluation of a s1 receptor radioligand with low lipophilicity as potent tumor imaging agent. J Med Chem 58:5395–5407

Yang S, Bhardwaj A, Cheng J et al (2007) Sigma receptor agonists provide neuroprotection *in vitro* by preserving *bcl-2*. Anesth Analg 104:1179–1184

Zhao J, Chang R, Carambot P et al (2005) Radiosynthesis and in vivo study of [^{18}F]1-(2-fluoroethyl)-4-[(cyanophenoxy)methyl]piperidine: a promising new sigma-1 receptor ligand. J Label Compd Radiopharm 48:547–555

Sigma-2 Receptors: An Emerging Target for CNS PET Imaging Studies

28

Aladdin Riad, Jinbin Xu, and Robert H. Mach

Contents

Abstract

The sigma-2 (σ2) receptor represents one of the most poorly understood proteins in cell biology. Although this receptor was identified through in vitro binding studies over 30 years ago, the molecular identity of this protein was not unambiguously determined until 2017. It is now known that the σ2 receptor is a pro-

A. Riad · R. H. Mach (✉)
Department of Radiology, Perelman School of Medicine, University of Pennsylvania, Philadelphia, PA, USA
e-mail: Aladdin.Riad@PennMedicine.UPenn.edu; rmach@pennmedicine.upenn.edu

J. Xu
Mallinckrodt Institute of Radiology, Washington University School of Medicine-St Louis, St. Louis, MO, USA
e-mail: jinbinxu@wustl.edu

973

tein called TMEM97 and that this protein forms a trimeric complex with PGRMC1 and the LDL receptor to increase the rate of internalization of lipoproteins. There is overwhelming data demonstrating that the σ2 receptor is an important biomarker of tumor cell proliferation, which is consistent with the lipoprotein uptake mechanism associated with this protein. In the CNS, σ2 receptor antagonists block Aβ1-42 oligomer synaptic dysfunction in transgenic mouse models of Alzheimer's disease and have shown promise in animal models of traumatic brain injury and alcohol abuse. These results clearly indicate that this protein is an important therapeutic target for the treatment of a variety of CNS conditions. These observations highlight the importance of having high affinity σ2-selective radiotracers for imaging this protein in vivo with PET.

Abbreviations

Aβ	Beta amyloid protein
CNS	Central nervous system
LDL	Low density lipoprotein
PET	Positron emission tomography
PGRMC1	Progesterone membrane binding component 1
TMEM97	Transmembrane protein 97
σ	Sigma

28.1 Introduction

The sigma (σ) receptors represent one of the most poorly understood protein families in cell biology. Their name was derived from their initial identification as a subtype of the opiate receptors (Martin et al. 1976). This characterization was based on the binding properties and behavioral properties of the benzomorphan analog SKF10047 and that these properties could be blocked by naltrexone, an opioid receptor antagonist. Subsequent studies revealed that the (−)-enantiomer of SKF10047 was a nonselective opioid ligand, acting as a partial agonist at mu and delta receptors, and an antagonist at kappa opioid receptors (Su 1982). On the other hand, (+)-SKF10047 had a high affinity for the σ receptor. By conducting a series of radioligand binding and photoaffinity labeling studies, Hellewell and Bowen were able to demonstrate that there were two subtypes of the σ receptor, σ1 and σ2 (Bowen et al. 1989; Hellewell and Bowen 1990). The σ1 receptor had a molecular weight of ~25 kDa, and [^{3}H](+)-SKF10047, [^{3}H](+)-pentazocine, and [^{3}H]DTG had a high affinity for this binding site. A second σ receptor was found to have a MW of ~21.5 kDa and had a high affinity for [^{3}H]DTG but did not bind the benzomorphan analogs [^{3}H](+)-pentazocine and [^{3}H](+)-SKF10047. This receptor was named the σ2 receptor (Hellewell and Bowen 1990).

Of the two receptor subtypes, much more attention has been placed on the σ1 versus σ2 receptor. This has resulted in publication of a number of key studies including its purification and cloning, resolution of the crystal structure as a homotrimeric complex, subcellular localization, molecular chaperone properties, and its ability to interact with and form heteromeric complexes with G proteins including the opiate and dopamine D2 receptors (Alon et al. 2017a; Beggiato et al. 2017; Borroto-Escuela et al. 2019; Hanner et al. 1996; Hayashi and Su 2007; Navarro et al. 2010; Schmidt et al. 2016). Although less is known about the structure and function of the σ2 receptor, a number of seminal studies have been recently reported that have led to a greater understanding of the function of this receptor in cell biology.

28.2   Pharmacological and Molecular Characterization of the σ2 Receptor

28.2.1 In Vitro Binding Studies

For many years, much of what was known about the σ2 receptor was obtained using radioligand binding studies with tritiated ligands. Photoaffinity labeling studies with [^{3}H]azido-DTG (Fig. 28.1) were able to determine that the molecular weight of the σ2 receptor was ~21.5 kDa, which was smaller than the σ1 receptor (Hellewell
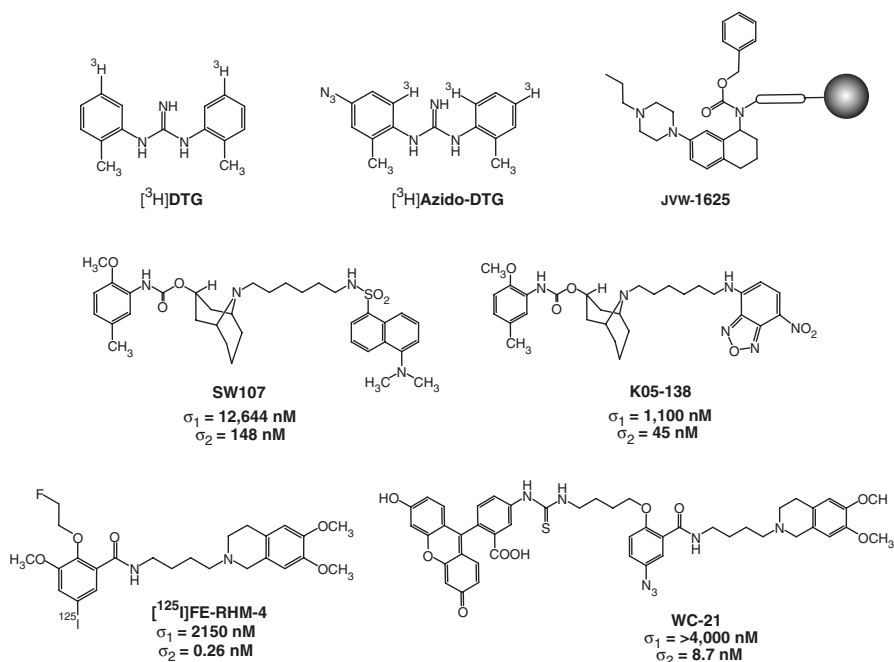
Fig. 28.1   Structures of the compounds and radioligands used to characterize the σ2 receptor

et al. 1994). In vitro binding studies with [³H]DTG in the presence of (+)-pentazo-cine to mask σ1 receptors were useful in studying the density of the protein in various tissues including cancer cells (Hellewell et al. 1994; Vilner et al. 1995). Radioligand binding assays with this ligand have also been instrumental in identifying compounds having a higher affinity and greater selectivity for σ2 versus σ1 receptors, which have served as more optimal ligands for in vitro and in vivo imaging studies.

One of the more important observations made with in vitro binding studies of [³H]DTG was that σ2 receptors were expressed in high density in a broad panel of cancer cell lines derived from both murine and human tumors (Vilner et al. 1995). This indicated that the σ2 receptor was a potential biomarker for differentiating tumors from the surrounding normal tissue. Another important observation was that the density of σ2 receptors was found to be tenfold higher in mouse mammary adenocarcinoma (66) cells when they were actively progressing through the cell cycle (i.e., proliferating) versus 66 cells that were driven into a state of quiescence (66Q cells) via nutrient deprivation (Mach et al. 1997). The density of σ2 receptors in proliferating 66 (66P) cells was also relatively high, ~one million copies/cell. Furthermore, the time interval for the downregulation of σ2 receptors once the 66 cells entered a quiescent state was ~5 days, which is consistent with the downregulation of a membrane-bound protein (Al-Nabulsi et al. 1999; Wheeler et al. 2000). Finally, the tenfold difference in σ2 receptor density between 66P and 66Q cells was observed in solid tumor xenografts, which indicated that this was not a tumor property limited to cell culture techniques (Shoghi et al. 2013; Wheeler et al. 2000).

28.2.2 Microscopy Studies

The next phase in the study of the σ2 receptor involved two-photon and confocal microscopy studies using fluorescently tagged small molecules possessing a high affinity for σ2 versus σ1 receptors. Although a number of these probes have been reported, studies that have yielded the most useful information have utilized the probes **SW-107** and **K05-138** in cancer cells in combination with a series of "tracker" dyes to determine the subcellular localization of the σ2-targeting fluorescent probes. In these studies, the fluorescent signal of the σ2 receptor ligand was co-localized with tracker dyes for lysosomes/endosomes (LysoTracker), endoplasmic reticulum (ER-Tracker), mitochondria (MitoTracker), and the plasma membrane (FM-1-43FX). These studies demonstrated a co-localization of the σ2 receptor fluorescent ligands with each of the different tracker dyes (Zeng et al. 2007, 2011). In addition, there was a rapid uptake of **K05-138** in time lapsed confocal microscopy studies, and this uptake could be delayed by incubation with the known endocytosis inhibitor phenylarsine oxide. These data indicated that the fluorescent probes undergo receptor-mediated endocytosis into endosomes and that once inside the cell, the fluorescent probes localize to the ER and mitochondria. The receptor-mediated endocytosis of the σ2 receptor fluorescent probes was also consistent with earlier reports of the localization of σ2

receptors in lipid rafts, which play and important role in membrane trafficking (Gebreselassie and Bowen 2004; Zeng et al. 2007).

The observation that the fluorescent probes **SW-107** and **K05-138** undergo receptor-mediated endocytosis and localization in mitochondria led to the use of the [3.3.1] aza-bicyclononane scaffold as a means for delivering anticancer drugs to cancer cells (Hornick et al. 2012; Mach et al. 2013). One of the more interesting results in this series of studies was the observation that this σ2 receptor scaffold increased the rate of uptake of gold nanocages by breast cancer cells; transmission electron microscopy determined that the gold nanocages have a size of ~50 nm and suggested that the "endogenous ligand" binding to the σ2 receptor is likely to have a high molecular weight (Sun et al. 2014). Binding to the σ2 receptor leads to the receptor-mediated internalization of this high molecular weight endogenous ligand into the endosomal compartment. This information was useful in ultimately identifying the structure of the σ2 receptor as discussed in detail below.

28.3   Identification of the σ2 Receptor and Its Putative Biological Function

28.3.1 Progesterone Receptor Membrane Component 1 (PGRMC1)

Although the above radioligand binding and microscopy studies were able to provide valuable information regarding the molecular weight and subcellular localization of the σ2 receptor, they did not address the most important questions: (1) What is the σ2 receptor? (2) What is its role in cell biology? (3) Why is this protein upregulated in proliferating cancer cells? The only way this could be accomplished was through the purification, sequencing and cloning of the σ2 receptor, and determining the biochemical pathways that utilize this protein.

In order to accomplish this goal, Xu and colleagues (2011) developed a photoaffinity probe based on the conformationally flexible benzamide analogs (Fig. 28.1). These compounds have been shown to have a high affinity for the σ2 versus σ1 receptor, and PET probes based on this class of compounds demonstrated promising results in PET imaging studies of the σ2 receptor (Tu et al. 2005, 2010). The photoaffinity probe also contained a FITC moiety; although it is typically used as a fluorescent probe, this moiety was chosen since there are highly specific antibodies for FITC that could be used to visualize photoaffinity-labeled proteins using classic molecular biology techniques. In this study, σ2 receptors in rat liver membrane homogenates, the tissue used in standard σ2 receptor binding assays, were labeled with the photoaffinty probe under a series of protein enrichment techniques. Western blot analysis using an anti-FITC antibody revealed a protein band having a molecular weight of ~24 kDa, which was larger than the 21.5 kDa band identified by Hellewell and Bowen (Hellewell et al. 1994). This protein was isolated and submitted to two different protein sequencing labs; there was only one protein common to both lists of candidate proteins, the progesterone receptor membrane component 1

or PGRMC1, which has also been termed the 25-Dx protein (Xu et al. 2011). Previous studies have shown that the molecular weight of the PGRMC1 (25-Dx protein) ranged between 22 and 25 kDa in polyacrylamide gels. Interestingly, the PGRMC1 was previously shown to be upregulated in a wide panel of tumors and was proposed as a biomarker for breast cancer (Neubauer et al. 2008). The characterization of protein expression levels of PGRMC1 in tumors on the Human Protein Atlas database paralleled very closely the density of σ2 receptors in cancer cells growing under cell culture techniques reported in the paper by Vilner et al. (1995). In addition, the PGRMC1 was thought to not be functionally active as a monomer but was thought to form either a homodimer in the internalization of heme or a partner protein with a number of other proteins including Insig-1, PAIR-BR1, and EGFR (Ahmed et al. 2010a, b; Cahill 2007).

Since the PGRMC1 was a known protein, it was possible to obtain a number of standard molecular biology reagents to study expression levels under a variety of experimental conditions. This led to a series of studies relating the binding of the radioiodinated σ2 ligand, [^{125}I]FE-RHM-4, to HeLa cells in which PGRMC1 was either transiently knocked down using siRNA for this protein or transiently upregulated via the transfection of HeLa cells with human PGRMC1 cDNA. Since it was not possible to isolate enough HeLa cells to conduct full Scatchard analysis of the siRNA or overexpression experiments, the binding studies were conducted using a single concentration of [^{125}I]FE-RHM-4, and the assumption was made that either knocking out or overexpressing PGRMC1 did not alter the Kd value of this radioligand.

In the siRNA experiments, the transient knockdown of PGRMC1 led to a reduction in binding of [^{125}I]FE-RHM-4. Similarly, transfection of human PGRMC1 cDNA in HeLa cells led to an increase in binding of this radioligand. However, the authors noticed that the level of binding of [^{125}I]FE-RHM-4 did not match the level of PGRMC1 protein measured via Western blot analysis (Xu et al. 2011). This disconnect between protein levels and radioligand binding data led the authors to conclude that the σ2 receptor was not directly the PGRMC1 but likely represented a binding site on a protein complex involving the PGRMC1 and one of its binding partners. Evidence consistent with the involvement of PGRMC1 with σ2 receptors was reported by Izzo et al. (2014b) and Yi et al. (2017).

In 2015, two papers were published that disputed the results reported by Xu et al. (2011). In the study reported by Abate and colleagues, a stable knockout or overexpression of PGRMC1 in the human breast cancer cell line, MCF-7 cells, did not affect the binding of [^{3}H]DTG (Abate et al. 2015). A similar result was reported by Ruoho and colleagues using NSC34 cells using overexpression and CRISPR to knockout the protein (Chu et al. 2015). Both papers stated that the conclusions reached by Xu et al. were incorrect, even though the authors never claimed that the PGRMC1 was the σ2 receptor (Xu et al. 2011). This misquoting of the conclusions stated in the Xu et al. paper has been repeated in subsequent review articles and editorial articles on the σ2 receptor (Blass and Rogers 2018; Hiranita 2016; Schmidt and Kruse 2019).

28.3.2 Identification of the Gene Encoding the σ2 Receptor

In 2017, Alon et al. published a seminal study that would provide key information to the identity and molecular function of the σ2 receptor (Alon et al. 2017b). In this paper, the authors used affinity chromatography in which the agarose beads were covalently modified with **JVW-1625**, a high affinity σ2 receptor ligand (Fig. 28.1). The authors were able to identify a small panel of candidate proteins from these chromatography experiments, and the protein that displayed high binding of [³H]DTG proved to be TMEM97, which has also been named MAC30, a membrane protein previously implicated in a number of cancers. TMEM97 is also a binding partner of the protein NPC1. NPC1 is a lysosomal cholesterol transporter, and loss of this protein leads to the fatal lysosomal storage disorder Niemann-Pick disease type C1.

The authors of this study found that siRNA knockdown of TMEM97 in PC-12 cells resulted in a large reduction in binding of [³H]DTG. Furthermore, overexpression of TMEM97 in sf9 cells, an insect cell line that does not express TMEM97, resulted in high binding of [³H]DTG. Overexpression of PGRMC1 in the sf9 cells did not result in an increase in binding of [³H]DTG, which was consistent with the data reported by Abate et al. (2015) and Chu et al. (2015). Finally, introduction of point mutations in several critical residues (Asp56 and Asp29) resulted in a loss of binding of [³H]DTG. Taken collectively, these data confirm that the molecular identification of the σ2 receptor protein, and the gene that encodes that protein, is TMEM97. This observation has led to this protein being termed "σ2 receptor/TMEM97" in some literature reports (Sahn et al. 2017; Scott et al. 2018a; Vazquez-Rosa et al. 2019a).

28.3.3 The Role of the σ2 Receptor in Cholesterol Trafficking

The data described above proved to be instrumental in the identification of the role of the σ2 receptor in cell biology. First, the identification of the σ2 receptor as TMEM97, and the association of this protein with NPC1, strongly implicated this receptor in cholesterol trafficking (Alon et al. 2017b). Second, identification of the σ2 receptor as a binding site in the PGRMC1 protein complex also implicated this protein in cholesterol trafficking since the PGRMC1 has been shown to interact with the LDL receptor, a key process in the cellular uptake of cholesterol (see review by Cahill 2007). Third, the increased rate of internalization of gold nanocages functionalized with the σ2 agonist, **SV119** (Sun et al. 2014), suggested that the endogenous ligand for the σ2 receptor had a high molecular weight; the size of LDL particles range between 22 and 27.5 nm, which is smaller than the size of the gold nanocage described above. Taken collectively, these data suggested that the PGRMC1 protein complex containing the "putative σ2 receptor binding site" consisted of a trimeric complex of σ2 receptor/TMEM97, PGRMC1, and the LDL receptor.

Using the above information, Riad et al. (2018) conducted a series of studies that confirmed the existence of this trimeric complex. Using HeLa cells and the CRISPR/cas 9 gene editing, this group found that a complete knockout of TMEM97 (TMEM97(−) cells) led to a complete loss of binding of [^{125}I]**RHM-4** and a dramatic (but not complete) reduction in the binding of [^{3}H]DTG (Fig. 28.2). A knockout of PGRMC1 in the HeLa cells (PGRMC1(−) cells) resulted in no change in the density of σ2 receptors measured with both radioligands but a significant *reduction in the Kd* value of both [^{125}I]**RHM-4** and [^{3}H]DTG. Finally, knocking out both TMEM97 and PGRMC1 in HeLa cells (i.e., double knockout or TMEM97(−)/PGRMC1(−) cells) had the same effect as knocking out only TMEM97 (Fig. 28.2).

The next series of studies centered on the uptake of LDL particles radiolabeled with [^{3}H]cholesterol (i.e., [^{3}H]LDL). Knocking out TMEM97 resulted in a dramatic reduction in the rate of uptake of [^{3}H]LDL by the HeLa cells. Furthermore, knocking out PGRMC1 resulted in the same reduction in rate of uptake of [^{3}H]LDL by HeLa cells. Knocking out both proteins (i.e., double knockout cells) had the same effect as knocking out either TMEM97 or PGRMC1. These data indicated that both TMEM97 and PGRMC1 are integral in the rapid uptake of LDL by the LDL receptor.
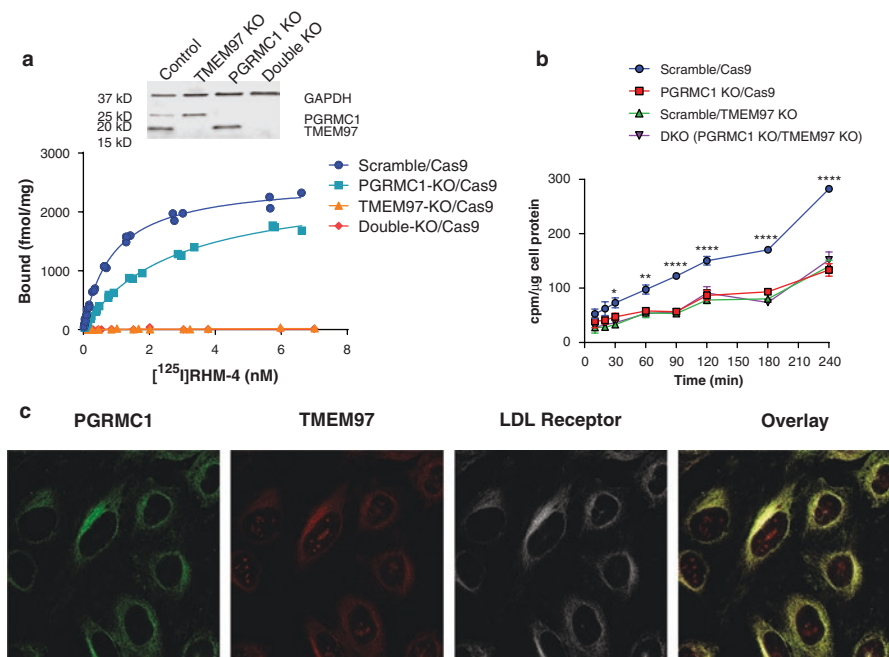
Fig. 28.2 Studies in CRISPR-edited HeLa cells confirming the existence of the TMEM97/σ2 receptor-PGRMC1-LDL receptor complex. (**a**) In vitro binding studies using [^{125}I]**RHM-4** as the radioligand. (**b**) Reduction in uptake of [^{3}H]LDL in the TMEM97/σ2 receptor, PGRMC1, and double k/o cells. (**c**) Fluorescence microscopy studies in HeLa cells showing the co-localization of the TMEM97/σ2 receptor-PGRMC1-LDL receptor complex

The third set of studies used a series of antibody labeling studies with confocal microscopy and proximity ligation assays (PLA) to determine the localization of these proteins within the cells (Fig. 28.2). Under serum-starved conditions, it is well established that the LDL receptor localizes on one side of the plasma membrane. A similar observation was made with the localization of both TMEM97 and PGRMC1. Co-localization studies suggested that all three proteins were co-localized. To better visualize the trimeric complex, the authors conducted a series of PLA experiments, a technique that is used to identify protein-protein interactions. A PLA signal was observed when cells were labeled with a pairwise combination of antibodies targeting LDL receptor-TMEM97, LDL receptor-PGRMC1, and TMEM97-PGRMC1. Knocking out TMEM97 eliminated the PLA signal from the LDL-TMEM97 and TMEM97-PGRMC1 labeled cells, but not the LDL receptor-PGRMC1 labeled cells. Similarly, knocking out PGRMC1 eliminated the PLA signal from LDL receptor-PGRMC1 and TMEM97-PGRMC1 cells, but not LDL receptor-TMEM97 labeled cells. Finally, the double knockout cells did not generate a PLA signal with any of the antibody combinations. *These data clearly demonstrate that the TMEM97, PGRMC1, and LDL receptor form a trimeric complex in HeLa cells and that this complex must be intact in order for there to be a rapid uptake of LDL by the cell.*

Figure 28.3 shows a structure of this trimeric complex that is consistent with the results described by Riad et al. (2018) and previous studies demonstrating that the
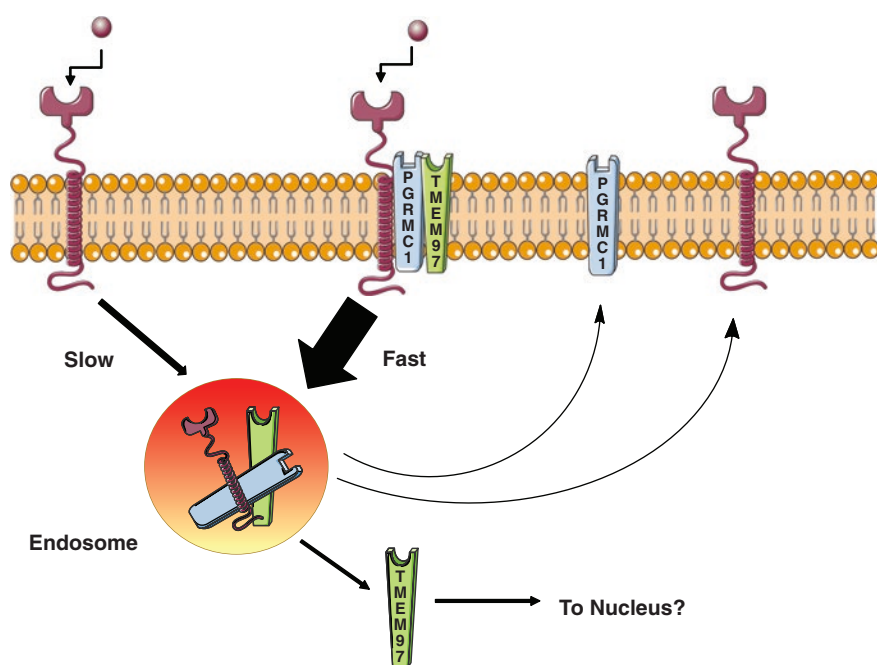
Fig. 28.3 Cartoon showing the hypothetical role of the TMEM97/σ2 receptor-PGRMC1-LDL receptor complex in the internalization of LDL in proliferating versus quiescent tumor cells

σ2 receptor is upregulated in proliferating versus quiescent cancer cells (Mach et al. 1997; Wheeler et al. 2000). Cholesterol is a key component of the cell membrane, and the demand for cholesterol is much higher in proliferating than in quiescent cells. Therefore, the "slow" uptake mechanism of LDL uptake is adequate to provide the cholesterol needed when cells are not actively dividing (i.e., quiescent or senescent cells). Consequently, the density of σ2 receptors/TMEM97 (and possibly PGRMC1) is low. However, when cells enter a proliferative state, this slow mechanism is not able to provide the amount of cholesterol needed for synthesis of the cell membrane and other cholesterol-rich organelles. Under these conditions, the "rapid" mechanism of LDL uptake is required, one that involves formation of a trimeric complex consisting of the LDL receptor, TMEM97, and PGRMC1. Therefore, there is an upregulation of the σ2 receptor/TMEM97 (and possibly PGRMC1) in order to increase the level of the trimeric complex in proliferating cells. This hypothesis of "fast" and "slow" uptake mechanisms of LDL is completely consistent with the data reported by Wheeler and colleagues and their characterization of the up- and down-regulation of the σ2 receptor in 66P and 66Q cells (Wheeler et al. 2000).

28.4   Role of the σ2 Receptor in the CNS

28.4.1 Pharmacological Studies

Although the σ2 receptor has been frequently associated with cancer cell biology because of its high density in proliferating breast cancer cells, σ2 receptor ligands have been shown to have pharmacological properties in the CNS. For example, Lu 28-179 (i.e., Siramesine), a high affinity σ2 receptor agonist having moderate selectivity versus σ1 receptors (Ki for σ2 receptor = 0.12 nM; Ki for σ2 receptor = 17 nM), was initially evaluated as an anxiolytic agent. Subsequent studies indicated that siramesine displayed antidepressant properties in rodents.

The σ2 receptor/PGRMC1 complex has been shown to play a role in neurodegenerative diseases, such as Alzheimer's disease, where σ2 receptor ligands have been found to reduce synaptic loss due to Aβ oligomers and facilitate neuroprotective and anti-inflammatory properties in models of neurodegeneration. For example, Izzo et al. conducted a series of experiments where they discovered that the σ2 receptor mediates Aβ42 oligomer binding to synaptic puncta on neurons (Izzo et al. 2014a, b). Their work describes that Aβ oligomers act as ligands for the σ2 receptor/PGRMC1 receptor complex and that σ2 expression is upregulated in cultured neurons upon exposure to Aβ oligomers. They reported that their series of compounds, which they described as antagonists for the σ2 receptor/PGRMC1 receptor complex, displaced bound oligomers in neuronal synapses and prevented further binding of Aβ42 oligomers in neuronal cultures; moreover, their studies showed that σ2 receptor/PGRMC1 complex antagonists inhibited oligomer-induced synaptic loss in neuronal cultures. Due to the ability of their compounds to displace pre-bound oligomers, they conclude that these σ2 ligands function as allosteric antagonists for the σ2 receptor/PGRMC1 receptor complex, rather than direct competitive antagonists. The compounds were able to enter the brain, have an 80% receptor occupancy of the σ2 receptor/PGRMC1 receptor complex, and,

importantly, restored memory deficits in the APP transgenic mouse model of Alzheimer's disease (AD). Phase 1 and 2 clinical trials of a compound designated **CT1812**, which was developed by Cognition Therapeutics, Inc., are currently ongoing in Alzheimer's disease patients.

Yi et al. showed that compounds in the norbenzomorphan class of σ2 receptor ligands modulate intracellular Ca^{2+} levels in the human SK-N-SH neuroblastoma cell line, resulting in an increased intracellular concentration (Yi et al. 2017). Dysregulation of Ca^{2+} homeostasis has been observed in neurodegenerative diseases such as AD, where Aβ oligomers cause dysregulation of Ca^{2+} signaling ultimately resulting in neurodegeneration. Their studies showed that a compound from this class of σ2 receptor ligands, **SAS-0132**, reduced neuroinflammation and reduced behavioral deficits in APP murine models, despite the fact that it had no effect upon Aβ burden or synaptic loss. Vazquez-Rosa et al. found that the σ2 receptor plays a role in other models of neurodegeneration such as traumatic brain injury (Vazquez-Rosa et al. 2019b). Rodents treated with another compound from their series, **DKR-1677**, showed reduced memory loss, axonal degeneration, and loss of neurons and oligodendrocytes.

The σ2 receptor has also been found to be a potential therapeutic target in the context of alcohol addiction. In a study from the same group, Scott et al. characterized a σ2 receptor specific ligand from the same series, **JVW-1034**, that enhanced behavioral performance in a *C. elegans* model of ethanol withdrawal (Scott et al. 2018b). This effect was attenuated when the worm orthologs of σ2 receptor-like protein or PGRMC1, Y38H6C.16, and VEM-1, respectively, were not present. They go on to show that targeting the σ2 receptor ligand with **JVW-1034** caused a reduction in voluntary ethanol intake in ethanol-dependent rats.

Taken together, these studies suggest that the σ2 receptor/PGRMC1 receptor complex represents a promising therapeutic target for ameliorating neurodegeneration, Aβ oligomer-induced synaptotoxicity, and the subsequent neuroinflammatory cascade that ultimately leads to cognitive impairment. The role of the σ2 receptor in facilitating cellular lipoprotein uptake via formation of a trimeric complex with PGRMC1 and the LDL receptor may also prove to be an important consideration in neurodegenerative therapeutics, as the apolipoprotein E4 allele is the greatest risk factor for development of Alzheimer's disease.

28.4.2 Autoradiography Studies

N-[4-(3,4-dihydro-6,7-dimethoxyisoquinolin-2(1H)-*yl*)butyl]-2-methoxy-5-methyl-benzamide (**RHM-1**), a conformationally flexible benzamide analogue, has been shown to have high affinity and selectivity for σ2 receptor versus σ1 receptor and the dopamine D_2 and D_3 receptors (Mach et al. 2004; Xu et al. 2005). Its high σ2 receptor affinity ($K_i < 10$ nM) and selectivity (σ1:σ2 ratio > 300) indicate that it's a useful radioligand to assess the σ2 receptors in the brain. Therefore, **RHM-1** was radiolabeled with tritium (specific activity = 80 Ci/mmol), and the binding of [^{3}H]**RHM-1** to σ2 receptors of aged human postmortem brain tissue (ranging from 84 to 96 years of age) was evaluated in vitro using quantitative autoradiography. Demographic details of the human brains are summarized in Table 28.1.

Table 28.1 Demographic details of human brains

Case number	Age (year)	Gender	Brain weight (g)	PMI (h)	Braak NFT	Braak amyloid	CDR
1	96	M	1165	12	1	0	0
2	90	M	1150	10	4	A	0
3	84	M	1010	5.5	1	B	0
4	91	M	1170	8.5	1	A	0

PMI postmortem interval, *CDR* clinical dementia rating
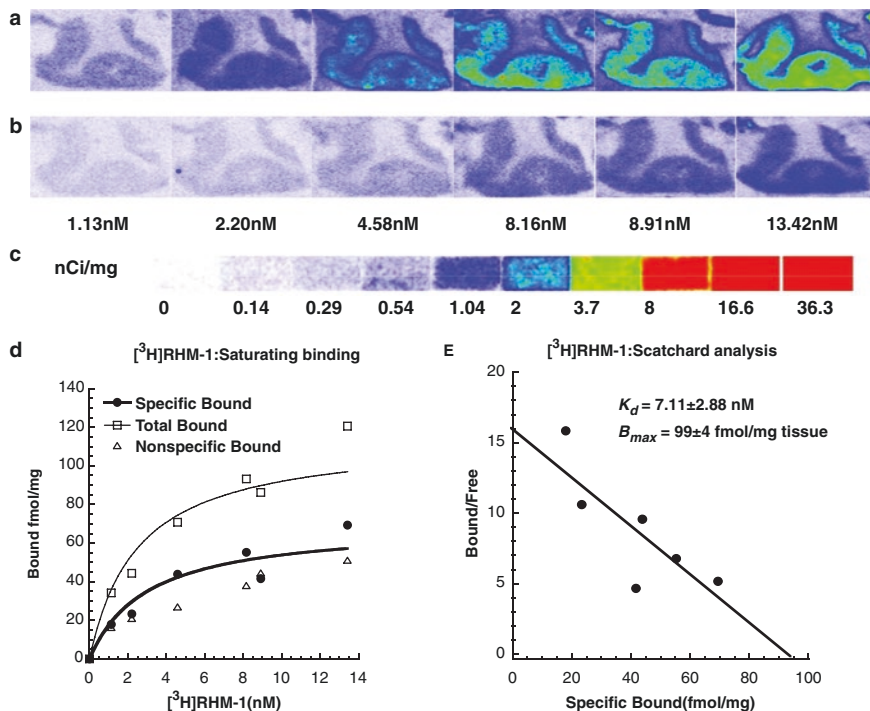
Fig. 28.4 Representative autoradiography saturation binding of [³H]**RHM-1** to σ2 receptors in the frontal cortex of a male cognitively healthy case. Representative autoradiograms show the binding of [³H]**RHM-1** to σ2 receptors under different radiotracer concentrations (panel **a**), Nonspecific binding was determined from adjacent tissue section which contained 1 uM siramesine to mask the σ2 receptor (panel **b**). [³H]Microscale standards (ranging from 0 to 36.3 nCi/mg) were also counted for the calibration of radioactivity (panel **c**). Quantitative autoradiography analysis of the saturation binding (panel **d**) and Scatchard plots (panel **e**) was performed to derive the binding densities (B_{max} values) and the dissociation constants (K_d values) from three sets of determinations

To measure the binding affinity, direct autoradiography saturation binding studies were conducted using [³H]**RHM-1** with a male brain (Fig. 28.4); the K_d values of the receptor-radioligand binding from Scatchard plots of [³H]**RHM-1** to human cortex are shown in Fig. 28.3. [³H]**RHM-1** binds with dissociation constant (K_d) of 7.11 nM to σ2 receptors in human frontal cortex.

To compare σ2 with σ1 receptors, direct autoradiography saturation binding studies were also conducted using the σ1-specific radioligand [³H](+)pentazocine in the adjacent tissue sections from the same subject. The K_d values of the receptor-radioligand binding from Scatchard plots of [³H](+)pentazocine to human cortex sections are shown in Fig. 28.5. [³H](+)pentazocine binds with dissociation constant (K_d) of 3.98 nM to σ1 receptors in human frontal cortex.

Autoradiography studies using single concentration radioligands of 8 nM [³H]**RHM-1** and 4 nM [³H](+)pentazocine were conducted in three additional male subjects, and the absolute σ2 and σ1 receptor density values (B_{max}) were calculated using the saturation binding isotherm (i.e., Michaelis-Menten equation): $B_{max} = B(1 + K_d/L)$, where B_{max} is the receptor density, B is the apparent binding density measured using single radioligand concentration, L is the radioligand concentration, and K_d is the equilibrium dissociation constant. In this study, the L and
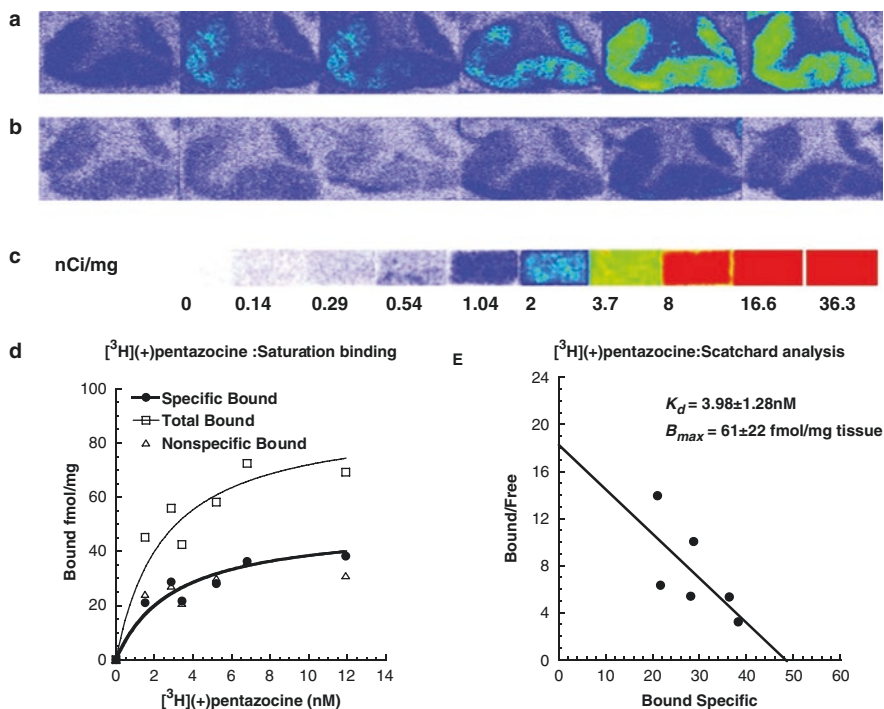
Fig. 28.5 Binding density and affinity of [³H](+)pentazocine to σ1 receptors in the adjacent sections of frontal cortex from the same male subject as shown in Fig. 28.1. Autoradiograms show the binding of [³H](+)pentazocine to σ1 receptors under different radiotracer concentrations (panel **a**). Nonspecific binding was determined from adjacent tissue section which contained 10 μM haloperidol to mask the σ1 receptor (panel **b**). [³H]Microscale standards (ranging from 0 to 36.3 nCi/mg) were also counted for the calibration of radioactivity (panel **c**). Quantitative analysis of the binding was performed to derive the saturation curve (panel **d**), and Scatchard plots (panel **e**) were used to determine the binding densities (B_{max} values) and dissociation constants (K_d values) from three sets of determinations

Table 28.2 Comparison of σ1 and σ2 receptor densities (fmol/mg) in the frontal cortex of aged male human brains

Density (fmol/mg tissue)	σ2 receptor	σ1 receptor	σ2/σ1 ratio	Age (year)
Male (n = 4)	106.2 ± 8	70.5 ± 10.5*	1.6 ± 0.3	90.3 ± 2.5

Data were obtained from aged male healthy brains (n = 4) and presented as mean value ± SEM
*Denotes $p < 0.05$, student t test, σ2 versus σ1

K_d values were 8 and 7.11 nM for σ2 receptors and 4 and 3.98 nM for σ1 receptors, which were determined using saturation binding assay as shown in Figs. 28.4 and 28.5.

σ2 and σ1 receptors are highly expressed in the frontal cortex of heathy control brains. σ2 density (106.2 ± 8 fmol/mg tissue) is higher than σ1 receptor density (70.5 ± 10.5) in the frontal cortex with a ratio of ~1.6-fold, summarized in Table 28.2. The high binding density of σ2 receptor in the aged brains suggests that σ2 receptor may play an important role in the brain disorders, and further studies in both male and female controls, Alzheimer's and Parkinson disease brains, will be important in understanding the regulation of σ2 receptor in central nervous disorders.

28.4.3 PET Radiotracers for Imaging the σ2 Receptor

To date, a large number of [11]C- and ^{18}F-labeled radiotracers having a high affinity for σ2 receptors and good selectivity versus the σ1 receptor have been evaluated in in vivo imaging studies. The majority of these studies have focused on tumor imaging studies because of the high correlation of σ2 receptor density and the proliferative statue (i.e., P: Q ratio) of the tumor. The only σ2-selective PET radiotracer translated to human imaging studies is [^{18}F]**ISO-1** (Fig. 28.6). A preliminary study of [^{18}F]**ISO-1** in patients diagnosed with either lymphoma or breast or head and neck cancer demonstrated that it was possible to separate patients into high and low proliferative status based on a comparison of the PET results with the Ki-67 score of the tumor upon histological analysis (Dehdashti et al. 2013). That is, [^{18}F]**ISO-1** had a higher uptake in patients having a Ki-67 score > 0.4 and a lower tracer uptake in tumors below this cutoff value. A follow-up study in breast cancer patients revealed that there was a good correlation of [^{18}F]**ISO-1** when compared with Ki-67 score (McDonald et al. 2020). However, the dynamic range for [^{18}F]**ISO-1** uptake in tumors having a high versus low Ki-67 was low, which is likely due to the low aggressive nature of breast cancer versus other cancers (McDonald et al. 2020). In addition, [^{18}F]**ISO-1** has a very low brain uptake, which has been attributed to it being a substrate for P-glycoprotein (Mach, unpublished data). Therefore, [^{18}F]**ISO-1** is not a suitable PET radiotracer for imaging σ2 receptors in the CNS.

A number of promising PET radiotracers for imaging σ2 receptors in the CNS have been reported in recent years. The first PET radiotracer worth noting is [^{11}C]**SA5845** (Fig. 28.6), which has a good affinity for σ2 receptors and modest affinity versus σ1 receptors (Kortekaas et al. 2008). PET imaging studies in
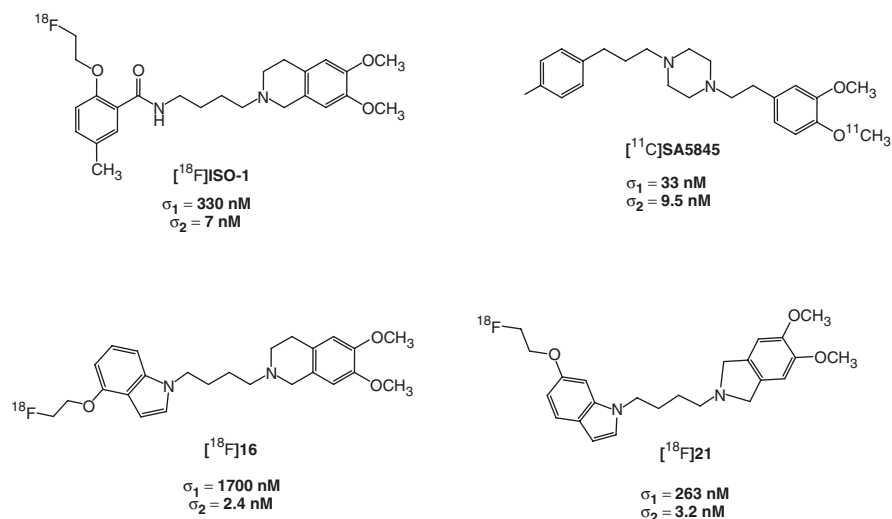
Fig. 28.6 Structures of representative PET radiotracers for imaging the σ2 receptor

nonhuman primates revealed high brain uptake of this radiotracer and kinetically irreversible binding to sigma receptors in vivo (Kortekaas et al. 2008). However, a potential limitation of this radiotracer is its relatively low selectivity versus σ1 receptors, which makes it difficult to identify changes in σ2 receptor density in CNS disorders.

Jia et al. (2019) and Wang et al. (2017) have recently reported two ^{18}F-labeled σ2-selective PET radiotracers that displayed a high uptake in both rodent and non-human primate brain (Fig. 28.6). Of the two PET radiotracers, [18F]**21** had the higher brain uptake. In vivo blocking studies and in vivo metabolite analysis indicated that [18F]**21** was specific for σ2 receptors; there were no radioactive metabolites of [18F]**21** observed in rodent brain, indicating that this radiotracer may be useful in quantitative PET imaging studies of σ2 receptors in humans.

28.5 Conclusions and Perspectives

The σ2 receptor has undergone a major scientific evolution in recent years. The initial recognition that this protein could serve as a receptor-based marker of the proliferative status of solid tumors resulted in an effort focused on the development of PET radiotracers for oncologic imaging studies. The molecular identification of the σ2 receptor as being a component of the TMEM97/σ2-PGRMC1-LDL receptor complex suggests that these PET imaging studies will be useful in evaluating the role of lipoprotein uptake in cell proliferation. Although promising results have been obtained in translational imaging studies with [18F]**ISO-1** in cancer patients, PET radiotracers having a higher affinity for σ2 receptors will likely be needed.

The recent studies showing that σ2 receptor ligands possess a diverse set of pharmacological properties in the CNS have opened a new avenue of research in PET probe development since many of the radiotracers used in the oncological imaging studies lacked either a high brain uptake or suitable σ2:σ1 receptor selectivity required for brain imaging studies. Two promising PET radiotracers were recently reported in imaging studies in rodents and nonhuman primates, but it is not clear if they are suitable for translational imaging studies in humans. The development of σ2 selective radiotracers for brain imaging studies will likely be an active area of research in the years to come.

References

Abate C, Niso M, Infantino V, Menga A, Berardi F (2015) Elements in support of the 'non-identity' of the PGRMC1 protein with the sigma2 receptor. Eur J Pharmacol 758:16–23

Ahmed IS, Rohe HJ, Twist KE, Craven RJ (2010a) Pgrmc1 (progesterone receptor membrane component 1) associates with epidermal growth factor receptor and regulates erlotinib sensitivity. J Biol Chem 285:24775–24782

Ahmed IS, Rohe HJ, Twist KE, Mattingly MN, Craven RJ (2010b) Progesterone receptor membrane component 1 (Pgrmc1): a heme-1 domain protein that promotes tumorigenesis and is inhibited by a small molecule. J Pharmacol Exp Ther 333:564–573

Al-Nabulsi I, Mach RH, Wang LM, Wallen CA, Keng PC, Sten K, Childers SR, Wheeler KT (1999) Effect of ploidy, recruitment, environmental factors, and tamoxifen treatment on the expression of sigma-2 receptors in proliferating and quiescent tumour cells. Br J Cancer 81:925–933

Alon A, Schmidt H, Zheng S, Kruse AC (2017a) Structural perspectives on Sigma-1 receptor function. Adv Exp Med Biol 964:5–13

Alon A, Schmidt HR, Wood MD, Sahn JJ, Martin SF, Kruse AC (2017b) Identification of the gene that codes for the sigma2 receptor. Proc Natl Acad Sci U S A 114(27):7160–7165

Beggiato S, Borelli AC, Borroto-Escuela D, Corbucci I, Tomasini MC, Marti M, Antonelli T, Tanganelli S, Fuxe K, Ferraro L (2017) Cocaine modulates allosteric D2-sigma1 receptor-receptor interactions on dopamine and glutamate nerve terminals from rat striatum. Mol Neurobiol 40:116–124

Blass BE, Rogers JP (2018) The sigma-2 (sigma-2) receptor: a review of recent patent applications: 2013–2018. Expert Opin Ther Pat 28:655–663

Borroto-Escuela DO, Narvaez M, Romero-Fernandez W, Pinton L, Wydra K, Filip M, Beggiato S, Tanganelli S, Ferraro L, Fuxe K (2019) Acute cocaine enhances dopamine D2R recognition and signaling and counteracts D2R internalization in Sigma1R-D2R heteroreceptor complexes. 56:7045-7055. Mol Neurobiol 56(10):7045–7055

Bowen WD, Hellewell SB, McGarry KA (1989) Evidence for a multi-site model of the rat brain sigma receptor. Eur J Pharmacol 163:309–318

Cahill MA (2007) Progesterone receptor membrane component 1: an integrative review. J Steroid Biochem Mol Biol 105:16–36

Chu UB, Mavlyutov TA, Chu ML, Yang H, Schulman A, Mesangeau C, McCurdy CR, Guo LW, Ruoho AE (2015) The Sigma-2 receptor and progesterone receptor membrane component 1 are different binding sites derived from independent genes. EBioMedicine 2:1806–1813

Dehdashti F, Laforest R, Gao F, Shoghi KI, Aft RL, Nussenbaum B, Kreisel FH, Bartlett NL, Cashen A, Wagner-Johnston N, Mach RH (2013) Assessment of cellular proliferation in tumors by PET using 18F-ISO-1. J Nucl Med 54:350–357

Gebreselassie D, Bowen WD (2004) Sigma-2 receptors are specifically localized to lipid rafts in rat liver membranes. Eur J Pharmacol 493:19–28

Hanner M, Moebius FF, Flandorfer A, Knaus HG, Striessnig J, Kempner E, Glossmann H (1996) Purification, molecular cloning, and expression of the mammalian sigma₁-binding site. Proc Natl Acad Sci U S A 93:8072–8077

Hayashi T, Su TP (2007) Sigma-1 receptor chaperones at the ER-mitochondrion interface regulate Ca(2+) signaling and cell survival. Cell 131:596–610

Hellewell SB, Bowen WD (1990) A sigma-like binding site in rat pheochromocytoma (PC12) cells: decreased affinity for (+)-benzomorphans and lower molecular weight suggest a different sigma receptor form from that of Guinea pig brain. Brain Res 527:244–253

Hellewell SB, Bruce A, Feinstein G, Orringer J, Williams W, Bowen WD (1994) Rat liver and kidney contain high densities of sigma-1 and sigma-2 receptors: characterization by ligand binding and photoaffinity labeling. Eur J Pharmacol 268:9–18

Hiranita T (2016) Identification of the Sigma-2 receptor: distinct from the progesterone receptor membrane component 1 (PGRMC1). J Alcohol Drug Depend 4:1–3

Hornick JR, Spitzer D, Goedegebuure P, Mach RH, Hawkins WG (2012) Therapeutic targeting of pancreatic cancer utilizing sigma-2 ligands. Surgery 152:S152–S156

Izzo NJ, Staniszewski A, Ta L, Fa M, Teich AF, Saeed F, Wostein H, Walko T 3rd, Vaswani A, Wardius M, Syed Z, Ravenscroft J, Mozzoni K, Silky C, Rehak C, Yurko R, Finn P, Look G, Rishton G, Safferstein H, Miller M, Johanson C, Stopa E, Windisch M, Hutter-Paier B, Shamloo M, Arancio O, LeVine H 3rd, Catalano SM (2014a) Alzheimer's therapeutics targeting amyloid beta 1–42 oligomers I: Abeta 42 oligomer binding to specific neuronal receptors is displaced by drug candidates that improve cognitive deficits. PLoS One 9:e111898

Izzo NJ, Xu J, Zeng C, Kirk MJ, Mozzoni K, Silky C, Rehak C, Yurko R, Look G, Rishton G, Safferstein H, Cruchaga C, Goate A, Cahill MA, Arancio O, Mach RH, Craven R, Head E, LeVine H 3rd, Spires-Jones TL, Catalano SM (2014b) Alzheimer's therapeutics targeting amyloid beta 1-42 oligomers II: Sigma-2/PGRMC1 receptors mediate Abeta 42 oligomer binding and synaptotoxicity. PLoS One 9:e111899

Jia H, Zhang Y, Huang Y (2019) Imaging sigma receptors in the brain: new opportunities for diagnosis of Alzheimer's disease and therapeutic development. Neurosci Lett 691:3–10

Kortekaas R, Maguire RP, van Waarde A, Leenders KL, Elsinga PH (2008) Despite irreversible binding, PET tracer [11C]-SA5845 is suitable for imaging of drug competition at sigma receptors-the cases of ketamine and haloperidol. Neurochem Int 53:45–50

Mach RH, Smith CR, Al-Nabulsi I, Whirrett BR, Childers SR, Wheeler KT (1997) Sigma-2 receptors as potential biomarkers of proliferation in breast cancer. Cancer Res 57:156–161

Mach RH, Huang Y, Freeman RA, Wu L, Vangveravong S, Luedtke RR (2004) Conformationally-flexible benzamide analogues as dopamine D₃ and sigma-2 receptor ligands. Bioorg Med Chem Lett 14:195–202

Mach RH, Zeng C, Hawkins WG (2013) The sigma2 receptor: a novel protein for the imaging and treatment of cancer. J Med Chem 56:7137–7160

Martin WR, Eades CG, Thompson JA, Huppler RE, Gilbert PE (1976) The effects of morphine- and nalorphine-like drugs in the nondependent and morphine-dependent chronic spinal dog. J Pharmacol Exp Ther 197:517–532

McDonald ES, Doot RK, Young AJ, Schubert EK, Pryma DA, Farwell MD, Tchou J, Nayak A, Ziober A, Feldman MD, DeMichele A, Clark AS, Shah PD, Lee H, Carlin SD, Mach RH, Mankoff DA (2020) Breast cancer (18)F-ISO-1 uptake as a marker of proliferation status. J Nucl Med 61(5):665–670

Navarro G, Moreno E, Aymerich M, Marcellino D, McCormick PJ, Mallol J, Cortes A, Casado V, Canela EI, Ortiz J, Fuxe K, Lluis C, Ferre S, Franco R (2010) Direct involvement of sigma-1 receptors in the dopamine D1 receptor-mediated effects of cocaine. Proc Natl Acad Sci U S A 107:18676–18681

Neubauer H, Clare SE, Wozny W, Schwall GP, Poznanovic S, Stegmann W, Vogel U, Sotlar K, Wallwiener D, Kurek R, Fehm T, Cahill MA (2008) Breast cancer proteomics reveals correlation between estrogen receptor status and differential phosphorylation of PGRMC1. Breast Cancer Res 10:R85

Riad A, Zeng C, Weng CC, Winters H, Xu K, Makvandi M, Metz T, Carlin S, Mach RH (2018) Sigma-2 receptor/TMEM97 and PGRMC-1 increase the rate of internalization of LDL by LDL receptor through the formation of a ternary complex. Sci Rep 8(1):16845

Sahn JJ, Mejia GL, Ray PR, Martin SF (2017) Sigma 2 receptor/Tmem97 agonists produce long lasting Antineuropathic pain effects in mice. ACS Chem Neurosci 8(8):1801–1811

Schmidt HR, Kruse AC (2019) The molecular function of sigma receptors: past, present, and future. Trends Pharmacol Sci 40:636–654

Schmidt HR, Zheng S, Gurpinar E, Koehl A, Manglik A, Kruse AC (2016) Crystal structure of the human sigma1 receptor. Nature 532:527–530

Scott LL, Sahn JJ, Ferragud A, Yen RC, Satarasinghe PN, Wood MD, Hodges TR, Shi T (2018a) Small molecule modulators of sigma2R/Tmem97 reduce alcohol withdrawal-induced behaviors. Neuropsychopharmacology 43(9):1867–1875

Scott LL, Sahn JJ, Ferragud A, Yen RC, Satarasinghe PN, Wood MD, Hodges TR, Shi T, Prakash BA, Friese KM, Shen A, Sabino V, Pierce JT, Martin SF (2018b) Small molecule modulators of sigma2R/Tmem97 reduce alcohol withdrawal-induced behaviors. Neuropsychopharmacology 43:1867–1875

Shoghi KI, Xu J, Su Y, He J, Rowland D, Yan Y, Garbow JR, Tu Z, Jones LA, Higashikubo R, Wheeler KT, Lubet RA, Mach RH, You M (2013) Quantitative receptor-based imaging of tumor proliferation with the sigma-2 ligand [(18)F]ISO-1. PLoS One 8:e74188

Su T-P (1982) Evidence for sigma opioid receptor: binding of [^{3}H]SKF-10047 to etorphine-inaccessible sites in Guinea-pig brain. J Pharmacol Exp Ther 223:284–290

Sun T, Wang Y, Wang Y, Xu J, Zhao X, Vangveravong S, Mach RH, Xia Y (2014) Using SV119-gold nanocage conjugates to eradicate cancer stem cells through a combination of photothermal and chemo therapies. Adv Healthc Mater 3:1283–1291

Tu Z, Dence CS, Ponde DE, Jones L, Wheeler KT, Welch MJ, Mach RH (2005) Carbon-11 labeled sigma-2 receptor ligands for imaging breast cancer. Nucl Med Biol 32:423–430

Tu Z, Xu J, Jones LA, Li S, Zeng D, Kung M-P, Kung HF, Mach RH (2010) Radiosynthesis and biological evaluation of a promising σ_2-receptor ligand radiolabeled with fluorine-18 or iodine-125 as a PET/SPECT probe for imaging breast cancer. Appl Radiat Isot 68:2268–2273

Vazquez-Rosa E, Watson MR, Sahn JJ, Hodges TR (2019a) Neuroprotective efficacy of a sigma 2 receptor/TMEM97 modulator (DKR-1677) after traumatic brain injury. ACS Chem Neurosci 10(3):1595–1602

Vazquez-Rosa E, Watson MR, Sahn JJ, Hodges TR, Schroeder RE, Cintron-Perez CJ, Shin MK, Yin TC, Emery JL, Martin SF, Liebl DJ, Pieper AA (2019b) Neuroprotective efficacy of a sigma 2 receptor/TMEM97 modulator (DKR-1677) after traumatic brain injury. ACS Chem Neurosci 10:1595–1602

Vilner BJ, John CS, Bowen WD (1995) Sigma-1 and sigma-2 receptors are expressed in a wide variety of human and rodent tumor cell lines. Cancer Res 55:408–413

Wang L, Ye J, He Y, Deuther-Conrad W, Zhang J, Zhang X, Cui M, Steinbach J, Huang Y, Brust P, Jia H (2017) (18)F-labeled indole-based analogs as highly selective radioligands for imaging sigma-2 receptors in the brain. Bioorg Med Chem 25:3792–3802

Wheeler KT, Wang LM, Wallen CA, Childers SR, Cline JM, Keng PC, Mach RH (2000) Sigma-2 receptors as a biomarker of proliferation in solid tumours. Br J Cancer 82:1223–1232

Xu J, Tu Z, Jones LA, Vangveravong S, Wheeler KT, Mach RH (2005) [^{3}H]N-[4-(3,4-dihydro-6,7-dimethoxyisoquinolin-2(1H)-yl)butyl]-2-methoxy-5-methylbenzamide: a novel sigma-2 receptor probe. Eur J Pharmacol 525:8–17

Xu J, Zeng C, Chu W, Pan F, Rothfuss JM, Zhang F, Tu Z, Zhou D, Zeng D, Vangveravong S, Johnston F, Spitzer D, Chang KC, Hotchkiss RS, Hawkins WG, Wheeler KT, Mach RH (2011) Identification of the PGRMC1 protein complex as the putative sigma-2 receptor binding site. Nat Commun 2:380

Yi B, Sahn JJ, Ardestani PM, Evans AK, Scott LL, Chan JZ, Iyer S, Crisp A, Zuniga G, Pierce JT, Martin SF, Shamloo M (2017) Small molecule modulator of sigma 2 receptor is neuroprotective and reduces cognitive deficits and neuroinflammation in experimental models of Alzheimer's disease. J Neurochem 140:561–575

Zeng C, Vangveravong S, Xu J, Chang KC, Hotchkiss RS, Wheeler KT, Shen D, Zhuang ZP, Kung HF, Mach RH (2007) Subcellular localization of sigma-2 receptors in breast cancer cells using two-photon and confocal microscopy. Cancer Res 67:6708–6716

Zeng C, Vangveravong S, Jones LA, Hyrc K, Chang KC, Xu J, Rothfuss JM, Goldberg MP, Hotchkiss RS, Mach RH (2011) Characterization and evaluation of two novel fluorescent sigma-2 receptor ligands as proliferation probes. Mol Imaging 10:420–433

PET Imaging of Synaptic Vesicle Protein 2A

29

Sjoerd J. Finnema, Songye Li, Zhengxin Cai, Mika Naganawa, Ming-Kai Chen, David Matuskey, Nabeel Nabulsi, Irina Esterlis, Sophie E. Holmes, Rajiv Radhakrishnan, Takuya Toyonaga, Yiyun Huang, and Richard E. Carson

Contents

S. J. Finnema (✉)
Department of Radiology and Biomedical Imaging, Yale Positron Emission Tomography Center, Yale University, New Haven, CT, USA

Integrated Science and Technology, Translational Imaging, AbbVie, North Chicago, IL, USA
e-mail: sjoerd.finnema@abbvie.com

S. Li · Z. Cai · M. Naganawa · M.-K. Chen · N. Nabulsi · T. Toyonaga · Y. Huang
Department of Radiology and Biomedical Imaging, Yale Positron Emission Tomography Center, Yale University, New Haven, CT, USA
e-mail: songye.li@yale.edu; jason.cai@yale.edu; mika.naganawa@yale.edu; ming-kai.chen@yale.edu; nabeel.nabulsi@yale.edu; takuya.toyonaga@yale.edu; henry.huang@yale.edu

D. Matuskey
Department of Radiology and Biomedical Imaging, Yale Positron Emission Tomography Center, Yale University, New Haven, CT, USA

Department of Psychiatry, Yale University, New Haven, CT, USA
e-mail: david.matuskey@yale.edu

I. Esterlis · S. E. Holmes · R. Radhakrishnan
Department of Psychiatry, Yale University, New Haven, CT, USA
e-mail: irina.esterlis@yale.edu; sophie.holmes@yale.edu; rajiv.radhakrishnan@yale.edu

R. E. Carson
Department of Radiology and Biomedical Imaging, Yale Positron Emission Tomography Center, Yale University, New Haven, CT, USA

Department of Biomedical Engineering, Yale University, New Haven, CT, USA
e-mail: richard.carson@yale.edu

Abstract

The synaptic vesicle protein 2A (SV2A) is an integral 12-transmembrane domain glycoprotein located in the membrane of synaptic vesicles and widely distributed throughout the brain. In 2004, SV2A was shown to be the molecular target of the antiepileptic drug levetiracetam. High-affinity SV2A ligands have been described by the pharmaceutical company UCB more recently, and this enabled the rapid development of SV2A positron emission tomography (PET) radioligands. Because synaptic vesicle proteins, such as SV2A, have previously been used as biomarkers of synaptic density, PET imaging of SV2A may have broad utility across neuropathological diseases. In this chapter we review the current status of SV2A PET imaging.

During the last few years, several SV2A radioligands have been synthesized and evaluated with PET in animals and human. Although [11C]levetiracetam was deemed an unsuitable radioligand, radiolabeled non-acetamide *racetams* (a class of drugs that contain the pyrrolidone moiety) such as [11C]UCB-J and more recently [18F]SynVesT-1 and [18F]SynVesT-2 provided high-quality brain PET imaging results across species. Regional brain SV2A levels were shown to closely correlate with those of synaptophysin, another commonly used marker for synaptic density. PET studies using SV2A-targeting antiepileptic drugs levetiracetam and brivaracetam confirmed that the radioligands bind specifically to SV2A and provided valuable insight in to the potential use of a reference region approach for quantification of brain PET signal. Several initial PET studies examining SV2A radioligand binding in patient groups have been reported, and SV2A was found to be reduced in disease-associated brain regions in epilepsy, Alzheimer's disease, major depressive disorder and posttraumatic stress disorder, Parkinson's disease, and schizophrenia.

In conclusion, PET imaging of SV2A has rapidly developed, and qualified radioligands are now available. Initial PET studies in humans indicate that SV2A loss might be specific to disease-associated brain regions and consistent with synaptic density loss. Future studies warrant the use of fluorine-18 labeled radioligands in larger patient cohorts to establish the clinical value of SV2A PET imaging and its potential for diagnosis and progression monitoring of neuropathological diseases, as well as efficacy assessment of disease-modifying therapies.

29.1 Synaptic Vesicle Protein 2

The synaptic vesicle protein 2 (SV2) constitutes a conserved protein family in vertebrates (Buckley and Kelly 1985) and is an integral 12-transmembrane domain glycoprotein (Bajjalieh et al. 1992) located on secretory vesicles of neurons and endocrine cells (Buckley and Kelly 1985; Floor and Feist 1989). The SV2 protein sequence has been found to be very similar to sequences of transporter proteins, and SV2 was therefore initially considered to be a vesicular transport protein (Bajjalieh et al. 1992; Feany et al. 1992). SV2 is critical for normal synaptic function and plays a role in vesicle trafficking and exocytosis (Nowack et al. 2010), although its exact functions remain to be fully elucidated (see for reviews Mendoza-Torreblanca et al. 2013; Bartholome et al. 2017).

Further characterization of the SV2 protein has resulted in the identification of three isoforms that share approximately 60% of their sequences (Bajjalieh et al. 1994; Janz and Sudhof 1999). The isoforms have a different regional distribution in the brain; SV2A is ubiquitously expressed in virtually all synapses, while SV2B is more restricted but present throughout the rat brain (Janz and Sudhof 1999; Bajjalieh et al. 1993, 1994). In contrast, SV2C was observed in only a few rat brain areas, including the globus pallidus, substantia nigra, midbrain, brainstem, and olfactory bulb (Janz and Sudhof 1999). On the neuronal level, SV2A is thought to be located in glutamatergic and GABAergic neurons, while SV2B might be more restricted to glutamatergic neurons and SV2C to GABAergic neurons (see for review Bartholome et al. 2017).

29.2 Development of SV2A PET Radioligands

In 2004, Lynch et al. demonstrated that SV2A was the molecular target of the antiepileptic drug levetiracetam (Lynch et al. 2004; Gillard et al. 2006). Considering the clinical success of levetiracetam as an effective antiepileptic drug, UCB started an extensive medicinal chemistry program to identify a novel generation of antiepileptic drugs with increased SV2A affinity and anti-seizure potency, ultimately resulting in the development of brivaracetam (Gillard et al. 2011; Klein et al. 2018).

As a first attempt to develop a SV2A PET radioligand, levetiracetam was labeled with carbon-11 as [^{11}C]levetiracetam (Fig. 29.1) (Cai et al. 2014) but was not evaluated further, probably due to its low binding affinity to SV2A (K_i = 1.74 μM) (Danish et al. 2017). In the meanwhile, high binding affinity SV2A-specific ligands with the pyrrolidinone pharmacophore were synthesized and evaluated as candidates for SV2A PET (Mercier et al. 2014, 2017). Three of the SV2A ligands described in the 2014 paper were labeled with carbon-11 or fluorine-18 as [^{11}C]UCB-A (Estrada et al. 2016), [^{18}F]UCB-H (Warnock et al. 2014; Becker et al. 2017; Warnier et al. 2016; Bretin et al. 2013), and [^{11}C]UCB-J (Nabulsi et al. 2016) (Fig. 29.1), and all were initially evaluated in nonhuman primates at the Yale PET Center.
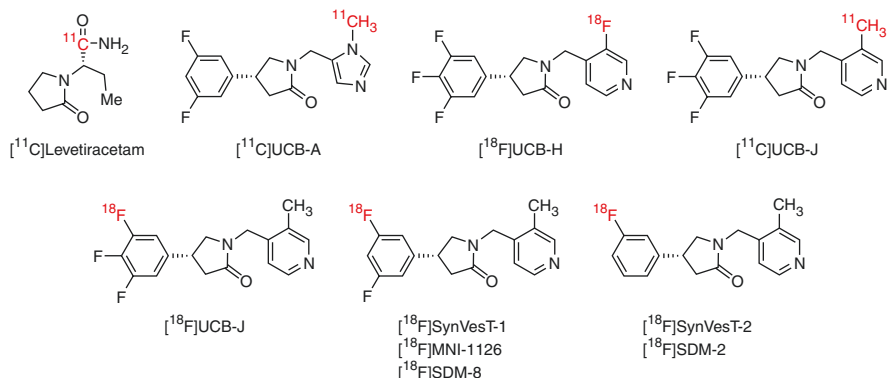
Fig. 29.1 Chemical structures of SV2A PET radioligands [11C]levetiracetam, [11C]UCB-A, [18F]UCB-H, [11C]UCB-J, [18F]UCB-J, [18F]SynVesT-1, and [18F]SynVesT-2. Modified from Cai et al. (2019)
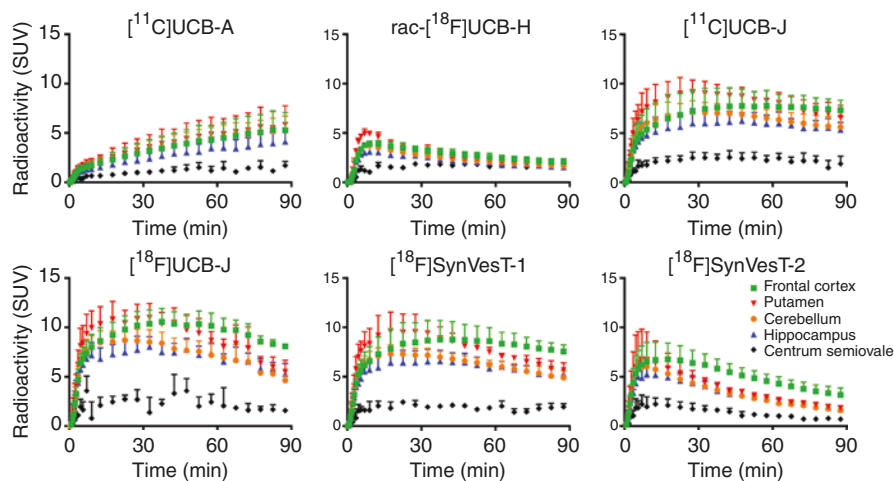
Fig. 29.2 Regional brain time-activity curves of SV2A PET radioligands [11C]UCB-A ($n = 5$), rac-[18F]UCB-H ($n = 2$), [11C]UCB-J ($n = 6$), [18F]UCB-J ($n = 4$), [18F]SynVesT-1 ($n = 3$), and [18F]SynVesT-2 ($n = 3$) evaluated in rhesus monkeys. Error bars (up) denote standard deviation. Modified from Cai et al. (2019)

The preclinical results demonstrated that [11C]UCB-J possessed the most suitable pharmacokinetic profile as a brain PET radioligand, i.e., rapid and high brain uptake, reversible binding kinetics, and relatively low nonspecific binding in white matter (Nabulsi et al. 2016), while [11C]UCB-A showed slower brain penetration and apparently irreversible kinetics in the brains of nonhuman primates, making quantitative analysis more challenging (Fig. 29.2). Furthermore, rac-[18F]UCB-H showed relatively low specific binding in the nonhuman primate brain, probably due to its lower binding affinity to SV2A ($pIC_{50} = 7.8$ for UCB-H vs. 8.2 for UCB-J)

(Mercier et al. 2014; Nabulsi et al. 2016). After translation to clinical studies, the human imaging data were highly consistent with preclinical data, reaffirming [^{11}C]UCB-J as an ideal imaging radioligand for SV2A in the brain (Finnema et al. 2016), with [^{11}C]UCB-A possessing slow binding kinetics (Lubberink et al. 2017) and [^{18}F]UCB-H low specific binding in the brain (Bahri et al. 2017), limiting both [^{11}C]UCB-A and [^{18}F]UCB-H as PET radioligands for quantifying SV2A in the brain.

As preliminary data of [^{11}C]UCB-J in preclinical and clinical PET studies were promising, fluorine-18 labeled SV2A radioligands became of interest as the short half-life of carbon-11 (20.4 min) limits the production of [^{11}C]UCB-J to PET centers with cyclotrons. Initial work focused on the synthesis of fluorine-18 labeled counterparts of UCB-J, i.e., [^{18}F]UCB-J (Fig. 29.1), and indeed [^{18}F]UCB-J provided very similar results as [^{11}C]UCB-J in nonhuman primates (Li et al. 2019b). However, due to the harsh labeling conditions and the need for chiral HPLC separation in the production of [^{18}F]UCB-J, the process was considered unsuitable for routine production supporting clinical studies. A second approach focused on the synthesis of mono- and di-fluorinated UCB-J analogs, i.e., [^{18}F]SynVesT-1 ([^{18}F]SDM-8, [^{18}F]MNI-1126) (Li et al. 2019a; Constantinescu et al. 2019) and [^{18}F]SynVesT-2 ([^{18}F]SDM-2) (Cai et al. 2020) (Fig. 29.1). In nonhuman primates, the brain pharmacokinetics of [^{18}F]SynVesT-2 were faster than [^{11}C]UCB-J (Fig. 29.2), while regional binding potential (BP_{ND}) values of the two radioligands were very similar. [^{18}F]SynVesT-1 possessed similar pharmacokinetic profile and higher BP_{ND} values as [^{11}C]UCB-J (Fig. 29.2). [^{18}F]SynVesT-1 was evaluated in humans and displayed outstanding imaging characteristics, i.e., very high brain uptake, fast and reversible kinetics, and excellent test-retest reproducibility and binding specificity to SV2A (Li et al. 2019c). Compared to [^{11}C]UCB-J, [^{18}F]SynVesT-1 displayed higher specific binding signals (i.e., BP_{ND}). Recent human studies with [^{18}F]SynVesT-2 showed slightly lower BP_{ND} but exhibited faster kinetics, as in nonhuman primates. The availability of these fluorine-18 labeled SV2A PET radioligands provides the opportunity for multicenter clinical validation of SV2A PET in a variety of neuropsychiatric disorders.

29.3   SV2A as a Biomarker of Synaptic Density

The human brain is estimated to contain close to 100 billion neurons (Azevedo et al. 2009), and with estimates of each neuron potentially contacting >1000 synapses, there might be >100 trillion synapses. Structural disturbances or reductions in synapses can result in dysfunctional neuronal signaling and in network dysfunctions. Synaptic vesicle proteins, such as SV2A, have previously been established as histological markers of synaptic density (De Camilli et al. 1983; Goelz et al. 1981; Masliah et al. 1990) due to their highly restricted localization to synaptic boutons. SV2A is a promising biomarker of synaptic density as it is ubiquitously and homogeneously present in synaptic vesicles (Bajjalieh et al. 1994) and has relative low variation in copy number per vesicle, i.e., SV2 was most "monodispersed" (Mutch et al. 2011).

To examine if [^{11}C]UCB-J binding to SV2A could be used as an index of synaptic density, a baboon (*Papio anubis*) underwent a [^{11}C]UCB-J PET measurement after which the animal was euthanized and the brain harvested for post-mortem tissue studies. Analysis of regional brain tissues confirmed that the PET-measured [^{11}C]UCB-J distribution volume (V_T) correlated well with the regional distribution of SV2A measured by radioligand homogenate binding assay (Fig. 29.3a) and western blot (Fig. 29.3b). Importantly, there was also good correlation between SV2A and the "gold standard" synaptic density marker synaptophysin in western blot (Fig. 29.3c) and confocal microscopy experiments, indicating that SV2A can be
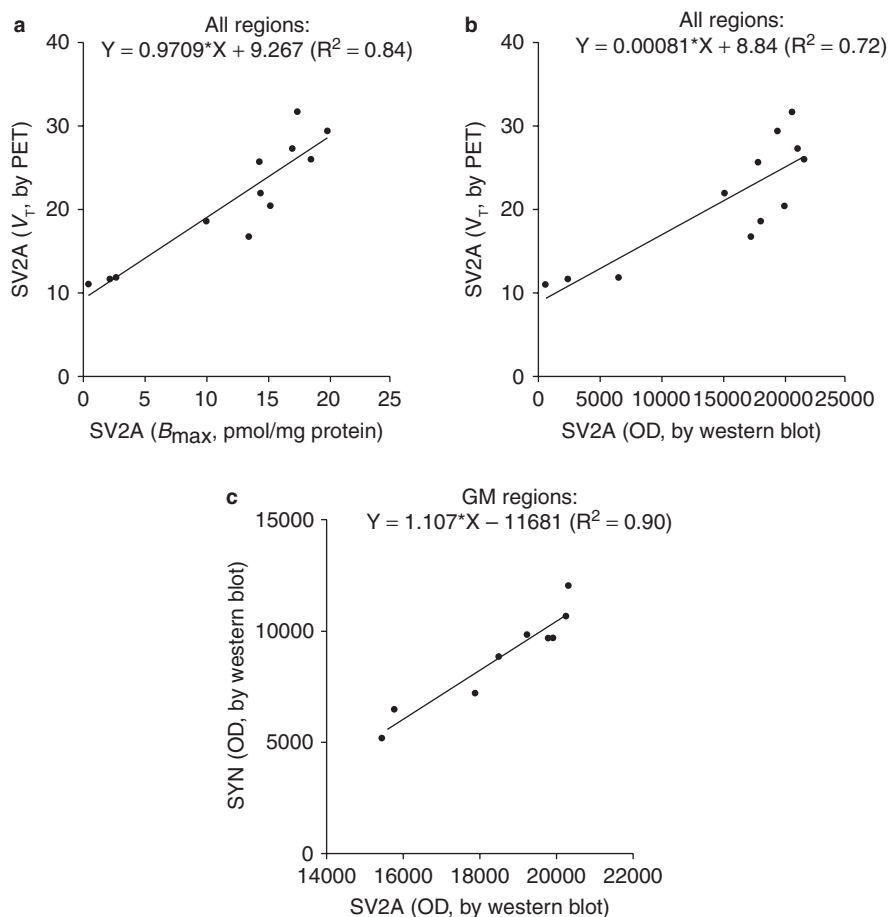
Fig. 29.3 (**a**) Correlation between regional in vitro SV2A (B_{max}) measured using tissue homogenate binding and in vivo SV2A (V_T by PET). Data are 12 brain regions. (**b**) Correlation between regional in vitro SV2A (optical density (OD) by western blot) and in vivo SV2A (V_T by PET). Data are 12 brain regions. (**c**) Correlation between in vitro SV2A and in vitro synaptophysin density in gray matter regions determined using western blot analyses. Data are nine brain regions. Modified from Finnema et al. (2016)

used as an alternative to synaptophysin for accurate quantification of synaptic density (Finnema et al. 2016). Analogous biochemical studies with resected human tissue following epilepsy surgery show promising results. Further studies with larger sample sets from post-mortem human tissue samples are required to more firmly establish the value of SV2A as a biomarker of synaptic density.

29.4   Quantification of SV2A PET Radioligands

Evaluation of the pharmacokinetic properties of SV2A PET radioligands in humans revealed that the best models to quantify regional V_T values require measurements of arterial input function: the one-tissue compartment model (1TC) for [^{11}C]UCB-J (Finnema et al. 2018; Koole et al. 2019; Mansur et al. 2020) and the two-tissue compartment model (2TC) or Logan graphical analysis for [^{18}F]UCB-H (Bahri et al. 2017). Furthermore, excellent test-retest reproducibility and low noise V_T parametric images can be obtained with the 1TC model for [^{11}C]UCB-J (Finnema et al. 2018).

Noninvasive imaging with [^{11}C]UCB-J would not only make blood sampling redundant but is also desired to increase subject comfort and simplify imaging protocols. It is also of interest to conduct parametric imaging to explore SV2A changes in the whole brain using statistical mapping in larger study cohorts. There are two promising kinetic analysis methods which could be used for noninvasive parametric imaging of [^{11}C]UCB-J: using the reference tissue model or the standard uptake value ratio (SUVR) approach. Before implementing these methods, identification of a reference tissue was needed first.

For noninvasive quantification of [^{11}C]UCB-J specific binding, the centrum semiovale (CS) has been proposed as a reference region based on in vitro data (Finnema et al. 2016), which showed negligible concentrations of SV2A in CS in baboons by biochemical methods. However, a reduction in [^{11}C]UCB-J uptake was observed in CS V_T in displacement studies with levetiracetam and brivaracetam in humans (Finnema et al. 2016, 2019). Further assessment of CS as a reference region in drug occupancy studies revealed that CS V_T overestimated the non-displaceable distribution volume (V_{ND}) (Rossano et al. 2019; Koole et al. 2019) but showed a significant correlation between CS V_T and gray matter V_{ND}, which suggests that the CS remains a promising proxy reference region (Rossano et al. 2019). To avoid a spill-in from surrounding gray matter uptake, a core area of the CS (volume, 2 mL) was determined based on a probability map. Increasing the number of ordered subset expectation maximization (OSEM) iterations decreased the CS V_T values (35–40% overestimation at 4 iterations of 30 subsets) (Rossano et al. 2019).

Since 1TC is the model of choice with arterial blood sampling, simplified reference tissue model (SRTM) and SRTM2 were expected to work well as reference tissue models, and SRTM2 would improve the statistical quality of parametric imaging over SRTM. It has been reported that SRTM2 worked well with a sufficiently long acquisition (80 or 90 min) (Mertens et al. 2020), on a GE Signa PET/MR system. For shorter acquisition duration, the variance of k_2' estimates (i.e., the efflux rate from the CS region of interest) in SRTM2 increased, and SRTM2 failed

more often (11% of the scans at 50 min acquisition). However, the use of higher-resolution PET system (HRRT, high-resolution research tomograph), combined with the use of a small core CS region (2 mL), produced a noisy CS time-activity curve (TAC). This affected the estimation performance of k_2'. However, the 1TC k_2 value of CS was similar between healthy controls and patients (healthy control, 0.029 ± 0.003; Alzheimer's disease (AD), 0.028 ± 0.005; all participants, 0.028 ± 0.004 [1/min]) (Naganawa et al. 2018b). Therefore, SRTM2 with population k_2' is a promising method to generate high-resolution parametric BP_{ND} images, although this approach will require validation in other populations.

The ratio of tissue activity to plasma activity (i.e., apparent V_T) overestimated the 1TC V_T at any time point in a 90 min scan after bolus injection (Naganawa et al. 2018a). This was the case in both healthy controls and patients. However, the overestimation in the target regions and reference region (i.e., CS) tended to cancel out while computing the SUVR value (i.e., ratio of target tissue activity to CS activity). The choice of the acquisition time window is critical to compute SUVR values, since SUVR values continued to increase monotonically over time throughout a 2 h scan. When comparing SUVR-1 values from several 30 min acquisition time windows with the 1TC BP_{ND} values, the best match was observed at 60–90 min post-injection in healthy controls (Mertens et al. 2020; Koole et al. 2019) and patients with various diseases (Naganawa et al. 2018a). Similar results have recently been found for [^{18}F]SynVesT-1, which should allow the use of SUVR for application in large studies evaluating the effect of drug treatment in neurodegenerative disorders.

Evaluation of the other radioligands has also been conducted for the imaging and quantification of SV2A in humans. As expected, [^{11}C]UCB-A displayed slow kinetics leading to unreliable estimates of binding parameters (Lubberink et al. 2017), while the specific binding of [^{18}F]UCB-H was low, with BP_{ND} below 1.0 for all regions (Bahri et al. 2017). For [^{18}F]SynVesT-1, evaluation in humans reveals tissue kinetics similar to that of [^{11}C]UCB-J (Li et al. 2019c) (Fig. 29.4). The 1TC model fits the regional time-activity curves well and provides reliable estimates of regional V_T values, which are lower than those of [^{11}C]UCB-J. However, regional BP_{ND} values of [^{18}F]SynVesT-1 estimated with CS as reference region are higher than those of [^{11}C]UCB-J (Table 29.1). Also similar to [^{11}C]UCB-J, 60 min of acquisition time was sufficient to estimate 1TC V_T values. As for [^{18}F]SynVesT-2, its tissue kinetics in humans are substantially faster than those of [^{11}C]UCB-J and [^{18}F]SynVesT-1 (Fig. 29.4). Regional V_T and BP_{ND} values are also lower. However, due to its fast kinetics, a relative short acquisition (i.e., 30 min) is sufficient for stable estimates of regional V_T values.

In summary, there are to date five radioligands available for imaging and quantification of SV2A in humans, with three of them ([^{11}C]UCB-J, [^{18}F]SynVesT-1, and [^{18}F]SynVesT-2) displaying excellent imaging characteristics of high and reversible brain uptake, excellent test-retest reproducibility, and high specific binding. Application of radiolabeled SV2A radioligands, especially [^{18}F]SynVesT-1 and [^{18}F]SynVesT-2, will advance our understanding of neurologic and psychiatric
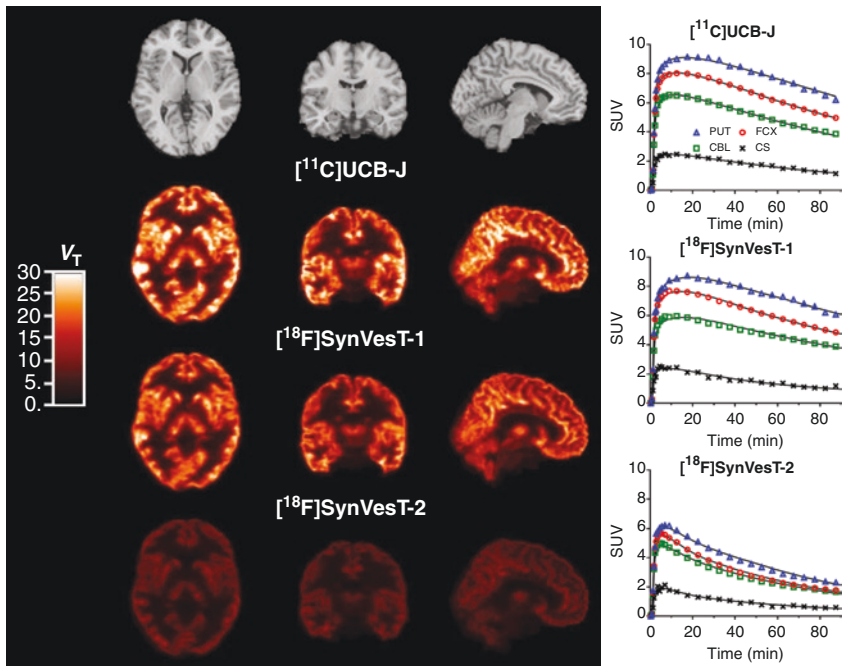
Fig. 29.4 Comparison of [^{11}C]UCB-J, [^{18}F]SynVesT-1, and [^{18}F]SynVesT-2 in one human subject. Left: MR and V_T images from PET measurements following injection of [^{11}C]UCB-J, [^{18}F]SynVesT-1, and [^{18}F]SynVesT-2. Right: Regional time-activity curves following injection of [^{11}C]UCB-J, [^{18}F]SynVesT-1, and [^{18}F]SynVesT-2. Solid lines represent the 1TC fit

disorders in large-scale longitudinal and cross-sectional studies in patient populations and facilitate evaluation of disease-modifying therapeutics.

29.5 PET Studies in Disease Populations

29.5.1 Epilepsy

Epilepsy is one of the most common neurological conditions with a prevalence of 0.5–1.0% (Bell and Sander 2001; Picot et al. 2008). It is characterized by spontaneous and recurrent seizures typically starting in a focal brain area referred to as the seizure onset zone (SOZ). Approximately 20–40% of patients develop drug-resistant epilepsy (Picot et al. 2008; Kwan and Brodie 2000; Cockerell et al. 1995) with a high incidence (50–70%) in temporal lobe epilepsy (TLE), the most common type of epilepsy in adults (Schmidt and Loscher 2005). In patients with medically refractory epilepsy, surgical resection of the epileptogenic tissue may provide high quality-of-life benefit (Jette et al. 2016). Identification of the SOZ can however be challenging and is typically guided by multi-modality data, including magnetic

Table 29.1 Comparison of BP_{ND} values of [^{11}C]UCB-J, [^{18}F]SynVesT-1, and [^{18}F]SynVesT-2 in humans

Radioligand	Thalamus	Putamen	Frontal	Parietal	Occipital	Temporal	Amygdala	Hippocampus	Caudate	Subjects
[^{11}C]UCB-J	2.22	3.69	3.15	3.37	3.37	3.61	2.95	2.18	2.58	$n = 3$
[^{18}F]SynVesT-1	2.92	4.48	4.01	4.38	4.34	4.63	4.06	2.84	3.39	$n = 6$
[^{18}F]SynVesT-2	1.94	3.02	2.40	2.48	2.43	2.71	2.31	1.59	1.59	$n = 3$

resonance (MRI) and PET imaging (Martinkovic et al. 2014). 2-Deoxy-2-^{18}F-fluoro-D-glucose ([18F]FDG) is the clinical standard PET radioligand, but other radioligands have shown promise for improved identification of the SOZ when compared to anatomical MRI (Theodore 2017).

SV2A is the binding site for the antiepileptic drugs levetiracetam and brivaracetam (Gillard et al. 2006; Lynch et al. 2004; Gillard et al. 2011). In vitro studies using resected brain tissue have shown that SV2A expression is reduced by 30–50% in the epileptogenic anterior temporal neocortex of patients with TLE (Feng et al. 2009). Similar reductions in SV2A have been observed in the hippocampus of TLE patients with hippocampal sclerosis using western blot analysis (Van Vliet et al. 2009) and quantitative mRNA expression (Crevecoeur et al. 2014). Furthermore, in rat models of epilepsy, SV2A loss has been shown to contribute to epileptogenesis and pharmacoresistance (Van Vliet et al. 2009; Hanaya et al. 2012; Wang et al. 2014). For instance, SV2A knockout mice manifest a severe seizure phenotype (Crowder et al. 1999; Janz et al. 1999).

In the first pilot study in subjects with TLE ($n = 3$), [11C]UCB-J binding was asymmetric in the mesial temporal lobe, consistent with SV2A loss in the ipsilateral mesial temporal lobe (Finnema et al. 2016). In a follow-up study, 11 subjects with TLE and medial temporal lobe sclerosis (MTS) and 11 control subjects were investigated (Finnema et al. 2017). In the TLE MTS subjects with hippocampal volumetric asymmetry of 25 ± 11%, [11C]UCB-J BP_{ND} values were lower in the sclerotic hippocampus when compared to control subjects (Fig. 29.5). Following partial volume correction, hippocampal [11C]UCB-J BP_{ND} asymmetry indices were 37 ± 19% in the hippocampus with very limited asymmetry in other brain regions. The corresponding asymmetry in hippocampal [18F]FDG uptake was 22 ± 7% and correlated
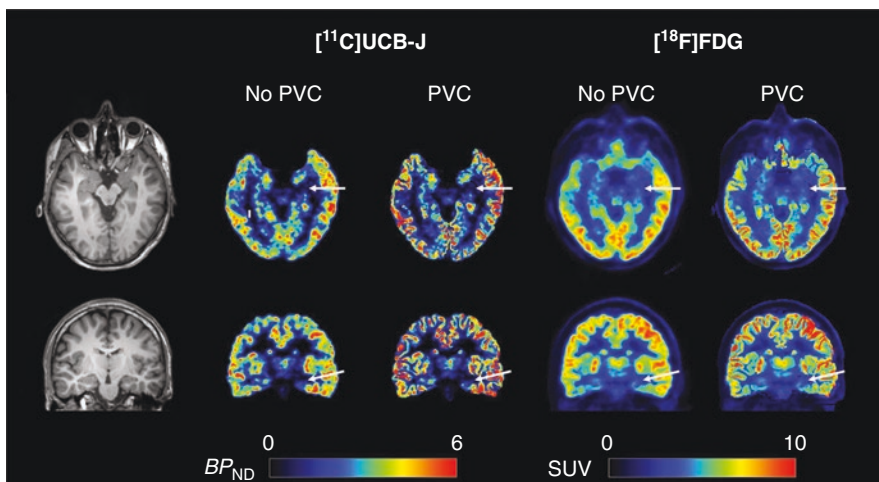
Fig. 29.5 Parametric images without and with partial volume correction (PVC) of [11C]UCB-J BP_{ND} (left) and [18F]FDG standard uptake values (SUV, right) reveal unilateral mesial temporal sclerosis (MTS) in a representative subject with temporal lobe epilepsy (TLE)

with that of [^{11}C]UCB-J BP_{ND} across subjects. Notably, hippocampal asymmetries in [^{11}C]UCB-J binding were 1.7-fold larger than those of [^{18}F]FDG uptake. In summary, [^{11}C]UCB-J binding was reduced in the seizure onset zone of TLE subjects with MTS. PET imaging of SV2A holds promise as a biomarker approach in the presurgical selection and evaluation of TLE patients and may improve the sensitivity of molecular imaging for SOZ detection. Future studies should evaluate SV2A imaging in patients with TLE without MTS and in extra temporal non-lesional epilepsy patients.

29.5.2 Alzheimer's Disease and Other Dementias

Aging is a normal physiologic process, which includes gradual decrease in cognitive function as compared to healthy young adults. Cognitive function refers to complex cortical functions predominantly relating to memory, language, judgment, reasoning, planning, behavior, and executional abilities. Dementia is abnormal cognitive decline that is greater than expected as compared to age-matched controls and often causes disability or affects the ability to independently perform daily living activities. Dementia has become a global public health issue with an increasingly aging population. Dementia can be attributed to many causes, the most common and devastating one is AD accounting for more than 50–60% of dementia, while 15–25% of cases are due to frontotemporal dementia (FTD) and dementia with Lewy bodies (DLB), respectively (Brown et al. 2014). In 2016, approximately 5.4 million Americans were estimated to have AD, and it was the sixth leading cause of death in the United States (Scheltens et al. 2016). The number of patients is expected to double by 2050 if no cure is identified (Alzheimer's-Association 2017).

From a diagnostic perspective, AD is increasingly viewed along a continuum from preclinical AD to mild cognitive impairment (MCI) and to AD dementia (Jack et al. 2011). The clinical dementia stage of AD is coupled to a distinct pathology with formation of plaques composed of β-amyloid, neurofibrillary tangles composed of hyperphosphorylated tau protein, and synaptic density loss (Overk and Masliah 2014). Synapses are crucial for cognitive function, and synaptic density loss is a robust and consistent pathology in AD (Selkoe 2002). Cognitive impairment in AD is closely associated with synaptic density loss in the cortex and limbic system (Terry et al. 1991; Dekosky and Scheff 1990; Dekosky et al. 1996; Hamos et al. 1989). Synaptic density damage induced by toxic Aβ oligomers is observed in the earliest stages of clinical AD with loss of synapses and several presynaptic proteins (Pham et al. 2010; Robinson et al. 2014; Beeri et al. 2012). However, the assessment of synapse loss and quantification of presynaptic proteins in AD could previously only be performed in post-mortem brain tissues. Thus, the ability to assess synaptic density in vivo would be extremely valuable in studies of AD as well as in monitoring the efficacy of potential therapies.

PET imaging is increasingly employed in AD studies to measure glucose metabolism (i.e., [^{18}F]FDG), β-amyloid, and neurofibrillary tangles (Mckhann et al. 2011).

[^{18}F]FDG PET is widely used clinically to differentiate AD from FTD and to track disease progression by measuring neuronal activity (Landau et al. 2011). However, [^{18}F]FDG is metabolized by both neurons and glial cells (astrocytes, microglia, and oligodendrocytes) and is not a direct biomarker of synaptic density. [^{18}F]FDG PET also has its limitations, e.g., brain [^{18}F]FDG uptake is affected by stimulation, medication, and blood glucose level (Ishibashi et al. 2015; Burns et al. 2013). Inadequate fasting in healthy subjects can result in false-positive findings of [^{18}F]FDG PET, similar to a pattern of AD (Ishibashi et al. 2015; Burns et al. 2013). SV2A imaging has potential to provide a direct indicator of synaptic density in AD.

In the first SV2A PET imaging study on quantitative assessment of synaptic density in AD using high-resolution PET, [^{11}C]UCB-J binding was compared in 10 AD and 11 cognitively normal (CN) subjects (Chen et al. 2018). All AD subjects were confirmed β-amyloid positive (Aβ+) by carbon-11 labeled Pittsburgh compound B ([^{11}C]PiB) PET and spanned the disease stages from amnestic mild cognitive impairment (MCI, $n = 5$) to mild dementia ($n = 5$). All CN subjects were confirmed Aβ–, and the two diagnostic groups were well balanced for age, sex, and education. The AD subjects had clinical characteristics typical of amnestic MCI and mild AD dementia with MMSE = 24.1 ± 4.8 and CDR-global = 0.75 ± 0.26 (Chen et al. 2018). Reduced [^{11}C]UCB-J binding in the hippocampus of AD was hypothesized based on early degeneration of entorhinal cortical cell projections to the hippocampus via the perforant pathway (Gomez-Isla et al. 1996; Braak et al. 2011) and hippocampal SV2A reductions observed in AD post-mortem studies (Robinson et al. 2014). A statistically significant reduction of BP_{ND} was found by 41% in the hippocampus of AD as compared to CN ($p = 0.011$) (Fig. 29.6).

The reduction of BP_{ND} in the hippocampus of AD was larger than the volume loss (22%) measured by MRI (Chen et al. 2018). Statistically significant correlations were found between synaptic density as measured by hippocampus BP_{ND} and the clinical cognitive tests including an episodic memory score (mean Z scores from LMII and RAVLT, $R = 0.53$, $p < 0.05$) and the clinical dementia rating sum of boxes (CDR-sb, $R = -0.70$, $p < 0.05$) (Chen et al. 2018). This study was the first demonstration of reduced synaptic density in the hippocampus of living AD subjects by SV2A PET imaging with [^{11}C]UCB-J.

More recently, Bastin and coworkers reported the evaluation of [^{18}F]UCB-H in 24 patients with MCI or AD (all Aβ+) and 19 healthy controls (Bastin et al. 2020). The distribution volume (V_T) of [^{18}F]UCB-H was lower in the hippocampus (31%, $d = 1.24$), cortical regions (11–18%, $d = 0.49$–0.69), and the thalamus (16%, $d = 0.73$). The difference in hippocampal binding was directly related to patients' cognitive decline and unawareness of memory problems. A similar significant reduction in [^{11}C]UCB-J binding (38%) in the hippocampus of AD ($n = 12$) as compared to CN ($n = 12$) was reported by the MINDMAPS consortium (Molecular Imaging of Neurodegeneration Mitochondria, Associated Proteins, Synapses) at the BrainPET 2019 conference (Venkataraman et al. 2019). They also presented a statistically significant reduction in other brain regions such as amygdala and associated cortical regions (~20%). However, the authors did indicate significant reduction
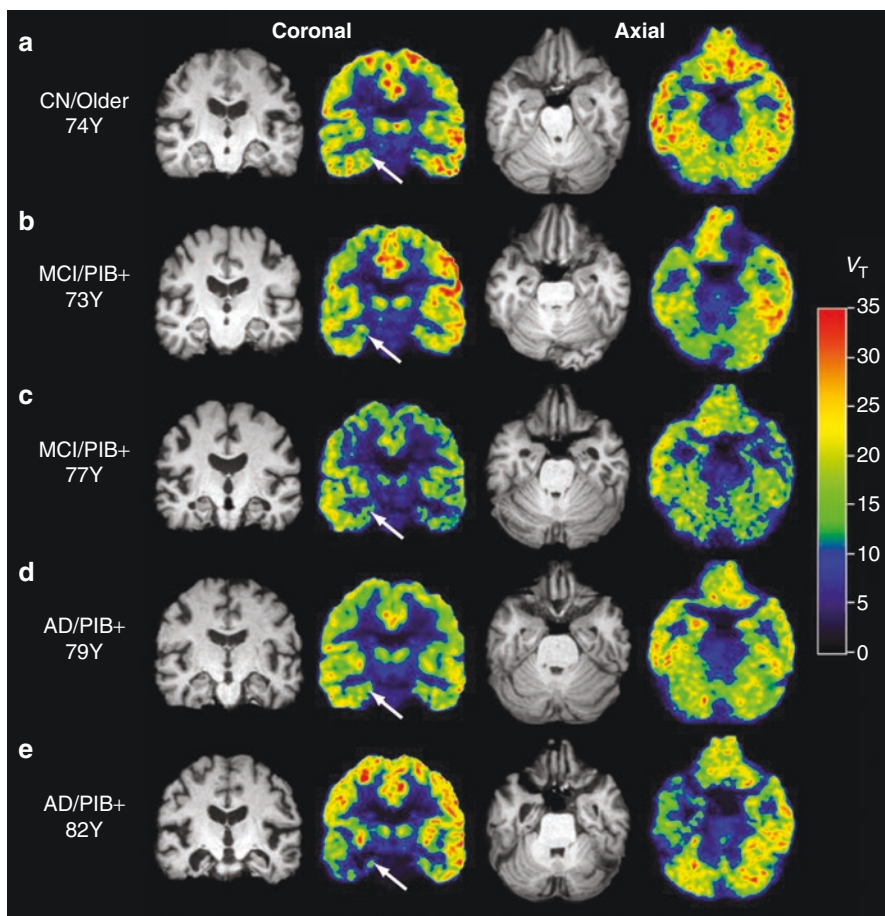
Fig. 29.6 Representative coronal images of [^{11}C]UCB-J parametric PET (V_T) in CN, MCI, and mild AD dementia. The CN participant had a negative [^{11}C]PiB scan and MCI/AD participants had positive [^{11}C]PiB scans. The pseudo-color in PET images represents the intensity of [^{11}C]UCB-J binding (V_T). Evident reduction of [^{11}C]UCB-J binding in the hippocampus of AD was noted as compared to CN (arrow denotes the right hippocampus). Adapted from Chen et al. (2018)

of [^{11}C]UCB-J binding (18%) in the cerebellum of AD, which is usually considered spared in AD. Therefore, more studies are needed to further establish the utility of SV2A PET in AD.

In addition to studying pathophysiology in AD, preclinical studies were conducted to explore the potential of SV2A PET imaging for evaluating AD treatment effects. In a recent PET study using an AD mouse model, longitudinal [^{11}C]UCB-J PET was performed to measure disease progression and treatment effects of saracatinib (Toyonaga et al. 2019). Saracatinib is a Fyn kinase inhibitor and has been investigated as potential therapeutic drug for AD. Saracatinib has been previously demonstrated to restore synaptic density loss in AD mice by post-mortem

immunohistochemistry for SV2A (Kaufman et al. 2015; Nygaard et al. 2014). In this study, nine wild-type (WT) mice and nine amyloid precursor protein and presenilin 1 double transgenic (APPswe/PS1ΔE9:APP/PS1) mice underwent [¹¹C]UCB-J PET at baseline, following treatment with saracatinib and during drug washout phase. At first the authors confirmed that [¹¹C]UCB-J uptake in hippocampus with normalized SUVR values at baseline was significantly lower in AD than WT mice (AD, 1.11 ± 0.04; WT, 1.15 ± 0.02, p = 0.033) (Toyonaga et al. 2019). Using SUVR-1 for the hippocampus, there was a significant difference at baseline (AD, 0.48 ± 0.13; WT, 0.65 ± 0.10, p = 0.017). Following 1 month of treatment with saracatinib, hippocampal SUVR values in AD mice were significantly increased (p = 0.037) (Toyonaga et al. 2019). Treatment effects from saracatinib may persist, as there were no significant differences between WT and AD mice after drug washout (Toyonaga et al. 2019). These results support the use of [¹¹C]UCB-J PET as a potential biomarker for detecting disease-specific synaptic deficits and to monitor treatment effects in AD.

In summary, [¹¹C]UCB-J PET provides a direct measure of SV2A and a proxy of synaptic density and therefore holds promise as a novel in vivo biomarker for AD. The potential clinical applications of SV2A PET imaging with [¹¹C]UCB-J in AD include the early detection of synaptic density loss as demonstrated by our pilot PET study in human and the monitoring of disease progression and the evaluation of synaptic rescue and recovery through therapeutic interventions as demonstrated by the PET study in an AD mouse model. SV2A PET could also be utilized as an outcome measure for trials of disease-modifying therapies, particularly those that target the preservation and restoration of synapses. For example, the effect of CT1812 (Elayta™, a sigma-2 receptor antagonist) treatment on brain synaptic density in participants with mild to moderate AD is currently being evaluated by CogRx (Cognition Therapeutics Inc.) in collaboration with Yale School of Medicine using [¹¹C]UCB-J-PET (NCT03493282).

29.5.3 Parkinson's Disease

Parkinson's disease (PD) is characterized as a neurodegenerative disease with predominant motor and non-motor symptoms. Despite well-documented dopamine neuron decreases, the etiology of PD is only partially understood. While studies have found cortical and limbic Lewy bodies or amyloid plaque pathology (Sabbagh et al. 2009), the wide range of clinical difficulties in PD have been proposed to represent varying rates and regional patterns of neurodegeneration. Furthermore, there is evidence of widespread brain pathology involving multiple transmitter systems and pathways, including the cholinergic, noradrenergic, and serotonergic systems and not just a single neural structure or neurotransmitter (i.e., substantia nigra and dopamine) (Todorova et al. 2014; Jellinger 2012; Picconi et al. 2012; Sauerbier et al. 2016).

Thus, examining synaptic density is exceedingly relevant in PD as current evidence has demonstrated synaptic changes in both animal models and post-mortem

patients with the disease, particularly in the later stages of PD when clinical manifestations develop and decreases in synaptic density are overwhelmingly prevalent (Picconi et al. 2012; Mathai et al. 2015; Hallett et al. 2005; Villalba and Smith 2013; Zaja-Milatovic et al. 2005). These synaptic losses have also been found outside of the nigrostriatal system and include non-dopamine neurons in the cortex, implicating widespread synaptic damage throughout the brain (Hou et al. 2010). In addition, accumulating evidence implicating gene mutations (e.g., α-synuclein and LRRK2) suggests that synaptic dysfunction is centrally involved in PD and that synaptic loss may be a characteristic in the pathogenesis of the disease (Picconi et al. 2012).

The Yale PET Center has recently reported a study with [^{11}C]UCB-J examining 12 PD subjects with mild bilateral disease compared to 12 demographically matched healthy controls (Matuskey et al. 2020). Lower SV2A BP_{ND} values were observed in all brain regions examined, with the largest differences in the brainstem regions including the substantia nigra (-45%; $p < 0.001$), red nucleus (-31%; $p = 0.03$), and locus coeruleus (-17%; $p = 0.03$) (Fig. 29.7a,b). Cortical areas also exhibited significantly lower BP_{ND} in PD subjects in the posterior cingulate cortex (-15%; $p = 0.01$), parahippocampal gyrus (-12%; $p < 0.01$), orbitofrontal cortex (-11%; $p = 0.01$), and ventromedial prefrontal cortex (-11%; $p = 0.02$; all p values are uncorrected) (Matuskey et al. 2020). This study provided the first in vivo evidence of decreased synaptic density in PD, and ongoing follow-up work focuses on the sensitivity and longitudinal dimensions of these findings.

29.5.4 Major Depressive Disorder

Stress has a profound impact on the human brain, affecting both its structure and function (Duman and Aghajanian 2012). Indeed, persisting levels of stress can lead to a loss of synapses in circuits underlying affective and cognitive processing, which is thought to contribute to the symptoms of major depressive disorder (MDD) and posttraumatic stress disorder (PTSD) (Duman et al. 2016) – disorders which are highly prevalent and debilitating, yet whose treatment is currently inadequate. Convergent research indicates that synaptic loss contributes to stress-related disorders such as MDD and PTSD, and lower synaptic density is consistently observed in preclinical models of chronic stress and depression (Duman and Aghajanian 2012; Liu and Aghajanian 2008; Kassem et al. 2013). A lower number of synaptic-function-related genes and synaptic signaling proteins have been demonstrated in post-mortem brain tissue of individuals with MDD (Kang et al. 2012; Feyissa et al. 2009; Duric et al. 2013), meanwhile MRI studies have consistently shown lower brain volume in the prefrontal cortex (PFC), anterior cingulate cortex (ACC), and hippocampus in both MDD (Price and Drevets 2010; Bora et al. 2012) and PTSD (Kühn and Gallinat 2013), likely in part due to synaptic and neuronal loss (Duman et al. 2016). Stress-related alterations in synaptic connections are also thought to contribute to the network dysfunction observed in both MDD (Scheinost et al. 2018; Kaiser et al. 2015; Murrough et al. 2016) and PTSD (Akiki et al. 2017). Increasing
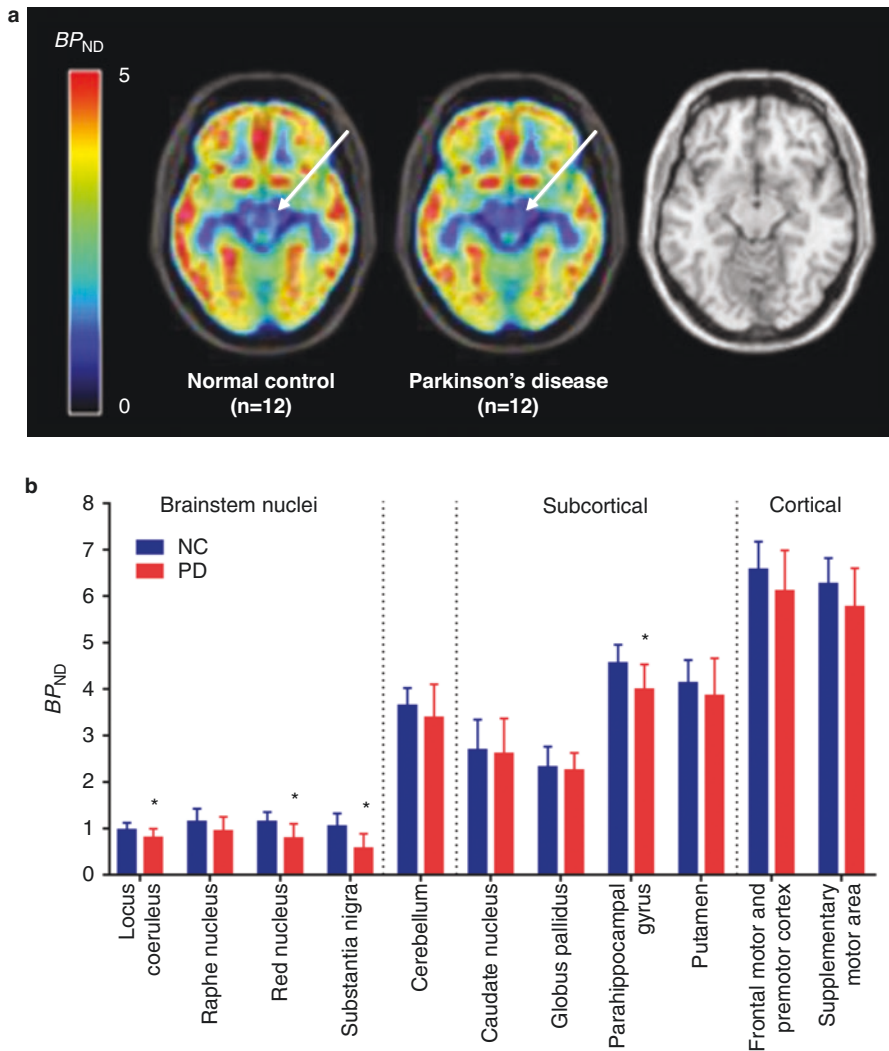
Fig. 29.7 (**a**) The midbrain area with arrows denoting the substantia nigra (SN) is shown on the averaged group BP_{ND} [^{11}C]UCB-J parametric images for normal control (left) and Parkinson's disease (center) subjects. Magnetic resonance imaging template is also shown for comparison purposes (right). Color scale denotes binding potential (BP_{ND}). (**b**) Region of interest analysis of binding potential (BP_{ND}) values for normal control (NC) and Parkinson's disease (PD) subjects. BP_{ND} values were lower across all primary brain regions between the NC and PD subjects. *Statistical significance at $p = 0.05$ or better on post hoc tests. Error bars denote standard deviation. Modified after Matuskey et al. (2020)

synaptic connections, therefore, appears to be a promising approach for the treatment of symptoms of MDD and PTSD which are often resistant to conventional antidepressants. In line with this, ketamine (an NMDA receptor antagonist with rapid antidepressant effect and recently approved by the FDA for treatment-resistant depression) is thought to exert its therapeutic effects in MDD (Mcgirr et al. 2015; Krystal et al. 2013; Esterlis et al. 2018) and PTSD (Feder et al. 2014) through restoration of synaptic connections (Li et al. 2010; Duman and Aghajanian 2012; Hare et al. 2017), thus adding further support to the notion that synaptic loss contributes to the neurobiology underlying depressive symptoms in these disorders. However, evaluation of synaptic density in MDD and PTSD has until now been confined to post-mortem and preclinical quantification.

In the first in vivo study to investigate synaptic density in depression, the relationship between [^{11}C]UCB-J binding and depression severity was evaluated in a transdiagnostic sample of 26 individuals with MDD and/or PTSD and compared to 21 healthy comparison (HC) subjects (Holmes et al. 2019). The primary outcome measure was V_T, calculated using a 1TC model with a metabolite-corrected arterial input function, in the dorsolateral PFC (dlPFC), ACC, and hippocampus. Loss of synaptic connections is likely to have consequences for network organization and function. Therefore, a secondary analysis was applied to examine intrinsic connectivity distribution (ICD) (Scheinost et al. 2012), a measure of whole-brain connectivity obtained via functional MRI (fMRI), and a follow-up seed connectivity was used to explore network alterations in relation to synaptic density and symptom severity. The primary finding was a negative correlation between [^{11}C]UCB-J V_T and symptoms of depression (measured using the Hamilton Depression Rating Scale; HAMD-17(Hamilton 1967)) across individuals with MDD and PTSD in dlPFC ($r = -0.63$, $p = 0.001$), ACC ($r = -0.63$, $p = 0.001$) and hippocampus ($r = -0.49$, $p = 0.01$), such that lower synaptic density was associated with more severe depression (Fig. 29.8a). There were no significant differences in [^{11}C]UCB-J V_T between the full clinical sample and HCs. However, after stratifying clinical subjects by severity of depressive symptoms, a significantly lower [^{11}C]UCB-J V_T was observed in individuals with higher depression severity vs. HCs across ROIs ($p = 0.005$; Fig. 29.8b,c), but no difference between mild depression and HC groups. Exploratory whole-brain functional connectivity analyses revealed significantly lower whole-brain functional connectivity in the dlPFC ($p < 0.05$, corrected) in the full clinical sample. Using the dlPFC as seed, a significant negative correlation was observed between dlPFC-posterior cingulate cortex (PCC) connectivity and SV2A density in the dlPFC ($r = -.60$, $p = 0.002$), as well as with depression severity ($r = 0.41$, $p = 0.042$) (Fig. 29.8d), suggesting that lower synaptic density in the dlPFC is associated with downstream network dysfunction. Specifically, it was demonstrated that higher connectivity between central nodes of the default mode network (PCC) and central executive network (dlPFC) is associated with higher depression severity. Importantly, these two networks are typically anticorrelated (Fox et al. 2005) and are thought to be "blurred" in depression, possibly reflecting a bias toward internal
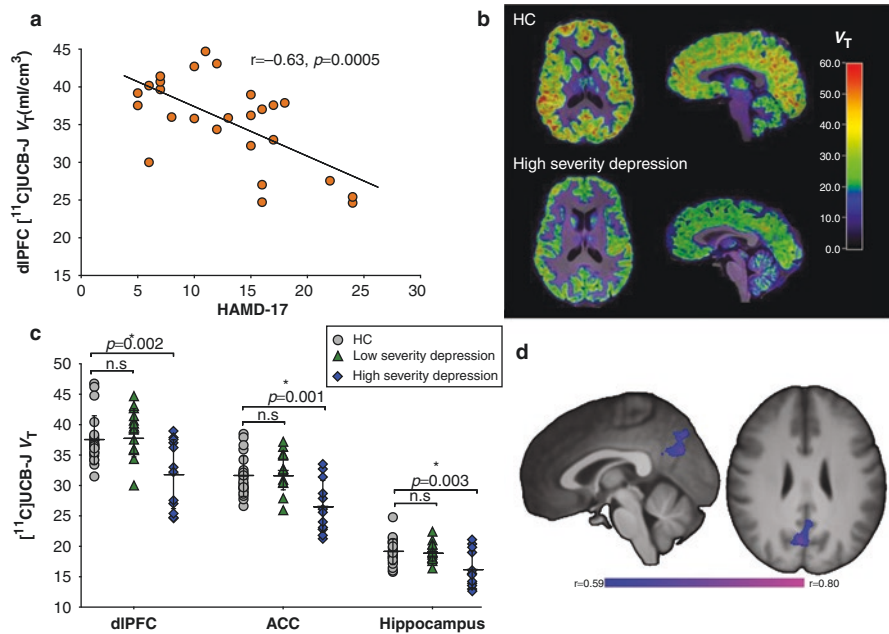
Fig. 29.8 (**a**) Correlation between dlPFC [^{11}C]UCB-J V_T and depression severity (as measured using the HAMD-17) across MDD and PTSD subjects ($n = 26$). Correlations were also significant in ACC and hippocampus. (**b**) Representative parametric V_T images registered to MR images from a HC subject (top) and a subject with high severity depression (bottom). (**c**) [^{11}C]UCB-J V_T in the dlPFC, ACC, and hippocampus across groups. The low severity group (in green; $n = 14$) consisted of participants with HAMD-17 scores <14 and the high severity group (in blue; $n = 12$) consisted of participants with HAMD-17 scores ≥14. (**d**) Negative correlation between dlPFC-PCC connectivity and dlPFC SV2A density in clinical subjects. Significant voxels represent those voxels whose connectivity with the dlPFC negatively correlates with [^{11}C]UCB-J V_T in the dlPFC. Adapted from Holmes et al. (2019)

thoughts at the expense of engagement with the external world (Anticevic et al. 2012). Taken together, the findings suggest that lower synaptic density in the dlPFC may underlie "blurring" of networks in depression, possibly reflecting reduced top-down control over network function.

In summary, the use of [^{11}C]UCB-J PET provided the first in vivo evidence of lower synaptic density in association with depressive severity in MDD and PTSD. Importantly, these findings provide further incentive to discover and evaluate treatment interventions that increase synaptic connections and reverse the loss of synapses caused by stress. Hopefully, SV2A PET imaging will aid in the search for targeted treatments that are critically needed to reduce the suffering and burden caused by depression.

29.5.5 Schizophrenia

Schizophrenia (SCZ) is a debilitating psychiatric disorder, of as yet unknown etiology, that affects about 1% of the general population and is associated with significant morbidity, health expenditure, and disability (Owen et al. 2016). Reduced dendritic spine density in several brain regions (Glantz and Lewis 2000; Garey 2010; Roberts et al. 2015; Bakhshi and Chance 2015; Osimo et al. 2019) is one of the most consistent neuropathological findings seen in post-mortem studies of SCZ. Additionally, post-mortem studies show lower expression of region-specific presynaptic transcripts/proteins (e.g., synaptophysin, SNAP-25, and rab3a) (Faludi and Mirnics 2011). Moreover, genetic studies in SCZ have implicated genes encoding presynaptic proteins (including syntaxin1a, SNAP-25) (Dyck et al. 2011; Ayalew et al. 2012) and relevant to synaptic integrity and function (e.g., ZNF804A, complement C4 gene) (Deans et al. 2017; Sekar et al. 2016). Thus, converging evidences implicate synaptic pathology in SCZ. In the meantime, a recent post-mortem study showed that lower synaptic spine density in SCZ was found specifically in immature spines rather than mature spines, suggesting that the synaptic density differences are not secondary to synaptic pruning (Macdonald et al. 2017), thereby raising the possibility that this finding is a result of disease-specific factors such as age at onset of illness, duration of illness, and illness severity.

Post-mortem studies are, however, confounded by a number of methodological limitations related to factors such as the mode of collection of specimens, post-mortem interval, storage, and nature of death (Harrison 2011). Additionally, it is challenging to address the confounding effects of disease-specific factors such as age at onset of illness, duration of illness, illness severity, effects of antipsychotic treatment, drugs/alcohol abuse, and tobacco use, all of which are common in SCZ (Harrison 2011). Furthermore, post-mortem findings cannot be related to concurrent measures of the illness, e.g., symptom severity or cognitive function.

Onwordi et al. recently reported the evaluation of [^{11}C]UCB-J in control subjects ($n = 18$) and SCZ patients on antipsychotic medication ($n = 18$) (Onwordi et al. 2020). A significant group difference and group-by-region interaction effect on V_T were found, with lower V_T values in the frontal (-13%, $p = 0.03$) and anterior cingulate (-13%, $p = 0.02$) cortices. Evaluation of distribution volume ratio (DVR) using the CS as a reference region resulted in significantly lower SV2A in frontal and anterior cingulate cortices and the hippocampus in SCZ. Exploratory analysis of additional brain regions also showed lower SV2A in the dorsolateral prefrontal and temporal cortices and occipital lobe in SCZ. Since SCZ patients were not drug-naïve, the authors examined the effect of antipsychotic drug administration on SV2A levels in rats using western blot, SV2A autoradiography, and confocal microscopy and found no significant effect of drug administration on SV2A outcome measures. This was the first PET study to demonstrate lower levels of a presynaptic protein marker in SCZ and confirmed previous post-mortem evidence. These preliminary findings demonstrate the utility of SV2A PET imaging to further understand the neurobiology of SCZ and warrant further evaluation in larger study cohorts.

29.6   Future Considerations

In summary, PET imaging of SV2A has been rapidly established during the last decade. High-quality PET radioligands labeled with carbon-11 and fluorine-18 have been developed and validated for application in human studies. The utility of SV2A as a marker of synaptic density is promising and warrants formal validation by comparison of in vivo SV2A PET signal to post-mortem evaluation of SV2A and synapse levels in the human brain. The first PET studies in patient groups indicate SV2A loss specific to disease-associated brain regions and consistent with synaptic density loss. Future studies may apply SV2A PET imaging to study neuronal development and neurodegeneration in the healthy and diseased brain. Further studies also warrant use of fluorine-18 labeled radioligands in larger patient cohorts to establish the clinical value of SV2A PET imaging and its potential for diagnosis and progression monitoring of neuropathological diseases, as well as assessment of drug treatment effects.

References

Akiki TJ, Averill CL, Abdallah CG (2017) A network-based neurobiological model of PTSD: evidence from structural and functional neuroimaging studies. Curr Psychiatry Rep 19:81

Alzheimer's-Association (2017) Alzheimer's disease facts and figures. Alzheimers Dement 13:325–373

Anticevic A, Cole MW, Murray JD et al (2012) The role of default network deactivation in cognition and disease. Trends Cogn Sci 16:584–592

Ayalew M, Le-Niculescu H, Levey DF et al (2012) Convergent functional genomics of schizophrenia: from comprehensive understanding to genetic risk prediction. Mol Psychiatry 17:887–905

Azevedo FA, Carvalho LR, Grinberg LT et al (2009) Equal numbers of neuronal and nonneuronal cells make the human brain an isometrically scaled-up primate brain. J Comp Neurol 513:532–541

Bahri MA, Plenevaux A, Aerts J et al (2017) Measuring brain synaptic vesicle protein 2A with positron emission tomography and [(18)F]UCB-H. Alzheimers Dement (N Y) 3:481–486

Bajjalieh SM, Peterson K, Shinghal R, Scheller RH (1992) SV2, a brain synaptic vesicle protein homologous to bacterial transporters. Science 257:1271–1273

Bajjalieh SM, Peterson K, Linial M, Scheller RH (1993) Brain contains two forms of synaptic vesicle protein 2. Proc Natl Acad Sci U S A 90:2150–2154

Bajjalieh SM, Frantz GD, Weimann JM, Mcconnell SK, Scheller RH (1994) Differential expression of synaptic vesicle protein 2 (SV2) isoforms. J Neurosci 14:5223–5235

Bakhshi K, Chance SA (2015) The neuropathology of schizophrenia: a selective review of past studies and emerging themes in brain structure and cytoarchitecture. Neuroscience 303:82–102

Bartholome O, Van Den Ackerveken P, Sanchez Gil J et al (2017) Puzzling out synaptic vesicle 2 family members functions. Front Mol Neurosci 10:148

Bastin C, Bahri MA, Meyer F et al (2020) In vivo imaging of synaptic loss in Alzheimer's disease with [18F]UCB-H positron emission tomography. Eur J Nucl Med Mol Imaging 47:390–402

Becker G, Warnier C, Serrano ME et al (2017) Pharmacokinetic characterization of [18F]UCB-H PET radiopharmaceutical in the rat brain. Mol Pharm 14:2719–2725

Beeri MS, Haroutunian V, Schmeidler J et al (2012) Synaptic protein deficits are associated with dementia irrespective of extreme old age. Neurobiol Aging 33(1125):e1–e8

Bell GS, Sander JW (2001) The epidemiology of epilepsy: the size of the problem. Seizure 10:306–314; quiz 315–6

Bora E, Fornito A, Pantelis C, Yücel M (2012) Gray matter abnormalities in major depressive disorder: a meta-analysis of voxel based morphometry studies. J Affect Disord 138:9–18

Braak H, Thal DR, Ghebremedhin E, Del Tredici K (2011) Stages of the pathologic process in Alzheimer disease: age categories from 1 to 100 years. J Neuropathol Exp Neurol 70:960–969

Bretin F, Warnock G, Bahri MA et al (2013) Preclinical radiation dosimetry for the novel SV2A radiotracer [^{18}F]UCB-H. EJNMMI Res 3:35

Brown RK, Bohnen NI, Wong KK, Minoshima S, Frey KA (2014) Brain PET in suspected dementia: patterns of altered FDG metabolism. Radiographics 34:684–701

Buckley K, Kelly RB (1985) Identification of a transmembrane glycoprotein specific for secretory vesicles of neural and endocrine cells. J Cell Biol 100:1284–1294

Burns CM, Chen K, Kaszniak AW et al (2013) Higher serum glucose levels are associated with cerebral hypometabolism in Alzheimer regions. Neurology 80:1557–1564

Cai H, Mangner TJ, Muzik O et al (2014) Radiosynthesis of ^{11}C-Levetiracetam: a potential marker for PET imaging of SV2A expression. ACS Med Chem Lett 5:1152–1155

Cai Z, Li S, Matuskey D, Nabulsi N, Huang Y (2019) PET imaging of synaptic density: a new tool for investigation of neuropsychiatric diseases. Neurosci Lett 691:44–50

Cai Z, Li S, Zhang W et al (2020) Synthesis and preclinical evaluation of an (18)F-labeled synaptic vesicle glycoprotein 2A PET imaging probe: [(18)F]SynVesT-2. ACS Chem Neurosci 11(4):592–603

Chen MK, Mecca AP, Naganawa M et al (2018) Assessing synaptic density in Alzheimer disease with synaptic vesicle glycoprotein 2A positron emission tomographic imaging. JAMA Neurol 75:1215–1224

Cockerell OC, Johnson AL, Sander JW, Hart YM, Shorvon SD (1995) Remission of epilepsy: results from the National General Practice Study of Epilepsy. Lancet 346:140–144

Constantinescu CC, Tresse C, Zheng M et al (2019) Development and in vivo preclinical imaging of fluorine-18-labeled synaptic vesicle protein 2A (SV2A) PET tracers. Mol Imaging Biol 21:509–518

Crevecoeur J, Kaminski RM, Rogister B et al (2014) Expression pattern of synaptic vesicle protein 2 (SV2) isoforms in patients with temporal lobe epilepsy and hippocampal sclerosis. Neuropathol Appl Neurobiol 40:191–204

Crowder KM, Gunther JM, Jones TA et al (1999) Abnormal neurotransmission in mice lacking synaptic vesicle protein 2A (SV2A). Proc Natl Acad Sci U S A 96:15268–15273

Danish A, Namasivayam V, Schiedel AC, Muller CE (2017) Interaction of approved drugs with synaptic vesicle protein 2A. Arch Pharm (Weinheim) 350:1700003

De Camilli P, Harris SM Jr, Huttner WB, Greengard P (1983) Synapsin I (protein I), a nerve terminal-specific phosphoprotein. II. Its specific association with synaptic vesicles demonstrated by immunocytochemistry in agarose-embedded synaptosomes. J Cell Biol 96:1355–1373

Deans PJ, Raval P, Sellers KJ et al (2017) Psychosis risk candidate ZNF804A localizes to synapses and regulates neurite formation and dendritic spine structure. Biol Psychiatry 82(1):49–61

Dekosky ST, Scheff SW (1990) Synapse loss in frontal cortex biopsies in Alzheimer's disease: correlation with cognitive severity. Ann Neurol 27:457–464

Dekosky ST, Scheff SW, Styren SD (1996) Structural correlates of cognition in dementia: quantification and assessment of synapse change. Neurodegeneration 5:417–421

Duman RS, Aghajanian GK (2012) Synaptic dysfunction in depression: potential therapeutic targets. Science 338:68

Duman RS, Aghajanian GK, Sanacora G, Krystal JH (2016) Synaptic plasticity and depression: new insights from stress and rapid-acting antidepressants. Nat Med 22:238

Duric V, Banasr M, Stockmeier CA et al (2013) Altered expression of synapse and glutamate related genes in post-mortem hippocampus of depressed subjects. Int J Neuropsychopharmacol 16(1):69–82

Dyck BA, Beyaert MG, Ferro MA, Mishra RK (2011) Medial prefrontal cortical synapsin II knock-down induces behavioral abnormalities in the rat: examining synapsin II in the pathophysiology of schizophrenia. Schizophr Res 130:250–259

Esterlis I, Dellagioia N, Pietrzak RH et al (2018) Ketamine-induced reduction in mGluR5 availability is associated with an antidepressant response: an [11 C] ABP688 and PET imaging study in depression. Mol Psychiatry 23(4):824–832

Estrada S, Lubberink M, Thibblin A et al (2016) [^{11}C]UCB-A, a novel PET tracer for synaptic vesicle protein 2 A. Nucl Med Biol 43:325–332

Faludi G, Mirnics K (2011) Synaptic changes in the brain of subjects with schizophrenia. Int J Dev Neurosci 29:305–309

Feany MB, Lee S, Edwards RH, Buckley KM (1992) The synaptic vesicle protein SV2 is a novel type of transmembrane transporter. Cell 70:861–867

Feder A, Parides MK, Murrough JW et al (2014) Efficacy of intravenous ketamine for treatment of chronic posttraumatic stress disorder: a randomized clinical trial. JAMA Psychiat 71:681–688

Feng G, Xiao F, Lu Y et al (2009) Down-regulation synaptic vesicle protein 2A in the anterior temporal neocortex of patients with intractable epilepsy. J Mol Neurosci 39:354–359

Feyissa AM, Chandran A, Stockmeier CA, Karolewicz B (2009) Reduced levels of NR2A and NR2B subunits of NMDA receptor and PSD-95 in the prefrontal cortex in major depression. Prog Neuropsychopharmacol Biol Psychiatry 33:70–75

Finnema SJ, Nabulsi NB, Eid T et al (2016) Imaging synaptic density in the living human brain. Sci Transl Med 8:348ra96

Finnema SJ, Detyniecki K, Chen MK et al (2017) Reduced SV2A binding in the seizure onset zone in temporal lobe epilepsy patients—a PET study with ^{11}C-UCB-J. J Nucl Med 58:632

Finnema SJ, Nabulsi NB, Mercier J et al (2018) Kinetic evaluation and test-retest reproducibility of [^{11}C]UCB-J, a novel radioligand for positron emission tomography imaging of synaptic vesicle glycoprotein 2A in humans. J Cereb Blood Flow Metab 38(11):2041–2052

Finnema SJ, Rossano S, Naganawa M et al (2019) A single-center, open-label positron emission tomography study to evaluate brivaracetam and levetiracetam synaptic vesicle glycoprotein 2A binding in healthy volunteers. Epilepsia 60:958–967

Floor E, Feist BE (1989) Most synaptic vesicles isolated from rat brain carry three membrane proteins, SV2, synaptophysin, and p65. J Neurochem 52:1433–1437

Fox MD, Snyder AZ, Vincent JL et al (2005) The human brain is intrinsically organized into dynamic, anticorrelated functional networks. Proc Natl Acad Sci U S A 102(27):9673–9678

Garey L (2010) When cortical development goes wrong: schizophrenia as a neurodevelopmental disease of microcircuits. J Anat 217:324–333

Gillard M, Chatelain P, Fuks B (2006) Binding characteristics of levetiracetam to synaptic vesicle protein 2A (SV2A) in human brain and in CHO cells expressing the human recombinant protein. Eur J Pharmacol 536:102–108

Gillard M, Fuks B, Leclercq K, Matagne A (2011) Binding characteristics of brivaracetam, a selective, high affinity SV2A ligand in rat, mouse and human brain: relationship to anti-convulsant properties. Eur J Pharmacol 664:36–44

Glantz LA, Lewis DA (2000) Decreased dendritic spine density on prefrontal cortical pyramidal neurons in schizophrenia. Arch Gen Psychiatry 57:65–73

Goelz SE, Nestler EJ, Chehrazi B, Greengard P (1981) Distribution of protein I in mammalian brain as determined by a detergent-based radioimmunoassay. Proc Natl Acad Sci U S A 78:2130–2134

Gomez-Isla T, Price JL, Mckeel DW Jr et al (1996) Profound loss of layer II entorhinal cortex neurons occurs in very mild Alzheimer's disease. J Neurosci 16:4491–4500

Hallett PJ, Dunah AW, Ravenscroft P et al (2005) Alterations of striatal NMDA receptor subunits associated with the development of dyskinesia in the MPTP-lesioned primate model of Parkinson's disease. Neuropharmacology 48:503–516

Hamilton M (1967) Development of a rating scale for primary depressive illness. Br J Soc Clin Psychol 6:278–296

Hamos JE, Degennaro LJ, Drachman DA (1989) Synaptic loss in Alzheimer's disease and other dementias. Neurology 39:355–361

Hanaya R, Hosoyama H, Sugata S et al (2012) Low distribution of synaptic vesicle protein 2A and synaptotagimin-1 in the cerebral cortex and hippocampus of spontaneously epileptic rats exhibiting both tonic convulsion and absence seizure. Neuroscience 221:12–20

Hare BD, Ghosal S, Duman RS (2017) Rapid acting antidepressants in chronic stress models: molecular and cellular mechanisms. Chronic Stress 1:2470547017697317

Harrison PJ (2011) Using our brains: the findings, flaws, and future of postmortem studies of psychiatric disorders. Biol Psychiatry 69:102–103

Holmes SE, Scheinost D, Finnema SJ et al (2019) Lower synaptic density is associated with depression severity and network alterations. Nat Commun 10:1529

Hou Z, Lei H, Hong S et al (2010) Functional changes in the frontal cortex in Parkinson's disease using a rat model. J Clin Neurosci 17:628–633

Ishibashi K, Onishi A, Fujiwara Y, Ishiwata K, Ishii K (2015) Relationship between Alzheimer disease-like pattern of ^{18}F-FDG and fasting plasma glucose levels in cognitively normal volunteers. J Nucl Med 56:229–233

Jack CR Jr, Albert MS, Knopman DS et al (2011) Introduction to the recommendations from the National Institute on Aging-Alzheimer's Association workgroups on diagnostic guidelines for Alzheimer's disease. Alzheimers Dement 7:257–262

Janz R, Sudhof TC (1999) SV2C is a synaptic vesicle protein with an unusually restricted localization: anatomy of a synaptic vesicle protein family. Neuroscience 94:1279–1290

Janz R, Goda Y, Geppert M, Missler M, Sudhof TC (1999) SV2A and SV2B function as redundant Ca^{2+} regulators in neurotransmitter release. Neuron 24:1003–1016

Jellinger KA (2012) Neuropathology of sporadic Parkinson's disease: evaluation and changes of concepts. Mov Disord 27:8–30

Jette N, Sander JW, Keezer MR (2016) Surgical treatment for epilepsy: the potential gap between evidence and practice. Lancet Neurol 15:982–994

Kaiser RH, Andrews-Hanna JR, Wager TD, Pizzagalli DA (2015) Large-scale network dysfunction in major depressive disorder: a meta-analysis of resting-state functional connectivity. JAMA Psychiat 72:603–611

Kang HJ, Voleti B, Hajszan T et al (2012) Decreased expression of synapse-related genes and loss of synapses in major depressive disorder. Nat Med 18:1413

Kassem MS, Lagopoulos J, Stait-Gardner T et al (2013) Stress-induced grey matter loss determined by MRI is primarily due to loss of dendrites and their synapses. Mol Neurobiol 47:645–661

Kaufman AC, Salazar SV, Haas LT et al (2015) Fyn inhibition rescues established memory and synapse loss in Alzheimer mice. Ann Neurol 77:953–971

Klein P, Diaz A, Gasalla T, Whitesides J (2018) A review of the pharmacology and clinical efficacy of brivaracetam. Clin Pharmacol 10:1–22

Koole M, Van Aalst J, Devrome M et al (2019) Quantifying SV2A density and drug occupancy in the human brain using [(11)C]UCB-J PET imaging and subcortical white matter as reference tissue. Eur J Nucl Med Mol Imaging 46:396–406

Krystal JH, Sanacora G, Duman RS (2013) Rapid-acting glutamatergic antidepressants: the path to ketamine and beyond. Biol Psychiatry 73:1133–1141

Kühn S, Gallinat J (2013) Gray matter correlates of posttraumatic stress disorder: a quantitative meta-analysis. Biol Psychiatry 73:70–74

Kwan P, Brodie MJ (2000) Early identification of refractory epilepsy. N Engl J Med 342:314–319

Landau SM, Harvey D, Madison CM et al (2011) Associations between cognitive, functional, and FDG-PET measures of decline in AD and MCI. Neurobiol Aging 32:1207–1218

Li N, Lee B, Liu R-J et al (2010) mTOR-dependent synapse formation underlies the rapid antidepressant effects of NMDA antagonists. Science 329:959–964

Li S, Cai Z, Wu X et al (2019a) Synthesis and in vivo evaluation of a novel PET radiotracer for imaging of synaptic vesicle glycoprotein 2A (SV2A) in nonhuman primates. ACS Chem Neurosci 10:1544–1554

Li S, Cai Z, Zhang W et al (2019b) Synthesis and in vivo evaluation of [^{18}F]UCB-J for PET imaging of synaptic vesicle glycoprotein 2A (SV2A). Eur J Nucl Med Mol Imaging 46:1952–1965

Li S, Naganawa M, Zheng M et al (2019c) First-in-human evaluation of ^{18}F-SDM-8, a novel radiotracer for PET imaging of synaptic vesicle glycoprotein 2A. J Nucl Med 60:49

Liu R-J, Aghajanian GK (2008) Stress blunts serotonin-and hypocretin-evoked EPSCs in prefrontal cortex: role of corticosterone-mediated apical dendritic atrophy. PNAS 105:359–364

Lubberink M, Appel L, Daging J et al (2017) Tracer kinetic analysis of the SV2A ligand ^{11}C-UCBA as a PET marker for synaptic density in humans. J Nucl Med 58:631

Lynch BA, Lambeng N, Nocka K et al (2004) The synaptic vesicle protein SV2A is the binding site for the antiepileptic drug levetiracetam. Proc Natl Acad Sci U S A 101:9861–9866

Macdonald ML, Alhassan J, Newman JT et al (2017) Selective loss of smaller spines in schizophrenia. Am J Psychiatry 174:586–594

Mansur A, Rabiner EA, Comley RA et al (2020) Characterization of 3 PET tracers for quantification of mitochondrial and synaptic function in healthy human brain: (18)F-BCPP-EF, (11)C-SA-4503, (11)C-UCB-J. J Nucl Med 61(1):96–103

Martinkovic L, Hecimovic H, Sulc V, Marecek R, Marusic P (2014) Modern techniques of epileptic focus localization. Int Rev Neurobiol 114:245–278

Masliah E, Terry RD, Alford M, Deteresa R (1990) Quantitative immunohistochemistry of synaptophysin in human neocortex: an alternative method to estimate density of presynaptic terminals in paraffin sections. J Histochem Cytochem 38:837–844

Mathai A, Ma Y, Pare JF et al (2015) Reduced cortical innervation of the subthalamic nucleus in MPTP-treated parkinsonian monkeys. Brain 138:946–962

Matuskey D, Tinaz S, Wilcox KC et al (2020) Synaptic changes in Parkinson disease assessed with in vivo imaging. Ann Neurol 87:329

Mcgirr A, Berlim M, Bond D et al (2015) A systematic review and meta-analysis of randomized, double-blind, placebo-controlled trials of ketamine in the rapid treatment of major depressive episodes. Psychol Med 45:693–704

Mckhann GM, Knopman DS, Chertkow H et al (2011) The diagnosis of dementia due to Alzheimer's disease: recommendations from the National Institute on Aging-Alzheimer's Association workgroups on diagnostic guidelines for Alzheimer's disease. Alzheimers Dement 7:263–269

Mendoza-Torreblanca JG, Vanoye-Carlo A, Phillips-Farfan BV, Carmona-Aparicio L, Gomez-Lira G (2013) Synaptic vesicle protein 2A: basic facts and role in synaptic function. Eur J Neurosci 38:3529–3539

Mercier J, Archen L, Bollu V et al (2014) Discovery of heterocyclic nonacetamide synaptic vesicle protein 2A (SV2A) ligands with single-digit nanomolar potency: opening avenues towards the first SV2A positron emission tomography (PET) ligands. ChemMedChem 9:693–698

Mercier J, Provins L, Valade A (2017) Discovery and development of SV2A PET tracers: potential for imaging synaptic density and clinical applications. Drug Discov Today Technol 25:45–52

Mertens N, Maguire RP, Serdons K et al (2020) Validation of parametric methods for [(11)C]UCB-J PET imaging using subcortical white matter as reference tissue. Mol Imaging Biol 22(2):444–452

Murrough JW, Abdallah CG, Anticevic A et al (2016) Reduced global functional connectivity of the medial prefrontal cortex in major depressive disorder. Hum Brain Mapp 37:3214–3223

Mutch SA, Kensel-Hammes P, Gadd JC et al (2011) Protein quantification at the single vesicle level reveals that a subset of synaptic vesicle proteins are trafficked with high precision. J Neurosci 31:1461–1470

Nabulsi NB, Mercier J, Holden D et al (2016) Synthesis and preclinical evaluation of ^{11}C-UCB-J as a PET tracer for imaging the synaptic vesicle glycoprotein 2A in the brain. J Nucl Med 57:777–784

Naganawa M, Gallezot JD, Finnema SJ et al (2018a) Simplified ^{11}C-UCB-J PET quantification evaluated in Alzheimer's disease, epilepsy, and healthy individuals. J Nucl Med 59:542. (abstract)

Naganawa M, Gallezot JD, Finnema SJ, et al (2018b) Strategies for simplified ^{11}C-UCB-J PET quantification: ratio and reference tissue methods. In: The XII international symposium of functional neuroreceptor mapping of the living brain (NRM18) OP30 (abstract)

Nowack A, Yao J, Custer KL, Bajjalieh SM (2010) SV2 regulates neurotransmitter release via multiple mechanisms. Am J Physiol Cell Physiol 299:C960–C967

Nygaard HB, Van Dyck CH, Strittmatter SM (2014) Fyn kinase inhibition as a novel therapy for Alzheimer's disease. Alzheimers Res Ther 6:8

Onwordi EC, Halff EF, Whitehurst T et al (2020) Synaptic density marker SV2A is reduced in schizophrenia patients and unaffected by antipsychotics in rats. Nat Commun 11:246

Osimo EF, Beck K, Reis Marques T, Howes OD (2019) Synaptic loss in schizophrenia: a meta-analysis and systematic review of synaptic protein and mRNA measures. Mol Psychiatry 24(4):549–561

Overk CR, Masliah E (2014) Pathogenesis of synaptic degeneration in Alzheimer's disease and Lewy body disease. Biochem Pharmacol 88:508–516

Owen MJ, Sawa A, Mortensen PB (2016) Schizophrenia. Lancet 388:86–97

Pham E, Crews L, Ubhi K et al (2010) Progressive accumulation of amyloid-beta oligomers in Alzheimer's disease and in amyloid precursor protein transgenic mice is accompanied by selective alterations in synaptic scaffold proteins. FEBS J 277:3051–3067

Picconi B, Piccoli G, Calabresi P (2012) Synaptic dysfunction in Parkinson's disease. Adv Exp Med Biol 970:553–572

Picot MC, Baldy-Moulinier M, Daures JP, Dujols P, Crespel A (2008) The prevalence of epilepsy and pharmacoresistant epilepsy in adults: a population-based study in a Western European country. Epilepsia 49:1230–1238

Price JL, Drevets WC (2010) Neurocircuitry of mood disorders. Neuropsychopharmacology 35:192

Roberts RC, Barksdale KA, Roche JK, Lahti AC (2015) Decreased synaptic and mitochondrial density in the postmortem anterior cingulate cortex in schizophrenia. Schizophr Res 168:543

Robinson JL, Molina-Porcel L, Corrada MM et al (2014) Perforant path synaptic loss correlates with cognitive impairment and Alzheimer's disease in the oldest-old. Brain 137:2578–2587

Rossano S, Toyonaga T, Finnema SJ et al (2019) Assessment of a white matter reference region for (11)C-UCB-J PET quantification. J Cereb Blood Flow Metab 2019:271678X19879230

Sabbagh MN, Adler CH, Lahti TJ et al (2009) Parkinson disease with dementia: comparing patients with and without Alzheimer pathology. Alzheimer Dis Assoc Disord 23:295–297

Sauerbier A, Jenner P, Todorova A, Chaudhuri KR (2016) Non motor subtypes and Parkinson's disease. Parkinsonism Relat Disord 22:S41

Scheinost D, Benjamin J, Lacadie C et al (2012) The intrinsic connectivity distribution: a novel contrast measure reflecting voxel level functional connectivity. NeuroImage 62:1510–1519

Scheinost D, Holmes SE, Dellagioia N et al (2018) Multimodal investigation of network level effects using intrinsic functional connectivity, anatomical covariance, and structure-to-function correlations in Unmedicated major depressive disorder. Neuropsychopharmacology 43(5):1119–1127

Scheltens P, Blennow K, Breteler MM et al (2016) Alzheimer's disease. Lancet 388:505–517

Schmidt D, Loscher W (2005) Drug resistance in epilepsy: putative neurobiologic and clinical mechanisms. Epilepsia 46:858–877

Sekar A, Bialas AR, De Rivera H et al (2016) Schizophrenia risk from complex variation of complement component 4. Nature 530:177–183

Selkoe DJ (2002) Alzheimer's disease is a synaptic failure. Science 298:789–791

Terry RD, Masliah E, Salmon DP et al (1991) Physical basis of cognitive alterations in Alzheimer's disease: synapse loss is the major correlate of cognitive impairment. Ann Neurol 30:572–580

Theodore WH (2017) Presurgical focus localization in epilepsy: PET and SPECT. Semin Nucl Med 47:44–53

Todorova A, Jenner P, Ray Chaudhuri K (2014) Non-motor Parkinson's: integral to motor Parkinson's, yet often neglected. Pract Neurol 14:310–322

Toyonaga T, Smith LM, Finnema SJ et al (2019) In vivo synaptic density imaging with (11) C-UCB-J detects treatment effects of saracatinib (AZD0530) in a mouse model of Alzheimer's disease. J Nucl Med 60:1780

Van Vliet EA, Aronica E, Redeker S, Boer K, Gorter JA (2009) Decreased expression of synaptic vesicle protein 2A, the binding site for levetiracetam, during epileptogenesis and chronic epilepsy. Epilepsia 50:422–433

Venkataraman AV, Mansur A, Lewis Y et al (2019) Evaluation of mitochondrial and synaptic function in Alzheimer's: a [^{18}F]BCPP-EF, [^{11}C]SA4503 and [^{11}C]UCB-J PET study. BrainPET, Yokohama

Villalba RM, Smith Y (2013) Differential striatal spine pathology in Parkinson's disease and cocaine addiction: a key role of dopamine? Neuroscience 251:2–20

Wang L, Shi J, Wu G, Zhou F, Hong Z (2014) Hippocampal low-frequency stimulation increased SV2A expression and inhibited the seizure degree in pharmacoresistant amygdala-kindling epileptic rats. Epilepsy Res 108:1483–1491

Warnier C, Lemaire C, Becker G et al (2016) Enabling efficient positron emission tomography (PET) imaging of synaptic vesicle glycoprotein 2A (SV2A) with a robust and one-step radiosynthesis of a highly potent ^{18}F-labeled ligand ([^{18}F]UCB-H). J Med Chem 59:8955–8966

Warnock GI, Aerts J, Bahri MA et al (2014) Evaluation of ^{18}F-UCB-H as a novel PET tracer for synaptic vesicle protein 2A in the brain. J Nucl Med 55:1336–1341

Zaja-Milatovic S, Milatovic D, Schantz AM et al (2005) Dendritic degeneration in neostriatal medium spiny neurons in Parkinson disease. Neurology 64:545–547

PET Imaging of Translocator Protein Expression in Neurological Disorders

30

David J. Brooks

Contents

Abstract

Microglia provide the intrinsic immune defence of the brain and are activated by any injurious process. As such they provide a non-specific marker of disease activity. Their function can be both detrimental and beneficial as they release cytokines which drive disease progression but also release restorative growth factors, help clear cellular debris and abnormal protein aggregations and can remodel connections as an adaptive response to brain damage. Activated microglia express translocator protein (TSPO), and this allows them to be imaged in vivo with positron emission tomography (PET) radioligands which are

D. J. Brooks (✉)
Faculty of Medicine, University of Newcastle Upon Tyne, Newcastle Upon Tyne, UK

Department of Nuclear Medicine, Aarhus University, Aarhus, Denmark
e-mail: David.Brooks@newcastle.ac.uk

substrates. In this review the role of TSPO imaging with PET is discussed in neurodegenerative and inflammatory brain diseases and in focal brain injury due to trauma or stroke.

30.1 Introduction

The 18 kDa translocator protein (TSPO), previously known as the peripheral benzo-diazepine receptor (PBR), is present in many peripheral organs including the liver, spleen, adrenals and myocardium (Banati 2002b). It is expressed only at low levels in a normal brain, but if microglial cells become activated, TSPO can be detected in their outer mitochondrial membrane. The TSPO serves a number of functions including transport of cholesterol, anions, nucleosides and porphyrins; maintenance of mitochondrial membrane potential; regulation of cell apoptosis and proliferation and immunomodulation (Papadopoulos et al. 2006). The protein expresses a bind-ing site for benzodiazepines and isoquinolines such as PK11195, and this has allowed the detection of TSPO expression in vivo with (R)-[11C]PK11195 PET. Newer PET biomarkers are now available to image TSPO expression which include phenoxyarylacetamides such as [11C]/[18F]DAA1106, [11C]PBR28, [18F]PBR06, [18F]PBR111 and [18F]FEPPA; pyrazolo-[1,5-a]-pyrimidines such as [11C]DPA713 and [18F]DPA714; the vinca alkaloid [11C]vinpocetine and the imid-azo-[1,2a]-pyridines [11C]/[18F]CLINDE (Dolle et al. 2009; Doorduin et al. 2008).

Microglia account for around 15% of the cerebral white cell population. They are normally in a resting state sending out long ramified processes which contact neigh-bouring neurones and astrocytes (Kreutzberg 1996; Ransohoff and Perry 2009). It is, therefore, likely that the function of resting microglia is to monitor changes in the local brain milieu—for a review see (Hanisch and Kettenmann 2007). Microglia are cells of monocyte lineage and are protected from antigens in the plasma by the blood-brain barrier. They form the natural immune defence of the brain, and expo-sure to plasma proteins such as fibrinogen following blood-brain barrier disruption, or to intrinsic excitotoxic agents such as raised glutamate, nitric oxide or cytokines, causes them to become activated taking on ameboid- or rod-like morphology. When activated, the microglia express MHC class 1 and 2 antigens and can release cyto-kines such as TNFα, IL1β and IL6, or growth factors such as TGF-β1. They may become phagocytic clearing cellular debris and stripping and remodelling synapses. It is now considered that activated microglia may exist as two primary phenotypes: M1 which is associated with the release of cidal cytokines so promoting cell dam-age and M2 which is associated with phagocytosis of dead tissue, synaptic remodel-ling and growth factor release promoting neurogenesis (Boche et al. 2013; Varnum and Ikezu 2012). These two primary phenotypes are thought to be interconvertible, have overlapping functions and predominate at different disease phases. It has been suggested that substrates binding to the TREM2 receptor on microglia promote acti-vation of the M2 phenotype (Li and Zhang 2018). After an acute stroke, activated microglia act locally to wall off, remove dead tissue and remodel connections, while

in chronic neurodegenerative diseases, they may release cytokines where disease is locally active but remodel distant connections in the brainstem and thalamus. The advent of TSPO PET agents has allowed us to image in life the distribution of activated microglia in the brain. Current TSPO PET ligands are unable to discriminate between M1 and M2 phenotypes and provide a measure of total activated microglia load rather than indicating whether their function is protective or toxic in nature.

30.2 Imaging TSPO with PET

The PET ligand that was initially used for imaging TSPO expression in the brain and has seen the greatest use is the isoquinoline (R)-[^{11}C]-PK11195. The rat unilateral facial nerve crush model results in activated microglia in the disconnected ipsilateral facial nucleus. Autoradiography studies have shown that [^{3}H]PK11195 binds selectively to these activated microglia which are involved in remodelling connections to restore facial muscle function (Banati et al. 1997). A human equivalent of this rodent model is Bell's palsy where the facial nerve becomes unilaterally compressed due to local inflammation and swelling as it passes through the auditory canal. (R)-[^{11}C]PK11195 PET studies have demonstrated tracer uptake in the facial nerve nucleus ipsilateral to the paralysed facial muscles (Banati 2002b). Human subjects with acquired upper limb amputations develop phantom limb phenomena where the absent limb still feels present but telescoped into the stump. In these subjects one can detect thalamic inflammation contralateral to the missing limb with (R)-[^{11}C]PK11195 PET (Banati 2002a). These studies, therefore, reveal the microglial activation resulting from the disconnection of brain nuclei due to peripheral injury, presumably playing an active role in the remodelling of connections. It remains to be determined whether these cells are primarily expressing an M2 phenotype.

   In the majority of brain disorders, (R)-[^{11}C]PK11195 PET reveals microglial activation due to both local disease activity and the effects of downstream disconnection. Additionally, as endothelial cells also express TSPO, tracer binding is seen in the lateral and sagittal venous sinuses, and this signal can spill over into adjacent brain tissue—particularly the cerebellum—due to the 4–5 mm spatial resolution of most commercial PET cameras. This makes quantitative modelling of brain (R)-[^{11}C]PK11195 PET problematic as there is no anatomical region that provides a pure tissue reference for non-specific tracer uptake though cerebellar grey matter has been used. The use of an arterial plasma input function with this tracer is also problematic as (R)-[^{11}C]PK11195 sticks to plastic tubing, making it difficult to obtain blood time-activity curves which allow an accurate measurement of peak height, delay and dispersion. For these reasons, a modelling approach has been developed that uses supervised cluster analysis to identify clusters of voxels that fall into six classes of brain uptake kinetics. One of these clusters represents a collection of grey matter voxels in the subject's brain that have a time-activity curve (TAC) similar to that of a normal grey matter TAC in a population of healthy controls, while another represents vascular binding (Anderson et al. 2007). The normal grey

matter reference cluster can be used to compute non-specific (R)-[^{11}C]PK11195 uptake in other brain clusters where specific tracer retention is occurring. At the same time, the vascular signal due to tracer binding, which shows the most rapid uptake, can be separated from adjacent brain parenchymal signal. The (R)-[^{11}C]PK11195 binding potentials (BPs) are then computed using a standard simplified reference tissue model (SRTM) with brain-specific and non-specific compartments. As (R)-[^{11}C]PK11195 binding increases in a normal thalamus and, to a lesser degree, cortex with age, it is important to age match healthy controls to patients when assessing levels of inflammation in disease states (Cagnin et al. 2001).

Recently, second-generation TSPO tracers have been developed which can have higher affinity and/or a lower non-specific signal in order to provide a more sensitive detection of microglial activation and facilitate modelling approaches. However, with these new tracers has come the realisation that TSPO PET imaging is influenced by TSPO gene polymorphisms expressed by individuals (Owen et al. 2012). The most influential of these is the rs6971 polymorphism where Ala147Thr substitutions result in homozygous subjects becoming low affinity binders of these newer TSPO ligands while heterozygotes express a mixture of TSPO with high and low affinity for these ligands. In Caucasian populations, around 60% of individuals are high, 10% low and 30% mixed affinity binders for the newer TSPO ligands. (R)-[^{11}C]PK11195 affinity for TSPO, however, appears to be less influenced by genotype (Owen et al. 2012), while [^{11}C]PBR28 shows a 75-fold difference in affinity for TSPO between high (Kd 4 nM) and low (Kd 300 nM) affinity binders. The PET tracers [^{11}C]DAA1106, [^{11}C]DPA713 and [^{18}F]PBR111 show 4–5-fold differences in affinity for TSPO between high and low binders. Mixed affinity binders express high and low affinity TSPO binding sites in equal proportions. If one is to use these newer TSPO PET markers, then low affinity binders will need to be excluded by prior genetic screening and patient and control populations matched for prevalence of mixed and high affinity binders. When interrogating associations between TSPO PET signals and pathology or clinical parameters, the variance due to TSPO polymorphisms may need to be corrected by ANCOVA.

Modelling the brain uptake kinetics of second-generation TSPO PET tracers has similar problems to those described previously for (R)-[^{11}C]PK11195. In practice cerebellar grey matter has often been employed as a tissue reference for non-specific binding for tracers such as [^{18}F]DPA714 and [^{11}C]PBR28 although this can lead to underestimations of specific binding in regions of interest. Supervised cluster analysis has also been applied to define reference clusters for individual patients and correct spill over of vascular signals. Arterial input functions have been also used in some series (Schain et al. 2018).

30.3 TSPO Imaging in Alzheimer's Disease

Dementia affects 10% of the over 60s, the prevalence rising to 30% by the ninth decade. It is characterised clinically by progressive impairment of memory, speech and perception along with personality change in the absence of altered conscious

level. Sixty percent of dementia cases have Alzheimer pathology characterised by extracellular fibrillar β-amyloid plaques and intra-neuronal neurofibrillary tangles of hyper-phosphorylated tau at post-mortem. Activated microglia are seen surrounding the neuritic amyloid plaques which target association cortex and cingulate but are less evident in the striatum where plaques are diffuse (Braak and Braak 1997; Dickson 1997). Activated microglia are also found in brain areas surrounding neurites with tau tangle pathology such as the entorhinal cortex and hippocampus.

Raised levels of microglial activation were first imaged in vivo in clinically diagnosed Alzheimer's disease (AD) patients with (R)-[^{11}C]PK11195 PET, binding potentials being raised by up to 50% in association cortex (Cagnin et al. 2001; Schuitemaker et al. 2013) (Fig. 30.1a). Uptake of the TSPO ligand [^{11}C]DAA1106 has also been reported to be elevated by up to 33% in AD (Yasuno et al. 2008). The cortical distribution of raised (R)-[^{11}C]PK11195 uptake parallels that of β-amyloid plaque deposition revealed with [^{11}C]PIB PET, a marker of fibrillar amyloid load
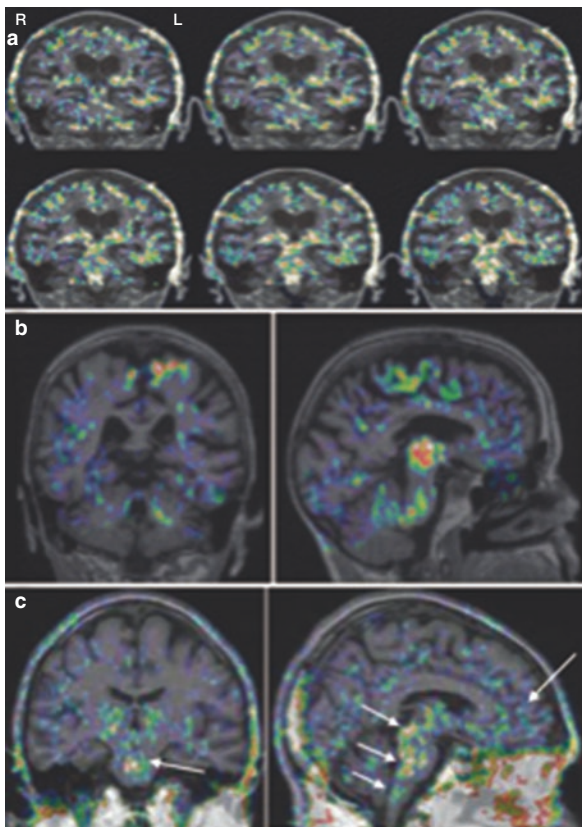
Fig. 30.1 (R)-[^{11}C]PK11195 PET images of microglial activation in patients with (**a**) Alzheimer's disease, (**b**) motor neuron disease, (**c**) Parkinson's disease, (**d**) multiple sclerosis

Fig. 30.1 (continued)

(Edison et al. 2007a), targeting association rather than primary areas. Levels of cortical (R)-[11C]PK11195 and [11C]PBR28 uptake in AD have been reported to correlate with cognitive impairment rated with the mini-mental state examination (MMSE) and CDR-SOB, but there was no correlation between amyloid load and cognitive status (Edison et al. 2007b; Kreisl et al. 2016; Yokokura et al. 2011). In established Alzheimer's disease, amyloid plaque load plateaus while cognitive ability declines, and these findings suggests that it may be the cortical microglial activation rather than amyloid plaques in AD that are detrimental to cognitive function, possibly due to cytokine release by cells exhibiting a cidal M1 phenotype. Along with the raised cortical TSPO signal, activated microglia can also be detected in the thalamus, cerebellum and brainstem of Alzheimer patients. As these subcortical areas are only targeted in late disease by plaques, the (R)-[11C]PK11195 signal there is likely to reflect microglial activation either due to local tau tangle disease or in response to cortical disconnection, the cells acting to remodel connections.

(R)-[11C]PK11195, [11C]DAA1106 and [18F]DPA714 PET have all been reported to detect the presence of microglial activation in a proportion of amnestic mild cognitive impairment (MCI) cases. These subjects have isolated progressive recall problems that are not severe enough to interfere with activities of daily living, but around 60% of these cases progress over 5 years to develop Alzheimer's disease (Petersen et al. 2001). In an initial small series, 60% of MCI cases showed evidence of amyloid plaque deposition with [11C]PIB PET and so represented prodromal Alzheimer's disease (pAD). (R)-[11C]PK11195 PET detected microglial activation in 40% of these amnestic MCI cases; that is two thirds of the pAD subjects (Okello et al. 2009). However, another series failed to detect microglial activation in amnestic MCI with (R)-[11C]PK11195 PET—possibly because these workers used a cerebellar reference rather than defining normal voxels with supervised cluster analysis (Schuitemaker et al. 2013). A group of seven MCI cases showed a significant mean of 27% increase in tracer uptake across brain regions when their TSPO was imaged with [11C]DAA1106 PET, and two cases individually had microglial activation elevated more than 2 SD above the control mean (Yasuno et al. 2012). Five of these seven MCI subjects with [11C]DAA1106 uptake raised more than 0.5 standard deviations above the normal mean progressed to develop dementia over a 2-year follow-up period.

More recently, Parbo and colleagues scanned 42 MCI cases with [11C]PiB and (*R*)-[11C]PK11195 PET (Parbo et al. 2017). Twenty-six (62%) of the cases had raised cortical [11C]PiB uptake, and 17 (65%) of these pAD cases had evidence of cortical inflammation. Clusters of correlated levels of amyloid and inflammation were found in the frontal, temporal and parietal cortex. In a follow-up study, tau tangle load was imaged with [18F]flortaucipir PET in a subgroup of 20 MCI cases and 6 AD patients (Parbo et al. 2018). While amyloid load and inflammation levels were again correlated in cortical clusters of voxels, there was surprisingly no correlation evident between tau tangle load and inflammation. However, a 2-year follow-up study on these subjects has now detected a correlation between cortical tau and inflammation levels in the MCI and early AD cohort though this was not evident at baseline (R Ismail, Brooks DJ. Neurobiology of Disease 2020;17(1):151).

Using [18F]DPA714 PET, Hamelin and colleagues have studied the levels of microglial activation in prodromal (38) and early clinical Alzheimer's disease (26) and its relationship with clinical progression (Hamelin et al. 2016). The presence of raised amyloid load was confirmed in all cases with [11C]PiB PET, and, based on their MMSE score changes over 2 years, the AD group was divided into fast and slow decliners. The levels of TSPO binding were determined as target region:cerebellar ratios, and findings for high and mixed affinity binders were combined. TSPO binding in AD was raised relative to healthy controls, and cortical levels correlated negatively with MMSE scores and hippocampal volume and positively with CDR-SOB ratings and [11C]PiB uptake. The slow and fast decliners had similar baseline levels of amyloid load, but baseline TSPO uptake was higher in the slow decliners. The authors suggested that microglial activation may be playing a protective role in early AD. In a follow-up study, these workers repeated [18F]DPA714 PET in their AD patients and control subjects and found a greater increase in inflammation in AD (Hamelin et al. 2018). However, the increase in [18F]DPA714 uptake was lower in those cases with higher baseline inflammation. The authors suggested that inflammation has two distinct profiles in AD, an initial protective profile followed by a detrimental effect on disease progression.

In favour of a protective role of inflammation in early AD, an [11C]PBR28 PET series in 37 MCI amyloid-positive cases has reported that levels of TSPO binding correlated positively with cortical and hippocampal volumes (Femminella et al. 2019). Here an arterial input function with Logan graphical analysis was employed to measure tracer volumes of distribution. Longitudinal data is not yet available for this cohort.

Recently, our group has followed 38 MCI cases over 2 years with [11C]PK11195 and [11C]PiB PET (Ismail R and Brooks DJ. Neurobiology of Disease 2020;17(1):151). Twenty-two of these MCI subjects also had [18F]flortaucipir PET to determine their tau tangle load. At baseline 23 MCI cases had raised and 15 cases had low/normal levels of cortical PiB uptake. Over 2 years the combined group of 38 MCI cases showed a rise in mean amyloid load but a decrease in mean cortical level of inflammation. In those 22 cases who had [18F]flortaucipir PET, their cortical tau tangle load increased over time. Seven of the low PiB cohort showed increasing tracer uptake over 2 years, three crossing into the abnormal range. These cases

showed a correlation between their cortical PiB uptake and inflammation levels in the absence of tau tangle deposition. In the MCI group with raised PiB, the level of inflammation correlated with tau tangle load. These findings suggest that inflammation plays a role both in early MCI when amyloid load is rising—possibly protective—and in later MCI when tau tangles are forming, possibly toxic. The relationship between pathology and cognitive status was also followed in this MCI cohort. Amyloid plaque load and levels of inflammation across cortical regions at baseline correlated with cognitive deficit, while tau load correlated most strongly at the 2-year follow-up time point.

30.4 Imaging Inflammation in Frontotemporal Dementia and ALS

Dementia with a frontotemporal phenotype comprises around 10% of later onset dementia cases, and clinically it presents as personality change, praxis and language difficulties with memory becoming impaired subsequently. Clinical phenotypes include behavioural variant frontotemporal dementia (bvFTD), semantic dementia (SD) where subjects cannot recall the features and uses of objects and progressive non-fluent aphasia and apraxia (PNFA). The pathology targets the frontal and inferior temporal lobes and most commonly involves TDP-43 protein inclusions when it can also be associated with ALS. Less commonly Pick bodies containing three-repeat tau isoforms or spongiform degeneration are present.

25–50% of FTD cases are genetic in origin, and multiple gene mutations have been implicated. Repeat expansions of the C9ORF72 gene are the most common genetic cause and are associated with TDP-43 inclusions as are mutations of the progranulin (GRN) gene. MAPT gene mutations can cause Pick body tau inclusion disease. Mutations of TREM2 have been associated with FTD implicating a role of inflammation (Zhang 2015). Presenilin gene mutations also can rarely cause FTD as can mutations of the mitochondrial CHCHD10 gene. FTD is usually younger onset than AD and rarely associated with amyloid plaque formation.

The first PET series to study inflammation reported raised frontotemporal uptake of (R)-[^{11}C]PK11195 in four idiopathic PFNA and a fifth bvFTD case (Cagnin et al. 2004). In some but not all regions, the inflammation was associated with cortical atrophy. More recently, increased [^{11}C]PBR28 uptake has been documented in bvFTD cortex targeting association areas in patterns matching the clinical phenotypes of the patients (Kim et al. 2019). Larger series including presymptomatic susceptibility gene carriers are required to determine whether inflammation precedes neuronal dysfunction and aberrant protein aggregation in FTD.

There is both a clinical and pathological overlap between frontotemporal dementia and motor neuron disease (amyotrophic lateral sclerosis). The neuropathology of both can be associated with cortical TDP-43 inclusions and spongiform degeneration, and neuropsychological and imaging studies have indicated that dysfunction extends beyond the motor system in ALS. In an early series, ten probable or definite (El Escorial criteria) ALS patients without dementia had (R)-[^{11}C]PK11195 PET (Turner

et al. 2004). Significantly increased microglial activation was seen in the motor cortex, brainstem, thalamus, dorsolateral prefrontal cortex and occipital lobes of the ALS patients compared with 14 healthy controls (Fig. 30.1b). There was a significant correlation between the severity of upper motor neuron signs on examination and levels of motor cortex (R)-[^{11}C]PK11195 uptake. More recently, ten non-demented patients with probable or definite ALS were enrolled prospectively and eight healthy controls matched for age had [^{18}F]DPA714 PET (Corcia et al. 2012). A significant increase of microglial activation was found in the ALS sample in primary motor, supplementary motor and temporal cortex. Longitudinal follow-up is required in these series to determine the predictive power of TSPO PET for dementia in ALS cases.

Alshikho and colleagues have scanned 53 ALS and 11 primary lateral sclerosis (PLS) cases with [^{11}C]PBR28 PET and compared their findings with those of 21 healthy controls (Alshikho et al. 2018). Inflammation was measured as cortical grey matter SUVRs with a cerebellar reference for non-specific signal. ALS and PLS cases both showed increased inflammation in pre-and post-central gyri along with cortical thinning. Cortical uptake of [^{11}C]PBR28 correlated negatively with ALSFRS-R disability ratings. No significant increase in pre- and post-central cortical [^{11}C]PBR28 was apparent over a 6-month follow-up although ALSFRS-R ratings continued to decline. The authors suggested [^{11}C]PBR28 PET could provide a useful biomarker of the efficacy of neuroprotective strategies in ALS.

30.5   Parkinson's Disease and TSPO Imaging

Parkinson's disease (PD) is the second most common neurodegenerative disorder after dementia, affecting around 1% of the over 60s. It manifests as asymmetrical limb bradykinesia, rigidity and tremor, and these symptoms are usually responsive to oral levodopa. The pathology is characterised by Lewy body inclusions in neurons and Lewy neurites which contain aggregated alpha-synuclein and neurofilaments.

While the dopamine neurons of the substantia nigra pars compacta are targeted by the Lewy body pathology, it is now thought that the pathology can start peripherally in the skin and gut and then track via the vagus nerve to affect the dorsal motor nucleus in the medulla and then ascend through the brainstem to the cortex in stages (Braak et al. 2004). In stage 2 the locus ceruleus, pedunculopontine nucleus and median raphe in the pons become involved, while the dopamine neurons of the substantia nigra pars compacta in the midbrain only become targeted in stage 3 along with the cholinergic nucleus basalis. The limbic cortex and cingulate are involved by stage 4 and the association and primary neocortex in stages 5 and 6.

At post-mortem microglial activation has been reported to accompany Lewy body pathology in affected subcortical and cortical regions (Imamura et al. 2003; McGeer et al. 1993). Aggregations of alpha-synuclein as oligomers and fibrils can stimulate microglial activation in vitro, but the relationship between inflammation and disease progression remains uncertain. In an initial PET study, it was reported that levels of increased midbrain (R)-[^{11}C]PK11195 uptake in PD patients correlated

with reductions in putamen dopamine transporter (DAT) binding measured with [^{11}C]CFT PET (Ouchi et al. 2005). The authors suggested that this provided evidence for involvement of microglia in the dopamine loss that characterises PD.

Later (R)-[^{11}C]PK11195 PET series, however, have failed to detect consistent microglial activation in the substantia nigra of PD cases or to replicate an association between midbrain (R)-[^{11}C]PK11195 signals and loss of dopaminergic function in PD. Gerhard and colleagues noted that PD patients showed significant striatal and frontotemporal (R)-[^{11}C]PK11195 uptake though this did not correlate with disease severity (Gerhard et al. 2006a) (Fig. 30.1c). Iannaccone and co-workers have reported increased (R)-[^{11}C]PK11195 binding in the putamen and the substantia nigra of early Parkinson's disease but did not detect inflammation in the cortex (Iannaccone et al. 2013). Measuring [^{11}C]PBR28 V_T with Logan graphical analysis using an arterial plasma input function, Varnas and co-workers (Varnas et al. 2019) were unable to detect any increase in microglial activation in their group of 16 PD patients (8 HABs and 8 MABs).

In contrast, using the second-generation TSPO marker [^{11}C]DPA713 PET, increased signal was detected in the temporal, parietal and occipital cortex of PD cases which increased over 1 year (Terada et al. 2016). This finding supports the report from Gerhard and suggests that microglia activation can involve the substantia nigra, striatum and association cortex and be present in the early stages of the disease even in the absence of dementia.

It is conceivable that the dopaminergic drugs used to treat PD may have an influence on levels of microglial activation. Although none of these dopaminergic agents directly act to suppress microglial activation, it has been suggested that both dopamine agonists and monoamine oxidase B inhibitors have neuroprotective properties (Schapira and Olanow 2004). This claim is, however, controversial, and currently there is no hard evidence that therapy for PD influences levels of the inflammatory response.

The widespread microglial activation seen in PD at post-mortem and the raised (R)-[^{11}C]PK11195 uptake seen in the brainstem, basal ganglia and cortical regions of non-demented cases with PET are all regions which are targeted by Lewy body pathology in later Braak stages. More recently we have noted that levels of striatal (R)-[^{11}C]PK11195 uptake in PD correlated with disability rated with the Unified Parkinson's Disease Rating Scale (UPDRS), while impaired verbal fluency was associated with raised frontal and insular (R)-[^{11}C]PK11195 activity (Simpson et al. 2012). This supports a role for microglial activation in driving disease activity and is in line with the dying back theory of PD pathology which suggests that nigrostriatal terminals may become dysfunctional ahead of nigral cell body loss.

Those few longitudinal studies that have reported (R)-[^{11}C]PK11195 uptake in PD suggest levels remain static over a 1–2-year follow-up period despite on-going clinical deterioration and loss of putamen [^{18}F]DOPA storage of PD cases (Gerhard et al. 2004; Terada et al. 2016). It has been suggested that cortical microglial activation is an early phenomenon in PD and may act to promote the superadded dementia that usually follows although levels of inflammation remain fixed. In favour of this viewpoint, it was noted that PD cases with late dementia had similar cortical levels of microglial activation to similarly disabled non-demented cases.

30.6   Atypical Parkinsonian Syndromes and TSPO Imaging

Neurodegenerative disorders that cause atypical parkinsonian disorders include multiple system atrophy (MSA) and progressive supranuclear palsy (PSP). MSA is associated with asymmetric parkinsonism along with early autonomic dysfunction, postural instability and ataxia. The pathology is characterised by argyrophilic glial cytoplasmic inclusions (GCIs) that contain alpha-synuclein and targets the substantia nigra, putamen, ponto-cerebellar connections and the lateral columns of the spinal cord. Microglial activation is known to be associated with MSA pathology, and (R)-[^{11}C]PK11195 PET has revealed raised TSPO binding in the putamen, pallidum, pons, substantia nigra and the dorsolateral prefrontal cortex at higher levels than that associated with PD (Gerhard et al. 2003). In a follow-up series of 14 MSA-P cases, Gerhard and colleagues again reported significant increases in microglial activation in the putamen ($p = 0.001$), pallidum ($p = 0.002$), precentral gyrus ($p = 0.004$), orbitofrontal cortex ($p = 0.006$), presubgenual anterior cingulate cortex ($p = 0.006$) and the superior parietal gyrus ($p = 0.007$) but now also the caudate nucleus ($p = 0.002$) (Kubler et al. 2019). The increases in (R)-[^{11}C]PK11195 binding potentials correlated with decreases in glucose utilisation in the putamen ($r = -0.78$, $p = 0.003$) and pallidum ($r = -0.77$, $p = 0.003$). No correlations between regional (R)-[^{11}C]PK11195 BPs and clinical parameters were found.

A proteolipid protein-alpha-synuclein overexpression (PLP-αSYN) transgenic mouse model of MSA showed a correlation between levels of nigral microglial activation and dopamine neurone loss (Stefanova et al. 2007). Minocycline suppressed the inflammation and preserved dopamine neurones in the mouse. A human trial was subsequently set up to determine whether minocycline had neuroprotective efficacy in MSA. The drug failed to alter disease progression at clinically licensed doses though MSA cases receiving active medication showed a 30% reduction in brain (R)-[^{11}C]PK11195 uptake relative to placebo-treated cases (Dodel et al. 2010).

Three PSP patients with Richardson syndrome who were studied with (R)-[^{11}C]PK11195 PET showed significantly increased signal in their caudate nucleus, putamen, pallidum, midbrain, substantia nigra, the frontal lobe and the cerebellum (Gerhard et al. 2006b). One of these patients was rescanned after 10 months, and the level of microglial activation had remained stable.

30.7   Detecting Preclinical Huntington's Disease Activity with TSPO PET

Huntington's disease is an autosomal dominant inherited progressive neurodegenerative disorder associated with motor, cognitive and psychiatric symptoms. It arises from an abnormal CAG triplet repeat expansion of the HTT gene on chromosome 4 which leads to an elongated polyglutamine chain at the terminus of the huntingtin protein. This results in cytoplasmic and intranuclear aggregations of huntingtin and progressive loss of medium spiny striatal GABA-ergic and cortical interneurons

(Sapp et al. 1997). The striatal output neurons express either dopamine D1 or D2 receptors depending on whether they are part of the direct or indirect pathway to the internal pallidum. Striatal dysfunction can be detected prior to symptom onset as a loss of availability of D1 and D2 sites for ligand binding (Andrews et al. 1999).

The loss of striatal and cortical neurons in HD is associated with microglial activation (Sapp et al. 2001) which can be detected in vivo with (R)-[^{11}C]PK11195 PET. Levels of striatal microglial activation correlate with loss of dopamine D2 receptor binding measured with [^{11}C]raclopride PET and with locomotor disability rated with the Unified Huntington's Disease Rating Scale (UHDRS) (Pavese et al. 2006). This suggests that microglial activation plays a role in driving the disease process. Supporting this viewpoint, (R)-[^{11}C]PK11195 PET studies have detected raised microglial activation in a majority of asymptomatic adult HD gene carriers in their fourth decade (Tai et al. 2007). Those asymptomatic carriers with raised TSPO expression also showed reduced dopamine D2 availability with [^{11}C]raclopride PET. Cortical microglial activation was also evident in pre-manifesting HD carriers confirming that this is not purely a basal ganglia disorder (Politis et al. 2011). Levels of striatal (R)-[^{11}C]PK11195 uptake have been shown to correlate with the predicted time of clinical disease onset (Politis et al. 2011; Tai et al. 2007).

Lois and colleagues have measured translocator protein (TSPO) expression in HD using [^{11}C]PBR28 PET. Regional signals were quantitated using SUVRs normalised to whole brain uptake with emission data acquired 60–90 min after intravenous radiotracer administration (Lois et al. 2018). Significant TSPO overexpression was detected in the putamen and pallidum of all the individual HD patients. Additionally, some HD patients showed elevated [^{11}C]PBR28 uptake in thalamic nuclei, the brainstem and red nuclei. Increased cortical inflammation was not reported in this series. The authors suggested that [^{11}C]PBR28 PET might prove a useful biomarker in clinical trials evaluating therapies targeting neuroinflammation.

30.8   Measuring Inflammation in Multiple Sclerosis

Multiple sclerosis (MS) is a disease characterised clinically by relapsing and remitting neurological episodes followed by a progressive phase of disability. Pathologically central inflammatory demyelination is seen as white matter plaques associated with axonal degeneration. MS targets young adults and is their most common cause of non-traumatic disability in the Western world (Compston and Coles 2008). Active plaques of demyelination contain blood-borne B and T lymphocytes and macrophages that have invaded via the disrupted blood-brain barrier. However, there is also an intrinsic immune reaction to the disease process manifested as involvement of activated microglia (Benveniste 2007). Post-mortem investigations have detected activated microglia not just in white matter plaques but also in cortex and apparently normal-appearing brain areas (De Groot et al. 2001; Peterson et al. 2001). In progressive MS activated microglia are seen surrounding the degenerating myelinated axons (Magliozzi et al. 2010).

(*R*)-[¹¹C]PK11195 PET has been used to demonstrate the extent of microglial activation in MS patients (Banati et al. 2000; Debruyne et al. 2003; Politis et al. 2012) (Fig. 30.1d). PET findings have been validated with [³H]PK11195 autoradiographic studies on human brain slices which showed that this tracer binds to activated microglia rather than activated astrocytes or lymphocytes in plaques of demyelination (Banati et al. 2000). PET reveals that not only can raised (*R*)-[¹¹C]PK11195 uptake be seen in active plaques which show raised T2 signal and gadolinium enhancement on MRI but also in normal-appearing white and grey matter (Banati et al. 2000; Debruyne et al. 2003; Versijpt et al. 2005; Politis et al. 2012). This finding supports the hypothesis that in early MS microglial activation may initiate the inflammatory process prior to invasion of the damaged blood-brain barrier by lymphocytes. The activated microglial load at baseline may well be the critical factor when predicting outcome in MS patients (Confavreux et al. 2000). (*R*)-[¹¹C]PK11195 uptake has been reported to be higher in secondary progressive than relapsing-remitting MS. Additionally, a significant correlation was reported between levels of (*R*)-[¹¹C]PK11195 binding in cortical grey matter and locomotor disability in patients with secondary progressive MS (Politis et al. 2012).

TSPO expression in MS has also been examined with [¹¹C]PBR28, [¹⁸F]DPA714 and GE180 PET. Oh and colleagues reported that global brain [¹¹C]PBR28 uptake was increased in their MS cohort and focal increases in binding, corresponding to areas of active inflammation and blood-brain barrier breakdown on gadolinium contrast-enhanced magnetic resonance imaging (MRI), were evident (Oh et al. 2010). Increases in [¹¹C]PBR28 binding preceded the appearance of contrast enhancement on magnetic resonance imaging in some lesions, suggesting that glial activation is an early phenomenon in MS lesion formation. In this series global levels of brain [¹¹C]PBR28 binding correlated with disease duration but not with locomotor disability. Herranz and colleagues have imaged nine relapsing-remitting multiple sclerosis (RRMS) and ten secondary progressive multiple sclerosis (SPMS) patients with [¹¹C]PBR28 PET and 7-Tesla (7 T) MRI (Herranz et al. 2019). Normal white matter signal was used as a reference tissue to compute SUVRs. Raised [¹¹C]PBR28 uptake was found in cortical lesions in both RRMS and SPMS but in the latter inflammation was also evident in normal-appearing cortex. It was noted that patients with higher levels of cortical inflammation had a worse clinical outcome. The same group also used [¹¹C]PBR28 PET to demonstrate significant cerebellar inflammation in RRMS and SPMS patients (Barletta et al. 2019). Levels of cerebellar [¹¹C]PBR28 uptake correlated with both physical disability and cognitive deficit.

The utility of the TSPO ligand, [¹⁸F]DPA-714, has been evaluated in primary and secondary progressive multiple sclerosis (PMS) (Hagens et al. 2018). Eight PMS cases and seven healthy controls had [¹⁸F]DPA-714 PET, and non-binders were excluded by prior genotyping for the presence of the rs6971 polymorphism. Regional time-activity curves (TACs) were kinetically modelled using a brain two-compartment model and a metabolite corrected plasma input function. Regional V_Ts were higher for high affinity (HABs) than mixed affinity binders (MABs) in both patient and normal groups, but [¹⁸F]DPA-714 PET was not able to discriminate

patients from healthy controls. The patients, however, only showed focally increased tracer uptake where T2 white matter lesions were seen on MRI. A drawback with [^{18}F]DPA-714 as a TSPO marker was felt to be its large non-displaceable background signal, rather similar to the situation seen with (R)-[^{11}C]PK11195.

30.9 Traumatic Brain Injury

Recovery from concussive traumatic brain injury (TBI) is highly variable. (R)-[^{11}C]PK11195 PET can detect the presence of microglial activation in many of these cases years after the original injury. In a recent series, ten patients had (R)-[^{11}C]PK11195 PET at least 11 months after moderate to severe TBI, and binding was calculated in and around the site of focal brain damage, and in selected distant and subcortical brain regions (Ramlackhansingh et al. 2011). Microglial activation was significantly raised in the thalami, putamen, occipital cortices and the posterior limb of the internal capsules after TBI though there was no increase in binding at the original site of the focal brain injury. Levels of thalamic (R)-[^{11}C]PK11195 uptake correlated with impairment on executive tasks but not with either time since the injury or the amount of structural brain injury. The authors concluded that increased microglial activation can persist up to 17 years after TBI in distant brain areas from the original focal lesion, particularly in subcortical regions. They suggested that a chronic inflammatory response to TBI develops over time and that anti-microglial strategies may still be beneficial months to years after the original insult. In a follow-up article, these workers showed that levels of thalamic inflammation correlated with levels of thalamo-cortical fibre damage measured with diffusion tensor imaging rather than cortical or thalamic lesions (Scott et al. 2015). Whether the persistent inflammation was beneficial to recovery or toxic remained uncertain.

30.10 Stroke and Microglial Activation

Stroke is associated with microglial activation both around the infarct, which develops within hours of the event, but also later in disconnected brain regions including the thalamus and brainstem. In an early series, six patients were examined with (R)-[^{11}C]PK11195 PET between 3 and 150 days after their infarct, and increased microglial activation was present in all the patients examined (Gerhard et al. 2005). In the first 6 days following the stroke, the focus of inflammation was generally smaller and found adjacent to the MRI lesion with little spatial overlap. The size of the local area of microglial activation then increased over the next months overlapping with the MRI lesion as the blood-brain barrier became disrupted and invasion by macrophages binding (R)-[^{11}C]PK11195 alongside local microglial activation occurred. By 6 months after the initial stroke, local microglial activation was subsiding, whereas distant areas of (R)-[^{11}C]PK11195 uptake could be seen beyond the

primary infarct site involving disconnected areas of the ipsilateral hemisphere including the thalamus and brainstem. The lesioned cortical area with high initial (*R*)-[^{11}C]PK11195 binding became atrophic during that 6-month interval as local inflammation regressed.

Thiel and colleagues used (*R*)-[^{11}C]PK11195 PET to prospectively image activated microglia in vivo 2 weeks and 6 months after acute subcortical stroke in humans to investigate their temporal dynamics and relate local and remote inflammation to pyramidal tract (PT) damage detected using diffusion tensor imaging (DTI) (Thiel et al. 2010). As reported previously, microglial activation increased and then regressed around the local lesion. In contrast, brainstem inflammation was only seen in cases with pyramidal tract damage on DTI and occurred later. The brainstem (*R*)-[^{11}C]PK11195 signal correlated positively with clinical outcome.

Recently Morris and co-workers used diffusion and perfusion MRI to define the ischemic penumbra around acute stroke and examined neuronal integrity with the GABA marker [^{11}C]flumazenil PET and microglial activation with (*R*)-[^{11}C]PK11195 PET (Morris et al. 2018). They found evidence of viable neurons in the penumbra in the absence of microglial activation. These workers concluded that viable penumbra may not require the presence of activated microglia during the stroke recovery phase.

30.11 Psychosis

Lewy body dementia and Parkinson's disease are associated with secondary psychosis related to their cortical pathology and possibly the presence of the cortical and limbic inflammation that can be detected in these disorders. Schizophrenia is a primary psychosis but has also been reported to be associated with brain inflammation at post-mortem. In an early series, seven schizophrenic patients in the recovery phase from a psychotic episode were studied with (*R*)-[^{11}C]PK11195 PET (Doorduin et al. 2009). Conventional T1- and T2-weighted MRI showed no significant abnormalities. PET revealed a 51% increase in mean hippocampal and a 30% increase in global cortical (*R*)-[^{11}C]PK11195 binding in the schizophrenic subjects compared with age-matched cortical controls. Three of the subjects individually showed significantly raised levels of cortical inflammation. Low-level inflammation in the cortex of schizophrenic cases in remission has also been reported (van Berckel et al. 2008). Doorduin and co-workers suggested that active episodes of psychosis may be related to increases in background inflammatory activity.

In contrast, using the second-generation TSPO marker [^{11}C]PBR28 with PET, Collste and colleagues detected reduced levels of binding (V_T) in 16 untreated schizophrenics recovering from their first psychotic episode (Collste et al. 2017). Brain tracer uptake was kinetically modelled using a two-compartmental approach with an arterial plasma input function. These workers suggested that the function of immune cells may be depressed in schizophrenia.

30.12 Conclusions

Microglial activation is a non-specific reaction to all forms of brain injury and can be detected with PET in inflammatory, vascular, traumatic, degenerative and, possibly, psychotic brain disorders. The role of activated microglia after stroke and trauma appears to be primarily restorative, the cells adopting a phagic phenotype removing debris and remodelling connections to disconnected regions. However, the ischemic penumbra surrounding infarcted tissue may not require activated microglia for its revival. In neurodegenerative diseases, the role of activated microglia is less certain. Initially these cells could act to ingest misfolded proteins and release growth factors, but in later disease this action could fail and local release of toxic cytokines predominate leading to neuronal death and disease progression. In downstream disconnected areas, microglia could be beneficial leading to remodelling of connections as an adaptive response.

Currently PET imaging of activated microglia relies on the use of TSPO radioligands. While these provide a valuable in vivo tool for detecting disease activity and tracking the progression of neuroinflammation, binding of second-generation ligands is influenced by the TSPO polymorphisms expressed by subjects—10% of Caucasians are non-affinity binder, 30% mixed affinity binders and 60% high affinity binders. As a consequence, despite its higher non-specific signal and rapid washout, (*R*)-[^{11}C]PK11195 PET still provides a reasonable approach for measuring brain inflammation as it is little affected by the TSPO polymorphisms expressed. While TSPO imaging reflects disease activity, it does not have diagnostic potential as raised microglial activation is not specific to any one neurological disorder. However, the early detection of microglia with PET provides a potential biomarker for establishing the presence of disease activity in at risk subjects and testing the efficacy of neuroprotective strategies designed to suppress the inflammatory response to local injury or neurodegenerative processes. In the future, hopefully, there will be development of both better TSPO tracers uninfluenced by the genotype along with other markers of microglial activation, such as cannabinoid CB2 expression, allowing us to improve our understanding of the role of activated microglia in CNS disease.

References

Alshikho MJ, Zurcher NR, Loggia ML et al (2018) Integrated magnetic resonance imaging and [(11) C]-PBR28 positron emission tomographic imaging in amyotrophic lateral sclerosis. Ann Neurol 83(6):1186–1197. https://doi.org/10.1002/ana.25251

Anderson AN, Pavese N, Edison P et al (2007) A systematic comparison of kinetic modelling methods generating parametric maps for [(11)C]-(R)-PK11195. NeuroImage 36(1):28–37. https://doi.org/10.1016/j.neuroimage.2007.02.017

Andrews TC, Weeks RA, Turjanski N et al (1999) Huntington's disease progression PET and clinical observations. Brain 122:2353–2363

Banati RB (2002a) Brain plasticity and microglia: is transsynaptic glial activation in the thalamus after limb denervation linked to cortical plasticity and central sensitisation? J Physiol Paris 96(3–4):289–299

Banati RB (2002b) Visualising microglial activation in vivo. Glia 40(2):206–217. https://doi.org/10.1002/glia.10144

Banati RB, Myers R, Kreutzberg GW (1997) PK ('peripheral benzodiazepine')—binding sites in the CNS indicate early and discrete brain lesions: microautoradiographic detection of [3H]PK11195 binding to activated microglia. J Neurocytol 26(2):77–82

Banati RB, Newcombe J, Gunn RN et al (2000) The peripheral benzodiazepine binding site in the brain in multiple sclerosis: quantitative in vivo imaging of microglia as a measure of disease activity. Brain 123(Pt 11):2321–2337

Barletta VT, Herranz E, Treaba CA et al (2019) Evidence of diffuse cerebellar neuroinflammation in multiple sclerosis by (11)C-PBR28 MR-PET. Mult Scler 26(6):1352458519843048. https://doi.org/10.1177/1352458519843048

Benveniste EN (2007) Role of macrophages/microglia in multiple sclerosis and experimental allergic encephalomyelitis. J Mol Med 75:165–173

Boche D, Perry VH, Nicoll JA (2013) Activation patterns of microglia and their identification in the human brain. Neuropathol Appl Neurobiol 39(1):3–18. https://doi.org/10.1111/nan.12011

Braak H, Braak E (1997) Frequency of stages of Alzheimer-related lesions in different age categories. Neurobiol Aging 18(4):351–357

Braak H, Ghebremedhin E, Rub U, Bratzke H, Del Tredici K (2004) Stages in the development of Parkinson's disease-related pathology. Cell Tissue Res 318(1):121–134

Cagnin A, Brooks DJ, Kennedy AM et al (2001) In-vivo measurement of activated microglia in dementia. Lancet 358(9280):461–467

Cagnin A, Rossor M, Sampson EL, Mackinnon T, Banati RB (2004) In vivo detection of microglial activation in frontotemporal dementia. Ann Neurol 56(6):894–897. https://doi.org/10.1002/ana.20332

Collste K, Plaven-Sigray P, Fatouros-Bergman H et al (2017) Lower levels of the glial cell marker TSPO in drug-naive first-episode psychosis patients as measured using PET and [(11)C]PBR28. Mol Psychiatry 22(6):850–856. https://doi.org/10.1038/mp.2016.247

Compston A, Coles A (2008) Multiple sclerosis. Lancet 372(9648):1502–1517. https://doi.org/10.1016/S0140-6736(08)61620-7

Confavreux C, Vukusic S, Moreau T, Adeleine P (2000) Relapses and progression of disability in multiple sclerosis. N Engl J Med 343(20):1430–1438. https://doi.org/10.1056/NEJM200011163432001

Corcia P, Tauber C, Vercoullie J et al (2012) Molecular imaging of microglial activation in amyotrophic lateral sclerosis. PLoS One 7(12):e52941. https://doi.org/10.1371/journal.pone.0052941

De Groot CJ, Bergers E, Kamphorst W et al (2001) Post-mortem MRI-guided sampling of multiple sclerosis brain lesions: increased yield of active demyelinating and (p)reactive lesions. Brain 124(Pt 8):1635–1645

Debruyne JC, Versijpt J, Van Laere KJ et al (2003) PET visualization of microglia in multiple sclerosis patients using [11C]PK11195. Eur J Neurol 10(3):257–264

Dickson DW (1997) The pathogenesis of senile plaques. J Neuropathol Exp Neurol 56(4):321–339

Dodel R, Spottke A, Gerhard A et al (2010) Minocycline 1-year therapy in multiple-system-atrophy: effect on clinical symptoms and [(11)C] (R)-PK11195 PET (MEMSA-trial). Mov Disord 25(1):97–107. https://doi.org/10.1002/mds.22732

Dolle F, Luus C, Reynolds A, Kassiou M (2009) Radiolabelled molecules for imaging the translocator protein (18 kDa) using positron emission tomography. Curr Med Chem 16(22):2899–2923

Doorduin J, de Vries EF, Dierckx RA, Klein HC (2008) PET imaging of the peripheral benzodiazepine receptor: monitoring disease progression and therapy response in neurodegenerative disorders. Curr Pharm Des 14(31):3297–3315

Doorduin J, de Vries EF, Willemsen AT, de Groot JC, Dierckx RA, Klein HC (2009) Neuroinflammation in schizophrenia-related psychosis: a PET study. J Nucl Med 50(11):1801–1807. https://doi.org/10.2967/jnumed.109.066647

Edison P, Archer H, Hinz R et al (2007a) Relationship between the distribution of microglial activation and amyloid deposition in Alzheimer's disease: an 11C-PK11195 and 11C-PIB PET study. J Neurol Neurosurg Psychiatry 78(2):219–219

Edison P, Archer HA, Hinz R et al (2007b) Amyloid, hypometabolism, and cognition in Alzheimer disease—an [11C]PIB and [18F]FDG PET study. Neurology 68(7):501–508

Femminella GD, Dani M, Wood M et al (2019) Microglial activation in early Alzheimer trajectory is associated with higher gray matter volume. Neurology 92(12):E1331–E1343. https://doi.org/10.1212/wnl.0000000000007133

Gerhard A, Banati RB, Goerres GB et al (2003) [(11C)(R)-PK11195 PET imaging of microglial activation in multiple system atrophy. Neurology 61(5):686–689

Gerhard A, Pavese N, Hotton GR et al (2004) Microglial activation in Parkinson's disease—its longitudinal course and correlation with clinical parameters: an [11C](R)—PK11195 PET study. Neurology 62(Suppl 5):A432

Gerhard A, Schwarz J, Myers R, Wise R, Banati RB (2005) Evolution of microglial activation in patients after ischemic stroke: a [(11C)(R)-PK11195 PET study. NeuroImage 24(2):591–595

Gerhard A, Pavese N, Hotton G et al (2006a) In vivo imaging of microglial activation with [(11C)(R)-PK11195 PET in idiopathic Parkinson's disease. Neurobiol Dis 21(2):404–412

Gerhard A, Trender-Gerhard I, Turkheimer F, Quinn NP, Bhatia KP, Brooks DJ (2006b) In vivo imaging of microglial activation with [(11C)(R)-PK11195 PET in progressive supranuclear palsy. Mov Disord 21(1):89–93

Hagens MHJ, Golla SV, Wijburg MT et al (2018) In vivo assessment of neuroinflammation in progressive multiple sclerosis: a proof of concept study with [(18)F]DPA714 PET. J Neuroinflammation 15(1):314. https://doi.org/10.1186/s12974-018-1352-9

Hamelin L, Lagarde J, Dorothee G et al (2016) Early and protective microglial activation in Alzheimer's disease: a prospective study using 18F-DPA-714 PET imaging. Brain 139(Pt 4):1252–1264. https://doi.org/10.1093/brain/aww017

Hamelin L, Lagarde J, Dorothee G et al (2018) Distinct dynamic profiles of microglial activation are associated with progression of Alzheimer's disease. Brain 141(6):1855–1870. https://doi.org/10.1093/brain/awy079

Hanisch UK, Kettenmann H (2007) Microglia: active sensor and versatile effector cells in the normal and pathologic brain. Nat Neurosci 10(11):1387–1394. https://doi.org/10.1038/nn1997

Herranz E, Louapre C, Treaba CA et al (2019) Profiles of cortical inflammation in multiple sclerosis by (11)C-PBR28 MR-PET and 7 tesla imaging. Mult Scler:1352458519867320. https://doi.org/10.1177/1352458519867320

Iannaccone S et al (2013) In vivo microglia activation in very early dementia with Lewy bodies, comparison with Parkinson's disease. Parkinsonism Relat Disord 19(1):47–52

Imamura K, Hishikawa N, Sawada M, Nagatsu T, Yoshida M, Hashizume Y (2003) Distribution of major histocompatibility complex class II-positive microglia and cytokine profile of Parkinson's disease brains. Acta Neuropathol (Berl) 106(6):518–526

Kim MJ, McGwier M, Jenko KJ et al (2019) Neuroinflammation in frontotemporal lobar degeneration revealed by (11) C-PBR28 PET. Ann Clin Transl Neurol 6(7):1327–1331. https://doi.org/10.1002/acn3.50802

Kreisl WC, Lyoo CH, Liow J-S et al (2016) 11 C-PBR28 binding to translocator protein increases with progression of Alzheimer's disease. Neurobiol Aging 44:53–61

Kreutzberg GW (1996) Microglia: a sensor for pathological events in the CNS. Trends Neurosci 19(8):312–318

Kubler D, Wachter T, Cabanel N et al (2019) Widespread microglial activation in multiple system atrophy. Mov Disord 34(4):564–568. https://doi.org/10.1002/mds.27620

Li JT, Zhang Y (2018) TREM2 regulates innate immunity in Alzheimer's disease. J Neuroinflammation 15(1):107. https://doi.org/10.1186/s12974-018-1148-y

Lois C, Gonzalez I, Izquierdo-Garcia D et al (2018) Neuroinflammation in Huntington's disease: new insights with (11)C-PBR28 PET/MRI. ACS Chem Neurosci 9(11):2563–2571. https://doi.org/10.1021/acschemneuro.8b00072

Magliozzi R, Howell OW, Reeves C et al (2010) A gradient of neuronal loss and meningeal inflammation in multiple sclerosis. Ann Neurol 68(4):477–493. https://doi.org/10.1002/ana.22230

McGeer P, Kawamata T, Walker DG, Akiyama H, Tooyama I, McGeer EG (1993) Microglia in degenerative disease. Glia 7:84–92

Morris RS, Simon Jones P, Alawneh JA et al (2018) Relationships between selective neuronal loss and microglial activation after ischaemic stroke in man. Brain 141(7):2098–2111. https://doi.org/10.1093/brain/awy121

Oh U, Fujita M, Ikonomidou VN et al (2010) Translocator protein PET imaging for glial activation in multiple sclerosis. J Neuroimmune Pharmacol 6:354. https://doi.org/10.1007/s11481-010-9243-6

Okello A, Edison P, Archer HA et al (2009) Microglial activation and amyloid deposition in mild cognitive impairment: a PET study. Neurology 72(1):56–62. https://doi.org/10.1212/01.wnl.0000338622.27876.0d

Ouchi Y, Yoshikawa E, Sekine Y et al (2005) Microglial activation and dopamine terminal loss in early Parkinson's disease. Ann Neurol 57(2):168–175

Owen DR, Yeo AJ, Gunn RN et al (2012) An 18-kDa translocator protein (TSPO) polymorphism explains differences in binding affinity of the PET radioligand PBR28. J Cerebr Blood Flow Metab 32(1):1–5. https://doi.org/10.1038/jcbfm.2011.147

Papadopoulos V, Baraldi M, Guilarte TR et al (2006) Translocator protein (18kDa): new nomenclature for the peripheral-type benzodiazepine receptor based on its structure and molecular function. Trends Pharmacol Sci 27(8):402–409. https://doi.org/10.1016/j.tips.2006.06.005

Parbo P, Ismail R, Hansen KV et al (2017) Brain inflammation accompanies amyloid in the majority of mild cognitive impairment cases due to Alzheimer's disease. Brain 140(7):2002–2011. https://doi.org/10.1093/brain/awx120

Parbo P, Ismail R, Sommerauer M et al (2018) Does inflammation precede tau aggregation in early Alzheimer's disease? A PET study. Neurobiol Dis 117:211–216. https://doi.org/10.1016/j.nbd.2018.06.004

Pavese N, Gerhard A, Tai YF et al (2006) Microglial activation correlates with severity in Huntington disease: a clinical and PET study. Neurology 66(11):1638–1643

Petersen RC, Doody R, Kurz A et al (2001) Current concepts in mild cognitive impairment. Arch Neurol 58(12):1985–1992

Peterson JW, Bo L, Mork S, Chang A, Trapp BD (2001) Transected neurites, apoptotic neurons, and reduced inflammation in cortical multiple sclerosis lesions. Ann Neurol 50(3):389–400

Politis M, Pavese N, Tai YF et al (2011) Microglial activation in regions related to cognitive function predicts disease onset in Huntington's disease: a multimodal imaging study. Hum Brain Mapp 32(2):258–270. https://doi.org/10.1002/hbm.21008

Politis M, Giannetti P, Su P et al (2012) Increased PK11195 PET binding in the cortex of patients with MS correlates with disability. Neurology 79(6):523–530. https://doi.org/10.1212/WNL.0b013e3182635645

Ramlackhansingh AF, Brooks DJ, Greenwood RJ et al (2011) Inflammation after trauma: microglial activation and traumatic brain injury. Ann Neurol 70(3):374–383. https://doi.org/10.1002/ana.22455

Ransohoff RM, Perry VH (2009) Microglial physiology: unique stimuli, specialized responses. Annu Rev Immunol 27:119–145. https://doi.org/10.1146/annurev.immunol.021908.132528

Sapp E, Schwarz C, Chase K et al (1997 Oct) Huntingtin localization in brains of normal and Huntington's disease patients. Ann Neurol 42(4):604–612

Sapp E, Kegel KB, Aronin N et al (2001) Early and progressive accumulation of reactive microglia in the Huntington disease brain. J Neuropathol Exp Neurol 60(2):161–172

Schain M, Zanderigo F, Ogden RT, Kreisl WC (2018) Non-invasive estimation of [(11)C]PBR28 binding potential. NeuroImage 169:278–285. https://doi.org/10.1016/j.neuroimage.2017.12.002

Schapira AH, Olanow CW (2004) Neuroprotection in Parkinson disease: mysteries, myths, and misconceptions. JAMA 291(3):358–364

Schuitemaker A, Kropholler MA, Boellaard R et al (2013) Microglial activation in Alzheimer's disease: an (R)-[(1)(1)C]PK11195 positron emission tomography study. Neurobiol Aging 34(1):128–136. https://doi.org/10.1016/j.neurobiolaging.2012.04.021

Scott G, Hellyer PJ, Ramlackhansingh AF, Brooks DJ, Matthews PM, Sharp DJ (2015) Thalamic inflammation after brain trauma is associated with thalamo-cortical white matter damage. J Neuroinflamm 12:224. https://doi.org/10.1186/s12974-015-0445-y

Simpson BS, Pavese N, Ramlackhansingh AF, Breen DP, Barker RA, Brooks DJ (2012) Clinical correlates of brain inflammation in Parkinson's disease: a PET study. Mov Disord 27(Suppl 1):775

Stefanova N, Reindl M, Neumann M, Kahle PJ, Poewe W, Wenning GK (2007) Microglial activation mediates neurodegeneration related to oligodendroglial alpha-synucleinopathy: implications for multiple system atrophy. Mov Disord 22(15):2196–2203. https://doi.org/10.1002/mds.21671

Tai YF, Pavese N, Gerhard A et al (2007) Microglial activation in presymptomatic Huntington's disease gene carriers. Brain 130:1759–1766

Terada T, Yokokura M, Yoshikawa E et al (2016) Extrastriatal spreading of microglial activation in Parkinson's disease: a positron emission tomography study. Ann Nucl Med 30(8):579–587. https://doi.org/10.1007/s12149-016-1099-2

Thiel A, Radlinska BA, Paquette C et al (2010) The temporal dynamics of poststroke neuroinflammation: a longitudinal diffusion tensor imaging-guided PET study with 11C-PK11195 in acute subcortical stroke. J Nucl Med 51(9):1404–1412. https://doi.org/10.2967/jnumed.110.076612

Turner MR, Cagnin A, Turkheimer FE et al (2004) Evidence of widespread cerebral microglial activation in amyotrophic lateral sclerosis: an [11C](R)-PK11195 positron emission tomography study. Neurobiol Dis 15(3):601–609

Van Berckel BN, Bossong MG, Boellaard R et al (2008) Microglia activation in recent-onset schizophrenia: a quantitative (R)-[11C]PK11195 positron emission tomography study. Biol Psychiatry 64(9):820–822. https://doi.org/10.1016/j.biopsych.2008.04.025

Varnas K et al (2019) PET imaging of [11C]PBR28 in Parkinson's disease patients does not indicate increased binding to TSPO despite reduced dopamine transporter binding. Eur J Nucl Med Mol Imaging 46(2):367–375

Varnum MM, Ikezu T (2012) The classification of microglial activation phenotypes on neurodegeneration and regeneration in Alzheimer's disease brain. Arch Immunol Ther Exp 60(4):251–266. https://doi.org/10.1007/s00005-012-0181-2

Versijpt J, Debruyne JC, Van Laere KJ et al (2005) Microglial imaging with positron emission tomography and atrophy measurements with magnetic resonance imaging in multiple sclerosis: a correlative study. Mult Scler 11(2):127–134

Yasuno F, Ota M, Kosaka J et al (2008) Increased binding of peripheral benzodiazepine receptor in Alzheimer's disease measured by positron emission tomography with [11C]DAA1106. Biol Psychiatry 64(10):835–841. https://doi.org/10.1016/j.biopsych.2008.04.021

Yasuno F, Kosaka J, Ota M et al (2012) Increased binding of peripheral benzodiazepine receptor in mild cognitive impairment-dementia converters measured by positron emission tomography with [(11)C]DAA1106. Psychiatry Res 203(1):67–74. https://doi.org/10.1016/j.pscychresns.2011.08.013

Yokokura M, Mori N, Yagi S et al (2011) In vivo changes in microglial activation and amyloid deposits in brain regions with hypometabolism in Alzheimer's disease. Eur J Nucl Med Mol Imaging 38(2):343–351. https://doi.org/10.1007/s00259-010-1612-0

Zhang J (2015) Mapping neuroinflammation in frontotemporal dementia with molecular PET imaging. J Neuroinflammation 12:108. https://doi.org/10.1186/s12974-015-0236-5

Toward Imaging Tropomyosin Receptor Kinase (Trk) with Positron Emission Tomography

31

Ralf Schirrmacher, Vadim Bernard-Gauthier,
Carolin Jaworski, Carmen Wängler, Björn Wängler,
and Justin Bailey

Contents

Abstract

The three tropomyosin receptor kinases (TrkA, B, and C) fulfill important roles within the central nervous system facilitating neuronal growth, neuronal survival, and neuronal differentiation during cell development at all ages of neuronal

R. Schirrmacher (✉) · C. Jaworski · J. Bailey
Division of Oncological Imaging, Department of Oncology, University of Alberta,
Edmonton, AB, Canada
e-mail: schirrma@ualberta.ca; cjaworsk@ualberta.ca; jjbailey@ualberta.ca

V. Bernard-Gauthier
Azrieli Centre for Neuro-Radiochemistry, Research Imaging Centre, Centre for Addiction
and Mental Health, Toronto, ON, Canada

C. Wängler
Biomedical Chemistry, Department of Clinical Radiology and Nuclear Medicine, Medical
Faculty Mannheim of Heidelberg University, Mannheim, Germany
e-mail: Carmen.Waengler@medma.uni-heidelberg.de

B. Wängler
Molecular Imaging and Radiochemistry, Department of Clinical Radiology and Nuclear
Medicine, Medical Faculty Mannheim of Heidelberg University, Mannheim, Germany
e-mail: Bjoern.Waengler@medma.uni-heidelberg.de

development. The downregulation of TrkA, B, and C has been identified as an important hallmark of a plethora of neurological diseases such as Alzheimer's disease (AD) and Parkinson's disease (PD). In oncology, Trks have been recognized as tumorigenic drivers. Full-length Trk as well as fusion proteins composed of the kinase portion of the full-length receptor and various other cancer-related proteins has been reported, and the targeting of these receptors for a contingent Trk-based therapy has recently caught momentum in the wake of precision medicine evolvement. Both in neurology and oncology, the spatiotemporal changes in Trk expression can only be reviewed via destructive and invasive methods such as taking a tumor biopsy. The quantification of Trk density in neurodegeneration (e.g., AD and PD) as well as cancer treatment, where therapeutic Trk target engagement of antineoplastic Trk inhibitors with Trk fusion proteins is the site of therapeutic action, has triggered the need for a noninvasive methodology to quantify Trk in vivo in these Trk-altering conditions. Positron emission tomography (PET), a noninvasive imaging methodology, relying on the highly sensitive detection of radiation, has the potential to take advantage of radioactively labeled probes binding to the kinase domain of Trk to not only reveal the location of Trk but allow for the quantification of receptor density. This article covers the most recent developments in Trk tracer evolution for PET imaging and their first human in vivo application.

31.1   The Role of Trk in Neurology and Oncology

The tropomyosin receptor kinases (TrkA, B, and C) constitute transmembrane glycoproteins which are encoded by their individual genes (NTRK1, 2, and 3). These kinases are composed of an extracellular domain (ECD) which is the target for the endogenous neurotrophins such as the nerve growth factor (NGF), binding to TrkA; the brain-derived neurotrophic factor (BDNF) and neurotrophin-4, binding to TrkB; and neurotrophin-3 engaging TrkC (Lessmann et al. 2003; Chao 1992, 2003; Kaplan and Miller 2000; Binder and Scharfman 2004). In addition to the ECD, all Trks possess an intracellular binding domain which encodes a tyrosine kinase binding site which primarily interacts with ATP as a binding substrate (Fig. 31.1a) (Reichardt 2006; Huang and Reichardt 2003). Ligand-induced dimerization of Trk activates the tyrosine kinase and mediates receptor transphosphorylation. In this activated state, the Trks immediately phosphorylate their endogenous substrates: Shc, phospholipase Cγ1 (PLC-γ 1), and the fibroblast growth factor receptor substrate 2 (FRS2/SNT1) (Kaplan and Miller 2000; Huang and Reichardt 2003; Yan et al. 2019; Poo 2001). In addition to the full-length Trks, truncated variants can be formed by alternative splicing which lack the intracellular kinase domain (Fig. 31.1b) (Fenner et al. 2014; Fenner 2012; Luberg et al. 2010). In the case of TrkB, the 90 kDa truncated isoform TrkB.t1, comprised of only the extracellular domain, is the most prominent differentially spliced variant. When ATP binds to the intracellular kinase domain, downstream signaling pathways are activated which control neuronal survival and
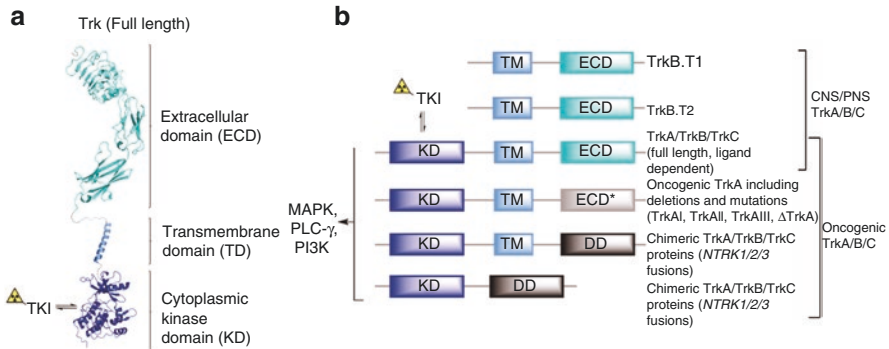
Fig. 31.1 Tertiary and domain structural representations of native and aberrantly expressed Trk proteins. (**a**) Structure (Massa et al. 2010) overview of the representative native TrkA receptor (TKI: tyrosine kinase inhibitor). (**b**) Domain representation of diverse oncogenic Trk proteins, including Trk splice variants and Trk fusion proteins. Dimerization and transautophosphorylation of Trk kinase domains leads to the activation of the downstream signaling pathways, including MAPK1, PI3-K/Akt, and PLC-γ1 (DD: dimerization domain). Reproduced with permission from R. Schirrmacher et al.; Pharmaceuticals (Basel), 2019, 12(1), 7–21

mediate embryonic, postnatal, and mature differentiation of the developing central and peripheral nervous system.

Aberrant or impaired expression/signaling of Trks within the central nervous system is connected to a variety of neuropathological abnormalities encompassing Alzheimer's disease (AD), Parkinson's disease (PD), and other neurodegenerative diseases (Zhang et al. 2012; Song et al. 2015; Murer et al. 2001; Reinhart et al. 2015; Oyesiku et al. 1999; Deng et al. 2007; Gupta et al. 2013). Convincing evidence points to a direct involvement of impaired TrkB and C signaling in AD. Confirmative studies gained through ex vivo analysis of brain tissue from AD patients demonstrated that TrkB levels are significantly reduced in the hippocampus and the frontal and temporal cortex of AD individuals (Ferrer et al. 1999). In addition, the progressive loss of TrkA, B, and C in basal forebrain cholinergic nuclei has been linked to the progression of AD (Allen et al. 1999; Savaskan et al. 2000). There is further evidence from transgenic mouse models of AD that treatment with Trk agonists increases the formation of dendritic spines in hippocampal and cortical regions (Castello et al. 2014; Li and Liu 2010; Nagahara and Tuszynski 2011; Devi and Ohno 2015). During agonist treatment, inhibition of neuronal apoptosis in ongoing neurodegeneration as a result of plaque deposition and neurofibrillary tangle formation results in improved spatial memory performance (Géral et al. 2013). However, there is currently no noninvasive way to follow the spatiotemporal changes of Trk densities over time. PET would provide a unique opportunity to track these dynamic changes without perturbing the underlying biochemistry and would connect disease progression or recession to a quantifiable visual signal provided by the PET camera. Besides an obvious interest in Trk radioligands for neurological imaging, the continuously growing interest in anti-Trk therapy in fusion cancers provides further incentive to develop Trk-radioligands for cancer staging and subsequent

therapeutic investigations after agonist therapy (Cocco et al. 2018). Such radioligands targeting Trks would have an important impact on patient care for individuals enrolled in NTRK fusion-positive cancer trial where pan-Trk inhibitors are administered as part of the treatment protocol (Lange and Lo 2018). The current practice is to acquire tumor biopsies and assay them for Trk occurrence, followed by next-generation sequencing or fluorescence in situ hybridization. This procedure is highly invasive and puts significant stress on the cancer patient. Radioactively labeled Trks have the potential to noninvasively quantify Trk present in tumor tissue and would alleviate an investigative burden from the patient. In addition, Trk PET imaging would significantly expedite Trk status stratification and patient sorting (Hsiao et al. 2019; Khotskaya et al. 2017).

NTRK fusions are generally a low-frequency occurrence in a variety of commonly known cancers, although they occur at a very high frequency in some rare neoplasms (Märkl et al. 2019). A prerequisite for all aforementioned applications is the development of selective pan-Trk inhibitors that can either be used in therapeutic scenarios or be translated into a functioning Trk radiotracer. Fortunately, recent research efforts from academia and industry have provided a great plethora of new Trk lead structures covering selective pan-Trk as well as TrkA subtype selective inhibitors. These inhibitors lay the foundation for efficient radiotracer development where medicinal chemistry provides the scaffold for further translational work into clinical PET tracer advancement. Trk radiotracers would be especially useful in the assessment of Trk status in the early clinical stages of cancer where the treatment regimen is set for the individual patient. Only patients who possess NTRK fusions are responsive to a Trk-inhibitor-driven therapy (Lange and Lo 2018). Patients undergoing Trk inhibitory therapy could be monitored for treatment response including possible downregulation of Trk receptors hampering a continuous therapy. Omitting sequential tumor biopsies as part of the treatment monitoring would benefit the patient by removing invasive procedures from the therapy plan. Radiolabeled Trk inhibitors for in vivo imaging would thus have a profound impact on patient care and disease control.

31.2 The History of Trk Radioligand Development

31.2.1 Positron Emission Tomography

The PET detection principle is based on the simultaneous detection of two gamma rays of 511 keV stemming from the annihilation of a positron and an electron (masses are converted into energy) using a PET camera. The positron originates from the radioactive decay of a positron-emitting radionuclide, which is integrated into the structure of the radioligand, and the electron is provided by the surrounding body tissue. The PET camera consists of multilayered ring-shaped arranged detectors surrounding the patient's body. Following the rule of conservation of momentum, the two gamma rays originating from the annihilation are leaving their point of origin in the opposite direction. Traveling with the speed of light, opposite detectors

can detect these two gamma rays in coincidence, drawing a virtual line of response between the two detectors activated. The origin of the positron annihilation consequently must be somewhere on that line of response, narrowed down by the time resolution of the used detector material. Accumulated information from all communicating detector pairs and applying mathematical reconstruction algorithms (e.g., filtered back projection) allow for the accurate reconstruction of the radioactivity distribution within the region of interest. PET's resolution depends primarily on the positron energy but also on the size of the detectors and the photomultipliers intensifying the relatively weak signal from the gamma ray interacting with the detector material. Preclinically, submillimeter resolution is achieved in animal PET imaging, whereas in a human clinical setting, millimeter resolution is routinely accomplished.

In order to gain the maximum information about a disease state from a radiotracer's binding characteristics, the compound used must comply with a few general criteria. Foremost, and this is an independent biological parameter, the molecular target concentration (e.g., TrkB) must be sufficiently high to generate a quantifiable radioactivity signal upon radiotracer binding. If the concentration of the receptor (B_{max}) is low, only tracers with a very high binding affinity will yield a detectable signal. The radiotracer concentration in the tissue of interest (e.g., the brain) must also be sufficiently high to guarantee binding, and radiotracer equilibrium conditions have to be established where the tracers k_{on} and k_{off} are the same. Tracer stability is also of utmost importance to preclude bio-active metabolite binding interference, complicating the kinetic analysis of the tracer binding pattern. Another important point is a tracer's on-target specificity. If the tracer binds to more than one target, reconstruction and image interpretation are very difficult to achieve since the only signal that is recorded is the radioactivity concentration in the tissue of interest. The PET camera does not distinguish between radioactivity signals coming from different target interactions. After careful consideration of all the above-mentioned points, the consequent question in the development of potential Trk radiotracers is which domain of the Trk receptor is suitable for targeting in order to answer a clinical question related to a specific disease?

31.2.2 The Tropomyosin Receptor and Its Targets: Extra- Vs. Intracellular Target Engagement

Trk possesses two very distinct binding sites: the extracellular binding domain (ECD), which is engaged by endogenous ligands, and an intracellular kinase binding site which binds ATP and significantly impacts tracer development. Furthermore, the TrkA/B/C isoforms and splice variants/fusion proteins found in certain cancers may complicate the in vivo PET imaging depending on the choice of target, extra- vs. intracellular. To illustrate this further, besides the full-length TrkA/B/C containing a fully functional extra- and intracellular domain, a variety of truncated isoforms missing the intracellular kinase domain have been identified for TrkB (TrkB.T1 and TrkB.T2). Their biological function is unclear and still under debate, but it is

accepted that these splice variants are not associated with neurodegeneration or function as oncogenic drivers. However, a most recent study revealed that astrocyte truncated-TrkB exerts a BDNF anti-apoptotic effect that leads to neuroprotection (Saba et al. 2018). Especially within the brain, the expression of the truncated isoforms on the protein level is much higher than that of the full-length, biologically active, TrkB. A radiotracer targeting the ECD of TrkB (e.g., radiolabeled BDNF) would not be able to distinguish between the full-length Trk protein and the truncated isoforms, and consequentially would overestimate the number of biologically active TrkB (Tejeda and Díaz-Guerra 2017). The combined PET signal resulting from the catalytically incompetent truncated isoforms, lacking the kinase domain, and the full-length TrkB would therefore erroneously overestimate the number of catalytically active Trk responsible for an array of downstream signaling on a molecular level. Such a tracer would be useless to investigate TrkB's role in neurodegeneration. In a cancer imaging situation where NTRK fusion proteins are present, an ECD radiotracer would be unable to engage this protein target because it lacks the cognate ectodomain. Besides these obvious hurdles, there are currently no compounds available which warrant a translation into a radiotracer as a result of their poor and challenging in vivo properties.

Our research group and collaborators recently demonstrated that radiolabeled fluorine-containing 7,8-dihydroxyflavon (7,8-DHF), which was reported to bind with high affinity to the ECD (Jang et al. 2010), was unsuitable as PET imaging agent for TrkB (Bernard-Gauthier et al. 2013). None of the reported 7,8-DHFs' basic biological properties could be reproduced (unpublished). In one of our preclinical PET imaging studies in healthy rats using 2-(4-[^{18}F]fluorophenyl)-7,8-dihydroxy-4H-chromen-4-one, we observed a low overall radioactivity uptake in the brain (SUV of 0.64) that was followed by a fast elimination, proving the inability of the DHF compounds to serve as a TrkB radioprobe. The plasma half-life was suboptimal at 4 min and suggests an extensive phase II metabolic breakdown accounting for the poor radiotracer properties. In support of our findings, Boltaev et al. most recently incontrovertibly demonstrated the absence of an interaction of these and other compounds with the ECD of TrkB, or any TrkB-related effects attributed to these compounds (Boltaev et al. 2017). Going from putative ECD binding drugs to inhibitors targeting the ATP binding site of the cytoplasmic kinase domains offers several advantages and at the same time adds some challenges to a PET imaging approach. Unfortunately, all Trks display a high homology within their kinome as well as within their Trk family sequence identity, adding an intrinsic challenge to any imaging regime. To achieve selectivity over at least other unrelated kinases, our group always tested the most promising compounds for PET tracer translation in a comprehensive kinase screening to ensure near exclusive binding to TrkA/B/C. All radiolabeled compounds reported so far are pan-Trk radioligands which insufficiently distinguish between the three subtypes. Fortunately, the local deposition of TrkB/C in comparison to TrkA in the human brain is very prominent, in theory yielding a target density-driven PET image of predominantly TrkB/C (Altar et al. 1991a, b; Merlio et al. 1992; Anderson et al. 1995). This would translate into an almost exclusive visualization and quantification of TrkB/C in the human
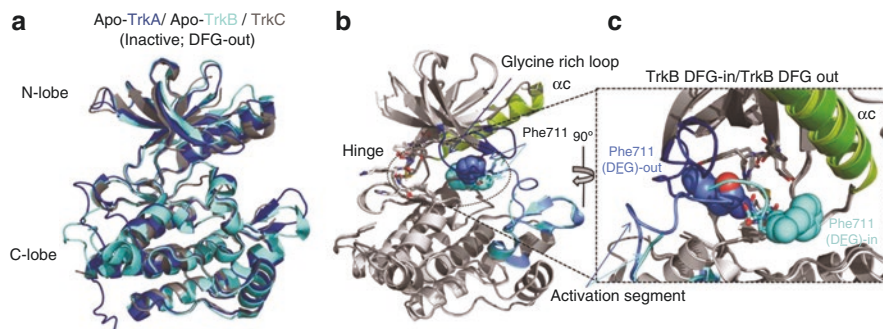
Fig. 31.2 Trk kinase domain. (**a**) Overlap of TrkA, TrkB, and TrkC kinase domains in the inactive DFG-out conformation (PDB: 4F0I, 4ASZ, 3V5Q). (**b**, **c**) Views of the conformational differences between "Asp-Phe-Gly" DFG-in and DFG-out TrkB. The Phe residues of the DFG triad are shown in spheres (PDB: 4AT3, 4AT5). Reproduced with permission from R. Schirrmacher et al.; Pharmaceuticals (Basel), 2019, 12(1), 7–21

brain. The imaging situation is further complicated by the fact that Trk kinases can exists in two distinct conformations, DFG-in, wherein the active kinase conformation is targeted by type-1 inhibitors, and DFG-out, which is the inactive conformation being engaged by type-2 inhibitors (Fig. 31.2a). Conformational rearrangements within the DFG motive grant access to a deep binding pocket that is favorably targeted by lipophilic moieties inherent of type-2 inhibitors (Fig. 31.2b, c). This extended binding mode for type-2 inhibitors enhances the residence time of the inhibitor at the kinase binding site via cooperative binding in comparison to type-1 inhibitors. Ultimately, only the final in vivo imaging study can reveal what type of radiolabeled inhibitor will be the most suitable for human Trk PET imaging. To investigate the relation of each binding mode to PET image quality, as well as the tracers' residence time and overall kinetic profile, we developed both type-1 and type-2 radiotracers. The following sections will give an overview of our efforts to preclinically, as well as clinically, introduce these novel Trk radiotracers to the imaging community, culminating in the two first human in vivo studies of a type-1 Trk radioligand in a healthy male subject.

31.2.2.1 Radioligands for Brain Imaging: General Considerations

When developing radiotracers for brain imaging, the chance of successful neurological PET imaging is significantly elevated by adhering to a few general principles guiding the structural composition of a potential radiotracer. The following parameters are cardinal points that should help streamlining the tracer design process (Van de Bittner et al. 2014). First and foremost, a radiotracer intended for neurologic PET imaging must cross the highly restricted blood-brain barrier (BBB) to bind to its target. As for Trk target binding, the tracer also has to overcome the neuron cell membrane to bind to the cytoplasmic binding site of the Trk kinase domain. To get a high contrast image, it is advantageous that the radioligand binds with high specificity to the target and only displays minor, or ideally no, nonspecific binding (a

feature rarely seen). A common denominator determining nonspecific binding is the tracer's lipophilicity, or $LogD_{7.4}$, granting passive diffusion through the cell membrane and if too high simultaneously increasing nonspecific binding and influencing the tracer's receptor binding potential ($BP = B_{max}/K_d > 10$). Further parameters, like susceptibility to active efflux from the brain compartment, the topological surface area (TSPA), and hydrogen bond donor characteristics, directly influence BBB penetration and binding specificity. Taken together, these considerations and parameters directly determine the quality of a potential PET tracer for neuroimaging.

31.2.2.2 Radioligands Based on the 4-Aza-2-Oxindole Scaffold

Following the above-outlined considerations, the first pan-Trk radiotracer developed was structurally based on reported 3-arylideneindolin-2-on Trk inhibitors belonging to the 4-aza-2-oxindole family. The well-characterized type-I inhibitor GW441756 was found to theoretically fulfill most of the parameters accounting for a viable PET neuro-tracer (Zhang et al. 2013; Pike 2009; Rankovic 2015) and was consequently translated into its ^{11}C-isotopologue and applied in autoradiography ex vivo binding studies as well as preclinical animal PET imaging. GW441756 was found to possess a half maximal inhibitory concentration (IC_{50}) of 29.6 nM for TrkA, and 6.7 nM and 4.6 nM for TrkB and TrkC, respectively (Wood et al. 2004). The ^{11}C-radiolabeling of GW441756 (Fig. 31.3a) was easily accomplished in high radiochemical yields (RCYs) by using standard ^{11}C-labeling methodology, although the labeled compound turned out to be a mixture of two distinct isomers, the E and Z isomer, of which only the Z isomer actively binds to the kinase domain (Bernard-Gauthier et al. 2015a). The E/Z ratio after synthesis was 1:1, accounting to 50% of the radioactivity signal stemming from the wrong isomer. In addition, the clinical translation of an impure tracer is very difficult from an image reconstruction and modeling point of view, not to mention the ethical challenge of injecting a useless impurity into a human subject. However, autoradiographic ex vivo imaging using the mixed isomers demonstrated competitive and replaceable binding, matching the almost ubiquitous distribution of TrkB/C throughout the brain.

Following these successful ex vivo investigations, E/Z-[^{11}C]GW441756 was injected into healthy Sprague-Dawley rats to investigate general tracer parameters
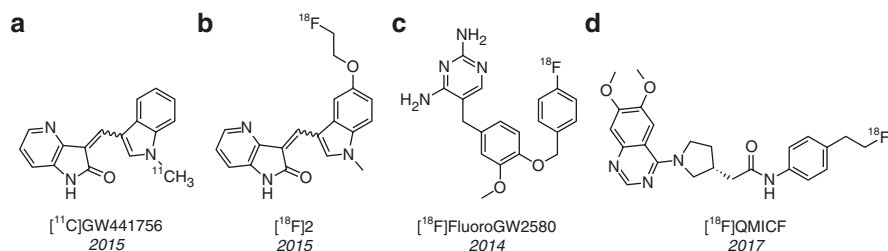
Fig. 31.3 Chemical structures of early Trk-targeted PET radioligands. (**a**, **b**) [11]C- and ^{18}F-labeled analogues of type-I inhibitor GW441756. (**c**, **d**) Type-II binding mode ^{18}F-labeled 2,4-diaminopyridines

such as BBB penetration and general full body biodistribution. Elucidated in PET baseline scans, it was observed that the tracer quickly entered the brain with an SUV peaking at 2 after 30 s, but was rapidly eliminated from the brain over the following 30 min. The distribution of the mixed tracer was uniform throughout the rodent brain generally matching the distribution of TrkB/C expression. A replacement study using a non-radioactive GW441756 yielded ambiguous results, although an indication of specific binding interaction was deduced from successful blocking of pulmonary radioactivity uptake. The attempted derivatization of the accessible 5-hydroxy moiety present in GW441756 with a ^{18}F-fluoroethyl appendix (Fig. 31.3b) delivered a highly kinase selective compound with generally favorable in vivo properties such as a low nano-molar binding affinity for all Trk subtypes. Unfortunately, the in vitro evaluation in rat plasma revealed a pronounced CYP450 metabolic susceptibility in contrast to the original unmodified compound precluding any further efforts to translate this ^{18}F-derivative into a PET tracer. An additional in vivo animal experiment confirmed a lack of in vivo blocking after pre-treatment with GW441756 and the presence of unidentified brain-penetrating metabolites preventing proper image interpretation. These accumulated data thwarted any further ambitions to translate compounds from the 3-indolydene 4-aza-2-oxindole scaffold into clinical PET tracers. Even though the labeled compounds showed a high selectivity and potency toward Trk, the unavoidable presence of the E isomer, formed by reaching a stable photostationary state, unwarranted any further research into potential PET tracer development.

31.2.2.3 Type-II Trk Inhibitors: 2,4-Diamionopyrimidine and Quinazoline-Derived Radiotracers

As mentioned above, type-II inhibitors targeting the DFG-out conformation are further capitalizing on the deep binding pocket made accessible by the DFG-in to DFG-out switch, leading to a longer residence time and improved overall kinetics. Compared to prototypical type-I inhibitors, type-II binding compounds are typically characterized by a linear, elongated structure which makes it possible to penetrate the lipophilic binding pocket residing alongside the DFG-out kinase binding domain. Type-II inhibitors thus display a higher average molecular weight and a higher hydrogen bond donor ability in comparison to type-I inhibitors which might translate into significantly different in vivo behavior, especially regarding brain imaging. Two structurally diverging type-II inhibitors appertaining to the class of 2,4-diaminopyridines (Bernard-Gauthier and Schirrmacher 2014) and quinazoline (Bernard-Gauthier et al. 2017a) have been converted into potential PET radiotracers, [^{18}F]FluoroGW2580 and [^{18}F]QMICF (Fig. 31.3c,d).

Extensive kinome vetting identified GW2580 as a dually active Trk as well as colony-stimulating factor-1 receptor (CSF-1R) inhibitor with a K_d of 630 nM for TrkA, 36 nM for TrkB, 120 nM for TrkC, and 2 nM for CSF-1R, representing one of the most kinome selective compounds known to date. In addition to this promising selectivity profile, preclinically acquired data on absorption, distribution, metabolism, and excretion (ADME) prompted us to approach the conversion of GW2580 into a PET radiotracer for both Trk and CSF-1R in vivo imaging. Imaging

of CSF-1R might be helpful in imaging tumor-infiltrating macrophages in cancer. We omitted the conversion of GW2580 into a structurally identical ^{11}C-isotopologue and instead opted for the introduction of ^{18}F to take full advantage of [18]F's superior PET imaging properties. A library of fluorinated GW2580 derivatives was synthesized and tested for their kinome selectivity and Trk binding affinities. Among these compounds, the most promising lead was converted into the ^{18}F-radiotracer, 5-(4-((4-[^{18}F]fluorobenzyl)oxy)-3-methoxybenzyl)pyrimidine-2,4-diamine ([^{18}F]FluoroGW2580) (Fig. 31.3c). However, the radiosynthesis of ([^{18}F]FluoroGW2580 proved to be challenging, involving several consecutive steps which included the synthesis of the 4-[^{18}F]fluorobenzylbromide prosthetic group for reaction with a phenolic precursor molecule (Lemaire et al. 2012). Naturally, this complex multistep synthesis provided the radiotracer in only limited amounts, unsuitable for any future clinical application. More recent ^{18}F-labeling efforts however introduced a simple one-step labeling procedure based on Cu-catalyzed late-state fluorination of a GW2580 boronic ester precursor, providing the radiotracer in just two steps in high RCYs (unpublished results).

Another more recent addition to the Trk tracer portfolio is the quinazoline motif-bearing type-II pan-Trk inhibitor [^{18}F]QMICF (Fig. 31.3d) constituting a dual Trk and FLT3 inhibitor. The compound exists in two different stereoisomers and extensive structure-activity studies identified the R isomer being the active TrkB inhibitor. Before engaging into radiolabeling, the actual positioning of the fluorine atom within the molecular structure had to be considered carefully to avoid a reduction in kinase inhibitory activity. Molecular modeling revealed that a derivatization of the allosteric pocket interacting portion of the molecule lends itself favorably to ^{18}F-labeling without compromising the binding interaction. The original lead structure that was chosen as a starting point for tracer development of [^{18}F]QMICF contained an isopropyl moiety connected to the 4-position of a benzene moiety. The isopropyl unit was replaced by a 2-fluoroethyl group of highly adaptable flexibility and able to protrude inside the allosteric binding pocket. The 2-fluoroethyl group provided a perfect opportunity to introduce the ^{18}F isotope by the simple nucleophilic substitution of a mesyl leaving group of the appropriate precursor molecule in 18% RCY. Yet, even the minor structural change from an isopropyl group to a 2-fluoroethyl moiety reduced the potency of Trk binding by a factor 10. A full kinase profiling of [^{19}F]QMICF demonstrated exceptional selectivity for Trk. In parallel, a Calcein-AM assay in P-gp-overexpressing MDCKII cells demonstrated only minor interaction with P-gp (P-glycoprotein), an important parameter for brain PET imaging. The tracer is currently being evaluated as a peripheral tumor imaging agent visualizing NTKR fusion proteins in cancer. Preclinical PET imaging in mice bearing TrkA-TPM3 overexpressing colon carcinoma KM12 tumor xenografts are ongoing in our lab and will soon be reported.

31.2.2.4   Toward Clinical Application: Synthesis of Imidazo[1,2-*b*] Pyridazine-Related Radioligands

The advent of imidazo[1,2-*b*]pyridazine-related inhibitors happened coincidentally with the increased clinical interest in Trk inhibitor therapy of cancers comprising

NTRK fusions. The existing portfolio of mainly nonselective pan-Trk inhibitors was not ideally suited to address the current need for a Trk inhibitor-based therapeutic regimen. Owing to their improved pan-Trk selectivity profile, and therefore enhanced potential for a specific Trk therapy without engaging other kinases, imidazo[1,2-*b*]pyridazine- and pyrazolo[1,5-*a*]pyrimidine-based inhibitors received increased attention from medicinal chemistry and industry Trk inhibitor programs. In 2014, our group and collaborators became aware of this trend, and we chose to focus our developmental efforts on these promising structural scaffolds for radiotracer development (Bernard-Gauthier et al. 2015b). When compared side by side with all other Trk inhibitors described so far (vide supra), the type-I pan-Trk inhibitors originating from the (2-pyrrolidin-1-yl)imidazo[1,2-*b*]pyridazine structural motif displayed the highest affinity with all three Trk subtypes and provided an advantageous starting point for PET probe development.

Our first step in the development of a new library of potential PET-suited compounds was to engage into extensive molecular modeling studies to reveal the best position for ^{18}F-introduction or ^{11}C-labeling into this chemical scaffold. These modeling efforts translated into a comprehensive library of compounds suitable for radiotracer development yielding compounds that showed the highest reported potency against TrkB/C to date (<200 pm). Among these compounds, two structures caught our attention, IPMIC6 and IPMICF10. Both compounds demonstrated favorable binding to all Trk subtypes, a high kinome selectivity, and their chemical nature allowed for an easy introduction of ^{18}F via nucleophilic substitution (Fig. 31.4a, b). The translation of both compounds into experimental radiotracers was straightforward, although the RCYs of the final products were rather low (3–8% RCY). Subjected to autoradiography using coronal rat brain slices, both radiotracers were able to accurately map the established brain distribution of TrkB/C receptors, in congruence with known mRNA and protein level expressions most prominent in cortical areas, the striatum, thalamus, and cerebellum.
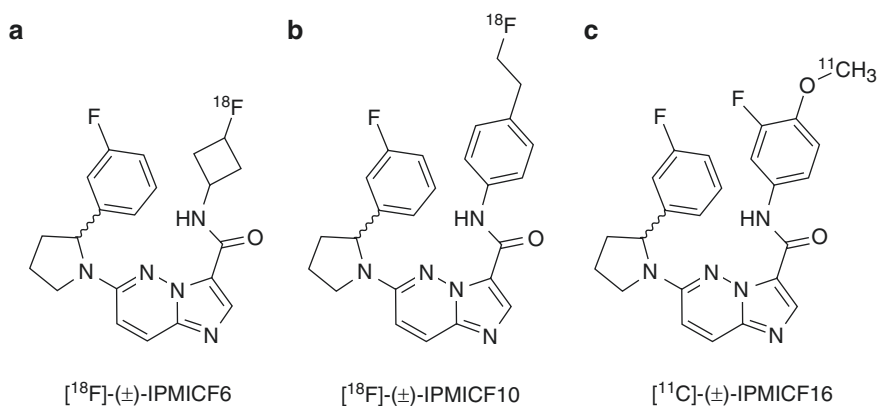

Fig. 31.4 Chemical structures of preclinical imidazo[1,2-*b*]pyridazine-based Trk-targeting PET radioligands. (**a**, **b**) ^{18}F-labeled racemic tracers. (**c**) ^{11}C-labeled racemic lead

Despite these encouraging preliminary results, we decided to focus our attention to another member of that library, IPMICF16, based on its highest scores in binding affinity and general physicochemical properties. The structure of IPMICF16 is perfectly suited for a simple ^{11}C-methylation using the most common ^{11}C-labeling synthon, [^{11}C]methyl iodide (Fig. 31.4c) (Bernard-Gauthier et al. 2017b). Initially, only the racemic IPMIC16 compound was evaluated, but based on structure/activity studies using computational chemistry, it became clear that only one isomer, namely, the *R* isomer, would be responsible for the high binding affinities observed. To confirm these computational results experimentally, both isomers of IPMICF16 were synthesized and evaluated for their binding potential. (*R*)-IPMICF16 demonstrated an exceptionally high binding affinity toward all Trk subtypes as well as showing an unexpected intra-Trk selectivity. IC_{50}s of 4.0, 0.2, and 0.1 nM for human TrkA, B, and C were experimentally determined in addition to observed inhibitory constants (K_i) of 2.80, 0.05, and 0.021 nM, respectively. Experimental studies confirmed our docking studies that only the *R* isomer possesses a high affinity to Trks. A full kinome analysis revealed an exceptional selectivity of (*R*)-IPMICF16 toward TrkB/C over 369 other targeted kinases prominent in the human brain. When reacting the desmethyl precursor of *R*-IPMICF16 with [^{11}C]methyl iodide in a single one-step reaction, RCYs of >10% were routinely achieved, enough for a non-human primate or even human PET study. Before planning non-human primate PET studies and a first-in-human study with [^{11}C]-(*R*)-IPMICF16, the radiosynthesis was established according to good manufacturing practices at four different production sites. Consequently, (*R*)-IPMICF was evaluated in vivo first in mice, then non-human primates, and finally in a healthy human subject.

When performing in vivo PET experiments in double knockout Mdr1a/b-Bcrp mice, it became obvious that [^{11}C]-(*R*)-IPMICF16 is a substrate for active efflux transporters such as P-gp and breast cancer resistance protein (Fig. 31.5). However, even after 60-min PET scanning time, the SUV in the rodent brain was still 0.4, pointing toward only a moderate efflux liability. In vivo PET blocking studies irrefutably confirmed specific binding of [^{11}C]-(*R*)-IPMICF16 to TrkB/C after challenging receptor binding by adding the clinically approved pan-Trk inhibitor

Fig. 31.5 Time-activity curve for [^{11}C]-(*R*)-IPMICF16 brain uptake in Mdr1a/b$^{(-/-)}$Bcrp$^{(-/-)}$ and FVB mice
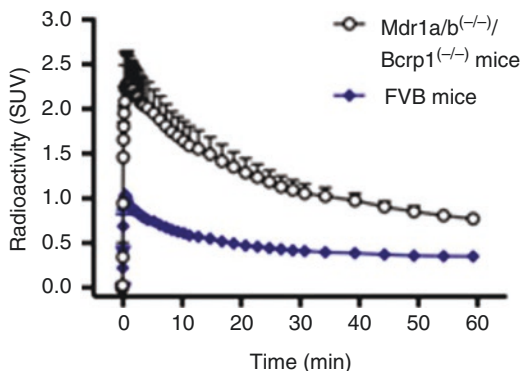
entrectinib. The blocking agent was injected intraperitoneally in high dose (350 mg/kg) as a result of its low BBB penetrating properties that were reported previously. Eighty-eight percent of the brain radioactivity signal could be blocked during these in vivo experiments.

These positive data in rodents prompted us to further evaluate this tracer in nonhuman primates (NHP). Interestingly, but not entirely unexpected due to known interspecies differences in biodistribution, the brain kinetics in NHP turned out to be significantly different than what we observed in mice. Even though the overall brain uptake was clearly slower than in mice, the overall tracer uptake in the brain was continuously rising without any detectable washout during the 60-min PET scan. Analysis of the regional tracer distribution in the NHP brain showed a high uptake in Trk-rich gray matter areas of the brain, reflecting the known distribution of TrkB/C in the NHP brain (highest uptake in the thalamus was SUV 0.8 (Fig. 31.6a)). In contrast to gray matter uptake, the white matter tracer accumulation was reduced in accordance with the near absence of Trk receptors in these regions. In comparison to the PET data obtained in rodents and the obvious efflux liability observed in this species, the PET data in NHP did not indicate a liability concern in higher species as a result of interspecies discrepancies.
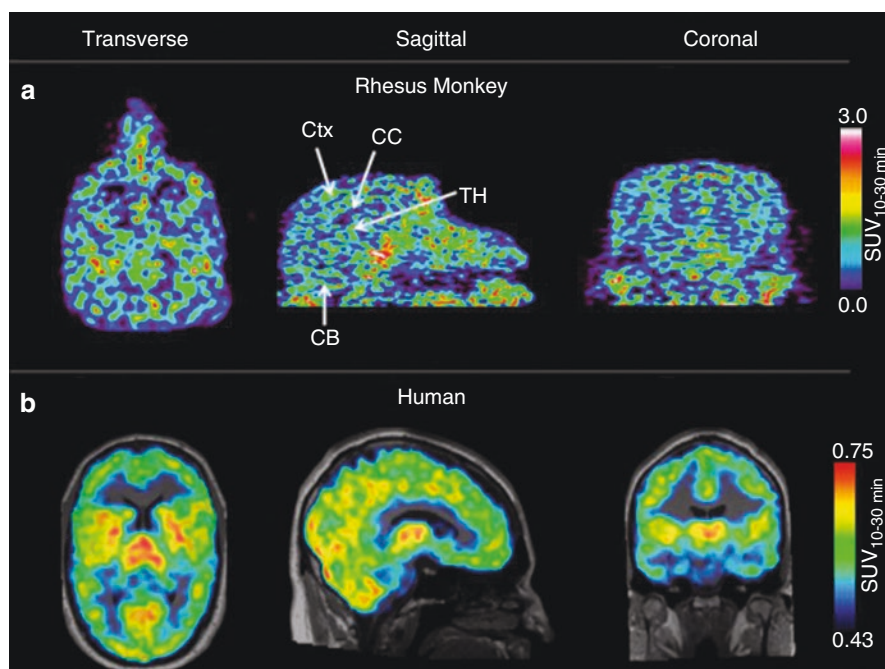
Fig. 31.6 In vivo PET imaging of $[^{11}C]$-(R)-IPMICF16. (**a**) Representative in vivo PET images in NHP. SUV summed over 30–60 min p.i. *CB* cerebellum, *CC* corpus callosum, *Ctx* cortex, *TH* thalamus. (**b**) Representative in vivo PET images in a healthy human brain with MRI overlay. Static SUV images averaged over 10–30 min p.i.

Motivated by these outcomes, the decision was made to evaluate (*R*)-[^{11}C]IPMICF16 for human brain PET imaging. This move was further substantiated by some very encouraging autoradiography results demonstrating that (*R*)-[^{11}C]IPMICF16 reflects the regionally specific and significant reduction of hippocampal TrkB/C concentrations in AD brain slices compared to healthy, age-matched control brains. The accumulation of [^{11}C]-(*R*)-IPMICF16 could be challenged in both AD brains and control brains using a structurally distinct pan-Trk inhibitor evidencing specific binding of [^{11}C]-(*R*)-IPMICF16 in the hippocampus and other TrkB/C-rich brain compartments. [^{11}C]-(*R*)-IPMICF16 was consequently injected into a 41-year-old healthy male subject (Bernard-Gauthier et al. 2017b). The radioactivity distribution principally matched the PET data acquired in NHP with a peak SUV of 1.5 after in the thalamus after a short tracer delivery phase of 25 s to the brain (Fig. 31.6b). After 60 min, equilibrium was reached, and a SUV in the thalamus of stable 0.7 was observed followed by a slow washout. The human PET data corresponded well to the previously acquired NHP PET data, reflecting equivalent topographical distribution of TrkB/C in all gray matter regions, as well as in white matter areas of low Trk occurrence. More importantly, the general brain distribution of [^{11}C]-(*R*)-IPMICF16 extracted from both in vivo studies corroborated the known biodistribution of TrkB/C allocated from ex vivo studies. The most pronounced uptake was found in the thalamus, followed by cerebral uptake and cortical accumulation of the tracer. No adverse effects after the injection of [^{11}C]-(*R*)-IPMICF16 were recorded, and the tracer is now ready for further clinical application. A larger follow-up study to fully characterize [^{11}C]-(*R*)-IPMICF16 in vivo is currently underway.

Based on our extensive previous computational studies which revealed an accurate picture of the structure-activity relationship of the Trk inhibitor binding site interaction, we aimed to modify [^{11}C]-(*R*)-IPMICF16 toward a possible ^{18}F-radiolabeled analogue, taking full advantage of the longer half-life and more optimal decay properties (e.g., lower positron energy yielding PET images of higher resolution) of ^{18}F. The structure of [^{11}C]-(*R*)-IPMICF16 lends itself perfectly to a ^{18}F-introduction via the so-called late-stage copper-catalyzed fluorination of aromatic non-activated boronic esters, a technique pioneered most recently by different radiochemistry groups (Preshlock et al. 2016; Brooks et al. 2014; Zlatopolskiy et al. 2015; Tredwell et al. 2014). Even so, this radiochemical methodology still has to cope with unwanted side reactions of boronic esters (e.g., protodeboronation during the radiofluorination contaminating the ^{18}F-tracer and reducing its molar activity (A_m)); it is one of the most valuable new additions to the growing portfolio of ^{18}F-labeling procedures and enables the ^{18}F-introduction into organic compounds that were previously regarded as challenging. However, the presence of a protodeboronated side product, having very similar physicochemical properties as the ^{18}F-fluorinated tracer, can significantly and undesirably compete for the ATP kinase binding site, reducing the quality of the PET image via receptor challenge.

Another main motivation to structurally amend IPMICF16 was the intention to reduce its efflux liability. The methoxy group close to the fluorine atom at the

aromatic amide fragment was clearly determined to be a major contributor to P-gp and BCRP efflux of the compound. The methoxy group was therefore removed yielding a pan-Trk inhibitor with increased subtype selectivity and a slightly decreased affinity for all Trk subtypes. The latter feature was welcome since a reduced, yet still high, affinity will more quickly achieve an equilibrium binding state. The resulting compound was named TRACK (the *R* isomer), and the ^{18}F-labeled isotopologue was obtained by late-stage copper-catalyzed fluorination of the corresponding boronic ester precursor in good RCY for clinical translation. The formation of a side product stemming from protodeboronation could not be separated during the radiofluorination reaction, yielding the radiotracer [^{18}F]TRACK with a low effective A_m of 15 GBq/µmol—too low for a clinical application and Trk visualization with PET. Fortunately, the use of a specialized HPLC column material, a pentafluorophenyl-modified stationary phase, achieved the baseline separation of [^{18}F]TRACK and the protodeboronation side product, resulting in high A_m of >100 GBq/µmol—sufficient for human application and complying to the tracer principle (Bernard-Gauthier et al. 2018).

During the planning phase of the human study and the acquisition of ethic approval, [^{18}F]TRACK was evaluated in the first study in a rhesus monkey affirming the uptake of [^{18}F]TRACK in TrkB/C-rich regions of the brain (Fig. 31.7a), reminiscent of the brain distribution profile of [^{11}C]-(*R*)-IPMICF16 in the same species yet with a slightly higher uptake in the cerebellum (SUV 0.9), thalamus (SUV 0.8) and cortex (SUV 0.6). The radioactivity uptake in white matter areas was comparable to [^{11}C]-(*R*)-IPMICF16. Most interestingly, the overall uptake kinetics of [^{18}F]TRACK were distinguishably different, hinting at a more reversibly binding radiotracer. As expected, injection of [^{18}F]TRACK of different A_m into the same NHP revealed the paramount importance of a high A_m for optimal PET image quality (Fig. 31.7a).

Most recently we reported on the first-in-human evaluation of [^{18}F]TRACK alongside with a thorough investigation of its CNS off-target engagement (Fig. 31.7b) (Bailey et al. 2019). TRACK demonstrated excellent kinome selectivity and high on-target in vitro potency for all three Trk subtypes (4.21, 0.15, and 0.31 nM for human TrkA, B, and C, respectively). The basic PET scan was performed in the same human subject that previously took part in the [^{11}C]-(*R*)-IPMICF16 PET study, enabling the best possible and accurate comparison between the two tracers. After injection of a bolus radioactivity of 185 MBq, the radioactivity concentration due to flow-related first pass peaked after 30 s and steadily increased over the first 20 min, after which the concentration was slowly decreasing. The tracer distribution in the human brain matched the regional distribution of TrkB/C accurately. In stark difference to [^{11}C]-(*R*)-IPMICF16, which demonstrated a steadily increasing accumulation of radioactivity in Trk-rich areas, [^{18}F]TRACK contrarily reached a plateau with no discernable washout between 5 and 60 min scan time. Human plasma analysis revealed only a minor metabolic fraction in addition to the unaltered tracer. [^{18}F]TRACK was 80% intact after 90 min post injection, rendering this tracer highly suitable for human brain PET imaging. In addition, no defluorination was observed attesting to the tracer's
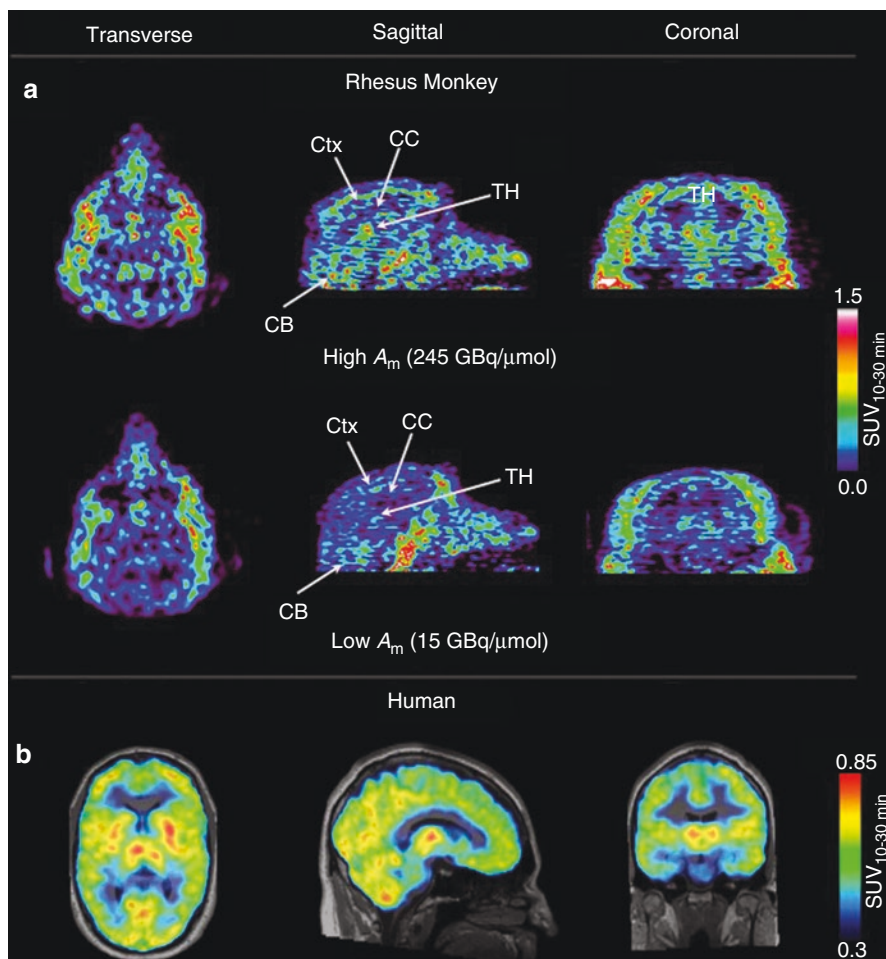
Fig. 31.7 In vivo PET imaging of [18F]TRACK (Bernard-Gauthier et al. 2018). (**a**) Representative in vivo PET images in an NHP brain at high and low effective A_m. SUV summed over 10–30 min p.i. *CB* cerebellum, *CC* corpus callosum, *Ctx* cortex, *TH* thalamus. (**b**) PET/T1MP-RAGE MRT in vivo overlay in a healthy human brain. Static SUV images averaged over 10–30 min p.i.

high in vivo stability and robustness. Several studies in human AD and MCI (mild cognitive impairment) patients are currently planned as well as a full characterization study of the whole body dosimetry of [18F]TRACK in healthy control subjects. As the contingent of newly disclosed Trk inhibitors grows over time (Bailey et al. 2017a, b), new lead compounds will be translated into potential radiotracers with a higher overall brain uptake (SUV >1) and longer residence time at the Trk receptor (type-II inhibitors).

31.3   Conclusion

The visualization and quantification of the Trk receptor system with potent and reversibly binding Trk radioligands is of undeniable importance to the investigation of neurodegenerative diseases such as AD and may become a diagnostic tool to assess and characterize Trk fusion proteins in cancer to support individualized Trk inhibitor-based therapies. The so far disclosed prototypical imaging probes [^{11}C]-(*R*)-IPMICF16 and [^{18}F]TRACK, although displaying a suboptimal brain uptake in humans (SUV brain <1), are certainly suitable to start the investigation whether Trk PET imaging constitutes a valuable tool for neuroimaging in the context of neurodegeneration and cancer Trk-fusion research. The most important goal is to find Trk radiotracers that display an improved general brain uptake surpassing the current generation of type-I ATP challenging probes. Macrocyclic pyrazolo[1,5-*a*]pyrimidines, such as LOXO-195, could delineate a seminal starting point for the development of a third generation of Trk imaging probes with improved physicochemical properties.

References

Allen SJ, Wilcock GK, Dawbarn D (1999) Profound and selective loss of catalytic TrkB immunoreactivity in Alzheimer's disease. Biochem Biophys Res Commun 264(3):648–651

Altar CA et al (1991a) Recombinant human nerve growth factor is biologically active and labels novel high-affinity binding sites in rat brain. Proc Natl Acad Sci U S A 88(1):281–285

Altar C et al (1991b) Medial-to-lateral gradient of neostriatal NGF receptors: relationship to cholinergic neurons and NGF-like immunoreactivity. J Neurosci 11(3):828–836

Anderson KD et al (1995) Differential distribution of exogenous BDNF, NGF, and NT-3 in the brain corresponds to the relative abundance and distribution of high-affinity and low-affinity neurotrophin receptors. J Comp Neurol 357(2):296–317

Bailey JJ et al (2017a) Tropomyosin receptor kinase inhibitors: an updated patent review for 2010-2016—part I. Expert Opin Ther Pat 27(6):733–751

Bailey JJ et al (2017b) Tropomyosin receptor kinase inhibitors: an updated patent review for 2010-2016—part II. Expert Opin Ther Pat 27(7):831–849

Bailey JJ et al (2019) First-in-human brain imaging of [18F]TRACK, a PET tracer for tropomyosin receptor kinases. ACS Chem Neurosci 10(6):2697–2702

Bernard-Gauthier V, Schirrmacher R (2014) 5-(4-((4-[18F]fluorobenzyl)oxy)-3-methoxybenzyl) pyrimidine-2,4-diamine: a selective dual inhibitor for potential PET imaging of Trk/CSF-1R. Bioorg Med Chem Lett 24(20):4784–4790

Bernard-Gauthier V et al (2013) Towards tropomyosin-related kinase B (TrkB) receptor ligands for brain imaging with PET: Radiosynthesis and evaluation of 2-(4-[18F]fluorophenyl)-7,8-dihydroxy-4H-chromen-4-one   and   2-(4-([N-methyl-11C]-dimethylamino)phenyl)-7,8-dihydroxy-4H-chromen-4-one. Bioorg Med Chem 21(24):7816–7829

Bernard-Gauthier V et al (2015a) Syntheses and evaluation of Carbon-11- and Fluorine-18-radiolabeled pan-tropomyosin receptor kinase (Trk) inhibitors: exploration of the 4-Aza-2-oxindole scaffold as Trk PET imaging agents. ACS Chem Neurosci 6(2):260–276

Bernard-Gauthier V et al (2015b) Development of subnanomolar radiofluorinated (2-pyrrolidin-1-yl)imidazo[1,2-*b*]pyridazine pan-Trk inhibitors as candidate PET imaging probes. MedChemComm 6(12):2184–2193

Bernard-Gauthier V et al (2017a) Design and synthesis of a fluorinated quinazoline-based type-II Trk inhibitor as a scaffold for PET radiotracer development. Bioorg Med Chem Lett 27(12):2771–2775

Bernard-Gauthier V et al (2017b) A Kinome-wide selective radiolabeled TrkB/C inhibitor for in vitro and in vivo neuroimaging: synthesis, preclinical evaluation, and first-in-human. J Med Chem 60(16):6897–6910

Bernard-Gauthier V et al (2018) Identification of [18F]TRACK, a Fluorine-18-labeled tropomyosin receptor kinase (Trk) inhibitor for PET imaging. J Med Chem 61(4):1737–1743

Binder DK, Scharfman HE (2004) Brain-derived neurotrophic factor. Growth Factors (Chur, Switzerland) 22(3):123–131

Boltaev U et al (2017) Multiplex quantitative assays indicate a need for reevaluating reported small-molecule TrkB agonists. Sci Signal 10(493):eaal1670

Brooks AF et al (2014) Late-stage [(18)F]fluorination: new solutions to old problems. Chem Sci 5(12):4545–4553

Castello NA et al (2014) 7,8-Dihydroxyflavone, a small molecule TrkB agonist, improves spatial memory and increases thin spine density in a mouse model of Alzheimer disease-like neuronal loss. PLoS One 9(3):e91453

Chao MV (1992) Neurotrophin receptors: a window into neuronal differentiation. Neuron 9(4):583–593

Chao MV (2003) Neurotrophins and their receptors: a convergence point for many signalling pathways. Nat Rev Neurosci 4(4):299–309

Cocco E, Scaltriti M, Drilon A (2018) NTRK fusion-positive cancers and TRK inhibitor therapy. Nat Rev Clin Oncol 15(12):731–747

Deng V et al (2007) FXYD1 is an MeCP2 target gene overexpressed in the brains of Rett syndrome patients and Mecp2-null mice. Hum Mol Genet 16(6):640–650

Devi L, Ohno M (2015) TrkB reduction exacerbates Alzheimer's disease-like signaling aberrations and memory deficits without affecting β-amyloidosis in 5XFAD mice. Transl Psychiatry 5(5):e562

Fenner BM (2012) Truncated TrkB: beyond a dominant negative receptor. Cytokine Growth Factor Rev 23(1):15–24

Fenner ME, Achim CL, Fenner BM (2014) Expression of full-length and truncated trkB in human striatum and substantia nigra neurons: implications for Parkinson's disease. J Mol Histol 45(3):349–361

Ferrer I et al (1999) BDNF and full-length and truncated TrkB expression in Alzheimer disease. Implications in therapeutic strategies. J Neuropathol Exp Neurol 58(7):729–739

Géral C, Angelova A, Lesieur S (2013) From molecular to nanotechnology strategies for delivery of Neurotrophins: emphasis on brain-derived neurotrophic factor (BDNF). Pharmaceutics 5(1):127–167

Gupta VK et al (2013) TrkB receptor signalling: implications in neurodegenerative, psychiatric and proliferative disorders. Int J Mol Sci 14(5):10122–10142

Hsiao SJ et al (2019) Detection of tumor NTRK gene fusions to identify patients who may benefit from tyrosine kinase (TRK) inhibitor therapy. J Mol Diagn 21(4):553–571

Huang EJ, Reichardt LF (2003) Trk receptors: roles in neuronal signal transduction. Annu Rev Biochem 72(1):609–642

Jang S-W et al (2010) A selective TrkB agonist with potent neurotrophic activities by 7,8-dihydroxyflavone. Proc Natl Acad Sci U S A 107(6):2687–2692

Kaplan DR, Miller FD (2000) Neurotrophin signal transduction in the nervous system. Curr Opin Neurobiol 10(3):381–391

Khotskaya YB et al (2017) Targeting TRK family proteins in cancer. Pharmacol Ther 173:58–66

Lange AM, Lo H-W (2018) Inhibiting TRK proteins in clinical cancer therapy. Cancers 10(4):105

Lemaire C et al (2012) Fast and reliable method for the preparation of ortho- and Para-[18F]fluorobenzyl halide derivatives: key intermediates for the preparation of no-carrier-added PET aromatic radiopharmaceuticals. J Fluor Chem 138:48–55

Lessmann V, Gottmann K, Malcangio M (2003) Neurotrophin secretion: current facts and future prospects. Prog Neurobiol 69(5):341–374

Li N, Liu G-t (2010) The novel squamosamide derivative FLZ enhances BDNF/TrkB/CREB signaling and inhibits neuronal apoptosis in APP/PS1 mice. Acta Pharmacol Sin 31(3):265–272

Luberg K et al (2010) Human TrkB gene: novel alternative transcripts, protein isoforms and expression pattern in the prefrontal cerebral cortex during postnatal development. J Neurochem 113(4):952–964

Märkl B, Hirschbühl K, Dhillon C (2019) NTRK-fusions—a new kid on the block. Pathol Res Pract 215(10):152572

Massa SM et al (2010) Small molecule BDNF mimetics activate TrkB signaling and prevent neuronal degeneration in rodents. J Clin Invest 120(5):1774–1785

Merlio JP et al (1992) Molecular cloning of rat trkC and distribution of cells expressing messenger RNAs for members of the trk family in the rat central nervous system. Neuroscience 51(3):513–532

Murer MG, Yan Q, Raisman-Vozari R (2001) Brain-derived neurotrophic factor in the control human brain, and in Alzheimer's disease and Parkinson's disease. Prog Neurobiol 63(1):71–124

Nagahara AH, Tuszynski MH (2011) Potential therapeutic uses of BDNF in neurological and psychiatric disorders. Nat Rev Drug Discov 10:209

Oyesiku NM et al (1999) Regional changes in the expression of neurotrophic factors and their receptors following acute traumatic brain injury in the adult rat brain. Brain Res 833(2):161–172

Pike VW (2009) PET radiotracers: crossing the blood-brain barrier and surviving metabolism. Trends Pharmacol Sci 30(8):431–440

Poo M-M (2001) Neurotrophins as synaptic modulators. Nat Rev Neurosci 2(1):24–32

Preshlock S, Tredwell M, Gouverneur V (2016) 18F-labeling of Arenes and Heteroarenes for applications in positron emission tomography. Chem Rev 116(2):719–766

Rankovic Z (2015) CNS drug design: balancing physicochemical properties for optimal brain exposure. J Med Chem 58(6):2584–2608

Reichardt LF (2006) Neurotrophin-regulated signalling pathways. Philos Trans R Soc B Biol Sci 361(1473):1545–1564

Reinhart V et al (2015) Evaluation of TrkB and BDNF transcripts in prefrontal cortex, hippocampus, and striatum from subjects with schizophrenia, bipolar disorder, and major depressive disorder. Neurobiol Dis 77:220–227

Saba J et al (2018) Astrocyte truncated tropomyosin receptor kinase B mediates brain-derived neurotrophic factor anti-apoptotic effect leading to neuroprotection. J Neurochem 146(6):686–702

Savaskan E et al (2000) Alterations in Trk a, Trk B and Trk C receptor immunoreactivities in parietal cortex and cerebellum in Alzheimer's disease. Eur Neurol 44(3):172–180

Song J-H, Yu J-T, Tan L (2015) Brain-derived neurotrophic factor in Alzheimer's disease: risk, mechanisms, and therapy. Mol Neurobiol 52(3):1477–1493

Tejeda GS, Díaz-Guerra M (2017) Integral characterization of defective BDNF/TrkB signalling in neurological and psychiatric disorders leads the way to new therapies. Int J Mol Sci 18(2):268

Tredwell M et al (2014) A general copper-mediated nucleophilic 18F fluorination of arenes. Angew Chem Int Ed Engl 53(30):7751–7755

Van de Bittner GC, Ricq EL, Hooker JM (2014) A philosophy for CNS radiotracer design. Acc Chem Res 47(10):3127–3134

Wood ER et al (2004) Discovery and in vitro evaluation of potent TrkA kinase inhibitors: oxindole and aza-oxindoles. Bioorg Med Chem Lett 14(4):953–957

Yan W et al (2019) Insights into current tropomyosin receptor kinase (TRK) inhibitors: development and clinical application. J Med Chem 62(4):1731–1760

Zhang F et al (2012) Roles of brain-derived neurotrophic factor/tropomyosin-related kinase B (BDNF/TrkB) signalling in Alzheimer's disease. J Clin Neurosci 19(7):946–949

Zhang L et al (2013) Design and selection parameters to accelerate the discovery of novel central nervous system positron emission tomography (PET) ligands and their application in the development of a novel phosphodiesterase 2A PET ligand. J Med Chem 56(11):4568–4579

Zlatopolskiy BD et al (2015) Copper-mediated aromatic radiofluorination revisited: efficient production of PET tracers on a preparative scale. Chem Eur J 21(15):5972–5979

Radioligand Development for PET Imaging of the Vesicular Acetylcholine Transporter (VAChT) in the Brain

32

Barbara Wenzel, Winnie Deuther-Conrad,
Matthias Scheunemann, and Peter Brust

Contents

Abstract

Nowadays, it is general consensus that the cholinergic transmission system in the brain is heavily involved in the development, progress, and therapy of certain neurodegenerative diseases. In particular cholinergic presynaptic components such as the acetylcholinesterase (AChE) or the vesicular acetylcholine transporter (VAChT) are considered to be affected by early changes in neuropathological processes as observed, e.g., in Alzheimer's disease (AD). The VAChT is a transmembrane protein located at synaptic vesicles and responsible for the

B. Wenzel (✉) · W. Deuther-Conrad · M. Scheunemann · P. Brust
Department of Neuroradiopharmaceuticals, Institute of Radiopharmaceutical Cancer
Research, Helmholtz-Zentrum Dresden-Rossendorf, Research Site Leipzig,
Leipzig, Germany
e-mail: b.wenzel@hzdr.de; w.deuther-conrad@hzdr.de; m.scheunemann@hzdr.de;
p.brust@hzdr.de

transport and storage of the neurotransmitter acetylcholine (ACh) in the vesicles. Therefore, the VAChT is regarded as a potential target for neuroimaging of cholinergic alterations with positron emission tomography. To date, the development of PET radioligands for this transporter is based on a single known lead compound named vesamicol. A challenge was arising due to the finding that vesamicol also binds to the sigma receptors which are partly co-localized with the VAChT in several brain regions. In the last three decades, a multitude of structural diverse vesamicol analogs has been designed resulting in a considerable number of [11]C- and ^{18}F-labeled PET as well as a few [123]/^{125}I-labeled SPECT tracers which were mainly preclinically evaluated. However, only very few of them had the potential for translation to human studies. Therefore, a routinely used VAChT PET imaging method could not be established in the clinics so far. However, first results of recently published studies using the potent candidate [^{18}F]FEOBV in patients with neuropathologies are very promising and possibly a breakthrough in this field.

This review addresses the efforts in ligand design and PET radioligand development for the VAChT with a special view on the difficulties arising from the lead compound vesamicol and its low selectivity.

32.1   Introduction

32.1.1 The Vesicular Acetylcholine Transporter

The vesicular acetylcholine transporter, coded by the gene *SLC18A3* (solute carrier family 18 member A3), belongs to the major facilitator superfamily (MFS). These transmembrane proteins are expressed in all organisms and transport dissolved small organic molecules across the cell membrane along a chemiosmotic gradient of either the solute itself (passive diffusion) or a second substrate (co-transport). In principle, all MFS transporters consist of 12 transmembrane helical sequences separated in two bundles of six N- and six C-terminal helices forming the cavity for the respective substrate (Bai et al. 2017).

Mainly related to neurotransmission in vertebrates, the transport of acetylcholine and other positively charged amine neurotransmitters from the cytoplasm into secretory vesicles is mediated by a specific subgroup of the MFS, the SLC18 transporters (Alexander et al. 2017). Multiple aspects of the history, function, and structure of these vesicular neurotransmitter transporters have recently been reviewed (Lawal and Krantz 2013; Anne and Gasnier 2014). The neurotransmitter ACh is the endogenous substrate of the VAChT which utilizes a proton gradient to mediate the vesicular storage of one molecule ACh by the antiport of two protons (Alexander et al. 2017; Eiden et al. 2004). First reports, indicating an active proton-driven uptake of

ACh into synaptic vesicles, date back to the 1980s (Koenigsberger and Parsons 1980; Michaelson and Angel 1981), followed soon by the identification of AH1853 (vesamicol) as potent inhibitor of this vesicular uptake of acetylcholine (Anderson et al. 1983; Carroll 1985) postulated by I. G. Marshall (1970) already in 1970.

With this tool in hands, biochemical research on structure-function aspects of the assumed VAChT, at first named "synaptic vesicle vesamicol receptor" (Bahr and Parsons 1986), was strongly stimulated. The cDNA encoding VAChT has been cloned in the early 1990s, initially in worms (Alfonso et al. 1993) and shortly after in mouse, rat, and humans (Bejanin et al. 1994; Erickson et al. 1994; Roghani et al. 1994) allowing detailed analyses of the binding sites of protons, ACh, and vesamicol (Song et al. 1997; Kim et al. 1999, 2000; Keller et al. 2000; Zhu et al. 2001; Khare et al. 2010). As one result it has been shown that vesamicol binds to an allosteric binding site of the VAChT and inhibits the ACh transport non-competitively (Marshall and Parsons 1987; Prior et al. 1992). Although no crystal structure has been reported so far, the group of S. Schuldiner created a homology model of the human VAChT (see Fig. 1 in Khare et al. 2010) based on the principle structure of MFS proteins, in particular the neurotransmitter transporters of the SLC18 family (Vardy et al. 2004; Elbaz et al. 2010).

As already mentioned, the VAChT couples the transport of acetylcholine into the synaptic vesicle with an efflux of protons. By this energy-dependent process, a remarkably high gradient of ACh can be obtained—from 1–4 mM in the cytoplasm up to 600 mM in the cytoplasmic vesicle (Parsons et al. 1993)—which is of crucial importance for unimpaired neurotransmission. Stimulated release of this highly concentrated ACh from vesicles of presynaptic neurons into the synaptic cleft results in local concentrations of up to 1 mM ACh which enable a prompt and efficient activation of postsynaptic receptors such as the nicotinic acetylcholine receptors (nAChRs) possessing EC_{50} values in the micromolar range (Zwart and Vijverberg 1998). Accordingly, VAChT expressed in neurons of the central, peripheral, autonomic, and somatic nervous system is a significant component of the ACh release cycle. Due to the presence of VAChT in particular brain regions (Erickson et al. 1994; Albin et al. 2018), it is obvious that dysfunction or attenuated expression affects cholinergic neurotransmission. Indeed, noninvasive imaging studies as well as postmortem investigations indicate a correlation between changes in the availability of intact VAChT and neuropathological processes related to abnormal cholinergic function such as neurodegenerative or depressive disorders in both preclinical animal models and patients (Bohnen et al. 2019; Smith et al. 2006; Chen et al. 2011; Mazere et al. 2013; Ruberg et al. 1990; Gilmor et al. 1998) as well as age-related physiological changes (Albin et al. 2018; Parent et al. 2012). Accordingly, the potential of VAChT as marker of the integrity of cholinergic pathways, in particular of presynaptic neurons, makes this protein an attractive target for the pharmacological research and the development of diagnostic techniques for a variety of brain diseases.

32.1.2 Vesamicol as Basis for the Development of Ligands Targeting the VAChT

The development of VAChT radioligands is mainly based on vesamicol (*trans*-2-(4-phenylpiperidino)cyclohexanol, Fig. 32.1) which was primarily developed already in the 1960s as an analgesic drug. Fundamental work was performed by Rogers et al. with the synthesis of a large number of structurally diverse vesamicol analogues and the determination of their potential to inhibit the [³H]ACh transport into synaptic vesicles isolated from the electric organ of *Torpedo californica* (Rogers et al. 1989). The group discovered some important features for obtaining a high binding affinity toward VAChT such as the *trans*-orientation of the hydroxy and the amino substituent at the cyclohexylring A of vesamicol (Fig. 32.1) and the enantioselectivity with *1R,2R*-(−)-vesamicol being 25-fold more potent than *1S,2S*-(+)-vesamicol. However, subsequent extensive research has shown that vesamicol additionally exhibits substantial affinity toward the σ₁ and σ₂ receptors, which are also expressed in cholinergic brain regions, thereby limiting the suitability of radiolabeled vesamicol itself as a specific VAChT imaging agent (Custers et al. 1997; Ogawa et al. 2013; Bouchard and Quirion 1997). Therefore, the VAChT ligand
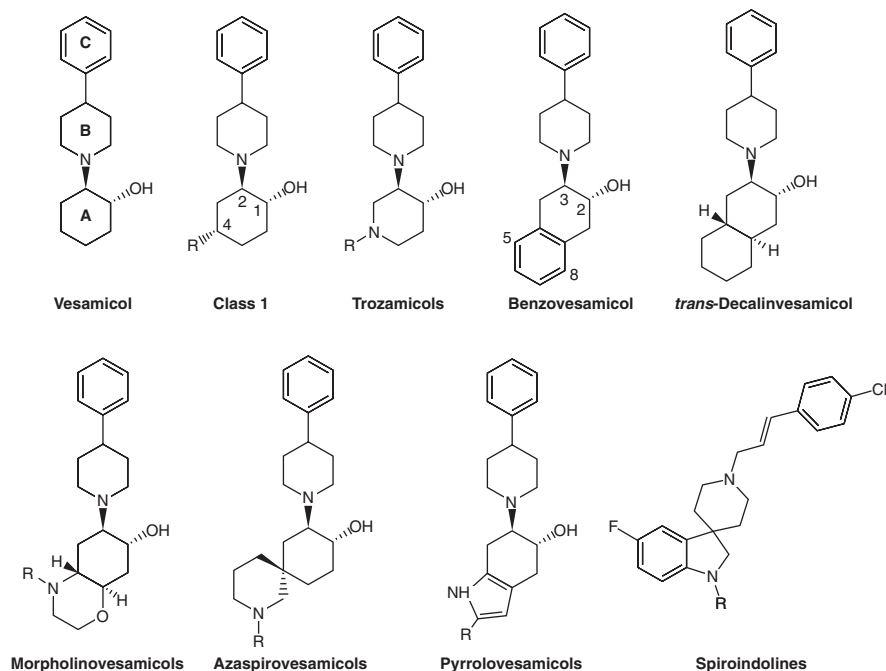
Fig. 32.1 Vesamicol, selected structurally diverse vesamicol analogs and spiroindolines as potential VAChT ligands

design has moved in the recent years away from focusing solely on VAChT binding toward additionally considering potential sigma receptor binding.

When summarizing the chemical efforts of the last three decades, it becomes obvious that structural modifications were performed at all three rings A, B, and C of the vesamicol skeleton (Fig. 32.1), which was also reviewed by Giboureau et al. (2010a). A tendency can be identified at which substitutions at ring A lead to considerably increased VAChT affinity while modifications in ring B and C are less favorable. This trend was supported by a 3D QSAR approach, giving more detailed insight into structural implications for high binding affinity (Szymoszek et al. 2008). By contrast, no general trend regarding sigma receptor affinity could be found based on the results of an extensive SAR study using data from a systematically modified compound library (Barthel et al. 2015).

Figure 32.1 shows some selected ligand classes which are characterized by quite interesting ring A modifications. One of the initial SAR findings was the favorable substitution in 4-position of the cyclohexylring A resulting in an increase of VAChT binding affinity. Known examples are fluoromethylvesamicol (FMV) (Rogers et al. 1993) and 4-*O*-fluorobenzylether vesamicol (Scheunemann et al. 2004) (class 1 in Fig. 32.1) as well as the 4-azavesamicol derivative fluorobenzyltrozamicol (FBT) (Efange et al. 1993). However, the obtained high binding affinity toward VAChT was accompanied by high affinity to at least one of the sigma receptors resulting in a low selectivity.

A milestone in the VAChT ligand development was the discovery of benzovesamicol (BV) which was achieved by the fusion of a benzene with the cyclohexylring A and resulting in one of the most potent VAChT ligands (Rogers et al. 1993). Despite the remaining non-negligible affinity toward the sigma receptors (Barthel et al. 2015), the selectivity of benzovesamicol significantly improved in comparison with vesamicol (Rogers et al. 1993) due to the 20-fold increase of VAChT affinity. Therefore this compound served later as basis for the development of several ^{18}F-labeled VAChT radioligands such as [^{18}F]FEOBV. Ring fusions were also performed with saturated ring systems resulting in structurally similar vesamicol analogs with high VAChT binding affinity such as the *trans*-decalinvesamicol (Rogers et al. 1993) and the morpholinovesamicol (Sorger et al. 2008, 2009) derivatives. Using spiro-ring fusion as another approach for obtaining conformational restriction resulted in the azaspirovesamicol derivatives (Wenzel et al. 2011) showing slightly lower VAChT affinity in comparison with benzovesamicol but negligible affinity toward sigma receptors. Unexpectedly low binding affinities for the VAChT were found for the pyrrolovesamicols characterized by the fusion of ring A with a five membered heteroaromatic ring system (Wenzel et al. 2012).

To our knowledge along with vesamicol, the spiroindoline type (Fig. 32.1) represents the only other class of compounds being reported to potentially exhibit VAChT binding in the nanomolar range (Sluder et al. 2012). In order to examine the potential of these spiroindolines as a new lead compound candidate for the development of VAChT PET ligands, selected derivatives were recently synthesized

(Lindemann et al. 2017). However, the compounds demonstrated only moderate VAChT binding affinity not suitable for PET imaging purposes. Interestingly, also these non-vesamicol based derivatives have binding affinity toward the two sigma receptor subtypes.

32.1.3 Considerations on Binding Affinity Data for VAChT Obtained In Vitro

The evaluation and discussion of published in vitro binding affinity data for the VAChT should be carried out with some caution because different K_i values (inhibition constants) are reported for identical compounds due to the use of different experimental protocols as also mentioned by Ogawa et al. in the recently published review (Ogawa and Shiba 2018). In general, radioligand displacement assays are utilized with $(-)$-[^{3}H]vesamicol as radioligand; however, the applied biological material differs regarding species and tissue. For example, the group of Rogers and Parsons initially used synaptic vesicles isolated from the electric organ of *Torpedo californica* and reported a K_i value of 1.0 nM for $(\pm)$-vesamicol (Rogers et al. 1993). By contrast, a K_i value of 33.9 nM was reported by the group of Shiba, using membrane preparations of the rat brain (Shiba et al. 2002; Kozaka et al. 2012). Furthermore, cell lines stably transfected with either rat (Barthel et al. 2015; Roghani and Carroll 2002) or human VAChT (Tu et al. 2009; Varoqui and Erickson 1996) are used by other research groups. As part of a comprehensive SAR study, our group recently devoted attention to this matter and investigated membranes obtained from the rat brain and PC-12 cells stably transfected with a cDNA of rat VAChT (rVAChT-PC12) and $(-)$-[^{3}H]vesamicol as radioligand (Barthel et al. 2015). As the main finding of this study, considerable differences of K_i values became apparent. For example, for $(\pm)$-benzovesamicol, K_i values of 1.3 nM with rVAChT-PC12 cells and 23.4 nM with the rat brain were obtained. Also, for $(\pm)$-vesamicol a higher binding affinity to rVAChT-PC12 cells (K_i of 47.4 nM) was observed compared to rat brain membranes with a K_i value of 84.2 nM. Since the two VAChT membrane preparations applied are of rat origin, comparable affinity data of the vesamicol derivatives could be expected. However, in comparison with rVAChT-PC12 cell homogenates, the rat brain is characterized by a much lower concentration of VAChT and the presence of a complex protein mixture. The latter becomes evident by the higher nonspecific binding of $(-)$-[^{3}H]vesamicol in brain membranes (>20%) compared to rVAChT-PC12 cell membranes (<5%). Furthermore, it has to be considered that $(-)$-[^{3}H]vesamicol is not selective due to its high affinity to sigma receptors which are widely distributed in the brain but rarely present in rVAChT-PC12 cells.

Finally, for a reasonable interpretation of VAChT binding affinity data, both species differences and the source of biological material should be considered. If and how these differences of the in vitro data correlate with in vivo PET imaging results would be interesting to explore.

32.2   Fluorine-18- and Carbon-11-Labeled PET Radioligands for Imaging the VAChT

Potential radiolabeled imaging agents for a quantitative visualization of the neuronal VAChT in living systems have to fulfil several criteria such as (1) high VAChT binding affinity in the low nanomolar range combined with high selectivity regarding sigma receptors, (2) low nonspecific binding, (3) no brain penetrant radiometabolites, (4) high blood-brain barrier permeability with a low potential for efflux transport, and (5) rapid clearance to reduce the radioactivity background in the target tissue. In order to fulfill the first criterion, the distribution of a VAChT selective PET probe in the brain should correspond with the known protein expression. Immunohistochemistry studies of rat brain material have confirmed the exclusive location of VAChT at cholinergic nerve terminals with high densities in the striatum, cortex, basal forebrain, hippocampus, thalamus, amygdala, and brain stem (Schäfer et al. 1998; Arvidsson et al. 1997; Weihe et al. 1996; Gilmor et al. 1996; Ichikawa et al. 1997).
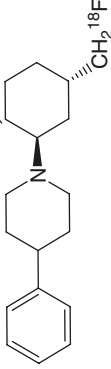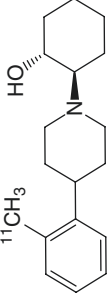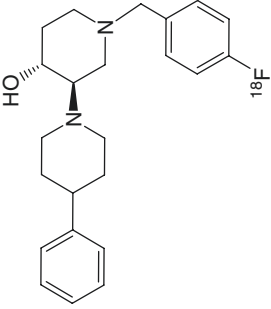
Despite the challenges in developing specific PET radioligands for imaging the VAChT in the brain, a considerable number of fluorine-18- and carbon-11-labeled tracers were synthesized and evaluated mainly in preclinical studies. These efforts have been reviewed in 2010 by Giboureau et al. (2010b) and recently by Ogawa and Shiba (2018). A summary of the most important compounds is given in Table 32.1 and discussed below within selected structural groups.
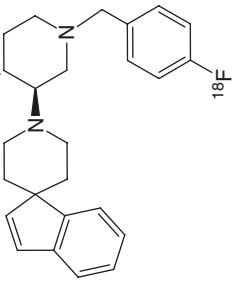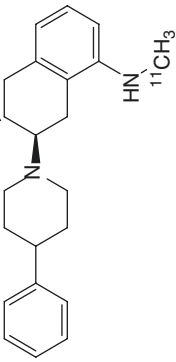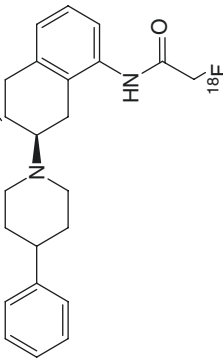
32.2.1 Vesamicol-Based PET Radioligands

(−)-[¹⁸F]FMV: The radiofluorinated fluoromethylvesamicol (−)-[¹⁸F]FMV was one of the first ¹⁸F-labeled VAChT PET radioligands and was developed by Widen and Rogers et al. in 1992 (Widen et al. 1992; Rogers et al. 1994). The (−)-enantiomer showed a distinctly higher affinity to the VAChT (IC_{50} = 5.1 nM) than the (+)-enantiomer (IC_{50} = 960 nM), determined on vesicles of the electric organ of *T. californica* (Hicks et al. 1991). PET studies in rats and non-human primates showed a rapid and high uptake of (−)-[¹⁸F]FMV in the brain which could be blocked by pre-injection of vesamicol (Widen et al. 1992). Compared to the cerebellum, a substantially higher uptake of the radiotracer was observed in representative cholinergic brain regions such as the striatum and cortex indicating specific binding. However, the kinetic analysis of the (−)-[¹⁸F]FMV distribution in rats led the authors conclude that the pharmacokinetic profile of the radiotracer is not suitable for an accurate quantification of the VAChT binding sites due to an irreversible binding pattern amongst others.

(−)-[¹¹C]OMV: Carbon-11-labeled *o*-methylvesamicol (−)-[¹¹C]OMV was reported in 2006 by Kawamura et al. (2006) and Shiba et al. (2006). In vitro binding studies revealed a high VAChT binding affinity of (−)-OMV (K_i = 6.7 nM) which was in the range of the binding affinity of (−)-vesamicol (K_i = 4.4 nM) determined

Table 32.1 In vitro binding affinity data and in vivo results of ^{11}C- and ^{18}F-labeled VAChT PET ligands and the selected SPECT tracer $(-)$-$[^{123/125}I]$IBVM
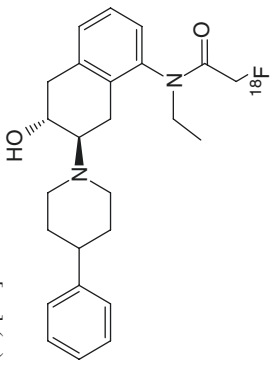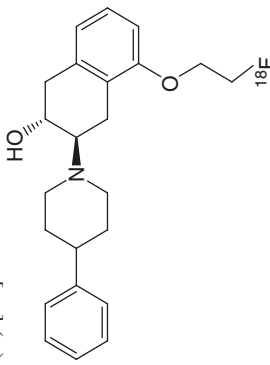
Compound name/structure	Binding affinity K_i, in nM			Main findings
	VAChT	σ_1	σ_2	
$(-)$-$[^{18}F]$FMV	5.1 ± 0.5^a (IC_{50})	n.r.	n.r.	High cerebral uptake in rats and non-human primates. Unfavorable kinetics with irreversible binding (Widen et al. 1992)
$(-)$-$[^{11}C]$OMV	6.7 ± 0.4^b	33.7 ± 5.9^c	266 ± 28^d	Nonspecific accumulation in the brain of rats and non-human primates due to additional binding to sigma receptors (Kawamura et al. 2006; Shiba et al. 2006, 2009)
$(+)$-$[^{18}F]$FBT	0.22 ± 0.05^a	21.6 ± 3.9^e	35.9 ± 6.3^d	High accumulation in basal ganglia of non-human primates with suitable kinetic profile. No radiometabolites within the brain. No further studies are reported, e.g., on specificity (Efange et al. 1993, 1994a; Mach et al. 1997; Voytko et al. 2001; Gage et al. 2000)
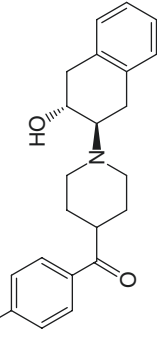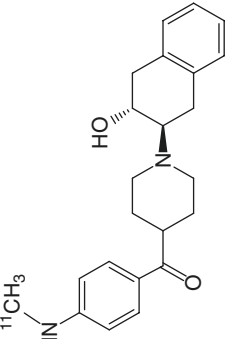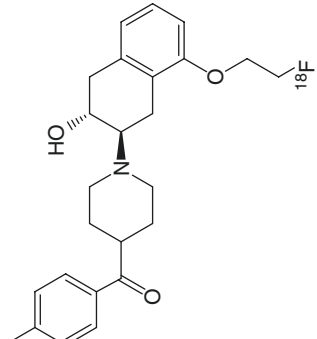
	0.44 ± 0.04[a]	48.7 ± 8.7[f]	32.5 ± 1.3[f]	Low basal ganglia-to-cerebellum ratio in non-human primates and rapid metabolism (Efange et al. 1994b, 1999)
(+)-[18F]Spiro-FBT				
(−)-[11C]MABV	n.r.	n.r.	n.r.	High accumulation in the striatum, cortex, and hippocampus of the mouse brain with suitable kinetic profile. No radiometabolites in the brain. No further studies performed (Kilbourn et al. 1990)
(−)-[18F]FAA	n.r.	n.r.	n.r.	Rapid metabolism in rats with the very likely formation of brain penetrant [18F]fluoroacetate (Rogers et al. 1994)

(continued)
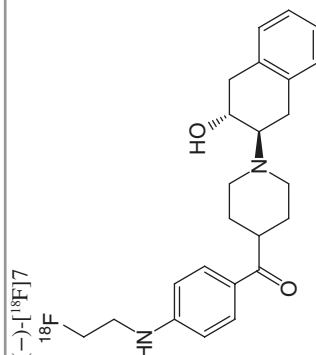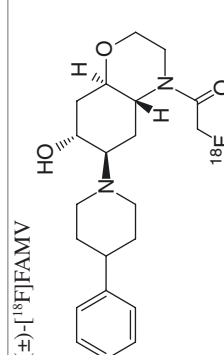
Table 32.1 (continued)
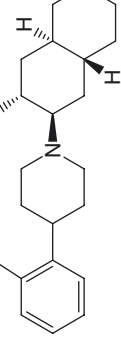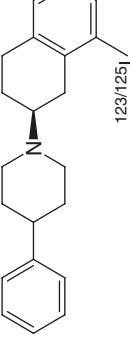
Compound name/structure	Binding affinity K_i in nM			Main findings
	VAChT	σ_1	σ_2	
(−)-[18F]NEFA	0.32 ± 0.04^a	n.r.	n.r.	High and specific accumulation in the striatum of non-human primates with suitable tracer kinetics. High striatal but low cortical uptake in human healthy subjects. No significant difference of binding pattern between healthy controls and AD patients (Rogers et al. 1993; Ingvar et al. 1993; Widen et al. 1993)
(−)-[18F]FEOBV	6.75 ± 2.02^g	2275 ± 390^h	2118 ± 1058^i	High and specific binding in the striatum, thalamus, amygdala, hippocampus, neocortical regions, rostral brain stem, and cerebellar cortex in healthy humans. First successful studies in patients with AD, DLB, and PD (Albin et al. 2018; Bohnen et al. 2019; Petrou et al. 2014; Aghourian et al. 2017; Schmitz et al. 2018; Nejad-Davarani et al. 2019; van der Zee et al. 2019; Mulholland et al. 1993, 1998; Helbert et al. 2019)

Compound				Comments
(−)-[18F]FBBV	4.1 ± 0.6^j	658 ± 118^e	319 ± 36^d	Low brain uptake in rats. High striatal uptake in non-human primates with moderate striatum to cerebellum ratio. No further studies reported (Tu et al. 2009)
(−)-[11C]TZ659	0.78 ± 0.07^l	992 ± 21^e	$11,443 \pm 690^d$	High striatal and specific binding in non-human primates with moderate striatum-to-cerebellum ratio. Suitable pharmacokinetic profile. Further studies proposed reg. suitability in humans (Li et al. 2013; Jin et al. 2016)
(−)-[18F]VAT	0.59 ± 0.06^j	$>10,000^e$	$>10,000^d$	High specific, striatal binding in non-human primates with suitable pharmacokinetics and dosimetry. Further studies are ongoing reg. suitability in humans (Jin et al. 2018; Tu et al. 2015)

(continued)

Table 32.1 (continued)

Compound name/structure	Binding affinity K_i in nM			Main findings
	VAChT	σ_1	σ_2	
(−)-[18F]7	0.31 ± 0.03[j]	1870 ± 250[e]	5480 ± 140[d]	High uptake in the striatum and thalamus in preliminary studies in non-human primates. Further characterization necessary (Yue et al. 2017)
(R,R)-[11C]HAPT	27.5[k]	>1000[c]	n.r.	High, specific, and stereospecific uptake in the putamen and caudate of non-human primates. Suitable metabolism profile. Further studies needed (Nishiyama et al. 2014)
(±)-[18F]FAMV	39.9 ± 5.9[i]	–	(>1500)[l]	Low but specific accumulation in the rat brain. Fast metabolic degradation with formation of brain penetrable radiometabolites (Sorger et al. 2008)

(±)-[^{18}F]FBMV	27.5 ± 8.8[i]	–	(>3000)[l]	Moderate, specific uptake in the rat brain. Reduction of tracer binding in rat model with cholinergic immunolesion. Suitable metabolism profile Preliminary PET imaging data from pig (Sorger et al. 2009)
(±)-[^{11}C]OMDV	11.9[b]	70.3[c]	43.6[d]	Relatively high brain uptake in rats. Moderate target to non-target ratios (Kitamura et al. 2016)
(−)-[$^{125/123}$I]IBVM	n.r.	n.r.	n.r.	High and specific binding in the striatum, thalamus, hippocampus, pons, and cerebellar vermis in healthy human. Promising results from first studies in patients with early AD and PD (Kuhl et al. 1994, 1996; Mazere et al. 2008, 2012; Jung et al. 1990, 1996; Van Dort et al. 1993; Sorger et al. 2000)

n.r. not reported

[a] K_i or IC_{50} values are determined using vesicles from the electric organ of *Torpedo californica* and (−)-[^{3}H]vesamicol

[b] K_i values are determined using cerebral membranes of rat and (−)-[^{3}H]vesamicol

[c] K_i values are determined using cerebral membranes of rat and (+)-[^{3}H]pentazocine
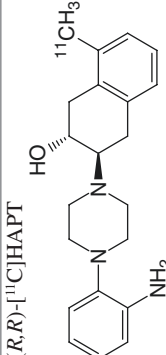
(continued)

Table 32.1 (continued)

Compound name/structure	Binding affinity K_i in nM			Main findings
	VAChT	σ_1	σ_2	

d K_i values are determined using liver membranes of rat and [³H]DTG with blocking σ_1 receptor sites using (+)-pentazocine

e K_i values are determined using brain membranes of guinea pig and (+)-[³H]pentazocine

f No exact assay information available

g K_i values are determined using PC12 cell membranes stably expressing rat VAChT and (−)-[³H]vesamicol

h K_i values are determined using cortex homogenates of rat and (+)-[³H]pentazocine

i K_i values are determined using liver membranes of rat and [³H]DTG with blocking of σ_1 receptor sites using dextrallorphan

j K_i values are determined using PC12 cell membranes stably expressing human VAChT and (−)-[³H]vesamicol

k K_i values are determined using cerebral membranes of rat and [³H]aminobenzovesamicol

l K_i values are determined using liver membranes of rat and [³H]DTG without blocking the σ_1 receptor sites

by using rat cerebral membranes (Shiba et al. 2006). However, this vesamicol analog possessed in vitro also considerable affinity toward the σ_1 receptor ($K_i = 33.7$ nM). The resulting low selectivity was reflected by further in vivo evaluation of (−)-[^{11}C]OMV (Kawamura et al. 2006). Biodistribution studies revealed an uptake of (−)-[^{11}C]OMV in the rat brain of 1.1%ID/g at 5 min p.i. which nearly remained on this level for 60 minutes. A significant inhibition of the uptake was not only observed by co-injection of (−)-vesamicol but also by the two sigma receptor ligands SA4503 and haloperidol (Kawamura et al. 2006). Furthermore, low striatum-to-cerebellum and cortex-to-cerebellum ratios of 1.5 and 1.2, respectively, have been obtained in subsequent PET studies in non-human primates (Shiba et al. 2009). The authors concluded that (−)-[^{11}C]OMV showed a high brain uptake and appropriate brain kinetics for a carbon-11-labeled radiopharmaceutical and suggested to use the tracer in a simultaneous imaging setup together with the sigma receptor ligand [^{11}C]SA4503 to differentiate between VAChT and sigma receptor binding.

32.2.2 Trozamicol-Based PET Radioligands

Another approach to develop VAChT radioligands was taken in the design and synthesis of vesamicol analogs by replacing the cyclohexyl ring A by a piperidine ring (see Fig. 32.1). Thus, the available amino nitrogen of the so-called trozamicols provides an easily accessible position for introduction of radiolabeled moieties.

(+)-[^{18}F]FBT: Fluorobenzyltrozamicol (FBT) was synthesized by Efange et al. in 1993 as a first example of the trozamicols (Efange et al. 1993). Interestingly, the (+)-enantiomer showed a higher affinity ($K_i = 0.22$ nM) than the (−)-enantiomer ($K_i = 16.0$ nM) determined later by Mach et al. on synaptic vesicles isolated from the electric organ of *T. californica* (Mach et al. 1997). This phenomenon was only observed for the trozamicol compound class. For all other vesamicol analogs, the (−)-enantiomer was found to be the more potent stereoisomer. The binding affinity of (+)-FBT was slightly higher compared to the affinity of (−)-vesamicol ($K_{i(ves)} = 1.0$ nM). A lower, but not negligible binding affinity of (+)-FBT was observed for the σ_1 ($K_i = 21.6$ nM) and σ_2 ($K_i = 35.9$ nM) receptors resulting in 98- and 160-fold ratio of VAChT/σ_1 and VAChT/σ_2 affinities, respectively. In vivo evaluation of (+)-[^{18}F]FBT in rats showed an initial brain uptake of 0.82%ID/g at 5 minutes decreasing to 0.27% ID/g at 3 h p.i (Efange et al. 1994a). The highest accumulation of activity was observed in the striatum and hippocampus, followed by moderate uptake in cortex and low uptake in the cerebellum resulting in a maximum striatum-to-cerebellum ratio of 2.8 at 3 h p.i. Sigma receptor binding appeared to account for only a small fraction of (+)-[^{18}F]FBT binding since pre-injected haloperidol had no significant effect on the binding in frontal cortex and hippocampus. PET imaging studies in non-human primates revealed a high accumulation and slow washout of (+)-[^{18}F]FBT from the basal ganglia with a continuously increasing basal ganglia-to-cerebellum ratio reaching 1.75 at 3 h p.i. (Mach et al. 1997). In contrast, the time-activity curves of cortical regions are in the same range as for the cerebellum. In this study no blocking experiments were performed in order to verify

the specificity of the radiotracer. (+)-[^{18}F]FBT was found to be similarly metabolized in both species, and the generated radiometabolites did not cross the blood-brain barrier (Mach et al. 1997). The reproducibility of the (+)-[^{18}F]FBT PET measurements in the basal ganglia was demonstrated in a separate study (Gage et al. 2000). The authors concluded that (+)-[^{18}F]FBT is a promising radiotracer for studying cholinergic terminal density with PET and indeed an age-dependent reduction of the binding of (+)-[^{18}F]FBT in the basal ganglia of aged rhesus monkeys could be demonstrated (Voytko et al. 2001). However, obtained individual differences require further investigations. To our knowledge, there are no reports on the application of (+)-[^{18}F]FBT in human studies despite the promising preclinical results. Tu and Mach et al. mentioned in a paper in 2009 (Tu et al. 2009) unpublished data which demonstrated unacceptably high nonspecific binding in human subjects.

(+)-Spiro-FBT: Fluorobenzyl spirotrozamicol (Spiro-FBT) was developed by Efange et al. in 1994 with the aim to design conformationally restricted vesamicol analogues maintaining an orthogonal orientation of the phenyl ring C and the piperidine ring B (Efange et al. 1994b). As also observed for FBT, (+)-Spiro-FBT showed a higher binding affinity (K_i = 0.44 nM) toward the VAChT than (−)-Spiro-FBT (K_i = 30.5 nM) (Efange et al. 1999). The affinity to sigma receptors was determined with K_i values of 48.7 and 32.5 nM for σ_1 and σ_2, respectively. Biodistribution studies with (+)-[^{18}F]Spiro-FBT in rats showed an initial brain uptake of 0.74% ID/g at 5 min p.i. The accumulation in the different brain regions striatum, hippocampus, cortex, and cerebellum was in a similar range of 0.66–0.84% ID/g at 5 min p.i. (Efange et al. 1999). However, due to different rates of washout, the striatum-to-cerebellum and hippocampus-to-cerebellum ratios increased from about 1.2 to 2.0 within 120 min p.i. Pretreatment with (+)-FBT reduced the uptake in most of the brain regions suggesting identical binding sites for these two ligands in vivo. PET studies in rhesus monkeys revealed a rapid accumulation of activity in the brain. However, the washout of (+)-[^{18}F]Spiro-FBT from the basal ganglia was more rapid displaying a lower basal ganglia-to-cerebellum ratio in comparison with (+)-[^{18}F]FBT. This unexpected result was explained by a fast metabolism of (+)-[^{18}F]Spiro-FBT with only 10% of intact tracer in the plasma at 10 min p.i. This led the authors to conclude that this radiotracer might be not suitable for PET imaging of the VAChT.

32.2.3 Benzovesamicol-Based PET Radioligands

Most of the PET radioligands developed for imaging of the VAChT are derived from benzovesamicol as this vesamicol analog demonstrated a very high binding affinity (K_i = 0.055 nM, on vesicles of *T. californica* Rogers et al. 1993).

(−)-[^{11}C]MABV: One of the first representatives is the carbon-11-labeled 5-(N-methylamino)benzovesamicol (−)-[^{11}C]MABV which was developed by Kilbourn et al. already in 1990 on the basis of 5-aminobenzovesamicol (ABV, Rogers et al. 1993; Kilbourn et al. 1990). Biodistribution studies in mouse showed

a very high radiotracer uptake in the striatum (8.1% ID/g at 45 min p.i.) followed by the cortex, hippocampus, and hypothalamus. A slower washout in these brain regions compared to the cerebellum resulted in striatum-to-cerebellum and cortex-to-cerebellum ratios of 13 and 5, respectively, at 75 min p.i. of (−)-[^{11}C]MABV. The accumulation in these brain regions was lower after pretreatment of (±)-vesamicol and showed stereoselectivity with higher uptake of the (−)-enantiomer compared to the (+)-enantiomer. A radiometabolite analysis of homogenized mouse brain tissue at 45 minutes p.i. of (−)-[^{11}C]MABV revealed the solely presence of the radiotracer. However, despite these promising results, the authors did not continue with this compound, and except an improved radiosynthesis protocol (Mulholland and Jung 1992), no further work on (−)-[^{11}C]MABV has been published.

[^{18}F]FAA and **[^{18}F]NEFA**: The *N*-[^{18}F]fluoroacetylated and *N*-ethyl-[^{18}F]fluoroacetylated 5-aminobenzovesamicol derivatives [^{18}F]FAA and [^{18}F]NEFA ($K_{i((±)-NEFA}$ = 0.32 nM Rogers et al. 1993) were developed by Rogers et al. (1994). PET studies of [^{18}F]FAA in rats in combination with the monitoring of arterial blood revealed a rapid metabolism with the very likely generation of [^{18}F]fluoroacetate, and therefore the authors excluded this radiotracer from further studies. By contrast, initial PET investigation of [^{18}F]NEFA in rats indicated a specific uptake in cerebral tissues and a higher metabolic stability due to the *N*-ethylation. Subsequent PET imaging studies in non-human primates (Ingvar et al. 1993) showed a stereoselective binding of (−)-[^{18}F]NEFA with a regional distribution pattern of striatum>cortex>cerebellum at late time points. The activity ratio of striatum to cerebellum increased continuously and reached a value in the range of 2.5–3 at 50 min p.i. The tracer binding could be selectively blocked but not displaced with vesamicol and remained unaffected by the pretreatment with the σ_1 receptor ligand pentazocine. The twofold increase of the striatum-to-cerebellum ratio in response to the pretreatment with haloperidol or raclopride suggested that blocking of the dopamine-D2 receptors stimulated the cholinergic system of the striatum. Therefore, a human PET study was performed on two healthy subjects and one AD patient (Widen et al. 1993). However, despite a high accumulation in the striatum, (−)-[^{18}F]NEFA showed no relevant binding in the cortex of the healthy subjects, and no difference was observed between healthy and diseased brain. Accordingly, the authors did not perform further studies with this radiotracer.

(−)-[^{18}F]FEOBV: One of the most investigated VAChT PET radioligands is the 5-[^{18}F]fluoroethoxy-substituted benzovesamicol [^{18}F]FEOBV which was developed by Mulholland et al. (1993, 1998). In a very fundamental study in rodents, this group investigated the regional distribution in the brain, stereospecificity, dosimetry, toxicity, pharmacological blocking effects, and the in vivo metabolism. (−)-[^{18}F]FEOBV demonstrated (1) a high brain uptake (2.68% ID/g at 5 min p.i.) with a strong cholinergic pattern of localization matching known distributions of other presynaptic cholinergic markers, (2) a favorable metabolism, and (3) no considerable interaction with dopamine or σ_1 receptor binding sites. The clearance of the radiotracer from the cerebellum was fast and slow from the striatum where the highest tracer accumulation was reached between 45 and 180 min p.i. (8–9% ID/g) with a maximum striatum-to-cerebellum ratio of about 5. Interestingly, to our knowledge,

no in vitro binding affinity data were reported at this time. Recently, our group together with Elsinga et al. investigated (−)-FEOBV (Helbert et al. 2019) and determined a K_i value of 6.75 nM toward the VAChT (on rVAChT PC12 cells). For σ_1 and σ_2 receptors, K_i values of about 2000 nM were determined (Helbert et al. 2019). These data correspond to the specific binding observed in the initial in vivo studies. The early results obtained by Mulholland et al. were later confirmed and the studies expanded to non-human primates demonstrating the potential of this radiotracer for imaging the VAChT in the brain (Kilbourn et al. 2009). Moreover, a correlation of reduced (−)-[^{18}F]FEOBV binding in the rat brain with aging as well as with cholinergic deficits caused by lesions was reported (Parent et al. 2012; Cyr et al. 2014). Because of these very promising preclinical findings, in vivo PET studies in human followed. In the recently published reports (Albin et al. 2018; Petrou et al. 2014), the authors describe a tracer distribution and regional density pattern which is highly consistent with the known distribution of cholinergic nerve terminals. Accordingly, highest binding was found in the striatum, followed by particular regions of the thalamus, amygdala, hippocampus, some neocortical regions, rostral brain stem, and some regions of the cerebellar cortex. The data also demonstrated that (−)-[^{18}F]FEOBV has an acceptable dosimetry and safety profile in human subjects (Petrou et al. 2014). Moreover, the results indicated an association of normal aging with regional reductions of (−)-[^{18}F]FEOBV binding in the striatum and some cortical regions (Albin et al. 2018). Finally, the authors concluded that PET imaging using (−)-[^{18}F]FEOBV provides more direct information about cholinergic terminal integrity than, for example, acetylcholinesterase-based PET methods as these are indirect markers because they reflect the activity of a hydrolytic enzyme which might be variable. With these satisfying results, a starting signal was given for using (−)-[^{18}F]FEOBV in clinical studies related to neuropathologies. Thus, in the last 2 years, patients suffering from AD (Aghourian et al. 2017; Schmitz et al. 2018), dementia with Lewy bodies (DLB) (Nejad-Davarani et al. 2019), Parkinson's disease (Bohnen et al. 2019; van der Zee et al. 2019), or REM sleep behavior disorder (Bedard et al. 2019) were investigated with (−)-[^{18}F]FEOBV PET. The therein described initial observations are very promising as it seems to be possible with this first selective VAChT radiotracer to distinguish between the participation of certain cholinergic regions or projections in the different neuropathologies probably due to the fact that the targeted protein is solely present in cholinergic nerve terminals. Further studies are needed now to, e.g., (1) better characterize the (−)-[^{18}F]FEOBV binding in diseases associated with cholinergic dysfunction, (2) to investigate the relationship between regional cholinergic alterations and clinical symptomatology, and (3) to compare (−)-[^{18}F]FEOBV PET to other imaging approaches with regard to a reliable disease discrimination.

[^{18}F]FBBV: In 2009, Tu et al. developed with [^{18}F]fluorobenzoylbenzovesamicol ([^{18}F]FBBV) the first representative of a new class of benzovesamicol derivatives, containing a carbonyl group between the fragments B and C of the vesamicol scaffold (Tu et al. 2009). Until 2018, this group and others reported on numerous ^{11}C- (Jin et al. 2016; Padakanti et al. 2014; Luo et al. 2018; Bergman et al. 2014) and ^{18}F-labeled (Jin et al. 2018; Yue et al. 2017; Luo et al. 2018; Yue et al. 2018)

compounds belonging to this class of which only the most potent candidates are reviewed here. The (−)-enantiomer of FBBV exhibited with a K_i value of 4.1 nM (on hVAChT PC12 cells) a high binding affinity to the VAChT accompanied by a high selectivity with K_i values of 658 and 319 nM for the σ_1 and σ_2 receptors, respectively (Tu et al. 2009). In vivo studies in rats revealed a moderate brain uptake of (−)-[^{18}F]FBBV with a maximum of 0.82% ID/g at 5 min p.i. reaching a striatum-to-cerebellum ratio of 1.8 at 30 min p.i. MicroPET imaging studies in non-human primates demonstrated a high uptake in the striatum (SUV_{max}(caudate) = 4.5 and SUV_{max}(putamen) = 5 at 30 min p.i.) with a maximum striatum-to-cerebellum ratio of 2.1 at 2 h. No attempts were made to perform blocking studies in order to prove the specificity of the radiotracer. The authors stated that (−)-[^{18}F]FBBV has excellent potential to be a novel PET tracer for clinical imaging of the VAChT; however, no further studies have been reported so far.

(−)-[^{11}C]TZ659: With the ^{11}C-labeled methylaminobenzoylbenzovesamicol (−)-[^{11}C]TZ659, Tu et al. developed another compound of the carbonyl group containing benzovesamicol class. This derivative is characterized by an excellent in vitro binding profile with K_i values of 0.78, 992, and 11,443 nM for the VAChT, σ_1, and σ_2 receptors, respectively (Li et al. 2013). Biodistribution studies in rats showed highest radiotracer accumulation in the striatum (0.6% ID/g at 30 min p.i.) reaching a striatum-to-cerebellum ratio of 3.75. An about twofold increase of brain uptake was observed due to the injection of the P-glycoprotein (P-gp) inhibitor cyclosporine indicating that (−)-[^{11}C]TZ659 might be a potential substrate of this drug efflux transporter (Li et al. 2013). Subsequent PET imaging studies in non-human primates showed a high retention of the radiotracer in the striatum with a maximum SUV of 4.5 at 20 min p.i. and a slow washout (Jin et al. 2016). This tracer binding could be blocked and displaced in a dose-dependent manner by (−)-vesamicol but not (+)-pentazocine. Fastest washout was observed for the cerebellum giving striatum-to-cerebellum ratios in the range of 1.8–2.4 from 60 to 110 min scanning time. From occupancy studies, an ED_{50} value of 0.0057 mg/kg of (−)-vesamicol for striatal VAChT was calculated (Jin et al. 2016). Based on these results, the authors intended to further investigate (−)-[^{11}C]TZ659 regarding its suitability for quantifying VAChT levels in human subjects and characterizing expression changes during disease progression or therapeutic treatment.

(−)-[^{18}F]VAT: Further exploration of the carbonyl-substituted benzovesamicols leads to (−)-[^{18}F]VAT which can be regarded as a structural merge of FEOBV and FBBV. The new derivative has an excellent in vitro binding profile with a K_i value of 0.59 nM for the VAChT and no binding affinity toward the σ_1 and σ_2 receptors (Tu et al. 2015). Interestingly, the introduction of the fluoroethoxy group in 5-position of the benzene ring of FBBV strongly diminished the binding to the sigma receptors, a phenomenon which was already observed for FEOBV. Biodistribution studies in rats showed highest regional radiotracer uptake in the striatum (0.9% ID/g at 30 min) reaching a striatum-to-cerebellum ratio of about 3 at 30 min (Tu et al. 2015). PET imaging and dosimetry studies in non-human primates were performed demonstrating the great potential of this radiotracer (Jin et al. 2018; Tu et al. 2015). Highest (−)-[^{18}F]VAT binding was observed in the striatum followed by the

thalamus, hippocampus, frontal cortex, and vermis corresponding to known distribution of cholinergic terminals. The peak of striatal uptake was already reached at 15 min p.i. of (−)-[^{18}F]VAT (SUV of 5) indicating a faster equilibrium compared to (−)-[^{18}F]FEOBV. Blocking with (−)-vesamicol significantly reduced the striatal uptake, while no change was observed in cerebellar regions. A metabolite analysis of arterial blood samples showed a decrease of parent radiotracer from 66% at 15 min to 16% at 90 minutes p.i. Moreover, different modeling methods were applied to estimate the VAChT levels in non-human primates, and a good reproducibility and reliability in repeated measurements were found. According to the authors, the clinical investigation of (−)-[^{18}F]VAT in patients with various neurodegenerative and neurological diseases is ongoing (Luo et al. 2018).

(−)-[^{18}F]7: A recently published derivative belonging to the carbonyl-containing benzovesamicols was obtained by replacement of the methyl group of (−)-[^{11}C]TZ659 by a fluoroethyl chain in order to obtain the corresponding ^{18}F-labeled radiotracer (−)-[^{18}F]7 (Yue et al. 2017). Also this compound showed very high binding affinity to the VAChT (K_i = 0.31 nM) and negligible affinities to the σ_1 and σ_2 receptors. Surprisingly, the radiosynthesis of (−)-[^{18}F]7 turned out to be rather challenging, and the deliverable activity was not sufficient for routine PET studies in non-human primates. Therefore, only two PET studies in a male macaque were performed with, however, quite promising results (Yue et al. 2017). The activity uptake peaked at about 10 min p.i. and was highest in the striatum (SUV$_{max}$: ~8) followed by the thalamus (SUV$_{max}$: ~7.5), cerebellum, hippocampus, and cortical regions. The washout was slowest from the striatum followed by the thalamus and very fast from the cerebellum resulting in striatum-to-cerebellum and thalamus-to-cerebellum ratios of about 3 and 2.3, respectively, at 60 minutes p.i. of (−)-[^{18}F]7. The authors intend to further characterize this radiotracer after improving the radiosynthesis procedure.

(R,R)-[^{11}C]HAPT: In 2014 Nishiyama et al. reported on [^{11}C]HAPT another ^{11}C-labeled benzovesamicol derivative bearing as ring B a piperazine instead of the piperidine ring in the vesamicol core (Nishiyama et al. 2014). Interestingly, the ^{11}C-methyl group is substituted in 8-position of the tetralin ring system which was described to be unfavorable compared to the 5-position in case of amino substitution like in aminobenzovesamicol (Rogers et al. 1989). The enantiomer (R,R)-[^{11}C]HAPT showed a considerably higher binding affinity for the VAChT (K_i = 27.5 nM on rat cerebral membranes) than the (S,S)-[^{11}C]HAPT (K_i = 699 nM) and a negligible affinity toward the σ_1 receptor. This was well reflected by the PET imaging studies in non-human primates (Nishiyama et al. 2014). While (R,R)-[^{11}C]HAPT was heterogeneously distributed in the brain with highest uptake in the putamen and caudate (SUV$_{max}$ at 20 min: 4 and 3.4, respectively), intermediate uptake in the thalamus and amygdala, lower uptake in cortical regions, and lowest in the cerebellum, the (S,S)-[^{11}C]HAPT showed a lower and homogeneous distribution in all brain regions. The preadministration of (−)-vesamicol induced a complete inhibition of (R,R)-[^{11}C]HAPT binding in all regions except the cerebellum. By contrast, no significant changes in tracer uptake were observed after preadministration of SA4503, a specific σ_1 receptor ligand. A metabolite analysis revealed a

fraction of 34% of parent radiotracer (*R,R*)-[^{11}C]HAPT in plasma, at 45 min p.i. The authors concluded that this radiotracer is a potential PET probe for quantification of the VAChT in the living brain.

32.2.4 Morpholinovesamicols

In an effort to develop selective VAChT radioligands keeping the favorable binding profile of benzovesamicol but possessing a more moderate lipophilicity, new structurally similar analogs were designed by fusing a morpholino instead of a benzene ring on ring A of the vesamicol skeleton. Moreover, the nitrogen atom of the morpholine system offers the possibility of a straightforward introduction of different fluoro-carrying functionalities. Thus, different morpholinovesamicol derivatives were developed, and two of them are radiofluorinated and preclinically evaluated (Sorger et al. 2008, 2009).

(±)-[^{18}F]FAMV: The [^{18}F]fluoroacetyl-substituted derivative (±)-[^{18}F]FAMV was published in 2008 by Sorger et al. and showed with a K_i value of 39.9 nM (on rVAChT PC12 cells) and low binding affinities toward the sigma receptors a good in vitro binding profile (Sorger et al. 2008). Injected into rats, (±)-[^{18}F]FAMV accumulated only to low amounts (0.12% ID/g at 5 min p.i.) but specifically in the brain as demonstrated by pretreatment with (−)-vesamicol (Sorger et al. 2008). Ex vivo autoradiography showed a heterogeneous uptake which was highest in the striatum followed by the cortical regions, hippocampus, and thalamus and lowest in the cerebellum. Region-to-cerebellum ratios at 1 h p.i. of (±)-[^{18}F]FAMV were 4.5 and 2 for the striatum and cortical regions, respectively. Metabolism studies revealed a fast degradation with the formation of brain penetrable radiometabolites, limiting the utility of this compound for in vivo studies.

[^{18}F]FBMV: With the [^{18}F]fluorobenzoyl-substituted derivative (±)-[^{18}F]FBMV, another morpholinovesamicol was developed exhibiting a slightly higher binding affinity toward the VAChT (K_i = 27.5 nM) and selectivity regarding the σ receptors compared to (±)-[^{18}F]FAMV (Sorger et al. 2009). Biodistribution studies in rats showed highest brain uptake of 0.17% ID/g at 5 min p.i. of (±)-[^{18}F]FBMV with a regional distribution at later time points which is typical for VAChT-containing brain regions (Sorger et al. 2009). At 1 h p.i., striatum-to-cerebellum and cortex-to-cerebellum ratios of about 3.4 and 1.8, respectively, were determined in ex vivo autoradiography experiments. Pretreatment with (−)-vesamicol inhibited the observed binding quantitatively resulting in a homogeneous tracer distribution in the brain. Investigation of (±)-[^{18}F]FBMV using a rat model with a specific cholinergic immunolesion revealed a reduced tracer binding by about 20% in particular in cortical brain regions. In metabolism studies in rats, parent radiotracer fractions of 79, 61, and 43% at 15, 60, and 120 minutes p.i. of (±)-[^{18}F]FBMV, respectively, were determined in plasma, and mainly intact radiotracer was detectable in the brain demonstrating a considerably higher in vivo stability compared to (±)-[^{18}F]FAMV. Preliminary PET studies were performed in pigs and revealed a desirable brain uptake of (±)-[^{18}F]FBMV with a regional distribution corresponding to

cholinergic nerve terminals. Co-administration of (±)-vesamicol resulted in a 60% reduction of radiotracer binding in the striatum; however, further studies are needed to better characterize this radiotracer.

32.2.5 Other Vesamicol Analogs

[^{11}C]OMDV: The ring-fused analog *trans*-decalinvesamicol (Fig. 32.1) was first synthesized by Rogers et al. (1993) and demonstrated an exceptional high binding affinity to the VAChT (K_i = 0.009 nM on vesicles of *T. californica*). However, the compound does not offer simple access for radiofluorination. Therefore, the group of K. Shiba (Kitamura et al. 2016) focused on ^{11}C-labeling by substituting a methyl group in *ortho* position of the phenyl ring as this position was shown to be more suitable than the *para* position when the *o*-methylvesamicol [^{11}C]OMV was developed (Shiba et al. 2006). Interestingly, the obtained OMDV showed still a high binding affinity toward the VAChT (K_i = 11.9 nM on rat cerebral membranes) but much lower than reported by Rogers et al. The binding affinities to the σ_1 and σ_2 receptors were determined to be 70.3 and 43.6 nM, respectively (Kitamura et al. 2016). Biodistribution studies in rats showed an initial uptake of 0.92% ID/g at 2 minutes p.i. of [^{11}C]OMDV in the cerebrum which decreased within 60 minutes to 0.44% ID/g. The regional activity distribution at 30 minutes p.i. was highest in the striatum (0.69% ID/g) followed by the cortex (0.62% ID/g) and the cerebellum with 0.50% ID/g resulting in a striatum-to-cerebellum ratio of 1.4. The uptake was inhibited in all three brain regions by co-injection of (−)-vesamicol. When (+)-pentazocine or the $\sigma_{1/2}$ receptor ligand (+)-3-PPP was administered, no significant changes were observed. These findings were confirmed by PET-CT studies in rats. However, the time-activity curves demonstrated rather low target-to-non-target ratios for the striatum and cortex during the scanning time of 35 minutes. In this study, the in vivo metabolism was not investigated. The authors concluded that [^{11}C]OMDV may be suitable for PET imaging of dementia; however, further evaluation of the radiotracer is necessary.

32.3 The Use of (−)-[^{123}/^{125}]Iodobenzovesamicol as SPECT Imaging Agent for VAChT

Several radioiodinated vesamicol analogs were developed for the use as SPECT imaging agents. Since this review is focused on PET radiopharmaceuticals, they are not listed here. However, because of the important findings obtained with (−)-[^{123}]iodobenzovesamicol in human studies, this section of our chapter concerns this SPECT tracer.

Jung et al. developed 5-[^{125}]iodobenzovesamicol ([^{125}I]IBVM) already in 1990 and investigated the biodistribution of this tracer in mice (Jung et al. 1990). The (−)-enantiomer showed a high accumulation in the striatum (6.26% ID/g) and the cortex (2.56% ID/g) and low uptake in the cerebellum (0.23% ID/g) at 4 h p.i. In

comparison, the accumulation of the (+)-enantiomer was much lower accompanied by a rather homogeneous distribution in the brain. Pretreatment with (−)-vesamicol reduced the striatal and cortical uptake of (−)-[^{125}I]IBVM considerably. A few years later, the same group established the radiosynthesis of the ^{123}I-labeled derivative (−)-[^{123}I]IBVM and demonstrated that the two radioiodinated compounds behave similarly in vivo (Van Dort et al. 1993). Sorger et al. evaluated (−)-[^{125}I]IBVM in a rat model with a cholinergic immunolesion showing a significantly reduced binding in the affected brain regions which corresponded to a reduced AChE binding as measured by AChE histochemical staining (Sorger et al. 2000). Moreover, (−)-[^{125}I]IBVM was found to specifically bind in cholinergic brain regions as demonstrated by blocking studies with (−)-vesamicol, haloperidol (dopamine D2 and sigma receptor ligand), and DTG ($\sigma_{1/2}$ receptor ligand) (Sorger et al. 2000).

Kuhl et al. reported in 1994 and 1996 on human studies investigating (−)-[^{123}I]IBVM in healthy subjects (Kuhl et al. 1994) and in AD and PD patients (Kuhl et al. 1996). While in mildly demented AD patients with an early onset a reduced (−)-[^{123}I]IBVM binding in the neocortex and hippocampus was observed, reductions were significant in temporal cortex and hippocampus in mild AD patients with a late onset. By contrast, when the dementia was severe, terminal deficits were extensive in all AD patients independent from the time of onset. More than 10 years later, Mazère et al. also reported on (−)-[^{123}I]IBVM SPECT imaging in patients with early Alzheimer's disease and demonstrated a decrease of tracer binding of 47–62% relative to healthy subjects which was specifically localized in the cingulate cortex and parahippocampal-amygdaloid complex (Mazere et al. 2008). The authors concluded that the results suggest the occurrence of cholinergic degeneration in the early stage of AD which is likely related to the impairment of the cognitive function. Therefore, the data support the cholinergic hypothesis (Bartus et al. 1982) suggesting that human cholinergic dysfunction is an early pathological feature of cognitive decline in AD. Further SPECT imaging studies with (−)-[^{123}I]IBVM in patients with progressive supranuclear palsy (Mazere et al. 2012) and multiple system atrophy (Mazere et al. 2013) followed in later years to evaluate the integrity of central cholinergic pathways.

32.4 Summary and Conclusion

The VAChT is a very attractive target for imaging cholinergic innervation as this transporter is exclusively expressed in the presynaptic part of cholinergic neurons. This makes the VAChT valuable for investigating, characterizing, and diagnosing brain diseases involving cholinergic dysfunction. As already concluded by Ogawa and Shiba (2018), this transporter additionally can be seen as an ideal imaging counterpart of other cholinergic elements such as acetylcholine receptors which are located post- and presynaptically and not only on cholinergic neurons.

However, the development of VAChT-specific PET radioligands is very challenging as it is based on the only known lead compound vesamicol. Because of the structural similarity of vesamicol to the pharmacophore of sigma receptor ligands,

the design of suitable derivatives has to be directed not only to the VAChT binding affinity but also to a high selectivity versus sigma receptors. This becomes evident by the numerous vesamicol-based ligands which often show binding affinities even in the nanomolar range in particular to σ_1 receptors. Sigma receptors are also distributed in cholinergic brain regions such as the thalamus, hippocampus, or striatum (Bouchard and Quirion 1997) and would therefore impair specific in vivo imaging. However, although structure-affinity relationship studies considering the three competing targets have been performed (Barthel et al. 2015), no clear indicators for constructive structural modifications could be revealed so far as also concluded by Giboureau et al. (2010a). A tendency for high affinity to VAChT was disclosed, but results for σ_1/σ_2 receptor binding in dependence on the molecular structure were inconsistent.

In conclusion, numerous PET radioligands for the VAChT have been developed, but with [^{18}F]NEFA and [^{18}F]FEOBV, only two of them were investigated in humans so far. Just recently, [^{18}F]FEOBV was translated into clinical application for investigation of patients with dementia. Additionally, human studies with the SPECT tracer (−)-[^{123}I]IBVM demonstrated the relevance of the VAChT for imaging cholinergic dysfunction already in the early stage of neurodegenerative diseases. Finally, the first published human data are very promising and give hope for a breakthrough of successful VAChT PET imaging in the brain and the implementation of this method in diagnosing and understanding cholinergic pathologies as appearing, e.g., in Alzheimer's disease.

References

Aghourian M, Legault-Denis C, Soucy JP, Rosa-Neto P, Gauthier S, Kostikov A, Gravel P, Bedard MA (2017) Quantification of brain cholinergic denervation in Alzheimer's disease using PET imaging with [^{18}F]FEOBV. Mol Psychiatry 22:1531–1538

Albin RL, Bohnen NI, Muller M, Dauer WT, Sarter M, Frey KA, Koeppe RA (2018) Regional vesicular acetylcholine transporter distribution in human brain: a [^{18}F]fluoroethoxybenzovesamicol positron emission tomography study. J Comp Neurol 526:2884–2897

Alexander SPH, Kelly E, Marrion NV, Peters JA, Faccenda E, Harding SD, Pawson AJ, Sharman JL, Southan C, Davies JA (2017) The concise guide to pharmacology 2017/18: transporters. Br J Pharmacol 174:S360–S446

Alfonso A, Grundahl K, Duerr JS, Han HP, Rand JB (1993) The *Caenorhabditis elegans* unc-17 gene: a putative vesicular acetylcholine transporter. Science 261:617–619

Anderson DC, King SC, Parsons SM (1983) Pharmacological characterization of the acetylcholine transport system in purified Torpedo electric organ synaptic vesicles. Mol Pharmacol 24:48–54

Anne C, Gasnier B (2014) Vesicular neurotransmitter transporters: mechanistic aspects. Curr Top Membr 73:149–174

Arvidsson U, Riedl M, Elde R, Meister B (1997) Vesicular acetylcholine transporter (VAChT) protein: a novel and unique marker for cholinergic neurons in the central and peripheral nervous systems. J Comp Neurol 378:454–467

Bahr BA, Parsons SM (1986) Demonstration of a receptor in Torpedo synaptic vesicles for the acetylcholine storage blocker l-trans-2-(4-phenyl[3,4-3H]-piperidino) cyclohexanol. Proc Natl Acad Sci U S A 83:2267–2270

Bai X, Moraes TF, Reithmeier RAF (2017) Structural biology of solute carrier (SLC) membrane transport proteins. Mol Membr Biol 34:1–32

Barthel C, Sorger D, Deuther-Conrad W, Scheunemann M, Schweiger S, Jäckel P, Roghani A, Steinbach J, Schüürmann G, Sabri O, Brust P, Wenzel B (2015) New systematically modified vesamicol analogs and their affinity and selectivity for the vesicular acetylcholine transporter—a critical examination of the lead structure. Eur J Med Chem 100:50–67

Bartus RT, Dean RL 3rd, Beer B, Lippa AS (1982) The cholinergic hypothesis of geriatric memory dysfunction. Science 217:408–414

Bedard MA, Aghourian M, Legault-Denis C, Postuma RB, Soucy JP, Gagnon JF, Pelletier A, Montplaisir J (2019) Brain cholinergic alterations in idiopathic REM sleep behaviour disorder: a PET imaging study with [18F]FEOBV. Sleep Med 58:35–41

Bejanin S, Cervini R, Mallet J, Berrard S (1994) A unique gene organization for two cholinergic markers, choline acetyltransferase and a putative vesicular transporter of acetylcholine. J Biol Chem 269:21944–21947

Bergman S, Estrada S, Hall H, Rahman R, Blomgren A, Larhed M, Svedberg M, Thibblin A, Wangsell F, Antoni G (2014) Synthesis and labeling of a piperazine-based library of 11C-labeled ligands for imaging of the vesicular acetylcholine transporter. J Label Compd Radiopharm 57:525–532

Bohnen NI, Kanel P, Zhou Z, Koeppe RA, Frey KA, Dauer WT, Albin RL, Müller MLTM (2019) Cholinergic system changes of falls and freezing of gait in Parkinson's disease. Ann Neurol 85:538–549

Bouchard P, Quirion R (1997) [3H]1,3-di(2-tolyl)guanidine and [3H](+)pentazocine binding sites in the rat brain: autoradiographic visualization of the putative sigma1 and sigma2 receptor subtypes. Neuroscience 76:467–477

Carroll PT (1985) The effect of the acetylcholine transport blocker 2-(4-phenylpiperidino) cyclohexanol (AH5183) on the subcellular storage and release of acetylcholine in mouse brain. Brain Res 358:200–209

Chen KH, Reese EA, Kim HW, Rapoport SI, Rao JS (2011) Disturbed neurotransmitter transporter expression in Alzheimer's disease brain. J Alzheimers Dis 26:755–766

Custers FG, Leysen JE, Stoof JC, Herscheid JD (1997) Vesamicol and some of its derivatives: questionable ligands for selectively labelling acetylcholine transporters in rat brain. Eur J Pharmacol 338:177–183

Cyr M, Parent MJ, Mechawar N, Rosa-Neto P, Soucy JP, Aliaga A, Kostikov A, Maclaren DA, Clark SD, Bedard MA (2014) PET imaging with [18F]fluoroethoxybenzovesamicol ([18F]FEOBV) following selective lesion of cholinergic pedunculopontine tegmental neurons in rat. Nucl Med Biol 41:96–101

Efange SM, Khare A, Parsons SM, Bau R, Metzenthin T (1993) Nonsymmetrical bipiperidyls as inhibitors of vesicular acetylcholine storage. J Med Chem 36:985–989

Efange SM, Mach RH, Khare A, Michelson RH, Nowak PA, Evora PH (1994a) p-[18F]fluorobenzyltrozamicol ([18F]FBT): molecular decomposition- reconstitution approach to vesamicol receptor radioligands for positron emission tomography. Appl Radiat Isot 45:465–472

Efange SM, Khare AB, Foulon C, Akella SK, Parsons SM (1994b) Spirovesamicols: conformationally restricted analogs of 2-(4-phenylpiperidino)cyclohexanol (vesamicol, AH5183) as potential modulators of presynaptic cholinergic function. J Med Chem 37:2574–2582

Efange SM, Nader MA, Ehrenkaufer RL, Khare AB, Smith CR, Morton TE, Mach RH (1999) (+)-p-([18F]fluorobenzyl)spirotrozamicol [(+)-[18F]spiro-FBT]: synthesis and biological evaluation of a high-affinity ligand for the vesicular acetylcholine transporter (VAChT). Nucl Med Biol 26:189–192

Eiden LE, Schäfer MK, Weihe E, Schütz B (2004) The vesicular amine transporter family (SLC18): amine/proton antiporters required for vesicular accumulation and regulated exocytotic secretion of monoamines and acetylcholine. Pflugers Arch 447:636–640

Elbaz Y, Danieli T, Kanner BI, Schuldiner S (2010) Expression of neurotransmitter transporters for structural and biochemical studies. Protein Expr Purif 73:152–160

Erickson JD, Varoqui H, Schafer MK, Modi W, Diebler MF, Weihe E, Rand J, Eiden LE, Bonner TI, Usdin TB (1994) Functional identification of a vesicular acetylcholine transporter and its expression from a "cholinergic" gene locus. J Biol Chem 269:21929–21932

Gage HD, Voytko ML, Ehrenkaufer RL, Tobin JR, Efange SM, Mach RH (2000) Reproducibility of repeated measures of cholinergic terminal density using [18F]-4-Fluorobenzyltrozamicol and PET in the Rhesus Monkey Brain. J Nucl Med 41:2069–2076

Giboureau N, Aumann KM, Beinat C, Kassiou M (2010a) Development of vesicular acetylcholine transporter ligands: molecular probes for Alzheimer's disease. Curr Bioact Compd 6:129–155

Giboureau N, Som IM, Boucher-Arnold A, Guilloteau D, Kassiou M (2010b) PET radioligands for the vesicular acetylcholine transporter (VAChT). Curr Top Med Chem 10:1569–1583

Gilmor ML, Nash NR, Roghani A, Edwards RH, Yi H, Hersch SM, Levey AI (1996) Expression of the putative vesicular acetylcholine transporter in rat brain and localization in cholinergic synaptic vesicles. J Neurosci 16:2179–2190

Gilmor ML, Counts SE, Wiley RG, Levey AI (1998) Coordinate expression of the vesicular acetylcholine transporter and choline acetyltransferase following septohippocampal pathway lesions. J Neurochem 71:2411–2420

Helbert H, Wenzel B, Deuther-Conrad W, Luurtsema G, Szymanski W, Brust P, Feringa B, Dierckx R, Elsinga P (2019) Pd catalyzed cross-coupling of [11C]MeLi and its application in the synthesis and evaluation of a potential PET tracer for the vesicular acetylcholine transporter (VAChT). J Label Compd Radiopharm 62:S238–S239

Hicks BW, Rogers GA, Parsons SM (1991) Purification and characterization of a nonvesicular vesamicol-binding protein from electric organ and demonstration of a related protein in mammalian brain. J Neurochem 57:509–519

Ichikawa T, Ajiki K, Matsuura J, Misawa H (1997) Localization of two cholinergic markers, choline acetyltransferase and vesicular acetylcholine transporter in the central nervous system of the rat: in situ hybridization histochemistry and immunohistochemistry. J Chem Neuroanat 13:23–39

Ingvar M, Stone-Elander S, Rogers GA, Johansson B, Eriksson L, Parsons SM, Widen L (1993) Striatal D2 acetylcholine interactions—PET studies of the vesamicol receptor. Neuroreport 4:1311–1314

Jin H, Zhang X, Yue X, Liu H, Li J, Yang H, Flores H, Su Y, Parsons SM, Perlmutter JS, Tu Z (2016) Kinetics modeling and occupancy studies of a novel C-11 PET tracer for VAChT in nonhuman primates. Nucl Med Biol 43:131–139

Jin H, Yue X, Liu H, Han J, Flores H, Su Y, Parsons SM, Perlmutter JS, Tu Z (2018) Kinetic modeling of [18F]VAT, a novel radioligand for positron emission tomography imaging vesicular acetylcholine transporter in non-human primate brain. J Neurochem 144:791–804

Jung YW, Van Dort ME, Gildersleeve DL, Wieland DM (1990) A radiotracer for mapping cholinergic neurons of the brain. J Med Chem 33:2065–2068

Jung YW, Frey KA, Mulholland GK, del Rosario R, Sherman PS, Raffel DM, Van Dort ME, Kuhl DE, Gildersleeve DL, Wieland DM (1996) Vesamicol receptor mapping of brain cholinergic neurons with radioiodine-labeled positional isomers of benzovesamicol. J Med Chem 39:3331–3342

Kawamura K, Shiba K, Tsukada H, Nishiyama S, Mori H, Ishiwata K (2006) Synthesis and evaluation of vesamicol analog (−)-o-[11C]methylvesamicol as a PET ligand for vesicular acetylcholine transporter. Ann Nucl Med 20:417–424

Keller JE, Bravo DT, Parsons SM (2000) Modification of cysteines reveals linkage to acetylcholine and vesamicol binding sites in the vesicular acetylcholine transporter of *Torpedo californica*. J Neurochem 74:1739–1748

Khare P, Ojeda AM, Chandrasekaran A, Parsons SM (2010) Possible important pair of acidic residues in vesicular acetylcholine transporter. Biochemistry 49:3049–3059

Kilbourn MR, Jung YW, Haka MS, Gildersleeve DL, Kuhl DE, Wieland DM (1990) Mouse brain distribution of a carbon-11 labeled vesamicol derivative: presynaptic marker of cholinergic neurons. Life Sci 47:1955–1963

Kilbourn MR, Hockley B, Lee L, Sherman P, Quesada C, Frey KA, Koeppe RA (2009) Positron emission tomography imaging of (2R,3R)-5-[^{18}F]fluoroethoxybenzovesamicol in rat and monkey brain: a radioligand for the vesicular acetylcholine transporter. Nucl Med Biol 36:489–493

Kim MH, Lu M, Lim EJ, Chai YG, Hersh LB (1999) Mutational analysis of aspartate residues in the transmembrane regions and cytoplasmic loops of rat vesicular acetylcholine transporter. J Biol Chem 274:673–680

Kim MH, Lu M, Kelly M, Hersh LB (2000) Mutational analysis of basic residues in the rat vesicular acetylcholine transporter. Identification of a transmembrane ion pair and evidence that histidine is not involved in proton translocation. J Biol Chem 275:6175–6180

Kitamura Y, Kozaka T, Miwa D, Uno I, Azim MA, Ogawa K, Taki J, Kinuya S, Shiba K (2016) Synthesis and evaluation of a new vesamicol analog o-[^{11}C]methyl-trans-decalinvesamicol as a PET ligand for the vesicular acetylcholine transporter. Ann Nucl Med 30:122–129

Koenigsberger R, Parsons SM (1980) Bicarbonate and magnesium ion-ATP dependent stimulation of acetylcholine uptake by Torpedo electric organ synaptic vesicles. Biochem Biophys Res Commun 94:305–312

Kozaka T, Uno I, Kitamura Y, Miwa D, Ogawa K, Shiba K (2012) Syntheses and in vitro evaluation of decalinvesamicol analogues as potential imaging probes for vesicular acetylcholine transporter (VAChT). Bioorg Med Chem 20:4936–4941

Kuhl DE, Koeppe RA, Fessler JA, Minoshima S, Ackermann RJ, Carey JE, Gildersleeve DL, Frey KA, Wieland DM (1994) In vivo mapping of cholinergic neurons in the human brain using SPECT and IBVM. J Nucl Med 35:405–410

Kuhl DE, Minoshima S, Fessler JA, Frey KA, Foster NL, Ficaro EP, Wieland DM, Koeppe RA (1996) In vivo mapping of cholinergic terminals in normal aging, Alzheimer's disease, and Parkinson's disease. Ann Neurol 40:399–410

Lawal HO, Krantz DE (2013) SLC18: vesicular neurotransmitter transporters for monoamines and acetylcholine. Mol Asp Med 34:360–372

Li J, Zhang X, Zhang Z, Padakanti PK, Jin H, Cui J, Li A, Zeng D, Rath NP, Flores H, Perlmutter JS, Parsons SM, Tu Z (2013) Heteroaromatic and aniline derivatives of piperidines as potent ligands for vesicular acetylcholine transporter. J Med Chem 56:6216–6233

Lindemann M, Deuther-Conrad W, Moldovan R, Sekhar KVGC, Brust P, Wenzel B (2017) Do spiroindolines have the potential to replace vesamicol as lead compound for the development of radioligands targeting the vesicular acetylcholine transporter? Bioorg Med Chem 25:5107–5113

Luo Z, Liu H, Jin H, Gu J, Yu Y, Kaneshige K, Perlmutter JS, Parsons SM, Tu Z (2018) Exploration of sulfur-containing analogues for imaging vesicular acetylcholine transporter in the brain. ChemMedChem 13:1978–1987

Mach RH, Voytko ML, Ehrenkaufer RL, Nader MA, Tobin JR, Efange SM, Parsons SM, Gage HD, Smith CR, Morton TE (1997) Imaging of cholinergic terminals using the radiotracer [^{18}F](+)-4-fluorobenzyltrozamicol: in vitro binding studies and positron emission tomography studies in nonhuman primates. Synapse 25:368–380

Marshall IG (1970) Studies on the blocking action of 2-(4-phenylpiperidino)cyclohexanol (AH5183). Br J Pharmacol 38:503–516

Marshall IG, Parsons SM (1987) The vesicular acetylcholine transport-system. Trends Neurosci 10:174–177

Mazere J, Prunier C, Barret O, Guyot M, Hommet C, Guilloteau D, Dartigues JF, Auriacombe S, Fabrigoule C, Allard M (2008) In vivo SPECT imaging of vesicular acetylcholine transporter using [^{123}I]-IBVM in early Alzheimer's disease. NeuroImage 40:280–288

Mazere J, Meissner WG, Mayo W, Sibon I, Lamare F, Guilloteau D, Tison F, Allard M (2012) Progressive supranuclear palsy: in vivo SPECT imaging of presynaptic vesicular acetylcholine transporter with [I-123]-iodobenzovesamicol. Radiology 265:537–543

Mazere J, Meissner WG, Sibon I, Lamare F, Tison F, Allard M, Mayo W (2013) [^{123}I]IBVM SPECT imaging of cholinergic systems in multiple system atrophy: a specific alteration of the ponto-thalamic cholinergic pathways (Ch5-Ch6). Neuroimage Clin 3:212–217

Michaelson DM, Angel I (1981) Saturable acetylcholine transport into purified cholinergic synaptic vesicles. Proc Natl Acad Sci U S A 78:2048–2052

Mulholland GK, Jung YW (1992) Improved synthesis of [^{11}C]methylaminobenzovesamicol. J Label Compd Radiopharm 31:253–259

Mulholland GK, Jung YW, Wieland DM, Kilbourn MR, Kuhl DE (1993) Synthesis of [^{18}F]fluoroethoxy-benzovesamicol, a radiotracer for cholinergic neurons. J Label Compd Radiopharm 33:583–591

Mulholland GK, Wieland DM, Kilbourn MR, Frey KA, Sherman PS, Carey JE, Kuhl DE (1998) [^{18}F]fluoroethoxy-benzovesamicol, a PET radiotracer for the vesicular acetylcholine transporter and cholinergic synapses. Synapse 30:263–274

Nejad-Davarani S, Koeppe RA, Albin RL, Frey KA, Müller MLTM, Bohnen NI (2019) Quantification of brain cholinergic denervation in dementia with Lewy bodies using PET imaging with [^{18}F]FEOBV. Mol Psychiatry 24:322–327

Nishiyama S, Ohba H, Kobashi T, Nakamasu Y, Nakao H, Ogata T, Kitashoji T, Tsukada H (2014) Development of novel PET probe [^{11}C](R,R)HAPT and its stereoisomer [^{11}C](S,S)HAPT for vesicular acetylcholine transporter imaging: a PET study in conscious monkey. Synapse 68:283–292

Ogawa K, Shiba K (2018) In vivo and in vitro characteristics of radiolabeled vesamicol analogs as the vesicular acetylcholine transporter imaging agents. Contrast Media Mol Imaging 2018:4535476

Ogawa K, Kanbara H, Kiyono Y, Kitamura Y, Kiwada T, Kozaka T, Kitamura M, Mori T, Shiba K, Odani A (2013) Development and evaluation of a radiobromine-labeled sigma ligand for tumor imaging. Nucl Med Biol 40:445–450

Padakanti PK, Zhang X, Jin H, Cui J, Wang R, Li J, Flores HP, Parsons SM, Perlmutter JS, Tu Z (2014) In vitro and in vivo characterization of two ^{11}C-labeled PET tracers for vesicular acetylcholine transporter. Mol Imaging Biol 16:773–780

Parent M, Bedard MA, Aliaga A, Soucy JP, Landry St-Pierre E, Cyr M, Kostikov A, Schirrmacher E, Massarweh G, Rosa-Neto P (2012) PET imaging of cholinergic deficits in rats using [^{18}F]fluoroethoxybenzovesamicol ([^{18}F]FEOBV). NeuroImage 62:555–561

Parsons SM, Prior C, Marshall IG (1993) Acetylcholine transport, storage, and release. Int Rev Neurobiol 35:279–390

Petrou M, Frey KA, Kilbourn MR, Scott PJH, Raffel DM, Bohnen NI, Muller MLTM, Albin RL, Koeppe RA (2014) In vivo imaging of human cholinergic nerve terminals with (−)-5-[^{18}F]fluoroethoxybenzovesamicol: biodistribution, dosimetry, and tracer kinetic analyses. J Nucl Med 55:396–404

Prior C, Marshall IG, Parsons SM (1992) The pharmacology of vesamicol: an inhibitor of the vesicular acetylcholine transporter. Gen Pharmacol 23:1017–1022

Rogers GA, Parsons SM, Anderson DC, Nilsson LM, Bahr BA, Kornreich WD, Kaufman R, Jacobs RS, Kirtman B (1989) Synthesis, in vitro acetylcholine-storage-blocking activities, and biological properties of derivatives and analogues of trans-2-(4-phenylpiperidino)cyclohexanol (vesamicol). J Med Chem 32:1217–1230

Rogers GA, Kornreich WD, Hand K, Parsons SM (1993) Kinetic and equilibrium characterization of vesamicol receptor-ligand complexes with picomolar dissociation-constants. Mol Pharmacol 44:633–641

Rogers GA, Stone-Elander S, Ingvar M, Eriksson L, Parsons SM, Widen L (1994) ^{18}F-labelled vesamicol derivatives: syntheses and preliminary in vivo small animal positron emission tomography evaluation. Nucl Med Biol 21:219–230

Roghani A, Carroll PT (2002) Analysis of uptake and release of newly synthesized acetylcholine in PC12 cells overexpressing the rat vesicular acetylcholine transporter (VAChT). Mol Brain Res 100:21–30

Roghani A, Feldman J, Kohan SA, Shirzadi A, Gundersen CB, Brecha N, Edwards RH (1994) Molecular cloning of a putative vesicular transporter for acetylcholine. Proc Natl Acad Sci U S A 91:10620–10624

Ruberg M, Mayo W, Brice A, Duyckaerts C, Hauw JJ, Simon H, LeMoal M, Agid Y (1990) Choline acetyltransferase activity and [³H]vesamicol binding in the temporal cortex of patients with Alzheimer's disease Parkinson's disease, and rats with basal forebrain lesions. Neuroscience 35:327–333

Schäfer MK-H, Eiden LE, Weihe E (1998) Cholinergic neurons and terminal fields revealed by immunohistochemistry for the vesicular acetylcholine transporter. I. Central nervous system. Neuroscience 84:331–359

Scheunemann M, Sorger D, Wenzel B, Heinitz K, Schliebs R, Klingner M, Sabri O, Steinbach J (2004) Synthesis of novel 4- and 5-substituted benzyl ether derivatives of vesamicol and in vitro evaluation of their binding properties to the vesicular acetylcholine transporter site. Bioorg Med Chem 12:1459–1465

Schmitz TW, Mur M, Aghourian M, Bedard MA, Spreng RN (2018) Longitudinal Alzheimer's degeneration reflects the spatial topography of cholinergic basal forebrain projections. Cell Rep 24:38–46

Shiba K, Yano T, Sato W, Mori H, Tonami N (2002) Characterization of radioiodinated (−)-ortho-iodovesamicol binding in rat brain preparations. Life Sci 71:1591–1598

Shiba K, Ogawa K, Ishiwata K, Yajima K, Mori H (2006) Synthesis and binding affinities of methylvesamicol analogs for the acetylcholine transporter and sigma receptor. Bioorg Med Chem 14:2620–2626

Shiba K, Nishyama S, Tsukada H, Ishiwata K, Kawamura K, Ogawa K, Mori H (2009) The potential of (−)-o-[¹¹C]methylvesamicol for diagnosing cholinergic deficit dementia. Synapse 63:167–171

Sluder A, Shah S, Cassayre J, Clover R, Maienfisch P, Molleyres LP, Hirst EA, Flemming AJ, Shi M, Cutler P, Stanger C, Roberts RS, Hughes DJ, Flury T, Robinson MP, Hillesheim E, Pitterna T, Cederbaum F, Worthington PA, Crossthwaite AJ, Windass JD, Currie RA, Earley FG (2012) Spiroindolines identify the vesicular acetylcholine transporter as a novel target for insecticide action. PLoS One 7:e34712

Smith R, Chung H, Rundquist S, Maat-Schieman ML, Colgan L, Englund E, Liu YJ, Roos RA, Faull RL, Brundin P, Li JY (2006) Cholinergic neuronal defect without cell loss in Huntington's disease. Hum Mol Genet 15:3119–3131

Song H, Ming G, Fon E, Bellocchio E, Edwards RH, Poo M (1997) Expression of a putative vesicular acetylcholine transporter facilitates quantal transmitter packaging. Neuron 18:815–826

Sorger D, Schliebs R, Kampfer I, Rossner S, Heinicke J, Dannenberg C, Georgi P (2000) In vivo [¹²⁵I]-iodobenzovesamicol binding reflects cortical cholinergic deficiency induced by specific immunolesion of rat basal forebrain cholinergic system. Nucl Med Biol 27:23–31

Sorger D, Scheunemann M, Grossmann U, Fischer S, Vercouillie J, Hiller A, Wenzel B, Roghani A, Schliebs R, Brust P, Sabri O, Steinbach J (2008) A new ¹⁸F-labeled fluoroacetylmorpholino derivative of vesamicol for neuroimaging of the vesicular acetylcholine transporter. Nucl Med Biol 35:185–195

Sorger D, Scheunemann M, Vercouillie J, Grossmann U, Fischer S, Hiller A, Wenzel B, Roghani A, Schliebs R, Steinbach J, Brust P, Sabri O (2009) Neuroimaging of the vesicular acetylcholine transporter by a novel 4-[¹⁸F]fluoro-benzoyl derivative of 7-hydroxy-6-(4-phenyl-piperidin-1-yl)octahydro-benzo[1,4]oxazines. Nucl Med Biol 36:17–27

Szymoszek A, Wenzel B, Scheunemann M, Steinbach J, Schüürmann G (2008) First CoMFA characterization of vesamicol analogs as ligands for the vesicular acetylcholine transporter. J Med Chem 51:2128–2136

Tu Z, Efange SMN, Xu J, Li S, Jones LA, Parsons SM, Mach RH (2009) Synthesis and in vitro and in vivo evaluation of ¹⁸F-labeled positron emission tomography (PET) ligands for imaging the vesicular acetylcholine transporter. J Med Chem 52:1358–1369

Tu Z, Zhang X, Jin H, Yue X, Padakanti PK, Yu L, Liu H, Flores HP, Kaneshige K, Parsons SM, Perlmutter JS (2015) Synthesis and biological characterization of a promising F-18 PET tracer for vesicular acetylcholine transporter. Bioorg Med Chem 23:4699–4709

van der Zee S, Vallez Garcia D, Elsinga PH, Willemsen ATM, Boersma HH, Gerritsen MJJ, Spikman JM, van Laar T (2019) [¹⁸F]Fluoroethoxybenzovesamicol in Parkinson's disease

patients: quantification of a novel cholinergic positron emission tomography tracer. Mov Disord 34:924–926

Van Dort ME, Jung YW, Gildersleeve DL, Hagen CA, Kuhl DE, Wieland DM (1993) Synthesis of the ^{123}I- and ^{125}I-labeled cholinergic nerve marker (−)-5-iodobenzovesamicol. Nucl Med Biol 20:929–937

Vardy E, Arkin IT, Gottschalk KE, Kaback HR, Schuldiner S (2004) Structural conservation in the major facilitator superfamily as revealed by comparative modeling. Protein Sci 13:1832–1840

Varoqui H, Erickson JD (1996) Active transport of acetylcholine by the human vesicular acetyl-choline transporter. J Biol Chem 271:27229–27232

Voytko ML, Mach RH, Gage HD, Ehrenkaufer RL, Efange SM, Tobin JR (2001) Cholinergic activity of aged rhesus monkeys revealed by positron emission tomography. Synapse 39:95–100

Weihe E, Tao-Cheng JH, Schäfer MK, Erickson JD, Eiden LE (1996) Visualization of the vesicular acetylcholine transporter in cholinergic nerve terminals and its targeting to a specific population of small synaptic vesicles. Proc Natl Acad Sci U S A 93:3547–3552

Wenzel B, Hiller A, Fischer S, Sorger D, Deuther-Conrad W, Scheunemann M, Brust P, Sabri O, Steinbach J (2011) In vitro binding profile and radiosynthesis of a novel ^{18}F-labeled azaspi-rovesamicol analog as potential ligand for imaging of the vesicular acetylcholine transporter. J Label Compd Radiopharm 54:426–432

Wenzel B, Li Y, Kraus W, Sorger D, Sabri O, Brust P, Steinbach J (2012) Pyrrolovesamicols: synthesis, structure, and VAChT binding of two 4-fluorobenzoyl regioisomers. Bioorg Med Chem Lett 22:2163–2166

Widen L, Eriksson L, Ingvar M, Parsons SM, Rogers GA, Stone-Elander S (1992) Positron emission tomographic studies of central cholinergic nerve terminals. Neurosci Lett 136:1–4

Widen L, Eriksson M, Ingvar M, Parsons M, Rogers GA, Stone-Elander S (1993) PET studies of central cholinergic nerve terminals in animals and man. J Cereb Blood Flow Metab 33:S300

Yue X, Jin H, Liu H, Luo Z, Zhang X, Kaneshige K, Flores HP, Perlmutter JS, Parsons SM, Tu Z (2017) Synthesis, resolution, and in vitro evaluation of three vesicular acetylcholine transporter ligands and evaluation of the lead fluorine-18 radioligand in a nonhuman primate. Org Biomol Chem 15:5197–5209

Yue X, Luo Z, Liu H, Kaneshige K, Parsons SM, Perlmutter JS, Tu Z (2018) Radiosynthesis and evaluation of a fluorine-18 labeled radioligand targeting vesicular acetylcholine transporter. Bioorg Med Chem Lett 28:3425–3430

Zhu H, Duerr JS, Varoqui H, McManus JR, Rand JB, Erickson JD (2001) Analysis of point mutants in the *Caenorhabditis elegans* vesicular acetylcholine transporter reveals domains involved in substrate translocation. J Biol Chem 276:41580–41587

Zwart R, Vijverberg HP (1998) Four pharmacologically distinct subtypes of alpha4beta2 nicotinic acetylcholine receptor expressed in *Xenopus laevis* oocytes. Mol Pharmacol 54:1124–1131

PET Imaging of Vesicular Monoamine Transporters

33

Michael R. Kilbourn

Contents

M. R. Kilbourn (✉)
University of Michigan Medical School, Ann Arbor, MI, USA
e-mail: mkilbour@umich.edu

Abstract

The vesicular monoamine transporter type 2 (VMAT2) is a protein specifically located in the membrane of neurotransmitter storage vesicles of monoaminergic neurons (dopamine, serotonin, norepinephrine, and histamine) and was considered as a potential marker for noninvasive in vivo imaging of changes in mono-aminergic innervation in human neurological diseases. Development efforts towards suitably radiolabeled compounds for in vivo imaging using positron emission tomography (PET) yielded optimized carbon-11 ((+)-α-[^{11}C]dihydro-tetrabenazine, DTBZ) and fluorine-18 (9-O-(3-[^{8}F]fluoropropyl)dihydrotetra-benazine, AV-133) radioligands. Applications of VMAT2 radioligand imaging in animal models (mouse, rat, pig and nonhuman primate) and human studies of numerous neurodegenerative diseases (e.g., Parkinson's and related movement disorders, dementia with Lewy bodies), psychiatric diseases (e.g., schizophrenia), and drug abuse (cocaine, methamphetamine) have demonstrated that in vivo imaging of the VMAT2 provides a powerful tool to investigate changes of mono-aminergic innervation in human disease conditions.

Abbreviations

AD	Alzheimer's disease
AMPH	Amphetamine
AMPT	Alpha-methyl-para-tyrosine
AV-133	9-(3-Fluoropropyl)-10-methoxy-3-(2-methylpropyl)-1,3,4,6,7,11b-hexahydrobenzo[*a*]quinolizin-2-ol
COC	Cocaine
DASB	3-Amino-4-(2-dimethylaminomethylphenylsulfanyl)-benzonitrile
DLB	Dementia with Lewy bodies
DOPA	3,4-Dihydroxyphenylalanine
DTBZ	Dihydrotetrabenazine: 9,10-dimethoxy-3-(2-methylpropyl)-1,3,4,6,7,11b-hexahydrobenzo[*a*]quinolizin-2-ol
FDG	2-Fluoro-2-deoxy-ᴅ-glucose
FluoroDOPA	6-Fluoro-3,4-dihydroxyphenylalanine
FPBM	2-(2′-((Dimethylamino)methyl)-4′-(3-fluoropropoxy)phenylthio)benzenamine
FTD	Frontotemporal dementia

HD   Huntington's disease
HED   Hydroxyephedrine
IBVM   Iodobenzovesamicol
MDMA   3,4-Methylenedioxy-*N*-methylamphetamine
METH   Methamphetamine
MPH   Methylphenidate
MPP+   1-Methyl-4-phenylpyridinium
MPTP   1-Methyl-4-phenyl-2,3,5,6-tetrahydropyridine
MSA   Multiple system atrophy
MTBZ   Methoxytetrabenazine
OPCA   Olivopontocerebellar atrophy
PD   Parkinson's disease
PDD   Parkinson's disease with dementia
PET   Positron emission tomography
PIB   Pittsburgh compound B
PMP   *N*-methylpiperidinyl propionate
PSP   Progressive supranuclear palsy
RAC   Raclopride
SCZ   Schizophrenia
SPECT   Single photon emission computed tomography
TBZ   Tetrabenazine: 3-isobutyl-9,10-dimethoxy-1,3,4,6,7,11b-hexahydro-
                pyrido[2,1-*a*]isoquinolin-2-one
TS   Tourette's syndrome
VAChT   Vesicular acetylcholine transporter
VGAT   Vesicular GABA transporter
VGLUT   Vesicular glutamate transporter
VMAT   Vesicular monoamine transporter

33.1   Introduction

The simplified view of neurotransmission in the brain involves the biosynthesis of
neurotransmitters, transporter-mediated uptake, and concentration of the neu-
rotransmitter molecules within vesicles located in presynaptic terminals, stimulated
release of the vesicular contents through calcium-induced fusion of synaptic vesi-
cles with the neuronal membrane and exocytotic release of neurotransmitters into
the synapse and binding of the released neurotransmitters to post-synaptic recep-
tors. The removal of the neurotransmitter from the synapse can result from
transporter-mediated reuptake of neurotransmitter back across the neuronal mem-
brane into the cytosol, intra-synaptic catabolism, or simply diffusion out of the syn-
aptic space. Those neurotransmitter molecules recovered from the synapse and
transported back into the presynaptic terminal can then be metabolically degraded
by cytosolic enzymes or repackaged into vesicles for future release.
Radiopharmaceutical chemists have targeted every one of these steps for

development of in vivo radioligands (Zimmer and Luxen 2012): in the dopaminergic system, for example, this has produced useful radiotracers for neurotransmitter synthesis (e.g., [18F]fluoroDOPA), post-synaptic receptor binding (e.g., [11C]raclopride), presynaptic reuptake (e.g., [11C]methylphenidate), and catabolism (e.g., [11C]deprenyl) (Brooks and Pavese 2011). The last target for PET radiotracer development has been the vesicular neurotransmitter transporters.

As a critical part of this process of neurotransmission, the vesicular neurotransmitter transporters are synaptic vesicle proteins that actively transport newly synthesized or recovered cytosolic neurotransmitter molecules across the vesicle lipid bilayer and into the lumen. Separate transporters are found for each of the major classical neurotransmitters: VMAT1 (*SLC18A1*) and VMAT2 (*SLC18A2*) for the monoamines, VAChT (*SLC18A3*) for acetylcholine, VGAT (*SLC32A1*) for inhibitory amino acids, and VGLUT (*SLC17A6, SLC17A7, SLC17A8*) for the vesicular glutamate transporters (Eiden et al. 2004; Gasnier 2004; Omote et al. 2011). These vesicular transporters are located in the membranes of vesicles located in presynaptic terminals and have been targeted as potential biomarkers of specific neuronal populations (although the possibility of neurons expressing more than one vesicular transporter cannot be discounted (Munster-Wandowski et al. 2016; Silm et al. 2019)). As such, vesicular transporter targets complement the more extensive efforts expended in radioligand development for the neuronal membrane neurotransmitter transporters (Brooks and Pavese 2011), a structurally unrelated family of proteins responsible for the reuptake of intra-synaptic neurotransmitters across the synaptic membrane and into the cytosol.

Only two vesicular neurotransmitter transporters, the VMAT2 and VAChT, have been successfully targeted for development of in vivo radioligands for human studies. The development and applications of VMAT2 radioligands are described in the following sections. In contrast to VMAT2 radiotracer development, a wider variety of compounds have been radiolabeled as prospective in vivo imaging agents for the VAChT, but only two ([123I]IBVM for single photon emission computed tomography, [18F]FEOBV for positron emission tomography) have reached the stage of achieving approvals for human studies (Kuhl et al. 1994; Petrou et al. 2012a). At present the development of in vivo radioligands for the VGAT and VGLUT transporters is severely limited by a lack of structures known to be high affinity inhibitors that might serve as templates for radiotracer design (Thompson et al. 2005).

33.2 Biology and Pharmacology of the Vesicular Monoamine Transporter Type 2

33.2.1 Molecular Biology of the VMAT2

The VMAT2 is part of the family of amine transporters (Eiden et al. 2004) and transports single positively charged amine substrates into vesicles with a concomitant

extrusion of two protons. The accumulation of monoamines is thus dependent on a pH gradient maintained by the action of a separate membrane-bound ATPase. A crystal structure of the VMAT2 has not yet been achieved, but homology modeling has suggested a 12-transmembrane domain configuration with both the amino and carboxyl terminal ends within the cytoplasm and a large intracellular loop between transmembrane domains I and II (Wimalasena 2010; Yaffe et al. 2018). The structure of VMAT2 is highly conserved across mammalian species (Schafer et al. 2013). VMAT2 is the form found in the neurons of the brain, although it is also expressed in nerves and exocrine cells in a variety of peripheral organs. The structurally related VMAT1 (with 40% sequence homology) is predominantly located in organs outside the brain with highest concentrations in the adrenals, although recent studies have suggested the presence of VMAT1 in the mammalian brain (Lohoff et al. 1712). A functional monoaminergic neuron consists of the VMAT2 co-expressed with the necessary neurotransmitter-specific biosynthetic enzymes and corresponding neuronal membrane reuptake transporter (e.g., dopaminergic neurons have tyrosine hydroxylase, DOPA decarboxylase, and the dopamine transporter (DAT)). Homozygous knockout of the VMAT2 is lethal in mice, but heterozygous knockouts survive with reduced filling of neuronal vesicles (Miller et al. 2001). Genetic variants in the human *SLC18A2* gene are rare and produce a severe infantile parkinsonian disorder termed brain dopamine-serotonin vesicular transport disease (Jacobsen et al. 2016).

33.2.2 Localization of the VMAT2 in Mammalian Brain

In vitro studies of rodent and human brain tissues using the VMAT2 ligand [^{3}H]dihydrotetrabenazine ([^{3}H]DTBZ, originally termed [^{3}H]TBZOH) have demonstrated the concentration of the transporter in brain regions rich in monoaminergic neuronal synapses, with the highest concentrations in the basal ganglia, intermediate in such cell bodies as the substantia nigra, and low in the cortex (Scherman and Raisman 1988) (Table 33.1). Radioligand binding in the striatum is predominantly (>95%) to dopaminergic terminals; in other brain regions binding is likely due to a mixture of dopaminergic, serotonergic, and adrenergic innervation. The high concentration of VMAT2 in the basal ganglia has also been demonstrated using immunochemical techniques and a specific hVMAT2 antibody (Tong et al. 2011). Postmortem studies in human brains using radioligand binding or immunochemical staining techniques have demonstrated the significant loss of VMAT2 in the basal ganglia in neurodegenerative diseases such as Parkinson's disease (Scherman et al. 1989; Miller et al. 1998). The extremely low levels of VMAT2 in regions such as the occipital cortex or cerebellar cortex have proven advantageous for in vivo imaging, as these regions can then be used to estimate nonspecific distribution of radioligands for pharmacokinetic modeling purposes.

Table 33.1 Regional in vitro and in vivo binding data for VMAT2 radioligands in mouse, rat, and human brains (DV_{total} = total distribution volume)

Mouse	fmol/mg protein (Scherman and Raisman 1988)	[^{11}C]TBZ % inj dose/g (DaSilva and Kilbourn 1992)
Striatum	1345	4.96
Thalamus	111	2.06
Hippocampus	141	2.01
Hypothalamus	411	2.96
Pons-medulla	167	1.96
Cortex (frontal)	115	1.91
Cerebellum	56	1.76
Rat	fmol/mg protein (Vander Borght et al. 1995a)	[^{11}C]DTBZ DV_{total} (Kilbourn et al. 2002)
Striatum	1199	7.35
Thalamus	111–669	2.80
Hippocampus	124	2.51
Hypothalamic nuclei	838	5.13
Pons-medulla	–	–
Cortex (frontal)	103	2.18
Cerebellum	60	2.07
Human	fmol/mg protein (Scherman and Raisman 1988)	[^{11}C]DTBZ D DV_{total} (Vander Borght et al. 1995b)
Caudate	742	12.5
Putamen	766	11.7
Hypothalamus	245	–
Hippocampus	–3	–
Thalamus	–	4.75
Cortex (frontal)	–7	4.16
Cerebellum	–	4.06

33.2.3 VMAT2 Substrates and Inhibitors

The VMAT2 transports a wide variety of molecules, including not only the classical neurotransmitters DA, NE, and 5-HT but also many biogenic amines, drugs of abuse (e.g., amphetamines), and neurotoxins (e.g., 1-methyl-4-phenylpyridinium, MPP+). Substrates for the VMAT2 have typical low binding affinities (>100 μM) but high rates of transport. The wide variety of compounds known to be antagonists for the receptors and neuronal membrane transporters for the monoamines are ineffective inhibitors of either VMAT2 transport function or high affinity radioligand binding to the VMAT2 (Wimalasena 2010; Gonzalez et al. 1994).

When development of in vivo VMAT2 radioligands was begun, the list of known medium to high affinity ligands (agonist or antagonist) for the VMAT2 was limited to reserpine, tetrabenazine, and ketanserin, and decades later this situation has not appreciably changed. Reserpine is a large (MW = 608) complex alkaloid with an extremely high affinity for VMAT2 (K_D = 0.3 nM) and is essentially an irreversible inhibitor with a protracted effect on brain VMAT2 (Naudon et al. 1995): those

properties made it a poor candidate for in vivo radioligand development. Ketanserin has a moderate affinity for the VMAT2 ($K_D = 45$ nM) but also high affinity for serotonin receptors, making it also a less than optimal target for development of an in vivo imaging agent. Attempts at modification of the ketanserin structure have failed to yield compounds with potential as higher affinity and more specific radioligands (Darchen et al. 1989; Provencher et al. 2018). A series of compounds derived from lobelane (1,4-diphenylalkylpiperidines) were reported to be potent inhibitors of vesicular dopamine uptake, but they have only moderate affinities (>200 nM) for inhibition of [³H]DTBZ binding (Zheng et al. 2005; Nickell et al. 2016) and did not inhibit in vivo VMAT2 binding in a rat model (Kilbourn et al. 2010). Most recently, a new lead compound GZ-11610 (R-3-(4-methoxyphenyl)-N-(1-phenylpropan-2-yl) propane-1-amine was reported as a high affinity ($K_i = 8.7$ nM) inhibitor of DA uptake by the VMAT2 (Lee et al. 2018), but the potential use as an in vivo radioligand has not been investigated.

Tetrabenazine (TBZ: 3-isobutyl-9,10-dimethoxy-1,3,4,6,7,11b-hexahydropyrido[2,1-a]isoquinolin-2-one, Fig. 33.1) is one of a series of benzoisoquinolines initially developed by Hoffman-LaRoche (Quinn et al. 1959). For decades after its clinical introduction, there had been little further examination of the structure-affinity relationships of such benzoisoquinolizines for the VMAT2, but prompted by the interest in developing optimal radioligands for imaging, a larger sets of derivatives of tetrabenazine have been recently synthesized and evaluated in vitro and in vivo. As described in the following sections, these efforts have led to stereospecific syntheses of TBZ and its primary metabolite dihydrotetrabenazine (DTBZ: 9,10-dimethoxy-3-(2-methylpropyl)-1,3,4,6,7,11b-hexahydrobenzo[a]quinolizin-2-ol, Fig. 33.1) and
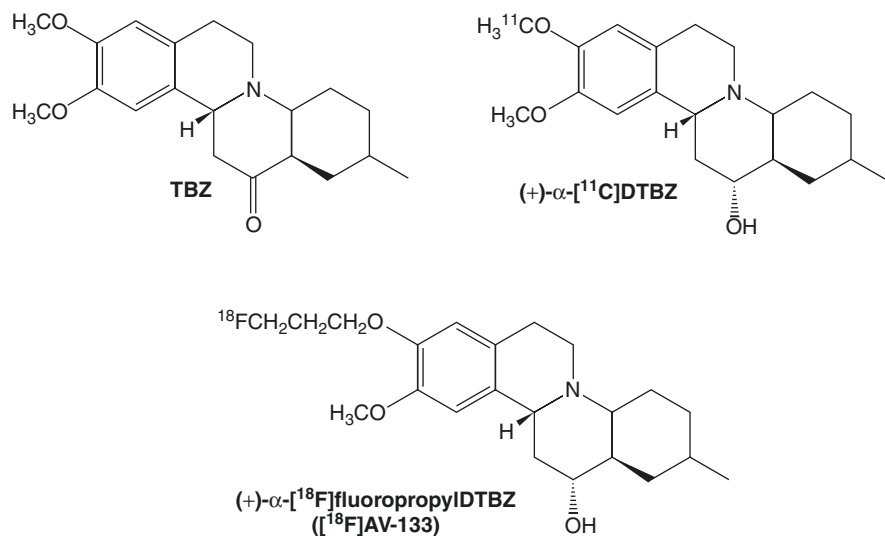
Fig. 33.1 Chemical structures for tetrabenazine (TBZ) and the two VMAT2 radioligands which have been most used for animal and human PET imaging studies, (+)-alpha-[¹¹C]DTBZ, and (+)-alpha-[¹⁸F]fluoropropylDTBZ ([¹⁸F]AV-133)

the modification of DTBZ with 2-alkyl substituents (Lee et al. 1996), altered 3-alkyl groups (Zheng et al. 2011), and substitutions of longer alkyl or fluoroalkyl chains for the 9-O-methyl substituent (Goswami et al. 2006; Hostetler et al. 2007).

33.3   VMAT2 Radioligands for Autoradiography

33.3.1 [³H]Tetrabenazine ([³H]TBZ)

Tritiated tetrabenazine was only recently reported (Rhee et al. 2011) using the catalytic reduction of a suitably constructed alkene precursor (1,3,4,6,7,11b-hexahydro-3-(2-methyl-2-propenyl)-9,10-dimethoxy-2-oxo-2H-benzo[a]quinolizine) with tritium gas to yield the [³H$_2$]tetrabenazine with a specific activity of 1850 GBq/mmol.

33.3.2 α-[³H]Dihydrotetrabenazine ([³H]DTBZ)

The tritiated form of α-dihydrotetrabenazine (originally termed TBZOH) was first reported in 1981 and prepared by the sodium borotritide reduction of the 2-ketone group of TBZ (Scherman et al. 1981). The radioligand was obtained as a mixture of the α- and β-isomers resulting from a non-stereospecific reduction of the ketone, and chromatographic purification likely gave the α-[³H]DTBZ (specific activity of 185–555 GBq/mmol) as a racemic mixture of enantiomers. The synthesis of the single isomer (+)-α -[³H]DTBZ (2*R*,3*R*,11b*R* configuration) was accomplished by O-methylation of (+)-α-9-O-desmethylDTBZ using [³H]methyl iodide, with a specific activity of 2923 GBq/mmol (Kilbourn and Sherman 1997). [³H]DTBZ remains the preferred in vitro radioligand for the VMAT2.

33.3.3 (±)-[³H]Methoxytetrabenazine ([³H]MTBZ)

In an attempt to prepare a radioligand with better long-term radiochemical stability than [³H]DTBZ, the derivative 2-(O-[³H]methyl)dihydrotetrabenazine ([³H]MTBZ, K_i = 3.9 nM) was prepared by alkylation (±)-α-DTBZ with tritiated methyl iodide (Vander Borght et al. 1995a). This tritiated molecule was considerably more stable and showed less radiolytic decomposition upon storage as compared to tritiated DTBZ.

33.3.4 [³H]/[¹²⁵I]Reserpine

Tritiated reserpine (292 Gbq/mmol) has been synthesized from [2,6-³H]3,4,5-trimethoxybenzoic acid and used for ex vivo autoradiography in rat brain. A radioiodinated reserpine derivative, 18-O-[3-(3-[¹²⁵I]iodo-4-azidophenyl-propionyl]methyl reserpate, has been used for photoaffinity labeling experiments with the VMAT2 (Sievert et al. 2007).

33.3.5 Radioiodinated Tetrabenazines

A radioiodinated derivative of tetrabenazine with an iodovinyl substituent at the 2-position was prepared in very high-specific activities (81,400 GBq/mmol) by an iododestannylation reaction (Kung et al. 1994) and obtained as a mixture of two isomers of which only one showed high affinity binding to the VMAT2 (K_D = 0.22 nM). The stereochemistries of the radioiodinated ligands have not been determined.

More recently, a 9-[131I]iodovinyl-DTBZ derivative was reported to show specific binding to the VMAT2 in rat brain using in vitro autoradiography (Cao et al. 2018). No in vivo studies have been reported.

33.3.6 Ketanserin Derivatives

Ketanserin is a moderate affinity (K_i = 45 nM) but nonspecific ligand for the VMAT2 (Darchen et al. 1988), and with appropriate pharmacological blocking of its other binding sites (e.g., serotonin receptors), two radioiodinated derivatives, 7-amino-8-[125I]iodoketanserin and 7-azido-8-[125I]iodoketanserin, have been used for in vitro autoradiography and photoaffinity labeling experiments (Darchen et al. 1989).

33.4 VMAT2 Radioligands for PET Imaging Studies

The development of VMAT2 radioligands for positron emission tomography (PET) began with the practical choice of TBZ as the initial target compound. The TBZ molecule has two phenolic methoxy groups suitable for radiolabeling using carbon-11 methyl iodide, and the resultant radioligand would be unchanged from the drug that had been in human use for decades; this avoided any worries about toxicology as the pharmacology and metabolism of the drug were very well-known.

33.4.1 [11C]Tetrabenazine ([11C]TBZ)

The labeling of tetrabenazine simply required removal of one of the O-methyl groups and replacement with the carbon-11 ($t_{1/2}$ = 20 min) labeled methyl group (DaSilva and Kilbourn 1992; DaSilva et al. 1993a). Although simple in concept, the cleavage of the phenolic methoxy group using reagents such as boron tribromide proved to be a difficult reaction and led to complex mixtures of the mono- and bis-demethylated products. Careful chromatography yielded a single pure product assigned as the 9-O-desmethyltetrabenazine, with the identification of the demethylation site (9 vs. 10) based on proton and carbon-13 NMR spectroscopy; that was later proved correct through a synthesis of 9-O-desmethyltetrabenazine by an independent and unambiguous route. The reaction of the free phenolic compound with [11C]methyl iodide under basic conditions gave the desired [11C]tetrabenazine in

modest yields and good specific activities (74000–92,500 GBq/mmol) (DaSilva et al. 1993a). At the time of its preparation and use in humans, [¹¹C]TBZ was obtained as a mixture of stereoisomers; based on later studies of DTBZ isomers (see below), the starting material and the final radiochemical product were both likely racemic mixtures of 3*R*,11b*R* and 3*S*,11b*S* enantiomers.

33.4.2 (±)-α-(9-O-[¹¹C]Methyl)Dihydrotetrabenazine ([¹¹C]DTBZ)

The consideration of the metabolic fate of TBZ in the human body led to the rapid realization that what was really desired for an in vivo imaging agent was the carbon-11 labeled DTBZ, which is formed by the action of carbonyl reductase in the liver and is the predominant chemical species in the bloodstream after administration of TBZ to rats or humans (Mehvar et al. 1987). That metabolite (previously termed TBZOH) had been used for years in tritiated form for in vitro studies of the VMAT2 (Scherman and Raisman 1988). The reduction of the ketone of TBZ by in vivo metabolism, or by chemical means in the laboratory, produces two isomers termed α- and β-DTBZ to denote the configuration of the newly created hydroxyl group. The α-isomer was identified as having the higher affinity in vitro for the VMAT2. The required precursor for radiolabeling was (±)-9-O-desmethylDTBZ, prepared in two steps from TBZ by reduction of the ketone followed by demethylation (Jewett et al. 1997). Alkylation with [¹¹C]methyl iodide produced (±)-α-(9-O-[¹¹C]methyl) DTBZ in moderate yields and useful specific activities (>59,200 GBq/mmol) but still as a racemic mixture of enantiomers.

33.4.3 2-(O-[¹¹C]Methyl)Dihydrotetrabenazine ([¹¹C]MTBZ)

In an attempt to alter and perhaps improve the metabolic disposition of VMAT2 radioligands, a new derivative with a [¹¹C]methoxy substituent at the 2-position was synthesized (DaSilva et al. 1993b). Prepared by reaction of (±)-DTBZ with [¹¹C]methyl iodide under strongly basic conditions, the radioligand 2-(O-[¹¹C]methyl) dihydrotetrabenazine (MTBZ: K_i = 3.9 nM) was successfully introduced into human studies (Vander Borght et al. 1995b). However, the radiochemical synthesis proved more difficult than the alkylation of the phenol (as done for [¹¹C]DTBZ), and with the development of (+)-α [¹¹C]DTBZ, MTBZ was not utilized further.

33.4.4 (+)-α-(9-O-[¹¹C]Methyl)Dihydrotetrabenazine ((+)-α-[¹¹C]DTBZ)

The last step in improvement of carbon-11 VMAT2 radiotracers was the development of (+)-α-(9-O-[¹¹C]methyl)DTBZ ((+)-α-[¹¹C]DTBZ, Fig. 33.1). That TBZ and its metabolite DTBZ were mixtures of stereoisomers which had been known for many years (Schwartz et al. 1966), but the isomers had not been isolated, and their

absolute configurations had not been determined. The enantiomers of racemic α-DTBZ were finally isolated by preparative chiral HPLC (Kilbourn et al. 1995a; Kilbourn et al. 1997) providing a high affinity (+)-isomer (K_i = 1 nM) and low affinity (−)-isomer (K_i = 2200 nM). Crystals of (−)-α-DTBZ were successfully grown for X-ray structural analysis, and the absolute stereochemistry of the isomers finally assigned: (2*R*,3*R*,11b*R*) for the (+)-isomer and (2*S*,3*S*,11b*S*) for the (−)-isomer (Kilbourn et al. 1997; Liu et al. 2012; Liu et al. 2013). The interest in the stereoisomers of DTBZ as imaging agents and potential drugs stimulated numerous new and improved synthetic routes to TBZ and DTBZ (Boldt et al. 2008; Paek et al. 2010; Rishel et al. 2009a) including the preparation and characterization of all eight possible DTBZ stereoisomers (Tridgett et al. 2008; Yu et al. 2010; Yao et al. 2011). Determination of the in vitro binding affinities have consistently shown that the isomer with the 2*R*,3*R*,11b*R* absolute stereochemistry is the highest affinity DTBZ ligand for the VMAT2 (Fig. 33.1).

The synthesis of (+)-α-[^{11}C]DTBZ required the preparation of the resolved (+)-isomer of the 9-O-desmethylDTBZ, which was first accomplished by a low-yield sequence using reduction of TBZ, isolation of the racemic α-isomer, chiral column HPLC resolution, and a modified demethylation reaction condition using sodium hydride/N-methylaniline/hexamethylphosphoramide (Kilbourn et al. 1997). The more recent improved synthetic routes to TBZ, (+)-α DTBZ, and (+)-α-9-O-desmethylDTBZ have made synthesis of the precursor much more practical. Alkylation of the desmethyl precursor with [^{11}C]methyl iodide (Jewett et al. 1997) or [^{11}C]methyl triflate (Zhang et al. 2012) provided a reliable route to preparation of (+)-α-[^{11}C]DTBZ in high average specific activities (370,000 GBq/mmol) and a defined 2*R*,3*R*,11b*R* stereochemistry.

33.4.5 (+)-α-(10-O-[^{11}C]Methyl)Dihydrotetrabenazine

The synthesis and in vivo evaluation of DTBZ labeled in the 10-methoxy position was recently accomplished (Huang et al. 2016). Racemic 10-O-desmethylDTBZ was resolved using fractional crystallization and then reduced to yield the desired (+)-α-(10-desmethyl)DTBZ. Alkylation with [^{11}C]methyl iodide formed (+)-α-(10-[^{11}C]methyl)DTBZ. MicroPET imaging in rat brains showed specific uptake in the striatum with striatum-to-cerebellum ratios reportedly higher than for the corresponding 9-[^{11}C]methoxyDTBZ. No human studies have been reported for this radiotracer.

33.4.6 Copper-64 Labeled Dihydrotetrabenazine

In an attempt to develop a VMAT2 radioligand labeled with a longer-lived PET radionuclide, a 2-amino derivative of DTBZ was conjugated with the chelating group 2,2′-(1,4,8,11-tetraazabicyclo[6.6.2]hexadecane-4,11-diyl)diacetic acid

(Kumar et al. 2014). Complexation of copper-64 yielded a radioligand with an in vitro IC_{50} of 16.8 nM. No in vivo studies of this radioligand have been reported.

33.4.7 Fluorine-18 Labeled Dihydrotetrabenazines

The application of VMAT2 imaging to widespread clinical care would require the availability of radioligands labeled with longer half-life radionuclides. Fortunately, development of fluorine-18 ($t_{1/2}$ = 109.6 min) labeled VMAT2 radioligands was able to build on the experience developed in the carbon-11 series.

The substitution of the 9-methoxy group of DTBZ with [18F]fluoroalkoxy groups resulted in the syntheses of 9-O-[18F]fluoromethyl-, 9-O-(2-[18F]fluoroethyl)- and 9-O-(3-[18F]fluoropropyl)DTBZ. The [18F]fluoromethyl derivative (K_i = 0.87) was prepared by O-alkylation of (+)-α-9-O-desmethylDTBZ with [18F]FCH$_2$Br under basic conditions (Hostetler et al. 2007). The [18F]fluoroethyl (K_i = 0.76 nM) and [18F]fluoropropyl (K_i = 0.56 nM) derivatives were first prepared in racemic form by [18F]fluoride ion displacement of the corresponding mesylates in specific activities >74,000 GBq/mmol (Goswami et al. 2006; Kung et al. 2007). Subsequently, stereospecific syntheses of (+)-α-9-O-(3-[18F]fluoropropyl)DTBZ (also termed [18F]AV-133: (2*R*,3*R*,11b*R*)-9-(3-[18F]fluoropropoxy)-10-methoxy-3-(2-methylpropyl)-1,3,4,6,7,11b-hexahydro-2*H*-benzo[*a*]quinolizin-2-ol)) from the corresponding chiral mesylate or tosylate were developed (Li et al. 2017), yielding the very high affinity (K_i = 0.1 nM) single isomer with specific activities of 55,000–74,000 GBq/mmol. As was expected, the (−)-α-(3-fluoropropyl)DTBZ isomer showed negligible affinity for VMAT2 (>3000 nM). Recently, attempts were made to reduce in vivo metabolism of the [18F]fluoroalkyl DTBZ radioligands using deuterium substitutions on the fluoroalkyl groups, but significant improvements of the radiotracer imaging properties were not achieved (Varone et al. 2012; Liu et al. 2018).

As of the start of 2019, the only fluorine-18 radioligand that had reached human studies was the [18F]fluoropropyl derivative [18F]AV-133. A variety of other compounds had, however, been synthesized and radiolabeled with fluorine-18. Replacement of the 2-hydroxyl group of DTBZ with a 2-fluoropropylamino group yielded a derivative with an in vitro K_i of 7 nM (as racemate) (Zhu et al. 2009). Substitution of the 2-hydroxyl function of 2-[18F]fluoropropyl-(+)-DTBZ with an epoxide ring provided a derivative with an excellent in vitro affinity (K_i = 0.08 ± 0.01 nM) (Kung et al. 2008). Attempts to change the 3-alkyl group resulted in reduced in vitro binding affinities (Zheng et al. 2011). A completely different approach to fluorine-18 labeled DTBZ molecules was reported in a series of patents (Kankanamalage et al. 2009; Rishel et al. 2009; Amarasinghe et al. 2009) that claimed a large number of fluorine-substituted (+)-α-DTBZ derivatives, but in vitro biological information is only available for a few of the compounds claimed: the 2-fluoroethynyl substituted DTBZ derivative showed reasonable affinity

(K_i = 19 nM), consistent with the earlier demonstration of bulk tolerance of reasonably small 2-alkyl substituents (Lee et al. 1996), and the 2-fluoroethoxy ether derivative had a good in vitro binding affinity of 3.2 nM, which was not significantly different than that previously obtained for the slightly smaller methyl ether derivative (Vander Borght et al. 1995a).

33.5 Evaluation of VMAT2 Imaging Radioligands in Animals

The evaluation of VMAT2 radioligands for pharmacological specificity, kinetics, sensitivity to endogenous neurotransmitters, propensity for up- or downregulation, and changes in models of human disease has been extensively pursued in both small and large animal models (Table 33.2).

33.5.1 Mouse Brain VMAT2 Studies

The mouse was utilized for the initial evaluation of [^{11}C]TBZ, where it was demonstrated that (a) the radioligand localized in regions of the brain containing high concentrations of the VMAT2, (b) localization was likely not specific only to dopaminergic neurons but, as expected, also due to noradrenergic and serotonergic innervation (Table 33.1), and (c) binding could be blocked by pharmacological doses of TBZ but not drugs that bound to the neuronal membrane dopamine transporter (DaSilva and Kilbourn 1992).

Subsequent studies (Table 33.2) of VMAT2 radioligands ([^{11}C]DTBZ, [^{11}C]MTBZ, and [^{18}F]AV-133) binding in the mouse brain demonstrated that simple

Table 33.2 Animal studies using VMAT2 radioligands

Species	Radioligands	Topic	Ref.
Mouse	[^{11}C]TBZ	First in vivo studies	DaSilva and Kilbourn (1992)
	[^{11}C]TBZ	Brain distribution in vivo, metabolism, dosimetry	DaSilva et al. (1994)
	[^{11}C]MTBZ	Study in *tottering* mice	Kilbourn et al. (1995b)
	(+)- and (−)-[^{11}C]DTBZ	Stereospecificity of in vivo binding	Kilbourn et al. (1995a)
	(±)-[^{11}C]MTBZ	Binding in different mouse strains	Kilbourn and Frey (1996)
	(±)-[^{11}C]MTBZ	Evaluation of DTBZ derivatives	Lee et al. (1996)
	(±)-[^{11}C]MTBZ	Binding site recovery after TBZ dose	Kilbourn (1997)
	(+)-[^{11}C]DTBZ,[^{11}C]MPH	Differential VMAT2, DAT binding in MPTP mice	Kilbourn et al. (2000)
	[^{18}F]FE-DTBZ, [^{18}F]FP-DTBZ	Evaluation of new fluoroalkyl DTBZ derivatives	Goswami et al. (2006)
	[^{18}F]AV-133	PET and in vitro autoradiography in MPTP mice	Chao et al. (2012)
	[^{18}F]AV-133	PET imaging of MPTP mice	Toomey et al. (2012)
	[^{18}F]AV-133	MPTP mice treated with magnolol	Weng et al. (2017a)
	(+)-[^{11}C]DTBZ	Effect of methcathinone	Asser et al. (1652)

Table 33.2 (continued)

Species	Radioligands	Topic	Ref.
Rat	[^{125}I]IodovinylTBZ	In vitro autoradiography	Kung et al. (1994)
	[^{3}H]MTBZ	Autoradiography: Effects of drug treatments	Vander Borght et al. (1995c)
	[^{3}H]MTBZ	Autoradiography in 6-OHDA lesioning	Vander Borght et al. (1995a)
	(±)-[^{11}C]DTBZ	Ex vivo studies: DA-ergic drug treatments	Kilbourn et al. (1996)
	[^{3}H]DTBZ	Bolus vs. equilibrium rat studies	Kilbourn and Sherman (1997)
	[^{3}H]DTBZ	Autoradiography in METH-treated rats	Frey et al. (1997)
	[^{3}H]MTBZ	In vitro studies: Effects of DA-ergic drug treatments	Kemmerer et al. (2003)
	(+)-[^{3}H]DTBZ, [^{3}H]MPH	Equilibrium infusion technique	Kilbourn et al. (2002)
	(+)-[^{3}H]DTBZ, (+)-[^{11}C]DTBZ	Long-term reproducibility ex vivo	Kilbourn (2004)
	(±)-[^{11}C]DTBZ	6-OHDA treated rats	Strome et al. (2000)
	[^{18}F]FP-DTBZ, (+)-[^{11}C]DTBZ	microPET imaging: Pharmacokinetics	Kilbourn et al. (2007)
	[^{18}F]FP-DTBZ (AV-133)	First brain uptake studies	Kung et al. (2007)
	(+)-[^{11}C]DTBZ	Unilateral 6-OHDA reproducibility	Sossi et al. (2007)
	(±)-[^{11}C]DTBZ	Effects of AMPT, AMPH	Tong et al. (2008)
	(+)-[^{11}C]DTBZ, [^{11}C]MPH	Sensitivity to DA levels	Kilbourn et al. (2010a)
	(+)-[^{11}C]DTBZ, [^{11}C]MPH, [^{11}C]RAC	Unilateral 6-OHDA: Effects of pramipexole and levodopa	Sossi et al. (2010a)
	[^{18}F]AV-133, [^{18}F]FPBM	Study of VMAT2 and SERT in 6-OHDA lesioned rat	Wang et al. (2010)
	(+)-[^{11}C]DTBZ	Competition by lobelane derivative	Kilbourn et al. (2010)
	(±)-[^{11}C]DTBZ	Intranigral lactacystin	Mackey et al. (2013)
	(±)-[^{11}C]DTBZ, [^{19}F]FDOPA	Longitudinal studies in unilateral 6-OHDA rats	Walker et al. (2013a)
	(±)-[^{11}C]DTBZ, [^{19}F]FDOPA	PET and DA microdialysis in 6-OHDA rats	Walker et al. (2013b)
	[^{18}F]AV-133, [^{19}F]AV-133	Compare LC-MS/MS for cold ligand vs. in vivo [^{18}F]ligand	Deng et al. (2014)
	(±)-[^{11}C]DTBZ, [^{18}F]FDOPA, [^{11}C]RAC	PET imaging normal rats	Lara-Camacho et al. (2014)
	10-[^{11}C]methoxy-DTBZ	PET in 6-OHDA rats	Li et al. (2014)
	(±)-[^{11}C]DTBZ	PET in over-expression of α-synuclein	Phan et al. (2017)
	[^{18}F]AV-133	Effect of impurity on brain binding	Wu et al. (2015)
	(±)-[^{11}C]DTBZ	Uni- and bilateral 6-OHDA lesions PET	Molinet-Dronda et al. (2015)
	[^{18}F]FP-DTBZ	Effects of anesthesia on imaging	Chen et al. (2016)
	10-([^{11}C]methoxy)-DTBZ	In vivo comparison with 9-([^{11}C]methoxy)DTBZ	Huang et al. (2016)
	[^{18}F]FP-DTBZ	PET after unilateral lactacystin injection	Weng et al. (2017b)
	(±)-[^{11}C]DTBZ	6-OHDA and lactacystin lesions	Mejias et al. (2016)
	(±)-[^{11}C]DTBZ	Test-retest reproducibility	Avendaño-Estrada and Ávila-Rodríguez (2018)
	d$_6$-[^{18}F]FP-DTBZ	Effects of deuteration on in vivo binding and metabolism	Liu et al. (2018)
	[^{18}F]FP-DTBZ	Longitudinal PET study	Jiang et al. (2018)

Table 33.2 (continued)

Species	Radioligands	Topic	Ref.
Minipigs	(+)-[¹¹C]DTBZ	Before and after lactacystin treatment	Lillethorup et al. (2018a)
	(+)-[¹¹C]DTBZ, [¹¹C]PK11195	Over-expression of α-synuclein	Lillethorup et al. (2018b)
	(+)-[¹¹C]DTBZ, [¹¹C]yohimbine, [¹¹C]DASB, [¹¹C]PK11195	Chronic lactacystin	Lillethorup et al. (2018c)
Guinea pigs	[¹⁸F]FP-DTBZ	Retina imaging and experimental myopia	Sun et al. (2018)
Primate	(±)-[¹¹C]TBZ	Normal and unilateral MPTP lesion	DaSilva et al. (1993c)
	[³H]DTBZ	In vitro after METH in baboons	Villemagne et al. (1998)
	(±)-[¹¹C]DTBZ	PET in METH treated monkeys	Fantegrossi et al. (2004)
	(+)-[¹¹C]DTBZ, [¹⁸F]FDOPA	Normal and MPTP lesioned	Doudet et al. (2006)
	(+)-[¹¹C]DTBZ, (±)-FP-DTBZ, (+)-FP-DTBZ	Comparison of pharmacokinetics via PET	Kilbourn et al. (2007))
	(+)-[¹¹C]DTBZ	Dosimetry study in baboon	Murthy et al. (2008)
	(+)-[¹¹C]DTBZ, [¹¹C]RAC, [¹¹C]PK11195, [¹¹C]WIN35428	Baboon chronic MPTP study	Chen et al. (2008)
	(+)-[¹¹C]DTBZ, [¹⁸F]FDOPA	Normal and MPTP lesioned	Collantes et al. (2008)
	(+)-[¹¹C]DTBZ, [¹⁸F]FDOPA	MPTP treated	Blesa et al. (2010)
	(+)-[¹¹C]DTBZ, [¹⁸F]FDOPA	Slow MPTP intoxication	Blesa et al. (2012)
	(+)-[¹¹C]DTBZ, [¹¹C]CFT	In vitro studies—Unilateral MPTP	Tian et al. (2012)
	(+)-[¹¹C]DTBZ, [¹¹C]CFT, [¹⁸F]FDOPA	MPTP monkey and study of apathy	Brown et al. (2012)
	(+)-[¹¹C]DTBZ, [¹¹C]CFT, [¹⁸F]FDOPA	MPTP monkey and in vitro nigral cell counts	Karimi et al. (2013b)
	(+)-[¹¹C]DTBZ, [¹⁸F]FDOPA	MPTP monkey the carboxyfullerene treatment	Dugan et al. (2014)
	[¹⁸F]AV-133	Progressive losses in MPTP monkey	Liu et al. (2014)
	(+)-[¹¹C]DTBZ, [¹¹C]CFT, [¹⁸F]FDOPA	MPTP monkey and in vitro biochemistry	Tian et al. (2014)
	(+)-[¹¹C]DTBZ, [¹¹C]CFT, [¹⁸F]FDOPA	MPTP monkey, various doses, apathy study	Tian et al. (2015)
	(+)-[¹¹C]DTBZ	Changes in chronic cocaine self-administration	Narendran et al. (2015)
	(+)-[¹¹C]DTBZ	Long-term reproducibility of PET measures	Kilbourn and Koeppe (2017)

measurement of tissue ratios between high (striatum) and low (cerebellum) regions of the mouse brain could be used to demonstrate the stereospecificity (Kilbourn et al. 1995a) and reversibility of [¹¹C]DTBZ binding to the VMAT2 [37]; measure decreases of VMAT2 binding sites after MPTP (1-methyl-4-phenyl-1,2,3,4-terahydropyridine) lesioning (Kilbourn et al. 2000; Chao et al. 2012; Toomey et al. 2012; Weng et al. 2017a) and shows increased in vivo binding in *tottering* mutant mice known to over-express the VMAT2 (Kilbourn et al. 1995b). In vivo measure of VMAT2 binding in MPTP-treated mice can also be used to evaluate potential therapeutic drug approaches (Weng et al. 2017a).

33.5.2 Rat Brain VMAT2 Studies

A larger number of studies of VMAT2 radioligands have been conducted in rats (for refs. see Table 33.2). These have utilized a variety of techniques, including (a) ex vivo measurements of tissue distributions following bolus injections, (b) ex vivo autoradiography of rat brain slices, (c) ex vivo determination of regional brain distributions after equilibrium infusions (Kilbourn et al. 2002), and (d) in vivo PET imaging studies including dynamic multi-tracer approaches (Sossi et al. 2009). Such studies consistently demonstrated the expected regional distribution of VMAT2 binding sites in the rat brain (Table 33.1), and studies of both the active and inactive stereoisomers of [^{11}C]DTBZ have shown that uptake and retention of VMAT2 radioligands in regions of the rat brain such as the cerebellum and the occipital cortex represents essentially negligible concentrations of the VMAT2 (Kilbourn et al. 2002), and thus those brain regions are suitable for estimations of nonspecific distributions of these radiotracers.

The sensitivity of measures of VMAT2 radioligand binding to regulation by chronic drug use has been examined both in vitro and in vivo, with decidedly mixed results. Several studies have demonstrated that chronic administration of such drugs as L-DOPA/benserazide, apomorphine, tetrabenazine, pramipexole, paroxetine, amphetamine, or cocaine did not alter in vitro levels of VMAT2 radioligand binding, nor was in vivo DTBZ binding altered by repeated administration of L-DOPA, deprenyl, or tetrabenazine (Kemmerer et al. 2003; Kilbourn et al. 1996; Schwartz et al. 2006; Vander Borght et al. 1995c; Vilpoux et al. 2000; Wilson and Kish 1996). These results supported the hypothesis that VMAT2 was a less regulated site than, for example, the neuronal membrane dopamine transporter for which changes could be seen following such drug treatments (Vander Borght et al. 1995c). In contrast, other studies have reported increases or decreases of VMAT2 radioligand binding after administration of some of the same or related drug substances (Schwartz et al. 2006; Frey et al. 1997; Sossi et al. 2010a). Drug effects can be dose-dependent, as seen for methamphetamine where reductions of VMAT2 binding are observed after neurotoxic but not lower behaviorally effective doses (Frey et al. 1997). For methcathinone (an analog of methamphetamine), an increase in VMAT2 radioligand binding was reported; that was attributed to a decrease of tissue dopamine levels and less competition of the neurotransmitter for the TBZ binding site on the VMAT2 (Asser et al. 1652). That was consistent with a few earlier studies in rats that supported a sensitivity of in vivo VMAT2 radioligand binding to drugs which directly decrease endogenous dopamine levels (e.g., α-methyl-p-tyrosine) (Kilbourn et al. 2008; Kilbourn et al. 2010a; Tong et al. 2008) or indirectly raise dopamine levels (pramipexole) (Sossi et al. 2010a). Those studies have indicated that alterations of vesicular dopamine concentrations may affect in vivo VMAT2 radioligand binding to the TBZ site located on the lumen surface of the vesicle, although it is noted that modest changes of in vivo radioligand binding (36% increase) required significant depletion of endogenous dopamine concentrations (>75%) in the rat brain.

To demonstrate losses of VMAT2 radioligand ([^{11}C]DTBZ or [^{18}F]AV-133) binding in rat models of neurodegeneration, investigators have widely used the

unilateral injection of 6-hydroxydopamine directly into the medial forebrain bundle (MFB: unilateral lesion) or the third ventricle (bilateral lesion) (for refs. see Table 33.2). This technique can produce a wide range of striatal lesions, from mild to severe, with a corresponding range of losses of VMAT2 radioligand binding. The decreased VMAT2 radioligand binding correlates with estimates of denervation from behavioral studies or in vitro autoradiographic studies of VMAT2 or DAT ligand binding. Using dynamic microPET imaging, the losses of radioligand binding were shown to be due to changes in numbers of VMAT2 binding sites (B_{max}) and not the apparent binding affinity (K_d^{app}) (Sossi et al. 2007). Used in combination with microPET studies with 6-[^{18}F]fluoroDOPA, the longitudinal changes in DA synthesis, and turnover and estimates of the compensatory changes in dopamine turnover (synthesis + vesicular trapping) after 6-OHDA lesions have been made (Walker et al. 2013a; Walker et al. 2013b).

Alternative models of dopaminergic degeneration in the rat brain have also been examined using VMAT2 radioligands. The stereotactic unilateral injection of lactacystin (a ubiquitin proteasome system inhibitor) into the substantia nigra produced dose-dependent decreases in VMAT2 radioligand binding (PET using [^{11}C]DTBZ or [^{18}F]AV-133) in the ipsilateral striatum, with losses of tyrosine hydroxylase immunoreactive cells (Mackey et al. 2013; Weng et al. 2017b). As a model of striatal dopaminergic terminal loss without nigral cell loss, the local unilateral injection of recombinant adeno-associated viral vectors coding for human α-synuclein produces α-synuclein deposits, motor impairments, and significant reductions in VMAT2 radioligand binding demonstrated both in vitro ([^{3}H]DTBZ autoradiography) and in vivo (^{11}C]DTBZ/PET) (Phan et al. 2017).

33.5.3 VMAT2 Radioligand Studies in Non-human Primates

A comprehensive autoradiographic study of the in vitro distribution of VMAT2 radioligand binding sites in the non-human primate brain is still missing from the literature, but specific binding in the caudate and putamen has been demonstrated (Chen et al. 2008; Tian et al. 2012; Blesa et al. 2012). The in vivo distribution of radiotracer binding would be expected to be consistent with the general distribution in mammalian brain as no significant species differences in brain VMAT2 distributions have been noted (Schafer et al. 2013). In contrast to the use of VMAT2 radioligands in rodent brain, all primate studies using PET radioligands have utilized in vivo imaging techniques (for refs. see Table 33.2). Such PET studies in normal primate brain have shown high binding in the striatal regions, with intermediate levels of radioactivity retention in the thalamus, hypothalamus, and midbrain cell bodies (raphe nucleus, locus ceruleus, substantia nigra), and negligible binding in cortex and cerebellum. The binding of [^{11}C]DTBZ and [^{18}F]AV-133 is stereospecific for the (+)-isomer ($2R$,$3R$,11bR-configuration) with low and uniform brain distribution of the corresponding inactive (−)-isomers (Kilbourn et al., unpublished data). A direct comparison of (+)-[^{11}C]DTBZ and [^{18}F]AV-133 demonstrated a higher striatal value for the distribution volume ratio (DVR, a measure of the specific

binding) for the fluorinated radioligand. A longitudinal study of (+)-[¹¹C]DTBZ binding in monkey brain has shown good reproducibility with little age effect over a 6-year span (8- to 14-year-old rhesus monkey) (Kilbourn and Koeppe 2017), although an age-dependent reduction of [¹¹C]DTBZ was noted by others when the comparison is made between young (8-year old) and older (22-year old) monkeys (Doudet et al. 2006).

To study dopaminergic degeneration in the monkey brain, investigators have uniformly utilized the MPTP lesion model. The initial demonstration of complete loss of VMAT2 radioligand binding in a monkey with a severe unilateral MPTP-induced lesion (DaSilva et al. 1993c) has been followed by numerous investigations in monkeys (Table 33.2) with either unilateral or bilateral lesions. Several studies have employed multi-tracer PET studies combining a VMAT2 radioligand ([¹¹C]DTBZ or [¹⁸F]AV-133) together with [¹⁸F]fluoroDOPA (a measure of dopamine synthesis and storage) and a DAT radioligand (e.g., [¹¹C]CFT), with some studies including postmortem tissue analyses (VMAT2 and DAT autoradiography, TH histochemistry, stereological cell counts in nigra: for references see Table 33.2). All studies have shown decreases of VMAT2 radioligand binding in MPTP-treated animals. The extent of the decreased VMAT2 binding correlates with the severity of the lesions, as indicated by losses of striatal dopamine (Karimi et al. 2013a) as well as changes in DAT radioligand binding or [¹⁸F]fluoroDOPA uptake and retention. In several studies, there is evidence to support that the in vivo measures with VMAT2 radioligands provided an earlier indication of loss of striatal dopaminergic terminals, as compared to DAT radioligands or [¹⁸F]fluoroDOPA uptake (Chen et al. 2008; Blesa et al. 2012; Doudet et al. 2006; Blesa et al. 2010).

The MPTP monkey model replicates most of the biochemical and behavioral changes of human PD, and the dosing of nonhuman primates with MPTP (Masilamoni and Smith 2018) provides a readily accessible and useful model to evaluate in vivo imaging radiotracers. The MPTP model provides a primate option for evaluation of potential pharmacological interventions to prevent or ameliorate dopaminergic degeneration, where PET imaging of the VMAT2 binding can serve as a biomarker (Dugan et al. 2014).

The MPTP intoxication model is thus widely used, but the potential of drugs of abuse to produce dopaminergic terminal losses has also been of interest. A single study of the potential changes of in vivo [¹¹C]DTBZ binding in a primate model of self-administration of methylenedioxymethamphetamine (MDMA) showed no evidence of dopaminergic degeneration in the striatum (Fantegrossi et al. 2004). In contrast, a postmortem study of amphetamine-treated baboons showed evidence for reduced binding of [³H]DTBZ to the VMAT2 (and reduced radioligand binding to the DAT) (Ricuarte et al. 2005). A PET imaging study of [¹¹C]DTBZ binding in monkeys after 16 months of cocaine self-administration demonstrated a significant (−25%) loss of striatal VMAT2 binding sites (Narendran et al. 2015): it was not determined if this was due to a downregulation of the VMAT2 or loss of dopaminergic terminals.

33.6 Applications of VMAT2 Radioligands in Human Imaging Studies

The first human studies of the VMAT2 using in vivo imaging with PET were reported in 1993 using racemic [^{11}C]tetrabenazine (Kilbourn et al. 1993), prompting additional years of radiotracer development culminating in the 2008 introduction into human use of a fluorine-18 labeled derivative, 9-(3-[^{18}F]fluoropropyl)-α-(+)-dihydrotetrabenazine ([^{18}F]AV-133) (Frey et al. 2008). The combination of improved VMAT2 radioligands with advancements in PET imaging instrumentation and image analysis resulted in significantly improved imaging of the transporter sites in the human brain (Fig. 33.2). As of the beginning of 2019, there were nearly 100 peer-reviewed publications using PET radioligands for VMAT2 imaging in humans, with thousands of subjects (Table 33.3). The majority of such studies have utilized [^{11}C]DTBZ, but there has been an increasing use of the fluorine-18 radioligand [^{18}F]AV-133.

33.6.1 Pharmacokinetic Studies of VMAT2 Radioligands in Normal Brain

The in vivo regional distribution of VMAT2 binding (Table 33.1) and pharmacokinetics of (+)-α-[^{11}C]DTBZ in the normal human brain have now been thoroughly studied. Initial evaluation of radioligand binding was done using bolus radiotracer

Fig. 33.2 Representative human PET images demonstrating how the development of better radioligands resulted in improvements of image quality and the estimation of specific binding (BP, binding potential) in normal subjects through the years

+/− [^{11}C]TBZ
BP = 0.96

+/− [^{11}C]DTBZ
BP = 1.49

+/− [^{11}C]DTBZ
BP = 2.56

+/− [^{18}F]AV-133
BP = 3.97
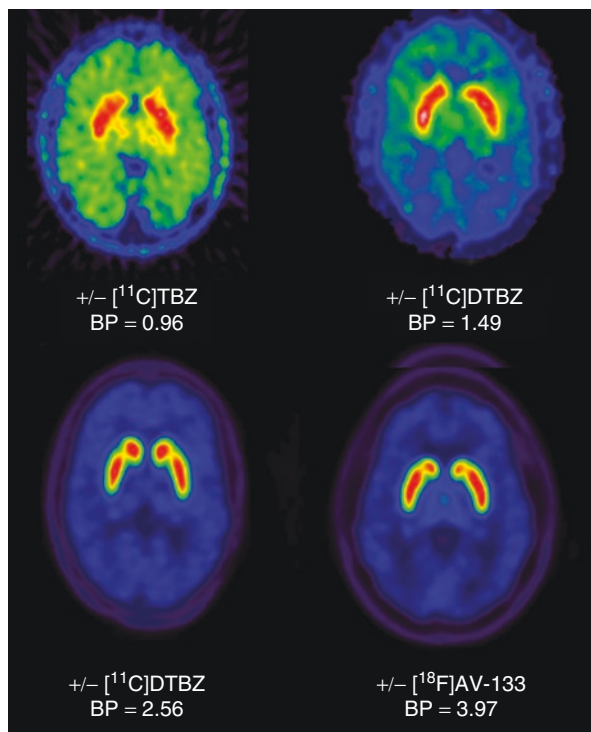
Table 33.3 Human studies using VMAT2 radioligands

Subjects	Radioligands	Topic	Year	Ref
3 NC	(±)[^{11}C]TBZ	First VMAT2 PET study	1993	Kilbourn et al. (1993)
6 NC	(±)[^{11}C]MTBZ	Evaluation of new VMAT2 ligand	1995	Vander Borght et al. (1995b)
15 NC, 7 PD	(±)[^{11}C]DTBZ	First PET study of VMAT2 in PD	1996	Frey et al. (1996)
9 NC, 8 OPCA, 4 MSA	(±)[^{11}C]DTBZ	Non-PD movement disorders	1996	Gilman et al. (1996)
7 NC	(+)[^{11}C]DTBZ	Eval of pharmacokinetic models	1996	Koeppe et al. (1996)
9 NC	(+)[^{11}C]DTBZ	Eval of equilibrium infusion PET	1997	Koeppe et al. (1997)
6 NC	(+)[^{11}C]DTBZ, (−)[^{11}C]DTBZ	Extrastriatal binding	1999	Koeppe et al. (1999)
22 NC, 8 TS	(+)[^{11}C]DTBZ	VMAT2 in Tourette's	1999	Meyer et al. (1999)
10 NC	(±)[^{11}C]DTBZ	Reproducibility studies	1999	Chan et al. (1999)
4 PDC	(+)[^{11}C]DTBZ	Paroxysmal dystonic choreoathetosis	1999	Bohnen et al. (1999)
64 NC, 19 HD	(+)[^{11}C]DTBZ	Huntington's disease	2000	Bohnen et al. (2000)
10 NC	(±)[^{11}C]DTBZ	Eval of pharmacokinetic models	2000	Sossi et al. (2000)
16 NC, 35 PD	(±)[^{11}C]DTBZ, [^{18}F]FDOPA, [^{11}C]MPH	Multi-tracer PET study in PD	2000	Lee et al. (2000)
16 NC, 16 BPD	(+)[^{11}C]DTBZ	Bipolar disorder	2000	Zubieta et al. (2000)
12 NC, 26 SCZ	(+)[^{11}C]DTBZ	Schizophrenia	2000	Taylor et al. (2000)
15 NC, 15 BPD, 12 SCZ	(+)-^{11}C]DTBZ	Comparison of VMAT2 in bipolar vs. schizophrenia	2001	Zubieta et al. (2001)
27 NC, 19 TS	(+)[^{11}C]DTBZ	VMAT2 in Tourette's	2003	Albin et al. (2003)
21 NC, 5 DRD	(±)[^{11}C]DTBZ, [^{18}F]FDOPA, [^{11}C]MPH	Multi-tracer study in Dopa-responsive dystonia	2003	De la Fuente-Fernandez et al. (2003a)
20 PD	(±)[^{11}C]DTBZ, [^{18}F]FDOPA, [^{11}C]MPH	Multi-tracer study in early vs. late onset PD	2003	De la Fuente-Fernandez et al. (2003b)
11 PD	(±)[^{11}C]DTBZ	Asymmetric PD and levodopa	2003	Kumar et al. (2003)
13 MSA	(+)[^{11}C]DTBZ, [^{123}I]IBVM	VMAT2 and VAChT in MSA	2003	Gilman et al. (2003)
19 NC, 20 DLB, 25 AD	(+)[^{11}C]DTBZ	VMAT2 in AD vs. DLB	2004	Gilman et al. (2004)

Table 33.3 (continued)

Subjects	Radioligands	Topic	Year	Ref
20 NC, 67 PD	(±)[^{11}C]DTBZ	Disease duration and striatal anteroposterior gradient	2004	Lee et al. (2004)
33 NC, 67 PD, 15 *LRRK2*	(+)[^{11}C]DTBZ, [^{18}F]FDOPA, [^{11}C]MPH	Multi-tracer study in *LRRK2* subjects	2005	Adams et al. (2005)
19 NC, 25 AD, 20 DLB, 7FTD	(+)[^{11}C]DTBZ	Use of BP and K$_1$ to differentiate dementias	2005	Koeppe et al. (2008)
10 NC, 9 PD, 8 PSP,10 MSA	(+)[^{11}C]DTBZ, [^{11}C]HED	Losses of brain VMAT2 and heart adrenergic innervation	2006	Raffel et al. (2006)
18 NC, 16 METH	(+)[^{11}C]DTBZ	Abstinent METH users	2006	Johanson et al. (2006)
75 NC, 31 PD	(+)[^{11}C]DTBZ	Age-related decline in NC: Losses in PD	2006	Bohnen et al. (2006)
2 *SPG3A*	(+)[^{11}C]DTBZ	*SPG3A* genetic mutations	2008	Albin et al. (2008)
14 NC, 16 METH	(+)[^{11}C]DTBZ	Binding in methamphetamine users	2008	Boileau et al. (2008)
33 NC, 27 PD	(+,−)[^{11}C]DTBZ	VMAT2 loss in early PD	2008	Martin et al. (2008)
15 NC, 44 PD	(+)[^{11}C]DTBZ	Study of VMAT2 and AChE in PD	2009	Bohnen et al. (2009)
28 NC, 33 TS	(+)[^{11}C]DTBZ	VMAT2 in Tourette's	2009	Meyer et al. (1999)
6 PD	(+)[^{11}C]DTBZ	Binding after acute levodopa	2009	De la Fuente-Fernandez et al. (2009)
36 PD	(+)[^{11}C]DTBZ	Increased loss in PD w/ dyskinesia	2009	Troiano et al. (2009)
78 PD	(±)[^{11}C]DTBZ, [^{11}C]MPH, [^{18}F] FDOPA	Longitudinal multi-tracer study	2009	Nandhagopal et al. (2011)
58 PD	(+)[^{11}C]DTBZ	Olfactory dysfunction in PD	2010	Bohnen et al. (2010)
33 NC	(±)[^{11}C]DTBZ, [^{11}C]MPH	Aging effects VMAT2 and DAT	2010	Troiano et al. (2010)
80 NC, 19 AD, 9 FTD, 5 DLB, 16 MCI	(+)[^{11}C]DTBZ, [^{18}F]FDG	Use of K$_1$ from DTBZ as surrogate for blood flow	2010	Albin et al. (2010)
9 NC	(+)[^{11}C]DTBZ	Effects of low-dose amphetamine	2010	Boileau et al. (2010)
9 NC	[^{18}F]AV-133	Human dosimetry study	2010	Lin et al. (2010)
8 *LRRK2*	(±)[^{11}C]DTBZ, [^{11}C]MPH [^{18}F] FDOPA	Multi-tracer study in *LRRK2* subjects	2010	Sossi et al. (2010b)

Table 33.3 (continued)

Subjects	Radioligands	Topic	Year	Ref
6 NC, 17 PD	[^{18}F]AV-133	Losses in PD	2010	Okamura et al. (2010)
73 PD	(+)[^{11}C]DTBZ	Leucoaraiosis in PD	2011	Bohnen et al. (2011)
75 dementia	(+)[^{11}C]DTBZ, [^{11}C]PIB	VMAT2 and amyloid to classify dementias	2011	Burke et al. (2011)
15 NC, 34 PD	(+)[^{11}C]DTBZ	Rhinorrhea in PD	2011	Chou et al. (2011)
35 NC, 78 PD	(±)[^{11}C]DTBZ	Progression of changes in young vs. older PD	2011	De la Fuente-Fernandez et al. (2011)
4 NC, 9 PD	[^{18}F]AV-133	Eval of imaging times for single-scan protocol	2011	Lin and Lin (2011)
10 NC, 10 AD, 20 PD, 9 DLB	[^{18}F]AV-133	Using VMAT2 to differentiate AD form DLB	2011	Villemagne et al. (2011)
10 NC, 9 DLB, 11 AD, 20 PD	[^{18}F]AV-133	Using VMAT2 to differentiate AD form DLB	2012	Villemagne et al. (2012)
35 NC, 78 PD	(±)[^{11}C]DTBZ, [^{18}F]FDOPA, [^{11}C]MPH	Longitudinal study of compensatory changes	2011	Nandhagopal et al. (2009)
4 NC, 9 PD	(+)[^{18}F]AV-133	Optimization of scan protocol	2011	Lin et al. (2011)
26 *LRRK2*	(±)[^{11}C]DTBZ	Losses in symptomatic *LRRK2*	2012	Aasly et al. (2012)
12 NC, 12 COC	(+)[^{11}C]DTBZ	Small losses in cocaine users	2012	Narendran et al. (2012a)
13 NC	(+)[^{11}C]DTBZ	Omega-3 supplementation	2012	Narendran et al. (2012b)
80 PD	(+)[^{11}C]DTBZ	Rapid eye movement disorder	2012	Kotagal et al. (2012)
51 PD	(+)[^{11}C]DTBZ, [^{11}C]DASB	Sleep disordered breathing	2012	Lelieveld et al. (2012)
40 PD-MCI	(+)[^{11}C]DTBZ, [^{11}C]PIB	VMAT2 and amyloid in PD w/MCI	2012	Petrou et al. (2012b)
32 NC, 125 PD	(+)[^{11}C]DTBZ, [^{11}C]PMP	VMAT2 and AChE –Gait speed correlation	2013	Bohnen et al. (2013)
22 NC	[^{18}F]AV-133	Normal brain distributions	2013	Lin et al. (2013)
148 PD	(+)[^{11}C]DTBZ, [^{11}C]PMP	PD and diabetes	2013	Kotagal et al. (2013)
18 PD	(+)[^{11}C]DTBZ	VMAT2 losses and levodopa	2013	Kwak et al. (2013)
44 PD	(+)[^{11}C]DTBZ, [^{11}C]PIB	Postural instability and gait	2013	Muller et al. (2013a)

Table 33.3 (continued)

Subjects	Radioligands	Topic	Year	Ref
25 NC, 124 PD	(+)[^{11}C]DTBZ, [^{11}C]PIB	VMAT2 and AChE in thalamus	2013	Muller et al. (2013b)
5 NC, 5 PD, 11 DLB, 10 AD	[^{18}F]AV-133 Florbetapir-F18	VMAT2 and amyloid in cognition	2014	Siderowf et al. (2014)
17 NC, 30 PD	[^{18}F]AV-133	Losses in early PD	2014	Lin et al. (2014)
8 NC, 10 PD	[^{18}F]AV-133 [^{99m}Tc] TRODAT-1	Comparison of VMAT2 and DAT losses in PD	2014	Hsiao et al. (2014a)
17 NC, 53 PD	[^{18}F]AV-133	Losses in advanced PD	2014	Hsiao et al. (2014b)
148 PD	(+)[^{11}C]DTBZ, [^{11}C]PMP	VMAT2 and AChE in PD w/diabetes	2014	Bohnen et al. (2014)
3 *DCTN1*	(+)[^{11}C]DTBZ, [^{18}F]FDOPA, [^{11}C]RAC, [^{11}C]DASB	Multi-tracer study in *DCTN1* genetic mutation	2014	Felicio et al. (2014)
49 NC, 83 PD	(+)[^{11}C]DTBZ	Cardiovascular risk	2014	Kotagal et al. (2014)
29 PD, 18 PD-MCI	(+)[^{11}C]DTBZ	Cognitive tests in MCI	2014	Chou et al. (2014)
8 NC, 8 PD, 4 Mn-intoxication	[^{18}F]AV-133	VMAT2 in Mn-intoxication	2015	Huang et al. (2015)
143 PD	(+)[^{11}C]DTBZ, [^{11}C]PMP	VMAT2 and AChE in cognition	2015	Bohnen et al. (2015)
9 NC, 18 PD	[^{18}F]AV-133	Decrease in CO-induced parkinsonism	2015	Chang et al. (2015)
48 PD	(+)[^{11}C]DTBZ	Exercise and symptom severity	2015	Snider et al. (2015)
133 PD	(+)[^{11}C]DTBZ	VMAT2 loss and fatigue in PD	2016	Chou et al. (2016)
22 NC, 28 METH, 9 COC	(+)[^{11}C]DTBZ	VMAT2 losses in cocaine and methamphetamine use	2016	Boileau et al. (2016)
4 NC, 22 PD	[^{18}F]AV-133	Correlations with CSF biomarkers	2016	Gao et al. (2016)
62 PD	(+)[^{11}C]DTBZ, [^{11}C]PIB, [^{11}C]PMP	Correlations with amyloidopathy	2016	Shah et al. (2016)
12 NC, 14 *22qII.2*	(+)[^{11}C]DTBZ	*22qII.2* genetic mutation effects on VMAT2	2017	Butcher et al. (2017)
49 PD	(+)[^{11}C]DTBZ	Color discrimination and PD	2017	Bohnen et al. (2017)
36 PD	(+)[^{11}C]DTBZ, [^{11}C]PIB	Hoeh and Yahr stage and amyloid burden	2017	Kotagal et al. (2017)

Table 33.3 (continued)

Subjects	Radioligands	Topic	Year	Ref
47 PD	[^{18}F]AV-133	Clinical impact in uncertain PD	2017	Alexander et al. (2017)
5 NC, 12 PD	[^{18}F]AV-133	Reproducibility study	2017	Wu et al. (2017)
13 PD, 16 *LRRK2*	(+)[^{11}C]DTBZ, [^{11}C]DASB	Dual VMAT2 and SERT study	2017	Wile et al. (2017)
9 NC, 15 PD, 17 *LRRK2*	(+)[^{11}C]DTBZ, [^{11}C]DASB	Pattern analysis of dual study	2018	Fu et al. (2018)
85 PD	[^{18}F]AV-133	Clinical impact in uncertain PD	2018	Xu et al. (2018)
26 NC,39 PD	[^{18}F]AV-133	Losses in PD	2018	Lung et al. (2018)
14 NC, 14 ND	(+)[^{11}C]DTBZ, [^{11}C]PMP	Study of peripheral neuropathy	2018	Beaulieu et al. (2018)
39 PD	(+)[^{11}C]DTBZ	Diagnostic utility in uncertain PD	2018	Perez-Lohman et al. (2018)
12 NC, 30 PD	(+)[^{11}C]DTBZ	VMAT2 loss in globus pallidus	2019	Cho et al. (2019)
75 NC, 129 PD	(+)[^{11}C]DTBZ	Combined with MRI diffusion imaging	2019	Yang et al. (2019)
8 PD	(+)[^{11}C]DTBZ	Implants of neural progenitor cells	2019	Madrazo et al. (2019)
7 PD	(+)[^{11}C]DTBZ	Deep brain stimulation study	2019	Smith et al. (2019)
15 PD	(+)[^{11}C]DTBZ, [^{11}C]MPH	Joint pattern analysis VMAT2 + DAT	2019	Fu et al. (2019)
21 NC. 37 PD	[^{18}F]AV-133	Correlations with nonmotor symptoms	2019	Shi et al. (2019)
83 NC, 84 PD	[^{18}F]AV-133	Constipation and inflammation	2019	Zhou et al. (2019)

injections, arterial blood sampling and determination of metabolite-corrected blood curves, and compartmental modeling to obtain estimates of binding potentials (BP) for [^{11}C]DTBZ in multiple regions of the human brain (Koeppe et al. 1996). (+)-α-[^{11}C]DTBZ is a reversibly binding radioligand also well suited for use in equilibrium infusion applications (Koeppe et al. 1997). Subsequent studies using injections of both the active and inactive stereoisomers, each in carbon-11 labeled form, provided direct evidence of very low binding of the radioligand in non-target regions such as the cerebellum and the occipital cortex (Koeppe et al. 1999), consistent with studies of immunoreactivity for VMAT2 (Tong et al. 2011) and in vitro autoradiographic studies (Scherman and Raisman 1988). The reproducibility of binding measures using [^{11}C]DTBZ in humans has been examined and found reliable, provided care is exercised in selecting appropriate reference regions (Chan et al. 1999).

The in vivo pharmacokinetics of the fluorine-18 labeled radiotracer ([^{18}F]AV-133) have similarly been evaluated using a variety of analysis methods (Frey et al. 2008;

Lin and Lin 2011; Lin et al. 2013; Okamura et al. 2010). Compartmental modeling of [^{18}F]AV-133 kinetics can be used to estimate regional binding potentials (BP) (Okamura et al. 2010), but the longer half-life of this radiotracer also permits a proposed use of delayed single-frame imaging protocols to estimate standard uptake value ratios (SUVr) as reasonable estimates of the specific binding of the radioligand (Lin and Lin 2011). Good reproducibility of such SUVr values has been demonstrated (Wu et al. 2017).

33.6.2 Aging

As many of the potential applications of VMAT2 imaging in neurodegenerative disease involve elderly populations (e.g., PD, AD), the possible effect of age-related declines in radioligand binding must be considered. Studies of aging effects in normal controls have however provided inconsistent results, showing both no decline of VMAT2 radioligand binding with age (Troiano et al. 2010) as well as a small but steady decrease of 0.5–0.77%/year (Frey et al. 1996; Bohnen et al. 2006). In a single study, a longitudinal study of the age-dependent losses of VMAT2 radioligand binding in early versus late onset PD subjects demonstrated a slower progression in the younger onset patients (De la Fuente-Fernandez et al. 2011). Age-related effects on radioligand binding remain a potential confound in imaging studies, and for that reason well-designed studies of VMAT2 changes in disease require the inclusion of appropriate age-matched control subjects.

33.6.3 Parkinson's Disease

By far, the single largest application of VMAT2 radioligand imaging has been in Parkinson's disease, with more than 50 published studies (for references see Table 33.3). The PET studies done with [^{11}C]DTBZ, and more recently [^{18}F]AV-133, have consistently shown decreases in radioligand binding in the striatal regions (caudate, putamen, nucleus accumbens, globus pallidus) (Table 33.4) . Significant losses of radioligand binding can be demonstrated in the presymptomatic phase, often with a unilateral presentation and observations of an anteroposterior gradient (losses in posterior putamen before the caudate nucleus and ventral striatum/nucleus accumbens) and progression to more severe and complete bilateral losses throughout the striatum in advanced disease (Fig. 33.3). The losses of VMAT2 radioligand binding can also be correlated with a variety of clinical observations (dyskinesias, olfaction, sleep disorders, gait, fatigue).

In order to more fully understand the biochemical changes in the human brain in the course of Parkinson's disease, numerous studies have utilized a multi-radiotracer approach by combining VMAT2 measures ([^{11}C [DTBZ or [^{18}F]AV-133) with imaging studies using radiotracers for the neuronal membrane dopamine transporter (DAT: [^{11}C]methylphenidate (MPH) or [^{99m}Tc]Trodat-1), dopamine synthesis

Table 33.4 In vivo binding estimates for (+)-α-[^{11}C]DTBZ and [^{18}F]AV-133 ((+)-α-(3-[^{18}F]fluoropropyl)DTBZ) in healthy controls (HC), Parkinson's disease (PD), dementia with Lewy bodies (DLB), and Alzheimer's disease (AD)

Ligand	Disease	Region	BP (binding potential) Mean (SD)
(+)-[^{11}C]DTBZ (Koeppe et al. 2008)	HC	Caudate nucleus	1.69 (0.23)
		Anterior putamen	2.00 (0.25)
		Posterior putamen	1.91 (0.25)
	PD	Caudate nucleus	0.93 (0.26)
		Anterior putamen	0.65 (0.21)
		Posterior putamen	0.43 (0.15)
	DLB	Caudate nucleus	0.87 (0.30)
		Anterior putamen	0.71 (0.21)
		Posterior putamen	0.57 (0.22)
	AD	Caudate nucleus	1.74 (0.35)
		Anterior putamen	2.06 (0.41)
		Posterior putamen	1.92 (0.42)
[^{18}F]AV-133 (Okamura et al. 2010)	HC	Caudate nucleus	2.53 (0.3)
		Anterior putamen	2.56 (0.3)
		Posterior putamen	2.53 (0.3)
	PD	Caudate nucleus	1.20 (0.5)
		Anterior putamen	0.66 (0.3)
		Posterior putamen	0.30 (0.2)
	DLB	Caudate nucleus	1.24 (0.6)
		Anterior putamen	0.90 (0.5)
		Posterior putamen	0.62 (0.5)
	AD	Caudate nucleus	2.83 (0.9)
		Anterior putamen	3.01 (0.9)
		Posterior putamen	2.87 (0.9)

([^{18}F]fluoroDOPA), dopamine receptors ([^{11}C]raclopride), serotonin reuptake (SERT: [^{11}C]DASB), acetylcholinesterase ([^{11}C]PMP), and amyloid burden ([^{11}C]PIB). Combination of [^{11}C]DTBZ with [^{18}F]fluoroDOPA and [^{11}C]MPH, all three of which measure aspects of presynaptic dopaminergic neurons, has demonstrated differential losses when comparing PD subjects at various stages of disease: investigators have proposed that VMAT2 measures appear the least subject to regulatory effects and may represent the most accurate measure of DA-ergic terminals, whereas these studies support that dopamine synthesis is upregulated (result: increased [^{18}F]fluoroDOPA uptake and retention) and the DAT is downregulated (result: decreased [^{11}C]MPH binding) (Nandhagopal et al. 2011; Lee et al. 2000). Such compensatory changes would work to maintain synaptic dopamine levels as terminals are lost to the disease process, but that conclusion is dependent on VMAT2 as a reliable marker of terminal density. A part of the rationale for development of VMAT2 radioligands was the hypothesis that the vesicular transporter, in comparison to measures of dopamine synthesis or the neuronal membrane dopamine transporter, would be more resistant to regulation of total numbers (B_{max}) in response to

Fig. 33.3 Representative human PET images of (+)-alpha-[¹¹C]DTBZ binding in normal controls (NC), Alzheimer's disease (AD), progressive supranuclear palsy (PSP), early and late Parkinson's disease (PD), and dementia with Lewy bodies disease (DLB)
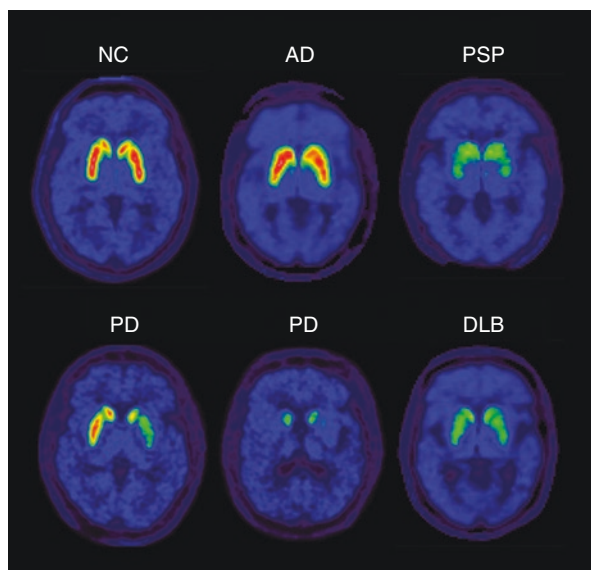
pharmacological treatments or compensatory changes in a disease process. Animal studies to evaluate that hypothesis have been inconsistent (see Sect. 33.5.2), and studies intended to perturb brain biochemistry are of course much harder to perform in living human subjects. The administration of amphetamine could lead to depletion of vesicular dopamine levels due to stimulant-induced release, but a low acute dose of amphetamine in human subjects was found to produce only a small (5%) decrease in radioligand binding to the VMAT2 (Boileau et al. 2010); whether the dose of amphetamine administered was adequate to reduce vesicular dopamine levels to an extent sufficient to subsequently reduce competition for radioligand binding remains an open question, as the effects of amphetamine on the VMAT2 are complex and dose-dependent (Reith and Gnegy 2020). It should be noted that in animals, demonstration of an effect of amphetamine required extensive depletion of tissue dopamine concentrations. The clinical equivalent of depletion of synaptic vesicle dopamine is the condition known as DOPA-responsive dystonia: the observation that in vivo binding of [¹¹C]DTBZ is increased in those subjects (De la Fuente-Fernandez et al. 2003a) was an indication that vesicular dopamine may compete for binding of radioligands to the TBZ site located on the inner surface of the vesicular membrane. However, in both these patients and in studies of dopamine-depleted rat brains, alterations of VMAT2 radioligand binding in vivo were shown after extensive or complete neurotransmitter depletion was accomplished, and the sensitivity of VMAT2 radioligand binding to smaller changes in dopamine levels remains to be determined. The potential effects of increased endogenous dopamine levels affecting human [¹¹C]DTBZ studies have been examined through acute administration of L-DOPA to subjects with advanced Parkinson's disease (De la Fuente-Fernandez et al. 2009), where significant decreases in radioligand binding in caudate and putamen were proposed to be due to the increases in vesicular

dopamine. Taken together, the animal and human studies involving manipulations of endogenous dopamine levels suggest that care should be taken to account for use of L-DOPA, or other dopamine-modifying drugs, when performing studies with VMAT2 radioligands.

Several studies have examined particular subsets of patients to probe different aspects of the disease. Examination of VMAT2 binding in a cohort of untreated early, untreated PD patients demonstrated that even in these subjects, there was a significant loss (>50%) of VMAT2 binding sites particularly in the putamen (Martin et al. 2008); a loss of DTBZ binding in the clinically unaffected side of PD patients has also been reported (Bohnen et al. 2006). In studies of unilateral Parkinsonism, the greater decrease of DTBZ binding on the more clinically affected side correlated with responsiveness to L-DOPA treatment (Kumar et al. 2003). A study of both the VMAT2 and the DAT in controls versus Parkinson's disease with dyskinesias showed no significant differences of DTBZ binding between groups but a difference in the ratio of dopamine transporter (DAT) to VMAT2 radioligand binding in the putamen, with ratios being significantly lower in the group having dyskinesias. The comparison of VMAT2 radioligand binding measurements with matched studies of the dopamine neuronal membrane transporter (DAT) and 6-[^{18}F]fluoroDOPA uptake in a large cohort of Parkinson's disease patients (De la Fuente-Fernandez et al. 2011) provided evidence that younger-onset subjects had better compensatory mechanisms operating to maintain the biochemical balance of the dopaminergic system as compared to late-onset PD patients. A longitudinal multi-tracer study of PD patients provided evidence for compensatory upregulation of the DAT radioligand binding and 6-[^{18}F]fluoroDOPA uptake in earlier stages of the disease, but that compensatory mechanisms decline with advanced neuronal losses as shown by extensive losses of [^{11}C]DTBZ binding. The numerous studies that have now compared multiple presynaptic radiotracers have clearly demonstrated differential rates and extents of losses between the measures of the VMAT2, the DAT, and dopamine synthesis.

The VMAT2 radioligands [^{11}C]DTBZ and [^{18}F]AV-133 have not reached routine use in the clinical management of Parkinson's disease, but studies have begun to evaluate the value of such imaging studies in situations where the diagnosis of PD is uncertain (Alexander et al. 2017; Xu et al. 2018).

33.6.4 Non-Parkinson Movement Disorders

Losses of in vivo VMAT2 radioligand binding have been observed in studies of less common neurodegenerative movement disorders (progressive supranuclear palsy (PSP), multiple system atrophy (MSA), and olivopontocerebellar atrophy (OPCA)) that share traits with idiopathic parkinsonism but express additional clinical symptoms. Involvement of the basal ganglia is generally observed, but the pattern of VMAT2 radioligand binding changes are different: for example, whereas in

idiopathic Parkinson's disease losses are earlier, asymmetric, and more predominant in the posterior putamen, in PSP there was observed a more uniform involvement of both the caudate and the putamen (Fig. 33.3) (Raffel et al. 2006). Similarly, VMAT2 radioligand binding is altered in MSA, OPCA, and other degenerative diseases involving monoaminergic nerve terminals of the basal ganglia (Gilman et al. 1996; Gilman et al. 2003).

33.6.5 Huntington's Disease

Huntington's disease (HD) is characterized by significant neuronal loss and atrophy in the caudate nucleus and putamen. A single study of [^{11}C]DTBZ binding in HD subjects showed reductions in total radioligand binding in caudate nucleus, anterior and posterior putamen, with losses most prominent in the posterior putamen (Bohnen et al. 2000). Within the study group, individuals with the akinetic-rigid phenotype (ADr) showed more significant losses of total radioligand binding than the subgroup with the chorea phenotype (HDc).

33.6.6 Dementia

The underlying biochemical changes in different clinical manifestations of dementia (Alzheimer's disease (AD), Parkinson's disease with dementia (PDD), and dementia with Lewy body disease (DLB)) do not uniformly involve the same degenerative pathways, and losses of VMAT2 are not uniform in the different dementias (Table 33.4). In Alzheimer's disease the striatal monoaminergic innervation is generally intact (Fig. 33.3), and no losses of in vivo VMAT2 radioligand binding have been reported (Gilman et al. 2004; Koeppe et al. 2008). In contrast, the basal ganglia are significantly affected in dementia with Lewy bodies, with losses of radioligand binding clearly evident throughout the caudate nucleus and putamen (Fig. 33.3); use of imaging techniques to clearly identify DLB vs. AD patients (Koeppe et al. 2008; Villemagne et al. 2011; Villemagne et al. 2012) has clinical impact, as DLB patients are subject to adverse reactions from dopaminergic treatments that might otherwise be useful for treatment of hallucinations or behavioral disturbances in AD patients. Finally, Parkinson's disease with dementia patients show the expected significant losses of striatal VMAT2 radioligand binding (Koeppe et al. 2008); the dementia is proposed to be associated with concurrent changes in the cholinergic system, which can sometimes be demonstrated by separate imaging studies with radiotracers for that neurotransmitter system (Bohnen and Frey 2007; Bohnen and Albin 2011). The combination of [^{11}C]DTBZ imaging studies with PET imaging of amyloid deposits using such radioligands as [^{11}C]PIB provides a method for classifications of dementia subjects which may not always agree with consensus clinical evaluations (Burke et al. 2011).

33.6.7 Genetic Diseases

There are several genetic mutations that have been examined using PET and VMAT2 radioligands. Mutations of the *LRRK2* protein (leucine-rich repeat kinase 2) produce L-DOPA responsive parkinsonism, and PET imaging was used to show decreases of [^{11}C]DTBZ, [^{18}F]fluoroDOPA, and [^{11}C]MPH in symptomatic subjects (Adams et al. 2005; Aasly et al. 2012). The Parkinson's disease phenotype of *22q11.2DS* produces clinical symptoms and response to treatment similar to PD, and preliminary imaging studies with [^{11}C]DTBZ showed the interesting results of increased radioligand binding in non-symptomatic gene carriers and the expected severe losses of VMAT2 binding in a subject with parkinsonism (Butcher et al. 2017). In a preliminary study (Felicio et al. 2014), three individuals with a mutation in the dynactin gene (*DCTN1*) that produces an autosomal dominantly inherited parkinsonism (and other clinical signs, including depression, forming Perry syndrome) were examined by PET with [^{11}C]DTBZ, [^{18}F]fluoroDOPA, [^{11}C]raclopride, and [^{11}C]DASB. In two clinically affected subjects, there was a large decrease in [^{11}C]DTBZ binding, a modest loss of [^{18}F]fluoroDOPA uptake, and normal to increased [^{11}C]RAC.

33.6.8 Environmental Toxins

PET imaging of [^{11}C]DTBZ binding has been utilized to evaluate the potential losses of dopaminergic innervation after environmental insults. Chronic excessive exposure to manganese produces some clinical signs similar to idiopathic Parkinson's disease, but the involvement of dopaminergic degeneration has not been firmly established. PET studies with [^{18}F]AV-133 showed no decreased VMAT2 binding, supporting the distinction between manganese intoxication and PD (Huang et al. 2015). In contrast, studies of [^{18}F]AV-133 binding in subjects with carbon monoxide-induced parkinsonism showed decreases in caudate and putamen, although the sparing of radioligand binding in the substantia nigra suggested a differential pathophysiology as compared to idiopathic PD (Chang et al. 2015).

33.6.9 Psychiatric Disease

A few studies have been completed looking at VMAT2 radioligand binding in schizophrenia and bipolar disorder type I. In schizophrenia, no differences in striatal or thalamic binding of VMAT2 radioligands was observed, but small increases in binding in the ventral brainstem of schizophrenics were observed relative to controls (Taylor et al. 2000; Zubieta et al. 2001). The importance of that observation is difficult to ascribe to any single neurotransmitter system, as that portion of the brain has cell bodies and projections for both serotonergic and dopaminergic neurons. For the bipolar disorder type I group, increases of VMAT2 binding in the thalamus relative to controls can at least be proposed not to be due to changes in dopaminergic

innervation, which is very low in that brain region, but to changes in the serotonergic and noradrenergic innervation (Zubieta et al. 2000).

The in vivo binding of VMAT2 radioligands has also been examined in Tourette's syndrome, and inconsistent results have been obtained, with the discrepant observations of both no changes (Meyer et al. 1999) and increased [¹¹C]DTBZ binding (Albin et al. 2003) attributed to the heterogeneity of Tourette's syndrome patient populations.

33.6.10   Drug Abuse

As many drugs which are abused are known to interact with the monoaminergic systems of the brain (e.g., amphetamine, methamphetamine, cocaine), the effects of such drug use on the in vivo binding of VMAT2 radioligands to monoaminergic terminals have been examined, with particular interest in the potential neurotoxic effects on monoaminergic terminals. Postmortem studies of chronic cocaine users have demonstrated both no changes in VMAT2 ligand binding or immunoreactivity (Staley et al. 1997) as well as modest decreases in VMAT2 radioligand binding (Wilson et al. 1996a; Little et al. 2003). In a PET study of cocaine users, reduced in vivo VMAT2 binding was shown in several striatal regions, suggesting either a compensatory downregulation of VMAT2 storage systems after drug use or a loss of dopaminergic terminals (Narendran et al. 2012a); which of these is occurring, and the clinical impact needs further study.

The effects of methamphetamine on striatal VAMT2 radioligand binding have been examined both in vitro and in vivo with conflicting results (Boileau et al. 2016, 2008; Wilson et al. 1996b; Johanson et al. 2006). Postmortem studies of methamphetamine users have not shown decreases in VMAT2 binding, but PET studies have shown both decreased (suggesting neurodegeneration) and increased [¹¹C]DTBZ binding (suggesting higher VMAT2 site availability due to lower DA levels). The effects of methamphetamine on the dopaminergic system and the VMAT2, and the potential neurotoxicity, are thus poorly understood (Kish et al. 2017).

33.7   Conclusions

In contrast to the development of radiopharmaceuticals for in vivo PET imaging of most other biochemical targets, where multiple competing radioligands have been synthesized and advanced through to human studies (e.g., dopamine receptors, amyloid imaging), the development of an in vivo imaging radiotracer for the VMAT2 has been focused on derivatives of a single basic structure that of tetrabenazine. The currently available radiotracers, (+)-α-[¹¹C]DTBZ and [¹⁸F]AV-133, present very favorable characteristics: good brain permeability, reversible kinetics, lack of interfering metabolites, well-known pharmacology, acceptable radiation dosimetry, and simple radiochemical preparation. In vivo human imaging of the vesicular

monoamine transporter 2 (VMAT2) will continue to be useful in studies of diseases involving changes of monoaminergic neuronal densities in the brain.

References

Aasly JO, Shi M, Sossi V et al (2012) Cerebrospinal fluid amyloid β and tau in *LRRK2* mutation carriers. Neurology 78:55–61

Adams JR, van Netten H, Schulzer M et al (2005) PET in *LRRK2* mutations: comparison to sporadic Parkinson's disease and evidence for presymptomatic compensation. Brain 128:2777–2785

Albin RA, Koeppe RA, Bohnen NI et al (2003) Increased ventral striatal monoaminergic innervation in Tourette syndrome. Neurology 61:310–315

Albin RL, Koeppe RA, Rainer S et al (2008) Normal dopaminergic nigrostriatal innervation in SPG3A hereditary spastic paraplegia. J Neurogenet 22:289–294

Albin RL, Koeppe RA, Burke JF et al (2010) Comparable results of FDG-PET CMRglu and DTBZ-PET K1 in evaluation of early dementia and mild cognitive impairment. Arch Neurol 67:440–446

Alexander PK, Lie Y, Jones G et al (2017) Management impact of imaging brain vesicular monoamine transporter type 2 in clinically uncertain parkisonian syndrome with 18F-AV-133 and PET. J Nucl Med 58:1815–1820

Amarasinghe K, Rishel M, Dinn S et al (2009) Fluorinated dihydrotetrabenazine ether imaging agents and probes. World Patent WO 2009/05520 A2

Asser A, Koks S, Snellman A et al (1652) Increased striatal VMAT2 binding in mice after chronic administration of methcathinone and magnesium. Brain Res 2016:97–102

Avendaño-Estrada A, Ávila-Rodríguez MA (2018) Reference tissue models in the assessment of [^{11}C]-DTBZ binding to the VMAT2 in rat striatum: a test-retest reproducibility study. Synapse 72:e22029

Beaulieu ML, Miller MITM, Bohnen NI (2018) Peripheral neuropathy is associated with more frequent falls in Parkinson's disease. Parkinsonism Relat Disord 54:46–50

Blesa J, Juri C, Collantes M et al (2010) Progression of dopaminergic depletion in a model of MPTP-induced parkinsonism in non-human primates. An ^{18}F-DOPA and ^{11}C-DTBZ study. Neurobiol Dis 38:456–463

Blesa J, Pifl C, Sánchez-González MA et al (2012) The nigrostriatal system in the presymptomatic and symptomatic stages in the MPTP monkey model: a PET, histological and biochemical study. Neurobiol Dis 48:79–91

Bohnen NI, Albin RL (2011) The cholinergic. System and Parkinson's disease. Behav Brain Res 221:564–573

Bohnen NI, Frey KA (2007) Imaging of cholinergic and monoaminergic neurochemical changes in neurodegenerative disorders. Mol Imaging Biol 9:243–257

Bohnen NI, Albin RL, Frey KA, Fink JK (1999) (+)-Alpha-[^{11}C]dihydrotetrabenazine PET imaging in familial paroxysmal choreoathetosis. Neurology 52:1067–1069

Bohnen NI, Koeppe RA, Mayer P et al (2000) Decreased striatal monoaminergic terminals in Huntington's disease. Neurology 54:1753–1759

Bohnen NI, Albin RL, Koeppe RA et al (2006) Positron emission tomography of monoaminergic vesicular binding in aging and Parkinson's disease. J Cereb Blood Flow Metab 26:1198–1212

Bohnen NI, Muller ML, Koeppe RA et al (2009) History of falls in Parkinson disease is associated with reduced cholinergic activity. Neurology 73:1670–1676

Bohnen NI, Muller ML, Kotagal V et al (2010) Olfactory dysfunction, central cholinergic integrity and cognitive impairment in Parkinson disease. Brain 133:1747–1754

Bohnen NI, Muller ML, Zarzhevsky N et al (2011) Leucoaraiosis, nigrostriatal denervation and motor symptoms in Parkinson's disease. Brain 134:2358–2365

Bohnen NI, Frey KA, Studenski S et al (2013) Gait speed in Parkinson disease correlates with cholinergic degeneration. Neurology 81:1611–1616

Bohnen NI, Kotagal V, Müller ML et al (2014) Diabetes mellitus is independently associated with more severe cognitive impairment in Parkinson disease. Parkinsonism Relat Disord 20:1394–1398

Bohnen NI, Albin RL, Müller ML et al (2015) Frequency of cholinergic and caudate nucleus dopaminergic deficits across the predemented cognitive spectrum of Parkinson disease and evidence of interaction effects. JAMA Neurol 72:194–200

Bohnen NI, Haugen J, Ridder A et al (2017) Color discrimination errors associate with axial motor impairments in Parkinson's disease. Mov Disord Clin Pract 4:864–869

Boileau I, Rusjan P, Houle S et al (2008) Increased vesicular monoamine transporter binding during early abstinence in human methamphetamine users: is VMAT2 a stable dopamine neuron marker? J Neurosci 28:9850–9856

Boileau I, Houle S, Rusjan PM et al (2010) Influence of a low dose of amphetamine on vesicular monoamine transporter binding: a PET (+)[^{11}C]DTBZ study in humans. Synapse 64:417–420

Boileau I, McCluskey T, Tong J et al (2016) Rapid recovery of vesicular dopamine levels in methamphetamine users in early abstinence. Neuropsychopharmacology 41:1179–1187

Boldt KG, Brine GA, Rehder K (2008) Synthesis of (+)-9-O-desmethyl-dihydrotetrabenazine, precursor for the high affinity VMAT2 imaging PET radioligand [^{11}C]-(+)-dihydrotetrabenazine. Org Prep Proced Int 40:379–384

Brooks DJ, Pavese N (2011) Imaging biomarkers in Parkinson's disease. Prog Neurobiol 95:614–628

Brown CA, Campbell MC, Karimi M et al (2012) Dopamine pathway loss in nucleus accumbens and ventral tegmental area predicts apathetic behavior in MPTP-lesioned monkeys. Exp Neurol 236:190–197

Burke JF, Albin RL, Koeppe RA et al (2011) Assessment of mild dementia with amyloid and dopamine terminal positron emission tomography. Brain 134:1647–1657

Butcher NJ, Marras C, Pondal M et al (2017) Neuroimaging and clinical features in adults with a 22q11.2 deletion at risk of Parkinson's disease. Brain 140:1371–1383

Cao L, Xie M, Zhao C et al (2018) Synthesis and preliminary evaluation of ^{131}I-9-iodovinyl-terabenazine targeting vesicular monoamine transporter 2. J Radioanal Nucl Chem 317:315–323

Chan GLY, Holden JE, Stoessl AJ et al (1999) Reproducibility studies with ^{11}C-DTBZ, a monoamine vesicular transporter inhibitor, in healthy human subjects. J Nucl Med 40:283–289

Chang CC, Hsiao IT, Huang SH et al (2015) ^{18}F-FP-(+)-DTBZ positron emission tomography detection of monoaminergic deficient network in patients with carbon monoxide related parkinsonism. Eur J Neurol 22:845–852. e59–60

Chao K-T, Tsao H-H, Weng Y-H et al (2012) Quantitative analysis of binding sites for 9-fluoropropyl-(+)-dihydrotetrabenazine ([^{18}F]AV-133) in a MPTP-lesioned PD mouse model. Synapse 66:823–831

Chen MK, Kuwabara H, Zhou Y et al (2008) VMAT2 and dopamine neuron loss in a primate model of Parkinson's disease. J Neurochem 105:78–90

Chen Z, Tang J, Liu C et al (2016) Effects of anesthetics on vesicular monoamine transporter type 2 binding to ^{18}F-FP-(+)-DTBZ: a biodistribution study in rat brain. Nucl Med Biol 43:124–129

Cho SS, Christopher L, Koshimori Y et al (2019) Decreased pallidal vesicular monoamine transporter type 2 availability in Parkinson's disease: the contribution of the nigropallidal pathway. Neurobiol Dis 124:176–182

Chou KL, Koeppe RA, Bohnen NI (2011) Rhinorrhea: a common nondopaminergic feature of Parkinson's disease. Mov Disord 26:320–323

Chou KL, Lenhart A, Koeppe RA et al (2014) Abnormal MoCA and normal range MMSE scores in Parkinson disease without dementia: cognitive and neurochemical correlates. Parkinsonism Relat Dis 20:1076–1080

Chou KL, Kotagal V, Bohnen NI (2016) Neuroimaging and clinical predictors of fatigue in Parkinson disease. Parkinsonism Relat Disord 23:45–49

Collantes M, Penuelas I, Alvarez-Erviti L et al (2008) Use of ^{11}C-(+)-alpha-dihydrotetrabenazine for the assessment of dopaminergic innervation in animal models of Parkinson's disease. Rev Esp Med Nucl 27:103–111

Darchen F, Scherman D, Laduron PM et al (1988) Ketanserin binds to the monoamine transporter of chromaffin granules and of synaptic vesicles. Mol Pharmacol 33:672–677

Darchen F, Masuo Y, Vial M et al (1989) Quantitative autoradiography of the rat brain vesicular monoamine transporter using the binding of [^{3}H]dihydrotetrabenazine and 7-amino-8-[^{125}I]iodoketanserin. Neuroscience 33:4341–4349

DaSilva JN, Kilbourn MR (1992) In vivo binding of [^{11}C]tetrabenazine to vesicular monoamine transporters in mouse brain. Life Sci 51:593–600

DaSilva JN, Kilbourn MR, Mangner TJ (1993a) Synthesis of [^{11}C]tetrabenazine, a vesicular monoamine uptake inhibitor, for PET imaging studies. Appl Radiat Isot 44:673–676

DaSilva JN, Kilbourn MR, Mangner TJ (1993b) Synthesis of a [^{11}C]methoxy derivative of α-dihydrotetrabenazine: a radioligand for studying the vesicular monoamine transporter. Appl Radiat Isot 44:1487–1489

DaSilva JN, Kilbourn MR, Domino EF (1993c) In vivo imaging of monoaminergic nerve terminals in normal and MPTP-lesioned primate brain using positron emission tomography (PET) and [^{11}C]tetrabenazine. Synapse 14:128–131

DaSilva JN, Kilbourn MR, Carey JE et al (1994) Characterization of [^{11}C]tetrabenazine as an in vivo radioligand for the vesicular monoamine transporter. Nucl Med Biol 21:151–156

De la Fuente-Fernandez R, Furtado S, Guttman M et al (2003a) VMAT2 binding is elevated in Dopa-responsive dystonia: visualizing empty vesicles by PET. Synapse 49:20–28

De la Fuente-Fernandez R, Lim AS, Sossi V et al (2003b) Age and severity of nigrostriatal damage at onset of Parkinson's disease. Synapse 47:152–158

De la Fuente-Fernandez R, Sossi V, McCormick S et al (2009) Visualizing vesicular dopamine dynamics in Parkinson's disease. Synapse 63:713–716

De la Fuente-Fernandez R, Schulzer M, Kuramoto L et al (2011) Age-specific progression of nigrostriatal dysfunction in Parkinson's disease. Ann Neurol 69:803–810

Deng A, Wu X, Zhou X et al (2014) Mapping the target localization and biodistribution of non-radiolabeled VMAT2 ligands in rat brain. AAPS J 16:592–599

Doudet DJ, Rosa-Neto P, Munk OL (2006) Effect of age on markers for monoaminergic neurons of normal and MPTP-lesioned rhesus monkeys: a multi-tracer PET study. NeuroImage 30:26–35

Dugan LL, Tian L, Quick KL et al (2014) Carboxyfullerene neuroprotection postinjury in parkinsonian nonhuman primates. Ann Neurol 76:393–402

Eiden LE, Schafer MK-H, Weihe E et al (2004) The vesicular amine transporter family (SLC18): amine/proton antiporters required for vesicular accumulation and regulated exocytotic secretion of monoamines and acetylcholine. Pflugers Arch Eur J Physiol 447:636–640

Fantegrossi WE, Woolverton WL, Kilbourn M et al (2004) Behavioral and neurochemical consequences of long-term intravenous self-administration of MDMA and its enantiomers by rhesus monkeys. Neuropsychopharmacology 29:1270–1281

Felicio AC, Dinelle K, Agarwal PA et al (2014) In vivo dopaminergic and serotenergic dysfunction in DCTN1 gene mutation carriers. Mov Disord 29:1197–1201

Frey KA, Koeppe RA, Kilbourn MR et al (1996) Presynaptic monoamine vesicles in Parkinson's disease and normal aging. Ann Neurol 40:873–884

Frey K, Kilbourn M, Robinson T (1997) Reduced striatal vesicular monoamine transporters after neurotoxic but not after behaviorally-sensitizing doses of methamphetamine. Eur J Pharm 334:273–279

Frey KA, Koeppe RA, Kilbourn MR et al (2008) Imaging VMAT2 in Parkinson's disease with [F-18]AV-133. J Nucl Med 49:5P

Fu JF, Klyuzhin I, Liu S et al (2018) Investigation of serotonergic Parkinson's disease-related covariance pattern using [^{11}C]-DASB/PET. Neuroimage Clin 19:652–660

Fu JF, Klyuzhin I, McKenzie J et al (2019) Joint pattern analysis applied to PET DAT and VMAT2 imaging reveals new insights into Parkinson's disease induced presynaptic alterations. NeuroImage Clin 23:101856

Gao R, Zhang G, Chen X et al (2016) CSF biomarkers and its associations with ^{18}F-AV-133 cerebral VMAT2 binding in Parkinson's disease—a preliminary report. PLoS One 11:e0164762

Gasnier B (2004) The SLC32 transporter, a key protein for the synaptic release of inhibitory amino acids. Pflugers Arch Eur J Physiol 447:756–759

Gilman S, Frey KA, Koeppe RA et al (1996) Decreased striatal monoaminergic terminals in olivopontocerebellar atrophy and multiple system atrophy demonstrated with positron emission tomography. Ann Neurol 40:885–892

Gilman S, Koeppe RA, Chervin RD et al (2003) REM sleep behavior disorder is related to striatal monoaminergic deficit in MSA. Neurology 61:29–34

Gilman S, Koeppe RA, Little R et al (2004) Striatal monoamine terminals in Lewy body dementia and Alzheimer's disease. Ann Neurol 55:774–780

Gonzalez AM, Walther D, Pazos A et al (1994) Synaptic vesicular monoamine transporter expression: distribution and pharmacologic profile. Mol Brain Res 22:219–226

Goswami R, Kung M-P, Ponde D et al (2006) Fluoroalkyl derivatives of dihydrotetrabenazine as PET imaging agents targeting vesicular monoamine transporters. Nucl Med Biol 33:685–694

Hostetler ED, Patel S, Guenther I et al (2007) Characterization of a novel F-18 labeled radioligand for VMAT2. J Label Compd Radiopharm 50:S330

Hsiao IT, Weng YH, Hsieh CJ et al (2014a) Correlation of Parkinson disease severity and ^{18}F-DTBZ positron emission tomography. JAMA Neurol 71:758–766

Hsiao I-T, Weng Y-H, Lin W-Y et al (2014b) Comparison of ^{99m}Tc-TRODAT-1 and ^{18}F-AV-133 imaging in healthy controls and Parkinson's disease patients. Nucl Med Biol 41:322–329

Huang CY, Liu CH, Tsao E et al (2015) Chronic manganism: a long-term follow-up study with a new dopamine terminal biomarker of ^{18}F-FP-(+)-DTBZ (^{18}F v-AV-133) brain PET scan. J Neurol Sci 353:102–106

Huang Z-R, Tsai C-L, Huang Y-Y et al (2016) A novel potential positron emission tomography imaging agent for vesicular monoamine transporter type 2. PLoS One 11:e0161295

Jacobsen JC, Wilson C, Cunningham V et al (2016) Brain dopamine-serotonin vesicular transport disease presenting as a severe infantile parkinsonian disorder. J Inherit Metab Dis 39:305–308

Jewett DM, Kilbourn MR, Lee LC (1997) A simple synthesis of [^{11}C]dihydrotetrabenazine. Nucl Med Biol 24:197–199

Jiang D, Lu X, Li Z et al (2018) Increased vesicular monoamine transporter 2 (VMAT2) and dopamine transporter (DAT) expression in adolescent brain development: a longitudinal microPET study in rodent. Front Neurosci 12:1052

Johanson C-E, Frey KA, Lundahl LH et al (2006) Cognitive function and nigrostriatal markers in abstinent methamphetamine abusers. Psychopharmacology 185:327–338

Kankanamalage K, Amarasinghe D, Rishel M et al (2009) Fluorinated dihydrotetrabenazine ether imaging agents and probes. US Patent 2009/0110636 A1

Karimi M, Tian LL, Brown CA et al (2013a) Validation of nigrostriatal PET measures: critical limits. Ann Neurol 73:390–396

Karimi M, Tian L, Brown CA et al (2013b) Validation of nigrostriatal positron emission tomography measures: critical limits. Ann Neurol 73:390–396

Kemmerer ES, Desmond TJ, Albin RL et al (2003) Treatment effects on nigrostriatal projection integrity in partial 6-OHDA lesions: comparison of L-DOPA and pramipexole. Exp Neurol 183:81–86

Kilbourn MR (1997) Time-dependent recovery of in vivo binding sites after drug dosing: a method for radiotracer evaluation. Nucl Med Biol 24:115–118

Kilbourn MR (2004) Long-term reproducibility of in vivo measures of specific binding of radioligands in rat brain. Nucl Med Biol 31:591–595

Kilbourn M, Frey K (1996) Striatal concentrations of vesicular monoamine transporters are identical in MPTP-sensitive (C57Bl/6) and -insensitive (CD-1) mouse strains. Eur J Pharmacol 307:227–232

Kilbourn MR, Koeppe RA (2017) A six-year longitudinal PET study of (+)-[^{11}C]DTBZ binding to the VMAT2 in monkey brain. Nucl Med Biol 55:34–37

Kilbourn M, Sherman P (1997) In vivo binding of (+)-α-[^{3}H]dihydrotetrabenazine to the vesicular monoamine transporter of rat brain: bolus vs. equilibrium studies. Eur J Pharm 331:161–168

Kilbourn MR, DaSilva JN, Frey KA et al (1993) In vivo imaging of vesicular monoamine transporters in human brain using [^{11}C]tetrabenazine and positron emission tomography. J Neurochem 60:2315–2318

Kilbourn MR, Lee L, Vander Borght T et al (1995a) Binding of α-dihydrotetrabenazine to the vesicular monoamine transporter is stereospecific. Eur J Pharm 278:249–252

Kilbourn MR, Sherman PS, Abbott LC (1995b) Mutant mouse strains as models for in vivo radiotracer evaluations: [^{11}C]methoxytetrabenazines ([^{11}C]MTBZ) in tottering mice. Nucl Med Biol 22:565–567

Kilbourn MR, Frey KA, Vander Borght T et al (1996) Effects of dopaminergic drug treatments on in vivo radioligand binding to brain vesicular monoamine transporters. Nucl Med Biol 23:467–471

Kilbourn MR, Lee LC, Jewett DM et al (1997) The absolute configuration of (+)-α-dihydrotetrabenazine, an active metabolite of tetrabenazine. Chirality 9:59–62

Kilbourn MR, Kuszpit K, Sherman P et al (2000) Rapid and differential losses of in vivo dopamine transporter (DAT) and vesicular monoamine transporter (VMAT2) radioligand binding in MPTP-treated mice. Synapse 35:250–255

Kilbourn MR, Sherman PS, Kuszpit K (2002) In vivo measures of dopaminergic radioligands in the rat brain:equilibrium infusion studies. Synapse 43:188–194

Kilbourn MR, Hockley B, Lee L et al (2007) Pharmacokinetics of [^{18}F]fluoroalkyl derivatives of dihydrotetrabenazine (DTBZ) in rat and monkey brain. Nucl Med Biol 34:233–237

Kilbourn MR, Butch ER, Desmond T et al (2008) Dopamine depletion increases in vivo [^{11}C]DTBZ binding in awake rat brain. NeuroImage 41(Suppl 2):T54

Kilbourn MR, Sherman P, Quesada C et al (2010) Effects of a lobelane derivative on [^{11}C]DTBZ binding to the VMAT2. NeuroImage 52(suppl 1):S568

Kilbourn MR, Butch ER, Desmond T et al (2010a) Dopamine depletion increases in vivo [^{11}C]dihydrotetrabenazine ([^{11}C]DTBZ) binding in rat striatum. Nucl Med Biol 37:3–8

Kish SJ, Boileau I, Callachan RC et al (2017) Brian dopamine neurone 'damage': methamphetamine users vs Parkinson's disease—a critical assessment of the evidence. Eur J Neurosci 45:58–66

Koeppe RA, Frey KA, Vander Borght TM et al (1996) Kinetic evaluation of [^{11}C]dihydrotetrabenazine by dynamic PET: measurement of the vesicular monoamine transporter. J Cereb Blood Flow Metab 16:1288–1299

Koeppe RA, Frey KA, Kume A et al (1997) Equilibrium versus compartmental analysis for assessment of the vesicular monoamine transporter using (+)-α-[^{11}C]dihydrotetrabenazine (DTBZ) and PET. J Cereb Blood Flow Metab 17:919–931

Koeppe RA, Frey KA, Kuhl DE et al (1999) Assessment of extrastriatal vesicular monoamine transporter binding site density using stereoisomers of [^{11}C]dihydrotetrabenazine. J Cereb Blood Flow Metab 19:1376–1384

Koeppe RA, Gilman S, Junck L et al (2008) Differentiating Alzheimer's disease from dementia with Lewy bodies and Parkinson's disease with (+)-[^{11}C]dihydrotetrabenazine positron emission tomography. Alzheimer's Dement 4:S67–S76

Kotagal V, Albin RL, Müller ML et al (2012) Symptoms of rapid eye movement sleep behavior disorder are associated with cholinergic denervation in Parkinson disease. Ann Neurol 71:560–568

Kotagal V, Albin RL, Muller ML et al (2013) Diabetes is associated with postural instability and gait difficulty in Parkinson disease. Parkinsonism Relat Disord 19:522–526

Kotagal V, Albin RL, Müller ML et al (2014) Modifiable cardiovascular risk factors and axial motor impairments in Parkinson disease. Neurology 82:1514–1520

Kotagal V, Bohnen NI, Müller ML et al (2017) Cerebral amyloid burden and Hoehn and Yahr stage 3 scoring in Parkinson disease. J Parkinsons Dis 7:143–147

Kuhl DE, Koeppe RA, Fessler JA (1994) In vivo mapping of cholinergic neurons in the human brain using SPECT and IBVM. J Nucl Med 53:405–410

Kumar A, Mann S, Sossi V et al (2003) [^{11}C]DTBZ-PET correlates of levodopa responses in asymmetric Parkinson's disease. Brain 126:2648–2655

Kumar A, Lo S-T, Oz OK et al (2014) Derivatization of (±)dihydrotetrabenazine for copper-64 labeling towards long-lived radiotracers for PET imaging of the vesicular monoamine transporter 2. Bioorg Med Chem Lett 24:5663–5665

Kung M-P, Canney DJ, Frederick D et al (1994) Binding of ^{125}I-iodovinyltetrabenazine to CNS vesicular monoamine transport sites. Synapse 18:225–232

Kung M-P, Hou C, Goswami R et al (2007) Characterization of optically resolved 9-fluoropropyl-dihydrotetrabenazine as a potential PET imaging agent targeting vesicular monoamine transporters. Nucl Med Biol 34:239–246

Kung M-P, Lieberman BP, Zhuang Z-P et al (2008) In vivo imaging of vesicular monoamine transporter 2 in pancreas using an ^{18}F epoxide derivative of tetrabenazine. Nucl Med Biol 35:825–837

Kwak Y, Bohnen NI, Muller MLT et al (2013) Striatal denervation pattern predicts levodopa effects on sequence learning in Parkinson's disease. J Mot Behav 45:423–429

Lara-Camacho VM, Avila-Garcia MC, Avila-Rodriguez MA (2014) Preclinical assessment of the dopaminergic system in rats by microPET using positron-emitting radiopharmaceuticals. AIP Conf Proc 1626:73

Lee LC, Vander Borght T, Sherman PS et al (1996) In vitro and in vivo studies of benzoisoquinoline ligands for the brain synaptic vesicle monoamine transporter. J Med Chem 39:191–196

Lee CS, Samii A, Sossi V et al (2000) In vivo positron emission tomographic evidence for compensatory changes in synaptic dopaminergic nerve terminals in Parkinson's disease. Ann Neurol 47:493–503

Lee CS, Schulzer M, de la Fuente-Fernandez R et al (2004) Lack of regional selectivity during the progression of Parkinson disease. Arch Neurol 61:1920–1925

Lee N-R, Zheng G, Crooks PA et al (2018) New scaffold for lead compounds to treat methamphetamine use disorders. AAPS J 20:29

Lelieveld IM, Müller ML, Bohnen NI et al (2012) The role of serotonin in sleep disordered breathing associated with Parkinson disease: a correlative [^{11}C]DASB PET imaging study. PLoS One 7:e40166

Li X, Chen Z, Tang J et al (2014) Synthesis and biological evaluation of 10-^{11}C-dihydrotetrabenazine as a vesicular monoamine transporter type 2 radioligand. Arch Pharm Chem Life Sci 347:313–319

Li X, Chen Z, Liu C et al (2017) Method development and validation for determination of p-toluenesulfonoxypropyl-(+)-dihydrotetrabenazine enantiomeric purity by HPLC on a chiral stationary phase. Chromatographia 80:483–488

Lillethorup TP, Glud AN, Alstrup AKO et al (2018a) Nigrostriatal proteasome inhibition impairs dopamine neurotransmission and motor function in minipigs. Exp Neurol 303:142–152

Lillethorup TP, Glud AN, Landeck N et al (2018b) In vivo quantification of glial activation in minipigs overexpressing human α-synuclein. Synapse 72:e22060

Lillethorup TP, Glud AN, Alstrup AKO et al (2018c) Longitudinal monoaminergic PET imaging of chronic proteasome inhibition in minipigs. Sci Rep 8:15715

Lin K-J, Weng Y-H, Wey S-P et al (2010) Whole-body biodistribution and radiation dosimetry of ^{18}F -FP-(+)-DTBZ (^{18}F-AV-133): a novel vesicular monoamine transporter 2 imaging agent. J Nucl Med 51:1480–1485

Lin K-J, Lin W-Y, Hsieh C-J et al (2011) Optimal scanning time window for ^{18}F-FP-(+)-DTBZ (^{18}F-AV-133) summed uptake measurements. Nucl Med Biol 38:1149–1155

Lin K-J, Weng Y-H, Hsieh C-J et al (2013) Brian imaging of vesicular monoamine transporter type 2 in healthy aging subjects by ^{18}F -FP-(+)-DTBZ PET. PLoS One 8:e75952

Lin S-C, Lin K-J, Hsiao I-T et al (2014) In vivo detection of monoaminergic degeneration in early Parkinson disease by ^{18}F-9-fluoropropyl-(+)-dihydrotetrabenazine PET. J Nucl Med 55:73–79

Little KY, Krolewski DM, Zhang L et al (2003) Loss of striatal vesicular monoamine transporter protein (VMAT2) in human cocaine users. Am J Psychiatry 160:47–55

Liu C, Chen Z, Li X et al (2012) A concise synthesis of tetrabenazine and its crystal structure. Mol Cryst Liq Cryst 557(1):39–49

Liu C, Chen Z, Li X et al (2013) (+)-9-Benzyloxy-α-dihydrotetrabenazine as an important intermediate for the VMAT2 imaging agents: absolute configuration and chiral recognition. Chirality 25:215–223

Liu Y, Yue F, Tang R et al (2014) Progressive loss of striatal dopamine terminals in MPTP-induced acute parkinsonism in cynamologous monkeys using vesicular monoamine transporter type 2 PET imaging ([18F]AV-133). Neurosci Bull 30:409–416

Liu F, Choi SR, Zha Z et al (2018) Deuterated [18F]-9-O-hexadeutero-3-fluoropropoxyl-(+)-dihydrotetrabenazine (D6-FP-(+)-DTBZ): a vesicular monoamine transporter 2 (VMAT2) imaging agent. Nucl Med Biol 57:42–49

Lohoff FW, Carr GV, Brookshire B et al (1712) Deletion of the vesicular monoamine transporter 1 (vmat1/slc18a1) gene affects dopamine signaling. Brain Res 2019:151–157

Lung H-J, Weng Y-H, Wen M-C (2018) Quantitative study of [18]F-(+)-DTBZ image: comparison of PET template-based and MRI based image analysis. Sci Rep 8:16027

Mackey S, Jing Y, Flores J et al (2013) Direct intranigral administration of an ubiquitin proteasome system inhibitor in rat: behavior, positron emission tomography, immunohistochemistry. Exp Neurol 247:19–24

Madrazo I, Kopyov O, Avila-Rodriguez MA et al (2019) Transplantation of human neural progenitor cells (NPC) into putamina of parkinsonian patients: a case series study, safety and efficacy four years after surgery. Cell Transplant 28:269–285

Martin W, Wieler M, Stoessl AJ et al (2008) Dihydrotetrabenazine positron emission tomography imaging in early, untreated Parkinson's disease. Ann Neurol 63:388–394

Masilamoni G, Smith Y (2018) Chronic MPTP administration regimen in monkeys: a model of dopaminergic and non-dopaminergic cell loss in Parkinson's disease. J Neural Transm 125:337–363

Mehvar R, Jamali F, Watson MWB et al (1987) Pharmacokinetics of tetrabenazine and its major metabolite in man and rat. Drug Metab Dispos 12:250–255

Mejias M, Yu J, Mackey S et al (2016) Interpreting DTBZ binding data in rodent: inherent variability and compensation. Synapse 70:147–152

Meyer P, Bohnen NI, Minoshima S et al (1999) Striatal presynaptic monoaminergic vesicles are not increased in Tourette's syndrome. Neurology 53:371–374

Miller GW, Erickson JD, Perez JT et al (1998) Immunochemical analysis of vesicular monoamine transporter (VMAT2) protein in Parkinson's disease. Exp Neurol 156:138–148

Miller GW, Wang YM, Gainetdinov RR et al (2001) Dopamine transporter and vesicular monoamine transporter knockout mice: implications for Parkinson's disease. Methods Mol Med 62:179–190

Molinet-Dronda F, Gago B, Quiroga-Varela A et al (2015) Monoaminergic PET imaging and histopathological correlation in unilateral and bilateral 6-hydroxydopamine lesioned rat models of Parkinson's disease: a longitudinal in-vivo study. Neurobiol Dis 77:165–172

Muller MLT, Frey KA, Petrou M et al (2013a) Amyloid and postural instability and gait difficulty in Parkinson's disease at risk for dementia. Mov Disord 28:296–301

Muller MLT, Albin RL, Kotagal V et al (2013b) Thalamic cholinergic innervation and postural sensory integration function in Parkinson's disease. Brain 136:3282–3289

Munster-Wandowski A, Zander J-F, Richter K et al (2016) Co-existence of functionally different vesicular neurotransmitter transporters. Front Synaptic Neurosci 8:4

Murthy R, Harris P, Simpson N et al (2008) Whole body [11C]-dihydrotetrabenazine imaging of baboons: biodistribution and human dosimetry estimates. Eur J Nucl Med Imaging 35:790–797

Nandhagopal R, Kuramoto L, Schulzer M et al (2009) Longitudinal progression of sporadic Parkinson's disease: a multi-tracer positron emission tomography study. Brain 132:2970–2979

Nandhagopal R, Kuramoto L, Schulzer M et al (2011) Longitudinal evolution of compensatory changes in striatal dopamine processing in Parkinson's disease. Brain 134:3290–3298

Narendran R, Lopresti BJ, Martinez D et al (2012a) In vivo evidence for low striatal vesicular monoamine transporter 2 (VMAT2) availability in cocaine abusers. Am J Psychiatry 169:55–63

Narendran R, Frankle WG, Mason NS et al (2012b) Improved working memory but no effect on striatal vesicular monoamine transporter type 2 after omega-3 polyunsaturated fatty acid supplementation. PLoS One 7:e46832

Narendran R, Jedema HP, Lopresti BJ et al (2015) Decreased vesicular monoamine transporter, type 2 availability in the striatum following chronic cocaine self-administration in nonhuman primates. Biol Psychiatry 77:488–492

Naudon L, Leroux-Nicollet I, Raisman-Vozari R et al (1995) Time course of modifications elicited by reserpine on the density and mRNA synthesis of the vesicular monoamine transporter, and on the density of the membrane dopamine uptake complex. Synapse 21:29–36

Nickell JR, Culver JP, Janganati V et al (2016) 1,4-Diphenylalkylpipridines: a new scaffold for the design of potent inhibitors of the vesicular monoamine transporter-2. Bioorg Med Chem Lett 26:2997–3000

Okamura N, Villemagne VL, Drago J et al (2010) In vivo measurement of vesicular monoamine transporter type 2 density in Parkinson disease with (18)F-AV-133. J Nucl Med 51:223–228

Omote H, Miyaji T, Juge N et al (2011) Vesicular neurotransmitter transporter: bioenergetics and regulation of glutamate transport. Biochemistry 50:5558–5565

Paek S-M, Kim N-J, Shin D et al (2010) A concise total synthesis of (+)-tetrabenazine and (+)-α-dihydrotetrabenazine. Chem Eur J 16:4623–4628

Perez-Lohman C, Kerik NE, Diaz-Meneses IE et al (2018) Diagnostic utility of [^{11}C]DTBZ positron emission tomography in clinically uncertain parkinsonism: experience of a single tertiary center. Rev Investig Clin 70:285–290

Petrou M, Koeppe R, Scott P et al (2012a) PET imaging of the vesicular acetylcholine transporter. J Nucl Med 53:290

Petrou M, Bohnen NI, Müller ML et al (2012b) Aβ-amyloid deposition in patients with Parkinson disease at risk for development of dementia. Neurology 79:1161–1167

Phan JA, Stokholm K, Zareba-Paslawska J et al (2017) Early synaptic dysfunction induced by α-synuclein in a rat model of Parkinson's disease. Sci Rep 7(1):6363

Provencher BA, Eshleman AJ, Johnson RA et al (2018) Synthesis and discovery of arylpiperidinylquinazolines: new inhibitors of the vesicular monoamine transporter. J Med Chem 61:9121–9131

Quinn GP, Shore PA, Brodie BB (1959) Biochemical and pharmacological studies of RO 1-9568 (Tetrabenazine), a non-indole tranquilizing agent with reserpine-like effects. J Pharmacol Exp Ther 127:103–109

Raffel DM, Koeppe RA, Little R et al (2006) PET measurement of cardiac and nigrostriatal denervation in parkinsonian syndromes. J Nucl Med 47:1769–1777

Reith MEA, Gnegy ME (2020) Molecular mechanisms of amphetamines. Handb Exp Pharmacol 258:265–297. https://doi.org/10.1007/164_2019_251

Rhee S-W, Ryan KJ, Tanga MJ (2011) Synthesis of ^{3}H-labeled tetrabenazine. J Label Compd Radiopharm 54:367–370

Ricuarte GA, Mechan AO, Yuan J et al (2005) Amphetamine treatment similar to that used in the treatment of adult attention-deficit/hyperactivity disorder damages dopaminergic nerve endings in striatum of adult nonhuman primates. J Pharmacol Exp Ther 315:91–98

Rishel MJ, Johnson BF, Kankanamalage K et al (2009) Alpha-fluoroalkyl dihydrotetrabenazine imaging agents and probes. US Patent 2009/0142276 A1

Rishel MJ, Amarasinghe KKD, Dinn SR et al (2009a) Asymmetric synthesis of tetrabenazine and dihydrotetrabenazine. J Org Chem 74:4001–4004

Schafer MK-H, Weihe E, Eiden LE (2013) Localization and expression of VMAT2 across mammalian species: a translational guide to its visualization and targeting in health and disease. Adv Pharmacol 68:319–334

Scherman D, Raisman R (1988) Ploska et al. [³H]Dihydrotetrabenazine, a new in vitro monoaminergic probe for human brain. J Neurochem 50:1131–1136

Scherman D, Jaudon P, Henry JP (1981) Binding of a tetrabenazine derivative to the monoamine transporter of the chromaffin granule membrane. C R Seances Acad Sci III 293:221–224

Scherman D, Desnos C, Darchen F et al (1989) Striatal dopamine deficiency in Parkinson's disease: role of aging. Ann Neurol 26:551–557

Schwartz DE, Bruderer H, Reider J et al (1966) Metabolic studies of tetrabenazine, a psychotropic drug in animals and man. Biochem Pharmacol 13:645–655

Schwartz K, Nachman R, Yossifoff M et al (2006) Cocaine, but not amphetamine, short term treatment elevates the density of rat brain vesicular monoamine transporter 2. J Neural Transm 114:427–430

Shah N, Frey KA, Muller MLT et al (2016) Striatal and cortical β-amyloidopathy and cognition in Parkinson's disease. Mov Disord 31:111–117

Shi X, Zhang Y, Xu S et al (2019) Decreased striatal vesicular monoamine transporter type 2 correlates with the nonmotor symptoms in Parkinson's disease. Clin Nucl Med 44:707–713

Siderowf A, Pontecorvo MJ, Shill HA et al (2014) PET imaging of amyloid with Florbetapir F 18 and PET imaging of dopamine degeneration with ¹⁸F-AV-133 (fluorbenazine) in patients with Alzheimer's disease and Lewy body disorders. BMC Neurol 14:79

Sievert MK, Hajipour AR, Ruoho AE (2007) Specific derivatization of the vesicular monoamine transporter with novel carrier-free radioiodinated reserpine and tetrabenazine photoaffinity labels. Anal Biochem 367:68–78

Silm K, Yang J, Marcott PF et al (2019) Synaptic vesicle recycling pathway determines neurotransmitter content and release properties. Neuron 22:786–800

Smith GS, Mills KA, Pontone GM et al (2019) Effect of STN DBS on vesicular monoamine transporter 2 and glucose metabolism in Parkinson's disease. Parkinsonism Relat Disord. https://doi.org/10.1016/j.parkreldis.2019.04.006

Snider J, Müller ML, Kotagal V et al (2015) Non-exercise physical activity attenuates motor symptoms in Parkinson disease independent from nigrostriatal degeneration. Parkinsonism Relat Disord 21(10):1227–1231

Sossi V, Holden JE, Chan G et al (2000) Analysis of four dopaminergic tracer kinetics using two different tissue input function methods. J Cereb Blood Flow Metab 20:653–660

Sossi V, Holden JE, Topping GJ et al (2007) In vivo measurement of density and affinity of the monoamine vesicular transporter in a unilateral 6-hydroxydopamine rat model of PD. J Cereb Blood Flow Metab 27:1407–1415

Sossi V, Dinelle K, Topping GJ (2009) Dopamine transporter relation to levodopa-derived synaptic dopamine in a rat model of Parkinson's: an in vivo imaging study. J Neurochem 109:85–92

Sossi V, Dinelle K, Schulzer M (2010a) Levodopa and pramipexole effects on presynaptic dopamine PET markers and estimated dopamine release. Eur J Nucl Med Mol Imaging 37:2364–2370

Sossi V, de la Fuentes-Fernandez R, Nandhagopal R et al (2010b) Dopamine turnover increases in asymptomatic *LRRK2* mutation carriers. Mov Disord 16:2717–2723

Staley JK, Talbot JZ, Ciliax BJ et al (1997) Radioligand binding and immunoautoradiographic evidence for a lack of toxicity to dopaminergic nerve terminals in human cocaine overdose victims. Brain Res 747:219–229

Strome E, Cepeda IL, Sossi V et al (2000) Evaluation of the integrity of the dopamine system in a rodent model of Parkinson's disease: small animal positron emission tomography compared to behavioral assessment and autoradiography. Mol Imaging Biol 8:292–299

Sun Y, Zhao N, Liu W et al (2018) Study of vesicular monoamine transporter 2 in myopic retina using [¹⁸F]FP-(+)-DTBZ. Mol Imaging Biol 20:771–779

Taylor SF, Koeppe RA, Tandon R et al (2000) In vivo measurement of the vesicular monoamine transporter in schizophrenia. Neuropsychopharmacology 23:667–675

Thompson CM, Davis E, Carrigan CN et al (2005) Inhibitor of the glutamate vesicular transporter (VGLUT). Curr Med Chem 12:2041–2056

Tian L, Karimi M, Loftin SK et al (2012) No differential regulation of dopamine transporter (DAT) and vesicular monoamine transporter 2 (VMAT2) binding in a primate model of Parkinson's disease. PLoS One 7(2):e31439

Tian L, Karimi M, Brown CA et al (2014) In vivo measures of nigrostriatal neuronal response to unilateral MPTP treatment. Brain Res 1571:49–60

Tian L, Xia Y, Flores HP et al (2015) Neuroimaging analysis of the dopaminergic basis for apathetic behaviors in an MPTP-lesioned primate model. PLoS One 10:e0132064

Tong J, Wilson AA, Boileau I et al (2008) Dopamine modulating drugs influence striatal (+)-[^{11}C]DTBZ binding in rats: VMAT2 binding is sensitive to changes in vesicular dopamine concentration. Synapse 62:873–876

Tong J, Boileau I, Furakawa Y et al (2011) Distribution of vesicular monoamine transporter 2 protein in human brain; implications for brain imaging studies. J Cereb Blood Flow Metab 31:2065–2075

Toomey JS, Bhatia S, Moon L et al (2012) PET imaging a MPTP-induced mouse model of Parkinson's disease using the fluoropropyl-dihydrotetrabenazine analog [^{18}F]-DTBZ (AV-133). PLoS One 7:e39041

Tridgett R, Turtle R, Johnston G (2008) Dihydrotetrabenazines and pharmaceutical compositions containing them. US Patent 2008/0108645 A1

Troiano AR, de la Fuentes-Fernandez R, Sossi V et al (2009) PET demonstrates reduced dopamine transporter expression in PD with dyskinesias. Neurology 72:1211–1216

Troiano AR, Schulzer M, De La Fuente-Fernandez R et al (2010) Dopamine transporter PET in normal aging: dopamine transporter decline and its possible role in preservation of motor function. Synapse 64:146–151

Vander Borght TM, Sima AAF, Kilbourn MR et al (1995a) [^{3}H]Methoxytetrabenazine: a high specific activity ligand for estimating monoaminergic neuronal integrity. Neuroscience 68:955–962

Vander Borght TM, Kilbourn MR, Koeppe RA et al (1995b) In vivo imaging of the brain vesicular monoamine transporter. J Nucl Med 36:2252–2260

Vander Borght TM, Kilbourn MR, Desmond TJ et al (1995c) The vesicular monoamine transporter is not regulated by dopaminergic drug treatments. Eur J Pharmacol 294:577–583

Varone A, Jahan M, Toth M et al (2012) PET imaging of VMAT2 with the novel radioligand [^{18}F]FE-DTBZ-d4 in non-human primates: comparison with [^{11}C]DTBZ and [^{18}F]FE-DTBZ. J Cereb Blood Flow Metab 32(Suppl 1):S113–S114

Villemagne V, Yuan J, Wong DF et al (1998) Brain dopamine neurotoxicity in baboons treated with doses of methamphetamine comparable to those recreationally abused by humans: evidence from [^{11}C]WIN-35,428 positron emission tomography studies and direct in vitro determinations. J Neurosci 18:419–427

Villemagne VL, Okamura N, Pejoska S et al (2011) In vivo assessment of vesicular monoamine transporter type 2 in dementia with Lewy bodies and Alzheimer disease. Arch Neurol 68:905–912

Villemagne VL, Okamura N, Pejoska S et al (2012) Differential diagnosis in Alzheimer's disease and dementia with Lewy bodies via VMAT2 and amyloid imaging. Neurodegener Dis 10:161–165

Vilpoux C, Leroux-Nicollet I, Naudon L et al (2000) Reserpine or chronic paroxetine treatments do not modify the vesicular monoamine transporter 2 expression in serotonin-containing regions of the rat brain. Neuropharmacology 39:1075–1082

Walker MD, Dinelle K, Kornelsen R et al (2013a) In-vivo measurement of LDOPA uptake, reserve and turnover in the rat brain using [^{18}F]FDOPA PET. J Cereb Blood Flow Metab 33:59–66

Walker MD, Dinelle K, Kornelsen R et al (2013b) Measuring dopaminergic function in the 6-OHDA-lesioned rat: a comparison of PET and microdialysis. EJNMMI Res 3:69

Wang JL, Oya S, Parhi AK et al (2010) In vivo studies of the SERT-selective [^{18}F]FPBM and VMAT2-selective [^{18}F]AV-133 radiotracers in a rat model of Parkinson's disease. Nucl Med Biol 37:479–486

Weng C-C, Chen Z-A, Chao K-T et al (2017a) Quantitative analysis of the therapeutic effect of magnolol on MPTP-induced mouse model of Parkinson's disease using in vivo ^{18}F-9-fluoropropyl-(+)-dihydrotetrabenazine PET imaging. PLoS One 12(3):e173503

Weng CC, Huang SL, Chen ZA et al (2017b) [^{18}F]FP-(+)-DTBZ PET study in a lactacystin treated rat model of Parkinson disease. Ann Nucl Med 31:506–513

Wile DJ, Agarwal PA, Schulzer M et al (2017) Serotonin transporter binding and motor onset of Parkinson's disease in asymptomatic LRRK2 mutation carriers: a cross-sectional study. Lancet Neurol 16:351–359

Wilson JM, Kish SJ (1996) The vesicular monoamine transporter, in contrast to the dopamine transporter, is not altered by chronic cocaine self-administration in the rat. J Neurosci 16:3507–3510

Wilson JM, Levey AI, Bergeron C et al (1996a) Striatal dopamine, dopamine transporter, and vesicular monoamine transporter in chronic cocaine users. Ann Neurol 40:428–439

Wilson JM, Kalasinsky KS, Levey AI et al (1996b) Striatal dopamine nerve terminal markers in human, chronic methamphetamine users. Nat Med 2:699–703

Wimalasena K (2010) Vesicular monoamine transporters: structure-function, pharmacology, and medicinal chemistry. Med Res Rev 31:483–519

Wu X, Zhou X, Zhang S et al (2015) Brain uptake of a non-radioactive pseudo-carrier and its effect on the biodistribution of [^{18}F]AV-133 in rat brain. Nucl Med Biol 42:630–636

Wu CH, Hsiao IT, Lin KJ et al (2017) Test and retest studies of ^{18}F-FP(+)-DTBZ brain PET imaging. J Neurol Sci 381:259

Xu SS, Alexander PK, Lie Y et al (2018) Diagnostic accuracy of imaging brain vesicular monoamine transporter type 2 (VMAT2) in clinically uncertain parkinsonian syndrome (CUPS): a 3-year follow-up study in community patients. BMJ Open 8:e025533

Yaffe D, Forrest LR, Shuldiner S (2018) The ins and outs of vesicular monoamine transporters. J Gen Physiol 150:671–682

Yang J, Archer DB, Burciu RG et al (2019) Multimodal dopaminergic and free-water imaging in Parkinson's disease. Parkinsonism Relat Disord 62:10–15

Yao Z, Wei X, Wu X et al (2011) Preparation and evaluation of tetrabenazine enantiomers and all eight stereoisomers of dihydrotetrabenazine as VMAT2 inhibitors. Eur J Med Chem 46:1841–1848

Yu Q, Luo W, Deschamps J, Holloway HW et al (2010) Preparation and characterization of tetrabenazine enantiomers against vesicular monoamine transporter 2. Med Chem Lett 1:105–109

Zhang J, Zhang X, Li Y et al (2012) Simple, rapid and reliable preparation of [^{11}C]-(+)-α-DTBZ of high quality for routine applications. Molecules 17:6697–6704

Zheng G, Dwoskin LP, Deaciuc AG et al (2005) Lobelane analogues as novel ligands for the vesicular monoamine transporter-2. Bioorg Med Chem 13:3899–3909

Zheng P, Lieberman BP, Choi SR et al (2011) Synthesis and biological evaluation of 3-alkyl-dihydrotetrabenazine derivatives as vesicular monoamine transporter-2 (VMAT2) ligands. Bioorg Med Chem Lett 21:3435–3438

Zhou Y, Su Y, Xu W et al (2019) Constipation increases disability and decreases dopamine levels in the nigrostriatal system through gastric inflammatory factors in Parkinson's disease. Curr Neurovasc Res 16:241. https://doi.org/10.2174/1567202616666190618170103

Zhu L, Liu J, Kung HF (2009) Synthesis and evaluation of 2-amino-dihydrotetrabenazine derivatives as probes for imaging vesicular monoamine transporter-2. Bioorg Med Chem Lett 19:5026–5028

Zimmer L, Luxen A (2012) PET radiotracers for molecular imaging in the brain: past, present and future. NeuroImage 61:363–370

Zubieta J-K, Hugulet P, Ohl LE et al (2000) High vesicular monoamine transporter binding in asymptomatic bipolar I disorder: sex differences and cognitive correlates. Am J Psychiatry 157:1619–1628

Zubieta J-K, Taylor SF, Huegulet P et al (2001) Vesicular monoamine transporter concentrations in bipolar disorder type I, schizophrenia, and healthy subjects. Biol Psychiatry 49:110–116